51ST INTERNATIONAL MICRO AND NANO ENGINEERING CONFERENCE

15 - 18 SEPTEMBER 2025

National Oceanography Centre
Southampton | United Kingdom

Organized by

Platinum

Gold

Silver

Bronze

Partner

THE ZEPLER CLEANROOMS

The Zepler Cleanrooms Complex
is a world-class facility advancing research and innovation in electronics, photonics, and nanotechnology, with unique capabilities in both wafer and fibre technologies, supporting both research and enterprise.

Our core expertise spans:

— Fibres & Communication
— Photonic Systems, Circuits & Sensors
— Quantum Devices
— Neuromorphic Memristors
— III-V Semiconductors

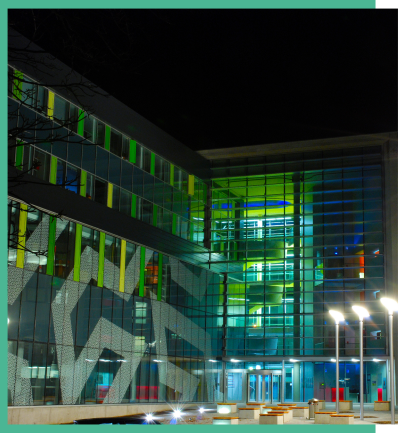

University of Southampton

CORNERSTONE

University of Glasgow

UKRI Science and Technology Facilities Council

SOUTHAMPTON NANOFABRICATION CENTRE

Open-source silicon photonics rapid prototyping

Through the **CORNERSTONE Foundry** we provide a variety of services:

- **Multi-project-wafer (MPW)**
- **Bespoke fabrication batches**
- **Deep-UV projection lithography**
- **E-Beam lithography**

Our technology platforms include:

- **Silicon-On-Insulator (SOI)**
- **Silicon Nitride**
- **Germanium-On-Silicon**
- **Suspended Silicon**

For CORNERSTONE services contact:
cornerstone@soton.ac.uk

Proof of Concept R&D to Low Volume Production

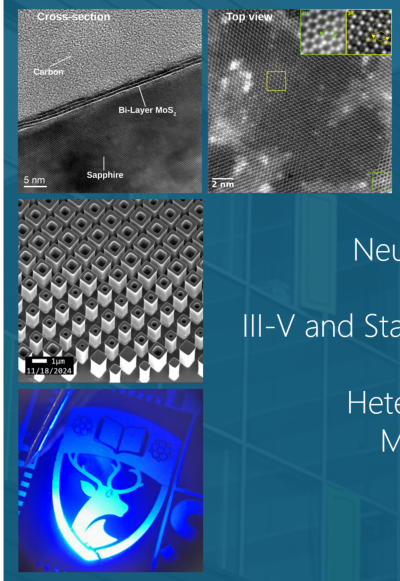

Quantum Devices
Metalenses
Nanoelectronics
Sensors
Neuromorphic Computing
Nanoelectronics
III-V and Standard Semiconductors
Memristors
Heterogeneous Integration
Micro and Nano-Fluidics
Micro-LEDs
Sensors
MEMS and NEMS
Photovoltaics
Ebeam Lithography
2D Materials

For bespoke fabrication services contact:
L.A.Boodhoo@southampton.ac.uk

Solutions for Innovation | JEOL

JBX-A9 SERIES

Electron Beam Lithography System

- High Precision and High Throughput Direct Writing System
- Built with JEOL's renowned Electron Optics for ultimate stability
- Loadable wafer up to 300 mm
- FOUP system optionally available
- In-line extendibility to other process tools such as coaters and developers
- Low power consumption
- Improved ease-of-use for all experience levels

MLA 150

MASKLESS ALIGNER

10 YEARS

LET'S CELEBRATE!

Join us for a cocktail at our booth.

Monday evening, 15/09/2025

Another reason to celebrate: **Greatscale (DWL 66⁺)** and **Decapede (NanoFrazor)**

HEIDELBERG INSTRUMENTS

Learn more about the MLA 150 at our anniversary page.

heidelberg-instruments.com

Multifunctional Electron Beam Lithography

RAITH

E—LINE

Better performance. Undreamt-of possibilities. True multifunctionality.

Maximum versatility for widest application bandwidth

Intuitive control, innovative capabilities

Upgradability for a system that evolves with your research

NEW E-LINE 100

raith.com/new-eline

ALLRESIST

Innovation
Creativity
Customer-specific solutions

Medusa 84 SiH – HSQ resist for highest resolution

Stabilized HSQ polymer, improved process- and storage-stability
Available in 4%, 8%, 12% and 22% HSQ in butyl acetate, ranging from 30 nm up to 800 nm thickness
Double coatable for extended thickness range of over 1400 nm

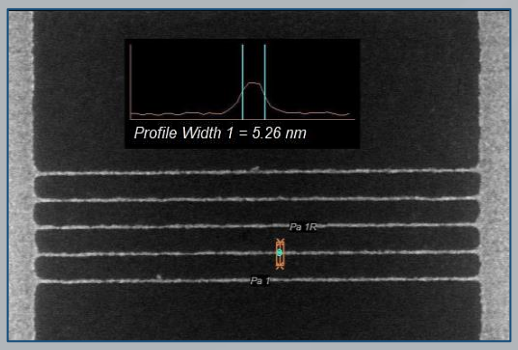

© Raith GmbH

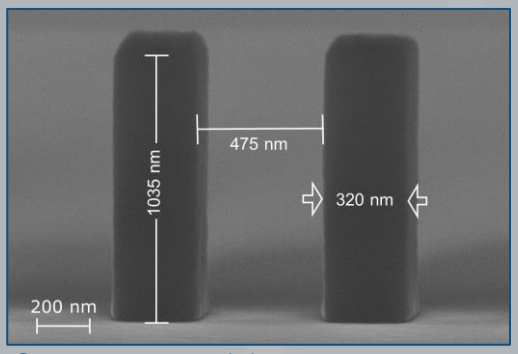

© Yurii Kutovyi, FZ Jülich

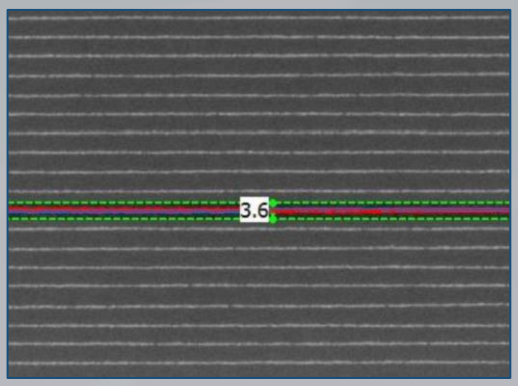

© Raith GmbH

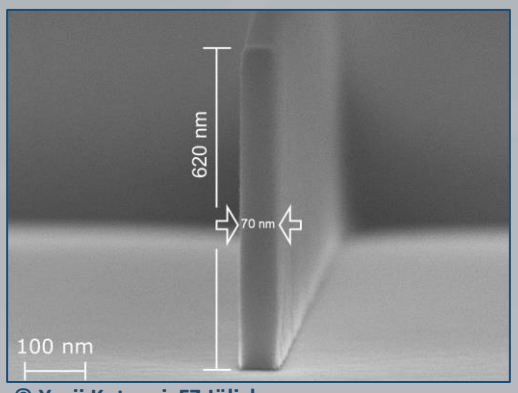

© Yurii Kutovyi, FZ Jülich

CSAR 62

highest resolution positive e-beam resist
suitable for single-layer liftoff

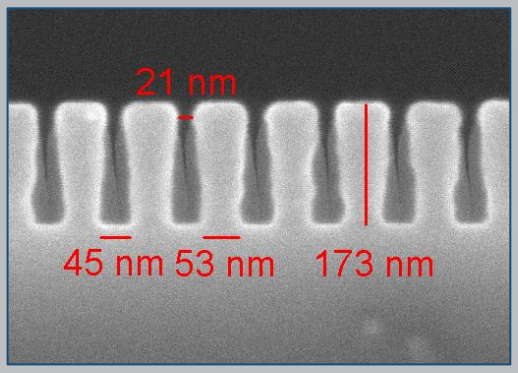

© CMAT, University Halle

Electra 94

conductive coating for charge dissipation
coatable on all e-beam resists from AR

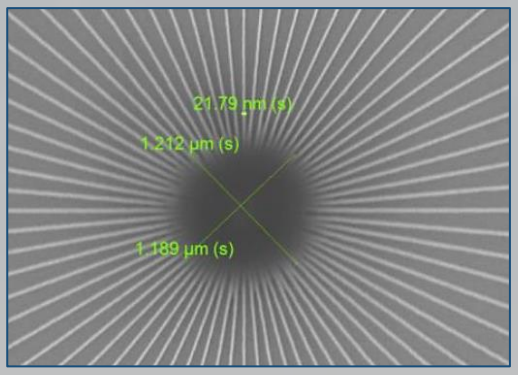

HSQ on quartz patterened with Electra 94 on top
© Bob Drent, AMOLF NanoLab Amsterdam

Allresist GmbH • Strausberg, Germany
www.allresist.com • info@allresist.de

STS ELIONIX

Electron Beam Lithography Systems

ELS-BODEN Series

MODULAR CONFIGURATION

- Acceleration Voltage (150, 125, 100 or 50 kV)
- Chamber/Stage Size (200 or 300 mm)
- Loading Mechanism (Single, Multi or Robot)

ELS-ORCA

REVOLUTIONARY 30kV EBL TOOL

- A Cost-Effective Cutting-Edge EBL Platform
- High Resolution SEM Imaging
- User Friendly 'elms' Software

FULLSTACK SOFTWARE (elms)

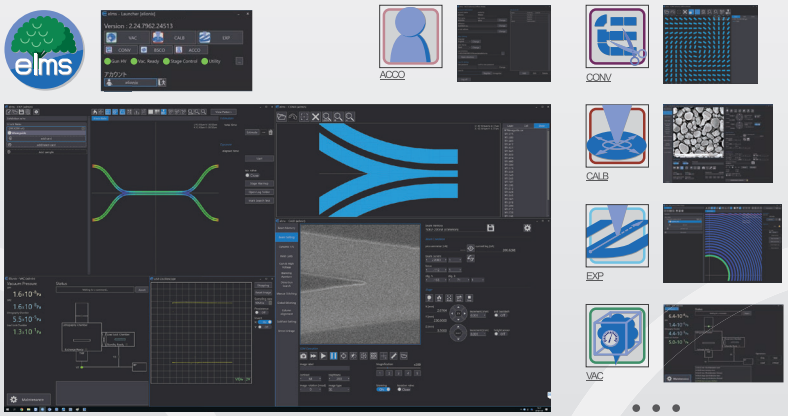

elionix lithography management System

STS-Elionix
118 Cedar Street
Wellesley Hills, MA 02481 USA

www.sts-elionix.com
+1 (978) 362-0510
sales@sts-elionix.com

GenISys
Advancing the Standard

Software for Advanced Lithography & Metrology

Based in Munich (Germany), GenISys develops, markets and supports software solutions for the optimization of lithography and inspection for nano-fabrication processes.

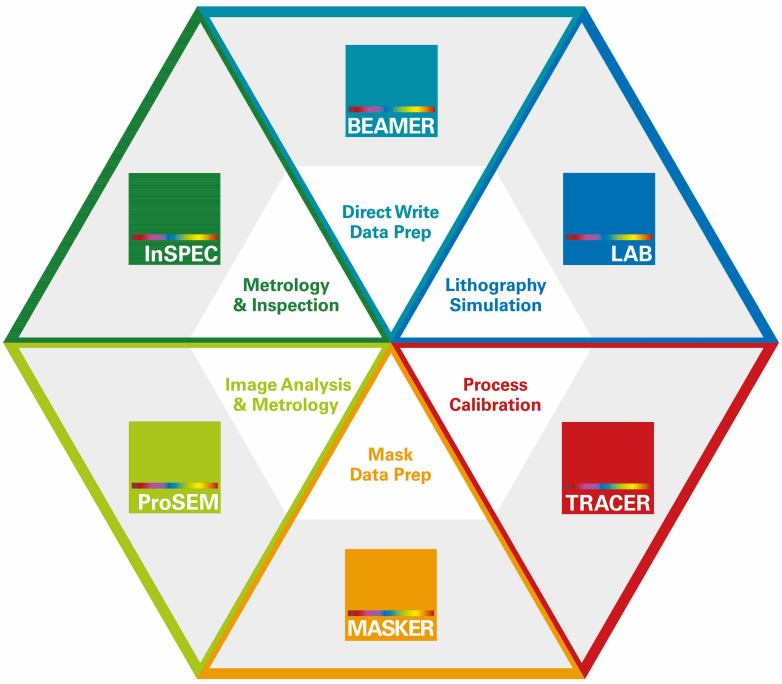

info@genisys-gmbh.com
www.genisys-gmbh.com

nanoscribe

Think big. Print nano.

Quantum X shape

Fastest and most accurate 3D printer in class

Your advantages at a glance

- High-speed 3D Microfabrication with 100 nm feature size control
- 200 typical mesoscale structures printable overnight
- Broad range of substrates and wafers up to 8”

nanoscribe.com

ies EQUIPMENT PARTNERS

EVG

Lithography
& Wafer Bonding

scia systems

Ion Beam Etch
& Deposition

Veeco

Atomic Layer
Deposition

Alpha Plasma

Resist Strip &
Surface Preparation

+44 (0)117 916 3663 | ies.co.uk/equipment-partners

AMO is a non-profit research company in the field of nanotechnology and acts as pathfinder for new technologies, bridging the gap between academic and industrial research. We are partners of innovators and translate the latest findings of research into new applications.

from lab to fab

We understand E-BEAM.

Beamfox

SOFTWARE FOR HIGH-PERFORMANCE
ELECTRON-BEAM LITHOGRAPHY

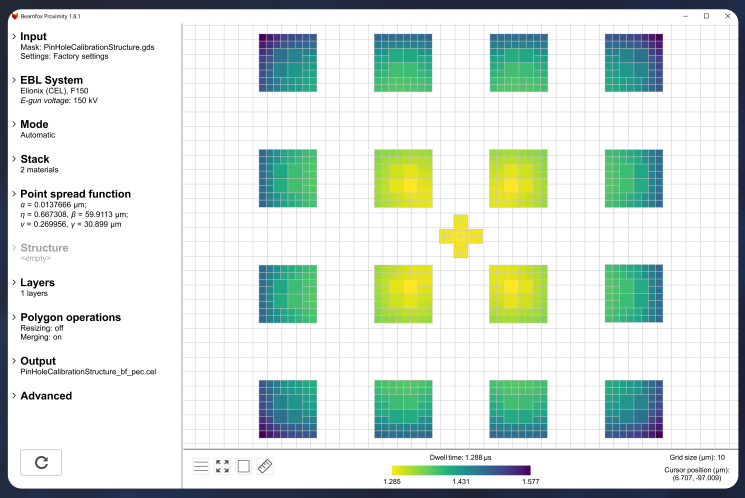

Beamfox Proximity - powerful proximity effect correction and data preparation for electron-beam lithography systems in a user-friendly software package.

Visit **beamfox.dk/downloads** to download your fully-featured, **30-day free trial.**

Let's Shape the Future, Together

micro resist technology

Materials and Technologies for Micro- and Nanofabrication

PFAS free - sustainable products @ MRT

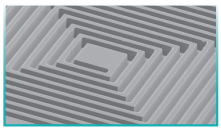

Let's talk about the alternative solutions for PFAS free photoresists and photopolymers we have been developed since many years

Transparent Polymer moulds

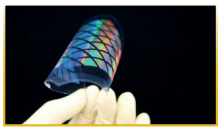

UV replication / imprint
OrmoStamp®FF

Hybrid Polymers

Microfluidic devices

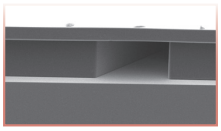

Capping / tenting of holes and channels
mr-LamiRes
SUEXTM, ADEXTM
MX5000, WBR2000

Scan me!

Inkjet printing

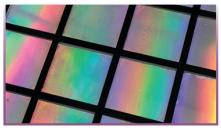

Inkjet dispensing for selective material deposition
mr-UVCur26SF
InkOrmo
InkEpo

Inkjet

Micro Optical Components

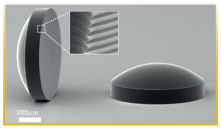

Microlens made of InkOrmo, with integrated nano grating by combination of inkjet dispensing and UV replication

Multilayer patterning

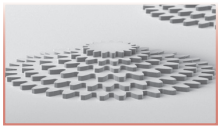

Multilayer pattern for complex 3D-architectures
mr-LamiRes
SUEXTM, ADEXTM
MX5000, WBR2000

Lift-Off Processing

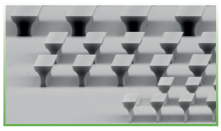

Single layer lift off pattern made by UV lithography in ma-N 1440

Flyer NR

UV-NIL, Photo-NIL

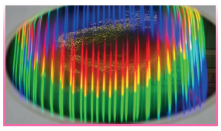

Etch mask
Micro / nanofabrication
mr-NIL200
mr-NIL210
mr-NIL212FC
mr-NIL6000E

NIL Materials

UV Lithography - Thick Film Processing

Pattern in 100µm thick positive tone resist
ma-P 1200 series
ma-P 1275HV

Flyer PR

E-beam / Deep UV lithography

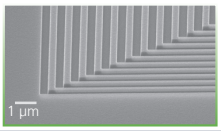

Etch mask
Stamp
Template manufacture
ma-N 2400
mr-EBL 6000

Thermal nanoimprint

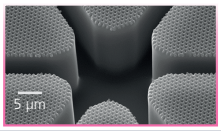

Etch mask
Micro / nanofabrication
Micro fluidic chips
mr-I 7000R / mr-I 8000R
mr-I 9000M / mr-I T85
SIPOL

Greyscale Lithography

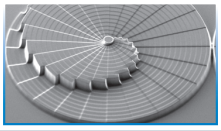

Master generation
Mould for electroplating
Mould for PDMS replication
ma-P 1200 series
ma-P 1275HV

Atomic layer etch achieves high accuracy and low damage with surface smoothing

OXFORD INSTRUMENTS

Excellent process etch uniformity for high performance p-GaN HEMTs and recessed gate MISHEMTs devices.

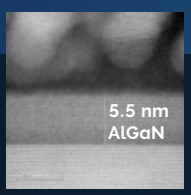

Remaining AlGaN thickness of 5 nm ±0.5 nm verified by TEM for 3 samples.

plasma.oxinst.com

amcoss
systems

Smart single wafer processing

Fully automated amc series

Coating
Developing
Lift-off
Etching
Cleaning
Heating/Cooling
Digital Process Control

Semi-automated amr series

MEMBER OF GROUP | LAB | semi MEMBER | SILICON SAXONY | Quality made in Austria

amcoss-systems.com

creative engineering and manufacturing

idonus

Equipment for microfabrication, processing, inspection and assembly

idonus specializes in the development and fabrication of manufacturing equipment for the MEMS and semiconductor industries.
The vertical integration of the company enables fast prototyping and shorter lead times for customers.

UV LED Mask Aligner for Photolithography Exposure

- Size: up to 600 x 600 mm
- Manual / Semi-automated / Fully-automated
- Modular system architecture
- Alignment precision: below 1 µm
- Custom-made solutions
- Cost efficient

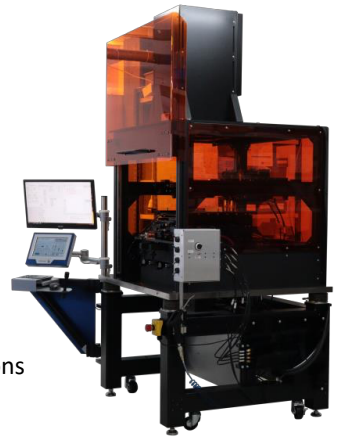

www.idonus.com • info@idonus.com • made in Switzerland

SmarAct | group

Your Partner for High Precision in Positioning, Automation and Metrology.

www.smaract.com

Table of Contents

Abstracts

Plenary 1 - Dr Drew Nelson

Building Globally Relevant Semiconductor Clusters and Their Relevance to the UK Semiconductor Strategy 3

Dr. Drew Nelson[1]

1. All Party Parliamentary Group on Semiconductors Advisory Board

Plenary 2 - Dr Naoto Horiguchi

CMOS scaling paradigm shift from CMOS 1.0 to CMOS 2.0 5

Dr. Naoto Horiguchi[1]

1. IMEC, Belgium

Plenary 3 - Prof Dinesh Pamunuwa

Edge Computing Platform based on Nanoelectromechanical Relays 7

Prof. Dinesh Pamunuwa[1]

1. University of Bristol

MNE Fellow Award: Prof Lars Montelius

Science in our time - for People, Planet and Prosperity 9

Prof. Lars Montelius[1]

1. Lund University

Oral Session 1A : Microsystem and MEMS Applications

Fabrication of Flexible III-Nitride MEMS Resonators by Lift-Off and Transfer onto Thin Metal Substrates 11

Mr. Ali Kassem[1], Dr. Rajat Gujrati [1], Mr. david bourrier [2], Dr. Cédric Ayela [3], Mr. Fabrice Mathieu [2], Prof. Isabelle Dufour [3], Prof. Liviu Nicu [2], Dr. Vishnu Ottapilakkal [1], Dr. Phuong Vuong [4], Prof. Suresh Sundaram [4], Prof. William Hunt [5], Prof. Abdallah Ougazzaden [5], Dr. Thierry Leichlé [5], Prof. Jean-Paul Salvestrini [1]

1. CNRS, IRL 2958 Georgia Tech-CNRS, Metz, France, 2. LAAS-CNRS, Université de Toulouse, CNRS, Toulouse, France, 3. Université de Bordeaux, Laboratoire IMS UMR-CNRS 5218, Talence, France, 4. Georgia Tech Europe, IRL 2958 Georgia Tech-CNRS, Metz, France, 5. Georgia Institute of Technology, School of Electrical and Computer Engineering, IRL 2958 Georgia Tech-CNRS, Atlanta, GA, USA

Probing Cell Mechanosensitivity in Microengineered 3D Scaffolds 13

Ms. Aída Gabriela Fernández Contreras[1], Ms. Chloé Viat [1], Prof. Boudewijn van der Sanden [2], Prof. Olivier Stephan [3], Prof. Jean-Hervé Tortai [1], Prof. Alice Nicolas [1]

1. LTM, 2. TIMC, 3. LiPhy

Wafer-scale transfer-free multi-layer graphene process for MEMS sensors 14
Prof. Sten Vollebregt[1]
1. Associate Professor

High Speed Nickel Electrodeposition in a Supercritical CO2 Emulsified Nickel Sulfamate Bath toward MEMS Applications 15
Mr. WENDING HOU[1], Dr. Tomoyuki Kurioka [1], Prof. Chun-Yi Chen [1], Prof. Masato Sone [1], Prof. Tso-Fu Mark Chang [1]
1. Institute of Science Tokyo

Oral Session 1B : Electron Beam Lithography

Precise Dimension Control of Narrow Gaps in High Density Pattern on InP-Based Substrate by Electron Beam Lithography 17
Mr. Hao Zhang[1], Dr. Jing Becker [2], Mr. Jan Ebbert [1], Mr. Tekin Kahilogullari [1], Dr. Daniel Ritter [2], Prof. Nils Weimann [1]
1. Components for High Frequency Electronics, Duisburg, 47057, University Duisburg Essen, 2. GenISys GmbH

Qualification of Direct Write E-beam Lithography Tools with Two-Dimensional Vernier Patterns 18
Dr. Alexei Bogdanov[1]
1. NTT Research Inc.

Direct Fabrication of 3-D PEDOT:PSS Nanostructures by Electron Beam Lithography 19
Mr. Yandong YANG[1], Prof. Shin'ichi Warisawa [1], Prof. Reo Kometani [1]
1. Graduate School of Frontier Sciences, The University of Tokyo

High Resolution Electron Beam Lithography Patterning for Advanced Grating Couplers 20
Ms. Pragya Sah[1], Mr. Radhakant Singh [1], Mr. Kai Zhang [1], Mr. Michael Möller [1], Dr. Rijil Thomas [1], Dr. Jens Bolten [1], Ms. Anastasiia Sorokina [2], Mr. Guochun Du [3], Mr. Carl Grimpe [3], Dr. Steffen Sauer [2], Dr. Elena Jordan [3], Prof. Stefanie Kroker [2], Prof. Tanja Mehlstaeubler [3], Dr. Stephan Suckow [1], Prof. Max Lemme [4]
1. AMO GmbH, 2. Technische Universität Braunschweig, 3. Physikalisch-Technische Bundesanstalt, 4. Chair of Electronic Devices, RWTH Aachen University

A novel patterning approach enabling consistent high aspect ratio nanostructures with functional tops 21
Mr. Bryan Benz[1], Prof. Marco Stampanoni [2], Prof. Martino Poggio [3], Dr. Lucia Romano [1]
1. Paul Scherrer Institute (PSI), 2. ETH Zürich, 3. University of Basel

Oral Session 1C : Electronics 1

P-channel Oxide Thin Film Transistors for CMOS Logic 23
Dr. Kham Niang [1], Dr. Ben Peek [2], Dr. James Parish [3], Prof. Paul Chalker [2], Prof. Andrew Johnson [3], Prof. Andrew Flewitt[1]
1. University of Cambridge, 2. University of Liverpool, 3. University of Bath

Electric Field Confinement-Induced Potentiation in Inert Mixed Ionic-Electronic Conducting Memristors 24
Dr. Philip Calado[1]
1. University of Southampton

Towards aluminium nitride on diamond surface acoustic wave devices 25
Dr. Jerome Cuenca [1], Dr. Soumen Mandal [1], Prof. Oliver Williams[1]
1. Cardiff University

Nanoscale Back-End-of-Line Silicon Carbide Memristor for Resistive Memory 26
Mr. Qin Liu[1], Dr. Omesh Kapur [1], Dr. Anushka Gangnaik [2], Dr. Ruomeng Huang [2], Prof. Kees de Groot [2]
1. School of Electronics and Computer Science, University of Southampton, Southampton SO17 1BJ, United Kingdom, 2. University of Southampton

2D Materials for Electrostrictive FET 27
Ms. Nigama Vykari Vajjula [1], Mr. Fitunerediate Gebeyehu [1], Prof. Ethan Ahn[1]
1. George Mason University

Oral Session 1D: Biodevices and Systems 1

Contactless Measurement of Radial Artery Pulse Waves Using an Acoustic Sensing System 29
Ms. Chaeeun Lee[1], Prof. Je Hoon Oh [1], Mr. Changwoo Cho [1]
1. Hanyang University

A microfluidic Cartilage-on-Chip platform for personalized cartilage transplant compatibility screening 30
Dr. Rahman Sabahi-Kaviani[1], Ms. Giorgia Mazzini [2], Ms. Emma Bristow [2], Dr. Cynthia Fehres [2], Prof. René Toes [2], Dr. Yolande Ramos [2], Prof. Ingrid Meulenbelt [2], Dr. Regina Luttge [1]
1. Eindhoven University of Technology, 2. Leiden University Medical Centre

A Microfluidic Device for Monitoring Functional Enzyme Activity of Primary Human Hepatocyte Spheroids Based on Cell-Secreted Extracellular Vesicles 31
Mr. Ehsanollah Moradi[1], Dr. Päivi Järvinen [1], Dr. Markus Haapala [1], Prof. Ossi Korhonen [2], Prof. Tiina Sikanen [1]
1. University of Helsinki, 2. University of Eastern Finland

Wavelength-selective photodetector for NADH fluorescence detection 32
Mr. Zhengwei Liao[1], Ms. Laura Cavedoni [1], Ms. Ceren Kutucu [1], Prof. Padmakumar Rao [1], Prof. Clementine Boutry [1], Prof. Filipe Arroyo Cardoso [1]
1. Delft University of Technology

Nano- and Microscale Aptamer Biosensors for Monitoring Biomarkers of Human Health 33
Prof. Nako Nakatsuka[1]
1. CHEMINA - EPFL

Poster Session 1

Ionic Liquids and Focused Ion Beams: Are all Ionic Liquids Adequate for Advanced FIB Micro- or Nano-engineering? 35
Dr. Jacques Gierak[1], Ms. Elinoa Sebag [2], Mr. Amir Goodwin [2], Mr. David Bouville [2], Dr. philippe Lesot [3], Dr. philippe Berdagué [3]
1. C2N-CNRS, 2. Centre de Nanosciences et de Nanotechnologies (C2N), Palaiseau, 91120, France, 3. ICMMO

Plasmonic aluminium nanogap creation by electromigration for plasmonic UV-Nanolithography 36
Mr. Jakob Nüßlein[1], Mr. Zhuoji Huang [1], Prof. Steffen Strehle [1]
1. Techische Universität Ilmenau

Improved Accuracy in Measuring the Dielectric Constant of Nanoparticles in Electrostatic Force Microscopy 37
Mr. Lukas Lehnert[1], Mr. Benjamin Baumann [1], Prof. Ronald Thoelen [2], Prof. Hildegard Moebius [1]
1. University of Applied Sciences Kaiserslautern, 2. Hasselt University

Effect of doping Nb on optical properties of Sea Urchin-like TiO2 Photocatalysis 38
Dr. Mariko Murayama[1], Prof. Xinwei Zhao [2], Prof. Taichiro Nishio [1]
1. Tokyo University of Science, 2. Henan University of Technology

PVDF-TrFE with suspended AlN particles: a polymer nano-composite with boosted ferroelectric properties 39
Dr. Wolfgang Hilber[1], Mr. Sebastian Lang [1], Prof. Bernhard Jakoby [1]
1. Johannes Kepler University Linz

Fabrication of Ferroelectric PVDF:TrFE Foil via Controlled Dewetting 40
Mr. Sebastian Lang[1], Dr. Wolfgang Hilber [1], Ms. Tina Mitteramskogler [1], Prof. Bernhard Jakoby [1]
1. Johannes Kepler University Linz

X-ray energy dependence of gold nanoparticle synthesis in X-ray radiolysis 41
Dr. Akinobu Yamaguchi[1], Dr. Kenji Hanada [2], Prof. Ikuo Okada [2], Dr. Hiroshi Sekiguchi [3], Dr. Ikuya Sakurai [4]
1. Toyo University, 2. Aichi Synchrotron Radiation Center, 3. Japan Synchrotron Radiation Research Institute, 4. Nagoya University

E-Beam Lithography Process Calibration with Minimum Number of SEM Images using Deep Learning 43
Mr. Burak Çoban[1], Mr. Suleyman Celik [2], Mr. Florian Imeri [3], Dr. Jan Klikovits [3], Dr. Klaus Gieb [3], Mr. Nezih Ünal [3]
1. İzmir Institute of Technology, 2. Sabanci University Nanotechnology Research and Application Center, 3. GenISys GmbH

Eco-friendly, bioinspired nanopattern for antifouling: Cicada wing-inspired nanostructures for marine applications 44
Mr. Zihao Zhao[1], Ms. Nan Liang [1], Prof. Shoso Shingubara [1], Prof. Tomohiro Shimizu [1], Prof. Takeshi Ito [1]
1. Kansai University

Electrochemical Investigation of $[Ru(bpy)_2(L)]^{2+}$ Complexes for Biosensor Applications: Insights into Rct Reduction Mechanism 45
Mr. Koki Yamashita[1], Prof. Tomohiro Shimizu [1], Prof. Shoso Shingubara [1], Mr. Hitoshi Ishida [1], Mr. Akinori Kuzuya [1], Prof. Takeshi Ito [1]
1. Kansai University

Bactericidal property of COP nanopillars dependent with their size 46
Mr. Gakuto Inoue[1]
1. Kansai University

Impact of microfabrication conditions on the oxygen depletion rate of thiol-enes 47
Dr. Markus Haapala[1], Dr. Päivi Järvinen [1], Dr. Iiro Kiiski [1], Prof. Tiina Sikanen [1]
1. University of Helsinki

Microstructuring of 3D Printed Ceramic Surfaces using Nanoimprint Lithography 48
Ms. Sonja Kopp [1], Dr. Abhijeet Lale [2], Ms. Viktorija Jonaityte [1], Dr. Michael Haslinger [1], Ms. Marta Bonora [3], Mr. Matthias Vostatek [3], Ms. Sarah Linnemeier [4], Prof. Marcus Granegger [4], Prof. Francesco Moscato [3], Dr. Martin Schwentenwein [2], Dr. Michael Muehlberger[1]
1. PROFACTOR GmbH, 2. Lithoz GmbH, 3. Center for Medical Physics and Biomedical Engineering, Medical University of Vienna, 4. Department of Cardiac Surgery, Medical University of Vienna

Post-etch Surface Modification for Sidewall Smoothing in Deep Reactive Ion Etched Silicon 49
Mr. Arjun Moothedath Sethumadhavan[1], Mr. Zhong Ren [1]
1. Oxford Instruments

Fabrication of fine metal patterns using solvent-soluble UV-curable resin 50
Mr. Satoshi Fujieda[1], Mr. Takeshi Osaki [2], Mr. Yukio Okado [2], Prof. Jun Taniguchi [1]
1. Tokyo University of Science, 2. Toyo Gosei Co., Ltd., Photosensitive Materials Research Center

Effect of Polyethylene Glycol on growth of Porous Silicon 51
Mr. XUMING ZHAO[1], Mr. Tomoya Okawa [1], Ms. Chenxin Zhong [1], Mr. koji akiyama [2], Mr. takeya inoue [2], Prof. Takeshi Ito [1], Prof. Shoso Shingubara [1], Prof. Tomohiro Shimizu [1]
1. Kansai University, 2. Tokyo Electron

Study of blob defectivity for different 248nm resist processes: influence of material chemistry, pattern types, bake and development conditions. 52
Mrs. Lucie BORGET[1], Mrs. Romane Francais [1], Mr. Loic Balme [1], Mr. Yohann Lebel [1], Mr. OLIVIER MERMET [1], Dr. Benedicte Mortini [1]
1. STMicroelectronics

Development of Microfluidic Flow Cells with Integrated Arrays of Freestanding Al_2O_3 Membranes for SEM Imaging 53
Mr. Jeremy Teuber[1], Mr. Tim Erichlandwehr [2], Mr. Rukan Nasri [2], Dr. Irene Fernandez [2]
1. Max-Planck-Institute for the Structure and Dynamics of Matter, 2. UHH

Fabrication of Flexible Printed In-Mold Electronic Devices 54
Dr. JEONGDAI JO[1], Mr. Pyoungwon Park [1], Dr. Taik-Min Lee [2], Dr. Inyoung Kim [2]
1. Korea Institute of Machinery and Materials (KIMM), 2. Korea Institute of Machinery & Materials (KIMM)

Bioinspired Nanospike Formation on the Surfaces of Commercial Plastic Plates Using Atmospheric-Pressure Low-Temperature Plasma 55
Dr. Masashi Yamamoto[1], Mr. Motoki Tanaka [2], Mr. Ayumu Takada [2], Dr. Atsushi Sekiguchi [3]
1. National Institute of Technology (KOSEN) Kagawa College, 2. National Institute of Technology, Kagawa College, 3. Litho Tech Japan Corporation

Impact of processing on the temperature-dependant behaviour of nano-structured Platinum thin films fabricated by Spark Ablation 56
Ms. Shatavisha Biswas[1], Prof. Sten Vollebregt [2]
1. PhD, 2. Associate Professor

Hierarchical structures fabricated for probiotic marine bacterial growth using hybrid methods for polymer replication 57
Ms. Yuyan Liu[1], Mr. Xavier Florensa [1], Mr. Euan McDonald [2], Prof. Paul Kempen [1], Prof. Claus Sternberg [1], Prof. Nikolaj Gadegaard [2], Prof. Lone Gram [1], Prof. Rafael Taboryski [1]
1. Technical University of Denmark, 2. The University of Glasgow

Fluorination of Ni Hard masks during Fluorine-Based DRIE: Structural and Spectroscopic Insights into NiF_2 Formation 58
Mr. Baptiste Fischer-Kaszuba [1], Dr. Amandine Andrieux-Ledier [2], Dr. Etienne Carré[1], Dr. Patrick Kayser [1], Dr. Pierre Lavenus [2], Mr. Jean-Sebastien Mérot [3], Dr. Frédéric Fossard [3], Dr. Thomas Baron [4]
1. DPHY, ONERA, Université Paris-Saclay, 92320 Châtillon, France, 2. DPHY, ONERA, Université Paris-Saclay, 3. Université Paris-Saclay, ONERA, CNRS, Laboratoire d'étude des microstructures (LEM), 4. Université Marie et Louis Pasteur, SUPMICROTECH, CNRS, Institut FEMTO-ST

On-CMOS 3D Platinum Electrodes Fabricated by Focussed-Ion Beam for Dielectrophoresis of DNA Towards an Electrokinetic Lab-on-CMOS 59
Dr. Lewis Keeble[1], Mr. Arthur Jaccottet [1], Mr. Daryl Ma [1], Dr. Jesus Rodriguez-Manzano [1], Prof. Pantelis Georgiou [1]
1. Imperial College London

Hybrid-Polymer Microring Resonator Arrays for Next-Generation Photoacoustic and Biosensing Applications 60
Dr. Santhosh Pandian [1], Ms. Marina Fetisova [2], Dr. Petri Karvinen [2], Dr. Paul Müellner [3], Dr. Moritz Eggeling [3], Dr. Rainer Hainberger [3], Mr. Evgenii Lepukhov[1], Prof. Tapio Niemi [1]
1. Tampere University, 2. University of Eastern Finland, 3. AIT Austrian Institute of Technology GmbH

Femtosecond laser inscription of optical waveguide in sapphire 61
Dr. Wei Lyu[1], Dr. Ding Zhao [1], Prof. Min Qiu [2]
1. Westlake Institute for Optoelectronics, 2. Westlake University

Effective diffusion barrier for Au/Ni thin films in quartz MEMS processing 62
Mr. Baptiste Fischer-Kaszuba[1], Dr. Amandine Andrieux-Ledier [1], Dr. Etienne Carré [1], Dr. Frédéric Fossard [2], Mr. Jean-Sebastien Mérot [2], Dr. Patrick Kayser [3], Dr. Pierre Lavenus [1], Dr. Thomas Baron [4]
1. DPHY, ONERA, Université Paris-Saclay, 2. Université Paris-Saclay, ONERA, CNRS, Laboratoire d'étude des microstructures (LEM), 3. DPHY, ONERA, Université Paris-Saclay, 92320 Châtillon, France, 4. Université Marie et Louis Pasteur, SUPMICROTECH, CNRS, Institut FEMTO-ST

Analysis and fabrication of electrothermal electrodes for micro and nanostructured sensors 63
Mr. Abel Palomas Jiménez[1], Dr. Michelle Cedeño [1], Ms. Ana Coloma Velez [1], Dr. Jorge Luis Villar [1], Dr. Manuel Domínguez-Pumar [1], Dr. Sandra Bermejo [1]
1. Universitat Politècnica de Catalunya - BarcelonaTech (UPC)

Ultra-thick grayscale ellipsoidal structures for X-ray focusing using scanning-laser direct write lithography 64
Dr. Giulia Malvicini[1], Prof. Helmut Schift [1]
1. Paul Scherrer Institute (PSI)

Effects of Annealing on Effective Young's Modulus of Ti/Au Multi-Layered Microcantilevers for MEMS Capacitive Accelerometers 65
Mr. Tatsuhiko Mori[1], Dr. Tomoyuki Kurioka [1], Mr. Shunkai Watanabe [1], Prof. Chun-Yi Chen [1], Prof. Tso-Fu Mark Chang [1], Prof. Katsuyuki Machida [1], Prof. Hiroyuki Ito [1], Prof. Yoshihiro Miyake [1], Prof. Masato Sone [1]
1. Institute of Science Tokyo

Development of an In Situ Microfluidic System for Real-Time Control of Porous Microspheres Fabrication 66
Mr. Ji Hwan Han[1], Mr. Min Chul Shin [1], Prof. Chul Min Kim [2], Prof. Gyu Man Kim [1]
1. Kyungpook National University, 2. Gyengsang National University

Slippery liquid-infused micropatterned surface for air-lifted analyte membrane formation 67
Mr. Seong Min Yoon[1], Prof. Young Tae Cho [1], Dr. Woo Young Kim [1], Mr. Chae Hyeok Yoon [1]
1. Changwon National University, Changwon

Mastering the growth of centimetric sp2-hybridized boron nitride films for optoelectronic devices 68
Dr. Laure Tailpied [1], Ms. Marjolaine Cornu [1], Dr. Frédéric Fossard [2], Mr. Jean-Sebastien Mérot [3], Ms. Chloe Grekobi [3], Mr. Jules Lagrave [3], Dr. Jean-Manuel Decams [4], Dr. Annick Loiseau [3], Dr. Amandine Andrieux-Ledier[5]
1. Université Paris-Saclay, ONERA, CNRS, Laboratoire d'étude des microstructures (LEM), 92322 Châtillon, France, 2. Université Paris-Saclay, ONERA, CNRS, Laboratoire d'étude des microstructures (LEM), 3. Université Paris-Saclay, ONERA, CNRS, Laboratoire d'étude des microstructures (LEM), 92322 Châtillon, 4. Annealsys, 139 rue des Walkyries, 34000 Montpellier, France, 5. DPHY, ONERA, Université Paris-Saclay, F-92322 Châtillon, France

Fabrication of slanted diffraction gratings by electron beam lithography with tilted angle exposure 69
Mr. Naoya Shibasaki[1], Prof. Jun Taniguchi [1]
1. Tokyo University of Science

Investigation of Pre-Stressed Membranes in Miniaturized Piezoresistive Diaphragm Pressure Sensors for Enhanced Sensitivity in High Vacuum 70
Dr. Jian LU[1], Dr. Lan ZHANG [1], Dr. Yuichi KURASHIMA [1], Dr. Hideki TAKAGI [1]
1. National Institute of Advanced Industrial Science and Technology (AIST)

Integration of a metal nano-antenna structure into silicon substrates using surface-activated room temperature bonding 71
Dr. Yuichi KURASHIMA[1], Dr. Takashi Matsumae [1], Mr. Atsuhiko Maeda [1], Dr. Masaaki Oshita [1], Dr. Hideki TAKAGI [1], Dr. Tetsuo Kan [2], Dr. Elyas Ashenafi Abadi [2], Dr. Daiji Noda [3], Mr. Ryo Ohta [3]
1. National Institute of Advanced Industrial Science and Technology (AIST), 2. The University of Electro-Communications, 3. Micromachine Center

Interface-Engineered Ferroelectric Tunnel Junctions with Ultra-High TER via Optimized P(VDF-TrFE) Crystallinity 72
Mr. Mohit Kumar Gautam[1], Dr. Roshni Satheesh-Babu [1], Dr. Ioannis Zeimpekis [1], Prof. Dimitra Georgiadou [1]
1. University of Southampton

Fabrication of metal nanodot arrays for LSPR biosensors with LOD of 1fg/mL using nanoimprint lithography process 74
Dr. JaeJong Lee[1], Dr. Narae Jo [2]
1. Korea Institute of Machinery and Materials (KIMM), 2. Korea Research Institute of Standards and Science

Study of the high-intensity reflection structure that used the speckle exposure method 75
Dr. Atsushi Sekiguchi[1]
1. Litho Tech Japan Corporation

Introducing ArF grayscale lithography for large-scale fabrication of submicronic 3D structures 76
Mr. Gaby Bélot[1], Mr. Sébastien Bérard-Bergery [1], Dr. Élodie Sungauer [1], Mr. Api Warsono [2], Dr. Arnaud Bazin [2], Dr. Aurélien Fay [2], Dr. Cécile Gourgon [3]
1. STMicroelectronics, 850 rue Jean Monnet, 38926 Crolles Cedex, France, 2. Univ. Grenoble Alpes, CEA, Leti, F-38000 Grenoble, France, 3. Université Grenoble Alpes, CNRS, CEA/LETI-Minatec, Grenoble INP, LTM, 17 Rue des Martyrs, Grenoble 38054, France

MoTe2-Based Memristor Fabrication with Scanning Probe Lithography 77
Ms. Busra Oyku Alan[1], Dr. Christoph Reuter [1], Dr. Ren Li [1], Prof. Steffen Strehle [1]
1. Techische Universität Ilmenau

Study on Micro Scale Surface Polishing and Modification of 3D Biodegradable Scaffolds using Electron Beam Treatment 78
Mr. JeongSik Noh[1], Prof. Jongsung Park [1]
1. Kyungpook National University

Micro-Mechanical Properties of Annealed Electrodeposited Gold for Design of MEMS Structural Components 79
Mr. Shota Iima[1], Dr. Tomoyuki Kurioka [2], Mr. Shota Kanno [2], Prof. Chun-Yi Chen [2], Prof. Tso-Fu Mark Chang [2], Prof. Katsuyuki Machida [2], Prof. Hiroyuki Ito [2], Prof. Yoshihiro Miyake [2], Prof. Masato Sone [2]
1. Institute of Integrated Research, Institute of Science Tokyo, 2. Institute of Science Tokyo

Scalable manufacturing processes for solid-state nanopores using Atomic Layer Deposition 80
Mr. Nico Rademacher[1], Ms. Stefanie Linda Stoll [1], Mrs. Anja Leibold [2], Mr. Michael Möller [1], Dr. Christoph Blattert [2], Dr. Jens Bolten [1], Prof. Max Lemme [1]
1. AMO GmbH, 2. Hahn-Schickard-Gesellschaft für angewandte Forschung e.V.

The Impact of Writing Field Stitching on Optical Losses in Electron Beam Fabricated Silicon-on-Insulator Waveguides 81
Mr. Maksim Lipkin[1], Mr. Michael Möller [1], Ms. Lisa Ehlert [1], Dr. Jens Bolten [1], Dr. Rijil Thomas [1], Dr. Stephan Suckow [1], Prof. Max Lemme [2]
1. AMO GmbH, 2. Chair of Electronic Devices, RWTH Aachen University

A Deep Learning-Based Photoresist Shrinkage Correction Method via Fusion of SEM Image and Scanning Parameter Features 82
Ms. Sa Liu [1], Dr. Yanan Zhu [2], Mr. Jiebin Niu [3], Prof. Diwei Zhou [4], Dr. Fuqin Deng [1], Prof. Zhuming Liu[2]
1. School of Electronics and Information Engineering,Wuyi University, 2. Institute of Semiconductors, Guangdong Academy of Sciences, 3. Institute of Microelectronics of the Chinese Academy of Sciences, 4. School of Science, Loughborough University

Fabrication and Nanoscale Characterization of Sidewall Roughness in SOI Waveguides 83
Dr. Magdalena Ulmeanu[1], Dr. Kate Stokes [1], Dr. Marta Kocun [2], Dr. Roger Proksch [2], Dr. Vlad Korolkov [3], Dr. Luis Perdigao [3], Dr. Jason Li [2], Dr. Gabriele Selvaggio [2], Mr. Zhong Ren [1]
1. Oxford Instruments Plasma Technology, 2. Oxford Instruments Asylum Research, 3. Oxford Instruments NanoAnalysis

Fabrication of hierarchical structures in a greyscale positive photoresist by applying two lithography methods in a single resist film 84
Dr. Christine Schuster [1], Dr. Anja Voigt[1], Dr. David Kuhness [2], Ms. Christine Prietl [2], Dr. Matej Goraus [3], Mr. Daniel Mrena [3], Prof. Dusan Pudis [3], Dr. Arne Schleunitz [1], Mrs. Gabi Grützner [1], Mr. Markus Postl [2]
1. micro resist technology GmbH, 2. Joanneum Research Forschungsgesellschaft mbH, 3. University of Zilina

200 kV E-beam Lithography for Patterning Thick Resist 85
Dr. Ying Tran[1], Dr. Kian Shen Kiang [1], Mr. Hitoshi Kato [2], Mr. Ryo Matsui [2], Mr. Yukinori Aida [2], Prof. Martin Charlton [1]
1. University of Southampton, 2. JEOL Ltd

Large-Scale Integrated Visible/Near-Infrared Multi-Channel Polarizer based on Sub-wavelength Metal Grating 86
Ms. Kangping Liu[1], Mr. Jinyu Guo [1], Mr. Wentao Yuan [1], Mr. Shuoqiu Tian [1], Mr. Hao Quan [1], Mr. Qiucheng Chen [1], Ms. Qingxin Wu [1], Ms. xunjia Zhao [1], Prof. Yifang Chen [1]
1. Fudan university

High Resolution Electron Beam Lithography for 10 nm Zone Plates with ultra-high aspect ratio 87
Ms. Qingxin Wu[1], Mr. Qiucheng Chen [1], Mr. Hao Quan [1], Ms. xunjia Zhao [1], Mr. Wentao Yuan [1], Mr. Shuoqiu Tian [1], Mr. Jinyu Guo [1], Ms. Kangping Liu [1], Prof. Yifang Chen [1]
1. Fudan university

Ultra high resolution and dense SiO2 gratings by electron beam lithography and dry-etch **88**
Mr. Sheng Tao[1], Prof. Yifang Chen [1], Mr. Shuoqiu Tian [1], Mr. Wentao Yuan [1], Mr. Jinyu Guo [1], Ms. Kangping Liu [1]
1. *Fudan university*

Ultrafast Single Germanium Nanowire Photodetectors **89**
Dr. Ahmad Echresh[1], Mr. Mohd Saif Shaikh [2], Mr. mircea-traian catuneanu [2], Prof. Manfred Helm [1], Dr. Shengqiang Zhou [1], Prof. Artur Erbe [1], Dr. Lars Rebohle [1], Prof. Kambiz Jamshidi [2], Dr. Yonder Berencen [1], Dr. Yordan M. Georgiev [1]
1. *Helmholtz-Zentrum Dresden-Rossendorf (HZDR),* ***2.*** *Technische Universität Dresden*

Substantial Ron,sp Reduction in a 1.2 kV SiC DMOSFET Using a Double-Epi Drift Layer **90**
Mr. Seung wan Jung[1]
1. *Pusan National University*

Development of a uniform cell dispersion structure in microfluidic channels with low cell loss **91**
Mr. Takumi Yamada[1], Mr. Akihito Kimura [1], Dr. Maho Kaminaga [1], Dr. Akira Kotani [1]
1. *National Institute of Technology (KOSEN) Toyota College*

3D-Printed Microfluidic Device for Biological Application **92**
Mr. Amlan Ashish[1], Prof. Gorachand Dutta [1]
1. *Indian Institute of Technology Kharagpur*

Tattoo Electrodes for Comfortable and Reliable Masticatory EMG Monitoring **93**
Ms. Núria Termes Español[1], Ms. Eva Casals [1], Ms. Yolanda Castillo [2], Prof. Raimon Jané [2], Ms. Rosa Villa [1], Mr. Anton Guimerà-Brunet [1], Ms. Gemma Gabriel [1]
1. *Institute of Microelectronics of Barcelona (IMB-CNM, CSIC),* ***2.*** *Universitat Politècnica de Catalunya - BarcelonaTech (UPC)*

Exploiting the dewetting instability of thin Ge films to develop a novel photonic platform **94**
Dr. Sonia Freddi[1], Dr. Nicoletta Granchi [2], Dr. Alessia Arrigoni [3], Mr. Michele Gherardi [4], Dr. Benedetta Squeo [3], Mr. Raffaele Giani [4], Dr. Alexey Fedorov [1], Dr. Laura Pasquardini [5], Dr. Lia Vanzetti [6], Prof. Maria Antonietta Vincenti [7], Dr. Mariacecilia Pasini [3], Prof. Francesca Intonti [2], Dr. Monica Bollani [1]
1. *Institute of Photonic and Nanotechnology (IFN) - CNR,* ***2.*** *LENS and Department of Physics and Astronomy, University of Florence,* ***3.*** *SCITEC-CNR,* ***4.*** *Politecnico di Milano,* ***5.*** *Indivenire s.r.l.,* ***6.*** *Center for Sensors and Devices, Fondazione Bruno Kessler,* ***7.*** *Università degli studi di Brescia*

Mechanically robust spin-on-glass packaging of hydrogenated amorphous silicon for harsh environment applications **95**
Mr. Junhwa Seong[1], Dr. Younghwan Yang [1], Mr. Youngsun Jeon [1], Prof. Junsuk Rho [1]
1. *Pohang University of Science and Technology*

Dynamic Electrical Conductivity of Ni-P/Nylon Yarns with Different Twist Number for Weavable Device **96**
Mr. Takumi Suda[1], Mr. Kazuhiro Shibata [1], Dr. Tomoyuki Kurioka [1], Prof. Katsunari Sato [2], Prof. Chun-Yi Chen [1], Ms. Nao Yoshida [2], Prof. Tso-Fu Mark Chang [1], Prof. Hiromichi Kurosu [2], Prof. Masato Sone [1]
1. *Institute of Science Tokyo,* ***2.*** *Nara Women's University*

Crystalline atomic layer–dielectric hybrid metasurfaces for high-efficiency visible metaphotoncis **97**
Mr. Junhwa Seong[1], Dr. Younghwan Yang [1], Mr. Youngsun Jeon [1], Prof. Junsuk Rho [1]
1. *Pohang University of Science and Technology*

Volatile Threshold Switching Characteristics of TiN/TaOx/TiN Selector Devices **98**
Ms. Zohreh Hajiabadi[1], Mr. Aiden Graham [1], Mr. Alexander-Hanyu Wang [1], Dr. Mari Napari [2], Prof. Dimitra Georgiadou [1], Prof. David Thomas [1], Prof. Harold Chong [1], Dr. Firman Simanjuntak [1]
1. *University of Southampton,* ***2.*** *King's College London*

Silicon-based metasurface polarizer supporting quasi-bound states in the continuum **99**
Prof. Maria Antonietta Vincenti [1], Dr. Luca Fagiani [2], Dr. Luca Bolzonello [3], Dr. Johann Osmond [3], Mr. Michele Gherardi [4], Dr. Sonia Freddi [5], Prof. Domenica de Ceglia [1], Prof. Niek van Hulst [3], Dr. Monica Bollani[6]
1. *Università degli studi di Brescia,* ***2.*** *Physic Department of Milano Politecnico, Milano, 20133, Italy,* ***3.*** *ICFO, The Barcelona Institute of Science and Technology, Barcellona, 08860, Spain,* ***4.*** *Politecnico di Milano,* ***5.*** *IFN-CNR,* ***6.*** *Institute of Photonic and Nanotechnology (IFN) - CNR*

Effect of excitation wavelength on micro-Raman thermometry for suspended silicon MEMS structures **100**
Dr. Masaki Shimofuri[1], Mr. Kanta Fujiwara [1], Dr. Amit Banergee [1], Dr. Jun Hirotani [1], Prof. Toshiyuki Tsuchiya [1]
1. *Kyoto University*

High-performance structures with photoimageable thick film pastes in low temperature cofiring ceramics for mmWave packages **101**
Ms. Lynn Möhring[1], Mr. Martin Ihle [1], Ms. Birgit Manhica [1], Dr. Stefan Körner [1], Dr. Uwe Partsch [1], Dr. Peter Uhlig [2], Mr. Enrico Tolin [2]
1. *Fraunhofer Institute of Ceramic Technologies and Systems IKTS,* ***2.*** *IMST GmbH*

Electrical Behavior of Rectifying and Ohmic Contacts on Lightly n-Doped Germanium **102**
Mr. Michele Gherardi[1], Dr. Sonia Freddi [2], Mr. Francesco Scali [1], Dr. Carlo Zucchetti [1], Prof. Federico Bottegoni [1], Prof. Giovanni Isella [1], Prof. Franco Ciccacci [1], Prof. Marco Finazzi [1], Dr. Alexey Fedorov [2], Dr. Monica Bollani [3]
1. *Politecnico di Milano,* ***2.*** *IFN-CNR,* ***3.*** *Institute of Photonic and Nanotechnology (IFN) - CNR*

Fabrication of Titanium-based Microneedles Array Using Wire Electrical Discharge Machining **103**
Mr. Min Chul Shin[1], Mr. Ji Hwan Han [1], Prof. Gyu Man Kim [1]
1. *Kyungpook National University*

Polymer-based MEMS microcantilever and microfluidic system for biochemical detection **104**
Dr. Pooja P. Kanade[1], Dr. Paul T. Baine [2], Dr. Briliant Adhi Prabowo [1], Dr. Arthur Lipinski [3], Dr. Jason Wiggins [1], Prof. Robert M. Bowman [1]
1. *School of Mathematics and Physics, Queen's University Belfast,* ***2.*** *School of Electronics, Electrical Engineering and Computer Science, Queen's University Belfast,* ***3.*** *Research Fellow*

Two-photon polymerization as mastering tool for nanoimprint lithography to produce microfluidic test devices **105**
Mr. Stjepan Perak [1], Ms. Sonja Kopp [2], Ms. Viktorija Jonaityte [2], Ms. Marta Bonora [3], Dr. Michael Muehlberger [2], Prof. Francesco Moscato [3], Dr. Markus Lunzer[1]
1. *UpNano GmbH,* ***2.*** *PROFACTOR GmbH,* ***3.*** *Center for Medical Physics and Biomedical Engineering, Medical University of Vienna*

Engineered magnetic quantum dot nanoprobes for multiplexed, equipment-free Alzheimer's diagnosis at point-of-care **106**
Dr. Anjum Qureshi [1], Dr. Javed H. Niazi[1]
1. *SUNUM - Sabanci University Nanotechnology Research & Application Center*

Quality Factor Engineering in NIR Optical Metasurfaces Using Ge2Sb2Te5 and Graphene 107
Dr. Seyed As'ad Amirhosseini [1], Mr. Daniyal Khoshmaram[2]
1. Department of Electrical and Computer Engineering, Isfahan University of Technology, Isfahan, Iran, 2. Department of Electrical Engineering, Amirkabir University of Technology, Tehran, Iran

Anomalous mapping between the Surface Charge and Ionic Conductance in Narrow Confinements 108
Mr. Debmalya Roy[1], Prof. Suman Chakraborty [1]
1. Indian Institute of Technology Kharagpur

Ultrasensitive, AI-integrated cyber-physical system for patient-specific CYFRA21-1 biomarker quantification 109
Mr. Biswadeep Roy[1], Dr. Abhisek Maikap [1], Prof. Soumen Das [1], Prof. Suman Chakraborty [1]
1. Indian Institute of Technology Kharagpur

Broadband Transmission Measurement for Ta2O5 Photonic Crystal Waveguide 111
Ms. Wenjie Wang[1], Prof. Martin Charlton [1]
1. University of Southampton

Fabrication of planar nanostructured SiC microelectrode arrays for long-lifetime neural interfaces 112
Dr. Fabrice Iacovella[1], Dr. Gwenaell Pound-Lana [1], Mr. Lucas Labbe [1], Mr. Sébastien Labau [1], Dr. Camille Petit-Etienne [1], Mr. Andrei Uvarov [2], Dr. Scott Greenhorn [3], Mr. Marcin Zielinski [4], Prof. Konstantinos Zekentes [3], Prof. Edwige Bano [3], Dr. Cécile Gourgon [1], Prof. Jumana Boussey [1]
1. Université Grenoble Alpes, CNRS, CEA/LETI-Minatec, Grenoble INP, LTM, 17 Rue des Martyrs, Grenoble 38054, France, 2. Plasma-therm Europe, Bernin, 38190, France, 3. Centre de Radiofréquences, Optique et Micro-nanoélectronique des Alpes, Grenoble, 38016, France, 4. NOVASiC, Le Bourget du Lac, 73375, France

Sub-wavelength grating polarizers in 1-D array focal plane for ultraviolet polarimetric detection 113
Mr. Jinyu Guo[1], Ms. Kangping Liu [1], Ms. Qingxin Wu [1], Mr. Qiucheng Chen [1], Mr. Hao Quan [1], Ms. xunjia Zhao [1], Prof. Yifang Chen [1]
1. Fudan university

Design and Fabrication of a 100mm-Diameter Pillar Metalens for High-Performance Mid-Infrared Imaging 114
Ms. Weilin Jin[1], Mr. Gaochen Dong [1], Ms. Zixuan Wang [1], Dr. Kian Shen Kiang [1], Prof. Jize Yan [1]
1. University of Southampton

Quantum Dot-Low Dimensional Material Hybrid Heterostructures for Physically Unclonable Optical Tags 115
Mr. Yueyu Guo[1], Ms. Syeda Ramsha Ali [1], Dr. Nema Abdelazim [2]
1. School of Electronics and Computer Science, University of Southampton, Southampton SO17 1BJ, United Kingdom, 2. University of Southampton

Modelling the Heat Distribution in Organ-on-a-Chip Systems Using Integrated Microheaters 116
Mr. Gabriel Ferreira[1], Dr. Patrícia Sousa [2], Prof. Rui Lima [1], Prof. Susana Catarino [1], Prof. Graça Minas [1]
1. University of Minho, 2. International Iberian Nanotechnology

Microfabricated Light Pipe for Sustainable and Lithography-Free SPR Sensor 117
Dr. Briliant Adhi Prabowo[1], Dr. Pooja P. Kanade [1], Dr. Fatemeh Moradiani [1], Dr. Arthur Lipinski [1], Dr. Paul T. Baine [2], Dr. Jason Wiggins [1], Prof. Robert M. Bowman [1]
1. School of Mathematics and Physics, Queen's University Belfast, 2. School of Electronics, Electrical Engineering and Computer Science, Queen's University Belfast

Dual-Path Anomaly Detection for Semiconductor Equipment: Toward Sensor-Level Intelligence in Digital Twin Manufacturing 118
Mr. Joon Soo Kim[1]
1. SUNG KYUN KWAN University / Samsung Electronics

Real-time lesion location detection system using Mu-metal and Hall sensor 119
Dr. Woojin Yun [1], Mr. Gapseop Sim[1], Prof. Hyeinjune Kim [2], Dr. Seung-Hwan Jung [3]
1. National Nanofab Center, 2. Seoul National University of Science and Technology, 3. GRIT Custom-IC

A Study on Focus Control Improvement in Response to Wafer Table Edge Wear in Photolithography Equipment 120
Mr. Kyunghwan Joo[1], Mr. Kwang Hoon Lee [2], Prof. Jae Wook Jeon [3]
1. SUNG KYUN KWAN University / Samsung Electronics, 2. Samsung Electronics, 3. Sungkyunkwan University

Automated Silicon Wafer Handling for Gravity Effect Compensation in High-Precision Horizontal Metrology 122
Mr. CESAR PEREZ DOMINGUEZ[1], Dr. JUAN TRUJILLO-SEVILLA [2], Dr. CARMELO MILITELLO-MILITELLO [3]
1. Wooptix, 2. WOOPTIX, 3. Universidad de La Laguna

A 10.94bit resolution measurement circuit for resistive sensors 123
Dr. xiaoming teng[1], Prof. yufeng zhang [1], Mr. haoyu liang [1]
1. MEMS Center, Harbin Institute of Technology

Device Variation Effect Simulation for SnOx Memristor-based Neural Networks 124
Mr. Aiden Graham[1], Ms. Zohreh Hajiabadi [1], Mr. Alexander-Hanyu Wang [1], Prof. Dimitra Georgiadou [1], Dr. Ruomeng Huang [1], Dr. Firman Simanjuntak [1]
1. University of Southampton

Eco-Friendly Functionalization of Graphene via Spark Ablation for Enhanced NO2 Gas Sensing Applications 125
Dr. Mudassir Husain[1], Dr. Leandro Sacco [2], Prof. Sten Vollebregt [3]
1. PhD, 2. VSParticle, 3. Associate Professor

Enhancing Overlay Accuracy through Transformation of Overlay Outliers caused by Wafer Local Defocus in Photolithography Scanner Calibration 126
Mr. Kwang Hoon Lee[1], Prof. Won Bo Lee [2]
1. Seoul National University / Samsung Electronics, 2. Seoul National University

Gas Sensors Based on MoS_2 Quantum Dots Deposited via Drop-Casting for Environmental Monitoring on Microfabricated Platforms 128
Ms. Andrea Carolina Villalvazo-Hidalgo[1], Dr. Orfil González-Reynoso [1], Ms. Martha Angelica Hidalgo-Ríos [1], Dr. Gregorio Guadalupe Carbajal-Arizaga [1], Dr. Mario Alberto García-Ramírez [1]
1. Universidad de Guadalajara

Real-Time Wireless Tremor Tracking System with V-Groove Crack Sensor 129
Mr. Jonghyeon Woo[1], Mr. JeongSik Noh [1], Prof. Jongsung Park [1]
1. Kyungpook National University

Microscope-based Multi-Analyte-Reflectance-Spectroscopy (μ-MARS) for multiplexed label free monitoring of immunoreactions 130
Dr. Grigorios Zisis [1], Dr. Dimitra Tsounidi [1], Dr. Georgios Koukouvinos [1], Dr. Panagiota Petrou [1], Dr. Ioannis Raptis[1]
1. NCSR Demokritos

CNFET fabrication for NO2 gas sensor recovery with local electrode heating 131
Ms. Ines Kraiem[1], Dr. Cosmin Ioan Roman [1], Mr. Andri Sigron [1], Dr. Miroslav Haluska [1], Prof. Christofer Hierold [1]
1. ETH Zürich

Selective Electrochemical Aptasensor Using Methylene Blue for Pseudomonas aeruginosa Detection in Mixed Bacterial Cultures 132
Ms. Somayeh Maghsoomi Taramsari[1]
1. University for Continuing Education Krems

Water-soluble holographic color prints from UV to visible for sustainable optical security device 133
Ms. Hyunjung Kang[1], Mr. Hongyoon Kim [1], Prof. Junsuk Rho [1]
1. Pohang University of Science and Technology

Dual functional filmy device for heat dissipation and power generation based on Bi2Te3 array with topological surface 134
Dr. YiHeng Zhao[1], Mr. Mingxue Li [1], Prof. yufeng zhang [2]
1. MEMS Center, Harbin Institute of Technology, Harbin 150001, China, 2. MEMS Center, Harbin Institute of Technology

A Modeling Study on Inorganic Chalcogenide Transport Layers in Sn-Based Perovskite Solar Cells 135
Mr. Daniyal Khoshmaram[1]
1. Department of Electrical Engineering, Amirkabir University of Technology, Tehran, Iran

Conformally-coated titanium carbide on structured pyrolytic carbon electrodes for lithium sulphur batteries 136
Mr. Owen Bell[1], Dr. Daniel Ho [2], Mrs. Nadira Palakkool [2], Dr. Mike Taverne [2], Dr. Kevin Chung-Che Huang [3], Prof. Vincent Barrioz [2], Dr. Yongtao Qu [2], Dr. Johnathan Mar [4], Dr. Tam Ho [2], Dr. Christopher Jones [5], Mr. Giray Kartopu [2]
1. PhD Student, 2. Northumbria University, 3. Southampton University, 4. Newcastle University, 5. Bristol University

A deeper dive into droplet and dust dynamics on commercially available solar panels 137
Mr. Anirban Roy[1], Mr. Rahul Roy [1], Dr. Chirodeep Bakli [1]
1. Indian Institute of Technology Kharagpur

All-in-one Microfluidic Platform for Single-Cell Environmental Phenotyping of Chlamydomonas reinhardtii 138
Mr. Alexandre Chargueraud[1], Dr. Lars Kool [2], Ms. Eliora Israelievitch [3], Dr. Alix Boulouis [3], Dr. Jacques FATTACCIOLI [4]
1. CPCV, Département de Chimie, Ecole Normale Supérieure, PSL Université, Sorbonne Université, CNRS, 75005 Paris, France, 2. Institut Pierre-Gilles de Gennes pour la Microfluidique, Paris, 75005, France, 3. Laboratoire de Biologie du Chloroplaste et Perception de la lumière chez les microalgues of the Institut de Biologie Physico-Chimique, Sorbonne Université, Paris, 75005, France, 4. CPCV, Département de Chimie, Ecole Normale Supérieure, PSL Université, Sorbonne Université, CNRS

Plenary 4 - Prof Shinichi Saito

Why Micro is different from Macro? A Challenge towards Macroscopic Quantum Technologies **140**
Dr. Shinichi Saito[1]
1. *Hitachi*

Plenary 5 - Prof Mariana Medina Sanchez

Medical Microrobots with Functional Nanomaterials for Precision Women's Healthcare **142**
Prof. Mariana Medina Sanchez[1]
1. *nanoGune*

Oral Session 2A: Nanoimprint and alternative lithography

Comparison of 2 processes based on NIL and lift-off for the fabrication of thick nano antennas for solar PV-TE applications **144**
Dr. Jean-Baptiste Doucet[1], Dr. Franck Carcenac [1], Dr. Leopold Boudier [1], Dr. Inès Revol [1]
1. *LAAS-CNRS*

Fine silver wiring using replica mold with light-shielding film **145**
Mr. Takumi Ashida[1], Prof. Jun Taniguchi [1]
1. *Tokyo University of Science*

Single-nm Mask Writing for Nanoimprint Lithography, as an Energy-Efficient Alternative to EUV **146**
Dr. James Owen[1], Mr. Robin Santini [1], Dr. John Randall [1]
1. *Zyvex Labs*

Optimization of grayscale direct-write laser lithography for the fabrication of large-area 2.5D molds for nanoimprint lithography **147**
Dr. Peng Tian[1], Dr. Maria Szola [1], Dr. Dimitrios Kazazis [1], Dr. Yasin Ekinci [1]
1. *Paul Scherrer Institute (PSI)*

Advanced Patterning For Smart Optical Devices: Integrating Inkjet Coating with Nanoimprinting for Precise Height Control and Minimal Residual Layers **148**
Mrs. Andrea Kronawitter[1], Mrs. Johanna Rimböck [1], Mrs. Lisa Vsetecka [1], Mrs. Thomas Achleitner [1], Mrs. Patrick Schuster [1], Mrs. Brid Connolly [2], Mr. Martin Sczyrba [3], Mr. Andreas Frangen [2]
1. *EV Group,* ***2.*** *Tekscend Photomasks Germany GmbH,* ***3.*** *AMTC Dresden*

Exploring water-soluble polymeric stamps for ultraviolet light nano-imprint lithography **150**
Mr. Haohui Yang[1], Mr. Anmol Gupta [1], Prof. Steffen Strehle [1]
1. *Techische Universität Ilmenau*

Fabrication and Evaluation of Curved Mirror for Co-packaged optics Using Photo Nanoimprint Technology **151**
Ms. Maaya Watanabe[1], Dr. Fumi Nakamura [2], Mr. Taro Itatani [2], Prof. Joji Maeda [1], Dr. Takeru Amano [2]
1. *Tokyo University of Science,* ***2.*** *National Institute of Advanced Industrial Science and Technology (AIST)*

Advances in parallelization of thermal scanning probe lithography and large-area patterning **152**
Ms. Julia Stark[1], Dr. Jana Chaaban [1], Mr. Kartik Buddha [1], Dr. Fabian Koenemann [1], Dr. Emine Çağın [1]
1. *Heidelberg Instruments*

Oral Session 2B: Photonics, Photonic structures and Metasurfaces

Sustainable manufacturing of optical metasurfaces for imaging, sensing and display 154
Prof. Junsuk Rho[1]
1. *Pohang University of Science and Technology*

A Novel Manufacturing Platform for Large-diameter Si Metalens using Deep-UV Lithography 155
Dr. Kai Sun[1], Dr. Xingzhao Yan [2], Mr. Jordan Scott [1], Dr. James Monks [3], Dr. Jun-Yu Ou [1], Prof. Otto Muskens [1]
1. *Physics and Astronomy, University of Southampton,* ***2.*** *Optoelectronics Research Centre, University of Southampton, SO17 1BJ, UK,* ***3.*** *Teledyne Qioptiq Ltd*

Understanding 3D Structural Control in Metasurface-Based Holographic Lithography 156
Mr. Jeevan Rois[1], Mr. Zesen Zhou [1], Dr. Matias Kagias [1]
1. *Lund University*

Fabrication of Substrates with Plasmonic Gold Nanostructures for Cellular Membrane Rupture 157
Mr. Christian Einsiedler[1], Dr. Franziska Marie Esmek [2], Mr. Rukan Nasri [3], Dr. Irene Fernandez [3]
1. *University of Hamburg, Hamburg Center for Ultrafast Imaging,* ***2.*** *University of Hamburg/Hamburg Center for Ultrafast Imaging,* ***3.*** *UHH/CUI*

Printable Spin-Multiplexed Metasurfaces for Ultraviolet Holographic Displays 158
Ms. Hyunjung Kang[1], Mr. Hongyoon Kim [1], Prof. Junsuk Rho [1]
1. *Pohang University of Science and Technology*

Embedded-Holey Metasurfaces for Enhanced Mechanical Robustness and Integration Compatibility 159
Ms. Zixuan Wang[1], Dr. Chuang Sun [1], Ms. Weilin Jin [2], Dr. Jun-Yu Ou [3], Dr. Kian Shen Kiang [2], Prof. Jize Yan [2]
1. *School of Electronics and Computer Science, University of Southampton, Southampton SO17 1BJ, United Kingdom,* ***2.*** *University of Southampton,* ***3.*** *Physics and Astronomy, University of Southampton*

Novel UV-curable organic-inorganic polymers for micro-optical and photonic components with enhanced reliability 160
Dr. Maria Russew [1], Dr. Alexander Plucinski[1], Dr. Thomas Wiglenda [1], Mr. Johannes Wolf [1], Dr. Arne Schleunitz [1], Mrs. Gabi Grützner [1]
1. *micro resist technology GmbH*

Oral Session 2C: Photonics and Optoelectronics

Monolithic Integration of GeV Centers in Ring Waveguides for Quantum Light Emission 162
Dr. Fatemeh Moradiani[1], Mr. Arran Ashfield [2], Dr. Arthur Lipinski [1], Prof. Robert M. Bowman [3], Dr. Hamidreza Siampour [4]
1. *Research Fellow,* ***2.*** *PhD Student,* ***3.*** *Professor,* ***4.*** *Lecturer*

Microsphere-assisted generation of localized optical emitters in 2D hexagonal boron nitride 163
Ms. XILIANG YANG[1], Dr. Sabina Caneva [1], Prof. Peter Steeneken [1], Prof. Dong Hoon Shin [2]
1. *Delft University of Technology,* ***2.*** *Korea University*

Chip-scale infrared Fourier-transform spectrometer based on nano-opto-electro-mechanical systems 164
Dr. Bingrui Lu[1], Dr. Babak Vosoughi Lahijani [1], Dr. Søren Engelberth Hansen [1], Dr. Thor August Schimmell Weis [1], Dr. Marcus Albrechtsen [1], Dr. Ali Nawaz Babar [1], Dr. Michael Juhl [1], Dr. Christian Anker Rosiek [1], Mr. Jesper Laurberg Sand [1], Mr. Bjarke Almer Frederiksen [1], Mr. Mathias Linde Holst Korsgaard [1], Mr. Nikolaj Balslev Hougs [1], Dr. Konstantinos Tsoukalas [1], Dr. Guillermo Arregui Bravo [1], Prof. Søren Stobbe [1]
1. *Technical University of Denmark*

Hydrophobic and Sticky Silver-Decorated Nanoimprinted ZnO Nanograss Substrates for Enhanced SERS Performance 165
Mr. Kuan-Ting Kuo [1], Prof. Wen-Huei Chang [2], Prof. Hsiang Chen [3], Mr. Jyun-Jie Chen [1], Prof. Chun-Hung Lin[4]
1. Department of Photonics, National Cheng Kung University, 2. Department of Applied Chemistry, National Pingtung University, 3. Department of Applied Materials and Optoelectronic Engineering, National Chi Nan University, 4. National Cheng Kung University

Antireflection of near-infrared light using a moth-eye structure film 166
Mr. Kei Hirata[1], Prof. Jun Taniguchi [1]
1. Tokyo University of Science

One-Step Printable Fabrication of Tantalum Pentoxide Metasurfaces for UV–Visible Optics 167
Ms. Eunji Lee[1], Prof. Junsuk Rho [2]
1. POSTECH, 2. Pohang University of Science and Technology

Red Emitting DBR Laser Array with 0.1 nm Wavelength Spacing Defined by Direct Write Ebeam Lithography 168
Dr. Olaf Brox[1], Dr. Jörg Fricke [1], Dr. Ralph-Stephan Unger [1], Dr. André Maaßdorf [1], Dr. Anna Mogilatenko [1], Mr. Maximilian Beier [1], Dr. Heike Christopher [1], Dr. Andrea Knigge [1], Dr. Hans Wenzel [1]
1. Ferdinand-Braun-Institut gGmbH

Anti-reflection and radiative cooling bifunctional polymer film fabricated via nanoimprint lithography and in situ boehmite formation by hydrothermal treatment 169
Ms. Nefeli Dimogerontaki[1], Dr. Nikolaos Mattheakakis [2], Dr. Nikos Papanikolaou [3], Dr. Nikolaos Kehagias [2]
1. Department of Physics, School of Applied Mathematical and Physical Sciences National Technical University of Athens, Zografou Campus, GREECE, 2. NCSR Demokritos, Institute of Nanoscience & Nanotechnology, P. Grigoriou 27 & Neapoleos Str., 15341 Ag. Paraskevi, Greece, 3. NCSR Demokritos

Oral Session 2D: Information Communication Technologies

Fabrication and Analysis of Self-Rolled-Up Polymer Ribbon Structure Based on Photosensitive Polyimide and Mechanical Debonding 171
Dr. HyungDal Park [1], Dr. Seonho Seok[2], Dr. Jinseok Kim [1]
1. Korea Institute of Science and Technology, 2. University-Paris-Saclay

Semiconductor Quantum Dots: From Tailored Synthesis to Advanced Sensing and Biosensing Applications 172
Dr. Javed H. Niazi[1]
1. SUNUM - Sabanci University Nanotechnology Research & Application Center

Adaptive Adhesion through Bio-Inspired Interlocking Micropatterns for Harsh Environments 173
Mr. Marco Bruno[1], Mr. Luigi Portaluri [2], Prof. Massimo De Vittorio [3], Prof. Stanislav Gorb [4], Prof. Michele Scaraggi [3]
1. Istituto Italiano di Tecnologia (IIT), 2. Department of Innovation Engineering, University of Salento, Lecce, LE, 73100, Italy, 3. Center for Biomolecular Nanotechnologies, Istituto Italiano di Tecnologia (IIT), 73010 Arnesano, LE, Italy, 4. University of Kiel

Single-Charge Detection in a Room Temperature Single-Electron Memory 174
Mr. Jingbo Chen[1], Dr. Wenkun He [1], Mr. Kai-Lin Chu [1], Dr. Mervyn Jones [1], Prof. Zahid Durrani [1]
1. Imperial College London

Design and characterization of surface acoustic wave on thin film lithium niobate on insulator for acousto-optic applications 175
Ms. Fatemeh Arefi[1], Dr. Ivan Prieto [1], Mr. Florian Hartmann [2], Mr. Silvan Stettler [2], Dr. Homa Zarebidaki [1], Mr. Hamed Sattari [1], Dr. Dara Bayat [1], Prof. Guillermo Villanueva [2], Dr. Michel Despont [1]
1. CSEM, 2. NEMS, EPFL

Nanofabrication of shadow masks for josephson-junction quantum devices 176
Dr. Rucha Deshpande[1], Prof. Rafael Taboryski [1], Prof. Thomas Sand Jespersen [1], Dr. Sabbir Ahmed Khan [2]
1. Technical University of Denmark, 2. Danmarks Nationale Metrologiinstitut

Oral Session 3A: UV, EUV, and two-photon lithography

EUV interference lithography at PSI: pushing the limits of resolution of next generation photolithography 178
Dr. Dimitrios Kazazis[1], Mr. Benjamin Bächtold [1], Mr. Stephan Maag [1], Mr. Marco Schneider [1], Mr. Achim Ammon [1], Mr. Emanuele Japichino [1], Mr. Lars Heller [1], Mr. Thierry Lachat [1], Mr. Michael Peters [1], Mr. Peter Heimgartner [1], Mrs. Michaela Vockenhuber [1], Mr. Markus Kropf [1], Mr. David Piguet [1], Dr. Yasin Ekinci [1], Dr. Iacopo Mochi [1]
1. Paul Scherrer Institute (PSI)

Towards sub-nm roughness in 3D topography for reflective X-ray focusing optics 179
Dr. Giulia Malvicini[1], Prof. Helmut Schift [1]
1. Paul Scherrer Institute (PSI)

Quantifying and overcoming wafer distortion on bonded wafers for deep-UV lithography 180
Dr. Jeroen Bolk [1], Dr. Sander Reniers[1], Mr. Stacey Martina [1], Dr. Sara Sequeira [1], Ms. Sruja Dave [1], Prof. Kevin Williams [1], Dr. Yuqing Jiao [1]
1. Eindhoven University of Technology

Pushing the Boundaries: in situ Development and Multi-Material Exchange for Two-Photon 3D Printing 181
Mr. Pratyaksh Yemulwar[1], Mr. Man-Ho Wong [1], Mr. Saurabh Karle [1], Mr. Josua Zschleile [1], Dr. Robert Kirchner [1]
1. HETEROMERGE Gmbh

Oral Session 3B: Advanced Nanofabrication I

Fabrication of arsenic-in-silicon single-electron transistors using scanning tunnelling microscopy hydrogen resist lithography 184
Dr. Kieran Spruce[1], Mr. Rajath Ravichandar [1], Dr. Patrick See [2], Dr. Mark Buitelaar [1], Dr. Taylor Stock [1], Prof. Neil Curson [1]
1. University College London, 2. NPL

Tailoring Vertical Gradients in Thin Films: Design and Fabrication 185
Dr. Xiangyu Chen[1]
1. Beihang University

Anti-virus performance of Si nanopillar array mimicking cicada wing surface 186
Prof. Takeshi Ito[1], Dr. Hitoshi Ishiguro [2], Prof. Tomohiro Shimizu [1], Prof. Shoso Shingubara [1]
1. Kansai University, 2. Kanagawa Institute of Industrial Science and Technology

3D structured local thin film deposition by Micro Direct Atomic Layer Deposition (µDALP™) 187
Mrs. Mira Baraket [1], Mr. Jesper Navne[2]
1. ATLANT 3D, 2. PhD

Oral Session 3C: Sustainable Devices and Process Technology

Shaping of a bio-sourced AESO polymer for micro-encapsulation purposes 189
Ms. Estelle Lu[1], Mr. Bruno Bresson [2], Dr. Jacques FATTACCIOLI [1]
1. CPCV, Département de Chimie, Ecole Normale Supérieure, PSL Université, Sorbonne Université, CNRS, 2. Laboratoire Sciences et Ingénierie de la Matière Molle, ESPCI Paris

Layer-by-layer functionalization of cotton fabric for enhanced electrokinetic energy harvesting 190
Mr. Aditya Patwari[1], Dr. Chirodeep Bakli [1], Prof. Suman Chakraborty [1]
1. Indian Institute of Technology Kharagpur

Process development for improved passivation in IBC Solar Cells 191
Mr. Jens Munk Nielsen[1], Dr. Rasmus Schmidt Davidsen [2], Prof. Stephan Sylvest Keller [1]
1. National Centre for Nano Fabrication and Characterization, DTU Nanolab, Technical University of Denmark, 2. Department of Electrical and Computer Engineering, Aarhus University

Inkjet printing of stealth nanobeacons 192
Dr. Akinobu Yamaguchi[1], Dr. Toshiya Yasunaga [2], Prof. Kyoko Namura [3], Prof. Motofumi Suzuki [3], Mr. Takao Fukuoka [3]
1. Toyo University, 2. Aichi Gakuin University, 3. Kyoto University

Oral Session 3D: Devices and Systems

Selective Laser Etching as a Key Enabler of Custom Silica-Based AFM Probes 195
Mr. koutayba saada [1], Mr. david bourrier [1], Ms. Juliette Lignieres [1], Dr. Etienne Dague [1], Dr. Laurent Malaquin[1]
1. LAAS-CNRS, Université de Toulouse, CNRS, Toulouse, France

Scalable Piezo-Optomechanical Transducer for Optical Readout of a Superconducting Qubit 196
Dr. Linh Nguyen[1]
1. QphoX

Nonlinear resonators based on nano optomechanical metamaterials 197
Ms. Ting Hou[1], Mr. Lifeng Bao [1], Dr. Jun-Yu Ou [2], Dr. Xin Zhou [3], Prof. Nobuhiko Nishiyama [4], Dr. Yoshishige Tsuchiya [1]
1. University of Southampton, 2. Physics and Astronomy, University of Southampton, 3. Université de Lille, 4. Institute of Science Tokyo

Carbon-based contacts for integrated nanoelectromechanical switches 198
Dr. Jens Bolten[1], Mr. Bartos Chmielak [1], Ms. Lisa Ehlert [1], Dr. Elliott Worsey [2], Ms. Yingying Li [3], Prof. Frank Niklaus [3], Prof. Dinesh Pamunuwa [2], Dr. Simon Bleiker [3], Prof. Max Lemme [1]
1. AMO GmbH, 2. University of Bristol, 3. Royal Institute of Technology (KTH)

Poster Session 2

Auxiliary-Ring-Assisted Fabrication of Hard X-ray Photon Sieves with Low Resist Wettability 200
Mr. Qiucheng Chen[1], Ms. Qingxin Wu [1], Mr. Hao Quan [1], Ms. xunjia Zhao [1], Mr. Jinyu Guo [1], Ms. Kangping Liu [1], Prof. Yifang Chen [1]
1. Fudan university

Electron beam-Simulation collaborative fabrication of zone plates with gradient duty cycle 201
Ms. xunjia Zhao[1], Mr. Hao Quan [1], Mr. Qiucheng Chen [1], Ms. Qingxin Wu [1], Mr. Wentao Yuan [1], Mr. Shuoqiu Tian [1], Mr. Jinyu Guo [1], Ms. Kangping Liu [1], Prof. Yifang Chen [1]
1. Fudan university

Room temperature Au-Au die bonding in ambient air via N_2 plasma treatment 202
Prof. RYO TAKIGAWA[1], Mr. Yunhan Fan [1], Mr. Kosei Matsunobu [1]
1. Kyushu University

Simulation-guided interpretation of scanning electron microscope images 203
Mr. Jianyao Jin[1], Dr. Timon Fliervoet [2], Dr. Kees Hagen [1]
1. Delft University of Technology, 2. ASML

Manufacturing and testing of ultra-low expansion glass based planar frame resonator 204
Mr. AHMAD ALI[1], Mr. Muhammad Awais Maqbool [1], Dr. Hamza Shakeel [1]
1. School of Electronics, Electrical Engineering and Computer Science, Queen's University Belfast

Investigation of Intra-Level Mix-and-Match lithography approach in AR-N 7520new for use in a Mix-and-Match grayscale lithography process 205
Mr. Markus Gottwald[1], Mr. Sebastian Schermer [1], Mr. Ritesh Ambar [1], Ms. Pia Kohlschreiber [1], Dr. Christian Helke [1], Mr. Harry Biller [2], Dr. Mandy Sendel [2], Dr. Danny Reuter [1]
1. Fraunhofer Institute for Electronic Nano Systems ENAS, 2. Allresist GmbH

Influence of substrate properties and addition of oxygen on the process of reactive ion etching to optimize the nanopatterning of silicon structures 206
Ms. Lenia Böhm[1], Ms. Pia Kohlschreiber [1], Mr. Micha Haase [1], Dr. Christian Helke [1], Dr. Danny Reuter [1]
1. Fraunhofer Institute for Electronic Nano Systems ENAS

Interposer Interconnects: An Important Step For Research and Industry 207
Dr. Omesh Kapur[1], Mr. Arvin Mallari [1], Dr. Anushka Gangnaik [2], Ms. Amanda Green [1], Dr. Ibrahim Sari [2], Mr. John Darlington [2], Dr. Liam Boodhoo [1]
1. School of Electronics and Computer Science, University of Southampton, Southampton SO17 1BJ, United Kingdom, 2. University of Southampton

Nanofabrication of monolithically integrated multilayer metasurfaces via fully CMOS-compatible processes 208
Mr. Yuntian Ye[1], Mr. Hao Peng [1], Dr. Shengqi Yin [2], Prof. Jize Yan [3], Dr. Kian Shen Kiang [2], Dr. Xu Fang [1]
1. School of Electronics and Computer Science, University of Southampton, Southampton SO17 1BJ, United Kingdom, 2. Optoelectronics Research Centre, University of Southampton, SO17 1BJ, UK, 3. University of Southampton

Single-Printed Nb2O5 UV-Visible Metasurfaces for Chiro-Optical Holography 209
Ms. Eunji Lee[1], Prof. Junsuk Rho [2]
1. POSTECH, 2. Pohang University of Science and Technology

Plasma-induced periodic surface structures on polymeric microfluidic channel sidewalls 210
Dr. Athina S. Kastania [1], Ms. Eleni Stai [1], Mr. Sotiris Mouchtouris [1], Dr. Vassilios Constantoudis [1], Prof. George Kokkoris [2], Dr. Pavlos Tsavalas [3], Dr. Konstantina Mergia [3], Dr. Gerburg Schider [4], Mr. Daniel Borstner [4], Mr. Philipp Melchior [4], Dr. Dieter Nees [4], Dr. Barbara Stadlober [4], Dr. Evangelos Gogolides[1], Dr. Angeliki Tserepi [1]
1. NCSR Demokritos, Institute of Nanoscience & Nanotechnology, P. Grigoriou 27 & Neapoleos Str., 15341 Ag. Paraskevi, Greece, 2. School of Chemical Engineering, National Technical University of Athens, Athens, 157 80, Greece, 3. NCSR Demokritos, Institute of Nuclear & Radiological Sciences and Technology, Energy & Safety, Ag. Paraskevi, 153 41, Greece, 4. Joanneum Research Forschungsgesellschaft mbH, Weiz, 8160, Austria

Scalable Multilayer Silicon Anode Architecture with Porosity Control via UV-NIL Roll-to-Plate Process for Enhanced Lithium-Ion Battery Performance 211
Ms. YU JU HAN[1], Ms. Seo Rim Park [1], Mr. Seong Min Yoon [1], Ms. Min Ju An [1], Prof. Yeon Guk Son [1], Prof. Young Tae Cho [1]
1. Changwon National University, Changwon

First results on vacuum-gas-controlled metal assisted chemical etching 212
Mr. Bryan Benz[1], Ms. Vahide Hosseini [2], Dr. Georg Umlauf [2], Mr. Toni Sandbrink-Koblenz [3], Dr. David Anderson [3], Dr. Danny Reuter [2], Dr. Christoph Robert Meinecke [2], Dr. Lucia Romano [1]
1. Paul Scherrer Institute (PSI), 2. Fraunhofer Institute for Electronic Nano Systems ENAS, 3. memsstar Ltd

OPTIMIZING RETICLE BASED HIGH THROUGHPUT I-LINE GRAYSCALE PROJECTION LITHOGRAHPHY FOR 3D STRUCTURES 213
Mr. Sebastian Schermer[1], Mr. Stephen DeMoor [2], Mr. Andrew Zanzal [2], Mr. Patrick Reynolds [2], Mr. Jens Bonitz [1], Mr. Jeremy Bieling [3], Dr. Christian Helke [4], Dr. Anja Voigt [5], Dr. Danny Reuter [4]
1. Fraunhofer Institute for Electronic Nano Systems, 2. Benchmark Technologies, 3. Technische Universität Chemnitz, 4. Fraunhofer Institute for Electronic Nano Systems ENAS, 5. micro resist technology GmbH

Ion Beam Planarization using Low-Viscosity, Non-Volatile Containing Polymer Coatings 214
Mr. Lukas Paul Lingenfelder[1]
1. Leibniz-Institut für Oberflächenmodifizierung e.V. (IOM)

The role of surface chemistry and morphology on adhesive wafer bonding 215
Mr. Duarte Silva[1], Dr. Tarni Aggarwal [1], Dr. Yuqing Jiao [1], Dr. Martijn Heck [1]
1. Eindhoven University of Technology

Sub-diffraction-limited nano-texturing on silicon by ultrafast lasers with MHz- burst mode 216
Mr. Pin-Yen Chen [1], Mr. You Yu-Sheng [2], Prof. Yuan-Jen Chang[3]
1. National Taipei University of Technology, Department of Mechanical Engineering, 2. National Taipei University of Technology, Graduate Institute of Manufacturing Technology, 3. National Taipei University of Technology

Fabrication of Micro-Lattice Filters for Particulate and Gas Emission Reduction 217
Ms. Seo Rim Park[1], Mr. Myung Seo Kim [2], Prof. Young Tae Cho [1]
1. Changwon National University, Changwon, 2. Changwon National University, Department of Mechanical Engineering

Microfluidic Devices Based on Deterministic Lateral Flow Displacement for Protein Separation 218
Ms. Nilüfer Tasli[1], Dr. Sadhana Tiwari [1], Dr. Irene Fernandez [2]
1. UHH, 2. UHH/CUI

Evaluation of Inorganic-organic Hybrid Resist Materials with ultrafast coherent high harmonic generation (HHG) EUV system 219
Dr. Hiroki Yamamoto[1]
1. National Institutes for Quantum Science and Technology (QST)

Graphene Electrodes for In-plane Electrochemical growth of TMDCs 220
Mr. Shaokai Song[1], Dr. Shibin Thomas [1], Dr. Nema Abdelazim [1], Dr. Sami Ramadan [2], Dr. Victoria Greenacre [1], Mr. Hongwei Zhang [1], Dr. Yisong Han [3], Prof. Richard Beanland [3], Prof. Gill Reid [1], Prof. Philip Bartlett [1], Prof. Kees de Groot [4], Dr. Yasir Noori [1]
1. University of Southampton, 2. Imperial College London, 3. University of Warwick, 4. School of Electronics and Computer Science, University of Southampton, Southampton SO17 1BJ, United Kingdom

A Technique for Simultaneous Embedding and Welding of Metal Nanowires on Polymer Surfaces for Flexible Conductors 221
Mr. sangmok Kim[1], Mr. Youngjae Nam [1], Prof. Joonwon Kim [1]
1. Pohang University of Science and Technology

Fabrication of a superhydrophobic surface with partially superhydrophilic regions and surface free energy comparison 222
Mr. Takuto Wakasa[1], Prof. Jun Taniguchi [1]
1. Tokyo University of Science

Design of an Antireflective Hierarchical Structure Based on Finite-Difference Time-Domain (FDTD) Simulation 223
Mr. YAONIEN TSAI[1], Mr. YENEN JUAN [1], Mr. GUOCHEN NIEH [1], Dr. YEEUCHANG LEE [1]
1. Chung Yuan Christian University

Fabrication of Broadband Antireflection Hierarchical Micro/Nano Structures Using Colloidal Lithography 224
Mr. YENEN JUAN[1], Mr. GUOCHEN NIEH [1], Mr. YAONIEN TSAI [1], Dr. YEEUCHANG LEE [1]
1. Chung Yuan Christian University

An e-beam lithographer's approach to evaluating a new HIMT DWL66+ direct laser writer for Mix&Match processes – resists, contrast curves, grayscale lithography, alignment, and developer test sticks 225
Dr. Silvia Diewald[1], Prof. Gernot Goll [1]
1. Karlsruhe Institute of Technology (KIT)

Direct data generation of wafer-scale metalens for e-beam exposure 226
Ms. Yixuan Zhao[1], Dr. Kian Shen Kiang [1], Prof. Jize Yan [1]
1. University of Southampton

Impact of PEALD Temperature on Al_2O_3 Gate Dielectric of ZnO-TFTs 227
Mr. Jiale Zeng[1], Dr. Ben Rowlinson [2], Dr. Omesh Kapur [1], Prof. Harold Chong [3]
1. School of Electronics and Computer Science, University of Southampton, Southampton SO17 1BJ, United Kingdom, 2. University of Edinburgh, 3. University of Southampton

Plasma-enhanced ALD of ultra-thin Al2O3 films for passivating contacts 228
Ms. Yaxin Zhan[1], Dr. Ben Rowlinson [2], Prof. Harold Chong [1], Dr. Stuart Boden [1]
1. University of Southampton, 2. University of Edinburgh

Inducing piezoelectricity in chitosan films by cathodic electrodeposition: challenging a new approach for wearable sensors' fabrication 229
Ms. Valeria D'Errico[1], Dr. Gaia de Marzo [2], Dr. Antonio Qualtieri [1], Dr. Luciana Algieri [3], Prof. Massimo De Vittorio [1]
1. Center for Biomolecular Nanotechnologies, Istituto Italiano di Tecnologia (IIT), 73010 Arnesano, LE, Italy, 2. IDUN section, Department of Health Technology, Technical University of Denmark, DK-2800 Kongens Lyngby, Denmark, 3. Department of Innovation Engineering, University of Salento, Lecce, LE, 73100, Italy

Synthesis of novel EB resist based on KrF resist system 230
Dr. Atsushi Sekiguchi[1]
1. Litho Tech Japan Corporation

Nanofabrication of Large, Stitch-free Diffractive Optics 231
Dr. Anna Casimiro[1], Dr. Sander Schellingerhout [1], Ms. Adriana Umbria [1], Dr. Kahraman Keskinbora [1]
1. Raith Laser Systems B.V.

Secondary particle detection for deterministic single ion implantation 232
Dr. Kristian Stockbridge[1], Dr. Ella Schneider [2], Dr. Gianfranco Arresta [1], Dr. David Cox [2]
1. Ionoptika Ltd, 2. University of Surrey

Control of the Scanning Tunnelling Microscope Based on Hybrid Gain Integrator Systems (HIGS) 233
Ms. Richa Mishra [1], Prof. S. O. Reza Moheimani[2]
1. The University of Texas at Dallas, 2. The Univeraity of Texas at Dallas

Towards single-electron devices based on SOI silicon nanowires: simulation and fabrication 234
Mr. Gabriele Petitto[1], Mr. Ziyin Sun [2], Dr. Jordi Antoja [2], Dr. Alberto del Moral [1], Dr. Albert Guerrero [3], Dr. Roser Mas [2], Dr. Alberto García-García [2], Prof. Joan Bausells [1], Prof. Francesc Pérez-Murano [1], Dr. Esteve Amat [1], Dr. Jordi Llobet [2]
1. Institute of Microelectronics of Barcelona (IMB-CNM, CSIC), 2. Institut de Microelectrònica de Barcelona, IMB-CNM (CSIC), Universitat Autònoma de Barcelona, Cerdanyola Del Vallès, 08193, Barcelona, Spain., 3. Instituto de Microelectrónica de Barcelona

A YOLOv8-Based Defect Inspection for Semiconductor 235
Mr. Xiaolong Guo [1], Dr. Yanan Zhu [2], Mr. Heming Wu [3], Prof. Diwei Zhou [4], Prof. Zhuming Liu[2]
1. School of Electronic Science and Engineering , South China Normal University, 2. Institute of Semiconductors, Guangdong Academy of Sciences, 3. Institute of Semiconductors, Guangdong Academy of Sciences,, 4. School of Science, Loughborough University

Two-dimensional arrays of InAs nanodots grown on inverted pyramid Si templates 236
Dr. Javier Bravo Larrea[1], Mr. David Bermudez [2], Mr. Lisandro Jofre [1], Dr. Paloma Tejedor [2]
1. NAITEC, 2. Instituto de Ciencia de Materiales de Madrid, CSIC, Madrid, 28049, Spain

EBIC measurement of the minority carriers diffusion length in a GaAs solar cell p-n junction 237
Dr. Anya Grushina[1], Mr. Karl Boche [1]
1. Imina Technologies

Preparation of Regrowth Interfaces in AlGaN/GaN Heterostructures Using Atomic Layer Etching for Ohmic Contact Formation 238
Dr. Aslanidis Evangelos[1], Dr. Adam Adikimenakis [1], Mr. Nikos Makris [1], Mr. Antonios Stavrinidis [1], Dr. George Konstantinidis [1]
1. Microelectronics Research Group (MRG), Institute of Electronic Structure and Laser (IESL), Foundation of Research & Technology Hellas (FORTH), Crete 70013, Greece;

Fabrication of coupled silicon nanoelectromechanical resonators with heavily doped silicon towards reservoir computing chip 240
Mr. Dai Ai[1], Ms. Ting Hou [2], Ms. Zixuan Wang [2], Dr. Kian Shen Kiang [2], Dr. Yoshishige Tsuchiya [2], Dr. Jun-Yu Ou [3]
1. School of Electronics and Computer Science, University of Southampton, Southampton, SO17 1BJ, UK, 2. University of Southampton, 3. Physics and Astronomy, University of Southampton

Vapor Phase Infiltration in Homopolymers and Block copolymers: A comparative study 241
Ms. Maria Teresa Elenes Cervantes[1], Ms. Olga Muntada [1], Dr. Sara Duran [1], Mr. Ricard Noy [1], Ms. Libertad Sole [1], Dr. Jordi Llobet [1], Prof. Francesc Perez-Murano [1], Dr. Marta Fernández-Regúlez [1]
1. Institute of Microelectronics of Barcelona (IMB-CNM, CSIC)

Epitaxial growth of InAs/InGaAs-Al nanowire hybrids for quantum computing applications 242
Dr. Paloma Tejedor[1], Dr. Beatriz Galiana [2], Mr. Gabriel Moraes [3], Dr. Eduardo J.H. Lee [3]
1. Instituto de Ciencia de Materiales de Madrid, CSIC, Madrid, 28049, Spain, 2. Universidad Carlos III de Madrid, 3. Departamento de Física de la Materia Condensada and Condensed Matter Physics Center (IFIMAC), Universidad Autónoma de Madrid, 28049 Madrid

Nanomechanical Mass Sensor: Integrating Nanoimprint Lithography with Flow-Through Gas Phase Deposition 243
Dr. Lucjan Grzegorzewski[1]
1. University of Hamburg

Nanoimprinted Multimode Polymer Waveguides with Integrated Bragg Gratings for Structural Health Monitoring 244
Dr. Michael Haslinger[1], Mr. Florian Egger [2], Ms. Viktorija Jonaityte [1], Prof. Vaclav Prajzler [3], Dr. Antreas Theodosiou [4], Dr. Michael Muehlberger [1]
1. PROFACTOR GmbH, 2. PROFACTOR GmbH, Im Stadtgut D1, 4407 Steyr, Austria, 3. Department of Microelectronics, Faculty of Electrical Engineering, Czech Technical University in Prague, Technicka 2, 168 27 Prague, Czech Republic, 4. Photonics Research Center (PRC), Lumoscribe Ltd, 12 Anthipoloxagou Georgiou Savva,8201 Geroskipou, Paphos, Cyprus

Advanced AFM Metrology of Vertical Structures: Sample Reorientation for Sidewall Surface Access 245
Dr. Paweł Janus [1], Dr. Krzysztof Domański [1], Dr. Adam Łaszcz [1], Dr. Andrzej Sierakowski [1], Ms. Magdalena Kucharska[1], Dr. Dariusz Szmigiel [1]
1. Institute of Microelectronics and Photonics

Processing Pathways for Transparent, Flexible Electrodes in Next-Generation Smart Windows 246
Dr. Michael Haslinger[1], Ms. Viktorija Jonaityte [1], Mr. Dorly Holzer-Harringer [2], Mr. Marcus Harringer [2], Dr. Florian Frischmann [3], Dr. Wenxing Huo [4], Dr. Martina Harnisch [5], Dr. Andreas Zimmermann [5], Dr. Michael Muehlberger [1]
1. PROFACTOR GmbH, 2. Almendo Technologies GmbH, Wolfschwangweg 216, 5084 Großgmain, Austria, 3. Bartenbach GmbH, Rinner Straße 14, 6071 Aldrans, Austria, 4. Department of Biomedical Engineering, Tianjin University, 92 Weijin Road, Tianjin 300072, China, 5. Sunplugged GmbH, Affenhausen 1, 6413 Wildermieming, Austria

Electrochemically growing morphology on micro structured 3D frameworks 247
Ms. Itishree Panda[1], Ms. Trina Dhara [1], Prof. Sunando DasGupta [1]
1. Indian Institute of Technology Kharagpur

Micro/Nano Thin-Film Coating Processes of Carbon Materials for Energy Devices 248
Dr. JEONGDAI JO[1]
1. Korea Institute of Machinery and Materials (KIMM)

Bulk Micro-Machining of SrTiO3 Substrates for Device Applications 249
Dr. Nicola Manca [1], Dr. Luca Pellegrino[1]
1. National Research Council

Towards EUV lithography with alternative sources: a proof-of-concept high-harmonic generation in gas-filled hollow waveguides driven by ultrafast infrared laser pulses 250
Dr. Sonia Freddi[1], Dr. Anna G. Ciriolo [1], Dr. Rebeca Martinez Vazquez [1], Prof. Salvatore Stagira [2], Dr. Monica Bollani [3]
1. *IFN-CNR,* ***2.*** *Politecnico di Milano,* ***3.*** *Institute of Photonic and Nanotechnology (IFN) - CNR*

Medusa 84 SiH, an alternative HSQ resist for realizing DFB lasers diodes 251
Mrs. Poojitha Sammeta[1], Dr. Olaf Brox [1], Dr. Pietro Della Casa [1], Mr. Dirk Rentner [1], Dr. Ralph-Stephan Unger [1], Dr. Hans Wenzel [1], Mr. Maximilian Schäfer [1], Dr. Andrea Knigge [1], Mr. Harry Biller [2], Mr. Matthias Schirmer [2]
1. *Ferdinand-Braun-Institut gGmbH,* ***2.*** *Allresist GmbH*

Integrated Microfabrication Capabilities for Life Science Applications: From Polymer Platforms to Active Micropumps 252
Mr. Robin de Bruijn[1], Ms. Marie Monchablon [1], Mr. Sander Visser [1], Ms. Laure van der Sanden [2], Dr. Hossein E. Amirabadi [2], Prof. Jaap den Toonder [1]
1. *Eindhoven University of Technology,* ***2.*** *ARTIC Technologies B.V.*

Engineering soft nanoscale surfaces force material interaction study 253
Dr. Martina Paraggio[1], Prof. Luigi Bruno [2], Dr. Chiara Morano [2], Ms. Maria Laura Coluccio [1], Ms. Francesca Gualtieri [3], Prof. CARMELA DE MARCO [3], Prof. Francesco Gentile [3]
1. *Magna Graecia University, Catanzaro,* ***2.*** *University of Calabria,* ***3.*** *Magna Græcia University of Catanzaro*

Isotopically pure Silicon-28 thin films for improved coherence times in silicon quantum technologies built by scanning tunnelling microscopy 254
Mr. Oisín FitzGerald[1], Dr. Taylor Stock [1]
1. *University College London*

Ultra-thick HSQ Resist for Optical Waveguide Grating Coupler Applications 255
Mr. Kun Zhang[1], Dr. Kian Shen Kiang [2], Dr. Ying Tran [3], Prof. David Thomson [3], Prof. Harold Chong [3]
1. *School of Electronics and Computer Science, University of Southampton, Southampton, SO17 1BJ, UK,* ***2.*** *Optoelectronics Research Centre, University of Southampton, Southampton, SO17 1BJ, UK,* ***3.*** *University of Southampton*

Integration of Interband Infrared Cascade Photodetector onto a SOI Platform for Gas Sensing 256
Mr. Daniel Adeyemi[1], Dr. Colin Mitchell [1], Prof. Goran Mashanovich [1], Dr. Milos Nedeljkovic [1]
1. *Optoelectronics Research Centre, University of Southampton, SO17 1BJ, UK*

Biofabrication of 3D Scaffolds and Functional Microstructures Using Two- Photon Lithography 257
Dr. Mario Kandra [1], Mr. Jáchym Podstránský[1]
1. *IQS nano s.r.o*

The modulation of X-ray by high resolution zone plates when volume diffraction effects dominate 258
Mr. Hao Quan[1], Dr. Xujie Tong [1], Mr. Qiucheng Chen [1], Ms. Qingxin Wu [1], Ms. xunjia Zhao [1], Mr. Shuoqiu Tian [1], Mr. Wentao Yuan [1], Mr. Jinyu Guo [1], Ms. Kangping Liu [1], Prof. Yifang Chen [1]
1. *Fudan university*

Microfluidic Mixing Induced by the Blinking-Two-Cilia System 259
Mr. Yangyu Duan[1], Mr. Ishu Aggarwal [2], Dr. Ye Wang [1], Prof. Patrick Onck [2], Prof. Jaap den Toonder [1]
1. *Eindhoven University of Technology,* ***2.*** *University of Groningen*

Neurohybrid interfaces via microstructured conductive hydrogels 260
Mr. Marco Buzio[1], Dr. Nevena Stajkovic [2], Dr. Valeria Criscuolo [2], Prof. Francesca Santoro [2]
1. a Institute of Biological Information Processing IBI-3, Forschungszentrum Juelich, 52428 Jülich, Germany, 2. Institute of Biological Information Processing IBI-3, Forschungszentrum Juelich, 52428 Jülich, Germany

Micropillars Based PDMS Lab-On-chip Device for Tryptic Digestion of Proteins for Proteomics 261
Dr. Sadhana Tiwari[1], Ms. Nilüfer Tasli [1], Dr. Manuela Moritz [2], Dr. Franziska Marie Esmek [3], Mr. Tim Erichlandwehr [1], Dr. Jan Hahn [2], Prof. Hartmut Schlüter [2], Dr. Irene Fernandez [4]
1. University of Hamburg, 2. Universitätsklinikum Hamburg-Eppendorf, 3. University of Hamburg/Hamburg Center for Ultrafast Imaging, 4. UHH

Method for high phase accuracy trimming of MZIs via Ge ion implantation and electrical annealing 262
Ms. April Logan[1], Dr. Xia Chen [1], Dr. Xingshi Yu [1], Ms. Weihong Shen [1], Dr. Xingzhao Yan [2], Dr. Weiwei Zhang [1], Prof. Goran Mashanovich [1], Prof. Graham Reed [1], Prof. David Thomson [2]
1. Optoelectronics Research Centre, University of Southampton, SO17 1BJ, UK, 2. University of Southampton

Microcavities to engineer dynamics in coupled E. coli oscillators 263
Mr. Kushal Swamy[1], Dr. Farbod Alijani [1]
1. Delft University of Technology

Manipulation of Liquid Marbles via Triboelectric Charging 264
Ms. Yuan-Hsuen Chou[1], Prof. Jiann Shieh [1]
1. National United University

An Extrusion Printed Lorentz Force Actuated Electromechanical Relay 265
Mr. Desmond Lagace [1], Dr. Cyrus Shafai[1]
1. University of Manitoba

Integrating Surface-Confined Molecular Motors into Microfluidic Platforms: Toward Automated, High-Throughput analysis of Actinomyosin in vitro motility Assays 266
Mr. Tim Erichlandwehr[1], Ms. Veronica Mieites [2], Mr. Jeremy Teuber [3], Mr. Rukan Nasri [4], Dr. Marko Usaj [5], Prof. Alf Månsson [5], Prof. Olga María Conde Portilla [2], Dr. Irene Fernandez-Cuesta [4]
1. UHH/DESY, 2. University of Cantabria, Photonics Engineering Group, 3. UHH/MPSD, 4. UHH/CUI, 5. Linnaeus University

Tuning fork optomechanical NIR antenna with integrated optical transmission line 267
Mr. Daniyal Khoshmaram[1], Dr. Xavier Borrisé [2], Prof. Joan Jose Garcia-Garcia [1], Mr. Raul Ruiz [1], Dr. Xavier Cartoixà [1], Dr. Gabriel Abadal [1]
1. Universitat Autonòma de Barcelona, 2. Catalan Institute of Nanoscience and Nanotechnology (ICN2) and Barcelona Institute of Science and Technology (BIST)

Low-Temperature Deposition of Metal Chalcogenides via Single-Source Precursors for Flexible Electronics 268
Ms. Sayali Harke [1], Ms. Suprabha Dixit [2], Dr. Chitra Gurnani[1], Dr. Ruomeng Huang [3], Dr. Omesh Kapur [4]
1. Ecole Centrale School of Engineering, Mahindra University, Hyderabad, 2. Ecole Centrale School of Engineering, Mahindra University, 3. University of Southampton, 4. School of Electronics and Computer Science, University of Southampton, Southampton SO17 1BJ, United Kingdom

Application of Integrated Electrode Fabrication Technique in Microfluidic lab-on-a-chip Devices for Single-Cell Analysis 269
Mr. Herbert Atrian-Garcia[1], Ms. Louise von Lacroix [1], Dr. Irene Fernandez [1], Mr. Rukan Nasri [1]
1. University of Hamburg

Preparation of Biocompatible Ag/Nylon Yarns Fabricated by Supercritical CO_2-assisted Ag Electroless Plating toward Weavable Devices 270

Mr. Tomoya Higashi[1], Dr. Tomoyuki Kurioka [2], Mr. Kazuhiro Shibata [2], Dr. Satoru Egawa [3], Prof. Toshitaka Yoshii [3], Prof. Chun-Yi Chen [2], Prof. Tso-Fu Mark Chang [2], Prof. Katsunari Sato [4], Prof. Hiromichi Kurosu [4], Prof. Masato Sone [2]

1. Institute of Innovative Research, Institute of Science Tokyo, 2. Institute of Science Tokyo, 3. Department of Orthopaedic Surgery, Institute of Science Tokyo, 4. Nara Women's University

Flexible AlScN Piezoelectric Films for Next-Generation Smart Biomedical Sensors 271

Dr. Padmalochan Panda[1], Dr. Gaia de Marzo [2], Dr. Luciana Algieri [3], Dr. Antonio Qualtieri [1], Dr. Francesco Rizzi [1], Prof. Michele Scaraggi [1], Dr. Vincenzo M. Mastronardi [3], Prof. Massimo De Vittorio [1]

1. Center for Biomolecular Nanotechnologies, Istituto Italiano di Tecnologia (IIT), 73010 Arnesano, LE, Italy, 2. IDUN section, Department of Health Technology, Technical University of Denmark, DK-2800 Kongens Lyngby, Denmark, 3. Department of Innovation Engineering, University of Salento, Lecce, LE, 73100, Italy

Monolithic All-Silicon Ring Resonator for Optical Modulation and Detection 272

Mr. Yifu Chen[1], Dr. Weiwei Zhang [1], Ms. Tzu-yun Chang [1], Ms. Hanuushah Vizabaskaran [1], Mr. James Le Besque [1], Dr. Xingzhao Yan [1], Dr. Martin Ebert [1], Prof. Callum Littlejohns [1], Prof. David Thomson [1]

1. Optoelectronics Research Centre, University of Southampton, SO17 1BJ, UK

InP Nanowire-Based Photoelectrical Detection of Single Particles and DNA in Nanofluidic Systems 273

Mr. Leon Seggering[1], Mr. Vidar Flodgren [2], Dr. Abhijit Das [2], Mr. Thomas Kjellberg Jensen [2], Dr. Joachim Elbeshausen Sestoft [3], Prof. Jesper Nygård [3], Prof. Anders Mikkelsen [2], Dr. Irene Fernandez-Cuesta [4]

1. UHH/DESY, 2. Lund University, 3. University of Copenhagen, 4. UHH/CUI

Ultrasensitive Raman Detection via Electrostatic Droplet Manipulation and Laser-Patterned Pinhole Concentration 274

Ms. Jia-yi Chen[1], Mr. Cheng-Han Yu [1], Prof. Jiann Shieh [1]

1. National United University

Scalable integration of III-V nanowire transistors for NMOS logic 275

Dr. Faris Abualnaja[1], Mr. Ibtisam Abbasi [1], Mr. Xiaofan Lin [1], Prof. Hoe Tan [2], Prof. Chennupati Jagadish [2], Prof. Hannah Joyce [1], Dr. Jack Alexander-Webber [1]

1. University of Cambridge, 2. The Australian National University

Piezoelectric microdevices for single-cell stimulation via ultrasound-driven ZnO nanosheets 276

Mx. Laura Lefaix[1], Mr. Marc Navarro [2], Prof. Jaume Esteve [1], Prof. Carme Nogués [3], Dr. Andreu Blanquer [4], Dr. Gonzalo Murillo [2]

1. Instituto de Microelectrónica de Barcelona, 2. Institute of Microelectronics of Barcelona (IMB-CNM, CSIC), 3. Universitat Autonòma de Barcelona, 4. Departament de Biologia Cel.lular, Fisiologia i Immunologia, Universitat Autonoma de Barcelona

Technological platforms for manufacturing semiconductor qubits 277

Dr. Alberto del Moral[1], Mx. Iker Uranga [1], Mr. Gabriele Petitto [1], Mr. Pol Gaya [1], Mr. Gorka Aizpurua-Iraola [1], Dr. Jordi Antoja [2], Dr. Esteve Amat [1], Dr. Jordi Llobet [2], Dr. Marta Fernández-Regúlez [1], Prof. Joan Bausells [1], Prof. Francesc Pérez-Murano [1]

1. Institute of Microelectronics of Barcelona (IMB-CNM, CSIC), 2. Institut de Microelectrònica de Barcelona, IMB-CNM (CSIC), Universitat Autònoma de Barcelona, Cerdanyola Del Vallès, 08193, Barcelona, Spain.

Double-Spot Detection in Nanochannels Enables Precise Velocity Profiling and Long-Term Stability Monitoring in Passive Micro- and Nanofluidic- Systems 278
Mr. Phil Grzybeck[1], Mr. lucjan Grzegorzewski [1], Mr. Leon Seggering [2], Dr. Franziska Marie Esmek [3], Dr. Irene Fernandez-Cuesta [4]
1. UHH, 2. UHH/DESY, 3. University of Hamburg/Hamburg Center for Ultrafast Imaging, 4. UHH/CUI

Synchronization of autonomous vibrating electrostatic MEMS torsional mirrors 279
Mr. Yuta Kawashima[1], Mr. Mikiya Oki [1], Dr. Amit Banergee [1], Dr. Jun Hirotani [1], Prof. Toshiyuki Tsuchiya [1]
1. Kyoto University

Solution-Processed UV-Vacuum-Heat (UVVH) Treated Mixed Size Zinc Oxide Nanoparticle Diode-like Device for Ion Sensing Applications 280
Mr. Mengyang Qu[1], Dr. Huanghao Dai [1], Dr. Omesh Kapur [2], Prof. Steve Beeby [1], Prof. Harold Chong [1]
1. University of Southampton, 2. School of Electronics and Computer Science, University of Southampton, Southampton SO17 1BJ, United Kingdom

PEGDA microfluidic-device featuring a Y-type shape for hydrogel microspheres synthesis analysis 281
Ms. Anayancy Itzel Villatoro Guillen[1], Dr. Orfil González-Reynoso [1], Ms. Andrea Carolina Villalvazo-Hidalgo [1], Dr. Alvaro de Jesús Martínez-Gómez [1], Dr. Antonio Romero-Estrada [1], Dr. Sergio Gómez-Salazar [1], Dr. Mario Alberto García-Ramírez [1]
1. Universidad de Guadalajara

Piezoresistivity in FEBID nanowires imaged via opMEMS straining 282
Dr. Bartosz Pruchnik [1], Ms. Magdalena Kucharska[2], Dr. Krzysztof Kwoka [1], Dr. Tomasz Piasecki [1], Dr. Soraya Sangiao [3], Prof. Jose Maria De Teresa [3], Mrs. Ewelina Gacka [1], Mr. Dominik Badura [1], Mr. Piotr Kunicki [1], Dr. Andrzej Sierakowski [2], Dr. Paweł Janus [2], Prof. Teodor Gotszalk [1]
1. Wrocław University of Science and Technology, 2. Institute of Microelectronics and Photonics, 3. Universidad de Zaragoza

Simulation of contact forces associated with contact wear in MEMS switches 283
Mr. Nasser Aldhahri[1], Prof. John Mcbride [2], Dr. Yoshishige Tsuchiya [1]
1. University of Southampton, 2. School of Engineering, University of Southampton

A Hybrid Superconductor/Nanomechanical Magnetic Field Detector for Biomagnetism 284
Dr. Luca Pellegrino[1]
1. National Research Council of Italy

Development of a 3-Channel Solar-Blind UV-C Sensor for Determining Source Location and Intensity 285
Dr. Keekeun Lee[1]
1. Ajou Unversity

Electrostatic Manipulation of Low Surface Tension Liquids on Silica Nanowire-based Slippery Liquid-infused Porous Surfaces 286
Mr. Ching Chi Lin[1], Mr. Yueh Tse Lin [1], Prof. Jiann Shieh [1]
1. National United University

Edge Engineering for Intrinsic Cold-metallic Injection Source in 2D FETs 287
Ms. Zhirong PENG[1], Mr. Ning JI [2], Mr. Jinchen Wei [1], Mr. Kwok-Ho Wong [1], Mr. Tin Shing Peter Ho [1], Prof. Lining Zhang [2], Prof. Mansun Chan [1]
1. The Hong Kong University of Science and Technology, 2. Peking University

Plasmonic antenna-VO2 hybrid metasurface for all-optical nonlinearity 288
Mr. Trubacs Daniel-Iosif[1], Dr. Kai Sun [1], Dr. Ioannis Zeimpekis [1], Prof. Otto Muskens [1]
1. University of Southampton

A massive-scale droplet microfluidic platform based on an active matrix of high-voltage thin-film transistors 289
Prof. Xing Cheng[1]
1. Southern University of Science and Technology

Vertically-Integrated VRRAM-Based Hardware Reservoir Computing System 290
Prof. Sungjun Kim[1]
1. Dongguk University

Optoelectronic Synaptic IGZO Transistor and Its Demonstration of Electrical and Optical Plasiticity for Light-Susceptive Processing-in-Memory 291
Prof. Myounggon Kang[1]
1. University of Seoul

Superhydrophobic Multifocal Microlens Array with Depth-of-Field Detection for Humid Environment 292
Dr. Hao Cao[1]
1. wuhan university

Prediction of Photo Lithography Equipment Wafer Moving Robot Errors Using ARIMA model 293
Mr. Kyunghwan Joo[1], Prof. Jae Wook Jeon [2]
1. SUNG KYUN KWAN University / Samsung Electronics, 2. Sungkyunkwan University

Optimisation of a Microfluidic Electrochemical Biosensor for E. coli Detection via ssDNA Hybridization and CRISPR/Cas-Based Sensing to Combat Sepsis 295
Mrs. Eleonora Quasso[1], Prof. Isabelle Le Potier [1], Dr. Hiu Mun Man [1], Dr. Hervé Jacquier [2], Dr. David Bikard [3], Dr. Laurent Thouin [4], Dr. Jean Gamby [1]
1. Université Paris-Saclay, Centre de Nanosciences et de Nanotechnologies, 2. Hôpital Henri Mondor, APHP, 3. Institut Pasteur, Université Paris Cité, 4. Ecole normale supérieure, PSL University, Sorbonne Université

Scalable Nanobubble Generation Using Centrifugal Micro-Porous Mesh Disc Technology 296
Mr. Bo-Wei Cheng [1], Prof. Yuan-Jen Chang [1], Prof. Chia-Lung Kuo [2], Dr. Kuen-Yi Wu [3], Prof. Chao-Ching Ho[1]
1. National Taipei University of Technology, 2. National Yunlin University of Science and Technology, 3. Rayzher Industrial Co., Ltd.

Refractive index controllable plasmonic color metasurfaces fabricated by combination of Nanoimprint lithography and Inkjet Printing 297
Ms. Nefeli Dimogerontaki[1], Dr. Nikolaos Mattheakakis [2], Ms. Narges Heidaryan [3], Ms. Sonja Kopp [3], Dr. Michael Muehlberger [3], Dr. Nikolaos Kehagias [2]
1. Department of Physics, School of Applied Mathematical and Physical Sciences National Technical University of Athens, Zografou Campus, GREECE, 2. NCSR Demokritos, Institute of Nanoscience & Nanotechnology, P. Grigoriou 27 & Neapoleos Str., 15341 Ag. Paraskevi, Greece, 3. PROFACTOR GmbH

Machine Learning Enabled Thermoelectric Device Design and Optimization 298
Mr. Haoji Yang[1], Dr. Yuxiao Zhu [2], Prof. Kees de Groot [2], Prof. Harold Chong [2], Dr. Ruomeng Huang [2]
1. School of Electronics and Computer Science, University of Southampton, Southampton SO17 1BJ, United Kingdom, 2. University of Southampton

Flexible, non-toxic SF radiochromic film based on 10,12-PCDA for on-site X-ray dosimetry 299
Mr. Naseer Ahmad [1], Mrs. Aida Visus [1], Mr. Salvador David Aznar [2], Prof. Gonzalo Guirado [3], Dr. Consuelo Guardiola [1], Dr. Xavier Muñoz Berbel [1], Dr. Silvia Mena Fernández[1]
1. Institute of Microelectronics of Barcelona (IMB-CNM, CSIC), 2. Instituto Murciano de Investigación y Desarrollo Agrario y Medioambiental, 3. Universitat Autonòma de Barcelona

Open Science & Technology: Microfluidic fluid handling 300
Dr. Lars Kool[1], Dr. Bertrand Cinquin [1]
1. Institut Pierre-Gilles de Gennes pour la Microfluidique, Paris, 75005, France

An Ultrasensitive TDSE/Au/SOD-based Electrochemical Sensing Platform for Real-Time Monitoring of Superoxide Ion at Cellular Level. 301
Mr. Pratyusa Mohapatra[1], Prof. Soumen Das [1]
1. Indian Institute of Technology Kharagpur

Simulation of physical reservoir computing based on nonlinear dynamics of nanoelectromechanical resonators 302
Mr. Lianghong Ye[1], Dr. Klaus-Peter Zauner [1], Dr. Mark Vousden [1], Mr. Yuta Kawashima [2], Prof. Toshiyuki Tsuchiya [2], Dr. Yoshishige Tsuchiya [1]
1. University of Southampton, 2. Kyoto University

Microfluidic chip for electrochemical detection of circulating miRNAs: real-sample testing of cardiac disease biomarkers 303
Ms. Anna Tarasova[1], Dr. Israël Mbomekallé [2], Prof. Sébastien Banzet [3], Dr. Hiu Mun Man [4], Prof. Isabelle Le Potier [4], Dr. Jean Gamby [4]
1. Université Paris-Saclay, Centre de Nanosciences et de Nanotechnologies (C2N), Palaiseau, 91120, France, 2. Institut de Chimie Physique d'Orsay (ICP), Orsay, 91400, France, 3. INSERM, Institut André Lwoff (IAL), Hôpital de Clamart, Clamart, 92140, France, 4. Université Paris-Saclay, Centre de Nanosciences et de Nanotechnologies

Optic Fibre Gas Sensor featuring MoS2 QD as an Active Layer 304
Dr. Mario Alberto García-Ramírez[1], Dr. Orfil González-Reynoso [1], Ms. Andrea Carolina Villalvazo-Hidalgo [1], Dr. Miguel Angel Bello-Jiménez [2], Dr. Abel García-Barrientos [2], Dr. Gregorio Guadalupe Carbajal-Arizaga [1]
1. Universidad de Guadalajara, 2. Universidad Autónoma de San Luis Potosí

Development kinetics of photoresist films using trimethyl-ammonium hydroxide (TMAH) aqueous developer contaminated with poly-hydroxy-styrene 305
Ms. Andreia Santos [1], Dr. Masahiko Harumoto[2], Dr. Yuqing Jin [3], Dr. Takahiro Kozawa [3]
1. SCREEN SPE, 2. SCREEN Semiconductor Solutions Co., Ltd, 3. SANKEN, Osaka Univ

Introducing a new era of green and functional biopolymeric surfaces 306
Dr. Dimosthenis Ioannou[1], Dr. Kosmas Ellinas [2], Dr. Alexandros Banis [1], Dr. Danai Ioanna Koukoumaki [3], Dr. Dimitris Sarris [3], Dr. Evangelos Gogolides [4]
1. Institute of Nanoscience and Nanotechnology, NCSR "Demokritos", 27 Neapoleos str & Patriarchou Grigoriou, Ag. Paraskevi, 153 41, Greece, 2. Laboratory of Advanced Functional Materials and Nanotechnology, Department of Food Science and Nutrition, School of the Environment, University of the Aegean, Leoforos Dimokratias 66, Myrina 81400, Lemnos, Greece, 3. Laboratory of Physico-Chemical and Biotechnological Valorization of Food By-Products, Department of Food Science & Nutrition, School of Environment, University of the Aegean, Leoforos Dimokratias 66, Myrina 81400, Lemnos, Greece, 4. NCSR Demokritos, Institute of Nanoscience & Nanotechnology, P. Grigoriou 27 & Neapoleos Str., 15341 Ag. Paraskevi, Greece

Pattern transfer by laser ablation: demonstration of a vacuumless process for micropatterning from lithographic masks 307
Dr. Klaus Zimmer[1], Dr. Joachim Zajadacz [2], Dr. Martin Ehrhardt [1], Dr. Pierre Lorenz [1], Dr. Tomi Smausz [3], Prof. Bela Hopp [3]
1. Leibniz Institute of Surface Engineering (IOM), 2. Leibniz Institute of Surface Engineering (IOM), Dep. Ultra-Precision Surfaces, 3. University of Szeged, Department of Optics and Quantum Electronics

Etching of optical glass by reactive plasmas at atmospheric pressure 308
Dr. Martin Ehrhardt [1], Mr. Robert Heinke [2], Dr. Pierre Lorenz [1], Prof. Thomas Arnold [3], Dr. Klaus Zimmer[1]
1. Leibniz Institute of Surface Engineering (IOM), 2. Leibniz Institute of Surface Engineering (IOM) and Technische Universität Dresden, 3. Technical University Dresden

From Waste to Resource: Engineering End-of-Life Graphite Anodes for Solid-State Hydrogen Storage 309
Mr. Mukhammed Kenzhebek[1]
1. National Laboratory Astana, Nazarbayev University

Low-Waste Fabrication of Flexible Carbon Electrodes: Capacitance Comparison of Inkjet-Printed and Laser-Induced Graphene with Ag Nanoparticles 310
Ms. Rou Xuan Goh [1], Mr. Ishant G. Patil [1], Dr. Suan Hui Pu [2], Dr. Suhana Sultan [3], Prof. Harold Chong [4], Dr. Ivan Ling[4]
1. Smart Manufacturing and Systems Research Group, University of Southampton Malaysia, 2. University of Southampton Malaysia, 3. Universiti Teknologi Malaysia, 4. University of Southampton

Mobile Ions Improve the Power Conversion Efficiency of Perovskite Solar Cells with Large Energetic Offsets 311
Ms. Lucy Hart [1], Mr. Fraser Angus [2], Ms. Yin Li [3], Mr. Abdul Kahleed [3], Dr. Philip Calado[4], Prof. James Durrant [5], Prof. Aleksandra Djurišić [3], Dr. Pablo Docampo [2], Dr. Piers Barnes [1]
1. Department of Physics, Imperial College London, 2. Department of Chemistry, University of Glasgow, 3. Department of Physics, The University of Hong Kong, 4. University of Southampton, 5. Department of Chemistry, Imperial College London

Heterogeneous Integration of Diamond 312
Dr. Soumen Mandal [1], Dr. Jerome Cuenca [1], Prof. Oliver Williams[1]
1. Cardiff University

Oral Session 4A: Advanced Nanofabrication II

Geometric optimization improves the performance of organic electrochemical transistors for bio-sensing applications 314
Dr. Noemi Cesario[1], Prof. Natalia Malara [2], Dr. Nicola Coppedè [3], Prof. Francesco Gentile [4]
1. Nanotechnology Research Center, Department of Experimental and Clinical Medicine, University "Magna Graecia" of Catanzaro, 88100 Catanzaro (Italy), 2. Department of Health Sciences, University Magna Graecia, Catanzaro, Italy, 3. IMEM-CNR Institute of Materials for Electronic and Magnetism, National research council, Parco area delle scienze 37/a 43124 Parma, 4. Magna Græcia University of Catanzaro

Introducing thermal scanning probe lithography into the fabrication of semiconductor quantum devices 315
Mx. Iker Uranga[1], Mr. Robin Erne [2], Dr. Jana Chaaban [2], Dr. Marta Fernández-Regúlez [1], Prof. Joan Bausells [1], Dr. Guido Rademaker [3], Dr. Emine Çağın [2], Prof. Francesc Pérez-Murano [1]
1. Institute of Microelectronics of Barcelona (IMB-CNM, CSIC), 2. Heidelberg Instruments, 3. CEA Leti

Fabrication of Vanadium Dioxide Resistors on Fully-released Polyimide Thin Films for High Strain Studies 316
Mr. Loïc Lahaye[1], Prof. Jean-Pierre Raskin [1], Prof. Denis Flandre [1]
1. *ICTEAM UCLouvain*

FabuBlox – An AI-driven Platform Connecting the Nanofabrication World 317
Dr. Jan Tiepelt[1], Dr. Josh Perozek [1], Mr. Jack Muller [1], Mr. Eyal Perry [1]
1. *FabuBlox Inc.*

Fabrication of Seamless, Homogenous Al2O3 Membranes by Gas-Phase-Deposition for highly stable Liquid Cells for Transmission Electron Microscopy 318
Ms. Nathalie Pranzner[1], Mrs. Judith Estengre Pérez [1], Mr. Jeremy Teuber [2], Mr. Rukan Nasri [3], Dr. Irene Fernandez [3], Prof. Arwen Pearson [1]
1. *University of Hamburg,* ***2.*** *Max-Planck-Institute for the Structure and Dynamics of Matter,* ***3.*** *UHH*

Localised O2 Plasma Treatment of AZO and Zn for Broadband Modulation of Optical and Radio Frequency Response. 319
Mr. Thomas Howe[1], Dr. Kai Sun [1], Prof. Otto Muskens [1], Prof. Kees de Groot [1]
1. *University of Southampton*

Single-Molecule Identification Using Plasmonic Nanopores and Ultrafast SERS 320
Dr. Kirill Khabarov[1], Ms. Ilaria Micol Baldi [1], Dr. Maria Blanco Formoso [1], Dr. Foroogh Khozeymeh Sarbishe [1], Dr. Giulia Bruno [1], Prof. Francesco Gentile [2], Dr. Francesco Tantussi [1], Prof. Francesco De Angelis [1]
1. *Istituto Italiano di Tecnologia (IIT),* ***2.*** *Magna Græcia University of Catanzaro*

Oral Session 4B: Advanced Nanofabrication and Characterisation

Ti-Ni-Cu shape memory alloy thin films with improved adhesion and controlled residual stress for MEMS applications 322
Dr. Elaheh Akbarnejad[1], Mr. Alan Savan [1], Mr. Gowtham Arivanandhan [2], Prof. Manfred Kohl [2], Prof. Alfred Ludwig [1]
1. *Ruhr University Bochum,* ***2.*** *Karlsruhe Institute of Technology (KIT)*

Temperature Homogenization for Local Electro-Thermal Annealing of Shape Memory Alloy Microstructures 323
Mr. Gowtham Arivanandhan[1], Dr. Elaheh Akbarnejad [2], Prof. Alfred Ludwig [2], Prof. Manfred Kohl [1]
1. *Karlsruhe Institute of Technology (KIT),* ***2.*** *Ruhr University Bochum*

3D Printing of MEMS Devices 324
Prof. Frank Niklaus[1]
1. *Royal Institute of Technology (KTH)*

Lightweight Machine-Learned Surrogate Models for Carrier Transport using Gradient-Boosted Feature Selection 325
Dr. Ben Rowlinson[1], Dr. Alexandros Keros [1], Prof. Subramanian Ramamoorthy [1], Prof. Jacqueline Cole [2], Prof. Themis Prodromakis [1]
1. *University of Edinburgh,* ***2.*** *University of Cambridge*

Breaking the Resolution Barrier: Phased Exposure Methodology for Precision Microfluidic Injection Moulding Tools 326
Mr. Euan McDonald[1], Mr. Pedro Duarte Menezes [1], Dr. Hojjat Madadi [2], Dr. Xin Li [2], Ms. Alysha Hunter [1], Prof. Daniel Mulvihill [1], Prof. Nikolaj Gadegaard [1]
1. The University of Glasgow, 2. Sphere Bio LTD

Ultra-precision diamond micro-grinding of integrated mirrors in silicon for quantum atomic technologies 327
Dr. Paul Gow[1], Mr. Joel Keen [2], Mr. Glenn Churchill [1], Prof. Corin Gawith [1], Prof. James Gates [1]
1. University of Southampton, 2. Optoelectronics Research Centre, University of Southampton, SO17 1BJ, UK

Magnetic artificial cilia to steer the locomotion of microswimmers 328
Dr. Zhiwei Cui[1], Mr. Kushal Swamy [1], Prof. Jaap den Toonder [2], Dr. Farbod Alijani [1]
1. Delft University of Technology, 2. Eindhoven University of Technology

Oral Session 4C: Electronics II

Mesoporous silica-based memristor for neuromorphic computing 330
Mr. Bohao Ding[1], Dr. Tongjun Zhang [1], Dr. Li Shao [1], Dr. Ayoub Jaafa [1], Prof. Andrew Hector [1], Dr. Ruomeng Huang [1]
1. University of Southampton

Novel Reagents for the Solution-processible Deposition of Low-dimensional Materials and their Composites for Flexible Memristors and Smart Sensors 331
Mrs. Trishala Desai[1], Dr. Chitra Gurnani [2]
1. Trishala Desai, 2. Ecole Centrale School of Engineering, Mahindra University, Hyderabad

Non-planar patterning of an Organic Electrochemical Transistor (OECT) on a tapered optical fiber-based neural interface 332
Mrs. Sneha Pottekkad[1], Dr. Stella Aslanoglou [1], Dr. Barbara Spagnolo [1], Dr. Antonio Qualtieri [1], Dr. Claudia Latte Bovio [1], Dr. Michele Di Lauro [2], Mr. Federico Rondelli [2], Dr. Fabio Biscarini [2], Prof. Massimo De Vittorio [1], Dr. Ferruccio Pisanello [1]
1. Center for Biomolecular Nanotechnologies, Istituto Italiano di Tecnologia (IIT), 73010 Arnesano, LE, Italy, 2. Istituto Italiano di Tecnologia (IIT)

Towards Additive Manufacturing and Conformal Metallization of 3D-Printed Antennas for Radar Applications 333
Dr. Michael Haslinger[1], Dr. Vaclav Prochazka [2], Mr. Peter Bauer [3], Dr. Dieter Holzinger [3], Mr. Jean Temga [4], Dr. Saeid Kameramzadeh [4]
1. PROFACTOR GmbH, 2. PROFACTOR GmbH, Im Stadtgut D1, 4407 Steyr, Austria, 3. TIGER Coatings GmbH & Co KG, Wels, 4600, Austria, 4. Millimeter Wave Technologies, Intelligent Wireless System, Silicon Austria Labs (SAL), 4040 Linz, Austria.

Adaptive Reservoir Computing with Electro-Optical and 3D Structured Memristor Hardware Platforms 334
Prof. Sungjun Kim[1]
1. Dongguk University

VO2-based memristor grown by ALD for neuromorphic computing 335
Mr. Bingkai Ding[1], Dr. Ruomeng Huang [1], Dr. Kai Sun [1], Prof. Kees de Groot [1]
1. University of Southampton

Enhancement of Data Retention Characteristics in 2D and 3D NAND Flash via Hydrogen Trap Engineering 336
Mr. Joongho Yoon[1], Mr. MinSung Song [1], Mr. HyunSuk Kim [1], Mr. EunJin Baek [1], Mr. KeeJeong Rho [1], Mr. JungGyu Kim [1], Mr. JongKwang Lim [1], Mr. YoungHo Kwon [1], Dr. YongSik Yim [1]
1. Samsung Electronics

Oral Session 4D: Sustainable Fabrication Processes I

Pattern transfer using atmospheric pressure plasma processes 338
Dr. Martin Ehrhardt [1], Mr. Robert Heinke [2], Dr. Pierre Lorenz [1], Mr. Visar Demiri [1], Dr. Joachim Zajadacz [3], Prof. Thomas Arnold [4], Dr. Klaus Zimmer[1]
1. Leibniz Institute of Surface Engineering (IOM), 2. Leibniz Institute of Surface Engineering (IOM) and Technische Universität Dresden, 3. Leibniz Institute of Surface Engineering (IOM), Dep. Ultra-Precision Surfaces, 4. Technical University Dresden

Towards Sustainable Electronics: Wafer-Scale Fabrication of Fully Biodegradable CMOS Devices 339
Ms. Laura Cavedoni[1], Mr. Zhengwei Liao [1], Mr. Yukun Lian [1], Mr. Francesco Stallone [1], Prof. Filipe Arroyo Cardoso [1], Prof. Clementine Boutry [1]
1. Delft University of Technology

Conductive carbon film growth from recycled plastics 340
Mr. Carlos Barbero Rodriguez[1], Dr. Geoff Fowler [1], Prof. Kristel Fobelets [1]
1. Imperial College London

Development of sustainable machining processes to manufacture vacuum cells for Quantum Technology 341
Mr. Joel Keen[1], Dr. Paul Gow [1], Mr. Glenn Churchill [1], Prof. Corin Gawith [1], Prof. James Gates [1]
1. University of Southampton

Energy-efficient optical crosslinking system for sustainability in ArFi lithography 342
Ms. SEUNGJOO BAEK[1], Ms. Elke Caron [1], Mr. Wesley Zanders [1], Ms. Andreia Santos [2], Dr. Masahiko Harumoto [3], Dr. Seonggil Heo [4], Mr. Jelle Vandereyken [4], Ms. Veerle Van Driessche [5], Mr. Douglas Guerrero [5]
1. Screen SPE Germany GmbH, 2. SCREEN SPE, 3. SCREEN Semiconductor Solutions Co., Ltd, 4. imec, 5. Brewer Science

Isotropic etching of suspended Si structures using a single-step, single-mask deep reactive ion etching process 343
Dr. Sarah Günther-Müller [1], Mr. Marius Hillebrand[2], Prof. Martin Hoffmann [2], Prof. Steffen Strehle [1]
1. Techische Universität Ilmenau, 2. Ruhr University Bochum

Designing for End-of-Life Electronics: Additive Manufacturing of conductive materials to enable 99% degradable High-Performance Printed Circuit Boards 344
Prof. Jeff Kettle[1], Dr. Jonathon Harwell [1]
1. University of Glasgow

Plenary Sessions

Plenary 6 - Dr Feras Alkhalil

Flexible Integrated Circuits Revolution: Innovative Manufacturing, Materials and Roadmaps 347
Dr. Feras Alkhalil[1]
1. PragmatIC Semiconductor

Elsevier YIA Talk - Dr Alexandros El Sachat

Engineering Thermal and Thermoelectric Transport in Two-dimensional (2D) Semiconductors and Devices 349

Dr. Alexandros El Sachat[1]

1. Institute of Nanoscience and Nanotechnology, NCSR "Demokritos", 27 Neapoleos str & Patriarchou Grigoriou, Ag. Paraskevi, 153 41, Greece

Oral Session 5A: Integrated System Processes

Microscale Patterning of Transparent Conductive Oxides (TCOs) Using High Precision Capillary Printing for Display Applications 351

Dr. Marc Pascual[1], Dr. Ludovic Hahn [2], Dr. Frederic Raynam [1], Mr. Nathan Bigan [1], Mr. Achille Guitton [1], Dr. Amin Mbarki [1], Dr. Tony Jullien [2], Dr. Chloe Guerin [2], Dr. Vincent Jousseaume [2]

1. Hummink, 2. CEA Leti

MULTILAYER POLYMER-BASED CANTILEVERS WITH MULTIPLE EMBEDDED PIEZORESISTIVE SENSORS FOR HIGH-SENSITIVITY ATOMIC FORCE MICROSCOPY 352

Mr. Ekin Asım Özek[1], Dr. Nahid Hosseini [1], Prof. Georg E. Fantner [1]

1. LBNI, EPFL

Pattern dependent micro needle formation in the SPPW process using a digital mask 353

Mr. Myung Seo Kim[1], Mr. Jun Ho Song [1], Ms. Seo Rim Park [1], Prof. Young Tae Cho [1]

1. Changwon National University, Changwon

Fabrication of Ultra-Scaled Back-End TiN Contacts in Silicon-Rich Oxide for High Density Memory Applications 354

Mrs. Christelle CHARPIN-NICOLLE[1], Mr. Gabriele NAVARRO [1], Mr. Antoine SALVI [1], Mrs. Catherine PELLISSIER [1], Mr. Pierre SIXT [1], Mr. Eric NGUYEN GIA CAN [1], Ms. Floriane BAUDIN [1], Ms. Cassandre BELUFFI [1], Mr. Richard SOUIL [1], Mr. Jean-Pierre NIETO [1], Mr. Dominique DESPOIS [1], Mr. Fabien LAULAGNET [1], Mr. Thomas MAGIS [1], Mr. Romuald BLANC [1], Mr. Olivier GLORIEUX [1], Mr. Grégory BONIFACE [1], Mr. Jean ROTTNER [1], Dr. Toshihiko Jimbo [2], Dr. Takashi Kojiri [2], Mr. Vincent BARRAL [1], Mr. François ANDRIEU [1]

1. CEA-Leti, Uni. Grenoble Alpes, 38000 Grenoble, France, 2. Zeon Corporation R&D Center, 1-2-1 Yako, Kawasaki-ku, Kawasaki, Kanagawa, 210-9507

Oral Session 5B: Biodevices and Systems II

Fabrication of Low-cost Microfluidic Devices for Point-of-Care Bacterial Diagnostics 356

Dr. Maria Szola[1], Dr. Peng Tian [1], Ms. Chang Liu [1], Dr. Aysegül Develioglu [1], Mr. Gabriel Weber [1], Mr. Marceau Brisselian Kamary [1], Dr. Thomas Mortelmans [1], Dr. Dimitrios Kazazis [1], Dr. Philipp Berger [1], Dr. Yasin Ekinci [1]

1. Paul Scherrer Institute (PSI)

Non-Invasive Label-Free Electrical and Optical Parrallel Recordings of Electrophysiological Action Potentials of hiPSC Cardiomyocytes 357

Dr. Julien Hurtaud[1], Dr. Alessio Boschi [1], Dr. Giuseppina Iachetta [1], Dr. Michele Dipalo [1], Prof. Francesco De Angelis [1]

1. Istituto Italiano di Tecnologia (IIT)

Biodegradable silk fibroin nanofiber-based microparticles for wound regeneration 358
Mr. Marc Navarro[1], Ms. Laia Bagur [1], Mr. Lasse Højlund Eklund Thamdrup [2], Dr. Fatemeh Ajalloueian [2], Mr. Salvador David Aznar [3], Dr. Xavier Muñoz Berbel [1], Dr. Anja Boisen [2], Dr. Andreu Blanquer [4], Dr. Gonzalo Murillo [1]
1. Institute of Microelectronics of Barcelona (IMB-CNM, CSIC), 2. IDUN section, Department of Health Technology, Technical University of Denmark, DK-2800 Kongens Lyngby, Denmark, 3. Instituto Murciano de Investigación y Desarrollo Agrario y Medioambiental, 4. Departament de Biologia Cel.lular, Fisiologia i Immunologia, Universitat Autonoma de Barcelona

Development of micron mist generating nebulizer 359
Mr. Taki Watanabe[1], Prof. Sho Amano [1], Prof. Yuichi Utsumi [1], Prof. Kazuhiro Kanda [1]
1. Laboratory of Advanced Science and Technology for Industry, University of Hyogo

Three-Dimensional Manipulation of Water Droplets via Spatially Patterned Triboelectric Charging 360
Mr. YU-CHIA CHEN[1], Mr. Cheng-Han Yu [1], Prof. Chin-Chi Hsu [1], Prof. Jiann Shieh [1]
1. National United University

Zero-power MEMS sensors for trees health monitoring 361
Ms. Zarina Nazyrova[1], Prof. Emile Martincic [1]
1. C2N Université Paris-Saclay

Oral Session 5C: Micro-Nano Systems I

CFET novel implementation to enhance IC integration level by stacking devices in a single vertical nanowire 363
Dr. Esteve Amat[1], Dr. Alberto del Moral [1], Prof. Joan Bausells [1], Prof. Francesc Pérez-Murano [1]
1. Institute of Microelectronics of Barcelona (IMB-CNM, CSIC)

Replaceable micromixer agitated by surface acoustic wave 364
Dr. Akinobu Yamaguchi[1], Mr. Masatoshi Takahashi [2], Dr. Satoshi Amaya [3], Prof. Tsunemasa Saiki [4]
1. Toyo University, 2. University of Hyogo, 3. University of Tokyo, 4. University of Fukuchiyama

Characterization and Thermo-mechanical Analysis for a Light-driven Liquid-crystal-elastomer-based Crawling Robot 366
Ms. Yen-Chun Chen[1], Prof. Yao-Joe Yang [1]
1. National Taiwan University

A MINIATURIZED KIRIGAMI SOFT GRIPPER INTEGRATED WITH SELF-SENSING CAPABILITY 367
Mr. Chia Yu Cho[1], Prof. Yao-Joe Yang [1]
1. National Taiwan University

Short-Channel Junctionless Nanowire Transistors 368
Mr. Sayantan Ghosh[1], Mr. Alessandro Puddu [1], Dr. Slawomir Prucnal [1], Dr. Ahmad Echresh [1], Prof. Artur Erbe [1], Dr. Yordan M. Georgiev [1]
1. Helmholtz-Zentrum Dresden-Rossendorf (HZDR)

Oral Session 5D: Electronic Sensors

A Saw-Tooth Slot Antenna Sensor for Dielectric Sensing 371
Dr. Hilary Scott Nkimbeng Cho [1], Prof. Jin Choi[1]
1. Michigan Technological University

Exploitation of Surface Acoustic Waves for the implementation of innovative sensing devices applied to the measurement of gas phase pollutants 372
Dr. Meddy Vanotti[1], Ms. Ghida Fawaz [1], Ms. Margerie Loze [2], Mr. Sacha Poisson [1], Dr. Stéphane Brandès [2], Dr. Laurie André [2], Dr. Nicolas Desbois [2], Prof. Claude P. Gros [2], Dr. Virginie Blondeau-Patissier [1]
1. Université Marie et Louis Pasteur, SUPMICROTECH, CNRS, Institut FEMTO-ST, 2. Université Bourgogne Europe

Tunable Nanoarchitectures in NiO/In2O3 Thin Films sensor: Thickness-Modulated Response Enhancement for Ultrafast Butanone Sensing 373
Prof. Zhenyu Yuan[1]
1. Northeastern university

Electric-field Sensor based on Graphene/MoS_2 Heterostructure for Lightning Forecast 375
Ms. Jiali Hu[1], Dr. Mohammad Razzakul Islam [1], Dr. Afsal Kareekunnam [1], Dr. Takeshi Kudo [2], Mr. Takeshi Maruyama [2], Prof. Masashi Akabori [1], Prof. Hiroshi Mizuta [1]
1. Japan Advanced Institute of Science and Technology, 2. Otowa Electric Co., Ltd.

Disposable electrode based iontronic pressure sensors and their potential applications in generative artificial intelligence 376
Mr. Changwoo Cho[1], Ms. Chaeeun Lee [1], Prof. Je Hoon Oh [1]
1. Hanyang University

High-Mobility of Amorphous-Crystalline Phase-Composite Indium Oxide for Thin Film Transistor Applications 377
Mr. Quang Khanh Nguyen[1], Prof. Myung Mo Sung [1]
1. Hanyang University

Oral Session 6A: Advanced Nanofabrication III

Sequential Infiltration Synthesis for Organized Nanostructure Fabrication 379
Dr. Gabriele Seguini[1]
1. IMM-CNR

Effect of Binary Mechanical Environment on T Cell Function 380
Mr. Jatin jawhir Pandit[1], Mr. Abed Al Kader Yassin [2], Dr. Carlos Ureña Martin [1], Dr. Guillaume Le Saux [1], Prof. Angel Porgador [2], Prof. Mark Schvartzman [1]
1. Department of Materials Engineering, Ben-Gurion University of the Negev, P.O. Box 653, Beer-Sheva 84105, Israel; Ilse Katz Institute for Nanoscale Science and Technology, 2. The Shraga Segal Department of Microbiology, Immunology, and Genetics Faculty of Health Sciences, Ben-Gurion University of the Negev, P.O. Box 653, Beer-Sheva 84105, Israel

Patterning on Living Tardigrades 381
Ms. Zhirong Yang[1], Dr. Shan Wu [1], Dr. Kang Zhao [1], Dr. Ding Zhao [1], Prof. Min Qiu [1]
1. Westlake University

Electrodeposition of conducting polymers on silicon towards integrated autonomous sensor systems 382
Dr. Tomoyuki Kurioka[1], Mr. Punvinai Vinaisuratern [1], Mr. Joji Higuchi [1], Mr. Keisuke Okamoto [1], Prof. Tso-Fu Mark Chang [1], Mr. Nasser Aldhahri [2], Prof. John Mcbride [3], Dr. Yoshishige Tsuchiya [2], Prof. Masato Sone [1]
1. Institute of Integrated Research, Institute of Science Tokyo, 2. School of Electronics and Computer Science, University of Southampton, Southampton SO17 1BJ, United Kingdom, 3. School of Engineering, University of Southampton

A Thick-Film Micro-Patterning Method for Organic Thermoelectric Materials Using O2 Plasma and Metal Masks 383
Mr. Shota SAWAYAMA[1], Dr. Qingshuo Wei [2], Prof. Daisuke Yamane [1]
1. Ritsumeikan University, 2. National Institute of Advanced Industrial Science and Technology (AIST)

Oral Session 6B: Micro-Nano Systems II

Making a Miniature Sun: Ultra High Temperature Carbon Devices 385
Prof. Oliver Williams[1]
1. Cardiff University

Mechanical and electrical contact testing for Pt/PEDOT/Si layered structures 386
Dr. Yoshishige Tsuchiya[1], Dr. Tomoyuki Kurioka [2], Mr. Punvinai Vinaisuratern [3], Mr. Joji Higuchi [3], Prof. Tso-Fu Mark Chang [2], Prof. Masato Sone [2], Mr. Nasser Aldhahri [1], Dr. Liam Boodhoo [4], Dr. Thomas Bull [5], Prof. Yan Yang [6], Prof. John Mcbride [5]
1. University of Southampton, 2. Institute of Science Tokyo, 3. Institute of Integrated Research, Institute of Science Tokyo, 4. School of Electronics and Computer Science, University of Southampton, Southampton SO17 1BJ, United Kingdom, 5. School of Engineering, University of Southampton, 6. TaiCaan Technologies

Wafer scale fabrication of pyrolytic carbon submicron gap membrane electrodes for electrochemical sensing 387
Dr. Nicolai Støvring[1], Dr. Pratik Kusumanchi [1], Ms. Estefany Ureta [1], Dr. Arto Heiskanen [2], Prof. Jenny Emnéus [2], Prof. Stephan Sylvest Keller [3]
1. DTU Nanolab, 2. DTU Bioengineering, Danmarks Tekniske Universitet (DTU), 2800 Kgs. Lyngby, Denmark, 3. National Centre for Nano Fabrication and Characterization, DTU Nanolab, Technical University of Denmark

Energy-Free Micro-Latching Mechanisms for Bidirectional SMA Actuators 388
Ms. Yizheng Liu[1], Mr. Vincent Gottwald [2]
1. Institut für Mikrosystemtechnik – IMTEK, Albert-Ludwigs-Universität Freiburg, Georges-Köhler-Allee 102, 79110 Freiburg, Germany, 2. Karlsruhe Institute of Technology (KIT)

Physical reservoir computing with MEMS torsional mirrors 389
Mr. Yuta Kawashima[1], Mr. Mikiya Oki [1], Dr. Jun-Yu Ou [2], Dr. Yoshishige Tsuchiya [3], Prof. Toshiyuki Tsuchiya [1]
1. Kyoto University, 2. Physics and Astronomy, University of Southampton, 3. University of Southampton

Oral Session 6C : Optical Sensors

Monitoring vibrational fingerprints of polypeptide monolayers by infrared plasmonic nanoantennas 391
Dr. Santos Merino[1], Dr. Alberto Villar [1], Dr. Ruth Díez [1], Dr. Gabriel Ortega [2], Dr. Mónica García-Mota [3], Dr. Anna Kimmel [3], Dr. Albert Guerrero [4], Dr. Jorge Espina [5], Dr. Mario Zapata [6], Prof. Javier Aizpurua [7]
1. Tekniker, 2. CIC bioGUNE, 3. Simune Atomistics, 4. Instituto de Microelectrónica de Barcelona, 5. Universidad de Oviedo, 6. Materials Physics Center, 7. Donostia International Physics Center

On-fiber printed polymeric tapers for chronically implantable neural interfaces 392
Dr. Stella Aslanoglou[1], Dr. Barbara Spagnolo [1], Dr. Cinzia Montinaro [1], Dr. Alberto Perna [2], Dr. João F. Ribeiro [2], Dr. Marco Pisanello [3], Dr. Luca Berdondini [2], Dr. Tommaso Fellin [2], Dr. Ferruccio Pisanello [1], Prof. Massimo De Vittorio [1]
1. Center for Biomolecular Nanotechnologies, Istituto Italiano di Tecnologia (IIT), 73010 Arnesano, LE, Italy, 2. Center for Convergent Technologies, Istituto Italiano di Tecnologia (IIT), 16163 Genova, Italy, 3. OptogeniX s.r.l., 73010 Arnesano, Italy

Detection of Phtalate release from plastic tubes using a NanoFabricated Surface Enhanced Raman Spectroscopy device 393
Mr. Sofien Ramos[1], Ms. Camille Blanc [2], Dr. Laurence Salomé [2], Dr. Philippe Louarn [3], Dr. Emmanuelle Trevisiol [4], Prof. Christophe Vieu [1]
1. LAAS-CNRS, 2. IPBS, 3. IRAP, 4. TBI

Detection of Polystyrene Microplastics via Surface-Enhanced Raman Scattering on Sticky Hydrophobic Nanopillar Substrates 394
Mr. Tzu-Yu Chiu[1], Prof. Wen-Huei Chang [2], Mr. Kuan-Ting Kuo [1], Mr. Yao-Ming Ku [1], Prof. Chih-Chia Huang [1], Prof. Chun-Hung Lin [1]
1. Department of Photonics, National Cheng Kung University, 2. Department of Applied Chemistry, National Pingtung University

Micro-optics Design and Preliminary Characterization of a Fiber-Optic SERS Probe for In Vivo Diagnostics 395
Ms. Yingwei Hou[1], Dr. Nilanjan Manda [1], Dr. Belal Ahmad [1], Dr. Jang Ah Kim [2], Dr. Alexander J Thompson [1]
1. Department of Surgery & Cancer, Imperial College London, London, United Kingdom., 2. Department of Mechanical Engineering, Imperial College London, London, United Kingdom.

Oral Session 6D: Advanced Nanofabrication IV

Ice lithography using Diobalt octa-carbonyl 397
Mr. Limin Qi[1], Dr. Dongli Liu [2], Dr. Ding Zhao [3], Prof. Min Qiu [1]
1. Westlake University, 2. Westlake Instruments (Hangzhou) Technology Co., Ltd, 3. Westlake Institute for Optoelectronics

Quasi-3D Nanoscale Fabrication: Precision Patterning and Modelling via Focused Ion Beam Implantation 398
Dr. Jordi Llobet [1], Dr. Jordi Antoja[1], Dr. Alberto del Moral [2], Mr. Marcel de la Vega Czarnecki [1], Ms. Marta Duch [1], Mr. Alessandro Cian [3], Mr. Elia Scattolo [3], Dr. Michele Crivellari [3], Dr. Xavier Borrisé [4], Dr. Damiano Giubertoni [3], Prof. Francesc Pérez-Murano [2]
1. Institut de Microelectrònica de Barcelona, IMB-CNM (CSIC), Universitat Autònoma de Barcelona, Cerdanyola Del Vallès, 08193, Barcelona, Spain., 2. Institute of Microelectronics of Barcelona (IMB-CNM, CSIC), 3. FBK, Fondazione Bruno Kessler, 4. Catalan Institute of Nanoscience and Nanotechnology (ICN2) and Barcelona Institute of Science and Technology (BIST)

Investigation of process windows for alternative non-toxic and metal ion free developer choline hydroxide for HSQ resist Medusa 84 SiH 399
Ms. Pia Kohlschreiber[1], Mr. Markus Gottwald [1], Dr. Christian Helke [1], Mr. Harry Biller [2], Dr. Mandy Sendel [2], Dr. Danny Reuter [1]
1. Fraunhofer Institute for Electronic Nano Systems ENAS, 2. Allresist GmbH

Resist-free and low-temperature micropatterning of IGZO using stencil lithography for electronic applications 400
Mr. Chenxiang Zhang[1], Prof. Giovanni Boero [1], Dr. Arnaud Bertsch [1], Prof. Jürgen Brugger [1]
1. Microsystems Laboratory, Ecole Polytechnique Fédérale de Lausanne (EPFL)

Papers

Plenary 1 - Dr Drew Nelson

Building Globally Relevant Semiconductor Clusters and Their Relevance to the UK Semiconductor Strategy 403
Dr. Drew Nelson[1]
1. All Party Parliamentary Group on Semiconductors Advisory Board

Plenary 2 - Dr Naoto Horiguchi

CMOS scaling paradigm shift from CMOS 1.0 to CMOS 2.0 405
Dr. Naoto Horiguchi[1]
1. IMEC, Belgium

Plenary 3 - Prof Dinesh Pamunuwa

Edge Computing Platform based on Nanoelectromechanical Relays 408
Prof. Dinesh Pamunuwa[1]
1. University of Bristol

MNE Fellow Award: Prof Lars Montelius

Science in our time - for People, Planet and Prosperity 410
Prof. Lars Montelius[1]
1. Lund University

Oral Session 1A : Microsystem and MEMS Applications

Fabrication of Flexible III-Nitride MEMS Resonators by Lift-Off and Transfer onto Thin Metal Substrates 412
Mr. Ali Kassem[1], Dr. Rajat Gujrati [1], Mr. david bourrier [2], Dr. Cédric Ayela [3], Mr. Fabrice Mathieu [2], Prof. Isabelle Dufour [3], Prof. Liviu Nicu [2], Dr. Vishnu Ottapilakkal [1], Dr. Phuong Vuong [4], Prof. Suresh Sundaram [4], Prof. William Hunt [5], Prof. Abdallah Ougazzaden [5], Dr. Thierry Leichlé [5], Prof. Jean-Paul Salvestrini [1]
1. CNRS, IRL 2958 Georgia Tech-CNRS, Metz, France, 2. LAAS-CNRS, Université de Toulouse, CNRS, Toulouse, France, 3. Université de Bordeaux, Laboratoire IMS UMR-CNRS 5218, Talence, France, 4. Georgia Tech Europe, IRL 2958 Georgia Tech-CNRS, Metz, France, 5. Georgia Institute of Technology, School of Electrical and Computer Engineering, IRL 2958 Georgia Tech-CNRS, Atlanta, GA, USA

Probing Cell Mechanosensitivity in Microengineered 3D Scaffolds 414
Ms. Aída Gabriela Fernández Contreras[1], Ms. Chloé Viat [1], Prof. Boudewijn van der Sanden [2], Prof. Olivier Stephan [3], Prof. Jean-Hervé Tortai [1], Prof. Alice Nicolas [1]
1. LTM, 2. TIMC, 3. LiPhy

Wafer-scale transfer-free multi-layer graphene process for MEMS sensors 416
Prof. Sten Vollebregt[1]
1. Associate Professor

High Speed Nickel Electrodeposition in a Supercritical CO2 Emulsified Nickel Sulfamate Bath toward MEMS Applications 418
Mr. WENDING HOU[1], Dr. Tomoyuki Kurioka [1], Prof. Chun-Yi Chen [1], Prof. Masato Sone [1], Prof. Tso-Fu Mark Chang [1]
1. Institute of Science Tokyo

Oral Session 1B : Electron Beam Lithography

Precise Dimension Control of Narrow Gaps in High Density Pattern on InP-Based Substrate by Electron Beam Lithography 421
Mr. Hao Zhang[1], Dr. Jing Becker [2], Mr. Jan Ebbert [1], Mr. Tekin Kahilogullari [1], Dr. Daniel Ritter [2], Prof. Nils Weimann [1]
1. Components for High Frequency Electronics, Duisburg, 47057, University Duisburg Essen, 2. GenISys GmbH

Qualification of Direct Write E-beam Lithography Tools with Two-Dimensional Vernier Patterns 423
Dr. Alexei Bogdanov[1]
1. NTT Research Inc.

Direct Fabrication of 3-D PEDOT:PSS Nanostructures by Electron Beam Lithography 425
Mr. Yandong YANG[1], Prof. Shin'ichi Warisawa [1], Prof. Reo Kometani [1]
1. Graduate School of Frontier Sciences, The University of Tokyo

High Resolution Electron Beam Lithography Patterning for Advanced Grating Couplers 427
Ms. Pragya Sah[1], Mr. Radhakant Singh [1], Mr. Kai Zhang [1], Mr. Michael Möller [1], Dr. Rijil Thomas [1], Dr. Jens Bolten [1], Ms. Anastasiia Sorokina [2], Mr. Guochun Du [3], Mr. Carl Grimpe [3], Dr. Steffen Sauer [2], Dr. Elena Jordan [3], Prof. Stefanie Kroker [2], Prof. Tanja Mehlstaeubler [3], Dr. Stephan Suckow [1], Prof. Max Lemme [4]
1. AMO GmbH, 2. Technische Universität Braunschweig, 3. Physikalisch-Technische Bundesanstalt, 4. Chair of Electronic Devices, RWTH Aachen University

A novel patterning approach enabling consistent high aspect ratio nanostructures with functional tops 429
Mr. Bryan Benz[1], Prof. Marco Stampanoni [2], Prof. Martino Poggio [3], Dr. Lucia Romano [1]
1. Paul Scherrer Institute (PSI), 2. ETH Zürich, 3. University of Basel

Oral Session 1C : Electronics 1

P-channel Oxide Thin Film Transistors for CMOS Logic 432
Dr. Kham Niang [1], Dr. Ben Peek [2], Dr. James Parish [3], Prof. Paul Chalker [2], Prof. Andrew Johnson [3], Prof. Andrew Flewitt[1]
1. University of Cambridge, 2. University of Liverpool, 3. University of Bath

Electric Field Confinement-Induced Potentiation in Inert Mixed Ionic-Electronic Conducting Memristors 434
Dr. Philip Calado[1]
1. University of Southampton

Towards aluminium nitride on diamond surface acoustic wave devices 436
Dr. Jerome Cuenca [1], Dr. Soumen Mandal [1], Prof. Oliver Williams[1]
1. Cardiff University

Nanoscale Back-End-of-Line Silicon Carbide Memristor for Resistive Memory 438
Mr. Qin Liu[1], Dr. Omesh Kapur [1], Dr. Anushka Gangnaik [2], Dr. Ruomeng Huang [2], Prof. Kees de Groot [2]
1. School of Electronics and Computer Science, University of Southampton, Southampton SO17 1BJ, United Kingdom, 2. University of Southampton

2D Materials for Electrostrictive FET 440
Ms. Nigama Vykari Vajjula [1], Mr. Fitunerediate Gebeyehu [1], Prof. Ethan Ahn[1]
1. George Mason University

Oral Session 1D: Biodevices and Systems 1

Contactless Measurement of Radial Artery Pulse Waves Using an Acoustic Sensing System 443
Ms. Chaeeun Lee[1], Prof. Je Hoon Oh [1], Mr. Changwoo Cho [1]
1. Hanyang University

A microfluidic Cartilage-on-Chip platform for personalized cartilage transplant compatibility screening 445
Dr. Rahman Sabahi-Kaviani[1], Ms. Giorgia Mazzini [2], Ms. Emma Bristow [2], Dr. Cynthia Fehres [2], Prof. René Toes [2], Dr. Yolande Ramos [2], Prof. Ingrid Meulenbelt [2], Dr. Regina Luttge [1]
1. Eindhoven University of Technology, 2. Leiden University Medical Centre

A Microfluidic Device for Monitoring Functional Enzyme Activity of Primary Human Hepatocyte Spheroids Based on Cell-Secreted Extracellular Vesicles 447
Mr. Ehsanollah Moradi[1], Dr. Päivi Järvinen [1], Dr. Markus Haapala [1], Prof. Ossi Korhonen [2], Prof. Tiina Sikanen [1]
1. University of Helsinki, 2. University of Eastern Finland

Wavelength-selective photodetector for NADH fluorescence detection 449
Mr. Zhengwei Liao[1], Ms. Laura Cavedoni [1], Ms. Ceren Kutucu [1], Prof. Padmakumar Rao [1], Prof. Clementine Boutry [1], Prof. Filipe Arroyo Cardoso [1]
1. Delft University of Technology

Nano- and Microscale Aptamer Biosensors for Monitoring Biomarkers of Human Health 451
Prof. Nako Nakatsuka[1]
1. CHEMINA - EPFL

Poster Session 1

Ionic Liquids and Focused Ion Beams: Are all Ionic Liquids Adequate for Advanced FIB Micro- or Nano-engineering? 453
Dr. Jacques Gierak[1], Ms. Elinoa Sebag [2], Mr. Amir Goodwin [2], Mr. David Bouville [2], Dr. philippe Lesot [3], Dr. philippe Berdagué [3]
1. C2N-CNRS, 2. Centre de Nanosciences et de Nanotechnologies (C2N), Palaiseau, 91120, France, 3. ICMMO

Plasmonic aluminium nanogap creation by electromigration for plasmonic UV-Nanolithography 455
Mr. Jakob Nüßlein[1], Mr. Zhuoji Huang [1], Prof. Steffen Strehle [1]
1. Techische Universität Ilmenau

Improved Accuracy in Measuring the Dielectric Constant of Nanoparticles in Electrostatic Force Microscopy 457
Mr. Lukas Lehnert[1], Mr. Benjamin Baumann [1], Prof. Ronald Thoelen [2], Prof. Hildegard Moebius [1]
1. University of Applied Sciences Kaiserslautern, 2. Hasselt University

Effect of doping Nb on optical properties of Sea Urchin-like TiO2 Photocatalysis 459
Dr. Mariko Murayama[1], Prof. Xinwei Zhao [2], Prof. Taichiro Nishio [1]
1. Tokyo University of Science, 2. Henan University of Technology

PVDF-TrFE with suspended AlN particles: a polymer nano-composite with boosted ferroelectric properties 461
Dr. Wolfgang Hilber[1], Mr. Sebastian Lang [1], Prof. Bernhard Jakoby [1]
1. Johannes Kepler University Linz

Fabrication of Ferroelectric PVDF:TrFE Foil via Controlled Dewetting 463
Mr. Sebastian Lang[1], Dr. Wolfgang Hilber [1], Ms. Tina Mitteramskogler [1], Prof. Bernhard Jakoby [1]
1. Johannes Kepler University Linz

X-ray energy dependence of gold nanoparticle synthesis in X-ray radiolysis 465
Dr. Akinobu Yamaguchi[1], Dr. Kenji Hanada [2], Prof. Ikuo Okada [2], Dr. Hiroshi Sekiguchi [3], Dr. Ikuya Sakurai [4]
1. Toyo University, 2. Aichi Synchrotron Radiation Center, 3. Japan Synchrotron Radiation Research Institute, 4. Nagoya University

E-Beam Lithography Process Calibration with Minimum Number of SEM Images using Deep Learning 467
Mr. Burak Çoban[1], Mr. Suleyman Celik [2], Mr. Florian Imeri [3], Dr. Jan Klikovits [3], Dr. Klaus Gieb [3], Mr. Nezih Ünal [3]
1. İzmir Institute of Technology, 2. Sabanci University Nanotechnology Research and Application Center, 3. GenISys GmbH

Eco-friendly, bioinspired nanopattern for antifouling: Cicada wing-inspired nanostructures for marine applications 469
Mr. Zihao Zhao[1], Ms. Nan Liang [1], Prof. Shoso Shingubara [1], Prof. Tomohiro Shimizu [1], Prof. Takeshi Ito [1]
1. Kansai University

Electrochemical Investigation of $[Ru(bpy)_2(L)]^{2+}$ Complexes for Biosensor Applications: Insights into Rct Reduction Mechanism 471
Mr. Koki Yamashita[1], Prof. Tomohiro Shimizu [1], Prof. Shoso Shingubara [1], Mr. Hitoshi Ishida [1], Mr. Akinori Kuzuya [1], Prof. Takeshi Ito [1]
1. Kansai University

Bactericidal property of COP nanopillars dependent with their size 473
Mr. Gakuto Inoue[1]
1. Kansai University

Impact of microfabrication conditions on the oxygen depletion rate of thiol-enes 475
Dr. Markus Haapala[1], Dr. Päivi Järvinen [1], Dr. Iiro Kiiski [1], Prof. Tiina Sikanen [1]
1. University of Helsinki

Microstructuring of 3D Printed Ceramic Surfaces using Nanoimprint Lithography 477
Ms. Sonja Kopp [1], Dr. Abhijeet Lale [2], Ms. Viktorija Jonaityte [1], Dr. Michael Haslinger [1], Ms. Marta Bonora [3], Mr. Matthias Vostatek [3], Ms. Sarah Linnemeier [4], Prof. Marcus Granegger [4], Prof. Francesco Moscato [3], Dr. Martin Schwentenwein [2], Dr. Michael Muehlberger[1]
1. PROFACTOR GmbH, 2. Lithoz GmbH, 3. Center for Medical Physics and Biomedical Engineering, Medical University of Vienna, 4. Department of Cardiac Surgery, Medical University of Vienna

Post-etch Surface Modification for Sidewall Smoothing in Deep Reactive Ion Etched Silicon 479
Mr. Arjun Moothedath Sethumadhavan[1], Mr. Zhong Ren [1]
1. Oxford Instruments

Fabrication of fine metal patterns using solvent-soluble UV-curable resin 481
Mr. Satoshi Fujieda[1], Mr. Takeshi Osaki [2], Mr. Yukio Okado [2], Prof. Jun Taniguchi [1]
1. Tokyo University of Science, 2. Toyo Gosei Co., Ltd., Photosensitive Materials Research Center

Effect of Polyethylene Glycol on growth of Porous Silicon 483
Mr. XUMING ZHAO[1], Mr. Tomoya Okawa [1], Ms. Chenxin Zhong [1], Mr. koji akiyama [2], Mr. takeya inoue [2], Prof. Takeshi Ito [1], Prof. Shoso Shingubara [1], Prof. Tomohiro Shimizu [1]
1. Kansai University, 2. Tokyo Electron

Study of blob defectivity for different 248nm resist processes: influence of material chemistry, pattern types, bake and development conditions. 485
Mrs. Lucie BORGET[1], Mrs. Romane Francais [1], Mr. Loic Balme [1], Mr. Yohann Lebel [1], Mr. OLIVIER MERMET [1], Dr. Benedicte Mortini [1]
1. STMicroelectronics

Development of Microfluidic Flow Cells with Integrated Arrays of Freestanding Al_2O_3 Membranes for SEM Imaging 487
Mr. Jeremy Teuber[1], Mr. Tim Erichlandwehr [2], Mr. Rukan Nasri [2], Dr. Irene Fernandez [2]
1. Max-Planck-Institute for the Structure and Dynamics of Matter, 2. UHH

Fabrication of Flexible Printed In-Mold Electronic Devices 489
Dr. JEONGDAI JO[1], Mr. Pyoungwon Park [1], Dr. Taik-Min Lee [2], Dr. Inyoung Kim [2]
1. Korea Institute of Machinery and Materials (KIMM), 2. Korea Institute of Machinery & Materials (KIMM)

Bioinspired Nanospike Formation on the Surfaces of Commercial Plastic Plates Using Atmospheric-Pressure Low-Temperature Plasma 491
Dr. Masashi Yamamoto[1], Mr. Motoki Tanaka [2], Mr. Ayumu Takada [2], Dr. Atsushi Sekiguchi [3]
1. National Institute of Technology (KOSEN) Kagawa College, 2. National Institute of Technology, Kagawa College, 3. Litho Tech Japan Corporation

Impact of processing on the temperature-dependant behaviour of nano-structured Platinum thin films fabricated by Spark Ablation 493
Ms. Shatavisha Biswas[1], Prof. Sten Vollebregt [2]
1. PhD, 2. Associate Professor

Hierarchical structures fabricated for probiotic marine bacterial growth using hybrid methods for polymer replication 495
Ms. Yuyan Liu[1], Mr. Xavier Florensa [1], Mr. Euan McDonald [2], Prof. Paul Kempen [1], Prof. Claus Sternberg [1], Prof. Nikolaj Gadegaard [2], Prof. Lone Gram [1], Prof. Rafael Taboryski [1]
1. Technical University of Denmark, 2. The University of Glasgow

Fluorination of Ni Hard masks during Fluorine-Based DRIE: Structural and Spectroscopic Insights into NiF_2 Formation 497
Mr. Baptiste Fischer-Kaszuba [1], Dr. Amandine Andrieux-Ledier [2], Dr. Etienne Carré[1], Dr. Patrick Kayser [1], Dr. Pierre Lavenus [2], Mr. Jean-Sebastien Mérot [3], Dr. Frédéric Fossard [3], Dr. Thomas Baron [4]
1. DPHY, ONERA, Université Paris-Saclay, 92320 Châtillon, France, 2. DPHY, ONERA, Université Paris-Saclay, 3. Université Paris-Saclay, ONERA, CNRS, Laboratoire d'étude des microstructures (LEM), 4. Université Marie et Louis Pasteur, SUPMICROTECH, CNRS, Institut FEMTO-ST

On-CMOS 3D Platinum Electrodes Fabricated by Focussed-Ion Beam for Dielectrophoresis of DNA Towards an Electrokinetic Lab-on-CMOS 499
Dr. Lewis Keeble[1], Mr. Arthur Jaccottet [1], Mr. Daryl Ma [1], Dr. Jesus Rodriguez-Manzano [1], Prof. Pantelis Georgiou [1]
1. Imperial College London

Hybrid-Polymer Microring Resonator Arrays for Next-Generation Photoacoustic and Biosensing Applications 501
Dr. Santhosh Pandian [1], Ms. Marina Fetisova [2], Dr. Petri Karvinen [2], Dr. Paul Müellner [3], Dr. Moritz Eggeling [3], Dr. Rainer Hainberger [3], Mr. Evgenii Lepukhov[1], Prof. Tapio Niemi [1]
1. Tampere University, 2. University of Eastern Finland, 3. AIT Austrian Institute of Technology GmbH

Femtosecond laser inscription of optical waveguide in sapphire 503
Dr. Wei Lyu[1], Dr. Ding Zhao [1], Prof. Min Qiu [2]
1. Westlake Institute for Optoelectronics, 2. Westlake University

Effective diffusion barrier for Au/Ni thin films in quartz MEMS processing 505
Mr. Baptiste Fischer-Kaszuba[1], Dr. Amandine Andrieux-Ledier [1], Dr. Etienne Carré [1], Dr. Frédéric Fossard [2], Mr. Jean-Sebastien Mérot [2], Dr. Patrick Kayser [3], Dr. Pierre Lavenus [1], Dr. Thomas Baron [4]
1. DPHY, ONERA, Université Paris-Saclay, 2. Université Paris-Saclay, ONERA, CNRS, Laboratoire d'étude des microstructures (LEM), 3. DPHY, ONERA, Université Paris-Saclay, 92320 Châtillon, France, 4. Université Marie et Louis Pasteur, SUPMICROTECH, CNRS, Institut FEMTO-ST

Analysis and fabrication of electrothermal electrodes for micro and nanostructured sensors 507
Mr. Abel Palomas Jiménez[1], Dr. Michelle Cedeño [1], Ms. Ana Coloma Velez [1], Dr. Jorge Luis Villar [1], Dr. Manuel Domínguez-Pumar [1], Dr. Sandra Bermejo [1]
1. Universitat Politècnica de Catalunya - BarcelonaTech (UPC)

Ultra-thick grayscale ellipsoidal structures for X-ray focusing using scanning-laser direct write lithography 509
Dr. Giulia Malvicini[1], Prof. Helmut Schift [1]
1. Paul Scherrer Institute (PSI)

Effects of Annealing on Effective Young's Modulus of Ti/Au Multi-Layered Microcantilevers for MEMS Capacitive Accelerometers 511
Mr. Tatsuhiko Mori[1], Dr. Tomoyuki Kurioka [1], Mr. Shunkai Watanabe [1], Prof. Chun-Yi Chen [1], Prof. Tso-Fu Mark Chang [1], Prof. Katsuyuki Machida [1], Prof. Hiroyuki Ito [1], Prof. Yoshihiro Miyake [1], Prof. Masato Sone [1]
1. Institute of Science Tokyo

Development of an In Situ Microfluidic System for Real-Time Control of Porous Microspheres Fabrication 513
Mr. Ji Hwan Han[1], Mr. Min Chul Shin [1], Prof. Chul Min Kim [2], Prof. Gyu Man Kim [1]
1. Kyungpook National University, 2. Gyengsang National University

Slippery liquid-infused micropatterned surface for air-lifted analyte membrane formation 515
Mr. Seong Min Yoon[1], Prof. Young Tae Cho [1], Dr. Woo Young Kim [1], Mr. Chae Hyeok Yoon [1]
1. Changwon National University, Changwon

Mastering the growth of centimetric sp2-hybridized boron nitride films for optoelectronic devices 517
Dr. Laure Tailpied [1], Ms. Marjolaine Cornu [1], Dr. Frédéric Fossard [2], Mr. Jean-Sebastien Mérot [3], Ms. Chloe Grekobi [3], Mr. Jules Lagrave [3], Dr. Jean-Manuel Decams [4], Dr. Annick Loiseau [3], Dr. Amandine Andrieux-Ledier[5]
1. Université Paris-Saclay, ONERA, CNRS, Laboratoire d'étude des microstructures (LEM), 92322 Châtillon, France, 2. Université Paris-Saclay, ONERA, CNRS, Laboratoire d'étude des microstructures (LEM), 3. Université Paris-Saclay, ONERA, CNRS, Laboratoire d'étude des microstructures (LEM), 92322 Châtillon, 4. Annealsys, 139 rue des Walkyries, 34000 Montpellier, France, 5. DPHY, ONERA, Université Paris-Saclay, F-92322 Châtillon, France

Fabrication of slanted diffraction gratings by electron beam lithography with tilted angle exposure 519
Mr. Naoya Shibasaki[1], Prof. Jun Taniguchi [1]
1. Tokyo University of Science

Investigation of Pre-Stressed Membranes in Miniaturized Piezoresistive Diaphragm Pressure Sensors for Enhanced Sensitivity in High Vacuum 522
Dr. Jian LU[1], Dr. Lan ZHANG [1], Dr. Yuichi KURASHIMA [1], Dr. Hideki TAKAGI [1]
1. National Institute of Advanced Industrial Science and Technology (AIST)

Integration of a metal nano-antenna structure into silicon substrates using surface-activated room temperature bonding 524
Dr. Yuichi KURASHIMA[1], Dr. Takashi Matsumae [1], Mr. Atsuhiko Maeda [1], Dr. Masaaki Oshita [1], Dr. Hideki TAKAGI [1], Dr. Tetsuo Kan [2], Dr. Elyas Ashenafi Abadi [2], Dr. Daiji Noda [3], Mr. Ryo Ohta [3]
1. National Institute of Advanced Industrial Science and Technology (AIST), 2. The University of Electro-Communications, 3. Micromachine Center

Interface-Engineered Ferroelectric Tunnel Junctions with Ultra-High TER via Optimized P(VDF-TrFE) Crystallinity 526
Mr. Mohit Kumar Gautam[1], Dr. Roshni Satheesh-Babu [1], Dr. Ioannis Zeimpekis [1], Prof. Dimitra Georgiadou [1]
1. University of Southampton

Fabrication of metal nanodot arrays for LSPR biosensors with LOD of 1fg/mL using nanoimprint lithography process 528
Dr. JaeJong Lee[1], Dr. Narae Jo [2]
1. Korea Institute of Machinery and Materials (KIMM), 2. Korea Research Institute of Standards and Science

Study of the high-intensity reflection structure that used the speckle exposure method 530
Dr. Atsushi Sekiguchi[1]
1. Litho Tech Japan Corporation

Introducing ArF grayscale lithography for large-scale fabrication of submicronic 3D structures 537
Mr. Gaby Bélot[1], Mr. Sébastien Bérard-Bergery [1], Dr. Élodie Sungauer [1], Mr. Api Warsono [2], Dr. Arnaud Bazin [2], Dr. Aurélien Fay [2], Dr. Cécile Gourgon [3]
1. STMicroelectronics, 850 rue Jean Monnet, 38926 Crolles Cedex, France, 2. Univ. Grenoble Alpes, CEA, Leti, F-38000 Grenoble, France, 3. Université Grenoble Alpes, CNRS, CEA/LETI-Minatec, Grenoble INP, LTM, 17 Rue des Martyrs, Grenoble 38054, France

MoTe2-Based Memristor Fabrication with Scanning Probe Lithography 539
Ms. Busra Oyku Alan[1], Dr. Christoph Reuter [1], Dr. Ren Li [1], Prof. Steffen Strehle [1]
1. Techische Universität Ilmenau

Study on Micro Scale Surface Polishing and Modification of 3D Biodegradable Scaffolds using Electron Beam Treatment 541
Mr. JeongSik Noh[1], Prof. Jongsung Park [1]
1. Kyungpook National University

Micro-Mechanical Properties of Annealed Electrodeposited Gold for Design of MEMS Structural Components 543
Mr. Shota Iima[1], Dr. Tomoyuki Kurioka [2], Mr. Shota Kanno [2], Prof. Chun-Yi Chen [2], Prof. Tso-Fu Mark Chang [2], Prof. Katsuyuki Machida [2], Prof. Hiroyuki Ito [2], Prof. Yoshihiro Miyake [2], Prof. Masato Sone [2]
1. Institute of Integrated Research, Institute of Science Tokyo, 2. Institute of Science Tokyo

Scalable manufacturing processes for solid-state nanopores using Atomic Layer Deposition 545
Mr. Nico Rademacher[1], Ms. Stefanie Linda Stoll [1], Mrs. Anja Leibold [2], Mr. Michael Möller [1], Dr. Christoph Blattert [2], Dr. Jens Bolten [1], Prof. Max Lemme [1]
1. AMO GmbH, 2. Hahn-Schickard-Gesellschaft für angewandte Forschung e.V.

The Impact of Writing Field Stitching on Optical Losses in Electron Beam Fabricated Silicon-on-Insulator Waveguides 547
Mr. Maksim Lipkin[1], Mr. Michael Möller [1], Ms. Lisa Ehlert [1], Dr. Jens Bolten [1], Dr. Rijil Thomas [1], Dr. Stephan Suckow [1], Prof. Max Lemme [2]
1. AMO GmbH, 2. Chair of Electronic Devices, RWTH Aachen University

A Deep Learning-Based Photoresist Shrinkage Correction Method via Fusion of SEM Image and Scanning Parameter Features 549

Ms. Sa Liu [1], Dr. Yanan Zhu [2], Mr. Jiebin Niu [3], Prof. Diwei Zhou [4], Dr. Fuqin Deng [1], Prof. Zhuming Liu[2]

1. School of Electronics and Information Engineering,Wuyi University, 2. Institute of Semiconductors, Guangdong Academy of Sciences, 3. Institute of Microelectronics of the Chinese Academy of Sciences, 4. School of Science, Loughborough University

Fabrication and Nanoscale Characterization of Sidewall Roughness in SOI Waveguides 551

Dr. Magdalena Ulmeanu[1], Dr. Kate Stokes [1], Dr. Marta Kocun [2], Dr. Roger Proksch [2], Dr. Vlad Korolkov [3], Dr. Luis Perdigao [3], Dr. Jason Li [2], Dr. Gabriele Selvaggio [2], Mr. Zhong Ren [1]

1. Oxford Instruments Plasma Technology, 2. Oxford Instruments Asylum Research, 3. Oxford Instruments NanoAnalysis

Fabrication of hierarchical structures in a greyscale positive photoresist by applying two lithography methods in a single resist film 553

Dr. Christine Schuster [1], Dr. Anja Voigt[1], Dr. David Kuhness [2], Ms. Christine Prietl [2], Dr. Matej Goraus [3], Mr. Daniel Mrena [3], Prof. Dusan Pudis [3], Dr. Arne Schleunitz [1], Mrs. Gabi Grützner [1], Mr. Markus Postl [2]

1. micro resist technology GmbH, 2. Joanneum Research Forschungsgesellschaft mbH, 3. University of Zilina

200 kV E-beam Lithography for Patterning Thick Resist 555

Dr. Ying Tran[1], Dr. Kian Shen Kiang [1], Mr. Hitoshi Kato [2], Mr. Ryo Matsui [2], Mr. Yukinori Aida [2], Prof. Martin Charlton [1]

1. University of Southampton, 2. JEOL Ltd

Large-Scale Integrated Visible/Near-Infrared Multi-Channel Polarizer based on Sub-wavelength Metal Grating 557

Ms. Kangping Liu[1], Mr. Jinyu Guo [1], Mr. Wentao Yuan [1], Mr. Shuoqiu Tian [1], Mr. Hao Quan [1], Mr. Qiucheng Chen [1], Ms. Qingxin Wu [1], Ms. xunjia Zhao [1], Prof. Yifang Chen [1]

1. Fudan university

High Resolution Electron Beam Lithography for 10 nm Zone Plates with ultra-high aspect ratio 559

Ms. Qingxin Wu[1], Mr. Qiucheng Chen [1], Mr. Hao Quan [1], Ms. xunjia Zhao [1], Mr. Wentao Yuan [1], Mr. Shuoqiu Tian [1], Mr. Jinyu Guo [1], Ms. Kangping Liu [1], Prof. Yifang Chen [1]

1. Fudan university

Ultra high resolution and dense SiO2 gratings by electron beam lithography and dry-etch 561

Mr. Sheng Tao[1], Prof. Yifang Chen [1], Mr. Shuoqiu Tian [1], Mr. Wentao Yuan [1], Mr. Jinyu Guo [1], Ms. Kangping Liu [1]

1. Fudan university

Ultrafast Single Germanium Nanowire Photodetectors 563

Dr. Ahmad Echresh[1], Mr. Mohd Saif Shaikh [2], Mr. mircea-traian catuneanu [2], Prof. Manfred Helm [1], Dr. Shengqiang Zhou [1], Prof. Artur Erbe [1], Dr. Lars Rebohle [1], Prof. Kambiz Jamshidi [2], Dr. Yonder Berencen [1], Dr. Yordan M. Georgiev [1]

1. Helmholtz-Zentrum Dresden-Rossendorf (HZDR), 2. Technische Universität Dresden

Substantial Ron,sp Reduction in a 1.2 kV SiC DMOSFET Using a Double-Epi Drift Layer 565

Mr. Seung wan Jung[1]

1. Pusan National University

Development of a uniform cell dispersion structure in microfluidic channels with low cell loss 567

Mr. Takumi Yamada[1], Mr. Akihito Kimura [1], Dr. Maho Kaminaga [1], Dr. Akira Kotani [1]

1. National Institute of Technology (KOSEN) Toyota College

3D-Printed Microfluidic Device for Biological Application 569
Mr. Amlan Ashish[1], Prof. Gorachand Dutta [1]
1. Indian Institute of Technology Kharagpur

Tattoo Electrodes for Comfortable and Reliable Masticatory EMG Monitoring 571
Ms. Núria Termes Español[1], Ms. Eva Casals [1], Ms. Yolanda Castillo [2], Prof. Raimon Jané [2], Ms. Rosa Villa [1], Mr. Anton Guimerà-Brunet [1], Ms. Gemma Gabriel [1]
1. Institute of Microelectronics of Barcelona (IMB-CNM, CSIC), 2. Universitat Politècnica de Catalunya - BarcelonaTech (UPC)

Exploiting the dewetting instability of thin Ge films to develop a novel photonic platform 573
Dr. Sonia Freddi[1], Dr. Nicoletta Granchi [2], Dr. Alessia Arrigoni [3], Mr. Michele Gherardi [4], Dr. Benedetta Squeo [3], Mr. Raffaele Giani [4], Dr. Alexey Fedorov [1], Dr. Laura Pasquardini [5], Dr. Lia Vanzetti [6], Prof. Maria Antonietta Vincenti [7], Dr. Mariacecilia Pasini [3], Prof. Francesca Intonti [2], Dr. Monica Bollani [1]
1. Institute of Photonic and Nanotechnology (IFN) - CNR, 2. LENS and Department of Physics and Astronomy, University of Florence, 3. SCITEC-CNR, 4. Politecnico di Milano, 5. Indivenire s.r.l., 6. Center for Sensors and Devices, Fondazione Bruno Kessler, 7. Università degli studi di Brescia

Mechanically robust spin-on-glass packaging of hydrogenated amorphous silicon for harsh environment applications 575
Mr. Junhwa Seong[1], Dr. Younghwan Yang [1], Mr. Youngsun Jeon [1], Prof. Junsuk Rho [1]
1. Pohang University of Science and Technology

Dynamic Electrical Conductivity of Ni-P/Nylon Yarns with Different Twist Number for Weavable Device 577
Mr. Takumi Suda[1], Mr. Kazuhiro Shibata [1], Dr. Tomoyuki Kurioka [1], Prof. Katsunari Sato [2], Prof. Chun-Yi Chen [1], Ms. Nao Yoshida [2], Prof. Tso-Fu Mark Chang [1], Prof. Hiromichi Kurosu [2], Prof. Masato Sone [1]
1. Institute of Science Tokyo, 2. Nara Women's University

Crystalline atomic layer–dielectric hybrid metasurfaces for high-efficiency visible metaphotoncis 579
Mr. Junhwa Seong[1], Dr. Younghwan Yang [1], Mr. Youngsun Jeon [1], Prof. Junsuk Rho [1]
1. Pohang University of Science and Technology

Volatile Threshold Switching Characteristics of TiN/TaOx/TiN Selector Devices 581
Ms. Zohreh Hajiabadi[1], Mr. Aiden Graham [1], Mr. Alexander-Hanyu Wang [1], Dr. Mari Napari [2], Prof. Dimitra Georgiadou [1], Prof. David Thomas [1], Prof. Harold Chong [1], Dr. Firman Simanjuntak [1]
1. University of Southampton, 2. King's College London

Silicon-based metasurface polarizer supporting quasi-bound states in the continuum 583
Prof. Maria Antonietta Vincenti [1], Dr. Luca Fagiani [2], Dr. Luca Bolzonello [3], Dr. Johann Osmond [3], Mr. Michele Gherardi [4], Dr. Sonia Freddi [5], Prof. Domenica de Ceglia [1], Prof. Niek van Hulst [3], Dr. Monica Bollani[6]
1. Università degli studi di Brescia, 2. Physic Department of Milano Politecnico, Milano, 20133, Italy, 3. ICFO, The Barcelona Institute of Science and Technology, Barcellona, 08860, Spain, 4. Politecnico di Milano, 5. IFN-CNR, 6. Institute of Photonic and Nanotechnology (IFN) - CNR

Effect of excitation wavelength on micro-Raman thermometry for suspended silicon MEMS structures 585
Dr. Masaki Shimofuri[1], Mr. Kanta Fujiwara [1], Dr. Amit Banergee [1], Dr. Jun Hirotani [1], Prof. Toshiyuki Tsuchiya [1]
1. Kyoto University

High-performance structures with photoimageable thick film pastes in low temperature cofiring ceramics for mmWave packages 587
Ms. Lynn Möhring[1], Mr. Martin Ihle [1], Ms. Birgit Manhica [1], Dr. Stefan Körner [1], Dr. Uwe Partsch [1], Dr. Peter Uhlig [2], Mr. Enrico Tolin [2]
1. Fraunhofer Institute of Ceramic Technologies and Systems IKTS, 2. IMST GmbH

Electrical Behavior of Rectifying and Ohmic Contacts on Lightly n-Doped Germanium 589
Mr. Michele Gherardi[1], Dr. Sonia Freddi [2], Mr. Francesco Scali [1], Dr. Carlo Zucchetti [1], Prof. Federico Bottegoni [1], Prof. Giovanni Isella [1], Prof. Franco Ciccacci [1], Prof. Marco Finazzi [1], Dr. Alexey Fedorov [2], Dr. Monica Bollani [3]
1. Politecnico di Milano, 2. IFN-CNR, 3. Institute of Photonic and Nanotechnology (IFN) - CNR

Fabrication of Titanium-based Microneedles Array Using Wire Electrical Discharge Machining 592
Mr. Min Chul Shin[1], Mr. Ji Hwan Han [1], Prof. Gyu Man Kim [1]
1. Kyungpook National University

Polymer-based MEMS microcantilever and microfluidic system for biochemical detection 594
Dr. Pooja P. Kanade[1], Dr. Paul T. Baine [2], Dr. Briliant Adhi Prabowo [1], Dr. Arthur Lipinski [3], Dr. Jason Wiggins [1], Prof. Robert M. Bowman [1]
1. School of Mathematics and Physics, Queen's University Belfast, 2. School of Electronics, Electrical Engineering and Computer Science, Queen's University Belfast, 3. Research Fellow

Two-photon polymerization as mastering tool for nanoimprint lithography to produce microfluidic test devices 596
Mr. Stjepan Perak [1], Ms. Sonja Kopp [2], Ms. Viktorija Jonaityte [2], Ms. Marta Bonora [3], Dr. Michael Muehlberger [2], Prof. Francesco Moscato [3], Dr. Markus Lunzer[1]
1. UpNano GmbH, 2. PROFACTOR GmbH, 3. Center for Medical Physics and Biomedical Engineering, Medical University of Vienna

Engineered magnetic quantum dot nanoprobes for multiplexed, equipment-free Alzheimer's diagnosis at point-of-care 598
Dr. Anjum Qureshi [1], Dr. Javed H. Niazi[1]
1. SUNUM - Sabanci University Nanotechnology Research & Application Center

Quality Factor Engineering in NIR Optical Metasurfaces Using Ge2Sb2Te5 and Graphene 600
Dr. Seyed As'ad Amirhosseini [1], Mr. Daniyal Khoshmaram[2]
1. Department of Electrical and Computer Engineering, Isfahan University of Technology, Isfahan, Iran, 2. Department of Electrical Engineering, Amirkabir University of Technology, Tehran, Iran

Anomalous mapping between the Surface Charge and Ionic Conductance in Narrow Confinements 602
Mr. Debmalya Roy[1], Prof. Suman Chakraborty [1]
1. Indian Institute of Technology Kharagpur

Ultrasensitive, AI-integrated cyber-physical system for patient-specific CYFRA21-1 biomarker quantification 604
Mr. Biswadeep Roy[1], Dr. Abhisek Maikap [1], Prof. Soumen Das [1], Prof. Suman Chakraborty [1]
1. Indian Institute of Technology Kharagpur

Broadband Transmission Measurement for Ta2O5 Photonic Crystal Waveguide 606
Ms. Wenjie Wang[1], Prof. Martin Charlton [1]
1. University of Southampton

Fabrication of planar nanostructured SiC microelectrode arrays for long-lifetime neural interfaces **608**
Dr. Fabrice Iacovella[1], Dr. Gwenaell Pound-Lana [1], Mr. Lucas Labbe [1], Mr. Sébastien Labau [1], Dr. Camille Petit-Etienne [1], Mr. Andrei Uvarov [2], Dr. Scott Greenhorn [3], Mr. Marcin Zielinski [4], Prof. Konstantinos Zekentes [3], Prof. Edwige Bano [3], Dr. Cécile Gourgon [1], Prof. Jumana Boussey [1]
1. Université Grenoble Alpes, CNRS, CEA/LETI-Minatec, Grenoble INP, LTM, 17 Rue des Martyrs, Grenoble 38054, France, 2. Plasma-therm Europe, Bernin, 38190, France, 3. Centre de Radiofréquences, Optique et Micro-nanoélectronique des Alpes, Grenoble, 38016, France, 4. NOVASiC, Le Bourget du Lac, 73375, France

Sub-wavelength grating polarizers in 1-D array focal plane for ultraviolet polarimetric detection **610**
Mr. Jinyu Guo[1], Ms. Kangping Liu [1], Ms. Qingxin Wu [1], Mr. Qiucheng Chen [1], Mr. Hao Quan [1], Ms. xunjia Zhao [1], Prof. Yifang Chen [1]
1. Fudan university

Design and Fabrication of a 100mm-Diameter Pillar Metalens for High-Performance Mid-Infrared Imaging **612**
Ms. Weilin Jin[1], Mr. Gaochen Dong [1], Ms. Zixuan Wang [1], Dr. Kian Shen Kiang [1], Prof. Jize Yan [1]
1. University of Southampton

Quantum Dot-Low Dimensional Material Hybrid Heterostructures for Physically Unclonable Optical Tags **614**
Mr. Yueyu Guo[1], Ms. Syeda Ramsha Ali [1], Dr. Nema Abdelazim [2]
1. School of Electronics and Computer Science, University of Southampton, Southampton SO17 1BJ, United Kingdom, 2. University of Southampton

Modelling the Heat Distribution in Organ-on-a-Chip Systems Using Integrated Microheaters **615**
Mr. Gabriel Ferreira[1], Dr. Patrícia Sousa [2], Prof. Rui Lima [1], Prof. Susana Catarino [1], Prof. Graça Minas [1]
1. University of Minho, 2. International Iberian Nanotechnology

Microfabricated Light Pipe for Sustainable and Lithography-Free SPR Sensor **617**
Dr. Briliant Adhi Prabowo[1], Dr. Pooja P. Kanade [1], Dr. Fatemeh Moradiani [1], Dr. Arthur Lipinski [1], Dr. Paul T. Baine [2], Dr. Jason Wiggins [1], Prof. Robert M. Bowman [1]
1. School of Mathematics and Physics, Queen's University Belfast, 2. School of Electronics, Electrical Engineering and Computer Science, Queen's University Belfast

Dual-Path Anomaly Detection for Semiconductor Equipment: Toward Sensor-Level Intelligence in Digital Twin Manufacturing **619**
Mr. Joon Soo Kim[1]
1. SUNG KYUN KWAN University / Samsung Electronics

Real-time lesion location detection system using Mu-metal and Hall sensor **621**
Dr. Woojin Yun [1], Mr. Gapseop Sim[1], Prof. Hyeinjune Kim [2], Dr. Seung-Hwan Jung [3]
1. National Nanofab Center, 2. Seoul National University of Science and Technology, 3. GRIT Custom-IC

A Study on Focus Control Improvement in Response to Wafer Table Edge Wear in Photolithography Equipment **623**
Mr. Kyunghwan Joo[1], Mr. Kwang Hoon Lee [2], Prof. Jae Wook Jeon [3]
1. SUNG KYUN KWAN University / Samsung Electronics, 2. Samsung Electronics, 3. Sungkyunkwan University

Automated Silicon Wafer Handling for Gravity Effect Compensation in High-Precision Horizontal Metrology **625**
Mr. CESAR PEREZ DOMINGUEZ[1], Dr. JUAN TRUJILLO-SEVILLA [2], Dr. CARMELO MILITELLO-MILITELLO [3]
1. Wooptix, 2. WOOPTIX, 3. Universidad de La Laguna

A 10.94bit resolution measurement circuit for resistive sensors 627
Dr. xiaoming teng[1], Prof. yufeng zhang [1], Mr. haoyu liang [1]
1. MEMS Center, Harbin Institute of Technology

Device Variation Effect Simulation for SnOx Memristor-based Neural Networks 629
Mr. Aiden Graham[1], Ms. Zohreh Hajiabadi [1], Mr. Alexander-Hanyu Wang [1], Prof. Dimitra Georgiadou [1], Dr. Ruomeng Huang [1], Dr. Firman Simanjuntak [1]
1. University of Southampton

Eco-Friendly Functionalization of Graphene via Spark Ablation for Enhanced NO2 Gas Sensing Applications 631
Dr. Mudassir Husain[1], Dr. Leandro Sacco [2], Prof. Sten Vollebregt [3]
1. PhD, 2. VSParticle, 3. Associate Professor

Enhancing Overlay Accuracy through Transformation of Overlay Outliers caused by Wafer Local Defocus in Photolithography Scanner Calibration 633
Mr. Kwang Hoon Lee[1], Prof. Won Bo Lee [2]
1. Seoul National University / Samsung Electronics, 2. Seoul National University

Gas Sensors Based on MoS_2 Quantum Dots Deposited via Drop-Casting for Environmental Monitoring on Microfabricated Platforms 635
Ms. Andrea Carolina Villalvazo-Hidalgo[1], Dr. Orfil González-Reynoso [1], Ms. Martha Angelica Hidalgo-Ríos [1], Dr. Gregorio Guadalupe Carbajal-Arizaga [1], Dr. Mario Alberto García-Ramírez [1]
1. Universidad de Guadalajara

Real-Time Wireless Tremor Tracking System with V-Groove Crack Sensor 637
Mr. Jonghyeon Woo[1], Mr. JeongSik Noh [1], Prof. Jongsung Park [1]
1. Kyungpook National University

Microscope-based Multi-Analyte-Reflectance-Spectroscopy (μ-MARS) for multiplexed label free monitoring of immunoreactions 639
Dr. Grigorios Zisis [1], Dr. Dimitra Tsounidi [1], Dr. Georgios Koukouvinos [1], Dr. Panagiota Petrou [1], Dr. Ioannis Raptis[1]
1. NCSR Demokritos

CNFET fabrication for NO2 gas sensor recovery with local electrode heating 641
Ms. Ines Kraiem[1], Dr. Cosmin Ioan Roman [1], Mr. Andri Sigron [1], Dr. Miroslav Haluska [1], Prof. Christofer Hierold [1]
1. ETH Zürich

Selective Electrochemical Aptasensor Using Methylene Blue for Pseudomonas aeruginosa Detection in Mixed Bacterial Cultures 643
Ms. Somayeh Maghsoomi Taramsari[1]
1. University for Continuing Education Krems

Water-soluble holographic color prints from UV to visible for sustainable optical security device 645
Ms. Hyunjung Kang[1], Mr. Hongyoon Kim [1], Prof. Junsuk Rho [1]
1. Pohang University of Science and Technology

Dual functional filmy device for heat dissipation and power generation based on Bi2Te3 array with topological surface 648
Dr. YiHeng Zhao[1], Mr. Mingxue Li [1], Prof. yufeng zhang [2]
1. MEMS Center, Harbin Institute of Technology, Harbin 150001, China, 2. MEMS Center, Harbin Institute of Technology

A Modeling Study on Inorganic Chalcogenide Transport Layers in Sn-Based Perovskite Solar Cells 650
Mr. Daniyal Khoshmaram[1]
1. Department of Electrical Engineering, Amirkabir University of Technology, Tehran, Iran

Conformally-coated titanium carbide on structured pyrolytic carbon electrodes for lithium sulphur batteries 652
Mr. Owen Bell[1], Dr. Daniel Ho [2], Mrs. Nadira Palakkool [2], Dr. Mike Taverne [2], Dr. Kevin Chung-Che Huang [3], Prof. Vincent Barrioz [2], Dr. Yongtao Qu [2], Dr. Johnathan Mar [4], Dr. Tam Ho [2], Dr. Christopher Jones [5], Mr. Giray Kartopu [2]
1. PhD Student, 2. Northumbria University, 3. Southampton University, 4. Newcastle University, 5. Bristol University

A deeper dive into droplet and dust dynamics on commercially available solar panels 655
Mr. Anirban Roy[1], Mr. Rahul Roy [1], Dr. Chirodeep Bakli [1]
1. Indian Institute of Technology Kharagpur

All-in-one Microfluidic Platform for Single-Cell Environmental Phenotyping of Chlamydomonas reinhardtii 657
Mr. Alexandre Chargueraud[1], Dr. Lars Kool [2], Ms. Eliora Israelievitch [3], Dr. Alix Boulouis [3], Dr. Jacques FATTACCIOLI [4]
1. CPCV, Département de Chimie, Ecole Normale Supérieure, PSL Université, Sorbonne Université, CNRS, 75005 Paris, France, 2. Institut Pierre-Gilles de Gennes pour la Microfluidique, Paris, 75005, France, 3. Laboratoire de Biologie du Chloroplaste et Perception de la lumière chez les microalgues of the Institut de Biologie Physico-Chimique, Sorbonne Université, Paris, 75005, France, 4. CPCV, Département de Chimie, Ecole Normale Supérieure, PSL Université, Sorbonne Université, CNRS

Plenary 4 - Prof Shinichi Saito

Why Micro is different from Macro? A Challenge towards Macroscopic Quantum Technologies 660
Dr. Shinichi Saito[1]
1. Hitachi

Plenary 5 - Prof Mariana Medina Sanchez

Medical Microrobots with Functional Nanomaterials for Precision Women's Healthcare 663
Prof. Mariana Medina Sanchez[1]
1. nanoGune

Oral Session 2A: Nanoimprint and alternative lithography

Comparison of 2 processes based on NIL and lift-off for the fabrication of thick nano antennas for solar PV-TE applications 665
Dr. Jean-Baptiste Doucet[1], Dr. Franck Carcenac [1], Dr. Leopold Boudier [1], Dr. Inès Revol [1]
1. LAAS-CNRS

Fine silver wiring using replica mold with light-shielding film 667
Mr. Takumi Ashida[1], Prof. Jun Taniguchi [1]
1. Tokyo University of Science

Single-nm Mask Writing for Nanoimprint Lithography, as an Energy-Efficient Alternative to EUV 669
Dr. James Owen[1], Mr. Robin Santini [1], Dr. John Randall [1]
1. Zyvex Labs

Optimization of grayscale direct-write laser lithography for the fabrication of large-area 2.5D molds for nanoimprint lithography 671
Dr. Peng Tian[1], Dr. Maria Szola [1], Dr. Dimitrios Kazazis [1], Dr. Yasin Ekinci [1]
1. Paul Scherrer Institute (PSI)

Advanced Patterning For Smart Optical Devices: Integrating Inkjet Coating with Nanoimprinting for Precise Height Control and Minimal Residual Layers 673
Mrs. Andrea Kronawitter[1], Mrs. Johanna Rimböck [1], Mrs. Lisa Vsetecka [1], Mrs. Thomas Achleitner [1], Mrs. Patrick Schuster [1], Mrs. Brid Connolly [2], Mr. Martin Sczyrba [3], Mr. Andreas Frangen [2]
1. EV Group, 2. Tekscend Photomasks Germany GmbH, 3. AMTC Dresden

Exploring water-soluble polymeric stamps for ultraviolet light nano-imprint lithography 675
Mr. Haohui Yang[1], Mr. Anmol Gupta [1], Prof. Steffen Strehle [1]
1. Techische Universität Ilmenau

Fabrication and Evaluation of Curved Mirror for Co-packaged optics Using Photo Nanoimprint Technology 677
Ms. Maaya Watanabe[1], Dr. Fumi Nakamura [2], Mr. Taro Itatani [2], Prof. Joji Maeda [1], Dr. Takeru Amano [2]
1. Tokyo University of Science, 2. National Institute of Advanced Industrial Science and Technology (AIST)

Advances in parallelization of thermal scanning probe lithography and large-area patterning 679
Ms. Julia Stark[1], Dr. Jana Chaaban [1], Mr. Kartik Buddha [1], Dr. Fabian Koenemann [1], Dr. Emine Çağın [1]
1. Heidelberg Instruments

Oral Session 2B: Photonics, Photonic structures and Metasurfaces

Sustainable manufacturing of optical metasurfaces for imaging, sensing and display 682
Prof. Junsuk Rho[1]
1. Pohang University of Science and Technology

A Novel Manufacturing Platform for Large-diameter Si Metalens using Deep-UV Lithography 683
Dr. Kai Sun[1], Dr. Xingzhao Yan [2], Mr. Jordan Scott [1], Dr. James Monks [3], Dr. Jun-Yu Ou [1], Prof. Otto Muskens [1]
1. Physics and Astronomy, University of Southampton, 2. Optoelectronics Research Centre, University of Southampton, SO17 1BJ, UK, 3. Teledyne Qioptiq Ltd

Understanding 3D Structural Control in Metasurface-Based Holographic Lithography 685
Mr. Jeevan Rois[1], Mr. Zesen Zhou [1], Dr. Matias Kagias [1]
1. Lund University

Fabrication of Substrates with Plasmonic Gold Nanostructures for Cellular Membrane Rupture 687
Mr. Christian Einsiedler[1], Dr. Franziska Marie Esmek [2], Mr. Rukan Nasri [3], Dr. Irene Fernandez [3]
1. University of Hamburg, Hamburg Center for Ultrafast Imaging, 2. University of Hamburg/Hamburg Center for Ultrafast Imaging, 3. UHH/CUI

Printable Spin-Multiplexed Metasurfaces for Ultraviolet Holographic Displays 689
Ms. Hyunjung Kang[1], Mr. Hongyoon Kim [1], Prof. Junsuk Rho [1]
1. Pohang University of Science and Technology

Embedded-Holey Metasurfaces for Enhanced Mechanical Robustness and Integration Compatibility 691
Ms. Zixuan Wang[1], Dr. Chuang Sun [1], Ms. Weilin Jin [2], Dr. Jun-Yu Ou [3], Dr. Kian Shen Kiang [2], Prof. Jize Yan [2]
1. School of Electronics and Computer Science, University of Southampton, Southampton SO17 1BJ, United Kingdom, 2. University of Southampton, 3. Physics and Astronomy, University of Southampton

Novel UV-curable organic-inorganic polymers for micro-optical and photonic components with enhanced reliability 693
Dr. Maria Russew [1], Dr. Alexander Plucinski[1], Dr. Thomas Wiglenda [1], Mr. Johannes Wolf [1], Dr. Arne Schleunitz [1], Mrs. Gabi Grützner [1]
1. micro resist technology GmbH

Oral Session 2C: Photonics and Optoelectronics

Monolithic Integration of GeV Centers in Ring Waveguides for Quantum Light Emission 696
Dr. Fatemeh Moradiani[1], Mr. Arran Ashfield [2], Dr. Arthur Lipinski [1], Prof. Robert M. Bowman [3], Dr. Hamidreza Siampour [4]
1. Research Fellow, 2. PhD Student, 3. Professor, 4. Lecturer

Microsphere-assisted generation of localized optical emitters in 2D hexagonal boron nitride 698
Ms. XILIANG YANG[1], Dr. Sabina Caneva [1], Prof. Peter Steeneken [1], Prof. Dong Hoon Shin [2]
1. Delft University of Technology, 2. Korea University

Chip-scale infrared Fourier-transform spectrometer based on nano-opto-electro-mechanical systems 700
Dr. Bingrui Lu[1], Dr. Babak Vosoughi Lahijani [1], Dr. Søren Engelberth Hansen [1], Dr. Thor August Schimmell Weis [1], Dr. Marcus Albrechtsen [1], Dr. Ali Nawaz Babar [1], Dr. Michael Juhl [1], Dr. Christian Anker Rosiek [1], Mr. Jesper Laurberg Sand [1], Mr. Bjarke Almer Frederiksen [1], Mr. Mathias Linde Holst Korsgaard [1], Mr. Nikolaj Balslev Hougs [1], Dr. Konstantinos Tsoukalas [1], Dr. Guillermo Arregui Bravo [1], Prof. Søren Stobbe [1]
1. Technical University of Denmark

Hydrophobic and Sticky Silver-Decorated Nanoimprinted ZnO Nanograss Substrates for Enhanced SERS Performance 702
Mr. Kuan-Ting Kuo [1], Prof. Wen-Huei Chang [2], Prof. Hsiang Chen [3], Mr. Jyun-Jie Chen [1], Prof. Chun-Hung Lin[4]
1. Department of Photonics, National Cheng Kung University, 2. Department of Applied Chemistry, National Pingtung University, 3. Department of Applied Materials and Optoelectronic Engineering, National Chi Nan University, 4. National Cheng Kung University

Antireflection of near-infrared light using a moth-eye structure film 704
Mr. Kei Hirata[1], Prof. Jun Taniguchi [1]
1. Tokyo University of Science

One-Step Printable Fabrication of Tantalum Pentoxide Metasurfaces for UV–Visible Optics 706
Ms. Eunji Lee[1], Prof. Junsuk Rho [2]
1. POSTECH, 2. Pohang University of Science and Technology

Red Emitting DBR Laser Array with 0.1 nm Wavelength Spacing Defined by Direct Write Ebeam Lithography **708**
Dr. Olaf Brox[1], Dr. Jörg Fricke [1], Dr. Ralph-Stephan Unger [1], Dr. André Maaßdorf [1], Dr. Anna Mogilatenko [1], Mr. Maximilian Beier [1], Dr. Heike Christopher [1], Dr. Andrea Knigge [1], Dr. Hans Wenzel [1]
1. *Ferdinand-Braun-Institut gGmbH*

Anti-reflection and radiative cooling bifunctional polymer film fabricated via nanoimprint lithography and in situ boehmite formation by hydrothermal treatment **710**
Ms. Nefeli Dimogerontaki[1], Dr. Nikolaos Mattheakakis [2], Dr. Nikos Papanikolaou [3], Dr. Nikolaos Kehagias [2]
1. *Department of Physics, School of Applied Mathematical and Physical Sciences National Technical University of Athens, Zografou Campus, GREECE,* ***2.*** *NCSR Demokritos, Institute of Nanoscience & Nanotechnology, P. Grigoriou 27 & Neapoleos Str., 15341 Ag. Paraskevi, Greece,* ***3.*** *NCSR Demokritos*

Oral Session 2D: Information Communication Technologies

Fabrication and Analysis of Self-Rolled-Up Polymer Ribbon Structure Based on Photosensitive Polyimide and Mechanical Debonding **713**
Dr. HyungDal Park [1], Dr. Seonho Seok[2], Dr. Jinseok Kim [1]
1. *Korea Institute of Science and Technology,* ***2.*** *University-Paris-Saclay*

Semiconductor Quantum Dots: From Tailored Synthesis to Advanced Sensing and Biosensing Applications **715**
Dr. Javed H. Niazi[1]
1. *SUNUM - Sabanci University Nanotechnology Research & Application Center*

Adaptive Adhesion through Bio-Inspired Interlocking Micropatterns for Harsh Environments **716**
Mr. Marco Bruno[1], Mr. Luigi Portaluri [2], Prof. Massimo De Vittorio [3], Prof. Stanislav Gorb [4], Prof. Michele Scaraggi [3]
1. *Istituto Italiano di Tecnologia (IIT),* ***2.*** *Department of Innovation Engineering, University of Salento, Lecce, LE, 73100, Italy,* ***3.*** *Center for Biomolecular Nanotechnologies, Istituto Italiano di Tecnologia (IIT), 73010 Arnesano, LE, Italy,* ***4.*** *University of Kiel*

Single-Charge Detection in a Room Temperature Single-Electron Memory **718**
Mr. Jingbo Chen[1], Dr. Wenkun He [1], Mr. Kai-Lin Chu [1], Dr. Mervyn Jones [1], Prof. Zahid Durrani [1]
1. *Imperial College London*

Design and characterization of surface acoustic wave on thin film lithium niobate on insulator for acousto-optic applications **720**
Ms. Fatemeh Arefi[1], Dr. Ivan Prieto [1], Mr. Florian Hartmann [2], Mr. Silvan Stettler [2], Dr. Homa Zarebidaki [1], Mr. Hamed Sattari [1], Dr. Dara Bayat [1], Prof. Guillermo Villanueva [2], Dr. Michel Despont [1]
1. *CSEM,* ***2.*** *NEMS, EPFL*

Nanofabrication of shadow masks for josephson-junction quantum devices **722**
Dr. Rucha Deshpande[1], Prof. Rafael Taboryski [1], Prof. Thomas Sand Jespersen [1], Dr. Sabbir Ahmed Khan [2]
1. *Technical University of Denmark,* ***2.*** *Danmarks Nationale Metrologiinstitut*

Oral Session 3A: UV, EUV, and two-photon lithography

EUV interference lithography at PSI: pushing the limits of resolution of next generation photolithography 725
Dr. Dimitrios Kazazis[1], Mr. Benjamin Bächtold [1], Mr. Stephan Maag [1], Mr. Marco Schneider [1], Mr. Achim Ammon [1], Mr. Emanuele Japichino [1], Mr. Lars Heller [1], Mr. Thierry Lachat [1], Mr. Michael Peters [1], Mr. Peter Heimgartner [1], Mrs. Michaela Vockenhuber [1], Mr. Markus Kropf [1], Mr. David Piguet [1], Dr. Yasin Ekinci [1], Dr. Iacopo Mochi [1]
1. Paul Scherrer Institute (PSI)

Towards sub-nm roughness in 3D topography for reflective X-ray focusing optics 727
Dr. Giulia Malvicini[1], Prof. Helmut Schift [1]
1. Paul Scherrer Institute (PSI)

Quantifying and overcoming wafer distortion on bonded wafers for deep-UV lithography 730
Dr. Jeroen Bolk [1], Dr. Sander Reniers[1], Mr. Stacey Martina [1], Dr. Sara Sequeira [1], Ms. Sruja Dave [1], Prof. Kevin Williams [1], Dr. Yuqing Jiao [1]
1. Eindhoven University of Technology

Pushing the Boundaries: in situ Development and Multi-Material Exchange for Two-Photon 3D Printing 732
Mr. Pratyaksh Yemulwar[1], Mr. Man-Ho Wong [1], Mr. Saurabh Karle [1], Mr. Josua Zschleile [1], Dr. Robert Kirchner [1]
1. HETEROMERGE Gmbh

Oral Session 3B: Advanced Nanofabrication I

Fabrication of arsenic-in-silicon single-electron transistors using scanning tunnelling microscopy hydrogen resist lithography 735
Dr. Kieran Spruce[1], Mr. Rajath Ravichandar [1], Dr. Patrick See [2], Dr. Mark Buitelaar [1], Dr. Taylor Stock [1], Prof. Neil Curson [1]
1. University College London, 2. NPL

Tailoring Vertical Gradients in Thin Films: Design and Fabrication 737
Dr. Xiangyu Chen[1]
1. Beihang University

Anti-virus performance of Si nanopillar array mimicking cicada wing surface 739
Prof. Takeshi Ito[1], Dr. Hitoshi Ishiguro [2], Prof. Tomohiro Shimizu [1], Prof. Shoso Shingubara [1]
1. Kansai University, 2. Kanagawa Institute of Industrial Science and Technology

3D structured local thin film deposition by Micro Direct Atomic Layer Deposition (µDALP™) 741
Mrs. Mira Baraket [1], Mr. Jesper Navne[2]
1. ATLANT 3D, 2. PhD

Oral Session 3C: Sustainable Devices and Process Technology

Shaping of a bio-sourced AESO polymer for micro-encapsulation purposes 743
Ms. Estelle Lu[1], Mr. Bruno Bresson [2], Dr. Jacques FATTACCIOLI [1]
1. CPCV, Département de Chimie, Ecole Normale Supérieure, PSL Université, Sorbonne Université, CNRS, 2. Laboratoire Sciences et Ingénierie de la Matière Molle, ESPCI Paris

Layer-by-layer functionalization of cotton fabric for enhanced electrokinetic energy harvesting 745
Mr. Aditya Patwari[1], Dr. Chirodeep Bakli [1], Prof. Suman Chakraborty [1]
1. Indian Institute of Technology Kharagpur

Process development for improved passivation in IBC Solar Cells 747
Mr. Jens Munk Nielsen[1], Dr. Rasmus Schmidt Davidsen [2], Prof. Stephan Sylvest Keller [1]
1. National Centre for Nano Fabrication and Characterization, DTU Nanolab, Technical University of Denmark, 2. Department of Electrical and Computer Engineering, Aarhus University

Inkjet printing of stealth nanobeacons 749
Dr. Akinobu Yamaguchi[1], Dr. Toshiya Yasunaga [2], Prof. Kyoko Namura [3], Prof. Motofumi Suzuki [3], Mr. Takao Fukuoka [3]
1. Toyo University, 2. Aichi Gakuin University, 3. Kyoto University

Oral Session 3D: Devices and Systems

Selective Laser Etching as a Key Enabler of Custom Silica-Based AFM Probes 752
Mr. koutayba saada [1], Mr. david bourrier [1], Ms. Juliette Lignieres [1], Dr. Etienne Dague [1], Dr. Laurent Malaquin[1]
1. LAAS-CNRS, Université de Toulouse, CNRS, Toulouse, France

Scalable Piezo-Optomechanical Transducer for Optical Readout of a Superconducting Qubit 754
Dr. Linh Nguyen[1]
1. QphoX

Nonlinear resonators based on nano optomechanical metamaterials 756
Ms. Ting Hou[1], Mr. Lifeng Bao [1], Dr. Jun-Yu Ou [2], Dr. Xin Zhou [3], Prof. Nobuhiko Nishiyama [4], Dr. Yoshishige Tsuchiya [1]
1. University of Southampton, 2. Physics and Astronomy, University of Southampton, 3. Université de Lille, 4. Institute of Science Tokyo

Carbon-based contacts for integrated nanoelectromechanical switches 758
Dr. Jens Bolten[1], Mr. Bartos Chmielak [1], Ms. Lisa Ehlert [1], Dr. Elliott Worsey [2], Ms. Yingying Li [3], Prof. Frank Niklaus [3], Prof. Dinesh Pamunuwa [2], Dr. Simon Bleiker [3], Prof. Max Lemme [1]
1. AMO GmbH, 2. University of Bristol, 3. Royal Institute of Technology (KTH)

Poster Session 2

Auxiliary-Ring-Assisted Fabrication of Hard X-ray Photon Sieves with Low Resist Wettability 761
Mr. Qiucheng Chen[1], Ms. Qingxin Wu [1], Mr. Hao Quan [1], Ms. xunjia Zhao [1], Mr. Jinyu Guo [1], Ms. Kangping Liu [1], Prof. Yifang Chen [1]
1. Fudan university

Electron beam-Simulation collaborative fabrication of zone plates with gradient duty cycle 763
Ms. xunjia Zhao[1], Mr. Hao Quan [1], Mr. Qiucheng Chen [1], Ms. Qingxin Wu [1], Mr. Wentao Yuan [1], Mr. Shuoqiu Tian [1], Mr. Jinyu Guo [1], Ms. Kangping Liu [1], Prof. Yifang Chen [1]
1. Fudan university

Room temperature Au-Au die bonding in ambient air via N_2 plasma treatment 765
Prof. RYO TAKIGAWA[1], Mr. Yunhan Fan [1], Mr. Kosei Matsunobu [1]
1. Kyushu University

Simulation-guided interpretation of scanning electron microscope images 767
Mr. Jianyao Jin[1], Dr. Timon Fliervoet [2], Dr. Kees Hagen [1]
1. Delft University of Technology, 2. ASML

Manufacturing and testing of ultra-low expansion glass based planar frame resonator 769
Mr. AHMAD ALI[1], Mr. Muhammad Awais Maqbool [1], Dr. Hamza Shakeel [1]
1. *School of Electronics, Electrical Engineering and Computer Science, Queen's University Belfast*

Investigation of Intra-Level Mix-and-Match lithography approach in AR-N 7520new for use in a Mix-and-Match grayscale lithography process 771
Mr. Markus Gottwald[1], Mr. Sebastian Schermer [1], Mr. Ritesh Ambar [1], Ms. Pia Kohlschreiber [1], Dr. Christian Helke [1], Mr. Harry Biller [2], Dr. Mandy Sendel [2], Dr. Danny Reuter [1]
1. *Fraunhofer Institute for Electronic Nano Systems ENAS,* ***2.*** *Allresist GmbH*

Influence of substrate properties and addition of oxygen on the process of reactive ion etching to optimize the nanopatterning of silicon structures 773
Ms. Lenia Böhm[1], Ms. Pia Kohlschreiber [1], Mr. Micha Haase [1], Dr. Christian Helke [1], Dr. Danny Reuter [1]
1. *Fraunhofer Institute for Electronic Nano Systems ENAS*

Interposer Interconnects: An Important Step For Research and Industry 775
Dr. Omesh Kapur[1], Mr. Arvin Mallari [1], Dr. Anushka Gangnaik [2], Ms. Amanda Green [1], Dr. Ibrahim Sari [2], Mr. John Darlington [2], Dr. Liam Boodhoo [1]
1. *School of Electronics and Computer Science, University of Southampton, Southampton SO17 1BJ, United Kingdom,* ***2.*** *University of Southampton*

Nanofabrication of monolithically integrated multilayer metasurfaces via fully CMOS-compatible processes 777
Mr. Yuntian Ye[1], Mr. Hao Peng [1], Dr. Shengqi Yin [2], Prof. Jize Yan [3], Dr. Kian Shen Kiang [2], Dr. Xu Fang [1]
1. *School of Electronics and Computer Science, University of Southampton, Southampton SO17 1BJ, United Kingdom,* ***2.*** *Optoelectronics Research Centre, University of Southampton, SO17 1BJ, UK,* ***3.*** *University of Southampton*

Single-Printed Nb2O5 UV-Visible Metasurfaces for Chiro-Optical Holography 779
Ms. Eunji Lee[1], Prof. Junsuk Rho [2]
1. *POSTECH,* ***2.*** *Pohang University of Science and Technology*

Plasma-induced periodic surface structures on polymeric microfluidic channel sidewalls 781
Dr. Athina S. Kastania [1], Ms. Eleni Stai [1], Mr. Sotiris Mouchtouris [1], Dr. Vassilios Constantoudis [1], Prof. George Kokkoris [2], Dr. Pavlos Tsavalas [3], Dr. Konstantina Mergia [3], Dr. Gerburg Schider [4], Mr. Daniel Borstner [4], Mr. Philipp Melchior [4], Dr. Dieter Nees [4], Dr. Barbara Stadlober [4], Dr. Evangelos Gogolides[1], Dr. Angeliki Tserepi [1]
1. *NCSR Demokritos, Institute of Nanoscience & Nanotechnology, P. Grigoriou 27 & Neapoleos Str., 15341 Ag. Paraskevi, Greece,* ***2.*** *School of Chemical Engineering, National Technical University of Athens, Athens, 157 80, Greece,* ***3.*** *NCSR Demokritos, Institute of Nuclear & Radiological Sciences and Technology, Energy & Safety, Ag. Paraskevi, 153 41, Greece,* ***4.*** *Joanneum Research Forschungsgesellschaft mbH, Weiz, 8160, Austria*

Scalable Multilayer Silicon Anode Architecture with Porosity Control via UV-NIL Roll-to-Plate Process for Enhanced Lithium-Ion Battery Performance 783
Ms. YU JU HAN[1], Ms. Seo Rim Park [1], Mr. Seong Min Yoon [1], Ms. Min Ju An [1], Prof. Yeon Guk Son [1], Prof. Young Tae Cho [1]
1. *Changwon National University, Changwon*

First results on vacuum-gas-controlled metal assisted chemical etching 785
Mr. Bryan Benz[1], Ms. Vahide Hosseini [2], Dr. Georg Umlauf [2], Mr. Toni Sandbrink-Koblenz [3], Dr. David Anderson [3], Dr. Danny Reuter [2], Dr. Christoph Robert Meinecke [2], Dr. Lucia Romano [1]
1. *Paul Scherrer Institute (PSI),* ***2.*** *Fraunhofer Institute for Electronic Nano Systems ENAS,* ***3.*** *memsstar Ltd*

OPTIMIZING RETICLE BASED HIGH THROUGHPUT I-LINE GRAYSCALE PROJECTION LITHOGRAHPHY FOR 3D STRUCTURES 787
Mr. Sebastian Schermer[1], Mr. Stephen DeMoor [2], Mr. Andrew Zanzal [2], Mr. Patrick Reynolds [2], Mr. Jens Bonitz [1], Mr. Jeremy Bieling [3], Dr. Christian Helke [4], Dr. Anja Voigt [5], Dr. Danny Reuter [4]
1. Fraunhofer Institute for Electronic Nano Systems, 2. Benchmark Technologies, 3. Technische Universität Chemnitz, 4. Fraunhofer Institute for Electronic Nano Systems ENAS, 5. micro resist technology GmbH

Ion Beam Planarization using Low-Viscosity, Non-Volatile Containing Polymer Coatings 789
Mr. Lukas Paul Lingenfelder[1]
1. Leibniz-Institut für Oberflächenmodifizierung e.V. (IOM)

The role of surface chemistry and morphology on adhesive wafer bonding 791
Mr. Duarte Silva[1], Dr. Tarni Aggarwal [1], Dr. Yuqing Jiao [1], Dr. Martijn Heck [1]
1. Eindhoven University of Technology

Sub-diffraction-limited nano-texturing on silicon by ultrafast lasers with MHz- burst mode 793
Mr. Pin-Yen Chen [1], Mr. You Yu-Sheng [2], Prof. Yuan-Jen Chang[3]
1. National Taipei University of Technology, Department of Mechanical Engineering, 2. National Taipei University of Technology, Graduate Institute of Manufacturing Technology, 3. National Taipei University of Technology

Fabrication of Micro-Lattice Filters for Particulate and Gas Emission Reduction 795
Ms. Seo Rim Park[1], Mr. Myung Seo Kim [2], Prof. Young Tae Cho [1]
1. Changwon National University, Changwon, 2. Changwon National University, Department of Mechanical Engineering

Microfluidic Devices Based on Deterministic Lateral Flow Displacement for Protein Separation 797
Ms. Nilüfer Tasli[1], Dr. Sadhana Tiwari [1], Dr. Irene Fernandez [2]
1. UHH, 2. UHH/CUI

Evaluation of Inorganic-organic Hybrid Resist Materials with ultrafast coherent high harmonic generation (HHG) EUV system 799
Dr. Hiroki Yamamoto[1]
1. National Institutes for Quantum Science and Technology (QST)

Graphene Electrodes for In-plane Electrochemical growth of TMDCs 801
Mr. Shaokai Song[1], Dr. Shibin Thomas [1], Dr. Nema Abdelazim [1], Dr. Sami Ramadan [2], Dr. Victoria Greenacre [1], Mr. Hongwei Zhang [1], Dr. Yisong Han [3], Prof. Richard Beanland [3], Prof. Gill Reid [1], Prof. Philip Bartlett [1], Prof. Kees de Groot [4], Dr. Yasir Noori [1]
1. University of Southampton, 2. Imperial College London, 3. University of Warwick, 4. School of Electronics and Computer Science, University of Southampton, Southampton SO17 1BJ, United Kingdom

A Technique for Simultaneous Embedding and Welding of Metal Nanowires on Polymer Surfaces for Flexible Conductors 803
Mr. sangmok Kim[1], Mr. Youngjae Nam [1], Prof. Joonwon Kim [1]
1. Pohang University of Science and Technology

Fabrication of a superhydrophobic surface with partially superhydrophilic regions and surface free energy comparison 805
Mr. Takuto Wakasa[1], Prof. Jun Taniguchi [1]
1. Tokyo University of Science

Design of an Antireflective Hierarchical Structure Based on Finite-Difference Time-Domain (FDTD) Simulation **807**
Mr. YAONIEN TSAI[1], Mr. YENEN JUAN [1], Mr. GUOCHEN NIEH [1], Dr. YEEUCHANG LEE [1]
1. *Chung Yuan Christian University*

Fabrication of Broadband Antireflection Hierarchical Micro/Nano Structures Using Colloidal Lithography **809**
Mr. YENEN JUAN[1], Mr. GUOCHEN NIEH [1], Mr. YAONIEN TSAI [1], Dr. YEEUCHANG LEE [1]
1. *Chung Yuan Christian University*

An e-beam lithographer's approach to evaluating a new HIMT DWL66+ direct laser writer for Mix&Match processes – resists, contrast curves, grayscale lithography, alignment, and developer test sticks **811**
Dr. Silvia Diewald[1], Prof. Gernot Goll [1]
1. *Karlsruhe Institute of Technology (KIT)*

Direct data generation of wafer-scale metalens for e-beam exposure **813**
Ms. Yixuan Zhao[1], Dr. Kian Shen Kiang [1], Prof. Jize Yan [1]
1. *University of Southampton*

Impact of PEALD Temperature on Al_2O_3 Gate Dielectric of ZnO-TFTs **815**
Mr. Jiale Zeng[1], Dr. Ben Rowlinson [2], Dr. Omesh Kapur [1], Prof. Harold Chong [3]
1. *School of Electronics and Computer Science, University of Southampton, Southampton SO17 1BJ, United Kingdom,* ***2.*** *University of Edinburgh,* ***3.*** *University of Southampton*

Plasma-enhanced ALD of ultra-thin Al2O3 films for passivating contacts **817**
Ms. Yaxin Zhan[1], Dr. Ben Rowlinson [2], Prof. Harold Chong [1], Dr. Stuart Boden [1]
1. *University of Southampton,* ***2.*** *University of Edinburgh*

Inducing piezoelectricity in chitosan films by cathodic electrodeposition: challenging a new approach for wearable sensors' fabrication **819**
Ms. Valeria D'Errico[1], Dr. Gaia de Marzo [2], Dr. Antonio Qualtieri [1], Dr. Luciana Algieri [3], Prof. Massimo De Vittorio [1]
1. *Center for Biomolecular Nanotechnologies, Istituto Italiano di Tecnologia (IIT), 73010 Arnesano, LE, Italy,* ***2.*** *IDUN section, Department of Health Technology, Technical University of Denmark, DK-2800 Kongens Lyngby, Denmark,* ***3.*** *Department of Innovation Engineering, University of Salento, Lecce, LE, 73100, Italy*

Synthesis of novel EB resist based on KrF resist system **821**
Dr. Atsushi Sekiguchi[1]
1. *Litho Tech Japan Corporation*

Nanofabrication of Large, Stitch-free Diffractive Optics **823**
Dr. Anna Casimiro[1], Dr. Sander Schellingerhout [1], Ms. Adriana Umbria [1], Dr. Kahraman Keskinbora [1]
1. *Raith Laser Systems B.V.*

Secondary particle detection for deterministic single ion implantation **825**
Dr. Kristian Stockbridge[1], Dr. Ella Schneider [2], Dr. Gianfranco Arresta [1], Dr. David Cox [2]
1. *Ionoptika Ltd,* ***2.*** *University of Surrey*

Control of the Scanning Tunnelling Microscope Based on Hybrid Gain Integrator Systems (HIGS) **826**
Ms. Richa Mishra [1], Prof. S. O. Reza Moheimani[2]
1. *The University of Texas at Dallas,* ***2.*** *The Univeraity of Texas at Dallas*

Towards single-electron devices based on SOI silicon nanowires: simulation and fabrication **828**
Mr. Gabriele Petitto[1], Mr. Ziyin Sun [2], Dr. Jordi Antoja [2], Dr. Alberto del Moral [1], Dr. Albert Guerrero [3], Dr. Roser Mas [2], Dr. Alberto García-García [2], Prof. Joan Bausells [1], Prof. Francesc Pérez-Murano [1], Dr. Esteve Amat [1], Dr. Jordi Llobet [2]
1. Institute of Microelectronics of Barcelona (IMB-CNM, CSIC), 2. Institut de Microelectrònica de Barcelona, IMB-CNM (CSIC), Universitat Autònoma de Barcelona, Cerdanyola Del Vallès, 08193, Barcelona, Spain., 3. Instituto de Microelectrónica de Barcelona

A YOLOv8-Based Defect Inspection for Semiconductor **830**
Mr. Xiaolong Guo [1], Dr. Yanan Zhu [2], Mr. Heming Wu [3], Prof. Diwei Zhou [4], Prof. Zhuming Liu[2]
1. School of Electronic Science and Engineering , South China Normal University, 2. Institute of Semiconductors, Guangdong Academy of Sciences, 3. Institute of Semiconductors, Guangdong Academy of Sciences,, 4. School of Science, Loughborough University

Two-dimensional arrays of InAs nanodots grown on inverted pyramid Si templates **832**
Dr. Javier Bravo Larrea[1], Mr. David Bermudez [2], Mr. Lisandro Jofre [1], Dr. Paloma Tejedor [2]
1. NAITEC, 2. Instituto de Ciencia de Materiales de Madrid, CSIC, Madrid, 28049, Spain

EBIC measurement of the minority carriers diffusion length in a GaAs solar cell p-n junction **834**
Dr. Anya Grushina[1], Mr. Karl Boche [1]
1. Imina Technologies

Preparation of Regrowth Interfaces in AlGaN/GaN Heterostructures Using Atomic Layer Etching for Ohmic Contact Formation **836**
Dr. Aslanidis Evangelos[1], Dr. Adam Adikimenakis [1], Mr. Nikos Makris [1], Mr. Antonios Stavrinidis [1], Dr. George Konstantinidis [1]
1. Microelectronics Research Group (MRG), Institute of Electronic Structure and Laser (IESL), Foundation of Research & Technology Hellas (FORTH), Crete 70013, Greece;

Fabrication of coupled silicon nanoelectromechanical resonators with heavily doped silicon towards reservoir computing chip **838**
Mr. Dai Ai[1], Ms. Ting Hou [2], Ms. Zixuan Wang [2], Dr. Kian Shen Kiang [2], Dr. Yoshishige Tsuchiya [2], Dr. Jun-Yu Ou [3]
1. School of Electronics and Computer Science, University of Southampton, Southampton, SO17 1BJ, UK, 2. University of Southampton, 3. Physics and Astronomy, University of Southampton

Vapor Phase Infiltration in Homopolymers and Block copolymers: A comparative study **840**
Ms. Maria Teresa Elenes Cervantes[1], Ms. Olga Muntada [1], Dr. Sara Duran [1], Mr. Ricard Noy [1], Ms. Libertad Sole [1], Dr. Jordi Llobet [1], Prof. Francesc Perez-Murano [1], Dr. Marta Fernández-Regúlez [1]
1. Institute of Microelectronics of Barcelona (IMB-CNM, CSIC)

Epitaxial growth of InAs/InGaAs-Al nanowire hybrids for quantum computing applications **842**
Dr. Paloma Tejedor[1], Dr. Beatriz Galiana [2], Mr. Gabriel Moraes [3], Dr. Eduardo J.H. Lee [3]
1. Instituto de Ciencia de Materiales de Madrid, CSIC, Madrid, 28049, Spain, 2. Universidad Carlos III de Madrid, 3. Departamento de Física de la Materia Condensada and Condensed Matter Physics Center (IFIMAC), Universidad Autónoma de Madrid, 28049 Madrid

Nanomechanical Mass Sensor: Integrating Nanoimprint Lithography with Flow-Through Gas Phase Deposition **844**
Dr. Lucjan Grzegorzewski[1]
1. University of Hamburg

Nanoimprinted Multimode Polymer Waveguides with Integrated Bragg Gratings for Structural Health Monitoring **846**

Dr. Michael Haslinger[1], Mr. Florian Egger [2], Ms. Viktorija Jonaityte [1], Prof. Vaclav Prajzler [3], Dr. Antreas Theodosiou [4], Dr. Michael Muehlberger [1]

1. PROFACTOR GmbH, 2. PROFACTOR GmbH, Im Stadtgut D1, 4407 Steyr, Austria, 3. Department of Microelectronics, Faculty of Electrical Engineering, Czech Technical University in Prague, Technicka 2, 168 27 Prague, Czech Republic, 4. Photonics Research Center (PRC), Lumoscribe Ltd, 12 Anthipoloxagou Georgiou Savva,8201 Geroskipou, Paphos, Cyprus

Advanced AFM Metrology of Vertical Structures: Sample Reorientation for Sidewall Surface Access **848**

Dr. Paweł Janus [1], Dr. Krzysztof Domański [1], Dr. Adam Łaszcz [1], Dr. Andrzej Sierakowski [1], Ms. Magdalena Kucharska[1], Dr. Dariusz Szmigiel [1]

1. Institute of Microelectronics and Photonics

Processing Pathways for Transparent, Flexible Electrodes in Next-Generation Smart Windows **850**

Dr. Michael Haslinger[1], Ms. Viktorija Jonaityte [1], Mr. Dorly Holzer-Harringer [2], Mr. Marcus Harringer [2], Dr. Florian Frischmann [3], Dr. Wenxing Huo [4], Dr. Martina Harnisch [5], Dr. Andreas Zimmermann [5], Dr. Michael Muehlberger [1]

1. PROFACTOR GmbH, 2. Almendo Technologies GmbH, Wolfschwangweg 216, 5084 Großgmain, Austria, 3. Bartenbach GmbH, Rinner Straße 14, 6071 Aldrans, Austria, 4. Department of Biomedical Engineering, Tianjin University, 92 Weijin Road, Tianjin 300072, China, 5. Sunplugged GmbH, Affenhausen 1, 6413 Wildermieming, Austria

Electrochemically growing morphology on micro structured 3D frameworks **853**

Ms. Itishree Panda[1], Ms. Trina Dhara [1], Prof. Sunando DasGupta [1]

1. Indian Institute of Technology Kharagpur

Micro/Nano Thin-Film Coating Processes of Carbon Materials for Energy Devices **855**

Dr. JEONGDAI JO[1]

1. Korea Institute of Machinery and Materials (KIMM)

Bulk Micro-Machining of SrTiO3 Substrates for Device Applications **857**

Dr. Nicola Manca [1], Dr. Luca Pellegrino[1]

1. National Research Council

Towards EUV lithography with alternative sources: a proof-of-concept high-harmonic generation in gas-filled hollow waveguides driven by ultrafast infrared laser pulses **859**

Dr. Sonia Freddi[1], Dr. Anna G. Ciriolo [1], Dr. Rebeca Martinez Vazquez [1], Prof. Salvatore Stagira [2], Dr. Monica Bollani [3]

1. IFN-CNR, 2. Politecnico di Milano, 3. Institute of Photonic and Nanotechnology (IFN) - CNR

Medusa 84 SiH, an alternative HSQ resist for realizing DFB lasers diodes **861**

Mrs. Poojitha Sammeta[1], Dr. Olaf Brox [1], Dr. Pietro Della Casa [1], Mr. Dirk Rentner [1], Dr. Ralph-Stephan Unger [1], Dr. Hans Wenzel [1], Mr. Maximilian Schäfer [1], Dr. Andrea Knigge [1], Mr. Harry Biller [2], Mr. Matthias Schirmer [2]

1. Ferdinand-Braun-Institut gGmbH, 2. Allresist GmbH

Integrated Microfabrication Capabilities for Life Science Applications: From Polymer Platforms to Active Micropumps **863**

Mr. Robin de Bruijn[1], Ms. Marie Monchablon [1], Mr. Sander Visser [1], Ms. Laure van der Sanden [2], Dr. Hossein E. Amirabadi [2], Prof. Jaap den Toonder [1]

1. Eindhoven University of Technology, 2. ARTIC Technologies B.V.

Engineering soft nanoscale surfaces force material interaction study 865
Dr. Martina Paraggio[1], Prof. Luigi Bruno [2], Dr. Chiara Morano [2], Ms. Maria Laura Coluccio [1], Ms. Francesca Gualtieri [3], Prof. CARMELA DE MARCO [3], Prof. Francesco Gentile [3]
1. Magna Graecia University, Catanzaro, 2. University of Calabria, 3. Magna Græcia University of Catanzaro

Isotopically pure Silicon-28 thin films for improved coherence times in silicon quantum technologies built by scanning tunnelling microscopy 868
Mr. Oisín FitzGerald[1], Dr. Taylor Stock [1]
1. University College London

Ultra-thick HSQ Resist for Optical Waveguide Grating Coupler Applications 870
Mr. Kun Zhang[1], Dr. Kian Shen Kiang [2], Dr. Ying Tran [3], Prof. David Thomson [3], Prof. Harold Chong [3]
1. School of Electronics and Computer Science, University of Southampton, Southampton, SO17 1BJ, UK, 2. Optoelectronics Research Centre, University of Southampton, Southampton, SO17 1BJ, UK, 3. University of Southampton

Integration of Interband Infrared Cascade Photodetector onto a SOI Platform for Gas Sensing 872
Mr. Daniel Adeyemi[1], Dr. Colin Mitchell [1], Prof. Goran Mashanovich [1], Dr. Milos Nedeljkovic [1]
1. Optoelectronics Research Centre, University of Southampton, SO17 1BJ, UK

Biofabrication of 3D Scaffolds and Functional Microstructures Using Two- Photon Lithography 874
Dr. Mario Kandra [1], Mr. Jáchym Podstránský[1]
1. IQS nano s.r.o

The modulation of X-ray by high resolution zone plates when volume diffraction effects dominate 876
Mr. Hao Quan[1], Dr. Xujie Tong [1], Mr. Qiucheng Chen [1], Ms. Qingxin Wu [1], Ms. xunjia Zhao [1], Mr. Shuoqiu Tian [1], Mr. Wentao Yuan [1], Mr. Jinyu Guo [1], Ms. Kangping Liu [1], Prof. Yifang Chen [1]
1. Fudan university

Microfluidic Mixing Induced by the Blinking-Two-Cilia System 878
Mr. Yangyu Duan[1], Mr. Ishu Aggarwal [2], Dr. Ye Wang [1], Prof. Patrick Onck [2], Prof. Jaap den Toonder [1]
1. Eindhoven University of Technology, 2. University of Groningen

Neurohybrid interfaces via microstructured conductive hydrogels 880
Mr. Marco Buzio[1], Dr. Nevena Stajkovic [2], Dr. Valeria Criscuolo [2], Prof. Francesca Santoro [2]
1. a Institute of Biological Information Processing IBI-3, Forschungszentrum Juelich, 52428 Jülich, Germany, 2. Institute of Biological Information Processing IBI-3, Forschungszentrum Juelich, 52428 Jülich, Germany

Micropillars Based PDMS Lab-On-chip Device for Tryptic Digestion of Proteins for Proteomics 882
Dr. Sadhana Tiwari[1], Ms. Nilüfer Tasli [1], Dr. Manuela Moritz [2], Dr. Franziska Marie Esmek [3], Mr. Tim Erichlandwehr [1], Dr. Jan Hahn [2], Prof. Hartmut Schlüter [2], Dr. Irene Fernandez [4]
1. University of Hamburg, 2. Universitätsklinikum Hamburg-Eppendorf, 3. University of Hamburg/Hamburg Center for Ultrafast Imaging, 4. UHH

Method for high phase accuracy trimming of MZIs via Ge ion implantation and electrical annealing 884
Ms. April Logan[1], Dr. Xia Chen [1], Dr. Xingshi Yu [1], Ms. Weihong Shen [1], Dr. Xingzhao Yan [2], Dr. Weiwei Zhang [1], Prof. Goran Mashanovich [1], Prof. Graham Reed [1], Prof. David Thomson [2]
1. Optoelectronics Research Centre, University of Southampton, SO17 1BJ, UK, 2. University of Southampton

Microcavities to engineer dynamics in coupled E. coli oscillators 886
Mr. Kushal Swamy[1], Dr. Farbod Alijani [1]
1. Delft University of Technology

Manipulation of Liquid Marbles via Triboelectric Charging **888**
Ms. Yuan-Hsuen Chou[1], Prof. Jiann Shieh [1]
1. *National United University*

An Extrusion Printed Lorentz Force Actuated Electromechanical Relay **890**
Mr. Desmond Lagace [1], Dr. Cyrus Shafai[1]
1. *University of Manitoba*

Integrating Surface-Confined Molecular Motors into Microfluidic Platforms: Toward Automated, High-Throughput analysis of Actinomyosin in vitro motility Assays **892**
Mr. Tim Erichlandwehr[1], Ms. Veronica Mieites [2], Mr. Jeremy Teuber [3], Mr. Rukan Nasri [4], Dr. Marko Usaj [5], Prof. Alf Månsson [5], Prof. Olga María Conde Portilla [2], Dr. Irene Fernandez-Cuesta [4]
1. *UHH/DESY,* ***2.*** *University of Cantabria, Photonics Engineering Group,* ***3.*** *UHH/MPSD,* ***4.*** *UHH/CUI,* ***5.*** *Linnaeus University*

Tuning fork optomechanical NIR antenna with integrated optical transmission line **894**
Mr. Daniyal Khoshmaram[1], Dr. Xavier Borrisé [2], Prof. Joan Jose Garcia-Garcia [1], Mr. Raul Ruiz [1], Dr. Xavier Cartoixà [1], Dr. Gabriel Abadal [1]
1. *Universitat Autonòma de Barcelona,* ***2.*** *Catalan Institute of Nanoscience and Nanotechnology (ICN2) and Barcelona Institute of Science and Technology (BIST)*

Low-Temperature Deposition of Metal Chalcogenides via Single-Source Precursors for Flexible Electronics **896**
Ms. Sayali Harke [1], Ms. Suprabha Dixit [2], Dr. Chitra Gurnani[1], Dr. Ruomeng Huang [3], Dr. Omesh Kapur [4]
1. *Ecole Centrale School of Engineering, Mahindra University, Hyderabad,* ***2.*** *Ecole Centrale School of Engineering, Mahindra University,* ***3.*** *University of Southampton,* ***4.*** *School of Electronics and Computer Science, University of Southampton, Southampton SO17 1BJ, United Kingdom*

Application of Integrated Electrode Fabrication Technique in Microfluidic lab-on-a-chip Devices for Single-Cell Analysis **898**
Mr. Herbert Atrian-Garcia[1], Ms. Louise von Lacroix [1], Dr. Irene Fernandez [1], Mr. Rukan Nasri [1]
1. *University of Hamburg*

Preparation of Biocompatible Ag/Nylon Yarns Fabricated by Supercritical CO_2-assisted Ag Electroless Plating toward Weavable Devices **900**
Mr. Tomoya Higashi[1], Dr. Tomoyuki Kurioka [2], Mr. Kazuhiro Shibata [2], Dr. Satoru Egawa [3], Prof. Toshitaka Yoshii [3], Prof. Chun-Yi Chen [2], Prof. Tso-Fu Mark Chang [2], Prof. Katsunari Sato [4], Prof. Hiromichi Kurosu [4], Prof. Masato Sone [2]
1. *Institute of Innovative Research, Institute of Science Tokyo,* ***2.*** *Institute of Science Tokyo,* ***3.*** *Department of Orthopaedic Surgery, Institute of Science Tokyo,* ***4.*** *Nara Women's University*

Flexible AlScN Piezoelectric Films for Next-Generation Smart Biomedical Sensors **902**
Dr. Padmalochan Panda[1], Dr. Gaia de Marzo [2], Dr. Luciana Algieri [3], Dr. Antonio Qualtieri [1], Dr. Francesco Rizzi [1], Prof. Michele Scaraggi [1], Dr. Vincenzo M. Mastronardi [3], Prof. Massimo De Vittorio [1]
1. *Center for Biomolecular Nanotechnologies, Istituto Italiano di Tecnologia (IIT), 73010 Arnesano, LE, Italy,* ***2.*** *IDUN section, Department of Health Technology, Technical University of Denmark, DK-2800 Kongens Lyngby, Denmark,* ***3.*** *Department of Innovation Engineering, University of Salento, Lecce, LE, 73100, Italy*

Monolithic All-Silicon Ring Resonator for Optical Modulation and Detection **904**
Mr. Yifu Chen[1], Dr. Weiwei Zhang [1], Ms. Tzu-yun Chang [1], Ms. Hanuushah Vizabaskaran [1], Mr. James Le Besque [1], Dr. Xingzhao Yan [1], Dr. Martin Ebert [1], Prof. Callum Littlejohns [1], Prof. David Thomson [1]
1. *Optoelectronics Research Centre, University of Southampton, SO17 1BJ, UK*

InP Nanowire-Based Photoelectrical Detection of Single Particles and DNA in Nanofluidic Systems 906
Mr. Leon Seggering[1], Mr. Vidar Flodgren [2], Dr. Abhijit Das [2], Mr. Thomas Kjellberg Jensen [2], Dr. Joachim Elbeshausen Sestoft [3], Prof. Jesper Nygård [3], Prof. Anders Mikkelsen [2], Dr. Irene Fernandez-Cuesta [4]
1. UHH/DESY, 2. Lund University, 3. University of Copenhagen, 4. UHH/CUI

Ultrasensitive Raman Detection via Electrostatic Droplet Manipulation and Laser-Patterned Pinhole Concentration 908
Ms. Jia-yi Chen[1], Mr. Cheng-Han Yu [1], Prof. Jiann Shieh [1]
1. National United University

Scalable integration of III-V nanowire transistors for NMOS logic 910
Dr. Faris Abualnaja[1], Mr. Ibtisam Abbasi [1], Mr. Xiaofan Lin [1], Prof. Hoe Tan [2], Prof. Chennupati Jagadish [2], Prof. Hannah Joyce [1], Dr. Jack Alexander-Webber [1]
1. University of Cambridge, 2. The Australian National University

Piezoelectric microdevices for single-cell stimulation via ultrasound-driven ZnO nanosheets 912
Mx. Laura Lefaix[1], Mr. Marc Navarro [2], Prof. Jaume Esteve [1], Prof. Carme Nogués [3], Dr. Andreu Blanquer [4], Dr. Gonzalo Murillo [2]
1. Instituto de Microelectrónica de Barcelona, 2. Institute of Microelectronics of Barcelona (IMB-CNM, CSIC), 3. Universitat Autonòma de Barcelona, 4. Departament de Biologia Cel.lular, Fisiologia i Immunologia, Universitat Autonoma de Barcelona

Technological platforms for manufacturing semiconductor qubits 914
Dr. Alberto del Moral[1], Mx. Iker Uranga [1], Mr. Gabriele Petitto [1], Mr. Pol Gaya [1], Mr. Gorka Aizpurua-Iraola [1], Dr. Jordi Antoja [2], Dr. Esteve Amat [1], Dr. Jordi Llobet [2], Dr. Marta Fernández-Regúlez [1], Prof. Joan Bausells [1], Prof. Francesc Pérez-Murano [1]
1. Institute of Microelectronics of Barcelona (IMB-CNM, CSIC), 2. Institut de Microelectrònica de Barcelona, IMB-CNM (CSIC), Universitat Autònoma de Barcelona, Cerdanyola Del Vallès, 08193, Barcelona, Spain.

Double-Spot Detection in Nanochannels Enables Precise Velocity Profiling and Long-Term Stability Monitoring in Passive Micro- and Nanofluidic- Systems 916
Mr. Phil Grzybeck[1], Mr. lucjan Grzegorzewski [1], Mr. Leon Seggering [2], Dr. Franziska Marie Esmek [3], Dr. Irene Fernandez-Cuesta [4]
1. UHH, 2. UHH/DESY, 3. University of Hamburg/Hamburg Center for Ultrafast Imaging, 4. UHH/CUI

Synchronization of autonomous vibrating electrostatic MEMS torsional mirrors 918
Mr. Yuta Kawashima[1], Mr. Mikiya Oki [1], Dr. Amit Banergee [1], Dr. Jun Hirotani [1], Prof. Toshiyuki Tsuchiya [1]
1. Kyoto University

Solution-Processed UV-Vacuum-Heat (UVVH) Treated Mixed Size Zinc Oxide Nanoparticle Diode-like Device for Ion Sensing Applications 920
Mr. Mengyang Qu[1], Dr. Huanghao Dai [1], Dr. Omesh Kapur [2], Prof. Steve Beeby [1], Prof. Harold Chong [1]
1. University of Southampton, 2. School of Electronics and Computer Science, University of Southampton, Southampton SO17 1BJ, United Kingdom

PEGDA microfluidic-device featuring a Y-type shape for hydrogel microspheres synthesis analysis 922
Ms. Anayancy Itzel Villatoro Guillen[1], Dr. Orfil González-Reynoso [1], Ms. Andrea Carolina Villalvazo-Hidalgo [1], Dr. Alvaro de Jesús Martínez-Gómez [1], Dr. Antonio Romero-Estrada [1], Dr. Sergio Gómez-Salazar [1], Dr. Mario Alberto García-Ramírez [1]
1. Universidad de Guadalajara

Piezoresistivity in FEBID nanowires imaged via opMEMS straining 924
Dr. Bartosz Pruchnik [1], Ms. Magdalena Kucharska[2], Dr. Krzysztof Kwoka [1], Dr. Tomasz Piasecki [1], Dr. Soraya Sangiao [3], Prof. Jose Maria De Teresa [3], Mrs. Ewelina Gacka [1], Mr. Dominik Badura [1], Mr. Piotr Kunicki [1], Dr. Andrzej Sierakowski [2], Dr. Paweł Janus [2], Prof. Teodor Gotszalk [1]
1. Wrocław University of Science and Technology, 2. Institute of Microelectronics and Photonics, 3. Universidad de Zaragoza

Simulation of contact forces associated with contact wear in MEMS switches 926
Mr. Nasser Aldhahri[1], Prof. John Mcbride [2], Dr. Yoshishige Tsuchiya [1]
1. University of Southampton, 2. School of Engineering, University of Southampton

A Hybrid Superconductor/Nanomechanical Magnetic Field Detector for Biomagnetism 928
Dr. Luca Pellegrino[1]
1. National Research Council of Italy

Development of a 3-Channel Solar-Blind UV-C Sensor for Determining Source Location and Intensity 930
Dr. Keekeun Lee[1]
1. Ajou Unversity

Electrostatic Manipulation of Low Surface Tension Liquids on Silica Nanowire-based Slippery Liquid-infused Porous Surfaces 932
Mr. Ching Chi Lin[1], Mr. Yueh Tse Lin [1], Prof. Jiann Shieh [1]
1. National United University

Edge Engineering for Intrinsic Cold-metallic Injection Source in 2D FETs 934
Ms. Zhirong PENG[1], Mr. Ning JI [2], Mr. Jinchen Wei [1], Mr. Kwok-Ho Wong [1], Mr. Tin Shing Peter Ho [1], Prof. Lining Zhang [2], Prof. Mansun Chan [1]
1. The Hong Kong University of Science and Technology, 2. Peking University

Plasmonic antenna-VO2 hybrid metasurface for all-optical nonlinearity 936
Mr. Trubacs Daniel-Iosif[1], Dr. Kai Sun [1], Dr. Ioannis Zeimpekis [1], Prof. Otto Muskens [1]
1. University of Southampton

A massive-scale droplet microfluidic platform based on an active matrix of high-voltage thin-film transistors 938
Prof. Xing Cheng[1]
1. Southern University of Science and Technology

Vertically-Integrated VRRAM-Based Hardware Reservoir Computing System 940
Prof. Sungjun Kim[1]
1. Dongguk University

Optoelectronic Synaptic IGZO Transistor and Its Demonstration of Electrical and Optical Plasiticity for Light-Susceptive Processing-in-Memory 942
Prof. Myounggon Kang[1]
1. University of Seoul

Superhydrophobic Multifocal Microlens Array with Depth-of-Field Detection for Humid Environment 944
Dr. Hao Cao[1]
1. wuhan university

Prediction of Photo Lithography Equipment Wafer Moving Robot Errors Using ARIMA model 948
Mr. Kyunghwan Joo[1], Prof. Jae Wook Jeon [2]
1. SUNG KYUN KWAN University / Samsung Electronics, 2. Sungkyunkwan University

Optimisation of a Microfluidic Electrochemical Biosensor for E. coli Detection via ssDNA Hybridization and CRISPR/Cas-Based Sensing to Combat Sepsis 950
Mrs. Eleonora Quasso[1], Prof. Isabelle Le Potier [1], Dr. Hiu Mun Man [1], Dr. Hervé Jacquier [2], Dr. David Bikard [3], Dr. Laurent Thouin [4], Dr. Jean Gamby [1]
1. Université Paris-Saclay, Centre de Nanosciences et de Nanotechnologies, 2. Hôpital Henri Mondor, APHP, 3. Institut Pasteur, Université Paris Cité, 4. Ecole normale supérieure, PSL University, Sorbonne Université

Scalable Nanobubble Generation Using Centrifugal Micro-Porous Mesh Disc Technology 952
Mr. Bo-Wei Cheng [1], Prof. Yuan-Jen Chang [1], Prof. Chia-Lung Kuo [2], Dr. Kuen-Yi Wu [3], Prof. Chao-Ching Ho[1]
1. National Taipei University of Technology, 2. National Yunlin University of Science and Technology, 3. Rayzher Industrial Co., Ltd.

Refractive index controllable plasmonic color metasurfaces fabricated by combination of Nanoimprint lithography and Inkjet Printing 954
Ms. Nefeli Dimogerontaki[1], Dr. Nikolaos Mattheakakis [2], Ms. Narges Heidaryan [3], Ms. Sonja Kopp [3], Dr. Michael Muehlberger [3], Dr. Nikolaos Kehagias [2]
1. Department of Physics, School of Applied Mathematical and Physical Sciences National Technical University of Athens, Zografou Campus, GREECE, 2. NCSR Demokritos, Institute of Nanoscience & Nanotechnology, P. Grigoriou 27 & Neapoleos Str., 15341 Ag. Paraskevi, Greece, 3. PROFACTOR GmbH

Machine Learning Enabled Thermoelectric Device Design and Optimization 956
Mr. Haoji Yang[1], Dr. Yuxiao Zhu [2], Prof. Kees de Groot [2], Prof. Harold Chong [2], Dr. Ruomeng Huang [2]
1. School of Electronics and Computer Science, University of Southampton, Southampton SO17 1BJ, United Kingdom, 2. University of Southampton

Flexible, non-toxic SF radiochromic film based on 10,12-PCDA for on-site X-ray dosimetry 958
Mr. Naseer Ahmad [1], Mrs. Aida Visus [1], Mr. Salvador David Aznar [2], Prof. Gonzalo Guirado [3], Dr. Consuelo Guardiola [1], Dr. Xavier Muñoz Berbel [1], Dr. Silvia Mena Fernández[1]
1. Institute of Microelectronics of Barcelona (IMB-CNM, CSIC), 2. Instituto Murciano de Investigación y Desarrollo Agrario y Medioambiental, 3. Universitat Autonòma de Barcelona

Open Science & Technology: Microfluidic fluid handling 960
Dr. Lars Kool[1], Dr. Bertrand Cinquin [1]
1. Institut Pierre-Gilles de Gennes pour la Microfluidique, Paris, 75005, France

An Ultrasensitive TDSE/Au/SOD-based Electrochemical Sensing Platform for Real-Time Monitoring of Superoxide Ion at Cellular Level. 962
Mr. Pratyusa Mohapatra[1], Prof. Soumen Das [1]
1. Indian Institute of Technology Kharagpur

Simulation of physical reservoir computing based on nonlinear dynamics of nanoelectromechanical resonators 964
Mr. Lianghong Ye[1], Dr. Klaus-Peter Zauner [1], Dr. Mark Vousden [1], Mr. Yuta Kawashima [2], Prof. Toshiyuki Tsuchiya [2], Dr. Yoshishige Tsuchiya [1]
1. University of Southampton, 2. Kyoto University

Microfluidic chip for electrochemical detection of circulating miRNAs: real-sample testing of cardiac disease biomarkers 966
Ms. Anna Tarasova[1], Dr. Israël Mbomekallé [2], Prof. Sébastien Banzet [3], Dr. Hiu Mun Man [4], Prof. Isabelle Le Potier [4], Dr. Jean Gamby [4]
1. Université Paris-Saclay, Centre de Nanosciences et de Nanotechnologies (C2N), Palaiseau, 91120, France, 2. Institut de Chimie Physique d'Orsay (ICP), Orsay, 91400, France, 3. INSERM, Institut André Lwoff (IAL), Hôpital de Clamart, Clamart, 92140, France, 4. Université Paris-Saclay, Centre de Nanosciences et de Nanotechnologies

Optic Fibre Gas Sensor featuring MoS2 QD as an Active Layer 968
Dr. Mario Alberto García-Ramírez[1], Dr. Orfil González-Reynoso [1], Ms. Andrea Carolina Villalvazo-Hidalgo [1], Dr. Miguel Angel Bello-Jiménez [2], Dr. Abel García-Barrientos [2], Dr. Gregorio Guadalupe Carbajal-Arizaga [1]
1. Universidad de Guadalajara, 2. Universidad Autónoma de San Luis Potosí

Development kinetics of photoresist films using trimethyl-ammonium hydroxide (TMAH) aqueous developer contaminated with poly-hydroxy-styrene 970
Ms. Andreia Santos [1], Dr. Masahiko Harumoto[2], Dr. Yuqing Jin [3], Dr. Takahiro Kozawa [3]
1. SCREEN SPE, 2. SCREEN Semiconductor Solutions Co., Ltd, 3. SANKEN, Osaka Univ

Introducing a new era of green and functional biopolymeric surfaces 972
Dr. Dimosthenis Ioannou[1], Dr. Kosmas Ellinas [2], Dr. Alexandros Banis [1], Dr. Danai Ioanna Koukoumaki [3], Dr. Dimitris Sarris [3], Dr. Evangelos Gogolides [4]
1. Institute of Nanoscience and Nanotechnology, NCSR "Demokritos", 27 Neapoleos str & Patriarchou Grigoriou, Ag. Paraskevi, 153 41, Greece, 2. Laboratory of Advanced Functional Materials and Nanotechnology, Department of Food Science and Nutrition, School of the Environment, University of the Aegean, Leoforos Dimokratias 66, Myrina 81400, Lemnos, Greece, 3. Laboratory of Physico-Chemical and Biotechnological Valorization of Food By-Products, Department of Food Science & Nutrition, School of Environment, University of the Aegean, Leoforos Dimokratias 66, Myrina 81400, Lemnos, Greece, 4. NCSR Demokritos, Institute of Nanoscience & Nanotechnology, P. Grigoriou 27 & Neapoleos Str., 15341 Ag. Paraskevi, Greece

Pattern transfer by laser ablation: demonstration of a vacuumless process for micropatterning from lithographic masks 974
Dr. Klaus Zimmer[1], Dr. Joachim Zajadacz [2], Dr. Martin Ehrhardt [1], Dr. Pierre Lorenz [1], Dr. Tomi Smausz [3], Prof. Bela Hopp [3]
1. Leibniz Institute of Surface Engineering (IOM), 2. Leibniz Institute of Surface Engineering (IOM), Dep. Ultra-Precision Surfaces, 3. University of Szeged, Department of Optics and Quantum Electronics

Etching of optical glass by reactive plasmas at atmospheric pressure 977
Dr. Martin Ehrhardt [1], Mr. Robert Heinke [2], Dr. Pierre Lorenz [1], Prof. Thomas Arnold [3], Dr. Klaus Zimmer[1]
1. Leibniz Institute of Surface Engineering (IOM), 2. Leibniz Institute of Surface Engineering (IOM) and Technische Universität Dresden, 3. Technical University Dresden

From Waste to Resource: Engineering End-of-Life Graphite Anodes for Solid-State Hydrogen Storage 979
Mr. Mukhammed Kenzhebek[1]
1. National Laboratory Astana, Nazarbayev University

Low-Waste Fabrication of Flexible Carbon Electrodes: Capacitance Comparison of Inkjet-Printed and Laser-Induced Graphene with Ag Nanoparticles 981
Ms. Rou Xuan Goh [1], Mr. Ishant G. Patil [1], Dr. Suan Hui Pu [2], Dr. Suhana Sultan [3], Prof. Harold Chong [4], Dr. Ivan Ling[4]
1. Smart Manufacturing and Systems Research Group, University of Southampton Malaysia, 2. University of Southampton Malaysia, 3. Universiti Teknologi Malaysia, 4. University of Southampton

Mobile Ions Improve the Power Conversion Efficiency of Perovskite Solar Cells with Large Energetic Offsets 983
Ms. Lucy Hart [1], Mr. Fraser Angus [2], Ms. Yin Li [3], Mr. Abdul Kahleed [3], Dr. Philip Calado[4], Prof. James Durrant [5], Prof. Aleksandra Djurišić [3], Dr. Pablo Docampo [2], Dr. Piers Barnes [1]
1. Department of Physics, Imperial College London, 2. Department of Chemistry, University of Glasgow, 3. Department of Physics, The University of Hong Kong, 4. University of Southampton, 5. Department of Chemistry, Imperial College London

Heterogeneous Integration of Diamond 985
Dr. Soumen Mandal [1], Dr. Jerome Cuenca [1], Prof. Oliver Williams[1]
1. Cardiff University

Oral Session 4A: Advanced Nanofabrication II

Geometric optimization improves the performance of organic electrochemical transistors for bio-sensing applications 988
Dr. Noemi Cesario[1], Prof. Natalia Malara [2], Dr. Nicola Coppedè [3], Prof. Francesco Gentile [4]
1. Nanotechnology Research Center, Department of Experimental and Clinical Medicine, University "Magna Graecia" of Catanzaro, 88100 Catanzaro (Italy), 2. Department of Health Sciences, University Magna Graecia, Catanzaro, Italy, 3. IMEM-CNR Institute of Materials for Electronic and Magnetism, National research council, Parco area delle scienze 37/a 43124 Parma, 4. Magna Græcia University of Catanzaro

Introducing thermal scanning probe lithography into the fabrication of semiconductor quantum devices 990
Mx. Iker Uranga[1], Mr. Robin Erne [2], Dr. Jana Chaaban [2], Dr. Marta Fernández-Regúlez [1], Prof. Joan Bausells [1], Dr. Guido Rademaker [3], Dr. Emine Çağın [2], Prof. Francesc Pérez-Murano [1]
1. Institute of Microelectronics of Barcelona (IMB-CNM, CSIC), 2. Heidelberg Instruments, 3. CEA Leti

Fabrication of Vanadium Dioxide Resistors on Fully-released Polyimide Thin Films for High Strain Studies 992
Mr. Loïc Lahaye[1], Prof. Jean-Pierre Raskin [1], Prof. Denis Flandre [1]
1. ICTEAM UCLouvain

FabuBlox – An AI-driven Platform Connecting the Nanofabrication World 994
Dr. Jan Tiepelt[1], Dr. Josh Perozek [1], Mr. Jack Muller [1], Mr. Eyal Perry [1]
1. FabuBlox Inc.

Fabrication of Seamless, Homogenous Al2O3 Membranes by Gas-Phase-Deposition for highly stable Liquid Cells for Transmission Electron Microscopy 996
Ms. Nathalie Pranzner[1], Mrs. Judith Estengre Pérez [1], Mr. Jeremy Teuber [2], Mr. Rukan Nasri [3], Dr. Irene Fernandez [3], Prof. Arwen Pearson [1]
1. University of Hamburg, 2. Max-Planck-Institute for the Structure and Dynamics of Matter, 3. UHH

Localised O2 Plasma Treatment of AZO and Zn for Broadband Modulation of Optical and Radio Frequency Response. 998
Mr. Thomas Howe[1], Dr. Kai Sun [1], Prof. Otto Muskens [1], Prof. Kees de Groot [1]
1. University of Southampton

Single-Molecule Identification Using Plasmonic Nanopores and Ultrafast SERS 1000
Dr. Kirill Khabarov[1], Ms. Ilaria Micol Baldi [1], Dr. Maria Blanco Formoso [1], Dr. Foroogh Khozeymeh Sarbishe [1], Dr. Giulia Bruno [1], Prof. Francesco Gentile [2], Dr. Francesco Tantussi [1], Prof. Francesco De Angelis [1]
1. Istituto Italiano di Tecnologia (IIT), 2. Magna Græcia University of Catanzaro

Oral Session 4B: Advanced Nanofabrication and Characterisation

Ti-Ni-Cu shape memory alloy thin films with improved adhesion and controlled residual stress for MEMS applications **1003**
Dr. Elaheh Akbarnejad[1], Mr. Alan Savan [1], Mr. Gowtham Arivanandhan [2], Prof. Manfred Kohl [2], Prof. Alfred Ludwig [1]
1. Ruhr University Bochum, 2. Karlsruhe Institute of Technology (KIT)

Temperature Homogenization for Local Electro-Thermal Annealing of Shape Memory Alloy Microstructures **1005**
Mr. Gowtham Arivanandhan[1], Dr. Elaheh Akbarnejad [2], Prof. Alfred Ludwig [2], Prof. Manfred Kohl [1]
1. Karlsruhe Institute of Technology (KIT), 2. Ruhr University Bochum

3D Printing of MEMS Devices **1007**
Prof. Frank Niklaus[1]
1. Royal Institute of Technology (KTH)

Lightweight Machine-Learned Surrogate Models for Carrier Transport using Gradient-Boosted Feature Selection **1008**
Dr. Ben Rowlinson[1], Dr. Alexandros Keros [1], Prof. Subramanian Ramamoorthy [1], Prof. Jacqueline Cole [2], Prof. Themis Prodromakis [1]
1. University of Edinburgh, 2. University of Cambridge

Breaking the Resolution Barrier: Phased Exposure Methodology for Precision Microfluidic Injection Moulding Tools **1010**
Mr. Euan McDonald[1], Mr. Pedro Duarte Menezes [1], Dr. Hojjat Madadi [2], Dr. Xin Li [2], Ms. Alysha Hunter [1], Prof. Daniel Mulvihill [1], Prof. Nikolaj Gadegaard [1]
1. The University of Glasgow, 2. Sphere Bio LTD

Ultra-precision diamond micro-grinding of integrated mirrors in silicon for quantum atomic technologies **1012**
Dr. Paul Gow[1], Mr. Joel Keen [2], Mr. Glenn Churchill [1], Prof. Corin Gawith [1], Prof. James Gates [1]
1. University of Southampton, 2. Optoelectronics Research Centre, University of Southampton, SO17 1BJ, UK

Magnetic artificial cilia to steer the locomotion of microswimmers **1014**
Dr. Zhiwei Cui[1], Mr. Kushal Swamy [1], Prof. Jaap den Toonder [2], Dr. Farbod Alijani [1]
1. Delft University of Technology, 2. Eindhoven University of Technology

Oral Session 4C: Electronics II

Mesoporous silica-based memristor for neuromorphic computing **1017**
Mr. Bohao Ding[1], Dr. Tongjun Zhang [1], Dr. Li Shao [1], Dr. Ayoub Jaafa [1], Prof. Andrew Hector [1], Dr. Ruomeng Huang [1]
1. University of Southampton

Novel Reagents for the Solution-processible Deposition of Low-dimensional Materials and their Composites for Flexible Memristors and Smart Sensors **1019**
Mrs. Trishala Desai[1], Dr. Chitra Gurnani [2]
1. Trishala Desai, 2. Ecole Centrale School of Engineering, Mahindra University, Hyderabad

Non-planar patterning of an Organic Electrochemical Transistor (OECT) on a tapered optical fiber-based neural interface 1021
Mrs. Sneha Pottekkad[1], Dr. Stella Aslanoglou [1], Dr. Barbara Spagnolo [1], Dr. Antonio Qualtieri [1], Dr. Claudia Latte Bovio [1], Dr. Michele Di Lauro [2], Mr. Federico Rondelli [2], Dr. Fabio Biscarini [2], Prof. Massimo De Vittorio [1], Dr. Ferruccio Pisanello [1]
1. Center for Biomolecular Nanotechnologies, Istituto Italiano di Tecnologia (IIT), 73010 Arnesano, LE, Italy, 2. Istituto Italiano di Tecnologia (IIT)

Towards Additive Manufacturing and Conformal Metallization of 3D-Printed Antennas for Radar Applications 1023
Dr. Michael Haslinger[1], Dr. Vaclav Prochazka [2], Mr. Peter Bauer [3], Dr. Dieter Holzinger [3], Mr. Jean Temga [4], Dr. Saeid Kameramzadeh [4]
1. PROFACTOR GmbH, 2. PROFACTOR GmbH, Im Stadtgut D1, 4407 Steyr, Austria, 3. TIGER Coatings GmbH & Co KG, Wels, 4600, Austria, 4. Millimeter Wave Technologies, Intelligent Wireless System, Silicon Austria Labs (SAL), 4040 Linz, Austria.

Adaptive Reservoir Computing with Electro-Optical and 3D Structured Memristor Hardware Platforms 1026
Prof. Sungjun Kim[1]
1. Dongguk University

VO2-based memristor grown by ALD for neuromorphic computing 1027
Mr. Bingkai Ding[1], Dr. Ruomeng Huang [1], Dr. Kai Sun [1], Prof. Kees de Groot [1]
1. University of Southampton

Enhancement of Data Retention Characteristics in 2D and 3D NAND Flash via Hydrogen Trap Engineering 1029
Mr. Joongho Yoon[1], Mr. MinSung Song [1], Mr. HyunSuk Kim [1], Mr. EunJin Baek [1], Mr. KeeJeong Rho [1], Mr. JungGyu Kim [1], Mr. JongKwang Lim [1], Mr. YoungHo Kwon [1], Dr. YongSik Yim [1]
1. Samsung Electronics

Oral Session 4D: Sustainable Fabrication Processes I

Pattern transfer using atmospheric pressure plasma processes 1032
Dr. Martin Ehrhardt [1], Mr. Robert Heinke [2], Dr. Pierre Lorenz [1], Mr. Visar Demiri [1], Dr. Joachim Zajadacz [3], Prof. Thomas Arnold [4], Dr. Klaus Zimmer[1]
1. Leibniz Institute of Surface Engineering (IOM), 2. Leibniz Institute of Surface Engineering (IOM) and Technische Universität Dresden, 3. Leibniz Institute of Surface Engineering (IOM), Dep. Ultra-Precision Surfaces, 4. Technical University Dresden

Towards Sustainable Electronics: Wafer-Scale Fabrication of Fully Biodegradable CMOS Devices 1034
Ms. Laura Cavedoni[1], Mr. Zhengwei Liao [1], Mr. Yukun Lian [1], Mr. Francesco Stallone [1], Prof. Filipe Arroyo Cardoso [1], Prof. Clementine Boutry [1]
1. Delft University of Technology

Conductive carbon film growth from recycled plastics 1036
Mr. Carlos Barbero Rodriguez[1], Dr. Geoff Fowler [1], Prof. Kristel Fobelets [1]
1. Imperial College London

Development of sustainable machining processes to manufacture vacuum cells for Quantum Technology 1038
Mr. Joel Keen[1], Dr. Paul Gow [1], Mr. Glenn Churchill [1], Prof. Corin Gawith [1], Prof. James Gates [1]
1. University of Southampton

Energy-efficient optical crosslinking system for sustainability in ArFi lithography **1040**
Ms. SEUNGJOO BAEK[1], Ms. Elke Caron [1], Mr. Wesley Zanders [1], Ms. Andreia Santos [2], Dr. Masahiko Harumoto [3], Dr. Seonggil Heo [4], Mr. Jelle Vandereyken [4], Ms. Veerle Van Driessche [5], Mr. Douglas Guerrero [5]
1. Screen SPE Germany GmbH, 2. SCREEN SPE, 3. SCREEN Semiconductor Solutions Co., Ltd, 4. imec, 5. Brewer Science

Isotropic etching of suspended Si structures using a single-step, single-mask deep reactive ion etching process **1042**
Dr. Sarah Günther-Müller [1], Mr. Marius Hillebrand[2], Prof. Martin Hoffmann [2], Prof. Steffen Strehle [1]
1. Techische Universität Ilmenau, 2. Ruhr University Bochum

Designing for End-of-Life Electronics: Additive Manufacturing of conductive materials to enable 99% degradable High-Performance Printed Circuit Boards **1044**
Prof. Jeff Kettle[1], Dr. Jonathon Harwell [1]
1. University of Glasgow

Plenary Sessions

Plenary 6 - Dr Feras Alkhalil

Flexible Integrated Circuits Revolution: Innovative Manufacturing, Materials and Roadmaps **1047**
Dr. Feras Alkhalil[1]
1. PragmatIC Semiconductor

Elsevier YIA Talk - Dr Alexandros El Sachat

Engineering Thermal and Thermoelectric Transport in Two-dimensional (2D) Semiconductors and Devices **1049**
Dr. Alexandros El Sachat[1]
1. Institute of Nanoscience and Nanotechnology, NCSR "Demokritos", 27 Neapoleos str & Patriarchou Grigoriou, Ag. Paraskevi, 153 41, Greece

Oral Session 5A: Integrated System Processes

Microscale Patterning of Transparent Conductive Oxides (TCOs) Using High Precision Capillary Printing for Display Applications **1051**
Dr. Marc Pascual[1], Dr. Ludovic Hahn [2], Dr. Frederic Raynam [1], Mr. Nathan Bigan [1], Mr. Achille Guitton [1], Dr. Amin Mbarki [1], Dr. Tony Jullien [2], Dr. Chloe Guerin [2], Dr. Vincent Jousseaume [2]
1. Hummink, 2. CEA Leti

MULTILAYER POLYMER-BASED CANTILEVERS WITH MULTIPLE EMBEDDED PIEZORESISTIVE SENSORS FOR HIGH-SENSITIVITY ATOMIC FORCE MICROSCOPY **1053**
Mr. Ekin Asım Özek[1], Dr. Nahid Hosseini [1], Prof. Georg E. Fantner [1]
1. LBNI, EPFL

Pattern dependent micro needle formation in the SPPW process using a digital mask **1055**
Mr. Myung Seo Kim[1], Mr. Jun Ho Song [1], Ms. Seo Rim Park [1], Prof. Young Tae Cho [1]
1. Changwon National University, Changwon

Fabrication of Ultra-Scaled Back-End TiN Contacts in Silicon-Rich Oxide for High Density Memory Applications **1057**
Mrs. Christelle CHARPIN-NICOLLE[1], Mr. Gabriele NAVARRO [1], Mr. Antoine SALVI [1], Mrs. Catherine PELLISSIER [1], Mr. Pierre SIXT [1], Mr. Eric NGUYEN GIA CAN [1], Ms. Floriane BAUDIN [1], Ms. Cassandre BELUFFI [1], Mr. Richard SOUIL [1], Mr. Jean-Pierre NIETO [1], Mr. Dominique DESPOIS [1], Mr. Fabien LAULAGNET [1], Mr. Thomas MAGIS [1], Mr. Romuald BLANC [1], Mr. Olivier GLORIEUX [1], Mr. Grégory BONIFACE [1], Mr. Jean ROTTNER [1], Dr. Toshihiko Jimbo [2], Dr. Takashi Kojiri [2], Mr. Vincent BARRAL [1], Mr. François ANDRIEU [1]
1. *CEA-Leti, Uni. Grenoble Alpes, 38000 Grenoble, France,* ***2.*** *Zeon Corporation R&D Center, 1-2-1 Yako, Kawasaki-ku, Kawasaki, Kanagawa, 210-9507*

Oral Session 5B: Biodevices and Systems II

Fabrication of Low-cost Microfluidic Devices for Point-of-Care Bacterial Diagnostics **1060**
Dr. Maria Szola[1], Dr. Peng Tian [1], Ms. Chang Liu [1], Dr. Aysegül Develioglu [1], Mr. Gabriel Weber [1], Mr. Marceau Brisselian Kamary [1], Dr. Thomas Mortelmans [1], Dr. Dimitrios Kazazis [1], Dr. Philipp Berger [1], Dr. Yasin Ekinci [1]
1. *Paul Scherrer Institute (PSI)*

Non-Invasive Label-Free Electrical and Optical Parrallel Recordings of Electrophysiological Action Potentials of hiPSC Cardiomyocytes **1062**
Dr. Julien Hurtaud[1], Dr. Alessio Boschi [1], Dr. Giuseppina Iachetta [1], Dr. Michele Dipalo [1], Prof. Francesco De Angelis [1]
1. *Istituto Italiano di Tecnologia (IIT)*

Biodegradable silk fibroin nanofiber-based microparticles for wound regeneration **1064**
Mr. Marc Navarro[1], Ms. Laia Bagur [1], Mr. Lasse Højlund Eklund Thamdrup [2], Dr. Fatemeh Ajalloueian [2], Mr. Salvador David Aznar [3], Dr. Xavier Muñoz Berbel [1], Dr. Anja Boisen [2], Dr. Andreu Blanquer [4], Dr. Gonzalo Murillo [1]
1. *Institute of Microelectronics of Barcelona (IMB-CNM, CSIC),* ***2.*** *IDUN section, Department of Health Technology, Technical University of Denmark, DK-2800 Kongens Lyngby, Denmark,* ***3.*** *Instituto Murciano de Investigación y Desarrollo Agrario y Medioambiental,* ***4.*** *Departament de Biologia Cel.lular, Fisiologia i Immunologia, Universitat Autonoma de Barcelona*

Development of micron mist generating nebulizer **1066**
Mr. Taki Watanabe[1], Prof. Sho Amano [1], Prof. Yuichi Utsumi [1], Prof. Kazuhiro Kanda [1]
1. *Laboratory of Advanced Science and Technology for Industry, University of Hyogo*

Three-Dimensional Manipulation of Water Droplets via Spatially Patterned Triboelectric Charging **1068**
Mr. YU-CHIA CHEN[1], Mr. Cheng-Han Yu [1], Prof. Chin-Chi Hsu [1], Prof. Jiann Shieh [1]
1. *National United University*

Zero-power MEMS sensors for trees health monitoring **1070**
Ms. Zarina Nazyrova[1], Prof. Emile Martincic [1]
1. *C2N Université Paris-Saclay*

Oral Session 5C: Micro-Nano Systems I

CFET novel implementation to enhance IC integration level by stacking devices in a single vertical nanowire **1075**
Dr. Esteve Amat[1], Dr. Alberto del Moral [1], Prof. Joan Bausells [1], Prof. Francesc Pérez-Murano [1]
1. *Institute of Microelectronics of Barcelona (IMB-CNM, CSIC)*

Replaceable micromixer agitated by surface acoustic wave **1077**
Dr. Akinobu Yamaguchi[1], Mr. Masatoshi Takahashi [2], Dr. Satoshi Amaya [3], Prof. Tsunemasa Saiki [4]
1. *Toyo University,* ***2.*** *University of Hyogo,* ***3.*** *University of Tokyo,* ***4.*** *University of Fukuchiyama*

Characterization and Thermo-mechanical Analysis for a Light-driven Liquid-crystal-elastomer-based Crawling Robot **1079**
Ms. Yen-Chun Chen[1], Prof. Yao-Joe Yang [1]
1. *National Taiwan University*

A MINIATURIZED KIRIGAMI SOFT GRIPPER INTEGRATED WITH SELF-SENSING CAPABILITY **1081**
Mr. Chia Yu Cho[1], Prof. Yao-Joe Yang [1]
1. *National Taiwan University*

Short-Channel Junctionless Nanowire Transistors **1083**
Mr. Sayantan Ghosh[1], Mr. Alessandro Puddu [1], Dr. Slawomir Prucnal [1], Dr. Ahmad Echresh [1], Prof. Artur Erbe [1], Dr. Yordan M. Georgiev [1]
1. *Helmholtz-Zentrum Dresden-Rossendorf (HZDR)*

Oral Session 5D: Electronic Sensors

A Saw-Tooth Slot Antenna Sensor for Dielectric Sensing **1086**
Dr. Hilary Scott Nkimbeng Cho [1], Prof. Jin Choi[1]
1. *Michigan Technological University*

Exploitation of Surface Acoustic Waves for the implementation of innovative sensing devices applied to the measurement of gas phase pollutants **1088**
Dr. Meddy Vanotti[1], Ms. Ghida Fawaz [1], Ms. Margerie Loze [2], Mr. Sacha Poisson [1], Dr. Stéphane Brandès [2], Dr. Laurie André [2], Dr. Nicolas Desbois [2], Prof. Claude P. Gros [2], Dr. Virginie Blondeau-Patissier [1]
1. *Université Marie et Louis Pasteur, SUPMICROTECH, CNRS, Institut FEMTO-ST,* ***2.*** *Université Bourgogne Europe*

Tunable Nanoarchitectures in NiO/In2O3 Thin Films sensor: Thickness-Modulated Response Enhancement for Ultrafast Butanone Sensing **1090**
Prof. Zhenyu Yuan[1]
1. *Northeastern university*

Electric-field Sensor based on Graphene/MoS_2 Heterostructure for Lightning Forecast **1092**
Ms. Jiali Hu[1], Dr. Mohammad Razzakul Islam [1], Dr. Afsal Kareekunnam [1], Dr. Takeshi Kudo [2], Mr. Takeshi Maruyama [2], Prof. Masashi Akabori [1], Prof. Hiroshi Mizuta [1]
1. *Japan Advanced Institute of Science and Technology,* ***2.*** *Otowa Electric Co., Ltd.*

Disposable electrode based iontronic pressure sensors and their potential applications in generative artificial intelligence **1094**
Mr. Changwoo Cho[1], Ms. Chaeeun Lee [1], Prof. Je Hoon Oh [1]
1. *Hanyang University*

High-Mobility of Amorphous-Crystalline Phase-Composite Indium Oxide for Thin Film Transistor Applications **1096**
Mr. Quang Khanh Nguyen[1], Prof. Myung Mo Sung [1]
1. *Hanyang University*

Oral Session 6A: Advanced Nanofabrication III

Sequential Infiltration Synthesis for Organized Nanostructure Fabrication 1099
Dr. Gabriele Seguini[1]
1. IMM-CNR

Effect of Binary Mechanical Environment on T Cell Function 1100
Mr. Jatin jawhir Pandit[1], Mr. Abed Al Kader Yassin [2], Dr. Carlos Ureña Martin [1], Dr. Guillaume Le Saux [1], Prof. Angel Porgador [2], Prof. Mark Schvartzman [1]
1. Department of Materials Engineering, Ben-Gurion University of the Negev, P.O. Box 653, Beer-Sheva 84105, Israel; Ilse Katz Institute for Nanoscale Science and Technology, 2. The Shraga Segal Department of Microbiology, Immunology, and Genetics Faculty of Health Sciences, Ben-Gurion University of the Negev, P.O. Box 653, Beer-Sheva 84105, Israel

Patterning on Living Tardigrades 1102
Ms. Zhirong Yang[1], Dr. Shan Wu [1], Dr. Kang Zhao [1], Dr. Ding Zhao [1], Prof. Min Qiu [1]
1. Westlake University

Electrodeposition of conducting polymers on silicon towards integrated autonomous sensor systems 1104
Dr. Tomoyuki Kurioka[1], Mr. Punvinai Vinaisuratern [1], Mr. Joji Higuchi [1], Mr. Keisuke Okamoto [1], Prof. Tso-Fu Mark Chang [1], Mr. Nasser Aldhahri [2], Prof. John Mcbride [3], Dr. Yoshishige Tsuchiya [2], Prof. Masato Sone [1]
1. Institute of Integrated Research, Institute of Science Tokyo, 2. School of Electronics and Computer Science, University of Southampton, Southampton SO17 1BJ, United Kingdom, 3. School of Engineering, University of Southampton

A Thick-Film Micro-Patterning Method for Organic Thermoelectric Materials Using O2 Plasma and Metal Masks 1106
Mr. Shota SAWAYAMA[1], Dr. Qingshuo Wei [2], Prof. Daisuke Yamane [1]
1. Ritsumeikan University, 2. National Institute of Advanced Industrial Science and Technology (AIST)

Oral Session 6B: Micro-Nano Systems II

Making a Miniature Sun: Ultra High Temperature Carbon Devices 1109
Prof. Oliver Williams[1]
1. Cardiff University

Mechanical and electrical contact testing for Pt/PEDOT/Si layered structures 1111
Dr. Yoshishige Tsuchiya[1], Dr. Tomoyuki Kurioka [2], Mr. Punvinai Vinaisuratern [3], Mr. Joji Higuchi [3], Prof. Tso-Fu Mark Chang [2], Prof. Masato Sone [2], Mr. Nasser Aldhahri [1], Dr. Liam Boodhoo [4], Dr. Thomas Bull [5], Prof. Yan Yang [6], Prof. John Mcbride [5]
1. University of Southampton, 2. Institute of Science Tokyo, 3. Institute of Integrated Research, Institute of Science Tokyo, 4. School of Electronics and Computer Science, University of Southampton, Southampton SO17 1BJ, United Kingdom, 5. School of Engineering, University of Southampton, 6. TaiCaan Technologies

Wafer scale fabrication of pyrolytic carbon submicron gap membrane electrodes for electrochemical sensing 1113
Dr. Nicolai Støvring[1], Dr. Pratik Kusumanchi [1], Ms. Estefany Ureta [1], Dr. Arto Heiskanen [2], Prof. Jenny Emnéus [2], Prof. Stephan Sylvest Keller [3]
1. DTU Nanolab, 2. DTU Bioengineering, Danmarks Tekniske Universitet (DTU), 2800 Kgs. Lyngby, Denmark, 3. National Centre for Nano Fabrication and Characterization, DTU Nanolab, Technical University of Denmark

Energy-Free Micro-Latching Mechanisms for Bidirectional SMA Actuators **1115**
Ms. Yizheng Liu[1], Mr. Vincent Gottwald [2]
1. Institut für Mikrosystemtechnik – IMTEK, Albert-Ludwigs-Universität Freiburg, Georges-Köhler-Allee 102, 79110 Freiburg, Germany, 2. Karlsruhe Institute of Technology (KIT)

Physical reservoir computing with MEMS torsional mirrors **1117**
Mr. Yuta Kawashima[1], Mr. Mikiya Oki [1], Dr. Jun-Yu Ou [2], Dr. Yoshishige Tsuchiya [3], Prof. Toshiyuki Tsuchiya [1]
1. Kyoto University, 2. Physics and Astronomy, University of Southampton, 3. University of Southampton

Oral Session 6C : Optical Sensors

Monitoring vibrational fingerprints of polypeptide monolayers by infrared plasmonic nanoantennas **1120**
Dr. Santos Merino[1], Dr. Alberto Villar [1], Dr. Ruth Díez [1], Dr. Gabriel Ortega [2], Dr. Mónica García-Mota [3], Dr. Anna Kimmel [3], Dr. Albert Guerrero [4], Dr. Jorge Espina [5], Dr. Mario Zapata [6], Prof. Javier Aizpurua [7]
1. Tekniker, 2. CIC bioGUNE, 3. Simune Atomistics, 4. Instituto de Microelectrónica de Barcelona, 5. Universidad de Oviedo, 6. Materials Physics Center, 7. Donostia International Physics Center

On-fiber printed polymeric tapers for chronically implantable neural interfaces **1122**
Dr. Stella Aslanoglou[1], Dr. Barbara Spagnolo [1], Dr. Cinzia Montinaro [1], Dr. Alberto Perna [2], Dr. João F. Ribeiro [2], Dr. Marco Pisanello [3], Dr. Luca Berdondini [2], Dr. Tommaso Fellin [2], Dr. Ferruccio Pisanello [1], Prof. Massimo De Vittorio [1]
1. Center for Biomolecular Nanotechnologies, Istituto Italiano di Tecnologia (IIT), 73010 Arnesano, LE, Italy, 2. Center for Convergent Technologies, Istituto Italiano di Tecnologia (IIT), 16163 Genova, Italy, 3. OptogeniX s.r.l., 73010 Arnesano, Italy

Detection of Phtalate release from plastic tubes using a NanoFabricated Surface Enhanced Raman Spectroscopy device **1124**
Mr. Sofien Ramos[1], Ms. Camille Blanc [2], Dr. Laurence Salomé [2], Dr. Philippe Louarn [3], Dr. Emmanuelle Trevisiol [4], Prof. Christophe Vieu [1]
1. LAAS-CNRS, 2. IPBS, 3. IRAP, 4. TBI

Detection of Polystyrene Microplastics via Surface-Enhanced Raman Scattering on Sticky Hydrophobic Nanopillar Substrates **1126**
Mr. Tzu-Yu Chiu[1], Prof. Wen-Huei Chang [2], Mr. Kuan-Ting Kuo [1], Mr. Yao-Ming Ku [1], Prof. Chih-Chia Huang [1], Prof. Chun-Hung Lin [1]
1. Department of Photonics, National Cheng Kung University, 2. Department of Applied Chemistry, National Pingtung University

Micro-optics Design and Preliminary Characterization of a Fiber-Optic SERS Probe for In Vivo Diagnostics **1128**
Ms. Yingwei Hou[1], Dr. Nilanjan Manda [1], Dr. Belal Ahmad [1], Dr. Jang Ah Kim [2], Dr. Alexander J Thompson [1]
1. Department of Surgery & Cancer, Imperial College London, London, United Kingdom., 2. Department of Mechanical Engineering, Imperial College London, London, United Kingdom.

Oral Session 6D: Advanced Nanofabrication IV

Ice lithography using Diobalt octa-carbonyl **1131**
Mr. Limin Qi[1], Dr. Dongli Liu [2], Dr. Ding Zhao [3], Prof. Min Qiu [1]
1. Westlake University, 2. Westlake Instruments (Hangzhou) Technology Co., Ltd, 3. Westlake Institute for Optoelectronics

Quasi-3D Nanoscale Fabrication: Precision Patterning and Modelling via Focused Ion Beam Implantation **1133**
Dr. Jordi Llobet [1], Dr. Jordi Antoja[1], Dr. Alberto del Moral [2], Mr. Marcel de la Vega Czarnecki [1], Ms. Marta Duch [1], Mr. Alessandro Cian [3], Mr. Elia Scattolo [3], Dr. Michele Crivellari [3], Dr. Xavier Borrisé [4], Dr. Damiano Giubertoni [3], Prof. Francesc Pérez-Murano [2]
1. *Institut de Microelectrònica de Barcelona, IMB-CNM (CSIC), Universitat Autònoma de Barcelona, Cerdanyola Del Vallès, 08193, Barcelona, Spain.,* ***2.*** *Institute of Microelectronics of Barcelona (IMB-CNM, CSIC),* ***3.*** *FBK, Fondazione Bruno Kessler,* ***4.*** *Catalan Institute of Nanoscience and Nanotechnology (ICN2) and Barcelona Institute of Science and Technology (BIST)*

Investigation of process windows for alternative non-toxic and metal ion free developer choline hydroxide for HSQ resist Medusa 84 SiH **1135**
Ms. Pia Kohlschreiber[1], Mr. Markus Gottwald [1], Dr. Christian Helke [1], Mr. Harry Biller [2], Dr. Mandy Sendel [2], Dr. Danny Reuter [1]
1. *Fraunhofer Institute for Electronic Nano Systems ENAS,* ***2.*** *Allresist GmbH*

Resist-free and low-temperature micropatterning of IGZO using stencil lithography for electronic applications **1137**
Mr. Chenxiang Zhang[1], Prof. Giovanni Boero [1], Dr. Arnaud Bertsch [1], Prof. Jürgen Brugger [1]
1. *Microsystems Laboratory, Ecole Polytechnique Fédérale de Lausanne (EPFL)*

Abstracts

Plenary 1 - Dr Drew Nelson

Building Globally Relevant Semiconductor Clusters and Their Relevance to the UK Semiconductor Strategy

Tuesday, 16th September - 09:00: Plenary 1 - Dr Drew Nelson (Plenary Hall) - Oral - Abstract ID: 464

Dr. Drew Nelson [1]

1. *All Party Parliamentary Group on Semiconductors Advisory Board*

This talk will illustrate the pathways to building powerful, globally relevant semiconductor clusters, using the Compound Semiconductor Cluster in South Wales as an exemplar. During the presentation, the various elements to creating a successful and sustainable semiconductor ecosystem will be explored, and the relevance of such clusters to the UK Semiconductor Strategy will be examined.

Plenary 2 - Dr Naoto Horiguchi

CMOS scaling paradigm shift from CMOS 1.0 to CMOS 2.0

Tuesday, 16th September - 09:45: Plenary 2 - Dr Naoto Horiguchi (Plenary Hall) - Oral - Abstract ID: 454

Dr. Naoto Horiguchi [1]

1. *IMEC, Belgium*

Current CMOS technologies are homogeneous in terms of devices (Si-based FinFETs to nanosheet) and interconnects (Cu-based dual damascene for signal and power lines) for almost all functions (high performance & low power logic, SRAM, I/O, …) (CMOS 1.0). Its homogeneity provides a good power performance-area trade-off so far. However, exploding demands for performance improvement in diverse applications (from mobile to HPC) make significant challenges in the homogeneous CMOS scaling approach. In this paper, we will discuss how to extend CMOS 1.0 scaling by introducing new device and interconnect architectures and how to bring CMOS scaling to the next level by combining heterogeneous technologies with CMOS 1.0 from system viewpoint (CMOS2.0).

Plenary 3 - Prof Dinesh Pamunuwa

Edge Computing Platform based on Nanoelectromechanical Relays

Tuesday, 16th September - 11:00: Plenary 3 - Prof Dinesh Pamunuwa (Plenary Hall) - Oral - Abstract ID: 455

Prof. Dinesh Pamunuwa [1]

1. *University of Bristol*

Electronics that operate at the edge of the network, especially in industrial and manufacturing applications, typically have stringent environmental and power restrictions that limit their usage. For example, existing transistor technology struggles to function at temperatures much beyond 125 °C; thus, the electronics in an aircraft engine controller (FADEC) sit much further away from the engine than the sensors and actuators, even though the controller efficiency is significantly reduced as a result. High levels of radiation, as for example found in the nuclear sector and aerospace, also introduce many faults, limiting the lifetime of electronics while increasing fabrication and packaging costs and weight; a simple processor can cost 10,000 times as much as its standard cost when qualified for space. Many such applications, including ones that require resilience to both high temperatures and radiation levels, can be found in the industrial IoT. Moreover, current leakage grows exponentially with temperature, increasing the challenge of embedding electronics at the edge.

MNE Fellow Award: Prof Lars Montelius

Science in our time - for People, Planet and Prosperity

Tuesday, 16th September - 11:45: MNE Fellow Award: Prof Lars Montelius (Plenary Hall) - Oral - Abstract ID: 457

Prof. Lars Montelius [1]

1. *Lund University*

Semiconductors power virtually all modern technologies — from smartphones and AI data centers to electric vehicles (EVs), industrial automation, and medical devices. As more industries digitize and automate, the need for advanced chips grows.

- AI Boom: Training and running large AI models (like ChatGPT) require massive computational power, driven by GPUs and AI-specific chips.
- EV & Mobility Shift: Electric and autonomous vehicles need significantly more chips than traditional cars — for sensors, power management, infotainment, etc.
- IoT Growth: Billions of devices (smart homes, factories, etc.) are connecting to the internet, all requiring semiconductors.

The COVID-19 pandemic and geopolitical tensions exposed the fragility of the global chip supply chain. Further, the Covid-19 pandemics painfully made us aware of the necessity of robust supply chains – and today we witness the resulting increased demand for national manufacturing capabilities of critical products. In addition, there is a worldwide increased political instability. Semiconductors are now considered strategic assets — much like oil in the 20th century.

Consequently, the global geo-political landscape is rapidly changing. But even larger, and a necessity for a sustained and prosperous life at our planet Earth, is the absolute requirement for a **green** transition **to be able to become a sustainable society**.

Nanotechnology is a Key Enabling Technology with promises for making solid contributions to the grand societal challenges of today, offering possibilities to address solutions for enabling sustainable energy supply on demand, clean water to everyone, novel e-care and e-health paradigms etc.

These major societal developments challenge society and will in turn challenge the present higher education systems as well as the industrial society. There will be an increased demand for transversal interdisciplinary participation to enable the needed disruptive innovations to happen.

Higher Educational Systems are key for addressing large societal challenges – and serve at large as igniters of changes. And presently there are urgent needs for novel solutions and incentives to recruit needed trans-disciplinary engagements and closer collaboration with the industrial fabric - as well as with society at large. **Simply put, there is a need to join forces to create a global systemic and inclusive Science, Technology, Society and Innovation pathway for People, Planet and Prosperity.**

Oral Session 1A : Microsystem and MEMS Applications

Fabrication of Flexible III-Nitride MEMS Resonators by Lift-Off and Transfer onto Thin Metal Substrates

Tuesday, 16th September - 14:00: Oral Session 1A : Microsystem and MEMS Applications (Plenary Hall) - Oral - Abstract ID: 129

Mr. Ali Kassem [1], ***Dr. Rajat Gujrati*** [1], ***Mr. david bourrier*** [2], ***Dr. Cédric Ayela*** [3], ***Mr. Fabrice Mathieu*** [2], ***Prof. Isabelle Dufour*** [3], ***Prof. Liviu Nicu*** [2], ***Dr. Vishnu Ottapilakkal*** [1], ***Dr. Phuong Vuong*** [4], ***Prof. Suresh Sundaram*** [4], ***Prof. William Hunt*** [5], ***Prof. Abdallah Ougazzaden*** [5], ***Dr. Thierry Leichlé*** [5], ***Prof. Jean-Paul Salvestrini*** [1]

1. *CNRS, IRL 2958 Georgia Tech-CNRS, Metz, France,* ***2.*** *LAAS-CNRS, Université de Toulouse, CNRS, Toulouse, France,* ***3.*** *Université de Bordeaux, Laboratoire IMS UMR-CNRS 5218, Talence, France,* ***4.*** *Georgia Tech Europe, IRL 2958 Georgia Tech-CNRS, Metz, France,* ***5.*** *Georgia Institute of Technology, School of Electrical and Computer Engineering, IRL 2958 Georgia Tech-CNRS, Atlanta, GA, USA*

This work presents a scalable wafer-level transfer method for fabricating crack-free III-N MEMS drum resonators on flexible metal substrates. By electroplating a metal stressor on III-N layer epitaxially grown atop a 2D h-BN release layer, thermal delamination allows seamless transfer of III-N layers to a flexible metal substrate. Freestanding MEMS resonators are released by etching the metal layer, with integrated electrodes used to actuate the MEMS at resonance. This simple methodology offers strong potential for next-generation sensors aimed at wearable and IoT applications.

Recent efforts have focused on integrating freestanding MEMS resonators onto flexible substrates using various approaches. Conventional methods involve direct fabrication on flexible substrates with sacrificial layers, but these cannot withstand high temperatures and are thus limited to polycrystalline materials [1]. Another approach involves fabricating the MEMS device on a rigid substrate before transferring it to a flexible one. This allows for high-performance materials like AlN and $LiNbO_3$, but faces challenges including complex release steps and poor scalability [2]. Advances have been made using 2D layer transfer techniques, where materials like hexagonal boron nitride (h-BN) help lift and transfer layers for MEMS processing [3]. In this study, a metal stressor serves both as a transfer aid and as the bottom contact/flexible substrate—an approach termed Self-Lift-Off and Transfer (SLOT) [4], adapted here for the first time for flexible MEMS resonators. We demonstrate that this process enables crack-free AlGaN/GaN and GaN MEMS resonators, with expected resonance behavior, on flexible metal substrates. The SLOT process for MEMS resonators on flexible metal substrate is shown in Figure 1. III-N layers are grown atop a 2D h-BN layer, followed by electroplating of a 30 µm Ni stressor. The III-N/Ni bilayer is then delaminated by heating the sapphire growth substrate at 100°C for 1 hour. Thermal expansion mismatch between the metal and sapphire creates compressive and tensile stress in the metal and substrate, respectively, leading to delamination due to the weak Van der Waals forces in the h-BN layer. After lift-off, Ti/Au electrodes are deposited and patterned. Wet etching of circular cavities in the Ni layer releases the III-N films, forming freestanding III-N drum structures with electrodes sandwiching the III-N bilayer for integrated actuation (Figure 1).

The resulting III-N MEMS were characterized using a laser Doppler vibrometer to observe their vibration modes (Figure 2). The first five modes of GaN circular resonators on Ni were detected, with frequencies of 542.7 kHz, 1.087 MHz, and 1.836 MHz for 100 µm diameter drum resonators. Finite element method (FEM) simulations, using a tensile stress of ~130 MPa in the GaN layer, accurately predicted these resonance modes, validating the experimental results. Several hundred resonators were successfully fabricated using the SLOT process, showing promising quality factors: Q = 153 (Mode 1), Q = 385 (Modes 2–3), and Q = 313 (Modes 4–5) for the 100 µm diameter drum GaN resonator. Compared to conventional techniques involving sacrificial layers or complex release steps, this method provides a cost-effective, scalable route for high-performance flexible III-N

MEMS resonators.
[1] H. Hamid et al., IEEE Sens. J., vol. 21, pp. 12606–12617, 2021.
[2] X. Sun, et al., Appl. Phys. Lett., 115, 093501, 2019.
[3] R. Gujrati, et al., Appl. Phys. Lett., 124(10), 104102, 2024.
[4] S. Karrakchou et al. ACS Applied Electronic Materials 2021 3 (6), 2614-2621

Probing Cell Mechanosensitivity in Microengineered 3D Scaffolds

Tuesday, 16th September - 14:15: Oral Session 1A : Microsystem and MEMS Applications (Plenary Hall) - Oral - Abstract ID: 163

Ms. Aída Gabriela Fernández Contreras [1], ***Ms. Chloé Viat*** [1], ***Prof. Boudewijn van der Sanden*** [2], ***Prof. Olivier Stephan*** [3], ***Prof. Jean-Hervé Tortai*** [1], ***Prof. Alice Nicolas*** [1]

1. *LTM,* ***2.*** *TIMC,* ***3.*** *LiPhy*

Our team has developed an optimized two-photon polymerization protocol to fabricate isometric 3D scaffolds with tunable geometry. Using 3T3 fibroblasts, we demonstrated that microstructural variations influence cell morphology and cytoskeletal organization. This platform facilitates controlled studies of cell–matrix interactions in biomimetic environments, thereby advancing mechanobiology research and tissue engineering developments.

Keywords: Two-photon lithography, 3D cellular scaffolds, Mechanobiology, Isometric microfabrication.

Wafer-scale transfer-free multi-layer graphene process for MEMS sensors

Tuesday, 16th September - 14:30: Oral Session 1A : Microsystem and MEMS Applications (Plenary Hall) - Oral - Abstract ID: 450

Prof. Sten Vollebregt [1]

1. *Associate Professor*

Graphene has unique properties that make it an attractive material for sensors or nano/micro-electro-mechanical systems (NEMS/MEMS). For sensors, especially those based on mechanical structures, graphene does not necessarily have to be single-layer to achieve good performance. Moreover, few or multi-layered graphene can enhance mechanical stability or processability, especially for large, suspended devices [1].

Chemical vapour deposition (CVD) on a metal catalyst is widely regarded as the most promising method for integrating graphene into semiconductor technology. A downside of CVD graphene is that it requires the transfer of the graphene from the catalyst. This step can introduce polymer contamination, cracks, and wrinkles. Another challenge is adhesion issues with the target substrate, mainly for non-flat substrates [2]. While significant progress has been made in CVD graphene and transfer [3,4], challenges remain, especially when creating suspended graphene devices.

As an alternative to transfer, we have developed a transfer-free method based on Mo as a catalyst [5]. By pre-patterning the catalyst, the graphene anchors to the substrate on the edges of the pattern, enabling lithographic control over the size and location. Furthermore, adhesion issues are circumvented by keeping the catalyst until the end of the fabrication. The limitation of the technology is that the growth is coupled to the target substrate. However, this is not an issue for MEMS devices, as it is customary in the industry to have a separate MEMS chip to form a system-in-package (SiP).

Here, we will show the latest advances in this platform's technology. These include wafer-scale graphene gas sensors on suspended micro-hotplates [6]. By using the transfer-free process, variation of the devices was minimized while the heater enabled fast recovery. We also have demonstrated the first wafer-scale graphene condenser microphones with high mechanical compliance, 10-100x higher than Si MEMS, while being ~9x smaller[7].

[1] S. Lukas et al., ACS Nano, 18 (2024) 25614

[2] S. Wagner et al., Microelectronic Engineering, 159 (2016), 108

[3] D. Neumaier et al., Nature Materials, 18 (2019), 525

[4] P.G. Steeneken et al., 2D Materials, 23 (2025), 014035

[5] S. Vollebregt et al., Proc. of IEEE MEMS (2016), 17-20

[6] L.N. Sacco and S. Vollebregt, Proc. of IEEE MEMS (2025)

[7] R. Pezone et al., Microsystems & Nanoengineering 10 (2024), 27

High Speed Nickel Electrodeposition in a Supercritical CO2 Emulsified Nickel Sulfamate Bath toward MEMS Applications

Tuesday, 16th September - 15:00: Oral Session 1A : Microsystem and MEMS Applications (Plenary Hall) - Oral - Abstract ID: 189

Mr. WENDING HOU [1], ***Dr. Tomoyuki Kurioka*** [1], ***Prof. Chun-Yi Chen*** [1], ***Prof. Masato Sone*** [1], ***Prof. Tso-Fu Mark Chang*** [1]

1. *Institute of Science Tokyo*

This study reports nickel electrodeposition using a supercritical CO_2-emulsified sulfamate bath. The electrodeposited-Ni obtained from the supercritical CO_2-emulsified sulfamate bath showed 1.6 times greater Vickers hardness than that obtained from the conventional sulfamate bath.

Oral Session 1B : Electron Beam Lithography

Precise Dimension Control of Narrow Gaps in High Density Pattern on InP-Based Substrate by Electron Beam Lithography

Tuesday, 16th September - 14:00: Oral Session 1B : Electron Beam Lithography (Charnock Lecture Theater) - Oral - Abstract ID: 294

Mr. Hao Zhang [1], ***Dr. Jing Becker*** [2], ***Mr. Jan Ebbert*** [1], ***Mr. Tekin Kahilogullari*** [1], ***Dr. Daniel Ritter*** [2], ***Prof. Nils Weimann*** [1]

1. *Components for High Frequency Electronics, Duisburg, 47057, University Duisburg Essen,* ***2.*** *GenISys GmbH*

A mid-range parameter was incorporated into proximity effect correction for transmission line method structures, yielding enhanced spatial uniformity, reduced current crowding, and improved accuracy in contact resistance extraction. Experimental results exhibited strong agreement with simulations, validating the efficacy of the refined electron beam lithography approach.

Qualification of Direct Write E-beam Lithography Tools with Two-Dimensional Vernier Patterns

Tuesday, 16th September - 14:15: Oral Session 1B : Electron Beam Lithography (Charnock Lecture Theater) - Oral - Abstract ID: 395

Dr. Alexei Bogdanov [1]

1. *NTT Research Inc.*

Electron-beam lithography (EBL) remains a cornerstone technique in advanced microfabrication, providing unparalleled resolution for nanoscale device patterning. The precise control of EBL tool parameters is paramount to achieving high production yields and maintaining the stringent quality requirements of fabricated components. In this regard, the two-dimensional (2D) Vernier approach has emerged as an effective metrological method for evaluating the critical performance attributes of Gaussian-beam direct-write systems. This methodology facilitates the accurate assessment of key parameters, including beam size and shape, internal overlay accuracy, field stitching performance in step-and-repeat configurations, and stripe stitching precision in step-and-scan operations.

In this work, we present the application of the 2D Vernier method for the qualification of a vector-scan Gaussian beam e-beam lithography tool. Scanning electron microscopy (SEM) was employed for the acquisition and analysis of Vernier patterns, enabling detailed evaluation of the tool's performance metrics. These measurements included the characterization of beam spot size and shape distribution across the scanning field, as well as the assessment of the tool's pattern placement accuracy.

The experimental results reveal that the 2D Vernier method achieves over an order of magnitude improvement in measurement accuracy across all evaluated parameters when compared to conventional qualification techniques. Notably, the 2D Vernier method uniquely enables precise measurements of the effective spot size and beam shape, surpassing the practical accuracy of existing approaches. Furthermore, placement accuracy, internal overlay precision, and field stitching accuracy were determined with sub-angstrom resolution, demonstrating the exceptional metrological capability of this method.

These findings highlight the efficacy of the 2D Vernier method in enhancing the precision and reliability of EBL tool characterization. By delivering superior measurement fidelity, this approach offers a robust framework for optimizing system performance and ensuring stringent quality control in electron-beam lithography processes.

Direct Fabrication of 3-D PEDOT:PSS Nanostructures by Electron Beam Lithography

Tuesday, 16th September - 14:30: Oral Session 1B : Electron Beam Lithography (Charnock Lecture Theater) - Oral - Abstract ID: 271

Mr. Yandong YANG [1], ***Prof. Shin'ichi Warisawa*** [1], ***Prof. Reo Kometani*** [1]

1. *Graduate School of Frontier Sciences, The University of Tokyo*

In this study, the EBL-based direct fabrication of the 3-D PEDOT:PSS nanostructure was achieved, and its exposure properties were analyzed, and effect of e-beam irradiation to the chemical state of PEDOT:PSS were evaluated by Raman spectroscopy.

High Resolution Electron Beam Lithography Patterning for Advanced Grating Couplers

Tuesday, 16th September - 14:45: Oral Session 1B : Electron Beam Lithography (Charnock Lecture Theater) - Oral - Abstract ID: 224

Ms. Pragya Sah [1], ***Mr. Radhakant Singh*** [1], ***Mr. Kai Zhang*** [1], ***Mr. Michael Möller*** [1], ***Dr. Rijil Thomas*** [1], ***Dr. Jens Bolten*** [1], ***Ms. Anastasiia Sorokina*** [2], ***Mr. Guochun Du*** [3], ***Mr. Carl Grimpe*** [3], ***Dr. Steffen Sauer*** [2], ***Dr. Elena Jordan*** [3], ***Prof. Stefanie Kroker*** [2], ***Prof. Tanja Mehlstaeubler*** [3], ***Dr. Stephan Suckow*** [1], ***Prof. Max Lemme*** [4]

1. *AMO GmbH,* ***2.*** *Technische Universität Braunschweig,* ***3.*** *Physikalisch-Technische Bundesanstalt,* ***4.*** *Chair of Electronic Devices, RWTH Aachen University*

Grating couplers (GCs) are crucial for coupling light into photonic integrated circuits. We focus on optimized fabrication of apodized GCs for near-infrared wavelengths. These offer improved coupling efficiency and directionality over conventional uniform GCs but require tighter critical dimension control, varying feature sizes, and high aspect ratios (~2.86). We address this by targeted modifications in resist, dose, and etching, thus reducing the minimum manufacturable ridges and trenches from 200nm and 90nm to 110nm and 50nm, respectively. The emission angle of these GCs shows strong agreement with simulation (-52.40° vs. -51.88°), which is significant for e.g., optical addressing of trapped ions.

A novel patterning approach enabling consistent high aspect ratio nanostructures with functional tops

Tuesday, 16th September - 15:00: Oral Session 1B : Electron Beam Lithography (Charnock Lecture Theater) - Oral - Abstract ID: 177

Mr. Bryan Benz [1], ***Prof. Marco Stampanoni*** [2], ***Prof. Martino Poggio*** [3], ***Dr. Lucia Romano*** [1]

1. *Paul Scherrer Institute (PSI),* ***2.*** *ETH Zürich,* ***3.*** *University of Basel*

A patterning approach to realize structures with ultra-high aspect ratio for MacEtch is presented. The silicon structures achieve aspect ratios up to 1’000:1 with widths of 100 nm and different top layer materials. These tops are placed prior to MacEtch and provide a functional aspect to the resulting structures.

Oral Session 1C : Electronics 1

P-channel Oxide Thin Film Transistors for CMOS Logic

Tuesday, 16th September - 14:00: Oral Session 1C : Electronics 1 (One Ocean Suite) - Oral - Abstract ID: 439

Dr. Kham Niang [1], Dr. Ben Peek [2], Dr. James Parish [3], Prof. Paul Chalker [2], Prof. Andrew Johnson [3], Prof. Andrew Flewitt [1]

1. *University of Cambridge,* ***2.*** *University of Liverpool,* ***3.*** *University of Bath*

In this work, promising precursors for the ALD deposition of SnO are explored. Sn (II) bis(*tert*-butoxide) is shown to produce TFTs following annealing at 250 – 350 ºC with a field effect mobility up to 2 cm^2 V^{-1} s^{-1} and a switching ratio between 10^3 and 10^4 [4]. By combining these devices with a-IGZO TFTs, all-oxide TFT-based CMOS inverters have been produced with a DC voltage gain of ~130 for a supply voltage of 4 V (Figure 1). The deposition of amorphous SnO (a-SnO) is also reported using another novel precursor with a growth rate that is over 4 times higher than typically-reported growth rates by ALD. Transfer characteristics of TFTs produced with this a-SnO are shown in Figure 2. These devices have a field effect mobility ~1 cm^2 V^{-1} s^{-1}, a threshold voltage close to 0 V and a switching ratio ~10^5. These devices are particularly attractive not only due to the good electrical characteristics, but also because of the fast deposition and the uniformity afforded by amorphous thin film semiconductors.

Electric Field Confinement-Induced Potentiation in Inert Mixed Ionic-Electronic Conducting Memristors

Tuesday, 16th September - 14:30: Oral Session 1C : Electronics 1 (One Ocean Suite) - Oral - Abstract ID: 419

Dr. Philip Calado [1]

1. *University of Southampton*

Memristors are two-terminal passive circuit elements characterised by their ability to change resistance in response to past electrical stimuli in such a way that the device current is a function of both the applied voltage and a history-dependent state variable.[1] Interconnecting an array of memristors produces a hardware neural network capable of in-memory computing with the potential to realize neuromorphic chips with improved energy efficiency, real-time learning and greater fault tolerance as compared to the current breed of silicon-based Artificial Intelligence accelerators.[2] Electronic currents within mixed ionic-electronic conductors (MIEC), such as hybrid organic-inorganic perovskites, can be modulated through the redistribution of slow moving ionic carriers, making them prime candidates for use as memristive materials.[3][4] Many challenges remain for the research field, however, including understanding the underlying memristive mechanisms, device stability, and state retention.

In this work, potentiation and depression of currents in inert perovskite memristors (IPMs), employing unreactive electrode materials[3], is successfully reproduced using a numerical drift-diffusion device simulator[5] and an analytical model. The memristor device models developed for the study include both electronic carriers and relatively high concentrations of intrinsic mobile ionic carriers (>10^{17} cm^{-3}), compensated by static counter ions, modelling Schottky defects. The results indicate that the potentiation and depression of currents observed within IPMs can be attributed to Schottky defect migration in response to the time-averaged internal electric field generated during a series of voltage pulses applied to the device. As defects migrate during potentiation, the potential drop across the perovskite layer becomes localised to the interfaces, increasing the magnitude of the electric field and associated electronic drift currents in these regions. This electric field confinement effect injects more electronic carriers into the field-free region, enabling higher diffusion currents. The models show that potentiation in IPMs can be explained by this effect as opposed to energetic (Schottky) barrier modulation.[6] Depression of currents is achieved via the inverse process during which the potential drop becomes spatially distributed across the device. Notably, the state variable controlling the resistance in IPMs is explicitly identified as the time-dependent ionic depletion width. These findings provide new insight into the resistive switching mechanism underlying inert MIEC memristors more generally and suggest new design strategies for the optimisation of real-world devices.

References

[1] L. O. Chua, IEEE Trans. Circuit Theory, 18(5) (1971) 507–519.

[2] S. Kumar et al., Nat. Rev. Mater., 7(7) (2022) 575–591.

[3] Z. Xiao and J. Huang, Adv. Electron. Mater., 2 (2016) 1–8.

[4] S. J. Kim et al., Nat. Nanotechnol., 20 (2025) 83–92.

[5] P. Calado et al., J. Comput. Electron., 21(4) (2022) 960–991.

[6] X. Guan et al., Adv. Funct. Mater., 28(3) (2018) 1704665.

Towards aluminium nitride on diamond surface acoustic wave devices

Tuesday, 16th September - 14:45: Oral Session 1C : Electronics 1 (One Ocean Suite) - Oral - Abstract ID: 435

Dr. Jerome Cuenca [1], ***Dr. Soumen Mandal*** [1], ***Prof. Oliver Williams*** [1]

1. *Cardiff University*

High-frequency communication devices rely on surface acoustic wave (SAW) filters due to their low insertion loss and high selectivity[1]. SAW devices can be fabricated on bulk or thin-film piezoelectric materials including lithium niobate ($LiNbO_3$), zinc oxide (ZnO), gallium nitride (GaN) and aluminium nitride (AlN), enabling acoustic wave generation through an interdigitated transducer. However, the maximum operating frequency is limited by the minimum feature size of the transducer fingers but ultimately, the acoustic velocity of the material (4,000 to 6,000 m/s) [2,3,4]. To overcome this, piezoelectric films need to be integrated with high velocity substrates such as diamond (12,000 m/s)[3], either through direct deposition or through wafer bonding.

In previous work, super-high-frequency SAW resonators have been fabricated on AlN/diamond heterostructures, operating beyond 10 GHz [3]. Previous work on AlScN, where the piezoelectric coupling coefficient is up to 4x greater than AlN, has also demonstrated gigahertz devices, although material deposition and integration is significantly more challenging[4]. Owing to the difficulty in direct heteroepitaxy of diamond on piezoelectric films, the film is typically deposited on a freestanding diamond either through sputtering or molecular beam epitaxy. However, this means that the film is inherently textured and granular where ideally single crystal films are preferred, so as to avoid any potential mechanical losses caused by grain boundaries and coupling losses due to an inhomogeneous piezoelectric film.

In this work, we present advancements in integrating diamond and AlN for high-performance surface acoustic wave (SAW) devices, with (1) preliminary investigations of SAW devices on single crystal AlN and (2) freestanding AlN on diamond plates through direct diamond growth on single crystal AlN (10x10 mm^2 area) for SAW devices. For this demonstration we use simple optical lithography to produce micron scale SAW devices with aim to directly compare AlN/Si and AlN/Diamond devices. We present finite element modelling of these simple structures to show the ~2x increase in frequency just by changing the substrate.

Nanoscale Back-End-of-Line Silicon Carbide Memristor for Resistive Memory

Tuesday, 16th September - 15:00: Oral Session 1C : Electronics 1 (One Ocean Suite) - Oral - Abstract ID: 298

Mr. Qin Liu [1], ***Dr. Omesh Kapur*** [1], ***Dr. Anushka Gangnaik*** [2], ***Dr. Ruomeng Huang*** [2], ***Prof. Kees de Groot*** [2]

1. *School of Electronics and Computer Science, University of Southampton, Southampton SO17 1BJ, United Kingdom,* ***2.*** *University of Southampton*

This report presents nanoscale silicon carbide memristors fabricated employing plasma-enhanced chemical vapour deposition (PECVD), explores their performance and proves their potential and development prospects for applications in resistive memory and neuromorphic computing.

2D Materials for Electrostrictive FET

Tuesday, 16th September - 15:15: Oral Session 1C : Electronics 1 (One Ocean Suite) - Oral - Abstract ID: 169

Ms. Nigama Vykari Vajjula [1], ***Mr. Fitunerediate Gebeyehu*** [1], ***Prof. Ethan Ahn*** [1]

1. *George Mason University*

In this work, the TMD heterostructure of MoS_2/$PtSe_2$ is finite-element simulated with a focus on electrostriction of MoS_2 and the strain-to-stress transfer on $PtSe_2$. Stress as high as 10^7 Pascal is induced on few-layer $PtSe_2$ for a nominal gate voltage of 1 V applied to monolayer MoS_2.

Oral Session 1D:
Biodevices and Systems 1

Contactless Measurement of Radial Artery Pulse Waves Using an Acoustic Sensing System

Tuesday, 16th September - 14:00: Oral Session 1D: Biodevices and Systems 1 (Seminar Room) - Oral - Abstract ID: 288

Ms. Chaeeun Lee [1], ***Prof. Je Hoon Oh*** [1], ***Mr. Changwoo Cho*** [1]

1. *Hanyang University*

In this work, we present a prototype system for the contactless acquisition of radial artery pulse waves using a smart speaker and microphone array. By leveraging this system, the full potential for non-invasive, contactless measurement of radial artery pulse waves can be realized, offering an accurate approach for cardiovascular monitoring.

A microfluidic Cartilage-on-Chip platform for personalized cartilage transplant compatibility screening

Tuesday, 16th September - 14:15: Oral Session 1D: Biodevices and Systems 1 (Seminar Room) - Oral - Abstract ID: 428

Dr. Rahman Sabahi-Kaviani [1]***, Ms. Giorgia Mazzini*** [2]***, Ms. Emma Bristow*** [2]***, Dr. Cynthia Fehres*** [2]***, Prof. René Toes*** [2]***, Dr. Yolande Ramos*** [2]***, Prof. Ingrid Meulenbelt*** [2]***, Dr. Regina Luttge*** [1]

1. *Eindhoven University of Technology,* ***2.*** *Leiden University Medical Centre*

Osteoarthritis (OA) is a leading cause of joint degeneration, often requiring joint replacement [1]. While iPSC-derived cartilage presents a promising regenerative alternative, its clinical success hinges on patient-specific compatibility and the risk of allograft rejection [2]. Existing Cartilage-on-Chip models have advanced the simulation of cartilage-bone interactions and mechanical stimuli [3–5], yet they fall short in assessing immune responses, leaving a gap in screening patient eligibility for cartilage transplantation.

To address this, we introduce a Cartilage-on-Chip screening platform that integrates microfluidic and microtunnel devices (MDs) [6]. Fabricated using photolithography and soft lithography techniques, MDs consist of PDMS structures bonded to glass substrates (Fig. 1a) [7]. These devices allow spatially controlled co-culture of iPSC-derived cartilage organoids (hiChOs), primary chondrocytes, synovial fluid, synovium, and immune cells such as T-cells (Fig. 1b). The microtunnel architecture supports diffusion-based signaling while preventing direct cell mixing, enabling physiologically relevant interaction studies under controlled conditions. The platform is modular and scalable, allowing for parallelized, high-throughput screening. Furthermore, its transparent PDMS-glass design permits live imaging and fluorescence-based readouts. Biocompatibility tests with patient-derived chondrocytes and iPSC-derived cartilage organoids demonstrated high survival rates (>80%) after 48 hours of co-culture, confirming the suitability of MDs for integrated biological assays.

Cytokine release is a hallmark of immune activation during allograft rejection, and electrochemical (EC) sensors provide a powerful method for cytokine detection [8]. While functionalized EC sensors offer high specificity for individual cytokines, non-functionalized sensors detect total cytokine mass, making them suitable for broad inflammation profiling due to their simpler design and fabrication. To enable real-time monitoring of immune responses, we developed a non-functionalized graphene-based electrochemical sensor [9] and integrated it into the MD platform (Fig. 2a–b). Initial validation using electrochemical impedance spectroscopy (EIS) on NaCl solutions with varying concentrations resulted in Bode and Nyquist plots exhibiting clear impedance shifts across concentrations (Fig. 3), confirming the sensor's sensitivity, reproducibility, and compatibility with the MD layout

In the next phase, we will test the sensor with cytokine-spiked media and apply it to co-culture assays involving hiChOs, primary chondrocytes, and immune cells to monitor dynamic immune responses. This integrated platform represents a step toward developing a clinically relevant pre-transplant screening tool to personalize regenerative joint therapies and improve the outcomes of cartilage implantation procedures.

[1] Loeser, Richard F., et al. *Arthritis and rheumatism* 64.6 (2012): 1697.

[2] Abe, Kengo, and Noriyuki Tsumaki. *Inflammation and Regeneration* 43.1 (2023): 56.

[3] Tuerlings, Margo, et al. *Advanced Materials Technologies* 7.8 (2022): 2101310.

[4] Paggi, Carlo Alberto, et al. *Lab on a Chip* 22.9 (2022): 1815-1828.

[5] Liu, Hao, et al. *Bioactive Materials* 33 (2024): 61-68.

[6] Bastiaens, Alex, et al. *Frontiers in Neuroscience* 14 (2020): 666.

[7] Sabahi-Kaviani, Rahman, et al., *In Preperation*.

[8] McCrae, Lauren E., et al. *Biosensors and Bioelectronics: X* 13 (2023): 100288.

[9] Khayamian, Mohammad Ali, et al. *RSC advances* 11.55 (2021): 34503-34515.

A Microfluidic Device for Monitoring Functional Enzyme Activity of Primary Human Hepatocyte Spheroids Based on Cell-Secreted Extracellular Vesicles

Tuesday, 16th September - 14:30: Oral Session 1D: Biodevices and Systems 1 (Seminar Room) - Oral - Abstract ID: 96

Mr. Ehsanollah Moradi [1], ***Dr. Päivi Järvinen*** [1], ***Dr. Markus Haapala*** [1], ***Prof. Ossi Korhonen*** [2], ***Prof. Tiina Sikanen*** [1]

1. *University of Helsinki,* ***2.*** *University of Eastern Finland*

Primary Human Hepatocytes (PHH) quickly lose liver-specific functions in traditional cultures, limiting their use in drug metabolism studies. Culturing PHH in a 3D format helps preserve their phenotype and provides an in vivo-like environment. This study explores using cell-secreted extracellular vesicles (EVs) to monitor metabolic enzyme activities in 3D cultured PHHs. EVs transfer cellular cargo that influences biological processes, but their isolation and characterization are complex. A new microdevice was developed for on-chip EV isolation and enzyme activity analysis in a single experiment. This device uses electrochemical impedance spectroscopy (EIS) and a micropillar array for EV quantitation and enrichment. It selectively immobilizes hepatocyte-secreted EVs using a HepPar1 antibody. The study found that EV and protein amounts increase during the initial days of 3D culture, stabilizing after nine days as spheroids mature. The microdevice's analysis showed that liver-specific EV profiles and CYP3A4 activities follow similar trends to total EVs and enzyme activities, indicating that 3D culture supports PHH stability. The microfluidics-assisted EV isolation method could noninvasively monitor cell culture maturation and differentiation. The system demonstrated robust EV immobilization efficiency and stability after cryopreservation, supporting its potential for technology transfer and scale-up.

Keywords: Primary Human Hepatocytes (PHH), Extracellular Vesicles (EVs), Electrochemical Impedance Spectroscopy (EIS), CYP3A4 activity, Freeze-Drying

Wavelength-selective photodetector for NADH fluorescence detection

Tuesday, 16th September - 14:45: Oral Session 1D: Biodevices and Systems 1 (Seminar Room) - Oral - Abstract ID: 321

Mr. Zhengwei Liao [1], ***Ms. Laura Cavedoni*** [1], ***Ms. Ceren Kutucu*** [1], ***Prof. Padmakumar Rao*** [1], ***Prof. Clementine Boutry*** [1], ***Prof. Filipe Arroyo Cardoso*** [1]

1. *Delft University of Technology*

NADH, a crucial molecule in cellular energy metabolism, provides valuable insight for disease diagnosis through non-invasive monitoring utilizing its fluorescence property. Here, we propose a backside-illuminated, wavelength-selective photodetector for NADH molecule fluorescence detection. The device adopted a transistor-like architecture, operating in the subthreshold regime. The detector substrate thickness was optimized to be 900 nm, balancing its high selectivity (470 nm over 350 nm photocurrent) of 115.1, together with a relatively strong 470 nm photocurrent of 1.83 nA. We achieved precise substrate thinning down to 900 nm using the shallow trench isolation feature as an etching ending point.

Nano- and Microscale Aptamer Biosensors for Monitoring Biomarkers of Human Health

Tuesday, 16th September - 15:00: Oral Session 1D: Biodevices and Systems 1 (Seminar Room) - Oral - Abstract ID: 441

Prof. Nako Nakatsuka [1]

1. *CHEMINA - EPFL*

Monitoring small molecules is essential for advancing diagnostics, therapeutics, and real-time health monitoring across a wide range of biomedical applications. Specifically in neuroscience, advancing our fundamental understanding of brain (dys)function requires the development of novel nanotools capable of monitoring chemical signaling in complex biological systems. Detecting small molecules in the brain is especially challenging due to low concentrations spanning orders of magnitude (picomolar to micromolar), limited mass and charge, and interference from high amounts of nonspecific molecules. Further, neurotransmitters co-exist with structurally similar metabolites across different brain regions. At the Laboratory of Chemical Nanotechnology (CHEMINA), we tackle this challenge by integrating DNA-based recognition elements called aptamers, into nano- and microscale biosensing platforms fabricated in-house. Aptamers are systematically designed oligonucleotide receptors that exhibit highly specific and selective recognition of targets. We employ aptamers designed to recognize small-molecule neurotransmitters such as serotonin and dopamine with high affinity and selectivity. We have developed nanoscale aptamer-modified nanopipettes with ~10 nm openings – approaching the spatial resolution of synapses where neurons communicate (~50 nm) – as well as microscale aptamer-functionalized field-effect transistors. Reversible target binding induces conformational changes in the aptamers, rearranging their negatively charged backbone, which are transduced into measurable electrical signals through the nanopore or across the semiconducting channel, respectively. Extensive characterization of these target-specific aptamer structural dynamics has provided fundamental insights into the signal transduction mechanisms underpinning our biosensing technologies. These findings lay the foundation for expanding this approach to a broad range of small-molecule targets – including sugars, amino acids, lipids, and hormones – relevant to diverse areas of human health.

Poster Session 1

Ionic Liquids and Focused Ion Beams: Are all Ionic Liquids Adequate for Advanced FIB Micro- or Nano-engineering?

Tuesday, 16th September - 16:00: Poster Session 1 - Poster - Abstract ID: 7

Dr. Jacques Gierak [1], ***Ms. Elinoa Sebag*** [2], ***Mr. Amir Goodwin*** [2], ***Mr. David Bouville*** [2], ***Dr. philippe Lesot*** [3], ***Dr. philippe Berdagué*** [3]

1. *C2N-CNRS,* ***2.*** *Centre de Nanosciences et de Nanotechnologies (C2N), Palaiseau, 91120, France,* ***3.*** *ICMMO*

In this work, we will present our efforts to re-invest the FIB micro-fabrication based on our recent development of space thruster based on multi-tip cell emitters capable of: i) achieving stable and long-lasting emission fluxes (125 **µA**/cm²), ii) beam energies around 10 keV, and iii) operation sequences with a constant polarity exceeding 15 minutes. It is indeed crucial for a FIB process to maintain the geometrical alignment of the emitter using transfer optics and maintain both the transported dose for the duration of the patterning sequence and the transported ions nature, charge and masses.

Plasmonic aluminium nanogap creation by electromigration for plasmonic UV-Nanolithography

Tuesday, 16th September - 16:00: Poster Session 1 - Poster - Abstract ID: 20

Mr. Jakob Nüßlein [1], ***Mr. Zhuoji Huang*** [1], ***Prof. Steffen Strehle*** [1]

1. *Techische Universität Ilmenau*

In our approach, we explore a strategy for the creation of nanogaps via electromigration in aluminium. Specifically, our contribution targets the design and implementation of plasmonic masks for sub-wavelength UV-lithography by room temperature electromigration investigating the associated limitations and parameter dependencies.

Improved Accuracy in Measuring the Dielectric Constant of Nanoparticles in Electrostatic Force Microscopy

Tuesday, 16th September - 16:00: Poster Session 1 - Poster - Abstract ID: 24

Mr. Lukas Lehnert [1], ***Mr. Benjamin Baumann*** [1], ***Prof. Ronald Thoelen*** [2], ***Prof. Hildegard Moebius*** [1]

1. *University of Applied Sciences Kaiserslautern,* ***2.*** *Hasselt University*

In this study, the influence of tip size in relation to particle size for measuring the dielectric constant of nanoparticles using the Electrostatic Force Microscopy (EFM) is investigated. This research shows that using a tip larger than the particle yields better accuracy when measuring the dielectric constant of nanoparticles.

Effect of doping Nb on optical properties of Sea Urchin-like TiO2 Photocatalysis

Tuesday, 16th September - 16:00: Poster Session 1 - Poster - Abstract ID: 26

Dr. Mariko Murayama [1], ***Prof. Xinwei Zhao*** [2], ***Prof. Taichiro Nishio*** [1]

1. *Tokyo University of Science,* ***2.*** *Henan University of Technology*

Sea urchin-like titanium dioxide (U-TiO_2) and niobium-doped U-TiO_2 (U-TiO_2: Nb) were successfully synthesized by a hydrothermal method. Both samples exhibited a consistent sea urchin-like structure with grown crystals in a specific direction.

Photocatalytic performance evaluated using Methylene Blue and UV-Vis revealed that U- TiO_2: Nb had better photodegradation activity with narrower E_g than that of U-TiO_2 and pristine TiO_2 powder. Even without doping Nb, U-TiO_2 showed improved photocatalytic performance, suggesting that the sea urchin-like structure led to improved light absorption efficiency, facilitated by the scattering of light through nanorods with the wide surface areas in the urchin-like samples. In addition, Nb doping resulted in increased conductivity, contributing to higher carrier concentration. This study highlights U-TiO_2: Nb as a promising photocatalyst with both high photocatalytic efficiency and easy recoverability.

The findings suggest its potential application in various environmental and industrial contexts require efficient and reusable photocatalytic materials.

PVDF-TrFE with suspended AlN particles: a polymer nano-composite with boosted ferroelectric properties

Tuesday, 16th September - 16:00: Poster Session 1 - Poster - Abstract ID: 27

Dr. Wolfgang Hilber [1], ***Mr. Sebastian Lang*** [1], ***Prof. Bernhard Jakoby*** [1]

1. *Johannes Kepler University Linz*

PVDF-TrFE, additively printed and embedded into the organic surface coating of metallic substrates, has been successfully used by our group for the realization of piezo- and pyroelectric transducers for various applications. Here we present an approach to boost the ferroelectric properties of the material while maintaining the achieved ease of processing, by adding highly ferroelectric ceramic AlN nano-particles that are uniformly incorporated into the PVDF-TrFE polymer matrix. In this way, a highly functional ferroelectric composite has been created, featuring a maximum polarization that exceeds that of the PVDF-TrFE base material by far.

Fabrication of Ferroelectric PVDF:TrFE Foil via Controlled Dewetting

Tuesday, 16th September - 16:00: Poster Session 1 - Poster - Abstract ID: 28

Mr. Sebastian Lang [1], ***Dr. Wolfgang Hilber*** [1], ***Ms. Tina Mitteramskogler*** [1], ***Prof. Bernhard Jakoby*** [1]

1. *Johannes Kepler University Linz*

Flexible electronics and sensor technologies are becoming increasingly important due to their wide-ranging applications in wearable devices, healthcare monitoring, environmental sensing, and industrial automation [1]. Especially poly(vinylidene-fluoride) (PVDF) and its copolymer with trifluoroethylene have been some of the most used polymers in force-sensing applications due to their strong piezoelectricity and wide range of ways of fabrication [2]. Usually, force sensors using PVDF are fabricated either by using a prefabricated and polarized large-scale foil, which is cut to size, creating fibers to embed into a polymer matrix or similar, or by printing the sensor and its electrodes directly onto the final substrate [3,4].

This work presents an alternative method for fabricating Poly(vinylidene fluoride–trifluoroethylene) (PVDF:TrFE) foils of arbitrary shape, size, and thickness via stencil printing and following controlled dewetting from the substrate. This foil could be used to fabricate various kinds of devices utilizing the chemical stability of PVDF, or flexible piezoelectric or ferroelectric sensors. Compared to utilizing a prefabricated foil, this approach does not require cutting the foil before the following steps or fixing it for any printing process. Subsequent printing of other functional materials allows for the fabrication of sensors on this fixed substrate to any shape and design desired[m1] . After all the printing steps are performed, the foil can be separated via dewetting, leaving the self-supported sensors ready for use.

The proposed process starts with stencil printing a layer of PVDF:TrFE onto a gold substrate. This step is identical to existing fabrication processes for rigid PVDF-based force sensors [5]. The substrate used is a printed circuit board (PCB) with a single large electrode coated with electroless nickel immersion gold (ENIG) as shown in Figure 1. Afterward, other necessary processing steps may be conducted to build the finished device which is still attached to the rigid substrate. An additional layer of PVDF:TrFE may be needed for passivation and protection from the chemicals used in the following steps. After these steps, a solution of acetone and gamma-butyrolactone (GBL) in a mixture of approximately 50:50 is applied to simultaneously soften the PVDF:TrFE layer and cause the first layer to dewet from the gold substrate. It is crucial to only add as little as necessary, as the PVDF:TrFE might get partially dissolved. Successful dewetting can be observed via a honeycomb-like structure appearing due to the detachment and slight expansion of the first PVDF:TrFE layer. The foil can then be cut free from any attachments (e.g., parts of the substrate that are not covered in ENIG) and then dried off in warm air.

This work has been partially supported by the State of Upper Austria in the frame of the Center for Symbiotic Mechatronics (of the Linz Center of Mechatronics, LCM).

X-ray energy dependence of gold nanoparticle synthesis in X-ray radiolysis

Tuesday, 16th September - 16:00: Poster Session 1 - Poster - Abstract ID: 29

Dr. Akinobu Yamaguchi [1], ***Dr. Kenji Hanada*** [2], ***Prof. Ikuo Okada*** [2], ***Dr. Hiroshi Sekiguchi*** [3], ***Dr. Ikuya Sakurai*** [4]

1. *Toyo University,* ***2.*** *Aichi Synchrotron Radiation Center,* ***3.*** *Japan Synchrotron Radiation Research Institute,* ***4.*** *Nagoya University*

Nanoparticles are of tremendous scientific and industrial importance owing to their unique physicochemical properties arising from their nanoscale dimensions. For example, gold nanoparticles in particular are used for colouration of stained glass in familiar applications and as a colouration mechanism in infectious disease testing kits. More recently, they have attracted attention for their use as molecular sensors utilising surface-enhanced Raman scattering, as well as for their use as nanotags, since they excite plasmon resonance.

Chemical synthesis methods are mostly used to produce nanoparticles. Recent reports on the feasibility of nanoparticle synthesis by photoexcited chemical reactions have attracted attention to mechanistic elucidation and applied research. In this study, research was carried out with the aim of conducting basic research to elucidate the mechanism and engineering applications of nanoparticle synthesis from liquid, especially by irradiating with X-rays. [1, 2] Their formation and the growth kinetics under synchrotron radiation (SR) X-ray irradition are governed by mechanisms that are linked to the photoelectric cross-section, especially focusing the probability of interaction of X-rays with matter. The knowledge of these interactions is crucial to optimizing experimental conditions to obtain the desired nanoparticles with desirable properties.

SR X-ray, with its high intensity, wide energy range, and tunable, has been a unique tool in the study of material science and nanotechnology. The applications of this in photochemical processes provide insight into radiation-induced reactions, especially in liquid-phase systems.

We demonstrated that direct monochromatic X-ray synchrotron irradiation induced the formation of gold nanoparticles and aggregates from a solution containing $Na_3Au(SO_3)_2$ in Aichi SR. The experiments were performed as schematically illustrated in Fig. 1, with monochromatic X-ray energy ranging from 6 keV to 20 keV. The silicon substrate was immersed in a $Na_3Au(SO_3)_2$ solution in a polyimide film container and irradiated with X-rays; after X-ray irradiation, the liquid was extracted and particle measurements were carried out using dynamic light scattering (DLS). In addition, the X-ray energy dependence of the size and shape of the nanoparticles produced was evaluated by scanning electron microscopy (SEM) observation of the nanoparticles adhered to the immersed silicon substrate surface. When X-rays are irradiated into the liquid, as shown in Fig. 2(a), ionisation of water is induced, ion reduction occurs and particle growth is promoted after nucleation. The relationship between X-ray energy and nucleation is then clarified.

Figures 2(b) to 2(d) show some of the SEM observations of nanoparticles immobilized on the silicon substrate after X-ray irradiation with energy of 6, 12 and 16 keV. Energy dispersive X-ray spectroscopy (EDX) measurements confirmed that these nanoparticles are composed of gold. The SEM images shown here are observations of areas where only relatively dispersed nanoparticles were observed. The locations where the nanoparticles have agglomerated are also assessed separately. The size of the nanoparticles was evaluated using ImageJ, resulting in a particle size distribution diagram as shown in Fig. 3.

The particle size and aggregation were observed to be strongly dependent on the X-ray energy. We have studied in detail the X-ray energy dependence of the particle sizes that make up the aggregates and those that are relatively isolated. We found that the isolated particle size is proportional to the X-ray photoelectric absorption cross section for Au. In other words, it was found that the primary formation and ripening process is triggered by the impact of X-rays on Au ions, which in turn initiates nucleation and particle growth as Au is reduced by the

surrounding radical electrons. The ability to control nanoparticle synthesis by X-ray photochemical reactions is expected to lead to developments in 3D printers and the synthesis of functional nanoparticles.

[1] A. Yamaguchi, T. Matsumoto, I. Okada, I. Sakurai and Y. Utsumi, Materials Chemistry and Physics 160 (2015) 205 – 211.

[2] A. Yamaguchi, I. Sakurai, I. Okada, H. Izumi, M. Ishihara, T. Fukuoka, S. Suzuki and Y. Utsumi, J. Synchrotron Radiation 27 (2020) 1008 – 1014.

E-Beam Lithography Process Calibration with Minimum Number of SEM Images using Deep Learning

Tuesday, 16th September - 16:00: Poster Session 1 - Poster - Abstract ID: 40

Mr. Burak Çoban [1], ***Mr. Suleyman Celik*** [2], ***Mr. Florian Imeri*** [3], ***Dr. Jan Klikovits*** [3], ***Dr. Klaus Gieb*** [3], ***Mr. Nezih Ünal*** [3]

1. *İzmir Institute of Technology,* ***2.*** *Sabanci University Nanotechnology Research and Application Center,* ***3.*** *GenISys GmbH*

We propose an efficient method for process calibration in Electron Beam Lithography with our compact 2D calibration pattern, aiming for minimal metrology effort. A machine learning model trained with a dataset of synthetic SEM images is applied for process parameter extraction and evaluated for prediction accuracy on real SEM images.

Eco-friendly, bioinspired nanopattern for antifouling: Cicada wing-inspired nanostructures for marine applications

Tuesday, 16th September - 16:00: Poster Session 1 - Poster - Abstract ID: 56

Mr. Zihao Zhao [1], ***Ms. Nan Liang*** [1], ***Prof. Shoso Shingubara*** [1], ***Prof. Tomohiro Shimizu*** [1], ***Prof. Takeshi Ito*** [1]

1. *Kansai University*

Inspired by cicada wings, nanopillar-patterned polymer surfaces demonstrated antifouling properties by combining nanoscale topography and surface energy modulation. These rigid, superhydrophobic surfaces resist biofouling without toxic coatings, offering a sustainable solution for marine and biomedical applications.

Electrochemical Investigation of $[Ru(bpy)_2(L)]^{2+}$ Complexes for Biosensor Applications: Insights into Rct Reduction Mechanism

Tuesday, 16th September - 16:00: Poster Session 1 - Poster - Abstract ID: 59

Mr. Koki Yamashita [1], ***Prof. Tomohiro Shimizu*** [1], ***Prof. Shoso Shingubara*** [1], ***Mr. Hitoshi Ishida*** [1], ***Mr. Akinori Kuzuya*** [1], ***Prof. Takeshi Ito*** [1]

1. *Kansai University*

$[Ru(bpy)_2dppz]^{2+}$ is well known as a DNA intercalator. Recently, it has been reported that Ru complex with redox mediator decrease the charge transfer resistance (R_{ct}) of electrochemical system. To discuss the impedance reductoin mechanism, we evaluated the R_{ct} depending on the concentration and the five types of Ru complex under the redox mediator $[Fe(CN)_6]^{3-/4-}$. The results showed that R_{ct} decreased with increasing Ru complex concentration, but the decrease rate is dependet with thier molecular structure.

Bactericidal property of COP nanopillars dependent with their size

Tuesday, 16th September - 16:00: Poster Session 1 - Poster - Abstract ID: 60

Mr. Gakuto Inoue [1]

1. *Kansai University*

Bactericidal performance was investigated by varying the dimensions of polymer nanopillars, which mimic the nanostructure of cicada wing surfaces. The polymer nanopillars were fabricated using thermal nanoimprint lithography (NIL) with anodized aluminum oxide (AAO) as the template. Bactericidal activity was evaluated using LIVE/DEAD Cell Viability Assays. The results indicated that as the contact between bacteria and the pillars decreased, bactericidal activity increased.

Impact of microfabrication conditions on the oxygen depletion rate of thiol-enes

Tuesday, 16th September - 16:00: Poster Session 1 - Poster - Abstract ID: 64

Dr. Markus Haapala [1], ***Dr. Päivi Järvinen*** [1], ***Dr. Iiro Kiiski*** [1], ***Prof. Tiina Sikanen*** [1]

1. *University of Helsinki*

Off-stoichiometric thiol-enes (OSTE) are an appealing microfabrication material owing to their tunable mechanical (bulk) and surface properties, supplemented by intrinsic oxygen scavenging ability. The purpose of this study was to examine how microfabrication conditions, including OSTE bulk composition and different post-processing methods, influence the oxygen depletion rate by OSTE polymers.

Microstructuring of 3D Printed Ceramic Surfaces using Nanoimprint Lithography

Tuesday, 16th September - 16:00: Poster Session 1 - Poster - Abstract ID: 68

Ms. Sonja Kopp [1], Dr. Abhijeet Lale [2], Ms. Viktorija Jonaityte [1], Dr. Michael Haslinger [1], Ms. Marta Bonora [3], Mr. Matthias Vostatek [3], Ms. Sarah Linnemeier [4], Prof. Marcus Granegger [4], Prof. Francesco Moscato [3], Dr. Martin Schwentenwein [2], Dr. Michael Muehlberger [1]

1. *PROFACTOR GmbH,* ***2.*** *Lithoz GmbH,* ***3.*** *Center for Medical Physics and Biomedical Engineering, Medical University of Vienna,* ***4.*** *Department of Cardiac Surgery, Medical University of Vienna*

Ceramic 3D printing or Lithography-based Ceramic Manufacturing (LCM) [1] is able to produce a wide range of ceramic components for various applications ranging from medical to aerospace. LCM distinguishes itself from other additive manufacturing (AM) techniques for ceramics by the high resolution and the absolutely isotropic and homogeneous microstructure that can be obtained by this process. The materials that are used in the LCM process are UV-curable suspensions that can comprise different ceramic particles. To obtain a fully inorganic final ceramic object, the parts have to be debinded and sintered. Extremely high densities of up to up to 99.9% can be obtained in this way. We are interested in using a ceramic material for applications in life sciences. Although the surface quality meets or exceeds the requirement for most applications and surface roughness R_a of 0.4µm can be achieved in the final part [2], in certain cases it can be interesting to add well defined microstructures on the surface.

We use UV-based nanoimprinting to achieve this, because on the one hand the LCM process is also based on UV-curable materials and on the other hand nanoimprinting is capable of also patterning non-flat surfaces [3,4]. We use flexible polymeric stamps (MD700) to do the nanoimprinting. In our work we compare two different UV-curable ceramic suspensions normally used for LCM, which were modified for the nanoimprint process: LithaLox 350, which is an alumina suspension, and LithaCon ATZ980 [5], which results in alumina-toughened zirconia after sintering. The imprinting is performed on unsintered 3D printed substrates (so-called green parts), resulting in an additional microstructured layer on top of the substrate.

For alumina the effect of grain growth can clearly be seen. There is a change in pattern shape due to the grain growth as well as additional surface roughness. It can however be noted that the roughness after sintering in the flat but imprinted areas is reduced as compared to the flat but just 3D-printed areas. The surface roughness in flat areas (as 3D-printed surface) is around R_a=377nm while in the areas where the surface has been modified by imprinting but without any additional microstructure (flat stamp, green areas) is R_a=279nm. For the ATZ the grain growth during sintering is significantly reduced. Dor the ATZ samples, a dramatically improved pattern fidelity after sintering could be obtained. We are now working on finding the resolution limit with these materials and will present additional results and discuss application scenarios.

The authors acknowledge funding from the OptiFlow3D project (FFG FO999891239).

[1] M. Schwentenwein, e.al., Advances in Science and Technology 88 (2014): 60–64.

[2] https://lithoz.com/en/materials/lithalox-350/

[3] M. Haslinger, et al., SPIE Proceedings Volume 11177 (EMLC 2019); 111770K (2019)

[4] A.R. Moharana, et al., Coatings. 10 (2020) 301.

[5] https://www.lithoz.com/en/materials/lithacon-atz-980/

Post-etch Surface Modification for Sidewall Smoothing in Deep Reactive Ion Etched Silicon

Tuesday, 16th September - 16:00: Poster Session 1 - Poster - Abstract ID: 69

Mr. Arjun Moothedath Sethumadhavan [1], ***Mr. Zhong Ren*** [1]

1. *Oxford Instruments*

Deep reactive ion etching (DRIE) is extensively used for creating deep trenches and vias, especially in micro-electromechanical systems and through silicon vias (TSVs). However, due to the alternating etch and passivation steps inherent to the DRIE process, scalloped sidewalls are formed, which can negatively impact device performance. In superconducting TSVs, such roughness on the sidewalls can lead to higher microwave losses and degrade the quality of superconducting films—an important concern in quantum systems. This work introduces a post-etch surface modification approach based on fluorine chemistry to smooth the sidewalls created by DRIE. The technique effectively removed scallops at the top of the vias and reduced scallop depth by approximately one-third in the middle and lower sections, resulting in average depth of 23 nm and 14 nm, respectively. We have implemented this smoothing process into the fabrication of niobium nitride superconducting TSVs, achieving a superconducting transition temperature of 10.7 K. These enhanced TSVs are well-suited for superconducting systems, particularly those operating at millikelvin temperatures, such as qubit shielding and signaling in superconducting qubit computing.

Fabrication of fine metal patterns using solvent-soluble UV-curable resin

Tuesday, 16th September - 16:00: Poster Session 1 - Poster - Abstract ID: 71

Mr. Satoshi Fujieda [1], ***Mr. Takeshi Osaki*** [2], ***Mr. Yukio Okado*** [2], ***Prof. Jun Taniguchi*** [1]

1. *Tokyo University of Science,* ***2.*** *Toyo Gosei Co., Ltd., Photosensitive Materials Research Center*

We demonstrated a lift-off process for fabricating fine metal patterns using PAK-YY01, a solvent-soluble UV-curable resin. Compared to etching, this method minimizes substrate damage and cost. The process enables high-resolution patterning with controllable thickness, offering a promising approach for efficient, low-cost nanofabrication in semiconductor and related applications.

Effect of Polyethylene Glycol on growth of Porous Silicon

Tuesday, 16th September - 16:00: Poster Session 1 - Poster - Abstract ID: 72

Mr. XUMING ZHAO [1], ***Mr. Tomoya Okawa*** [1], ***Ms. Chenxin Zhong*** [1], ***Mr. koji akiyama*** [2], ***Mr. takeya inoue*** [2], ***Prof. Takeshi Ito*** [1], ***Prof. Shoso Shingubara*** [1], ***Prof. Tomohiro Shimizu*** [1]

1. *Kansai University,* ***2.*** *Tokyo Electron*

Through-silicon via (TSV) technology plays a critical role in integrated circuit (IC) packaging by enabling vertical interconnects essential for three-dimensional system integration. Anodized porous silicon (PSi) exhibits a high specific surface area and controllable pore morphology. The vertically aligned pores of PSi, featuring tunable aspect ratios and compatibility with low-cost electrochemical processing, provide a viable approach for TSV fabrication. The work of Nenzi et al. has explored the use of electrochemically etched porous silicon in TSV-related processes and demonstrated the potential for forming ordered vertical pore arrays under controlled conditions. However, achieving precise control of pore morphology to satisfy the structural and integration requirements of TSV remains a major technical hurdle.

This study introduces polyethylene glycol (PEG), a common wet etching additive, into the anodization process in an attempt to reduce sidewall roughness in high aspect ratio porous silicon structures. Compared to conventional additives such as DMF and ethanol , PEG shows a distinct effect on pore morphology, leading to improved sidewall smoothness under certain conditions and suggesting potential benefits for preparation of straight and vertical Si pore for TSV application.

Study of blob defectivity for different 248nm resist processes: influence of material chemistry, pattern types, bake and development conditions.

Tuesday, 16th September - 16:00: Poster Session 1 - Poster - Abstract ID: 75

Mrs. Lucie BORGET [1], ***Mrs. Romane Francais*** [1], ***Mr. Loic Balme*** [1], ***Mr. Yohann Lebel*** [1], ***Mr. OLIVIER MERMET*** [1], ***Dr. Benedicte Mortini*** [1]

1. *STMicroelectronics*

Blob defects, also called satellite defects, are micron-size, disc-shaped residues with a thickness of a few nanometers, as illustrated in Figure 1 [1,2]. They are described in the literature as partially soluble polymers/ photoresist aggregates that adhere to the wafer at the end of the lithographic process, during the wafer drying step [3].
Although they are generally not considered a killer defect, their presence in high quantities degrades the accuracy of in-line defectivity controls to the extent that –in the worst cases – the control can become totally ineffective.
In this work, we evaluate several different formulations of 248nm resists for implant levels under conditions that were initially known to be especially prone to generating blob defects. Indeed, we observe that this defectivity mode is strongly dependent on layer design such as mask transmission rate and the amount of photoresist that must be dissolved by the developer solution. For our most blob-sensitive lithographic levels, our first finding was that blob defects are present regardless of the resist formulation. Therefore, process tunings have been investigated to decrease the density of blob defects. We will present results obtained by varying the bake conditions, especially Post Exposure Bake, as well as development and rinse sequences.
After conducting bake experiments, although we were able to correlate a relationship between blob reduction and completion of the deprotection reaction measured by thermogravimetry analysis, we pointed out a trade-off between the formation of blob defects due to partially deprotected polymer chains and the ultimate lithographic performance of the photoresist (resolution, resist profiles, process window). To overcome this limitation, we focused on optimizing the development and rinse steps. As a result, we achieved a significant reduction in defect density from about 3 defect/cm² to 0.02 defect/cm², down to a level that allows accurate post-lithography inline defectivity monitoring (cf Figure 2).
[1] J. Erhardt, K. Phan and J. Cheng, “An investigation of circular resist residue defects in the development of a flash memory process flow,” 2001 IEEE/SEMI Advanced Semiconductor Manufacturing Conference (IEEE Cat. No.01CH37160), Munich, Germany, 2001, pp. 231-236, doi: 10.1109/ASMC.2001.925651
[2] Chih-Chieh Yu, Mars Yang, Elvis Yang, T. H. Yang, K. C. Chen, Chih-Yuan Lu, “Pattern dependent satellite defects in via lithography”, Proceedings Volume 8325, Advances in Resist Materials and Processing Technology XXIX; 83252K (2012) https://doi.org/10.1117/12.915572
[3] Yuko Ono, Takeshi Shimoaoki, Ryoichiro Naito, Junichi Kitano, “Behavior of chemically amplified resist defects in TMAH solution: III”, Proceedings Volume 5376, Advances in Resist Technology and Processing XXI; (2004) https://doi.org/10.1117/12.534982

Development of Microfluidic Flow Cells with Integrated Arrays of Freestanding Al_2O_3 Membranes for SEM Imaging

Tuesday, 16th September - 16:00: Poster Session 1 - Poster - Abstract ID: 85

Mr. Jeremy Teuber [1], ***Mr. Tim Erichlandwehr*** [2], ***Mr. Rukan Nasri*** [2], ***Dr. Irene Fernandez*** [2]

1. *Max-Planck-Institute for the Structure and Dynamics of Matter,* ***2.*** *UHH*

We present a scalable fabrication method for microfluidic flow cells integrating freestanding, electron-transparent Al_2O_3 membranes compatible with scanning electron microscopy (SEM). The membranes are selectively opened within sealed microchannels, forming well-defined windows with customizable shape, size, and placement. Up to 200 windows can be integrated simultaneously. The devices are fabricated using UV nanoimprint lithography, flow-through gas-phase deposition, and multilayer structuring. We demonstrate membrane transparency by SEM imaging of polystyrene beads and gold nanoparticles inside the channels. This platform enables real-time, high-resolution observation of nanoscale processes in liquid environments, offering new opportunities for advanced in situ studies.

Fabrication of Flexible Printed In-Mold Electronic Devices

Tuesday, 16th September - 16:00: Poster Session 1 - Poster - Abstract ID: 86

Dr. JEONGDAI JO [1], ***Mr. Pyoungwon Park*** [1], ***Dr. Taik-Min Lee*** [2], ***Dr. Inyoung Kim*** [2]

1. *Korea Institute of Machinery and Materials (KIMM),* ***2.*** *Korea Institute of Machinery & Materials (KIMM)*

The increasing focus on sustainable manufacturing in the electronics industry has created a demand for environmentally friendly technologies [1, 2, 3]. In response to this need, In-Mold Electronics (IME), which integrates plastic molding with printed electronics, has emerged as a sustainable manufacturing solution. In-Mold Electronics (IME), which integrates plastic molding with printed electronics, has emerged as a sustainable manufacturing solution. IME not only addresses the functional requirements, such as reduced weight and increased flexibility, but also aligns with the broader trend toward sustainable mass production. [4, 5, 6].

There are two primary methods for manufacturing 3D electronic products: creating the curved product first and then applying printed electrodes by the non-contact printing method, or printing conductive patterns first on a film, followed by thermoforming. In this work, the aim was to fabricate a device on a 3D mold to address the deformation of printed circuits in the IME process.

In this study, printing conductive patterns first on a film, followed by thermoforming for ease of manufacturing and ability to produce fine patterns. Our experimental setup for the 3D IME consists of several steps: paste preparation, screen printing, thermoforming, and LED devices attachment. Initially, 3D IME devices was fabricated on a Polyethylene Terephthalate Glycol (PETG) substrate using a thermoforming approach, the silver paste was dispersed using a mixer. This prepared ink was then patterned onto a PETG substrate through the screen printing process. Following this, the substrate with the printed electrodes was directly mounted to the thermoforming machine. Once thermoforming was completed, LEDs were attached to the thermoformed circuit to verify functionality. Results demonstrated that the 3D IME circuit demonstrated elongation in length ranging and after thermoforming, confirming its stretchability. This approach effectively eliminated cracks on the circuit and optimized the manufacturing process for 3D electronic structural devices.

This research was supported by the National Research Council of Science & Technology(NST) (No. CAP22083-300) and the National Research Foundation of Korea(NRF) (No. RS-2023-00222166) grant by the Korea government (MSIT) and the Korea government(MOTIE) (No. RS-2024-00470021).

Bioinspired Nanospike Formation on the Surfaces of Commercial Plastic Plates Using Atmospheric-Pressure Low-Temperature Plasma

Tuesday, 16th September - 16:00: Poster Session 1 - Poster - Abstract ID: 92

Dr. Masashi Yamamoto [1], ***Mr. Motoki Tanaka*** [2], ***Mr. Ayumu Takada*** [2], ***Dr. Atsushi Sekiguchi*** [3]

1. *National Institute of Technology (KOSEN) Kagawa College,* ***2.*** *National Institute of Technology, Kagawa College,* ***3.*** *Litho Tech Japan Corporation*

In recent years, bioinspired materials have garnered significant attention due to their potential in functional surface design. Cicada wings exhibit antibacterial properties due to nanospike structures. Previous studies have replicated such nanostructures on silicon substrates using photolithographic techniques developed for semiconductor fabrication. However, these approaches are constrained by substrate shape, size, and the need for specialized equipment, limiting scalability for practical applications. This study examined a simple method using atmospheric-pressure low-temperature plasma to form nanospikes on commercial plastic plates (PMMA, PET, PC, PVC). All materials successfully developed nanospikes, with sizes correlating to their thermal properties. PC and PET showed finer structures due to higher thermal stability, while PVC formed larger spikes likely because of thermal crosslinking. These findings suggest that resin properties influence nanospike formation, offering a practical approach for bioinspired surfaces.

Impact of processing on the temperature-dependant behaviour of nano-structured Platinum thin films fabricated by Spark Ablation

Tuesday, 16th September - 16:00: Poster Session 1 - Poster - Abstract ID: 93

Ms. Shatavisha Biswas [1], ***Prof. Sten Vollebregt*** [2]

1. *PhD,* ***2.*** *Associate Professor*

This study investigates the influence of processing conditions on the performance of nanostructured platinum thin films prepared by spark ablation, focusing on optimizing them as resistive temperature detectors. The spark-ablated platinum nanoparticles were deposited through impaction printing, thus enabling direct sensor patterning without complex processing steps. It was found that higher deposition speeds led to sparse, thermally unstable films, with 1 mm/min concluded as the optimal speed. The TCR increased with the film thickness, with a mean TCR of 2.17 x 10^{-3} /^{o}C achieved for an 8-trace film (around 350 nm) annealed at 600^{o}C.

Hierarchical structures fabricated for probiotic marine bacterial growth using hybrid methods for polymer replication

Tuesday, 16th September - 16:00: Poster Session 1 - Poster - Abstract ID: 106

Ms. Yuyan Liu [1], ***Mr. Xavier Florensa*** [1], ***Mr. Euan McDonald*** [2], ***Prof. Paul Kempen*** [1], ***Prof. Claus Sternberg*** [1], ***Prof. Nikolaj Gadegaard*** [2], ***Prof. Lone Gram*** [1], ***Prof. Rafael Taboryski*** [1]

1. *Technical University of Denmark,* ***2.*** *The University of Glasgow*

Several species of marine bacteria from the Roseobacter group have been identified as producers of the antibacterial compounds tropodithietic acid (TDA). In certain species, the TDA production is clearly facilitated when bacteria form biofilm on a surface rather than existing in the planktonic state [1]. Micropatterned polymeric surfaces have been investigated to support bacterial growth and TDA production, with varying patterns yielding different levels of TDA production [2]. Consequently, screening micropattern designs for optimal TDA production is essential. In this study, we present hybrid methods to fabricate hierarchical structures across multiple size scales through polymer replication, with the goal of supporting roseobacter biofilm growth.

Here we developed a hybrid fabrication method that combines the strengths of clean room fabrication and 3D printing techniques, providing a flexible and high-resolution fabrication approach. To start with, we fabricate the micro-patterned silicon wafer in the clean room, subsequently, we cast a relief in polydimethylsiloxane (PDMS) using the microfabricated wafer as a mold. We first 3D print the mold base, where at specific stages we pause the 3D printing to transfer the PDMS-based micropatterns into the mold. The printing then resumes, layering additional material over the transferred micropatterns to create inlet ports (Figure 1a). Scanning electron microscopy (SEM) micrographs, as shown in Figure 1b, show the transferred micropatterns on the fabricated mold. The resulting micropatterned mold serves as a negative relief for the injection molding of the microfluidic flow cell. This hybrid approach provides a highly flexible prototyping method to facilitate biofilm growth studies, enabling the integration of custom micropatterns at desired locations.

In yet another approach, we introduce nanoscale roughness to the patterned microstructures through the novel uses of polystyrene (PS) nanoparticles. PS beads are distributed on a flat polypropylene (PP) surface before imprinting with a microfabricated Si mold (Figure 2a). During imprinting [3], the PS beads are pressed into PP. The PS beads are then softened and removed by acetone, leaving nanoscale indentations that generate additional random textures to create the final hierarchical surface structure (Figure 2b and 2c). This additive approach efficiently introduces nanoscale roughness to existing microstructure designs during polymer replication.

Future research will focus on evaluating fabricated hierarchical structures, incorporating micro- and nanoscale features, through biological experiments involving probiotic marine bacterial biofilm growth. Figure 3 illustrates bacterial growth on microstructures, including hexagonal pits and pillars.

Fluorination of Ni Hard masks during Fluorine-Based DRIE: Structural and Spectroscopic Insights into NiF_2 Formation

Tuesday, 16th September - 16:00: Poster Session 1 - Poster - Abstract ID: 113

Mr. Baptiste Fischer-Kaszuba [1], Dr. Amandine Andrieux-Ledier [2], Dr. Etienne Carré [1], Dr. Patrick Kayser [1], Dr. Pierre Lavenus [2], Mr. Jean-Sebastien Mérot [3], Dr. Frédéric Fossard [3], Dr. Thomas Baron [4]

1. *DPHY, ONERA, Université Paris-Saclay, 92320 Châtillon, France,* ***2.*** *DPHY, ONERA, Université Paris-Saclay,* ***3.*** *Université Paris-Saclay, ONERA, CNRS, Laboratoire d'étude des microstructures (LEM),* ***4.*** *Université Marie et Louis Pasteur, SUPMICROTECH, CNRS, Institut FEMTO-ST*

Deep Reactive Ion Etching (DRIE) is widely used in the MEMS fabrication due to its excellent etching capabilities, including high selectivity, vertical sidewalls, and compatibility with a broad range of substrate materials [1]. Fluorine-based plasmas, in particular, enable the etching of various substrates such as silicon, lithium niobate, glass, and, as in our case, quartz. To achieve deeper etching or higher selectivity than what polymer masks allow, metallic hard masks such as aluminum or nickel are often employed. However, under moderated temperatures (a few hundred degrees Celsius) and in the presence of fluorinated gases, these metallic masks can react and be contaminated by fluorine ions [2-3]. Key characteristics of the chemical compounds formed remains unexplored (thickness, crystallinity…). This lack of knowledge means that optimal solutions cannot be applied to remove them and leads to unwanted residues on the MEMS devices.

In this study, we examine the structural and compositional evolution during fluorine-based plasma etching of a nickel PVD-sputtered hard mask, deposited on quartz. For that purpose, we performed characterization, from the macroscopic to the atomic scale, by optical microscopy, scanning and transmission electron microscopes (SEM, TEM), Energy Dispersive, X-ray photoelectron and Electron Energy Loss spectroscopies (EDS, XPS and EELS). Our results reveal the formation of a uniform layer, composed of Ni and F, tens of nanometers thick, depending on the etching conditions (Figure 1). This layer exhibits high crystallinity, with a 1:2 stoichiometry consistent with NiF_2 and lattice parameters matching those expected from single-crystal X-ray diffraction reference data [4]. This structural quality enabled us to record, for the first time to our knowledge, the electron energy loss spectrum (EELS) of crystalline NiF_2. As this fluorinated layer is insoluble in water or nitric acid—unlike pure Ni—we also propose a gentle, accessible method for its removal, which allow us to obtain a MEMS quartz wafer without any nickel hard-mask residues.

On-CMOS 3D Platinum Electrodes Fabricated by Focussed-Ion Beam for Dielectrophoresis of DNA Towards an Electrokinetic Lab-on-CMOS

Tuesday, 16th September - 16:00: Poster Session 1 - Poster - Abstract ID: 115

Dr. Lewis Keeble [1], ***Mr. Arthur Jaccottet*** [1], ***Mr. Daryl Ma*** [1], ***Dr. Jesus Rodriguez-Manzano*** [1], ***Prof. Pantelis Georgiou*** [1]

1. *Imperial College London*

Biosensing based on complementary metal-oxide-semiconductor (CMOS) technology has become a powerful tool for diagnostic devices. There are now opportunities to move sample preparation onto CMOS microchips by using electrokinetics, but this comes with challenges surrounding CMOS-compatible fabrication processes, electrode stability, and electrokinetic efficiency.

To overcome these challenges, this paper demonstrates the fabrication of 3D platinum electrodes on-CMOS using focussed ion beam (FIB) deposition. A 6µm tall square pillar electrode, with a 5µm base, was connected to an electroless nickel immersion gold-plated CMOS bondpad, separated by 2µm from a line electrode.

Upon application of a 4V, 500Hz signal, DNA was trapped between the electrodes under dielectrophoresis (DEP). This was the first demonstration of DEP trapping on-CMOS using 3D electrodes and provides an approach to develop systems to test on-CMOS electrokinetics, towards creating sample-to-result electrokinetic lab-on-CMOS diagnostic devices.

Hybrid-Polymer Microring Resonator Arrays for Next-Generation Photoacoustic and Biosensing Applications

Tuesday, 16th September - 16:00: Poster Session 1 - Poster - Abstract ID: 116

Dr. Santhosh Pandian [1], Ms. Marina Fetisova [2], Dr. Petri Karvinen [2], Dr. Paul Müellner [3], Dr. Moritz Eggeling [3], Dr. Rainer Hainberger [3], Mr. Evgenii Lepukhov [1], Prof. Tapio Niemi [1]

1. *Tampere University,* ***2.*** *University of Eastern Finland,* ***3.*** *AIT Austrian Institute of Technology GmbH*

Polymer materials have enhanced photonics integrated circuits by providing a broad wavelength range, low absorption, diverse material choices, and cost-effective fabrication processes [1,2]. Polymer-based microring resonators (MRRs) are important for optical communications and medical diagnostics [3,4]. They are also used as compact ultrasonic detectors in photoacoustic imaging [5]. Our objective is to apply these MRRs for photoacoustic imaging of drug-tolerant persister cells in breast cancer [6]. Recently, we have prepared and characterized single MRRs [7]. The angular field-of-view of a single MRR ultrasound detector depends on the signal frequency and the ring diameter. For imaging with a single ring, either the imaged area is limited, or the sample or detector must be movable to extend the area. Alternatively, an array of MRRs can be sequentially interrogated to image a larger area in a fixed setup. In this work, we report on the fabrication and optical performance characterization of an array of 16 MRRs. We employ nanoimprint lithography (NIL), which is recognized for its high resolution, precision, and cost-efficiency in patterning structures [1,3].

The MRRs were fabricated on a 500 µm thick silicon wafers with a 2 µm thermal oxide layer serving as lower cladding (n=1.453) by means of UV-NIL using hybrid polymer ORMOCORE^{TM} as waveguide layer (n=1.543). Figure 1a shows an example of a single MRR. PDMS (n=1.40) was spin-coated as top-cladding. The design of the waveguide core is 1.2 µm high and 1 µm wide with a 5 µm thick PDMS top cladding. The residual layer on both sides of the imprinted waveguide is a critical process related parameter that we aim to minimize. In our NIL process, we achieve a thickness of 80-300 nm. Figure 1b, exemplarily shows the SEM image of a sample with a residual layer thickness of approximately 80 nm. To extend the detection area we designed a 4×4 array of rings with 400 µm spacing (see Fig. 2a). Each ring has a slightly different diameter to separate the resonance wavelengths. The row starts with rings having a 120 µm diameter, increasing by 20 nm per ring. Optical modelling shows that these values correspond to a free spectral range (FSR) of 1.01 nm and a resonance shift by 0.13 nm per ring. A single input waveguide is split up twice through a 1×2 splitter, resulting in four distinct rows. Signals from each of these rows are detected individually. This array configuration offers scalability and enables multiplexed detection over an area of approximately 2.7×2.7 mm², enhancing advanced photoacoustic imaging applications. The characterization of the MRR array fabricated on a silica-on-silicon sample is performed using a wavelength tunable laser. Figure 2b plots the transmission spectra for the MRRs along the four rows. The resonance of each ring is clearly separated by 0.07-0.3 nm inside FSR of approximately 1.07 nm. The Q-factors of the resonances range from 5.8 to 7.5×10^4, which aligns with our previous measurements [7]. The resonance performance is consistent across the array elements, which reflects the uniform fabrication quality over the area of the array in terms of waveguide thickness and width as well as residual layer thickness. The spectral transmission results confirm that MRR detectors can be scaled into parallel detection schemes potentially enhancing the spatial resolution and image acquisition speed. Moreover, the well-defined resonances with high extinction ratios across the rows highlight the potential of hybrid-polymer MRR arrays as highly sensitive and scalable platforms for photoacoustic imaging and biosensing applications.

Femtosecond laser inscription of optical waveguide in sapphire

Tuesday, 16th September - 16:00: Poster Session 1 - Poster - Abstract ID: 118

Dr. Wei Lyu [1], ***Dr. Ding Zhao*** [1], ***Prof. Min Qiu*** [2]

1. *Westlake Institute for Optoelectronics,* ***2.*** *Westlake University*

Femtosecond laser direct inscription creates optical waveguides in transparent materials, overcoming challenges like crack formation in sapphire crystals. Using a 1030 nm, 130 fs pulse laser, this study fabricates precise waveguides with controlled refractive index modification. The depressed cladding waveguide supports single-mode propagation at 1550 nm, suitable for optical communications. Surface waveguides show potential for sensing in extreme environments due to sapphire's stability. This technique advances robust photonic devices.

Effective diffusion barrier for Au/Ni thin films in quartz MEMS processing

Tuesday, 16th September - 16:00: Poster Session 1 - Poster - Abstract ID: 123

Mr. Baptiste Fischer-Kaszuba [1], ***Dr. Amandine Andrieux-Ledier*** [1], ***Dr. Etienne Carré*** [1], ***Dr. Frédéric Fossard*** [2], ***Mr. Jean-Sebastien Mérot*** [2], ***Dr. Patrick Kayser*** [3], ***Dr. Pierre Lavenus*** [1], ***Dr. Thomas Baron*** [4]

1. *DPHY, ONERA, Université Paris-Saclay,* ***2.*** *Université Paris-Saclay, ONERA, CNRS, Laboratoire d'étude des microstructures (LEM),* ***3.*** *DPHY, ONERA, Université Paris-Saclay, 92320 Châtillon, France,* ***4.*** *Université Marie et Louis Pasteur, SUPMICROTECH, CNRS, Institut FEMTO-ST*

The fabrication of MEMS on hard substrates like quartz, fused silica or lithium niobate often relies on Deep Reactive Ion Etching (DRIE), where metal hard masks such as nickel [1], chromium [2], and aluminum [3] are used for their high etch resistance and selectivity. However, these masks present challenges, especially in multilayer metallization for electrodes. A key issue is the interdiffusion of metals—particularly chromium and gold—into the nickel layer. This diffusion leads to a degradation of the Cr/Au layer morphology after nickel removal and can deteriorate the electrical and mechanical performance of the device. Addressing this interlayer diffusion is essential to maintain structural integrity and reliability in MEMS processes.

The aim of this study is to investigate the behavior in Cr/Au/Ni multilayer stacks deposited on quartz substrates under DRIE processing conditions, using carbon-fluorinated gases and low operating temperature (100-300°C). For that purpose, we used high-resolution electron microscopy to analyze morphological and elemental composition along the process. We present a detailed analysis of metal diffusion pathways in these thin film structures as seen in figure 1. This study reveals that diffusion along grain boundaries and in between column microstructure of the Cr/Au/Ni multilayers on quartz dominate. This agrees with the literature, showing that diffusion short-circuit prevails over bulk diffusion within our temperature range [4].

In the end, based on the results of the study, we're able to propose a diffusion barrier consisting of an evaporated alumina (Al_2O_3) ceramic layer sandwiched between gold and nickel layers. Under our DRIE conditions, we demonstrate a complete suppression of the Au/Ni interdiffusion (Fig. 2). This approach thus offers a robust, scalable solution to enhance material stability and reliability in MEMS fabrication using metallic hard masks and multilayer electrode systems.

Analysis and fabrication of electrothermal electrodes for micro and nanostructured sensors

Tuesday, 16th September - 16:00: Poster Session 1 - Poster - Abstract ID: 136

Mr. Abel Palomas Jiménez [1], ***Dr. Michelle Cedeño*** [1], ***Ms. Ana Coloma Velez*** [1], ***Dr. Jorge Luis Villar*** [1], ***Dr. Manuel Domínguez-Pumar*** [1], ***Dr. Sandra Bermejo*** [1]

1. *Universitat Politècnica de Catalunya - BarcelonaTech (UPC)*

This work presents the development and thermal characterization of microfabricated electrothermal devices on borosilicate glass for localized heating applications. Metallic electrodes generate heat through Joule effect to enable the degradation of target compounds. The fabrication integrates cleanroom processes including physical vapor deposition of copper, photolithography, and nickel electroplating. Finite element simulations (COMSOL) were combined with experimental measurements to analyze temperature distribution and optimize design. Results show strong agreement between simulation and experiments, achieving controlled heating above hundreds of degrees Celsius. The findings provide insights into thermal behavior at the microscale, guiding future integration of these devices into complex sensor systems.

Ultra-thick grayscale ellipsoidal structures for X-ray focusing using scanning-laser direct write lithography

Tuesday, 16th September - 16:00: Poster Session 1 - Poster - Abstract ID: 137

Dr. Giulia Malvicini [1], ***Prof. Helmut Schift*** [1]

1. *Paul Scherrer Institute (PSI)*

Ellipsoidal mirrors are ideal focusing elements for X-ray beams, as rays emitted from one focal point reflect off the internal surface and converge precisely at the second focus. Conventional fabrication methods, such as thermally drawn glass capillaries, offer excellent surface smoothness (RMS roughness < 1 nm) but lack flexibility for tailoring complex geometries.

We present an alternative approach using direct laser writing lithography (DWL) to fabricate freeform three-dimensional (3D) ellipsoidal structures in thick photoresist. By modulating local exposure doses across the resist surface, grayscale lithography enables smooth, continuous topographies derived from computer-aided designs. Using the DWL 66+ system with 1024 grayscale values (GVs) and the thick resist *mr-P 22G_XP*, we fabricated ellipsoidal profiles up to 80 µm deep in 100 µm resist layers, with potential for deeper structures.

To ensure durability and reusability, the resist patterns were transferred into PMMA substrates using nanoimprinting with hybrid materials such as *OrmoComp*® or *OpTool*®. This enables the creation of long-lasting masters for further pattern replication. Surface characterization by confocal microscopy, white light interferometry, and atomic force microscopy (AFM) confirmed the accuracy and smoothness of the fabricated structures. The resulting surfaces exhibit low roughness, making this method promising for advanced X-ray optics requiring customized shapes and high optical quality.

Ellipsoidal X-ray mirrors were fabricated using direct laser writing in thick grayscale resist with 1024 grayscale levels. The resulting 3D structures, with depths up to 100 µm, were transferred into durable hybrid polymers via nanoimprinting. Surface analysis confirmed low roughness, demonstrating suitability for high-precision X-ray optics applications.

Effects of Annealing on Effective Young's Modulus of Ti/Au Multi-Layered Microcantilevers for MEMS Capacitive Accelerometers

Tuesday, 16th September - 16:00: Poster Session 1 - Poster - Abstract ID: 140

Mr. Tatsuhiko Mori [1], ***Dr. Tomoyuki Kurioka*** [1], ***Mr. Shunkai Watanabe*** [1], ***Prof. Chun-Yi Chen*** [1], ***Prof. Tso-Fu Mark Chang*** [1], ***Prof. Katsuyuki Machida*** [1], ***Prof. Hiroyuki Ito*** [1], ***Prof. Yoshihiro Miyake*** [1], ***Prof. Masato Sone*** [1]

1. *Institute of Science Tokyo*

This study investigates the effect of annealing temperature on the effective Young's modulus of electrodeposited-Au microcantilevers with Ti/Au multi-layered structures, which are used as spring components in capacitive MEMS accelerometers. The effective Young's modulus is evaluated by the resonance frequency method using a laser Doppler vibrometer (LDV). The effective Young's modulus of the micro-cantilevers decreases with increases in the annealing temperature.

Development of an In Situ Microfluidic System for Real-Time Control of Porous Microspheres Fabrication

Tuesday, 16th September - 16:00: Poster Session 1 - Poster - Abstract ID: 144

Mr. Ji Hwan Han [1], ***Mr. Min Chul Shin*** [1], ***Prof. Chul Min Kim*** [2], ***Prof. Gyu Man Kim*** [1]

1. *Kyungpook National University,* ***2.*** *Gyengsang National University*

Porous microspheres with controlled internal structures have been considered as a potential platform to overcome the limitations of conventional solid microspheres [1, 2]. They offer a high surface area, excellent permeability, and the ability to protect encapsulated cells and bioactive molecules, making them highly attractive for biomedical applications such as tissue engineering and regenerative therapy [3]. However, most existing microfluidic approaches rely on injecting pre-mixed polymer and porogen phases, which leads to fixed internal morphology and limits the controllability of pore formation during the microsphere preparation process [4].

To address this challenge, we developed an in situ microfluidic system that enables the fabrication of highly porous polycaprolactone (PCL) microspheres with tunable pore sizes. In this system, PCL and camphene (CAMP) solutions are introduced independently and mixed directly within curved microchannels before droplet formation, eliminating the need for pre-mixing. The overall configuration of the microfluidic device and the mechanism of pore formation based on camphene crystallization and sublimation are shown in Figure 1.

Microspheres were fabricated using 3 wt.% PCL and 20 wt.% CAMP in dichloromethane as the dispersed phase, and PVA in water as the continuous phase. By adjusting the flow rate ratios of the polymer and porogen (PCL:CAMP = 1:1, 2:1, 3:1), we were able to precisely control both particle size and internal pore structure. Optical microscopy and field-emission scanning electron microscopy (FE-SEM) images confirmed these morphological differences, as presented in Figure 2.

To investigate the biological response to pore size variation, porous microspheres with three distinct pore sizes were subcutaneously implanted into animal tissue. Histological staining and immunofluorescence imaging revealed that microspheres with larger pores promoted more favorable tissue integration, enhanced cell infiltration, and exhibited reduced inflammatory responses compared to those with smaller pores (Figure 3).

These results should provide a clear basis for designing microsphere-based scaffolds with tunable biological interactions, highlighting the significance of pore structure control in future biomedical applications.

Acknowledgement:

This work was supported by the National Research Foundation of Korea (NRF) grant funded by the Korean government (MSIT) (No. 2019R1I1A1A01063257, RS-2023-00208717 and RS-2024-00406223), and by the Korea Institute for Advancement of Technology (KIAT) grant funded by the Ministry of Trade, Industry and Energy (MOTIE) (No. RS-2022-KI002563, HRD Program for Industrial Innovation).

Slippery liquid-infused micropatterned surface for air-lifted analyte membrane formation

Tuesday, 16th September - 16:00: Poster Session 1 - Poster - Abstract ID: 145

Mr. Seong Min Yoon [1], ***Prof. Young Tae Cho*** [1], ***Dr. Woo Young Kim*** [1], ***Mr. Chae Hyeok Yoon*** [1]

1. *Changwon National University, Changwon*

In this study, we utilized a hexagonal grid pattern on a slippery to confine colloidal solutions into narrow regions. The confined colloidal solution forms a membrane on the fabricated surface, which can be employed as a high-sensitivity sensing substrate.

Mastering the growth of centimetric sp2-hybridized boron nitride films for optoelectronic devices

Tuesday, 16th September - 16:00: Poster Session 1 - Poster - Abstract ID: 147

Dr. Laure Tailpied [1], Ms. Marjolaine Cornu [1], Dr. Frédéric Fossard [2], Mr. Jean-Sebastien Mérot [3], Ms. Chloe Grekobi [3], Mr. Jules Lagrave [3], Dr. Jean-Manuel Decams [4], Dr. Annick Loiseau [3], Dr. Amandine Andrieux-Ledier [5]

1. *Université Paris-Saclay, ONERA, CNRS, Laboratoire d'étude des microstructures (LEM), 92322 Châtillon, France,* ***2.*** *Université Paris-Saclay, ONERA, CNRS, Laboratoire d'étude des microstructures (LEM),* ***3.*** *Université Paris-Saclay, ONERA, CNRS, Laboratoire d'étude des microstructures (LEM), 92322 Châtillon,* ***4.*** *Annealsys, 139 rue des Walkyries, 34000 Montpellier, France,* ***5.*** *DPHY, ONERA, Université Paris-Saclay, F-92322 Châtillon, France*

In the recent years, sp²-hybridized boron nitride (sp^2-BN) has been identified as a key component for the development of high-performance 2D material platforms towards applied devices. Its unique properties - including a large band gap (> 6 eV), chemical inertness, atomically flat surface free of dangling bonds and small lattice mismatch with graphene (less than 1.7%) [1] - give it a pivotal role in van der Waals heterostructures elaboration. Indeed, sp²-BN has been identified as the ideal insulating substrate and encapsulating layer to achieve the highest mobility or best optical properties in graphene or other 2Ds channels, with strong implications for efficient electronic, optoelectronic and spintronic devices [2]. However, realising the potential of BN-based electronic platforms requires continuous, atomically flat BN films on a large-scale with a controlled thickness ranging from a monolayer to 50 nm, depending on the targeted application. To date, proof-of-principle demonstrations showing ultimate performance have been obtained using exfoliated flakes from high-quality bulk crystals. This fabrication method seems unsuitable for practical applications due to the low yield and quality limitations of the nanosheets produced, such as the small lateral size, lack of homogeneity and thickness control [3]. In parallel, large-scale synthesis is being developed, in particular by MBE, ALD and CVD [4]. However, real control of film thickness with high crystalline quality has not yet been achieved.

In this context, the aim of the research we have undertaken is to develop the synthesis by chemical vapor deposition of multilayer sp²-hybridized BN films with structural specifications that meet these requirements. In collaboration with Annealsys, we have developed an epitaxial growth process on Ni (111) substrates on the centimeter scale, using borazine molecule as a source of boron and nitrogen atoms [5]. We have characterised the structure and the quality of BN films from the centimetre to the atomic scale using a wide range of techniques (OM, SEM, TEM, AFM, Raman spectroscopy) and in a quantitative manner. We show that by adjusting the synthesis parameters, we can obtain BN films with controlled thicknesses between 2 and 10 layers, homogeneous over several mm^2 with the same crystalline orientation and a hexagonal or rhombohedral stacking sequence. These are essential control points for the future integration of BN films into large-scale devices with other 2D materials.

[1] T. Niu et al. Prog.Surf.Sci. 90, 2015, 21-45

[2] K. K. Kim et al. Chem. Soc. Rev. 2018, 47, 6342-6369

[3] R. Frisenda et al. *Chem. Soc. Rev.*, 2018 ,47, 53-68

[4] A. Rigosi *et al* 2021 *J. Phys. Mater. 4* 032003

[5] L.Tailpied et al. Cryst. Growth Des. 2024, 24, 18, 7432–7444

Fabrication of slanted diffraction gratings by electron beam lithography with tilted angle exposure

Tuesday, 16th September - 16:00: Poster Session 1 - Poster - Abstract ID: 160

Mr. Naoya Shibasaki [1], ***Prof. Jun Taniguchi*** [1]

1. *Tokyo University of Science*

EBL from an oblique angle was used to improve the fabrication flow of slanted gratings. The effect of PEB was verified and the aspect was improved at 10 kV. As a result, the suppression of forward scattering was confirmed and aspect ratio of 2 or higher was achieved.

Investigation of Pre-Stressed Membranes in Miniaturized Piezoresistive Diaphragm Pressure Sensors for Enhanced Sensitivity in High Vacuum

Tuesday, 16th September - 16:00: Poster Session 1 - Poster - Abstract ID: 165

Dr. Jian LU [1], ***Dr. Lan ZHANG*** [1], ***Dr. Yuichi KURASHIMA*** [1], ***Dr. Hideki TAKAGI*** [1]

1. *National Institute of Advanced Industrial Science and Technology (AIST)*

The piezoresistive diaphragm pressure sensor stands out for its unique advantage of being independent of the gas type in the vacuum chamber and for offering a wider measurement range, making it widely used in the semiconductor industry for process monitoring and various other applications. Our previous study demonstrated a miniaturized piezoresistive diaphragm pressure sensor, which exhibited a high sensitivity of 4.1 μV/(V·Pa) in the pressure range of 10 Pa to 100 Pa, with a measurement range extending up to atmospheric pressure. However, it was found that the stress state of the membrane of the diaphragm near the neutral surface can significantly affect the overall performance of the sensor, particularly when the measured pressure P approaches the sealed cavity pressure P_0. This effect becomes more significant when the cavity is created by anodic bonding between silicon and glass, as opposed to Au-Au bonding between silicon chips, in order to reduce process difficulties and production costs. Although the structural engineering of sensing diaphragms has been extensively studied over the past decades, this work focuses on investigating membrane pre-stress as a means to achieve enhanced sensitivity under high-vacuum conditions. Further evaluation results and detailed discussions will be presented at the conference.

Integration of a metal nano-antenna structure into silicon substrates using surface-activated room temperature bonding

Tuesday, 16th September - 16:00: Poster Session 1 - Poster - Abstract ID: 166

Dr. Yuichi KURASHIMA [1], ***Dr. Takashi Matsumae*** [1], ***Mr. Atsuhiko Maeda*** [1], ***Dr. Masaaki Oshita*** [1], ***Dr. Hideki TAKAGI*** [1], ***Dr. Tetsuo Kan*** [2], ***Dr. Elyas Ashenafi Abadi*** [2], ***Dr. Daiji Noda*** [3], ***Mr. Ryo Ohta*** [3]

1. *National Institute of Advanced Industrial Science and Technology (AIST),* ***2.*** *The University of Electro-Communications,* ***3.*** *Micromachine Center*

This study demonstrates the integration of metal nano-antenna into Si substrates for silicon-based IR detectors. Pt patterns were fabricated on a Si substrate and bonded to another Si substrate using surface-activated room temperature bonding. To promote the formation of platinum silicide, the bonded samples were annealed at 400 °C for 20 minutes in a nitrogen atmosphere. Infrared camera imaging, transmission electron microscopy (TEM), and energy-dispersive X-ray (EDX) analysis confirmed defect-free bonding and uniform adhesion. Post-annealing, the Pt layer thickness nearly doubled, with EDX indicating successful silicidation. This integration technique is expected to increase the IR detection sensitivity of Si-based IR detectors because of increasing the photocurrent extraction area.

Interface-Engineered Ferroelectric Tunnel Junctions with Ultra-High TER via Optimized P(VDF-TrFE) Crystallinity

Tuesday, 16th September - 16:00: Poster Session 1 - Poster - Abstract ID: 167

Mr. Mohit Kumar Gautam [1], ***Dr. Roshni Satheesh-Babu*** [1], ***Dr. Ioannis Zeimpekis*** [1], ***Prof. Dimitra Georgiadou*** [1]

1. *University of Southampton*

Ferroelectric tunnel junctions (FTJs) are emerging as key building blocks for next-generation non-volatile memory and neuromorphic computing systems due to their low-power operation, non-destructive readout, scalability, and ability to exhibit memristive behaviour [1]. In particular, polymer-based ferroelectrics, such as poly(vinylidene fluoride-trifluoroethylene) (P(VDF-TrFE)), offer unique advantages, including mechanical flexibility and low-temperature processability, making them ideal candidates for integration into flexible electronics and hardware-efficient neuromorphic platforms. This work aims to develop high-performance coplanar nanogap electrode-based organic polymer ferroelectric tunnel junctions (FTJs) with high tunnel electroresistance (TER) ratio.

The 10-nm separated Al/Au nanogap electrodes are fabricated using adhesion lithography technique [2], and PVDF(TrFE) polymer film was deposited via spin-coating its solution in different solvents, such as cyclopentanone (CP), dimethylformamide (DMF), and dimethyl sulfoxide (DMSO), followed by annealing at 100 °C, 120 °C, 140 °C, and 160 °C for 2 hours in a glove box at ~3 mbar pressure (**Figure 1A**). A comprehensive structural analysis was made with grazing incidence X-ray diffraction (XRD), aimed at optimising β-phase crystallinity, which is essential for robust ferroelectric behaviour.

The asymmetric I–V characteristic displayed in **Figure 1B** is due to the unequal energy barrier modulation at the two metal-ferroelectric interfaces, i.e., gold and aluminium with P(VDF-TrFE). At the aluminium contact, a native Al_2O_3 layer introduces a fixed tunnelling barrier that remains largely insensitive to polarisation switching. In contrast, the Au/P(VDF-TrFE) interface is more electrostatically coupled to the ferroelectric layer, allowing significant modulation of the energy barrier during switching. When the polarisation points toward the Al electrode, negative bound charges reduce the effective barrier height at the Al_2O_3 interface, enhancing carrier tunnelling and producing a low-resistance state. Reversing the polarisation shifts the barrier modulation toward the Au interface, increasing the effective potential barrier and leading to a suppressed current or high-resistance state. This interfacial asymmetry in barrier height and screening efficiency is key to the polarisation-dependent resistive switching and the resulting ultra-high TER ratio of ~8×10^6 at 4V [3]. **Figures 2A-C** present grazing incidence XRD patterns of PVDF-TrFE thin films spin-coated on glass substrates using three different solvents and annealed at various temperatures. The β-phase peak at $2\theta \approx 19.8°$ becomes sharper and more intense with temperature, peaking at 140 °C. CP-based films (**Figure 2C**) exhibit the highest intensity and narrowest peaks, indicating superior β-phase crystallinity. At 160 °C, reduced peak intensity suggests thermal degradation. **Figure 2D** compares XRD patterns of CP-processed films on gold and aluminium substrates. Both support β-phase formation, but gold yields stronger, sharper peaks, particularly at 140 °C, and maintains higher crystallinity at 160 °C. Crystallite size analysis (**Tables 1** and **2**) supports these observations: CP films on gold reach ~14 nm across all temperatures, while aluminium films drop from ~12 nm at 140 °C to ~9 nm at 160 °C. These results confirm the significant influence of solvent and substrate on the crystallinity and thermal stability of PVDF-TrFE films.

In summary, the combination of a coplanar nanogap architecture, polarisation-driven tunnelling modulation, and structurally optimised P(VDF-TrFE) films enables ultra-high TER performance in ferroelectric tunnel junctions. These findings demonstrate the critical role of interface and crystallinity engineering in advancing low-temperature, flexible FTJ devices for future non-volatile memory and neuromorphic computing applications.

References:

[1] Park, Sung Hyuk, et al. “Ferroelectric tunnel junctions: promise, achievements and challenges.” *Journal of Physics D: Applied Physics* (2024).

[2] Semple, James, et al. “Large-area plastic nanogap electronics enabled by adhesion lithography.” *npj Flexible Electronics* 2.1 (2018): 18.

[3] Kumar, Manasvi, et al. “Colossal tunneling electroresistance in co-planar polymer ferroelectric tunnel junctions.” *Advanced Electronic Materials* 6.2 (2020): 1901091.

Fabrication of metal nanodot arrays for LSPR biosensors with LOD of 1fg/mL using nanoimprint lithography process

Tuesday, 16th September - 16:00: Poster Session 1 - Poster - Abstract ID: 170

Dr. JaeJong Lee [1], ***Dr. Narae Jo*** [2]

1. *Korea Institute of Machinery and Materials (KIMM),* ***2.*** *Korea Research Institute of Standards and Science*

Nanoimprint lithography is a promising technology capable of rapidly and easily generating patterns over large areas at a lower cost compared to other lithography methods. As advancements in biosensor technology continue, there is an increasing demand for diverse nanostructures and nanoscale patterns. In particular, the LSPR(Localized Surface Plasmon Resonance) utilizes the phenomenon that occurs in nano-sized metals. To make an LSPR biosensor chip, a nano-sized metal array should be implemented in a large area substrate. In order to fabricate the nanoscale patterns on the substrate, the nanoimprint technology is one of good solutions. The silicon master's hole pattern with a diameter of 150nm, pitch of 300nm, and depth of 150nm, coated with UV resin (PFPE), was covered with Polycarbonate (PC) film and irradiated with UV light to fabricate a replica mold. Thermoplastic resin (Poly (methyl methacrylate (PMMA), mr-I PMMA 35k200) was spin-coated onto a glass substrate, and imprinting was conducted at 130°C and 5 bar pressure. After cooling and detachment of the replica mold, a chromium layer was deposited to protect the resin during O2 plasma etching. Subsequently, a Ti/Au(1/20nm) layer was deposited via e-beam evaporation, followed by lift-off with acetone solution. It was confirmed that the created sensor chip exhibited the LSPR phenomenon and was used to detect AFP (α-fetoprotein), a liver cancer marker. It was possible to detect the LSPR wavelength peak with a change amount depending on the concentration, and the limit of detection (LOD) was 1fg/ml. These nanostructure arrays fabricated through imprinting can serve not only as biosensors but also as a variety of optical components

Study of the high-intensity reflection structure that used the speckle exposure method

Tuesday, 16th September - 16:00: Poster Session 1 - Poster - Abstract ID: 176

Dr. Atsushi Sekiguchi [1]

1. *Litho Tech Japan Corporation*

Cases have been reported of pedestrians being injured when they collided with vehicles while walking at night. While having pedestrians wear reflectors can help, drivers must often be quite close before the reflected light becomes visible, because the reflector does not have a structure that generates high-intensity reflections. We therefore considered using lithography technology to create a reflection structure that can generate high-intensity reflections visible from greater distances.

Specifically, we developed a high-intensity reflection structure by using a photoresist with controlled molecular weight distribution and performing speckle exposure（Fig-1）｛1｝.

We applied an F2 resist with controlled molecular weight distribution onto an Si substrate and performed speckle exposure and development. The structure obtained was irradiated with white LED light to observe the reflections. The results indicated success in creating a structure that reflects light with high intensity. Additionally（Fig-2）, we performed theoretical verification by carrying out simulations of the molecular size and reflectivity, the results of which are also reported here.

Introducing ArF grayscale lithography for large-scale fabrication of submicronic 3D structures

Tuesday, 16th September - 16:00: Poster Session 1 - Poster - Abstract ID: 179

Mr. Gaby Bélot [1], ***Mr. Sébastien Bérard-Bergery*** [1], ***Dr. Élodie Sungauer*** [1], ***Mr. Api Warsono*** [2], ***Dr. Arnaud Bazin*** [2], ***Dr. Aurélien Fay*** [2], ***Dr. Cécile Gourgon*** [3]

1. *STMicroelectronics, 850 rue Jean Monnet, 38926 Crolles Cedex, France,* ***2.*** *Univ. Grenoble Alpes, CEA, Leti, F-38000 Grenoble, France,* ***3.*** *Université Grenoble Alpes, CNRS, CEA/LETI-Minatec, Grenoble INP, LTM, 17 Rue des Martyrs, Grenoble 38054, France*

The growth of the 3D microfabrication field is fueled by the needs of various applications, ranging from optics, to microfluidics, MEMS or photonics. Following the global trend of micro-components, 3D structures are often not spared by the wish for miniaturization. On the industrial side, this objective rhymes with a requirement for a high resolution, large scale and low-cost 3D microfabrication process. Grayscale PhotoLithography (GPL) is a derivative of classical photolithography, using low-contrast photoresist and unresolved binary masks to perform the fabrication of 3D structures in a single lithography step, thus offering the desired high throughput. The goal of this work is to propose an extension of the GPL technology by the transition to a 193nm dry photolithography process, for which a relevant low contrast photoresist has been developed. The objective is a proof of concept for the high-volume manufacturing of various submicronic 3D features. A dedicated binary photomask has been designed following previously established best practices, the recourse to curvilinear sub-resolution mask features is also investigated. A new ArF photoresist formulation has been developed to meet the requirement in terms of dose sensitivity and coating thickness. This material is shown to display the desired response through the progressive behavior of its contrast curve. The combination of these two achievements enabled performing the first state of the art ArF Grayscale lithography process. The patterning of various submicronic resist patterns is demonstrated through tilted SEM inspection. The viability of the G-ArF process as a strong contestant for the large-scale patterning of submicronic 3D structures is proved. Moreover, this study opens the door to many further developments regarding this technology and its future applications.

MoTe2-Based Memristor Fabrication with Scanning Probe Lithography

Tuesday, 16th September - 16:00: Poster Session 1 - Poster - Abstract ID: 181

Ms. Busra Oyku Alan [1], ***Dr. Christoph Reuter*** [1], ***Dr. Ren Li*** [1], ***Prof. Steffen Strehle*** [1]

1. *Techische Universität Ilmenau*

This study explores using scanning probe lithography (SPL) with local anodic oxidation (LAO) to fabricate 2H-$MoTe_2$-based memristors for neuromorphic computing. SPL-LAO creates nanoscale trenches to facilitate conductive filament formation. Memristor devices showed resistive switching, confirmed through I-V sweeps, conductive AFM, and Raman spectroscopy.

Study on Micro Scale Surface Polishing and Modification of 3D Biodegradable Scaffolds using Electron Beam Treatment

Tuesday, 16th September - 16:00: Poster Session 1 - Poster - Abstract ID: 182

Mr. JeongSik Noh [1], ***Prof. Jongsung Park*** [1]

1. *Kyungpook National University*

This study introduces an electron beam post-processing method that enhances surface smoothness, dimensional accuracy, and mechanical strength of 3D printed scaffolds, specifically demonstrated on PLA vascular stents. The technique is rapid, batch-processable, and applicable to both polymers and metals, with potential for broad biomedical implant use.

Micro-Mechanical Properties of Annealed Electrodeposited Gold for Design of MEMS Structural Components

Tuesday, 16th September - 16:00: Poster Session 1 - Poster - Abstract ID: 183

Mr. Shota Iima [1], ***Dr. Tomoyuki Kurioka*** [2], ***Mr. Shota Kanno*** [2], ***Prof. Chun-Yi Chen*** [2], ***Prof. Tso-Fu Mark Chang*** [2], ***Prof. Katsuyuki Machida*** [2], ***Prof. Hiroyuki Ito*** [2], ***Prof. Yoshihiro Miyake*** [2], ***Prof. Masato Sone*** [2]

1. *Institute of Integrated Research, Institute of Science Tokyo,* **2.** *Institute of Science Tokyo*

This study investigates the effects of annealing on the micro-mechanical properties of electrodeposited gold used in MEMS accelerometers. Gold films were electrodeposited and annealed at 200 °C and 300 °C. Micro-compression tests revealed that annealing decreased the yield stress due to grain growth, but the flow stress at 6% strain was maintained at 200 °C. The relationship between grain size and stress was analyzed, showing that while the yield stress did not clearly follow the Hall-Petch relationship, the flow stress did. The results suggest that annealing at 200 °C effectively removes impurities without significantly compromising mechanical strength.

Scalable manufacturing processes for solid-state nanopores using Atomic Layer Deposition

Tuesday, 16th September - 16:00: Poster Session 1 - Poster - Abstract ID: 202

Mr. Nico Rademacher [1], ***Ms. Stefanie Linda Stoll*** [1], ***Mrs. Anja Leibold*** [2], ***Mr. Michael Möller*** [1], ***Dr. Christoph Blattert*** [2], ***Dr. Jens Bolten*** [1], ***Prof. Max Lemme*** [1]

1. *AMO GmbH,* ***2.*** *Hahn-Schickard-Gesellschaft für angewandte Forschung e.V.*

A reliable, scalable, and cost-effective fabrication method for solid-state nanopores is essential for their application in genome sequencing and biomedical research. This work employs electron beam lithography (EBL) to prototype structures with various edge lengths, followed by atomic layer deposition (ALD) to precisely reduce the pore size. Silicon chips with silicon dioxide and a 50 nm low-stress silicon nitride membrane were used. The process allows controlled customization of solid-state nanopores for specific applications like protein or molecule detection without relying on high-resolution lithography techniques.

The Impact of Writing Field Stitching on Optical Losses in Electron Beam Fabricated Silicon-on-Insulator Waveguides

Tuesday, 16th September - 16:00: Poster Session 1 - Poster - Abstract ID: 206

Mr. Maksim Lipkin [1], ***Mr. Michael Möller*** [1], ***Ms. Lisa Ehlert*** [1], ***Dr. Jens Bolten*** [1], ***Dr. Rijil Thomas*** [1], ***Dr. Stephan Suckow*** [1], ***Prof. Max Lemme*** [2]

1. *AMO GmbH,* ***2.*** *Chair of Electronic Devices, RWTH Aachen University*

This study investigates how electron-beam lithography field stitching errors affect optical waveguides. By introducing controlled artificial defects, we analyze their impact on light propagation. Results reveal measurable losses from even 2.5 nm offsets, establishing critical fabrication tolerances for maintaining waveguide performance. The work provides guidelines for optimizing nanophotonic device fabrication.

A Deep Learning-Based Photoresist Shrinkage Correction Method via Fusion of SEM Image and Scanning Parameter Features

Tuesday, 16th September - 16:00: Poster Session 1 - Poster - Abstract ID: 209

Ms. Sa Liu [1], Dr. Yanan Zhu [2], Mr. Jiebin Niu [3], Prof. Diwei Zhou [4], Dr. Fuqin Deng [1], Prof. Zhuming Liu [2]

1. *School of Electronics and Information Engineering,Wuyi University,* ***2.*** *Institute of Semiconductors, Guangdong Academy of Sciences,* ***3.*** *Institute of Microelectronics of the Chinese Academy of Sciences,* ***4.*** *School of Science, Loughborough University*

A deep learning model is developed to predict the unshrunk state of photoresist images based on SEM data and process parameters, addressing an image-to-image regression task. By correcting shrinkage introduced during the SEM metrology process, the method improves measurement accuracy and offers a new solution to enhance photolithography quality.

Fabrication and Nanoscale Characterization of Sidewall Roughness in SOI Waveguides

Tuesday, 16th September - 16:00: Poster Session 1 - Poster - Abstract ID: 214

Dr. Magdalena Ulmeanu [1], ***Dr. Kate Stokes*** [1], ***Dr. Marta Kocun*** [2], ***Dr. Roger Proksch*** [2], ***Dr. Vlad Korolkov*** [3], ***Dr. Luis Perdigao*** [3], ***Dr. Jason Li*** [2], ***Dr. Gabriele Selvaggio*** [2], ***Mr. Zhong Ren*** [1]

1. *Oxford Instruments Plasma Technology,* ***2.*** *Oxford Instruments Asylum Research,* ***3.*** *Oxford Instruments NanoAnalysis*

We demonstrate the capacitive plasma etching of Si waveguides using the Si-on-Insulator (SOI) platform. These results establish a reliable baseline for evaluating process-induced sidewall variations and offer critical feedback for further process refinement and modelling of optical losses in high-confinement SOI waveguides.

Fabrication of hierarchical structures in a greyscale positive photoresist by applying two lithography methods in a single resist film

Tuesday, 16th September - 16:00: Poster Session 1 - Poster - Abstract ID: 216

Dr. Christine Schuster [1], Dr. Anja Voigt [1], Dr. David Kuhness [2], Ms. Christine Prietl [2], Dr. Matej Goraus [3], Mr. Daniel Mrena [3], Prof. Dusan Pudis [3], Dr. Arne Schleunitz [1], Mrs. Gabi Grützner [1], Mr. Markus Postl [2]

1. *micro resist technology GmbH,* ***2.*** *Joanneum Research Forschungsgesellschaft mbH,* ***3.*** *University of Zilina*

Combined micro and nanoscale structures integrate different functions in one surface.
Larger microscale wave patterns from Direct Write Lithography were combined with Laser Interference Lithography nanoscale gratings. Fabricated in mr-P 22G_XP, a photoresist prototype enabling very deep greyscale patterns, these hierarchical structures expand possible pattern size combinations and multifunctional applications.

200 kV E-beam Lithography for Patterning Thick Resist

Tuesday, 16th September - 16:00: Poster Session 1 - Poster - Abstract ID: 222

Dr. Ying Tran [1], ***Dr. Kian Shen Kiang*** [1], ***Mr. Hitoshi Kato*** [2], ***Mr. Ryo Matsui*** [2], ***Mr. Yukinori Aida*** [2], ***Prof. Martin Charlton*** [1]

1. *University of Southampton,* ***2.*** *JEOL Ltd*

Electron beam lithography (EBL) enables nano-scale patterning for applications such as photonics and electronics, but 100 kV systems face challenges such as secondary electron back-scatter, charging effects, and limited etch transfer due to thin resist masks.

High-resolution patterns require a trade-off between resist thickness and feature depth. New 200 kV EBL systems, like the JEOL JBX-8100FS G3, improve vertical side wall profiles and aspect ratios in thick resists, confirmed by simulations and SEM images of exposed features on 10 μm thick PMMA.

Large-Scale Integrated Visible/Near-Infrared Multi-Channel Polarizer based on Sub-wavelength Metal Grating

Tuesday, 16th September - 16:00: Poster Session 1 - Poster - Abstract ID: 230

Ms. Kangping Liu [1], ***Mr. Jinyu Guo*** [1], ***Mr. Wentao Yuan*** [1], ***Mr. Shuoqiu Tian*** [1], ***Mr. Hao Quan*** [1], ***Mr. Qiucheng Chen*** [1], ***Ms. Qingxin Wu*** [1], ***Ms. xunjia Zhao*** [1], ***Prof. Yifang Chen*** [1]

1. *Fudan university*

Linear polarization is the simplest form of polarized light whose electric field vector is in the plane perpendicular to the direction of propagation. It can help people get the information more accurately by using polarizers to process the optical information. Extensive applications of polarimetric detection in visible/near-infrared wavelengths can be found in resource exploration, material analysis and Marine pollution detection. Sub-wavelength metal grating with the advantages of miniaturization and integration with focal plane array of detectors on one chip, possesses promising prospect for future multi-channel on-chip polarizers[1]. This work successfully fabricate polarizers with three channels through polarization of 0°, -60°, and 60° in the visible and near-infrared bands. Each channel has at least 150 μm × 15 mm of grating coverage area achieving large-scale linear polarizers on silicon-based photodetector chips. Finite difference time domain (FDTD) is utilized to obtain the structure parameters of the aluminum (Al) grating with balance between efficiency and process complexity[2,3]. Electron beam lithography (EBL) on bilayer resist for pattern definition and lift-off for pattern transfer are carried out for the metal polarizers. Transmittance and extinction ratio (ER) through the gratings are characterized in visible/near-infrared bands.

In order to reduce the influence of stray light, chromium (Cr) is used as a shield to form the light slits. Metal wire grids with different polarization directions are required to cover each light slit. The schematic diagram of the integrated three-channels polarizer and an additional slit for benchmark on the detector is shown in Fig. 1. According to the simulation results shown in Figure 2(a) and Fig. 2(b), it is determined that with a period of less than 150 nm the structure has a TM wave transmittance greater than 60% and a good ER operating in the visible/near-infrared band. According to the results shown in Fig. 2(c) and Fig. 2(d), with 150 nm period and 75 nm line width, the grating can achieve a transmittance over 60% and a ER above 100:1 when the height exceeds 100 nm. This work adopted a double-layer Polymethylmethacrylate (PMMA) lift-off technology due to its small period. As is shown in Fig. 3, PMMA (100K) was selected as the bottom resist and PMMA (950K) as the top. The experimental results are shown in Fig. 4 which has Al wire grids with directions of 0°, -60°, and 60°. Results obtained from the final test is illustrated in Fig. 5, showing that the transmittance of TM can exceed 70% and ER can be greater than 50:1 over the range of 650 nm to 900 nm.

Reference:

1 Feng, B. *et al.* Precision integration of grating-based polarizers onto focal plane arrays of near-infrared photovoltaic detectors for enhanced contrast polarimetric imaging. *Int. J. Extreme Manuf.* **3** (2021). https://doi.org/10.1088/2631-7990/abf5c8

2 Yang, Z. *et al.* Optimization study of metallic sub-wavelength gratings as the polarizer in infrared wavelengths. *Appl Opt* **59**, 1253-1258 (2020). https://doi.org/10.1364/AO.378636

3 Yang, Z. *et al.* A study of nano-structural effect on the polarization characteristics of metallic sub-wavelength grating polarizers in visible wavelengths. *Microelectronic Engineering* **227** (2020). https://doi.org/10.1016/j.mee.2020.111327

High Resolution Electron Beam Lithography for 10 nm Zone Plates with ultra-high aspect ratio

Tuesday, 16th September - 16:00: Poster Session 1 - Poster - Abstract ID: 231

Ms. Qingxin Wu [1], ***Mr. Qiucheng Chen*** [1], ***Mr. Hao Quan*** [1], ***Ms. xunjia Zhao*** [1], ***Mr. Wentao Yuan*** [1], ***Mr. Shuoqiu Tian*** [1], ***Mr. Jinyu Guo*** [1], ***Ms. Kangping Liu*** [1], ***Prof. Yifang Chen*** [1]

1. *Fudan university*

High-resolution Fresnel zone plates are urgently needed by X-ray nanoprobes for important applications in material and life science, biology, medical diagnosis, new energy resources and integrated chips, etc. Although 10 nm resolution zone plates have been reported by double-patterning technology, the diffraction efficiency remains limited to about 1% [1], primarily due to defects and imperfection in the structure. The technology of high-efficiency 10 nm zone plates using electron beam lithography (EBL) remains challenging. In this paper, an optimized exposure strategy for 10 nm resolution HSQ zone plate template is presented. Careful Monte Carlo simulations for achieving ultra high dense pattern were carried out to compare original with optimized exposure methods. High-quality zone plates with 10 nm linewidth and vertical sidewalls were successfully replicated using the optimized dose distribution combined with our hot development process [2].

To eliminate proximity effect on the dense pattern, the designed linewidths of both zones and ribs are reduced to 5 nm. Fig. 1 presents scanning electron microscope (SEM, ZEISS Sigma 300 HD) images of 10 nm HSQ zone plate templates fabricated by state-of-the-art beam-writer, JBX6300FS, with exposure doses of 20000 μC/cm² (Fig. 1a-c) and 25000 μC/cm² (Fig. 1d-f). While 10 nm lines are visible in high-magnification images (Fig. 1a), defects are observed in outer zones (Fig. 1b). The 45° tilted view (Fig. 1c) reveals uneven exposure patterns, with over exposed intersections and under exposed zone regions. These defects significantly affect zone height uniformity and diffraction efficiency.

An optimized exposure strategy was developed (Fig. 2), incorporating two key modifications. First, zone linewidths (6 nm) were increased relative to ribs (2 nm) to enhance dose concentration in zone areas. Second, relief holes were introduced at zone-rib intersections to reduce proximity effects. Monte Carlo simulations are employed to calculate the isoenergy contours, showing concentrated charge density at intersections in the original design (Fig. 2a) versus uniform distribution across zones in the optimized pattern (Fig. 2b). Using this strategy, we successfully fabricated defect-free 10 nm HSQ zone plate templates with 180 nm height and 1:3 duty cycle, as demonstrated in Fig. 3a.

In conclusion, 10 nm HSQ zone plate templates with 180 nm height and 1:3 duty cycle is successfully fabricated by electron beam lithography. With the assistance of hot developing and optimized exposure process, well-defined zone plate profiles are achieved. Our in-house developed calculation method shows an efficiency over 3% of the 10 nm HSQ zone plates.

[1] R. Benedikt et al., Microelectronic Eng., 191 (2018) 91–96.

[2] Y. Chen et al., Microelectron. Eng., 83 (2006) 4-9.

Ultra high resolution and dense SiO2 gratings by electron beam lithography and dry-etch

Tuesday, 16th September - 16:00: Poster Session 1 - Poster - Abstract ID: 232

Mr. Sheng Tao [1], ***Prof. Yifang Chen*** [1], ***Mr. Shuoqiu Tian*** [1], ***Mr. Wentao Yuan*** [1], ***Mr. Jinyu Guo*** [1], ***Ms. Kangping Liu*** [1]

1. *Fudan university*

This work focuses on nanofabrications of highly dense SiO_2 gratings by electron beam lithography (EBL) together with reactive ion etch (RIE), using ZEP520A as etching mask. The final task of the work is to achieve 14 nm lines/14 nm spaces with the height around 35 nm, which will sit on the top of quartz. SiO_2 based gratings are crucial in various optical applications such as spectroscopy, optical communication, and optical sensors. It can also be applied as nanoimprint templates for high resolution patterning. ZEP520A was used as etching mask because of its high resolution, high sensitivity, high contrast and high resistivity to plasma etch.

In this research, systematic processes were studied to explore the processing window. A 140 nm - thick layer of ZEP520A was coated onto a SiO_2 substrate. Electron beam lithography (JEOL JBX - 6300FS) was applied for exposure, and then development in O-Xylene. Reactive ion etch was carried out in Plasma lab system 100, where CHF_3 was employed as etching gases. Various parameters such as gas flow rate, pressure, and power were systematically varied to optimize the etching process.

The results indicate that under optimized conditions (etching power of 200 W, SF_6 flow rate of 0 SCCM, CHF_3 flow rate of 30 SCCM, etching time of 30 s, and pressure of 4 Pa), ZEP520A can be efficiently used as an etching mask to achieve the SiO2 based grating with good side-wall verticality. SEM characterization confirmed that the fabricated grating structures exhibited excellent verticality and uniform periodic arrangement.

Further analysis revealed that introducing SF_6 increases the etching rate of SiO_2 but leds to significant consumption of ZEP520A, making this approach unsuitable for the etching process. As shown in Figure (b), the pattern morphology remained largely unchanged before and after photoresist removal, indicating complete etching of the ZEP520A photoresist within 30 seconds. Regarding pressure, it was observed that the etching rate and verticality first increased and then decreased with increasing pressure. Notably, at pressures of 4 - 5 Pa, the etching exhibited better verticality, as evidenced by the combination of Figure (c) and Figure (e). Figure (d) illustrates that the effective etching of grating structures occurred within the blue region (SF_6 flow rate of 0 – 5 SCCM). When the gas flow rate exceeded 5 SCCM, the ZEP520A photoresist was consumed too rapidly to function properly, resulting in uniform etching across the entire plane.

Overall, this study demonstrates that using ZEP520A photoresist as an etching mask in the etching process can produce high quality SiO_2 gratings, providing a reliable technical approach for manufacturing high resolution SiO2 based nanoimrint templates. Future work will focus on how to reduce the dimension of the graing linewidth for 14 nm lines/spaces grating in quartz.

Keywords: SiO_2 grating; electron beam lithography, reactive ion etch, nanoimprint templates, ZEP520A

Ultrafast Single Germanium Nanowire Photodetectors

Tuesday, 16th September - 16:00: Poster Session 1 - Poster - Abstract ID: 15

Dr. Ahmad Echresh [1], ***Mr. Mohd Saif Shaikh*** [2], ***Mr. mircea-traian catuneanu*** [2], ***Prof. Manfred Helm*** [1], ***Dr. Shengqiang Zhou*** [1], ***Prof. Artur Erbe*** [1], ***Dr. Lars Rebohle*** [1], ***Prof. Kambiz Jamshidi*** [2], ***Dr. Yonder Berencen*** [1], ***Dr. Yordan M. Georgiev*** [1]

1. *Helmholtz-Zentrum Dresden-Rossendorf (HZDR),* ***2.*** *Technische Universität Dresden*

Semiconductor nanowire-based photodetectors with high sensitivity and rapid photoresponse in the near-infrared (NIR) spectrum are essential for applications in optical communication switches, as well as environmental and atmospheric sensing [1-3]. These devices exploit the high surface-to-volume ratio, quantum confinement effects, and the tunable bandgap of nanowires to achieve enhanced responsivity, fast response times, and broad spectral sensitivity, including in the NIR region [4]. Recently, there has been growing interest in the development of photodetectors that can operate at zero bias, making them more suitable for portable, low-power applications. Such self-powered photodetectors, which utilize the photovoltaic effect, can be categorized into Schottky junctions, p–n junctions, and photoelectrochemical cells [5]. Among various semiconductor materials, germanium nanowires (Ge NWs) offer distinct advantages for optoelectronic applications, including high carrier mobility, compatibility with silicon-based complementary metal-oxide-semiconductor (CMOS) technology, and a lower bandgap compared to silicon [6]. However, despite these promising properties, research on the fabrication and photoresponse characteristics of axial p–n junctions in single Ge NWs remains limited, necessitating further investigation.

This study presents the top-down fabrication of axial p–n junction along single Ge NWs and investigates their photoresponse characteristics in the NIR spectral range. The fabricated devices exhibit rectifying current-voltage behavior with a high rectification ratio in dark conditions (Fig. 1a). Under 850 nm wavelength laser illumination at reverse bias, the devices achieve a responsivity of 1.72 AW^{-1} (Fig. 1b), a low noise-equivalent power of 5.68×10^{-11} $W/\sqrt{Hz}$ (Fig. 2a), and a high-frequency response of 2.85 GHz (Fig. 2b), characterized by a 3dB cut-off frequency. The enhanced sensitivity of Ge NW-based photodetectors is attributed to the presence of a radial built-in electric field, which extends the carrier lifetime, while their nanoscale dimensions result in minimal capacitance, enabling ultrafast response times. These findings hold significant promise for the development of high-speed, energy-efficient photodetectors, with potential applications in next-generation optical communication systems and integrated optoelectronic technologies.

Substantial Ron,sp Reduction in a 1.2 kV SiC DMOSFET Using a Double-Epi Drift Layer

Tuesday, 16th September - 16:00: Poster Session 1 - Poster - Abstract ID: 46

Mr. Seung wan Jung [1]

1. *Pusan National University*

This study proposes a 1.2 kV SiC DMOSFET using a double-epi structure with a deep, highly doped upper drift layer to reduce on-resistance (Ron,sp). The structure improves current conduction, reduces Ron,sp by 40%, and maintains a safe breakdown voltage, achieving enhanced efficiency and performance.

Development of a uniform cell dispersion structure in microfluidic channels with low cell loss

Tuesday, 16th September - 16:00: Poster Session 1 - Poster - Abstract ID: 53

Mr. Takumi Yamada [1], ***Mr. Akihito Kimura*** [1], ***Dr. Maho Kaminaga*** [1], ***Dr. Akira Kotani*** [1]

1. *National Institute of Technology (KOSEN) Toyota College*

This study presents a low-loss cell seeding method for microfluidic devices using a micropillar array and microballoon actuators. The pillars induce random flow for uniform cell dispersion, while actuators switch the channel width to collect residual cells. Effectiveness was validated by cell distribution and flow analysis using particle image velocimetry.

3D-Printed Microfluidic Device for Biological Application

Tuesday, 16th September - 16:00: Poster Session 1 - Poster - Abstract ID: 62

Mr. Amlan Ashish [1], ***Prof. Gorachand Dutta*** [1]

1. *Indian Institute of Technology Kharagpur*

The study focuses on the fabrication of 3D-printed microfluidic device using an acrylate-based resin and DLP technique to investigate the influence of different growth media under constant flow condition responsible for bacterial adhesion and subsequent biofilm formation. It can be customizable to understand the capability of different bacteria forming biofilm.

Tattoo Electrodes for Comfortable and Reliable Masticatory EMG Monitoring

Tuesday, 16th September - 16:00: Poster Session 1 - Poster - Abstract ID: 73

Ms. Núria Termes Español [1]***, Ms. Eva Casals*** [1]***, Ms. Yolanda Castillo*** [2]***, Prof. Raimon Jané*** [2]***, Ms. Rosa Villa*** [1]***, Mr. Anton Guimerà-Brunet*** [1]***, Ms. Gemma Gabriel*** [1]

1. *Institute of Microelectronics of Barcelona (IMB-CNM, CSIC),* ***2.*** *Universitat Politècnica de Catalunya - BarcelonaTech (UPC)*

This study introduces an ultrathin, wireless electronic tattoo for non-invasive electromyographic recordings of masticatory muscles. Made with stretchable materials via screen-printing, this technology matches commercial electrodes in performance and offers a miniaturizable, user-friendly solution for long-term electrophysiological monitoring in both clinical and home settings.

Exploiting the dewetting instability of thin Ge films to develop a novel photonic platform

Tuesday, 16th September - 16:00: Poster Session 1 - Poster - Abstract ID: 91

Dr. Sonia Freddi [1], ***Dr. Nicoletta Granchi*** [2], ***Dr. Alessia Arrigoni*** [3], ***Mr. Michele Gherardi*** [4], ***Dr. Benedetta Squeo*** [3], ***Mr. Raffaele Giani*** [4], ***Dr. Alexey Fedorov*** [1], ***Dr. Laura Pasquardini*** [5], ***Dr. Lia Vanzetti*** [6], ***Prof. Maria Antonietta Vincenti*** [7], ***Dr. Mariacecilia Pasini*** [3], ***Prof. Francesca Intonti*** [2], ***Dr. Monica Bollani*** [1]

1. *Institute of Photonic and Nanotechnology (IFN) - CNR,* ***2.*** *LENS and Department of Physics and Astronomy, University of Florence,* ***3.*** *SCITEC-CNR,* ***4.*** *Politecnico di Milano,* ***5.*** *Indivenire s.r.l.,* ***6.*** *Center for Sensors and Devices, Fondazione Bruno Kessler,* ***7.*** *Università degli studi di Brescia*

This work investigates from a fundamental point of view the dewetting features of thin germanium films, following the morphological and chemical evolution upon annealing, from flat films to islands creation. Then, coupling EBL and RIE to pattern Ge films and controlling the annealing parameters, ordered array of islands that support optical Mie resonances are created. The presence of Mie responances are proven theoretically and experimentally. Finally, these islands are selectively functionalized for sensing applications, demonstrating also how nitrogen atmosphere improves the process efficiency.

Mechanically robust spin-on-glass packaging of hydrogenated amorphous silicon for harsh environment applications

Tuesday, 16th September - 16:00: Poster Session 1 - Poster - Abstract ID: 95

Mr. Junhwa Seong [1], ***Dr. Younghwan Yang*** [1], ***Mr. Youngsun Jeon*** [1], ***Prof. Junsuk Rho*** [1]

1. *Pohang University of Science and Technology*

Metalenses—ultrathin planar lenses composed of nanostructured metasurfaces—are poised to revolutionize optical systems due to their compact form factor and advanced functionalities, including aberration correction, field-of-view expansion, and tunable focusing [1]. Despite their exceptional optical performance, their widespread deployment in real-world applications remains hindered by a critical weakness: structural fragility in harsh environments. Nanostructures on exposed surfaces are prone to detachment or degradation under mechanical stress and contamination, severely impairing device performance [2]. In this work, we introduce a comprehensive fabrication platform for encapsulated, self-cleaning, and mechanically robust metalenses by integrating hydrogenated amorphous silicon (a-Si:H) with a spin-on-glass (SoG) packaging technique. By optimizing plasma-enhanced chemical vapor deposition (PECVD) conditions—including chamber pressure, temperature, and gas flow ratios—we engineer a-Si:H films exhibiting an exceptionally high refractive index of n = 3.23 with near-zero optical losses at visible wavelengths (635 nm). This high-index contrast between meta-atoms and the SoG background enables strong light confinement, supporting efficient phase modulation and waveguiding critical for high-performance metalens operation. We demonstrate that the encapsulated metalenses achieve a calculated polarization conversion efficiency of 97.2%, substantially outperforming conventional unencapsulated structures. More importantly, mechanical durability was validated by a rigorous sonication test using coarse sand particles, where unencapsulated devices were visibly damaged and functionally degraded, whereas encapsulated devices preserved both their structure and optical focusing capability over extended exposure times. In addition, our encapsulation strategy allows for post-fabrication control of surface wettability, enabling both hydrophilic and hydrophobic states without impairing optical function. We exploit this property to realize passive self-cleaning metalenses, wherein hydrophobic treatment causes water droplets to roll off the surface, removing particulates and contaminants. This is particularly advantageous for long-term deployment in outdoor or industrial optical systems, where manual cleaning is impractical. The proposed platform is fully compatible with CMOS processes and scalable for wafer-level manufacturing, opening the door to commercial applications in augmented reality optics, LiDAR sensors, biomedical imaging systems, and more. Our findings represent a key step toward the practical realization of ruggedized, multifunctional metasurfaces, bridging the gap between nanophotonics research and real-world implementation.

[1] M. Khorasaninejad et al., Science (2016) 352, 1190-1194.

[2] Y. Yang et al., ACS Nano (2025) 19, 3008-3018.

Dynamic Electrical Conductivity of Ni-P/Nylon Yarns with Different Twist Number for Weavable Device

Tuesday, 16th September - 16:00: Poster Session 1 - Poster - Abstract ID: 99

Mr. Takumi Suda [1], ***Mr. Kazuhiro Shibata*** [1], ***Dr. Tomoyuki Kurioka*** [1], ***Prof. Katsunari Sato*** [2], ***Prof. Chun-Yi Chen*** [1], ***Ms. Nao Yoshida*** [2], ***Prof. Tso-Fu Mark Chang*** [1], ***Prof. Hiromichi Kurosu*** [2], ***Prof. Masato Sone*** [1]

1. *Institute of Science Tokyo,* ***2.*** *Nara Women's University*

We report the dynamic electrical resistance changes of Ni-P/Nylon yarns with various twist numbers under both loading and unloading conditions. The yarns are fabricated via supercritical CO_2-assisted Ni-P electroless plating. Under unloading conditions, the Ni-P/Nylon yarns exhibit higher electrical resistance than under loading conditions. A higher twist number is beneficial in suppressing the variation in electrical resistance during mechanical movement.

Crystalline atomic layer–dielectric hybrid metasurfaces for high-efficiency visible metaphotoncis

Tuesday, 16th September - 16:00: Poster Session 1 - Poster - Abstract ID: 101

Mr. Junhwa Seong [1], ***Dr. Younghwan Yang*** [1], ***Mr. Youngsun Jeon*** [1], ***Prof. Junsuk Rho*** [1]

1. *Pohang University of Science and Technology*

Metasurfaces, composed of subwavelength-scale nanostructures, have emerged as compelling candidates for flat optical components due to their ability to control amplitude, phase, and polarization of light with compact form factors [1]. However, the practical adoption of visible metasurfaces has been impeded by several critical limitations, including low efficiency, high-temperature fabrication requirements, and incompatibility with CMOS processes [2]. In this work, we present a scalable platform for large-area, high-efficiency hybrid metasurfaces based on directly crystallized TiO_2 atomic layers deposited on SiO_2 nanostructures via plasma-enhanced atomic layer deposition (PEALD). By tuning deposition parameters such as temperature, plasma power, and exposure duration, we achieve a refractive index as high as 2.78 at 400 nm, enabling near-unity efficiency across the visible spectrum. Specifically, the metasurfaces demonstrate cross-polarization transmittance (CPT) values of 75% (blue), 95% (green), and 95% (red). These structures are used to fabricate 5 mm-aperture metalenses that achieve diffraction-limited imaging performance. Compared to conventional sol-gel or amorphous TiO_2 approaches, our method eliminates shrinkage and high-temperature annealing (>600 °C), significantly simplifying the manufacturing process [3]. The use of SiO_2 as the core material enhances thermal and mechanical stability, provides CMOS compatibility, and offers reliable integration into semiconductor workflows [4]. This approach also enables extended functionality, such as operational wavelength tuning via alternative coatings, or multilayer stacking for photonic crystal or Bragg reflector architectures. Our study demonstrates a practical pathway for low-cost, high-performance metasurface production, suitable for integration in AR/VR optics, full-color display technologies, and LiDAR systems. This work establishes a robust platform for next-generation flat optics with strong industrial scalability.

[1] N. Yu et al., Science (2011) 334, 333-337.

[2] J. Seong et al., Int. J. Precis. Eng. Manuf. – Green Technol. (2024) 11, 685-706

[3] R. C. Develin et al., Proc. Natl. Acad. Sci. 113 (2016), 10473-10478.

[4] J.-S. Park et al., ACS Nano 18 (2024), 3187-3198.

Volatile Threshold Switching Characteristics of TiN/TaOx/TiN Selector Devices

Tuesday, 16th September - 16:00: Poster Session 1 - Poster - Abstract ID: 104

Ms. Zohreh Hajiabadi [1], ***Mr. Aiden Graham*** [1], ***Mr. Alexander-Hanyu Wang*** [1], ***Dr. Mari Napari*** [2], ***Prof. Dimitra Georgiadou*** [1], ***Prof. David Thomas*** [1], ***Prof. Harold Chong*** [1], ***Dr. Firman Simanjuntak*** [1]

1. *University of Southampton,* ***2.*** *King's College London*

Addressing sneak path currents, which are unintended currents flowing through non-selected cells in crossbar arrays, presents a critical challenge in large-scale artificial neural networks [1]. This work introduces a TaOx-based selector that can overcome this challenge while simultaneously providing tunable temporal characteristics essential for synaptic functions. The fabrication process involved creating a TiN(60nm)/TaOx(11nm)/TiN (60nm) stack structure. TiN electrodes were deposited via DC magnetron sputtering (Angstrom Engineering) using titanium targets in a nitrogen atmosphere, while the TaOx dielectric layer was formed through plasma-enhanced atomic layer deposition (Oxford Instruments FlexAL, ICP source) at 200◦C using PDMAT precursor with O2 plasma cycles. The resulting architecture (Fig. 1.a) features 55×55 device arrays with well-defined top and bottom electrodes that sandwich the active TaOx layer. Thickness uniformity mapping of the TaOx layer across 180 measurement points (Fig. 1.b) revealed variations from 68.36Å to 146.33Å, with an average thickness of 118.48Å, (σ = 20.03Å).

DC electrical measurements revealed asymmetric threshold behavior, triggering voltages at -2V and +1V for negative and positive bias regimes, respectively (Fig. 2). The devices exhibited maximum currents of 2×10−5A during positive bias and 5×10−7A during negative bias, confirming their suitability for one-diode, one-memristor (1D1M) architectures. A key discovery emerged through transient electrical testing under controlled conditions (pulse amplitude: -2V, duration: 10µs, base voltage: -0.1V, gap: 100ns) (see Fig. 3.a), demonstrating that decay time constants could be manipulated by adjusting measurement range settings (Fig.3b-d). At a 1µA current range, devices showed extended decay profiles, while a 100µA range produced accelerated response transitions, similar to biological synapse adaptation mechanisms, without requiring structural modifications [2]. Additional tests examining voltage amplitude dependencies from +1V to +3V (Fig. 4a-c) and -1V to -3V (Fig. 5a-c) demonstrated that various stimulus intensities can affect the decay ratio of the device. This behavior is particularly valuable for implementing spike-timing-dependent plasticity in artificial neural networks, where timing and amplitude of pre- andpost-synaptic pulses directly influence synaptic weight changes [3].

A depth profile analysis of X-ray photoelectron spectroscopy (XPS) (Fig. 6a) confirms well-defined interfaces with expected atomic percentages between layers, validating the fabrication process. High-resolution Ta 4f spectra (Fig. 6b) show a Ta 4f7/2 peak at 26.03 eV, consistent with Ta2O5 formation, with the expected ∼1.9 eV spin–orbit splitting and 4:3 area ratio [4].

The ability to externally control the temporal response characteristics positions these devices as promising candidates for next-generation neuromorphic computing platforms. Using measurement parameters to adjust timing behaviors, these selectors enable the implementation of essential neuromorphic functions while maintaining fabrication consistency and operational stability.

Silicon-based metasurface polarizer supporting quasi-bound states in the continuum

Tuesday, 16th September - 16:00: Poster Session 1 - Poster - Abstract ID: 114

Prof. Maria Antonietta Vincenti [1], ***Dr. Luca Fagiani*** [2], ***Dr. Luca Bolzonello*** [3], ***Dr. Johann Osmond*** [3], ***Mr. Michele Gherardi*** [4], ***Dr. Sonia Freddi*** [5], ***Prof. Domenica de Ceglia*** [1], ***Prof. Niek van Hulst*** [3], ***Dr. Monica Bollani*** [6]

1. *Università degli studi di Brescia,* ***2.*** *Physic Department of Milano Politecnico, Milano, 20133, Italy,* ***3.*** *ICFO, The Barcelona Institute of Science and Technology, Barcellona, 08860, Spain,* ***4.*** *Politecnico di Milano,* ***5.*** *IFN-CNR,* ***6.*** *Institute of Photonic and Nanotechnology (IFN) - CNR*

This study introduces ultra-compact all-dielectric silicon metasurfaces that manipulate light polarization by exploiting quasi-bound states in the continuum (q-BICs). Fabricated using standard nanolithography techniques, these structures enable precise polarization control without prior knowledge of the input state, showing strong experimental agreement with simulated transmission spectra.

Effect of excitation wavelength on micro-Raman thermometry for suspended silicon MEMS structures

Tuesday, 16th September - 16:00: Poster Session 1 - Poster - Abstract ID: 117

Dr. Masaki Shimofuri [1], ***Mr. Kanta Fujiwara*** [1], ***Dr. Amit Banergee*** [1], ***Dr. Jun Hirotani*** [1], ***Prof. Toshiyuki Tsuchiya*** [1]

1. *Kyoto University*

The effect of excitation laser wavelength on micro-Raman thermometry for suspended silicon MEMS structures was investigated. Unlike the thermo-reflectance method, which is highly sensitive to structural tilt and movement, micro-Raman thermometry is more robust and suitable for high-precision thermometry for them, but, its measurement accuracy is typically limited to around 1 K. In this paper, we compared 488 nm and 688 nm lasers and demonstrated that the 633 nm laser achieved a measurement accuracy of ±0.35 K with a measurement time of 5 seconds, representing a 7-fold improvement in accuracy over the 488 nm laser.

High-performance structures with photoimageable thick film pastes in low temperature cofiring ceramics for mmWave packages

Tuesday, 16th September - 16:00: Poster Session 1 - Poster - Abstract ID: 120

Ms. Lynn Möhring [1], ***Mr. Martin Ihle*** [1], ***Ms. Birgit Manhica*** [1], ***Dr. Stefan Körner*** [1], ***Dr. Uwe Partsch*** [1], ***Dr. Peter Uhlig*** [2], ***Mr. Enrico Tolin*** [2]

1. *Fraunhofer Institute of Ceramic Technologies and Systems IKTS,* ***2.*** *IMST GmbH*

The demand for products that are as multifunctional and compact as possible beside the reduction of process costs in favour of smaller carbon footprint to meet the requirements of sustainable development moved into focus in recent years. LTCC (low-temperature co-fired ceramics) materials offers significant advantages including three-dimensional, hermetical sealing of packages and outstanding high-frequency characteristics such as a very low dielectric loss and a comparable low and stable permittivity in a in a wide temperature range. This abstract is intended to provide an overview regarding the further development of photoimageable thick film pastes for laser direct imaging (LDI) and high-frequency LTCC materials.

Electrical Behavior of Rectifying and Ohmic Contacts on Lightly n-Doped Germanium

Tuesday, 16th September - 16:00: Poster Session 1 - Poster - Abstract ID: 127

Mr. Michele Gherardi [1], ***Dr. Sonia Freddi*** [2], ***Mr. Francesco Scali*** [1], ***Dr. Carlo Zucchetti*** [1], ***Prof. Federico Bottegoni*** [1], ***Prof. Giovanni Isella*** [1], ***Prof. Franco Ciccacci*** [1], ***Prof. Marco Finazzi*** [1], ***Dr. Alexey Fedorov*** [2], ***Dr. Monica Bollani*** [3]

1. *Politecnico di Milano,* ***2.*** *IFN-CNR,* ***3.*** *Institute of Photonic and Nanotechnology (IFN) - CNR*

Germanium has recently gained significant attention in varius fields, including electronic, photonic, spintronics and quantum communication. However, low-resistivity ohmic contacts remain a challenge, for n-type Ge. This work focuses on the fabrication of a spintronic device on lightly doped n-type Ge in which both rectifying and non-rectifying contacts were obtained by electron beam lithography and electron beam evaporation. Specific nanofabrication details, along with electrical measurement performed at room temperature, will be presented.

Fabrication of Titanium-based Microneedles Array Using Wire Electrical Discharge Machining

Tuesday, 16th September - 16:00: Poster Session 1 - Poster - Abstract ID: 131

Mr. Min Chul Shin [1], ***Mr. Ji Hwan Han*** [1], ***Prof. Gyu Man Kim*** [1]

1. *Kyungpook National University*

Wire Electrical Discharge Machining (WEDM) is a non-contact machining technique that precisely removes material through controlled electrical discharges between a wire electrode and a conductive workpiece. It is particularly suitable for fabricating micro-scale features in high-hardness materials, making it attractive for micro/nano engineering and biomedical device manufacturing. Titanium alloys are widely used in biomedical applications such as implants and microneedles due to their excellent biocompatibility, mechanical strength, and corrosion resistance [1][2].

In this study, we report the fabrication of titanium-based microneedle arrays using WEDM, and investigate the effect of machining conditions on the formation quality. Brass wire electrodes with a diameter of 250 μm were used to machine 1-mm thick titanium substrates in kerosene dielectric fluid. Key parameters such as voltage (300 - 350 V) and capacitance (0.05 - 0.47 μF) were varied to optimize the dimensional precision and surface integrity of the fabricated microneedle structures.

The machined structures were characterized using Field-Emission Scanning Electron Microscopy (FE-SEM) to observe tip sharpness, surface roughness, and uniformity. Comparative evaluation before and after parameter optimization showed a significant improvement in microneedle shape consistency and reduction of burr formation. Higher discharge energy tended to cause surface melting and dimensional deviations, while optimized settings enabled the reliable production of high-aspect-ratio microneedles with sharp, well-defined tips.

The results demonstrate that WEDM offers a controllable and effective method for fabricating titanium microneedle arrays, with tunable process parameters that influence structural quality. This approach provides a practical pathway for manufacturing next-generation microneedle devices for transdermal drug delivery and biomedical sensing applications [3][4].

Acknowledgement:

This work was supported by the National Research Foundation of Korea (NRF) grant funded by the Korean government (MSIT) (No. RS-2023-00208717 and RS-2024-00406223), and by the Korea Institute for Advancement of Technology (KIAT) grant funded by the Ministry of Trade, Industry and Energy (MOTIE) (No. RS-2022-KI002563, HRD Program for Industrial Innovation).

Polymer-based MEMS microcantilever and microfluidic system for biochemical detection

Tuesday, 16th September - 16:00: Poster Session 1 - Poster - Abstract ID: 134

Dr. Pooja P. Kanade [1], ***Dr. Paul T. Baine*** [2], ***Dr. Briliant Adhi Prabowo*** [1], ***Dr. Arthur Lipinski*** [3], ***Dr. Jason Wiggins*** [1], ***Prof. Robert M. Bowman*** [1]

1. *School of Mathematics and Physics, Queen's University Belfast,* ***2.*** *School of Electronics, Electrical Engineering and Computer Science, Queen's University Belfast,* ***3.*** *Research Fellow*

This work presents a polymer-based MEMS microcantilever integrated within a 3D-printed microfluidic system for biochemical detection. The device features four polymer microcantilevers embedded with a strain sensor. Fabrication was achieved through photolithography, followed by enclosing in a microfluidic chip. The system demonstrates potential for scalable, cost-effective biochemical sensing.

Two-photon polymerization as mastering tool for nanoimprint lithography to produce microfluidic test devices

Tuesday, 16th September - 16:00: Poster Session 1 - Poster - Abstract ID: 148

Mr. Stjepan Perak [1], Ms. Sonja Kopp [2], Ms. Viktorija Jonaityte [2], Ms. Marta Bonora [3], Dr. Michael Muehlberger [2], Prof. Francesco Moscato [3], Dr. Markus Lunzer [1]

1. *UpNano GmbH,* ***2.*** *PROFACTOR GmbH,* ***3.*** *Center for Medical Physics and Biomedical Engineering, Medical University of Vienna*

2-photon polymerization (2PP) is a high-resolution 3D printing technology that is very useful for creating master structures for nanoimprint lithography (NIL). Microstructures on the surfaces of medical devices can help prevent blood clotting. We use these techniques to manufacture microfluidic devices for testing the interaction of blood platelets with microstructured surfaces.

Engineered magnetic quantum dot nanoprobes for multiplexed, equipment-free Alzheimer's diagnosis at point-of-care

Tuesday, 16th September - 16:00: Poster Session 1 - Poster - Abstract ID: 151

Dr. Anjum Qureshi [1], ***Dr. Javed H. Niazi*** [1]

1. *SUNUM - Sabanci University Nanotechnology Research & Application Center*

Abstract

This work introduces a bio-inspired nanomaterial design utilizes the unique optical and magnetic properties of engineered quantum dots (QDs) to revolutionize point-of-care (PoC) diagnostics. At its core, the technology harnesses nature-mimicking hierarchical assembly, integrating multicolored colloidal QDs and superparamagnetic quantum dots (MQDs) into an immuno-optomagnetic nanosystem capable of rapid, multiplexed biomarker detection. The QD-MQD hybrid nanoarchitecture draws inspiration from biological recognition processes, where antibody-functionalized nanoparticles emulate the specificity of immune complexes while enabling tunable photonic and magnetic responses.

Central to this nanoarchitecture is the precise nanoscale engineering of core-shell-shell CdSe/CdS/ZnS QDs, optimized for aqueous stability, minimized photobleaching, and enhanced serum compatibility through polyglycine coatings. The MQDs are synthesized via colloidal and chemical cross-linking routes, yielding a combination of size-tunable fluorescence (450-650 nm) with superparamagnetism, which enables simultaneous magnetic enrichment and optical signaling. Unlike conventional diagnostic probes, these nanostructures eliminate the need for external separation steps or complex instrumentation by performing all-in-solution detection in microliter-scale volumes.

The bio-inspired assay design mirrors natural antibody-antigen interactions, where non-magnetic QDs (emitting at l_1) first capture target analytes (e.g., amyloid-b, tau proteins) to form fluorescent "Complex 1", which then recruits spectrally distinct MQDs (l_2) via sandwich immunoassays. This generates a magneto-optical "Complex 2" detectable in real-time (<20 min) through direct fluorescence readouts. This system achieves multiplexing by exploiting QD color-coding (e.g., red for colloidal QDs and green for MQDs or vice versa as shown for Ab1-42 in **Figure 1(a-c**) and for tau-protein in **Figure 2(a-c)** without cross-talk, enabled by precise spectral separation.

The developed optically tunable nano-biosystem addresses longstanding gaps in early detection of Alzheimer's disease (AD) and its role in rapid diagnosis [1]. Traditional AD biomarkers are typically identified post-symptomatically via MRI or invasive cerebrospinal fluid assays. Here, the QD-MQD nano-biosystem detects pathogenic amyloid-b (both b1-40 and b1-42 forms) and tau proteins in serum at clinically relevant concentrations (<10 pg/mL), correlating with neuronal dysfunction. The equipment-free workflow, conducted entirely in microtubes, reduces costs and complexity while outperforming existing in vitro diagnostics in speed and sensitivity.

Quality Factor Engineering in NIR Optical Metasurfaces Using Ge2Sb2Te5 and Graphene

Tuesday, 16th September - 16:00: Poster Session 1 - Poster - Abstract ID: 154

Dr. Seyed As'ad Amirhosseini [1], ***Mr. Daniyal Khoshmaram*** [2]

1. *Department of Electrical and Computer Engineering, Isfahan University of Technology, Isfahan, Iran,* ***2.*** *Department of Electrical Engineering, Amirkabir University of Technology, Tehran, Iran*

We propose an optically reconfigurable metasurface that utilizes graphene heaters for dynamic control of the phase of Ge2Sb2Te5 (GST) through Joule heating. This design achieves a tunable phase modulation range of 0° to 300° for reflected waves at a wavelength of 1.55 μm by varying the crystallization levels of GST. The incorporation of graphene enhances plasmonic effects, optimizing absorption and facilitating effective phase manipulation. Our simulations indicate significant potential for applications in electro-optical devices, such as LiDAR and beam steering.

Anomalous mapping between the Surface Charge and Ionic Conductance in Narrow Confinements

Tuesday, 16th September - 16:00: Poster Session 1 - Poster - Abstract ID: 157

Mr. Debmalya Roy [1], ***Prof. Suman Chakraborty*** [1]

1. *Indian Institute of Technology Kharagpur*

Fluid flow within narrow biological and bio-analytical confinements, such as nanopores, ion channels, or lab-on-chip devices, is strongly governed by the wall-fluid interfacial properties, particularly the surface charge density. This interfacial charge shapes the electric potential across the electrical double layer, playing a pivotal role in phenomena such as electroosmosis, electrokinetic energy conversion, and the electrophoretic transport of biomolecules under extreme confinement conditions [1–4]. A widely adopted approach for determining the surface charge density involves measuring the ionic conductance of an electrolyte within these narrow confinements [5–7]. This total conductance is commonly decomposed into the bulk and surface contributions, with the surface component directly linked to the surface charge. Conventionally, this relationship is simplified by assuming that the interfacial charge is exactly neutralized by an equal number of counterions, resulting in a presumed linear dependence of the surface conductance on surface charge density [2,8]. However, such a simplification markedly deviates from the ionic distribution as obtained from a fully-coupled Poisson-Nernst Planck theory. This deficit in the traditional simplified model stems from the consideration of the predominant role of the counterion in the ionic current estimation, commonly ignoring the role of the co-ions on the same. To address this limitation, we demonstrate here that, contrary to the commonly assumed linear relationship, surface conductance scales quadratically with the surface charge density at the leading order (Figure 1). This non-linear dependence arises because interfacial charges simultaneously increase the counterion concentration and decrease the co-ion concentration. This redistribution adheres to the Boltzmann distribution when convective ionic currents are negligible across the electric double layer, where the odd-order terms, such as the linear components, cancel each other out due to symmetry in the counterion and co-ion responses. As a result, the net increase in charge carriers is captured by the even powers of surface charge density, with the quadratic term being dominant. Additionally, in the presence of electroosmotic flow orthogonal to the electric double layer potential field (commonly in the axial direction of a fluidic confinement), the local ionic current density is further influenced. An applied axial electric field mobilizes the excess charge within the electrical double layer, contributing an extra component to the ionic current. This contribution can be estimated by integrating the product of fluid velocity and excess volumetric charge density in the double layer, both of which scale linearly with the surface charge density at leading order. Consequently, the electroosmotic component of the current also exhibits a quadratic dependence on the surface charge. Together, these observations challenge the traditional linear model of surface conductance in confined systems. Instead, our analysis reveals a fundamentally quadratic scaling law. This theoretical framework was validated using continuum simulations based on the full Poisson-Nernst-Planck model coupled with Navier-Stokes equations (PNP-NS Simulations, see figure 1). This key insight that surface conductance scales quadratically with surface charge density provides a more accurate means of determining surface charge in nanoconfined environments, thereby advancing a wide range of applications including energy conversion, iontronics, desalination, and biomolecule sensing technologies.

Ultrasensitive, AI-integrated cyber-physical system for patient-specific CYFRA21-1 biomarker quantification

Tuesday, 16th September - 16:00: Poster Session 1 - Poster - Abstract ID: 158

Mr. Biswadeep Roy [1], ***Dr. Abhisek Maikap*** [1], ***Prof. Soumen Das*** [1], ***Prof. Suman Chakraborty*** [1]

1. *Indian Institute of Technology Kharagpur*

Early detection of non-small cell lung cancer (NSCLC) is critical for improving survival rates but remains challenging due to the sub-nanomolar concentrations of tumor-specific biomarkers in early disease stages and the limitations of conventional diagnostics. Standard techniques such as liquid chromatography-mass spectrometry (LC-MS) and enzyme-linked immunosorbent assay (ELISA) provide high specificity but rely on centralized laboratories, specialized personnel, and extended processing times, limiting their practicality in decentralized, point-of-care (POC) settings. To address this gap, we present a compact, cyber-physical diagnostic platform for rapid, quantitative, and ultrasensitive detection of Cytokeratin-19 fragment (CYFRA21-1), a clinically validated NSCLC biomarker, particularly relevant for squamous cell carcinoma. Elevated CYFRA21-1 levels reflect tumor burden, disease progression, and therapeutic response, making it a promising target for early cancer screening. The platform integrates three key components: (i) a nanotechnology-enhanced biosensor based on surface-functionalized Green-Carbon Dots (G-CDs) (**Figure 1(a)**), (ii) a portable, smartphone-based fluorescence microscope, and (iii) an artificial intelligence (AI) engine driven by a convolutional neural network (CNN) that incorporates patient-specific data. The carbon dots, modified with amine and carboxyl groups for antibody (Ab) conjugation, exhibit absorption at 360 nm and 440 nm as observed in the UV-Vis spectroscopy (**Figure 1(b)**) and dual-emission fluorescence at 450 nm and 550 nm as observed in the photoluminescence (PL) response (**Figure 1(c)**), enabling ratiometric quantification and minimizing background interference. Embedded within a lateral flow microfluidic strip, these probes enable plasma separation and immunoassay reactions in a single, disposable chip, eliminating the need for external sample preparation. The PL response of the G-CD-conjugated antibody-antigen complex is measured across varying antigen concentrations to investigate its fluorescence characteristics and integrate these findings into our portable microscopy system (**Figure 1(d)**). Successful conjugation of CYFRA21-1 Ab with G-CD is validated by Fourier-transform infrared (FTIR) spectroscopy, which reveals a characteristic peak near 2940 cm^{-1} corresponding to N–H stretching vibrations (**Figure 1(e)**). Fluorescence signals are captured using a miniaturized optical module with a 450 nm light source, band-pass filters, and a CMOS sensor integrated with a smartphone. This portable microscopy system achieves high spatial resolution (**Figure 2A**) while maintaining low power consumption. A mobile application supports automated image acquisition, background correction, and signal normalization, ensuring consistent performance in diverse environments (**Figure 2B**). A distinguishing feature of the system is its AI-driven analytics layer, which uses a CNN trained on multimodal datasets combining fluorescence intensity profiles with clinical metadata such as patient age, sex, smoking history, and geographical data. This integration enables dynamic calibration of diagnostic thresholds, improving sensitivity and specificity by accounting for patient-specific variability. The model adapts classification criteria based on longitudinal patterns, reducing false positives in benign conditions and false negatives in early or asymptomatic cases. Validation studies with human plasma samples spiked with CYFRA21-1 demonstrate a detection limit as low as 0.1 ng/mL, significantly surpassing standard ELISA sensitivity thresholds, which typically detect levels above 1.0 ng/mL. The complete diagnostic workflow, from sample application to result generation, is achieved within 10 minutes- a substantial improvement over traditional methods. The platform's low-cost, disposable chips and smartphone-compatible interface ensure scalability and affordability for large-scale deployment. Designed for decentralized healthcare environments, it aligns with global health priorities to democratize cancer diagnostics and reduce diagnostic delays in underserved populations. Future versions will enable multiplexed detection of additional NSCLC biomarkers and incorporate cloud-based telemedicine fea-

tures for remote consultation and real-time data integration, supporting personalized clinical decision-making.

Broadband Transmission Measurement for Ta2O5 Photonic Crystal Waveguide

Tuesday, 16th September - 16:00: Poster Session 1 - Poster - Abstract ID: 178

Ms. Wenjie Wang [1], ***Prof. Martin Charlton*** [1]

1. *University of Southampton*

Low-loss waveguides are essential components in silicon photonics. Photonic crystals (PhCs) enable control of light via photonic band gaps (PBGs), and their integration into photonic crystal waveguides (PhCWs) introduces slow light effects, enhancing light–matter interaction and nonlinear processes. However, characterizing slow light in the time domain remains challenging. Here, we demonstrate broadband transmission measurements of Ta_2O_5 PhCWs, providing an efficient method to identify the PBG and support future slow light studies.

Fabrication of planar nanostructured SiC microelectrode arrays for long-lifetime neural interfaces

Tuesday, 16th September - 16:00: Poster Session 1 - Poster - Abstract ID: 198

Dr. Fabrice Iacovella [1], ***Dr. Gwenaell Pound-Lana*** [1], ***Mr. Lucas Labbe*** [1], ***Mr. Sébastien Labau*** [1], ***Dr. Camille Petit-Etienne*** [1], ***Mr. Andrei Uvarov*** [2], ***Dr. Scott Greenhorn*** [3], ***Mr. Marcin Zielinski*** [4], ***Prof. Konstantinos Zekentes*** [3], ***Prof. Edwige Bano*** [3], ***Dr. Cécile Gourgon*** [1], ***Prof. Jumana Boussey*** [1]

1. *Université Grenoble Alpes, CNRS, CEA/LETI-Minatec, Grenoble INP, LTM, 17 Rue des Martyrs, Grenoble 38054, France,* ***2.*** *Plasma-therm Europe, Bernin, 38190, France,* ***3.*** *Centre de Radiofréquences, Optique et Micro-nanoélectronique des Alpes, Grenoble, 38016, France,* ***4.*** *NOVASiC, Le Bourget du Lac, 73375, France*

This work focuses on the fabrication planar of Micro-Electrode Arrays (MEA) for neural interfaces fully based on biocompatible SiC. To increase their surface area, the electrodes are nanostructured with nanopillar arrays. An increase of almost 5 times of the recorded electrochemical signal intensity is expected.

Sub-wavelength grating polarizers in 1-D array focal plane for ultraviolet polarimetric detection

Tuesday, 16th September - 16:00: Poster Session 1 - Poster - Abstract ID: 199

Mr. Jinyu Guo [1], ***Ms. Kangping Liu*** [1], ***Ms. Qingxin Wu*** [1], ***Mr. Qiucheng Chen*** [1], ***Mr. Hao Quan*** [1], ***Ms. xunjia Zhao*** [1], ***Prof. Yifang Chen*** [1]

1. *Fudan university*

Polarizers are indispensable optics in optical systems and networks. Ultraviolet (UV) polarizers rely on their unique ability to modulate polarization, and are especially irreplaceable in the fields of spectral analysis, industrial inspection and biomedicine. Unfortunately, conventional polarizers are bulky, expensive, and operate with very small acceptance angles. Thin-film polymer polarizers have major reliability problems at UV wavelengths. Sub-wavelength wire-grid polarizers in ultraviolet wavelength band provide great advantages in terms of thinness, low cost, large working reception angle, high durability against both ultraviolet radiation and temperature.

This work presents a process for sub-wavelength gratings of aluminum (Al) in three directions on fused silica by electron beam lithography (EBL) and lift-off process. For achieving both high transmittance and high extinction ratio, the period and height of the grating are optimized by Finite-Difference Time-Domain (FDTD) simulation. Al grating with a duty cycle of 50% at 150 nm period and a height of ~100 nm was finally realized. Spectrometer test characterizes that its transmittance in the 385 nm is greater than 55%, and the extinction ratio is greater than 10:1.

Fig. 1 illustrates the process of fabricating Al wire-grid gratings on fused silica. It should be noted that after the resist coating is completed, a 10 nm Al needs to be evaporated on the top to eliminate the charge accumulation effect during the electron beam exposure on the less conductive substrate, in order to ensure high-precision exposure. After exposure, the 10 nm Al needs to be removed using an alkaline solution before proceeding to the development process. Fig. 2shows the systematic simulation results of transmittance and extinction ratio of the Al wire-grid gratings at a UV wavelength of 385 nm, as function of pitch from 50 to 200 nm and height from 10 to 200 nm. Based on our previous experience, a fixed duty cycle (i.e., width of the wire divided by the pitch) of 50% for the Al nanowire grid were used. At a height of 100 nm, good transmittance (>70%) is obtained over the simulated pitch range. For shorter pitch and higher metal thicknesses, better extinction ratio can be obtained (as indicated by the arrow in Fig. 2b). More specifically, the transmittance and and extinction ratio of 300 nm-900 nm of the rectangular configuration at a fixed metal height of 100 nm and a period of 150 nm are shown in Fig. 3. It can be seen that a transmittance of 76% and an extinction ratio of 143 can be obtained in the 385 nm band. From this result, this Al wire grid gratings can also be used as a polarizer in the visible and near-infrared bands, and the performance will become better. SEM photos and optical characterization results of the fabricated Al gratings are elucidated in Fig. 4, where it can be seen that obtained Al gratings with 50% duty cycle, a period of 150 nm and a height of ~100 nm by adjusting the dose and designed linewidths in different directions. The expected performance was achieved at 350-700 nm. The average transmittance around 385 nm was 55% with an extinction ratio of more than 10. At 678 nm, a transmittance of 79% and an extinction ratio of 58 were measured. The difference between the characterization and simulation results comes from the non-rectangular configuration of the Al grating cross section, which greatly affects the extinction ratio.

In summary, dense sub-wavelength Al grating polarizers are fabricated and applied to 1-D array focal plane for UV polarization detection by electron beam lithography. The process preserves the original optical properties of the metal, allowing for high edge quality metal gratings and further application to smaller period grating realizations to enhance the polarized performance.

Design and Fabrication of a 100mm-Diameter Pillar Metalens for High-Performance Mid-Infrared Imaging

Tuesday, 16th September - 16:00: Poster Session 1 - Poster - Abstract ID: 208

Ms. Weilin Jin [1], ***Mr. Gaochen Dong*** [1], ***Ms. Zixuan Wang*** [1], ***Dr. Kian Shen Kiang*** [1], ***Prof. Jize Yan*** [1]

1. *University of Southampton*

We demonstrate a 100 mm-diameter mid-infrared metalens at 10 μm, fabricated using CMOS-compatible processes. To overcome data and fabrication challenges, a parallel layout generation strategy reduced file size from 64 GB to 293 MB in under 5 minutes. Through a 4f imaging system, the metalens successfully captured mid-infrared images, showcasing large-scale fabrication feasibility.

Quantum Dot-Low Dimensional Material Hybrid Heterostructures for Physically Unclonable Optical Tags

Tuesday, 16th September - 16:00: Poster Session 1 - Poster - Abstract ID: 215

Mr. Yueyu Guo [1], ***Ms. Syeda Ramsha Ali*** [1], ***Dr. Nema Abdelazim*** [2]

1. *School of Electronics and Computer Science, University of Southampton, Southampton SO17 1BJ, United Kingdom,* ***2.*** *University of Southampton*

We present a portable, secure authentication tag based on low dimensional material heterostructures. Integrated quantum dots with 2D materials offers distinct PL response to ensures robustness, uniqueness for anti-counterfeiting applications. This hybrid system enables smartphone-based verification using broadband flashlights by enhancing spectral selectivity and generating unique optical fingerprints.

Modelling the Heat Distribution in Organ-on-a-Chip Systems Using Integrated Microheaters

Tuesday, 16th September - 16:00: Poster Session 1 - Poster - Abstract ID: 218

Mr. Gabriel Ferreira [1], ***Dr. Patrícia Sousa*** [2], ***Prof. Rui Lima*** [1], ***Prof. Susana Catarino*** [1], ***Prof. Graça Minas*** [1]

1. *University of Minho,* ***2.*** *International Iberian Nanotechnology*

Microfluidic systems with integrated heating elements are increasingly applied in lab-on-a-chip and organ-on-a-chip technologies. In OoC devices, precise temperature control is vital for cell viability. Combining microheaters with sensors, and using multiphysics simulations, enables accurate prediction and management of temperature distributions within microfluidic environments. In this study, the authors investigated the thermal performance and flow dynamics of microfabricated OoC chamber structures.

Microfabricated Light Pipe for Sustainable and Lithography-Free SPR Sensor

Tuesday, 16th September - 16:00: Poster Session 1 - Poster - Abstract ID: 219

Dr. Briliant Adhi Prabowo [1], ***Dr. Pooja P. Kanade*** [1], ***Dr. Fatemeh Moradiani*** [1], ***Dr. Arthur Lipinski*** [1], ***Dr. Paul T. Baine*** [2], ***Dr. Jason Wiggins*** [1], ***Prof. Robert M. Bowman*** [1]

1. *School of Mathematics and Physics, Queen's University Belfast,* ***2.*** *School of Electronics, Electrical Engineering and Computer Science, Queen's University Belfast*

Introduction: Surface plasmon resonance (SPR) sensors have emerged as essential tools for label-free, real-time monitoring of molecular interactions, with wide-ranging applications in medical diagnostics, environmental monitoring, and pharmaceutical development[1]. Despite their advantages, traditional SPR systems often require complex prism-based optical components and rely heavily on lithography-based fabrication methods[2]. These limitations result in high production costs, significant chemical waste, and poor scalability, ultimately hindering widespread deployment and field integration.

In this work, we present a next-generation SPR sensor platform that overcomes these bottlenecks through a novel light-pipe-based architecture and a sustainable, non-lithographic microscale manufacturing approach. The innovation centers on the replacement of conventional prism couplers with a custom-designed microfabricated light pipe, which enables angular coupling of light to the plasmonic interface within a compact form factor[3]. This light pipe structure was optimized using Zemax ray tracing simulations, allowing precise modeling and tuning of internal reflections, beam angles, and coupling conditions to ensure optimal excitation of surface plasmons on the metallic sensing layer.

Fabrication Method: Fabrication was achieved using a two-tier strategy. First, two-photon polymerisation was used to rapidly prototype high-resolution micro-optical structures with sub-micron fidelity. For scaling beyond prototyping, we developed a pick-and-place micro-templating method that assembles optical and plasmonic components without lithography, wet chemistry, or masks. This fully dry and additive process eliminates the need for photoresists, solvents, and spin coating, thereby dramatically reducing chemical waste and energy consumption. Our approach promotes not only sustainability but also democratisation of SPR technology by removing the dependency on high-cost cleanroom processes.

Results: The resulting SPR device integrates a gold-coated plasmonic surface within a monolithic platform that supports microfluidic compatibility and maintains robust optical alignment tolerances. Preliminary experimental evaluations confirm that the sensor structure achieves a well-constructed device on par with conventional Kretschmann-based SPR systems, while offering substantial improvements in scalability, portability, manufacturability, and environmental footprint.

Summary: Overall, this work introduces a fundamentally new design and fabrication paradigm for SPR sensors, targeting the convergence of high performance, scalability, and eco-friendly production. The proposed system opens avenues for affordable, field-deployable biochemical sensing platforms, offering a significant step toward decentralised diagnostics and sustainable photonic device manufacturing.

Dual-Path Anomaly Detection for Semiconductor Equipment: Toward Sensor-Level Intelligence in Digital Twin Manufacturing

Tuesday, 16th September - 16:00: Poster Session 1 - Poster - Abstract ID: 17

Mr. Joon Soo Kim [1]

1. *SUNG KYUN KWAN University / Samsung Electronics*

With the advancement of smart manufacturing technologies, the integration of process and equipment operations via digital twins is emerging as a core strategy in the semiconductor industry. In particular, Fault Detection and Classification (FDC) data, collected in real-time from thousands of sensors within the fab, serves as a precise digital representation of equipment states and forms the basis of anomaly detection systems that act as quality defense mechanisms. However, most deployed systems rely on static thresholds and univariate statistical techniques, which are structurally limited in capturing dynamic patterns. Semiconductor equipment undergoes physical changes due to degradation over time and periodic (PM) or breakdown maintenance (BM), resulting in evolving sensor interactions. Additionally, recipe modifications, process parameter tuning, and production optimization induce nonlinear, time-dependent variations, which static threshold-based systems fundamentally struggle to detect.

To address these limitations, we propose Dual-Path Anomaly Detection, a sensor-aware anomaly detection architecture that integrates graph modeling of sensor interactions with patch-level analysis of process transitions, reflecting both the structural nature of FDC data and the operational context of semiconductor equipment. First, in the Graph Neural Network Modeling path, we focus on the dynamic correlations among sensors that vary depending on recipe conditions, equipment modes, and maintenance history (PM/BM). These shifting correlations are challenging to model using conventional multivariate or univariate time-series methods. To this end, we define a Dynamic Sensor Graph, where each sensor is represented as a node and pairwise correlations as edges, and apply Graphormer, a Transformer-based graph model. Leveraging flexible receptive fields and attention-based message passing, it effectively captures condition-dependent, concurrent sensor interactions as observed in real fab environments. This enhances the precision of detecting complex, relation-based anomaly patterns arising within semiconductor tools. Second, in the Patch-Level Modeling path, we account for the discrete nature of semiconductor process time-series data, which exhibits abrupt distributional shifts due to recipe transitions, equipment status changes, wafer transport, and loading events. Rather than treating the entire sequence as a continuous stream, we automatically identify change-points corresponding to these transitions and segment the data into meaningful units, or patches. Each patch encapsulates a distinct process context and is treated as a token that captures both local features and inter-patch transitions. A Transformer-based sequence model is then employed to learn the nonlinear temporal dynamics across patches. This approach allows the model to effectively reflect the fragmented flow of data induced by process state changes in real manufacturing environments. Finally, the outputs from the graph neural network modeling and patch-level modeling paths are integrated through a late fusion strategy, enabling robust detection of complex, time-dependent anomalies within semiconductor equipment.

We validate our approach using the public UCI SECOM dataset, achieving performance improvements of up to 20.3% in F1-score and 17.8% in AUPRC over LSTM baselines. We also evaluate a lightweight GCN+TCN model suitable for resource-constrained environments, demonstrating balanced performance. This study goes beyond applying AI to manufacturing data; it integrates semiconductor domain expertise into a practical detection system that reflects real-time variability and engineer judgment, supporting the Sensing Intelligence Layer in digital twin architectures.

Real-time lesion location detection system using Mu-metal and Hall sensor

Tuesday, 16th September - 16:00: Poster Session 1 - Poster - Abstract ID: 18

Dr. Woojin Yun [1], ***Mr. Gapseop Sim*** [1], ***Prof. Hyeinjune Kim*** [2], ***Dr. Seung-Hwan Jung*** [3]

1. *National Nanofab Center,* ***2.*** *Seoul National University of Science and Technology,* ***3.*** *GRIT Custom-IC*

In case of laparoscopic or surgical operation after general endoscopy, position marking technology is becoming more important from medical staff in diverse fields for accurate judgment and successful operation of the lesion site during laparotomy or incision surgery at a transferred medical center. At present, the position of lesion is indicated by tattooing method through ink, but the position indicated by this method is unclear or invisible at 22% and the visibility at the time of procedure is difficult in 31.5%. As a result, it can lead wrong surgery. In this paper, we have developed a detection system for the lesion in the human body, which overcomes the conventional ink marking method, through the use of mu-metal which can magnetize and sensor system to detect it.

A Study on Focus Control Improvement in Response to Wafer Table Edge Wear in Photolithography Equipment

Tuesday, 16th September - 16:00: Poster Session 1 - Poster - Abstract ID: 23

Mr. Kyunghwan Joo [1], ***Mr. Kwang Hoon Lee*** [2], ***Prof. Jae Wook Jeon*** [3]

1. *SUNG KYUN KWAN University / Samsung Electronics,* ***2.*** *Samsung Electronics,* ***3.*** *Sungkyunkwan University*

• Purpose of the work;

The continuous scaling of semiconductor devices necessitates highly precise focus control technologies in photolithography equipment. In particular, the 300 mm wafer table experiences continuous wear during repetitive wafer handling process, which causes focus imbalance. Continuous wear of the wafer table causes edge-roll-off (ERO) at the edge of the wafer, which reduces the uniformity of the critical dimension (CD) of the device and causes serious defects such as pattern bridge defect. This ultimately leads to serious problems that lead to a decrease in semiconductor production yield. However, most existing process control systems rely on average correction based on wafer center focus information, and thus have limitations in sufficiently responding to local deterioration phenomena occurring at the edge. To address this technological gap, this study investigated an advanced focus management method that can accurately quantify, monitor, and predictively respond to focus deterioration due to wafer table edge wear. In particular, by focusing on measuring the 140 to 147 mm wafer radius section, the foundation has been established for precise analysis of local defocus changes and resulting pattern quality degradation, and the goal is to present a practical solution that can contribute to increased productivity and improved equipment reliability.

• Novelty of the work with respect to the state of the art;

This study introduced Geometry-based Optical Focus Metrology (GOFM) to overcome the limitations of existing focus management technology and to enhance wafer edge focus monitoring, and implemented it as an original edge monitoring system applicable to actual semiconductor production environments. GOFM constructed an asymmetric pattern based on diffraction through an Optical Diffraction Metrology Mark (ODMM) etched on a reticle, and measured the subtle asymmetry of the Side Wall Angle (SWA) by analyzing the diffraction light using scatterometry. The ODMM mark has been experimentally optimized under various pitch conditions, and can be used to measure and compensate for the Z/Ry Tilt of the entire wafer table area by converting the difference in intensity between the +1st and -1st order diffracted light into a quantitative index of focus sensitivity. The technology can go beyond focus measurement centered on the wafer table center and also serve as a precise sensor for detecting edge focus variation, so that the degree of physical wear at the wafer table edge can be indirectly quantified. In particular, by separately analyzing the 140~147mm and 144~147mm radius sections, which are sensitive to wear among the edge areas, and proposing new indices such as Range Percentile 97% and Focus Slope*3, the sensitivity and prediction accuracy were improved. This methodology is a monitoring technology that can detect CD deterioration due to edge wear early and respond in advance, and can contribute not only to improving process yield but also to optimizing equipment maintenance cycles.

• Results of the work.

As a result of this study, it was possible to match the defocus index of 97% of the Range Percentile in the 140–147 mm radius area of the wafer table and the defocus value at the 147 mm radius point when the critical dimension (CD) quality spec is exceeded due to wafer edge deterioration, and based on this, it was possible to establish an edge-roll-off management standard that can detect and prevent edge pattern quality deterioration in advance. In addition, we applied the GOFM-based focus management system to an actual mass production environment and obtained and analyzed long-term data for about one year. As a result, we were able to secure consistency and stability of wafer edge focus management. In addition, we verified that the consistency between the center focus and the edge focus increased even after the wafer table was replaced, proving the reliability and repro-

ducibility of the developed edge monitoring system. It showed the possibility of quantitatively analyzing the wear trend of each equipment and using it to predict equipment replacement time and establish maintenance optimization strategies. This monitoring system can be effectively used to detect and manage focus imbalance problems caused by wafer edge wear in actual semiconductor manufacturing sites, and as a result, it is expected to greatly contribute to maintaining consistency in device quality and improving production yield.

Automated Silicon Wafer Handling for Gravity Effect Compensation in High-Precision Horizontal Metrology

Tuesday, 16th September - 16:00: Poster Session 1 - Poster - Abstract ID: 63

Mr. CESAR PEREZ DOMINGUEZ [1], ***Dr. JUAN TRUJILLO-SEVILLA*** [2], ***Dr. CARMELO MILITELLO-MILITELLO*** [3]

1. *Wooptix,* ***2.*** *WOOPTIX,* ***3.*** *Universidad de La Laguna*

Gravitational deformation affects the accuracy of silicon wafer metrology in horizontal setups. This work presents an automated handling system that eliminates manual wafer rotation, improving repeatability, reducing contamination, and enabling gravity compensation using Wave Front Phase Imaging (WFPI). The system supports multiple wafer sizes and allows accurate, efficient surface reconstruction in a horizontal configuration, addressing key challenges in semiconductor manufacturing.

A 10.94bit resolution measurement circuit for resistive sensors

Tuesday, 16th September - 16:00: Poster Session 1 - Poster - Abstract ID: 65

Dr. xiaoming teng [1], ***Prof. yufeng zhang*** [1], ***Mr. haoyu liang*** [1]

1. *MEMS Center, Harbin Institute of Technology*

This paper presents a novel circuit fabricated in standard 180nm CMOS technology for resistance measurement. It consists of four modules: a 2^{nd}-order temperature-curvature compensation bandgap with base-current compensation, an auto-zero offset-stabilized amplifier, a damped-SC based variable gain amplifier with an auto gain control loop, and a 12-bit SAR ADC. Simulation shows that the resolution of the whole circuit can reach 10.94bit. The chip is $2.4mm^2$ and the simulated power consumption of the chip is only 67.7 μA.

Device Variation Effect Simulation for SnOx Memristor-based Neural Networks

Tuesday, 16th September - 16:00: Poster Session 1 - Poster - Abstract ID: 74

Mr. Aiden Graham [1], ***Ms. Zohreh Hajiabadi*** [1], ***Mr. Alexander-Hanyu Wang*** [1], ***Prof. Dimitra Georgiadou*** [1], ***Dr. Ruomeng Huang*** [1], ***Dr. Firman Simanjuntak*** [1]

1. *University of Southampton*

SnOx-based memristors were fabricated and evaluated for CNN performance. Devices with a Ti barrier showed reduced noise and more symmetric nonlinearity. Simulations revealed that fixed nonlinearity had minimal performance impact, while cycle-to-cycle variability significantly reduced CNN accuracy, highlighting sensitivity to device-level variations.

Eco-Friendly Functionalization of Graphene via Spark Ablation for Enhanced NO2 Gas Sensing Applications

Tuesday, 16th September - 16:00: Poster Session 1 - Poster - Abstract ID: 84

Dr. Mudassir Husain [1]***, Dr. Leandro Sacco*** [2]***, Prof. Sten Vollebregt*** [3]

1. *PhD,* ***2.*** *VSParticle,* ***3.*** *Associate Professor*

This work reports, for the first time, the use of spark ablation with impaction printing to selectively deposit silver (Ag) and gold (Au) nanoparticle (NP) functionalization on single-layer graphene (SLG)-based gas sensors. This method avoids lithography and chemical processes, maintaining the device's quality while potentially lowering the fabrication costs. Ag-decorated sensors reveal a three-fold improvement in nitrogen dioxide (NO_2) gas response over pristine-SLG sensors. We demonstrate detection capabilities down to 50 ppb at room temperature, negating the requirement for external thermal or photoactivation. In contrast to pristine or Au-decorated SLG sensors, Ag-decorated devices exhibit 96% recovery at room temperature (RT). These results highlight the potential of using spark ablation with impaction printing for functionalizing graphene-based sensors.

Enhancing Overlay Accuracy through Transformation of Overlay Outliers caused by Wafer Local Defocus in Photolithography Scanner Calibration

Tuesday, 16th September - 16:00: Poster Session 1 - Poster - Abstract ID: 138

Mr. Kwang Hoon Lee [1], ***Prof. Won Bo Lee*** [2]

1. *Seoul National University / Samsung Electronics,* ***2.*** *Seoul National University*

• Purpose of the work

In semiconductor photolithography, overlay refers to the misalignment error in the X and Y directions between successive patterned layers on a wafer. It is a critical metric that directly impacts both the functional integrity and yield of chips. In advanced memory processes, scanner overlay margins have become extremely tight, where even sub-nm deviations can result in significant device failures. To control such precision, scanner systems perform regular XY calibrations to generate tool-specific overlay compensation models. However, the test tool wafers used for calibration are subject to surface contamination and physical wear over repeated exposures in High Volume Manufacturing (HVM), leading to localized defocus conditions. These local defocus effects manifest as overlay outliers, which distort the calibration model and degrade compensation accuracy. In severe cases, they necessitate wafer rework or recalibration, resulting in productivity losses and increased tool downtime. This study proposes a robust outlier transformation method based on a 10-parameter linear regression model, designed to detect and correct overlay outliers generated during scanner XY calibration. The method replaces erroneous data points with statistically valid values, thereby preserving overlay budget integrity and minimizing operational losses. Importantly, the proposed approach is implemented entirely through software, requiring no hardware modifications or sensor upgrades, and can significantly enhance lithography overlay control and manufacturing stability.

• Novelty of the work with respect to the state of the art

Conventional overlay control methods typically rely on indirect improvements such as enhanced metrology accuracy, photomask heating compensation, or process-level tuning. Direct compensation of overlay anomalies using raw scanner calibration data remains highly limited—primarily due to restricted access to internal data structures. In high-volume manufacturing (HVM) environments, this limitation makes it challenging to independently identify and correct overlay outliers generated during calibration. In this work, we developed a proprietary data parsing engine to structurally decode the scanner's XY calibration dataset. Using this parsed data, we systematically modeled the detection and transformation of overlay outliers. A total of eight correction approaches—including missing data handling, linear regression-based modeling, and machine learning algorithms—were benchmarked. Among them, the 10-parameter linear regression model achieved optimal performance in terms of statistical consistency and cosine similarity to reference profiles. Notably, the solution can detect and transform outliers directly within the scanner data pipeline, without altering scanner architecture or hardware. This enables meaningful improvements in overlay accuracy at the tool level, and more importantly, shifts control capabilities from equipment suppliers to end users. This represents a key advancement in lithography process flexibility and technical self-reliance in semiconductor manufacturing.

• Results of the work

The proposed methodology was experimentally validated across multiple scanner platforms operating in a high-volume manufacturing environment. During periodic XY calibration, a substantial amount of overlay vector data was collected and analyzed. Using point-to-point delta mapping, local defocus-induced overlay outliers were statistically identified on a per-wafer basis. Outlier detection thresholds were examined across multiple statistical bands, and an optimal filtering criterion was established based on operational robustness. Identified outliers were treated through missing data imputation, and eight different transformation models were applied

to reconstruct the overlay map. Among them, the 10-parameter linear regression model exhibited the most stable and consistent performance. It demonstrated high correlation with a golden reference wafer—both in terms of cosine similarity and residual analysis—validating its effectiveness as a correction strategy. Furthermore, the proposed method was shown to reduce unnecessary calibration retries and improve scanner operation stability, resulting in a measurable improvement in overlay performance consistency. Given its data-driven nature and compatibility with current tool infrastructure, the method is expected to be highly applicable to sub-10nm lithography nodes and next-generation platforms such as EUV and High-NA scanners. It also offers meaningful scalability for broader integration into overlay correction workflows.

Gas Sensors Based on MoS_2 Quantum Dots Deposited via Drop-Casting for Environmental Monitoring on Microfabricated Platforms

Tuesday, 16th September - 16:00: Poster Session 1 - Poster - Abstract ID: 141

Ms. Andrea Carolina Villalvazo-Hidalgo [1], ***Dr. Orfil González-Reynoso*** [1], ***Ms. Martha Angelica Hidalgo-Ríos*** [1], ***Dr. Gregorio Guadalupe Carbajal-Arizaga*** [1], ***Dr. Mario Alberto García-Ramírez*** [1]

1. *Universidad de Guadalajara*

Here, we present a scalable MoS_2 quantum dot-based gas sensor for NO_2 and CO_2 detection. Synthesized hydrothermally and integrated via drop-casting onto microfabricated IDEs, the device shows distinct responses and promising sensitivity. It offers a low-cost, efficient platform for atmospheric monitoring.

Real-Time Wireless Tremor Tracking System with V-Groove Crack Sensor

Tuesday, 16th September - 16:00: Poster Session 1 - Poster - Abstract ID: 171

Mr. Jonghyeon Woo [1], ***Mr. JeongSik Noh*** [1], ***Prof. Jongsung Park*** [1]

1. *Kyungpook National University*

This study introduces a wearable, wireless sensor using a PDMS-based V-groove crack structure for early Parkinson's tremor detection. Integrated with BLE and analyzed via a Hidden Markov Model, it enables accurate, low-cost monitoring with minimal data and computational needs, offering the potential for diagnosis and neurological health applications.

Microscope-based Multi-Analyte-Reflectance-Spectroscopy (μ-MARS) for multiplexed label free monitoring of immunoreactions

Tuesday, 16th September - 16:00: Poster Session 1 - Poster - Abstract ID: 172

Dr. Grigorios Zisis [1], ***Dr. Dimitra Tsounidi*** [1], ***Dr. Georgios Koukouvinos*** [1], ***Dr. Panagiota Petrou*** [1], ***Dr. Ioannis Raptis*** [1]

1. *NCSR Demokritos*

A novel biosensing approach, μ-MARS, that integrates Multi-Area Reflectance Spectroscopy with an optical microscope is introduced. During bioreactions, reflectance spectra obtained from chips with two SiO_2 areas of different thickness modified with different biorecognition molecules are collected through a dedicated aperture array and are guided to a spectrometer for further analysis enabling the monitoring of the respective bioreactions. The μ-MARS principle was evaluated through imunochemical detection of one and two analytes demonstrating the potential of this appoach for accurate muliplexed determinations.

CNFET fabrication for NO2 gas sensor recovery with local electrode heating

Tuesday, 16th September - 16:00: Poster Session 1 - Poster - Abstract ID: 191

Ms. Ines Kraiem [1], ***Dr. Cosmin Ioan Roman*** [1], ***Mr. Andri Sigron*** [1], ***Dr. Miroslav Haluska*** [1], ***Prof. Christofer Hierold*** [1]

1. *ETH Zürich*

This paper presents a novel gas sensor recovery approach for Carbon Nanotube Field Effect Transistor (CNFET) nitrogen dioxide (NO2) sensors, relying on the local heating of the transistor's Source (S) and Drain (D) electrodes. By fabricating split S and D electrodes, a current can be passed through them, heating the electrodes metal by Joule heating and the carbon nanotube suspended on top of them. We show that in two different CNFET devices electrode heating enables sensor recovery within 10 seconds. The temperature reached by the carbon nanotube (CNT) is estimated by simulating the Joule heating of the contact electrodes during local electrode heating (EH) pulses.

Selective Electrochemical Aptasensor Using Methylene Blue for Pseudomonas aeruginosa Detection in Mixed Bacterial Cultures

Tuesday, 16th September - 16:00: Poster Session 1 - Poster - Abstract ID: 11

Ms. Somayeh Maghsoomi Taramsari [1]

1. *University for Continuing Education Krems*

This study presents an electrochemical aptasensor for the rapid and sensitive detection of *Pseudomonas aeruginosa*, a clinically significant pathogen. The sensor utilizes the F23 aptamer immobilized on disposable gold screen-printed electrodes (Au-SPEs) and employs methylene blue (MB) as a redox indicator to enhance signal sensitivity. Square wave voltammetry (SWV) demonstrated a strong correlation between bacterial concentration and current peak reduction, achieving a detection limit of 8 CFU·mL^{-1}. The aptasensor exhibited excellent selectivity against interfering bacteria and was successfully tested in tap water samples, demonstrating its potential for real-time monitoring in clinical, food safety, and environmental applications.

Water-soluble holographic color prints from UV to visible for sustainable optical security device

Tuesday, 16th September - 16:00: Poster Session 1 - Poster - Abstract ID: 50

Ms. Hyunjung Kang [1], ***Mr. Hongyoon Kim*** [1], ***Prof. Junsuk Rho*** [1]

1. *Pohang University of Science and Technology*

We developed eco-friendly, water-soluble QR codes with holographic and structural color functionalities using biopolymer–TiO_2 nanocomposites. Fabricated via nanoimprint lithography, these labels enable anti-counterfeiting, humidity sensing, and recyclability, offering a sustainable solution for smart optical security and packaging.

Dual functional filmy device for heat dissipation and power generation based on Bi2Te3 array with topological surface

Tuesday, 16th September - 16:00: Poster Session 1 - Poster - Abstract ID: 88

Dr. YiHeng Zhao [1], ***Mr. Mingxue Li*** [1], ***Prof. yufeng zhang*** [2]

1. *MEMS Center, Harbin Institute of Technology, Harbin 150001, China,* ***2.*** *MEMS Center, Harbin Institute of Technology*

With rapid development of integrated circuit (IC) technology, the continuous improvement in computational density and power consumption has created an urgent demand for highly integrated thermal management systems. In this work, bismuth telluride with topological surface is used to prepare a functional thin film that can both realize heat dissipation and waste heat conversion for power generation. The proposed device shows significant potential for enhancing heat dissipation in high-power-density ICs and enabling waste heat recovery and utilization.

A Modeling Study on Inorganic Chalcogenide Transport Layers in Sn-Based Perovskite Solar Cells

Tuesday, 16th September - 16:00: Poster Session 1 - Poster - Abstract ID: 155

Mr. Daniyal Khoshmaram [1]

1. *Department of Electrical Engineering, Amirkabir University of Technology, Tehran, Iran*

Tin-based perovskites have emerged as promising candidates for photovoltaic applications. This work introduces a strategy to improve both the stability and efficiency of pure Sn-based perovskite solar cells (PSCs), achieving results comparable to conventional structures by utilizing inorganic chalcogenide electron transport layers (ETLs) and hole transport layers (HTLs).

Conformally-coated titanium carbide on structured pyrolytic carbon electrodes for lithium sulphur batteries

Tuesday, 16th September - 16:00: Poster Session 1 - Poster - Abstract ID: 164

Mr. Owen Bell [1], ***Dr. Daniel Ho*** [2], ***Mrs. Nadira Palakkool*** [2], ***Dr. Mike Taverne*** [2], ***Dr. Kevin Chung-Che Huang*** [3], ***Prof. Vincent Barrioz*** [2], ***Dr. Yongtao Qu*** [2], ***Dr. Johnathan Mar*** [4], ***Dr. Tam Ho*** [2], ***Dr. Christopher Jones*** [5], ***Mr. Giray Kartopu*** [2]

1. *PhD Student,* ***2.*** *Northumbria University,* ***3.*** *Southampton University,* ***4.*** *Newcastle University,* ***5.*** *Bristol University*

This study explores Py-C/TiC/S cathodes for Li-S batteries, enhancing electrochemical performance and stability. Using 3D structures and advanced fabrication techniques, the cathodes show improved conductivity, reduced polysulphide shuttling, higher capacity retention, and longer cycle life, highlighting their potential for high-performance Li-S batteries.

A deeper dive into droplet and dust dynamics on commercially available solar panels

Tuesday, 16th September - 16:00: Poster Session 1 - Poster - Abstract ID: 203

Mr. Anirban Roy [1], ***Mr. Rahul Roy*** [1], ***Dr. Chirodeep Bakli*** [1]

1. *Indian Institute of Technology Kharagpur*

Efficient cleaning of solar panels is required for better performance. Towards this, we suggest a suitable droplet dispensing height for either targeted cleaning (displacing dust from a spot of smaller size) or bulk area cleaning. We further quantify the amount of dust displaced in each case using image processing.

All-in-one Microfluidic Platform for Single-Cell Environmental Phenotyping of Chlamydomonas reinhardtii

Tuesday, 16th September - 16:00: Poster Session 1 - Poster - Abstract ID: 213

Mr. Alexandre Chargueraud [1], ***Dr. Lars Kool*** [2], ***Ms. Eliora Israelievitch*** [3], ***Dr. Alix Boulouis*** [3], ***Dr. Jacques FATTACCIOLI*** [4]

1. *CPCV, Département de Chimie, Ecole Normale Supérieure, PSL Université, Sorbonne Université, CNRS, 75005 Paris, France,* ***2.*** *Institut Pierre-Gilles de Gennes pour la Microfluidique, Paris, 75005, France,* ***3.*** *Laboratoire de Biologie du Chloroplaste et Perception de la lumière chez les microalgues of the Institut de Biologie Physico-Chimique, Sorbonne Université, Paris, 75005, France,* ***4.*** *CPCV, Département de Chimie, Ecole Normale Supérieure, PSL Université, Sorbonne Université, CNRS*

This work presents a reusable microfluidic platform for environmental monitoring using *Chlamydomonas reinhardtii*, a model microalga. It enables sequential trapping, high-resolution analysis, and controlled release of individual cells under dynamic conditions. Designed for long-term assays of stress response, viability, and photosynthetic activity, the device offers a powerful tool to study microalgal responses to environmental fluctuations and contaminants.

Plenary 4 - Prof Shinichi Saito

Why Micro is different from Macro? A Challenge towards Macroscopic Quantum Technologies

Wednesday, 17th September - 08:00: Plenary 4 - Prof Shinichi Saito (Plenary Hall) - Oral - Abstract ID: 13

Dr. Shinichi Saito [1]

1. *Hitachi*

We developed an SU(N) representation theory to describe both spin and orbital angular momentum of coherent photons and experimentally demonstrated their controls over a full Poincaré sphere. We found Stokes parameters are spin expectation values by SU(2) wavefunctions, which exhibit non-trivial topological features like a torus, a Möbius strip, and a bosonic Dirac cone. We also ascribed topological colour charge to photonic orbital angular momentum, whose SU(3) states are shown on a Gell-Mann hypersphere in SO(8). We also realised photonic SU(4) states of singlet and triplet states, which were successfully projected into SU(2)×SU(2) states by a rotated polariser.

Plenary 5 - Prof Mariana Medina Sanchez

Medical Microrobots with Functional Nanomaterials for Precision Women's Healthcare

Wednesday, 17th September - 08:45: Plenary 5 - Prof Mariana Medina Sanchez (Plenary Hall) - Oral - Abstract ID: 460

Prof. Mariana Medina Sanchez [1]

1. *nanoGune*

Owing to their active propulsion and high thrust forces, nanomaterial-enhanced microrobots hold significant promises for next-generation assisted reproduction techniques, offering more targeted, efficient, and less invasive approaches to gamete and embryo manipulation, ultimately aiming to improve pregnancy success rates by providing a more natural environment for development. Beyond reproduction, they open new avenues for precision drug delivery in gynecological health, particularly in addressing cancers of the reproductive tract. In this context, we have exploited sperm cells as biohybrid drug carriers, taking advantage of on their unique ability to load high amounts of anticancer drugs without compromising viability or motility, their natural adaptation to swim against backflows in viscoelastic media, and their intrinsic capacity to fuse with cancer cells for highly localized drug delivery. By actively navigating to deep-seated or otherwise inaccessible disease sites, such microrobots enable therapeutic interventions that minimize systemic side effects while maximizing efficacy. Incorporating functional nanomaterials with magnetic, plasmonic, and acoustic properties further enhances their biomedical potential, allowing precise and minimally invasive remote control through external fields and improved visualization in scattering tissues via ultrasound and photoacoustic imaging. Moreover, functionalization with nanocarriers such as polymersomes and liposomes substantially increases therapeutic payloads while enabling finely tunable release strategies. Together, these advances position medical microrobots as transformative tools for women's health and beyond, reshaping therapeutic paradigms through targeted, minimally invasive, and patient-centered interventions.

Oral Session 2A: Nanoimprint and alternative lithography

Comparison of 2 processes based on NIL and lift-off for the fabrication of thick nano antennas for solar PV-TE applications

Wednesday, 17th September - 10:00: Oral Session 2A: Nanoimprint and alternative lithography (Plenary Hall) - Oral - Abstract ID: 440

Dr. Jean-Baptiste Doucet [1], ***Dr. Franck Carcenac*** [1], ***Dr. Leopold Boudier*** [1], ***Dr. Inès Revol*** [1]

1. *LAAS-CNRS*

Combining photovoltaic cells with thermoelectric generators could enhance solar energy efficiency using a nanostructured photothermal interface based on metal nano antennas. Nanoimprint lithography and lift-off can produce them. We report here on the comparison of two processes we developed and on the successful 150-200 nm thick metal lift off.

Fine silver wiring using replica mold with light-shielding film

Wednesday, 17th September - 10:15: Oral Session 2A: Nanoimprint and alternative lithography (Plenary Hall) - Oral - Abstract ID: 21

Mr. Takumi Ashida [1], ***Prof. Jun Taniguchi*** [1]

1. *Tokyo University of Science*

We have developed a process to fabricate the CNP (Combined nanoimprint lithography) mask without deposition and transfer silver ink wiring using it without generating residual film, which has been a problem in conventional nanoimprint lithography. In addition, complex silver ink patterns were transferred and their conductivity was verified.

Single-nm Mask Writing for Nanoimprint Lithography, as an Energy-Efficient Alternative to EUV

Wednesday, 17th September - 10:30: Oral Session 2A: Nanoimprint and alternative lithography (Plenary Hall) - Oral - Abstract ID: 394

Dr. James Owen [1], ***Mr. Robin Santini*** [1], ***Dr. John Randall*** [1]

1. *Zyvex Labs*

We are developing a process to create single-nm linewidth Nanoimprint Lithography templates starting with atomically-precise STM patterns. Selective ALD of TiO_2 followed by RIE transfers the STM pattern into a Si Nanoimprint template. Linewidths down to 11 nm were demonstrated in previous work, comparable to the limit for E-beam lithography, now we are extending this down to 5 nm linewidth, narrower than is possible with EUV.

Optimization of grayscale direct-write laser lithography for the fabrication of large-area 2.5D molds for nanoimprint lithography

Wednesday, 17th September - 10:45: Oral Session 2A: Nanoimprint and alternative lithography (Plenary Hall) - Oral - Abstract ID: 240

Dr. Peng Tian [1], ***Dr. Maria Szola*** [1], ***Dr. Dimitrios Kazazis*** [1], ***Dr. Yasin Ekinci*** [1]

1. *Paul Scherrer Institute (PSI)*

We investigate the usage of grayscale direct-write laser lithography for the fabrication of 2.5D large-area master molds for nanoimprint lithography, to reach larger pattern depth and higher throughput. With our comprehensively optimised process, “resist masters” were reproducibly fabricated and effectively used for replication of the patterns to daughter stamps.

Advanced Patterning For Smart Optical Devices: Integrating Inkjet Coating with Nanoimprinting for Precise Height Control and Minimal Residual Layers

Wednesday, 17th September - 11:00: Oral Session 2A: Nanoimprint and alternative lithography (Plenary Hall) - Oral - Abstract ID: 49

Mrs. Andrea Kronawitter [1], ***Mrs. Johanna Rimböck*** [1], ***Mrs. Lisa Vsetecka*** [1], ***Mrs. Thomas Achleitner*** [1], ***Mrs. Patrick Schuster*** [1], ***Mrs. Brid Connolly*** [2], ***Mr. Martin Sczyrba*** [3], ***Mr. Andreas Frangen*** [2]

1. *EV Group,* ***2.*** *Tekscend Photomasks Germany GmbH,* ***3.*** *AMTC Dresden*

Nanostructured surfaces are integral to various industries, including semiconductors, sensors, and biomedical applications. Nanoimprint lithography (NIL) is a pivotal technique for the precise patterning of nanostructures onto materials such as silicon, compound semiconductors, glasses, and polymers. Leading manufacturers in augmented reality, optical sensors, and biomedical chip production are increasingly implementing NIL, acknowledging its significant advantages in the fabrication of advanced devices.

Traditionally, imprint materials (polymers) are applied using spin coating. However, evolving applications require more precise control over the residual layer thickness to accommodate different master form factors, as well as improved efficiency and sustainability in resin usage. Inkjet coating, which allows for the printing of patterns with lateral resolution and variable thicknesses in a single process step, offers a promising coating alternative for NIL [1]. This method could facilitate the development of new applications while enhancing sustainability by reducing material consumption.

This study explores the integration of NIL with inkjet coating for the fabrication of non-functional grating structures, commonly employed in waveguides for AR devices. The master template, manufactured by Tekscend Photomask and utilized in this work, illustrated in Figure 1(a), comprises three distinct grating regions (refer to Figure 1(b) and 1(c)):

- the incouple (IC) grating: staircase structures
- the expander (EPE) grating: binary gratings with a linear depth profile ranging from 60 nm to 160 nm
- the outcouple (OC) grating: slanted gratings with a nonlinear depth profile spanning from 50 nm to 200 nm
- along with variations in duty cycle

First, initial NIL imprints on 6-inch silicon wafers with a uniform resin layer were generated, applied via spin coating. The resulting nanoimprints, shown in Figure 2(a-d), successfully replicated all three test gratings with strong adhesion to the substrate. The staircase, the binary and the slanted grating structures were accurately molded using NIL. Cross-sectional analysis revealed that the residual layer thickness ranged from 308 nm to 377 nm, depending on the fill factors at different positions within the gratings. This variation, coupled with the overall high residual layer thickness, is unsuitable for achieving optimal optical performance in smart devices. In order to achieve a thinner and more uniform residual layer, inkjet coating was utilized to modify the film thickness prior to the imprinting process. To do so, a grayscale image of the master layout was generated, and grayscale inkjet coating (which employs variable drop sizes to produce different gray levels) was applied to create a resin layer with thickness variations across the wafer. The NIL process was subsequently performed on the inkjet coated wafers (instead of using spin coated wafers). Cross-sectional analysis of the resulting imprints, shown in Figure 3(a-d), confirmed successful replication of the structures with high pattern fidelity. All of the three complex grating designs were precisely replicated using NIL in conjunction with inkjet coating. The polymer showed excellent fluidic and filling properties after the inkjet coating and soft bake processes, with no observable change in adhesion. Compared to the spin coated imprints, the inkjet coated imprints demonstrated

a more uniform and thinner residual layer across all grating types. The residual layer thickness ranged from 49 nm to 60 nm, which is more suitable for the optical performance required in augmented reality (AR) devices.

[1] J. Rimböck, P. Schuster, L. Vsetecka, and C. Thanner, “UV Nanoimprint Lithography—Impact of Coating Techniques on Pattern Quality,” Nanomanufacturing, vol. 4, pp. 69-80, 2024.

Exploring water-soluble polymeric stamps for ultraviolet light nano-imprint lithography

Wednesday, 17th September - 11:15: Oral Session 2A: Nanoimprint and alternative lithography (Plenary Hall) - Oral - Abstract ID: 201

Mr. Haohui Yang [1], ***Mr. Anmol Gupta*** [1], ***Prof. Steffen Strehle*** [1]

1. *Techische Universität Ilmenau*

Ultraviolet nanoimprint lithography (UV-NIL) is a cost-effective, parallel, and 3D micro-nano manufacturing technique. However, the demolding process may damage the cured photoresist structures. Our research aims to reduce demolding stress by using polyvinyl alcohol (PVA) as a soft stamp material and investigating turbulence-induced elution on the PVA surface.

Fabrication and Evaluation of Curved Mirror for Co-packaged optics Using Photo Nanoimprint Technology

Wednesday, 17th September - 11:30: Oral Session 2A: Nanoimprint and alternative lithography (Plenary Hall) - Oral - Abstract ID: 156

Ms. Maaya Watanabe [1], ***Dr. Fumi Nakamura*** [2], ***Mr. Taro Itatani*** [2], ***Prof. Joji Maeda*** [1], ***Dr. Takeru Amano*** [2]

1. *Tokyo University of Science,* **2.** *National Institute of Advanced Industrial Science and Technology (AIST)*

Co-packaging optics using silicon photonics is one of the promised solutions for increasing AI workloads, and micro-mirror is key component for optical re-distribution there. In this work, we introduced nanoimprint technology for fabrication 3D curved mirrors to enable high throughput, and demonstrated mirror fabrication in several imprint condition. Polydimethylsiloxane mold was prepared from master mold with 27 curved mirrors formed by two photon polymerization-based 3D printing. The mirrors were successfully transferred to UV curable polymer at mold loads of approximately 100, 200, 300, and 400 kPa. At 200 kPa, where a stable residual layer thickness of 1.62 μm was obtained, the mirrors were fabricated with an average height reduction of 5.8%.

Advances in parallelization of thermal scanning probe lithography and large-area patterning

Wednesday, 17th September - 11:45: Oral Session 2A: Nanoimprint and alternative lithography (Plenary Hall) - Oral - Abstract ID: 103

Ms. Julia Stark [1], ***Dr. Jana Chaaban*** [1], ***Mr. Kartik Buddha*** [1], ***Dr. Fabian Koenemann*** [1], ***Dr. Emine Çağın*** [1]

1. *Heidelberg Instruments*

The new generation of the NanoFrazor enables precise surface nanostructuring with parallel thermal scanning probe lithography, achieving ten times higher throughput. Ideal for large-area applications like metasurfaces and nanometer-precise grayscale holography, it combines advanced patterning capabilities with user-friendly operation for efficient and scalable nanofabrication.

Oral Session 2B: Photonics, Photonic structures and Metasurfaces

Sustainable manufacturing of optical metasurfaces for imaging, sensing and display

Wednesday, 17th September - 10:00: Oral Session 2B: Photonics, Photonic structures and Metasurfaces (Charnock Lecture Theater) - Oral - Abstract ID: 445

Prof. Junsuk Rho [1]

1. *Pohang University of Science and Technology*

Metamaterials and metasurfaces are novel optical components composed of nanostructure arrays. They offer the advantage of an ultracompact form factor and can image submicron objects with resolution approaching the diffraction limit of light. The scope of this imaging extends from simple microscopes to more advanced light imaging applications such as 3D sensors, LiDAR, bio-imaging, and cameras. The wavelength range of imaging is also diversifying to support various imaging applications. Metalenses operating in the UV region enable high-resolution imaging due to the short wavelength of light. In the visible light spectrum, metalenses can be used for imaging in VR/AR displays. Near-infrared metalenses have potential applications in night vision devices and endoscopes. The wavelength range extends further to include the ultrasound region, where it can be used in photoacoustic microscopy. Additionally, elastic metalenses can be applied for energy harvesting, and acoustic metalenses can be used to focus sound waves. Furthermore, metalenses can perform imaging with various functionalities. They can tune their focal length, demonstrate trichannel imaging based on spin, and even image single photons emitted from a source. While metalenses operate across various wavelengths and offer diverse functionalities for numerous imaging applications, their design is currently not scalable, making large-area designs computationally heavy and expensive. To address this, efficient computational methods like RCWA and AI/DB-based design approaches have been developed . However, even with advances in large-area design capabilities, their commercialization has been hindered by manufacturing limitations such as high cost and low throughput. To reduce the production cost of metalenses, nanoimprint lithography has been employed. To address the low refractive index of conventional imprint resins, high-refractive-index particles are incorporated, creating a one-step printable platform On the other hand, ArF photolithography has been used to overcome low throughput and produce large-area metasurfaces at wafer scale. However, due to the high manufacturing costs associated with this method, research has been conducted on mass-producing metasurfaces by using wafer-scale nanoimprint technology to replicate metasurfaces initially created through photolithography. These scalable manufacturing approaches are expected to propel metalenses beyond the research level and into practical applications.

A Novel Manufacturing Platform for Large-diameter Si Metalens using Deep-UV Lithography

Wednesday, 17th September - 10:30: Oral Session 2B: Photonics, Photonic structures and Metasurfaces (Charnock Lecture Theater) - Oral - Abstract ID: 132

Dr. Kai Sun [1], ***Dr. Xingzhao Yan*** [2], ***Mr. Jordan Scott*** [1], ***Dr. James Monks*** [3], ***Dr. Jun-Yu Ou*** [1], ***Prof. Otto Muskens*** [1]

1. *Physics and Astronomy, University of Southampton,* ***2.*** *Optoelectronics Research Centre, University of Southampton, SO17 1BJ, UK,* ***3.*** *Teledyne Qioptiq Ltd*

We demonstrate 40 mm diameter Si-based metalenses, based on our novel designs and fabrication. With full CMOS compatibility, the metalens diameter has been increased over the exposure field size (25 mm X 33 mm) and the technique can be further scaled up.

Understanding 3D Structural Control in Metasurface-Based Holographic Lithography

Wednesday, 17th September - 10:45: Oral Session 2B: Photonics, Photonic structures and Metasurfaces (Charnock Lecture Theater) - Oral - Abstract ID: 228

Mr. Jeevan Rois [1], ***Mr. Zesen Zhou*** [1], ***Dr. Matias Kagias*** [1]

1. *Lund University*

This study analyzes dielectric metasurfaces for holographic lithography, focusing on material compatibility with lithographic wavelengths and robust unit cell designs. We identify combinations that enable 3D periodic structures with sub-micrometer features, offering high tunability and low sensitivity to meta-atom dimensional variations within a few nanometers, ensuring fabrication tolerance.

Keywords: Dielectric metasurface, Holographic lithography, Damascene lithography, 3D Morphology, Diffraction efficiency

Fabrication of Substrates with Plasmonic Gold Nanostructures for Cellular Membrane Rupture

Wednesday, 17th September - 11:00: Oral Session 2B: Photonics, Photonic structures and Metasurfaces (Charnock Lecture Theater) - Poster - Abstract ID: 382

Mr. Christian Einsiedler [1], ***Dr. Franziska Marie Esmek*** [2], ***Mr. Rukan Nasri*** [3], ***Dr. Irene Fernandez*** [3]

1. *University of Hamburg, Hamburg Center for Ultrafast Imaging,* ***2.*** *University of Hamburg/Hamburg Center for Ultrafast Imaging,* ***3.*** *UHH/CUI*

We present plasmonic substrates for selective, laser-induced cell membrane rupture, using nanolithography-patterned gold nanostructures and Au nanoparticle-embedded polymers. Three fabrication methods are compared and optically characterized via dark-field spectroscopy. Preliminary results show successful cell seeding and laser-induced membrane damage. Ongoing work focuses on optimizing conditions for localized single-cell lysing.

Printable Spin-Multiplexed Metasurfaces for Ultraviolet Holographic Displays

Wednesday, 17th September - 11:15: Oral Session 2B: Photonics, Photonic structures and Metasurfaces (Charnock Lecture Theater) - Oral - Abstract ID: 51

Ms. Hyunjung Kang [1], ***Mr. Hongyoon Kim*** [1], ***Prof. Junsuk Rho*** [1]

1. *Pohang University of Science and Technology*

We demonstrate scalable, spin-multiplexed ultraviolet metaholograms using printable ZrO_2-based nanocomposites. The metasurfaces generate polarization-dependent holographic images with high efficiency via single-step nanoimprint lithography, offering a cost-effective and mass-producible platform for secure optical encryption.

Embedded-Holey Metasurfaces for Enhanced Mechanical Robustness and Integration Compatibility

Wednesday, 17th September - 11:30: Oral Session 2B: Photonics, Photonic structures and Metasurfaces (Charnock Lecture Theater) - Oral - Abstract ID: 316

Ms. Zixuan Wang [1], ***Dr. Chuang Sun*** [1], ***Ms. Weilin Jin*** [2], ***Dr. Jun-Yu Ou*** [3], ***Dr. Kian Shen Kiang*** [2], ***Prof. Jize Yan*** [2]

1. *School of Electronics and Computer Science, University of Southampton, Southampton SO17 1BJ, United Kingdom,* ***2.*** *University of Southampton,* ***3.*** *Physics and Astronomy, University of Southampton*

This work proposes embedded-holey metasurfaces that enhance mechanical stability and surface uniformity. We fabricated and experimentally compared three types of metasurfaces with key fabrication process differences, demonstrating that all designs exhibit comparable optical performance. The proposed embedded-holey metasurface overcomes the limitations of conventional designs, enabling the realization of scalable commercialization.

Novel UV-curable organic-inorganic polymers for micro-optical and photonic components with enhanced reliability

Wednesday, 17th September - 11:45: Oral Session 2B: Photonics, Photonic structures and Metasurfaces (Charnock Lecture Theater) - Poster - Abstract ID: 211

Dr. Maria Russew [1], ***Dr. Alexander Plucinski*** [1], ***Dr. Thomas Wiglenda*** [1], ***Mr. Johannes Wolf*** [1], ***Dr. Arne Schleunitz*** [1], ***Mrs. Gabi Grützner*** [1]

1. *micro resist technology GmbH*

Novel applications for micro optical and photonics components for example, in the field of automotive ligthing, drive the research for highly reliable optical materials. In this contribution, we will present further advanced organic-inorganic hybrid polymers with reduced yellowing behavior to meet these strict requirements.

Oral Session 2C: Photonics and Optoelectronics

Monolithic Integration of GeV Centers in Ring Waveguides for Quantum Light Emission

Wednesday, 17th September - 10:00: Oral Session 2C: Photonics and Optoelectronics (One Ocean Suite) - Oral - Abstract ID: 130

Dr. Fatemeh Moradiani [1], ***Mr. Arran Ashfield*** [2], ***Dr. Arthur Lipinski*** [1], ***Prof. Robert M. Bowman*** [3], ***Dr. Hamidreza Siampour*** [4]

1. *Research Fellow,* ***2.*** *PhD Student,* ***3.*** *Professor,* ***4.*** *Lecturer*

We demonstrate a room-temperature single-photon source by coupling GeV center emission into surface plasmon polariton modes via a ring-waveguide resonator. The device exhibits an 11-fold emission enhancement at 602.35 nm with $Q \approx 200$ and $g^2(0) \approx 0.2$, confirming spectrally narrow, bright, and stable single-photon emission.

Microsphere-assisted generation of localized optical emitters in 2D hexagonal boron nitride

Wednesday, 17th September - 10:15: Oral Session 2C: Photonics and Optoelectronics (One Ocean Suite) - Oral - Abstract ID: 55

Ms. XILIANG YANG [1], ***Dr. Sabina Caneva*** [1], ***Prof. Peter Steeneken*** [1], ***Prof. Dong Hoon Shin*** [2]

1. *Delft University of Technology,* ***2.*** *Korea University*

Crystal defects in hexagonal boron nitride (hBN) are emerging as versatile nanoscale optical probes with a wide application profile, spanning the fields of nanophotonics, biosensing, bioimaging and quantum information processing. However, generating these crystal defects as reliable optical emitters remains challenging due to the need for deterministic defect placement and precise control of the emission area. Here, we demonstrate an approach that integrates microspheres with hBN optical probes to enhance both defect generation and optical signal readout. This technique harnesses microspheres to amplify light-matter interactions at the nanoscale through two mechanisms: focused femtosecond (fs) laser irradiation into a photonic nanojet (PNJ) for highly localized defect generation, and enhanced light collection via the whispering gallery mode (WGM) effect. Our microsphere-assisted defect generation method reduces the emission area by a factor of 5 and increases the fluorescence collection efficiency by approximately 10 times compared to microsphere-free samples. These advancements in defect generation precision and signal collection efficiency open new possibilities for optical emitter manipulation in hBN, with potential applications in quantum technologies and nanoscale sensing.

Chip-scale infrared Fourier-transform spectrometer based on nano-opto-electro-mechanical systems

Wednesday, 17th September - 10:30: Oral Session 2C: Photonics and Optoelectronics (One Ocean Suite) - Oral - Abstract ID: 356

Dr. Bingrui Lu [1], ***Dr. Babak Vosoughi Lahijani*** [1], ***Dr. Søren Engelberth Hansen*** [1], ***Dr. Thor August Schimmell Weis*** [1], ***Dr. Marcus Albrechtsen*** [1], ***Dr. Ali Nawaz Babar*** [1], ***Dr. Michael Juhl*** [1], ***Dr. Christian Anker Rosiek*** [1], ***Mr. Jesper Laurberg Sand*** [1], ***Mr. Bjarke Almer Frederiksen*** [1], ***Mr. Mathias Linde Holst Korsgaard*** [1], ***Mr. Nikolaj Balslev Hougs*** [1], ***Dr. Konstantinos Tsoukalas*** [1], ***Dr. Guillermo Arregui Bravo*** [1], ***Prof. Søren Stobbe*** [1]

1. *Technical University of Denmark*

This work presents a chip-scale near-infrared Fourier-transform spectrometer (FTS) using a Mach-Zehnder interferometer (MZI) on a nano-opto-electro-mechanical system (NOEMS). Light enters through a grating coupler, splits via an inverse-designed beamsplitter, and travels through tunable slot-waveguides actuated by low-voltage comb drives. The compact SOI-based design is promising for portable spectroscopy for clinical and industrial applications.

Hydrophobic and Sticky Silver-Decorated Nanoimprinted ZnO Nanograss Substrates for Enhanced SERS Performance

Wednesday, 17th September - 10:45: Oral Session 2C: Photonics and Optoelectronics (One Ocean Suite) - Oral - Abstract ID: 175

Mr. Kuan-Ting Kuo [1], Prof. Wen-Huei Chang [2], Prof. Hsiang Chen [3], Mr. Jyun-Jie Chen [1], Prof. Chun-Hung Lin [4]

1. *Department of Photonics, National Cheng Kung University,* ***2.*** *Department of Applied Chemistry, National Pingtung University,* ***3.*** *Department of Applied Materials and Optoelectronic Engineering, National Chi Nan University,* ***4.*** *National Cheng Kung University*

Patterned ZnO nanograss substrates, crafted via nanoimprint lithography and hydrothermal growth, and silver-decorated, exhibit enhanced SERS sensitivity for malachite green detection. The grating-mediated architecture boosts plasmonic interaction. Over time, increased hydrophobicity enhances molecule retention. This scalable platform shows potential for competitive sensitivity and stability in future diverse sensing applications.

Antireflection of near-infrared light using a moth-eye structure film

Wednesday, 17th September - 11:00: Oral Session 2C: Photonics and Optoelectronics (One Ocean Suite) - Oral - Abstract ID: 58

Mr. Kei Hirata [1], ***Prof. Jun Taniguchi*** [1]

1. *Tokyo University of Science*

A moth-eye structure was obtained by irradiating oxygen ions onto glassy carbon.
The moth-eye structure was destroyed when the ICP RF power was 600 W or higher.
The anti-reflection performance was best at 500 W, but the transmittance dropped.
Even those that maintained high transmittance had anti-reflection of near-infrared light.

One-Step Printable Fabrication of Tantalum Pentoxide Metasurfaces for UV–Visible Optics

Wednesday, 17th September - 11:15: Oral Session 2C: Photonics and Optoelectronics (One Ocean Suite) - Oral - Abstract ID: 275

Ms. Eunji Lee [1], ***Prof. Junsuk Rho*** [2]

1. *POSTECH,* ***2.*** *Pohang University of Science and Technology*

Broadband metasurfaces capable of precise electromagnetic wave control from the ultraviolet (UV) to the visible range enable multi-spectral photonic applications. We present a one-step nanoimprint process using particle-embedded resin (PER) for fabricating Ta_2O_5-based UV-visible metasurfaces. By carefully tuning fabrication conditions, we achieved high-fidelity patterning with adjustable refractive index. This method enables direct replication of UV–visible metaholograms and metalenses, simplifying fabrication while preserving optical performance, and offering a scalable route toward cost-effective mass production.

Red Emitting DBR Laser Array with 0.1 nm Wavelength Spacing Defined by Direct Write Ebeam Lithography

Wednesday, 17th September - 11:30: Oral Session 2C: Photonics and Optoelectronics (One Ocean Suite) - Poster - Abstract ID: 54

Dr. Olaf Brox [1], ***Dr. Jörg Fricke*** [1], ***Dr. Ralph-Stephan Unger*** [1], ***Dr. André Maaßdorf*** [1], ***Dr. Anna Mogilatenko*** [1], ***Mr. Maximilian Beier*** [1], ***Dr. Heike Christopher*** [1], ***Dr. Andrea Knigge*** [1], ***Dr. Hans Wenzel*** [1]

1. *Ferdinand-Braun-Institut gGmbH*

We present a red emitting distributed Bragg reflector diode laser array (DBR array) designed for digital holography on technical and biological surfaces. Controlled but small wavelengths differences are requested for digital holography to generate long synthetical wavelengths. Here we test ebeam direct write lithography to realize 0.1 nm wavelength spacing between adjacent emitters. Dimensions and optoelectronic performances make the fabricated DBR array an excellent light source for digital holographic systems.

Anti-reflection and radiative cooling bifunctional polymer film fabricated via nanoimprint lithography and in situ boehmite formation by hydrothermal treatment

Wednesday, 17th September - 11:45: Oral Session 2C: Photonics and Optoelectronics (One Ocean Suite) - Oral - Abstract ID: 274

Ms. Nefeli Dimogerontaki [1], ***Dr. Nikolaos Mattheakakis*** [2], ***Dr. Nikos Papanikolaou*** [3], ***Dr. Nikolaos Kehagias*** [2]

1. *Department of Physics, School of Applied Mathematical and Physical Sciences National Technical University of Athens, Zografou Campus, GREECE,* ***2.*** *NCSR Demokritos, Institute of Nanoscience & Nanotechnology, P. Grigoriou 27 & Neapoleos Str., 15341 Ag. Paraskevi, Greece,* ***3.*** *NCSR Demokritos*

A bifunctional polymer film with micro- and nano-structured features was fabricated via nanoimprint lithography and Aluminum hydrothermal treatment. The film exhibits anti-reflective behavior in the visible range and enhanced thermal emissivity in the infrared, enabling passive radiative cooling for solar absorbers. This scalable method offers potential for energy-efficient optical and thermal management applications.

Oral Session 2D: Information Communication Technologies

Fabrication and Analysis of Self-Rolled-Up Polymer Ribbon Structure Based on Photosensitive Polyimide and Mechanical Debonding

Wednesday, 17th September - 10:00: Oral Session 2D: Information Communication Technologies (Seminar Room) - Poster - Abstract ID: 107

Dr. HyungDal Park [1], Dr. Seonho Seok [2], Dr. Jinseok Kim [1]

1. *Korea Institute of Science and Technology,* ***2.*** *University-Paris-Saclay*

This paper presents a new technique to fabricate a rolled-up ribbon structure based on conventional photo patterning of photosensitive polyimide (PSPI) on the Si substrate and mechanical debonding by using lowered interface energy. Compared with the reported rolled-up structuring techniques based on wet sacrificial etch, the proposed technique uses interface energy reduction of polymer material with thin gold metal layer as function of time. In case of polymer rolled-up structuring, wet sacrificial etch can modify the mechanical characteristics of the polymer material itself and different etch rate could invoke unwanted rolled-up shape. Besides, modeling and simulation have been conducted to understand the behavior of the rolled-up structure. It was found that a single polymer layer coated on the Si substrate has opposite stresses, or top surface of the polymer has compressive stress, while bottom surface of the polymer has tensile one due to difference of CTE with Si substrate. Therefore, rolled-up shape has been made after the debonding of the polymer ribbon from the Si substrate.
The self-rolled-up structures have been used for unconventional 3D devices such as transformer, MEMS switch and have been frequently implemented with bi-layered thin film through wet sacrificial etch, laser processes [1-3]. Existing processes would create unwanted rolled-up modes especially . Fig. 1 shows the twisted self-rolled-up polymer ribbon when wet sacrificial etch has been applied to release polymer ribbons. Note that the dimension of the sample is 50 mm x 5 mm x 5 mm. To overcome the issue related with sacrificial release, a mechanical debonding rolled-up process has been proposed as depicted in Fig. 2. Mechanical debonding using blade insertion between polymer layer and gold thin film has been used. It was found that the interface energy has been degraded as function of time and thus blade insertion has been used to initiate self-rolled-up polymer structure. The rolled-up structure has been implemented by applying mechanical force debonding the polymer surface from the gold metal layer. Fig. 3 shows the fabrication results of the self-rolled-up polyimide structure. To understand the rolled-up behavior, FEM (Finite Element Method) modeling and simulation has been conducted and the rolled-up of the polymer layer has been successfully reproduced as shown in Fig. 4. The material properties are 6.0 MPa of Young's modulus, 52 ppm of the thermal expansion coefficient (CTE) and the thermal stress of the polymer ribbon has been defined by temperature. As shown in Fig. 4 (a), the polymer ribbon was self-rolled-up due to the applied thermal stresses. Thus, it was found that stress gradient has been created between top surface and bottom surface of the polymer layer patterned on the Si substrate. By consequence, it is considered that top-half of the polymer is in compressive stress, while bottom-half is in tensile stress. Besides, it was found that the maximum rolled-up diameter can be extracted as function of the thermal stress as shown in Fig. 4 (b). This self-rolled-up polymer structure would be evolved to develop a novel medical device such as cylindrical-type interfaces for various sensors in near future.

Semiconductor Quantum Dots: From Tailored Synthesis to Advanced Sensing and Biosensing Applications

Wednesday, 17th September - 10:15: Oral Session 2D: Information Communication Technologies (Seminar Room) - Oral - Abstract ID: 444

Dr. Javed H. Niazi [1]

1. *SUNUM - Sabanci University Nanotechnology Research & Application Center*

Semiconductor quantum dots (QDs) are nanoscale materials with exceptional size-tunable optical and electronic properties, governed by quantum confinement effects. Their synthesis follows either top-down (e.g., lithography, etching) or bottom-up approaches (e.g., colloidal, hydrothermal methods), with the latter offering superior control over size, crystallinity, and surface functionalization. Core-shell structures, surface passivation, and biofunctionalization further enhance their photoluminescence efficiency, stability, and specificity making them ideal for optoelectronic and biomedical applications.

This talk will explore the evolution of QD synthesis techniques, emphasizing scalable production of high-quality QDs (e.g., CdSe@CdS@ZnS core-shell-shell nanostructures) and their integration into cutting-edge sensing platforms. A key focus will be on immuno-optomagnetic point-of-care (PoC) biosensors, where magnetic QDs (MQDs)- QDs coated with magnetic nanoparticles to combine optical and magnetic properties. These enable rapid, multiplexed detection of disease biomarkers (e.g., breast cancer's Her2, and Alzheimer's Ab1-42, tau protein) in complex biological samples (e.g., serum, saliva) with visible results in 10-30 min. The talk will demonstrate a novel PoC assay combining multicolored QDs and magnetic separation for real-time analysis without complex equipment, enabling low-cost, rapid diagnostics.
Applications span clinical diagnostics (chronic diseases), environmental monitoring (pathogens/toxins), and personalized medicine, demonstrating QDs' versatility as high-performance fluorescent nanoprobes. The talk bridges fundamental nanoscience with translational applications, offering insights into next-generation QD-based technologies for early disease diagnosis and on-site monitoring. The talk will conclude with future directions in scalable nanomaterial engineering, multiplexed PoC systems, and AI-integrated biosensing, underscoring QDs' transformative role in healthcare solutions.

Adaptive Adhesion through Bio-Inspired Interlocking Micropatterns for Harsh Environments

Wednesday, 17th September - 10:45: Oral Session 2D: Information Communication Technologies (Seminar Room) - Oral - Abstract ID: 376

Mr. Marco Bruno [1], ***Mr. Luigi Portaluri*** [2], ***Prof. Massimo De Vittorio*** [3], ***Prof. Stanislav Gorb*** [4], ***Prof. Michele Scaraggi*** [3]

1. *Istituto Italiano di Tecnologia (IIT),* ***2.*** *Department of Innovation Engineering, University of Salento, Lecce, LE, 73100, Italy,* ***3.*** *Center for Biomolecular Nanotechnologies, Istituto Italiano di Tecnologia (IIT), 73010 Arnesano, LE, Italy,* ***4.*** *University of Kiel*

Adhering in harsh conditions, such as wet, dusty, or low-surface-energy environments, is essential for technologies in surgery, robotics, and aerospace. Biological systems achieve this through surface structures that enable interlocking via friction and stored elastic energy. This study introduces a nature-inspired, reversible adhesion strategy, validated experimentally and theoretically, offering reliable alternatives where standard adhesives fail.

Single-Charge Detection in a Room Temperature Single-Electron Memory

Wednesday, 17th September - 11:00: Oral Session 2D: Information Communication Technologies (Seminar Room) - Poster - Abstract ID: 180

Mr. Jingbo Chen [1], ***Dr. Wenkun He*** [1], ***Mr. Kai-Lin Chu*** [1], ***Dr. Mervyn Jones*** [1], ***Prof. Zahid Durrani*** [1]

1. *Imperial College London*

A room-temperature (RT) single-electron memory cell in silicon, with one, or a few, electrons/bit, is demonstrated. The device uses two RT dopant atom quantum dot single-electron transistors (SETs), with one SET used to trap charge on a nanoscale memory node via the Coulomb blockade effect, and the other to sense this with single-electron precision. The memory cell is fabricated in silicon-on-insulator material via electron beam lithography. Memory operation is verified by measurement of single-electron charge hysteresis on the memory node, demonstrating RT single-electron memory operation.

Design and characterization of surface acoustic wave on thin film lithium niobate on insulator for acousto-optic applications

Wednesday, 17th September - 11:15: Oral Session 2D: Information Communication Technologies (Seminar Room) - Poster - Abstract ID: 392

Ms. Fatemeh Arefi [1], ***Dr. Ivan Prieto*** [1], ***Mr. Florian Hartmann*** [2], ***Mr. Silvan Stettler*** [2], ***Dr. Homa Zarebidaki*** [1], ***Mr. Hamed Sattari*** [1], ***Dr. Dara Bayat*** [1], ***Prof. Guillermo Villanueva*** [2], ***Dr. Michel Despont*** [1]

1. *CSEM,* ***2.*** *NEMS, EPFL*

This study investigates optimizing surface acoustic waves (SAWs) on X-cut LNOI for acousto-optic applications by analyzing Rayleigh and shear horizontal modes and tuning key design parameters to enhance SAW device performance.

Nanofabrication of shadow masks for josephson-junction quantum devices

Wednesday, 17th September - 11:30: Oral Session 2D: Information Communication Technologies (Seminar Room) - Oral - Abstract ID: 345

Dr. Rucha Deshpande [1], ***Prof. Rafael Taboryski*** [1], ***Prof. Thomas Sand Jespersen*** [1], ***Dr. Sabbir Ahmed Khan*** [2]

1. *Technical University of Denmark,* **2.** *Danmarks Nationale Metrologiinstitut*

We demonstrate new material platform based on poly-Si shadow masks for insitu post processing of III/V nanowires (InAs) used for josephson-junction quantum devices. Poly-Si material allows for high-aspect ratio and sub-100 nm feature sizes, suitable for shadow patterns. It allows for cleaner interfaces by elimination of resist type residues, which supports the purity required for quantum device processes.

Oral Session 3A: UV, EUV, and two-photon lithography

EUV interference lithography at PSI: pushing the limits of resolution of next generation photolithography

Wednesday, 17th September - 13:30: Oral Session 3A: UV, EUV, and two-photon lithography (Plenary Hall) - Oral - Abstract ID: 355

Dr. Dimitrios Kazazis [1], ***Mr. Benjamin Bächtold*** [1], ***Mr. Stephan Maag*** [1], ***Mr. Marco Schneider*** [1], ***Mr. Achim Ammon*** [1], ***Mr. Emanuele Japichino*** [1], ***Mr. Lars Heller*** [1], ***Mr. Thierry Lachat*** [1], ***Mr. Michael Peters*** [1], ***Mr. Peter Heimgartner*** [1], ***Mrs. Michaela Vockenhuber*** [1], ***Mr. Markus Kropf*** [1], ***Mr. David Piguet*** [1], ***Dr. Yasin Ekinci*** [1], ***Dr. Iacopo Mochi*** [1]

1. *Paul Scherrer Institute (PSI)*

Building on 20+ years of research, PSI is advancing EUV interference lithography with a new tool offering excellent thermal and mechanical stability. It aims to push resolution beyond the state of the art, enabling advanced materials development for high and hyper NA EUV lithography as well as soft X-ray wavelengths.

Towards sub-nm roughness in 3D topography for reflective X-ray focusing optics

Wednesday, 17th September - 13:45: Oral Session 3A: UV, EUV, and two-photon lithography (Plenary Hall) - Oral - Abstract ID: 351

Dr. Giulia Malvicini [1], ***Prof. Helmut Schift*** [1]

1. *Paul Scherrer Institute (PSI)*

Fabricating ultra-smooth, 3D surfaces for X-ray and EUV optics remains challenging, as these components require surface roughness below 1 nm to minimize scattering losses. We present a grayscale lithography process using scanning-laser direct write lithography (DWL) to pattern 100 µm-thick mr-P 22G_XP photoresist. This method enables complex sloped geometries but introduces artifacts from dose quantization and field stitching. By maximizing GVs and applying an N-overlap exposure strategy, these artifacts are largely suppressed, achieving an RMS roughness of ~5 nm as measured by laser scanning confocal microscopy (LSCM) and confirmed by atomic force microscopy (AFM). AFM analysis showed ~2.3 nm RMS roughness in unexposed resist and ~4.5 nm in exposed regions, with residual roughness attributed to the intrinsic properties of the Novolak-based resist. To further reduce roughness, resist patterns were transferred into PMMA using nanoimprinting, followed by selective thermal reflow at 110°C. This process decreased RMS roughness by 2 nm without altering slope geometry, demonstrating a pathway toward sub-nm surface quality. The combined approach of optimized exposure and post-processing offers a scalable route to produce large-area, freeform optical components suitable for EUV and soft X-ray focusing applications.

Quantifying and overcoming wafer distortion on bonded wafers for deep-UV lithography

Wednesday, 17th September - 14:00: Oral Session 3A: UV, EUV, and two-photon lithography (Plenary Hall) - Oral - Abstract ID: 125

Dr. Jeroen Bolk [1], ***Dr. Sander Reniers*** [1], ***Mr. Stacey Martina*** [1], ***Dr. Sara Sequeira*** [1], ***Ms. Sruja Dave*** [1], ***Prof. Kevin Williams*** [1], ***Dr. Yuqing Jiao*** [1]

1. *Eindhoven University of Technology*

To enable low-cost and high-yield manufacturing, fabrication methods of InP membrane photonics need to adopt industrial lithography methods. This transition requires to be performed without sacrificing the required resolution and overlay, while addressing membrane specific-challenges such as front- to back-side overlay, membrane bonding accuracy, and distortion. In this work, we present the efforts to quantify and mitigate these challenges to enable a route towards membrane technology with wafer-scale, 193 nm ArF projection lithography.

Pushing the Boundaries: in situ Development and Multi-Material Exchange for Two-Photon 3D Printing

Wednesday, 17th September - 14:15: Oral Session 3A: UV, EUV, and two-photon lithography (Plenary Hall) - Oral - Abstract ID: 77

Mr. Pratyaksh Yemulwar [1], ***Mr. Man-Ho Wong*** [1], ***Mr. Saurabh Karle*** [1], ***Mr. Josua Zschleile*** [1], ***Dr. Robert Kirchner*** [1]

1. *HETEROMERGE Gmbh*

Three-dimensional (3D) laser micro- and nano-printing has advanced dramatically over the last two decades, from a theoretically appealing novelty to a durable, flexible, financially viable, and widely used technology. Originally developed as a scientific curiosity, it has now become a mainstay in a variety of sectors due to its dependability and adaptability [1]. It has a wide range of applications, including but not limited to 3D photonics, individual micro-optics, complete micro-optical systems, and 3D-printed micromachines. One of its distinguishing aspects is the ability to combine different materials into a single printing process improving the utility and flexibility the technology. This latest feature is especially important for the development of composite materials, digital ("voxelated") materials, multi-material devices, and structures with customizable characteristics adapted to specific applications. [2, 4].

In this study, we aimed to advance the state-of-the art by fabricate with more than two materials, as well as to introduce an in situ rinsing (development) step in between the exchange of one material to another. This will support more diverse material combinations with even more stable structures. The technology base is a new, new version of a multi-material exchange system (MergeOne, HETEROMERGE GmbH) [3] in conjunction with a PP GT2 3D micro-nano-printer (Nanoscribe GmbH & Co KG). We used commercial three different materials and a solvent in one single print-run (IP-PDMS: Nanoscribe; MXpure: HETEROMERGE, isopropanol: MERCK).

We created microstructures with diameters of roughly 200 µm diameter and 100 µm height using material combinations with significant difference in viscosity (IPA: 2.1 mPas, IP-PDMS: 100 mPas, MX535: 900 mPas) and properties (hydrophobic vs. hydrophilic). Using the multi-material exchange system (as shown in Fig. 1), we conducted a thorough examination of structure evolution during the exchange process. Our findings gave important insights into the real-time exchange phenomena that occur during the two-photon polymerization (2PP)-based 3D printing process. We have tested various complicated designs to better understand flow behavior and structure formation. This helped to establish a technique for universally removing material from the deadzone of the microstructure (Fig. 2) during the exchange process, which was not possible without solvent rinsing process before. This significantly improved the multi-material printing for those distinct materials. Dead-zones in the vicinity of the microstructure, particularly in regions upstream and downstream of the flow direction is eliminated thus providing proper and non-contaminated exchange of materials (Fig. 3).

Typical parameter settings are about 200 mbar for IP-PDMS, 300 mbar for MXpure, 60 mbar IPA injection as well as for -100 mbar for IP-PDMS, -100 mbar for MXpure, and -100 mbar for IPA volume synchronized removal. Typical process times varied between. 10 to 15 min for one material exchange step (e.g. IP-PDMS vs IPA or IPA vs. MXpure). This has to be compared to about 60 min of process time of standard manual process (MXpure printing, 30 min IPA development, IP-PDMS printing, 30 min IPA development). This provides an improvement of a factor of ten just on the development process using the novel three-channel print-head. The consumed IPA volume is below 5 ml compared to 2x20 ml for a manual process, providing a factor of 40 improvement strongly supporting sustainable processing. Based on our observations, strategies and recipes for the multi-material printing are developed for an efficient printing of composite structures.

[1] A. Jaiswal et al., iScience 26(4), (2023) 106374.

[2] Y. Gao et al., SPIE (2021).

[3] R. Kirchner et al., in Proc. SPIE PC12412 (2023), PC1241206.
[4] P. Yemulwar et al., J VAC SCI TECHNOL B 43(2), (2025) 022602.

Oral Session 3B: Advanced Nanofabrication I

Fabrication of arsenic-in-silicon single-electron transistors using scanning tunnelling microscopy hydrogen resist lithography

Wednesday, 17th September - 13:30: Oral Session 3B: Advanced Nanofabrication I (Charnock Lecture Theater) - Oral - Abstract ID: 420

Dr. Kieran Spruce [1], ***Mr. Rajath Ravichandar*** [1], ***Dr. Patrick See*** [2], ***Dr. Mark Buitelaar*** [1], ***Dr. Taylor Stock*** [1], ***Prof. Neil Curson*** [1]

1. *University College London,* ***2.*** *NPL*

Silicon devices incorporating single dopant atoms as the active components have applications in quantum computing where the dopants provide electron or nuclear spin qubits, or quantum simulators where the dopant atoms are used to create artificial lattices. Scanning tunnelling microscopy hydrogen resist lithography (STM-HRL) makes it possible to fabricate such devices, and historically all such devices have been made using phosphorus-in-silicon. Recent studies, however, have found that the dopant arsenic shows superior incorporation precision (~97%) and placement accuracy [1], compared to phosphorus (~70%) [2], with the implication that arsenic-in-silicon is more suitable for scaling to large numbers of single atom devices.

This work demonstrates the first successful implementation of atomically precise arsenic-in-silicon device fabrication using STM-HRL. We have fabricated and measured the first arsenic-based quantum dot single-electron transistors (QD SETs), and in so doing we have developed new fabrication strategies that form part of our developing process for creating scalable atomic-scale quantum devices in silicon. We have advanced the general STM-HRL device fabrication methodology in two ways. Firstly, we have developed a novel three-way SET architecture, see Figure 1 upper panel, that enables comparison of multiple tunnel junctions with identical fabrication parameters, all within a single device structure, providing direct insights into electron transport characteristics such as gap resistance and dot capacitance. Secondly, we eliminate unwanted incorporation of arsenic atoms from the precursor gas arsine (AsH3) by introducing a pre-dosing step, of the phosphorus precursor gas phosphine (PH3), to block silicon adsorption sites where spurious arsenic dopants may be introduced into the surface.

Comprehensive electrical characterisation of the arsenic SETs, conducted in a dilution refrigerator at milli-Kelvin temperatures, revealed clear Coulomb blockade behaviour across all junctions, see Figure 1 lower panel. Our arsenic-based SETs achieved performance metrics comparable to similar phosphorus devices, with charging energies ranging from 8-19 meV and consistent lever arms of approximately 0.04. Gap resistances varied with junction geometry rather than dopant type, ranging from 1 to 40 MΩ. Notably, compared to phosphorus-based devices, the arsenic-based QD SETs reveal additional features in their Coulomb diamond measurements, including substructures within blockade regions that indicate electron tunnelling processes to/from near-by dopants.

The demonstration of an arsenic-in-silicon SET presented here, combined with the enhanced precision in dopant placement that arsenic offers, provides a robust foundation to scalable qubits, where each qubit is effectively an SET island consisting of a single atom. This work addresses critical challenges in quantum computing hardware development in silicon and presents a clear path toward higher-yield, more complex device architectures using multiple dopant precursors.

[1] T. J. Z. Stock et al., Advanced Materials, 36 (2024)

[2] J. A. Ivie et al., Phys. Rev. Applied 16, 054037 (2021)

Tailoring Vertical Gradients in Thin Films: Design and Fabrication

Wednesday, 17th September - 13:45: Oral Session 3B: Advanced Nanofabrication I (Charnock Lecture Theater) - Oral - Abstract ID: 10

Dr. Xiangyu Chen [1]

1. *Beihang University*

Differential laser sintering of multicomponent nanoparticles offers a versatile and cost-effective approach for fabricating high-performance gradient films, widely used in thermoelectric devices, mechanical components, and biosensors. However, spontaneous gradient formation hinders precise control over film composition and performance. This study introduces a novel gradient composition control method based on heavy nanoparticle composition ratios and develops a vertical energy distribution theory by integrating radiation and heat transfer theories. This approach provides technical and theoretical support for achieving high-lifetime gradient films with efficient processing.

Anti-virus performance of Si nanopillar array mimicking cicada wing surface

Wednesday, 17th September - 14:00: Oral Session 3B: Advanced Nanofabrication I (Charnock Lecture Theater) - Oral - Abstract ID: 14

Prof. Takeshi Ito [1], ***Dr. Hitoshi Ishiguro*** [2], ***Prof. Tomohiro Shimizu*** [1], ***Prof. Shoso Shingubara*** [1]

1. *Kansai University,* ***2.*** *Kanagawa Institute of Industrial Science and Technology*

Many researchers have been reported about the bactericidal and antibacterial effects of nanostructures. On the other hand, there are few reports regarding their effects on viruses. In this study, we fabricated Si nanostructures and evaluated their anti-virus performance changing with their pitch and height. As the results, extremely high antiviral activity for influenza A was observed only when the pitch was 200 nm. Additionally, regarding the height, it was found that antiviral activity appeared when the height was 200 nm or more.

3D structured local thin film deposition by Micro Direct Atomic Layer Deposition (µDALP™)

Wednesday, 17th September - 14:15: Oral Session 3B: Advanced Nanofabrication I (Charnock Lecture Theater) - Oral - Abstract ID: 8

Mrs. Mira Baraket [1], ***Mr. Jesper Navne*** [2]

1. *ATLANT 3D,* ***2.*** *PhD*

Advancements in chemical and physical deposition techniques for thin films and coatings are paramount for academic research and industrial applications in many technologies such as electronics, energy, and MEMS. Recent trends point to deposition technologies that combine flexibility, scalability, and material versatility. While traditional methods like Chemical Vapor Deposition (CVD) and Atomic Layer Deposition (ALD) offer high-quality film deposition, they often face challenges in patterning, complex structure fabrication, and process adaptability. Overcoming these limitations typically requires additional pre- or post-processing steps (such as lithography), which increase both processing time and cost, limiting their efficiency for next-generation applications.

Here, we introduce Micro Direct Atomic Layer Processing (µDALP™), a novel, atmospheric-pressure, direct-write deposition technology that expands ALD into localized, high-precision thin film printing (Figure 1). Unlike conventional ALD, µDALP™ enables complex structured coatings and seamless material transitions. Moreover, it allows deposition in ambient pressure, eliminating vacuum-related throughput limitations, and eliminates the need for lithography for some applications, significantly enhancing scalability for industrial applications. In particular, µDALP™ allows 3D designs with sub-nanometer control over the thickness profile of the film (Figure 2), making structures such as gradients, wells, and combs accessible easily.

µDALP™ adaptability and versatility open new possibilities for designing, developing, and producing next-generation thin film-based devices. By leveraging µDALP™'s capability for pre-programming the print shape and material transitions during deposition, we significantly accelerate device validation and optimization, dramatically reducing R&D costs.

In this talk, we will present the key advantages of µDALP™ for disruptive devices, multi-material integration, rapid material discovery, and direct-write patterning of functional thin films.

Oral Session 3C: Sustainable Devices and Process Technology

Shaping of a bio-sourced AESO polymer for micro-encapsulation purposes

Wednesday, 17th September - 13:30: Oral Session 3C: Sustainable Devices and Process Technology (One Ocean Suite) - Oral - Abstract ID: 200

Ms. Estelle Lu [1], ***Mr. Bruno Bresson*** [2], ***Dr. Jacques FATTACCIOLI*** [1]

1. *CPCV, Département de Chimie, Ecole Normale Supérieure, PSL Université, Sorbonne Université, CNRS,* ***2.*** *Laboratoire Sciences et Ingénierie de la Matière Molle, ESPCI Paris*

This study explores the use of bio-based AESO coming from vegetal oil for microencapsulation via microfluidics. The focus is on the fabrication process and on the physicochemical properties of the particles, namely the permeability behavior. Results highlight AESO's potential as a sustainable materials with further tunable properties currently under investigation.

Layer-by-layer functionalization of cotton fabric for enhanced electrokinetic energy harvesting

Wednesday, 17th September - 13:45: Oral Session 3C: Sustainable Devices and Process Technology (One Ocean Suite) - Oral - Abstract ID: 111

Mr. Aditya Patwari [1], ***Dr. Chirodeep Bakli*** [1], ***Prof. Suman Chakraborty*** [1]

1. *Indian Institute of Technology Kharagpur*

In pursuit of renewable and sustainable energy solutions, we developed a bioinspired cotton-based device through layer-by-layer surface functionalization using PDADMAC and silica nanoparticles to enhance electrokinetic energy conversion. Mimicking the mechanism of plant transpiration, the device generates electricity via microscale, capillary-driven streaming potential, achieving twice the output compared to pristine cotton and enabling efficient, continuous operation without any external power input.

Process development for improved passivation in IBC Solar Cells

Wednesday, 17th September - 14:00: Oral Session 3C: Sustainable Devices and Process Technology (One Ocean Suite) - Oral - Abstract ID: 43

Mr. Jens Munk Nielsen [1], ***Dr. Rasmus Schmidt Davidsen*** [2], ***Prof. Stephan Sylvest Keller*** [1]

1. *National Centre for Nano Fabrication and Characterization, DTU Nanolab, Technical University of Denmark,* ***2.*** *Department of Electrical and Computer Engineering, Aarhus University*

Our study focuses on optimizing the dielectric passivation stack in our interdigitated back contact (IBC) solar cells. We achieved a low surface recombination velocity of 1.86 cm/s with a symmetrical Al_2O_3 and a:SiNx:H stack indicating promising results towards efficient solar cells

Inkjet printing of stealth nanobeacons

Wednesday, 17th September - 14:15: Oral Session 3C: Sustainable Devices and Process Technology (One Ocean Suite) - Oral - Abstract ID: 30

Dr. Akinobu Yamaguchi [1], ***Dr. Toshiya Yasunaga*** [2], ***Prof. Kyoko Namura*** [3], ***Prof. Motofumi Suzuki*** [3], ***Mr. Takao Fukuoka*** [3]

1. *Toyo University,* ***2.*** *Aichi Gakuin University,* ***3.*** *Kyoto University*

Counterfeit and imitation products are becoming a significant problem with the rise of e-commerce. Counterfeit medicines pose health risks and will endanger life. To fight counterfeiting, various anticounterfeiting technologies have been suggested and developed. Apart from anticounterfeiting, there are also proposals to tack products to conduct market research, recycle materials and hold products accountable. This trend is known as digital product passporting, and there is demand for research and development of technology to attach mechanisms to products for covert tracking.

Recently, to achieve the combat the counterfeiting and digital product passporting, microtaggants and RFID have attracted much attention. Among them, we have developed stealth nanobeacons composed of self-assemblies of colloidal gold nanoparticles with reporter molecules. These stealth nanobeacons produce characteristic surface-enhanced Raman scattering (SERS) signals with long-term stability. [1, 2] The distinguishable SERS signals can be rapidly detected. If a stealth nanobeacon can be inked and printed, it can carry a great deal of information and can be incorporated into authentication systems related with the anticounterfeiting and digital product passporting etc.

Here, we prepared an ink by mixing normal inkjet printing ink with the stealth nanobeacons. Using a special inkjet printer, we print it and evaluate the print characteristics. Stealth nanobeacons were prepared by mixing 4, 4'-bipyridine (4bpy) with gold nanoparticles that had been prepared via a citric acid reduction of an aqueous gold chloride solution. Nanobeacons are gold nanoparticle aggregates with indefinite shapes that are dispersed in a metastable state in solution. Figure 1 shows a typical absorption spectra of nanobeacons with various shpaes: (i) relatively dispersive, (ii) chain-like structure, and (iii) flocculated agglomerate. There may be cases in which the nanobeacons form clusters with each other or the nanobeacons are larger in size. In this study, the ultrasonic oscillating element homogenizer NR-50M (Microtec Co., Ltd, Chiba, Japan) was used for 10 min, as schematically shown in Fig. 2. Two solution types containing the adjusted stealth nanobeacons were prepared: 1) Stealth nanobeacon solution with no treatment: ultrapure water = 1:1, and 2) Stealth nanobeacon homogenized solution: ultrapure water = 1:1. In addition, we also prepared inks by mixing the yellow and magenta inks from a commercial inkjet printer with the homogenized stealth nanobeacon solution at a ratio of 1:1. Inkjet printing was performed using a special inkjet printer. The spatical districation of the SERS signal varied based on the printing conditions were investigated by a Raman microscopy. The printing conditions for the inkjet printer were set at a 15 μm nozzle diameter, a 20 V discharge voltage, and a 1 kHz cycle rate, and the number of shots (i.e., the number of times that a spot is printed) was adjusted. All inkjet printing experiments and observation evaluations were conducted at room temperature in atmospheric air.

Figure 3 shows comparison of inkjet printed surface of a paper with various number of shots N = (a) 100, (b) 50, (c) 30, and (d) 10 to examine the dependence of the printing characteristics on N. By comparing the opitcal photographs in Figs. 3(A) and 3(B), it was found that the shapaes of the printed dots can be discerned when N is 10. As the number of shots increases, the dot shape structures can no longer be distingushed. The results of microscopic Raman mapping at 1600 cm^{-1} peaks of the SERS signal from the nanobeacon shown in Fig. 3(C). Comparing these results with and without homogenising treatment, it was found that the homogenised ink was spatially more uniformly dispersed. Inkjet printing was also possible for mixed inks with yellow and magenta inks. It was found that SERS signals could be detected from these prints even with a simple portable Raman spectrometer with low sensitivity. In addition, it was found that even with a tenfold dilution of the nanobeacon

concentration, the SERS signal could be detected by micro Raman spectral mapping, as shown in Fig. 3(D). Successful inkjet printing of nanobeacon-containing inks. This shows promise for development into a new information tracking system.

This work was supported by Innovative Science and Technology Initiative for Security Grant Number JPJ004596, ATLA, Japan.

[1] T. Fukuoka, T. Yasunaga, K. Namura, M. Suzuki, A. Yamaguchi, Advanced Materials Interfaces (2023) 2300157.
[2] T. Fukuoka, T. Yasunaga, K. Namura, M. Suzuki, A. Yamaguchi, Sci. Rep. 12 (2022) 985.

Oral Session 3D: Devices and Systems

Selective Laser Etching as a Key Enabler of Custom Silica-Based AFM Probes

Wednesday, 17th September - 13:30: Oral Session 3D: Devices and Systems (Seminar Room) - Poster - Abstract ID: 185

Mr. koutayba saada [1], ***Mr. david bourrier*** [1], ***Ms. Juliette Lignieres*** [1], ***Dr. Etienne Dague*** [1], ***Dr. Laurent Malaquin*** [1]

1. *LAAS-CNRS, Université de Toulouse, CNRS, Toulouse, France*

We demonstrate the 3D manufacturing of silica-based AFM probes using Selective-Laser-Etching. Functional cantilevers with thicknesses ranging from 50 µm down to 1 µm and spring constants ranging from 0.02 N/m to 85 N/m were successfully fabricated. These probes were validated for high-resolution surface imaging and mechanical characterization of biological cells.

Scalable Piezo-Optomechanical Transducer for Optical Readout of a Superconducting Qubit

Wednesday, 17th September - 13:45: Oral Session 3D: Devices and Systems (Seminar Room) - Poster - Abstract ID: 97

Dr. Linh Nguyen [1]

1. *QphoX*

Quantum computing is rapidly advancing, with superconducting qubits being strong candidates despite scaling challenges due to cryogenic space limits. This work introduces a compact, bidirectional microwave-to-optics quantum transducer that connects microwave and optical photons through a mechanical resonator. Using a demolition readout technique, we achieve a single-shot optical readout fidelity of 81%. Our results show the potential of piezo-optomechanical transduction to overcome cryogenic constraints, offering a viable approach for low-dissipation operation of large quantum processors.

Nonlinear resonators based on nano optomechanical metamaterials

Wednesday, 17th September - 14:00: Oral Session 3D: Devices and Systems (Seminar Room) - Oral - Abstract ID: 336

Ms. Ting Hou [1], ***Mr. Lifeng Bao*** [1], ***Dr. Jun-Yu Ou*** [2], ***Dr. Xin Zhou*** [3], ***Prof. Nobuhiko Nishiyama*** [4], ***Dr. Yoshishige Tsuchiya*** [1]

1. *University of Southampton,* ***2.*** *Physics and Astronomy, University of Southampton,* ***3.*** *Université de Lille,* ***4.*** *Institute of Science Tokyo*

We present a novel nonlinear optomechanical resonator integrated with nanophotonic metamaterials, aiming to enhance the transduction efficiency of nanoscale mechanical motion and to investigate its nonlinear dynamic characteristics. Nonlinear dynamics are demonstrated through reflective optical amplitude–frequency responses under varying excitation voltages.

Carbon-based contacts for integrated nanoelectromechanical switches

Wednesday, 17th September - 14:15: Oral Session 3D: Devices and Systems (Seminar Room) - Oral - Abstract ID: 33

Dr. Jens Bolten [1], ***Mr. Bartos Chmielak*** [1], ***Ms. Lisa Ehlert*** [1], ***Dr. Elliott Worsey*** [2], ***Ms. Yingying Li*** [3], ***Prof. Frank Niklaus*** [3], ***Prof. Dinesh Pamunuwa*** [2], ***Dr. Simon Bleiker*** [3], ***Prof. Max Lemme*** [1]

1. *AMO GmbH,* ***2.*** *University of Bristol,* ***3.*** *Royal Institute of Technology (KTH)*

We present the fabrication of nanoelectromechanical (NEM) switch contacts using nanocrystalline graphite (NCG) on a commercial back-end-of-line (BEOL) foundry platform.

A tailored plasma-enhanced vapor phase deposition (PECVD) process was developed to achieve selective NCG deposition, maximizing material thickness at contact areas while minimizing it elsewhere. Subsequently, a two-step inductively coupled plasma reactive ion etching (ICP-RIE) process was employed to precisely remove unwanted NCG, preserving the desired contact layer thickness.

Initial characterization of the fabricated NEM switches demonstrates device functionality, validating our proposed fabrication methodology. Detailed descriptions of the optimized deposition process and etching strategy are provided.

Poster Session 2

Auxiliary-Ring-Assisted Fabrication of Hard X-ray Photon Sieves with Low Resist Wettability

Wednesday, 17th September - 15:00: - Poster

Mr. Qiucheng Chen [1], ***Ms. Qingxin Wu*** [1], ***Mr. Hao Quan*** [1], ***Ms. xunjia Zhao*** [1], ***Mr. Jinyu Guo*** [1], ***Ms. Kangping Liu*** [1], ***Prof. Yifang Chen*** [1]

1. *Fudan university*

Photon sieves as diffractive optics are becoming more and more important for high-resolution hard X-ray imaging, offering design flexibility and compatibility with synchrotron beamlines. To enhance image contrast and suppress background noise, central and outer blocking layers are often applied. A straightforward approach is to define both the sieve and stop layers in a single lithographic step, but this can be limited by strong backscattered electron and extended writing time over large areas. Alternatively, two-step electron beam lithography often fails on dense, high-aspect-ratio gold structures due to poor resist wettability, leading to incomplete coverage (Fig. 2).

This work presents a ring-assisted two-step fabrication strategy to overcome these technical issues. A key innovation is the introduction of a 30 μm-wide gold auxiliary ring positioned concentrically around the photon sieve (Fig. 3). This low-aspect-ratio structure improves resist wettability and enables structural compatibility with overlay processing. By decoupling the high-resolution sieve patterning from the large-area stop layer definition, the second lithography step can be performed using a chemically amplified resist, significantly improving fabrication throughput. The specific fabrication steps are detailed as follows (Fig. 1).

In the first step, a 1.9 μm-thick PMMA resist (MW: 350 k) was spin-coated on a 100 nm-thick silicon nitride membrane and baked at 180 °C for 5 minutes. Electron beam lithography was performed at 100 kV with a 7 nm Gaussian beam and 500 pA current, using a dose of 1500 μC/cm². After development in MIBK:IPA (1:3) at 23 °C, gold was electroplated in a $K_3Au(SO_3)_2$ solution at 50 °C with a constant 3 μA current. The resist was stripped in acetone at 50 °C, yielding a photon sieve with a central stop. (Fig. 4(a-b))

In the second step, a 2 μm-thick UV5 resist was applied and prebaked at 115 °C for 90 seconds. Using the membrane edge for alignment, a second e-beam exposure was performed under the same beam conditions with a reduced dose of 30 μC/cm². Post-exposure bake and development were conducted at 115 °C and in TMAH:H_2O (1:8) for 60 seconds, respectively. A second gold electroplating step was then carried out under the same current, followed by resist removal in acetone at 50 °C. This method enabled successful overlay of the outer stop onto the photon sieve, despite the poor resist wettability on the high-aspect-ratio gold structures.

Using this method, a photon sieve with a minimum pillar diameter of 140 nm and a height of 1.8 μm was successfully fabricated (Fig. 5), and the overlay of blocking layers onto these low-wettability structures was reliably achieved. After the second exposure and development, the auxiliary ring and UV5 resist effectively protected the gold pillars (Fig. 4(c-d)). Notably, the process does not require conventional alignment marks; the membrane edge served as a reference, and the overlay error was effectively compensated by the auxiliary ring. Furthermore, the use of a chemically amplified resist for defining the large-area outer stop reduced the second exposure time to just 15 minutes, greatly enhancing fabrication efficiency without compromising accuracy.

In summary, the proposed auxiliary-ring-assisted two-step process enables accurate and efficient fabrication of photon sieves with integrated blocking layers, even on low-wettability, high-aspect-ratio structures. This method is fully compatible with existing lithography infrastructure and can be extended to other nanostructured devices requiring multilayer alignment and resist protection.

Electron beam-Simulation collaborative fabrication of zone plates with gradient duty cycle

Wednesday, 17th September - 15:00: - Poster

Ms. xunjia Zhao [1], ***Mr. Hao Quan*** [1], ***Mr. Qiucheng Chen*** [1], ***Ms. Qingxin Wu*** [1], ***Mr. Wentao Yuan*** [1], ***Mr. Shuoqiu Tian*** [1], ***Mr. Jinyu Guo*** [1], ***Ms. Kangping Liu*** [1], ***Prof. Yifang Chen*** [1]

1. *Fudan university*

Despite nanofabrication technology has advanced for X-ray Fresnel zone plates from hundreds nm of the outermost zone width down to sub-10 nm, extremely limited diffraction efficiency is still a big issue. For example, for the 100 nm resolution zone plate, the efficiency is merely around 5%. It has always been the bottle-neck to the technical development and applications of X ray microscopy as a whole because of the low efficiency. Enhance the resolution as well as the efficiency at the same time is urgently needed. The limited efficiency is generally caused by limited zone plate height, the zone material defects, the rectangular zone shape and the imperfection in nanofabrication.

This work tackles the efficiency issue by focusing on the duty circle ratio (the ratio of the outmost zone width/the air gap), which is one of the key factors in determining the efficiency. In the fabrication of gold-based Fresnel zone plates, systematic investigations into the mechanisms of duty cycle shift caused by imperfection in electron beam lithography (EBL) and e-beam resist thermal reflow were conducted, using the software of TRACER for electron trajectory simulation and LAB for resist profile modeling. This approach enables precise control and fabrication of zone plates with gradient duty cycles (1:1→4:1). Furthermore, employing the Beam Propagation Method (BPM) to simulate diffraction optical fields of zone plates with varying duty cycles reveals the influence mechanisms of duty cycle variations (within 1:1-5:1 range) on focal spot positions and focusing efficiency. Figure1 presents the fabricated 100 nm hard X-ray zone plates with 1.3 μm height and the 1:1 duty cycle. Figure 2 presents the zone plates with various duty cycle from 1:1 up to 5:1 for our experimental study of duty cycle dependent efficiency. Experimental verification is still underway and the results shall be presented elsewhere.

Room temperature Au-Au die bonding in ambient air via N_2 plasma treatment

Wednesday, 17th September - 15:00: - Poster

Prof. RYO TAKIGAWA [1], ***Mr. Yunhan Fan*** [1], ***Mr. Kosei Matsunobu*** [1]

1. *Kyushu University*

This presentation focuses on ambient room temperature Au-Au die bonding via N_2 plasma treatment for surface activation of Au thin film. In addition, its bond quality was investigated in details. The bond strength of over 68 MPa could be achieved, indicating the sufficient bond strength for device applications.

Simulation-guided interpretation of scanning electron microscope images

Wednesday, 17th September - 15:00: - Poster

Mr. Jianyao Jin [1], ***Dr. Timon Fliervoet*** [2], ***Dr. Kees Hagen*** [1]

1. *Delft University of Technology,* ***2.*** *ASML*

To reliably interpret scanning electron microscope (SEM) images, accurate knowledge is needed of the interaction of electrons with matter. The progressive miniaturization of semiconductor devices for example has increased the importance of such electron beam inspection and metrology technology. We have developed an open-source simulation tool, Nebula, intended to simulate SEM images. Although the tool contains the best possible physics models to describe the electron scattering in materials there is still room for improvement, for instance concerning the scattering of low energy electrons (< 100 eV). Low energy electron scattering is a significant contributor to SEM image signal, and may gain importance as SEM inspection tools work at lower energies, i.e. < 500 eV.

Manufacturing and testing of ultra-low expansion glass based planar frame resonator

Wednesday, 17th September - 15:00: - Poster

Mr. AHMAD ALI [1], ***Mr. Muhammad Awais Maqbool*** [1], ***Dr. Hamza Shakeel*** [1]

1. *School of Electronics, Electrical Engineering and Computer Science, Queen's University Belfast*

In this work, we demonstrated a wet etching method for fabrication of 500 µm thick ultra-low expansion glass based planar frame resonator. Fabricated resonator performed well in air with a quality factor of 3,416. The quality of surface can be improved by increasing the thickness of polysilicon masking layer.

Investigation of Intra-Level Mix-and-Match lithography approach in AR-N 7520new for use in a Mix-and-Match grayscale lithography process

Wednesday, 17th September - 15:00: - Poster

Mr. Markus Gottwald [1], ***Mr. Sebastian Schermer*** [1], ***Mr. Ritesh Ambar*** [1], ***Ms. Pia Kohlschreiber*** [1], ***Dr. Christian Helke*** [1], ***Mr. Harry Biller*** [2], ***Dr. Mandy Sendel*** [2], ***Dr. Danny Reuter*** [1]

1. *Fraunhofer Institute for Electronic Nano Systems ENAS,* ***2.*** *Allresist GmbH*

Intra-Level Mix-and-Match Lithography combines the advantages of multiple exposures types, in this case high-throughput i-line wafer stepper and high-resolution e-beam while mitigating their respective disadvantages. Augmenting this process to create 2.5D/3D structures via grayscale lithography has promising possibilities. We present results showing this strategy is viable in AR-N 7520new photoresist.

Influence of substrate properties and addition of oxygen on the process of reactive ion etching to optimize the nanopatterning of silicon structures

Wednesday, 17th September - 15:00: - Poster

Ms. Lenia Böhm [1], ***Ms. Pia Kohlschreiber*** [1], ***Mr. Micha Haase*** [1], ***Dr. Christian Helke*** [1], ***Dr. Danny Reuter*** [1]

1. *Fraunhofer Institute for Electronic Nano Systems ENAS*

This study investigates the influence of oxygen in the gas flow of the reactive ion etching process while additionally varying the utilized substrates which exhibit different crystal orientations and electrical resistivities. The aim is to improve the quality of the fabricated structures by analyzing their line edge roughness and dimensions.

Interposer Interconnects: An Important Step For Research and Industry

Wednesday, 17th September - 15:00: - Poster

Dr. Omesh Kapur [1], ***Mr. Arvin Mallari*** [1], ***Dr. Anushka Gangnaik*** [2], ***Ms. Amanda Green*** [1], ***Dr. Ibrahim Sari*** [2], ***Mr. John Darlington*** [2], ***Dr. Liam Boodhoo*** [1]

1. *School of Electronics and Computer Science, University of Southampton, Southampton SO17 1BJ, United Kingdom,* ***2.*** *University of Southampton*

This work presents scalable fabrication processes for partial and through-hole interposers with integrated copper vias and redistribution layers. Designed for academic and industrial use, the platform enables UK-based research in advanced semiconductor packaging, supporting system-level interconnect studies and bridging the gap between device fabrication and 2.5D/3D integration.

Nanofabrication of monolithically integrated multilayer metasurfaces via fully CMOS-compatible processes

Wednesday, 17th September - 15:00: - Poster

Mr. Yuntian Ye [1], ***Mr. Hao Peng*** [1], ***Dr. Shengqi Yin*** [2], ***Prof. Jize Yan*** [3], ***Dr. Kian Shen Kiang*** [2], ***Dr. Xu Fang*** [1]

1. *School of Electronics and Computer Science, University of Southampton, Southampton SO17 1BJ, United Kingdom,* ***2.*** *Optoelectronics Research Centre, University of Southampton, SO17 1BJ, UK,* ***3.*** *University of Southampton*

We have developed a novel metasurface stacking methodology that is fully compatible with standard Complementary Metal-Oxide-Semiconductor（CMOS） processes, advancing the mass production and commercialization of metasurface technologies.

Single-Printed Nb2O5 UV-Visible Metasurfaces for Chiro-Optical Holography

Wednesday, 17th September - 15:00: - Poster

Ms. Eunji Lee [1], ***Prof. Junsuk Rho*** [2]

1. *POSTECH,* ***2.*** *Pohang University of Science and Technology*

A single-step nanoimprint process using Nb_2O_5-based particle-embedded resin enables scalable fabrication of UV–visible metasurfaces. Fine-tuned nanoparticle concentration and process conditions ensure high-fidelity pattern transfer. The approach supports broadband phase modulation and spin-selective holography, offering a practical route to printable chiral photonic devices for applications such as secure optical encryption.

Keywords:
UV-visible metasurface, nanoimprint lithography, particle-embedded resin, metasurface encryption, particle swarm optimization, chiro-optical holography

Plasma-induced periodic surface structures on polymeric microfluidic channel sidewalls

Wednesday, 17th September - 15:00: - Poster

Dr. Athina S. Kastania [1], Ms. Eleni Stai [1], Mr. Sotiris Mouchtouris [1], Dr. Vassilios Constantoudis [1], Prof. George Kokkoris [2], Dr. Pavlos Tsavalas [3], Dr. Konstantina Mergia [3], Dr. Gerburg Schider [4], Mr. Daniel Borstner [4], Mr. Philipp Melchior [4], Dr. Dieter Nees [4], Dr. Barbara Stadlober [4], Dr. Evangelos Gogolides [1], Dr. Angeliki Tserepi [1]

1. *NCSR Demokritos, Institute of Nanoscience & Nanotechnology, P. Grigoriou 27 & Neapoleos Str., 15341 Ag. Paraskevi, Greece,* ***2.*** *School of Chemical Engineering, National Technical University of Athens, Athens, 157 80, Greece,* ***3.*** *NCSR Demokritos, Institute of Nuclear & Radiological Sciences and Technology, Energy & Safety, Ag. Paraskevi, 153 41, Greece,* ***4.*** *Joanneum Research Forschungsgesellschaft mbH, Weiz, 8160, Austria*

Plasma-induced surface roughness on polymeric surfaces perpendicularly placed on plasma electrode was recently investigated revealing periodic nanoripples converting to more isotropic patterns when moving upwards. Herein, imprinted polymeric microfluidic channels are plasma treated and the roughened sidewall surfaces form similar nanoripples, however covering most of the sidewall, exploitable in microfluidics.
Keywords: plasma etching, polymer substrates, microfluidic sidewalls, nanoripples, metrological analysis

Scalable Multilayer Silicon Anode Architecture with Porosity Control via UV-NIL Roll-to-Plate Process for Enhanced Lithium-Ion Battery Performance

Wednesday, 17th September - 15:00: - Poster

Ms. YU JU HAN [1], ***Ms. Seo Rim Park*** [1], ***Mr. Seong Min Yoon*** [1], ***Ms. Min Ju An*** [1], ***Prof. Yeon Guk Son*** [1], ***Prof. Young Tae Cho*** [1]

1. *Changwon National University, Changwon*

This study addresses the problems of volume expansion, nonuniform solid electrolyte interface (SEI) formation, and dendrite growth leading to performance degradation of silicon (Si)-based anodes in lithium ion batteries. A multilayer anode structure was developed using a roll-to-plate process based on UV nanoimprint lithography (UV-NIL), which is advantageous for large-area production. The anode consists of two layers. The first layer contains Si, carbon, and UV-curable resin for strong adhesion, and the second layer is fabricated by blending polyethylene glycol (PEG) and UV-curable resin and has a porous planar structure that suppresses dendrite growth. The porosity of the second layer was controlled by adjusting the molecular weight and mixing ratio of PEG. The battery cycle performance trend according to the porosity was analyzed, and it was found that the porosity reduced the dendrite formation. The relationship between the porosity and dendrite suppression was confirmed by scanning electron microscopy (SEM) analysis. This scalable approach provides a promising solution to improve the performance and safety of Si-based lithium ion batteries.

First results on vacuum-gas-controlled metal assisted chemical etching

Wednesday, 17th September - 15:00: - Poster

Mr. Bryan Benz [1], ***Ms. Vahide Hosseini*** [2], ***Dr. Georg Umlauf*** [2], ***Mr. Toni Sandbrink-Koblenz*** [3], ***Dr. David Anderson*** [3], ***Dr. Danny Reuter*** [2], ***Dr. Christoph Robert Meinecke*** [2], ***Dr. Lucia Romano*** [1]

1. *Paul Scherrer Institute (PSI),* ***2.*** *Fraunhofer Institute for Electronic Nano Systems ENAS,* ***3.*** *memsstar Ltd*

Metal assisted chemical etching of silicon is a plasma-free, local electroless etching method promising high aspect ratio nano-structuring capabilities in the gas-phase. The first results of a collaboration between Fraunhofer ENAS, Paul-Scherrer Institute and memsstar Ltd. are presented here, opening new opportunities for these innovative technologies for research and industry.

OPTIMIZING RETICLE BASED HIGH THROUGHPUT I-LINE GRAYSCALE PROJECTION LITHOGRAHPHY FOR 3D STRUCTURES

Wednesday, 17th September - 15:00: - Poster

Mr. Sebastian Schermer [1], ***Mr. Stephen DeMoor*** [2], ***Mr. Andrew Zanzal*** [2], ***Mr. Patrick Reynolds*** [2], ***Mr. Jens Bonitz*** [1], ***Mr. Jeremy Bieling*** [3], ***Dr. Christian Helke*** [4], ***Dr. Anja Voigt*** [5], ***Dr. Danny Reuter*** [4]

1. *Fraunhofer Institute for Electronic Nano Systems,* ***2.*** *Benchmark Technologies,* ***3.*** *Technische Universität Chemnitz,* ***4.*** *Fraunhofer Institute for Electronic Nano Systems ENAS,* ***5.*** *micro resist technology GmbH*

In this work a reticle based i-line projection grayscale lithography (3D fabrication process) is analyzed, and optimized to obtain low surface roughness grayscale pattern. The i-line grayscale exposure requires specialized reticles to vary the light intensity, thereby achieving different height levels in the resist layer. This work now focuses on process optimization of resist surface roughness after development, the dependency of pixel size and methods to reduce the surface roughness of grayscale patterns. The NIKON NSR2205i11D i-line stepper is used together with a specialized grayscale reticle from Benchmark Technologies.

Ion Beam Planarization using Low-Viscosity, Non-Volatile Containing Polymer Coatings

Wednesday, 17th September - 15:00: - Poster

Mr. Lukas Paul Lingenfelder [1]

1. *Leibniz-Institut für Oberflächenmodifizierung e.V. (IOM)*

This paper presents new developments for ion beam planarization of optical surfaces. In ion beam planarization, thin, usually polymeric, sacrificial layers are applied to the surfaces to be planarized. Subsequently, an ion beam etching step is used to transfer the levelled surfaces into the optical surface. In general, the smoothing effect decreases very strongly with the spatial wavelength of the roughness components. This is caused by the loss of solvent in the photoresist during the coating step.
It is shown how the smoothing effect can be significantly increased by using the solvent-rich nanoimprint resist Amonil and how larger spatial wavelengths can also be smoothed. The smoothing behavior is investigated for pre-structured Si wafers with line pattern of lateral structure sizes up to 450 µm and surface amplitude of 20 nm. The ion beam etching transfer is carried out with a broad beam ion source of the Kaufman type, whereby the influence of the etch selectivity (Si to photoresist) on the achievable degree of planarization is investigated. To further improve the planarization level and etch resistance of the resist UV flood exposure, pre-tempering, and post-tempering are examined.

The role of surface chemistry and morphology on adhesive wafer bonding

Wednesday, 17th September - 15:00: - Poster

Mr. Duarte Silva [1], ***Dr. Tarni Aggarwal*** [1], ***Dr. Yuqing Jiao*** [1], ***Dr. Martijn Heck*** [1]

1. *Eindhoven University of Technology*

Adhesive wafer bonding via ultra-thin DVS-BCB is a an attractive technique for heterogeneously integrated photonics. However, such regime becomes increasingly intolerant to particle contamination, and understanding and optimizing the bonding interface properties becomes paramount to ensure a high adhesion energy. In this work, we have studied different adhesive bonding layer stacks and we assess their effectiveness by monitoring defect sizes. Additionally, we perform XPS and AFM measurements of the surfaces to reveal the main contributors for adhesion. With our results, we demonstrate improved adhesion for rough and hydroxyl-rich surfaces, paving the way for improved bonding strength and higher quality bonds, particularly for ultra-thin DVS-BCB bonding.

Sub-diffraction-limited nano-texturing on silicon by ultrafast lasers with MHz- burst mode

Wednesday, 17th September - 15:00: - Poster

Mr. Pin-Yen Chen [1], ***Mr. You Yu-Sheng*** [2], ***Prof. Yuan-Jen Chang*** [3]

1. *National Taipei University of Technology, Department of Mechanical Engineering,* ***2.*** *National Taipei University of Technology, Graduate Institute of Manufacturing Technology,* ***3.*** *National Taipei University of Technology*

In this paper, we have proposed to utilize ultrafast lasers in burst mode and form sub-diffraction-limited nanostructures on silicon surfaces. We employed a technique of overlapping dual orthogonally polarized femtosecond laser beams. A minimum line width of 435.5 nm was achieved with direct laser machining.

Fabrication of Micro-Lattice Filters for Particulate and Gas Emission Reduction

Wednesday, 17th September - 15:00: - Poster

Ms. Seo Rim Park [1], ***Mr. Myung Seo Kim*** [2], ***Prof. Young Tae Cho*** [1]

1. *Changwon National University, Changwon,* ***2.*** *Changwon National University, Department of Mechanical Engineering*

Micro-lattice filters fabricated using DLP or metal FFF 3D printing were developed for diesel emission reduction. Utilizing CuO, Mn, and Pt catalysts, the filters exhibited high particulate matter capture and catalytic efficiency under low pressure drop. Their open-cell architecture enables stable operation, offering a compact alternative to conventional monolith-based systems for diesel generator applications.

Microfluidic Devices Based on Deterministic Lateral Flow Displacement for Protein Separation

Wednesday, 17th September - 15:00: - Poster

Ms. Nilüfer Tasli [1], ***Dr. Sadhana Tiwari*** [1], ***Dr. Irene Fernandez*** [2]

1. *UHH,* ***2.*** *UHH/CUI*

Deterministic lateral flow displacement (DLD) microfluidic devices enable efficient particle separation. In this work, chips are fabricated by photolithography and reactive ion etching, followed by direct UV imprinting. The microfluidic devices can separate beads by size and the beads can be functionalized, allowing precise and sensitive protein separation.

Evaluation of Inorganic-organic Hybrid Resist Materials with ultrafast coherent high harmonic generation (HHG) EUV system

Wednesday, 17th September - 15:00: - Poster

Dr. Hiroki Yamamoto [1]

1. *National Institutes for Quantum Science and Technology (QST)*

In the realization of patterning feature sizes of sub-10 nm in semiconductor devices, it is essential to get new resist design strategies such as inorganic-organic hybrid resist materials for extreme ultraviolet (EUV) lithography. However, it is challenging for fundamental researchers to develop EUV resist materials due to the difficulty in obtaining experimental time for EUV exposure and limited EUV exposure tools, which are very expensive. Recently, we developed ultra-fast coherent EUV system based on high harmonics generation (HHG) and applied to EUV resist evaluation. In this study, the sensitivity of inorganic-organic hybrid resist materials known as metal-oxo clusters was evaluated by using this HHG EUV system. The obtained sensitivities were found to be comparable to the sensitivities obtained by conventional EUV flood exposure tool. It is concluded that the developed coherent HHG EUV system is very useful for sensitivity measurement of EUV resists and developing new EUV resists.

Graphene Electrodes for In-plane Electrochemical growth of TMDCs

Wednesday, 17th September - 15:00: - Poster

Mr. Shaokai Song [1], ***Dr. Shibin Thomas*** [1], ***Dr. Nema Abdelazim*** [1], ***Dr. Sami Ramadan*** [2], ***Dr. Victoria Greenacre*** [1], ***Mr. Hongwei Zhang*** [1], ***Dr. Yisong Han*** [3], ***Prof. Richard Beanland*** [3], ***Prof. Gill Reid*** [1], ***Prof. Philip Bartlett*** [1], ***Prof. Kees de Groot*** [4], ***Dr. Yasir Noori*** [1]

1. *University of Southampton,* ***2.*** *Imperial College London,* ***3.*** *University of Warwick,* ***4.*** *School of Electronics and Computer Science, University of Southampton, Southampton SO17 1BJ, United Kingdom*

Short-channel effects in field-effect transistors have intensified interest in two-dimensional (2D) materials, particularly transition metal dichalcogenides (TMDCs), due to their potential to mitigate these effects. A significant challenge in TMDC-based transistors is the high contact resistance at metal-semiconductor interfaces, often attributed to van der Waals interactions between layers. Electrodeposition emerges as an industrially compatible technique offering unique advantages for scaling 2D heterostructures. We designed and transferred novel patterns onto graphene substrates, enabling lateral electrodeposition of TMDCs. Through iterative optimization of fabrication processes, including lithography, lift-off, and etching—we overcame challenges related to pattern fidelity and material compatibility. High-quality graphene substrates have beenprepared for subsequent TMDC deposition. Our next step involves utilizing these graphene electrodes to deposit various TMDCs and their heterojunctions, aiming to explore diverse applications. Additionally, we have mastered mechanical exfoliation techniques to fabricate comparable transistors, providing benchmarks for evaluating the performance of our electrodeposited structures.

A Technique for Simultaneous Embedding and Welding of Metal Nanowires on Polymer Surfaces for Flexible Conductors

Wednesday, 17th September - 15:00: - Poster

Mr. sangmok Kim [1], ***Mr. Youngjae Nam*** [1], ***Prof. Joonwon Kim*** [1]

1. *Pohang University of Science and Technology*

We present a fabrication technique for flexible electrodes, in which AgNWs are simultaneously welded and embedded into a PDMS matrix, achieving high conductivity and mechanical robustness through junction welding and mechanical interlocking. This approach is suitable for pressure sensors requiring stable operation under repeated pressure and EMI.

Fabrication of a superhydrophobic surface with partially superhydrophilic regions and surface free energy comparison

Wednesday, 17th September - 15:00: - Poster

Mr. Takuto Wakasa [1], ***Prof. Jun Taniguchi*** [1]

1. *Tokyo University of Science*

Inspired by the tenebrionid beetle, we fabricated a surface with superhydrophilic patterns on a superhydrophobic background using photolithography and UV-NIL. Contact angle measurements showed surface free energy is tunable by hydrophilic area ratio. Future work explores effects of pattern size and distribution at constant area ratio.

Design of an Antireflective Hierarchical Structure Based on Finite-Difference Time-Domain (FDTD) Simulation

Wednesday, 17th September - 15:00: - Poster

Mr. YAONIEN TSAI [1], ***Mr. YENEN JUAN*** [1], ***Mr. GUOCHEN NIEH*** [1], ***Dr. YEEUCHANG LEE*** [1]

1. *Chung Yuan Christian University*

This study, based on the wave optics of subwavelength structures, proposes a hierarchical structure that combines two periodicities 0.5 μm and 2 μm to form anti-reflective bands. FDTD simulations demonstrate that the hierarchical structure effectively suppresses higher-order diffraction and further reduces reflectance through Mie scattering and multiple internal reflection effects, thereby achieving low reflectance across a broad wavelength range.

Fabrication of Broadband Antireflection Hierarchical Micro/Nano Structures Using Colloidal Lithography

Wednesday, 17th September - 15:00: - Poster

Mr. YENEN JUAN [1], ***Mr. GUOCHEN NIEH*** [1], ***Mr. YAONIEN TSAI*** [1], ***Dr. YEEUCHANG LEE*** [1]

1. *Chung Yuan Christian University*

Single-scale subwavelength structures exhibit antireflective properties, their effectiveness is typically limited to specific wavelength ranges, making them unsuitable for broadband applications. In this study, we developed hierarchical micro/nano subwavelength structures using colloidal lithography to achieve high-efficiency, broadband antireflection performance spanning from the visible to the near- and mid-infrared spectral regions.

An e-beam lithographer's approach to evaluating a new HIMT DWL66+ direct laser writer for Mix&Match processes – resists, contrast curves, grayscale lithography, alignment, and developer test sticks

Wednesday, 17th September - 15:00: - Poster

Dr. Silvia Diewald [1], ***Prof. Gernot Goll*** [1]

1. *Karlsruhe Institute of Technology (KIT)*

Exposing a sample fast with high resolution and accuracy is a lithographer's dream (or at least for someone working at a service facility in a university setting catering mostly to master and PhD students demanding exactly that). Mix&Match processes which combine the high resolution and accuracy of e-beam lithography (EBL) with the speed of optical lithography (OL) in a single process run seem a natural fit. However, the time-consuming fabrication of masks for ever-evolving designs and the challenge to actually align EBL and OL exposures with sufficient precision seem to have hindered the wide-spread adoption in our facility.

Getting a new direct laser writer (DLW), a Heidelberg Instruments DWL66$^+$, literally installed two doors down will pique even the interest of the resident e-beam operator. So, intrigued by its 375 nm laser option for higher resolution, standard grayscale capabilities and higher speed (compared to its more than 20 years old predecessor), a vague (and in hindsight certainly naïve) idea formed to use a DLW in conjunction with EBL in Mix&Match processes to overcome some of the downsides of the SÜSS MA6 Maskaligner that was almost exclusively used for the OL part before. To test the feasibility of such an endeavor, several aspects have been investigated: EBL resists in DLW, OL resists for EBL, one-step patterning of alignment marks in the EBL exposure and their use as field alignment marks in the immediately following DLW step, potential of grayscale lithography (and ways to prevent visible stripe borders in the remaining resist), finding suitable developing recipes for the prevalent materials in the lab (and a handy tool, a "developer test stick", to simply monitor the correct ratio in diluted and self-mixed developers).

Direct data generation of wafer-scale metalens for e-beam exposure

Wednesday, 17th September - 15:00: - Poster

Ms. Yixuan Zhao [1], ***Dr. Kian Shen Kiang*** [1], ***Prof. Jize Yan*** [1]

1. *University of Southampton*

To avoid large-size files to store layouts, we developed a “MetalensGenerator” module using BEAMER scripts, which directly generates metalens layout data for e-beam exposure. The module generates and processes metalens patterns in .togobject format, eliminating the need for data format conversions and contributing to fabricating high-resolution, wafer-scale metalenses.

Impact of PEALD Temperature on Al_2O_3 Gate Dielectric of ZnO-TFTs

Wednesday, 17th September - 15:00: - Poster

Mr. Jiale Zeng [1], ***Dr. Ben Rowlinson*** [2], ***Dr. Omesh Kapur*** [1], ***Prof. Harold Chong*** [3]

1. *School of Electronics and Computer Science, University of Southampton, Southampton SO17 1BJ, United Kingdom,* ***2.*** *University of Edinburgh,* ***3.*** *University of Southampton*

Aluminium Oxide (Al_2O_3) is widely adopted as a gate insulator in both thin-film transistors (TFTs) and metal-oxide-semiconductor field-effect transistors (MOSFETs) due to its wide bandgap, low leakage current, excellent thermal stability, good interface quality, and moderate dielectric constant. Moreover, Al_2O_3 offers significant advantages for thermosensitive applications such as flexible electronics, transparent electronic devices and low-temperature oxide semiconductors, owing to its high compatibility with atomic layer deposition (ALD) processes and its ability to be processed at low deposition temperatures. The material quality of Al_2O_3 thin films deposited in isolation at different temperatures has been systematically investigated. However, studies focusing solely on Al_2O_3 thin films are often insufficient to reflect their impact on device platforms, as the overall improvement of device performance is essential for advancing their practical applications. Many studies employ post-annealing to enhance the Al_2O_3/semiconductor interface, though such high-temperature processes are incompatible with thermosensitive applications. Therefore, it is necessary to investigate how deposition temperature affects device characteristics within a suitable process window (150°C–300°C). This study provides experimental guidance for the process optimization of low-temperature oxide electronic devices.

Plasma-enhanced ALD of ultra-thin Al2O3 films for passivating contacts

Wednesday, 17th September - 15:00: - Poster

Ms. Yaxin Zhan [1], ***Dr. Ben Rowlinson*** [2], ***Prof. Harold Chong*** [1], ***Dr. Stuart Boden*** [1]

1. *University of Southampton,* ***2.*** *University of Edinburgh*

Discussions on using Al_2O_3 as a surface passivation material primarily focus on thicker layers, whereas the method required for achieving the surface cleanliness necessary for 1–2 nm deposition entails a complex cleaning procedure. This work proposes strategies that simplify the fabrication of dual-purpose Al_2O3 tunnelling barriers and passivation layers.

Inducing piezoelectricity in chitosan films by cathodic electrodeposition: challenging a new approach for wearable sensors' fabrication

Wednesday, 17th September - 15:00: - Poster

Ms. Valeria D'Errico [1], ***Dr. Gaia de Marzo*** [2], ***Dr. Antonio Qualtieri*** [1], ***Dr. Luciana Algieri*** [3], ***Prof. Massimo De Vittorio*** [1]

1. *Center for Biomolecular Nanotechnologies, Istituto Italiano di Tecnologia (IIT), 73010 Arnesano, LE, Italy,* ***2.*** *IDUN section, Department of Health Technology, Technical University of Denmark, DK-2800 Kongens Lyngby, Denmark,* ***3.*** *Department of Innovation Engineering, University of Salento, Lecce, LE, 73100, Italy*

Polymers appear as an interesting alternative to piezo-ceramics for applications in wearable sensors field. The present work focuses on chitosan, a bio-based polymer, exploring cathodic electrodeposition as a method to improve its piezoelectric properties and, at the same time, to get better control in chitosan films production.

Synthesis of novel EB resist based on KrF resist system

Wednesday, 17th September - 15:00: - Poster

Dr. Atsushi Sekiguchi [1]

1. *Litho Tech Japan Corporation*

As EB resists are mainly used to make photomasks, their usage is overwhelmingly smaller compared to semiconductor resists and resist manufacturers have not put much effort into their development for mass production such as KrF resists

On the other hand, EB exposure using direct writing is very important for device prototyping, because it allows maskless pattern formation. In this work, we try to synthesize EB resists using monomers that are the base of KrF resists. As shown in Fig.1, we use4-Ethenylphenol acetate (M1) as the base monomer, and we use 1-Ethylcyclohexyl methacrylate (M15) and tert-Butyl methacrylate (M18) as the protecting groups, respectively. By alternating the polymerization ratio of the monomers, monomers with different properties were synthesized and EB resists were produced by adding PAG to the synthesized polymers, where the PAG used in this work is generally known to be effective for even EB exposure system [1].

Figure 2 shows the sensitivity curves for KrF exposure of polymers with different polymerization ratios. Screening was performed in advance using KrF exposure to determine the optimal polymerization ratio.

Figure 3 shows the results of an electron beam exposure experiment on a material that showed relatively good properties when polymerized with KrF. The result shows that the synthesized resin is also be used for EB exposure.

In the presentation we will apply novel deep learning system to optimize polymerization ratio [2] and show the pattern formation performance in EB exposure using computational lithography investigations.

Nanofabrication of Large, Stitch-free Diffractive Optics

Wednesday, 17th September - 15:00: - Poster

Dr. Anna Casimiro [1], ***Dr. Sander Schellingerhout*** [1], ***Ms. Adriana Umbria*** [1], ***Dr. Kahraman Keskinbora*** [1]

1. *Raith Laser Systems B.V.*

Diffractive optics are ubiquitous in various applications from X-ray imaging to interferometric measurements. Their performance is tightly linked to the structural fidelity achieved during fabrication. Traditionally, these structures are created using direct-write lithography within a single writefield. However, when the desired size of the optical device exceeds the maximum writefield size of a particular fabrication method, the design has to be broken into sub-fields in a matrix form, each of which is exposed sequentially. This process introduces stitching artifacts in the xy-plane at the boundaries of each writefield compromising optical performance of the fabricated device [1].

In this work, we demonstrate a stitch-free fabrication method using a maskless laser beam lithography (LBL) tool with a split-stage exposure strategy. Unlike systems that rely on beam scanning, this approach keeps the laser beam stationary with respect to the optical axis and precisely moves the sample underneath using a synchronized motion of scan (y-axis) and step (x-axis) stages (Figure 1). In each pass of the scan stage, one column of pattern data is exposed. This strategy enables seamless exposure of entire patterns, effectively making the writefield as large as the pattern itself and consequently eliminates stitching artifacts.

We demonstrate the lack of stitching artifacts by doing extensive metrology on various types of diffractive structures including diffraction gratings, variable pitched gratings, and Fresnel Zone Plates (FZP) using a split-stage maskless LBL tool. Moreover, we compare the results of infinitesimal stitching artifacts (20-30 nm) that are intentionally introduced in control samples, to the samples that are 100 % stitch-free. This stitch-free exposure strategy has many benefits in applications where the structural quality is paramount. These applications include micro-diffractive optics or integrated photonic circuit elements such as waveguides where avoiding scattering losses induced by stitching is vital.

[1] M.Gnan et al., CLEO/Europe and IQEC 2007 Conference Digest, (Optica Publishing Group, 2007).

Secondary particle detection for deterministic single ion implantation

Wednesday, 17th September - 15:00: - Poster

Dr. Kristian Stockbridge [1], ***Dr. Ella Schneider*** [2], ***Dr. Gianfranco Arresta*** [1], ***Dr. David Cox*** [2]

1. *Ionoptika Ltd,* ***2.*** *University of Surrey*

For single ion implantation achieved via detection of secondary charged particles (SCPs), detection efficiency is limited by poor SCP yield and/or suboptimal detector arrangement. Decoupling these effects is needed to characterise exclusively the detector performance. Methods to enhance SCP yield and alternative detection methods exist for unavoidably poor yield materials.

Control of the Scanning Tunnelling Microscope Based on Hybrid Gain Integrator Systems (HIGS)

Wednesday, 17th September - 15:00: - Poster

Ms. Richa Mishra [1], ***Prof. S. O. Reza Moheimani*** [2]

1. *The University of Texas at Dallas,* ***2.*** *The Univeraity of Texas at Dallas*

Linear controllers, such as integral (I) control and proportional-integral (PI) control, have been widely employed to regulate the tunneling current in the scanning tunneling microscope (STM). Although several alternative control methodologies have been proposed in the literature, many lack accompanying imaging results to substantiate their efficacy [1]. Control of the STM Feedback loop based on a linear controller and striking a balance between a fast transient response and closed-loop stability robustness could be challenging [2], leading to a degradation of reference tracking performance. There has been a growing shift toward adopting nonlinear and hybrid control techniques to address the limitations of linear controllers. These advanced approaches could offer enhanced adaptability, improved dynamic performance, and greater robustness, without imposing excessive control effort.

We propose a novel STM z-axis feedback control method inspired by the Hybrid Integrator-Gain System (HIGS)-I control, as shown in Fig. 1(a). This control constitutes an advanced switching strategy that can surpass the performance limitations typically associated with classical linear control techniques [3]. Unlike conventional Linear Time-Invariant (LTI) integral action, which introduces a fixed phase lag of 90°, the HIGS approach imposes a reduced phase lag of approximately 38.15°, thereby contributing to improved phase margin and enhanced closed-loop stability robustness, as shown in Fig. 1(b). HIGS generates a continuous yet inherently non-smooth control signal by switching between integral and gain modes. By alternating between these two modes, HIGS-I effectively mitigates the detrimental effects commonly associated with pure integral action, such as pronounced oscillations near resonant frequencies, while ensuring system stability. The HIGS element is combined with LTI filters C1 and C2 to obtain a smooth control signal. The placement order of the filters is crucial for HIGS to function properly [3].

We conducted several experiments to investigate the efficacy of HIGS-I control compared to I-control. The results in Fig. 2 demonstrate the images obtained with both controllers on the same surface area. We observe higher oscillation levels in the topography and current signal profile data in Figs. 1 (a)-(b) (left) as compared to Figs. 2 (a)-(b) (right). We continued to scan the same area to demonstrate how a change of controller alters the tip behavior, as shown in a set of images in Figs. 3 (a)-(b) (left) where we change control from HIGS-I to I control. We observe that the tip starts to oscillate as the control changes to an I-controller, and an improved behavior is observed when the control is changed from I to HIGS-I control, as shown in Figs. 3 (c)-(d) (right). Another experiment we performed to compare the performance of HIGS-I control over I-control was to scan the surface at a higher scan speed of 500 nm/s, compared to the regular scanning speed of 200 nm/s. The scan data show much improved performance with the HIGS-I controller compared to when only I-control is implemented, as shown in Figs. 3 1(a) & (b) (left). By comparing all the results presented, we can conclude that HIGS-I is a competitive and superior control method compared to linear controls for z-axis control of STM, as it provides more stability and better tracking conditions, even at high scan speeds. From the perspective of designing the HIGS-I controller, we only need to tune the gain parameter once the rest of the parameters of the C1 and C2 filters are fixed. Within this frequency range, HIGS-I can provide sufficient phase margin even in the presence of unknown disturbances, unlike a PI controller, where two parameters will be required to tune to obtain a comparable phase margin.

Towards single-electron devices based on SOI silicon nanowires: simulation and fabrication

Wednesday, 17th September - 15:00: - Poster

Mr. Gabriele Petitto [1], ***Mr. Ziyin Sun*** [2], ***Dr. Jordi Antoja*** [2], ***Dr. Alberto del Moral*** [1], ***Dr. Albert Guerrero*** [3], ***Dr. Roser Mas*** [2], ***Dr. Alberto García-García*** [2], ***Prof. Joan Bausells*** [1], ***Prof. Francesc Pérez-Murano*** [1], ***Dr. Esteve Amat*** [1], ***Dr. Jordi Llobet*** [2]

1. *Institute of Microelectronics of Barcelona (IMB-CNM, CSIC),* ***2.*** *Institut de Microelectrònica de Barcelona, IMB-CNM (CSIC), Universitat Autònoma de Barcelona, Cerdanyola Del Vallès, 08193, Barcelona, Spain.,* ***3.*** *Instituto de Microelectrónica de Barcelona*

Silicon-on-insulator (SOI) nanowires are emerging as promising platforms for single-electron devices, leveraging long coherence times and compatibility with semiconductor fabrication techniques. This study combines advanced TCAD simulations with precision nanofabrication to develop and characterise SOI-based single-electron transistors. Fabricated test devices demonstrate the viability paving the way for advancements in quantum transport applications at the nanoscale.

A YOLOv8-Based Defect Inspection for Semiconductor

Wednesday, 17th September - 15:00: - Poster

Mr. Xiaolong Guo [1], Dr. Yanan Zhu [2], Mr. Heming Wu [3], Prof. Diwei Zhou [4], Prof. Zhuming Liu [2]

1. *School of Electronic Science and Engineering , South China Normal University,* ***2.*** *Institute of Semiconductors, Guangdong Academy of Sciences,* ***3.*** *Institute of Semiconductors, Guangdong Academy of Sciences,,* ***4.*** *School of Science, Loughborough University*

To address the challenges posed by increasingly smaller defect sizes, complex structural patterns, and elevated noise interference, we present an enhanced YOLOv8 model incorporating a novel hybrid loss function that combines Focal Loss and CIoU Loss. The proposed YOLOv8-based framework demonstrates significant potential for SEM defect inspection

Two-dimensional arrays of InAs nanodots grown on inverted pyramid Si templates

Wednesday, 17th September - 15:00: - Poster

Dr. Javier Bravo Larrea [1], ***Mr. David Bermudez*** [2], ***Mr. Lisandro Jofre*** [1], ***Dr. Paloma Tejedor*** [2]

1. *NAITEC,* ***2.*** *Instituto de Ciencia de Materiales de Madrid, CSIC, Madrid, 28049, Spain*

Our work study selective growth of InAs nanodots on Si inverted pyramids patterned by laser interference lithography and wet etching. Growth conditions, especially GaAs buffer layers and high As/III flux ratios, critically affect morphology, enabling defect-free nanodots while suppressing unwanted GaAs nanowires on specific Si facets.

EBIC measurement of the minority carriers diffusion length in a GaAs solar cell p-n junction

Wednesday, 17th September - 15:00: - Poster

Dr. Anya Grushina [1], ***Mr. Karl Boche*** [1]

1. *Imina Technologies*

This poster shows how electron beam induced current (EBIC) with calibrated signal acquisition can be used to measure the minority charge carrier diffusion length at the p-n junction of a solar cell. Our setup enabled us to calculate the diffusion length of minority charge carriers, amounting to 570 nm, which is within the expected range for such devices. We also estimate that the surface recombination velocity is close to zero, which suggests a low density of defects in the semiconductor layer of the solar cell.

Preparation of Regrowth Interfaces in AlGaN/GaN Heterostructures Using Atomic Layer Etching for Ohmic Contact Formation

Wednesday, 17th September - 15:00: - Poster

Dr. Aslanidis Evangelos [1], ***Dr. Adam Adikimenakis*** [1], ***Mr. Nikos Makris*** [1], ***Mr. Antonios Stavrinidis*** [1], ***Dr. George Konstantinidis*** [1]

1. *Microelectronics Research Group (MRG), Institute of Electronic Structure and Laser (IESL), Foundation of Research & Technology Hellas (FORTH), Crete 70013, Greece;*

Atomic Layer Etching (ALE) has emerged as a critical technique for achieving ultra-precise, damage-free surface modification in III-nitride semiconductor devices [1, 2]. In high-electron-mobility transistors (HEMTs) based on GaN/AlGaN heterostructures, the control of etch depth and surface quality is essential for subsequent epitaxial regrowth processes. This is particularly relevant in the formation of low-resistance ohmic contacts through selective regrowth of heavily doped n++ GaN in the source/drain access regions [3, 4]. Conventional dry etching techniques often introduce plasma-induced damage, surface roughness, and compositional changes which can degrade regrowth interface quality and device performance. ALE offers a promising alternative by enabling atomic-scale layer removal with minimal surface damage, thereby preserving the integrity of the underlying crystal structure and enabling high-quality regrowth.

While ALE has been explored for surface smoothing and damage mitigation in GaN devices, its targeted use as a regrowth interface preparation method for forming n++ GaN ohmic contacts remains largely unexplored. This work demonstrates a robust ALE-enabled etch technique, validated by atomic force microscopy (AFM) and Reflection high-energy electron diffraction (RHEED), that yields atomically smooth surfaces conducive to high-quality epitaxial regrowth for low-resistance ohmic contact formation. To investigate the ohmic contact a TLM sample was fabricated. The process flow begins with mesa isolation performed by BCl_3/Cl_2-based dry etching in an ICP-RIE system. A 250 nm silicon nitride (SiN) hard mask was then deposited via PECVD, followed by selective patterning using SF_6 plasma to define regrowth regions. To prepare the surface for regrowth, the GaN cap and AlGaN barrier layers were removed using an ALE etching technique. This technique was developed in a regular ICP-RIE tool and consisting of consecutive cycles of Cl_2 gas and low-energy Ar plasma sputtering. The Cl_2 gas reacts with the GaN surface creating Gallium chlorites [2] which can be easily removed by the low energy Ar ions. The etching was found to be around 3 monolayers of GaN per cycle (Figure 1a) and has very good synergy of 95.6%. The ALE process was selected for its ability to minimize surface damage while achieving high uniformity and smoothness suitable for epitaxial regrowth. The surface RMS roughness was measured by AFM and found 0.35 nm. The etching depth was carefully controlled to terminate just below the AlGaN barrier, enabling access to the 2DEG through the exposed sidewall. Without the ALE technique the precision of the etching depth and the smoothness of the etched surface will not be possible. The samples were then cleaned using a piranha solution, followed by the deposition of a 50 nm molybdenum layer on the sample backside via electron-beam evaporation to facilitate thermal handling. Samples were then introduced into a molecular beam epitaxy (MBE) system, where they underwent ex-situ chemical cleaning and in-situ thermal desorption under ultra-high vacuum. The substrate temperature was gradually increased to 680 °C under Ga-rich conditions to initiate two-dimensional (2D) epitaxial growth of a highly doped n+ GaN layer. Regrowth GaN layer was 65 nm thick with doping of $1.5\times10^{20}\,cm^{-3}$. RHEED patterns remained streaky throughout growth, confirming layer-by-layer growth and a smooth surface. AFM analysis of the regrown regions revealed an atomically smooth surface with RMS roughness as low as 0.28 nm (Figure 2), validating the effectiveness of the ALE-based etch in preserving surface quality. In contrast, GaN grown on the SiN mask surface was polycrystalline, with RMS roughness exceeding 22 nm (Figure 2). This unwanted material was subsequently removed through a standard

lift-off process. The final step was the deposition of the overlay Ti and Au at the top of the regrowth GaN and the dc characterization of the TLMs where excellent ohmic contact behavior was observed (Figure 3). This work demonstrates the advantages of ALE for preparing regrowth interfaces in GaN-based devices. Such accuracy and surface quality would not be attainable using conventional etching methods, highlighting the importance of the ALE approach and paving the way for its integration into HEMT fabrication for high-frequency RF applications.
This project was funded from the European Union's Project "POWERSAT" under the grant agreement No [101162320]

Fabrication of coupled silicon nanoelectromechanical resonators with heavily doped silicon towards reservoir computing chip

Wednesday, 17th September - 15:00: - Poster

Mr. Dai Ai [1], ***Ms. Ting Hou*** [2], ***Ms. Zixuan Wang*** [2], ***Dr. Kian Shen Kiang*** [2], ***Dr. Yoshishige Tsuchiya*** [2], ***Dr. Jun-Yu Ou*** [3]

1. *School of Electronics and Computer Science, University of Southampton, Southampton, SO17 1BJ, UK,* ***2.*** *University of Southampton,* ***3.*** *Physics and Astronomy, University of Southampton*

This work demonstrates the design and fabrication of silicon nanoelectromechanical resonators. Single and coupled nanobeam devices were fabricated with expected resonances at VHF band and smallest feature size of 70 nm. These suspended nanobeam devices aim to enable nanomechanical sensors and energy-efficient reservoir computing chips.

Vapor Phase Infiltration in Homopolymers and Block copolymers: A comparative study

Wednesday, 17th September - 15:00: - Poster

Ms. Maria Teresa Elenes Cervantes [1], ***Ms. Olga Muntada*** [1], ***Dr. Sara Duran*** [1], ***Mr. Ricard Noy*** [1], ***Ms. Libertad Sole*** [1], ***Dr. Jordi Llobet*** [1], ***Prof. Francesc Perez-Murano*** [1], ***Dr. Marta Fernández-Regúlez*** [1]

1. *Institute of Microelectronics of Barcelona (IMB-CNM, CSIC)*

We investigate the vapor phase infiltration of Al_2O_3 into PS-b-PMMA block copolymers and PMMA homopolymers under different conditions. Cross-sectional STEM reveals differences in the infiltration profile. Directed self-assembly via graphoepitaxy enables ordered nanostructures and facilitates structural analysis. After removing the polymer matrix, suspended inorganic nanostructures emerge, showing potential for NEMS and sensing applications.

Epitaxial growth of InAs/InGaAs-Al nanowire hybrids for quantum computing applications

Wednesday, 17th September - 15:00: - Poster

Dr. Paloma Tejedor [1], ***Dr. Beatriz Galiana*** [2], ***Mr. Gabriel Moraes*** [3], ***Dr. Eduardo J.H. Lee*** [3]

1. *Instituto de Ciencia de Materiales de Madrid, CSIC, Madrid, 28049, Spain,* ***2.*** *Universidad Carlos III de Madrid,* ***3.*** *Departamento de Física de la Materia Condensada and Condensed Matter Physics Center (IFIMAC), Universidad Autónoma de Madrid, 28049 Madrid*

Hybrid superconductor-semiconductor nanowires hold great promise for fault-tolerant quantum computation. We describe here the VLS growth of core-shell InAs/InGaAs-Al nanowires by MBE. We discuss the effect of growth parameters on nanowire density, morphology, structure, and composition as well as the electron mobility and weak anti-localization effect arising from the spin orbit interaction.

Nanomechanical Mass Sensor: Integrating Nanoimprint Lithography with Flow-Through Gas Phase Deposition

Wednesday, 17th September - 15:00: - Poster

Dr. Lucjan Grzegorzewski [1]

1. *University of Hamburg*

We demonstrate a rapid, wafer-scale method—UV nanoimprint lithography plus pressure-driven Al_2O_3 coating—for producing hollow nanochannel resonators. Under vacuum readout, these double-clamped beams attain Q>1,000 and ~100 ag mass-resolution at MHz frequencies, enabling scalable, multiplexed buoyant-mass sensing of nanoparticles in liquids.

Nanoimprinted Multimode Polymer Waveguides with Integrated Bragg Gratings for Structural Health Monitoring

Wednesday, 17th September - 15:00: - Poster

Dr. Michael Haslinger [1], ***Mr. Florian Egger*** [2], ***Ms. Viktorija Jonaityte*** [1], ***Prof. Vaclav Prajzler*** [3], ***Dr. Antreas Theodosiou*** [4], ***Dr. Michael Muehlberger*** [1]

1. *PROFACTOR GmbH,* ***2.*** *PROFACTOR GmbH, Im Stadtgut D1, 4407 Steyr, Austria,* ***3.*** *Department of Microelectronics, Faculty of Electrical Engineering, Czech Technical University in Prague, Technicka 2, 168 27 Prague, Czech Republic,* ***4.*** *Photonics Research Center (PRC), Lumoscribe Ltd, 12 Anthipoloxagou Georgiou Savva,8201 Geroskipou, Paphos, Cyprus*

Photonics has enabled highly sensitive optical sensors across integration, sensing, LED, and laser technologies. In structural health monitoring, Fiber Bragg Gratings (FBGs) detect temperature, stress, and strain via wavelength shift, intensity, and polarization changes in optical waveguides. Building on recent advances in roll-to-roll and roll-to-plate nanoimprint lithography (NIL), we have fabricated multimode polymer waveguides (50 × 50 µm² core, 250 µm pitch) and imprinted Bragg gratings in an inorganic–organic hybrid polymer (n = 1.5464 at 850 nm) with UV-cured cladding (n = 1.5069 at 850 nm). Dimensions and grating profiles were verified by optical microscopy and AFM, and alternative bio-based photopolymers were assessed for sustainability. Optical losses were measured via the cut-back method, while finite-difference time-domain simulations in Meep modelled mode propagation and dispersion. We present optimized NIL-fabricated FBG designs minimizing loss and maximizing sensitivity, alongside a comparison of laser-inscribed versus NIL-fabricated load sensors. This work demonstrates a cost-effective, scalable, and eco-friendly platform for polymer-based photonic sensors, with broad applications in industrial, environmental, and composite-embedded monitoring.

Advanced AFM Metrology of Vertical Structures: Sample Reorientation for Sidewall Surface Access

Wednesday, 17th September - 15:00: - Poster

Dr. Paweł Janus [1]***, Dr. Krzysztof Domański*** [1]***, Dr. Adam Łaszcz*** [1]***, Dr. Andrzej Sierakowski*** [1]***,***
Ms. Magdalena Kucharska [1]***, Dr. Dariusz Szmigiel*** [1]

1. *Institute of Microelectronics and Photonics*

In this study, we present techniques for the high-precision characterization of sidewall roughness in vertically etched structures. The investigation is based on atomic force microscopy (AFM) imaging using standard probe tips. To enable accurate and reproducible measurements, cross-sectional sample preparation was carried out using either focused ion beam (FIB) milling or a combination of plasma and chemical etching, depending on the material system and structural requirements. The proposed characterization technique is essential for the accurate evaluation of sidewall roughness in plasma etched passive photonic structures, such as germanium and silicon waveguides, grating couplers, and optical filters.

Processing Pathways for Transparent, Flexible Electrodes in Next-Generation Smart Windows

Wednesday, 17th September - 15:00: - Poster

Dr. Michael Haslinger [1], ***Ms. Viktorija Jonaityte*** [1], ***Mr. Dorly Holzer-Harringer*** [2], ***Mr. Marcus Harringer*** [2], ***Dr. Florian Frischmann*** [3], ***Dr. Wenxing Huo*** [4], ***Dr. Martina Harnisch*** [5], ***Dr. Andreas Zimmermann*** [5], ***Dr. Michael Muehlberger*** [1]

1. *PROFACTOR GmbH,* ***2.*** *Almendo Technologies GmbH, Wolfschwangweg 216, 5084 Großgmain, Austria,* ***3.*** *Bartenbach GmbH, Rinner Straße 14, 6071 Aldrans, Austria,* ***4.*** *Department of Biomedical Engineering, Tianjin University, 92 Weijin Road, Tianjin 300072, China,* ***5.*** *Sunplugged GmbH, Affenhausen 1, 6413 Wildermieming, Austria*

Smart windows are dynamic glazing systems that regulate light and heat transmission while offering enhanced functionalities such as energy efficiency and smart home integration. Transparent conductive layers (TCLs) are essential components in these systems, traditionally relying on indium tin oxide (ITO). However, ITO's brittleness and limited availability have driven the search for alternatives. Silver nanowire networks and metal nanomeshes have emerged as promising candidates, combining high electrical conductivity, optical transparency, and mechanical flexibility. This work presents a nanoimprint lithography–based fabrication process for metal nanomeshes with various patterns, achieving conductivity comparable to ITO while maintaining transparency and stretchability. The developed nanomeshes and nanowire networks provide a viable alternative TCL for flexible smart window applications.

Electrochemically growing morphology on micro structured 3D frameworks

Wednesday, 17th September - 15:00: - Poster

Ms. Itishree Panda [1], ***Ms. Trina Dhara*** [1], ***Prof. Sunando DasGupta*** [1]

1. *Indian Institute of Technology Kharagpur*

Controlling electrochemical deposit growth is vital for batteries as well as micro/nano manufacturing. This work demonstrates, through real-time visualization, that altering the underlying structured electrode significantly impacts the spatiotemporal evolution of the deposit interface, highlighting electrode architecture as a powerful tool for regulating the deposition behavior.

Micro/Nano Thin-Film Coating Processes of Carbon Materials for Energy Devices

Wednesday, 17th September - 15:00: - Poster

Dr. JEONGDAI JO [1]

1. *Korea Institute of Machinery and Materials (KIMM)*

For high-power secondary batteries, research on various types of contacts of the electrode-current collector interface is required, and primer coating layer using carbon materials is required for strong adhesion of the electrode-current collector interface.

To verify the effect of primer coating layer, carbon materials for high power secondary battery current collector were coated with an ultra-thin film using blade coating, slot die coating, and spray coating. First, an aluminum (Al) foil with a carbon black paste of 18-19 wt%/58.8 cPs was coated using a blade coater. A carbon black paste of 18-19 wt%/ 58.8 cPs was coated with a thin film using a blade coating process, and it was confirmed that a thin film of several μm to several hundreds of nm was uniformly coated on an area of 11 cm in width and length of 8 cm. The average thickness of the coating was 3 to 5 μm (measured by 9 points) and coating uniformity was 9% (standard deviation) as a result of measuring the coating thickness with a surface profiler. When 4.5 wt% carbon black paste was coated in a thin film, the average thickness of 1 μm to 500nm was measured, although there was a slight difference depending on the conditions of drying/curing conditions. The sheet resistance for each sample was measured, and although there was a difference according to wt%, it was ~ 6 mΩ/sq.

Second, the viscosity and solid content ox-SWCNT paste + PVdF (NMP) were coated using a blade coater, and it was confirmed that a thin film of 1 μm to 500 nm was uniformly coated. As a result of coating the Al foil on a large area, a thickness of 500nm was shown and the uniformity was confirmed to be within about 5%. Carbon black paste and ox-SWCNT paste + PVdF (NMP) were coated with a thin film using a slot die, and it was confirmed that a thin film of several μm to several hundreds of nm was uniformly coated in an area of 11 cm in width and 8 cm in length. Carbon black paste of 9 wt%, 6 wt%, and 4.5 wt% and ox-SWCNT paste + PVdF (NMP) were coated with a thin film with ink in the same area with a slot die, and the electrode thickness was measured to be an average thickness of 1 μm to 500 nm. The sheet resistance for each sample was measured, and there was a difference according to wt%, and it was 6 mΩ/sq or less.

Finally, the carbon material was thin-film coated using a spray coater, and the spray coating properties were confirmed according to the temperature change of the substrate, and the conditions for the uniformity of the coating according to the number of coatings were found.

This research was supported by the National Research Council of Science & Technology (NST) (No. CAP22083-300), the National Research Foundation of Korea (NRF) (No. RS-2023-00222166), and the Korea government (MOTIE) (No. RS-2024-00470021).

Bulk Micro-Machining of SrTiO3 Substrates for Device Applications

Wednesday, 17th September - 15:00: - Poster

Dr. Nicola Manca [1], ***Dr. Luca Pellegrino*** [1]

1. *National Research Council*

Advanced fabrication protocols are instrumental to the development of new experiments and device prototypes. For long time complex oxides micro-fabrication was limited to surface micro-machining of thin films by chemical or physical etching or lift-off. More recently, the possibility to exfoliate complex oxide heterostructures from their growth substrate by using a water-soluble buffer layer opened the opportunity to manipulate complex oxides in a similar fashion to Van der Waals materials.

Here, we further extend this tool-box by presenting a set of fabrication protocols to realize fully suspended micro-structures from complex oxides thin films by etching through the full thickness of their growth substrate [1]. These methods rely on the selective chemical etching of $SrTiO_3$ by HF and the use of double-polished STO substrates. These allow for the growth of epitaxial oxide thin films on both sides which are employed as hard masks and/or device layers to realize fully suspended oxide membranes. We will present different examples of possible device geometry, such as trampolines, sealed membranes, or even the substrate itself carved into suspended resonant devices. These simple geometries can be employed to realize more advanced device prototypes by stacking thin layers of crystalline complex oxides havind different functional properties, such as high-Tc superconductivity or magnetism [2, 3].

Acknowledgement

This project has received funding from the European Union's Horizon 2020 research and innovation programme under Grant Agreement No. 828784 (www.oxinems.eu). This work was also funded by the European Union - NextGenerationEU and by the Ministry of University and Research (MUR), National Recovery and Resilience Plan (NRRP), Mission 4, Component 2, Investment 1.5, project "RAISE - Robotics and AI for Socio-economic Empowerment" (ECS00000035).

[1] N. Manca et al., Adv. Sci. 12 (2025) 2412683.

[2] N. Manca et al., Adv. Funct. Mater. **34** (2024) 2403155.

[3] N. Manca et al., ACS Sens. (2025).

Towards EUV lithography with alternative sources: a proof-of-concept high-harmonic generation in gas-filled hollow waveguides driven by ultrafast infrared laser pulses

Wednesday, 17th September - 15:00: - Poster

Dr. Sonia Freddi [1], ***Dr. Anna G. Ciriolo*** [1], ***Dr. Rebeca Martinez Vazquez*** [1], ***Prof. Salvatore Stagira*** [2], ***Dr. Monica Bollani*** [3]

1. *IFN-CNR,* ***2.*** *Politecnico di Milano,* ***3.*** *Institute of Photonic and Nanotechnology (IFN) - CNR*

This study presents a proof-of-concept setup for compact extreme ultraviolet (EUV) lithography using high-harmonic generation (HHG) in gas-filled microstructured photonic devices. Unlike traditional, large-scale EUV systems, this approach aims for a more scalable and sustainable alternative. Early results demonstrate efficient EUV generation and successful preliminary photolithographic patterning using a Ti:Sapphire laser and argon-filled microfluidic sources. While development is ongoing, these initial findings highlight the feasibility of integrated, compact EUV systems for next-generation nanofabrication.

Medusa 84 SiH, an alternative HSQ resist for realizing DFB lasers diodes

Wednesday, 17th September - 15:00: - Poster

Mrs. Poojitha Sammeta [1], ***Dr. Olaf Brox*** [1], ***Dr. Pietro Della Casa*** [1], ***Mr. Dirk Rentner*** [1], ***Dr. Ralph-Stephan Unger*** [1], ***Dr. Hans Wenzel*** [1], ***Mr. Maximilian Schäfer*** [1], ***Dr. Andrea Knigge*** [1], ***Mr. Harry Biller*** [2], ***Mr. Matthias Schirmer*** [2]

1. *Ferdinand-Braun-Institut gGmbH,* ***2.*** *Allresist GmbH*

Distributed feedback (DFB) lasers are attractive for communication, atomic clocks and spectroscopy applications. DFB laser diodes are compact and easy to handle. Edge emitting DFB laser diodes were initially fabricated and characterized using hydrogen silesequioxane (HSQ) electron beam resist. HSQ resist is expensive and has a low shelf life. In addition, HSQ resist also utilizes a harmful solvent - methyl isobutyl ketone (MIBK). To overcome the shortcomings of HSQ resist an alternative hydrogen silsesquioxane polymer based MEDUSA 84 SiH by Allresist GmbH (Germany) was tested. In this work frame, edge emitting DFB lasers were fabricated with Medusa 84 SiH resist and were characterized. From the laser output performance it was seen that Medusa 84 SiH is an equivalent replacement for similar HSQ variants resist without compromising in the quality of the DFB laser performance.

Integrated Microfabrication Capabilities for Life Science Applications: From Polymer Platforms to Active Micropumps

Wednesday, 17th September - 15:00: - Poster

Mr. Robin de Bruijn [1], ***Ms. Marie Monchablon*** [1], ***Mr. Sander Visser*** [1], ***Ms. Laure van der Sanden*** [2], ***Dr. Hossein E. Amirabadi*** [2], ***Prof. Jaap den Toonder*** [1]

1. *Eindhoven University of Technology,* ***2.*** *ARTIC Technologies B.V.*

MicroFab Lab supports microfabrication for life sciences, integrating cleanroom processes, 3D polymer fabrication, laser micromachining, and biological workflows. We highlight a cilia-actuated micropump embedded in a 96-well-compatible MAC plate, enabling gentle, programmable flow for 3D cultures. This showcases our capacity to prototype complex, application-driven microsystems for biomedical research.

Engineering soft nanoscale surfaces force material interaction study

Wednesday, 17th September - 15:00: - Poster

Dr. Martina Paraggio [1], ***Prof. Luigi Bruno*** [2], ***Dr. Chiara Morano*** [2], ***Ms. Maria Laura Coluccio*** [1], ***Ms. Francesca Gualtieri*** [3], ***Prof. CARMELA DE MARCO*** [3], ***Prof. Francesco Gentile*** [3]

1. *Magna Graecia University, Catanzaro,* ***2.*** *University of Calabria,* ***3.*** *Magna Grœcia University of Catanzaro*

The study presents the design and characterization of nano-structured PDMS substrates with independently tunable stiffness and roughness, used to investigate their effects on cell behavior. Through cell tracking algorithms, the research explores how engineered surfaces influence adhesion and migration, supporting advanced applications in cancer research and biomaterials.

Isotopically pure Silicon-28 thin films for improved coherence times in silicon quantum technologies built by scanning tunnelling microscopy

Wednesday, 17th September - 15:00: - Poster

Mr. Oisín FitzGerald [1], ***Dr. Taylor Stock*** [1]

1. *University College London*

Silicon spin-based quantum computers suffer from short coherence times due to the Silicon-29 isotope. Isolating qubits from this noise source is critical for achieving high-fidelity, error-resistant computation. This work addresses the challenge of growing isotopically enriched Si-28 while ensuring compatibility with the strict thermal budget for STM quantum device fabrication.

Ultra-thick HSQ Resist for Optical Waveguide Grating Coupler Applications

Wednesday, 17th September - 15:00: - Poster

Mr. Kun Zhang [1], ***Dr. Kian Shen Kiang*** [2], ***Dr. Ying Tran*** [3], ***Prof. David Thomson*** [3], ***Prof. Harold Chong*** [3]

1. *School of Electronics and Computer Science, University of Southampton, Southampton, SO17 1BJ, UK,* ***2.*** *Optoelectronics Research Centre, University of Southampton, Southampton, SO17 1BJ, UK,* ***3.*** *University of Southampton*

We present a robust fabrication process for ultra-thick Hydrogen Silsesquioxane (HSQ) resist structures for optical coupler applications. To overcome the limitation of conventional SiO_2 deposition in waveguide regions, experiments of ultra-thick HSQ deposition including exposure dose stability, soft baking and development were done to address the challenge of this novel resist. A controlled ramp baking strategy minimizes cracking, while optimized electron-beam doses (400–700 μC/cm²) and development times ($\geq$3 minutes in TMAH-0.26N) enable a stable pattern transfer during the process. Inspection after fabrication confirms that the HSQ layer exhibits a refractive index of 1.38 at 1550nm, while a simulation underwent with data collected demonstrates a grating coupler efficiency of 23%.This method provides a practical approach to using a thick HSQ layer as an isolated mesa SiO cladding in photonic devices.

Integration of Interband Infrared Cascade Photodetector onto a SOI Platform for Gas Sensing

Wednesday, 17th September - 15:00: - Poster

Mr. Daniel Adeyemi [1], ***Dr. Colin Mitchell*** [1], ***Prof. Goran Mashanovich*** [1], ***Dr. Milos Nedeljkovic*** [1]

1. *Optoelectronics Research Centre, University of Southampton, SO17 1BJ, UK*

Silicon photonics has proven industrial applications for communication, such as in data centres at the 1550nm and 1310nm wavelengths. Additionally, there is much interest at higher wavelengths where there is significant potential for silicon photonic systems for integrated sensing circuits in the mid infrared as it overlaps with the finger-print wavelength range (). This spectral range is where molecules can be identified due to their distinct absorption spectrum generated by the characteristic resonant frequencies of their structure. Within the fingerprint spectrum there are distinct absorption peaks for substances such as methane, carbon dioxide, nitrous oxide, phenytoin and more. To exploit this capacity, we can utilise absorption spectroscopy which involves measuring the change in transmission once a gas interacts with light of a specific wavelength.

Traditional gas sensing system can be bulky, require cooling, are expensive, difficult to integrate into other systems and consequently have comparatively short lifetimes especially in harsh environments such as might be encountered for oceanography as an example investigated here. On-chip absorption spectroscopy has been increasingly desirable as it addresses these issues. This is because it does not utilise a chemical reaction to detect a molecule increasing the sensor lifetime, has excellent chemical specificity and good sensitivity.

Furthermore, on-chip absorption spectroscopy allows for the electronic components to be integrated for greater performance into a smaller package with improved mechanical stability, reduced weight etc. To achieve this, it is desirable to integrate mid-infrared lasers and detectors onto the same chip making use of the excellent optical properties of III-V materials and the compatibility of silicon with CMOS processes allowing for the production of low cost, high performance photonic circuits. However, for on-chip sensing it is also beneficial that these devices can operate at, or close to, room temperature whilst maintaining performance, as cooling is difficult to achieve on such a small scale.

We present a methodology to integrate a 12-stage interband cascade infrared photodetector (ICIP) supplied by the University of Würzburg onto a SOI platform for a collaboration with the National Oceanography Centre[1] to produce gas sensors for oceanography. This is to be achieved using a hybrid flip chip bonding approach utilising etched support structures and AuSn solder for contacting between the two components. In addition, we present waveguides designed for operation at three wavelengths to sense and measure the concentrations of methane (3.3 μm), atmospheric absorption (3.8 μm) and carbon dioxide (4.3 μm). In order to achieve these goals, we have designed novel self-aligned double etch gratings for the each of the wavelengths under test for coupling directly to the detector above.

The device will be tested by coupling the light from a free space laser into the waveguides where it will pass through spiral waveguides of varying lengths (5 mm, 1 cm and 4 cm). This will allow us to evaluate the change in sensitivity with differing path lengths whilst maintaining a compact structure and decoupling any free space effects. To reduce free space absorption further, we have also designed and constructed a gas cell to evaluate this system maximising the path length exposed to the gas under test.

References

[1] A. Bader, F. Rothmayr, N. Khan, J. Koeth, F. Hartmann, and S. Höfling, “Detectivity enhancement by double radiation pass in interband cascade infrared photodetectors,” *Applied Physics Letters,* vol. 123, no. 14, 2023, doi: 10.1063/5.0165187.

Biofabrication of 3D Scaffolds and Functional Microstructures Using Two- Photon Lithography

Wednesday, 17th September - 15:00: - Poster

Dr. Mario Kandra [1], ***Mr. Jáchym Podstránský*** [1]

1. *IQS nano s.r.o*

Two-photon lithography (TPL) has gained increasing attention as a direct laser writing technique capable of producing three-dimensional microstructures with sub-micrometer precision. Unlike traditional lithographic methods—such as electron beam lithography or nanoimprint lithography—which are typically limited to two-dimensional patterning and require vacuum conditions or multiple processing steps, TPL allows the generation of freeform 3D architectures in a single-step process under ambient conditions[1]. This capability enables the creation of structures with complex topologies, variable porosity, and internal heterogeneity, features that are particularly valuable in biomedical applications where physical microenvironments influence cellular responses. An additional advantage of TPL lies in its ability to perform multilayer structuring within a continuous writing sequence, enabling the spatial organization of different functionalities within a single construct[2]. Despite known limitations related to processing speed and material throughput, the high resolution and design flexibility of TPL make it a valuable tool for applications in tissue modeling, biointerfaces, and microfluidic systems.

While existing research has largely concentrated on optimizing material systems and process parameters, our work focuses on expanding the functional scope of TPL toward the fabrication of integrated components for biological microsystems. In contrast to conventional techniques that often require multiple fabrication and assembly steps, we apply TPL to produce not only scaffolds but also additional functional microstructures—such as semi-permeable membranes, compartmentalizing barriers, and microfilters— directly within microfluidic layouts. This approach allows for precise spatial alignment of structural and fluidic features during fabrication and facilitates the creation of customizable, monolithic devices[3]. The novelty of our work lies in leveraging TPL's 3D capabilities to enable multifunctional integration within a single platform, enhancing both design flexibility and reproducibility for organ-on-chip and related applications.

We demonstrate the fabrication of scaffold architectures with controlled geometry suitable for incorporation into microfluidic systems. These scaffolds can be spatially defined relative to the chip's fluidic channels and structural elements. In addition, we show that TPL can be used to fabricate auxiliary features such as filters and membranes within the same fabrication sequence. This co-fabrication approach reduces reliance on manual assembly and alignment while enabling the production of complex, modular biological devices. Our results highlight the potential of TPL as a versatile tool for creating integrated bio-microdevices with precise control over both structural design and functional layout.

The modulation of X-ray by high resolution zone plates when volume diffraction effects dominate

Wednesday, 17th September - 15:00: - Poster

Mr. Hao Quan [1], ***Dr. Xujie Tong*** [1], ***Mr. Qiucheng Chen*** [1], ***Ms. Qingxin Wu*** [1], ***Ms. xunjia Zhao*** [1], ***Mr. Shuoqiu Tian*** [1], ***Mr. Wentao Yuan*** [1], ***Mr. Jinyu Guo*** [1], ***Ms. Kangping Liu*** [1], ***Prof. Yifang Chen*** [1]

1. *Fudan university*

In this paper, utilizing beam propagation method (BPM), we construct the whole optical field, especially the field coming out from the zone plates and the field at the focal plane, to describe a more clear and vivid physical scene, which may explain how the individual zone works and how to optimize the focusing performances including resolution, efficiency, imaging contrast. To validate the simulation results, we fabricated an X-ray zone plate with outermost zone width is 15 nm utilizing e-beam lithography and zone-doubling technique and conducted transmitting imaging at Shanghai Synchrotron Radiation Facility (SSRF).

Microfluidic Mixing Induced by the Blinking-Two-Cilia System

Wednesday, 17th September - 15:00: - Poster

Mr. Yangyu Duan [1], ***Mr. Ishu Aggarwal*** [2], ***Dr. Ye Wang*** [1], ***Prof. Patrick Onck*** [2], ***Prof. Jaap den Toonder*** [1]

1. *Eindhoven University of Technology,* ***2.*** *University of Groningen*

We simulate a novel blinking-two-cilia system (BTCS) to study microfluidic mixing in a closed space. By varying inter-cilia distance, blinking cycle frequency, and actuation patterns, we find that co-rotating cilia with relatively smaller spacing and lower blinking cycle frequency more effectively enhance mixing. This work offers valuable insights for designing future microfluidic mixers.

Neurohybrid interfaces via microstructured conductive hydrogels

Wednesday, 17th September - 15:00: - Poster

Mr. Marco Buzio [1], ***Dr. Nevena Stajkovic*** [2], ***Dr. Valeria Criscuolo*** [2], ***Prof. Francesca Santoro*** [2]

1. *a Institute of Biological Information Processing IBI-3, Forschungszentrum Juelich, 52428 Jülich, Germany,* ***2.*** *Institute of Biological Information Processing IBI-3, Forschungszentrum Juelich, 52428 Jülich, Germany*

We developed a light-based method to fabricate soft, conductive, and biodegradable 3D microstructures by combining PEDOT:PSS with gelatin. Using two-photon polymerization, we achieved high-resolution patterning of hydrogels with tunable electrical and mechanical properties. This fabrication strategy enables the creation of next-generation neurohybrid interfaces that closely mimic living tissue.

Micropillars Based PDMS Lab-On-chip Device for Tryptic Digestion of Proteins for Proteomics

Wednesday, 17th September - 15:00: - Poster

Dr. Sadhana Tiwari [1], ***Ms. Nilüfer Tasli*** [1], ***Dr. Manuela Moritz*** [2], ***Dr. Franziska Marie Esmek*** [3], ***Mr. Tim Erichlandwehr*** [1], ***Dr. Jan Hahn*** [2], ***Prof. Hartmut Schlüter*** [2], ***Dr. Irene Fernandez*** [4]

1. *University of Hamburg,* ***2.*** *Universitätsklinikum Hamburg-Eppendorf,* ***3.*** *University of Hamburg/Hamburg Center for Ultrafast Imaging,* ***4.*** *UHH*

A PDMS-based lab-on-a-chip device with high-aspect-ratio micropillars was developed for efficient on-chip trypsin digestion for proteomics applications. The micropillar architecture enhanced enzyme immobilization and mass transfer, improving digestion efficiency. Immobilized trypsin remained active for about a week under refrigerated conditions, enabling multiple uses and effective peptide analysis by mass spectrometry.

Method for high phase accuracy trimming of MZIs via Ge ion implantation and electrical annealing

Wednesday, 17th September - 15:00: - Poster

Ms. April Logan [1], ***Dr. Xia Chen*** [1], ***Dr. Xingshi Yu*** [1], ***Ms. Weihong Shen*** [1], ***Dr. Xingzhao Yan*** [2], ***Dr. Weiwei Zhang*** [1], ***Prof. Goran Mashanovich*** [1], ***Prof. Graham Reed*** [1], ***Prof. David Thomson*** [2]

1. *Optoelectronics Research Centre, University of Southampton, SO17 1BJ, UK,* ***2.*** *University of Southampton*

This work presents a method of phase trimming Ge ion implanted silicon waveguides via on chip microheaters with the aim of achieving a higher phase tuning accuracy than has previously been demonstrated. A minimum phase trimming accuracy of 0.0054π and an average resolution of phase trimming of 0.0007π were achieved.

Microcavities to engineer dynamics in coupled E. coli oscillators

Wednesday, 17th September - 15:00: - Poster

Mr. Kushal Swamy [1], ***Dr. Farbod Alijani*** [1]

1. *Delft University of Technology*

In this work, we engineered order out of the chaotic swimming dynamics of *E. coli* bacteria, taming their random motion and developing a platform that allows for phase synchronization of single *E. coli* cells. Circular microcavities were used to isolate *E. coli* cells that swim along the cavity wall, resulting in self-sustained oscillations. Connecting these cavities by microchannels yielded synchronization patterns with phase slips. Previous studies have shown the presence of emergent nonlinear phenomena such as self-organization in confinement and advances are being made in the construction of microfluidic devices for artificial microswimmers. Our work supplements these observations, showing that spontaneous order can be engineered in microswimmers found in nature and can be controlled at the level of single cells.

Manipulation of Liquid Marbles via Triboelectric Charging

Wednesday, 17th September - 15:00: - Poster

Ms. Yuan-Hsuen Chou [1], ***Prof. Jiann Shieh*** [1]

1. *National United University*

We present a triboelectric approach for manipulating liquid marbles (LMs) on superhydrophobic glass. Using a charged PTFE rod, LMs are guided, merged, and controlled from both sides of the substrate. This simple, contactless method enables scalable LM manipulation, offering new possibilities for open-surface digital microfluidic applications.

An Extrusion Printed Lorentz Force Actuated Electromechanical Relay

Wednesday, 17th September - 15:00: - Poster

Mr. Desmond Lagace [1], ***Dr. Cyrus Shafai*** [1]

1. *University of Manitoba*

This work presents a millimeter-scale microelectromechanical (MEM) relay fabricated via extrusion printing techniques. The proposed relay features double-sided extrusion printing of silver conductive ink on a polyimide substrate. It utilizes a spring-suspended Lorentz actuator crossbar released via laser micromachining on one side and a relay contact on the other. This method of fabrication realizes a rapidly manufacturable and low-cost alternative to traditional lithographic processes used for MEMS development. The relay exhibits comparable, and, in some cases, superior performance metrics compared to commercially available relays, including switching time, power consumption, contact resistance, and maximum dc load current.

Integrating Surface-Confined Molecular Motors into Microfluidic Platforms: Toward Automated, High-Throughput analysis of Actinomyosin in vitro motility Assays

Wednesday, 17th September - 15:00: - Poster

Mr. Tim Erichlandwehr [1], ***Ms. Veronica Mieites*** [2], ***Mr. Jeremy Teuber*** [3], ***Mr. Rukan Nasri*** [4], ***Dr. Marko Usaj*** [5], ***Prof. Alf Månsson*** [5], ***Prof. Olga María Conde Portilla*** [2], ***Dr. Irene Fernandez-Cuesta*** [4]

1. *UHH/DESY,* ***2.*** *University of Cantabria, Photonics Engineering Group,* ***3.*** *UHH/MPSD,* ***4.*** *UHH/CUI,* ***5.*** *Linnaeus University*

Lab-on-a-chip devices miniaturize complex lab functions onto portable platforms, with great potential in biomedical diagnostics and environmental monitoring. A key challenge remains the active, selective transport of nanoscale cargo independently of bulk fluid flow. To address this, we integrate surface-bound molecular motor systems with microfluidic channels designed for analyte capture and directed transport. Specifically, myosin motors adsorbed on hydrophobic surfaces propel actin filaments (AFs), which are partially biotinylated (5–20%) to enable cargo pick-up of biotinylated molecules (e.g., fluorescent DNA oligos) via a biotin-streptavidin-biotin linkage.

For robust and reproducible surface preparation, we established a rapid gas-phase silanization protocol using silanes such as TMCS, FOTCS, and FDDTCS, achieving uniform hydrophobic functionalization of glass or polymer substrates in under 10 minutes. Surface quality was validated through AFM and water contact angle measurements. The resulting coatings support high AF motility with average speeds of 3.5 ± 1.1 µm/s and motile filament ratios up to 91%.

We further integrated a rapid UV-nanoimprint lithography process to create confinement channels in under two minutes, preserving AF motility within topographically and chemically defined regions. This expands compatibility with complex chip geometries from earlier studies.

To overcome the bottleneck of low-throughput manual filament analysis, we implemented an automated pipeline capable of tracking hundreds of filaments per assay across varying conditions. Benchmarking showed strong agreement with manual analysis and offered scalable, unbiased quantification of motility and cargo binding. This platform unites functional biomolecular transport with fast fabrication and high-throughput analytics, laying groundwork for applications of motor proteins in diagnostic technologies.

Tuning fork optomechanical NIR antenna with integrated optical transmission line

Wednesday, 17th September - 15:00: - Poster

Mr. Daniyal Khoshmaram [1], ***Dr. Xavier Borrisé*** [2], ***Prof. Joan Jose Garcia-Garcia*** [1], ***Mr. Raul Ruiz*** [1], ***Dr. Xavier Cartoixà*** [1], ***Dr. Gabriel Abadal*** [1]

1. *Universitat Autonòma de Barcelona,* ***2.*** *Catalan Institute of Nanoscience and Nanotechnology (ICN2) and Barcelona Institute of Science and Technology (BIST)*

The work presents a redesigned NEMSTENNA device that converts near-infrared (NIR) radiation into mechanical motion using plasmonic nanoantennas and lateral-moving nano-cantilevers in a tuning fork configuration. This architecture simplifies fabrication (eliminates dual alignment) and improves performance. A monolithic optical transmission line (OTL) patterned in a Au/Si_3N_4 bilayer connects to a nanodipole antenna resonant at 1.55 μm, with electrostatic forces generated by the induced voltage driving lateral deflection.

Fabrication uses a 6-step FIB milling process with precise current and resolution control. COMSOL simulations model the electromagnetic field, voltage-induced forces, and mechanical response. Narrower feed gaps increase electric field and deflection (up to 13 nm at 7.5 mW input), though at the cost of transmission efficiency. Optimization of gap size and dipole length is key for balancing field enhancement and signal transmission.

Low-Temperature Deposition of Metal Chalcogenides via Single-Source Precursors for Flexible Electronics

Wednesday, 17th September - 15:00: - Poster

Ms. Sayali Harke [1], Ms. Suprabha Dixit [2], Dr. Chitra Gurnani [1], Dr. Ruomeng Huang [3], Dr. Omesh Kapur [4]

1. *Ecole Centrale School of Engineering, Mahindra University, Hyderabad,* ***2.*** *Ecole Centrale School of Engineering, Mahindra University,* ***3.*** *University of Southampton,* ***4.*** *School of Electronics and Computer Science, University of Southampton, Southampton SO17 1BJ, United Kingdom*

Single-source precursors enabled low-temperature deposition of metal chalcogenide films, demonstrating excellent resistive switching on both flexible and rigid substrates. Devices exhibited synaptic behavior, mechanical robustness, and scalability, highlighting their potential for neuromorphic computing. This approach offers a promising pathway for future energy-efficient, flexible, and intelligent electronic systems.

Application of Integrated Electrode Fabrication Technique in Microfluidic lab-on-a-chip Devices for Single-Cell Analysis

Wednesday, 17th September - 15:00: - Poster

Mr. Herbert Atrian-Garcia [1], ***Ms. Louise von Lacroix*** [1], ***Dr. Irene Fernandez*** [1], ***Mr. Rukan Nasri*** [1]

1. *University of Hamburg*

In this work we present the fabrication of a microfluidic device consisting of two parts: the fluidic device with microchannels and the ultra-flat coverslip (sealing component), with integrated microelectrodes, for the analysis of the mechanical properties of single cells. In our device, the drop of the electrical current caused by the deformation of individual cancer cells as they flow along several microchannels and expansion chambers, so squeezing and expanding, will be measured with the integrated electrodes.

Preparation of Biocompatible Ag/Nylon Yarns Fabricated by Supercritical CO_2-assisted Ag Electroless Plating toward Weavable Devices

Wednesday, 17th September - 15:00: - Poster

Mr. Tomoya Higashi [1], ***Dr. Tomoyuki Kurioka*** [2], ***Mr. Kazuhiro Shibata*** [2], ***Dr. Satoru Egawa*** [3], ***Prof. Toshitaka Yoshii*** [3], ***Prof. Chun-Yi Chen*** [2], ***Prof. Tso-Fu Mark Chang*** [2], ***Prof. Katsunari Sato*** [4], ***Prof. Hiromichi Kurosu*** [4], ***Prof. Masato Sone*** [2]

1. *Institute of Innovative Research, Institute of Science Tokyo,* ***2.*** *Institute of Science Tokyo,* ***3.*** *Department of Orthopaedic Surgery, Institute of Science Tokyo,* ***4.*** *Nara Women's University*

Ag-coated Nylon yarns were prepared via supercritical CO_2-assisted catalyzation using $Pd(hfa)_2$, followed by a silver electroless plating . Yarns with Twist numbers ranging from 0 to 865 T/m were examined to investigate the influence of twist on electrical conductivity. Resistance measurements showed that higher Twist numbers led to increased silver coverage and reduced resistance. Optical microscopy confirmed more extensive silver deposition with increasing twist. Under repeated strain cycling, Ag-coated yarns exhibited a notable resistance increase upon release, indicating deformation-sensitive conductive behavior. These findings support future applications in stretchable and weavable bioelectronic systems.

Flexible AlScN Piezoelectric Films for Next-Generation Smart Biomedical Sensors

Wednesday, 17th September - 15:00: - Poster

Dr. Padmalochan Panda [1], ***Dr. Gaia de Marzo*** [2], ***Dr. Luciana Algieri*** [3], ***Dr. Antonio Qualtieri*** [1], ***Dr. Francesco Rizzi*** [1], ***Prof. Michele Scaraggi*** [1], ***Dr. Vincenzo M. Mastronardi*** [3], ***Prof. Massimo De Vittorio*** [1]

1. *Center for Biomolecular Nanotechnologies, Istituto Italiano di Tecnologia (IIT), 73010 Arnesano, LE, Italy,* ***2.*** *IDUN section, Department of Health Technology, Technical University of Denmark, DK-2800 Kongens Lyngby, Denmark,* ***3.*** *Department of Innovation Engineering, University of Salento, Lecce, LE, 73100, Italy*

We report the room-temperature deposition and characterization of Sc-doped AlN films on both rigid and flexible substrates for smart health monitoring. The films exhibit enhanced piezoelectric response and mechanical flexibility, supporting their integration into smart patch sensors and advancing next-generation AlScN-based biomedical devices on flexible platforms.

Monolithic All-Silicon Ring Resonator for Optical Modulation and Detection

Wednesday, 17th September - 15:00: - Poster

Mr. Yifu Chen [1], ***Dr. Weiwei Zhang*** [1], ***Ms. Tzu-yun Chang*** [1], ***Ms. Hanuushah Vizabaskaran*** [1], ***Mr. James Le Besque*** [1], ***Dr. Xingzhao Yan*** [1], ***Dr. Martin Ebert*** [1], ***Prof. Callum Littlejohns*** [1], ***Prof. David Thomson*** [1]

1. *Optoelectronics Research Centre, University of Southampton, SO17 1BJ, UK*

We demonstrate an all-silicon, reconfigurable microring device supporting both high-speed modulation and photodetection. It achieves 55 GHz EO bandwidth with 6.6 V·mm efficiency, and 23 GHz OE bandwidth with up to 0.97 A/W responsivity, making it highly suitable for scalable WDM and programmable photonic circuits.
Key words: silicon photonics, microring modulator, photodetector, CMOS-compatible, reconfigurable device, WDM, high-speed optical I/O

InP Nanowire-Based Photoelectrical Detection of Single Particles and DNA in Nanofluidic Systems

Wednesday, 17th September - 15:00: - Poster

Mr. Leon Seggering [1], ***Mr. Vidar Flodgren*** [2], ***Dr. Abhijit Das*** [2], ***Mr. Thomas Kjellberg Jensen*** [2], ***Dr. Joachim Elbeshausen Sestoft*** [3], ***Prof. Jesper Nygård*** [3], ***Prof. Anders Mikkelsen*** [2], ***Dr. Irene Fernandez-Cuesta*** [4]

1. *UHH/DESY,* ***2.*** *Lund University,* ***3.*** *University of Copenhagen,* ***4.*** *UHH/CUI*

We present a nanofluidic device integrating photo-excitable InP nanowires for electrical detection of particles and DNA. The device combines precise nanowire alignment, fluidics, and PCB readout. Initial results confirm photocurrent response under laser excitation. Future work targets single-particle detection for high-throughput biomolecular sensing.

Ultrasensitive Raman Detection via Electrostatic Droplet Manipulation and Laser-Patterned Pinhole Concentration

Wednesday, 17th September - 15:00: - Poster

Ms. Jia-yi Chen [1], ***Mr. Cheng-Han Yu*** [1], ***Prof. Jiann Shieh*** [1]

1. *National United University*

We demonstrate ultrasensitive molecular detection by electrostatically guiding analyte-containing droplets into laser-patterned pinholes on a superhydrophobic glass surface. Drying forms coffee-ring stains that concentrate molecules and nanoparticles, enhancing Raman signals. This precise, flexible method enables detection of R6G down to 10^{-12} M, with potential for digital microfluidics applications.

Scalable integration of III-V nanowire transistors for NMOS logic

Wednesday, 17th September - 15:00: - Poster

Dr. Faris Abualnaja [1], ***Mr. Ibtisam Abbasi*** [1], ***Mr. Xiaofan Lin*** [1], ***Prof. Hoe Tan*** [2], ***Prof. Chennupati Jagadish*** [2], ***Prof. Hannah Joyce*** [1], ***Dr. Jack Alexander-Webber*** [1]

1. *University of Cambridge,* ***2.*** *The Australian National University*

In this work, we demonstrate scalable III-V InAs nanowire inverters using enhancement- and depletion-mode transistors with controlled diameters. Partially automated fabrication enables logic circuits with rail-to-rail output and RC-limited frequency response. These results highlight the potential of III-V nanowires for compact, low-power electronics.

Piezoelectric microdevices for single-cell stimulation via ultrasound-driven ZnO nanosheets

Wednesday, 17th September - 15:00: - Poster

Mx. Laura Lefaix [1], ***Mr. Marc Navarro*** [2], ***Prof. Jaume Esteve*** [1], ***Prof. Carme Nogués*** [3], ***Dr. Andreu Blanquer*** [4], ***Dr. Gonzalo Murillo*** [2]

1. *Instituto de Microelectrónica de Barcelona,* ***2.*** *Institute of Microelectronics of Barcelona (IMB-CNM, CSIC),* ***3.*** *Universitat Autonòma de Barcelona,* ***4.*** *Departament de Biologia Cel.lular, Fisiologia i Immunologia, Universitat Autonoma de Barcelona*

Silicon microtechnology enables the scalable fabrication of cytocompatible microdevices for wireless electrical stimulation. Microdevices smaller than a cell allow accurate interaction with single cells. By integrating piezoelectric nanostructures that can be actuated by ultrasound within the biomedical range in the microdevice, cells could be electrically stimulated. In this work, this electrical stimulation was observed to trigger intracellular Ca^{2+} entry through membrane channels, promoting cell excitation.

Technological platforms for manufacturing semiconductor qubits

Wednesday, 17th September - 15:00: - Poster

Dr. Alberto del Moral [1], ***Mx. Iker Uranga*** [1], ***Mr. Gabriele Petitto*** [1], ***Mr. Pol Gaya*** [1], ***Mr. Gorka Aizpurua-Iraola*** [1], ***Dr. Jordi Antoja*** [2], ***Dr. Esteve Amat*** [1], ***Dr. Jordi Llobet*** [2], ***Dr. Marta Fernández-Regúlez*** [1], ***Prof. Joan Bausells*** [1], ***Prof. Francesc Pérez-Murano*** [1]

1. *Institute of Microelectronics of Barcelona (IMB-CNM, CSIC),* ***2.*** *Institut de Microelectrònica de Barcelona, IMB-CNM (CSIC), Universitat Autònoma de Barcelona, Cerdanyola Del Vallès, 08193, Barcelona, Spain.*

An overview of various semiconductor qubit platforms is presented, with special interest in electrostatic quantum dot-based qubits. We present results on the fabrication steps adapted from CMOS technology like the characterization of the gate oxide, the structural and electrical characterization of MOSFET devices at low temperatures and structural characterization of single electron transistor devices, validating our qubit device fabrication process.

Double-Spot Detection in Nanochannels Enables Precise Velocity Profiling and Long-Term Stability Monitoring in Passive Micro- and Nanofluidic- Systems

Wednesday, 17th September - 15:00: - Poster

Mr. Phil Grzybeck [1], ***Mr. lucjan Grzegorzewski*** [1], ***Mr. Leon Seggering*** [2], ***Dr. Franziska Marie Esmek*** [3], ***Dr. Irene Fernandez-Cuesta*** [4]

1. *UHH,* ***2.*** *UHH/DESY,* ***3.*** *University of Hamburg/Hamburg Center for Ultrafast Imaging,* ***4.*** *UHH/CUI*

Recent advances in nanofabrication have enabled the development of nanofluidic devices capable of detecting single biomolecules like DNA. In such devices, coiled DNA enters nanochannels from one microchannel to another, requiring linearization due to strong confinement. Traditional single-spot fluorescence detection provides valuable data but is limited by its dependence on peak shape, which is sensitive to external factors like flow fluctuations and buffer conditions.

We present a dual-spot laser detection approach that allows direct measurement of particle velocity within a nanochannel. By extracting peak-to-peak time intervals from two laser spots, we accurately determine individual translocation speeds and use this information to correct peak widths, decoupling shape artifacts from particle size.

To assess long-term stability and buffer-dependent flow behavior, we conducted 60-minute measurements using linearized DNA (2686 bp) in varying TBE buffer concentrations (0.5×, 0.25×, 0.1×). Velocity-corrected data revealed consistent peak width distributions across all conditions, demonstrating improved measurement robustness.

Our results show that double-spot detection ensures reproducible, comparable data over long durations and under varying conditions. This approach supports the development of simple, mobile, and pump-free platforms for single-molecule DNA diagnostics.

Synchronization of autonomous vibrating electrostatic MEMS torsional mirrors

Wednesday, 17th September - 15:00: - Poster

Mr. Yuta Kawashima [1], ***Mr. Mikiya Oki*** [1], ***Dr. Amit Banergee*** [1], ***Dr. Jun Hirotani*** [1], ***Prof. Toshiyuki Tsuchiya*** [1]

1. *Kyoto University*

We report synchronization of electrostatic MEMS torsional micromirrors using forced synchronization for high-performance optical systems with large scan angle, high speed, and high resolution. By applying an external force signal to a 1×2 micromirror array autonomously oscillated via a phase-locked loop, we confirmed the vibration frequencies of both mirrors matched.
Key words: electrostatic MEMS tortional mirror, autonomous oscillation, forced synchronization

Solution-Processed UV-Vacuum-Heat (UVVH) Treated Mixed Size Zinc Oxide Nanoparticle Diode-like Device for Ion Sensing Applications

Wednesday, 17th September - 15:00: - Poster

Mr. Mengyang Qu [1], ***Dr. Huanghao Dai*** [1], ***Dr. Omesh Kapur*** [2], ***Prof. Steve Beeby*** [1], ***Prof. Harold Chong*** [1]

1. *University of Southampton,* ***2.*** *School of Electronics and Computer Science, University of Southampton, Southampton SO17 1BJ, United Kingdom*

Zinc oxide nanoparticles (ZnO NPs), as an n-type semiconductor, have garnered significant research interest due to their low toxicity, environmentally friendly fabrication processes, and wide bandgap [1]. The deposition of ZnO NP films can be achieved via solution-based methods that eliminate the need for high-temperature processes. Such solution-processing techniques offer broad applicability, suitable for fabricating electronic devices on various substrates. However, solution-deposited ZnO NPs typically exhibit high resistivity and limited electrical stability, primarily attributed to the adsorption of atmospheric oxygen molecules, which trap electrons within the nanoparticles and reduce carrier concentration [1,2].

The UV-Vacuum-Heating (UVVH) process has been demonstrated to remove adsorbed ionized oxygen, thereby decreasing the film's resistivity. When combined with ethylene-vinyl alcohol (EVOH) passivation, this low-resistivity state can be maintained for up to two months [3]. Li et al. have further reported that the adsorption process can be modulated by an applied electric field [4]. Consequently, it is hypothesized that the resistivity at the interface between low- and high-resistivity ZnO NPs films can be influenced by the bias voltage, which modulates the adsorption and desorption of oxygen molecules on the nanoparticle surfaces. The fabrication process achieves a diode-like ZnO NPs device, which has potential applications for ion sensing.

We successfully demonstrated a diode-like ZnO NPs through a solution-based deposition method and a UVVH process. The device's diode-like behavior was attributed to the adsorption and desorption of the oxygen molecules on the interface between low- and high-ZnO NPs films. The threshold voltage was 1.3 V for pH 9 solution applied and increased with the low pH solution applied, achieving a sensitivity of 233 mV/pH.

PEGDA microfluidic-device featuring a Y-type shape for hydrogel microspheres synthesis analysis

Wednesday, 17th September - 15:00: - Poster

Ms. Anayancy Itzel Villatoro Guillen [1], ***Dr. Orfil González-Reynoso*** [1], ***Ms. Andrea Carolina Villalvazo-Hidalgo*** [1], ***Dr. Alvaro de Jesús Martínez-Gómez*** [1], ***Dr. Antonio Romero-Estrada*** [1], ***Dr. Sergio Gómez-Salazar*** [1], ***Dr. Mario Alberto García-Ramírez*** [1]

1. *Universidad de Guadalajara*

The microfluidics devices offer remarkable flexibility, integration capability, improved precision, and efficient raw materials use. Implementation of different channel sizes and geometries is key to generate mono-disperse droplets. The microfluidics operation relies on the viscous forces interplay, capillary forces, nozzle diameter, surface tension between the dispersed and continuous phases. Polyethylene glycol diacrylate (PEGDA) is a polymeric material used in tissue engineering and biomedical applications due to its biocompatibility and ability to form three-dimensional networks through photopolymerization. In this study a numerical analysis was performed in order to find the ideal conditions for the PEGDA hydrogel microspheres formation by using different flow rates featuring a Y-microfluidic device by considering a prepolymer PEGDA hydrogel solution as the dispersed phase and mineral oil as the continuous one. As a result, the numerical analysis shows that the small-size microspheres diameter (200 to 600 μm) is inversely proportional to the flow rate increase for the continuous phase while the dispersed-phase flow rate is kept constant. On the other hand, by decreasing the continuous flow rate, it does not generate the microsphere due to it agglomerates the dispersed phase. In contrast, the increment on the continuous flow rate allow to form ovals due to the drift that present the dispersed phase. The application milestone is focused on drug delivery such as in cancer treatments in order to improve the efficiency and reduce the side effects such as cytotoxic ones. By having the smaller the particle, the most efficient it can be.

Piezoresistivity in FEBID nanowires imaged via opMEMS straining

Wednesday, 17th September - 15:00: - Poster

Dr. Bartosz Pruchnik [1], Ms. Magdalena Kucharska [2], Dr. Krzysztof Kwoka [1], Dr. Tomasz Piasecki [1], Dr. Soraya Sangiao [3], Prof. Jose Maria De Teresa [3], Mrs. Ewelina Gacka [1], Mr. Dominik Badura [1], Mr. Piotr Kunicki [1], Dr. Andrzej Sierakowski [2], Dr. Paweł Janus [2], Prof. Teodor Gotszalk [1]

1. *Wrocław University of Science and Technology,* ***2.*** *Institute of Microelectronics and Photonics,* ***3.*** *Universidad de Zaragoza*

Piezoresistivity is the property that enables the resistive measurement of mechanical displacement in solid structures. Electrical strain measurements are used in nanoscopy, nanomechanical sensors and environmental and embedded devices. Piezoresistivity is characterised by the gauge factor (GF), which relates the change in resistance to strain. Typically, it does not exceed 100 nm. However, it is predicted that it may be elevated in one-dimensional structures, namely nanowires. The term ‘giant piezoresistivity’ is used for a GF greater than 1000.

Conversely, bottom-up nanofabrication enables the development of localised nanowire structures. Focused electron beam induced deposition (FEBID) allows multiple materials to be deposited, including metal-carbon composites (Me(C)). The spatial resolution is better than 2 nm, with a minimal nanostructure diameter of 8 nm. Me(C) materials consist of carbon nanograins embedded in a carbon matrix. This non-uniform structure is predicted to exhibit piezoresistivity and potentially giant piezoresistivity.

Here, we report the measurement of giant piezoresistivity in FEBID-developed tungsten-carbon (T(C)) nanowires. GF values exceeding 1000 and reaching 6700 were encountered with a few-fold change in resistance over elongation under 1000 ppm. We compare the piezoresistive properties of these materials with those of platinum-carbon (Pt(C)) and cobalt (Co), which also exhibit significant GF values, reaching 400. We discuss the possible underlying physical mechanism, which we believe to be the composite nano-grain structure of the materials combined with their heavily limited physical dimensions.

The measurement setup was based on the opMEMS design, which operates within the Lab-in-SEM. Nanowires with diameters below 20 nm and lengths below 100 nm were deposited in the area of interest of the opMEMS. The opMEMS was then statically actuated, while the resistance of the nanowire was simultaneously measured. All electrical signals were controlled by a source measurement unit (SMU). The elongation was derived by measuring the displacement of the opMEMS with a laser Doppler vibrometer (LDV). The displacement difference across the region of interest was measured and normalized.

Simulation of contact forces associated with contact wear in MEMS switches

Wednesday, 17th September - 15:00: - Poster

Mr. Nasser Aldhahri [1], ***Prof. John Mcbride*** [2], ***Dr. Yoshishige Tsuchiya*** [1]

1. *University of Southampton,* ***2.*** *School of Engineering, University of Southampton*

Understanding wear behaviour is crucial for enhancing MEMS contact switch reliability. This study simulates contact forces and wear effects for a model of MEMS contact switches. Increase of the contact force in response to wear-induced deflection suggests that the voltage to maintain stable conduction can be reduced with wear.

A Hybrid Superconductor/Nanomechanical Magnetic Field Detector for Biomagnetism

Wednesday, 17th September - 15:00: - Poster

Dr. Luca Pellegrino [1]

1. *National Research Council of Italy*

Current commercial setups for magnetoencephalography (MEG) use helmets comprising superconducting quantum interference devices (SQUIDs) made of low critical temperature superconductors. SQUID sensors are barely robust to static and pulsed magnetic fields, such as the ones used in Ultra-Low Field Magnetic Resonance Imaging (MRI) and especially Transcranial Magnetic Stimulation (TMS). For this reason, integration of MEG with these techniques in a unique system at present has not yet been achieved.

Our purpose is to develop a magnetic field sensor with sensitivity of the order of 10fT/sqrt(Hz) to measure the magnetic field of the human brain and at the same time quickly recovering in a strong applied field (» 1 T). This sensor would be suitable for an on-scalp MEG system integrated with multiple imaging modalities to image brain activity and connectivity with high spatial and temporal resolution. We are developing a hybrid device by coupling a high-Q micro/nanomechanical (M/NEMS) resonator having a magnetic element to a high-Tc superconducting magnetic field focuser in series to a pick-up loop that collects the external magnetic field. The biomagnetic field induces a supercurrent in the loop, which has a geometry designed to generate a strong non-uniform magnetic field in the proximity of the magnetic element of the resonator. The resonance frequency of the resonator is modified by this magnetic coupling and detected by a fiber-optic interferometer. Optomechanical detection of biomagnetic fields has the advantage of reducing the crosstalk between the channels with respect to electrical detection. This feature requires the development of a cheap, robust and scalable optomechanical platform for a future M/NEMS-based helmet. We discuss the basic working principle of this hybrid sensor and the advancements made so far for the realization and characterization of the first device prototypes as well for the realization of the optomechanical platform that will host the first magnetometer to be characterized in operative environment.

This project has received funding from the European Union's Horizon 2020 research and innovation programme under Grant Agreement No. 828784 (www.oxinems.eu). This work was also funded by the European Union - NextGenerationEU and by the Ministry of University and Research (MUR), National Recovery and Resilience Plan (NRRP), Mission 4, Component 2, Investment 1.5, project "RAISE - Robotics and AI for Socio-economic Empowerment" (ECS00000035).

[1] Patents no. US11415642 and EP3896470B1 "A device for sensing a magnetic field".

Development of a 3-Channel Solar-Blind UV-C Sensor for Determining Source Location and Intensity

Wednesday, 17th September - 15:00: - Poster

Dr. Keekeun Lee [1]

1. *Ajou Unversity*

This study presents a high-performance solar-blind UV-C corona sensor using b-Ga_2O_3/Al_2O_3 integrated with a surface acoustic wave (SAW) platform, achieving sub-second response times and a detection limit of 0.1 μW/cm². A 3-channel electronic interface enables real-time localization and intensity mapping of corona discharges. The sensor demonstrates excellent sensitivity, stability, and long-term reliability, validated through multi-channel testing for accurate UV-C corona detection and positioning.

Electrostatic Manipulation of Low Surface Tension Liquids on Silica Nanowire-based Slippery Liquid-infused Porous Surfaces

Wednesday, 17th September - 15:00: - Poster

Mr. Ching Chi Lin [1], ***Mr. Yueh Tse Lin*** [1], ***Prof. Jiann Shieh*** [1]

1. *National United University*

We present a transparent SLIPS surface made by infusing lubricant into silica nanowire-coated glass. This design lowers sliding angles and enables electrostatic manipulation of water, ethanol, and acetone droplets. Using a triboelectrically charged PTFE rod and programmable platform, droplets are precisely guided—even across defects and from the backside of the glass.

Edge Engineering for Intrinsic Cold-metallic Injection Source in 2D FETs

Wednesday, 17th September - 15:00: - Poster

Ms. Zhirong PENG [1], ***Mr. Ning JI*** [2], ***Mr. Jinchen Wei*** [1], ***Mr. Kwok-Ho Wong*** [1], ***Mr. Tin Shing Peter Ho*** [1], ***Prof. Lining Zhang*** [2], ***Prof. Mansun Chan*** [1]

1. *The Hong Kong University of Science and Technology,* ***2.*** *Peking University*

For further improving the energy efficiency of modern transistors, suppressing thermionic carrier injection is a potential strategy against Boltzmann limit. Two-dimensional (2D) devices have remarkable eletrostatic controllability while off-state leakage current is still limited by conventional “hot” metal contacts with thermal broadening of the Fermi-Dirac distribution [1]. Cold metal sources filter out high-energy carriers by sharp decline in density of states (DOS) near the Fermi level (E_F), thus suppressing the thermal tail effect [2]. Experimentally, the graphene nanoribbon has demonstrated its potential as cold source [3], while MoS2 nanoribbons are still mainly applied to channel [4]. Herein, the cold metal characteristics of zigzag-oriented (ZZ) MoS_2 NR is realized by edge engineering. With a significant conduction gap above the Fermi level, the hot electrons can be filtered out at off-state, leading to low electronic transmission.

The ZZ MoS_2 NRs are established as shown in Fig. 1a. Both edges of ZZ MoS_2 NR are ended at sulfur (S) atoms for a better stability, and passivated with pseudo-hydrogen to eliminate dangling bonds while preserving the metallic character of pristine ZZ edges. The ZZ MoS_2 NRs with different width, in the range of 1 nm to 10 nm, are constructed and named as ZZ_N (N=1, 2, 3…), where N denotes the number of Mo-S hexagon rings along x direction. Both un-passivated and passivated ZZ MoS_2 NRs structures exhibit metallic characteristics (Fig. 1b and 1d), which are different from their host 2D structures. In the passivated structure, a conduction gap (E_{CG}) of ~0.467 eV emerges, endowing the ZZ MoS_2 NR with cold source characteristics in n-type devices. The E_{CG} is caused by the pulled-down energy level (marked in green and orange respectively in the band structure), corresponding to the partial charge density plotted in Fig. 1c and 1e. The edge S atoms exhibit two types of coordination: S_1 atoms bonded to one Mo atom and S_2 atoms bonded to two Mo atoms. Upon passivation, a sharper downward energy shift of S_1-derived states can be witnessed than that of S_2-related states due to additional bond formation, consequently results in E_{CG} and thus the cold metallic characteristic.

It is notable that the cold metal properties of ZZ MoS_2 NRs can be extended ranging from 1 nm to 10 nm with the same cold metal formation mechanism (see Fig. 2a and 2b). This band originates from the Mo edge near the S_1 sites (Fig. 1c and 1e), giving further assurance of the metallicity of the ZZ MoS_2 NRs. Fig. 2c plots the lower (E_L) and upper (E_H) bounds of the E_C as a function of width. The presence of a clear E_{CG} above the Fermi level across all widths confirms that the cold metallic feature persists over a wide range of lateral dimensions. Fig. 2d shows the total energy of each structure as a function of nanoribbon width. The total energy of the ZZ MoS_2 NR is linearly correlated with the width, implying similar electronic structure as it scales.

With metallic ZZ_5 as intrinsic source, the cold-sourced device can be constructed as shown in Fig. 3a. Due to a distinct energy window above the Fermi level where the DOS are significantly low, the hot electrons are cut with small gate voltage (Fig. 3b), leading to suppressed hot thermal tail effect. As a result, an electrons filter window can also be observed in the transmission spectrum (Fig. 3c). This energy-selective transmission mechanism underpins the superior performance of cold-metallic sources in minimizing off-state leakage current. To conclude, we proposed that intrinsic cold-metallic ZZ MoS_2 NR can function as the source in MoS_2-based transistors via edge engineering. With an energy gap of ~0.467 eV above the Fermi level, the high-energy electrons can be effectively filtered out at off state. Its robustness is well maintained across a width range of 1 nm to 10 nm, underscoring its potential for continuously scaled low-power device applications.

Plasmonic antenna-VO2 hybrid metasurface for all-optical nonlinearity

Wednesday, 17th September - 15:00: - Poster

Mr. Trubacs Daniel-Iosif [1], ***Dr. Kai Sun*** [1], ***Dr. Ioannis Zeimpekis*** [1], ***Prof. Otto Muskens*** [1]

1. *University of Southampton*

The benefits brought by the current Artificial Intelligence (AI) come at a great energy cost, with AI systems demanding ever-increasing computational power. A solution to this problem is photonic computing, which promises to have a much smaller carbon footprint than electronics. While many photonic devices have already been developed to emulate their electronic counterparts, all-optical non-linearity in their design - which is a key requirement for implementing AI algorithms – remains a challenge.

Vanadium dioxide (VO_2) is a promising candidate in this area, as its ultrafast metal-insulator transition (MIT) can be induced all-optically [1] and its switching behavior can be tuned when combined with plasmonic antennas [2]. In this work, we demonstrate that a plasmonic antenna-VO_2 hybrid metasurface exhibits a strong and tunable all-optical nonlinear response to the power of incident light measured on the sample. Unlike many other past works, where many external stimuli are required to induce the MIT, we have used a single source of light: a 1550 nm laser.

A full fabrication flow process of the VO_2 device is shown in Figure 1. Fabrication started with a 1 mm-thick glass substrate, onto which electron-beam resist (ZEP520A) was spin-coated and patterned to form the antenna shapes. Next, a gold (Au) layer of thickness 45 nm was formed using electron-beam evaporation. The deposited Au layer was then lifted-off in N-Methyl-2-pyrrolidone (NMP) solvent at room temperature. Afterward, VO_2 with a thickness of about 40 nm was deposited through atomic layer deposition (ALD). The ALD growth parameters were reported in a previous publication [3]. After deposition, the VO_2 was annealed in oxygen to crystallize VO_2 into VO_2(M1), giving the material its crucial phase-transition capabilities.

The fabricated devices consist of 36 square arrays each in size of 120 μm × 120 μm (Figure 2 left), with the length (L) and dimer gap (DG) of the antennas being varied between the square arrays, whilst the width of the antennas (W) and the gap (G) between them stayed constant (Figure 2 right).

Optical characterization, using Fourier Transform Infrared Spectroscopy, shows that the C21 antennas are resonant at ∼2 μm, while the C22-C25 antennas are resonant at ∼1.2 μm. By modulating the power of a 1550 nm pump laser polarized along the antenna's long axis (Figure 3), optical switching is induced with the MIT in VO_2 being observed at ~30 mW. When the bare film is patterned with Au antennas, the switching threshold can be reduced to as low as ∼10 mW. More interestingly, in the C21 array, which has a lower frequency resonance than the other antennas, the MIT happens continuously. Unlike the other sharp transitions, this response can be more suited to emulate smooth nonlinear functions.

The development of a reliable optical nonlinearity is crucial for advancing photonic computing. Our results indicate that VO_2-based plasmonic metasurfaces can provide a strong and tunable optical response to devices working at telecom wavelengths. Moreover, by carefully tuning the antenna's shape for specific resonances, the nonlinear optical response can be made into a smooth function, more closely matching activation functions used in neural networks.

[1]. J. Parra et al, Scientific Reports 15, 5608 (2025).

[2]. K. Sun et al, Nanophotonics 11, 17, (2022): 4101-4114.

[3]. O.Muskens et al, Light Science and Applications 5, e16173 (2016)

A massive-scale droplet microfluidic platform based on an active matrix of high-voltage thin-film transistors

Wednesday, 17th September - 15:00: - Poster

Prof. Xing Cheng [1]

1. *Southern University of Science and Technology*

Droplet-based digital microfluidics are useful alternative to channel-based continuous flow microfluidics. Particularly, droplets actuated by EWOD or DEP forces allow facile manipulation of droplets in large scale using microfabricated electrode arrays. In recent years, electrode arrays driven by active-matrix thin-film transistors (TFTs) are gaining increasing attention due to its automatic operation and potential in scalability. However, current TFTs from flat panel display industry operates at a voltage of 40-60 volts, and this voltage level is often insufficient in driving droplets with less polarity, which sometimes requires a driving voltage of more than 100 volts. Additionally, droplet heating required in applications such as on-chip PCR often expedite the threshold voltage shift in TFTs and render the TFTs unusable after prolonged period of heating and electrical biasing.
To address the limitations of current TFTs in actuating digital microfluidic platform, we design, fabricate and tested a new architecture of TFTs. The cross-sectional view of the new design and a fabricated device based on a-Si is shown in Fig. 1. By splitting channel into two sections and employing internal floating back gates, the new device can withstand high source-drain voltage while approximately maintains the same source-drain current level. Electrical characterizations of the device are shown in Fig. 2. The transfer curve (top left) and the output curve (top right) show a well-behaved a-Si TFT. The high-voltage biasing in Fig. 2 (bottom left) shows the new device can withstand up to ~ 390 volts before breakdown, which has much better high-voltage performance compared to conventional device structure. The device after breakdown is shown in Fig. 2 (bottom right).
A 400x400 AM array of electrodes driven by our high-voltage TFTs is fabricated through a multi-project on glass (MPG) program from Tianma (Fig. 3). With custom-built peripheral electronics and user-interface software, we build a droplet microfluidic platform, which is capable of fully automatic actuation of hundreds of droplets. By utilizing AI imaging sensing, we achieve droplet splitting with high accuracy (~2% CV). We also demonstrate that biologically meaningful applications such as sample preparations for genomics and proteomics analysis can be completed reliably on our platform.

Vertically-Integrated VRRAM-Based Hardware Reservoir Computing System

Wednesday, 17th September - 15:00: - Poster

Prof. Sungjun Kim [1]

1. *Dongguk University*

This work demonstrates a novel hardware-oriented reservoir computing architecture that simultaneously satisfies the requirements for short-term temporal processing and long-term state retainability. By leveraging the dual-mode behavior of a single memory cell, the system achieves high computational efficiency, reduced training overhead, and minimal power usage, in a highly scaled physical area. These technological advancements lay the groundwork for manufacturable realization of compact, reliable, and energy-efficient neuromorphic processors capable with higher autonomy in the resource-limited environments

Optoelectronic Synaptic IGZO Transistor and Its Demonstration of Electrical and Optical Plasiticity for Light-Susceptive Processing-in-Memory

Wednesday, 17th September - 15:00: - Poster

Prof. Myounggon Kang [1]

1. *University of Seoul*

The optoelectronic IGZO synaptic transistor in this work has exhibited stable and reproducible dual-mode operations through electrical and optical pathways, effectively emulating the essential synaptic functions. Highlights are shed on its strong potential for integration into low-power, hardware-oriented neuromorphic systems requiring multi-modal input sensitivity and cognitive adaptability, while offering high compatibility with processing-in-memory (PIM) architectures presumably having optical input layer capable of improving the system compactness, minimizing the amount of data transmission, and reducing energy consumption. Through the results, it has been demonstrated that it is possible to move beyond conventional research on electrical neuron and synaptic devices enabling broader applicability across various domains by PIM AI.

Superhydrophobic Multifocal Microlens Array with Depth-of-Field Detection for Humid Environment

Wednesday, 17th September - 15:00: - Poster

Dr. Hao Cao [1]

1. *wuhan university*

Microlens array (MLA) has been widely applied in augmented reality and optical imaging. When used in humid environment or medical endoscopy, MLA needs to be both superhydrophobic and multifocal. However, it is not easy to achieve both superhydrophobic and multifocal function by integrating superhydrophobic and multifocal structures on the same surface by means of a simple, efficient and precise method. In this paper, the superhydrophobic multifocal MLA with superhydrophobic property and multifocal function is successfully designed for preparation based on a method of 3D lithography and soft lithography. The 3D lithography can further help the preparation of multifocal MLA with varying aperture and multi-step superhydrophobic structure with round doom. The superhydrophobic multifocal MLA with periods 50 μm and 120 μm has perfect superhydrophobic property. The water droplet can slide and bounce off the surface at a roll angle of less than 12.9° with both multifocal and integrated imaging function, as well as up to 397 μm Depth-of-Field (DOF) detection range, this greatly exceeds the conventional MLA. The perfect superhydrophobic and optical property can be achieved in extremely humid environment. The superhydrophobic multifocal MLA proposed in this paper has a promising prospect in actual practices.

Prediction of Photo Lithography Equipment Wafer Moving Robot Errors Using ARIMA model

Wednesday, 17th September - 15:00: - Poster

Mr. Kyunghwan Joo [1], ***Prof. Jae Wook Jeon*** [2]

1. *SUNG KYUN KWAN University / Samsung Electronics,* ***2.*** *Sungkyunkwan University*

• Purpose of the work;

The purpose of this study is to develop a method for predicting unexpected failures of the wafer load robot of semiconductor exposure equipment in advance and improve the operational efficiency and productivity of the equipment. In the semiconductor manufacturing process, the photo process is a key process that accurately forms a circuit pattern on a thin film-formed wafer, and in particular, the stability and accuracy of the exposure process directly affect the product quality and production yield. The wafer load robot of the photo lithography DUV model mainly uses a 3-DoF SCARA type robot, and is responsible for repeatedly moving the wafer to an accurate position. Since this robot has a structural weakness in the vertical (Z-axis) load when the robot extends in the direction of wafer movement, lightweight and durable ceramic materials are used, but fatigue accumulation and tilt phenomenon of the robot arm and gripper occur due to continuous mechanical load and repetitive movement. Such mechanical deterioration and tilt phenomenon of the robot cause a decrease in overlay accuracy and unexpected downtime of the equipment, which affects the operational efficiency of the production line.

• Novelty of the work with respect to the state of the art;

Previously, facility maintenance was focused on periodic inspections and responses to equipment failures, which limited the ability to recognize and respond to sudden and rapid component deterioration early. To overcome these problems, this study developed a deterioration prediction system for a wafer transfer robot based on the ARIMA (Autoregressive Integrated Moving Average) model. The core of this system is the wafer exchange safety sensor, which measures the tilt of the robot and gripper in real time and stops the equipment when the error limit is exceeded. However, the existing method collected wafer exchange safety sensor data only during periodic inspections, making it difficult to respond immediately to changes in the positions of the robot arm and gripper. However, in this study, we implemented a technology to collect the measurements of the wafer exchange safety sensor in real time, visualize them in the form of time series data, and monitor and predict changes. To this end, the robot and gripper tilt values were extracted from the error log, and in this process, it was recognized that the tilt change occurred rapidly when a failure occurred along with the drift due to mechanical deterioration, so the extracted values were plotted as a line chart in time series to detect the tilt change, and the ARIMA model was applied to predict the abnormally fluctuating results. In order for the ARIMA model to improve the prediction accuracy, the equipment predicted to be defective was selected as a model, and the performance of the failure prediction model was evaluated through the prediction results according to the parameter setting values of the three main parameters (p: AR, d: difference, q: MA) and actual observation data, and as a result, the Forecast (5,2,1) model, which showed the most similar prediction performance to the actual operation data, was selected and applied to the equipment, and the prediction accuracy was improved through this.

• Results of the work.

Based on the prediction system developed through this study, a preemptive response standard for replacing the robot in advance was established when the monthly tilt change of the wafer robot exceeds 0.5 mrad. After applying the system to the production site, it contributed to reducing the sudden stoppage of the equipment through prediction-based activities. These results led to increased operational efficiency of the production line and reduced maintenance costs, and it is expected to greatly contribute to improving the stability and produc-

tivity of equipment operation in the long term. We plan to conduct continuous research to further improve the accuracy and reliability of the future sudden failure prediction system, and in particular, we will consider ways to contribute to the establishment of autonomous manufacturing based on real-time cause analysis of predicted problems and an automated response system.

Optimisation of a Microfluidic Electrochemical Biosensor for E. coli Detection via ssDNA Hybridization and CRISPR/Cas-Based Sensing to Combat Sepsis

Wednesday, 17th September - 15:00: - Poster

Mrs. Eleonora Quasso [1], ***Prof. Isabelle Le Potier*** [1], ***Dr. Hiu Mun Man*** [1], ***Dr. Hervé Jacquier*** [2], ***Dr. David Bikard*** [3], ***Dr. Laurent Thouin*** [4], ***Dr. Jean Gamby*** [1]

1. *Université Paris-Saclay, Centre de Nanosciences et de Nanotechnologies,* ***2.*** *Hôpital Henri Mondor, APHP,* ***3.*** *Institut Pasteur, Université Paris Cité,* ***4.*** *Ecole normale supérieure, PSL University, Sorbonne Université*

This thesis aims to develop a biosensor to detect *Escherichia coli*, focusing on antibiotic-resistant strains causing sepsis. Using ssDNA and CRISPR/Cas methods on platinum and platinum/graphene electrodes, respectively, it targets the blaCTX-M-8 gene. Devices are tested via electrochemical techniques and COMSOL simulations to optimize probe density, balancing sensitivity and sensibility.

Scalable Nanobubble Generation Using Centrifugal Micro-Porous Mesh Disc Technology

Wednesday, 17th September - 15:00: - Poster

Mr. Bo-Wei Cheng [1], ***Prof. Yuan-Jen Chang*** [1], ***Prof. Chia-Lung Kuo*** [2], ***Dr. Kuen-Yi Wu*** [3], ***Prof. Chao-Ching Ho*** [1]

1. *National Taipei University of Technology,* ***2.*** *National Yunlin University of Science and Technology,* ***3.*** *Rayzher Industrial Co., Ltd.*

This study presents a centrifugal-driven nanobubble generation system utilizing micro-porous rotational discs for efficient and scalable nanobubble production. By enhancing gas-liquid interactions through centrifugal force, the system achieves stable, uniformly sized nanobubbles without requiring additional gas propulsion, offering significant energy efficiency and scalability benefits.

Refractive index controllable plasmonic color metasurfaces fabricated by combination of Nanoimprint lithography and Inkjet Printing

Wednesday, 17th September - 15:00: - Poster

Ms. Nefeli Dimogerontaki [1], ***Dr. Nikolaos Mattheakakis*** [2], ***Ms. Narges Heidaryan*** [3], ***Ms. Sonja Kopp*** [3], ***Dr. Michael Muehlberger*** [3], ***Dr. Nikolaos Kehagias*** [2]

1. *Department of Physics, School of Applied Mathematical and Physical Sciences National Technical University of Athens, Zografou Campus, GREECE,* ***2.*** *NCSR Demokritos, Institute of Nanoscience & Nanotechnology, P. Grigoriou 27 & Neapoleos Str., 15341 Ag. Paraskevi, Greece,* ***3.*** *PROFACTOR GmbH*

A scalable, cost-effective method for plasmonic color tuning using UV nanoimprint lithography, aluminum deposition, and inkjet printing on PET substrates. Color shifts were achieved by varying the refractive index of cover layers and the method was tested with inkjet pinting. This method enables customizable color control for applications in anti-counterfeiting, information security, and micro-scale optical encoding.

Machine Learning Enabled Thermoelectric Device Design and Optimization

Wednesday, 17th September - 15:00: - Poster

Mr. Haoji Yang [1], ***Dr. Yuxiao Zhu*** [2], ***Prof. Kees de Groot*** [2], ***Prof. Harold Chong*** [2], ***Dr. Ruomeng Huang*** [2]

1. *School of Electronics and Computer Science, University of Southampton, Southampton SO17 1BJ, United Kingdom,* ***2.*** *University of Southampton*

Thermoelectric (TE) technology has gained significant attention due to its ability to convert heat into electricity and vice versa, offering potential for sustainable energy solutions such as waste heat recovery, clean energy generation, and efficient cooling [1]. TE devices typically consist of n-type and p-type semiconductors connected by metal interconnects and capped with ceramic plates, as shown in Figure 1(a). These devices are classified into thermoelectric generators (TEGs), which convert heat into electricity, and thermoelectric coolers (TECs), which use electrical energy to provide cooling [2]. However, the low efficiency of both TEGs (around 10%) [3] and TECs (often lower than 10%) [4] limits their wider use. Improving the performance of TE devices involves two main approaches: developing better thermoelectric materials and optimizing the device design. While tools like COMSOL Multiphysics, based on the finite element method (FEM), are commonly used for design optimization, they are computationally expensive and time-consuming for iterative simulations [5]. Therefore, more efficient optimization methods are needed to enhance TE device performance.

To address the efficiency limitations of thermoelectric (TE) devices, we present a novel machine learning-based approach that integrates artificial neural networks (ANNs) with genetic algorithms (GAs) to effectively optimize both the geometry and operating conditions of thermoelectric generators (TEGs) and thermoelectric coolers (TECs). As shown in Figure 1(b) and 1(c), the ANN is trained using datasets obtained from COMSOL simulations and achieves prediction accuracy exceeding 98% for TEGs (Figure 2(a)). The model demonstrates excellent agreement with COMSOL results, with R^2 values above 0.999 for both maximum power density (PD_max) and efficiency (η), as illustrated in Figure 2(b–c) [6]. Following training, the GA is employed to explore the design space and determine optimal parameters, with sample results displayed in Figure 3. This approach was also applied to segmented TEGs (STEGs), where the ANN achieved a similar prediction accuracy of 98% and R^2 values over 0.99 for PD_max [7]. Additionally, we extended this method to optimize photovoltaic-thermoelectric generator (PV-TEG) systems, where the ANN reached 98.8% accuracy and R^2 of 0.999 for both power density and the average PV cell temperature [8]. In parallel, we applied the same strategy to TEC optimization, which is equally critical for TE device performance. The ANN developed for TECs achieved over 99% prediction accuracy, with R^2 values surpassing 0.999 for both the cooling and heat dissipation side temperatures. These results demonstrate the effectiveness and versatility of our approach in optimizing various TE systems under different conditions. The optimized device dimensions align with typical fabrication standards for both TEGs and TECs, with TE leg height, width, and depth all within the 0.1–10 mm range, ensuring manufacturability while maximizing thermoelectric performance.

We will present the performance of our artificial neural network model for both TEGs and TECs, comparing the results with those from the COMSOL model under various conditions. Additionally, we will highlight the superior simulation speed by predicting millions of results to generate mapping images. The application of a genetic algorithm in this research to identify optimal parameters will also be discussed. This work bridges the gap between high-fidelity simulation and real-time optimization, providing a scalable framework for next-generation TE device optimization.

Flexible, non-toxic SF radiochromic film based on 10,12-PCDA for on-site X-ray dosimetry

Wednesday, 17th September - 15:00: - Poster

Mr. Naseer Ahmad [1], Mrs. Aida Visus [1], Mr. Salvador David Aznar [2], Prof. Gonzalo Guirado [3], Dr. Consuelo Guardiola [1], Dr. Xavier Muñoz Berbel [1], Dr. Silvia Mena Fernández [1]

1. *Institute of Microelectronics of Barcelona (IMB-CNM, CSIC),* ***2.*** *Instituto Murciano de Investigación y Desarrollo Agrario y Medioambiental,* ***3.*** *Universitat Autonòma de Barcelona*

X-rays play a crucial role in various fields, including medicine, forensic science, security screening, scientific research, sterilization, and industrial applications, due to their ability to penetrate materials and provide detailed information[1-3]. In medicine, X-rays are particularly important for imaging, disease detection, and therapies such as cancer treatment[4]. However, excessive exposure to X-rays poses significant health risks, including tissue damage, DNA mutations, infertility, birth defects, skin burns, impaired vision, and carcinogenesis[5]. Accurate dosimetry is essential to ensure radiation safety. Yet, conventional dosimeters, such as thermoluminescent and semiconductor-based sensors, along with current commercial dosimetry films, often suffer from limitations like rigidity, high costs, and complex fabrication processes, making them less suitable for real-time, on-site detection[6].

In view of these facts, we report a novel flexible and biocompatible X-ray dosimeter based on silk fibroin films incorporating 10,12-pentacosadiynoic acid (PCDA). Upon irradiation, PCDA undergoes topo-chemical polymerization, resulting in changes in the optical density (OD) of the film. A clear linear relationship between absorbed dose (0–50 Gy) and ΔOD after irradiation has been established (Figure 1). Compared to other polymer-based membranes, these films are more biocompatible and mechanically robust: their flexibility has been tested, revealing measurable differences in mechanical properties before and after irradiation (Figure 2). In order to enable real-time, label-free, on-site dosimetry, a conductive sensor has been developed by integrating screen printed electrodes onto the PCDA–silk fibroin film. We explore for the first time the potential correlation between PCDA polymerization and changes in electrical impedance measured by electrochemical impedance spectroscopy (EIS). This correlation between impedance variation and radiation dose highlights the potential of this system for non-optical readout of radiochromic films (Figure 3).

Overall, this work advances the development of flexible, cost-effective, and biocompatible dosimeter films by introducing a new impedance-based readout method. The approach paves the way for integrating similar radiochromic films into portable microfabricated devices for medical dose monitoring and environmental radiation detection.

Open Science & Technology: Microfluidic fluid handling

Wednesday, 17th September - 15:00: - Poster

Dr. Lars Kool [1], ***Dr. Bertrand Cinquin*** [1]

1. *Institut Pierre-Gilles de Gennes pour la Microfluidique, Paris, 75005, France*

We developed standardized drivers for fluid handling using μManager, an open-source platform for microscopy automation. With these drivers, it is possible to develop device-agnostic applications that can easily be shared for increased accessibility, transparency and standardization. Furthermore, this also enables the use of real-time image analysis to control fluid-flow.

An Ultrasensitive TDSE/Au/SOD-based Electrochemical Sensing Platform for Real-Time Monitoring of Superoxide Ion at Cellular Level.

Wednesday, 17th September - 15:00: - Poster

Mr. Pratyusa Mohapatra [1], ***Prof. Soumen Das*** [1]

1. *Indian Institute of Technology Kharagpur*

Biological oxidative stress is a critical contributor to the pathogenesis of various life-threatening diseases, such as cancer and neurodegenerative disorders. This oxidative stress is primarily driven by the excessive generation of reactive oxygen species (ROS), among which superoxide anion (O_2^-) serves as the initial form that propagates the formation of more reactive ROS through various interactions. Therefore, detecting superoxide at the cellular level is crucial for controlling the overall ROS-induced stress. However, its detection is particularly challenging due to its short lifespan and high reactivity. Herein, we report the development of an ultrasensitive, planar electrode for the precise detection of superoxide ions in biological systems. The sensor fabrication consists of a thermal vapour deposition-based silver electrode (TDSE) on a polystyrene substrate, which is further functionalized with ultra-small gold nanoparticles (AuNPs) conjugated with superoxide dismutase (SOD) to enhance electrochemical activity and sensitivity[2]. TDSE exhibited superior conductivity and catalytic performance compared to various commercial carbon and gold electrodes, also demonstrated in multiple studies. After completing comprehensive physical and electrochemical characterization, the TDSE/Au/SOD sensor was employed for electrochemical detection. The resulting TDSE/Au/SOD sensor demonstrated a limit of detection (LOD) of 0.1 μM and excellent sensitivity in detecting chemically synthesized superoxide ions. Comprehensive evaluations of selectivity, sensitivity, reliability, and reproducibility were conducted, establishing the sensor as a high-performance platform. Finally, the TDSE/Au/SOD sensor was successfully used to detect superoxide at cellular levels across different cell lines (Hela and L929), exhibiting minimal interference within the cellular environment. The work established the efficacy of TDSE/Au/SOD for real-time monitoring of superoxide concentrations in biological systems, advancing research into ROS-related cellular processes and disease mechanisms.

Simulation of physical reservoir computing based on nonlinear dynamics of nanoelectromechanical resonators

Wednesday, 17th September - 15:00: - Poster

Mr. Lianghong Ye [1], ***Dr. Klaus-Peter Zauner*** [1], ***Dr. Mark Vousden*** [1], ***Mr. Yuta Kawashima*** [2], ***Prof. Toshiyuki Tsuchiya*** [2], ***Dr. Yoshishige Tsuchiya*** [1]

1. *University of Southampton,* ***2.*** *Kyoto University*

Reservoir computing is a neuromorphic computing paradigm that can be realised using Nano-electromechanical systems (NEMS) resonators, which promise higher operating frequencies, lower power consumption and smaller device footprint compared with alternative physical reservoirs. This research demonstrates the efficacy of computing using NEMS resonators by simulating a parity benchmarking task.

Microfluidic chip for electrochemical detection of circulating miRNAs: real-sample testing of cardiac disease biomarkers

Wednesday, 17th September - 15:00: - Poster

Ms. Anna Tarasova [1], ***Dr. Israël Mbomekallé*** [2], ***Prof. Sébastien Banzet*** [3], ***Dr. Hiu Mun Man*** [4], ***Prof. Isabelle Le Potier*** [4], ***Dr. Jean Gamby*** [4]

1. *Université Paris-Saclay, Centre de Nanosciences et de Nanotechnologies (C2N), Palaiseau, 91120, France,* ***2.*** *Institut de Chimie Physique d'Orsay (ICP), Orsay, 91400, France,* ***3.*** *INSERM, Institut André Lwoff (IAL), Hôpital de Clamart, Clamart, 92140, France,* ***4.*** *Université Paris-Saclay, Centre de Nanosciences et de Nanotechnologies*

We present the validation of microfluidic electrochemical biosensor for label-free, simultaneous detection of miR-1 and miR-133a – key cardiac biomarkers. The device integrates platinum microelectrodes within a microfluidic channel to enhance sensitivity and minimize sample volume. Detection of hybridisation event via electrochemical methods reaches attomolar sensitivity without amplification. The release of miRNAs was induced by notexin insertion into mice muscles. The sensor differentiates damage levels and matches RT-qPCR trends, confirming the miRNAs release even for the lowest lesion. Compact microdevice enables rapid, real-time analysis for point-of-care cardiac diagnostics.

Optic Fibre Gas Sensor featuring MoS2 QD as an Active Layer

Wednesday, 17th September - 15:00: - Poster

Dr. Mario Alberto García-Ramírez [1], ***Dr. Orfil González-Reynoso*** [1], ***Ms. Andrea Carolina Villalvazo-Hidalgo*** [1], ***Dr. Miguel Angel Bello-Jiménez*** [2], ***Dr. Abel García-Barrientos*** [2], ***Dr. Gregorio Guadalupe Carbajal-Arizaga*** [1]

1. *Universidad de Guadalajara,* ***2.*** *Universidad Autónoma de San Luis Potosí*

Bio-related sensors are key for a broad variety of fields such as industrial plants, hospitals, airports, among others. Most of them are electronic-based that require a close spot as well as an array to get enough information to be measured and analysed. In this matter, we are proposing a heterodox bio sensor based on an optic fibre array. We are considering an optic fibre featuring a set of four tapers featuring a 60 um thick at 2 cm in length in a transition of 1 cm each whilst a separation among them of 10 cm is presented as schematically is shown in Fig. 1. Once the tapers are generated, through an in-house deposition system, a thin layer of MoS2 quantum dots is deposited (Fig. 2). In order to get the desired biomolecule, we functionalised two taper sections with different bio-receptors and two to measure whole environment as a differential one. MoS2 quantum dots is an in-house synthesised material through a hydrothermal technique where it is possible to get it as a monolayer dispersion. The deposition process is as follows, the optic fibre is covered in a positive photoresist to protect whole fibre, the mask is located at each taper in order to properly deposit the MoS2, once deposited, the photoresist is developed and the material is exposed (Fig. 3). To measure it, we are using a 980 nm laser to read the state for each taper and according to the tuning bio-molecule to analyse. We obtained promising results to measure two different biomolecules in a harsh environment.

Development kinetics of photoresist films using trimethyl-ammonium hydroxide (TMAH) aqueous developer contaminated with poly-hydroxy-styrene

Wednesday, 17th September - 15:00: - Poster

Ms. Andreia Santos [1], ***Dr. Masahiko Harumoto*** [2], ***Dr. Yuqing Jin*** [3], ***Dr. Takahiro Kozawa*** [3]

1. *SCREEN SPE,* ***2.*** *SCREEN Semiconductor Solutions Co., Ltd,* ***3.*** *SANKEN, Osaka Univ*

The semiconductor industry's pursuit of sustainability requires the reduction of chemical waste and the implementation of greener processes. Tetramethylammonium hydroxide (TMAH) at 2.38 wt% concentration is widely used as a developer in photolithography, but its toxicity and environmental impact pose significant challenges [1]. Recycling TMAH on coater-developer tracks could be a promising solution, but it requires a comprehensive understanding of the interactions between TMAH and photoresist materials, as it is crucial to efficiently remove organic and inorganic impurities that leach to the developer chemical during the development process.

In this work, we initiate a fundamental investigation into the dissolution dynamics of 3 different photoresist polymer models in TMAH solutions using the quartz crystal microbalance (QCM) method [2-4]. The QCM measurement enables real-time monitoring of mass changes on a sensor surface, allowing precise measurements of dissolution rates and the identification of any alterations due to contamination. To simulate a recycling scenario, we checked how TMAH solutions contaminated with different poly(4-hydroxystyrene) (PHS) amounts affect the dissolution behaviour of each photoresist, providing insights into the interactions between the developer and photoresist components.

Our findings reveal that the presence of dissolved PHS in the developer solution significantly influences the dissolution dynamics of each model-resist: the dissolution rate significantly decreases once PHS is added in the developer solution, with higher concentrations of PHS resulting in a corresponding decrease in dissolution (Fig. 1). These results underscore the importance of effective purification strategies to remove organic contaminants from used developer solutions and emphasize the importance of understanding resist-developer interactions to develop recycling protocols that ensure both environmental sustainability and process reliability.

Introducing a new era of green and functional biopolymeric surfaces

Wednesday, 17th September - 15:00: - Poster

Dr. Dimosthenis Ioannou [1], ***Dr. Kosmas Ellinas*** [2], ***Dr. Alexandros Banis*** [1], ***Dr. Danai Ioanna Koukoumaki*** [3], ***Dr. Dimitris Sarris*** [3], ***Dr. Evangelos Gogolides*** [4]

1. *Institute of Nanoscience and Nanotechnology, NCSR "Demokritos", 27 Neapoleos str & Patriarchou Grigoriou, Ag. Paraskevi, 153 41, Greece,* ***2.*** *Laboratory of Advanced Functional Materials and Nanotechnology, Department of Food Science and Nutrition, School of the Environment, University of the Aegean, Leoforos Dimokratias 66, Myrina 81400, Lemnos, Greece,* ***3.*** *Laboratory of Physico-Chemical and Biotechnological Valorization of Food By-Products, Department of Food Science & Nutrition, School of Environment, University of the Aegean, Leoforos Dimokratias 66, Myrina 81400, Lemnos, Greece,* ***4.*** *NCSR Demokritos, Institute of Nanoscience & Nanotechnology, P. Grigoriou 27 & Neapoleos Str., 15341 Ag. Paraskevi, Greece*

Polymeric materials have long dominated the market of functional surfaces, accompanied by the rapidly increasing production of disposable plastic products and the excessive use of fossil resources. As a result, the necessity for alternative production models has emerged and the development of integrated biorefinery concepts within the circular bioeconomy era could provide a solution to this urgent problem. In this work, we demonstrate an approach to fabricate sustainable bacterial cellulose (BC) surfaces, to which we also tune the structural and chemical properties on demand using plasma nanotechnology, aiming for superhydrophobicity. As a result, the plasma-treated biopolymeric samples feature consistent surface topography with dense textures of similar sizes, very high water contact angles and very low hysteresis. Thus, the proposed surfaces are promising candidates for a new era of green and functional biopolymeric surfaces.

Pattern transfer by laser ablation: demonstration of a vacuumless process for micropatterning from lithographic masks

Wednesday, 17th September - 15:00: - Poster

Dr. Klaus Zimmer [1], ***Dr. Joachim Zajadacz*** [2], ***Dr. Martin Ehrhardt*** [1], ***Dr. Pierre Lorenz*** [1], ***Dr. Tomi Smausz*** [3], ***Prof. Bela Hopp*** [3]

1. *Leibniz Institute of Surface Engineering (IOM),* ***2.*** *Leibniz Institute of Surface Engineering (IOM), Dep. Ultra-Precision Surfaces,* ***3.*** *University of Szeged, Department of Optics and Quantum Electronics*

Pattern transfer of lithographically fabricated pattern into the functional surface is a basic process for micropatterning. Here an alternative, sustainable approach using pulsed laser radiation is proposed and demonstrated. Experimentally the transfer of lithographic pattern with micron dimensions is shown and the most important features of the pattern transfer process are summarized.

Etching of optical glass by reactive plasmas at atmospheric pressure

Wednesday, 17th September - 15:00: - Poster

Dr. Martin Ehrhardt [1]***, Mr. Robert Heinke*** [2]***, Dr. Pierre Lorenz*** [1]***, Prof. Thomas Arnold*** [3]***,***
Dr. Klaus Zimmer [1]

1. *Leibniz Institute of Surface Engineering (IOM),* ***2.*** *Leibniz Institute of Surface Engineering (IOM) and Technische Universität Dresden,* ***3.*** *Technical University Dresden*

Etching of glass materials with atmospheric plasma technologies is challenging due to the chemical composition of glass that contain different metal oxides that form non-volatile reaction products during fluorine plasma etching. Laser-induced plasmas and reactive atmospheric plasma jets are utilised for glass etching. The characteristics of the etching process and the achievable surfaces are discussed in the presentation.

From Waste to Resource: Engineering End-of-Life Graphite Anodes for Solid-State Hydrogen Storage

Wednesday, 17th September - 15:00: - Poster

Mr. Mukhammed Kenzhebek [1]

1. *National Laboratory Astana, Nazarbayev University*

Spent LIB graphite anodes, structurally modified by cycling, are upcycled for hydrogen storage. A selective heat treatment removes binders while preserving lithium, enhancing physisorption and chemisorption. Further exfoliation, doping, and metal decoration improve adsorption properties, positioning the material as a multifunctional platform for solid-state hydrogen storage.

Low-Waste Fabrication of Flexible Carbon Electrodes: Capacitance Comparison of Inkjet-Printed and Laser-Induced Graphene with Ag Nanoparticles

Wednesday, 17th September - 15:00: - Poster

Ms. Rou Xuan Goh [1], Mr. Ishant G. Patil [1], Dr. Suan Hui Pu [2], Dr. Suhana Sultan [3], Prof. Harold Chong [4], Dr. Ivan Ling [4]

1. *Smart Manufacturing and Systems Research Group, University of Southampton Malaysia,* ***2.*** *University of Southampton Malaysia,* ***3.*** *Universiti Teknologi Malaysia,* ***4.*** *University of Southampton*

Sustainable fabrication methods for flexible electronics are critical to advancing low-energy, low-waste technologies. This study investigates the electrochemical performance of reduced graphene oxide (rGO) and laser-induced graphene (LIG) electrodes, fabricated using environmentally friendly methods: inkjet printing and laser scribing, respectively. Both materials were further enhanced by the incorporation of silver (Ag) nanoparticles, known to improve conductivity and charge storage through synergistic interactions with graphene's conductive network. Inkjet-printed rGO electrodes were fabricated on polyethylene terephthalate (PET) substrates using a 50 wt.% rGO and 50 wt.% Ag nanoparticle ink. LIG electrodes were produced by CO_2 laser scribing on polyimide (PI) films and subsequently modified via drop-casting of an Ag nanoparticle solution. Cyclic voltammetry was conducted in a standard three-electrode configuration using 1 M KCl electrolyte to evaluate interfacial capacitance. The results demonstrate that Ag loading significantly improves the capacitance of both electrode types, with inkjet-printed rGO in an offset Ag configuration achieving a maximum interfacial capacitance of 0.0025 mF/cm² representing a fivefold improvement over its non-loaded counterpart and a 6.5% enhancement compared to aligned Ag configurations. LIG electrodes exhibited a 5.6% capacitance increase upon Ag loading. These findings highlight the potential of low-energy, scalable techniques for producing high-performance, flexible energy storage devices. The demonstrated enhancements through Ag integration provide a promising pathway for further research into sustainable, high-efficiency capacitive materials for next-generation electronics.

Mobile Ions Improve the Power Conversion Efficiency of Perovskite Solar Cells with Large Energetic Offsets

Wednesday, 17th September - 15:00: - Poster

Ms. Lucy Hart [1], Mr. Fraser Angus [2], Ms. Yin Li [3], Mr. Abdul Kahleed [3], Dr. Philip Calado [4], Prof. James Durrant [5], Prof. Aleksandra Djurišić [3], Dr. Pablo Docampo [2], Dr. Piers Barnes [1]

1. *Department of Physics, Imperial College London,* ***2.*** *Department of Chemistry, University of Glasgow,* ***3.*** *Department of Physics, The University of Hong Kong,* ***4.*** *University of Southampton,* ***5.*** *Department of Chemistry, Imperial College London*

Metal halide perovskites have attracted significant research attention as photovoltaic materials for next generation solar cells, with the best lab-scale devices achieving power conversion efficiencies comparable to incumbent silicon solar cell technology (~26%).[1][2] However, the underlying device physics of perovskite solar cells (PSCs) is substantially different to that of previous generations of photovoltaics, owing to the presence of high concentrations of mobile ionic (Schottky) defects in the perovskite layer, which redistribute to screen internal electric fields.[3][4][5] Consequently, new design criteria must be established to optimise the performance of PSCs.

In this recently published study[6] we use the open-source mixed ionic-electronic device simulation software Driftfusion[7] to show that, while the presence of mobile ionic defects tends to reduce short-circuit current due to screening of the internal field, it boosts the open circuit voltage (V_{OC}) relative to otherwise identical devices without mobile ions as illustrated in Fig 1a. We find that redistribution of mobile ions under steady-state operation leads to the largest improvement in V_{OC} where a large energetic offset exists to the transport layers and when interfacial recombination is the dominant loss pathway (see Fig 1b). These criteria are both met in many high-performing devices. The improvement in V_{OC} arises because, once V_{OC} surpasses the flat-band condition in the active layer (V_{flat}), ionic carriers screen the reverse electric field that would otherwise drive minority carriers to the interfaces, thus reducing surface recombination currents.

We verified our predictions experimentally by using short voltage pulses to measure the current density-voltage characteristics of a set of PSCs (Figs 2a and 2b). By switching rapidly between read and set voltages, the redistribution of mobile ions was minimised during the measurements. Using this technique, we estimated the pre-bias voltage corresponding to V_{flat} and a uniform ion distribution in the perovskite layer. As the performance of a device in this state is theoretically equivalent to an otherwise identical device without mobile ionic defects, these results allowed us to isolate the influence of ionic redistribution on device performance. (Figs 2c-e). Our results demonstrate that ionic modulation of recombination currents increases the range of transport layer energy offsets where it is possible to achieve high performance results and imply new design strategies for PSCs.

References

[1] H. Min et al., Nature, 598 (2021) 444–450.

[2] Park, J et al., Nature, 616 (2023) 724–730.

[3] A. Senocrate et al., Angew. Chem., Int. Ed., 56 (2017) 7755–7759.

[4] N. E. Courtier et al., Energy Environ. Sci., 12 (2019) 396–409.

[5] D. Moia and J. Maier, ACS Energy Lett., 6 (2021) 1566–1576.

[6] L. Hart et al., Energy Environ. Sci., 17 (2024) 7107-7118.

[7] P. Calado et al., J. Comput. Electron., 21 (2022) 960–991.

Heterogeneous Integration of Diamond

Wednesday, 17th September - 15:00: - Poster

Dr. Soumen Mandal [1], ***Dr. Jerome Cuenca*** [1], ***Prof. Oliver Williams*** [1]

1. *Cardiff University*

The integration of diamond with other materials offers immense potential for extreme applications due to diamond's unique properties—such as exceptional thermal conductivity, electrical insulation, and room-temperature single-photon emission—but also presents significant challenges, primarily stemming from its low thermal expansion coefficient and difficulty in doping. These challenges complicate direct growth on non-diamond substrates, which expand more under heat and often lack chemical compatibility with carbon. The research focuses on direct diamond growth using nanodiamond seeding and interlayers on various substrates, with AlN being the only one to support thick diamond films without interlayers. Issues like poor adhesion and substrate degradation under high-temperature CVD conditions limit broader application. Consequently, direct bonding—requiring ultra-smooth surfaces and covalent interface formation—has emerged as a promising alternative, with chemical mechanical polishing enabling atomically smooth diamond surfaces and current efforts aimed at achieving room-temperature bonding to expand integration possibilities.

Oral Session 4A: Advanced Nanofabrication II

Geometric optimization improves the performance of organic electrochemical transistors for bio-sensing applications

Thursday, 18th September - 08:30: Oral Session 4A: Advanced Nanofabrication II (Plenary Hall) - Oral - Abstract ID: 431

Dr. Noemi Cesario [1], ***Prof. Natalia Malara*** [2], ***Dr. Nicola Coppedè*** [3], ***Prof. Francesco Gentile*** [4]

1. *Nanotechnology Research Center, Department of Experimental and Clinical Medicine, University "Magna Graecia" of Catanzaro, 88100 Catanzaro (Italy),* ***2.*** *Department of Health Sciences, University Magna Graecia, Catanzaro, Italy,* ***3.*** *IMEM-CNR Institute of Materials for Electronic and Magnetism, National research council, Parco area delle scienze 37/a 43124 Parma,* ***4.*** *Magna Græcia University of Catanzaro*

We investigate the influence of PEDOT:PSS channel thickness on the sensitivity of organic electrochemical transistors (OECTs) for NaCl detection. Devices with varied thicknesses (400 nm–3.5 µm) show that thicker films enhance modulation and reduce time constants, enabling improved discrimination of electrolyte concentrations via scalable microfabrication techniques.

Introducing thermal scanning probe lithography into the fabrication of semiconductor quantum devices

Thursday, 18th September - 08:45: Oral Session 4A: Advanced Nanofabrication II (Plenary Hall) - Oral - Abstract ID: 340

Mx. Iker Uranga [1], ***Mr. Robin Erne*** [2], ***Dr. Jana Chaaban*** [2], ***Dr. Marta Fernández-Regúlez*** [1], ***Prof. Joan Bausells*** [1], ***Dr. Guido Rademaker*** [3], ***Dr. Emine Çağın*** [2], ***Prof. Francesc Pérez-Murano*** [1]

1. *Institute of Microelectronics of Barcelona (IMB-CNM, CSIC),* ***2.*** *Heidelberg Instruments,* ***3.*** *CEA Leti*

The goal of this work is to benchmark the placement accuracy of the NanoFrazor tool in semiconductor quantum devices. Samples from CSIC and CEA-Leti have been patterned by NanoFrazor. Placement error for CSIC samples is sub-10 nm for 64% of patterns analyzed, and for 73% of patterns from CEA-Leti samples.

Fabrication of Vanadium Dioxide Resistors on Fully-released Polyimide Thin Films for High Strain Studies

Thursday, 18th September - 09:00: Oral Session 4A: Advanced Nanofabrication II (Plenary Hall) - Oral - Abstract ID: 338

Mr. Loïc Lahaye [1], ***Prof. Jean-Pierre Raskin*** [1], ***Prof. Denis Flandre*** [1]

1. *ICTEAM UCLouvain*

We demonstrate the fabrication of vanadium dioxide resistors on fully-released polyimide thin film for high strain studies (ε>0.1%). Raman spectroscopy is used to check the stoichiometry of the deposited film. IV measurements show a proper reversible metal-to-insulator transition which proves that the transfer does not hinder the material fundamental properties.

FabuBlox – An AI-driven Platform Connecting the Nanofabrication World

Thursday, 18th September - 09:15: Oral Session 4A: Advanced Nanofabrication II (Plenary Hall) - Oral - Abstract ID: 334

Dr. Jan Tiepelt [1], ***Dr. Josh Perozek*** [1], ***Mr. Jack Muller*** [1], ***Mr. Eyal Perry*** [1]

1. *FabuBlox Inc.*

FabuBlox is an AI-driven platform standardizing nanofabrication process design, simulation, and tool capability management across facilities. With features like automated cross-section generation, fab tracking, and its embedded AI engine, it streamlines collaboration and accelerates innovation. The long-term vision for the platform is to connect facilities, suppliers, and fabless companies in a unified marketplace. Similarly, FabuBlox Hub Portals enable fab networks to unify capabilities in one central node.

Fabrication of Seamless, Homogenous Al2O3 Membranes by Gas-Phase-Deposition for highly stable Liquid Cells for Transmission Electron Microscopy

Thursday, 18th September - 09:30: Oral Session 4A: Advanced Nanofabrication II (Plenary Hall) - Oral - Abstract ID: 308

Ms. Nathalie Pranzner [1], ***Mrs. Judith Estengre Pérez*** [1], ***Mr. Jeremy Teuber*** [2], ***Mr. Rukan Nasri*** [3], ***Dr. Irene Fernandez*** [3], ***Prof. Arwen Pearson*** [1]

1. *University of Hamburg,* ***2.*** *Max-Planck-Institute for the Structure and Dynamics of Matter,* ***3.*** *UHH*

Balancing stability and electron transparency is one of the greatest challenges in the fabrication of liquid cells for transmission electron microscopy. We present here a fabrication method based on gas-phase-deposition enabling the production of polymer-based liquid cells sealed by a continuous aluminium oxide membrane for high stability under vacuum conditions.

Localised O2 Plasma Treatment of AZO and Zn for Broadband Modulation of Optical and Radio Frequency Response.

Thursday, 18th September - 09:45: Oral Session 4A: Advanced Nanofabrication II (Plenary Hall) - Oral - Abstract ID: 41

Mr. Thomas Howe [1], ***Dr. Kai Sun*** [1], ***Prof. Otto Muskens*** [1], ***Prof. Kees de Groot*** [1]

1. *University of Southampton*

As the development of smart cities continues, the increasing amount of electromagnetic pollution hinders progress by impacting device performance and integrity. In this work, we present our novel O_2 plasma treatment on AZO and Zn, showcasing its potential for metamaterial applications in optically transparent broadband EMI shielding.

Single-Molecule Identification Using Plasmonic Nanopores and Ultrafast SERS

Thursday, 18th September - 10:00: Oral Session 4A: Advanced Nanofabrication II (Plenary Hall) - Oral - Abstract ID: 9

Dr. Kirill Khabarov [1], ***Ms. Ilaria Micol Baldi*** [1], ***Dr. Maria Blanco Formoso*** [1], ***Dr. Foroogh Khozeymeh Sarbishe*** [1], ***Dr. Giulia Bruno*** [1], ***Prof. Francesco Gentile*** [2], ***Dr. Francesco Tantussi*** [1], ***Prof. Francesco De Angelis*** [1]

1. *Istituto Italiano di Tecnologia (IIT),* ***2.*** *Magna Græcia University of Catanzaro*

Surface-Enhanced Raman Spectroscopy (SERS) enables single-molecule detection with high accuracy and rapid response, offering unique vibrational fingerprints for molecular identification. We present a novel approach for biopolymer sequencing using permeable plasmonic membranes and real-time microsecond SERS detection with Single-Photon Avalanche Diode cameras. Molecules translocate through nanopores, allowing sequential spectral acquisition and unambiguous identification. We demonstrate accurate detection of nucleosides and peptides, achieving >89% classification accuracy at a single-molecule level. Our method enhances molecular discrimination, operates label-free, and achieves picomolar sensitivity, paving the way for next-generation sequencing and disease diagnostics with unprecedented precision.

Oral Session 4B: Advanced Nanofabrication and Characterisation

Ti-Ni-Cu shape memory alloy thin films with improved adhesion and controlled residual stress for MEMS applications

Thursday, 18th September - 08:30: Oral Session 4B: Advanced Nanofabrication and Characterisation (Charnock Lecture Theater) - Oral - Abstract ID: 237

Dr. Elaheh Akbarnejad [1], ***Mr. Alan Savan*** [1], ***Mr. Gowtham Arivanandhan*** [2], ***Prof. Manfred Kohl*** [2], ***Prof. Alfred Ludwig*** [1]

1. *Ruhr University Bochum,* ***2.*** *Karlsruhe Institute of Technology (KIT)*

This work investigates the possibility of coating Ti-Ni-Cu SMA film onto Si nanohinges with properties investigations and enhancing the SMA film adhesion to the selected substrate by reducing residual stress levels using substrate bias during the magnetron sputtering deposition process. The results support the development of TiNiCu-based actuators down to the scale of 150 nm.

Temperature Homogenization for Local Electro-Thermal Annealing of Shape Memory Alloy Microstructures

Thursday, 18th September - 08:45: Oral Session 4B: Advanced Nanofabrication and Characterisation (Charnock Lecture Theater) - Oral - Abstract ID: 266

Mr. Gowtham Arivanandhan [1], ***Dr. Elaheh Akbarnejad*** [2], ***Prof. Alfred Ludwig*** [2], ***Prof. Manfred Kohl*** [1]

1. *Karlsruhe Institute of Technology (KIT),* ***2.*** *Ruhr University Bochum*

We present a novel design strategy for achieving uniform temperature profiles upon direct Joule heating required for local electro-thermal annealing of shape memory alloy (SMA) microstructures. This strategy is validated for a Ti–Ni–Cu/Si microactuator consisting of coupled microbridges and co-integrated heating circuits fabricated by electron beam lithography and magnetron sputtering. Our research is motivated by the need for ultra-compact, bidirectional, and bistable actuators capable of producing large strokes in the order of several percent of the actuator length. Although antagonistic SMA beams have enabled buckling bistable actuation at the macroscale, scaling down to micrometer dimensions poses significant challenges. These include fabrication limitations, inhomogeneous temperature profiles, and difficulties in achieving antagonistic shape setting of SMA microbridges. In particular, conventional high-temperature annealing procedures being essential for shape setting of SMA microstructures induce undesired thermal stress in the neighbouring silicon microstructures. Local electrothermal annealing may overcome these issues, however, Joule heating may cause large temperature gradients. In this work, we mitigate these challenges by introducing a design that enables temperature homogenization during local annealing to confine the heat treatment to target regions and later on during selective actuation of antagonistic SMA microstructures with enhanced phase transformation.

3D Printing of MEMS Devices

Thursday, 18th September - 09:00: Oral Session 4B: Advanced Nanofabrication and Characterisation (Charnock Lecture Theater) - Oral - Abstract ID: 451

Prof. Frank Niklaus [1]

1. *Royal Institute of Technology (KTH)*

Traditional semiconductor manufacturing processes enable mass production of MEMS (Micro-Electro-Mechanical Systems) with high efficiency. However, these methods are not well-suited for fabricating complex MEMS components in smaller quantities, making it challenging to serve applications that require fewer than 5,000 to 10,000 units annually. To address this gap, 3D printing offers a promising alternative for producing MEMS with complex structures at low to medium volumes. In this talk, we will share our work on 3D-printing microstructures using polymer and glass materials, and explore how these techniques can be applied to develop functional MEMS devices for specialized use cases.

Lightweight Machine-Learned Surrogate Models for Carrier Transport using Gradient-Boosted Feature Selection

Thursday, 18th September - 09:30: Oral Session 4B: Advanced Nanofabrication and Characterisation (Charnock Lecture Theater) - Oral - Abstract ID: 105

Dr. Ben Rowlinson [1], ***Dr. Alexandros Keros*** [1], ***Prof. Subramanian Ramamoorthy*** [1], ***Prof. Jacqueline Cole*** [2], ***Prof. Themis Prodromakis*** [1]

1. *University of Edinburgh,* ***2.*** *University of Cambridge*

Machine learned (ML) surrogate models of material properties have gathered increasing attention in the engineering community in recent years, primarily due to beneficial scaling properties (O(n)), compared to first-principles approaches which often range from $O(n^3)$ to $O(n^7)$. An ML surrogate model is inherently only as effective as the underlying training dataset. As such, recent progress in large-scale standardised datasets has enabled increasingly accurate thermodynamic stability and property predictions using ML surrogate models. As semiconductor device engineers, arguably the most critical electronic property is hole and electron mobility (μ_h and μ_e). However, carrier transport is significantly more computationally intensive than properties such as energy above convex hull of stability (E_{hull}) and electronic bandgap (E_g). Therefore, lightweight surrogate models for mobility are becoming desirable for material screening and high-throughput "inverted pyramid" design-to-device pipelines. In this work, we propose interpretable ML surrogate models for E_g, μ_h and μ_e prediction based on chemically-relevant compositional features.

Breaking the Resolution Barrier: Phased Exposure Methodology for Precision Microfluidic Injection Moulding Tools

Thursday, 18th September - 09:45: Oral Session 4B: Advanced Nanofabrication and Characterisation (Charnock Lecture Theater) - Oral - Abstract ID: 347

Mr. Euan McDonald [1], ***Mr. Pedro Duarte Menezes*** [1], ***Dr. Hojjat Madadi*** [2], ***Dr. Xin Li*** [2], ***Ms. Alysha Hunter*** [1], ***Prof. Daniel Mulvihill*** [1], ***Prof. Nikolaj Gadegaard*** [1]

1. *The University of Glasgow,* ***2.*** *Sphere Bio LTD*

Masked Stereolithography (mSLA) 3D printing offers numerous advantages for microfluidic applications, including design flexibility and rapid prototyping capabilities suitable for injection moulding [1]. However, conventional mSLA approaches utilise uniform exposure calibration regardless of feature size and geometry, fundamentally limiting resolution and feature accuracy for high-precision microfluidics. With standard techniques, features below 100µm in the XY plane are particularly challenging to reproduce accurately, regardless of Z resolution capabilities. This work presents an optimised phased exposure methodology that significantly extends the capabilities of commercial mSLA systems to achieve previously unattainable feature sizes—down to 30µm—and accuracy without specialised equipment.

Our approach introduces three key innovations: feature-specific exposure control, component-wise exposure of intersecting features, and critical sequencing of exposure order. Building upon previous work demonstrating how spatially controlled exposure can enhance resolution in fully 3D printed microfluidics [2], we apply and extend these principles specifically for injection moulding tooling. Unlike conventional methods that expose entire layers uniformly, we selectively control exposure parameters for specific feature sizes and geometries. More importantly, we demonstrate that intersecting microfluidic features (such as droplet generator nozzles) can be decomposed into separate components and exposed sequentially for superior dimensional control. Critical features are prioritised in the exposure sequence, with smaller, geometry-sensitive features exposed first, followed by less critical larger features.

Experimental validation with 60µm droplet generator nozzles demonstrated that phased exposure produced channels with mean height of 62.2µm (±0.258µm) and width of 66.9µm (±10µm), compared to non-optimised approaches yielding 43.2µm (±1.2µm) height and 97.0µm (±12.7µm) width. Microscopy confirmed elimination of rounded corners at channel intersections, achieving sharp junctions critical for consistent droplet generation. The resulting injection moulding tools enabled same-day production of fully functional high accuracy microfluidic devices in commercial thermoplastics (PS and COC). From initial design to testable device, the entire process requires just over 3.5 hours—1 hour for design and exposure planning, 2 hours for mould fabrication, 1 minute cycle for injection moulding, and 30 minutes for assembly and bonding. This represents a paradigm shift compared to traditional injection moulding tooling, which typically requires weeks to months of lead time at costs orders of magnitude higher.

This methodology seamlessly integrates into an end-to-end manufacturing workflow for microfluidic devices, supporting production of up to 500 devices per mould. Current limitations include the need for material-specific calibration and manual exposure editing, presenting opportunities for future automation and further miniaturisation beyond the current 30µm feature size achievement.

Ultra-precision diamond micro-grinding of integrated mirrors in silicon for quantum atomic technologies

Thursday, 18th September - 10:00: Oral Session 4B: Advanced Nanofabrication and Characterisation (Charnock Lecture Theater) - Oral - Abstract ID: 220

Dr. Paul Gow [1]***, Mr. Joel Keen*** [2]***, Mr. Glenn Churchill*** [1]***, Prof. Corin Gawith*** [1]***, Prof. James Gates*** [1]

1. *University of Southampton,* ***2.*** *Optoelectronics Research Centre, University of Southampton, SO17 1BJ, UK*

We present vacuum cell components fabricated in 6mm thick silicon using diamond micro-grinding tools. Features include apertures, vias, and low chipping suitable for bonding. We also present ductile machining to produce optical-grade mirrors internal to the vacuum cell frames, with angles not restricted to crystal planes as in etching.

Magnetic artificial cilia to steer the locomotion of microswimmers

Thursday, 18th September - 10:15: Oral Session 4B: Advanced Nanofabrication and Characterisation (Charnock Lecture Theater) - Oral - Abstract ID: 253

Dr. Zhiwei Cui [1], ***Mr. Kushal Swamy*** [1], ***Prof. Jaap den Toonder*** [2], ***Dr. Farbod Alijani*** [1]

1. *Delft University of Technology,* ***2.*** *Eindhoven University of Technology*

In this study, we integrate magnetic artificial cilia within microfabricated cavities to investigate their effect on the dynamics of microswimmers. When actuated, the cilia generate external harmonic force inside the cavities, which alters the behavior of the microswimmers. These findings contribute to the development of active microenvironments for biomedical microrobotics.

Oral Session 4C: Electronics II

Mesoporous silica-based memristor for neuromorphic computing

Thursday, 18th September - 08:30: Oral Session 4C: Electronics II (Seminar Room) - Oral - Abstract ID: 358

Mr. Bohao Ding [1], ***Dr. Tongjun Zhang*** [1], ***Dr. Li Shao*** [1], ***Dr. Ayoub Jaafa*** [1], ***Prof. Andrew Hector*** [1], ***Dr. Ruomeng Huang*** [1]

1. *University of Southampton*

Neuromorphic computing is a novel approach inspired by the structure and function of neurons and synapses in the human brain, aiming to overcome the limitations of traditional Von Neumann architectures and improve energy efficiency for data-intensive tasks like machine learning. Diffusive memristors, known for their ability to mimic complex synaptic plasticity, have gained significant attention, especially when based on mesoporous materials that offer rapid electron transport and high surface-to-volume ratios. Incorporating porous structures into the electrolyte layer allows precise regulation of ion dynamics through controlled pore geometry, essential for nano- and atomic-scale control.

In this study, we developed a diffusive memristor using 3D-structured mesoporous silica ($mSiO_2$) via a cost-effective, vacuum-free sol–gel process. The device exhibits both volatile and non-volatile resistive switching, tunable by the applied compliance current. The fast mobility of Ag+ ions within the porous network enables short-term memory functionality. By engineering the porosity, pore orientation, and electrode materials, we further control ion migration and synaptic behavior, such as postsynaptic currents and relaxation times.

Additionally, we fabricated crossbar architectures to improve scalability and integrated these memristors into reservoir computing systems, achieving high classification accuracy. These findings demonstrate the potential of mesoporous silica-based memristors to advance scalable, energy-efficient neuromorphic systems and open new avenues for future research.

Novel Reagents for the Solution-processible Deposition of Low-dimensional Materials and their Composites for Flexible Memristors and Smart Sensors

Thursday, 18th September - 08:45: Oral Session 4C: Electronics II (Seminar Room) - Oral - Abstract ID: 229

Mrs. Trishala Desai [1], ***Dr. Chitra Gurnani*** [2]

1. *Trishala Desai,* ***2.*** *Ecole Centrale School of Engineering, Mahindra University, Hyderabad*

This work highlights the solution-processible synthesis of cellulose-MXene composite hydrogels and NiS_2 nanostructures for advanced flexible electronics. These materials facilitate scalable, cost-effective fabrication of high-performance resistive memory devices, synaptic mimics, and breath sensors, exhibiting exceptional sensitivity, mechanical durability, and biocompatibility. This study pioneers sustainable, multifunctional solutions for wearable healthcare and IoT applications, integrating nanomaterials with cutting-edge technologies.

Non-planar patterning of an Organic Electrochemical Transistor (OECT) on a tapered optical fiber-based neural interface

Thursday, 18th September - 09:00: Oral Session 4C: Electronics II (Seminar Room) - Oral - Abstract ID: 386

Mrs. Sneha Pottekkad [1], ***Dr. Stella Aslanoglou*** [1], ***Dr. Barbara Spagnolo*** [1], ***Dr. Antonio Qualtieri*** [1], ***Dr. Claudia Latte Bovio*** [1], ***Dr. Michele Di Lauro*** [2], ***Mr. Federico Rondelli*** [2], ***Dr. Fabio Biscarini*** [2], ***Prof. Massimo De Vittorio*** [1], ***Dr. Ferruccio Pisanello*** [1]

1. *Center for Biomolecular Nanotechnologies, Istituto Italiano di Tecnologia (IIT), 73010 Arnesano, LE, Italy,* ***2.*** *Istituto Italiano di Tecnologia (IIT)*

In this work, we demonstrate, for the first time, a strategy for the integration of an Organic electrochemical transistor (OECT) on the highly non-planar surface of a tapered optical fiber (TF)-based neural interface for simultaneous performance of optogenetic stimulation and neurochemical sensing.

Towards Additive Manufacturing and Conformal Metallization of 3D-Printed Antennas for Radar Applications

Thursday, 18th September - 09:15: Oral Session 4C: Electronics II (Seminar Room) - Oral - Abstract ID: 401

Dr. Michael Haslinger [1], ***Dr. Vaclav Prochazka*** [2], ***Mr. Peter Bauer*** [3], ***Dr. Dieter Holzinger*** [3], ***Mr. Jean Temga*** [4], ***Dr. Saeid Kameramzadeh*** [4]

1. *PROFACTOR GmbH,* ***2.*** *PROFACTOR GmbH, Im Stadtgut D1, 4407 Steyr, Austria,* ***3.*** *TIGER Coatings GmbH & Co KG, Wels, 4600, Austria,* ***4.*** *Millimeter Wave Technologies, Intelligent Wireless System, Silicon Austria Labs (SAL), 4040 Linz, Austria.*

Additive manufacturing via stereolithography (SLA) enables rapid, lightweight fabrication of volumetric waveguides, antenna structures, and a WR12 Butler matrix. Post-print metallization—using dip coating, electroplating, and electroless plating with silver or copper—yields continuous conductive surfaces essential for wave propagation. We introduce SLA resins optimized for millimeter-wave operation and evaluate coating uniformity in high-aspect-ratio channels. High-frequency measurements demonstrate return losses, bandwidths, and radiation patterns. These results demonstrate that SLA combined with advanced metallization delivers rapid prototyping of volumetric waveguide antennas.

Adaptive Reservoir Computing with Electro-Optical and 3D Structured Memristor Hardware Platforms

Thursday, 18th September - 09:30: Oral Session 4C: Electronics II (Seminar Room) - Oral - Abstract ID: 452

Prof. Sungjun Kim [1]

1. *Dongguk University*

The reservoir computing (RC) is an emerging neuromorphic paradigm designed to efficiently process temporal and sequential data by projecting inputs into a high-dimensional dynamic state space using a nonlinear, fixed reservoir. Unlike traditional recurrent neural networks, RC simplifies training by decoupling memory and learning; only the readout layer is trained, significantly reducing computational cost. To implement RC at the hardware level, our research focuses on developing adaptive memory-based platforms with coexisting short-term and long-term memory capabilities. These platforms leverage various emerging memory technologies, including 2D planar resistive switching memories (RRAM), ferroelectric tunnel junctions (FTJs), and 3D vertically stacked RRAM and ferroelectric capacitor arrays.

Volatile memory elements exhibiting tunable short-term memory (STM) dynamics were implemented using oxygen-rich TiO_x layers and metastable defect configurations. These devices showed conductance decay characteristics modulated by the magnitude and duration of electrical or optical stimuli. We demonstrated their potential as nonlinear dynamic reservoirs capable of capturing complex temporal features. On the other hand, non-volatile memory arrays served as readout layers, where precision weight updates were achieved via an Incremental Step Pulse with Verify Algorithm (ISPVA), enabling up to 4-bit multilevel conductance states with high yield (>98%) across memristor arrays (e.g., 24×24 cells).

Moreover, we explored RGB-sensitive optical reservoir computing by integrating light-activated memristors with gold nanoparticles and ferroelectric switching layers. These devices enabled wavelength-dependent modulation of conductance and supported direct color image classification without pre-processing, achieving 97.99% accuracy on the Fruits-360 dataset and 96.37% on MNIST using simple MLP classifiers. Additionally, the monolithic integration of STM (TiN-BE) and LTM (W-BE) VRRAM cells within a unified 3D array offers a scalable architecture for full RC implementation.

Overall, our hardware platforms represent a holistic approach to physical reservoir computing, combining materials engineering, device design, and circuit integration. These systems are highly applicable to energy-efficient neuromorphic processors for edge computing, real-time biosignal analysis, and intelligent sensing systems. By tailoring volatility, optical sensitivity, and structural integration, we pave the way toward fully functional, hardware-implemented reservoir computing systems.

VO2-based memristor grown by ALD for neuromorphic computing

Thursday, 18th September - 09:45: Oral Session 4C: Electronics II (Seminar Room) - Oral - Abstract ID: 329

Mr. Bingkai Ding [1], ***Dr. Ruomeng Huang*** [1], ***Dr. Kai Sun*** [1], ***Prof. Kees de Groot*** [1]

1. *University of Southampton*

Drawing inspiration from the efficiency of brain, we developed ALD-grown VO_2 memristors that exhibit volatile, threshold-switching behavior closely mimicking neuronal and synaptic functions. These devices offer excellent uniformity, scalability, and reproducible electrical performance at room temperature, highlighting their potential for energy-efficient neuromorphic computing.

Enhancement of Data Retention Characteristics in 2D and 3D NAND Flash via Hydrogen Trap Engineering

Thursday, 18th September - 10:00: Oral Session 4C: Electronics II (Seminar Room) - Oral - Abstract ID: 389

Mr. Joongho Yoon [1], ***Mr. MinSung Song*** [1], ***Mr. HyunSuk Kim*** [1], ***Mr. EunJin Baek*** [1], ***Mr. KeeJeong Rho*** [1], ***Mr. JungGyu Kim*** [1], ***Mr. JongKwang Lim*** [1], ***Mr. YoungHo Kwon*** [1], ***Dr. YongSik Yim*** [1]

1. *Samsung Electronics*

In this study, we investigate the impact of hydrogen on data retention characteristics in both planar (2D) and vertical (3D) NAND flash memory. Through modeling of hydrogen behavior and implementation of trap engineering techniques, we achieved significant improvements in data retention. Hydrogen incorporation prior to cell contact formation serves to suppress cell-to-cell interference by increasing charge traps. Subsequently, outgassing processes are applied post cell contact formation to remove excess hydrogen, thereby stabilizing long-term data retention. Structural modifications—such as partial removal of the blocking SiN layer—facilitate hydrogen exhaust pathways. Experimental results down to sub-2xnm technology nodes demonstrate that this approach is effective in enhancing retention characteristics and is highly applicable to advanced vertical NAND architectures.

Oral Session 4D: Sustainable Fabrication Processes I

Pattern transfer using atmospheric pressure plasma processes

Thursday, 18th September - 08:30: Oral Session 4D: Sustainable Fabrication Processes I (One Ocean Suite) - Oral - Abstract ID: 367

Dr. Martin Ehrhardt [1], Mr. Robert Heinke [2], Dr. Pierre Lorenz [1], Mr. Visar Demiri [1], Dr. Joachim Zajadacz [3], Prof. Thomas Arnold [4], Dr. Klaus Zimmer [1]

1. *Leibniz Institute of Surface Engineering (IOM),* ***2.*** *Leibniz Institute of Surface Engineering (IOM) and Technische Universität Dresden,* ***3.*** *Leibniz Institute of Surface Engineering (IOM), Dep. Ultra-Precision Surfaces,* ***4.*** *Technical University Dresden*

Pattern transfer of masked substrates is usually performed by plasma etching technologies that, however, requires vacuum whereby processing limitation in time, cost, sample size and throughput may appear. Therefore, two approaches for atmospheric plasma-based pattern transfer processes were studied. Experimentally, the pattern transfer of micron sized lines into fused silica is shown and the most important characteristics of the r process and the achievable surfaces are given.

Towards Sustainable Electronics: Wafer-Scale Fabrication of Fully Biodegradable CMOS Devices

Thursday, 18th September - 08:45: Oral Session 4D: Sustainable Fabrication Processes I (One Ocean Suite) - Oral - Abstract ID: 277

Ms. Laura Cavedoni [1], ***Mr. Zhengwei Liao*** [1], ***Mr. Yukun Lian*** [1], ***Mr. Francesco Stallone*** [1], ***Prof. Filipe Arroyo Cardoso*** [1], ***Prof. Clementine Boutry*** [1]

1. *Delft University of Technology*

The growing environmental impact of electronic devices underscores the urgent need for sustainable alternatives. We present a wafer-scale, fully biodegradable CMOS fabrication process compatible with standard foundry techniques. Using ultra-thin silicon substrates, molybdenum interconnects, and biodegradable dielectrics, we demonstrate the fabrication of a biodegradable NMOS transistor. Process simulations guided dopant implantation to ensure reliable operation in ultra-thin silicon. The fabricated devices exhibit an on/off ratio >10^3 and a threshold voltage of ~2.8 V. While further optimization is needed, this work represents a significant step toward scalable, sustainable electronics.

Conductive carbon film growth from recycled plastics

Thursday, 18th September - 09:00: Oral Session 4D: Sustainable Fabrication Processes I (One Ocean Suite) - Oral - Abstract ID: 150

Mr. Carlos Barbero Rodriguez [1], ***Dr. Geoff Fowler*** [1], ***Prof. Kristel Fobelets*** [1]

1. *Imperial College London*

A method for growth of conductive carbon layers on silicon from polystyrene is demonstrated. Placing p-Si or n-Si and polystyrene in a tube furnace at high temperature (700, 800 and 900 °C) under N_2 flow, a carbon film is grown on Si. The effect of process temperature on film properties and microstructure is studied.

Development of sustainable machining processes to manufacture vacuum cells for Quantum Technology

Thursday, 18th September - 09:15: Oral Session 4D: Sustainable Fabrication Processes I (One Ocean Suite) - Oral - Abstract ID: 32

Mr. Joel Keen [1], ***Dr. Paul Gow*** [1], ***Mr. Glenn Churchill*** [1], ***Prof. Corin Gawith*** [1], ***Prof. James Gates*** [1]

1. *University of Southampton*

Future quantum technologies require wafer-based fabrication of millimetre-scale vacuum cells with nanometric surface quality and three-dimensional optical access. This is both challenging for cleanroom fabrication and for sustainability. In this work, we propose an optimised hybrid machining process with waterjet rough cutting and diamond finish grinding to achieve optical interfaces.

Energy-efficient optical crosslinking system for sustainability in ArFi lithography

Thursday, 18th September - 09:30: Oral Session 4D: Sustainable Fabrication Processes I (One Ocean Suite) - Oral - Abstract ID: 332

Ms. SEUNGJOO BAEK [1], ***Ms. Elke Caron*** [1], ***Mr. Wesley Zanders*** [1], ***Ms. Andreia Santos*** [2], ***Dr. Masahiko Harumoto*** [3], ***Dr. Seonggil Heo*** [4], ***Mr. Jelle Vandereyken*** [4], ***Ms. Veerle Van Driessche*** [5], ***Mr. Douglas Guerrero*** [5]

1. *Screen SPE Germany GmbH,* ***2.*** *SCREEN SPE,* ***3.*** *SCREEN Semiconductor Solutions Co., Ltd,* ***4.*** *imec,* ***5.*** *Brewer Science*

With increasing global emphasis on climate change and sustainability, the semiconductor industry is actively seeking ways to minimize its environmental impact. Reducing greenhouse gas (GHG) emissions and adopting greener processes have become essential priorities in achieving long-term sustainability. Energy efficiency is a critical focus area in the chip manufacturing, as electricity consumption is recognized as one of the most significant challenges due to its resource-intensive nature. Lithography tools, in particular, contribute heavily to energy usage, requiring substantial power to operate effectively. The conventional lithographic process for curing underlayer materials relies on heat applied through a hotplate, which is dependent on elevated temperatures to achieve film densification. The high temperatures required for thermal baking of underlayer materials and the need to maintain elevated target temperatures significantly contribute to energy consumption in track systems, raising concerns about energy usage.

SCREEN introduced an innovative energy-saving process utilizing light, integrated into SCREEN's DT-3000 track, as an energy-efficient alternative to conventional baking process for baking underlayer materials using heat on the hotplate in exposure extreme ultraviolet (EUV) lithography. [1-3] This novel technique has successfully demonstrated significant energy-conservation and rapid processing at room temperature while maintaining lithographic performance. Following this initial success, we have extended the evaluation of this technology to ArF immersion (ArFi) lithography, which remains widely used in the semiconductor industry. By applying optical crosslinking to ArFi processes, we aim to demonstrate that this approach is not limited to EUV but can also deliver environmental and process integration advantage across multiple lithography platforms.

In this work, we assessed the patterning performance of the optical crosslinking system using light-curable underlayer materials, which achieved full crosslinking at 200mJ/cm^2, in ArFi lithography. The patterning results from the after-development inspection (ADI) process on a pitch 90 nm line-and-space (L/S) structure with a critical dimension (CD) of 41 nm demonstrate that the optical crosslinking process shows competitive patterns compared to the conventional thermal crosslinking system (Fig 1). To further validate this approach, we advanced the study to contact hole (CH) patterns on a pitch 100 nm targeting a CD of 50 nm and observed improved pattern performance, including dose to size, depth of focus (DOF) and exposure latitude (EL), as shown in Fig 2. Fig 3 shows that the optical crosslinking process demonstrated energy savings of 75% for spin-on carbon (SOC) and 60% for spin-on glass (SOG) compared to thermal-curable underlayers, without compromising lithographic performance. These findings highlight the potential of optical crosslinking as a sustainable and process-compatible solution for next-generation lithography, enabling reduced environmental impact while maintaining pattern quality.

Isotropic etching of suspended Si structures using a single-step, single-mask deep reactive ion etching process

Thursday, 18th September - 09:45: Oral Session 4D: Sustainable Fabrication Processes I (One Ocean Suite) - Oral - Abstract ID: 159

Dr. Sarah Günther-Müller [1], ***Mr. Marius Hillebrand*** [2], ***Prof. Martin Hoffmann*** [2], ***Prof. Steffen Strehle*** [1]

1. *Techische Universität Ilmenau,* ***2.*** *Ruhr University Bochum*

The development of efficient and cost-effective fabrication techniques is essential in advancing microelectromechanical systems (MEMS). This work introduces a simplified process for producing suspended silicon structures using a single-mask approach combined with deep reactive ion etching (DRIE). By strategically alternating between isotropic and anisotropic etching steps, both single- and multi-level released structures can be achieved without the need for multiple masks or complex processing sequences. Demonstrated on both bulk silicon and silicon-on-insulator (SOI) substrates, the method enables the fabrication of high-aspect-ratio structures with lateral dimensions down to 3–5 µm. Scanning electron microscopy confirms the successful release and definition of intricate features. The process also allows precise control over structure height and level separation.

Designing for End-of-Life Electronics: Additive Manufacturing of conductive materials to enable 99% degradable High-Performance Printed Circuit Boards

Thursday, 18th September - 10:00: Oral Session 4D: Sustainable Fabrication Processes I (One Ocean Suite) - Oral - Abstract ID: 463

Prof. Jeff Kettle [1], ***Dr. Jonathon Harwell*** [1]

1. *University of Glasgow*

For more than 50 years, advances in electronics have transformed every socioeconomic sector. However, this progress has largely been driven by technical or economic requirements rather than sustainability, leading to unsustainable practices with unintended consequences. In response, interest has grown in recyclable, or degradable electronics to address the escalating e-waste challenge, which is anticipated to grow significantly over the next decade and beyond. Yet, achieving high-resolution circuits with bulk-metal performance and environmentally benign end-of-life (EoL) pathways has remained a significant challenge.

Here, we report printed circuit board (PCB) assemblies in which 99.7% of the mass degrades into benign products under both controlled laboratory and soil environments, enabling circularity of integrated circuits (ICs) and reducing significantly the waste generated by the electronics. Our approach uses a “growth-and-transfer” method, where a conductive zinc (Zn) layer is electroplated onto a sacrificial carrier substrate and subsequently transferred onto a biodegradable substrate. This process yields track resolutions as fine as 5 μm, a sheet resistance of 3 mΩ/square, and a shelf life exceeding one year; an order of magnitude higher resolution than conventional subtractive PCBs made using Copper.

To demonstrate viability, we fabricated PCB-based touch sensor circuits embedding a microcontroller and amplifier to drive an LED. Their functionality, lifetime performance, and degradability were evaluated. Results show that the PCBs fully degrade within 450 hours in a soil composter or within 30 minutes under laboratory conditions using an acetic acid solution. Life Cycle Assessments (LCAs) of this manufacturing approach, benchmarked against conventional FR-4 copper (FR-4-Cu) PCBs, reveal a 79% reduction in Global Warming Potential and significant improvements across other environmental impact categories.

Moreover, this method facilitates the recovery of high-value components such as ICs and LEDs for recycling. Our findings demonstrate a scalable and new pathway to reduce e-waste, enhance component recovery and lower the overall environmental footprint of electronics throughout their entire lifecycle, while ensuring that, even if discarded in landfills, PCBs degrade into harmless end products.

Plenary Sessions

Plenary 6 - Dr Feras Alkhalil

Flexible Integrated Circuits Revolution: Innovative Manufacturing, Materials and Roadmaps

Thursday, 18th September - 11:00: Plenary 6 - Dr Feras Alkhalil (Plenary Hall) - Oral - Abstract ID: 458

Dr. Feras Alkhalil [1]

1. *PragmatIC Semiconductor*

Pragmatic Semiconductor's innovative approach to semiconductor manufacturing enables ultra-thin, flexible, low carbon and low-cost integrated circuits. In this talk we will provide an overview of our vision, our unique technology and will showcase how our innovative approach to manufacturing drives our flexible integrated circuit products and applications roadmap.

Elsevier YIA Talk - Dr Alexandros El Sachat

Engineering Thermal and Thermoelectric Transport in Two-dimensional (2D) Semiconductors and Devices

Thursday, 18th September - 11:45: Elsevier YIA Talk - Dr Alexandros El Sachat (Plenary Hall) - Oral - Abstract ID: 459

Dr. Alexandros El Sachat [1]

1. *Institute of Nanoscience and Nanotechnology, NCSR "Demokritos", 27 Neapoleos str & Patriarchou Grigoriou, Ag. Paraskevi, 153 41, Greece*

We present a comprehensive overview of three interrelated scientific investigations that collectively address the engineering of thermal and thermoelectric transport in two-dimensional (2D) materials and devices. The first study demonstrates the successful realization of large area cross-plane thermal insulation by engineering ultra-thin lattice mismatched epitaxial van der Waals heterostructures [1]. In the second study, we systematically study the temperature-dependent in-plane and cross-plane thermal conductivity in nanopatterned suspended MoS and supported WS_2 films with varying thickness in a wide temperature range (80-460 K). The research uncovers that nanopatterning is an efficiency approach to create 2D heat-routing structures that effectively confine and guide heat flow in prespecified directions [2]. Additionally, we find that WS_2 exhibits an exceptionally high in-plane thermal conductivity, ~1000 $Wm^{-1}K^{-1}$ at 80 K and tunable thermal anisotropy, i.e. increases from 30 (460 K) to 78 (80 K), which is observed to originate from the strong reduction of the out-of-plane component triggered by the onset of the quasi ballistic transport regime. Last, we investigate local thermal and thermoelectric transport [3] on devices based on nanopatterned $SnSe_2$. We found that while thermal transport varies on distances of a few tens of nanometres, the modification of Seebeck coefficient expands on much larger distance with the characteristic Seebeck exponential "decay length" being on the order of 1 μm. By selecting appropriate density and diameter of the nanofabricated patterns, we demonstrate the possibility to create large areas of Seebeck coefficient modification. Collectively, these works advance thermal management technologies and foster the design of customized thermoelectric devices.

References

[1] E. Chavez-Angel et al., Nano Letters 23, 6883–6891 (2023)

[2] P. Xiao et al. Science Advances, 10, 13, (2024)

[3] Harzheim et al. Nano Letters 18 (12), 7719-7725 (2018)

Oral Session 5A: Integrated System Processes

Microscale Patterning of Transparent Conductive Oxides (TCOs) Using High Precision Capillary Printing for Display Applications

Thursday, 18th September - 14:00: Oral Session 5A: Integrated System Processes (Plenary Hall) - Oral - Abstract ID: 12

Dr. Marc Pascual [1], ***Dr. Ludovic Hahn*** [2], ***Dr. Frederic Raynam*** [1], ***Mr. Nathan Bigan*** [1], ***Mr. Achille Guitton*** [1], ***Dr. Amin Mbarki*** [1], ***Dr. Tony Jullien*** [2], ***Dr. Chloe Guerin*** [2], ***Dr. Vincent Jousseaume*** [2]

1. *Hummink,* ***2.*** *CEA Leti*

Thin films of **Transparent Conductive Oxides (TCOs)** are widely used as electrodes and optical filters in display devices. Although **Indium Tin Oxide (ITO)** is commonly used today, alternative materials like **Zinc Oxide (ZnO)** and **Tin Dioxide (SnO_2)** show promise. However, patterning these materials at the micrometer scale remains a challenge.

To address this, **High Precision Capillary Printing (HPCaP) technology** is employed. This technique prints thin polymer masking layers on a **silicon (Si)** sample before applying a TCO layer using **Atomic Layer Deposition (ALD)**. Inspired by atomic force microscopy, **HPCaP** enables the printing of polymer melts and nanoparticle inks at the micrometer scale, without damaging the substrate.

In our experiments, we printed three different polymers—**PMMA (15k molecular weight)**, **PVP (40k molecular weight)**, and **SU8 2002**—to assess their ability to prevent the growth of **ZnO** during the ALD process. All three polymers successfully inhibited ZnO growth. Once the polymers were removed, the resulting patterns had pixel sizes smaller than **5 µm**.

While this technique is not yet suitable for mass production, it shows great potential for **prototyping and repairing** TCO-based display devices.

MULTILAYER POLYMER-BASED CANTILEVERS WITH MULTIPLE EMBEDDED PIEZORESISTIVE SENSORS FOR HIGH-SENSITIVITY ATOMIC FORCE MICROSCOPY

Thursday, 18th September - 14:15: Oral Session 5A: Integrated System Processes (Plenary Hall) - Oral - Abstract ID: 383

Mr. Ekin Asım Özek [1], ***Dr. Nahid Hosseini*** [1], ***Prof. Georg E. Fantner*** [1]

1. *LBNI, EPFL*

A polymer–semiconductor–ceramic AFM cantilever integrates dual embedded piezoresistive sensor layers for differential self-sensing. Fabricated via low-temperature wafer bonding, the device achieves 40 nm/V deflection sensitivity and 335 kHz resonance frequency—doubling sensitivity over single-sensor designs—enabling compact, laser-free AFM operation in ambient and fluidic environments with scalable MEMS-compatible fabrication.

Pattern dependent micro needle formation in the SPPW process using a digital mask

Thursday, 18th September - 14:30: Oral Session 5A: Integrated System Processes (Plenary Hall) - Oral - Abstract ID: 300

Mr. Myung Seo Kim [1], ***Mr. Jun Ho Song*** [1], ***Ms. Seo Rim Park*** [1], ***Prof. Young Tae Cho*** [1]

1. *Changwon National University, Changwon*

To address the need for efficient high-aspect-ratio fabrication, the SPPW process enables single-exposure structuring via nonlinear photopolymerization. This study reduces mask-related costs by employing a DMD-based digital mask and purposefully utilizes aggregation phenomena to fabricate microneedles, transforming a structural drawback into a functional design strategy.

Fabrication of Ultra-Scaled Back-End TiN Contacts in Silicon-Rich Oxide for High Density Memory Applications

Thursday, 18th September - 15:00: Oral Session 5A: Integrated System Processes (Plenary Hall) - Oral - Abstract ID: 174

Mrs. Christelle CHARPIN-NICOLLE [1], ***Mr. Gabriele NAVARRO*** [1], ***Mr. Antoine SALVI*** [1], ***Mrs. Catherine PELLISSIER*** [1], ***Mr. Pierre SIXT*** [1], ***Mr. Eric NGUYEN GIA CAN*** [1], ***Ms. Floriane BAUDIN*** [1], ***Ms. Cassandre BELUFFI*** [1], ***Mr. Richard SOUIL*** [1], ***Mr. Jean-Pierre NIETO*** [1], ***Mr. Dominique DESPOIS*** [1], ***Mr. Fabien LAULAGNET*** [1], ***Mr. Thomas MAGIS*** [1], ***Mr. Romuald BLANC*** [1], ***Mr. Olivier GLORIEUX*** [1], ***Mr. Grégory BONIFACE*** [1], ***Mr. Jean ROTTNER*** [1], ***Dr. Toshihiko Jimbo*** [2], ***Dr. Takashi Kojiri*** [2], ***Mr. Vincent BARRAL*** [1], ***Mr. François ANDRIEU*** [1]

1. *CEA-Leti, Uni. Grenoble Alpes, 38000 Grenoble, France,* ***2.*** *Zeon Corporation R&D Center, 1-2-1 Yako, Kawasaki-ku, Kawasaki, Kanagawa, 210-9507*

We fabricated ultra-scaled back-end TiN contacts, down to 30 nm, in Silicon-Rich Oxide (SRO) for high density memory applications. A dedicated oxide, Silicon-Rich Oxide, SiOx (x<2) was developed; its stability (index and thickness) over time and within temperature was demonstrated. A combination of two TiN deposition processes was found to correctly fill small vias, and a range of thicknesses was optimized for minimizing SRO consumption, lower than 3.3 nm. Extensive morphological characterizations (TEM, EDX and AFM analyses) were conducted, highlighting a TiN consumption in vias less than 5 nm. Electrical functionality could be demonstrated, whatever the size of the device.

Oral Session 5B:
Biodevices and Systems II

Fabrication of Low-cost Microfluidic Devices for Point-of-Care Bacterial Diagnostics

Thursday, 18th September - 14:00: Oral Session 5B: Biodevices and Systems II (Charnock Lecture Theater) - Oral - Abstract ID: 251

Dr. Maria Szola [1], ***Dr. Peng Tian*** [1], ***Ms. Chang Liu*** [1], ***Dr. Aysegül Develioglu*** [1], ***Mr. Gabriel Weber*** [1], ***Mr. Marceau Brisselian Kamary*** [1], ***Dr. Thomas Mortelmans*** [1], ***Dr. Dimitrios Kazazis*** [1], ***Dr. Philipp Berger*** [1], ***Dr. Yasin Ekinci*** [1]

1. *Paul Scherrer Institute (PSI)*

This work introduces a cost-effective, portable microfluidic device for rapid bacterial detection and identification. Utilizing advanced fabrication, the device enables size-based bacterial trapping and multiplexed analysis, with potential for clinical use.

Non-Invasive Label-Free Electrical and Optical Parrallel Recordings of Electrophysiological Action Potentials of hiPSC Cardiomyocytes

Thursday, 18th September - 14:15: Oral Session 5B: Biodevices and Systems II (Charnock Lecture Theater) - Oral - Abstract ID: 313

Dr. Julien Hurtaud [1], ***Dr. Alessio Boschi*** [1], ***Dr. Giuseppina Iachetta*** [1], ***Dr. Michele Dipalo*** [1], ***Prof. Francesco De Angelis*** [1]

1. *Istituto Italiano di Tecnologia (IIT)*

TOXFREE devices integrate optical and electrical readouts thus enabling in-vitro simultaneous label-free, non-invasive cardiotoxicity testing on hiPSC cardiomyocytes. This technology enhances the current state of art and could potentially improve drug approval rates by detecting side effects early.

Biodegradable silk fibroin nanofiber-based microparticles for wound regeneration

Thursday, 18th September - 14:30: Oral Session 5B: Biodevices and Systems II (Charnock Lecture Theater) - Oral - Abstract ID: 337

Mr. Marc Navarro [1], ***Ms. Laia Bagur*** [1], ***Mr. Lasse Højlund Eklund Thamdrup*** [2], ***Dr. Fatemeh Ajalloueian*** [2], ***Mr. Salvador David Aznar*** [3], ***Dr. Xavier Muñoz Berbel*** [1], ***Dr. Anja Boisen*** [2], ***Dr. Andreu Blanquer*** [4], ***Dr. Gonzalo Murillo*** [1]

1. *Institute of Microelectronics of Barcelona (IMB-CNM, CSIC),* ***2.*** *IDUN section, Department of Health Technology, Technical University of Denmark, DK-2800 Kongens Lyngby, Denmark,* ***3.*** *Instituto Murciano de Investigación y Desarrollo Agrario y Medioambiental,* ***4.*** *Departament de Biologia Cel.lular, Fisiologia i Immunologia, Universitat Autonoma de Barcelona*

Biodegradable microparticles made from electrospun silk fibroin nanofibers were developed for ultrasound-induced cell stimulation to enhance wound regeneration. Characterization confirmed β-sheet crystallization and high cell viability of keratinocytes and fibroblasts. The scaffold-like microparticles exhibit piezoelectric properties suitable for biomedical applications, supporting sustainable, bio-integrated electronic systems.

Development of micron mist generating nebulizer

Thursday, 18th September - 14:45: Oral Session 5B: Biodevices and Systems II (Charnock Lecture Theater) - Oral - Abstract ID: 109

Mr. Taki Watanabe [1], ***Prof. Sho Amano*** [1], ***Prof. Yuichi Utsumi*** [1], ***Prof. Kazuhiro Kanda*** [1]

1. *Laboratory of Advanced Science and Technology for Industry, University of Hyogo*

Our group developed a mesh nebulizer using a micro-perforated filter with submicron apertures, achieving generation of mist droplets with a medium diameter of 1.53 µm. Over 70% of droplets were $\leq$2 µm, and 20% were submicron-sized, enabling effective deep-lung delivery and outperforming conventional nebulizers.

Three-Dimensional Manipulation of Water Droplets via Spatially Patterned Triboelectric Charging

Thursday, 18th September - 15:00: Oral Session 5B: Biodevices and Systems II (Charnock Lecture Theater) - Oral - Abstract ID: 108

Mr. YU-CHIA CHEN [1], ***Mr. Cheng-Han Yu*** [1], ***Prof. Chin-Chi Hsu*** [1], ***Prof. Jiann Shieh*** [1]

1. *National United University*

Droplet manipulation is vital in fields like microfluidics, diagnostics, and precision manufacturing, yet traditional methods are limited to in-plane systems. We present a platform for programmable, three-dimensional droplet control using electrostatic forces and a superhydrophobic glass substrate. Water droplets, naturally carrying a positive charge when dispensed, are guided by negative charges induced on the glass through controlled water injection and PTFE-based triboelectric charging. A custom system integrates PTFE plates onto a 3D printer, enabling precise droplet movement in multiple orientations, including horizontal sliding, vertical lifting, and lateral transfer. The glass surface, made via CVD-grown silica nanowires, ensures low adhesion and supports high mobility. This platform enables mixing, targeted placement, and microscale chemical reactions, offering a versatile solution for open-space droplet manipulation, with significant implications for lab-on-a-chip systems and advanced microscale processing.

Zero-power MEMS sensors for trees health monitoring

Thursday, 18th September - 15:15: Oral Session 5B: Biodevices and Systems II (Charnock Lecture Theater) - Oral - Abstract ID: 35

Ms. Zarina Nazyrova [1], ***Prof. Emile Martincic*** [1]

1. *C2N Université Paris-Saclay*

Applications based on MEMS play a crucial role for the industry and have grown significantly for the last decades. This can provide important solutions for various fields especially for precision agriculture development. Global warming provokes stronger heat waves, and it is important to protect and adapt the agricultural sector. To prevent early wilting process, this is essential to monitor plants. In this work is presented the passive MEMS sensor based on piezoelectric material to detect the cavitation events.

Oral Session 5C:
Micro-Nano Systems I

CFET novel implementation to enhance IC integration level by stacking devices in a single vertical nanowire

Thursday, 18th September - 14:00: Oral Session 5C: Micro-Nano Systems I (Seminar Room) - Oral - Abstract ID: 312

Dr. Esteve Amat [1], ***Dr. Alberto del Moral*** [1], ***Prof. Joan Bausells*** [1], ***Prof. Francesc Pérez-Murano*** [1]

1. *Institute of Microelectronics of Barcelona (IMB-CNM, CSIC)*

CFET circuit implementation has emerged as a promising option to increase the ICs integration level. 3D configurations using vertical device topology are considered the next step to improve the performance of electronic devices/circuits. Relevant reduction in area and power consumption can be achieved.

Replaceable micromixer agitated by surface acoustic wave

Thursday, 18th September - 14:15: Oral Session 5C: Micro-Nano Systems I (Seminar Room) - Oral - Abstract ID: 31

Dr. Akinobu Yamaguchi [1], ***Mr. Masatoshi Takahashi*** [2], ***Dr. Satoshi Amaya*** [3], ***Prof. Tsunemasa Saiki*** [4]

1. *Toyo University,* ***2.*** *University of Hyogo,* ***3.*** *University of Tokyo,* ***4.*** *University of Fukuchiyama*

Lab-on-a-Chip (LOC) has attracted much attention in the fields of medicine, environmental measurement, and biochemistry etc. In LOC, the micropumps commonly used in unit chemical operations include mechanical diaphragm pumps and non-mechanical electro-osmotic pumps. These pumps are simple to use, but have the disadvantages of residual fluid in the tubing and pump and a larger system. A new pump proposal is therefore requested. Pumping mechanisms using surface acoustic waves (SAWs) are attracting attention as new pumps. [1, 2] Until now, many research groups demonstrated fluid drive, droplet transfer, continuous fluid pumping on a single chip and mixing. However, depending on the fluid used, the substrate can become contaminated and cannot be used again, because the microfluidic channels are directly formed on the piezoelectric substrate for SAW excitation and the liquid is directly manipulated on the substrate.

In the present study, a mixing system with SAWs was fabricated by means of interdigital transducer (IDT) electrodes arranged with a shifted central axis, and a coupling liquid was introduced between the SAW-excited substrate and the mixing vessel to enable separation of the substrate and vessel, as shown in Fig. 1(a). A jig was arranged to transmit the SAW propagation to the mixing vessel via the coupling solution and at the same time to position the mixing vessel so that it is not driven out of position by the SAW. An optical photograph of the completed system is shown in Fig. 1(b). When the aluminium (Al) vessel is placed on top of the coupling solution and jig and the SAW is driven, longitudinal wave propagation of the SAW occurs and the liquid in the Al vessel is driven as shown in Fig. 1(c). The driving force from the opposing SAW exerts a swirling force on the liquid in the Al vessel, so that the liquid in the Al vessel can mix. The system was fabricated onto the 500-μm-thick piezoelectric $LiNbO_3$substrate using a combination of semiconductor lithography, a lift-off process and 3D printer jig fabrication. The pitch and aperture width of IDT are set to be 200 μm and 6.0 mm with log 20, respectively.

To demonstrate and characterise the mixing system, water was used as the coupling liquid and zirconia ball with a diameter of 900 μm were floated in an Al vessel. Figure 2(a) shows snapshots of the swirling behaviour at an input power of 0.1 W. Figure 3(b) shows the time dependence of the area velocity for the input power of 0.1, 0. 3, and 0.5 W. The area velocity of the ball becomes stable and almost constat in about 3 seconds after the start of power application to the IDT.

From the snapshots, kinetic energy due to swirling behaviour is evaluated as physical energy. Based on the law conservation of angular momentum, the kinetic energy, , is given by , where , , and are the mass of zirconia ball, radius of ball rotation assumed that the ball is swirling in a nearly circular motion, and area velocity, respectively. The input power dependence is measured by applying powers of 0.1, 0.2, 0.3, 0.4, and 0.5 W to the IDT. We estimated input power dependence of kinetic energy, as plotted on Fig. 2(c). The results show that the output can have a nearly linear rotation behaviour with the respect to the input power. Next, in order to consider the optimisation of the coupling liquid, the mixing characteristics of different specific gravities of the coupling liquid were investigated. The method of investigation was based on the previous evaluation method, where NaCl was dissolved in the coupling liquid and the swirling characteristics of the zirconia balls in relation to the specific gravity of the coupling liquid were evaluated. The dependence of the evaluated physical energy on NaCl is shown in Fig. 3. The results show that there was almost no change in the swirling properties in the 0 - 20% concentration range where the evaluation was carried out.

This study shows that by introducing a SAW propagation mechanism with coupling liquids, a contamination-free and interchangeable mixing system can be achieved.

[1] L. Schmid and T. Franke, Lab Chip 13, 1691 (2013).

[2] M. Takahashi, A. Yamaguchi, Y. Utsumi, M. Takeo, S. Amaya, H. Sakamoto, and T. Saiki, J. Photopolym. Sci. Technol. 35, 147 (2022).

Characterization and Thermo-mechanical Analysis for a Light-driven Liquid-crystal-elastomer-based Crawling Robot

Thursday, 18th September - 14:30: Oral Session 5C: Micro-Nano Systems I (Seminar Room) - Oral - Abstract ID: 273

Ms. Yen-Chun Chen [1], ***Prof. Yao-Joe Yang*** [1]

1. *National Taiwan University*

This work presents the thermo-mechanical analysis and characterization of a light-driven crawling soft robot. The device is made of liquid crystal elastomer (LCE) coated with an efficient photothermal film, and is capable of rapid locomotion and turning directions. The proposed LCE device consists of two small front legs, two large rear legs, and a concave cargo platform connecting the legs. The device locomotion, which is inspired by the principle of snake rectilinear movement, is generated by activating the rear legs with periodic NIR illumination. The thermo-mechanical analysis was performed using a commercially-available finite element tool. Thermal response of the device was also measured using an infrared imager. The simulated results were also validated by measurement. The performance of the device locomotion under different NIR intensities was also characterized and discussed.

A MINIATURIZED KIRIGAMI SOFT GRIPPER INTEGRATED WITH SELF-SENSING CAPABILITY

Thursday, 18th September - 14:45: Oral Session 5C: Micro-Nano Systems I (Seminar Room) - Oral - Abstract ID: 289

Mr. Chia Yu Cho [1], ***Prof. Yao-Joe Yang*** [1]

1. *National Taiwan University*

This work presents a miniaturized electrothermally-driven soft actuator based on Kirigami structure. The proposed device is capable of generating large deformations, but also possesses self-sensing capability for structure deformation. The device comprises a liquid crystal elastomer (LCE) layer serving as the active material for generating deformation, and a conductive composite layer (CCL) serving as a piezoresistive sensing material for detecting deformations. Inspired by the art of Kirigami, monolithically micromachined flat structures can smoothly transform between 2D and 3D shapes. The gripper was capable of grasping and lifting objects of different sizes. The relationships between structure deformation and resistance change were measured. The capabilities of displacement tracking and touch detection were also demonstrated.

Short-Channel Junctionless Nanowire Transistors

Thursday, 18th September - 15:00: Oral Session 5C: Micro-Nano Systems I (Seminar Room) - Oral - Abstract ID: 79

Mr. Sayantan Ghosh [1], ***Mr. Alessandro Puddu*** [1], ***Dr. Slawomir Prucnal*** [1], ***Dr. Ahmad Echresh*** [1], ***Prof. Artur Erbe*** [1], ***Dr. Yordan M. Georgiev*** [1]

1. *Helmholtz-Zentrum Dresden-Rossendorf (HZDR)*

The relentless demand for miniaturized, high-speed, and energy-efficient electronic systems continues to drive the semiconductor industry's pursuit of aggressive device scaling, as projected by Moore's Law [1]. However, the physical and technological limitations of traditional planar transistors at sub-nanometer nodes necessitate the exploration of alternative device architectures. Junctionless nanowire transistors (JNTs) have emerged as a promising candidate owing to their superior electrostatic gate control, intrinsic scalability, and simplified fabrication requirements. Silicon (Si) nanowires, with their reduced dimensionality, enhance gate controllability and enable higher sensitivity, making them ideal for next-generation applications. A defining characteristic of JNTs is the absence of pn-junctions within the channel, which allows for a uniformly doped active region [2]. This eliminates the need for complex doping profiles, thereby simplifying the fabrication process and improving manufacturability. Furthermore, short-channel JNTs offer the potential for high-density integration with reduced power consumption, primarily due to their inherently low leakage currents [3].

In this work, short-channel Si JNT devices are fabricated and characterized using a top-down approach. The devices are created on silicon-on-insulator (SOI) substrates with a 20 nm-thick n-doped (~5 x 1018 cm-3) Si layer and a 100 nm buried oxide. Nanowires with a fixed width and height of 20 nm and channel lengths from 1000 nm to 50 nm are patterned by electron beam lithography (EBL) and etched using reactive ion etching. A 3 nm SiO2 layer is grown by rapid thermal oxidation (RTO) for surface passivation, followed by deposition of a 7 nm Al2O3 gate dielectric via atomic layer deposition (ALD). Nickel (Ni) source/drain contacts (100 nm) are sputtered, and TiN top gates are defined using EBL, metal sputtering, and lift-off process [4]. Figure 1 presents the schematic of the short-channel JNT device, along with SEM images of the smallest device (50 nm channel length) and a 1000 nm device featuring a TiN top gate. Electrical characterization of short-channel JNT is initially performed using back-gate modulation. Transfer characteristics, obtained by sweeping the back-gate voltage (VBG) from –30 to 30 V at the constant drain bias (VDS) of 0.5 V, exhibit pronounced ambipolar behaviour (Figure 2a) across all channel lengths (1000 nm to 50 nm). This ambipolarity is observed to resemble reconfigurable FET (RFET) behavior more than that of conventional JNTs [5]. The 50 nm device exhibits an ION/IOFF ratio exceeding 107, indicating strong gate control at scaled dimensions. A positive threshold shift is consistently observed, likely due to charge trapping introduced during the ALD process. To investigate the origin of ambipolarity, output characteristics are analyzed. Schottky barrier-limited conduction is confirmed for electron conduction (Figure 2c), while predominantly ohmic conduction is observed for holes (Figure 2d), suggesting Fermi level pinning near the valence band due to interface traps. Top-gated characteristics measured for the 50 nm device (Figure 2b) further validate the true junctionless mode of operation, with prominent unipolar behaviour with strong electrostatic modulation. Extracted parameters across various channel lengths (Figure 3) show that device performance improves with scaling. The 50 nm JNT demonstrates an ION/IOFF ratio of 1.1 x 105 and a subthreshold swing (SS) of 231 mV/dec—among the best reported for CMOS-compatible, top-down fabricated short-channel JNTs. In conclusion, scaling to shorter channel lengths significantly enhances electrostatic control, demonstrating that JNTs are a promising solution for continued transistor miniaturization. Their simplified fabrication process and effective gate modulation at nanoscale dimensions make them well-suited for future technology nodes. As a next step, these short-channel devices will be investigated for gas sensing applications under various gaseous environments [6], leveraging their high sensitivity and strong electrostatic control for real life practical deployment.

[1] Moore, G.E., Proceedings of the IEEE, 1998. 86(1).
[2] Duffy, R., ECS Transactions, 2016. 72(4).
[3] Colinge, J.-P., et al., Nature Nanotechnology, 2010. 5(3).
[4] Ghosh, S., et al., Device Research Conference, 2024.
[5] Ghosh, S., et al., ACS Applied Electronic Materials, 2023.
[6] Vardhan, V., et al., ACS Applied Materials & Interfaces, 2023.

Oral Session 5D: Electronic Sensors

A Saw-Tooth Slot Antenna Sensor for Dielectric Sensing

Thursday, 18th September - 14:00: Oral Session 5D: Electronic Sensors (One Ocean Suite) - Oral - Abstract ID: 267

Dr. Hilary Scott Nkimbeng Cho [1], ***Prof. Jin Choi*** [1]

1. *Michigan Technological University*

This work introduces a novel saw-tooth slot antenna sensor designed to enhance electric field concentration within the sensing region, addressing the critical need for high-sensitivity performance in dielectric sensing applications. Although slot antennas have been widely developed for various sensing applications [1]–[3], improving the sensitivity of the slot area itself has not been fully explored. Specifically, in [1], an array of narrow rectangular slots was employed for yeast detection, but without any modifications to enhance the electric field concentration within the slots. In [2], a wide slotted region of 11 mm was introduced into a patch antenna to improve sensitivity; however, increasing the slot width was found to reduce electric field concentration, thereby diminishing sensing effectiveness. Similarly, in [3], a wide slot was used for sweat sensing, which again resulted in lower E-field confinement and reduced sensing performance. Based on the aformentioned designs, there is need for a new approach that strengthens electric field localization.

The proposed antenna consists of a saw-tooth slot etched into the ground plane on the top surface of a single-layer Rogers RO4003 substrate, which has a thickness of 0.508 mm and dimensions of 48 × 48 mm². A microstrip feedline with a matching stub is placed on the bottom side to efficiently excite the slot and improve impedance matching, as shown in Fig. 1(a) and (b), respectively. Rogers RO4003 was chosen for its low dielectric loss, stable permittivity, and excellent mechanical properties, ensuring consistent sensor performance and minimal signal degradation. In the sensing setup illustrated in Fig. 1(c) and (d), a dielectric layer representing the material under test is placed above the slot to simulate different sensing conditions.

To evaluate the effect of slot geometry on sensing performance, three slot configurations were compared: a rectangular slot, a wide saw-tooth slot, and a narrow saw-tooth slot as shown in Fig. 2(a), (b) and (c) respectively. Among them, the narrow saw-tooth slot demonstrated superior resonance characteristics and improved impedance matching, as shown in Fig. 2(d). Electric field analysis in Fig. 3 further revealed that the narrow saw-tooth configuration achieved the highest relative field concentration approximately 7.4 times greater than the rectangular slot and 1.5 times greater than the wide saw-tooth slot. This enhancement is attributed to the sharp, confined geometry of the narrow saw-tooth slot.

Sensing performance was tested by placing various porous polymer materials—polyimide (ε_r=4.3), polystyrene (ε_r=2.6), and polyethylene (ε_r=2.25) as well as liquid materials such as distilled water(ε_r=81), and vinegar (ε_r=24.1) over the slot region, as shown in Fig.1(c). Each material caused a shift in the resonance frequency shift due to changes in the effective dielectric constant as illustrated in Fig.4. This frequency shift occurs because the material near the slot alters the effective dielectric constant, thereby modifying the electrical length of the antenna. As the effective permittivity increases, the resonant frequency decreases, based on $f_r^2 \sim 1/\varepsilon_{ff}$ where f_r is the resonance frequency and ε_{ff} is the effective dieletric constant.

This work presents a novel narrow saw-tooth slot antenna sensor designed to enhance electric field confinement and achieve high sensitivity for dielectric sensing applications. The proposed structure demonstrates improved field localization and distinct resonance frequency shifts in response to different dielectric materials, confirming its effectiveness. Future work will focus on experimental validation of the simulation results, fabrication of the antenna prototype, and integration into compact wireless sensing platforms for potential applications in environmental monitoring and gas sensing.

Exploitation of Surface Acoustic Waves for the implementation of innovative sensing devices applied to the measurement of gas phase pollutants

Thursday, 18th September - 14:15: Oral Session 5D: Electronic Sensors (One Ocean Suite) - Oral - Abstract ID: 149

Dr. Meddy Vanotti [1], ***Ms. Ghida Fawaz*** [1], ***Ms. Margerie Loze*** [2], ***Mr. Sacha Poisson*** [1], ***Dr. Stéphane Brandès*** [2], ***Dr. Laurie André*** [2], ***Dr. Nicolas Desbois*** [2], ***Prof. Claude P. Gros*** [2], ***Dr. Virginie Blondeau-Patissier*** [1]

1. *Université Marie et Louis Pasteur, SUPMICROTECH, CNRS, Institut FEMTO-ST,* ***2.*** *Université Bourgogne Europe*

The topic of health issues related to air pollution has been taking over international headlines. Gaseous pollutants and Particulate Matter (PM) represent a threat not only to human health but also to that of animals and plants. Here we propose to show how the diverse properties of Surface Acoustic Waves (SAW) can be exploited in different ways to further develop innovative air quality monitoring solutions.

Tunable Nanoarchitectures in NiO/In2O3 Thin Films sensor: Thickness-Modulated Response Enhancement for Ultrafast Butanone Sensing

Thursday, 18th September - 14:30: Oral Session 5D: Electronic Sensors (One Ocean Suite) - Oral - Abstract ID: 42

Prof. Zhenyu Yuan [1]

1. *Northeastern university*

This study aims to develop high-performance butanone gas sensors by introducing a gas-liquid interfacial self-assembly technique to construct heterojunction-sensitive thin films, addressing the limited gas permeability of traditional thick-film metal oxide semiconductor (MOS) sensors. By synergizing heterojunction interface engineering with interfacial self-assembly innovation, this work provides a novel strategy for designing highly sensitive and integrable gas sensors. The proposed self-assembly technique enables large-area, controllable film fabrication without complex equipment, demonstrating unique potential for flexible sensing and MEMS integration.

Monodispersed $Ni(OH)_2$/InOOH heterojunction microspheres were synthesized via a solvothermal method, with surface oxygen adsorption properties optimized by adjusting the Ni/In atomic ratio (0–5%). Leveraging interfacial engineering at the gas-liquid boundary, surfactant (Hypermer 2296)-mediated modulation enabled the formation of dense monolayer films (>10 cm^2), overcoming the thickness control limitations of conventional spin/dip-coating methods (see Fig 1a). The layer-by-layer (LbL) self-assembly technique was further employed to precisely regulate film thickness, systematically investigating the structure-response relationship between film layers and butanone sensing performance at the test platform (see Fig 1b).

A series of characterizations verified the successful preparation of monolayer and multilayer NiO/In_2O_3 heterogeneous thin films. The heterojunction construction between NiO and In_2O_3 significantly governed the morphological evolution of the monolayer microspheres. SEM analysis (see Fig 2a) revealed that increasing NiO content slightly enlarged microsphere diameters while suppressing surface protrusions and alleviating agglomeration. Optimal heterojunction engineering was achieved at 3% NiO, yielding monodisperse microspheres with minimal aggregation, where surface microprotrusions (40–50 nm height) and nanoscale roughness synergistically amplified the specific surface area, enhancing gas adsorption capacity. XPS analysis revealed that NiO incorporation (3% Ni/In ratio) boosted chemisorbed oxygen (O_C) content from 39.80% to 46.79% (see Fig 2b), creating abundant active sites for gas adsorption. Cross-sectional SEM characterization confirmed the formation of monolayer films and multilayer structures via LbL assembly, achieving thickness control from ~300 nm (1L) to ~3 μm (10L), as shown in Fig 2c.

The 3% NiO/In_2O_3 heterojunction thin film achieved breakthrough gas-sensing performance through synergistic heterojunction engineering and morphology optimization (see Fig 3a). It exhibited an ultrafast response time of 1.3 s to 50 ppm butanone at 220°C, enabled by hierarchical nanoparticle-assembled microspheres with high surface accessibility and reduced agglomeration. Simultaneously, the heterojunction-enhanced specificity delivered a 3.2× higher response to butanone (192.86 vs. 60 for pure In_2O_3) with minimal cross-sensitivity to 10 interfering gases, while microprotrusions and agglomeration-free monolayers facilitated ultrasensitive detection down to 750 ppb butanone (response: 4.66). Furthermore, the sensor demonstrated robust reliability.

The gas-liquid self-assembled NiO/In_2O_3 films exhibited thickness-dependent sensing performance for butanone (see Fig 3b). The optimal 5-layer film (NiO/In_2O_3-5L) achieved a response of 235.7 to 50 ppm butanone at 200°C, outperforming 1L (192.86) and 10L (198) films. This ‘rise-then-fall’ trend stems from a balance between enhanced active sites (increasing layers) and gas diffusion limitations (excessive thickness). The 5L films also demonstrated ultrafast response (1.3 s) and sub-ppm detection (6–750 ppb). Simultaneously, the multilayer films retained robust selectivity and reliability, further validating their adaptability to complex sensing envi-

ronments.

Thicker films reduced baseline resistance (R_a) by widening conductive channels (1L: ~300 nm; 5L: ~1.5 μm), but excessive layers (10L) caused electron transport saturation. The 5L architecture optimally balances gas accessibility, charge transfer efficiency, and active site density, positioning it as a benchmark for tunable, high-performance sensing interfaces.

Electric-field Sensor based on Graphene/MoS_2 Heterostructure for Lightning Forecast

Thursday, 18th September - 14:45: Oral Session 5D: Electronic Sensors (One Ocean Suite) - Oral - Abstract ID: 22

Ms. Jiali Hu [1], ***Dr. Mohammad Razzakul Islam*** [1], ***Dr. Afsal Kareekunnam*** [1], ***Dr. Takeshi Kudo*** [2], ***Mr. Takeshi Maruyama*** [2], ***Prof. Masashi Akabori*** [1], ***Prof. Hiroshi Mizuta*** [1]

1. *Japan Advanced Institute of Science and Technology,* ***2.*** *Otowa Electric Co., Ltd.*

A graphene/MoS_2 heterostructure device is developed to boost carrier mobility through low-resistance contact and strain-induced band modulation, enabling ultra-sensitive electric field detection with a detection limit of ~100 V/m. This work offers a new approach for low-power, ultra-sensitive lightning detection.

Graphene/MoS_2 heterostructure, tensile strain, carrier mobility, electric field sensing

Disposable electrode based iontronic pressure sensors and their potential applications in generative artificial intelligence

Thursday, 18th September - 15:00: Oral Session 5D: Electronic Sensors (One Ocean Suite) - Oral - Abstract ID: 270

Mr. Changwoo Cho [1], ***Ms. Chaeeun Lee*** [1], ***Prof. Je Hoon Oh*** [1]

1. *Hanyang University*

This study presents a disposable Hanji-based pressure sensor and TimeGAN-based data augmentation to enable non-invasive, continuous blood pressure monitoring. The sensor captures radial pulse signals with high sensitivity, while TimeGAN generates realistic waveform-BP pairs, addressing scarcity and enhancing deep learning accuracy for cardiovascular disease detection and monitoring.

High-Mobility of Amorphous-Crystalline Phase-Composite Indium Oxide for Thin Film Transistor Applications

Thursday, 18th September - 15:15: Oral Session 5D: Electronic Sensors (One Ocean Suite) - Poster - Abstract ID: 94

Mr. Quang Khanh Nguyen [1], ***Prof. Myung Mo Sung*** [1]

1. *Hanyang University*

Indium oxide (InO_x) exhibits high electron mobility and optical transparency, ideal for advanced thin-film transistors (TFTs). However, its performance is often constrained by excessive carrier concentration and challenges in crystallization control. In this study, we demonstrate the fabrication of exceptionally smooth indium oxide (InO_x) thin films with an amorphous/nanocrystal phase-composite structure using high-pressure atomic layer deposition (ALD) for the first time (Figure 1). By employing bis(trimethylsilyl)amidodiethyl indium (InCA-1) and hydrogen peroxide (H_2O_2) vapor at pressures over 100 times higher than conventional ALD, we achieved ultrafast growth rates at low temperatures [1]. Systematic control of deposition temperature and film thickness enabled precise tuning of carrier concentration and crystallinity. Notably, lower temperatures suppressed both carrier concentration and crystallization, yielding films with enhanced electronic properties. An optimized 7.0 nm-thick InO_x film deposited at 110 °C exhibited excellent field-effect transistor (FET) performance, with an electron mobility (μ_e) of 61.1 $cm^2\ V^{-1}\ s^{-1}$ and an on/off current ratio of ~0.9×10^6 (Figure 2-3). The phase-composite structure, consisting of nanocrystals embedded in an amorphous matrix, facilitates efficient charge transport via resonant hybridization, forming delocalized electronic states [2-3]. These InO_x films also exhibit high optical transparency, uniform surface coverage, mechanical flexibility, and environmental stability. This high-pressure ALD approach overcomes previous limitations in InO_x film processing and unlocks new possibilities for next-generation flexible and transparent electronics.

Oral Session 6A: Advanced Nanofabrication III

Sequential Infiltration Synthesis for Organized Nanostructure Fabrication

Thursday, 18th September - 16:00: Oral Session 6A: Advanced Nanofabrication III (Plenary Hall) - Oral - Abstract ID: 453

Dr. Gabriele Seguini [1]

1. *IMM-CNR*

Sequential infiltration synthesis (SIS) is a three-dimensional growth process derived from atomic layer deposition (ALD) on polymers. SIS permits to grow inorganic materials into polymeric films. SIS into self-assembled block copolymers (BCP) offers the possibility to fabricate inorganic nanostructures starting from nanostructured organic templates. The fine-tuning of the dimensions of the resulting nanostructures can be achieved by proper selection of the SIS process conditions. In particular, the sequential reaction steps of the SIS process allow tuning the dimensions of the nanostructured material adjusting the number of SIS cycles. This capability to achieve a fine tuning of the dimensions of the resulting inorganic nanostructures is fundamental to make this technology suitable for the different target applications. At the same time, this step-by-step growth of the inorganic nanostructure allows us to obtain information about the progressive mass uptake of the inorganic component into the polymer matrix and to delve into the growth mechanism. In this work, Al_2O_3 dot, antidot, or lamellae arrays were synthetized by infiltration of trimethylaluminum and water precursors into out of plane cylinder or lamellae forming poly(styrene-*block*-methyl methacrylate) (PS-*b*-PMMA) BCP thin films. Collected data provided information about the mechanism governing the effective incorporation of Al_2O_3 into the PMMA component of the BCP thin films. Overall, this study collects exhaustively the infiltration behavior in different PS-*b*-PMMA nanostructures and consequently improves the application of SIS generated masks from PS-*b*-PMMA in industrial lithographic processes.

Effect of Binary Mechanical Environment on T Cell Function

Thursday, 18th September - 16:30: Oral Session 6A: Advanced Nanofabrication III (Plenary Hall) - Oral - Abstract ID: 234

Mr. Jatin jawhir Pandit [1], ***Mr. Abed Al Kader Yassin*** [2], ***Dr. Carlos Ureña Martin*** [1], ***Dr. Guillaume Le Saux*** [1], ***Prof. Angel Porgador*** [2], ***Prof. Mark Schvartzman*** [1]

1. *Department of Materials Engineering, Ben-Gurion University of the Negev, P.O. Box 653, Beer-Sheva 84105, Israel; Ilse Katz Institute for Nanoscale Science and Technology,* ***2.*** *The Shraga Segal Department of Microbiology, Immunology, and Genetics Faculty of Health Sciences, Ben-Gurion University of the Negev, P.O. Box 653, Beer-Sheva 84105, Israel*

Recent studies indicate that T cells are mechanosensitive, and their activation depends on the mechanical properties of their environment, including target cells, professional antigen-presenting cells, and surrounding tissues. This mechanosensing was demonstrated *ex vivo* by showing that T cells activated on surfaces of varying stiffness adjust their responses accordingly. However, in all these studies, T cells were stimulated *ex vivo* by **homogeneous** mechanical environments, whereas their natural environment can be **heterogeneous**, providing multiple mechanical stimuli simultaneously. For example, antigen-presenting cells such as dendritic cells, macrophages, and B cells, as well as endothelial cells within blood vessels, expose T cells to different mechanical cues, often at the same time. In bones, T cells encounter both the cortical bone, with elasticity in the range of tens of GPa, and the bone marrow, with elasticity in the range of a few kPa. Similarly, tumor tissue comprises multiple components with varying elasticities: tumor cells (~1–10 kPa), fibroblasts (~5–10 kPa), immune cells (~100 Pa), and extracellular matrix, whose primary components include fibronectin (~1–15 MPa) and collagen (~5–10 GPa). This raises a long-standing question: **when T cells receive two or more mechanical stimuli simultaneously, do they average their responses to these stimuli, or does one stimulus dominate**? Addressing this question has so far been limited due to the lack of *ex vivo* model environments capable of delivering simultaneous mechanical stimuli.

Here, we engineered a novel model system for T cell stimulation that mimics the mechanical complexity of the T cell environment and studied its effects on T cell activation. The system consisted of a micropattern of alternating soft and stiff microdomains. The micropattern was fabricated by photolithographic patterning of silica lines, which were then mechanically embedded within soft polydimethylsiloxane (PDMS). The pattern was uniformly functionalized with activating and costimulatory ligands essential for biochemical signaling. T cells were plated on these patterns as well as on homogeneous soft and stiff surfaces for comparison. We found that T cells did not average the mechanical signals. Instead, they responded similarly to those on a homogeneously soft surface, exhibiting lower activation compared to those on a stiff surface. Interestingly, long-term exposure to these patterns enhanced the proliferation of central memory and effector T cell phenotypes, similar to the response observed in stiff environments. These findings reveal the non-linear nature of T cell mechanosensing and suggest that mechanical heterogeneity plays a critical role in modulating T cell responses. This provides new insights into T cell activation and has potential implications for immunotherapies.

[1] J.J Pandit., Acta Biomaterialia Volume 195 (2025), 83-93.

Patterning on Living Tardigrades

Thursday, 18th September - 16:45: Oral Session 6A: Advanced Nanofabrication III (Plenary Hall) - Oral - Abstract ID: 61

Ms. Zhirong Yang [1], ***Dr. Shan Wu*** [1], ***Dr. Kang Zhao*** [1], ***Dr. Ding Zhao*** [1], ***Prof. Min Qiu*** [1]

1. *Westlake University*

Conventional micro/nanofabrication techniques exhibit significant limitations when applied to fragile biological specimens with non-planar topological morphologies. Ice lithography enables in situ patterning of nanostructures on extremophilic organisms such as tardigrades. Such a biocompatible fabrication paradigm establishes a novel methodology for direct bioelectronic interface engineering and nanodevice integration on biological specimens.

Electrodeposition of conducting polymers on silicon towards integrated autonomous sensor systems

Thursday, 18th September - 17:00: Oral Session 6A: Advanced Nanofabrication III (Plenary Hall) - Oral - Abstract ID: 304

Dr. Tomoyuki Kurioka [1], ***Mr. Punvinai Vinaisuratern*** [1], ***Mr. Joji Higuchi*** [1], ***Mr. Keisuke Okamoto*** [1], ***Prof. Tso-Fu Mark Chang*** [1], ***Mr. Nasser Aldhahri*** [2], ***Prof. John Mcbride*** [3], ***Dr. Yoshishige Tsuchiya*** [2], ***Prof. Masato Sone*** [1]

1. *Institute of Integrated Research, Institute of Science Tokyo,* ***2.*** *School of Electronics and Computer Science, University of Southampton, Southampton SO17 1BJ, United Kingdom,* ***3.*** *School of Engineering, University of Southampton*

This work reports the heterogeneous integration of conducting polymers onto the silicon substrate via the direct electrodeposition of conducting polymers on the silicon substrate. The effects of the passed amount of charge for the electrodeposition on the morphologies and electrical conductivity of the electrodeposited conducting polymer films are investigated. These properties of the conducting polymer vary, depending on the chemical structures of the repeating units of the conducting polymers.

A Thick-Film Micro-Patterning Method for Organic Thermoelectric Materials Using O2 Plasma and Metal Masks

Thursday, 18th September - 17:15: Oral Session 6A: Advanced Nanofabrication III (Plenary Hall) - Oral - Abstract ID: 343

Mr. Shota SAWAYAMA [1], ***Dr. Qingshuo Wei*** [2], ***Prof. Daisuke Yamane*** [1]

1. *Ritsumeikan University,* ***2.*** *National Institute of Advanced Industrial Science and Technology (AIST)*

A thick-film micro-patterning method for organic thermoelectric materials was developed using O_2 plasma and metal masks. PEDOT:PSS and PBFDO films over 15 µm thick were patterned successfully. Diluted etchant and ethanol cleaning reduced delamination. PBFDO showed strong adhesion, validating this method for robust, micro-patterned organic thermoelectric device fabrication.

Oral Session 6B: Micro-Nano Systems II

Making a Miniature Sun: Ultra High Temperature Carbon Devices

Thursday, 18th September - 16:00: Oral Session 6B: Micro-Nano Systems II (Charnock Lecture Theater) - Oral - Abstract ID: 424

Prof. Oliver Williams [1]

1. *Cardiff University*

In this work we demonstrate MEMS hotplates based on boron doped diamond thin film technology. The active heating element of these hotplates is diamond alone, significantly reducing the stresses induced by thermal expansion and thus increasing the maximum operating temperature dramatically. Temperatures exceeding 2700 K were reached with millisecond response times.

Mechanical and electrical contact testing for Pt/PEDOT/Si layered structures

Thursday, 18th September - 16:15: Oral Session 6B: Micro-Nano Systems II (Charnock Lecture Theater) - Oral - Abstract ID: 402

Dr. Yoshishige Tsuchiya [1], ***Dr. Tomoyuki Kurioka*** [2], ***Mr. Punvinai Vinaisuratern*** [3], ***Mr. Joji Higuchi*** [3], ***Prof. Tso-Fu Mark Chang*** [2], ***Prof. Masato Sone*** [2], ***Mr. Nasser Aldhahri*** [1], ***Dr. Liam Boodhoo*** [4], ***Dr. Thomas Bull*** [5], ***Prof. Yan Yang*** [6], ***Prof. John Mcbride*** [5]

1. *University of Southampton,* ***2.*** *Institute of Science Tokyo,* ***3.*** *Institute of Integrated Research, Institute of Science Tokyo,* ***4.*** *School of Electronics and Computer Science, University of Southampton, Southampton SO17 1BJ, United Kingdom,* ***5.*** *School of Engineering, University of Southampton,* ***6.*** *TaiCaan Technologies*

A contact resistance with force test and a hot switching test are done for a Pt/PEDOT/Si layered structure. With the contact force of 1 mN, the contact resistance is 120 Ω. The step-like contact voltage in hot switching suggests boiling of the conductive surface and formation of molten metal bridges.

Wafer scale fabrication of pyrolytic carbon submicron gap membrane electrodes for electrochemical sensing

Thursday, 18th September - 16:30: Oral Session 6B: Micro-Nano Systems II (Charnock Lecture Theater) - Oral - Abstract ID: 264

Dr. Nicolai Støvring [1], ***Dr. Pratik Kusumanchi*** [1], ***Ms. Estefany Ureta*** [1], ***Dr. Arto Heiskanen*** [2], ***Prof. Jenny Emnéus*** [2], ***Prof. Stephan Sylvest Keller*** [3]

1. *DTU Nanolab,* ***2.*** *DTU Bioengineering, Danmarks Tekniske Universitet (DTU), 2800 Kgs. Lyngby, Denmark,* ***3.*** *National Centre for Nano Fabrication and Characterization, DTU Nanolab, Technical University of Denmark*

Submicron gap electrically separated electrodes can be employed to drastically enhance current signals for electrochemical sensors by a phenomenon known as redox cycling. Here, an analyte is repeatedly oxidized and reduced between the electrodes effectively amplifying the signal each time. Realizing submicron gap electrodes in a membrane-based format could further improve these sensor architectures by offering flexible electrodes coupled with higher flow rates through the submicron gaps for redox cycling. Pyrolytic carbon (PyrC) has been shown to offer high structural strength making it ideal for enabling thin membrane electrodes with submicron gaps. In this work we demonstrate the wafer-scale fabrication of large area, 4 mm diameter, membrane PyrC electrodes separated by a submicron insulating layer. Furthermore, we elucidate some of the ongoing challenges in fabrication of these devices due to the high-temperature and reactive ion etching process as well as required through wafer electrical contacts.

Energy-Free Micro-Latching Mechanisms for Bidirectional SMA Actuators

Thursday, 18th September - 16:45: Oral Session 6B: Micro-Nano Systems II (Charnock Lecture Theater) - Oral - Abstract ID: 195

Ms. Yizheng Liu [1], ***Mr. Vincent Gottwald*** [2]

1. *Institut für Mikrosystemtechnik – IMTEK, Albert-Ludwigs-Universität Freiburg, Georges-Köhler-Allee 102, 79110 Freiburg, Germany,* ***2.*** *Karlsruhe Institute of Technology (KIT)*

This work presents reversible, energy-free micro-latching systems using polymers for microscale actuation. A passive adhesive mechanism and an active paraffin-based interlock provide reliable retention without continuous power. CHic-crosslinkable polymers enable tunable, durable adhesion, offering a material-driven, energy-efficient solution for programmable mechanical locking in microscale systems.

Physical reservoir computing with MEMS torsional mirrors

Thursday, 18th September - 17:00: Oral Session 6B: Micro-Nano Systems II (Charnock Lecture Theater) - Oral - Abstract ID: 36

Mr. Yuta Kawashima [1], ***Mr. Mikiya Oki*** [1], ***Dr. Jun-Yu Ou*** [2], ***Dr. Yoshishige Tsuchiya*** [3], ***Prof. Toshiyuki Tsuchiya*** [1]

1. *Kyoto University,* ***2.*** *Physics and Astronomy, University of Southampton,* ***3.*** *University of Southampton*

This paper reports on physical reservoir computing (PRC) using an electrostatic MEMS mirror demonstrating enhanced memory capacities at resonance for the first time. We evaluated the learning performance of this novel computing system both numerically and experimentally. Both results demonstrate the effectiveness of PRC using a MEMS mirror.

Key words: physical reservoir computing, MEMS tortional mirror

Oral Session 6C : Optical Sensors

Monitoring vibrational fingerprints of polypeptide monolayers by infrared plasmonic nanoantennas

Thursday, 18th September - 16:00: Oral Session 6C : Optical Sensors (One Ocean Suite) - Oral - Abstract ID: 184

Dr. Santos Merino [1], ***Dr. Alberto Villar*** [1], ***Dr. Ruth Díez*** [1], ***Dr. Gabriel Ortega*** [2], ***Dr. Mónica García-Mota*** [3], ***Dr. Anna Kimmel*** [3], ***Dr. Albert Guerrero*** [4], ***Dr. Jorge Espina*** [5], ***Dr. Mario Zapata*** [6], ***Prof. Javier Aizpurua*** [7]

1. *Tekniker,* ***2.*** *CIC bioGUNE,* ***3.*** *Simune Atomistics,* ***4.*** *Instituto de Microelectrónica de Barcelona,* ***5.*** *Universidad de Oviedo,* ***6.*** *Materials Physics Center,* ***7.*** *Donostia International Physics Center*

This study employs resonant Surface-Enhanced Infrared Absorption (SEIRA) to detect the vibrational fingerprints of the TRP-cage, one of the smallest known proteins to adopt a stable, cooperative, and compact fold. Ab initio calculations based on Density Functional Theory (DFT) were used to identify the vibrational signatures of the protein's Amide I band, specifically associated with C=O and R–C=O stretching modes. The Finite Element Method (FEM) was then used to design gold nanoantennas with electromagnetic responses tuned to these target vibrational modes. A customized biofunctionalization strategy was developed to enable free molecular vibration while ensuring consistent protein orientation upon binding to the gold surface. The functionalized substrate was integrated into a microfluidic chip, and light absorption was characterized using Fourier-transform infrared spectroscopy (FTIR). Both cooperative and localized vibrational modes were identified, and absorbance signal was calculated, revealing features corresponding to decoupled and coupled vibrational modes within the Amide I band.

On-fiber printed polymeric tapers for chronically implantable neural interfaces

Thursday, 18th September - 16:15: Oral Session 6C : Optical Sensors (One Ocean Suite) - Oral - Abstract ID: 388

Dr. Stella Aslanoglou [1], ***Dr. Barbara Spagnolo*** [1], ***Dr. Cinzia Montinaro*** [1], ***Dr. Alberto Perna*** [2], ***Dr. João F. Ribeiro*** [2], ***Dr. Marco Pisanello*** [3], ***Dr. Luca Berdondini*** [2], ***Dr. Tommaso Fellin*** [2], ***Dr. Ferruccio Pisanello*** [1], ***Prof. Massimo De Vittorio*** [1]

1. *Center for Biomolecular Nanotechnologies, Istituto Italiano di Tecnologia (IIT), 73010 Arnesano, LE, Italy,* ***2.*** *Center for Convergent Technologies, Istituto Italiano di Tecnologia (IIT), 16163 Genova, Italy,* ***3.*** *OptogeniX s.r.l., 73010 Arnesano, Italy*

In this work, we demonstrate a method for the fabrication of soft and flexible polymeric air-clad tapers using two-photon polymerization (2PP) in a single processing step and investigate their prospective use in chronically implantable neural interfaces.

Detection of Phtalate release from plastic tubes using a NanoFabricated Surface Enhanced Raman Spectroscopy device

Thursday, 18th September - 16:30: Oral Session 6C : Optical Sensors (One Ocean Suite) - Oral - Abstract ID: 263

Mr. Sofien Ramos [1], ***Ms. Camille Blanc*** [2], ***Dr. Laurence Salomé*** [2], ***Dr. Philippe Louarn*** [3], ***Dr. Emmanuelle Trevisiol*** [4], ***Prof. Christophe Vieu*** [1]

1. *LAAS-CNRS,* ***2.*** *IPBS,* ***3.*** *IRAP,* ***4.*** *TBI*

Our analytical devices use a superhydrophobic fluidic concentrator to focus analytes onto a SERS-active area (Ag nanoparticles). In this work, we confidently demonstrate our ability to detect phthalic acid at 1 nM and 1 fM in ultrapure water, and clearly identify its release from polypropylene tubes after one week of storage at 37 °C.

Keywords: SERS, Superhydrophobic surface, Phtalate detection

Detection of Polystyrene Microplastics via Surface-Enhanced Raman Scattering on Sticky Hydrophobic Nanopillar Substrates

Thursday, 18th September - 16:45: Oral Session 6C : Optical Sensors (One Ocean Suite) - Oral - Abstract ID: 39

Mr. Tzu-Yu Chiu [1], ***Prof. Wen-Huei Chang*** [2], ***Mr. Kuan-Ting Kuo*** [1], ***Mr. Yao-Ming Ku*** [1], ***Prof. Chih-Chia Huang*** [1], ***Prof. Chun-Hung Lin*** [1]

1. *Department of Photonics, National Cheng Kung University,* ***2.*** *Department of Applied Chemistry, National Pingtung University*

This study improves SERS sensitivity and reproducibility for nanoplastic detection using a sticky hydrophobic SU-8 nanopillar substrate, NaCl aggregators, and gold nanoparticles. The scalable substrate promotes effective nanoparticle aggregation and clustering, enhancing detection performance. This robust approach supports sensitive, consistent nanoplastic detection for environmental monitoring and health risk assessment.

Micro-optics Design and Preliminary Characterization of a Fiber-Optic SERS Probe for In Vivo Diagnostics

Thursday, 18th September - 17:00: Oral Session 6C : Optical Sensors (One Ocean Suite) - Poster - Abstract ID: 70

Ms. Yingwei Hou [1], ***Dr. Nilanjan Manda*** [1], ***Dr. Belal Ahmad*** [1], ***Dr. Jang Ah Kim*** [2], ***Dr. Alexander J Thompson*** [1]

1. *Department of Surgery & Cancer, Imperial College London, London, United Kingdom.*, ***2.*** *Department of Mechanical Engineering, Imperial College London, London, United Kingdom.*

We present a forward-viewing SERS probe featuring a gold-coated micro-optic cap with a SERS array, fabricated via two-photon polymerization. The design enhances Raman signal detection and supports integra tion with complex fiber optics. Comparative analysis confirms its feasibility for low-background, minimally invasive diagnostics using hollow-core and advanced optical fibers.

Oral Session 6D: Advanced Nanofabrication IV

Ice lithography using Diobalt octa-carbonyl

Thursday, 18th September - 16:00: Oral Session 6D: Advanced Nanofabrication IV (Seminar Room) - Oral - Abstract ID: 122

Mr. Limin Qi [1], ***Dr. Dongli Liu*** [2], ***Dr. Ding Zhao*** [3], ***Prof. Min Qiu*** [1]

1. *Westlake University,* ***2.*** *Westlake Instruments (Hangzhou) Technology Co., Ltd,* ***3.*** *Westlake Institute for Optoelectronics*

Ice lithography is an eco-friendly nanofabrication method that enables electron beam patterning on curved surfaces. This study explores dicobalt octa-carbonyl ($Co_2(CO)_8$) as a novel metal-organic precursor. Using a micromachined Joule-Thomson cryocooler to maintain the substrate at ~106 K, $Co_2(CO)_8$ vapor was condensed and patterned via electron beam exposure, followed by thermal desorption. Cobalt-based nanostructures with sub-100 nm resolution were achieved using doses around 10 mC/cm². Electrical and optical measurements confirm their functional properties, demonstrating the technique's potential for advanced electronic and photonic applications.

Quasi-3D Nanoscale Fabrication: Precision Patterning and Modelling via Focused Ion Beam Implantation

Thursday, 18th September - 16:15: Oral Session 6D: Advanced Nanofabrication IV (Seminar Room) - Poster - Abstract ID: 341

Dr. Jordi Llobet [1], Dr. Jordi Antoja [1], Dr. Alberto del Moral [2], Mr. Marcel de la Vega Czarnecki [1], Ms. Marta Duch [1], Mr. Alessandro Cian [3], Mr. Elia Scattolo [3], Dr. Michele Crivellari [3], Dr. Xavier Borrisé [4], Dr. Damiano Giubertoni [3], Prof. Francesc Pérez-Murano [2]

1. *Institut de Microelectrònica de Barcelona, IMB-CNM (CSIC), Universitat Autònoma de Barcelona, Cerdanyola Del Vallès, 08193, Barcelona, Spain.,* ***2.*** *Institute of Microelectronics of Barcelona (IMB-CNM, CSIC),* ***3.*** *FBK, Fondazione Bruno Kessler,* ***4.*** *Catalan Institute of Nanoscience and Nanotechnology (ICN2) and Barcelona Institute of Science and Technology (BIST)*

In this work, we present recent advances in the development and modelling of quasi-3D silicon nanostructures defined by focused ion beam (FIB) technologies together with wet etching. We report the use of focused Au+ and Ga+ ion implantation to create hard masks for nanolithography on silicon, focusing on the modelling of the implantation and etching processes to control the thickness and height/depth to the ultimate sub-nm range.
We successfully demonstrated the development and modelling of silicon nanostructures using FIB implantation with both Ga and Au ion species. Through the detailed process-calibration experiments and the development of predictive algorithms, we achieved precise control over the etching behavior of ion-implanted silicon in TMAH, enabling the fabrication of highly defined, suspended 3D nanostructures.

Investigation of process windows for alternative non-toxic and metal ion free developer choline hydroxide for HSQ resist Medusa 84 SiH

Thursday, 18th September - 16:30: Oral Session 6D: Advanced Nanofabrication IV (Seminar Room) - Oral - Abstract ID: 297

Ms. Pia Kohlschreiber [1], ***Mr. Markus Gottwald*** [1], ***Dr. Christian Helke*** [1], ***Mr. Harry Biller*** [2], ***Dr. Mandy Sendel*** [2], ***Dr. Danny Reuter*** [1]

1. *Fraunhofer Institute for Electronic Nano Systems ENAS,* ***2.*** *Allresist GmbH*

Choline hydroxide – a non-toxic, metal ion free, strong aqueous base – is investigated as developer for HSQ resist Medusa84 SiH, a high-resolution negative tone electron beam lithography resist, aiming to replace toxic tetramethyl ammonium hydroxide (TMAH). So far, 40 nm isolated lines at comparatively low doses were developed with choline hydroxide.

Resist-free and low-temperature micropatterning of IGZO using stencil lithography for electronic applications

Thursday, 18th September - 16:45: Oral Session 6D: Advanced Nanofabrication IV (Seminar Room) - Oral - Abstract ID: 261

Mr. Chenxiang Zhang [1], ***Prof. Giovanni Boero*** [1], ***Dr. Arnaud Bertsch*** [1], ***Prof. Jürgen Brugger*** [1]

1. *Microsystems Laboratory, Ecole Polytechnique Fédérale de Lausanne (EPFL)*

Stencil lithography enables micrometer-scale, near-room-temperature patterning of IGZO on biodegradable substrates without wet processing. We demonstrate RF sputtering and IBE through SiN_x stencils, achieving ~5 µm resolution and preserving electrical performance. Tunable carrier density (10^{19} cm^{-3}) and mobility (~20 $cm^2/V{\cdot}s$) highlight its potential for sustainable TFT fabrication.

Papers

Plenary 1 - Dr Drew Nelson

Building Globally Relevant Semiconductor Clusters and Their Relevance to the UK Semiconductor Strategy

Drew Nelson
Chair of UK Semiconductor Strategy
All Party Parliamentary Group on Semiconductors Advisory Board, United Kingdom

Abstract

This talk will illustrate the pathways to building powerful, globally relevant semiconductor clusters, using the Compound Semiconductor Cluster in South Wales as an exemplar. During the presentation, the various elements to creating a successful and sustainable semiconductor ecosystem will be explored, and the relevance of such clusters to the UK Semiconductor Strategy will be examined.

Plenary 2 - Dr Naoto Horiguchi

CMOS scaling paradigm shift from CMOS 1.0 to CMOS 2.0

Naoto Horiguchi, Julien Ryckaert

imec, Leuven, 3001, Belgium
e-mail: naoto.horiguchi@imec.be

Introduction

Current CMOS technologies are homogeneous in terms of devices (Si-based FinFETs to nanosheet) and interconnects (Cu-based dual damascene for signal and power lines) for almost all functions (high performance & low power logic, SRAM, I/O, ...) (CMOS 1.0). Its homogeneity provides a good power-performance-area trade-off so far. However, exploding demands for performance improvement in diverse applications (from mobile to HPC) make significant challenges in the homogeneous CMOS scaling approach. In this paper, we will discuss how to extend CMOS 1.0 scaling by introducing new device & interconnect architectures and how to bring CMOS scaling to the next level by combining heterogeneous technologies with CMOS 1.0 from system viewpoint (CMOS2.0).

CMOS 1.0 extension by new device and interconnect architectures

For further CMOS 1.0 scaling, CMOS device architecture is being transitioned from FinFET to nanosheet in industry today to improve electrostatics and drive current per device footprint by stacked gate-all-around nanosheet channels [1]. For ultimate CMOS device scaling, complementary FET (CFET), which has stacked NMOS-PMOS nanosheet architecture, is investigated (Fig. 1) [2]. In addition to the new device architectures, backside power delivery network (BSPDN) (Fig. 2) is proposed [3] and will be combined with advanced device architectures [4]. BSPDN reduces IR drop/power and improves scaling by separating narrow signal lines in frontside and wide power lines in backside. BSPDN is a critical step toward CMOS 2.0 to introduce heterogeneity in interconnect, to enable fine pitch vertical interconnect, and to open opportunities to use backside for CMOS scaling, for example, by introducing signal interconnect, MIM caps, ESD diodes and devices on backside [5].

From CMOS 1.0 to CMOS 2.0

General purpose CMOS 1.0 scaling by using a single device & interconnect architecture is successful for > 50 years. However, due to recent diverse applications with stringent power/performance/area requirements, the general-purpose CMOS scaling is getting less and less efficient. For example, it is harder and harder to provide both logic and SRAM scaling. It is also difficult to meet device target for both low power, such as mobile, and high performance, such as HPC. High power consumption in HPC with homogeneous CMOS devices is one of the biggest concerns.

We are trying to solve the conflicting requirements in CMOS 1.0 by segmenting functions (logic, SRAM, I/O, ...) in a system-on-chip, implementing the segmented functions with best technologies, and connecting them vertically with recent backside technologies, 3D bonding or sequential 3D integration (Fig. 3) [6]. We refer to this CMOS scaling approach as CMOS 2.0. CMOS 2.0 provides not only logic-SRAM chip stacking, which is used in production already, but also high performance logic- high density logic chip stacking, which could provide better power-performance-area trade-off than general-purpose CMOS 1.0 (Fig. 4). Even in CMOS 2.0, continuous CMOS 1.0 scaling is required to improve transistor density by using new lithography, new device & interconnect architectures, which enhances system-on-chip function. CMOS 2.0 could accept non-Si technologies, for example, IGZO, 2D materials, and ferroelectric by combining them with Si-based CMOS technologies with 3D bonding if they are specialized for certain functions. CMOS 2.0 will try to provide more heterogeneous CMOS platforms for better CMOS scaling.

[1] J. Jeong et al., VLSI 2023. G. Yeap et al., IEDM 2024.
[2] S. Liao et ai., IEDM 2024. A. Vandooren et al., IEDM 2024.
[3] D. Prasad et al., IEDM 2019.
[4] M. Shamanna et al., VLSI 2023. K. Fischer et al., VLSI 2025.
[5] H. Lin et al., VLSI 2021. R. Chen et al., VLSI 2022. K. Serbulova et a., VLSI 2022.
[6] J. Ryckaert et al., EDTM 2024.

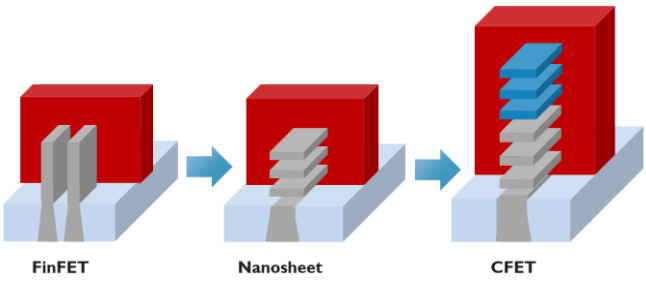

Figure 1. CMOS device architecture evolution from FinFET to nanosheet and CFET

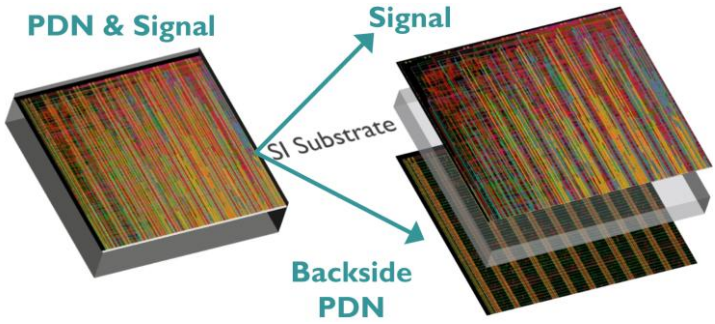

Figure 2. Backside power delivery network

Figure 2. CMOS scaling key options from past (transistor/interconnect), today (standard cells (DTCO)) to future (system on chips (STCO))

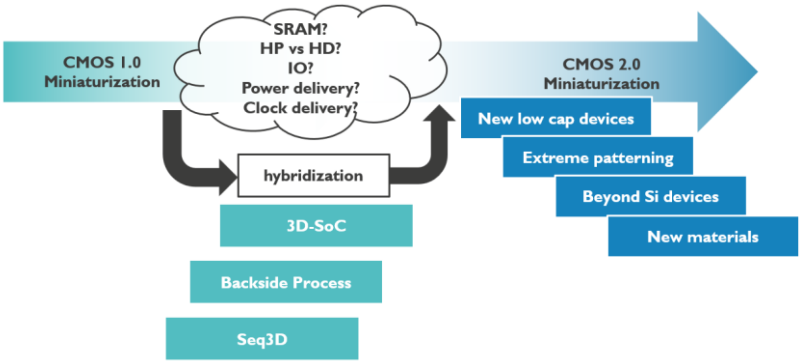

Figure 3. Transition from CMOS 1.0 to CMOS 2.0

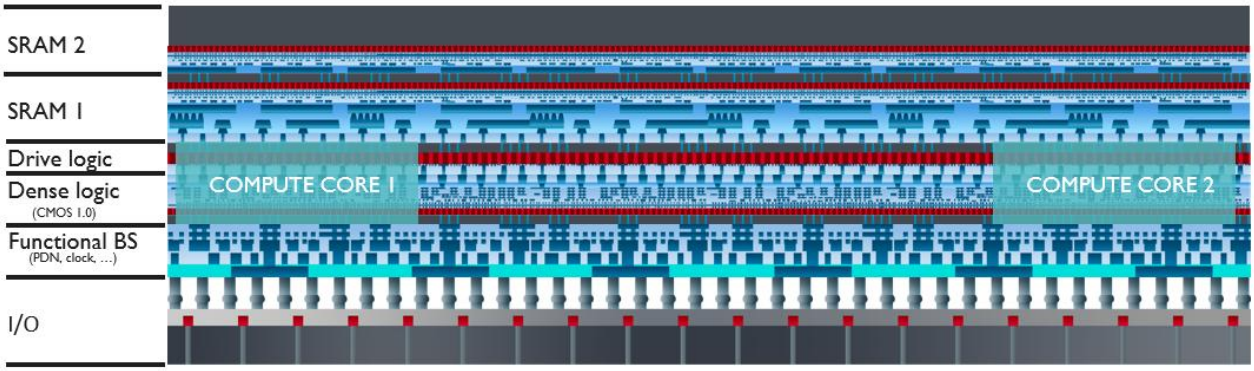

Figure 4. CMOS 2.0 architecture example. Each layer has specialized devices for target functions.

Plenary 3 - Prof Dinesh Pamunuwa

Edge Computing Platform based on Nanoelectromechanical Relays

Dinesh Pamunuwa, University of Bristol, UK

Abstract

Electronics that operate at the edge of the network, especially in industrial and manufacturing applications, typically have stringent environmental and power restrictions that limit their usage. For example, existing transistor technology struggles to function at temperatures much beyond 125 °C; thus, the electronics in an aircraft engine controller (FADEC) sit much further away from the engine than the sensors and actuators, even though the controller efficiency is significantly reduced as a result. High levels of radiation, as for example found in the nuclear sector and aerospace, also introduce many faults, limiting the lifetime of electronics while increasing fabrication and packaging costs and weight; a simple processor can cost 10,000 times as much as its standard cost when qualified for space. Many such applications, including ones that require resilience to both high temperatures and radiation levels, can be found in the industrial IoT. Moreover, current leakage grows exponentially with temperature, increasing the challenge of embedding electronics at the edge.

Electromechanical relays by contrast are inherently high-temperature capable, up to 300 °C, and can cope with radiation levels that are two orders of magnitude higher. All of this harsh-environment capability comes with zero energy consumption in the off state and abrupt on-off transitions, regardless of the environmental conditions. Thus, using nanoscale relays instead of transistors as digital switches holds out the potential of building a new class of harsh-environment capable processors with integrated sensing and zero standby power for these existing and emerging edge computing applications.

In this talk, I will introduce a hardware platform that we have developed for nanoelectromechanical (NEM) switch-based computing, covering devices to circuits to large-scale integration, as well as modelling, simulation and design and programming tools. I will discuss our innovations in switch contact coating, relay and circuit designs, and computer architecture which eliminates the memory communication bottleneck, that allow the unique attributes of NEM relays to be leveraged to build efficient FPGAs with integrated non-volatile memory and sensing. Using this platform we are building NEM switch-based prototypes for IoT type applications, as well as hot zones and radiation heavy environments where conventional electronics cannot operate.

MNE Fellow Award: Prof Lars Montelius

Science in our time - for People, Planet and Prosperity

Lars Montelius

Department of Physics, Division of Solid State Physics and NanoLund, the center for research, education and innovation within nanoscience at Lund University, Sweden.

Former Director–General of the International Iberian Nanotechnology Laboratory, headquartered in Braga, Portugal.

Abstract:

Semiconductors power virtually all modern technologies — from smartphones and AI data centers to electric vehicles (EVs), industrial automation, and medical devices. As more industries digitize and automate, the need for advanced chips grows.

- AI Boom: Training and running large AI models (like ChatGPT) require massive computational power, driven by GPUs and AI-specific chips.
- EV & Mobility Shift: Electric and autonomous vehicles need significantly more chips than traditional cars — for sensors, power management, infotainment, etc.
- IoT Growth: Billions of devices (smart homes, factories, etc.) are connecting to the internet, all requiring semiconductors.

The COVID-19 pandemic and geopolitical tensions exposed the fragility of the global chip supply chain. Further, the Covid-19 pandemics painfully made us aware of the necessity of robust supply chains – and today we witness the resulting increased demand for national manufacturing capabilities of critical products. In addition, there is a worldwide increased political instability. Semiconductors are now considered strategic assets — much like oil in the 20th century.

Consequently, the global geo-political landscape is rapidly changing. But even larger, and a necessity for a sustained and prosperous life at our planet Earth, is the absolute requirement for a **green** transition **to be able to become a sustainable society**.

Nanotechnology is a Key Enabling Technology with promises for making solid contributions to the grand societal challenges of today, offering possibilities to address solutions for enabling sustainable energy supply on demand, clean water to everyone, novel e-care and e-health paradigms etc.

These major societal developments challenge society and will in turn challenge the present higher education systems as well as the industrial society. There will be an increased demand for transversal interdisciplinary participation to enable the needed disruptive innovations to happen.

Higher Educational Systems are key for addressing large societal challenges – and serve at large as igniters of changes. And presently there are urgent needs for novel solutions and incentives to recruit needed trans-disciplinary engagements and closer collaboration with the industrial fabric - as well as with society at large. **Simply put, there is a need to join forces to create a global systemic and inclusive Science, Technology, Society and Innovation pathway for People, Planet and Prosperity.**

Oral Session 1A : Microsystem and MEMS Applications

Fabrication of Flexible III-Nitride MEMS Resonators by Lift-Off and Transfer onto Thin Metal Substrates

A. Kassem[1], R. Gujrati[1], D. Bourrier[2], C. Ayela[3], F. Mathieu[2], I. Dufour[3], L. Nicu[2], V. Ottalapikkal[1], P. Vuong[1, 4], S. Sundaram[1, 4, 5], W. Hunt[5], A. Ougazzaden[1, 5], T. Leichlé[1, 5]**, J.P. Salvestrini[1, 4, 5]**

[1] CNRS, IRL 2958 Georgia Tech-CNRS, Metz, France
[2] LAAS-CNRS, Toulouse, France
[3] Université de Bordeaux, Laboratoire IMS UMR-CNRS 5218, Talence, France
[4] Georgia Tech Europe, IRL 2958 Georgia Tech-CNRS, Metz, France
[5] Georgia Institute of Technology, School of Electrical and Computer Engineering, IRL 2958 Georgia Tech-CNRS, Atlanta, GA, USA
**Corresponding Authors: Jean-Paul.Salvestrini@georgiatech-metz.fr; thierry.leichle@cnrs.fr

This work presents a scalable wafer-level transfer method for fabricating crack-free III-N MEMS drum resonators on flexible metal substrates. By electroplating a metal stressor on III-N layer epitaxially grown atop a 2D h-BN release layer, thermal delamination allows seamless transfer of III-N layers to a flexible metal substrate. Freestanding MEMS resonators are released by etching the metal layer, with integrated electrodes used to actuate the MEMS at resonance. This simple methodology offers strong potential for next-generation sensors aimed at wearable and IoT applications.

Recent efforts have focused on integrating freestanding MEMS resonators onto flexible substrates using various approaches. Conventional methods involve direct fabrication on flexible substrates with sacrificial layers, but these cannot withstand high temperatures and are thus limited to polycrystalline materials [1]. Another approach involves fabricating the MEMS device on a rigid substrate before transferring it to a flexible one. This allows for high-performance materials like AlN and $LiNbO_3$, but faces challenges including complex release steps and poor scalability [2]. Advances have been made using 2D layer transfer techniques, where materials like hexagonal boron nitride (h-BN) help lift and transfer layers for MEMS processing [3]. In this study, a metal stressor serves both as a transfer aid and as the bottom contact/flexible substrate—an approach termed Self-Lift-Off and Transfer (SLOT) [4], adapted here for the first time for flexible MEMS resonators. We demonstrate that this process enables crack-free AlGaN/GaN and GaN MEMS resonators, with expected resonance behavior, on flexible metal substrates. The SLOT process for MEMS resonators on flexible metal substrate is shown in Figure 1. III-N layers are grown atop a 2D h-BN layer, followed by electroplating of a 30 µm Ni stressor. The III-N/Ni bilayer is then delaminated by heating the sapphire growth substrate at 100°C for 1 hour. Thermal expansion mismatch between the metal and sapphire creates compressive and tensile stress in the metal and substrate, respectively, leading to delamination due to the weak Van der Waals forces in the h-BN layer. After lift-off, Ti/Au electrodes are deposited and patterned. Wet etching of circular cavities in the Ni layer releases the III-N films, forming freestanding III-N drum structures with electrodes sandwiching the III-N bilayer for integrated actuation (Figure 1).

The resulting III-N MEMS were characterized using a laser Doppler vibrometer to observe their vibration modes (Figure 2). The first five modes of GaN circular resonators on Ni were detected, with frequencies of 542.7 kHz, 1.087 MHz, and 1.836 MHz for 100 µm diameter drum resonators. Finite element method (FEM) simulations, using a tensile stress of ~130 MPa in the GaN layer, accurately predicted these resonance modes, validating the experimental results. Several hundred resonators were successfully fabricated using the SLOT process, showing promising quality factors: Q = 153 (Mode 1), Q = 385 (Modes 2–3), and Q = 313 (Modes 4–5) for the 100 µm diameter drum GaN resonator. Compared to conventional techniques involving sacrificial layers or complex release steps, this method provides a cost-effective, scalable route for high-performance flexible III-N MEMS resonators.

[1] H. Hamid et al., IEEE Sens. J., vol. 21, pp. 12606–12617, 2021.
[2] X. Sun, et al., Appl. Phys. Lett., 115, 093501, 2019.
[3] R. Gujrati, et al., Appl. Phys. Lett., 124(10), 104102, 2024.
[4] S. Karrakchou et al. ACS Applied Electronic Materials 2021 3 (6), 2614-2621

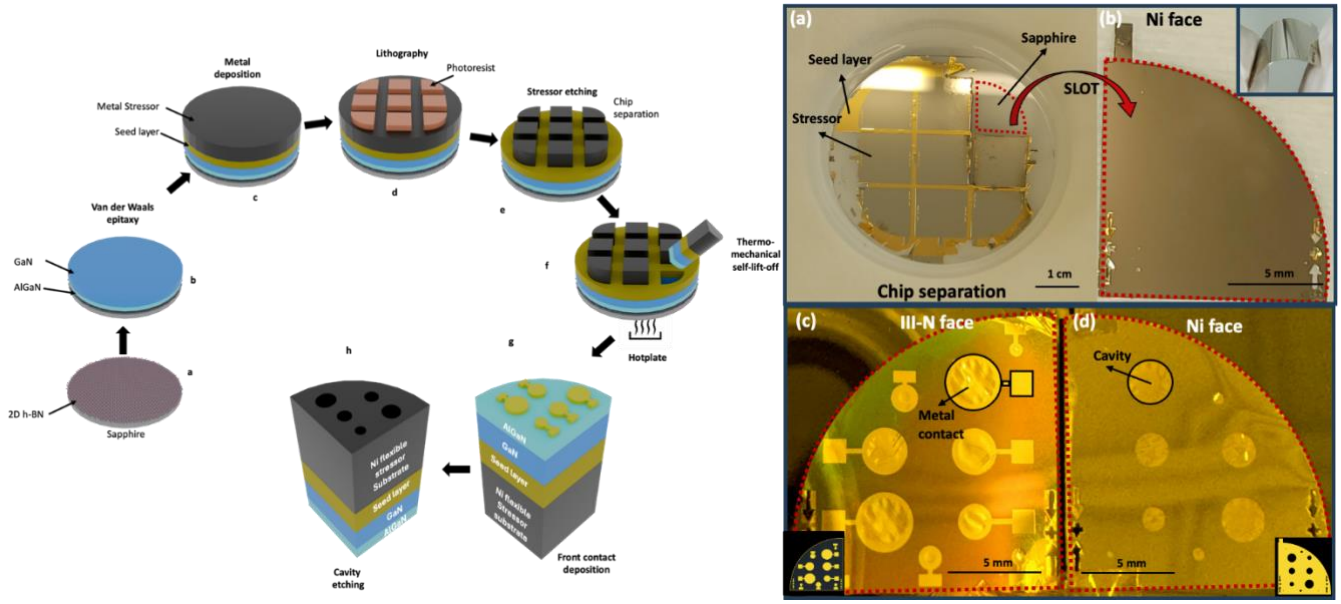

Figure 1. (Left) Process for the fabrication of III-N MEMS on flexible metal substrates. (a) MOVPE growth of a 3nm 2D h-BN release layer on a 2-inch sapphire growth substrate. (b) Van der Waals epitaxy of III-N epilayer. (c) Deposition of metal seed layer followed by electrodeposition of a 30 µm-thick Ni stressor layer. (d,e) 12 x 12 mm^2 chips definition and separation by photolithography and wet etching of the metal layer. (f) Thermally activated mechanical self-exfoliation (SLOT) of the chips. (g) Deposition and patterning of the metal front contact on the III-N layer, followed by the release of the III-N membrane on the opposite side through etching of the metal. (Right) (a) Eight III-N chips on a 2-inch sapphire substrate; (b) a single chip released via SLOT process; (c) integrated actuation with front metal contacts deposition on the III-N side; (d) freestanding III-N layers after Ni-side etching.

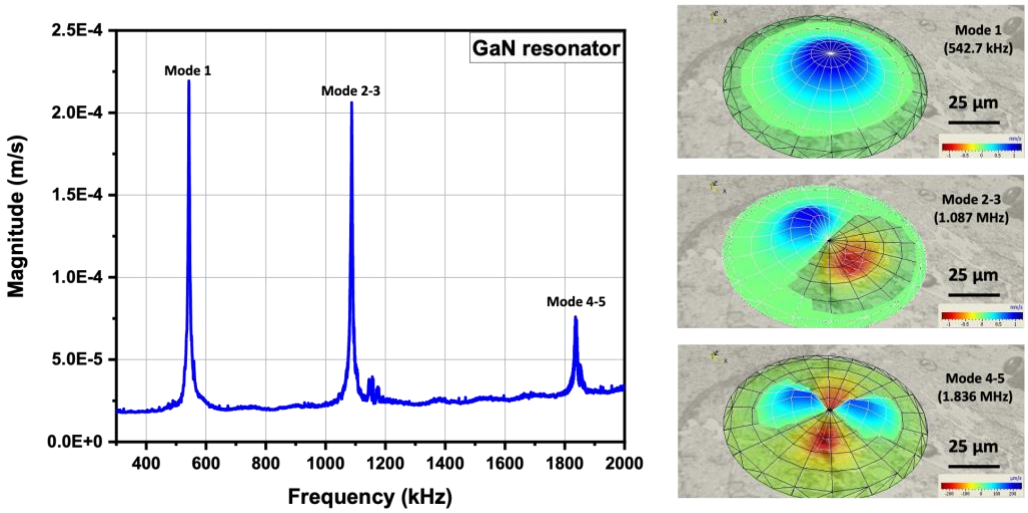

Figure 2. Typical resonance spectrum of a 340 nm thick, 100 µm diameter GaN MEMS and its corresponding vibration modes. The plotted velocity magnitude is the mean value of the velocity magnitude at each point of measurement.

Probing Cell Mechanosensitivity in Microengineered 3D Scaffolds

Aída Gabriela Fernández Contreras [a], Chloé Viat [a], Boudewijn van der Sanden [b], Olivier Stephan [c], Jean-Hervé Tortai [a], Alice Nicolas [a]

[a] Université Grenoble Alpes, CNRS, LTM, Grenoble, 38000, France
[b] Université Grenoble Alpes, CNRS, TIMC-IMAG, Grenoble, 38000, France
[c] Université Grenoble Alpes, CNRS, LiPhy, Grenoble, 38000, France
e-mail: aida-gabriela.fernandezcontreras@cea.fr
Keywords: Two-photon lithography, 3D cellular scaffolds, Mechanobiology, Isometric microfabrication.

Cells in the body are embedded within a dynamic and structurally complex network known as the extracellular matrix (ECM). Beyond providing structural support, the ECM has mechanical cues, such as stiffness and geometry, that influence essential cellular processes, including adhesion, migration, and proliferation. This interaction is bidirectional, as cells are able to generate tension and actively remodel the ECM [1].

In vitro models constitute essential resources employed to study cell-ECM interactions in a controlled manner. However, the use of traditional models based on two-dimensional (2D) rigid surfaces often leads to results that poorly translate to in vivo and clinical settings. In contrast, three-dimensional (3D) models, with tunable microscale architecture and stiffness, enable the recapitulation of physical properties of the native ECM, thereby establishing a more physiologically relevant environment for cell studies [2].

Traditional techniques for the fabrication of 3D scaffolds include solvent casting, freeze-drying, phase separation, and electrospinning. While these methods enable the creation of structures with high porosity and large surface area that promote cell adhesion, precise control over the scaffold architecture and pore size is limited. Additive Manufacturing techniques allow the production of precise structures with controllable and complex architecture based directly on computer-aided design models, achieving higher repeatability and precision. Two-photon polymerization (TPP) is an additive manufacturing technique that stands out for its sub-micrometer resolution, enabling the fabrication of highly detailed 3D scaffolds. It uses a focused femtosecond laser to polymerize a photosensitive resist only at the focal volume, known as a voxel, building 3D structures voxel-by-voxel, granting high control over geometry and stiffness [3].

However, this voxel-by-voxel approach also raises challenges, especially in terms of high fabrication time and inherent anisotropy due to the ellipsoidal shape of the voxel. This results in vertically elongated structures along the optical (z) axis, which can introduce directional biases [4]. Therefore, replicating isometric 3D structures with precise stiffness and geometry remains technically challenging.

In this work, a TPP-based protocol was developed to create isometric, cage-like 3D scaffolds using OrmoComp, a commercial photoresist. Design and fabrication parameters were optimized to balance structural fidelity with reduced fabrication time. This allowed us to recapitulate horizontal and vertical beams with identical cross-sections, with dimensions ranging from 2 to 10 µm. The resulting architectures featured cavity sizes ranging from 20 to 40 µm. The dimensional precision was confirmed via scanning electron microscopy (SEM) (Figure 1) and confocal microscopy. The resulting 3D microfabricated system enables independent control over geometry, subcellular-scale stiffness, and global structural stiffness, allowing systematic modulation of mechanical cues across scales.

3T3 fibroblasts were cultured in the printed scaffolds and analyzed using high-resolution two-photon microscopy (Figure 2) for live imaging and 3D reconstruction. Cells were tracked within the 3D scaffolds; morphological differences were observed depending on beam thickness: on 2 µm beams, fibroblasts adopted a narrow, elongated shape, with thin protrusions aligned to the beams, often limited to spanning single cavity regions. On 5 and 7 µm beams, cells exhibited moderate spreading, forming broader extensions that bridged multiple beams. In contrast, on scaffolds with 10 µm beams, fibroblasts adopted a well-spread shape, with robust actin stress fibers bridging different levels, reflecting more stable scaffold engagement. These findings underscore how microstructural geometry and stiffness can modulate cellular behavior, including cytoskeletal organization, morphology, and potentially downstream processes such as migration and proliferation.

By leveraging TPP and innovative design strategies, this work introduces a versatile and biomimetic platform to dissect cell-matrix interactions in geometrically controlled environments and to translate this knowledge into developments in fields such as tissue engineering and drug development through more physiologically relevant in vitro models.

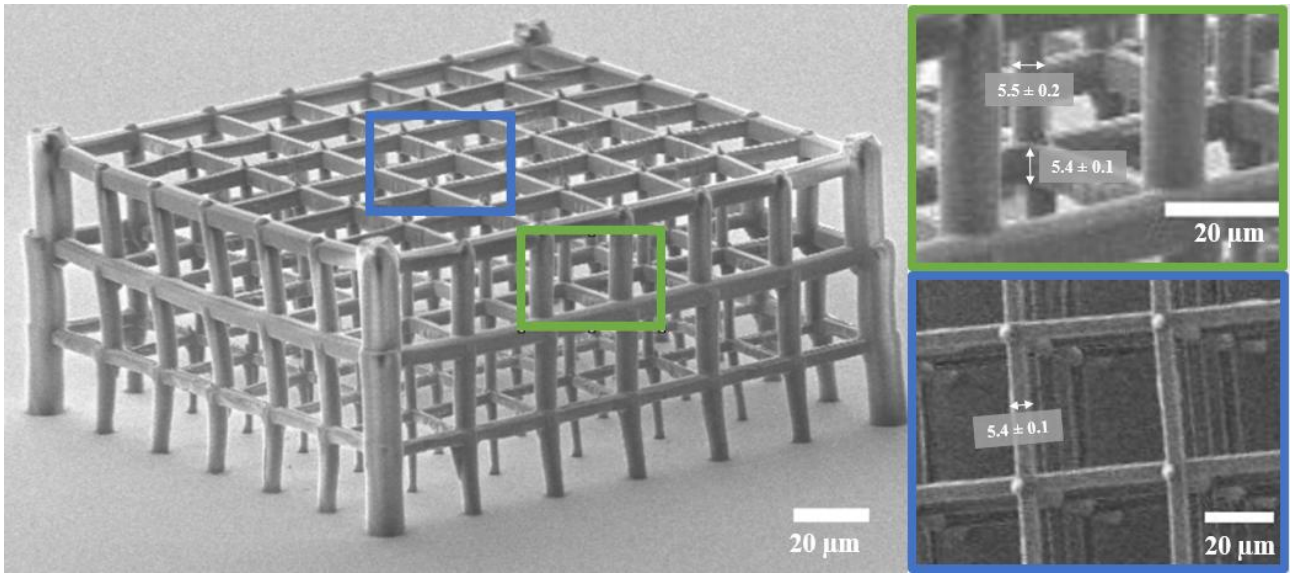

Figure 1. SEM image of 3D scaffold with 5 µm beams. Colored frames highlight top (blue) and side (green) views, showing consistent beam dimensions and confirming structural isometry.

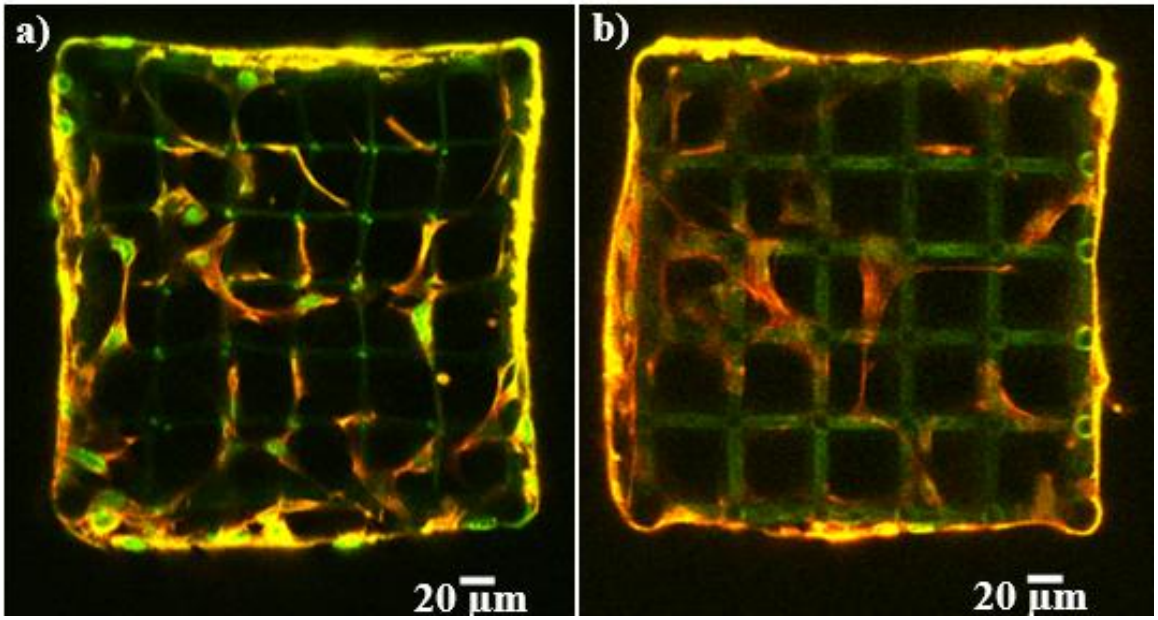

Figure 2. Two-photon microscopy images (λ = 800 nm) of fixed 3T3 fibroblasts stained with SPY555-actin (red) on OrmoComp scaffolds (green) with 40 µm cavities and beam widths of (a) 2 µm and (b) 10 µm, showing distinct 3D cell distribution and morphology as a function of scaffold architecture.

[1] Y. Shou et al., Adv. Sci. 10 (21) (2023) 2300670.
[2] R. Shyam, L.V.K. Reddy, A. Palaniappan, Int. J. Mol. Sci. 24 (3) (2023) 1912.
[3] L. Bourdon, J.-C. Maurin, K. Gritsch, A. Brioude, V. Salles, ACS Biomater. Sci. Eng. 4 (12) (2018) 3927–3938.
[4] N. Barin et al., Small 18 (49) (2022) 2204485.

Wafer-scale transfer-free multi-layer graphene process for MEMS sensors

Sten Vollebregt, R. Pezone, M. Husain, T. An, L.N. Sacco

Microelectronics Department, Delft University of Technology, Delft, 2628 CD, The Netherlands
e-mail: s.vollebregt@tudelft.nl

Graphene has unique properties that make it an attractive material for sensors or nano/micro-electro-mechanical systems (NEMS/MEMS). For sensors, especially those based on mechanical structures, graphene does not necessarily have to be single-layer to achieve good performance. Moreover, few or multi-layered graphene can enhance mechanical stability or processability, especially for large, suspended devices [1].

Chemical vapour deposition (CVD) on a metal catalyst is widely regarded as the most promising method for integrating graphene into semiconductor technology. A downside of CVD graphene is that it requires the transfer of the graphene from the catalyst. This step can introduce polymer contamination, cracks, and wrinkles. Another challenge is adhesion issues with the target substrate, mainly for non-flat substrates [2]. While significant progress has been made in CVD graphene and transfer [3,4], challenges remain, especially when creating suspended graphene devices.

As an alternative to transfer, we have developed a transfer-free method based on Mo as a catalyst [5]. By pre-patterning the catalyst, the graphene anchors to the substrate on the edges of the pattern, enabling lithographic control over the size and location. Furthermore, adhesion issues are circumvented by keeping the catalyst until the end of the fabrication. The limitation of the technology is that the growth is coupled to the target substrate. However, this is not an issue for MEMS devices, as it is customary in the industry to have a separate MEMS chip to form a system-in-package (SiP).

Here, we will show the latest advances in this platform's technology. These include wafer-scale graphene gas sensors on suspended micro-hotplates (Fig. 1) [6]. By using the transfer-free process, variation of the devices was minimized while the heater enabled fast recovery. We also have demonstrated the first wafer-scale graphene condenser microphones with high mechanical compliance, 10-100x higher than Si MEMS, while being ~9x smaller (Fig. 2) [7].

[1] S. Lukas et al., ACS Nano, 18 (2024) 25614
[2] S. Wagner et al., Microelectronic Engineering, 159 (2016), 108
[3] D. Neumaier et al., Nature Materials, 18 (2019), 525
[4] P.G. Steeneken et al., 2D Materials, 23 (2025), 014035
[5] S. Vollebregt et al., Proc. of IEEE MEMS (2016), 17-20
[6] L.N. Sacco and S. Vollebregt, Proc. of IEEE MEMS (2025)
[7] R. Pezone et al., Microsystems & Nanoengineering 10 (2024), 27

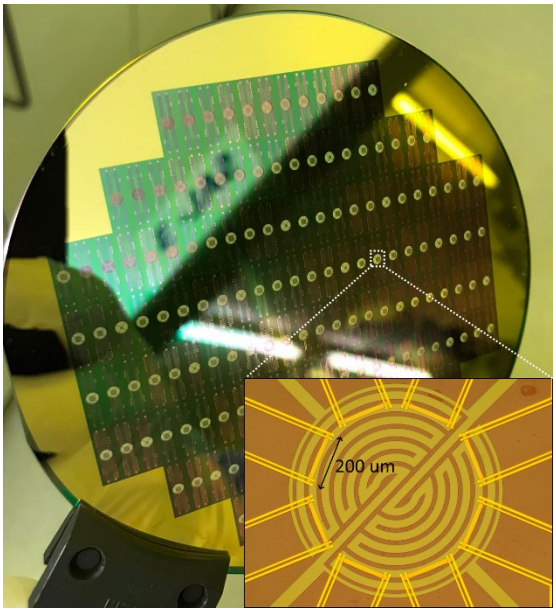

Figure 1. A 100 mm wafer with 156 suspended micro-hotplates. On each hotplate, up to 8 graphene strips are placed (inset).

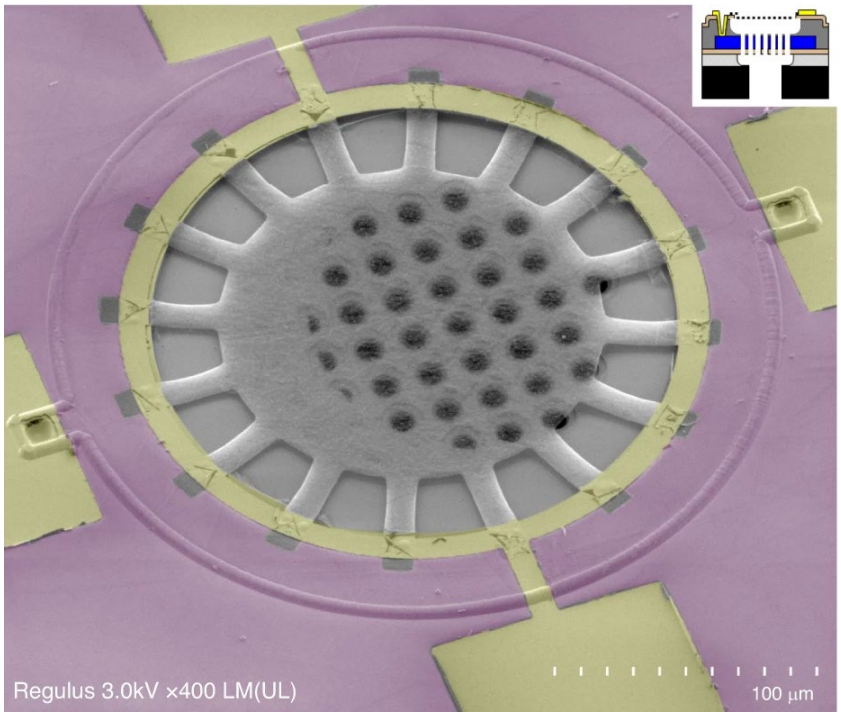

Figure 2. False colour scanning electron microscopy image of a 220 µm diameter, 7 nm thick, suspended graphene condenser microphone with poly-Si backplate. Inset: schematic cross-section of the device.

High Speed Nickel Electrodeposition in a Supercritical CO_2 Emulsified Nickel Sulfamate Bath toward MEMS Applications

Wending Hou [a,b], Tomoyuki Kurioka [a,b], Chun-Yi Chen [a], Masato Sone [a,b], Tso-Fu Mark Chang [a,b]
[a] *Materials and Structures Laboratory, Institute of Integrated Research, Institute of Science Tokyo, Kanagawa 226-8501, Japan*
[b] *Laboratory for Future Interdisciplinary Research of Science and Technology, Institute of Integrated Research, Institute of Science Tokyo, Kanagawa 226-8501, Japan*
email：hou@ames.pi.titech.ac.jp

Microelectromechanical systems (MEMS)-based sensors are widely recognized for their high accuracy in measuring motion, pressure, and temperature, highlighting their importance in modern technology. The flexibility and scalability of MEMS continue to drive advancements in their design and manufacturing. Since the early 2000s, efforts have been made to introduce supercritical carbon dioxide (SC-CO_2) emulsion into electrodeposition processes, aiming to take advantage of its unique properties, such as low viscosity and high diffusivity, to improve plating outcomes [1, 2] Studies involving the nickel Watts bath under supercritical conditions have shown improvements in surface smoothness and grain refinement [3, 4]. These findings have led to notable advancements in electroplated nickel for MEMS components, particularly in applications requiring high surface quality and fine microstructures.

However, despite the growing interest in electrodeposition with SC-CO_2 emulsion, investigations into behaviors of SC-CO_2 emulsified nickel sulfamate bath remain relatively limited. Unlike the Watts bath, the sulfamate bath allows the application of a high current density that leads to a high deposition rate. Generally, electrodeposition at a high current density results in defective surfaces and low current efficiency, which limit practical applications.

This study focuses on electrodeposition with SC-CO_2 emulsified nickel sulfamate bath and evaluating the influences of controlled parameters such as current density and CO_2 volume fraction. The electrodeposition was conducted at 14 MPa and 55 °C in a stainless steel cell of 50 ml. The total electric charge was 216 C, and the current density was varied from 0.03 A/cm^2 to 0.4 A/cm^2. Fig. 1 shows the reaction apparatus. To clarify the effects of the SC-CO_2 emulsion, conventional electrodeposition was also conducted.

Figs. 2 and 3 show optical microscopic images of nickel films from conventional electrodeposition and electrodeposition with the SC-CO_2 emulsion, respectively. Conventional electrodeposition at 0.24 A/cm^2 resulted in rough surfaces with defects, such as pinholes. In contrast, electrodeposition with the SC-CO_2 emulsion produced smooth surfaces at a high current density of 0.4 A/cm2. Fig. 4 shows the Faraday efficiency (FE) values for conventional electrodeposition and electrodeposition with the SC-CO_2 emulsion. The FE of the electrodeposition with the SC-CO_2 emulsion is lower than that of conventional electrodeposition. H_2 evolution is a common side reaction in nickel electrodeposition, and the removal of H_2 bubbles from the cathode is promoted by the SC-CO_2 emulsion. This results in better surface conditions but also promotes H_2 evolution, which lowers the FE. Nevertheless, the FE remains decent, and the defect-free surface condition is promising for the high-speed fabrication of MEMS components.

References:
[1] H. Yoshida *et al.*, *Surf. Coat. Technol.* 173 (2023) 285–292.
[2] H. Yoshida *et al.*, *Thin Solid Films* 446 (2004) 194–199.
[3] T.-F. M. Chang *et al.*, *Electrochim. Acta* 55 (2010) 6469–6475.
[4] T.-F. M. Chang *et al.*, *Microelectron. Eng.* 88 (2011) 2225–2228.

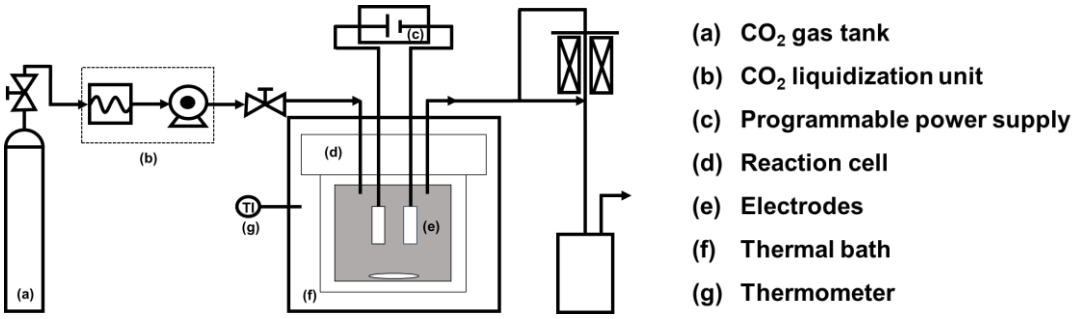

Figure 1. Reaction apparatus

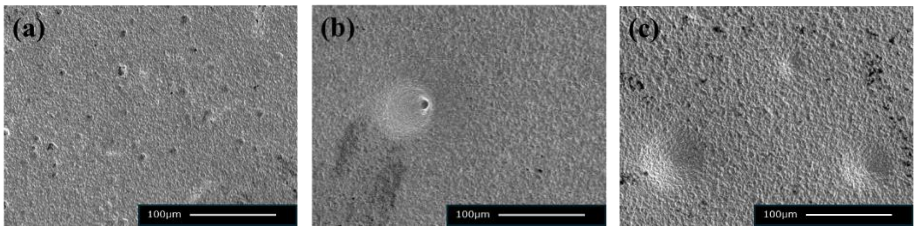

Figure 2. Optical microscopic images of nickel films by conventional electrodeposition of sulfamate bath at different current densities: (a)0.14 A/cm^2, (b)0.24 A/cm^2, (c)0.36 A/cm^2

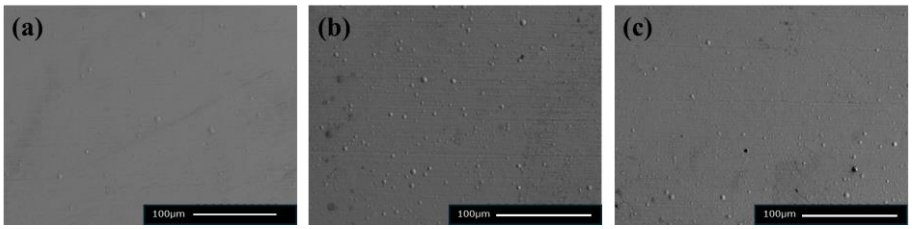

Figure 3. Optical microscopic images of nickel films by electrodeposition in the SC-CO_2 emulsion of sulfamate bath at different current densities: (a)0.14 A/cm^2, (b)0.36 A/cm^2, (c)0.4 A/cm^2

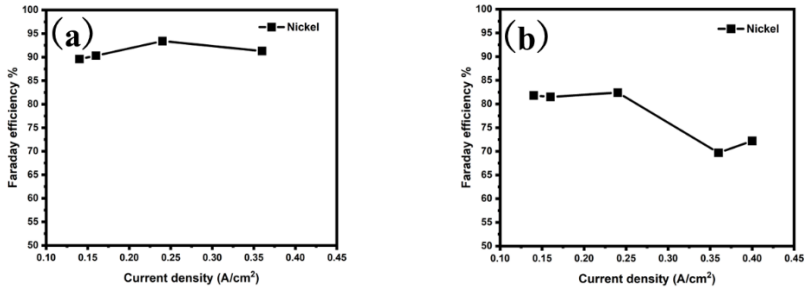

Figure 4. Faraday efficiency values of (a) conventional electrodeposition and (b) SC-CO_2 emulsion electrodeposition

Oral Session 1B : Electron Beam Lithography

Precise Dimension Control of Narrow Gaps on InP-Based Substrate by Electron Beam Lithography

Hao Zhang [a], Jing Becker [b], Jan Ebbert [a], Tekin Kahilogullari [a], Daniel Ritter [b], Nils Weimann [a]

[a] Components for High Frequency Electronics, Duisburg, 47057, Germany
[b] GenISys GmbH, Munich, 82008, Germany
e-mail: hao.zhang@uni-due.de

In the fabrication of III-V high-frequency devices, the quality of the metal–semiconductor contact plays a critical role in determining the device's ultimate high-frequency performance. Accurate and reliable measurement of contact resistance is therefore essential. The refined transmission line method (TLM) has demonstrated the ability to provide consistent and precise results, particularly when the specific contact resistivity is on the order of 10^{-8} Ω·cm² [1]. Due to their inherently high-density and tight-spacing nature, TLM structures pose significant challenges in patterning and measurement. When exposed on InP substrates using electron beam lithography (EBL), variations in pad spacing of up to ~20% have been observed between the center and edges of the array. This spatial non-uniformity leads to uneven current distribution (current crowding), which introduces systematic errors into the resistance measurement [2]. In this work, we incorporate an additional mid-range parameter into the proximity effect correction (PEC) process, aiming to improve uniformity in current flow across the TLM structure and thereby enhance the accuracy of contact resistance extraction.

In this study, PMMA 950K was used as the electron beam resist for metal lift-off. The substrate was a 450 µm thick InP wafer. Electron beam lithography was carried out using a JEOL JBX-8100FS system, operating at an acceleration voltage of 100 kV and a beam current of 15 nA. Exposure parameters (base line, figure 2) were based on previously calibrated values for PMMA [3]. For the modified proximity effect correction, an additional mid-range component was introduced, with the gamma range set between 1 and 10 µm, and the mid-range correction parameter (nue) varied between 0.1 and 1. Scanning electron microscopy (SEM) imaging was performed using a JEOL IT800 system. Feature spacing measurements were conducted using the ProSEM® from GenISys GmbH to ensure precise evaluation of pattern fidelity and proximity correction performance.

The spacing between the central and edge regions of all structures were measured and compared. Each spacing value is based on the average of at least 1000 measurements. The results show that after including the mid-range correction, the difference in spacing between the edge and central areas significantly decreased, with most values falling below 100 nm, and in some cases, even below 5 nm. Among all parameter sets, the best performance was observed when gamma was 7 µm. In this case, when nue ranged from 0.1 to 0.6, nearly all spacing differences were below 7 nm. Furthermore, a 2D ebeam simulation with BEAMER® from GenISys GmbH using this parameter set was compared with the experimental results, showing excellent agreement in terms of trend, which confirms the reliability of the measurements.

[1] Mark J.W.Rodwell et al., "Submicron Scaling of HBTs", in IEEE Transactions on Electron Devices, Vol. 48, Issue. 11, November 2001.
[2] Haw-Jye Ueng et al., "Error analysis leading to design criteria for transmission line model characterization of ohmic contacts", in IEEE Transactions on Electron Devices, Vol. 48, No. 4, pp. 758-766, April 2001
[3] U. Hofmann et al., A novel method to find the best (iso-focal) process point in electron beam lithography, GenISys White Paper.

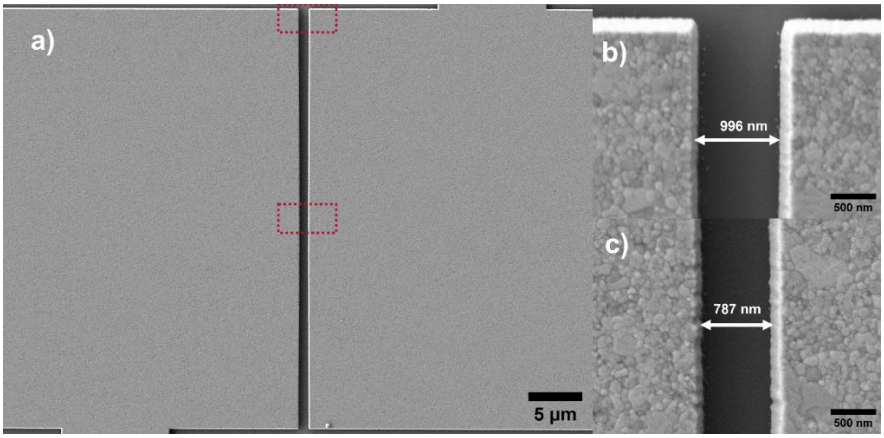

Figure 1. *a) SEM image of a TLM structure with a designed spacing of 1 µm on a InP substrate; b) the edge region, where the measured spacing is 996 nm; c) the central region with a spacing 787 nm.*

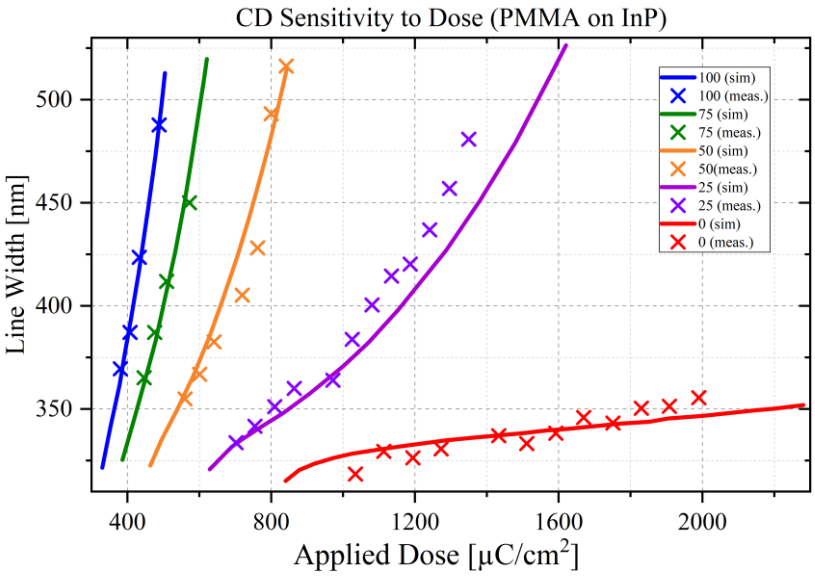

Figure 2. *Measured linewidth (cross) as a function of dose and density, with a model overlaid (lines). 0-100 present the pattern density in %. The calibrated results are used as the base line for exposure.*

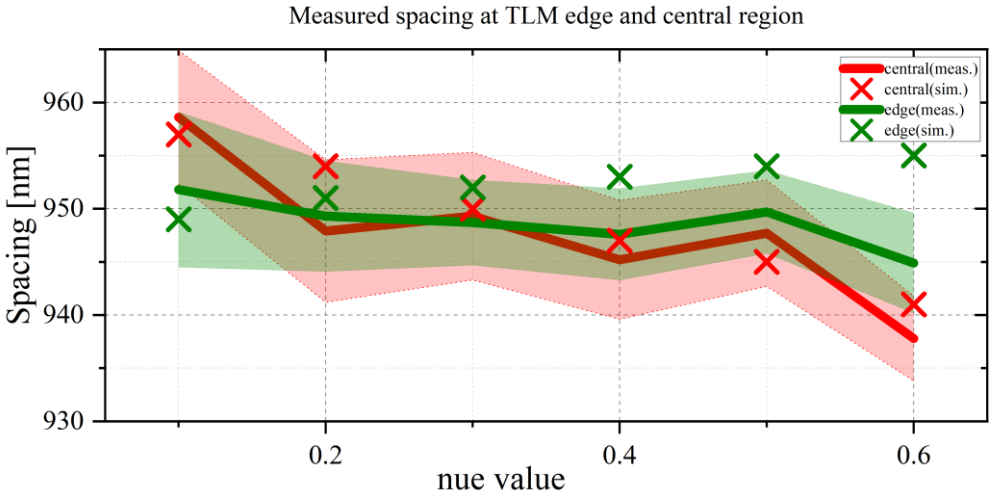

Figure 3. *For gamma = 7 µm, a comparison is made between the central and edge regions over the nue range from 0.1 to 0.6. Solid lines represent measured values, the shaded regions next to the lines indicate the first deviation, while the markers denote structures simulated using BEAMER.*

Direct Fabrication of 3-D PEDOT:PSS Nanostructures by Electron Beam Lithography

Yandong Yang, Shin'ichi Warisawa, Reo Kometani

Graduate School of Frontier Sciences, The University of Tokyo
5-1-5, Kashiwanoha, Kashiwa-shi, Chiba 277-8563, Japan
email: yang-yandong@s.h.k.u-tokyo.ac.jp

Keywords: Electron beam lithography, PEDOT:PSS, 3-D nanostructure, exposure property, chemical state

Currently, Poly(3,4-ethylenedioxythiophene):polystyrene sulfonate (PEDOT:PSS) has become a key material for constructing functional device, such as flexible sensing device and actuator [1], because of its conductivity (conductive polymer), transparency, flexibility, electrically contractile, and active optoelectronic tunability [2]. To unlock the full potential of PEDOT:PSS in sensing and integrated microsystems, advanced patterning and three-dimensional (3D) fabrication techniques are crucial. PEDOT:PSS has previously been shown to behave as a negative-tone resist on electron beam lithography (EBL)[3, 4]. EBL is useful as a research tool. [3, 4]. However, the fabrication of the 3-D PEDOT:PSS nano- and microstructure has not been reported. In this study, the EBL-based direct fabrication of the 3-D PEDOT:PSS nanostructure was tried, and its exposure properties and effect of e-beam irradiation to the chemical state of PEDOT:PSS were evaluated.

Figure 1(a) shows a fabrication process for the 3-D PEDOT:PSS nanostructure. Because the exposure depth varies depending on the acceleration voltage (Acc. V), a low Acc. V is useful for exposing the surface of the PEDOT:PSS film, and a high Acc. V is effective for exposing the PEDOT:PSS film deeply. Therefore, selection of Acc. V enables us to form the 3-D nanostructure, as shown in Fig. 1(a). All processes were carried out employing commercial PEDOT:PSS (Ossila PH1000). PEDOT:PSS films with a thickness of about 2350 nm were prepared on Si substrate using a 10 times multi spin-coating approach. The spin-coating process consisted of two steps: (1) 90 s at 2000 rpm for a stable film surface and (2) 150 s at 4000 rpm to promote solvent evaporation. The films were sufficiently dried for 24 h. In this study, e-beam with Acc. V of 5 kV and 20 kV were used for the fabrication of a suspended structure and supporting structures, respectively. The exposure dose for suspended and supporting structures were 100 $\mu C/cm^2$. The exposed samples were developed with deionized water for 12 min, and then rinsed in isopropanol alcohol for 40 s. Figure 1(b) shows a SEM image of an example of a suspended structure as the 3-D PEDOT:PSS nanostructure. We demonstrated that the proposed method enables us to achieve the 3-D nanostructure. And, Fig. 2(a) shows the relationship between the width and thickness of the suspended structure at Acc. V of 5 kV. And, the contrast curve at 20 kV Acc. V consists of two linear regions, as shown in Fig. 2 (b). We suggest that the non-linear is closely associated with the surface enrichment behavior of PSS. And, the sensitivity at Acc. V of 20 kV is calculated to be 384.2 $\mu C/cm^2$.

Raman spectroscopy was employed to characterize the chemical states of PEDOT:PSS exposed by electron beam with Acc. V of 5 kV and 20 kV. The PEDOT:PSS thin films utilized in this study were prepared by single spin-coating, with a thickness of 98 nm. The patterns for characterization were prepared by e-beam with the dose of 100 $\mu C/cm^2$. As shown in Fig. 3, it is observed that (1) the main peak C_α=$C_{\beta\ (symmetrical)}$ shifts to a higher wavenumber with increasing Acc. V, (2) $I_{_580}/I_{_1432}$ and $I_{_990}/I_{_1432}$ decrease when Acc. V is increasing, showing the π-conjugation length of PEDOT decreases, and e-beam exposure might cause C-S bond cleavage. Additionally, $I_{_1500}/I_{_1432}$ decreases as Acc.V increases. It suggests that the e-beam exposure leads to cross-linking of PEDOT. However, the spectrum did not change significantly enough to completely carbonize PEDOT:PSS using the e-beam. Although detailed evaluation of the material properties is required, the 3-D structure fabricated using the electron beam mostly retains the PEDOT:PSS structure.

Direct fabrication of PEDOT:PSS suspended nanostructures using EBL was demonstrated, and the effect of electron beam exposure on the chemical state was explored. This work provides significant insights for the precise fabrication of the 3D PEDOT:PSS nanostructures.

[1] F. Hu et al., Front. Robot. AI. 6 (2019) 114.
[2] H. Zhang et al., ACS Appl. Mater. 16 (2) (2016) 2554-2563.
[3] S. Doshi et al., Nanophotonics.13 (12) (2024) 2271-2280.
[4] Y. Yang et al., JSAP. Conference. (2025) 17p-K507-3.

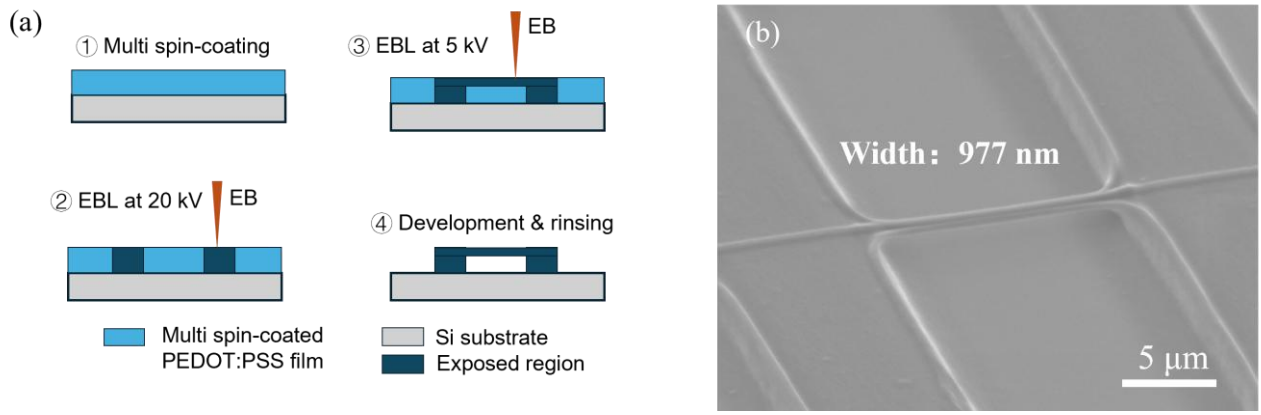

Figure 1. EBL-based direct fabrication of the 3-D PEDOT:PSS nanostructure: (a) Fabrication process of the 3-D nano- and microstructure. (b) SEM image of a suspended structure as the 3-D nanostructure. The length, width and thickness of the suspended structure were 14.7 μm, 977 nm and 410 nm, respectively. The height of supporting structure was 2147 nm.

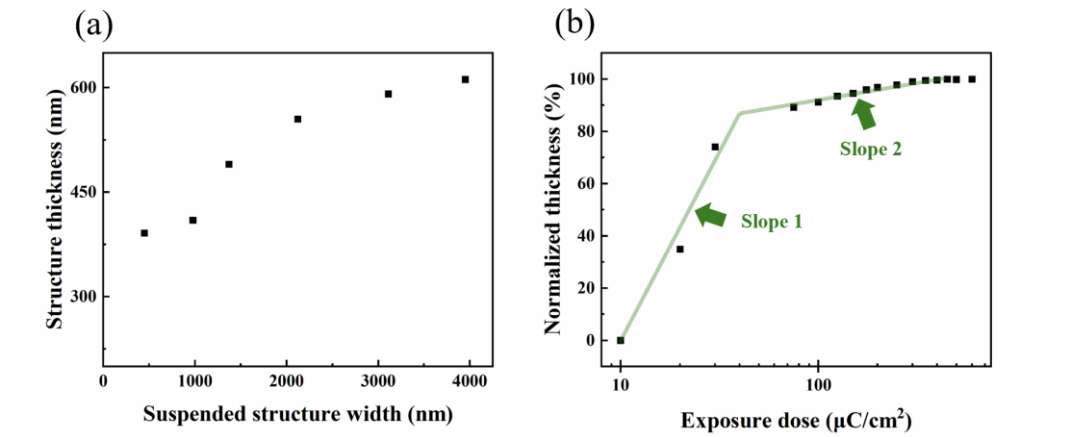

Figure 2. Exposure characteristics: (a) Thickness variation of suspended structure with structure width at Acc. V of 5 kV. (b) Contrast curve of PEDOT:PSS on Si substrate at Acc. V of 20 kV.

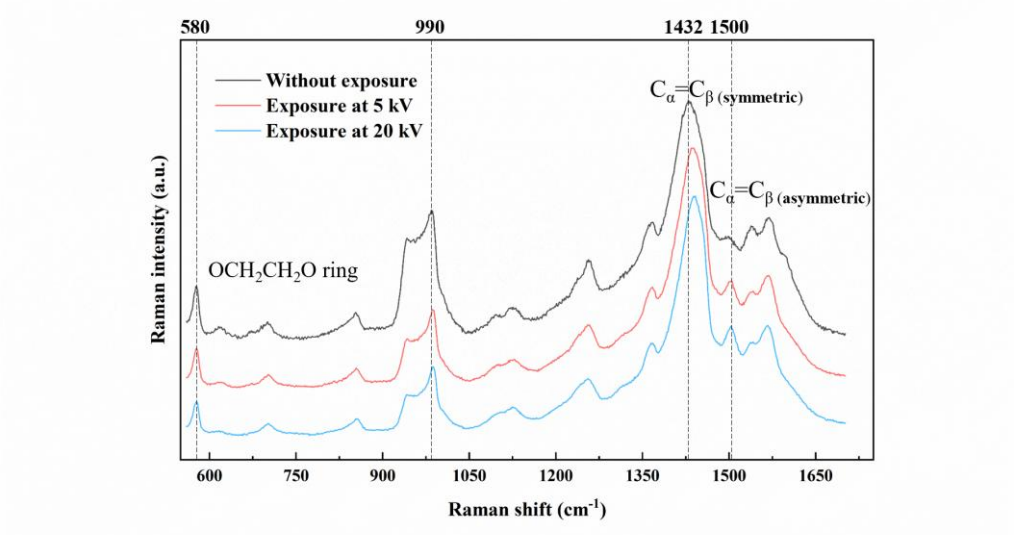

Figure 3. Evaluation of effect of e-beam irradiation to chemical state of PEDOT:PSS by Raman spectroscopy. In this Raman spectroscopy, a laser with a wavelength of 532 nm was used.

High Resolution Electron Beam Lithography Patterning for Advanced Grating Couplers

Pragya Sah[a,b], Radhakant Singh[a,b], Kai Zhang[a,b], Michael Möller[a], Rijil Thomas[a], Jens Bolten[a], Anastasiia Sorokina[c,d,e], Guochun Du[c], Carl-Frederik Grimpe[c], Steffen Sauer[c,d,e], Elena Jordan[c], Stefanie Kroker[c,d,e], Tanja E. Mehlstäubler[c,f,g], Stephan Suckow[a], Max C. Lemme[a,b]

[a] AMO GmbH, Aachen, 52074, Germany
[b] Chair of Electronic Devices, RWTH Aachen University, Aachen, 52074, Germany
[c] Physikalisch-Technische Bundesanstalt, Braunschweig, 38116, Germany
[d] Technische Universität Braunschweig, Institute of Semiconductor Technology, 38106, Germany
[e] Laboratory for Emerging Nanometrology (LENA), Braunschweig, 38106, Germany
[f] Leibniz Universitat Hannover, Institut fur Quantenoptik, Hannover, 30167, Germany
[g] Leibniz Universitat Hannover, Laboratorium fur Nano- und Quantenengineering, 30167, Germany
e-mail: max.lemme@eld.rwth-aachen.de; suckow@amo.de;

Silicon nitride (Si_3N_4) is a mature and versatile photonic platform with applications from data communication and spectroscopy to quantum computing, optogenetics, and meta-surface optics [1-5]. Grating couplers (GCs) are essential for coupling light in and out of photonic integrated circuits (PICs). Uniform GCs with constant periods and duty cycles are easy to fabricate if the lithography resolution is sufficient. However, they suffer from limited coupling efficiency and beam shaping control. This is particularly problematic for future applications in quantum computing, where trapped ions must be addressed precisely with light emitted from GCs [3], [8].

We have used apodized GCs with variable period and duty cycle to address this shortcoming. However, they add fabrication complexities because of tighter critical dimension requirements and the presence of features with different dimensions within the same GC. This is particularly critical at shorter wavelengths that require photonic structures of 150 – 200 nm feature size. We propose a mix-and-match fabrication scheme, where apodized GCs are fabricated via electron beam lithography (EBL), and waveguides are patterned with optical lithography. Our work focuses on optimizing the EBL resist, exposure dose, and etch process to reliably fabricate these high-resolution and high-efficiency apodized GC structures.

GCs operating in the near-infrared (NIR) spectral range (760–1650 nm) were made from a 200 nm thick Si_3N_4 film deposited on a 3 µm-thick buried oxide (BOX). Si_3N_4 was selected owing to its mature integration with silicon semiconductor technology and its wide optical transparency in wavelengths from 400 nm to 2.3 µm. The apodized GCs were subsequently defined using EBL. Efficient coupling required small features with high aspect ratios, i.e., ~2.86 without resist and ~8.57 with a 400 nm PMMA resist. Our apodized GC design consists of 85 nm to 255 nm wide ridges and 75 to 195 nm trenches. These parameters were chosen for the targeted wavelength, emission angle, and beam waist for each GC. Such flexible designs required determining the optimal exposure dose for different GCs with a wide range of feature dimensions. Moreover, managing mechanical instability and aspect ratio-dependent etching (ARDE) effects added to the fabrication complexity.

Our experiments identified three key optimizations that were instrumental in achieving our objectives: **(1) Resist optimization:** Replacing PMMA with a more chemically resistant resist, AR-P 6200, offered improved selectivity (0.89 to 1.25), yielding larger maximum etch depth or better resolution via thinner resist layers. This reduced the required resist thickness to just 350 nm for etching 200 nm deep into Si_3N_4, and, additionally, reduced the ARDE effect (**Figure 1**). **(2) Dose optimization:** Implementing the proximity effect correction for EBL helped to resolve the apodized GC design. However, for optimum results, we determined the appropriate dose for different GC designs, categorized by minimum feature size and fill factor, and exposed them with different doses in a single multipass exposure. **(3) Etching optimization:** The addition of ~10% O_2 in our CHF_3-based Si_3N_4 reactive ion etching (RIE) recipe [9] resulted in steeper sidewalls without significantly compromising the selectivity. This further helped in yielding target feature sizes close to design and optical performance close to simulation **(Figure 2)**.

We measured an emission angle of -51.88° and a beam waist of 14.5 x 23.82 µm^2 from the fabricated GCs, which is in strong agreement with the simulated angle of -52.40° and beam-waist of 15 x 22 µm^2 (**Figure *2***), thereby demonstrating the reliability of our fabrication approach.

Keywords: Apodized grating couplers, electron beam lithography, high aspect ratio features, ion traps

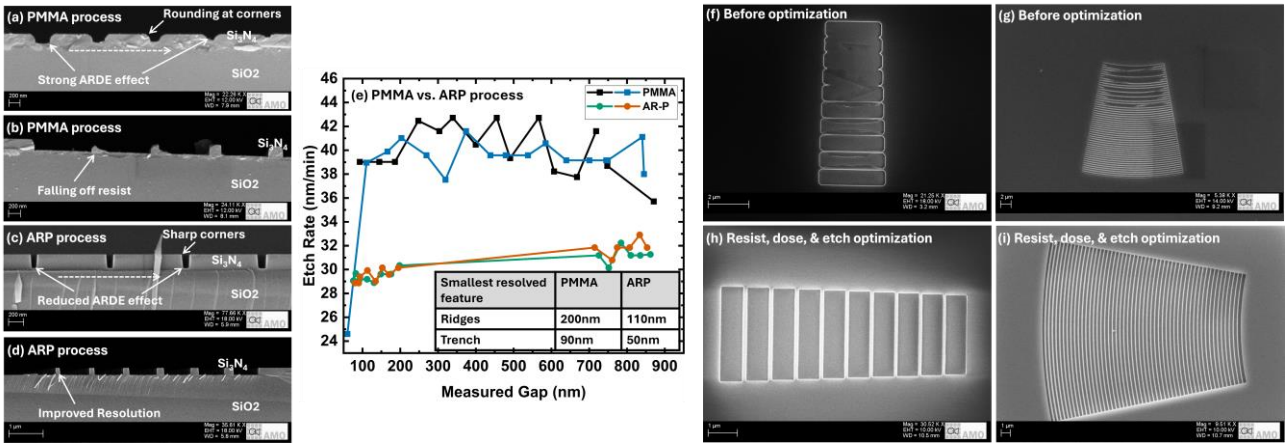

Figure 1: (a,b) Strong ARDE effect and mechanical instability of small features with PMMA for high aspect ratio features; (c,d) Improvement in minimum feature size (from 200 nm and 90 nm to 110 nm and 50 nm for ridges and trenches, respectively) and less profound ARDE effect with AR-P 6200 optimization; (e) Etch performance of PMMA vs AR-P 6200 against the fabricated trench dimensions highlighting (i) lower etch rate of AR-P 6200 and (ii) more uniform etch rate of AR-P 6200 across all the tested trench sizes; (f,g) Top view scanning electron microscope (SEM) image of GCs with small pillar and small trench features before optimization; (h,i) Top view SEM image of GCs with small pillar and small trench GCs after optimization.

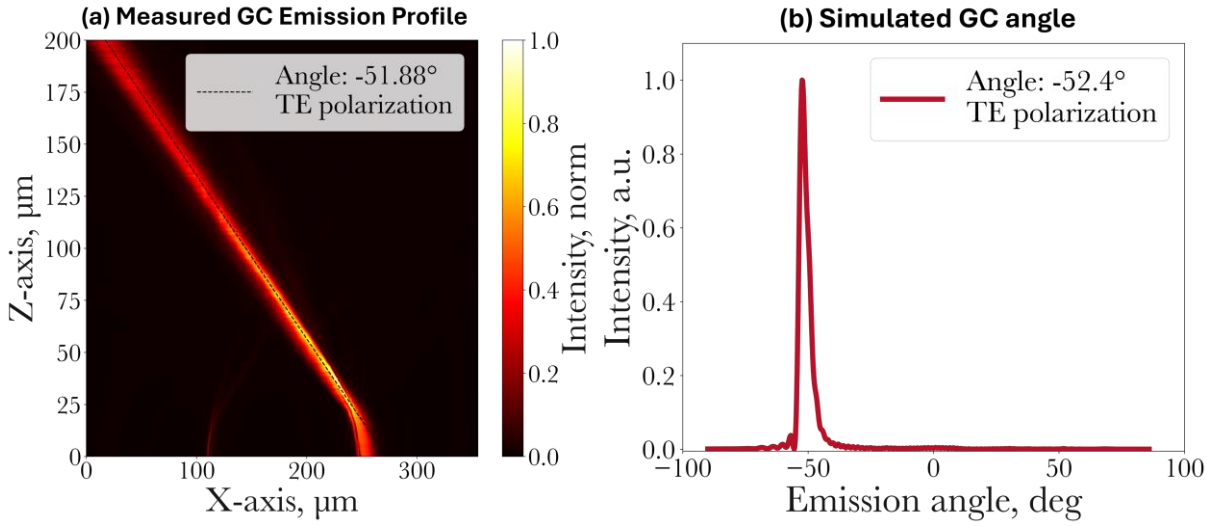

Figure 2: (a) Measured emission profile and angle of an exemplary GC for 760 nm with TE polarization at the WG compared to (b) the simulated GC emission angle.

References:

[1] Rahim *et al.*, *IEEE Journal of Selected Topics in Quantum Electronics*, vol. 25, no. 5, pp. 1–18, Sep. 2019
[2] A. Z. Subramanian *et al.*, *Photon. Res., PRJ*, vol. 3, no. 5, pp. B47–B59, Oct. 2015
[3] K. K. Mehta *et al.*, *Nature Nanotech*, vol. 11, no. 12, pp. 1066–1070, Dec. 2016
[4] L. Hoffman *et al.*, *IEEE Photonics Journal*, vol. 8, no. 5, pp. 1–11, Oct. 2016
[5] I. H. Syed *et al.*, in *2023 IEEE 23rd International Conference on Nanotechnology (NANO)*, Jul. 2023, pp. 983–987
[6] D. J. Blumenthal *et al.*, *Proceedings of the IEEE*, vol. 106, no. 12, pp. 2209–2231, Dec. 2018
[7] X. Chen *et al.*, *IEEE Photonics Technology Letters*, vol. 22, no. 15, pp. 1156–1158, Aug. 2010
[8] K. K. Mehta *et al.*, *Sci Rep*, vol. 7, no. 1, p. 2019, May 2017
[9] J. Sun *et al.*, *Vacuum*, vol. 207, p. 111650, Jan. 2023

A novel patterning approach enabling consistent high aspect ratio nanostructures with functional structuring

B. Benz [a,b,c], M. Stampanoni [c,d], M. Poggio [a,b], L. Romano [c,d]

[a] University of Basel, Basel, 4001, Switzerland
[b] Swiss Nanoscience Institute, Basel, 4001, Switzerland
[c] Paul Scherrer Institute, Villigen, 5232, Switzerland
[d] Institute for Biomedical Engineering at University and ETH Zürich, Zürich, 8092, Switzerland
e-mail: bryan.benz@psi.ch

Metal assisted chemical etching (MacEtch) can be used to create Si nanostructures with ultra-high aspect ratio. Its applications range from a broad spectrum, including solar cells, batteries, X-ray optics [2], wires for bio-surfaces, and sensors [1]. These applications often require structures that are made of more than just Si. With a reduction in size and an increase in aspect ratio, the deposition of these materials proves challenging. Examples are cantilevers for magnetic force measurement [3]. They require very high aspect ratio wires with sections in the nanometer scale and magnetic tips. Creating structures in the required aspect ratio is not trivial and the deposition of a tip after etching is an open issue. MacEtch in vapor phase [4] can solve both issues at once.

MacEtch is a plasma free, anisotropic chemical etching method that uniquely defies the isotropic nature of conventional wet etching, through local catalyzed electrochemistry. An oxidant is reduced at the catalyst surface and the silicon substrate underneath the catalyst layer is oxidized and subsequently removed by an etchant, usually HF. Inspired by vapor phase HF etching of SiO_2 releasing structures for micro-electromechanical systems, vapor-MacEtch delivers the etchant to the substrate surface in the vapor phase instead of the liquid phase. Oxygen from the air is used as oxidant with platinum as catalyst [5]. Since it is a "dry" process, it can be used for stiction sensitive applications without the need for supercritical drying steps.

We present here a new patterning method – called interlayer patterning – to realize nanostructures more consistently for vapor MacEtch and enable the structuring of functional tips. The main challenge of a lift-off-based patterning is the poor yield, especially with noble metals, since the deposition is usually done by physical evaporation that might reflow the resist pattern. Overcoming lift-off by patterning an interlayer (Figure 1) allows for a clean pattern transfer with high uniformity. Figure 2 show some examples of patterned and etched arrays of nanostructures: h-bars, lines and nanowires. In addition, the method allows to be used in two complementary ways, which change the region to be exposed in electron beam lithography. This has the same effect as changing from negative to positive resist without changing the resist itself. This method can be further used to create structures with functional tips like magnetic materials and metal-oxide stacks. Such structures were successfully created with aspect ratio of up to 1'000:1 and feature sizes down to 100 nm (Figure 2d, 2e). The ordered array of wires has been patterned by electron beam lithography with 100 nm sized holes spaced at 50 µm distance. The catalyst has been treated by thermal de-wetting to create random distributed holes with size smaller than 10 nm to favor the diffusion of the reactants between the main ordered wires. The random holes create also wires with thickness smaller than 10 nm during MacEtch that are consumed during the long etching process (> 10 hr) so that the remaining structures are only the main ordered wires. EDX analyses indicate the interlayer material is present only in the multi-layer tip. This shows the potential of MacEtch not only as a cost-effective alternative to reactive ion etching for high-aspect-ratio structures but also as a tool to create multi-layer functional structures.

[1] R. P. Srivastava and D. Y. Khang, Adv. Mat. 47 (2021) 2005932.
[2] L. Romano and M. Stampanoni, Micromachines 11 (2020) 589.
[3] F.R. Braakman and M. Poggio Nanotechnology 30 (2019) 332001.
[4] L. Romano et al., Nanoscale Horizon 5 (2020) 869-879.
[5] Z. Shi et al., Materials Science in Semiconductor Processing 157 (2023) 107311.

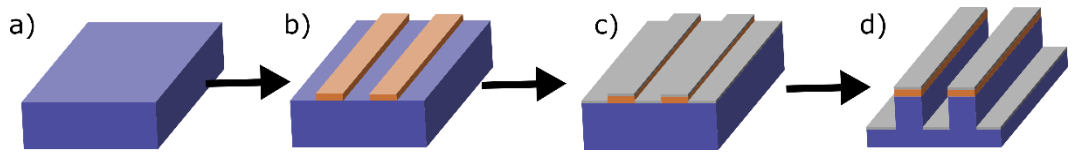

Figure 1. Process flow of the vapor MacEtch process: a) taking a silicon substrate (blue) on which b) an interlayer not reactive to MacEtch (orange) is deposited and patterned by electron beam lithography. Afterwards c) the Pt catalyst (gray) is deposited and then d) the structure is exposed to HF in vapor phase and O_2, realizing the MacEtch process: the substrate in contact with the catalyst is etched. With the catalyst progressively sinking down into the substrate, high aspect ratio silicon structures are obtained with the original pattern and a tip consisting of the interlayer and the Pt catalyst.

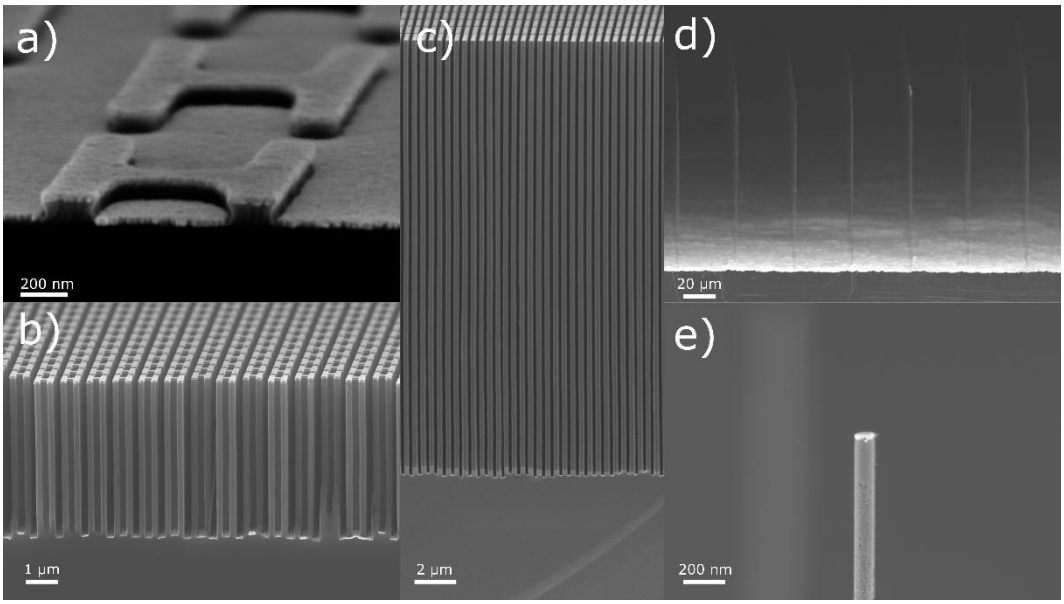

Figure 2. SEM in cross-section of various nanostructures by vapor-MacEtch; a) 200 nm h-bar structures with tips before etching; b) 200nm h-bar etched structures (aspect ratio 25:1); c) 200 nm lines without tips after etching (aspect ratio 100:1); d) 100 nm wide and 100 µm tall wires (aspect ratio 1’000:1); e) zoomed in image of the tip of an etched 100nm-wide nanowire in d) showing a 40 nm-thick layer on top of the wire.

Oral Session 1C : Electronics 1

P-channel Oxide Thin Film Transistors for CMOS Logic

K. M. Niang [a], B. Peek [b], J. Parish [c], P. Chalker [b], A. Johnson [c], A. J. Flewitt [a]

[a] Electrical Engineering Division, Cambridge University, Cambridge, CB3 0FA, UK
[b] School of Engineering, University of Liverpool, Liverpool, L69 3BX, UK
[c] Department of Chemistry, University of Bath, Bath, BA2 7AX, UK
e-mail: ajf23@cam.ac.uk

Thin film transistors (TFTs) employing amorphous indium gallium zinc oxide (a-IGZO) as the channel semiconductor are widely used in the display industry as a result of their good stability, exceptionally low off-state current and good mobility (typically well over 10 $cm^2 V^{-1} s^{-1}$). In addition, deposition is possible at room temperature by sputtering [1]. This has resulted in significant interest in using a-IGZO beyond the field of displays, including digital logic circuits on flexible substrates for applications such as smart packaging. An example of this is the recent report of a ARM-based microprocessor based on an NMOS architecture on a flexible substrate [2]. However, the future development of such flexible logic systems is limited by the high power consumption of NMOS architectures, and CMOS is now required. This necessitates both a p-channel and n-channel TFT, but p-type doping of a-IGZO and similar materials is not possible as a result of fundamental physical limitations [3].

Tin monoxide (SnO) has emerged as a promising p-type thin film oxide semiconductor that would complement a-IGZO well in TFT-based CMOS logic circuits as a result of its relatively high hole mobility which results from s relatively less localized valence band maximum which is dominated by hybridized O 2*p* states and Sn 5*s* states. Although there has been some success in sputter-deposition of p-type SnO, reproducibility has proved to be challenges because of the multiple valence states that Sn can possess. Better control of valency is possible using atomic layer deposition (ALD) through the use of precursors such as bis(1-dimethylamino-2-methyl-2-propoxy)tin where the Sn atom is already in the 2+ valence state that is required to form SnO.

In this work, other promising precursors for the ALD deposition of SnO are explored. Sn (II) bis(*tert*-butoxide) is shown to produce TFTs following annealing at 250 – 350 ºC with a field effect mobility up to 2 $cm^2 V^{-1} s^{-1}$ and a switching ratio between 10^3 and 10^4 [4]. By combining these devices with a-IGZO TFTs, all-oxide TFT-based CMOS inverters have been produced with a DC voltage gain of ~130 for a supply voltage of 4 V (Figure 1). The deposition of amorphous SnO (a-SnO) is also reported using another novel precursor with a growth rate that is over 4 times higher than typically-reported growth rates by ALD. Transfer characteristics of TFTs produced with this a-SnO are shown in Figure 2. These devices have a field effect mobility ~1 $cm^2 V^{-1} s^{-1}$, a threshold voltage close to 0 V and a switching ratio ~10^5. These devices are particularly attractive not only due to the good electrical characteristics, but also because of the fast deposition and the uniformity afforded by amorphous thin film semiconductors.

[1] Nomura, K., *et al.*, *Nature*, **432**, 488 (2004)
[2] Biggs, J., *et al.*, *Nature*, **595**, 532 (2021)
[3] Robertson, J. and Clark, S.J., *Phys. Rev. B*, **83**, 075205 (2011)
[4] Gomersall, D.E., *et al.*, *J. Mater. Chem. C*, **11**, 5740 (2023)

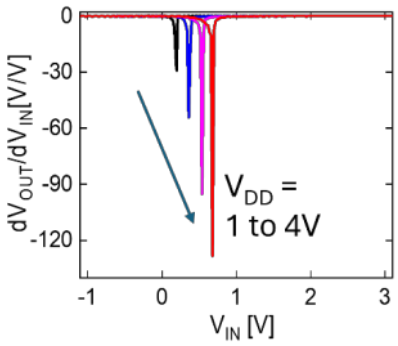

Figure 1. DC voltage gain of a CMOS inverter employing an SnO p-channel TFT and an a-IGZO n-channel TFT.

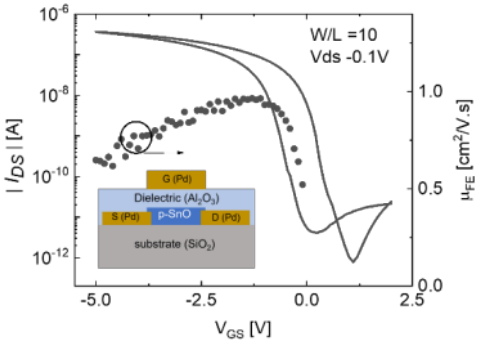

Figure 2. transfer characteristics of a top gate a-SnO TFT.

Electric Field Confinement-Induced Potentiation in Inert Mixed Ionic-Electronic Conducting Memristors

Philip Calado

School of Electronics and Computer Science,
University of Southampton, Southampton, SO17 1BJ, UK
e-mail: p.calado@soton.ac.uk

Memristors are two-terminal passive circuit elements characterised by their ability to change resistance in response to past electrical stimuli in such a way that the device current is a function of both the applied voltage and a history-dependent state variable.[1] Interconnecting an array of memristors produces a hardware neural network capable of in-memory computing with the potential to realize neuromorphic chips with improved energy efficiency, real-time learning and greater fault tolerance as compared to the current breed of silicon-based Artificial Intelligence accelerators.[2] Electronic currents within mixed ionic-electronic conductors (MIEC), such as hybrid organic-inorganic perovskites, can be modulated through the redistribution of slow moving ionic carriers, making them prime candidates for use as memory materials in memristive devices.[3][4] Many challenges remain for the research field, however, including understanding the underlying resistive switching mechanisms, device stability, and state retention.

In this work, increases and decreases in currents (potentiation and depression) in inert perovskite memristors (IPMs), employing unreactive electrode materials[3], are successfully reproduced using a numerical drift-diffusion device simulator[5] and an analytical model (Figs 1 and 2). The memristor device models developed for the study include both electronic carriers and relatively high concentrations of intrinsic mobile ionic carriers ($n_{SD} > 10^{17}$ cm^{-3}), compensated by static counter ions, modelling Schottky defects. The results indicate that the potentiation and depression of currents observed within IPMs can be attributed to Schottky defect migration in response to the time-averaged internal electric field generated during a series of voltage pulses applied to the device. As defects migrate during potentiation, the potential drop across the perovskite layer becomes localised to the interfaces, increasing the magnitude of the electric field and associated electronic drift currents in these regions (see Fig 2a). This electric field confinement effect injects more electronic carriers into the field-free region, enabling higher diffusion currents. The models show that potentiation in IPMs can be explained by this effect as opposed to energetic (Schottky) barrier modulation.[6] Depression of currents is achieved via the inverse process during which the potential drop becomes spatially distributed across the device. Notably, the state variable controlling the resistance in IPMs is explicitly identified as the time-dependent ionic depletion width (Figs 2a and 2b). These findings provide new insight into the resistive switching mechanism underlying inert MIEC memristors more generally and suggest new design strategies for the optimisation of real-world devices.

References

[1] L. O. Chua, IEEE Trans. Circuit Theory, 18(5) (1971) 507–519.
[2] S. Kumar et al., Nat. Rev. Mater., 7(7) (2022) 575–591.
[3] Z. Xiao and J. Huang, Adv. Electron. Mater., 2 (2016) 1–8.
[4] S. J. Kim et al., Nat. Nanotechnol., 20 (2025) 83–92.
[5] P. Calado et al., J. Comput. Electron., 21(4) (2022) 960–991.
[6] X. Guan et al., Adv. Funct. Mater., 28(3) (2018) 1704665.

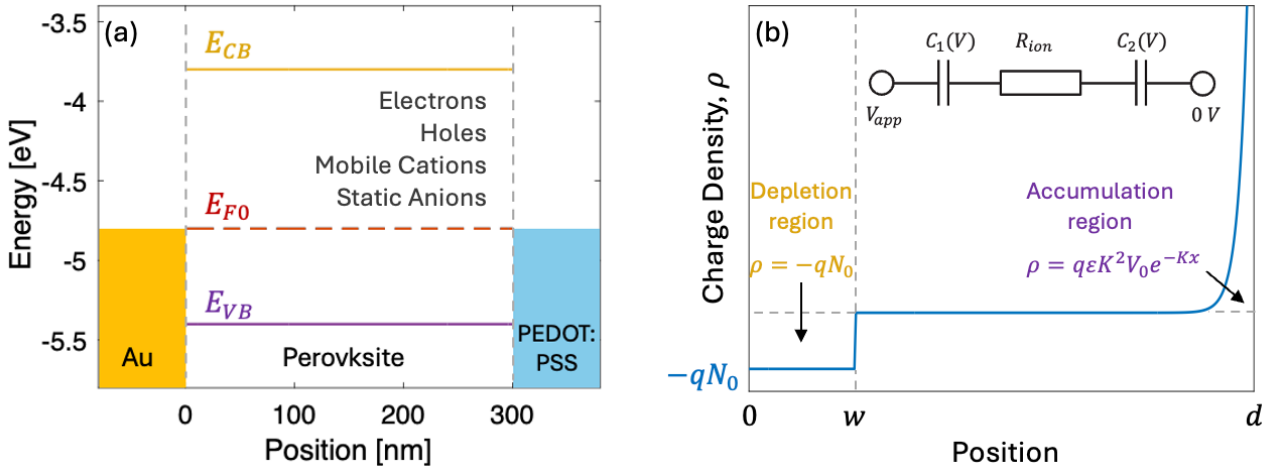

Figure 1. Schematics of the models. (a) Energy level diagram of the simulated MIEC device at equilibrium. E_{CB}, E_{VB}, and E_{F0} are the conduction band, valence band, and equilibrium Fermi energies respectively. (b) Schematic of ionic space charge as a function of position x for the analytical model. In the accumulation region the small voltage approximation to the charge density ρ is used. For the depleted region, a uniform charge density across the depletion width w is assumed. N_0 denotes is the intrinsic Schottky defect density. Inset: The equivalent circuit model used for time evolution.

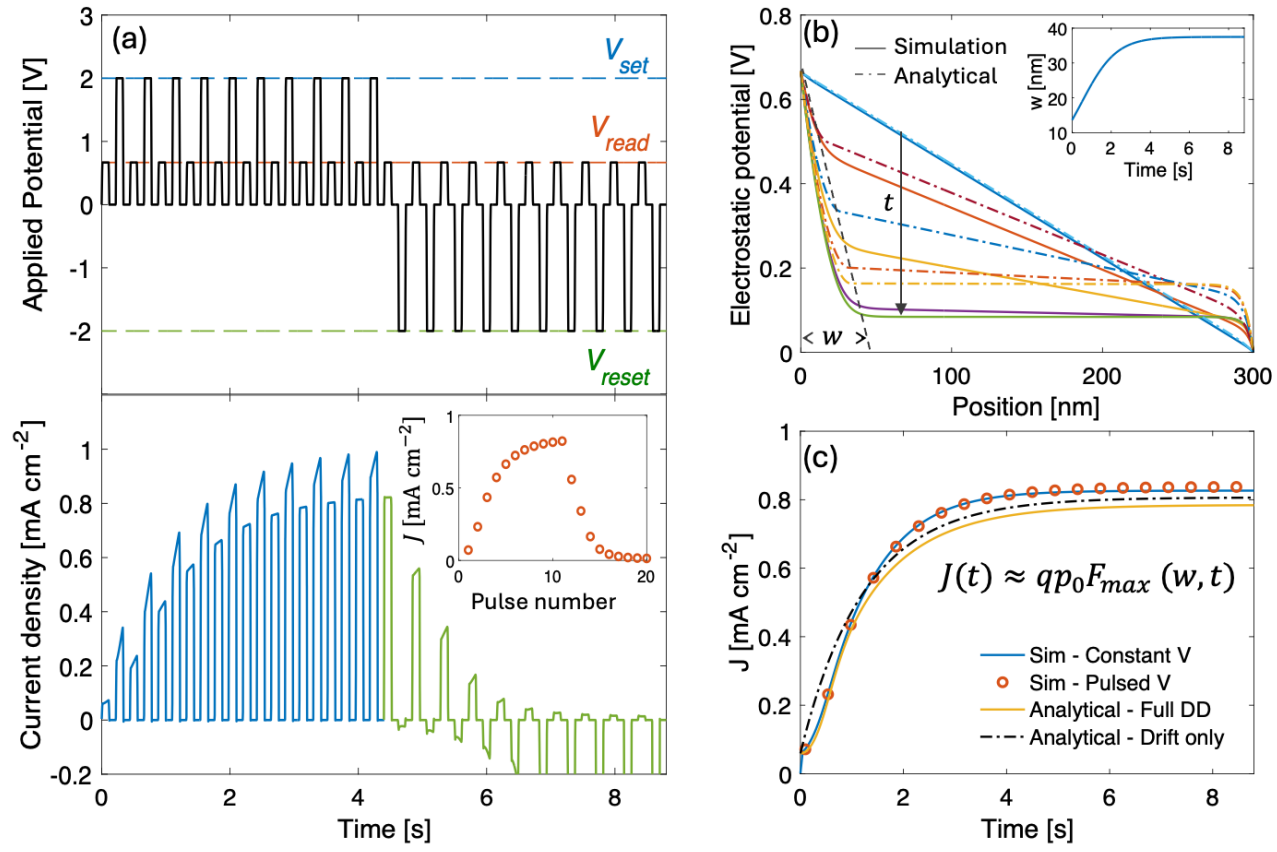

Figure 2. Potentiation and depression in the simulated and analytical models. (a) Pulsed potential scheme and output current density for the simulated inert perovskite memristor. The potential scheme consists of 10 potentiation and read cycles followed by 10 depression and read cycles. The resulting current density $J(t)$ exhibits potentiation and depression. Inset: J extracted from the penultimate data point of each read pulse. (b) Numerical simulation and analytical solutions to the electric potential profiles as a function of time following a jump in voltage from short circuit to $v = -0.67\ V$. Inset: The ionic depletion width transient. (c) Current density transients for the different models. At high injection the J is proportional to the electric field at the electrode interfaces F_{max}, defined by the depletion width w.

Towards aluminium nitride on diamond surface acoustic wave devices

Jerome A. Cuenca[a], Soumen Mandal[a], Oliver A. Williams[a]

[a] Cardiff University, Cardiff, CF24 3AA, United Kingdom
e-mail: williamso@cardiff.ac.uk

High-frequency communication devices rely on surface acoustic wave (SAW) filters due to their low insertion loss and high selectivity[1]. SAW devices can be fabricated on bulk or thin-film piezoelectric materials including lithium niobate ($LiNbO_3$), zinc oxide (ZnO), gallium nitride (GaN) and aluminium nitride (AlN), enabling acoustic wave generation through an interdigitated transducer. However, the maximum operating frequency is limited by the minimum feature size of the transducer fingers but ultimately, the acoustic velocity of the material (4,000 to 6,000 m/s) [2,3,4]. To overcome this, piezoelectric films need to be integrated with high velocity substrates such as diamond (12,000 m/s)[3], either through direct deposition or through wafer bonding.

In previous work, super-high-frequency SAW resonators have been fabricated on AlN/diamond heterostructures, operating beyond 10 GHz [3]. Previous work on AlScN, where the piezoelectric coupling coefficient is up to 4x greater than AlN, has also demonstrated gigahertz devices, although material deposition and integration is significantly more challenging[4]. Owing to the difficulty in direct heteroepitaxy of diamond on piezoelectric films, the film is typically deposited on a freestanding diamond either through sputtering or molecular beam epitaxy. However, this means that the film is inherently textured and granular where ideally single crystal films are preferred, so as to avoid any potential mechanical losses caused by grain boundaries and coupling losses due to an inhomogeneous piezoelectric film.

In this work, we present advancements in integrating diamond and AlN for high-performance surface acoustic wave (SAW) devices, with (1) preliminary investigations of SAW devices on single crystal AlN and (2) freestanding AlN on diamond plates through direct diamond growth on single crystal AlN (10x10 mm^2 area) for SAW devices. For this demonstration we use simple optical lithography to produce micron scale SAW devices with aim to directly compare AlN/Si and AlN/Diamond devices. We present finite element modelling of these simple structures to show the ~2x increase in frequency just by changing the substrate.

[1] Y. Takagaki, P. V. Santos, E. Wiebicke, O. Brandt, H.P. Schönherr, K.H. Ploog, Superhigh-frequency surface-acoustic-wave transducers using AlN layers grown on SiC substrates, Appl. Phys. Lett. 81 (2002) 2538–2540. https://doi.org/10.1063/1.1509471.

[2] O. Zywitzki, T. Modes, S. Barth, H. Bartzsch, P. Frach, Effect of scandium content on structure and piezoelectric properties of AlScN films deposited by reactive pulse magnetron sputtering, Surf. Coatings Technol. 309 (2017) 417–422. https://doi.org/10.1016/j.surfcoat.2016.11.083.

[3] G. Rodríguez-Madrid, G.F. Iriaróte, J. Pedros, O.A. Williams, D. Brink, F. Calle, Super-high-frequency SAW resonators on AlN/diamond, IEEE Electron Device Lett. 33 (2012) 495–497. https://doi.org/10.1109/LED.2012.2183851.

[4] M. Yuan, D. Van Dinh, S. Mandal, O.A. Williams, Z. Chen, O. Brandt, P.V. Santos, Generation of GHz surface acoustic waves in (Sc,Al)N thin films grown on free-standing polycrystalline diamond wafers by plasma-assisted molecular beam epitaxy, J. Phys. D. Appl. Phys. 57 (2024) 495103. https://doi.org/10.1088/1361-6463/ad76ba.

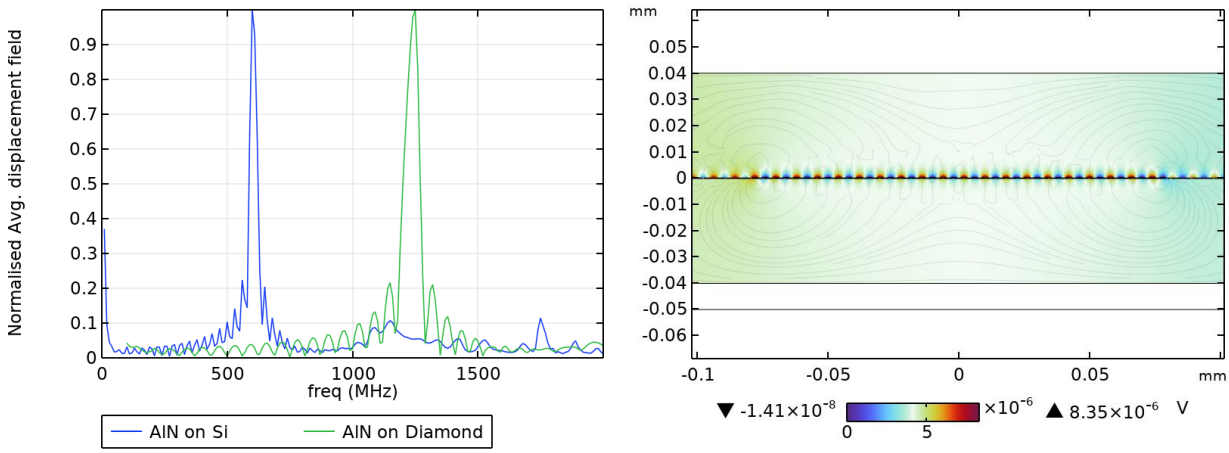

Figure 1. Finite element modelling results of SAW devices of AlN on Si and Diamond showing the normalized displacement field within the AlN layer as a function of frequency (left) and the electric potential distribution on resonance (right)

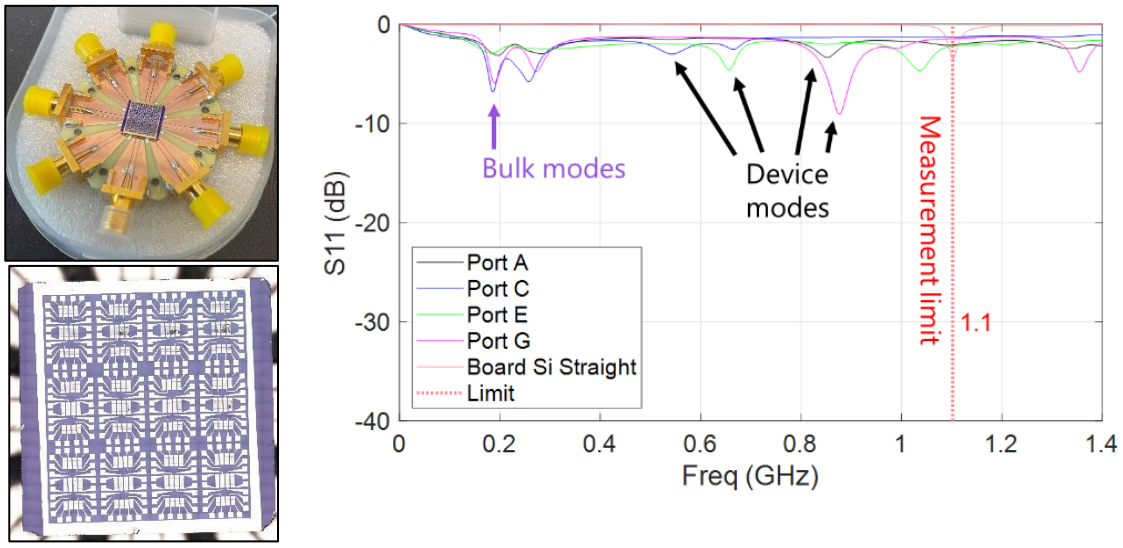

Figure 2. Photograph of AlN on Si SAW device showing the launcher board (top-left) the 10x10mm AlN/Si substrate (bottom-left) and 1-port reflection measurements of devices (right)

Nanoscale Back-End-of-Line Silicon Carbide Memristor for Resistive Memory

Qin Liu [a], Omesh Kapur [a], Anushka Gangnaik [a], Ruomeng Huang [a], C.H. Kees de Groot [a]

[a] University of Southampton, Southampton, SO17 1BJ, England
e-mail: ql4u22@soton.ac.uk

With the development of artificial intelligence and big data technologies, the density and complexity of data are increasing abruptly, leading to extensive research on next-generation non-volatile memory to achieve area-efficient and power-efficient in-memory computing [1]. Resistive Random-Access Memory (RRAM) is a popular candidate for the next generation of non-volatile memory because of its switching performance and scaling potential. RRAM is usually a simple metal-insulator-metal sandwich structure, where top electrode metal ions are injected into the dielectric layer and migrate to form or rupture conductive filaments between the two electrodes when applying an external electric field, allowing the device to switch between low resistance state (LRS) and high resistance state (HRS). In addition, RRAM cells have potential to be integrated directly into CMOS low K/Cu interconnect to reduce latency in connectivity constrained computational devices, and by stacking memory directly on top of logic to reduce a chip's footprint, improving a faster overall performance [2].

Amorphous silicon carbide (SiC) is a back-end-of-line (BEOL) material in the CMOS industry and is regarded as the interconnection dielectric material for third-generation semiconductors. In our previous work, we demonstrated that bilayer SiC/Si memristors (schematic shown in Figure 1a) can achieve one billion switching cycles with an ON/OFF ratio of ca. two orders of magnitude (Figure 1b), and exhibit multiple resistive states switching by controlling the pulse conditions such as pulse endurance and amplitude (Figure 1c), proving the potential for high-performance applications [3]. We demonstrated single-layer silicon carbide memristors with neuromorphic behaviour. By applying DC and AC bias, we modulated the multi-resistive states to mimic the synaptic features of the human brain, including short-term plasticity (STP), spike-voltage-dependent plasticity (SVDP), etc. These devices also successfully simulated learning-forgetting-relearning processes [4] and can be used as the physical reservoir to implement a reservoir computing system for pattern recognition, achieving high accuracy [5]. All of the above works showed the potential of SiC memristors for non-volatile memory and neuromorphic computing applications.

Based on these advancements, we now present the first nanoscale SiC-based memristor (schematic shown in Figure 2a). Decreasing the physical size of the memristors is crucial for making the memristors more compatible with CMOS technology, lowering the area cost and reducing the power consumption. Our device utilizes SiC as the dielectric layer with Cu top electrodes and W bottom electrodes. The SiC layer is deposited by plasma-enhanced chemical vapour deposition (PECVD). The flatness of the contact area between the bottom electrodes and the SiC layer is optimised using an in-laid W electrode to strengthen the control of conductive filaments. The width of the interconnect lines of our memristor array is varied from 320 nm to 5 nm by e-beam lithography. The devices are fabricated in both crosspoint and crossbar arrays (Figure 2b and 2c), enabling a comparative analysis of single-bit and 0.25kb chip architectures.

References:

[1] Z. Wang et al., Nature Reviews Materials, 5, (2020), 173-195.
[2] R. Cao et al., IEEE Electron Device Letters, 38, (2017), 1371-1374.
[3] O. Kapur et al., Scientific Reports, 14, (2024), 14008.
[4] O. Kapur et al., Advanced Electronic Materials, 8, (2022), 2200312.
[5] D. Guo et al., Materials Advances, 4, (2023), 5305-5313.

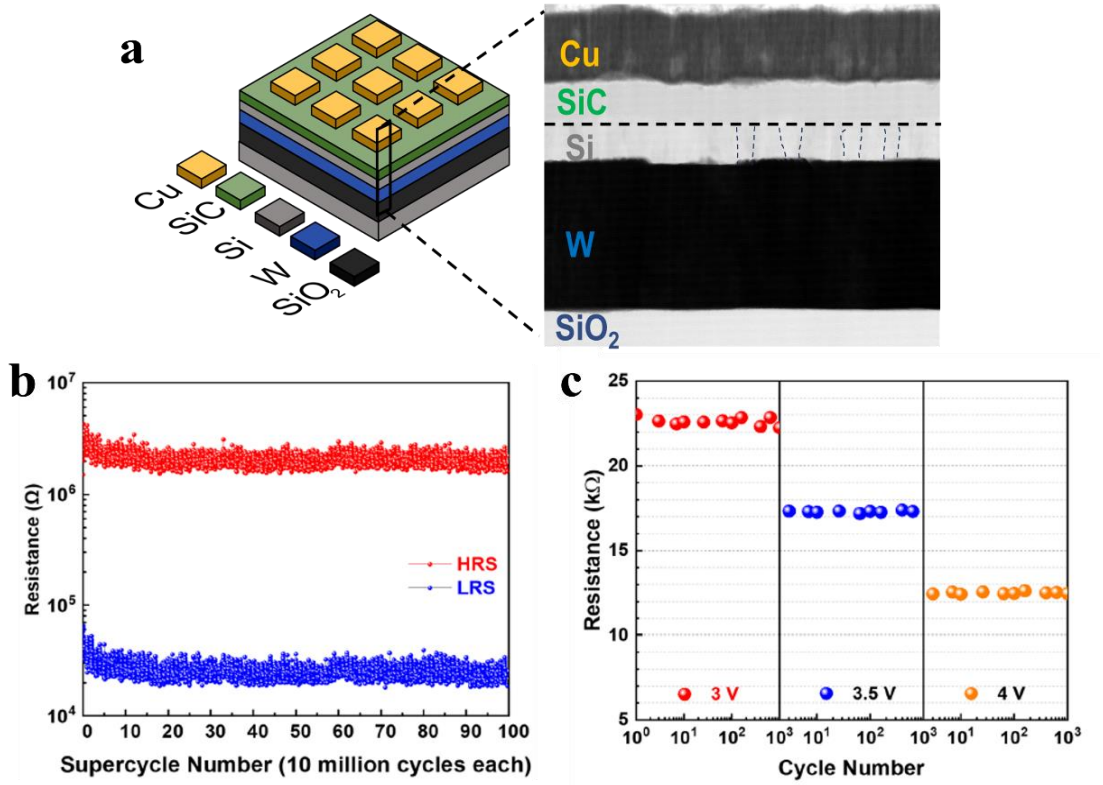

Figure 1. (a) Schematic of the bilayer SiC/Si memristor, (b) The endurance of 1 billion cycles using a pulsed training scheme, (c) Multiple LRS of 1000 cycles each using different pulse amplitudes [3].

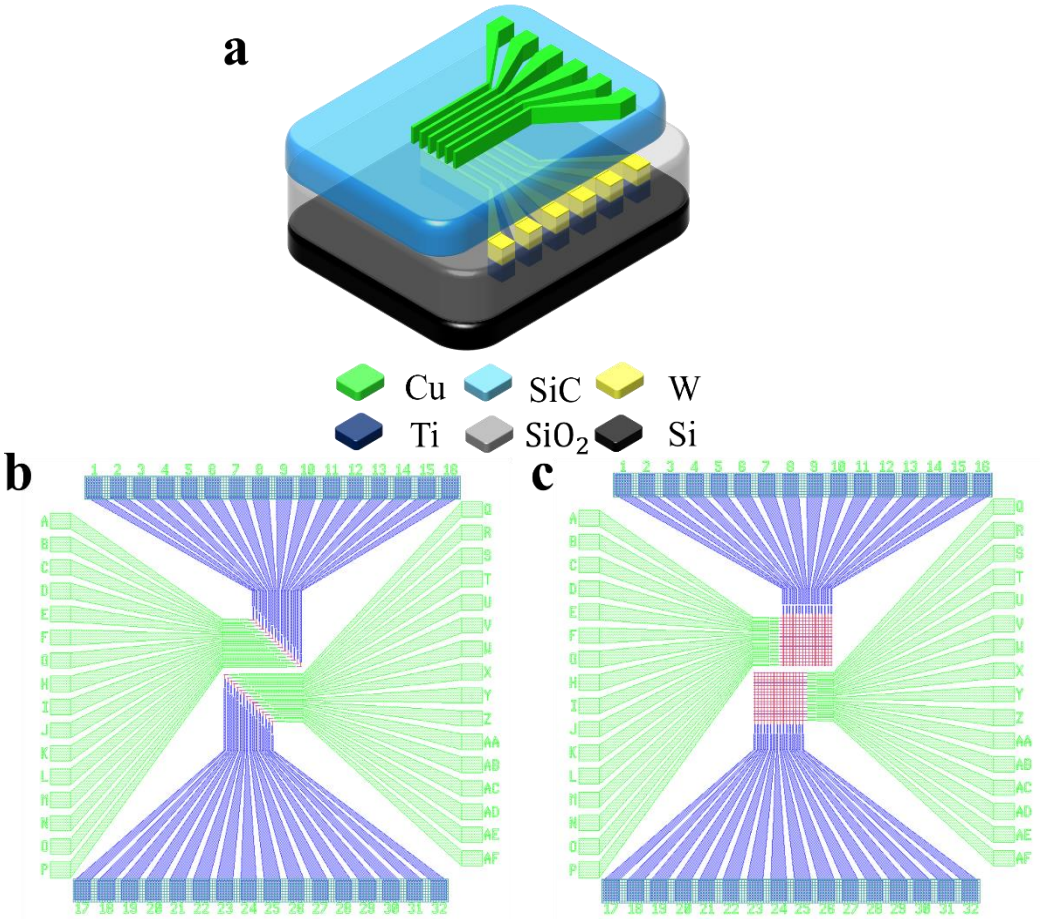

Figure 2. (a) Schematic of the Cu/SiC/W memristor array structure, and the chip layout of (b) Single-bit crosspoint array, (c) 0.25Kb crossbar array.

2D Materials for Electrostrictive FET

Nigama V. Vajjula, Fitunerediate G. Gebeyehu, and Ethan C. Ahn
George Mason University, Fairfax, VA 22030, USA
e-mail: eahn7@gmu.edu

Purpose: Layered nanomaterials have existed for more than a century. However, only recently, researchers have begun to realize the true potential of these 2D material systems **[1-2]**. Among a rich spectrum of 2D inorganic materials, transition metal dichalcogenides (TMDs) have been extensively studied owing to their unique physical properties alongside the ultimate thickness dimension **[3]**. In particular, we note that the interplay between electrical and mechanical effects in 2D materials remains relatively unexplored despite its great potential to advance emerging computing paradigms. Electrostrictive FET (E-FET) **[4-5]** is a new class of field-effect transistors (FETs) based on piezoelectricity and strain modulation of constituent materials. In this work, we propose an idea of using 2D materials as key to implement E-FETs by finite-element simulating the TMD heterostructure of MoS_2/$PtSe_2$ with a focus on electrostriction of MoS_2 that induces stress on $PtSe_2$. Learnings from and methodologies of this study are applicable to other various TMD heterostructures, and researchers in the field are expected to re-think about and experimentally explore 2D materials for E-FET.

Novelty: In 2013, a theoretical framework for E-FET was first reported by opening a new pathway to steep subthreshold slope (< 60 mV/decade) devices **[4]**. In 2016, an idea of using 2D materials as a bandgap-engineered channel material was introduced for E-FET **[6]**. However, because the electrostrictive material was still modeled as a conventional bulk piezoelectric material, a fundamental question of "how can an electrostrictive material be best interfaced with a channel material?" still remained unanswered. One study in 2017 has experimentally demonstrated an E-FET device with black phosphorus (BP) as a channel material **[7]**. However, in this work the strain was applied through the substrate bending other than the electrostriction effect; therefore, this BP-based E-FET may find its best application in sensing rather than computation. Since then, to date no one has experimentally demonstrated the E-FET device that is capable of low power logic operations due to limited understanding of material requirements for such a device. In this context, our work is sharply distinguished from any previous works because (1) both the materials for electrostriction and stress-induced conductivity modulation are made of 2D materials and (2) this material stack can feature maximum strain-to-stress transfer due to van der Waals interfaces that allow clean stacking of atomically thin layers.

Results: The COMSOL Multiphysics was used as a finite-element (FE) simulation tool to examine the electromechanics in the proposed TMD heterostructure stack (**Fig. 1**). Our simulative study successfully estimated the stress (Pascal, N/m^2) induced on the 2D channel ($PtSe_2$) layer while demonstrating the scaling trend of the 2D piezoelectric material (MoS_2) layer. Our choice of MoS_2/$PtSe_2$ as a flagship structure has the following reasoning. MoS_2 has been one of the earliest discovered 2D piezoelectric materials **[8-9]** owing to broken inversion symmetry in odd-layered MoS_2, including the monolayer (d_{33} ~ 2.8 pm/V **[10]**). Being air-stable, MoS_2 transistors have already been demonstrated **[11-12]**. $PtSe_2$ is emerging with a rare combination of high mobility, excellent air-stability, and low-temperature growth **[13]**. Therefore, with further in-depth studies on MoS_2/$PtSe_2$ interfaces **[14]** and strain modulation of $PtSe_2$ **[15]**, the simulated structure will serve as an ideal material platform for E-FET. **Fig. 2** shows the FE simulation results on the gate voltage (1 V)-induced (von Mises) stress on the order of 10^7 N/m^2 for the stack of [W (10 nm)/monolayer MoS_2 (t_1 = 0.65 nm)/few-layer $PtSe_2$ (t_2 = 6.5 nm)/Si (25 nm)]. **Fig. 3** further displays a simulated phase diagram for the 6.5 nm MoS_2 layer, suggesting that for a given electrical potential, the stress due to electrostrictive deformation of the MoS_2 layer is larger at positions closer to the MoS_2 bottom surface (i.e., the MoS_2 and $PtSe_2$ interface). Lastly, **Fig. 4** investigates how the stress on $PtSe_2$ varies with the MoS_2 layer thickness. Both the strong piezoelectricity and electric field make the use of monolayer MoS_2 the best suited for the purpose of maximizing the stress on $PtSe_2$ and thus implementing the E-FET.

References: **[1]** E. Ahn, *npj 2D Mater. Appl.* **4**, 17 (2020) **[2]** A. K. Katiyar et al., *Chem. Rev.* **124**, 318 (2024) **[3]** S. Manzeli et al., *Nat. Rev. Mater.* **2**, 17033 (2017) **[4]** T. van Hemert et al., *IEEE Trans. Elec. Dev.* **60**, 3265 (2013) **[5]** M. K. Anam et al., *Sci. Rep.* **10**, 14636 (2020) **[6]** S. Das, *Sci. Rep.* **6**, 34811 (2016) **[7]** Z. Zhang et al., *Nano Lett.* **17**, 6097 (2017) **[8]** W. Wu et al., *Nat.* **514**, 470 (2014) **[9]** H. Zhu et al., *Nat. Nanotechnol.* **10**, 151 (2015) **[10]** M. Haque et al., *Mater. Today* **47**, 69 (2021) **[11]** B. Radisavljevic et al., *Nat. Nanotechnol.* **6**, 147 (2011) **[12]** A. Nourbakhsh et al., *Nano Lett.* **16**, 7798 (2016) **[13]** M. S. Shawkat et al., *ACS Appl. Mater. Interfaces* **12**, 14341 (2020) **[14]** T. Gui et al., *Mater. Design* **238**, 112722 (2024) **[15]** H. Jeon et al., *ACS Nano* **19**, 9107 (2025)

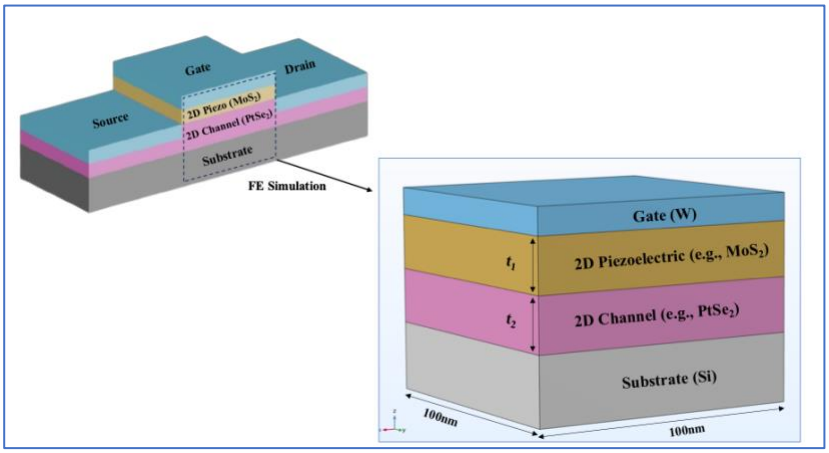

Figure 1. A 3-dimensional schematic of the proposed E-FET device structure. The FE (finite-element) simulation is carried out on the 2D material stack highlighted in a dashed zone. The thicknesses of the substrate (Si) and gate electrode (W) layers are fixed at 25 nm and 10 nm, respectively. t_1 and t_2 vary in the simulation along with varying physical parameters.

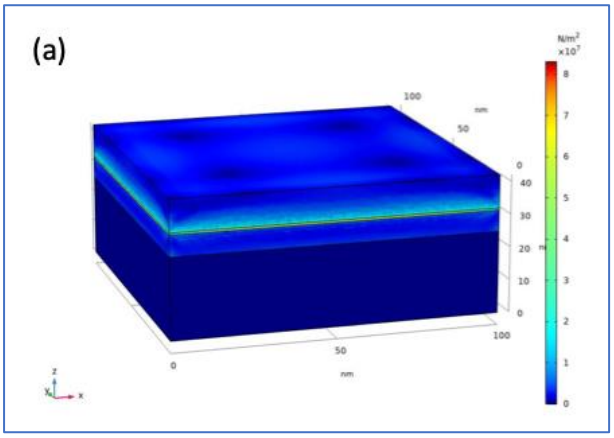

Figure 2a. The gate voltage-induced stress levels (Pascal, N/m^2) for the whole [electrode/TMD heterostructure/substrate] stack. Even with a small gate voltage bias applied (1 V as the nominal supply voltage), considerably high stresses on the order of 10^7 Pascal are induced owing to the sharp interface assumed in the simulation.

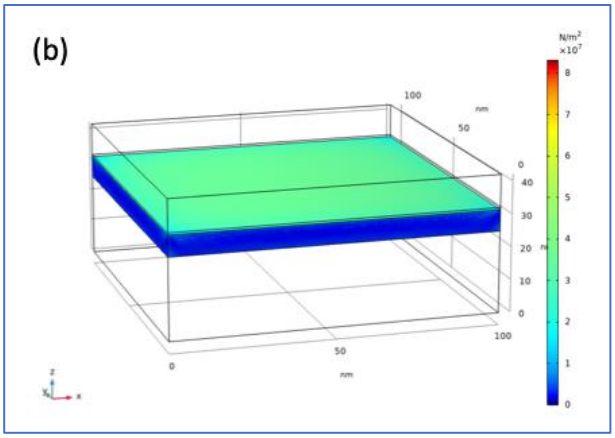

Figure 2b. The gate voltage-induced stress levels (Pascal, N/m^2) for the few-layer $PtSe_2$ (6.5 nm). The maximum stress occurs at the top surface of the $PtSe_2$ layer along the z-axis.

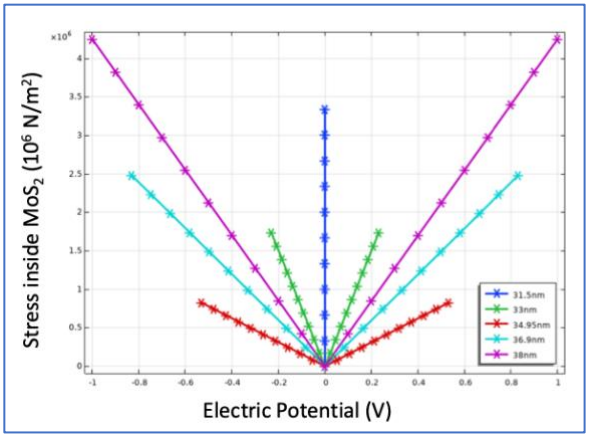

Figure 3. The phase diagram of the 2D piezoelectric layer (6.5 nm-thick MoS_2) for varying z-positions. The z-coordinates of 31.5 and 38 nm are at the bottom and top surfaces, respectively. It is found that higher stresses are induced at near the MoS_2 bottom surface for the same potential value, which is transferred to $PtSe_2$ for conductivity modulation.

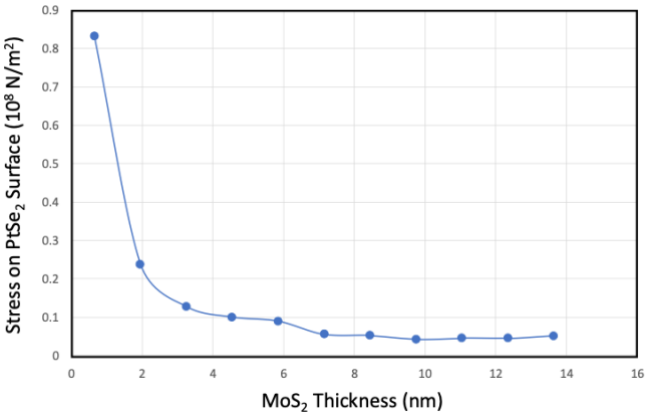

Figure 4. The MoS_2 thickness dependence of the maximum stress induced at the $PtSe_2$ surface. Literature-benchmarked d_{33} values of MoS_2 are incorporated in the simulation.

Oral Session 1D:
Biodevices and Systems 1

Contactless Measurement of Radial Artery Pulse Waves Using an Acoustic Sensing System

Chaeeun Lee, Changwoo Cho and Je Hoon Oh

Department of Mechanical Engineering and BK21 FOUR ERICA-ACE Center, Hanyang University, Ansan, Gyeonggi-do, 15588, Republic of Korea
E-mail: jehoon@hanyang.ac.kr

The radial artery pulse waveform contains critical hemodynamic information, including cardiac output, arterial stiffness, and vascular resistance [1]. Consequently, continuous and accurate monitoring of wrist pulse waves is increasingly regarded as a key element in personalized and preventive healthcare. Despite its clinical significance, however, the precise acquisition of radial artery pulse waveforms remains technically challenging. These signals typically exhibit low amplitude, making them highly susceptible to external noise and degradation. Moreover, they are sensitive to preload conditions and display considerable inter-pulse variability due to physiological fluctuations and subject movement. Additional factors such as sensor misalignment, inconsistent contact pressure, and variations in skin condition can further distort the signal, complicating reliable and repeatable measurements.

These challenges pose major obstacles to developing robust and user-friendly pulse wave monitoring systems that are practical for real-world applications. In response, recent research has increasingly focused on non-contact sensing technologies, particularly those utilizing acoustic wave detection [2, 3]. Acoustic-based remote sensing methods have attracted attention for their ability to non-invasively capture bio-signals in a comfortable and continuous manner. By leveraging the built-in microphones and speakers of widely available consumer devices such as smartphones, tablets, and smart speakers, these techniques offer a practical and unobtrusive solution for health monitoring. As a result, they represent a promising direction for the next generation of accessible, non-contact biosignal measurement systems.

In this study, we experimentally verified the feasibility of non-contact pulse wave detection. Utilizing commercial microphone array and speaker, we successfully acquired radial pulse waveforms, demonstrating the potential of acoustic-based remote sensing for reliable and accessible continuous pulse wave monitoring.

As illustrated in **Figure 1**, an frequency modulated continuous wave (FMCW) signal is transmitted toward the radial artery phantom vessel using a commercial speaker (AS07808AS-R, PUI Audio), and the reflected signals are captured by a microphone array (UMA-8 USB mic array, mini DSP). An intermediate frequency (IF) signal is first generated by mixing the transmitted and received signals. This IF signal is then sampled using an analog-to-digital converter for further processing. The beat frequency of the IF signal provides an approximate estimation of the target distance, while the phase of the IF signal is highly sensitive to fine displacement changes [4]. Therefore, precise extraction of the IF signal phase is performed. The spatial domain is divided into multiple range–azimuth bins, and the bin containing the strongest pulsatile motion is identified. The phase signal extracted from the pulse bin is then processed using a Kalman filter-based tracking algorithm, ultimately allowing us to obtain the final pulse waveform.

To extract the pulse wave, a phantom vessel of the radial artery was fabricated using a liquid-assisted dip coating technique [5]. The artificial vessel was made of PDMS, with an approximate Young's modulus of 2 MPa, a diameter of 4 mm, and a thickness of 300 μm (**Figure 2(a)**). To simulate the pulsatile motion of the artificial vessel, the flow and pressure waveforms were controlled by the motor of the blood circulation simulator through PWM (pulse-width modulation) control. The speaker and microphone array were mounted on a semicircular acrylic jig, maintaining an angle of 60 degrees (**Figure 2(b)**).

The pulse wave in the radial artery is generated by the overlap of reflected pulse waves, resulting in a characteristic waveform with three distinct peaks. These peaks correspond to the initial forward wave, the first reflected wave, and the second reflected wave (**Figure 2(c)**). When the pulse wave was measured using the contactless method, three distinct peaks, typically observed in the radial artery pulse wave, were clearly detected. To validate this, the non-contact pulse wave measurements were compared with the traditional contact-based measurements. After varying the pressure within the normal blood pressure range of 120/80 mmHg, it was confirmed that the pulse waveforms obtained from both methods were very similar (**Figure 2(d)**). This suggests that the contactless measurement technique can effectively replicate the pulse wave behavior seen in traditional contact-based methods, offering a promising alternative for non-invasive pulse wave analysis.

References
[1] J. Kromka et al., Measurement 219 (2023) 113174.
[2] A. Wang et al., Commun. Biol. 4 (2021) 319.
[3] T. Tran et al., Sensors 24 (2024) 382.
[4] Z. Bai et al., Biomed. Signal Process. Control 106 (2025) 107718.
[5] Y. Kim et al., Adv. Mater. Technol. 8 (2023) 230073.

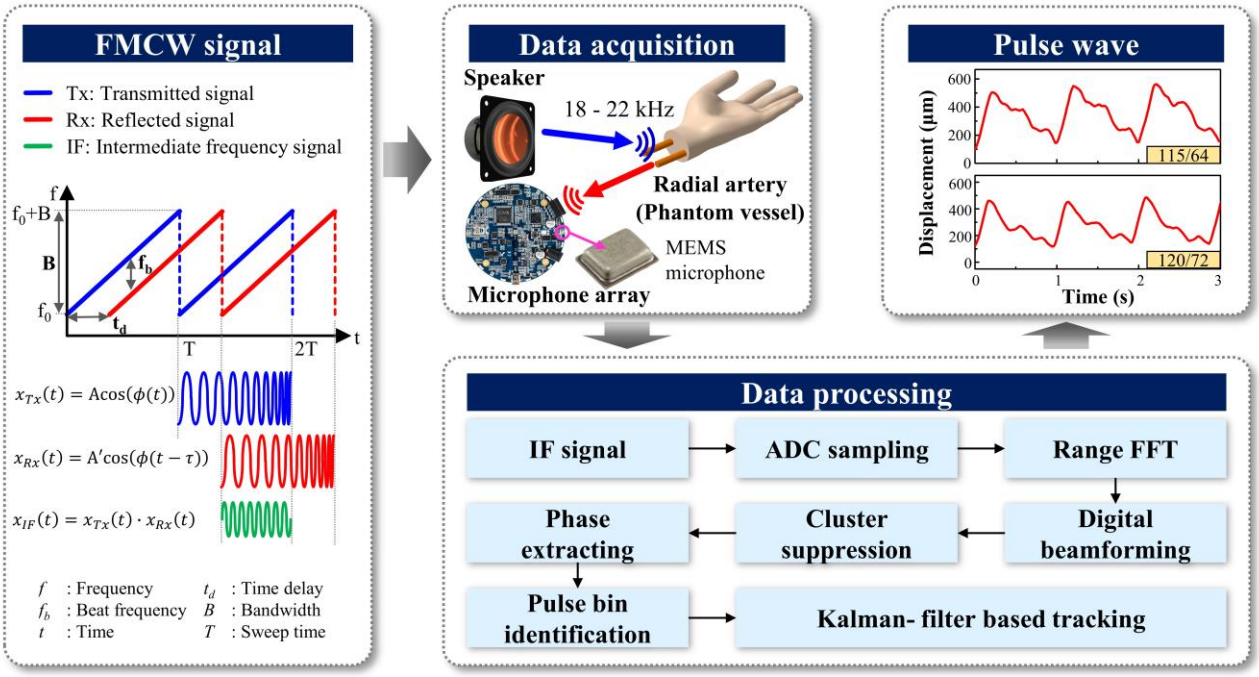

Figure 1. Processing flow of the contactless pulse wave measurement system based on FMCW signal, including data acquisition, data processing, and pulse wave extraction.

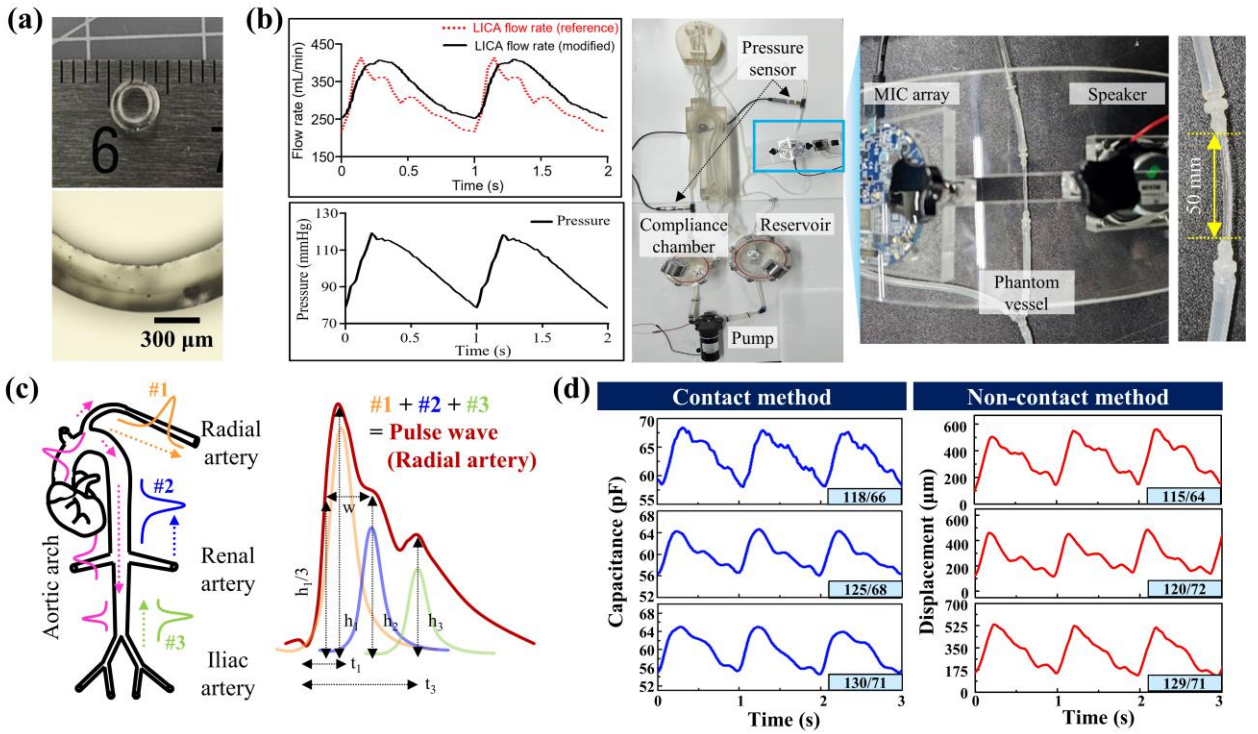

Figure 2. Photographs of **(a)** the radial artery phantom vessel and **(b)** the experimental setup used for contactless pulse wave measurement. **(c)** Pulse wave formation in the radial artery. (d) Comparison of pulse wave obtained using (left) a contact method based on capacitance sensing and (right) a contactless method based on displacement measurements.

A microfluidic Cartilage-on-Chip platform for personalized cartilage transplant compatibility screening

Rahman Sabahi-Kaviani [a], Giorgia Mazzini [b], Emma J. Bristow [c], Cynthia M. Fehres [c], René E. M. Toes [c], Yolande F.M. Ramos [b], Ingrid Meulenbelt [b], and Regina Luttge [a]

[a] Neuro-Nanoscale Engineering, Department of Mechanical Engineering, and Institute of Complex Molecular Systems, Eindhoven University of Technology, Eindhoven, 5612AZ, the Netherlands
[b] Biomedical Data Sciences, Section Molecular Epidemiology, Leiden University Medical Centre, Leiden, The Netherlands
[c] Department of Rheumatology, Leiden University Medical Center, Leiden, The Netherlands
e-mail: r.luttge@tue.nl

Osteoarthritis (OA) is a leading cause of joint degeneration, often requiring joint replacement [1]. While iPSC-derived cartilage presents a promising regenerative alternative, its clinical success hinges on patient-specific compatibility and the risk of allograft rejection [2]. Existing Cartilage-on-Chip models have advanced the simulation of cartilage-bone interactions and mechanical stimuli [3–5], yet they fall short in assessing immune responses, leaving a gap in screening patient eligibility for cartilage transplantation.

To address this, we introduce a Cartilage-on-Chip screening platform that integrates microfluidic and microtunnel devices (MDs) [6]. Fabricated using photolithography and soft lithography techniques, MDs consist of PDMS structures bonded to glass substrates (Fig. 1a) [7]. These devices allow spatially controlled co-culture of iPSC-derived cartilage organoids (hiChOs), primary chondrocytes, synovial fluid, synovium, and immune cells such as T-cells (Fig. 1b). The microtunnel architecture supports diffusion-based signaling while preventing direct cell mixing, enabling physiologically relevant interaction studies under controlled conditions. The platform is modular and scalable, allowing for parallelized, high-throughput screening. Furthermore, its transparent PDMS-glass design permits live imaging and fluorescence-based readouts. Biocompatibility tests with patient-derived chondrocytes and iPSC-derived cartilage organoids demonstrated high survival rates (>80%) after 48 hours of co-culture, confirming the suitability of MDs for integrated biological assays.

Cytokine release is a hallmark of immune activation during allograft rejection, and electrochemical (EC) sensors provide a powerful method for cytokine detection [8]. While functionalized EC sensors offer high specificity for individual cytokines, non-functionalized sensors detect total cytokine mass, making them suitable for broad inflammation profiling due to their simpler design and fabrication. To enable real-time monitoring of immune responses, we developed a non-functionalized graphene-based electrochemical sensor [9] and integrated it into the MD platform (Fig. 2a–b). Initial validation using electrochemical impedance spectroscopy (EIS) on NaCl solutions with varying concentrations resulted in Bode and Nyquist plots exhibiting clear impedance shifts across concentrations (Fig. 3), confirming the sensor's sensitivity, reproducibility, and compatibility with the MD layout

In the next phase, we will test the sensor with cytokine-spiked media and apply it to co-culture assays involving hiChOs, primary chondrocytes, and immune cells to monitor dynamic immune responses. This integrated platform represents a step toward developing a clinically relevant pre-transplant screening tool to personalize regenerative joint therapies and improve the outcomes of cartilage implantation procedures.

[1] Loeser, Richard F., et al. *Arthritis and rheumatism* 64.6 (2012): 1697.
[2] Abe, Kengo, and Noriyuki Tsumaki. *Inflammation and Regeneration* 43.1 (2023): 56.
[3] Tuerlings, Margo, et al. *Advanced Materials Technologies* 7.8 (2022): 2101310.
[4] Paggi, Carlo Alberto, et al. *Lab on a Chip* 22.9 (2022): 1815-1828.
[5] Liu, Hao, et al. *Bioactive Materials* 33 (2024): 61-68.
[6] Bastiaens, Alex, et al. *Frontiers in Neuroscience* 14 (2020): 666.
[7] Sabahi-Kaviani, Rahman, et al., *In Preperation*.
[8] McCrae, Lauren E., et al. *Biosensors and Bioelectronics: X* 13 (2023): 100288.
[9] Khayamian, Mohammad Ali, et al. *RSC advances* 11.55 (2021): 34503-34515.

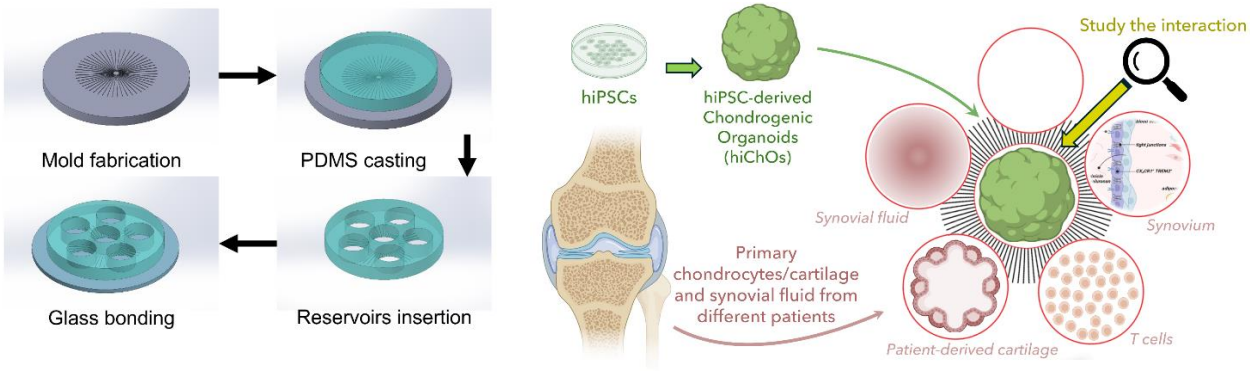

(a) **(b)**

Figure 1. (a) Schematic of the fabrication process of MD using soft lithography [7]. The PDMS-based compartments are bonded to a glass substrate to form an optically transparent and biocompatible chip. (b) Conceptual illustration of the MD application for co-culturing iPSC-derived cartilage organoids (hiChOs), primary chondrocytes, synovial fluid, synovium and T-cells.

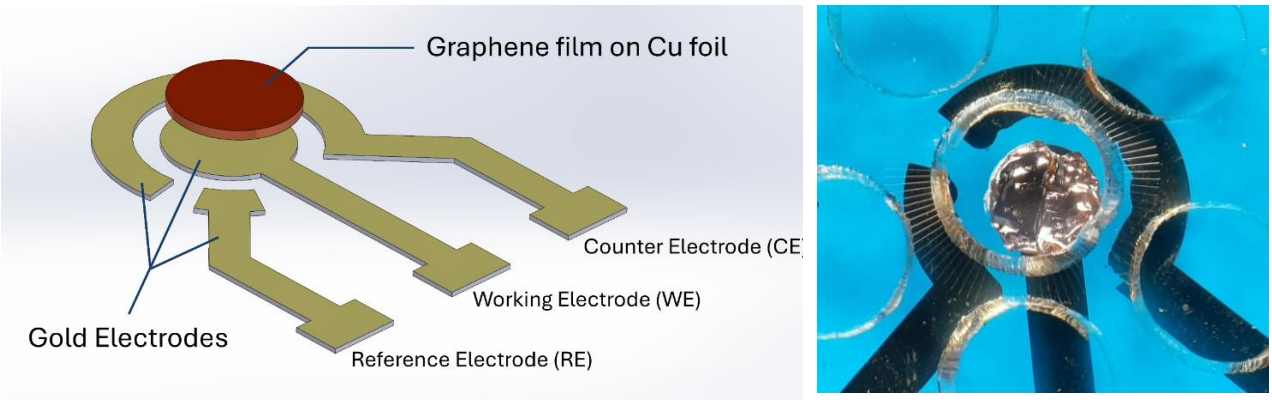

(a) **(b)**

Figure 2. (a) The design of a graphene-based electrochemical sensor fabricated to detect total cytokine mass via impedance spectroscopy. The sensor uses a graphene sensing layer on a gold electrode, enabling label-free, non-functionalized detection. (b) Sensor integrated into the MD platform to enable on-chip co-culture and real-time sensing of cytokine release under physiologically relevant conditions.

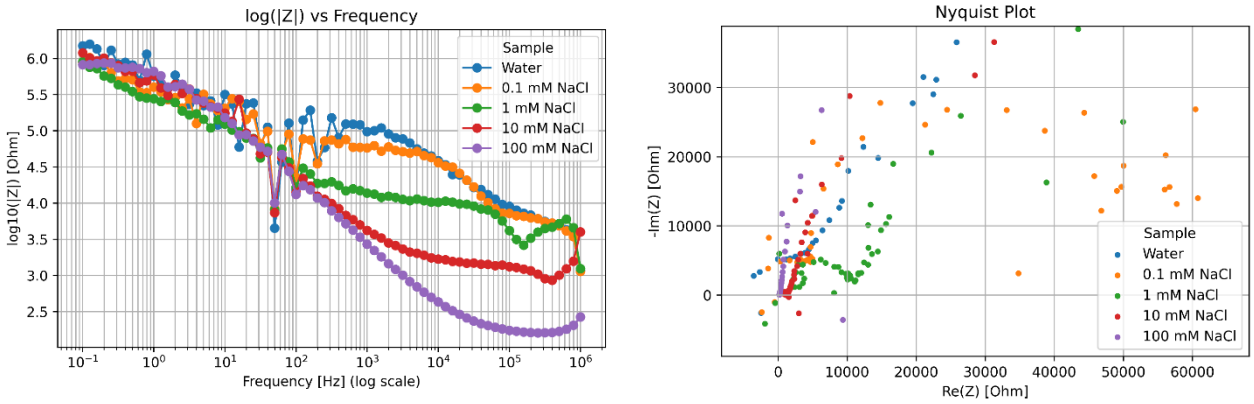

Figure 3. Bode and Nyquist plots demonstrate clear and reproducible impedance distinctions across NaCl concentrations (0–100 mM), especially at higher frequencies, confirming the graphene-based sensor's sensitivity and suitability for integration into the MD platform.

A Microfluidic Device for Monitoring Functional Enzyme Activity of Primary Human Hepatocyte Spheroids Based on Cell-Secreted Extracellular Vesicles

E. Moradi [a], P. Järvinen [a], M. Haapala [a], O. Korhonen [b], T. Sikanen [a]

[a] Faculty of Pharmacy, Drug Research Program, University of Helsinki, Helsinki, 00790, Finland
[b] Faculty of Health Sciences, School of Pharmacy, University of Eastern Finland, Kuopio, 70210, Finland
e-mail: tiina.sikanen@helsinki.fi

Primary Human Hepatocytes (PHH) rapidly lose their liver-specific functions, including metabolic enzyme activity, in conventional cultures, limiting their application for drug metabolism studies. [1] Culturing PHH cells in a 3D format can offer a platform to preserve the PHH phenotype and provide cells with an in vivo-like microenvironment. [2] The purpose of this study was to evaluate the feasibility of cell-secreted extracellular vesicles (EVs) for monitoring the metabolic enzyme activities of 3D cultured PHHs. The EVs are membranous structures that transfer cellular cargo (including proteins and enzymes) influencing various biological processes such as cell-cell signaling and metabolic activities. [3,4] However, cell-type selective EV isolation, quantitation and characterization with respect to exosomal enzyme activities is time-consuming and laborious, requiring many purification, enrichment, and analysis steps. [5]

In this study, we used a newly developed microdevice [6] for on-chip EV isolation, quantitation, and enzyme activity assaying in a single microfluidic experiment. This microdevice comprises integrated electrochemical impedance spectroscopy (EIS) electrodes and a dense micropillar array channel (15,360 pillars; 4×30×0.18 mm^3, W×L×H), for EV quantitation and enrichment, respectively (Fig 1A). For cell-type selective EV immobilization onto the chip, the electrodes and the pillar array are coated with protein A/G and the liver-selective HepPar1 antibody (Fig 1B).

The cell-secreted EVs were isolated from culture media collected on different days of the 3D PHH spheroid culture (Fig 2A) and pre-purified with commercial ExoEasy kit. The total EV counts and protein concentrations in the media were determined based on nanoparticle tracking analysis and Pierce™ BCA kits, respectively (Fig 2B). The cytochrome P450 (CYP) activity of the PHH spheroids was determined using the Luciferin-IPA assay (a selective CYP3A4 marker, Promega; Figure 2C). Next, the pre-treated culture media were applied onto the HepPar1-coated microdevices to isolate and immobilize only hepatocyte-secreted EVs via immunocapturing (Fig 1B). The concentration of HepPar1(+)-EVs was determined based on the change in the on-chip EIS signal before and after EV immobilization. The CYP3A4 enzyme activities of the immunocaptured EVs were determined by infusing 3 µM Luciferin-IPA through the device at a constant flow rate (1.25 µL/min) and measuring the Luciferin metabolite concentration in the chip effluent (Fig 2D).

Our results demonstrate that the cumulative amount of hepatocyte-secreted EVs, as well as the total EV protein amount, increase during the first days of 3D culture, when the spheroids evolve, but plateaus after nine days, suggesting that the spheroids reach a more stable and mature state (Fig 2B). This conclusion is supported by the fact that beyond Day 9 of the PHH spheroid culture, there is very little variation in the CYP3A4 activity (Fig 2C). The on-chip analysis of HepPar1(+)-EVs reveals that the profile of liver-specific EVs and their CYP3A4 activities follow similar trends, as those of total EVs and cellular enzyme activities, respectively (Fig 2E), confirming that the 3D culture slows down PHH dedifferentiation and supports de novo protein synthesis.

Overall, our results suggest that the microfluidics-assisted EV isolation and characterization could be a viable, new tool to monitor the maturation and (de)differentiation of in vitro cell cultures noninvasively based on the cell-secreted EVs in the culture media. To further assess the technology readiness, we also evaluated the chip-to-chip repeatability in terms of EV immobilization efficiency (based on EIS; Fig 3A) as well as the shelf-life of biofunctionalized chips following cryopreservation of protein A/G and HepPar1 coated microdevices by freeze-drying and their subsequent storing at room temperature (protected from light and moisture). Our data demonstrates no significant loss of EV immobilization efficiency for at least 3 months storage, neither based on EIS (Fig 3B) nor CYP3A4 activity of the immobilized EVs (Fig 3C), suggesting that the system is robust with a view to technology transfer and scale-up.

References:

[1] Handin, N., et al., iScience, 2021. 24(11).
[2] Abuwatfa, W., et al. J. Biomed. Sci., 2024. 31(1).
[3] Chen, B.-Y., et al., Clin. Chim. Acta., 2019. 493.
[4] Balaphas, A., et al. Liver Int., 2019. 39(10).
[5] Kumari, S., et al., Biomolecules, 2024. 14(12).
[6] Moradi, E, et al. ISEV Meeting, 2024.

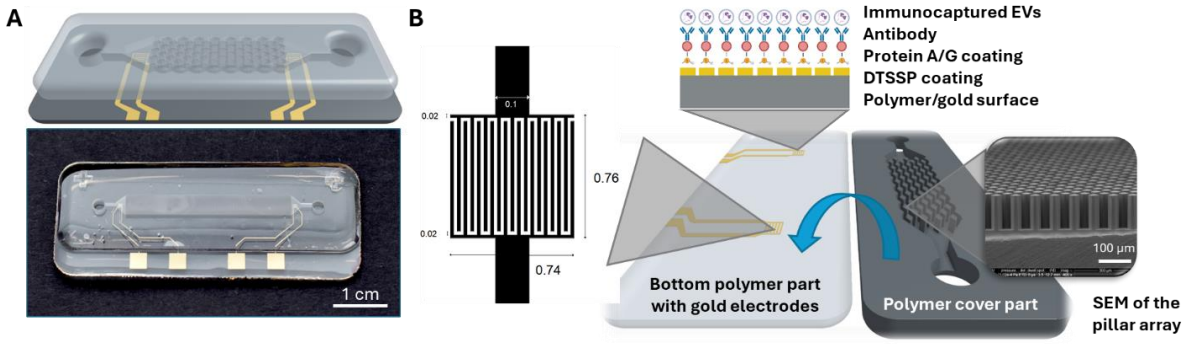

Figure 1. The microfluidic device. (A) 3D schematic and a photograph of the microdevice made from off-stoichiometric thiol-ene (100:125) with integrated gold electrodes. (B) The CAD design of the EIS electrodes and the surface biofunctionalization applied onto the microdevice.

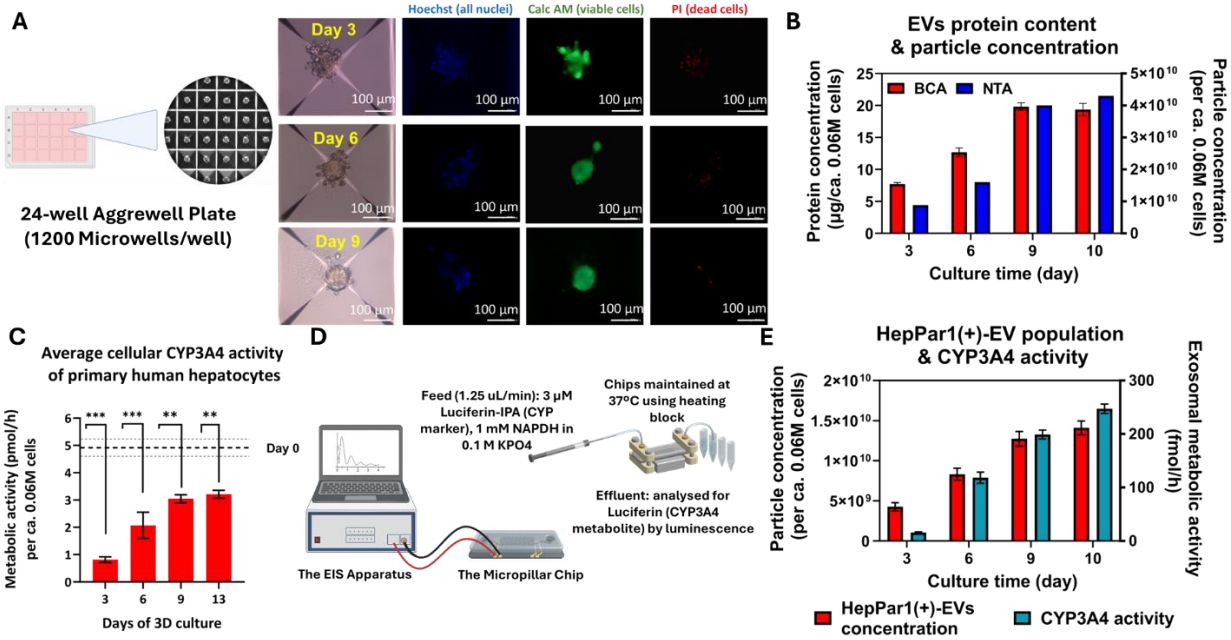

Figure 2. Evaluation of PHH maturation in 3D cultures based on cell-secreted EVs. (A) Cell viability in the 3D PHH spheroids cultured on Aggrewell plate for three, six or nine days. (B) The total EV amount and total EV protein content in the media collected from PHH culture. (C) Cellular CYP3A4 activity in PHH spheroids on different days of the 3D culture. (D) The measurement setup for on-chip EIS and flow-through CYP activity determination of immunocaptured HepPar1(+)-EVs. (E) The concentration and CYP3A4 activity of immunocaptured HepPar1(+)-EVs in the PHH culture media. The error bars represent the deviation between n=3 measurements in each case.

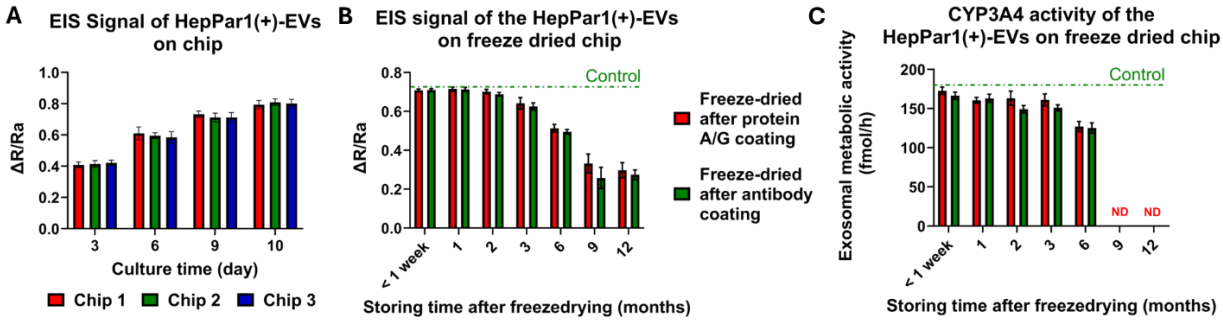

Figure 3. Robustness of the microfluidic EV measurements. (A) The repeatability of HepPar1(+)-EV immobilization based on EIS analysis on three replicate devices. (B-C) The impact of storing time on the EV immobilization efficiency of the freeze-dried protein A/G- or HepPar1-coated microdevices, stored at room temperature until use, and evaluated based on the on-chip EIS (B) and CYP3A4 activity (C) of HepPar1(+)-EVs collected on Day 9 of the 3D culture. The error bars represent the deviation between n=6 (A,B) or n=3 (C) measurements.

Wavelength-selective photodetector for NADH fluorescence detection

Z. Liao [a,b]*, L. Cavedoni [a,b], *C. Kutucu* [b], *P. R. Rao* [a], *C. Boutry* [b], *F.* A. *Cardoso* [a]

[a] Electronic Instrumentation Laboratory (EI), Department of Microelectronics, TU Delft, 2628CD, Netherlands
[b] Electronic Components, Technology and Materials Laboratory (ECTM), Department of Microelectronics, TU Delft, 2628CD, Netherlands
* Zhengwei Liao (z.liao@tudelft.nl)

Cellular metabolism supplies the energy required for most biological processes, and its alteration is a hallmark of diseases such as cancer and diabetes.[1] Specifically, nicotinamide adenine dinucleotide (NADH) plays a central role in cellular energy metabolism. Label-free, non-invasive monitoring of NADH has been demonstrated using fluorescence sensing, where NADH emits light at 470 nm when excited by 350 nm light. [1,2] However, detecting the 470 nm fluorescence requires filtering out the 350 nm excitation light. This is typically achieved using interference and absorption filters. But monolithically integrating filters with photodetectors is hindered by the need for complex optics for interference filters and the lack of efficient thin-film absorption filters. To overcome this challenge, Si-based devices were proposed for wavelength-selective sensing, relying on the absorption of Si for different wavelengths.[3] Researchers developed fluorescence sensors with a photogate structure for wavelength-sensitive fluorescence detection, but 350 nm filtering remains unexplored.[4]

Here, we propose a backside-illuminated, wavelength-selective photodetector for NADH fluorescence detection. The device adopted a transistor-like architecture (Fig. 1), operating in the subthreshold regime ($V_g < V_{th}$), allowing tunable depletion width beneath the gate. Positive biasing of the n+ implants (V_r) establishes a fixed depletion width in the reverse-biased pn junction between the implant and the bulk p-doped Si. In this biasing configuration, the depletion region width beneath the gate is controlled by the gate voltage V_g, provided $0 < V_g < V_{th}$ (Fig.1). Under backside illumination, photons reaching the depletion region beneath the gate generates a photocurrent (I_{lum}) flowing toward the reverse-biased n^+-wells. In Si, the penetration depth of 470 nm photons (i.e, 1226 nm for 90% of the photons) is ~56 times greater than the penetration depth of 350 nm photons (i.e., 22 nm for 90% of the photons). Consequently, by tuning the Si thickness to ~1 μm, fluorescent emission photons from NADH (470 nm) are able to reach the depletion region and generate photocurrent. The excitation photons (350 nm), however, creates electron-holes pairs near the surface, which recombine without reaching the depletion region beneath the gate, thus not contributing to the photocurrent. To demonstrate the operation, we performed SPECTRA simulations (Fig. 2). In these simulations, the device dimensions were 5 μm for the n-well width, 150 μm and 800 μm for the channel length and width, respectively, and the substrate thickness varied from 0.7 μm to 5 μm. For this geometry, we identified an optimum V_r =1.64 V and V_g = 1.3 V. As the substrate thickness increased from 0.7 μm to 0.9 μm, the selectivity of 470 nm over 350 nm improved from 11.3 to 115.1, while the photocurrent generated by 470 nm photons remained stable (Fig. 2b). Beyond a Si thickness of 900 nm, the photocurrent generated by 470 nm and 350 nm photons decreased equally, thus maintaining the same selectivity. Therefore, the proposed photodetector requires a substrate thickness of 900 nm to attain wavelength selectivity of 115.1 while still producing a current of 1.83 nA.

Fabricating a 900 nm device from standard 290 μm bulk silicon wafers was the main challenge addressed in this work. In a standard CMOS process, we introduced a process step that etched 1.2 μm deep shallow trench isolation (STI) on the wafer frontside. Then, the Si substrate was thinned by etching the backside of the wafer and using the STI as an optical endpoint for etching. The backside etch began with TMAH wet etching of 280 μm of the substrate, achieving a smooth landing morphology. The remaining 9 μm of Si were etched using SF_6/O_2 reactive ion etching (RIE) until the STI was optically observed (Fig.3). By optimizing the SF_6/O_2 ratio, pressure, and power, we obtained a surface roughness of 6.94 nm_{rms} after 9 μm dry etching.

In conclusion, this paper proposes a novel wavelength-selective photodetector for NADH fluorescence monitoring. To fabricate this sensor, we developed a new Si thinning method that uses STI as an etch stop point to achieve precise substrate thinning down to micrometer levels.

[1] Song, A et al., Communications Biology. 7 (2024) 428.
[2] Sasagawa, K et al., Electron Comm Jpn. 141 (2021) 71-76.
[3] Wang, H et al., Int J Thermophys. 34 (2013) 213–225.
[4] Y.J. Choi et al., Sensors and Actuators B. 256 (2018) 38–47.

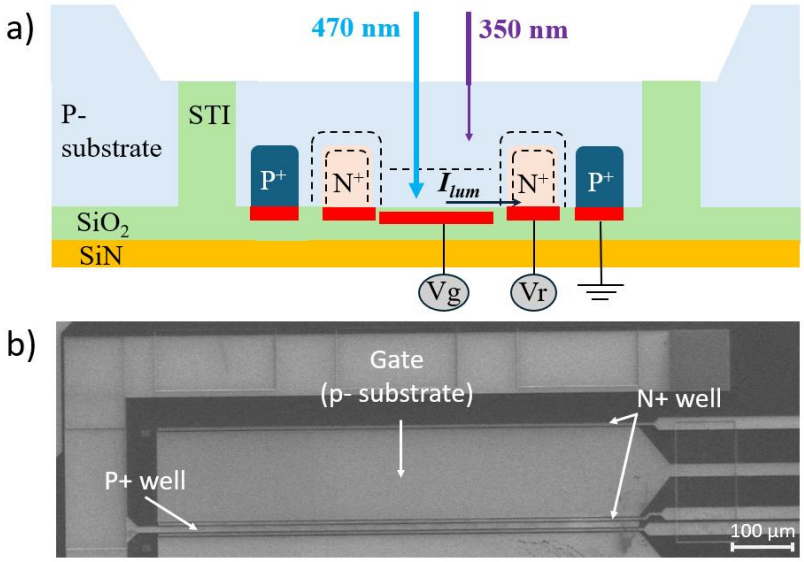

Figure 1. (a) Schematic illustration of the cross-section structure and (b) SEM picture showing the planar structure of the wavelength-selective photodetector.

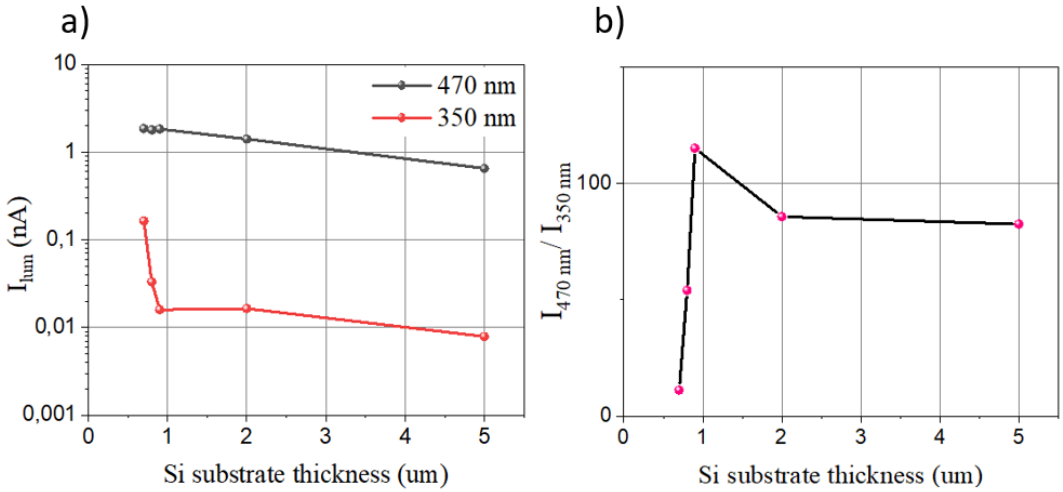

Figure 2. (a) The absolute values of simulated photocurrent (I_{lum}) of the designed photodiode in SPECTRA for two wavelengths (470 nm and 350 nm) at a power intensity of 20 µW/m^2. (b) Selectivity of 470 nm photocurrent ($I_{470\ nm}$) over 350 nm ($I_{350\ nm}$) as a function of different Si substrate thicknesses for the same illumination conditions as (a).

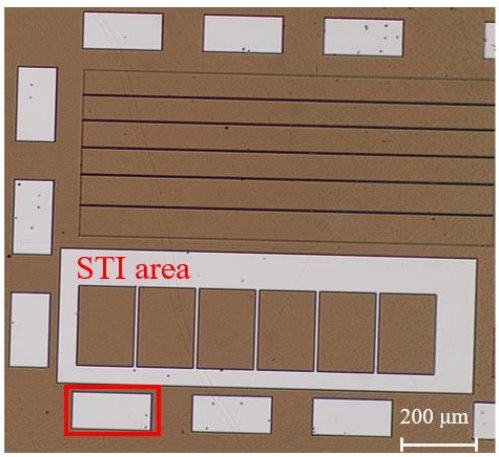

Figure 3. Optical picture of backside thinned Si when reaching STI ending point.

Nano- and Microscale Aptamer Biosensors for Monitoring Biomarkers of Human Health

Nako Nakatsuka

Monitoring small molecules is essential for advancing diagnostics, therapeutics, and real-time health monitoring across a wide range of biomedical applications. Specifically in neuroscience, advancing our fundamental understanding of brain (dys)function requires the development of novel nanotools capable of monitoring chemical signaling in complex biological systems. Detecting small molecules in the brain is especially challenging due to low concentrations spanning orders of magnitude (picomolar to micromolar), limited mass and charge, and interference from high amounts of nonspecific molecules. Further, neurotransmitters co-exist with structurally similar metabolites across different brain regions. At the Laboratory of Chemical Nanotechnology (CHEMINA), we tackle this challenge by integrating DNA-based recognition elements called aptamers, into nano- and microscale biosensing platforms fabricated in-house. Aptamers are systematically designed oligonucleotide receptors that exhibit highly specific and selective recognition of targets. We employ aptamers designed to recognize small-molecule neurotransmitters such as serotonin and dopamine with high affinity and selectivity. We have developed nanoscale aptamer-modified nanopipettes with ~10 nm openings – approaching the spatial resolution of synapses where neurons communicate (~50 nm) – as well as microscale aptamer-functionalized field-effect transistors. Reversible target binding induces conformational changes in the aptamers, rearranging their negatively charged backbone, which are transduced into measurable electrical signals through the nanopore or across the semiconducting channel, respectively. Extensive characterization of these target-specific aptamer structural dynamics has provided fundamental insights into the signal transduction mechanisms underpinning our biosensing technologies. These findings lay the foundation for expanding this approach to a broad range of small-molecule targets – including sugars, amino acids, lipids, and hormones – relevant to diverse areas of human health.

Poster Session 1

Ionic Liquids and Focused Ion Beams: Are all Ionic Liquids Adequate for Advanced FIB Micro- or Nano-engineering?

Jacques Gierak [a-b], Elinoa Sebag [a-b], Amir Goodwin [a-b], David Bouville [a-b], Philippe Lesot [b-c], Philippe Berdagué [c]

[a] C2N, Pole instrumentation, Univ. Paris-Saclay, 10 Boulevard Thomas Gobert 91120 Palaiseau, France.
[b] Centre National de la Recherche Scientifique (CNRS), 3, Rue Michel Ange, 75016 Paris, France.
[c] Equipe RMN en Milieu Orienté, Institut de Chimie Moléculaire et des Matériaux d'Orsay (ICMMO), UMR-CNRS 8182, Faculté des Sciences, Site Henri Moissan, 17 Avenue des Sciences, 91400 Orsay, France.

Keywords: FIB, micro-fabrication, Electro-HydroDynamic, Ionic Liquids
Email: jacques.gierak@cnrs.fr

Traditionally, focused ion beam machining has been associated with device editing, direct prototyping and nanofabrication [**1**], a domain where ablation or modification of material must be finely controlled to achieve desired pattern placement, design fidelity and efficiency.

Several years ago, Ionic Liquids (ILs) i.e. a molten salt at room temperature with appreciable electrical conductivity, were proposed as a feed material for Electro-HydroDynamic (EHD) Ion Sources. These Ionic Liquid Ion Sources (ILISs) have promisingly paved the way for broadening ion species and beam characteristics. It has been demonstrated that by adjusting the emission current from an IL-based ion source, the emission beam can be varied from pure molecular ions with extremely low emission currents down to **nA** to charged clusters beams allowing higher etch rates or surface planarization effects [**2**]. In addition, the attractive possibility to emit positive or negative molecular ions on-demand has opened up new insights and prospects for modelling or functionalising chemical surfaces (**Figure 1**). ILISs are therefore unique molecular species in their ability to produce high-brightness beams of complex organic and inorganic molecular and mono-atomic ions in a wide range of currents.

The ionic composition depends on the structure of the IL and can be represented schematically as a structure $[A]^+ [B]^-$, where A is the cation and B the anion. Therefore, the emission characteristics of an ILIS operated in the pure ion emission regime relies on the depletion of the emitted ion either [A]+ or [B]-, and the accumulation of counter-ions at the very top of the ionic liquid-emitting structure. In practice, the more cation or anion is emitted (as a function of time or flux), the more degraded the IL will become for a given emission current value. Thus, in the case of $Emi^+BF_4^-$, this chemical degradation was found to cause browning of the IL combined with solid deposits as well as conductive whiskers growing from the free liquid surface of the emitter.

Adding to this first difficulty, the Taylor cone formation as observed on ILIS [**3**] does not match the classical EHD emitter profile denoted as the Taylor Cone or "cusp on a cone". In the ILIS-based operation, the cusp is an elongated filament, which is highly mobile in response to the highly dense cloud of emitted ions located by essence just above its apex (**µA** currents from nanometer-sized dimensions). This jet-like filament is difficult to stabilize both in position (x, y, z) and in emitted fluxes values at acceptable values for FIB instruments. So alternative ion sources geometries, ionic liquids characteristics and FIB optics designs are required to exploit the promises of ILIS-FIB technologies for the main foreseen market, *i.e.* semiconductor editing applications.

In this work, we will present our efforts to re-invest the FIB micro-fabrication based on our recent development of space thruster based on multi-tip cell emitters capable of: i) achieving stable and long-lasting emission fluxes (125 **µA**/cm²), ii) beam energies around 10 keV, and iii) operation sequences with a constant polarity exceeding 15 minutes. It is indeed crucial for a FIB process to maintain the geometrical alignment of the emitter using transfer optics and maintain both the transported dose for the duration of the patterning sequence and the transported ions nature, charge and masses.

We will examine our ILIS operational tests results, based on the monitoring of the emitted flux over time, the coloration of IL-based fuel and a molecular analysis using ^1H and ^{19}F NMR spectroscopy (**Figure 2**).

Finally, we describe our preliminary studies to propose relevant task-oriented ILs capable of moving towards innovative applications with modern challenges such as chemical direct patterning by FIB.

[1] J. Gierak, Nanofabrication, 1, 35, (2014).
[2] S. Guilet et al. Microelectronic Engineering, 88, 1968, (2011).
[3] A. M. Gañán-Calvo et al., Sci. Rep. 6, 32357, (2016).

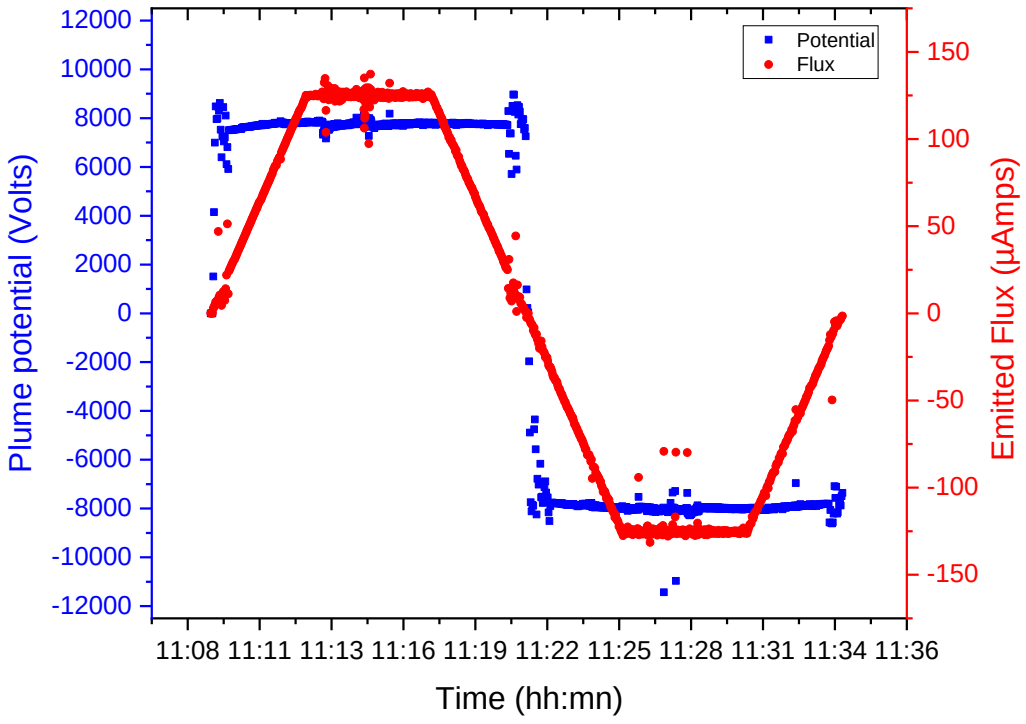

Figure 1. Bipolar Emission/Current characteristic of a **ILIS**-based multi-tips emitter ($Emi^+BF_4^-$).

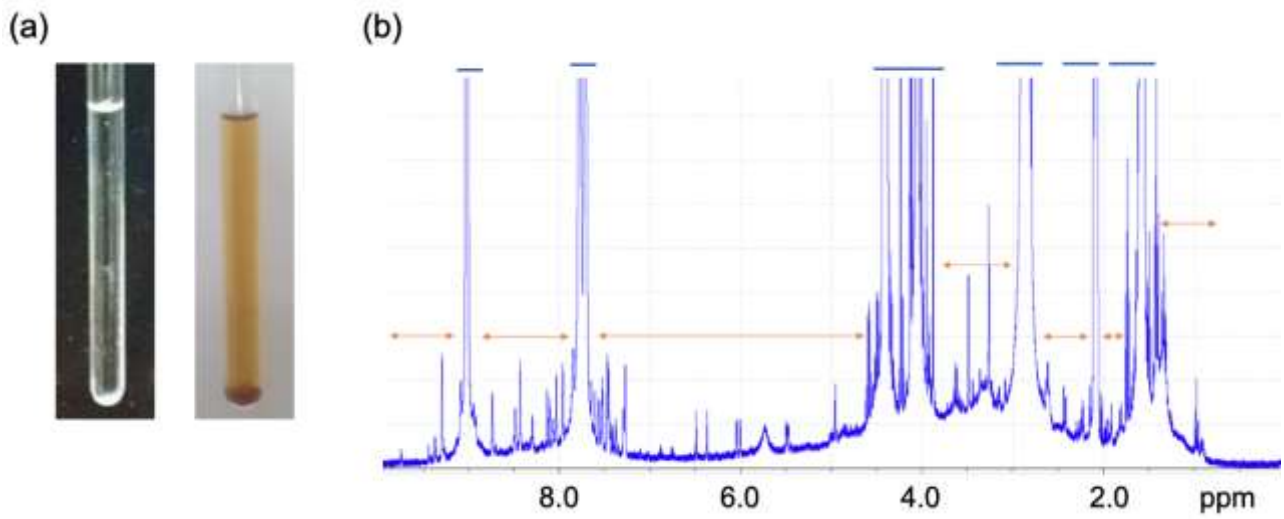

Figure 2. (a) Illustration of the degradation of $EmiBF_4$ leading to a brown solution in acetone-d_6 with unsoluble residues obtained with **EHD** operation for a total duration of 30 mins. (b) 600 MHz ^1H NMR spectrum showing multiple resonances associated with degradation species (red arrows) generated during the EHD process.

Plasmonic aluminium nanogap creation by electromigration for plasmonic UV-Nanolithography

Jakob Nüßlein[a], Zhuoji Huang[a], Steffen Strehle[a]
[a] Department of Microsystem Technology TU Ilmenau, Ilmenau, 98693, Germany
e-mail: jakob.nuesslein@tu-ilmenau.de

Electromigration induces the movement of atoms in a conductor due to momentum transfer between electrons and lattice atoms, which can lead in case of mass flow gradients to void and hillock formation. [1] Although typically an undesirable effect, electromigration can be leveraged to create nanostructures, such as nanogaps, as, for instance, required for plasmonic sensing applications.

In our contribution, we explore aluminum nanogap implementation for the design of so-called plasmonic masks as required in plasmonic nanolithography. Plasmonic nanolithography can overcome the diffraction limit of conventional photolithography by using surface plasmon polariton interference to achieve high spatial exposure and resolution. Due to the strong near-field localization in small nanogaps, the electromagnetic field at the nanogap positions is enhanced. Such nanogaps are typically based on gold and fabricated using complex methods such as focused ion beam milling or e-beam lithography. [2]

In our approach, we explore a strategy for the creation of nanogaps via electromigration in aluminium. Specifically, our contribution targets the design and implementation of plasmonic masks for sub-wavelength UV-lithography by room temperature electromigration investigating the associated limitations and parameter dependencies. For our studies, we used four inch diameter Si wafers as substrate material equipped with 500 nm thick silicon dioxide films that were created by a wet oxidation process at 1050 °C for 65 minutes. This oxide film was required to be sufficiently comparable with respect to the interface properties to quartz glass, which is later used as a substrate material for plasmonic lithography masks. For the plasmonic experiments, aluminium interconnects for electromigration experiments were created by a conventional lift-off process utilizing standard UV-laser-lithography with a negative tone photoresist (LNR003), followed by thermal e-beam evaporation of aluminium and a resist lift-off step. In the evaporation process, a slow evaporation rate of 0.04 to 0.05 nm/s was used to obtain a smoother surface, as a high surface roughness can affect the electromigration process. As part of this research, the electromigration effects on different junctions with contact pad spacings of 60 µm, 100 µm and 150 µm have been analysed at room temperature. SEM images of these junctions are shown in Figure 1 a)-c). The upper left side in all images in Figure 1 is used as the cathode and the lower right side was the anode.

We used a theoretical approach to obtain the necessary parameters for the different electromigration effects. To calculate these values, being shown in Table 1, we used the geometric values of the junctions obtained from SEM images in addition to material parameters following the approach presented in reference [1]. We explored two approaches, the constant current approach and the constant voltage approach. For both strategies, a Keithley 4200 SCS was used to apply the current or voltage to the test structure to perform the electromigration experiments. During the experiment, the corresponding voltage or current was monitored. When the respective value suddenly dropped to zero, voltage or current application was immediately stopped, as this meant that a gap had formed in the aluminium interconnect. The separated junctions after the electromigration can be seen in Figure 1 d)-e) for the constant voltage mode and the junction breaks closer to the cathode side. With the second approach, the constant current mode, as shown in Figure 1 g)-i), the junction breaks closer to the center part. Some of these gaps appear to be formed with a mixture of thermo- and stressmigration of the material and an electromigration process also due Joule heating. The formation of hillocks at the anode side indicates that electromigration is present.

To support and verify our experimental data, we have also performed numerical simulations. The simulations are based on the finite element method (FEM) and were realized using COMSOL Multiphysics as FEM software. A representative model for the simulations is shown in Figure 2 a), which uses a simplification with the geometric values of one of the created junctions that can be seen in 2b). In 2c) and 2d) the results show that in an initial state of electromigration the highest current densities are at the edges. Consequently, in the experiments, the fracture was observed closer to the cathode side and not in the middle part (Figure 1d)-1e)).

[1] I. A. Blech, J. Appl. Phys., Vol. 47, no. 4, (1976) S. 1203–1208
[2] F. Hong et al, Adv. Optical Mater. 7 (14), (2019) S.1801653

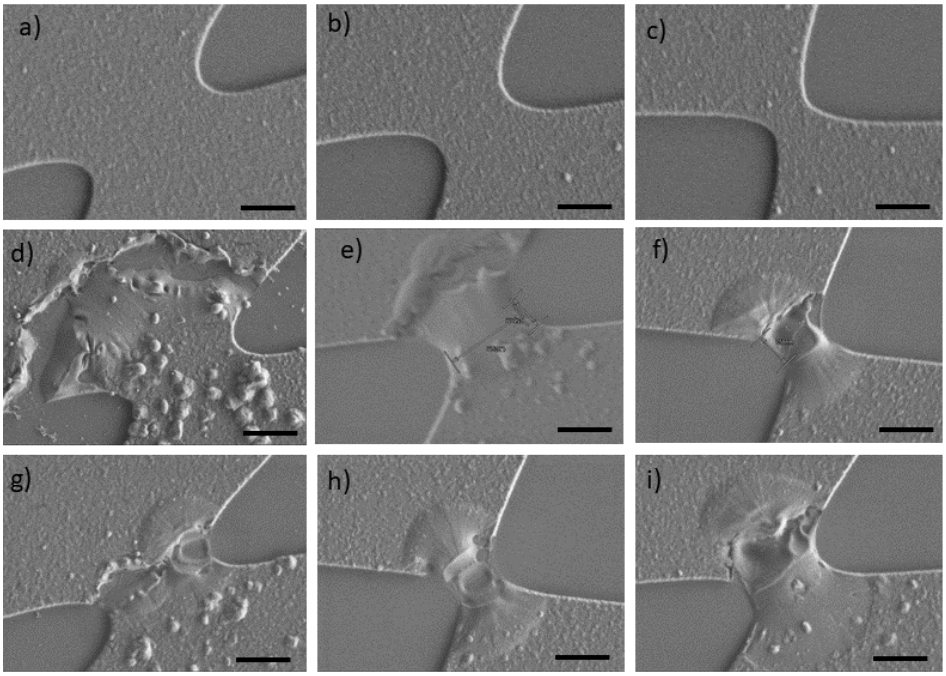

Figure 1. SEM images visualizing the observed electromigration effects in aluminum interconnects with narrowed regions and distances of the contact pads of: 60 µm (first column), 100 µm (second column), 150 µm (third column). SEM before the process in a)-c), with constant voltage in d)-f) and with constant current in g)-h) all scalebars are 1 µm.

Length [µm]	Current [mA]	Absolut resistance [Ω]	Voltage [mV]
60	59	$R_{20\ ℃} = 0.08$	$U_{min} = 4.7$
		$R_{660\ ℃} = 0.28$	$U_{max} = 16.5$
100	35	$R_{20\ ℃} = 0.13$	$U_{min} = 4.6$
		$R_{660\ ℃} = 0.45$	$U_{max} = 15.8$
150	26	$R_{20\ ℃} = 0.18$	$U_{min} = 4.7$

Table 1. Calculated results of the lowest required current and voltage for electromigration as well as the absolute resistances for the analyzed structures following the approach in reference [1].

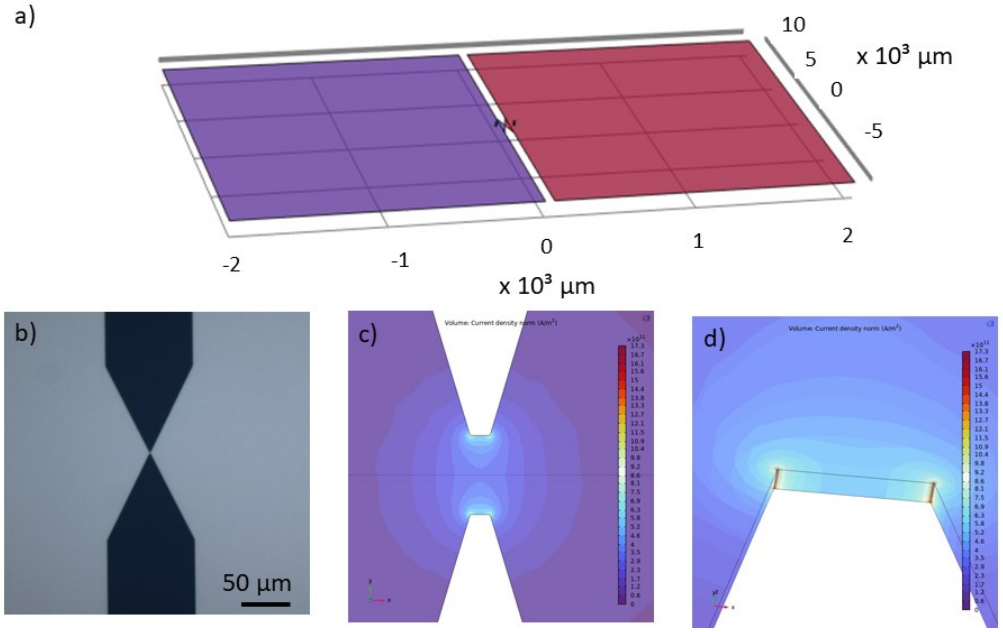

Figure 2 Simulation of the electromigration process. In a) the created model based on the microscope image of a structure shown in b). The close ups in c) and d) show that the highest current density occurs in the edges of the junction.

Improved Accuracy in Measuring the Dielectric Constant of Nanoparticles in Electrostatic Force Microscopy

Lukas Lehnert[a], Benjamin Baumann[a], Ronald Thoelen[b], and Hildegard Möbius[a,*]

[a]Department of Computer Sciences and Micro Systems Technology, University of Applied Sciences Kaiserslautern, Zweibrücken, Germany
[b]Institute for Materials Research, Hasselt University, Hasselt, Belgium
[*]E-mail: hildegard.moebius@hs-kl.de

Keywords: Electrostatic Force Microscopy, nanoparticles, dielectric constant, characterization and analytical techniques

Electrostatic Force Microscopy (EFM) is a widely recognized method for characterizing the local electrostatic properties of materials at nanometer range. In this technique, the tip and substrate form a capacitor whose capacitance is sensitive to changes in charge distribution or variations in dielectric properties during surface scanning. Theoretical modeling of this capacitance can be achieved through analytical evaluations of the tip-sample interaction, 3D-FEM simulations [1], or utilizing a parallel plate capacitor model [2]. When characterizing 3D-structures (e.g. nanoparticles) with EFM an additional complexity arises due to the changes in capacitance caused by variable tip-to-sample distances. A commonly adopted approach to mitigate this topographic effect is to hold the tip at a constant height, disregarding the topography of the sample, also called linear mode. Often, the influence of tip size relative to particle size is neglected [2, 3] or a given model is only valid within specific constraints of tip and particle dimensions [1].
In this study we introduce a straightforward sectionwise-defined model using a parallel plate capacitor model as illustrated in Figure 1. The approximation of the tip-substrate interaction as a parallel plate capacitor is an established method for characterizing nanoparticles [2]. This model distinguishes two primary conditions: $A_{Tip} < A_{Particle}$ and $A_{Tip} > A_{Particle}$. The electrostatic force gradient which corresponds to the second derivative of the parallel plate capacitors capacitance is proportional to the phaseshift of the tip's oscillation. This is described by Equation 1 when $A_{Tip} < A_{Particle}$ and Equation 2 when $A_{Tip} > A_{Particle}$. It should be noted that when $A_{Tip} > A_{Particle}$ the phaseshift is influenced only by the nanoparticle's size leading to no variation in phaseshift as a function of the ratio $A_{Tip}/A_{Particle}$.

$$\Delta\Phi_{el} = -\frac{Q}{k}\varepsilon_0(V_{DC} - V_{CPD})^2 \left(\frac{A_{Tip}}{(z+\frac{d}{\varepsilon_P})^3} - \frac{A_{Tip}}{(z+d)^3}\right) \tag{1}$$

$$\begin{aligned}\Delta\Phi_{el} &= -\frac{Q}{k}\varepsilon_0(V_{DC} - V_{CPD})^2 \left(\frac{A_{Particle}}{(z+\frac{d}{\varepsilon_P})^3} + \frac{A_{Tip} - A_{Particle}}{(z+d)^3} - \frac{A_{Tip}}{(z+d)^3}\right) \\ &= -\frac{Q}{k}\varepsilon_0(V_{DC} - V_{CPD})^2 \left(\frac{A_{Particle}}{(z+\frac{d}{\varepsilon_P})^3} - \frac{A_{Particle}}{(z+d)^3}\right)\end{aligned} \tag{2}$$

with $\Delta\Phi_{el}$ as phaseshift [°], A_{Tip} the interaction area of tip [m^2],$A_{Particle}$ the interaction area of particle [m^2], Q the quality factor, k the spring constant of the cantilever [N m^{-1}], ε_0 the electric field constant [F m^{-1}], V_{DC} the tip voltage [V], V_{CPD} contact potential difference [V], z lift height above the particle [m], d particle diameter [m] and ε_P dielectric constant of the nanoparticle.

For measuring the dielectric constant of nanoparticles it is important to consider variations in tip size arising from deformation [1]. Determining the dielectric constant when A_{Tip} is smaller than $A_{Particle}$ depends on the precise knowledge of the tip radius. Therefore, $A_{Particle}$ has to be smaller than A_{Tip} to ensure robust measurements. This is an important consideration when measuring the dielectric constant of nanoparticles of varying sizes.
These effects are shown in Figure 2. Here the phaseshift is depicted as a function of $A_{Tip}/A_{Particle}$, based on variations in tip size and particle size. Figure 2(a) shows the calculated phaseshift when the diameter d of a SiO2 nanoparticle is varied from 40 nm to 140 nm with a tip radius ranging from 1 to 100 nm including the convolution of tip and particle. In Figure 2(b) this hypothesis is experimentally validated through EFM experiments utilizing CoCr-coated tips with varying radii (MESP-V2 ($r_{Tip} = 31\ nm$) and MESP-HM-V2 ($r_{Tip} = 62\ nm$) from Bruker Inc.) on 75 ± 5 nm SiO2 nanoparticles with a lift height above the particle of 50 nm. Thus, measuring the dielectric constant with a tip size larger than the size of the nanoparticle dramatically improves accuracy.

References

[1] L. Fumagalli, D. Esteban-Ferrer, A. Cuervo, J. L. Carrascosa, and G. Gomila. Label-free identification of single dielectric nanoparticles and viruses with ultraweak polarization forces. *Nat. Mater.*, 11(9):808–16, 2012.

[2] Marc Fuhrmann, Alexander Krivcov, Anna Musyanovych, Ronald Thoelen, and Hildegard Möbius. The role of nanoparticles on topographic cross-talk in electric force microscopy and magnetic force microscopy. *Phys. Status Solidi A*, 217(13), 2020.

[3] S. Belaidi, P. Girard, and G. Leveque. Electrostatic forces acting on the tip in atomic force microscopy: Modelization and comparison with analytic expressions. *J. Appl. Phys. (Melville, NY, U. S.)*, 81(3):1023–1030, 1997.

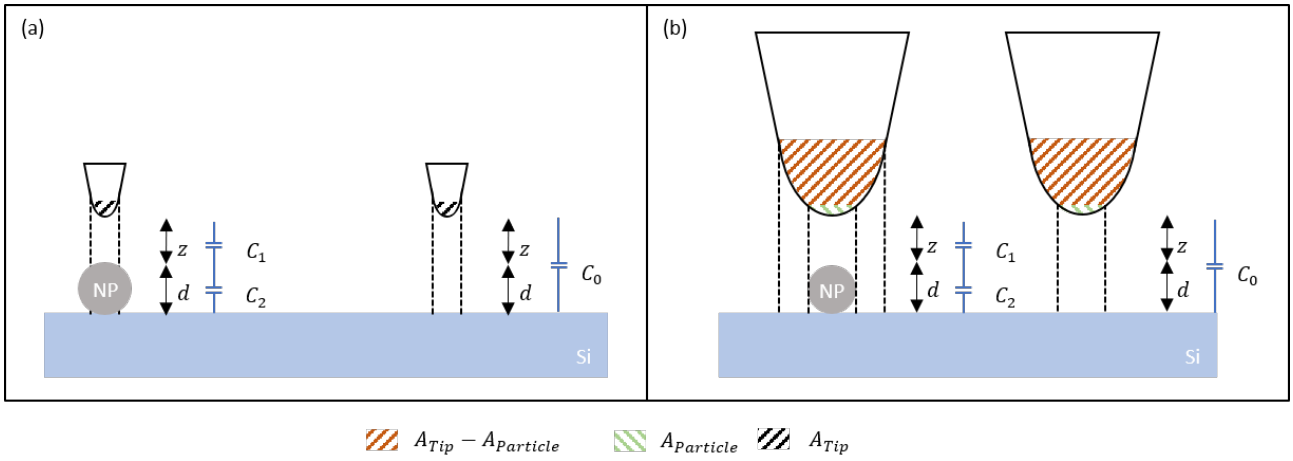

Figure 1: Schematic of capacitor circuit diagram to calculate phaseshift in linear mode measurements for (a) $A_{Tip} < A_{Particle}$ and (b) $A_{Tip} > A_{Particle}$

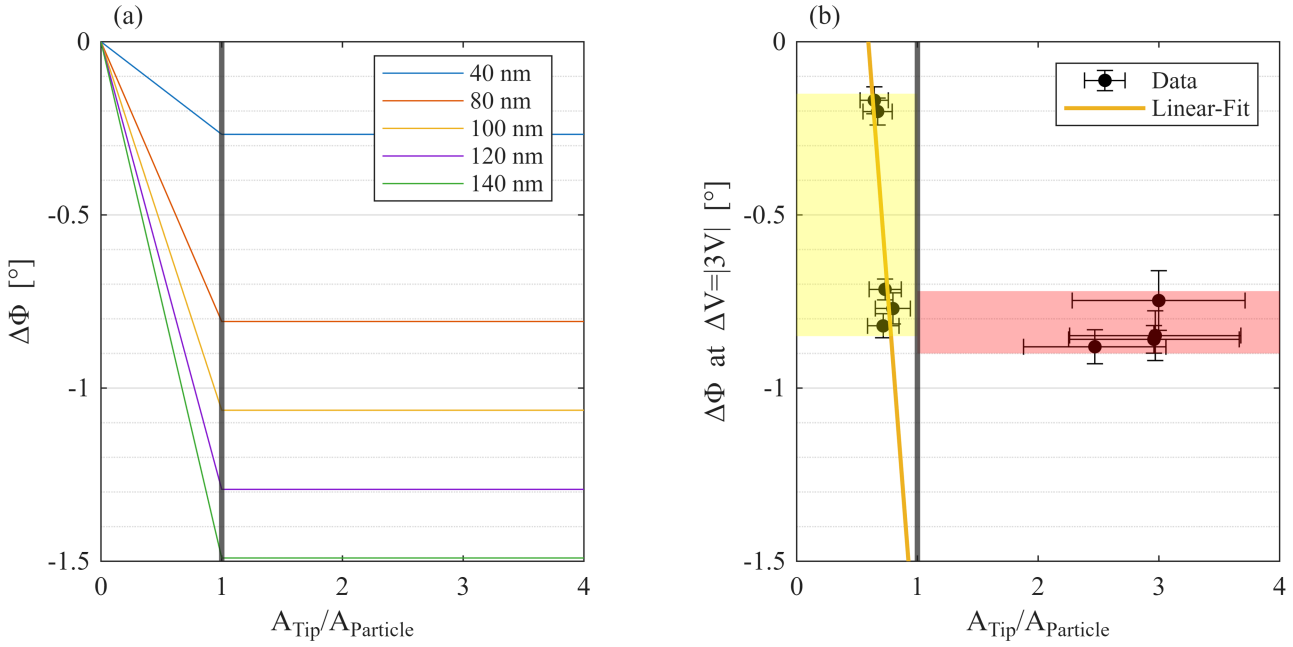

Figure 2: (a) Calculated phaseshift over $A_{Tip}/A_{Particle}$ for tip radii from 1 to 100 nm with variation in particle size d (40, 80, 100, 120, 140 nm) and ε_P=4; (b) Measured phaseshift of SiO2 nanoparticles ($d = 73 - 78\ nm$) with a lift height above the particle of 50 nm using CoCr-coated tips (MESP-V2 ($r_{Tip} = 31\ nm$) and MESP-HM-V2 ($r_{Tip} = 62\ nm$) from Bruker Inc.)

Effect of doping Nb on optical properties of Sea Urchin-like TiO_2 Photocatalysis

Mariko Murayama [a, b], Xinwei Zhao [c], Taichiro Nishio [a]

[a] Tokyo University of Science, Tokyo, 1638601, Japan
[b] Toyo University Research Institute of Industrial Technology, Saitama, 3508585, Japan
[c] R&D Center for Advanced Energy Materials, Henan University of Technology, Henan, 450001, China
e-mail: nishio@rs.tus.ac.jp

Titanium dioxide (TiO_2) for environmental applications has been widely investigated for a long time because of its excellent properties of high chemical stability, low toxicity, and relatively high photocatalytic activity. The photocatalytic activity of TiO_2 is determined by the specific surface area, crystallinity, crystallite size, crystal structure, surface defects, and electron–hole recombination rate. This means that there are many factors that influence photocatalytic performance, such as the specific surface area, size of particle/crystallite, pore volume and structure, crystalline phase, and the exposed surface facets [1]. TiO_2 in zero to three dimensions has been widely studied for photocatalytic applications. For example, Sea urchin-like TiO_2 (U-TiO_2) micro- or nanoparticles assembled with nanorods, show promising potential for improving light absorption efficiency by increasing surface area and inducing light scattering. They exhibit minimal aggregation and are easily separated from solutions [2, 3]. However, there are barriers to better performance: the process for forming nanorods with high crystallinity has not been established and the shape of the nanorods reduces carrier mobility. In addition, the wide bandgap of TiO_2 (3.2 eV for brookite and anatase, 3.0 eV for rutile) limits their photocatalytic performance. Niobium (Nb)-doped TiO_2 thin films are an alternative to ITO which is currently one of the most practical transparent conducting oxides. Doping Nb into TiO_2 can be expected to adjust the bandgap width, covering a range from visible to ultraviolet light, and to enhance the electrical conductivity by supplying electrons from Nb^{5+}. In this paper, we have attempted to dope Nb into TiO_2 while maintaining it in the sea urchin form.

Sea Urchin-shaped TiO_2 and TiO_2:Nb (U-TiO_2 and U-TiO_2:Nb) were synthesised by the hydrothermal synthesis method using TiO_2 or TiO_2:Nb powder. Prior to the hydrothermal process, TiO_2 and TiO_2:Nb powders were prepared. TiO_2 powder was purchased from Teika Corporation and TiO_2:Nb powder was synthesized as follows: Titanium (IV) isopropoxide ($Ti(OiPr)_4$) was dissolved in ethanol and niobium ethoxide ($Nb(OC_2H_5)_5$) was added and the mixed solution was heated in an autoclave at 200°C for 24 h to promote the reaction. 0.5 g of TiO_2 or TiO_2: Nb powder was added to a NaOH solution and ultrasonicated for 30 min. The mixture was then transferred to an autoclave and heated at 120°C for 24 h. The resulting precipitate was extracted, dried at 60°C for 1 h, and then subsequently mixed with a solution of NaOH and H_2O_2 (30 % mass). The mixture was stirred, transferred to a Teflon-lined stainless-steel autoclave, and heated at 150°C for 8 hours, followed by cooling to room temperature. To remove most of the sodium ions, the precipitate was further washed with deionised water until the pH of the supernatant approached 7.0. Finally, the synthesised product was dried at 60°C for 1 h and calcined at 400°C for 1 h, respectively. The crystal size and structure of the samples were determined using X-ray diffraction (XRD). The morphology and microstructure of the samples were characterized by a scanning electron microscopy (SEM). The identification of elements present including ionization and defects were characterised by X-ray photoelectron spectroscopy (XPS). UV-Vis spectroscopy was carried out to estimate the bandgap energy and the photocatalytic degradation of Methylene Blue (MB) solution of the samples.

Figure 1 shows SEM images of U-TiO_2 and U-TiO_2:Nb. The samples obtaining the sea urchin-form suggest that they have a large specific surface area for dye adsorption, edge nano ribbons can enhance light scattering ability, and accelerating electron transfer. The optical absorption spectra (indicate of the bandgap, Eg) are illustrated in Fig. 2 determining to be 3.20, 3.15, and 3.10 eV for TiO_2, U-TiO_2 and U-TiO_2: Nb suggesting Nb doping successfully narrowed the TiO_2 bandgap. Since Nb^{5+} ions in TiO_2 are donors, it can be assumed that the dopant-related level is located under the conduction band within the TiO_2 bandgap. Each doping level of Nb may affect the electronic structure of TiO_2.

[1] K. Nakata et al., J Photochem. and Photobio. C: Photochem. Rev. 13 (2012) 3, 169-189.
[2] Wu, Z. et al., Particuology (2014) 15, 61-70.
[3] Yan, T. et al., J. Hazard. Mater. 186 (2011) 1, 272-279.

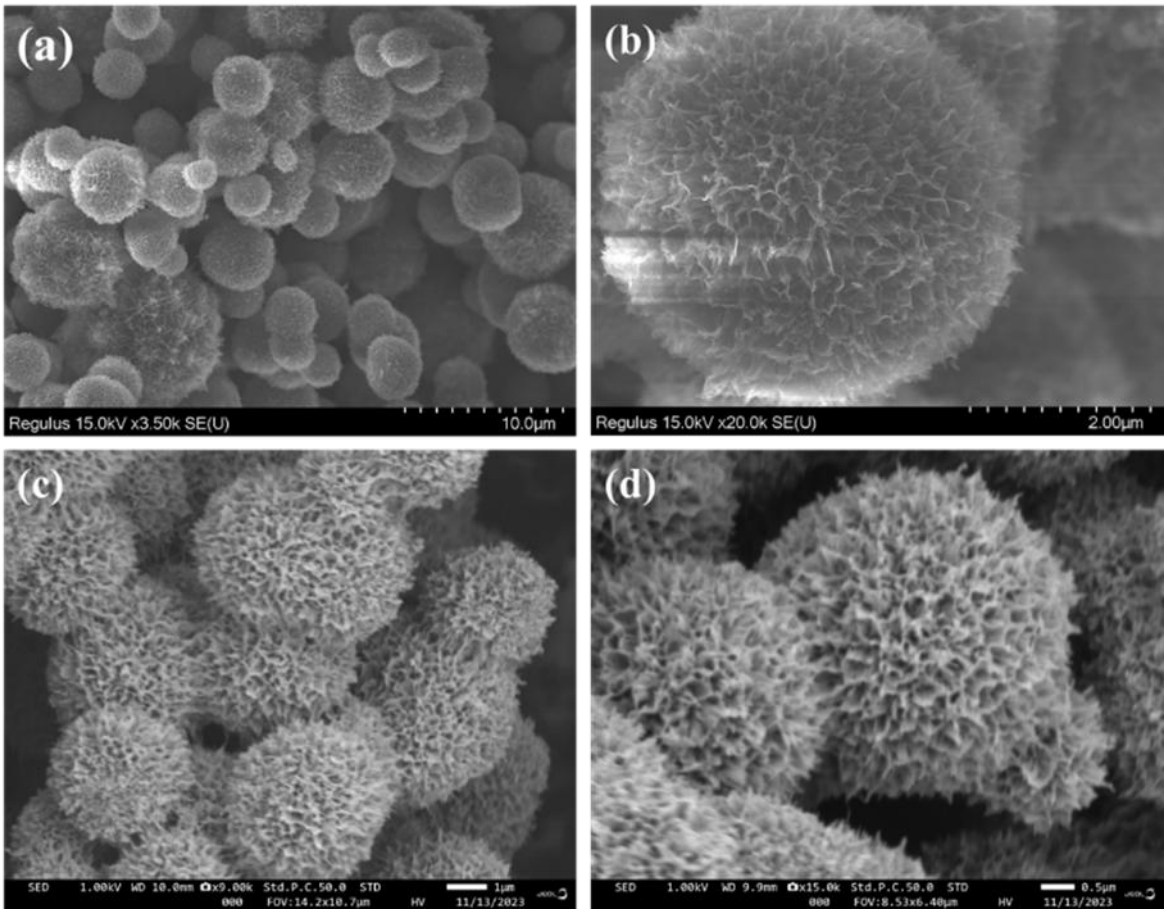

Figure 1. SEM images and magnified SEM images of (a), (b) U-TiO_2 and (c), (d) U- TiO_2: Nb.

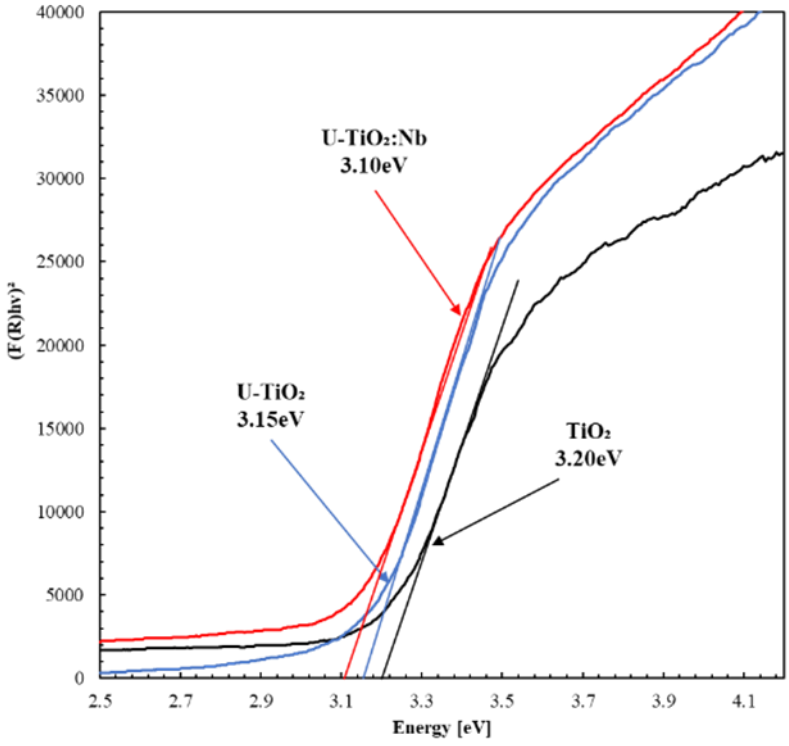

Figure 2. Absorption spectra of TiO_2 powder, U-TiO_2 and U-TiO_2:Nb.

PVDF-TrFE with suspended AlN particles: a polymer nano-composite with boosted ferroelectric properties

Wolfgang Hilber [a], Sebastian Lang [a], and Bernhard Jakoby [a]

[a] Institute for Microelectronics and Microsensors, JKU Linz, 4040 Linz, Austria
e-mail: wolfgang.hilber@jku.at

PVDF-TrFE, additively printed and embedded into the organic surface coating of metallic substrates, has been successfully used by our group for the realization of piezo- and pyroelectric transducers for various applications. Here we present an approach to boost the ferroelectric properties of the material while maintaining the achieved ease of processing, by adding highly ferroelectric ceramic AlN nano-particles that are uniformly incorporated into the PVDF-TrFE polymer matrix. In this way, a highly functional ferroelectric composite has been created, featuring a maximum polarization that exceeds that of the PVDF-TrFE base material by far.

The polymeric compound poly[(vinylidenefluoride)-cotrifluoroethylene], abbreviated PVDF-TrFE, exhibits piezo- and pyroelectric properties after polarization when deposited on surfaces as a thin film [1]. PVDF-TrFE granulate has been dissolved in a mixture of γ-butyrolactone (GBL) and acetone to achieve an appropriate viscosity for processing, and additively printed mainly via screen- and stencil-print for realization of various transducer concepts so far. For example, as depicted in Fig. 1, it has been used to embed ferroelectric transducers into the organic coating of sheet steel [2].
Here, as a further step, in order to improve performance and sensitivity of the functional polymer, we have created a composite of PVDF-TrFE and ferroelectric Aluminum-nitride (AlN) nano-particles that features enhanced physical properties. Following the concept of '*hard magnetic soft materials*' [3], smart composites that consist of a mechanically soft polymer impregnated with hard magnetic filler particles, a functional composite consisting of AlN nano-particles (featuring diameters below 100 nm), and PVDF-TrFE solution at a dry weight ratio of PVDF-TrFE : AlN ~ 1 : 3.5 has been created, that by analogy can be interpreted as a '*hard ferroelectric soft material*'.
At first the AlN particles were dissolved in acetone in an ultrasonic bath, and subsequently mixed into the polymer solution by using a magnetic stirrer. The prepared composite has then been printed on test substrates, PCB boards with a smooth and Au-plated copper layer, for electrical characterization. Figure 2 shows pictures of the resulting microstructure taken with a scanning electron microscope (SEM). The images clearly show the hosting PVDF-TrFE polymer network, as well as the distribution of AlN particles in the x-ray photoelectron spectroscopy (XPS) images. On the one hand, it can be seen that the particles are indeed homogeneously distributed over the whole layer, but on the other hand, the pictures also reveal that clustering of the particles up to a few micrometers in size occurs.
Finally, Figure 3 depicts the measured polarization hysteresis of the created PVDF-TrFE / AlN composite compared to pure PVDF-TrFE polymer. It is clearly visible, that the hysteresis of the composite is much more pronounced, with a maximum polarization, respectively surface charge density, that exceeds the value of the base polymer almost by a factor of eight.

Summarizing we have shown that, by adding AlN nanoparticles to a printable PVDF-TrFE polymer solution, the ferroelectric properties can be enhanced considerably, while keeping the materials ease of processing with standard additive printing methods. The devised composite material may be utilized for the realization of ferroelectric transducers with increased sensitivity and performance.

[1] S. Bauer and F. Bauer, Piezoelectric polymers and their applications, in: Piezoelectricity, Springer Berlin Heidelberg (2008) 157–177.
[2] W. Hilber, H. Enser, M. Knoll, C. Offenzeller and B. Jakoby, Embedded Transducers in Polymeric Coatings on Metallic Substrates, IEEE Sensors Journal 21.11 (2021) 12444-12456.
[3] P. Narayanan, R. Pramanik and A. Arockiarajan, Hard magnetics and soft materials - a synergy, Smart Materials and Structures 33.4 (2024) 043001.

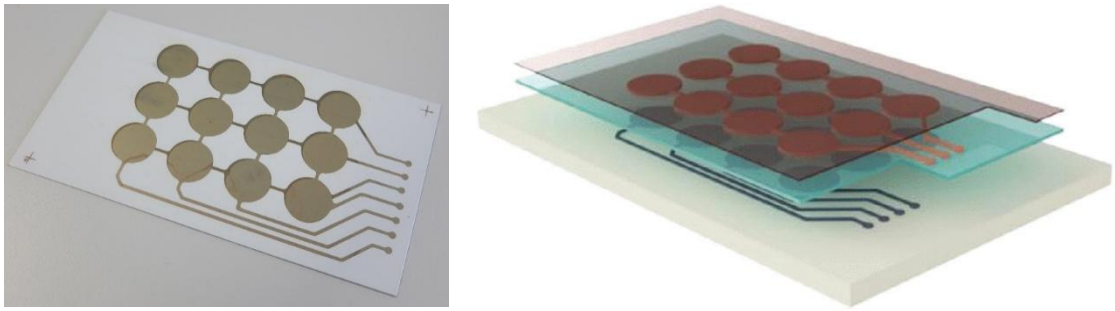

Figure 1. Example of previously realized transducers with printed PVDF-TrFE: 3x4 matrix of piezo- and pyroelectric sensors embedded into the organic coating of sheet steel (left: fabricated sample, right: schematic showing top and bottom electrode, the PVDF-TrFE in between, and a protective layer on top).

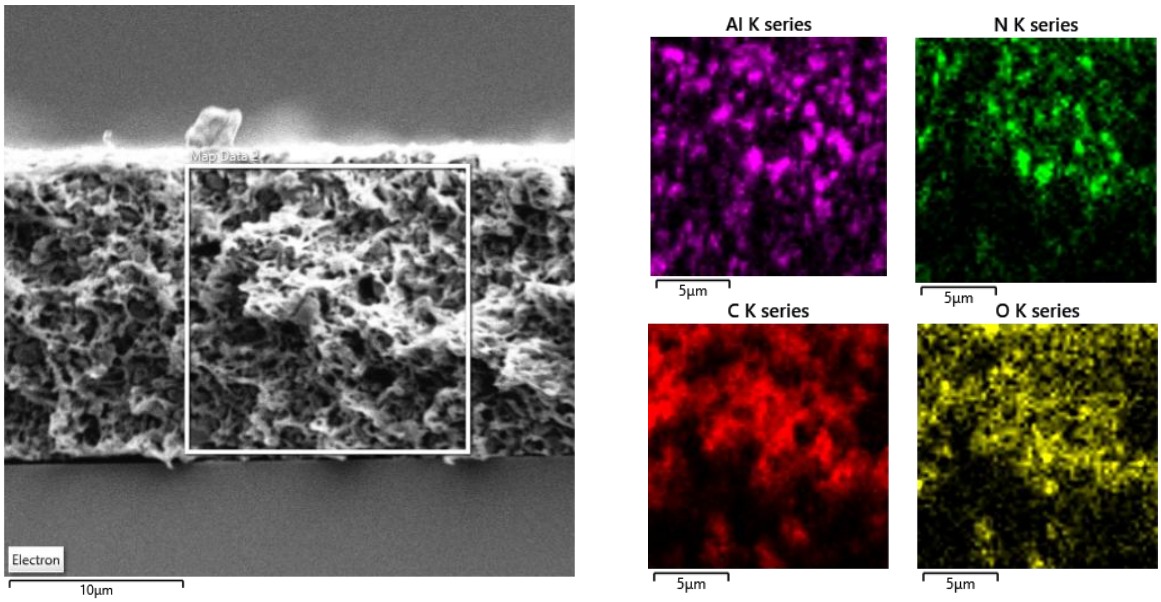

Figure 2. SEM analysis of the developed PVDF-TrFE / AlN nanocomposite: (left) SEM image of the cross-section, (right) XPS analysis of the indicated cutout showing the material distribution, Al and N in the top row reflecting the nano-particles, C and O in the bottom row reflecting the polymer.

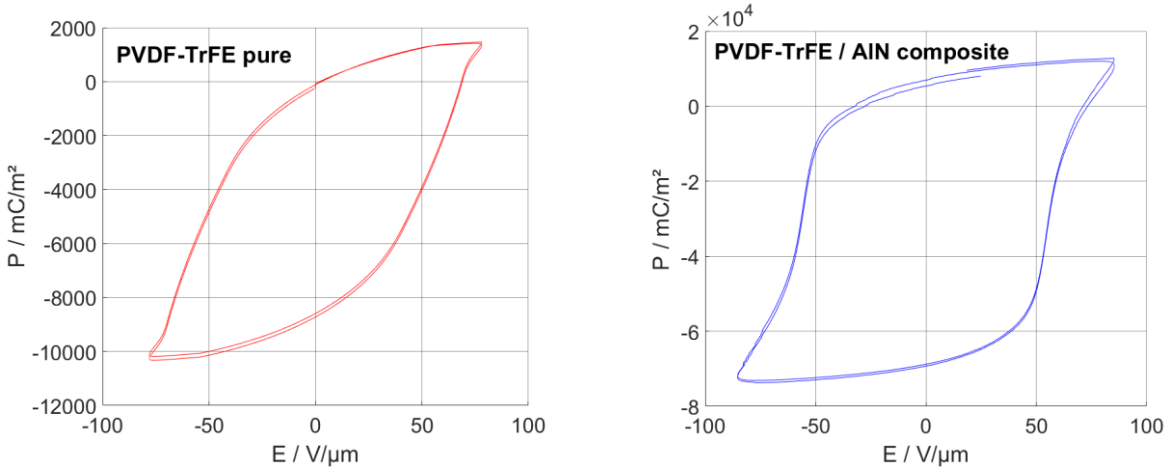

Figure 3. Measured polarization hysteresis for the created PVDF-TrFE / AlN composite (right) and pure PVDF-TrFE (left). Note the more pronounced hysteresis as well as the multiple times higher polarization of the printable nano-composite.

Fabrication of Ferroelectric PVDF:TrFE Foil via Controlled Dewetting

Sebastian Lang [a], Wolfgang Hilber [a], Tina Mitteramskogler [a], Bernhard Jakoby [a]

[a] Institute for Microelectronics and Microsensors, Johannes Kepler University Linz, Linz, 4040, Austria
e-mail: sebastian.lang@jku.at

Flexible electronics and sensor technologies are becoming increasingly important due to their wide-ranging applications in wearable devices, healthcare monitoring, environmental sensing, and industrial automation [1]. Especially poly(vinylidene-fluoride) (PVDF) and its copolymer with trifluoroethylene have been some of the most used polymers in force-sensing applications due to their strong piezoelectricity and wide range of ways of fabrication [2]. Usually, force sensors using PVDF are fabricated either by using a prefabricated and polarized large-scale foil, which is cut to size, creating fibers to embed into a polymer matrix or similar, or by printing the sensor and its electrodes directly onto the final substrate [3,4].

This work presents an alternative method for fabricating Poly(vinylidene fluoride–trifluoroethylene) (PVDF:TrFE) foils of arbitrary shape, size, and thickness via stencil printing and following controlled dewetting from the substrate. This foil could be used to fabricate various kinds of devices utilizing the chemical stability of PVDF, or flexible piezoelectric or ferroelectric sensors. Compared to utilizing a prefabricated foil, this approach does not require cutting the foil before the following steps or fixing it for any printing process. Subsequent printing of other functional materials allows for the fabrication of sensors on this fixed substrate to any shape and design desired. After all the printing steps are performed, the foil can be separated via dewetting, leaving the self-supported sensors ready for use.

The proposed process starts with stencil printing a layer of PVDF:TrFE onto a gold substrate. This step is identical to existing fabrication processes for rigid PVDF-based force sensors [5]. The substrate used is a printed circuit board (PCB) with a single large electrode coated with electroless nickel immersion gold (ENIG) as shown in Figure 1. Afterward, other necessary processing steps may be conducted to build the finished device, which is still attached to the rigid substrate. An additional layer of PVDF:TrFE may be needed for passivation and protection from the chemicals used in the following steps. After these steps, a solution of acetone and gamma-butyrolactone (GBL) in a mixture of approximately 50:50 is applied to simultaneously soften the PVDF:TrFE layer and cause the first layer to dewet from the gold substrate. It is crucial to only add as little as necessary, as the PVDF:TrFE might get partially dissolved. Successful dewetting can be observed via a honeycomb-like structure appearing due to the detachment and slight expansion of the first PVDF:TrFE layer. The foil can then be cut free from any attachments (e.g., parts of the substrate that are not covered in ENIG) and then dried off in warm air.

This work has been partially supported by the State of Upper Austria in the frame of the Center for Symbiotic Mechatronics (of the Linz Center of Mechatronics, LCM).

[1] A. Ahmed, S. Sharma, B. Adak, M.M. Hossain, A.M. LaChance, S. Mukhopadhyay, L. Sun, Two-dimensional MXenes: New frontier of wearable and flexible electronics, InfoMat 4 (2022) e12295. https://doi.org/10.1002/inf2.12295.
[2] Y. Wu, Y. Ma, H. Zheng, S. Ramakrishna, Piezoelectric materials for flexible and wearable electronics: A review, Materials & Design 211 (2021) 110164. https://doi.org/10.1016/j.matdes.2021.110164.
[3] W. Hilber, H. Enser, M. Knoll, C. Offenzeller, B. Jakoby, Embedded Transducers in Polymeric Coatings on Metallic Substrates, IEEE Sensors Journal 21 (2021) 12444–12456. https://doi.org/10.1109/JSEN.2021.3057664.
[4] E. Ragonese, M. Fattori, E. Cantatore, Printed Organic Electronics on Flexible Foil: Circuit Design and Emerging Applications, IEEE Transactions on Circuits and Systems II: Express Briefs 68 (2021) 42–48. https://doi.org/10.1109/TCSII.2020.3040707.
[5] S. Lang, W. Hilber, H. Enser, T. Mitteramskogler, B. Jakoby, Embedding PVDF-Based Force Sensors in Stacked Printed Circuit Boards, IEEE Sensors Letters 8 (2024) 1–4. https://doi.org/10.1109/LSENS.2024.3440477.

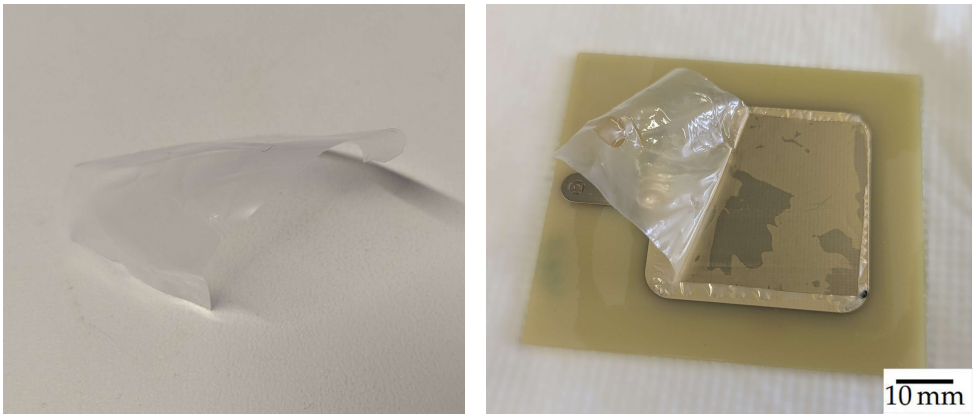

Figure 1. An early sample of fabricated foil (left) freely placed on a table, and a sample still partially attached to the substrate (right). The right figure still shows the honeycomb-like structure on the edges, where the foil was cut. The foil is still wet in the right figure and therefore slightly wrinkled; the left sample is already dried. The right figure also shows that a part of the PVDF:TrFE remains attached to the substrate. The reason is that the PVDF:TrFE area is bigger than the ENIG area. The PVDF:TrFE layer can contact the FR4 polymer, which offers a better bond. Therefore, the layer is cut with a scalpel to remove the desired piece of foil.

Figure 2. Full dewetting of a single PVDF:TrFE layer on the used PCB substrates. A distinct honeycomb-like structure can be seen, which seems to stem from the simultaneous expansion of the PVDF:TrFE layer and detachment from the ENIG. The layer still mostly contacts the surface (left), but there are cases where it already starts lifting, creating a bubble-like texture (right).

X-ray energy dependence of gold nanoparticle synthesis in X-ray radiolysis

Akinobu Yamaguchi [a], Kenji Hanada [b], Ikuo Okada [b], Hiroshi Sekiguchi [c], Ikuya Sakurai [d]

[a] Toyo University, Kawagoe, 350-8585, Japan
[b] Aichi Synchrotron Radiation Center, Seto, 489-0965, Japan
[c] Japan Synchrotron Radiation Research Institute, Sayo, 679-5198, Japan
[d] Nagoya University, Nagoya, 464-8603, Japan
e-mail: yamaguchi054@toyo.jp

Nanoparticles are of tremendous scientific and industrial importance owing to their unique physicochemical properties arising from their nanoscale dimensions. For example, gold nanoparticles in particular are used for colouration of stained glass in familiar applications and as a colouration mechanism in infectious disease testing kits. More recently, they have attracted attention for their use as molecular sensors utilising surface-enhanced Raman scattering, as well as for their use as nanotags, since they excite plasmon resonance.

Chemical synthesis methods are mostly used to produce nanoparticles. Recent reports on the feasibility of nanoparticle synthesis by photoexcited chemical reactions have attracted attention to mechanistic elucidation and applied research. In this study, research was carried out with the aim of conducting basic research to elucidate the mechanism and engineering applications of nanoparticle synthesis from liquid, especially by irradiating with X-rays. [1, 2] Their formation and the growth kinetics under synchrotron radiation (SR) X-ray irradition are governed by mechanisms that are linked to the photoelectric cross-section, especially focusing the probability of interaction of X-rays with matter. The knowledge of these interactions is crucial to optimizing experimental conditions to obtain the desired nanoparticles with desirable properties.

SR X-ray, with its high intensity, wide energy range, and tunable, has been a unique tool in the study of material science and nanotechnology. The applications of this in photochemical processes provide insight into radiation-induced reactions, especially in liquid-phase systems.

We demonstrated that direct monochromatic X-ray synchrotron irradiation induced the formation of gold nanoparticles and aggregates from a solution containing $Na_3Au(SO_3)_2$ in Aichi SR. The experiments were performed as schematically illustrated in Fig. 1, with monochromatic X-ray energy ranging from 6 keV to 20 keV. The silicon substrate was immersed in a $Na_3Au(SO_3)_2$ solution in a polyimide film container and irradiated with X-rays; after X-ray irradiation, the liquid was extracted and particle measurements were carried out using dynamic light scattering (DLS). In addition, the X-ray energy dependence of the size and shape of the nanoparticles produced was evaluated by scanning electron microscopy (SEM) observation of the nanoparticles adhered to the immersed silicon substrate surface. When X-rays are irradiated into the liquid, as shown in Fig. 2(a), ionisation of water is induced, ion reduction occurs and particle growth is promoted after nucleation. The relationship between X-ray energy and nucleation is then clarified.

Figures 2(b) to 2(d) show some of the SEM observations of nanoparticles immobilized on the silicon substrate after X-ray irradiation with energy of 6, 12 and 16 keV. Energy dispersive X-ray spectroscopy (EDX) measurements confirmed that these nanoparticles are composed of gold. The SEM images shown here are observations of areas where only relatively dispersed nanoparticles were observed. The locations where the nanoparticles have agglomerated are also assessed separately. The size of the nanoparticles was evaluated using ImageJ, resulting in a particle size distribution diagram as shown in Fig. 3.

The particle size and aggregation were observed to be strongly dependent on the X-ray energy. We have studied in detail the X-ray energy dependence of the particle sizes that make up the aggregates and those that are relatively isolated. We found that the isolated particle size is proportional to the X-ray photoelectric absorption cross section for Au. In other words, it was found that the primary formation and ripening process is triggered by the impact of X-rays on Au ions, which in turn initiates nucleation and particle growth as Au is reduced by the surrounding radical electrons. The ability to control nanoparticle synthesis by X-ray photochemical reactions is expected to lead to developments in 3D printers and the synthesis of functional nanoparticles.

[1] A. Yamaguchi, T. Matsumoto, I. Okada, I. Sakurai and Y. Utsumi, Materials Chemistry and Physics 160 (2015) 205 – 211.
[2] A. Yamaguchi, I. Sakurai, I. Okada, H. Izumi, M. Ishihara, T. Fukuoka, S. Suzuki and Y. Utsumi, J. Synchrotron Radiation 27 (2020) 1008 – 1014.

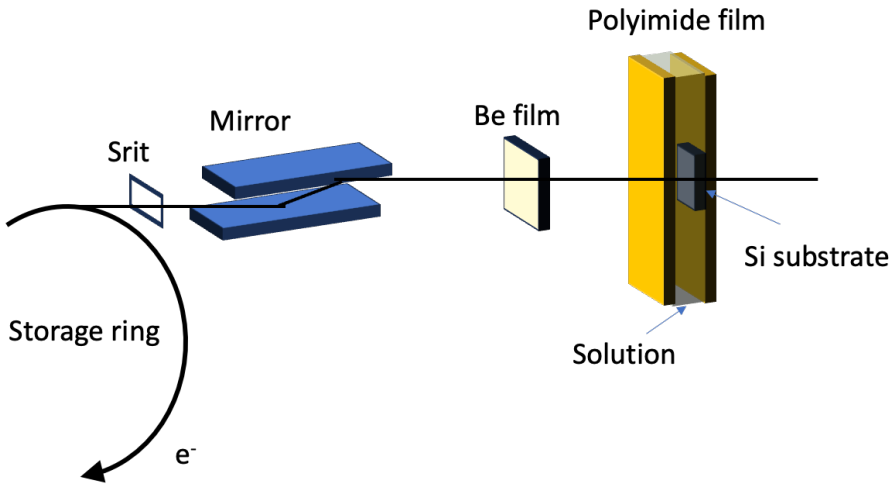

Figure 1. Schematic diagram of experimental setup for monochromatic X-ray radiolysis.

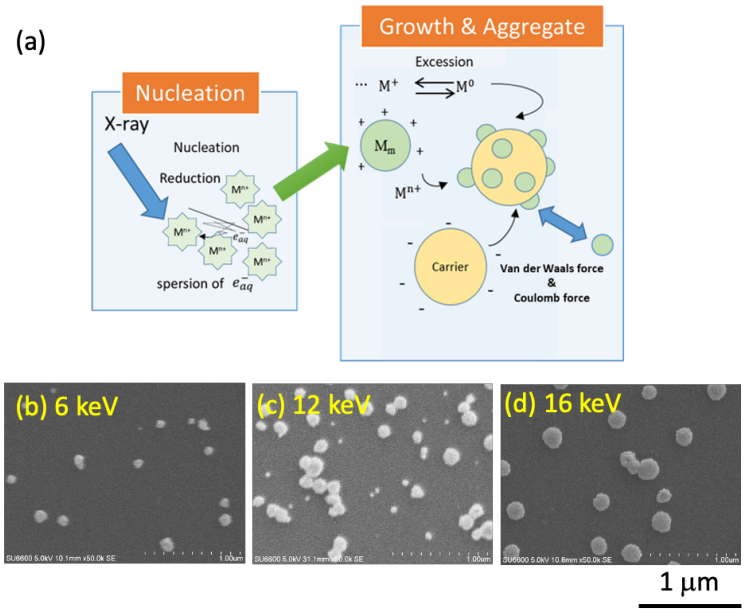

Figure 2. (a) Schematic diagram of the process of nucleation and particle growth by X-ray irradiation. SEM images of nanoparticles adhered to a silicon substrate at X-ray energies of (b) 6, (c) 12 and (d) 16 keV, respectively.

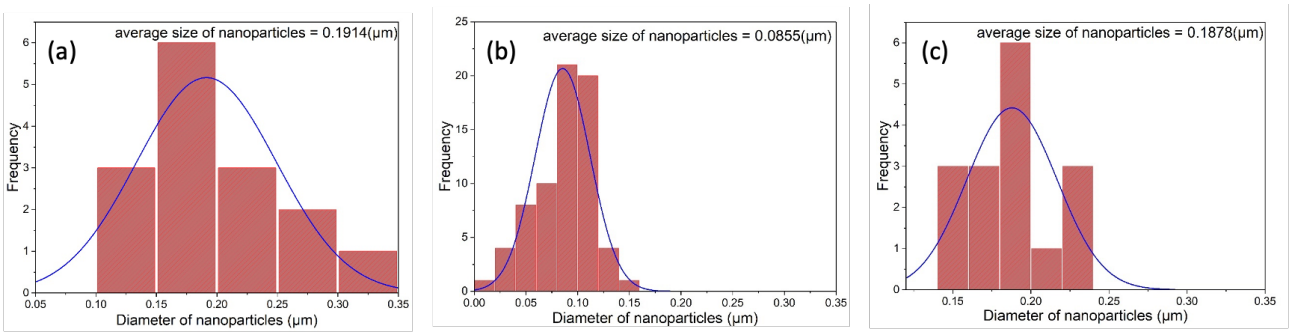

Figure 3. Histograms of particle size distribution at X-ray energy of (a) 6 , (b) 12, and (c) 16 keV.

E-Beam Lithography Process Calibration with Minimum Number of SEM Images using Deep Learning

Burak Çoban [a], Süleyman Çelik [b] Florian Imeri [c], Jan Klikovits [c], Klaus Gieb [c], Nezih Ünal [c]

[a] İzmir Institute of Technology, İzmir, 35430, Türkiye
[b] Sabanci University Nanotechnology Research and Application Center - SUNUM, İstanbul, 34956, Türkiye
[c] GenISys GmbH, Unterhaching, 82008, Germany
e-mail: burakcoban@std.iyte.edu.tr

Electron Beam Lithography (EBL) plays a crucial role in high-resolution nanofabrication, but its accuracy is highly affected by proximity effect caused by electron scattering and complex process effects, which arise from different fabrication steps such as resist development and etching. Electron scattering can be modelled by Monte-Carlo simulation, leading to a point-spread function (PSF) for the proximity effect correction (PEC) [1]. Due to the lack of a physics-based model for the resist development or etching, precise experimental calibration of process correction parameters is required. The state-of-the-art process calibration [2] is based on SEM imaging and measuring critical dimensions (CDs) of about 50 lines in a calibration pattern (see Fig. 1) after exposure, development and pattern transfer (etching or lift-off). This procedure uses only one-dimensional (1D) structures for calibration and can be improved in efficiency by using 2D calibration patterns, thereby reducing both the metrology effort and metrology-induced noise. This study investigates the application of machine learning techniques for image processing in EBL process calibration using only a minimum number of 2D SEM images.

We propose a smart 2D calibration pattern (see Fig. 2) designed to fit within the field of view (FOV) of a typical SEM. This compact design consists of a 7x7 array of dose-varied squares at the center and density variation in the surroundings to capture a wide variety of e-beam and process effects. It aims to provide enhanced accuracy for capturing 2D effects, and its compact form also allows seamless integration with machine learning models. Next, we employed a deep learning model to capture and map the image data to continuous correction parameters. The model was trained with a dataset of synthetic SEM images based on simulated data from our lithography simulation software, LAB [3]. Synthetic SEM images were generated with exposure parameters varied within physically relevant ranges. Simulation parameters were used as labels for the images during training. To ensure that the generated SEM images closely resemble real-world data, we introduced signal variations such as different contrast levels, noise, rotation and scaling.

We present the application of our trained model to real SEM images. A detailed evaluation and discussion of its performance and efficiency is presented. We also highlight the potential of machine learning techniques for enabling more efficient and data-driven process control in Electron Beam Lithography.

[1] Hofmann U. et. al. From ghost to state-of-the-art process corrections – PEC enabled e-beam nanofabrication, Micro and Nanoengineering Volume 25, Dec 2024, 100286
[2] G. Lopez et al, Isofocal Dose Based Proximity Effect Correction - Tolerance to the Effective Process Blur. Journal of Vacuum Science & Technology B 35, 06G505, 2017
[3] LAB is a 3D lithography simulation software of GenISys GmbH (www.genisys-gmbh.com)

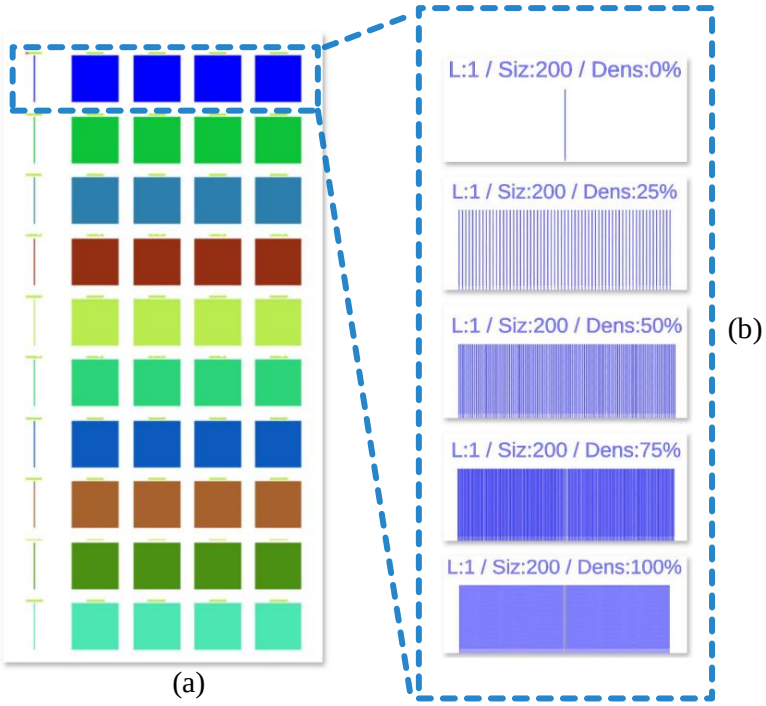

Figure 1. State-of-the-art calibration pattern with different base doses (a) and different background densities (%0-%25-%50-%75-%100) (b).

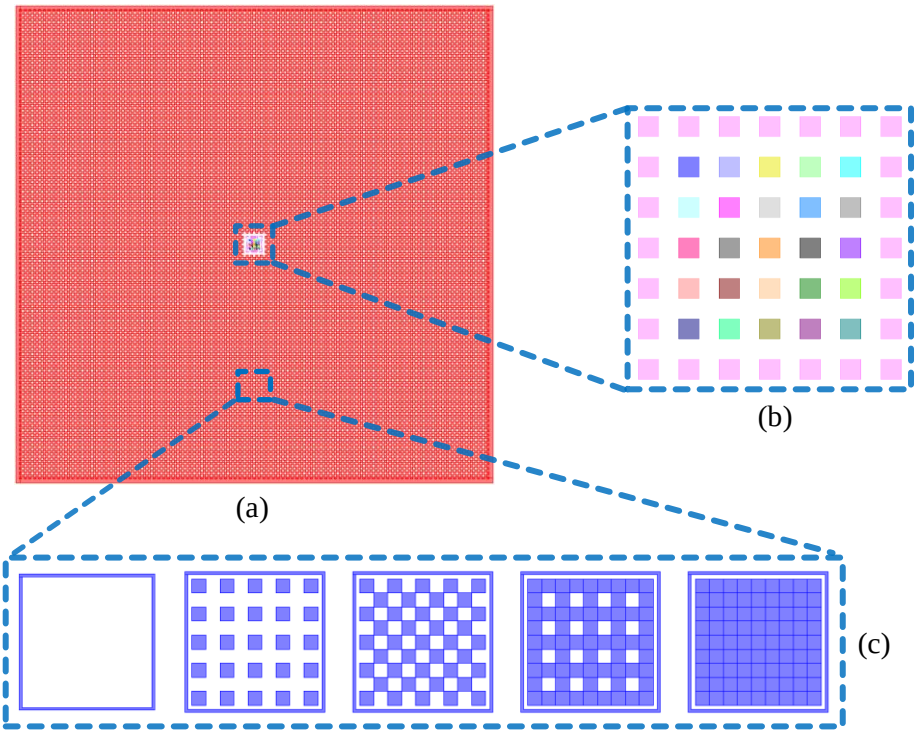

Figure 2. 2D calibration pattern (a) with 7x7 array of squares at the center (b) and different background densities in the surroundings (%0-%25-%50-%75-%100) (c).

Eco-friendly, bioinspired nanopattern for antifouling: Cicada wing-inspired nanostructures for marine applications

Zihao Zhao, Nan Liang, Tomohiro Shimizu, Shoso Shigubara, Takeshi Ito※

Graduate School of Science and Engineering, Kansai University, Suita-shi, Osaka, 564-8680, Japan
e-mail: t.ito@kansai-u.ac.jp

Biofouling challenges industries like marine coatings, biomedical devices, and water treatment, leading to efficiency loss and environmental concerns from toxic biocides. Researchers are developing non-toxic, durable fouling-release (FR) coatings, such as PDMS and fluoropolymers, which leverage low surface energy and elasticity for easy fouling removal. However, a universal antifouling solution remains challenging due to diverse environmental conditions and organisms [1]. *Chlorella vulgaris* (*C. vulgaris*) was chosen for a case study in this work due to its size (diameter of 2~10 μm), which aids in developing a broadly applicable antifouling strategy.

This study investigates an innovative surface engineering method to impart FR properties to mechanically rigid polymer surfaces. The experimental method combines nanoscale topography, surface energy modulation, and apparent elasticity reduction. Specifically, we aim to demonstrate that high-hardness polymer films can achieve FR properties. These properties, typically found in soft elastomers, are realized here through nanotechnology-enabled surface modification. In this study, we utilized anodic oxidation to fabricate manometer-scale porous surfaces on an aluminum sheet, which served as a mold to prepare resin nanostructures. Additionally, we employed thermal nanoimprint lithography (T-NIL) to replicate these structures onto cyclo olefin polymer (COP) surfaces, generating large-area nano-pillars inspired by cicada wing topography [2].

In this work, the heights of nanopillars were controlled from 200 nm to 350 nm, with a fixed diameter (100 nm) and pitch (center-to-center distance, 200 nm). The wettability measurement results indicated their superhydrophobicity, i.e., their achievement of the Cassie-Baxter state. Furthermore, only the dispersion component of surface energy (i.e., critical surface energy) of 27 mN/n was detected (Table 1), which achieved the FR of the Baier curve [3]. Additionally, previous studies [2][4] indicated that the nanopillar surface (NPS) decreased the surface elastic modulus (local elastic modulus). Our study reveals a fundamental paradigm shift in antifouling surface design: mechanical softness is not essential for effective FR. Instead, we demonstrate that NPSs decrease the apparent plane strain modulus, mimicking the compliance of soft elastomers while preserving the mechanical robustness of rigid substrates. Key findings include:

- Critical surface energy (20–30 mN/m) and incorporating micro/nanoscale roughness work together to enhance FR, diminish microbial adhesion, and enable biofilm detachment (Table 1).
- NPSs have much lower biofouling adhesion than unstructured ones, based on the PCRR, which shows the force needed for cell pull-out from various COP surfaces (Fig 1).
- COP films exhibit high hardness. Nanoscale topography induces localized deformation, altering surface adhesion mechanics, as shown in Fig 2.

Our findings show that topographical modifications alone can achieve and enhance biofouling resistance, eliminating the need for chemically active coatings or soft materials. They open doors for eco-friendly, robust antifouling solutions across the marine, biomedical, and industrial sectors. Our work challenges traditional antifouling methods and creates a durable, high-performance FR surface modification method. Combining advanced nanostructure fabrication with surface energy management offers a sustainable, non-toxic alternative for industries facing persistent biofouling issues.

[1] H. Qiu et al., Prog. Polym. Sci. 127 (2022) 101516.
[2] Z. Zhao et al., Environ. Sci. Nano 11 (2024) 4359-4371.
[3] R. E. Baier, J. Mater. Sci.: Mater. Med. 17 (2006) 1057-1062.
[4] Y. Matsushita et al., Colloids Surf. B Biointerfaces 250 (2025) 114560.

Table 1. Wettability of COP flat and NPSs [2]. WCA and DCA stand for water and diiodomethane contact angle, respectively. The letter h in sample names indicates pillar height.

Sample	Contact Angle (°)		Surface free energy (mN/m)					
			Owens-Wendt method			Kaelble-Uy method		
	WCA	DCA	d	h	total	d	p	total
Flat COP	96.4 ± 1.0	41.3 ± 0.7	39.1 ± 1.0	0.2 ± 0.1	39.3 ± 1.0	39.7 ± 0.5	0.2 ± 0.1	39.9 ± 0.5
COP h200	146.6 ± 1.3	18.0 ± 2.0	27.9 ± 1.0	0.0 ± 0.0	27.9 ± 1.0	28.2 ± 0.4	0.0 ± 0.0	28.2 ± 0.4
COP h250	152.8 ± 1.6	13.0 ± 3.0	27.2 ± 1.0	0.0 ± 0.0	27.2 ± 1.0	27.4 ± 0.4	0.0 ± 0.0	27.4 ± 0.4
COP h300	148.8 ± 6.1	12.6 ± 0.4	28.1 ± 1.7	0.0 ± 0.0	28.1 ± 1.7	28.3 ± 1.4	0.0 ± 0.0	28.3 ± 1.4
COP h350	154.0 ± 3.8	15.2 ± 2.2	26.7 ± 1.2	0.0 ± 0.0	26.7 ± 1.2	26.9 ± 0.8	0.0 ± 0.0	26.9 ± 0.8

※d: dispersive component
※h: hydrogen bonds component
※p: polar component

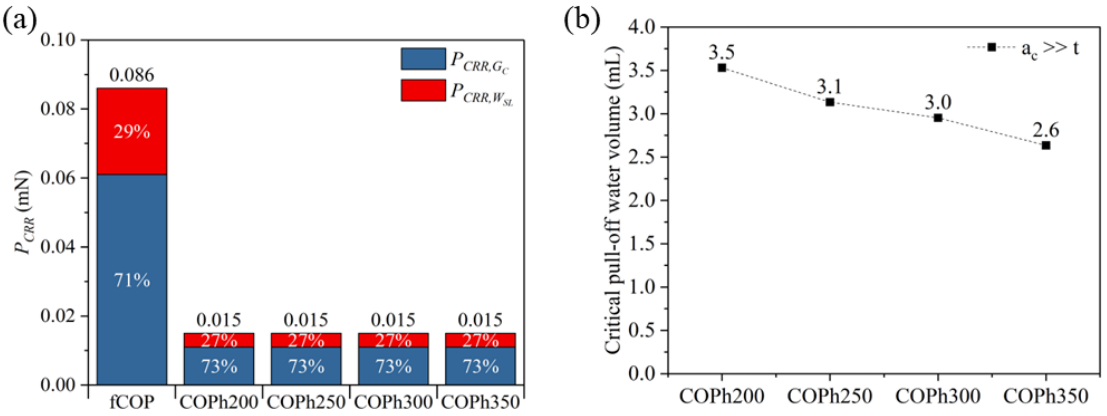

Figure 1. (a) Total critical release-resistance force (P_{CRR}) on different COP samples. (b) Critical pull-off volumes of water required in the fouling-release process on NPSs. G_C and W_{SL} stand for critical surface tension and work of adhesion, respectively. fCOP denotes the flat COP sample, and "h" refers to nanopillar height, e.g., COPh200 means 200 nm height of NPS.

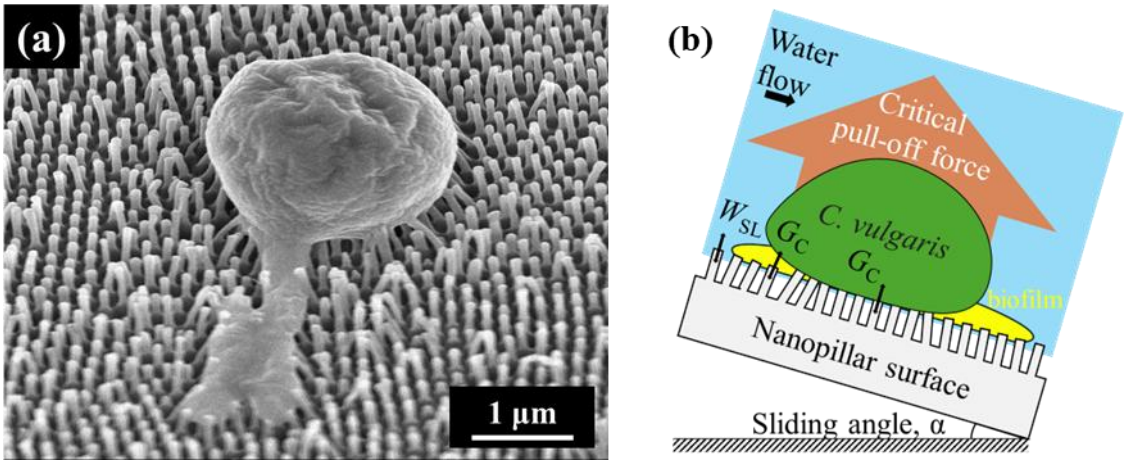

Figure 2. (a) SEM image of a *C. vulgaris* cell on the NPS (COPh350), and (b) Schematic of fouling-release process on NPS.

Electrochemical Investigation of $[Ru(bpy)_2(L)]^{2+}$ Complexes for Biosensor Applications: Insights into Rct Reduction Mechanism

Koki Yamashita, Tomohiro Shimizu, Shoso Shingubara, Hitoshi Ishida, Akinori Kuzuya, Takeshi Ito

Graduate School of Science and Engineering, Kansai University, Suita, Osaka, Japan

e-mail : t.ito@kansai-u.ac.jp

Abstract

$[Ru(bpy)_2dppz]^{2+}$ is well known as a DNA intercalator. Recently, it has been reported that Ru complex with redox mediator decrease the charge transfer resistance (R_{ct}) of electrochemical system. To discuss the impedance reductoin mechanism, we evaluated the R_{ct} depending on the concentration and the five types of Ru complex under the redox mediator $[Fe(CN)_6]^{3-/4-}$. The results showed that R_{ct} decreased with increasing Ru complex concentration, but the decrease rate is dependet with thier molecular structure.

Keywords—Ru complex; biosensors; electrochemical measurements

Introduction

Biosensors, which detect target biomolecules such as biomarker, are essential technologies to maintain a healthy lifestyle. In this study, we focus on an electrochemical impedance spectroscopy (EIS)-based biosensor, since this method is simple and rapid detection method with high sensitivity. In previous studies, electrochemical biosensors have used biomolecules immobilized on the electrode, but their preservation and durability remain challenges [1]–[3]. Nobusawa et al. developed a non-immobilization detection system to quantify PCR products using EIS with $[Fe(CN)_6]^{3-/4-}$ and the ruthenium (Ru) complex $[Ru(bpy)_2(dppz)]^{2+}$ as a DNA intercalator. [4]. The redox reaction of $[Fe(CN)_6]^{3-/4-}$ on the electrode surface generates charge transfer resistance (R_{ct}), which was significantly reduced upon addition of the Ru complex. However, the mechanism behind this R_{ct} reduction remains unclear. Therefore, we synthesized various $[Ru(bpy)_2(L)]^{2+}$ complexes (Fig. 1) and investigated their effect on R_{ct} to explore the cause of impedance decrease.

Experimental

We measured electrochemical behaviors using three electrodes system composed of Au working electrode (WE) with a diameter of 1.6 mm, Pt wire counter electrode (CE) and Ag/AgCl reference electrode (RE) using an electrochemical analyzer. After the WE was polished with alumina powder (0.05 μm diameter) for 5 min, it was ultrasonically cleaned with ethanol and pure water for 5 min in order. Then, the electrodes were set on an electrochemical cell (volume: 3 ml). The WE was electrochemically cleaned using cyclic voltammetry (CV) in a H_2SO_4 (0.5 M) solution with a sweep rate of 100 mV/s for 15 times from 0 to 1.6 V vs. RE. Next, we measured electrochemical impedance spectroscopy (EIS) of a measurement buffer with 1 mM of $[Fe(CN)_6]^{3-/4-}$ in the PCRi. Here, EIS was performed around the open potential until the Nyquist plots were stabilized. Five Ru complexes were dissolved into DMSO, and then they were added sequentially into the measurement buffer and the EIS measurements were repeated until stabilized with the same condition as above.

Results and Discussions

Example of the Nyquist plots dependent with the addition of $[Ru(bpy)_2(thdppz)]^{2+}$ was shown in Fig. 2. When the concentration of the Ru complex increased, the diameter of the semicircle, meaning R_{ct}, decreased drastically. After the similar measurements were performed for all complexes, we estimated the R_{ct} by fitting the Nyquist plots with the equivalent circuit model. Since the initial values of the R_{ct}, meaning the Ru complex concentration of 0 μM, were different for each, the rate of change in R_{ct} due to the addition of Ru complexes with regards to its initial value was plotted on Fig. 3. The results indicate that a structure with three interconnected benzene rings would be important for reducing the charge transfer resistance.

[1] M. Govindhan et al., Biosens. Bioelectron., 103 (2018) 113-129.
[2] Y. Cheng et al., Anal. Chim. Acta., 887 (2015) 17-37.
[3] J. Tiwari et al., ACS Nano, 10 (2016) 46-80.
[4] K. Nobusawa et al., Anal. Chem., 94 (2022) 7747-7751.

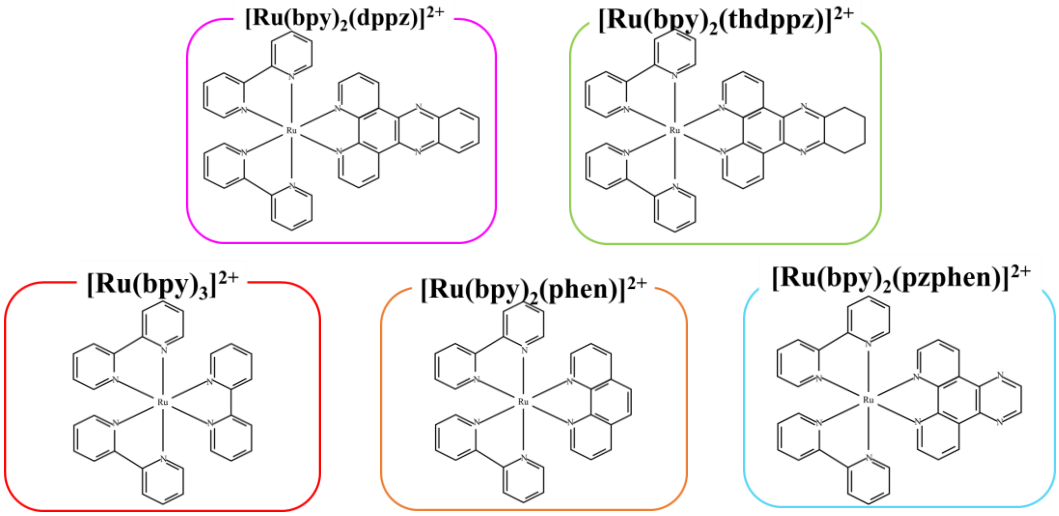

Figure 1. Schematic diagrams of the Ru complexes used.

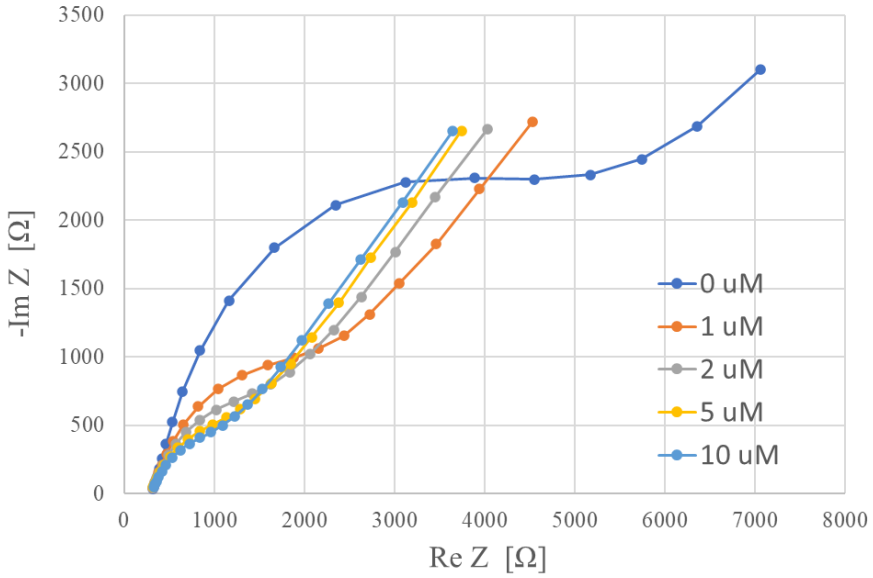

Figure 2. Nyquist plots dependent with the concentration of $[Ru(bpy)2(thdpz)]^{2+}$.

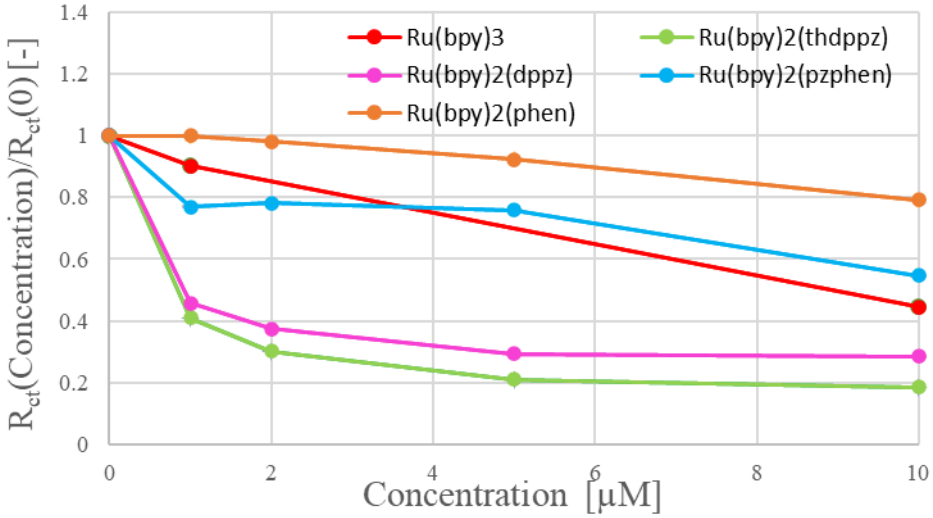

Figure 3. Rate of R_{ct} change with addition of Ru complexes.

Bactericidal property of COP nanopillars dependent with their size

Gakuto Inoue [a], Tomohiro Shimizu [a], Shoso Shingubara [a], Takeshi Ito [a] *

[a] Grad. School of Science and Eng., Kansai Univ., 3-3-35 Yamate-cho, Suita-shi, Osaka 564-8680 Japan
e-mail: k771151@kansai-u.ac.jp

Abstract Text
Bactericidal performance was investigated by varying the dimensions of polymer nanopillars, which mimic the nanostructure of cicada wing surfaces. The polymer nanopillars were fabricated using thermal nanoimprint lithography (NIL) with anodized aluminum oxide (AAO) as the template. Bactericidal activity was evaluated using LIVE/DEAD Cell Viability Assays. The results indicated that as the contact between bacteria and the pillars decreased, bactericidal activity increased.

1. Introduction.

Nano- and microscopic patterns found in nature exhibit a variety of beneficial functions. For example, the wings of cicadas and dragonflies are covered with nano-sized bumps, which contribute to their bactericidal and antimicrobial properties [1]. Physical antimicrobial properties represent a promising new tool to tackle against antimicrobial drug-resistant (AMR) bacteria. The number of deaths caused by AMR infections, as initially reported by O'Neill, was estimated to exceed 0.7 million [2]. Only four years after this report, the number had risen to 1.27 million. Therefore, new non-chemically driven antimicrobial technologies are needed. Nanostructures compose of silicon, titanium, and polymers have been reported to exhibit bactericidal effects [3]. More recently, there are increasing reports of nanostructures on polymer surfaces showing bactericidal effects [4]. Polymers have the advantage of being versatile because, unlike Si, they have excellent processability and are flexible. However, the dimensions of nanostructures exhibiting bactericidal properties have not been optimized. Therefore, this study focused on the contact area between bacteria and nanostructures by changing the pitch of the nanopillars. The aim of this study is to fabricate polymer nanopillars with varying dimensions, develop a simple model of bacteria and nanopillars, and clarify the characteristics of structures that exhibit a high bactericidal effect based on the contact area between bacteria and nanopillars.

2. Experiments.

The polymer nanopillars were fabricated using thermal nanoimprint lithography (NIL) with anodized aluminum oxide (AAO) as the template. AAO templates with regularly arranged nanoholes were prepared by a two-step anodic oxidation method. First, the Al plate surface was planarized by electropolishing. Next, anodic oxidation and wet etching were performed to obtain different parameters (pitch: 100–300 nm; depth: 100–300 nm; diameter: 50–200 nm). The hole spacing and depth of the nanoholes can be controlled by varying the electrolyte, the applied voltage and the time for anodic oxidation. Nanoholes were imprinted on polymer (cyclo-olefin polymer: COP) films using thermal nanoimprint lithography. Bactericidal performance of the fabricated polymer nanopillars were evaluated using LIVE/DEAD assay.

3. Results and discussion.

Fig. 1 shows SEM images of AAO templates with controlled hole spacing. Regularly arranged nanoholes with hole spacing of approximately 100 nm, 200 nm and 300 nm, respectively, were observed. Fig. 2 shows SEM images of polymer nanopillars transferred onto the COP film using AAO as the template. The dimensions of the polymer nanopillars closely match those of the AAO template, indicating that the template was transferred accurately. Fig. 3 shows simple models to calculate the contact rate of the pillars with a rod shape bacteria (0.5 μm × 2 μm). The results show that the lower the contact rate between the pillars and the bacteria, the higher the bactericidal effect.

[1] E.P. Ivanova et al., Small 8 (2012) 489-2494.
[2] C.J.L. Murray et al., LANCET 399 (2022) 629-655, 399.
[3] C.D. Bandara et al., ACS Appl. Mater. Interfaces 9 (2017) 6746-6760.
[4] Q. Cui et al., ACS Appl. Nano Mater. 3 (2020) 4599–4609.

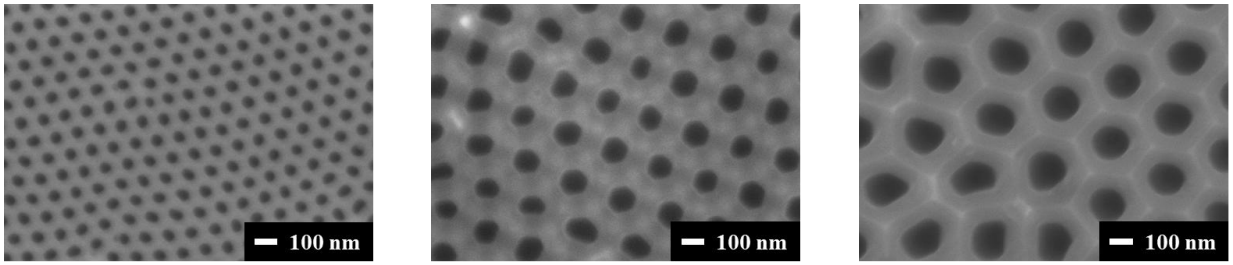

(a) Pitch 100 nm
Diameter 50 nm

(b) Pitch 200 nm
Diameter 100 nm

(c) Pitch 300 nm
Diameter 150 nm

Fig. 1 SEM images of the AAO templates

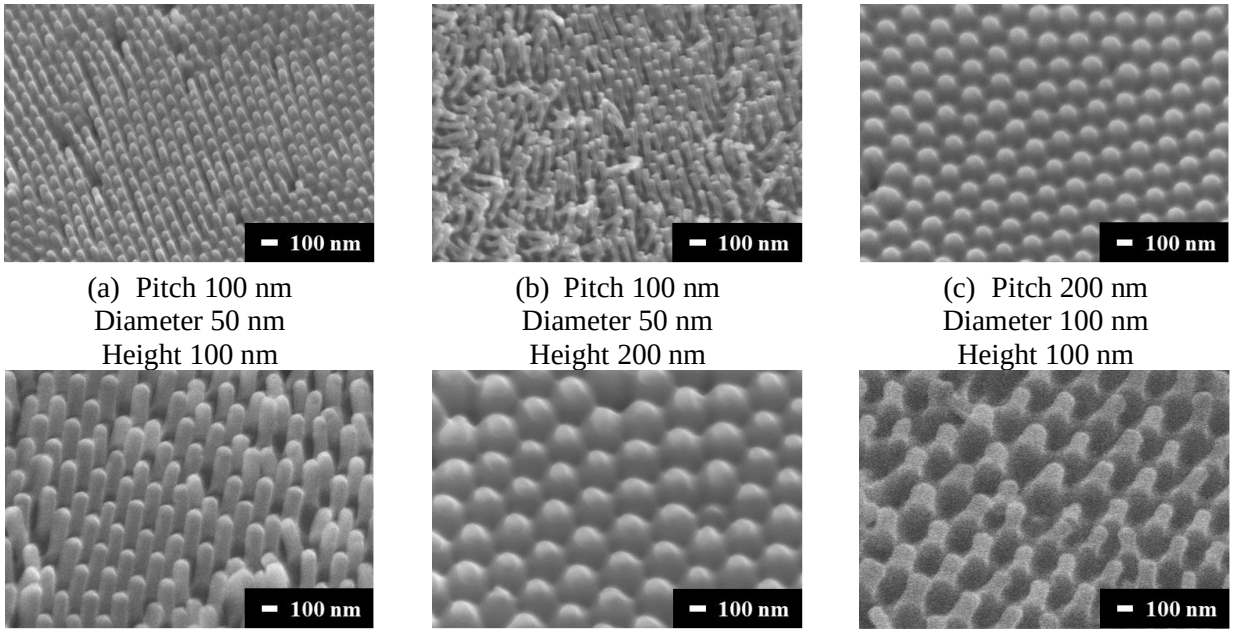

(a) Pitch 100 nm
Diameter 50 nm
Height 100 nm

(b) Pitch 100 nm
Diameter 50 nm
Height 200 nm

(c) Pitch 200 nm
Diameter 100 nm
Height 100 nm

(d) Pitch 200 nm
Diameter 100 nm
Height 300 nm

(e) Pitch 300 nm
Diameter 100 nm
Height 100 nm

(f) Pitch 300 nm
Diameter 100 nm
Height 300 nm

Fig.2 Bird's view SEM images of COP nanopillars

(a) Simple model of bacteria (green) and nanopillars (blue)
(Pitch 300 nm, Diameter 200 nm)

(b) Simple model of bacteria (green) and nanopillars (blue)
(Pitch 300 nm, Diameter 200 nm)

Fig.3 Sterilization effect of polymer nanopillars based on a simple model

Impact of microfabrication conditions on the oxygen depletion rate of thiol-enes

M. Haapala [a], P. Järvinen [a], I. Kiiski [a], T. Sikanen [a]

[a] Faculty of Pharmacy, Drug Research Program, University of Helsinki, Helsinki, 00790, Finland
e-mail: tiina.sikanen@helsinki.fi

Off-stoichiometric thiol-ene (OSTE) polymers have emerged as an appealing material for rapid prototyping of microfluidic devices owing to their tunable mechanical (bulk) properties and surface chemistry that enables further biofunctionalization reactions [1]. A particularly intriguing property of OSTE polymers is their intrinsic oxygen scavenging ability [2], which facilitates establishment of spatial and time-dependent oxygen gradients within OSTE microchannels [3]. Combining this ability with microfluidic cell cultures could enable recreation of physiological oxygen environment on chip, such as hypoxic conditions or oxygen gradients relevant for, e.g., tumor microenvironment or metabolic zonation of the liver, respectively.

The purpose of this study was to examine how microfabrication conditions, including OSTE bulk composition and different post-processing methods, influence the oxygen depletion rate by OSTE polymers. For this purpose, we fabricated 1.7-mm-thick OSTE plates (10×45 mm^2, w×L; Fig. 1A) via UV-replicamolding, by mixing PETMP (tetrathiol) and TATATO (triene) monomers in different stoichiometric ratios, casting this mixture on a PDMS mold, and UV curing from one side for 5 min (Dymax EC5000, 225 mW/cm^2). Where indicated, the OSTE plates were additionally post-processed by heat (100°C, 2 h) or UV (Dymax +5 min) from the opposite side, or by oxygen plasma (500 mTorr O_2, 30 W, 5 min) from both sides. Oxygen depletion rates were determined by immersing the OSTE plates in deionized water in air-tight containers equipped with ground glass joints and PreSens SP-PSt7-10-NAU sensors connected to EOM-O2-FDM meter (Fig. 1A).

Our results confirm that thiol-rich OSTE compositions have a long-lasting (at least ~96h) ability to scavenge dissolved oxygen with a highly repeatable depletion rate from plate-to-plate and batch-to-batch (Figure 1B). Addition of a photoinitiator (here, 0.1% TPO-L) to the monomer mixture did not significantly change the depletion rate (Fig 1B) but statistically significant differences were observed between the thiol-rich and stoichiometric and allyl-rich compositions (Fig. 2A). However, all compositions efficiently scavenged oxygen in closed containers, unless the bulk polymer was post-processed by heat. This yielded significantly lower oxygen depletion rates with no statistical difference between the different heat-treated compositions (Fig 2A).

Like many other polymers, native OSTE surfaces are not necessarily cell compatible. So far, conclusive results cannot be drawn based on the prevailing literature, but it has been shown that post-processing by plasma [4] or UV [5] can increase cell viability on OSTE microdevices. Our results also confirmed that heat treatment reduces the number of apoptotic cells on OSTE surfaces, yielding cell viability similar to that of commercial culture dishes (Fig. 2B). The cell viability was assessed using OSTE disks (Ø 35 mm) prepared by UV-replica molding similarly to the test plates and attached to culture dishes with 1% (m/v, aq.) agar. Among these post-processing options, UV treatment was shown to reduce the oxygen depletion rate significantly when compared with native untreated plates but less than heat treatment (Fig. 2C). Interestingly, plasma-treated OSTE plates exhibited similar oxygen depletion rate to that of native plates, suggesting that there could be a window of opportunity to fabricate cell-compatible OSTE surfaces while retaining the oxygen scavenging ability inherent to this polymer family.

Finally, the impact of interfacial processes on the oxygen depletion rate of OSTE microfluidic devices was assessed by infusing a 1 mg/mL solution (aq.) of commercial oxygen-sensitive nanoparticles (OXNANO, Pyro Science) through the micropillar chip at different flow rates and measuring the oxygen concentration at the chip outlet with a Piccolo2 oxygen meter (Fig. 3A). Comparison of the oxygen concentrations measured on chip with those predicted based on the oxygen depletion rates derived from the static assay setup revealed that interfacial mass transfer is likely to further enhance oxygen scavenging in flow-through conditions (Fig. 3B).

[1] D. Sticker et al., ACS Appl. Mater. Interfaces 12 (2020) 10080-10095.
[2] D. Sticker et al., ACS Appl. Mater. Interfaces 11 (2019) 9730-9739.
[3] I. Kiiski et al., Lab Chip 21 (2021) 1820-1831; Z. Yuan et al., Microfluid. Nanofluid. 26 (2022) 42.
[4] T.F. Chen et al., Mater. Sci. Eng. C 79 (2017) 613-621; K. Piironen et al., MicroTAS (2019) 316-317.

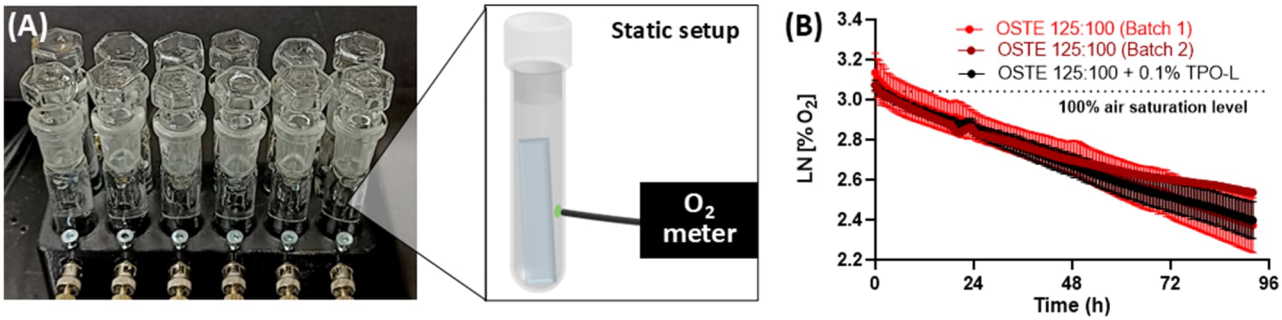

Figure 1. Determination of oxygen depletion rate in static conditions. (A) Photograph and schematic of the closed container setup. (B) Oxygen depletion rate of two thiol-rich (+25 mol-% over allyl) OSTE 125:100 batches (n=3 each) with and without photoinitiator (0.1% TPO-L).

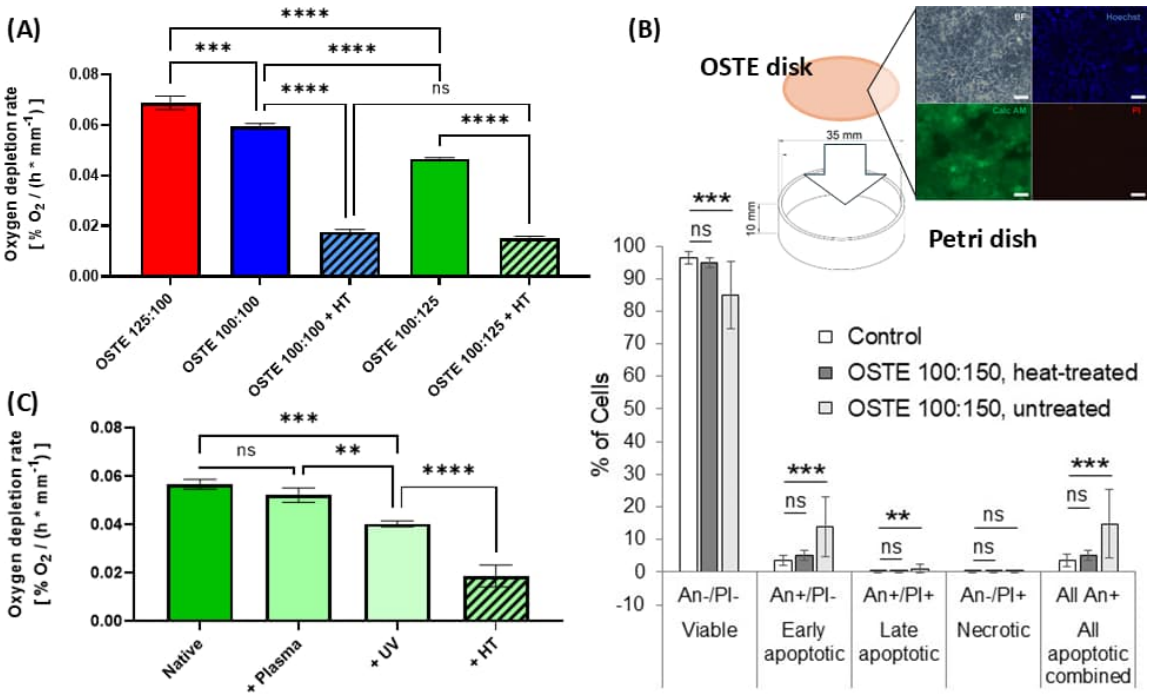

Figure 2. Impact of bulk composition and post-processing. (A) Oxygen depletion rates of OSTE plates prepared using different thiol:allyl ratios with and without heat treatment. (B) Huh7 cell viability on heat-treated and native (untreated) allyl-rich OSTE 100:150 surfaces, based on Annexin/propodium iodide (An/PI) staining. (C) Impact of post-processing methods on the oxygen depletion rate of OSTE allyl-rich OSTE 100:125 plates. The oxygen depletion rates in (A) and (C) are normalized to the OSTE surface-to-volume ratio (A/V 0.1 mm^{-1}) of the static assay setup.

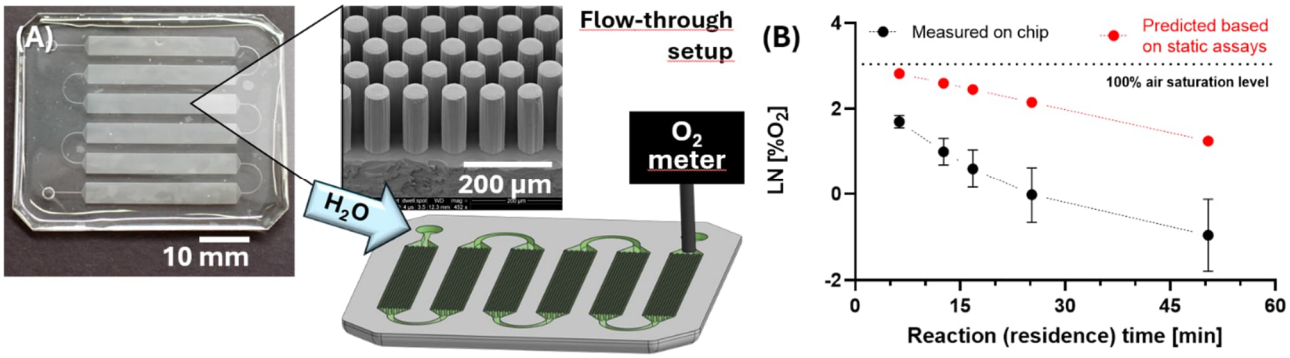

Figure 3. Determination of oxygen depletion rate in microfluidic conditions. (A) Photograph and schematic of the micropillar chip and the flow-through assay setup. (B) Measured oxygen concentration as a function of residence time (i.e., flow rate) at the outlet of a thiol-rich OSTE chip vs. predicted oxygen concentration calculated based on the depletion rate of OSTE 125:100 composition measured in static conditions (Fig. 2A), the reaction (residence time), and the surface-to-volume ratio (A/V 31 mm^{-1}) of the micropillar chip.

Microstructuring of 3D Printed Ceramic Surfaces using Nanoimprint Lithography

S. Kopp[a], A. Lale[b], V. Jonaityte[a], M. J. Haslinger[a], M. Bonora[c], M. Vostatek[c], S. Linnemeier[d], M. Granegger[d], F. Moscato[c,e,f], M. Schwentenwein[b], M. M. Mühlberger[a]

[a] PROFACTOR GmbH, Steyr, 4407, Austria
[b] Lithoz GmbH, Vienna, 1060, Austria
[c] Center for Medical Physics and Biomedical Engineering, Medical University of Vienna, 1090, Austria
[d] Department of Cardiac Surgery, Medical University of Vienna, Vienna, 1090, Austria
[e] Ludwig Boltzmann Institute for Cardiovascular Research, Vienna, 1090, Austria
[f] Austrian Cluster for Tissue Regeneration, Vienna, 1090, Austria
e-mail: michael.muehlberger@profactor.at

Ceramic 3D printing or Lithography-based Ceramic Manufacturing (LCM) [1] is able to produce a wide range of ceramic components for various applications ranging from medical to aerospace. LCM distinguishes itself from other additive manufacturing (AM) techniques for ceramics by the high resolution and the absolutely isotropic and homogeneous microstructure that can be obtained by this process. The materials that are used in the LCM process are UV-curable suspensions that can comprise different ceramic particles. To obtain a fully inorganic final ceramic object, the parts have to be debinded and sintered. Extremely high densities of up to up to 99.9% can be obtained in this way. We are interested in using a ceramic material for applications in life sciences. Although the surface quality meets or exceeds the requirement for most applications and surface roughness R_a of 0.4µm can be achieved in the final part [2], in certain cases it can be interesting to add well defined microstructures on the surface.

We use UV-based nanoimprinting to achieve this, because on the one hand the LCM process is also based on UV-curable materials and on the other hand nanoimprinting is capable of also patterning non-flat surfaces [3,4]. We use flexible polymeric stamps (MD700) to do the nanoimprinting. In our work we compare two different UV-curable ceramic suspensions normally used for LCM, which were modified for the nanoimprint process: LithaLox 350, which is an alumina suspension, and LithaCon ATZ980 [5], which results in alumina-toughened zirconia after sintering. The imprinting is performed on unsintered 3D printed substrates (so-called green parts), resulting in an additional microstructured layer on top of the substrate.

Figure 1 shows an alumina sample after sintering. The effect of grain growth can clearly be seen. There is a change in pattern shape due to the grain growth as well as additional surface roughness. It can however be noted that the roughness after sintering in the flat but imprinted areas is reduced as compared to the flat but just 3D-printed areas. The surface roughness in flat areas (as 3D-printed surface) is around R_a=377nm while in the areas where the surface has been modified by imprinting but without any additional microstructure (flat stamp, green areas) is R_a=279nm. For the ATZ the grain growth during sintering is significantly reduced, as can be seen in Figure 2, where an alumina sample (left) is compared to an ATZ sample (right). Figure 3 shows two ATZ samples, as-imprinted on the left side and after sintering on the right side; compare also Figure 1 left and Figure 3 right to see the dramatically improved pattern fidelity for the ATZ after sintering. We are now working on finding the resolution limit with these materials and will present additional results and discuss application scenarios.

The authors acknowledge funding from the OptiFlow3D project (FFG FO999891239).

[1] M. Schwentenwein, e.al., Advances in Science and Technology 88 (2014): 60–64.
[2] https://lithoz.com/en/materials/lithalox-350/
[3] M. Haslinger, et al., SPIE Proceedings Volume 11177 (EMLC 2019); 111770K (2019)
[4] A.R. Moharana, et al., Coatings. 10 (2020) 301.
[5] https://www.lithoz.com/en/materials/lithacon-atz-980/

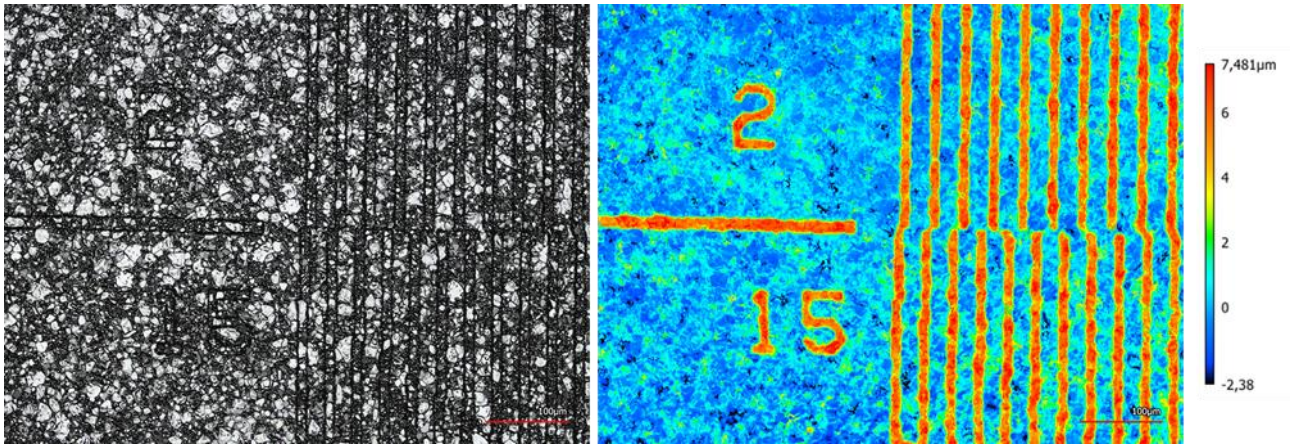

Figure 1. Laser scanning microscope images of micropatterned sintered alumina surfaces. Left: greyscale version highlighting the ceramic grains, right: false color image. Scale bars are 100µm.

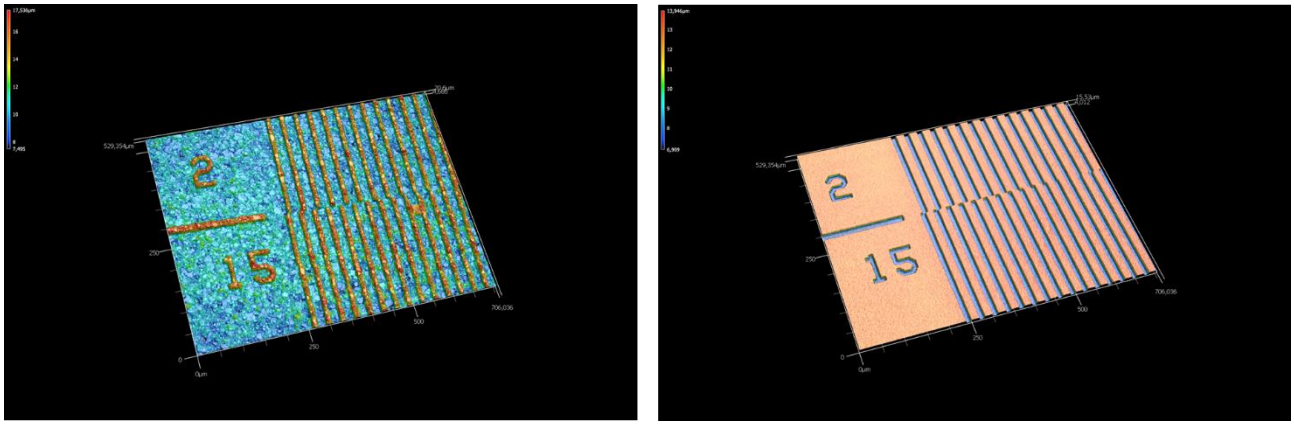

Figure 2. 3D plots of laser scanning microscope images of two different ceramic surfaces. Left: alumina, with significant grain growth visible, right alumina toughened zirconia (ATZ), with no microscopic grain growth.

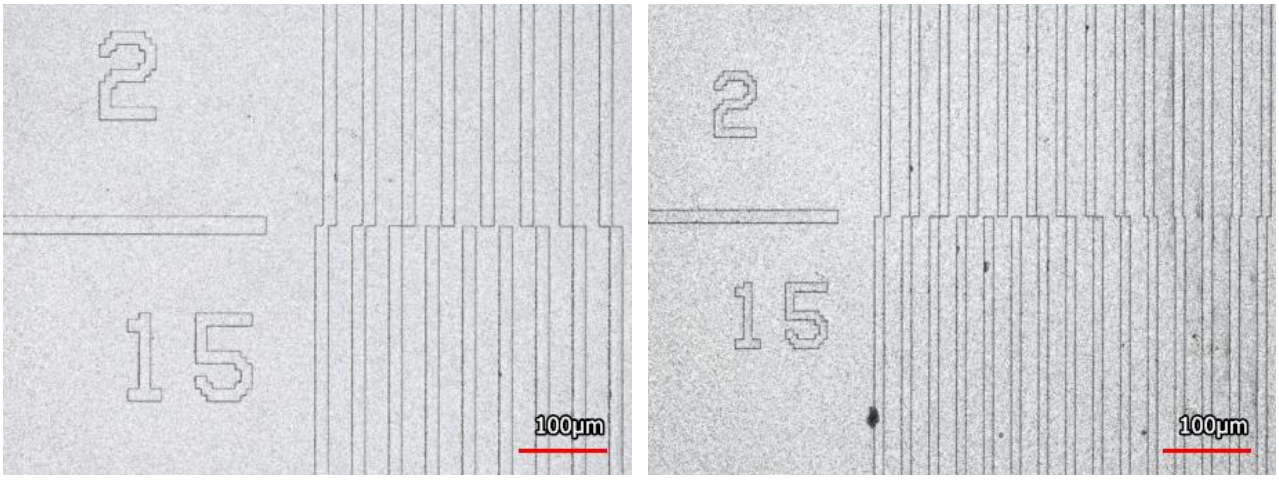

Figure 3. images of ATZ samples: left as imprinted , right: after sintering. The scale bars are 100µm in each image, the field of view is the same for both images. The shrinkage that occurs during sintering can be well seen.

Post-etch Surface Modification for Sidewall Smoothing in Deep Reactive Ion Etched Silicon

Arjun Moothedath and Zhong Ren

Oxford Instruments Plasma Technology, Severn Beach, Bristol BS35 4GG United Kingdom
e-mails: Arjun.moothedath@oxinst.com; Zhong.ren@oxinst.com

Key words: Deep reactive ion etching, Scallop smoothing, Time-multiplexed process.

Among dry etching techniques, deep reactive ion etching (DRIE) is the most widely used process for creating deep trenches and holes, particularly in applications like micro-electromechanical systems (MEMS) micromachining and through silicon vias (TSVs) [1]. DRIE operates through a pulsed, time-multiplexed etching method known as the Bosch process [2], which alternates between etching and passivation steps to achieve vertical trench profiles [3]. However, due to the cyclic nature of these etch and deposition steps, the technique inherently results in scalloped sidewalls, which can negatively impact device performance. For instance, the rough silicon sidewalls can introduce interface charges and undesired capacitance, thereby degrading the efficiency of silicon diodes [4]. Additionally, in superconducting TSVs, higher microwave losses and reduced superconducting film quality can be caused by sidewall roughness [5], where they are used for interconnection in quantum applications. Recently, the Bosch-based advanced DRIE tools have significantly improved control over sidewall roughness by adjusting the process parameters [6][7]. Nevertheless, these methods decreased the etching rate and selectivity [8].

This study introduces an effective scallop smoothing technique using fluorine chemistry, conducted entirely on a DRIE tool (Oxford Instruments, Estrelas). The experiments were carried out on 150 mm silicon wafers patterned with 20 µm square holes and coated with a 10 µm thick photoresist mask. Initially, the wafers were etched using a time-multiplexed Bosch process employing C_4F_8-SF_6 gases. The system's rapid radio frequency (RF) matching units (<10 millisecond response time) along with digital mass flow controllers (<100 millisecond switching time) facilitated precise control over process parameters. Prior to applying the scallop smoothing process, the remaining mask and polymer residue formed during the deposition steps of Bosch process were removed via an O_2 plasma ashing treatment. Figure 1.a illustrates the overall cross-section of the etched hole following ashing. All processing steps were conducted within the same system with necessary procedures.

The etched feature exhibited an aspect ratio of approximately 10:1. After the ashing process, scallop depths measured at three distinct sections of the holes are shown in Figure 2. To achieve smoother sidewalls, the ashed wafer was treated with CF_4/O_2 plasma with a gas ratio of 1:4 for a duration of 20 minutes at room temperature. The plasma was primarily powered by an inductively coupled plasma source with low bias RF power to enhance the isotropic etching of silicon while minimizing ion bombardment. The fluorine radicals react with the silicon surface to form SiF_x (where $x \leq 3$) [9]. Some byproducts are combined with O_2 forming SiO_xF_y layer over the silicon surface. An increased oxygen concentration in the plasma controls the silicon etch rate and facilitates the formation of activated SiO_xF_y layer within the scallops. Hence, sharp peaks of the scallops will be etched more rapidly than their valley regions. This step effectively eliminated all scallops at the top and reduced their depth to 26 nm in the middle and 14 nm at the bottom as depicted in Figure 3. This significant reduction in the scallop size is illustrated in Figure 1.b. The process slightly enlarged hole dimensions by an additional 400 nm and further etched to several microns' depth. This technique has been successfully employed to fabricate the high-quality niobium nitride superconducting TSVs and obtained a transition temperature (T_c) of 10.7 K [10]. These TSVs with elevated T_c values find applications across various superconducting domains, including millikelvin temperature scenarios such as qubit shielding and signaling in superconducting qubit computing, as well as superconducting nanowire single photon detector, quantum transduction, single flux quantum logic circuits and other applications operating at temperatures ranging from 4 K to 10 K.

[1] Wu, Banqiu, Ajay Kumar, and Sharma Pamarthy. "High aspect ratio silicon etch: A review." *Journal of applied physics* 108.5 (2010).
[2] Parasuraman, Jayalakshmi, et al. "Deep reactive ion etching of sub-micrometer trenches with ultra high aspect ratio." *Microelectronic engineering* 113 (2014): 35-39.
[3] Huff, Michael. "Recent advances in reactive ion etching and applications of high-aspect-ratio microfabrication." *Micromachines* 12.8 (2021): 991.
[4] Voss, Lars F., et al. "Smooth Bosch etch for improved Si diodes." *IEEE electron device letters* 34.10 (2013): 1226-1228.
[5] Grigoras, Kestutis, et al. "Qubit-compatible substrates with superconducting through-silicon vias." *IEEE Transactions on Quantum Engineering* 3 (2022): 1-10.
[6] Richter, Karola, André Mocker, and Johann-Wolfgang B. "High quality semicontinuous deep reactive ion etching of silicon for the creation of x-ray lenses." *Journal of Vacuum Science & Technology B* 35.3 (2017).
[7] Moothedath, Arjun, and Zhong Ren. "Enhanced plasma etching using nonlinear parameter evolution." *Micro and Nano Engineering* 25 (2024): 100288.
[8] Hsin, Yu-Chen, et al. "Effects of etch rate on scallop of through-silicon vias (TSVs) in 200mm and 300mm wafers." *2011 IEEE 61st Electronic Components and Technology Conference (ECTC)*. IEEE, 2011.
[9] Knizikevičius, R. "Real dimensional simulation of silicon etching in CF4+O2 plasma." *Applied surface science* 201.1-4 (2002): 96-108.
[10] Ren, Zhong, et al. "Plasma Processes for Vertical Niobium Nitride Superconducting Through Silicon Vias." *IEEE Electron Device Letters* (2025): 175-178.

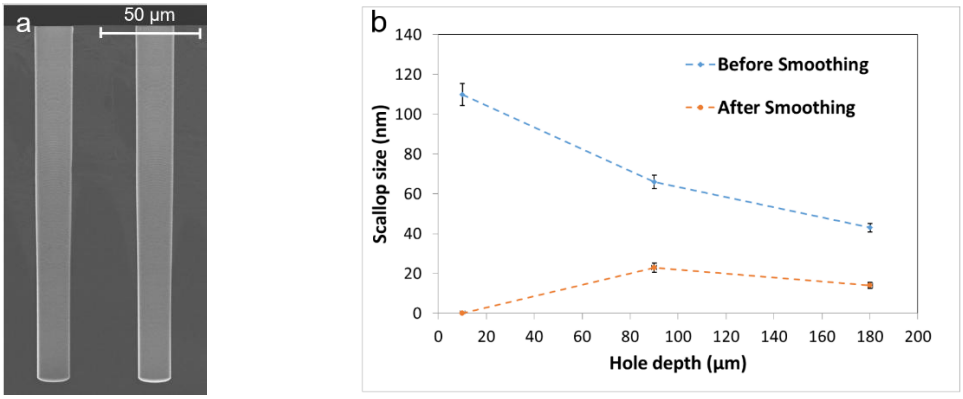

Figure 1. (a) Cross-section of etched holes; (b) Graph illustrating reduction in scallop size after smoothing with respect to etching depth

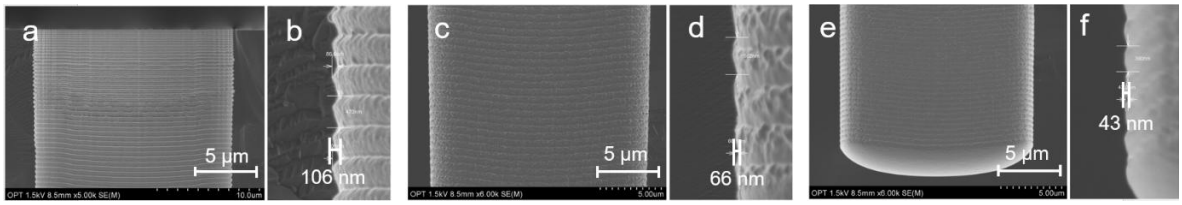

Figure 2. Holes without plasma smoothing: (a) SEM images showed cross-section at the top; (b) showed the sidewall roughness with scallops measuring 106 nm at the top; (c) SEM images showed cross-section at the middle; (d) showed the sidewall roughness with scallops measuring 66 nm at the middle; (e) SEM images showed cross-section at the bottom; (f) showed the sidewall roughness with scallops measuring 43 nm at the bottom

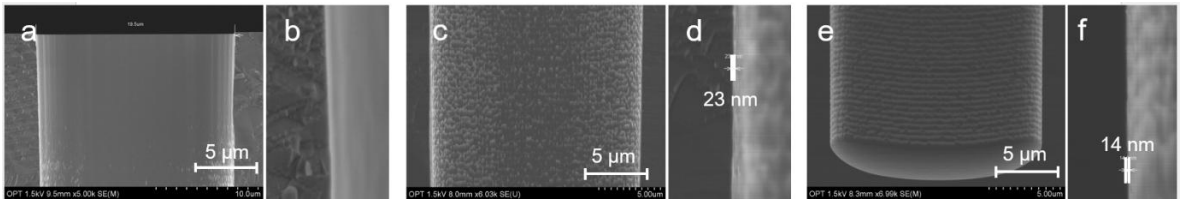

Figure 3. Holes after smoothing: (a) SEM images showed cross-section at the top; (b) showed the scallop-free sidewall at the top; (c) SEM images showed cross-section at the middle; (d) showed the sidewall roughness measuring 23 nm at the middle; (e) SEM images showed cross-section at the bottom; (f) showed the sidewall roughness measuring 14 nm at the bottom

Fabrication of fine metal patterns using solvent-soluble UV-curable resin

Satoshi Fujieda[1*], Takeshi Osaki[2], Yukio Okado[2], Jun Taniguchi[1]

[1]Department of Applied Electronics, Tokyo University of Science, Tokyo, 125-8585, Japan
[2]Toyo Gosei Co., Ltd., Photosensitive Materials Research Center,
4-2-1 Wakahagi, Inzai-shi, Chiba, 270-1609, Japan
*e-mail: 8125532@ed.tus.ac.jp

1. Introduction

Nanoimprinting is a technique used in the process of transferring a nanometer-sized pattern onto a resin between the mold and the substrate. This technique was first proposed by Chou et al. in 1995. It is low-cost and yet has a sufficiently high throughput [1]. There are also methods of fabricating metal patterns. For example, metal patterns are fabricated by etching and lift-off process. Etching is a processing technique that selectively removes material from the substrate surface according to a pre-formed pattern. This is an important technology as a means of miniaturizing and increasing the integration of semiconductor devices [2]. Lift-off, on the other hand, involves depositing a film of material on a pre-formed pattern and peeling off the unwanted portions with resist. This is a technique to obtain a desired pattern. Especially in the case of the etching process, the substrate is damaged, and the cost is high. The lift-off process, however, causes less damage to the substrate and is less expensive, resulting in higher productivity. Therefore, in this study, we fabricated fine metal patterns by the lift-off process using PAK-YY01(Toyo Gosei, Co., Ltd), which is solvent-soluble UV-curable resin.

2. Experiment

Figure 1 shows the process of applying HSQ (Hydrogen Silsesquixane) resist on a quartz substrate to create a pillar-shaped mold. First, HSQ resist was applied on the quartz substrate. Next, after an initial rotation of 300 rpm for 3 seconds, spin coating was performed at this rotation of 3000 rpm for 2 minutes. Baking was performed on a hot plate at 120℃ for 2 minutes. After the ESPACER 300Z (Showa Denko Inc.) was applied, it was spin coated at 3000 rpm 5 minutes. Electron beam lithography (EBL, ELS-7500M, ELIONIX Inc.) was performed the acceleration voltage of 50 kV, the current value of 10 pA, and dose of 200 μC/cm^2. Subsequently, the ESPACER was then removed with a pure water solution and developed with TMAH (Tetramethylammonium Hydroxide) for 1 minute. Next, mold release treatment was performed. Finally, it was soaked in 1% release coating agent (Optool DSX, Daikin Co. Ltd.) 3 hours of liquid phase treatment was performed, after 5 minutes bake treatment at 120℃ on a hot plate, the mold was rinsed with fluorosurf for 1 minute. **Figure 2** shows the lift-off process, in which PAK-YY01 was dropped into the fabricated mold, transferred to the silicon substrate, and platinum (Pt) was deposited. First, PAK-YY01 was dropped onto the fabrication mold. Next, the transfer was performed to the silicon substrate. At this time, the irradiance was 50 mW/cm^2, the irradiation time was 10 seconds, and pressure of 100 Pa was applied. After that, the substrate was immersed in a solvent prepared at a ratio of water: PGME = 1: 4 for 5 minutes to remove a residual layer. Then, Pt was deposited on it. After that, this sample was immersed in acetone for 15 minutes, then this sample was dried on a hot plate at 40℃ for 15 minutes. Finally, this sample was immersed in ZED-N50 solution for 5 minutes to dissolve PAK-YY01 and then obtained metal patterns.

3. Result

First, before and after soaking for 5 minutes at a ratio of water: PGME = 1: 4 is shown in (**Figure3**(a), (b)) and (**Figure3**(c), (d)). This process was performed to remove the residual layer that remains after the PAK-YY01 resin was transferred to the silicon substrate. Comparing **Figure 3**(a) and (c), a slight deformation in the hole shape was observed. This indicates that it was dissolved. Furthermore, it was also confirmed that the remaining film was also removed. **Figure 4** shows the appearance after lift-off of a pillar-shaped pattern with a diameter of 150 nm and a pitch of 500 nm and a diameter of 50 nm and a pitch of 100 nm. From the point of **Fig. 4**, the lift-off process was able to fabricate a pillar-shaped pattern in metal. In **Figure 4**(a) and (b), metal deposition was performed for 15 minutes. In **Figure 4**(c) and (d), metal deposition was performed for 30 minutes. This also shows that the height of the metal pattern can be easily selected by simply changing the time of metal deposition when the desired height of the metal pattern is to be obtained.

4. Conclusion

By using PAK-YY01, a solvent-soluble UV-curable resin, and UV-NIL, fabrication of metal nano patterns by lift-off is possible. The merit of this process is removal of residual layer and cured UV-curable resin can be removed by only solvent immersion.

[1] Nobuji Sakai, *J. Photopol. Sci. Technol.*, Volume22, Number2 (2009)
[2] Kazuo Nojiri, *Springer*, Number2014949262

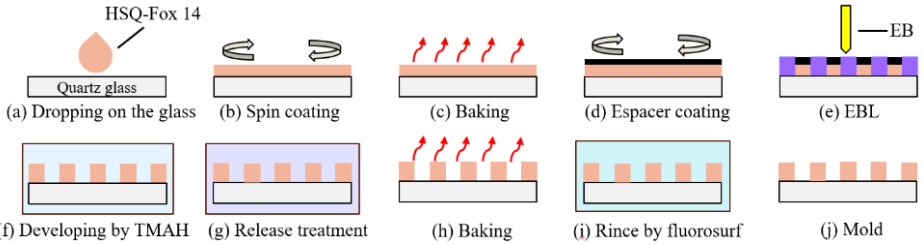

Fig 1. The process of applying HSQ resist on a quartz substrate to create pillar-shaped mold

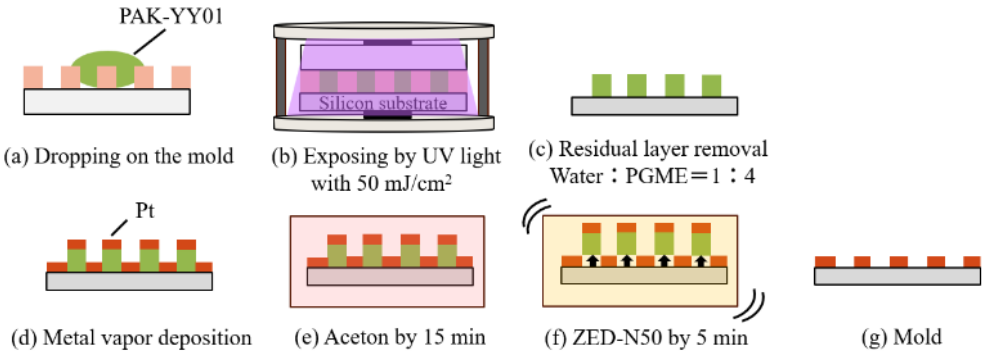

Fig 2. PAK-YY01 was dropped into the fabricated mold, transferred to the silicon substrate, and showed the lift-off process

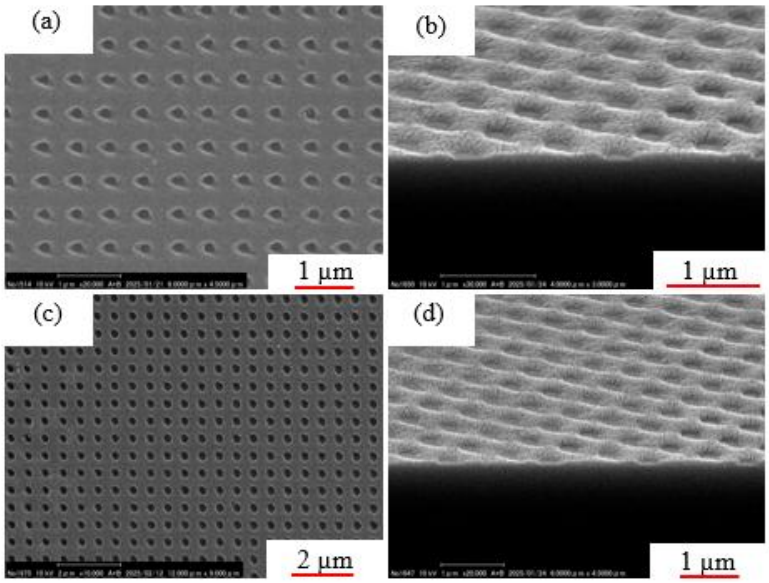

Fig 3. (a) Top view by SEM after transfer to silicon substrate. (b) Top view by SEM from an angle (c) Top view by SEM after immersion in water : PGME = 1 : 4 ratio for 5 minutes. (d) Top view by SEM from an angle under the same conditions.

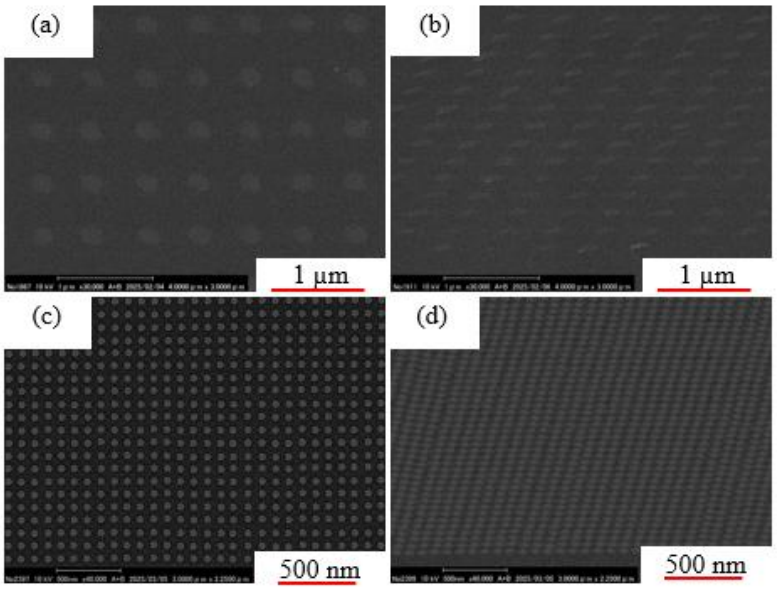

Fig 4. (a) Pattern with a diameter of 150 nm and a pitch of 500 nm, observed from the top surface by SEM after lift-off. (b) Observed from an angle by SEM. (c) Pattern with a diameter of 50 nm and a pitch of 100 nm, observed from the top surface by SEM after lift-off. (d) Same conditions, observed from an angle by SEM, observed from an oblique angle.

Effect of Polyethylene Glycol on growth of Porous Silicon

Xuming Zhao [a], Okawa Tomoya [a], Chenxin Zhong [a], Koji Akiyama [b], Takeya Inoue [b], Takeshi Ito [a], Shoso Shingubara [a], Tomohiro Shimizu [a]

[a] Kansai Univ. Suita-shi,564-8680, Osaka, Japan
[b] Tokyo Electron Ltd. Akasaka Biz Tower,5-3-1 Akasaka, Minato-ku, Tokyo, Japan
Email:shimi@kansai-u.ac.jp

1. Introduction

Through-silicon via (TSV) technology plays a critical role in integrated circuit (IC) packaging by enabling vertical interconnects essential for three-dimensional system integration. Anodized porous silicon (PSi) exhibits a high specific surface area and controllable pore morphology. The vertically aligned pores of PSi, featuring tunable aspect ratios and compatibility with low-cost electrochemical processing, provide a viable approach for TSV fabrication [1-2]. The work of Nenzi et al. has explored the use of electrochemically etched porous silicon in TSV-related processes and demonstrated the potential for forming ordered vertical pore arrays under controlled conditions [1]. However, achieving precise control of pore morphology to satisfy the structural and integration requirements of TSV remains a major technical hurdle.
This study introduces polyethylene glycol (PEG), a common wet etching additive, into the anodization process in an attempt to reduce sidewall roughness in high aspect ratio porous silicon structures. Compared to conventional additives such as DMF and ethanol [1–5], PEG shows a distinct effect on pore morphology, leading to improved sidewall smoothness under certain conditions and suggesting potential benefits for preparation of straight and vertical Si pore for TSV application.

2.Experimental Methods

Porous silicon (PSi) was fabricated by electrochemical anodization of p-type silicon in an HF-based electrolyte, using polyethylene glycol (PEG), dimethylformamide (DMF), and a PEG-DMF mixture as additives. Prior to anodization, the silicon substrates were sequentially cleaned by immersion in acetone and ethanol with ultrasonic agitation to remove organic contaminants. After rinsing with deionized water, the substrates were immersed in the 1 % HF solution for 10 minutes to remove the native silicon oxide layer. After the final rinse and drying, a layer of Ga-In alloy was applied to the backside of each substrate to ensure reliable electrical contact with the copper support plate. Anodization was carried out for 30 minutes at constant voltages ranging from 1 to 3 V with three-electrode electrochemical cell. A platinum plate was used as the counter electrode, and an Ag/AgCl electrode served as the reference to ensure accurate monitoring of potential and current during the process. The effects of PEG, DMF, and their combination on pore formation were investigated under different voltages and compared based on current-time characteristics, cyclic voltammetry (CV), and scanning electron microscopy (SEM) analysis of pore morphology.

3.Results and Discussion

Fig.1 and fig.2 show cross-sectional SEM images of PSi samples prepared by anodization at a constant voltage of 3V with different additive. The vertical micron-size Si pore structure was observed in both samples. The diameter and depth of Si pores were 3~5 and 120~150 μm for DMF, 3~5 and 120~130 μm for DMF-PEG. Compared to DMF, DMF-PEG, improvement of pore morphology was observed for DMF-PEG sample, resulting in smoother sidewalls and enhanced verticality. This suggests that PEG may modify electrolyte properties, potentially effect pore formation dynamics during anodization. Additionally, the PEG-

DMF mixture further suppressed growth of pore, indicating its potential for pore depth control. These results highlight PEG's effectiveness in forming uniform, high aspect ratio porous silicon.

[1] P. Nenzi et al. Proc. Electronic Components and Technology Conference (ECTC) (2013) 2201-2207.
[2] T. Urata et al. ECS J. Solid State Sci. Technol. 5 (2016) 250-255.
[3] J.-C. Lin et al. Electrochem. Soc. 155 (2008) D436–D442.
[4] F. Ronkel et al. J. Porous Mater. 7, 11–16 (2000).
[5] K. Uehira et al., Chem. Lett. 45, 1171–1173 (2016).

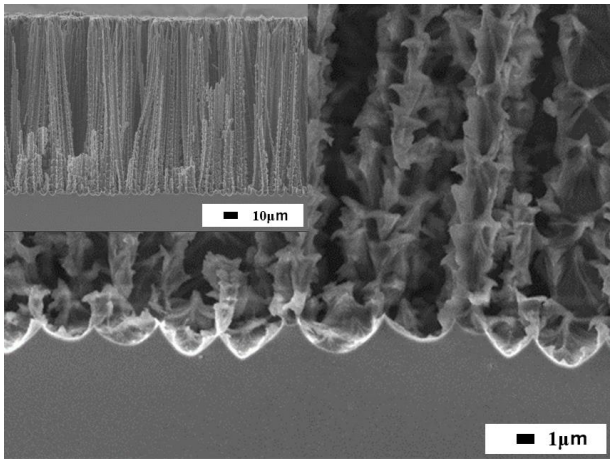

Fig.1 Cross-sectional SEM images of PSi samples prepared by anodization at a constant voltage of 3V under DMF-based electrolyte

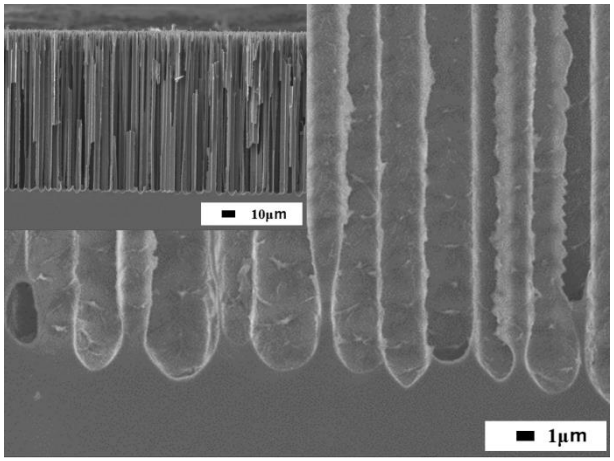

Fig.2 Cross-sectional SEM images of PSi samples prepared by anodization at a constant voltage of 3V under DMF-PEG mixed electrolyte.

Study of blob defectivity for different 248nm resist processes: influence of material chemistry, pattern types, bake and development conditions.

Authors : Lucie Borget, Romane Français, Loic Balme, Yohann Lebel, Olivier Mermet, Benedicte Mortini

Blob defects, also called satellite defects, are micron-size, disc-shaped residues with a thickness of a few nanometers, as illustrated in Figure 1 [1,2]. They are described in the literature as partially soluble polymers/ photoresist aggregates that adhere to the wafer at the end of the lithographic process, during the wafer drying step [3].

Although they are generally not considered a killer defect, their presence in high quantities degrades the accuracy of in-line defectivity controls to the extent that –in the worst cases – the control can become totally ineffective.

In this work, we evaluate several different formulations of 248nm resists for implant levels under conditions that were initially known to be especially prone to generating blob defects. Indeed, we observe that this defectivity mode is strongly dependent on layer design such as mask transmission rate and the amount of photoresist that must be dissolved by the developer solution. For our most blob-sensitive lithographic levels, our first finding was that blob defects are present regardless of the resist formulation. Therefore, process tunings have been investigated to decrease the density of blob defects. We will present results obtained by varying the bake conditions, especially Post Exposure Bake, as well as development and rinse sequences.

After conducting bake experiments, although we were able to correlate a relationship between blob reduction and completion of the deprotection reaction measured by thermogravimetry analysis, we pointed out a trade-off between the formation of blob defects due to partially deprotected polymer chains and the ultimate lithographic performance of the photoresist (resolution, resist profiles, process window). To overcome this limitation, we focused on optimizing the development and rinse steps. As a result, we achieved a significant reduction in defect density from about 3 defect/cm^2 to 0.02 defect/cm^2, down to a level that allows accurate post-lithography inline defectivity monitoring (cf Figure 2).

[1] J. Erhardt, K. Phan and J. Cheng, "An investigation of circular resist residue defects in the development of a flash memory process flow," 2001 IEEE/SEMI Advanced Semiconductor Manufacturing Conference (IEEE Cat. No.01CH37160), Munich, Germany, 2001, pp. 231-236, doi: 10.1109/ASMC.2001.925651

[2] Chih-Chieh Yu, Mars Yang, Elvis Yang, T. H. Yang, K. C. Chen, Chih-Yuan Lu, “Pattern dependent satellite defects in via lithography”, Proceedings Volume 8325, Advances in Resist Materials and Processing Technology XXIX; 83252K (2012) https://doi.org/10.1117/12.915572

[3] Yuko Ono, Takeshi Shimoaoki, Ryoichiro Naito, Junichi Kitano, “Behavior of chemically amplified resist defects in TMAH solution: III”, Proceedings Volume 5376, Advances in Resist Technology and Processing XXI; (2004) https://doi.org/10.1117/12.534982

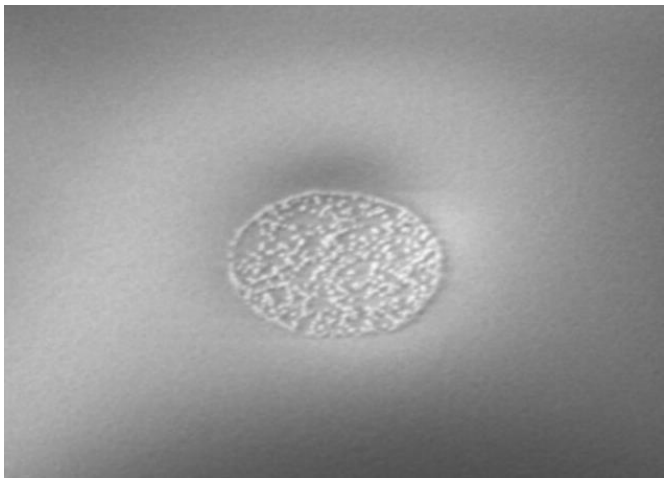

Figure 1 : Blob defect onto the remaining resist film (Resist C).
Diameter of the defect is few microns.

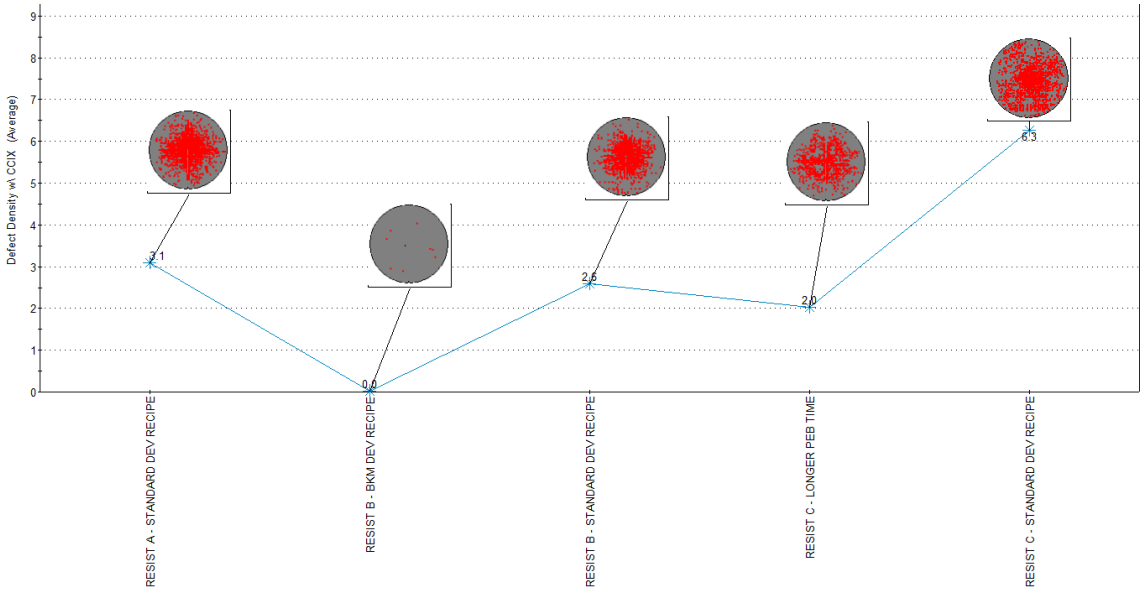

Figure 2 : Blob defect density as a function of the resist formulation, the bake process or the development recipe.

Development of Microfluidic Flow Cells with Integrated Arrays of Freestanding Al_2O_3 Membranes for SEM Imaging

Jeremy Teuber[a], Tim Erichlandwehr[b], Rukan Nasri[b], Irene Fernandez-Cuesta[b]

[a] Max-Planck-Institute for the Structure and Dynamics of Matter, 22761, Hamburg, Germany
[b] Institut für Nanostruktur- und Festkörperphysik, Universität Hamburg, 20146 Hamburg, Germany

E-Mail: jeremy.teuber@uni-hamburg.de

Scanning electron microscopy (SEM) enables high-resolution imaging of nanoscale structures and can be extended to study dynamic processes in liquid environments using integrated microfluidics [1]. However, many existing systems are limited in geometry, lack flexible membrane integration, and are costly to fabricate.

We present a fabrication strategy for microfluidic devices with integrated, freestanding Al_2O_3 membranes that are transparent to electrons. A central feature of our approach is the ability to selectively open these windows within sealed channels, resulting in freestanding, well-defined structures. Their shape, size, and placement can be precisely tailored, offering high flexibility in design. The resulting devices function as compact SEM-compatible flow cells, combining electron transparency with passive flow-based particle delivery.

The fluidic devices were fabricated via direct UV nanoimprint (NIL) [2]. A master stamp was first defined on a silicon wafer using photolithography and reactive ion etching (RIE), and replicated into a flexible PDMS stamp. This stamp was used to imprint microchannel structures into a UV-curable polymer (OrmoStamp from micro resist technology GmbH) coated on a polycarbonate (PC) substrate (Fig. 1a). The channel system was then enclosed with a multilayer polymer coverslip (Fig. 1(b)). To render the microchannels electron-transparent, a conformal Al_2O_3 layer was deposited on the inner surfaces via flow-through gas-phase deposition (GPD) using a custom-built system (Fig. 1(c)) [3]. The film thickness could be controlled by adjusting the precursor flow and the deposition time. Subsequently, a 100 nm copper layer was sputtered onto the coverslip (Fig. 1(d)), followed by spin-coating and patterning of a photoresist (S1813) using a photomask and mask aligner. After development, copper was selectively etched with $Fe(NO_3)_3$ to define window regions. Reactive ion etching (RIE) was then used to remove the underlying coverslip material and expose the Al_2O_3 membrane windows (Fig. 1(e)). In the final step, residual photoresist and copper were removed by oxygen plasma and wet etching, respectively (Fig. 1(f)).

As illustrated in Fig. 2(a), microchannels connect the inlet and outlet, with dimensions of 10 µm in width and 1 µm in height. A photomask containing 10 µm-wide rectangular features was used to pattern the coverslip, creating 10 µm × 10 µm openings at the intersections with the underlying microchannels (highlighted in purple in Fig. 2(b,c)). This approach enables the simultaneous fabrication of up to 200 electron-transparent windows, as shown in Fig. 2(b). A magnified view of an individual window is presented in Fig. 2(c). We have also observed that the fluidic device remains functional after the whole fabrication process – we have flown water stained with rhodamine, and observed it flowing under the windows, which withstand the hydrostatic pressure.

To demonstrate the electron transparency of the Al_2O_3 membrane, polystyrene beads and gold nanoparticles were flown through the microchannels. Upon drying, the particles adhered to the inner walls of the coated channels. Fig. 3(a) presents a schematic of the microchannel with the exposed Al_2O_3 membrane and the deposited particles underneath. SEM images in Fig. 3(b,c) show polystyrene beads and gold nanoparticles, respectively, imaged through the membrane at 10 kV. Fig. 3(d–f) displays the same region imaged at accelerating voltages of 3 kV, 10 kV, and 20 kV. The increased number of visible particles at higher acceleration voltages shows that deeper electron penetration increases the image contrast. The SEM images can confirm that the deposited Al_2O_3 membrane is electron transparent and the sample can be used as flow cell in an electron microscope. In the near future, these devices will enable real-time observation of nanoscale dynamics in liquid, under near-native conditions and opens new possibilities for advanced in situ experiments.

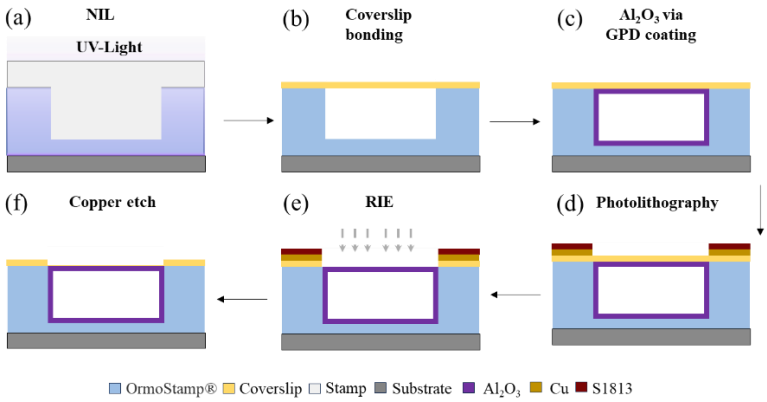

Figure 1. Schematic illustration of the sample fabrication process. (a) Microchannels are fabricated via nanoimprint lithography (NIL) in OrmoStamp®, where a UV-curable polymer is cast onto a substrate with predefined holes. (b) A polymer coverslip is applied to seal the fluidic system. (c) The sample is placed in a custom-built gas-phase deposition (GPD) reactor to deposit an electron transparent Al_2O_3 layer onto the inner surface of the enclosed channels. (d) A copper layer and photoresist are deposited on the coverslip, and photolithography is used to structure windows above the microchannels. Copper is selectively removed in these regions using $Fe(NO_3)_3$. (e) Reactive ion etching (RIE) is used to etch away the coverslip, creating free-standing Al_2O_3 windows. (f) The remaining photoresist and copper surrounding the windows are removed via O_2 plasma and $Fe(NO_3)_3$ treatment.

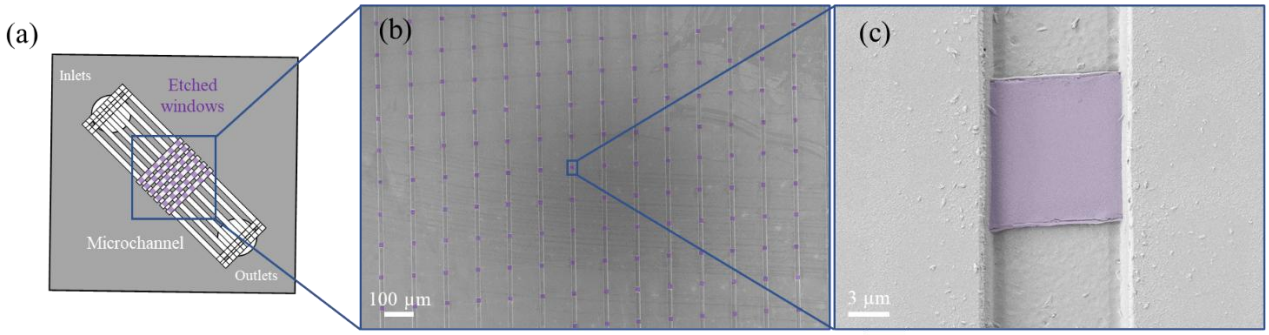

Figure 2. Microchannel flow cell with (a) shows a sketch of the fluidic structure on the substrate with inlets and outlets. To pattern the coverslip, a photomask with 10 µm-wide rectangular features was used, arranged such that their intersection with the underlying microchannel resulted in 10 µm × 10 µm openings (shown in purple). (b) Scanning electron microscope (SEM) image of the free-standing, electron-transparent windows. This design enables the simultaneous fabrication of multiple windows. (c) Magnified SEM image of a single window acquired at an accelerating voltage of 10 kV.

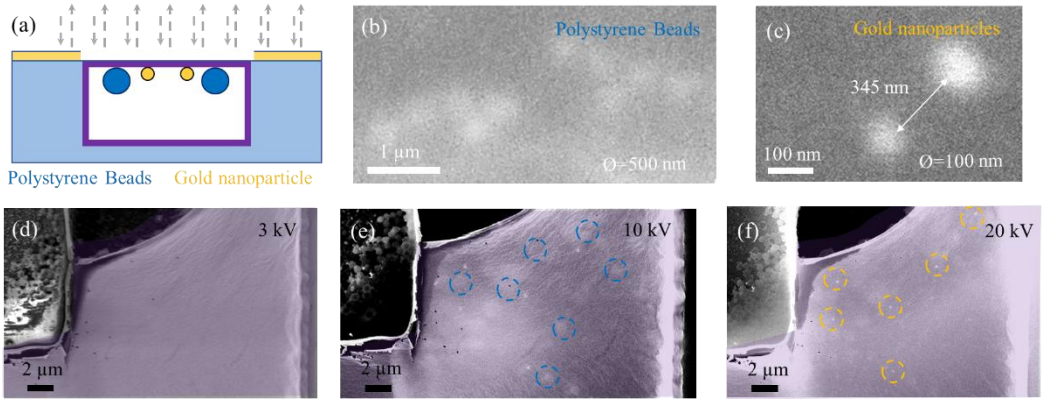

Figure 3. Evaluation of electron transparency in Al_2O_3-coated microchannels. (a) Schematic illustration of an electron-transparent microchannel containing polystyrene beads and gold nanoparticles. (b) SEM image of polystyrene beads observed through the Al_2O_3 window at 10 kV. (c) SEM image of gold nanoparticles through the same window at 10 kV. (d–f) SEM images of a free-standing Al_2O_3 window acquired at different accelerating voltages (3 kV, 10 kV, 20 kV), demonstrating that both polystyrene beads and gold nanoparticles become increasingly visible at higher voltages.

[1] Yoon, A. et al. (2001). Dynamic Imaging of Nanostructures in an Electrolyte with a Scanning Electron Microscope. *Microscopy and Microanalysis, 27(1),* 121-128. Doi 10.1017/S1431927620024769
[2] I. Fernandez-Cuesta et al., J. Vac. Sci. Technol. B (2011) 29 06F801.
[3] M. Müller et al., DE 102020102076A1 (2020) Hamburg, Germany, Deutsches Patent- und Markenamt.

Fabrication of Flexible Printed In-Mold Electronic Devices

Jeongdai Jo [a], Pyoungwon Park [a], Taik-Min Lee [a], and Inyoung Kim [a]

[a] Korea Institute of Machinery & Materials, 34103, Republic of Korea
e-mail: micro@kimm.re.kr

The increasing focus on sustainable manufacturing in the electronics industry has created a demand for environmentally friendly technologies [1, 2, 3]. In response to this need, In-Mold Electronics (IME), which integrates plastic molding with printed electronics, has emerged as a sustainable manufacturing solution. In-Mold Electronics (IME), which integrates plastic molding with printed electronics, has emerged as a sustainable manufacturing solution. IME not only addresses the functional requirements, such as reduced weight and increased flexibility, but also aligns with the broader trend toward sustainable mass production. [4, 5, 6].

There are two primary methods for manufacturing 3D electronic products: creating the curved product first and then applying printed electrodes by the non-contact printing method, or printing conductive patterns first on a film, followed by thermoforming. In this work, the aim was to fabricate a device on a 3D mold to address the deformation of printed circuits in the IME process.

In this study, printing conductive patterns first on a film, followed by thermoforming for ease of manufacturing and ability to produce fine patterns. Our experimental setup for the 3D IME consists of several steps: paste preparation, screen printing, thermoforming, and LED devices attachment. Initially, 3D IME devices was fabricated on a Polyethylene Terephthalate Glycol (PETG) substrate using a thermoforming approach, the silver paste was dispersed using a mixer. This prepared ink was then patterned onto a PETG substrate through the screen printing process. Following this, the substrate with the printed electrodes was directly mounted to the thermoforming machine. Once thermoforming was completed, LEDs were attached to the thermoformed circuit to verify functionality. Results demonstrated that the 3D IME circuit demonstrated elongation in length ranging and after thermoforming, confirming its stretchability. This approach effectively eliminated cracks on the circuit and optimized the manufacturing process for 3D electronic structural devices.

This research was supported by the National Research Council of Science & Technology(NST) (No. CAP22083-300) and the National Research Foundation of Korea(NRF) (No. RS-2023-00222166) grant by the Korea government (MSIT) and the Korea government(MOTIE) (No. RS-2024-00470021).

[1] Muhammad Irfan et al., Precision Engineering and Manufacturing–Green Technology. (2025) https://doi.org/10.1007/s40684-025-00713-4
[2] Phung, T. H et al., Flexible and Printed Electronics, 6(2), (2021). 024001.
[3] Ghaffarzadeh, K., & Collins, R. et al., IDTechEx. https://www.idtechex.com/en/research-report/in-mold-electronics-2020-2030-technology-market-forecasts-players/722
[4] Beltrão, M. et al., Polymer Engineering & Science, 62(4), (2022) 967
[5] Lall, P. et al., Proceedings of the ASME 2023 International Technical Conference and Exhibition on Packaging and Integration of Electronic and Photonic Microsystems. (2023)
[6] Srinivasan, K. P., & Muthuramalingam, T., Journal of Physics: Conference Series, 1969, 012064 (2021).

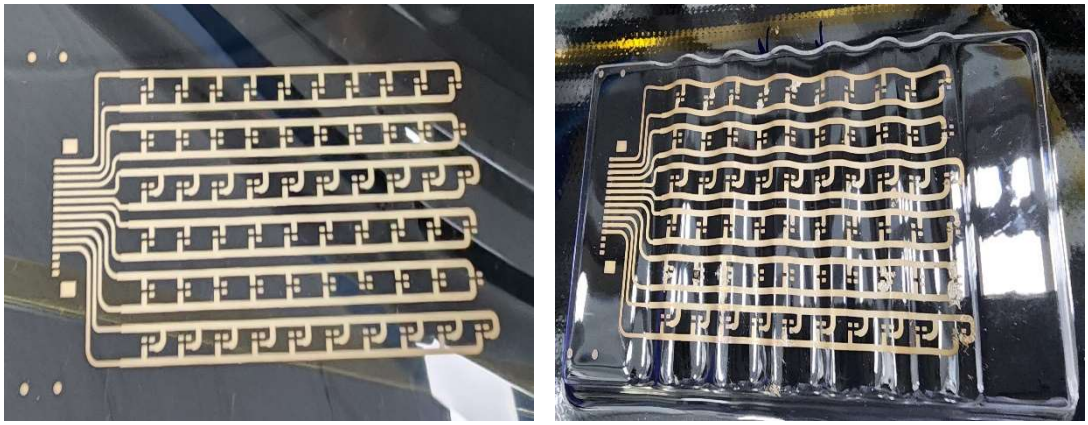

Figure 1. Screen printed circuit and 3D thermoformed electronic device.

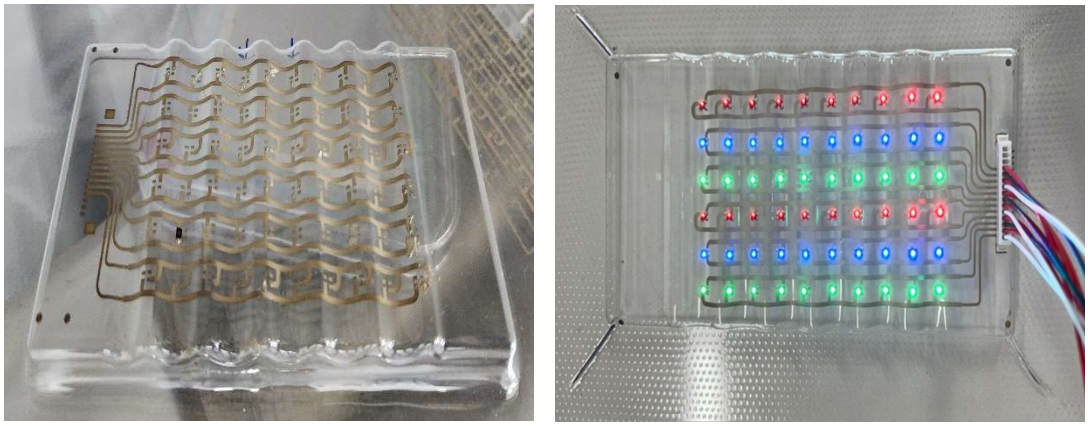

Figure 2. The LED attached on 3D electronic device and the RGB LED array in the completed circuit layout.

Bioinspired Nanospike Formation on the Surfaces of Commercial Plastic Plates Using Atmospheric-Pressure Low-Temperature Plasma

Masashi Yamamoto [a], Motoki Tanaka [a], Ayumu Takada [a], Atsushi Sekiguchi [b, c]

[a] National Institute of Technology, Kagawa College, 335 Chokushi-cho, Takamatsu, Kagawa 761-8058, Japan
[b] Litho Tech Japan Corporation, 2-6-6 Namiki, Kawaguchi, Saitama, 332-0034, Japan
[c] Osaka Metropolitan University, 3-3-138 Sugimoto-cho, Sumiyoshi-ku, Osaka 558-8585, Japan
e-mail: m-yamamoto@t.kagawa-nct.ac.jp

In recent years, bioinspired materials have garnered significant attention due to their potential in functional surface design. Among various natural templates, we focused on the antibacterial properties of cicada wings. Notably, the surface of the *Cryptotympana facialis* (Kumazemi) wing exhibits exceptional antibacterial activity, attributed to its distinctive needle-like nanostructures, known as nanospike structures (Figure 1). Previous studies have replicated such nanostructures on silicon substrates using photolithographic techniques developed for semiconductor fabrication [1, 2]. However, these approaches are constrained by substrate shape, size, and the need for specialized equipment, limiting scalability for practical applications.

To breakthrough these limitations, we have been developing micro-nano-structuring techniques based on atmospheric-pressure low-temperature plasma. In our previous work presented at MNE2024, we demonstrated that nanospike structures mimicking those found on cicada wings could be successfully fabricated on solvent-cast polymer films, resulting in surfaces with excellent antibacterial properties [3]. In the present study, to further enhance industrial applicability, we investigated the feasibility of forming nanospike structures on four types of commercially available plastic plates: PMMA (poly(methyl methacrylate)), PET (poly(ethylene terephthalate)), PC (polycarbonate), and PVC (poly(vinyl chloride)). Thickness of substrates were 2-3 mm. The atmospheric-pressure low-temperature plasma was generated using a He/O_2 gas mixture and a 13.56 MHz RF power source. Surface morphologies before and after plasma treatment were analyzed using atomic force microscopy (AFM).

Nanospike structures were successfully formed on all resin surfaces, as shown in Table 1. The micropores on the untreated surfaces might play a role of a starting point for the nanospike formation [4]. The full width at half maximum (FWHM) of the nanospikes followed the order: PC (≈ 0.05 μm) < PET (≈ 0.1 μm) < PMMA (≈ 0.2 μm) < PVC (≈ 0.4 μm), which may correlate with the thermal decomposition properties of the resins: PVC (200-260 °C) < PMMA (200-300 °C) < PET (≈ 350 °C) < PC (≈ 450 °C). PC and PET, containing aromatic rings, are structurally stable, whereas PMMA and PVC are vinyl polymers with main-chain scission and main-chaincrosslinking mechanisms, respectively [5]. PVC, despite its lower thermal resistance, may exhibit enhanced plasma durability because of thermal crosslinking.

These findings could suggest that the thermal and chemical properties of the resins influence nanospike formation. This study contributes to the industrial application of biomimetics by demonstrating a simple nanospike fabrication method using atmospheric-pressure low-temperature plasma. A part of this work was supported by JSPS KAKENHI Grant Number 22K04251.

[1] E. P. Ivanova *et al.*, *small* **8**, 2489 (2012).
[2] K. Itoh, *Fragrance Journal* **2018-6**, 51 (2018).
[3] M. Yamamoto *et al.*, *MNE 2024*, Sep. 16th-19th, TP4 (2024).
[4] M. Yamamoto *et al.*, *J. Photopolym. Sci. Technol.* 34, 385 (2021).
[5] A. A. Miller *et al.*, *J. Polym. Sci.* 14, 530 (1954).

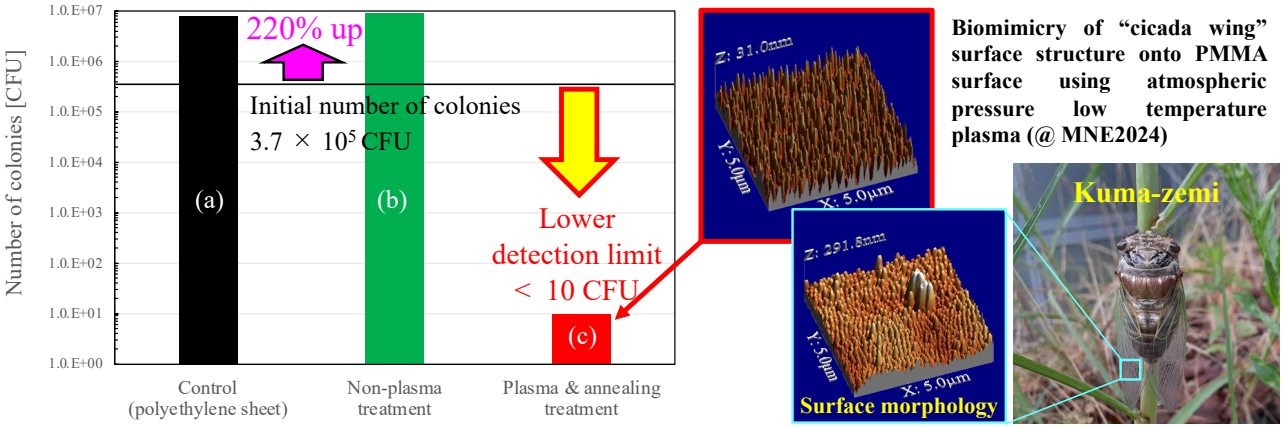

Figure 1. Antimicrobica performance of the PMMA film surface evaluated by the ISO 22196 test using *Escherichia coli* (NBRC 3972). (a) Control (polyethylene sheet), (b) Untreated PMMA, (c) Plasma-treated and annealed PMMA.

Table 1. Surface morphologies of plastic plates irradiated by an atmospheric-pressure low-temperature plasma.

Plastics	Surface morphologies
PMMA: poly (methyl methacrylate) 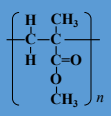	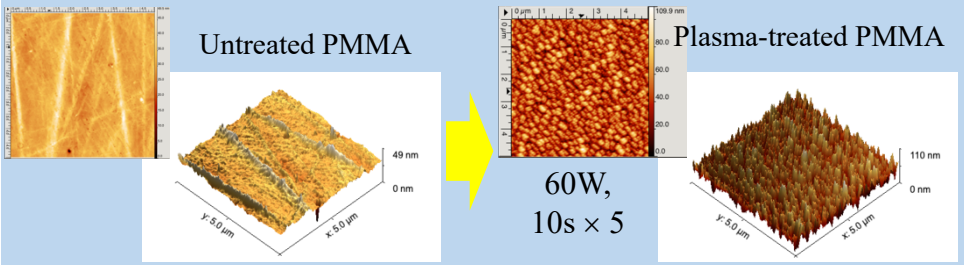
PET: poly (ethylene terephthalate 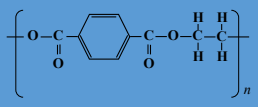	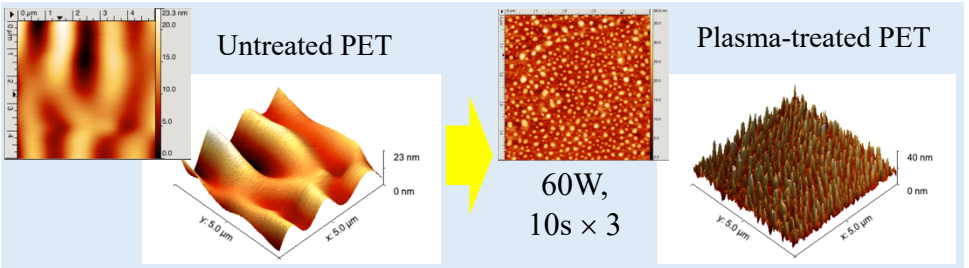
PC: polycarbonate 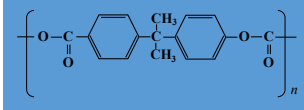	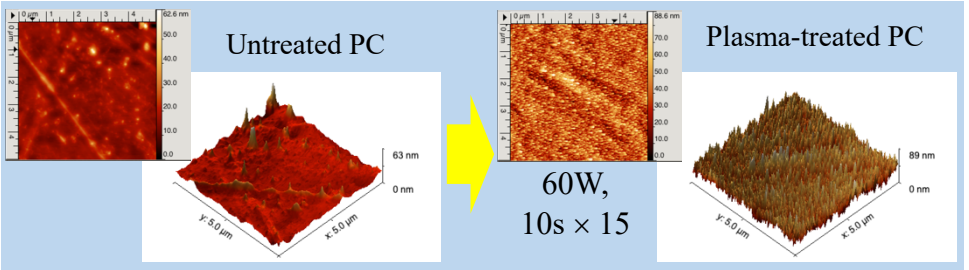
PVC: poly (vinyl chloride) 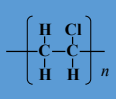	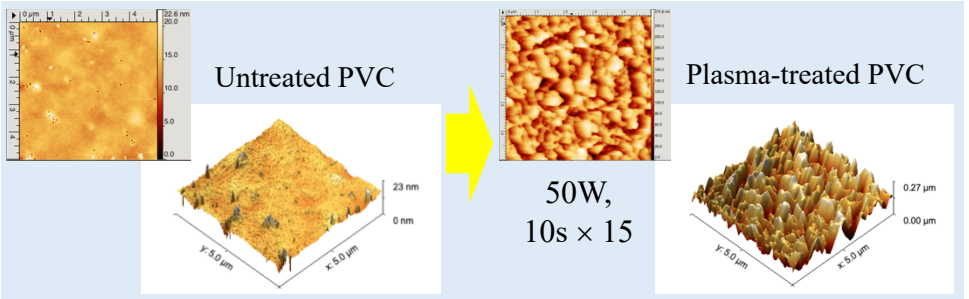

Impact of processing on the temperature-dependant behaviour of nanostructured Platinum thin films fabricated by Spark Ablation

Shatavisha Biswas [a], and Sten Vollebregt [a]
[a] Delft University of Technology, Delft, 2628 CD Delft, Netherlands
E-mail: s.vollebregt@tudelft.nl

This paper reports a systematic study of the processing parameters for fabricating nanostructured platinum (Pt) thin films via spark ablation, with the goal of optimizing their performance as resistive temperature detectors (RTDs). Spark Ablation is a dry and versatile chemical-free technique that requires only a controlled, atmospheric-pressure gaseous environment and a pair of electrically conductive electrodes for the synthesis of nanoparticles [1]. In this study, Pt nanoparticles (NPs) were generated using spark ablation, and then deposited through impaction printing (illustrated in Figure 1). The novelty of this work lies in the comprehensive understanding of how the key printing parameters can be precisely tuned to engineer the electrical and thermal behavior of the printed films for RTD applications. This study marks a step forward towards eliminating the need for lithographic or wet-chemical processing steps, thus enabling direct patterning of the functional sensor on the desired substrate and providing a more efficient alternative to the conventional fabrication methods.

A spark ablation generator (VSP G1, VSParticle B.V.) equipped with a pair of 99.999% pure platinum electrodes was used to produce pure Pt nanoparticles (NPs). Nitrogen served as the carrier gas at a flow rate of 1.5 L/min. For deposition, a nozzle with a throughput of 0.08 L/min was utilized, with programmable XYZ motion for pattern control. It is to be noted that, at high spark energy, unwanted clusters and overspray of NPs across the printed trace were found. This was due to the increased particle generation at higher spark energies, which heightened the likelihood of particle collisions while in the aerosol state. Thus, to avoid non-uniform layer thicknesses, an optimized spark current of 5 mA and voltage of 1 kV were used. Prior to the temperature-dependent studies, the printed films were annealed at 600 °C for approximately 1 hour to enhance interparticle contact and prevent particle fusing during testing.

To investigate the influence of printing speed on the properties of spark-ablated Pt films, deposition rates ranging from 0.3 mm/min (lowest possible) to 1 mm/min were tested. Although the films printed at speeds above 1 mm/min exhibited higher resistivity, they were found to be sparse, exhibiting increased inter-particle separation, which could potentially compromise their thermal stability. Based on the findings (Figure 2), the deposition speed of 1 mm/min was chosen as the optimized condition, ensuring an efficient processing time while achieving a high sheet resistance (~259.4 Ω/sq), preffered for enhanced sensitivity. XRD analysis confirmed that the deposition speed has no significant effect on the grain size, with the average size of the unnannealed Pt NPs being 2.3 nm. To further optimize the performance of the printed Pt films, the effect of film thickness was explored. Temperature-dependant studies revealed that the temperature coefficient of resistance (TCR) increases with the increasing thickness of the Pt layer (Figure 3(a)). This could be attributed to the fact that for thin metallic films, when the grain size and thickness drops below or is comparable to the mean free path of the charge carriers, grain boundary scattering becomes dominant (also known as the size effect). Moreover, the presence of a greater number of isolated Pt islands in thinner films increases surface scattering and further contributes to the reduction of TCR. A mean TCR of 2.17 x 10^{-3} /°C has been achieved for the film printed with 8-layer traces at the optimized processing conditions. However, when the Pt film thickness exceeds 500 nm, delamination is observed during annealing, which is likely induced by thermal stress.

Studies are ongoing with the aim to further optimize the film properties, geometry of the RTD and assess its performance at elevated temperatures. The relatively high TCR and linearity (Figure 3(b)) observed at such low film thickness as compared to existing technologies [2, 3] coupled with the simplicity of the fabrication process, highlights the strong potential of spark-ablated Pt films for temperature-sensing applications.

References:

[1] P. Pál et al., Chemosensors, 11(3) (2023), p.180.
[2] Y. Zeng et al., ACS Applied Materials & Interfaces, 15(1) (2022), pp.2172-2182.
[3] W. Lv et al., Materials Letters, 309 (2022), p.131313.

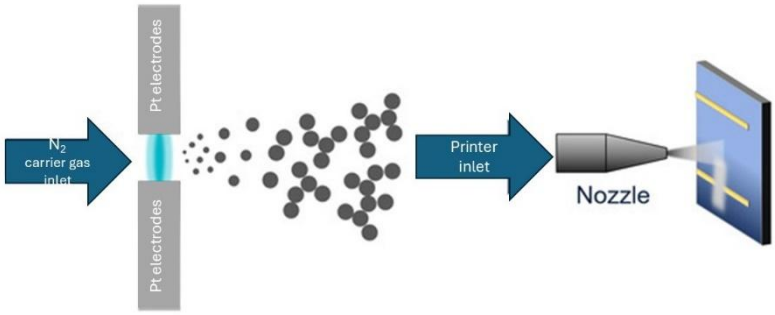

Figure 1. Schematic of the experimental setup

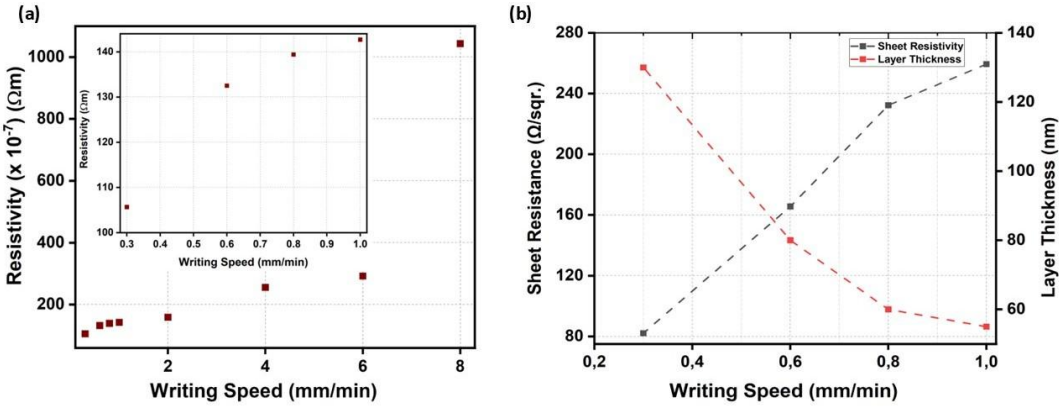

Figure 2. (a) Variation of film resistivity at different printing speeds, (b) Variation of sheet resistance and layer thickness at varying printing speeds

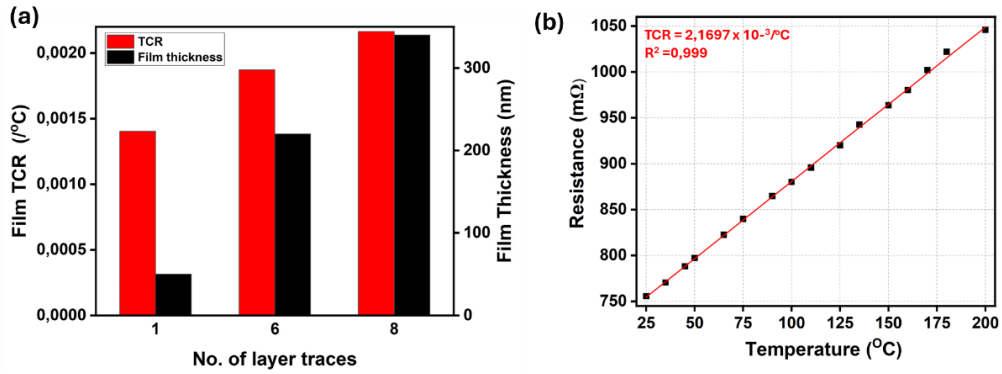

Figure 3. (a) Mean TCR of the films printed with different layer thickness, (b) Temperature-dependent resistance variation of the film printed with 8-layer traces

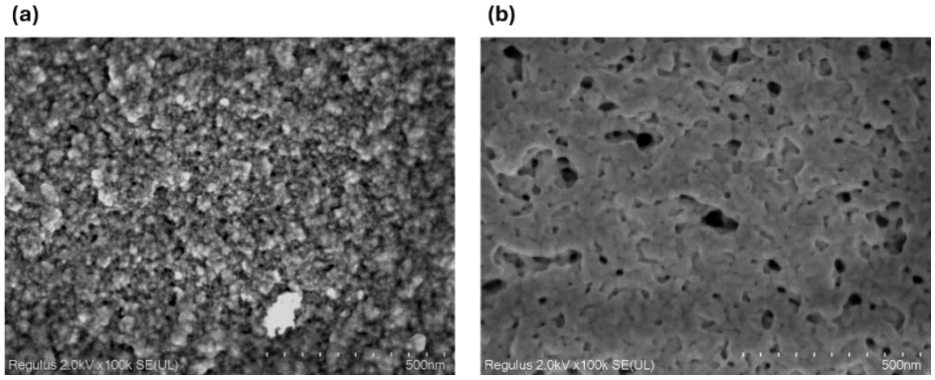

Figure 4. SEM micrograph of the 8-layer traces film printed at 1mm/min Before annealing, (b) Post-annealing, at 600 °C for 1 hr

Hierarchical structures fabricated for probiotic marine bacterial growth using hybrid methods for polymer replication

Yuyan Liu [a], Xavier F. Florensa [b], Euan McDonald [c], Paul Kempen [a], Claus Sternberg [b], Nikolaj Gadegaard [c], Lone Gram [b], and Rafael Taboryski [a]

[a] National Centre for Nano Fabrication and Characterization, DTU, Kgs. Lyngby, 2800, Denmark
[b] Department of Biotechnology and Biomedicine, DTU, Kgs. Lyngby, 2800, Denmark
[c] Biomedical Engineering, The University of Glasgow, Glasgow, G12 8LT, Scotland

e-mail: rata@dtu.dk

Several species of marine bacteria from the Roseobacter group have been identified as producers of the antibacterial compounds tropodithietic acid (TDA). In certain species, the TDA production is clearly facilitated when bacteria form biofilm on a surface rather than existing in the planktonic state [1]. Micropatterned polymeric surfaces have been investigated to support bacterial growth and TDA production, with varying patterns yielding different levels of TDA production [2]. Consequently, screening micropattern designs for optimal TDA production is essential. In this study, we present hybrid methods to fabricate hierarchical structures across multiple size scales through polymer replication, with the goal of supporting roseobacter biofilm growth.

Here we developed a hybrid fabrication method that combines the strengths of clean room fabrication and 3D printing techniques, providing a flexible and high-resolution fabrication approach. To start with, we fabricate the micro-patterned silicon wafer in the clean room, subsequently, we cast a relief in polydimethylsiloxane (PDMS) using the microfabricated wafer as a mold. We first 3D print the mold base, where at specific stages we pause the 3D printing to transfer the PDMS-based micropatterns into the mold. The printing then resumes, layering additional material over the transferred micropatterns to create inlet ports (Figure 1a). Scanning electron microscopy (SEM) micrographs, as shown in Figure 1b, show the transferred micropatterns on the fabricated mold. The resulting micropatterned mold serves as a negative relief for the injection molding of the microfluidic flow cell. This hybrid approach provides a highly flexible prototyping method to facilitate biofilm growth studies, enabling the integration of custom micropatterns at desired locations.

In yet another approach, we introduce nanoscale roughness to the patterned microstructures through the novel uses of polystyrene (PS) nanoparticles. PS beads are distributed on a flat polypropylene (PP) surface before imprinting with a microfabricated Si mold (Figure 2a). During imprinting [3], the PS beads are pressed into PP. The PS beads are then softened and subsequently removed by acetone, leaving behind nanoscale indentations that generate additional random textures to create the final hierarchical surface structure (Figure 2b and 2c). This additive approach efficiently introduces nanoscale roughness to existing microstructure designs during polymer replication.

Future research will focus on evaluating fabricated hierarchical structures, incorporating micro- and nanoscale features, through biological experiments involving probiotic marine bacterial biofilm growth. Figure 3 illustrates bacterial growth on microstructures, including hexagonal pits and pillars.

[1] D'Alvise, P.W.; Magdenoska, O.; Melchiorsen, J.; Nielsen, K.F.; Gram, L. *Environ. Microbiol.* 2014, 16, 1252–1266.

[2] Droumpali, A.; Liu, Y.; Ferrer-Florensa, X.; Sternberg, C.; Dimaki, M.; Andersen, A.J.C.; Strube, M.L.; Kempen, P.J.; Gram, L.; Taboryski, R. *RSC Adv.* 2023, 13, 33159–33166.

[3] Liu, Y., Ferrer-Florensa, X., Sternberg, C., Kempen, P., Schift, H., Gram, L., & Taboryski, R. *Nanomanufacturing*, 2024, 4(4), 202-213.

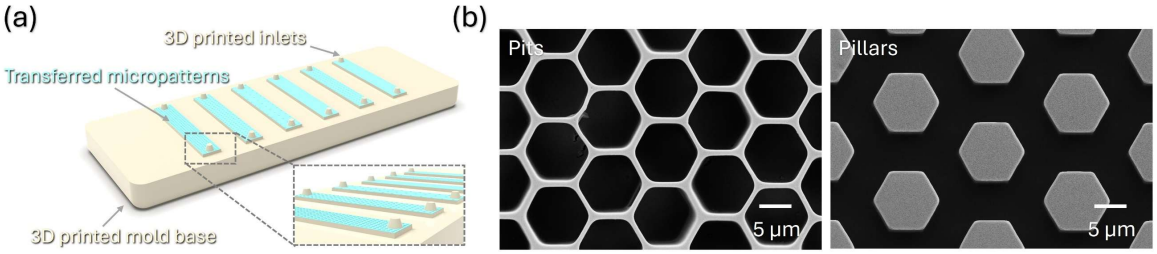

Figure 1. Hierarchical structured molds fabricated using clean room fabrication and 3D printing hybrid methods. (a) Schematic representation of a fabricated mold. (b) Scanning electron microscopy (SEM) of transferred microstructures on 3D-printed mold base.

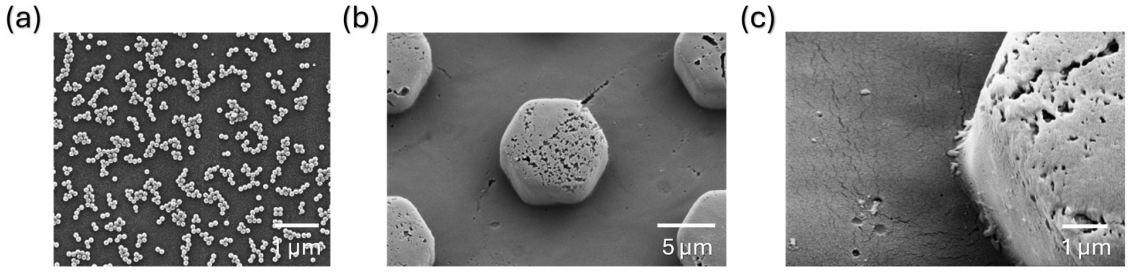

Figure 2. SEM micrographs of hierarchical structures fabricated using clean room fabrication and nano beads hybrid method. (a) Polystyrene (PS) nano beads distributed on the flat polypropylene (PP) surface. (b) Microstructured PP surface featuring nano-scale roughness. (c) A close-up observation on the roughness.

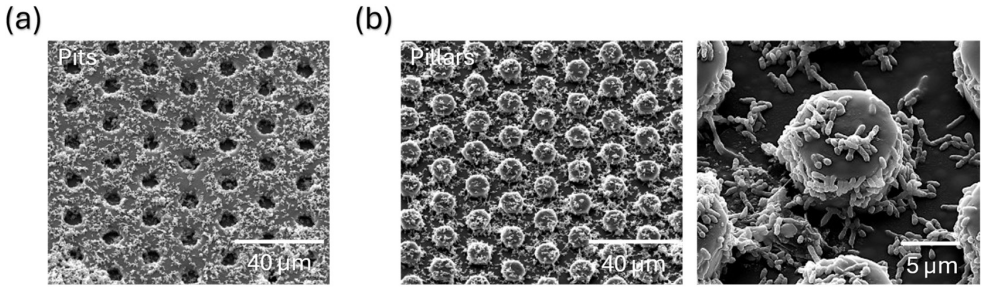

Figure 3. SEM micrographs of marine bacterial growth on the structured polymer surfaces.

Fluorination of Ni Hard masks during Fluorine-Based DRIE: Structural and Spectroscopic Insights into NiF_2 Formation

Baptiste Fischer-Kaszuba[1*], Amandine Andrieux-Ledier[1], Etienne Carré[1], Patrick Kayser[1], Pierre Lavenus[1], Frédéric Fossard[2], Jean-Sébastien Mérot[2], Thomas Baron[3].

[1] DPHY, ONERA, Université Paris-Saclay, 92320 Châtillon, France.

[2] Université Paris-Saclay, ONERA, CNRS, Laboratoire d'étude des microstructures (LEM), 92322 Châtillon, France.

[3] Université Marie et Louis Pasteur, SUPMICROTECH, CNRS, Institut FEMTO-ST, F-25000 Besançon, France.

e-mail: baptiste.fischer-kaszuba@onera.fr

Deep Reactive Ion Etching (DRIE) is widely used in the MEMS fabrication due to its excellent etching capabilities, including high selectivity, vertical sidewalls, and compatibility with a broad range of substrate materials [1]. Fluorine-based plasmas, in particular, enable the etching of various substrates such as silicon, lithium niobate, glass, and, as in our case, quartz. To achieve deeper etching or higher selectivity than what polymer masks allow, metallic hard masks such as aluminum or nickel are often employed. However, under moderated temperatures (a few hundred degrees Celsius) and in the presence of fluorinated gases, these metallic masks can react and be contaminated by fluorine ions [2-3]. Key characteristics of the chemical compounds formed remains unexplored (thickness, crystallinity…). This lack of knowledge means that optimal solutions cannot be applied to remove them and leads to unwanted residues on the MEMS devices.

In this study, we examine the structural and compositional evolution during fluorine-based plasma etching of a nickel PVD-sputtered hard mask, deposited on quartz. For that purpose, we performed characterization, from the macroscopic to the atomic scale, by optical microscopy, scanning and transmission electron microscopes (SEM, TEM), Energy Dispersive, X-ray photoelectron and Electron Energy Loss spectroscopies (EDS, XPS and EELS). Our results reveal the formation of a uniform layer, composed of Ni and F, tens of nanometers thick, depending on the etching conditions (Figure 1). This layer exhibits high crystallinity, with a 1:2 stoichiometry consistent with NiF_2 and lattice parameters matching those expected from single-crystal X-ray diffraction reference data [4]. This structural quality enabled us to record, for the first time to our knowledge, the electron energy loss spectrum (EELS) of crystalline NiF_2. As this fluorinated layer is insoluble in water or nitric acid—unlike pure Ni—we also propose a gentle, accessible method for its removal, which allow us to obtain a MEMS quartz wafer without any nickel hard-mask residues.

References:

[1] S. Queste, G. Ulliac, J. C. Jeannot, and C. K. Malek, DRIE of non-conventional materials: first results, pp. 171-174 (2008).

[2] D. Senthilkumar, K. L. T. Shee and B. S. S. C. Rao, IEEE 24th Electronics Packaging Technology Conference (EPTC), Singapore, pp. 175-178 (2022).

[3] R. Ettouri, T. Tillocher, P. Lefaucheux, B. Boutaud, V. Fernandez, N. Fairley, C. Cardinaud, A. Girard, and R. Dussart, Surface and Interface Analysis 54, 134 (2022).

[4] J. W. Stout, S. A. Reed, The crystal structure of MnF_2, FeF_2, CoF_2, NiF_2 and ZnF_2, J. Am. Chem. Soc., 76, 21, 5279-5281 (1954).

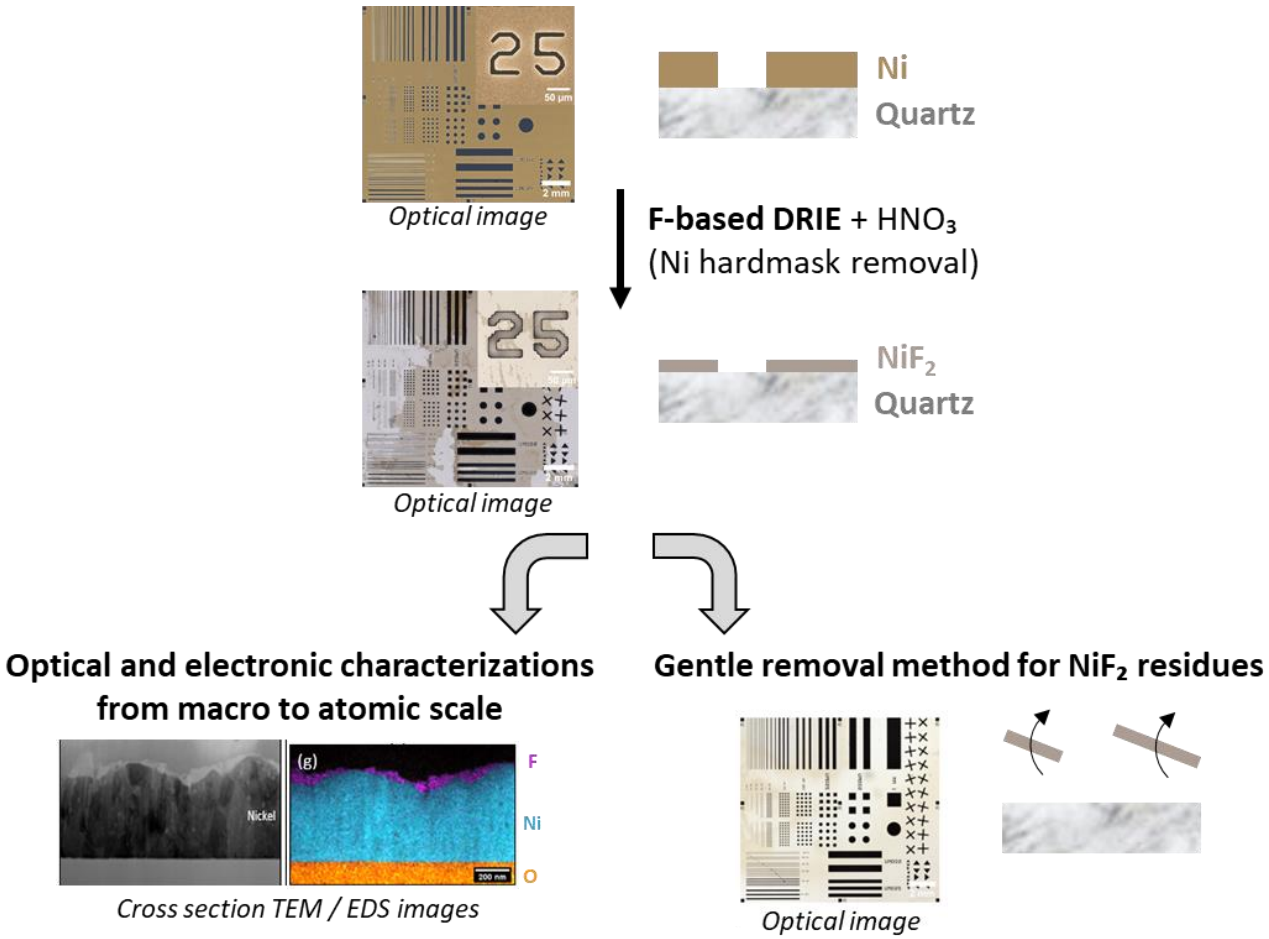

Figure 1: Fluorination of the Ni mask using F-based plasma, multiscale investigation and gentle removal of the resulting NiF_2.

On-CMOS 3D Platinum Electrodes Fabricated by Focussed-Ion Beam for Dielectrophoresis of DNA Towards an Electrokinetic Lab-on-CMOS

Lewis Keeble [a], Arthur Jaccottet [a], Daryl Ma [a], Jesus Rodriguez Manzano [b], Pantelis Georgiou [a]
[a] Department of Electrical and Electronic Engineering, Imperial College London, London, SW7 2AZ, UK
[b] Department of Infectious Disease, Imperial College London, London, W12 0NN, UK
e-mail: lewisaskeeble@gmail.com

Introduction: The continued rise in the use of complementary metal-oxide-semiconductor (CMOS) technology to form highly adept biosensing platforms for the diagnosis of infectious diseases has brought with it unparalleled scalability of production and device accessibility. Yet, preparation of samples for testing is typically conducted separately to the CMOS microchip, either by an attached microfluidic system or by the user. This increases manufacturing complexity and device size or increases chances of incorrect tests through user error or contamination. The ideal device would see the sample preparation system integrated as part of the microchip to process samples for testing in-situ: A lab-on-CMOS system.

Electrokinetics, including dielectrophoresis (DEP), have shown significant promise in performing sample preparation tasks and are ideal for integration with CMOS technology because both utilize electric potentials. An issue with electrokinetic lab-on-CMOS systems in the literature is that the electrodes reside underneath a passivating layer and are thus separated from the sample under testing [1]. This reduces the electrokinetic forces that can be exerted, which is acceptable for cell-based applications but not when working with smaller targets such as DNA that require larger field gradients. However, exposing the electrodes to the electrolyte brings challenges, as the high conductivity solutions encountered within biological applications catalyse electrode-spoiling reactions. Another pitfall of the electrodes used in the literature is their planar profile, which significantly limits the range of electrokinetic forces and results in the low efficiency and throughput of such systems [2]. There is a clear need for the production of CMOS-compatible electrodes with a 3D profile that are stable within high conductivity media and capable of high throughput.

This study will use focused-ion beam (FIB) deposition of platinum to produce 3D platinum electrodes on-CMOS for the first time. Whilst the FIB fabrication method is not currently scalable, useful on-CMOS 3D electrode systems can be created using this method to provide proof-of-concept studies for new electrokinetic lab-on-CMOS devices.

Approach: A microchip was designed with bond-pads on which the 3D electrodes were based, connected to bondpads on the microchip periphery for wirebonded connections to a printed circuit board. The aluminium metallization of the bond-pads contains an insulating oxide layer that would prevent electrical connection to the 3D electrodes. This oxide layer was removed with etching in sodium hydroxide and nitric acid, before a double zincation process. To raise the level of the metallization to the top of the passivating layer of the microchip, an electroless nickel, immersion gold process was run [3].

Platinum deposition was conducted using a FIB with a gas injection system. A vaporised precursor is introduced to the deposition area which degrades into metallic platinum after collision with an ion. This process was used to create a 5µmx5µm square pillar connected by a 100nm thick line to a bond-pad. Opposite the pillar, a 100nm thick line electrode was deposited, with a 2µm gap between the pillar. To ensure that the two electrodes were not shorted by platinum depositing between them (Figure 1), a trench was etched in a 10nA FIB (Figure 2). The two electrodes were connected to a function generator which applied 4V at 500Hz with opposite polarization. 40pM 45kbp λ-DNA was fluorescently dyed with YOYO-1 Iodide at a ratio of 1 dye molecule per 10 base pairs. The DNA was imaged using a Zeiss Axiozoom v1.6 upright fluorescent microscope.

Results: The fabricated 3D electrode reached a height of 5-6µm as measured with a profilometer. The line electrodes successfully scaled the small height between the gold bond-pad and the passivation, ensuring successful electrical connection. Upon application of the voltage to the electrodes, DNA was concentrated by dielectrophoresis between the electrodes (Figure 3). When the voltage was removed, the DNA diffused away from this region, indicating that DNA was not bonding with the platinum electrodes. This is the first demonstration of DEP of DNA using FIB-fabricated electrodes.

References: [1] W. Lin et al., *IEEE International Symposium on Circuits and Systems* (2024) 1-5

[2] L. Keeble et al., *International Conference and Exhibition on New Actuator Systems and Applications* (2024) 13-16

[3] Lewis Keeble et al., Electrochimica Acta 477 (2024)

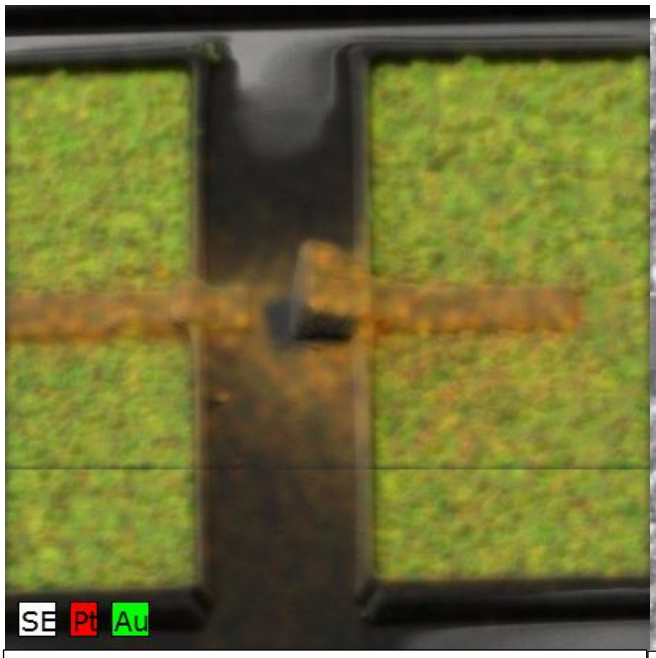

Figure 1: EDX image with SEM overlay showing the gold-plated bondpads and 3D Pt electrode, with Pt deposited between the electrode pair.

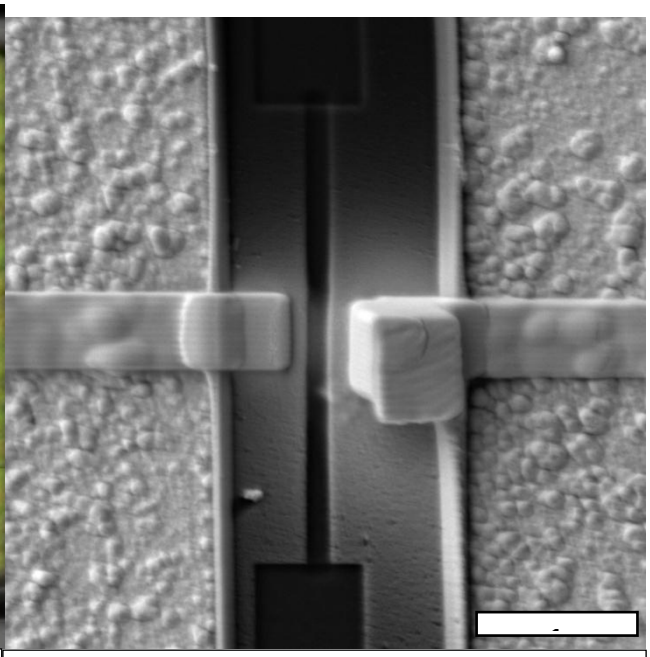

Figure 2: SEM image of the final electrode system, with etched trench between electrodes.

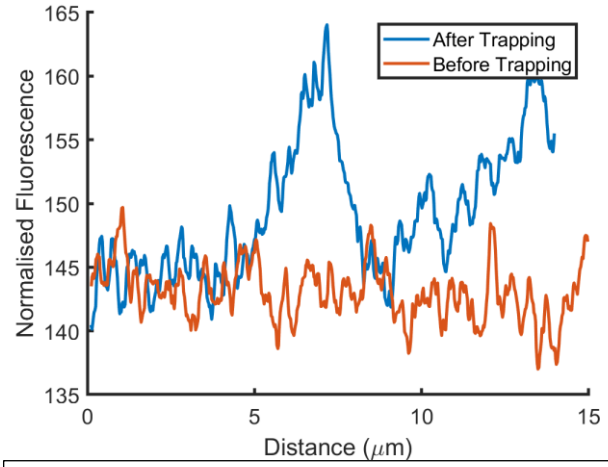

Figure 3: Fluorescence profile across the electrode pair (**red**) before and (**blue**) after the voltage is applied to the electrode. The profile after trapping is normalised against the average fluorescence before trapping.

Hybrid-Polymer Microring Resonator Arrays for Next-Generation Photoacoustic and Biosensing Applications

Santhosh Pandian [a], Marina Fetisova [b], Petri Karvinen [b], Paul Müllner [c], Moritz Eggeling [c], Rainer Hainberger [c], Evgenii Lepukhov [a], Tapio Niemi [a]

[a] Nanophotonics Group, Tampere University, Tampere, FI-33720, Finland
[b] Centre for Photonics Sciences, University of Eastern Finland, Joensuu, FI-80101, Finland
[c] Molecular Diagnostics, AIT Austrian Institute of Technology GmbH, Vienna, 1210, Austria
e-mail: santhosh.pandian@tuni.fi

Polymer materials have enhanced photonics integrated circuits by providing a broad wavelength range, low absorption, diverse material choices, and cost-effective fabrication processes [1,2]. Polymer-based microring resonators (MRRs) are important for optical communications and medical diagnostics [3,4]. They are also used as compact ultrasonic detectors in photoacoustic imaging [5]. Our objective is to apply these MRRs for photoacoustic imaging of drug-tolerant persister cells in breast cancer [6]. Recently, we have prepared and characterized single MRRs [7]. The angular field-of-view of a single MRR ultrasound detector depends on the signal frequency and the ring diameter. For imaging with a single ring, either the imaged area is limited, or the sample or detector must be movable to extend the area. Alternatively, an array of MRRs can be sequentially interrogated to image a larger area in a fixed setup. In this work, we report on the fabrication and optical performance characterization of an array of 16 MRRs. We employ nanoimprint lithography (NIL), which is recognized for its high resolution, precision, and cost-efficiency in patterning structures [1,3].

The MRRs were fabricated on a 500 µm thick silicon wafers with a 2 µm thermal oxide layer serving as lower cladding (n=1.453) by means of UV-NIL using hybrid polymer ORMOCORE™ as waveguide layer (n=1.543). Figure 1a shows an example of a single MRR. PDMS (n=1.40) was spin-coated as top-cladding. The design of the waveguide core is 1.2 µm high and 1 µm wide with a 5 µm thick PDMS top cladding. The residual layer on both sides of the imprinted waveguide is a critical process related parameter that we aim to minimize. In our NIL process, we achieve a thickness of 80-300 nm. Figure 1b, exemplarily shows the SEM image of a sample with a residual layer thickness of approximately 80 nm. To extend the detection area we designed a 4×4 array of rings with 400 µm spacing (see Fig. 2a). Each ring has a slightly different diameter to separate the resonance wavelengths. The row starts with rings having a 120 µm diameter, increasing by 20 nm per ring. Optical modelling shows that these values correspond to a free spectral range (FSR) of 1.01 nm and a resonance shift by 0.13 nm per ring. A single input waveguide is split up twice through a 1×2 splitter, resulting in four distinct rows. Signals from each of these rows are detected individually. This array configuration offers scalability and enables multiplexed detection over an area of approximately 2.7×2.7 mm², enhancing advanced photoacoustic imaging applications. The characterization of the MRR array fabricated on a silica-on-silicon sample is performed using a wavelength tunable laser. Figure 2b plots the transmission spectra for the MRRs along the four rows. The resonance of each ring is clearly separated by 0.07-0.3 nm inside FSR of approximately 1.07 nm. The Q-factors of the resonances range from 5.8 to 7.5×10^4, which aligns with our previous measurements [7]. The resonance performance is consistent across the array elements, which reflects the uniform fabrication quality over the area of the array in terms of waveguide thickness and width as well as residual layer thickness. The spectral transmission results confirm that MRR detectors can be scaled into parallel detection schemes potentially enhancing the spatial resolution and image acquisition speed. Moreover, the well-defined resonances with high extinction ratios across the rows highlight the potential of hybrid-polymer MRR arrays as highly sensitive and scalable platforms for photoacoustic imaging and biosensing applications.

[1] R. Morarescu, et al., ICTON IEEE. (2015) 1-4.
[2] R. Landgraf, et al., Advanced Sensor Systems and Applications. 8561 (2012) 135-146.
[3] R. Kirchner et al., Journal of Lightwave Technology. 32 (2014) 1674-1681.
[4] Y. Liang et al., Sensors. 19 (2019) 181.
[5] H. Li et al., Nature Communications. 10 (2019) 4277.
[6] M. Liu et al., Journal of Physics: Photonics. 3 (2021) 021001.
[7] S. Pandian et al., 49th International Conference on Micro and Nano Engineering. (2023).

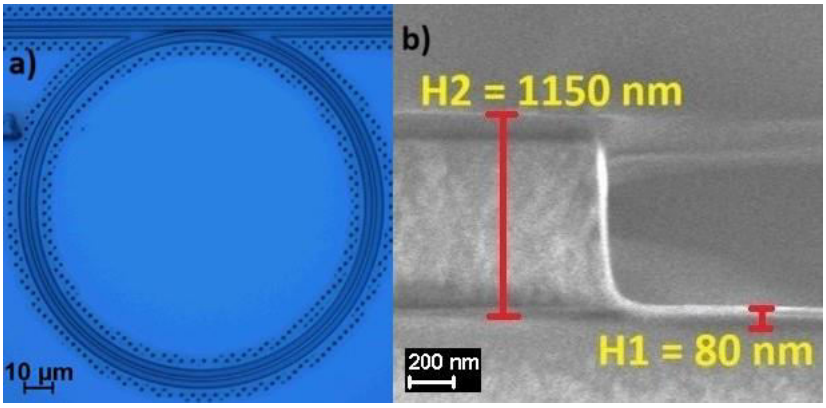

Figure 1. a) MRR with 120 µm diameter fabricated by UV-NIL. The dot pattern close to the waveguide structures can avoid disruption of the waveguides in the case of bubble formation during the NIL process. b) SEM image of the waveguide cross-section, revealing a residual layer thickness of ca. 80 nm.

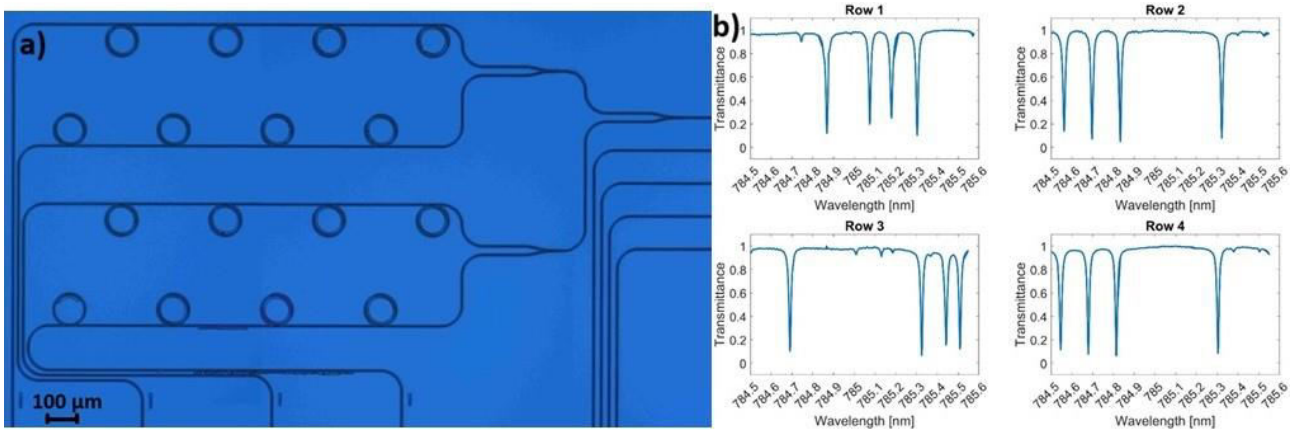

Figure 2. a) Microscope image of an MRR array with 120 µm diameter rings, waveguides and 1×2 splitters. b) Transmission spectra from four rows within one FSR.

Femtosecond laser inscription of optical waveguide in sapphire

Wei Lyu [a], Ding Zhao [a*], Min Qiu [a,b*]

[a] Zhejiang Key Laboratory of 3D Micro/Nano Fabrication and Characterization, Westlake Institute for Optoelectronics, Fuyang, Hangzhou 311421, China
[b] Key Laboratory of 3D Micro/Nano Fabrication and Characterization of Zhejiang Province, School of Engineering, Westlake University, Hangzhou 310030, China
e-mail: zhaoding@westlake.edu.cn (D.Z.), qiu_lab@westlake.edu.cn (M.Q.)

In the research of photonic device fabrication, femtosecond laser direct inscription has emerged as a powerful technique for creating optical waveguides in transparent materials, including glass, polymers, and crystals [1,2]. However, processing photonic devices in such hard and brittle crystals still presents several technical challenges, such as crack formation and cumulative heat effects [3]. To overcome these challenges, this study demonstrates the fabrication of optical waveguides in sapphire (Al_2O_3) crystals using a femtosecond laser with a 1030 nm wavelength and 130 fs pulse width, irradiated both inside and on the surface of the material (see Fig1). This method allows for the precise and controlled modification of the material's refractive index, enabling the formation of complex photonic structures. The depressed cladding waveguide, a key structure fabricated using this technique, features a central core with a higher refractive index surrounded by a lower-index cladding, effectively guiding light through the core with minimal loss [4]. Experimental results confirm that the fabricated waveguides, both buried and surface, support single-mode propagation at 1550 nm (the telecommunication wavelength) (see Fig2). Moreover, the surface waveguides exhibit potential for near- and mid-infrared sensing applications, particularly in extreme environments (e.g., high temperature, radiation, or corrosive conditions), owing to sapphire's exceptional chemical and thermal stability. This research not only highlights the technical feasibility of such waveguides but also opens new avenues for the development of robust, high-efficiency photonic devices in various applications, including optical communications and sensing technologies.

Key words: femtosecond laser, direct inscription, optical waveguide, crystal, sapphire, near-IR/mid-IR

References:
[1] R. R. Gattass et al., Nat. Photonics 2 (2008) 219–225.
[2] F. Chen et al., Laser & Photonics Rev. 8 (2014) 251-275.
[3] L. Li et al., Adv. Photon. 4 (2022) 024002.
[4] J. P. Bérubé et al., Opt. Lett. 44 (2019) 37-40.

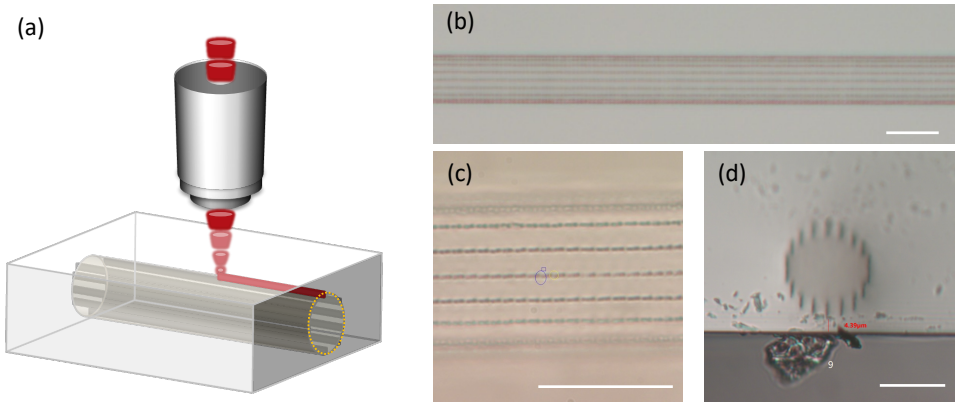

Figure 1. (a) Schematic illustration of femtosecond laser direct writing for fabricating waveguides in sapphire. The focused laser beam modifies the material's refractive index, creating regions with lower refractive indices compared to the unmodified areas, which is essential for the formation of depressed cladding waveguides. (b) Top-view optical microscope image of a depressed cladding waveguide. (c) Enlarged view of the top-view optical microscope image, further emphasizing the high resolution and accuracy of the fabrication process. (d) Side-view optical microscope image of a depressed cladding waveguide. Scale bar: 20 µm.

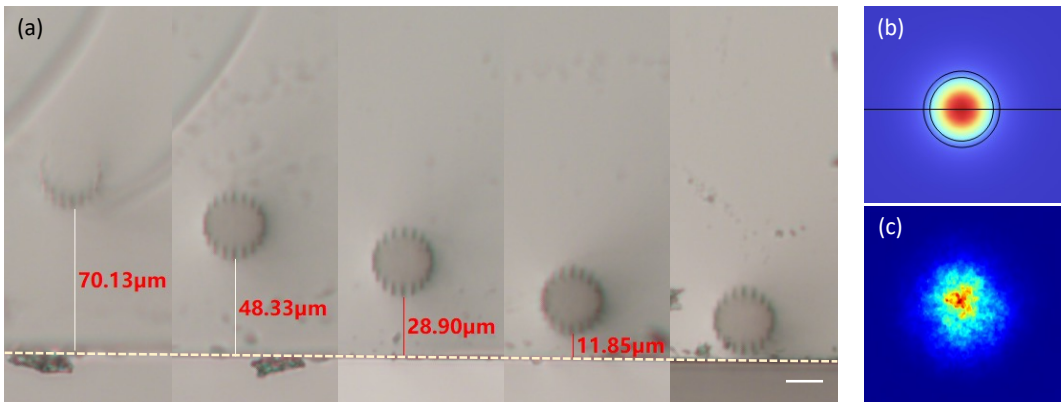

Figure 2. (a) Side-view optical microscope image of depressed cladding waveguides at different depths, within the sapphire (Al_2O_3) crystal, gradually approaching the surface (the yellow dash line). The region below the dashed line represents the air environment. This image highlights the precise control of the femtosecond laser direct writing technique in creating waveguides at specific depths. Scale bar: 20 µm. (b) Simulated single-mode light transmission in a depressed cladding waveguide. The simulation demonstrates the confinement of the light within the core region, with minimal leakage into the surrounding cladding. (c) Experimental measurement of single-mode light at the output of waveguide with a 1550 nm wavelength. The measurement confirms that the waveguide successfully transmits the near-infrared (NIR) light in a single mode, validating the effectiveness of the femtosecond laser direct writing technique in creating high-quality optical waveguides.

Effective diffusion barrier for Au/Ni thin films in quartz MEMS processing

Baptiste Fischer-Kaszuba[a], Amandine Andrieux-Ledier[a], Etienne Carre[a], Frédéric Fossard[b], Jean-Sebastien Mérot[b], Pierre Lavenus[a], Thomas Baron[c]

[a] *DPHY, ONERA, Université Paris-Saclay, 92320 Châtillon, France*

[b] *Université Paris-Saclay, ONERA, CNRS, Laboratoire d'étude des microstructures (LEM), 92322 Châtillon, France*

[c] *Université Marie et Louis Pasteur, SUPMICROTECH, CNRS, Institut FEMTO-ST, F-25000 Besançon, France*

e-mail : baptiste.fischer-kaszuba@onera.fr

The fabrication of MEMS on hard substrates like quartz, fused silica or lithium niobate often relies on Deep Reactive Ion Etching (DRIE), where metal hard masks such as nickel [1], chromium [2], and aluminum [3] are used for their high etch resistance and selectivity. However, these masks present challenges, especially in multilayer metallization for electrodes. A key issue is the interdiffusion of metals—particularly chromium and gold—into the nickel layer. This diffusion leads to a degradation of the Cr/Au layer morphology after nickel removal and can deteriorate the electrical and mechanical performance of the device. Addressing this interlayer diffusion is essential to maintain structural integrity and reliability in MEMS processes.

The aim of this study is to investigate the behavior in Cr/Au/Ni multilayer stacks deposited on quartz substrates under DRIE processing conditions, using carbon-fluorinated gases and low operating temperature (100-300°C). For that purpose, we used high-resolution electron microscopy to analyze morphological and elemental composition along the process. We present a detailed analysis of metal diffusion pathways in these thin film structures as seen in figure 1. This study reveals that diffusion along grain boundaries and in between column microstructure of the Cr/Au/Ni multilayers on quartz dominate. This agrees with the literature, showing that diffusion short-circuit prevails over bulk diffusion within our temperature range [4].

In the end, based on the results of the study, we're able to propose a diffusion barrier consisting of an evaporated alumina (Al_2O_3) ceramic layer sandwiched between gold and nickel layers. Under our DRIE conditions, we demonstrate a complete suppression of the Au/Ni interdiffusion (Fig. 2). This approach thus offers a robust, scalable solution to enhance material stability and reliability in MEMS fabrication using metallic hard masks and multilayer electrode systems.

[1] S. Queste, et al., «DRIE of non-conventional materials: first results» 2008.
[2] T. Ujiie, et al., «Fabrication of quartz microcapillary electrophoresis chips using plasma etching» 2000.
[3] V. Bliznetsov, H. M. Lin, Y. J. Zhang et D. Johnson, «Deep SiO2 etching with Al and AlN masks for MEMS devices» 2015.
[4] P. Guiraldenq, «Diffusion in metals» 1994

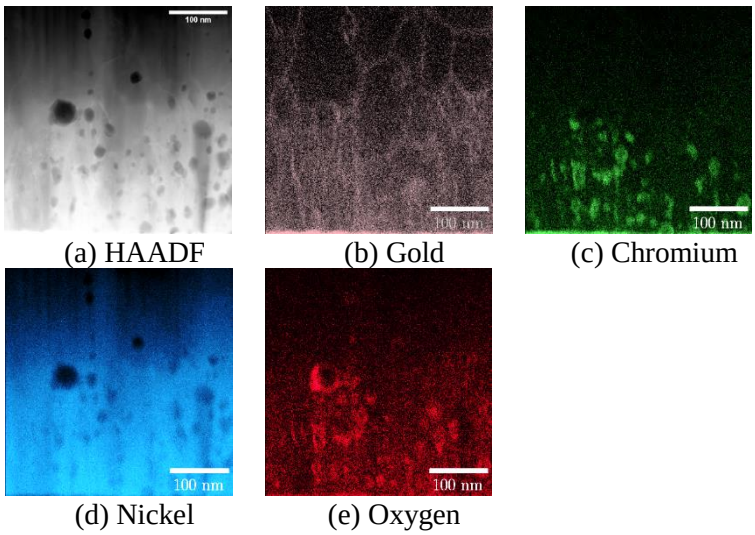

(a) HAADF (b) Gold (c) Chromium

(d) Nickel (e) Oxygen

Figure 1. State of multilayer system after DRIE processing characterized by TEM microscopy; the nickel layer showed significant degradation, including disjointed columns, porosity, and visible grain boundaries. EDS analysis confirmed that both gold and chromium diffused into the nickel, primarily along grain boundaries and porous areas. Chromium exhibited a dual behavior, diffusion along grain boundaries and segregation into porosity.

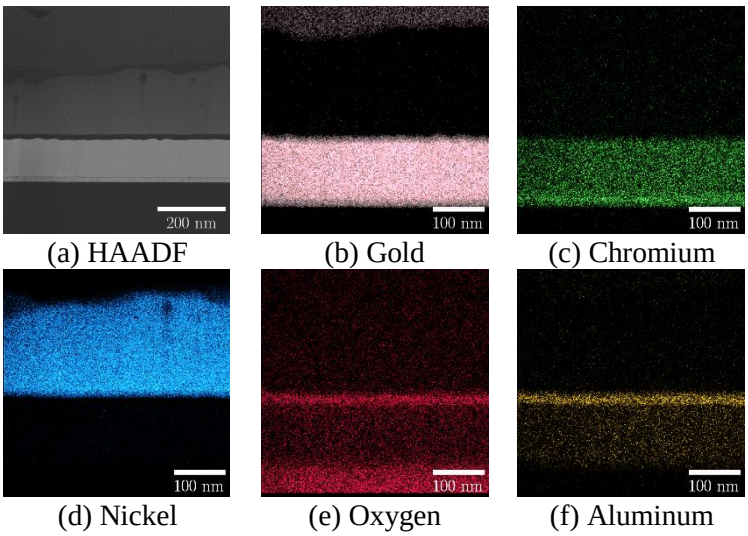

(a) HAADF (b) Gold (c) Chromium

(d) Nickel (e) Oxygen (f) Aluminum

Figure 2. State of multilayer system with alumina diffusion barrier after DRIE processing characterized by TEM microscopy. EDS analysis confirmed that the gold and chromium had not diffused into the nickel and that the alumina barrier remained intact. Nevertheless, chromium and gold interdiffused as expected.

Analysis and fabrication of electrothermal electrodes for micro and nanostructured sensors

Abel Palomas [a], Michelle Cedeño [a], Ana Coloma Vélez [a], Jorge Luis Villar [a], Manuel Domínguez-Pumar [a], Sandra Bermejo [a]

[a] Universitat Politècnica de Catalunya (UPC), Micro and Nanotechnologies Group (MNT), Barcelona, 08034, Spain
e-mail: abel.palomas@estudiantat.upc.edu

Purpose of the work

The aim of this work is to develop and thermally characterize a microfabricated electrothermal device designed for localized heating applications. Built on borosilicate glass substrates, the device incorporates metallic electrodes that generate heat through Joule effect when a voltage is applied. This heating capability is intended for enabling the thermal degradation of selected compounds in potential future applications. The primary objective is to evaluate the temperature distribution and thermal efficiency of the system, combining multiphysics simulations with experimental measurements. With these simulations, it is also studied the micro and nano structure of the ceramic part of the sensor. This part is a nano-voided structure capable of trapping the compounds. The study focuses on understanding the thermal behavior at the microscale to guide future design optimizations and integration into complex microdevices.

Novelty of the work with respect to the state of the art

This research presents a dedicated thermal study of a microfabricated platform manufactured entirely using cleanroom processes. The choice of borosilicate glass provides thermal and chemical stability, while the use of copper electrodes reinforced with nickel via electroplating enhances both electrical conductivity and durability under thermal cycling. The fabrication steps include substrate sandblasting to promote adhesion, sequential cleaning, physical vapor deposition of copper, photolithographic patterning, wet chemical etching, and electroplating of nickel.

The novelty lies in the comprehensive thermal approach combining fabrication with predictive modeling. Finite element simulations using COMSOL Multiphysics were performed to simulate temperature gradients, heat distribution, and current flow under varying electrical conditions. An example can be seen in Figure 1. These simulations provide a design framework for adjusting geometries and materials to achieve optimal heat control in microscale systems. These simulations also reflect the evolution of the temperature inside the structure, showing how it behaves related to the temperature.

Results of the work

The fabricated devices showed good mechanical adhesion and reliable electrical performance. Thermocouple-based measurements confirmed that temperatures exceeding hundreds of Celsius can be achieved in a controlled and repeatable manner with moderate voltage inputs. Experimental data closely matched the results obtained through simulation, validating the thermal model used.

Temperature maps obtained from simulation revealed areas of concentrated heating (hot spots), along with lateral thermal gradients, offering insight into how design modifications can influence heat spread and intensity. These findings are key for future versions of the device aiming to deliver more uniform or spatially selective heating. Regarding the ceramic structure, the temperature profile remains approximately linear across its volume, indicating minimal thermal dissipation. This behavior is desirable, as it ensures uniform heating throughout the structure.

This work was conducted as part of project TED2021-131552B-C22. This is a project founded by «Proyectos Estratégicos Orientados a la Transición Ecológica y a la Transición Digital» 2021

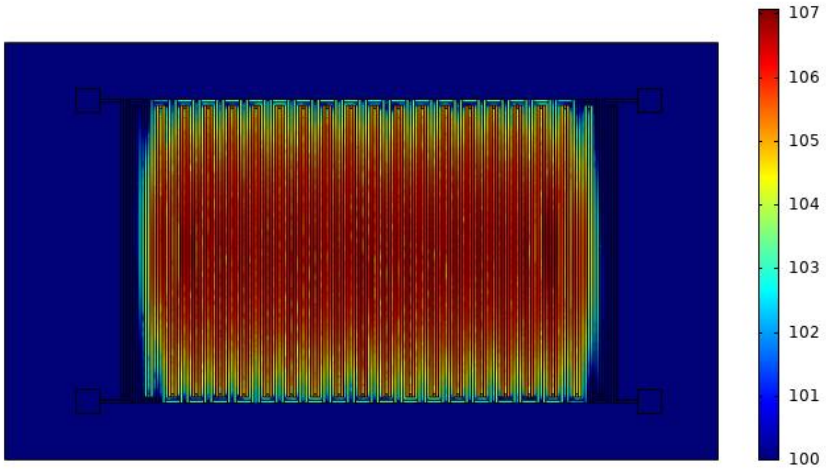

Figure 1. Finite element simulations using COMSOL Multiphysics. This simulation represents the temperature distribution among the electrodes when 5 V are applied. The room temperature considered is 25ºC

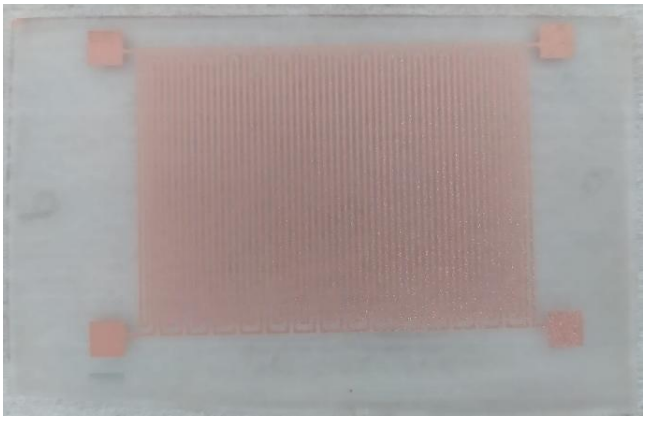

Figure 2. Copper electrodes before the electroplating process.

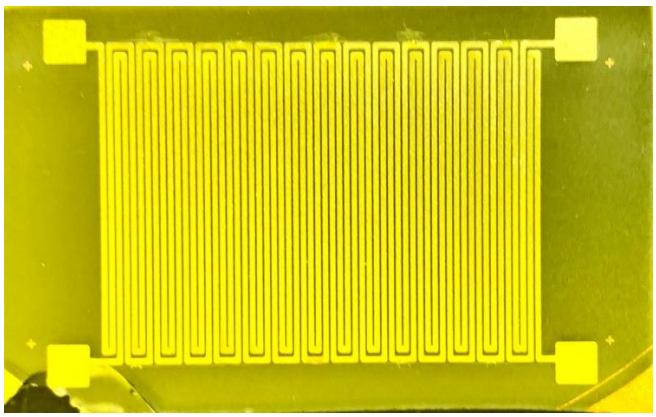

Figure 3. Final structure of the electrothermal sensor.

Ultra-thick grayscale ellipsoidal structures for X-ray focusing using scanning-laser direct write lithography

Giulia Malvicini[1,*], Muhammad Refatul Haq[1], Jan Erjawetz[2], Helmut Schift[1]

[1] Paul Scherrer Institute, Laboratory for Nano and Quantum Technologies, 5232 Villigen PSI, Switzerland
[2] XRnanotech, Parkstrasse 1, 5234 Villigen, Switzerland
e-mail: giulia.malvicini@psi.ch

Keywords: Grayscale lithography, Direct write lithography, X-ray optics, surface roughness.

Ellipsoidal or parabolic mirrors, serve as highly efficient focusing elements for X-ray beams. In a perfect ellipsoid, rays emitted from one focal point reflect off the internal surface and converge precisely at the second focal point, enabling sharp and efficient beam focusing (Fig. 1) [1]. In contrast, a parabolic mirror focuses collimated (parallel) incoming rays to a single focal point, making it especially suitable for distant or quasi-collimated X-ray sources. In practice, however, only a partial section of the ellipsoid or paraboloid – is fabricated and used in grazing-incidence geometry. Conventional methods, such as thermal drawing of glass capillaries, provide excellent surface quality with RMS roughness below 1 nm [1], but they offer limited flexibility in shaping complex focusing geometries.

Scanning-laser direct write lithography (DWL) offers an attractive alternative for the fabrication of customized three-dimensional (3D) surfaces. By exposing photosensitive materials with varying local doses, structures with continuous topographies can be created directly from computer-aided designs. In positive-tone photoresists, the exposed regions are selectively removed during development, revealing the desired 3D profile without the need for additional etching steps [2].

The purpose of this work is to develop a flexible, high-precision fabrication method, using grayscale DWL in thick photoresist, for freeform X-ray reflective focusing mirrors, overcoming the geometric limitations of conventional methods. [2]. By modulating the local exposure dose in a positive-tone resist (*mr-P 22G_XP*, micro resist technology GmbH) with up to 1024 grayscale values, we achieve smooth, continuous topographies with depths exceeding 80 µm, with potential extension beyond 200 µm [4]. The process allows the translation of computer-aided designs into 3D optical surfaces. The only required calibration step is determining the resist's contrast curve, i.e., the developed thickness as a function of dose, where each dose level corresponds directly to a grayscale value in the exposure file. The challenge lies, besides the processing of thick Novolak-based grayscale resists, in the generation of surfaces that are free from writing artifacts (stitching lines, steps) and enable postprocessing using established pattern transfer (replication) and smoothening (selective thermal reflow) processes down to the material limits, which is below 1 nm. The 3D profiles on ellipsoidal and lenses fabricated in mr-P_22G_XP using the described process in shown in Figure 3. Surface characterization revealed an RMS roughness of approximately 5 nm.

To enhance durability and enable reuse, the photoresist structures are first transferred into UV-curable, hybrid polymers such as OrmoComp (micro resist technology GmbH) and GMN-PS90 (OpTool AP), which serve as intermediate masters. These materials offer several advantages: they are flexible, inexpensive, easy to replicate, and capable of preserving high-resolution features. Additionally, they are less sensitive to particle contamination and can be UV-transparent. From these hybrid polymer masters further replications can be generated in PMMA substrates or other target materials as needed. The full fabrication process is shown in Fig. 2. The transfer process preserves both fine topographical features and global form accuracy..

Surface characterization was performed using laser scanning confocal microscopy (LSCM) and white light interferometry (WLI) to assess the structure accuracy and slope continuity. This process demonstrates that direct laser writing in thick photoresist layers, followed by transfer into hybrid materials, is a promising approach to fabricate customized 3D ellipsoidal mirrors, combining design flexibility, long-term stability, and optical surface quality required for advanced X-ray focusing applications.

[1] H. Yumoto *et al.,* Sci. Rep. **7** (2017) 16408.
[2] J. Erjawetz, D. Collé, G. Ekindorf, *et al.,* Micro- and Nanoeng. 15, 100137 (2022).
[3] Project CAPOFOX (CAPillary Optics for FOcusing of X-rays) by Swiss Nano Science Institute
[4] C. Schuster, G. Ekindorf, A. Voigt, *et al.,* Proc. SPIE 124970P (2023) 14 pp

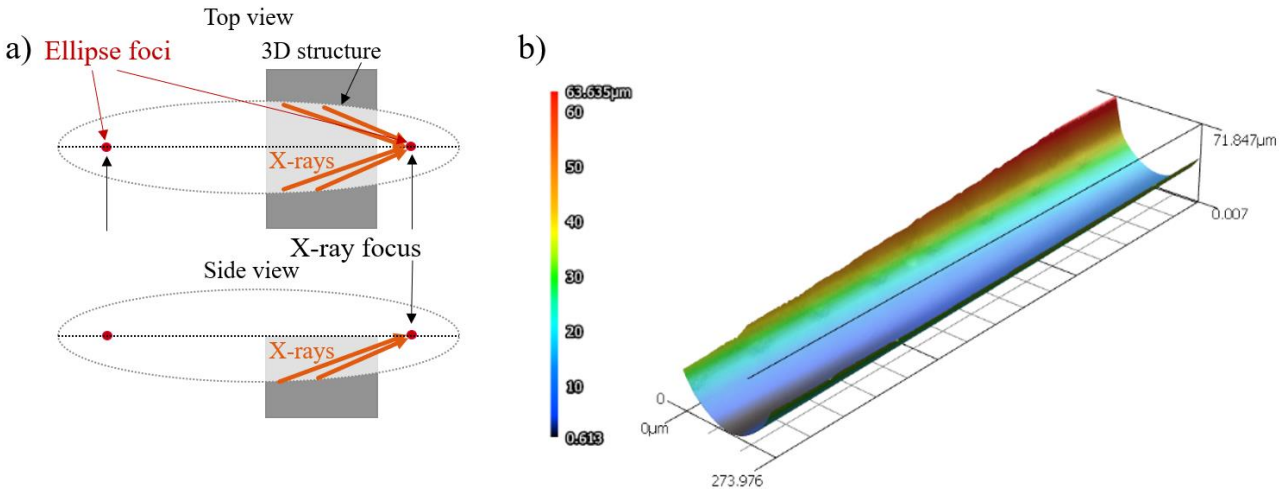

Figure 1. a) Schematic side and top view of an ideal ellipsoidal mirror, showing the reflection of x-rays from the source (first focal point) to the focus (second focal point). b) 3D confocal measurement of a fabricated 80 µm-thick ellipsoidal section in 100 µm-thick resist.

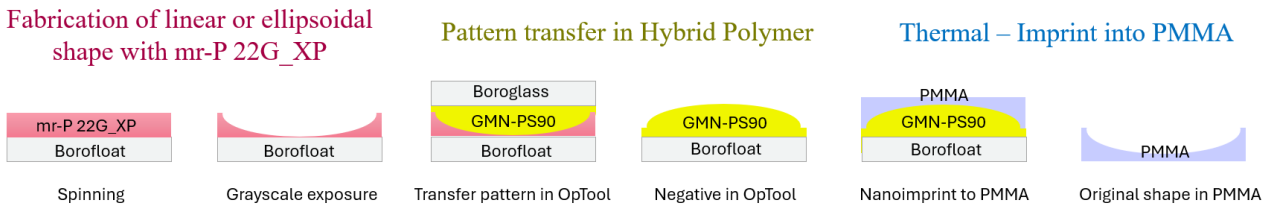

Figure 2. (a) Schematic of the fabrication process: exposure of *mr-P 22G_XP* grayscale resist via DWL, followed by development and pattern transfer into PMMA using hybrid polymers (*GMN-PS90* / *OrmoComp*) as imprint materials.

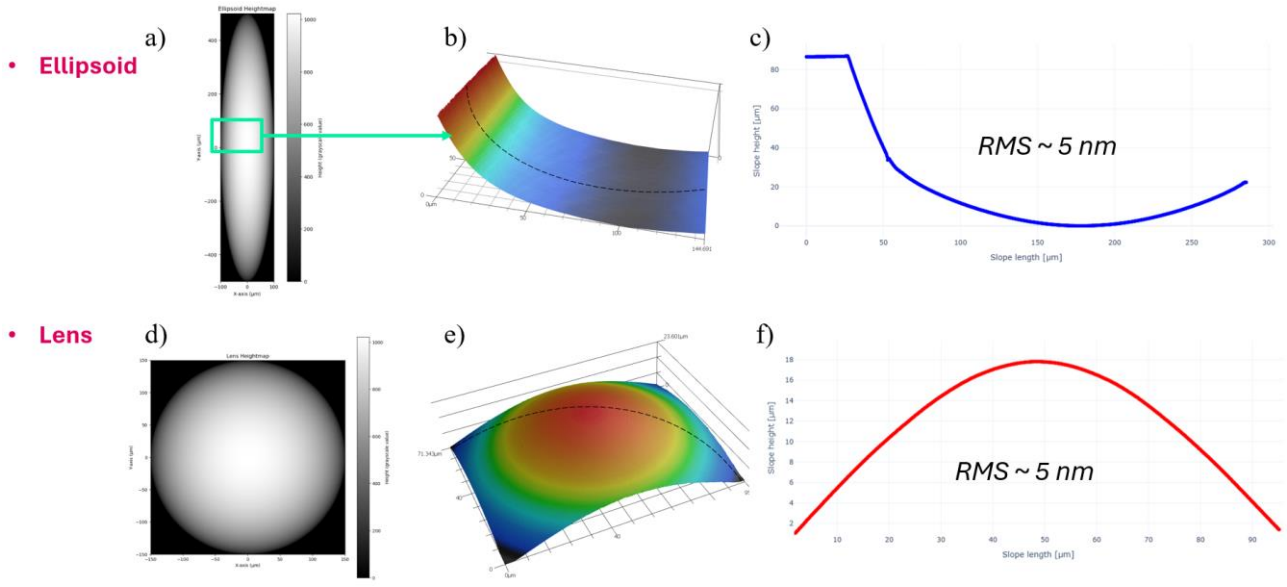

Figure 3. (a) Example grayscale dose distribution used to fabricate an ellipsoidal and lens structure, highlighting the 3D surface profiles. Ellipsoid (concave) and spherical lens (convex) in mr-P 22G XP. (b) Measured 3D profiles of a fabricated ellipsoid and plano-convex lens with laser scanning confocal microscopy. c) cross-sectional 2D profiles.

Effects of Annealing on Effective Young's Modulus of Ti/Au Multi-Layered Microcantilevers for MEMS Capacitive Accelerometers

Tatsuhiko Mori [a], Tomoyuki Kurioka [a], Shunkai Watanabe [a], Chun-Yi Chen [a], Tso-Fu Mark Chang [a], Katsuyuki Machida [a], Hiroyuki Ito [a], Yoshihiro Miyake [b], Masato Sone [a]

[a] Institute of Integrated Research, Institute of Science Tokyo, Yokohama 226-8501, Japan
[b] Department of Computer Science, Institute of Science Tokyo, Yokohama 226-8501, Japan
e-mail: mori@ames.pi.titech.ac.jp

Micro-electro-mechanical systems (MEMS) accelerometers are widely used in various applications [1]. In medical applications, MEMS accelerometers in the small size with high resolution and sensitivity are promising for the early diagnosis of serious diseases. To realize this, we have developed capacitive MEMS accelerometers with electrodeposited-Au proof mass using multi-layer technologies (Au-MEMS). The high density of Au enables both miniaturization and high sensitivity by suppressing Brownian noise [1].

Annealing is effective in removing the impurities (e.g., H_2 and H_2O) from the Au-MEMS, which can suppress the drift phenomena during the operation of the Au-MEMS [2]. The suppression of the drift phenomena is expected to improve its sensing accuracy. On the other hand, annealing often results in changes in the mechanical properties of metallic materials because their grain size is increased. Because the Au-MEMS is fabricated using Ti/Au multi-layer technologies, the annealing is expected to change the mechanical properties of the electrodeposited-Au components installed into the Au-MEMS.

In this work, we report the effects of the annealing of the electrodeposited-Au microcantilevers with Ti/Au multi-layered structures on their effective Young's modulus (E_{eff}). The cantilever structures can be regarded as a model structure of the spring component connected to the movable electrode; thus, the E_{eff} affects the sensitivity of the Au-MEMS. Therefore, it is crucial to evaluate the effects of the annealing on the E_{eff} of the electrodeposited-Au microcantilevers with Ti/Au multi-layered structure.

According to the literature [3], Ti/Au microcantilevers with a 5 μm-beam thickness and a 40 μm-beam width were fabricated. The beam lengths (L) were designed to be 600 μm, 800 μm, and 1000 μm, respectively (Figure 1). These cantilevers were annealed at 150 °C, 200 °C, or 300 °C. After annealing, their resonance frequency (f_c) was measured by using a laser Doppler vibrometer (LDV) with the application of 10 V between the bottom surface of the microcantilevers and the fixed electrode (Figure 2). E_{eff} was calculated based on the following equation [4]:

$$f_{\mathrm{c}} = 0.16154 \frac{t}{L^2} \sqrt{\frac{E_{\mathrm{eff}}}{\rho}}$$

where f_c is the resonance frequency, t is the beam-thickness (5 μm), L is the cantilever length, ρ is the density of Au, and E_{eff} is the effective Young's modulus.

Figure 3(a–c) shows the resonance frequency f_c plotted against $1/L^2$ for each annealing condition. Regardless of the annealing temperature, a good linear relationship between f_c and $1/L^2$ was observed. E_{eff} was calculated using the approximate linear fittings obtained from the least-squares approximation method for the plots of f_c. Figure 3d shows the relationship between E_{eff} of the Ti/Au microcantilevers and the annealing temperature. The increase in the annealing temperature led to a decrease in their E_{eff}, presumably due to the facilitation of the grain growth of the electrodeposited-Au layer.

In conclusion, we successfully evaluated the effects of the annealing temperature on the E_{eff} of the Ti/Au microcantilevers. Their E_{eff} was decreased by annealing them at a higher temperature. The lower E_{eff} is advantageous for improving the sensitivity of the Au-MEMS for the acceleration sensing. Therefore, annealing is found to be a powerful approach not only to suppress the drift phenomena of the Au-MEMS, but also to improve its sensitivity.

Acknowledgments: We appreciate T. Sakai, S. Iida, and T. Konishi at NTT-AT Corp. for their technical support. This work was supported by JST, CREST Grant Number JPMJCR21C5, Japan.

References:

[1] K. Machida et al., *ECS Trans.* 61 (2014) 21.
[2] A. Onishi et al., *Jpn. J. Appl. Phys.* 61 (2022) SD1028..
[3] S. Watanabe et al., *Micro Nano Eng.* 23 (2024) 100249.
[4] C.-W. Baek et al., *Sensors Actuators A Phys.* 117 (2005) 17–27.

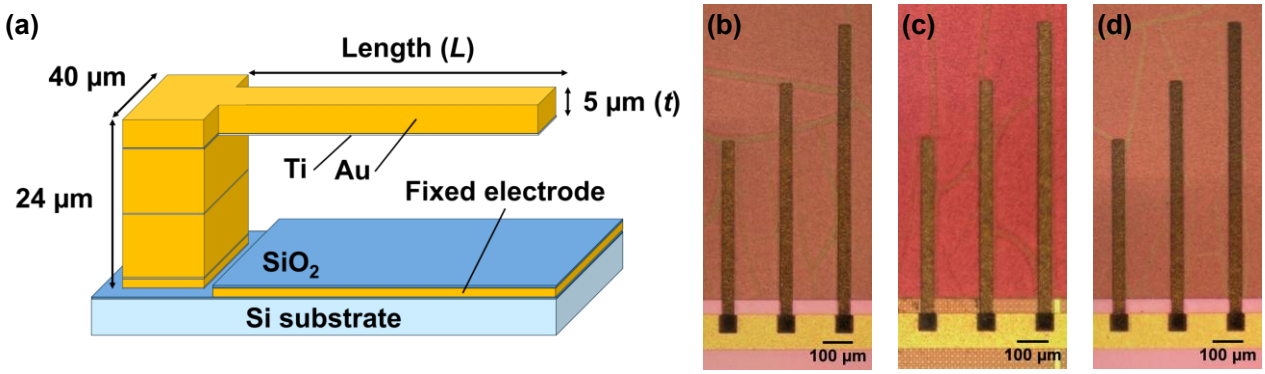

Figure 1. (a) Schematic illustration of the Ti/Au microcantilever. (b–d) Optical microscope images of the microcantilevers after annealing at (b) 150 °C, (c) 200 °C, and (d) 300 °C, respectively.

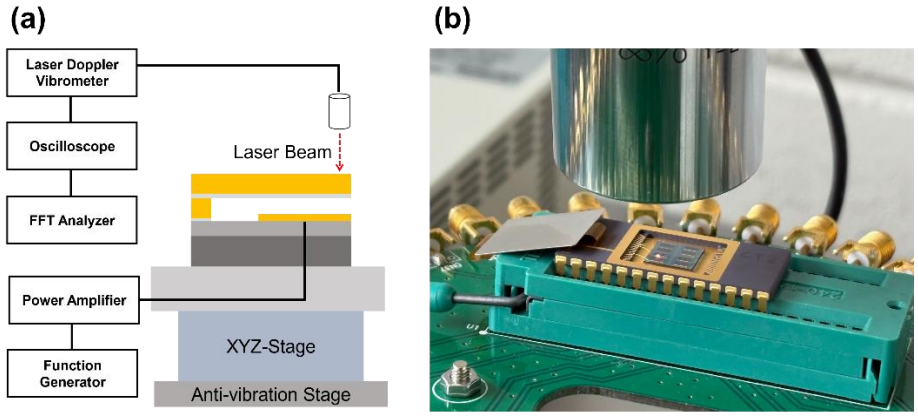

Figure 2. (a) Schematic and (b) photograph of the measurement setup for evaluating the resonance frequency f_c of the Ti/Au microcantilever using a laser Doppler vibrometer (LDV).

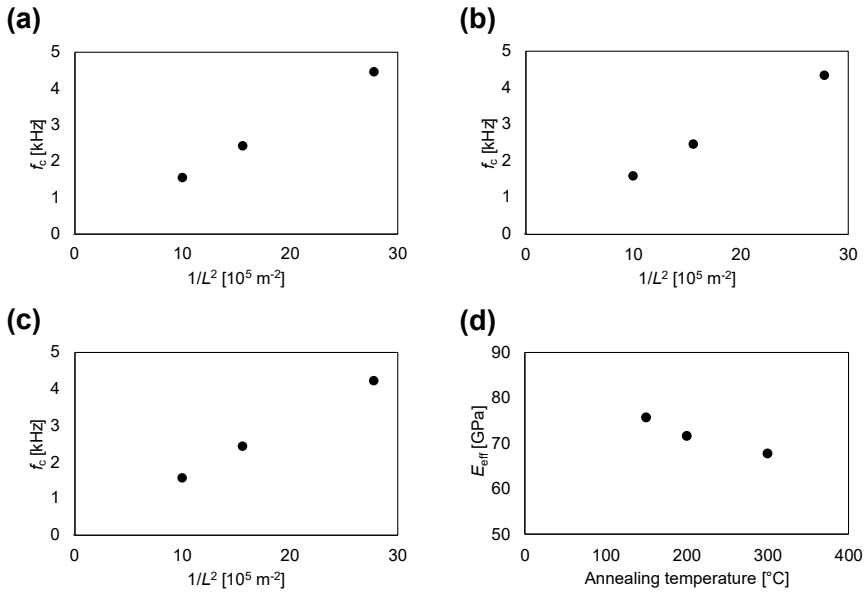

Figure 3. (a–c) Plots of resonance frequency f_c versus $1/L^2$ for Ti/Au microcantilevers annealed at (a) 150 °C, (b) 200 °C, and (c) 300 °C, respectively. (d) Effective Young's modulus E_{eff} as a function of annealing temperature.

Development of an In Situ Microfluidic System for Real-Time Control of Porous Microspheres Fabrication

Ji Hwan Han [a], Min Chul Shin [a], Chul Min Kim[b], Gyu Man Kim [a]

[a] School of Mechanical engineering, Kyungpook National University, Republic of Korea
[b] Department of Mechatronics Engineering, Gyeongsang National University, Republic of Korea
e-mail: gyuman.kim@knu.ac.kr

Porous microspheres with controlled internal structures have been considered as a potential platform to overcome the limitations of conventional solid microspheres [1, 2]. They offer a high surface area, excellent permeability, and the ability to protect encapsulated cells and bioactive molecules, making them highly attractive for biomedical applications such as tissue engineering and regenerative therapy [3]. However, most existing microfluidic approaches rely on injecting pre-mixed polymer and porogen phases, which leads to fixed internal morphology and limits the controllability of pore formation during the microsphere preparation process [4].

To address this challenge, we developed an in situ microfluidic system that enables the fabrication of highly porous polycaprolactone (PCL) microspheres with tunable pore sizes. In this system, PCL and camphene (CAMP) solutions are introduced independently and mixed directly within curved microchannels before droplet formation, eliminating the need for pre-mixing. The overall configuration of the microfluidic device and the mechanism of pore formation based on camphene crystallization and sublimation are shown in Figure 1.

Microspheres were fabricated using 3 wt.% PCL and 20 wt.% CAMP in dichloromethane as the dispersed phase, and PVA in water as the continuous phase. By adjusting the flow rate ratios of the polymer and porogen (PCL:CAMP = 1:1, 2:1, 3:1), we were able to precisely control both particle size and internal pore structure. Optical microscopy and field-emission scanning electron microscopy (FE-SEM) images confirmed these morphological differences, as presented in Figure 2.

To investigate the biological response to pore size variation, porous microspheres with three distinct pore sizes were subcutaneously implanted into animal tissue. Histological staining and immunofluorescence imaging revealed that microspheres with larger pores promoted more favorable tissue integration, enhanced cell infiltration, and exhibited reduced inflammatory responses compared to those with smaller pores (Figure 3).

These results should provide a clear basis for designing microsphere-based scaffolds with tunable biological interactions, highlighting the significance of pore structure control in future biomedical applications.

Acknowledgement:
This work was supported by the National Research Foundation of Korea (NRF) grant funded by the Korean government (MSIT) (No. 2019R1I1A1A01063257, RS-2023-00208717 and RS-2024-00406223), and by the Korea Institute for Advancement of Technology (KIAT) grant funded by the Ministry of Trade, Industry and Energy (MOTIE) (No. RS-2022-KI002563, HRD Program for Industrial Innovation).

[1] Y. Cai et al., Int. J. Nanomed. 8 (2013) 1111–1120.
[2] D. G. Ghosh Dastidar et al., Int. J. Pharm. 548 (2018) 34–48.
[3] C. M. Kim et al., Int. J. Precis. Eng. Manuf. 16 (2015) 2545–2551.
[4] J. H. Han et al., Colloids Surf. A Physicochem. Eng. Asp. 708 (2025) 135918.

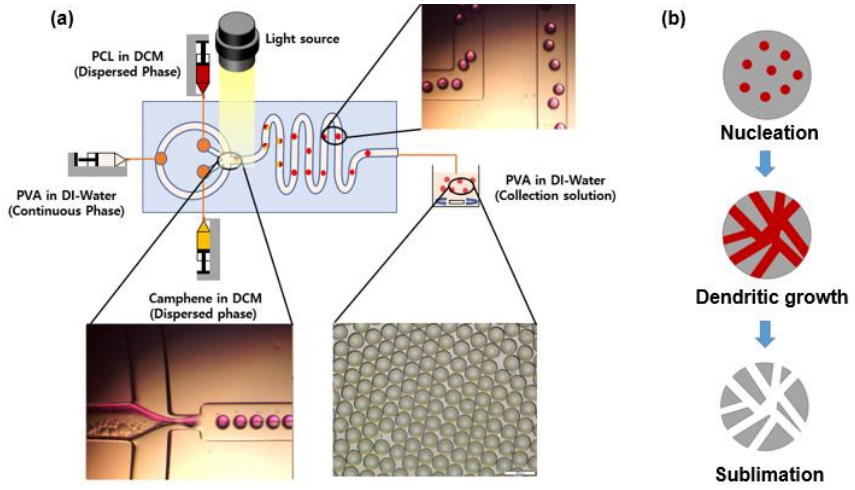

Figure 1. Schematics of the generation process of highly porous microspheres with controllable pores by an in situ microfluidic system: (a) overall microfluidic system, (b) pore structure generation process.

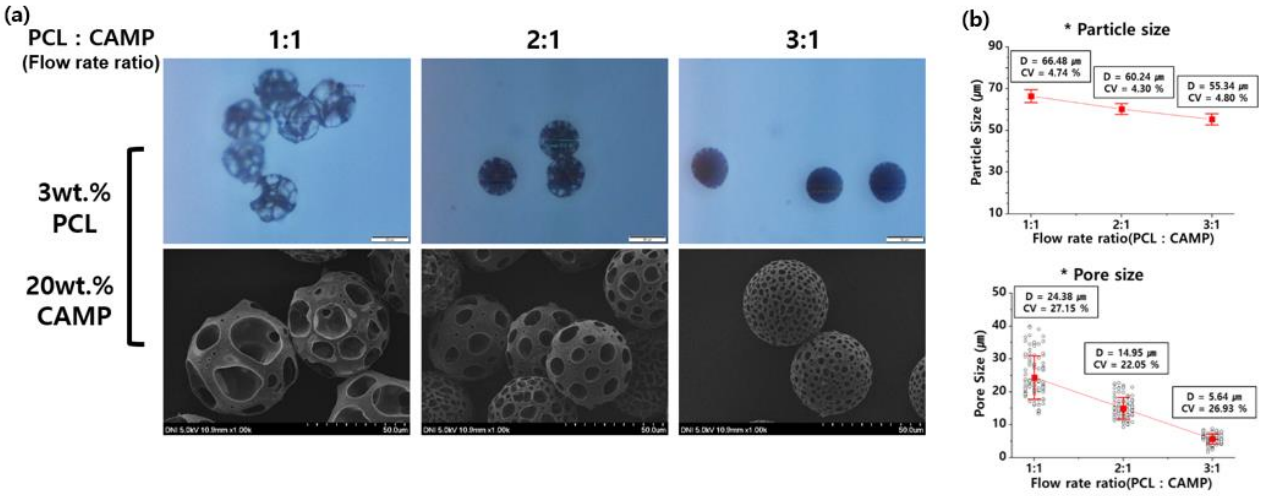

Figure 2. (a) Optical and FE-SEM images of PCL porous microspheres prepared according to flow rate ratio. (b) Graph of the PCL porous microspheres size according to the ratio of each flow rate (PCL : CAMP = 1:1, 2:1, 3:1)

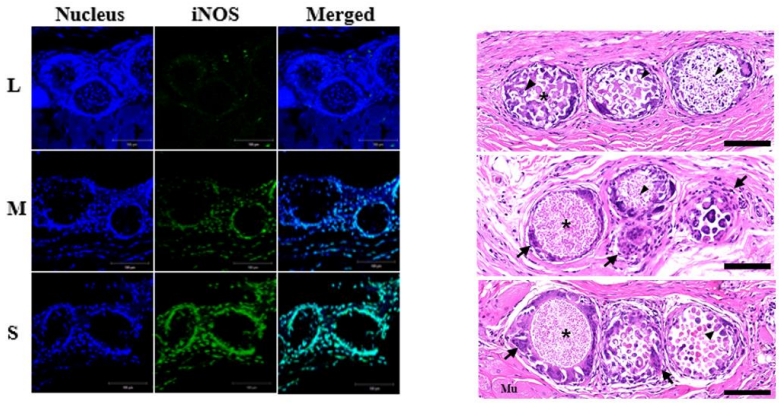

Figure 3. (a) The immunofluorescence microscopic images of inflammation related proteins iNOS expression in the subcutaneous tissue of the porous microsphere injected rat
(b) The representative histological images of in vivo biocompatibility analysis for microsphere (*; Porous MS. arrows; inflammatory cells. arrowheads: cells infiltrated in Porous MS .Mu; muscle tissue, HE; Hematoxylin-Eosin stain, MT; Masson-Trichrome stain, scale bar indicated 50 μm)

Slippery liquid-infused micropatterned surface for air-lifted analyte membrane formation

Seong Min Yoon [a], Woo Young Kim [a], Chae Hyeok Yoon [a], Young Tae Cho [a]

[a] Changwon National University, Changwon, 51139, Republic of Korea
e-mail: ytcho@changwon.ac.kr

Keywords : Slippery interface, Microstructure, Droplet evaporation, Membrane formation, High-sensitive

The drying process of droplets containing non-volatile solutes has significant potential in sensing applications such as disease diagnostics and hazardous substance detection [1]. Accordingly, interest in analyzing the evaporation dynamics of such droplets has been steadily growing. Typically, colloidal droplets leave behind a "coffee-ring" pattern in which particles accumulate near the three-phase contact line upon evaporation. However, this pattern can vary depending on the physicochemical properties of the colloidal solution and its interaction with the substrate. When particles are unevenly distributed over a wide area, as in the coffee-ring pattern, it can lead to signal distortion and reduced reproducibility during detection, ultimately lowering the sensitivity of the sensor [2]. Therefore, forming a particle deposition pattern that is uniform and highly localized is essential for enhancing sensing performance. To address this challenge, extensive research has focused on modifying substrate surface properties to overcome the limitations of conventional detection. For example, micropatterned surface can increase the contact angle and reduce the contact area between the droplet and the substrate [3]. Alternatively, slippery liquid-infused porous surfaces (SLIPS) can minimize contact line pinning, allowing droplets to contract and concentrate particles in a smaller area [4]. However, these approaches often suffer from overlapping signals between the residual particles and the substrate after evaporation, thereby compromising both sensitivity and reproducibility. However, these approaches often suffer from overlapping signals between the residual particles and the substrate after evaporation, thereby compromising both sensitivity and reproducibility.

Using UV nanoimprint lithography (UV NIL), we fabricated a hexagonal grid pattern on a polydimethylsiloxane (PDMS)-based organogel substrate [5]. A lubricant layer was applied to the patterned surface, followed by UV exposure to induce the formation of PDMS brushes, thereby imparting slippery properties. To evaluate the aggregation behavior, we deposited sessile droplets of deionized water containing polystyrene nanoparticles and measured the time-dependent contact angle, contact diameter, and aggregation area. Experiments were conducted under identical conditions on hydrophilic and hydrophobic patterns for comparison, and the results showed that particle aggregation was most narrowly concentrated on the slippery pattern (**Figure 1**). In addition, the slippery pattern induced the formation of air pockets, leading to the development of a membrane over the pattern during droplet evaporation (**Figure 2**). These results demonstrate the potential of the substrate as a SERS platform capable of enhancing detection sensitivity and reproducibility, thereby overcoming the limitations of conventional detection methods

Acknowledgement
This work was supported by the National Research Foundation of Korea(NRF) grant funded by the Korea government(MSIT)(No. RS-2023-00238462, RS-2019-NR040067) and Korea Institute for Advancement of Technology (KIAT) grant funded by the Korean government (MOTIE) (141588607, Additive Manufacturing Technology Innovation Alliance for Aerospace/Small Modular Reactor/Defense Industry).

References
[1] Yakhno, T. A et al., Tech. Phys. 55 (2010) 929–935.
[2] Lian. H et al., Appl. Surf. Sci. 499 (2020)143826.
[3] J. E. George et al., Sens. Actuators B Chem. 272 (2018) 485-493.
[4] S. Yang et al., Proc. Natl. Acad. Sci. 113.2 (2016) 268–273.
[5] Zhao. X et al., ACS nano. 15 (2021) 13559-13567.

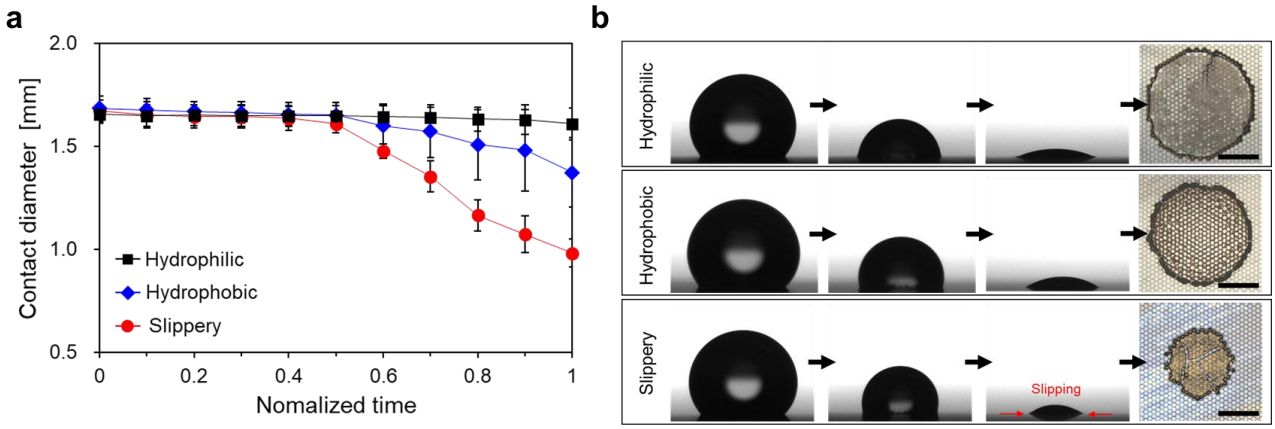

Figure 1. a) Contact diameter of a colloidal droplet over time on hydrophilic, hydrophobic and slippery micropatterned surfaces. b) Evaporation of colloidal droplet and top-view images of the resulting evaporation on hydrophilic, hydrophobic and slippery micropatterned surfaces (scale bar: 500 µm).

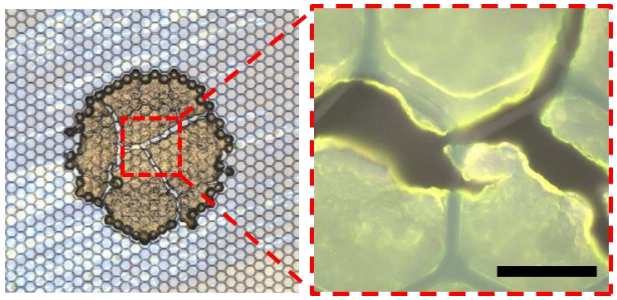

Figure 2. Top-view image of a membrane formed on a micropatterned slippery surface (scale bar: 20 µm).

Mastering the growth of centimetric sp^2-hybridized boron nitride films for optoelectronic devices

L. Tailpied [a], M. Cornu [a], F. Fossard [a], J.-S. Mérot [a], C. Grekobi [a], J. Lagrave [a]
J.-M. Decams [b], A. Loiseau [a], A. Andrieux-Ledier [c]

[a] *Université Paris-Saclay, ONERA, CNRS, Laboratoire d'étude des microstructures (LEM), 92322 Châtillon*
[b] *Annealsys, 139 rue des Walkyries, 34000 Montpellier, France*
[c] *DPHY, ONERA, Université Paris-Saclay, F-92322 Châtillon, France*

e-mail: amandine.andrieux@onera.fr

In the recent years, sp²-hybridized boron nitride (sp^2-BN) has been identified as a key component for the development of high-performance 2D material platforms towards applied devices. Its unique properties - including a large band gap (> 6 eV), chemical inertness, atomically flat surface free of dangling bonds and small lattice mismatch with graphene (less than 1.7%) [1] - give it a pivotal role in van der Waals heterostructures elaboration. Indeed, sp²-BN has been identified as the ideal insulating substrate and encapsulating layer to achieve the highest mobility or best optical properties in graphene or other 2Ds channels, with strong implications for efficient electronic, optoelectronic and spintronic devices [2]. However, realising the potential of BN-based electronic platforms requires continuous, atomically flat BN films on a large-scale with a controlled thickness ranging from a monolayer to 50 nm, depending on the targeted application. To date, proof-of-principle demonstrations showing ultimate performance have been obtained using exfoliated flakes from high-quality bulk crystals. This fabrication method seems unsuitable for practical applications due to the low yield and quality limitations of the nanosheets produced, such as the small lateral size, lack of homogeneity and thickness control [3]. In parallel, large-scale synthesis is being developed, in particular by MBE, ALD and CVD [4]. However, real control of film thickness with high crystalline quality has not yet been achieved.

In this context, the aim of the research we have undertaken is to develop the synthesis by chemical vapor deposition of multilayer sp²-hybridized BN films with structural specifications that meet these requirements. In collaboration with Annealsys, we have developed an epitaxial growth process on Ni (111) substrates on the centimeter scale, using borazine molecule as a source of boron and nitrogen atoms [5]. We have characterised the structure and the quality of BN films from the centimetre to the atomic scale using a wide range of techniques (OM, SEM, TEM, AFM, Raman spectroscopy) and in a quantitative manner. We show that by adjusting the synthesis parameters, we can obtain BN films with controlled thicknesses between 2 and 10 layers, homogeneous over several mm^2 with the same crystalline orientation and a hexagonal or rhombohedral stacking sequence. These are essential control points for the future integration of BN films into large-scale devices with other 2D materials.

[1] T. Niu et al. Prog.Surf.Sci. 90, 2015, 21-45
[2] K. K. Kim et al. Chem. Soc. Rev. 2018, 47, 6342-6369
[3] R. Frisenda et al. *Chem. Soc. Rev.*, 2018 ,47, 53-68
[4] A. Rigosi et al 2021 J. Phys. Mater. *4* 032003
[5] L.Tailpied et al. Cryst. Growth Des. 2024, 24, 18, 7432–7444

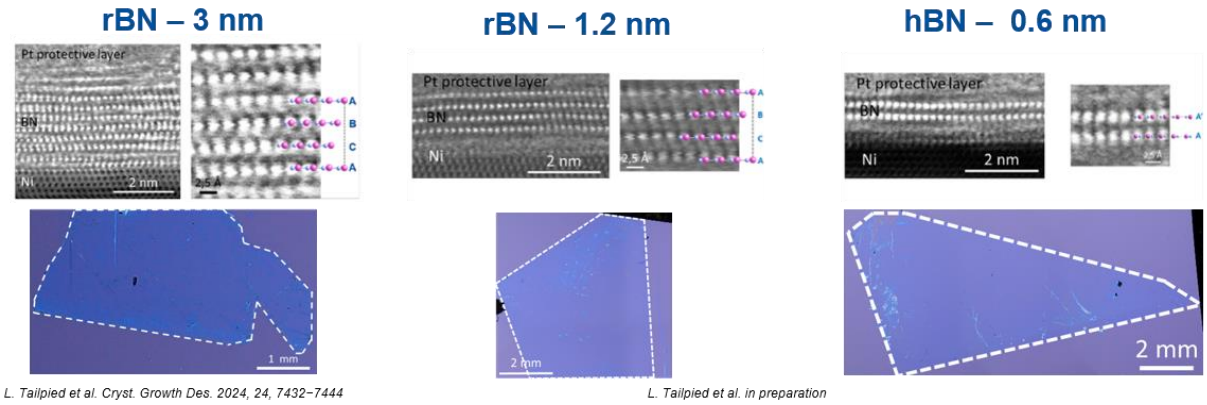

Figure 1. (top) High resolution STEM image in cross-section of the sp^2-hybridized boron nitride films synthesized by CVD on nickel (111) substrate, showing the different thicknesses and stacking sequence that can be obtained by varying the synthesis parameters. (bottom) Optical microscopy images showing homogeneous centimetric BN films transferred onto 90 nm SiO_2/Si substrate for devices fabrication

Fabrication of slanted diffraction gratings by electron beam lithography with tilted angle exposure

Naoya SHIBASAKI [a] and Jun TANIGUCHI [a*]

[a] Department of Applied Electronics, Tokyo University of Science
[*] e-mail:junt@te.noda.tus.ac.jp

1. Introduction

In recent years, with the development of three-dimensional (3D) technology, virtual reality (VR) and augmented reality (AR) glasses, which are the next generations displays, are becoming smaller and more popular [1]. The slanted diffraction gratings have the function which conveys information to wear's eyes. The slanted diffraction gratings (SDG) can be fabricated by Ultraviolet Nanoimprint lithography (UV-NIL) in a high refractive index resin using a working stamp [2]. The master mold for the slanted diffraction grating is fabricated using electron beam lithography (EBL) and reactive-ion beam etching (RIBE) at an oblique incident angle [2]. As this method requires many flows, we tried to fabricate the SDG mold directly using EBL for 45-degree tilted substrate. This process can save the RIBE process. In this study, the effect of acceleration voltage was investigated.

2. Experiment

Figure 1 shows a fabrication process of slanted diffractive grating. Positive tone EB resist (ZEP520A) was dropped onto the silicon substrate, then, spin coated at an initial rotation of 500 rpm for 5 s and at a main rotation of 3000 rpm for 120s (Fig. 1(1)). The Si substrate was baked at 80°C for 5 minutes the first time and 120°C for 20 minutes the second time. Then, thickness of this resist was measured with a contact step meter α-step (KLA-Tencor Japan) and confirmed to be about 400 nm. The substrate was installed in EBL machine with titled angle of 45° and EBL with acceleration voltage of 4 or 10 kV was carried out (Fig. 1(2)). The condition when drawing patterns at 4 kV were a L&S pattern with a line width of 90 nm and an interval of 270 nm, and a L&S pattern with a line width of 180 nm and an interval of 270 nm. And the Dose amount are 15, 20, 25 μC/cm^2. It is known that post exposure bake (PEB) condition at 120℃ for 10 minutes improves the development resolution [3]. To fabricate an aspect ratio of 2, the 10 kV drawing patterns were a L&S pattern with a line width of 90 nm and an interval of 360 nm. We compared how drawing at 45° angle affects development, with and without PEB at this condition (Fig. 1(3)). After these molds were developed with ZED-N50 (Zeon Corporation) for 30 seconds and rinsed with 2-propanol (Fig.1(4)). Platinum coating is applied to the molds release process, and the molds were then immersed in 1 wt% release coating agent (Optool DSX-E, Daikin Industries.) for 3 hours and baked at 120℃ for 5 minutes (Fig.1(5)). These molds were transferred to UV-curable resin (PAK-01CL, Toyo Gosei Co. Ltd.) by UV-NIL.

3. Result

Figure 2 shows transferred PAK-01CL SDG from the mold which was made with 4 kV, 20 dose and the drawing design was a L&S pattern with a line width of 180 nm and an interval of 270 nm. Widths of PAK-01 CL were wider than the design values. Also, the angles were slightly off from 45°. This is thought to be because of the forward scattering of EB. But Fig.2(a) had a suppression of angular and line width errors. Figure 3 shows transferred PAK-01CL SDG from the mold, which was made with 10 kV, 40 dose and the drawing design was a L&S pattern with a line width of 90 nm and an interval of 360 nm. The transferred PAK01-CL SDG had a height of 400 nm, a line width of 170 nm, a space of 257 nm, and an aspect ratio of 2 or greater.

4. Conclusion

We have transferred the SDG pattern from the mold which was fabricated by EBL with 45° tilted substrate. In Fig.2(a), the replicated slanted gratings with PEB can suprress the angular and line width errors. PEB is useful for high resolusion and 10 kV acceralation is enough to fabricate aspect ratio of 2 SDG mold.

Reference

[1] Zhitian Shi et al., Applied Surface Science, **588** (2022) 1-10
[2] Tapani Levola, Pasi laakkonen, Optical Society of America, **15** (2007) 2067-2074
[3] Hidetatsu Miyoshi, Jun Taniguchi, Microelectronic Engineering, **143**(2015) 48-54

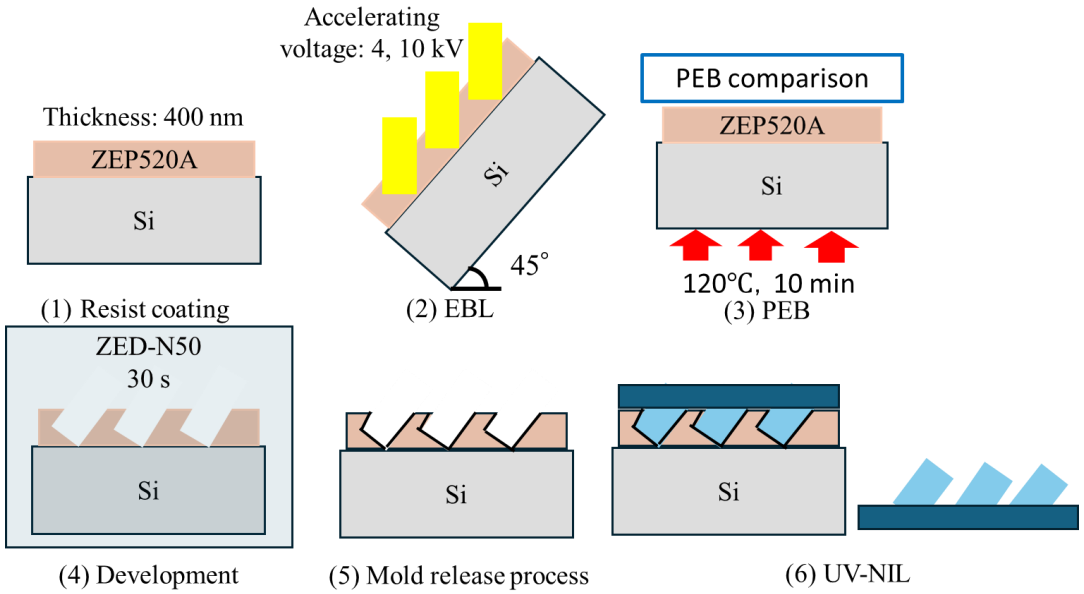

Figure 1. Fabrication process of slanted diffractive gratings.

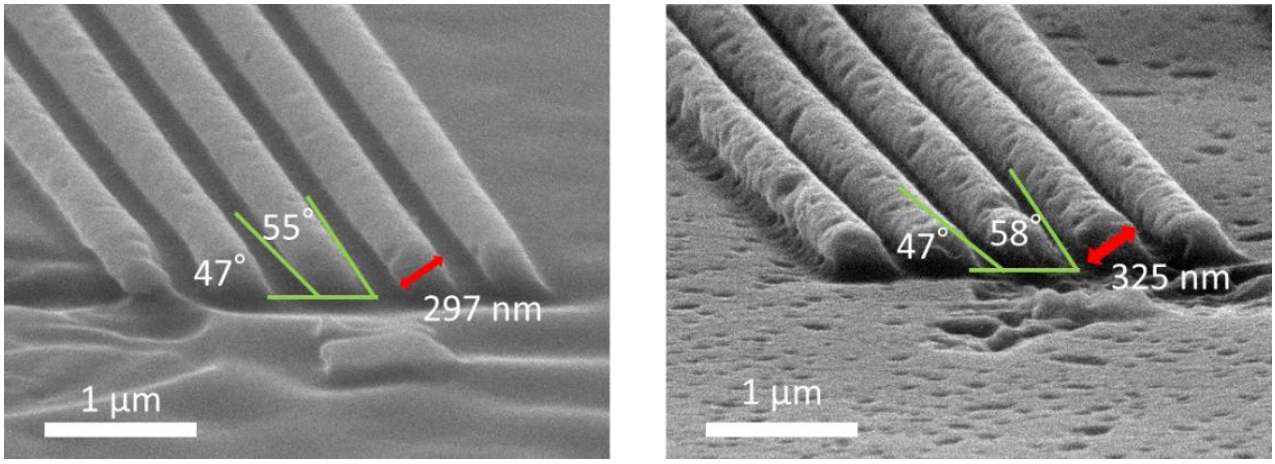

(a) (b)

Figure 2. Transferred PAK-01CL SDG at 4 kV, 20 dose and 180 nm line with design.
(a) with PEB (b) without PEB

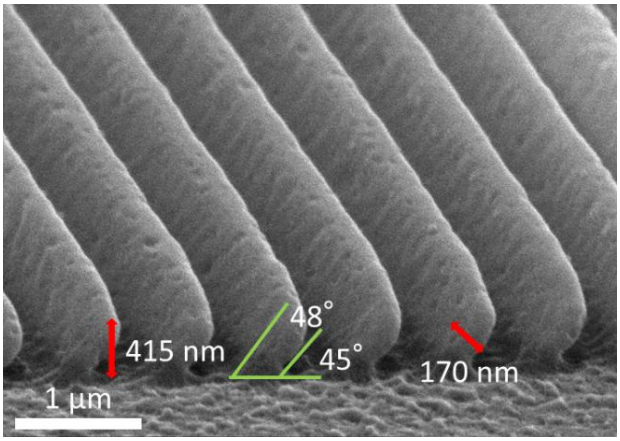

Figure 3. Transferred PAK-01CL slanted diffraction gratins at 10 kV, 90 nm line with design with PEB.

Abstract
EBL from an oblique angle was used to improve the fabrication flow of slanted gratings. The effect of PEB was verified and the aspect ratio was improved at 10 kV. As a result, the suppression of forward scattering was confirmed and an aspect ratio of 2 or higher was achieved.

Investigation of Pre-Stressed Membranes in Miniaturized Piezoresistive Diaphragm Pressure Sensors for Enhanced Sensitivity in High Vacuum

Jian Lu, Lan Zhang, Yuichi Kurashima, Hideki Takagi

National Institute of Advanced Industrial Science and Technology (AIST), Tsukuba, 305-8564, Japan
e-mail: jian-lu@aist.go.jp

The piezoresistive diaphragm pressure sensor stands out for its unique advantage of being independent of the gas type in the vacuum chamber and for offering a wider measurement range, making it widely used in the semiconductor industry for process monitoring and various other applications [1]. Our previous study demonstrated a miniaturized piezoresistive diaphragm pressure sensor, which exhibited a high sensitivity of 4.1 μV/(V·Pa) in the pressure range of 10 Pa to 100 Pa, with a measurement range extending up to atmospheric pressure [2][3]. However, it was found that the stress state of the membrane of the diaphragm near the neutral surface can significantly affect the overall performance of the sensor, particularly when the measured pressure P approaches the sealed cavity pressure P_0 [3]. This effect becomes more significant when the cavity is created by anodic bonding between silicon and glass, as opposed to Au-Au bonding between silicon chips, in order to reduce process difficulties and production costs. Although the structural engineering of sensing diaphragms has been extensively studied over the past decades [4], this work focuses on investigating membrane pre-stress as a means to achieve enhanced sensitivity under high-vacuum conditions.

Fig. 1 presents a schematic illustration of our miniaturized piezoresistive diaphragm pressure sensor, in which the membrane is formed from the active silicon layer of a silicon-on-insulator (SOI) wafer. Prior to anodic bonding with a 700 μm-thick glass wafer at the pressure of ~1 kPa (P_0), the SOI wafer was thinned to a thickness of 300 μm. A pre-stressed layer was designed on the membrane surface to ensure smoother transitions between upward (+) and downward (−) bendings, and is thereby expected to mitigate the effects of thermal mismatch stress between the silicon and the underlying glass [5], as well as the intrinsic stress of the active silicon layer [6]. The three-dimensional morphology of the membrane was observed using a laser confocal scanning microscope (VK-X3000, Keyence Corp.), as described in [3]. As shown in fig. 2, the sensors were packaged and subsequently set up in a vacuum chamber for evaluation of pressure dependency.

The estimated stresses of the 30 nm-thick TEOS SiO_2, 500 nm-thick TEOS SiO_2, and 50 nm-thick plasma-enhanced Si_3N_4 layers were approximately 80 MPa (tensile), 100 MPa (compressive), and 300 MPa (tensile), respectively. The measured 3D morphology of the membrane in fig. 3 clearly reveals that tensile stress (fig. 3(b) and 3(d)) may significantly facilitate smoother and more gradual transitions as the measured pressure P approaches the cavity pressure P_0. In contrast, when using the pre-stressed layer with compressive stress (fig. 3(c)), the membrane exhibits abrupt changes between upward (+) and downward (−) bending. The pressure-dependent deformation of the membranes with different pre-stress layers applied is summarized in fig. 4, which shows that all membranes saturated at approximately -21 μm of downward bending under atmospheric pressure.

Fig. 3 and fig. 4 indicate that the membrane without any pre-stressed layer also exhibits smooth pressure-dependent deformation. However, as shown in fig. 5, many of those sensors display an 'abrupt change in output' a few days after the assembly, which is believed to result from variations in the intrinsic stress of the active silicon layer across the SOI wafer [6], as well as gradual stress relaxation over time. Fig. 6 and fig. 7 suggest that high sensitivity and repeatability can be achieved across the full measurement range by sensors employing 30 nm-thick SiO_2 or 50 nm-thick Si_3N_4 layers, without any 'abrupt change in output.' Although the output levels are different, likely due to the distinct material properties of TEOS SiO_2 and plasma-enhanced Si_3N_4. Long-term evaluation is currently ongoing to better understand the underlying physics and assess suitability for practical applications. The results presented in this paper are valuable to relevant communities from both engineering and practical application perspectives. Further evaluation results and detailed discussions will be presented at the conference.

[1] A.S. Fiorillo, C.D. Critello, S.A. Pullano et al., Sens. Actuators A Phys., 281 (2018) 156–175.
[2] J.Lu, L.Zhang, Y.Kurashima et al., in Proceedings MNE2023, Berlin, Germany (2023) 789.
[3] J.Lu, L.Zhang, Y.Kurashima et al., in Proceedings MNE2024, Montpellier, France (2024) 39.
[4] V.C.Thakar, B.N.Patel, P.K.Karsh, Materials Today: Proceedings 65 (2022) 3683-3687.
[5] X.Zheng, W.Chen, X.Chen, in Proceedings NEMS 2010, Xiamen, China (2010) 524-527.
[6] H.Yang, M.Liu, Y.Zhu et al., Micromachines 14 (2023) 1510.

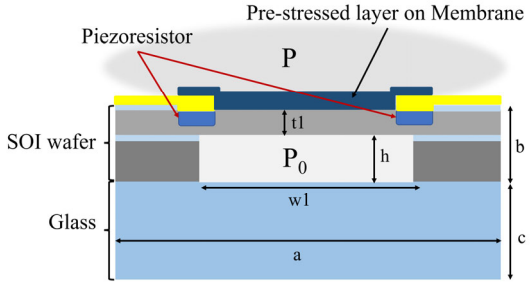

Figure 1. Schematic view of our diaphragm sensor structure. A pre-stressed layer was designed on the membrane surface to ensure smoother transitions between upward (+) and downward (-) bendings.

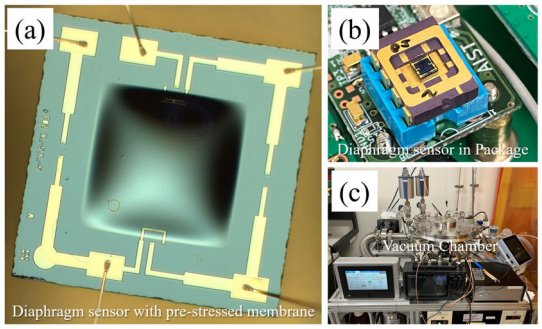

Figure 2. Photo of our fabricated sensor (a), wire-bonded into a ceramic package (b), and then set up in a vacuum chamber for evaluation (c).

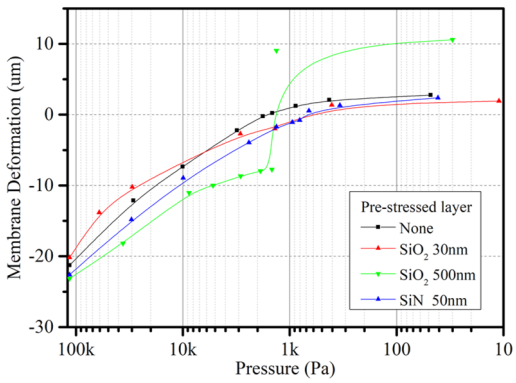

Figure 4. Membrane bending measured at various pressures P, with different pre-stress layers applied.

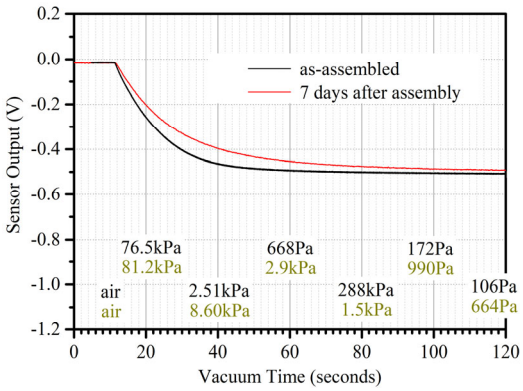

Figure 6. Measured sensor output versus pressure when using a 30nm-thick SiO_2 pre-stressed layer.

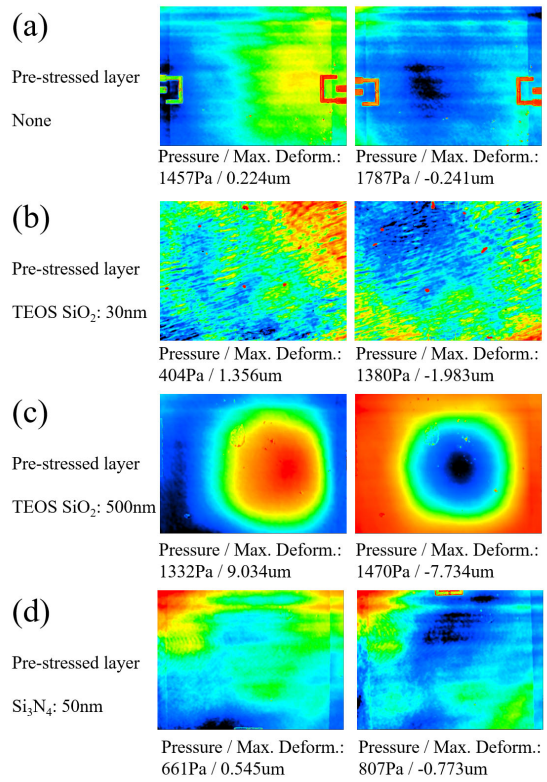

Figure 3. 3D morphology of the membrane before and after the deformation change from upward (+) to downward (-) bending as the measured pressure P approaches the cavity pressure P_0.

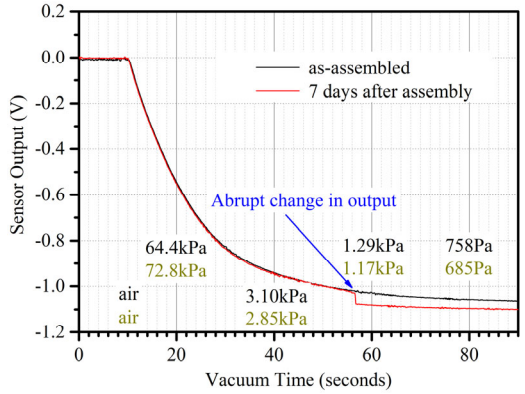

Figure 5. Measured sensor output versus pressure without using pre-stressed layer.

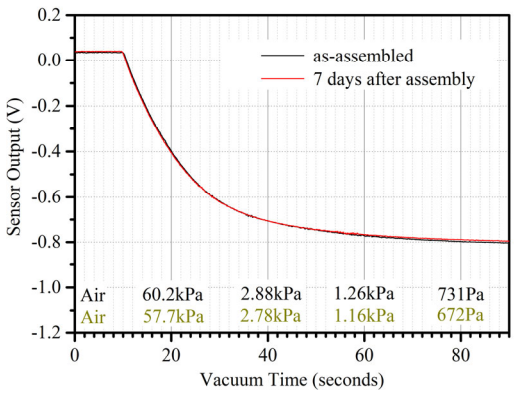

Figure 7. Measured sensor output versus pressure when using a 50nm-thick Si_3N_4 pre-stressed layer.

Integration of a metal nano-antenna structure into silicon substrates using surface-activated room temperature bonding

Yuichi Kurashima [a], Takashi Matsumae [a], Atsuhiko Maeda [a], Masaaki Oshita [a], Hideki Takagi [a]
Tetsuo Kan [b], Elyas Ashenafi Abadi [b], Daiji Noda [c], Ryo Ohta [c]

[a] National Institute of Advanced Industrial Science and Technology (AIST), Tukuba-city, 305-8564, Japan
[b] The University of Electro-Communications, Chofu-city, 182-8585, Japan
[c] Micromachine Center, Chiyoda-ward, 101-0026, Japan
e-mail: y-kurashima@aist.go.jp

Silicon-based near-infrared (IR) detection has attracted significant research interest across various fields. We have developed infrared detectors by fabricating periodic hole structures-approximately 100 nm in diameter and 500 nm in depth on the surface of Si, and embedding metal within these structures. [1] This approach is based on the principle of surface plasmon resonance, wherein carriers (electrons or holes) on the surface of metal nano-antennas resonate and oscillate, resulting in the absorption of IR light energy. The hot carriers generated by the absorbed IR light can overcome the Schottky energy barrier at the metal nano-antennas-Si interface and be detected as a photocurrent. To enhance the sensitivity of IR detection by increasing the photocurrent extraction area, we propose integration of the metal nano-antenna into the Si substrate by bonding the metal nano-antenna on a Si substrate to another Si substrate, as illustrated in Fig. 1. [2] In this report, we primarily evaluate the bonding characteristics between Si and the metal nano-antenna.

Pt patterns with a thickness of 20 nm were fabricated on an 8-inch Si wafer. Line-and-space (L&S) patterns with a width of 1 μm were designed at the center as dummy structures representing the metal nano-antenna structures used for IR light detection. A Pt thin film was incorporated around the central IR detection area to prevent uneven pressure during the bonding process. Two Pt line patterns extended from the IR detection region was connect to the two electrode pads. Samples cut from 8-inch Si wafer were thoroughly cleaned to remove residues (such as photoresist remaining), which could cause defects during the bonding process. The Pt-patterns on Si substrate were then bonded to the 4-inch Si wafers using surface-activated room temperature bonding. The bonding was performed under a load of 3000 N for 60 seconds. The bonded sample was annealed at 400 °C for 20 minutes in a nitrogen atmosphere to induce the formation of platinum silicide. The bonded interfaces were subsequently evaluated using an IR camera, transmission electron microscopy (TEM) and energy-dispersive X-ray (EDX) spectroscopy.

Fig. 2 shows an IR camera image between the 4-inch Si wafer and the Si substrate with the Pt patterns. There are no defects that can be seen by the IR camera, indicating that the entire wafer was uniformly bonded. Although the L&S pattern itself cannot be observed due to its small 1 μm scale, the around wiring and electrode pad regions appear distinctly different in color from the Pt-deposited areas, owing to the absence of Pt in those regions. Fig. 3(a) shows a TEM image of the interface bonded by the surface-activated bonding room temperature bonding, while Fig. 3(b) presents a TEM image of the interface after annealing at 400 °C for 20 minutes in a nitrogen atmosphere. In both images, the Pt patterns are clearly observed between the two Si substrates, and the bonding interfaces-both the Pt-Si interface and the interface between the deposited Pt film and the Si substrate-exhibit adhesion with no voids. In Fig. 3(b), the Pt region appears to have expanded to approximately twice the thickness observed in Fig. 3(a). Point elemental analysis was confirmed that the Pt had undergone silicidation as shown in Fig. 3(c), indicating that the observed expansion in the Pt region is attributable to the formation of platinum silicide.

Pt patterns as dummy structure representing the metal nano-antenna structure were fabricated on a Si substrate and bonded to another Si substrate using the surface-activated room temperature bonding. The bonding interface was found to be adhered with no voids or other defects caused by bonding process. In addition, annealing treatment of the bonded sample resulted in silicidation of the Pt pattern in Si.

Acknowledgments: This paper is based on results obtained from a project, JPNP14004, commissioned by the New Energy and Industrial Technology Development Organization (NEDO)

[1] S. Yasunaga et al., Adv. Mater. Interfaces 7 (2020) 2001039.
[2] H. Takagi et al., Jpn. J. Appl. Phys. Vol. 38 (1999) L1559.

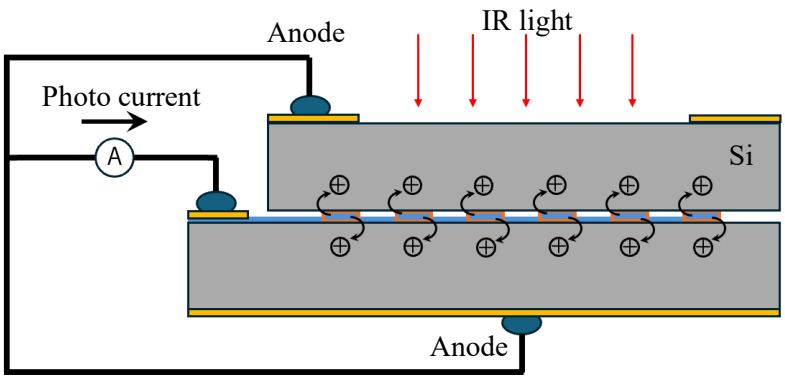

Figure 1. Schematic illustration of our proposed IR detection structure. The metal nano-antenna is sandwiched between Si substrates by a bonding process.

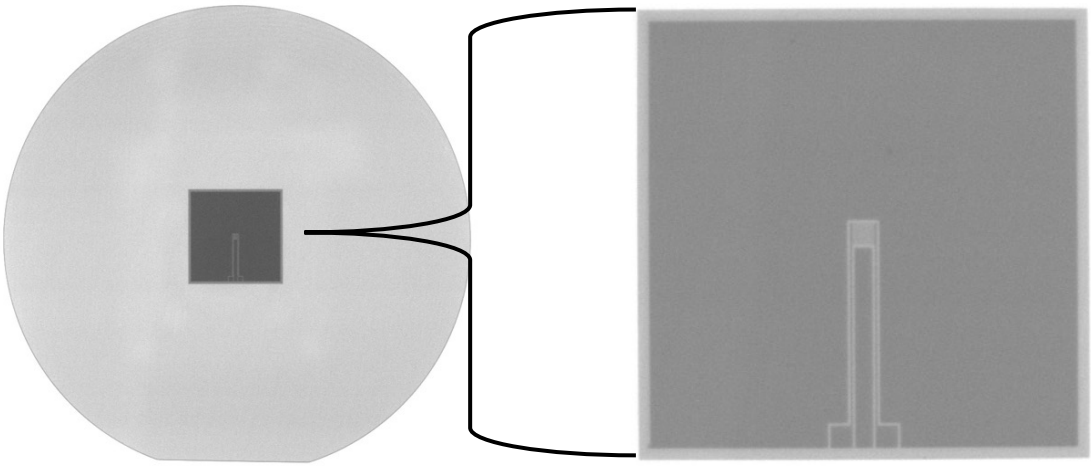

Figure 2. Infrared camera image of the sample bonded with a 4-inch Si wafer and a Si substrate with Pt patterns.

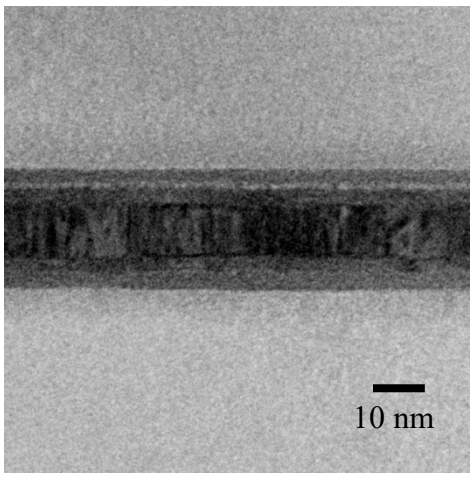

(a) Bonding interface after room temperature bonding.

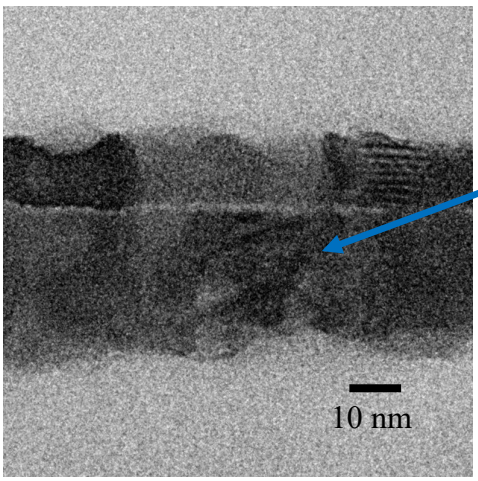

(b) Bonding interface after annealing at 400 °C for 20 minutes.

Element	Weight %	Atomic %
O K	0.2	1.4
Si K	11.4	46.3
Ar K	0.3	0.9
Pt M	88.1	51.5
Total	100	100

(c)Results of point elemental analysis by EDX.

Figure 3. Cross sectional TEM images of bonding interface. Point elemental analysis result by EDX.

Interface-Engineered Ferroelectric Tunnel Junctions with Ultra-High TER via Optimised P(VDF-TrFE) Crystallinity

Mohit Kumar Gautam[a], Roshni Babu[a], Ioannis Zeimpekis[a], Dimitra Georgiadou[a]

[a] School of Electronics and Computer Science, University of Southampton, Southampton, SO17 1BJ, United Kingdom
e-mail: D.Georgiadou@soton.ac.uk

Ferroelectric tunnel junctions (FTJs) are emerging as key building blocks for next-generation non-volatile memory and neuromorphic computing systems due to their low-power operation, non-destructive readout, scalability, and ability to exhibit memristive behaviour [1]. In particular, polymer-based ferroelectrics, such as poly(vinylidene fluoride-trifluoroethylene) (P(VDF-TrFE)), offer unique advantages, including mechanical flexibility and low-temperature processability, making them ideal candidates for integration into flexible electronics and hardware-efficient neuromorphic platforms. This work aims to develop high-performance coplanar nanogap electrode-based organic polymer ferroelectric tunnel junctions (FTJs) with high tunnel electroresistance (TER) ratio.

The 10-nm separated Al/Au nanogap electrodes are fabricated using adhesion lithography technique [2], and PVDF(TrFE) polymer film was deposited via spin-coating its solution in different solvents, such as cyclopentanone (CP), dimethylformamide (DMF), and dimethyl sulfoxide (DMSO), followed by annealing at 100 °C, 120 °C, 140 °C, and 160 °C for 2 hours in a glove box at ~3 mbar pressure (**Figure 1A**). A comprehensive structural analysis was made with grazing incidence X-ray diffraction (XRD), aimed at optimising β-phase crystallinity, which is essential for robust ferroelectric behaviour.

The asymmetric I–V characteristic displayed in **Figure 1B** is due to the unequal energy barrier modulation at the two metal-ferroelectric interfaces, i.e., gold and aluminium with P(VDF-TrFE). At the aluminium contact, a native Al_2O_3 layer introduces a fixed tunnelling barrier that remains largely insensitive to polarisation switching. In contrast, the Au/P(VDF-TrFE) interface is more electrostatically coupled to the ferroelectric layer, allowing significant modulation of the energy barrier during switching. When the polarisation points toward the Al electrode, negative bound charges reduce the effective barrier height at the Al_2O_3 interface, enhancing carrier tunnelling and producing a low-resistance state. Reversing the polarisation shifts the barrier modulation toward the Au interface, increasing the effective potential barrier and leading to a suppressed current or high-resistance state. This interfacial asymmetry in barrier height and screening efficiency is key to the polarisation-dependent resistive switching and the resulting ultra-high TER ratio of ~8×10^6 at 4V [3].

Figures 2A-C present grazing incidence XRD patterns of PVDF-TrFE thin films spin-coated on glass substrates using three different solvents and annealed at various temperatures. The β-phase peak at $2\theta \approx 19.8°$ becomes sharper and more intense with temperature, peaking at 140 °C. CP-based films (**Figure 2C**) exhibit the highest intensity and narrowest peaks, indicating superior β-phase crystallinity. At 160 °C, reduced peak intensity suggests thermal degradation. **Figure 2D** compares XRD patterns of CP-processed films on gold and aluminium substrates. Both support β-phase formation, but gold yields stronger, sharper peaks, particularly at 140 °C, and maintains higher crystallinity at 160 °C. Crystallite size analysis (**Tables 1** and **2**) supports these observations: CP films on gold reach ~14 nm across all temperatures, while aluminium films drop from ~12 nm at 140 °C to ~9 nm at 160 °C. These results confirm the significant influence of solvent and substrate on the crystallinity and thermal stability of PVDF-TrFE films.

In summary, the combination of a coplanar nanogap architecture, polarisation-driven tunnelling modulation, and structurally optimised P(VDF-TrFE) films enables ultra-high TER performance in ferroelectric tunnel junctions. These findings demonstrate the critical role of interface and crystallinity engineering in advancing low-temperature, flexible FTJ devices for future non-volatile memory and neuromorphic computing applications.

References:

[1] Park, Sung Hyuk, et al. "Ferroelectric tunnel junctions: promise, achievements and challenges." *Journal of Physics D: Applied Physics* (2024).

[2] Semple, James, et al. "Large-area plastic nanogap electronics enabled by adhesion lithography." *npj Flexible Electronics* 2.1 (2018): 18.

[3] Kumar, Manasvi, et al. "Colossal tunneling electroresistance in co-planar polymer ferroelectric tunnel junctions." *Advanced Electronic Materials* 6.2 (2020): 1901091.

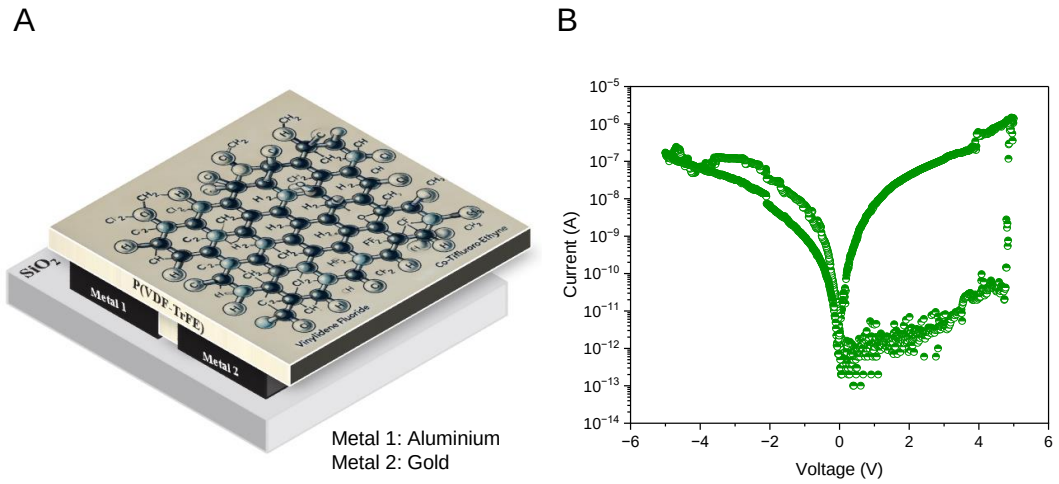

Figure 1: (A) 3D schematic of the proposed device. (B) I–V characteristics of the FTJs devices.

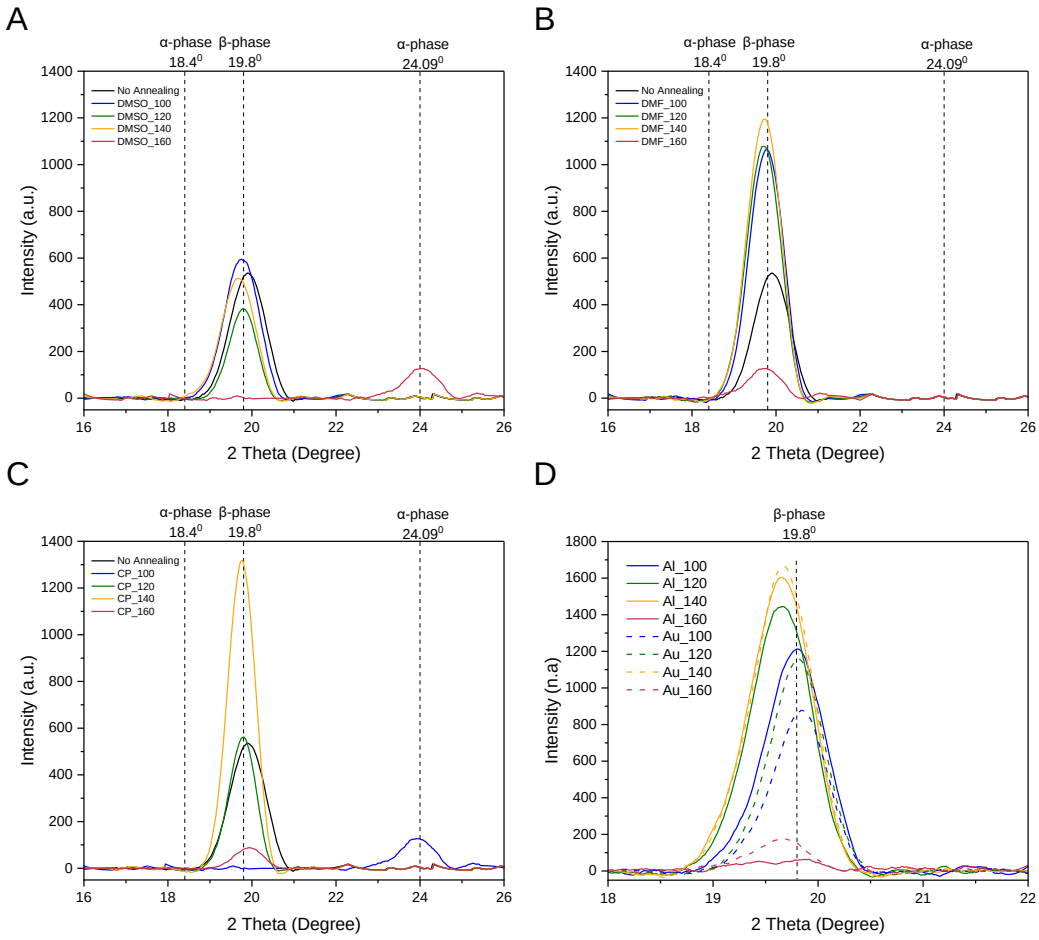

Figure 2: X-ray diffraction pattern of PVDF-TrFE thin film on glass substrate for (**A**) dimethyl sulfoxide (DMSO), (**B**) dimethylformamide (DMF) and (**C**) Cyclopentanone (CP) solvents, annealed at 100°C, 120°C,140°C and 160°C for 2 hours in a glove box at ~3mbar pressure. (**D**) X-ray diffraction pattern of PVDF-TrFE thin film on Aluminium and Gold substrate for Cyclopentanone (CP) solvent, annealed at 100°C, 120°C,140°C and 160°C for 2 hours in a glove box at ~3 mbar pressure.

Table 1: *Crystallite size of PVDF(TrFE)at various solvents and T*

Crystallite Size	100ºC	120ºC	140ºC	160ºC
CP (nm)	~11	~11	~12	~11
DMF (nm)	~9	~9	~9	~9
DMSO (nm)	~9	~11	~9	~12

Table 2: *Crystallite size of PVDF(TrFE) in CP on Al and Au*

Crystallite Size	100 ºC	120 ºC	140 ºC	160 ºC
Al (nm)	~12	~12	~12	~9
Au (nm)	~14	~14	~14	~13

Fabrication of metal nanodot arrays for LSPR biosensors with LOD of 1fg/mL using nanoimprint lithography process

Narae Jo [a], Jaejong Lee [b]

[a] Korea Research Institute of Standards and Science (KRISS), Daejeon 34113, South Korea

[b] Korea Institute of Machinery and Materials, 156 Gajeongbuk-ro, Yoseong-gu, Daejeon, 34103, South Korea

e-mail: jjlee@kimm.re.kr

Abstract

Nanoimprint lithography is a promising technology capable of rapidly and easily generating patterns over large areas at a lower cost compared to other lithography methods. As advancements in biosensor technology continue, there is an increasing demand for diverse nanostructures and nanoscale patterns. In particular, the LSPR(Localized Surface Plasmon Resonance) utilizes the phenomenon that occurs in nano-sized metals. To make an LSPR biosensor chip, a nano-sized metal array should be implemented in a large area substrate. In order to fabricate the nanoscale patterns on the substrate, the nanoimprint technology is one of good solutions. The silicon master's hole pattern with a diameter of 150nm, pitch of 300nm, and depth of 150nm, coated with UV resin (PFPE), was covered with Polycarbonate (PC) film and irradiated with UV light to fabricate a replica mold. Thermoplastic resin (Poly (methyl methacrylate (PMMA), mr-I PMMA 35k200) was spin-coated onto a glass substrate, and imprinting was conducted at 130°C and 5 bar pressure. After cooling and detachment of the replica mold, a chromium layer was deposited to protect the resin during O2 plasma etching. Subsequently, a Ti/Au(1/20nm) layer was deposited via e-beam evaporation, followed by lift-off with acetone solution. It was confirmed that the created sensor chip exhibited the LSPR phenomenon and was used to detect AFP (α-fetoprotein), a liver cancer marker. It was possible to detect the LSPR wavelength peak with a change amount depending on the concentration, and the limit of detection (LOD) was 1fg/ml. These nanostructure arrays fabricated through imprinting can serve not only as biosensors but also as a variety of optical components

[1] Haes, A.J.,VanDuyne,R.P., J.Am.Chem.Soc.124, 2002, 10596–10604.

[2] Lee, S.-W.,Lee,K.-S.,Ahn,J.,Lee,J.-J.,Kim,M.-G.,Shin,Y.-B., ACS Nano, 2011, 897–904.

[3] Johnson, P.B.,Christy,R.W., Phys.Rev.B.6, 1972, 4370–4379.

[4] Cegielski, Piotr Jacek, et al., Microelectronic Engineering 197, 2018, 83-86.

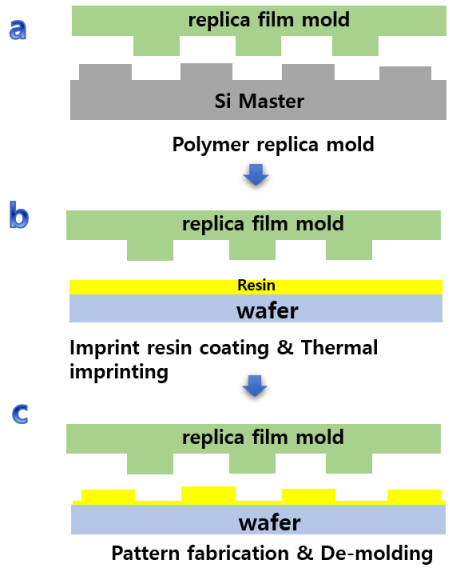

Fig. 1. Diagrams of (a) imprint process

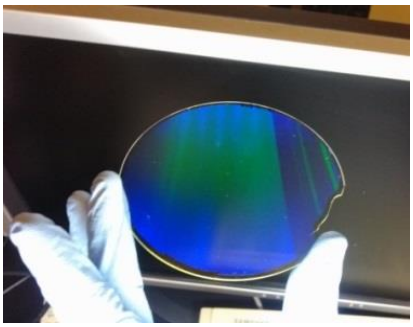

Fig. 2. Results of imprinting hexagonal structure hole arrays

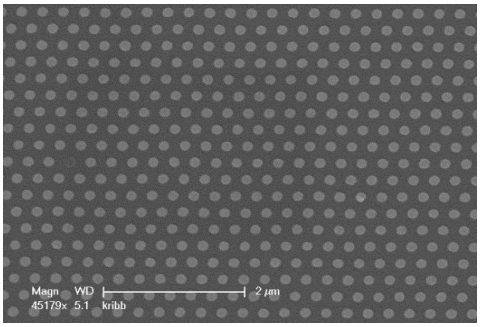

Fig3. SEM image of metal nanodot array

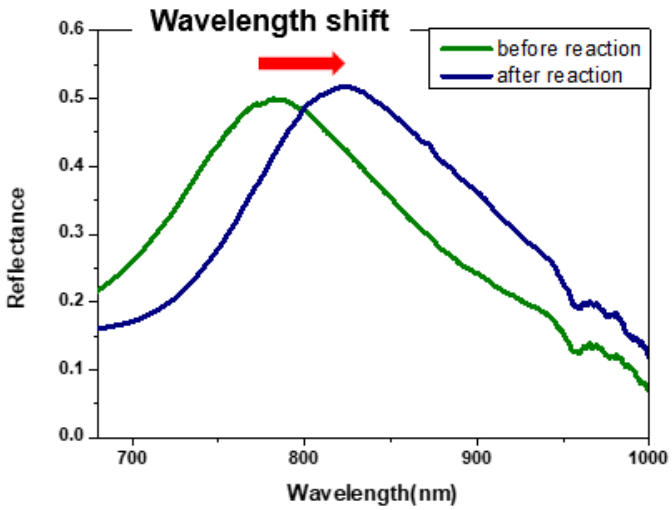

Fig4. LSPR wavelength peak change graph for AFP detection at 10ng/ml concentration

Study of the High-intensity Reflection Structure that used the Speckle Exposure Method

Atsushi Sekiguchi[1*, 2], Tomoki Iwaoka[3], Hiroshi Kobayashi[3], Toshiyuki Horiuchi[3], Ryouichi Tomomatsu[2], Yoshihiko Hirai[1] and Masaaki Yasuda[1]

[1] Osaka Metropolitan University, Graduate School of Engineering,
1-1 Gakuen-cho, Naka-ku, Sakai, Osaka 599-8531, Japan
[2] Litho Tech Japan Corporation, Nanoscience Laboratories,
2-6-6 Namiki, Kawaguchi, Saitama 332-0034, Japan
[3] Tokyo Denki University, Department of Advanced Machinery Engineering, Graduate School of Engineering,
5 Senju-Asahi-cho, Adachi-ku, Tokyo 120-8551, Japan
**sekiguchi-pdg@ltj.co.jp*

Cases have been reported of pedestrians being injured when they collided with vehicles while walking at night. While having pedestrians wear reflectors can help, drivers must often be quite close before the reflected light becomes visible, because the reflector does not have a structure that generates high-intensity reflections. We therefore considered using lithography technology to create a reflection structure that can generate high-intensity reflections visible from greater distances. Specifically, we developed a high-intensity reflection structure by using a photoresist with controlled molecular weight distribution and performing speckle exposure. We applied an F-2 resist with controlled molecular weight distribution onto an Si substrate and performed speckle exposure and development. The structure obtained was irradiated with white LED light to observe the reflections. The results indicated success in creating a structure that reflects light with high intensity. Additionally, we performed theoretical verification by carrying out simulations of the molecular size and reflectivity, the results of which are also reported here.
Keywords: Speckle exposure, Molecular weight distribution control, White LED light source, Biomimetics, High-intensity reflection structure

1. Introduction

Cases have been reported of pedestrians being injured when they collided with vehicles while walking at night. While having pedestrians wear reflectors can help, drivers must often be quite close before the reflected light becomes visible, because the reflector does not have a structure that generates high-intensity reflections. We therefore considered using lithography technology to create a reflection structure capable of generating high-intensity reflections with a similar shine as that given off by the jewel beetle (Fig. 1). (Chrysochroa fulgidissima) that are visible from greater distances.

Specifically, we developed a high-intensity reflection structure by using a polymer with controlled molecular weight distribution and performing speckle exposure. More specifically, we applied each of a polymer with controlled molecular weight distribution and a polymer without controlled molecular weight distribution onto an Si substrate and performed speckle exposure and development. We then irradiated the structures obtained with white LED light and observed the reflections. The results indicated that, by synthesizing a tandem-structured polymer with controlled molecular weight distribution, we had successfully created a structure that reflects light with high intensity. Additionally, we performed theoretical verification by carrying out simulations of the molecular size and reflectivity, the results of which are also reported here.

2. Synthesis of a polymer with controlled molecular weight distribution

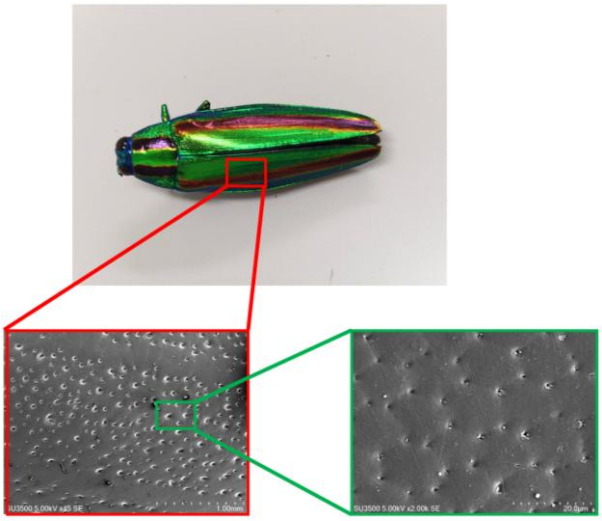

Fig. 1. Jewel beetle and its wing structure.

To create a structure with a reflection structure resembling the wings of a jewel beetle, we synthesized a polymer with controlled molecular size. We began by synthesizing a novolak resin. We placed meta-cresol 54 g (0.5 mol), para-cresol 54 g (0.5 mol), oxalic acid 0.284 g (0.012 mol), and pure water into a reaction flask, then gradually added 73 g (0.9 mol) of 37 wt.% formalin to the mixture over a period of 40 minutes while heating to 90 °C. The ratio of cresol to formalin at this time was 0.75. We maintained the mixture at 90 °C for 3 hours while stirring slowly to allow the methylolation reaction to proceed under catalysis of oxalic acid. We then added PGMEA and 5% oxalic acid solution and heated the mixture to promote polymerization through a condensation reaction. We allowed the polymerization to proceed for 10 more hours while slowly stirring the mixture at 90 °C. (It shows Fig. 2). [1-17]

We neutralized the polymer solution obtained with 5 % sodium hydroxide solution, then rinsed it with water to remove the oxalic acid catalyst. Dehydration was then performed with an evaporator.

Next, we performed fractionation to increase the molecular weight of the resin. Fractionation involves rinsing a resin with a solvent to dissolve and extract the low molecular weight components into the solvent, thereby separating the target component. The novolak resin solution obtained was transferred to a separating funnel, after which we added PGMEA and n-heptane at a ratio of resin : PGMEA : n-heptane = 1:5:6 by weight. We agitated the mixture for 3 minutes before allowing it to stand to separate the solution into two layers.

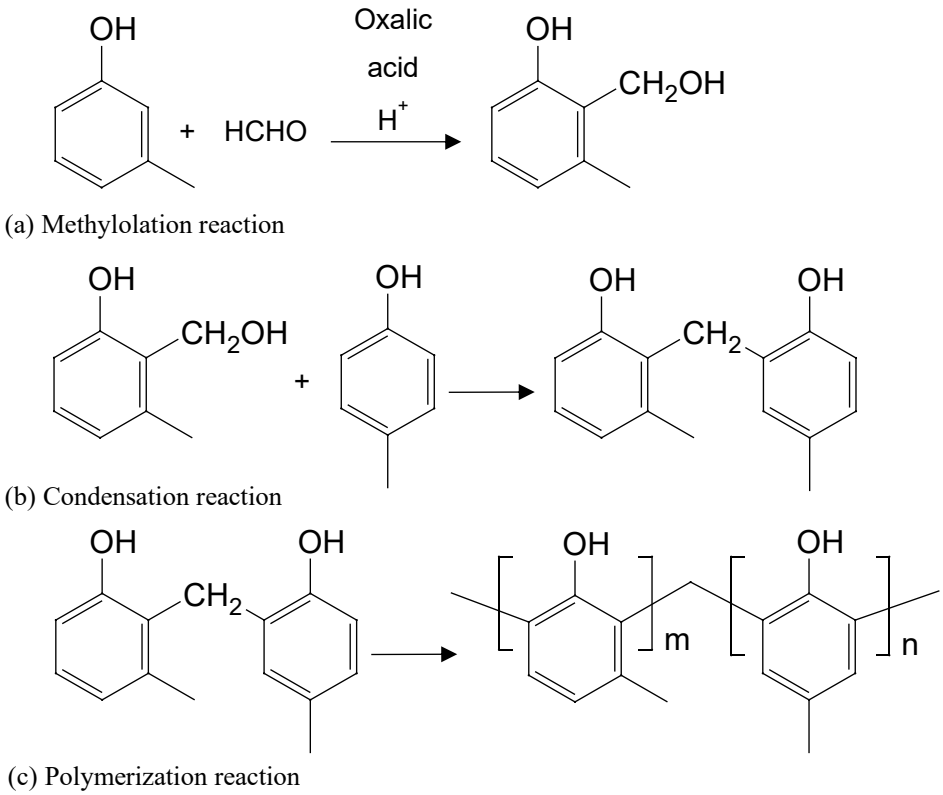

Fig. 2. Polymer synthesis.

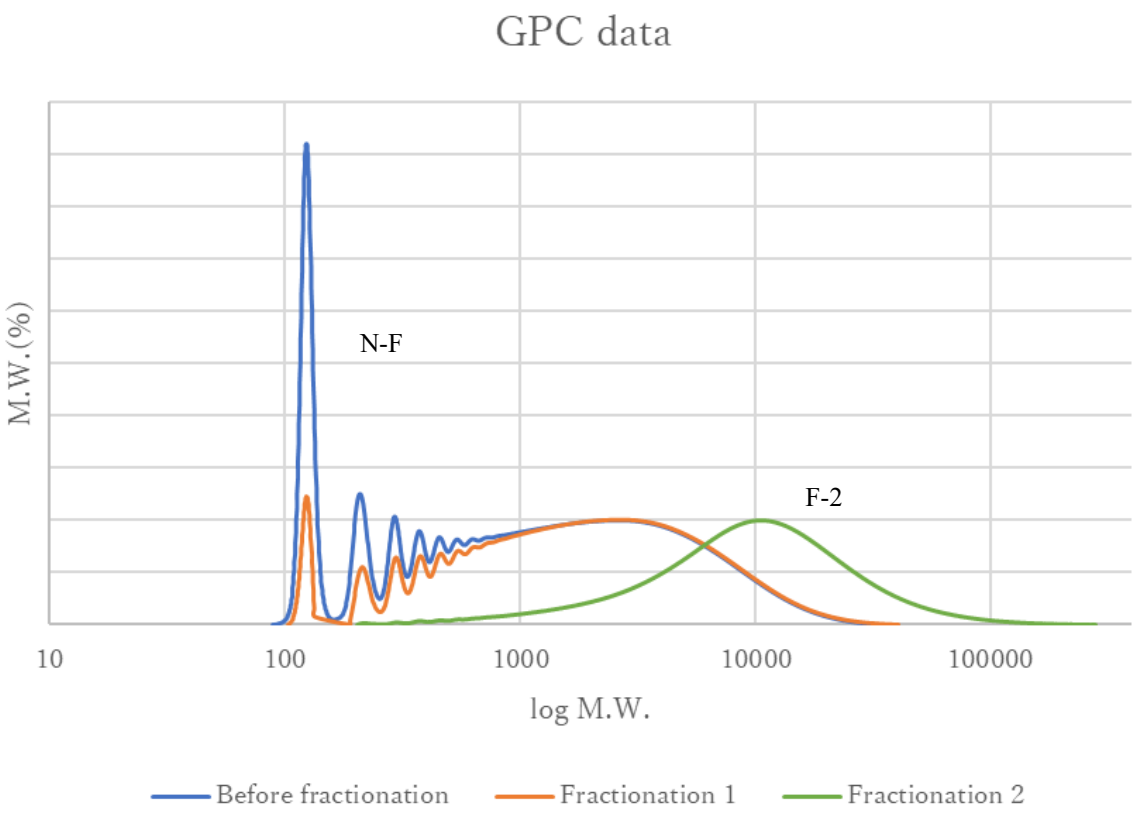

Fig. 3. GPC measurement results for the polymer before and after fractionation.

The upper layer is the n-heptane layer, in which the low molecular weight components are dissolved, while the lower layer is the PGMEA layer, in which the intermediate and high molecular weight components are dissolved. The fractionated resin solution can be obtained by separating the lower layer and removing the n-heptane using an evaporator. By repeating this fractionation process two more times while changing the ratio of PGMEA to n-heptane, we can remove the intermediate molecular weight components. We could finally obtain a polymer consisting only of high molecular weight components (F-2). We added a photosensitive material to the polymer before and after fractionation to produce resists. (It shows Fig. 3).

We added a photosensitive material to the above polymer at a ratio of 20 % by weight to obtain the

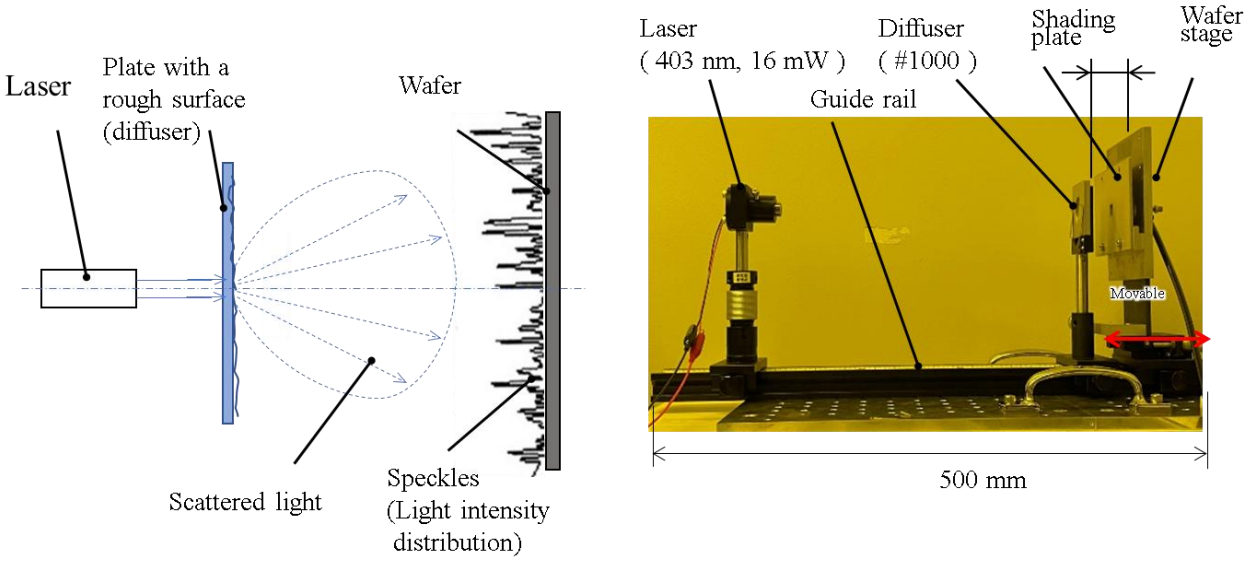

Fig. 4. Speckle exposure principle and equipment.

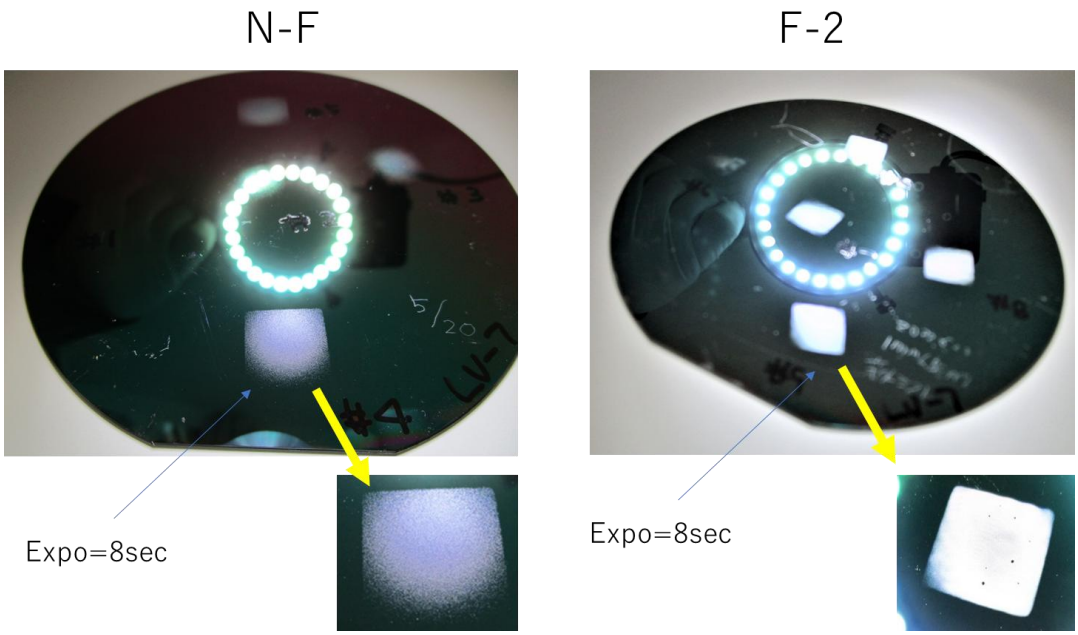

Fig. 5. Reflections of white light from the structures after speckle exposure and development.

resist material. The resist made of the polymer before fractionation is referred to as N-F and the resist made of the polymer after two fractionation steps as F-2.

3. Speckle exposure equipment

Figure 4 shows the outline and appearance of the speckle exposure equipment. The speckle exposure equipment is a system capable of performing exposure with random patterns. This system consists of a laser diode with a wavelength of 403 nm and an output of 16 mW, a diffuser plate (#1000, manufactured by SIGMAKOKI Co., Ltd.), and a wafer stage. The wafer is held in place by a vacuum chuck. They are linearly fixed on a guide rail [18-21].

To grasp the patterning characteristics efficiently and systematically, we performed experiments using a single wafer under various exposure conditions. We placed a shading plate in front of the wafer stage to confine the exposure to a 10-mm square area. The laser and the diffuser were separated by a space to allow the installation of additional collector lenses, as needed. This configuration allowed adjustment of the distance L between the diffuser plate and the wafer to any distance from 45 mm to 200 mm.

4. Experiments

We performed speckle exposure using non-fractionated (N-F) and twice-fractionated (F-2) resists.

We coated an Si substrate with each of these resists. The pre-bake conditions were 100 °C for 60 seconds. The film thickness was adjusted to 1,000 nm. We performed speckle exposure for 8 seconds for each resist and performed baking at 110 °C for 60 seconds after the exposure. The film was developed in an alkaline developer of 2.38 % TMAH for 60 seconds. We irradiated white light onto the resulting structures to observe the reflections (Fig. 5).

We found that the F-2 resist structure shines whiter than the N-F resist structure. Figure 6 shows the results of the F-2 resist subjected to 12-second exposure. The intensity of the reflected light from the F-2 resist exposed for 12 seconds was found to be even higher.

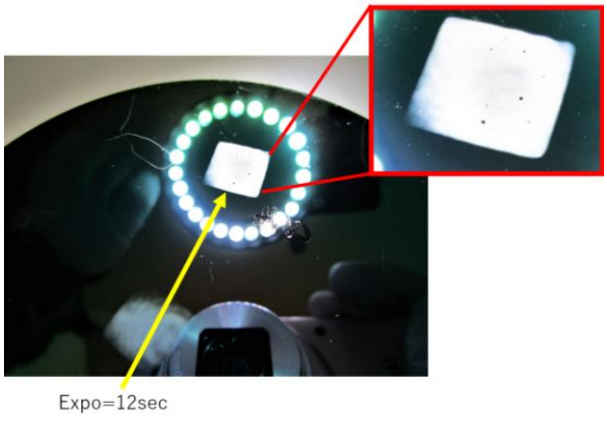

Fig. 6. Reflection from the substrate after development of F-2 resist exposed for 12 seconds.

5. Discussion

Figure 7 shows the results of SEM observations of the N-F and F-2 resist structures following development. It was found that a random structure forms on the surface of the resist pattern by speckle exposure. We observed that a nano-protrusion structure on the scale of 10 to 20 nm had formed on the surface of the speckle structure of the F-2 resist when observed at a high magnification of 100,000x. This structure is believed to result from having only high molecular weight components remaining in the resist after the removal of low molecular weight components by fractionation. Particle diameters ranged from 10 to 20 nm, approximately the same size as a single molecule of novolak resin. We will now discuss the reasons for the higher reflection intensity of the F-2 resist.

The SEM observation results show that a nanostructure on the scale of 10 to 20 nm forms on the surface of the F-2 resist pattern. When white light is incident on this structure, diffuse reflection is intensified, thereby increasing the reflection intensity (It shows Fig. 8).

6. Reflection simulations

We then simulated how reflection intensity is increased by the scale of the nanostructure.

We carried out analysis using the Lumerical FDTD (finite difference time domain) method [22-24]. This is generally a time series analysis method for simulating the propagation of electromagnetic waves and their interactions by discretizing the Maxwell equations with a fine mesh (lattice points) in space and time and calculating

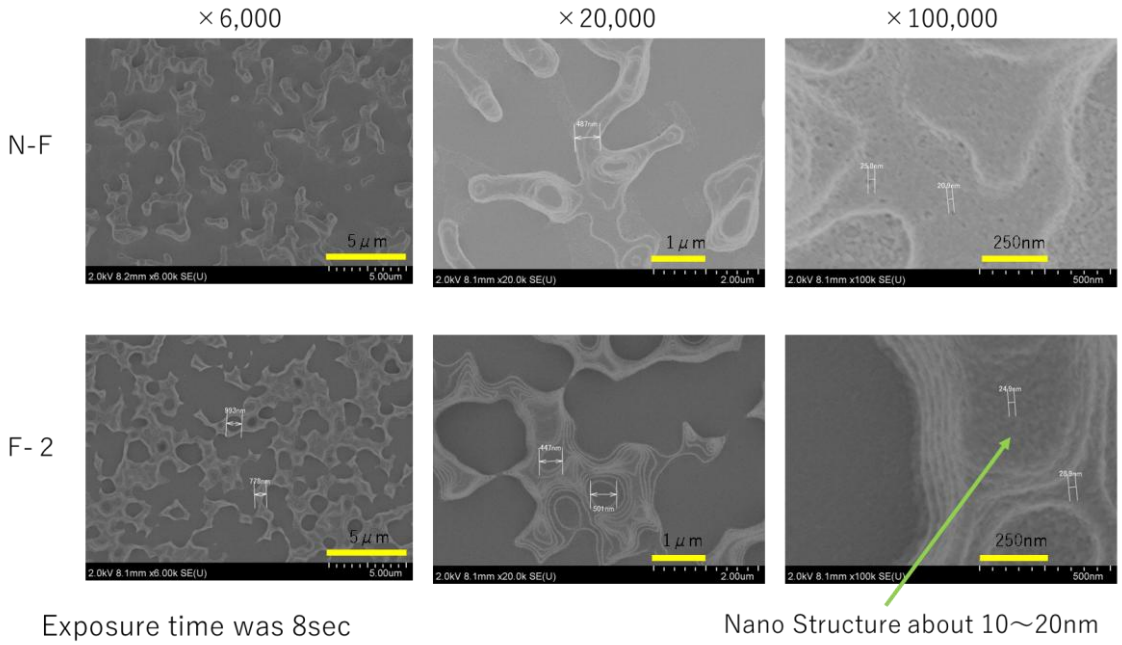

Fig. 7. Results of SEM observations of the structures after development.

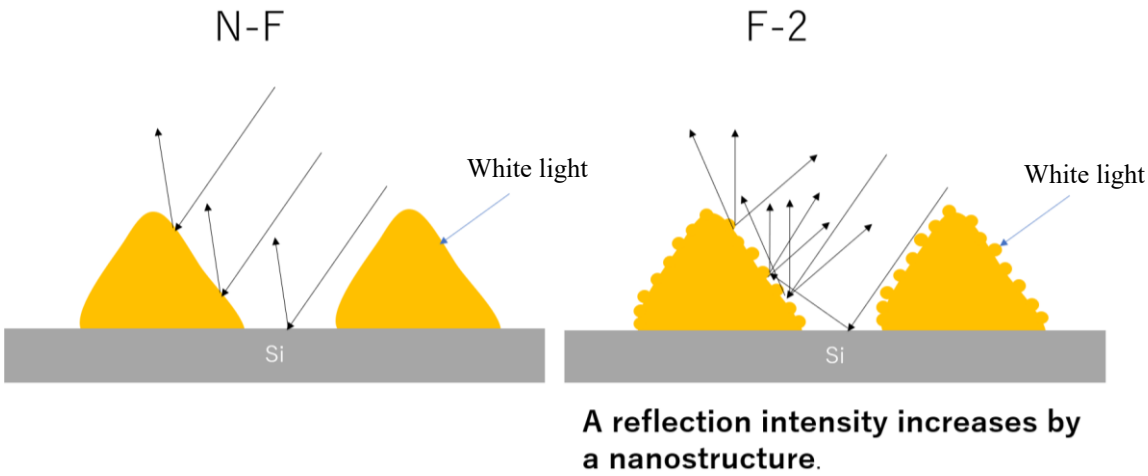

Fig. 8. Schematic diagram explaining higher reflection intensity of F-2 resist structure after development.

their changes using finite differences by approximation.

The following equations (1) to (3) were solved for the analysis:

$$\frac{\partial \vec{D}}{\partial t} = \nabla \times \vec{H} \quad (1)$$

$$\vec{D}(\omega) = \varepsilon_0 \varepsilon_\gamma(\omega)\vec{E}(\omega) \quad (2)$$

$$\frac{\partial \vec{H}}{\partial t} = -\frac{1}{\mu_0}\nabla \times \vec{E} \quad (3)$$

The behavior of electromagnetic waves can be analyzed by differentiating the above equations using the electric and magnetic fields arranged in a spatial lattice called the Yee cell and solving them in time and space. Figure 9 shows the model for analyzing the behavior of electromagnetic waves and the structural model used.

The visible light was assumed to enter the hemispherical particle at an angle. We varied the height, diameter, and interval of the hemispherical particles and calculated the reflection intensity when light of 500 nm to 800 nm was irradiated (Fig. 10).

The results showed higher reflectivity at smaller particle diameters in both of the case in which the particle interval was set to 10 nm and the case in which the particle diameter, particle height, and interval were set to be the same. This confirmed the reason why the reflection intensity was higher in the F-2 resist, which had a particle diameter of 10 to 20 nm.

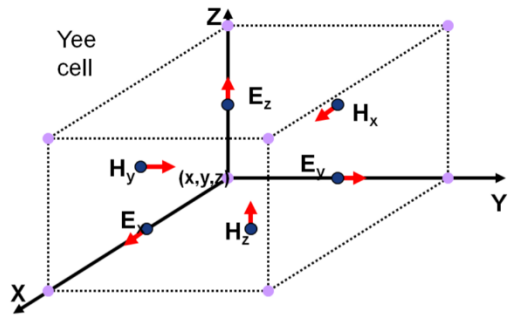

(a) Model used to analyze the behavior of electromagnetic waves

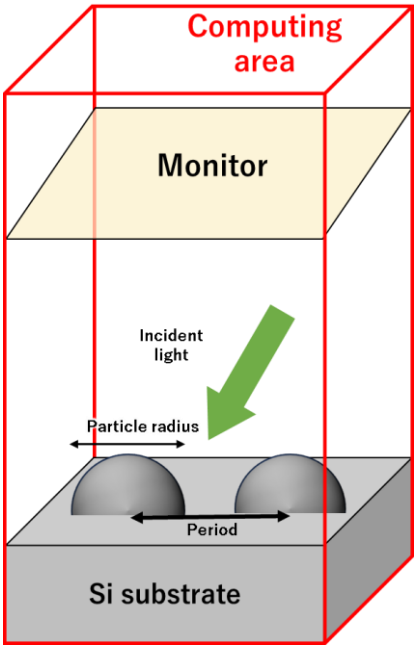

(b) Structural model used in the calculations

Fig. 9. Electromagnetic wave behavior analysis model and model structure.

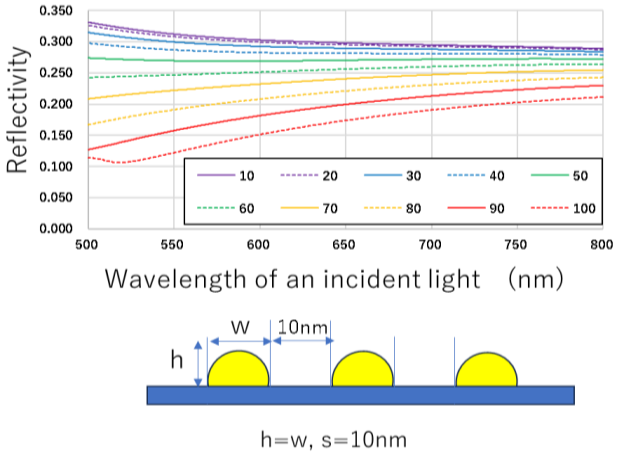

(a) Case in which the particle interval was set to 10 nm

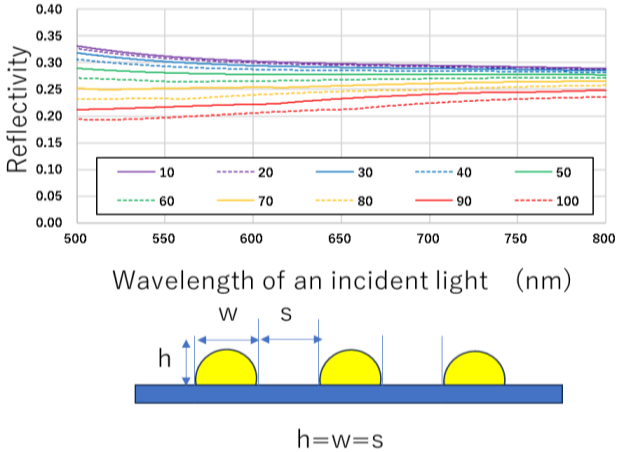

(b) Case in which the particle diameter, height, and interval were set to be the same

Fig. 10. Results of spectral irradiance calculations.

7. Summary

We developed a high-intensity reflection structure by performing speckle exposure on a polymer with controlled molecular weight distribution. We applied to an Si substrate a polymer with controlled molecular weight distribution and a polymer without controlled molecular weight distribution and performed speckle exposure and development. We then irradiated the structures obtained with white LED light and observed the reflections. The results indicated success in creating a structure that reflects light with high intensity, using the polymer with controlled molecular weight distribution. We also performed theoretical verification by carrying out simulations of the molecular size and reflectivity. The simulations also confirmed that higher reflection intensity can be achieved with smaller particle diameters.

Acknowledgements

We are grateful to Dr. Hanabata of the Photofunctional Materials Research Co., Ltd. who provided guidance for material synthesis for this study.

References

1. Ralph Dammel: *Tutorial texts in optical engineering v. TT, SPIE*, (1993).
2. R. Dammel, *"diazonaphthoquinone based resist" SPIE TT.*, **11** (1993).
3. H. Ito and C. G. Willson, *Technical Papers of SPE Regional Technical Conference on Photopolymers, Society of Plastics Engineers*, 331 (1982): *polym. Eng. Sci.*, **23** (1983) 1012.
4. H. Ito and C. G. Wilson, *In polymers in Electronics, T. Davidson, Ed., American chemical Society*, (1984) 11.
5. R. D. Allen, G. M. Wallraff, W. D. Hinsberg, and L. L. Simpson, *J. Vac. Sci. Technol.*, **B9**, (1991) 3357.
6. N. Abe, S. Takechi, Y. Kaimoto, M. Takahashi, and K. Nozaki, *J. Photopolym. Sci. Technol.*, **8** (1995) 637.
7. T. Watanabe, H. Kinoshita, N. Sakaya, T. Shoki, and S. Y. Lee, *Jpn. J. Appl. phys.*, **44** (2005) 5556.
8. K. Hamamoto, T. Watanabe, H. Tsubakino, H. Kinoshita, T. Shoki, and M. Hosoya, "Fine Pattern Replication by EUV Lithography", *J. Photopolym. Sci. Technol.*, **14** (2001) 567.
9. M. Hanabata, A. Furuta, and Y. Uemura, Proc. SPIE, **631** (1986) 76.
10. M. Hanabata, A. Furuta, Y. Uemura, *Proc. of SPIE*, **771** (1987) 85.
11. M. Hanabata, Y. Uemura, A. Furuta, *Proc. of SPIE*, **920** (1988) 349.
12. M. Hanabata and A. Furuta, *Proc. SPIE*, **1262** (1990) 476.
13. M. Hanabata, F. Oi, and A. Furuta, *Proc. SPIE*, **1466** (1991) 132.
14. A. Sekiguchi, C. A. Mack, Y. Minami, and T. Matsuzawa, Proc. SPIE, **2725** (1996) 49.
15. M. Yamamoto, R. Kitai, H. Horibe, A. Sekiguchi, and H. Tanaka, J. Photopolym. Sci. Technol., **22** (2009) 357.
16. A. Sekiguchi, Y. Matsumoto, H. Tanaka, T. Horiuchi, and Y. Sensu, *Proc. SPIE*, **9779** (2016) 55.
17. A. Sekiguchi, Y. Matsumoto, Y. Sensu, S. Takei, and M. Hanabata, H. Tanaka, *Proc. SPIE*, **10146** (2017) 101461K-1.
18. H. Kobayashi, T. Iwaoka, K. Oi, and T. Horiuchi, *J. Photopolym. Sci. Technol.*, **34** (2021) 35.
19. T. Iwaoka, T. Horiuchi, and H. Kobayashi, *J. Photopolym. Sci. Technol.*, **36** (2023) 403.
20. H. Kobayashi, M. Kataoka, S. Komiya, T. Iwaoka, K. Oi, and T. Horiuchi, *J. Photopolym. Sci. Technol.*, **37** (2024) 15.
21. Y. Kikuchi, R. Taura, K. Oi, T. Iwaoka, T. Horiuchi, and H. Konbayashi, *J. Photopolym. Sci. Technol.*, **37** (2024) 423.
22. Dennis M. Sullivan, *Electromagnetic simulation using the FDTD method. New York: IEEE Press Series*, (2000).
23. Allen Taflove, Computational Electromagnetics: *The Finite-Difference Time-Domain Method. Boston: Artech House*, (2005).
24. Stephen D. Gedney, *Introduction to the Finite-Difference Time-Domain (FDTD) Method for Electromagnetics. Morgan & Claypool publishers*, (2011).

Introducing ArF grayscale lithography for large-scale fabrication of submicronic 3D structures

BÉLOT Gaby[a], BÉRARD-BERGERY Sébastien[a], SUNGAUER Élodie[a], WARSONO Api[b], BAZIN Arnaud[b], FAY Aurélien[b], GOURGON Cécile[c]

[a] STMicroelectronics, 850 rue Jean Monnet, 38926 Crolles Cedex, France
[b] Univ. Grenoble Alpes, CEA, Leti, F-38000 Grenoble, France
[c] Université Grenoble Alpes, CNRS, CEA/LETI-Minatec, Grenoble INP, LTM, 17 Rue des Martyrs, Grenoble 38054, France
Corresponding author e-mail: gaby.belot@st.com

Background: The growth of the 3D microfabrication field is fueled by the needs of various applications, ranging from optics, to microfluidics, MEMS or photonics. Following the global trend of micro-components, 3D structures are often not spared by the wish for miniaturization. On the industrial side, this objective rhymes with a requirement for a high resolution, large scale and low-cost 3D microfabrication process. Grayscale PhotoLithography (GPL) is a derivative of classical photolithography, using low-contrast photoresist and unresolved binary masks to perform the fabrication of 3D structures in a single lithography step, thus offering the desired high throughput. In practice, the recourse to non-resolved mask patterns is made to modulate the mask transmission (its "gray-scale"), which allows a locally variable effective dose transmitted to the photoresist. This method has been proved efficient on 300 mm wafers in the realization of 3D morphologies down to the 2 µm scale thanks to an i-line process [1-2]. There is however a demand for submicronic 3D patterns, which cannot be addressed by the current state of the art processes [3-4].

Aim: The goal of this work is to propose an extension of the GPL technology by the transition to a 193nm dry photolithography process, for which a relevant low contrast photoresist has been developed. The main objective is a proof of concept of the Grayscale ArF (G-ArF) process serving an improvement of the resolution for the high-volume manufacturing of various submicronic 3D features.

Approach: First off, a dedicated binary photomask has been designed following previously established best practices [5]. The recourse to curvilinear sub-resolution mask features, shown of Fig.1 is also investigated and proposed as an enlargement of the mask data preparation methods. The multi-beam written mask, containing various original designs, has then been used to expose a low-contrast ArF photoresist. The latter is shown to have a progressive behavior in the 0 to 60 mJ/cm² dose interval. The contrast curve of the photoresist has been determined both via clear field exposures (Fig.2) and by measuring grayscale-patterned pillars using mechanical profilometry [5]. The observation of grayscale-patterned submicronic 3D structures will be conducted via tilted Scanning Electron Microscopy (tilted SEM) and 3D Atomic Force Microscopy (3D AFM).

Results: First off, a new ArF photoresist formulation has been developed to meet the requirement in terms of dose sensitivity and coating thickness. This material is shown to display the desired response through the progressive behavior of its contrast curve. Then, a binary mask has been designed with respect to challenging dimensional constraints in order to stay non-resolved. The combination of these two achievements enabled performing the first state of the art ArF Grayscale lithography process. The patterning of various submicronic resist patterns is demonstrated through tilted SEM inspection.

Conclusion: The viability of the G-ArF process as a strong contestant for the large-scale patterning of submicronic 3D structures is proved. Moreover, this study opens the door to many further developments regarding this technology and its future applications.

Keywords: grayscale lithography, ArF, 3D patterning, curvilinear mask

References:

[1] Chevalier, Pierre, et al. "Rigorous model-based mask data preparation algorithm applied to grayscale lithography for the patterning at the micrometer scale." Journal of Microelectromechanical Systems 30.3 (2021): 442-455.

[2] Allouti, Nacima, et al. "Grayscale lithography process study for sub 5µm microlens patterns." Novel Patterning Technologies for Semiconductors, MEMS/NEMS, and MOEMS 2019. Vol. 10958. SPIE, 2019.

[3] Schneider, Jens, et al. "Revival of grayscale technique in power semiconductor processing under low-cost manufacturing constraints." 34th European Mask and Lithography Conference. Vol. 10775. SPIE, 2018.

[4] Bélot, Gaby, et al. "3D structures sidewalls tuning using smart grayscale photolithography mask strategies." 39th European Mask and Lithography Conference (EMLC 2024). Vol. 13273. SPIE, 2024.

[5] Bélot, Gaby, et al. "Rethinking mask strategies for high vertical resolution grayscale lithography." Photomask Japan 2024: XXX Symposium on Photomask and Next-Generation Lithography Mask Technology. Vol. 13177. SPIE, 2024.

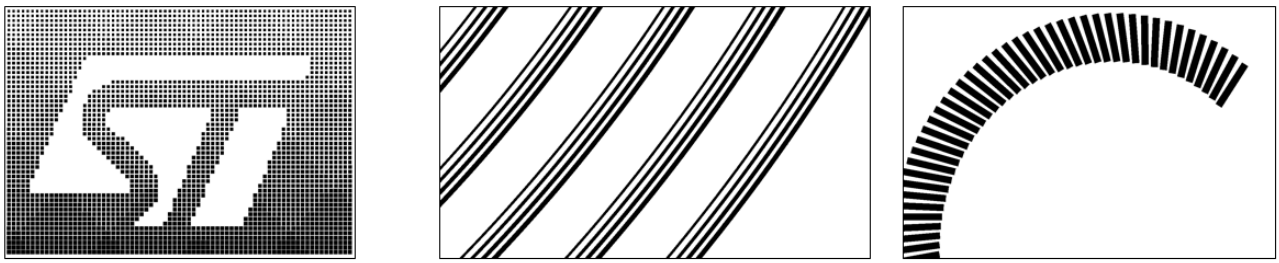

Figure 1. Example of G-ArF mask (a) manhattan and (b) curvilinear designs

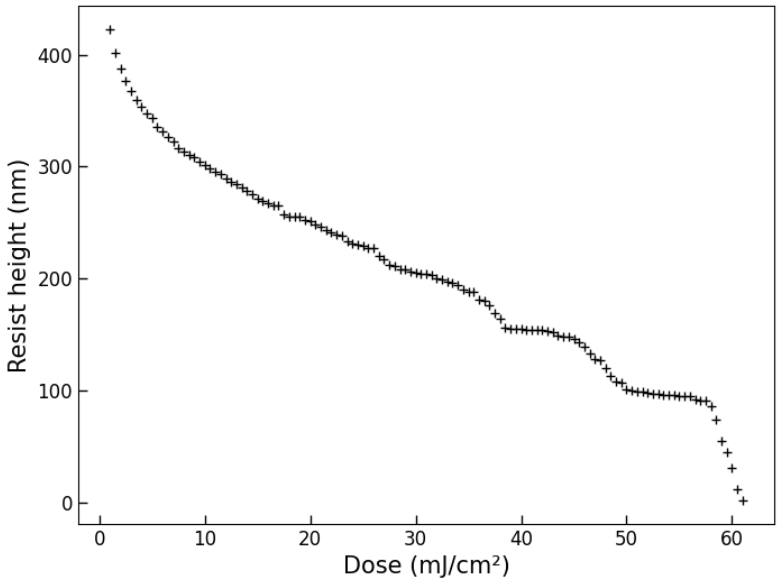

Figure 2. Contrast curve of the G-ArF photoresist

$MoTe_2$-Based Memristor Fabrication with Scanning Probe Lithography

Büsra Öykü Alan, Christoph Reuter, Ren Li, Steffen Strehle

TU Ilmenau, Institute of Micro- and Nanotechnologies, Microsystems Technology Group, Ilmenau, Germany
e-mail: buesra-oeyk.alan@tu-ilmenau.de

Neuromorphic computing offers a scalable, energy-efficient solution to the data processing challenges inherent in von Neumann architectures [1]. As key components in neuromorphic architectures, memristors mimic synaptic functions in biological networks by adjusting their resistance based on external inputs. In this context, two-dimensional (2D) materials have emerged as promising candidates for memristor fabrication. Nevertheless, these devices still suffer from device-to-device variability, which could be mitigated by introducing nanoscale structures [2].

This work studies the potential of scanning probe lithography (SPL) based on local anodic oxidation (LAO) to advance the fabrication of 2H-$MoTe_2$-based memristive devices. SPL-LOA represents in this context a high-resolution, high-accuracy, mask-free and overall gentle nanofabrication approach. Molybdenum ditelluride ($MoTe_2$) is a 2D material and transition metal dichalcogenide that offers tuneable semiconducting (2H) and metallic (1T) phase states, and enables efficient, low-power switching [3].
LOA-SPL enabled in our studies the creation of nanoscale trenches in 2H-$MoTe_2$ that promote the conductive filament formation through localized conductive paths and by the reduced material thickness, as shown in Fig.1(a-b). The fabricated devices, see Fig.1a and b, consist of bottom electrodes fabricated on a Si/SiO_2 substrate by direct writing laser lithography, thermal Cr/Au (10 nm/50 nm) e-beam deposition, and lift-off technique. $MoTe_2$ nanosheets were mechanically exfoliated and subsequently transferred onto the bottom electrodes, followed by a cleaning (acetone, isopropanol and deionized water) and annealing (at 200 °C, under Ar and N_2 gases) conditioning. The transferred nanosheets were inspected by atomic force microscopy (AFM) to assess their quality and subsequently patterned through SPL-LAO. SPL-LAO patterning was achieved with an Asylum Research Cypher by applying a bias voltage in AC mode to the sample and conductive silicon cantilever probes to locally oxidize the $MoTe_2$ surface. The oxidized areas were subsequently etched using deionized water. The oxidation parameters were studied for precise fabrication without damaging the nanosheets considering the following parameter space: frequency 1–100 Hz, pulse width 1–10 ms, lithography set point 20–50 mV, humidity 40–43 %, velocity 20–50 nm/s, and bias voltage 10–20 V. After SPL-LAO and etching, post-inspection was realized again by AFM. The top electrodes consisted of a 50 nm thick Ag thin film and were patterned using again direct writing laser lithography, e-beam evaporation, and lift-off technique.

To characterize the memristor behaviour, *I-V* sweeps were performed with a manual probe station. A forming voltage of 1.8 V was observed with a compliance current of 900 µA during SET to prevent irreversible device breakdown. SET voltages ranged from 0.5 to 0.8 V across four cycles, while RESET voltages were observed between -0.5 and -0.3 V as shown in Fig. 3. Variability in SET voltages across cycles likely stems from the stochastic nature of filament formation mechanism. The experiments are completed by conductive AFM and Raman spectroscopy to confirm the filament formation.

[1] T. Li, *Highlights Sci. Eng. Technol.*, vol. 87, pp. 186–191, Mar. 2024.
[2] K. C. Kwon, J. H. Baek, K. Hong, S. Y. Kim, and H. W. Jang, *Nano-Micro Lett.*, vol. 14, no. 1, p. 58, Dec. 2022.
[3] H.-K. He *et al.*, *Mater. Horiz.*, vol. 9, no. 3, pp. 1036–1044, 2022.

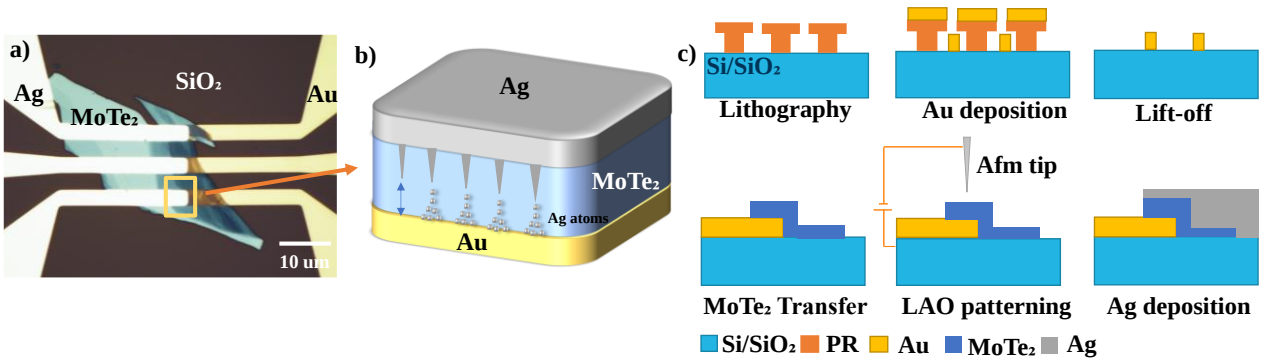

Figure 1. a) Optical image of a fabricated memristive device (Ag/$MoTe_2$/Au), b) Schematic of the proposed device architecture and switching mechanism, c) schematic fabrication steps of the memristive device.

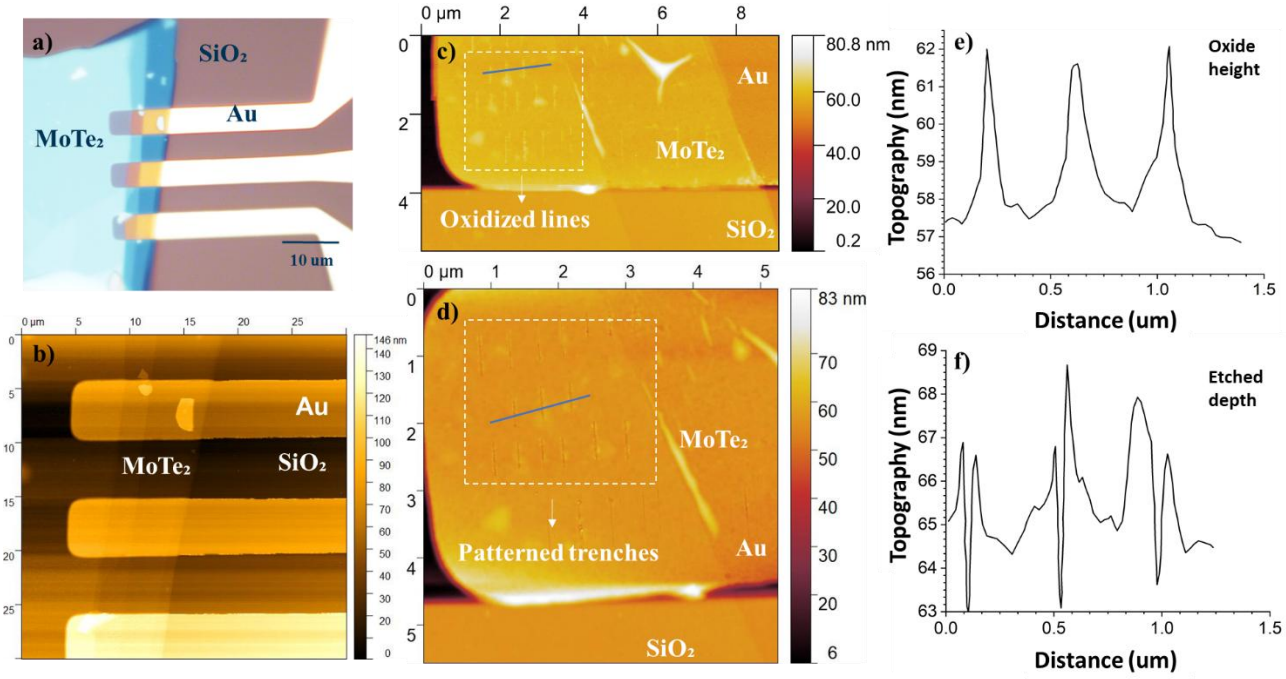

Figure 2. SPL-LAO memristor fabrication: a-b) optical and AFM images bottom electrodes and transferred $MoTe_2$ nanosheets, c) AFM image taken after LAO ($MoTe_2$ thickness 8 nm) using frequency 10 Hz, pulse width 10 ms, setpoint 20 mV, velocity 30 nm/s and bias voltage 12 V, d) AFM image taken after etching in deionized water for 2 minutes, e) AFM line profile, as indicated in c) and d), showing the height of oxidized structures, f) AFM line profile showing the depth of the created trenches after etching.

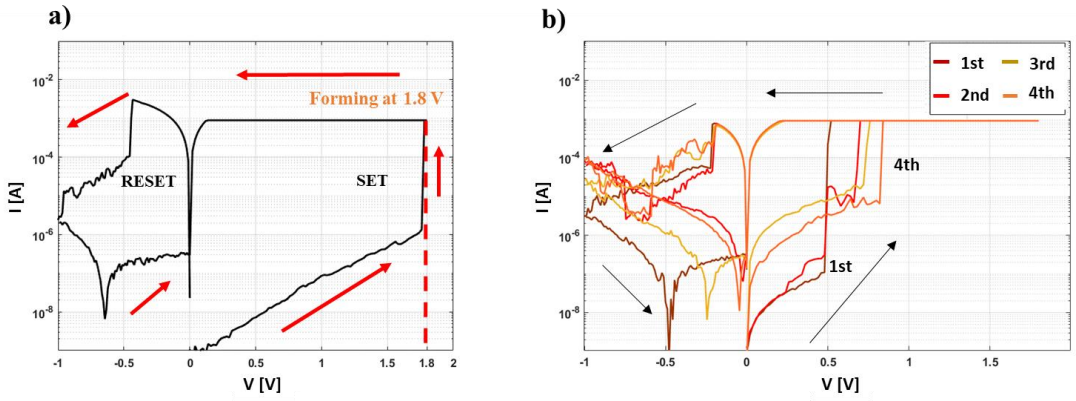

Figure 3. Electrical memristor characterization: a) I-V curve showing the filament formation process at 1.8 V, compliance current 900 µA, $MoTe_2$ thickness is 14 nm, b) I-V curve of 4 cycles after filament forming, sweeping 1.8V to -1 V at 900 µA (legend shows color scheme for different cycles).

Study on Micro Scale Surface Polishing and Modification of 3D Biodegradable Scaffolds using Electron Beam Treatment

Jeongsik Noh [a], Jongsung Park [a, b]

[a] Department of Precision Mechanical Engineering, Kyungpook National University, Sangju, 37224, Korea
[b] Convergence Research Center of Mechanical and Chemical Engineering, Kyungpook National University, Sangju, 37224 Korea
e-mail: jpark40@knu.ac.kr

The advantages of 3D printing technology is that it can easily process the desired shapes and produce complex geometric structures. However, it has a rough surface and poor dimensional accuracy, which is unsuitable for fields that require high precision. In specially, it has rough surface and insist extra burr during the printing process. For this reason, 3D printed biomedical scaffolds require post-processing to achieve high precision dimensions and smooth surfaces. This paper presents a technique that allows electron beam processing to physically and chemically modify the surface of a 3D printed biomedical scaffold. The process presented is both easy to polish to smooth the surface of the printed scaffold and can process a large number of samples in a short time. Various biomedical implant devices can utilize this process, which can be applied to various metal materials and polymer printing. The electron beam process we presented uses only heat treatment using electrons, ensuring that any side effects that may arise in clinical trials based on materials can be completely eliminated.

Electron beam treatment is appropriate for post-processing stents with complex three-dimensional shapes because it is done on the entire sample with a plasma environment. In addition, it has the advantages of a short process time (sub microseconds) and the ability to batch process multiple stent samples. In a plasma environment, irradiated electrons are accelerating to the stent in a few microseconds and colliding with the stent surface in a short period of time. This impact energy heats the stent surface and melts it to a depth of hundreds of nanometers. When this process is repeated multiple times, the melted surface hardens to form a smooth surface. Moreover, we increase the irradiation time, which causes the stent material to evaporate due to the accelerated electron energy. As these results, the stent strut thickness can be precisely adjusted in a process. This process can be applied not only to polymers but also to metal stents processed using a varying technique such as laser or EDM (Electrical discharge machining). Additionally, the surface can be modified to be hydrophilic or hydrophobic by certain plasma gas.

To evaluation the effectiveness, a vascular PLA (Polylactic acid) stent was made using a 3D printer and then post-processed. The vascular stents are inserted into blood vessels with a diameter of several millimeters. So, it needs to have high strength, high dimensional precision, and low surface roughness. Through an electron beam processing, we verified the surface roughness of vascular stents, the thickness control of stent struts required by the FDA regulation, and the welding strength of each struts.

Figure 1 shows a schematic diagram of the electron beam equipment used in this study. The 3D printed stent is attached to a substrate and the process proceeds by exposure to Ar or O_2 plasma. In this study, PLA polymer was employed, and the printing results are shown in Figure 2. As shown in the picture, unnecessary burrs, etc. are generated after printing, and these can be completely removed through electron beam processing. Also, SEM image of the stent circular ring and the bridge connecting the ring, and each bridge was completely welding using an electron beam. As from the results of the joint strength test between struts before and after electron beam treatment, and it was confirmed that the joint strength was improved by about two times after electron beam treatment. Figure 3 shows the results of the stent strut thickness change, and it was confirmed that the thickness of the stent strut can be effectively controlled according to the number of electron beam irradiation times.

[1] J. Kim et al., Corros. Sci., 89 (2014) 179-788
[2] X. Tong et al., Chen, Mater. Lett., 341 (2023) 134261

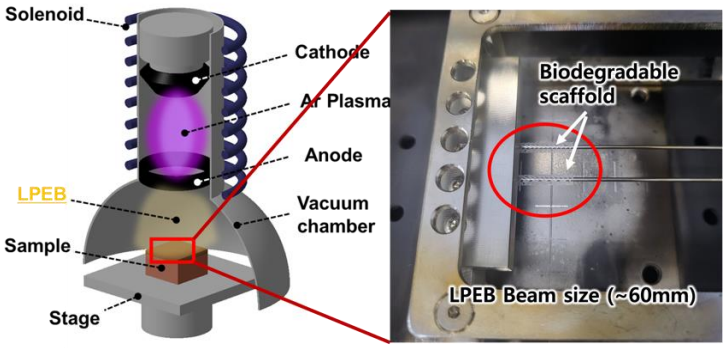

Figure 1. Schematic diagram of the experimental setups for the electron beam irradiations.

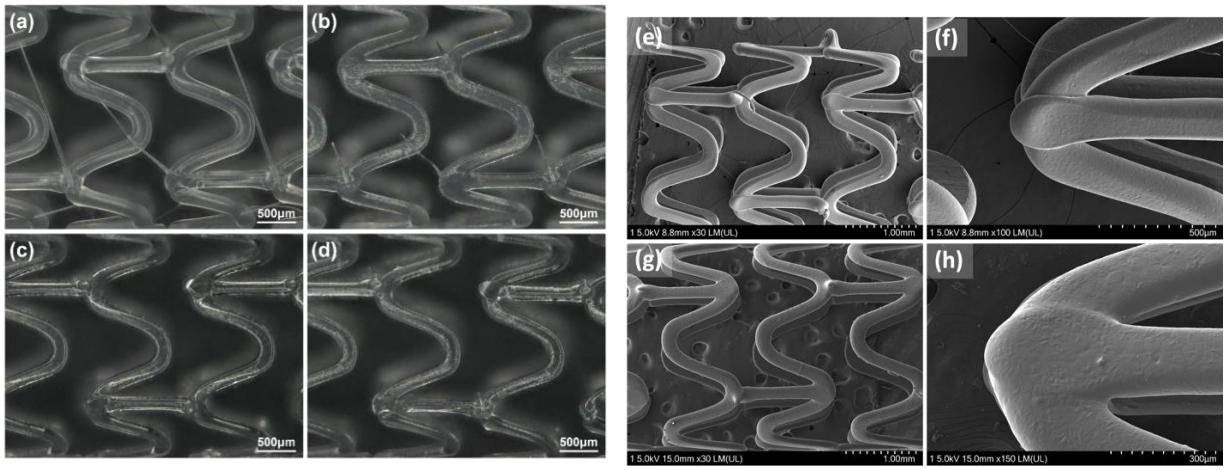

Figure 2. (a) and (b) photograph of the before treated of 3D printed PLA stent (c) and (d) the after electron beam treated photograph. The surface roughness is decreased and removed burr. (e) and (f) photograph of the before treated of 3D printed PLA stent. Unnecessary burrs and printing connections are not fully connected. (g) and (h) the after electron beam treated photograph. Every part cannot find burr and fully connected each printed wire.

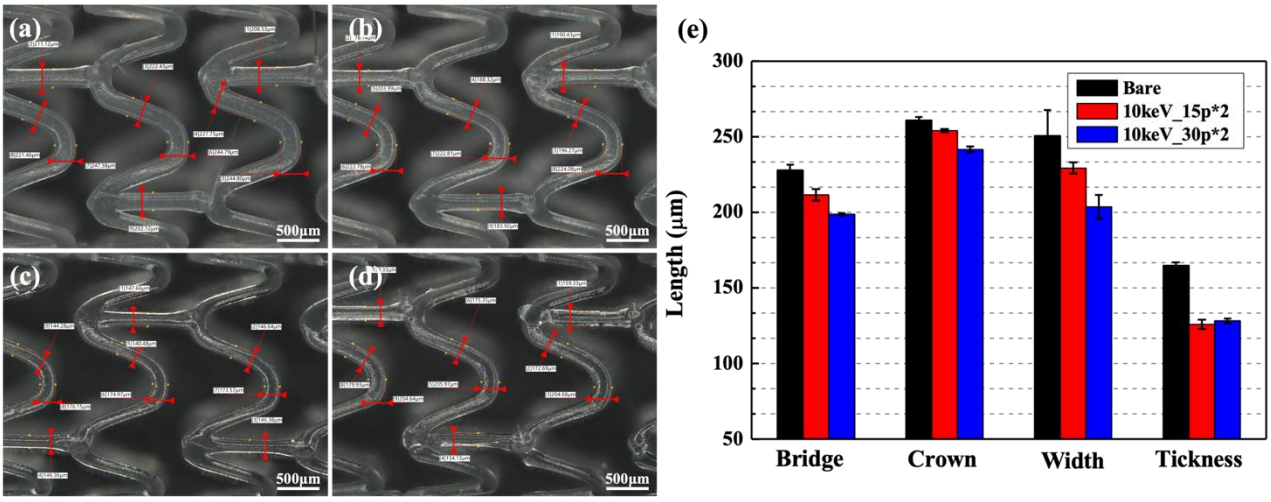

Figure 3. (a) and (b) photograph of the before treated of 3D printed PLA stent. Average stent strut width about 220μm. (c) and (d) the electron beam treated a PLA stent photograph. The width decreasing about 60μm. (d) The graph shows changes in stent struts according to various process conditions.

Micro-Mechanical Properties of Annealed Electrodeposited Gold for Design of MEMS Structural Components

Shota Iima[1], Tomoyuki Kurioka[1], Shota Kanno[1], Chun Yi-Chen[1], Tso-Fu Mark Chang[1], Katsuyuki Machida[1], Hiroyuki Ito[1], Yoshihiro Miyake[2], Masato Sone[1]

[1] Institute of Integrated Research, Institute of Science Tokyo, Yokohama, 226-8501, Japan
[2] Department of Computer Science, Institute of Science Tokyo, Yokohama, 226-8501, Japan
e-mail: iima@ames.pi.titech.ac.jp

The application of electrodeposited gold materials to the proof mass of capacitive MEMS (Micro-Electro-Mechanical Systems) accelerometers contributes to the suppression of Brownian noise, achieving miniaturization and high sensitivity simultaneously [1]. Capacitive MEMS accelerometers with gold proof mass (Au-MEMS) utilizing multi-layered technologies can detect sub-micro level acceleration, yet they suffer from drift phenomena during operation caused by impurities from the manufacturing process [2]. These impurities can be removed by annealing [3], which leads to the suppression of drift phenomena [2]. However, annealing raises another concern: the mechanical strength of electrodeposited gold materials at the micro-scale may be reduced due to increased grain size. Although the micro-mechanical properties of electrodeposited gold materials have been studied [4,5], those prepared using the same manufacturing procedures for Au-MEMS have never been examined. The effects of annealing on these materials also remain unexplored. Therefore, this study aims to evaluate the effects of annealing on the micro-mechanical properties of electrodeposited gold materials fabricated by the MEMS manufacturing process.

A Ti/Au layer (Ti: 0.1 μm, Au: 0.07 μm) was deposited on a SiO_2/Si substrate via evaporation, followed by the electrodeposition of a 30 μm-thick gold film. The electrodeposited gold films were annealed at either 200 °C or 300 °C for 30 minutes and then cooled to room temperature. Samples without annealing were denoted as sample-non, while those subjected to annealing at 200 °C or 300 °C were denoted as sample-200 and sample-300, respectively. Gold micro-pillars (10 μm × 10 μm × 20 μm) were fabricated using focused ion beam (FIB) system and subjected to micro-compression tests at a strain rate of 2.5×10^{-3} s^{-1}.

Figure 1 shows SEM images of the gold micro-pillars before and after the micro-compression test. A barrel-like ductile deformation occurred after the compression test, consistent with previous works [4,5]. Figure 2 presents the engineering stress (σ)-engineering strain (ε) curves obtained from the compression test: the yield stress (σ_y) was defined as the 0.2% offset yield strength, measuring 330 MPa for sample-non, 185 MPa for sample-200, and 178 MPa for sample-300. The σ_y of sample-non exceeded that of bulk gold (55-220 MPa) [6], while those of sample-200 and sample-300 did not exceed that of bulk gold, indicating that annealing decreased the σ_y. Grain sizes of sample-non, sample-200, and sample-300 were calculated to be 17.2, 19.4, and 23.2 nm, respectively, based on XRD results (Figure 3) and Scherrer's formula. The decrease in σ_y was due to grain growth caused by annealing. Conversely, when comparing the flow stress of samples at 6% strain (σ_6), that of sample-200 was close to sample-non. Figure 4 illustrates the relationship between the inverse-square root of average grain size ($d^{-1/2}$ [$nm^{-1/2}$]) and both σ_y and σ_6. Interestingly, the correlation between $d^{-1/2}$ and σ_y was not obvious, while the correlation between $d^{-1/2}$ and σ_6 followed the Hall-Petch relationship [7].

In conclusion, we clarified the effects of annealing on the micro-mechanical properties of electrodeposited gold. The yield stress decreased to 55% of that of the non-annealed sample due to annealing, while the flow stress at 6% strain remained despite annealing at 200 °C. Therefore, we concluded that 200 °C is the promising temperature for impurity removal without decreasing micro-mechanical properties.

Acknowledgements: This work was supported by JST, CREST Grant Number JPMJCR21C5, Japan.

References:

[1] D. Yamane et al., Appl. Phys. Lett. 104 (2014) 074102; [2] A. Onishi et al., Jpn. J. Appl. Phys. 61 (2022) SD1028; [3] T. Akiyama et al., Micro Nano Eng. 20 (2023) 100219; [4] T. Omura et al., Surf. Coat. Technol. 436 (2022) 128315; [5] S. Kanno et al., Micro Nano Eng. 23 (2024) 100254; [6] H. D. Espinosa et al., J. Mech. Phys. Solids 52 (2004) 667–689; [7] J. R. Greer et al., Prog. Mater. Sci. 56 (2011) 654–724.

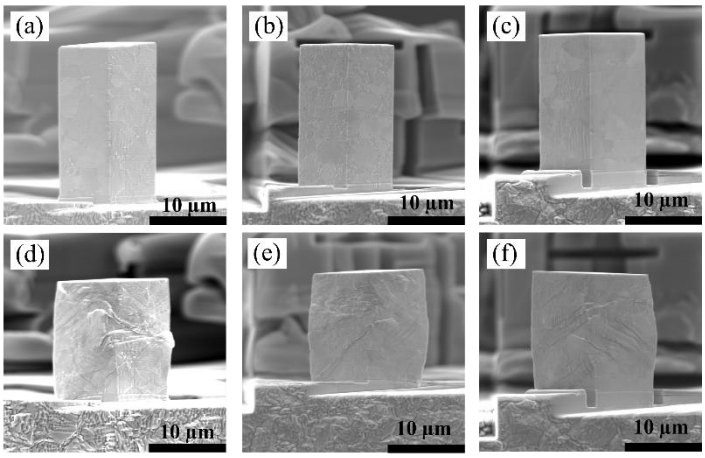

Figure 1. SEM images (a, b, c) before and (d, e, f) after the micro-compression tests for (a, d) sample-non, (b, e) sample-200, and (c, f) sample-300.

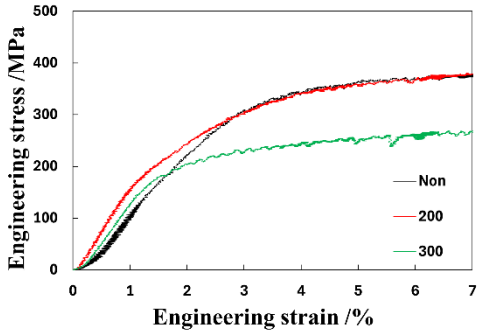

Figure 2. Engineering stress-engineering strain curves of gold micro-pillars at a strain rate of 2.5×10^{-3} s^{-1}.

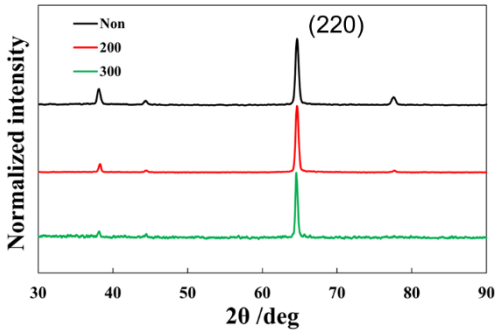

Figure 3. X-ray diffraction patterns of the electrodeposited gold samples: sample-non (black line), sample-200 (red line), and sample-300 (green line).

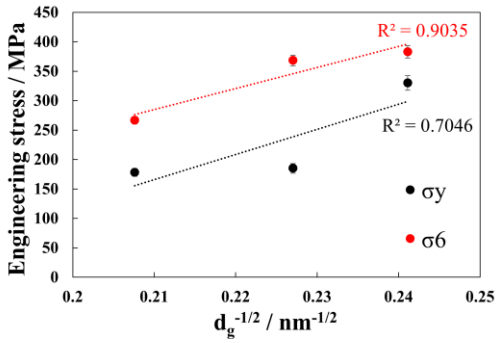

Figure 4. Relationship between the inverse-square root of the average grain size ($d_g^{-1/2}$ [$nm^{-1/2}$]) and yield stress (σ_y) (black dots) or flow stress at 6% strain (σ_6) (red dots).

Scalable manufacturing processes for solid-state nanopores using Atomic Layer Deposition

Nico Rademacher [a,*], Stefanie L. Stoll [a], Anja Leibold [b], Michael Möller [a], Christoph Blattert [b], Jens Bolten [a,*], Max Lemme [a,c]

[a] AMO GmbH, Aachen, 52074, Germany
[b] Hahn-Schickard-Gesellschaft für angewandte Forschung e.V., Villingen-Schwenningen, 78052, Germany
[c] Chair of Electronic Devices, RWTH Aachen University, Aachen, 52074, Germany
e-mail: rademacher@amo.de, bolten@amo.de

A reliable, scalable and cost-effective fabrication route is mandatory to exploit the scientific and commercial potential of solid-state nanopores in genome sequencing, biomedical research or protein analysis [1,2]. A number of methods are available to produce such nanopores, which are typically less than 100 nm in diameter [3]. These methods are often based on electron beam lithography (EBL) [4] or transmission electron microscopy (TEM) [5]. However, EBL or drilling with a TEM limit the throughput and industrial scalability. Here, we use EBL as a flexible and maskless method for prototyping of structures in the range of 250 nm, followed by an atomic layer deposition process to reduce the pore size to the targeted range below 100 nm with high precision.

We used silicon (Si) chips with thin films of 200 nm of silicon dioxide (SiO_2) and 50 nm of low stress silicon nitride (SiN_x). The SiO_2 was thermally grown and the SiN_x was deposited using low pressure chemical vapor deposition (LPCVD) at 840°C. Next, the Si was etched wet-chemically and the SiO_2 was etched by vapor hydrogen fluoride (HF) from the backside to create a 10×10 µm² SiN_x membrane. PMMA was spin-coated onto the samples and squares of 250 nm designed edge length were patterned using EBL. Subsequently, the PMMA was developed and the holes were etched into the membrane using a fluoroform (CHF_3)-based etching process. A schematic of the membrane and the target nanopore application are illustrated in Figures 1a and b, respectively. Scanning electron microscope (SEM) images were then taken to verify and measure the structure and size of the etched nanopores. The etched nanopores have edge lengths of ~250 nm (see examples in Figures 2a and 3a). Aluminum oxide (Al_2O_3) was deposited onto the substrate by atomic layer deposition (ALD) using a Trimethylaluminium (TMA) precursor, an oxygen plasma and a total of 700 cycles, resulting in a thickness of ~85 nm (see Figure 1a). The deposition rate was measured by ellipsometry on an unstructured Si sample processed together with the nanopore samples.

Subsequently, SEM images were taken to measure the nanopores after the ALD process (Figures 2b and 3b). The originally designed square shape was retained, confirming uniform deposition. The measurements show that the edges of the nanopores in the two examples shifted inwards by approximately 83 nm to 88 nm. These values are in good agreement with the layer thickness confirmed by ellipsometry.

We demonstrated an industry-standard ALD process to reduce the size of nanopores from lithography-defined edge lengths of 250 nm down to 80 to 90 nm in a highly controlled manner. The process facilitates the precise customization of solid-state nanopores for specific applications in protein or molecule detection [6,7] on an industrial scale. The combination of a lithography process and a subsequent ALD deposition relax lithography process control requirements, increasing overall critical dimension (CD) control for small nanopores.

This work was financially supported by the German Federal Ministry of Education and Research (BMBF) under the Cluster4Future project nanodiag BW (03ZU1208BC & 03ZU1208BA).

[1] Y. Wang, Y. Zhao, A. Bollas, Y. Wang, K.F. Au, Nat Biotechnol 39 (2021) 1348–1365.
[2] Y.-L. Ying, Z.-L. Hu, S. Zhang, Y. Qing, A. Fragasso, G. Maglia, A. Meller, H. Bayley, C. Dekker, Y.-T. Long, Nat. Nanotechnol. 17 (2022) 1136–1146.
[3] B.N. Miles, A.P. Ivanov, K.A. Wilson, F. Doğan, D. Japrung, J.B. Edel, Chem. Soc. Rev. 42 (2013) 15–28.
[4] M. Graf, 2D Nanopores: Fabrication, Energy Harvesting and Field-Effect Sensing, Lausanne, EPFL, 2019.
[5] S.J. Heerema, L. Vicarelli, S. Pud, R.N. Schouten, H.W. Zandbergen, C. Dekker, ACS Nano 12 (2018) 2623–2633.
[6] Z. Yuan, C. Wang, X. Yi, Z. Ni, Y. Chen, T. Li, Nanoscale Res Lett 13 (2018) 56.
[7] H. Liu, Q. Zhou, W. Wang, F. Fang, J. Zhang, Small 19 (2023) 2205680.

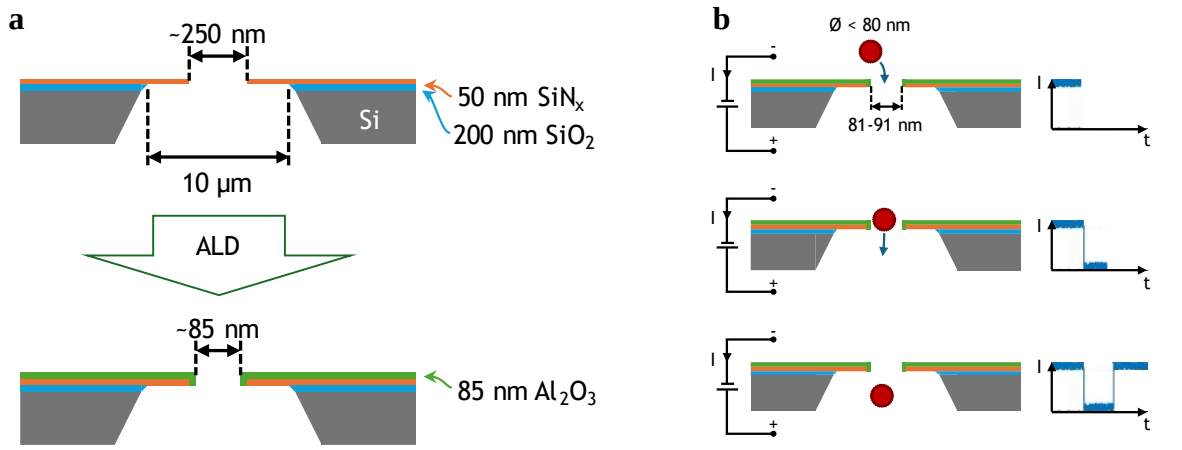

Figure 1: **a** Schematic of the dimensions of the Nanopores before and after the ALD process. **b** Schematics of the measurement principle of a nanopore detecting a particle.

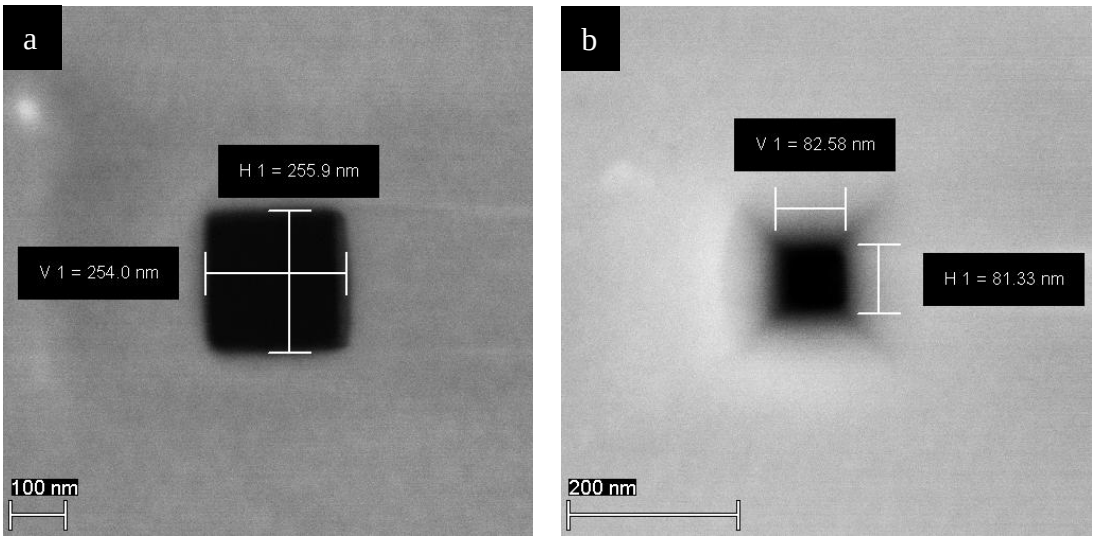

Figure 2. Sample #4554: SEM images of the nanopore in SiN_x (a) before and (b) after ALD deposition of 85 nm Al_2O_3.

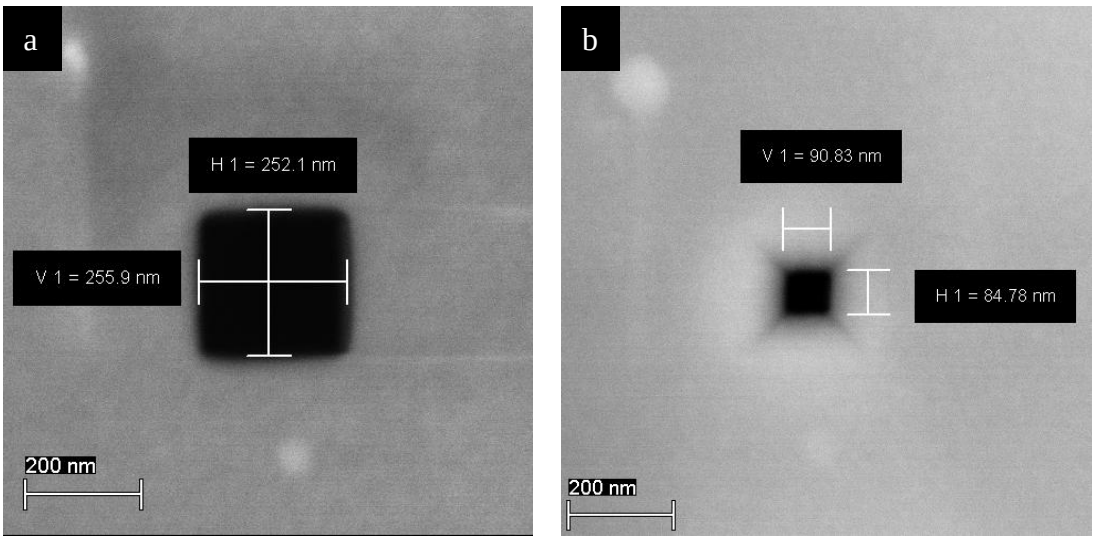

Figure 3. Sample #4654: SEM images of the nanopore in SiN_x (a) before and (b) after ALD deposition of 85 nm Al_2O_3.

The Impact of Writing Field Stitching on Optical Losses in Electron Beam Fabricated Silicon-on-Insulator Waveguides

Maksim Lipkin [a,b], Michael Möller [a], Lisa Ehlert [a], Jens Bolten [a], Rijil Thomas [a], Stephan Suckow [a], Max Lemme [a,b]

[a] AMO GmbH, Otto-Blumenthal-Straße 25, 52074 Aachen, Germany
[b] Chair of Electronic Devices, RWTH Aachen University, Otto-Blumenthal-Straße 25, 52074 Aachen, Germany
E-mail: Suckow@amo.de

Introduction: Electron-beam lithography (EBL) offers flexible prototyping through its direct-write capability. This patterning approach employs a series of adjacent writing fields that are stitched together during exposure. Imperfections at these boundaries - called stitching errors – can occur from stage displacements, beam inaccuracies, field distortion or field miscalibrations. Although techniques like multipass writing and dynamic field positioning [1] were developed to improve general stitching accuracy in EBL, the quantitative relationship between stitching errors and performance of photonic waveguides (WGs) fabricated using EBL as a patterning technique remains poorly understood [2 – 3].
This work systematically investigates how stitching errors from EBL affect optical WG performance by introducing artificial stitching errors in the lateral directions in WGs of varying lengths, analyzed via the cutback method. The layout included artificial EBL stitching offsets of 0 nm (reference), 2.5 nm, 5 nm, 7.5 nm, 10 nm, 15 nm, and 20 nm, replicated on two nominally identical 2×2 cm² dies.

Fabrication: The fabrication process was carried out on a 150 mm SOI wafer featuring a 220 nm silicon device layer on top of a 3 µm thick buried oxide layer. WG patterns were exposed in hydrogen silsesquionxane resist (HSQ) employing a Raith RAITH EBPG 5200 EBL system. The EBL system was operated at 100 kV acceleration voltage using a 160 µm main field size. Exposure patterning employed a 5 nm beam step size with 1 nA beam current. Layouts were fractured in GenISys BEAMER using four passes at a 50% main field overlap in high resolution mode [4]. The patterns were etched in a reactive ion etching (RIE) process using HBr as main etching agent, fully etching through the 220 nm silicon. The resulting WGs were 450 nm wide. A resulting WG structure with an artificial stitching offset of 20 nm is presented in Fig. 1. In a subsequent EBL step, grating couplers were defined using the positive tone resist polymethyl methacrylate (PMMA) and patterned into the silicon layer through RIE using a mixture of SF_6 and C_4F_8 gases.

Measurements and Results: A polarization-maintaining fiber was cleaved, positioned, and tilted to the vertical axis by the optimum coupling angle of 16° above the input grating coupler to inject TE-polarized light into the WG. A tunable continuous-wave laser (1520–1620 nm) served as the source, with its polarization adjusted to the TE mode using an external fiber polarization controller. At the output, the light was collected via a multimode fiber aligned at the same 16° angle, and the optical power was measured using an optical power meter [5]. The transmission spectra of 2 cm long WGs were measured for stitching offsets of 0 nm (reference), 2.5 nm, 5 nm, 7.5 nm, 10 nm, and 15 nm (Fig. 2a). Dotted lines mark the average transmission for each offset. In Fig. 3 the resulting average transmission values (blue dots) were plotted as a function of stitching offsets and fitted with a quadratic curve. A quadratic dependence was chosen because scattering due to sidewall roughness is expected to scale quadratically, as described by Tien's formula [6].

Discussion: The average transmission of the 2 cm WG (c.f. Fig. 3) reveals a systematic dependence on field stitching offsets, with average transmission declining quadratically as the offset increase. Even sub-10 nm offsets introduce measurable transmission losses in WGs compared to the reference value, revealing the critical role of EBL precision for photonic device performance. Notably, stitching-induced transmission losses become statistically significant at offsets as small as 2.5 nm, suggesting that conventional high-end EBL systems with typical 10 nm stitching specifications are insufficient for very low loss photonic applications (e.g. quantum photonics) or require careful optimizations of stitching and writing field size.

Acknowledgments: This work has been funded by the BMBF under grant agreement no. 13N16347 (QSPEC).

[1] S. Thoms, Electron Beam Lithography, Nanofabrication Handbook. (CRC Press, 2012).
[2] A. Bogdanov et al., J. Vac. Sci. Technol. B. 30 (2012) 031606.
[3] M. Gnan et al., J. Vac. Sci. Technol. B. 25 (2007) 2034–2037.
[4] W. Henschel et al., J. Vac. Sci. Technol. B. 21 (2003) 2018–2025.
[5] R. Singh et. al., Opt. Express 32 (2024) 46522-46528.
[6] R. J. Deri et. al., IEEE J. Quantum Electron (1991) 626-640.

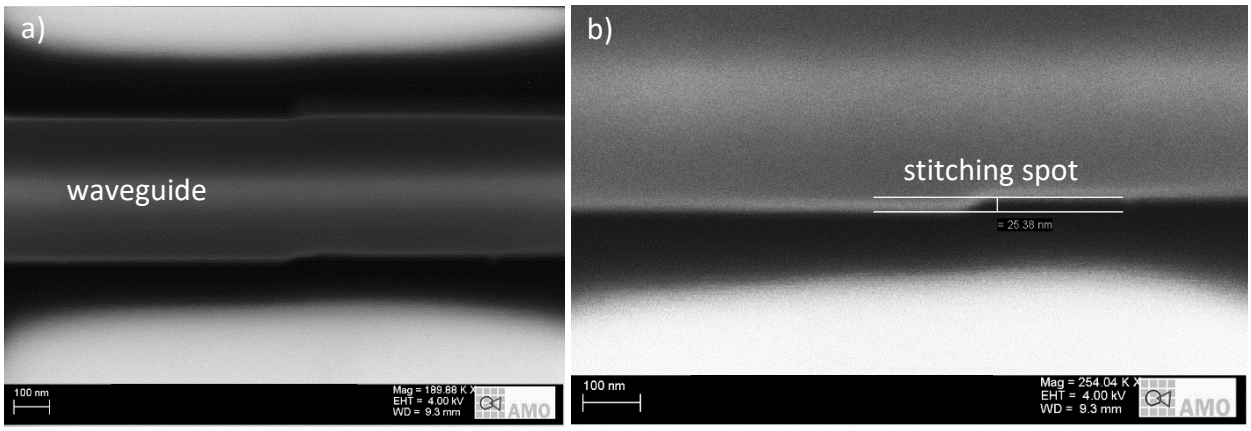

Figure 1. a) Scanning electron micrograph of a 450 nm wide waveguide in top view. Artificial stitching offset of 20 nm highlighted in b).

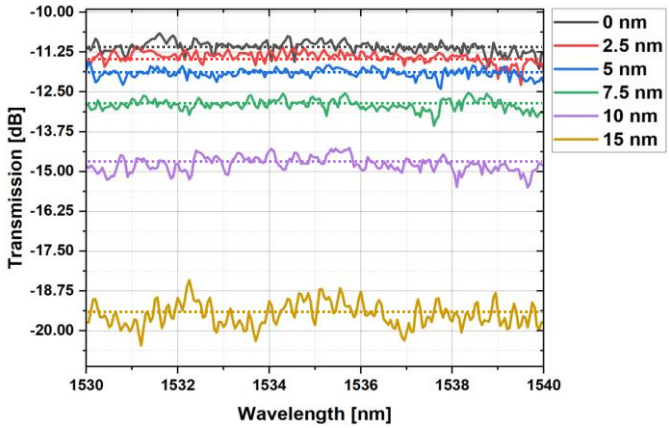

Figure 2. Measured transmission spectra of a 2 cm long waveguide for stitching offsets from 0 nm (reference) to 15 nm. Dotted lines indicate average transmission values.

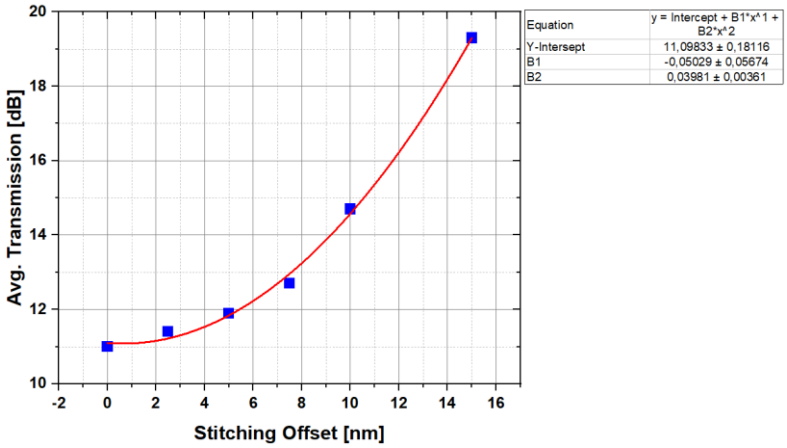

Figure 3. Average transmission as a function of stitching offset (blue dots) and corresponding quadratic fit.

A Deep Learning-Based Photoresist Shrinkage Correction Method via Fusion of SEM Image and Scanning Parameter Features

Sa Liu [b], Yanan Zhu [a], Jiebin Niu[c], Diwei Zhou[d], Fuqin Deng [b], Zhuming Liu [a]

[a] Institute of Semiconductors, Guangdong Academy of Sciences, Guangzhou, 510650, China
[b] School of Electronics and Information Engineering,Wuyi University, Jiangmen, 529000, China
[c] Institute of Microelectronics of the Chinese Academy of Sciences, Beijing, 100029, China
[d] School of Science, Loughborough University, Leicester, LE11 3TU, UK

e-mail: liuzhuming@gdisit.com

In semiconductor manufacturing, photolithography is a critical process for transferring nanoscale patterns onto substrates, and metrology based on scanning electron microscope (SEM) is a key technique to evaluate the quality of the photolithography. However, photoresist materials often experience shrinkage due to electron beam irradiation, leading to discrepancies between the captured images and the actual structures. This shrinkage not only hampers accurate assessment of photolithographic quality but also adversely affects subsequent fabrication steps [1]. Therefore, developing techniques to predict the unshrunk state of photoresist images is essential for enhancing the precision and efficiency of the lithography process. This paper presents a deep learning-based model that predicts the unshrunk state of photoresist structures from SEM images. Framed as an image-to-image regression task, the proposed model comprises four main components: an image encoder, a parameter encoder, a feature fusion module, and a decoder, as illustrated in Figure 1. The image encoder extracts hierarchical representations from SEM inputs, while the parameter encoder embeds key experimental settings such as electron beam dose, acceleration voltage, and scan count into a latent feature space. These two feature streams are then integrated by the fusion module, which captures the interactions between visual and contextual information. Finally, the decoder reconstructs the predicted unshrunk image from the combined features. The model takes as input both the SEM image and a vector of associated SEM parameters. Experimental results demonstrate that the proposed method accurately restores the original, unshrunk morphology of photoresist patterns, offering a robust and scalable solution for improving metrology precision in advanced photolithography.

[1] Park S, Nir I R, Kwak S, et al. Efficient way of reducing contaminant induced by interactions between EUV photoresist and electron beam in CD-SEM: the route to carryover free SEM metrology[C]//Metrology, Inspection, and Process Control XXXIX. SPIE, 2025, 13426: 162-171.

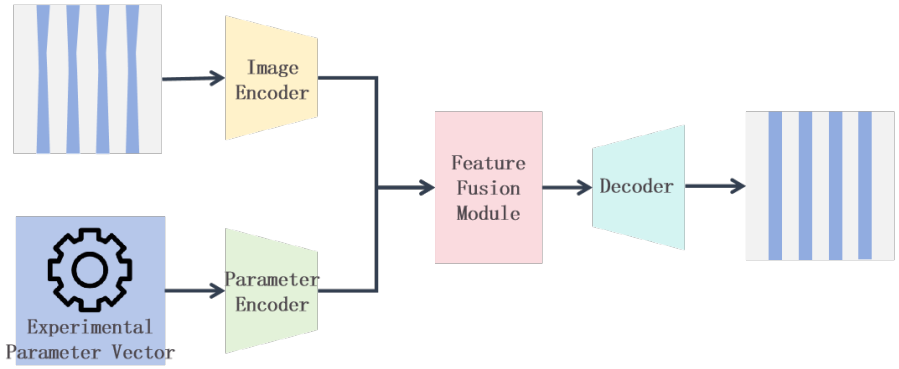

Figure 1. Schematic of the proposed deep learning-based model for predicting unshrunk photoresist images. The model consists of an image encoder, a parameter encoder, a feature fusion module, and a decoder, designed to integrate SEM image features and process parameters for generating unshrunk photoresist predictions.

Fabrication and Nanoscale Characterisation of Sidewall Roughness in SOI Waveguides

Magdalena Ulmeanu[a], Kate Stokes[a], Marta Kocun[b], Roger Proksch[b], Vlad Korolkov[c], Luis Perdigao[c]
Jason Li[b], Gabriele Selvaggio[b] and Zhong Ren[a]
[a]Oxford Instruments Plasma Technology, Severn Beach, Bristol, BS35 4GG, UK;
[b]Oxford Instruments Asylum Research, Santa Barbara, California, 93117, USA;
[c]Oxford Instruments NanoAnalysis, High Wycombe, Bucks, HP12 3SE, UK.
e-mails: magdalena.ulmeanu@oxinst.com; zhong.ren@oxinst.com

Key words: plasma etching, silicon photonics, line edge roughness, atomic force microscopy

Strip (or rib) waveguides in silicon-on-insulator (SOI) strongly confine light in sub-micron cross sections due to the high Si–air/SiO_2 refractive index contrast [1]. This strong confinement, while advantageous for compact photonic integration, also amplifies propagation losses caused by increased modal interaction with waveguide sidewalls—particularly sensitive to imperfections at the material interface [2]. These losses scale with the square of the sidewall surface roughness [3]. Current state-of-the-art fabrication methods use electron-beam (e-beam) or deep ultraviolet lithography combined with plasma-based dry etching to define waveguide features [1]. However, these processes inherently introduce line-edge roughness (LER) along the etched sidewalls. LER is typically assessed using critical-dimension scanning electron microscopy (SEM) [4], though such measurements are localised and limited in scope. In practice, many researchers infer roughness indirectly via optical loss analysis. The full statistical distribution of sidewall roughness remains elusive due to limited spatial access and resolution. Emerging tools like three-dimensional atomic force microscopy (AFM) now enable sidewall access using tilted scanning mechanisms [5], yet these systems are expensive and often entail trade-offs in versatility.

Our experiments were performed on 75 mm SOI wafers, each composed of a 220 nm thick top silicon device layer and a 2 µm buried oxide layer. The waveguide patterns were defined using ZEP520A e-beam resist of 600 nm thickness. A range of waveguide widths, between 400 nm and 600 nm, was written via high-resolution e-beam lithography, ensuring fidelity in pattern transfer. Etching depths were controlled using a laser interferometer, allowing real-time monitoring of the etch progress, as illustrated in Figure 1(a). The silicon etching process employed a fluorine-based chemistry, utilising SF_6 for etching and C_4F_8 as a passivating gas to maintain sidewall verticality. This gas combination was chosen not only for etching rate and selectivity but also for its non-toxic properties and fine-tunability. To achieve the desired etch profiles, particularly in critical regions such as the coupling sections [1], we optimised multiple etching parameters. Chamber pressure and radio frequency power were reduced enabling finer control over ion energy and mean free path within the plasma. This tuning was instrumental in maintaining verticality of sidewalls and minimising undercut. As a result, we consistently achieved well-defined profiles with a critical lateral dimension of approximately 100 nm and nearly vertical sidewalls, as shown in Figure 1(b). The reproducibility and stability of the process were confirmed across multiple wafers, demonstrating the robustness of the fabrication method.

To quantitatively characterise the resulting sidewall roughness, we employed an advanced AFM, the Jupiter XR system from Oxford Instruments Asylum Research, as depicted in Figure 2. A variety of AFM probes were selected based on their suitability for different structural features: Olympus AC160 probes were used to scan general sidewalls with moderate aspect ratios; Olympus AC55 probes were employed for capturing shallow and fine surface features; and high-aspect-ratio Nanotools NT EBD4-200 probes were specifically used for profiling deep, narrow structures such as grating couplers and sub-100 nm gaps [6]. Waveguide samples were mounted on a wedge stage to facilitate tilting, allowing the AFM probe to physically access sidewalls that are otherwise inaccessible in conventional top-down scanning. The tilt angle was adjusted individually for each structure. For comprehensive measurement, both sidewalls of a waveguide were imaged: after scanning one side, the sample was rotated 180 degrees to expose and scan the opposite face. Each side was scanned at three distinct longitudinal locations along the waveguide, and at each location, three replicate scans were performed to ensure statistical confidence and reproducibility.

Raw AFM data were first processed using Gwyddion software to eliminate long-range waviness and other artifacts caused by stage tilt or probe approach angle. This filtering process allowed extraction of the intrinsic roughness from the topographical data. Subsequent roughness analysis was performed using Oxford Instruments Asylum's Maps software [6]. The surface roughness values were summarised in Table 1. Our measurements showed that the root-mean-square roughness after plasma etching was consistently around 400 picometers, confirming the high surface quality achievable with our optimised process. These results establish a reliable baseline for evaluating process-induced sidewall variations and offer critical feedback for further process refinement and modelling of optical losses in high-confinement SOI waveguides.

[1] W. Bogaerts et al, Proc. SPIE 5956 (2005) 59560 R.
[2] P. K. Tien, Appl. Opt. 10 (1971) 2395.
[3] K. Lee et al, Appl. Phys. Lett. 77 (2000) 1617.
[4] J. S. Villarrubia et al, Surf. Interface Anal. 37 (2005) 951-958.
[5] S. Yoo et al. Appl. Microsc. (2022) 52:1.
[6] M. Kocun et al, Proc. SPIE 13414 (2025) 134140A.

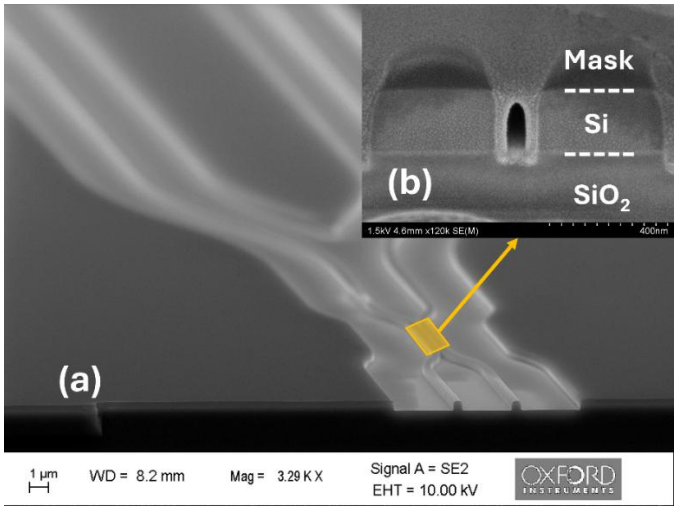

Figure 1. SEM images of etched strip waveguides on 220 nm SOI wafers: (a) silicon etching rate ~50 nm/min, with a selectivity to e-beam resist greater than 1:1; (b) vertical profile at the coupler section with a 100 nm gap, revealed through focused ion beam polishing following platinum metal deposition in the gap.

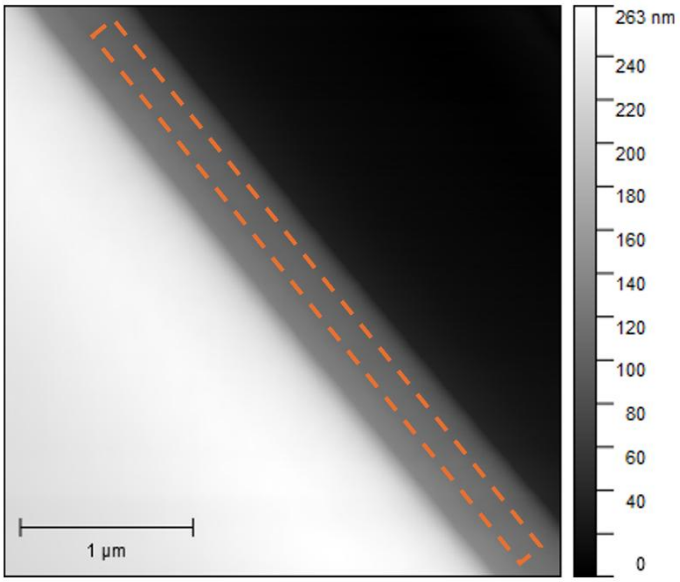

Figure 2. AFM image of the waveguide sidewall (highlighted area)

Parameter	Value
Roughness average (R_a)	325.967 pm
Root-mean-square roughness (R_q)	411.210 pm
Maximum height of the roughness (R_t)	2.00171 nm
Maximum roughness valley depth (R_v)	1.23745 nm
Maximum roughness peak height (R_p)	764.263 pm

Table 1. AFM measurement data of sidewall roughness

Fabrication of hierarchical structures in a greyscale positive photoresist by applying two lithography methods in a single resist film

Christine Schuster [a], Anja Voigt [a], David Kuhness [b], Christine Prietl [b], Matej Goraus [c], Daniel Mrena [c], Dusan Pudis [c], Arne Schleunitz [a], Gabi Gruetzner [a], Markus Postl [b]

[a] micro resist technology GmbH, Berlin, 12555, Germany
[b] Joanneum Research Forschungsgesellschaft mbH, Weiz, 8160, Austria
[c] University of Zilina, Faculty of Electrical Engineering and Information Technology, Zilina, 01026, Slovakia
e-mail: c.schuster@microresist.de

Photoresists especially designed for the use in greyscale lithography have been described previously, e.g. in [1], [2]. This type of lithography allows the manufacture of intricate 2.5D microstructures. These structures, once transferred into permanent materials, are highly versatile, finding applications in optical industries, high-end virtual reality displays, and beyond. Even more complex patterns combine 2D/2.5D features at micro and nanoscale. Such combined – i.e. hierarchical – structures in different sizes offer enhanced functional properties, such as light manipulation, mechanical strength, and energy efficiency [3], [4] etc. They generally allow multifunctionality – different functions induced in one surface topography.

Here, Direct Write Lithography, DWL, was used to manufacture larger microscale patterns, combined with Laser Interference Lithography, LIL, which enables the fabrication of large-area periodic nanoscale patterns. First results with this innovative lithography method combination using the conventional greyscale resist ma-P 1275G with a lower greyscale pattern height were presented in [6]. In this contribution we focus on the fabrication of hierarchical wave structures in mr-P 22G_XP – a photoresist prototype by micro resist technology GmbH. With its ability to achieve greyscale depths exceeding 100 µm ([5]), mr-P 22G_XP significantly broadens the scope for pattern size combinations and hence, facilitates even more multifunctional applications.

In first experiments with mr-P 22G_XP, DWL with 405 nm laser exposure was used to manufacture 85 µm deep, 280 µm wide wave patterns. A 1 µm wide grating on the surface of these large patterns was fabricated by 405 nm LIL with a development step after each exposure. First tests with a LIL pattern just 500 nm wide on the surface of a larger pattern created with DWL were also successful, and as found in [6], light diffraction and unwanted interference effects did not disturb the writing process of the patterns in the chosen dimensions. The only influence of the pattern manufactured first was the fact that the oblique incidence of light on the slopes of the large DWL structures causes slightly tilted LIL patterns. Hierarchical patterning for defined applications will show if this has an effect on the respective functionalities aimed at – and possibly has to be dealt with, e.g. by tilting the substrate during LIL.

This work was carried out in the frame of the EU-funded research project OPTIMAL (Automated Maskless Laser Lithography Platform for First Time Right Mixed Scale Patterning) which aims at integrating the different laser lithography technologies DWL, two-photon polymerization, and LIL, and inline quality monitoring, including self-learning algorithms to optimize the virtual photomask, in one platform to fabricate master structures for pattern transfer [7] – and will be presented in the context of this initiative.

[1] C. Schuster et al., “Positive greyscale photoresist for 3D patterning by direct writing or greyscale mask lithography”, 41st Micro and Nano Engineering Conference, The Hague, The Netherlands, 2015
[2] C. Schuster et al., “Advancing greyscale lithography and pattern transfer of 2.5D structures using ma-P 1200G resist series”, Whitepaper
[3] L.-Y. Li et al., ACS Nano 19(6) (2025) 6426–6436. PMID: 39912931.
[4] J. Huang et al., Chemical Engineering Journal 499 (2024) 156472.
[5] C. Schuster et al., Proc. SPIE 12497, Novel Patterning Technologies 2023, 124970P
[6] C. Schuster et al., “Generation of hierarchical riblet structures by combining direct write lithography and laser interference lithography in greyscale positive photoresists”, 50th Conference on Micro and Nano Engineering (MNE 2024), Montpellier, France, 2024
[7] https://www.optimal-project.eu/

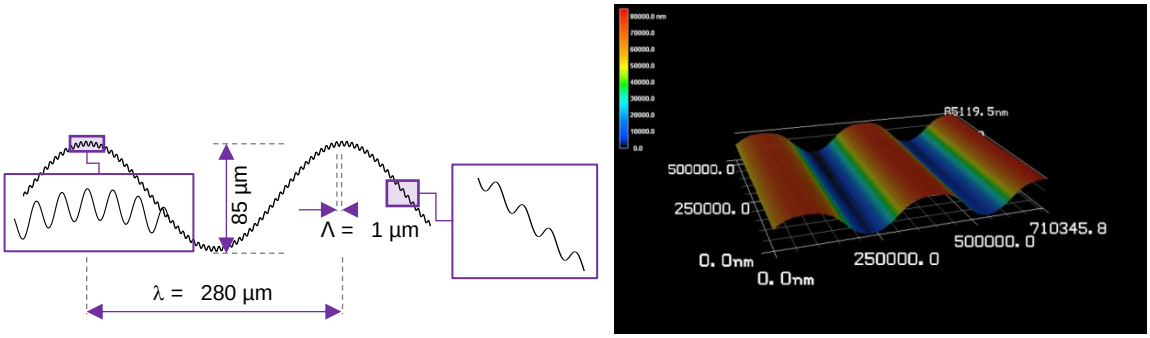

Figure 1. Optical pattern assessment of 1 µm grating by LIL surface modulation on 85 µm deep 280 µm wide DWL wave pattern in mr-P 22G_XP (Left: Scheme of the wave patterns and grating, Right: Confocal laser microscope image);
Top vs. slope LIL gratings: Slope grating slightly tilted due to the oblique incidence of light

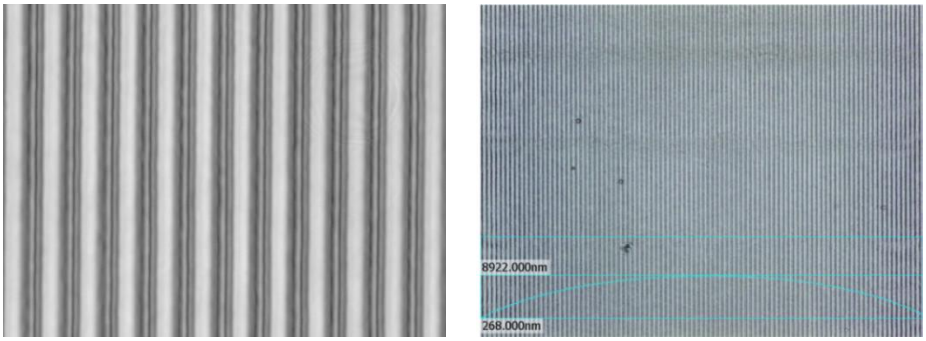

Figure 2. Confocal laser microscope pictures of the 280 µm wide wave patterns with the 1 µm grating on its surface in mr-P 22G_XP (Right: Upper ~ 8 µm)

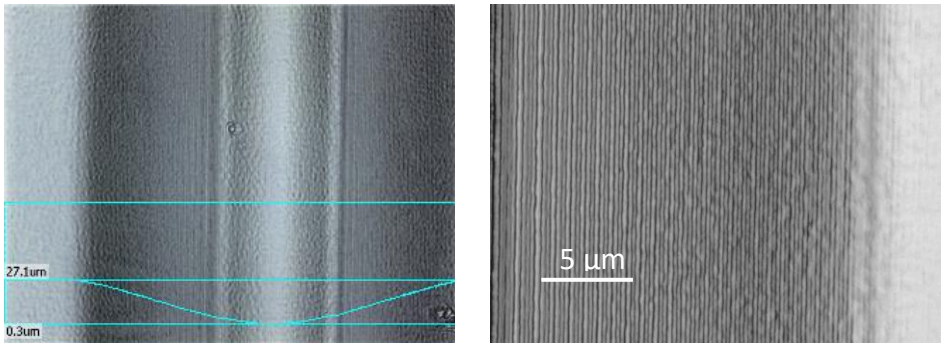

Figure 3. Confocal laser microscope picture of 500 nm LIL-fabricated gratings as surface topography on ~ 80 µm wide, ~ 27 µm deep DWL-manufactured wave patterns in mr-P 22G_XP (left), Detailed view (right),

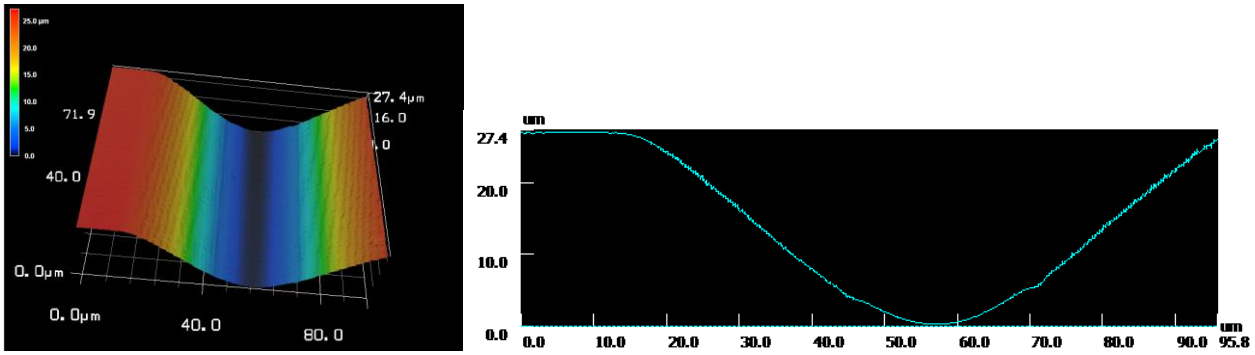

Figure 4. Optical pattern assessment of the 500 nm grating on the larger DWL pattern (cf. Figure 3, Left: Total, right: Scan across the hierarchical pattern)

200 kV E-beam Lithography for Patterning Thick Resist

Ying Tran [a], Kian Shen Kiang [a], Hitoshi Kato [b], Ryo Matsui [b], Hiroshi Ozawa [b], Yukinori Aida [b], Martin Charlton [a]
[a] University of Southampton, Highfield, Southampton, SO17 1BJ, UK
[b] JEOL Ltd, Akishima, Tokyo 196-8558, Japan
e-mail: D.T.Tran@soton.ac.uk

Electron beam lithography (EBL) is a key technique for fabricating nano-scale structures for applications such as photonics [1] and advanced electronics [2]. Although EBL systems operating at 100 kV have excellent resolution (typically 10 – 15 nm), issues of secondary electron back-scatter and material charging effects, limit pattern resolution and fidelity [3].

Another important consideration is the subsequent process flow. Resist mask thickness and feature aspect-ratio limits the transfer of high-resolution patterns to underlying material layers. For example, Diffractive Optic Elements (DOE), Meta-Lenses and Silicon photonics waveguide devices often have requirement to etch sub 50 nm features cleanly through 220 – 1200 nm thick Si/ SiO2/SiN waveguide layers. Sacrificial underlying hard–mask layers help improve achievable feature aspect ratio in the etched layers but complicates the process flow. Feature aspect-ratio combined with resist etch durability remains a limiting factor, determining the thickness of mask that can be used. The compromise is always etch depth vs feature size since high resolution patterns require very thin resist and consequently thin sacrificial mask layers.

Recently new EBL systems operating at 200 kV (JEOL JBX-8100FS G3 EBL) have emerged, and we are very happy to be the first to evaluate this equipment. High acceleration voltage can potentially mitigate these challenges, improving resolution and feature sidewall profile for thick resist.

In this work, we compare line exposures at both 100 kV and 200 kV in 5 μm and 10 μm thick PMMA on silicon. Monte Carlo simulation (Genisys Tracer software) was used to model the expected energy distribution (***Figure 1***). Colours of the energy distribution show that for 100 kV there is a higher energy density at the bottom of the resist leading to a broader profile, whilst at 200 kV the profile is less steep. Comparisons were made to the exposure results via cross-sectional scanning electron microscopy (SEM) images (***Figure 2***). While both voltages allowed nanoscale patterning, both SEMs and simulations confirmed that the 200 kV beam condition produced noticeably more vertical resist profiles achieving roughly double the aspect ratio.

These results highlight the potential of high-voltage EBL for fabricating high aspect ratio nano-scale features in thick resist and are expected to aid pattern transfer expanding the capabilities of nanofabrication for research and development in areas such as photonics, data communication, energy harvesting, sensors and monitoring devices.

Reference

[1] Wenjie Wang et al., J. Vac. Sci. Technol. A, 43, (2025), 023405
[2] Y.P. Lin et al., Microelectron. Eng., 98 (2012), pp. 386-390.
[3] R. Wüest et al., Photonics and Nanostructures - Fundamentals and Applications, 7 (2009), pp 212-219.

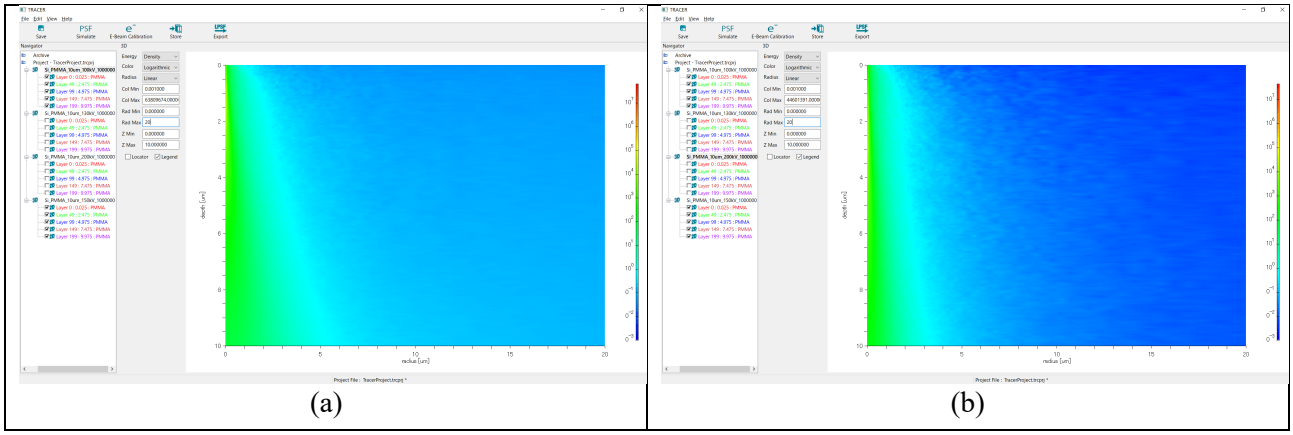

(a) (b)

Figure 1: Simulation results for 10 μm PMMA on silicon, comparison of (a) 100 kV and (b) 200 kV

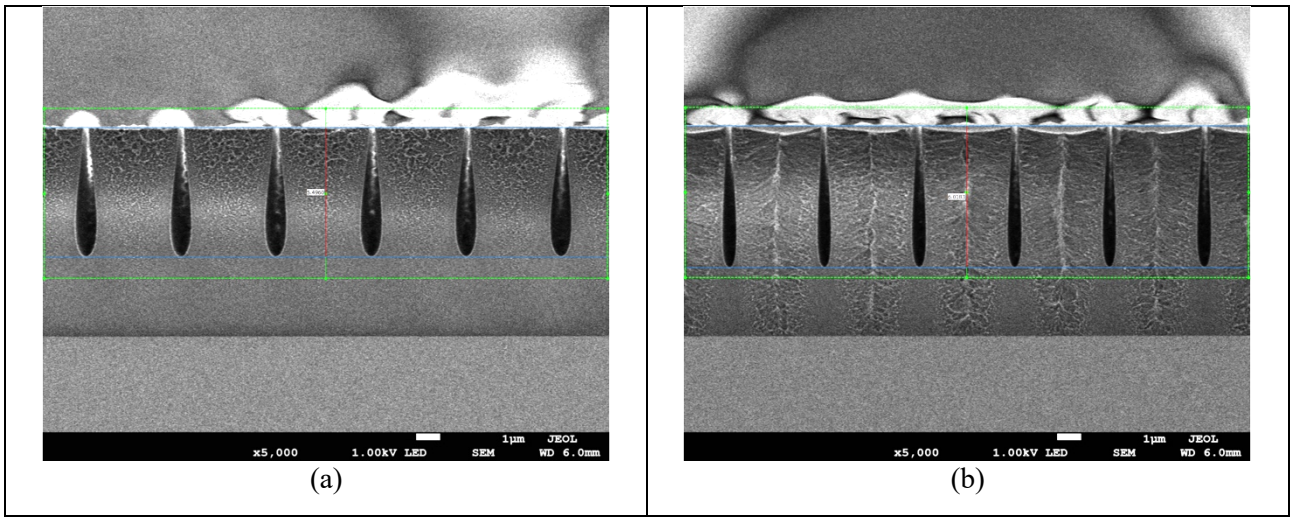

(a) (b)

Figure 2: SEM cross – section of 10 nm designed lines, exposed on 10 µm PMMA at (a)100 kV and (b)200 kV using a dose of 44000 µC/cm^2.

Large-Scale Integrated Visible/Near-Infrared Multi-Channel Polarizer based on Sub-wavelength Metal Grating

Kangping Liu[a,b], Jinyu Guo[a,b], Wentao Yuan[a,b], Shuoqiu Tian[a,b], Hao Quan[a,b], Qiucheng Chen[a,b], Qingxin Wu[a,b], Xunjia Zhao[a,b], Sheng Tao, Yifang Chen[a,b,*]

[a] Nanolithography and Application Research Group, School of Information Science and Technology, Fudan University, Shanghai 200433, China

[b] Shanghai Key Laboratory of Metasurfaces for Light Manipulation, Fudan University, Shanghai 200433, China

e-mail: * yifangchen@fudan.edu.cn

Abstract

Linear polarization is the simplest form of polarized light whose electric field vector is in the plane perpendicular to the direction of propagation. It can help people get the information more accurately by using polarizers to process the optical information. Extensive applications of polarimetric detection in visible/near-infrared wavelengths can be found in resource exploration, material analysis and Marine pollution detection. Sub-wavelength metal grating with the advantages of miniaturization and integration with focal plane array of detectors on one chip, possesses promising prospect for future multi-channel on-chip polarizers[1]. This work successfully fabricate polarizers with three channels through polarization of 0°, -60°, and 60° in the visible and near-infrared bands. Each channel has at least 150 μm × 15 mm of grating coverage area achieving large-scale linear polarizers on silicon-based photodetector chips. Finite difference time domain (FDTD) is utilized to obtain the structure parameters of the aluminum (Al) grating with balance between efficiency and process complexity[2,3]. Electron beam lithography (EBL) on bilayer resist for pattern definition and lift-off for pattern transfer are carried out for the metal polarizers. Transmittance and extinction ratio (ER) through the gratings are characterized in visible/near-infrared bands.

In order to reduce the influence of stray light, chromium (Cr) is used as a shield to form the light slits. Metal wire grids with different polarization directions are required to cover each light slit. The schematic diagram of the integrated three-channels polarizer and an additional slit for benchmark on the detector is shown in Fig. 1. According to the simulation results shown in Figure 2(a) and Fig. 2(b), it is determined that with a period of less than 150 nm the structure has a TM wave transmittance greater than 60% and a good ER operating in the visible/near-infrared band. According to the results shown in Fig. 2(c) and Fig. 2(d), with 150 nm period and 75 nm line width, the grating can achieve a transmittance over 60% and a ER above 100:1 when the height exceeds 100 nm. This work adopted a double-layer Polymethylmethacrylate (PMMA) lift-off technology due to its small period. As is shown in Fig. 3, PMMA (100K) was selected as the bottom resist and PMMA (950K) as the top. The experimental results are shown in Fig. 4 which has Al wire grids with directions of 0°, -60°, and 60°. Results obtained from the final test is illustrated in Fig. 5, showing that the transmittance of TM can exceed 70% and ER can be greater than 50:1 over the range of 650 nm to 900 nm.

Reference:

1 Feng, B. *et al.* Precision integration of grating-based polarizers onto focal plane arrays of near-infrared photovoltaic detectors for enhanced contrast polarimetric imaging. *Int. J. Extreme Manuf.* **3** (2021). https://doi.org/10.1088/2631-7990/abf5c8

2 Yang, Z. *et al.* Optimization study of metallic sub-wavelength gratings as the polarizer in infrared wavelengths. *Appl Opt* **59**, 1253-1258 (2020). https://doi.org/10.1364/AO.378636

3 Yang, Z. *et al.* A study of nano-structural effect on the polarization characteristics of metallic sub-wavelength grating polarizers in visible wavelengths. *Microelectronic Engineering* **227** (2020). https://doi.org/10.1016/j.mee.2020.111327

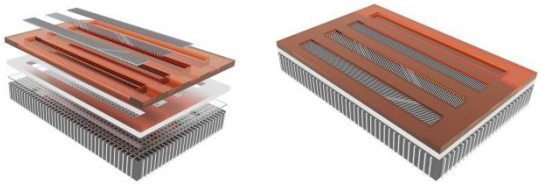

Figure 1. The process of fabrication.

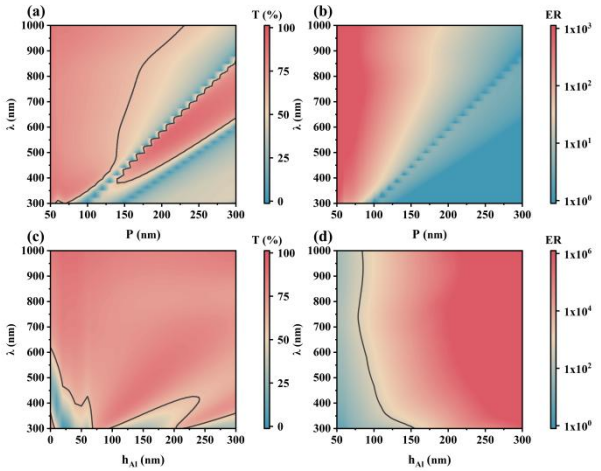

Figure 2. FDTD results of transmittance and the extinction ratio.

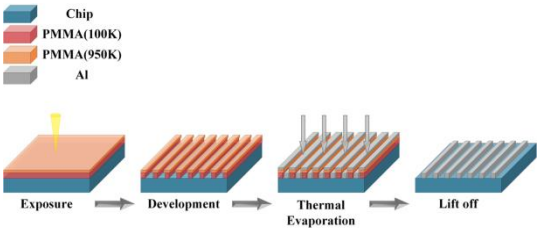

Figure 3. The process of fabrication.

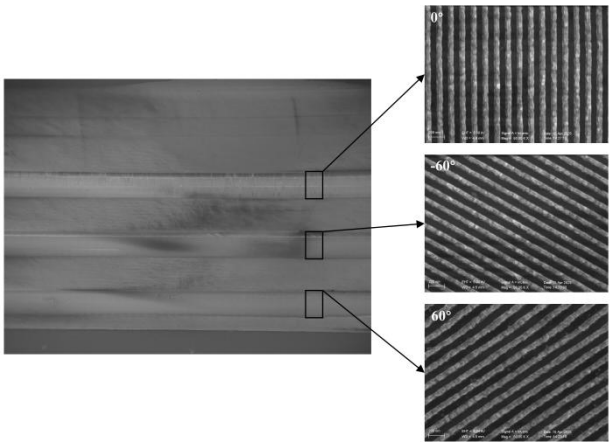

Figure 4. The SEM photos of fabricated 0°, -60◦ and 60◦ orientated gratings with a consistent 75 nm line width and 150 nm pitch in Al gratings.

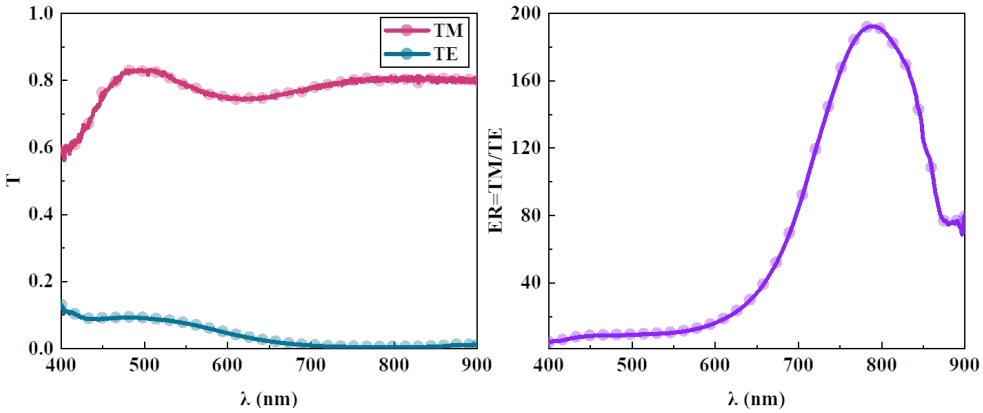

Figure 5. Optical test result.

High Resolution Electron Beam Lithography for 10 nm Zone Plates with ultra-high aspect ratio

Qingxin Wu, Qiucheng Chen, Hao Quan, Xunjia Zhao, Wentao Yuan, Shuoqiu Tian, Jinyu Guo, Kangping Liu, and Yifang Chen*

Nanolithography and Application Research Group, School of Information Science and Technology, Fudan University, Shanghai, China; Shanghai Key Laboratory of Metasurfaces for Light Manipulation, Fudan University, Shanghai, China.
e-mail: yifangchen@fudan.edu.cn

Keywords: electron beam lithography, Fresnel zone plate, soft X ray, 10 nm resolution, high aspect ratio.

High-resolution Fresnel zone plates are urgently needed by X-ray nanoprobes for important applications in material and life science, biology, medical diagnosis, new energy resources and integrated chips, etc. Although 10 nm resolution zone plates have been reported by double-patterning technology, the diffraction efficiency remains limited to about 1% [1], primarily due to defects and imperfection in the structure. The technology of high-efficiency 10 nm zone plates using electron beam lithography (EBL) remains challenging. In this paper, an optimized exposure strategy for 10 nm resolution HSQ zone plate template is presented. Careful Monte Carlo simulations for achieving ultra high dense pattern were carried out to compare original with optimized exposure methods. High-quality zone plates with 10 nm linewidth and vertical sidewalls were successfully replicated using the optimized dose distribution combined with our hot development process [2].

To eliminate proximity effect on the dense pattern, the designed linewidths of both zones and ribs are reduced to 5 nm. Fig. 1 presents scanning electron microscope (SEM, ZEISS Sigma 300 HD) images of 10 nm HSQ zone plate templates fabricated by state-of-the-art beam-writer, JBX6300FS, with exposure doses of 20000 μC/cm² (Fig. 1a-c) and 25000 μC/cm² (Fig. 1d-f). While 10 nm lines are visible in high-magnification images (Fig. 1a), defects are observed in outer zones (Fig. 1b). The 45° tilted view (Fig. 1c) reveals uneven exposure patterns, with over exposed intersections and under exposed zone regions. These defects significantly affect zone height uniformity and diffraction efficiency.

An optimized exposure strategy was developed (Fig. 2), incorporating two key modifications. First, zone linewidths (6 nm) were increased relative to ribs (2 nm) to enhance dose concentration in zone areas. Second, relief holes were introduced at zone-rib intersections to reduce proximity effects. Monte Carlo simulations are employed to calculate the isoenergy contours, showing concentrated charge density at intersections in the original design (Fig. 2a) versus uniform distribution across zones in the optimized pattern (Fig. 2b). Using this strategy, we successfully fabricated defect-free 10 nm HSQ zone plate templates with 180 nm height and 1:3 duty cycle, as demonstrated in Fig. 3a.

In conclusion, 10 nm HSQ zone plate templates with 180 nm height and 1:3 duty cycle is successfully fabricated by electron beam lithography. With the assistance of hot developing and optimized exposure process, well-defined zone plate profiles are achieved. Our in-house developed calculation method shows an efficiency over 3% of the 10 nm HSQ zone plates.

[1] R. Benedikt et al., Microelectronic Eng., 191 (2018) 91–96.
[2] Y. Chen et al., Microelectron. Eng., 83 (2006) 4-9.

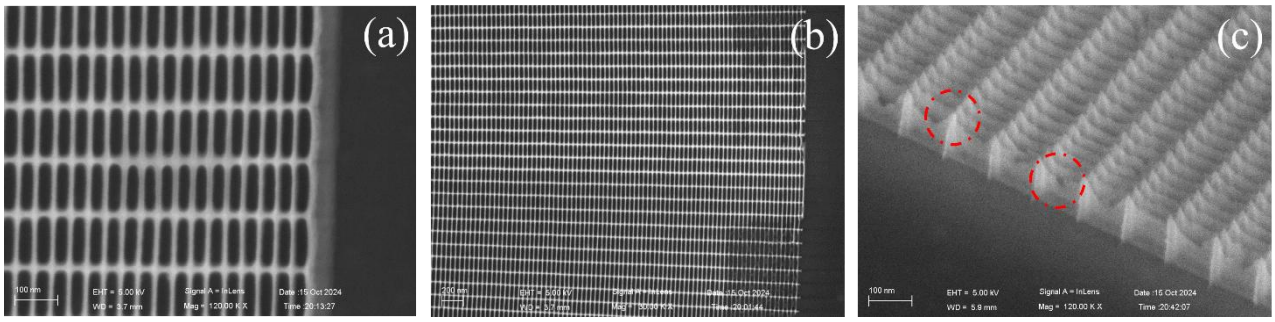

Figure 1. SEM images of the fabricated 10 nm zone plate in 180 nm thick HSQ resist without the optimized exposed process, with many fabrication imperfections. The designed widths of both the outermost zones and ribs are 5 nm

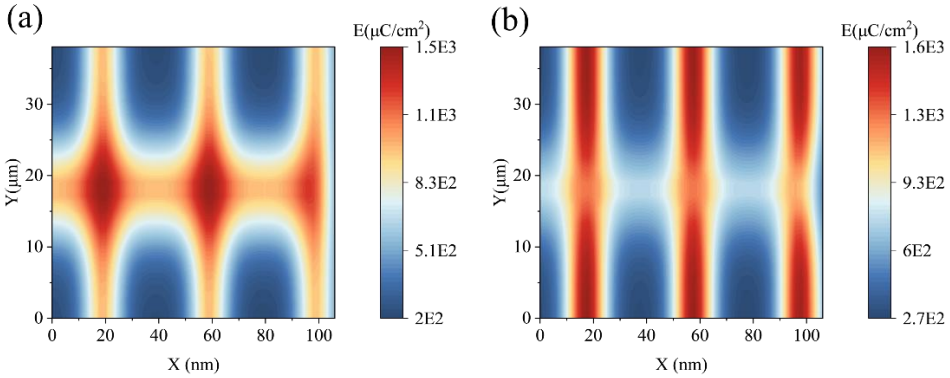

Figure 2. Comparison of (a) original and (b) optimized exposure patterns for 10 nm HSQ zone plate fabrication, with corresponding Monte Carlo-simulated isoenergy contours after e-beam exposure.

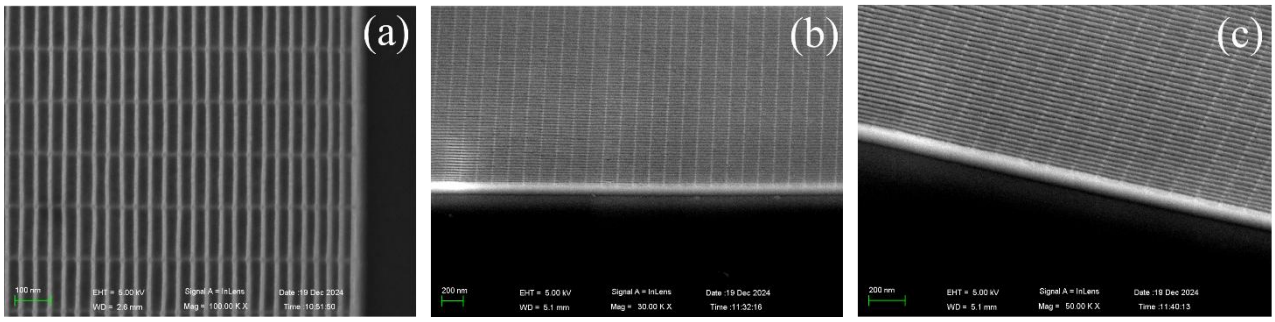

Figure 3. SEM images of the fabricated 10 nm resolution zone plate in 180 nm thick HSQ resist with the optimized exposed process, showing the reliable profiles with vertical sidewalls and without residual resist.

Ultra high resolution and dense SiO_2 gratings by electron beam lithography and dry-etch

Sheng Tao [a, b], Wentao Yuan [a, b], Shuoqiu Tian [a, b], Kangping Liu [a, b], Guojin Yu [a, b], Yifang Chen [a, b, *]

[a] *Nanolithography and Application Research Group, School of Information Science and Technology, Fudan University, Shanghai, China*
[b] *Shanghai Key Laboratory of Metasurfaces for Light Manipulation, Fudan University, Shanghai, China*

Abstract

This work focuses on nanofabrications of highly dense SiO_2 gratings by electron beam lithography (EBL) together with reactive ion etch (RIE), using ZEP520A as etching mask. The final task of the work is to achieve 14 nm lines/14 nm spaces with the height around 35 nm, which will sit on the top of quartz. SiO_2 based gratings are crucial in various optical applications such as spectroscopy, optical communication, and optical sensors. It can also be applied as nanoimprint templates for high resolution patterning. ZEP520A was used as etching mask because of its high resolution, high sensitivity, high contrast and high resistivity to plasma etch.

In this research, systematic processes were studied to explore the processing window. A 140 nm - thick layer of ZEP520A was coated onto a SiO_2 substrate. Electron beam lithography (JEOL JBX - 6300FS) was applied for exposure, and then development in O-Xylene. Reactive ion etch was carried out in Plasma lab system 100, where CHF_3 was employed as etching gases. Various parameters such as gas flow rate, pressure, and power were systematically varied to optimize the etching process.

The results indicate that under optimized conditions (etching power of 200 W, SF_6 flow rate of 0 SCCM, CHF_3 flow rate of 30 SCCM, etching time of 30 s, and pressure of 4 Pa), ZEP520A can be efficiently used as an etching mask to achieve the SiO_2 based grating with good side-wall verticality. SEM characterization confirmed that the fabricated grating structures exhibited excellent verticality and uniform periodic arrangement.

Further analysis revealed that introducing SF_6 increases the etching rate of SiO_2 but leds to significant consumption of ZEP520A, making this approach unsuitable for the etching process. As shown in Figure (b), the pattern morphology remained largely unchanged before and after photoresist removal, indicating complete etching of the ZEP520A photoresist within 30 seconds. Regarding pressure, it was observed that the etching rate and verticality first increased and then decreased with increasing pressure. Notably, at pressures of 4 - 5 Pa, the etching exhibited better verticality, as evidenced by the combination of Figure (c) and Figure (e). Figure (d) illustrates that the effective etching of grating structures occurred within the blue region (SF_6 flow rate of 0 – 5 SCCM). When the gas flow rate exceeded 5 SCCM, the ZEP520A photoresist was consumed too rapidly to function properly, resulting in uniform etching across the entire plane.

Overall, this study demonstrates that using ZEP520A photoresist as an etching mask in the etching process can produce high quality SiO_2 gratings, providing a reliable technical approach for manufacturing high resolution SiO_2 based nanoimrint templates. Future work will focus on how to reduce the dimension of the graing linewidth for 14 nm lines/spaces grating in quartz.

Keywords: SiO_2 grating; electron beam lithography, reactive ion etch, nanoimprint templates, ZEP520A

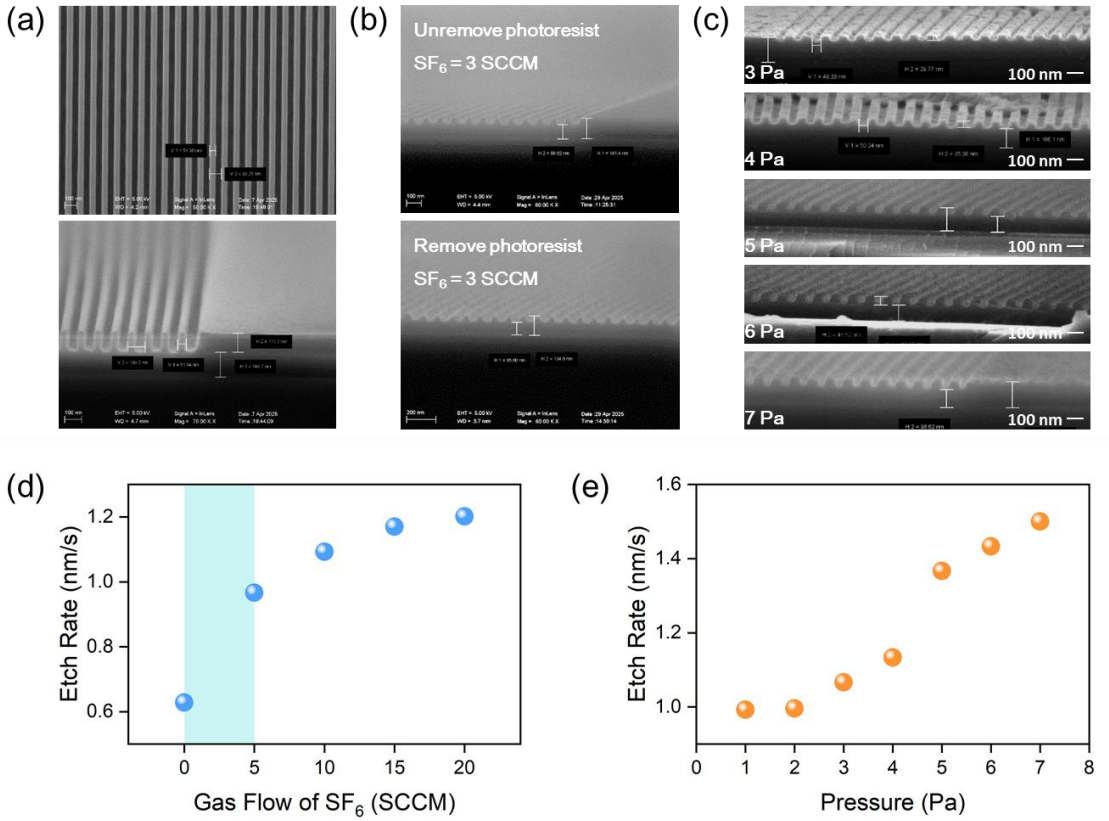

Figure 1. (a) SEM plan-view (upper) and cross-sectional (lower) images after EBL exposure and development; **(b)** SEM cross-sectional images after etching with SF_6 flow of 3 SCCM, with photoresist remaining (upper) and removed (lower); **(c)** Cross-sectional images after etching at pressures ranging from 3 to 7 Pa (from top to bottom); **(d)** Effect of SF_6 gas flow rate on SiO_2 etch rate; **(e)** Effect of etching pressure on SiO_2 etch rate.

Ultrafast Single Germanium Nanowire Photodetectors

Ahmad Echresh [a,b], Mohd Saif Shaikh [a], Mircea Traian Cauneanu [b], Manfred Helm [a,b], Shengqiang Zhou [a], Artur Erbe [a,b] , Lars Rebohle [a], Kambiz Jamshidi [b], Yonder Berencén [a], Yordan M. Georgiev [a,c]

[a] Institute of Ion Beam Physics and Materials Research, Helmholtz-Zentrum Dresden-Rossendorf (HZDR), Dresden, 01328, Germany
[b] Technische Universität Dresden, 01062 Dresden, Germany
[c] Institute of Electronics at the Bulgarian Academy of Sciences, Sofia, 1784, Bulgaria
e-mail: a.echresh@hzdr.de

Abstract

Semiconductor nanowire-based photodetectors with high sensitivity and rapid photoresponse in the near-infrared (NIR) spectrum are essential for applications in optical communication switches, as well as environmental and atmospheric sensing [1-3]. These devices exploit the high surface-to-volume ratio, quantum confinement effects, and the tunable bandgap of nanowires to achieve enhanced responsivity, fast response times, and broad spectral sensitivity, including in the NIR region [4]. Recently, there has been growing interest in the development of photodetectors that can operate at zero bias, making them more suitable for portable, low-power applications. Such self-powered photodetectors, which utilize the photovoltaic effect, can be categorized into Schottky junctions, p–n junctions, and photoelectrochemical cells [5]. Among various semiconductor materials, germanium nanowires (Ge NWs) offer distinct advantages for optoelectronic applications, including high carrier mobility, compatibility with silicon-based complementary metal-oxide-semiconductor (CMOS) technology, and a lower bandgap compared to silicon [6]. However, despite these promising properties, research on the fabrication and photoresponse characteristics of axial p–n junctions in single Ge NWs remains limited, necessitating further investigation.

This study presents the top-down fabrication of axial p–n junction along single Ge NWs and investigates their photoresponse characteristics in the NIR spectral range. The fabricated devices exhibit rectifying current–voltage behavior with a high rectification ratio in dark conditions (Fig. 1a). Under 850 nm wavelength laser illumination at reverse bias, the devices achieve a responsivity of 1.72 AW^{-1} (Fig. 1b), a low noise-equivalent power of 5.68×10^{-11} W/√Hz (Fig. 2a), and a high-frequency response of 2.85 GHz (Fig. 2b), characterized by a 3dB cut-off frequency. The enhanced sensitivity of Ge NW-based photodetectors is attributed to the presence of a radial built-in electric field, which extends the carrier lifetime, while their nanoscale dimensions result in minimal capacitance, enabling ultrafast response times. These findings hold significant promise for the development of high-speed, energy-efficient photodetectors, with potential applications in next-generation optical communication systems and integrated optoelectronic technologies.

[1] R. LaPierre, M. Robson, K. Azizur-Rahman, P. Kuyanov, Journal of Physics D: Applied Physics 50 (2017), 123001.
[2] W. Tian, Y. Wang, L. Chen, L. Li, Small 13 (2017), 1701848.
[3] L. Shen, H. Qian, Y. Yang, Y. Ma, J. Deng, Y. Zhang, J. Phys. Chem. C 127 (2023), 11328.
[4] J. Sun, M. Han, Y. Gu, Z.-x. Yang, H. Zeng, Advanced Optical Materials 6 (2018), 1800256.
[5] L. Peng, L. Hu, X. Fang, Advanced Functional Materials 24 (2014), 2591.
[6] J. W. John, V. Dhyani, Y. M. Georgiev et al., ACS Applied Electronic Materials 2 (2020), 1934.

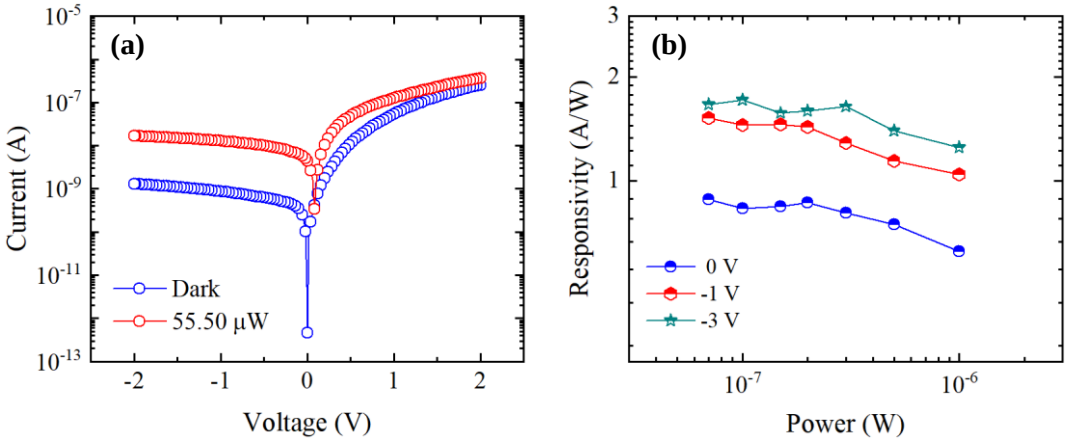

Figure 1. (a) Semi-log current−voltage characteristics of a single Ge NW-based p–n junction in dark conditions and under illumination of an 850 nm wavelength laser @ 55.50 μW. (b) Responsivity of the Ge NW photodetector as a function of illumination power of an 850 nm wavelength laser at zero and applied bias.

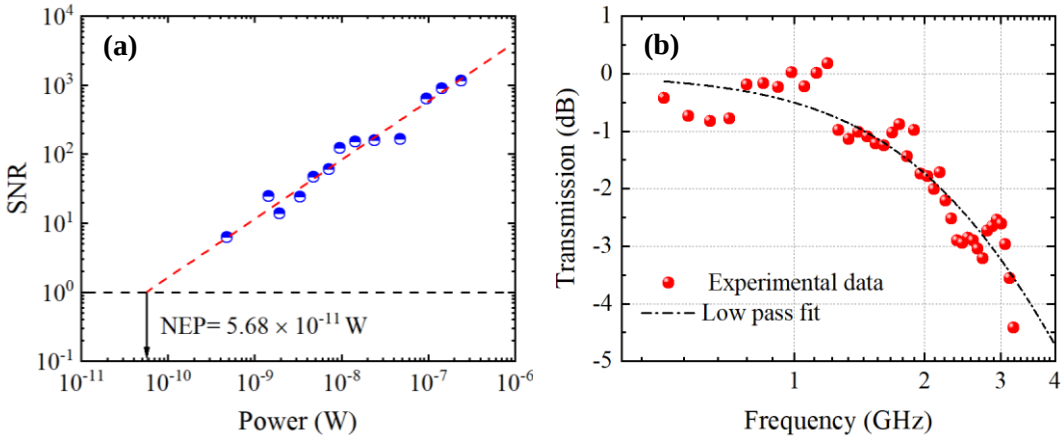

Figure 2. (a) Signal-to-noise (SNR) ratio as a function of laser power, and (b) frequency-response of the single Ge NW photodetector under pulsed photo-irradiation of an 850 nm wavelength laser at a reverse bias of 3V. A low-pass filter was used to fit the experimental data and to extract the 3dB cut-off frequency.

Substantial $R_{on,sp}$ Reduction in a 1.2 kV SiC DMOSFET Using a Double-Epi

Seungwan Jung[1], Gyuhyeok Kang[2], Dusan Baek[1], Sangyeob Kim[1], Sumin Park[1], Hyowon Yoon[1] and Ogyun Seok[1]
[1] Pusan National University, Busan, 46241, Republic of Korea
[2] Kumoh National Institute of Technology, Gumi, 39177, Republic of Korea
E-mail: ogseok@pusan.ac.kr

This study proposes a 1.2 kV Silicon Carbide (SiC) DMOSFET featuring a deep, highly doped upper drift layer formed under the P-base using a double-epi structure to reduce the on-resistance ($R_{on,sp}$). SiC offers superior performance compared to conventional Si-based MOSFETs and IGBTs due to its wide bandgap (~3.26 eV), high critical electric field (~3 MV/cm), and excellent thermal conductivity (~3.7 W/cm·K). These characteristics enable enhanced switching speed, thermal management, and voltage blocking capability, making SiC MOSFETs ideal for high-power and high-efficiency applications. Therefore, reducing $R_{on,sp}$ is crucial to further improving the efficiency of SiC DMOSFETs and requires structural optimizations. Previous studies have attempted to optimize $R_{on,sp}$ by adjusting key design parameters of the JFET region, such as doping concentration, width, and depth. Although deep ion implantation into the JFET region could further reduce $R_{on,sp}$, the inherent limitation of ion implantation depth in SiC makes it difficult to achieve a sufficient doping profile [1]. The proposed structure improves current conduction due to the upper drift layer with high doping concentration, which results in a reduction in $R_{on,sp}$. Additionally, this design offers cost advantages by eliminating the need for patterning and ion implantation processes in the JFET region. The highly doped region also facilitates recombination at a shallower depth, resulting in a lower forward voltage drop (V_F) [2]. Moreover, this structure suppresses bipolar degradation by reducing hole injection into the drift region. The electrical characteristics of the proposed upper drift DMOSFET with a double-epi structure were compared to those of a conventional DMOSFET using TCAD simulations. In addition, parametric variations of the upper drift structure were conducted to evaluate and analyze its impact on key electrical characteristics.

The cross-sectional view of the structures used in the study are shown in Figure.1, and the specifications show in Table I. Figure. 2 shows the difference in current density between structures (a) and (b) under V_{GS} = 15 V and V_{DS} = 20 V conditions. Structure (b) exhibits a more widely spreaded current density distribution due to the presence of the highly doped upper drift region. The characteristics of (b) structure according to thickness of upper drift are summarized in Table II. The doping concentration of the upper drift layer was determined based on the average doping level of the JFET region in the conventional reference structure. As the thickness of the upper layer increases, the expansion of the highly doped region leads to a reduction in $R_{on,sp}$. Additionally, the influence of the doping concentration in the upper drift region on device characteristics is presented in Table III. The doping concentration of the upper drift was determined using the average value of the reference JFET doping levels. To investigate the effects of doping concentration in the upper drift region, its thickness was fixed at 1.6 μm. Structure (b) employing the double-epi technique reduced $R_{on,sp}$ by up to 37.5 % relative to the reference device. As the upper drift doping concentration increased and reached 5×10^{16} cm^{-3}, the resistance dropped to 2.28 mΩ·cm^2. As the doping concentration increases, structure (b) shows a lower $R_{on,sp}$, confirming the effectiveness of the resistance reduction. However, overall structure (b) exhibits a lower breakdown voltage (BV) than structure (a) due to the suppression of depletion region expansion at the PN junction between the P-well and the upper drift region. Figure 3 illustrates the maximum electric field of structures (a) and (b) under V_{GS} = 0 V and V_{DS} = 1200 V. While structure (b) generally has a lower breakdown voltage than structure (a), Figure 3 shows that the peak electric field in structure (b) remains below ~2.58 MV/cm, indicating it operates within a safe electric field range. Also the body diode characteristics of both structures are presented in Tables II and III. Structure (b) demonstrates a lower forward voltage drop (V_F) compared to structure (a), due to a shallower recombination depth and reduced resistance component caused by the highly doped deep JFET. When simulating the 1.2 kV SiC DMOSFET using a double-epi structure with an upper drift layer, excellent results were achieved in terms of $R_{on,sp}$, while maintaining an appropriate BV.

This work was supported by Korea Institute for Advancement of Technology(KIAT) grant funded by the Korea Government(MOTIE) (RS-2025-02214408, HRD Program for Industrial Innovation) and IITP(Institute for Information & Communications Technology Planning & Evaluation) under the ITRC(Information Technology Research Center) support program(IITP-2025-RS-2024-00438288, 0.5) grant funded by the Korea government(MSIT)

[1] D. kim, et al., IEEE J-EDS, (2022)
[2] J. Qian, et al., Micromachines, (2024)

Table I. The specification of strctures

Parameter	Value
Cell Pitch [μm]	5
JFET Depth [μm]	1.1~1.2
JFET Width [μm]	0.6
Channel Length [μm]	0.4
Poly-Si Gate Width [μm]	3
N-drift Concentration [cm^{-3}]	8×10^{15}
Total drift layer thickness [μm]	10
Upper drift layer thickness [μm]	1.2, 1.6, 2.0
Upper drift layer concentration [cm^{-3}]	3.0×10^{16},4.0×10^{16}, 5.0×10^{16}

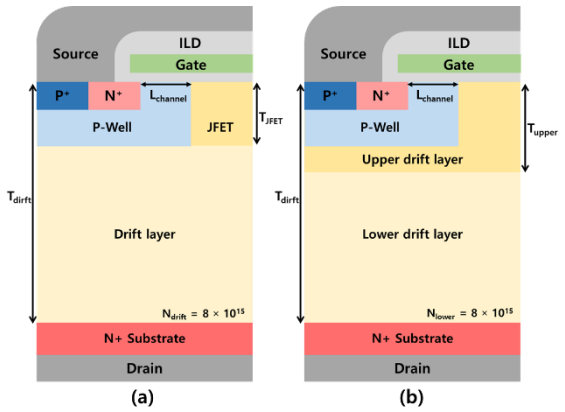

Figure 1. Cross-sectional views of the (a) SiC conventional DMOSFET, (b) SiC DMOSFET using upper drift layer

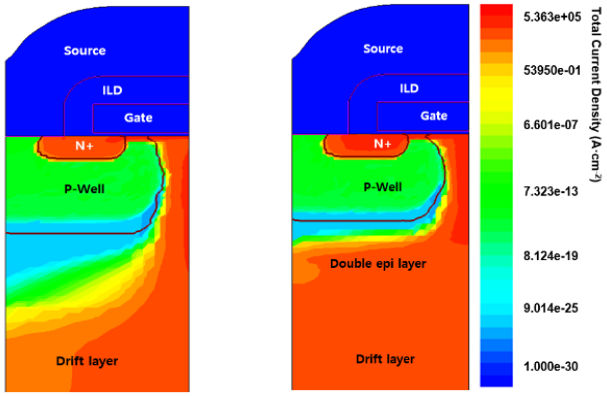

Figure 2. The defference of current density about the (a) SiC conventional DMOSFET and (b) SiC DMOSFET using upper drift layer when V_{DS} = 20 V, V_{GS} = 15 V

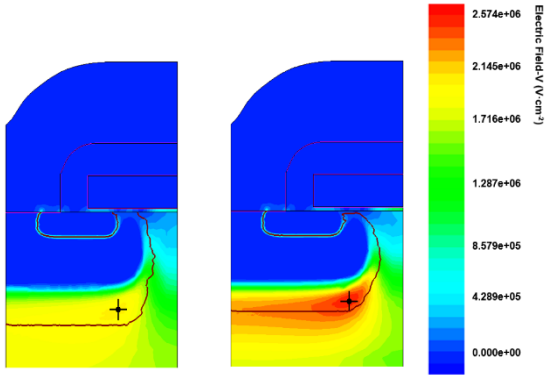

Figure 3. Max electric field of the (a) SiC conventional DMOSFET and (b) SiC DMOSFET using upper drift layer when V_{GS} = 0 V, V_{DS} = 1200 V

Table II. The characteristics of the structure (a) and (b) according to upper drift layer thickness

Type	T_{JFET} [μm]	T_{upper} [μm]	N_{JFET} [cm^{-3}]	N_{upper} [cm^{-3}]	V_{th} [V]	$R_{on,sp}$ [mΩ·cm^2]	BV [V]	V_F [V]
(a)	1.1	-	5×10^{16}	-	4.17	3.65	1533	–2.40
(b)	-	1.2	-	5×10^{16}	3.86	3.34	1487	–2.32
	-	1.6	-	5×10^{16}	3.87	2.28	1403	–2.30
	-	2.0	-	5×10^{16}	3.73	2.12	697.5	–2.24

Table III. The characteristics of the structure (a) and (b) according to upper drift layer doping concentration

Type	T_{JFET} [μm]	T_{upper} [μm]	N_{JFET} [cm^{-3}]	N_{upper} [cm^{-3}]	V_{th} [V]	$R_{on,sp}$ [mΩ·cm^2]	BV [V]	V_F [V]
(a)	1.1	-	5×10^{16}	-	4.17	3.65	1533	–2.40
(b)	-	1.6	-	3×10^{16}	4.19	3.04	1454	–2.42
	-	1.6	-	4×10^{16}	4.05	2.58	1408	–2.36
	-	1.6	-	5×10^{16}	3.87	2.28	1403	–2.30

Development of a uniform cell dispersion structure in microfluidic channels with low cell loss

YAMADA Takumi[a], KIMURA Akihito [a], KAMINAGA Maho [a], KOTANI Akira [a],
[a] National Institute of Technology (KOSEN) Toyota College, Toyota-city, postal code:471-8525, Japan
e-mail: d2409@toyota.kosen-ac.jp
keyword: Microfluidics, PIV, Cell dispersion, Micropillar array, Cell flow

• Purpose of the work:

The purpose of this study is to develop a uniform cell seeding method with low cell loss that is applicable to experiments using rare cells in microfluidic devices. Maintaining a constant cell density in the microchamber is pivotal to achieving reproducible cell experiments. Despite the numerous advantages of performing cellular experiments in a microchamber, achieving uniform cell distribution can be challenging owing to the low Reynolds number of the microfluidic system. In this study, we proposed a method for achieving homogeneous cell dispersion in microfluidic devices with low cell loss, particularly applicable to experiments with rare cells. A micropillar array (MPA) placed upstream of the microchamber generated a random flow of cells, resulting in uniform cell dispersion (Figure 1). The repetitive clogging and releasing of cell flow between the micropillars generated random flow. To resolve the issue of cells remaining between markedly narrow pillars, a microballoon actuator was used to switch the width of the flow path between cell dispersion and residual cell collection. Herein, the performance of a cell dispersion technique incorporating microballoon actuators was confirmed based on the degree of cell dispersion and flow visualized using particle image velocimetry (PIV).

• Novelty of the work with respect to the state of the art:

Several methods have been developed to ensure uniform cell distribution in microfluidic channels, which can be divided into two types. One method involves the uniform patterning of cell adhesion sites at the bottom of the microchamber [1], while the other utilizes the uniform distribution of microstructures that trap cells within the microchamber [2]. Using these techniques, the cells can be uniformly aligned with simple microstructures. However, adhesion sites and the microstructure itself act as obstacles that impact cell properties, such as cell differentiation, morphology, proliferation, adhesion, and gene expression [3]. These limitations often prevent accurate assessment of cellular activity. Consequently, we previously proposed a technique in which MPAs were placed in front of a cell culture region [4]. However, this technique has the disadvantage of a low cell passage rate of 30% due to the very narrow pillar spacing (5 μm), preventing its application to rare cells. Therefore, we developed the first homogeneous cell dispersion method that does not impact the cells and can be used for rare cell assessment.

• Results of the work.

Using a pressurized microballoon, the cell dispersion performance of the microfluidic device with micropillar gaps of 200 μm, which is sufficient for cell passage, was examined. Figure 2 presents the results of the cell distribution ratio in the range of 500 μm downstream of the MPA. The introduced cells spread to the area near the channel wall, which can be difficult to reach using conventional cell introduction. After cell introduction, the balloon pressure returned to atmospheric pressure, and purified water was introduced to collect the remaining cells between the micropillars. The residual cell area between the pillars was measured before and after cell collection to calculate the cell recovery rate. The recovery rate of the new device was 84.4%, indicating a 2.5-fold improvement over that of the conventional device (30%).

To evaluate cell dispersion in the microfluidic device, PIV analysis was performed to quantitatively clarify the flow of dispersed cells with different MPA parameters using a high-speed camera (DITECT, HAS-U2) and a PIV analysis software (Flownizer2D). The filming conditions were 150 fps, 1920 ×1080 resolution, and a channel flow velocity of ~ 0.918 mm/s. Figure 3a presents the results of the PIV analysis of the video in Figure 3b at 150 FPS and 3000 frames. Additionally, we confirmed that vectors of cell flow diverge in part of the MPA, suggesting that the pillars can alter cell flow.

References

[1] M. Kaminaga et al., Micromachines, 6 (2015) 409-422.
[2] L. Gonzalez-Macia et al., Analyst, 135 (2010) 845-867.
[3] J. Nilsson et al., Anal. Chim. Acta 649 (2009) 141–157.
[4] A. M. Ross et al., Small, 8 (2012) 336–355.

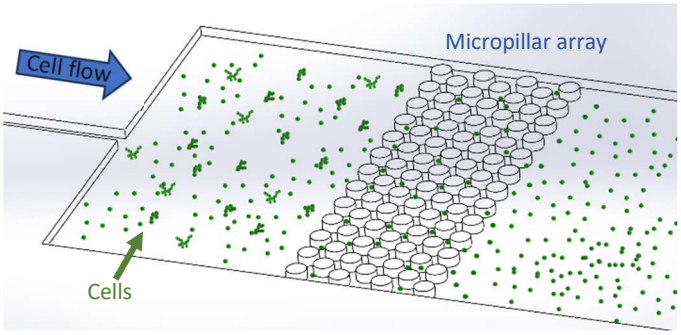

Figure 1. Micropillar array in a microfluidic device.

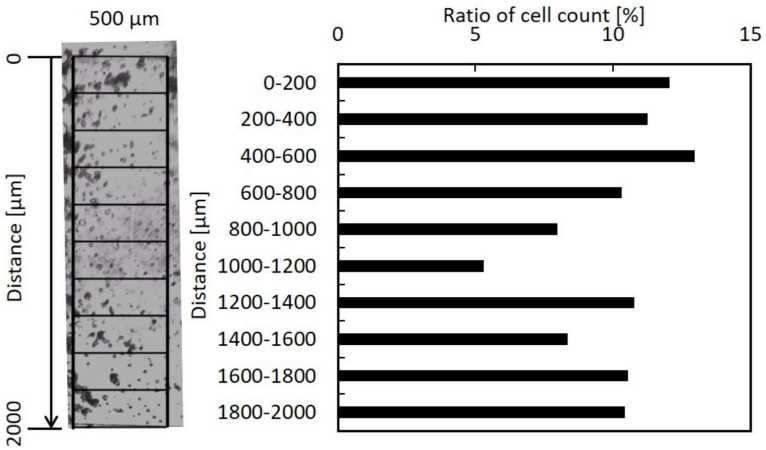

Figure 2. The ratio of cell distribution in the range of 500 µm downstream of the micropillar array.

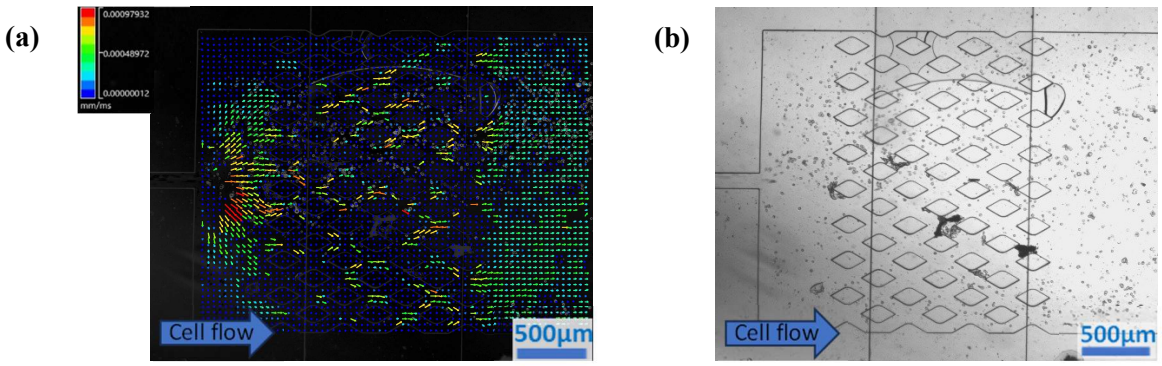

Figure 3. (a) Results of the PIV analysis of the video in Figure 3b at 150 FPS, 3000 frames. **(b)** Experiment of cells passing through the micropillar array.

3D-Printed Microfluidic Device for Biological Application

Amlan Ashish[1,2], Gorachand Dutta[1]*
[1]NanoBiosensors and Biodevices Lab, School of Medical Sciences and Technology, Indian Institute of Technology Kharagpur, Kharagpur-721302, India.
[2]Advanced Technology Development Centre (ATDC), Indian Institute of Technology Kharagpur, Kharagpur-721302, India.
[3] Department of Chemical Engineering, Indian Institute of Technology Kharagpur, Kharagpur-721302, India

*Corresponding author: g.dutta@smst.iitkgp.ac.in

The majority of microfluidic devices are made using the gold standard PDMS material because of their high resolution and transparency.[1] However, there are still an adequate number of barriers hindering their commercial scalability due to high costs and complex lab requirements, potentially impeding their widespread adoption in biological research. In contrast, three-dimensional (3D) printing [2] is evolving into a ground-breaking technique in the medical and biological domain. Notably, digital light processing (DLP) [3] has revolutionized the low-cost and high-resolution fabrication of microfluidic devices by offering a convenient method for producing assembly-free, customizable and intricate designs. [4]

This is a first report where an acrylate-based resin is used for the development of 3D-printed microfluidic device using DLP technique to investigate the influence of different growth media under constant flow rate condition responsible for bacterial adhesion and subsequent biofilm formation. This platform can be customizable to understand the capability of different bacteria to form biofilm and the effect of a specific molecule of interest adhered on the bacteria. Unlike static assay, where there is limited growth nutrient, this system can continuously provide nutrients for growth.

The resin material was characterized using X-ray photoelectron spectroscopy (XPS), Fourier transform infrared spectroscopy (FTIR), atomic force microscopy (AFM), universal testing machine (UTM), micro-CT and surface profilometry. The presence of urethane stretching and acrylate twisting was confirmed by FTIR analysis. AFM results indicated a favourable surface roughness (0.072 μm) conducive to bacterial adhesion. The bacterial growth was studies for an extended time period as shown in Figure 1. As the culture time increased, the density of adhered bacteria also increased. The density of adhesion was higher at the bottom surface of the chamber due to lower shearing forces compared to the sidewalls. Mechanical testing demonstrated adequate strength, measuring at 18.9 ± 3.2 MPa, essential for maintaining structural integrity. The height of the channel was estimated to be 500 μm from profilometry analysis and the overall dimensions of the channel were confirmed using micro-CT imaging. The data revealed that this material is not only bio-compatible for bacterial growth but also serves as a novel model system for studying bacterial adhesion and biofilm formation in micro-confinement. These findings were further supported by computational fluid dynamics (CFD) simulations, which helped in visualizing the bacterial flow patterns and analyzed shear stress distribution. The shear stress profile demonstrates that, with elevated stress observed in the inlet and outlet sections and a decrease in the central channel. A uniform shear stress (0.004 Pa) along the channel walls, relatively higher than in the central region where shear stress is minimal, promoting bacterial adhesion and biofilm formation, illustrated in Figure 2.

[1] J.C. McDonald, G.M. Whitesides, Poly(dimethylsiloxane) as a material for fabricating microfluidic devices, Acc. Chem. Res. 35 (2002) 491–499.

[2] B.C. Gross, J.L. Erkal, S.Y. Lockwood, C. Chen, D.M. Spence, Evaluation of 3D printing and its potential impact on biotechnology and the chemical sciences, Anal. Chem. 86 (2014) 3240–3253.

[3] C.I. Rogers, K. Qaderi, A.T. Woolley, G.P. Nordin, 3D printed microfluidic devices with integrated valves, Biomicrofluidics 9 (2015).

[4] S.C. Ligon, R. Liska, J. Stampfl, M. Gurr, R. Mülhaupt, Polymers for 3D Printing and Customized Additive Manufacturing, Chem. Rev. 117 (2017) 10212–10290.

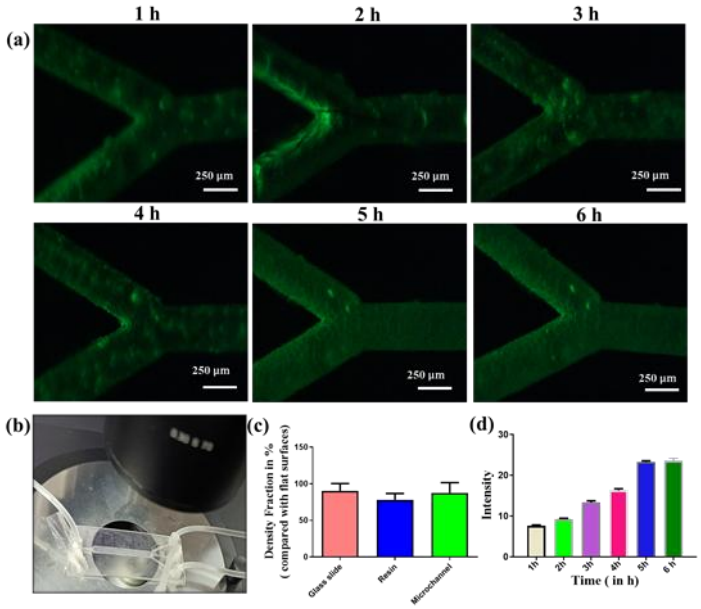

Figure 1. Cell adhesion experiment in microfluidic device (a) time chase adhesion study of *E. coli* under fluorescent microscope, (b) real photo of the experimental setup, (c) analysis of cell density in different surfaces, and (d) fluorescent intensity plot of time chase bacterial adhesion.

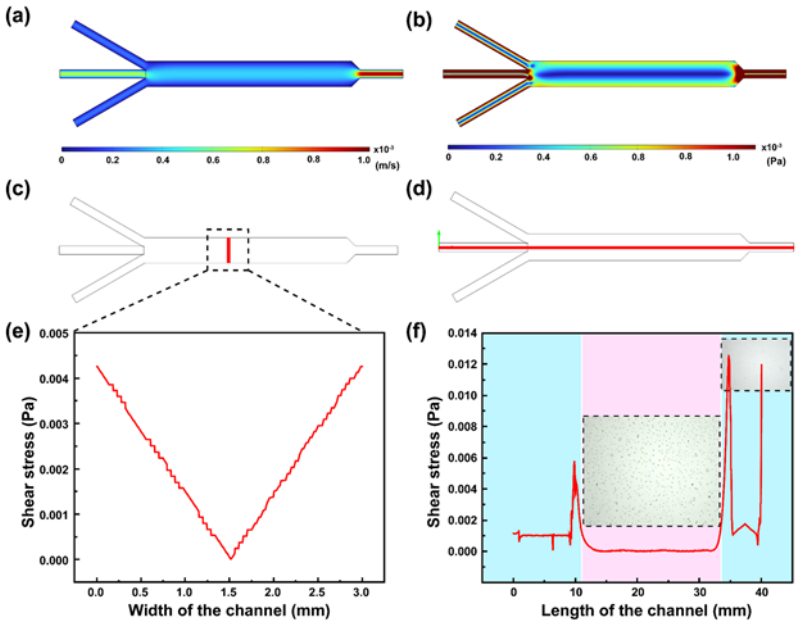

Figure 2. (a) velocity profile, (b) shear stress profile, (c) vertical cross-section at middle of the observation channel, (d) horizontal cross-section at middle of the observation channel, (e) x y graph of shear stress, and (f) variation of shear stress along the length of the channel.

Tattoo Electrodes for Comfortable and Reliable Masticatory EMG Monitoring

Núria Termes [a], *Eva Casals* [a], *Yolanda Castillo* [b,c,d], *Raimon Jané* [b,c,d], *Rosa Villa* [a,d], *Anton Guimera-Brunet* [a,d], *Gemma Gabriel* [a,d]

[a] Instituto de Microelectrónica de Barcelona, IMB-CNM (CSIC), Bellaterra, 08193, Spain
[b] Universitat Politècnica de Catalunya - BarcelonaTech (UPC), Barcelona, 08034, Spain
[c] Institute for Bioengineering of Catalonia (IBEC), Barcelona, 08028, Spain
[d] Centro de Investigación Biomédica en Red en Bioingeniería, Biomateriales y Nanomedicina (CIBER-BBN), Madrid, 28029, Spain
e-mail: nuria.termes@imb-cnm.csic.es

Keywords: e-tattoo, electrophysiology, wireless, screen-printing, conformable

With healthcare moving towards a patient-centred approach, wearables are becoming crucial by enabling real-time monitoring of biological signals, providing a more comfortable user experience and easier home-based settings. Electronic tattoos (e-tattoos) are a new class of wearable devices that aim to mimic the physical properties of the epidermis. By being lightweight, ultrathin and flexible, these sensors can comfortably cover the human skin surface with a non-invasive but intimate connection to record biopotentials [1]. However, reaching stable operation over the usage time is a significant challenge due to their exposure to substantial environmental stress, such as mechanical deformations caused by muscle activity. To overcome these issues, printing technology is one reliable alternative to obtain flexible and comfortable electrode arrays, as previously demonstrated by Hanein group [2]. Therefore, this work aims to develop wireless tattoo skin electrodes for comfortable electrophysiological recordings in a non-clinical environment.

We present an optimized fabrication protocol that allows the development of soft and conformable e-tattoos. In particular, this study displays an e-tattoo of 4 electrodes (Fig 1) that are 3 mm in diameter, conceived for measuring the masticatory electromyographic (EMG) activity. A thin, stretchable polyurethane (TPU) film of 50 µm was used as the substrate. The electrode traces were printed applying stretchable conductive silver (Ag) ink, while silver/silver chloride (Ag/AgCl) ink was used to print the electrodes. Traces were passivated with a double-sided adhesive film used to later attach the e-tattoo to the skin, containing pre-defined openings that expose the electrode area. Prior to skin application, a conductive gel is spread over the electrode area to ensure reliable electrical contact. Finally, the terminal pads were bonded to a flexible printed circuit board (PCB) using conductive paste, and the interface was sealed with silicone sealant. To enable signal acquisition, a dedicated acquisition system is being developed, aiming for minimal size and maximum power efficiency. The complete setup is displayed in Fig 2a.

The Ag/AgCl electrodes were electrochemically characterized by measuring the impedance spectroscopy (Fig 2b) and the open circuit potential of both electrode-electrolyte and electrode-skin interfaces. The electrical integrity of the junction between the e-tattoo and the flexible PCB was evaluated under different bending conditions. Additionally, a comparative study of conductive commercial gels and creams was conducted to identify the most suitable hydrogel to be applied at the tattoo electrode area, ensuring stable, long-term signal recording with minimal hydrogel evaporation.

Although the e-tattoo can be used to record various electrophysiological signals, this study demonstrates the feasibility of using these comfortable e-tattoos for masticatory muscle recordings and conducts a first evaluation of their EMG recording capabilities. The presented e-tattoo is specifically designed to cover the area over the masseter and temporalis muscles. Its performance was evaluated against commercial Ag/AgCl electrodes during different chewing tasks, using a commercial acquisition device. Results demonstrated an excellent correlation (0.95) between the EMG signals from the tattoo and the reference electrodes (Fig 3).

In summary, the proposed approach for e-tattoo electrodes offers multiple advantages, including versatile designs that can be adapted to different recording areas through screen-printing technology. Additionally, the electrodes can be further miniaturized, opening new opportunities for fabricating tattoos for high-density EMG (HD-EMG). This enables the exploration of more detailed EMG features and paves the way for advanced, non-invasive monitoring in both clinical and home-based settings.

[1] K. De Guzman and A. Morrin, “Screen-printed Tattoo Sensor towards the Non-invasive Assessment of the Skin Barrier,” *Electroanalysis*, vol. 29, no. 1, pp. 188–196, Jan. 2017, doi: 10.1002/elan.201600572.

[2] L. Bareket *et al.*, “Temporary-tattoo for long-term high fidelity biopotential recordings,” *Sci Rep*, vol. 6, May 2016, doi: 10.1038/srep25727.

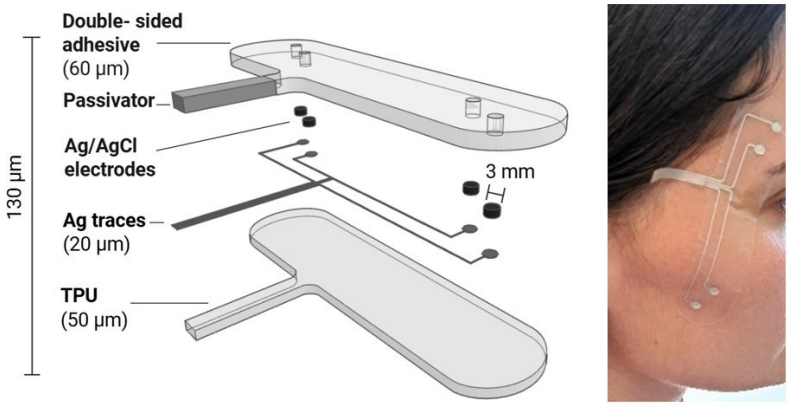

Figure 1. a Illustration of the layers of an e-tattoo and **b** its placement over the temporalis and masseter muscles of a subject.

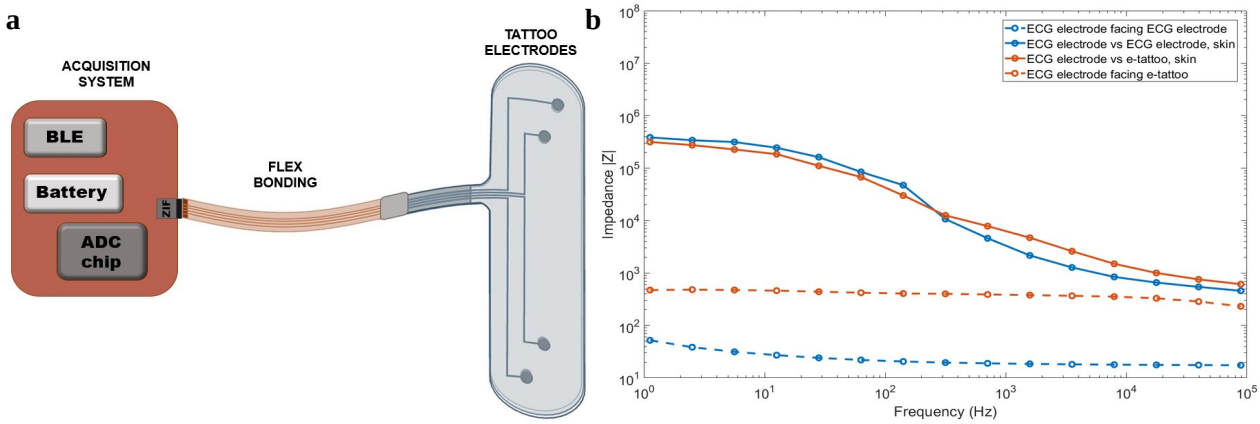

Figure 2. a E-tattoo setup for signal recording. E-tattoo bounded to a flexible PCB and connected to an electronic acquisition system. **b** Impedance comparison between the e-tattoo and a commercial Ag/AgCl electrode. Impedance magnitude as a function of frequency for both electrodes, measured in two configurations: applied on human skin and placed facing each other.

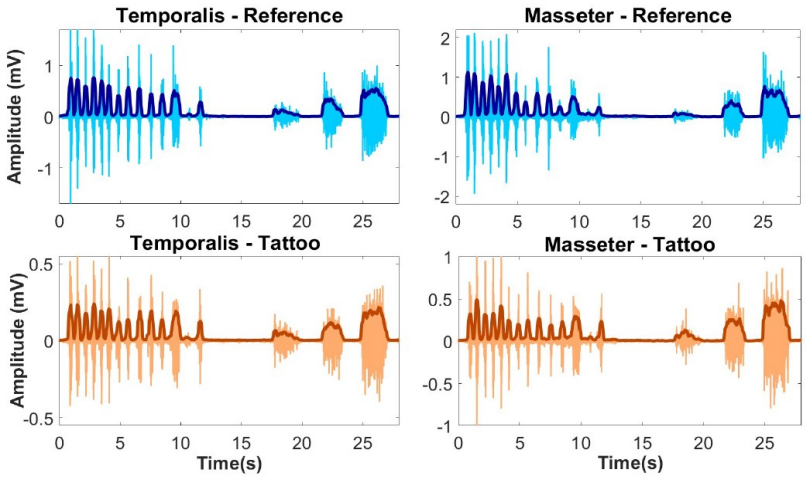

Figure 3. Segment of EMG signals showing temporalis and masseter activity during eating and chewing at different intensities, comparing e-tattoo and reference electrodes.

Exploiting the dewetting instability of thin Ge films to develop a novel photonic platform

Sonia Freddi [a], Nicoletta Granchi [b], Alessia Arrigoni [c], Michele Gherardi [d], Benedetta Squeo [c], Raffaele Giani [d], Alexey Fedorov [a], Laura Pasquardini [e,f], Lia Vanzetti [g], Maria Antonietta Vincenti [h], Mariacecilia Pasini [c], Francesca Intonti [b], Monica Bollani [a].

[a] Institute of Photonic and Nanotechnology (IFN)- CNR, LNESS laboratory, Como, 22100 Italy
[b] LENS and Department of Physics and Astronomy, University of Florence, Sesto Fiorentino, Italy
[c] Institute of Chemical Sciences and Technologies (SCITEC) – CNR, Milano, 20133, Italy
[d] Department of Physics, Politecnico di Milano, Milan, 20133 Italy
[e] Indivenire srl, Trento, Italy
[f] Department of Engineering, University of Campania Luigi Vanvitelli, Aversa, Italy
[g] Fondazione Bruno Kessler, Sensors and Devices Center, Trento, Italy
[h] Department of Information Engineering, University of Brescia, Brescia, Italy

e-mail: sonia.freddi@cnr.it, sonia.freddi@ifn.cnr.it

Thin solid films are metastable in the as-deposited state, and when heated to sufficiently high temperatures, they will dewet to form islands. This process, known as solid state dewetting (SSD), is driven by surface energy minimization and occurs via surface diffusion [1]. During thermal treatment, thin film evolves forming at first holes, which expand on the film surface favoring the rupture of the film. Isolated structures can then grow from the film breaking [2]. Dewetted structures can be exploited in several applications, including flexible photonics [2], photocatalysis [3] or dielectric Mie resonators [4].

Among the dewetting systems reported in the literature, ultra-thin crystalline silicon-on-insulator (SOI) films have been largely studied, and they are considered as a model system for investigating and studying SSD [1,2]. Recently, SiGe dewetting, i.e. SiGe structures directly formed on an insulating and optically transparent substrate, has been efficiently exploited to realize arrays of nanostructures with typical footprint ranging from few nm up to several μm [5].

On the contrary, despite the relevance of germanium for photonics, in particular since it allows detection in a near and mid infrared frequency, the investigation of its dewetting features is not yet complete and a deep understanding of the process is still missing.

Here, we study from a fundamental point of view, the evolution of an amorphous-Ge-based thin film (a-Ge) on a 250 nm of silicon dioxide and a silicon box, and we investigate morphological and chemical properties of the dewetted islands (Figure 1-a), exploiting several techniques, including scanning electron microscopy (SEM), atomic force microscopy (AFM), transmission electron microscopy (TEM), reflection high-energy electron diffraction (RHEED) and electron energy loss spectroscopy (EELS) [6]. In particular we disclose the crystallinity of the Ge islands after the annealing process, and we prove the composition, excluding a diffusion of the silicon dioxide underneath the a-Ge layer into the obtained Ge islands.

Full control over the final outcomes of SSD is obtained by introducing ad hoc features within the etched patches, thus guiding SSD fronts toward precise and reproducible shapes. So, to enhance the inherent spatial correlations into a true long-range ordering, SDD is also performed on a previously patterned a-Ge film achieved by a combination of electron beam lithography (EBL) and reactive ion etching (RIE). A cleaning step before the annealing process is carried out using acetone and hydrogen peroxide (H_2O_2 30% in vol for 2 sec). Theoretical calculations, coupled with dark field experimental evidence, demonstrate that the obtained dewetted Ge islands support Mie resonances (Figure 1-b).

These dewetted sensors, which rely on strong Mie-type optically induced resonances, are subsequently functionalized with appropriate organic linkers to achieve high selectivity, aiming at potential sensing applications [7]. Our focus is on the selective functionalization of Ge-based-patterned alloys, using a custom-made thiol-based luminescent molecule: 6-[2,7-bis[5-(5-hexyl-2-thienyl)-2-thienyl]-9-(6-sulfanylhexyl) fluoren-9-yl] hexane-1-thiol. This process selectively targets Ge-rich regions while leaving Si-rich areas unaffected. We highlight the detrimental effect of oxygen during the functionalization process, as its presence leads to reduced substrate coverage. To counteract this effect, we demonstrated that carrying out the process under a nitrogen atmosphere significantly improves functionalization efficiency.

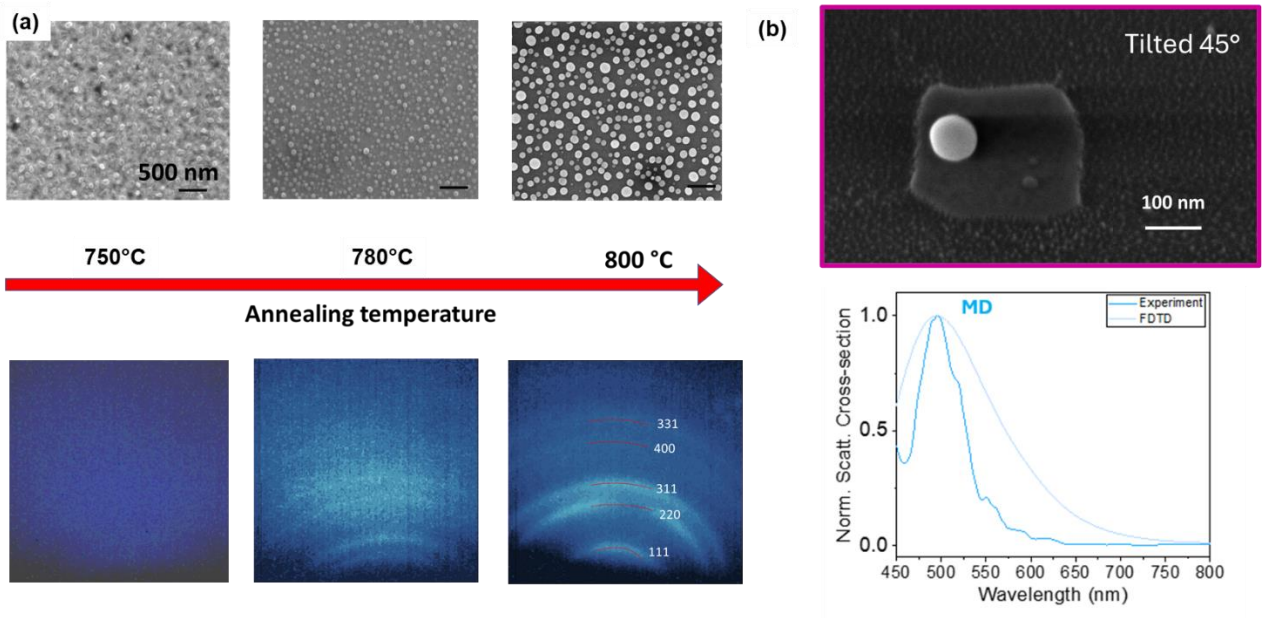

Figure 1 a) SEM images (upper side) and RHEED images (lower side) collected on Ge film annealed at different temperatures. b) SEM tilted image of a single Ge-island obtained from an annealing of a previously patterned a-Ge square (upper side). Simulation and experimental dark field data proof the presence of magnetic dipole (MD) resonance (lower side).

References

[1] M. Naffouti et al., Science Advances (2017), 3, 11, eaao1472.
[2] A. Benali et al., J. Phys.: Photonics (2020), 2, 015002.
[3] M. Altomare et al., Chem Sci (2016), 7(12), 6865-6886.
[4] N. Granchi et al., Opt Express (2023), 31, 5, 9007.
[5] M. Bollani et al., Nature Comm (2019), 10, 5632.
[6] S. Freddi et al., Mater Sci Semicond Process (2024), 174, 108228.
[7] A. Arrigoni, et al., Chemistry Proceedings (2024), 16(1), 21.

Acknowledgements

This work is supported by the PNRR project NQSTI - Spoke_7_National_Quantum Science and Technology, by the PRIN PNRR 2022 “ACONITE” grant n° P2022HRTYH, and by the CNR project “EPOCALE” (2022 – 2025).
S.F, M.G. and M.B. acknowledge Polifab, the micro and nanofabrication facility of Politecnico di Milano, for supporting the devices characterization.

Mechanically robust spin-on-glass packaging of hydrogenated amorphous silicon for harsh environment applications

Junhwa Seong[a], Younghwan Yang[a], Dohyun Kang[a], Junsuk Rho[abcd]

[a]Department of Mechanical Engineering, Pohang University of Science and Technology (POSTECH), Pohang 37673, Republic of Korea
[b]Department of Chemical Engineering, Pohang University of Science and Technology (POSTECH), Pohang, 37673, Republic of Korea
[c]Department of Electrical Engineering, Pohang University of Science and Technology (POSTECH), Pohang, 37673, Republic of Korea
[d]POSCO-POSTECH-RIST Convergence Research Center for Flat Optics and Metaphotonics, Pohang 37673, Republic of Korea
e-mail: jsrho@postech.ac.kr;

Metalenses—ultrathin planar lenses composed of nanostructured metasurfaces—are poised to revolutionize optical systems due to their compact form factor and advanced functionalities, including aberration correction, field-of-view expansion, and tunable focusing [1]. Despite their exceptional optical performance, their widespread deployment in real-world applications remains hindered by a critical weakness: structural fragility in harsh environments. Nanostructures on exposed surfaces are prone to detachment or degradation under mechanical stress and contamination, severely impairing device performance [2]. In this work, we introduce a comprehensive fabrication platform for encapsulated, self-cleaning, and mechanically robust metalenses by integrating hydrogenated amorphous silicon (a-Si:H) with a spin-on-glass (SoG) packaging technique. By optimizing plasma-enhanced chemical vapor deposition (PECVD) conditions—including chamber pressure, temperature, and gas flow ratios—we engineer a-Si:H films exhibiting an exceptionally high refractive index of n = 3.23 with near-zero optical losses at visible wavelengths (635 nm). This high-index contrast between meta-atoms and the SoG background enables strong light confinement, supporting efficient phase modulation and waveguiding critical for high-performance metalens operation. We demonstrate that the encapsulated metalenses achieve a calculated polarization conversion efficiency of 97.2%, substantially outperforming conventional unencapsulated structures. More importantly, mechanical durability was validated by a rigorous sonication test using coarse sand particles, where unencapsulated devices were visibly damaged and functionally degraded, whereas encapsulated devices preserved both their structure and optical focusing capability over extended exposure times. In addition, our encapsulation strategy allows for post-fabrication control of surface wettability, enabling both hydrophilic and hydrophobic states without impairing optical function. We exploit this property to realize passive self-cleaning metalenses, wherein hydrophobic treatment causes water droplets to roll off the surface, removing particulates and contaminants. This is particularly advantageous for long-term deployment in outdoor or industrial optical systems, where manual cleaning is impractical. The proposed platform is fully compatible with CMOS processes and scalable for wafer-level manufacturing, opening the door to commercial applications in augmented reality optics, LiDAR sensors, biomedical imaging systems, and more. Our findings represent a key step toward the practical realization of ruggedized, multifunctional metasurfaces, bridging the gap between nanophotonics research and real-world implementation.

[1] M. Khorasaninejad et al., Science (2016) 352, 1190-1194.
[2] Y. Yang et al., ACS Nano (2025) 19, 3008-3018.

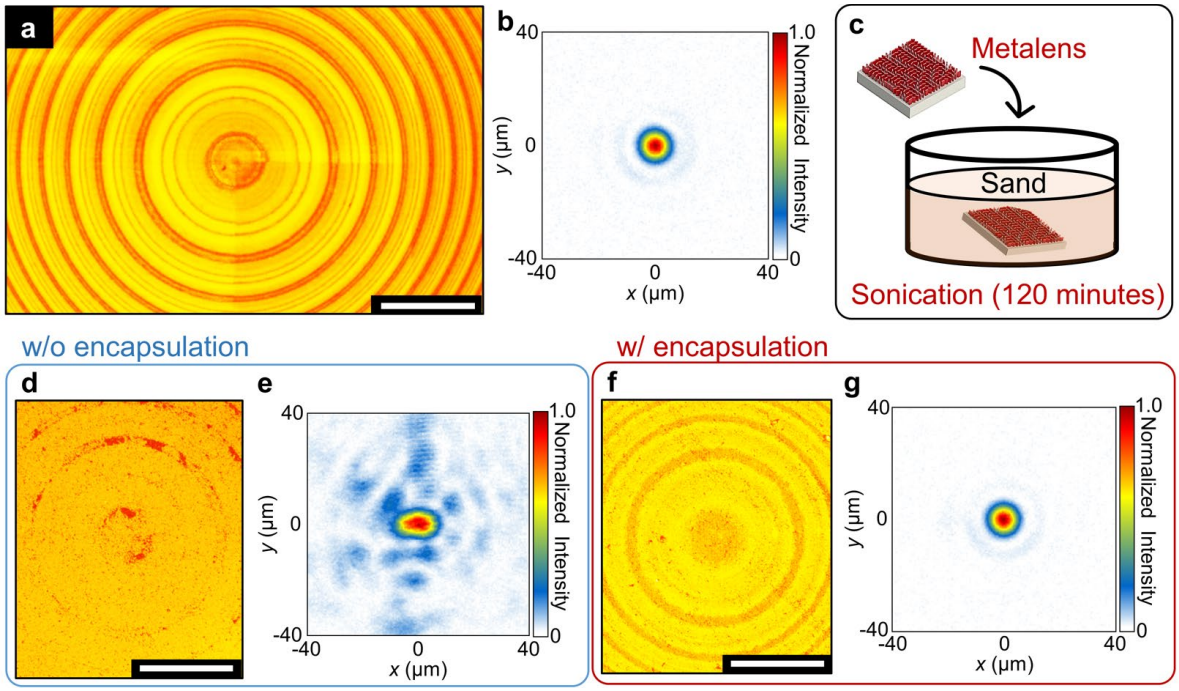

Figure 1. Mechanical Durability of Metalenses. (a) Optical microscope (OM) image illustrates the fabricated metalenses prior to encapsulation. (b) The corresponding beam intensity profile is recorded to assess optical performance. (c) To evaluate mechanical resilience, the metalenses are subjected to sonication while immersed in sand. A comparison is drawn between (d, e) unencapsulated and (f, g) encapsulated metalenses after 120 minutes of sonication. The unencapsulated samples display clear signs of physical degradation, as seen in (d) the OM image and (e) the disrupted beam profile. In contrast, the encapsulated metalenses maintain structural integrity and consistent optical performance, as confirmed by (f) the post-sonication OM image and (g) the preserved beam profile. All scale bars represent 150 μm.

Dynamic Electrical Conductivity of Ni-P/Nylon Yarns with Different Twist Number for Weavable Device

Takumi Suda[a], Kazuhiro Shibata[a], Tomoyuki Kurioka[a], Katsunari Sato[b]
Chun-Yi Chen[a], Tso-Fu Mark Chang[a], Nao Yoshida[b], Hiromichi Kurosu[b], Masato Sone[a]

[a] Institute of Integrated Research, Institute of Science Tokyo, Yokohama, 226-8501, Japan
[b] Cooperative Major in Human Centered Engineering, Nara Women's University, Nara 630-8506 Japan
e-mail: suda@ames.pi.titech.ac.jp

Weavable device is a multifunctional wearable device fabricated by weaving various functional yarns into a single piece of fabric. This approach enables the integration of various functional yarns, realizing the wearable devices with advanced multifunctionality beyond the conventional ones. Functional yarns—particularly metallized polymer fibers—hold great promise in achieving this goal. However, achieving both sufficient conductivity and good adhesion between the deposited metal layer and the polymer yarns remains challenging, due to the difference in the mechanical characteristics between the metal and polymer yarns.

On the other hand, we have developed the metallization of polymer yarns by performing the supercritical carbon dioxide ($scCO_2$)-assisted Ni-P electroless plating [1]. Generally, since yarns are used in a twisted state, the Twist number, defined as the number of twists per meter (T/m), is used to represent their degree of twist, which is known to affect their mechanical properties [2]. Recently, we have also discovered the influence of the Twist number of Nylon yarns on the electrical conductivity of the Ni-P/Nylon yarns [3]. In practical viewpoints, weavable devices are believed to have two conditions accompanying the body movements; that is, loading (stretched) and unloading (relaxed) conditions. Regardless of the conditions of the metallized yarns, their electrical conductivity should be maintained to enable the operation of the weavable devices. Therefore, it is important to evaluate the dynamic electrical conductivity of the metallized yarns between the loading and the unloading conditions. In this work, we report the change in the electrical resistance of the Ni-P/Nylon yarns with different Twist numbers under the loading and the unloading conditions.

Following the previously reported procedure [3], Ni-P/Nylon yarns with different Twist numbers were fabricated. The electrical resistance of the Ni-P/Nylon yarns under the loading and the unloading conditions was measured using the two-terminal method. The distance between the zigs was set to 5.0 cm for the measurement of the Ni-P/Nylon yarns under the loading conditions (Figure 1(a)), while that was set to 4.0 cm for the measurement of the Ni-P/Nylon yarns under the unloading conditions (Figure 1(b)). The distance between the zigs was changed by moving the left part at 2.0 cm/s. A total of 20 cycles of the two-terminal measurements under the loading and the unloading conditions were repeated.

Figure 2 shows the relationship between the changes in the electrical resistance of the Ni-P/Nylon with 455 T/m of Twist number or with 740 T/m of Twist number under the loading and the unloading conditions. Regardless of the Twist number, their electrical resistance under the unloading condition was higher than those under the loading condition. The average electrical resistance recorded over the 20 cycles for each Ni-P/Nylon with different Twist number is shown in Figure 3. It can be seen that as the Twist number increases, their electrical resistance decreased under both the loading and the unloading conditions. The difference in their electrical resistance between the two conditions decreased with the increase in their Twist number. Figure 4 shows the optical microscope (OM) images of the Ni-P/Nylon yarns with 455 T/m of Twist number or with 865 T/m of Twist number before and after the experiments. The diameter of the Ni-P/Nylon yarns with 455 T/m of Twist number became broadened after the 20 cycles of the two-terminal measurements. On the other hand, that with 865 T/m of Twist number was hardly changed. These observations indicated that the Ni-P/Nylon yarns with lower Twist number was more prone to fraying. As yarns became more frayed, the electrical connection between each Ni-P/Nylon yarn would decrease, which is considered to lead to decrease in electrical conductivity. The higher Twist number is considered to be contributed to the suppression of the fray of the Ni-P/Nylon yarns under the unloading conditions, which resulted in few changes in their electrical resistance between two conditions.

References

[1] H. Kondo, et al., *J. Supercrit. Fluids* **2025**, *218*, 106501.
[2] H. M. Hsiung, et al., *EMCS.* **2016**, 1660-1663.
[3] K. Shibata et al., *Micro Nano Eng.* **2025**, *submitted*.

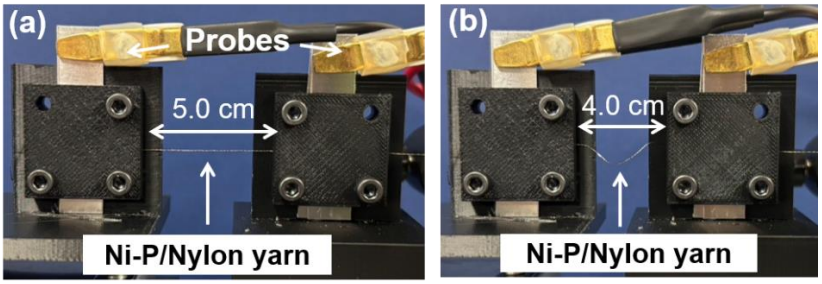

Figure 1. Photos of a Ni-P/Nylon fiber (a) under loading, and (b) under unloading

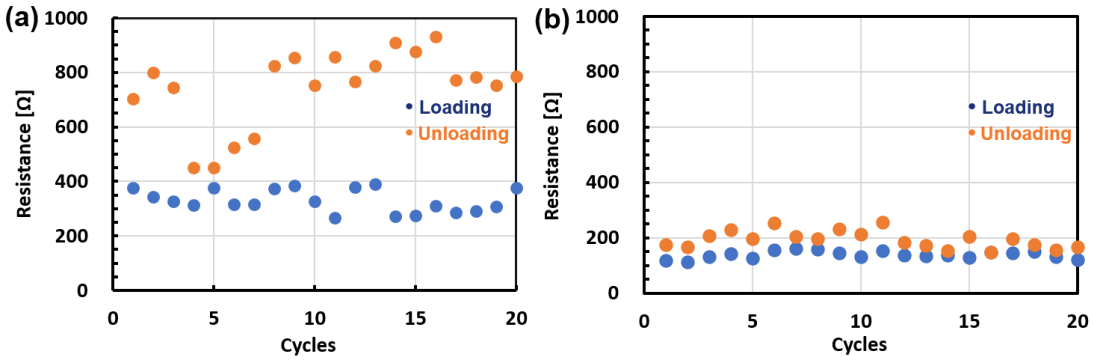

Figure 2. Electrical resistance measurements under 20 cycles of loading and unloading (a) 455 T/m, (b) 740 T/m

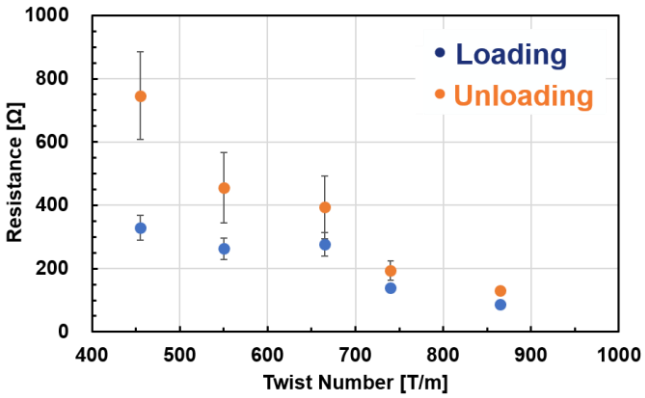

Figure 3. Surface electrical resistance of Ni-P/Nylon threads under loading and unloading

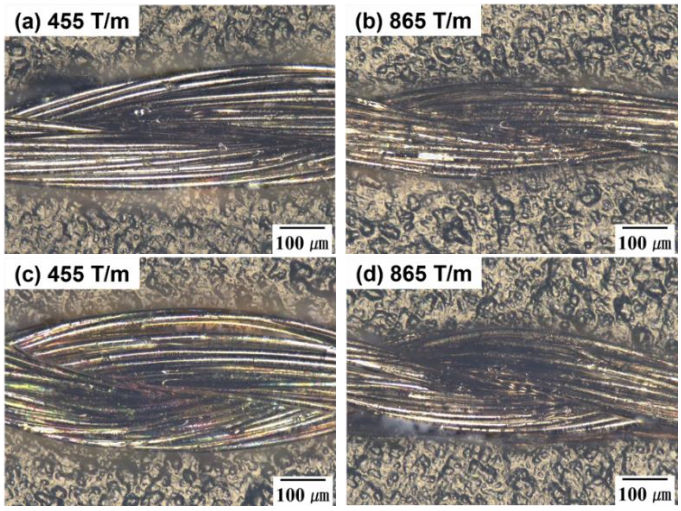

Figure 4. Optical microscope image of Ni-P/Nylon (a)(b) Before testing, (c)(d) After testing

Crystalline atomic layer–dielectric hybrid metasurfaces for high-efficiency visible metaphotoncis

Junhwa Seong[a], Younghwan Yang[a], Youngsun Jeon[a], Junsuk Rho[abcd]

[a]Department of Mechanical Engineering, Pohang University of Science and Technology (POSTECH), Pohang 37673, Republic of Korea
[b]Department of Chemical Engineering, Pohang University of Science and Technology (POSTECH), Pohang, 37673, Republic of Korea
[c]Department of Electrical Engineering, Pohang University of Science and Technology (POSTECH), Pohang, 37673, Republic of Korea
[d]POSCO-POSTECH-RIST Convergence Research Center for Flat Optics and Metaphotonics, Pohang 37673, Republic of Korea
e-mail: jsrho@postech.ac.kr;

Metasurfaces, composed of subwavelength-scale nanostructures, have emerged as compelling candidates for flat optical components due to their ability to control amplitude, phase, and polarization of light with compact form factors [1]. However, the practical adoption of visible metasurfaces has been impeded by several critical limitations, including low efficiency, high-temperature fabrication requirements, and incompatibility with CMOS processes [2]. In this work, we present a scalable platform for large-area, high-efficiency hybrid metasurfaces based on directly crystallized TiO_2 atomic layers deposited on SiO_2 nanostructures via plasma-enhanced atomic layer deposition (PEALD). By tuning deposition parameters such as temperature, plasma power, and exposure duration, we achieve a refractive index as high as 2.78 at 400 nm, enabling near-unity efficiency across the visible spectrum. Specifically, the metasurfaces demonstrate cross-polarization transmittance (CPT) values of 75% (blue), 95% (green), and 95% (red). These structures are used to fabricate 5 mm-aperture metalenses that achieve diffraction-limited imaging performance. Compared to conventional sol-gel or amorphous TiO_2 approaches, our method eliminates shrinkage and high-temperature annealing (>600 °C), significantly simplifying the manufacturing process [3]. The use of SiO_2 as the core material enhances thermal and mechanical stability, provides CMOS compatibility, and offers reliable integration into semiconductor workflows [4]. This approach also enables extended functionality, such as operational wavelength tuning via alternative coatings, or multilayer stacking for photonic crystal or Bragg reflector architectures. Our study demonstrates a practical pathway for low-cost, high-performance metasurface production, suitable for integration in AR/VR optics, full-color display technologies, and LiDAR systems. This work establishes a robust platform for next-generation flat optics with strong industrial scalability.

[1] N. Yu et al., Science (2011) 334, 333-337.
[2] J. Seong et al., Int. J. Precis. Eng. Manuf. – Green Technol. (2024) 11, 685-706
[3] R. C. Develin et al., Proc. Natl. Acad. Sci. 113 (2016), 10473-10478.
[4] J.-S. Park et al., ACS Nano 18 (2024), 3187-3198.

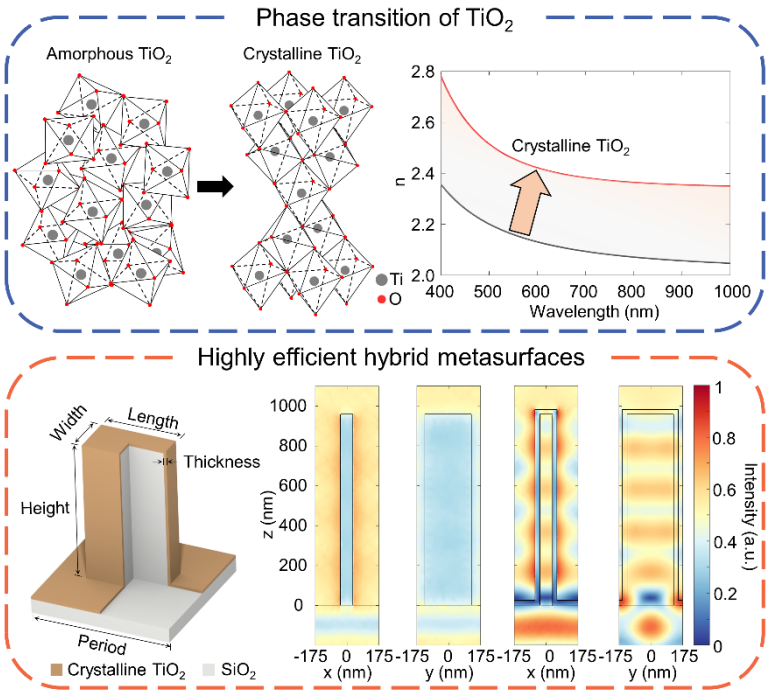

Figure 1. Schematic of high-efficiency hybrid metasurface via phase transition to crystalline TiO_2

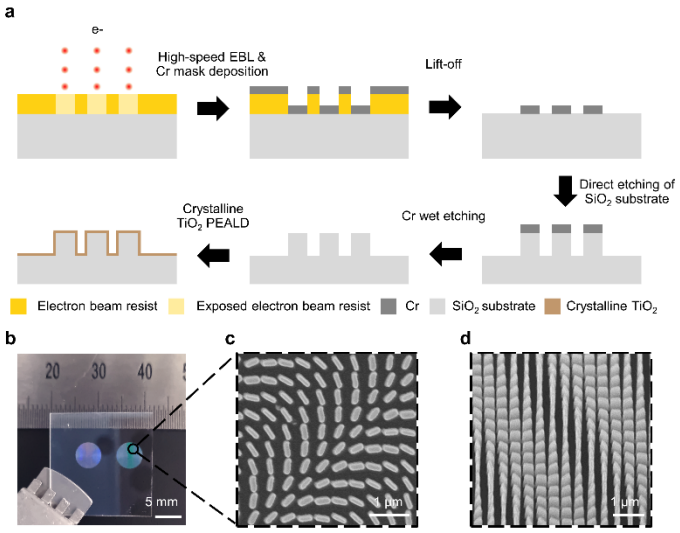

Figure 1. Development of large-aperture hybrid metalenses. a, Illustration of the fabrication process for hybrid metalenses utilizing a SiO_2 substrate combined with crystalline materials. b, Optical image showing a completed metalens with a diameter of 5 mm. c–d, Scanning electron microscope (SEM) images of the fabricated structure captured from (c) an angled bird's-eye view and (d) a 30°-tilted perspective.

Volatile Threshold Switching Characteristics of TiN/TaO_x/TiN Selector Devices

Zohreh Hajiabadi [a], Aiden Graham [a], Alexander-Hanyu Wang [a], Mari Napari [b], Dimitra G. Georgiadou [c], David B. Thomas [a], Harold M. H. Chong [a], Firman Simanjuntak [a]

[a] Sustainable Electronic Technologies, University of Southampton, SO171BJ, UK
[b] Department of Physics, King's College London, WC2R 2LS, UK
[c] Smart Electronic Materials and Systems, University of Southampton, SO171BJ, UK
email: f.m.simanjuntak@soton.ac.uk

Addressing sneak path currents, which are unintended currents flowing through non-selected cells in crossbar arrays, presents a critical challenge in large-scale artificial neural networks [1]. This work introduces a TaO_x-based selector that can overcome this challenge while simultaneously providing tunable temporal characteristics essential for synaptic functions. The fabrication process involved creating a TiN(60nm)/TaO_x(11nm)/TiN (60nm) stack structure. TiN electrodes were deposited via DC magnetron sputtering (Angstrom Engineering) using titanium targets in a nitrogen atmosphere, while the TaO_x dielectric layer was formed through plasma-enhanced atomic layer deposition (Oxford Instruments FlexAL, ICP source) at 200°C using PDMAT precursor with O_2 plasma cycles. The resulting architecture (Fig. 1.a) features 55×55 device arrays with well-defined top and bottom electrodes that sandwich the active TaO_x layer. Thickness uniformity mapping of the TaO_x layer across 180 measurement points (Fig. 1.b) revealed variations from 68.36Å to 146.33Å, with an average thickness of 118.48Å, ($\sigma = 20.03$Å).

DC electrical measurements revealed asymmetric threshold behavior, triggering voltages at -2V and +1V for negative and positive bias regimes, respectively (Fig. 2). The devices exhibited maximum currents of 2×10^{-5}A during positive bias and 5×10^{-7}A during negative bias, confirming their suitability for one-diode, one-memristor (1D1M) architectures. A key discovery emerged through transient electrical testing under controlled conditions (pulse amplitude: -2V, duration: 10μs, base voltage: -0.1V, gap: 100ns) (see Fig. 3.a), demonstrating that decay time constants could be manipulated by adjusting measurement range settings (Fig.3b-d). At a 1μA current range, devices showed extended decay profiles, while a 100μA range produced accelerated response transitions, similar to biological synapse adaptation mechanisms, without requiring structural modifications [2]. Additional tests examining voltage amplitude dependencies from +1V to +3V (Fig. 4a-c) and -1V to -3V (Fig. 5a-c) demonstrated that various stimulus intensities can affect the decay ratio of the device. This behavior is particularly valuable for implementing spike-timing-dependent plasticity in artificial neural networks, where timing and amplitude of pre- and post-synaptic pulses directly influence synaptic weight changes [3].

A depth profile analysis of X-ray photoelectron spectroscopy (XPS) (Fig. 6a) confirms well-defined interfaces with expected atomic percentages between layers, validating the fabrication process. High-resolution Ta 4f spectra (Fig. 6b) show a Ta $4f_{7/2}$ peak at 26.03 eV, consistent with Ta_2O_5 formation, with the expected $\sim$1.9 eV spin–orbit splitting and 4:3 area ratio [4].

The ability to externally control the temporal response characteristics positions these devices as promising candidates for next-generation neuromorphic computing platforms. Using measurement parameters to adjust timing behaviors, these selectors enable the implementation of essential neuromorphic functions while maintaining fabrication consistency and operational stability.

[1] Y.C. Chen et al., *Micromachines* **12**(1), 50 (2021).
[2] K.A. Campbell et al., *Front. Bioeng. Biotechnol.* **4**, 97 (2016).
[3] B. Taylor et al., *2021 IEEE Int. Symp. Circuits Syst.*, 1- 5 (2021).
[4] M. Napari et al., *Electron. Mater. Lett.* **20**(4), 363–371 (2024).

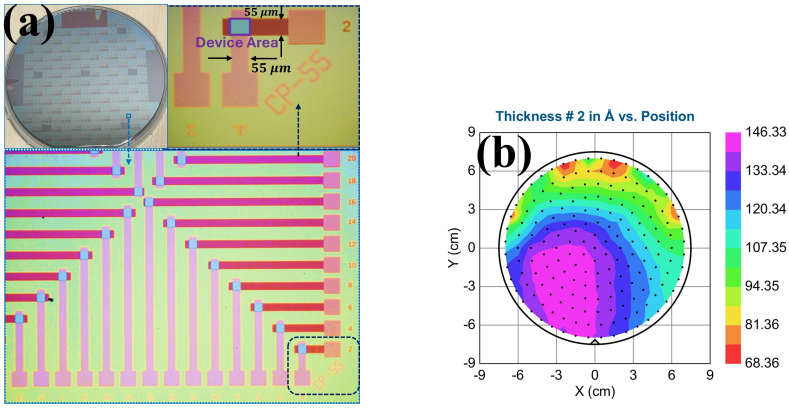

Fig. 1. (a) Fabrication flow from wafer to device level, showing TiN/TaO_x/TiN structure with zoomed sections of the 55×55 array and individual devices. (b) Thickness uniformity map of the TaO_x layer deposited via ALD on SiO_2/Si.

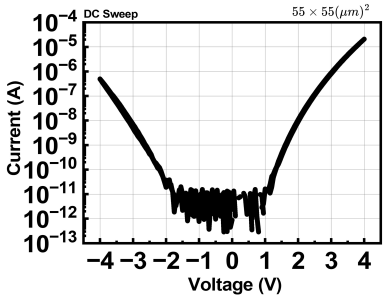

Fig. 2. DC I-V curve of a single 55 × 55 μm^2 device.

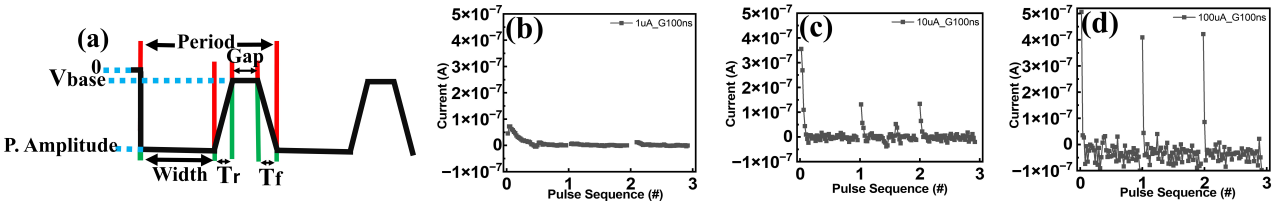

Fig. 3. (a) Pulse waveform, (b-d) Current vs. pulse sequence for three pulses at current ranges of 1μA, 10μA, and 100μA.

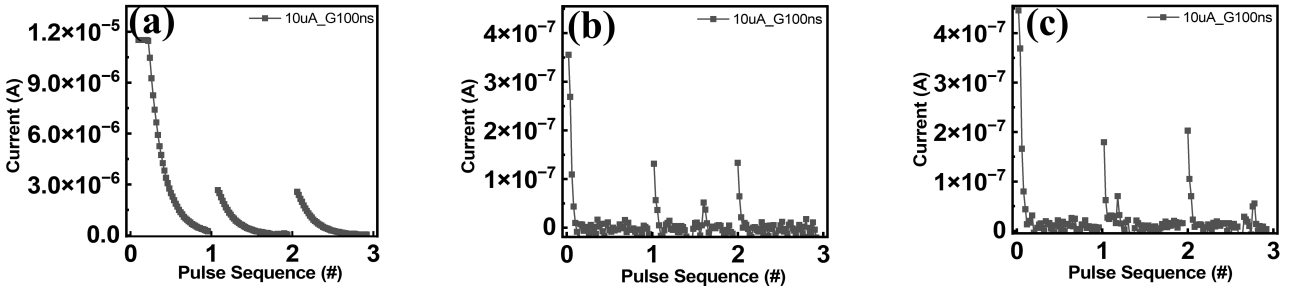

Fig. 4. (a-c) Effect of negative pulse amplitude variation from -1V to -3V on device response using 10μA current range.

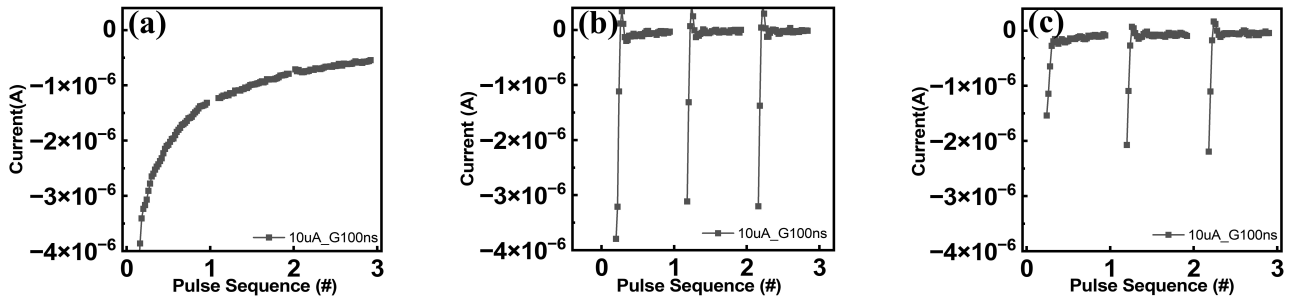

Fig. 5. (a-c) Effect of positive pulse amplitude variation from +1V to +3V on device response using 10μA current range.

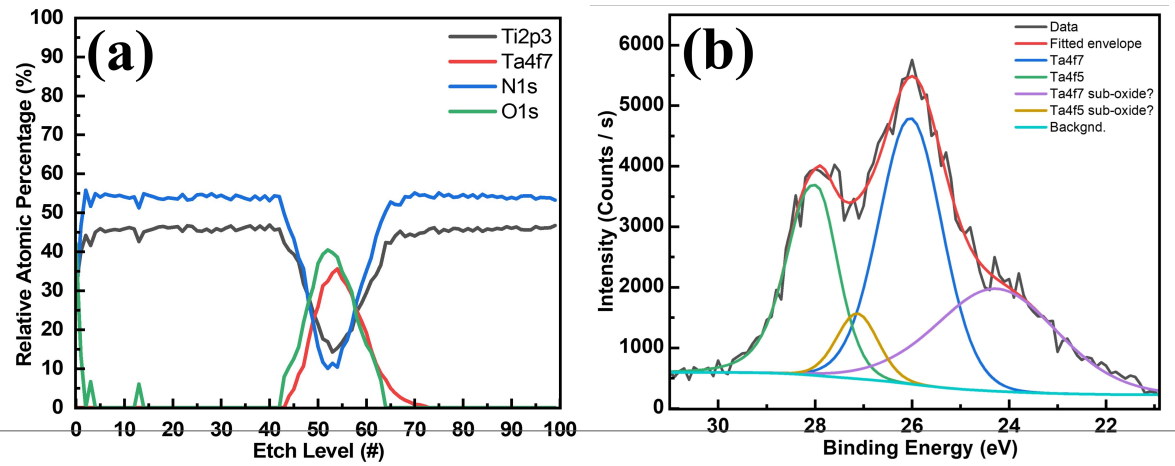

Fig. 6. (a) XPS Depth profile of the TiN/TaO_x/TiN structure. (b) Ta4f and N1s (inset) XPS spectra of 11nm TaO_x layer deposited via ALD on SiO_2 wafer.

Silicon-based metasurface polarizer supporting quasi-bound states in the continuum

Maria Antonietta Vincenti [a], Luca Fagiani [b], Luca Bolzonello [c], Johann Osmond [c], Michele Gherardi [b], Sonia Freddi [d], Domenico de Ceglia [a], Niek van Hulst [c], Monica Bollani [d]

[a] Department of Information Engineering, University of Brescia, 25123, Italy
[b] Physic Department of Milano Politecnico, Milano, 20133, Italy
[c] ICFO, The Barcelona Institute of Science and Technology, Barcellona, 08860, Spain
[d] Institute of Photonics and Nanotechnology (IFN) – CNR, LNESS, Como, 22100, Italy

e-mail: monica.bollani@ifn.cnr.it

Manipulating light polarization is essential for a wide range of applications, including quantum communications, sensing, imaging, and material characterization [1]. Traditional approaches, such as cascading waveplates, are not suitable for chip-scale integration, prompting a persistent search for compact and integrable alternatives. This has led to various solutions aimed at minimizing the footprint of polarization control devices. Examples include structures based on photonic crystals, metallic gratings, nanoparticles, and epsilon-near-zero materials [1,2].

Metasurfaces have recently emerged as powerful platforms for polarization detection and control at the nanoscale. However, current metasurface-based polarizers are typically limited to converting incident light into a single linear polarization state, with only moderate spectral tunability [3,4]. In this work, we present two ultra-compact, all-dielectric metasurfaces capable of converting arbitrary input polarizations into either horizontal or vertical linear polarization, without requiring prior knowledge of the input state [5]. This is achieved by exciting symmetry-protected quasi-bound states in the continuum (q-BICs) within carefully engineered metasurfaces.

Our optical modulators are based on silicon-on-insulator (SOI), leveraging silicon's mature fabrication processes, high refractive index, and strong third-order nonlinear susceptibility. The symmetry breaking necessary to excite q-BICs is introduced by alternating the width of adjacent silicon nanobars in the array. In the SOI metasurface, which consists of silicon nanobars with a periodicity of $p = 600$ nm, widths $D_1 = 150$ nm and $D_2 = 90$ nm (asymmetry factor $\alpha = 0.4$), and height $h = 145$ nm, positioned on a 2 μm SiO_2 substrate, we identify five distinct q-BICs in the near-infrared range. Each mode exhibits strong electric field enhancement and topological features characteristic of q-BICs.

The silicon-based nanostructure was fabricated using standard nanofabrication techniques, including electron-beam lithography (EBL) and inductively coupled plasma reactive ion etching (ICP-RIE) [6]. A single layer of positive resist (PMMA) was spin-coated onto the SOI wafer to a thickness of 80 nm and patterned via EBL using acceleration voltages of 30 kV or 50 kV. The applied dose ranged from 330 μC/cm² to 480 μC/cm² depending on the voltage. After development in a 1:3 MIBK/IPA solution for 90 seconds, a 45 nm layer of silica was deposited by electron-beam evaporation to form a hard mask, which remained after the lift-off process.

The SOI structures were then patterned using ICP-RIE with C_4F_8 and SF_6 gases. Different dry etching processes were explored to optimize the verticality of the nanobar sidewalls. In particular, the introduction of oxygen cleaning steps during the etching cycles will be described, highlighting the role of cleaning in removing the polymer that forms during the dry etching process. The SiO_2 mask was subsequently removed with a brief (20 s) dip in 5% HF solution. To enhance transmission measurements, the backside of the sample was mechanically polished. The remaining organic residues were removed via a 10-minute hot bath in acetone and isopropanol, followed by oxygen plasma cleaning.

Fabrication imperfections, such as variations in the gap size, etching irregularities, or deviations in the asymmetry factor, were also modeled. Specifically, the optical performance of non-ideal metasurfaces was simulated by varying the geometrical parameters affected by fabrication tolerances. Transmission spectra were both simulated and experimentally measured under normal incidence with two orthogonal linear polarizations, for different structural asymmetries. The experimental results show excellent agreement with the simulations and demonstrate that the incoming linear polarization can be selectively suppressed whenever a q-BIC resonance is excited [6].

Figure 1 summarizes the main results.

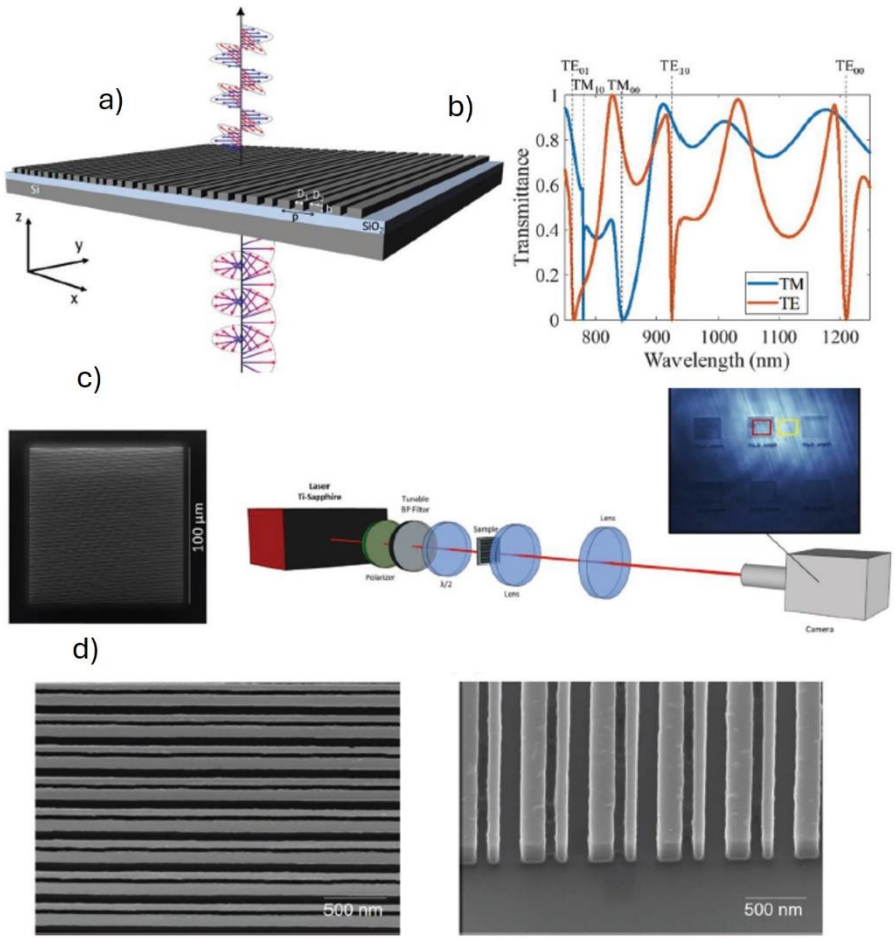

Figure 1: a) Working principle of the frequency selective polarization controller: a Si-based nanostructure supporting q-BICs converts arbitrarily polarized incoming light into linearly polarized light; b) Transmission spectra for incoming TE (red line - electric field oriented along *y*) and TM (blue line - electric field oriented along *x*) polarizations and five q-BICs can be identified. SEM characterization in top-view of the overall c) 100 μ m2 Si device. On the right, sketch of the optical setup, with a highlight on the main optical features used. d) SEM zoom of the inner region of the nanostructure from top and tilted view.

References:

[1] Y. Guo, et al., Advanced Optical Materials 7, 1801453, 2019.
[2] K.I. Okhlopkov, et al., Nano Letters, 21, 24, 10438–10445, 2021.
[3] N. Y and F. Capasso, Nature Materials, 13, 139-150, 2014.
[4] A. Tognazzi, et al., Optics Express Vol. 29, Issue 8, 11605, 2021.
[5] L. Fagiani, et al., Adv. Optical Mater., 2301456, 2023.

We acknowledge partial funding from NATO SPS Grant no. G5984, from Ministero dell'Istruzione, dell'Università e della Ricerca (Grant nos. PNRR PE0000023 NQSTI and PRIN Grant no.2022YJ5AZH).

Effect of excitation wavelength on micro-Raman thermometry for suspended silicon MEMS structures

Masaki Shimofuri[a], Kanta Fujiwara[a], Amit Banargee[a], Jun Hirotani[a], Toshiyuki Tsuchiya[a]
[a]Kyoto University, Kyoto, 615-8540, Japan
e-mail: m_shimofuri@nms.me.kyoto-u.ac.jp

Abstract Text

The effect of excitation laser wavelength on micro-Raman thermometry for suspended silicon MEMS structures was investigated. Unlike the thermo-reflectance method, which is highly sensitive to structural tilt and movement, micro-Raman thermometry is more robust and suitable for high-precision thermometry for them, but, its measurement accuracy is typically limited to around 1 K. In this paper, we compared 488 nm and 688 nm lasers and demonstrated that the 633 nm laser achieved a measurement accuracy of ±0.35 K with a measurement time of 5 seconds, representing a 7-fold improvement in accuracy over the 488 nm laser.

Background / State of the art

Measuring the local temperature of suspended structures in silicon MEMS is crucial for improving the reliability of sensors and actuators.[1] Patterned resistance thermometer requires the patterning of metal and wiring for measurements.[2] The thermo-reflectance method requires a reflective metal and is highly sensitive to structural tilt and positional variations.[2] Thus, neither method is suitable for suspended structure thermometry. Micro-Raman thermometry is a non-contact, high-spatial-resolution thermometry, which utilizes the temperature dependence of Raman scattering. Since it is based on lattice vibrations, a geometrically robust property, it is less affected by structural tilt or slight positional variations.[3] Furthermore, silicon exhibits strong Raman activity, so no additional processing is required. However, the achievable measurement accuracy has traditionally been limited to around 1 K due to the inherently weak Raman signal. In this study, we particularly focus on the excitation laser wavelength to improve this limited measurement accuracy.

Description of method

The effect of excitation wavelength on measurement accuracy was evaluated by comparing measurements with 488 nm and 633 nm lasers. The micro-Raman spectrometer was Horiba LabRAM HR-800, and a 488 nm sapphire laser and a 633 nm He-Ne laser were used for excitation. A 40x objective lens with correction collar was used for focusing. MEMS device has the structure supported by four 310 μm long folded flexure beams (Fig.1) and was fabricated from a SOI wafer with 5μm-thick device layer, 2μm-thick BOX layer, and 400μm-thick handle layer. The device was placed in a vacuum chamber with a window (Fig. 2), and Raman thermometry was performed on the suspended structure through the window while the backside of the device was controlled at 40-80°C. For spectral calibration, a Ne lamp plasma line was used for the 488 nm excitation, and a plasma line of the He-Ne laser itself was used for the 633 nm excitation.

Experimental Result

The results obtained using the two excitation lasers are shown in Fig.3. The horizontal axis represents time, and the vertical axis indicates the measured temperature. To convert the Raman spectrum peak shift to temperature, the last 10 data points at each temperature were averaged and used for linear regression. As shown in Fig. 3, the 633 nm laser exhibits smaller variance and higher precision compared to the 488 nm laser. The standard deviation was 2.5 K for the 488 nm laser and 0.35 K for the 633 nm laser. In addition, the measurement drift over 630 minutes was sufficiently small: 0.14 K for the 488 nm laser and 0.45 K for the 633 nm laser. Although the drift observed with the 633 nm laser appears relatively large, it is likely due to insufficient thermal stabilization time. This “apparent drift” can be further reduced by allowing a longer stabilization period. These results demonstrate that the 633 nm excitation laser enables higher-precision measurements compared to the 488 nm laser, indicating that the selection of excitation wavelength significantly affects measurement accuracy.

Acknowledgements

This research was supported by HONMAMON co-creative research program between HORIBA and Kyoto Univ.

[1] Y. Xu et al., Heliyon, vol. 10, no. 5, p. e27481, 2024.
[2] O. Chaalal, BJSTR, vol. 40, no. 3, 2021.
[3] T. Tsuchiya et al., JMEMS, vol. 25, no. 1, pp. 188–196, 2016.

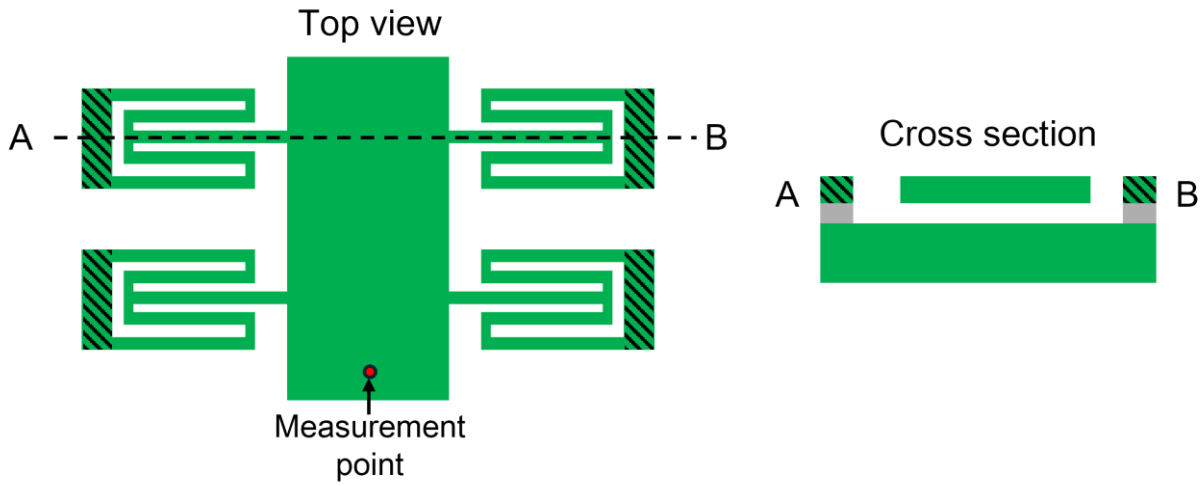

Figure 1. Schematic image of the suspended silicon MEMS structure.

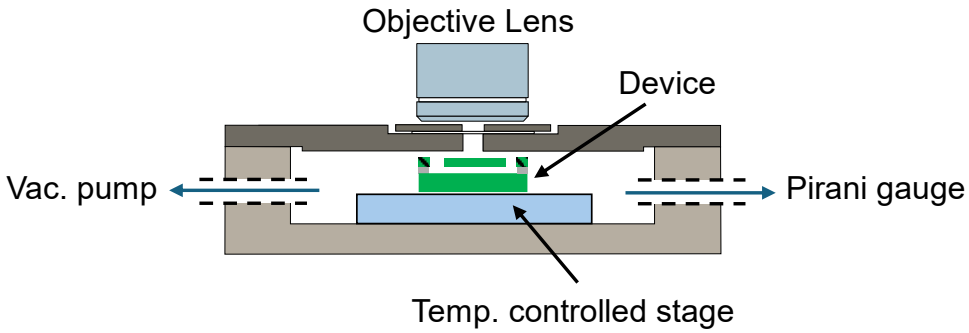

Figure 2. Schematic image of vacuum chamber with a sapphire window. MEMS device was placed on a temperature-controlled stage.

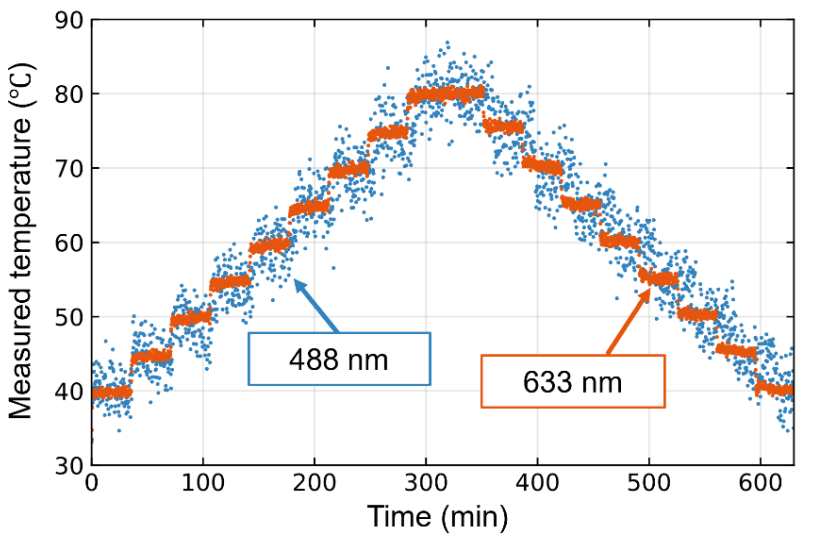

Figure 3. Comparison of micro-Raman thermometry results obtained using 488 nm and 633 nm excitation lasers. The horizontal axis represents time, and the vertical axis indicates the measured temperature converted from Raman spectra peak shift.

High-performance structures with photoimageable thick film pastes in low temperature cofiring ceramics for mmWave packages

Lynn Möhring [a], Martin Ihle [a], Birgit Manhica [a], Stefan Körner [a], Uwe Partsch [a], Peter Uhlig [b], Enrico Tolin [b]

[a] Fraunhofer Institute of Ceramic Technologies and Systems IKTS, Dresden, 01277, Germany
[b] IMST GmbH, Kamp-Lintfort, 47475, Germany
e-mail: lynn.moehring@ikts.fraunhofer.de

The demand for products that are as multifunctional and compact as possible beside the reduction of process costs in favour of smaller carbon footprint to meet the requirements of sustainable development moved into focus in recent years. One area of particular interest is energy-efficient wireless communication systems, which are essential for the Internet of Things (IoT), object identification and localisation for autonomous vehicles.
LTCC (low-temperature co-fired ceramics) materials offers significant advantages including three-dimensional and hermetical sealing of packages [1], which make it particularly attractive for use in harsh environmental conditions. Additionally, they offer outstanding high-frequency characteristics such as a very low dielectric loss and a comparable low and stable permittivity in a in a wide temperature range [2]. Conventional manufacturing methods on LTCC such as screen-printing limits the miniaturization due to the inability to print very fine (<50 µm). Other special solutions like aerosol-jet printing do offer the possibility of finer structuring, but there are significant disadvantages in terms of edge quality and layer thickness.
Due these facts, the development of fineline patterning processes using photoimageable (PI) thick film pastes on LTCC has played a major role over the last 25 years, enabling resolutions down to 50 micrometers [3,4]. Since 2019 Fraunhofer IKTS has developed thick film pastes which are photoimageable and allowing structural geometries down to 20 µm lines and spaces [5].
The PI technology is based on a UV-curable organic vehicle in which the functional inorganic components like metals, alloys, oxides, glasses and additives are mixed. The pastes were applied with standard screen printing as a full area or a rough structure. The required design is than applied via exposure using LDI or a photo mask. Areas that have not been exposed are then removed using spray development. In the final step of sintering all organic components are burned out and a dense pore-free functional layer is created. For a better understanding, the full photo imageable process chain is shown in Fig. 1.
In addition to the advantage that the current developed pastes do not require a yellow room, the main advantage over screen printing are the small line space resolutions and the high edge quality which can be achieved (Fig. 2). Compared to conventional thin-film lithography, fewer and less elaborate process steps are necessary. This minimises the amount of material required, as well as the amount of waste produced and the energy costs. This technology bridges the gap between conventional thick-film and thin-film technology by combining the advantages of both while reducing the disadvantages.
One of the most important points for using the PI technology especially the LDI in LTCC multilayer technology is the possibility of local shrinkage adjustments. The LDI process allows a high degree of geometric freedom and gives the opportunity to adapt the design almost at will. These advantages are important when sintering LTCC green films, because of their inhomogeneous and batch-dependent shrinkage which can lead to deviations in millimeter range on a substrate. This is a significant disadvantage, especially for applications in the high-frequency range, which is solved by using the LDI.
This abstract is intended to provide an overview regarding the further development of these pastes for laser direct imaging (LDI) and high-frequency LTCC materials. For the following work Vibrantz LTCC A6M-E was chosen as a substrate material because of their low dielectric constant and loss tangent at high frequencies. An important point for paste development is the adaptation of shrinkage to the co-sintering profile and the shrinkage of the tape during this process. Shrinkage curves of the green tape in the form of a laminate, tape powder and dried pastes in the temperature profile of the sintering were used for the adjustment. The adjustment is done via the solid components, whereby both their content and particle distribution are varied to adjust the start of sintering and the total shrinkage. In addition, the focus is on maintaining the exposure and development properties. The results can be seen in Fig. 3, show a close start of sintering of the paste (approx. 580°C) to substrate material (approx. 650 °C). Furthermore, the total shrinkage of the sample (18 %) is between the measured values of green tape (22.5 %) and tape powder (15.5 %).

Figure 4 shows the difference between a paste with adjusted shrinkage and one without. In the case of the paste without adjustment, a higher surface roughness and holes in the conductor track can be seen. The main cause of this is the different shrinkage of substrate and tape, which can be minimized with an appropriate adjustment.

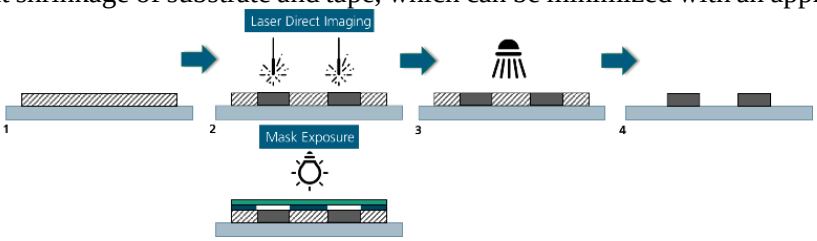

Figure 1. PI technology process chain: 1. Screen printing of full area or rough structure. 2. Exposure using UV-Laser or photo mask. 3. Development using spray ablation method. 4. Developed structures.

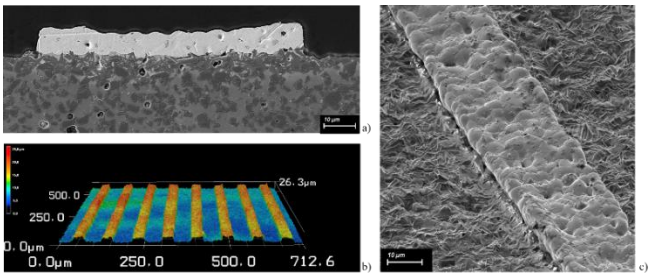

Figure 2. Images of sintered silver PI paste on LTCC (sintered GT951) exposed with LDI. a) cross section FESEM image of 90 µm conductor line. b) surface topography image of 30 µm conductor lines. c) crossbeam FESEM image of 25 µm conductor line.

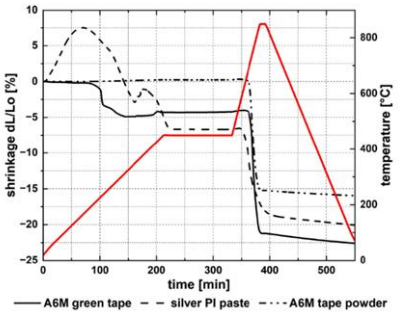

Figure 3. Shrinkage curves of LTCC A6M green tape, adjusted silver PI paste and LTCC A6M tape powder.

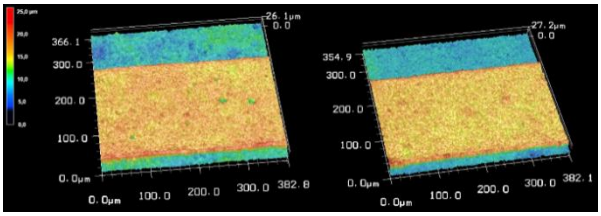

Figure 4. Surface topography images of sintered silver PI pastes on sintered LTCC A6M-E. left: Paste without shrinkage adjustment, right: Paste with shrinkage adjustment.

[1] J. Müller et al., "Fineline structuring on LTCC-substrates for 60 GHz line coupled filters," 18th European Microelectronics & Packaging Conference, Brighton, UK, 2011, pp. 1-5.

[2] M. V. Jacob, J. Mazierska, M. Bialkowski, “Measurement of complex permittivity of low temperature co-fired ceramic at cryogenic temperatures,” Advances in Electronic Ceramic Materials: Ceramic Engineering and Science Proceedings, vol. 26. Wiley, 2005.

[3] B. E. Taylor, L. Bidwell, A. Lawrence “New photoimageable LTCC technology for making a wide range of ceramic architectures and circuits” International Conference on High Density Interconnect and Systems Packaging. SPIE Proceedings, vol. 4428, 2001, pp.89-92.

[4] J. Müller, R. Perrone et al. “Comparison of High-Resolution Patterning Technologies for LTCC Microwave Circuits.” Journal of Microelectronics and Electronic Packaging 4 (3), 2007, pp. 99–104.

[5] K. Reinhardt; Fotostrukturierbare Pasten – Neuste Innovationen in der Fineline-Dickschichttechnik; PLUS 2/2022, Februar 2022, Band 24, p. 217-219

Germanium has recently gained significant attention in varius fields, including electronic, photonic, spintronics and quantum communication. However, low-resistivity ohmic contacts remain a challenge, for n-type Ge. This work focuses on the fabrication of a spintronic device on lightly doped n-type Ge in which both rectifying and non-rectifying contacts were obtained by electron beam lithography and electron beam evaporation. Specific nanofabrication details, along with electrical measurement performed at room temperature, will be presented.

Electrical Behavior of Rectifying and Ohmic Contacts on Lightly n-Doped Germanium

M. Gherardi[1,2], S. Freddi[2], F. Scali[1], C. Zucchetti[1], F. Bottegoni[1], G. Isella[1], F. Ciccacci[1], M. Finazzi[1], A. Federov[2], M. Bollani[2]

[1] Department of Physics, Politecnico di Milano, Piazza Leonardo Da Vinci 32, 20133 Milano, Italy

[2] CNR - IFN, LNESS Laboratory, Via Anzani 42, 22100 Como, Italy

michele.gherardi@polimi.it

In recent years, there has been a growing interest in the use of germanium for a wide range of applications. Owing to its lower effective mass and higher carrier mobility compared to silicon, Ge-based electronic devices offer the potential for high-speed operation combined with reduced power consumption. [1].

The integration of germanium into silicon photonics has enabled the development of high-performance photodetectors, lasers, and modulators [2]. Moreover, germanium exhibits a long spin lifetime and efficient generation of non-equilibrium spin populations via optical excitation, making it a promising material for spintronic applications [3].

For all these applications, the ability to fabricate both rectifying and Ohmic contacts on the same platform is particularly advantageous. Germanium is strongly affected by Fermi-level pinning (with a pinning factor $S \approx 0.05 – 0.07$), and its charge neutrality level lies approximately 0.09 eV above the valence band. As a result, metal contacts on p-type Ge with doping concentrations above 10^{14} cm^{-3} exhibit Ohmic behavior at room temperature. In contrast, n-type Ge is characterized by a Schottky barrier that is largely insensitive to the metal work function, posing significant challenges for practical applications. To address this issue, various strategies have been investigated, including surface passivation and the introduction of interfacial layers such as Ge_3N_4, black phosphorus, or ZnO. Although these methods help reduce Fermi-level pinning, they often result in relatively high specific contact resistance ($\rho_c > 10^{-6}$ $\Omega \cdot cm^2$).

Increasing doping concentration narrows the Schottky barrier width, thereby facilitating electron tunneling across the barrier. The direct deposition of Ni on n-type Ge has been shown to yield Ohmic contacts with a specific contact resistance as low as 2.3×10^{-7} $\Omega \cdot cm^2$. While this approach achieves the lowest ρ_c, it necessitates highly doped Ge ($N_d > 10^{19}$ cm^{-3}) ($Nd > 10^{19}$ cm^{-3}) [5]. For moderately doped n-type Ge ($Nd \approx 10^{18}$ cm^{-3}), AgSb alloys have been demonstrated to form effective Ohmic contacts by locally enhancing the Ge doping level [6].

In this work we present the fabrication of a spintronic device on lightly n-doped Ge ($Nd \approx 10^{15}$ cm^{-3}) featuring both rectifying and non-rectifying contacts. These contacts were defined using photolitography and fabricated by electron beam evaporation. Ohmic contacts were realized by evaporating AgSb alloys (99% Ag, 1% Sb), followed by annealing in Ar/H_2 atmosphere (Figure 1). A temperature range between 380 °C and 450 °C was investigated, and the process was optimized to achieve resistances below 100 kΩ. At a fixed temperature, the annealing time was also systematically studied in order to reduce the resistance. In contrast, Schottky contacts are formed by the evaporation of Pt or Ti without any annealing treatments. Systematic electrical measurements were conducted at room temperature to validate the fabrication process (Figure 2). Finally, the entire fabrication process was demonstrated using a nanolithography approach (electron beam lithography at 30kV), followed by evaporation steps and thermal treatments, in order to prove the feasibility of transferring two types of contacts even onto areas smaller than 200 nm^2.

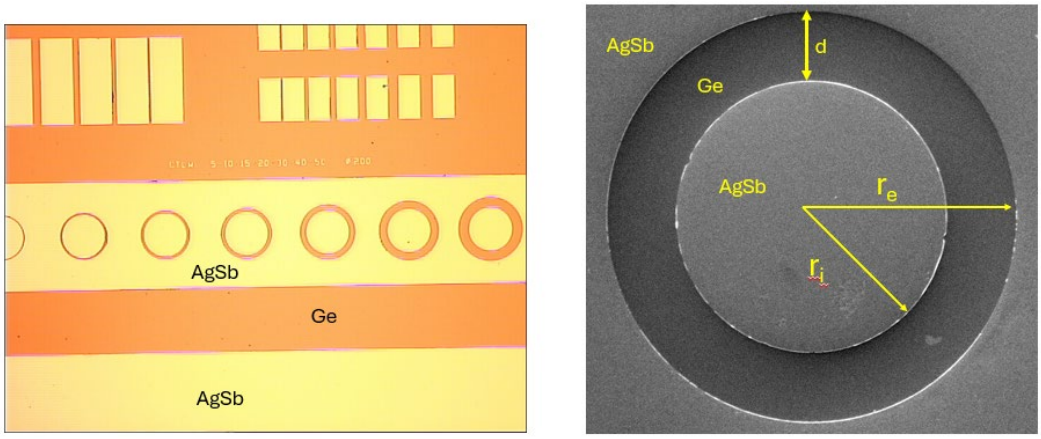

Figure 1: a) Optical image of the CTLM structures fabricated by optical lithography and electron beam evaporation. b) SEM image of a single CTLM structure in which the main geometrical features are highlighted.

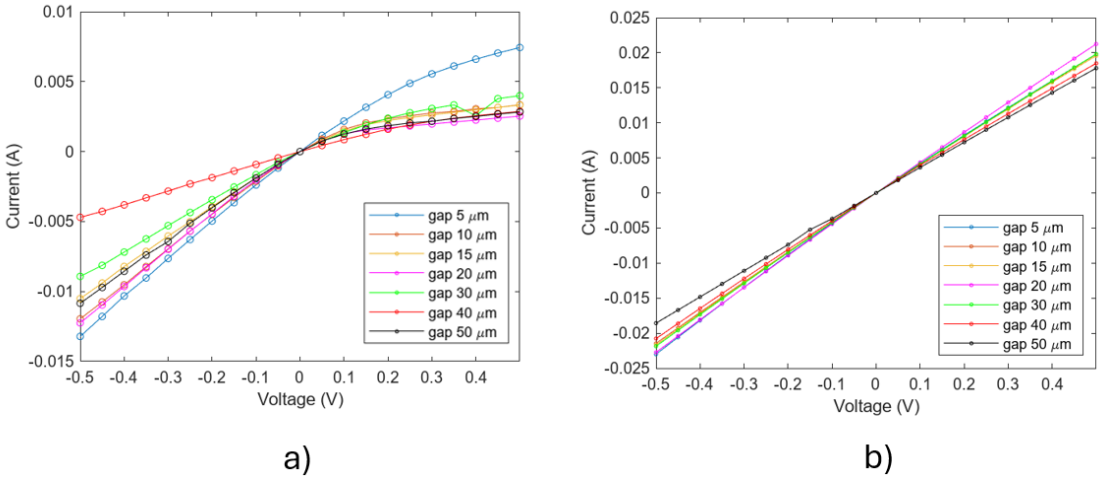

Figure 2: I-V curve of the CTLM structures after Rapid Thermal Annealing for 10' in Ar/H_2 atmosphere at different temperatures: a) 350°C (rectifying contact) and b) 450°C (non-rectifying contact).

[1] R. Pillarisetty, Nature 479, 324–328 (2011)
[2] D. Marris-Morini et al., Nanophotonics, 7(11), 1781-1793 (2018)
[3] C. Zucchetti et al., APL Materials 10, 011102 (2022)
[4] G. Scappucci et al., Nature Reviews Materials 6, 926–943 (2021)
[5] K. Gallacher et al., Appl. Phys. Lett. 100, 022113 (2012)
[6] D.C.S Dumas et al., Appl. Phys. Lett. 104, 162101 (2014)

We acknowledge funding from Ministero dell'Istruzione, dell'Università e della Ricerca PRIN Grant no.20222LPKZR.

Fabrication of Titanium-based Microneedles Array Using Wire Electrical Discharge Machining

Min Chul Shin [a], Ji Hwan Han [a], Gyu Man Kim [a]

[a] School of Mechanical engineering, Kyungpook National University, Republic of Korea
e-mail: gyuman.kim@knu.ac.kr

Wire Electrical Discharge Machining (WEDM) is a non-contact machining technique that precisely removes material through controlled electrical discharges between a wire electrode and a conductive workpiece. It is particularly suitable for fabricating micro-scale features in high-hardness materials, making it attractive for micro & nano engineering and biomedical device manufacturing. Titanium alloys are widely used in biomedical applications such as implants and microneedles due to their excellent biocompatibility, mechanical strength, and corrosion resistance [1][2].

In this study, we report the fabrication of titanium-based microneedle arrays using WEDM, and investigate the effect of machining conditions on the formation quality. Brass wire electrodes with a diameter of 250 μm were used to machine 1-mm thick titanium substrates in kerosene dielectric fluid. Key parameters such as voltage (300 - 350 V) and capacitance (0.05 - 0.47 μF) were varied to optimize the dimensional precision and surface integrity of the fabricated microneedle structures.

The machined structures were characterized using Field-Emission Scanning Electron Microscopy (FE-SEM) to observe tip sharpness, surface roughness, and uniformity. Comparative evaluation before and after parameter optimization showed a significant improvement in microneedle shape consistency and reduction of burr formation. Higher discharge energy tended to cause surface melting and dimensional deviations, while optimized settings enabled the reliable production of high-aspect-ratio microneedles with sharp, well-defined tips.

The results demonstrate that WEDM offers a controllable and effective method for fabricating titanium microneedle arrays, with tunable process parameters that influence structural quality. This approach provides a practical pathway for manufacturing next-generation microneedle devices for transdermal drug delivery and biomedical sensing applications [3][4].

Acknowledgement:
This work was supported by the National Research Foundation of Korea (NRF) grant funded by the Korean government (MSIT) (No. RS-2023-00208717 and RS-2024-00406223), and by the Korea Institute for Advancement of Technology (KIAT) grant funded by the Ministry of Trade, Industry and Energy (MOTIE) (No. RS-2022-KI002563, HRD Program for Industrial Innovation).

References:

[1] J. Yang, C. Liu, H. Sun, et al., The progress in titanium alloys used as biomedical implants: From the view of reactive oxygen species, Front. Bioeng. Biotechnol. 10 (2022) 1092916.

[2] E. Marin, Biomedical Applications of Titanium Alloys: A Comprehensive Review, Mater. 17 (2023) 114.

[3] P.T. McCarthy, K.J. Otto, M.P. Rao, Robust penetrating microelectrodes for neural interfaces realized by titanium micromachining, Biomed. Microdevices 13 (2011) 503–515.

[4] S.K. Chaubey, K. Gupta, A review on Wire-EDM of bio titanium, Rep. Mech. Eng. 4 (2023) 141–152.

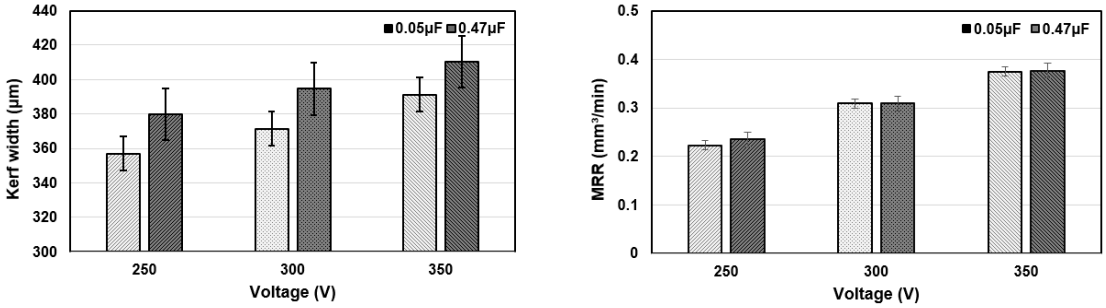

Figure 1. Kerf width and material removal rate (MRR) of titanium as a function of discharge voltage and capacitance during WEDM.

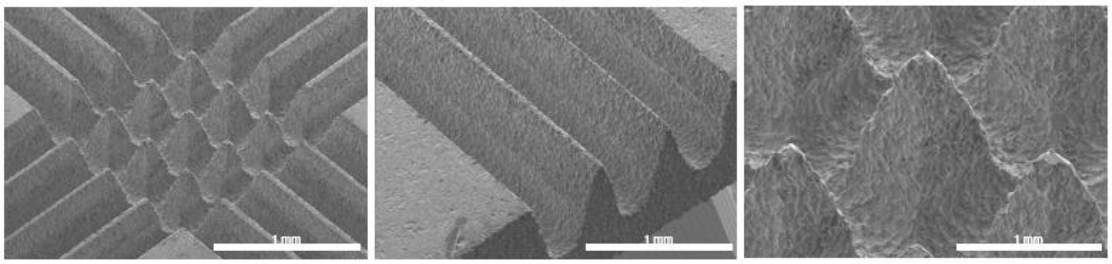

Figure 2. FE-SEM images showing titanium microneedle arrays fabricated by wire electrical discharge machining (WEDM)

Polymer-based MEMS microcantilever and microfluidic system for biochemical detection

Pooja P. Kanade[a], Paul T. Baine[b], Briliant Prabowo[a], Arthur Lipinski[a], Jason Wiggins[a], Robert M. Bowman[a]

[a] School of Mathematics and Physics, Queen's University Belfast, Belfast BT7 1NN, United Kingdom
[b] School of Electronics, Electrical Engineering and Computer Science, Queen's University Belfast, Belfast BT7 1NN, United Kingdom
e-mail: p.kanade@qub.ac.uk

Microelectromechanical systems (MEMS)-based sensors are widely used for a variety of applications, including electronics, space technology, and medical interventions. [1-2] MEMS cantilevers can be useful tool in biochemical detection, due to the adsorption of molecules of the surface of the cantilever, thereby measuring the change in surface stress. [3] Predominantly, silicon and silicon nitride based cantilevers have been introduced for biochemical detection. These materials have high Young's moduli, are expensive, and require complex manufacturing processes for microfabrication to achieve the desired accuracy. Instead of silicon and silicon nitride, photo-patternable polymer materials have a much lower Young's modulus and are easy to fabricate. [4-5]

This work introduces a polymer-based MEMS microcantilever device in a microfluidic channel for biochemical detection. The novelty of this work lies in the easy fabrication of polymer microcantilevers and the integration of the polymer microcantilevers in the 3D printed microfluidic channel. Figure 1 shows the schematic of the proposed system. Four polymer microcantilevers are placed in a microfluidic channel. A strain sensor is patterned on each microcantilever in the half-bridge configuration of the Wheatstone bridge. The microcantilever device is bonded to a patterned glass, which is then wire bonded to a custom-made printed circuit board. The surface of the cantilevers is activated before enclosing it in a microfluidic chamber.

The cantilever is first analyzed using simulation studies for the effect of external force on its deformation. Figure 2 shows the results of the simulation carried out using COMSOL Multiphysics. The dimension of the cantilever are 300 µm x 110 µm x 2.5 µm. As can be observed from the figure, the stress is maximum at the fixed end of the cantilever and gradually reduces as it moves toward the free end of the cantilever. Based on the simulation results, we designed the strain sensor to cover up to half of the length of the cantilever.

Figure 3 shows the microscope images of the fabricated device containing four microcantilevers. The devices were fabricated on a silicon dioxide wafer using photolithography, wet etching and lift-off techniques. First, the microcantilever layer was pattern using a thin SU-8 photoresist. Next, the sensors were patterned in the half bridge configuration of the Wheatstone bridge using Ti/Pd. The contact pads were then patterned using Ti/Au. The sensor and contact pads were then isolated using a layer of SU-8. Lastly, a body layer was formed using a thicker SU-8 to provide strength to the cantilever body. The device was then released from the silicon dioxide sacrificial layer using the buffered oxide etchant (BOE) (6:1). The released microcantilever device was then thermally bonded to a pattern glass. This device has potential for mass production with high reliability in bulk fabrication and repeatability.

References:
[1] Bruno et al. Adv. Sci. 8 (2021) 2100627.
[2] Dong et al. ACS Sens. 6(10) (2021) 3556-3563.
[3] Kosaka et al. Nat. Nanotechnol. 9 (2014) 1047-1053.
[4] Kanade et al. Small 20(33) (2024) 2311274.
[5] Kanade et al. Biosens Bioelectron. 216 (2022) 114675.

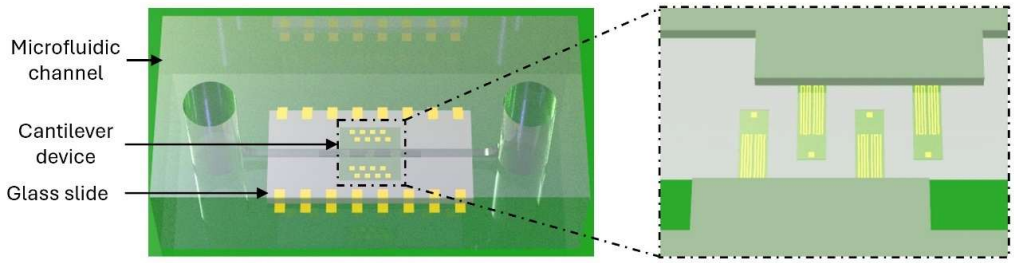

Figure 1. Schematic of the proposed cantilever-based device embedded in a microfluidic channel. Four cantilevers can simultaneously measure the strain generated by the antibodies.

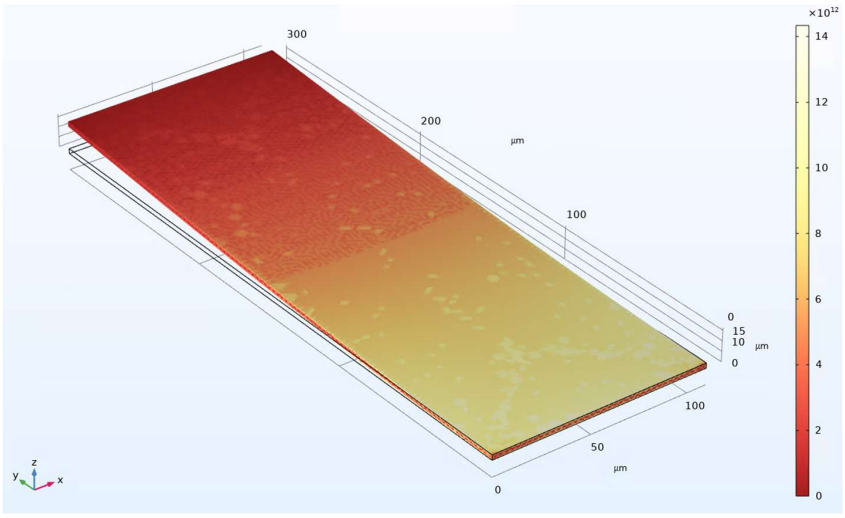

Figure 2. Simulation results of the stress generated on the polymer cantilever.

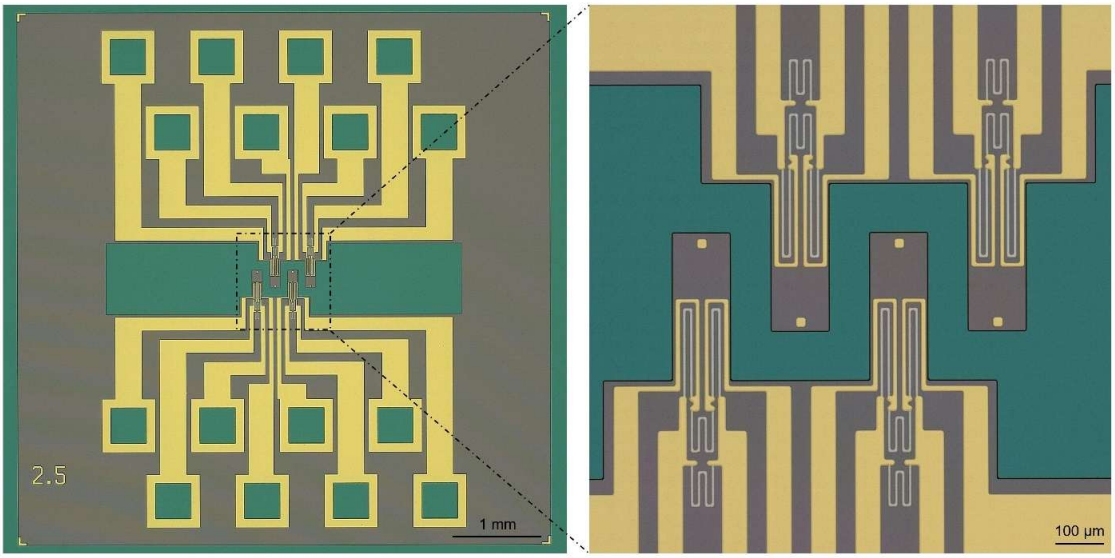

Figure 3. Microscope image of the fabricated four-cantilever device using photolithography.

Two-photon polymerization as mastering tool for nanoimprint lithography to produce microfluidic test devices

Stjepan Perak [a], Sonja Kopp [b], Viktorija Jonaityte [b], Marta Bonora [c,d,e], Michael M. Muehlberger [b], Francesco Moscato [c,d,e], Markus Lunzer [a]

[a] UpNano GmbH, Vienna, 1030, Austria
[b] PROFACTOR GmbH, Steyr-Gleink, 4407, Austria
[c] Center for Medical Physics and Biomedical Engineering, Medical University of Vienna, 1090, Austria
[d] Ludwig Boltzmann Institute for Cardiovascular Research, Vienna, 1090, Austria
[e] Austrian Cluster for Tissue Regeneration, Vienna, Austria
e-mail: markus.lunzer@upnano.com

UV-based Nanoimprint lithography (NIL) is a micro- and nano-replication technology, which offers very high resolution and high process flexibility 0. Its applications span various fields, including optics and life sciences. A critical aspect of the NIL process chain is the availability of high-quality masters, which are essential for the fabrication of NIL stamps. A key advantage of NIL is the capability to replicate complex structures in a single processing step [2]. We use two-photon polymerization (2PP) to fabricate such complex masters in high quality with high flexibility [3]. This sub-micrometer resolution, high-precision 3D printing technology uses nonlinear two-photon absorption to initiate polymerization in a photosensitive resin, making it ideal for biomedical, photonic and microengineering applications.

An application that demonstrates the potential of combining NIL and 2PP is the investigation of microstructured surfaces as antithrombogenic tools. Cardiovascular devices, such as implantable blood pumps, trigger the activation of platelets due to the iterative contact between blood cells and artificial device surfaces. The use of microstructures may help to reduce platelet adhesion and thus prevent blood clotting on these surfaces. Here, we test the hemocompatibility of microstructured surfaces in both semi-static and dynamic flow conditions. For this purpose, master microstructures were fabricated using the 2PP 3D printing system NanoOne 1000 (UpNano GmbH; Figure 1a) equipped with a 40× objective (NA 1.4, Olympus) in Vat mode (Figure 1b) [4]. The master microstructures as well as adjacent flat reference surfaces with an area of 4 x 4 mm^2 each (Figure 2a-b) were printed using UpNano's *Adaptive Resolution* 2PP technology. This approach enables the selective and dynamic application of high-resolution and high-throughput print parameters, thereby significantly reducing print time while preserving localized high-resolution. This multi-step approach of combining 2PP and NIL was first utilized to manufacture multiple samples, used to evaluate the antithrombogenic potential of microstructured surfaces with blood platelets in low-shear environment experiments. Subsequently, dynamic experiments were performed within microfluidic chips to simulate in vivo pump flow shear conditions. These microfluidic devices were fabricated in a manual step & repeat NIL process using PDMS stamps (Sylgard 184) and OrmoComp® (micro resist technology GmbH) as imprint material. NIL replication allows to obtain a large number of samples with different geometries for single-use experiments (Figure 2c-f) as well as the production of complex microfluidic test devices (Figure 3a-c).

The multi-step integration of 2PP, NIL, and PDMS casting has proven to be an efficient and economically viable process for the fabrication and replication of micropatterned surfaces and complex microfluidic devices for studying the interactions of microstructured surfaces and blood platelets. This approach is particularly advantageous in scenarios in which a large number of samples is required, e.g. when various geometries and dimensions are tested, or when test devices cannot be reused. We have demonstrated versatility in manufacturing samples for both static and dynamic experiments simulating physiological and non-physiological blood flow conditions. By enabling high-throughput fabrication of precisely engineered test-devices, our multi-step manufacturing process holds significant potential for optimizing cardiovascular devices more efficiently. Ultimately, it contributes to reducing thrombosis risk and improving the clinical outcomes for pediatric heart patients.

We gratefully acknowledge funding for the project OptiFlow3D (FFG Grant FO999891239).

[1] H. Schift, Journal of Vacuum Science & Technology B, 26 (2008) 458-480.
[2] M. Muehlberger, Nanomanufacturing, 2 (2022) 17-40.
[3] H. Wang, et al., Adv. Funct. Mater. 33 (2023) 2214211.
[4] T. Koch, et al., Adv. Mater. 36 (2024) 2308497.

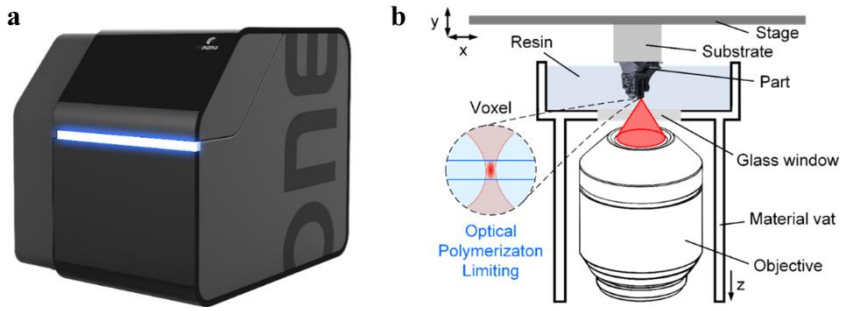

Figure 1. a: High-resolution two-photon polymerization (2PP) 3D printing system NanoOne 1000 (UpNano GmbH). **b:** Vat mode: A resin vat equipped with a high precision glass window is positioned above the objective, preventing contact with the resin and preserving the focusing power of the objective. The part is printed layer by layer, with the part being drawn out of the resin vat while maintaining a constant distance between the current print layer and the objective. This approach ensures consistently high precision throughout the printing process, guaranteeing optimal printing conditions. Additionally, due to the nonlinear nature of the excitation, a continuous liquid film persists between the part and the glass window, enabling a fast print process.

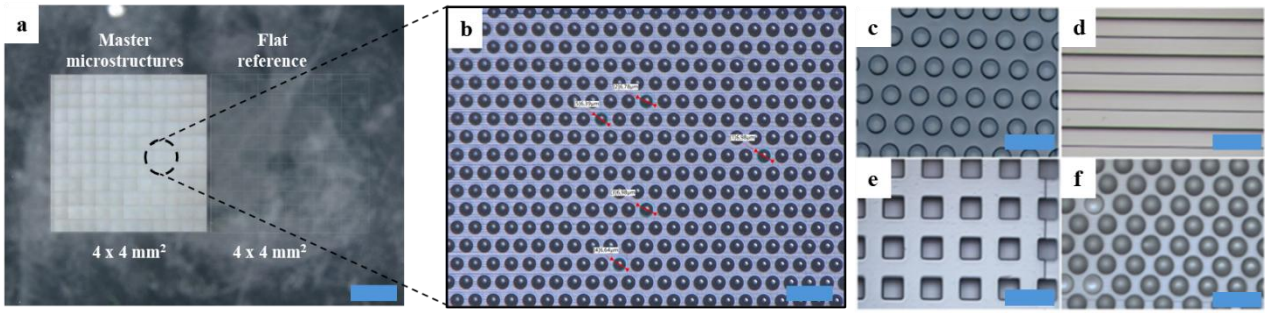

Figure 2. a: Light microscopy image (Keyence VHX-7000) of a 2PP 3D printed 4 x 4 mm^2 master microstructure pattern of small spheres (d = 6 µm), and a flat reference surface of the same area next to it (scale bar a-b: 1000 µm). **b:** Detailed image of the small spheres (scale bar: 20 µm). Light microscopy images (Keyence VHX-7000) of NIL replicated microstructures of **c:** large cones (d = 24 µm, h = 36 µm), **d:** large riblets (width = 24 µm, h = 12 µm), **e**: large grids (width = 24 µm, h = 12 µm) and **f:** large hemispheres (d = 24 µm), all in top view (scale bar c-f: 100 µm).

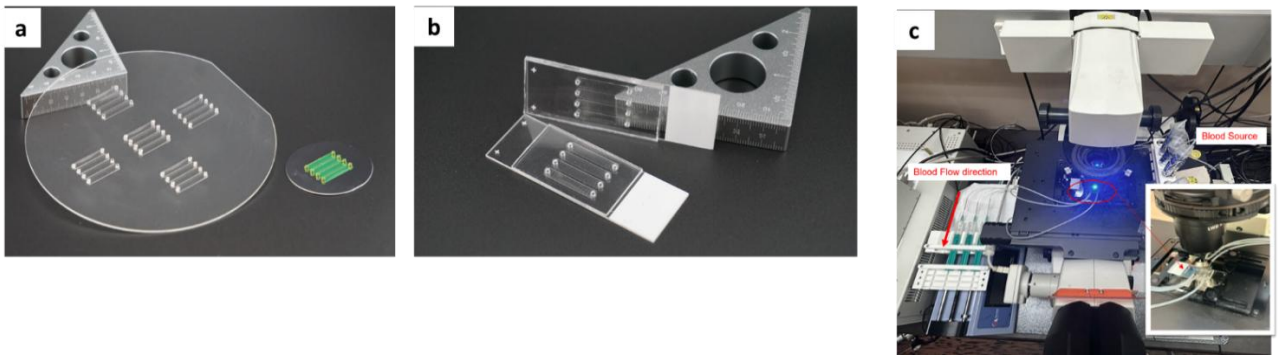

Figure 3. a: Master structures for PDMS casting: 2PP printed master (green) and replicated step & repeat samples (transparent). **b:** Microfluidic flow chambers replicated in OrmoComp®. **c:** Microfluidic setup: the flow chamber containing microchannels is placed under a fluorescent microscope and blood platelets are recorded via staining.

Engineered magnetic quantum dot nanoprobes for multiplexed, equipment-free Alzheimer's diagnosis at point-of-care

Anjum Qureshi [a], Javed H. Niazi [a]

[a]SUNUM - Sabanci University Nanotechnology Research and Application Center, Istanbul, 34956, Turkiye
e-mail: anjum@sabanciuniv.edu ; javed@sabanciuniv.edu

Abstract

This work introduces a bio-inspired nanomaterial design utilizes the unique optical and magnetic properties of engineered quantum dots (QDs) to revolutionize point-of-care (PoC) diagnostics. At its core, the technology harnesses nature-mimicking hierarchical assembly, integrating multicolored colloidal QDs and superparamagnetic quantum dots (MQDs) into an immuno-optomagnetic nanosystem capable of rapid, multiplexed biomarker detection. The QD-MQD hybrid nanoarchitecture draws inspiration from biological recognition processes, where antibody-functionalized nanoparticles emulate the specificity of immune complexes while enabling tunable photonic and magnetic responses.

Central to this nanoarchitecture is the precise nanoscale engineering of core-shell-shell CdSe/CdS/ZnS QDs, optimized for aqueous stability, minimized photobleaching, and enhanced serum compatibility through poly-glycine coatings. The MQDs are synthesized via colloidal and chemical cross-linking routes, yielding a combination of size-tunable fluorescence (450-650 nm) with superparamagnetism, which enables simultaneous magnetic enrichment and optical signaling. Unlike conventional diagnostic probes, these nanostructures eliminate the need for external separation steps or complex instrumentation by performing all-in-solution detection in microliter-scale volumes.

The bio-inspired assay design mirrors natural antibody-antigen interactions, where non-magnetic QDs (emitting at λ_1) first capture target analytes (e.g., amyloid-β, tau proteins) to form fluorescent "Complex 1", which then recruits spectrally distinct MQDs (λ_2) via sandwich immunoassays. This generates a magneto-optical "Complex 2" detectable in real-time (<20 min) through direct fluorescence readouts. This system achieves multiplexing by exploiting QD color-coding (e.g., red for colloidal QDs and green for MQDs or vice versa as shown for Aβ1-42 in **Figure 1(a-c**) and for tau-protein in **Figure 2(a-c)** without cross-talk, enabled by precise spectral separation.

The developed optically tunable nano-biosystem addresses longstanding gaps in early detection of Alzheimer's disease (AD) and its role in rapid diagnosis [1]. Traditional AD biomarkers are typically identified post-symptomatically via MRI or invasive cerebrospinal fluid assays. Here, the QD-MQD nano-biosystem detects pathogenic amyloid-β (both β1-40 and β1-42 forms) and tau proteins in serum at clinically relevant concentrations (<10 pg/mL), correlating with neuronal dysfunction. The equipment-free workflow, conducted entirely in microtubes, reduces costs and complexity while outperforming existing in vitro diagnostics in speed and sensitivity.

References: [1] J. H. Niazi KM and A. Qureshi. (2025) US20250020671A1.

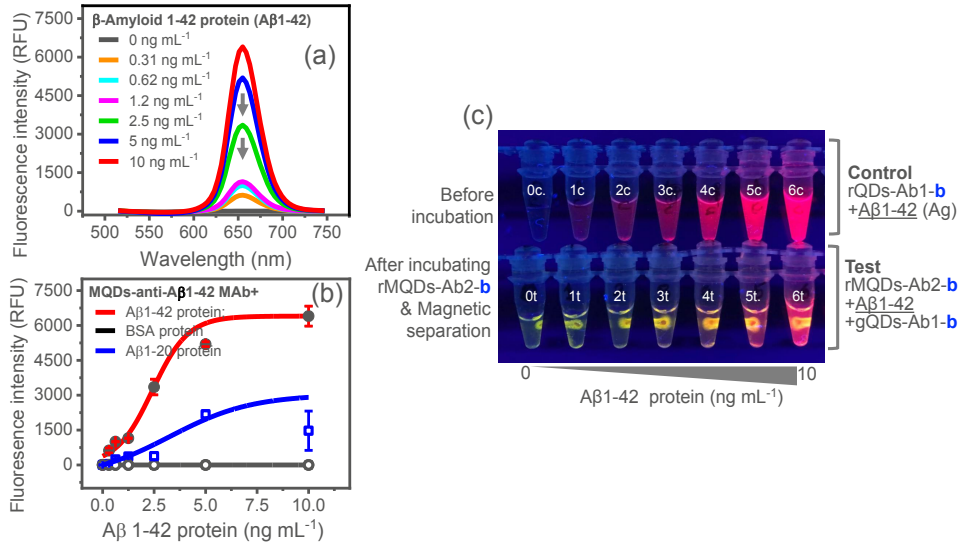

Figure 1. Binding reactions between bio-activated rQDs-Ab1-b (red) and Aβ1-42 protein, which is then recruited by analyte-specific gMQDs (green) to sandwich and change to a tertiary color (yellow) only when Aβ1-42 is present. (a). Changes in fluorescence intensity observed from fluorescence spectra of test samples calculated for bound fractions. (b) Non-linear regression fit of fluorescence intensity data extracted at a wavelength (655 nm) that showed no binding with BSA but partially bind to an analogous protein Aβ1-20 indicating the specificity of the reaction to Aβ protein fragments. (c) Images of reaction microtubes captured using a smartphone after incubation of control and test reaction tubes and after magnetic separation showing clear capturing of Aβ1-42 analyte that saturated at 10 ng mL^{-1}.

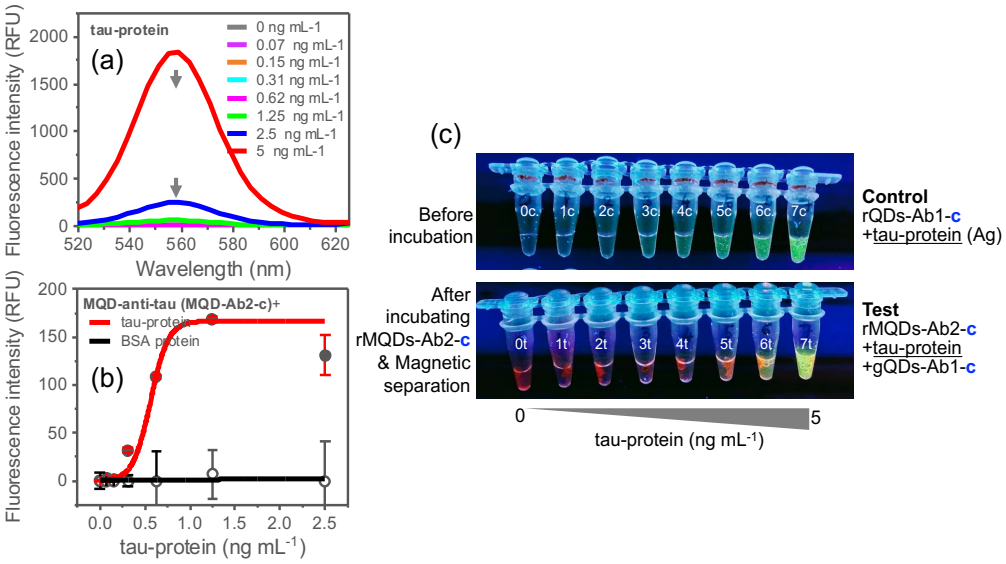

Figure 2. Binding reactions between bio-activated gQDs-Ab1-c (green) and tau-protein, which is then recruited by analyte-specific rMQDs-Ab2-c (green) to sandwich and change to a tertiary color (orange) only when tau-protein is present. (a) Changes in fluorescence intensities from fluorescence spectra of residual samples from reaction tubes after magnetic separation. (b) Calculated bound fluorescence intensities with varying analyte concentrations showing saturation at 1.25 ng mL^{-1} tau-protein with no non-specific binding with BSA. (c) Images of reaction microtubes captured by a smartphone camera showing controls containing green non-magnetic QDs-Ab1-c with respect to increasing concentrations of analyte (tau-protein) from 0 (blank) to 5 ng mL^{-1} tau-protein and after incubation with constant amounts of red-MQDs-Ab2-c followed by magnetic separation showing capturing of analyte and saturation.

Quality Factor Engineering in NIR Optical Metasurfaces Using $Ge_2Sb_2Te_5$ and Graphene

Seyed As'ad Amirhosseini
Department of Electrical and Computer Engineering, Isfahan University of Technology, Isfahan, Iran,
sa.amirhoseyni@ec.iut.ac.ir

Daniyal Khosh Maram
Department of Electrical Engineering, Amirkabir University of Technology, Tehran, Iran
danialkhoshmaram@aut.ac.ir

Abstract

We propose an optically reconfigurable metasurface that utilizes graphene heaters for dynamic control of the phase of $Ge_2Sb_2Te_5$ (GST) through Joule heating. This design achieves a tunable phase modulation range of 0° to 300° for reflected waves at a wavelength of 1.55 μm by varying the crystallization levels of GST. The incorporation of graphene enhances plasmonic effects, optimizing absorption and facilitating effective phase manipulation. Our simulations indicate significant potential for applications in electro-optical devices, such as LiDAR and beam steering.

Introduction

Metasurfaces—2D analogs of metamaterials—enable sub-wavelength light control [1], providing applications in beam shaping, and energy harvesting [2]. However, traditional static metasurfaces are limited by their fixed optical properties, highlighting the need for reconfigurable designs. Phase-change materials (PCMs) like $Ge_2Sb_2Te_5$ (GST) are promising due to their ability to transition between amorphous and crystalline states, significantly altering their refractive index. This work proposes a method for optically reconfigurable metasurfaces that utilize graphene heaters for dynamic control of the GST phase.

Materials and Design

The proposed metasurface consists of a GST nanoribbon structure layered with graphene as illustrated in Fig. 1. As shown in Fig. 2, by applying required bias voltages to the graphene, Joule heating induces phase transitions in the GST, controlling its optical properties. The metasurface includes Si and SiO_2 spacer layers and a gold substrate. The permittivity of GST in both amorphous and crystalline states is determined using experimentally obtained refractive index data [3]. Key parameters include the height of the GST nanoribbons, Fig. 3, the air gap width, the lattice constant, and the thicknesses of the Si, SiO_2, and gold layers.

Simulation and Results

The optical performance of the metasurface was simulated using finite element analysis with a transverse magnetic (TM) plane wave incident normally on the structure. By controlling the crystallization percentage of the GST through biasing the graphene layer, we achieved a tunable phase shift of up to 300 degrees in the reflected wave, shown in Fig. 4(b). Additionally, the plasmonic effects exhibited by graphene generated surface plasmon polaritons (SPPs), shown in Fig. 5, that enhanced absorbance rates, shown in Fig. 4(a), facilitating efficient phase changes, Fig. 4(b). The integration of graphene heaters with GST metasurfaces provides a dynamic reconfiguration platform for various nanophotonic applications, including electro-optical uses such as beam steering, as shown in Fig. 6, in LiDAR systems. The simulation results, Fig. 2- Fig. 6, indicate that careful control of GST crystallization levels enables fine-tuning of reflected light properties.

Conclusions

We have developed a novel method for designing optically reconfigurable metasurfaces using graphene heaters to control GST phase transitions. This approach achieves tunable optical properties with high efficiency. The tunability and efficiency of this design offer significant potential for advancing technologies such as beam steering, and energy harvesting.

References

[1] S. Abdollahramezani *et al.*, *Reconfigurable multifunctional metasurfaces*, Nanophotonics, 3883–3893, 2022.
[2] O. Abed and L. Yousefi, *Tunable metasurfaces with phase change materials*, Opt. Express, pp. 33876–33889, 2020.
[3] L. Adnane, PhD thesis, 2018.

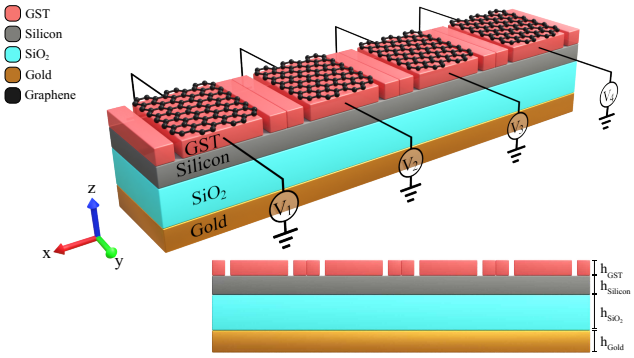

Fig. 1. Schematic of the array cell (metasurface) of our proposed GST-based metasurface with graphene.

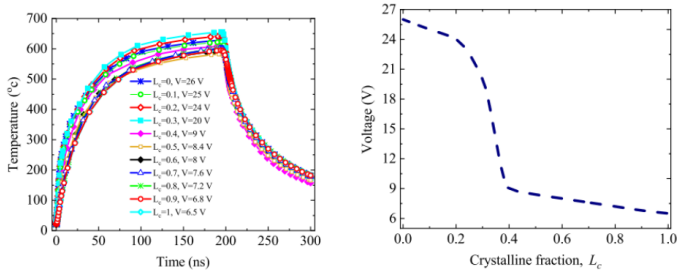

Fig. 2. Required voltage for achieving the melting temperature of amorphous surfaces on various crystalline fractions (a) at different times, and (b) for different crystalline metasurfaces.

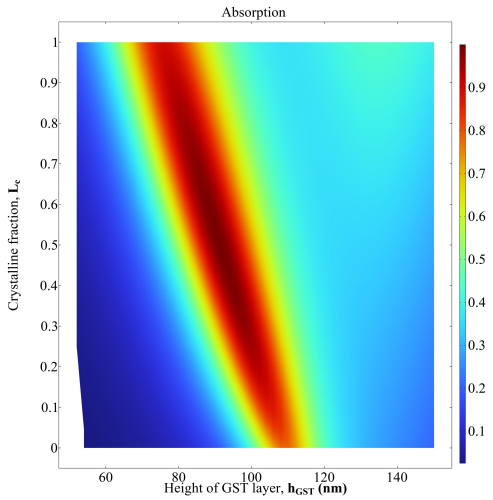

Fig. 3. Absorption spectrum of the metasurface: for various heights of the GST and crystallinity percentages ranging from 0 to 1.

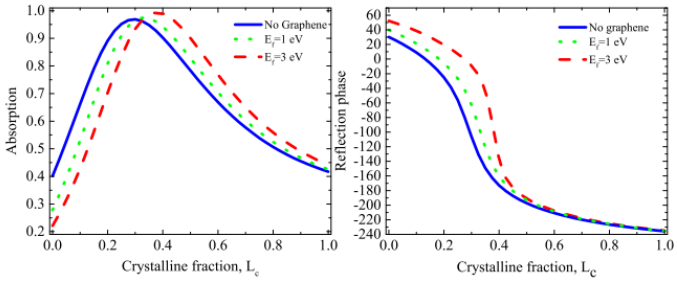

Fig. 4. (a) Optical absorption spectrum and (b) phase reflection diagram of the proposed single cell at a wavelength of 1550 nm as a function of different crystallinity percentages and Fermi-level of the graphene layer.

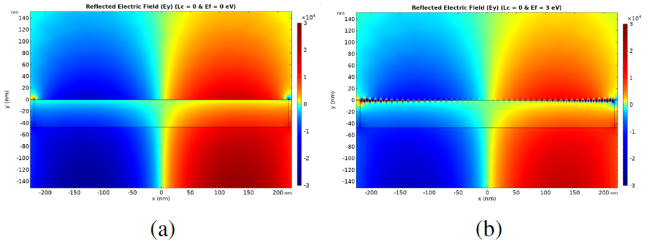

Fig. 5. (a) Ey distribution at Lc = 0 and Ef = 0 eV. At this Fermi level, no surface plasmon polaritons (SPP) will form. (b) Ey distribution at Lc = 0 and Ef = 3 eV. At this Fermi level, due to the transition of graphene to a semimetallic state, surface plasmon polaritons (SPP) have formed.

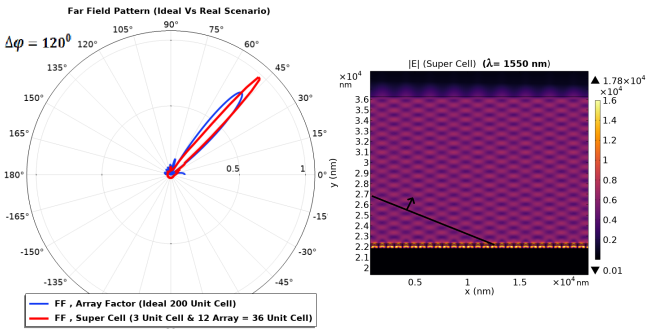

Fig. 6. Far-field radiation patterns and electric field distributions of the metasurface at different phase differences and angles. In the case of $\Delta\phi = 120°$, $\theta_r = 42.8°$.

Anomalous mapping between the Surface Charge and Ionic Conductance in Narrow Confinements

Debmalya Roy [a], Suman Chakraborty [a]

[a] Department of Mechanical Engineering, Indian Institute of Technology Kharagpur, WB, India
e-mail: suman@mech.iitkgp.ac.in

Fluid flow within narrow biological and bio-analytical confinements, such as nanopores, ion channels, or lab-on-chip devices, is strongly governed by the wall-fluid interfacial properties, particularly the surface charge density. This interfacial charge shapes the electric potential across the electrical double layer, playing a pivotal role in phenomena such as electroosmosis, electrokinetic energy conversion, and the electrophoretic transport of biomolecules under extreme confinement conditions [1–4]. A widely adopted approach for determining the surface charge density involves measuring the ionic conductance of an electrolyte within these narrow confinements [5–7]. This total conductance is commonly decomposed into the bulk and surface contributions, with the surface component directly linked to the surface charge. Conventionally, this relationship is simplified by assuming that the interfacial charge is exactly neutralized by an equal number of counterions, resulting in a presumed linear dependence of the surface conductance on surface charge density [2,8]. However, such a simplification markedly deviates from the ionic distribution as obtained from a fully-coupled Poisson-Nernst Planck theory. This deficit in the traditional simplified model stems from the consideration of the predominant role of the counterion in the ionic current estimation, commonly ignoring the role of the co-ions on the same. To address this limitation, we demonstrate here that, contrary to the commonly assumed linear relationship, surface conductance scales quadratically with the surface charge density at the leading order (Figure 1). This non-linear dependence arises because interfacial charges simultaneously increase the counterion concentration and decrease the co-ion concentration. This redistribution adheres to the Boltzmann distribution when convective ionic currents are negligible across the electric double layer, where the odd-order terms, such as the linear components, cancel each other out due to symmetry in the counterion and co-ion responses. As a result, the net increase in charge carriers is captured by the even powers of surface charge density, with the quadratic term being dominant. Additionally, in the presence of electroosmotic flow orthogonal to the electric double layer potential field (commonly in the axial direction of a fluidic confinement), the local ionic current density is further influenced. An applied axial electric field mobilizes the excess charge within the electrical double layer, contributing an extra component to the ionic current. This contribution can be estimated by integrating the product of fluid velocity and excess volumetric charge density in the double layer, both of which scale linearly with the surface charge density at leading order. Consequently, the electroosmotic component of the current also exhibits a quadratic dependence on the surface charge. Together, these observations challenge the traditional linear model of surface conductance in confined systems. Instead, our analysis reveals a fundamentally quadratic scaling law. This theoretical framework was validated using continuum simulations based on the full Poisson-Nernst-Planck model coupled with Navier-Stokes equations (PNP-NS Simulations, see figure 1). This key insight that surface conductance scales quadratically with surface charge density provides a more accurate means of determining surface charge in nanoconfined environments, thereby advancing a wide range of applications including energy conversion, iontronics, desalination, and biomolecule sensing technologies.

[1] L. Bocquet, E. Charlaix, Nanofluidics, from bulk to interfaces, Chem. Soc. Rev. 39 (2010) 1073–1095. https://doi.org/10.1039/B909366B.

[2] D. Stein, M. Kruithof, C. Dekker, Surface-Charge-Governed Ion Transport in Nanofluidic Channels, Phys. Rev. Lett. 93 (2004) 035901. https://doi.org/10.1103/PhysRevLett.93.035901.

[3] S. Chakraborty, C. Bakli, D. Roy, A. Chaudhuri, A. Guha, A. Patwari, Electrokinetic energy harvesting over nanometer and sub-nanometer scales, Appl. Phys. Rev. 12 (2025) 11305. https://doi.org/10.1063/5.0241150.

[4] L. Xue, H. Yamazaki, R. Ren, M. Wanunu, A.P. Ivanov, J.B. Edel, Solid-state nanopore sensors, Nat. Rev. Mater. 5 (2020) 931–951. https://doi.org/10.1038/s41578-020-0229-6.

[5] C.L. Ritt, J.P. de Souza, M.G. Barsukov, S. Yosinski, M.Z. Bazant, M.A. Reed, M. Elimelech,

Thermodynamics of Charge Regulation during Ion Transport through Silica Nanochannels, ACS Nano. 16 (2022) 15249–15260. https://doi.org/10.1021/acsnano.2c06633.

[6] R. Fan, S. Huh, R. Yan, J. Arnold, P. Yang, Gated proton transport in aligned mesoporous silica films, Nat. Mater. 7 (2008) 303–307. https://doi.org/10.1038/nmat2127.

[7] S. Qin, D. Liu, G. Wang, D. Portehault, C.J. Garvey, Y. Gogotsi, W. Lei, Y. Chen, High and Stable Ionic Conductivity in 2D Nanofluidic Ion Channels between Boron Nitride Layers, J. Am. Chem. Soc. 139 (2017) 6314–6320. https://doi.org/10.1021/jacs.6b11100.

[8] R.B. Schoch, P. Renaud, Ion transport through nanoslits dominated by the effective surface charge, Appl. Phys. Lett. 86 (2005) 1–3. https://doi.org/10.1063/1.1954899.

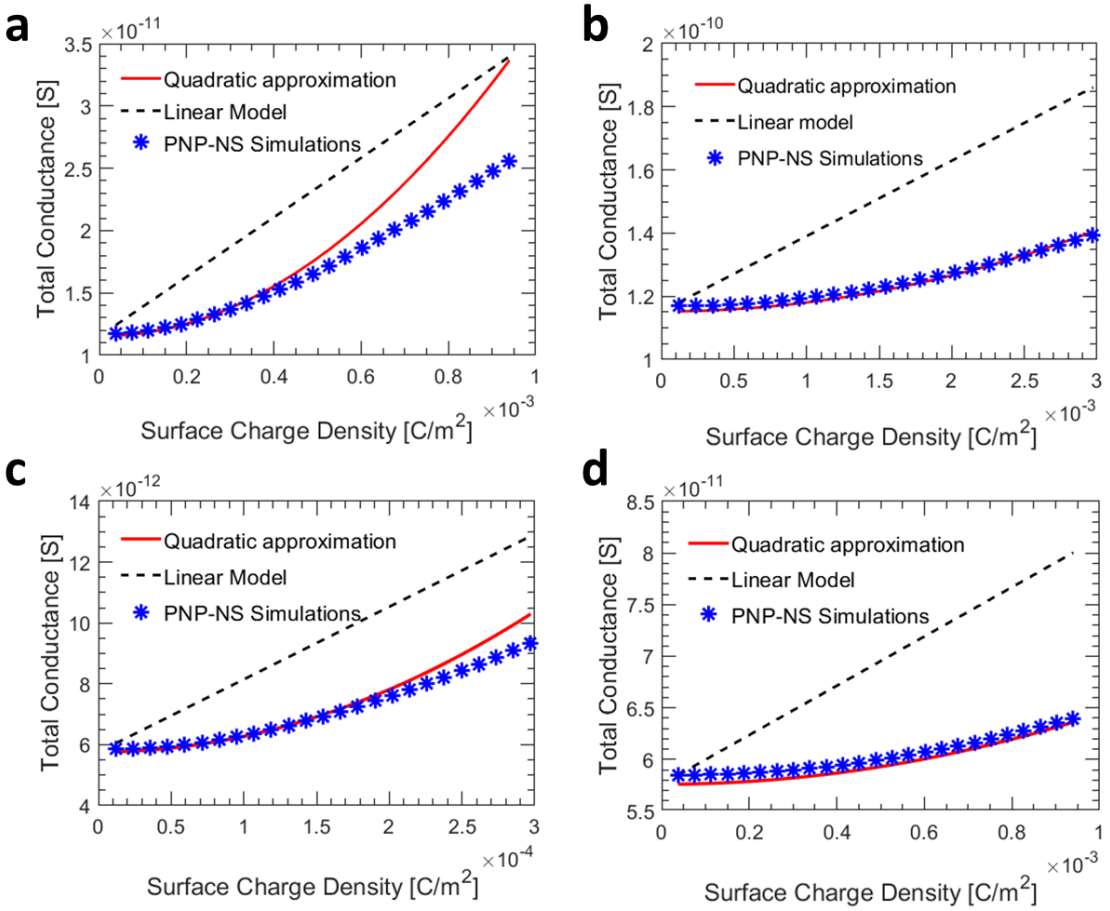

Figure 1. Total conductance is plotted against surface charge density for cylindrical nanochannels of diameters, (a-b) 10 nm and (c-d) 50 nm, and lengths, (a-b) 100 nm and (c-d) 500 nm. Bulk electrolyte concentration is (a) 1 mM, (b) 10 mM, (c) 0.1 mM and (d) 1 mM respectively. The quadratic approximation is a better tool for estimating surface charge density than the linear model.

Ultrasensitive, AI-integrated cyber-physical system for patient-specific CYFRA21-1 biomarker quantification

Biswadeep Roy[1,2], Abhisek Maikap[1], Soumen Das[2], Suman Chakraborty[1]

[1]*Department of Mechanical Engineering, Indian Institute of Technology Kharagpur, Kharagpur 721302, India*
[2] *School of Medical Science and Technology, Indian Institute of Technology Kharagpur, Kharagpur 721302, India*
Corresponding author Email: biswadeeproy84@gmail.com

Early detection of non-small cell lung cancer (NSCLC) is critical for improving survival rates but remains challenging due to the sub-nanomolar concentrations of tumor-specific biomarkers in early disease stages and the limitations of conventional diagnostics. Standard techniques such as liquid chromatography-mass spectrometry (LC-MS) and enzyme-linked immunosorbent assay (ELISA) provide high specificity but rely on centralized laboratories, specialized personnel, and extended processing times, limiting their practicality in decentralized, point-of-care (POC) settings. To address this gap, we present a compact, cyber-physical diagnostic platform for rapid, quantitative, and ultrasensitive detection of Cytokeratin-19 fragment (CYFRA21-1), a clinically validated NSCLC biomarker, particularly relevant for squamous cell carcinoma. Elevated CYFRA21-1 levels reflect tumor burden, disease progression, and therapeutic response, making it a promising target for early cancer screening. The platform integrates three key components: (i) a nanotechnology-enhanced biosensor based on surface-functionalized Green-Carbon Dots (G-CDs) (**Figure 1(a)**), (ii) a portable, smartphone-based fluorescence microscope, and (iii) an artificial intelligence (AI) engine driven by a convolutional neural network (CNN) that incorporates patient-specific data. The carbon dots, modified with amine and carboxyl groups for antibody (Ab) conjugation, exhibit absorption at 360 nm and 440 nm as observed in the UV-Vis spectroscopy (**Figure 1(b)**) and dual-emission fluorescence at 450 nm and 550 nm as observed in the photoluminescence (PL) response (**Figure 1(c)**), enabling ratiometric quantification and minimizing background interference. Embedded within a lateral flow microfluidic strip, these probes enable plasma separation and immunoassay reactions in a single, disposable chip, eliminating the need for external sample preparation. The PL response of the G-CD-conjugated antibody-antigen complex is measured across varying antigen concentrations to investigate its fluorescence characteristics and integrate these findings into our portable microscopy system (**Figure 1(d)**). Successful conjugation of CYFRA21-1 Ab with G-CD is validated by Fourier-transform infrared (FTIR) spectroscopy, which reveals a characteristic peak near 2940 cm^{-1} corresponding to N–H stretching vibrations (**Figure 1(e)**). Fluorescence signals are captured using a miniaturized optical module with a 450 nm light source, band-pass filters, and a CMOS sensor integrated with a smartphone. This portable microscopy system achieves high spatial resolution (**Figure 2A**) while maintaining low power consumption. A mobile application supports automated image acquisition, background correction, and signal normalization, ensuring consistent performance in diverse environments (**Figure 2B**). A distinguishing feature of the system is its AI-driven analytics layer, which uses a CNN trained on multimodal datasets combining fluorescence intensity profiles with clinical metadata such as patient age, sex, smoking history, and geographical data. This integration enables dynamic calibration of diagnostic thresholds, improving sensitivity and specificity by accounting for patient-specific variability. The model adapts classification criteria based on longitudinal patterns, reducing false positives in benign conditions and false negatives in early or asymptomatic cases. Validation studies with human plasma samples spiked with CYFRA21-1 demonstrate a detection limit as low as 0.1 ng/mL, significantly surpassing standard ELISA sensitivity thresholds, which typically detect levels above 1.0 ng/mL. The complete diagnostic workflow, from sample application to result generation, is achieved within 10 minutes- a substantial improvement over traditional methods. The platform's low-cost, disposable chips and smartphone-compatible interface ensure scalability and affordability for large-scale deployment. Designed for decentralized healthcare environments, it aligns with global health priorities to democratize cancer diagnostics and reduce diagnostic delays in underserved populations. Future versions will enable multiplexed detection of additional NSCLC biomarkers and incorporate cloud-based telemedicine features for remote consultation and real-time data integration, supporting personalized clinical decision-making.

[1] B. Roy, A. Maikap, S. Das, S. Chakraborty, Simultaneous detection of trace protein biomarkers from a single drop of blood using AI-enhanced smartphone-based digital microscopy, Biosens. Bioelectron. 276 (2025) 117259. https://doi.org/10.1016/j.bios.2025.117259.

[2] A. Maikap, B. Roy, N. De, S. Samanta, S. Chakraborty, Paper strips functionalized with a mixture of ZnO nanotubes and Mn_3O_4 nanoparticles for simultaneous separation of blood plasma and detection of physiological iron level, ACS Appl. Nano Mater. (2024). https://doi.org/10.1021/acsanm.4c00844.

[3] T. Li, Q. Xie, Y.Y. Fang, Prognostic value of CYFRA 21-1 and Ki67 in advanced NSCLC patients with wild-type EGFR, BMC Cancer 23 (2023) 295. https://doi.org/10.1186/s12885-023-10767-9.

[4] X. Sun, F. Fang, J. Na, R. Yan, Y. Huang, Z. Zhou, Y. Zhao, G. Li, Fluorescent "turn-on" aptamer sensor for sensitive and reliable detection of Golgi glycoprotein 73 based on nitrogen-doped graphene quantum dots and molybdenum disulfide nanosheets, J. Pharm. Biomed. Anal. 225 (2023) 115215. https://doi.org/10.1016/j.jpba.2022.115215.

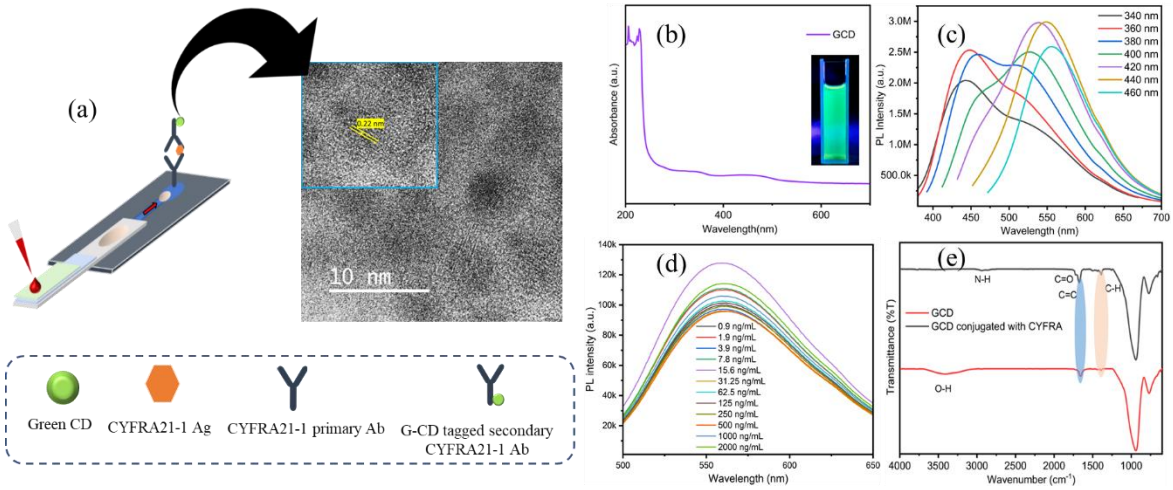

Figure 1: Morphological and spectroscopic characterizations of G-CD. (a) The detection strip facilitating in-situ blood plasma separation and sensing (on the left). The TEM images of G-CD. The average particle size is 4.5± 0.8 nm (on the right). Inset: the HRTEM images of G-CD show a single type of lattice fringe with an interplanar distance of 0.22 nm. (b) UV-Visible spectroscopic response of of G-CD. Inset: digital image of G-CD under excitation. (c) PL response characteristics of G-CD under various excitation wavelengths. (d) PL response characteristics of G-CD with variable antigen concentrations. (e) FTIR spectra of G-CD and G-CD tagged CYFRA21-1 conjugates.

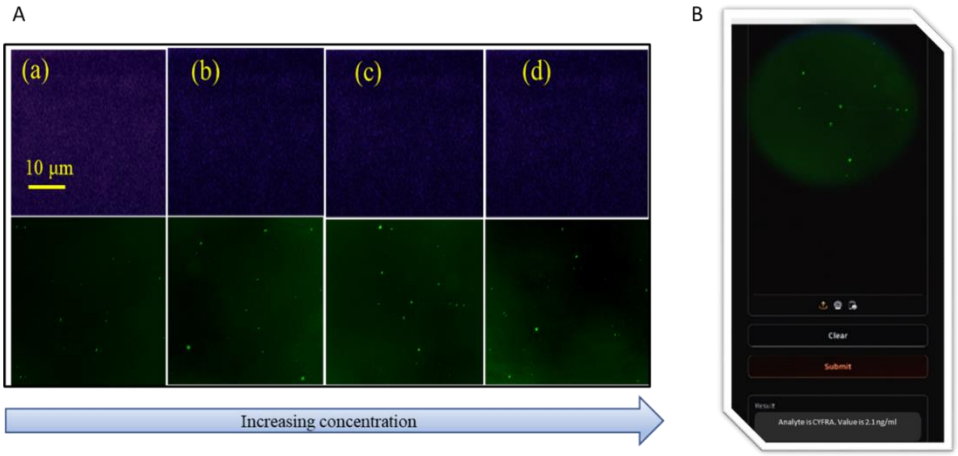

Figure 2: A. Fluorescent images of tagged antigen-antibody complexes. Each column displays two images: blank sample (top) and G-CD tagged CYFRA21-1 sample (bottom). Scale bar: 10 µm. Fluorescent images at (a) 0.9 ng/mL, (b) 15.6 ng/mL, (c) 31.2 ng/mL, and (d) 62.5 ng/mL concentration. B. The Android App interface integrated with AI model for real-time processing, quantification and decision-making.

Broadband Transmission Measurement for Ta_2O_5 Photonic Crystal Waveguide

W. Wang [a], M. Shayesteh [a], G. Churchill [b], M. D. B. Charlton [a]

[a] School of Electronics and Computer Science, University of Southampton, Southampton, SO17 1BJ, UK
[b] Optoelectronics Research Centre, University of Southampton, Southampton SO17 1BJ, UK.
e-mail: ww2m19@soton.ac.uk

Introduction

Low-loss waveguides are essential components in silicon photonics. Photonic crystals (PhCs) enable control of light via photonic band gaps (PBGs) [1], and their integration into photonic crystal waveguides (PhCWs) introduces slow light effects, enhancing light–matter interaction and nonlinear processes [2]. However, characterizing slow light in the time domain remains challenging. Here, we demonstrate broadband transmission measurements of Ta_2O_5 PhCWs, providing an efficient method to identify the PBG and support future slow light studies.

Fabrication and experiment

A 2 µm thick SiO_2 layer was thermally grown on a Si wafer via wet oxidation. A 450 nm Ta_2O_5 film was subsequently deposited by reactive sputtering (Helios ProXL, Leybold Optics). PhC patterns within the Ta_2O_5 PhCWs were defined using electron beam lithography (EBL), followed by ICP etching (ICP-RIE 180, Oxford Instruments) [3]. Figure 1 shows SEM images of the fabricated Ta_2O_5 PhCW. Tapered wire waveguides are used for efficient coupling light into and out of the PhCW. Figure 1(i) displays the tapered waveguide, while (ii) shows the junction between the taper and the PhCW. The whole structure is coated with ~500 nm of SiO_2, partially filling the PhCs and leaving visible voids that indicate its position. Figure 1(iii) presents a cross-sectional view of the PhCW, showing incomplete infiltration of SiO_2 into the PhCs. Figure 2 shows the experimental setup for broadband transmission measurements of the Ta_2O_5 PhCW. A tunable laser system (RegA 9000 + Vitesse + OPA 9400, Coherent; 480–700 nm and 933–2300 nm) and a supercontinuum white laser source (SuperK EVO, NKT Photonics; 415–2250 nm) were used. A top-view camera (uEye UI124xSE-C, IDS) ensured proper light coupling, while a side-view camera (uEye UI124XSE-NIR, IDS) monitored the mode profile. Example images from both views are attached. Transmission spectra were collected with a spectrometer (iHR320, HORIBA; 200–1700 nm).

Results and discussion

Figure 3(i) shows the simulated transmission of a Ta_2O_5 PhCW (pitch: 330 nm, hole diameter: 230 nm, length: 0.4 mm), indicating a TE-mode PBG from 500-720 nm and a TM-mode PBG from 700-850 nm. Measured propagation losses for the green (565 nm) and yellow (585 nm) wavelengths are 4.1 dB/cm and 7.7 dB/cm, respectively. Figure 3(ii) presents the stitched transmission spectra measured under TM polarization using the tunable laser centered at green, yellow, orange, and red. By stitching PhCW transmission measurements across multiple wavelength ranges and referencing the laser source spectrum, the normalized broadband transmission can be obtained. Alternatively, a supercontinuum white-light source provides a complementary method for broadband transmission measurement. In this approach, a single measurement yields transmission data across a wide spectral range, eliminating the need for wavelength stitching.

Conclusion

The fabricated Ta_2O_5 PhCWs were characterized using a broadband optical transmission setup. Preliminary measurements demonstrate transmission through a 0.4 mm-long Ta_2O_5 PhCW, featuring a photonic crystal lattice with a pitch of 330 nm and hole diameter of 230 nm, using laser sources centered at green, yellow, orange and red wavelengths.

[1] J. D. Joannopoulos, S. G. Johnson, J. N. Winn, and R. D. Meade, *Photonic Crystals: Molding the Flow of Light, Second Edition*. 2008.

[2] M. A. Butt, S. N. Khonina, and N. L. Kazanskiy, 'Recent advances in photonic crystal optical devices: A review', *Opt Laser Technol*, vol. 142, p. 107265, Oct. 2021, doi: 10.1016/J.OPTLASTEC.2021.107265.

[3] W. Wang, L. Arzubiaga, M. Shayesteh, S. Fenner, O. Clark, and M. D. B. Charlton, 'Anisotropic Ta2O5 photonic crystal waveguide etching using inductively coupled plasma etching', *Journal of Vacuum Science & Technology A*, vol. 43, no. 2, p. 23405, Mar. 2025, doi: 10.1116/6.0004211.

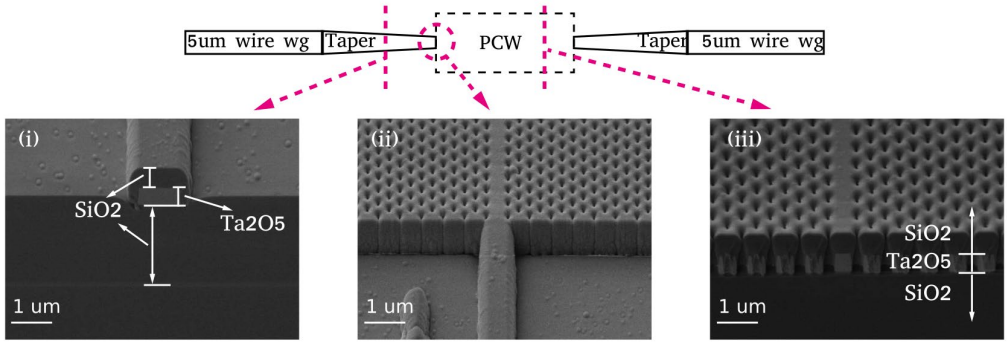

Figure 1. Ta_2O_5 PCW SEM images (i) tapered wire waveguide (ii) junction of wire waveguide and the PhCW (iii) cross-section of the PhCW

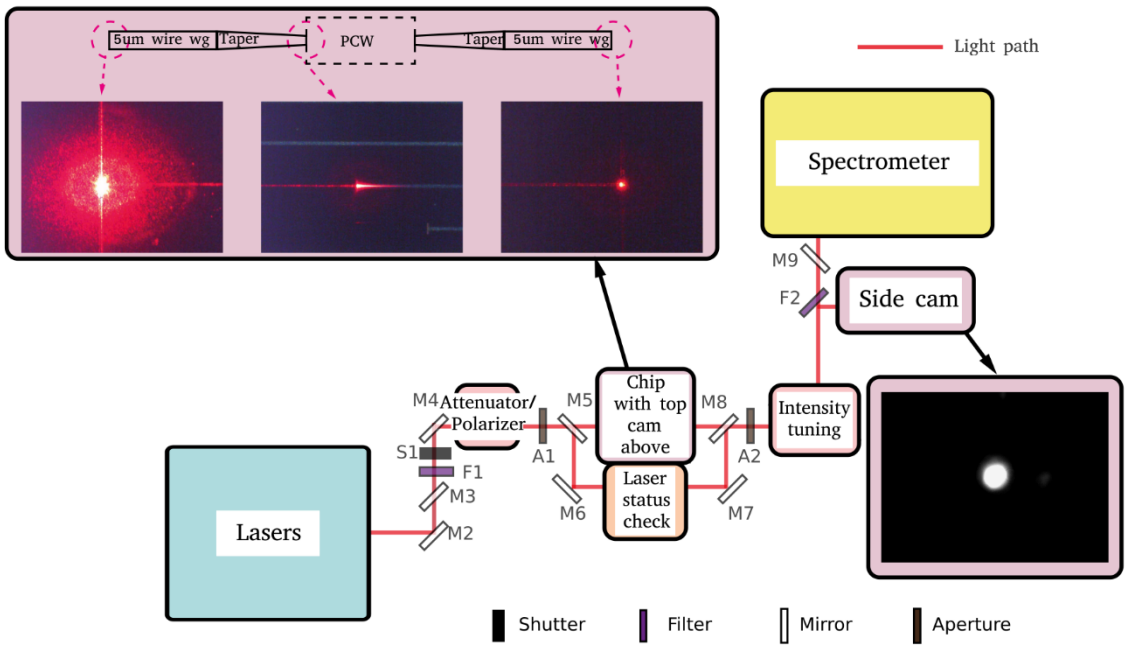

Figure 2. Experimental setup for broadband transmission measurements of the Ta_2O_5 PhCW

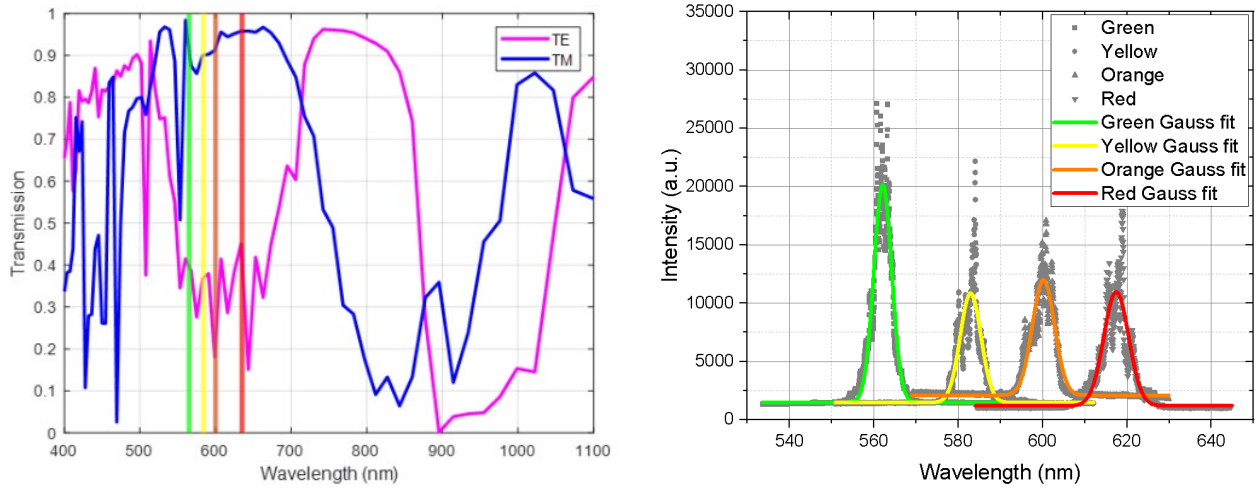

(i) (ii)

Figure 3. (i) Transmission simulation for Ta_2O_5 PhCW (ii) Transmission stitching for a Ta_2O_5 PhCW operating in TM polarization, with excitation lasers centered at wavelengths of 565 nm (Green), 585 nm (Yellow), 600 nm (Orange), and 618 nm (Red). The PhCW features a pitch of 330 nm, hole diameter of 230 nm, and a length of 0.4 mm.

Fabrication of planar nanostructured SiC microelectrode arrays for long-lifetime neural interfaces

F. Iacovella [a], G. Pound-Lana [a], L. Labbe [a], S. Labau [a], C. Petit-Etienne [a], A. Uvarov [b], S. Greenhorn [c], M. Zielinski [d], K. Zekentes [c,e], E. Bano [c], C. Gourgon [a] and J. Boussey [a]

[a] LTM, CNRS, CEA/LETI- Minatec, Grenoble INP-Univ. Grenoble Alpes, Grenoble, 38054, France
[b] Plasma-therm Europe, Bernin, 38190, France
[c] Centre de Radiofréquences, Optique et Micro-nanoélectronique des Alpes, Grenoble, 38016, France
[d] NOVASiC, Le Bourget du Lac, 73375, France
[e] Foundation for Research and Technology – Hellas, Heraklion, 70013, Greece
e-mail: fabrice.iacovella@cea.fr

Brain Computer Interfaces (BCI) offer interesting perspectives for the motricity or speech rehabilitation of people suffering from severe impairment of the central nervous system. BCI's reliability is to a large extent relying on the recording of the excitation potentials of the brain [1]. Various implantable neural interfaces based on conductive materials and polymers have been fabricated so far. Nevertheless, body inflammatory and rejection reactions as well as the degradation of the polymer insulating layers strongly limit their lifetime [2]. In this context, SiC has appeared as a promising alternative for the fabrication of neural interfaces due to its chemical inertness and biocompatibility [3]. Moreover, the possibility of tuning the surface Young modulus by surface functionalization could reduce the elasticity mismatch with the brain tissues and thus mitigate the body rejection response [2,4]. Finally, full SiC based neural interfaces can be envisaged relying on both conductive and insulating SiC layers which can be obtained combining different growth methods such as epitaxy and Plasma Enhanced Chemical Vapor Deposition (PECVD).

In this work we fabricated a series of Micro-Electrode Arrays (MEA) fully based on SiC. For the active sensing area, we used a stack of semi-insulating and n-doped 4H-SiC layers epaxially grown by NOVASiC at the surface of a n-doped 4H-SiC bulk substrate (Fig 1A). While standard npn vertical junction structures have been proven for the fabrication of MEA, we use a Vanadium doped semi-insulating layer (carrier concentration ~ 10^{16} cm^{-3}) to ensure the reduction of the cross-talk between adjacent electrodes. The different fabrication steps are summarized in Fig 1B. The MEA are shaped using a Cr hard mask patterned by optical lithography. The hard mask patterns are transferred to the conductive SiC epilayer using a dry etching process in an Inductively Coupled Plasma system (Fig 1C). Dry etching is an efficient technique that allows the shaping of SiC epilayers of different thicknesses ranging from a few hundred nm up to more than 10µm. A thin layer of insulating amorphous SiC (a-SiC) is deposited over all the wafer surface area by PECVD to protect the electrode tracks. Openings through a-SiC at the electrodes and pads areas are performed by dry etching (Fig 1D). The intensity of the recorded signal is proportional to the electrode surface area. We propose to increase the effective surface area of the 90µm-diameter electrodes by nanostructuring them. To this end, an array of nanopillars of 100nm-diameter is patterned using e-beam lithography and Hydrogen Silses-Quioxane (HSQ) based resist. The nanostructuration of the 90µm-diameter electrodes requires an adequate adjustment of the exposure dose in order to ensure a homogeneous coverage with the HSQ nanopillars (Fig 2A). The HSQ mask is first transferred to a Cr hard mask before being transferred to the SiC epilayer (Figs 2B and C). We will present our first fabrications runs where 500nm-height SiC nanopillars arrays have been fabricated over the full electrode surface area. Given the nanopillar dimensions and lattice structure, an almost 5-time increase of the recorded electrochemical signal intensity is expected in comparison with a non-nanostructured microelectrode.

This study has received funding from the French National Research Agency under the project SiCNeural (ANR Grant number ID ANR-21-CE19-0054-01) and by the French National Research Agency in the framework of the "Investissement d'avenir" program (ANR-15-IDEX-02). The authors would like to thank the French national nanofabrication network (RENATECH) and the Upstream Technological Platform (PTA) for their assistance and technical support.

[1] W.A. Awuah et al., World Neurosurg. 189 (2024) 138-153
[2] K. Liu et al., Mater. Adv. 5 (2024) 4958-4973
[3] S.E. Saddow, Micromachines 13 (2022) 346
[4] M. Rosso et al., Langmuir 24 (2008) 4007-4012

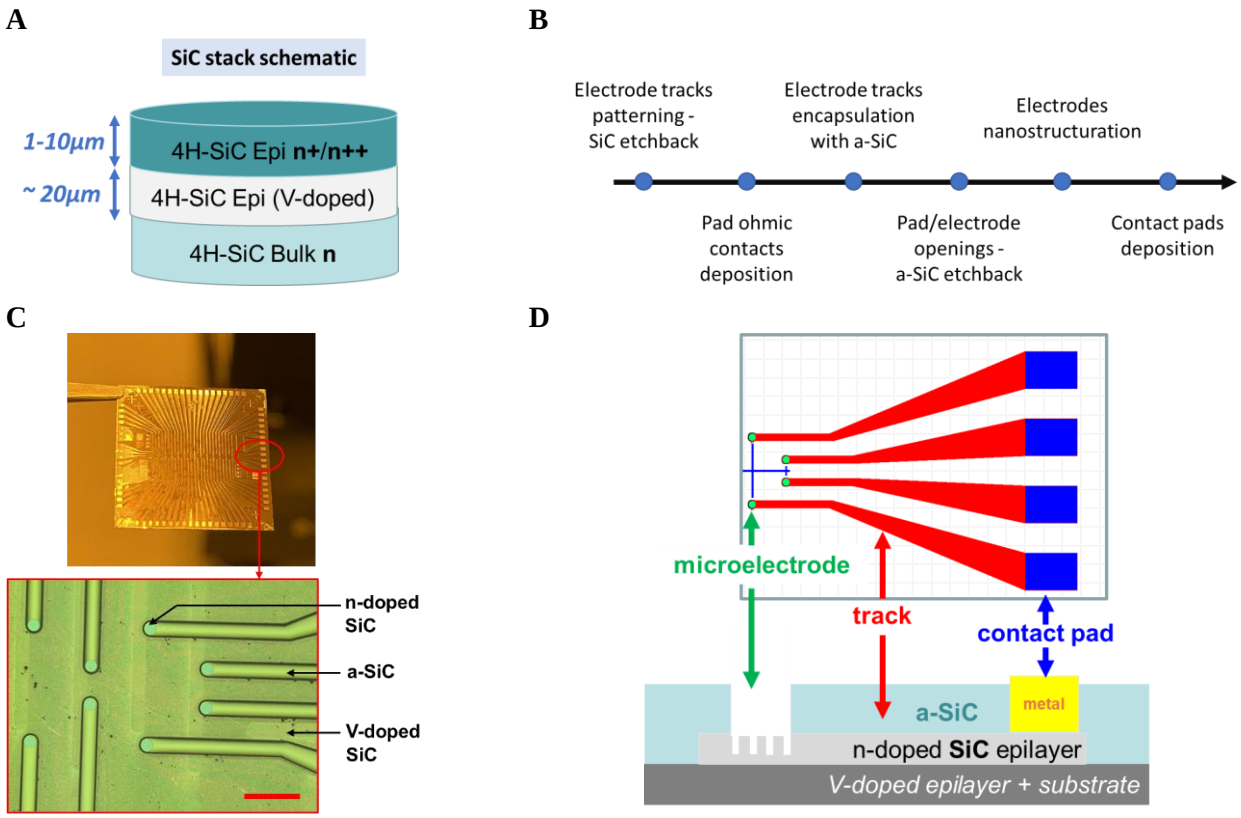

Figure 1. A) Schematic of the SiC stack used for the fabrication of the MEA. B) Fabrication process flow of the SiC based MEA. C) Picture of a fabricated MEA device and zoom-in on the microelectrode area. Scale bar: 400µm. D) Schematic transversal cut of a MEA device.

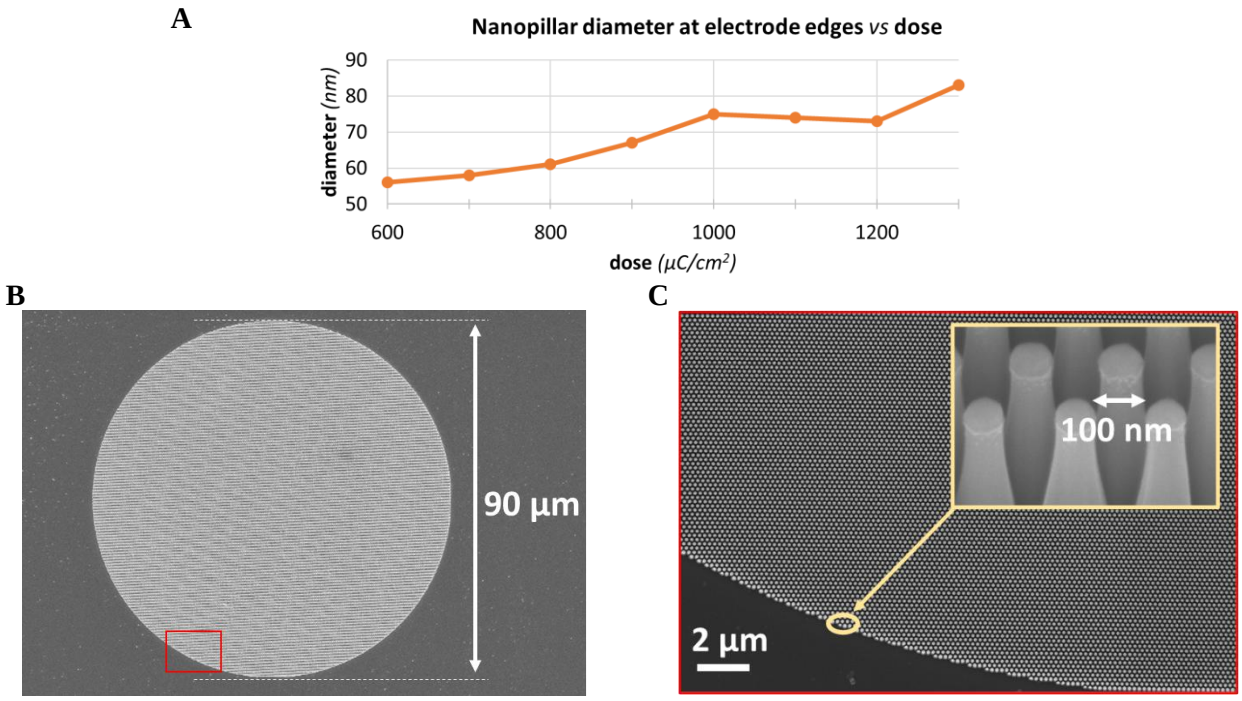

Figure 2. A) Evolution of the HSQ nanopillar diameter as a function of the exposure dose. The measurement is performed using SEM at the edges of the patterned area. B) SEM picture of SiC nanopillars covering a surface area similar to the 90µm-diameter electrodes of the MEA. C) Zoom-in on the area indicated by the red square in B. Insert: SEM picture taken with tilt angle of the SiC nanopillars.

Sub-wavelength grating polarizers in 1-D array focal plane for ultraviolet polarimetric detection

Jinyu Guo [a,b], Kangping Liu [a,b], Qingxin Wu [a,b], Qiucheng Chen [a,b], Hao Quan [a,b], Xunjia Zhao[a, b] and Yifang Chen [a,b,*]

[a] Nanolithography and Application Research Group, School of Information Science and Technology, Fudan University, Shanghai, 200433, China

[b] Shanghai Key Laboratory of Metasurfaces for Light Manipulation, Fudan University, Shanghai, 200433, China

e-mail: yifangchen@fudan.edu.cn

Keywords: ultraviolet polarization, electron beam lithography, lift-off, line array focal plane imaging

Abstract

Polarizers are indispensable optics in optical systems and networks. Ultraviolet (UV) polarizers rely on their unique ability to modulate polarization, and are especially irreplaceable in the fields of spectral analysis, industrial inspection and biomedicine. Unfortunately, conventional polarizers are bulky, expensive, and operate with very small acceptance angles. Thin-film polymer polarizers have major reliability problems at UV wavelengths. Sub-wavelength wire-grid polarizers in ultraviolet wavelength band provide great advantages in terms of thinness, low cost, large working reception angle, high durability against both ultraviolet radiation and temperature.

This work presents a process for sub-wavelength gratings of aluminum (Al) in three directions on fused silica by electron beam lithography (EBL) and lift-off process. For achieving both high transmittance and high extinction ratio, the period and height of the grating are optimized by Finite-Difference Time-Domain (FDTD) simulation. Al grating with a duty cycle of 50% at 150 nm period and a height of ~100 nm was finally realized. Spectrometer test characterizes that its transmittance in the 385 nm is greater than 55%, and the extinction ratio is greater than 10:1.

Fig. 1 illustrates the process of fabricating Al wire-grid gratings on fused silica. It should be noted that after the resist coating is completed, a 10 nm Al needs to be evaporated on the top to eliminate the charge accumulation effect during the electron beam exposure on the less conductive substrate, in order to ensure high-precision exposure. After exposure, the 10 nm Al needs to be removed using an alkaline solution before proceeding to the development process. Fig. 2shows the systematic simulation results of transmittance and extinction ratio of the Al wire-grid gratings at a UV wavelength of 385 nm, as function of pitch from 50 to 200 nm and height from 10 to 200 nm. Based on our previous experience, a fixed duty cycle (i.e., width of the wire divided by the pitch) of 50% for the Al nanowire grid were used. At a height of 100 nm, good transmittance (>70%) is obtained over the simulated pitch range. For shorter pitch and higher metal thicknesses, better extinction ratio can be obtained (as indicated by the arrow in Fig. 2b). More specifically, the transmittance and and extinction ratio of 300 nm-900 nm of the rectangular configuration at a fixed metal height of 100 nm and a period of 150 nm are shown in Fig. 3. It can be seen that a transmittance of 76% and an extinction ratio of 143 can be obtained in the 385 nm band. From this result, this Al wire grid gratings can also be used as a polarizer in the visible and near-infrared bands, and the performance will become better. SEM photos and optical characterization results of the fabricated Al gratings are elucidated in Fig. 4, where it can be seen that obtained Al gratings with 50% duty cycle, a period of 150 nm and a height of ~100 nm by adjusting the dose and designed linewidths in different directions. The expected performance was achieved at 350-700 nm. The average transmittance around 385 nm was 55% with an extinction ratio of more than 10. At 678 nm, a transmittance of 79% and an extinction ratio of 58 were measured. The difference between the characterization and simulation results comes from the non-rectangular configuration of the Al grating cross section, which greatly affects the extinction ratio.

In summary, dense sub-wavelength Al grating polarizers are fabricated and applied to 1-D array focal plane for UV polarization detection by electron beam lithography. The process preserves the original optical properties of the metal, allowing for high edge quality metal gratings and further application to smaller period grating realizations to enhance the polarized performance.

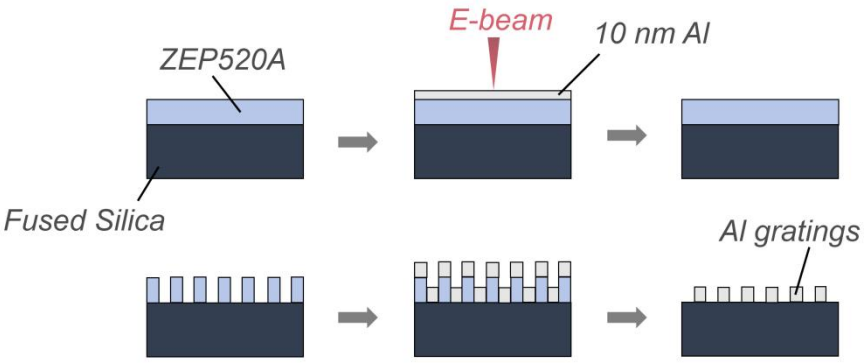

Fig.1 Process flow diagram for sub-wavelength Al grating polarizers

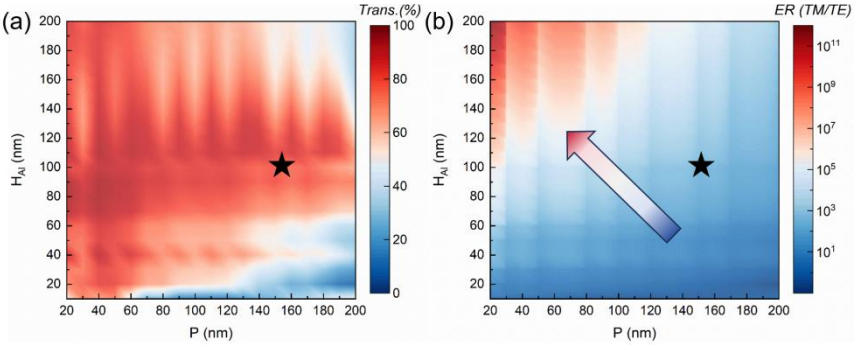

Fig.2 The systematic simulations of Al wire-grid polarization properties as the function of height and period at the wavelength of 385 nm.

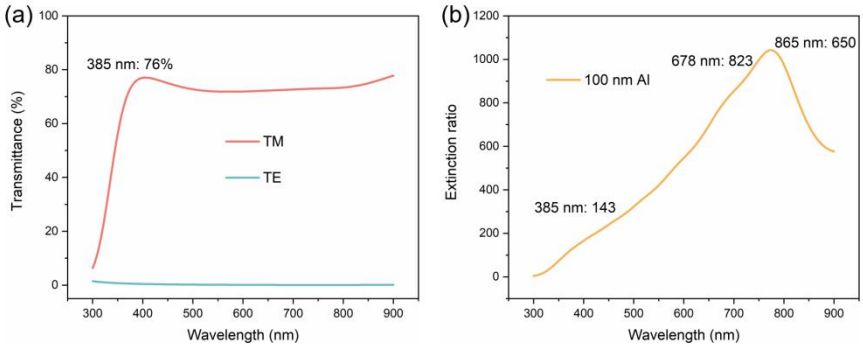

Fig.3 Simulated transmittance and extinction ratio of Al gratings with a fixed structure of 150 nm period and 100 nm height.

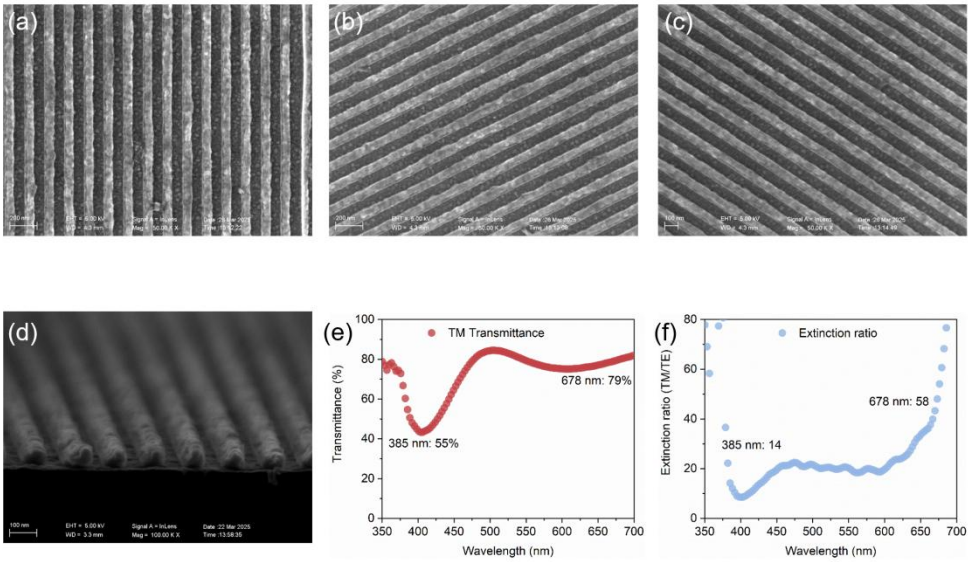

Fig.4 SEM photos and optical characterization results of fabricated Al gratings by lift-off process.

Design and Fabrication of a 100mm-Diameter Pillar Metalens for High-Performance Mid-Infrared Imaging

Weilin Jin, Gaochen Dong, Zixuan Wang, Kian Shen Kiang, Jize Yan*

School of Electronics and Computer Science, University of Southampton, Southampton, SO17 1BJ, UK
e-mail: *j.yan@southampton.ac.uk

As a new class of flat optical devices with submillimeter thickness [1], metalenses enable control of light's amplitude, phase, and polarization via subwavelength nanostructures. In astronomy and environmental monitoring, larger lens diameters usually increase volume and weight [2]. Metalenses, with ultracompact form factors, provide lightweight, space-saving alternatives to bulky optics. Yet, most high-performance metalenses remain millimeter-scale, restricted by data storage and fabrication limits in defining billions of nanostructures [3]. Park et al. demonstrated a 100 mm visible metalens using stitched DUV lithography, but nonuniform fidelity across stitched fields persists [1]. Therefore, reducing data volume while ensuring uniform pattern quality across large apertures is essential for efficient layout handling and improved nanostructure definition.

For our 100mm-diameter metalens, the design includes 4.9×10^8 silicon nanopillars. Conventional methods for generating this size layout require exceeding 10 hours and consume approximately 100 GB of such number of pillars [3]. Processing such large files at high resolution presents significant challenges for electron-beam lithography (EBL). To address this issue, we implemented a parallel strategy to reduce both the running time and file size. This approach involves dividing the layout into multiple sub-layouts of equal area and assigning them to different computing nodes for parallel generation separately and aggregation. Using this method, we generated the layout within 5 minutes and reduced full file size from 30GB to 293MB in OASIS format. This strategy not only accelerates pattern generation but also reduces data handling overhead during the EBL writing process.

We fabricated mid-infrared metalens with a 100 mm diameter and a thickness of 0.725 mm, achieving 12cm focal length at a wavelength of 10 μm through CMOS-compatible processes. The fabrication workflow (Fig.1) involved uniform hard mask deposition, precision electron-beam lithography with calibrated exposure dose and beam current for pattern uniformity across the full wafer, 80 °C-controlled lift-off, and deep reactive ion etching (DRIE). The DRIE process was iteratively optimized by tuning temperature, etching duration, and RF power, yielding vertical sidewalls with angles exceeding 89°. Structural fidelity was monitored using optical microscopy, ellipsometry, and SEM. As shown in Fig. 2a and 2b, the metalens consists of a uniform array of silicon nanopillars arranged in a 4 μm-period. Due to varying gap sizes between pillars, the etch depths range from 5 to 6 μm. This geometry enables full 0–2π phase modulation (Fig. 2d).

The imaging experimental setup and results are shown in Figure 3. The metalens was integrated as the first element of a standard 4f imaging system, where two lenses are placed at a distance equal to the sum of their focal lengths (Figure 3a). Due to sensor size limitations, the metalens need to collect and collimate infrared light from distant objects, then refocus it onto the thermal imager sensor at the image plane via a 10μm filter and a secondary lens. Using this system, we captured mid-infrared images of patterned metal board placed in front of 100°C hot water. This is the first demonstration of a 100mm-scale metalens operating at a 10μm wavelength, marking a significant step toward scalable, wafer-scale metasurface optics for infrared imaging and sensing applications.

We acknowledge support from the Henry Royce Institute (Research Equipment Access Scheme) for DRIE access at the Leeds Nanotechnology Cleanroom; EPSRC Grant Number EP/P022464/1

[1] She, Alan, et al. "Large area metalenses: design, characterization, and mass manufacturing." Optics Express 26.2 (2018): 1573-1585.
[2] Park, Joon-Suh, et al. "All-glass 100 mm Diameter Visible Metalens for Imaging the Cosmos." ACS Nano 18.4 (2024): 3187-3198.
[3] Sun, Chuang, Ou, Jun-Yu, Kiang, Kian Shen and Yan, Jize (2024) RAM-adaptive parallel generating and minimizing the layout file of wafer-scale metalens. 50th International Micro and Nano Engineering Conference, Montpellier, France, Montpellier, France. 16 - 19 Sep 2024.

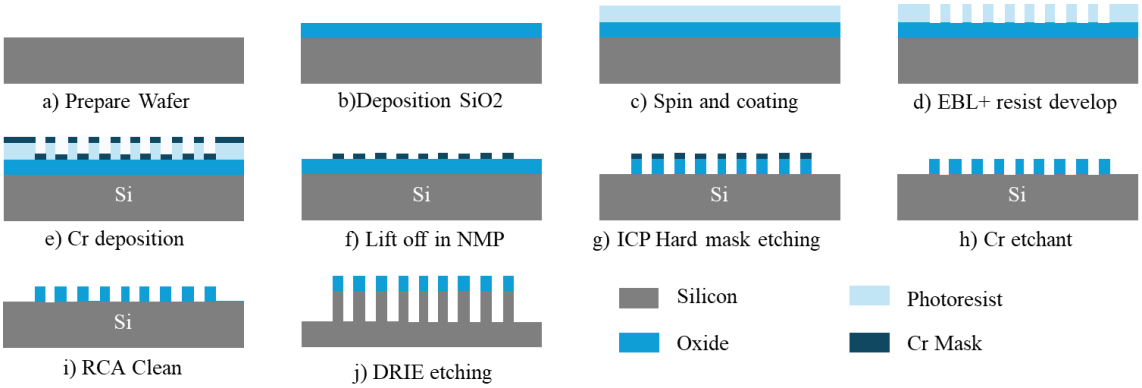

Figure 1. Fabrication process flow for the patterned silicon structure: (a) wafer preparation, (b) SiO2 deposition, (c) resist spin-coating, (d) EBL and development, (e) Cr deposition, (f) lift-off in NMP, (g) ICP oxide hard mask etching, (h) Cr removal, (i) RCA clean, and (j) DRIE of silicon. Legend: silicon (grey), oxide (blue), photoresist (light blue), Cr mask (dark blue).

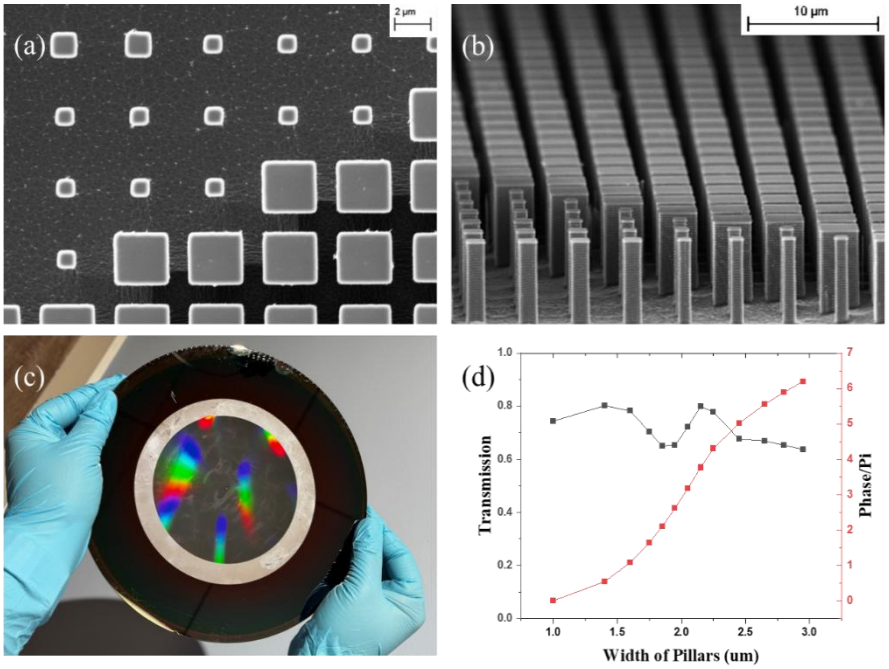

Figure 2. (a) Top-view SEM of the metalens. (b) Tilted-view SEM of DRIE-etched silicon showing vertical sidewalls. (c) Real picture of a large metalens. (d) Normalized transmission (black) and phase (red) versus width of pillars.

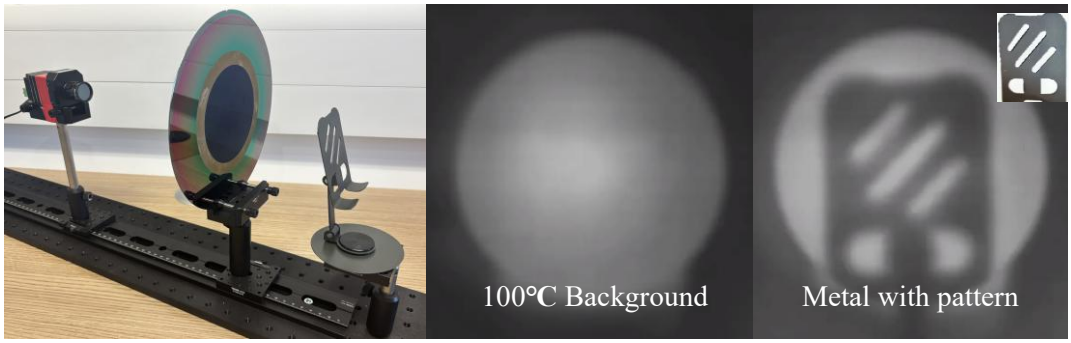

Figure 3. Experimental demonstration of mid-infrared imaging using a large-area metalens. (Left) Measurement setup showing the metalens mounted on an optical rail with a mid-infrared camera, imaging for patterned metal board. (Middle) Reference thermal image of the background at 100 °C. (Right) Thermal image of the patterned metal board, showing clear contrast and edge definition enabled by the metalens.

Quantum Dot-Low Dimensional Material Hybrid Heterostructures for Physically Unclonable Optical Tags

Yueyu Guo [a], Syeda Ramsha Ali [a], Nema Abdelazim [a],

[a] School of Electronics and Computer Science, University of Southampton, Southampton, SO17 1BJ, United Kingdom

e-mail: yg5g20@soton.ac.uk

Abstract

Ensuring product authenticity has become increasingly critical due to rising threats from counterfeit products. Authentication tags are essential tools for verifying product genuineness, but traditional solutions often lack robustness, uniqueness, or convenience for quick verification. Physical unclonable functions are security primitives that exploit the inherent physical randomness. They can provide unique and unclonable responses ideal for secure product authentication. Recently, low-dimensional nanomaterials such as colloidal quantum dots (QDs) have merged as promising candidates for creating optical PUF tags, due to their size-tunable optical properties, distinct excitation-dependent emission characteristics, and highly unique photoluminescent fingerprints[1]. However, authenticating these tags using smartphones remains challenging, as mobile flashlights typically produce broadband excitation, complicating the verification process.

This project presents a novel QDs-based authentication tag (QD-ID tag) integrated with low-dimensional heterostructures, enabling portable and fast authentication through smartphone flashlights. $CuInS_2$ QDs are chosen for their distinct PL response and non-toxicity. They are coupled with monolayer molybdenum disulfide (MoS_2), a two-dimensional (2D) material chosen for its robust second-harmonic generation (SHG) and efficient charge transfer[2]. The integration of MoS_2 effectively enhances authentication accuracy by filtering broad spectral illumination from smartphone flashlights and transmitting the optimal excitation wavelength to the QDs. Additionally, interfacial coupling between the 0D and the 2D material promotes charges and energy transfer, producing unique, reproducible, and unclonable optical responses.

The proposed hybrid structure includes a protective polymethylmethacrylate (PMMA) layer for mechanical robustness and environmental stability. Characterization and verification processes involve Raman microscopy to confirm the integrity and optical quality of MoS_2 and photoluminescence (PL) spectroscopy to acquire the distinctive emission patterns of both quantum dots and the heterostructure. Data processing procedures extract critical parameters including emission peak wavelength, intensity and full width at half maximum (FWHM) from the acquired PL spectra. These parameters are digitized into unique patterns or matrices and stored within a reference database. During verification, users employ smartphones to excite tags, capturing PL responses which are digitally compared against database references to confirm product authenticity instantly.

This quantum dot and low dimensional approach offers a robust, secure and portable authentication solution fully compatible with smartphone technologies, significantly enhancing product verification reliability and user-friendly applications.

References:

[1] M. J. Fong *et al.*, *Sci. Rep.*, 12 (2022) 16919.
[2] A. J. Goodman, N. S. Dahod, and W. A. Tisdale, *J. Phys. Chem. Lett.*, 9 (2018) 4227–4232.

Modelling the Heat Distribution in Organ-on-a-Chip Systems Using Integrated Microheaters

Gabriel M. Ferreira [a, b], Patrícia C. Sousa [b], R. A. Lima [c, d], Susana O. Catarino [a,e], Graça Minas [a, e]

[a]Microelectromechanical Systems Research unit (CMEMS-UMinho), School of Engineering, Campus de Azurém, University of Minho, 4800–058 Guimarães, Portugal
[b]INL - International Iberian Nanotechnology Laboratory, Braga, 4715-330, Portugal
[c]METRICS, University of Minho, Guimarães, Portugal
[d]CEFT, Faculty of Engineering of the University of Porto, Porto, Portugal
[e]LABBELS—Associate Laboratory, 4800–122 Braga, Portugal
e-mail: id10786@alunos.uminho.pt

Microfluidic systems with integrated heating transducers are of growing interest for applications in biochemical sensing, lab-on-a-chip and organ-on-a-chip (OoC) technologies [1]. Particularly, in OoC systems, temperature monitoring is crucial to maintain the cultured cells in a well-defined microenvironment for proper growth [2]. This monitoring can be achieved through temperature control systems combining microheaters and microsensors. Numerical simulation of these systems, based on multiphysics simulation tools, allow for an adequate prediction of the temperature distributions within the microfluidic module.

In this study, we investigated the thermal performance and flow dynamics of microfabricated OoC chamber structures, with particular emphasis on the effect of flow rates on the temperature distributions. The analysis was conducted using numerical simulations in COMSOL Multiphysics v5.3.

The modelled geometry consists of four polydimethylsiloxane (PDMS) micro-wells bonded into a 600 µm silicon substrate thickness [3]. Each well is 3 mm deep and includes an integrated thin platinum (Pt) heater with 200 nm in thickness, along with a 500 nm SiO_2 insulating layer (Figure 1). The simulations explore a range of inlet flow rates (100, 300 and 500 µL/min) and heating power conditions, for different electrical currents applied to each heater. Temperature profiles were extracted for different flow rates, and comparisons were made between inlet and outlet temperatures for multiple configurations. Firstly, the temperature produced by the microheaters was evaluated under a stationary flow in the chamber. The results showed that the temperature in the chamber, not only result from the main heater (positioned directly under that chamber), but it is also influenced by the adjacent heaters. Figure 2 (a1) presents the thermal distribution generated by microheater 4 (I4), with a maximum temperature of 42 °C in the corresponding chamber, when a current of 50 mA is applied. Good temperature uniformity is visible throughout the entire volume of the chamber (Figure 2 (a2)). However, despite the adjacent heaters being turned off (no current applied), the other chambers are still affected by the activated microheater. This implies that, to achieve the targeted temperature in each microheater, it will be necessary to adjust the current applied to each microheater. Results also show that, the greater the number of microheaters turned on, the more uniform the temperature becomes along the microchannels (Figure 2 (b1, b2)). Furthermore, the effect of the flow rate in the temperature was studied. Figure 3 shows that, as the flow rate increases, temperature uniformity in chamber 2 (microheater 2 on, with 50 mA) decreases, although heat becomes more widely distributed along the microchannels. Additionally, the overall device temperature decreases with higher flow rates due to increased heat dissipation caused by the fluid. This study highlights the temperature effects caused by microheaters in an OoC setup, considering microfluidic geometry, materials, and fluid dynamics. It provides valuable guidelines for the thermal design and optimization of microdevices in Organ-on-a-chip systems.

[1] Q. Wu *et al.*, "Organ-on-a-chip: Recent breakthroughs and future prospects," *Biomed. Eng. Online*, vol. 19, no. 1, pp. 1–19, 2020, doi: 10.1186/s12938-020-0752-0.

[2] G. M. Ferreira *et al.*, "Numerical simulation, fabrication, and characterization of a heating system for integration into an Organ-on-a-Chip," *Sensors Actuators A Phys.*, vol. 363, no. September, p. 114699, Dec. 2023, doi: 10.1016/j.sna.2023.114699.

[3] V. Carvalho *et al.*, "Numerical evaluation and experimental validation of fluid flow behavior within an organ-on-a-chip model," *Comput. Methods Programs Biomed.*, vol. 243, p. 107883, Jan. 2024, doi: 10.1016/j.cmpb.2023.107883.

Acknowledgements:Work supported by PTDC/EEI-EEE/2846/2021 project (https://doi.org/10.54499/PTDC/EEI-EEE/2846/2021) and 2022.06207.PTDC (https://doi.org/10.54499/2022.06207.PTDC) through national funds (OE), within the scope of the Scientific Research and Technological Development Projects (IC&DT) program in all scientific domains (PTDC), through the Foundation for Science and Technology, I.P. (FCT, I.P). The authors acknowledge the partial financial support within the R&D Unit Project Scope: UIDB/04436/2020, UIDP/04436/2020 and LA/P/0029/2020. GMF thanks FCT for Ph.D. grant, reference 2022.10519.BD.

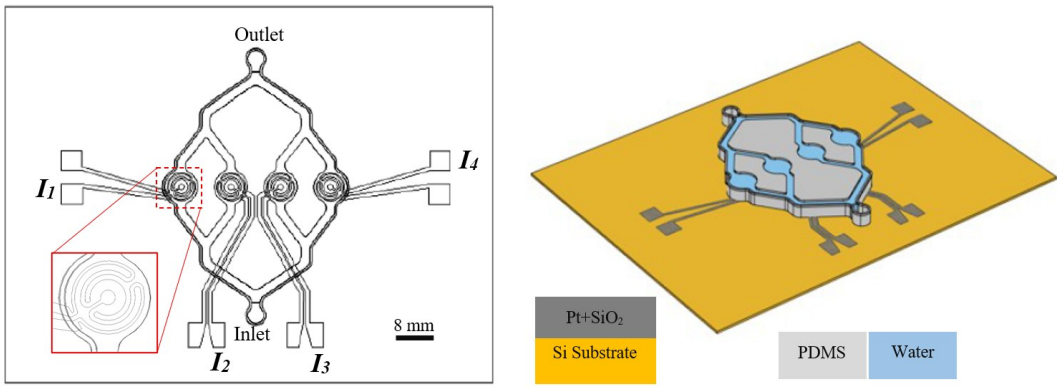

Figure 1. Geometry for the OoC device modelled in COMSOL Multiphysics. On the left, the top view of the layout, featuring four integrated microheaters (I1 to I4) positioned in individual chambers along the microchannel, between the inlet and outlet. On the right, a 3D schematic illustrates the multilayer structure of the device, composed of a Si substrate with Pt microheaters and SiO_2 layer, a PDMS layer forming the microchannels, and water-filled chambers (Water).

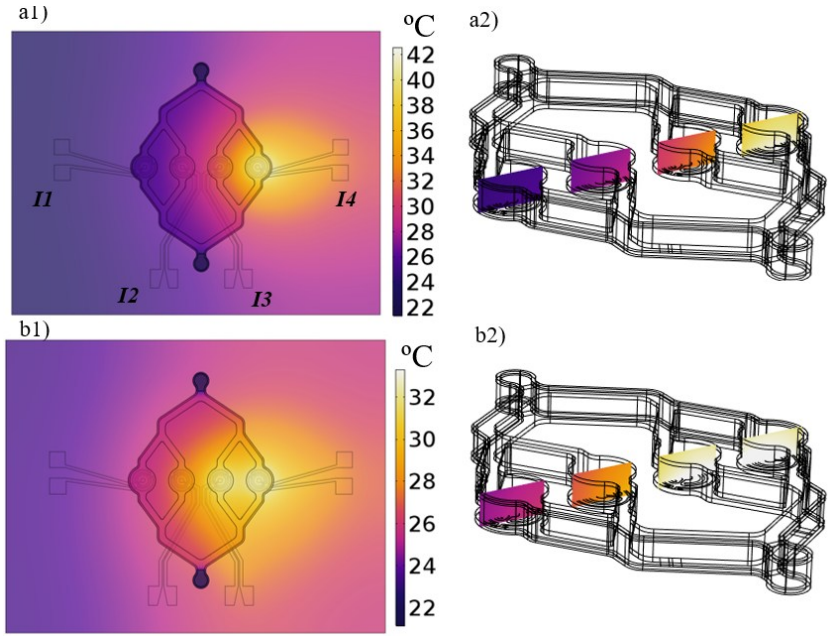

Figure 2 (a1) Top view of the temperature field when microheater I4 is activated with a current of 50 mA. **(a2)** 3D temperature distribution highlighting heat propagation in the corresponding chamber and partial thermal influence on adjacent chambers. **(b1)** Temperature field when microheaters I3 and I4 are activated with a current of 30 mA each. **(b2)** Corresponding 3D view, evidencing the combined thermal effect of both heaters and the temperature distribution within the structure.

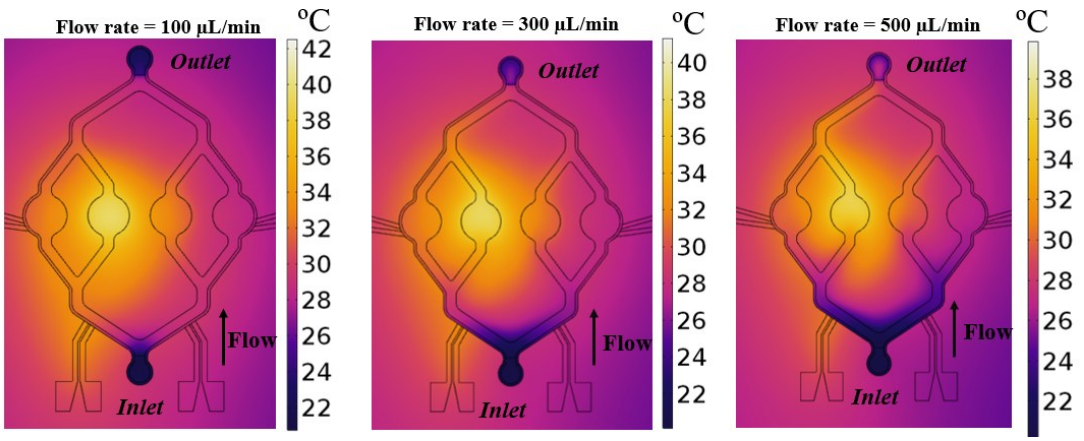

Figure 3 Temperature distribution maps in the OoC device under different flow rates (100, 300, and 500 µL/min) when microheater 2 is on, with an input current of 50 mA.

Microfabricated Light Pipe for Sustainable and Lithography-Free SPR Sensor

Briliant Prabowo [a], Arthur Lipinski [a], Pooja Kanade [a], Fatemeh Moradiani [a], Paul Baine [b], Jason Wiggins [a], Robert Bowman [a]

[a] Smart Nano NI, School of Mathematics and Physics, Queen's University Belfast, BT7 1NN, United Kingdom
[b] Queen's Advanced Microengineering Centre, School of Electronics, Electrical Engineering and Computer Science, Queen's University Belfast, Belfast, BT9 5AG, United Kingdom
e-mail: b.prabowo@qub.ac.uk

Abstract

Introduction: Surface plasmon resonance (SPR) sensors have emerged as essential tools for label-free, real-time monitoring of molecular interactions, with wide-ranging applications in medical diagnostics, environmental monitoring, and pharmaceutical development[1]. Despite their advantages, traditional SPR systems often require complex prism-based optical components and rely heavily on lithography-based fabrication methods[2]. These limitations result in high production costs, significant chemical waste, and poor scalability, ultimately hindering widespread deployment and field integration.

In this work, we present a next-generation SPR sensor platform that overcomes these bottlenecks through a novel light-pipe-based architecture and a sustainable, non-lithographic microscale manufacturing approach. The innovation centers on the replacement of conventional prism couplers with a custom-designed microfabricated light pipe, which enables angular coupling of light to the plasmonic interface within a compact form factor[3]. This light pipe structure was optimized using Zemax ray tracing simulations, allowing precise modeling and tuning of internal reflections, beam angles, and coupling conditions to ensure optimal excitation of surface plasmons on the metallic sensing layer.

Fabrication Method: Fabrication was achieved using a two-tier strategy. First, two-photon polymerisation was used to rapidly prototype high-resolution micro-optical structures with sub-micron fidelity. For scaling beyond prototyping, we developed a pick-and-place micro-templating method that assembles optical and plasmonic components without lithography, wet chemistry, or masks. This fully dry and additive process eliminates the need for photoresists, solvents, and spin coating, thereby dramatically reducing chemical waste and energy consumption. Our approach promotes not only sustainability but also democratization of SPR technology by removing the dependency on high-cost cleanroom processes.

Results: The resulting SPR device integrates a gold-coated plasmonic surface within a monolithic platform that supports microfluidic compatibility and maintains robust optical alignment tolerances. Preliminary experimental evaluations confirm that the sensor structure achieves a well-constructed device on par with conventional Kretschmann-based SPR systems, while offering substantial improvements in scalability, portability, manufacturability, and environmental footprint.

Summary: Overall, this work introduces a fundamentally new design and fabrication paradigm for SPR sensors, targeting the convergence of high performance, scalability, and eco-friendly production. The proposed system opens avenues for affordable, field-deployable biochemical sensing platforms, offering a significant step toward decentralised diagnostics and sustainable photonic device manufacturing.

Reference:

[1] B.A. Prabowo, P.D. Cabral, P. Freitas, E. Fernandes, The Challenges of Developing Biosensors for Clinical Assessment: A Review, Chemosensors 9 (2021) 299. https://doi.org/10.3390/chemosensors9110299.

[2] B.A. Prabowo, A. Purwidyantri, K.-C.C. Liu, Surface Plasmon Resonance Optical Sensor: A Review on Light Source Technology, Biosensors (Basel) 8 (2018) 80. https://doi.org/10.3390/bios8030080.

[3] B.A. Prabowo, A Light Guiding System for Photonic Applications, GB2501573.6., 2025.

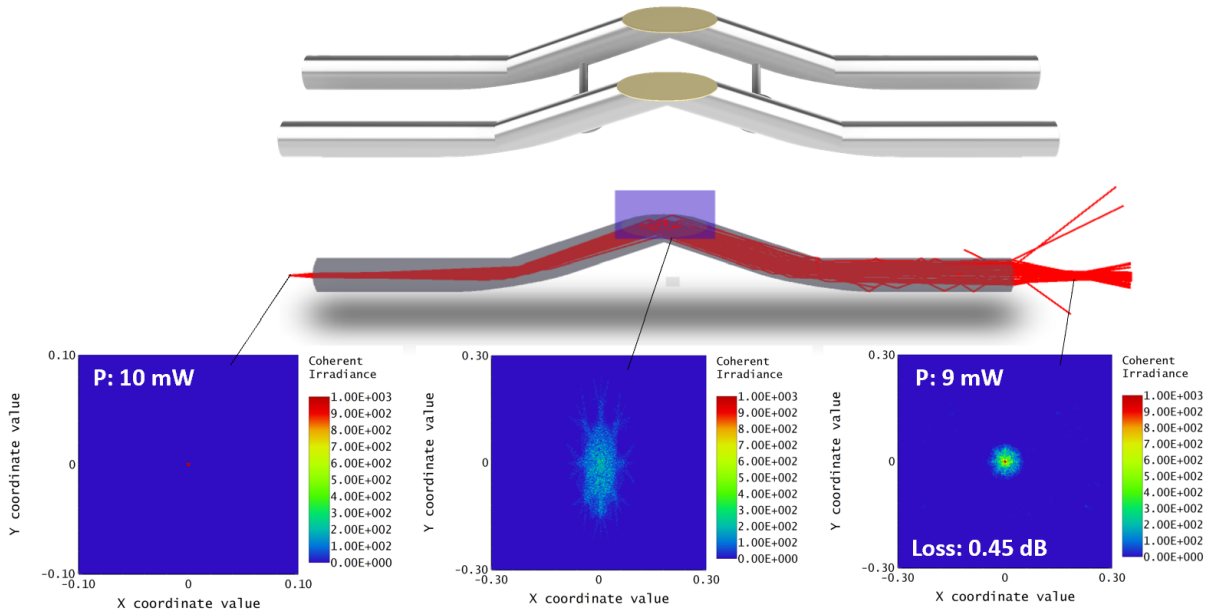

Figure 1. Low loss light-pipe SPR utilizing Kretschmann configuration, simulated by Zemax ray tracing simulation.

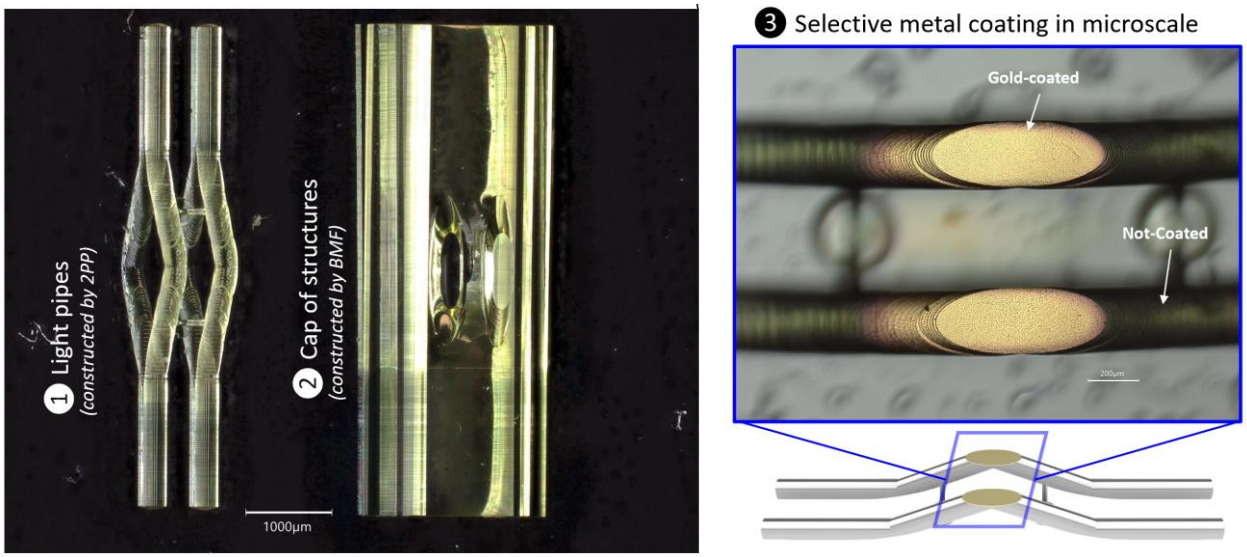

Figure 2. (1) Image of fabricated lightpipe on silicon and (2) the micro-template for non-lithography coating. (3) The sensing coating from micro-template over the light-pipe structure.

Dual-Path Anomaly Detection for Semiconductor Equipment: Toward Sensor-Level Intelligence in Digital Twin Manufacturing

Joon Soo Kim [a b], Jae Wook Jeon [c]

[a] Department of Semiconductor and Display Engineering, Sungkyunkwan University, Suwon, 16419, Korea
[b] Samsung Institute of Technology, Samsung Electronics, *Yongin*, 17113, Korea
[c] Department of Electrical and Computer Engineering, Sungkyunkwan University, Suwon, 16419,Korea
e-mail: chejunes@gmail.com

Purpose of the work

With the advancement of smart manufacturing technologies, the integration of process and equipment operations via digital twins is emerging as a core strategy in the semiconductor industry. In particular, Fault Detection and Classification (FDC) data, collected in real-time from thousands of sensors within the fab, serves as a precise digital representation of equipment states and forms the basis of anomaly detection systems that act as quality defense mechanisms. However, most deployed systems rely on static thresholds and univariate statistical techniques, which are structurally limited in capturing dynamic patterns. Semiconductor equipment undergoes physical changes due to degradation over time and periodic (PM) or breakdown maintenance (BM), resulting in evolving sensor interactions. Additionally, recipe modifications, process parameter tuning, and production optimization induce nonlinear, time-dependent variations, which static threshold-based systems fundamentally struggle to detect.

Novelty of the work

To address these limitations, we propose Dual-Path Anomaly Detection, a sensor-aware anomaly detection architecture that integrates graph modeling of sensor interactions with patch-level analysis of process transitions, reflecting both the structural nature of FDC data and the operational context of semiconductor equipment. First, in the Graph Neural Network Modeling path, we focus on the dynamic correlations among sensors that vary depending on recipe conditions, equipment modes, and maintenance history (PM/BM). These shifting correlations are challenging to model using conventional multivariate or univariate time-series methods. To this end, we define a Dynamic Sensor Graph, where each sensor is represented as a node and pairwise correlations as edges, and apply Graphormer, a Transformer-based graph model. Leveraging flexible receptive fields and attention-based message passing, it effectively captures condition-dependent, concurrent sensor interactions as observed in real fab environments. This enhances the precision of detecting complex, relation-based anomaly patterns arising within semiconductor tools. Second, in the Patch-Level Modeling path, we account for the discrete nature of semiconductor process time-series data, which exhibits abrupt distributional shifts due to recipe transitions, equipment status changes, wafer transport, and loading events. Rather than treating the entire sequence as a continuous stream, we automatically identify change-points corresponding to these transitions and segment the data into meaningful units, or patches. Each patch encapsulates a distinct process context and is treated as a token that captures both local features and inter-patch transitions. A Transformer-based sequence model is then employed to learn the nonlinear temporal dynamics across patches. This approach allows the model to effectively reflect the fragmented flow of data induced by process state changes in real manufacturing environments. Finally, the outputs from the graph neural network modeling and patch-level modeling paths are integrated through a late fusion strategy, enabling robust detection of complex, time-dependent anomalies within semiconductor equipment.

Results of the work

We validate our approach using the public UCI SECOM dataset, achieving performance improvements of up to 20.3% in F1-score and 17.8% in AUPRC over LSTM baselines. We also evaluate a lightweight GCN+TCN model suitable for resource-constrained environments, demonstrating balanced performance. This study goes beyond applying AI to manufacturing data; it integrates semiconductor domain expertise into a practical detection system that reflects real-time variability and engineer judgment, supporting the Sensing Intelligence Layer in digital twin architectures.

References

[1] A Generalization of Transformer Networks to Graphs
DWIVEDI, Vijay Prakash; BRESSON, Xavier. A generalization of transformer networks to graphs. arXiv preprint arXiv:2012.09699, 2020.
[2] DGTR: Dynamic Graph Transformer for Rumor Detection
WEI, Siqi, et al. DGTR: Dynamic graph transformer for rumor detection. Frontiers in Research Metrics and Analytics, 2023, 7: 1055348.
[3] Learning Graph Structures with Transformer for Multivariate Time-Series Anomaly Detection in IoT
CHEN, Zekai, et al. Learning graph structures with transformer for multivariate time-series anomaly detection in IoT. IEEE Internet of Things Journal, 2021, 9.12: 9179-9189.

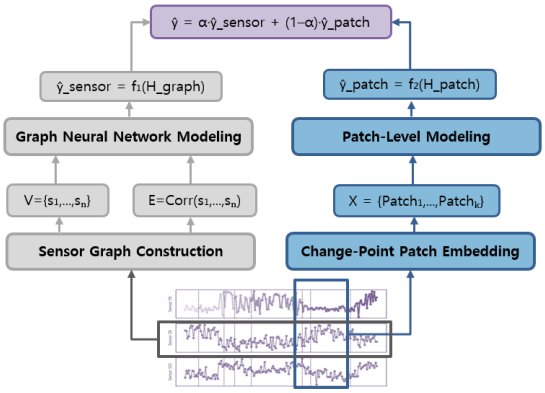

Figure 1. Overview of the proposed Dual-Path Anomaly Detection structure.
The left path models dynamic correlations among sensors using a graph neural network based on sensor-wise interactions, the right path segments the time-series into change-point-based patches and models transitions via a Transformer.

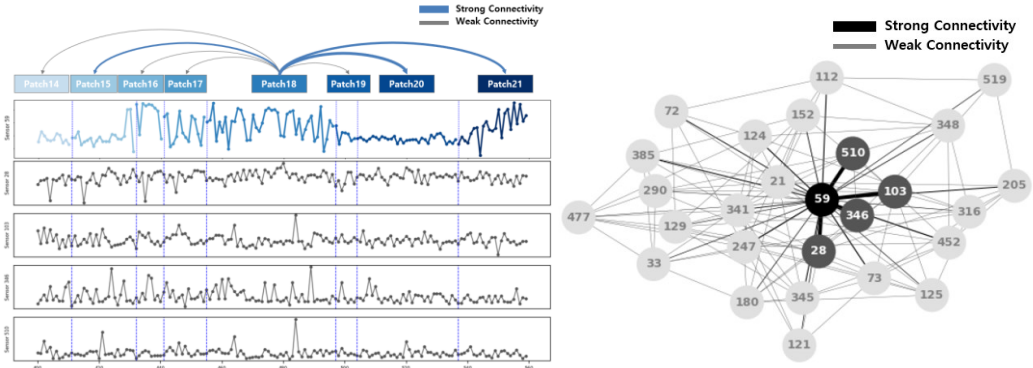

Figure 2. Illustration of inter-patch connectivity (left) and sensor graph structure (right).
Patches segmented by change-points are shown with strong/weak connectivity visualized by arrow thickness. Sensor nodes are modeled as a dynamic graph with varying connectivity strength, enabling both temporal and relational patterns to be captured jointly.

Models	Sensor Relationship Modeling(Vertical)	Dynamic Patch Modeling(Horizontal)	F1-score	AUPRC
Baseline(LSTM)	-	LSTM	0.62	0.55
Ours (Optimal)	Graphormer	Transformer	0.82	0.78
Ours (Efficient)	GCN	TCN	0.77	0.76
Ablation Study (No Sensor Relation)	-	TCN	0.61	0.63

Figure 3. Performance comparison across different model configurations.
Ours(Graphormer + Transformer) achieves the best overall results, while the efficient model (GCN + TCN) strikes a good balance between performance and efficiency. Patch-level modeling alone also outperforms the LSTM baseline in AUPRC, highlighting its suitability for imbalanced scenarios such as semiconductor anomaly detection.

Real-time lesion location detection system using Mu-metal and Hall sensor

Gapseop Sim [a], Hyeonjune Kim [b], Seung-Hwan Jung [c] and Woojin Yun [a]

[a] National Nanofab Center, Daejeon, 34141, Korea
[b] Seoul National University of Science and Technology, Seoul, 01811, Korea
[c] GRIT Custom-IC, Seoul, 07292, Korea
e-mail: woojunyun@nnfc.re.kr

Abstract
In case of laparoscopic or surgical operation after general endoscopy, position marking technology is becoming more important from medical staff in diverse fields for accurate judgment and successful operation of the lesion site during laparotomy or incision surgery at a transferred medical center. At present, the position of lesion is indicated by tattooing method through ink, but the position indicated by this method is unclear or invisible at 22% and the visibility at the time of procedure is difficult in 31.5%. As a result, it can lead wrong surgery. In this paper, we have developed a detection system for the lesion in the human body, which overcomes the conventional ink marking method, through the use of mu-metal which can magnetize and sensor system to detect it.

Figure 1 is a lesion location detection system. Figure 2 is a block diagram of a sensor detection system using Mu-metal. The sensor detection system consists of three parts: a marker part, a sensor detection part, and a signal processing part. A magnet was attached to the metal to make it magnetic, and it is used as a marker in the detection system. The sensor detection part consists of a hall sensor, an accelerometer, a MUX, a level shifter, and an amplifier. Also, the signal processing part consists of digital signal processing, distance conversion, power, LED, and USB etc.
Mu-metal must be implemented with a flexible material so that it can be attached to the probe marker in various shapes. For this purpose, polyimide and Ni/Co metal was deposited to implement magnetic Mu-metal. Figure 3 is a manufacturing process of Mu-metal and final product. Figure 4 is a circuit diagram and a lesion detection system board. It consists of a sensor section that detects magnetic markers, a power section, an MCU section, and a Bluetooth section for communication.

Table 1 is measurement results which compare the distance and MCU output value according to the type of marker. A three different sized markers were used, and it can be seen that the measurement is accurate from 0 to 20 mm. In this paper, we fabricated a high-capacity Mu-metal using a semiconductor process that is easy to mass-produce. We implemented a system that can easily detect the fabricated Mu-metal using a Hall sensor. This allows for more accurate identification of lesion locations than using conventional ink marking methods.

[1] P. Puangmali, K. Althoefer, L. D. Seneviratne, D. Murphy, and P. Dasgupta, “State-of-the-art in force and tactile sensing for minimally invasive surgery,” *IEEE Sensors J.*, vol. 8, no. 4, pp. 371_381, Apr. 2008.
[2] G. Niu, B. Pan, Y. Fu, and C. Qu, “Development of a new medical robot system for minimally invasive surgery,” *IEEE Access*, vol. 8, pp. 144136_144155, 2020.
[3] X. Tian and Y. Xu, “Low delay control algorithm of robot arm for minimally invasive medical surgery,” *IEEE Access*, vol. 8, pp. 93548_93560, 2020.
[4] N. Bandari, J. Dargahi, and M. Packirisamy, “Tactile sensors for minimally invasive surgery: A review of the State-of-the-art, applications, and perspectives,” *IEEE Access*, vol. 8, pp. 7682_7708, 2020.

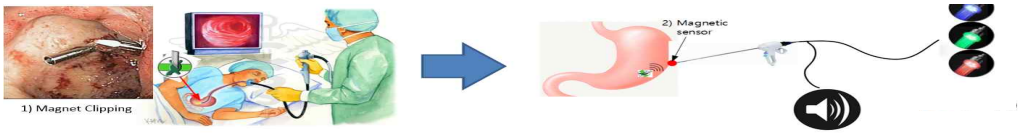

Figure 1. Schematic diagram of the lesion location detection system

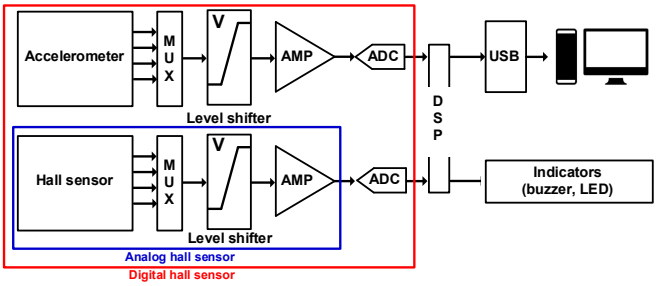

Figure 2. Block diagram of a sensor detection system

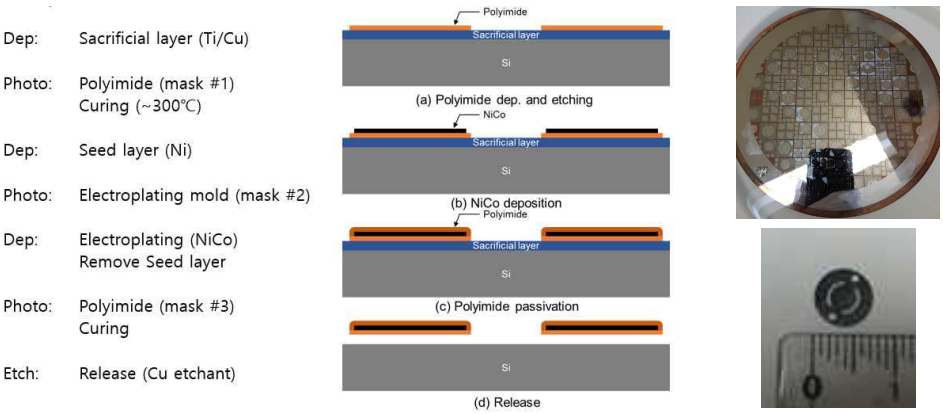

Figure 3. Process diagram for manufacturing Mu-metal

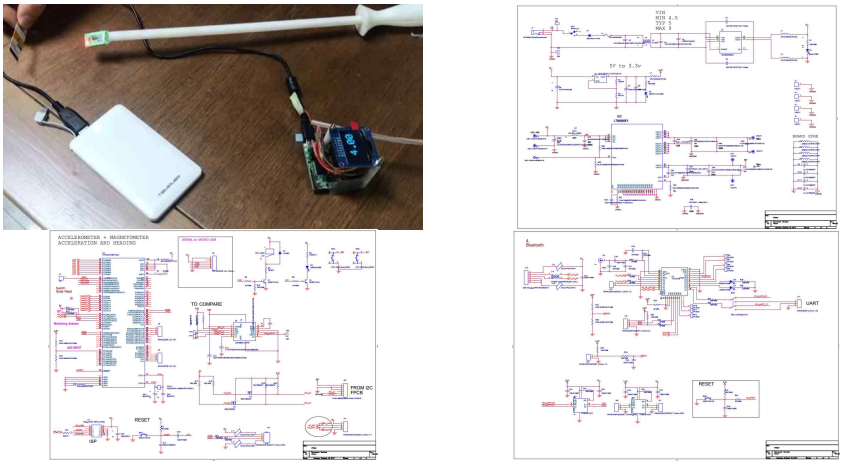

Figure 4. Process diagram for manufacturing Mu-metal

Table 1. Measurement results according to marker type and distance

	Marker 1	Marker 2	Marker 3
5 mm	44523	44518	44508
10 mm	44535	44527	44527
15 mm	44538	44532	44530
20 mm	44541	44535	44535

A Study on Focus Control Improvement in Response to Wafer Table Edge Wear in Photolithography Equipment

Kyunghwan Joo [a, b], Kwang Hoon Lee [b], Prof. Jae Wook Jeon [c]

[a] Department of Semiconductor and Display Engineering, Sungkyunkwan University, Suwon, 16419, Korea
[b] Samsung Institute of Technology, Samsung-ro 1, Giheung-gu, Yongin-si, Gyeonggi-do, 17113, Republic of Korea
[c] Department of Electrical and Computer Engineering, Sungkyunkwan University, Suwon, 16419, Korea

e-mail: okata2000@g.skku.edu

• Purpose of the work;

The continuous scaling of semiconductor devices necessitates highly precise focus control technologies in photolithography equipment. In particular, the 300 mm wafer table experiences continuous wear during repetitive wafer handling process, which causes focus imbalance. Continuous wear of the wafer table causes edge-roll-off (ERO) at the edge of the wafer, which reduces the uniformity of the critical dimension (CD) of the device and causes serious defects such as pattern bridge defect. This ultimately leads to serious problems that lead to a decrease in semiconductor production yield. However, most existing process control systems rely on average correction based on wafer center focus information, and thus have limitations in sufficiently responding to local deterioration phenomena occurring at the edge. To address this technological gap, this study investigated an advanced focus management method that can accurately quantify, monitor, and predictively respond to focus deterioration due to wafer table edge wear. In particular, by focusing on measuring the 140 to 147 mm wafer radius section, the foundation has been established for precise analysis of local defocus changes and resulting pattern quality degradation, and the goal is to present a practical solution that can contribute to increased productivity and improved equipment reliability.

• Novelty of the work with respect to the state of the art;

This study introduced Geometry-based Optical Focus Metrology (GOFM) to overcome the limitations of existing focus management technology and to enhance wafer edge focus monitoring, and implemented it as an original edge monitoring system applicable to actual semiconductor production environments. GOFM constructed an asymmetric pattern based on diffraction through an Optical Diffraction Metrology Mark (ODMM) etched on a reticle, and measured the subtle asymmetry of the Side Wall Angle (SWA) by analyzing the diffraction light using scatterometry. The ODMM mark has been experimentally optimized under various pitch conditions, and can be used to measure and compensate for the Z/Ry Tilt of the entire wafer table area by converting the difference in intensity between the +1st and -1st order diffracted light into a quantitative index of focus sensitivity. The technology can go beyond focus measurement centered on the wafer table center and also serve as a precise sensor for detecting edge focus variation, so that the degree of physical wear at the wafer table edge can be indirectly quantified. In particular, by separately analyzing the 140~147mm and 144~147mm radius sections, which are sensitive to wear among the edge areas, and proposing new indices such as Range Percentile 97% and Focus Slope*3, the sensitivity and prediction accuracy were improved. This methodology is a monitoring technology that can detect CD deterioration due to edge wear early and respond in advance, and can contribute not only to improving process yield but also to optimizing equipment maintenance cycles.

• Results of the work.

As a result of this study, it was possible to match the defocus index of 97% of the Range Percentile in the 140–147 mm radius area of the wafer table and the defocus value at the 147 mm radius point when the critical dimension (CD) quality spec is exceeded due to wafer edge deterioration, and based on this, it was possible to establish an edge-roll-off management standard that can detect and prevent edge pattern quality deterioration in advance. In addition, we applied the GOFM-based focus management system to an actual mass production environment and obtained and analyzed long-term data for about one year. As a result, we were able to secure consistency and stability of wafer edge focus management. In addition, we verified that the consistency between the center focus and the edge focus increased even after the wafer table was replaced, proving the reliability and reproducibility of the developed edge monitoring system. It showed the possibility of quantitatively analyzing the wear trend of each equipment and using it to predict equipment replacement time

and establish maintenance optimization strategies. This monitoring system can be effectively used to detect and manage focus imbalance problems caused by wafer edge wear in actual semiconductor manufacturing sites, and as a result, it is expected to greatly contribute to maintaining consistency in device quality and improving production yield.

[1] Keisuke Ehara, et al "CD and defect improvement challenges for immersion processes," Proc. SPIE 7273, Advances in Resist Materials and Processing Technology XXVI, 727322(1 April 2009)

[2] Jan Mulkens, et al. "Holistic optimization architecture enabling sub-14-nm projection lithography", Journal of Micro/Nanolithography, MEMS, and MOEMS Vol. 13, Issue 1 (Jan 2014)

[3] Yen-Jen Chen, et al. "Enhanced methodology of focus control and monitoring of scanner tool," Proc. SPIE 10145, Metrology, Inspection, and Process Control for Microlithography XXXI, 101452K (28 March 2017)

[4] Ben F. Noyes III, Babak Mokaberi, et al, "Applications of on-product diffraction-based focus metrology in logic high volume manufatcuring" Proc. SPIE 9778, Metrology, Inspection, and Process Control for Microlithography XXX, 97782V (8 March 2016)

[5] Hugo Cramer, Stefan Petra, et al, "Intra-field patterning control using highspeed and small-target optical metrology of CD and focus", SPIE 9424 (2025)

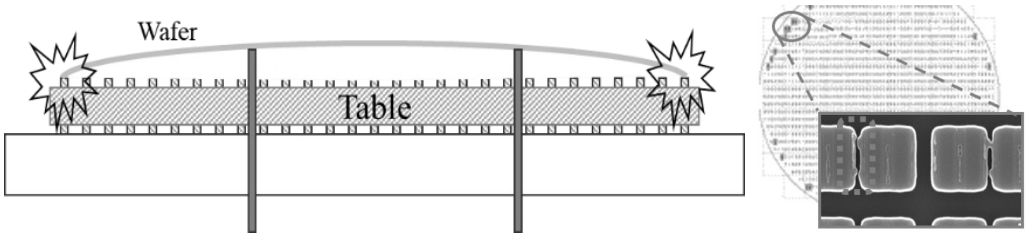

Figure 1. Photo lithography equipment wafer table edge wearing and pattern bridge defect

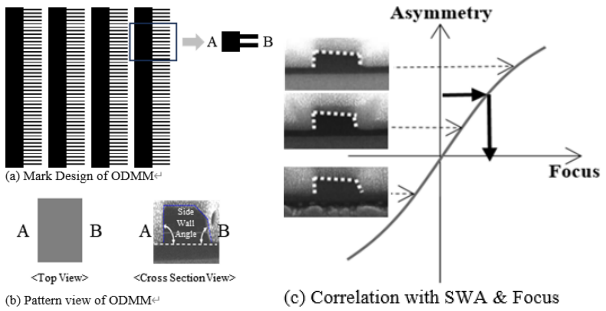

Figure 2. Principle of GOFM converging focus using ODMM

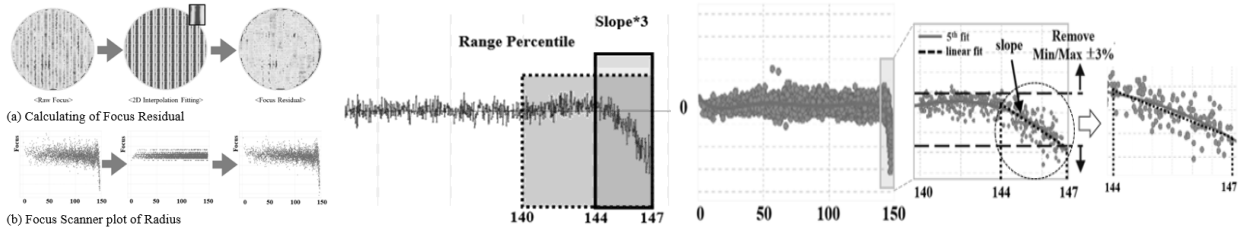

Figure 3. Data processing of wafer table edge-roll-off

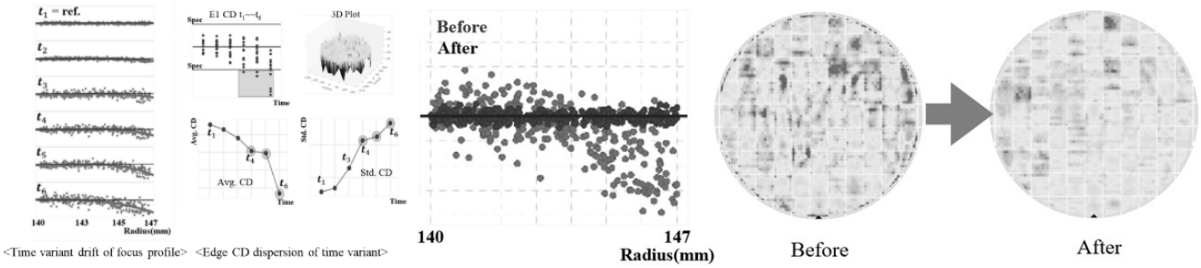

Figure 4. Focus profile and edge cd dispersion over time during 1year(t1~t6) and edge focus residual after wafer table replacement

Automated Silicon Wafer Handling for Gravity Effect Compensation in High-Precision Horizontal Metrology

César Pérez-Domínguez [a, b], Juan Trujillo-Sevilla [b], Carmelo Militello-Militello [a]
[a] Universidad de La Laguna, San Cristóbal de La Laguna, 38200, Spain
[b] Wooptix, San Cristóbal de La Laguna, 38200, Spain
e-mail: cesar.perez.dominguez@wooptix.com

The measurement of silicon wafers geometry in a horizontal configuration is inherently affected by gravitational deformation, preventing the direct acquisition of the free-form shape without additional correction strategies. This deformation introduces systematic errors that compromise metrology accuracy, making compensation techniques necessary to obtain reliable results. One of the optical methods used for wafer shape characterization is Wave Front Phase Imaging (WFPI), which reconstructs surface topography by capturing the intensity distribution of reflected light at multiple optical planes [1]. Although WFPI enables precise measurements, when applied in a horizontal setup, it remains susceptible to gravitational distortions, requiring additional strategies to eliminate these effects. A method proposed by Trujillo-Sevilla et al. [2] addresses this issue by relying on multiple rotated measurements to compensate for gravity-induced deformation. While effective in theory, its implementation presents several drawbacks: it requires manual handling of the wafer, leading to inconsistencies and repeatability issues, while also increasing the risk of contamination due to direct contact. Moreover, the sequential nature of the process significantly slows down acquisition, making it less suitable for high-throughput semiconductor manufacturing.

An alternative approach is to perform measurements in a vertical configuration, where gravitational deformation is minimized, improving shape accuracy [3]. However, many semiconductor processes, such as wafer bonding, chemical mechanical planarization (CMP), and lithography, require wafers to remain horizontal, making in-situ metrology in this orientation essential. In these cases, achieving high-precision measurements while compensating for gravity remains a key challenge.

To address these limitations, an automated wafer handling system (**Fig. 1**) has been developed, eliminating manual intervention while ensuring accurate metrology. Automating wafer positioning and rotation improves repeatability, reduces operator variability, and minimizes contamination risks by preventing direct wafer contact. The elimination of manual rotations also enhances throughput, enabling faster and more efficient measurements without compromising accuracy.

Designed primarily for 300 mm wafers, the system also supports 200 mm and 150 mm wafers, as well as bonded wafers, making it a versatile solution. By integrating automation into wafer metrology, this approach augments precision, reliability, and efficiency, addressing the challenges of horizontal measurement. Its implementation represents a significant advancement in semiconductor manufacturing, providing a scalable and robust solution for high-precision applications.

The effectiveness of the compensation strategy, combined with the WFPI technique, is demonstrated through the results presented in **Figs. 2 and 3**. In the first one, the wafer geometry measured in the horizontal configuration clearly exhibits the characteristic sagging due to gravitational deformation, while in the second, after applying the gravity removal process, the same wafer displays a significantly flatter and more symmetric topography that aligns with the expected free-form shape. These results validate the correction approach and confirm its capability to mitigate gravity-induced errors in horizontal wafer metrology, enabling accurate surface reconstruction without altering the measurement configuration, and demonstrating the practical value of the implemented system.

[1] Juan M. Trujillo-Sevilla, et.al. "Wave front phase imaging for silicon wafer metrology"; https://doi.org/10.1117/12.2632499
[2] Trujillo-Sevilla, J.M., Gaudestad, J., Rodríguez-Ramos, J.M. A Theoretical Method for Removal of Gravity-Induced Effects in Silicon Wafer Geometry Measurements. Appl. Sci. 2022, 12, 9049. https://doi.org/10.3390/app12189049
[3] O. Gaudestad, M. Jiménez, K. I. Kurtev, J. M. Trujillo-Sevilla, G. C. Luis and J. M. Ramos-Rodríguez, "3D Shape Measurements of Patterned Silicon Wafers,", doi:10.1109/ASMC61125.2024.10545453.

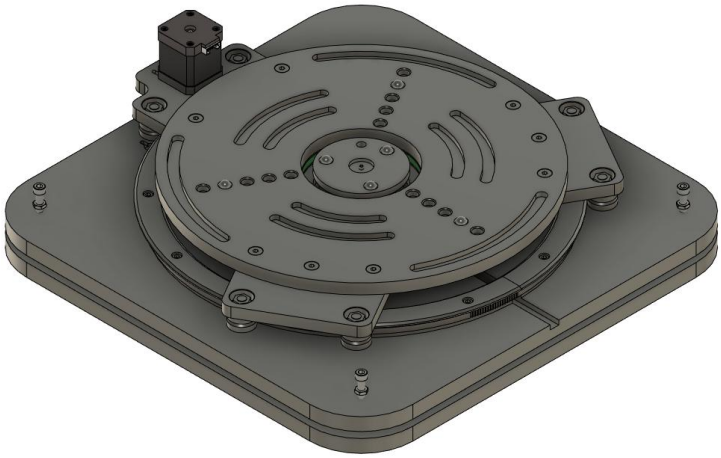

Figure 1. Automated horizontal silicon wafer holder

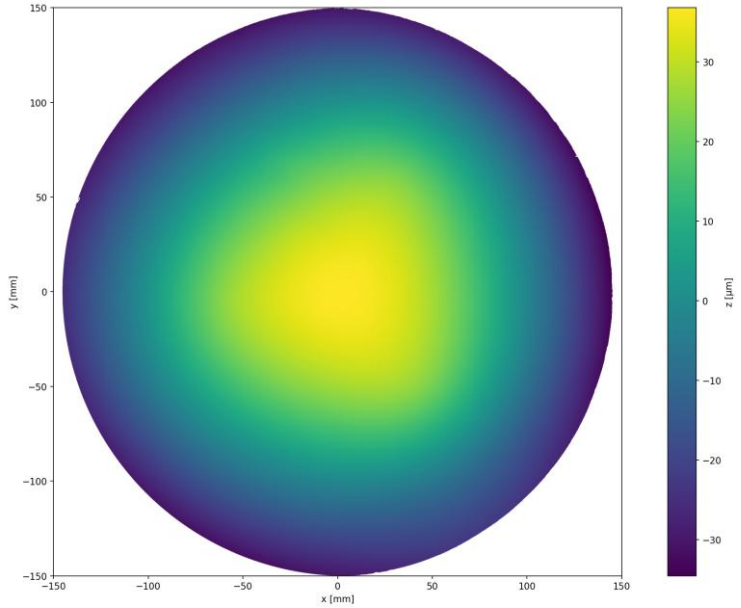

Figure 2. Wafer geometry under gravitational effect

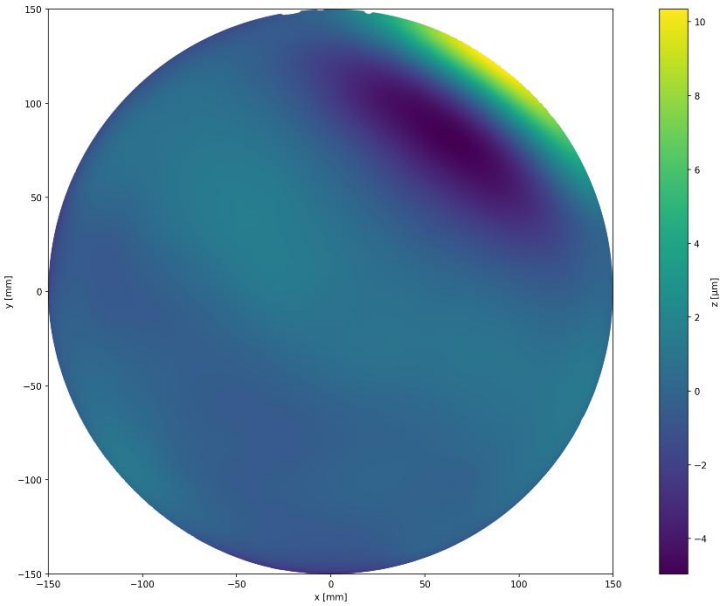

Figure 3. Wafer geometry after gravity compensation

A 10.94bit resolution measurement circuit for resistive sensors

Xiaoming Teng [a], Haoyu Liang [a], Yufeng Zhang [a]

[a] Harbin Institute of Technology, Harbin, 150001, China
e-mail: yufeng_zhang@hit.edu.cn

With the rapid development of sensing technology, various kinds of sensors have been increasingly used in production. Among them, one typical example is the resistive sensor, which has been widely used in temperature measurement, pressure sensing, toxic gas identification and so on. There are two main traditional methods for sensor resistance measurement, one is using R-V conversion circuit and analog-to-digital converter (ADC) to directly convert the resistance into digital output codes, the other is using oscillation circuit to convert the resistance into frequency of output codes. However, the former method usually has a high complexity for the design of signal processing and algorithms circuits, and the latter method often suffers from the variation of process, voltage, and temperature (PVT), which limits its accuracy of measurement.

This paper presents a novel circuit fabricated in standard 180nm CMOS technology for resistance measurement. The block diagram of the proposed circuit is shown in fig.1. It consists of four modules: a 2^{nd}-order temperature-curvature compensation bandgap with base-current compensation, an auto-zero offset-stabilized amplifier, a damped-SC based variable gain amplifier with an auto gain control loop, and a 12-bit SAR ADC. The bandgap shown in fig.2 provides a reference current independent of supply and temperature for the whole circuit. The offset-stabilized amplifier adopts the auto-zero stabilized amplifier structure to reduce the impact of 1/f noise and offset voltage caused by main amplifier on resistance measurement. To improve the stability of the circuit, we adopt the closed-loop structure for measurement. The variable gain amplifier shown in fig. 3 consists of three parts: 2 stages amplifier, quantifier, and logic update circuit. It can amplify the input signal to the ideal level automatically according to the timing diagram. The output signal will be quantified by a 12-bit SAR ADC, and transmitted to the host computer.

Compared to the previous work, this paper adopts the auto-zero offset-stabilized structure to realize the high precision measurement. What's more, a novel damped-SC based variable gain amplifier with an auto gain control loop is presented in this study for signal amplification to reach the maximum input range of ADC. For better process compatibility, a novel base-current compensation technique as well as a trim resistor is adopted in the design of 2^{nd}-order temperature-curvature compensation bandgap. Simulation shows that the temperature coefficient of improved bandgap reference can reach 1.27 ppm/°C. The auto-zero offset-stabilized circuit can reduce the offset voltage to 273μV with just 11.8μV ripples, which has an advantage over the previous work. The simulation result is shown in fig.4 and comparison with previous work is displayed in table.1. On the whole, processed by the variable gain amplifier and ADC, the resolution of the whole circuit can reach 10.94bit. The chip is 2.4mm^2 and the simulated power consumption of the chip is only 67.7 μA.

[1] Fatema A, Navnit A, Devendra D, et al. A combined capacitance and resistance digital readout circuit for sensory nodes[C]//2021 IEEE Sensors. IEEE, 2021: 1-4.

[2] George A K, Shim W, Kung J, et al. A 46-nF/10-MΩ range 114-aF/0.37-Ω resolution parasitic-and temperature-insensitive reconfigurable RC-to-digital converter in 0.18-μm CMOS[J]. IEEE Transactions on Circuits and Systems I: Regular Papers, 2021, 69(3): 1171-1184.

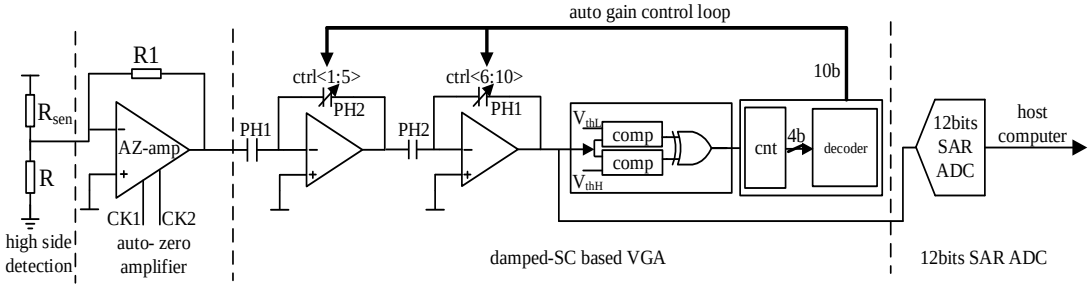

Fig 1. Structure of proposed bandgap with base-current compensation

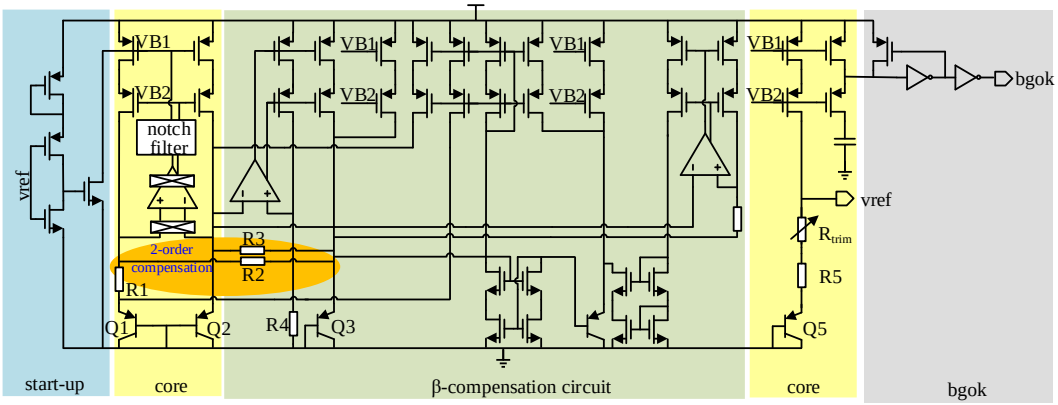

Fig 2. Structure of proposed bandgap with base-current compensation

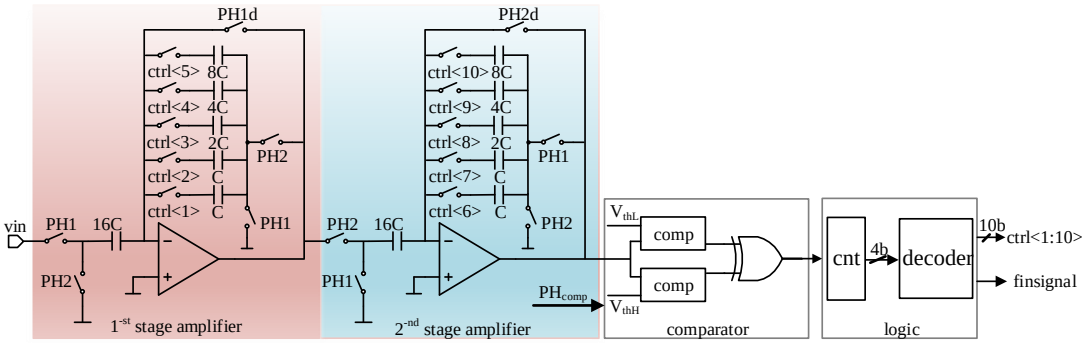

Fig 3. Structure of proposed damped-SC based VGA

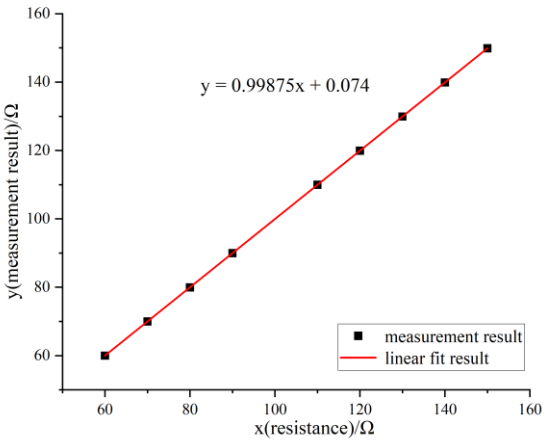

Fig 4. Simulation of the proposed circuit

Table 1. Performance comparison

	[1]	[2]	This Work
Process	0.18μm	0.18μm	0.18μm
Range(Ω)	1~30	15~90K	40~260
resolution	12bit	0.37Ω	10.94bit
non-linearity	0.57%	0.05%	0.096%
Power(W)	126m	140μ	121.9μ
Area(mm^2)	3.2	0.175	2.4

Device Variation Effect Simulation for SnOx Memristor-based Neural Networks

Aiden Graham [a], Zohreh Hajiabadi [a], Alexander-Hanyu Wang [a], Dimitra G. Georgiadou [b], Ruomeng Huang [a], Firman Simanjuntak [a]

[a] Sustainable Electronic Technologies, University of Southampton, SO171BJ, UK
[b] Smart Electronic Materials and Systems, University of Southampton, SO171BJ, UK
email: f.m.simanjuntak@soton.ac.uk

Memristors are of great interest for neuromorphic computing. Memristors can be fabricated in different structures; however, the nanofabrication methods have inherent variation between devices, arrays and wafers, and thus, more complex algorithms are often utilised to mitigate low performance yield. In this work, we fabricated SnOx-based memristors and studied the impact of device variations on the convolution neural network (CNN) computation. SnOx-based memristors are promising candidates for physical neural networks because of the ability to integrate with mature CMOS technology [1].

Ag(top electrode)/Ti/SnOx/TiN(bottom electrode) devices were fabricated using physical vapor deposition and lithography techniques. A control sample made without Ti barrier layer between the top electrode and SnOx switching layer was also fabricated. The devices made without and with Ti barrier layer are denoted as Device A and Device B, respectively. Both designs exhibited resistive switching and responded to synaptic inputs with potentiation and depression cycles (see Fig. 1). XPS analysis showed partial oxidation of the Ti barrier layer and a high oxide concentration at the layer interfaces (see Fig. 2).

The input was 2V amplitude, 100-pulse cycles, applied in alternating polarities. The pulse responses of Device B experience less noise compared to Device A, especially in the potentiated half-cycle. The nonlinearity of Device B devices appeared closer to symmetry than Device A. Therefore, the dynamics of Device B was used to simulate the CNN.

CNNs are important for computer vision and the CIFAR-10 dataset is a standard dataset for computer vision applications [2]. The dataset was divided 5:1 training images to testing images. The network structure is form of a 2D-Convolution layer paired with a ReLU Activation layer followed by a 2D-MaxPool layer. This structure is repeated thrice (see Fig. 3d). Each node in the network is assigned a nonlinearity value based on the runtime parameters. Through the gradient calculation, the nonlinearity is applied to the weight update.

Device B was cycled ten times, and nonlinearity was measured for each potentiation and depression half-cycle. The mean nonlinearity and its distribution between devices and across cycles were calculated and used as simulation parameters. Ideal devices with zero nonlinearity were simulated as a benchmark. One simulation sampled node nonlinearity from a normal distribution based on the average four-layer device, while another used unique nonlinearity values at each cycle using the within-device distribution.

The fixed nonlinearity network initially underperformed the benchmark by $\approx 5\%$, but this discrepancy dropped below 2% after 200 training epochs (Fig. 3b), suggesting further learning could mitigate device nonlinearity effects. However, the network with variable nonlinearity diverged from the benchmark, stabilizing at $\approx 23\%$ lower accuracy (Fig. 3c), indicating that CNNs are sensitive to device behaviour variability (Fig. 3a).

[1] W. Jiang, B. Xie, C.-C. Liu, and Y. Shi, "Integrating memristors and CMOS for better AI," *Nat. Electron.*, vol. 2, pp. 376–377, Sept. 2019.

[2] V. Thakkar, S. Tewary, and C. Chakraborty, "Batch normalization in convolutional neural networks — a comparative study with cifar-10 data," in *2018 Fifth International Conference on Emerging Applications of Information Technology (EAIT)*, pp. 1–5, 2018.

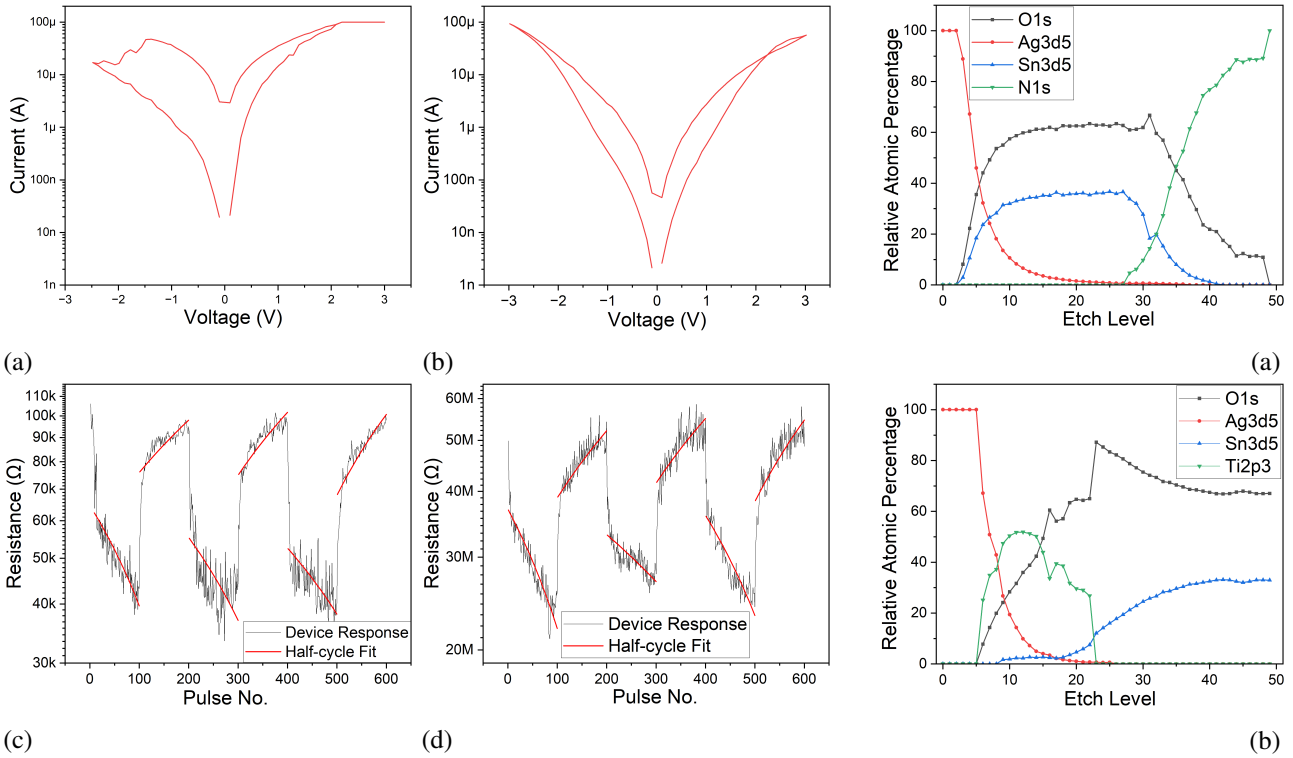

Figure 1: (a) & (b) show the resistive switching characteristics of Device A and B, respectively. (c) & (d) display the synaptic behaviour of Device A and B, respectively. Illustrative linear fits for each half-cycle are overlaid.

Figure 2: Depth profiles of relative atomic percentages obtained via XPS for Device A (a) and Device B (b) layer structures.

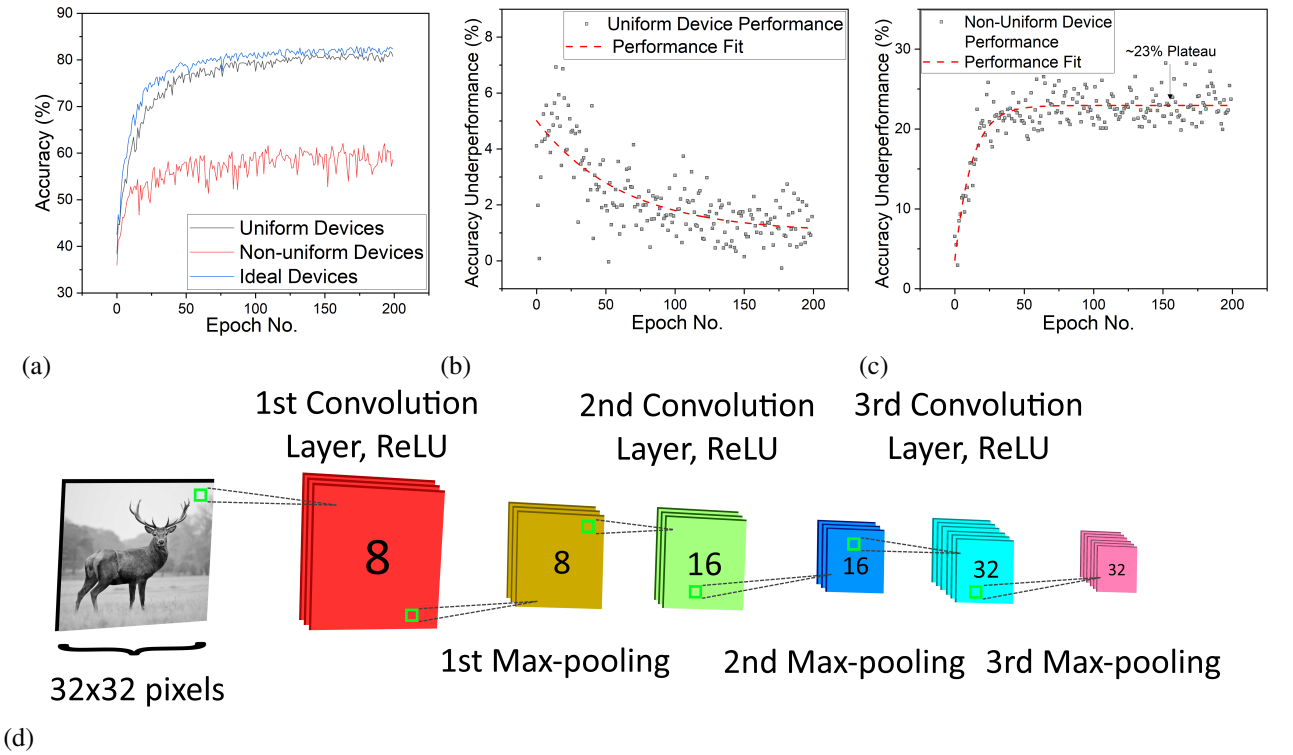

Figure 3: (a) compares the test simulations to the benchmark over 200 training epochs. (b) & (c) show the relative underperformance of the uniform devices and the non-uniform devices over 200 training epochs, respectively. (d) illustrates the repeating network structure of the CNN hidden layers.

Eco-Friendly Functionalization of Graphene via Spark Ablation for Enhanced NO_2 Gas Sensing Applications

Mudassir Husain, Leandro Nicolas Sacco, and Sten Vollebregt

Department of Microelectronics, Delft University of Technology, Delft 2628 CD, The Netherlands
e-mail: s.vollebregt@tudelft.nl

Air pollution remains one of the most critical environmental issues in modern society [1]. Nitrogen dioxide (NO_2) is a highly reactive and toxic gas predominantly released from the combustion of fossil fuels and the burning of organic biomass [2]. Even at concentrations as low as 1 ppm, NO_2 can cause significant harm to the human respiratory system [3]. Consequently, precise and continuous monitoring of even trace-level concentrations of NO_2 is essential for effective air quality assessment, public health safeguarding, and environmental regulation [4]. However, current sensors are typically not sufficiently sensitive, power-hungry, bulky and/or too expensive. Nanomaterial-based sensors hold the potential to tackle these limitations. Especially 2D materials like graphene are of interest for their potential to allow detection at room temperature, but sensitivity, selectivity, and recovery still require improvements. Functionalization of the graphene has been proposed as a method to achieve this [5].

This work reports the use of spark ablation with impaction printing to selectively deposit silver (Ag) and gold (Au) nanoparticles (NP) on single-layer graphene (SLG) based gas sensors for enhanced NO_2 gas sensing. This method avoids lithography and chemical processes, maintaining the device's quality while potentially lowering fabrication costs [6]. Ag-decorated sensors reveal a three-fold improvement in NO_2 gas response over pristine-SLG sensors. We demonstrate detection capabilities down to 50 ppb at room temperature (RT), negating the external thermal or photoactivation requirement. In contrast to pristine or Au-decorated SLG sensors, Ag-decorated devices exhibit 96% recovery at RT.

All graphene-based sensors were decorated utilizing impaction printing methods based on spark ablation using different stage speeds (Fig. 1) . Fig. 2 shows the scanning electron microscope (SEM) image before (D1) and after the decoration of Ag and Au -NPs (D2-D5). Using different printing speeds, three Ag-NP sensors with a surface coverage of 3.5% (D3), 2% (D4) and 0.8% (D5) were fabricated. Similarly, three devices were printed for Au-NPs. However, Au-NP decorated devices did not show any response against the NO_2 gas. Therefore, only one Au device (D2) is shown for comparison. Fig. 3 represents the two-probe I-V measurements. The response is Ohmic, and the sparse nanoparticles do not create a measurable change in resistance. Gas sensing measurements were performed against 1 ppm NO_2 at 80°C using 99.999% N_2 as a carrier for all sensors (Fig. 4, top). Pristine SLG (D1) exhibited scarce recovery, with an average response in all cycles of 2.2%. Interestingly, D3, D4 and D5 have an average response of 5.94%, 6.14%, and 5.22%, respectively, indicating a three-fold enhancement in response (Fig. 4, bottom). Moreover, a 96% recovery was observed after the initial pulse, which strongly contrasts with the device (D1). Fig. 5 depicts the change in resistance of the device (D4) at various NO_2 concentrations (50 –1000) ppb at RT and 80°C. Compared to RT, the device at 80°C shows a higher baseline resistance and a more noticeable resistance decline during the NO_2 gas exposure, indicating that higher temperatures improve the efficacy of NO_2 adsorption and charge transfer. As a result, the device can detect NO_2 concentrations as low as 50 ppb, even at RT. The inset graph demonstrates the device's responses against NO_2 concentrations after the 1st NO_2 pulse. The computed response at 80°C was 2.5 times greater than RT, highlighting the considerable enhancement in gas response by temperature. Based on these results, Ag-decorated devices exhibit great potential to detect low NO_2 concentrations and improve recovery at RT.

[1] A. Kampa et al., Environ. Pollut. 151 (2008) 362−367.
[2] I.S. Saggu et al., ACS Sens., 8 (2023) 243-253.
[3] J.Z. Ou et al., ACS Nano 9 (2015) 10313−10323.
[4] J. Wu et al., ACS Appl. Mater. Interfaces 11 (2019) 2364−2373.
[5] M. Kodu et al., Appl. Phys. Lett. 109 (2016) 113108.
[6] A. Schmidt-Ott, Spark Ablation: Building Blocks for Nanotechnology, Jenny Stanford Publishing, NY, 2019.

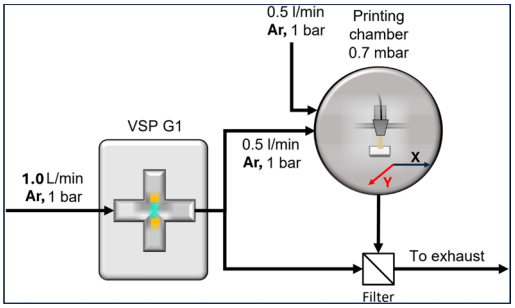

Figure 1. An Ar carrier gas is used in the VSParticle G1 to create an aerosol by spark ablating the metal electrodes. Part of this gas is directed to the P1 printer chamber with a nozzle and impacted on the sample placed on an x-y stage.

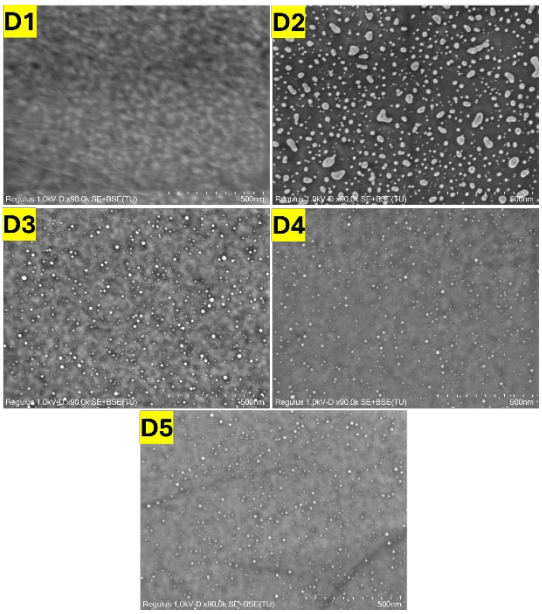

Figure 2: Top surface SEM images: (D1) pristine graphene, (D2) after Au-NPs decoration with an area coverage of 15.5%, and after Ag-NPs decoration with an area coverage of 3.5% (D3), 2% (D4) and 0.8% (D5), respectively. The coverage area was extracted using ImageJ.

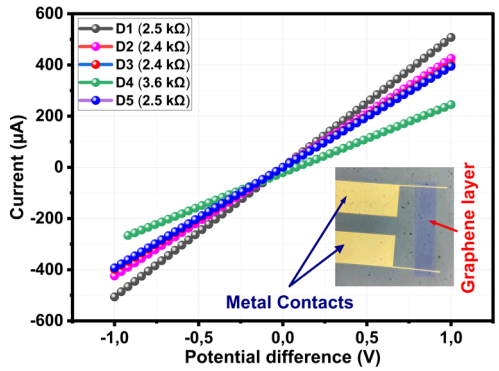

Figure 3: I-V characteristic of all devices with dimensions of 1000 × 200 µm as shown in the inset. The devices display Ohmic behaviour. Furthermore, the functionalization has no measurable impact on the resistance.

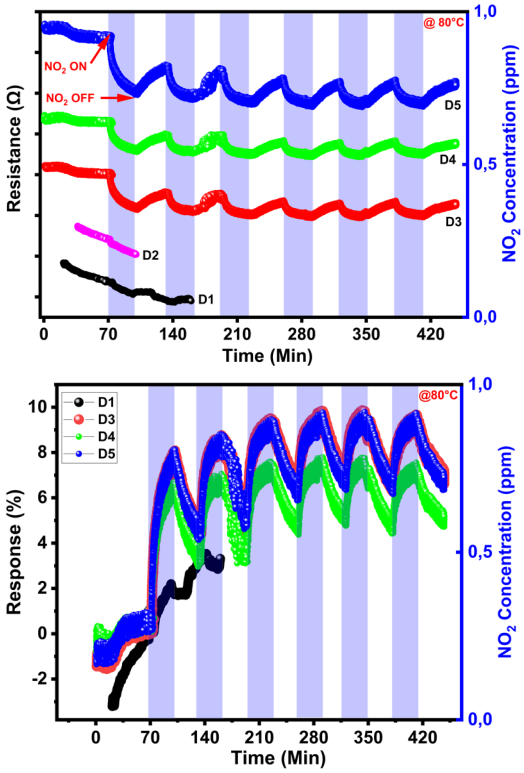

Figure 4. NO_2 gas sensing behaviour of all five sensors. Top: repeatability of the sensing devices towards 1 ppm NO_2 pulses (shaded area) with the chip at 80°C. Bottom: Calculated response of the sensing film. Here, the response is calculated using the formula: response (%) = $\{(R_{air} - R_{gas})/R_{air}\} \times 100$. Where R_{gas} is resistance when the target gas is injected and R_{air} is the resistance before the first NO_2 pulse.

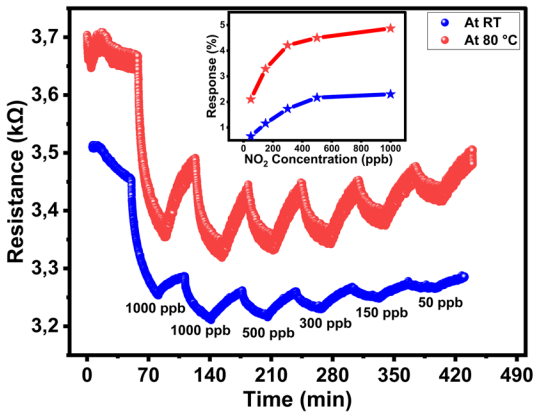

Figure 5: variation of resistance of device D4 at RT (blue) and 80°C (red) against different concentrations of NO_2, ranging from 50-1000 ppb. Inset: responses of the device vs. concentrations after the 1st NO_2 pulse.

Enhancing Overlay Accuracy through Transformation of Overlay Outliers caused by Wafer Local Defocus in Photolithography Scanner Calibration

Kwang Hoon Lee [a, b, c], Prof. Won Bo Lee [a]

[a] Department of Chemical and Biological Engineering, Seoul National University, Seoul 08826, Korea
[b] Samsung Institute of Technology, Yongin 17113, Korea
[c] Department of Memory Photo Technology Team, Samsung Electronics, Hwasung 18448, Korea
e-mail: kh1103.lee@snu.ac.kr

• Purpose of the work

In semiconductor photolithography, overlay refers to the misalignment error in the X and Y directions between successive patterned layers on a wafer. It is a critical metric that directly impacts both the functional integrity and yield of chips. In advanced memory processes, scanner overlay margins have become extremely tight, where even sub-nm deviations can result in significant device failures. To control such precision, scanner systems perform regular XY calibrations to generate tool-specific overlay compensation models. However, the test tool wafers used for calibration are subject to surface contamination and physical wear over repeated exposures in High Volume Manufacturing (HVM), leading to localized defocus conditions. These local defocus effects manifest as overlay outliers, which distort the calibration model and degrade compensation accuracy. In severe cases, they necessitate wafer rework or recalibration, resulting in productivity losses and increased tool downtime. This study proposes a robust outlier transformation method based on a 10-parameter linear regression model, designed to detect and correct overlay outliers generated during scanner XY calibration. The method replaces erroneous data points with statistically valid values, thereby preserving overlay budget integrity and minimizing operational losses. Importantly, the proposed approach is implemented entirely through software, requiring no hardware modifications or sensor upgrades, and can significantly enhance lithography overlay control and manufacturing stability.

• Novelty of the work with respect to the state of the art

Conventional overlay control methods typically rely on indirect improvements such as enhanced metrology accuracy, photomask heating compensation, or process- level tuning. Direct compensation of overlay anomalies using raw scanner calibration data remains highly limited —primarily due to restricted access to internal data structures. In high- volume manufacturing (HVM) environments, this limitation makes it challenging to independently identify and correct overlay outliers generated during calibration. In this work, we developed a proprietary data parsing engine to structurally decode the scanner' s XY calibration dataset. Using this parsed data, we systematically modeled the detection and transformation of overlay outliers. A total of eight correction approaches —including missing data handling, linear regression- based modeling, and machine learning algorithms —were benchmarked. Among them, the 10-parameter linear regression model achieved optimal performance in terms of statistical consistency and cosine similarity to reference profiles. Notably, the solution can detect and transform outliers directly within the scanner data pipeline, without altering scanner architecture or hardware. This enables meaningful improvements in overlay accuracy at the tool level, and more importantly, shifts control capabilities from equipment suppliers to end users. This represents a key advancement in lithography process flexibility and technical self-reliance in semiconductor manufacturing.

• Results of the work

The proposed methodology was experimentally validated across multiple scanner platforms operating in a high- volume manufacturing environment. During periodic XY calibration, a substantial amount of overlay vector data was collected and analyzed. Using point- to-point delta mapping, local defocus- induced overlay outliers were statistically identified on a per-wafer basis. Outlier detection thresholds were examined across multiple statistical bands, and an optimal filtering criterion was established based on operational robustness. Identified outliers were treated through missing data imputation, and eight different transformation models were applied to reconstruct the overlay map. Among them, the 10-parameter linear regression model exhibited the most stable and consistent performance. It demonstrated high correlation with a golden reference wafer— both in terms of cosine similarity and residual analysis —validating its effectiveness as a correction strategy. Furthermore, the proposed method was shown to reduce unnecessary calibration retries and improve scanner operation stability, resulting in a measurable improvement in overlay performance consistency. Given its data-driven nature and compatibility with current tool infrastructure, the method is expected to be highly applicable.

to sub-10nm lithography nodes and next-generation platforms such as EUV and High-NA scanners. It also offers meaningful scalability for broader integration into overlay correction workflows.

[1] Onur Demirer. Overlay control improvements through dynamic sampling. SPIE 12955, Metrology, Inspection, and Process Control XXXVIII, 1295527 (9 April 2024)
[2] Ik-Hyun Jeong, ASML. Improved wafer alignment model algorithm for better on-product overlay, Proc. SPIE 10961, Optical Microlithography XXXII, 109610A (2019)
[3] Joel Peterson. Lithography overlay control improvement using patterned wafer geometry for sub-22nm technology nodes. Proc. SPIE 9424, Metrology, Inspection, and Process Control for Microlithography XXIX, 94240N, 2015
[4] Timothy Wiltshire. Advanced overlay control in volume manufacturing IEEE/SEMI Advanced Semiconductor Manufacturing Conference, Saratoga Springs, NY, USA, 2011

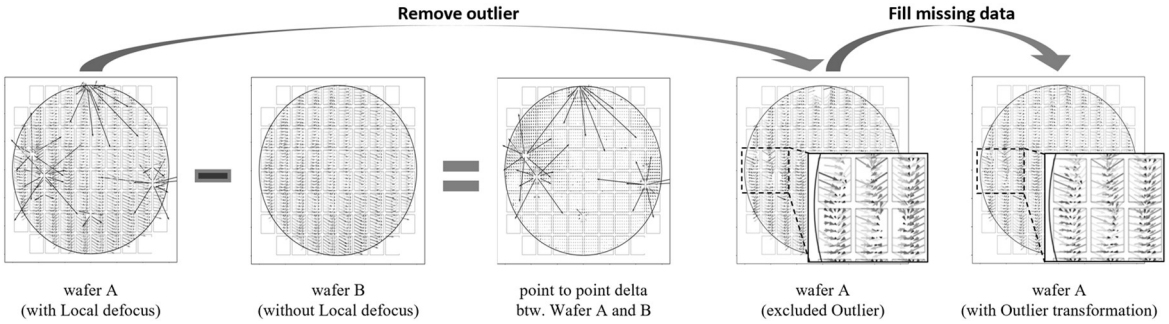

Figure 1. Flow chart of outlier detection and transformation (wafer A: contaminated, wafer B: reference). The transformation step was performed using a 10-parameter linear regression modeling method.

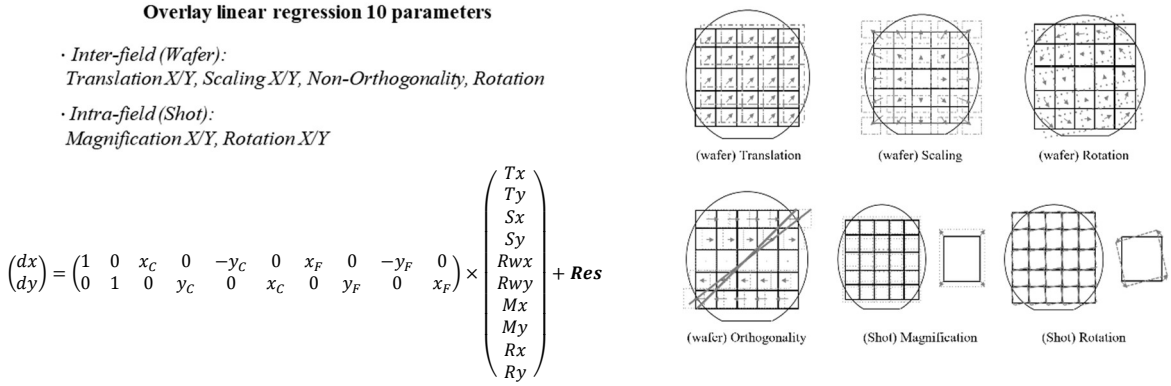

Figure 2. 10-parameter linear regression matrix and XY direction vector illustrations of individual terms

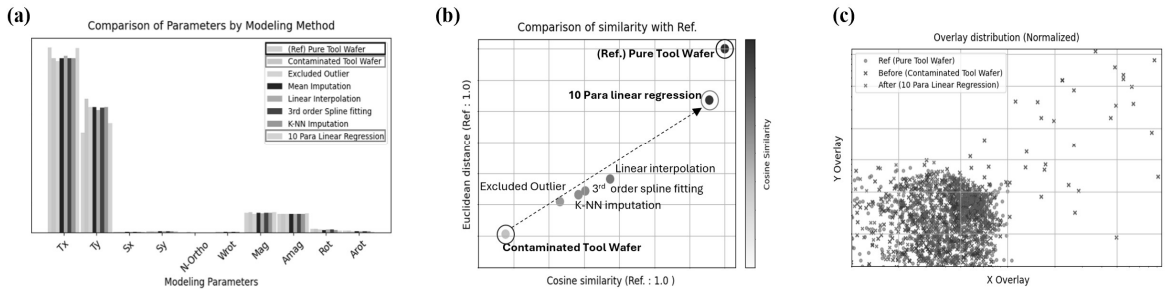

Figure 3. Evaluation of overlay modeling performance and transformation effect.
(a) Comparison of overlay using 8 modeling methods, high similarity in the 10-parameter linear regression.
(b) improvement from contaminated data quantified by Cosine similarity and Euclidean distance.
(c) Overlay distribution before and after transformation in the 10-parameter linear regression

Gas Sensors Based on MoS_2 Quantum Dots Deposited via Drop-Casting for Environmental Monitoring on Microfabricated Platforms

Villalvazo-Hidalgo Andrea Carolina, González-Reynoso Orfil, Carbajal-Arizaga Gregorio Guadalupe, Hidalgo-Rios Martha Angélica and García-Ramírez Mario Alberto

[a] University Center for Applied Sciences and Engineering, Guadalajara University, Guadalajara, Jalisco, 44430, México
e-mail: mario.garcia@academicos.udg.mx

Keywords: MoS_2, quantum dots, gas sensor, NO_2, CO_2, hydrothermal synthesis

The ability to swiftly detect atmospheric pollutants is a necessary feature of any monitoring tools available to use in the environment today. Atmospheric nitrogen dioxide (NO_2) and carbon dioxide (CO_2) are especially relevant components to address for public health and climate change. This is why, we are proposing a MoS_2-based gas sensor [1]. The gas sensor was fabricated by using a hydrothermal in-house-development synthesis method for obtaining molybdenum disulfide (MoS_2) quantum dots (QDs) and its applicational use in a micro-fabricated sensing platforms with an efficiently easy drop-casting method. The synthesis was performed at 120 °C for 24 hours, which resulted in QDs that were <3 nm in average diameter. The platform was fabricated on a Si/SiO_2 substrate (1x1 cm^2) that used interdigitated gold electrodes (IDE) (see Fig. 1).
The structural and chemical characterization were provided through X-ray diffraction (XRD) & UV-Vis (see Figs. 2 & 3). It shows MoS_2 crystallized that feature key optical and chemical properties for sensing applications. The fabricated device exhibited distinct electrical responses to gases such as NO_2 and CO_2. The combination of accessible synthesis, direct deposition and high sensitivity positions allows this platform as a promising and scalable solution for urban environmental monitoring applications.

[1] Chen, T.-M., Kuschner, W. G., Gokhale, J., & Shofer, S. (2007) 249–256.

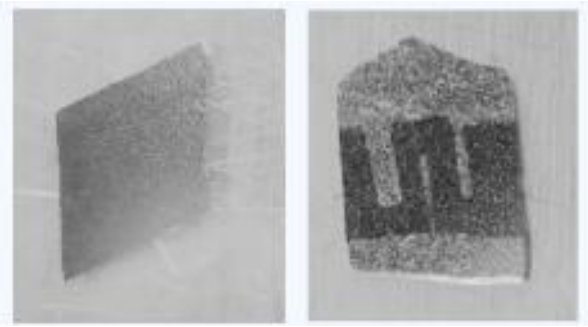

Figure 1. Before-and-after comparison of the sensor chip. The left image shows the untreated substrate, while the right displays the same chip after microfabrication with interdigitated gold electrodes and the deposition of MoS_2 quantum dots as the sensing layer

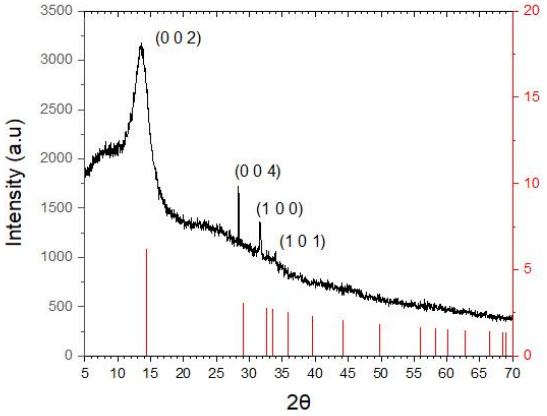

Figure 2. X-ray diffraction (XRD) pattern of hydrothermally synthesized MoS_2 quantum dots

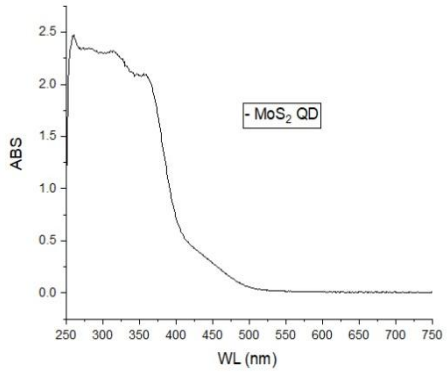

Figure 3. UV–Vis absorption spectrum of MoS_2 quantum dots synthesized via hydrothermal method.

Real-Time Wireless Tremor Tracking System with V-Groove Crack Sensor

Jonghyeon Woo, Jeongsik Noh, Jongsung Park

Department of Precision Mechanical Engineering, Kyungpook National University, Sangju, 37224, KOREA
e-mail: jpark40@knu.ac.kr

Parkinson's Disease (PD) is a chronic neurodegenerative disorder that induces various motor symptoms, including tremors [1]. Physicians typically assess disease severity using the Unified Parkinson's Disease Rating Scale (UPDRS) [2]. However, this process often relies on visual observation, which limits the objectivity and accuracy of quantifying tremor severity [3]. Among the four types of tremor patterns defined by the Movement Disorder Society (MDS), the postural tremor which exhibits a frequency similar or slightly higher than that of rest tremor poses a diagnostic challenge due to its subtle and hard-to-discern rhythmic characteristics [4].

To address these limitations, this study presents a compact, biocompatible, and wireless sensor system designed for the early detection and quantification of Parkinsonian tremors. Unlike conventional diagnostic methods that require in-clinic assessments and struggle to detect fine and intermittent muscle movement [5], the proposed device enables continuous and low-cost monitoring in daily life. The fabrication process incorporates standard MEMS techniques, including silicon wet etching, PDMS casting, and metal sputtering. The sensor is fabricated using a PDMS (polydimethylsiloxane)-based V-groove structure with a sputtered metal layer, designed to produce linear and repeatable changes in resistance in response to tensile deformation. The V-groove geometry concentrates stresses within a localized region, promoting crack initiation in the metal layer, promoting microcracks in the metal layer that converts minute tremors into measurable electrical signals.

The mechanical evaluation confirmed excellent durability, sensitivity, and negligible hysteresis over 1,000 cyclic loading tests. Furthermore, the sensor demonstrated high linearity in resistance change corresponding to repetitive strain conditions, verifying its reliability for long-term use. Using an ESP32 microcontroller with an integrated BLE system, tremor data were wirelessly collected and analyzed. For data analysis, a Hidden Markov Model (HMM) was employed to classify and quantify tremor patterns. HMM was chosen because of its effective ability to handle time-series data with relatively small datasets, making it well-suited for early-stage research and practical implementations where large-scale labeled data is typically limited [6]. Also, compared to other machine learning approaches such as LSTM, HMM offers significantly faster training times as well as lower computational requirements [6], ensuring efficient usage of our applications. After the tremor data was collected and preprocessed, the model was trained and showed high accuracy and F1 scores.

The classification performance was illustrated through feature extraction visualizations and confusion matrices, demonstrating the effectiveness of the proposed method in distinguishing different types of tremors. In conclusion, this sensor system provides a scalable, low-cost alternative for tremor monitoring, with potential applications in early PD diagnosis, treatment evaluation, rehabilitation, and broader neurological health monitoring.

[1] L. Shargel, Comprehensive Pharmacy Review, (Pennsylvania, Philadelphia, 2008).
[2] C. G Goetz et al., Mov. Disord. 23 (2008) 2129–2170.
[3] K. P Bhatia et al., Mov Disord. 33 (2018) 75–87.
[4] D. Belvisi et al., Parkinsonism & Related Disorders. 36 (2017) 41–46.
[5] B. Vescio et al., Front Neurol. 12 (2021).
[6] M. Panzer, Machine Learning, Optimization, and Big Data, (Volterra, Italy, 2016).

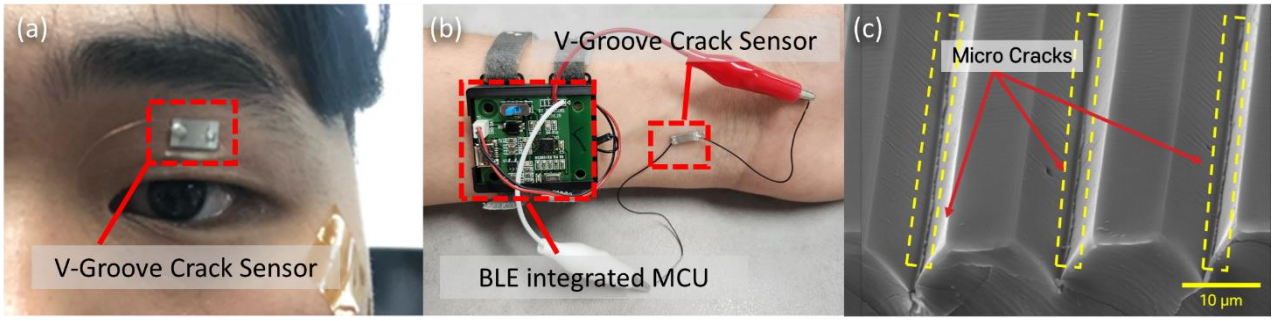

Figure 1. Photograph and microscopic images of the fabricated V-groove crack sensor.
(a) Optical image of V-groove based PDMS crack sensor attached around the eye area for facial tremor detection. (b) Photograph of the wearable system with a Bluetooth Low Energy (BLE)-integrated microcontroller unit (MCU), worn on the wrist. The V-groove crack sensor is attached onto the skin for tremor signal acquisition. (c) SEM image of the V-groove sensor after nano metal crack formation, depicts distinct fractures in the metal layer induced by tensile strain.

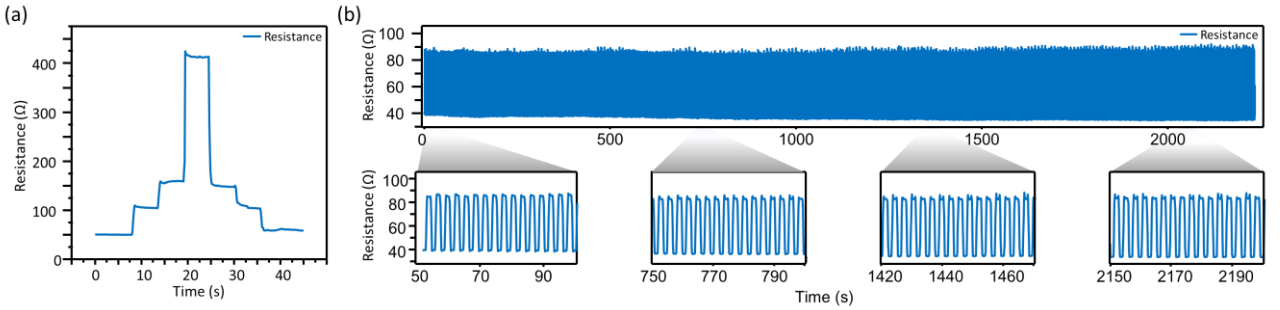

Figure 2. The performance of the PDMS based V-groove crack sensor under different conditions
(a) Preliminary sensing characteristics of the V-groove-crack sensor. (Moving step: 0.25 mm and Maximum moving displacement: 0.75 mm (b) Evaluation of repeatability and long-term durability of the fabricated V-groove crack sensor under a displacement of 0.25 mm tension, 0.25 mm compression.

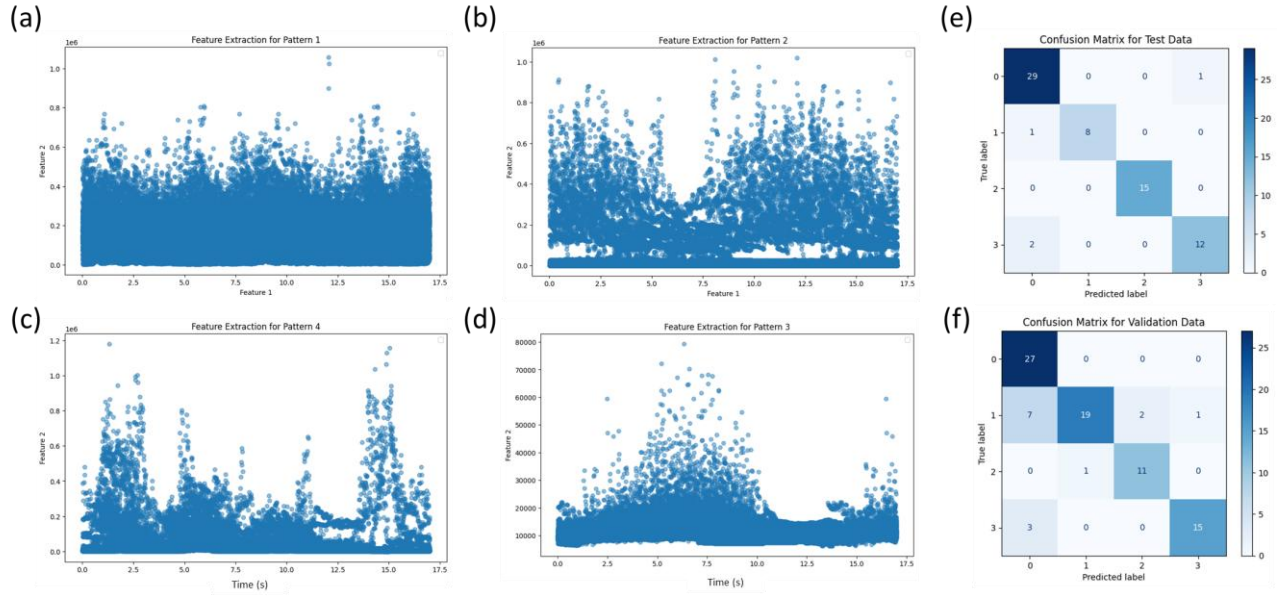

Figure 3. Feature extraction results and performance analysis
Figures (a–d) present the visualization of extracted features, showing key tremor characteristics and patterns. Figure (e) shows the confusion matrix for the test data, while Figure (f) displays the confusion matrix for the validation data, illustrating the classification performance of the HMM-based model and its effectiveness in distinguishing different tremor patterns.

Microscope-based Multi-Analyte-Reflectance-Spectroscopy (μ-MARS) for multiplexed label free monitoring of immunoreactions

G. Zisis[1], D. Tsounidi[2], G. Koukouvinos[2], P. Petrou[2], I. Raptis[1]

[1] Institute of Nanoscience & Nanotechnology, NCSR 'Demokritos', Athens, Greece
[2] Institute of Nuclear & Radiological Sciences & Technology, Energy & Safety, NCSR 'Demokritos, Greece
e-mail: i.raptis@inn.demokritos.gr

Optical biosensors are the most widely used type of biosensor due to their advantages in rapid, accurate, and label-free monitoring of bioreactions, as well as their ability to quantify minute concentrations of analytes. Despite these strengths, a major challenge remains in achieving multi-analyte detection—a crucial capability for applications in clinical diagnostics, food safety, and environmental monitoring. The development of multi-analyte biosensors could enable faster and more comprehensive analyses while also reducing overall analytical costs. One promising approach is White Light Reflectance Spectroscopy (WLRS), a powerful label-free detection method. WLRS monitors biomolecular interactions by tracking shifts in the interference spectrum generated when broadband light is reflected off a silicon chip topped with a silicon dioxide (SiO_2) layer [1]. To address the need for multi-analyte detection, a modified version of WLRS, known as Multi-Area Reflectance Spectroscopy (MARS), has been introduced. MARS utilizes three-dimensional structuring of the SiO_2 layer on silicon, enabling the simultaneous monitoring of multiple bioreactions with a single reflection probe and no moving components. This technique has been successfully demonstrated in the simultaneous detection of two mycotoxins in food samples [2]. This overlap complicates spectral analysis and limits the number of analytes that can be measured simultaneously.

In the present work, a radical principle of operation for fast and accurate multi-analyte determination of analytes is introduced, namely μ-MARS, by combining MARS with a standard optical microscope. In μ-MARS a dedicated optical module is mounted to any conventional reflectance optical microscope and converted it to a powerful optical tool for multi-analyte determinations resolving the limitations of MARS (limited number of analytes, limited tolerance in the placement of biosensing chip with respect to reflection probe, etc.). In μ-MARS approach, silicon chips with two or four sensing areas, each one consisting of SiO_2 layers of different thickness, are employed for the simultaneous detection of two or more analytes. Each area is functionalized with a specific antibody against to a particular analyte. These sensing areas are illuminated through the light source of the microscope and the reflected light goes through a dedicated aperture array (that defines the number of sensing areas) and is guided to a spectrometer for further analysis (Fig. 1). The fabrication flow-chart of the sensing chip is illustrated in Fig. 2 and includes cycles of opening of sensing areas through etching of Si_3N_4 layer followed by thermal oxidation. In addition, in Fig. 3, a microscope image with the areas from which the reflectance is collected and a typical reflectance spectrum is illustrated. The sensing chip is 15 mm × 5 mm in size and accommodate 4 sensing areas each one of them with different SiO_2 thickness and size of 4 mm × 2 mm. Using the aperture array, the reflected light comes only from the sensing areas and provides high tolerance in the placement of the sensing chip under the objective lens improving the reliability and accuracy of the detection against MARS method.

The μ-MARS sensing method was evaluated through a non-competitive immunoassay for detection of C-reactive protein (CRP). It was found that the signals obtained from the two sensing areas, when only one of them was modified with the antibody against CRP, were identical. Additionally, the signals obtained when both areas were modified with the specific antibody were the same, ensuring that there is no bias in the signals from the two sensing areas. Finally, to demonstrate the multi-analyte determination capabilities of the proposed sensing approach, antibodies against two different complement components, namely C3b and total complement complex (TCC), were immobilized onto the two sensing areas and the chips were used for detection of both proteins in complement-activated serum. These results highlight the potential of μ-MARS for multi-analyte biosensing applications in complex media with high specificity and sensitivity.

[1] D. Tsounidi, G. Koukouvinos, V. Christianidis, E. Legaki, V. Giogli, K. Panagiotopoulou, S. Taka, Z. Ekaterinidi, S. Kakabakos, I. Raptis, P. Petrou Biosensors 11 (2021) 268
[2] V. Anastasiadis, G. Koukouvinos, P.S. Petrou, A. Economou, M. Harjanne, P. Heimala, D. Goustouridis, I. Raptis, S.E. Kakabakos Biosens. Bioelectron. 153 (2020) 112035

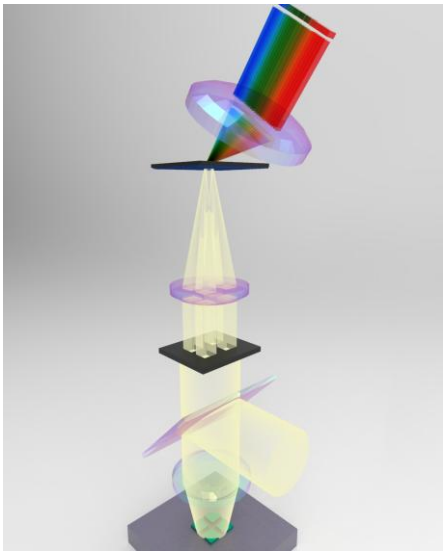

Figure 1. Principle of operation of the Microscope-based Multi-Analyte-Reflectance-Spectroscopy (μ-MARS) detection method.

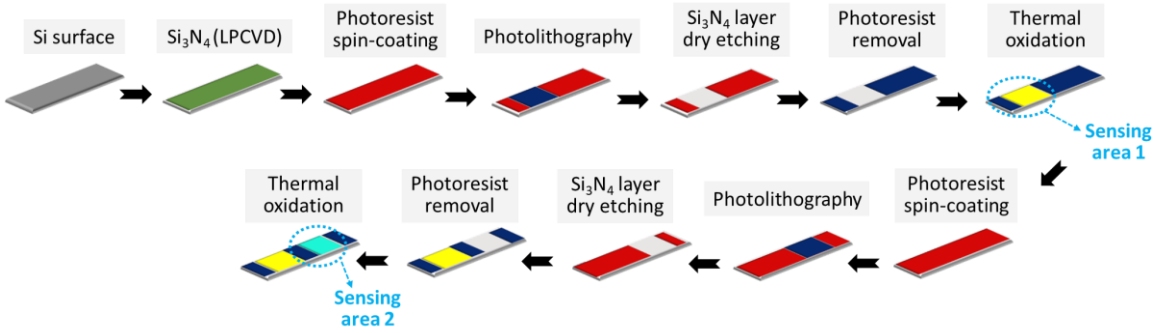

Figure 2. Schematic of the chip fabrication process for the preparation of μ-MARS biosensing chips with two sensing areas of SiO_2 of different thickness. The processing steps of opening of Si3N4 area, thermal oxidation and resist removal can be repeated to add more sensing areas on the same chip.

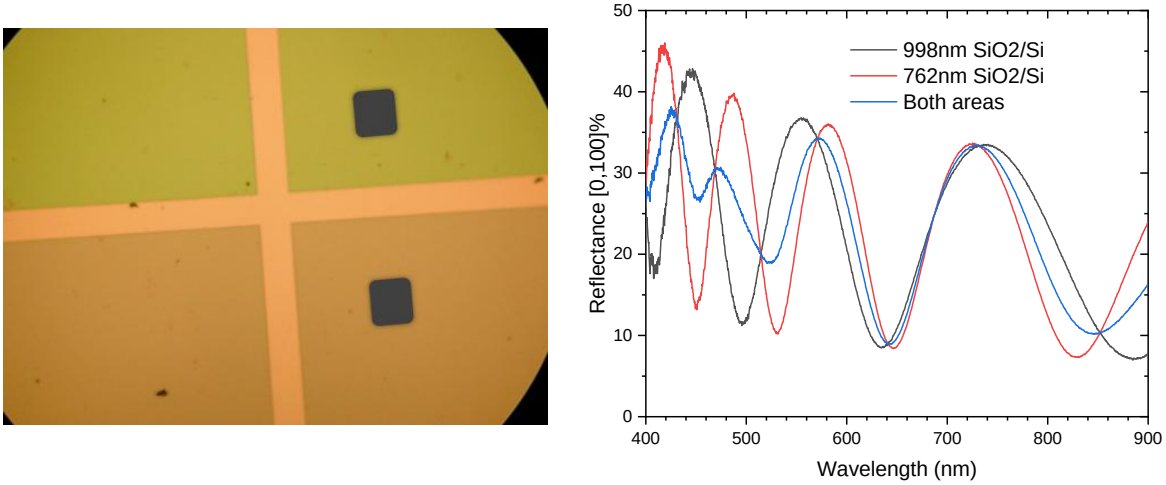

Figure 3. (a) Microscope photo of the sensing areas of the chip. (b) Reflectance spectra collected from each sensing area of different SiO_2 thickness and from both sensing areas combined.

CNFET fabrication for NO_2 gas sensor recovery with local electrode heating

Ines Kraiem [a], Cosmin Ioan Roman [a], Andri Sigron [a], Miroslav Haluska [a], Christofer Hierold [a]

[a] ETH Zurich, Micro- and Nanosystems, Zurich, Postal code, Switzerland
e-mail: ikraiem@ethz.ch

Abstract

This paper presents a novel gas sensor recovery approach for Carbon Nanotube Field Effect Transistor (CNFET) nitrogen dioxide (NO_2) sensors, relying on the local heating of the transistor's Source (S) and Drain (D) electrodes. By fabricating split S and D electrodes, a current can be passed through them, heating the electrodes metal by Joule heating and the carbon nanotube suspended on top of them. We show that in two different CNFET devices electrode heating enables sensor recovery within 10 seconds. The temperature reached by the carbon nanotube (CNT) is estimated by simulating the Joule heating of the contact electrodes during local electrode heating (EH) pulses.

Introduction

CNFETs achieve low-power NO_2 detection with high sensitivity. Progress has been made in the sensor readout and recovery schemes based on self-heating [1], with excellent limit-of-detection. Drift is still a potential challenge, since self-heating cannot desorb molecules close to contact regions which are colder. In the following, a potential sensor reset technique is presented that uses a similar device design to the one presented in [2], where Woo. et al. show that a U-shaped electrode design can reduce the contact resistance in devices with substrate-bound CNTs. In our work, suspended-CNT devices are locally heated to induce a fast desorption of the molecules from the CNFET.

Methodology:

Design and Fabrication: Figure 1 (a) shows the fabrication process of CNFET sensor devices with split electrodes. Starting with a Si/SiO_2 wafer, two e-beam lithography steps are carried out, the first one to define the distance between the suspended CNT channel and the gate electrode G (in our case 200 nm), and a second for the metallization of the S, D, and G electrodes. A photolithography step is performed afterwards to allow the elevation of the device structure, by etching 30 µm into the Si substrate using the Bosch process. The elevation of S and D electrodes allows the clean mechanical dry transfer of an individual CNT as explained in [3]. The results of the device fabrication are shown in the SEM image of figure 1 (b), and (c) where an individual suspended CNT can be seen on the S and D split electrodes.

Measurements: During gas measurements, the G voltage V_g is swept from -10 to 10V and transfer characteristics (TC) of the CNFET are recorded (I_s versus V_g) at $V_D = 0.3V$, whereby the split electrodes are shorted (figure 2 (c) left). To induce a quick gas molecule desorption EH voltage pulses are applied to the outer electrodes (figure 2 (c) right) while the inner ones are shorted to induce Joule heating in both S and D. The split electrodes are designed to be thinner outside the area of the suspended CNT to ensure the CNT is sufficiently heated without submitting it to a high potential difference. The potential drop experienced by the CNT is expected to stay well below 1V for V_{EH} up to 3V, as can be seen in the simulation results in figure 4 (a).

Results and Discussion

Figure 2 shows the effect of EH on the transfer characteristics of device 1 (a) and device 2 (b). After EH, both V_{th} and the shape of the slope in the transistor's on-state are recovered. Figure 3 shows the results of gas measurements with EH pulses of 10 seconds using $V_{EH} = 1V$ (a) and $V_{EH} = 2V$ (b). With 1V pulses the channel current around the original threshold voltage is not recovered to its baseline after EH pulses, whereas with 2V pulses the sensor signal is lowered after each pulse, whereby device 1 fully and device 2 partially recovers. A simulation of the S and D surface temperature was performed and is shown in Figure 4 (b). A difference of about 70°C in the electrode's temperature is expected when applying 1V and 2V pulses. The results suggest that a temperature of over 100°C need to be reached by the S and D electrodes to induce complete desorption of NO_2 molecules from the CNT surface. The split electrode design opens an opportunity to control the temperature of the CNT during EH by controlling V_{EH} and the electrodes geometry and can thus be a way to study the desorption dynamics of different molecules from a suspended CNT in a CNFET gas sensor.

[1] S. Jung et al., Adv. Sensor Res. 3 (2024) 2300081.
[2] Y. Woo et al., Nanotechnology 18 (2007) 095203.
[3] M. Muoth and C. Hierold, IEEE MEMS (Paris, 2012) 1352-1355.

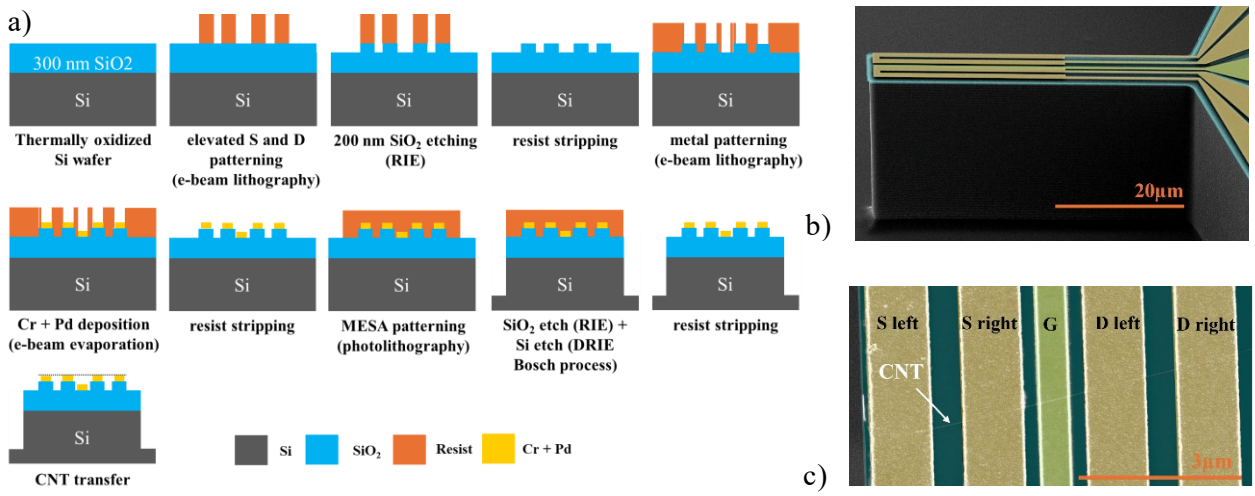

Figure 1. CNFET sensor device with local electrode heating structure. a) Fabrication process. The S and D electrodes are split to allow local electrode heating. b) SEM of CNFET device. C) SEM top view of CNFET after CNT transfer showing an individual CNT suspended over the G electrode.

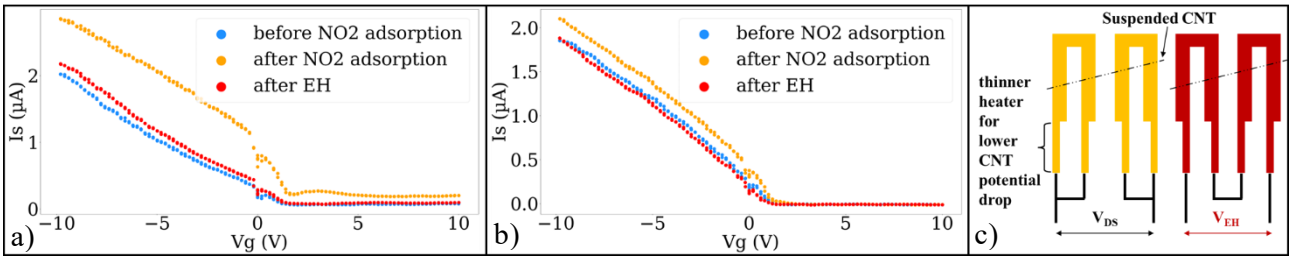

Figure 2. Transfer characteristics of the CNFET sensor at $V_D = 0.3V$ pre gas exposure (blue), after exposure to 500 ppb NO_2 (yellow), and after local EH (red) with $V_{EH} = 2V$ for device 1 (a) and device 2 (b). c) Measurement scheme for transfer characteristics (left, yellow) and electrode heating (right, red).

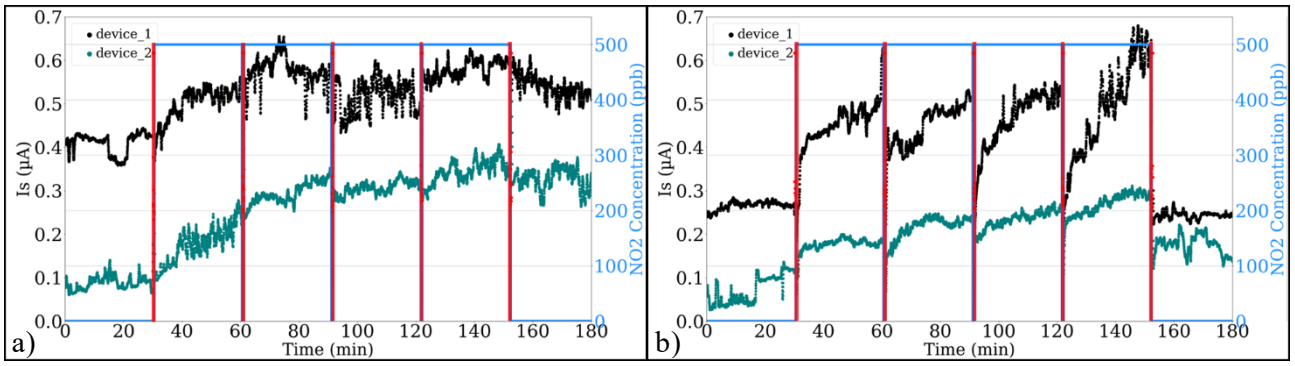

Figure 3. Channel current at pre-gas exposure V_{th} versus time (equivalent to V_{th} change over time) for device 1 (top curve, black) and device 2 (bottom curve, teal), and NO_2 concentration (blue). EH pulses of 10s (in red bars) are applied with a) V_{EH}=1V and b) $V_{EH} = 2V$, corresponding to 3mW and 12mW peak power.

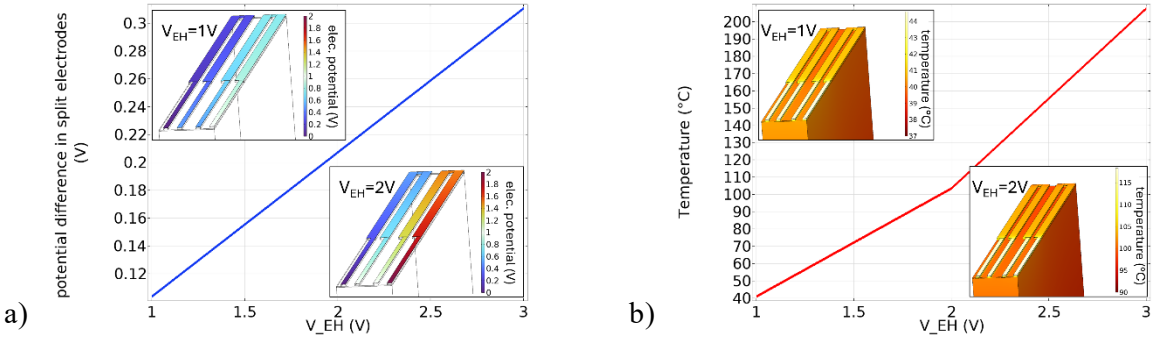

Figure 4. COMSOL simulations of a) expected potential drop over the CNT during EH for different V_{EH}, and b) expected temperature reached by the electrodes for different V_{EH}.

Selective Electrochemical Aptasensor Using Methylene Blue for *Pseudomonas aeruginosa* Detection in Mixed Bacterial Cultures

Somayeh Maghsoomi [a, b], Mai-Lan Pham[a] , Martin Brandl[a], Julia Walochnik[b].

[a] Center for Water and Environmental Sensors, Department for Integrated Sensor Systems, University for Continuing Education Krems, Dr.-Karl-Dorrek-Straße 30, 3500 Krems an der Donau, Austria.

[b] Institute of Specific Prophylaxis and Tropical medicine, Medical University of Vienna, Kinderspitalgasse 15, 1090 Vienna, Austria.

somayeh.maghsoomi.taramsari@donau-uni.ac.at

This study presents a sensitive electrochemical aptasensor for rapid detection of *Pseudomonas aeruginosa*, a clinically important environmental pathogen. The developed biosensor is based on the F23 aptamer immobilized on disposable gold screen-printed electrodes (Au-SPEs), employing methylene blue (MB) as an electrochemical redox indicator to enhance detection sensitivity. This study aims to improve the accuracy, selectivity, and practical applicability of *P. aeruginosa* detection through a novel aptasensing approach[1,2].

Unlike conventional methods, the aptasensor is efficient, low-cost, and portable approach for the rapid identification of *P. aeruginosa*. The incorporation of MB as an exogenous redox indicator significantly amplifies the electrochemical response, thereby enhancing both sensitivity and specificity. The aptasensor achieves an impressive limit of detection (LOD) of 8 CFU·mL^{-1}, surpassing several existing electrochemical detection platforms in terms of analytical performance[1].

The successful fabrication of the aptasensor was validated through scanning electron microscopy (SEM) imaging and cyclic voltammetry (CV) characterization, confirming efficient aptamer immobilization and the functional role of MB in signal enhancement. Square wave voltammetry (SWV) measurements demonstrated a robust and linear correlation between bacterial concentration and current peak reduction, enabling precise quantification of *P. aeruginosa* across diverse sample matrices. The aptasensor exhibited excellent selectivity, effectively differentiating *P. aeruginosa* from other bacterial species, including *Escherichia coli*, *Staphylococcus aureus*, *Pseudomonas putida*, and *Enterococcus faecalis*. Furthermore, its application in tap water samples demonstrated strong potential for point-of-care pathogen monitoring in both clinical and environmental settings[1].

This work represents a significant advancement in biosensing technologies, providing a highly sensitive and selective detection method for *P. aeruginosa*. The developed aptasensor holds promise for real-time monitoring applications in medical diagnostics, food safety assessment, and water quality surveillance, thereby contributing to improved public health and environmental safety measures. Despite the relatively lower signal gain for *P. aeruginosa* compared to some interfering bacteria, the aptasensor demonstrated excellent specificity and a very low detection limit (8 CFU·mL^{-1}). These characteristics highlight its practical potential for rapid, on-site detection of *P. aeruginosa* in clinical and environmental settings, contributing to improved public health and safety[1].

References

1. Maghsoomi, S., Walochnik, J., Brandl, M. & Pham, M. L. A Novel Methylene Blue Indicator-Based Aptasensor for Rapid Detection of Pseudomonas aeruginosa. *Int J Mol Sci* **25**, (2024).

2. Wang, K. Y., Zeng, Y. L., Yang, X. Y., Li, W. B. & Lan, X. P. Utility of aptamer-fluorescence in situ hybridization for rapid detection of Pseudomonas aeruginosa. *European Journal of Clinical Microbiology and Infectious Diseases* **30**, 273–278 (2011).

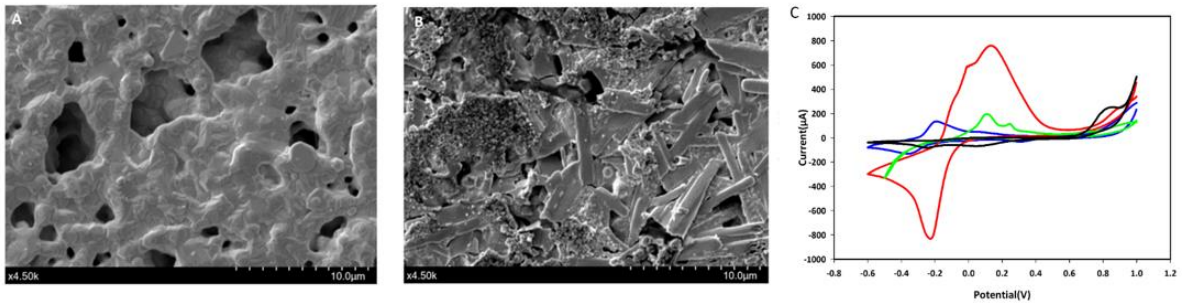

Fig. 1. SEM micrograph of (a) the bare Au-SPEs; (b) the modified Au-SPEs by assembly of F23 aptamer on the surface of Au-SPEs; (c) cyclic voltammogram of the bare Au-SPEs (black) measured in the electrolyte lacking MB, the bare Au-SPEs measured in the electrolyte supplemented with MB (blue), the modified Au-SPEs measured in the electrolyte lacking MB (green) and the modified Au-SPEs measured in the electrolyte supplemented with MB (red) within scan ranges from −0.6 to +1.0 V at a scan rate of 50 mV•s^{-1}.

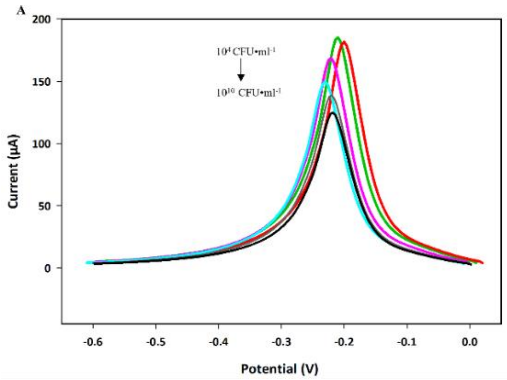

Fig. 2. SWV characteristic of the aptasensor in Tris buffer (pH 6.0) containing 50 mM MB after 1 hour incubation with various concentrations of *P. aeruginosa* ATCC27853, measured: (green) 10^4 CFU•ml^{-1}; (red) 10^6 CFU•ml^{-1}; (pink) 10^7 CFU•ml^{-1}; (blue) 10^8 CFU•ml^{-1}; (gray) 10^9 CFU•ml^{-1}; (black) 10^{10} CFU•ml^{-1}.

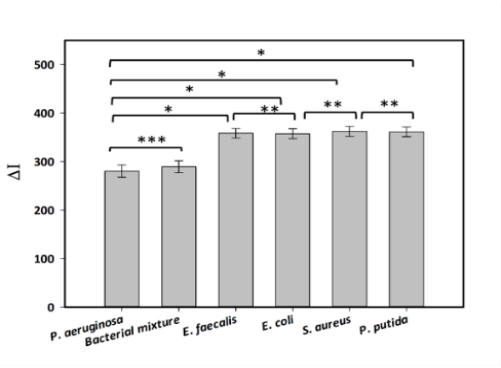

Fig. 3. Selectivity and specificity of the aptasensor in the presence of P. aeruginosa, E. coli, E. faecalis, S. aureus, P. putida, and a bacterial mixture (1.6×10^9 CFU·mL^{-1}). Statistical analysis was performed using one-way ANOVA with Tukey's post-hoc test ($p < 0.001$ considered significant; $p = 0.917$; *$p = 0.430$).

Table 1: Electrochemical signal obtained from aptasensors incubated with interfering bacteria and measured in the electrolyte supplemented with or without MB.

Bacteria	**ΔI (μA)**		
	Without MB	*With MB*	*Signal gain (%)*
P. aeruginosa	133.931 ± 5.155	280.387 ± 12.633	47.633 ± 2.175
Bacterial mixture	134.272 ± 4.714	283.433 ± 9.776	47.346 ± 1.651
E. coli	173.531 ± 5.879	358.644 ± 9.699	48.389 ± 1.347
E. faecalis	172.001 ± 6.148	357.479 ± 10.363	48.121 ± 1.349
S. aureus	178.024 ± 5.606	362.551 ± 10.466	49.112 ± 1.309
P. putida	176.440 ± 5.66	361.563 ± 10.066	48.807 ± 1.314

ΔI represent the current difference with and without bacterial incubation. The lower ΔI observed for *P. aeruginosa* likely reflects differences in aptamer binding efficiency or cell surface interaction.

Water-soluble holographic color prints from UV to visible for sustainable optical security device

Hyunjung Kang[1], Hongyoon Kim[1], Junsuk Rho[1*]

[1]Department of Mechanical Engineering, Pohang University of Science and Technology (POSTECH), Pohang-si, 37673, Republic of Korea

**Corresponding author E-mail: jsrho@postech.ac.kr*

Ensuring product authenticity and environmental sustainability has become increasingly important in the face of expanding counterfeiting and packaging waste. While metasurface-based optical security systems offer tamper resistance and visual versatility, their practical deployment remains limited due to high fabrication costs, low throughput, and lack of eco-friendly materials. In this work, we present a multifunctional optical security platform based on water-soluble holographic color print-based QR codes (**Figure 1**). The core of this system is a biocompatible nanocomposite composed of hydroxypropyl cellulose (HPC) and titanium dioxide (TiO_2) nanoparticles, offering a high refractive index (~1.9) and near-zero extinction coefficient across the ultraviolet (UV) to visible spectrum. The nanocomposite is patterned using scalable nanoimprint lithography (NIL) without requiring secondary etching or deposition, enabling large-area, substrate-independent fabrication. The metasurface design integrates Mie and lattice resonances with geometric phase control to simultaneously achieve vivid RGB coloration and full-phase holography. A supercell rotation strategy enables efficient polarization-sensitive hologram encoding while maintaining high color fidelity. Four optimized meta-atoms were designed for red (635 nm), green (532 nm), blue (450 nm), and UV (375 nm) wavelengths, achieving conversion efficiencies of 20–23% in the visible and 7% in the UV, while generating spectrally isolated structural colors. The fabricated QR codes incorporate RGB/UV metaholograms into position detection patterns, producing spin-dependent holographic images with dual-functionality under white and polarized light. These features support intuitive authentication and increased resistance against QR spoofing and duplication. Moreover, the QR code is biodegradable and fully dissolves in water, providing an environmentally friendly labeling solution compatible with curved or flexible packaging (**Figure 2**). Its nanostructures irreversibly degrade when exposed to high humidity (≥80% RH for 12 hours), making it a passive indicator for improper storage conditions. This irreversible degradation, combined with reversible color shifts under transient humidity exposure, enables its dual role as a sensor and security tag. The proposed platform addresses pressing needs in secure labeling, real-time quality indication, and sustainable packaging, paving the way for next-generation optical security devices in logistics, pharmaceuticals, and high-value consumer goods.

[1] J. Kim et al., Nature Food, 5 (2024), 293-300

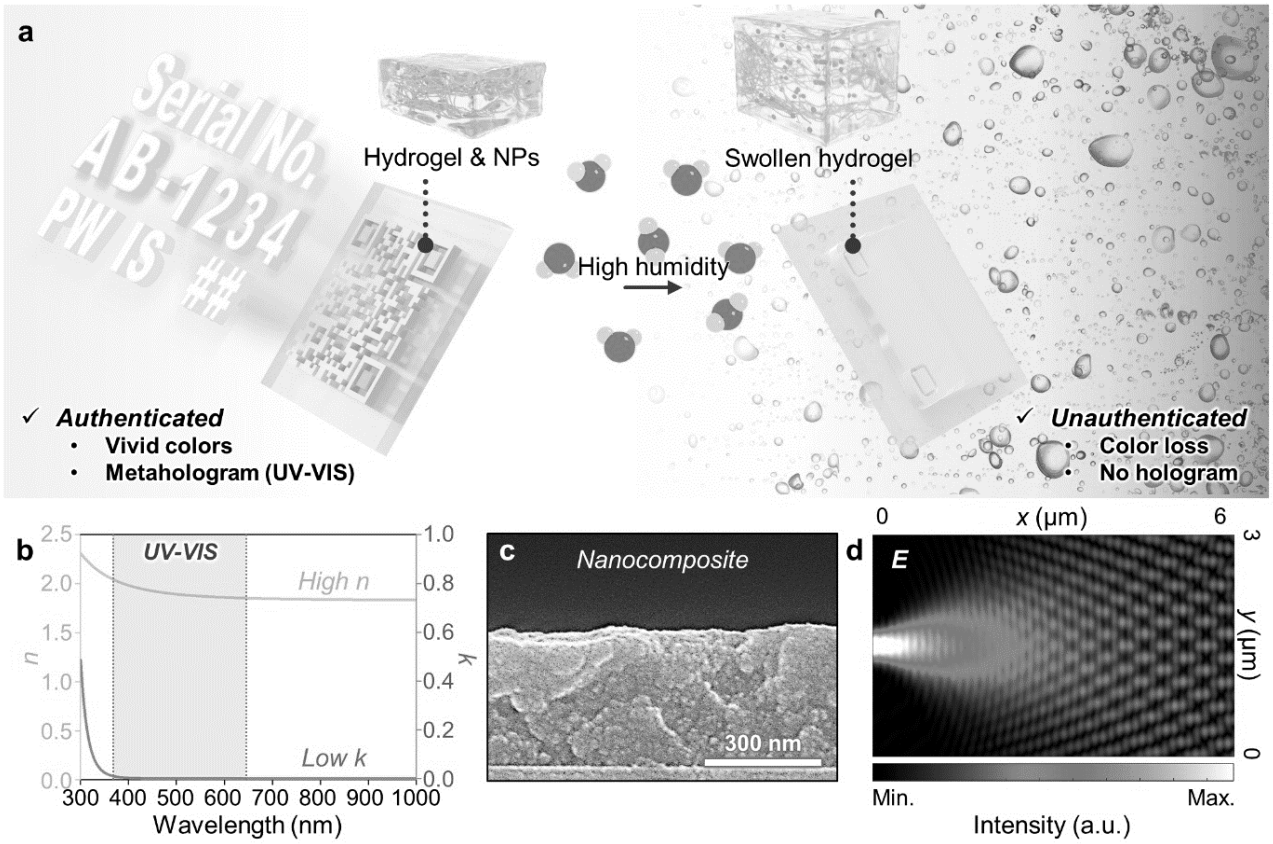

Figure 1. Characterization of the water-soluble nanocomposite. (**a**) Schematic of the QR code based on water-soluble holographic color prints. (**b**) Measured refractive index of the nanocomposite containing 75 wt% TiO2 nanoparticles. (**c**) Scanning electron microscopy (SEM) image of the nanocomposite film cross-section. (d) Scattering effect in the 75wt% nanocopmosite film analyzed 2D finite element simulations of Gaussian beam propagation.

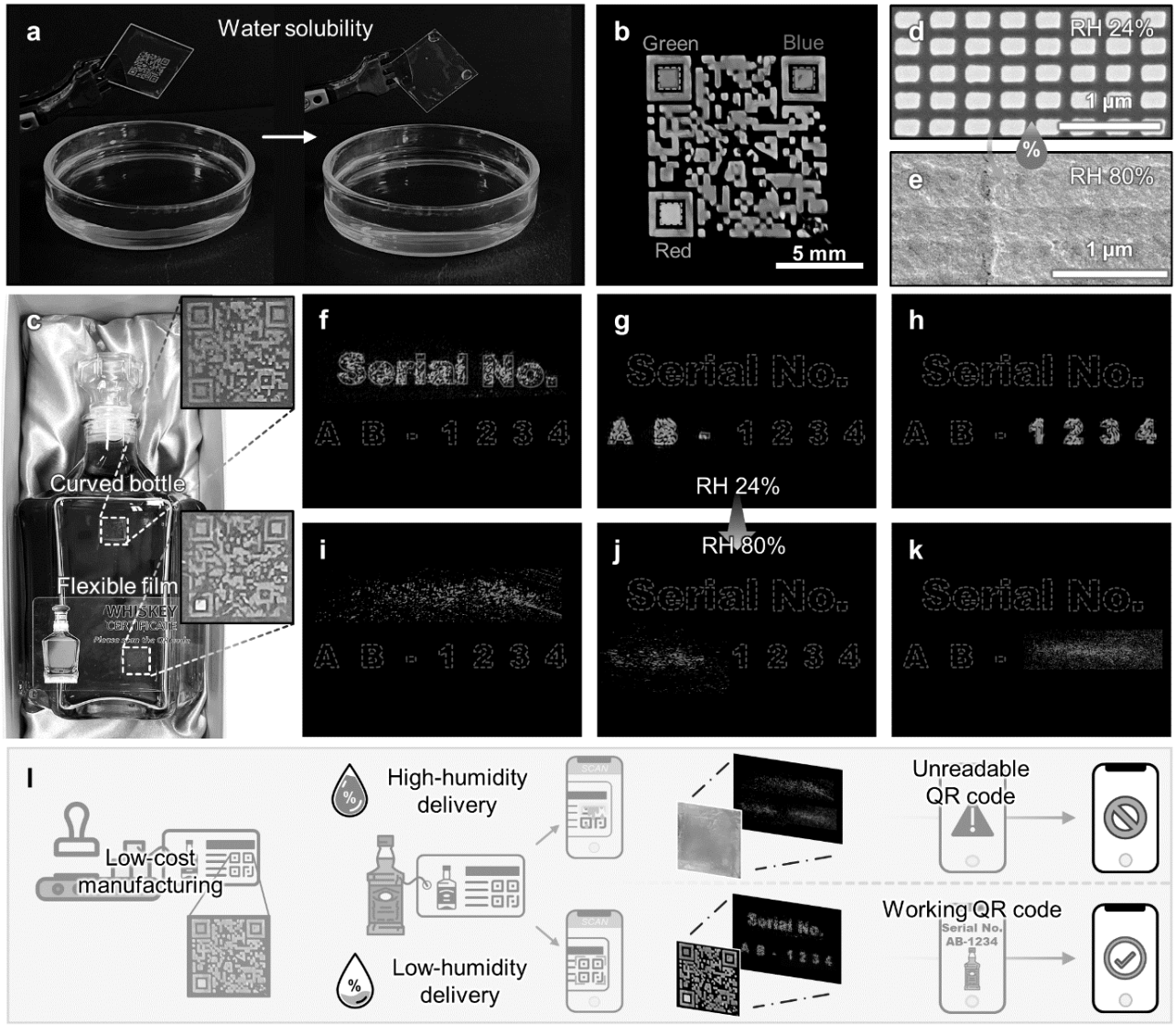

Figure 2**. Holographic QR code for sustainable and enhanced optical security. (a)** Sequential photographs demonstrating the water-solubility of the QR code. **(b)** Photograph of an RGB holographic color print-based QR code. **(c)** Printed QR codes on a curved glass bottle and a flexible plastic film. Scanning electron microscopy (SEM) images of the QR code **(d)** before (RH 24%) and **(e)** after exposure to RH 80% for 12 hours. Measured **(f)** red, **(g)** green, and **(h)** blue holographic images at RH 24%, and **(i–k)** corresponding images after exposure to RH 80%. **(l)** Schematic illustration of the proposed sustainable optical security system.

Dual functional filmy device for heat dissipation and power generation based on Bi_2Te_3 array with topological surface

Yiheng Zhao[1], Mingxue Li[1], Yufeng Zhang[1]

[1]Harbin Institute of Technology, School of Astronautics, Harbin,150001, China
e-mail: li_mingxue@hit.edu.cn

Keywords: thin films; thermoelectrics; magnetron sputtering

With rapid development of integrated circuit (IC) technology, the continuous improvement in computational density and power consumption has created an urgent demand for highly integrated thermal management systems[1]. One of the effective ways to realize high heat flux dissipation of power devices is to introduce integrated material thin film of high thermal conductivity benefitting from the near-junction low thermal resistance mechanism, such as single-crystal diamond film[2].Although heat can be effectively dissipated, the abundant energy contained therein is wasted. Thermoelectric materials[3] offer a dual-functional green energy solution by converting waste heat gradients into electrical energy, simultaneously achieving efficient thermal management and sustainable power supply. In this work, bismuth telluride with topological surface is used to prepare a functional thin film that can both realize heat dissipation and waste heat conversion for power generation.

The topological bandgap on the material surface opens under specific infrared irradiation, enabling heat dissipation via photon emission or phonon vibrations. Simultaneously, bismuth telluride (Bi_2Te_3), as an exceptional thermoelectric material, converts a portion of the thermal energy into electrical power. In order to increase the output voltage, an array structure consisting of multiple thin film generating units is employed. In this work, a finite element simulation model was established to optimize the thickness, distribution, and area of the device. The Bi_2Te_3 film device with both functions of heat dissipation and power generation were fabricated via magnetron sputtering technology, which unit size is 1.2*1.2 mm and overall size is 30 * 20 mm. Experimental results demonstrate that the fabricated Bi_2Te_3 films achieve a maximum output power of approximately 77 pW. When placed on a 50°C heating stage, the temperature of the sputtered film sample was reduced by 5°C compared to the non-sputtered reference. The proposed device shows significant potential for enhancing heat dissipation in high-power-density ICs and enabling waste heat recovery and utilization.

[1] M. Zhang et al., *Device*, 2 (2024) 100367.
[2] C. Zhang et al., *J. Mater. Sci.*, 58 (2023) 3485–3507.
[3] P. Wu et al., *Int. J. Thermophys.*, 42 (2021) 111.

Figure 1. Insert a concise explanation of figure 1 here. Figure may be color or grayscale and should include a scale bar where relevant.

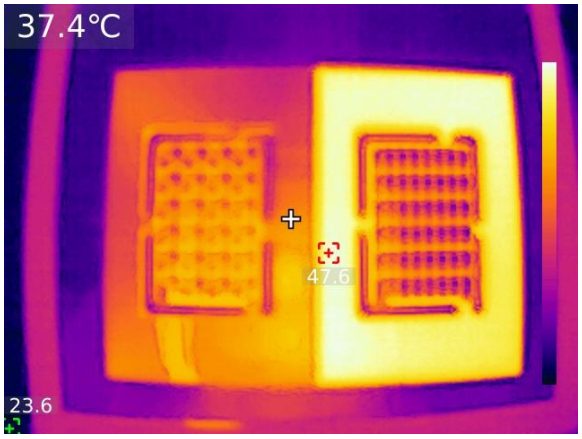

Figure 2. Insert a concise explanation of figure 1 here. Figure may be color or grayscale and should include a scale bar where relevant.

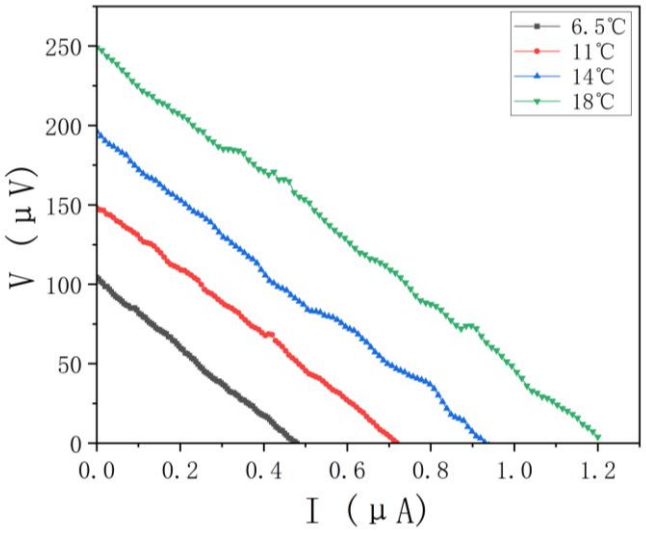

Figure 3. Current-Voltage curves of the device under varying temperature differences (ΔT)

A Modeling Study on Inorganic Chalcogenide Transport Layers in Sn-Based Perovskite Solar Cells

Daniyal Khosh Maram
Department of Electrical Engineering, Amirkabir University of Technology, Tehran, Iran
Danialkhoshmaram@aut.ac.ir

Abstract

Tin-based perovskites have emerged as promising candidates for photovoltaic applications. This work introduces a strategy to improve both the stability and efficiency of pure Sn-based perovskite solar cells (PSCs), achieving results comparable to conventional structures by utilizing inorganic chalcogenide electron transport layers (ETLs) and hole transport layers (HTLs).

Introduction

Tin (Sn) is considered one of the most promising alternatives to lead (Pb) in perovskite solar cells due to its narrower energy band gap, which is closer to the Shockley–Queisser limit (1.2-1.4 eV), as well as its higher mobility and longer carrier lifetime. However, a significant challenge in achieving high efficiency with Sn-based perovskite solar cells (PSCs) is the lack of electron and hole transport materials that have well-matched energy bands with the active layers in typical n-i-p or p-i-n architectures. This mismatch leads to energy barriers at the interfaces. Furthermore, the rapid oxidation of Sn results in poor stability and efficiency. Therefore, exploring new carrier transport materials with compatible energy levels is crucial for improving both the efficiency and stability of Sn-based PSCs.

Model

The effects of certain phenomena, mechanisms, or material parameters are often derived from experimental results. Numerical simulations can be used to better interpret these measurements and evaluate the performance of a solar cell. SCAPS-1D, due to its close alignment with experimental data, is considered superior to other software for modeling solar cells. The $J-V$ (current density-voltage) characteristics and quantum efficiency (QE) are the most commonly used data to validate numerical models. The modeling is conducted by simultaneously solving Poisson's equation, the continuity equation, and the drift-diffusion equation.

Discussion

According to Fig. 1, our modeling results are in agreement with the reported results from Ref. [2]. Subsequently, the $J-V$ and quantum efficiency (QE) characteristics of different inorganic chalcogenide HTLs and ETLs—including CZTS and SnS for the HTL, and SnO_2, SnS_2, and TiO2 for the ETL—have been investigated using a validated modeling setup. Among the different modeling cases, the PSC structure (FTO/SnS2(Spray)/Sn-perovskite/SnS/Au) achieves a power conversion efficiency (PCE) of 6.97%, making it the highest-performing PSC. The fill factor (FF), PCE, open-circuit voltage (Voc), and short-circuit current density (Jsc) for each case are shown in Fig. 1, Fig. 3, and Fig. 5. Additionally, the $J-V$ and QE characteristics for all modeling cases are presented in Fig. 1 to Fig. 6.

Conclusion

Inorganic chalcogenide materials, including CZTS and SnS for the HTL, and SnO_2, SnS_2, and TiO_2 for the ETL, have been investigated as potential candidates for improving HTL/ETL performance in numerical modeling. The results were compared with previously reported findings. In conclusion, we demonstrated that altering the inorganic chalcogenide HTL/ETL materials significantly affects cell performance. A maximum efficiency of 6.97% was achieved for the (FTO/SnS_2(Spray)/Sn-perovskite/SnS/Au) PSC structure, which is 1.53% higher than the reference case's PCE of 5.44%. This improvement is attributed to better band alignment and reduced Sn oxidation, leading to enhanced stability.

Word count: 491

References

[1] Yu, Bin-Bin et al, *Heterogeneous 2D/3D Tin-Halides ... Breaking 14%*, Advanced Materials, (2021).
[2] F. Hao et al, *Anomalous Band ...in Solar Cells*, JACS, (2014).

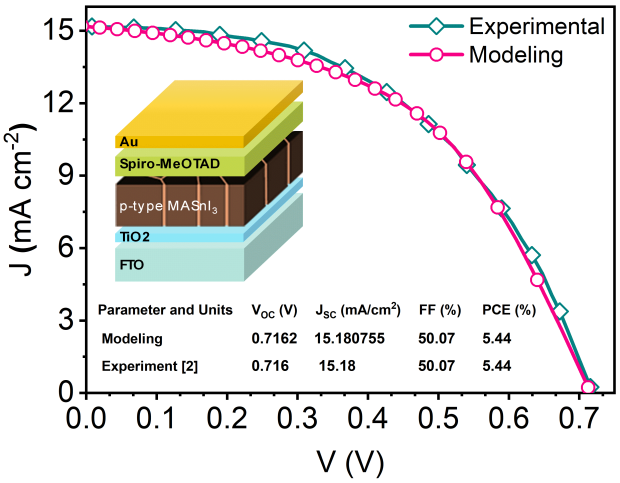

Fig. 1. $J-V$ characteristics obtained from our modeling and experimental data reported in [2].

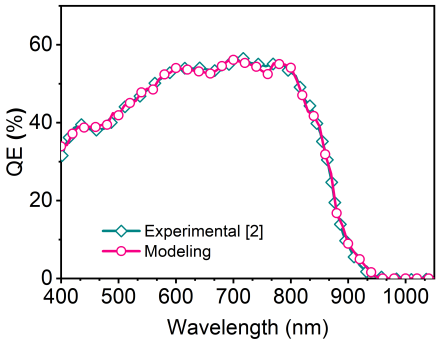

Fig. 2. QE curves obtained from our modeling and experimental data reported in [2].

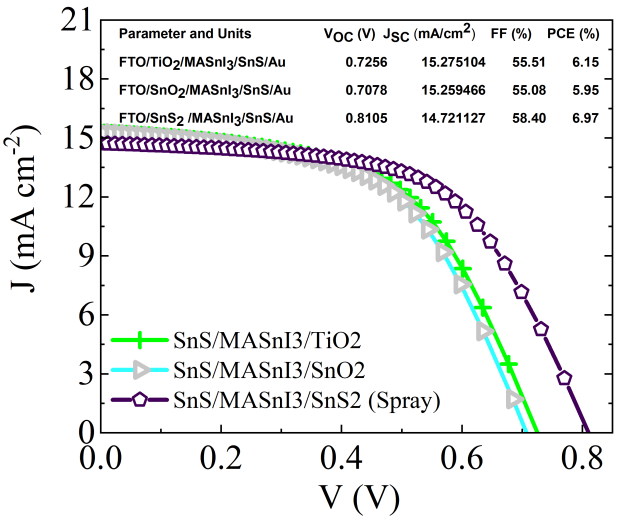

Fig. 3. $J-V$ characteristics obtained from modeling of perovskite solar cell with SnS based HTL with inorganic ETLs including TiO_2, SnO_2 and SnS_2.

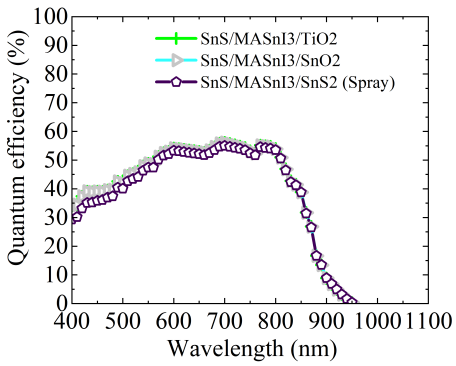

Fig. 4. QE characteristics obtained from modeling of perovskite solar cell with SnS based HTL with inorganic ETLs including TiO_2, SnO_2 and SnS_2.

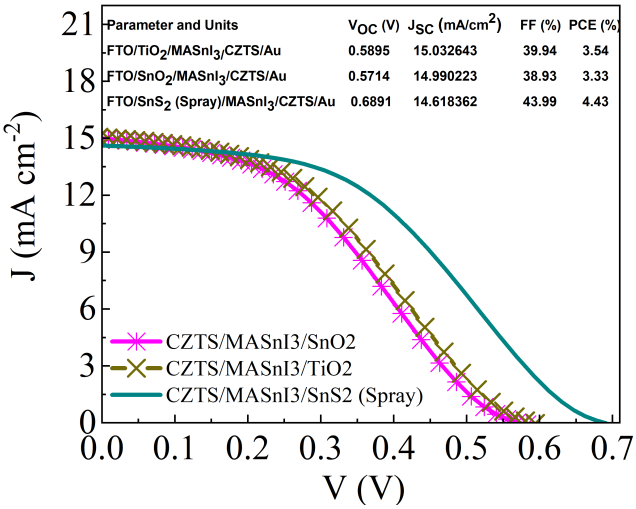

Fig. 5. $J-V$ characteristics obtained from modeling of perovskite solar cell with CZTS based HTL with inorganic ETLs including TiO_2, SnO_2 and SnS_2.

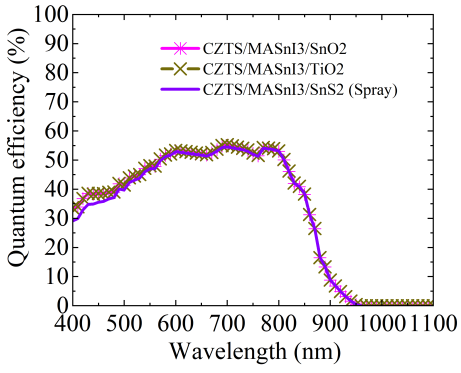

Fig. 6. QE characteristics obtained from modeling of perovskite solar cell with CZTS based HTL with inorganic ETLs including TiO_2, SnO_2 and SnS_2.

Conformally-coated titanium carbide on structured pyrolytic carbon electrodes for lithium sulphur batteries

Owen George Bell[a], Nadira M. Palakkool[a], Mike Taverne[a], Tam Ho[a], Johnathan Mar[c], Christopher Jones[d], Giray Kartopu[a], Yongtao Qu[a], Vincent Barrioz[a], Guillaume Zoppi[a], Kevin Chung-Che Huang[b], Yung-Ling Daniel Ho[a]

[a] Northumbria University, Newcastle Upon-Tyne, NE1 8ST, England
[b] Southampton University, SO17 1BJ, England
[c] Newcastle University, Newcastle Upon-Tyne, NE1 7RU, England
[d] Bristol University, Bristol, BS8 1QU

e-mail: owen2.bell@northumbria.ac.uk

Key words: Lithium sulphur batteries, pyrolytic carbon, titanium carbide, metal sulphides, electrode stability, 3D structures,

Alternative renewable energy solutions (ARES) have garnered vast amounts of attention recently, due to growing concerns about pollution, global warming, and emerging energy crises. Because of the intermittent nature of many mature ARES, improvement in battery technology is vital to ensure growing storage capacity requirements are satisfied, guaranteeing minimal energy loss from lack of storage capacity and allowing for on-demand energy usage.

Lithium-sulphur (Li-S) batteries have been pegged to outperform lithium-ion batteries in the future, due to a high theoretical energy density ($2600 Wh Kg^{-1}$) and specific capacity ($1675 Ah Kg^{-1}$) [1]. To realise this, challenges such as reaction rates, electrode stability, resistance to volume expansion caused differences in density between sulphur and its reduced discharge product Li_2S, and availability of reactants over many cycles, must be overcome [2].

In this study, we investigate the application of Py-C/TiC/S cathodes in Li-S batteries. Innovative cathode design enhances the electrochemical performance and stability of Li-S batteries. Using pyrolytic carbon (Py-C) enhanced with titanium carbide (TiC) and sulphur (S), we achieved considerably improved conductivity and sulphide utilisation. Results demonstrate that Py-C/TiC/S cathodes suffer much less from polysulphide shuttle effect, leading to higher capacity retention and longer cycle life. This work highlights the potential of Py-C/TiC/S cathodes in advancing the development of high-performance Li-S batteries.

To achieve this, this study investigates a variety of 3D structures for cathode electrodes, such as rod connected diamond (RCD), with the goal of increased surface area, energy density, life cycle safety, and higher resistance to expansion during lithiation. Fabrication techniques include 3D direct laser printing, followed by thermal annealing, chemical vapour deposition (CVD) growth, electrodeposition, dry etching, and doping. Structured materials developed in this study include pyrolytic carbon [3], TiC and metal sulphides (TiS_2[4], MoS_2), which have shown significant improvements in the electrochemical performance of Li-S batteries.

References

[1] S. S. Zhang, "Liquid electrolyte lithium/sulfur battery: Fundamental chemistry, problems, and solutions," *Journal of Power Sources*, vol. 231, pp. 153–162, Jun. 2013, doi: 10.1016/J.JPOWSOUR.2012.12.102.

[2] J. Cabana, L. Monconduit, D. Larcher, and M. R. Palacín, "Beyond intercalation-based Li-ion batteries: The state of the art and challenges of electrode materials reacting through conversion reactions," *Advanced Materials*, vol. 22, no. 35, Sep. 2010, doi: 10.1002/adma.201000717.

[3] Y. Gao, Z. Pan, J. Sun, Z. Liu, and J. Wang, "High-Energy Batteries: Beyond Lithium-Ion and Their Long Road to Commercialisation," Dec. 01, 2022, *Springer Science and Business Media B.V.* doi: 10.1007/s40820-022-00844-2.

[4] H. Kim, Y. Son, and C. Jo, "Free-Standing Carbon Materials for Lithium Metal Batteries," Sep. 16, 2024, *John Wiley and Sons Inc*. doi: 10.1002/celc.202400209.

[5] J. G. Wang, K. Xie, and B. Wei, "Advanced engineering of nanostructured carbons for lithium-sulfur batteries," Jul. 01, 2015, *Elsevier Ltd*. doi: 10.1016/j.nanoen.2015.05.006.

[6] Y. J. Choi, Y. D. Chung, C. Y. Baek, K. W. Kim, H. J. Ahn, and J. H. Ahn, "Effects of carbon coating on the electrochemical properties of sulfur cathode for lithium/sulfur cell," in *Journal of Power Sources*, Elsevier B.V., Oct. 2008, pp. 548–552. doi: 10.1016/j.jpowsour.2008.02.053.

[7] J. Balach, J. Linnemann, T. Jaumann, and L. Giebeler, "Metal-based nanostructured materials for advanced lithium-sulfur batteries," 2018, *Royal Society of Chemistry*. doi: 10.1039/C8TA07220E.

[8] M. Wang *et al.*, "Theoretical investigation on the strain engineering control of TiC as tunable high-efficiency bifunctional cathode materials for Lithium–Sulfur batteries," *Appl Surf Sci*, vol. 656, May 2024, doi: 10.1016/j.apsusc.2024.159714.

[9] Z. Liang *et al.*, "Sulfur cathodes with hydrogen reduced titanium dioxide inverse opal structure," *ACS Nano*, vol. 8, no. 5, pp. 5249–5256, May 2014, doi: 10.1021/nn501308m.

[10] Z. Z. Yang *et al.*, "Hierarchical TiO2 spheres as highly efficient polysulfide host for lithium-sulfur batteries," *Sci Rep*, vol. 6, Mar. 2016, doi: 10.1038/srep22990.

[11] J. Tang *et al.*, "Two-dimensional materials towards separator functionalization in advanced Li-S batteries," Dec. 07, 2021, *Royal Society of Chemistry*. doi: 10.1039/d1nr05489a.

[12] L. Hu *et al.*, "Double-Shelled NiO-NiCo2O4 Heterostructure@Carbon Hollow Nanocages as an Efficient Sulfur Host for Advanced Lithium–Sulfur Batteries," *Adv Energy Mater*, vol. 8, no. 23, Aug. 2018, doi: 10.1002/aenm.201800709.

[13] Z. W. Seh *et al.*, "Two-dimensional layered transition metal disulphides for effective encapsulation of high-capacity lithium sulphide cathodes," *Nat Commun*, vol. 5, 2014, doi: 10.1038/ncomms6017.

[14] K. Xie *et al.*, "Fabrication of a novel TiO2/S composite cathode for high performance lithium-sulfur batteries," *RSC Adv*, vol. 5, no. 94, pp. 77348–77353, Sep. 2015, doi: 10.1039/c5ra13823j.

[15] M. P. C. Taverne *et al.*, "Conformal CVD-Grown MoS2 on Three-Dimensional Woodpile Photonic Crystals for Photonic Bandgap Engineering," *ACS Applied Optical Materials*, vol. 1, no. 5, pp. 990–996, May 2023, doi: 10.1021/acsaom.3c00055.

A deeper dive into droplet and dust dynamics on commercially available solar panels

Anirban Roy [a], Rahul Roy [a] and Chirodeep Bakli [a]

[a] Thermofluidics and Nanotechnology for Sustainable Renewable Energy Systems Laboratory, School of Energy Science and Engineering, IIT Kharagpur, Kharagpur, 721302, India
e-mail: chirodeep@iitkgp.ac.in

Accessibility and abundance of solar radiation have made solar photovoltaic systems the most preferred way to transition to renewable energy. However, the efficiency of these solar PV systems gets hampered significantly due to the accumulation of atmospheric dust on panel surfaces[1,2]. Researchers have suggested strategies to mitigate dust from solar panels, which involves modification of the surface to make it superhydrophobic with the help of some coating or inscribing nanostructures on the surface[3,4]. This would allow water to roll off the panel, collecting dirt from the solar panel surface, thereby cleaning it. Likewise, many such studies have been previously reported that discuss droplet and dust dynamics on hydrophobic surfaces in depth[5,6]. However, most commercially deployed solar panels utilize glass cover, which is inherently hydrophilic in nature. Moreover, modifying the surface would hamper its optical properties leading to poor transmission and absorption of light leading to reduced efficiency of the solar panel. Given the above-mentioned factors, it is important to understand the droplet and dust dynamics of the commercially available solar panels, which are hydrophilic in nature, and specify a way to clean the surface efficiently without changing its surface properties. At the same time, it is essential to optimize the spraying parameters like height, droplet size and frequency so as to optimize cleaning and active energy consumption. Towards this, we study the droplet and dust dynamics when a water droplet falls on a commercially available solar PV panel (Frontech Model ECO 005). We analyze and suggest the suitable droplet impact height for two cases- maximum cleaning and quickest cleaning- without changing the surface properties of the solar panel. Further, we also quantify the amount of dust particles mitigated from the surface with the help of image processing and present a configuration for attaining maximum cleaning efficiency. The dispensing setup is powered by a syringe pump (Harvard PHD Ultra) dispensing at a volume flow rate of 1 ml/min through a tip of 1 mm diameter. The dispensing is stopped once the droplet detaches from the tip. The field of observation is illuminated using an LED light source (Nanlite Forza 60 II), and the impact process is captured using a high-speed camera (Phantom Miro C211). The impact height (H) is varied from 5 cm to 15 cm while the tilt angle (θ) is varied from 0 ° to 20 °. The schematic of the experimental setup is shown in Fig 1. Figure 2 represents the comparison of the spreading characteristics of the droplet impacting from a height of 10 cm on a solar panel oriented horizontally ($\theta = 0$ °). The comparison is shown up to the instant corresponding to the maximum extent of droplet spreading. Upon impact, the droplet displaces the dust from the surface as the droplet spreads. The spreading time is thus an important parameter as it determines how fast the panel will get cleaned. For comparison across various cases, we consider the ratio of time taken by the droplet to spread up to the maximum extent on the dusty panel (t) and clean panel (t'). It can be observed from Fig 3 that the presence of dust causes the time taken to attain maximum spreading, increase. A significant rise in the spreading time ratio (t/t') is observed beyond $\theta = 10°$ for H = 10 cm and 15 cm, in contrast to a minor decline at H = 5 cm. This is attributed to lower kinetic energy at the instant of impact for H = 5 cm compared to the other two cases. As the droplet has lower kinetic energy during impact, it tends to stay on the surface and spread evenly. This leads to quicker cleaning although the area covered is less. When the droplet has higher kinetic energy, it tends to slide down the plane upon impact instead of spreading thus leading to an augmented area of cleaning. It can thus be concluded that if the requirement is to displace dust from a spot of smaller size, a lower impact height should be preferred, while a higher impact height is required for removing dust over a greater area as it enables sliding motion post-impact. To further quantify the amount of dust displaced, we perform image processing to calculate the same.

References:

[1] J. Chen, et al. Energy 194 (2020) 116915.
[2] W. Zhao, et al. Energy 233 (2021) 121240.
[3] G. Hassan et al., Solar Energy 277 (2024) 112728.
[4] D. Zhang et al. Solar Energy 265 (2023) 112077
[5] J. S. Wang et al., Powder Technology 452 (2025) 120536
[6] C. Yan et al., Solar Energy Materials and Solar Cells 286 (2025) 113570.

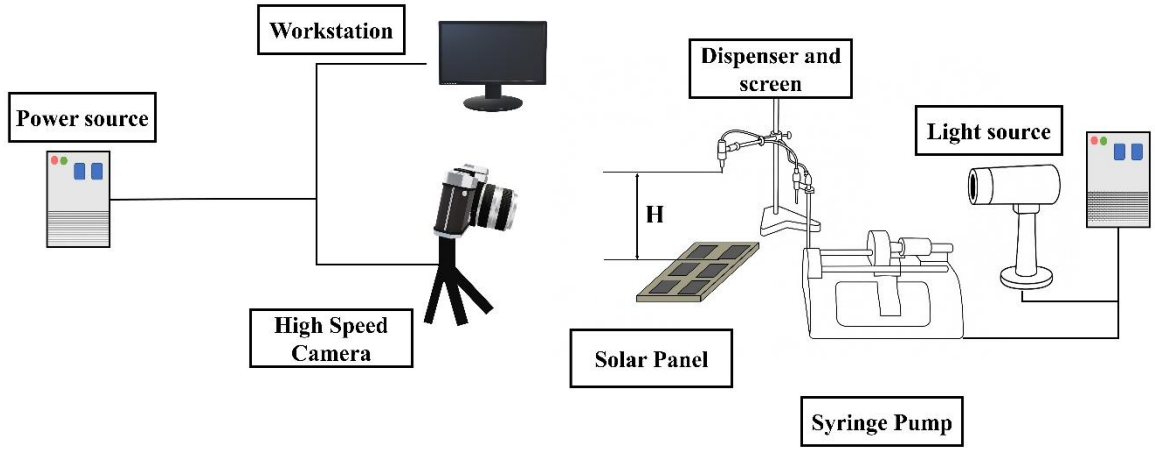

Figure 1. Schematic diagram of the experimental setup

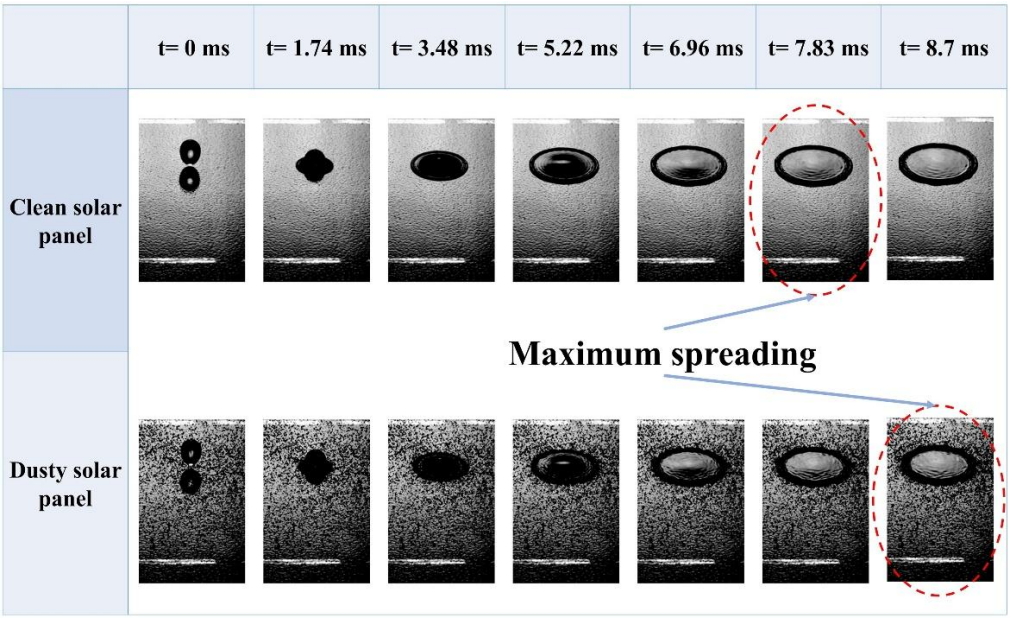

Figure 2. Comparison of spreading characteristics of droplet on clean and dusty solar panel for H = 10 cm and θ = 0 ° for different time instant.

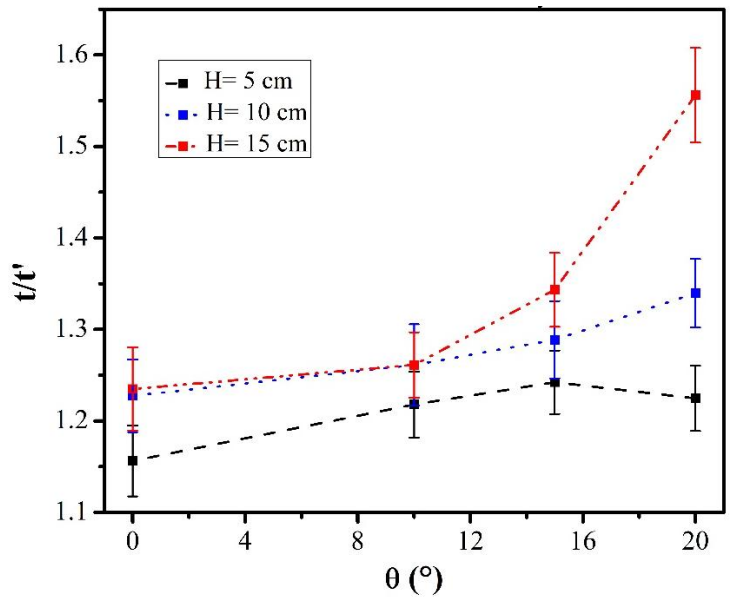

Figure 3. Variation of droplet spreading time ratio (t/t') with tilt angle (θ) for different droplet impact heights (H).

All-in-one Microfluidic Platform for Single-Cell Environmental Phenotyping of Chlamydomonas reinhardtii

Alexandre CHARGUERAUD [a,b], Lars KOOL[b], Eliora ISRAELEVITCH [c], Alix BOULOUIS [c] and Jacques FATTACCIOLI [a,b]

[a] UMR 8228 CPCV, Département de Chimie, École Normale Supérieure, PSL Université, 24 rue Lhomond, 75005 Paris, France.
[b] Institut Pierre-Gilles de Gennes pour la Microfluidique, Paris, 75005, France
[c] Laboratoire de Biologie du Chloroplaste et Perception de la lumière chez les microalgues of the Institut de Biologie Physico-Chimique, Sorbonne Université, Paris, 75005, France

e-mail: alexandre.chargueraud@ens.psl.eu

Microalgae are emerging as powerful indicators of aquatic ecosystem health, thanks to their sensitivity to environmental fluctuations and their diverse physiological responses. Among them, *Chlamydomonas reinhardtii* [1] is a well-characterized model organism, offering valuable insights into photosynthesis, nutrient sensing, stress tolerance, and cellular metabolism. To fully harness this potential, there is a growing need for tools [2] that enable precise, high-resolution phenotyping at the single-cell level.

Here, we present a multifunctional microfluidic platform specifically designed for non-motile *Chlamydomonas reinhardtii* that enables stable trapping, real-time optical monitoring, and controlled release of trapped cells (Fig.1). Inspired by Pachinko-style trap arrays [3] and implemented using a pneumatically actuated PDMS bilayer structure [4], the device (Fig.2) allows long-term observation under dynamic environmental conditions. Each trap can capture and retain 8 µm microalgae while maintaining optical accessibility for high-resolution imaging.

The system is supported by a custom user interface for intuitive control and synchronization of fluidic and imaging operations (Fig.3). It could be fully compatible with a range of cellular assays, including measurements of viability, photosynthetic activity, lipid accumulation, stress response, and intracellular content dynamics. This flexibility enables researchers to investigate microalgal behavior under varying conditions of light, nutrients, or pollutants.

By bridging microfluidic engineering and environmental monitoring, our platform provides a scalable and reusable solution for studying functional heterogeneity within microalgal populations. It paves the way for the selection and engineering of resilient strains and for advancing our understanding of microalgal roles in ecosystem dynamics and sustainability applications.

[1] S.P. Slocombe et al., Fixing the Broken Phosphorus Cycle: Wastewater Remediation by Microalgal Polyphosphates, Front. Plant Sci. 11 (2020) 982.

[2] H.S. Kim et al., Microfluidic systems for microalgal biotechnology: A review, Algal Res. 30 (2018) 149–161.

[3] O. Mesdjian et al., Enhancing the capture efficiency and homogeneity of single-layer flow-through trapping microfluidic devices using oblique hydrodynamic streams, Microfluid. Nanofluidics 25 (2021) 91.

[4] A. Abrishamkar et al., Microfluidic Pneumatic Cages: A Novel Approach for In-chip Crystal Trapping, Manipulation and Controlled Chemical Treatment, J. Vis. Exp. (2016).

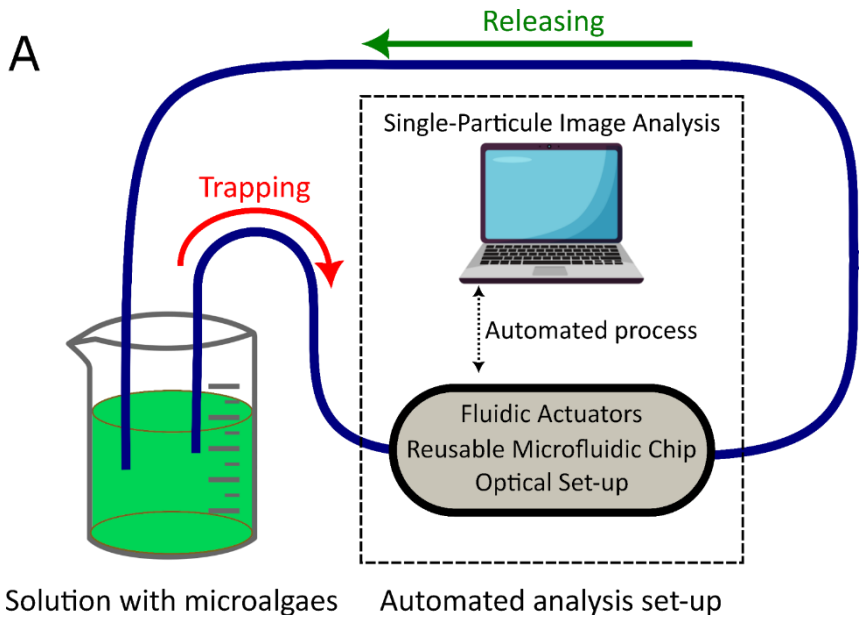

Figure 1. Schematic of the Automated Solution Analysis Device. This figure illustrates a use case involving a reconfigurable trap matrix. A solution containing microalgaes is analyzed by the device, which extracts and characterizes a significant number of cells before reinjecting them into the solution. This process can be repeated as many times as needed, depending on the experiment chosen by the user.

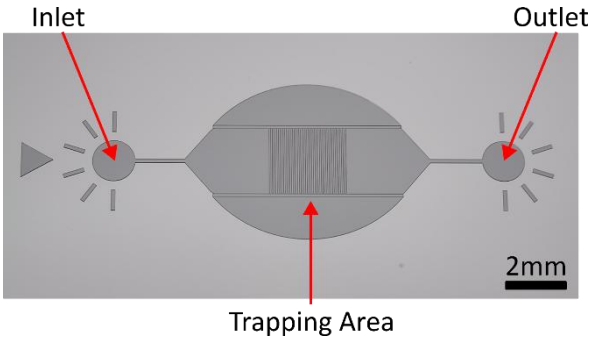

Figure 2. Photograph of the microfluidic chip wafer. This design has been optimized for trap-and-release cycles

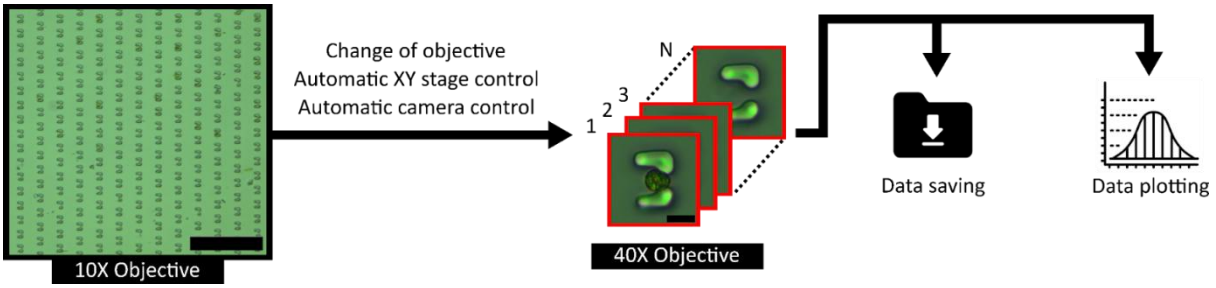

Figure 3. Images and scheme of the automated analysis process of the microalgal solution. Scale bar 10x : 200 µm; scale bar 40x : 10 µm.

Plenary 4 - Prof Shinichi Saito

Why Micro is different from Macro? A Challenge towards Macroscopic Quantum Technologies

Shinichi Saito

Research & Development Group, Hitachi, Ltd., Tokyo 185-8601, Japan.
e-mail: shinichi.saito.qt@hitachi.com

We consider why microscopic quantum mechanics seems to be different from macroscopic classical mechanics by using coherent photons emitted from a standard laser source. The coherent states describe quantum states of macroscopic number of photons, paving a way to realise macroscopic quantum technologies.

The first step is to achieve an arbitrary SU(2) rotations for coherent photons in experiments. We propose to call our device as a Poincaré rotator [1-3], since we can realise an arbitrary SU(2) operation for the polarisation state. The active Poincaré rotator operations are shown in Fig. 1. The phase-shifter operations were confirmed (Fig. 1 (a)-(c)) simply by splitting HV states using a polarisation-beam-splitter (PBS), followed by the phase-shifts of $LiNbO_3$ optical modulators, and recombined by a polarisation-beam-combiner (PBC). The amplitudes of HV states were controlled by the rotator operations (Fig. 1 (d)-(f)) by using another phase-shifter together with 2 quarter-wave-plates (QWPs). At this moment, the fidelity is as low as 90%, which was limited by expected deviations of rotation angles in achromatic wave-plates. By combining the phase-shifter and the rotator, we could realise arbitrary SU(2) states of polarisation, which corresponds to a single qubit operation. It is worth for noting that the rotation axis is rotated for the rotator operation of Fig. 1 (d) upon the phase-shift, while the phase-shifter operation is always along the S_1 axis due to the splitting by the PBS at the fixed directions. This naturally allows us to control both polar and azimuthal angles on the Poincaré sphere. As a demonstration of the Poincaré rotator, we have tried to draw the fullerene C_{60} (Fig. 1 (g) and (h)) and the coastline of the earth (Fig. 1 (i)) on the Poincreé sphere. The operation speed of 5 MHz was limited by the performance of electronics, used for this study, such as arbitrary-wave-form generators and amplifiers.

We have also realised Stokes parameters can fully span the three-dimensional Euclidean space, which we call Stokes space, since we are dealing with the macroscopic number of photons due to Bose-Einstein statistics, and the radius of the Poincaré sphere corresponds to the number of photons. Consequently, we can realise topologically non-trivial structures [1-3] as trajectories. Examples of topological polarisation states are shown in Fig. 2. The torus can be realised by a polarisation independent splitter and a combiner, together with a phase-shifter and a rotator. The splitter separates the input ray into two rays, and one of the ray is phase-shifted by half-wave-plates (HWPs), while the other ray is kept its polarisation state, and then they are recombined at the combiner [1-3].This simple set-up allows us to realise the interference to change the amplitude, which changes the radius of the trajectory to form a circle. Then, we can subsequently rotate the polarisation state along the direction perpendicular to the radius, to form a torus in the Stokes space (Fig. 2 (a)). We can confirm the torus, in a fibre-optic polarisation interferometer, together with passive optical components to use HWPs and QWPs. We can also realise more complex structures, such as a Möbius strip (Fig. 2 (b)) [1-3] and a bosonic Dirac cone (Fig. 2 (c)) [1-3], whose node must exist at the edge to change from a topologically non-trivial torus to a topologically trivial sphere, satisfying the Gauss-Bonnet theorem to account for the bulk-edge correspondence.

The final challenge is to realise macroscopic singlet and triplet states by using both spin and orbital angular momentum of coherent photons. These states were previously called as classical entangled states, while we think it is more suitable to call them as macroscopic quantum states, since they are described by internal degrees of freedom in quantum coherent states. As we have confirmed both theoretically and experimentally, coherent photons have both spin and orbital angular momentum, which at least forms SU(2)×SU(2) states, as far as they are independently controlled. We have experimentally realised these states by using Poincaré rotator together with the vortex lenses. In order to confirm the realisations of these states, we have projected the SU(4) states into SU(2)×SU(2) states by a linear polariser (Fig. 3).

[1] S. Saito, Front. Phys. **11**, 1225419; 1225346; 1225360; 1225387; 1225462; 1225488; 1289062 (2023); **11**, 1225334 (2024).
[2] S. Saito, Results. Phys. **59**, 107567; **61**, 107745 (2024).
[3] S. Saito, Heliyon **10**, e28367; e34423 (2024).

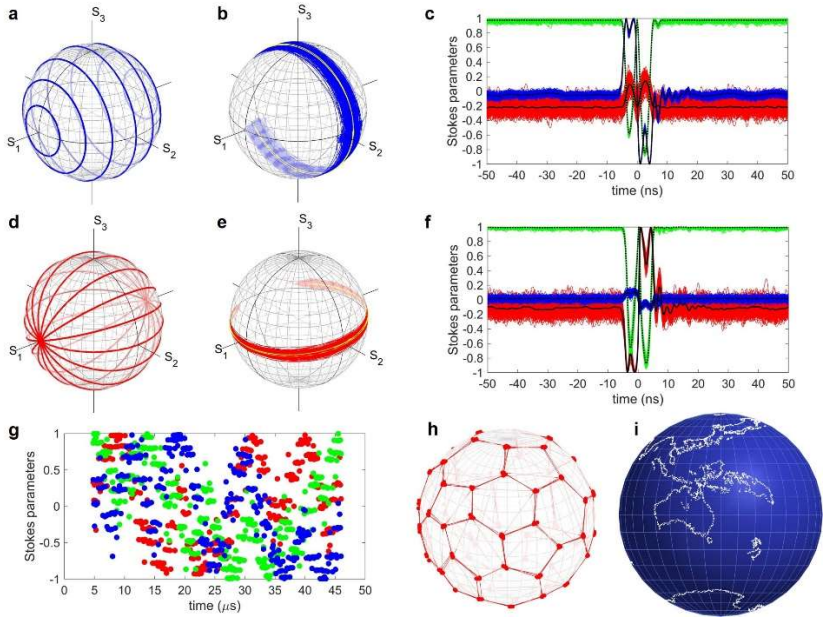

Figure 1. Poincaré rotator to realise an arbitrary SU(2) operation for spin states of coherent photons, using a laser with the wavelength of 1533nm. (a) and (d) simulated trajectories for phase-shifter and rotator operations, respectively. (b) and (c) phase-shifter operations, and (e) and (f) rotator operations, obtained by the input voltage of 4.6V applied to optical modulators. (g) and (h) fullerene C_{60}, and (i) the earth corresponding to 9,865 points, operated at 5 MHz with the duty cycle of 5%. Stokes parameters of S_1 (red), S_2 (green), and S_3 (blue) are shown in (c), (f), and (g).

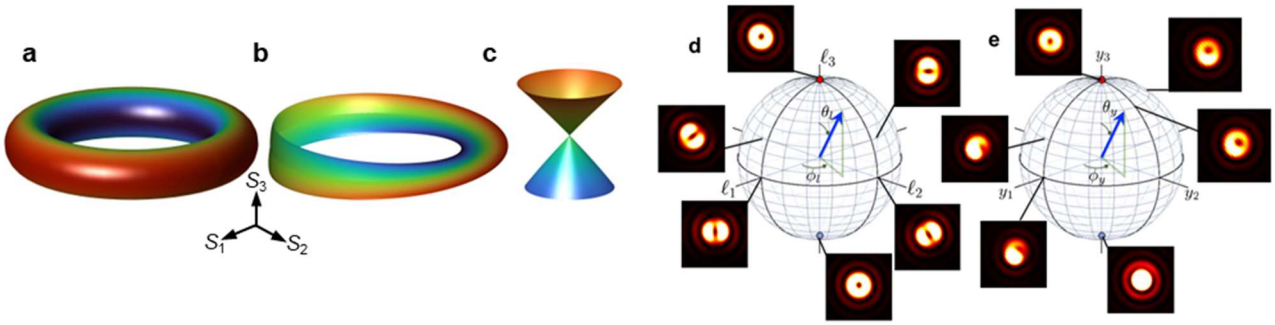

Figure 2. Topological polarisation states. Stokes parameters were theoretically calculated for (a) a torus, (b) a Möbius strip, and (c) a bosonic Dirac cone. (d) and (e) Gell-Mann parameters to characterise the SU(3) states of coherent photons, which are realised by superposition states of left- and right-vortexed states and a Gaussian state. (d) Orbital angular momentum, $\boldsymbol{\ell} = (\ell_1, \ell_2, \ell_3)$, and (e) hyperspin, $\mathbf{y}=(y_1,y_2,y_3)$. A laser with the wavelength of 532nm was used and far-field images were taken.

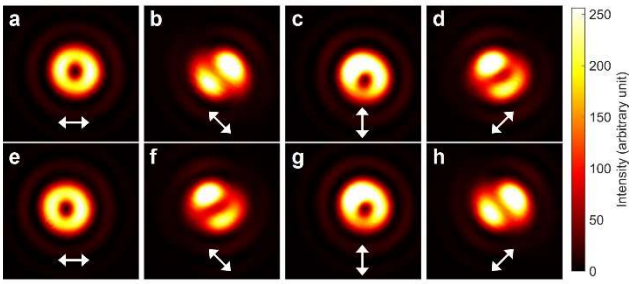

Figure 3. Macroscopic singlet and triplet states of coherent photons, from a laser with the wavelength of 532nm. Far-field images were taken for (a)-(d) singlet states, and (e)-(h) triplet states. Arrows indicate the projected direction for the polarisation. The chirality is not obvious for (a) and (e) right vortexed state, and (c) and (g) left vortexed state. On the other hand, the directions of dipoles are clearly perpendicular to the polarisation for singlet states of (b) and (d), while the directions of dipoles are aligned to the polarisation for triplet states of (f) and (h).

Plenary 5 - Prof Mariana Medina Sanchez

Medical Microrobots with Functional Nanomaterials for Precision Women's Healthcare

Mariana Medina Sanchez
Centro de Investigación Cooperative (CIC) nanoGUNE, Tolosa Hiribidea,
Donostia / San Sebastian

Owing to their active propulsion and high thrust forces, nanomaterial-enhanced microrobots hold significant promises for next-generation assisted reproduction techniques, offering more targeted, efficient, and less invasive approaches to gamete and embryo manipulation, ultimately aiming to improve pregnancy success rates by providing a more natural environment for development. Beyond reproduction, they open new avenues for precision drug delivery in gynecological health, particularly in addressing cancers of the reproductive tract. In this context, we have exploited sperm cells as biohybrid drug carriers, taking advantage of on their unique ability to load high amounts of anticancer drugs without compromising viability or motility, their natural adaptation to swim against backflows in viscoelastic media, and their intrinsic capacity to fuse with cancer cells for highly localized drug delivery. By actively navigating to deep-seated or otherwise inaccessible disease sites, such microrobots enable therapeutic interventions that minimize systemic side effects while maximizing efficacy. Incorporating functional nanomaterials with magnetic, plasmonic, and acoustic properties further enhances their biomedical potential, allowing precise and minimally invasive remote control through external fields and improved visualization in scattering tissues via ultrasound and photoacoustic imaging. Moreover, functionalization with nanocarriers such as polymersomes and liposomes substantially increases therapeutic payloads while enabling finely tunable release strategies. Together, these advances position medical microrobots as transformative tools for women's health and beyond, reshaping therapeutic paradigms through targeted, minimally invasive, and patient-centered interventions.

Oral Session 2A: Nanoimprint and alternative lithography

Comparison of 2 processes based on NIL and lift-off for the fabrication of thick nano antennas for solar PV-TE applications

Jean-Baptiste Doucet [a], Franck Carcenac [a], Leopold Boudier [a], Inès Revol [a]

[a] LAAS-CNRS, Université de Toulouse, Toulouse, 31400, France
e-mail : jbdoucet@laas.fr

Since conventional solar cells do not absorb the near-infrared and infrared solar spectrum, improving efficiency by combining a photovoltaic cell with a thermoelectric generator in a hybrid energy device is a promising approach. A propitious method to enhance the conversion efficiency of this device involves implementing a nanostructured photothermal interface between the solar cell and the thermoelectric generator. In this respect, diabolo-shaped nickel nano antennas are a good candidate for such interfaces, and they can be created using electron-beam lithography and lift-off techniques [1]. However, we require a faster and more cost-effective lithography method to address the demands of large surface areas at reduced costs.

Although nanoimprint lithography has proven to be an efficient method to combine with lift-off for metal deposition as early as 1995[2], it was only suitable for very thin layers at that time. Bilayer or trilayer lift-off processes have been investigated subsequently to achieve thicker depositions, and commercial solutions are proposed, but the targeted metal deposition thickness is only 40 nm[3].

For efficient photothermal conversion, a metal thickness of at least 150 nm is required, while the neck of a typical diabolo structure needs to be as narrow as 50 nm.

We present here both bilayer and trilayer lift-off processes that we developed, along with the results we obtained using these processes for depositing metals with thicknesses of 150 nm and above.

Both processes rely on soft nanoimprint lithography [4] combining thermal imprinting in a polymer foil with a UV nanoimprint step, based on a simple methacrylate homemade photoresist, with the secondary polymer mold. For the lift-off, we investigated several hard layer/sacrificial underlayer combinations.

Although the bilayer process does not meet the needs for high aspect ratios and sub-100 nm definition, it is simpler and involves a wet etching step instead of a dry etching one, and might be of interest for larger structures. When we use our trilayer nanoimprint and lift of process on silicon or fused silica, it shows that thicknesses above 150 nm and even 200 nm can be achieved. The definition of the diabolo antennas is similar to what is obtained with electron beam lithography, including the 50 nm large neck (see Figs 1, 2 and 3).

This work was supported by the LAAS-CNRS micro and nanotechnologies platform, a member of the French RENATECH network, and the French Agence Nationale de la Recherche (ANR), under grant ANR-21-CE50-0003 (project HYDRES).

[1] Hanauer et al., Photothermal Conversion of Solar Infrared Radiation by Plasmonic Nanoantennas for Photovoltaic-Thermoelectric Hybrid DevicesACS Applied Energy Materials 2023, 6, 2128.
[2] S. Chou, et al., Imprint of sub-25 nm vias and trenches in polymers, Appl. Phys. Lett. 67 (21) (1995)
[3] T. Handte, et al., Manufacturing of nanostructures with high aspect ratios using soft UV-nanoimprint lithography with bi-and trilayer resist systems, Micro Nano Eng., 14 (2022)
[4] S. Pelloquin, et al., Soft mold NanoImprint Lithography: a versatile tool for sub-wavelength grating applications, Microsyst. Technol. 1–8 (2018).

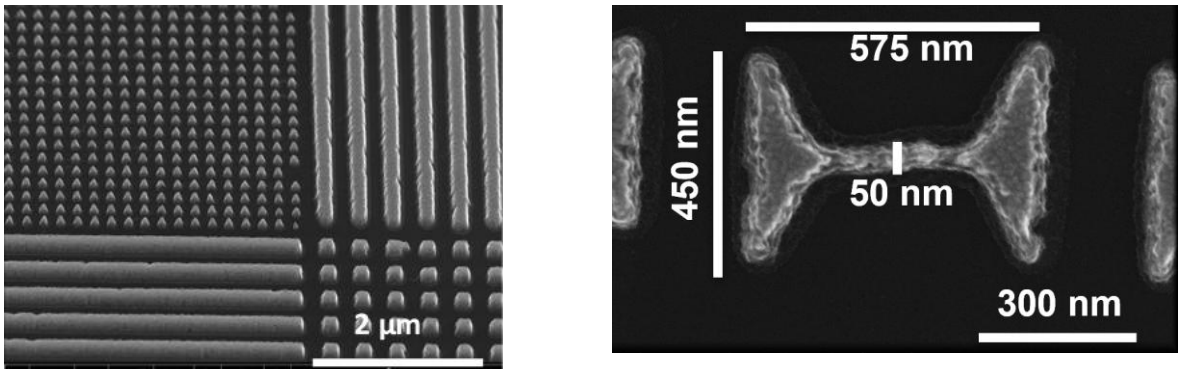

Figure 1. SEM images of Ni structures made by NIL and our trilayer lift-off process on silicon. Tilted view of various shapes (left), vertical view of diabolo (right)

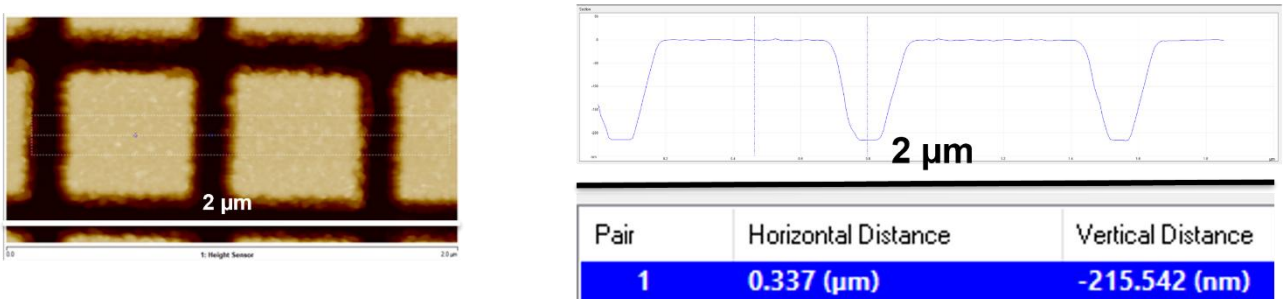

Figure 2. AFM image of Ni antennas made by NIL and our trilayer lift-off process on fused silica showing that a thickness of more than 200 nm can be reached

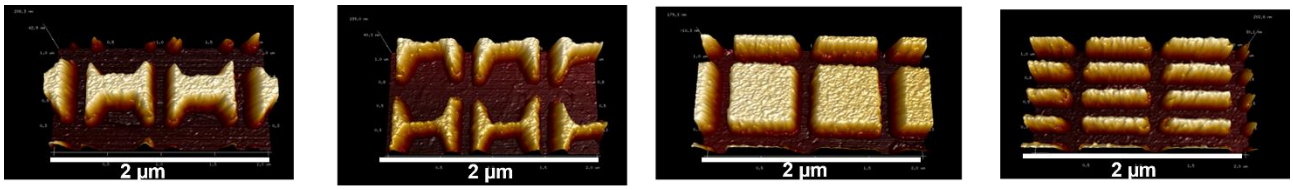

Figure 3. AFM images of various antennas obtained by > 200 nm Ni deposit after NIL and our trilayer lift-off process on fused silica

Fine silver wiring using replica mold with light-shielding film

Takumi Ashida, Jun Taniguchi

Department of Applied Electronics, Tokyo University of Science, Tokyo, 125-8585, Japan
e-mail: 8121003@ed.tus.ac.jp

1. Introduction

With the recent development of the information society, the industrial sector is required to miniaturize wiring. Nanoimprint lithography is one of the methods for forming fine wiring, and it is a technology that can achieve high throughput since there is no process for depositing metal [1]. Conventional nanoimprint lithography has the disadvantage of leaving excess resin at the bottom of the transferred pattern, known as residual film, but the Combined-nanoimprint-and-photolithography (CNP) method solves this problem [2]. The CNP method is a technique that suppresses the generation of residual film by placing a light-blocking metal layer on top of the transfer mold. Since the conventional CNP method requires metal deposition and etching processes on a quartz substrate to create the metal layer, in this study, the CNP mask was fabricated by scooping up the silver paste fired on the master mold with UV curable resin. We have made the CNP mask on a flexible polyester film, which is called a hybrid soft mask mold (HSMM), and performed silver micro wiring using the HSMM.

2. Experiments

First, SU-8 was applied on the silicon substrate to make a master mold and spin-coated to achieve uniform film thickness. The film was baked at 95 ℃ for 10 min to remove solvent. Photolithography was performed at a dose of 98.4 mJ/cm^2 followed by baking at 95 ℃, 3 min. Finally, the master mold was developed in SU-8Developer for 4 minutes and rinsed with pure water. To fabricate HSMM, silver paste (Smart Screen F, GenesInk Inc.) was dropped onto a master mold patterned of SU-8, vacuumed, and the thickness of the silver paste was adjusted by spin-coating. It was baked at 150 ℃ for 5 minutes and then baked at 85 ℃ for 5 minutes while the PET film was pressed against the master mold. This process separated the silver paste into the top and bottom of the master mold, and only the top portion was removed. By dropping UV curable resin (PARQIT OEX-028-X433-3, Autex Inc.) on the master mold and scooping up the silver paste with polyester film, HSMM was completed. Next, silver wiring was performed using HSMM as shown in Fig. 1. Photosensitive silver ink (LCAG-140K2, Toray Inc.) was dropped onto the release-treated HSMM (Fig. 1(a)), then these were bonded to the substrate as shown in Fig. 1(b), and the resin was made uniform by using a roll press (Fig. 1(c)). Two types of substrates, silicon and quartz, were used, and each was treated with silane coupling. The HSMM was then placed on a buffer material and UV irradiated to the silver ink while applying pressure (500 N) using a parallel plate press (Fig 1(d)). The irradiation dose was 240 mJ/cm^2 for transferring the pattern to the silicon substrate and 100 mJ/cm^2 for the quartz substrate due to the different adhesion of the two substrates. Finally, the HSMM was released from the mold, and the pattern was developed with Na_2CO_3 and rinsed with pure water to remove the uncured silver ink (Fig 1(e)). Fig. 2(a) shows a silver ink pattern transferred onto a silicon substrate using HSMM. The width, pitch, and height of this pattern were 4.0μm, 14.7 μm, and 5.5 μm. Fig. 2(b) shows the pattern without HSMM. Comparing Fig. 2(a) and (b), a pattern with no residual film was produced when HSMM was used. Fig. 2(c) shows a silver ink pattern transferred onto a quartz substrate using HSMM. The width, pitch, and height of this pattern were 2.1 μm, 15.1 μm, 4.5 μm. Comparing (a) and (c), the silver ink pattern on the silicon substrate with a larger irradiation dose has a larger line width than that on the silicon substrate with a smaller irradiation dose. Fig. 2(d) shows the HSMM. The line width, pitch, and height at the bottom of the pattern were 4.4 μm, 15.2 μm, and 4.2 μm, respectively, indicating that the transferred silver ink pattern had wider line width, wider pitch, and lower height. Fig. 3 shows an SEM image of a more complex silver ink pattern than L/S transferred on a silicon substrate. From images (b) and (c), the width, pitch, and height of this pattern were 20.3μm, 78.0μm, and 4.08μm, respectively. The conductivity was measured as shown in (d), and the resistivity was 34 kΩ.

3. Conclusion

CNP mask was fabricated without evaporation or etching, and silver ink patterns could be transferred without residual film using it. In addition, we were able to measure the conductivity of this silver ink pattern, which suggests that HSMM can be used in the wiring process.

[1] S. Y. Chou et al., J. Vac. Sci. Technol. B14 (1996) 4129-4133.
[2] X. Cheng, L. J. Cho, Microelectron. Eng. 71 (2004) 277-282.

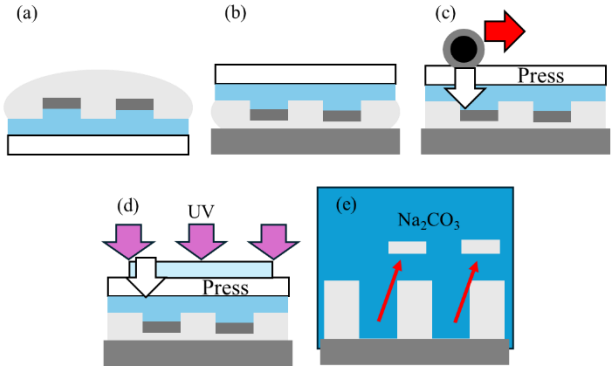

Fig 1. Process of non-residual film patterning using HSMM. (a): Drop of silver ink against HSMM; (b): Bonding HSMM and substrate; (c): Flattening silver ink using a roll press; (d): UV irradiation with pressing; (e): Develop and rinse.

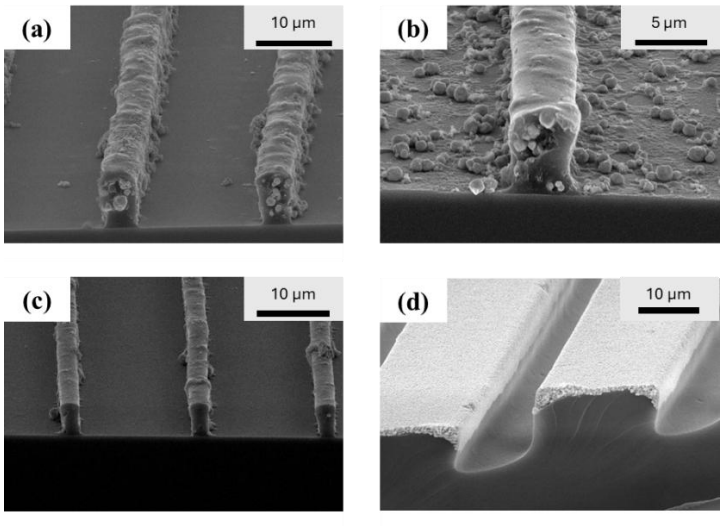

Fig 2. Silver ink patterns and HSMM. (a): Silver ink pattern transferred onto silicon substrate using HSMM; (b): Silver ink pattern transferred on silicon substrate without HSMM; (c): Transfer of silver ink pattern on quartz substrate using HSMM; (d): Cross section of hybrid soft mask mold.

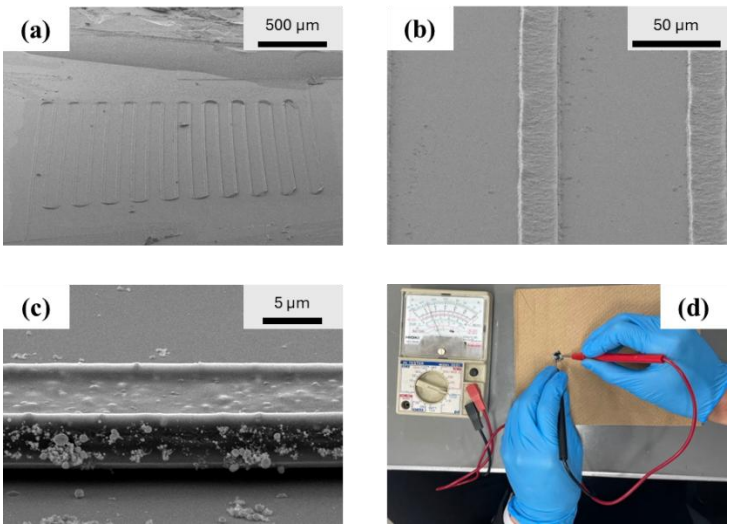

Fig 3. Complex silver ink line using HSMM. (a): Appearance of silver ink wiring; (b): Wiring line width; (c): Wiring height; (d): Confirmation of conductivity using a tester.

Single-nm Mask Writing for Nanoimprint Lithography, as an Energy-Efficient Alternative to EUV

James H.G. Owen, R. Santini and J. N. Randall

Zyvex Labs, 1301 N. Plano Rd, Richardson TX 75081, USA

For both technical and economic reasons, it is likely that the current ASML EUV tools will be the last photolithography technology to push to higher resolutions. The industry does not appear to expect any significant downscaling of devices beyond what will be possible with the ASML High-NA EUV tool which has a resolution of 8 nm. Furthermore, the DOE Advanced Materials and Manufacturing Technologies Office (AMMTO) sponsored Semiconductor Industry Energy Efficiency Scaling (EES2) roadmap has identified Extreme Ultraviolet Lithography (EUV) as a significant contributor to the energy budget of advanced digital electronics, which is increasing dramatically with each generation. Strikingly, EUV is so inefficient that only about 0.04% of the beam energy actually affects the resist.

The EES2 roadmap identifies the replacement of EUV with Nanoimprint lithography (NIL) as a key takeaway. NIL offers equal and better resolution and precision than EUV, with up to 90% lower energy costs, resulting in lower costs of production. However, NIL uses a 1x mold of the pattern to be printed on the wafer as a mask and the best resolution of the current mask writers, using E-Beam lithography (EBL), is 15 nm, and has also reached the end of feasible resolution improvements.

This means that it is critical to develop a mask writing technology with better resolution than EBL, to make adoption of NIL feasible. The masks must have resolution at least as good as the High NA EUV tool's 8nm for NIL to be widely adopted.

We have previously shown[Ballard2014] that ultrahigh-precision NIL templates can be made by writing sub-nm precision patterns on Si(001) using H Depassivation Lithography (HDL), followed by selective growth via atomic layer deposition (ALD) of a hard mask such as TiO_2, which is then used as an etch mask for Reactive Ion Etching (RIE) to form a Si template, replicating the STM pattern. [Fig.1] which will be used to pattern devices on the die or wafer scale.

In previous work, we demonstrated 11 nm linewidths [Fig.2], we are now working to extend these results to sub-10 nm feature sizes, down to 5 nm in the lateral dimension after the RIE step [Fig.3]. This process would achieve finer resolution than is possible with EBL, allowing masks to be made for NIL to achieve lithography at higher resolutions and precision than is possible with EUV, and with greater design freedom. In order to achieve the throughput required to be industrially relevant, we have been exploring high-speed STM lithography, and plan to develop a multitip STM tool using compact MEMS actuators.

J. B. Ballard et al., "Pattern transfer of hydrogen depassivation lithography patterns into silicon with atomically traceable placement and size control," J. Vac. Sci. Technol. B, **32**, (4), p. 041804, Jul. 2014.

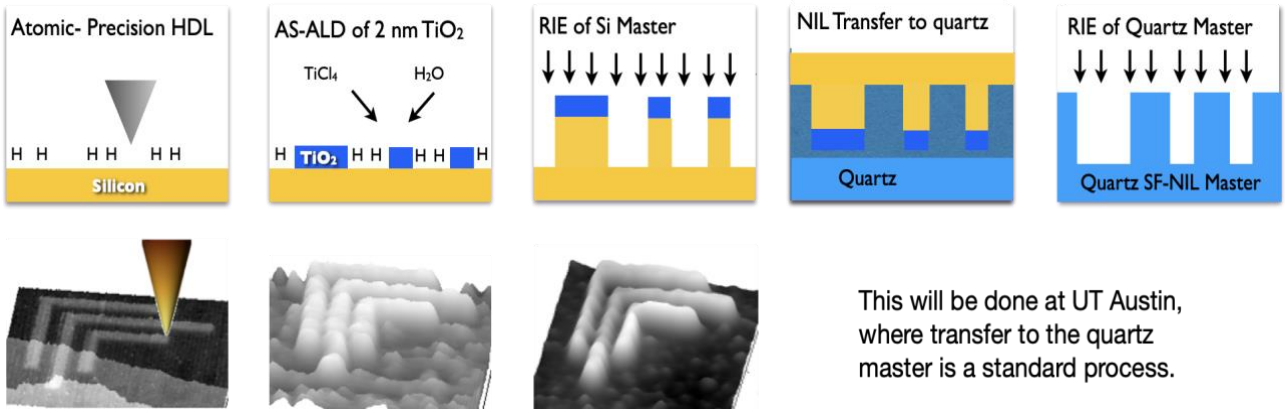

Fig. 1: Our overall process. (From left): Sub-nm precision patterns written using H Depassivation Lithography on Si(001):H. Atomic Layer Deposition of TiO_2 etch mask. Reactive Ion Etching with to make a Si master. The next step is to use Nanoimprint Lithography and RIE to produce a quartz master.

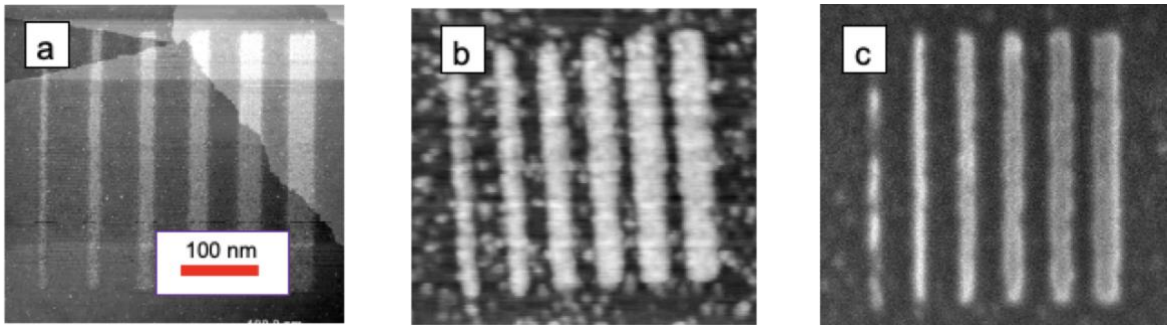

Fig. 2: Linewidth experiment. (a): STM pattern. (b): After ALD. (c): After RIE. For lines below 10 nm, it was found that the hard mask was not very robust, and was damaged by the RIE. The data also indicates that while the ALD process broadens the features, RIE returns them to the original width. These experiments are being repeated with cleaner, neater lithography in order to determine the minimum feasible linewidth. [Ballard 2014]

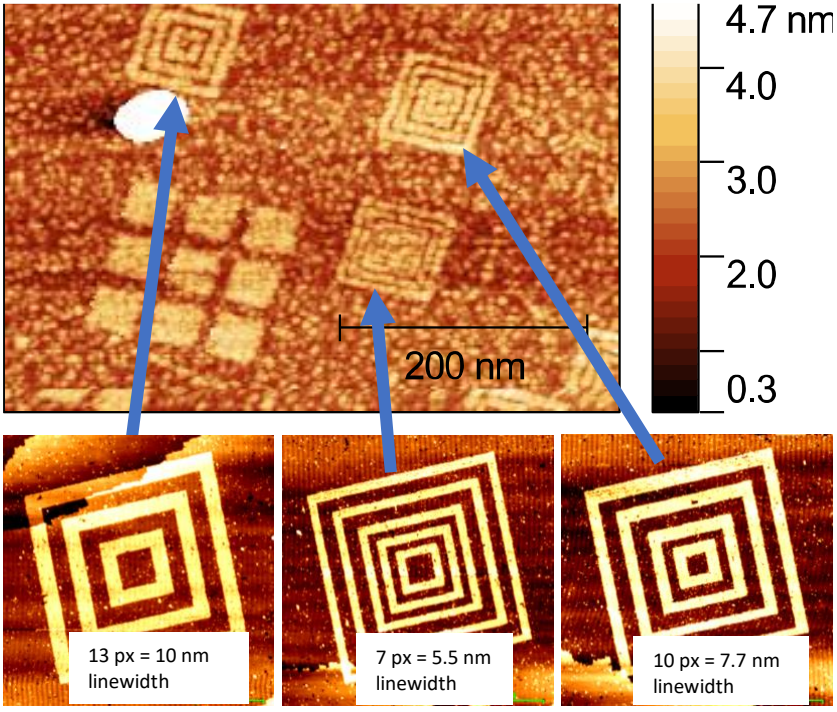

Fig. 3: AFM image of HDL-patterned features after ALD of 2 nm TiO_2.
The sets of concentric squares can be identified from their locations as sets of 7.10,13 px wide squares (1 px = 0.768 nm), making 5.5, 7.7 & 10 nm linewidths.
The original STM lithography patterns are shown below.

Optimization of grayscale direct-write laser lithography for the fabrication of large-area 2.5D molds for nanoimprint lithography

Peng Tian, Maria Szola, Dimitrios Kazazis, and Yasin Ekinci

Laboratory for X-ray Nanoscience and Technologies, Paul Scherrer Institute, 5232 Villigen, Switzerland
e-mail: peng.tian@psi.ch

Key words: grayscale lithography, nanoimprint, 2.5D, contrast curve optimisation, master stamp

Grayscale lithography (GSL) is a technology in which a photoresist film is exposed by electrons or photons with a modulated dose, leading to a varying surface topography after the wet development step. GSL has been used effectively to fabricate micro-optical elements like microlens arrays [1-3] and freeform metasurfaces [4], while these applications have become increasingly relevant, accompanying the booming demand of virtual reality (VR) and augmented reality (AR) technologies. Moreover, GSL is an ideal technique for the quick, low-cost, and versatile fabrication of large-area masters for nanoimprint lithography (NIL). The combination of GSL and NIL facilitates the replication of complex 2.5D structures, enabling applications like diffractive optical elements [5], MEMS [6, 7], and biomedical microdevices [8].

Grayscale writing can be realized across different lithography technologies, namely electron-beam, direct laser writing, and photolithography. Electron-beam lithography (EBL) is a very versatile and widely-used technique for the fabrication of grayscale structures [5, 8] owing to its ability to provide nanoscale resolution. However, EBL is not ideal for commercial applications due to its low throughput. Particularly for grayscale applications, EBL faces serious limitations in terms of the maximum structure depth that can be achieved with an electron beam. In this work, we investigate the use of direct-write laser lithography (DWL) for grayscale patterning, using resist films with thicknesses ranging between 10~15 μm. We demonstrate that DWL-based GSL is capable of producing 2.5D patterns with high throughput and relatively low cost to be used as reusable replication master stamps for NIL (see Fig 1).

However, despite all the aforementioned advantages, grayscale patterning requires careful optimisation at each step of the process from resist spin-coating to exposure and development and it must be meticulously planned to obtain acceptable reproducibility. A critical point to properly tune the grayscale patterning process is the shape of the resist contrast curve (CC) i.e. the plot of the remaining resist thickness versus the exposure dose (or gray value). Ideally, for GSL the CC should be as linear as possible, unlike binary lithography where a highly non-linear and sharp CC is needed. However, in practice, CCs of photoresists used in GSL often show some inherent nonlinearities mainly at the low-dose regime (see Fig 2). These nonlinearities, if not addressed, can lead to significant deviations from the designed structures especially for the shallow-depths of the fabricated patterns. The shape of the CC can be affected by several exposure settings such as the intensity of the light that is used during exposure, but is also largely affected by processing parameters such as resist thickness, soft baking conditions, development time, and any delay between these steps. Furthermore, surface roughness could become an important issue at shallow depths and have detrimental effects on the performance of the device, we have done a number of investigations on it and in the process of improving it.

In our work, we have found that the waiting time after the exposure and before the development can greatly impact the shape of the CC (see Fig 2), while the effect of film quality and resist aging are also addressed. We employ targeted optimization of our process to achieve high-quality and reproducible grayscale patterns with low roughness at wafer scale. With our comprehensively optimised process, “resist masters” were reproducibly fabricated and effectively used for replication of the patterns to daughter stamps for NIL.

[1] S.L.Aristizabal et al., Opt. Eng. 52(2013) 125101.
[2] A. Bouchouri et al., Micromachines 15(2024) 866.
[3] C. Hung et al., Opt. Express 33(2025) 7723-7739.
[4] H. Zheng et al., ACS Photonics 8(2021) 1824–1831.
[5] M.-A. Mattelin et al., Proc. SPIE 11292 (2020) 1129204.
[6] X. Fan et al., Microelectron. J. 37 (2006) 121–126.
[7] I.S. Garcia et al., J. Manuf. Process. 116 (2024) 202–209.
[8] T. Mortelmans et al., ACS Appl. Nano Mater. 5 (2022) 517−526.

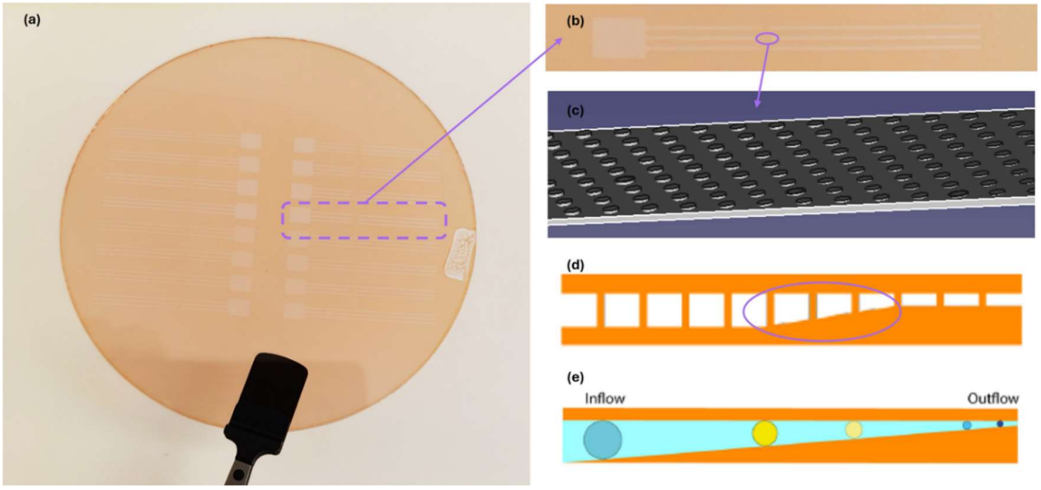

Figure 1. (a) A finished "resist master". 16 2.5D microfluidic devices, each consisting of three parallel channels (b) were fabricated on a 4" glass wafer. Each channel has grayscale wedge, shown in its 3D design (c), as well as pillars of gradually changing heights. The pillars work as support of the top part of the device, as shown in (d), and the sealed channel will trap and sort particles depending on their sizes (e).

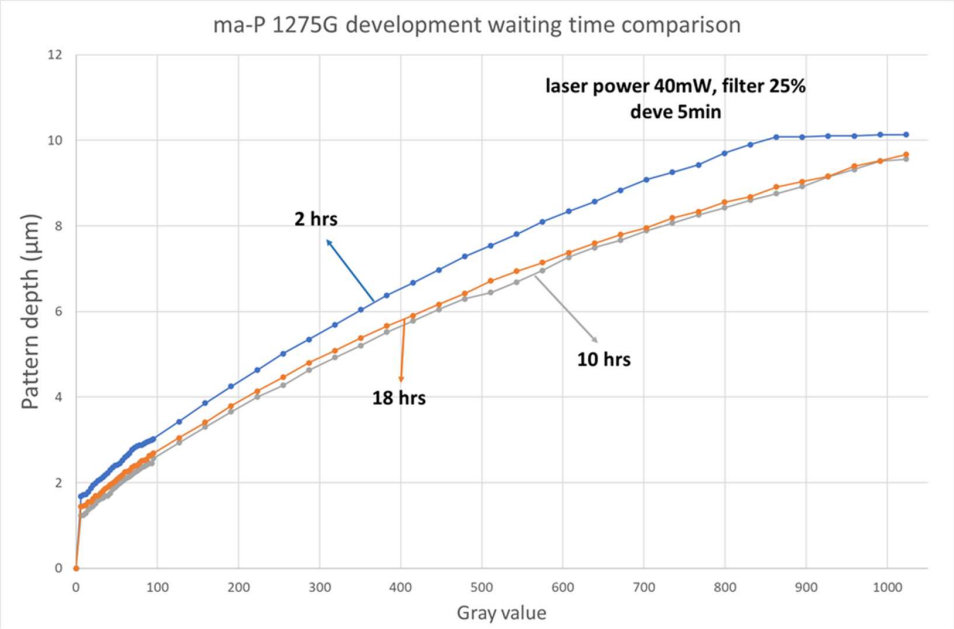

Figure 2. The impact of exposure-development waiting time on the shape of CC, as well as the non-linear part of CC at low GV regime. Note that the Y axis is pattern depth instead of remaining thickness, in order to remove the visually misleading effect stemming from the different thickness of resist films.

Advanced Patterning For Smart Optical Devices: Integrating Inkjet Coating with Nanoimprinting for Precise Height Control and Minimal Residual Layers

Patrick Schuster[a], Johanna Rimböck[a], Lisa Vsetecka[a], Thomas Achleitner[a], Andrea Kneidinger[a]
Brid Connolly[b], Martin Sczyrba[c], Andreas Frangen[b]

[a]EV Group, 4782 St. Florian am Inn, Austria
[b]Tekscend Photomasks Germany GmbH, 01109 Dresden, Germany
[c] AMTC Dresden, 01109 Dresden, Germany

Nanostructured surfaces are integral to various industries, including semiconductors, sensors, and biomedical applications. Nanoimprint lithography (NIL) is a pivotal technique for the precise patterning of nanostructures onto materials such as silicon, compound semiconductors, glasses, and polymers. Leading manufacturers in augmented reality, optical sensors, and biomedical chip production are increasingly implementing NIL, acknowledging its significant advantages in the fabrication of advanced devices.

Traditionally, imprint materials (polymers) are applied using spin coating. However, evolving applications require more precise control over the residual layer thickness to accommodate different master form factors, as well as improved efficiency and sustainability in resin usage. Inkjet coating, which allows for the printing of patterns with lateral resolution and variable thicknesses in a single process step, offers a promising coating alternative for NIL [1]. This method could facilitate the development of new applications while enhancing sustainability by reducing material consumption.

This study explores the integration of NIL with inkjet coating for the fabrication of non-functional grating structures, commonly employed in waveguides for AR devices. The master template, manufactured by Tekscend Photomask and utilized in this work, illustrated in Figure 1(a), comprises three distinct grating regions (refer to Figure 1(b) and 1(c)):

- the incouple (IC) grating: staircase structures
- the expander (EPE) grating: binary gratings with a linear depth profile ranging from 60 nm to 160 nm
- the outcouple (OC) grating: slanted gratings with a nonlinear depth profile spanning from 50 nm to 200 nm
- along with variations in duty cycle

First, initial NIL imprints on 6-inch silicon wafers with a uniform resin layer were generated, applied via spin coating. The resulting nanoimprints, shown in Figure 2(a-d), successfully replicated all three test gratings with strong adhesion to the substrate. The staircase, the binary and the slanted grating structures were accurately molded using NIL. Cross-sectional analysis revealed that the residual layer thickness ranged from 308 nm to 377 nm, depending on the fill factors at different positions within the gratings. This variation, coupled with the overall high residual layer thickness, is unsuitable for achieving optimal optical performance in smart devices.

In order to achieve a thinner and more uniform residual layer, inkjet coating was utilized to modify the film thickness prior to the imprinting process. To do so, a grayscale image of the master layout was generated, and grayscale inkjet coating (which employs variable drop sizes to produce different gray levels) was applied to create a resin layer with thickness variations across the wafer. The NIL process was subsequently performed on the inkjet coated wafers (instead of using spin coated wafers). Cross-sectional analysis of the resulting imprints, shown in Figure 3(a-d), confirmed successful replication of the structures with high pattern fidelity. All of the three complex grating designs were precisely replicated using NIL in conjunction with inkjet coating. The polymer showed excellent fluidic and filling properties after the inkjet coating and soft bake processes, with no observable change in adhesion. Compared to the spin coated imprints, the inkjet coated imprints demonstrated a more uniform and thinner residual layer across all grating types. The residual layer thickness ranged from 49 nm to 60 nm, which is more suitable for the optical performance required in augmented reality (AR) devices.

[1] J. Rimböck, P. Schuster, L. Vsetecka, and C. Thanner, "UV Nanoimprint Lithography—Impact of Coating Techniques on Pattern Quality," Nanomanufacturing, vol. 4, pp. 69-80, 2024.

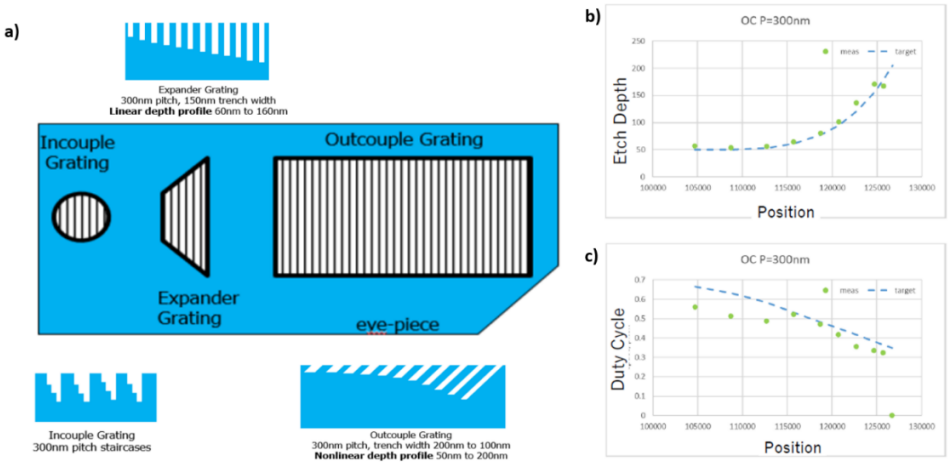

*Figure 1 TEKSCEND Photomask master template (**a**) schematic drawing with (**b**) nonlinear depth profile and (**c**) a variation of the duty cycle of the slanted gratings within the outcouple (OC) grating*

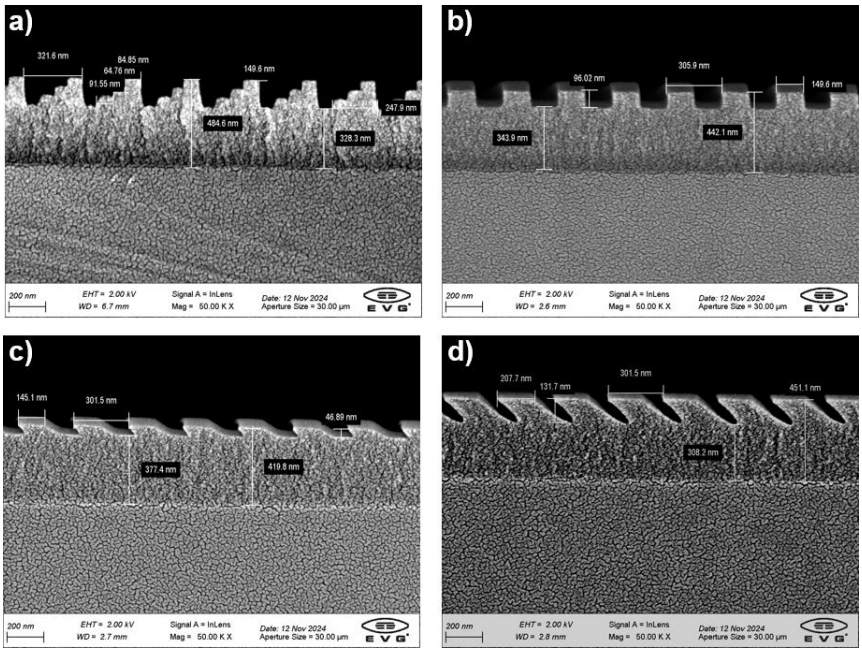

*Figure 2 SEM images of NIL imprint with spin coated resin: (**a**) incouple grating, (**b**) expander grating, (**c**) & (**d**) outcouple grating*

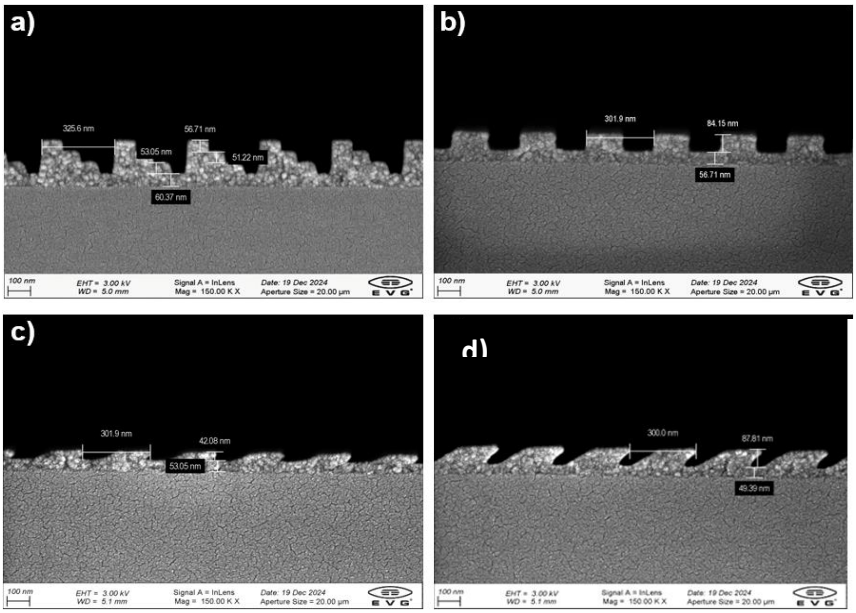

*Figure 3 SEM images of imprint with inkjet coated resin (**a**) incouple grating, (**b**) expander grating and (**c**) & (d) outcouple grating*

Exploring water-soluble polymeric stamps for ultraviolet light nano-imprint lithography

Haohui Yang [a], Anmol Gupta[a], Steffen Strehle [a],

[a] Technische Universität Ilmenau, Ilmenau, 98693, Germany
e-mail: haohui.yang@tu-ilmenau.de

Abstract:

Ultraviolet light nano-imprint lithography (UV-NIL) offers parallel, 3D and low-cost micro-nano manufacturing that bypasses the optical diffraction if compared with optical lithography. However, UV-NIL requires adequately patterned stamps and stamp demolding procedures. Our research focuses within this scope particularly on reducing the stress during the demolding process between soft UV-NIL stamps and the cured photoresist to reduce the risk of a damage of cured photoresist structures. We explored in this regard water-soluble polyvinyl alcohol (PVA) as soft stamp material and specifically the elution caused by a turbulent water flow shear force on the PVA surface. The turbulent flow regime was obtained by an in-house designed setup and nozzle as shown in Figure 1 (a).

Water-soluble polymer materials were previously suggested for UV-NIL [1] and it was demonstrated that the stamps can be indeed dissolved in water for demolding with low stress on the surface of the cured photoresist. They can thus replace for some cases potentially the traditional external force demold process. In addition, PVA materials will also produce noticeable swelling and elution in water. These phenomena are affected by the material preparation process based on PVA colloidal solution as different crosslinking processes of PVA affect its mechanical properties [2] and lead subsequently to different swelling and elution phenomena. In former experiments shown by Otsuka et al. [3], a limited amount of water resulted in a PVA gel that will first swell to an equilibrium state and then elute to an equilibrium state. However, when water is periodically renewed to dissolve the PVA gel, the elution process will continue after the swelling process is completed. Sonego J Met al. [4] discussed as release kinetics of PVA in Water swelling diffusion, followed by a disruption by erosion, and at last massive dissolution. Therefore, before PVA dissolves in water, swelling, erosion and other factors have already caused dissociation of the PVA tissue. Underwater adhesives [5] exhibited the above swelling, erosion, etc. behavior of PVA in water causing the PVA surface adhesion to fail before complete hydrolysis. Based on this, we propose a method to remove the PVA soft stamp when the adhesion between PVA and the cured photo resist fails through the surface shear force of the flow field (Figure 1 (b)), thereby facilitating and accelerating the demolding process.

The workflow is shown in Figure 2. With respect to mechanical properties, optical properties and other factors, we selected a PVA powder with medium molecular weight (Sigma-Aldrich®, Mw 85,000-124,000, 99+% hydrolyzed) for the experiments and used physical crosslinking and stirred PVA and water at 90 °C and 1200 rpm for 2 h to obtain a 10 wt% PVA colloidal solution, degas 24h in vacuum desiccator. The crosslinking method of PVA has a significant influence on the PVA properties. Usually, the methods are divided into physical and chemical crosslinking. Physical crosslinking creates hydrogen bonds between or within molecules and its products can be readily dissolved. In contrary, chemical crosslinking creates covalent bonds and its products are more stable [6]. Place the master stamp at the bottom of the mold container and pour the PVA colloid solution inside. After 48 hours of drying under atmospheric pressure at 20 °C, separate the PVA layer and cut off the structure area as the PVA soft stamp. The PVA soft stamp is fixed to the glass holder with adhesive layers (UV curing tape and X8 Gel pak®) to perform UV exposure at 4.5N force on a wafer which spin-coated with OrmoComp® photoresist. After half an hour of UV exposure, the photosensitive surface of UV curing tape lost its stickiness, and after another 20 min of hard baking, the adhesive layers used for holding soft stamp can be easily removed. In next step the imprinted substrate with the soft stamp can be placed into the nozzle and water piping system going the water flow removal process.

The experimental results under turbulent flow conditions (Reynolds number considered) show that, approximately 15 mm × 15 mm size PVA soft stamp can be removed in about 90 min with 50 °C hot DI water using a flow rate of 3 L/min. Finally, we replicated the microstructure from the master stamp successfully and maintained the integrity of the surface topography (Figure 3). Based on our workflow, we can control the soft PVA stamp removal process, which is the foundation to realize the development of a UV-NIL manufacturing process for multi-imprint, high aspect ratio structures, and further types of free-form surface structures. Using turbulent flow with different flow rates or using turbulent flow for PVA gel layer dissolution should in future allow us to gain enhanced control over the removal process.

Reference

[1] Choi, H., et al. Real. of high HAR metalenses by facile NIL using WSS. PhotoniX 4, 18 (2023).
[2] Chen Y, et al. Syn. and Prop. of PVA HGs with Str. and Tgh. Polymer Testing, 2022, 108: 107516.
[3] Otsuka E, et al. Elut. of Polym. from physically cross-linked PVA Gels. Soft Matter, 2010, 6(24): 6155-6159.
[4] Sonego M, et al. Highly structured PVA PCs: tuning inherent Stab. and RK in water. ACS omega, 2018, 3(2): 2390-2395.
[5] H. L. Fan, et al. Bioinspired Underwater Adhesives. Adv. Mater. 2021, 33, 2102983.
[6] Suzuki A, et al. Sw. and Mech. Prop. of PC-PVA HGs. Proc. Inst. Mech. Eng. H: J. Eng. Med., 2015, 229(12): 828-844.

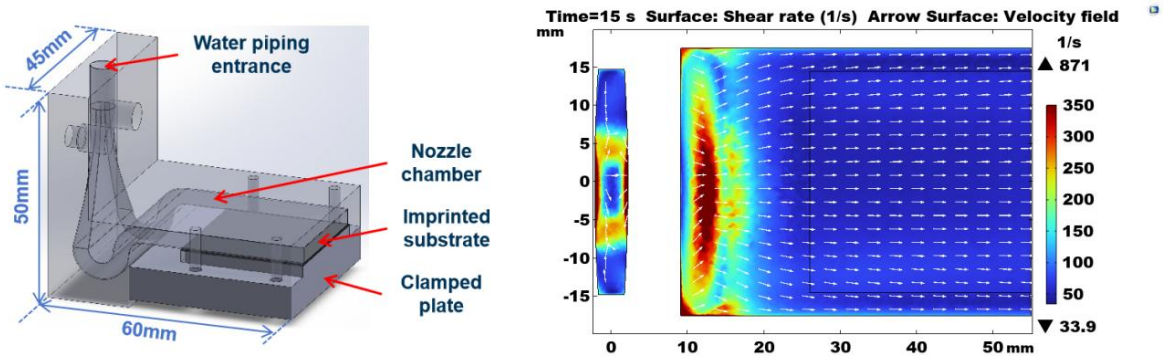

（a） (b)

Figure 1. 3D Design of the nozzle and flow field simulations: (a) 3D-CAD sketch of the nozzle and the PVA stamp dissolution chamber; (b) COMSOL® CFD simulation, shows the time average shear force distribution of flow field on the PVA soft stamp's surface from the bottom view.

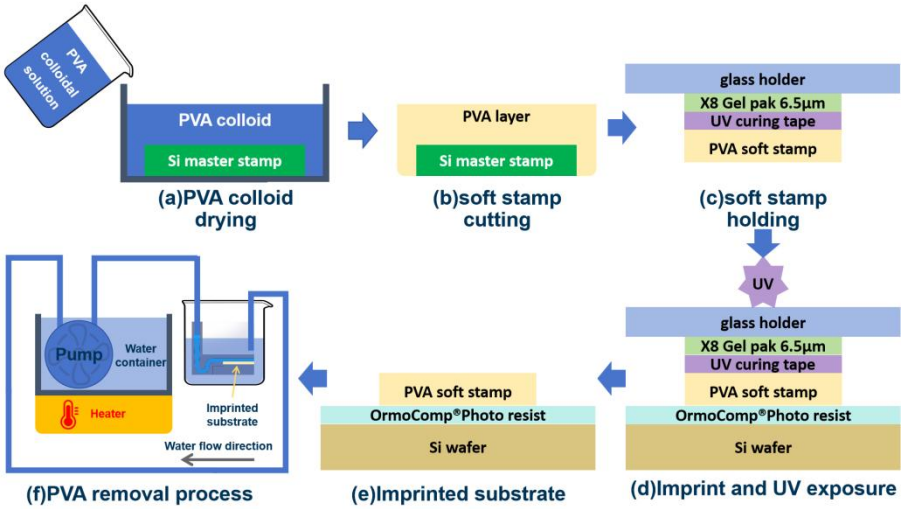

Figure 2. Process workflow of the water-soluble PVA stamps for UV-NIL: (a) PVA soft stamp drying and (b) cutting; (d)Imprinting with spin-coated OrmoComp® photo resist on Si substrate; (e) The UV curing tape lost adhesion, PVA soft stamp released on the imprinted substrate;(f) Placed imprinted substrate into nozzle and use water flow remove the PVA soft stamp.

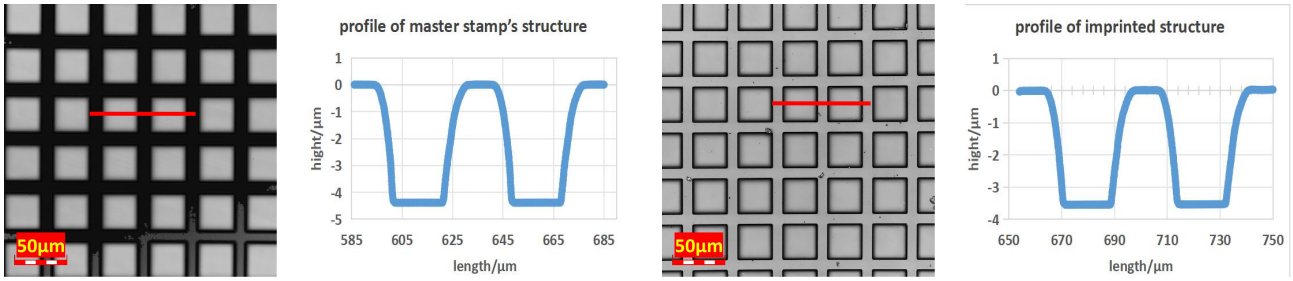

(a) (b) (c) (d)

Figure 3. Measurement result: (a) Target structure on master stamp and (b) cross-section measured by probe scanning; (c) The structure replicated on photo-resist and (d) cross-section measured by probe scanning.

Fabrication and Evaluation of Curved Mirror for Co-packaged optics Using Photo Nanoimprint Technology

Maaya Watanabe[1], Fumi Nakamura[2], Taro Itatani[2], Joji Maeda[1] and Takeru Amano[2]

[1]Graduate School of Science and Technology, Tokyo University of Science,
2641 Yamazaki, Noda, Chiba 278-8510, Japan

[2]The National Institute of Advanced Industrial Science and Technology (AIST)
1-1-1 Umezono, Tsukuba, Ibaraki 305-8568, Japan
e-mail: 7325627@ed.tus.ac.jp

With the recent rapid growth of artificial intelligence, the speed of cloud/edge computing has been increasing. Co-packaged optics (CPO) are expected to be key technologies of device implementation enabling high bandwidth and low power consumption [1]. Overview of Co-packaged optics is depicted in Fig. 1(a), where semiconductor devices and optical elements are integrated on the same substrate. One of technical challenges of CPO is the realization of optical In/Out to/from photonic integrated circuits. We have proposed and demonstrated a mirror-based optical re-distribution as shown in Fig 1 (b) [2]. The use of 3D micro-mirrors enables compact and wavelength-insensitive optical In/Out. Although laser direct writing technologies such as UV grayscale lithography [3] and two photon 3D printing [4] achieve high-precision microfabrication, they are not suitable for mass production. In this study, the fabrication of 3D curved mirrors for optical re-distribution was demonstrated using photo nanoimprint technology. The technology enables the transfer of 3D structures from a mold to a photo-curable resist, and it is well suited for efficient 3D microfabrication [5].

The fabrication process of curved mirrors using the imprint technology is shown in Fig. 2. In the proposed process, a PDMS (photo-curable polydimethylsiloxane) mold was used as a replica mold for imprinting, considering its transferability and gas permeability. The master mold was fabricated using two-photon grayscale lithography. It consisted of nine groups, each containing three mirrors arranged with 1 mm spacing both vertically and horizontally. The average height and radius of curvature of the 27 mirrors are 13.7 μm and 46.7 μm, respectively. As shown in Fig. 2(a), the replica mold was fabricated by pouring PDMS into the master mold and then exposed. The fabrication process of the curved mirror is shown in Fig. 2(b). A polymer resist (OrmoClear®FX) is spin-coated onto a 4-inch silicon substrate, and a replica mold was stamped and exposed to fabricate a curved mirror. Imprinting was performed while varying the load applied to the mold at approximately 100, 200, 300, and 400 kPa, and all of 27 mirrors were transferred at all load conditions. The heights of the mirrors fabricated at each load were measured using a laser microscope. The average mirror heights were 13.1, 12.9, 12.6, and 12.3 μm, respectively. Micrographs and 3D surface profile of the curved mirrors imprinted at a load of 100 kPa are shown in Figs. 3(a). Fig.3(b) shows a comparison of the cross-sectional profiles along A-A' with the master mold, replica mold, and mirrors fabricated under each applied load. As shown in Fig. 3(b), the height of the mirror decreases as the load applied to the mold increases. Also, measuring the radius of curvature from the cross-sectional profiles, the radius of curvature was 45.9 μm for the master mold, 59.8 μm for the replica mold, and 52.5, 60.1, 66.5, and 74.7 μm for the mirrors imprinted at 100, 200, 300, and 400 kPa, respectively. This shows that increasing the load applied to the mold during imprinting results in a collapse of the shape of the fabricated curved mirrors. Fig. 3(c) shows the results of nine measurement points of the residual layer around the curved mirrors fabricated at each load and confirms that the residual layer becomes thinner and more uniform in thickness as the load increases. Based on these results, we conclude that the optimal imprinting load is 200 kPa, where deformation from the master mold is minimal and residual layer is reduced. Future work will focus on evaluating the acceptable range of mirror shape variation for practical optical re-distribution applications.

[1] R. Mahajan et al., Journal of Lightwave Technology, vol. 40, no. 2, pp. 379-392, 15 Jan.15, 2022
[2] A. Noriki, et al, 2020 European Conference on Optical Communications, Tu2C-5, Belgium, 2020.
[3] Grushina, Anya. "Direct-write grayscale lithography" Advanced Optical Technologies, vol. 8, no. 3-4, 2019, pp. 163-169.
[4] V. Hahn, T. Messer, N.M. Bojanowski et al., "Two-step absorption instead of two-photon absorption in 3D nanoprinting", Nat. Photon., vol. 15, pp. 932-938, 2021
[5] F. Nakamura, et al., Electronic Components and Technology Conference (ECTC), 2024, pp. 1404-1408.

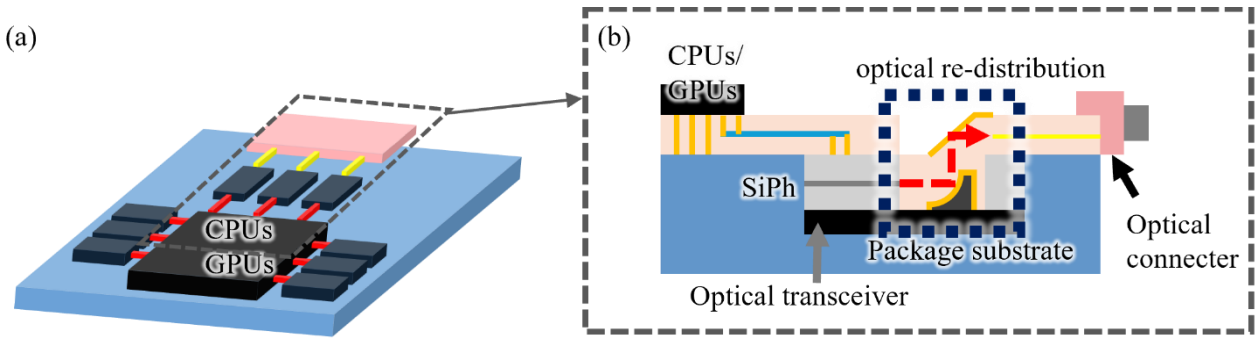

Fig.1(a) Overview of Co-packaged optics (CPO) architecture,
(b) cross-sectional view of the mirror-based optical re-distribution in CPO.

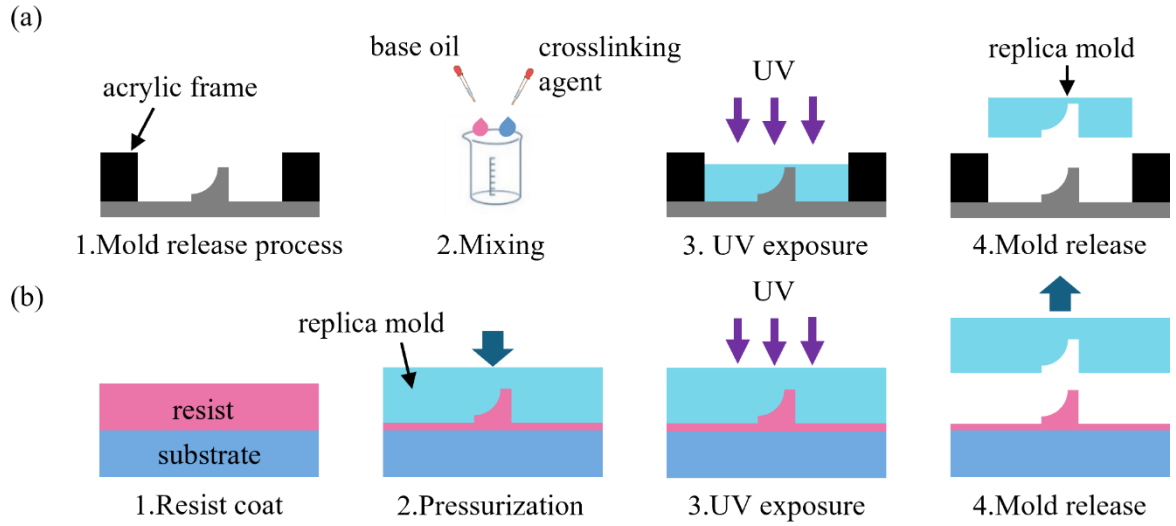

Fig.2:Fabrication process for curved mirror using imprint technology,
(a) process for replica mold, (b) imprint process.

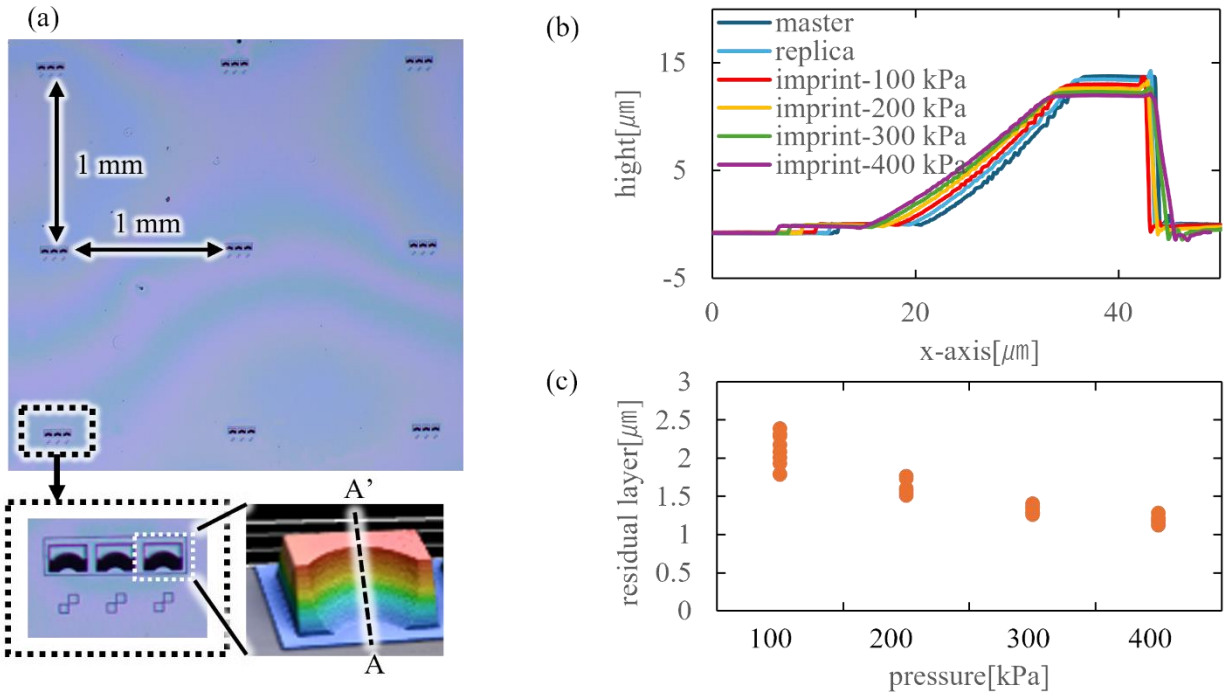

Fig.3 Result of mirror fabrication by imprint technology, (a) micrographs and 3D surface profiles of the curved mirrors imprinted at 100 kPa, (b) cross-sectional profiles along A-A' at master mold, replica mold and imprint mirror, (c) thickness of the residual layer around the curved mirrors.

Advances in parallelization of thermal scanning probe lithography and large-area patterning

Julia Stark[a], Jana Chaaban[a], Kartik Buddha[a], Fabian Könemann[a], Emine Çağın[a]

[a] Heidelberg Instruments Nano AG, Bändliweg 30, 8048 Zürich, Switzerland
e-mail: julia.stark@himt.ch

Thermal scanning probe lithography (t-SPL) is a direct-write nanolithography technique used by the NanoFrazor from Heidelberg Instruments to generate and inspect nanoscale structures by scanning with an ultrasharp tip over a sample surface. With a thermal stimulus, the hot tip can perform various local modifications to the sample via material removal, conversion, or addition [1].

Through localized thermal heating t-SPL enables high-resolution, damage-free patterning. Utilizing a closed-loop feedback mechanism for precise depth control, the NanoFrazor enables high-resolution nanolithography, including nanometer precise grayscale features. Additionally, the tool can be integrated into inert atmospheres in gloveboxes for applications using sensitive materials. This unique NanoFrazor technology enables new application areas and novel research in a wide range of material systems. Challenging applications in fields such as nanophotonics, quantum electronics, nanobiosystems and emerging materials research have been demonstrated [2,3].

Parallelization of thermal scanning probe lithography and faster electronics are now available for the first time in the new generation of the tool. Fully parallel operation of the NanoFrazor decapede module is now enabled by simultaneous patterning of ten thermal cantilevers with independent feedback control (see Figure 1). Together with smart handling of large designs, breakthroughs in throughput and maximum lithography area are possible. This allows for precise patterning of nanostructures over large areas, interesting for example in photonics applications [4].

The focus of this talk will be on large-area patterning with the NanoFrazor. Consistent repeated patterning of nanostructures over a large area has been demonstrated for metasurface applications. A metalens consisting of rectangular elements ranging from 100 nm to 250 nm in size over a total area of 690 µm x 690 µm has been patterned with the single-tip configuration. As can be seen in Figure 2, the patterned rectangular indentations have been transferred in an image reversal process to obtain pillars etched in silicon. The full metalens consists of almost 2 million individual elements, shown in Figure 3.

With the decapede module and an array of ten cantilevers operating in parallel the writing time for such metasurfaces is significantly reduced and much larger areas can be patterned. In this talk, I will present recent advances and applications for parallel writing. These include arrays of nanoholes for bio applications and differently sized bowtie structures for nanophotonics applications.

[1] S. T. Howell et al., Microsystems & Nanoengineering 6, 1 (2020), 21.
[2] E. Albisetti et al., Nat Rev Methods Primers 2, 32 (2022).
[3] N. Lassaline, J. Phys. Mater 7 (2023) 015008.
[4] N. Marcucci et al., Nanophotonics 12, 6 (2023) 1091-1140.

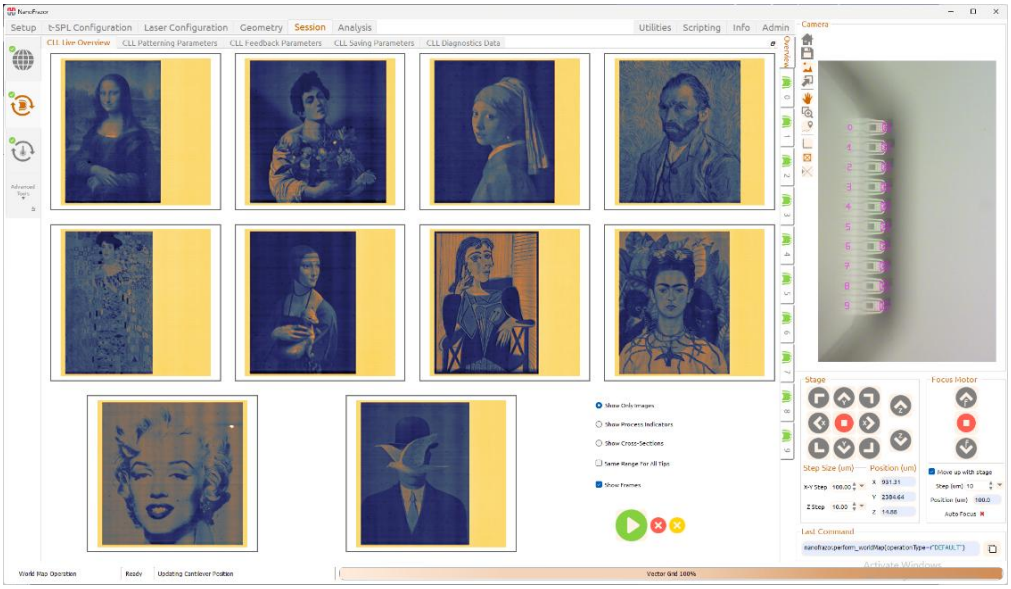

Figure 1. Software view showing the topography data of ten different artworks patterned in parallel with the NanoFrazor decapede module. This nanometer precise grayscale patterning is done by ten independently controlled thermal cantilevers. Each artwork has a length of 30 µm and a depth range of 25-60 nm.

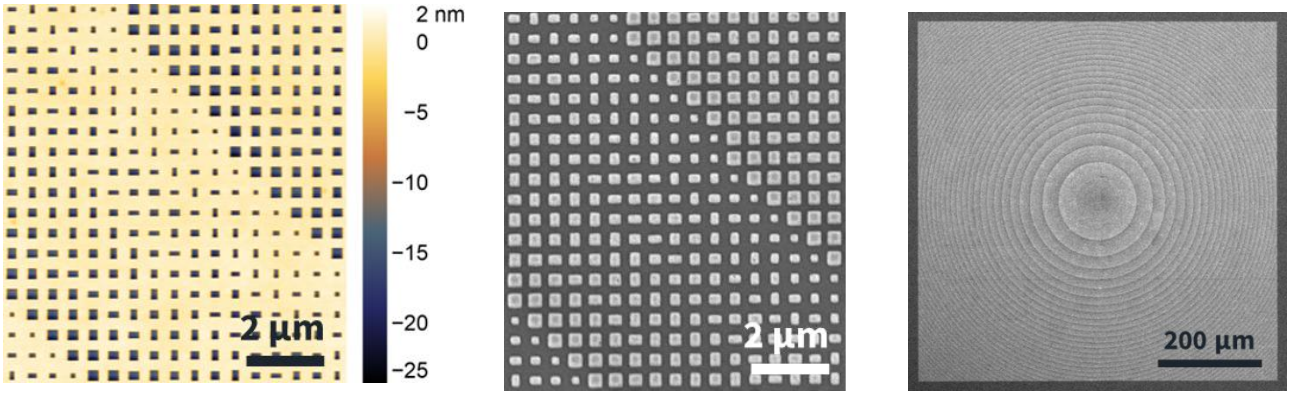

Figure 2. Left: Topography image of the patterned resist surface after thermal scanning probe lithography. Middle: SEM image of the same structures after full pattern transfer and etching pillars into the silicon substrate. Right: SEM image of the full metalens containing nanostructures etched in silicon.

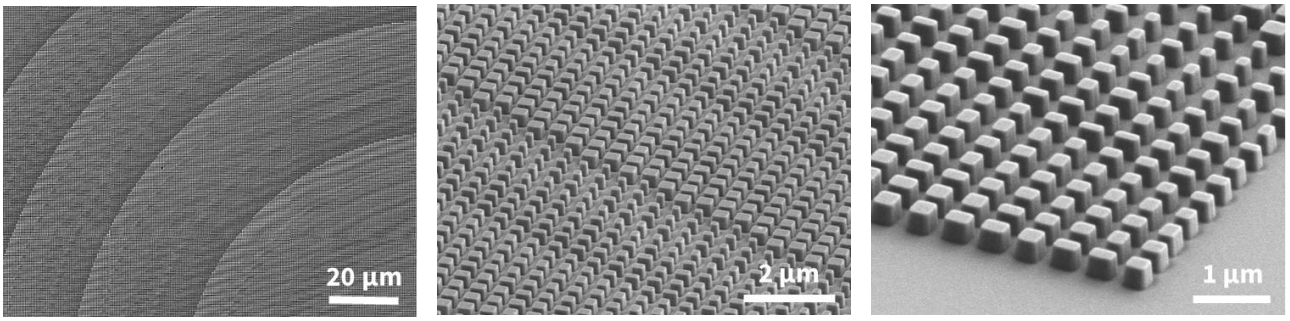

Figure 3. SEM images of the metalens shown in Figure 2, highlighting the NanoFrazor capability of creating dense nanostructures over a large area.

Oral Session 2B: Photonics, Photonic structures and Metasurfaces

Sustainable manufacturing of optical metasurfaces for imaging, sensing and display

Junsuk Rho
Department of Mechanical Engineering, Pohang University of Science and Technology (POSTECH), Pohang-si, 37673, Republic of Korea
E-mail: jsrho@postech.ac.kr

Metamaterials and metasurfaces are novel optical components composed of nanostructure arrays. They offer the advantage of an ultracompact form factor and can image submicron objects with resolution approaching the diffraction limit of light. The scope of this imaging extends from simple microscopes to more advanced light imaging applications such as 3D sensors, LiDAR, bio-imaging, and cameras. The wavelength range of imaging is also diversifying to support various imaging applications. Metalenses operating in the UV region enable high-resolution imaging due to the short wavelength of light. In the visible light spectrum, metalenses can be used for imaging in VR/AR displays. Near-infrared metalenses have potential applications in night vision devices and endoscopes. The wavelength range extends further to include the ultrasound region, where it can be used in photoacoustic microscopy. Additionally, elastic metalenses can be applied for energy harvesting, and acoustic metalenses can be used to focus sound waves. Furthermore, metalenses can perform imaging with various functionalities. They can tune their focal length, demonstrate trichannel imaging based on spin, and even image single photons emitted from a source. While metalenses operate across various wavelengths and offer diverse functionalities for numerous imaging applications, their design is currently not scalable, making large-area designs computationally heavy and expensive. To address this, efficient computational methods like RCWA and AI/DB-based design approaches have been developed . However, even with advances in large-area design capabilities, their commercialization has been hindered by manufacturing limitations such as high cost and low throughput. To reduce the production cost of metalenses, nanoimprint lithography has been employed. To address the low refractive index of conventional imprint resins, high-refractive-index particles are incorporated, creating a one-step printable platform On the other hand, ArF photolithography has been used to overcome low throughput and produce large-area metasurfaces at wafer scale. However, due to the high manufacturing costs associated with this method, research has been conducted on mass-producing metasurfaces by using wafer-scale nanoimprint technology to replicate metasurfaces initially created through photolithography. These scalable manufacturing approaches are expected to propel metalenses beyond the research level and into practical applications.

A Novel Manufacturing Platform for Large-diameter Si Metalens using Deep-UV Lithography

K. Sun [a], X. Yan [b], J. Scott [a], J. N. Monks [c], J. Y. Ou [a] and O. L. Muskens [a]

[a] Physics and Astronomy, University of Southampton, UK
[b] Optoelectronics Research Center, University of Southampton, UK
[c] Teledyne Qioptiq ltd, UK
e-mail: k.sun@soton.ac.uk

Abstract
With the adoption of artificial metasurfaces, the metalenses are developed through phase-shifts control by different nano-features [1]. Although metalenses have been widely demonstrated through e-beam lithography as a lab solution, it is still challenging to use Deep UV lithography to make metalenses with suitability of mass production. Recently, we have demonstrated that large-area and wafer-scale metal oxide metasurface can be reliably manufactured using DUV lithography [2]. In this work, we demonstrate 40 mm diameter Si-based metalenses, based on our novel designs and fabrication. With full CMOS compatibility, the metalens diameter has been increased over the exposure field size (25 mm X 33 mm) and the technique can be further scaled up.

The fabrication process flow is briefly described here. Firstly, alignment marks were defined through DUV lithography and then plasma etched into silicon. Then, based on the pre-defined alignment marks, the DUV lithography was performed by aligning to the alignments, with rotation applied to save reticles. Figure 1 shows the photo of a wafer with nine metalenses over a 200 mm Si substrate with the Nikon DUV scanner and TEL track as the background. The manufacturing method is ready for volume-up metalens production for its compatibility with the automatic system.

The manufactured metalenses were SEM inspected for etching control and optically characterized for focusing efficiency and optical performance including wavefront measurements. Figure 2 shows further characterizations of manufactured metalenses. For each metalens, four DUV exposures were given with 90-degree rotations (a). Due to its large diameter size, only the metalens central region is shown (b), with ring-like patterns from its design for optical phase coverage. A bit exposure border can be identified at vertical and horizontal orientation. From the SEM image at the exact metalens center, square rings can be identified with the central ring formed by 4-exposure stitching, and 4-exposure field as four quadrants in this image. Square rings are well-defined even cross-exposure borders with a stitching error of less than 100 nm. The metalens edge cross exposure is also presented in (c). The solid and hollow squares are all well-defined with very little deformation. This indicates the reliability of using the multi-exposure stitching technique.

The manufactured metalenses were laser-diced and optically mounted into a commercial long-wave infrared (LWIR) camera as its main focusing lens (d). Figure 2(e) presents a typical infrared image for a researcher standing before a tree. Significant fine details can be identified with trunks and fingers.

We report our latest works on large-diameter infrared silicon metalens manufacturing using production-ready deep-UV lithography. We have demonstrated a multi-stitching exposure technique to form metalenses beyond the exposure field limit. We will then disclose a few world first demonstrations in terms of nanostructure formation and optical functions enabled by our novel manufacturing process.

[1] Brongersma et al., Nature Reviews Electrical Engineering, 2 (2025) 125–143.
[2] Sun et al., Adv. Optical Mater., (2022) 2200452.

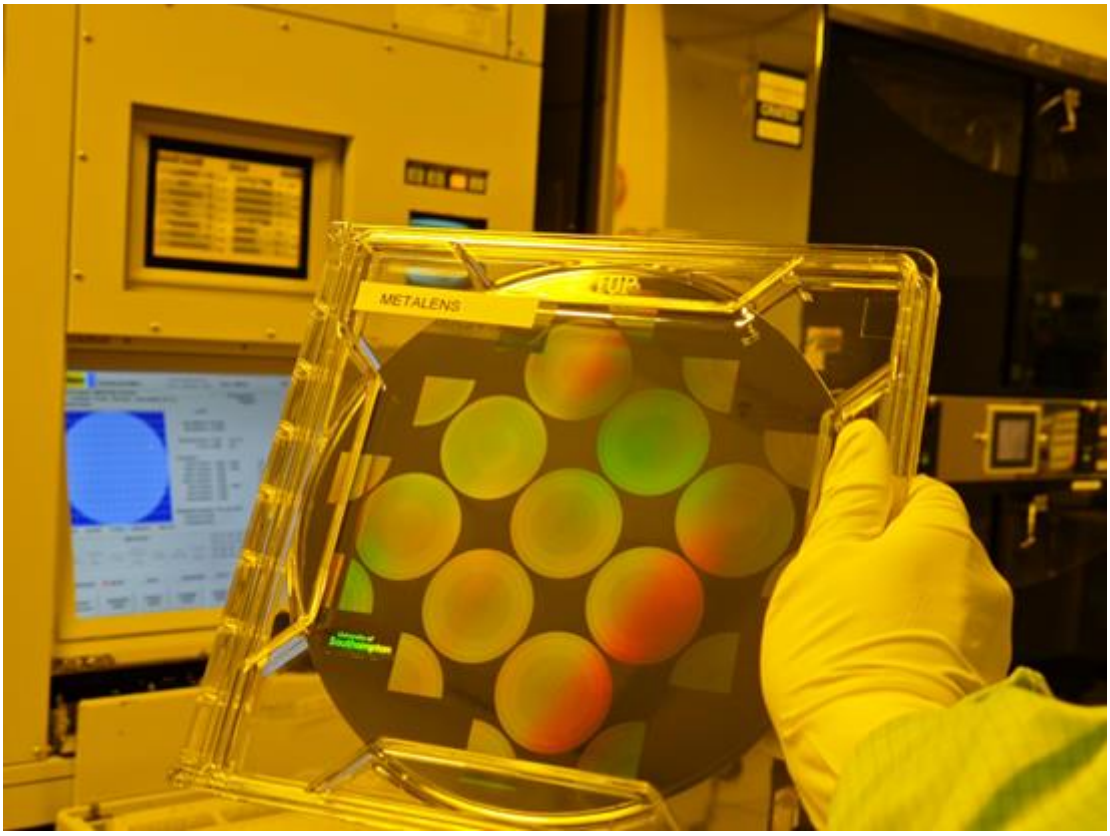

Figure 1. A typical photograph of metalenses waferscale over an 8-inch silicon substrate in front of Deep UV scanner and Track with the individual metalens diameter of 40 mm.

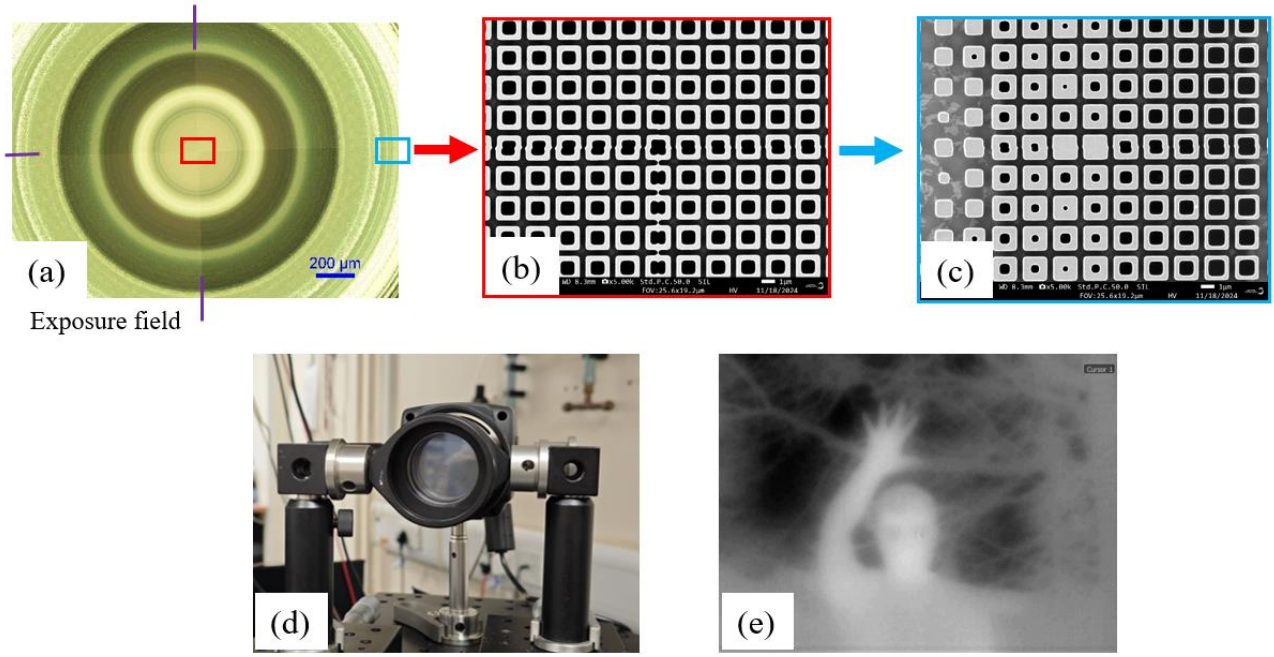

Figure 2. (a) micrograph of metalens center, (b) SEM image at the metalens center with 4 exposure stitching, (c) SEM image at the metalens edge with 2 exposure stitching, (d) diced metalens mounted on infrared camera and (e) real-world performance on a human standing in front of trees.

Understanding 3D Structural Control in Metasurface-Based Holographic Lithography

Jeevan Rois [a,b], Zesen Zhou [a,b], Matias Kagias [a,b]
[a] Division of Synchrotron Radiation Research and NanoLund, Lund University, Lund, Sweden
[b]Wallenberg Initiative Materials Science for Sustainability, Lund University, Lund, Sweden
e-mail: jeevan.rois@fysik.lu.se

One emerging application of optical metasurfaces is their use in holographic lithography as masks for generating 3D complex light intensity patterns [1] that can be printed in thick layers of photoresist. Recent work demonstrated that this approach can be utilized for fabricating centimeter scale 3D architected structures with high energy absorption capacity [2]. Other promising applications include 3D photonic crystals. For such applications, a high feature fidelity and pattern uniformity is critical. This can only be achieved by a spatially consistent optical response of the metasurface. Nonetheless, the remarkable tunability of metasurfaces can be counterproductive in these applications, since fine dimensional variations due to fabrication inconsistencies can lead to significantly different optical responses.

This study provides a systematic sensitivity analysis of dielectric metasurfaces for holographic lithography. We focus on the selection of appropriate dielectric materials as well as unit cell designs that produce 3D periodic structures with sub-micrometer periodicities. Material selection is narrowed down by choosing dielectrics that are compatible with lithographic wavelengths. Our goal is to uncover material and unit cell design combinations that allow for significant tunability while are fairly insensitive to meta-atom dimensional variations in the range of single digit nanometers.

Finite difference time domain (FDTD) simulations were used to calculate the field profile, diffraction efficiency, and 3D light distribution for several metasurface unit cells. We have chosen 400 nm high nanopillars as the meta-atoms. In figure 1. we show one of the investigated patterns for which we calculated diffraction efficiencies normalized by the (0,0) order for TiO_2 (n = 2.66 at 405 nm) and HfO_2 (n = 2.02 at 405 nm) under 405 nm plane wave illumination by varying the pillar radius between 50 nm and 80 nm. For TiO_2 orders (1,0) and (0,1) are highly sensitive in the radius range of 50 nm to 65 nm and their efficiency changes by 6.98 % per nm and 6.78 % per nm, respectively. In contrast, for HfO_2 the (1,0) and (0,1) orders again show the highest sensitivity, but the efficiency change is only 0.106 % per nm and 0.113 % per nm, respectively. The 3D morphologies corresponding to each radii shows that HfO_2 exhibits strong tolerance to nanofabrication imperfections, offering a favorable balance between control over diffraction efficiencies and is comparatively insensitive to nanofabrication defects. This robustness is attributed to the weaker electromagnetic field confinement within HfO_2 nanopillars, making them less sensitive to fabrication-induced defects. In contrast, TiO_2 provides greater tunability, enabling the realization of more complex 3D nanostructures due to its stronger field confinement and higher refractive index. We further developed a metasurface fabrication process that combines low-temperature atomic layer deposition (ALD) of HfO_2 with damascene lithography [3]. The fabrication process flow is described in fig 2. Currently metasurface prototypes are being optically tested to demonstrate their suitability for holographic lithography.

[1]. S.M. Kamali, E. Arbabi, H. Kwon, & A. Faraon, Metasurface-generated complex 3-dimensional optical fields for interference lithography, Proc. Natl. Acad. Sci. U.S.A. 116 (43) 21379-21384 (2019).

[2]. Kagias, M., Lee, S., Friedman, A. C., Zheng, T., Veysset, D., Faraon, A., & Greer, J. R, Metasurface-Enabled holographic lithography for Impact-Absorbing nanoarchitected sheets. Advanced Materials, 35 (2023).

[3]. Zhang, C., Divitt, S., Fan, Q. et al. Low-loss metasurface optics down to the deep ultraviolet region. Light Sci Appl 9, 55 (2020).

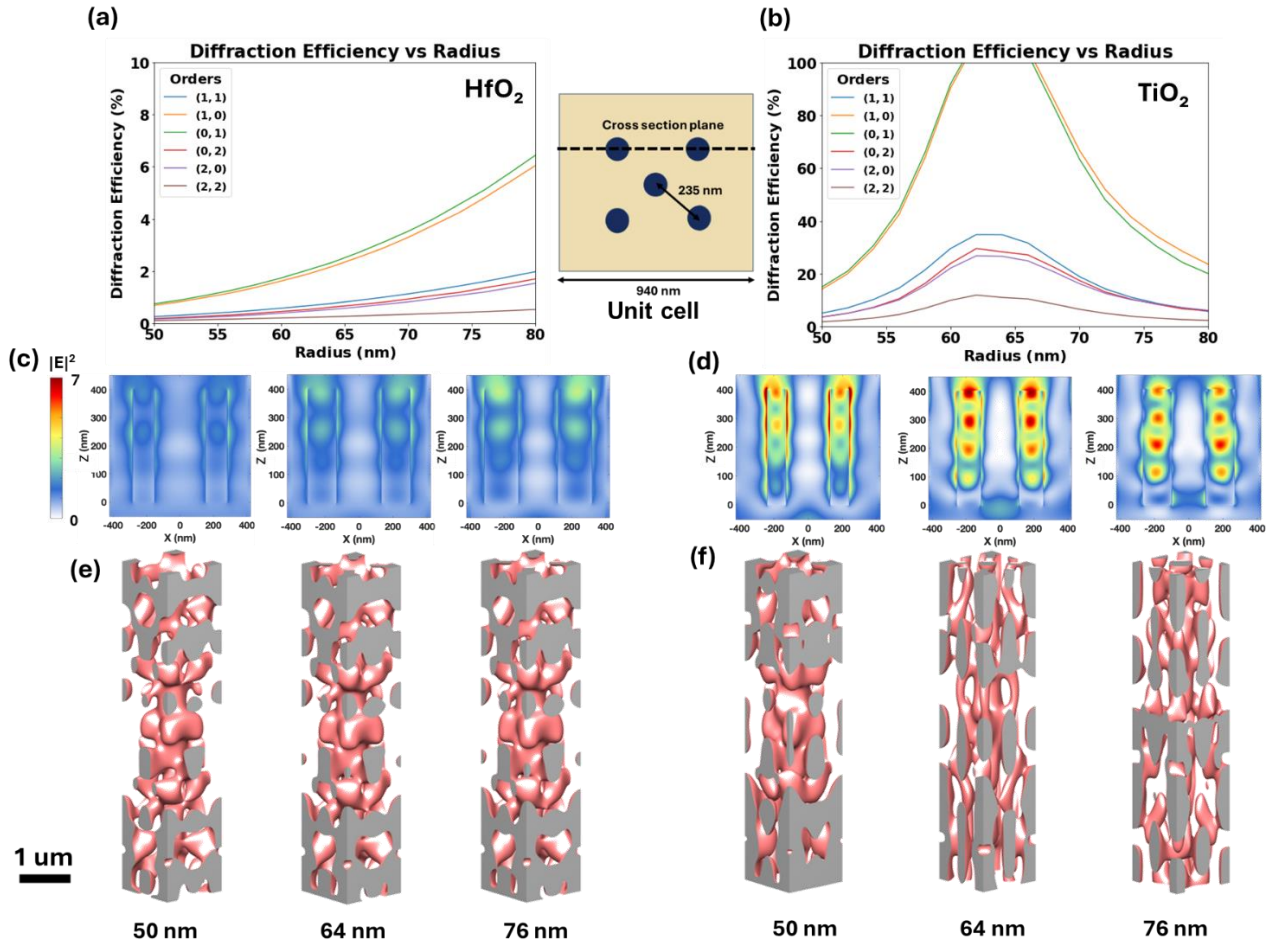

Fig.1 (a),(b) Comparison of diffraction efficiency as a function of meta-atom radius for HfO_2 and TiO_2 respectively in a cross-shaped metasurface unit cell. (c),(d) Representative electric field intensity distribution of XZ crossectional plane of the metasurface unit cell for HfO_2 and TiO_2 respectively. (e),(f) The corresponding 3D morphologies are shown for radii of 50 nm, 64 nm, and 76 nm for HfO_2 and TiO_2 respectively. The light intensity threshold was set to be 1.1 and 0.7 for HfO_2 and TiO_2 respectively.

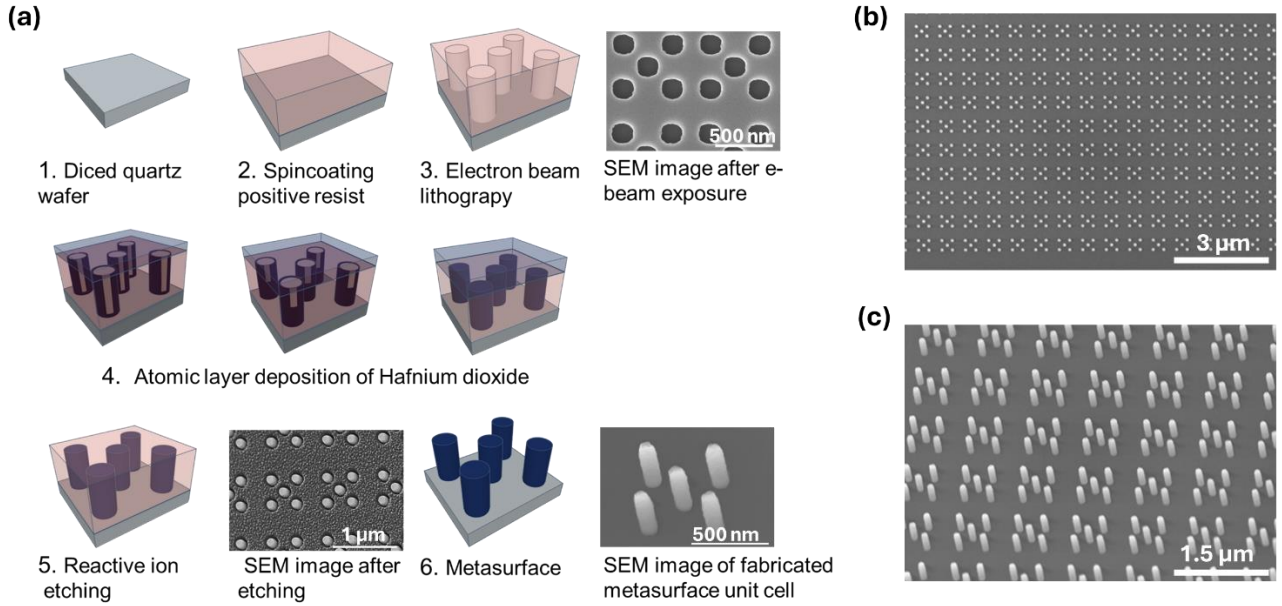

Fig. 2 (a) Metasurface fabrication process flow using damascene lithography. (b) Fabricated HfO_2 metasurface topview. (c) Fabricated HfO_2 metasurface tilted view at 30.9° angle.

Fabrication of Substrates with Plasmonic Gold Nanostructures for Cellular Membrane Rupture

Christian Einsiedler [a], Franziska Esmek [a,b], Rukan Nasri [a,b] Irene Fernandez-Cuesta [a,b]
[a] University of Hamburg, HARBOR, Hamburg, 22761, Germany
[b] Hamburg Center for Ultrafast Imaging
e-mail: christian.einsiedler@uni-hamburg.de

Cell lysing is a critical step in molecular cell biology. Biomedicine is shifting towards single cell analysis, which is revolutionizing what we know, for example, about heterogeneity in tumors and tissues, but this calls for new techniques, including single cell manipulation and lysing. Chemical lysing is often used for this purpose, but is not suitable for addressing single, individual cells, especially when they are all captured withing the same device. Thus, physical lysing methods, like those based on using lasers or intense optical fields are becoming increasingly interesting, since they could allow for selective membrane disruption. The localized surface plasmon resonance (LSPR) of nanoscale gold structures has attracted significant attention in this respect due to its capacity to convert optical energy into heat at the nanoscale.[1]

Our goal is to employ LSPR-induced photothermal effects triggered by pulsed laser irradiation to denaturate proteins, with the ultimate aim of achieving selective, local cell membrane rupture (Fig. 1a). In this work, we propose three different methods to prepare substrates with metal (gold) nanostructures, which can then be used to deposit cells on them. Two of them are based on gold nanostructures made by nanolithography, which has the advantage of allowing for precise and tailored nanostructure patterning, but with the disadvantage of being time and labor intensive. These can be used either directly as patterned on an inorganic, rigid substrate (approach 1, Fig. 1b), or transferred into a flexible, polymer substrate (approach 2, Fig. 1c). Approach 3 (Fig 1d) is based on using colloidal gold nanoparticles instead, embedded into a polymer coverslip. This approach does not offer such versatility in sizes, shapes or specific geometries and layouts, but is cheaper and simpler. This toolbox of approaches leverages the strong dependence of LSPR characteristics on the geometry and size of gold nanostructures, requiring precise fabrication and optical characterization.

Transparent and biocompatible substrates are crucial for this setup; indium tin oxide (ITO)-coated glass substrates were selected for their conductivity, biocompatibility, and superior gold adhesion. Different shaped nanostructures, like stars, rods, rings, or bowtie antennas, ranging from 100 - 1000 nm in width (with features as small as 40 nm) and a thickness of 20 nm were fabricated by electron beam lithography on PMMA onto ITO/glass, gold sputtering and gentle lift-off in acetone (Fig. 1b). This method allows to pattern the gold nanostructures directly on the substrate, without using adhesion layers, ensuring that the absorption capabilities of the gold structures and the associated induction of the E-field and thus temperature increase are not impaired.[2] These substrates can be used directly (approach 1), or the nanostructures can be transferred into a polymer coverlip (approach 2). For this, OrmoStamp (micro resist technology GmbH) is poured onto the substrate, pressed with another glass plate, cured under UV light, and then the thin OrmoStamp film is peeled from the glasses (Fig. 1c), to obtain a substrate that can even be used as a coverslip to seal microfluidic devices in the future. [3]

To identify resonant conditions, the gold nanostructures were characterized using dark-field spectroscopy. We observe a scattering peak at around 600 nm, which exact position depends on the dimensions of the gold rings, as expected (Fig. 2). This characterization will enable us to tune the excitation wavelenght to maximize interaction with the nanoparticles.

As an alternative, low cost fabrication method, 150 nm colloidal Au nanoparticles were embedded in an OrmoStamp coverslip. For this, glass slides were UV-ozone treated, spincoated with citrate-stabilized Au NP solution and then a drop of OrmoStamp casted, and another glass slide placed on top and UV cured (Fig. 1c).

Cells were seeded onto substrates and incubated for 2-3 hours to ensure proper adhesion. Figure 3 shows preliminary results of laser induced damage on colon cancer cells (CaCo cell line). Figure 3 (a) shows cells before (left) and after (right) pulsed laser irradiation (SuperK FIANIUM), with an emission set at λ=533nm ($\pm$50nm), where a significant reduction in size can be observed due to laser-induced damage. In figure 3 (b,c), spots on the cells membrane done by pulsed laser irradiation can be observed. In the next steps, we will study the effect of the nanoparticles for physical lysing of the cells. Preliminary tests show that it is possible to seed the cells on the substrates with the nanostructures (Fig. 3c) (ITO substrate with gold rings, in this specific case). Laser damage tests will be done next, and results presented at the conference.

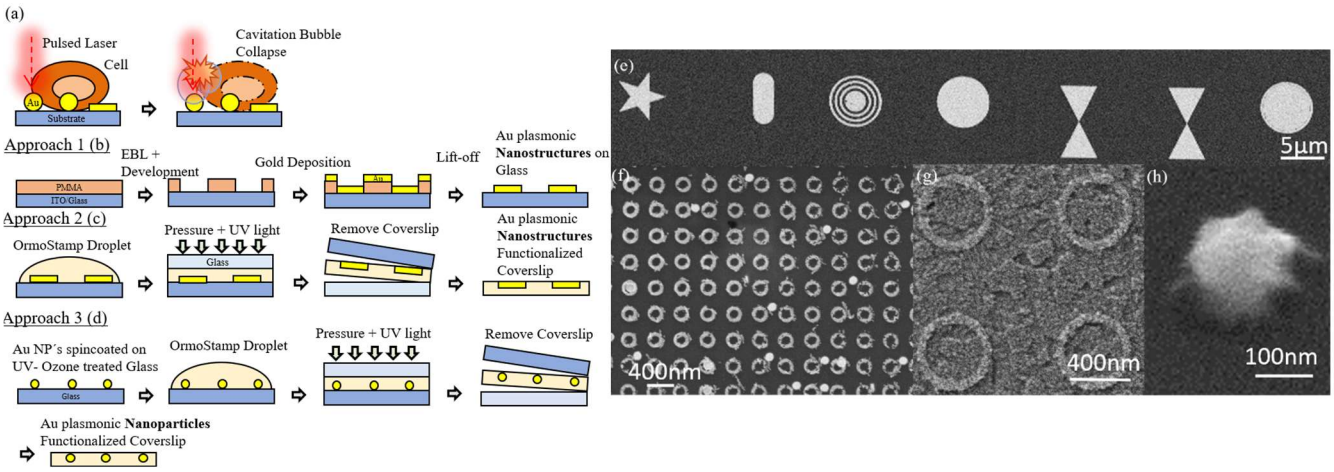

Figure 1: (a) Goal of the work: cells deposited on the substrate are exposed to pulsed laser irradiation, leading to photothermal effects and cellular membrane rupture, enhanced by plasmonic particles. (b) Substrate fabrication, approach 1: Au nanostructures on ITO/glass. (c) Approach 2: Au nanostructures embedded in OrmoStamp. (d) Approach 3: colloidal Au nanoparticles embedded in OrmoStamp. (e) SEM images of gold microstructures with corners and gaps, embedded in OrmoStamp. (f) Array of nano-rings embedded in OrmoStamp (g) Array of rings on ITO/glass. (h) Star shaped colloidal Au nanoparticle embedded in OrmoStamp.

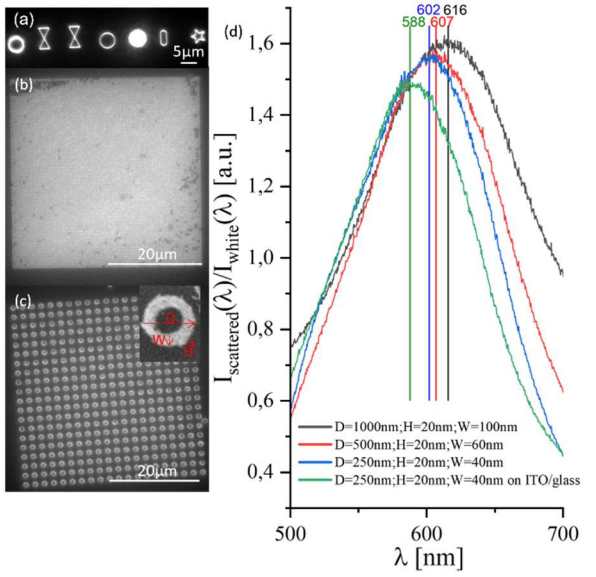

Figure 2: Micro- and nanostructures embedded in OrmoStamp under darkfield microscope: (a) Different shapes of Au nanostructures. (b) Array of D=250nm Au rings. (c) Array of D=1000nm Au rings and SEM image of such ring showing the respective dimensions (inset). Scattering spectra measurements. (d) Scattering spectra of ring arrays of different dimensions in OrmoStamp and on ITO/glass and the respective scattering peaks. The spectrum red-shifts for larger ring diameter and OrmoStamp as sorrounding media.

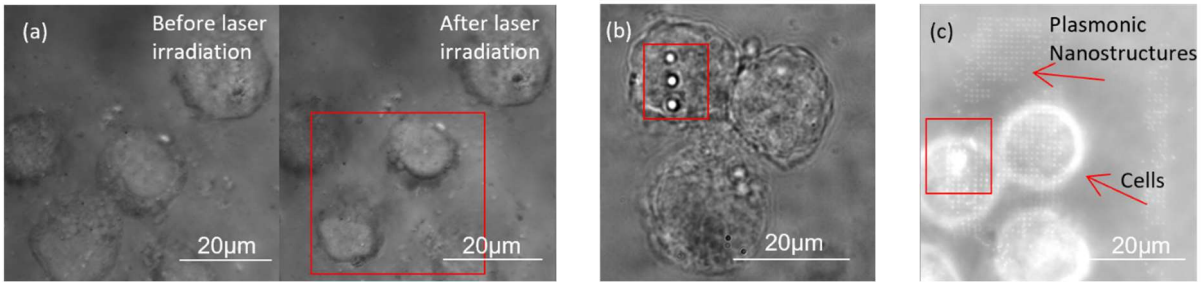

Figure 3: CaCo cells on different substrates under darkfield microscope. (a) Significant size reduction of cells deposited on Au nanoparticle cover slip after laser irradiation. (b) Three marks created by laser irradiation on the membrane of a cell deposited (c) Cells on top of an array of Au rings on ITO/glass with D=250nm. The pulsed laser marked also this cell.

[1] Jinxing Chen, Zuyang Ye et al. Small Science, 1, 2, 2 2021
[2] Mengjie Zheng, Yujia Yang et al. Microelectronic Enginerring, 233, 9 2020
[3] H. A. Garcia et al, Poster presentation at MNE, 2024

Printable Spin-Multiplexed Metasurfaces for Ultraviolet Holographic Displays

Hyunjung Kang[1], Hongyoon Kim[1], Kyungtae Kim[1], Junsuk Rho[1*]

[1]Department of Mechanical Engineering, Pohang University of Science and Technology (POSTECH), Pohang-si, 37673, Republic of Korea

**Corresponding author E-mail: jsrho@postech.ac.kr*

Ultraviolet (UV) metasurfaces are emerging as powerful platforms for high-resolution holography and secure optical encryption due to their ability to manipulate light with subwavelength precision. However, their practical implementation is hindered by material limitations, complex fabrication processes, and poor scalability. To overcome these challenges, we present a spin-multiplexed UV metahologram fabricated via a high-throughput, printable nanoimprint lithography (NIL) process, based on a zirconium dioxide (ZrO_2) particle-embedded resin (PER) (**Figure 1**). The PER material exhibits a high refractive index (~1.8) and negligible extinction coefficient at 320 nm, addressing the transparency and index constraints of conventional imprint resins. We exploit both propagation and geometric phase to achieve spin multiplexing, enabling distinct holographic images under left- and right-circularly polarized UV illumination. Anisotropic meta-atoms are designed and optimized to provide independent phase control for each spin state. A library of eight meta-atoms is selected to span the full 2π phase range with average phase errors below 0.09π and polarization conversion efficiencies up to 62%. The metasurfaces are fabricated using a single-step NIL process on centimeter-scale substrates without secondary etching or deposition steps, demonstrating excellent scalability and compatibility with curved surfaces. Experimental validation confirms the successful generation of two independent holographic images (**Figure 2**): a “warning message” under left-circular polarization (LCP) and a “sun” symbol under right-circular polarization (RCP), with measured efficiencies of 56.23% and 57.28%, respectively. The imprinted nanostructures exhibit sub-80 nm resolution and aspect ratios exceeding 10, confirming the precision of the NIL process. This work demonstrates a robust, scalable, and cost-effective route for fabricating spin-multiplexed UV metasurfaces and marks a significant advance toward the commercialization of multifunctional metasurface

[1] H. Kang et al., ACS Nano 18 (2024), 21504-21511

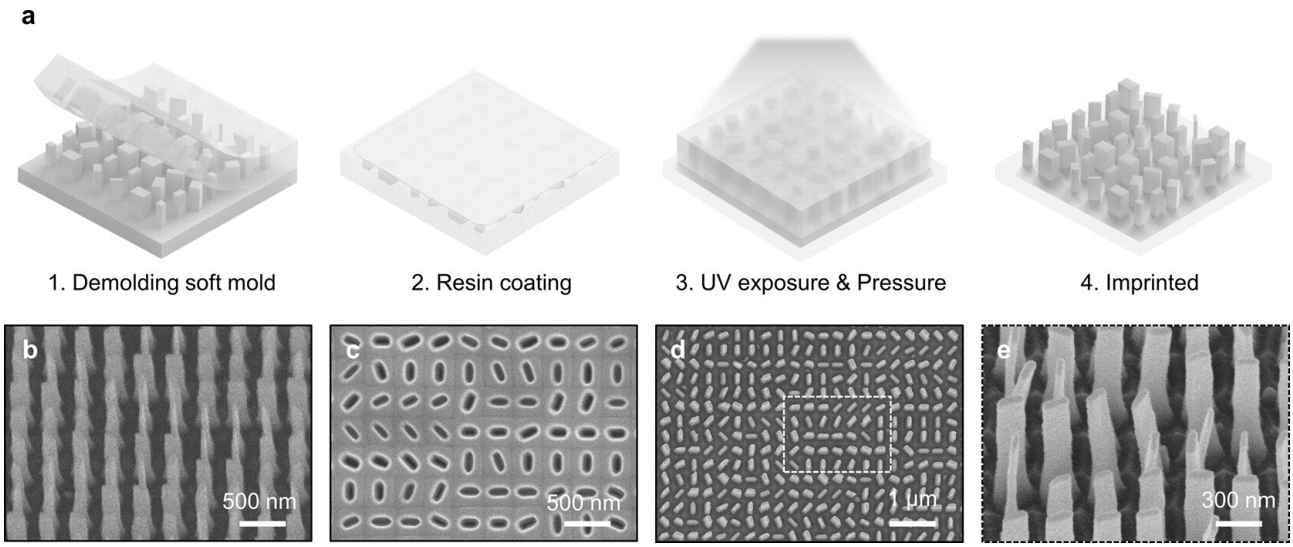

Figure 1. Fabrication of ZrO_2 PER-Based UV Metaholograms. (**a**) Schematic illustrating the nanoimprint lithography process employing ZrO_2 PER for the fabrication of spin-multiplexed UV metaholograms. SEM images of (**b**) the master mold, (**c**) the soft mold, and (**d, e**) the imprinted ZrO_2 PER -based metaholograms designed at $\lambda = 320$ nm.

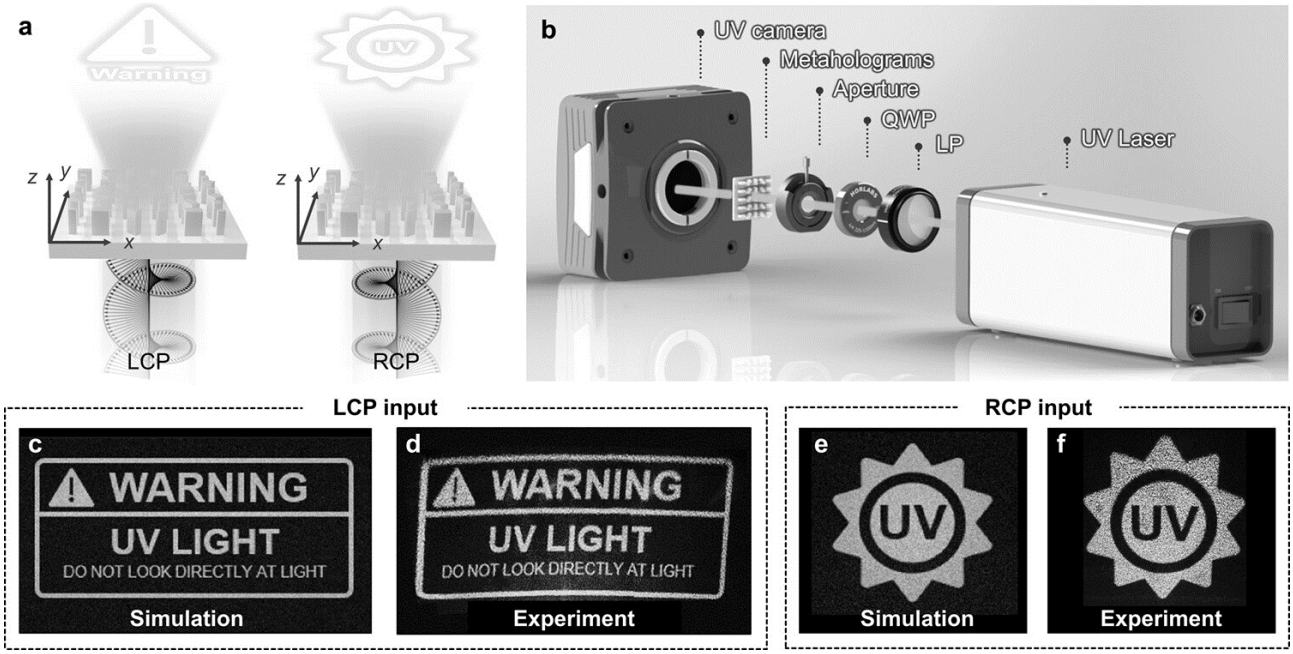

Figure 2. Demonstration of ZrO_2 PER-Based Spin-Multiplexed UV Metaholograms. (**a**) Schematic of holographic images projected by the spin-multiplexed UV metaholograms under left circularly polarized (LCP) and right circularly polarized (RCP) light illumination at $\lambda = 320$ nm. (**b**) Optical setup for measuring ZrO_2 PER-based metaholograms (LP: linear polarizer; QWP: quarter-wave plate; UV camera: sCMOS camera). (**c**) Simulated and (**d**) measured holographic images projected by the metaholograms under LCP light illumination. (**e**) Simulated and (**f**) measured holographic images projected by the metaholograms under RCP light illumination.

Embedded-Holey Metasurfaces for Enhanced Mechanical Robustness and Integration Compatibility

Zixuan Wang [a], Chuang Sun [a], Weilin Jin [a], Jun-Yu Ou [b], Kian Shen Kiang [a], Jize Yan [a]

[a] School of Electronics and Computer Science, University of Southampton, Southampton, SO17 1BJ, UK
[b] School of Physics and Astronomy, University of Southampton, Southampton, SO17 1BJ, UK
e-mail: ksk@ecs.soton.ac.uk; j.yan@southampton.ac.uk

Metasurfaces are periodically placed subwavelength structures which have an extraordinary ability to precisely manipulate multiple characteristics of light, including amplitude, phase, polarization, and frequency [1] by designing the geometrical parameters and distribution of these nanostructures. Owing to their extraordinary light-manipulation capabilities, metasurfaces have attracted extensive research attention and have significant progress across various fields. However, the mass production and commercialization of conventional pillar-based metasurfaces are constrained by the structural fragility of the nanopillars, especially as the aspect ratio increases. A larger aspect ratio generally enables broader phase coverage and provides greater flexibility in optical modulation. However, an excessively high aspect ratio in nanostructures will lead to fabrication challenges and make them more susceptible to damage during fabrication and operation. Moreover, the discontinuous surfaces further complicate photonic integration, thereby limiting their application in compact, chip-scale optical systems.

To overcome these fabrication and structural limitations, Lim et al. proposed hole-based metasurface architecture that enables the realization of higher aspect ratios while preserving optical performance [2]. However, despite the enhanced resistance to structural collapse, hole-based metasurfaces still suffer from mechanical fragility due to their hollow geometry and exhibit poor surface uniformity. Therefore, the hole-based design does not fundamentally resolve the challenges associated with robustness and integration in large-scale flat-optics devices.

In this work, we propose and experimentally demonstrate an embedded-holey metasurfaces filled with a SiO_2 layer, which further enhances device robustness and durability while maintaining high optical performance. We fabricated three types of metasurfaces based on different structural designs to make comparison: pillar-based, hole-based, and embedded-holey metasurfaces. As shown in Figure 2, all three metasurfaces were fabricated using electron-beam lithography (EBL) with ZEP520A resist for pattern definition. For the pillar-based design (blue box), a Cr layer was deposited after EBL and used as a hard mask for Reactive-ion etching (RIE). In contrast, the hole-based design (green box) was pre-deposited a SiO_2 layer as the etch mask, which enabled direct transfer of hole patterns after resist development. The embedded-holey metasurface (red box) follows the same steps as the hole-based process but includes one additional SiO_2 deposition step after etching to fill the nanoholes.

As shown in Figures 3, our design demonstrates similar focal spot size and quality compared to the other two, validating its optical performance. Experimental results show that the focal points of the three types of metasurfaces are located at 1.18 mm, 1.19 mm, and 1.18 mm, respectively, where the minimum spot size is achieved (FWHM = 1.68 μm for three types metasurfaces). Calculated results indicate that the effective numerical apertures (NAs) of the metasurfaces are 0.24, which matches the diffraction limit. Furthermore, the depth of focus was measured to be 165 μm, 160 μm, and 160 μm for the three designs, respectively.

In summary, conventional pillar-based metasurfaces suffer from structural fragility, poor surface uniformity, and limited integration capability. Hole-based designs partially improve mechanical robustness through their high-aspect-ratio geometry, but they remain possibility to collapse and still lack surface planarity. In contrast, our design achieves a high aspect ratio, mechanical stability, and surface flatness while maintaining excellent optical performance. Therefore, our proposed architecture enables the realization of future large-scale commercialization and widespread adoption of robust flat-optics devices.

[1] A. Arbabi, Y. Horie, M. Bagheri, and A. Faraon, "Dielectric metasurfaces for complete control of phase and polarization with subwavelength spatial resolution and high transmission," Nat. Nanotechnol. 10, 937–943 (2015).
[2] S. W. D. Lim, M. L. Meretska, and F. Capasso, "A High Aspect Ratio Inverse-Designed Holey Metasurface," Nano Lett. 21, 8642–8649 (2021).

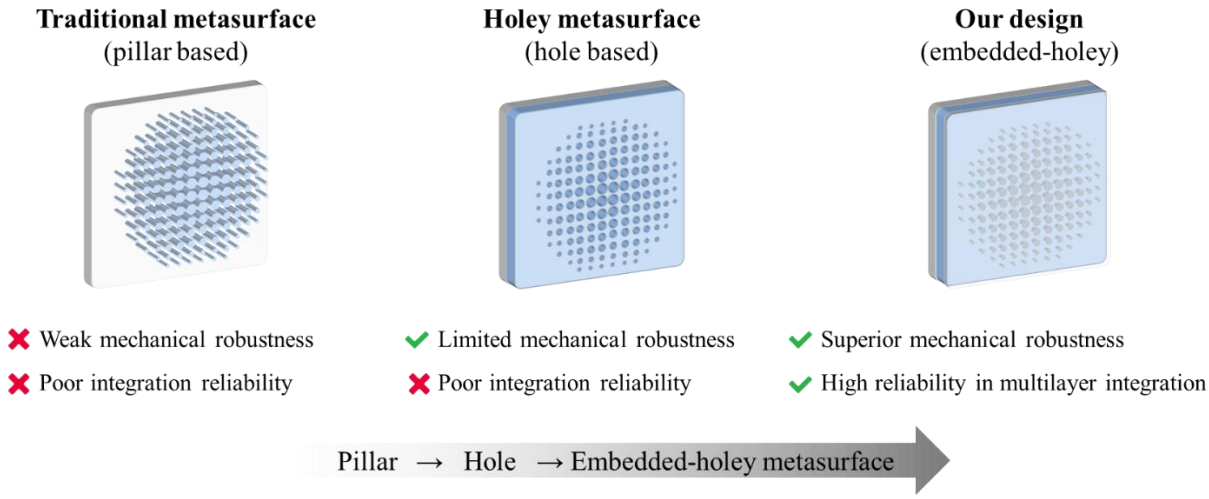

Figure 1. Comparison of three metasurface architectures: Traditional pillar-based metasurface (left), hole-based metasurface (middle), and the proposed embedded-holey metasurface (right).

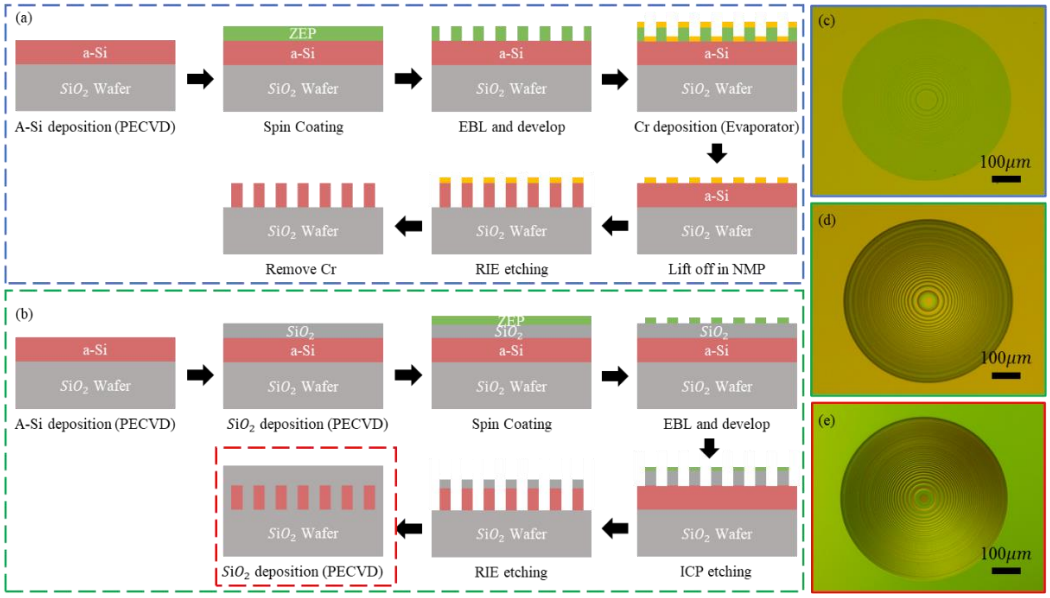

Figure 2. Fabrication process and corresponding optical microscope images of three types of metasurfaces. (a) The blue dashed box shows the process for the pillar-based metasurface; (b) the green dashed box corresponds to the hole-based metasurface and the a embedded-holey metasurface (deposition step is shown in red dashed box). The microscope images of metasurfacees with a corresponding color respectively.

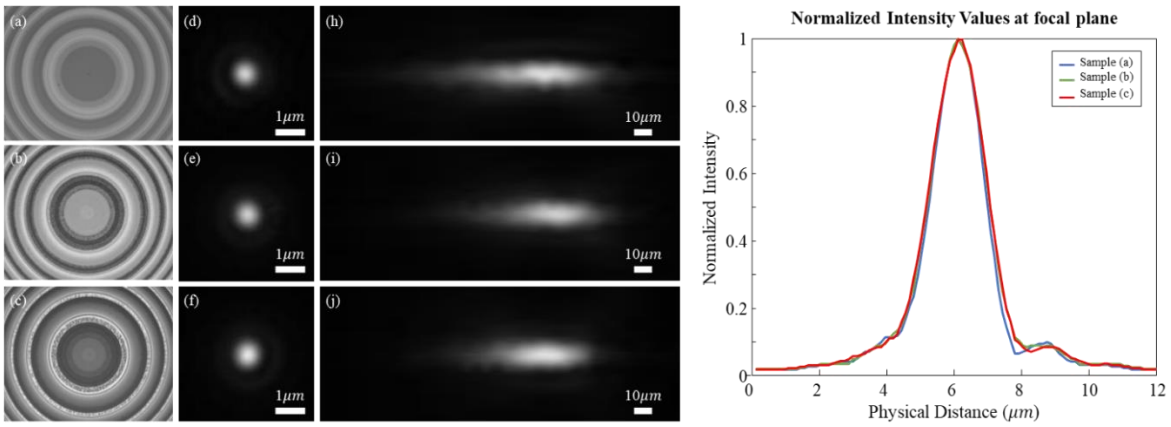

Figure 3. Optical characterization results of pillar-based metasurface, hole-based metasurface, and embedded-holey metasurface. (a-c) are the optical images; (d-f) are the focal points in XY-plane; (h-j) focusing process along z direction; (l) the normalized intensity distribution of focal points at XY-plane.

Novel UV-curable organic-inorganic polymers for micro-optical and photonic components with enhanced reliability

M. Russew[a], A. Plucinski[a], T. Wiglenda[a] J. Wolf[a], A. Schleunitz[a], G. Grützner[a]

a - micro resist technology GmbH, Berlin, Germany

e-mail: A.Plucinski@microresist.de

Novel micro-optical applications in the automotive sector and the need for new materials for the photonic applications, drive the research for further advanced optical materials meeting extended reliability standards in this industries. In this contribution, we highlight our latest material developments for the class of UV-curable organic-inorganic hybrid polymers meeting these strict criteria on temperature stability, optical transmission and non-yellowing behaviour. Also, these newly developed prototypes show excellent reliability and high transmission from the visible to the NIR wavelength region making them superior over generic polymers.

The material class of hybrid polymers has gained industrial relevance due to their unique opportunity of combining glass like properties with wafer-level processing options known from UV-curable polymeric materials.[1] Their hybridity is derived from the covalent connection of the siloxane backbone with organic side chains. Due to the synthesis via sol-gel approach, isotropic materials with excellent optical properties and high physical stability arise. Along other features, their superb transmission from the visible to the NIR wavelength range and quasi non-existing birefringence make them highly suitable for micro-lenses and arrays, optical waveguides, diffractive optical element and others optical components.

Trends towards miniaturization of optical elements is not limited to the automotive sector. Also in the data and telecommunication field, increasing demands for low loss and high reliability are driving research for materials with ever better resistance to temperatures, humidity and radiation, and at the same time maintaining excellent transmission. The flexibility of sol-gel synthesis makes it possible to adjust the final properties of the material to meet the evolving needs of novel applications, such as vehicle lighting using micro-optics or data and telecommunications based on photonics.

Polymers, for example in applications such as automotive projection systems, must pass demanding standards of reliability testing as the lifespan of these devices is ideally several decades. Therefore, accelerated aging tests are carried out in harsh environments. As the result of our research, we introduce our latest innovation from the hybrid polymer material class, the product OrmoEndur_XP, which was specifically designed to meet these optical requirements and reliability criteria of automotive materials. Excellent transmission, non-yellowing behaviour and thermal shock testing play a crucial role. By fundamentally changing the composition and synthesis conditions, we could achieve substantial improvement of the aging behaviour. Figure 1 shows results from imprintability tests and figure 2 the results of the optical testing of 500 µm thick films after 1000 h at high temperature storage at 130 °C and moist heat storage (85 °C/85% rH). The graphs indicate a significant improvement compared to standard hybrid polymers used in consumer electronics. At the same time, we were able to maintain the fast UV-curing behaviour and imprint performance that is essential for high-throughput wafer-level optics.

A second set of prototypes was developed to address the growing interest of polymeric waveguides as optical interconnects. Here, the material intrinsic optical loss as well as a refractive index adapted to the glass fiber are key material features. In Tab. 1 a comparison between standard waveguide hybrid polymers OrmoCore and OrmoClad, and newly developed OrmoCoreLL_XP and OrmoClad_LL_XP is shown. We could successfully decrease the intrinsic material optical loss down to 0.05 dB/cm for 1310 nm and 0.09 db/cm for 1550 nm. At the same time the absolute refractive index was lowered to match the optical fiber, which reduces incoupling losses in the device. Also these two new prototypes show similar results in reliability testing which will be further discussed in this contribution.

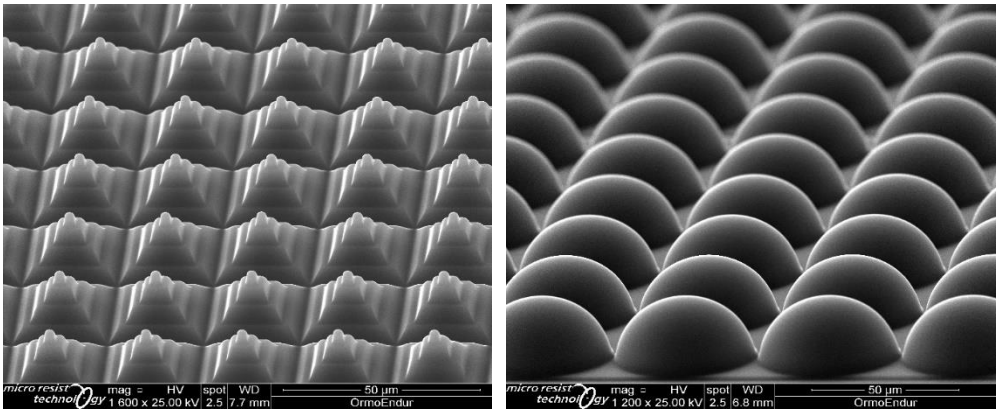

Figure 1. Left side: OrmoEndur_XP imprint of stepped pyramids (width 20 µm, hight 25 µm). Right side: OrmoEndur_XP imprint of micro lens arrays (d = 50 µm, hight 25 µm).

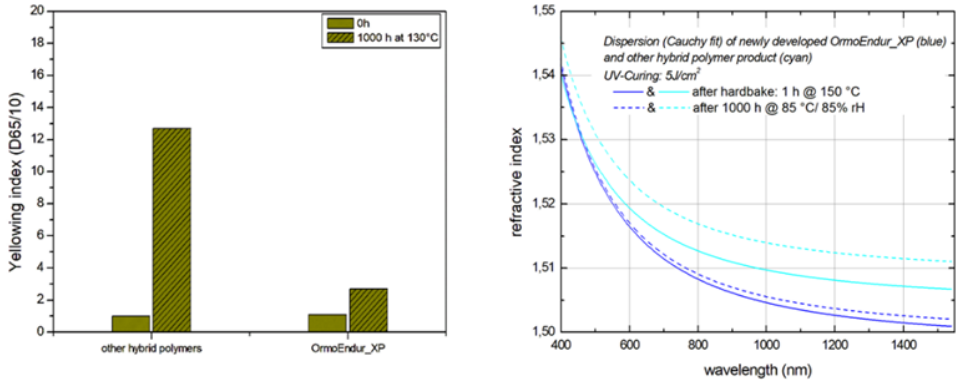

Figure 2. Left side: Yellowing index of the newly developed OrmoEndur_XP compared to the standard hybrid polymer after 1000 hours of high temperature storage at 130 °C (film thickness ~500µm). Right side: Dispersion of OrmoEndur_XP before and after moist heat storage (85 °C/ 85% rH).

	OrmoCore	**OrmoClad**	**OrmoCoreLL_XP**	**OrmoCladLL_XP**
Optical Loss @1330/1550 nm (dB/cm)	0.3/0.7	0.3/0.5	0.05/0.09	0.2/0.3
%T @ 400 nm (300 µm ft)	90*	90*	96	96
%T @ 400 nm (300 µm ft) after 1000h at 130 °C	n.d.	n.d.	93	91
n_D (solidified)	1.55	1.53	1.45	1.41

Table 1. Basic optical properties and reliability data of newly developed optical waveguide materials OrmoCoreLL_XP and OrmoCladLL_XP in comparison to standard hybrid polymer waveguide materials OrmoCore and OrmoClad. *150 µm film thickness

[1] Herder, M., Klein, J.J., Vogler, M., Russew, MM., Schleunitz, A., Grützner, G. (2021). „Hybrid Polymers for Conventional and Additive Manufacturing of Microoptical Elements". In: Heinrich, A. (eds) 3D Printing of Optical Components. Springer Series in Optical Sciences, vol 233. Springer, Cham.

Oral Session 2C: Photonics and Optoelectronics

Monolithic Integration of GeV Centers in Ring Waveguides for Quantum Light Emission

Fatemeh Moradiani [a], Ruairi Conlon [a], Arran Ashfield [a], Arthur Lipinski [a], Robert M. Bowman [a], Hamidreza Siampour [a*]

[a] Center for Quantum Materials and Technology, School of Mathematics and Physics, Queen's University Belfast, University Road, Belfast, BT7 1NN, United Kingdom
e-mail: h. siampour@qub.ac.uk

Room-temperature single-photon sources present a sustainable pathway for scalable quantum technologies, offering low-energy operation, integration-ready platforms, and long-term photostability. We report a single-photon source in which emission from a GeV color center is coupled into propagating surface plasmon polariton (SPP) modes through a cavity resonator. This coupling leads to spectral narrowing of the emitter's broad emission and enhances the photon extraction efficiency through the plasmonic cavity. A 100 nm silver layer is sputtered onto a silicon substrate as a base layer. Gold alignment markers (4 μm) are fabricated via electron beam lithography (EBL) by patterning PMMA, followed by development, 40 nm gold sputtering, and a lift-off process. GeV centers are subsequently spin-coated onto the sample, and their positions are identified using confocal spectroscopy. Ring waveguide resonators are then defined by patterning the negative resist hydrogen silsesquioxane (HSQ) at the nanoparticle locations. Figure 1(a) and (b) show the schematic and SEM image of the fabricated device. The width, height, and the radius of the ring resonator are 250 nm, 180 nm, and 2.5um respectively.

Single germanium-vacancy (GeV) centers serve as bright, spectrally narrow, and stable single-photon sources, making them well-suited for highly integrated photonic circuits. Scanning electron microscopy (SEM) images of GeV centers embedded in crystalline nanodiamonds (NDs) are shown in Figure 2(a), with particle sizes ranging from 20 nm to 200 nm. The second-order correlation, $g^2(0)$, measurement, presented in Figure 2(b) with maximum intensity observed at the zero-phonon line (ZPL) of $\lambda = 602$ nm.

To enhance the coupling efficiency of GeV centers to the resonant cavity, a ring-waveguide resonator was designed to operate at the zero-phonon line (ZPL) of GeV centers at 602 nm. The transmission spectrum of the fabricated device was measured using a supercontinuum laser spanning wavelengths from 580 to 650 nm. The results confirm a resonant wavelength at 602.35 nm, with a free spectral range (FSR) of 13.85 nm. The ring-waveguide exhibits a quality factor (Q) of 200, enabling an 11-fold enhancement of single-photon emission rates. This enhancement, along with directional control of emission, is achieved through precise design and alignment of the resonator with the GeV centers.

The $g^2(0)$ of the GeV center was measured before and after coupling to the resonator using optical excitation via confocal microscopy. A continuous-wave (CW) 532 nm laser was used to excite the GeV centers through a 100× objective lens with a numerical aperture of 0.9 (green path in Figure 3). Photon statistics were recorded using a Hanbury Brown and Twiss (HBT) setup, collecting emission through the same objective (red path in Figure 3). Our measurements show an antibunching dip with $g^{(2)}(0) < 0.5$ for isolated color centers, and a value of $g^{(2)}(0) \approx 0.2 \pm 0.05$ for GeV centers embedded in the resonant cavity, confirming single-photon emission characteristics.

[1] K. Snow et al., *Frontiers in Physics* 12 (2024): 1475071.
[2] H. Siampour et al., *Acs Photonics* 4.8 (2017): 1879-1884.
[3] H. Siampour et al., *Light: Science & Applications* 7.1 (2018): 61.
[4] H. Siampour et al., *Nanophotonics* 9.4 (2020): 953-962.

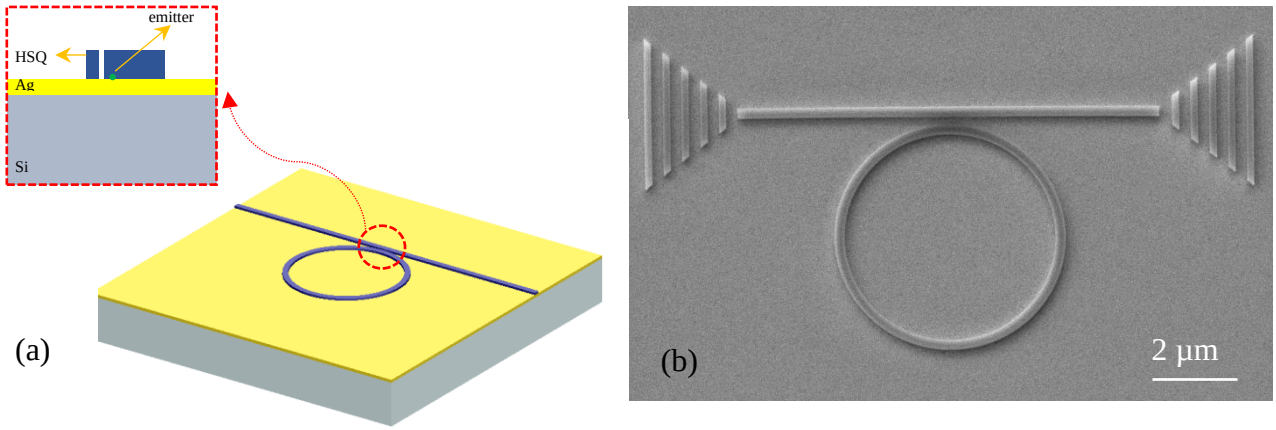

Figure 1. (a) Schematic illustration of the single quantum source device. The device consists of a GeV centers in a nanodiamond, which serves as the emitter, embedded in a plasmonic ring resonator cavity. **(b)** SEM image of the fabricated plasmonic ring-waveguide cavity using HSQ. The radius, width, and thickness of the ring are 2.5 µm, 250 nm, and 180 nm, respectively.

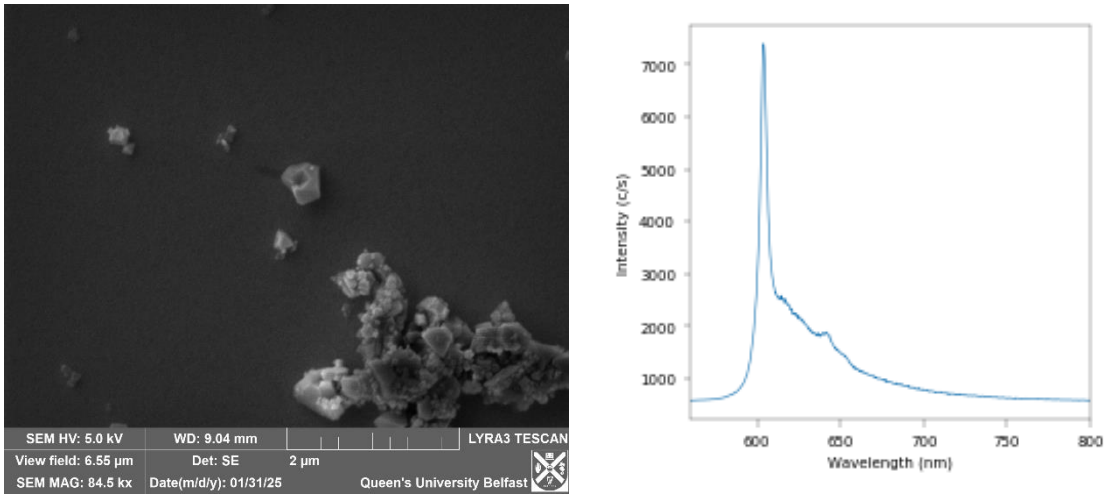

Figure 2. (a) SEM image of GeV centers in nanodiamonds. The particle sizes range from 20 nm to 200 nm. **(b)** Second order correlation measurement results taken for the GeV nanodiamond.

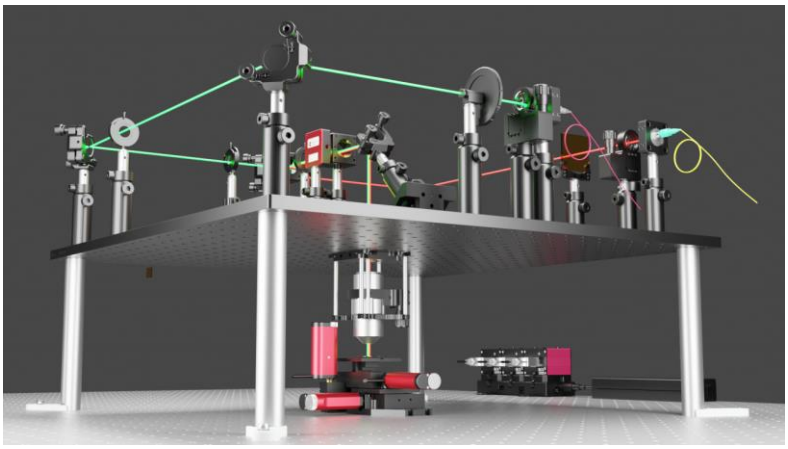

Figure 3. Schematic of the experimental setup for characterization of the single quantum source. The 532 nm CW laser is focused on the surface of the emitter through the 100x objective with 0.9 numerical aperture (green path). The luminance of the emitter then collected through the same objective and collected through the HBT setup to measure the $g^{(2)}$ (0)-factor of the device.

Microsphere-assisted generation of localized optical emitters in 2D hexagonal boron nitride

Xiliang Yang [a], Dong Hoon Shin [b], Kenji Watanabe [c], Takashi Taniguchi [c], Peter G. Steeneken [a], Sabina Caneva [a]*

[a] Department of Precision and Microsystems Engineering, Delft University of Technology, Delft, 2628 CD,The Netherlands.
[b] Department of Electronics and Information Engineering, Korea University, Sejong, 30019, Republic of Korea.
[c] National Institute for Materials Science, 1-1 Namiki, Tsukuba, Ibaraki 305-0044 Japan.
s.caneva@tudelft.nl

Abstract: Crystal defects in hexagonal boron nitride (hBN) are emerging as versatile nanoscale optical probes with a wide application profile, spanning the fields of nanophotonics, biosensing, bioimaging and quantum information processing. However, generating these crystal defects as reliable optical emitters remains challenging due to the need for deterministic defect placement and precise control of the emission area. Here, we demonstrate an approach that integrates microspheres with hBN optical probes to enhance both defect generation and optical signal readout. This technique harnesses microspheres to amplify light-matter interactions at the nanoscale through two mechanisms: focused femtosecond (fs) laser irradiation into a photonic nanojet (PNJ) for highly localized defect generation, and enhanced light collection via the whispering gallery mode (WGM) effect. Our microsphere-assisted defect generation method reduces the emission area by a factor of 5 and increases the fluorescence collection efficiency by approximately 10 times compared to microsphere-free samples. These advancements in defect generation precision and signal collection efficiency open new possibilities for optical emitter manipulation in hBN, with potential applications in quantum technologies and nanoscale sensing.

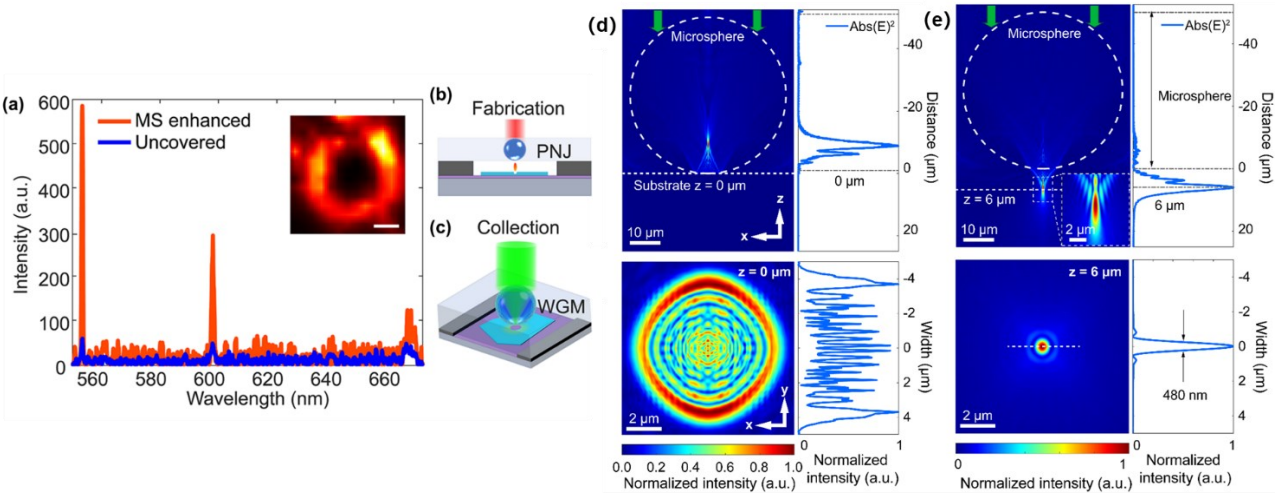

Figure 1. Schematic diagram of microsphere-assisted fs-laser fabrication collection of hBN emitters. (a) PL spectra of hBN emitters fabricated via microsphere-PDMS membrane (MPM) fs-laser, comparing MPM-covered and uncovered cases. Inset: PL maps of the irradiated hBN emitters rings. (b) Experimental design of the MPM with spacer over the hBN flake surface on the SiO2/Si substrate. Microsphere enhancement of the fs-laser focus to PNJ. [1] (c) Illustration of the spatial emission distribution of hBN emitters with a microsphere, where emitted photons are coupled to the microsphere via WGM and re-radiated at an engineered angle that falls within the collection range of the objective lens. [2] (d) Light distribution in the xz-plane/xy-plane and intensity distribution along the z-axis /y-axis with direct contact between the MPM and the substrate. (e) Light distribution in the xz-plane/xy-plane and intensity distribution along the z-axis/y-axis with a 6 μm distance between hBN and microsphere.

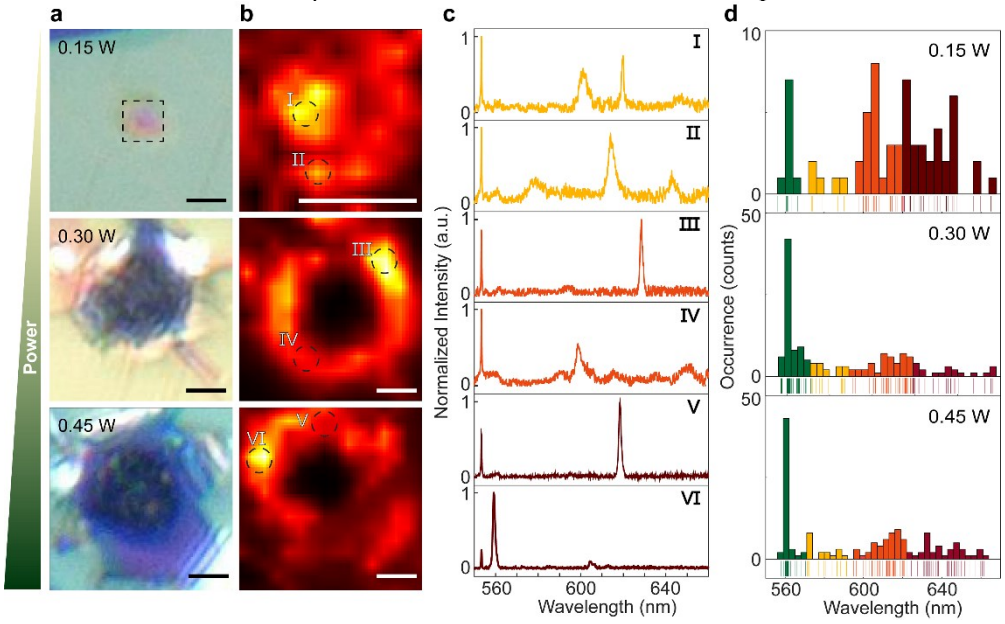

Figure 2. (a) Optical images of the defects of different sizes generated by MPM fs-laser with powers of 0.15, 0.3, 0.45 W. Scale bar: 3 μm. (b) The corresponding PL maps of the irradiated areas in (a). Scale bar: 3 μm. (c) Emission spectra of six representative emitters, as labelled in (b). The 550 nm peak in all panels arises from the Raman contribution. (d) Histograms of the emitters ZPLs, categorized by different colour ranges. Bin size: 3 nm [3]

[1] C. Xing et al., ACS Appl Mater Interfaces, vol. 9, no. 38, pp. 32896-32906, 2017.
[2] L. Yang et al., Advanced Optical Materials, vol. 7, no. 24, 2019.
[3] T. T. Tran et al., Nat Nanotechnol, vol. 11, no. 1, pp. 37-41, 2016.

Chip-scale infrared Fourier-transform spectrometer based on nano-opto-electro-mechanical systems

Bingrui Lu [a], Babak Vosoughi Lahijani [a, b], Søren E. Hansen [a], Thor A. S. Weis [a], Marcus Albrechtsen [a], Ali N. Babar [a, b], Michael Juhl [a], Christian A. Rosiek [a], Jesper L. Sand [a], Bjarke A. Frederiksen [a], Mathias L. H. Korsgaard [a], Nikolaj B. Hougs [a], Konstantinos Tsoukalas [a], Guillermo Arregui [a], and Søren Stobbe [a, b]

[a] DTU Electro, Department of Electrical and Photonics Engineering,
Technical University of Denmark, Ørsteds Plads 343, DK-2800 Kgs. Lyngby, Denmark.
[b] NanoPhoton - Center for Nanophotonics, Technical University of Denmark,
Ørsteds Plads 345A, DK-2800 Kgs. Lyngby, Denmark
e-mail: binlu@dtu.dk

Miniaturized near-infrared spectrometers are compact, fast, and energy-efficient, allowing for rapid analysis in a label-free and non-invasive manner. These advantages bring them great potential for applications in clinical diagnostics, food monitoring, forensic analysis, and health care [1]. A chip-scale spectrometer based on a mature silicon platform could solve the scalability issue for production in a cost-effective way.

In this work, we present a Mach-Zehnder interferometer (MZI) based chip-scale Fourier-transform spectrometer for the near-infrared wavelength on a nano-opto-electro-mechanical system (NOEMS) as shown in Fig. 1. The spectrometer is built from a silicon-on-insulator (SOI) substrate with the device patterned into the 220 nm silicon layer on top of the 2 µm buried oxide (BOX) layer. The incoming light is coupled into the spectrometer through a grating coupler [2] and then split into two separate paths with varying optical path lengths through an inverse-designed beamsplitter (Fig. 2) [3]. Each optical path contains a slot-mode waveguide consisting of two silicon beams separated by a gap that is tunable by a series of comb drive actuators driven by electric voltages (Fig. 3) [4]. For the chip integration and packaging, the grating couplers are covered by 2.25 µm of glass to enable optical fiber attachment, whereas the moving components and the electrical contacts are exposed to the environment as indicated by false colors in Fig. 1. Upon application of a voltage up to 10 V, the actuators modulate the waveguide slot gap with displacements on the order of tens of nanometers, which shifts the effective refractive index by ~0.6, thereby modifying the optical path length. Routing electrical and photonic signals in a single device layer requires electrical isolation trenches to intersect with waveguides. For this purpose, an inverse-designed electrical-photonic-circuit crossing is implemented [5, 6]. At the end of the two paths, the light is recombined in- or out-of-phase, and an interferogram in Fig. 4 through the output grating coupler can be obtained.

As near-infrared spectroscopy continues to grow in importance across biomedical and industrial sectors, this NOEMS-based FTS represents a promising step toward miniaturized, high-performance, low-cost, and energy-efficient spectral analysis tools, paving the way for next-generation ultra-compact point-of-care and on-site diagnostic solutions.

[1] Z. Yang et al., Science 371 (2021), abe0722.
[2] S. E. Hansen et al., Optics Express 31.11 (2023) 17424-17436.
[3] S. E. Hansen et al., Materials for Quantum Technology 4.1 (2024) 016201.
[4] T. A. S. Weis et al., arXiv preprint arXiv:2307.01122 (2023).
[5] B. Vosoughi Lahijani et al., arXiv preprint arXiv:2204.14257 (2022)..
[6] B. Lu et al., Proceedings of MNE2024. (2024).

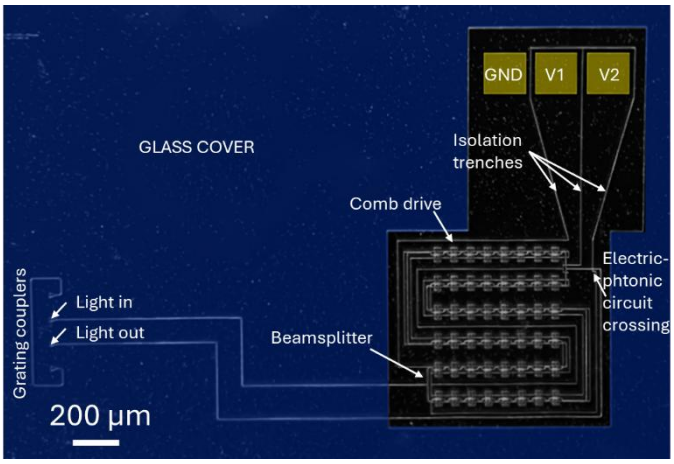

Figure 1. An optical Microscope image of a chip layout with false coloring. The yellow color represents the metal contacts, and the blue area is the glass-covered region.

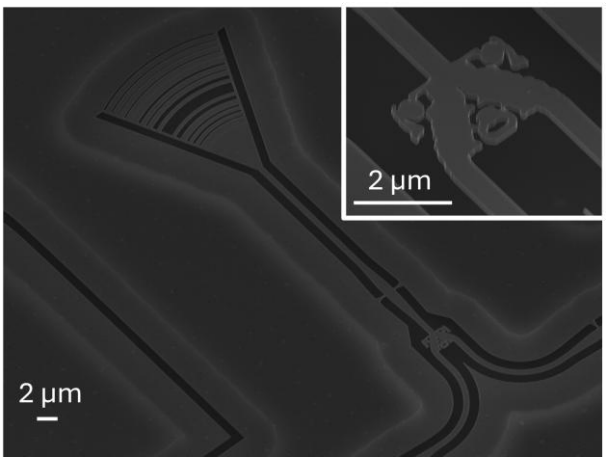

Figure 2. An electric scanning microscope (SEM) image of a grating coupler and an inverse-designed beamsplitter for the incoming light.

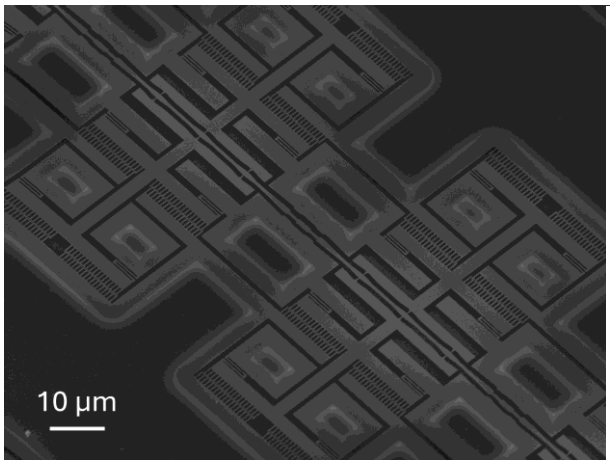

Figure 3. An SEM image of two sets of comb drives to electric-mechanically tune the gap size of the slot-mode waveguide.

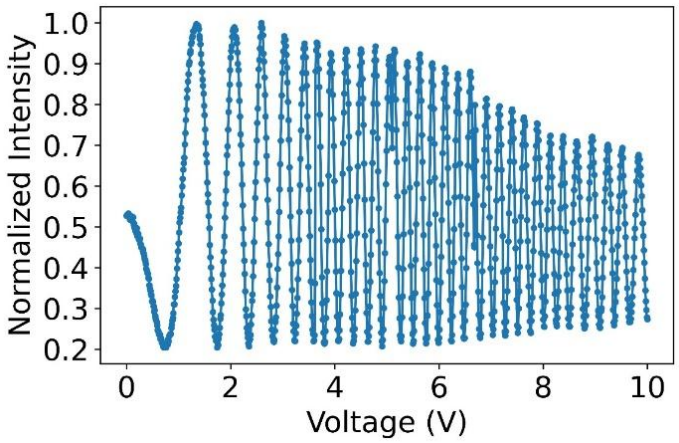

Figure 4. A measured interferogram at the wavelength of 1550 nm for one of the fabricated devices.

Hydrophobic and Sticky Silver-Decorated Nanoimprinted ZnO Nanograss Substrates for Enhanced SERS Performance

Kuan-Ting Kuo [a], Wen-Huei Chang [b]*, Hsiang Chen [c], Jyun-Jie Chen [a], Chun-Hung Lin [a]*

[a] Department of Photonics, National Cheng Kung University, Tainan 70101, Taiwan
[b] Department of Applied Chemistry, National Pingtung University, Pingtung 90003, Taiwan
[c] Department of Applied Materials and Optoelectronic Engineering, National Chi Nan University, Nantou 54561, Taiwan
e-mail: whchang@mail.nptu.edu.tw, chlin@ncku.edu.tw

Zinc oxide (ZnO) nanorods possess unique physical, chemical, and optical properties that make them attractive for optoelectronic and sensing applications. Among these, vertically aligned ZnO nanostructures offer high surface area and excellent molecule-substrate interaction, making them highly suitable for surface-enhanced Raman scattering (SERS). Building on our previous work [1], where nanoimprinted ZnO nanograss demonstrated broadband photodetection in the UV-visible spectrum, we repurposed the same platform for SERS detection. This transition highlights the adaptability and multifunctionality of the ZnO nanograss system.

In this study, we fabricated silver-decorated, sub-micron patterned ZnO nanograss substrates using nanoimprint lithography (NIL) combined with hydrothermal growth. A schematic of the fabrication process is shown in Fig. 1. NIL enabled precise spatial control over nanorod growth, confining it to predefined regions to form uniform nanograss structures. SEM images (Fig. 2a, 2b) confirmed the selective growth of ZnO nanorods on a 1000 nm periodic 1D grating pattern with an approximate line width of 500 nm. Following the deposition of a 30 nm silver film, top- and cross-sectional SEM images (Fig. 2c, 2d) showed a uniform distribution of silver nanoparticles (AgNPs). The optical image at the top of Fig. 2d further confirms the uniformity of the grating-patterned ZnO nanograss over a 5 mm × 5 mm area.

Characterization using SEM, EDS, XRD, and XPS confirmed the morphology and composition of the substrates. In addition, substrate hydrophobicity, influenced by dark storage conditions, was found to significantly affect SERS performance. Freshly prepared ZnO substrates exhibited moderate hydrophobicity, with contact angles around 93.5° (Fig. 3a), attributed to surface roughness. After three months of dark storage, the contact angles increased to approximately 144°, indicating enhanced hydrophobicity (Fig. 3b). Water droplets remained pinned on the surface even at tilt angles of 90° and 180°, as shown in Fig. 3c and 3d, reflecting strong adhesion behavior. Fig. 3e shows the SERS spectra of 10^{-8} M malachite green (MG) molecules on ZnO nanograss substrates stored for one day and three months. The sticky hydrophobic surface facilitated the localization and retention of analyte molecules, thereby enhancing SERS signal intensity.

SERS spectra of MG molecules at concentrations from 10^{-8} M to 10^{-14} M (Fig. 4a) showed a consistent decrease in signal intensity with dilution. Nonetheless, the characteristic Raman peaks, as previously reported at 1173, 1366, and 1615 cm^{-1} [2], remained clearly detectable at 10^{-14} M, establishing this as the substrate's limit of detection. Below this concentration, the signal was indistinguishable from background noise. A strong linear correlation ($R^2 = 0.992$; Fig. 4b) between MG concentration and Raman intensity at 1615 cm^{-1} confirmed reliable quantification. The ZnO nanograss architecture enhanced grating-mediated excitation of localized surface plasmon resonance, improving interaction between incident light and the plasmonic surface. The proposed energy band alignment (Fig. 4c) suggests that Raman enhancement arises from a combination of electromagnetic and chemical mechanisms, with charge transfer likely contributing significantly.

Compared to other ZnO-based SERS platforms, our AgNP-decorated, patterned ZnO nanograss demonstrates competitive sensitivity, long-term stability, and reproducibility. This cost-effective, scalable platform shows significant potential for applications in chemical, environmental, and biochemical sensing.

[1] M.-H. Li, J.-J. Chen, Y.-S. Chen, S.-T. Lin, B.-H. Lin, M.-Y. Kuo, C.-H. Lin, H. Chen, J. Han, Development of a broadband photodetector utilizing ZnO nanorods with grating structure fabricated via nanoimprint lithography, Sensors and Actuators A: Physical 375 (2024) 115530.
[2] W.-H. Chang, S.-Q. Zhang, Z.-Y. Yang, C.-H. Lin, Inverted Pyramid Nanostructures Coupled with a Sandwich Immunoassay for SERS Biomarker Detection, Nanomaterials 15(1) (2025) 64.

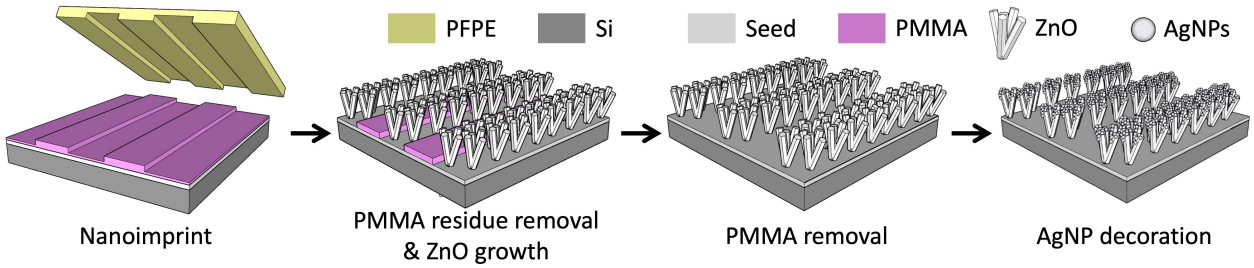

Figure 1. Schematic illustration of the fabrication process for the AgNP-decorated, site-selective ZnO nanograss substrate.

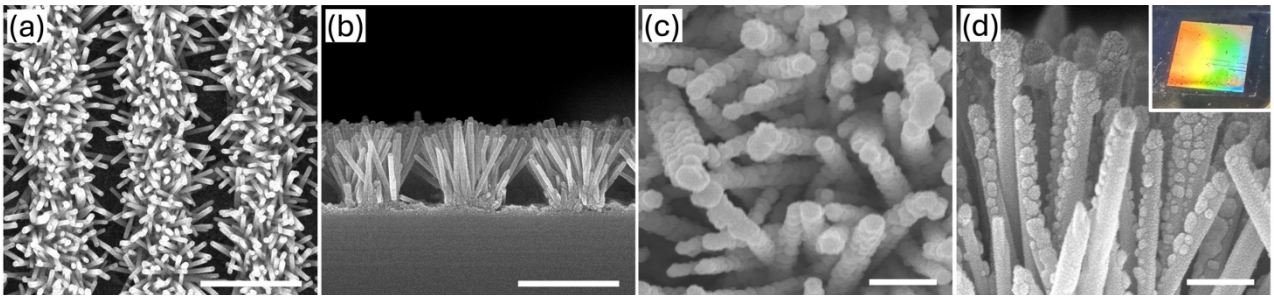

Figure 2. Morphology of ZnO nanograss. (a, b) SEM images showing selective growth of ZnO nanograss on a 1000 nm periodic 1D grating with ~500 nm line width. (c, d) Top and cross-sectional SEM images after deposition of a 30 nm Ag film. The optical image in the inset of (d) shows uniform patterning over a 5 mm × 5 mm area. Scale bars: 1 μm in (a, b); 200 nm in (c, d).

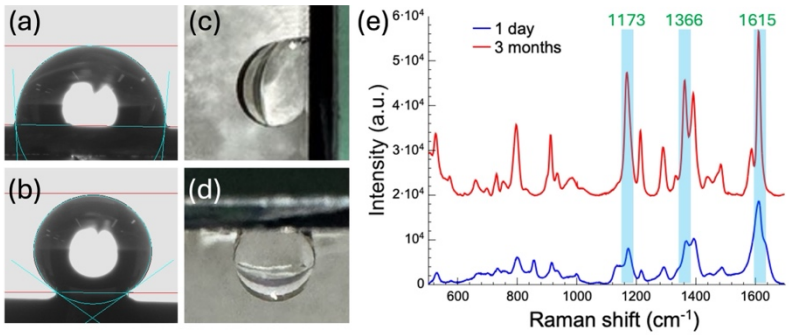

Figure 3. Wettability and SERS performance of AgNP-decorated ZnO nanograss with a 1200 nm grating period. (a) Contact angle of freshly prepared substrate (93.5°). (b) Contact angle after three months of dark storage (144°). (c, d) Images of a 10 μL water droplet on the three-month stored substrate at tilt angles of 90° and 180°, respectively. (e) SERS spectra of 10^{-8} M MG molecules on substrates stored for one day and three months, averaged from five positions along the coffee ring.

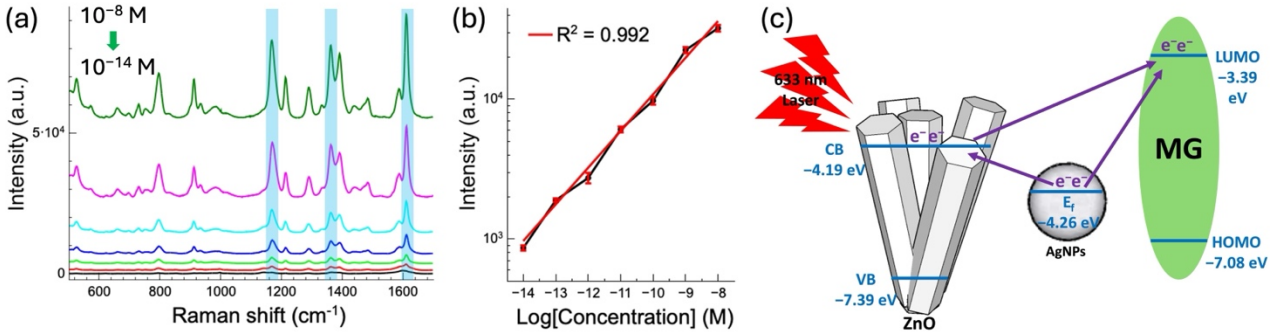

Figure 4. Sensitivity of the SERS substrate with a 1200 nm 1D grating. (a) SERS spectra of MG molecules at concentrations from 10^{-8} M to 10^{-14} M. (b) Linear correlation ($R^2 = 0.992$) between MG concentration and SERS intensity at 1615 cm^{-1}. (c) Schematic of energy band alignment among ZnO, AgNPs, and MG molecules.

Antireflection of near-infrared light using a moth-eye structure film

Kei Hirata [a], Jun Taniguchi [a*]

[a] Department of Applied Electronics, Tokyo University of Science, Tokyo, 125-8585, Japan
[*] e-mail: junt@te.noda.tus.ac.jp

1. Introduction

The moth-eye structure is a biomimetic structure that has anti-reflection properties over a wide wavelength range. It is also known that the wavelength range in which reflection is prevented changes depending on the height and pitch of the structure. Our previous research has shown that a moth-eye structure can be created by irradiating oxygen ions onto glassy carbon (GC) [1]. Then, an antireflection film has been transferred by Ultraviolet nanoimprint lithography (UV-NIL) using fabricated GC moth-eye structure as a mold. The transferred antireflection film has low reflection at visible light wavelength [2]. In recent years, the number of devices that use near-infrared wavelengths, such as LiDAR, has been increasing, leading to a growing need for anti-reflection of near-infrared light. In this study, reflection properties of GC's moth-eye structure and transferred film were examined at near-infrared range.

2. Experiment

First, we investigated the limit at which a moth-eye structure could be obtained on GC when the oxygen ion irradiation was increased. An inductively coupled plasma (ICP) device (EIS-700, Elionix.inc.) was used for oxygen ion irradiation. The ICP RF power was changed to 300, 400, 500, 600, and 700 W, and the sample RF power was fixed at 50 W, the oxygen flow rate at 50 sccm, and the processing time at 10 min. As a result, when the ICP RF power was 600 W or more, the moth-eye structure was destroyed, and anti-reflection properties were not obtained. Next, the moth-eye structures with ICP RF powers of 300, 400, and 500 W were subjected to a release treatment, and the properties of three types of films were investigated by transferring each of them with a transparent UV-curable resin by UV-NIL. First, the reflectance and transmittance of the prepared films were measured using a UV-Vis-NIR spectrophotometer (Solid Spec-3700, Shimadzu.co). The optical properties were measured from 300 nm to 1600 nm at 0.5 nm intervals. The reflectance was measured by tilting the sample by 5 degrees. The top and cross sections of the prepared film were also observed using a scanning electron microscope (SEM, ERA-8800FE, Elionix.inc) to measure the height and pitch of the moth-eye structure.

3. Result

Figure 1 shows a comparison of the cross-sectional SEM images of the GC moth-eye structure and the transferred moth-eye film. The height of the transferred moth-eye structure was lower than that of the GC moth-eye structure because of shrink of UV curable resin. The heights of moth-eye structure were increased with increasing ICP RF power in both cases. Figure 2 shows a comparison of the top view SEM images of the GC moth-eye structure and transferred moth-eye films. The pitches were also increased with increasing ICP RF power. Figure 3 shows the reflectance of the transferred moth-eye structure film. The noise between 850 nm and 1000 nm wavelengths is due to detector switching. As the wavelength increases, the film with a larger height and pitch of the moth-eye structure has a lower reflectance. In addition, when the ICP RF power was 500 W, the reflectance of shorter wavelength was decreased. Figure 4 shows the transmittance of the transferred moth-eye structure film. When the ICP RF power was 500 W, the transmittance of shorter wavelength side was decreased in spite of low reflectance. The reason for this is that, as can be seen from the SEM photograph, the tips of the needles are attached, and this structure increases scattering, which is thought to result in reduced transmission even though reflectance is low.

4. Conclusion

When fabricating a GC moth-eye, the higher the RF power of the ICP, the less the near-infrared reflection can be suppressed, but the transmission also decreases. Therefore, the optimal RF power is 300 to 400 W. In addition, a transparent film could be transferred from the made GC moth-eye mold by UV-NIL.A transferred moth-eye structure film can prevent reflection of near-infrared light. This will also prevent the reflection of near-infrared rays and enable lower power consumption for light sources.

[1] J. Taniguchi, Y. Kamiya, T. Ohsaki, N. Sakai, *Microelectronic Engineering,* **87** (2010) 859-863.
[2] T. Yano, H. Sugawara, J. Taniguchi, *Micro and Nano Engineering,* **9** (2020) 100077.

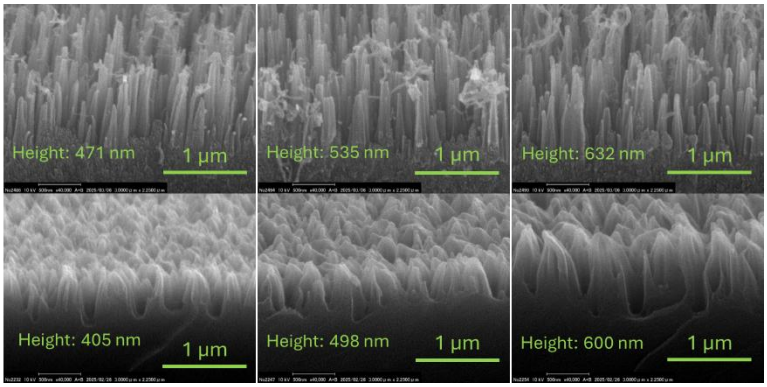

Figure 1. Cross-sectional SEM images of the moth-eye structure
Upper: GC mold, Lower: Transferred film, Left: ICP RF power: 300W, Centre: 400 W, Right: 500 W

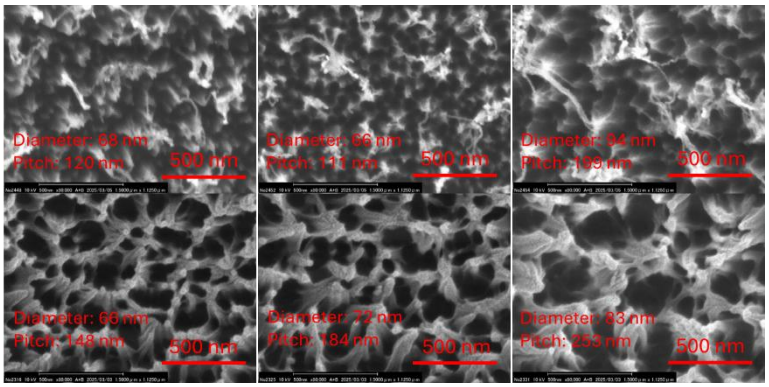

Figure 2. Top view SEM images of the moth-eye structure
Upper: GC mold, Lower: Transferred film, Left: ICP RF power: 300W, Centre: 400 W, Right: 500 W

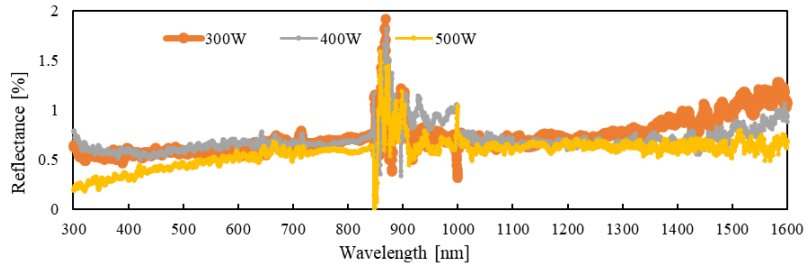

Figure 3. Reflectance of the transferred film

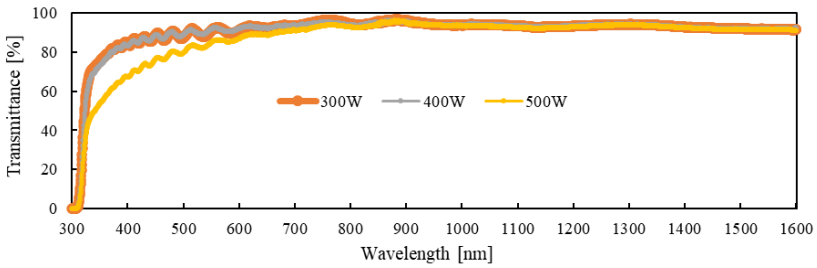

Figure 4. Transmittance of the transferred film

One-Step Printable Fabrication of Tantalum Pentoxide Metasurfaces for UV–Visible Optics

Eunji Lee [a+] *and Junsuk Rho* [a,b,c,d,e*]

[a]Department of Chemical Engineering, Pohang University of Science and Technology (POSTECH), Pohang 37673, Republic of Korea

[b]Department of Mechanical Engineering, Pohang University of Science and Technology (POSTECH), Pohang 37673, Republic of Korea

[c]Department of Electrical Engineering, Pohang University of Science and Technology (POSTECH), Pohang 37673, Republic of Korea

[d]POSCO-POSTECH-RIST Convergence Research Center for Flat Optics and Metaphotonics, Pohang 37673, Republic of Korea

[e]National Institute of Nanomaterials Technology (NINT), Pohang 37673, Republic of Korea

E-mail: jsrho@postech.ac.kr

The fabrication of high-performance optical metasurfaces demands materials with exceptional optical properties and scalable manufacturing processes. Tantalum pentoxide (Ta_2O_5), with its high refractive index and low optical absorption, is an attractive candidate for UV-visible applications. However, conventional Ta_2O_5 metasurface fabrication relies on complex, multi-step processes involving high-temperature deposition and anisotropic etching, limiting scalability and cost-effectiveness [1].

To overcome these limitations, we present a one-step nanoimprint lithography (NIL) process employing a novel particle-embedded resin (PER) formulation for direct patterning of Ta_2O_5-based metasurfaces. This technique enables the replication of diverse subwavelength nanostructures with feature sizes down to ~80 nm in a single imprint step using soft molds, substantially reducing fabrication complexity compared to conventional approaches. Simulations indicate that the PER- Ta_2O_5 structures exhibit favorable optical properties across the UV–visible range, with calculated conversion efficiencies exceeding 83%, depending on the design. The versatility of the method is demonstrated through the fabrication of holographic elements and metalenses, confirming its applicability to functional photonic devices.

This scalable and reproducible NIL process provides a practical route for integrating high-index materials into simplified manufacturing workflows, offering potential for low-cost production of advanced optics in applications such as compact sensors and AR/VR systems.

[1] C. Zhang et al., Light Sci. Appl. 13 (2024) 23.

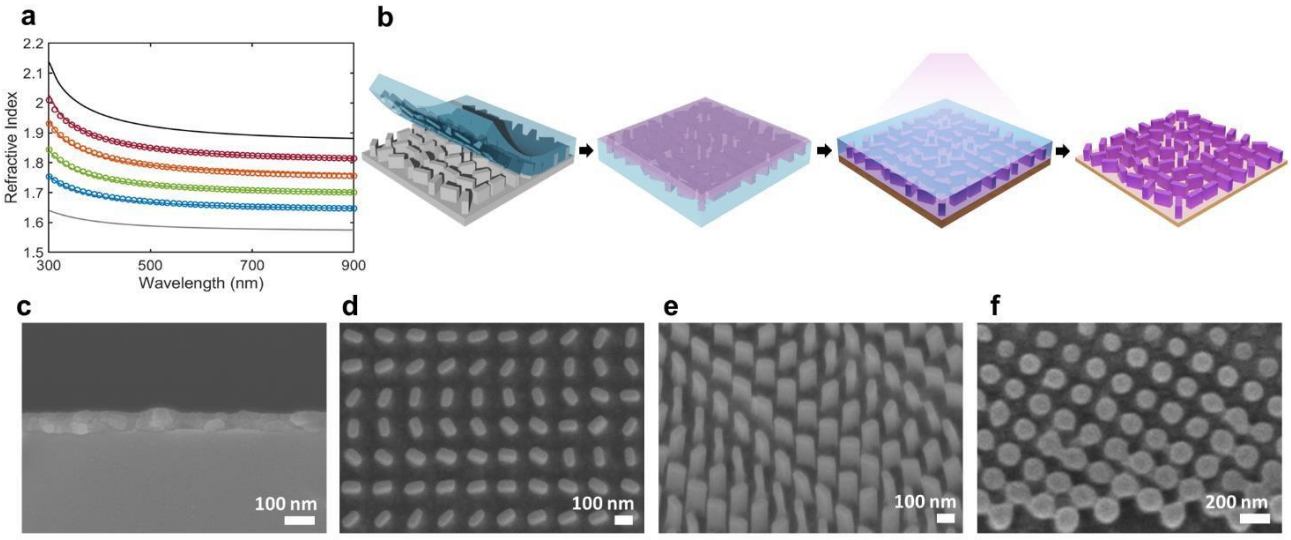

Figure 1. (a) Measured refractive indices of Ta_2O_5 PER films with varying nanoparticle concentrations (solid lines: calculated refractive indices, dotted lines: measured refractive indices, red line: 80 wt% Ta_2O_5 PER, orange line: 66.7 wt%, green line: 50 wt%, blue line: 33.3 wt%). (b) Schematic illustration of the one-step nanoimprint lithography (NIL) process using a soft mold and PER-Ta_2O_5 formulation to directly replicate subwavelength nanostructures. (c) SEM image of cross-sectional view showing uniform layer formation, (d) top and (e) side views of Ta_2O_5 PER imprinted nanopillar arrays, and (f) circular pillar array.

Red Emitting DBR Laser Array with 0.1 nm Wavelength Spacing Defined by Direct Write Ebeam Lithography

O. Brox [a], J. Fricke [a], R.-S. Unger [a], A. Maaßdorf [a], A. Mogilatenko [a], M. Beier [a], H. Christopher [a], A. Knigge [a], and H. Wenzel [a]

[a] Ferdinand-Braun-Institut (FBH), Berlin, Germany
e-mail: olaf.brox@fbh-berlin.de

We present a distributed Bragg reflector diode laser array (DBR array) designed for digital holography on technical and biological surfaces. Compared to DBR arrays developed earlier [1] we shift towards shorter wavelengths around 662 nm (i) for increased penetration depth into biological tissue and (ii) for better adjustment options of the holographical systems (visible light). Integration of optical gratings into edge emitting diode lasers is a prerequisite for holographic applications, because it stabilizes emission wavelengths and reduces linewidths. We apply high order surface gratings [2] and focus on their definition with ebeam lithography, since it allows flexible control of the periods for different vertical laser structures. Controlled but small wavelengths differences are requested for digital holography to generate long synthetical wavelengths [3]. Here we test ebeam direct write lithography to realize 0.1 nm wavelength spacing between adjacent emitters. Since current and temperature influence the emission wavelengths of DBR lasers the wavelength spacing should be obtained at similar operation points of the individual emitters.

Figure 1 shows the fabricated DBR array. The array with a footprint of 3.5 x 0.8 mm^2 is mounted p-side up on C-mount and contains four 3.5 µm wide ridge waveguides (RW) for fundamental lateral mode operation. Each emitter consists of an active and a grating section with lengths of 2.0 mm and 1.0 mm, respectively. The 0.5 mm long area behind the grating sections serves as the fan-out for the p-metal contacts. For the definition of the surface gratings we apply a hard mask that is structured with ebeam (Vistec SB251) and ZEP resist before it is transferred to the surface of the 3-inch wafer [2]. The gratings have periods of 1029.43 nm, 1029.62 nm, 1029.84 nm and 1030.01 nm (10^{th} grating order) and the width of the grating slits in the hard mask was adjusted to 200 nm. The depth of the slits influences the reflectivity of the grating. Based on simulations with a mode expansion tool the target depth of the grating slits in the vertical laser structure is 1.40 µm. We measured a depth of around 1.37 µm on a FIB-cut in the lateral center of the RW (Fig. 2) and conclude from simulations that the power reflectivity of the DBR gratings is in the range of 0.8. After manufacturing the gratings, a standard RW process was applied. For measurements the array was facet coated to provide power reflectivities of 0.3 and < 10^{-3} for the front and rear facet, respectively. Figure 3 summarizes the Light-Current-curves (L-I-curves) for single emitter operation. The threshold currents for all emitters are around 60 mA and at 150 mA pump current the optical power is above 70 mW. The optical spectra show single mode behavior with an optical side mode suppression of 60 dB (Fig. 4). Switching from single emitter to simultaneous operation of several emitters was investigated also and shows no significant changes in the optoelectronic performances. The peak wavelengths over pump current are summarized in Fig. 5. At a pump current of 130 mA the spectral distance of adjacent emitters is between 0.089 nm and 0.123 nm. The current range without DBR mode jumps is about 20 mA and allows 0.03 nm wide mode hop free tuning for further fine adjustment of the wavelength spacing.

In this study we successfully applied direct write ebeam lithography to fabricate a high-performance red emitting DBR array with a wavelength spacing around 0.1 nm. Dimensions and optoelectronic performances make the array an excellent light source for digital holographic systems.

[1] O Brox et al 2015 Electronics Letters 51, 17 DOI 10.1049/el.2015.2030
[2] J Fricke et al 2012 Semicond. Sci. Technol. 27 055009 DOI 10.1088/0268-1242/27/5/055009
[3] A Gröger et al 2023 J. Eur. Opt. Society-Rapid Publ., 19, 25 DOI 10.1051/jeos/2023024

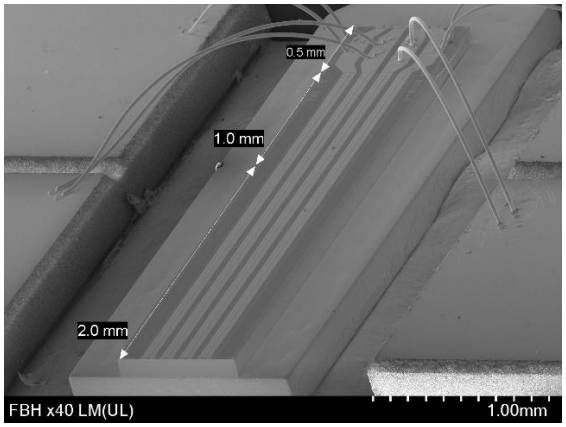

Fig. 1 DBR array with four RW emitters (spacing 127.5 µm). Lenghts are 2.0 and 1.0 mm for the active and the grating sections, respectively.

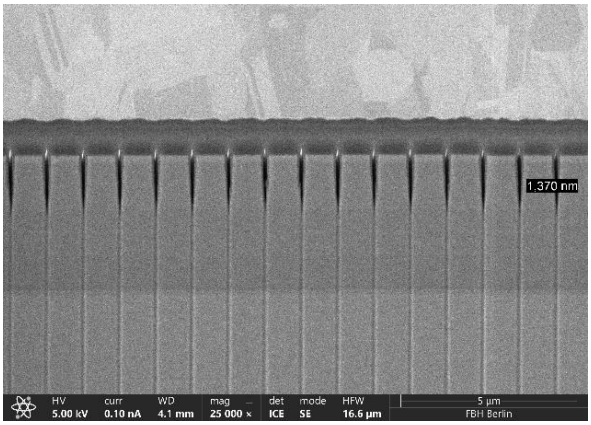

Fig. 2 Grating section: SEM of a FIB-cut in the lateral center of the 3.5 µm wide RW.

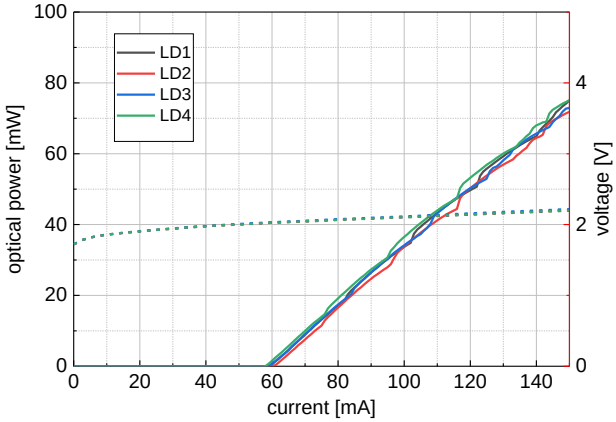

Fig. 3 L-I-curves of the four emitters of the DBR array.

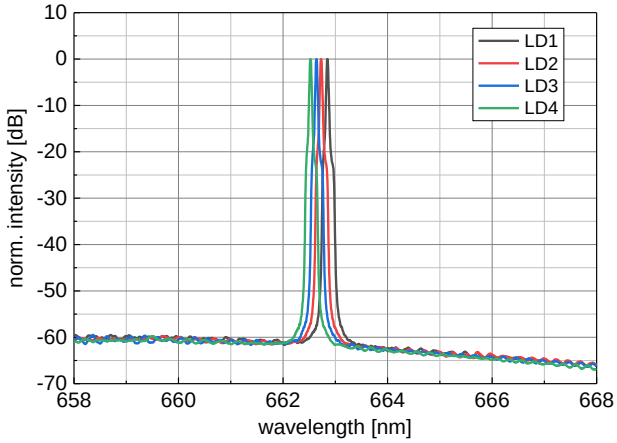

Fig. 4 Optical spectra at pump a current of 130 mA.

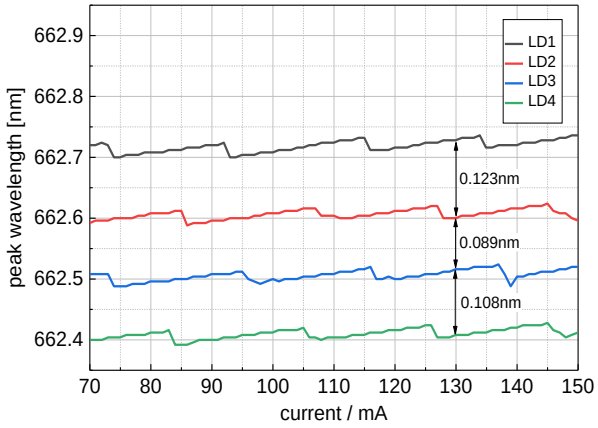

Fig. 5 Measured peak wavelengths over pump current. Each emitter is pumped separately. All measurements at 25 °C.

Anti-reflection and radiative cooling bifunctional polymer film fabricated via nanoimprint lithography and in situ boehmite formation by hydrothermal treatment

N. Dimogerontaki [1,2], N. Matthaiakakis [2], N. Papanikolaou[2], N. Kehagias[2]

[1]*Department of Physics, School of Applied Mathematical and Physical Sciences National Technical University of Athens, Zografou Campus, GREECE*
[2]*NCSR Demokritos, Institute of Nanoscience & Nanotechnology, P. Grigoriou 27 & Neapoleos Str., 15341 Ag. Paraskevi, Greece*

e-mail: nefelidimogerontaki@mail.ntua.gr

Radiative cooling is a passive cooling process where a surface dissipates heat by emitting infrared radiation to the cold outer space through the wavelengths where the atmosphere is transparent, called, the atmospheric transparency window, without consuming energy. Recently it has emerged as a promising cooling strategy for energy-efficient devices, particularly in outdoor environments where solar absorbers, such as solar cells, can experience significant heat buildup. To address this, visible transparent radiative coolers have been developed by engineering the surface of transparent materials to increase their emissivity, with most relying on silica (SiO_2) due to its stability, abundance, and non-toxicity. However, fabricating efficient photonic structures on SiO_2 typically involves costly and time-consuming processes like photolithography and etching, limiting scalability.[1] In this work, we introduce a scalable, transparent, micro/nano structured polymer film designed to enhance both infrared emissivity and visible-light transmittance when applied to soda-lime glass substrate. The film features a periodic micropillar array fabricated via UV light assisted nanoimprint lithography. A hybrid organic-inorganic UV curable resist was used throughout our experiments which has a high infrared emissivity due to its vibrational resonances from its silicon-oxygen and silicon-organic bonds.[2] Furthermore, its hybrid nature ensures both flexibility and fabrication ease combined with stability in outdoor conditions. After the imprinting process, a 30 nm aluminum (Al) layer was deposited on the micropatterned structures. After a hydrothermal treatment the thin Al layer transformed into boehmite creating a hierarchical micro/nano structured topography fig. 1(a-c).

The resulting composite film achieves a graded refractive index between air and glass, acting as an anti-reflective layer in the visible range [3]. The addition of the boehmite nanoscale roughness on the micropillar array reduces the total reflectivity by 3% while the micro pillars enhance the emissivity of glass in the atmospheric transparency window (7-14μm) from 0.88 to 0.97 (fig. 1d). This is attributed to the porous nano-morphology of the boehmite and the diffractive behavior of the periodic microstructure, which supports multi-order diffraction modes in infrared wavelengths [4]. Compared to bare glass and unstructured films, the micro/nano structured surface demonstrates significantly improved optical performance, as confirmed by visible transparency and infrared emissivity measurements shown in figure 2(a) and (b). Figure 2(a) shows the increased transmittance of the micro-nano structured polymer film compared to the microstructured. The apparent decreased transmittance in the micro structured and micro/nano structured samples compared to the unstructured sample and bare glass is due to diffraction effects from the microstructures, as seen in the inset image, where light is scattered into multiple angles beyond the detector's collection range. This dual-functional composite film provides an efficient and scalable approach to transparent radiative cooling, with broad potential for applications in solar energy systems and thermally sensitive outdoor devices.

Acknowledgments: This work has been funded under the National Recovery and Resilience Plan (Greece 2.0) Basic Research Financing Action (Horizontal support of all Sciences) Sub-action II Funding Projects in Leading-Edge Sectors for Hellenic Foundation for Research & Innovation Research Projects to support Faculty Members and Researchers. Project Number: 015117, Acronym: Multicool. The authors would like to thank the company Nanotypos for providing access to their equipment.

[1] Z. Ding *et al.*, "Designer SiO2 Metasurfaces for Efficient Passive Radiative Cooling," *Adv. Mater. Interfaces*, vol. 11, no. 3, pp. 1–14, 2024, doi: 10.1002/admi.202300603.
[2] S. Obi, "Replicated Optical microsctructure in Hybrid polymers: Process technology and applications," 2006.
[3] T. Ishiguro, T. Hori, and Z. Qiu, "Antireflective coating using aluminum hydroxide formed by hydrothermal treatment of sputtered aluminum films," *J. Appl. Phys.*, vol. 106, no. 2, pp. 0–3, 2009, doi: 10.1063/1.3181057.
[4] M. Gao *et al.*, "Approach to fabricating high-performance cooler with near-ideal emissive spectrum for above-ambient air temperature radiative cooling," *Sol. Energy Mater. Sol. Cells*, vol. 200, no. December 2018, p. 110013, 2019, doi: 10.1016/j.solmat.2019.110013.

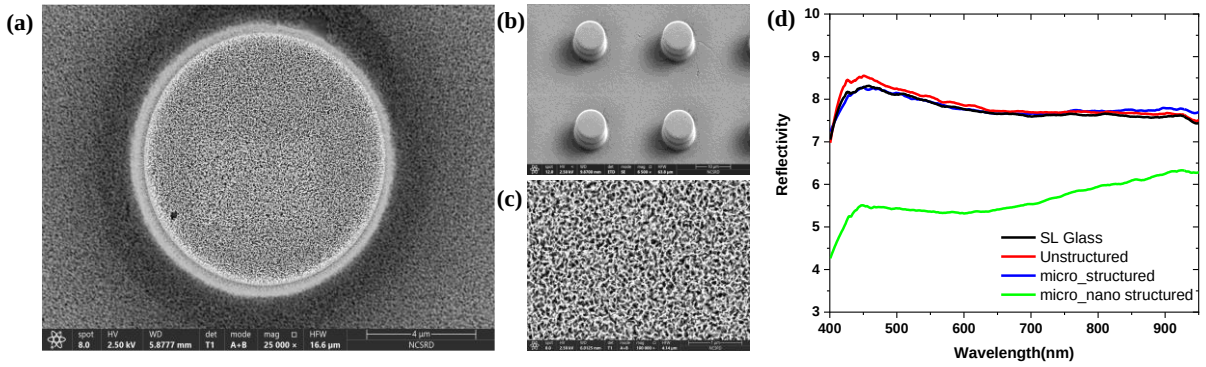

Figure 1. (a-c) Top view scanning electron microscope (SEM) images of boehmite nano roughness formed on top of the micro structured polymer film (a) Top view of a micropillar with nano roughness (b) tilted view periodic micropillar grating (c)boehmite nano roughness on a bare glass substrate (d) total reflectivity of bare soda lime glass compared to the unstructured polymer film, the micro structured and micro-nano structured with boehmite.

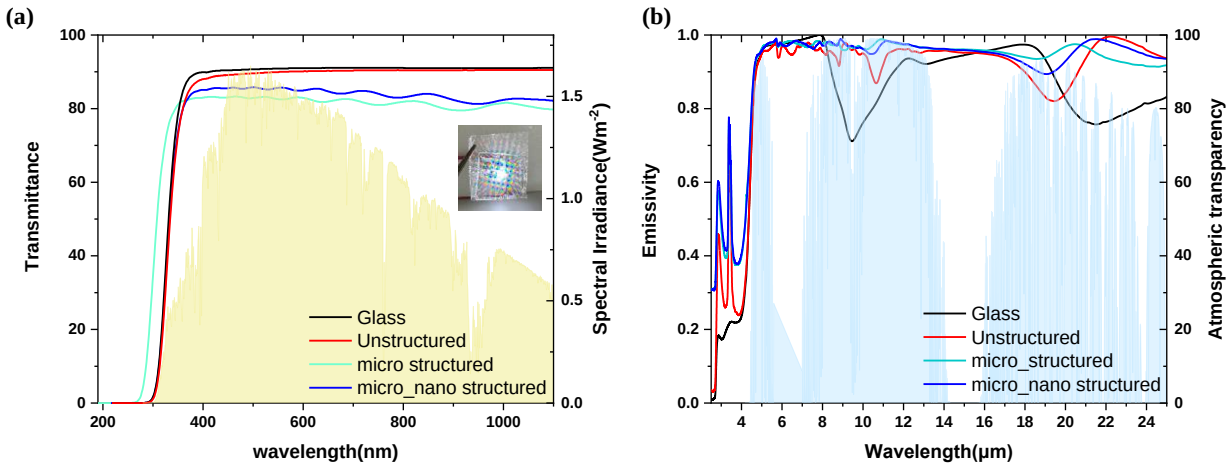

Figure 2. (a) UV-Visible transparency and (b) Infrared emissivity measurements of the bare glass substrate, the glass with the unstructured polymer, the microstructured polymer film and the microstructured polymer film with boehmite nano roughness.

Oral Session 2D: Information Communication Technologies

Fabrication and Analysis of Self-Rolled-Up Polymer Ribbon Structure Based on Photosensitive Polyimide and Mechanical Debonding

HyungDal Park[a†], Seonho Seok[b*], and Jinseok Kim[a*]

[a]Center for Bionics, Korea Institute of Science and Technology
[b]Center for Nanoscience and Nanotechnology (C2N), University-Paris-Saclay
e-mail: seonho.seok@c2n.upsaclay.fr, jinseok@kist.re.kr

Abstract
This paper presents a new technique to fabricate a rolled-up ribbon structure based on conventional photo patterning of photosensitive polyimide (PSPI) on the Si substrate and mechanical debonding by using lowered interface energy. Compared with the reported rolled-up structuring techniques based on wet sacrificial etch, the proposed technique uses interface energy reduction of polymer material with thin gold metal layer as function of time. In case of polymer rolled-up structuring, wet sacrificial etch can modify the mechanical characteristics of the polymer material itself and different etch rate could invoke unwanted rolled-up shape. Besides, modeling and simulation have been conducted to understand the behavior of the rolled-up structure. It was found that a single polymer layer coated on the Si substrate has opposite stresses, or top surface of the polymer has compressive stress, while bottom surface of the polymer has tensile one due to difference of CTE with Si substrate. Therefore, rolled-up shape has been made after the debonding of the polymer ribbon from the Si substrate.

The self-rolled-up structures have been used for unconventional 3D devices such as transformer, MEMS switch and have been frequently implemented with bi-layered thin film through wet sacrificial etch, laser processes [1-3]. Existing processes would create unwanted rolled-up modes especially . Fig. 1 shows the twisted self-rolled-up polymer ribbon when wet sacrificial etch has been applied to release polymer ribbons. Note that the dimension of the sample is 50 mm x 5 mm x 5 μm. To overcome the issue related with sacrificial release, a mechanical debonding rolled-up process has been proposed as depicted in Fig. 2. Mechanical debonding using blade insertion between polymer layer and gold thin film has been used. It was found that the interface energy has been degraded as function of time and thus blade insertion has been used to initiate self-rolled-up polymer structure. The rolled-up structure has been implemented by applying mechanical force debonding the polymer surface from the gold metal layer. Fig. 3 shows the fabrication results of the self-rolled-up polyimide structure. To understand the rolled-up behavior, FEM (Finite Element Method) modeling and simulation has been conducted and the rolled-up of the polymer layer has been successfully reproduced as shown in Fig. 4. The material properties are 6.0 MPa of Young's modulus, 52 ppm of the thermal expansion coefficient (CTE) and the thermal stress of the polymer ribbon has been defined by temperature. As shown in Fig. 4 (a), the polymer ribbon was self-rolled-up due to the applied thermal stresses. Thus, it was found that stress gradient has been created between top surface and bottom surface of the polymer layer patterned on the Si substrate. By consequence, it is considered that top-half of the polymer is in compressive stress, while bottom-half is in tensile stress. Besides, it was found that the maximum rolled-up diameter can be extracted as function of the thermal stress as shown in Fig. 4 (b). This self-rolled-up polymer structure would be evolved to develop a novel medical device such as cylindrical-type interfaces for various sensors in near future.

[1] Y. Chen, M. Tan, R. Yang, C. K. W. Lee, H. Zhong, Y. Xu, Y. Huang, M. Tang, M. G. Li, Adv. Funct. Mater. 2024, 34, 2400090.
[2] Bajwa, R., Saleh, H., Shojaeian, M. et al. Microsyst Nanoeng 9, 74 (2023).
[3] Wen Huang, Seid Koric, Xin Yu, K. Jimmy Hsia, and Xiuling Li *Nano Letters* **2014** *14* (11), 6293-6297

(a) Maximally twisted polymer ribbon (b) Minimally twisted polymer ribbon

Figure 1. Twisted polymer ribbons when sacrificial etch has been used for release

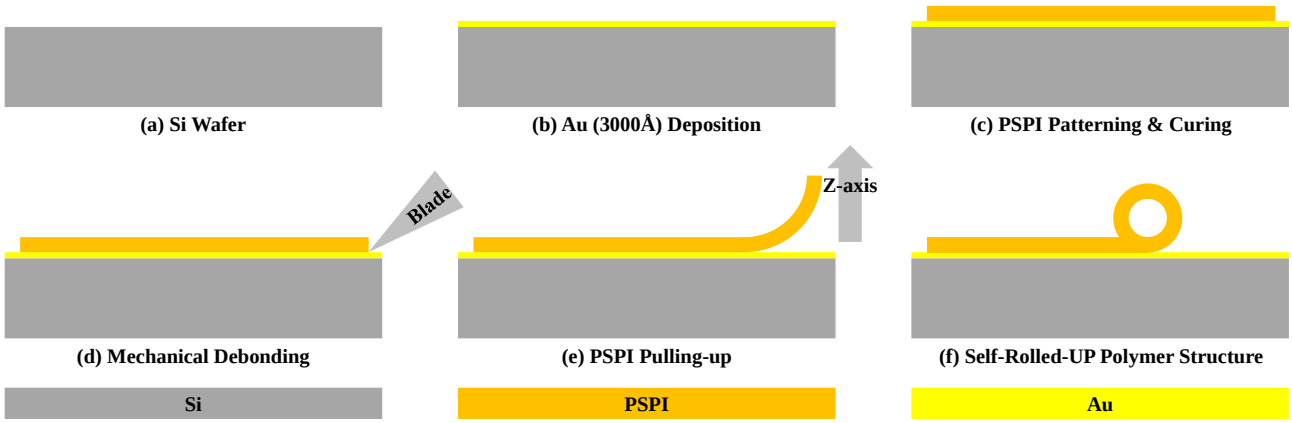

Figure 2. Fabrication process for self-rolled-up based on interfacial mechanical debonding

Figure 3. Self-rolled-up polymer ribbon (overall view and cross-sectional view)

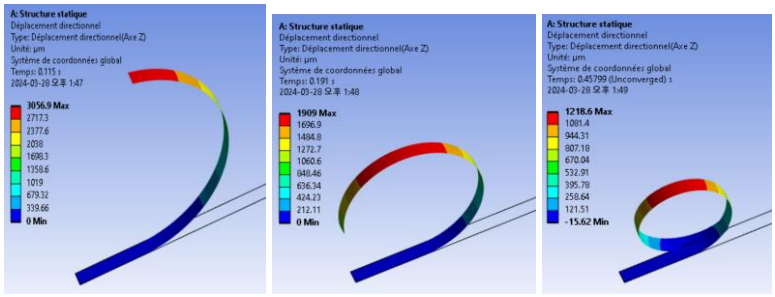

(a) Self-rolled-up simulation result

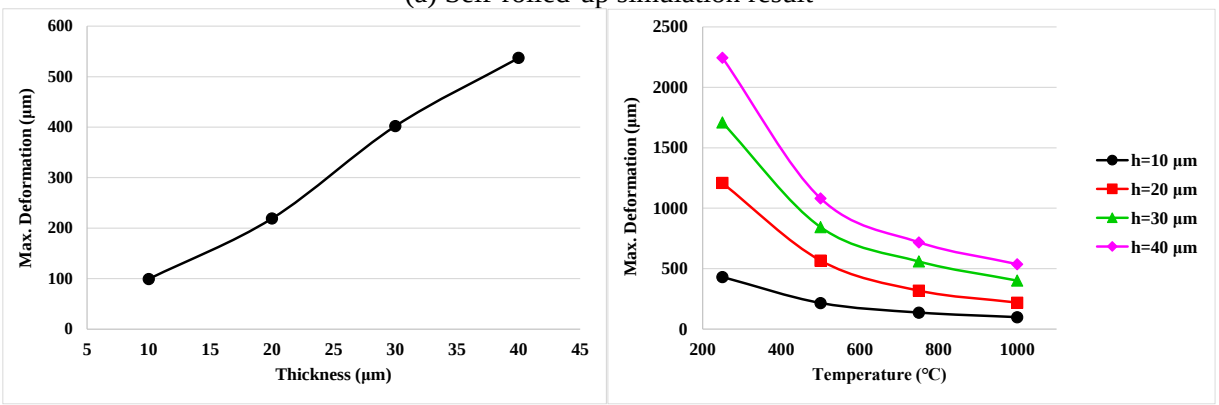

(b) Parametric studies: thickness and stresses

Figure 4. FEM modeling and simulation results

Invited Talk – MNE-2025

Semiconductor Quantum Dots: From Tailored Synthesis to Advanced Sensing and Biosensing Applications

Speaker: Dr. Javed H. Niazi

SUNUM – Sabanci University Nanotechnology Research & Application, Tuzla, Istanbul

Abstract

Semiconductor quantum dots (QDs) are nanoscale materials with exceptional size-tunable optical and electronic properties, governed by quantum confinement effects. Their synthesis follows either top-down (e.g., lithography, etching) or bottom-up approaches (e.g., colloidal, hydrothermal methods), with the latter offering superior control over size, crystallinity, and surface functionalization. Core-shell structures, surface passivation, and biofunctionalization further enhance their photoluminescence efficiency, stability, and specificity making them ideal for optoelectronic and biomedical applications.

This talk will explore the evolution of QD synthesis techniques, emphasizing scalable production of high-quality QDs (e.g., CdSe@CdS@ZnS core-shell-shell nanostructures) and their integration into cutting-edge sensing platforms. A key focus will be on immuno-optomagnetic point-of-care (PoC) biosensors, where magnetic QDs (MQDs)- QDs coated with magnetic nanoparticles to combine optical and magnetic properties. These enable rapid, multiplexed detection of disease biomarkers (e.g., breast cancer's Her2, and Alzheimer's Aβ1-42, tau protein) in complex biological samples (e.g., serum, saliva) with visible results in 10-30 min. The talk will demonstrate a novel PoC assay combining multicolored QDs and magnetic separation for real-time analysis without complex equipment, enabling low-cost, rapid diagnostics.

Applications span clinical diagnostics (chronic diseases), environmental monitoring (pathogens/toxins), and personalized medicine, demonstrating QDs' versatility as high-performance fluorescent nanoprobes. The talk bridges fundamental nanoscience with translational applications, offering insights into next-generation QD-based technologies for early disease diagnosis and on-site monitoring. The talk will conclude with future directions in scalable nanomaterial engineering, multiplexed PoC systems, and AI-integrated biosensing, underscoring QDs' transformative role in healthcare solutions.

Adaptive Adhesion through Bio-Inspired Interlocking Micropatterns for Harsh Environments

Marco BRUNO[1,*], Luigi Portaluri[1], Massimo DE VITTORIO[1], Stanislav GORB[2], Michele SCARAGGI[1]

[1]University of Salento, Department of Engineering for Innovation, Lecce, Italy
[2]Kiel University, Department of Functional Morphology and Biomechanics, Kiel, Germany
*Corresponding authors: marco.bruno@iit.it michele.scaraggi@unisalento.it

Mechanical adhesion, found in nature, offers reliable, reversible bonding in contaminated environments [1]. It uses surface protrusions to store elastic energy, enabling strong, adaptable interlocking not fully exploited in current technologies. Applications include medical devices, underwater systems, robotics, and space tech [2]. Bioinspired designs use micro-needles, pillars, and shapes to enhance contact [3], [4], with dynamic forms (e.g., inflatable structures) enabling switchable adhesion. Unlike environmentally sensitive dry or suction adhesives [5] mechanical interlocking resists contaminants and allows precise control of bond strength. Though models address specific geometries, they often simplify and ignore multi-contact behavior. Advancing theory and design is key to robust, versatile adhesion systems.

This work analyzes single-pair interactions between double conical microgeometries, selected for their tunable radius R and opening angles α, β, which affect strength, attachment, and detachment. The developed quasi-static contact model uses a Winkler foundation, Coulomb friction, and van der Waals adhesion. Figure 1 defines geometry, forces (Fn, Ft, Fy, Fel), penetration (δ), contact radius (a), radius (R), distance (y), and angles (α, β). Interactions are treated independently; dense systems assume a constant lattice distance I_0, implying infinite rod stiffness. For a Winkler foundation without adhesion, the normal force in a cylindrical contact is given by [6]. Following the schematic in Figure 1, it is possible to write the momentum equation in the vertical (out-of-plane) direction, thus relating the out-of-plane force to the deformation of the contacting cones. Though complex microgeometries require numerical methods (e.g., FEM), the multiscale approach used here remains valid. To solve the system, contact parameters (length l, penetration δ) must relate to cone positioning (in-plane distance I, out-of-plane distance y). This relationship is discontinuous, varying by contact region, as seen in attachment force data (Figure 2, left). These geometrically derived relations are available in [7]. Our normalized parametric study shows that force increases with R/l_0, indicating higher adhesion in densely packed structures, explaining the high density of these structures in natural systems.

Surface energy (Δγ) has minimal impact on out-of-plane force (Fy). A Hertzian model including surface energy [8] requires numerical integration along the contact line to relate Fy and y. As shown in Figure 2 (right), removing local adhesion changes little, confirming that geometry and friction dominate performance. Friction indeed is crucial in resisting detachment and boosting adhesion, though it increases engagement force. Unlike van der Waals-based adhesives, interlocking remains effective in contaminated or wet conditions. Friction, though affected by cleanliness or humidity, is not nullified. It also sets the critical tip angle (α) for jamming in double cones, influencing stick-slip or buckling. Accurate friction characterization is key for proper design. Figure 3 shows that higher friction increases pull-off pressure and mechanical adhesion energy.

This study presents a new reversible fastener geometry and clarifies how shape, friction, and surface energy affect interlocking adhesion. Tuning microgeometry enables controlled adhesion. Experiments in dry, wet, and dusty environments confirm the robustness of double-cone interlockers. These findings support their use in fields where adhesives fail, such as automation, biomedicine, and harsh conditions. Geometry and friction are key to reliable mechanical adhesion.

[1] E. Gorb and S. Gorb, “Contact separation force of the fruit burrs in four plant species adapted to dispersal by mechanical interlocking,” *Plant Physiol. Biochem.*, vol. 40, no. 4, pp. 373–381, 2002, doi: 10.1016/S0981-9428(02)01381-5.

[2] C. Lee, A. C. Via, A. Heredia, D. A. Adjei, and M. D. Bartlett, “Octopus-Inspired Adhesives with Switchable Attachment to Challenging Underwater Surfaces,” *Adv. Sci.*, vol. 12, no. 1, p. 2407588, 2025, doi: https://doi.org/10.1002/advs.202407588.

[3] C. Lee *et al.*, “Bioinspired materials for underwater adhesion with pathways to switchability,” *Cell Reports Phys. Sci.*, vol. 4, no. 10, 2023.

[4] Y. Li *et al.*, “Triple-Bioinspired Shape Memory Microcavities with Strong and Switchable

Adhesion," *ACS Nano*, vol. 17, no. 23, pp. 23595–23607, 2023, doi: 10.1021/acsnano.3c06651.
[5] M. Zhu, F. Zhang, and X. Chen, "Bioinspired Mechanically Interlocking Structures," *Small Struct.*, vol. 1, no. 3, pp. 1–8, 2020, doi: 10.1002/sstr.202000045.
[6] K. L. Johnson, K. Kendall, and A. A. D. Roberts, "Surface energy and the contact of elastic solids," *Proc. R. Soc. London. A. Math. Phys. Sci.*, vol. 324, no. 1558, pp. 301–313, 1971.
[7] M. Bruno, L. Portaluri, M. De Vittorio, S. Gorb, M. Scaraggi, Bio-Inspired Interlocking Micro-Patterning for Tunable, Switchable and Selective Adhesion in Wet and Dusty Environments. *Small* 2025, 2410527.
[8] M. K. Chaudhury, T. Weaver, C. Y. Hui, and E. J. Kramer, "Adhesive contact of cylindrical lens and a flat sheet," *J. Appl. Phys.*, vol. 80, no. 1, pp. 30–37, 1996.

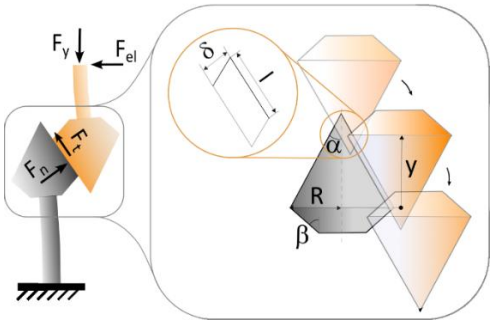

Figure 1. Kinematics of double conical interlockers showing penetration (δ), contact length (l), out-of-plane distance (y), radius (R), tip angle (α), base angle (β), and a free body diagram with forces: out-of-plane (Fy), in-plane (Fel), normal (Fn), and tangential (Ft).

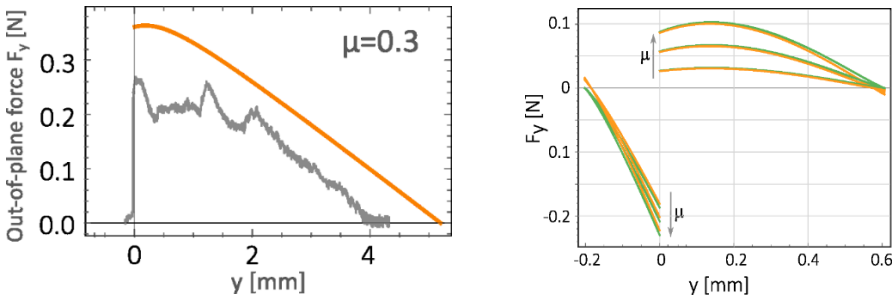

Figure 2. (left) Comparison between numerical and experimental out-of-plane force during approaching motion of a single pair of conical interlockers; **(right)** Predicted detachment force (Fy) of a soft double cone interlocker at different friction coefficients (μ = 0, 0.2, 0.4), and surface energies (Δγ = 10^{-3} N/m , 10 N/m)

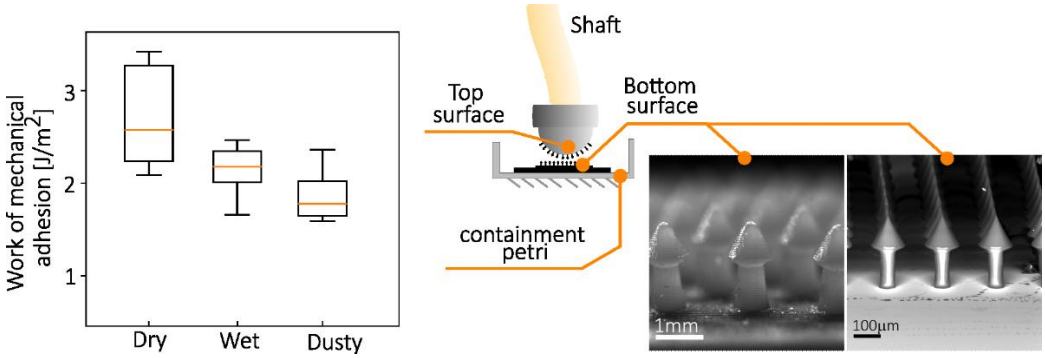

Figure 3. (right) Experimental setup, microscope image of 3D-printed samples and SEM image of 2 photon lithography samples; The out-of-plane force has been measured via a load cell placed on the support shaft. **(left)** Box-plots (n=10) show mechanical adhesion work in dry, wet (distilled water), and dusty (talc) conditions.

Single-Charge Detection in a Room Temperature Single-Electron Memory

Jingbo Chen [a], Wenkun He [a], Kai-Lin Chu [a], Mervyn Jones [a], Zahid Durrani [a]
[a] Department of Electronic and Electrical Engineering, Imperial College London, South Kensington, London, SW7 2AZ, UK
e-mail: Jingbo.chen23@imperial.ac.uk

Quantum effect devices are of great interest in the development of few- and single- electron, highly scaled memory devices [1-2]. These devices store information down to the one electron level [3] using the Coulomb Blockade effect, and quantum-confined discrete energy states. Single-electron storage at room-temperature (RT) can occur in sub-10 nm scale memory nodes [4] or interface traps [5] and may even be observed in highly scaled 3D NAND Flash memory [6]. However, these approaches rely mainly on small memory node sizes and do not exploit the precise control over single electrons enabled by single-electron transistors (SETs) [2]. Past work has shown SET based memory cell operation, however these devices operated mainly at cryogenic temperature [2, 7].

In this work, we have fabricated single-electron memory (SEM) cells based on dopant atom point-contact quantum dot (QD) SETs [8] in silicon-on-insulator (SOI) material, for room temperature (RT) operation. Two QD SETs define a memory cell (Fig. 1(a)), the first (the 'control SET') to trap electrons one by one on a nanoscale memory node via the SET's Coulomb blockade, and the second (the 'sense SET') to measure the trapped charge by operating as a single-electron detector. A current hysteresis loop, with single-electron switches, is measured in the sense-SET current at RT, as the word-line voltage biasing the control-SET is cycled.

Figure 1(a) shows a schematic diagram of the SEM cell, defined in the top Si layer of SOI material (Phosphorous doped ~10^{19}/cm^3, via ion-implantation). SET operation is based on single-electron charging of dopant atom QDs embedded within the point-contact of the SET. Room-temperature operation occurs due to the ultra-small, ~1 nm, dimensions of the QDs, creating large single-electron energies, ~0.1 eV >> k_BT =26 meV at RT. Single-electron charge transfer from a word-line (WL) occurs, across the control SET, onto a nanoscale memory node. Memory node charge is detected by the capacitively-coupled sense-SET. A node gate (N_g) is used to tune the control SET and further manipulate memory charge. Figure 1(b) shows a scanning-electron micrograph of the SEM. The SEM was defined using high-resolution electron beam lithography (EBL) and subsequent oxidation to reduce point-contact channel volumes to the sub-10 nm scale. Figure 2(a) shows the RT drain-source current I_{ds} vs. drain (V_{ds}) and side gate (V_{gs}) voltage for the sense SET, as V_{gs} is swept from 0.4 – 0.56 V. Coulomb blockade of current is observed for small V_{ds} magnitude, with blockade width modulated by V_{gs} (Fig. 2(a)). The corresponding single-electron oscillations in I_{ds} are shown in Fig. 2(b), where each oscillation corresponds to the addition of an electron onto the sense SET QD. Biasing the sense SET near a single-electron oscillation enables single electron detection of charge on the nearby memory node.

Figure 3 shows the RT sense SET current I_{ds} vs. word-line voltage V_w characteristics, at selected values of sense SET bias V_{ds}. Cycling V_w leads to single electron trapping/de-trapping on the memory node, with the charge states separated by Coulomb blockade in the control SET. Figures 3(a) and (b) show complete hysteresis loops for I_{ds}. Current switches correspond to single electrons added to the memory node. These lead to hysteresis loops, e.g. the loop between V_w = 2-3 V in (a), and two loops, between V_w = 0-1 V and 1-2 V in (b). A wider, multi-electron hysteresis is seen in (c). The hysteresis loops and current switches demonstrate the storage, and detection, of single-electrons stored on the memory node of the SEM, at RT.

The authors acknowledge support from the Engineering and Physical Sciences Research Council (EPSRC) under the UK EPSRC Single Atom Quantum Electronics project (EP/V030035/1).

References:

[1] A. Srivastava and S. Mohanty, Eds., *Advanced Technologies for Next Generation Integrated Circuits*. IET, 2020.
[2] Z. A. K. Durrani, *Single-electron devices and circuits in silicon*. London: Imperial College Press, 2010.
[3] W. Si, J. Li, G. Li, C. Jia, and X. Guo, *J. Mater. Chem. C*, vol. 12, no. 3, pp. 751–764, 2024.
[4] K. Yano *et al.*, *Proc. IEEE*, vol. 87, no. 4, pp. 633–651, Apr. 1999.
[5] S. Tiwari, F. Rana, H. Hanafi, A. Hartstein, E. F. Crabbé, and K. Chan, *Applied Physics Letters*, vol. 68, no. 10, pp. 1377–1379, Mar. 1996.

[6] C. Monzio Compagnoni *et al.*, *IEEE Electron Device Lett.*, vol. 36, no. 2, pp. 132–134, Feb. 2015.
[7] A. Nasri, A. Boubaker, and A. Kalboussi, *Discov Electron*, vol. 2, no. 1, p. 12, Mar. 2025.
[8] Z. Durrani *et al.*, *Journal of Applied Physics*, vol. 124, no. 14, p. 144502, Oct. 2018.

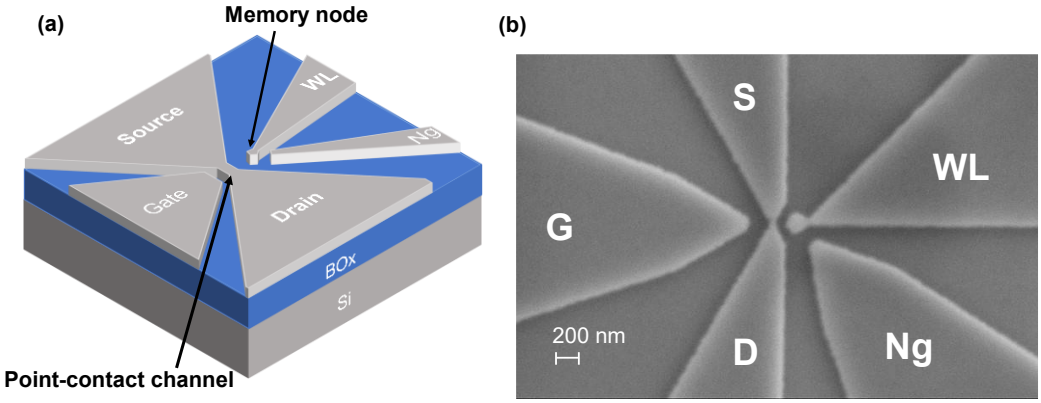

Figure 1. a) Schematic diagram of the SEM, the black arrows indicating the memory node and point-contact channel. **b)** Scanning-electron micrograph of the SEM device with a memory node ~ 150 nm, attached to a word line (WL) and its adjacent node gate (N_g).

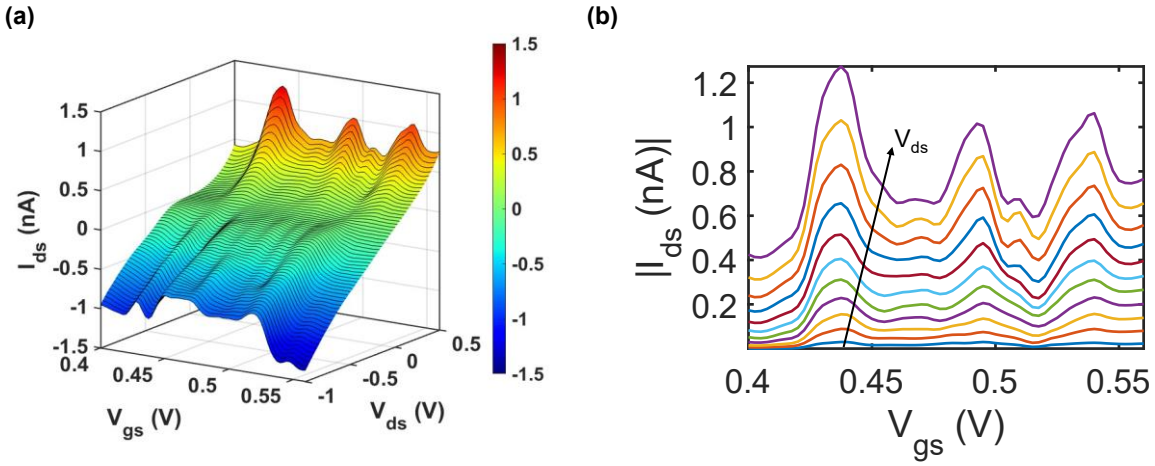

Figure 2. a) I_{ds} versus V_{gs} and V_{ds} for a sense SET. **b)** I_{ds} versus V_{gs} shows Coulomb oscillations. V_{ds} increases from 0 to 0.5 V, in steps of 0.05 V marked by a black arrow.

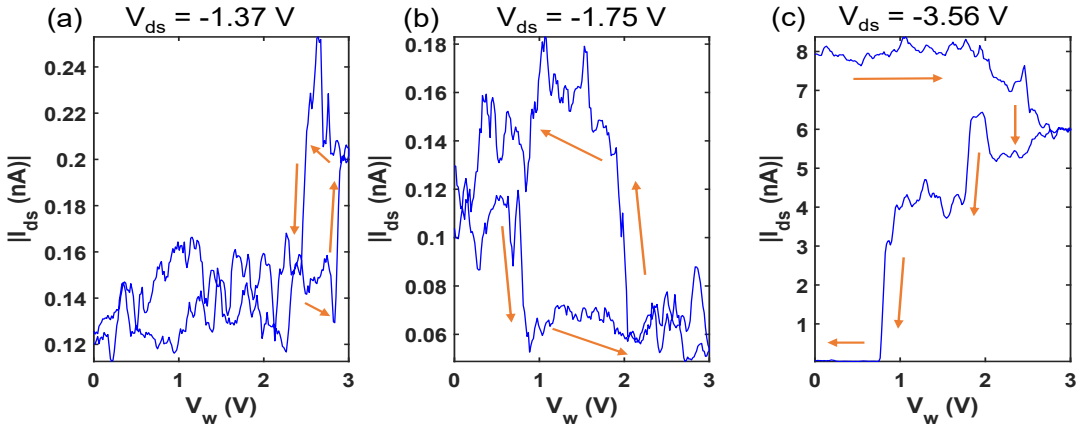

Figure 3. Charge detection via I_{ds} against V_w, with orange arrows indicating charge sweep direction, at selected V_{ds} = **a)** -1.37 V, **b)** -1.75 V and **c)** -3.56 V. Closed hysteresis loops observed in **a)** and **b)**. An 'open loop' with a larger current is seen in **c)** due to higher V_{ds}.

Design and characterization of surface acoustic wave on thin film lithium niobate on insulator for acousto-optic applications

Fatemeh Arefi[a,b], Ivan prieto[a], Florian Hartmann[b], Silvan Stettler[b], Hamed Sattari [a], Homa Zarebidaki[a], Dara Bayat[a], Guillermo Villanueva[b], Michel Despont[a]

[a] Swiss Center for Electronics and Microtechnology (CSEM), Neuchatel, 2002, Switzerland
[b] Advanced NEMS Group, École Polytechnique Fédérale de Lausanne (EPFL), Lausanne, 1015, Switzerland
e-mail: fatemeh.arefi@csem.ch

Motivation

Surface acoustic wave (SAW) plays a critical role in various applications, including acousto-optic modulators (AOMs). Thin-film lithium niobate (TFLN) on insulator has attracted significant interest for SAW devices and integrated photonic components due to its excellent piezoelectric and optical properties [1][2]. However, the use of SAWs for AOMs on LNOI is typically limited to Rayleigh modes, largely constrained by the underlying silicon dioxide layer [3]. This study aims to evaluate and fabricate various SAW devices, including Rayleigh and shear horizontal modes on X-cut TFLN on insulator applicable for AOM applications. The study explores design and fabrication aspects, including metallization, TFLN thickness, SAW wavelength, and propagation orientation, with the goal of identifying the configuration that maximizes acoustic and optical interactions.

Methodology

SAW can be effectively generated using interdigital transducers (IDTs), as shown in Figure 1-a, on piezoelectric substrates such as TFLN. The pitch of the IDTs directly determines the acoustic wavelength and, consequently, the operating frequency of the SAW device [3]. In this work, both fabrication and simulation of IDTs were carried out on X-cut TFLN with varying pitch sizes, targeting a frequency range from a few hundred MHz to GHz. For SAW characterization, initial 2D unit cell simulations were performed using the finite element method (FEM) in COMSOL Multiphysics. As illustrated in Figure 1-c, high-resolution IDTs were fabricated using a lift-off process based on a bilayer resist stack of PMMA495 and PMMA950, patterned via electron beam lithography. A 10 nm chromium adhesion layer was deposited, followed by varying thicknesses of aluminium and gold using electron beam evaporation. Metal lift-off was performed using Microposit 1165 at 70 °C. This fabrication approach provides well-defined IDTs down to a pitch of 150 nm, which is essential for efficient SAW excitation at high frequencies. A scanning electron microscope (SEM) image of the fabricated IDTs is shown in Figure 1-b, confirming the fidelity and resolution of the structures across various pitches.

Result

The phase velocity and effective electromechanical coupling coefficient (K_{eff}^2) are critical metrics for optimizing SAW-based AOMs. Low phase velocity enhances SAW confinement within TFLN, while high K_{eff}^2 ensures efficient electrical-to-acoustic energy conversion. In the initial phase of this study, a SAW device was fabricated and characterized on X-cut 600-nm-thick TFLN on 4.7 μm buried oxide layer along Z axis, an orientation widely used for AOM application due to its high photoelastic coefficient. As demonstrated in Figure *2*-a, the experimental output strongly confirmed the simulation result (shown in Figure *2*-b), showing weak excitation of Rayleigh waves in this direction, with K_{eff}^2 below 0.5% and relatively high phase velocity, which leads to acoustic leakage into the buried oxide layer. Building on the validated simulation approach, further simulations revealed (demonstrated in Figure *2*-c and Figure *2*-d) strong excitation of SH-waves along the Y + 170° axis with K_{eff}^2 higher than 20% and an effective generation of Rayleigh near the Y + 35° axis with 4% efficiency of K_{eff}^2. These results highlight the potential of these orientations for AOM applications. Additional simulations (shown in Figure *2*-e and Figure *2*-f) demonstrate that gold electrodes exhibited a significantly higher K_{eff}^2 compared to aluminum, due to gold's higher conductivity and mass loading. However, further studies are underway to evaluate the impact of mass loading of gold compared to aluminium on SAW propagation losses. The study is ongoing and aims to evaluate the previously mentioned parameters to enhance SAW confinement and improve AOM performance.

Reference

[1] Y. Qi and Y. Li, "Integrated lithium niobate photonics," Nanophotonics, vol. 9, no. 6, pp. 1287–1320, 2020.
[2] L. Shao et al., "Integrated microwave acousto-optic frequency shifter on thin-film lithium niobate," Opt. Express, vol. 28, no. 16, pp. 23728–23738, 2020.
[3] K. Hashimoto, "Surface acoustic wave (SAW) devices," in Ultrasonic Transducers, Elsevier, 2012, pp. 331–373.

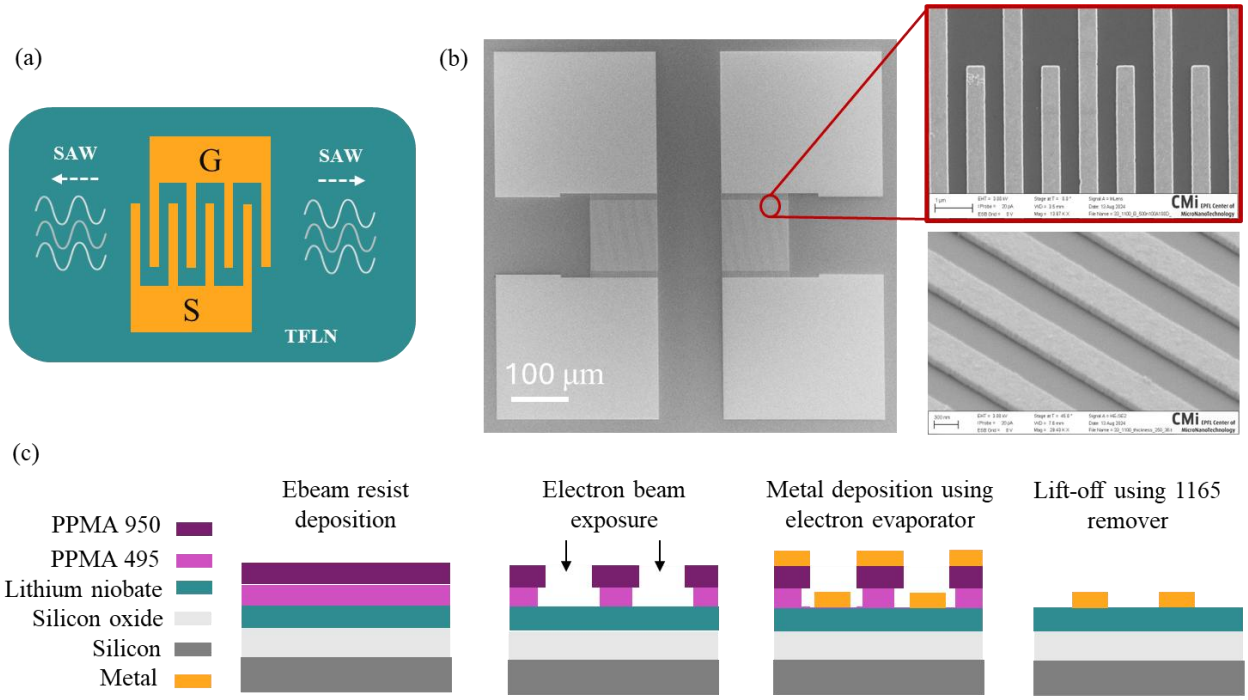

Figure 1: (a) Schematic of an interdigital transducer (IDT) fabricated on top of a thin-film lithium niobate (TFLN) substrate. (b) Process flow diagram illustrating the fabrication steps of the IDT. (c) Scanning electron microscope (SEM) image of an IDT with a 1 µm pitch.

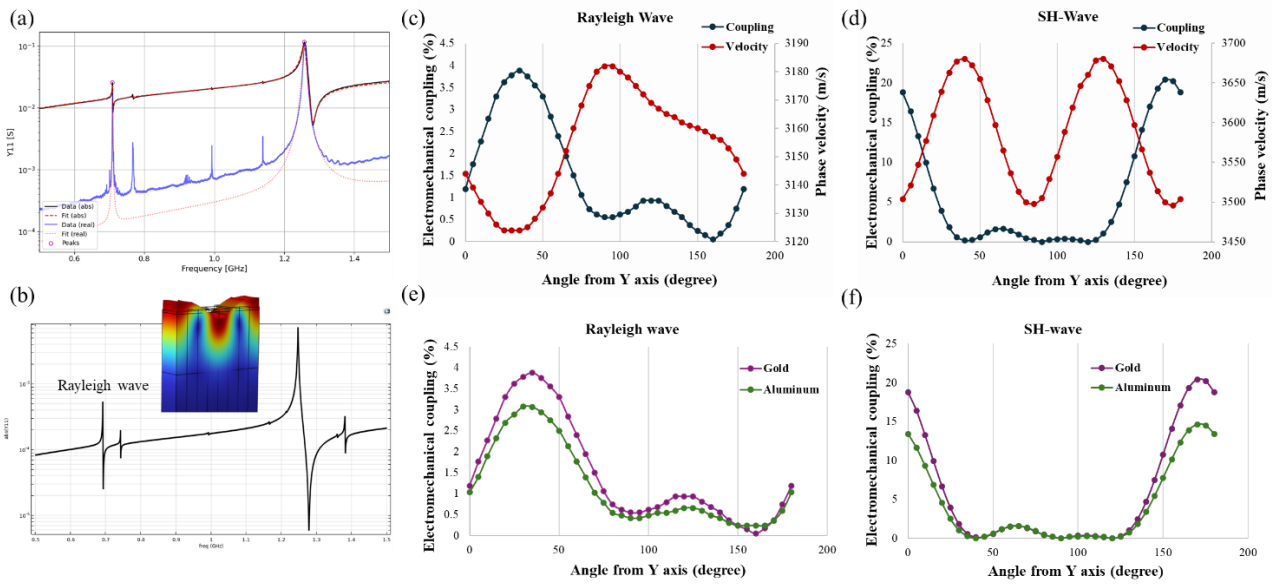

Figure 2: (a) Measured admittance response of an interdigital transducer on TFLN on insulator platform with 4 µm wavelength. (b) Simulated admittance response of the same IDT structure. The electromechanical coupling and phase velocity of (c) Rayleigh wave and (d) SH-wave across various propagation orientations on the TFLN substrate. The effect of Metallization (e) gold vs (f) aluminum on electromechanical coupling across various orientations on X-cut TFLN on insulator platform.

Nanofabrication of shadow masks for josephson-junction quantum devices

Rucha A. Deshpande [a], Sabbir Khan [b], Thomas Sand Jespersen [a], Rafael Taboryski [a]

[a] Technical University of Denmark, Lyngby, 2800, Denmark
[b] Dansk Fundamental Metrology, Hørsholm, 2970, Denmark
e-mail: rucha@dtu.dk

Keywords: quantum devices, multi-step nanofabrication, selective area growth (SAG), III/V nanowires

Abstract: We demonstrate new material platform based on poly-Si shadow masks for insitu post processing of III/V nanowires (InAs) used for josephson-junction quantum devices. Poly-Si material allows for high-aspect ratio and sub-100 nm feature sizes, suitable for shadow patterns. It allows for cleaner interfaces by elimination of resist type residues, which supports the purity required for quantum device processes.

Introduction: Conventional nanofabrication, where processing of III/V nanowires involves multiple stacks of post processing is detrimental to the purity of interfaces required for quantum devices. This can be overcome by shadow structures, which project selective open areas, where deposition of metals for contacts and other functions can be performed insitu without breaking the ultrahigh vacuum and clean conditions. Engineering the shadow structures to obtain better feature sizes is challenging due to requirement of high aspect ratio and small feature sizes of ~20 nm in precision. Material platform that can support such dimensions over wafer scale uniformity and contamination free substrate interfaces is essential for developing shadow mask multi-functional patterns. Recent studies show shadow mask composed of SiO_2 and Si_3N_4, fabricated for SAG III/V nanowires. [1, 2] We demonstrate the poly-Si based shadow masks, which is more robust platform compared to plain oxides and nitrides as the polycrystallinity of the material can be tuned based on deposition parameters and its dry etching can be controlled precisely.

Fabrication: We follow a process flow as shown in Figure 1b, followed by the schematic shown in Figure 1a. The first column describes the processes for obtaining SAG patterns, which exposes GaAs interface for III/V nanowire growth. The second column shows the shadow mask fabrication processes using poly-Si, which is currently under optimization.

Experiments and results: The shadow masks as obtained until step xi of process flow shown in Figure 1b, are transferred to MBE chamber for III/V nanowire growth. Next, shadow obtained for different angles of rotation of the sample can be probed for its efficiency of suitable metal deposition, for which we use Al as an example. Preliminary calculations for the shadow based minimum separation distances obtained for the patterns are shown in Figure 2a and 2b. These calculations do not consider the redeposition of the metal on the shadow masks, which can further distort the desired deposition dimensions. To assess these and other such issues, preliminary resist-based patterns as shown in Figure 2c are obtained for testing the shadow deposition dynamics. These will be followed by actual poly-Si based shadow masks, and cryogenic characterization of final device will be performed as proof of principle efficiency assessment of the newly developed poly-Si based shadow mask platform.[3]

References:

[1] A. Goswami, et al., Sn/InAs josephson junction on selective area grown nanowireswith in situ shadowed superconductor evaporation. *N. Lett.*. **2023**, 23, 7311-7318.
[2] D. J. Carrad, et al., Shadow epitaxy for in situ growth of generic semiconductor/superconductor hybrids. *Adv. Mater.* **2020**, 32, 1908411.
[3] D. Olsteins, et al., Cryogenic multiplexing using selective area grown nanowires. *Nat. Comm.* **2023**, 14, 7738.

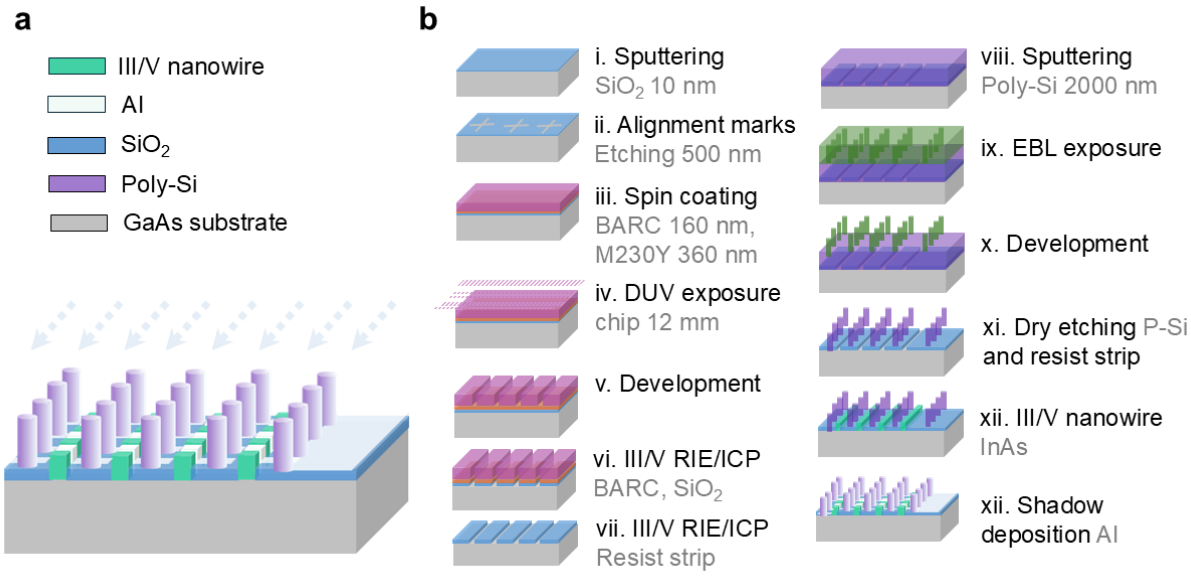

Figure 1. Process flow. (a) Shadow mask schematic. (b) Fabrication steps. Steps xii and xiii are performed insitu in MBE chamber at DFM. Steps i-xi are performed in DTU Nlab cleanroom.

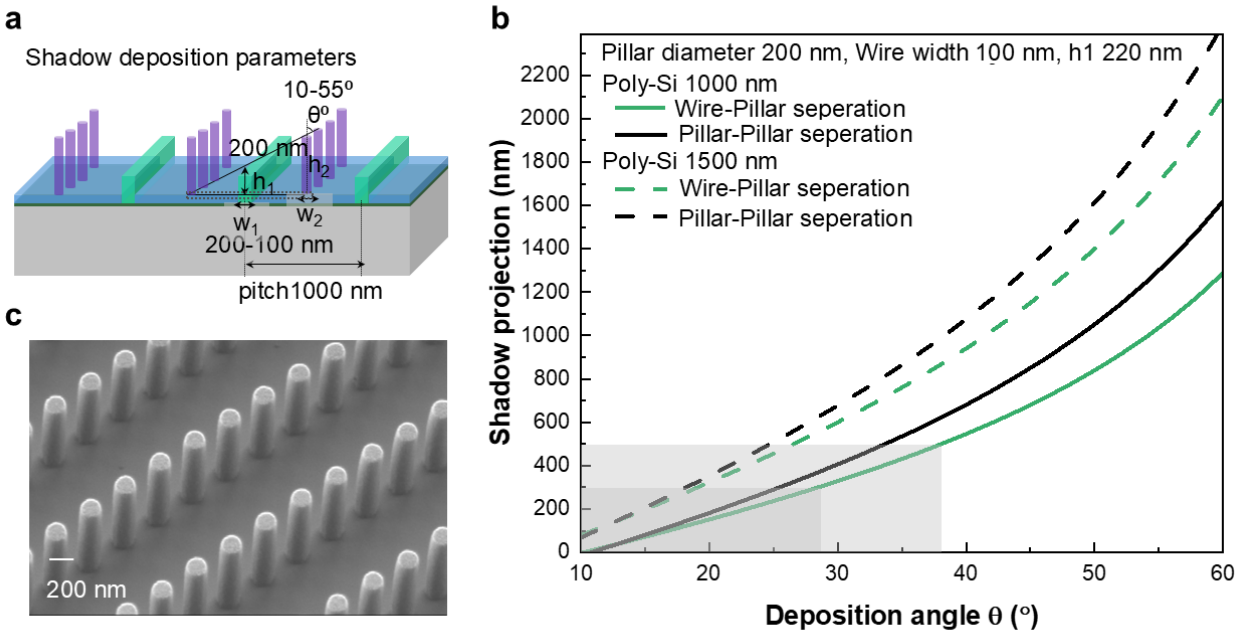

Figure 2. Parameters and results. (a) Schematic of dimensions of device that define the projection parameters. (b) Geometrical calculations of projection distances vs the deposition angle. The areas marked in grey color determine the range of angles for which the projection distance is too small to perform efficient masking for two different P-Si heights of 1000 and 1500 nm, respectively. (c) SEM image of preliminary patterning using resist, to be continued to be optimized for full process flow explained in Figure 1b.

Oral Session 3A: UV, EUV, and two-photon lithography

EUV interference lithography at PSI: pushing the limits of resolution of next generation photolithography

D. Kazazis, B. Bächtold, S. Maag, M. Schneider, A. Ammon, E. Japichino, L. Heller, T. Lachat, M. Peters, P. Heimgartner, M. Vockenhuber, M. Kropf, D. Piguet, Y. Ekinci, I. Mochi

[a] Paul Scherrer Institute, Villigen PSI, 5232, Switzerland
e-mail: dimitrios.kazazis@psi.ch

Extreme ultraviolet lithography (EUVL) [1] has recently been embraced by the semiconductor industry as the foremost lithography technology for pushing the miniaturization of semiconductor devices in accordance with Moore's law. By utilizing shorter wavelengths, EUVL enables the creation of nanoscale features with greater precision compared to earlier lithography techniques. The move towards scanners with high NA optics has already been decided and the new tools are expected to enter production between 2025-2026. Meanwhile, discussions on even higher NA optics (hyper NA) have already started with the goal to push the EUV technology beyond 2036.

The extreme ultraviolet interference lithography (EUV-IL) endstation of the XIL-II beamline at the Paul Scherrer Institute in Switzerland has served the scientific community for more than 20 years [2]. In particular, the contribution of the EUV-IL endstation to the development of novel photoresist materials suitable for EUV lithography towards high NA and the demonstration of resistless patterning has been remarkable [3,4]. In this EUV-IL system, polarized EUV light with a wavelength between 2.5-16 nm (typically 13.5 nm) irradiates special transmissive diffraction gratings, and the mutually coherent diffracted beams interfere and generate periodic aerial images with pitch and wavelength-independent contrast as shown in Fig. 1a. Using transmission gratings we have pushed the resolution down to half pitch (HP) 6 nm [5]. More recently, using a mirror-based setup shown (Fig. 1b), we achieved HP resolution down to 5 nm [6] (Fig. 2).

While the Swiss light source (SLS) is undergoing a major upgrade (SLS 2.0 project [7]), a new and more advanced endstation is under development. A schematic of the new EUV-IL tool is shown in Fig. 3a along with its main components. A schematic of the optical payload inside the chamber is shown in the cross-section of Fig. 3b. The aim of the new design is to overcome the limiting factors of the tool's performance in terms of resolution: thermal and mechanical drifts and vibrations. It is designed to achieve sub-nanometer stability (<1 nm) over a one-minute period, which exceeds the typical exposure duration. The system will be equipped with a load-lock for increased throughput. In addition, the wafer can thermalize inside the load-lock to the desired temperature and then be loaded into the exposure chamber with minimal heat transfer from and to it. The temperature of the wafer will be kept practically constant to ensure the wafer to mask position is kept to within less than 1 nm. The tool will support 200 mm wafers and offer multiple operation modes including interference lithography with transmissive diffraction gratings and with the PSI mirror interference setup as well as direct writing with Fresnel zone plates or Bessel beams, and arbitrary patterning with holography.

The new EUV lithography tool of PSI is expected to have high impact in the EUV community by pushing the resolution of photon-based lithography even further and towards the theoretical limit of EUV-IL of 3.5 nm HP, at the standard EUV wavelength of 13.5 nm. The system will enable research beyond the state of the art not only for the development of EUV materials for high and hyper NA EUV lithography but also for wavelengths in the soft X-ray regime.

[1] D. Kazazis *et al.,* Nat. Rev. Methods Primers 4 (2024) 84.
[2] N. Mojarad, J. Gobrecht, and Y. Ekinci, Microelectron. Eng. 143 (2015) 143.
[3] A. Develioglu *et al.*, Proc. SPIE 12750 (2023) 1275008.
[4] L.-T. Tseng *et al.*, Sci. Adv. 9 (2023) eadf5997.
[5] D. Fan and Y. Ekinci, J. Micro/Nanolith. MEMS MOEMS 15 (2016) 033505.
[6] I. Giannopoulos *et al.*, Nanoscale 16 (2024) 15533.
[7] P. R. Willmott and H. Braun, Synchrotron Radiat. News 37 (2024) 24.

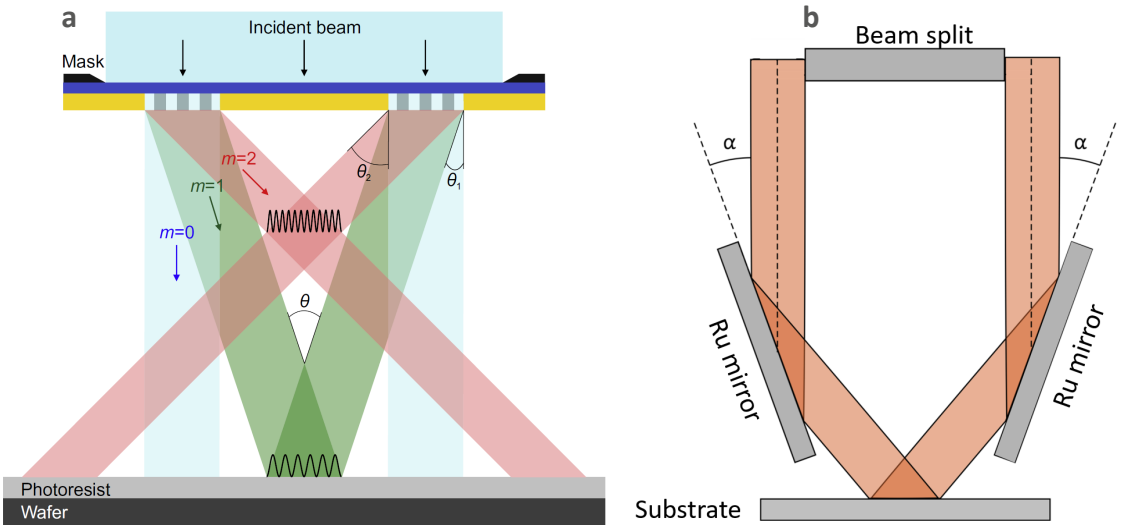

Figure 1. a. A schematic of interference lithography showing first and second order diffraction for two mutually coherent beams. **b.** Schematic of the mirror-based interference lithography setup.

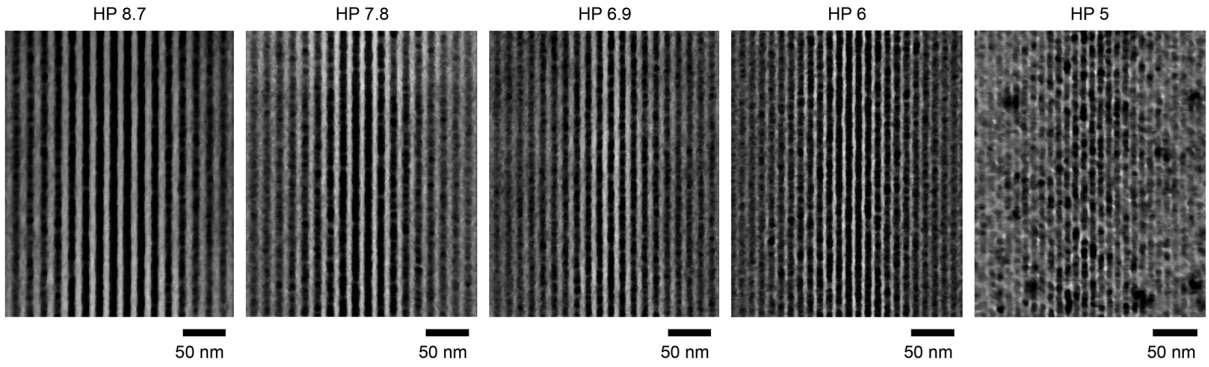

Figure 2. SEM images of exposed HSQ photoresist using the mirror-based interference lithography setup for half pitches down to 5 nm [6].

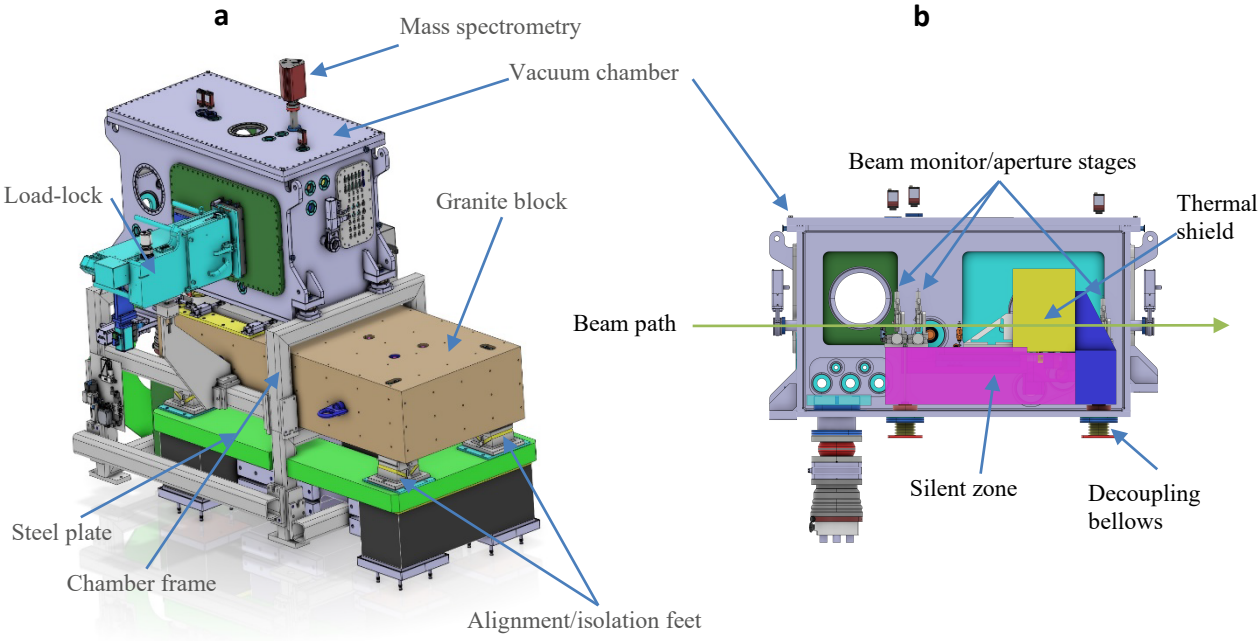

Figure 3. a. Schematic of the new EUV-IL tool with its main components and **b.** a cross section of the chamber showing the optical payload inside the chamber.

Towards sub-nm roughness in 3D topography for reflective X-ray focusing optics

Giulia Malvicini[1,*], Dogukan Güçtemur[2], Sina Saxer[2], Jan Erjawetz[3], Helmut Schift[1]

[1] Paul Scherrer Institute, Laboratory for Nano and Quantum Technologies, 5232 Villigen PSI, Switzerland
[2] FHNW School of Life Sciences, Hofackerstrasse 30, 4132 Muttenz, Switzerland
[3] XRnanotech, Parkstrasse 1, 5234 Villigen, Switzerland
e-mail: giulia.malvicini@psi.ch

X-rays span wavelengths ranging from 10 pm to 10 nm, so reflective or focusing optical components must have surface roughness well below these values, typically below 1 nm, to minimize scattering losses. Fabricating such ultra-smooth surfaces with complex 3D shapes remains a significant challenge. Such components are essential for advanced applications including synchrotron beamlines, extreme ultraviolet (EUV) lithography optics, X-ray microscopy among others [1].

We demonstrate a grayscale lithography process for fabricating smooth, sloped 3D structures in 100 µm-thick mr-P 22G_XP photoresist (micro resist technology GmbH) using scanning-laser direct write lithography (DWL) with up to 1024 grayscale values (GVs). A key limitation of this approach is the formation of staircase artifacts due to dose quantization and stitching effects between writing fields. Surface analysis revealed three main contributors to roughness: (a) vertical stripes from stitching, (b) horizontal steps from grayscale discretization, and (c) the intrinsic roughness of the resist itself, which is ~4 nm [2]. The aim of this research is to eliminate artifacts (a) and (b) by optimization of the writing process, and (c) by choosing appropriate processing parameters and choice of material. On top of this, measurement techniques capable of quantitatively assessing the quality (RMS roughness) of polymeric surfaces with deep 3D profiles must be adopted.

Fig. 1 presents a comparison of slopes generated with different numbers of grayscale values (64, 256 and 1024), with and without the N-over strategy, which uses overlapping multiple exposures to suppress stitching lines and enhance surface continuity. When using the maximum number of available GVs and the N-over strategy, the first two artifacts are mostly overcome, leading to a residual roughness of ~5 nm, initially measured by laser scanning confocal microscopy (LSCM), and subsequently confirmed by atomic force microscopy (AFM). That roughness could be attributed purely to the resist itself, identifying a fundamental material limit, likely due to the Novolak-based composition of mr-P 22G_XP.

AFM was employed to evaluate the surface roughness of patterned resist regions (Fig. 2). AFM provided high-resolution measurements of the surface roughness, although it is limited in application by scan area and the steepness of the slope. The results revealed RMS roughness values of ~4.5 nm in exposed regions (Fig. 2). While this level of smoothness is acceptable for many optical applications, it is still above the threshold required for EUV or soft X-ray optics. To overcome this, we transferred the resist patterns into PMMA via nanoimprinting, followed by a thermal reflow process at a temperature of 110°C, below the glass transition temperature (T_g=122°C) to reduce surface roughness without compromising the overall slope geometry. This selective reflow process (TASTE) [3], enabled by the linear polymer chains of PMMA in contrast to the large Novolak molecules, resulted in significant smoothing RMS reduction of 3 nm (Fig.3b) and points toward a viable route for reducing local nano-roughness below the intrinsic DWL resist limit.

Together, these results highlight a fabrication workflow that addresses both resolution and roughness limitations in grayscale lithography. By combining exposure strategies with material transfer and thermal smoothing, we offer a pathway to producing large-area, freeform 3D surfaces suitable for advanced optical systems, particularly for applications in EUV and soft X-ray focusing. Further optimization seems possible, based on the sub-nm replication fidelity obtained in PMMA.

[1] H. Yumoto *et al.*, Sci. Rep. **7** (2017) 16408.
[2] Dammel, R., SPIE Tutorial Texts TT11, SPIE Optical Engineering Press, (1993)
[3] Schleunitz, *et al. Nano Convergence* 1, 7 (2014)

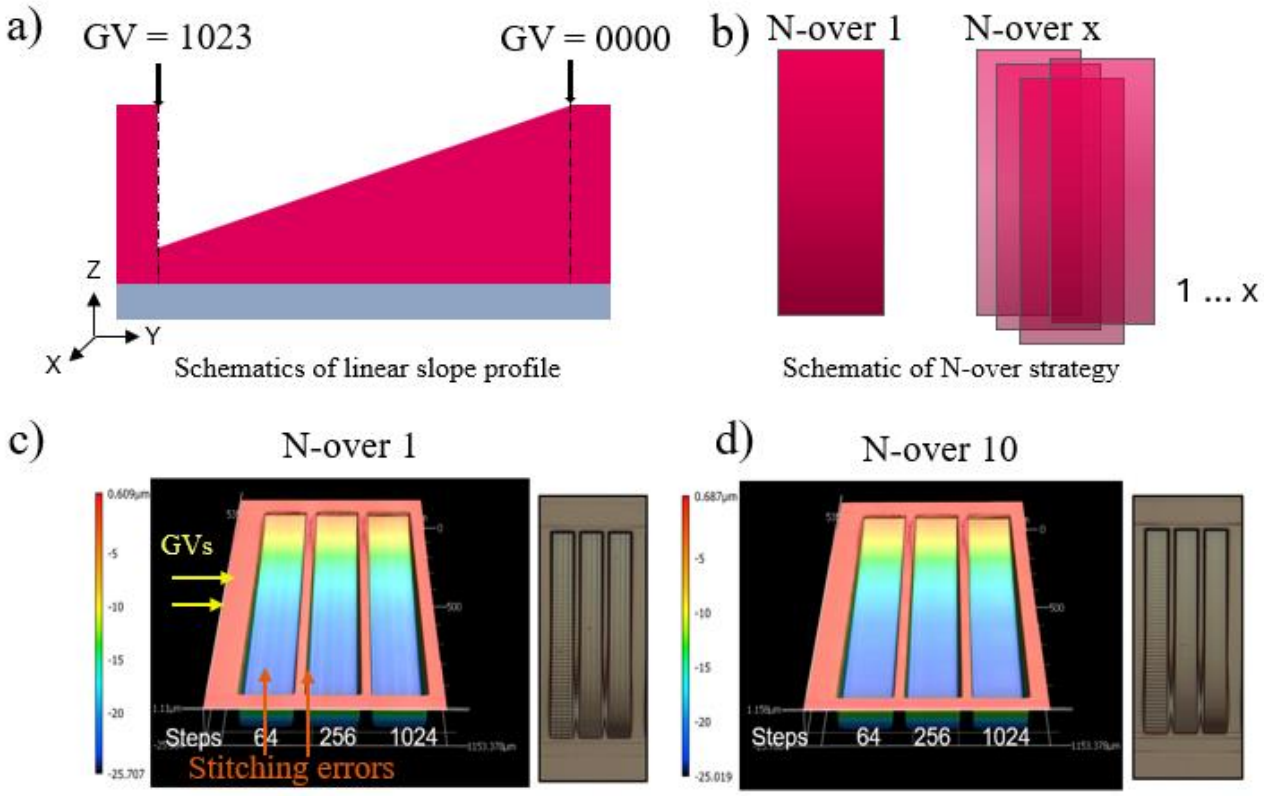

Figure 1. (a) Schematic of a linear grayscale slope generated using 1024 grayscale values (GVs). (b) Illustration of the N-over writing strategy, where overlapping exposure zones are used to mitigate stitching artifacts between adjacent writing fields (c) Comparison of linear slopes fabricated in *mr-P 22G_XP* with 64, 256 and 1024 GVs (measured by LSCM), with both N-over 1 and (d) N-over 10.

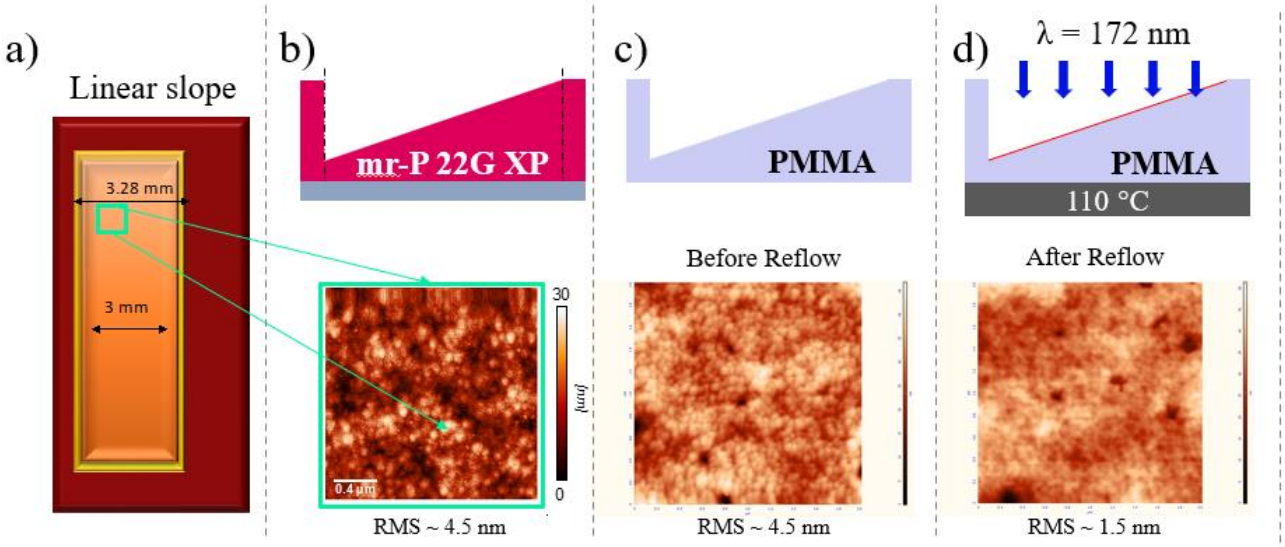

Figure 2. (a) Schematic of the wide linear slope indicating AFM measurement positions: light green rectangle highlights a patterned area (b), (c), (d) Schematic and roughness (AFM measurement) of *mr-P 22G_XP*, PMMA (pattern transfer through thermal imprint from *mr-P 22G_XP*) before and after thermal reflow, respectively. The roughness decreases down to ~1.5 nm after thermal reflow. The area of the AFM measurements is 2x2 μm^2.

Quantifying and overcoming wafer distortion on bonded wafers for deep-UV lithography

Jeroen Bolk[a], Sander Reniers[a], Stacey Martina[a], Sara Sequeira[a], Sruja Dave[a], Kevin Williams[a], Yuqing Jiao[a]

[a] Eindhoven University of Technology, Eindhoven, 5612 AP, The Netherlands
e-mail: j.bolk@tue.nl

Heterogeneous integration merges technologies of different material systems using wafer-bonding techniques that pose unique challenges. InP membrane photonics are developed to enable the miniaturization of photonic integrated circuits (PICs) through a high index contrast waveguide platform, with integrated lasers, detectors and phase shifter components. The platform that is developed at the Eindhoven University of Technology is called Indium-Phosphide-Membrane-on-Silicon (IMOS) [1]. In this platform, the membrane is attached to a silicon carrier substrate by an adhesive polymer layer: benzo-cyclo-butene (BCB), which is shown in Fig. 1.
Although some of the PIC layers on the InP membrane are fabricated before bonding, several layers also need to be fabricated afterwards from the backside of the membrane after removing the bulk substate. The temperature involved in the bonding process and the difference in thermal expansion coefficients of the carrier substrate, the adhesive layers, and the InP membrane, results in strain when the materials are fixated and return to room temperature. This gives rise to membrane expansion up to 320 ppm, and non-linear distortions in the coordinate system of the pre-bonding layers [1] that need to be compensated in the post-bonding layers to achieve precise sub-100 nm overlay. In previous work on double-sided membrane processing, electron beam lithography (EBL) was used to achieve good overlay through localized alignment for individual exposure fields. EBL can be precise but unfortunately sacrifices in throughput making it an unattractive candidate for large-scale manufacturing. Projection lithography can combine high resolution with throughput but typically uses global wafer-scale alignment models to achieve overlay with previous layers, making it harder to mitigate bonded-wafer coordinate system distortions.
In a proof-of-concept study, we used an ASML PAS5500 /1100B DUV scanner to read redesigned alignment markers that were fabricated before bonding, and processed in such a way, to become readable from the backside of the membrane, after bonding and removing the substrate (Figure 2).
We used the obtained data to determine the membrane distortions, and to expose the aligned post bonding layers. The coordinate systems pre- (Layer 1) and post-bonding (Layer 2) were compared to determine the overlay capabilities of this fabrication method (Figure 3).
Based on the initial result, we prepared a custom reticle design, to increase the measurement density by an order of magnitude, and to mimic 15x15 mm image field exposures required for wafer-scale volume processing. With a traditional 6-parameter model [2] based on alignment to the first frontside layer, overlay was determined on more than 1400 marker pairs successfully, with an overlay result below 300 nm in X and Y (Figure 4). Although this result does not yet meet the goals of sub-100 nm overlay precision, it demonstrates the viability of the method to visualize and quantify the wafer-scale membrane distortions and overlay result.
In future work, a batch of wafers will be processed to obtain a better understanding of the wafer-to-wafer reproducibility of the distortion signatures, and to assess industrial solutions to mitigate non-linear and non-uniform distortions. In this assessment a feed-forward method based on known distortion signatures of a wafer will be compared to real-time method where high-order alignment models can be applied and weighted evaluation of markers can be performed based on distance from the exposure location.

We would like to acknowledge the collaboration and contribution to this work by the ASML MPS Applications team, specifically: Chanho Ryu and Saulo Moura.

[1] Y. Jiao et al., “InP membrane integrated photonics research,” Semicond. Sci. Technol., vol. 36, no. 1, p. 013001, Jan. 2020, doi: 10.1088/1361-6641/abcadd.
[2] Abdi, S., et al. "High-Precision Mapping and Analysis of Wafer-Scale Distortions in InP Membranes to Si 3D Integration." IEEE Access (2024).

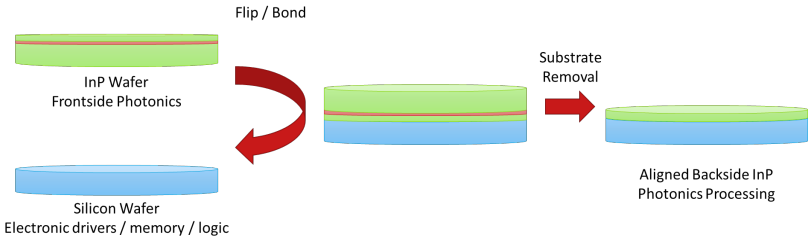

Figure 1. Bonding of a front-side processed InP wafer to a Silicon carrier wafer with an adhesive BCB layer. After the bonding process, the bulk-substrate of the InP wafer is removed up until and including the sacrificial etch-stop layer leaving the Silicon carrier wafer with the thin InP membrane on top for continued processing from the backside of the membrane.

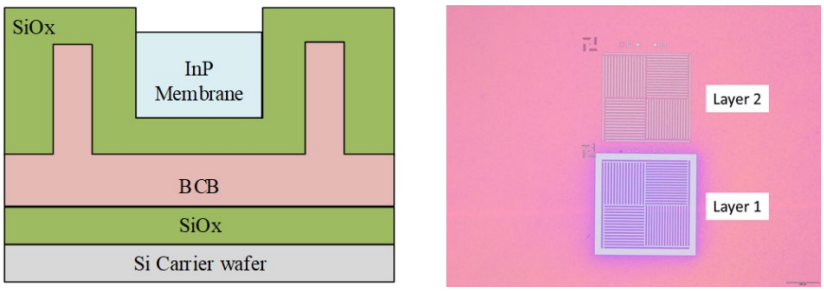

Figure 2. Schematic cross-section of a single post-bonding marker grating period as read with the scanner from the backside (left), and a photograph of the fabrication result with a pre- (Layer 1) and post-bonding (Layer 2) marker-pair to quantify the overlay (right).

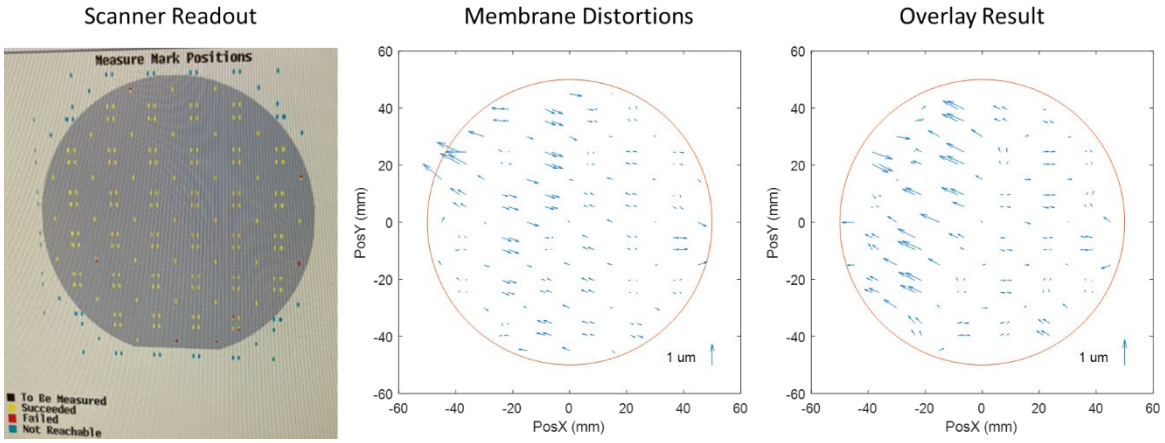

Figure 3. Proof-of-concept readout result (left), the membrane distortion vectors from the measured L1 markers (center) and overlay result as relative distortion vectors of L2 to L1 (right).

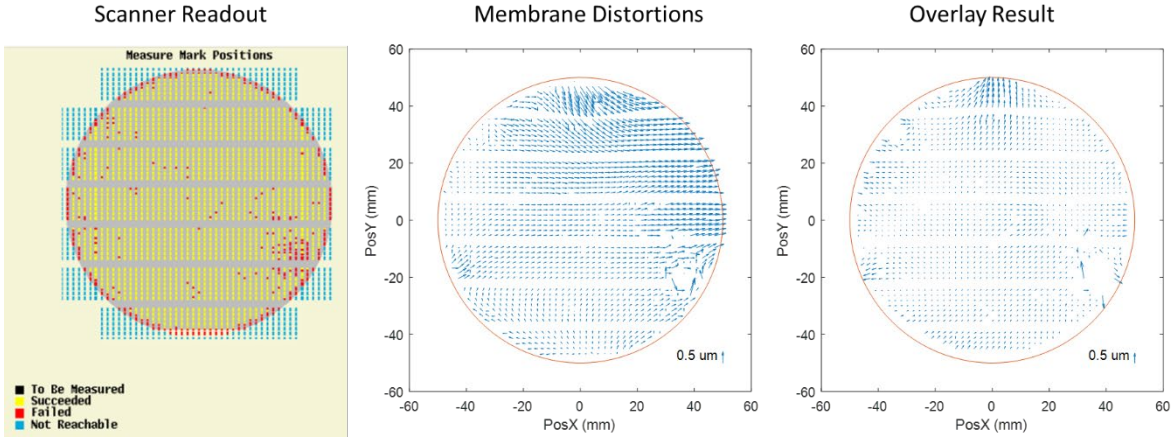

Figure 4. High-density readout result (left), the membrane distortion vectors from the measured L1 markers (center) and overlay result as relative distortion vectors of L2 to L1 (right).

Pushing the Boundaries: *in situ* Development and Multi-Material Exchange for Two-Photon 3D Printing

Pratyaksh Yemulwar[1, 2, a)], Man-Ho Wong[1)], Saurabh Karle[1)], Josua Zscheile[1)], Robert Kirchner[1)]
[1]*HETEROMERGE GmbH, Gostritzer Str. 61, 01217 Dresden, Germany*
[2]*Center for Advancing Electronics Dresden, TU Dresden, Helmholtz Str. 18, 01069 Dresden, Germany*

[a)]*pratyaksh.yemulwar@heteromerge.com*

Three-dimensional (3D) laser micro- and nano-printing has advanced dramatically over the last two decades, from a theoretically appealing novelty to a durable, flexible, financially viable, and widely used technology. Originally developed as a scientific curiosity, it has now become a mainstay in a variety of sectors due to its dependability and adaptability [1]. It has a wide range of applications, including but not limited to 3D photonics, individual micro-optics, complete micro-optical systems, and 3D-printed micromachines. One of its distinguishing aspects is the ability to combine different materials into a single printing process improving the utility and flexibility the technology. This latest feature is especially important for the development of composite materials, digital ("voxelated") materials, multi-material devices, and structures with customizable characteristics adapted to specific applications. [2, 4].

In this study, we aimed to advance the state-of-the art by fabricate with more than two materials, as well as to introduce an in situ rinsing (development) step in between the exchange of one material to another. This will support more diverse material combinations with even more stable structures. The technology base is a new, new version of a multi-material exchange system (MergeOne, HETEROMERGE GmbH) [3] in conjunction with a PP GT2 3D micro-nano-printer (Nanoscribe GmbH & Co. KG). We used three different commercial materials and a solvent in one single print-run (IP-PDMS: Nanoscribe; MX535: HETEROMERGE, isopropanol: MERCK).

We created microstructures with diameters of roughly 200 µm diameter and 100 µm height using material combinations with significant difference in viscosity (IPA: 2.1 mPas, IP-PDMS: 100 mPas, MX535: 900 mPas) and properties (hydrophobic vs. hydrophilic). Using the multi-material exchange system (as shown in Fig. 1), we conducted a thorough examination of structure evolution during the exchange process. Our findings gave important insights into the real-time exchange phenomena that occur during the two-photon polymerization (2PP)-based 3D printing process. We have tested various complicated designs to better understand flow behavior and structure formation. This helped to establish a technique for universally removing material from the deadzone of the microstructure (Fig. 2) during the exchange process, which was not possible without solvent rinsing process before. This significantly improved the multi-material printing for those distinct materials. Dead-zones in the vicinity of the microstructure, particularly in regions upstream and downstream of the flow direction is eliminated thus providing proper and non-contaminated exchange of materials (Fig. 3).

Typical parameter settings are about 200 mbar for IP-PDMS, 300 mbar for MXpure, 60 mbar for IPA injection as well as -100 mbar for IP-PDMS, -100 mbar for MXpure, and -100 mbar for IPA volume synchronized removal. Typical process times varied between. 10 to 15 min for one material exchange step (e.g. IP-PDMS vs. IPA or IPA vs. MXpure). This has to be compared to about 60 min of process time of standard manual process (MXpure printing, 30 min IPA development, IP-PDMS printing, 30 min IPA development). This provides an improvement of a factor of ten just on the development process using the novel three-channel print-head. The consumed IPA volume is below 5 ml compared to 2x20 ml for a manual process, providing a factor of 40 improvement strongly supporting sustainable processing. Based on our observations, strategies and recipes for the multi-material printing are developed for an efficient printing of composite structures.

[1] A. Jaiswal et al., iScience 26(4), (2023) 106374.
[2] Y. Gao et al., SPIE (2021).
[3] R. Kirchner et al., in Proc. SPIE PC12412 (2023), PC1241206.
[4] P. Yemulwar et al., J VAC SCI TECHNOL B 43(2), (2025) 022602.

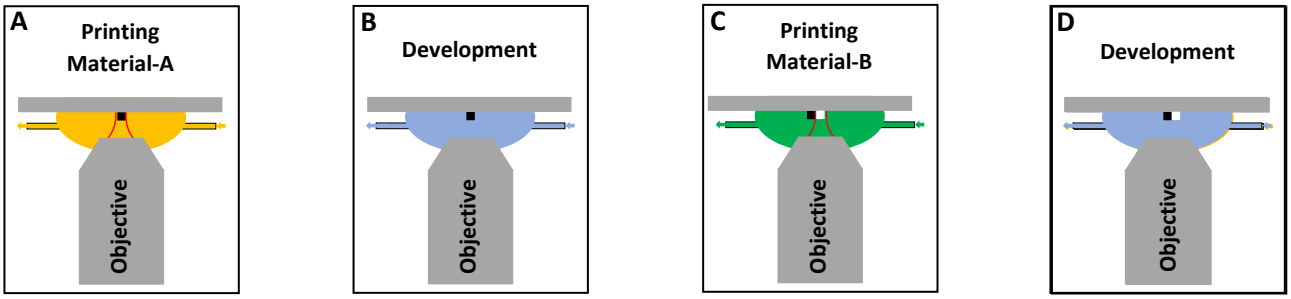

Figure 1: Schematic representation of *in-situ* material exchange through the HETEROMERGE printhead during writing using an open fluidic system to inject liquid and to actively remove liquid with a volume synchronized inward and outward flow. (A) Fabrication with material-A. (B) Development after fabrication of microstructure with printing material-A. (C) Exchange and fabrication with material-B. (D) Final development of fabricated micro-structure. (D) Final development of fabricated micro-structure.

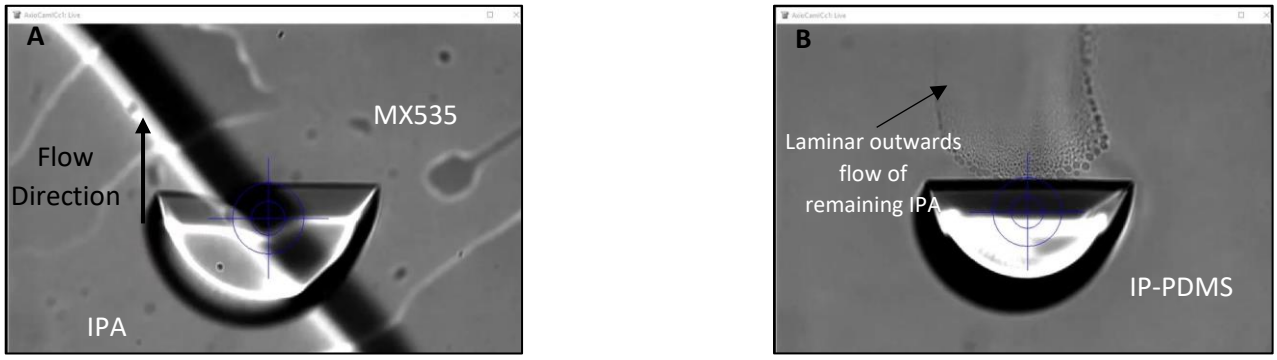

Figure 2: (A) The flow of IPA replacing MX535 can be observed along with clear visual of phase separation between both the materials across the microstructure during development of printed microstructure that was done during the printing process. (B) Laminar flow of IPA towards the end of exchange of IPA with IP-PDMS towards the end of successful development behind the microstructure can be observed. Here the bubbles can be seen due to the mixing of IPA with IP-PDMS.

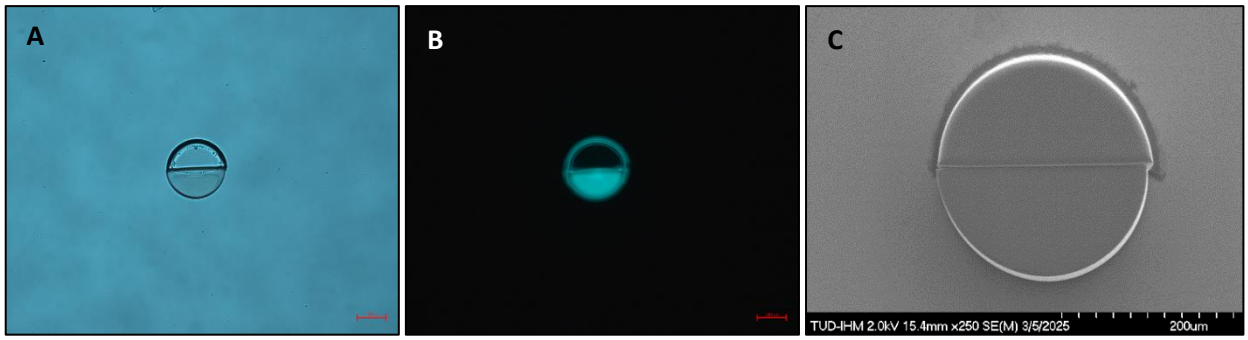

Figure 3: (A) Optical microscopy imaging of fabricated microstructure with the bottom part being fabricated with MX535 and the top part being fabricated with IP-PDMS. (B) Fluorescence imaging of microstructure in 38 HE Green Fluorescence Protein (GFP) filter as the MX535 is visible in the green spectrum whereas the IP-PDMS is not visible in the same filter set. (C) SEM image of the microstructure where both the materials can be distinguished by their slight surface texture variation.

Oral Session 3B: Advanced Nanofabrication I

Fabrication of arsenic-in-silicon single-electron transistors using scanning tunnelling microscopy hydrogen resist lithography

Kieran J. Spruce [a], Raj Ravichandar [a], Patrick See[b], Mark R. Buitelaar [a], Taylor J. Z. Stock [a], Neil J. Curson [a]
[a] UCL, London, WC1E 6BT
[b] NPL, Middlesex, TW11 0LW

e-mail: Kieran.spruce.20@ucl.ac.uk

Abstract Text

Silicon devices incorporating single dopant atoms as the active components have applications in quantum computing where the dopants provide electron or nuclear spin qubits, or quantum simulators where the dopant atoms are used to create artificial lattices. Scanning tunnelling microscopy hydrogen resist lithography (STM-HRL) makes it possible to fabricate such devices, and historically all such devices have been made using phosphorus-in-silicon. Recent studies, however, have found that the dopant arsenic shows superior incorporation precision (~97%) and placement accuracy [1], compared to phosphorus (~70%) [2], with the implication that arsenic-in-silicon is more suitable for scaling to large numbers of single atom devices.

This work demonstrates the first successful implementation of atomically precise arsenic-in-silicon device fabrication using STM-HRL. We have fabricated and measured the first arsenic-based quantum dot single-electron transistors (QD SETs), and in so doing we have developed new fabrication strategies that form part of our developing process for creating scalable atomic-scale quantum devices in silicon. We have advanced the general STM-HRL device fabrication methodology in two ways. Firstly, we have developed a novel three-way SET architecture, see Figure 1 upper panel, that enables comparison of multiple tunnel junctions with identical fabrication parameters, all within a single device structure, providing direct insights into electron transport characteristics such as gap resistance and dot capacitance. Secondly, we eliminate unwanted incorporation of arsenic atoms from the precursor gas arsine (AsH3) by introducing a pre-dosing step, of the phosphorus precursor gas phosphine (PH3), to block silicon adsorption sites where spurious arsenic dopants may be introduced into the surface.

Comprehensive electrical characterisation of the arsenic SETs, conducted in a dilution refrigerator at milli-Kelvin temperatures, revealed clear Coulomb blockade behaviour across all junctions, see Figure 1 lower panel. Our arsenic-based SETs achieved performance metrics comparable to similar phosphorus devices, with charging energies ranging from 8-19 meV and consistent lever arms of approximately 0.04. Gap resistances varied with junction geometry rather than dopant type, ranging from 1 to 40 MΩ. Notably, compared to phosphorus-based devices, the arsenic-based QD SETs reveal additional features in their Coulomb diamond measurements, including substructures within blockade regions that indicate electron tunnelling processes to/from near-by dopants.

The demonstration of an arsenic-in-silicon SET presented here, combined with the enhanced precision in dopant placement that arsenic offers, provides a robust foundation to scalable qubits, where each qubit is effectively an SET island consisting of a single atom. This work addresses critical challenges in quantum computing hardware development in silicon and presents a clear path toward higher-yield, more complex device architectures using multiple dopant precursors.

[1] T. J. Z. Stock et al., *Advanced Materials,* 36 (2024)
[2] J. A. Ivie et al., *Phys. Rev. Applied* 16, 054037 (2021)

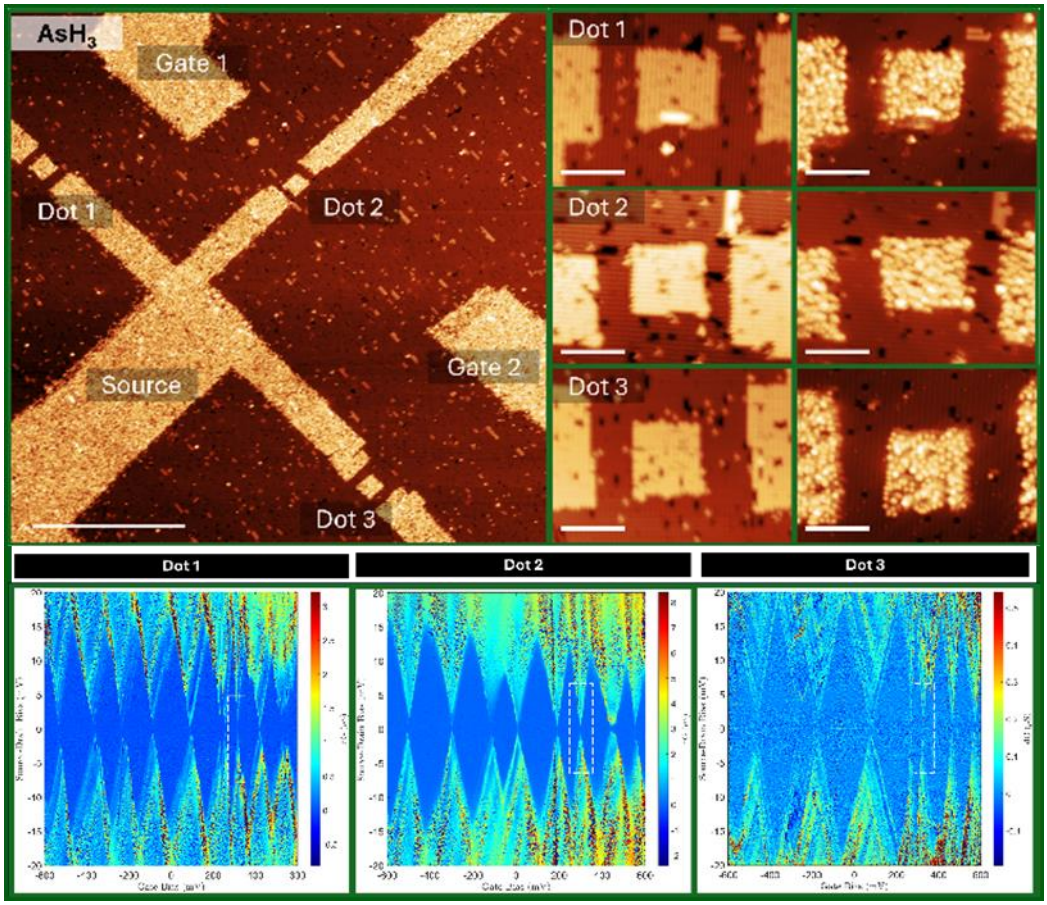

Figure 1. Upper panel: STM data showing an arsenic-in-silicon three-way single electron transistor. Left hand image shows the full three-way device, right hand shows detail of each junction before and after dosing with AsH_3. Lower panel: DC measurements of all three tunnel junctions showing characteristic SET Coulomb diamonds.

Tailoring Vertical Gradients in Thin Films: Design and Fabrication

Xiangyu Chen [a], Jianqin Zhu [a], Zhi Tao [a], Lu Qiu [a]
[a] Beihang University, Beijing, 100191, China
e-mail: qiulu@buaa.edu.cn

Keywords: Nanoparticles, Inkjet printing, Laser sintering, Gradient films

Purpose of the work. Differential laser sintering of multicomponent nanoparticles with distinct properties is a high-degree-of-freedom and cost-effective strategy for fabricating high-performance gradient films, widely applied in thermoelectric devices [1], mechanical components [2], and biosensors [3]. However, due to the spontaneity of gradient formation[4], precise control over the compositional and performance gradients of the films remains challenging. Conventional Physical Vapor Deposition (PVD) techniques suffer from long processing times and numerous interfacial defects, limiting the lifespan and economic viability of gradient films [5]. Therefore, there is an urgent need to develop new manufacturing pathways for high-lifetime gradient films with convenient processing.

Novelty of the work with respect to the state of the art. To address this challenge, this study proposes a gradient composition control method based on a heavy nanoparticle composition ratio and develops a vertical energy distribution theory applicable to gradient films by combining radiation and heat transfer theories, providing technical support and theoretical guidance for the heavy nanoparticle composition ratio control strategy and the laser vertical energy distribution theory.

Results of the work. Through inkjet printing and laser sintering, gradient films with compositional and property gradients were successfully fabricated. The study revealed that as the mass fraction of heavy particles (W nanoparticles) increases, the cumulative intensity of W elements in the film gradually increases, showing significant gradient characteristics in the lower half of the film (Figure 1). According to the fundamental principles of radiative heat transfer, a theoretical model was developed to predict the vertical distribution of laser energy as a function of thickness-dependent absorbance variations. This model enabled the prediction of laser energy distribution across different thicknesses, as illustrated in Figure 2.
Furthermore, the validity of the laser vertical energy distribution theory was experimentally verified through FIB-SEM characterization. The experimentally measured densification curves were found to be in excellent agreement with the theoretical vertical energy distribution curves, as shown in Figure 3.
This study proposed a gradient particle deposition control method based on the proportion of heavy particles, achieving full control over the component proportions of the entire film. By combining radiation and heat transfer theories, a vertical energy distribution model for laser differential absorption of multicomponent particles was developed, and the reasonableness of the theory was validated through micro-morphological characterization. The research findings provide a foundation for subsequent engineering applications and theoretical optimization.

[1] X. Liu, X. Shen, L. Gong, Multi-scale thermodynamic analysis method for 2D SiC/SiC composite turbine guide vanes. Chinese Journal of Aeronautics, 2018, 31(1): 117-25.
[2] Y. Lu, P. Sun, X. Yang, Review of Research Progress in Nontraditional Machining of Ultrahigh-Temperature Ceramic Matrix Composites. Coatings, 2023, 13(1).
[3] M. Zeng, Y. Du, Q. Jiang, High-throughput printing of combinatorial materials from aerosols. Nature, 2023, 617(7960): 292-8.
[4] X. Chen X, L. Qiu, M. Zhang, Nanoparticle-reinforced SiOC ceramic matrix composite films with structure gradient fabricated by inkjet printing and laser sintering. Communications Materials, 2024, 6(3).
[5] P. Ren, Study of high-temperature oxidation behavior of sputtered nanocrystalline low-expansion cermet coatings, Ph.D. Thesis, School of Energy and Power Engineering, University of Chinese Academy of Sciences, 2016.

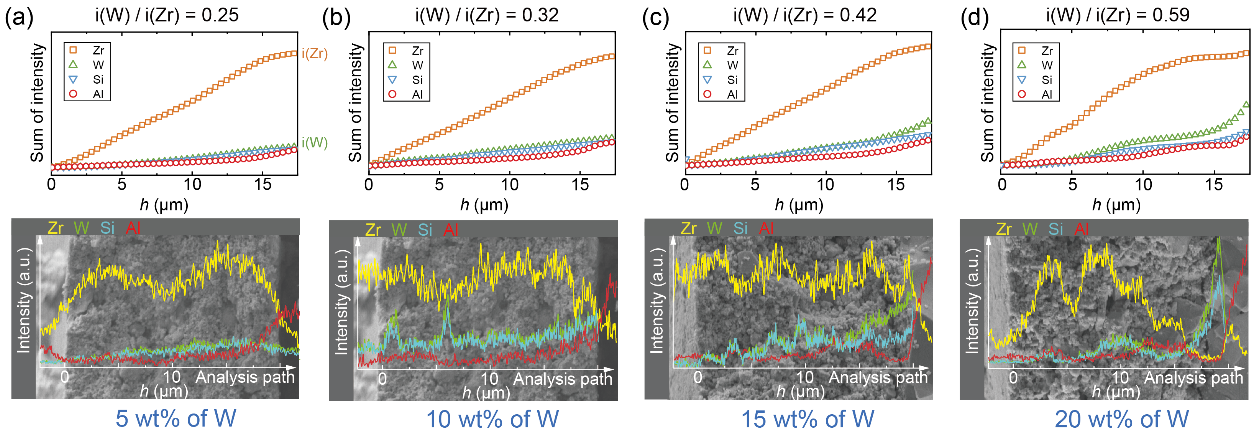

Figure 1. (a-d) illustrates that the ratio of heavy particles (W nanoparticles) modulates the gradient composition of the films. With an increasing proportion of W particles, the W content within the films gradually increases, accompanied by enhanced aggregation characteristics of the W-rich lower layer.

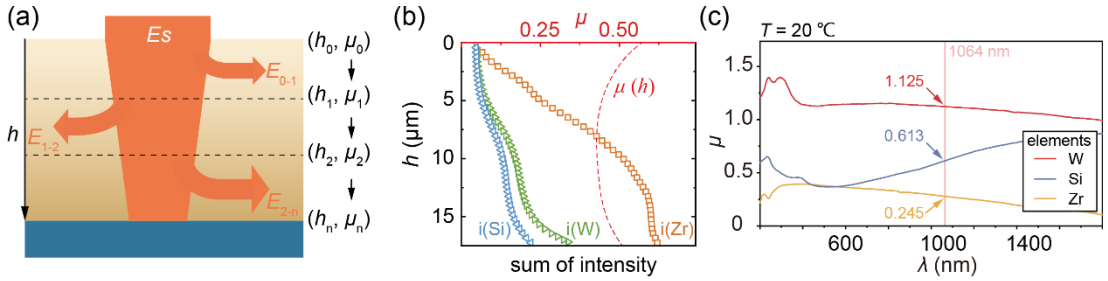

Figure 2. (a) Schematic representation of differential laser energy absorption along the vertical cross-section of a gradient-component film. (b) Depth-dependent variation of Zr, W, and Si elemental concentrations, accompanied by attenuation coefficient curves derived from the average absorbance (c) of each element as a function of film depth.

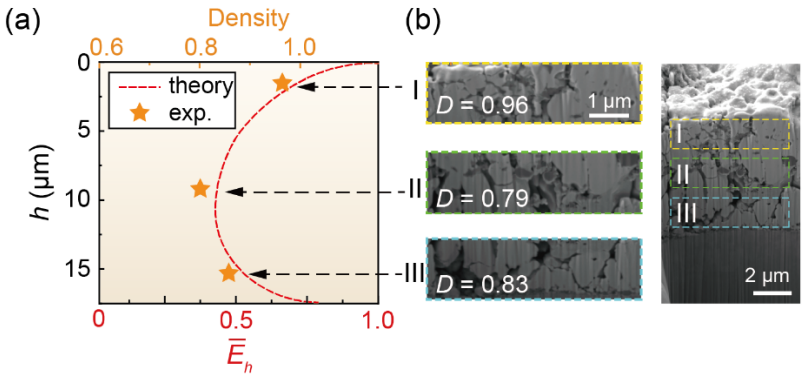

Figure 3. (a) The theoretical model for predicting the vertical energy distribution of the laser, (b) the variation in film density at different depths, as determined by FIB-SEM characterization, aligns well with the theoretical energy distribution curves, thereby validating the rationality of the proposed theory.

Anti-virus performance of Si nanopillar array mimicking cicada wing surface

Takeshi Ito [a] *, Hitoshi Ishiguro [b], Tomohiro Shimizu [a], Shoso Shingubara [a]

[a] Grad. School of Science and Eng., Kansai Univ., 3-3-35 Yamate-cho, Suita-shi, Osaka 564-8680 Japan
[b] Kanagawa Institute of Industrial Science and Technology, 3-25-13 Tonomachi, Kawasaki, Kanagawa
e-mail: t.ito@kansai-u.ac.jp

Abstract Text

Many researchers have been reported about the bactericidal and antibacterial effects of nanostructures. On the other hand, there are few reports regarding their effects on viruses. In this study, we fabricated Si nanostructures and evaluated their anti-virus performance changing with their pitch and height. As the results, extremely high antiviral activity for influenza A was observed only when the pitch was 200 nm. Additionally, regarding the height, it was found that antiviral activity appeared when the height was 200 nm or more.

1. Introduction.

Nano- and microscopic patterns found in nature exhibit a variety of beneficial functions. For example, the wings of cicadas and dragonflies are covered with nano-sized bumps, which contribute to their bactericidal and antimicrobial properties [1]. Inspired by these results, many researchers have been reported about the bactericidal and antibacterial effects of nanostructures [2, 3], which occurs through physical action, stretching the cell membrane of adhered bacterial cell. On the other hand, there are few reports regarding their effects on viruses. However, in medical practice, prevention of infections against both bacteria and viruses is a necessity. In this study, we fabricated Si nanostructures and evaluated their anti-virus performance changing with their pitch and height.

2. Experiments.

The nanopillar patterning was performed using colloidal lithography, and nanostructures were formed utilizing metal-assisted chemical etching (MachEtch). Si substrates (100) was set to 3 cm square. Firstly, Poly-styrene (PS) beads were spincoated on the Si substrate. Here, the diameter of the PS beads was varied at 100, 200, 300, 500, and 1000 nm, respectively. After the O_2 Plasma etching of the PS beads to decrease their diameter, Au thin film for a catalyst on the MachEtch was deposited on the sample surface. Finally, MachEtch was performed so that the etching depth was varied from 100 to 400 nm.

The antiviral test was conducted based on ISO 181814 (plaque assay method). The virus evaluated in this study was the enveloped virus, Influenza A. Anti-virus activity was calculated using an equation as below.

Ainti-virus activity = log(virus infection rate at the begiging of the test) -
log(virus infection rate after 2 hours incuvation)

3. Results and discussion.

Figure 1 shows an example of an SEM image of the fabricated nanostructures. As you can see, the nanostructures were fabricated regularly and uniformly. Figure 2 presents the antiviral activity values when the height was fixed at 200 nm, and the pitch was varied. Figure 3 shows the antiviral activity values when the pitch was fixed at 200 nm, and the height was varied. From these results, it was found that an extremely high antiviral activity was observed only when the pitch was 200 nm. Additionally, regarding the height, it was found that antiviral activity appeared when the height was 200 nm or more. These results clarify that antiviral properties can be exhibited solely by the physical shape of the nanostructures. However, the mechanism behind this effect is currently unknown.

[1] E.P. Ivanova et al., Small 8 (2012) 489-2494.
[2] Z. Zhao et al., ACS Appl. Nanomater. (2024) 14040-14049.
[3] Y. Matushita et al., Colloids nad Surfaces B: Biointerfaces (2025) 114560.

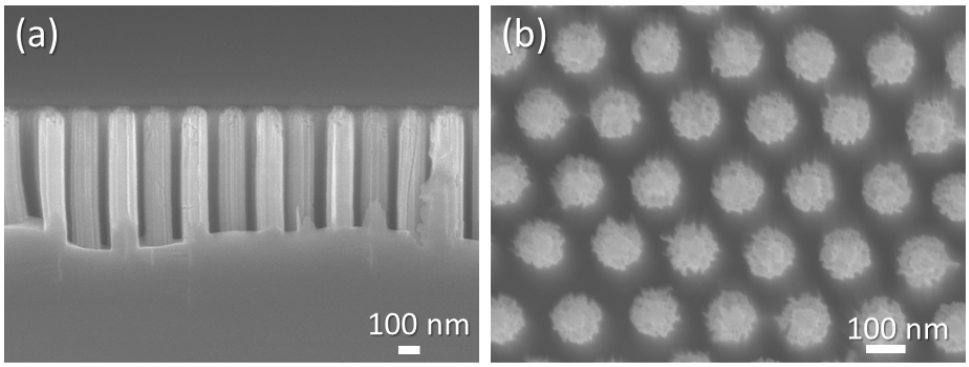

Figure 1. SEM images of the Si nanopillars with the height of 400 nm (left) and the pitch of 200 nm (right).

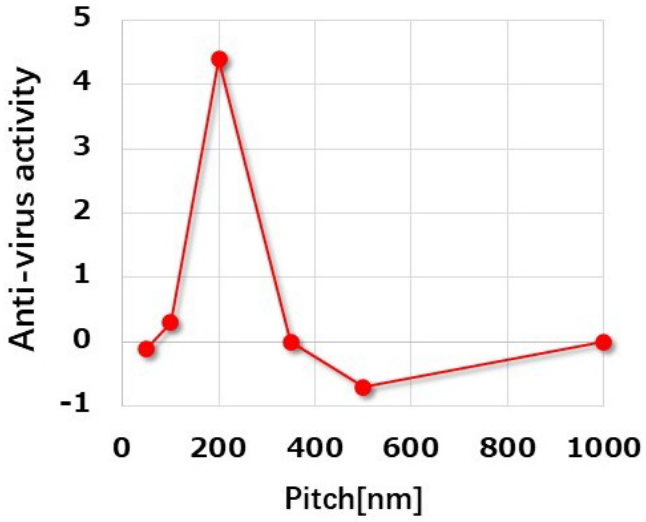

Figure 2. Anti-virus activity of Si nanopilalrs dependent with pillar pitch.

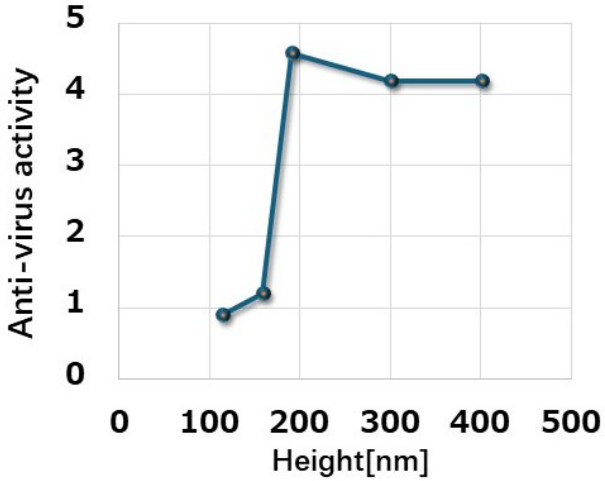

Figure 3. Anti-virus activity of Si nanopilalrs dependent with pillar height.

3D structured local thin film deposition by Micro Direct Atomic Layer Deposition (µDALP™)

Simone Santucci, Mira Baraket and Maksym Plakhotnyuk
ATLANT 3D, Taastrup, Denmark
E-mail: mbar@atlant3d.com

Advancements in chemical and physical deposition techniques for thin films and coatings are paramount for academic research and industrial applications in many technologies such as electronics, energy, and MEMS. Recent trends point to deposition technologies that combine flexibility, scalability, and material versatility. While traditional methods like Chemical Vapor Deposition (CVD) and Atomic Layer Deposition (ALD) offer high-quality film deposition, they often face challenges in patterning, complex structure fabrication, and process adaptability. Overcoming these limitations typically requires additional pre- or post-processing steps (such as lithography), which increase both processing time and cost, limiting their efficiency for next-generation applications.

Here, we introduce Micro Direct Atomic Layer Processing (µDALP™), a novel, atmospheric-pressure, direct-write deposition technology that expands ALD into localized, high-precision thin film printing (Figure 1). Unlike conventional ALD, µDALP™ enables complex structured coatings and seamless material transitions. Moreover, it allows deposition in ambient pressure, eliminating vacuum-related throughput limitations, and eliminates the need for lithography for some applications, significantly enhancing scalability for industrial applications. In particular, µDALP™ allows 3D designs with sub-nanometer control over the thickness profile of the film (Figure 2), making structures such as gradients, wells, and combs accessible easily.

µDALP™ adaptability and versatility open new possibilities for designing, developing, and producing next-generation thin film-based devices. By leveraging µDALP™'s capability for pre-programming the print shape and material transitions during deposition, we significantly accelerate device validation and optimization, dramatically reducing R&D costs.

In this talk, we will present the key advantages of µDALP™ for disruptive devices, multi-material integration, rapid material discovery, and direct-write patterning of functional thin films..

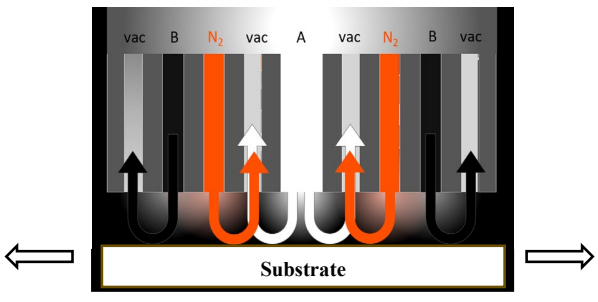

Figure 1: Microreactor nozzle scheme.

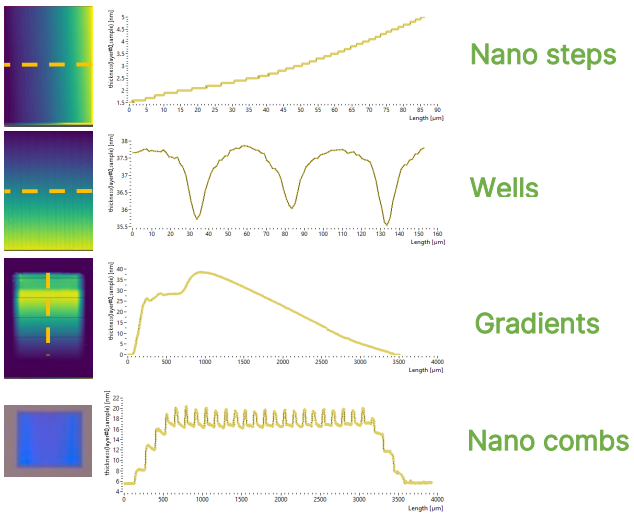

Figure 2: Thickness profile of thin film samples deposited by µDALP™.

Oral Session 3C: Sustainable Devices and Process Technology

Shaping of a bio-sourced AESO polymer for micro-encapsulation purposes

E. Lu[1, 2]*, B. Bresson[3], J. Fattaccioli[1, 2]

[1]CPCV, Département de Chimie, Ecole Normale Supérieure, PSL Université, Sorbonne Université, CNRS, 75005 Paris, France
[2]Institut Pierre-Gilles de Gennes pour la Microfluidique, 75005 Paris, France
[3]Laboratoire Sciences et Ingénierie de la Matière Molle, ESPCI Paris, 10 rue Vauquelin, Cedex 75231 Paris, France
*estelle.lu@ens.psl.eu

Keywords : materials, polymer, bio-based, microfluidics, micro-encapsulation

With the increasing environmental concerns, the polymers field is shifting towards more sustainable practices across various applications, such as additive manufacturing [1]. In particular, the growth of bio-based polymers is gradually replacing those derived from petrochemical sources [2]. This rapid development has been facilitated by the abundant availability of renewable resources.

Namely, soybean oil has emerged as a resource for green polymers. As a matter of fact, recent research has focused on exploiting polymers derived from acrylated epoxidized soybean oil (AESO) [3]. While few studies have proposed AESO for microencapsulation applications [4], the physicochemical properties of the resulting particles have not been extensively investigated.

In our work, we demonstrate the use of AESO as a bio-based polymer for microencapsulation using microfluidics systems, with the aim of better understanding its properties in the form of microcapsules such as the permeability or the swelling. A microfluidic double flow focusing system (Figure 1.a) was used to generate the particles (Figure 1.b). The microchip utilized here is divided into two sections: one for generating the double emulsion and another for UV-induced polymerization of the thermoset shell.

To optimize the process, magnetic particles were incorporated into the inner phase of the capsules to differentiate them from plain AESO particles, thereby improving capsule yielding. Sorting optimization was conducted by studying various parameters, including the concentration of magnetic particles (Figure 3.b) or the optimal distance between the magnet and the sample during sorting.

The fabrication of these capsules enabled a thorough characterization of their properties to better comprehend their behaviors, and thus enhance their potential applications. Specifically, we studied their permeability using microfluidics (Figure 4.a) and fluorescent-labeled molecules, analyzing the interaction between the aqueous core and the surrounding environment (Figure 4.b). Introducing molecules with different hydrodynamic radii in the continuous phase (Figure 4.c) revealed varying kinetics of core labeling, thereby highlighting the permeability of the particles (Figure 4.d). Controlling this property could be valuable for applications such as reagent trapping and controlled releasing. Additional tunable features with similar potential, such as the shell's swelling dynamics, are also being explored.

[1] C. Vazquez-Martel et al., ACS Sustainable Chem. & Eng. 9 (2021) 16840-16848.

[2] G. Karmakar et al., Polymers. 13 (2021) 1333.

[3] C. Hu, Versatile Biobased Particles of Acrylate Vegetable Oils: Synthesis and Applications Ph.D. Thesis, Chemistry Department, Ecole Normale Supérieure, 2022.

[4] L.R. de Souza et al., Sustainability. 14, 13556 (2022) 13556.

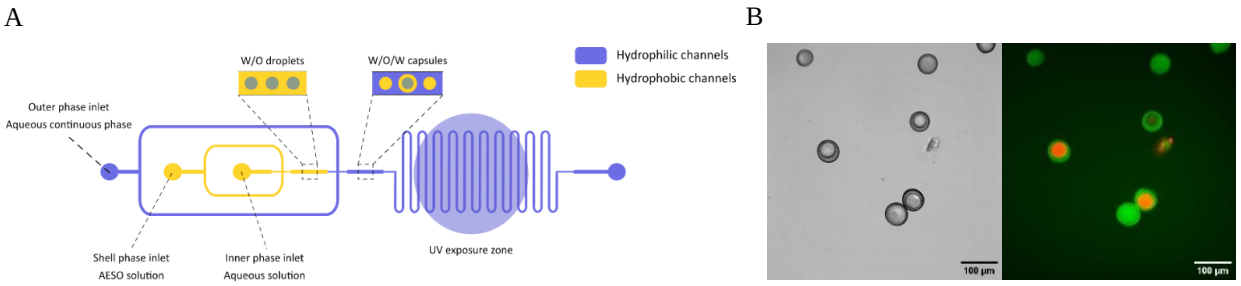

Figure 1: (a) Microfluidic chip for the encapsulation and photopolymerization process (b) Brightfield and GFP imaging of AESO microparticles and capsules by confocal microscopy

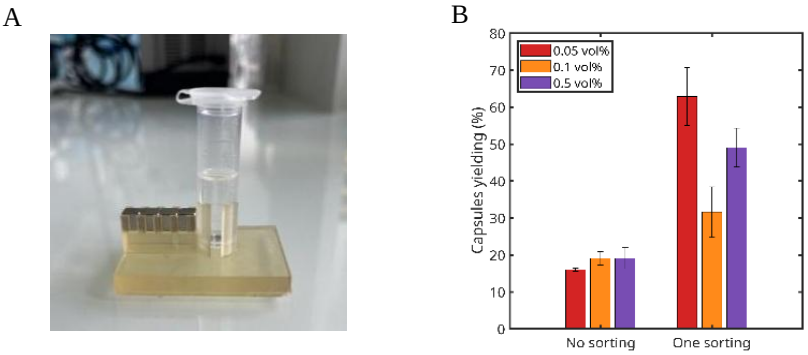

Figure 2: (a) Magnetic sorting setup (b) Influence of the magnetic particles concentration on the sorting yielding

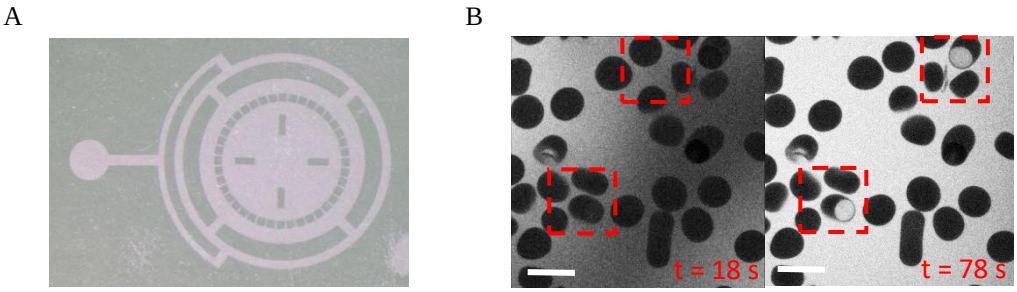

C

Mw (kDa)	Rh (nm)
4	1.4
10	2.2
250	11.3
2000	26.9

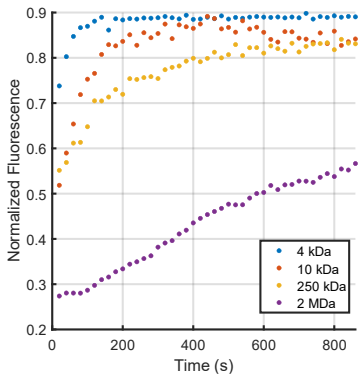

Figure 4: (a) Microfluidic design for the permeability analysis (b) Confocal imaging of the capsules' fluorescent marking with Dextran-FITC (4kDa). Scale bar: 100 µm (c) Dextran-FITC of different molecular weights with the corresponding hydrodynamic radius (d) Fluorescent monitoring of Dextran-FITC marking at different molecular weights

Layer-by-layer functionalization of cotton fabric for enhanced electrokinetic energy harvesting

Aditya Patwari [a], Chirodeep Bakli [b], and Suman Chakraborty [c]

[a] Advanced Technology Development Centre, Indian Institute of Technology Kharagpur, Kharagpur 721302, India.
[b] School of Energy Science and Engineering, Indian Institute of Technology Kharagpur, Kharagpur 721302, India.
[c] Department of Mechanical Engineering, Indian Institute of Technology Kharagpur, Kharagpur 721302, India.
e-mail: suman@mech.iitkgp.ac.in

In the milieu of rapid depletion of fossil fuels and corresponding environmental effects, the search for sustainable and renewable energy sources has gained urgency. To this end, numerous hydroelectric technologies have recently emerged owing to the natural abundance of water [1]. Water can be continuously pumped in a controlled direction through intricately shaped cotton fabric via capillary action, mimicking the natural transpiration process observed in plants. Subsequently, this water flow through microscale conduits formed within the cotton fabric network can be harnessed to generate electrical energy via electrokinetic effects, specifically through streaming potential. This phenomenon refers to the electrical potential difference that develops across the ends of micro/nano-conduits due to preferential transport of ions of either positive or negative polarity. However, prevailing attempts to harvest energy with similar approaches have largely remained inefficient, restricting the lab-to-industry translation of the technology. The underlying electrokinetic effects can be augmented by tuning the electric properties of the porous structure or altering fluid rheology [2]. In this work, we employ a layer-by-layer coating technique to functionalize the cotton fabric with a bilayer consisting of a PDADMAC (cationic polyelectrolyte) layer and a silica nanoparticle layer, as illustrated in Figure 1(a), intending to tailor the surface properties. The functionalized cotton is then shaped into a bioinspired design comprising (i) a root section that draws water from the reservoir, (ii) a trunk part consisting of microfluidic channels formed by confined pathways within the coated cotton fabric, and (iii) a leaf part that facilitates water evaporation by drawing ambient thermal energy, thereby maintaining continuous fluid flow without the need for any input mechanical power (refer to Figure 1 (b)). The fabricated device can generate electrical power as soon as the capillary infiltration reaches the top electrode. Figure 2 demonstrates the water infiltration states (photographic and infrared camera images) at the onset of capillary action (t = 0 s) and at the instant when the generated open-circuit voltage begins to plateau (t = 200 s). This saturated open circuit voltage is sustained for as long as the continuous transpiration-driven fluid flow is maintained. In Figure 3, we compare the streaming potential generated over time by pristine cotton and functionalized cotton. The functionalization process nearly doubles the streaming potential (i.e., from 0.2 V to 0.4 V). The observed performance enhancement arises from two key effects induced by surface functionalization: firstly, the increased magnitude of surface zeta potential due to inclusion of silica nanoparticles that have higher zeta potential than cellulose (cotton fabric) [3,4], secondly, the presence of trapped spherical nanoparticles increases the effective surface area in contact with the flowing water. Both effects contribute to a stronger electrokinetic response of the device. Additionally, the sandwiched PDADMAC layer, a polycation, electrostatically anchors the negatively charged silica nanoparticles to the cotton fabric, enhancing the device's stability during prolonged use. Summarily, we demonstrate a novel yet facile surface functionalization strategy to enhance electrokinetic energy conversion, paving the way for the development of efficient microfluidic energy harvesting systems.

References:

[1] S. Chakraborty et al., Applied Physics Reviews 12 (2025) 011305.
[2] A. Patwari et al., Analytica Chimica Acta 1321 (2024) 342997.
[3] A.M. Grancarić et al., AUTEX Research Journal 23 (2023) 184–192.
[4] M. Zhao et al., Materials 11 (2018) 1385.

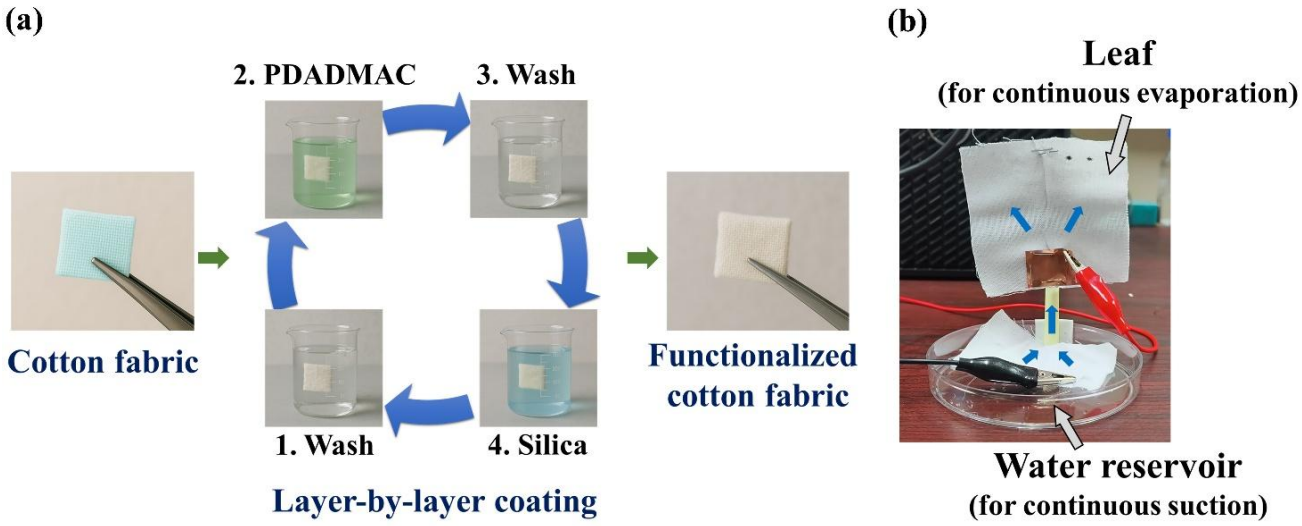

Figure 1. Device fabrication and working principle (a) cotton fabric functionalization process (b) fabricated device illustrating water transport through transpiration mechanism.

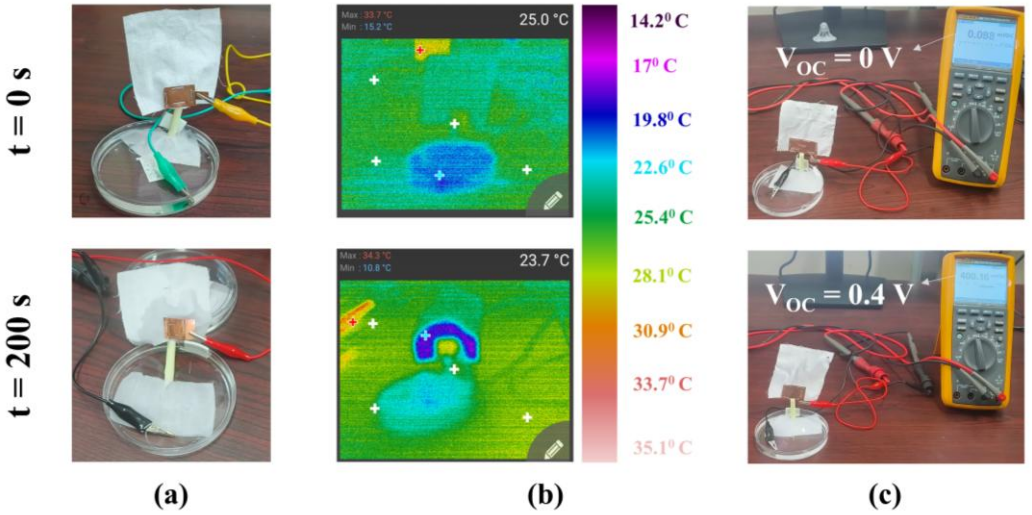

Figure 2. Device operation at different time instants (a) photographic images (b) Infrared (IR) images revealing the progression of water infiltration (c) corresponding open-circuit voltage (V_{OC}) generated.

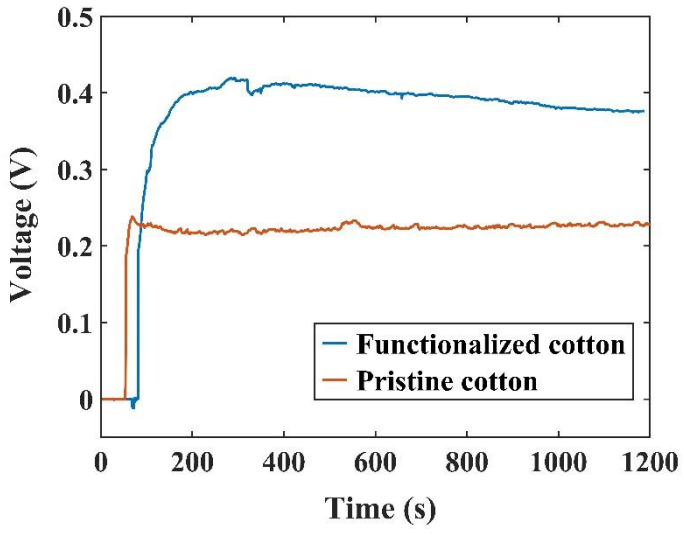

Figure 3. Temporal evolution of generated open circuit voltage.

Process development for improved passivation in IBC Solar Cells

Jens Munk Nielsen [a], Rasmus Schmidt Davidsen [b], Stephan Sylvest Keller [a]

[a] National Centre for Nano Fabrication and Characterization, DTU Nanolab, Technical University of Denmark, Kongens Lyngby, 2800, Denmark
[b] Department of Electrical and Computer Engineering, Aarhus University, Aarhus N, 8200, Denmark
e-mail: jemunk@dtu.dk

Interdigitated back contact (IBC) solar cells are pivotal in advancing silicon solar cells towards their theoretical efficiency limits [1]. The lack of reflective front metal contacts results in exceptional optical properties which make it a compelling architecture for both industry and research institutions. In our study, we implemented a process to realize IBC solar cells with focus on optimization of the dielectric passivation stack. Symmetrically passivated lifetime and pre-metallization samples yielded promising results from quasi-steady-state photoconductance (QSSPC) measurements. Specifically, undiffused thinned Czochralski(CZ) wafers with a symmetrical Al_2O_3 and a:SiN_x:H stack exhibited a low surface recombination velocity of 1.86 cm/s. Furthermore, pre-metallization with patterned emitter and back surface fields (BSF) demonstrated a minority carrier lifetime of 622 µs.

The solar cell fabrication process, illustrated in Figure 1, is largely based on the work by Franklin et al [2]. It begins with 4-inch n-type DSP CZ-grown Si <100> wafers, which are thinned down from 350 µm to 260 µm using 80°C 28 wt% KOH, followed by cleaning in sulfuric acid and ammonium peroxydisulfate solution. A standard RCA procedure is performed before the wet oxidation at 1050°C for 30 min to form the dopant diffusion mask. The n+ doping pattern is transferred into the oxide using maskless lithography and bHF etching, followed by another RCA procedure before the doping with POCl at 950°C for 20 min. After stripping the phosphorous oxide in HF, a drive-in wet oxidation is performed at 1050°C for 30 min. The p+ doping pattern is transferred into the new oxide by photolithography and bHF etching, Another RCA procedure is performed and is followed by deposition of boron-containing silicon oxide (BSG) in an SPTS Multiplex PECVD tool and subsequent drive-in at 900°C during a dry oxidation for 100 min. All oxides are removed in a bHF bath, followed by RCA cleaning and deposition of 30 nm Al_2O_3 in a Picosun R200 ALD chamber, capped with 60 nm a:SiN_x:H from PECVD. Point contacts are defined using photolithography and wet etched using bHF, with metallization achieved through e-beam evaporation of 600 nm Al and liftoff process. Post-deposition annealing at 400°C for 30 minutes is used to activate the passivation and improve the formation of the Al contacts. All the high temperature processes are done in horizontal quartz tube furnaces (HQTF) from Tempress, and they all feature a 20 min annealing process after the main process

Preliminary quality control measurements were done on a wafer that featured no point contact opening and no liftoff process. This wafer showed an implied open circuit voltage of 696mV, implied fill factor of 81.83, and a carrier lifetime of 622 µs using QSSPC on a Sinton WCT120. The lifetime was also measured using microwave photoconductivity decay (µ-PCD) using an MDPmap from Freiberg Instruments. This lifetime mapping showed a similar median lifetime of 630 µs see Fig.2 (Left). Next external quantum efficiency (EQE) was measured on the finished solar cell, see Fig.2 (Right), using a QEXL from PV measurements. Integrating the EQE yielded a short circuit current density of 7.57 mA/cm^2. These first results on full devices showed conflicting data. The lifetime measurements show a well passivated wafer, but the EQE indicates that we have a low collection efficiency especially for shorter wavelengths, which could be explained by high front surface recombination. Attempts at gathering IV curves were made. The result was irregular and noisy curves. We currently don’t know the root cause for this behaviour and have thus decided to not include it. Future work will focus on identifying the loss mechanisms in these devices in order to close the gap towards the current state of the art devices.

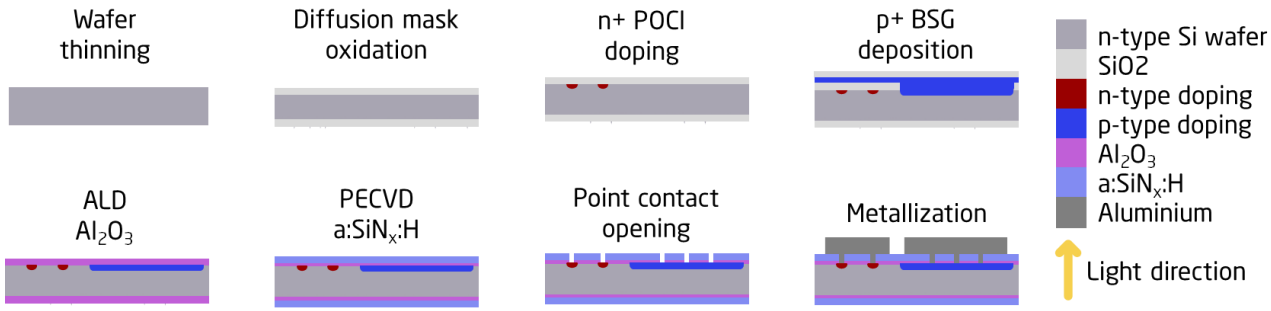

Figure 1. Sketch of the solar cell process flow. Omitted are patterning steps which are done using UV-lithography, and the pattern transfer is done using bHF to etch the dielectrics.

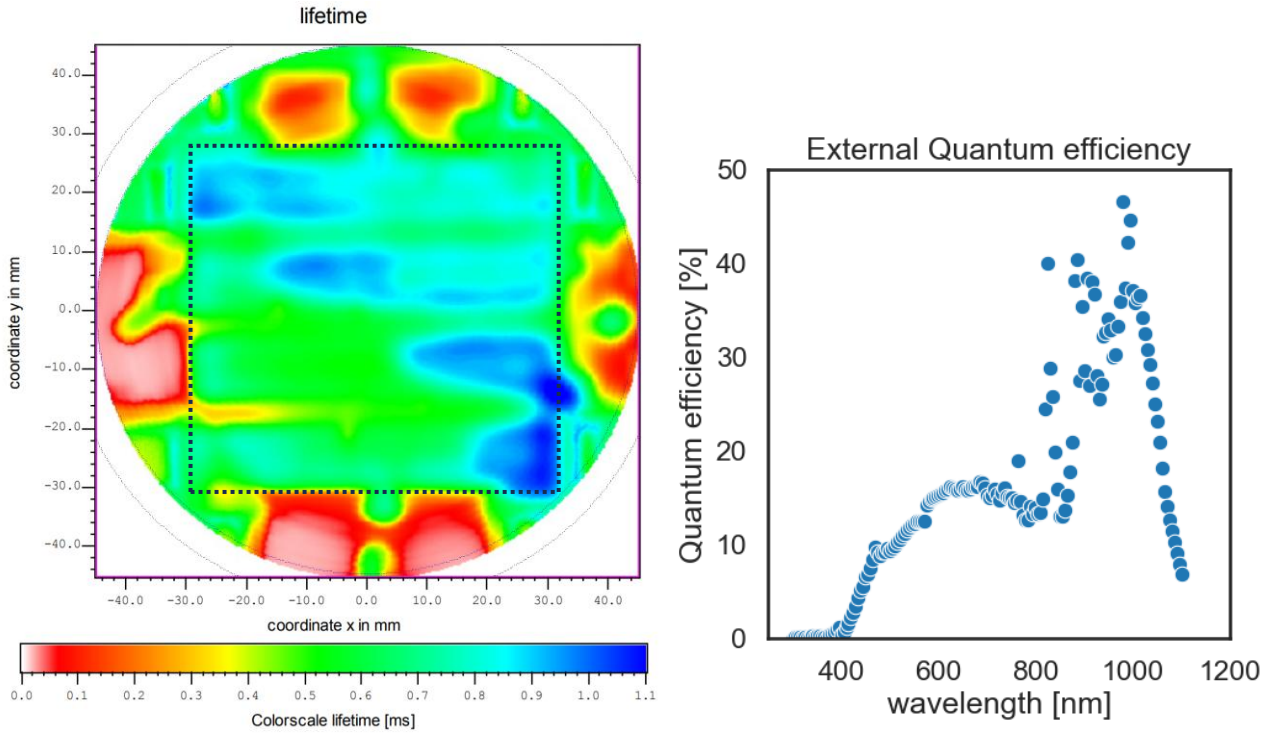

Figure 2. (Left) µ-PCD map of the pre-metallization wafer. The 4-inch wafer features 24 devices arranged in a 4 x 6 matrix in the centre of the wafer as indicated by the dashed box. (Right) External quantum efficiency measurements on a single finished solar cell measured using QEXL from PV Measurements.

[1] P. Procel-Moya, Y. Zhao, O. Isabella, Unlocking the potential of carrier-selective contacts: Key insights for designing c-Si solar cells with efficiency beyond 28%, Solar Energy Materials and Solar Cells, Volume 285, 2025, 113504

[2] E. Franklin et al., Design, fabrication and characterisation of a 24.4% efficient interdigitated back contact solar cell, Prog. Photovolt: Res. Appl. 24.4 (2016) 411-427

Inkjet printing of stealth nanobeacons

Akinobu Yamaguchi [a], Toshiya Yasunaga [b], Kyoto Namura [c], Motofumi Suzuki [c], Takao Fukuoka [c, d]

[a] Toyo University, Kawagoe, 350-8585, Japan
[b] Aichi Gakuin University, Nagoya, 464-8650, Japan
[c] Kyoto University, Kyoto, 615-8540, Japan
[d] Archilys Corporation, Kyoto, 600-8813, Japan
e-mail: yamaguchi054@toyo.jp

Counterfeit and imitation products are becoming a significant problem with the rise of e-commerce. Counterfeit medicines pose health risks and will endanger life. To fight counterfeiting, various anticounterfeiting technologies have been suggested and developed. Apart from anticounterfeiting, there are also proposals to tack products to conduct market research, recycle materials and hold products accountable. This trend is known as digital product passporting, and there is demand for research and development of technology to attach mechanisms to products for covert tracking.

Recently, to achieve the combat the counterfeiting and digital product passporting, microtaggants and RFID have attracted much attention. Among them, we have developed stealth nanobeacons composed of self-assemblies of colloidal gold nanoparticles with reporter molecules. These stealth nanobeacons produce characteristic surface-enhanced Raman scattering (SERS) signals with long-term stability. [1, 2] The distinguishable SERS signals can be rapidly detected. If a stealth nanobeacon can be inked and printed, it can carry a great deal of information and can be incorporated into authentication systems related with the anticounterfeiting and digital product passporting etc.

Here, we prepared an ink by mixing normal inkjet printing ink with the stealth nanobeacons. Using a special inkjet printer, we print it and evaluate the print characteristics. Stealth nanobeacons were prepared by mixing 4, 4'-bipyridine (4bpy) with gold nanoparticles that had been prepared via a citric acid reduction of an aqueous gold chloride solution. Nanobeacons are gold nanoparticle aggregates with indefinite shapes that are dispersed in a metastable state in solution. Figure 1 shows a typical absorption spectra of nanobeacons with various shpaes: (i) relatively dispersive, (ii) chain-like structure, and (iii) flocculated agglomerate. There may be cases in which the nanobeacons form clusters with each other or the nanobeacons are larger in size. In this study, the ultrasonic oscillating element homogenizer NR-50M (Microtec Co., Ltd, Chiba, Japan) was used for 10 min, as schematically shown in Fig. 2. Two solution types containing the adjusted stealth nanobeacons were prepared: 1) Stealth nanobeacon solution with no treatment: ultrapure water = 1:1, and 2) Stealth nanobeacon homogenized solution: ultrapure water = 1:1. In addition, we also prepared inks by mixing the yellow and magenta inks from a commercial inkjet printer with the homogenized stealth nanobeacon solution at a ratio of 1:1. Inkjet printing was performed using a special inkjet printer. The spatical districation of the SERS signal varied based on the printing conditions were investigated by a Raman microscopy. The printing conditions for the inkjet printer were set at a ϕ15 μm nozzle diameter, a 20 V discharge voltage, and a 1 kHz cycle rate, and the number of shots (i.e., the number of times that a spot is printed) was adjusted. All inkjet printing experiments and observation evaluations were conducted at room temperature in atmospheric air.

Figure 3 shows comparison of inkjet printed surface of a paper with various number of shots N = (a) 100, (b) 50, (c) 30, and (d) 10 to examine the dependence of the printing characteristics on N. By comparing the opitcal photographs in Figs. 3(A) and 3(B), it was found that the shapaes of the printed dots can be discerned when N is 10. As the number of shots increases, the dot shape structures can no longer be distingushed. The results of microscopic Raman mapping at 1600 cm^{-1} peaks of the SERS signal from the nanobeacon shown in Fig. 3(C). Comparing these results with and without homogenising treatment, it was found that the homogenised ink was spatially more uniformly dispersed. Inkjet printing was also possible for mixed inks with yellow and magenta inks. It was found that SERS signals could be detected from these prints even with a simple portable Raman spectrometer with low sensitivity. In addition, it was found that even with a tenfold dilution of the nanobeacon concentration, the SERS signal could be detected by micro Raman spectral mapping, as shown in Fig. 3(D). Successful inkjet printing of nanobeacon-containing inks. This shows promise for development into a new information tracking system.

This work was supported by Innovative Science and Technology Initiative for Security Grant Number JPJ004596, ATLA, Japan.

[1] T. Fukuoka, T. Yasunaga, K. Namura, M. Suzuki, A. Yamaguchi, Advanced Materials Interfaces (2023) 2300157.
[2] T. Fukuoka, T. Yasunaga, K. Namura, M. Suzuki, A. Yamaguchi, Sci. Rep. 12 (2022) 985.

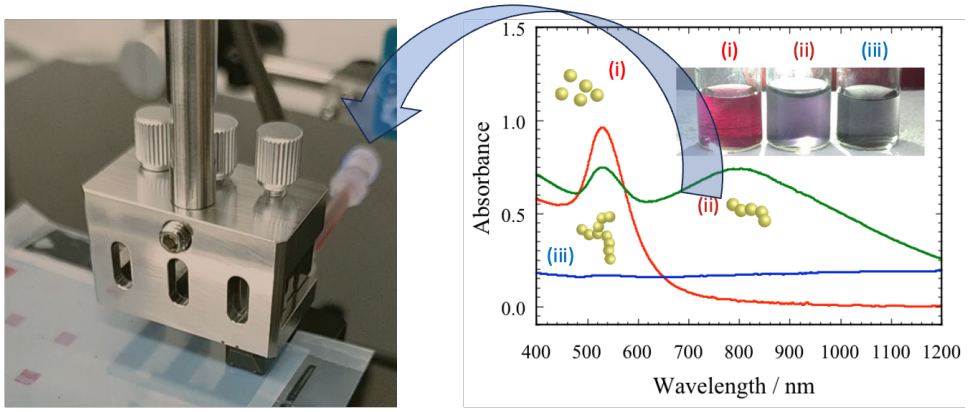

Figure 1. Photograph of inkjet head and optical absorption spectra of SERS active nanostructures. Inkjet printing of (ii) solution.

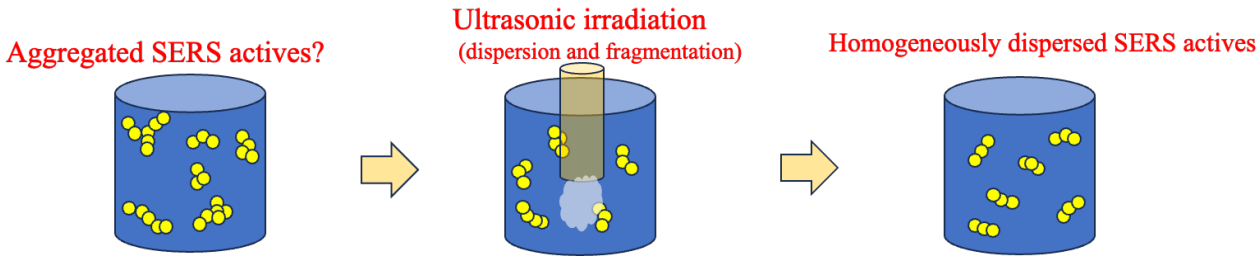

Figure 2. Overview of the homogenisation process with regard to SERS active structures.

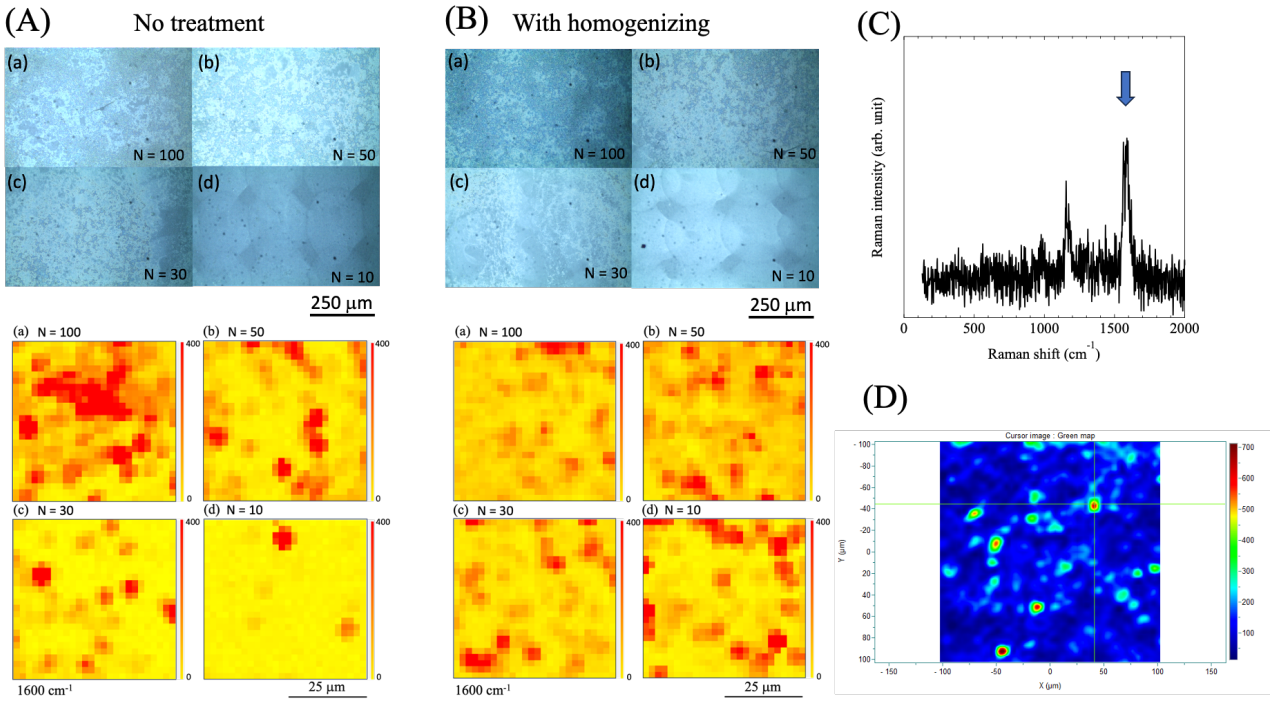

Figure 3. Observation of the inkjet-printed surface by optical microscopy and microscopic Raman mapping: (A) with no treatment (B) with homogenisation treatment (C) Raman spectrum of the SERS active aggregates, microscopic Raman mapping was performed at peak of 1600 cm^{-1} indicated by an arrow. (D) Mapping with another micro-Raman spectroscopy of the tenfold diluted ink.

Oral Session 3D: Devices and Systems

Selective Laser Etching as a Key Enabler of Custom Silica-Based AFM Probes

Koutayba SAADA[a], David BOURRIER[a], Juliette LIGNIERES[a], Etienne DAGUE[a], Laurent MALAQUIN[a]

[a] LAAS-CNRS, Université de Toulouse, CNRS, Toulouse, France
E-mail : laurent.malaquin@laas.fr - etienne.dague@laas.fr

Atomic force microscopy (AFM) is a high-resolution scanning probe technique that enables surface imaging and mechanical property measurements at the nanoscale. The probe acts as a force sensor and nanoscale interaction tool that plays a critical role in the technique's sensitivity and precision. By modifying probe's design, material or functionalisation, AFM can be adapted to a wide range of applications. For instance, high-speed AFM uses short, high-resonance frequency probes to study protein and enzyme dynamics[1]. FluidFM incorporates microchannel probes, enabling controlled liquid delivery, nano-injection, and nano-extraction into and from cells [2], [3].

Conventional fabrication techniques for probes, that rely on silicon or silicon nitride bulk micromachining, generally requires complex fabrication processes associated to low throughput and limited geometric flexibility [4], [5]. These limitations have driven the development of innovative AFM cantilevers made of silica glass through a novel, cost-effective approach that offers benefits such as chemical inertness, biocompatibility, reduced fabrication time and design flexibility due to isotropic etching of the glass to accommodate a wide range of applications. Our innovative approach involved the fabrication using selective laser etching (SLE), a subtractive laser technology capable of producing complex 3D glass structures with micron-level precision. The process consisted in 3 sequential steps: i) laser irradiation, ii) KOH etching, and iii) Ti/Au metallization. It begins by irradiating the transparent material with a focused femtosecond (*fs*) laser beam at 1030 nm, inducing localized modifications. The laser then writes the desired structure spot-by-spot in three dimensions (Fig. 1a). Following *fs* Laser irradiation, the irradiated volume was etched in a 6 mol/l KOH solution at 90°C for 5 hours (Fig. 1b). Upon completion, Ti/Au (10nm/30nm) deposition was performed to enable AFM laser reflection. This process yields a probe ready for integration into AFM system (Fig. 1c).

To accommodate a diverse range of applications, including material surface characterization and imaging of live soft cells, various cantilever dimensions have been fabricated. The cantilever lengths range from 500 µm to 1 mm, widths from 30 to 40 µm and thicknesses from 50 µm down to 1 µm (Fig. 1d, e, f). This dimensional range results in spring constants ranging from 0.02 N/m to 85 N/m that covers the typical range of stiffnesses addressed by current AFM probes. For the tip design, pyramidal probes with heights ranging from 10 µm to 30 µm and tip radii as small as 50 nm have been produced (Fig. 1h, i). Additionally, spherical tips with diameters ranging from 10 to 25 µm were developed (Fig. 1g). To validate the functionality of the cantilevers, topographical measurements, force spectroscopy, and imaging were performed on various calibration gratings and on living cells using both pyramidal and spherical tips. (Fig. 2a,b,c,d) shows the dimensional analysis of the calibration gratings with pitch sizes of 5 µm, and depths of 200 nm. (Fig. 2e,f,g,h) demonstrate the capacity of the spherical tips to investigate the mechanical properties of individual living cells PC3-GFP cells immobilized on a Petri dish. The spherical tip enabled controlled and precise probing of the cellular structures with indentation depth of 1.32 µm and measured cell stifness of 2.4 nN/µm confirming data recently obtained with commercial probes in some of our recent work [6].

These innovative silica glass AFM cantilevers present several key advantages, including ease of chemical functionalization, optical transparency, and biocompatibility, rendering them ideal for biological applications. Additionally, the fabrication approach offers the flexibility to produce cantilevers with a high aspect ratio, low stiffnesses and to integrate tips with customizable geometries, such as pyramidal, spherical, or tapered configurations. Condensing the process into three steps, reduces the fabrication time and cost while minimizing reliance on complex equipment and cleanroom facilities.

[1] T. Ando et al., Annu. Rev. Biophys. 42 (2013) 393–414.
[2] A. Meister et al., Nano Lett. 9 (2009) 2501–2507.
[3] O. Guillaume-Gentil et al., Cell 166 (2016) 506–516.
[4] F. J. Giessibl, Rev. Mod. Phys. 75 (2003) 949–983.
[5] A. S. Algamili et al., Nanoscale Res. Lett. 16 (2021) 16.
[6] O. Thomas-Chemin et al., ACS Appl. Mater. Interfaces 16 (2024) 44504–44517.

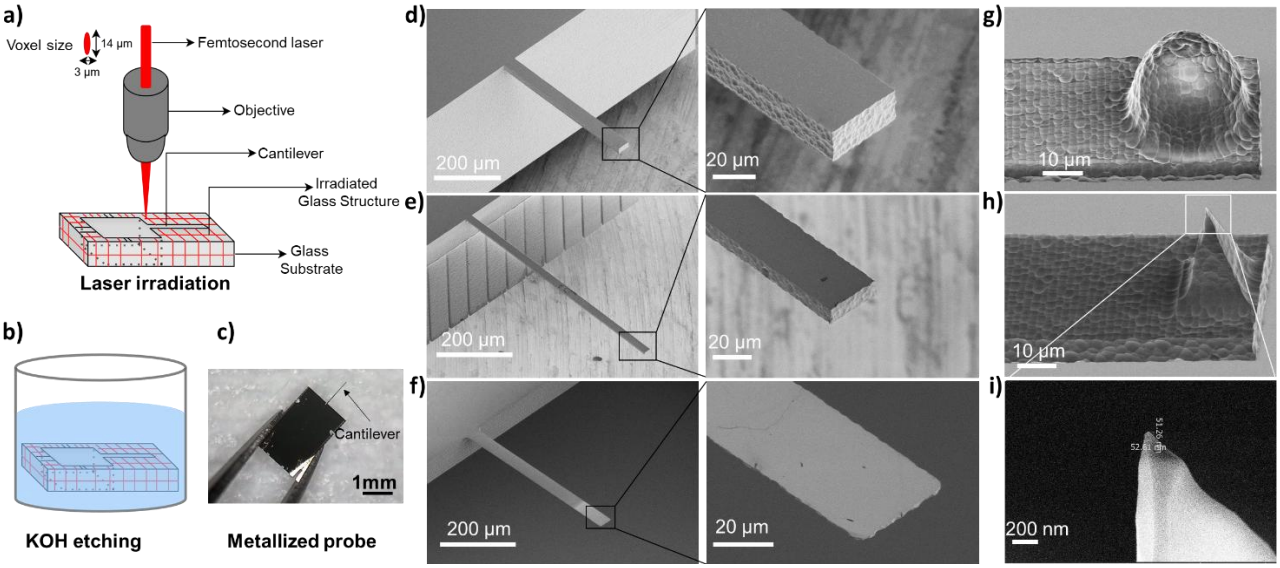

Figura 1 (a) Femtosecond laser writing of the cantilever structure.(b) KOH wet etching process. (c) Entire probe gripped by pliers prior to AFM integration. (d-e-f-g-h-i) SEM images of glass cantilevers: (d) Rectangular cantilever (20 µm thickness, 40 µm width, 500 µm length). (e) Rectangular cantilever (10 µm thickness, 30 µm width, 1 mm length). (f) Rectangular cantilever (1 µm thickness, 40 µm width, 500 µm length). (g) Rectangular cantilever (7 µm thickness, 40 µm width, 1 mm length) with a spherical tip (15 µm diameter).(h) Rectangular cantilever (10 µm thickness, 40 µm width, 1 mm length) with a cylindrical tip (30 µm height). (i) Tip radius (50 nm) of the cantilever shown in (h).

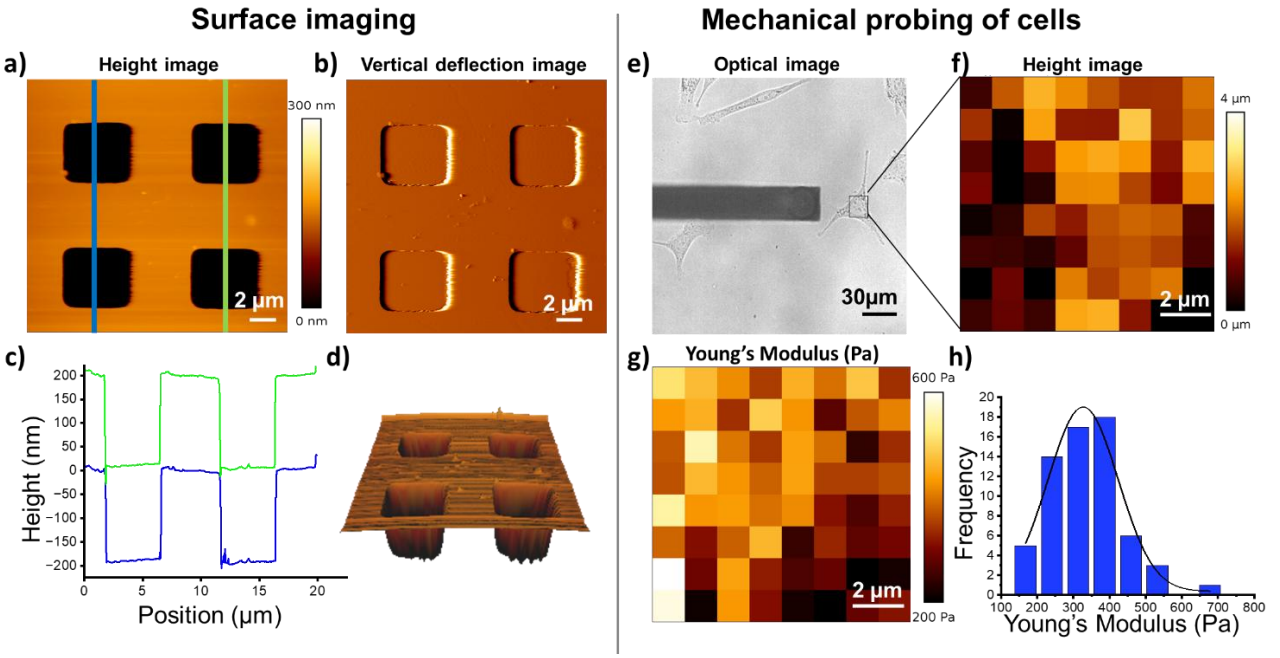

Figura 2 (a–d) Images of the calibration grid (Calibration Gratings, P/N 498-000-026; Digital Instruments, NY) with a 10 µm pitch and 200 nm step height, imaged in contact mode using a glass rectangular cantilever (10 µm thickness, 40 µm width, 1 mm length) with a cylindrical tip (25 µm height) and a spring constant of 0.919 N/m.(a) Height image. (b) Vertical deflection image. (c) Topographical profile along the blue and green lines shown in (a). (d) 3D surface image. Contact mode imaging parameters: setpoint – 2 nN, line rate – 0.8 lines/s, resolution – 512 × 512 pixels. (e–h) Images of a PC3-GFP cell immobilized on a Petri dish acquired using force mapping mode with a glass rectangular cantilever (8 µm thickness, 30 µm width, 1 mm length) with a spherical tip (20 µm diameter) and a spring constant of 0.2 N/m. (e) Optical image showing the cell and the cantilever. (f) Height image (10 × 10 µm²) of the selected cell region indicated by the square in (e). (g) Young's modulus map with an average value of 373 Pa. (h) Quantitative analysis of the cell's young's modulus. Force mapping parameters: setpoint – 3 nN, Z-length – 5 µm, Z-speed – 10 µm/s, contact time – 0.01 s, scan size – 10 µm, resolution – 8 × 8 pixels.

Scalable Piezo-Optomechanical Transducer for Optical Readout of a Superconducting Qubit

P. L. Nguyen [a], T. C. van Thiel [a], M. J. Weaver [a], F. Berto [a], P. Duivestein [a], M. Lemang [a], K. L. Schuurman[a], M. Žemlička [a], F. Hijazi [a], A. C. Bernasconi [a], C. Ferrer [a], E. Cataldo [a], E. Lachman [b], M. Field [b], Y. Mohan[b], F. K. de Vries [c], C. C. Bultink [c], J. C. van Oven [c], J. Y. Mutus [b], R. Stockill [a] & S. Gröblacher [a]

[a] QphoX B.V., Delft, the Netherlands
[b] Rigetti Computing Inc., Berkeley, CA, USA
[c] Qblox B.V., Delft, the Netherlands
e-mail: linh@qphox.eu; rob@qphox.eu; simon@qphox.eu

Key words: Microwave-to-optics transducer, piezo-optomechanical coupling, qubit readout

Quantum computing is rapidly advancing as a key technology of the future, with superconducting qubits, operating at cryogenic temperatures, emerging as promising building blocks [1]. However, scaling remains a challenge, due to limited space within dilution refrigerators [2]. One potential solution to overcome this limitation is using quantum transducers to up-convert the readout signal from a superconducting qubit to the optical domain, removing the need for cryogenic amplification, and routing the signal out of the cryostat via low-thermal conductivity optical fibers. Numerous efforts are ongoing to explore different transduction approaches [3].

In this work, we present a quantum microwave-to-optics transducer that operates by mediating the coupling between microwave and optical photons through a mechanical resonator [4]. We design and fabricate transducers composed of three primary components, as illustrated in Figure 1. The first component is a superconducting resonator that enables the coupling of microwave photons between a 50-Ω transmission line and a high-impedance piezoelectric device. The resonator's frequency is tunable via magnetic field, allowing matching with the mechanical mode frequency of the device. The second part is a piezoelectric block, electrically contacted on both sides and positioned at the end of the microwave resonator. The coupling between microwave and mechanical mode (electromechanical coupling) is achieved via the piezoelectric effect. The last component is a suspended silicon nanobeam with a short phononic waveguide which converts the mechanical mode into an optical signal (optomechanical coupling) using the photoelastic effect. Our transducer enables bidirectional, coherent conversion and offers high scalability, with a footprint of less than 0.15 mm² and a minimal optical pump power.

Figure 2(a) presents the bidirectional microwave-to-optics conversion spectrum for various detunings of the transducer microwave resonator, measured under a continuous 3.1 μW red-detuned optical pump tone. A peak efficiency of -24.8 dB (0.33%) is extracted at 5.1978 GHz, exhibiting minimal sensitivity to the detuning of the microwave resonator over a range of tens of megahertz. We observe a linear increase in efficiency within the range of optical pump powers investigated (Figure 2(c)). The realisation of efficient conversion at the qubit-readout frequency is a result of the large transduction bandwidth, owing to the strong piezoelectric coupling in the device. At the maximum optical power of 31 μW, efficiencies of 4% and 2% are extracted at the peak conversion and qubit readout frequencies, respectively. In addition, high-power qubit readout was performed using microwave signals only and via up-conversion to the optical domain in the transducer, yielding readout fidelities of 87% and 81%, respectively, as shown in Figure 3(a-d). Characterization of T_1 and T_2* reveals no statistical change with 60 dB of isolation between the transducer and qubit readout resonator (Figure 3(e,f)), highlighting the importance of a modular approach of qubit and transduction technology for the practical scaling of quantum computers.

[1] M. Kjaergaard et al., Superconducting Qubits: Current State of Play, Annual Review of Condensed Matter Physics, 11 (2020), 369–395.
[2] H. K. Warner et al., Coherent control of a superconducting qubit using light, Nat. Phys. (2025).
[3] N. Lauk et al., Perspectives on Quantum Transduction, Quantum Sci. Technol. 5(2) (2020).
[4] M. J. Weaver et al., An Integrated Microwave-to-Optics Interface for Scalable Quantum Computing. Nat. Nanotechnol. 19 (2) (2024), 166–172.

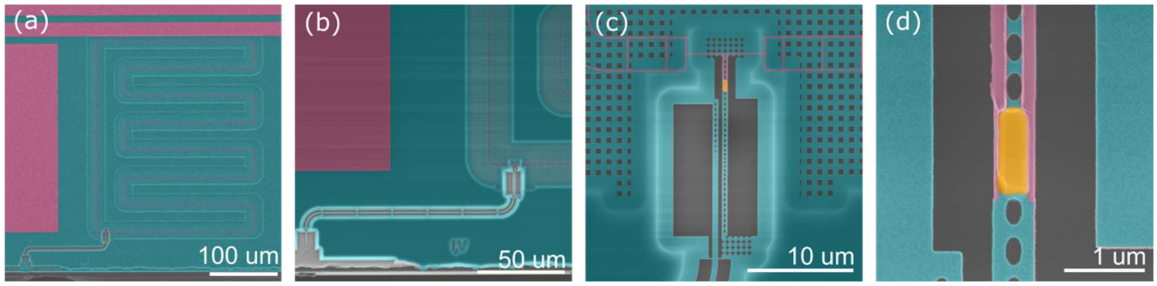

Figure 1. Scanning electron microscope images of a representative transducer with increasing magnification. The microwave resonator and the electrodes are colored in magenta. The piezoelectric block and silicon nanobeam are shown in yellow and cyan, respectively.

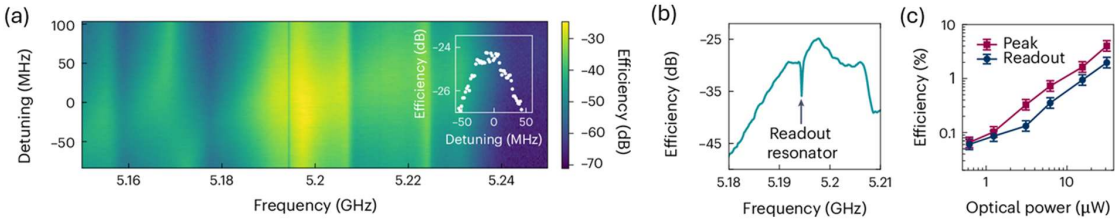

Figure 2. Transducer performance. (a) Continuous-tone bidirectional transduction efficiency under an optical pump power of 3.1 μW, plotted as a function of signal frequency and of microwave resonator detuning from the peak transduction frequency. The inset depicts a vertical linecut crossing the point of optimum efficiency. (b) A horizontal linecut shows a dip at 5.1944 GHz which corresponds to the readout resonator of the qubit. (c) Transduction efficiency as a function of optical pump power: the purple and blue lines represent the peak conversion efficiency and the efficiency at the qubit readout frequency, respectively.

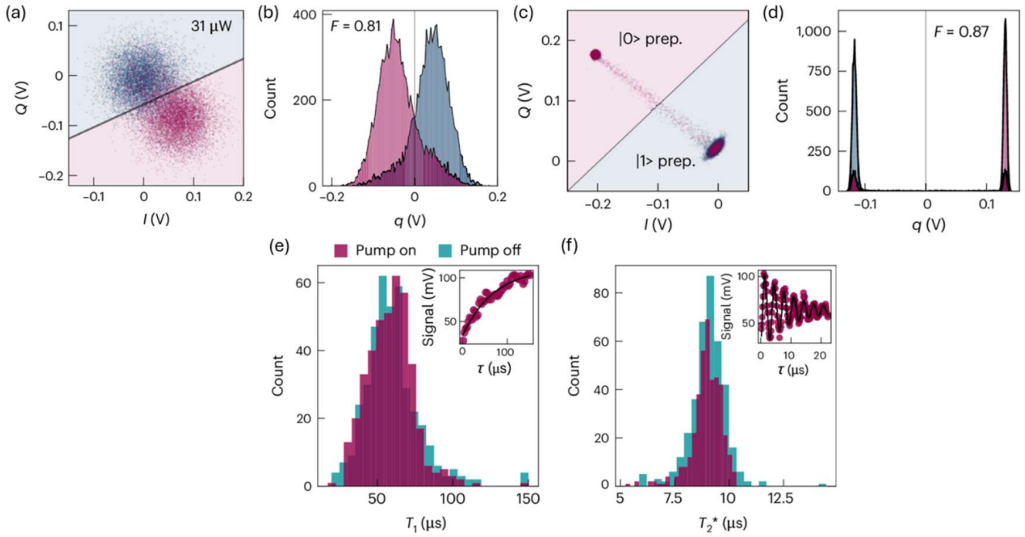

Figure 3. Statistical characterization of 10,000 single-shot microwave readout measurements (a), and optical readout measurements under 31 μW optical pump power (c) in phase space. The data from (a) and (c) are binned by the distance to a linear decision boundary q to obtain (b) and (d) respectively. (e,f) Absence of pump-induced decoherence. Statistical distributions of 401 T_1 measurements (e), and 401 T_2* measurements (f) with a 3.1 μW optical pump on (purple) and off (cyan). The insets in both panels depict respective example curves with the optical pump on.

Nonlinear resonators based on nano optomechanical metamaterials

Ting Hou [a], Lifeng Bao [a], Jun-Yu Ou [a], Xin Zhou [b], Nobuhiko Nishiyama [c], and Yoshishige Tsuchiya [a]
[a] University of Southampton, Southampton, SO17 1BJ, United Kingdom
[b] Université de Lille, CNRS, F-59000 Lille, France
[c] Institute of Science Tokyo, Tokyo 152-8550, Japan
e-mail: T.Hou@soton.ac.uk

Technology to integrate micro- and nano-electromechanical systems (MEMS/NEMS) with photonics on the semiconductor platform is promising for novel functional devices in the next generation. A good example is the emergence of Nano-Opto-Electro-Mechanical Systems (NOEMS) [1] where better controllability of light signals at high speed and low power consumption is expected. On the other hand, nonlinear response of nanoscale devices is attracting much attention in terms of its usefulness to improve the performance of specific devices such as resonant mass sensors [2] or of the requirement for particular applications such as coupled-oscillator-based physical reservoir computing [3]. Ben et al. [4] have observed and analysed the nonlinear resonance of Si NEMS beam resonators, while a general issue for practical application is the low energy efficiency of electromechanical transduction. In this study, we propose a novel nonlinear optomechanical resonator integrated with nanophotonic metamaterials as an attempt to improve signal transduction efficiency of nanoscale mechanical motion and investigate its nonlinear characteristics.

This work is based on the technology developed Ou et al [5]. The nano-optomechanical metamaterial shown in Figure 1a consists of a continuous plasmonic metallic "meander near the wire" pattern fabricated on a grid of flexible dielectric strings. These strings, nanobeams have picogram-scale mass and mechanical resonances in the megahertz range. When a few volts are applied between adjacent nanobeams, an electrostatic attraction of a few nano-Newtons is generated. This force pulls the nanobeams closer together within the plane of the metamaterial, narrowing the gap between them. This mechanical movement significantly alters the resonant optical behavior of the meander structure by influencing the excitation of a plasmonic mode. As a result, the metamaterial enables reversible modulation of transmission and reflection with megahertz bandwidth. Figure 1b and 1c shows the scanning electron microscope images of an array of nano-optomechanical metamaterial and a pair of double-beam resonators.

The finite element electromagnetic simulation of the optical reflection spectra of the designed nanostructure with varying displacement is shown in Figure 2a where the reflection spectra were calculated for displacements ranging from 0 nm to 100 nm. These simulations provide insight into the modulation behaviour of the optical reflective response as the structural gap changes. The two standard telecom wavelengths of 1310 nm and 1550 nm are indicated as the red dashed line. Figure 2b plots the normalized reflection intensity as a function of displacement at the two selected wavelengths, which is related to the sensitivity. The inset images in Figure 2b provide further insight into plasmonic mechanisms by showing simulated electric field distributions for structures with gaps of 125 nm and 25 nm. As the gap decreases, the confinement of the plasmonic field intensifies, resulting in a significant increase in the field power strength due to stronger near-field coupling between the nanostructures. Figure 3 displays the reflective optical intensity amplitude–frequency response curves with different excitation voltages, revealing characteristic signatures of nonlinear dynamic behaviour. At a low excitation voltage of 1.4 V (Figure 3a), the system exhibits a symmetric Lorentzian resonance profile. When the driving voltage is increased to 1.5 V, as shown in Figure 3b, the system begins to exhibit nonlinear features, represented as an asymmetric line shape of the resonance in the optical reflection intensity and emerging hysteresis depending on the direction of the frequency sweep. Note that the appearance of the asymmetry and hysteric behaviour in Figure 3b is different from what is expected from the solution of the nonlinear Duffing oscillator equation, which might be caused by the complexity of the resonator structure. The demonstrated nonlinear dynamic response is a foundational property for future applications of NOEMS in integrated photonic circuits or optical information processing.

Acknowledgements: This work is partially supported by Chist-Era NOEMIA (CHIST-ERA-21-NOEMS-004) and EPSRC-JST UK-Japan Semiconductor HetMEPS.

References: [1] L. Midolo et al., Nature Nanotechnology 13 (2018) 11-18.[2] N. Kacem et al., J. Micromech. Microeng. 20 (2010) 045023. [3] J. C. Coulombe et al., PLoS One, 12 (2017) e0178663. [4] F. Ben et al., Micro and Nano Engineering 19 (2023) 100212. [5] J.-Y.Ou et al., Nature Nanotechnology 8 (2013) 252-255.

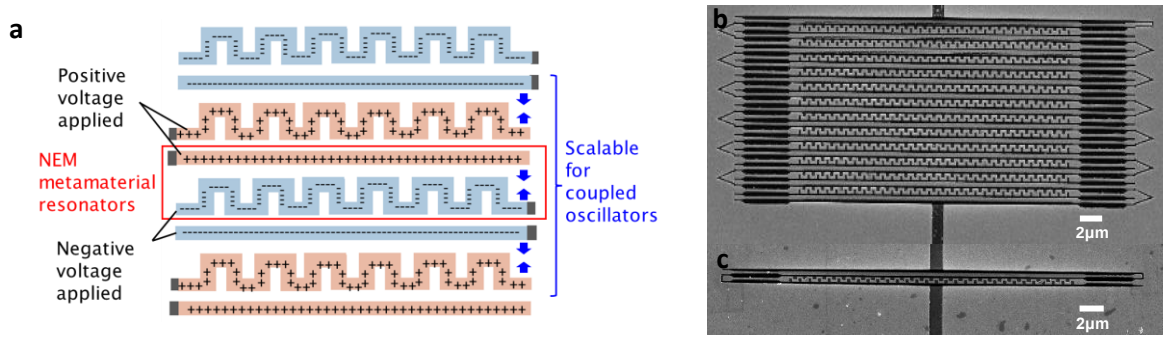

Figure 1. (a) A schematic diagram of a coupled oscillator based on nano-optomechanical metamaterial. SEM image of a fabricated (b) array of 12 nano-optomechanical metamaterial resonators and (c) a pair of metamaterial resonators.

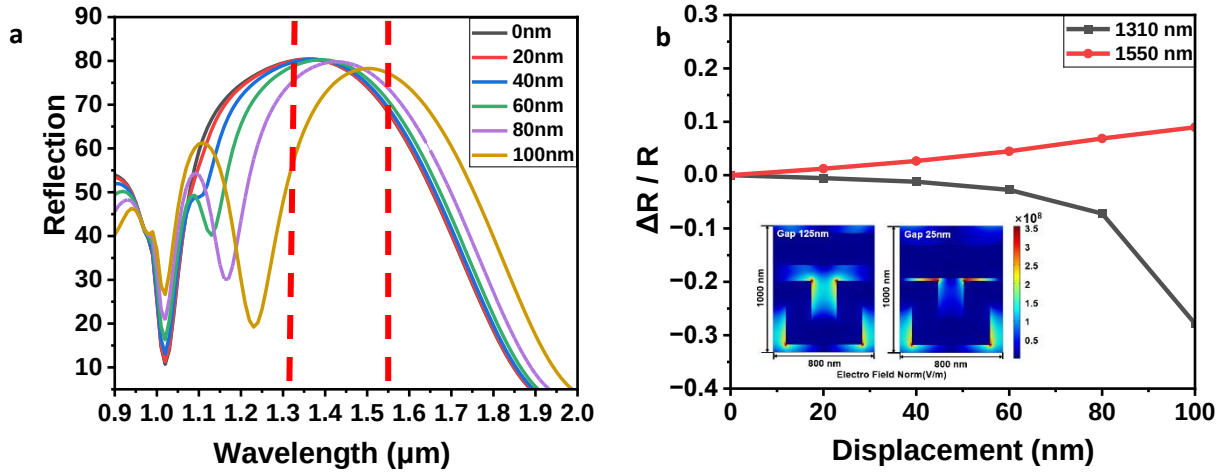

Figure 2. (a) Simulated reflection spectra as the displacements of the beam are changed from 0 to 100 nm, (b) The normalised reflection for each wavelength relevant to the displacement sensitivity, inset figure is simulated plasmonic field distribution for a device with the gap of 125 nm and 25 nm.

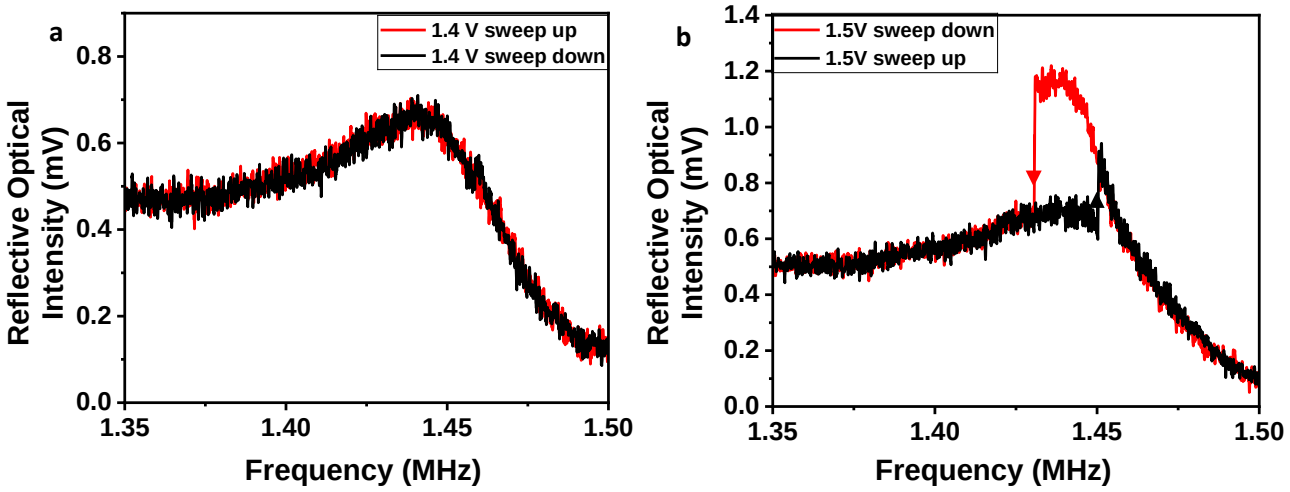

Figure 3. Reflective optical response of the single nano-optomechanical metamaterial resonator to a drive frequency sweep for a fixed drive amplitude of 1.4V(a) and 1.5V(b).

Carbon-based contacts for integrated nanoelectromechanical switches

J. Bolten[a], B. Chmielak[a], L. Ehlert[a], E. Worsey[b], Y. Li[c], F. Niklaus[c], D. Pamunuwa[b], S. J. Bleiker[c], M.C. Lemme[a,d]

[a] AMO GmbH, 52074 Aachen, Germany
[b] School of Electrical, Electronic and Mechanical Engineering, University of Bristol, Bristol BS8 1UB, U.K.,
[c] Division of Micro and Nanosystems, Royal Institute of Technology (KTH), Stockholm 114 28, Sweden
[d] Chair of Electronic Devices, RWHT Aachen University, 52074 Aachen, Germany

e-mail: bolten@amo.de

Edge computing, i.e., collecting and processing data where it is created, is an essential element in energy-efficient and sustainable transformation into a data-driven society.

Complementary Metal Oxide Semiconductor (CMOS) technology enables such computing applications; however, CMOS is unsuitable for harsh environments often found in industrial applications. Furthermore, edge computing often has extreme demands on energy efficiency, beyond even what low-power CMOS circuits can deliver. Nanoelectromechanical system (NEMS) based electronics utilizes mechanical switches operated through electrostatic actuation. They exhibit high resilience to extreme temperatures and radiation and can have zero standby power [1].

NEMS electronics can be employed where environmental conditions prohibit CMOS devices and leakage power limits device operation [2]. One prerequisite for the widespread use of NEMS switches in harsh environments is a reliable contact material that can withstand millions of switching cycles. Nanocrystalline graphite (NCG) coating has enabled microelectromechanical system (MEMS) switches with a critical dimension (CD) of 2 µm, achieving over 2.8 million fast, hot-switching cycles [3]. Here, we demonstrate NCG as a NEMS switch contact material with CDs below 200 nm.

We used a 3-terminal NEMS switch design and a fabrication and integration strategy adopted from [4] (see schematic in Fig. 1). The switches were made from silicon-on-insulator (SOI) wafers with a device layer that is 250 nm thick. After patterning and structuring using inductively coupled plasma reactive ion etching (ICP-RIE), NCG was deposited using chemical vapor deposition. The process was tuned for a high sidewall deposition rate, adapted from [3]. In our NEMS switch design, the actuator beam moves in-plane so that the beam tips form the contact surfaces of the devices. Hence, a thicker NCG layer on the sidewalls should significantly increase the number of hot-switching cycles. The chamber pressure was the most critical parameter to achieve good sidewall coverage, with higher pressures resulting in an increased sidewall deposition rate. The optimum chamber pressure was 2000 mTorr, which resulted in a top surface to sidewall deposition ratio of the NCG of ~1:3. Increasing the chamber pressure further led to unstable processing conditions. The resulting deposition profile for the optimum chamber pressure is shown in Fig. 2.

The samples were then further processed using an anisotropic two-step ICP-RIE process to remove the NCG on the top surfaces while maintaining good sidewall coverage. Therefore, first a purely physical Ar-based etching step was used to remove overhanging NCG features formed at the top corners of the Si structures (Fig. 3). A second, mixed physical/chemical Ar/O_2 process step was then performed to etch the remaining NCG from all top surfaces. The etching time for the first step was twice that of the second step for best results. The optimum flow ratio between Ar and O_2 in the second RIE was 1:2.

The NEMS switches were finalized with several process steps, including a vapor phase HF release etch. A fully fabricated 7-terminal switch is shown in the scanning electron microscope (SEM) image in Fig. 4. The switches were electrically characterized, as shown in the example of drain current versus gate voltage (I-V) curve for one switching cycle in Fig. 5.

This demonstrates that NCG is a viable contact solution not only for larger MEMS switches with CDs of a few micrometers but also for NEMS devices with much smaller CDs in the range of a few 100 nm, hence offering the potential to be used in high density integrated NEMS circuitry.

This work was supported by the i-EDGE project, which has received funding from the European Union (grant number 101092018), the Swiss State Secretariat for Education, Research and Innovation (SERI) and UK Research and Innovation (UKRI) under the UK government's Horizon Europe funding guarantee (grant numbers 10061130 and 10063023).

[1] Y. Li *et al.*, "Integrated 4-terminal single-contact nanoelectromechanical relays implemented in a silicon-on-insulator foundry process," *Nanoscale*, vol. 15, no. 43, pp. 17335–17341, 2023, doi: 10.1039/D3NR03429A.
[2] S. Ha *et. al.*, "Compact NEMS FPGA design for harsh environment and low power requirement," in *2013 Transducers & Eurosensors XXVII: The 17th International Conference on Solid-State Sensors, Actuators and Microsystems (TRANSDUCERS & EUROSENSORS XXVII)*, Barcelona, Spain: IEEE, Jun. 2013, pp. 2369–2372. doi: 10.1109/Transducers.2013.6627282.
[3] S. Rana *et al.*, "Nano-crystalline graphite for reliability improvement in MEM relay contacts," *Carbon*, vol. 133, pp. 193–199, Jul. 2018, doi: 10.1016/j.carbon.2018.03.011.
[4] D. Pamunuwa *et al.*, "Hardware Platform for Edge Computing Based on Nanoelectromechanical Relays," in *2023 22nd International Conference on Solid-State Sensors, Actuators and Microsystems (Transducers)*, Jun. 2023, pp. 537–541. Accessed: Apr. 22, 2025. [Online]. Available: https://ieeexplore.ieee.org/abstract/document/10516972/authors

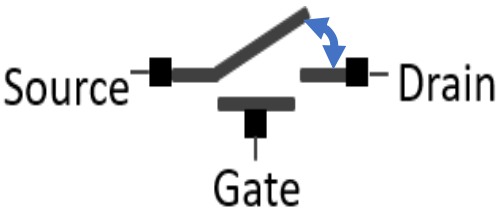

Figure 1. Schematic of a 3-terminal NEMS switch.

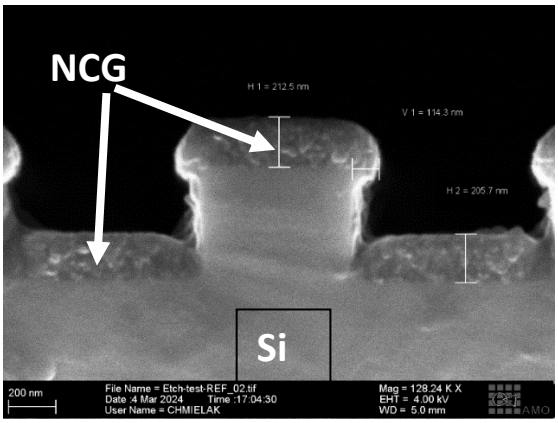

Figure 2. SEM cross sectional micrograph of an NCG layer after deposition on a test sample.

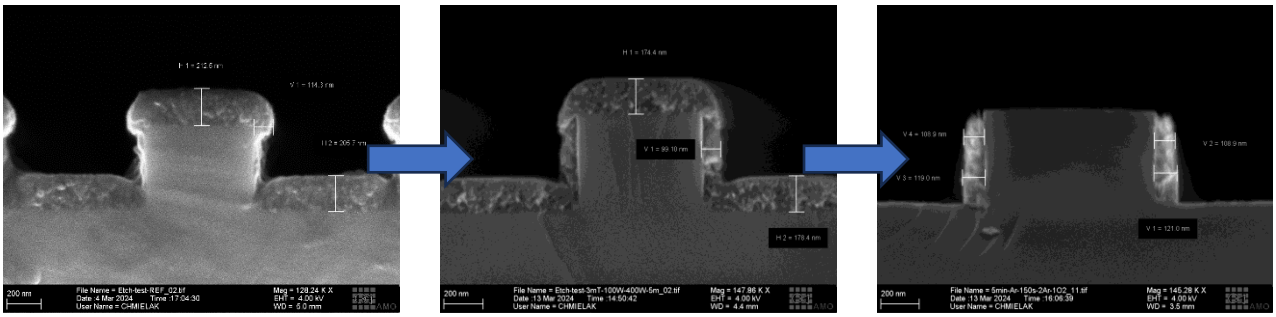

Figure 3. Process sequence of the two-step NCG ICP-RIE etching process. From left to right: Initial NCG profile after deposition, profile after first purely physical Ar etching step, profile after second mixed Ar/O_2 etching step.

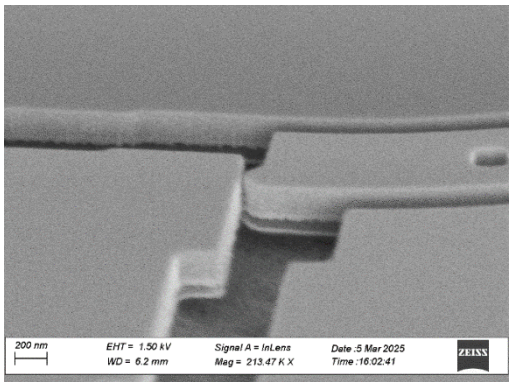

Figure 4. Semi-cross-sectional SEM micrograph of a functional 7-terminal NEMS switch with NCG contact coatings after vHF release etch.

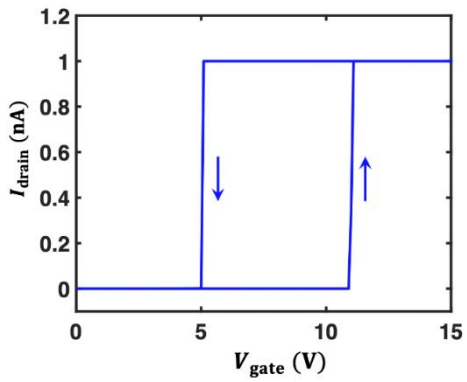

Figure 5. Result of initial electrical functionality test.

Poster Session 2

Auxiliary-Ring-Assisted Fabrication of Hard X-ray Photon Sieves with Low Resist Wettability

Qiucheng Chen, Qingxin Wu, Hao Quan, Xunjia Zhao, Jinyu Guo, Kangping Liu and Yifang Chen*

Nanolithography and Application Research Group, Shanghai Key Laboratory of Metasurfaces for Light Manipulation, School of Information Science and Technology, Fudan University, Shanghai, China

e-mail: yifangchen@fudan.edu.cn

Keywords: photon sieve, overlay lithography, low-wettability structures, auxiliary ring, hard X-ray optics

Photon sieves as diffractive optics are becoming more and more important for high-resolution hard X-ray imaging, offering design flexibility and compatibility with synchrotron beamlines. To enhance image contrast and suppress background noise, central and outer blocking layers are often applied. A straightforward approach is to define both the sieve and stop layers in a single lithographic step, but this can be limited by strong backscattered electron and extended writing time over large areas. Alternatively, two-step electron beam lithography often fails on dense, high-aspect-ratio gold structures due to poor resist wettability, leading to incomplete coverage (Fig. 2).

This work presents a ring-assisted two-step fabrication strategy to overcome these technical issues. A key innovation is the introduction of a 30 μm-wide gold auxiliary ring positioned concentrically around the photon sieve (Fig. 3). This low-aspect-ratio structure improves resist wettability and enables structural compatibility with overlay processing. By decoupling the high-resolution sieve patterning from the large-area stop layer definition, the second lithography step can be performed using a chemically amplified resist, significantly improving fabrication throughput. The specific fabrication steps are detailed as follows (Fig. 1).

In the first step, a 1.9 μm-thick PMMA resist (MW: 350 k) was spin-coated on a 100 nm-thick silicon nitride membrane and baked at 180 °C for 5 minutes. Electron beam lithography was performed at 100 kV with a 7 nm Gaussian beam and 500 pA current, using a dose of 1500 μC/cm². After development in MIBK:IPA (1:3) at 23 °C, gold was electroplated in a $K_3Au(SO_3)_2$ solution at 50 °C with a constant 3 μA current. The resist was stripped in acetone at 50 °C, yielding a photon sieve with a central stop. (Fig. 4(a-b))

In the second step, a 2 μm-thick UV5 resist was applied and prebaked at 115 °C for 90 seconds. Using the membrane edge for alignment, a second e-beam exposure was performed under the same beam conditions with a reduced dose of 30 μC/cm². Post-exposure bake and development were conducted at 115 °C and in TMAH:H_2O (1:8) for 60 seconds, respectively. A second gold electroplating step was then carried out under the same current, followed by resist removal in acetone at 50 °C. This method enabled successful overlay of the outer stop onto the photon sieve, despite the poor resist wettability on the high-aspect-ratio gold structures.

Using this method, a photon sieve with a minimum pillar diameter of 140 nm and a height of 1.8 μm was successfully fabricated (Fig. 5), and the overlay of blocking layers onto these low-wettability structures was reliably achieved. After the second exposure and development, the auxiliary ring and UV5 resist effectively protected the gold pillars (Fig. 4(c-d)). Notably, the process does not require conventional alignment marks; the membrane edge served as a reference, and the overlay error was effectively compensated by the auxiliary ring. Furthermore, the use of a chemically amplified resist for defining the large-area outer stop reduced the second exposure time to just 15 minutes, greatly enhancing fabrication efficiency without compromising accuracy.

In summary, the proposed auxiliary-ring-assisted two-step process enables accurate and efficient fabrication of photon sieves with integrated blocking layers, even on low-wettability, high-aspect-ratio structures. This method is fully compatible with existing lithography infrastructure and can be extended to other nanostructured devices requiring multilayer alignment and resist protection.

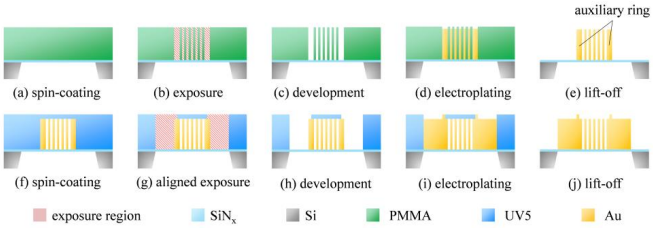

Fig. 1. The schematic of the process flow.

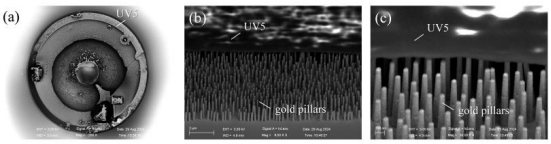

Fig. 2. SEM images of aligned overlay on low-wettability gold pillars.

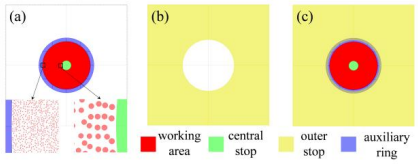

Fig. 3. Design layout of auxiliary ring, central stop and outer stop.

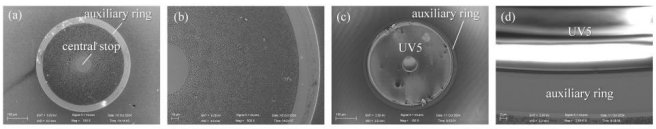

Fig. 4. Fabrication of a photon sieve assisted by auxiliary ring. (a–b) SEM images after the first EBL and gold electroplating. (c–d) SEM images after the second exposure and development.

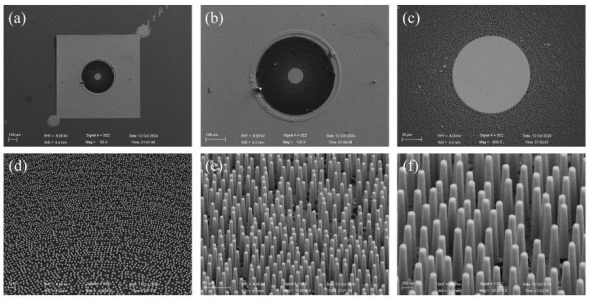

Fig. 5. SEM images of a photon sieve with central and outer stops.

Electron beam-Simulation collaborative fabrication of zone plates with gradient duty cycle

Xunjia Zhao, Hao Quan, Qiucheng Chen, Qingxin Wu, Wentao Yuan, Shuoqiu Tian, Kangping Liu, Jinyu Guo, and Yifang Chen*

Nanolithography and Application Research Group, School of Information Science and Technology, Fudan University, Shanghai, China; Shanghai Key Laboratory of Metasurfaces for Light Manipulation, Fudan University, Shanghai, China.
e-mail: yifangchen@fudan.edu.cn

Keywords: X-ray Fresnel zone plate, focusing/imaging efficiency, duty circle ratio, simulation, electron beam lithography,

Despite nanofabrication technology has advanced for X-ray Fresnel zone plates from hundreds nm of the outermost zone width down to sub-10 nm, extremely limited diffraction efficiency is still a big issue. For example, for the 100 nm resolution zone plate, the efficiency is merely around 5%. It has always been the bottle-neck to the technical development and applications of X ray microscopy as a whole because of the low efficiency. Enhance the resolution as well as the efficiency at the same time is urgently needed. The limited efficiency is generally caused by limited zone plate height, the zone material defects, the rectangular zone shape and the imperfection in nanofabrication.

This work tackles the efficiency issue by focusing on the duty circle ratio (the ratio of the outmost zone width/the air gap), which is one of the key factors in determining the efficiency. In the fabrication of gold-based Fresnel zone plates, systematic investigations into the mechanisms of duty cycle shift caused by imperfection in electron beam lithography (EBL) and e-beam resist thermal reflow were conducted, using the software of TRACER for electron trajectory simulation and LAB for resist profile modeling. This approach enables precise control and fabrication of zone plates with gradient duty cycles (1:1→4:1). Furthermore, employing the Beam Propagation Method (BPM) to simulate diffraction optical fields of zone plates with varying duty cycles reveals the influence mechanisms of duty cycle variations (within 1:1-5:1 range) on focal spot positions and focusing efficiency. Figure1 presents the fabricated 100 nm hard X-ray zone plates with 1.3 μm height and the 1:1 duty cycle. Figure 2 presents the zone plates with various duty cycle from 1:1 up to 5:1 for our experimental study of duty cycle dependent efficiency. Experimental verification is still underway and the results shall be presented elsewhere.

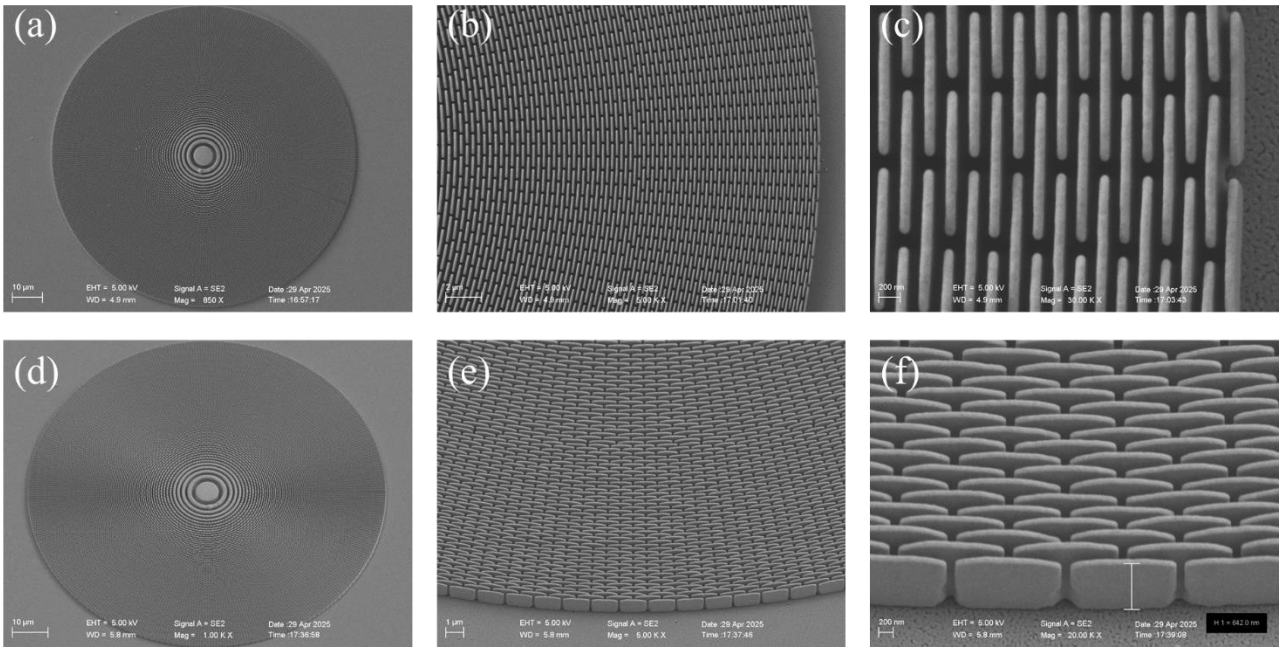

Figure 1. SEM images of the fabricated gold-based 100 nm zone plate.

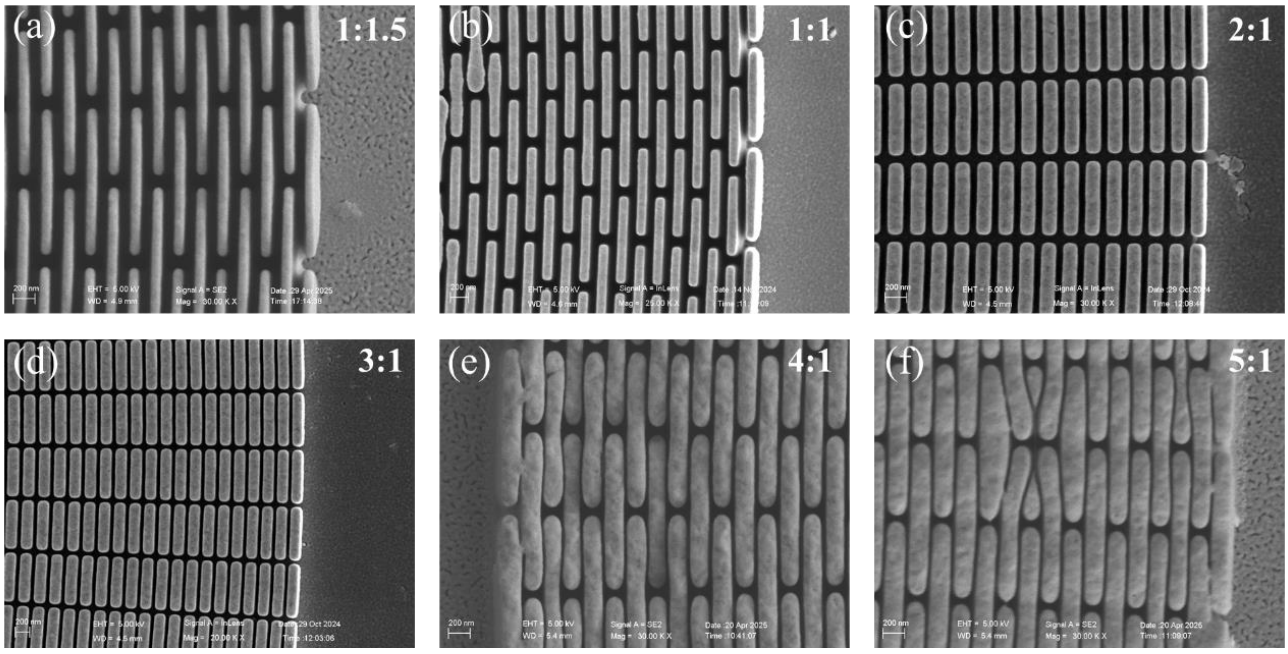

Figure 2. SEM images of the fabricated gold-based 100 nm zone plates with gradient duty cycles.

Room temperature Au-Au die bonding in ambient air via N_2 plasma treatment

Fan Yunhan, Kosei Matsunobu, Ryo Takigawa

Graduate School of Information Science and Electrical Engineering, Kyushu University, 7-3-1 Motooka, Nishi-ku, Fukuoka 819-0395, Japan

e-mail: fan.yunhan.627@m.kyushu-u.ac.jp

Due to the excellent property of Au being resistant to oxidation in atmospheric conditions, the low-temperature bonding technology based on surface activated bonding methods becomes possible in ambient atmospheric condition. This Au-Au bonding technology has been applied in the packaging of MEMS, electronics, and photonics devices [1,2]. Typically, Ar plasma treatment is commonly used as a surface activation for Au-Au bonding. To date, the use of surface activated direct bonding method with Ar plasma treatment at room temperature in ambient air using Au ultrathin films was recently shown to result in reliable Au–Au bonding [3]. In additions, comparative study of Ar and O_2 plasma treatments has been reported, and the effectiveness of Ar plasma treatments was verified. Here, we focus on ambient room temperature Au-Au die bonding via N_2 plasma treatment for surface activation of Au thin film. In addition, its bond quality was investigated in details.

The samples used in bonding experiment were 10 mm-square or 6 mm-square Si chips. On the surface of the 10 mm square chip, 4 nm-thick Ti and 50 nm-thick Au films were formed by the standard sputtering. On the 6 mm squared chip, the patterned 4 nm-thick Ti and 50 nm-thick Au films with a diameter of 4.5 mm were formed by conventional photolithography and sputtering. The bonding experiment is as followed. Firstly, N_2 plasma treatment was performed to remove the organic contaminants on Au surface before bonding. Then, bonding experiment was carried out at room temperature with the bonding pressure of 12.6 MPa in ambient air using a die bonder. Au-Au die bonding was successfully achieved at ambient room temperature using N_2 plasma treatment (Plasma power: 100 W). Atomic Force Microscope (AFM) analysis was used to measure the surface morphology of Au films before and after N_2 plasma treatments, as shown in **Figure 1(a)** and **Figure 2**. These results revealed that N_2 plasma treatment had a slight impact on the surface roughness. Grain size on the bonding surface has an important influence on room temperature direct bonding, proving that the larger the grain size, the stronger the bonding strength [4]. Figure 1 (b) shows the grain size of Au films before and after N_2 plasma treatment were estimated based on the AFM images, as shown in **Figure 1(b)**. It is confirmed that the grain size decreases with increasing plasma irradiation time. Next, the bonding experiment was carried out for 3 times using a die bonder, and the shear strength was measured, and the bond strength was measured by the die shear tests, whose result is shown in **Figure 3**. In the plasma irradiation time of 120 s, the strong bonding strength could not be achieved since the surface roughness increased and the grain size decreased. On the other hands, the plasma irradiation time of 120s demonstrated that the bond strength exceeded 68 MPa, indicating the sufficient bond strength for device applications.

These results suggest the potential that surface activated bonding method with N_2 plasma treatment is effective for room temperature direct bonding of Au ultrathin films.

Acknowledgement

Part of this work was financially supported by JSPS KAKENHI (Grant Numbers JP 24H00318 and JP21KK0255) and JST CREST (Grant Number JPMJCR2103). and JST CRONOS (Grant Number JPMJCS24N5).

References

[1] E Higurashi et al., IEEE Journal of Selected Topics in Quantum Electronics.15 (2009) 1500.
[2] R Takigawa et al., IEEE Journal of Selected Topics in Quantum Electronics. 17 (2011) 652.
[3] M Yamamoto et al., Micromachines. 10 (2019) 119.
[4] H. Takagi et al., Jpn. J. Appl. Phys. 37 (1998) 4197.

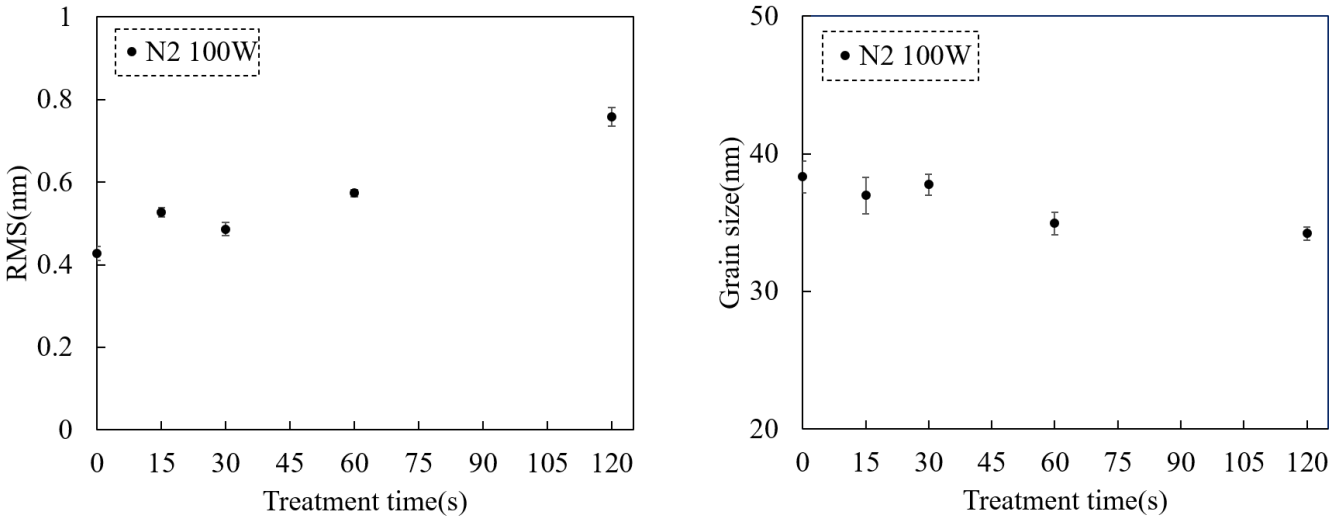

(a) (b)

Figure 1. (a) Measured surface roughness vs. N_2 plasma treatment time
(b) Measured surface grain size vs. N_2 plasma treatment time

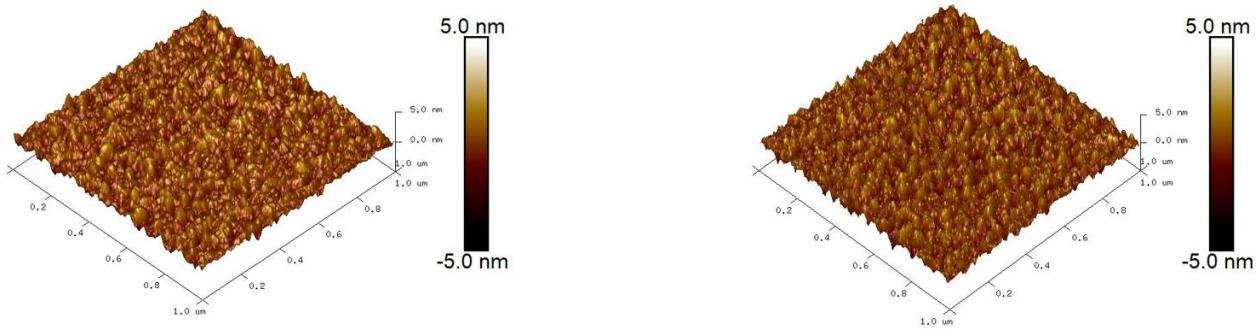

RMS: 0.427nm RMS: 0.527nm

(a) (b)

Figure 2. AFM images of Au thin films (a) Untreatment, (b) Plasma treatment time: 15s.

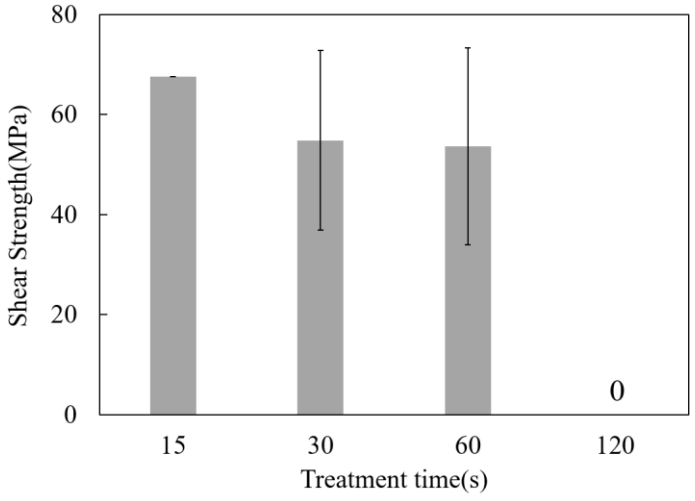

Figure 3. Measured shear strength vs. plasma treatment time

Simulation-guided interpretation of scanning electron microscope images

J. Jin [a], T. Fliervoet [a,b], C.W.Hagen [a]

[a] Delft university of technology, fac. Applied sciences, dept. imaging physics, Lorentzweg 1, 2628 CJ Delft, The Netherlands
[b] ASML Research, De Run 6501, 5504 DR Veldhoven, The Netherlands
e-mail: j.jin-1@tudelft.nl

Keywords: Monte Carlo simulation, SEM, electron-matter interaction, electron yields, low energy scattering, Nebula

To reliably interpret scanning electron microscope (SEM) images, accurate knowledge is needed of the interaction of electrons with matter. The progressive miniaturization of semiconductor devices for example has increased the importance of such electron beam inspection and metrology technology. We have developed an open-source Monte Carlo simulation tool, Nebula [1], intended to simulate SEM images. The tool contains the best possible physics models to describe electron scattering in materials, such as the Penn model for inelastic scattering, Mott cross sections for high energy elastic scattering (> 200 eV), electron-acoustic phonon scattering for low energies (< 100 eV), and a quantum mechanical boundary crossing model. Despite this, there is still room for improvement, for example concerning the low-energy scattering range (< 100 eV), as in this range certain model assumptions break down, other potentially important physics models are missing, and models disagree with each other (see Figure 1). These issues lead to noticeable deviations between simulated and experimental results and thus the unreliability of the simulator. For instance, the cross sections for the interaction of electrons with acoustic phonons proposed by different authors [2,3,4] differs by up to an order of magnitude (Fig. 1b), leading to different simulated low-energy SEM images. Further, band structure related effects may become increasingly important to take into account at lower energies, whereas Nebula currently contains a free electron model for all materials.

Before implementing more detailed physics models, we can already judge the effect of altering the various scattering cross sections in the current version of Nebula on simulated electron yields / images, by artificially modifying the calculated electron mean free paths (MFPs) to mimic the deviations between models. We simulated the total electron yield (TEY) for gold at 1 keV primary energy, applying multiplication factors to three different scattering models, mimicking differences between various models in literature (Figure 2). Gold was chosen because it is a conductive metal that does not easily form oxide layers, as secondary electron emission yields are highly affected by surface composition [6]. We found that it is hard to find reliable experimental TEY data in mutual agreement [5,6,7], and therefore it is also hard to conclude which physics models need most attention to improve. We also evaluated the effects of model uncertainty on simulated SEM images, by simulating 100 eV landing energy images of a flat silicon sample with holes of varying edge profile, depth and side-wall angle (Figure 3). The different modifications to the MFPs result in noticeably different images, and in particular the measured average grey values in the holes deviates significantly. This leads to differences in for example the measured critical dimension (CD), i.e. diameter of the holes. In addition, we will present data on the influence of the low-energy physics model choices on electron energy spectra, angular and spatial emission distributions and electron trajectories inside the sample.

We conclude that it is imperative to work on better low-energy scattering models to obtain more reliable simulated SEM images and with that a better fundamental understanding of real SEM images.

[1] Nebula (https://nebula-simulator.github.io). Published as L. van Kessel and C.W. Hagen, SoftwareX **12**, 100605 (2020).
[2] Schreiber, E. and Fitting, H.-J. (2002). *J. Electron Spectrosc.*, *124*, 25–37.
[3] Akkerman, A. and Murat, M. (2015). *NIM B*, *350*, 49–54. https://doi.org/10.1016/j.nimb.2015.03.024
[4] Salvat, F., Jablonski, A., Powell, C. J. (2005). *Computer Physics Communications*, *165*, 157–190.
[5] Walker, C. G. H. et al. (2008). *Scanning*, *30*, 365–380. https://doi.org/10.1002/sca.20124
[6] He, Y. et al. (2020). *Applied Surface Science*, *520*, 146320. https://doi.org/10.1016/j.apsusc.2020.146320
[7] Bronstein I. M. and Fraiman, B.S. (1969), "Vtorichnaya Elektronnaya Emissiya", (Nauka: Moskva), 340
[8] van Kessel, L. C. P. M. (2022). *Physics and applications of electron-matter interaction simulations*. PhD Thesis, TU Delft, https://repository.tudelft.nl/record/uuid:a8c16a82-e5aa-492a-88d1-72276b8328f1

Public

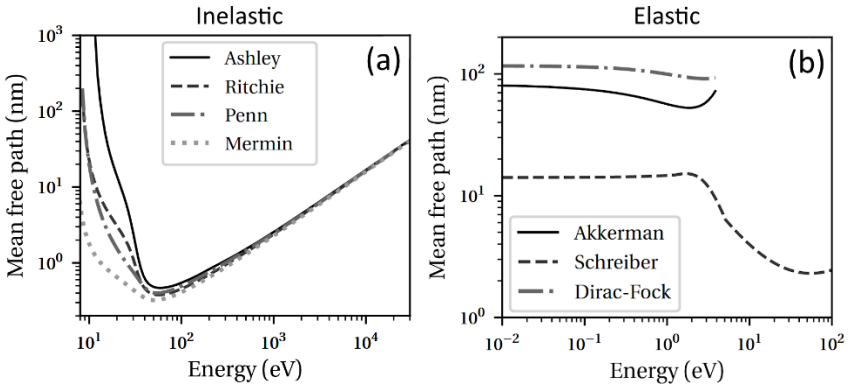

Figure 1. Model Disagreements [8]: Different models in literature for inelastic (a) and elastic (b) scattering produce different mean free path values at low energies. These can differ up to 2 orders of magnitude.

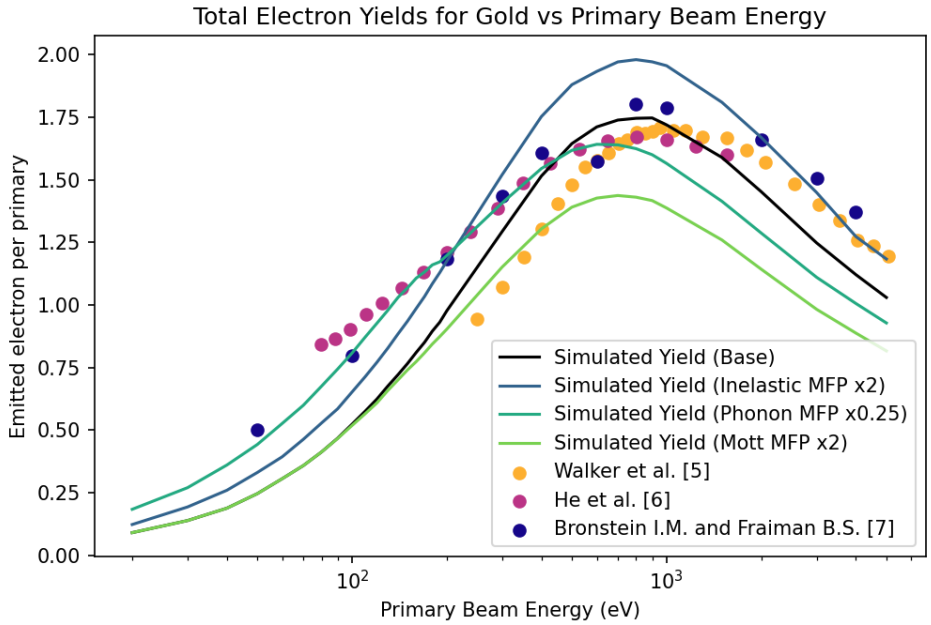

Figure 2. Total Electron Yield: Effect of changing the calculated mean free path of different scattering models on the total electron yield for gold (Base), by a multiplication factor of 2 or 0.25. Experimental data is shown as dots, simulated data as curves.

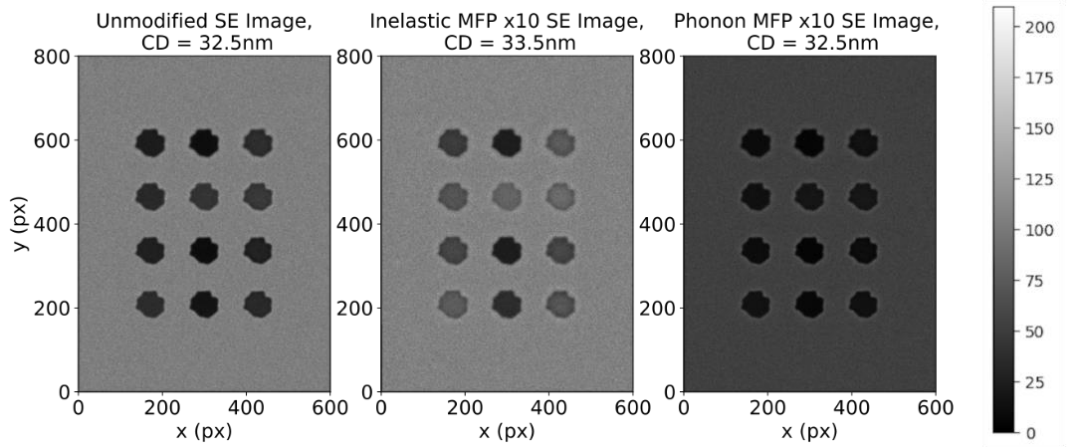

Figure 3. Images: Effect on a simulated secondary electron image (left) of changing the calculated inelastic (middle) and phonon (right) mean free path by a multiplication factor of 10. The simulated geometry is a flat silicon sheet with holes of varying edge profile, depth and side-wall angle, imaged at 100 eV landing energy. CD is the critical dimension (diameter), as measured from the images, averaged over all holes.

Public

Manufacturing and testing of ultra-low expansion glass based planar frame resonator

Ahmad Ali[a], Muhammad Awais Maqbool[a] and Hamza Shakeel[a]
[a] Queen's University Belfast, Belfast, BT7 1NN, United Kingdom
e-mail: H.Shakeel@qub.ac.uk

Introduction:

Glass based microelectromechanical system (MEMS) resonators – especially fused silica (FS) glass is getting importance because of a very low coefficient of thermal expansion (CTE) of FS compared to silicon. Resonators made of materials with low CTE operate well at elevated temperatures and are better suited for high precision applications. Similarly, ultra-low expansion (ULE) glass with an order of magnitude lower CTE compared to FS is also gaining traction recently for MEMS applications. It is worth noting that more work related to FS [1] is published compared to ULE glass. In [2], Weigel et al. proposed a method in which they utilized a deep reactive ion etching based method for reducing ULE wafer thickness from 500 µm to 100 µm. Researches has also utilized micro-blowing technique for ULE glass which is a well-known method for fused silica substrates for fabrication of 3D structures [3]. In our work, we utilized LPCVD polysilicon, thick photoresist, and a wet etching process to etch through 500 µm ULE substrate for fabrication of millimeter sized planar frame resonator (PFR) structure.

Methodology:

A 500 µm thick PFR geometry with optimized dimensions is shown in Fig 1. The fabrication process starts with a piranha cleaning of substrates in 1:1 mixture of H_2SO_4:H_2O_2. After cleaning, a layer of approximately 2.4 µm of LPCVD polysilicon is deposited on both side of the substrate followed by spin coating of AZ9260 photoresist with a thickness of ~12 µm. Afterwards, the photoresist is patterned using a conventional photolithography process followed by etching of exposed polysilicon in 40:100:6 solution of H_2O: HNO_3: HF for 1 minute. In the next step, the patterned ULE glass is etched in 50% solution of hydrogen chloride (HCL) acid which yields an etch rate of ~ 2.3 µm/min. During etching, solution is stirred continuously, and ULE wafer is cleaned with deionized wafer after every 15 minutes. To release fabricated wafer, a layer of coated photoresist is removed with fuming nitric acid followed by etching of the remaining polysilicon film. Fig. 2 shows a schematic of the fabrication process utilized for ULE wafer.

Results and Discussion:

PFR geometry was first simulated and optimized in COMSOL Multiphysics. The experimental setup utilized for measuring performance of PFR in air comprises of a Laser Doppler Vibrometer (LDV), LDV controller, piezo actuator and function generator (FG) as shown in Fig 3(a). A frequency sweep was applied to an actuator with the help of FG for the desired range of frequencies to find the required mode of resonance. Vibration amplitude of PFR increases significantly at resonance mode of vibration and decays exponentially which was captured by vibrometer as shown in Fig 3(b).

Our fabricated device performed well and has outperformed metrics compared to silicon and fused silica devices tested in air. After fabrication, we observed cracks on the surface of the resonator which we believe is a limiting factor for current design. We believe increasing the thickness of deposited polysilicon layer can solve this problem. For the next step, we are planning to increase the thickness of polysilicon and test new devices in vacuum.

Conclusion:

We have demonstrated a wet etching of a 500 µm thick ULE glass substrate using 50% HF solution with a controlled etch profile. Although there are cracks observed after etching still our fabricated device showed a good Q factor of 3,416.

References:

[1] H. Luo, Y. Zhang, J. Yu, X. Dong, and T. Zhou, "Additive, subtractive and formative manufacturing of glass-based functional micro/nanostructures: a comprehensive review," *Materials & Design,* vol. 233, p. 112285, 2023.

[2] C. Weigel *et al.*, "Ultralow expansion glass as material for advanced micromechanical systems," *Advanced Engineering Materials,* vol. 25, no. 9, p. 2201873, 2023.

[3] D. Senkal, M. Ahamed, A. A. Trusov, and A. M. Shkel, "High temperature micro-glassblowing process demonstrated on fused quartz and ULE TSG," *Sensors and Actuators A: Physical,* vol. 201, pp. 525-531, 2013.

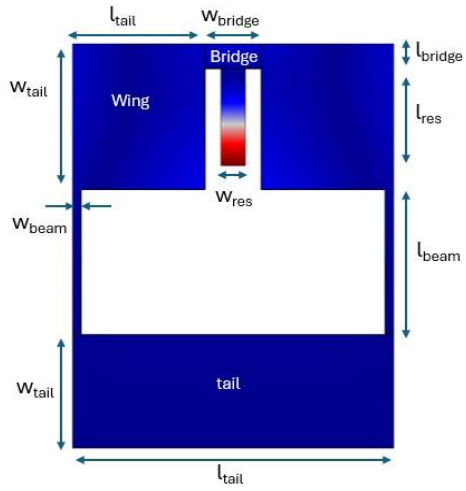

(a)

Table-1

	length (mm)	width (mm)
tail	20	7
wing	9	8.25
bridge	3.5	1.5
resonator	6	1.5
beam	6.7	0.5

(b)

Figure 1. (a) Out of plane mode of PFR at simulated resonance frequency of 9143 Hz (b) Table-1 showing dimensions of PFR

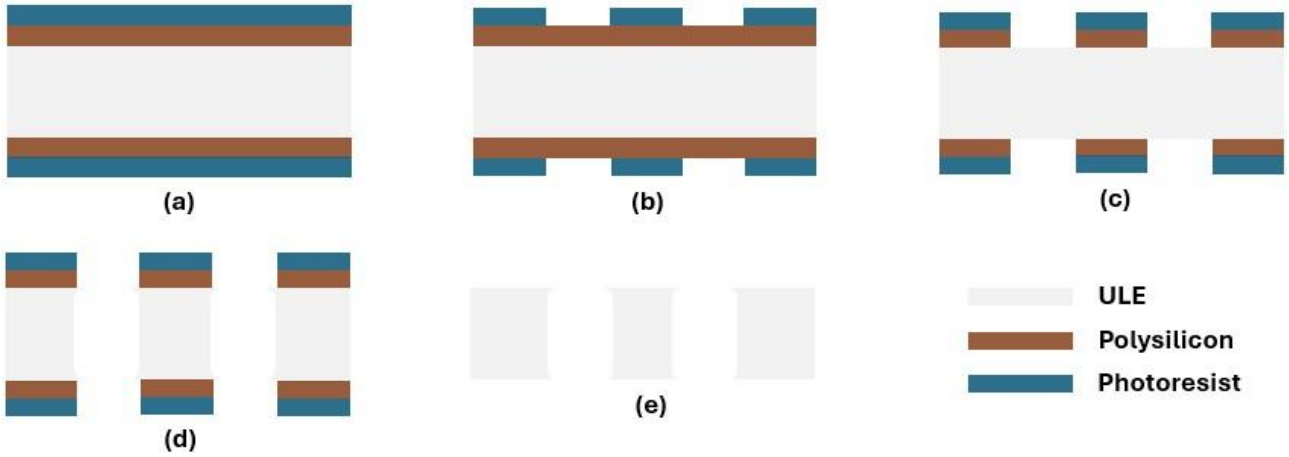

Figure 2. Fabrication process for ULE Glass PFR. (a) Deposition of polysilicon and spin coating photoresist on both sides of wafer (b) Photoresist patterning using lithography process. (c) Polysilicon etching conducted using H_2O: HNO_3: HF. (d) Through wafer etching of 500 µm thick ULE substrate with 50% HF solution. (e) Final device after photoresist removal performed using fuming nitric acid followed by the etching of polysilicon layer.

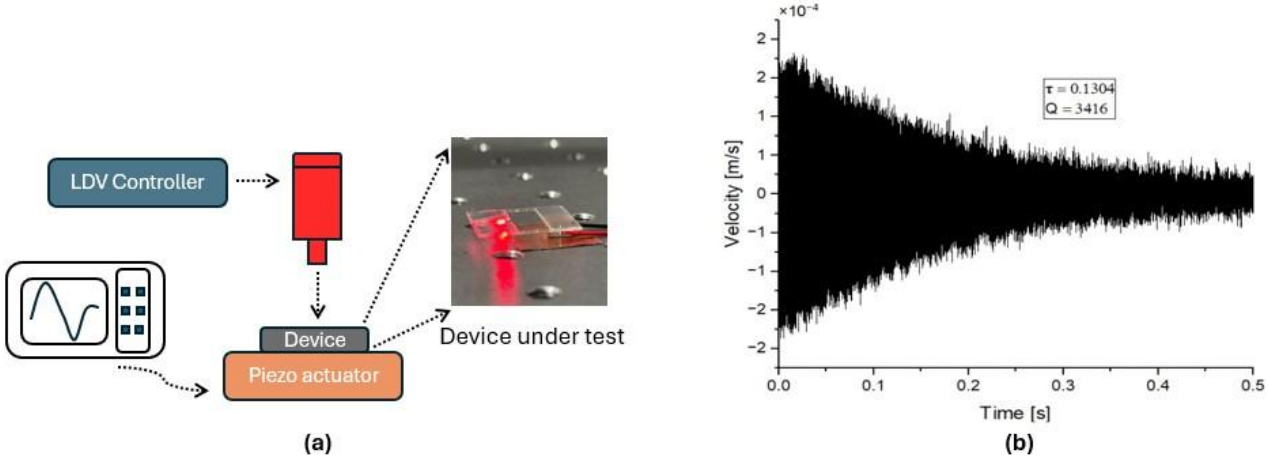

Figure 3. (a) Schematic showing setup used for testing of PFR in air. (b) Ringdown measurement for fabricated PFR at resonant frequency of 8,344 Hz and quality factor of 3,416.

Investigation of Intra-Level Mix-and-Match lithography approach in AR-N 7520new for use in a Mix-and-Match grayscale lithography process

M. Gottwald[a], S. Schermer[a], R. Ambar[a], P. Kohlschreiber[a], C. Helke[a,b], H. Biller[c], M. Sendel[c] and D. Reuter[a,b]

[a]Fraunhofer Institute for Electronic Nano Systems (ENAS), Chemnitz, Germany
[b]Technische Universität Chemnitz, Center for Micro- and nanotechnologies (ZfM), Chemnitz, Germany
[c]Allresist GmbH, Strausberg, Germany

e-mail: markus.gottwald@enas.fraunhofer.de

In recent years a multitude of patterning techniques to fabricate 2.5D and 3D structures for different applications have gained traction [1,2]. Some of the most prominent candidates, direct laser writing (DLW) and grayscale electron beam lithography (EBL) suffer from very long fabrication times, making them expensive and unviable for large scale production. It is a challenge to fulfill the ever-increasing demand for 2.5D structures in (multi) lens arrays, photonic integrated circuits (PICs) and (O)MEMS with the mentioned processes. Nano Imprint Lithography (NIL) offers a high-throughput solution, but needs high-precision masters which have to be fabricated first for each new layout, thus reducing flexibility [3]. Recently, a process for grayscale lithography using an i-line wafer stepper has been presented, which in turn has drawbacks in the minimal achievable resolution [4].
Intra-Level Mix-and-Match is the combination of two lithographic processes in a single resist layer to take advantage of the benefits of both exposures while simultaneously minimizing their disadvantages [5,6]. Combinations of e-beam and i-line wafer stepper lithography show significant improvements with regards to total processing time but allow for lower minimal structure size.
In this work we present process developments for use of the negative-tone resist AR-N 7520new by Allresist GmbH in a grayscale intra-level mix-and-match lithography process combining i-line wafer stepper lithography and electron beam lithography. Resist thicknesses of 500 nm and 900 nm were chosen to provide more options for structure transfer into the substrate material in a later etching step. The i-line (UV) lithography is performed in a Nikon NSR 2205i11D wafer stepper, a high throughput tool. Grayscale lithography with this wafer stepper can be achieved using specialized masks with sub-resolution features that modify the transmission based on a model of the contrast curve. Electron beam exposure was done in a Vistec SB254 shaped beam tool with 50 kV acceleration voltage. Exposing 2.5D structures via grayscale lithography with this tool requires specialized data preparation including non-Manhattan fracturing and dose modulation (including Proximity Effect Correction) fitted once again to a model of the contrast curve. These techniques for grayscale lithography were presented in previous works [7].
The two exposures were analyzed independently to record contrast curves which show different resist heights depending on the dose / transmission. The remaining resist height after development in AR 300-47 (TMAH 0.20n) was measured using profilometry and confocal microscopy. As visible in Figures 1 and 2, the AR-N 7520new resist shows a shallow contrast curve for both exposure types, making it a potential candidate for a mix-and-match extension to existing grayscale lithography processes. Investigations of such a complimentary grayscale approach are currently underway and show promising preliminary results.

[1] Grushina, A. "Direct-write grayscale lithography." Advanced Optical Technologies 8.3-4, 163-169 (2019).
[2] McKenna, C., et al. "Maskless direct write grayscale lithography for MEMS applications." 2010 18th Biennial University/Government/Industry Micro/Nano Symposium. IEEE, (2010).
[3] Thrun, Xaver, et al. "15 days electron beam exposure for manufacturing of large area silicon based NIL master." Microelectronic engineering 110 (2013): 119-122.
[4] Schermer, s., et al. "2.5 D-Patterning via i-line grayscale exposure for photonic structures and micro lens arrays." Novel Patterning Technologies 2024. Vol. 12956. SPIE, 2024.
[5] Gersborg-Hansen, M., et al. "Combined electron beam and UV lithography in SU-8." Microelectronic Engineering 84.5-8 (2007): 1058-1061.

[6] Helke, C., et al. "Intra-level mix and match lithography with electron beam lithography and i-line stepper combined with resolution enhancement for structures below the CD-limit." Micro and Nano Engineering 19 (2023): 100189.
[7] Hartmann, S., et at. "2.5D Patterning of photonic structures by electron beam-based grayscale lithography processes." 51st International Micro and Nano Engineering Conference (2024)

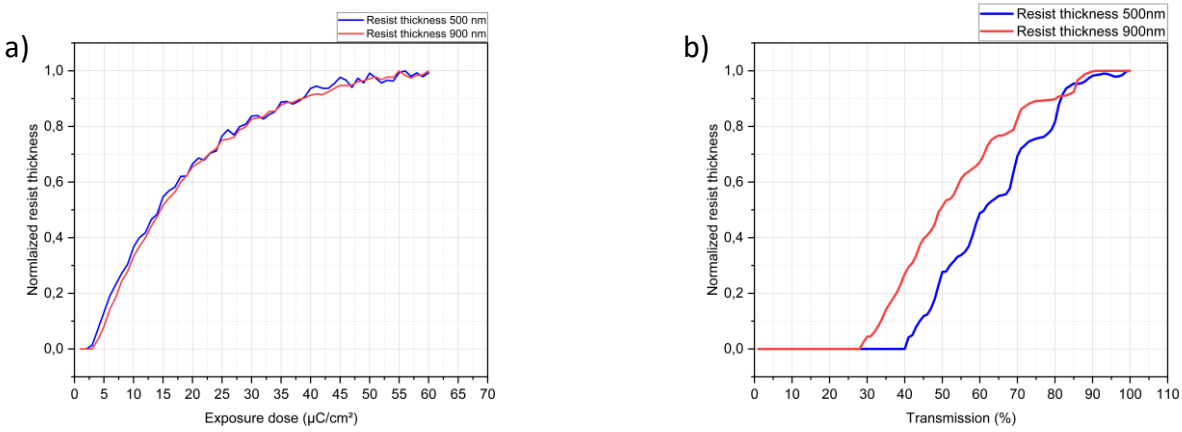

Figure 1. Contrast curves of AR-N 7520new at 500 nm and 900 nm thickness based on a) exposure dose for e-beam exposure and b) transmittivity of a specialized grayscale mask in i-line

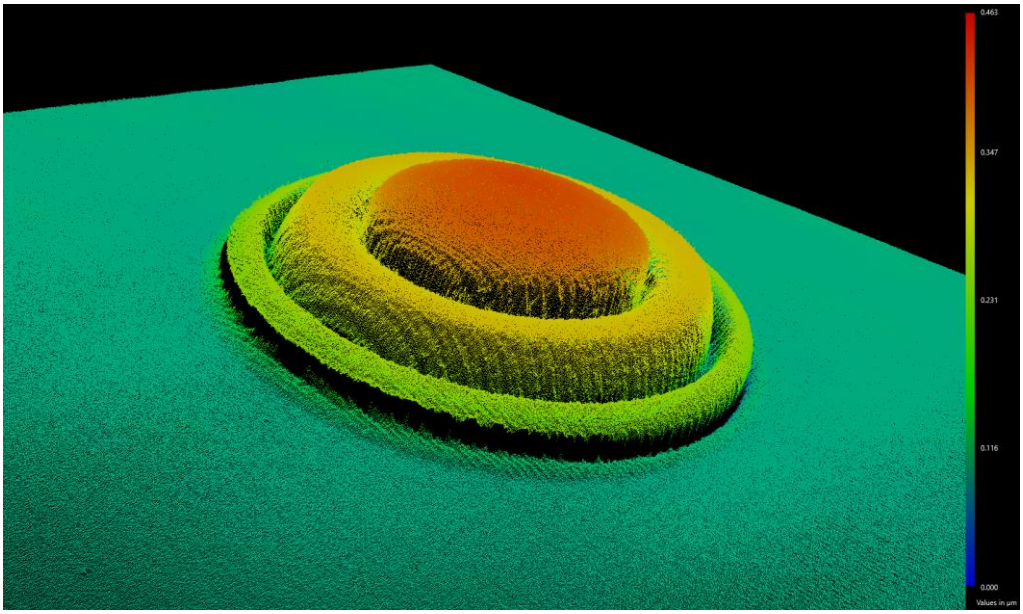

Figure 2. 3D point cloud taken by confocal microscopy measurement of a 3D lens-like structure (200 µm diameter) in 500 nm AR-N 7520new resist exposed with i-line through a specialized grayscale mask

Influence of substrate properties and addition of oxygen on the process of reactive ion etching to optimize the nanopatterning of silicon structures

L. Böhm [a], P. Kohlschreiber [a], M. Haase [a,b], C. Helke [a,b], D. Reuter [a,b]

[a] Fraunhofer Institute for Electronic Nano Systems (ENAS), Chemnitz, 09126, Germany
[b] Technische Universität Chemnitz, Center for Micro- and Nanotechnologies (ZfM), Chemnitz, 09126, Germany
pia.kohlschreiber@enas.fraunhofer.de

This study investigates the effects of different substrates on reactive ion etching (RIE) for the nanopatterning of silicon while also varying the volumetric flow rate of the oxygen in the gas flow of the RIE process. Differing calibration structures in the desired range of 50 nm to 200 nm were investigated with the aim of improving their quality by analyzing their features sizes and especially their line edge roughness.
The silicon substrates used exhibited varying crystal orientations and electrical resistivities: one substrate with (111) orientation and an electrical resistivity $\rho \leq 0.005$ Ωcm, one substrate with (100) orientation and ρ between 0.01 Ωcm and 0.02 Ωcm and one substrate with (100) orientation and an $\rho \geq 10$ Ωcm. All the examined substrates were p-doped. For the lithography, the resist AR-P 6200 by Allresist GmbH was applied and the exposure of the electron beam lithography on a Vistec SB254 followed with a dose of 170 µC/cm². After developing the resist, the substrates were etched by a RIE process in the AMAT Centura 5200. The composition of the etching gases is being varied by increasing the volumetric flow rate of oxygen in the gas flow. For each etching variation 15 sccm SF_6 is used. The first etching variation is using additionally 45 sccm Ar. The second variation is composed of additionally 5 sccm O_2 and 40 sccm Ar and the third variation is using 8 sccm O_2 and 37 sccm Ar in addition. After conducting the etching process, the resist was removed in a two-step process by plasma and wet removal.
The investigated structures were vertical and horizontal lines with a desired line width of 50 nm and 100 nm and squares with a desired edge length of 100 nm and 200 nm. To investigate the structures, measurements were realized by using a CD-SEM after the e-beam lithography step as well as after the resist removal. For the lines, the critical line width (CLW) and line edge roughness (LER) were measured, whereas for the squares, their vertical and horizontal critical dimensions (CD) were measured. Moreover, after completing the process flow, the wafers were fractured to image the cross-section of the wafer via SEM.
The results show that, despite the differing properties of the substrates, no significant influence on the structure transfer could be detected. Surprisingly, neither the electrical resistivity nor the crystal orientation of the substrates had a significant effect on the achieved structures (see Fig 1) although we expected to see at least minor differences [1,2]. These observations were made for all the measured structures.
Instead, it was observed that the varying process parameters of the RIE were crucial for the quality of the structure transfer. While increasing the volumetric flow rate of oxygen in the gas flow of the RIE the LER could be decreased significantly as previously shown in [3]. This led to a better quality of the structures which was noticeably measurable and visible (see Figs 1 and 2, respectively). Additionally, it was observed that the lateral etching rate was accelerated by increasing the oxygen over the etching variations which was expected as seen in [4].
These findings indicate that structure transfer is primarily determined by the optimization of the RIE process parameters, which is important for future developments in the field of nanopatterning. In particular, effects caused by the properties of silicon can be disregarded for the nanopatterning of Si with E-beam and RIE if the substrates have similar electrical resistivities regardless of the crystal orientation.

[1] H.F. Winters and D. Haarer, Physical Review B. 36 (1987) 6613-6623.
[2] H. Jansen et al., Journal of Micromechanics and Microengineering. 6 (1996) 14-28.
[3] S.A. Rasgon, Origin, evolution, and control of sidewall line edge roughness transfer during plasma etching, Ph.D. Thesis, Department of Chemical Engineering, Massachusetts Institute of Technology, 2005.
[4] J.W. Coburn and H.F. Winters, Plasma etching – a discussion of mechanisms, in: Critical Reviews in Solid State and Materials Sciences, 10(2), 119-141.

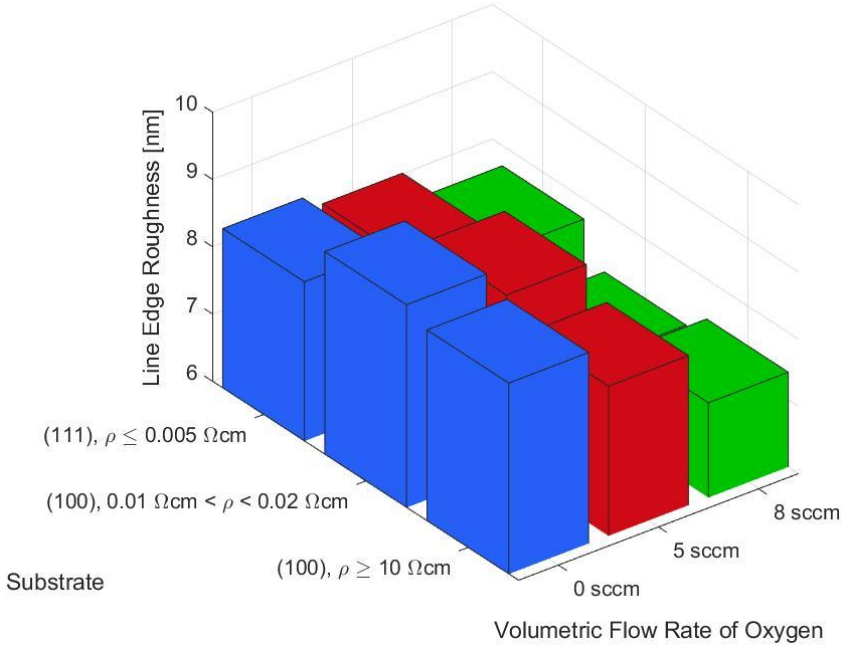

Figure 1. Line edge roughness depending on the substrate and the volumetric flow rate of oxygen in the process of reactive ion etching.

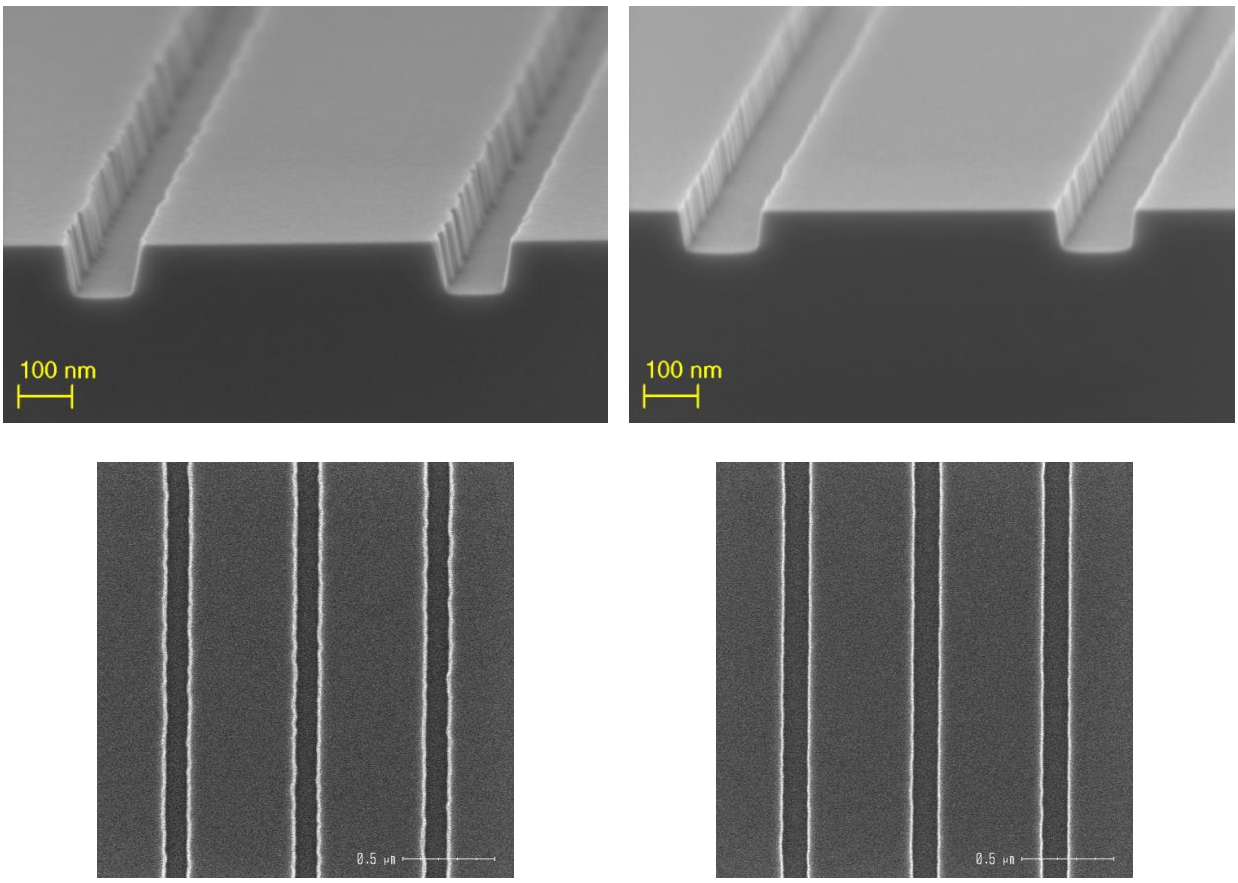

Figure 2. Top) SEM images of the etched lines with a desired line width of 100 nm in the silicon substrate with (100) orientation and an electrical resistivity ≥ 10 Ωcm. Bottom) CD-SEM images of the same structures and substrate. The scale bars correspond to 500 nm. Left) 0 sccm oxygen were utilized in the RIE process. Right) 8 sccm oxygen were utilized in the RIE process.

Interposer Interconnects: An Important Step For Research and Industry

Omesh Kapur [a], Arvin Cedric Mallari[a], Anushka Gangnaik[a], Amanda Green[a], Ibrahim Sari[a], John Darlington[a], Liam Boodhoo[a]

[a] University of Southampton, Southampton, SO17 1BJ, England
e-mail: o.r.kapur@soton.ac.uk

Interposers are planar and vertical copper interconnect structures that connect billions of transistors. They are essential components of modern semiconductor packaging, enabling electrical connectivity between logic dies, memory stacks, and I/O blocks[1]. Integrated during the back-end-of-line (BEOL) process, interposers are increasingly critical for sustaining system performance as CMOS scaling approaches physical and economic limits. At advanced nodes, interconnect bottlenecks such as increased resistance, signal delay, and thermal density pose major challenges[2,3]. While device miniaturisation has driven decades of progress, innovations in packaging, particularly 2.5D and 3D integration, are now key to further advancement[4].

Despite their industrial significance, interposer research is limited in academic settings, especially in the UK, where access to non-industrial fabrication capabilities remains scarce. Establishing scalable processes for interposer prototyping within research institutions is critical for bridging the gap between single-device fabrication and system-level packaging, and for supporting studies of emerging interconnect and memory architectures unsuitable for high-volume environments [5,6].

In this work, we report the development of fabrication processes for both partial and through-hole interposers on 4-inch and 8-inch silicon wafers. Partially-etched interposers, also known as blind-vias (Figure 1) and through-etched interposers, also known as through-vias (Figure 2), incorporate vertical copper vias through the wafer to enable out-of-plane connectivity. Process optimisation focused on eliminating voids and air entrapment in copper structures to ensure continuous electrical paths. Mechanical polishing was refined to achieve planar surface contacts suitable for further integration.

Redistribution layers (RDLs) were integrated into both interposer types (Figure 3) to enable comprehensive electrical characterisation, including continuity testing and resistance mapping across wafer-scale samples. SEM and profilometry were used to assess structural integrity, while four-point probe analysis was employed for electrical validation. Comparative evaluations highlight the process-dependent performance trade-offs between interposer types.

This work establishes a reproducible platform for non-industrial and industrial interposer fabrication, enabling UK-based academic researchers to contribute to CMOS packaging innovation and to explore interconnect-driven system scaling beyond the limitations of transistor miniaturisation.

References:

[1] J. P. Soulié et al., Journal of Applied Physics, 136, (2024) 171101
[2] R. H. Havemann etal., Proceedings of the IEEE, 89, (2001) 586-601
[3] D. Gall et al., MRS Bulletin, 46, (2021) 959-966
[4] S. A. Chew et al., Nature Reviews Electrical Engineering. (2024) 71-72.
[5] O. Kapur et al., Advanced Electronic Materials, 8, (2022), 2200312.
[6] O. Kapur, Scientific Reports, 14, (2024), 14008.

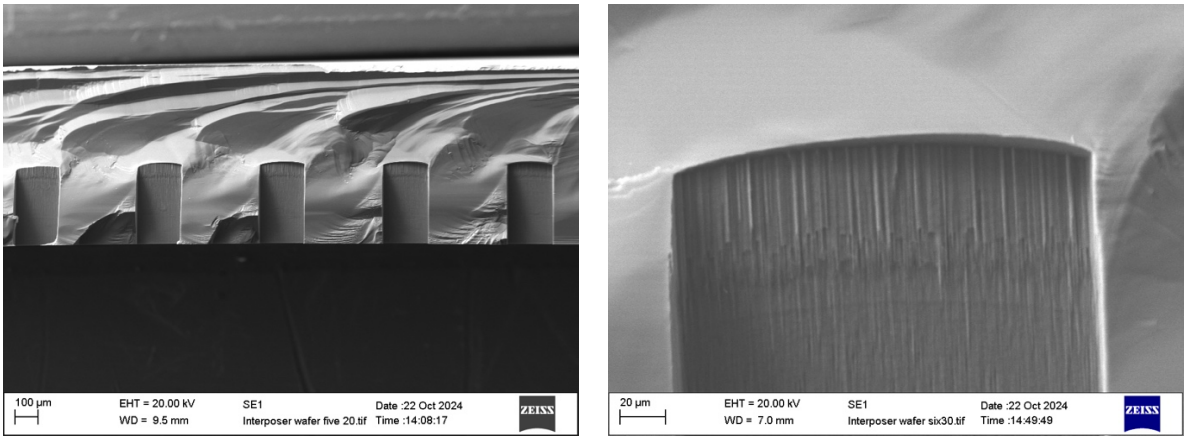

Figure 1. Scanning Electron Micrograph of partial interposer vias with a seed metal pre-electrodeposition (a) 5 partial vias with a seed metal deposited (b) zoomed-in interposer.

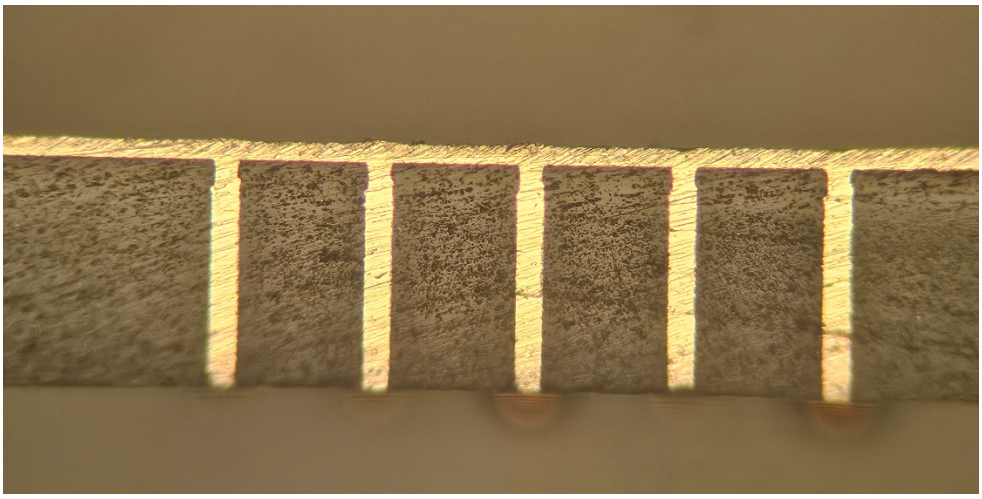

Figure 2. Optical micrograph of 30 µm through-via interposer post-electroplating.

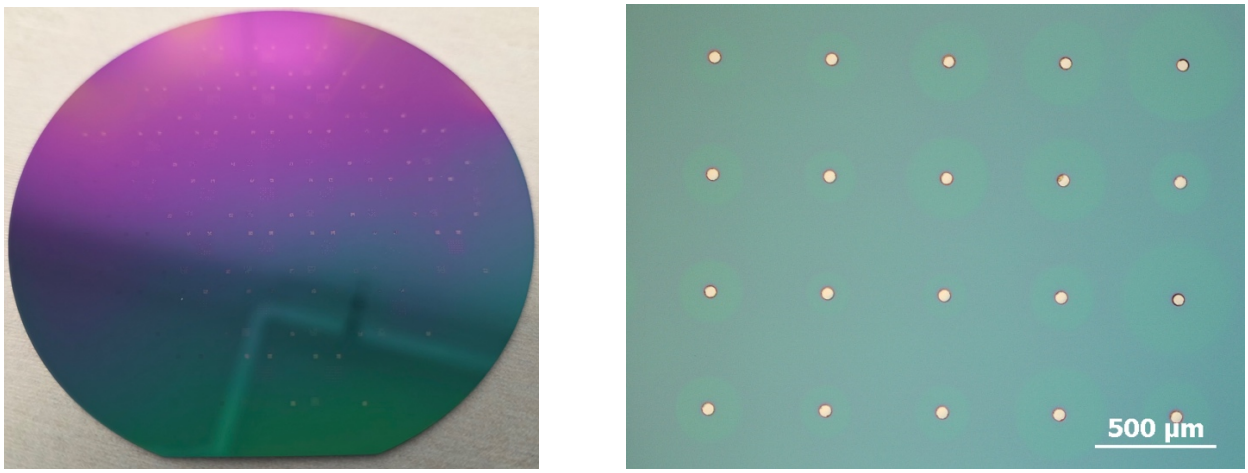

Figure 3. (a) 4-inch through-via interposer (b) Optical Micrograph of a single chip from the 4 inch wafer

Nanofabrication of monolithically integrated multilayer metasurfaces via fully CMOS-compatible processes

Yuntian Ye [a], Hao Peng [a], Shengqi Yin [b], Jize Yan[a], Kian Shen Kiang [b], Xu Fang [a*]
[a] School of Electronics and Computer Science, University of Southampton, Southampton, SO17 1BJ, UK
[b] Optoelectronics Research Center, University of Southampton, Southampton, SO17 1BJ, UK
e-mail: x.fang@soton.ac.uk

Abstract: We have developed a novel metasurface stacking methodology that is fully compatible with standard Complementary Metal-Oxide-Semiconductor（CMOS） processes, advancing the mass production and commercialization of metasurface technologies.

Metasurfaces are planar arrays of subwavelength nanostructures that enable precise control over the amplitude, phase, polarization, spectrum, and propagation direction of light. These capabilities have been extensively explored over the past decade, leading to a wide range of potential applications, including ultra-thin imaging lenses, holography, and vortex beam light sources [1].

Regardless of these progresses, recent studies have highlighted inherent limitations of monolayer metasurfaces in their light manipulation capabilities. These limitations are primarily due to intrinsic constraints in light-matter interactions imposed by monolayer meta-atom designs, which cannot be fully compensated for using advanced design methods such as multiplexing and machine learning-based inverse design. Similar to conventional optics, multilayer metasurfaces offer enhanced light manipulation capabilities, as each additional layer introduces new degrees of freedom. This enables advanced functionalities such as wide field-of-view imaging, where focusing and phase correction, two essential components of wavefront shaping, are implemented using two different metasurfaces [2].

Multilayer metasurfaces can be categorized into two types: multi-wafer cascaded configurations and monolithically integrated configurations. The former resembles traditional optical assemblies, where multiple metasurfaces are precisely aligned to achieve the desired function [3]. Although easier to fabricate, this approach is limited by its large spatial footprint and stringent alignment requirements. In contrast, monolithically integrated multilayer metasurfaces consolidate all layers onto a single substrate, greatly improving device compactness and eliminating alignment issues.

We have focused on the nanofabrication of monolithically integrated multilayer metasurfaces. Due to the potential importance of this type of metasurface, numerous nanofabrication methodologies have been explored. For instance, Reference [4] reported metasurfaces fabricated on both sides of a thick substrate, where the large and fixed distance between the two layers limits the applications of this method. References [5] and [6] used spin-coated polymers and thermal curing to create a flat silicon oxide intermediate layer, on which the second layer of metasurface was fabricated. References [7] and [8] used polymers such as PDMS and PMMA for metasurface encapsulation and stacking. Reference [9] used a special photoresist as an intermediate layer. These methods employed materials or processes that are not standard in semiconductor foundries, which can significantly increase the complexity and cost of mass production.

In contrast to these existing approaches, our nanofabrication methodology is fully CMOS-compatible. The critical step in our approach is chemical mechanical polishing (CMP), used to planarize a buffer layer before the fabrication of a second layer of metasurface. CMP is a standard semiconductor fabrication process that synergizes chemical etching and mechanical grinding to achieve high-precision planarization of wafer surfaces. Figures 1 and 2 show the morphology of a sample fabricated following this methodology. The fabrication of the first metasurface layer followed a standard process that utilized electron beam lithography (EBL). Subsequently, a 2.2 μm thick SiO_2 buffer layer was deposited via plasma-enhanced chemical vapor deposition (PECVD) over the nanostructures. Planarization was then carried out using CMP with a 50% colloidal silica slurry, resulting in a highly flat top surface of the buffer layer (Figure 1). The second metasurface layer was subsequently fabricated following the same procedure as the first.

Acknowledgements: This work was supported by EPSRC (EP/Z535813/1) and the Leverhulme Trust (RPG-2025-211).

[1] J. Hu, S. Bandyopadhyay, Y.-h. Liu, L.-y. Shao, A Review on Metasurface: From Principle to Smart Metadevices, Front. Phys. 8 (2021) 586087.
[2] F. Yang, M. Y. Shalaginov, H. Lin, S. An, A. Agarwal, H. Zhang, C. Rivero-Baleine, T. Gu, J. Hu, Wide field-of-view metalens: a tutorial, Adv. Photon. 5 (2023) 033001.
[3] F. Mei, G. Qu, X. Sha, J. Han, M. Yu, H. Li, Q. Chen, Z. Ji, J. Ni, C.-W. Qiu, Q. Song, Y. Kivshar, S. Xiao, Cascaded metasurfaces for high-purity vortex generation, Nat. Commun. 14 (2023) 6410.
[4] B. Groever, W.T. Chen, F. Capasso, Meta-Lens Doublet in the Visible Region, Nano Lett. 17 (2017) 4902–4907.
[5] J. Tan, R. Pan, Y. Xiang, Z. Tang, B. Wang, J. Li, Unilateral Asymmetric Radiation in Bilayer Metasurfaces, Adv. Funct. Mater. (2025) 2501156.
[6] Y. Bao, F. Nan, J. Yan, X. Yang, C.-W. Qiu, B. Li, Observation of full-parameter Jones matrix in bilayer metasurface, Nat. Commun. 13 (2022) 7550.
[7] J. Zhou, I. I. Kravchenko, H. Wang, J. R. Nolen, G. Gu, J. Valentine, Multilayer Noninteracting Dielectric Metasurfaces for Multiwavelength Metaoptics, Nano Lett. 18 (2018) 7529-7537.
[8] Y. Zhou, I.I. Kravchenko, H. Wang, H. Zheng, G. Gu, J. Valentine, Multifunctional metaoptics based on bilayer metasurfaces, Light Sci. Appl. 8 (2019) 80.
[9] L. Deng, Z. Li, Z. Zhou, Z. He, Y. Zeng, G. Zheng, S. Yu, Bilayer-Metasurface Design, Fabrication, and Functionalization for Full-Space Light Manipulation, Adv. Opt. Mater. 10 (2022) 2102179.

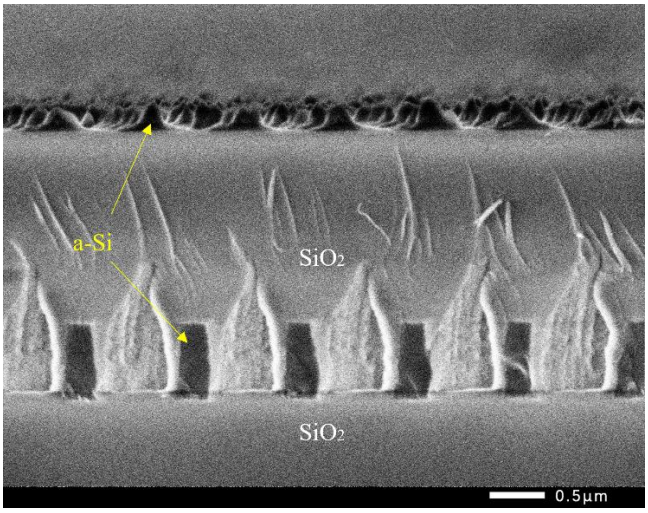

Figure 1. Cross-sectional SEM image of the double-layer metasurface fabricated using CMP planarization. The two metasurface layers, composed of amorphous silicon (a-Si) nanostructures, are separated by a SiO_2 buffer layer. CMP was employed to planarize this buffer layer. The features visible within the buffer layer are cleaving-induced fractures resulting from the wafer cross-sectioning process.

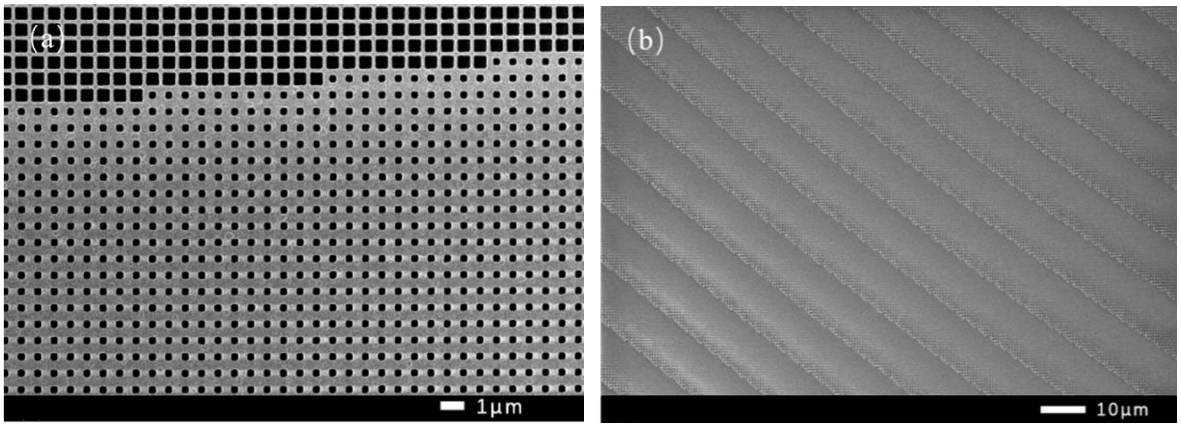

Figure 2. Planar view of the two metasurface layers. (a) Bottom layer, imaged prior to deposition of the SiO_2 buffer layer. (b) Top layer, imaged after completion of the nanofabrication process.

Single-Printed Nb2O5 UV-Visible Metasurfaces for Chiro-Optical Holography

Eunji Lee [a+], *Chanwoong Park* [b+], *Hongyoon Kim*[c], *Heon Lee* [b,d]* *and Junsuk Rho* [a,c,e,f,g]*

[a]Department of Chemical Engineering, Pohang University of Science and Technology (POSTECH), Pohang 37673, Republic of Korea

[b]Department of Materials Science and Engineering, Korea University, Seoul 02841, Republic of Korea

[c]Department of Mechanical Engineering, Pohang University of Science and Technology (POSTECH), Pohang 37673, Republic of Korea

[d]ZERC, Seoul 02841, Republic of Korea

[e]Department of Electrical Engineering, Pohang University of Science and Technology (POSTECH), Pohang 37673, Republic of Korea

[f]POSCO-POSTECH-RIST Convergence Research Center for Flat Optics and Metaphotonics, Pohang 37673, Republic of Korea

[g]National Institute of Nanomaterials Technology (NINT), Pohang 37673, Republic of Korea

E-mail: heonlee@korea.ac.kr, jsrho@postech.ac.kr

The scalable fabrication of broadband metasurfaces operating from the ultraviolet (UV) to visible wavelengths remains a major challenge in nanophotonics. Existing nanoparticle-embedded resists (nano-PERs) typically exhibit optimized performance over limited spectral ranges and often suffer from low refractive indices or increased optical losses outside their target band. Conventional lithographic techniques, such as electron beam lithography offers high resolution but lack scalability due to cost and low throughput. Here, we introduce a novel Nb2O5-based nano-PER that simultaneously addresses material and processing limitations. This PER formulation supports single-step nanoimprint lithography (NIL) for chiral metasurfaces, enabling full-spectrum phase modulation across the UV-visible region. Geometric parameters of the meta-atoms were optimized through particle swarm optimization (PSO) in combination with rigorous coupled-wave analysis (RCWA), enabling broadband and polarization-selective operation with enhanced conversion efficiency . Compared to previously reported PERs, the Nb2O5-based system achieves both high refractive index and minimal absorption, resulting in superior simulated conversion efficiency and polarization-selective holographic reconstruction (See Fig 1).

Furthermore, particle concentration and processing parameters were finely tuned to ensure high-fidelity pattern transfer via single-step NIL, validating the feasibility of imprinting high-resolution chiral metasurfaces using nano-PER. (See Fig 2). The metasurface selectively reconstructs encoded holographic information under right-circularly polarized (RCP) light, while effectively suppressing it under left-circularly polarized (LCP) incidence (See Fig 3). This spin-selective behavior demonstrates significant potential for advanced optical security and anti-counterfeiting technologies. By integrating high-index Nb2O5 nanoparticles into a scalable NIL platform, this work presents a versatile and practical route toward next-generation broadband photonic devices that overcome the limitations of spectral narrowness and multi-step processing.

[1] J. Kim et al., Laser Photonics Rev. 16 (2022) 2200098.

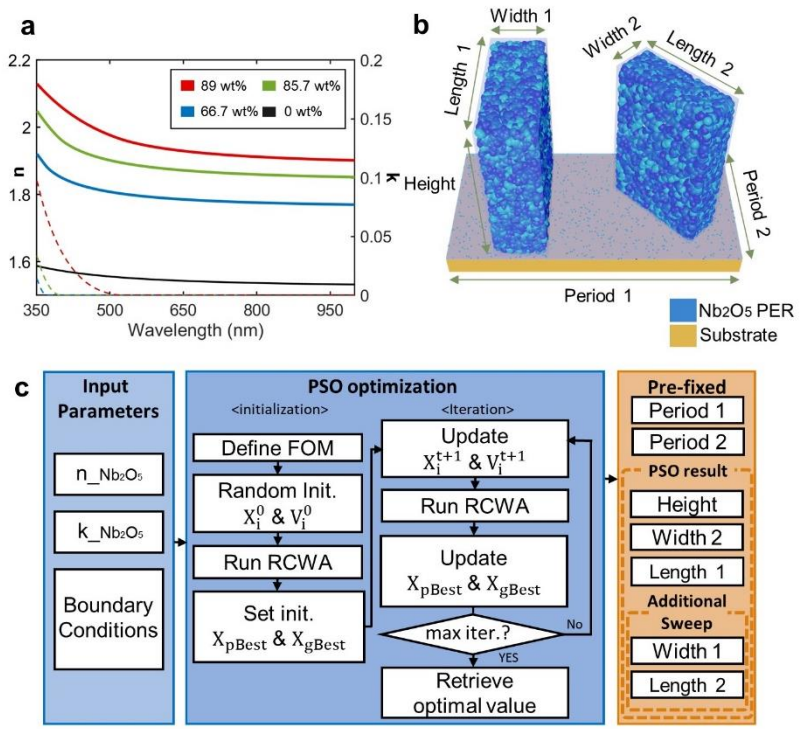

Figure 1. (a) Measured refractive indices of Nb_2O_5 PER films with varying nanoparticle concentrations. (b) Schematic of the Nb_2O_5 PER diatomic meta-atom structure. (c) Particle swarm optimization (PSO) flowchart used for the meta-atom design.

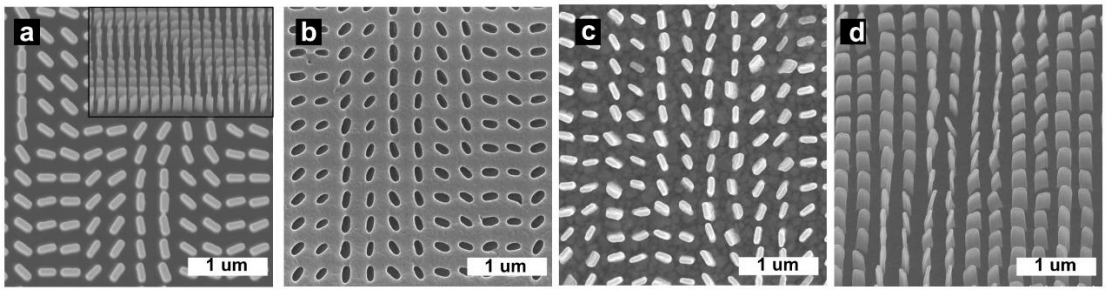

Figure 2. Scanning electron microscope images of the fabricated (c) master mold, (d) soft mold, (e) top view, and (f) tilted view of the imprinted metahologram.

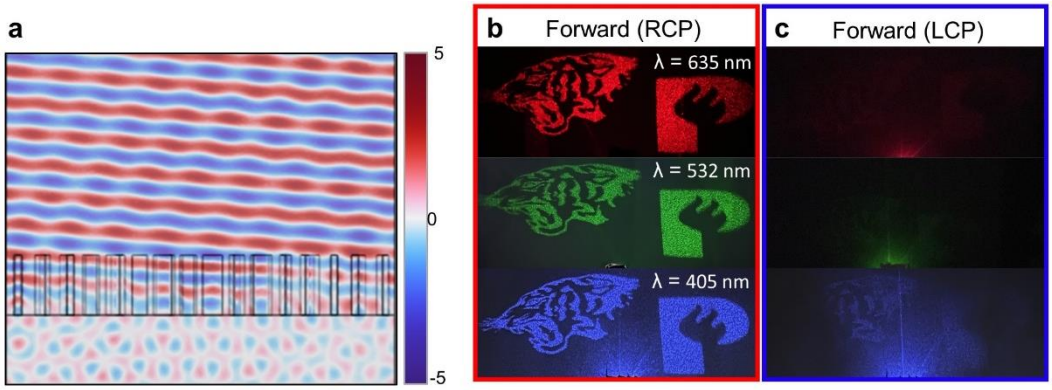

Figure 3. (a) Simulated electric field distribution under right circularly polarized (RCP) incidence in the forward direction. Measured holographic images for forward propagation under (b) RCP and (c) LCP incidence

Plasma-induced periodic surface structures on polymeric microfluidic channel sidewalls

A.S. Kastania [a], E. Stai [a,b], S. Mouchtouris [a,c], V. Constantoudis [a], G. Kokkoris [c], P. Tsavalas [d], K. Mergia [d], G. Schider [e], D. Borstner [e], P. Melchior [e], D. Nees [e], B. Stadlober [e], E. Gogolides [a], A. Tserepi [a]

[a] Institute of Nanoscience and Nanotechnology, NCSR "Demokritos", Agia Paraskevi, 15341, Greece
[b] Department of Physics, National and Kapodistrian University of Athens, Athens, 15784, Greece
[c] School of Chemical Engineering, National Technical University of Athens, Athens, 157 80, Greece
[d] Institute of Nuclear & Radiological Sciences and Technology, Energy & Safety, NCSR "Demokritos", Agia Paraskevi, 153 41, Greece
[e] Joanneum Research Forschungsgesellschaft MbH, Weiz, 8160, Austria
e-mail: a.tserepi@inn.demokritos.gr, a.kastania@inn.demokritos.gr
Keywords: plasma etching, polymer substrates, microfluidic sidewalls, nanoripples, metrological analysis

It is well-known that plasma treatment of polymer substrates generates surface roughness, the dimensions and morphology of which are influenced by the specific substrate material and the plasma processing parameters. Substrates that are horizontally oriented with respect to the electrode in the plasma reactor, such as big flat substrates and bottom surfaces of microfluidic channels, have been extensively examined in previous studies [1,2]. Recently, the formation of surface roughness on polymeric surfaces perpendicularly placed on the electrode plane was investigated [3], revealing anisotropic patterns in the form of periodic nanoripples on the sample surface adjacent to the electrode (plasma-induced periodic surface structures, PIPSS) converting into a more isotropic roughness on the sample surface away from the electrode. However, the surface roughness formed during plasma etching on the sidewalls of microfluidic channels is not yet as well-studied. To this end, imprinted polymeric microfluidic channels are plasma treated within a custom-fabricated plasma reactor [4] and the roughened surfaces are characterized using SEM. Microfluidics with such roughened sidewalls can be utilized for better mixing as well as regulating biomolecule or cell adhesion, proliferation, and cell fate specification.

The roughness observed on the microfluidic sidewall surfaces, assessed through SEM imaging (Fig. 1), exhibits different morphology compared to the previously reported horizontal surfaces, but it is similar to that of the PIPSS [3] on plasma treated polymeric flat surfaces perpendicularly placed to the electrode. The images demonstrate that the surface topography exhibits a roughness variation versus distance along the sidewall, transitioning from perpendicularly oriented nanoripples near the channel bottom to a more isotropic roughness toward the upper surface of the sidewall. Quite interestingly, the nanoripples appear to cover a larger area of the sidewall and the corresponding surface roughness variation is not as extensive on the channel walls as on the perpendicularly oriented substrate surfaces; the nanoripples near the channel bottom extend upwards over most of the surface area of the sidewall. Only a small part of the microfluidic sidewall surface appears to have isotropic roughness *(about 20% depending on the plasma process time)*. The anisotropy index A, obtained from two-dimensional Fourier analysis of SEM images (Fig. 2), quantitatively reflects both the anisotropy and the variation in roughness along the sidewall surface. In the near future, to illuminate the mechanism for nanoripple formation and roughness spatial variation on the microfluidic sidewall surfaces, a modelling framework, consisting of a reactor scale model and a Monte Carlo model for the calculation of particle trajectories [5], will be utilized towards prediction of the angular and energy distribution of ions reaching the microfluidic sidewalls.

This work is supported by the EU Horizon Pathfinder project VortexLC ("Vortex enhanced liquid chromatography for HbA1c monitoring based diabetes management in a globalized setting", contract No 101047029, www.vortexlc.com).

[1] K. Tsougeni et al., Sensors and Actuators B: Chemical 288 (2019) 171-179.
[2] A. S. Kastania et al., Biomed. Microdevices 22, 44 (2020).
[3] A. S. Kastania et al., Adv. Eng. Mater., 27, 2402729 (2025).
[4] A. Zeniou et al., Nanotechnology 32, 235305 (2021).
[5] S. Mouchtouris et al., Plasma Process. Polym. 14, 1600147 (2017).

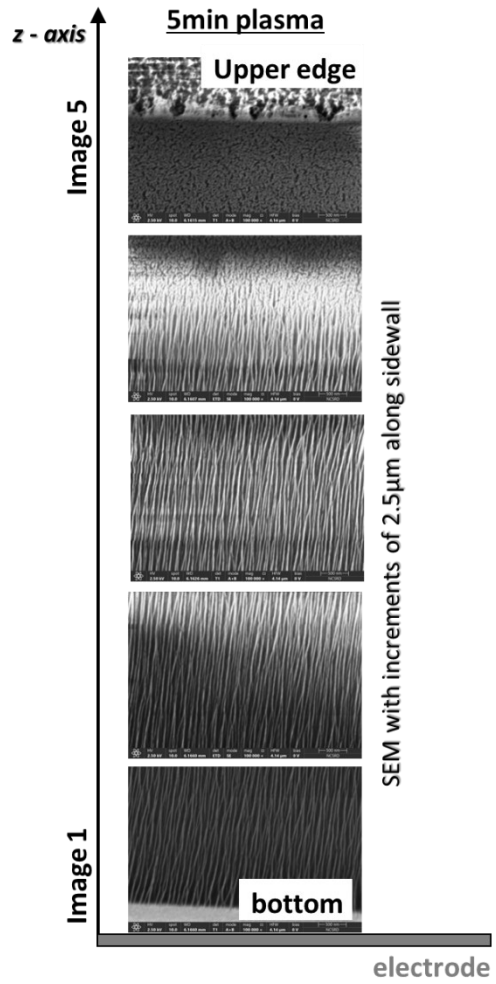

Figure 1. SEM images (at 45º views) of the sidewall of a plasma treated microfluidic channel wall after plasma roughening of an imprinted resin on PET, in RIE mode for 5 min, at increments of 2.5 µm along the sidewall.

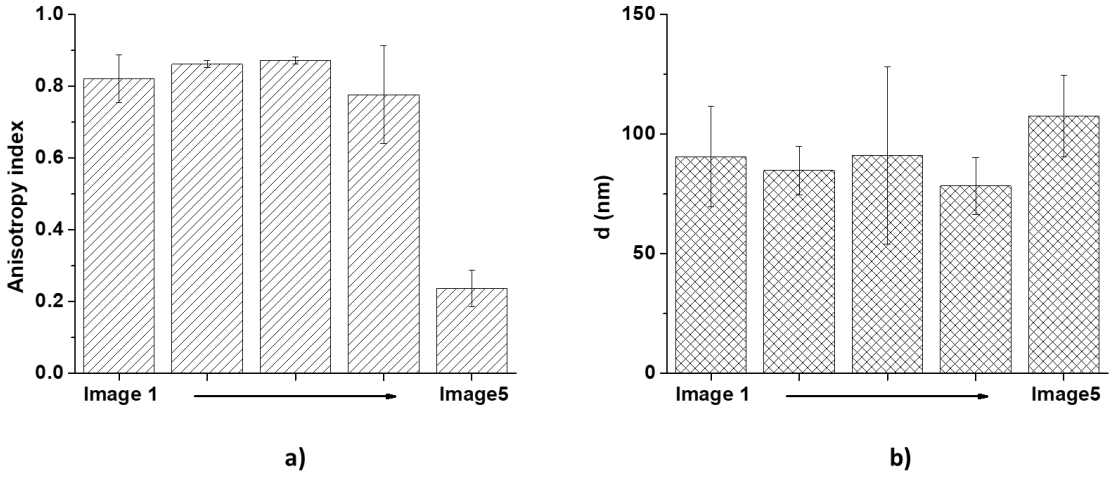

Figure 2. (a) Anisotropy index A and (b) ripple period (center-to-center distance) calculated for SEM images 1-5 of Fig. 1 for the channel sidewalls with increasing distance from the channel bottom.

Scalable Multilayer Silicon Anode Architecture with Porosity Control via UV-NIL Roll-to-Plate Process for Enhanced Lithium-Ion Battery Performance

Yu Ju Han [a], Seo Rim Park [a], Seong Min Yoon [a], Min Ju An [a], Yeon guk Son [a], Young Tae Cho [a]

[a] Changwon National University, Changwon, 51139, Republic of Korea
e-mail: ytcho@changwon.ac.kr

keywords : Silicon anode, Lithium-ion battery, Dendrite, UV-NIL, Porous structure

Silicon, as an anode material for lithium-ion batteries, offers an exceptionally high theoretical capacity, making it a promising candidate for next-generation energy storage devices. However, Si-based anodes experience severe performance degradation during cycling due to significant volumetric expansion, leading to structural failure, uneven formation of the solid electrolyte interphase (SEI), and dendrite growth. Specifically, the volumetric expansion of silicon causes particle fracture and loss of electrical contact. If the SEI forms unevenly, it can create electrically insulating layers, reducing ionic conductivity and decreasing reaction efficiency. Furthermore, uncontrolled dendrite growth on the anode surface can result in localized short circuits, threatening the safety and reliability of the battery. These challenges pose major obstacles to the practical application of silicon as an anode material.

In this study, to address these challenges, a multilayer anode structure was designed using a UV-nanoimprint lithography (UV-NIL) based Roll-to-Plate process, enabling uniform large-area application. The Roll-to-Plate process offers high productivity and allows for the consistent formation of fine structures through UV-NIL, making it highly scalable for commercial applications. Figure 1 illustrates the schematic of the fabrication process.

The anode structure consists of two layers. In the first layer, silicon, carbon, and UV-curable resin were used as a binder, ensuring stable particle dispersion and strong adhesion to the cu foil. In the second layer, a porous planar structure was formed by mixing UV-curable resin with polyethylene glycol (PEG), which effectively suppressed dendrite growth caused by volumetric expansion. This dual-layer design enhances the structural stability of the anode, while the porous structure in the second layer provides efficient ion transport pathways, improving overall battery performance.

The cycling performance tests were conducted as shown in Table 1, using bare Cu as a reference for comparison. The porosity of the porous structure was controlled by adjusting the molecular weight of PEG and its mixing ratio with the UV-curable resin. The effects of porosity on battery cycling performance and dendrite growth tendencies were systematically analyzed.

It was observed that increasing porosity led to changes in lithium-ion diffusion pathways, and the impact of these structural differences on cycling performance was quantitatively evaluated. Furthermore, dendrite growth patterns were visually examined using scanning electron microscopy (SEM), providing direct insight into the relationship between porosity variations and dendrite formation.

This study presents a novel approach for effectively suppressing dendrite growth in silicon-based anodes using a UV-NIL-based Roll-to-Plate process, enabling scalable large-area application. By systematically analyzing the impact of porous structure design on battery performance, this research offers valuable insights into optimizing anode architecture for enhanced electrochemical performance.

The proposed process demonstrates not only the potential for high-performance lithium-ion battery development but also provides a scalable and commercially viable fabrication technique. These findings are expected to make a significant contribution to the advancement of next-generation energy storage devices, ensuring both improved performance and efficient large-scale production.

Acknowledgement
This work was supported by the National Research Foundation of Korea(NRF) grant funded by the Korea government(MSIT)(NRF 2023R1A2C3006499, RS-2019-NR040067) and the Korea Institute for Advancement of Technology (KIAT) grant funded by the Korean government (MOTIE) (141588607, Additive Manufacturing Technology Innovation Alliance for Aerospace/Small modular reactor/Defense industry).

References

[1] Son, Yeonguk, et al. "High energy density anodes using hybrid Li intercalation and plating mechanisms on natural graphite." Energy & environmental science 13.10 (2020): 3723-3731.

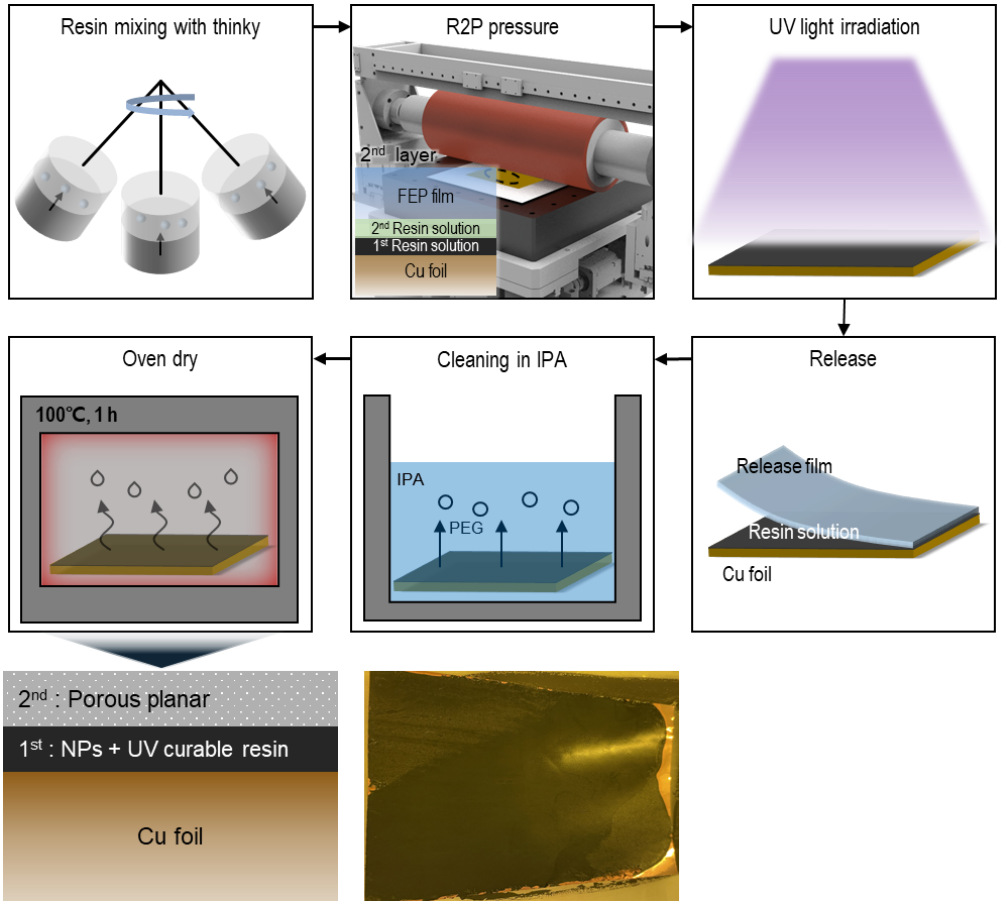

Figure 1. Schematic of the UV-NIL-Based Specimen Fabrication Process

Half cell assembly

Cell type	2032-type coin cell
Working electrode	Cu current collector,14 pi
Counter electrode	Li metal, 16 pi
Separator	Glass fiber
Electrolyte	1.3 M $LiPF_6$ in EC/EMC/DEC=3:5:2 + $LiBF_4$ 0.2 %+ FEC 10% + VC 0.5 %+ SN 3 %+ PS 1 %

Electrochemical measurement

	Formation test	Cycle test
C-rate	0.1 C (10 h)	0.5 C (2 h)
Lithiation	1 mAh/cm^2 capacity cut off	
Delithiation	1.5 V voltage cut off	

Table 1. Electrochemical Performance Evaluation Conditions for Cycling Test

First results on vacuum-gas-controlled metal assisted chemical etching

B. Benz [a,b] , V. Hosseini [c,d], G. Umlauf [c], T. Sandbrink-Koblenz [e], D. Anderson [e], D. Reuter [c,d]
Ch. Meinecke [c,d], L. Romano [b]

[a] University of Basel & Swiss Nanoscience Institute, Basel, 4001, Switzerland
[b] ETH Zürich & Paul Scherrer Institute, Villigen, 5232, Switzerland
[c] Fraunhofer Institute for Electronic Nano Systems (FhI ENAS), 09126 Chemnitz, Germany
[d] Center for Micro and Nano Technologies (ZfM), Chemnitz University of Technology, 09126 Chemnitz, Germany
[e] memsstar Ltd, 1 Fleming Road, EH54 7BN, Livingston, UK.
e-mail: lucia.romano@pis.ch; christoph.robert.meinecke@enas.fraunhofer.de

MacEtch is a fluorocarbon chemicals-free, plasma-free, local electroless etching method promising high aspect ratio nano-structuring capabilities of different semiconductors that is gaining quite relevant attention in the recent literature for several applications, spanning from silicon photonics to bio-sensors, solar cells and X-ray optics [1-5]. MacEtch of silicon is an etching mechanism based on the selective silicon etching by means of hydrofluoric acid that occurs locally at the contact interface between the silicon substrate and a metal catalyst. The catalyst reacts with an oxidant injecting positive charge carriers into the silicon substrate that is subsequently oxidized and removed by hydrofluoric acid. The etchant and the oxidant are here provided in a gas phase with controlled flow and concentration allowing the MacEtch reaction to occur in a programmable way [6]. This enables to achieve extremely high aspect ratio, so far demonstrated up to 10’000:1 [5].

The research institutes Fraunhofer ENAS (Chemnitz, Germany) and the Paul-Scherrer Institute (PSI, Switzerland) are pleased to announce the launch of their new research cooperation in the field of gas-phase metal assisted chemical etching (MACE, MacEtch) technologies. This partnership aims to develop innovative solutions in micro and nano manufacturing and further explore the potential of these technologies in semiconductor applications. memsstar Ltd., a leading provider of etch and deposition equipment to researchers and manufacturers of semiconductors and Microelectromechanical systems (MEMS), is supporting the research by further developing their Orbis tool platform specifically for the dedicated use of gas-phase MacEtch processes based, opening new opportunities for these innovative technologies at industrial scale.

Already in the early stages of the collaboration, the research team achieved very promising results with huge aspect ratio (at least 500:1) silicon nanowires, indicating an incredible development potential. Figure 1 shows: just etched silicon grating for PSI X-ray optics; Si nanowires as small as 10 nm in section lying on the metal catalyst and the happy crew in the clean room of the center for micro and nanotechnologies / Fraunhofer ENAS after the first successful experiment in March 2025. The tool has a large area wafer capability (8-inch wafer scale) with a substrate temperature up to 90 °C. Etching uniformity, reproducibility and etching recipes are currently under development.

[1] A. Mateen, et al., ChemSusChem 18 (2025) e202400777.
[2] S. Surdo, et al., Small 20 (2024) 2400499.
[3] M. Michalska, et al., Advanced Functional Materials 33 (2023) 2212660.
[4] H. Cho, et al., Advanced Functional Materials n/a (2025) 2502010.
[5] L. Romano, et al., Nanoscale Horiz 5 (2020) 869-879.
[6] L.L. Janavicius, et al., Applied Physics Reviews 10 (2023) 011409.

Figure 1. Etched silicon grating for PSI X-ray optics; cross-section SEM of Si nanowires as small as 10 nm in section lying on the metal catalyst; happy crew in the clean room of Fraunhofer ENAS after the first successful experiment in March 2025 (from bottom-left clockwise: Vahide Hosseini (Fraunhofer ENAS & Univ.Chemnitz); Toni Sandbrink-Koblenz (memsstar Ltd.); Lucia Romano (ETHZ & PSI); Bryan Benz (Univ. Basel & PSI); David Anderson (memsstar Ltd.) and Christoph R. Meinecke (Fraunhofer ENAS & Univ.Chemnitz)).

OPTIMIZING RETICLE BASED HIGH THROUGHPUT I-LINE GRAYSCALE PROJECTION LITHOGRAHPHY FOR 3D STRUCTURES

Sebastian Schermer [a], Stephen DeMoor [c], Andrew Zanzal [c], Patrick Reynolds [c], Jens Bonitz [a], Jeremy Bieling [b], Christian Helke [a,b], Anja Voigt [d] and Danny Reuter [a,b]

[a] Fraunhofer Institute for Electronic Nanosystems ENAS, Chemnitz, 09126, Germany
[b] Chemnitz University of Technology, Center for Microtechnologies, Chemnitz, 09126, Germany
[c] Benchmark Technologies, 7 Kimball Lane, Building E Lynnfield, MA 01940, USA
[d] Micro Resist Technology (MRT) GmbH, Köpenicker Str. 325, 12555 Berlin, Germany
e-mail: sebastian.schermer@enas.fraunhofer.de

In this work a reticle based i-line projection grayscale lithography (3D fabrication process) is analyzed, and optimized to obtain low surface roughness grayscale pattern. The impact of the pixel size (reticle) on the resist roughness and structure fidelity after the development will be evaluated. The ideal pixel size depending on the structure dimension will be determined. In addition, a DOE study on different annealing steps in order to smoothen the resist after the development will be conducted.

Grayscale lithography is used for patterning of 3D structures directly into the photoresist layer. This method is divided in two groups, mask (or reticle) based [1,2] and maskless technologies [3,4]. Maskless technologies suffer on the lack of high throughput [3,4]. Reticle based offers the same throughput like a standard binary i-line projection exposure. Also, established i-line projection stepper tools often used in the industry, can be "upgraded" to grayscale tools with specialized reticles [2]. This opens up new possibilities for MEMS design, integrating of optical elements like lenses and the manufacturing of microsystems in general. Another option for creating lenses is the use of binary lithography in combination with a reflow process [5]. The i-line grayscale exposure requires specialized reticles to vary the light intensity, thereby achieving different height levels in the resist layer. The general process was evaluated and already published [3], but the roughness was not analyzed yet.

This work now focusses on process optimization of resist surface roughness after development, the dependency of pixel size and methods to reduce the surface roughness of grayscale patterns. The NIKON NSR2205i11D i-line stepper is used together with a specialized grayscale reticle. This reticle contains pixelated sub-resolutions features to control the light passing through the reticle. The sub-resolution features are arranged in a defined pixel size on the reticle. Within this pixel size one gray level is obtained by varying the fill factor. The pixel size also has an impact on the structure, fidelity and roughness, this impact needs to be investigated. By reducing the pixel size, smaller resist pattern feature sizes can be realized. At the same time, a lower pixel size leads to less available gray levels, since the area to modulate the light intensity is smaller. A low roughness of the resist patterns is beneficial, since it will be directly transferred via etching into the layer/substrate. The influence of the reticle pixel size will be investigated, as well as the impact of different annealing steps as a post development treatment. Test pads for roughness measurements, which are flat plateaus exposed with 50 % of the dose, were integrated on the reticle. In these experiments the ma-P 1211G resist from micro resist technology is used. Figure 1 to 3 shows different 3D structures exposed with the specialized grayscale reticle. In Figure 2 a SEM image of different adjacent height levels without any spacing is illustrated. A SEM image of tuned sidewalls with a defined slope is shown in Figure 3. Both structures of interest for MEMS fabrication. The roughness of the resist was analyzed by automatic CD-AFM measurements of 2 µm x 2 µm squared arrays on the "roughness pads" (Figure 5). The graph in Figure 4 shows the roughness measurement before annealing for 0.2 µm and 0.4 µm pixel sizes. For 0.2 µm pixel size the mean roughness Ra over all 13 wafers is 3.9 nm, while the value for 0.4 µm is about 15 % higher at 4.6 nm. In Table 1 the planned annealing parameters are shown. This experiment will be carried out currently, afterwards the measurements in Figure 4, CD-AFM and SEM will be redone and evaluated.

[1] Schuster, Christine, et al. "Advancing greyscale lithography and pattern transfer of 2.5 D structures using ma-P 1200G resist series." (2022).
[2] Schermer, S., et al. "2.5 D-patterning via i-line grayscale exposure for photonic structures and micro lens arrays." Novel Patterning Technologies 2024. Vol. 12956. SPIE, (2024).

[3] Grushina, A. "Direct-write grayscale lithography." Advanced Optical Technologies 8.3-4, 163-169 (2019).
[4] McKenna, C., et al. "Maskless direct write grayscale lithography for MEMS applications." 2010 18th Biennial University/Government/Industry Micro/Nano Symposium. IEEE, (2010).
[5] Bonitz, J., et al. "Scalable fabrication approach and fill factor optimization for single pixel microlens arrays." *Journal of Vacuum Science & Technology B* 42.6 (2024).

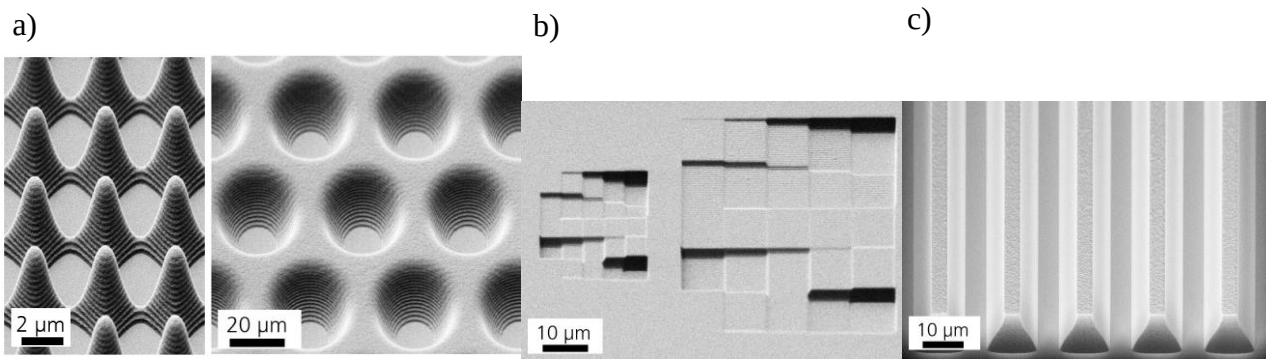

Figure 1. SEM image of exposed 3D structures in 1.8 µm thick ma-P 1215G resist, a) concave and convex lenses, b) different height levels (stairs) and c) tuned sidewalls in 7.8 µm ma-P 1275G resist.

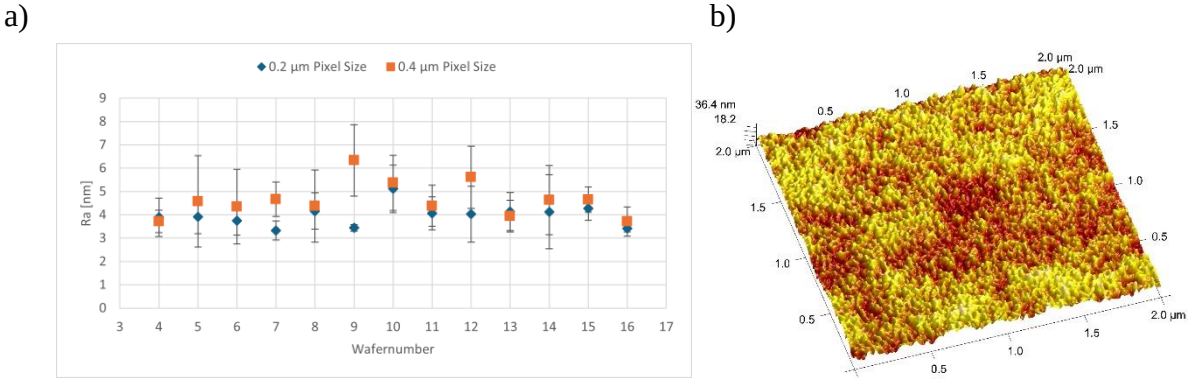

Figure 2. a) Resist Roughness R_a (after litho and before annealing) measured for the 0.2 µm pixel size (blue) and the 0.4 µm pixel over a total number of 13 Wafer. All Wafers are coated with ma-P 1211G with a resist thickness of 1.3 µm. The error bars are based on the max-min value; b) 2 µm x 2 µm height map measured with CD-AFM, pixel size of 0.4 µm. Max-Min Value of 29.9 nm

Table 1: Annealing Parameter in a convection oven;(r.t.= Room Temperature)

Wafer No.	**Temperature Step**
4 + 5	r.t. → 80 °C in 30 min Hold for 30 min @ 80 °C
6 + 7	r.t. → 90 °C in 30 min Hold for 30 min @ 90 °C
8 + 9	r.t. → 100 °C in 30 min Hold for 30 min @ 100 °C
10 + 11	r.t. → 110 °C in 30 min Hold for 30 min @ 110 °C
12 + 13	r.t. → 120 °C in 30 min Hold for 30 min @ 120 °C
14 + 15	r.t. → 130 °C in 30 min Hold for 30 min @ 130 °C

Ion Beam Planarization using Low-Viscosity, Non-Volatile Containing Polymer Coatings

L. P. Lingenfelder [a], J. Zajadacz [a], G. Dornberg [a], A. Finzel [a], D. Schäfer [b], T. Hänsel [b], F. Frost [a]

[a] Leibniz-Institut für Oberflächenmodifizierung e.V. (IOM), Leipzig, 04318, Germany
[b] NTG Neue Technologien GmbH & Co. KG, Gelnhausen, 63571, Germany

e-mail: lukasp.lingenfelder@iom-leipzig.de

The manufacture of metal optics for high-precision optical processes is one of the key technologies in numerous growth markets. Coated or uncoated precision metal mirrors in various sizes and shapes are used wherever high performance, complex component shapes, temperature stability, low weight with high strength or simply the economic method of production preclude the use of glass optics. Such optics are manufactured on ultra-precise diamond turning machines, which guarantee the required surface accuracy for different surface shapes (flat, aspherical or free-form surfaces). However, diamond turning creates regular patterns (turning marks) on the machined surface and thus a residual roughness that limits the performance of the optics by scattering. One process to further reduce surface roughness is the process of ion beam planarization [1].

In ion beam planarization [2], thin, usually polymeric, sacrificial layers are applied to the surfaces to be planarized. Subsequently, an ion beam etching step is used to transfer the leveled surfaces to the optical surface (Figure 1). Ideally, the etch rate selectivity (substrate material to polymer layer) is set to about 1 by optimizing ion beam parameters. Previous work has shown that this can reduce the roughness of diamond-turned NiP, for example, to approximately 30% of the initial value [3]. The degree of smoothing that can be achieved depends essentially on the leveling effect of the polymer layer, which is particularly limited by the evaporation of the solvent. This study demonstrates that the smoothing effect can be significantly increased by using the solvent-rich, non-volatile nanoimprint resist Amonil. Due to the remaining solvent after coating, the resist is still able to level, filling long-wavelength structures better than ordinary coatings. The smoothing behavior is investigated for pre-structured Si wafers with line patterns of lateral structure sizes up to 450 µm and a surface amplitude of 10 nm. Several pre-processing steps were conducted to increase etch stability and optimize etch rates toward a selectivity of one. The ion beam etching transfer is carried out with a broad beam ion source of the Kaufman type, whereby the influence of the etch selectivity (Si to photoresist) on the achievable degree of planarization is investigated.

The evolution of the surface topography of a typical Si test structure with a 20 µm period during a complete planarization cycle (initial profile in Si (A), after resist coating (B), as well as (C) after the adjusted ion beam planarization step) is summarized in Figure 2. The initial roughness of the Si test structure was reduced here to 3.7% of the initial value in a single process run. Figure 3 shows the achievable degrees of planarization (DoP) as a function of the spatial wavelength (period) of the structures. Up to a period of 30 µm, degrees of planarization < 10% can be achieved, and even spatial wavelengths of up to 150 µm can be flattened in this way. Additionally, Figure 4 illustrates the planarization results with a Ni-P sample.

Acknowledgements: The work was carried out within the joint project IONENPLAN, which was funded by the BMBF within the funding measure "KMU innovativ" (FKZ 02P19K551).

[1] Johnson, Leo F., and K. A. Ingersoll. "Ion polishing with the aid of a planarizing film." Applied Optics 22.8 (1983): 1165-1167.
[2] Frost, F., et al. "Large area smoothing of surfaces by ion bombardment: fundamentals and applications." Journal of Physics: Condensed Matter 21.22 (2009): 224026.
[3] Li, Yaguo, Hideo Takino, and Frank Frost. "Characteristics of diamond turned NiP smoothed with ion beam planarization technique." Journal of the European Optical Society-Rapid Publications 13 (2017): 1-5.

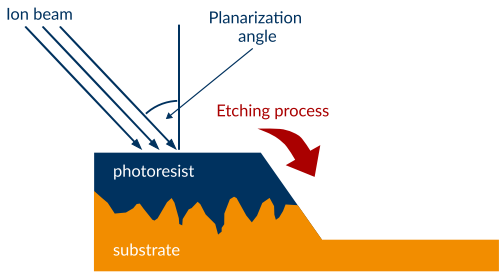

Figure 1. Schematic representation of the planarization process. A substrate material coated with photoresist is etched using RIBE. If the etch rate of the resist and the substrate are the same, the smooth surface of the resist is transferred into the substrate.

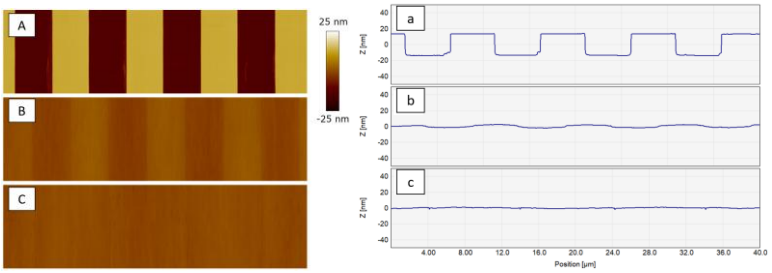

Figure 2. AFM 3D-images of a pre-structured Si-sample with a period of 20 µm before the planarization process (A) with an x-averaged profile (a); after coating with Amonil (B) and (b); after RIBE etching step (C) and (c).

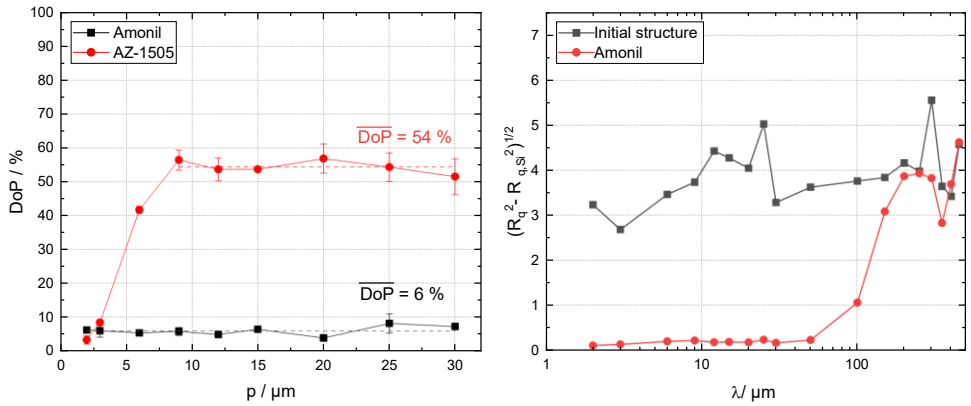

Figure 3. The degree of planarization (DoP) after applying the resist Amonil and AZ-1505 dependent on the lateral structure size is shown (left). Increased flowing-time of the after coating of Amonil improves the DoP, even for higher spatial wavelengths (right). The starting material was a silicon wafer structured with binary steps.

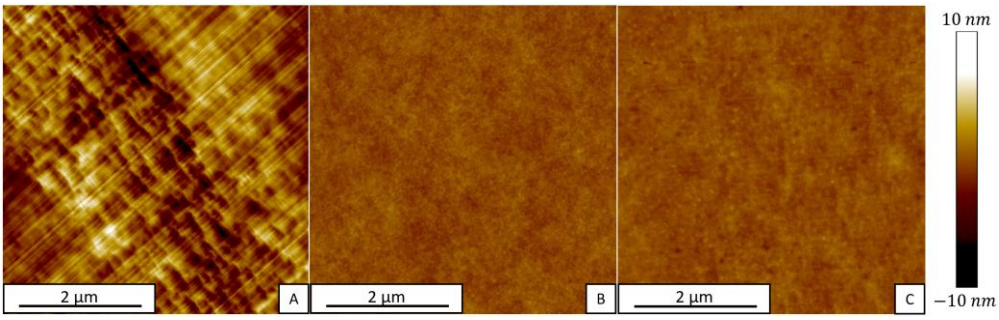

Figure 4. AFM images of a nickel-phosphorus sample before the planarization process (A), after coating with Amonil (B), and after RIBE etching step (C).

The role of surface chemistry and morphology on adhesive wafer bonding

Duarte J.F. da Silva [a], Tarni Aggarwal [a], Yuqing Jiao [a], Martijn J. R. Heck [a]

[a] Department of Electrical Engineering, Eindhoven University of Technology, Eindhoven, The Netherlands
e-mail: d.j.fernandes.da.silva@tue.nl

Adhesive wafer bonding via DVS-BCB (divinylsiloxane-bis-benzocyclobutene) is of high relevance owing to its superior bond strength, void-free interfaces, high degree of planarization, its chemical resistance and thickness control via dilution. These properties make it attractive for heterogeneously integrated Si, Si_3N_4, and III-V photonics where their waveguides must be within 100s of nanometers in order to ensure low interlayer coupling loss. With ultra-thin DVS-BCB bonding, however, particle contamination becomes a priority as even micron-sized particles can lead to millimeter-sized defects [1]. The size of these defects can be minimized by improving the adhesion between the bonding interfaces, which can be achieved via adhesion promoters, such as AP3000 [2]. This chemical is based on vinyltriacetoxysilane chemistry and, upon coating, the silanol bonds in the acetoxy groups will condense with hydroxyl groups at the bonding interface forming a strong covalent bond. Then, the vinyl groups will react with the o-xylylene rings of the BCB thus linking the adhesive to the semiconductor. The success of this adhesion promoter has allowed us to reliably bond virtually any pair of surfaces. Despite this, the optimization of surface properties like chemistry and morphology in adhesive bonding remains elusive even for well established bonding interfaces, which becomes paramount when working with thinner adhesive thicknesses so as to maximize adhesion.

In this work, we aim to understand how the surface chemistry and morphology of different surfaces interacting with AP3000 and the adhesive thickness will affect the overall adhesion. Therefore, we have tested four bonding stacks: i) InP + BCB (70nm) + Si, ii) InP + AP3000 + BCB(70nm) + AP3000 + Si, iii) InP + AP3000 + BCB(200nm) + AP3000 + Si and iv) InP + SiO_2 (10nm) + AP3000 + BCB(200nm) + AP3000 + SiO_2 (10nm) + Si. In these samples, the InP and Si wafer surfaces have been exposed to an O_2 RIE plasma at 200°C for 5 minutes at 1000W prior to AP3000 spin coating or SiO2 deposition. Additionally, we have performed x-ray photoelectron spectroscopy (XPS) on Si and InP wafers for different surface treatments, along with atomic force microscopy (AFM) measurements for surface roughness. Finally, in order to assess the adhesion energy of each bonded sample, we make use of the relation between particle size and defect radius developed in [3], as illustrated in figure 1. In our first sample, small particles cause large defects due to weak physical bonding. Sample ii), with AP3000, shows smaller defects, highlighting the benefit of covalent bonding. In sample iii), tripling the adhesive thickness reduces the sensitivity to particle height, as only a fraction of each particle punctures the InP membrane. XPS measurements show the InP surface is In-rich, suggesting an In-based oxide with mostly In–OH groups. These react with AP3000 to form In–O–Si or P–O–Si bonds, which are expected to be weaker than Si–O–Si bonds based on the In-O, P-O and Si-O dissociation energies (360, 596, and 798 kJ/mol, respectively [3]). Such chemistry confirms the native oxides in bare InP as an unsuitable bonding layer. Finally, in sample iv), 10 nm PECVD SiO_2 layers and subsequent thermal treatment (280°C, 3 h) lead to the smallest defects. XPS and AFM measurements suggest two reasons: 1) PECVD SiO_2 has an increased Si–OH content (see figure 2 and table 1), enabling stronger siloxane bonding with AP3000; and 2) the PECVD SiO_2 surface is ~10× rougher, increasing surface area and thus AP3000 retention, evidenced by higher surface carbon content.

In summary, we have studied different adhesive bonding layer stacks, and we demonstrate improved adhesion for rough and hydroxyl-rich surfaces. Deposition of PECVD SiO_2 prior to bonding will yield good results, but we expect improvements by harnessing surface plasma activation techniques, thus paving the way for improved bonding strength and higher quality bonds, particularly for ultra-thin DVS-BCB bonding.

References

[1] - Roelkens, G., 2007. PhD thesis, Universiteit Gent.
[2] - Im, J. et al. 1999., in: Proceedings International Symposium on Advanced Packaging Materials. Processes, Properties and Interfaces, pp. 53–56.
[3] - Speight, J.G. (Ed.), 2017. BOND LENGTHS AND STRENGTHS, in: Lange's Handbook of Chemistry. McGraw-Hill Education, New York.

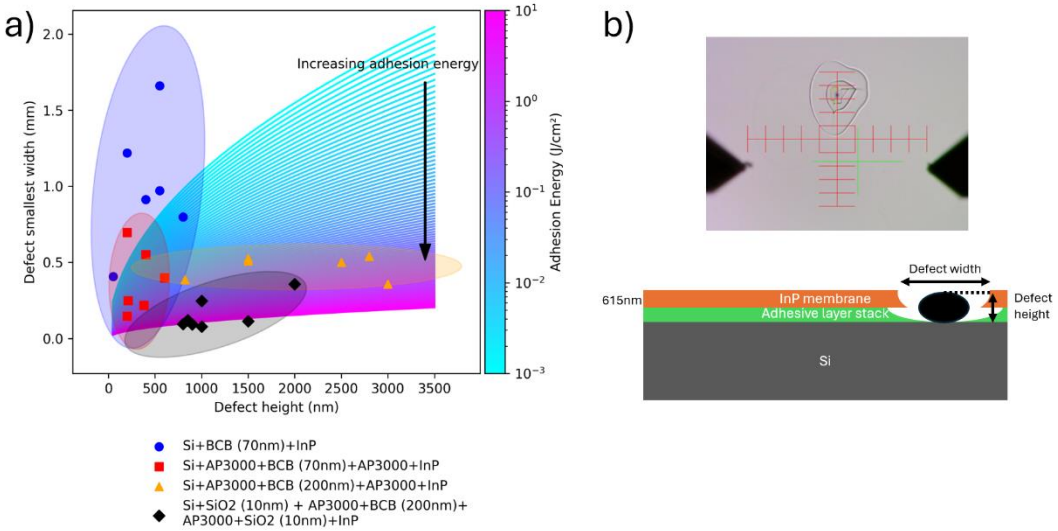

Fig. 1 – a) Analysis of the defect size as a function of the defect height as illustrated in b), where in the top is the view of a profilometer, and in the bottom an illustration of the physical system. Colored curves are theoretical predictions based on mechanical analysis for wafer bonding (see [1]).

	O 1s analysis		Full spectrum analysis	AFM analysis 1x1um
Processing step	Si-OH atomic %	SiO2 atomic %	Carbon atomic %	Surface roughness (nm)
Bare Si	0.00	100.00	5.27	0.3*
Bare Si+O2 plasma	3.40	96.60	0.49	
Bare Si+O2 plasma+AP3000	0.00	100.00	2.82	
Bare Si+O2 plasma+SiO2	16.95	83.05	0.77	3.46
Bare Si+O2 plasma+SiO2+AP3000	0.00	100.00	10.94	
Bare Si+O2 plasma+SiO2+O2 plasma	29.29	70.71	0.75	
Bare Si+O2 plasma+SiO2+O2 plasma+AP3000	0.00	100	10.53	

Table 1 – Summary of the results from XPS and AFM measurements on a Si wafer for various processing steps. The Si surface roughness is an estimation as the value is taken from the measurement of a DSP InP wafer surface.

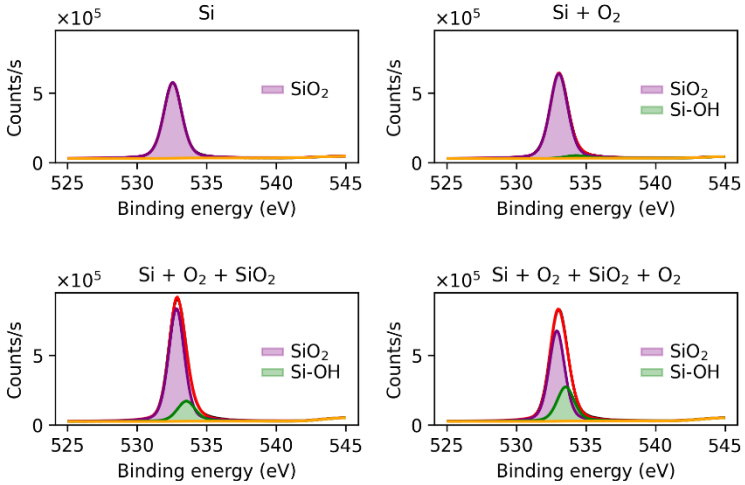

Fig. 2 – Deconvoluted O 1s XPS spectrum for the different Si surface treatment.

Sub-diffraction-limited nano-texturing on silicon by ultrafast lasers with MHz burst mode

Pin-Yen Chen, Yu-Sheng You, Yuan-Jen Chang*

Institute of Manufacturing Technology, National Taipei University of Technology, Taipei 10608 Taiwan
*e-mail: yjchang@ntut.edu.tw

In recent decades, with the rapid advancements in technology, the demand for applications of nano-texturing and nano-devices has been steadily increasing. Currently, techniques to fabricate nano-textures on material surfaces include photolithography, ion milling, or laser nanofabrication. Photolithography is the primary method for producing large-area nanostructures; however, its drawback lies in the high cost. Ion milling offers high resolution, but it is limited by its low fabrication efficiency. On the other hand, laser processing enables rapid, large-area fabrication of nanotextures with material flexibility, allowing the formation of sub-100 nm structures by laser-induced periodic surface structures (LIPSS) [1] to overcome the constraint of the optical diffraction limit ($\lambda/2$). In this paper, we have proposed to utilize ultrafast lasers in burst mode and form sub-diffraction-limited nanostructures on silicon surfaces.

To fabricate structures smaller than half of the laser wavelength, we employ a technique of overlapping dual orthogonally polarized femtosecond laser beams [2,3]. Our laser system operates at a central wavelength of 1030 nm, with a pulse duration of 350 fs, delivering a maximum power of 5 W at a repetition rate of 300 kHz, and is focused using an objective lens (NA = 0.65). The spot size after the objective lens is 1.45 μm. The experimental setup is shown in Figure 1. The repetition rates of 4 kHz, 5 kHz, and 6 kHz and the pulse energies at 400, 500, 555.6, and 583.3 nJ were applied to our experiments. Combined with MHz-burst mode (50 ns interval between shots), we draw circular patterns with a diameter of 200 μm on silicon using a galvanometer and a translation stage and measured the line width of circles.

The experimental results showed that at fluence of 57.4 J/cm^2 (600 nJ/pulse, 3.6 mm/s, 5 kHz), the linewidth at the top of the circle was 1.139 μm, and it was 1.016 μm at the bottom. Meanwhile, the linewidths were 1.295 μm and 0.916 μm at the most left and right of the circle, respectively. We found that at the top and bottom of the circle, increasing the burst mode with the same pulse energy reduced the line width efficiently, as shown in Figure 2. SEM images revealed that under a repetition rate of 4 kHz, a power of 2 mW (47.56 J/cm^2), and a burst mode of 1, a minimum line width of 435.5 nm was achieved at the right side of the circle, as shown in Figure 3. In Table 1, we can see that the line width at the top and bottom of our circle is slightly larger than that on the most left and right of circles. This is because the scanning direction is parallel to the polarization direction when passing through the left and right sides of the circle, resulting in a smaller line width. These findings contribute to advancing the development of micro- and nanostructure fabrication by exploring the interplay between laser parameters and material properties, with potential applications in nanotechnology and photonics.

[1] Huang, M., Zhao, F., Cheng, Y., Xu, N., and Xu, Z., "Origin of Laser-Induced near-Subwavelength Ripples: Interference between Surface Plasmons and Incident Laser," *ACS Nano*, 2009, 3 (12), 4062–4070.
[2] Lin, Z., Ji, L., and Hong, M., "Approximately 30 nm Nanogroove Formation on Single Crystalline Silicon Surface under Pulsed Nanosecond Laser Irradiation," *Nano Lett.*, 2022, 22, 7005−7010.
[3] Lin, Z., Liu, H., Ji, L., Lin, W., and Hong, M., "Realization of ∼10 nm Features on Semiconductor Surfaces via Femtosecond Laser Direct Patterning in Far Field and in Ambient Air," *Nano Lett.*, 2020, 20, 4947−4952.

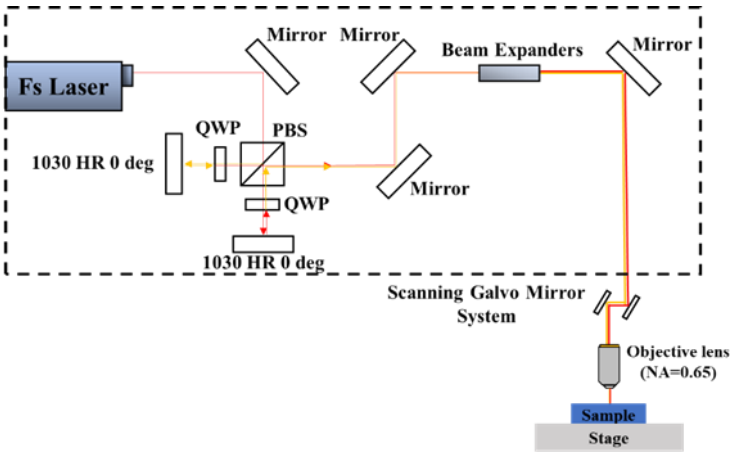

Figure 1. The experimental setup of ultrafast laser machining with objective lens.

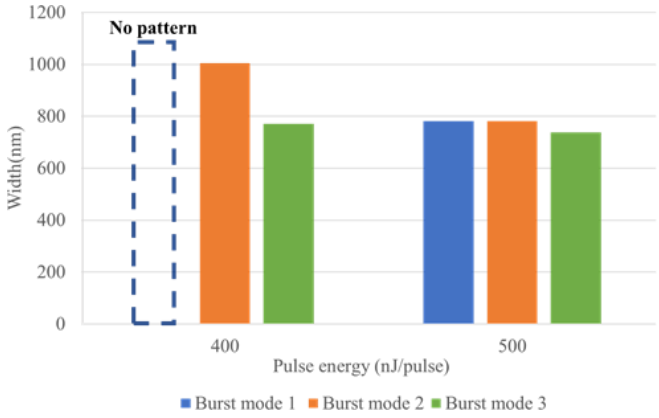

Figure 2. The relationship between burst mode and the resulting line width.

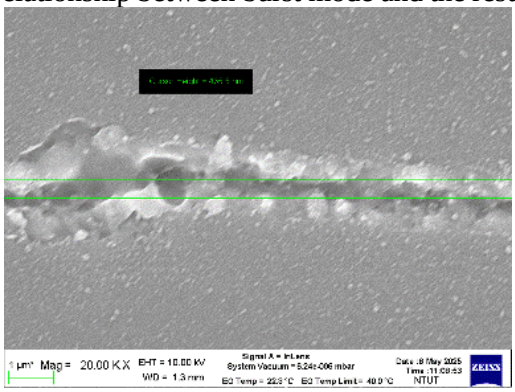

Figure 3. Bottom of circle at divided frequency of 4 kHz, 2 mW (500 nJ/pulse), and burst mode 1

Table 1. Linewidth with different laser parameters at different positions of machined circles.

	Top	Bottom	Left	Right
5k, 2mW(400nJ/pulse), Burst mode 1 38.31 J/cm²	NA	NA	NA	NA
5k, 4mW(400nJ/pulse), Burst mode 2 76.63 J/cm²	815.1 nm	1005 nm	926.8 nm	603 nm
5k, 6mW(400nJ/pulse), Burst mode 3 144.94 J/cm²	937.9 nm	770.4 nm	826.3 nm	547.1 nm
4k, 2mW(500nJ/pulse), Burst mode 1 47.56 J/cm²	1195 nm	781.6 nm	558.3 nm	435.5 nm
4k, 4mW(500nJ/pulse), Burst mode 2 95.12 J/cm²	1038 nm	781.6 nm	558.1 nm	725.8 nm
4k, 6mW(500nJ/pulse), Burst mode 3 142.69 J/cm²	859.8 nm	736.9 nm	714.6 nm	748.1 nm

Fabrication of Micro-Lattice Filters for Particulate and Gas Emission Reduction

Seo Rim Park [a], Myung Seo Kim [a], Young Tae Cho [a]

[a] Changwon National University, Changwon, 51139, Republic of Korea
e-mail: ytcho@changwon.ac.kr

keywords : Micro-lattice structures, Diesel emission reduction, Particulate matter filtration, Catalytic conversion

Emissions and particulate matter (PM) from diesel generators are major contributors to air pollution, prompting ongoing efforts to develop technologies for their reduction. Among the commonly used approaches are diesel oxidation catalysts (DOC) and selective catalytic reduction (SCR) systems, both of which use ceramic monoliths coated with noble metal catalysts such as Pt and Rh. Diesel particulate filters (DPF) also employ monoliths, where alternating inlet and outlet channels are blocked to force exhaust gases through porous ceramic walls. However, these systems have several limitations, including the high cost of catalysts, the presence of dead zones within housings, and increased device size and weight. In particular, DPFs can cause high back pressure and suffer performance loss if PM is not properly regenerated, leading to channel blockage.

To address these issues, this study proposes a compact particulate filter incorporating a micro-lattice structure with low density and high surface area, aiming to improve catalytic conversion and reduce pressure drop. Micro-lattices feature overhanging and intricate geometries that are difficult to fabricate using conventional methods. Therefore, we utilized either digital light processing (DLP) or metal fused filament fabrication (FFF) 3D printing to fabricate polymer- and copper-based micro-lattice filters. A heat-resistant photopolymer resin was used for DLP printing, suitable for exhaust temperatures around 300 °C. Since direct catalyst printing is limited, catalytic materials such as CuO, Mn, and Pt were either incorporated into the resin or applied onto the printed lattice templates through dip-coating. [1,2].

Octet-truss and Kelvin lattice types were selected based on simulation results showing catalytic conversion efficiencies exceeding 90% [3], and their performance was compared with conventional monoliths. As catalyst materials, titanium dioxide (TiO_2) was used for photocatalytic decomposition of VOCs, NO_x, and SO_x under UV light, while copper oxide (CuO) was applied for redox-based removal of harmful gases at lower temperatures.

Performance tests were conducted using real exhaust gases from a diesel generator. Gas concentration and pressure drop were measured before and after the filter. The micro-lattice filters achieved more than 70% PM capture efficiency under low-pressure-drop conditions and demonstrated higher catalytic performance than monoliths. This is attributed to the complex 3D flow paths of the micro-lattices, which promote uniform gas distribution and increase the effective reaction surface. Moreover, the open-cell structure allows continuous flow even when some passages are blocked by PM, thereby maintaining stable operation. In conclusion, this study presents a micro-lattice-based filtration system with improved performance and reduced device size, which may be applicable to emergency and industrial diesel generator systems.

Acknowledgement
This work was supported by the National Research Foundation of Korea(NRF) grant funded by the Korea government(MSIT)(No. RS-2023-00238462, RS-2019-NR040067) and Korea Institute for Advancement of Technology (KIAT) grant funded by the Korean government (MOTIE) (141588607, Additive Manufacturing Technology Innovation Alliance for Aerospace/Small Modular Reactor/Defense Industry).

References
[1] D. H. Kim et al., APL Materials. 12.2 (2024)
[2] S. R. Park et al., Journal of the Korean Society for Precision Engineering 38.9 (2021): 631-637.
[3] G. H. Jeong et al., Energies 15.12 (2022): 4200.

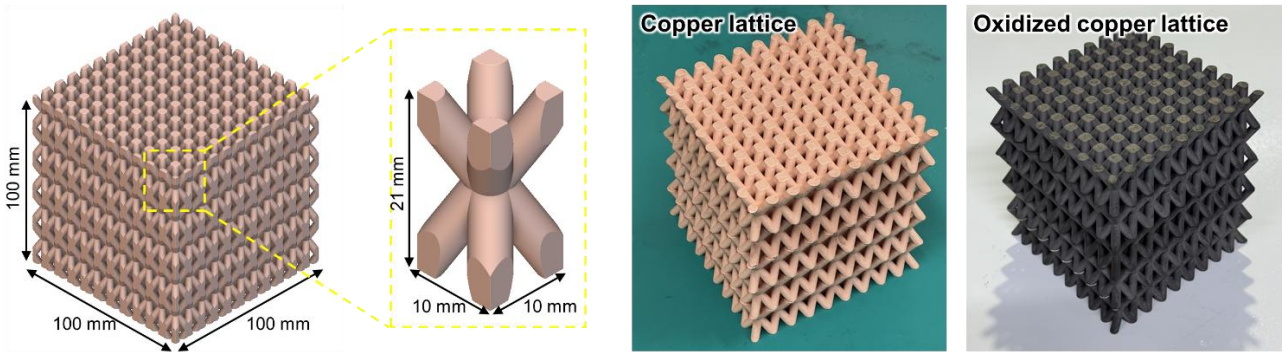

Figure 1. BCC lattice fabricated using copper and the corresponding copper oxide lattice.

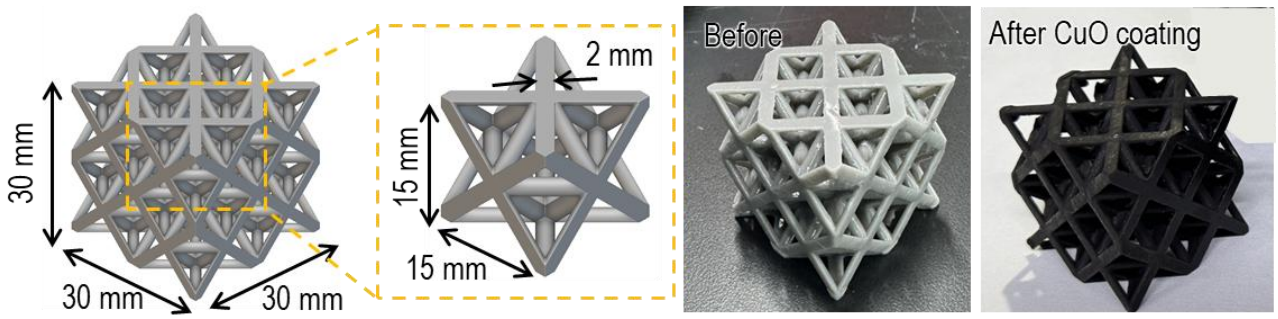

Figure 2. Octet-truss dip-coated with CuO mixture.

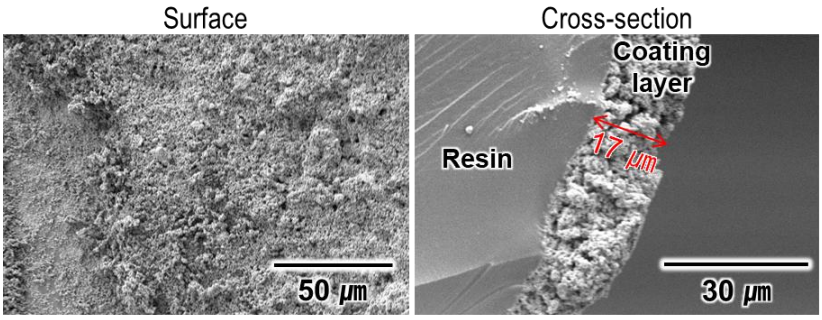

Figure 3. SEM images of CuO-coated microlattice (surface and cross-section).

Microfluidic Devices Based on Deterministic Lateral Flow Displacement for Protein Separation

Nilüfer Tasli [a], Sadhana Tiwari [a], Irene Fernandez-Cuesta [a, b]

[a] University of Hamburg, Hamburg, 20148, Germany
[b] Hamburg Center for Ultrafast Imaging
e-mail: niluefer.tasli@studium.uni-hamburg.de

Deterministic lateral flow displacement (DLD) has been widely used since 2004 for separating bioparticles such as blood cells, parasites, bacteria and exosomes in microfluidic devices. This method enables size-, charge-, and shape-based separation, making it highly promising for medical diagnostics. DLD operates across a broad particle size range from millimeters to nanometers. It offers sensitive, precise separation, which is particularly advantageous for point-of-care applications [1-2].

Protein separation is a key step in molecular biology. Conventional techniques used for protein separation and enrichment, such as size exclusion chromatography, ion exchange chromatography, centrifugation, and affinity chromatography often require large sample volumes and result in significant sample loss. In contrast, DLD-based microfluidic devices provide rapid, sensitive, robust, and cost-effective separations with minimal sample loss and high throughput [1-2].

In this work, we propose using a single-use fluidic chip made by direct UV imprinting for separation of beads, which can be further functionalized to capture specific proteins from a liquid sample. For making such devices, it is critical that the upper surface remains flat and smooth, since rough surfaces will prevent further fluidic device sealing and will result in liquid leakage. For this, we use a double replication approach, where we first make a silicon stamp and etch the microchannels into it, then make a negative replica of it, which is then used as the active stamp for making the devices by direct UV imprinting [3]. In this process, the upper surface will then be a replica from the original, ultra-smooth silicon wafer. For this, the silicon stamp was fabricated using photolithography and RIE. A silicon wafer was spin-coated with S1813 positive photoresist to a thickness of 13000 Å, soft-baked at 115 ℃ for 60 s, and exposed to UV light for 7 s through an aligned mask. The structure was developed in MF-319 for 60 s, followed by reactive ion etching (SF_6/C_4F_8, 60 min). OrmoStamp could not be used to make the negative stamp, since imprinting the micropillars is problematic due to air trapping. Instead, PDMS at a 1:10 ratio was used to copy the silicon stamp. The fluidic devices were made in OrmoStamp prepared by direct UV imprinting (500 mJ/cm^2 dose). The surface of the fluidic sample was activated using oxygen plasma and then sealed with a thin OrmoStamp coverslip (see Fig 1).

Fig 2A shows an image of the silicon stamp. The microchannel is 500 μm in width and 5000 μm in length, mostly covered by micropillars. Three microchannels (50 μm wide, 24 μm deep) are used to connect to three liquid inlets: one to flow the mixed liquid sample (middle one) and the two outer ones for liquid focusing. The three microchannel outlets enable collection of the separated particles with distinct size fractions. Figure 2B shows an image of the micropillars, with information on the DLD parameters: $D_C = 1.4 \cdot d \cdot (\Delta\lambda/\lambda)^{0.48}$, where D_C is the critical diameter (7.83 μm), d is the gap distance (17.73 μm), $\Delta\lambda$ is the vertical offset between adjacent pillars (3.42 μm), and λ is the center-to-center pillar distance (37.75 μm) [4]. In this specific device, pillars have a diameter of 20 μm and a height of 24 μm (see Fig 2C).

The critical diameter determines particle trajectories. Particles larger than the D_C follow a displacement mode, while smaller particles migrate in a zigzag mode. Precise adjustment of the critical diameter improves separation efficiency and throughput. Figure 3A shows the flow paths of beads with different sizes. As a proof-of-concept, a mixture of 1 μm and 10 μm green fluorescent microbeads was introduced into the device. Larger beads ($> D_C$) were displaced to the upper outlet, while smaller beads ($< D_C$) migrated to the middle outlet, confirming size-based separation. Ongoing work will focus on further exploiting the device for capturing and separating proteins. This will involve conjugating functionalized fluorescent beads with antibodies specific to the target protein. The target proteins will be bound to these antibody-coated beads (see Fig 3B).

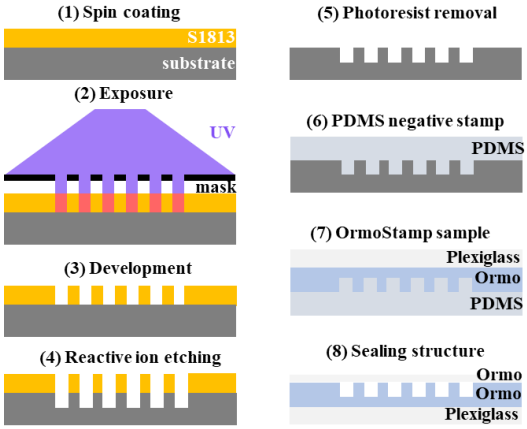

Figure 1. Fabrication process for making the silicon stamp, the PDMS negative stamp and the OrmoStamp microfluidic samples, including sealing them with a coverslip.

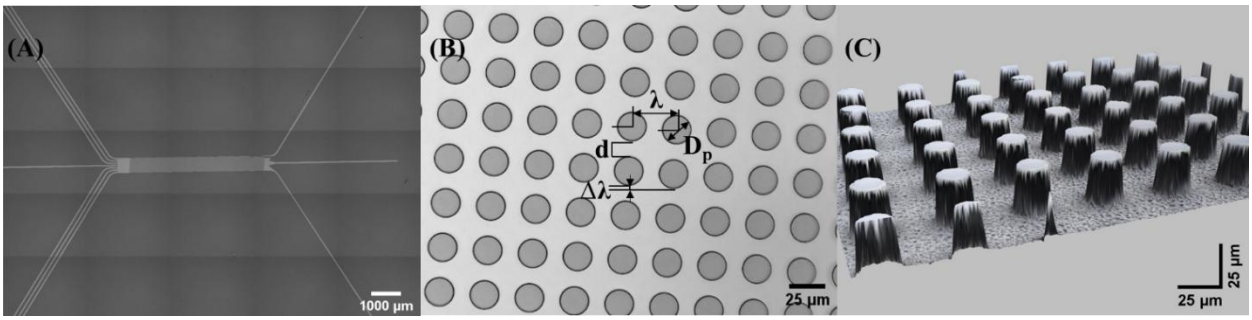

Figure 2. Images of the silicon masterstamp and the OrmoStamp sample obtained with a confocal microscope. (A) Overview of the structure of the DLD device. (B) Detail of the pillars in the microchannel, and DLD parameters: d is the gap distance, $\Delta\lambda$ is the vertical offset between adjacent pillars, λ is the center-to-center distance between pillars, and D_p is the pillar diameter. (C) Image of the pillars on the OrmoStamp fluidic chip with a height of 23.96 µm.

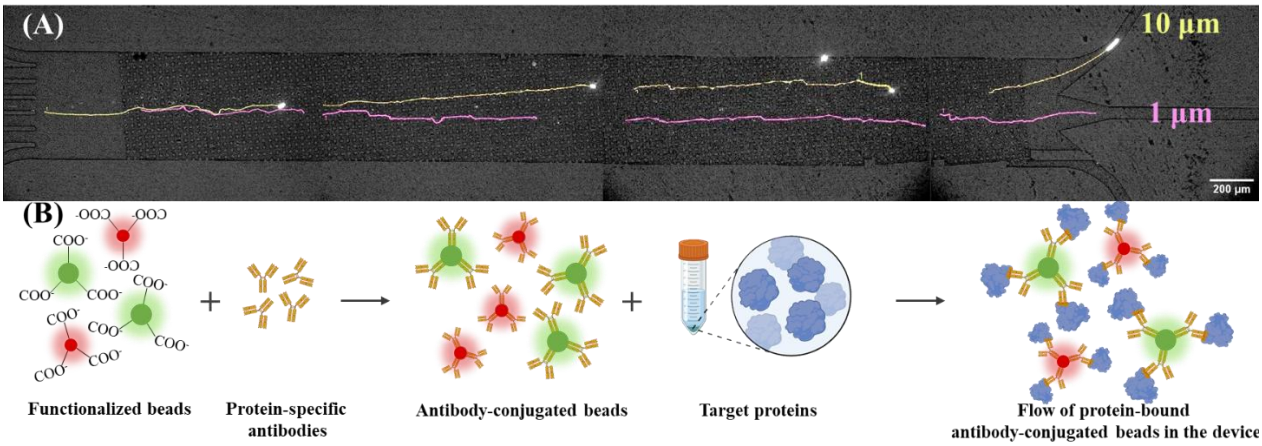

Figure 3. (A) Flow paths of 1 µm and 10 µm beads in the DLD microfluidic device, showing that larger and smaller beads follow different flow trajectories and can be collected at different outlets. (B) Strategy for binding proteins to beads.

References:

[1] Y. Zhang et al., Nano-Micro Lett. (2019) 11:77.
[2] S. Shikha and Y. Zhang et al., Nature communications (2018) 9:1254.
[3] Y. Nakai et al., J. Vac. Sci. Technol. B 29 (2011) 011005.
[4] S. Quian and F. Li et al., Scientific reports (2018) 8:3618.

Evaluation of Inorganic-organic Hybrid Resist Materials with ultrafast coherent high harmonic generation (HHG) EUV system

Hiroki Yamamoto1[a], Masahiko Ishino2[b], Thanh-Hung Dinh1[b]

[a] *Takasaki Institute for Advanced Quantum Science, National Institutes for Quantum Science and Technology (QST), 1233 Watanukimachi, Takasaki, Gunma 370-1292, Japan*
[2] *Kansai Institute for Photon Science (KPSI), National Institutes for Quantum Science and Technology (QST), 8-1-7 Umemidai, Kizugawa, Kyoto 619-0215, Japan*
e-mail: yamamoto.hiroki@qst.go.jp

The advent of the digital society has resulted in an unprecedented increase in the demand for high-performance electronic products such as smart phones, computers, and so on. The ongoing progress in the semiconductor industry leads to continual device miniaturization, which improves the performance of semiconductor devices. Up to now, lithography has been the main driving force behind this progress. Since 2019, the semiconductor industry has adopted extreme ultraviolet (EUV) lithography that has a wavelength of 13.5 nm in high-volume production lines [1]. Currently, the development of high-numerical aperture (high-NA) EUV exposure tools is also in progress to propel further miniaturization [2].

For high-NA EUV lithography, superior resist materials and processes are required. The resolution target of resist materials has been set to 8.4 nm half-pitch (hp) for dynamic random access memory (DRAM) by 2031. Although a high-NA EUV tool has potential for resolving less than hp 8.4 nm line-and-space patterns, the resist materials suitable for high-NA EUV have not been developed yet [3].

In the realization of patterning feature sizes of sub-10 nm in semiconductor devices, it is essential to get new resist design strategies such as inorganic-organic hybrid resist materials for extreme ultraviolet (EUV) lithography. However, it is challenging for fundamental researchers to develop EUV resist materials due to the difficulty in obtaining experimental time for EUV exposure and limited EUV exposure tools, which are very expensive. Recently, we developed ultra-fast coherent EUV system based on high harmonics generation (HHG) and applied to EUV resist evaluation. In this study, the sensitivity of inorganic-organic hybrid resist materials known as metal-oxo clusters was evaluated by using this HHG EUV system.

Some types of inorganic-organic hybrid resist materials (Zr- based and Hf-based oxo clusters) were synthesized using the sol-gel method. Resist solutions were spin-coated onto Si substrates and they were exposed to EUV HHG radiation. Typical spectra of the focused HHG beam shown as blue lines in Fig. 1 were calculated from the measured input HHG spectra (green line) and the mirror reflectance (red line). The inset of Fig. 1 shows a 2D image of the high-order harmonics around 13.5 nm after passing through two Zr filters and being reflected by a Mo/Si multilayer flat mirror. They were exposed to HHG EUV by changing the exposure position and time. After the exposure, they were immersion-developed in cyclohexanone for 30 s and then dried with an air duster. Resist film thickness was measured with a stylus profilometer (BRUKER, Dektak XT) to obtain sensitivity curves. Also, line profiles were examined using an optical microscope (BX-53M with Flovel FR-400C, Olympus) and LEXT nano search microscope (OLS4500, Olympus).

The line structure dimensions were characterized by optical microscopy. The six black lines appeared on the irradiated Hf-based oxo clusters film after development and black line patterns were observed as shown in Fig. 2 (a). Relatively well-formed lines were obtained after development. Line length was roughly estimated from optical microscope images. The average line length was c.a. 3 mm. In order to measure the line width accurately, AFM was used. Fig. 2 (b) shows AFM image of the line pattern upon exposed to HHG EUV for 4 mins using LEXT nano search microscope. The line widths were estimated by analyzing the 3-dimentional profiles. The fluence was converted to exposure dose using exposure time and these values to make sensitivity curves of hybrid inorganic-organic resists. Fig. 3 shows the sensitivity curves of hybrid inorganic-organic resi sts with different metal core ((a) Zr-based, and (b) Hf-based oxo clusters) upon exposure to EUV after development. Their thicknesses of spin-coated resists were 50 nm, The obtained sensitivities were found to be comparable to the sensitivities obtained by conventional EUV flood exposure tool. It is concluded that the developed coherent HHG EUV system is very useful for sensitivity measurement of EUV resists and developing new EUV resists.

[1] E. Verhoeven, R. Schuurhuis, M. Mastenbroek, P. Jonkers, F. Bornebroek, A. Minnaert, H. Dijck, P. Yaghoobi, G. Fisser., P. Tayebati, K. Hummler, R. Es, *Proc. SPIE*, **11609** (2021) 1160908.

[2] J. Schoot, S. Lok, E. Setten, R. Maas, K. Troost, R. Peeters, J. Finders, J. Stoeldraijer, J. Benschop, P. Graeupner, P. Kuerz, E. Kaiser, T. Stammler, *Proc. SPIE*, **11609** (2021) 1160905.
[3] T. P. Allenet, M. Vockenhuber, C.-K. Yeh, J. G. Santaclara, L. Lent-Protasova, and Y. Ekinci, *Proc. SPIE*, **11854** (2021) 118540N.

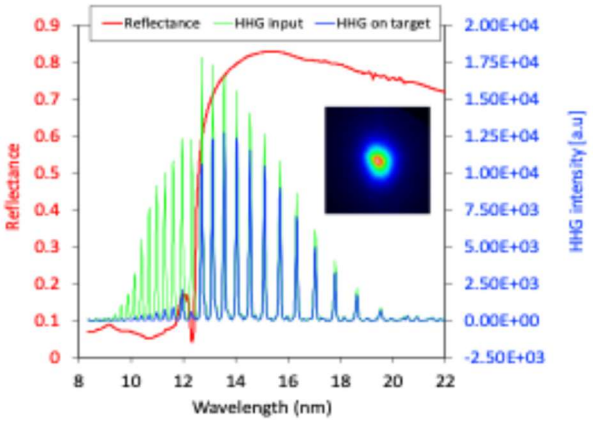

Figure 1. Typical spectrum of the HHG beam used for evaluating resist sensitivity. The inset shows a typical beam profile of the high harmonics around 13.5 nm.

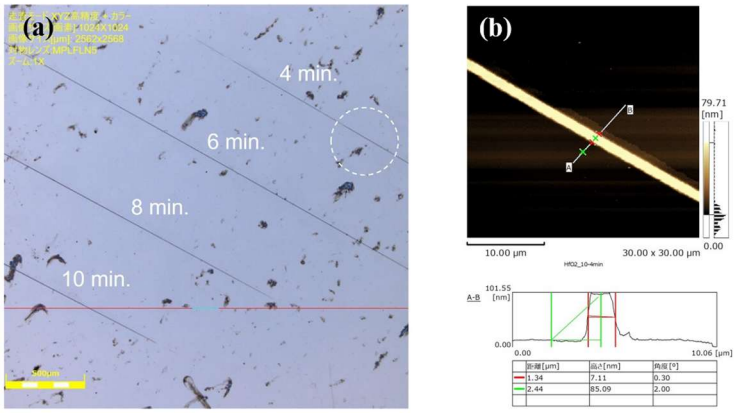

Figure 2. (a) Optical micrographs of six black lines on the irradiated Hf-based oxo clusters film after development and (b) AFM image of black line- pattern of Hf-based oxo clusters after development.

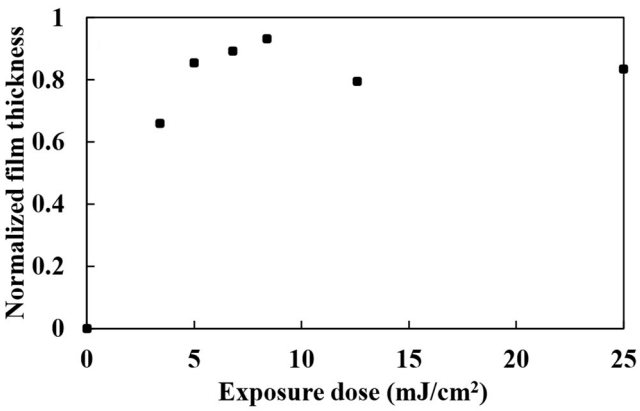

Figure 3. Sensitivity curves of hybrid inorganic-organic resists with Zr-based, oxo clusters upon exposure to EUV after development.

Graphene Electrodes for In-plane Electrochemical growth of TMDCs

Shaokai Song [a], Shibin Thomas [a], Nema Abdelazim [a], Sami Ramadan [b], Victoria Greenacre [c], Hongwei Zhang [a], Yisong Han [c], Richard Beanland [c], Gill Reid [c], Philip N Barlett [c], Kees de Groot [c], Yasir J Noori [c]

[a] School of Electronics and Computer Science, School of Chemistry, University of Southampton, Southampton, UK
[b] Department of material, Imperial College, London, UK
[c] Department of Physics, University of Warwick, Coventry, UK
e-mail: y.j.noori@southampton.ac.uk

Short-channel effects in field-effect transistors have intensified interest in two-dimensional (2D) materials, particularly transition metal dichalcogenides (TMDCs), due to their potential to mitigate these effects. A significant challenge in TMDC-based transistors is the high contact resistance at metal-semiconductor interfaces, often attributed to van der Waals interactions between layers. Electrodeposition emerges as an industrially compatible technique offering unique advantages for scaling 2D heterostructures. We designed and transferred novel patterns onto graphene substrates, enabling lateral electrodeposition of TMDCs. Through iterative optimization of fabrication processes, including lithography, lift-off, and etching—we overcame challenges related to pattern fidelity and material compatibility. High-quality graphene substrates have been prepared for subsequent TMDC deposition. Our next step involves utilizing these graphene electrodes to deposit various TMDCs and their heterojunctions, aiming to explore diverse applications. Additionally, we have mastered mechanical exfoliation techniques to fabricate comparable transistors, providing benchmarks for evaluating the performance of our electrodeposited structures.

[1] N. M. Abdelazim et al., "Lateral growth of MoS2 2D material semiconductors over an insulator via electrodeposition," Advanced Electronic Materials, vol. 7, no. 9, p. 2100419, 2021.
[2] Y. Noori et al., "Electrodeposited WS2 monolayers on patterned graphene," 2D Materials, vol. 9, no. 1, p. 015025, 2021.
[3] Y. Noori, S. Thomas, and S. Ramadan, "ACS Appl. Mater," Interface, vol. 12, p. 49786, 2020.
[4] S. Thomas et al., "Tungsten disulfide thin films via electrodeposition from a single source precursor," Chemical Communications, vol. 57, no. 79, pp. 10194-10197, 2021.
[5] P. N. Bartlett et al., "Molecular precursors for the electrodeposition of 2D-layered metal chalcogenides," Nature Reviews Chemistry, pp. 1-14, 2025.

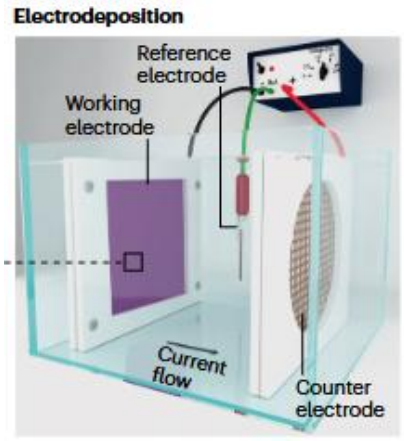

Figure 1. schematic illustration of a three-electrode electrodeposition setup with a substrate.

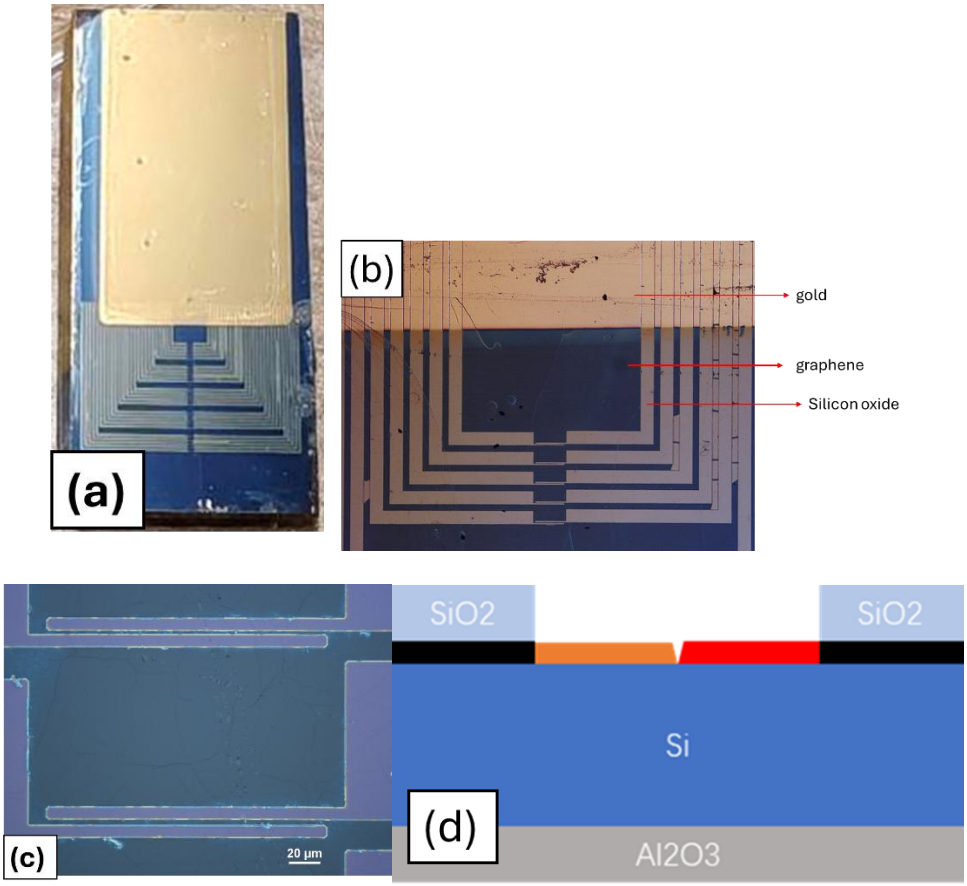

Figure 2. (a) image of a fabricated graphene substrate designed for lateral growth; (b) microscope image of the fabricated graphene samples, indicating the materials included; (c) microscope image of the fabricated graphene electrode structure, showing four adjacent electrodes with a design flow similar to (b); (d) schematic diagram of a transistor structure utilizing graphene, where the black region represents graphene, and the orange and red blocks denote heterojunctions generated laterally by graphene.

A Fabrication Technique for Simultaneous Embedding and Welding of Metal Nanowires on Polymer Surfaces for Flexible Conductors

Sangmok Kim [a], Youngjae Nam [a] and Joonwon Kim [a]

[a] Department of Mechanical Engineering, Pohang University of Science and Technology (POSTECH), Pohang, 37673, Republic of Korea
e-mail: joonwon@postech.ac.kr

Keywords: Fabrication technique, embedding + welding, flexible conductor, high conductivity

As interest in flexible electronic devices continues to grow,[1] the demand for flexible pressure sensors, key components of these systems, has amplified. These sensors have shown great potential for integration into applications such as electronic skin (E-skin),[2] flexible touch displays,[3] and wearable health-monitoring systems.[4] To meet the performance requirements of these applications, flexible pressure sensors must incorporate robust and highly conductive electrodes that can operate reliably under repetitive high pressure and electromagnetic interference (EMI).[5]

To address these requirements, recent studies have focused on embedding metal nanowires (MWs) into polymer matrix to develop flexible electrode.[6] This approach takes advantage of mechanical interlocking between MWs and the polymer to maintain electrical conductivity without loss or delamination of the MWs, while preserving the polymer's intrinsic properties and ductility. As a result, robust and reliable flexible electrodes can be fabricated. Despite these advantages, such approaches still face challenges in achieving high electrical conductivity due to point contacts between MWs, which limit device performance.

In this study, we propose a fabrication technique that simultaneously welds MWs and embeds them onto the polymer network surface, thereby achieving both mechanical durability and high electrical conductivity. Silver nanowires (AgNWs) and thermocurable polydimethylsiloxane (PDMS) were selected as the conductive MWs and polymer, respectively. The process involves poly(1,1,2,2-tetrafluoroethylene) (PTFE) coating of the substrate, followed by vacuum casting and annealing at 200 °C for 1 min to weld the AgNWs and partially cure the PDMS. Complete curing at 70 °C for 2 h enables the AgNWs to be firmly anchored into the PDMS through mechanical interlocking.

Figure 1 shows a schematic of the fabrication technique. A 1 wt% PTFE solution was coated onto the substrate to lower surface energy and reduce adhesion with the AgNW layer. The PTFE-coated substrate was then treated with air plasma to facilitate uniform dispersion of the IPA-based AgNW solution, which was subsequently spray-coated onto the substrate. (Figure 1a). The PDMS prepolymer was subsequently dispensed onto the AgNWs-coated substrate (Figure 1b), followed by vacuum casting at −0.9 bar for 30 min to ensure successful infiltration of the prepolymer into the AgNWs layer (Figure 1c). Annealing was then conducted at 200 °C for 1 min, which simultaneously welded the AgNWs and partially cured the PDMS (Figure 1d). Complete curing of the PDMS was then carried out in a oven at 70 °C for 2 h, allowing the AgNWs to become firmly anchored to the PDMS networks through mechanical interlocking. And then, the cured PDMS was easily peeled off from the substrate due to the low surface energy of PTFE layer (Figure 1e). Finally, a flexible electrode embedded with welded AgNWs was fabricated (Figure 1f).

Figure 2 presents SEM images of AgNWs networks. The spray-coated AgNWs remain unwelded at their junctions, resulting in point contacts that limit electrical conductivity (Figure 2a). Annealing at 200 °C for 1 min (Figure 2b) induced complete welding at the junctions, significantly enhancing electrical connectivity. In contrast, extending the annealing time to 2 min caused spheroidization and disconnection at multi-wire junctions (Figure 2c), disrupting electrical pathways and degrading conductivity due to Rayleigh instability.[7]

Figure 3 shows resistance changes in AgNW embedded flexible electrodes, indicating improved electrical conductivity via AgNWs welding. Minimum resistance was observed after annealing at 200 °C for 1 min, reduced to about 20% of that of unwelded AgNWs. Annealing exceeding 1 min led to increased resistance due to spheroidization and disconnection within the AgNW network, consistent with the SEM images.

We demonstrate that simultaneous welding and embedding of AgNWs into the PDMS matrix enables the fabrication of flexible electrodes with high conductivity and mechanical robustness, suitable for pressure sensors requiring stable operation under repeated pressure and EMI.

[1] H. Yang et al., Small methods 2 (2018) 1700259.
[2] B. Wang et al., Adv. Mater. 31 (2019) 1901408.
[3] N. M. Nair et al., ACS Appl. Mater. Interfaces 13 (2021) 34550.
[4] X. Wang et al., Small 13 (2017) 1602790.
[5] D. J. Won et al., ACS Appl. Electron. Mater. 2 (2020) 846.
[6] S. Kim et al., Small methods (2025) 2401839.
[7] M. E. Toimil Molares et al., Appl. Phys. Lett. 85 (2004) 5337.

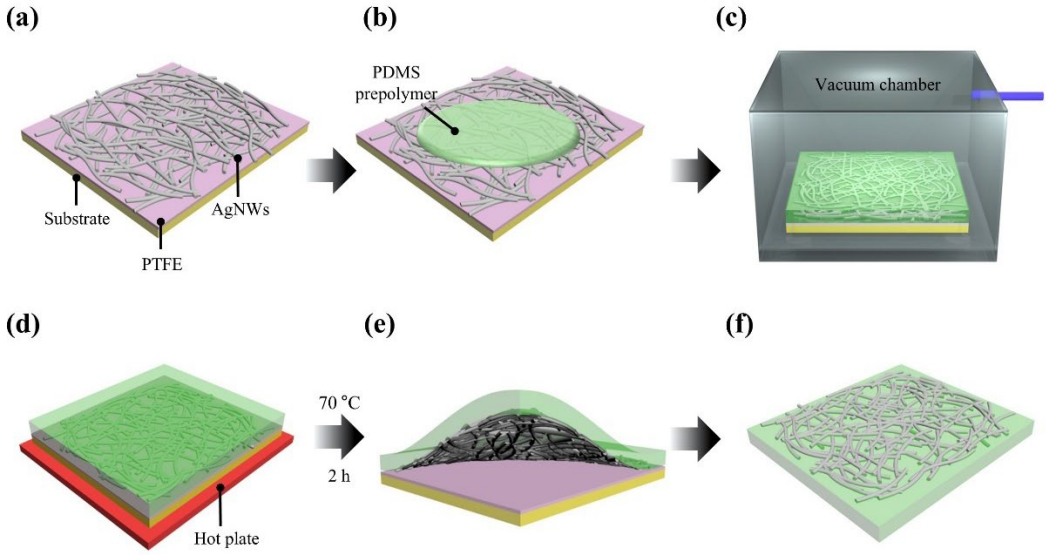

Figure 1. Schematic of the embedding process of welded AgNWs using the proposed fabrication technique. a) Spray coated AgNWs on the PTFE-coated substrate. b) Dispensing PDMS prepolymer on the AgNW-coated substrate. c) Infiltration of the prepolymer into the AgNW layer using vacuum casting. d) Annealing for the simultaneous welding of AgNWs and the partial curing of the PDMS prepolymer. e) Complete curing of the prepolymer, flexible electrodes were peeled off from the substrate. f) Final flexible electrodes.

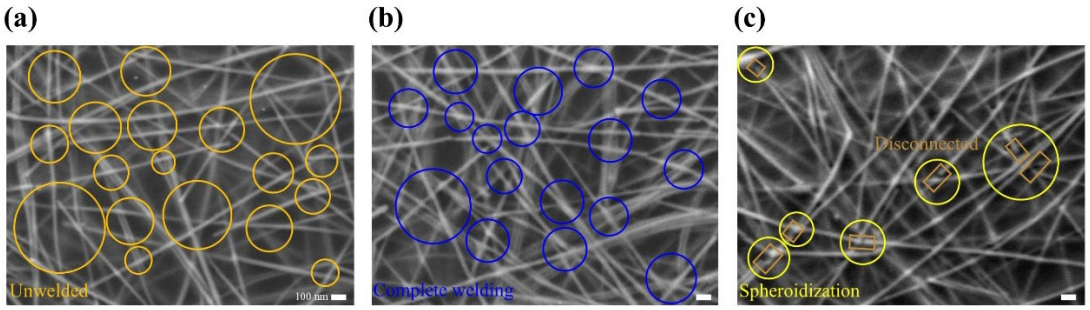

Figure 2. SEM images of AgNWs networks on fabricated flexible electrode surfaces. a) as spray-coated; after annealing at 200 °C for b) 1 min and c) 2 min.

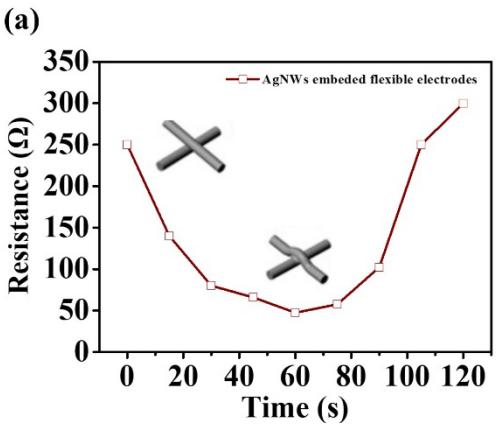

Figure 3. Changes in the resistance of AgNWs embedded flexible electrodes as a function of time at 200 °C.

Fabrication of a superhydrophobic surface with partially superhydrophilic regions and surface free energy comparison

Takuto Wakasa, Jun Taniguchi

Department of Applied Electronics, Tokyo University of Science, Tokyo, 125-8585, Japan
e-mail: junt@te.noda.tus.ac.jp

1. Introduction

The tenebrionid beetle, which inhabits the Namib Desert, collects water from fog using a uniquely structured surface on its elytra. This surface features regularly arranged hydrophilic regions on a hydrophobic background, allowing airborne microdroplets to grow on the hydrophilic sites and eventually fall off[1]. In this study, we investigated the wettability of droplets on surfaces with contrasting wettability. A structured surface was fabricated by applying a moth-eye structure across a predominantly hydrophobic surface that included patterned hydrophilic regions. This design enhanced the wettability contrast [2], making its effects more discernible. The evaluation was conducted by calculating the surface free energy based on the contact angles measured after dispensing solution droplets onto the surface.

2. Experiments

The fabrication process of a structured surface with superhydrophobic properties and selectively modified superhydrophilic regions is illustrated in Figure 1. A moth-eye structure was fabricated with an inductively coupled plasma (ICP) system (EIS-700, ELIONIX Co., Ltd.), followed by treatment with a silane coupling agent (Optool UD-509, Daikin Industries, Ltd.). A positive-type photoresist (PMER P-CY 1000, Tokyo Ohka Kogyo Co., Ltd.) was dropped onto the mold, and a polyester film (Cosmoshine A 4300, Toyobo Co., Ltd.), polypropylene (PP) film, and glass plate were sequentially layered. The stack was pressed for one minute to fill the resist into the moth-eye structures. After removing the glass plate and films, the resist surface was planarized via spin coating. The sample was prebaked at 130 °C for 3 minutes. UV exposure was performed using a photomask with a pattern of circular opaque areas of diameter D arranged in a pitch P. Post-exposure bake (PEB) was carried out at 80 °C for 3 minutes. Development was conducted using tetramethylammonium hydroxide (TMAH; NMD-3 2.38%, Tokyo Ohka Kogyo Co., Ltd.) for 2 minutes, followed by a fresh solution exchange and a secondary development for 1 minute. A UV-curable resin containing fluorine compounds was then dispensed onto the mold. A polyester film, PP film, and glass plate were sequentially layered and pressed under vacuum for 1 minute. After removing the PP film, the resin was cured by UV exposure (dose: 375 mJ/cm²). The cured film was then peeled off from the mold and heated at 80 °C for 30 minutes to bleed the fluorinated material to the surface.

Figure 2 shows SEM images of the fabricated surface with D = 500 μm and P = 1000 μm. Dark areas correspond to superhydrophilic regions, where moth-eye structures several hundred nanometers in height were observed. The surrounding regions remained superhydrophobic, also exhibiting nanostructured moth-eye features. Next, to calculate the surface free energy, droplets of water and diiodomethane (1 μL each) and ethylene glycol (5 μL) were deposited on structured surfaces with D = 75 μm and P ranging from 150 to 1275 μm, and their contact angles were measured. The results are summarized in Table 1. When the ratio of the hydrophilic region to the total surface area decreased by ~20%, the surface free energy increased by 26–56%. A trend of increasing surface free energy with decreasing hydrophobic area fraction was observed.

3. Conclusion

We drew inspiration from the capabilities of the tenebrionid beetle and investigated the wettability of surfaces with contrasting wettability characteristics. Using photolithography and UV-NIL, we successfully fabricated a structured surface with superhydrophilic patterns on a superhydrophobic surface. The surface free energy was evaluated through contact angle measurements. It was found that the overall surface free energy can be controlled by adjusting the ratio of hydrophilic regions to the total surface area. Future work will investigate the effects of further reducing the area ratio, and altering the size and distribution of the hydrophilic regions while maintaining the same area ratio.

[1] A.R. Parker and C.R. Lawrence, *Nature*, **414** (2001) 33.
[2] R. N. Wenzel, *Ind. Eng. Chem.*, **28** (1936) 988.

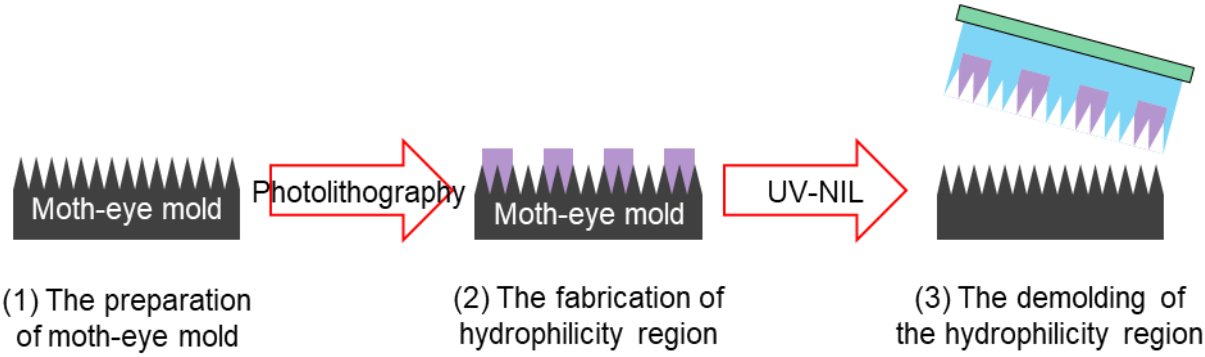

Fig 1. Process of the structured surface with superhydrophobic properties and selectively modified superhydrophilic regions

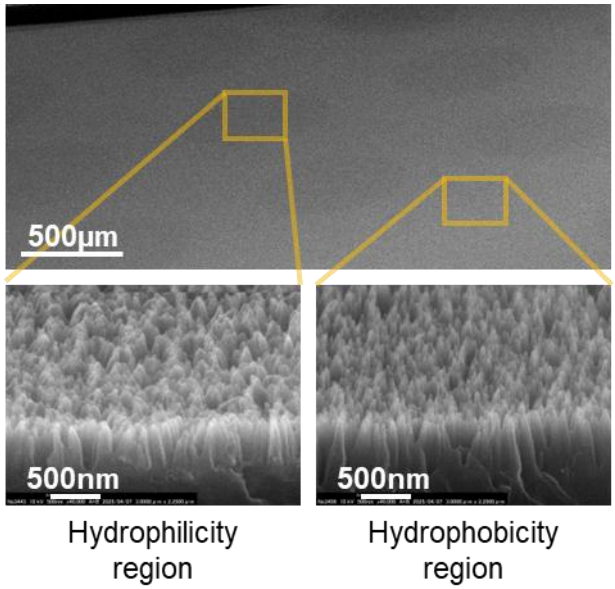

Fig 2. SEM images of the structured surface with superhydrophobic properties and selectively modified superhydrophilic regions (D = 500 μm and P = 1000 μm).

Table 1. Hydrophobicity and surface free energy of the structured surface with superhydrophobic properties and selectively modified superhydrophilic regions (D = 75 μm and P ranging from 150 to 1275 μm).
The drop volume of ethylene glycol alone is 5 μL, while that of the other solutions is 1 μL.

		The ratio of the hydrophobic region to the total surface area /%	C.A. /deg			Surface free energy /mNm^{-1}		
			Water	Diiodom-ethane	Ethylene glycol	Acid-base	Kaelble-Uy	Wu
P /μm	150	80.37	149.9	131.7	136.8	1.4	1.4	4.3
	375	96.86	153.5	135.7	136.8	1.0	0.9	3.6
	750	99.21	153.5	135.7	137.2	1.0	0.9	3.6
	1275	99.73	153.5	136.0	137.2	1.0	0.9	3.5
Hydrophobic moth-eye		100.00	154.3	136.5	137.4	0.9	0.9	3.4

Design of an Antireflective Hierarchical Structure Based on Finite-Difference Time-Domain (FDTD) Simulation

Yao-Nien Tsai*, Guo-Chen Nieh , Yen-En Juan, and Yeeu-Chang Lee**

Department of Mechanical Engineering, Chung Yuan Christian University, Chung Li 32023, TAIWAN
*e-mail: s30546202@gmail.com **e-mail: yclee@cycu.edu.tw
Keywords: Hierarchical Structure , Finite-Difference Time-Domain (FDTD), Antireflection

Abstract:

The excellent antireflective performance of subwavelength structures is explained by the Effective Medium Theory (EMT), where the structure and air form an effective medium with averaged optical properties. A gradual change in the fill factor from top to bottom results in a graded refractive index, which reduces Fresnel reflections[1].

However, the single-period structures still exhibit noticeable reflectance peaks at specific wavelengths. To achieve broadband anti-reflection, we based our design on the wave optics of subwavelength structures and combined the two structural scales to fabricate hierarchical micro/nanostructures. The optical behavior of these subwavelength components was analyzed using FDTD) simulations. Figure 1 shows the hierarchical structure and its corresponding parameters. Single-crystalline silicon was used as the material, with the micro structure serving as the base layer of the hierarchy, and densely packed nanostructures were arranged on the top. From Figure 2, it can be observed that the single-period 2 μm structure exhibits distinct reflectance peaks at wavelengths shorter than 2 μm, which are attributed to diffraction effects. This phenomenon occurs when the periodic structure satisfies the grating equation, leading to the emergence of higher-order diffraction modes (m = ±1, ±2, …) [2]. The grating equation is as follows:

$$d(n_0 sin\theta_0 + nsin\theta) = m\lambda_0$$

The variables in the grating equation are defined as follows: d is the grating period, θ_o and θ are the incident and diffraction angles, respectively, and n_o and n are the refractive indices of the incident and diffracted media. A structure with a period of 2 μm corresponds to a grating period d = 2 μm. When the incident angle θ_o = 90°, higher-order diffraction occurs in air for wavelengths $\lambda_o \leq$ 2 μm. Similarly, for the 0.5 μm structure, higher-order diffraction arises at $\lambda_o \leq$ 0.5 μm.

In the hierarchical structure, where both periodicities are combined, the interference coupling of specific diffraction orders is disrupted, effectively suppressing higher-order diffraction that would otherwise occur for wavelengths below 2 μm and 0.5 μm. The integration of both structures not only reduces high-order diffraction but also enhances broadband anti-reflective performance. Specifically, the 0.5 μm structure provides a low-reflectance band across the visible to near-infrared range, compensating for the higher reflectance of the 2 μm structure at shorter wavelengths. Conversely, the 2 μm structure offers anti-reflective performance in the short-wave infrared region. This behavior can be attributed to the Mie scattering theory, which predicts that when the incident wavelength is comparable to the structural feature size, the incident light is redirected upon entering the material, thereby reducing specular reflection and interface-related interference. Moreover, the geometric features of the structure facilitate multiple internal reflections, further decreasing the reflectance and allowing electromagnetic waves to penetrate the material more easily [3].

Reference:

[1] N. Shanmugam, R. Pugazhendhi, R. M. Elavarasan, P. Kasiviswanathan and N. Das, 2020 “Anti-reflectivecoating materials: A holistic review from PV perspective”, Energies, 13, 2631.

[2] L. M. Yang, C.Y. Pan, F.P. Lu, C.W. Chang, S.W. Feng, and L.W. Tu, 2015 ″Anti-reflection sub-wavelength structures design for InGaN-based solar cells performed by the finite-difference-time-domain (FDTD) simulation method ″ , Optics & Laser Technology, 67 , 72-77

[3] K. Zhou, Y. P. Yuan, C. L. Wang and J. M. Chen, 2024 “Large-area broadband ultralow reflectance biomimetic structures silicon via femtosecond laser inducing and chemical etching” Journal of Manufacturing Processes, 132 , 122-129.

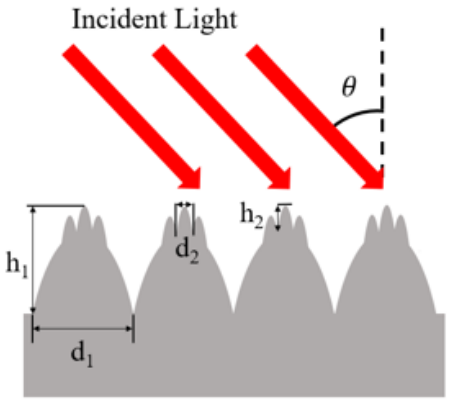

Incident light angle (θ)	**0°**
Incident light wavelength (μm)	0.4～5
Height(h_1) and width(d_1) of hierarchical structure(μm)	2、2
Height(h_2) and width(d_2) of nanostructure(nm)	0.75、0.5

Figure 1. Hierarchical structure simulation moldel and parameters of hierarchical structure

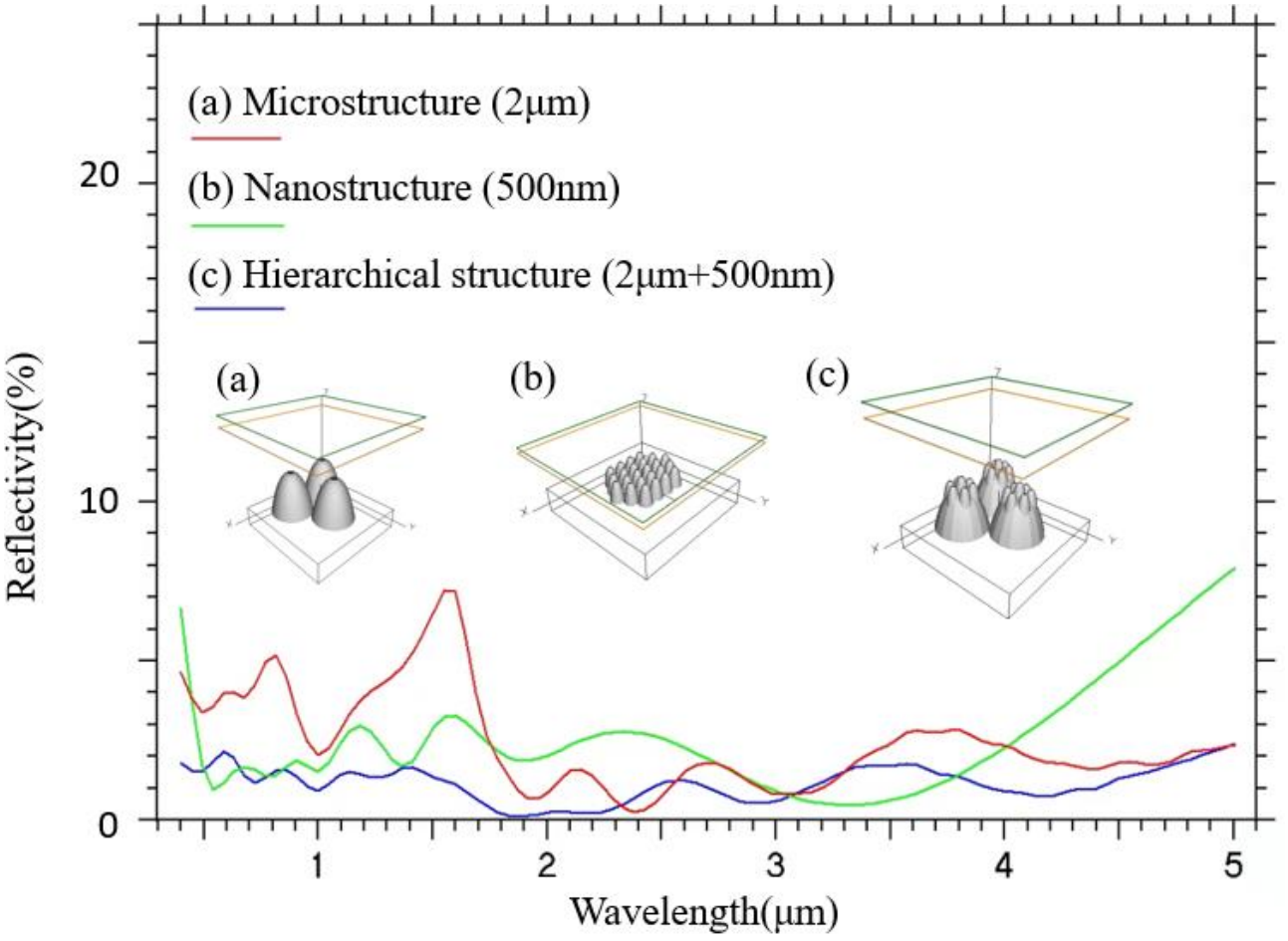

Figure 2. FDTD simulation of reflectance spectrum for micro, nano and hierarchical structures

Fabrication of Broadband Antireflection Hierarchical Micro/Nano Structures Using Colloidal Lithography

Yen-En Juan*, Guo-Chen Nieh , Yao-Nien Tsai and Yeeu-Chang Lee**
Department of Mechanical Engineering, Chung Yuan Christian University, Chung Li 32023, TAIWAN
*e-mail: juanian1258@gmail.com**e-mail: yclee@cycu.edu.tw
Keywords: Antireflection Structure, Hierarchical Structure, Colloidal Lithography

Abstract:
Moth-eye structures (subwavelength structures) effectively reduce reflection and enhance light transmission owing to their graded refractive index [1]. However, a moth-eye structure with a single diameter and periodicity generally exhibits optimal antireflection performance only within a specific wavelength range corresponding to its structural dimensions. When the incident wavelength is shorter than the structural size, diffraction and scattering lead to higher-order diffraction; conversely, when the wavelength is much longer, interference due to surface reflection causes oscillations in the reflectance. These effects limit the broadband antireflection performance of single-feature-sized moth-eye structures. In this study, hierarchical moth-eye antireflective structures were fabricated by combining colloidal lithography with reactive ion etching (RIE) [2], thereby forming hierarchical moth-eye antireflective surfaces with structural features of varying diameters or heights that enable broadband antireflection.
First, 2.2 μm diameter polystyrene (PS) microspheres were deposited on a silicon substrate via gas-liquid interface deposition, forming a close-packed hexagonal monolayer. As shown in Fig. 1, these microspheres served as etching masks in an RIE process using Ar (75 sccm), O_2 (30 sccm), and SF_6 (30 sccm) gases at a pressure of 20 mTorr and a power of 100 W for 5 min, producing truncated microstructures. They serve as the bases of the hierarchical system and provide structural support. Subsequently, 600 nm PS nanospheres were deposited onto the microstructures and etched under Ar (50 sccm), O_2 (30 sccm), and SF_6 (30 sccm) at 24.6 mtorr and 100 W power for 3 min. This step produced nanoscale subwavelength structures on a microscale base, enhancing the surface detail and refractive index gradation. The final surface consists of continuous microscale features overlaid with nanoscale textures.
As shown in Fig. 2, we fabricated (a) a single-diameter 600 nm tapered structure, (b) a single-diameter 2.2 μm truncated structure, and (c) a hierarchical micro/nano structure. As shown in Fig. 3, the 0.6 μm tapereted structure exhibited favorable antireflection performance between 500 and 1100 nm, consistent with the subwavelength behavior. However, a pronounced reflectance peak appeared near 400 nm owing to high-order diffraction when the size of the structure exceeded the wavelength. The 2.2 μm truncated structure, expected to function as a subwavelength structure in the 1500–1900 nm range, failed to show low reflectance in this region. This is attributed to its flat-topped incomplete geometry, which does not support a smooth refractive index transition.
Our results demonstrate that the hierarchical structure, formed by integrating features of different sizes, achieves multiscale refractive index gradation. This configuration not only suppresses the reflectance across the entire spectrum, maintaining values below 1.5% from 350 to 2500 nm, but also compensates for the respective reflectance peaks and dips of the constituent structures, resulting in broadband antireflection performance.

References:
[1]N.Shanmugam, R. Pugazhendhi, R. M. Elavarasan,P.Kasiviswanathan and N. Das, Anti-Reflective Coating Materials:A Holistic Review from PV Perspective. Energies 2020, 13, 2631.
[2]D. Schmelz, G. Jia, T. Käsebier, J. Plentz, U.D. Zeitner, Antireflection Structures for VIS and NIR on Arbitrarily Shaped Fused Silica Substrates with Colloidal Polystyrene Nanosphere Lithography. Micromachines 2023, 14, 1204.

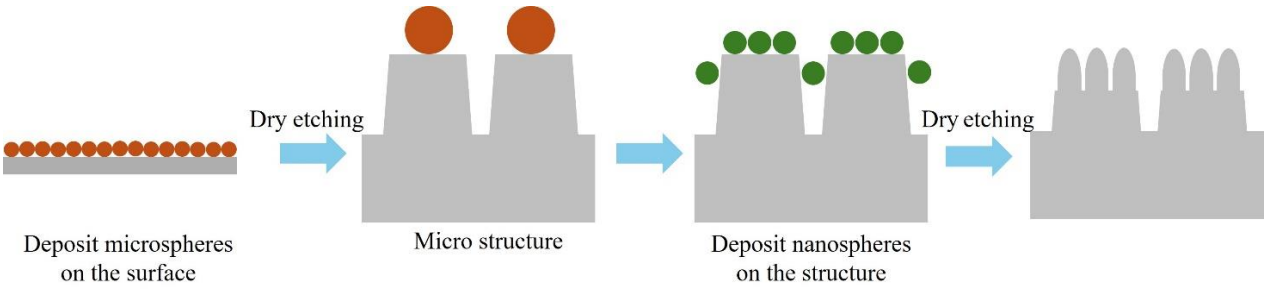

Figure 1. Fabrication process of hierarchical structures.

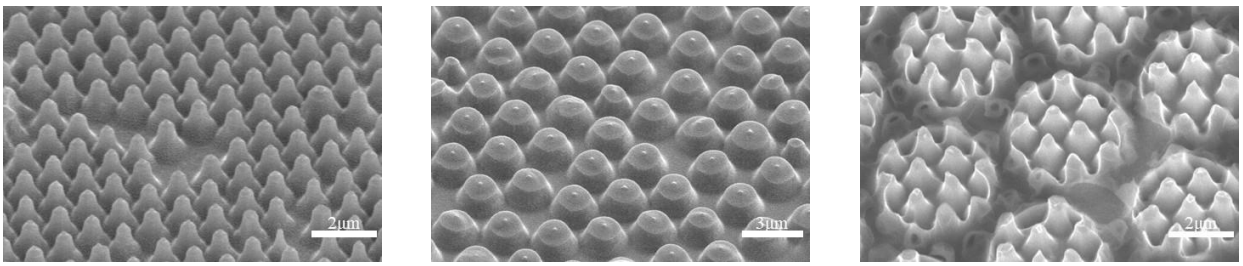

(a) (b) (c)

Figure 2. SEM images of (a) 600 nm tapered structure, (b) 2.2 μm truncated structure, (c) hierachical micro/nano structure.

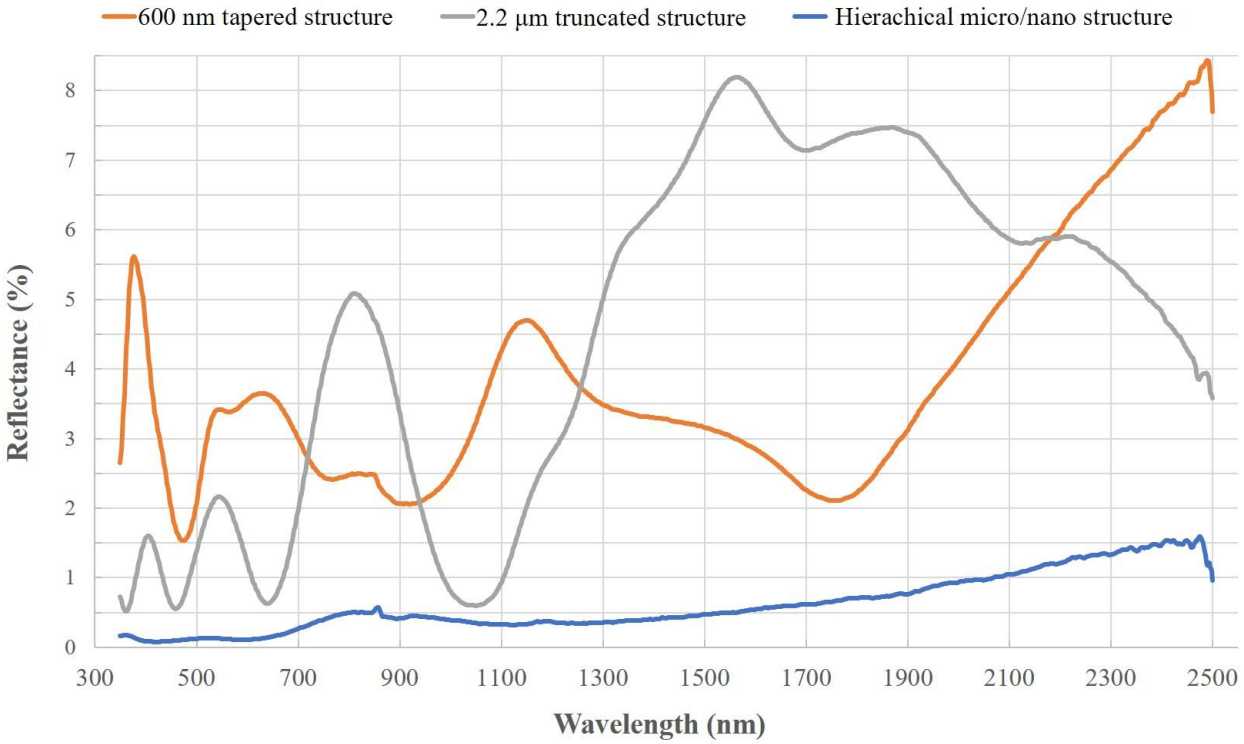

Figure 3. Reflectance measurements of 600 nm tapered structure, 2.2 μm truncated structure, and hierachical micro/nano structure.

An e-beam lithographer's approach to evaluating a new HIMT DWL66$^+$ direct laser writer for Mix&Match processes – resists, contrast curves, grayscale lithography, alignment, and developer test sticks

Silvia Diewald [a], Gernot Goll [a]

[a] Center for Functional Nanostructures – Nanostructure Service Laboratory (CFN-NSL), Karlsruhe Institute of Technology (KIT), 76131 Karlsruhe, Germany
e-mail: silvia.diewald@kit.edu

Exposing a sample fast with high resolution and accuracy is a lithographer's dream (or at least for someone working at a service facility in a university setting catering mostly to master and PhD students demanding exactly that). Obviously, high resolution is the domain of e-beam lithography (EBL). Even with a several years old lower-tier model like the JEOL JBX-5500ZD in our lab, structure sizes of 50 nm are routinely achieved – and 10 nm are possible with some effort. Marker structures with reasonably good quality provided, reaching overlay accuracies far better than 100 nm in multi-step fabrication processes are also an advantage of using EBL. Exposure speed, however, is not its strong point – especially when having to rely on an older tool with limited capabilities in regard to deflector frequency (12 MHz in our case) and maximum current (20 nA according to the manufacturer at least). But that's exactly where optical lithography (OL) usually shines. Thus, combining these in a Mix&Match process seems a natural fit: sparsely-distributed EBL-exposed fine structures (e.g., Josephson junctions in superconducting qubits) are complemented by less-critical large structures (e.g., interconnecting contact pads) exposed with an OL tool in the same process run with one and the same resist layer without any in-between developing. Eliminating an additional process step not only saves time but also prevents, e.g., undesired oxide barriers from forming between fine and coarse structures that could later adversely affect the performance of the fabricated devices.

So far, a SÜSS MA6 Maskaligner (upgraded with an additional deep UV source to also allow patterning of PMMA and PMMA-co-MAA resists) has been almost exclusively used as the OL tool in our lab for Mix&Match exposures. In spite of the aforementioned advantages and the extremely competitive exposure times (compared to EBL or direct laser writing (DLW) with an older Heidelberg Instruments DWL66), the actual number of users employing a Mix&Match process remained quite low. The most important reasons seem the time required to produce a mask – something that's necessary quite often in research settings with ever-evolving designs – and the challenge to actually align EBL and OL exposures precisely enough. So, a lot of designs are still completely exposed by EBL due to its flexibility and despite the long exposure times.

Observing the delivery of a new Heidelberg Instruments DWL66$^+$ (replacing the more than 20 years old DWL66) literally only two doors down, of course, piqued the curiosity of the resident EBL operator. Intrigued by its 375 nm laser option for higher resolution, standard grayscale capabilities and higher speed (compared to its predecessor), a vague (and, in hindsight, certainly naïve) idea formed to use DLW in conjunction with EBL in Mix&Match processes. To test the feasibility of such an endeavor, several aspects have been investigated:

- performance of EBL resists (which should ensure high-resolution patterning of fine EBL structures) for DLW with 375 nm (between the more common 405 nm "h-line" and 365 nm "i-line" OL tools)
- testing common OL resists for EBL (desperate search for a "universal" positive-tone resist)
- determining contrast curves to check for "grayscale potential" and suitable exposure parameters
- employing multiple "staggered" grayscale exposures in an attempt to reduce visible stripe borders
- visibility of EBL-exposed (but not developed) marker structures in DWL66$^+$ cameras used for alignment
- developing recipes compatible with materials used in established EBL-based processes (including "developer test sticks", a simple tool to monitor the strength of diluted or self-mixed developers)

As expected, the positive-tone EBL resists PMMA, PMMA-co-MAA and CSAR 62 (Allresist GmbH) are not sensitive to exposure with the 375 nm laser, however, both novolak-based negative-tone resist series ma-N2400 (micro resist technology GmbH) and AR-N7520 new (Allresist GmbH) show even some potential for grayscale lithography according to their contrast curves (see Fig. 1). For higher doses AR-N7520 new tends to puff out while ma-N2400 seems to shrink. Overexposed EBL marks in both resists are visible and can be used for alignment. S1800 G2 (DuPont), a positive-tone OL resist, offers some interesting possibilities for structuring since its novolak nature makes it a negative-tone resist for EBL. An example is shown in Fig. 2 where positive and negative behavior are combined to check the alignment between EBL and DLW step.

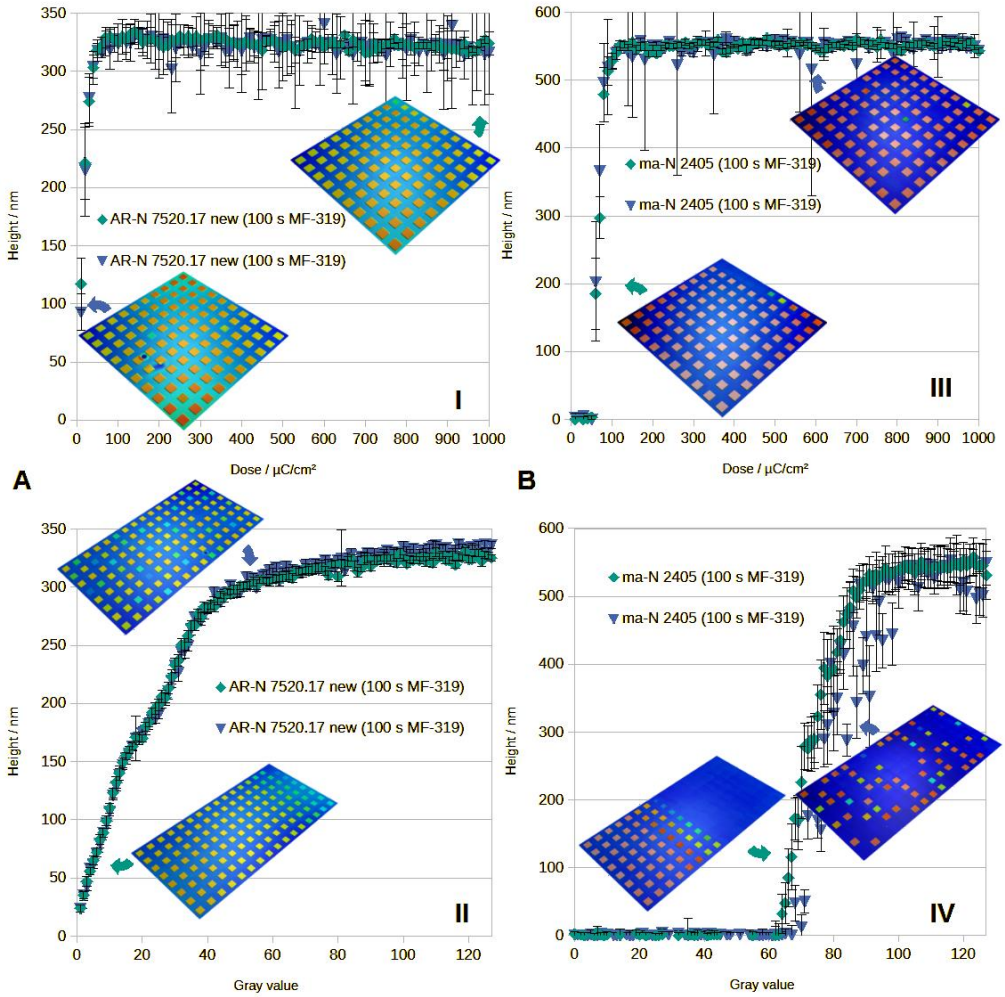

Figure 1. Measured contrast curves for (A) AR-N7520.17 new (I: EBL 50 kV, 20 nA, II: DLW 2 mm write-head, 70 mW laser power, 5 % transmission) and (B) ma-N2405 (III: EBL 50 kV, 20 nA, IV: DLW 2 mm write-head, 70 mW laser power, 50 % transmission) developed for 100 s with MF-319 (DuPont) at RT.

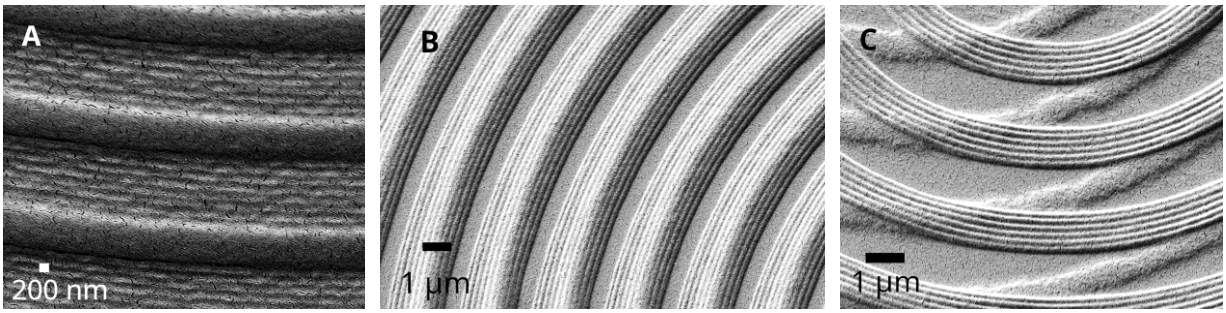

Figure 2. Scanning electron microscope (SEM) pictures showing bundles of 100 nm EBL spirals covered or complemented by wider single-line DLW spirals in S1805 as examples for a more (A, B) and less (C) successful alignment attempt between EBL and DLW exposures. The tested field alignment procedure of the DWL66$^+$ makes use of overexposed marks recognized by the frontside camera and written during the immediately preceding EBL exposure. Spirals are chosen as test design because any misalignment is easily spotted. S1805 acts as negative resist in EBL but as positive resist in OL. The samples shown here were developed after the DLW exposure for 40 s in a 3:2 mixture of AZ Developer and water and sputtered with 20 nm of gold before SEM investigations.

Direct data generation of wafer-scale metalens for e-beam exposure

Yixuan Zhao [a], Kian Shen Kiang [a], Jize Yan [a]
[a] School of Electronics and Computer Science, University of Southampton, Southampton, SO17 1BJ, UK
e-mail: J.Yan@southampton.ac.uk

Metalenses are two-dimensional arrangements of subwavelength meta-atoms that can focus light to a subwavelength spot and modulate various properties of light waves [1]. To fabricate nanometer-scale meta-atoms, high-resolution lithography techniques are required, such as electron beam (e-beam) lithography. Previous workflows for generating files for e-beam exposure rely on intermediate file formats such as GDSII or OASIS to store layouts, followed by data format conversion and pattern processing in software [2,3]. As the layouts typically involve millions or even billions of meta-atoms, especially for high-resolution and large-area designs, file sizes could reach hundreds of gigabytes, increasing memory costs and processing time during multiple steps [3-4].

For a 50mm metalens, the layout file size in GDSII format exceeds 200GB [4]. By saving in OASIS format, it is reduced to 4.3GB, but file sizes of 150mm, 200mm, and 300mm metalens are 40GB, 72GB, and 160GB based on calculation [3]. Such sizes exceed the handling capability of the processing tools. To avoid large-size files, we developed a "MetalensGenerator" module using BEAMER scripts, which directly generates metalens layout data for e-beam exposure. The module generates and processes metalens patterns in .togobject format, eliminating the need for data format conversions. Our method enables users to skip large intermediate layout files and fabricate high-resolution, wafer-scale metalenses.

We apply this method to design a polarization-independent metalens based on the propagation phase. Each unit cell consists of a rectangular nanopillar whose width is designed to achieve the desired discrete phase shift. By mapping the target phase profile onto the width of nanopillars, we generate and directly output the data in a format ready for e-beam exposure. This approach ensures efficient and flexible data generation for arbitrary metalenses. We demonstrate the method by fabricating a 2mm-diameter silicon nitride metalens working at 520nm, illustrating its practicality for small-scale production and its scalability to larger metalens layouts.

Figure 1a and 1b compare the workflows of previous multi-step methods using intermediate layouts with the 'MetalensGenerator' approach, demonstrating both the consistency of the generated patterns compared to previous methods and the significant improvements in data generation efficiency. Figure 1c shows the full lens layout and zoomed-in image of pattern distribution in files for e-beam exposure. Figure 2 shows the flowchart of how the polarization-independent metalens layout is generated and converted into e-beam compatible files using the Python-based 'MetalensGenerator' module. Figure 3a shows that the meta-atom library consists of 7 width values ranging from 120nm to 280nm, providing high transmission and 2π phase coverage with a period of 350nm at the working wavelength of 520nm. Fig. 3b and 3c illustrate the optical and SEM images of a fabricated 2mm metalens (after lift-off) based on the layout file generated using our method.

We acknowledge support from EPSRC Grant (EP/V000624/1).

[1] Y. Peng, et al., Laser Photonics Rev. 18 (2024) 2300731.
[2] J.S. Park, et al., ACS Nano 18 (2024) 3187–3198.
[3] C. Sun, et al., RAM-adaptive parallel generating and minimizing the layout file of wafer-scale metalens (2024), 50th International Micro and Nano Engineering Conference
[4] A. She, et al., Opt. Express 26 (2018) 1573–1585.

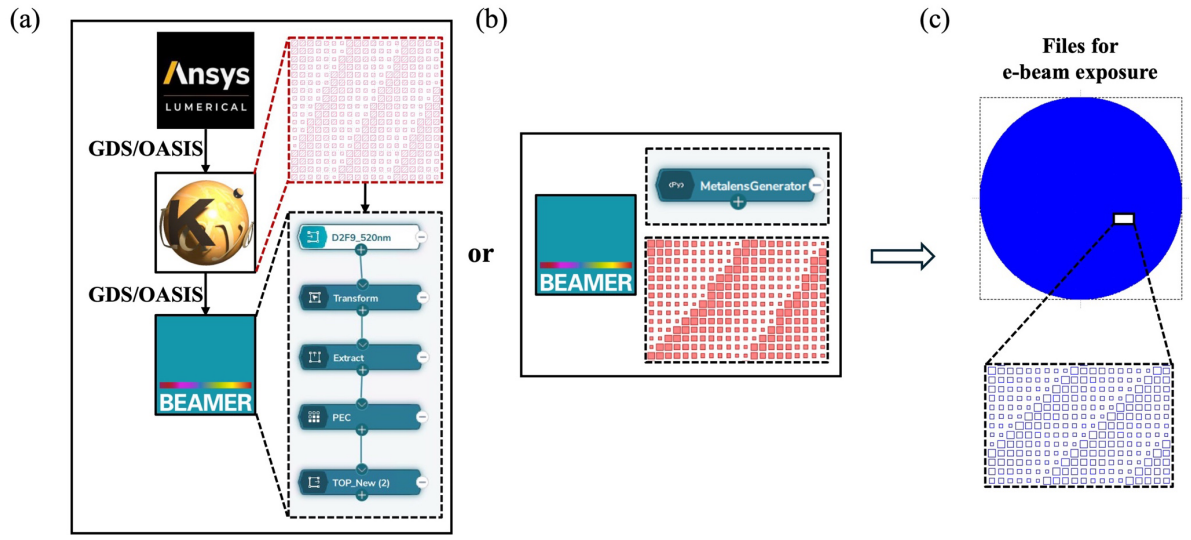

Figure 1. (a) Conventional workflow and (b) our method to generate e-beam compatible files (c) full lens layout and zoomed-in pattern distribution

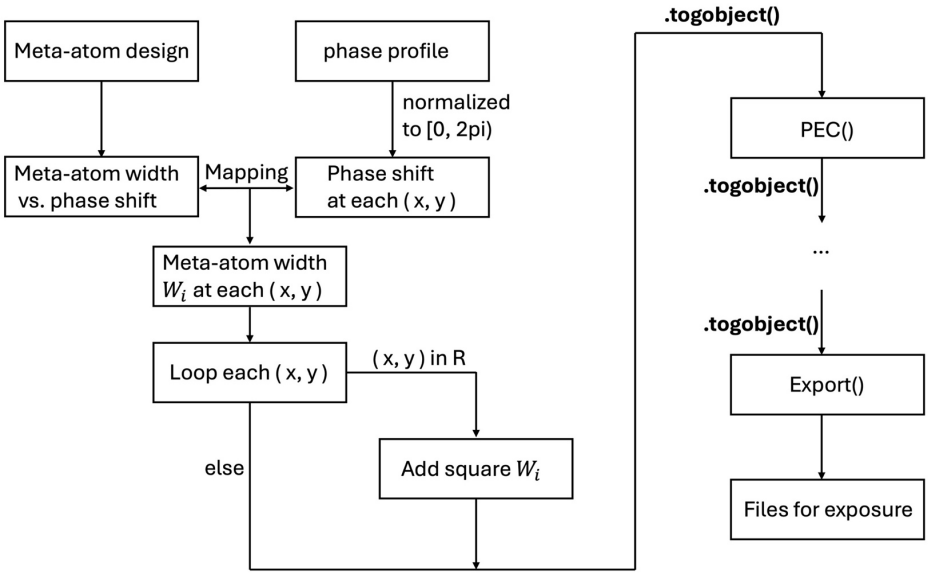

Figure 2. Flowchart of working principle in 'MetalensGenerator'

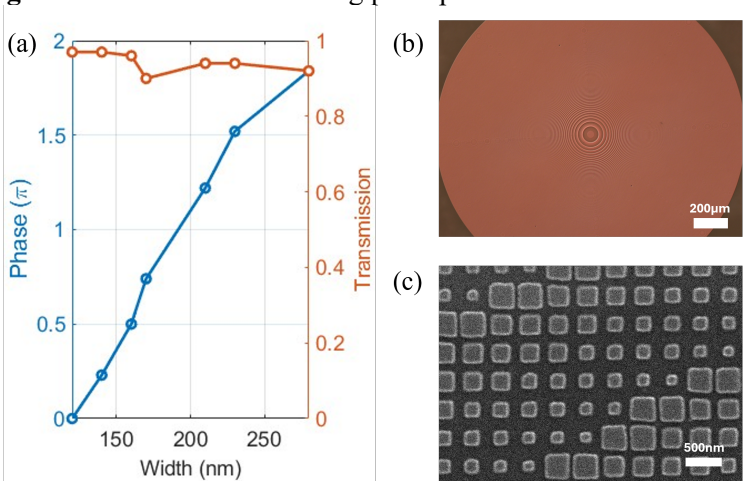

Figure 3. 2mm metalens design and fabrication results (a) meta-atom library working at 520nm (b) optical microscope and (c) SEM images of the sample (after lift-off)

Impact of PEALD Temperature on Al_2O_3 Gate Dielectric of ZnO-TFTs

J. Zeng [a], B.D. Rowlinson [a, b], O. Kapur [a] and H.M.H. Chong [a]

[a] School of Electronics and Computer Science, University of Southampton, SO17 1BJ, UK
[b] Centre for Electronic Frontiers, University of Edinburgh, Edinburgh, EH9 3BF, UK
e-mail: jz2g19@soton.ac.uk

Introduction: Aluminium Oxide (Al_2O_3) is widely adopted as a gate insulator in both thin-film transistors (TFTs) and metal-oxide-semiconductor field-effect transistors (MOSFETs) due to its wide bandgap, low leakage current, excellent thermal stability, good interface quality, and moderate dielectric constant. Moreover, Al_2O_3 offers significant advantages for thermosensitive applications such as flexible electronics, transparent electronic devices and low-temperature oxide semiconductors, owing to its high compatibility with atomic layer deposition (ALD) processes and its ability to be processed at low deposition temperatures. The material quality of Al_2O_3 thin films deposited in isolation at different temperatures has been systematically investigated [1-3]. However, studies focusing solely on Al_2O_3 thin films are often insufficient to reflect their impact on device platforms, as the overall improvement of device performance is essential for advancing their practical applications. Many studies employ post-annealing to enhance the Al_2O_3/semiconductor interface, though such high-temperature processes are incompatible with thermosensitive applications. Therefore, it is necessary to investigate how deposition temperature affects device characteristics within a suitable process window (150°C–300°C). This study provides experimental guidance for the process optimization of low-temperature oxide electronic devices.

Fabrication Process: The ZnO TFTs (Fig. 1) were fabricated on a 150 mm p-type silicon wafer. A 30 nm Al_2O_3 gate insulator (225 cycles) and a 40 nm ZnO channel layer (333 cycles) were consecutively deposited by plasma-enhanced atomic layer deposition (PE-ALD) without breaking the vacuum [4], using trimethylaluminium (TMA) as the precursor for Al_2O_3 and diethylzinc (DEZ) for ZnO. Then, the ZnO channel was patterned by wet etching in 1:1000 HCL: H_2O. Finally, 5 nm of titanium (Ti) and 150 nm of aluminium (Al) were deposited by RF magnetron sputtering and patterned using a lift-off process to form the source/drain (S/D) electrodes.

Results: Figure 2(a, c) presents the extracted threshold voltages (V_{TH}) of ZnO TFTs under various Al_2O_3 deposition temperatures (150–300 °C). All channel widths exhibit a similar temperature-dependent trend, with V_{TH} reaching its minimum value of -3.8 V in the 200–250 °C. However, significant variation in V_{TH} across channel widths is observed at 200 °C, while improved uniformity is achieved near 250 °C. As shown in Figure 2(b, d), the gate leakage current (I_{gmax}) increases with deposition temperature. This may be caused by the thinner Al_2O_3 grown at higher temperatures, which enhance leakage pathways [1,3]. The increased variation across channel widths further suggests degraded device uniformity and compromised dielectric reliability. Figure 3(a) shows the high-frequency (100 kHz) C–V characteristics of Al_2O_3/p-type Si MIS capacitors under different PE-ALD deposition temperatures, in order to evaluate the dielectric properties of Al_2O_3 and the hysteresis behavior induced by trapped charges within the Al_2O_3 layer. The hysteresis window increases with temperature, indicating enhanced charge trapping due to a higher density of interface traps. Figure 3(b) confirms that ΔV grows consistently with deposition temperature, particularly in the depletion region. These results suggest that excessive ALD temperatures may degrade interface quality despite improvements in bulk film density. The most promising process appears to be 150 °C, balancing interface quality and film densisty to produce stable V_{TH} and low I_{gmax}.

Summary: A PE-ALD temperature of Al_2O_3 for 150°C is promising to improve the threshold voltage characteristics, device uniformity, low gate leakage current, and better hysteresis performance without post-annealing. This makes it highly suitable for low-temperature, flexible, or back-end-of-line (BEOL) integrated electronics. Further work will address C-V measurements of the Al2O3/ZnO interface and its impact on the electrical characteristics of ZnO-TFTs.

[1] S. Kim et al. Scientific Reports 12, no. 5124, DOI: 10.1038/s41598-022-09054-7, (2022).
[2] M. A. Botzakaki et al. J. Vac. Sci. Technol. A, vol 36, issue 1, DOI: 10.1116/1.5003375 , (2018).
[3] M. D. Groner et al. Chemistry of Materials, vol. 16, issue 4, DOI: 10.1021/cm0304546, (2004).
[4] J. Zeng, B. D. Rowlinson, H. M. H. Chong, et al, MNE 2023, Berlin, Germany, (2023).

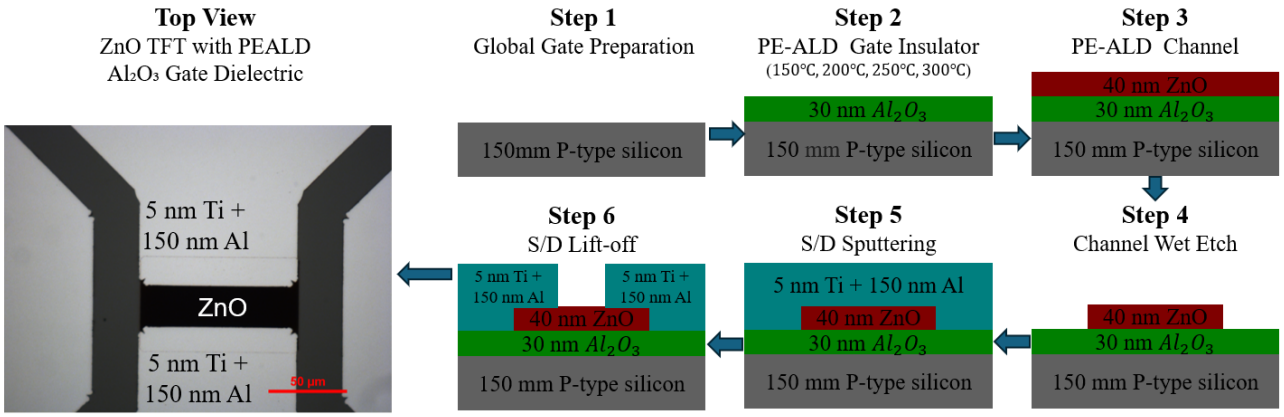

Figure 1. Fabrication process flow of the global bottom-gate ZnO thin-film transistor (TFT). Four different temperatures (150℃, 200℃, 250℃, and 300℃) were applied during the Al_2O_3 gate dielectric formation in Step 2. The ZnO channel layer is deposited immediately after the Al_2O_3 layer without breaking the vacuum. The top view on the left shows the final device structure.

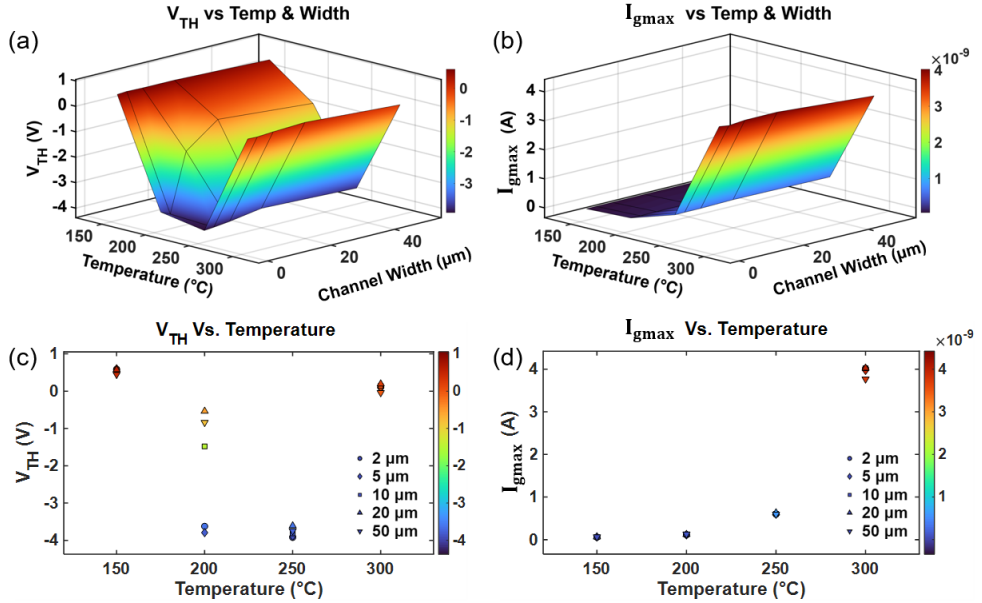

Figure 2. Temperature and channel width dependence of threshold voltage (V_{TH}) and maximum gate leakage current (I_{gmax}) in ZnO TFTs under a drain voltage (V_D) of 0.5V. (a) 3D surface plot of V_{TH} as a function of temperature (150 °C-300 °C) and channel width (2 μm-50 μm). (b) 3D surface plot of I_{gmax} under the same conditions. (c) Scatter plot of V_{TH} vs. Temperature for different channel widths, (d) scatter plot of I_{gmax} vs. Temperature showing width-dependent behaviour.

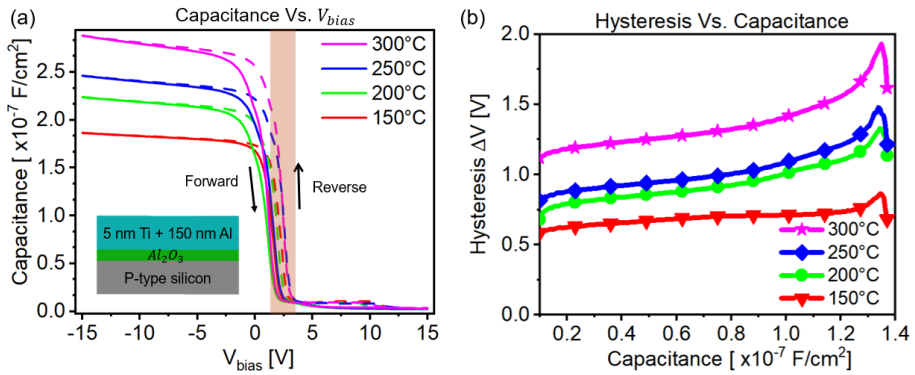

Figure 3. (a) High-frequency C-V characteristics of Al_2O_3/p-type Si MIS capacitors with Al_2O_3 gate dielectrics deposited at different ALD temperatures (150 °C to 300 °C). Forward and reverse sweep directions are indicated by the shaded region highlights the significant hysteresis that occurs. (b) Hysteresis voltage (ΔV) as a function of normalised capacitance, reflecting the voltage-dependent response of interface traps. The results demonstrate the impact of deposition temperature on interface quality in Al_2O_3-based MIS structures.

Plasma-enhanced ALD of ultra-thin Al_2O_3 films for passivating contacts

Yaxin Zhan[a], Ben D. Rowlinson[a,b], Harold M. H. Chong[a], Stuart A. Boden[a]

[a] School of Electronics and Computer Science, University of Southampton, Southampton, SO17 1BJ, UK
[b] Centre for Electronic Frontiers, University of Edinburgh, Edinburgh, EH9 3BF, UK

e-mail: yz41n21@soton.ac.uk

Introduction

Passivating contacts have emerged as a promising solution to push the efficiency of silicon-based solar cells to the theoretical efficiency limit of 29.4% [1]. Typically, an ultra-thin film of dielectric (1~2 nm) serves as a tunnelling barrier, separating carriers to reduce the surface recombination velocity (SRV). However, a trade-off is often presented between achieving high passivation quality with thicker films and maintaining carrier tunnelling with ultra-thin films. Aluminium oxide (Al_2O_3) is recognised as a candidate tunnelling oxide material due to its beneficial properties in reducing SRV and robust passivation quality. Atomic layer deposition (ALD) of Al_2O_3 is a surface-limited technique capable of achieving high-quality, ultra-thin layers in a scalable manner. Discussions on using Al_2O_3 as a surface passivation material primarily focus on thicker layers around 20 nm, while the standard RCA cleaning method used is often unsuitable for ultra-thin film applications. While the method in [2] achieves the surface cleanliness required for 1–2 nm deposition, this technique involves a complex cleaning procedure. This work proposes strategies that simplify the fabrication of dual-purpose Al_2O_3 tunnelling barriers and passivation layers. The SRV at the Si/Al_2O_3 interface is quantitatively analysed using effective carrier lifetime measurements to quantify surface quality.

Fabrication

Low resistivity (~2 Ω·cm) *n*-type *c*-Si wafers (280 μm) with crystal orientation of (1 0 0) were used. The effective carrier lifetime measurement requires samples with identical passivation quality on both sides (as per Fig.1). The wafers were first immersed in a standard RCA1 solution at 80°C for 10 minutes to remove surface organic particles. Then the samples were dipped into 20:1 HF for 30 seconds to remove the oxide contamination generated during RCA1 treatment. The wafers are then treated using RCA2 solution at 80°C for 10 minutes to remove surface metallic particles. The final cleaning step uses fresh 7:1 HF or 20:1 HF solutions to remove any oxidation. The cleaned wafers were immediately transferred into the load lock of the ALD system. Layers of Al_2O_3 with thicknesses between 1 nm and 20 nm were deposited on both sides of the wafer at 200°C using an O_2 plasma and trimethylaluminium (TMA) precursor, with a deposition rate of ~0.106 nm/cycle. Following the deposition step, the samples were annealed in a rapid thermal annealer (RTA) at 450°C for 20 minutes under N_2 ambient [2, 3].

Characterisation

Photoconductance decay (PCD) effective lifetime measurements were performed using a Sinton WCT-120 lifetime tester. Each result was averaged over 10 successive measurements and is assumed to be accurate to ± 8% [4]. Fig.2 demonstrates that for Al_2O_3 films thicker than 5 nm the effective lifetime remains relatively stable (1.1 ms). A 7:1 HF solution before the ALD process generally results in better passivation than a 20:1 HF pre-treatment. Particularly for 1.0 nm Al_2O_3, the effective lifetime discrepancy between 7:1 and 20:1 HF spans approximately an order of magnitude. This suggests the cleanliness of the surface before deposition plays a significant role in determining the subsequent Al_2O_3 quality. Photoluminescence (PL) Spectroscopy measurements are performed using the CellSpot-EL/PL tool. Darker regions correspond to areas where non-radiative, defect-assisted carrier recombination dominates, indicative of poorer passivation (Fig.3 a-c). The PL intensity generally increases and stabilises with the increase in thickness (Fig.3 d). For 1.3 nm and 1.5 nm, the fluctuation in the PL intensities indicates inferior passivation. Among ultra-thin Al_2O_3 films, 1.7 nm is an optimised choice, offering acceptable PL intensity and thus a relatively well-passivated surface.

Conclusion

Our findings suggest that an interfacial layer thickness of 1.7 nm of Al_2O_3 may be optimal for minimising SRV in tunnelling barrier applications for passivating contacts.

[1] A. Richter *et al.*, *IEEE Journal of Photovoltaics*, 2013. DOI: 10.1109/JPHOTOV.2013.2270351
[2] N. E. Grant *et al.*, *Applied Surface Science*, 2024. DOI: 10.1016/j.apsusc.2023.158786
[3] B. Hoex *et al.*, *Applied Physics Letters*, 2006. DOI: 10.1063/1.2240736
[4] A. L. Blum *et al.*, *IEEE Journal of Photovoltaics*, 2013. DOI: 10.1109/JPHOTOV.2013.2284375

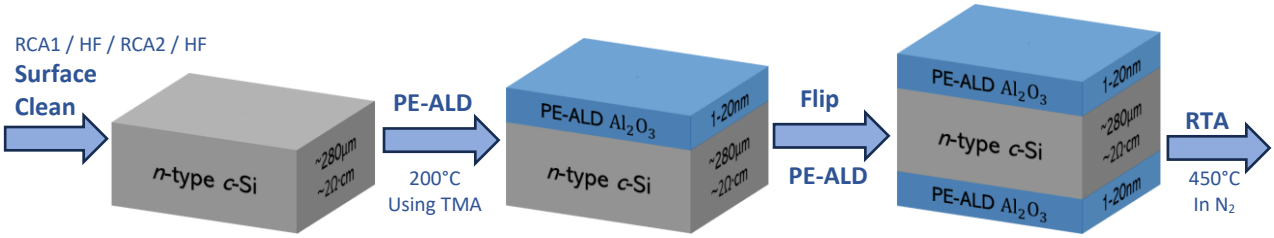

Figure 1 Schematic diagrams of the fabrication process for symmetrical Al_2O_3 passivated structure.

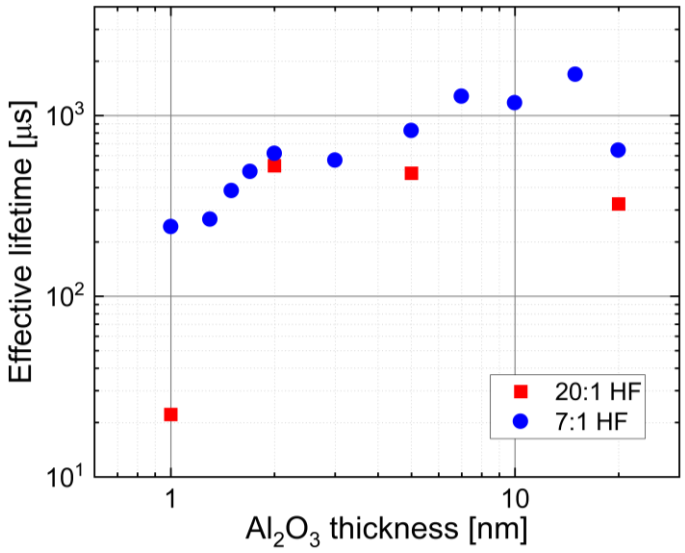

Figure 2 Effective lifetime (at $\Delta n = 10^{15}$ cm^{-3}) with variable Al_2O_3 thicknesses under different pre-treatments.

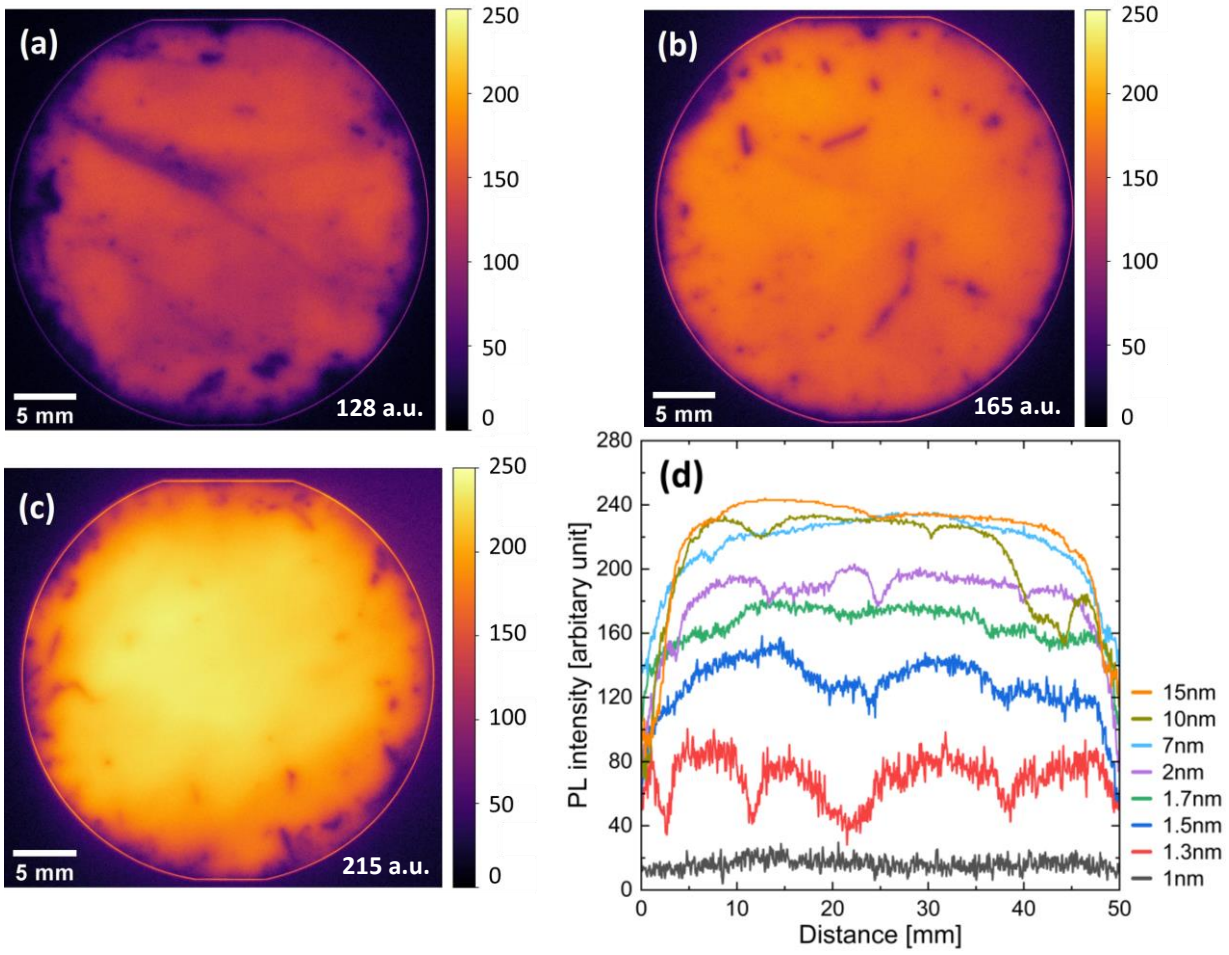

Figure 3 Photoluminescence (PL) results and mean PL intensity of the sample surface with **a.** 1.5 nm, **b.** 1.7 nm and **c.** 7 nm Al_2O_3. **d.** PL intensity along the same cutline for different Al_2O_3 passivation layer thicknesses.

Inducing piezoelectricity in chitosan films by cathodic electrodeposition: challenging a new approach for wearable sensors' fabrication

Valeria D'Errico [a, b], Gaia de Marzo [b, c], Antonio Qualtieri [b], Luciana Algieri [a], Massimo De Vittorio [a, b, c]

[a] Dipartimento di Ingegneria dell'Innovazione, Università del Salento, Lecce (LE), 73100, Italy
[b] Center for Biomolecular Nanotechnologies, Istituto Italiano di Tecnologia, Arnesano (LE), 73010, Italy
[c] Department of Health Technology, Technical University of Denmark, Kongens Lyngby, 2800, Denmark
e-mail: valeria.derrico@iit.it

Nowadays, real-time health monitoring is a largely investigated research topic, aiming to improve early diagnosis. In this context, wearable sensors represent a helpful and advanced instrument. They are often based on ceramic materials, much appreciated for their piezoelectric efficiency, but unfavourable for their rigidity, hard processing and high cost.
Intending to overcome traditional piezo-ceramics drawbacks, recent studies are evaluating polymers as a possible alternative due to their biocompatibility and sustainability, seeking new strategies to enhance their relatively low piezoelectric coefficient.
Moving in this direction, the present work explores cathodic electrodeposition (ED) as an unexplored approach to improve piezoelectric properties in chitosan films.
ED has already been widely performed for chitosan processing [1 - 4], but, to the best of our knowledge, it has never been considered to optimize piezoelectric properties in thin films.
Until now, just a few techniques have been tested for similar purposes, such as solvent casting followed by NaOH neutralization [5]. However, they demonstrate reduced possibilities for standardization and reproducible production on industrial scale due to the inherent process features.
Conversely, ED looks attractive for its adjustability by numerous parameters (such as voltage, time, electrolyte solution), allowing it to be tuned on the basis of the desired material properties [6 - 7]. Moreover, ED could offer a chance to fabricate chitosan films directly on the electrode intended to be employed in the final device, thus simplifying the fabrication process.
In accordance with this last issue, we have chosen gold-covered flexible substrates as electrodes (see Fig 1), matching the needs of biocompatibility and skin compliance required by wearable sensors.
By exploiting an electrolyte solution of chitosan and acetic acid, ED has been carried out under different voltages and times. Then, the realized films have been characterized with a focus on piezoelectric properties.
The piezoelectric coefficient (d_{33}) has been evaluated by means of an innovative set-up, specifically developed for soft thin films under weak mechanical loads [8]. The resulting values have proved the piezoelectricity of the electrodeposited chitosan films (see Fig 2). This assessment is consistent with the presence of Maltese crosses inside the films, identified by polarized light microscope (see Fig 3). Such structures, in fact, indicate the presence of polymer crystallization, which is a favourable condition to piezoelectricity generation.
These preliminary results enable to take a step forward in the improvement of the features of biopolymers to apply them in sensors technology, showing they can act as functional materials also in fields far from biology and tissue engineering.

[1] V. D. Patake et al., SN Applied Sciences (2019) 1:1063
[2] Y. Cheng et al., Materials Letters 87 (2012) 97-100
[3] Z. Geng et al., J. Mater. Chem. B, 2016, 4, 3331
[4] Y. Cheng et al., Soft Matter, 2010, 6, 3177-3183
[5] G. de Marzo et al., Adv. Electron. Mater. (2022) 2200069
[6] E. J. Choi et al., Materials Today, Vol. 62, 2023
[7] M. M. Momeni and Z. Tahmasebi, Inorganic Chemistry Communications 125 (2021) 108445
[8] G. de Marzo et al., Materials & Design 247 (2024) 113399

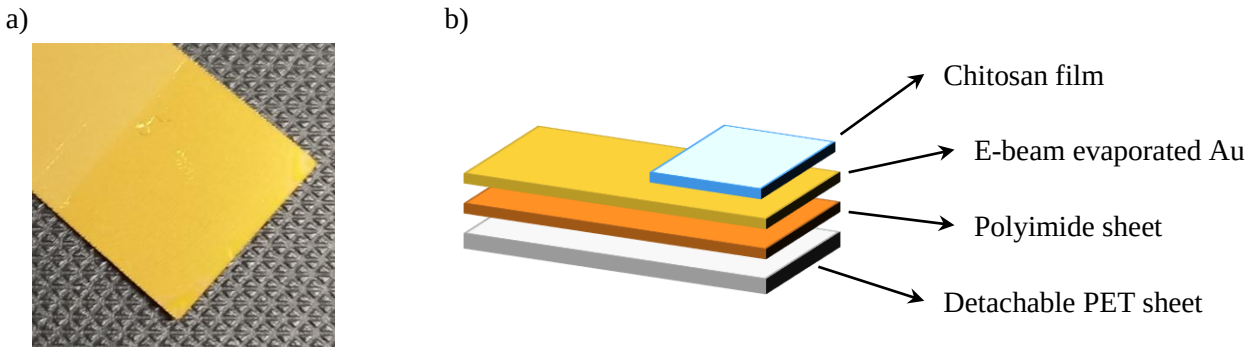

Figure 1. Chitosan film electrodeposited on gold-covered flexible electrode (Au e-beam evaporated on polyimide sheet) (a) and sample structure with explanation of the involved materials (b).

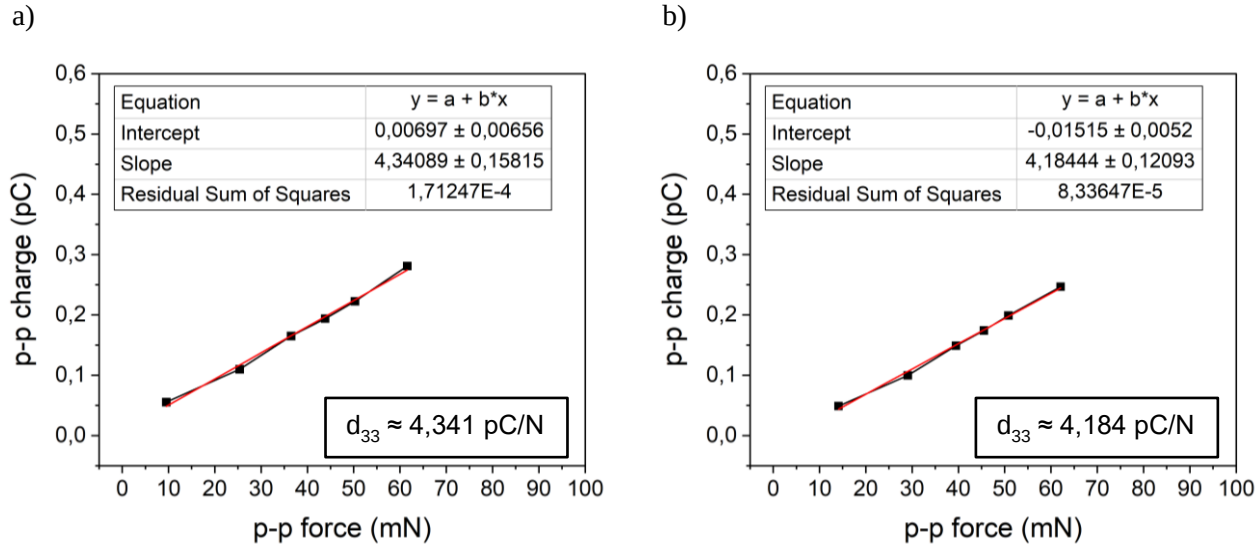

Figure 2. Piezoelectric coefficient (d_{33} [pC/N]) of chitosan films obtained by electrodeposition on gold-covered flexible electrodes at 3 V (a) and 6 V (b) for 10 minutes.

Figure 3. Chitosan film observed by polarized light microscope (100x) with detection of Maltese crosses.

Synthesis of novel EB resist based on KrF resist system

Atsushi SEKIGUCHI[1,2], Chen TANG[1], Yoshihiko HIRAI[1] and Masaaki YASUDA[1]

1 Osaka Metropolitan University, Graduate School of Engineering
1-1 Gakuen-cho, Naka-ku, Sakai, Osaka 599-8531, Japan

2 Litho Tech Japan Corporation, Nanoscience Laboratories
2-6-6 Namiki, Kawaguchi, Saitama 332-0034, Japan

Abstract

As EB resists are mainly used to make photomasks, their usage is overwhelmingly smaller compared to semiconductor resists and resist manufacturers have not put much effort into their development for mass production such as KrF resists

On the other hand, EB exposure using direct writing is very important for device prototyping, because it allows maskless pattern formation. In this work, we try to synthesize EB resists using monomers that are the base of KrF resists. As shown in Fig.1, we use4-Ethenylphenol acetate (M1) as the base monomer, and we use 1-Ethylcyclohexyl methacrylate (M15) and tert-Butyl methacrylate (M18) as the protecting groups, respectively. By alternating the polymerization ratio of the monomers, monomers with different properties were synthesized and EB resists were produced by adding PAG to the synthesized polymers, where the PAG used in this work is generally known to be effective for even EB exposure system [1].

Figure 2 shows the sensitivity curves for KrF exposure of polymers with different polymerization ratios. Screening was performed in advance using KrF exposure to determine the optimal polymerization ratio.

Figure 3 shows the results of an electron beam exposure experiment on a material that showed relatively good properties when polymerized with KrF. The result shows that the synthesized resin is also be used for EB exposure.

In the presentation we will apply novel deep learning system to optimize polymerization ratio [2] and show the pattern formation performance in EB exposure using computational lithography investigations.

Keywords: EB resist、polymer synthesis、EB exposure、KrF exposure、sensitive characteristics、Deep learning

Reference

[1] D. Shimizu, et al., JSR TECHNICAL REVIEW No.114(2007)11 in Japanese.
[2] C. Tang, et al., J. Vac. Sci. Technol. B 42, (2024) 062606.

Fig.1 Monomers used in this work

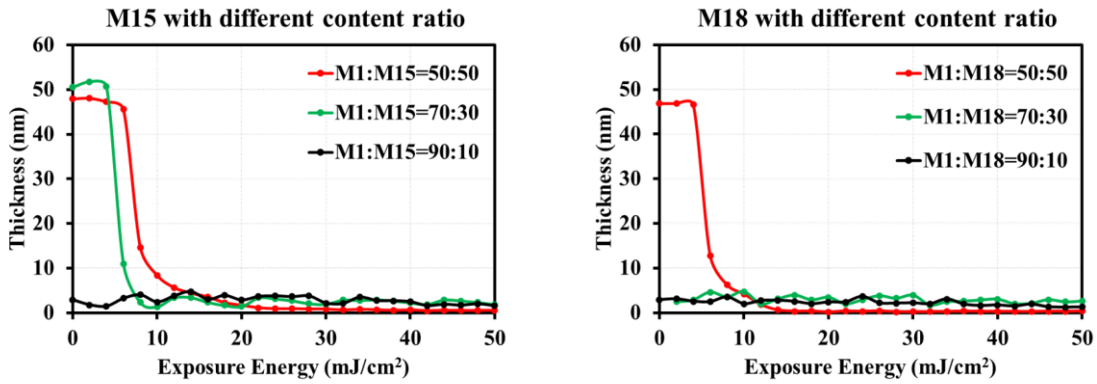

F.g2 Dependence of sensitivity curves on polymerization ratio (KrF exposure)

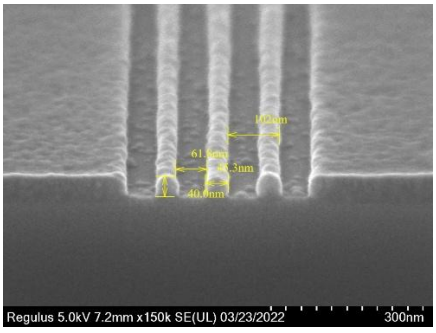

Fig.3 Experiment result by Electron beam exposure (M1:M15=70:30)

Nanofabrication of Large, Stitch-free Diffractive Optics

Anna Casimiro, Sander Schellingerhout, Adriana Umbria, Kahraman Keskinbora

RAITH Laser Systems B.V., Eindhoven, 5657 EH, The Netherlands
e-mail: anna.casimiro@raith.com

Diffractive optics are ubiquitous in various applications from X-ray imaging to interferometric measurements. Their performance is tightly linked to the structural fidelity achieved during fabrication. Traditionally, these structures are created using direct-write lithography within a single writefield. However, when the desired size of the optical device exceeds the maximum writefield size of a particular fabrication method, the design has to be broken into sub-fields in a matrix form, each of which is exposed sequentially. This process introduces stitching artifacts in the xy-plane at the boundaries of each writefield compromising optical performance of the fabricated device [1].

In this work, we demonstrate a stitch-free fabrication method using a maskless laser beam lithography (LBL) tool with a split-stage exposure strategy. Unlike systems that rely on beam scanning, this approach keeps the laser beam stationary with respect to the optical axis and precisely moves the sample underneath using a synchronized motion of scan (y-axis) and step (x-axis) stages (Figure 1). In each pass of the scan stage, one column of pattern data is exposed. This strategy enables seamless exposure of entire patterns, effectively making the writefield as large as the pattern itself and consequently eliminates stitching artifacts.

We demonstrate the lack of stitching artifacts by doing extensive metrology on various types of diffractive structures including diffraction gratings, variable pitched gratings, and Fresnel Zone Plates (FZP) using a split-stage maskless LBL tool. Moreover, we compare the results of infinitesimal stitching artifacts (20-30 nm) that are intentionally introduced in control samples, to the samples that are 100 % stitch-free. This stitch-free exposure strategy has many benefits in applications where the structural quality is paramount. These applications include micro-diffractive optics or integrated photonic circuit elements such as waveguides where avoiding scattering losses induced by stitching is vital.

[1] M.Gnan et al., CLEO/Europe and IQEC 2007 Conference Digest, (Optica Publishing Group, 2007).

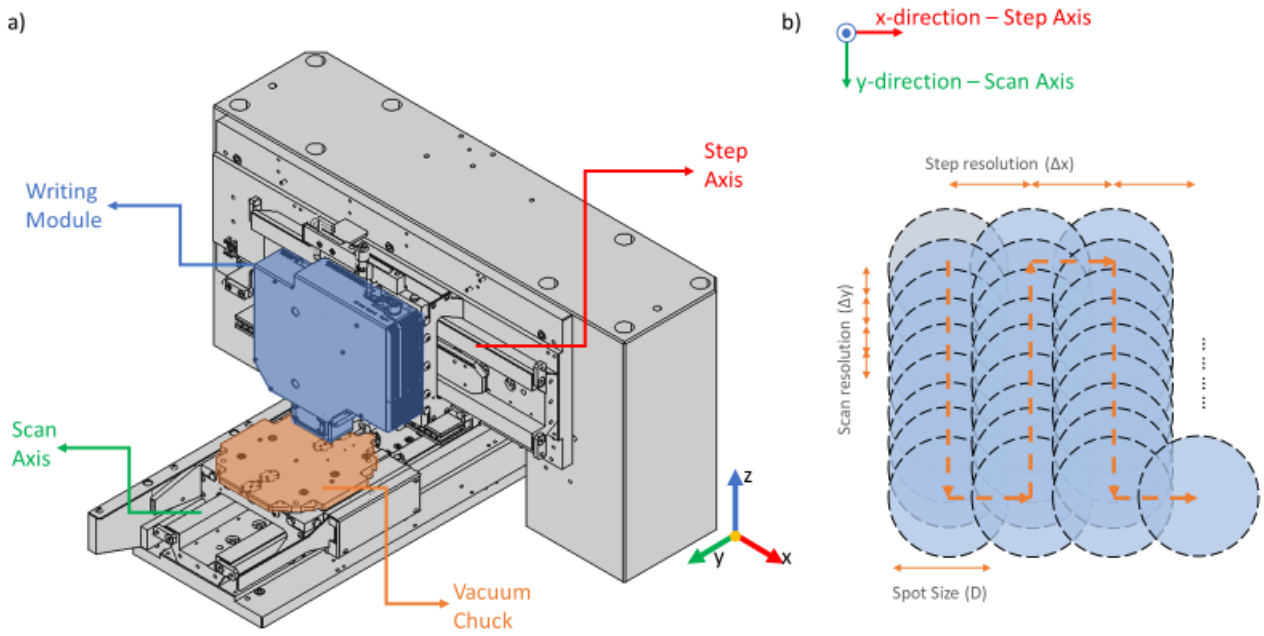

Figure 1: Schematic description of the split-stage concept. a) The diagram shows the scan and step stages as well in relation to the optical module and the substrate chuck. b) Pictographic representation of the split-stage exposure strategy.

Secondary particle detection for deterministic single ion implantation

K. Stockbridge [a], E. Schneider [b], G. Arresta [a], D. Cox [b]

[a] Ionoptika Ltd, Eastleigh, SO53 4BZ, UK
[b] University of Surrey, Guildford, GU2 7XH, UK
e-mail: k.stockbridge@ionoptika.co.uk

Techniques for deterministic implantation of single ions are currently of high interest for quantum applications that rely on the engineering of single defects in solids such as single photon emitters and solid-state qubits. The Ionoptika QOne single ion implanter achieves deterministic implantation by secondary charged particle (SCP) detection. Provided the ion beam/implant energy/target material combination results in a sufficiently high SCP yield, detection efficiencies up to 100% are possible and have been demonstrated.

Determining the detection efficiency of an ion/target system is vital in calculating the expected error-rate for a particular implant job. A <100% detection efficiency may be the result of low SCP yield (material physics limits) and/or poor conversion of generated particles to detected signal (sub-optimal detector configuration). Separating these two effects is required to fully understand and characterise the performance of the detectors independently of ion/target materials used.

For situations where poor SCP yield is the significant factor limiting high detection efficiency, methods to improve the SCP yield have been investigated e.g., by implanting through thin, high yield deposited material. Alternative detection modes e.g., ion beam induced charge (IBIC), have also been demonstrated in the QOne system.

Control of the Scanning Tunnelling Microscope Based on Hybrid Gain Integrator Systems (HIGS)

Richa Mishra [a], S. O. R. Moheimani [a]

[a] The University of Texas at Dallas, Richardson, TX 75080 USA
e-mail: reza.moheimani@utdallas.edu

Abstract:

Linear controllers, such as integral (I) control and proportional-integral (PI) control, have been widely employed to regulate the tunneling current in the scanning tunneling microscope (STM). Although several alternative control methodologies have been proposed in the literature, many lack accompanying imaging results to substantiate their efficacy [1]. Control of the STM Feedback loop based on a linear controller and striking a balance between a fast transient response and closed-loop stability robustness could be challenging [2], leading to a degradation of reference tracking performance. There has been a growing shift toward adopting nonlinear and hybrid control techniques to address the limitations of linear controllers. These advanced approaches could offer enhanced adaptability, improved dynamic performance, and greater robustness, without imposing excessive control effort.

We propose a novel STM z-axis feedback control method inspired by the Hybrid Integrator-Gain System (HIGS)-I control, as shown in Fig. 1(a). This control constitutes an advanced switching strategy that can surpass the performance limitations typically associated with classical linear control techniques [3]. Unlike conventional Linear Time-Invariant (LTI) integral action, which introduces a fixed phase lag of 90°, the HIGS approach imposes a reduced phase lag of approximately 38.15°, thereby contributing to improved phase margin and enhanced closed-loop stability robustness, as shown in Fig. 1(b). HIGS generates a continuous yet inherently non-smooth control signal by switching between integral and gain modes. By alternating between these two modes, HIGS-I effectively mitigates the detrimental effects commonly associated with pure integral action, such as pronounced oscillations near resonant frequencies, while ensuring system stability. The HIGS element is combined with LTI filters C_1 and C_2 to obtain a smooth control signal. The placement order of the filters is crucial for HIGS to function properly [3].

We conducted several experiments to investigate the efficacy of HIGS-I control compared to I-control. The results in Fig. 2 demonstrate the images obtained with both controllers on the same surface area. We observe higher oscillation levels in the topography and current signal profile data in Figs. 1 (a)-(b) (left) as compared to Figs. 2 (a)-(b) (right). We continued to scan the same area to demonstrate how a change of controller alters the tip behavior, as shown in a set of images in Figs. 3 (a)-(b) (left) where we change control from HIGS-I to I control. We observe that the tip starts to oscillate as the control changes to an I-controller, and an improved behavior is observed when the control is changed from I to HIGS-I control, as shown in Figs. 3 (c)-(d) (right). Another experiment we performed to compare the performance of HIGS-I control over I-control was to scan the surface at a higher scan speed of 500 nm/s, compared to the regular scanning speed of 200 nm/s. The scan data show much improved performance with the HIGS-I controller compared to when only I-control is implemented, as shown in Figs. 3 1(a) & (b) (left). By comparing all the results presented, we can conclude that HIGS-I is a competitive and superior control method compared to linear controls for z-axis control of STM, as it provides more stability and better tracking conditions, even at high scan speeds. From the perspective of designing the HIGS-I controller, we only need to tune the gain parameter once the rest of the parameters of the C_1 and C_2 filters are fixed. Within this frequency range, HIGS-I can provide sufficient phase margin even in the presence of unknown disturbances, unlike a PI controller, where two parameters will be required to tune to obtain a comparable phase margin.

[1] A. I. Oliva, M. Aguilar, J. L. Pena, and E. Anguiano, “Experimental determination of the parameters of the feedback system of a scanning tunnelling microscope,” Measurement Science and Technology, vol. 8, no. 5, pp. 501–507, 1997.

[2] I. Ahmad, A. Voda, G. Besancon, and G. Buche, “Robust digital control approach for high performance tunneling current measurement system,” Control Engineering Practice, vol. 20, no. 7, pp.643–653, 2012.

[3] van den Eijnden, S. J. A. M. (2022). Hybrid Integrator-Gain Systems: Analysis, Design, and Applications. [Ph.D. Thesis 1 (Research TU/e / Graduation TU/e), Mechanical Engineering]. Eindhoven University of Technology.

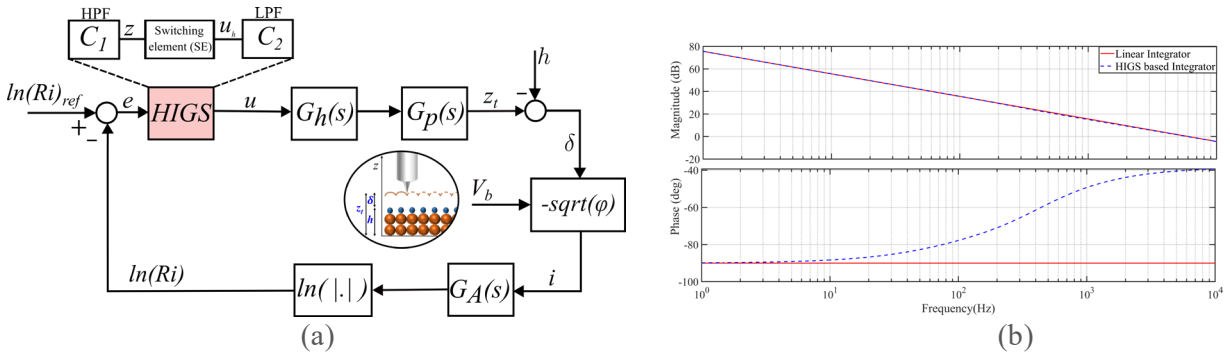

Figure 1. (a) The control block diagram of the z-axis of STM using the HIGS controller. This control has three critical elements: C_1, an LTI filter with high-pass characteristics; a switching element, which allows us to switch between integration and gain mode; and C_2, an LTI filter with low-pass characteristics. The high voltage amplifier, G_h, amplifies the controller command, which drives the piezo-actuator, G_p. The i changes momentarily when the tip encounters an unknown surface feature, h. This change is regulated by the controller HIGS by adjusting the tip-sample gap z_t (shown as δ in the figure). The preamplifier $G_A(s)$ converts the sub-nanometer range i to a measurable voltage. (b) Bode plot of the Integral controller (I) and the HIGS-based integrator for the same gain, optimized for better tracking.

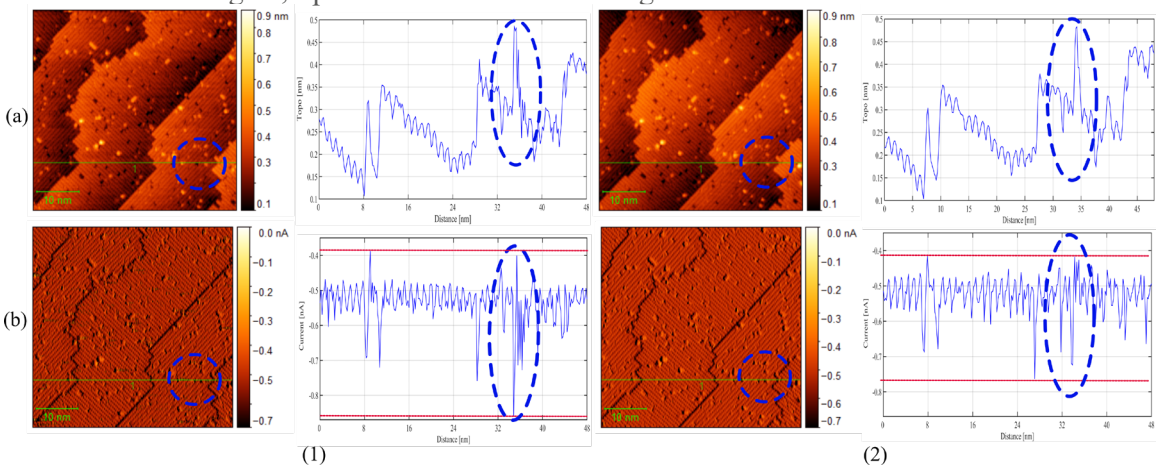

Figure 2. The image dataset to compare the performance of the integral controller and the HIGS-based integral controller. (Left) 1(a) Topography and 1(b) Current image and profile data when we use an integral controller. (Right) 2(a). Topography and 2(b). Current image and profile data when the controller is HIGS-I.

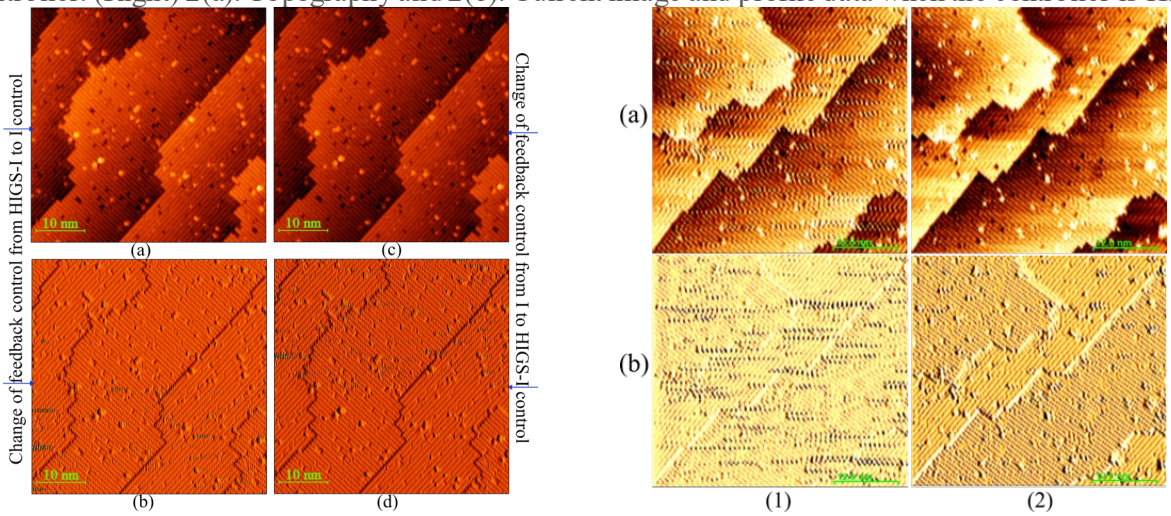

Figure 3. The image dataset (left) to compare the performance of the integral controller (I) and the HIGS-based I controller. (a) Topography and (b) Current data when the controller is switched from HIGS-I to I. (c) Topography and (d) Current data when the controller is switched from I to HIGS-I. (Right) The feedback loop is closed on ln(Ri), and the scanning speed is 500 nm/sec. 1(a) Topography and, 1(b) Current on I controller feedback loop. 2(a) Topography, 2(b) Current on HIGS based integral feedback loop.

Towards single-electron devices based on SOI silicon nanowires: simulation and fabrication

G. Petitto, Z. Sun, J. Antoja-Lleonart, A. del Moral, A. Guerrero, R. Mas, A. García-García, J. Bausells, F. Pérez-Murano, E. Amat, J. Llobet

Institute of Microelectronics of Barcelona (IMB-CNM CSIC), Bellaterra, 08193, Catalonia, Spain.
e-mail: jordi.llobet@imb-cnm.csic.es

Abstract. Silicon-on-insulator (SOI) nanowires are emerging as promising platforms for single-electron devices, leveraging long coherence times and compatibility with semiconductor fabrication techniques. This study combines advanced TCAD simulations with precision nanofabrication to develop and characterize SOI-based single-electron transistors. Fabricated test devices demonstrate the viability paving the way for advancements in quantum transport applications at the nanoscale.

Introduction. Silicon-based quantum devices offer long coherence times and seamless integration with existing semiconductor processes, making them promising candidates for quantum computing. Spin qubits can be engineered using electrostatic quantum dots or single donor atoms. Nevertheless, their fabrication presents some challenges, e.g. nanometer-scale electrode arrays, precise doping control, and robust quantum confinement structures. Recent research has focused on single-electron transistor (SET) [1] and silicon nanowire (SiNW) platforms [2], leveraging techniques such as electron beam lithography [3], directed self-assembly [4], and focused ion beam implantation [5] to enhance fabrication precision.

Device structure. The studied structures are based on SOI SiNW fabricated on wafers with a 50 nm silicon layer atop a 400 nm buried oxide (BOX). The key device parameters are an intrinsic SiNW 4 μm length, a gate oxide of 6.5 nm, and precisely engineered barriers (i.e. width: 30 nm, thickness: 50 nm) to enhance confinement. Fig. 1 shows the 2D and cross-section sketches of the SiNW-based device. By mean of two barrier voltages (V_g) applied on both planar gates the conduction can be tuned. The plunge gate voltage (V_{lead}) applied on the additional general gate located on top shifts the electric field over the channel.

TCAD simulations. We conducted 3D TCAD simulations using Sentaurus from Synopsys [6]. A semi-classical model was employed, solving carrier continuity equations for electrons and holes alongside the Poisson equation via a Newton-like solver. The simulations incorporated Fermi-Dirac statistics and accounted for incomplete ionization of dopants. To improve convergence at cryogenic temperatures, we adopted the hydrodynamic transport model with a quasi-stationary temperature ramp. The tunneling rate was computed using the WKB approximation. Fig. 2.a presents a 2D cross-section of the device, illustrating the electron tunneling rate through the potential barriers induced by the barrier gates. In this simulation, the device operated with a lead voltage above threshold (V_{lead} = 2.0 V), while barrier gates (V_b) were held at 0 V to induce local depletion in the channel. Fig. 2.b shows the conduction band profile (corresponding to the 1D cut along the channel shown in Fig. 1.a, marked by red dashed line) as a function of temperature.

Manufactured and measured devices. The fabrication process employs negative resist AR-N 7520.07, enabling both optical lithography for large patterns and electron beam lithography (EBL) for nanoscale features, without requiring intermediate development of the resist. After exposure and development, the remaining resist serves as a mask for silicon pattern transfer via reactive ion etching. The SiNW operates as an active channel, with source and drain electrodes defined by degenerately doped silicon implanted with boron to ensure efficient charge injection. Meanwhile, the nanowire remains undoped, enabling controlled electron confinement. A thermally grown SiO_2 layer serves as the gate dielectric, with up to six aluminum gates defined through EBL to provide flexible electrostatic control. Fig. 3.a presents an initial test device featuring a single aluminum gate on top a 6.5 nm gate oxide. The cross-section of a similar device (Fig. 3.b) highlights the gate oxide and Al-gate layers covering the SiNW. Next steps are oriented to finalize the multigate SiNWs and their electrical characterization at room temperature.

Conclusions. The integration of SiNW architecture, precision gate engineering, and selective ion implantation establishes a robust framework for exploring nanoscale electronic phenomena and quantum transport mechanisms. TCAD simulations refine barrier and lead electrode design, optimize dimensions, and enhance convergence by lowering temperature. Fabrication employs a mix-and-match approach for wafer-level SiNW production, with selective ion implantation doping the source and drain while preserving the NW channel. A flexible layout can accommodate up to six gates or barriers, supporting future advancements in single-electron devices, nanoelectronics, and quantum technologies.

Ref. [1] F. Bersano *et al.*, *ESSCIRC*, pp. 49-52 (2022). **[2]** R. Maurand *et al.*, *Nature Comm.*, **1**3575 (2016). [3] F. Abualnaja *et al. Appl. Phys. Lett.* **122**, 233504 (2023). **[4]** C. Pinto-Gómez *et al. Polymers* **12**, 2432 (2020). **[5]** J. Llobet *et al. Appl. Phys. Lett.* **107**, 223501 (2015). **[6]** Sentaurus Device, v. K-2022.06-SP2, 2022.

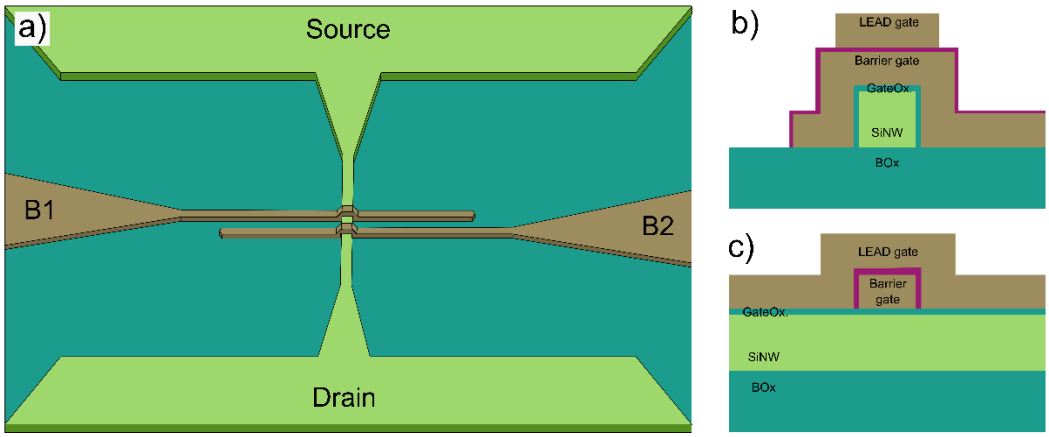

Fig. 1. *Schematic Representation of the Device. (a) Tilted perspective illustrating the SiNW, which serves as the transistor channel, along with two top-barrier gates. For clarity, dielectrics and the top-lead gate are omitted. (b) Horizontal cross-section detailing the gate oxide, the barrier gate B1, a thin alumina layer, and the top-lead gate. (c) Vertical cross-section providing insight into the device structural arrangement.*

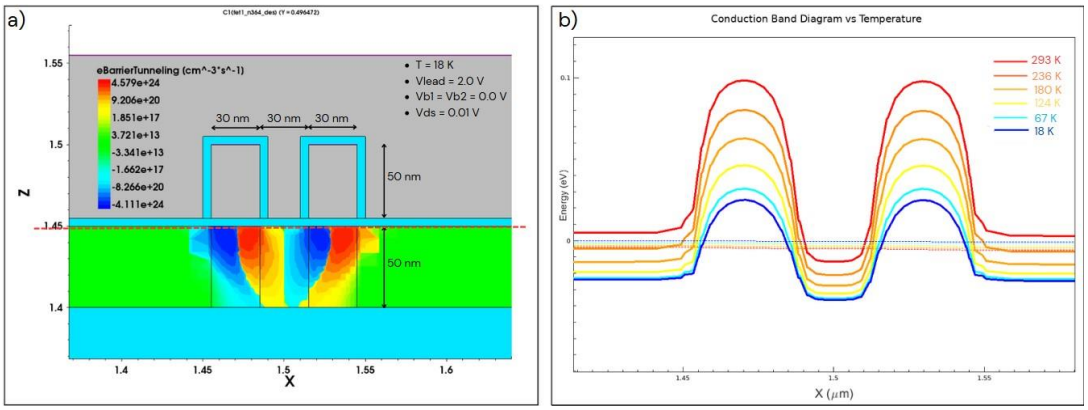

Fig. 2. *TCAD simulations.* ***a)*** *Cross-sectional view of the simulated dual-gate device, showing a color map of the electron tunneling rate through the barriers — i.e., the rate at which electrons disappear (negative values, corresponding to blue regions) and appear (positive values, red regions) in the conduction band of the channel due to tunneling.* ***b)*** *Conduction band profiles (solid lines) and electron quasi-Fermi levels (dashed lines) at different temperatures.*

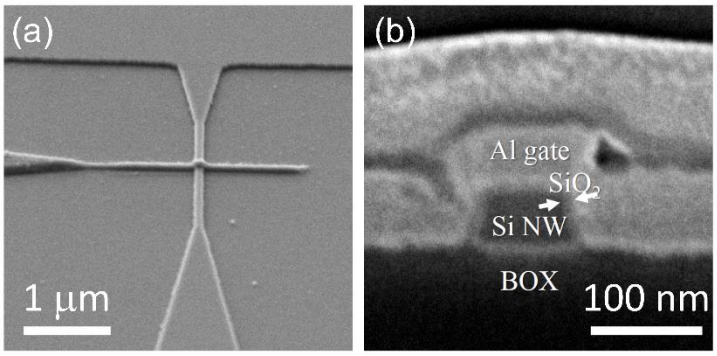

Fig. 3. *SiNW with a top Al gate.* ***a)*** *SEM image of a fabricated SiNW-based test device, featuring a narrow aluminum gate on top a 6.5 nm gate oxide layer.* ***b)*** *SEM/FIB cross-sectional view of a similar SiNW structure, highlighting the thermally grown gate oxide and aluminum gate on top of the nanowire.*

A YOLOv8-Based Defect Inspection for Semiconductor

Xiaolong Guo [b], Yanan Zhu [a], Heming Wu [a], Diwei Zhou[c], Zhuming Liu [a]

[a] Institute of Semiconductors, Guangdong Academy of Sciences, Guangzhou, 510650, China
[b] School of Electronic Science and Engineering (School of Microelectronics), South China Normal University, Foshan 528225, China
[c] School of Science, Loughborough University, Leicester, LE11 3TU, UK

e-mail: liuzhuming@gdisit.com

In semiconductor manufacturing, defect inspection based on scanning electron microscope (SEM) images is critical for ensuring high yield and product quality [1]. This paper proposes a deep learning framework based on YOLOv8 for high-resolution SEM image defect inspection. To address the challenges posed by increasingly smaller defect sizes, complex structural patterns, and elevated noise interference, we present an enhanced YOLOv8 model incorporating a novel hybrid loss function that combines Focal Loss and CIoU Loss. This improvement introduces tunable parameters to reduce the loss weight of easily classified samples while integrating center-point distance and aspect ratio constraints into the IoU metric, thereby enhancing defect localization accuracy and balancing inspection precision with computational efficiency. First, a comprehensive SEM image dataset is constructed, containing diverse defect types such as bridging, line collapse, gaps, and micro-bridges, with precise annotations. The dataset covers varying noise levels and defect densities to strengthen the model's generalization capability. During fine-tuning, data diversity is augmented through techniques including random cropping, rotation, flipping, and color jittering, improving the model's adaptability to different imaging conditions. The modified YOLOv8 model, equipped with the proposed loss function, is trained on this custom SEM dataset. Further optimization of model performance is achieved by hyperparameter tuning, such as adjusting the learning rate and training epochs, ensuring robust performance across diverse scenarios. The proposed YOLOv8-based framework demonstrates significant potential to deliver an efficient and accurate solution for SEM defect inspection in advanced semiconductor manufacturing.

[1] Kim, J., Kim, S., Kwon, N., Kang, H., Kim, Y., and Lee, C., “Deep learning based automatic defect classification in through-silicon via process: Fa: Factory automation,” in [2018 29th Annual SEMI Advanced Semiconductor Manufacturing Conference (ASMC)], 35–39 (2018).

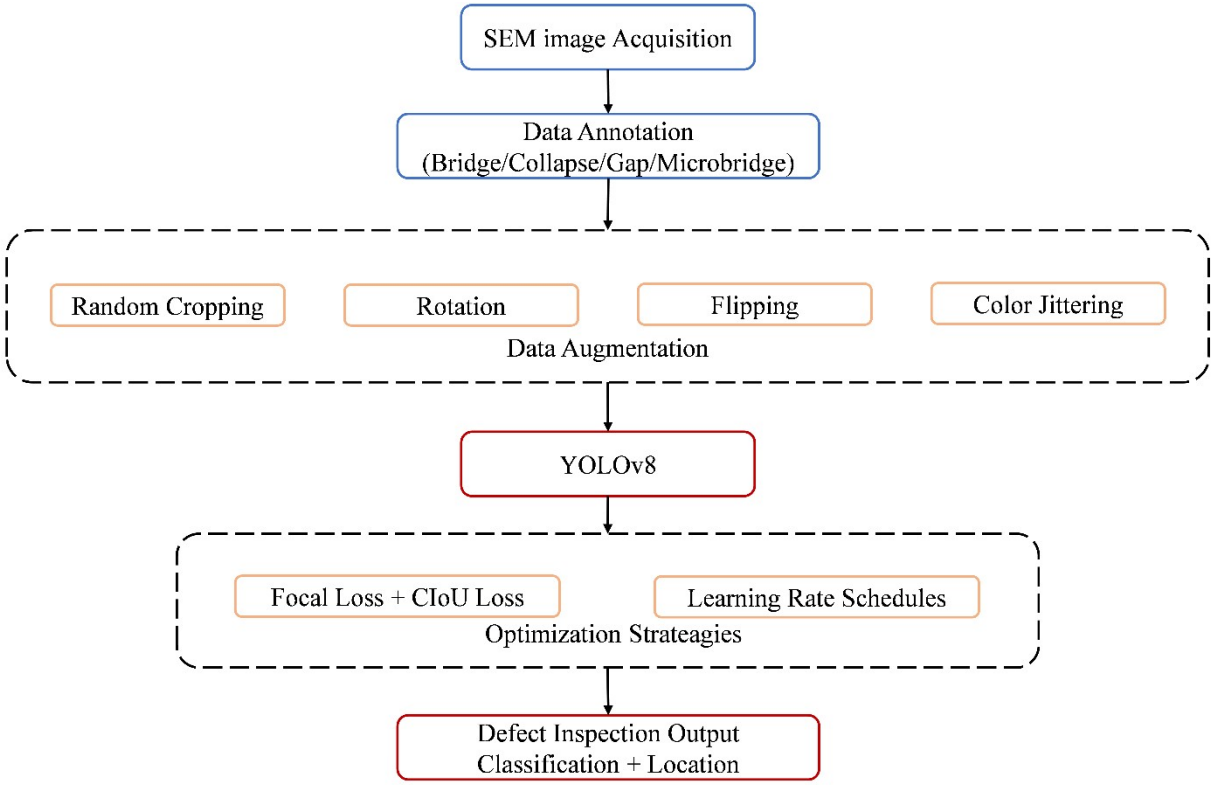

Figure 1. Schematic of the proposed deep learning-based framework for high-precision SEM image defect inspection. The framework comprises a customized SEM image dataset, a data augmentation module , a novel loss function, and hyperparameter optimization components, designed to enhance the inspection accuracy and computational efficiency for various defect types in SEM images.

Two-dimensional arrays of InAs nanodots grown on inverted pyramid Si templates

Javier Bravo[a], David Bermúdez[b], Lisandro Jofre[a], Paloma Tejedor[b]
[a]NAITEC, Pamplona, 31006, Spain
[b]Instituto de Ciencia de Materiales de Madrid, CSIC, Madrid, 28049, Spain
e-mail: jbravo@naitec.es

InAs nanodots are the basic elements of a variety of photonic and quantum devices. For many of these devices the formation of periodic one- or two-dimensional arrays of InAs nanostructures [1] over large areas, ideally integrated into Si substrates, is a requirement. Different nanolithographic techniques have been applied to fabricate nanopatterned Si templates to achieve precise site control of InAs nucleation by selective epitaxial growth. Among them, high-resolution Lloyd's mirror laser interference lithography (LIL) [2] offers a key advantage: it enables the creation of highly uniform, periodic nanostructures across centimeter-scale areas in a single process, without stitching artifacts, as it relies on recording an interference pattern.

In this work, we study the selective growth of InAs nanodots on inverted pyramids fabricated on Si wafers by laser interference nanolithography and wet etching. LIL is employed to define arrays of nanoholes in a photoresist, which are subsequently transferred to an underlying SiO_2 mask (previously deposited on Si) using reactive ion etching (RIE). These nanoholes in the SiO_2 layer are then used as a mask for anisotropic KOH etching to form inverted nanopyramids on the Si substrate [3].

We have investigated the effect of the main growth parameters on the selectivity, morphology, and structure of InAs/GaAs nanocrystals grown by hydrogen-assisted molecular beam epitaxy (H-MBE) on the nanofabricated Si templates. High-resolution scanning electron microscopy (HRSEM) and X-ray diffraction (HRXRD) techniques have demonstrated that the deposition of an ultra-thin (1 nm) GaAs buffer layer prior to epitaxial growth of InAs and the utilization of As/III flux ratios above 25 are crucial to obtain strained and coherent (defect-free) InAs nanodots selectively nucleated on the (001) nanofacets of the nanostructured Si substrate. The InAs/GaAs nanodots are 30-100 nm in size and are mainly bounded by (110), (311) and (001) facets. Lowering the As/III flux ratio below 25 has also shown to induce the secondary nucleation of GaAs nanowires on the (111) facets of the Si template during high-temperature steps of the growth process.

[1] P. Tejedor, E. García Tabares, L. Vázquez, B. Galiana, B. J. García, Appl. Surf. Sci. 616 (2023) 156518, 1-9.
[2] S. Dominguez, I, Cornago, J. Bravo, J. Pérez-Conde, H.J. Choi, J.G. Kim, G. Barbastathis, J. Vac Sci & Tech B, 32(3) (2014), 030602.
[3] S. Domínguez, I. Cornago, O. García, M. Ezquer, M.J. Rodríguez, A.R. Lagunas, J. Pérez-Conde, J. Bravo, Phot and Nanost-Funds and Apps 10.1 (2012): 46-53.

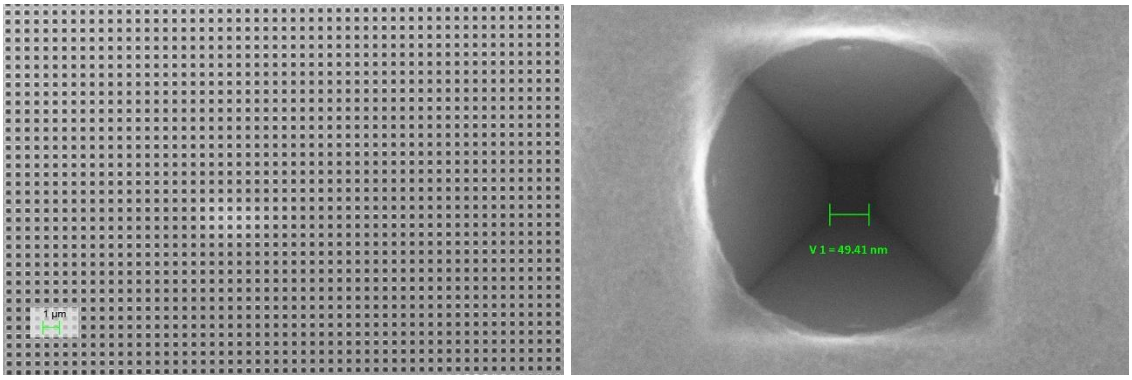

Figure 1. Plan-view HR-SEM image of the 2D array of inverted nanopyramids after the KOH etching. Left: low magnification view. Right: detailed view of one of the inverted nanopyramids.

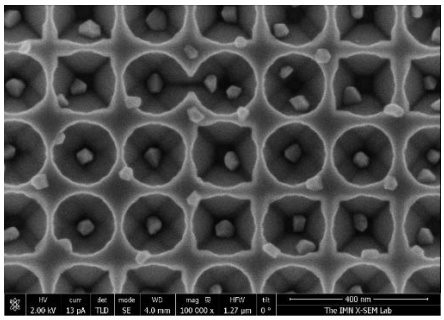

Figure 2. Plan-view HR-SEM image of the 2D array of InAs nanodots nucleated on the GaAs-coated Si template

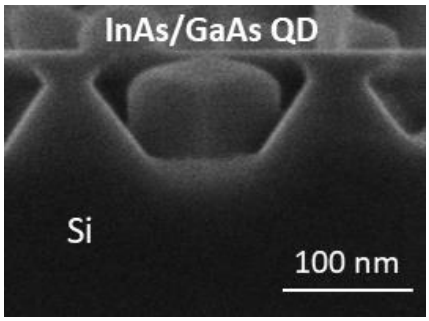

Figure 3. Cross-section HR-SEM image of an InAs nanodot grown on the (001) facet of an inverted pyramid of the GaAs-coated Si template

EBIC measurement of the minority carriers diffusion length in a GaAs solar cell p-n junction

Anya Grushina [a], Karl Boche [a]
[a] Imina Technologies, Cugy VD, 1054, Switzerland
e-mail: grushina@imina.ch

Electron beam current collection techniques are widely used to study semiconductor devices and to localize defects. Electron beam induced current (EBIC) can help to quantify carrier mobility, diffusion lengths, recombination processes, and defect distribution within the material [1]. This information is crucial for understanding the performance and quality of semiconductor devices, which, in turn, leads to improved design and fabrication processes. To obtain specific parameters describing the charge carrier dynamics, one needs to associate accurate current values with each pixel of the EBIC image [2].

Here, we present how calibrated EBIC signal acquisition can be used to measure the minority charge carrier diffusion length at the p-n junction of a solar cell. Their diffusion length, or lifetime, is related to defects or dislocation density in a semiconductor.

We collected EBIC signal from a GaAs solar cell cross-section, the schematic of the experiment is shown in Fig. 1, and the EBIC signal is shown in Fig. 2. Thanks to a well-calibrated EBIC signal acquisition module, we obtained accurate pixel current values for all amplification configurations and could quantify the device characteristics.

We collected 50 line-profiles of the EBIC signal (Fig 3) and used them to calculate the diffusion length of minority charge carriers, which amounted to 570 nm, which is within the expected range for such devices. We also estimated that the surface recombination velocity is close to zero, which suggests a low density of defects in the semiconductor layer of the solar cell.

[1] G. Moldovan, The emergence of electrical analysis in electron microscopy, Microscopy and Analysis, 2020.
[2] D. Chan, V. Ong, A direct method for the extraction of diffusion length and surface recombination velocity from an EBIC line scan, IEEE transactions on electron devices, 1995.

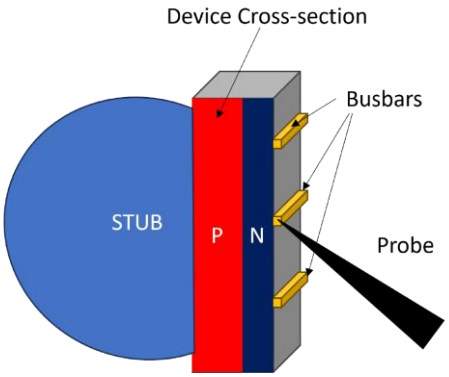

Figure 1. Sketch of the sample geometry as viewed from the top, with the device glued onto the SEM stub with the p-n junction facing the electron beam, and the busbars located on the vertical surface of the sample, easily reachable by the probes

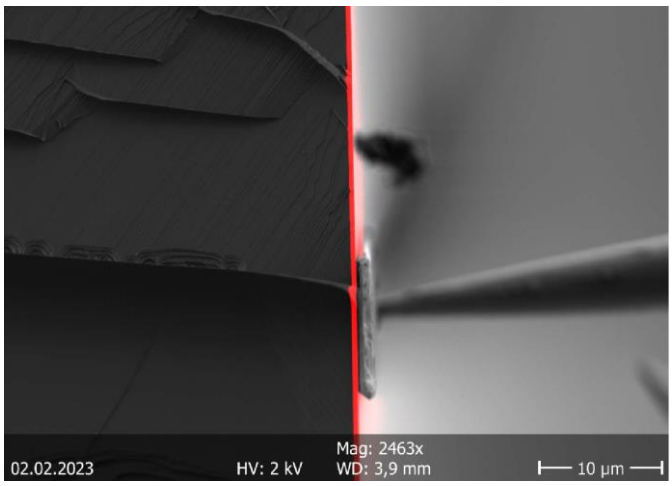

Figure 2. EBIC image of the solar cell p-n junction cross-section.

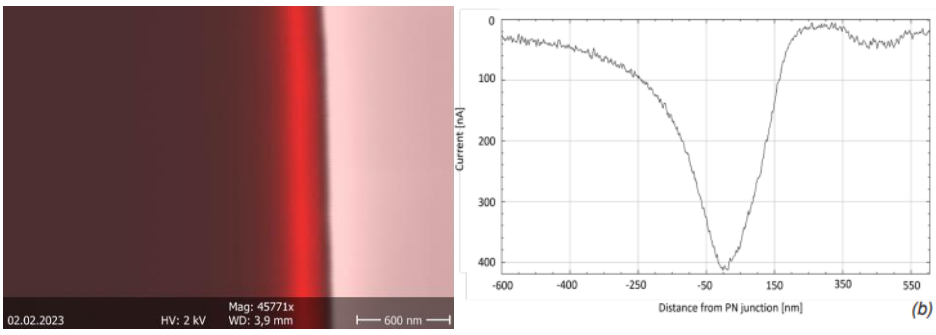

Figure 3. (left) Zoom into the area producing EBIC signal from Fig.2, across which the line-profiles were collected; **(right)** Average of 50 line-profiles of electron beam induced current across the p-n juction

Preparation of Regrowth Interfaces in AlGaN/GaN Heterostructures Using Atomic Layer Etching for Ohmic Contact Formation

E. Aslanidis[a], A. Adikimenakis [a], N. Makris[a], A. Stavrinidis [a], G. Konstantinidis [a]

[a] Microelectronics Research Group (MRG), Institute of Electronic Structure and Laser (IESL), Foundation of Research & Technology Hellas (FORTH), Crete 70013, Greece;
e-mail: e.aslanidis@iesl.forth.gr

Atomic Layer Etching (ALE) has emerged as a critical technique for achieving ultra-precise, damage-free surface modification in III-nitride semiconductor devices [1, 2]. In high-electron-mobility transistors (HEMTs) based on GaN/AlGaN heterostructures, the control of etch depth and surface quality is essential for subsequent epitaxial regrowth processes. This is particularly relevant in the formation of low-resistance ohmic contacts through selective regrowth of heavily doped n++ GaN in the source/drain access regions [3, 4]. Conventional dry etching techniques often introduce plasma-induced damage, surface roughness, and compositional changes which can degrade regrowth interface quality and device performance. ALE offers a promising alternative by enabling atomic-scale layer removal with minimal surface damage, thereby preserving the integrity of the underlying crystal structure and enabling high-quality regrowth.

While ALE has been explored for surface smoothing and damage mitigation in GaN devices, its targeted use as a regrowth interface preparation method for forming n++ GaN ohmic contacts remains largely unexplored. This work demonstrates a robust ALE-enabled etch technique, validated by atomic force microscopy (AFM) and Reflection high-energy electron diffraction (RHEED), that yields atomically smooth surfaces conducive to high-quality epitaxial regrowth for low-resistance ohmic contact formation. To investigate the ohmic contact a TLM sample was fabricated. The process flow begins with mesa isolation performed by BCl_3/Cl_2-based dry etching in an ICP-RIE system. A 250 nm silicon nitride (SiN) hard mask was then deposited via PECVD, followed by selective patterning using SF_6 plasma to define regrowth regions. To prepare the surface for regrowth, the GaN cap and AlGaN barrier layers were removed using an ALE etching technique. This technique was developed in a regular ICP-RIE tool and consisting of consecutive cycles of Cl_2 gas and low-energy Ar plasma sputtering. The Cl_2 gas reacts with the GaN surface creating Gallium chlorites [2] which can be easily removed by the low energy Ar ions. The etching was found to be around 3 monolayers of GaN per cycle (Figure 1a) and has very good synergy of 95.6%. The ALE process was selected for its ability to minimize surface damage while achieving high uniformity and smoothness suitable for epitaxial regrowth. The surface RMS roughness was measured by AFM and found 0.35 nm. The etching depth was carefully controlled to terminate just below the AlGaN barrier, enabling access to the 2DEG through the exposed sidewall. Without the ALE technique the precision of the etching depth and the smoothness of the etched surface will not be possible. The samples were then cleaned using a piranha solution, followed by the deposition of a 50 nm molybdenum layer on the sample backside via electron-beam evaporation to facilitate thermal handling. Samples were then introduced into a molecular beam epitaxy (MBE) system, where they underwent ex-situ chemical cleaning and in-situ thermal desorption under ultra-high vacuum. The substrate temperature was gradually increased to 680 °C under Ga-rich conditions to initiate two-dimensional (2D) epitaxial growth of a highly doped n+ GaN layer. Regrowth GaN layer was 65 nm thick with doping of 1.5×10^{20} cm^{-3}. RHEED patterns remained streaky throughout growth, confirming layer-by-layer growth and a smooth surface. AFM analysis of the regrown regions revealed an atomically smooth surface with RMS roughness as low as 0.28 nm (Figure 2), validating the effectiveness of the ALE-based etch in preserving surface quality. In contrast, GaN grown on the SiN mask surface was polycrystalline, with RMS roughness exceeding 22 nm (Figure 2). This unwanted material was subsequently removed through a standard lift-off process. The final step was the deposition of the overlay Ti and Au at the top of the regrowth GaN and the dc characterization of the TLMs where excellent ohmic contact behavior was observed (Figure 3). This work demonstrates the advantages of ALE for preparing regrowth interfaces in GaN-based devices. Such accuracy and surface quality would not be attainable using conventional etching methods, highlighting the importance of the ALE approach and paving the way for its integration into HEMT fabrication for high-frequency RF applications.

This project was funded from the European Union's Project "POWERSAT" under the grant agreement No [101162320]

[1] Guan, Lulu, Xingyu Li, Dongchen Che, Kaidong Xu, and Shiwei Zhuang. "Plasma atomic layer etching of GaN/AlGaN materials and application: An overview." Journal of Semiconductors 43, no. 11 (2022): 113101.

[2] Kauppinen, Christoffer, Sabbir Ahmed Khan, Jonas Sundqvist, Dmitry B. Suyatin, Sami Suihkonen, Esko I. Kauppinen, and Markku Sopanen. "Atomic layer etching of gallium nitride (0001)." Journal of Vacuum Science & Technology A 35, no. 6 (2017).

[3] Hickman, Austin, et al. "High breakdown voltage in RF AlN/GaN/AlN quantum well HEMTs." IEEE Electron Device Letters 40.8 (2019): 1293-1296.

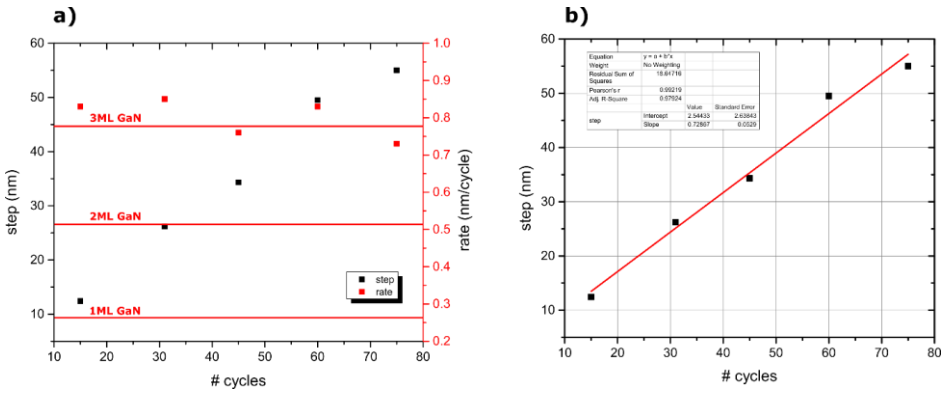

Figure 1. a) Graph showing step height as a function of the number of ALE cycles. Black dots represent the step height, while red dots indicate the etching rate. The graph also marks the thicknesses of one, two, and three monolayers of GaN (0.259 nm, 0.518 nm, and 0.777 nm, respectively). b) Step height vs. cycles graph, demonstrating the linearity of the ALE recipe.

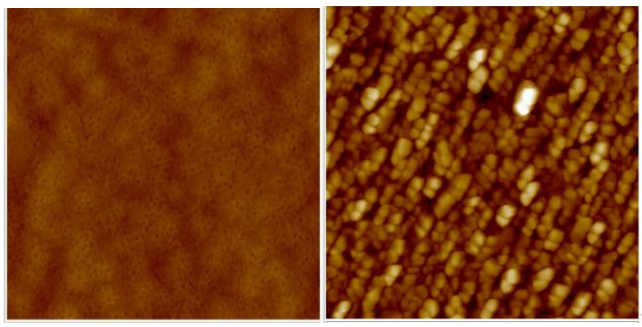

Figure 2. AFM pictures of the regrown n+ GaN film (left) and n+ GaN film grown on the SiN mask (right)

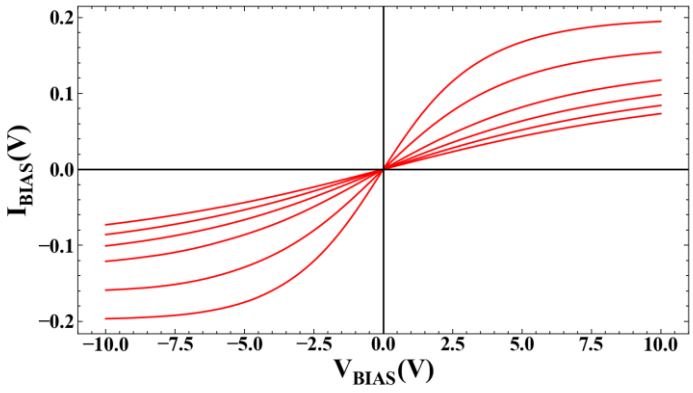

Figure 3. Ohmic contact behavior the regrown n+ GaN in TLM measurements

Fabrication of coupled silicon nanoelectromechanical resonators with heavily doped silicon towards reservoir computing chip

Dai Ai [a*], Ting Hou [a], Zixuan Wang [a], Kian Shen Kiang [a], Yoshishige Tsuchiya [a] and Jun-Yu Ou [b]

[a] School of Electronics and Computer Science, University of Southampton, Southampton, SO17 1BJ, UK
[b] School of Physics and Astronomy, University of Southampton, Southampton, SO17 1BJ, UK
*e-mail: da1r23@soton.ac.uk

Physical Reservoir Computing (PRC) is a form of physical computing applied within the framework of Reservoir Computing, a machine learning paradigm that simplifies and accelerates computation by using untrained, recurrently connected networks—known as reservoirs—and training only the output layer [1]. PRC enhances this concept by replacing the traditional neural network reservoir with a real physical dynamical system, requiring training solely at the readout stage. This approach enables greater node density, faster operation, and reduced power consumption, particularly when integrated with advanced micro- and nanofabrication technologies. Among the various scalable networks of micro/nanoscale nonlinear physical nodes, coupled nonlinear mechanical oscillator networks have shown promise. Coulombe et al. [2] demonstrated through numerical simulations that such networks can serve as energy-efficient physical reservoirs. These systems can be realized using Duffing nonlinear oscillators, which are compatible with silicon-based Micro- and Nano-Electro-Mechanical Systems (M/NEMS) technologies [3,4]. Here, we design and fabricate single and coupled silicon nanoelectromechanical resonators with heavily doped silicon operating at VHF range.

We first design our nanomechanical resonators with finite element method using COMSOL Multiphysics. The silicon single beam nanomechanical resonator with the length of 7.4 µm, width of 600 nm and height of 300 nm provides the fundamental out-of-plane resonance at 47.5 MHz, shown in Fig1 b. The double beam with the same dimensions of single beams are coupled with a mechanical link of 70 nm width and length of 2 microns. The coupled double beam device is resonated at 58.6 MHz according to our simulation, shown in Fig 1d.

Nanomechancial resonators are fabricated on silicon-on-insulator (SOI) wafers following a standard top-down nanofabrication process, shown in Fig 2. The silicon device layer with thickness of 300 nm were first doped by ion implantation. The next process starts with spin coating a 400-nm-thick ZEP520A photoresist layer. Electron beam lithography defines the resonator geometry by patterning the top 300 nm of the silicon device layer. After development, a dry etching with reactive ion etching (RIE) was used to transfer the pattern into the top silicon, with the remaining ZEP520A layer acting as a hard mask. A 400 nm silicon dioxide layer was then deposited by Plasma-Enhanced Chemical Vapor Deposition (PECVD) to serve as a protective layer for post process. The second electron beam lithography was used to define windows above the nanomechancial resonator beams, followed by RIE to locally remove the silicon dioxide in the exposed areas. This step exposes both the beam structures and the underlying sacrificial layer, while other regions remain protected. Finally, the sacrificial layer below the beams is removed by a vapor-phase etch using 50% hydrofluoric acid (HF-VPE) at 40 °C, resulting in suspended resonator structures. The optical images of single nanobeam (Fig. 2b) and double nanobeam devices (Fig. 2c) were taken with the magnification of 150x. Our single and coupled double beam devices were imaged using scanning electron microscope. Figure 3a shows the single nanobeam device with two side gates with a gap between the beam and gate of 100 nm. We observed a clear undercut showing the suspension of the nanobeam device. The coupled double beam with the mechanical coupling link is with the dimension of 70 nm width and 2 microns length and thinness of 300 nm.

In summary, we successfully fabricated single and coupled double nanobeam devices with expected mechanical resonance frequency of 47.5 MHz and 58.6 MHz. we aim to drive such device electrically with the side gates offering control of nonlinearity as a fundamental component for a future energy-efficient reservoir computing chip.

Acknowledgements: This work is partially supported by CHIST-ERA NOEMIA (CHIST-ERA-21-NOEMS-004) by EPSRC (EP/X03495X/1) and UK-Japan Semiconductor HetMEPS by EPSRC-JST.

References : [1] Tanaka et al, Neural Networks 115 (2019) 100. [2]J. C. Coulombe et al., PLoS One, 12 (2017) e0178663. [3] Csada et al., Appl. Phys. Rev. 7 (2020) 011302 [4] F. Ben et al., Micro and Nano Engineering 19 (2023) 100212.

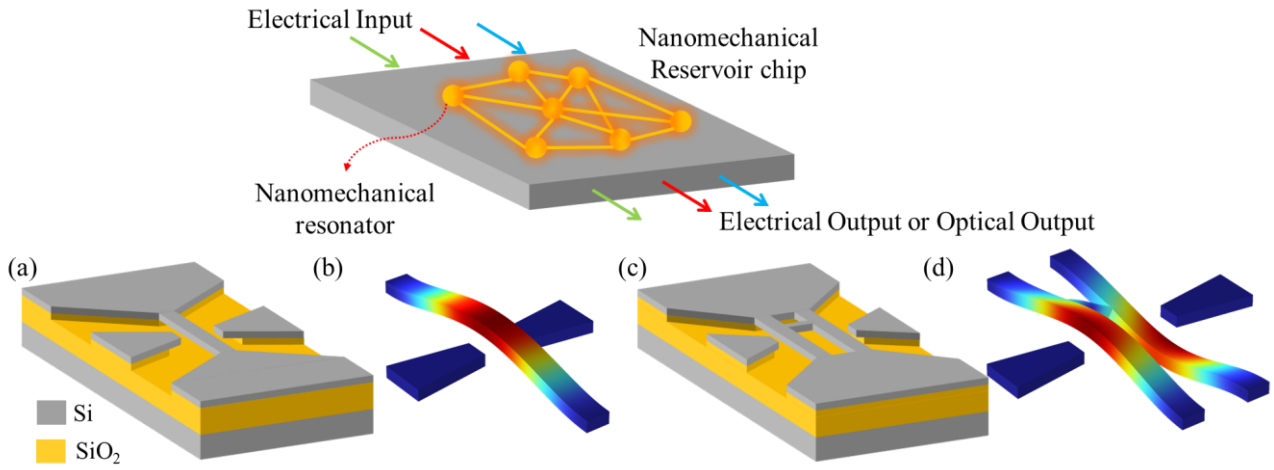

Figure 1. Conceptual illustration of nanomechanical reservoir computing chip. (a) a single beam nanomechancial resonator with fixed side gate. (b) a single nanobeam resonated at 47.5 MHz (c) a coupled double beam nanomechancial resonator with side gate (d) a coupled double beam resonator resonated at 58.6MHz.

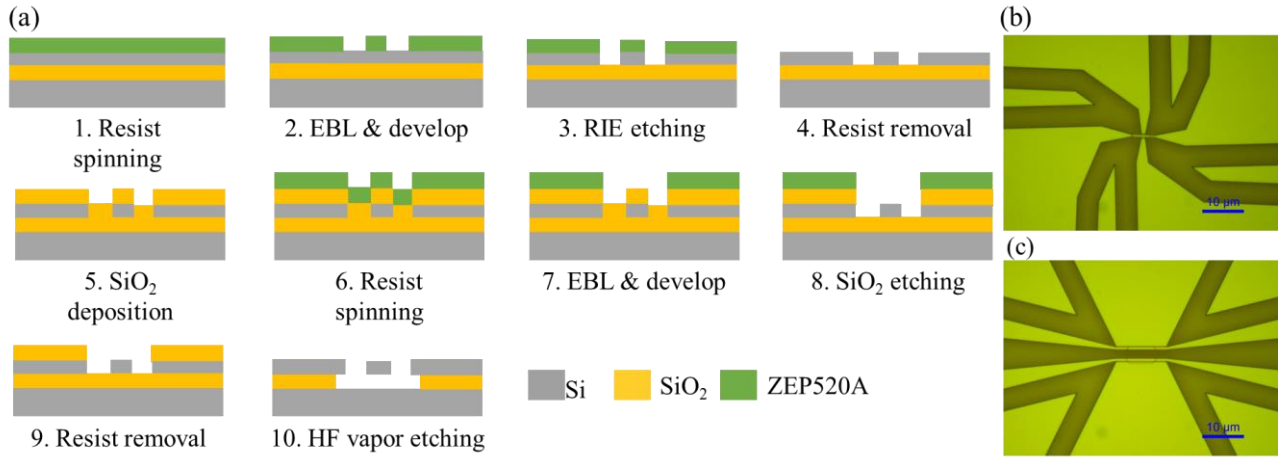

Figure 2. Fabrication of nanobeam mechanical resonators (a) Fabrication process flow for suspended nanobeam resonators using electron beam lithography, reactive ion etching and HF vapor etching. (b) optical image of a single beam resonator and (c) a double beam resonator. The scale bar is 10 µm.

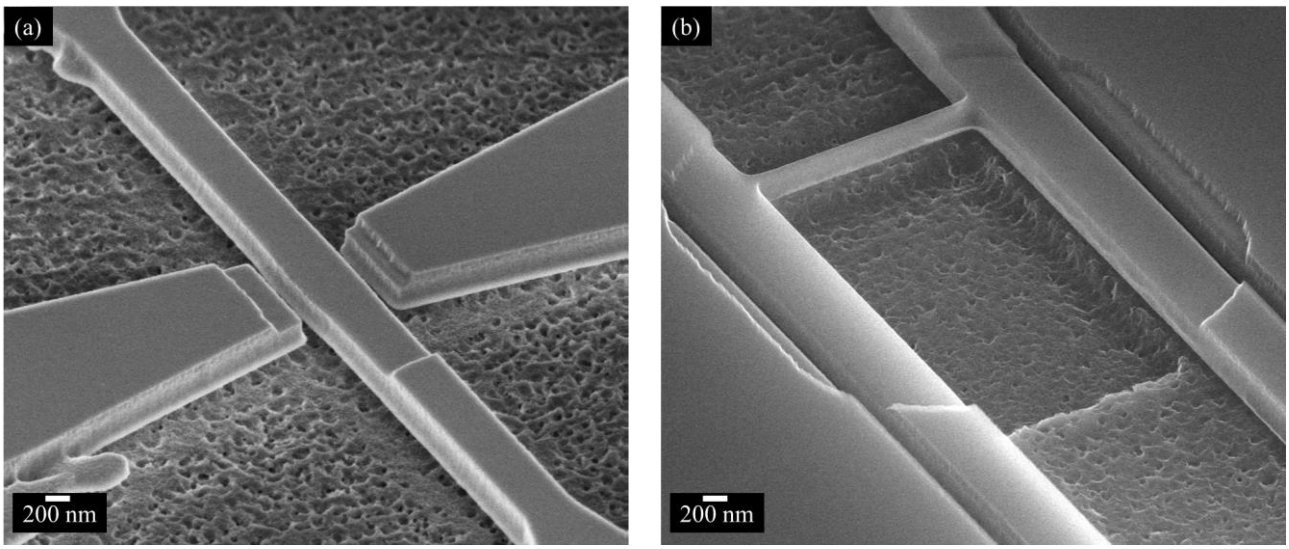

Figure 3. Fabrication results of nanomechanical resonators. (a) a single beam resonator (b) a coupled double beam resonator with coupling beam width of 70 nm and length of 2 µm. The scale bar is 200 nm.

Vapor Phase Infiltration in Homopolymers and Block copolymers: A comparative study

María Teresa Elenes*, Olga Muntada*, Sara Durán, Ricard Noy, Libertad Solé, Jordi Llobet, Francesc Perez-Murano, Marta Fernandez-Regulez
* *These two authors contributed equally to the work*
Institute of Microelectronics of Barcelona (IMB-CNM, CSIC), 08193 Cerdanyola del Valles, Spain

e-mail: marta.fernandez@imb-cnm.csic.es

Vapor phase infiltration (VPI) of polymeric templates is a versatile and emerging technique with broad applicability for the engineering of hybrid organic-inorganic materials [1]. Originating from atomic layer deposition (ALD) processes, VPI relies on the ability of gaseous precursors to diffuse into polymeric matrices and react selectively with functional polar groups, resulting in the incorporation of inorganic material throughout their polymeric structure. This approach has been successfully employed to enhance properties such as mechanical stiffness, etch resistance, and optical contrast, making VPI particularly attractive for application in lithography, sensor devices. photonics, and advanced nanomanufacturing.[2]

When applied to self-assembled block copolymer (BCPs), polymers composed of two or more covalently bounded blocks that microphase separate into periodic nanostructures, VPI offers a route to create well-defined hybrid or inorganic nanostructures with precise special organization. The selective infiltration of specific blocks containing polar functional groups within the BCP allows for material contrast at the nanoscale. However, despite the growing interest, a comprehensive understanding of the infiltration mechanisms in BCPs remains incomplete. Factors such as polymer morphology, domain size, and interfacial interactions with the precursors significantly influence the outcome, yet systematic studies addressing these parameters are still limited.

In this work, we investigate the kinetics of Al_2O_3 infiltration process into Polystyrene-*block*-Polymethylmethacrylate (PS-*b*-PMMA) block copolymer (BCP) thin films with different morphologies and periodicities using trimethylaluminium (TMA) and water precursors under different conditions. A comparative analysis with PMMA homopolymer films is also presented, highlighting the differences in behavior between homopolymer and BCP systems. To this end, cross-sectional scanning electron microscopy (STEM) analysis is performed on both systems to evaluate the infiltration depth. For the BCPs, aligned lamellas are obtained by directed self-assembly (DSA) to facilitate cross-sectional imaging to improve contrast between domains, following the process depicted in Figure 1a. In this case, this is achieved by graphoepitaxy. First, guiding patterns consisting of narrow SiO_2 lines are created by electron beam lithography (EBL) on hydrogen silsesquioxane (HSQ) resist layer [3]. Proper functionalization of the surface before BCP self-assembly allows to achieve the perpendicular lamellar orientation observed. Finally, PMMA block is selectively infiltrated with Al_2O_3 reproducing the original pattern defined by the self-assembled BCPs.

Consistent with previously reported [4, 5], a slightly deeper infiltration is expected in BCP systems. This is attributed to two main factors: (i) the increased interfacial area in the nanostructurated BCP morphology, which facilitates precursor access to PMMA domains; and (ii) the ability of TMA to diffuse through PS domains without reacting, reaching buried PMMA regions more effectively. In contrast, in PMMA homopolymer thin films the precursor can only enter through the top surface and reacts immediately, limiting the penetration depth.

Figure 1.d shows images of the BCP after DSA, after infiltration and after removing the PS. Interestingly, the line edge roughness has been reduced and, as the PMMA block infiltration does not occur within the full depth of the PMMA lamella,, inorganic structures appear suspended after polymer matrix removal. This incomplete vertical infiltration, combined with the regular nanoscale arrangement, opens up opportunities for fabricating suspended metal oxide nanowires or other free-standing architectures with potential applications in NEMS or sensing.

[1] Q. Peng et al. ACS Nano 5 (2011) 6, 4600- 4606
[2] A. Subramanian et al. Nanotechnol. (2021) 3, 766690
[3] S. Gottlieb et al. Mol. Syst. Des. Eng. (2019), 4, 175-185
[4] E. Cara et al. ACS Appl. Polym. Mater. (2023) 5, 2079 – 2087
[5] G. Seguini et al. ACS Appl. Nano Mater. (2022), 5, 7, 9818 - 9828

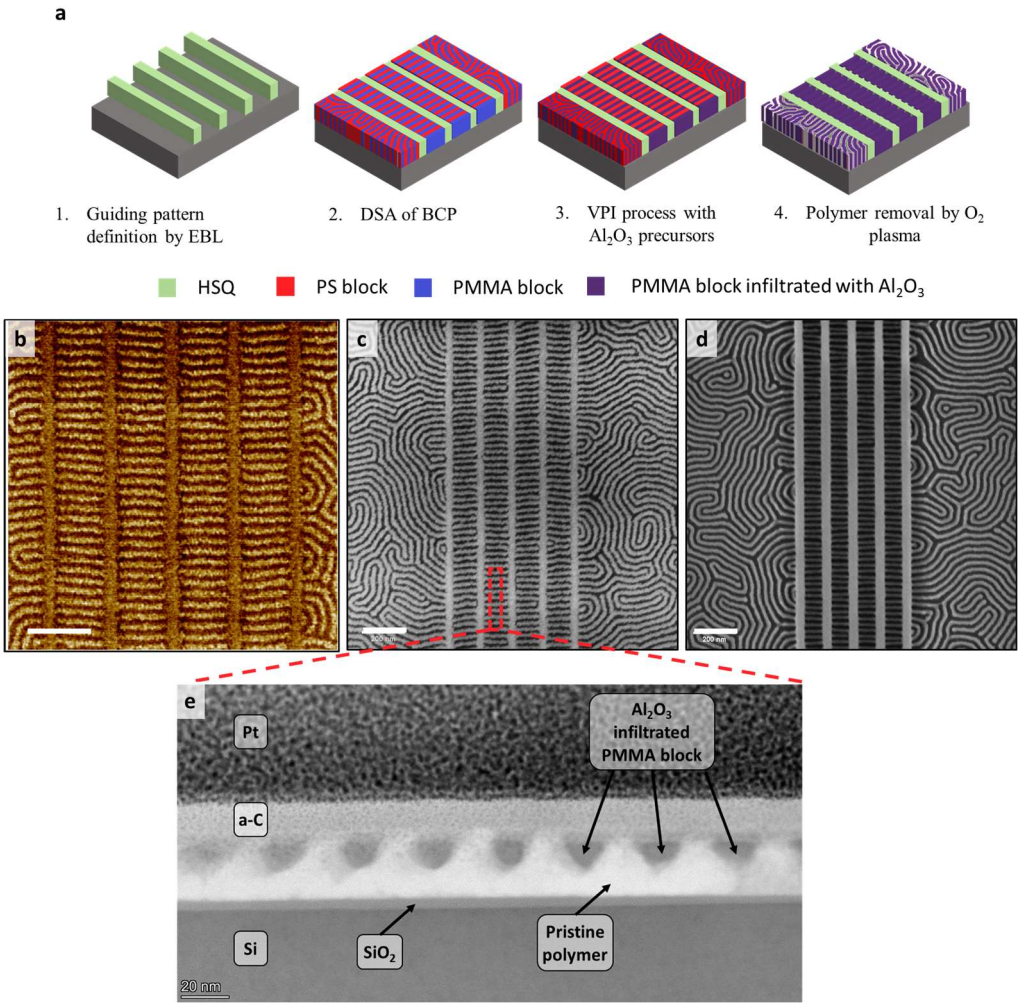

Figure 1. a) Process flow for the fabrication of horizontally aligned Al_2O_3 nanowires using DSA of lamellar PS-b-PMMA and 12 cycles of VPI, b) AFM phase image of the BCP after DSA on HSQ guiding patterns, c) and d) SEM images of the BCP infiltrated with Al_2O_3 before and after oxygen plasma respectively and e) Bright field STEM cross-section of sample c. The period of the lamellar PS-b-PMMA BCP is 30 nm and the scale bar in AFM and SEM images is 200 nm

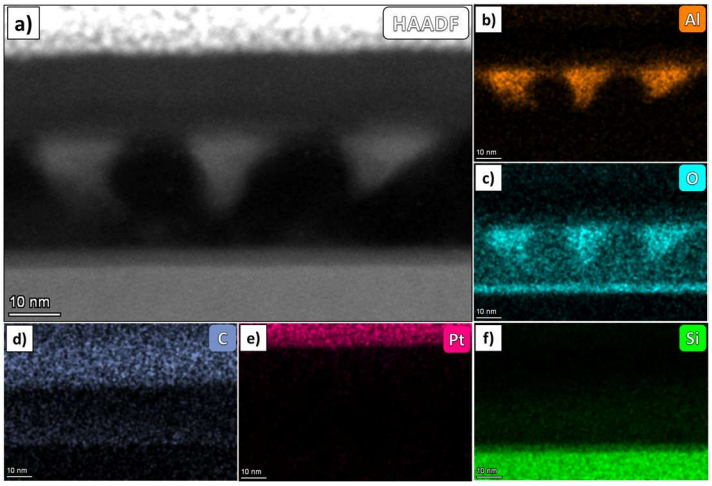

Figure 2. EDX analysis of aligned BCPs after VPI process a) High-angle annular dark-field STEM (HAADF) b) – f) EDX elemental maps showing the distribution of individual elements: Al, O, C, Pt and Si respectively. The sample was prepared using the same process described in figure 1.

Epitaxial growth of InAs/InGaAs-Al nanowire hybrids for quantum computing applications

P. Tejedor[a], B. Galiana[b], G. Moraes[c] and E.J.H. Lee[c]

[a]Instituto de Ciencia de Materiales de Madrid, CSIC, Sor Juana Inés de la Cruz 3, 28049 Madrid, Spain
[b]Universidad Carlos III de Madrid, Av. de la Universidad, 30, 28911 Leganés, Madrid, Spain
[c]Departamento de Física de la Materia Condensada and Condensed Matter Physics Center (IFIMAC), Universidad Autónoma de Madrid, 28049 Madrid, Spain

e-mail: ptejedor@icmm.csic.es

Hybrid superconductor-semiconductor nanowires are an interesting platform to explore one-dimensional topological superconductivity and Majorana zero modes (MZMs), holding great promise for the realization of fault-tolerant quantum computation [1]. The introduction of a potential barrier between the semiconductor and the top superconducting layer, aimed at tuning the tunneling between both regions, has been reported to increase electron mobility, and is expected to minimize the "metallization" of the semiconductor, which can suppress properties such as the spin-orbit interaction [2,3]. However, the effect of inserting a barrier in hybrid nanowires has not been sufficiently explored despite its potential benefits for device performance.

We describe here the *in situ* growth of core-shell InAs/$In_xGa_{1-x}As$-Al nanowires by molecular beam epitaxy, using a Au-catalyzed vapor-liquid-solid (VLS) process. The process includes a high temperature step at 450-500ºC for axial growth of the InAs core followed by a low temperature step at 390ºC for radial growth of an ultra-thin (<6 nm) $In_xGa_{1-x}As$ barrier (x=0.5-0.75) with V/III atomic flux ratios between 5 and 30. Subsequently, the III-V nanowire is coated with a full shell of Al at temperatures close to 0ºC (Figure 1). By using high-resolution scanning electron microscopy (HRSEM), high-resolution transmission electron microscopy (HRTEM) techniques and real-time reflective high-energy electron diffraction (RHEED) we have investigated the effect of V/III atomic flux ratio, nucleation/growth temperature and growth rate on the density, morphology and crystal structure of the hybrid nanowires. The nanowire density and the rate of axial growth increase with the V/III atomic ratio up to a value of 25 and decrease at higher values, pointing to a diffusion–limited process (Figure 2). By tuning the main growth parameters InAs/$In_xGa_{1-x}As$ nanowires with high aspect ratios and different crystal phases have been obtained: pure wurtzite nanowires free of stacking faults have been grown at high temperatures and low V/III flux ratios, while zinc-blende nanowires can exhibit twinned (111) planar defects. STEM-EDX analysis has shown an abrupt InAs/$In_xGa_{1-x}As$ interface and a modulated In composition in the ternary alloy (Figure 3). The Al shell deposited on the core nanowires shows a granular morphology, whose roughness varies with thickness and In content in the underlying III-V alloy. We also present the low-temperature transport characterization performed on the grown nanostructures. In particular, we discuss the results of magneto-transport measurements carried out to estimate the mobility of the nano-devices, as well as to study the weak anti-localization effect arising due to spin-orbit interaction.

[1] S. Das Sarma, M. Freedman, and C. Nayak, npj Quantum Inf. 1 (2015) 15001.
[2] E. Prada, P. San-José, M.W.A. de Moor, A. Geresdi, E.J.H. Lee *et al*., Nat. Rev. Phys. 2 (2020) 575-594.
[3] J. Shabani, M. Kjaergaard, H.J. Suominen, Y. Kim, F. Nichele, et al., Phys. Rev. B93 (2016) 155402.

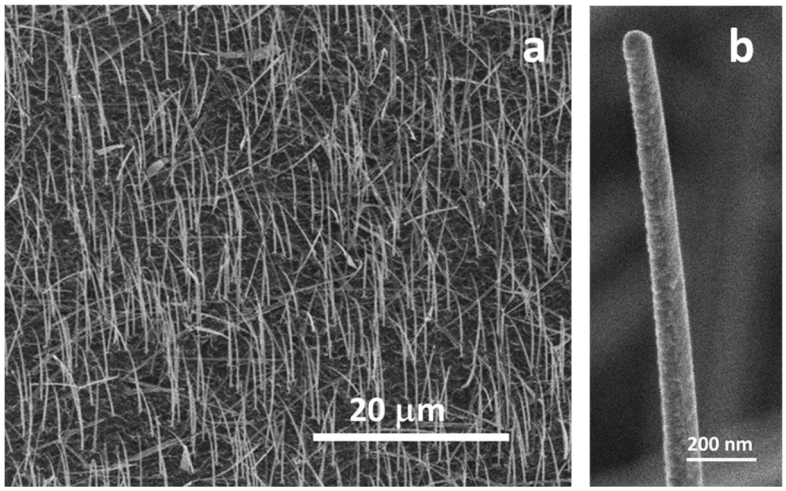

Figure 1. HRSEM images of (a) self-organized InAs/$In_{0.5}Ga_{0.5}As$/Al nanowire hybrids grown on GaAs(111)B substrates and (b) detail of a hybrid showing the Au nanoparticle used as catalyst. (Tilt: 30º)

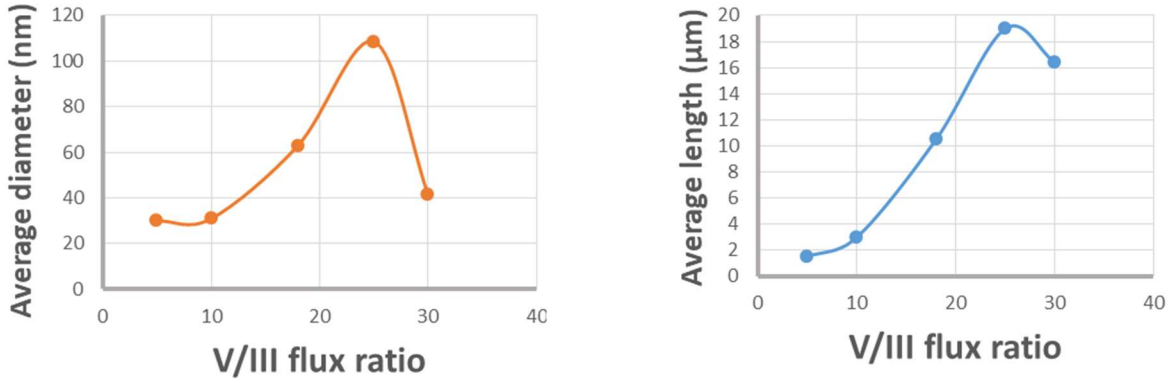

Figure 2. Dependence of InAs/$In_{0.5}Ga_{0.5}As$ nanowire average diameter and length on V/III atomic flux ratio

Z	Element	Family	Atomic Fraction (%)	Atomic Error (%)	Mass Fraction (%)	Mass Error (%)	Fit Error (%)
31	Ga	K	4.68	0.53	3.46	0.39	2.92
33	As	K	46.09	4.14	36.61	3.91	0.62
49	In	L	49.23	4.09	59.93	3.94	0.21

Z	Element	Family	Atomic Fraction (%)	Atomic Error (%)	Mass Fraction (%)	Mass Error (%)	Fit Error (%)
31	Ga	K	2.15	0.25	1.60	0.18	1.69
33	As	K	50.09	4.23	39.98	4.09	0.23
49	In	L	47.76	4.20	58.42	4.10	0.35

Figure 3. HRTEM-HAADF image and STEM EDX elemental analysis of the InAs core nanowire and the surrounding InGaAs barrier

Nanomechanical Mass Sensor: Integrating Nanoimprint Lithography with Flow-Through Gas Phase Deposition

Lucjan Grzegorzewski [a], Manuel Mueller [a], Jeremy Teuber [a], Irene Fernandez-Cuesta [a]
[a] Hamburg Advanced Research Centre for Bio-Organic Chemistry (HARBOR, Universität Hamburg, Hamburg, 20146, Germany
e-mail: lucjan.grzegorzewski@uni-hamburg.de

Keywords: Microfluidic mass sensing, Micro-nanofluidics, Mechanical resonator

Vacuum-operated hollow nanochannel resonators (HNRs) have emerged as a promising platform for label-free, single-particle mass spectrometry in liquids, enabling real-time buoyant weighing of cells, virions, extracellular vesicles, and individual macromolecules. Classical silicon-based HNRs, pioneered by Burg and Manalis, already achieve zeptogram sensitivity but require time-consuming multi-mask lithography, which is essential for defining nanostructures, deep reactive-ion etching, and single-clamped beam geometries that limit mechanical robustness and integration versatility [2–4].

Here, we introduce a new fabrication architecture based on UV nanoimprint lithography (NIL), which replicates complex micro- and nanostructures in seconds. This is paired with conformal, pressure-driven, flow-through gas-phase deposition (ft-GPD) to coat the interior of 500 nm-wide nanochannels with 30–50 nm of Al_2O_3—an order of magnitude faster than stop-flow atomic layer deposition (ALD) [1]. A single imprint step on a 4-inch wafer can produce over 200 fully released devices complete with alignment-free fluidic interfaces.

Figure 2a shows optical micrographs of the sample before and after suspension via trench etching. Figure 2b presents SEM images of a released beam, confirming uniform coating across the full chip area.

Resonator readout employs a combined scattering/interferometric scheme (Figure 1a). A 632.8 nm HeNe laser is focused on the suspended HNR beam; oscillations modulate scattered light and interference between the beam and substrate reflections. A polarizing beamsplitter directs the returning signal to a fast photodiode, and a lock-in amplifier extracts the resonance peak. A piezo actuator drives the mechanical mode, while a custom aluminum holder seals the chip at ~10^{-3} mbar for ultra-fast sample exchange and leaves microfluidic ports open for liquid injection.

Mechanical spectra (Figure 2c) reveal a fundamental mode at 2.65 MHz with Q≈200 under a 50 µW laser. A single 10 mW, 20 s laser-cleaning pulse raises Q to 1290. From the left flank of the resonance curve for a 35 µm-wide beam, we extract a calibration slope $\Delta f/\Delta V$ = 3.2 kHz/mV and measure amplitude noise of 25 µV at 10 kHz bandwidth (frequency noise ~80 Hz). Using the small-mass approximation yields a mass-detection limit of ~100 attograms at 10 kHz bandwidth.

By coupling NIL with ft-GPD, this workflow paves the way for disposable, multiplexed HNR arrays for single-particle mass spectrometry in liquids. Ongoing efforts aim to achieve 10–20 MHz beam designs, pushing resolution below 10 attograms.

[1] M. Müller, The fabrication of hollow nanochannel resonators via UV-imprinting and conformal gas-phase deposition, Ph.D. Thesis, Dr. Hut Verlag, 2024.
[2] T. P. Burg, M. Godin, S. M. Knudsen, W. Shen, G. Carlson, J. S. Foster, K. Babcock, and S. R. Manalis, Weighing of biomolecules, single cells and single nanoparticles in fluid, Nature 446 (2007) 1066–1069.
[3] A. Martín-Pérez, D. Ramos, J. Tamayo and M. Calleja, Nanomechanical molecular mass sensing using suspended microchannel resonators, Sensors 21 (2021) 3337.
[4] J. Lee, W. Shen, K. Payer, T. P. Burg and S. R. Manalis, Toward attogram mass measurements in solution with suspended nanochannel resonators, Nano Lett. 10 (2010) 2537–2542.

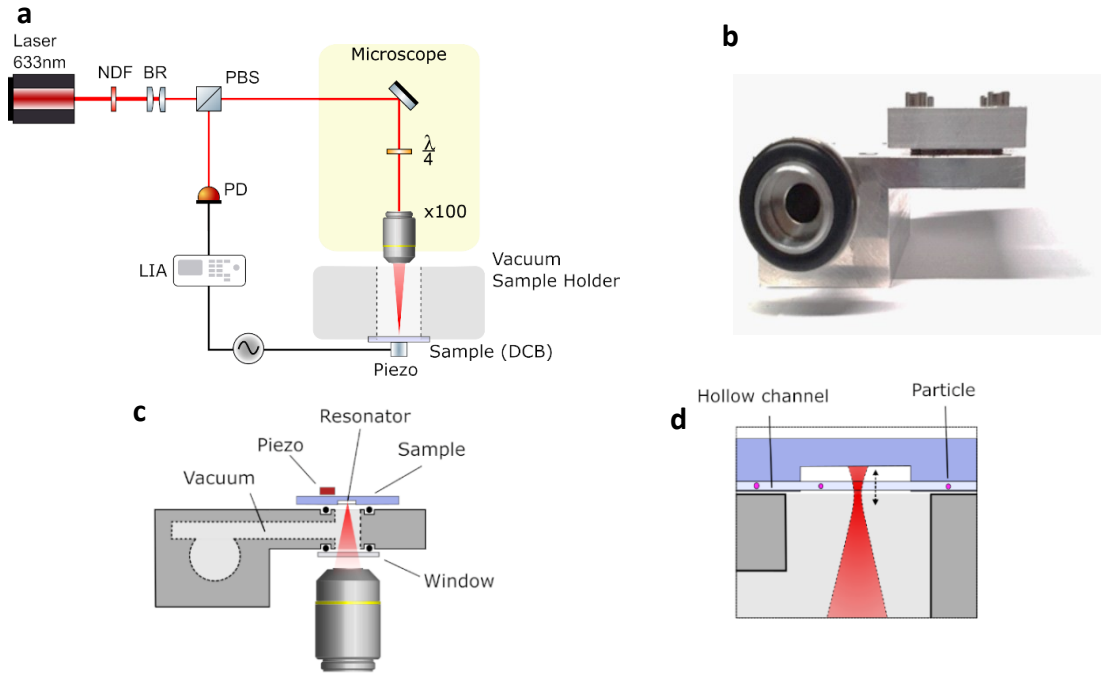

Figure 1. a, Schematic overview of the setup. **b**, side-view image of the vacuum holder. **c**, side-view image of the holder. **d**, zoomed view of the laser focused on the oscillating hollow channel.

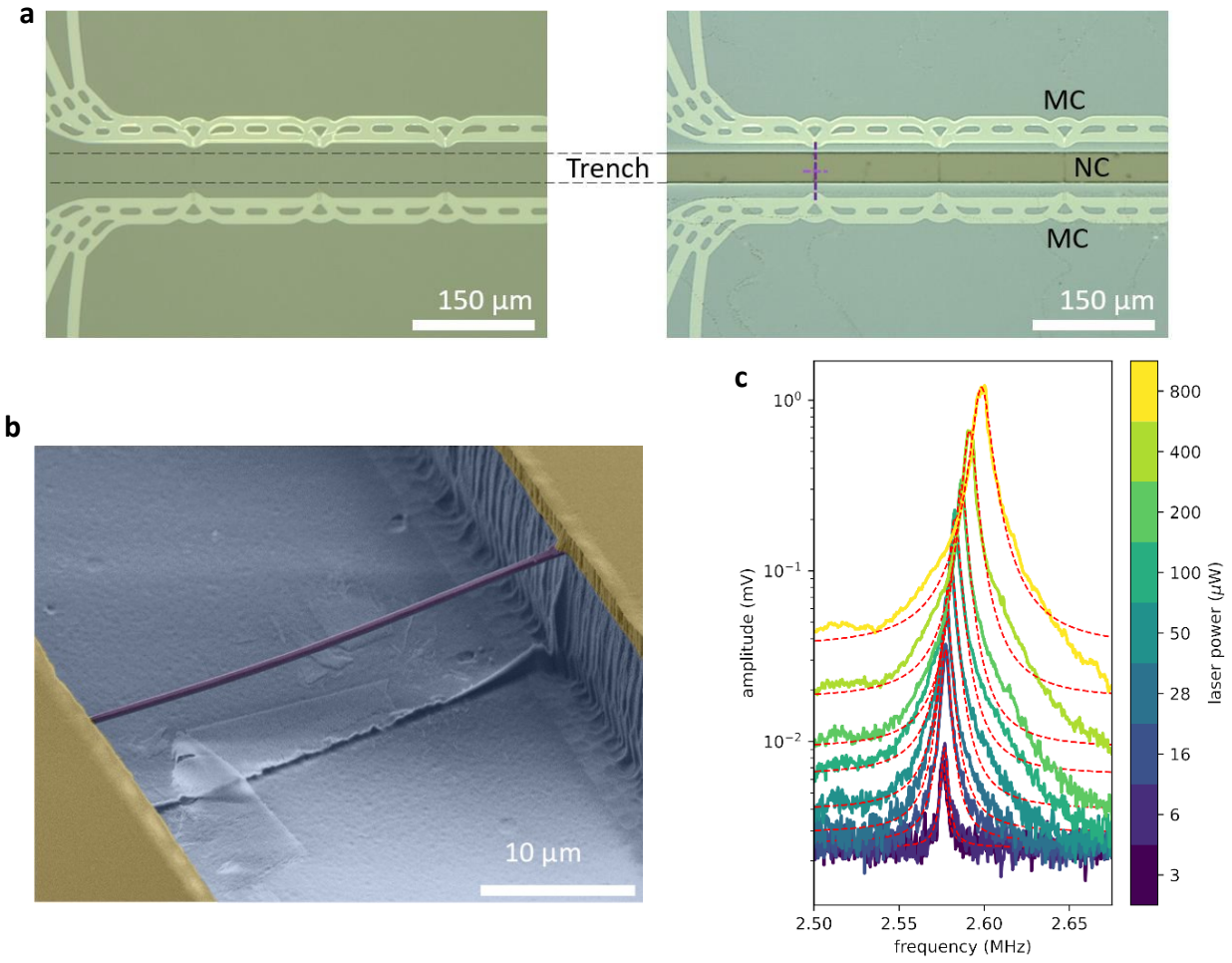

Figure 2. a, Microscope image before (left) and after (right) suspension of the resonator. **b**, SEM image of a suspended hollow microchannel. **c**, Resonance frequency in response to an increased laser power measured with the setup displayed in Fig. 1a.

Nanoimprinted Multimode Polymer Waveguides with Integrated Bragg Gratings for Structural Health Monitoring.

Florian Egger [a,b], Michael J. Haslinger [a], Viktorija Jonaityte [a], Vaclav Prajzler [c], Antreas Theodosiou [d] and Michael Mühlberger [a]

[a] PROFACTOR GmbH, Im Stadtgut D1, A-4407 Steyr-Gleink, Austria
[b] Division of Semiconductor Physics, Institute of Semiconductor and Solid State Physics, Johannes Kepler University Linz, Altenberger Straße 69, 4040 Linz, Austria
[c] Department of Microelectronics, Faculty of Electrical Engineering, Czech Technical University in Prague, Technicka 2, 168 27 Prague, Czech Republic
[d] Photonics Research Center (PRC), Lumoscribe Ltd, 12 Anthipoloxagou Georgiou Savva,8201 Geroskipou, Paphos, Cyprus

e-mail: michael.haslinger@profactor.at

Photonics has revolutionized modern technology, particularly the fields of photonic integration, sensing, LED (Light Emitting Diodes), and laser technology, enabling the development of highly sensitive optical sensors. [1]. For structural health monitoring, Fiber Bragg Grating (FBGs) sensors are of great interest [2] enabling high sensitivity measurements of the temperature, strain and pressure among others in real time.
Recent research on polymer waveguides has led to the development of advanced methods such as roll-to-roll (R2R) and roll-to-plate (R2P) nanoimprinting (NIL) and is presented in Figure 1 (a-k) [3]. Building on this preparatory work, a NIL based fabrication of multimode waveguides as well as the realization of FBGs could be realized. The multimode waveguides have dimensions of 50 × 50 µm² (height × width), with a channel pitch of 250 µm, and exhibit good quality (Figure 1 l-m). The dimensions of the waveguides and the imprinted Bragg grating were inspected using an optical microscope and AFM. For the fabrication, an inorganic-organic hybrid polymer with a refractive index of 1.5464 at 850 nm was used for the core layer, while a UV photopolymer with a refractive index of 1.5069 at 850 nm was used for the cladding layer [3]. In addition, several bio-based photopolymers have been tested for their suitability and will be presented. Examples are presented in Figure 2.
To optically characterize multimode optical waveguides fabricated using NIL, the cut-back method is employed to measure optical losses. This method involves comparing the power transmitted through the waveguide at two different lengths to determine its propagation loss. Modelling multimode waveguides is performed using the finite-difference time-domain (FDTD) method to solve Maxwell's equations in a discretized space-time grid in Meep [4, 5]. The computational domain is defined with appropriate boundary conditions. The electromagnetic field evolution is computed over time, enabling analysis of mode propagation, interference, and dispersion effects. Simulation results, including field distributions and transmission characteristics, can be extracted and visualized for performance evaluation.
Multimode waveguide and FBG fabrication using a Nanoimprint Lithography process will be presented, together with optical characterizations and simulations as well as an optimized Bragg grating design, focusing on minimizing losses and improving sensitivity. In addition, we will compare laser inscribed and NIL fabricated FBG load sensors. The presented research explores cost-effective and eco-friendly polymer-based solutions for photonic sensors, highlighting their potential for scalable production and broad applications in industrial and environmental monitoring, including the use of bio-based materials as sustainable alternatives for multimode waveguide and FBGs, to be used in biobased composite parts.

Acknowledgements
This work has been funded by the European Union (Grant Agreement No 101136335) and by CTU grant no. SGS23/181/OHK3/3T/13.

[1] M. A. Butt, et al. Photonics sensors: A perspective on current advancements, emerging challenges, and potential solutions (Invited), Physics Letters A, 516, 129633, 2024
[2] Kinet, Damien, et al. "Fiber Bragg grating sensors toward structural health monitoring in composite materials: Challenges and solutions." Sensors 14.4 (2014): 7394-7419.
[3] V. Prajzler, et al. Optical Polymer Waveguides Fabricated by Roll-to-Plate Nanoimprinting Technique. Nanomaterials, 11, 724. 2021

[4] https://meep.readthedocs.io/en/master/Introduction/
[5] A. Oskooi, D. Roundy, M. Ibanescu, P. Bermel, J.D. Joannopoulos, and S.G. Johnson, "MEEP: A flexible free-software package for electromagnetic simulations by the FDTD method," Computer Physics Communications, Vol. 181, pp. 687-702 (2010)

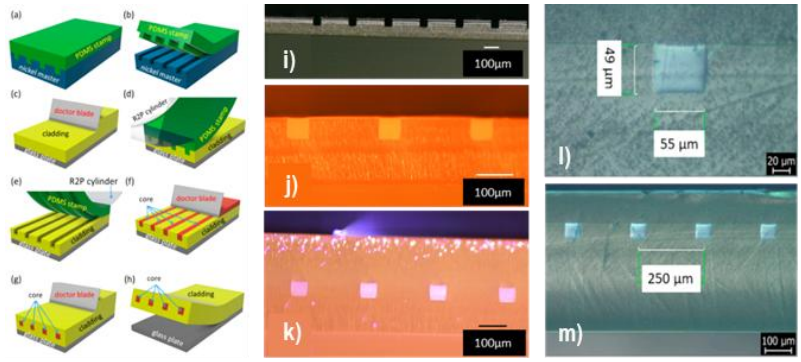

Figure 1 (left)Fabrication process of the multimode optical waveguides using Nanoimprint process [3] has been established and further developed. (centre) (I,j,k,) Microscope images representing certain fabrication steps, representing fabrication step e), f), and h). (right) (l,m) Cross section detail on fabricated waveguides including measurements representing fabrication step h).

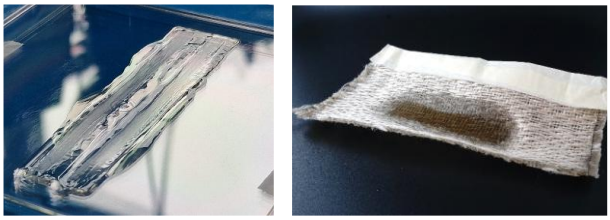

Figure 2 (left) fabrication of optical multimode waveguide on glass substrates. (right) Process development on flax based (bio-based) substrates.

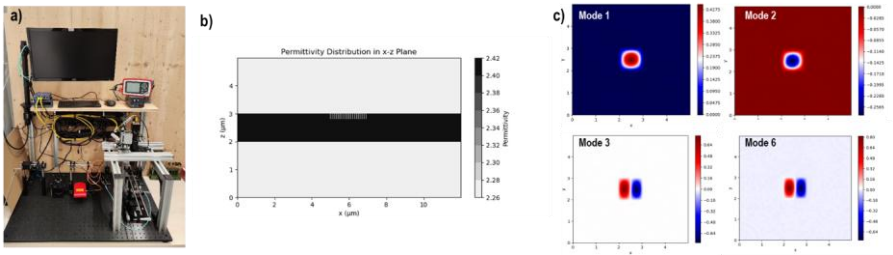

Figure 3 (a) Optical setup for waveguide characterization at PROFACTOR by using the cut-back method. (b) Simulation of a multimode waveguide in MEEP software including a FBG for 1550 nm. (c) Optical mode simulations in a polymer waveguide of 10x10 µm².

Advanced AFM Metrology of Vertical Structures: Sample Reorientation for Sidewall Surface Access

Paweł Janus , Krzysztof Domański, Adam Łaszcz, Andrzej Sierakowski, Magdalena Kucharska, Dariusz Szmigiel
Łukasiewicz Research Network, Institute of Microelectronics and Photonics, al. Lotników 32/46, Warszawa, 02-668, Poland
e-mail: krzysztof.domanski@imif.lukasiewicz.gov.pl

Keywords: AFM, sidewall roughness, 3D metrology, sidewall measurement, integrated photonics

In this study, we present techniques for the high-precision characterization of sidewall roughness in vertically etched structures. The investigation is based on atomic force microscopy (AFM) imaging using standard probe tips. To enable accurate and reproducible measurements, cross-sectional sample preparation was carried out using either focused ion beam (FIB) milling or a combination of plasma and chemical etching, depending on the material system and structural requirements. These approaches allow for clean exposure of the sidewalls with minimal morphological distortion. The proposed characterization technique is essential for the accurate evaluation of sidewall roughness in plasma etched passive photonic structures, such as germanium and silicon waveguides, grating couplers, and optical filters. Sidewall roughness in these structures increases transmission losses and significantly impairs the optical performance of monolithically integrated photonic devices. More accuracy in roughness assessment will enable more effective tuning and control of plasma etching parameters, thereby improving device yield and performance.

Conventional AFM technology enables three-dimensional characterization of nanometer-scale structures, providing precise depth measurements even for high-aspect-ratio features, as well as accurate evaluation of micro-roughness on horizontal surfaces such as top and bottom facets. AFM probes are less effective at imaging undercut sidewalls or accurately quantifying vertical sidewall roughness at the nanoscale due to limitations such as tip geometry, finite aspect ratio, and the effect of tip sliding on the edges. Cantilevers with special tip geometry - such as flared tips, carbon nanotube tips, sharpened tips, or visible apex probes - are employed to scan sidewalls and undercut features [1-3]. This method is often combined with tilting the cantilever probe or performing slow scans in a 'step-in' mode using point-by-point mapping [2]. While these probes improve accessibility to vertical or recessed structures, they remain not sufficient for high-precision sidewall roughness measurements. An alternative approach for sidewall characterization involves tilting the sample itself, e.g. using a variable-angle sample holder [4]. Although this technique simplifies probe configuration and enhances access to vertical features, it may limit access to some regions of larger samples.

Due to the relatively smooth sidewall surfaces of the photonic structures, we adopted an approach in which the waveguides were removed from the original substrate by selectively etching the surrounding material. The structures were then transferred onto a holder and positioned on their side. This orientation enabled direct imaging of the sidewalls using standard AFM techniques. In the paper we present of analysis of AFM imaging of waveguide sidewalls using three variants of samples preparation: wet etching of buried silicon dioxide (Fig.1), dry etching of the silicon substrate, and FIB milling of the same material (Fig. 2). Fig. 3 and 4 compare AFM analysis of Si waveguides etched on SOI substrates, viewed from the sidewall and the top, respectively. In the 3D AFM images shown in Fig. 3 and 4, the vertical scale has been adjusted (cropped) to highlight details of the investigated surfaces. The average roughness (Sa) of the plasma etched sidewall was found to be approximately an order of magnitude greater (4.5 nm) than that of the top polished surface (400 pm). Sample preparation for AFM using FIB techniques can introduce surface contamination. Gallium beam etching during FIB processing may result in the redeposition of both substrate material and gallium ions onto the sample. Additionally, during Pt sputtering, used to attach the sample to the substrate, Pt may be deposited onto adjacent areas of the sample surface. Therefore, in this study, we compare results obtained from samples prepared using different methods, with particular attention to potential contamination introduced during processing.

[1] S. Hosaka , T. Morimoto , H. Kuroda , Y. Minomoto , Y. Kembo , H. Koyabu , New AFM imaging for observing a high aspect structure, Appl. Surf. Sci. 188 , 467 (2002)

[2] K. Murayama et al, Side-Wall Measurement using Tilt-Scanning Method in Atomic Force Microscope Jpn. J. Appl. Phys. 45 5423–5428 (2006)

[3] Byoung-Woon Ahn, et al, Automated measurement and analysis of sidewall roughness using three-dimensional atomic force microscopy, Applied Microscopy 52(1), 1-8 (2022)

[4] M. Fouchier, E. Pargon, B. Bardet; An atomic force microscopy-based method for line edge roughness measurement. J. Appl. Phys. 113, 104903 (2013)

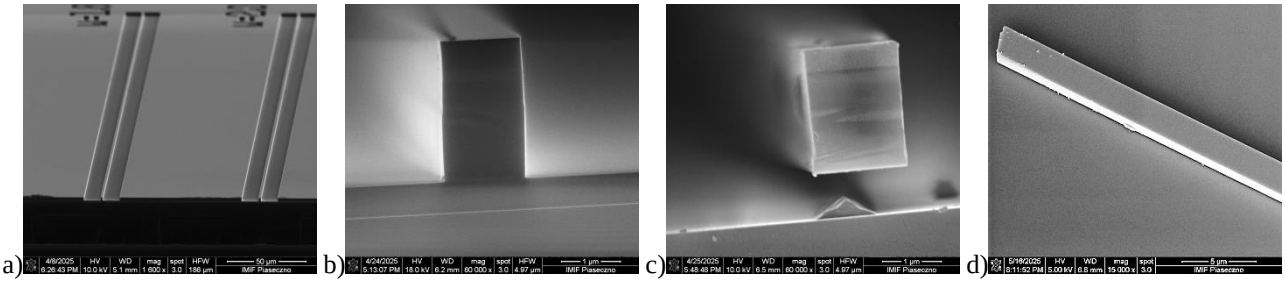

Figure 1. Transfer of Si waveguides from the SOI substrate by selectively etching of BOX layer: a) test structure, b) cross-section of the waveguide, c) cross-section of the waveguide after BOX layer etching, d) waveguide transferred onto PMMA layer

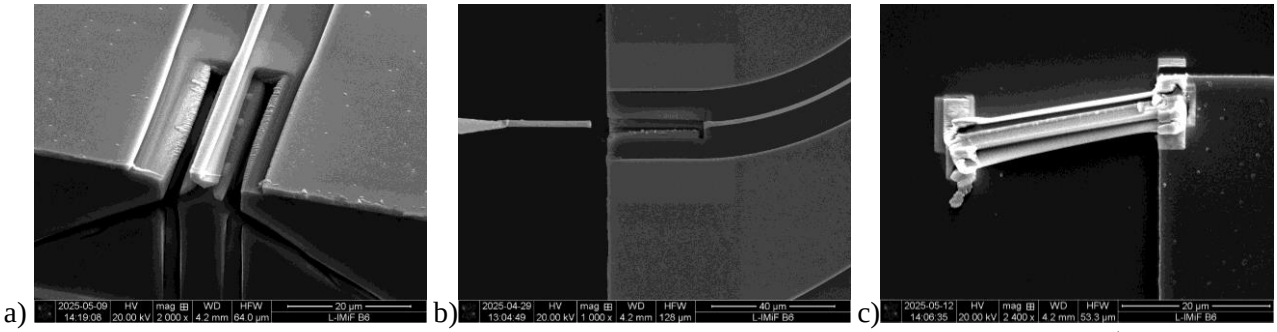

Figure 2. Transfer of Ge waveguide using FIB milling technique: a) trenches milled by Ga^+ beam, b) waveguide attached to the micromanipulator, c) waveguide clamped on both ends by Pt deposition

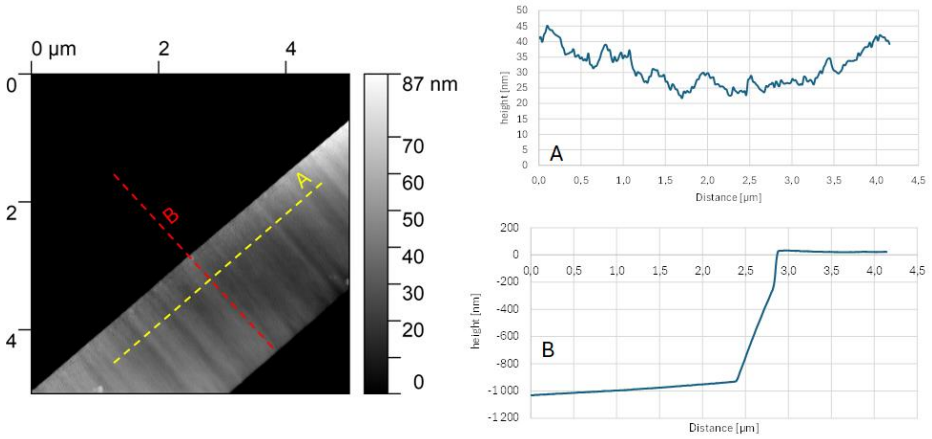

Figure 3. AFM analysis (tapping mode) of the sidewall (plasma etched) surface of Si waveguide. The observed inclination in the sample profile is attributed to non-uniform adhesion to the 200 nm-thick PMMA layer, likely due to deformation introduced during the sample pressing. Average roughness (Sa) ~ 4.5 nm

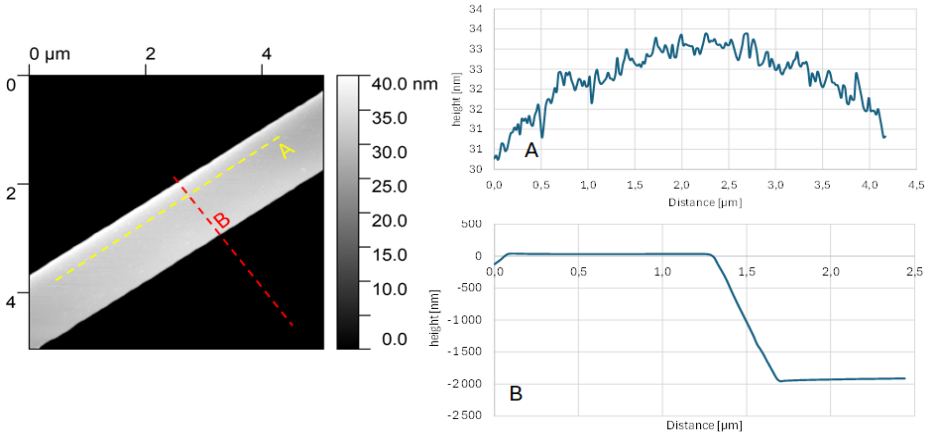

Figure 4. AFM analysis (tapping mode) of the top (polished) surface of Si waveguide. The difference in horizontal and vertical dimensions relative to the sample shown in Fig. 3 indicates that the sample is rotated by 90° compared to the orientation of the previous structure. Average roughness (Sa) on the strip ~ 400 pm

Processing Pathways for Transparent, Flexible Electrodes in Next-Generation Smart Windows

Michael J. Haslinger [a], Jonaityte Viktorija [a], Dorly Holzer-Harringer [b], Florian Frischmann [c], Marcus Harringer [b], Martina Harnisch [d], W.Huo [e], Andreas Zimmermann [d] and Michael Mühlberger [a]

[a] PROFACTOR GmbH, Im Stadtgut D1, 4407 Steyr-Gleink, Austria

[b] Almendo Technologies GmbH, Wolfschwangweg 216, 5084 Großgmain, Austria

[c] Bartenbach GmbH, Rinner Straße 14, 6071 Aldrans, Austria

[d] Sunplugged GmbH, Affenhausen 1, 6413 Wildermieming, Austria

[e] Department of Biomedical Engineering, Tianjin University, 92 Weijin Road, Tianjin 300072, China

e-mail: Michael.Haslinger@Profactor.at

Smart windows generally refer to dynamic or switchable glazing systems that actively regulate light and heat transmission. More broadly, they include any window offering enhanced functionalities—such as energy efficiency, sensing, energy harvesting, or smart home integration. A key component in these systems is the transparent conductive layer (TCL), which provides both electrical conductivity and optical transparency. While indium tin oxide (ITO) has been the standard TCL material due to its excellent performance, its brittleness and limited indium supply have spurred the development of alternative materials.

Among the most promising candidates are silver nanowire networks and nanomeshes—also referred to as metal nanowire meshes or grid electrodes. These architectures consist of interconnected metal nanowires, typically composed of silver or copper, with feature sizes ranging from the nanometer scale up to several tens of micrometers. Despite these advantages, scaling up production remains a challenge, particularly in achieving uniformity, reproducibility, and long-term operational stability [3, 4].

A nanoimprint lithography–based process was developed for the fabrication of metal nanomeshes with various patterns. The optical and electrical properties of random, hexagonal, and Penrose-style nanomeshes were investigated. Conductivity levels comparable to ITO were achieved by the nanomesh structures, while high optical transparency was maintained. Additionally, mechanical flexibility and stretchability are exhibited, making them suitable for use in flexible and curved electronic devices. Examples are shown in Figure 1 and Figure 2.

We present an alternative to ITO for transparent conductive layers, based on nanomeshes and nanowire networks, for smart window applications. The approach combines nanoimprinting and channel filling using silver nanoparticle-based and silver nanowire materials to fabricate conductive yet highly transparent meshes on transparent substrates.

The authors acknowledge funding from the Smart-Win project (FFG 891144).

[1] ‘Smart Windows: Electro-, Thermo-, Mechano-, Photochromics, and Beyond - Ke - 2019 - Advanced Energy Materials - Wiley Online Library’. Accessed: Feb. 28, 2024.

[2] H. H. Khaligh, K. Liew, Y. Han, N. M. Abukhdeir, and I. A. Goldthorpe, ‘Silver nanowire transparent electrodes for liquid crystal-based smart windows’, *Sol. Energy Mater. Sol. Cells*, vol. 132, pp. 337–341, 2015.

[3] H. B. Lee, W.-Y. Jin, M. M. Ovhal, N. Kumar, and J.-W. Kang, ‘Flexible transparent conducting electrodes based on metal meshes for organic optoelectronic device applications: a review1’, Accessed: Feb. 28, 2024.

[4] M. J. Haslinger *et al.*, ‘Development of a Soft UV-NIL Step&Repeat and Lift-Off Process Chain for High Speed Metal Nanomesh Fabrication’, *Nanotechnology*, 2020, doi: 10.1088/1361-6528/ab9130.

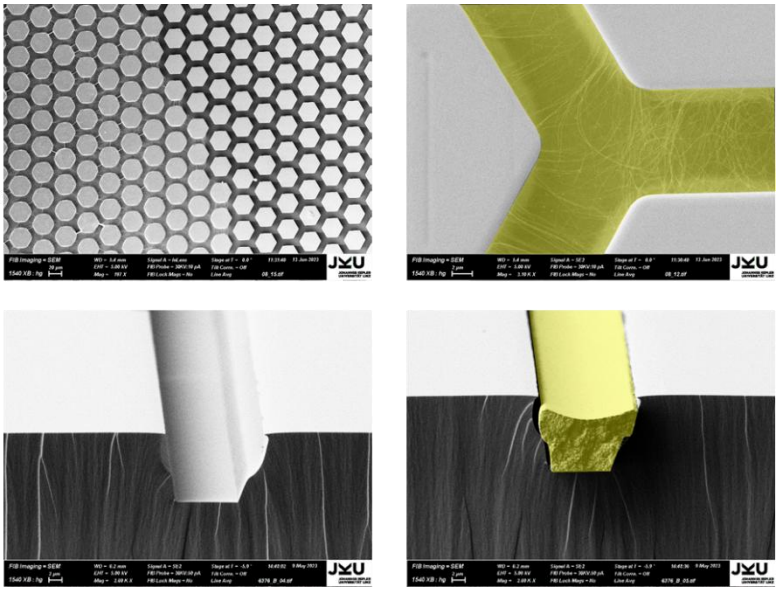

Figure 1. Examples of metal nanomeshes are fabricated using silver nanowires and silver nanoparticles on pre-structured substrates fabricated via nanoimprint lithography (NIL).

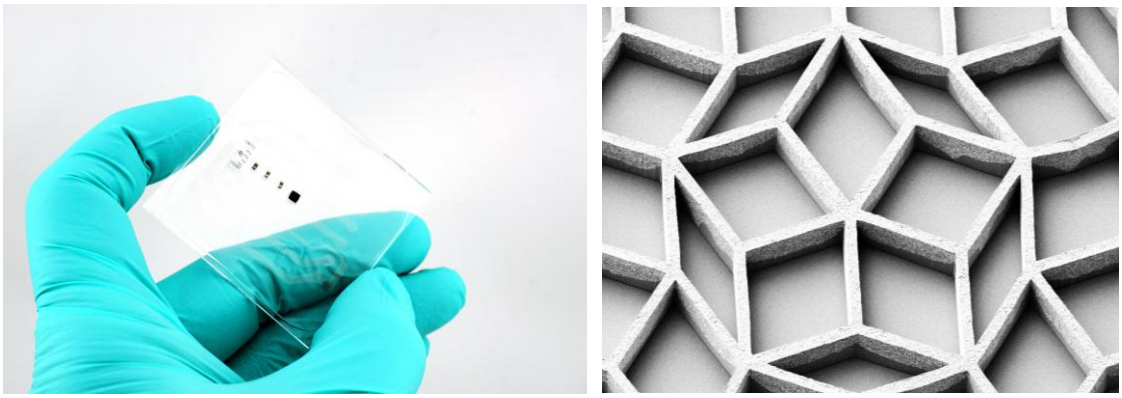

Figure 2. Photographs of transparent sensor module PCB on glass equipped with temperature and humidity sensors, as well as LEDs, designed for placement on a smart window (left). Close-up of a transparent conductive micromesh with a Penrose layout (right).

Smart windows are dynamic glazing systems that regulate light and heat transmission while offering enhanced functionalities such as energy efficiency and smart home integration. Transparent conductive layers (TCLs) are essential components in these systems, traditionally relying on indium tin oxide (ITO). However, ITO's brittleness and limited availability have driven the search for alternatives. Silver nanowire networks and metal nanomeshes have emerged as promising candidates, combining high electrical conductivity, optical transparency, and mechanical flexibility. This work presents a nanoimprint lithography–based fabrication process for metal nanomeshes with various patterns, achieving conductivity comparable to ITO while maintaining transparency and stretchability. The developed nanomeshes and nanowire networks provide a viable alternative TCL for flexible smart window applications.

Electrochemically growing morphology on micro structured 3D frameworks

Itishree panda[1], Trina Dhara[1], Sunando DasGupta*[1]
[1]Departement of Chemical Engineering, Indian Institute of Technology Kharagpur, India
Email: ipanda56@gmail.com

To cope up with the surge in energy demand, metal anode free batteries are increasingly replacing the conventional metal ion batteries due to their higher specific energy density. During electrochemical charging of solid-state batteries, metal ions (Ca, Mg, Na, K, Li) get deposited on the current collector as pure metallic anode[1,2]. The plating of the active material experiences a dynamic nonplanar metal front evolution as a result of localized current distribution. The metal anode undergoes expansion/shrinkage during charging/discharging, eventually structurally hampering the battery. Although the use of different electrolytes, electrolyte additives, and charging protocols etc. have proven to be beneficial in combating the anode deformation and undesirable metallic growth up to some extent, a favorable design in 3D current collectors situated below the metal anode will further alleviate the issues[2]. Moreover, a rough current collector enables void free electrical contact with the anode and prevents delamination of the anode while discharging[3]. Herein, morphology dependent electrodeposition of copper on structured thin metallic frameworks is explored that may provide insights in designing the current collectors. Dynamic hydrogen bubble template (DHBT) method is utilized to fabricate micro structured copper electrodes. A schematic of the experimental setup (see Figure 1a) is presented where an in-situ side view 2D visualization of the dynamic evolution front (metallic copper) atop the fabricated surfaces (pillar like (S1) and, honeycomb circular walls (S2), (see Figure 1b, c)) is done. Distinct morphologies (Mossy or compact structures) in the growth front at t=5 and 10seconds are observed (Figure 1d, e). The spatiotemporally varying deposit front is captured via videography and the frames are analyzed to quantify the space averaged growth height, growth velocity as well as the interfacial evenness (termed as tortuosity). The time evolution of all these characterized parameters is presented in Figure 2a, b and c respectively. A compact growth front with higher tortuosity is observed on the surface containing pillars (S1) whereas a faster growth with reduced tortuosity is observed for the honeycomb structure (S2). It is hypothesized that increase in the number of active sites, structure mediated minimized effective current density and homogenous distribution of incoming metal atoms over the entire area cumulatively manifests itself in the compact metallic growth. The findings highlight how the 3D architecture of an underlying electrode—beyond just its material properties—can be used to guide and regulate electrochemical growth processes.

Keywords: Rough micro structured electrode, 3D current collector, Dynamic hydrogen bubble template, electrochemical deposit interface

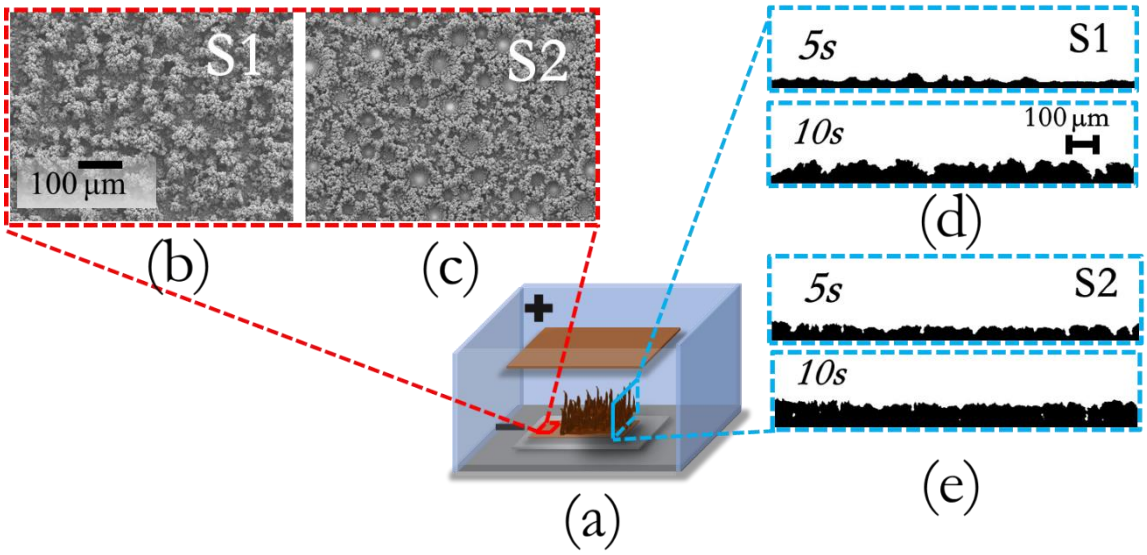

Figure 1 a) Schematic illustration of the experimental electrochemical setup on which the micro structured surfaces with **b)** pillar like units (S1) and **c)** honeycomb circular walls (S2) are employed as the negative electrode. Atop the structures, a dynamic metallic growing front atop **d)** S1 and **e)** S2 can be seen for t = 5 and 10s (scale bar 100µm).

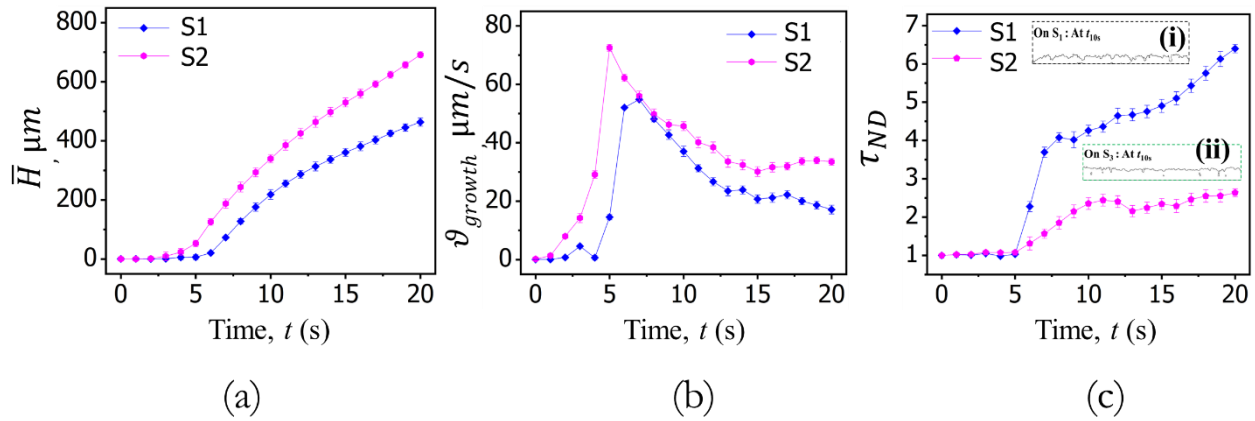

Figure 2 The mechanistic transitions of the growth front atop S1 and S2 is characterized in terms of average growth height ($\overline{H}$), growth velocity (ϑ_{growth}) and tortuosity (τ_{ND}). **a)** The deposit height remains higher for S2 relative to S1 until 20 seconds. **b)** The growth velocity (i.e. the rate of change of growth height) on S2 reaches a greater peak in comparison to S1. **c)** The deposit on S1 remains significantly high tortuous than S2. The insets i and ii present the outlined interfaces of the deposit on S1 and S2 at t = 10s respectively.

References

1. Liu W, Liu P, Mitlin D. Tutorial review on structure-dendrite growth relations in metal battery anode supports. *Chem Soc Rev*. 2020;49(20):7284-7300. doi:10.1039/d0cs00867b
2. Zhu P, Gastol D, Marshall J, Sommerville R, Goodship V, Kendrick E. A review of current collectors for lithium-ion batteries. *J Power Sources*. 2021;485. doi: 10.1016/j.jpowsour.2020.229321
3. Zeng Z, Barai P, Lee SY, et al. Electrode roughness dependent electrodeposition of sodium at the nanoscale. *Nano Energy*. 2020;72. doi: 10.1016/j.nanoen.2020.104721

Micro/Nano Thin-Film Coating Processes of Carbon Materials for Energy Devices

Jeongdai Jo [a] Joon Young Cho [a], and Pyoungwon Park [a]

[a] Korea Institute of Machinery & Materials, 34103, Republic of Korea
e-mail: micro@kimm.re.kr

For high-power secondary batteries, research on various types of contacts of the electrode-current collector interface is required, and primer coating layer using carbon materials is required for strong adhesion of the electrode-current collector interface [1, 2]. To verify the effect of primer coating layer, carbon materials for high power secondary battery current collector were coated with an ultra-thin film using blade coating, slot die coating, and spray coating.

First, an aluminum (Al) foil with a carbon black paste of 18-19 wt%/58.8 cPs was coated using a blade coater. A carbon black paste of 18-19 wt%/58.8 cPs was coated with a thin film using a blade coating process, and it was confirmed that a thin film of several μm to several hundreds of nm was uniformly coated on an area of 11 cm in width and length of 8 cm. The average thickness of the coating was 3 to 5 μm (measured by 9 points) and coating uniformity was 9% (standard deviation) as a result of measuring the coating thickness with a surface profiler. A carbon black paste of 9 wt% was coated on the same area with a thin film, and the coating thickness was measured and the average thickness was 1 to 1.5 μm, and when a carbon black paste of 6 wt% was coated with a thin film, the average thickness was 1 μm. When 4.5 wt% carbon black paste was coated in a thin film, the average thickness of 1 μm to 500nm was measured, although there was a slight difference depending on the conditions of drying/curing conditions. The sheet resistance for each sample was measured, and although there was a difference according to wt%, it was ~ 6 mΩ/sq.

Second, the viscosity and solid content ox-SWCNT paste + PVdF (NMP) were coated using a blade coater, and it was confirmed that a thin film of 1 μm to 500 nm was uniformly coated. As a result of coating the Al foil on a large area, a thickness of 500nm was shown and the uniformity was confirmed to be within about 5%. Carbon black paste and ox-SWCNT paste + PVdF (NMP) were coated with a thin film using a slot die, and it was confirmed that a thin film of several μm to several hundreds of nm was uniformly coated in an area of 11 cm in width and 8 cm in length. The average thickness of the electrode was 1 to 3 μm (measured by 9 points) and coating uniformity 5% (standard deviation) as a result of measuring the electrode thickness with a Surface profiler. Carbon black paste of 9 wt%, 6 wt%, and 4.5 wt% and ox-SWCNT paste + PVdF (NMP) were coated with a thin film with ink in the same area with a slot die, and the electrode thickness was measured to be an average thickness of 1 μm to 500 nm. The sheet resistance for each sample was measured, and there was a difference according to wt%, and it was 6 mΩ/sq or less.

Finally, the carbon material was thin-film coated using a spray coater, and the spray coating properties were confirmed according to the temperature change of the substrate, and the conditions for the uniformity of the coating according to the number of coatings were found.

This research was supported by the National Research Council of Science & Technology (NST) (No. CAP22083-300), the National Research Foundation of Korea (NRF) (No. RS-2023-00222166), and the Korea government (MOTIE) (No. RS-2024-00470021).

[1] Journal of Power Sources 406 (2018) 7–17
[2] Journal of Electroanalytical Chemistry 973 (2024) 118661

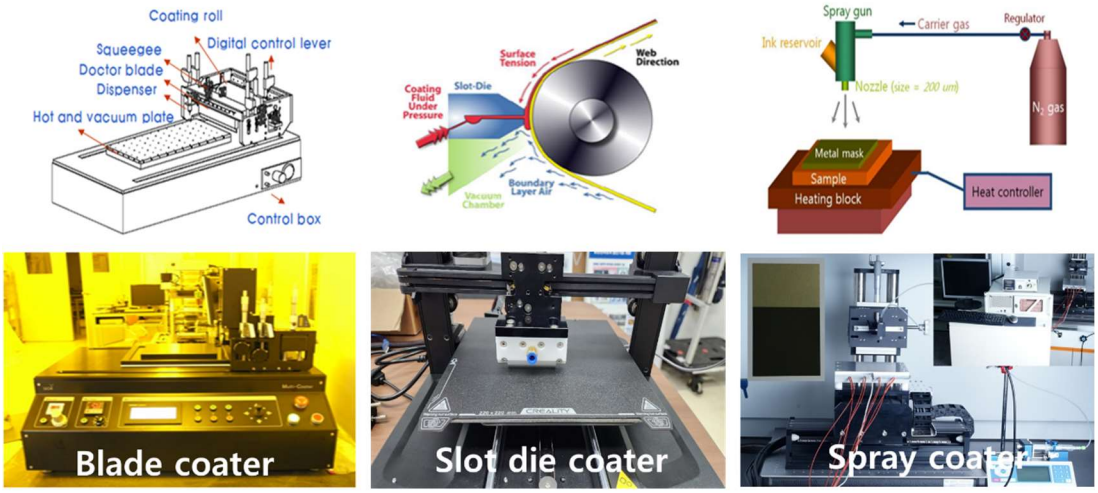

Figure 1. Thin-film coating processes using blade coating, slot die coating, and spray coating.

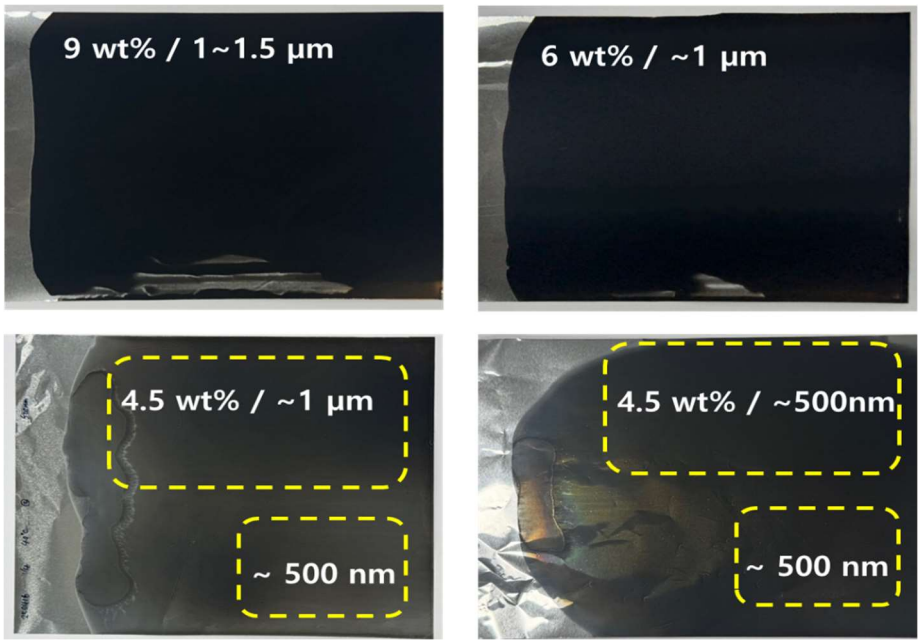

Figure 2. Coated micro/nano thin-film using carbon materials.

Bulk Micro-Machining of $SrTiO_3$ Substrates for Device Applications

Nicola Manca[1,2], Alejandro E. Plaza[1,2], Leonélio Cichetto Jr.[1], Warner J. Venstra[3], Daniele Marré[4,1], and Luca Pellegrino[1,2]

[1] CNR-SPIN, C.so F. M. Perrone, 24, Genova, 16152, Italy
[2] RAISE Ecosystem, Genova, Italy
[3] Quantified Air BV, Langegracht 70, Leiden, 2312NV, The Netherlands
[4] Dipartimento di Fisica, Università degli Studi di Genova, Genoa, 16146, Italy
e-mail: nicola.manca@spin.cnr.it

Advanced fabrication protocols are instrumental to the development of new experiments and device prototypes. For long time complex oxides micro-fabrication was limited to surface micro-machining of thin films by chemical or physical etching or lift-off. More recently, the possibility to exfoliate complex oxide heterostructures from their growth substrate by using a water-soluble buffer layer opened the opportunity to manipulate complex oxides in a similar fashion to Van der Waals materials.

Here, we further extend this tool-box by presenting a set of fabrication protocols to realize fully suspended micro-structures from complex oxides thin films by etching through the full thickness of their growth substrate [1]. These methods rely on the selective chemical etching of $SrTiO_3$ by HF and the use of double-polished STO substrates. These allow for the growth of epitaxial oxide thin films on both sides which are employed as hard masks and/or device layers to realize fully suspended oxide membranes. We will present different examples of possible device geometry, such as trampolines, sealed membranes, or even the substrate itself carved into suspended resonant devices. These simple geometries can be employed to realize more advanced device prototypes by stacking thin layers of crystalline complex oxides havind different functional properties, such as high-Tc superconductivity or magnetism [2, 3].

Acknowledgement
This project has received funding from the European Union's Horizon 2020 research and innovation programme under Grant Agreement No. 828784 (www.oxinems.eu). This work was also funded by the European Union - NextGenerationEU and by the Ministry of University and Research (MUR), National Recovery and Resilience Plan (NRRP), Mission 4, Component 2, Investment 1.5, project "RAISE - Robotics and AI for Socio-economic Empowerment" (ECS00000035).

[1] N. Manca et al., Adv. Sci. 12 (2025) 2412683.
[2] N. Manca et al., Adv. Funct. Mater. **34** (2024) 2403155.
[3] N. Manca et al., ACS Sens. (2025).

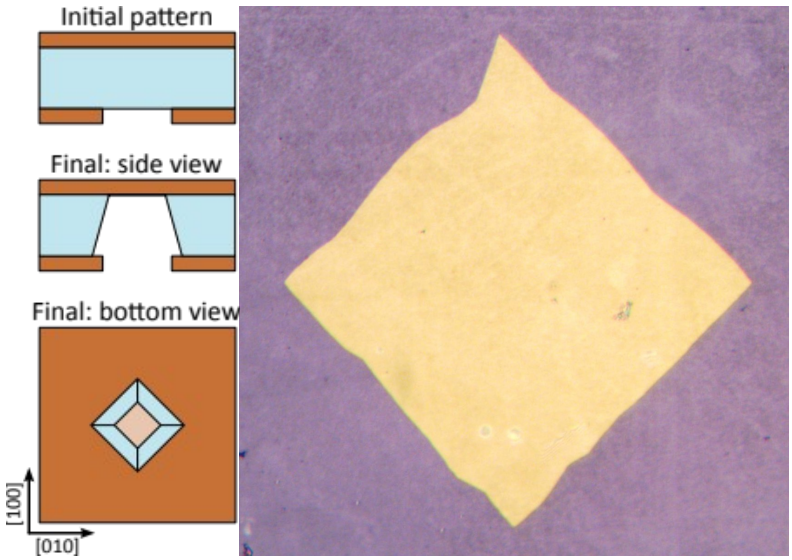

Figure 1. (left) Schematic illustration and (right) optical micrograph in reflected light of a 100 nm-thick suspended (La,Sr)MnO_3 membrane obtained by back-side etching of the SrTiO3(001) substrate. In the illustration the LaSrMnO3 is brown and the SrTiO3 is light blue. In the picture the suspended LaSrMnO3 is yellow and the clamped LaSrMnO3 is purple.

Towards EUV lithography with alternative sources: a proof-of-concept high-harmonic generation in gas-filled hollow waveguides driven by ultrafast infrared laser pulses

Sonia Freddi [a], Anna G. Ciriolo [b], Rebeca Martínez Vázquez [b], Salvatore Stagira [c], Monica Bollani [a].

[a] Institute of Photonic and Nanotechnology (IFN)- CNR, LNESS laboratory, Como, 22100 Italy
[b] Institute of Photonic and Nanotechnology (IFN)- CNR, Piazza Leonardo da Vinci, Milano, 20133 Italy
[c] Department of Physics, Politecnico di Milano, Piazza Leonardo da Vinci, Milano, 20133 Italy

e-mail: sonia.freddi@cnr.it, sonia.freddi@ifn.cnr.it

Extreme ultraviolet (EUV) lithography has recently attracted significant attention for advanced semiconductor manufacturing, enabling patterning at sub-10 nm scales. Nevertheless, current state-of-art implementation often relies on large-scale, complex infrastructures, such as plasma-based EUV sources and high-vacuum optical beamlines, which present considerable challenges related to cost, energy consumption, and system scalability [1,2]. As the demand for ever-finer resolution and more sustainable nanofabrication grows, the exploration of alternative, compact EUV generation methods are both timely and essential [2].

Here, we present the development of a proof-of-concept experimental setup that leverages ultrafast laser-driven high-harmonic generation (HHG) in gas-filled microstructured photonic devices to produce coherent EUV radiation (Figure 1a).

Although technical implementation is still ongoing, particularly the commissioning of a custom-made laser source, we had already demonstrated the viability of several key concepts, including efficient generation of EUV radiation in waveguide-based microfluidic glass device by HHG in a quasi-phase matching regime [3] and the realization of embedded nanometric hollow channels for EUV light manipulation [4].

In particular, initial steps toward functional demonstrations have been performed with proof-of-concept EUV photolithographic tests. A commercial negative resist (SX AR-N 8250.06) was selected following feasibility and market analyses, consistent with common practices in lithographic process development where resist performance, availability, and cost-effectiveness are critical factors. Spin coating tests were performed to optimize the film thickness within the range of 100–320 nm, and the resulting films were characterized using scanning electron microscopy (SEM) to evaluate their morphology and uniformity. The irradiation tests were carried out exploiting a Ti:Sapphire-driven HHG beamline with a microfluidic source filled with argon gas, optimized under vacuum at 100 mbar. This source enables HHG emission up to 60 eV, with a maximum photon flux at 40 eV corresponding to 10^12 photons/sec. We anticipate a spectral extension to >90 eV once the custom-made laser source becomes operational.

The setup included a sample holder mounted on motorized rotation and translation stages, enabling precise spatial alignment with the beam. An in-situ imaging system (2f-2f configuration) was used to monitor the exposure area, while sample positioning was pre-aligned using a pinhole and a strongly attenuated beam.

Initial exposures were performed with and without the presence of the fundamental 800-nm light, exploiting a 100 nm aluminium filter to isolate the EUV component. Samples were exposed for different time steps, i.e. 1–30 minutes. Clear lithographic features were observed on the sample exposed for 30 minutes with EUV only, and partial pattern formation was detected on samples with shorter or mixed exposure. The damage to the filter in later tests revealed the strong influence of residual IR on resist response, underscoring the importance of reliable IR suppression.

While these are preliminary stages, they are the proof of critical transition from component-level research to system-level integration. The realization of compact, integrated demonstrators for EUV photolithography points toward a future where high-resolution nanofabrication becomes more accessible, sustainable, and modular, unlocking new avenues in both industrial and scientific domains.

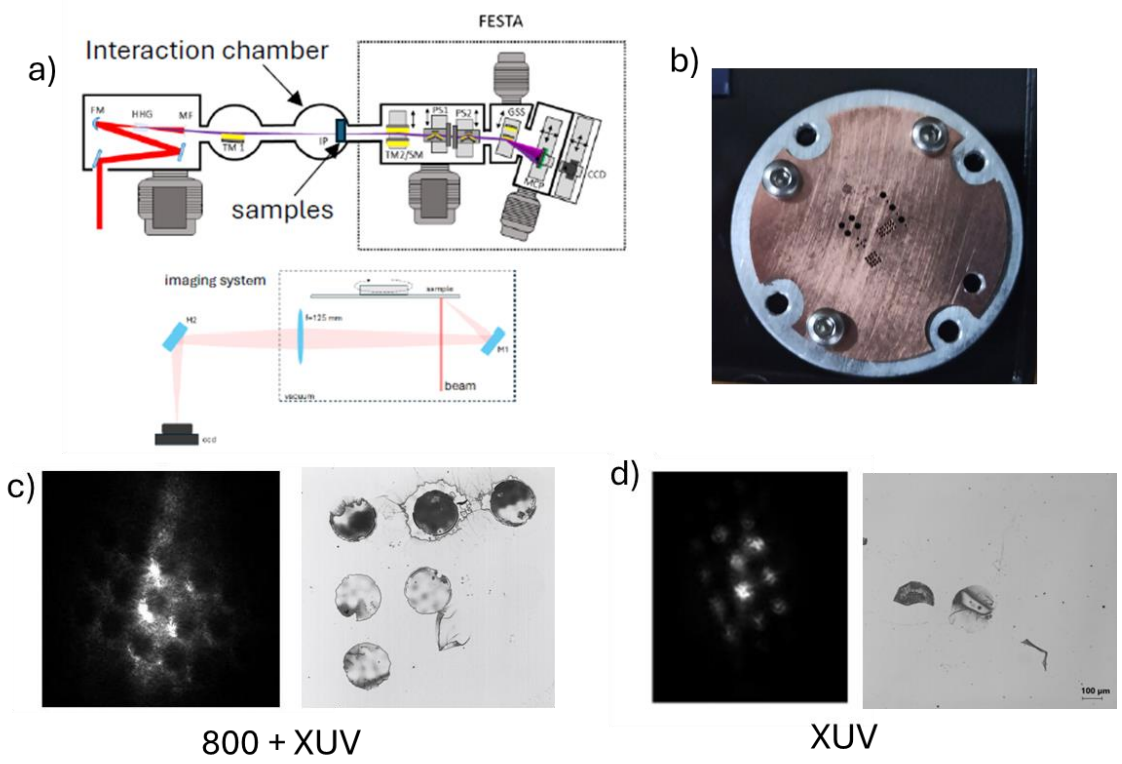

Figure1: Set up (a) and physical mask (b) exploited for the lithography process. c) left side: image of the mask area illuminated by the 800-nm light and XUV; right side: optical image of the pattern obtained on the sample after development. d) left side: image of the mask area illuminated by the XUV source; right side: optical image of the pattern obtained on the sample after development.

References

[1] Timurdogan, E., Sadri, D. (2021). Extreme ultraviolet (EUV) lithography: A review on technology and challenges. *Journal of Micro/Nanolithography, MEMS, and MOEMS*, *20*(2), 021202.

[2] Levinson, H. J. (2025). Challenges and limits to patterning using extreme ultraviolet lithography. *Journal of Micro/Nanopatterning, Materials, and Metrology*, *24*(1), 011005-011005.

[3] Ciriolo, A. G., Martínez Vázquez, R., Crippa, G., Devetta, M., Faccialà, D., Barbato, P., ... & Stagira, S. (2022). Microfluidic devices for quasi-phase-matching in high-order harmonic generation. *APL Photonics*, 7(11).

[4] Barbato, Pasquale, Roberto Osellame, and Rebeca Martínez Vázquez. (2024) Femtosecond laser nanomachining of high-aspect-ratio channels in bulk fused silica. *Advanced Materials Technologies* 9.18, 2400240.

Acknowledgements

This research has received funding from the European Union Horizon 2020 Research and Innovation Program under Grant Agreement No. 964588 (XPIC).

Medusa 84 SiH, an alternative HSQ resist for realizing DFB lasers diodes

P. Sammeta [a], O. Brox [a], D. Rentner [a], P. Della Casa [a], R.-S. Unger [a],
H. Wenzel [a], M. Schäfer [a], A. Knigge [a], H. Biller [b], M. Schirmer [b]

[a] Ferdinand- Braun-Institut (FBH), Berlin, 12489, Germany
[b] Allresist GmbH, Strausberg, 15344, Germany
e-mail: Poojitha.Sammeta@FBH-Berlin.de

In this paper we investigate the performance of the edge emitting distributed feedback (DFB) lasers fabricated using hydrogen silsesquioxane (HSQ) polymer-based electron beam resist Medusa 84 SiH by Allresist GmbH (Germany). DFB laser realized with hydrogen silsesquioxane resist were analyzed and presented in [1]. Limited shelf life of HSQ resist poses a concern while producing high-quality DFB lasers. In order to make the DFB fabrication process more reliable and cost-effective, an HSQ resist variant Medusa 84 SiH – SX AR-N 8400.08 was tested. In addition, the solvent used for Medusa 84 SiH is butyl acetate thereby avoiding a health hazardous solvent methyl isobutyl ketone (MIBK) which is commonly used for HSQ resist [2].

The first epitaxial growth step by metalorganic vapour-phase epitaxy (MOVPE) on a n-GaAs substrate terminates with InGaP/GaAs/InGaP grating layers. The DFB lasers were designed for an emission wavelength of 1064 nm. Grating lines of period 330 nm and width of 90 nm were patterned into 100 nm thick Medusa 84 SiH resist using e-beam lithography (Raith EBPG 5200) operating at 100 keV. The writing time (~12.5 hrs for a 3-inch wafer) was similar to the writing time of the process with different HSQ resist (~12 hrs). A post development bake at 120 °C was carried out to for an improved plasma etch resistance. The gratings were then plasma etched and the resist was removed with diluted hydrofluoric (HF) acid, followed by 10 mins DI water rinse. Fig. 1 exhibits an SEM micrograph of gratings taken after the dry etching and cleaning step. The gratings were finally buried during the second regrowth step, thereby completing the vertical laser epitaxial stack. The SEM image displayed in Fig. 2 showcases the cross-section of the gratings realized with Medusa 84 SiH resist. From the SEM micrograph it can be seen that there are less morphological defects at the interface indicating a good regrowth interface.

The DFB laser diodes of cavity length 1500 µm and 2.2 µm ridge width were facet coated with the front and rear facet reflectivity of 0% and 96%, respectively. Continuous wave measurements were then carried out on bar level. The output power and applied voltage versus injection current are shown in Fig. 3(a). The output spectrum for different injection current can be seen in Fig. 3(b). The output results were found to be similar to the results of the DFB laser fabricated with the other HSQ resist. In this work frame a DFB process fabricated with Medusa 84 SiH was developed and analyzed as an alternative source of HSQ resist. The results presented in this paper corroborate that the Medusa 84 SiH by Allresist GmbH is an equivalent replacement for similar HSQ variants resist without compromising in the quality of the DFB laser performance.

[1] O. Brox “Buried grating fabrication process for 7xx nm DFB laser diodes,” MNE 2024 - 50th International Micro and Nano Engineering Conference (MNE2024), Montpellier, France.
[2] O. R. Opaluch et al., “Medusa 84 SiH- A novel high selectivity electron beam resist for diamond quantum technologies”, 2025, DOI 10.48550/arXiv.2503.04845.

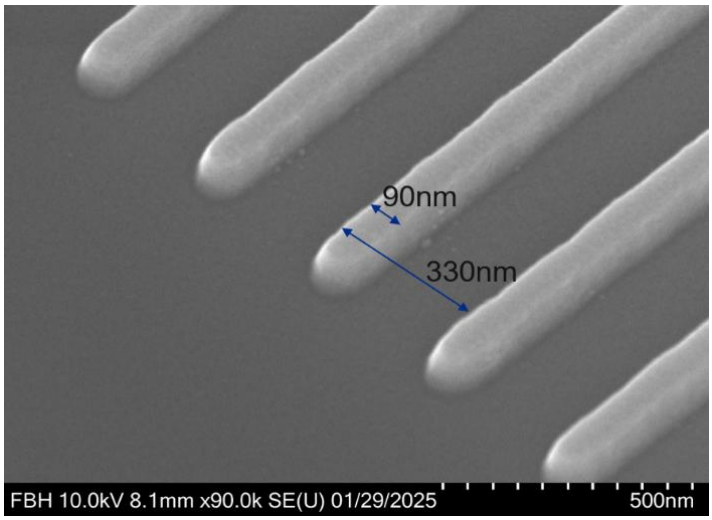

Figure 1. SEM micrograph at 30° tilt of the gratings post plasma etching and Medusa 84 SiH resist removal.

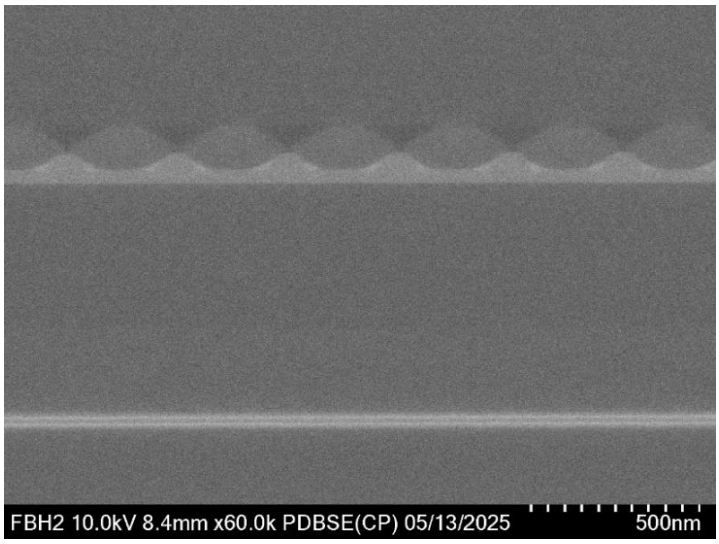

Figure 2. SEM (BSE) image of the gratings cross-section.

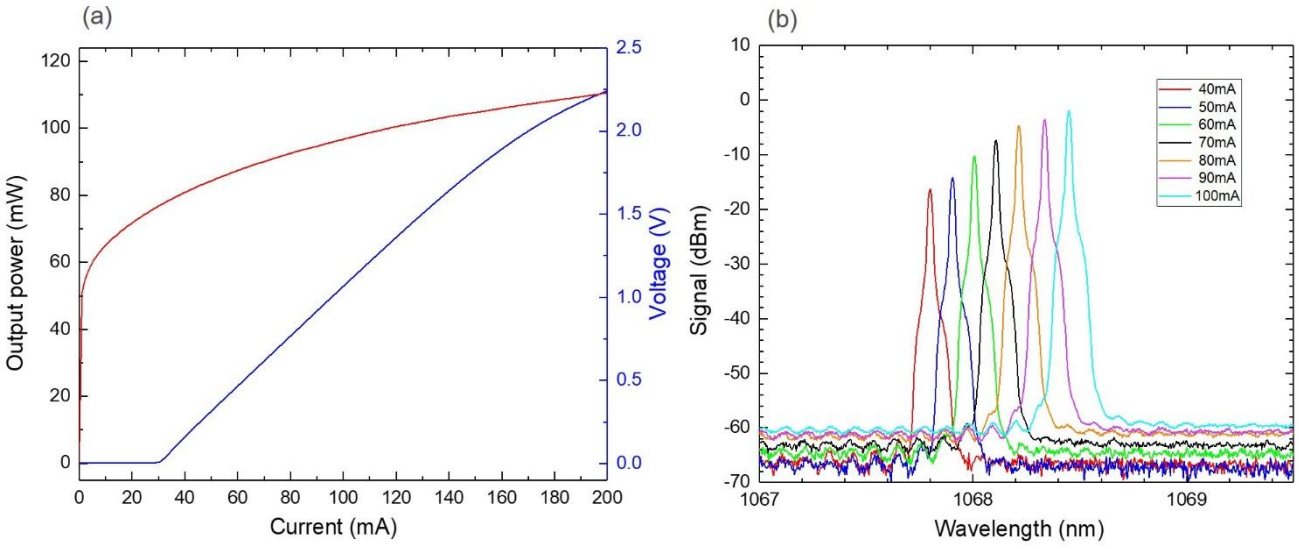

Figure 3. Measurement results, output PI and VI curve (a) and the optical spectra as a function of injection current (b).

Integrated Microfabrication Capabilities for Life Science Applications: From Polymer Platforms to Active Micropumps

Robin de Bruijn[1], Marie Monchablon[123], Sander Visser[123], Laure van der Sanden[2], Hossein E. Amirabadi[24], Jaap M.J. den Toonder[123]

[1] Department of Mechanical Engineering, Eindhoven University of Technology, Eindhoven, the Netherlands
[2] ARTIC Technologies B.V., Eindhoven, the Netherlands
[3] Institute for Complex Molecular Systems, Eindhoven University of Technology, Eindhoven, the Netherlands
[4] AZAR Innovations, Utrecht, the Netherlands
e-mail: r.d.bruijn2@tue.nl

MicroFab Lab is a microfabrication facility embedded in the Microsystems group at Eindhoven University of Technology, supporting the development of advanced micro- and nanosystems for life science and biomedical applications. The facility integrates polymer and 3D microfabrication, cleanroom-based lithographic processing, femtosecond laser micromachining, and advanced actuation and modeling. Its focus is on translating microsystem innovations into usable prototypes for cell biology, diagnostics, and organ-on-chip research.

MicroFab Lab's infrastructure spans five core capabilities: (1) cleanroom processing including lithography, RIE, and thin-film deposition; (2) polymer and 3D fabrication for rapid prototyping of microfluidic systems and organ-on-chip platforms; (3) laser micromachining with sub-micron resolution enabled by the FEMTOprint system; (4) biological laboratory facilities for integration with cell-based assays; and (5) computational tools for multiphysics modeling and design optimization. This range enables researchers and industrial partners to develop complex microsystems from early-stage concept to functional prototype. The facility is especially suited for interdisciplinary applications combining biology, mechanics, and microfabrication.

This submission will present an overview of our capabilities, specifically highlighting a recent case where microactuation was combined with 3D microfabrication in a high-throughput cell culture platform. The developed device—known as the MAC plate—integrates a cilia-inspired magnetic micropump with a polymer-based multiwell plate format. The goal was to enable controlled, gentle flow in each well while maintaining compatibility with robotic pipetting and imaging workflows.

The system preserves standard workflows from the widely adopted 96-well format but adds programmable flow control. This is realized by placing the MAC plate on a magnetic actuator system that drives embedded artificial cilia to generate physiological flow. Our results show that the actuation system can deliver targeted flow rates suitable for long-term culture and mechanobiological stimulation of 3D models.

The novelty of the MAC plate lies in its seamless integration of microactuated flow in a user-friendly platform without requiring additional tubing or external connections. This approach opens new directions for scalable, high-content screening of dynamic microenvironments in biology.

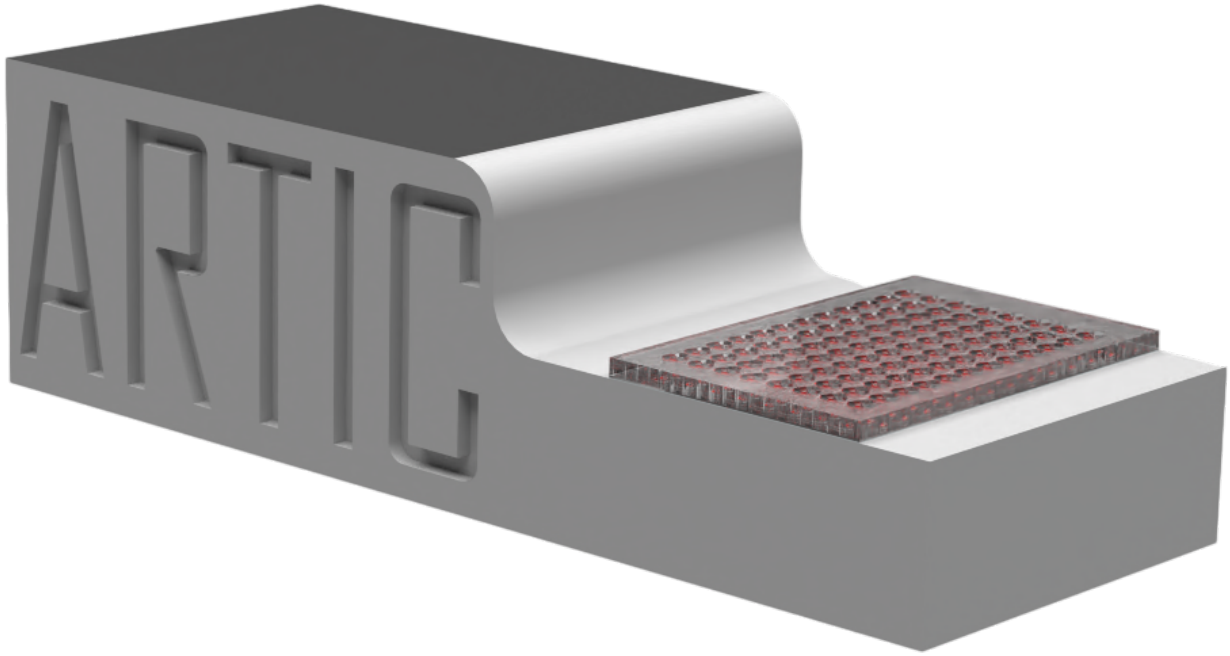

Figure 1. Representative image from the MAC plate platform showing cilia micropump integration and system compatibility.

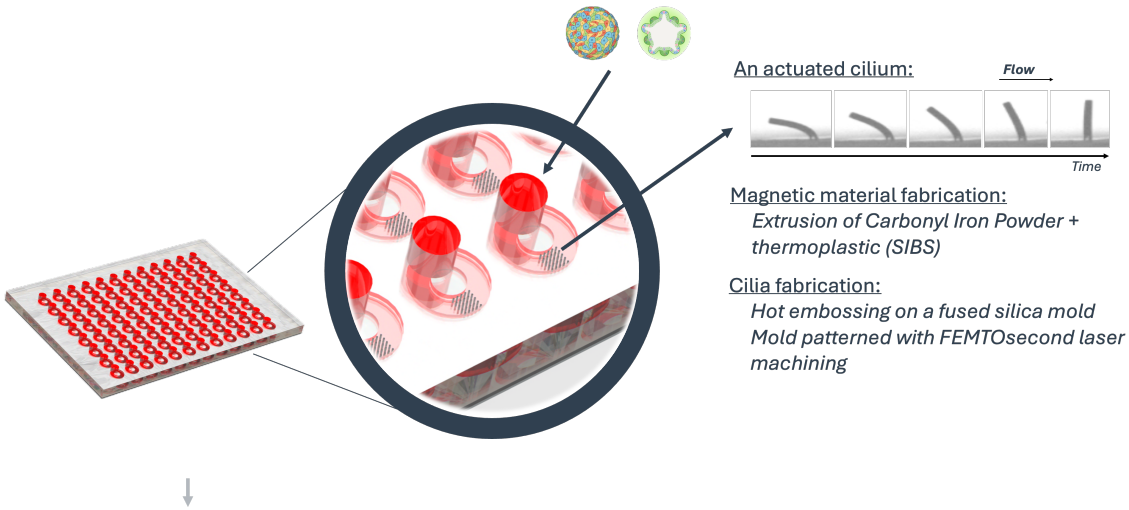

Figure 2. The MAC plate expanded showing the 3D cell culture chambers and the cilia pump section.

Engineering soft nanoscale surfaces force material interaction study

M. Paraggio [a, b], L. Bruno [c], C. Morano [c], M. L. Coluccio [a, b], F. Gualtieri [b], C. De Marco [b, d], F. Gentile [a, b]

[a] Nanotechnology Research Center, "Magna Graecia" University of Catanzaro, 88100 Catanzaro, Italy

[b] Department of Experimental and Clinical Medicine, "Magna Graecia" University of Catanzaro, 88100 Catanzaro, Italy

[c] Department of Mechanical Engineering, Energy Engineering and Management, University of Calabria, 87036 Rende, Italy

[d] Interdepartmental Center of Services (CIS), Omics and Biobank, "Magna Graecia" University of Catanzaro, 88100 Catanzaro, Italy

e-mail: martina.paraggio@unicz.it

Several studies focusing on the influence of nano-topography on cell adhesion and clustering [1] have recently demonstrated that both the nanometric-scale geometry and the mechanical properties of surfaces significantly affect cellular behavior, modulating and possibly enhancing adhesion, growth, proliferation, and migration. Among other things, engineered materials can amplify phenotypic differences between cell lines, highlighting latent or pathological properties [2]. As for an example, among the several different studies that have examined the influence of surface geometry on cell behavior, research reported in references [2], [3], [4] has illustrated that neuroblastoma cells cultured on random rough surfaces tend to cluster together —a behavior that is not observed when the same cells are cultured on flat surfaces. Thanks to their ability to drive cell behavior, from adhesion, to clustering, to migration, similar engineered surfaces found application in a variety of fields, spanning diagnostics [5], bioengineering [6], tissue engineering, biosensing [7] and nanomedicine [8] where they have been exploited, for example, for the early detection of cancer cells or to assess the efficacy of pharmacological or nanotechnological treatments on cultured tissues or cells. The present study focused on the design, fabrication and characterization of nano-structured poly-dimethyl-siloxane (PDMS) substrates, where surface roughness and stiffness - key parameters in tissue engineering - were independently controlled. Silicon substrates were patterned via chemical etching in a 50% w/w KOH solution, varying the etching time - between 0 and 60 min - to obtain surfaces with roughness in the 3-100 nm range. The samples obtained by etching silicon were characterized by optical profilometry and atomic force microscopy (AFM). AFM images were further analyzed using the software Gwyddion, which enabled to extract from data surface topography metrics, including the average surface roughness (Ra) and the maximum height (Max) - providing a detailed description of surface topography. Early results indicated that increasing the exposure time to the KOH solution leads to a progressive increase of Ra and Max, from 3 nm to around 100 nm, eventually reaching a steady state value (**Figure 1a**). This is further confirmed by the quantitative analysis reported in the diagram in **Figure 1b**, suggesting a direct relationship between etching time and topographical metrics Ra and Max of the sample surface. Rough silicon samples were then used as a mold for PDMS casting – this enabled to easily transfer the topography of the rigid silicon mold to soft PDMS samples, where the value of Young's modulus could be regulated by simply adjusting the proportion of the liquid PDMS base and of the curing agent set in the curing phase. The quality of replication was assessed using a variety of techniques, including 2D contact profiling, 3D optical profilometer, and atomic force microscopy (AFM). Of these, 2D contact profiling enables fast, reliable and robust topography measures, but is limited to linear scan of samples, moreover, the non-zero force exerted from the stylus on the samples may introduce artifacts in case of excessively compliant substrates. On the other hand, optical and AFM techniques – while significantly slower – allow for whole field analysis of samples, operate in non-contact mode, and can measure surface profile with – under some circumstances – sub-nanometer resolution. The possibility of measuring sample areas over region of interest with tunable size is especially important given the random nature of the etching of the silicon mold, that typically results in surfaces with relevant variations of heights. The stiffness of the PDMS substrates was modulated by adjusting the ratio (r:1) between the polymer base and the solidifying agent, here adjusted as 7:1, 10:1, and 13:1.

This variation enabled the fabrication of substrates with elastic moduli (Young's modulus) falling in the 1–2.5 MPa range, in line with previous reports [1]. We then evaluated the influence of substrate parameters on cellular behavior by examining the migration of OVCAR-429 cells - a human ovarian carcinoma cell line – on PDMS substrates. In an exploratory experimental campaign, we modulated sole stiffness in nominally flat PDMS samples (without roughness) and left the surface topography unchanged. A standard 6-well plate served as control. Cells were maintained in culture and observed continuously for 48 hours using the Leica Microsystems Thunder Imaging System. The recorded videos were analyzed using cell tracking algorithms

developed in Python, which allowed individual cell trajectories to be extracted, and the movement parameters quantified, including cell-path length, displacement, migration speed, diffusivity, and the number of adherent cells. **Figure 2a** shows a representative time sequence of frames acquired over 48 hours, showing cellular movement and morphological evolution. **Figure 2b** illustrates the resulting trajectories of OVCAR-429 cells cultured on substrates with a 1:10 ratio, revealing active and well-defined migratory behavior. Stemming from these preliminary results, an extended experimental campaign that will be performed over time, will systematically investigate the synergistic effects of nano-topography and surface elasticity on cell behavior, dissecting whether there exist optimal combinations of the parameters that amplify cell response. This comprehension of cell-material interaction can be used to segregate between healthy and non-healthy cells, from different tissues – including lung, colon, breast, ovary, CNS – by simply observing how their phenotypic and functional traits vary on precisely engineered materials.

Keywords: Material stiffness, polymeric surfaces, nano-roughness, cell migration, cell-material interaction, tissue engineering.

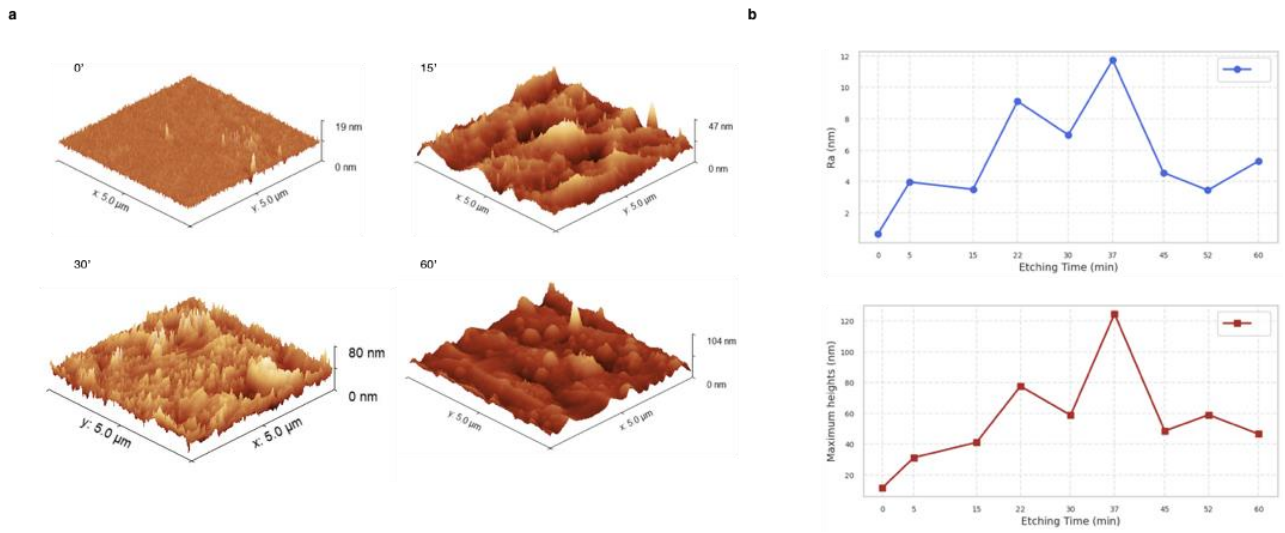

Figure 1: AFM imaging of Silicon surfaces etched with 50% KOH for different times (0, 15, 30, 60 min), showing a progressive increase of Ra over time (**a**). Quantitative analysis of Ra and Maximum heights (**b**).

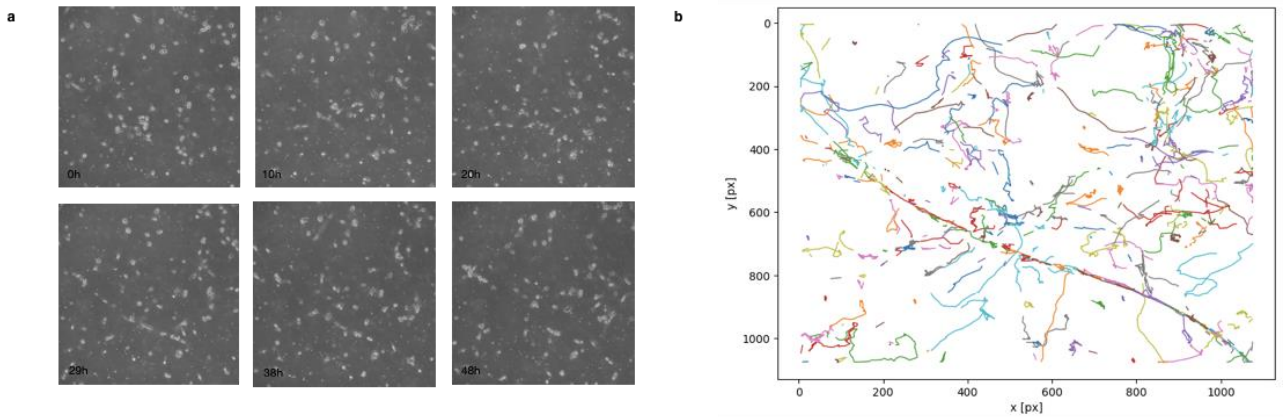

Figure 2: Representative time sequence of frames acquired over 48h, showing cellular movement and morphological evolution (**a**). Resulting trajectories of OVCAR-429 cells cultured on substrates with a 1:10 ratio, revealing active and well-defined migratory behavior (**b**).

References

[1] G. Marinaro *et al.*, "The role of elasticity on adhesion and clustering of neurons on soft surfaces," *Commun Biol*, vol. 7, no. 1, Dec. 2024, doi: 10.1038/s42003-024-06329-9.

[2] F. Gentile, “Cell aggregation on nanorough surfaces,” *J Biomech*, vol. 115, Jan. 2021, doi: 10.1016/j.jbiomech.2020.110134.
[3] V. Onesto *et al.*, “Cortical-like mini-columns of neuronal cells on zinc oxide nanowire surfaces,” *Sci Rep*, vol. 9, no. 1, Dec. 2019, doi: 10.1038/s41598-019-40548-z.
[4] V. Onesto *et al.*, “Nano-topography Enhances Communication in Neural Cells Networks,” *Sci Rep*, vol. 7, no. 1, Dec. 2017, doi: 10.1038/s41598-017-09741-w.
[5] F. Pagliari *et al.*, “Nano-Topography Enhanced Topological-Cell-Analysis in Radiation-Therapy,” *Adv Healthc Mater*, 2025, doi: 10.1002/adhm.202405187.
[6] C. J. Bettinger, R. Langer, and J. T. Borenstein, “Engineering substrate topography at the Micro- and nanoscale to control cell function,” Jul. 13, 2009. doi: 10.1002/anie.200805179.
[7] S. Salmasi, “Role of nanotopography in the development of tissue engineered 3D organs and tissues using mesenchymal stem cells,” *World J Stem Cells*, vol. 7, no. 2, p. 266, 2015, doi: 10.4252/wjsc.v7.i2.266.
[8] L. A. Walsh, J. L. Allen, and T. A. Desai, “Nanotopography applications in drug delivery,” Dec. 02, 2015, *Taylor and Francis Ltd*. doi: 10.1517/17425247.2015.1103734.

Isotopically pure Silicon-28 thin films for improved coherence times in silicon quantum technologies built by scanning tunnelling microscopy

Oisín FitzGerald [a], Taylor Stock-[a]
[a] University College London, London, WC1E 7JE, UK
e-mail: oisin.fitzgerald.23@ucl.ac.uk

Silicon-based quantum computers can, in principle, be fabricated using scanning tunnelling microscopy hydrogen resist lithography (STM-HRL) to place individual donor atoms with atomic precision into a silicon lattice [1]. Spin-qubit quantum processors built this way, in natural silicon, have spin coherence times that are limited by interactions with the non-zero nuclear spin of the Silicon-29 isotope. Isolating qubits from this noise source is critical for achieving high-fidelity, error-resistant computation. By reducing the Si-29 concentration to sub-100 ppm, the coherence time of an electron spin from a phosphorus impurity can be improved from milliseconds to about 2 seconds [2]. This work addresses the challenges of developing isotopically enriched Si-28 buffer layers that are compatible with the strict thermal budget required for atomic precise quantum device fabrication using STM-HRL. We use time-of-flight secondary ion mass spectrometry (ToF-SIMS) and silicon self-diffusion modelling to explore intermixing between a purified buffer layer and a natural substrate during flash annealing and balance this with the thermal processing conditions required to produce the atomically clean Si(001) surfaces that are needed for STM-HRL.

[1] Kane, B. E. (1998). A silicon-based nuclear spin quantum computer. NATURE, 393, 133–137
[2] Tyryshkin, A. M. et al. Electron spin coherence exceeding seconds in high-purity silicon. Nature 11, 143–147 (2011).

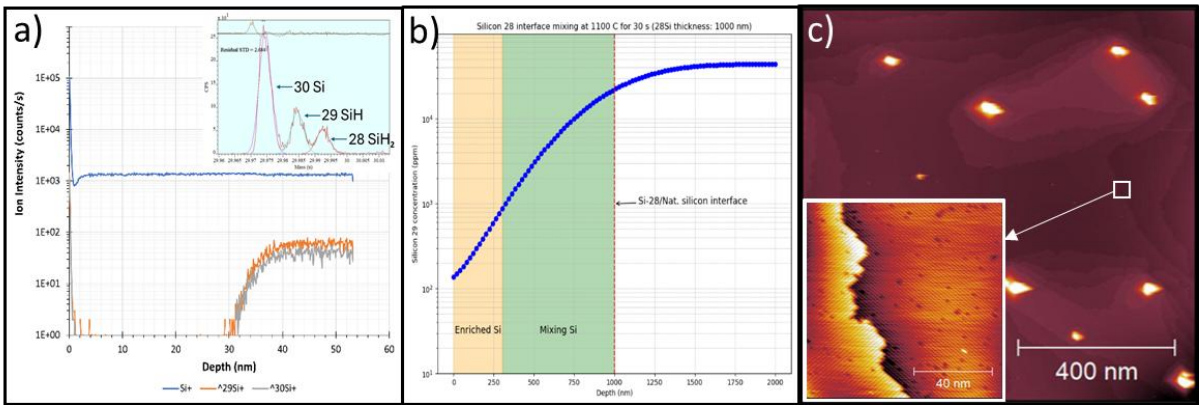

Figure 1. a) ToF-SIMS peak fitting (inset) for precise depth profiling of Si-28 buffer layers grown on natural silicon. b) Silicon self-diffusion model showing migration of Si-29 from a natural silicon substrate into the pure Si-28 during heating to 1100 °C for 30 s. c) STM images of a Si(001) sample after flash annealing to 1100 °C for 30 s. 1 um scale image shows low density oxide/carbide contaminants, while the 100 nm scale (inset) shows atomically clean silicon.

Ultra-thick HSQ Resist for Optical Waveguide Grating Coupler Applications

Kun Zhang [a*], Kian Shen Kiang [b], Ying Tran [a], David J. Thomson [b], Harold M. H. Chong [a]

[a] School of Electronics and Computer Science, University of Southampton, Southampton, SO17 1BJ, UK
[b] Optoelectronics Research Centre, University of Southampton, Southampton, SO17 1BJ, UK

e-mail: kz6u22@soton.ac.uk

Optical devices often employ a thin cladding layer in the waveguiding region for applications such as thermal optic switching or sensing. However, unlike the active waveguiding area, the cladding above the grating coupler requires at least three times as thick as the grating core to achieve efficient coupling. Surface above the grating coupler becomes uneven when a thin cladding layer is deposited, which leads to low coupling efficiency. To address this, a thicker silicon dioxide layer is required above the grating region to improve surface uniformity and enhance light coupling efficiency. Conventional SiO2 deposition methods are unsuitable for this purpose due to their planar deposition nature and the subsequent complex dry etch required for waveguiding region.

To address these challenges, an approach using an ultra-thick Hydrogen Silsesquioxane (HSQ) resist directly patterned onto the grating region via electron-beam lithography is introduced. While thin HSQ is well-known for its electron-beam sensitivity, achieving successful pattern transfer with ultra-thick HSQ (1.35 μm) presents unique challenges related to the stability of the electron-beam exposure dose, as well as the baking and development processes. Therefore, this work focuses on developing a robust pattern transfer process for ultrathick HSQ using electron-beam lithography, specifically tailored for optical coupler applications. The impact of ramp baking temperature and electron-beam dose is also investigated on the thick HSQ resist.

The schematic diagram of the fabrication process flow of the ultra-thick HSQ on the grating structures is shown in Figure 1. A 28% HSQ (EM Resist Ltd.), which provides a thickness ranging from 800 nm to 1400 nm, is used in the work. For testing purposes, we applied a 2000 rpm speed to get a 1000nm thick HSQ. Owing to the proposed ultra-thick HSQ layer, a lower soft bake temperature was adopted to prevent potential issues. In research done by Shen et al, [1] and Ali et al, [2], they found out that 90 ℃ can still lead to a premature crosslink within HSQ, while Jin et al, [3] also applied a curve operation ends at 90 ℃. Since then, temperatures near 90 ℃ were used for soft baking. An initial ramp curve soft-bake strategy was used to avoid cracks, as shown in Figure 2, but cracks appeared after soft-baking process, especially at the corner of the chip (30 mm × 40 mm). With 70-second development in TMAH-0.26 N after E-beam lithography, it can be easily observed that the resist is not fully developed. Four chip-sized wafers were then reprocessed with spin coating at 4000 rpm. A slower ramp soft baking was used (shown in Figure 3), and different developing times were applied on the chips. Microscope observation indicated that, except for the 70-second development, all other samples showed better development quality. When the development time reached 10 minutes, delamination of the HSQ layer was observed. Widths of backscattered areas detected under a microscope are provided in a diagram (Figure 4). Ellipsometry indicates that the thickness of HSQ after process is 1.35 μm (400 μC/cm2 and 6-minute development). With a refractive index of 1.38 at the wavelength of 1550 nm measured under ellipsometer, this resist exhibits optical properties like those of deposited silica. A simulation ran on Lumerical software with 220 nm fully etched grating coupler structure, shows that the coupling efficiency is approximately 23%. Figure 5 shows the optical microscope images of grating couplers with the HSQ mesa layer.

Preliminary results show that thick HSQ is a promising cladding layer for optical coupling. Despite a potential cracking of 28% HSQ during soft baking, an exposure dose of 400-700 μC/cm2 and development in TMAH for at least 3 minutes yield well-defined large-area patterns with clear edges. For finer structures, higher exposure doses and longer development times tend to produce better results. It is important to note that excessive development time in TMAH-0.26N leads to delamination of the exposed HSQ.

[1] J. Shen *et al., J. Vac. Sci. Technol. B,* vol. 37, issue 2, 2019, doi: 10.1116/1.5079657.
[2] A. Al-Moathin *et al., J. Vac. Sci. Technol. B,* vol. 37, no. 6, 2019, doi: 10.1116/1.5123286.
[3] F. Jin *et al., Nat. Commun.,* vol. 13, issue 1, doi: 10.1038/s41467-022-29036-7

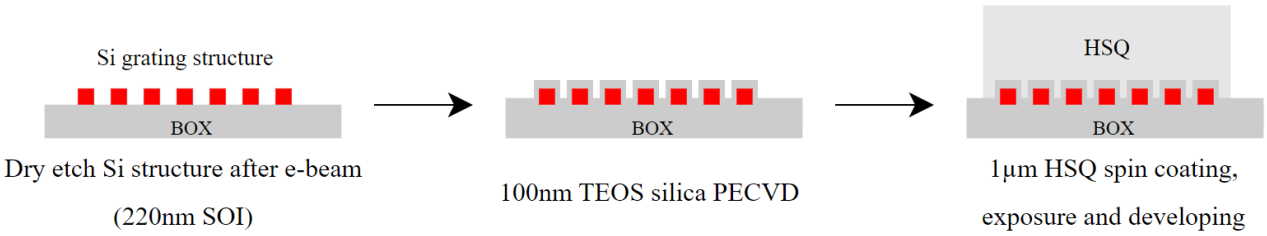

Figure 1. Fabrication process for grating planarization by HSQ.

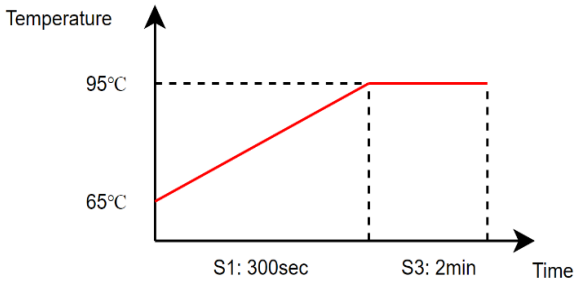

Figure 2. Ramp curve for soft-bake process.

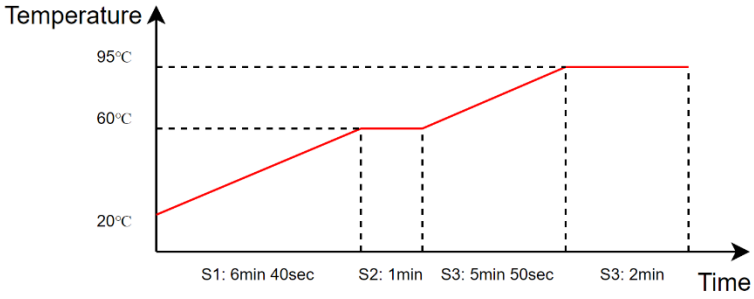

Figure 3. Slow ramp curve for 1.35μm HSQ soft-bake process.

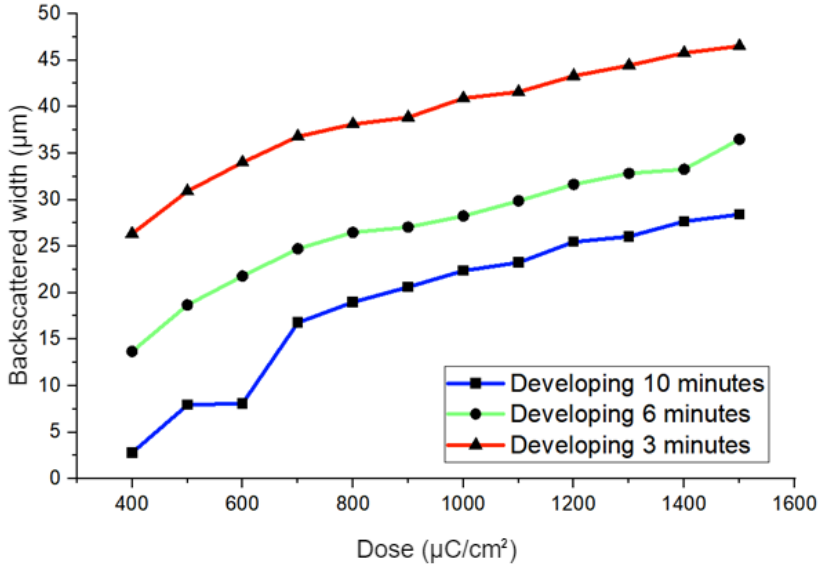

Figure 4. Width of backscattered area with different dose and development times.

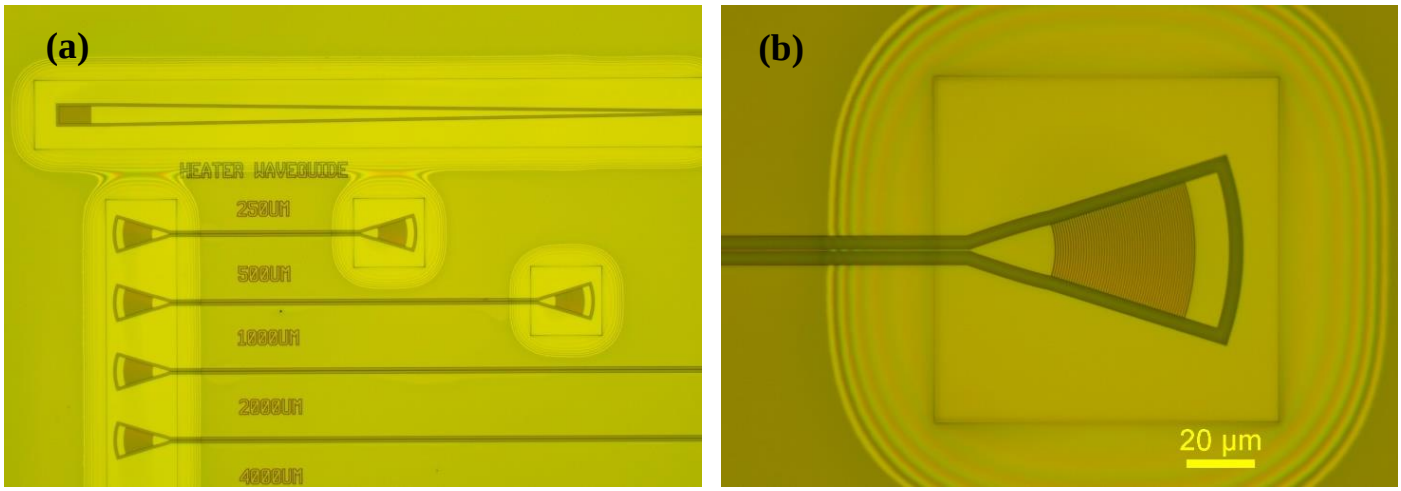

Figure 5. (a) Image of HSQ applied on grating area; **(b)** HSQ mesa on grating structure.

Integration of Interband Infrared Cascade Photodetector onto a SOI Platform for Gas Sensing

Daniel Adeyemi[1], Milos Nedeljkovic[1], Goran Mashanovich[1], Colin Mitchell*[1]

[1]Optoelectronics Research Centre, University of Southampton, University Road, Southampton, Hampshire SO17 1BJ, UK

Corresponding author*: c.j.mitchell@soton.ac.uk

Silicon photonics has proven industrial applications for communication, such as in data centres at the 1550nm and 1310nm wavelengths. Additionally, there is much interest at higher wavelengths where there is significant potential for silicon photonic systems for integrated sensing circuits in the mid infrared where it overlaps with the finger-print wavelength range ($2-10\mu m$). This spectral range is where molecules can be identified due to their distinct absorption spectra generated by the characteristic resonant frequencies of their structure. To exploit this capacity, we can utilise absorption spectroscopy which involves measuring the change in transmission once, for example, a gas interacts with light of a specific wavelength.

Traditional gas sensing system can be bulky, require cooling, are expensive, difficult to integrate into other systems and consequently have comparatively short lifetimes especially in harsh environments such as might be encountered for oceanography as an example investigated here. On-chip absorption spectroscopy has been increasingly desirable as it addresses these issues. Additionally, chemical reactions are not used to detect a molecule, which increases the sensor lifetime.

On-chip absorption spectroscopy allows for the electronic components to be integrated into a smaller package with improved mechanical stability, reduced weight etc. To achieve this, it is desirable to integrate mid-infrared lasers and detectors onto the same chip making use of the excellent optical properties of III-V materials and the compatibility of silicon with CMOS processes allowing for the production of low cost, high performance photonic circuits. However, for on-chip sensing it is also beneficial that these devices can operate at, or close to, room temperature whilst maintaining performance, as cooling is difficult to achieve on such a small scale.

We present a methodology to integrate a 12-stage interband cascade infrared photodetector (ICIP), supplied by the University of Würzburg, onto a SOI platform for a collaboration with the National Oceanography Centre[1] to produce gas sensing circuits for oceanography. This is to be achieved using a hybrid flip chip bonding approach utilising etched support structures and AuSn solder for contacting between the two components. In addition, we present waveguides designed for operation at three wavelengths to sense and measure the concentrations of methane (3.3 μm), atmospheric transmission (3.8 μm) and carbon dioxide (4.3 μm). In order to achieve these goals we have designed novel self-aligned double etch gratings for the each of the wavelengths under test for coupling directly to the detector above.

The device will be tested by coupling the light from a free space laser into the waveguides where it will pass through spiral waveguides of varying lengths (5 mm, 1 cm and 4 cm). This will allow us to evaluate the change in sensitivity with differing path lengths whilst maintain a compact structure and decoupling any free space effects. To reduce free space absorption further we have also designed and constructed a gas cell to evaluate this system minimising the path length exposed to the gas under test.

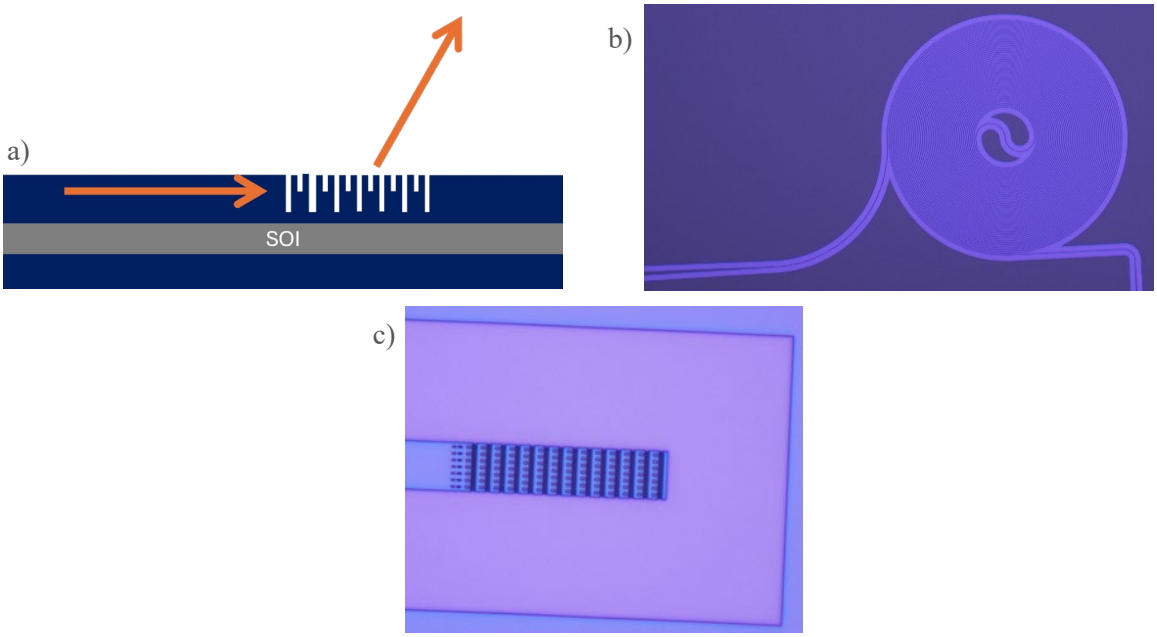

Fig. 1. a) Self-aligned double-etch grating, b) Microscope image of fabricated grating, c) Microscope image of fabricated waveguide spiral

Acknowledgements:
The ICIPs used in this collaboration were designed and fabricated at the University of Würzburg

References

[1] A. Bader, F. Rothmayr, N. Khan, J. Koeth, F. Hartmann, and S. Höfling, "Detectivity enhancement by double radiation pass in interband cascade infrared photodetectors," *Applied Physics Letters,* vol. 123, no. 14, 2023, doi: 10.1063/5.0165187.

Biofabrication of 3D Scaffolds and Functional Microstructures Using Two-Photon Lithography

Kandra M. [a], Podstránský J. [a], Stříteský S. [a], Matějka M. [a]

[a] IQS nano s.r.o, City, 250 68, Husinec – Řež, Czech republic
e-mail: mario.kandra@iqsnano.com

Two-photon lithography (TPL) has gained increasing attention as a direct laser writing technique capable of producing three-dimensional microstructures with sub-micrometer precision. Unlike traditional lithographic methods—such as electron beam lithography or nanoimprint lithography—which are typically limited to two-dimensional patterning and require vacuum conditions or multiple processing steps, TPL allows the generation of freeform 3D architectures in a single-step process under ambient conditions[1]. This capability enables the creation of structures with complex topologies, variable porosity, and internal heterogeneity, features that are particularly valuable in biomedical applications where physical microenvironments influence cellular responses. An additional advantage of TPL lies in its ability to perform multilayer structuring within a continuous writing sequence, enabling the spatial organization of different functionalities within a single construct[2]. Despite known limitations related to processing speed and material throughput, the high resolution and design flexibility of TPL make it a valuable tool for applications in tissue modeling, biointerfaces, and microfluidic systems.

While existing research has largely concentrated on optimizing material systems and process parameters, our work focuses on expanding the functional scope of TPL toward the fabrication of integrated components for biological microsystems. In contrast to conventional techniques that often require multiple fabrication and assembly steps, we apply TPL to produce not only scaffolds but also additional functional microstructures—such as semi-permeable membranes, compartmentalizing barriers, and microfilters—directly within microfluidic layouts. This approach allows for precise spatial alignment of structural and fluidic features during fabrication and facilitates the creation of customizable, monolithic devices[3]. The novelty of our work lies in leveraging TPL's 3D capabilities to enable multifunctional integration within a single platform, enhancing both design flexibility and reproducibility for organ-on-chip and related applications.

We demonstrate the fabrication of scaffold architectures with controlled geometry suitable for incorporation into microfluidic systems. These scaffolds can be spatially defined relative to the chip's fluidic channels and structural elements. In addition, we show that TPL can be used to fabricate auxiliary features such as filters and membranes within the same fabrication sequence. This co-fabrication approach reduces reliance on manual assembly and alignment while enabling the production of complex, modular biological devices. Our results highlight the potential of TPL as a versatile tool for creating integrated bio-microdevices with precise control over both structural design and functional layout.

[1] A. Jaiswal, C. K. Rastogi, S. Rani, G. P. Singh, S. Saxena, S. Shukla, *iScience* **2023**, *26*, 106374.
[2] S. O'Halloran, A. Pandit, A. Heise, A. Kellett, *Advanced Science* **2023**, *10*, 2204072.
[3] C. Maibohm, O. F. Silvestre, J. Borme, M. Sinou, K. Heggarty, J. B. Nieder, *Sci Rep* **2020**, *10*, 8740.

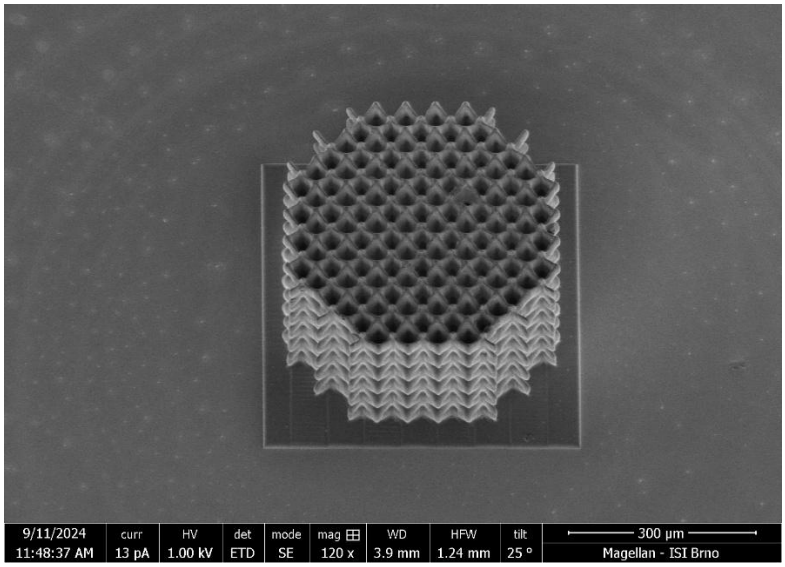

Figure 1. Well-defined scaffold fabricated by two photon lithography

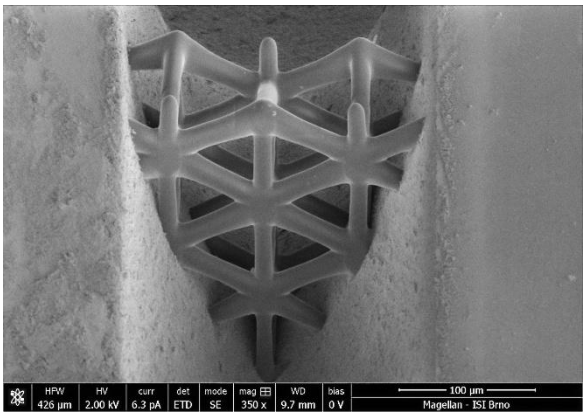

Figure 2. Microfilter incorporated into fluidic channel

The modulation of X-ray by high resolution zone plates when volume diffraction effects dominate

Hao Quan, Xujie Tong, Qiucheng Chen, Qingxin Wu, Xunjia Zhao, Shuoqiu Tian, Wentao Yuan, Jinyu Guo, Kangping Liu and Yifang Chen*
Nanolithography and Application Research Group, School of Information Science and Technology, Fudan University, Shanghai, 200090, China
Shanghai Key Laboratory of Metasurfaces for Light Manipulation, Fudan University, Shanghai, 200090, China
e-mail: *yifangchen@fudan.edu.cn*

X-ray microscopy occupies a unique position in terms of resolution, bridging the gap between optical microscopy and electron microscopy. Moreover, X-ray microscopy demonstrates distinctive advantages due to its interaction with diverse materials, thereby providing a wealth of physical and chemical information about specimens. For decades, researchers pursuing high-quality imaging have concentrated on improving efficiency and resolution based on Kirz's theory [1], which is an effective way to calculate focusing efficiency with different zone plates profiles. However, besides the focusing efficiency, Kirz's method is not able to deal with other characters of optical field including the size of focal spot, the phase distribution, the near field around the zone plates, etc. What's worse, when volume diffraction effects (VDE) are dominant, the efficiency predicted by Kirz's method will deviated significantly from the experimental value, which has been theoretically discussed and some satisfied mathematical results are given [2-4]. The influence of VDE on efficiency can be characterized by Klein-Cook parameter [5]:

$$Q = \frac{\pi}{2(1-\delta)} \frac{\lambda t_{zp}}{dr_N^2}.$$

With Q > 1indicating that VDE must be considered. With the width of the outermost ring dr_N^2 approaching 10 nm, which indicating that imaging resolution approaching 10 nm, Q commonly turns out to be over 10 given that X-ray zone plates usually needs a large thickness t_{zp} compared with dr_N^2 because of the high energy of X-ray. Since researchers realized that in high resolution zone plates, volume diffraction prevented focusing efficiency from further improvement, design of slant zone plates has been proposed and investigated, in which the rectangle zones are slant, especially the outer zones, to meet the Bragg's law. The slant structure and the introduction of Bragg's law suggest that the high-resolution X-ray zone plates are no longer considered as a super thin optics which is the precondition of Kirz's theory. Instead, the modulation process in the journey X-ray travels through the zone plates must be taken into consideration.

In this paper, utilizing beam propagation method (BPM), we construct the whole optical field, especially the field coming out from the zone plates and the field at the focal plane, to describe a more clear and vivid physical scene, which may explain how the individual zone works and how to optimize the focusing performances including resolution, efficiency, imaging contrast. To validate the simulation results, we fabricated an X-ray zone plate with outermost zone width is 15 nm utilizing e-beam lithography and zone-doubling technique and conducted transmitting imaging at Shanghai Synchrotron Radiation Facility (SSRF).

[1]Kirz, J., Phase zone plates for x rays and the extreme uv. Journal of the Optical Society of America, 1974. 64(3): p. 301-309. https://doi.org/10.1364/JOSA.64.000301
[2]Maser, J. and G. Schmahl, Coupled wave description of the diffraction by zone plates with high aspect ratios. Optics Communications, 1992. 89(2): p. 355-362. https://doi.org/https://doi.org/10.1016/0030-4018(92)90182-Q
[3]Schneider, G., S. Rehbein, and S. Werner, Volume Effects in Zone Plates, in Modern Developments in X-Ray and Neutron Optics, A. Erko, et al., Editors. 2008, Springer Berlin Heidelberg: Berlin, Heidelberg. p. 137-171.
[4]Li, K., et al., Tunable hard x-ray nanofocusing with Fresnel zone plates fabricated using deep etching. Optica, 2020. 7(5): p. 410-416. https://doi.org/10.1364/OPTICA.387445
[5]Klein, W.R. and B.D. Cook, Unified Approach to Ultrasonic Light Diffraction. IEEE Transactions on Sonics and Ultrasonics, 1967. 14(3): p. 123-134. https://doi.org/10.1109/T-SU.1967.29423

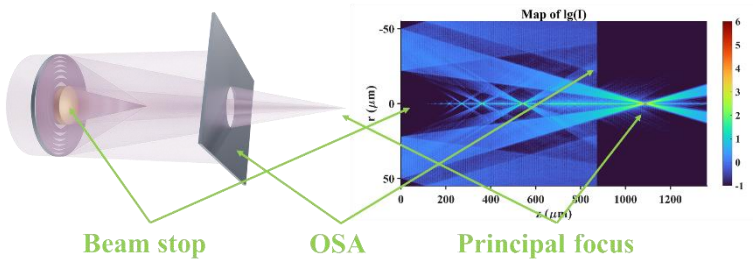

Figure 1. Schematic and simulation results of the light path for zone plates focusing and imaging.

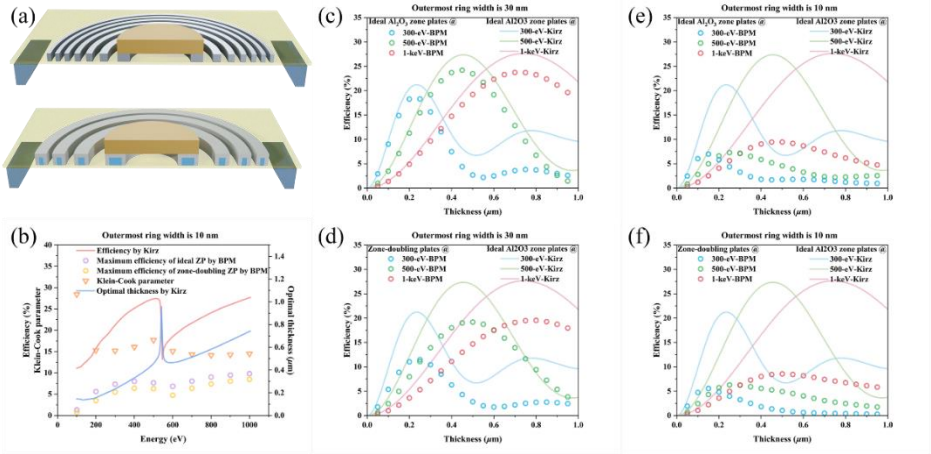

Figure 2. Efficiency comparison between Kirz's method and QDHT-BPM. (a) two structures that simulated by BPM: the gray material is Al_2O_3 and the blue one is HSQ; (b) the maximum efficiency under optimal thickness calculated by the two methods and the Klein-Cook parameter under the optimal conditions; (c)-(f) the efficiency under different thickness, energy and outermost ring width, calculated by the both methods.

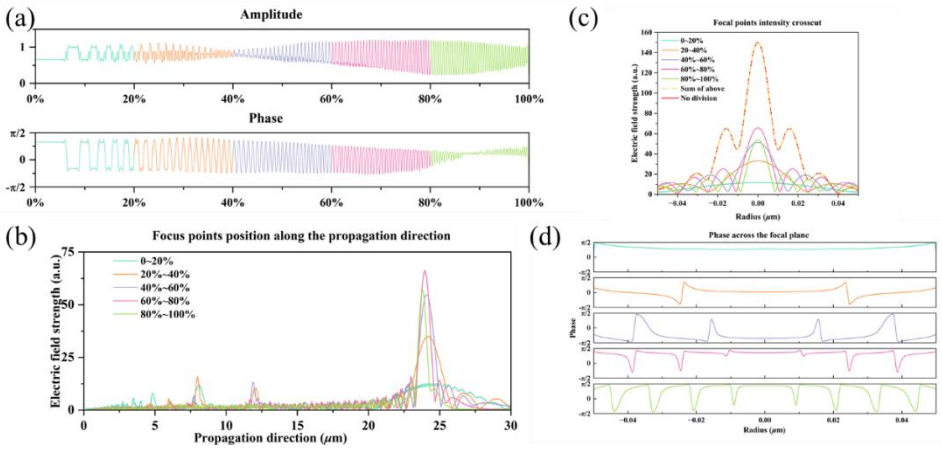

Figure 3. (a) the amplitude and phase out from the ZP (near field); (b) focus points position along the propagation direction; (c) the crosscut of focal points intensity; (d) the crosscut of focal points phase. In (b), (c) and (d), the focuses from separated regions are shown independently.

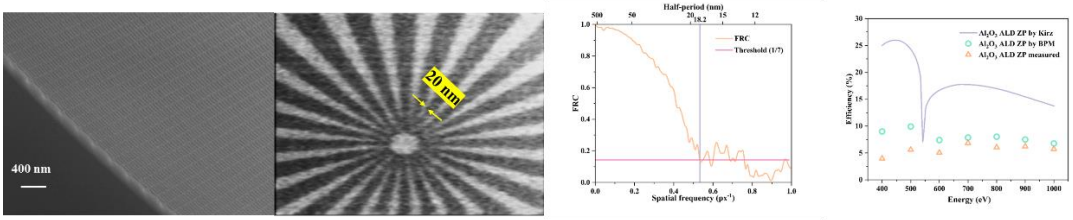

Figure 4. 15 nm-resolution Al_2O_3 zone plates and resolution and efficiency characterization

Microfluidic Mixing Induced by the Blinking-Two-Cilia System

Yangyu Duan [a,b], Ishu Aggarwal [c], Ye Wang [a,b], Patrick R. Onck [c] and Jaap M.J. den Toonder [a,b]

[a] Department of Mechanical Engineering, Eindhoven University of Technology, Eindhoven, 5600 MB, The Netherlands
[b] Institute for Complex Molecular Systems, Eindhoven University of Technology, Eindhoven, 5600 MB, The Netherlands
[c] Zernike Institute for Advanced Materials, University of Groningen, Groningen, 9747 AG, The Netherlands
e-mail: y.duan@tue.nl

Effective microfluidic mixing within a closed chamber is essential for various (bio)chemical and medical applications [1], enabling rapid, precise, and low-volume analysis. However, the absence of turbulence in such systems severely limits mixing efficiency. As a result, leveraging time-dependent intersecting streamlines has become the core mechanism for inducing chaotic mixing at such scale [2]. Artificial-cilia-driven flows have great potential for enhancing microfluidic mixing [3]. Yet, the fundamental understanding and optimization of the 3D mixing induced by a small number of artificial cilia remain unexplored.

Inspired by the classical blinking vortex model [4], we developed a novel blinking-two-cilia system (BTCS) through simulation by first calculating the elemental flow induced by one cilium performing a tilted conical motion (TCM), for varying cilium location within a circular microfluidic chamber. Based on Stokes flow theory, the full BTCS-driven flow field is then reconstructed through linear superposition of elemental flows generated by two symmetrically placed cilia (see Fig. 1(a)–(d)). Although previous work has preliminarily demonstrated the mixing potential of BTCS, its investigation was limited to a few specific 2D cases involving different beating times of two flap-shaped cilia [5]. Here, we further refine the parameter settings and systematically explore the effects of actuation patterns, inter-cilia distance β and blinking cycle frequency f_b^* (see Fig. 1(e)) on mixing performance, providing a deeper insight into BTCS-driven 3D mixing.

BTCS-driven flow patterns are observed by tracking tracer particles with two different colors, initially distributed in a half-half configuration. Each blinking cycle consists of the same number (N_c) of TCM performed alternately by each cilium, generating localized vortices shaped by the cilium's specific motion, spatial location and the N_c performed. Partial overlap between these alternating vortices creates regions of stretching and folding, causing chaotic advection. Across various β - f_b^* combinations, four representative blinking vortex patterns are identified (see Fig. 2). Among them, co-rotating vortex pairs facilitate stronger flow intersection from early stages, while separated counter-rotating pairs do not contribute to mixing. These observations are further supported by quantifying the normalized mixing number m/m_0 [6] over N_t=600 TCM cycles (see Fig. 3). A effectively-mixed state is defined when this value drops below 0.08, and the required number of cycles, N_m, is used to assess global mixing efficiency (see Fig. 4). The results show that the mixing is more effective in the lower β region (0.17~0.33) than in the higher region, with the optimal value at β =0.33. Meanwhile, co-rotating BTCS outperforms counter-rotating ones. While the influence of f_b^* varies across parameter combinations, f_b^* =0.01 yields the best mixing performance in general. The optimal mixing performance is achieved when β = 0.33 and f_b^* = 0.010 with co-rotating BTCS, when the time to reach the effectively-mixed state is minimized.

These simulation results demonstrate that BTCS-driven flows significantly enhance global mixing in a closed chamber and offer valuable insights for optimizing artificial-cilia-driven micromixers. Experimental validation of this BTCS is underway to translate these findings toward practical microfluidic applications.

[1] H. Kim, et al., Science. 352 (2016) 691–694
[2] Sturman R, et al., The Mathematical Foundations of Mixing. Cambridge University Press; 2006:31-58.
[3] T. ul Islam, et al., Microscopic artificial cilia – a review, Lab Chip 22 (2022) 1650–1679.
[4] H. Aref, Stirring by chaotic advection, J. Fluid Mech. 143 (1984) 1–21.
[5] N. Banka, et al., Individually Controllable Magnetic Cilia: Mixing Application, Journal of Medical Devices 11 (2017) 031003.
[6] Z.B. Stone, H.A. Stone, Imaging and quantifying mixing in a model droplet micromixer, Physics of Fluids 17 (2005) 063103.

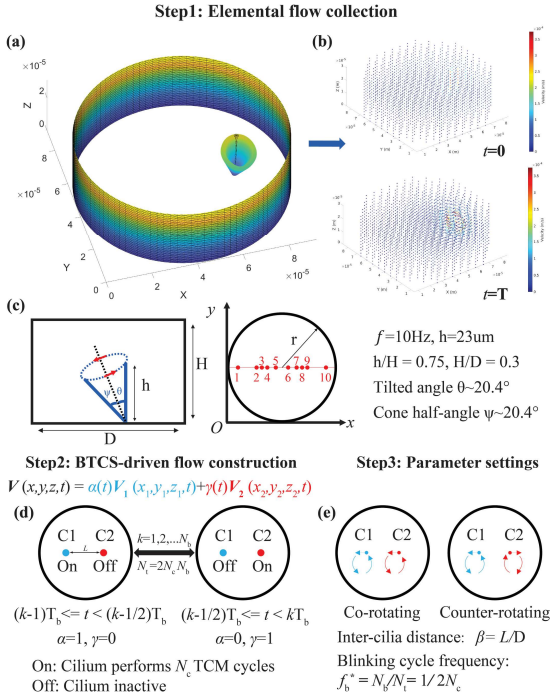

Figure 1. Simulation setup for the BTCS-driven flow. (a) Schematic of TCM induced by a single cilium. (b) Tracer particles distribution resulting from the elemental flow field at t=0 and t=T. (c) Geometry and the kinematics configuration of the cilium-chamber, with ten representative cilium locations used for building the elemental flow library. (d) Schematic of the BTCS model and the flow field reconstruction method based on superposition of elemental flows. Here, N_c denotes the number of TCM cycles performed by each cilium per blinking cycle, N_b is the total number of blinking cycles, and N_t is the total number of TCM cycles. (e) Overview of the two actuation patterns and the key parameters, inter-cilia distances β and blinking cycle frequency f_b^*, varied in this study.

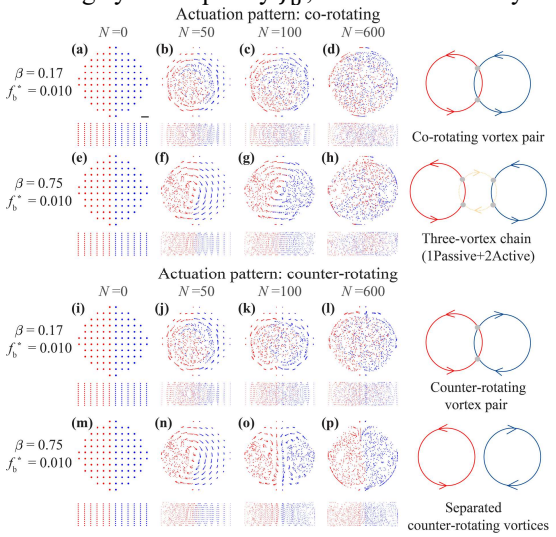

Figure 2. Time evolution of the distribution of tracer particles, projected onto the XY plane (top) and the XZ plane (bottom), within the BTCS over N_t = 600 TCM cycles. Scale bars: 10 um. Panels (a–h) and (i–p) correspond to co-rotating and counter-rotating actuation patterns, respectively. Each 4-panel block shows snapshot at N=0, 50, 100 and 600 for representative cases: (a–d): β = 0.17, f_b^* = 0.010; (e–h): β = 0.75, f_b^* = 0.010. The same layout is applied to counter-rotating cases in (i–p). Rightmost sketches summarize four representative vortex patterns for two actuation patterns, under relatively small and large β (from top to bottom).

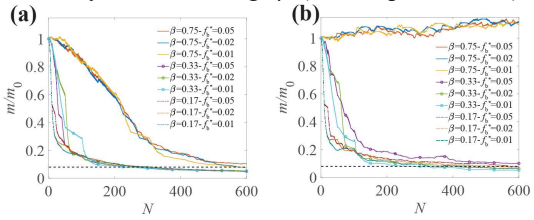

Figure 3. Mixing numbers normalized to their initial value, m/m_0, as function of the number of cycles for cilia performing TCM in the BTCS. (a) and (b) correspond to co-rotating and counter-rotating actuation patterns, respectively. Each panel shows curves corresponding to 9 typical β - f_b^* combinations. Mixing number is defined as $m = \sum_{i=1}^{i=n} \frac{\min(|x_i - x_j|)^2}{n}$, where j=1,2,…,n (n is the total number of same-color particles). The black dashed lines indicate the threshold of effectively-mixed state, defined in this study as m/m_0 = 0.08.

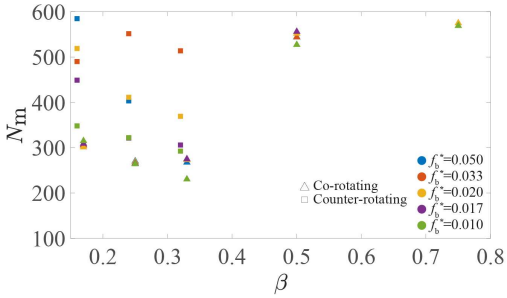

Figure 4. Cycles required to reach the effectively-mixed state N_m across parameter groups in the BTCS. Filled Triangles and open squares represent co-rotating and counter-rotating pattern, respectively. N_m denotes the cycle at which m/m_0 first drops below 0.08 (see Fig 3(a) and 3(b)). A small horizontal offset (jitter=0.01) is applied to the counter-rotating data to avoid overlap.

Neurohybrid interfaces *via* microstructured conductive hydrogels

Marco Buzio [a, b], Nevena Stajkovic [a, b], Valeria Criscuolo [a, b], Francesca Santoro [a, b]

[a] Institute of Biological Information Processing IBI-3, Forschungszentrum Juelich, 52428 Jülich, Germany
[b] Neuroelectronic Interfaces, Faculty of Electrical Engineering and IT, RWTH, 52074 Aachen, Germany
e-mail: buzio@nei.rwth-aachen.de

The integration of bioelectronics with living systems is gradually transforming how interfaces between the human body and machines are designed, making them more adaptive and responsive [1,2]. Conductive hydrogels, hydrophilic cross-linked polymeric networks, are emerging as key materials for the development of tissue-like and seamlessly integrated electronic devices, serving as an effective bridge between traditional rigid electronics and soft biological tissues and organs, thus addressing the inherent mechanical mismatch [3]. Organic mixed ionic-electronic conductors, such as poly(3,4-ethylenedioxythiophene) polystyrene sulfonate (PEDOT:PSS), play a pivotal role in this context by mediating signal transduction across the biotic and abiotic domains [4]. Such materials are introduced as electroactive components to craft pristine or doped polymeric conductive hydrogels overcoming inorganic materials limitations. One of the key challenges is developing engineering strategies to precisely shape conductive polymeric materials in three dimensions (3D) at the micro- and nanoscale, while also integrating both biological and physical cues to better mimic the native environment. To enhance bio-integration and signal fidelity, it is critical that the mechanical properties of the cell-material interface match those of the target tissues [3]. Typically, conductive polymers are non-photo-patternable, requiring soft lithography or inkjet printing to create 3D structures, which limit architectural and geometric precision. Light-assisted fabrication can overcome these limitations, enabling rapid prototyping of scaffolds and microelectrodes. In this work, we present a strategy for fabricating soft, biomimetic, and micro structured conductive hydrogels via two-photon polymerization (2PP) lithography (Fig 1a). By structuring gelatin-based hydrogels, chosen for their cell-adhesive properties and enzymatically degradable peptide sequences, we achieve high-resolution and customizable 3D architectures. Incorporation of PEDOT:PSS yields a photo patternable, conductive hydrogel with tunable mechanical properties, promoting low-impedance cell adhesion and enhanced signal transduction (Fig 1b). The fabricated structures were thoroughly characterized using optical and electron microscopy. Mechanical investigation revealed a Young's modulus of approximately 1 kPa (Fig 1c), indicating the material's mechanical softness. Electrochemical impedance spectroscopy showed that the hydrogel's impedance could be tuned by adjusting the PEDOT:PSS content (Fig 1d), enabling customizable electrical properties. Additionally, biocompatibility tests conducted with the immortalized hippocampal rat neuronal cell line HT-22 and primary rat cortical neurons demonstrated preserved cell viability on the patterned substrates, supporting the material's potential for neuroelectronic applications. This platform provides a versatile route for engineering soft, biomimetic, and electroconductive 3D interfaces tailored to various scales and applications, from electrode coatings and neural scaffolds to tissue engineering and bioelectronic medicine. Our approach paves the way toward a new generation of transient, adaptive, and biologically integrated devices.

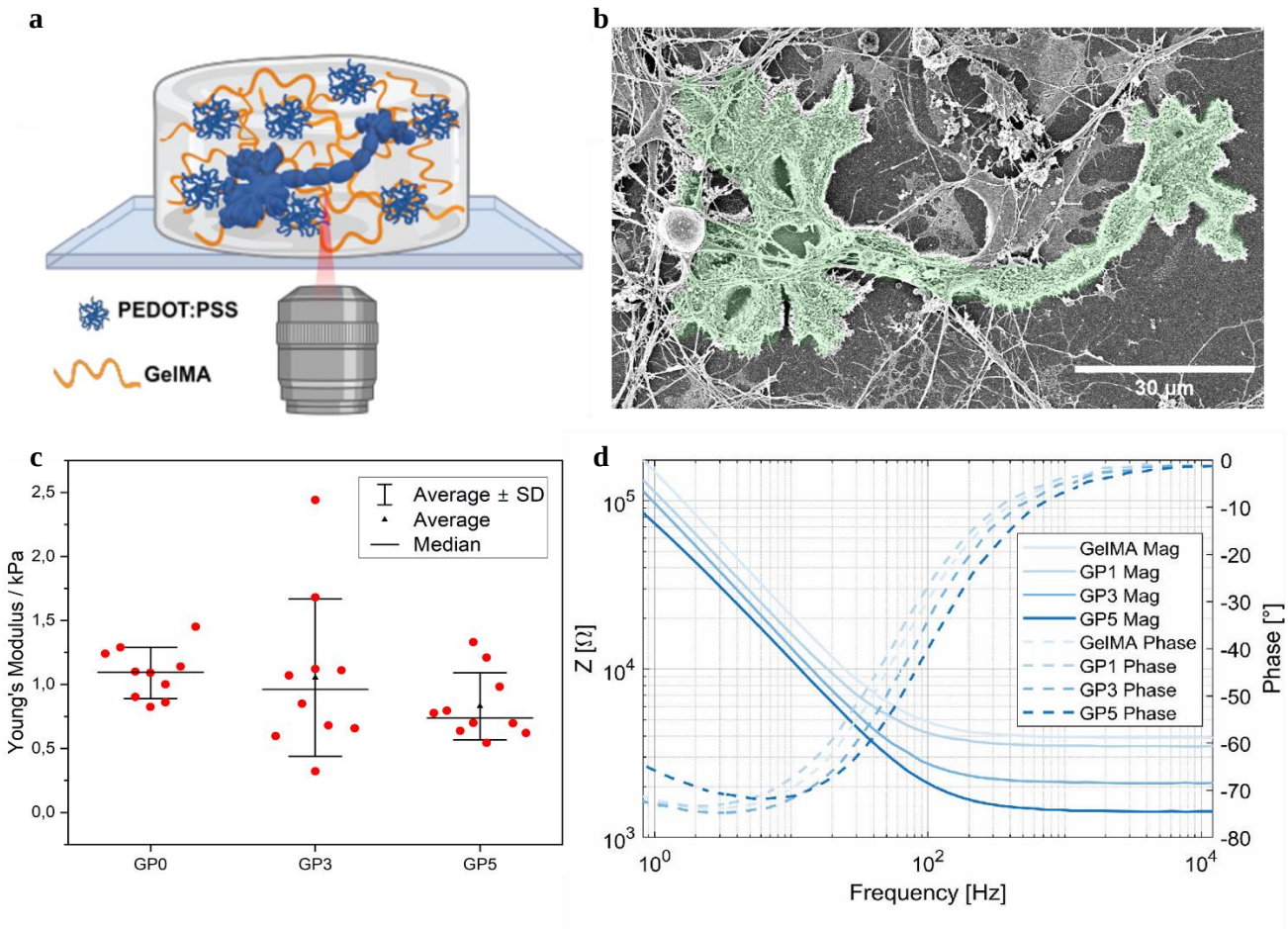

Figure 1 (a) Two-photon polymerization lithography of conductive hydrogels. **(b)** Micro structured hydrogel (false colored in green) interfacing with living cells. **(c)** Young's moduli derived from microgels' nanoindentation. **(d)** Electrochemical impedance spectroscopy of developed hydrogels.

[1] A. Carnicer-Lombarte, G.G. Malliaras, D.G. Barone, The Future of Biohybrid Regenerative Bioelectronics, Advanced Materials 37 (2025) 2408308. https://doi.org/10.1002/adma.202408308.
[2] A.E. Rochford, A. Carnicer-Lombarte, V.F. Curto, G.G. Malliaras, D.G. Barone, When Bio Meets Technology: Biohybrid Neural Interfaces, Advanced Materials 32 (2020) 1903182. https://doi.org/10.1002/adma.201903182.
[3] T.N. Tra, K. Fidanovski, D. Mawad, Bioelectronic Hydrogels: Exemplifying the Synergy Between Biopolymers and Conjugated Polymers, Macromolecular Materials and Engineering n/a (n.d.) 2500019. https://doi.org/10.1002/mame.202500019.
[4] J. Rivnay, S. Inal, B.A. Collins, M. Sessolo, E. Stavrinidou, X. Strakosas, C. Tassone, D.M. Delongchamp, G.G. Malliaras, Structural control of mixed ionic and electronic transport in conducting polymers, Nat Commun 7 (2016) 11287. https://doi.org/10.1038/ncomms11287.

Micropillars Based PDMS Lab-On-chip Device for Tryptic Digestion of Proteins for Proteomics

Sadhana Tiwari [a], Nilüfer Tasli [a], Manuela Moritz [b], Franziska Esmek [a,c], Tim Erichlandwehr [a], Jan Hahn [b], Hartmut Schlüter [b] and Irene Fernandez-Cuesta [a,c]

[a] University of Hamburg, Hamburg, 20146, Germany
[b] Universitätsklinikum Hamburg-Eppendorf, Hamburg, 20246, Germany
[c] Hamburg Center for Ultrafast Imaging, Hamburg, 22607, Germany
e-mail: sadhana.tiwari@uni-hamburg.de

Trypsin digestion is a key step in proteomic workflows, where proteins are enzymatically cleaved into peptides suitable for mass spectrometry analysis. Novel applications in cell and molecular biology often require manipulation and analysis of lower amounts of samples, pushing for the development of novel technologies. Devices such as glass fiber-based microreactors [1], PDMS porous reactors for tear fluid analysis [2], and centrifugal microfluidic platforms for serum digestion [3], demonstrate effective integration with downstream analytical workflows like capillary electrophoresis and mass spectrometry. Despite these advances, challenges such as enzyme leaching, incomplete digestion of complex proteins and protein adsorption to microchannel surfaces persist. Additionally, the full integration of upstream and downstream steps remains a key technical hurdle [4]. Lab-on-a-chip devices are a promising approach, where microfluidic channels allow for much faster processing times, while requiring minute amounts of liquid. On-chip trypsin digestion has thus emerged as a vital step in these miniaturized systems. In this step, the enzyme is immobilised on the surface, and the proteins in solution are digested as they flow through. Thus, microfluidic structures with a high surface area are critical, to maximize the amount of trypsin in the channels. However, laminar flow, typical in such small channels can be detrimental, as it limits the amount of liquid that comes into close contact with the immobilized enzyme.

Incorporating regularly spaced, high-aspect-ratio micropillars significantly increases the accessible surface area for trypsin immobilisation and improves mixing and mass transfer within laminar flow, thereby strengthening enzyme-substrate interactions and enhancing digestion efficiency. Moreover, the planar and open architecture of micropillars-based device is easier to integrate with downstream modules like MS interfaces and in monolithic lab-on-a-chip designs.

In this work we present a reusable microfluidic device for rapid and efficient on-chip trypsin digestion for proteomics. The microfluidic lab-on-a-chip consists of two parts; a structured layer and a cover layer (coverslip), both made of PDMS. To optimize the device morphology and digestion time, we have fabricated devices containing four individual microfluidic structures with different morphologies:(1) a meandering microchannel, (2) a microchannel with an incubation chamber with “big” pillars (Ø173 µm), (3) a similar chamber with “small” pillars (Ø35 µm) and (4) a control chamber similar to the other ones, but without pillars (Fig.1). The devices are fabricated by molding the PDMS via imprint lithography. For this, master stamps are fabricated using either electron beam lithography, photolithography followed by reactive ion etching to make positive stamps or by photolithography on SU-8 for negative stamps. Figure 1C and D show the micropillars in one of the PDMS devices, characterized by 3D-microscopy and profilometry.
After the fabrication of the devices, surface functionalisation for trypsin immobilation followed by protein injection for digestion is carried out in the sealed device. The Surface functionalisation and trypsin immobilisation was confirmed with water contact angle measurements and EDX analysis respectively (Fig. 2). For the initial optimization experiments BSA is used for digestion. The liquid sample was injected into the sample inlet of the device, using a pump it was pulled to the digestion chamber and after 15 min incubation, it was collected. Mass spectrometeric analysis was used to detect the tryptic peptides.

Our results demonstrate that integrating micropillars into the digestion chamber significantly enhances digestion efficiency, as evidenced by the increased number of tryptic peptides detected via MALDI-TOF analysis (Fig. 3). This enhancement is attributed to the larger immobilisation surface and improved convective transport facilitated by the micropillar architecture. Moreover, the immobilised trypsin retained enzymatic activity for up to one week when stored at 4 °C, supporting the device’s reusability and stability for proteomic applications.

References:
[1] Peterson et al., Anal. Chem. 74(16) 2002, 4081-4088. A.
[2] Kecskemeti et al., Prot. Clin. Appl. 11, 2017, 1700055.
[3] Klatt et al., Lab on a Chip 20(16) 2020, 2937–2945.
[4] Lazar et al., Anal. Chem. 92(1) 2019, 169–182.

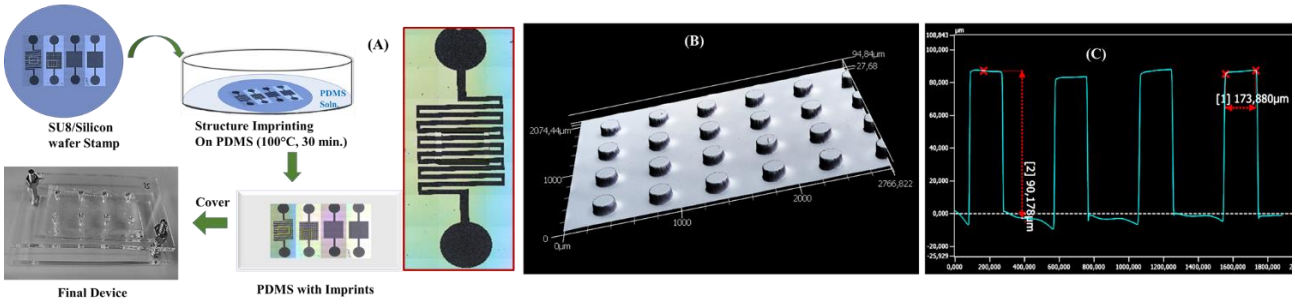

Figure 1. Overview of fabrication of the micropillar-based PDMS device and characterization of its topography. (A) Fabrication workflow starting from Si wafer with SU8 (negative photoresist) as working stamp for the microfluidic structure imprinting, magnified image of meandering str. (inset) (B) 3D-microscopic image of the device chamber with micropillars and (C) profile measurements of the PDMS micropillars.

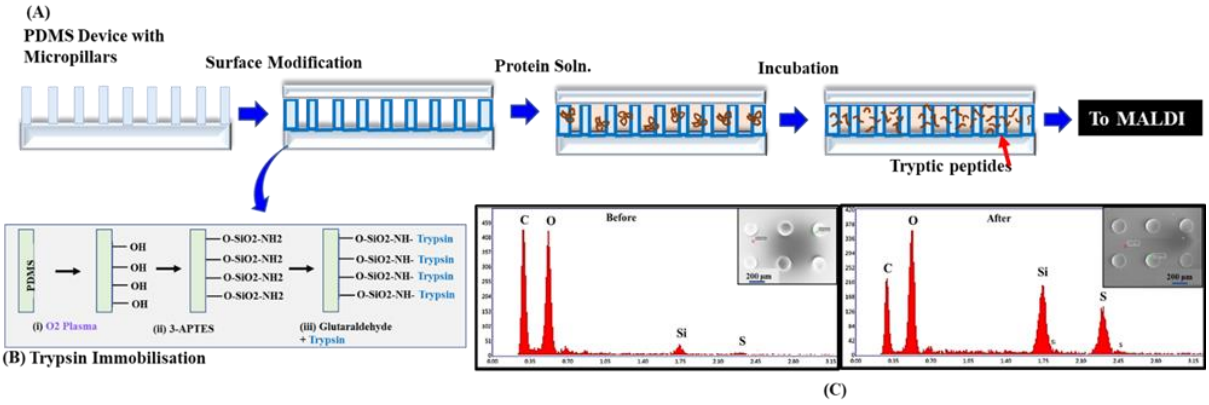

Figure 2. (A) Workflow of trypsin mediated digestion of proteins, e.g. BSA and illustration of method adopted for trypsin immobilisation on micropillars based device. (B) Schematic of surface functionalization: (i) activation with O2 Plasma, (ii) incubation with 3-APTES and (III) Crosslinking of trypsin via glutaraldehyde. (C) EDX spectra of the protein incubation chamber with micropillars before (left) and after trypsin immobilisation (right).

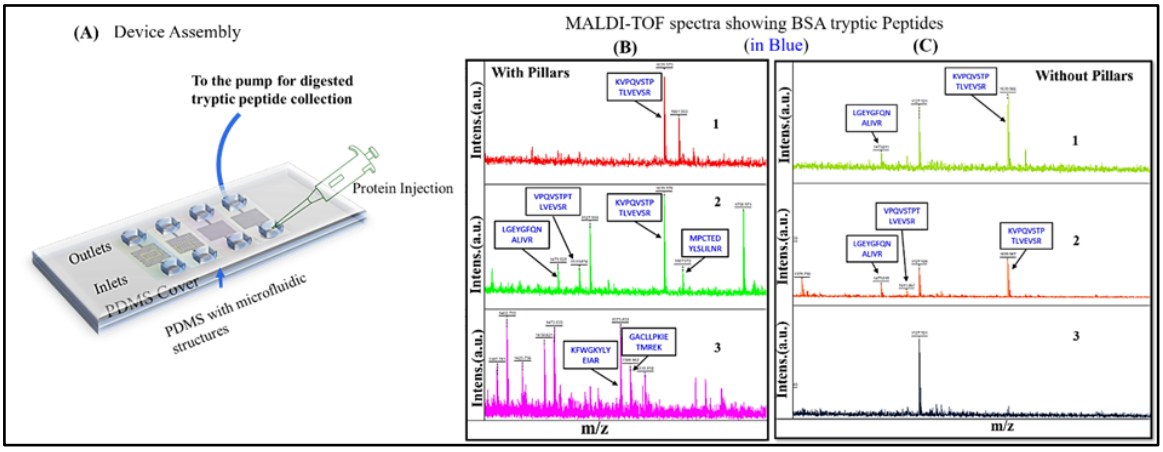

Figure 3. (A) Schematic of working PDMS device with four microfluidic structures (meander, big pillars, small pillars and no pillars), containing immobilised trypsin. MALDI spectra of the effluent of BSA passing the channel structures with big pillars (B) and without pillars (C).

Method for high phase accuracy trimming of MZIs via Ge ion implantation and electrical annealing

April M. Logan [a], Xia Chen [a], Xingshi Yu [a], Weihong Shen [a], Xingzhao Yan [a], Weiwei Zhang [a], Goran Z. Mashanovich [a], Graham T. Reed [a], David J. Thomson [a]
[a] Optoelectronics Research Centre, University of Southampton, Southampton SO17 1BJ, UK
e-mail: aml4g19@soton.ac.uk

Phase tuning is essential for many silicon photonic devices to correct phase errors that have occurred due to fabrication variations. Currently microheaters are commonly used to thermally tune devices however this requires a constant power to be supplied to the components, which makes it unattractive for large-scale circuits with many hundreds or thousands of components. Ge ion implantation and annealing is a method that can be used to create trimmable components in which the refractive index of the implanted waveguides can be permanently changed after fabrication, without requiring a constant power to maintain the tuning (it is non-volatile). This method is therefore also suitable for the creation of large-scale programmable circuits.

Ge ion implantation causes lattice damage to the crystalline structure of the silicon waveguide and at a certain implantation dose, it will become amorphous (as it is 100% damaged) which results in an increase of the refractive index to 3.96 [1]. Annealing the implanted silicon above 400°C, will cause the silicon to begin to recrystallize and its refractive index will start to decrease. Fully annealing at temperatures between 600°C to 700°C [2] allows the refractive index to be recovered (3.48). Therefore by partially annealing, it is possible to tune the refractive index across a range of values. Annealing can be done electrically (via microheaters fabricated on chip) or with a specialized laser setup. Trimming with microheaters can be carried out at the wafer scale [3] or after packaging each die and can be carried out in parallel, decreasing the time it takes to trim or program large circuits.

Localized sections of Ge ion implanted waveguides can be introduced in various components to make them phase trimmable or programmable, for example, ring resonators [3, 4] and directional couplers [5] but in this work MZIs (Mach-Zehnder Interferometers) were used (Figure 1). High trimming accuracy is important to ensure the desired phase can be closely reached. This work puts forward a method of electrical annealing using voltage pulses that provides a higher trimming accuracy than previously demonstrated (0.025π was demonstrated in [6] via laser annealing and $<0.01\pi$ was demonstrated in [3] via electrical annealing).

The method to electrically anneal the MZIs involved sending a series of voltage pulses to the microheater. Between successive pulses a voltage step was applied which was dependent on the average phase change brought about by the previous three voltage pulses as summarized in Table 1. Figures 2a and 2b show the accumulative phase change and the phase change between successive voltage pulses using this process respectively. Figure 2a also shows the voltage being applied across the microheater during the entire annealing process. Annealing began at a power of approximately 35mW and the device was fully annealed at a power of approximately 110mW.

Conclusion:
This work presents a method for annealing Ge ion implanted waveguides which can be used for phase trimming or creating programmable photonic components with high resolution of phase tuning. Using the developed electrical annealing process a minimum phase accuracy of 0.0054π was demonstrated, with potential for a much higher phase accuracy in the future.

[1] Yu et al, Journal of Lightwave Technology. 39, 15 (2022)
[2] Yu et al, Micromachines. 13, 291 (2022)
[3] Jayatilleka et al, Journal of Lightwave Technology. 39, 15 (2022)
[4] Milosevic et al, IEEE Journal Of Selected Topics In Quantum Electronics. 24, 4 (2018)
[5] Chen et al, Optics Express. 28, 12 (2020)
[6] Chen et al, Photonics Research. 5, 6 (2017)

Acknowledgments: EU Project DOLORES (101130178). Royal Society URF (UF150325).

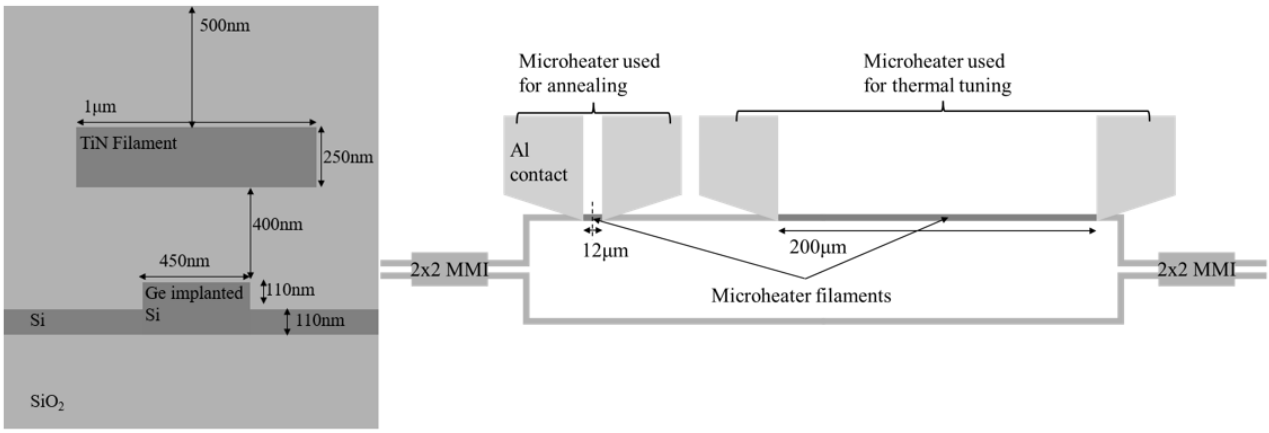

Figure 1. The cross-section (left) is taken at the dotted line on the diagram of the MZIs used in this work (right). The cross section is of a Ge ion implanted waveguide with a microheater filament above it. The MZI has two microheaters over its upper arm, the first is above a 12µm long implanted section of waveguide and is used for electrical annealing. The second (200µm) long microheater is above unimplanted waveguide and was used for thermal tuning.

Thresholds for the average phase change from the previous three voltage pulses, Δφ (radians)	The next voltage step (mV)
Δφ > 0.012	-1.2
0.012 > Δφ > 0.006	0
0.006 > Δφ > 0.001	0.6
0.001> Δφ	10

Table 1. Table displaying the thresholds for the average phase change brought about by the previous three voltage pulses that will determine what voltage step is taken next.

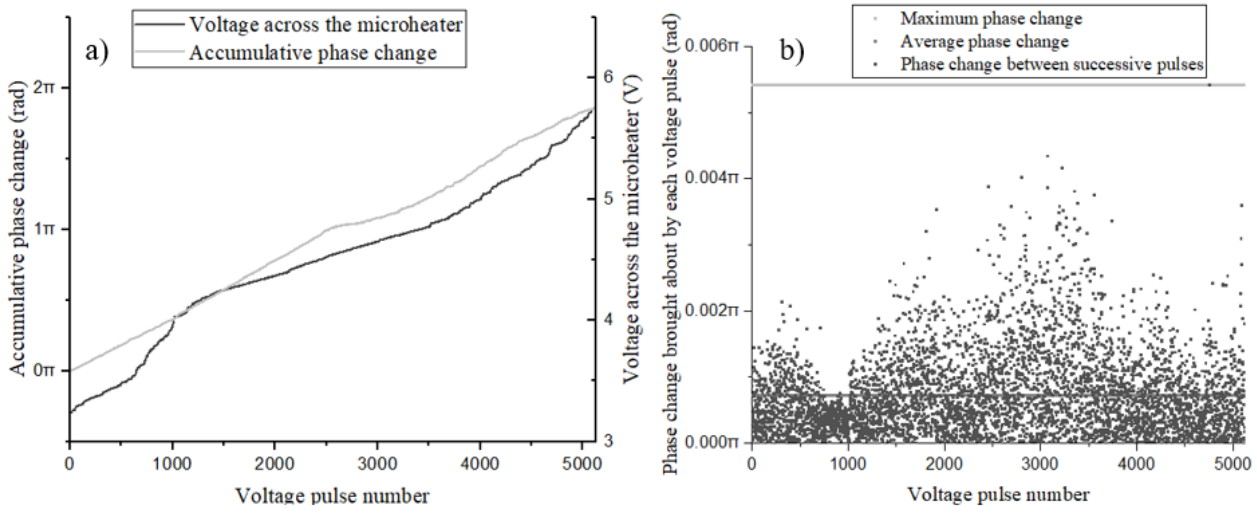

Figure 2. a) Graph showing the voltage being applied across the microheater (for electrical annealing) at each voltage pulse and the accumulative phase change being brought about by the annealing. **b)** Graph showing the phase change measured between successive pulses.

Microcavities to engineer dynamics in coupled *E. coli* oscillators

Kushal Swamy [a], Farbod Alijani [a]

[a] Delft University of Technology, Delft, 2628 CD, The Netherlands
e-mail: k.swamy@tudelft.nl

In this work, we engineered order out of the chaotic swimming dynamics of *E. coli* bacteria, taming their random motion and developing a platform that allows for phase synchronization of single *E. coli* cells [1]. Circular microcavities were used to isolate *E. coli* cells that swim along the cavity wall, resulting in self-sustained oscillations. Connecting these cavities by microchannels yielded synchronization patterns with phase slips. Previous studies have shown the presence of emergent nonlinear phenomena such as self-organization in confinement [2] and advances are being made in the construction of microfluidic devices for artificial microswimmers [3]. Our work supplements these observations, showing that spontaneous order can be engineered in microswimmers found in nature and can be controlled at the level of single cells.

To tame the Brownian motion of *E. coli* cells, we developed an assay made of circular PDMS microcavities of depth 2.5 μm and varying diameters. Initial molds were prepared from 500 μm thick silicon wafers with a 285nm thick layer of silicon dioxide. The wafers were patterned by electron beam lithography followed by reactive ion etching, resulting in a feature height of 2.5 μm for PDMS casting. Pre-polymer PDMS was mixed with curing agent in 4:1 ratio, stirred and then degassed in a vacuum chamber for 10–15 min. A small amount of PDMS was carefully dipped in the center of one of the structures of the patterned wafer and a 1mm thick, 22 × 22mm glass slide was placed on the droplet, spreading it over the patterned wafer structure. The assembly was subsequently baked at 90°C for 2.5h in an oven. Prior to baking, the silicon wafer was pre-treated with (Tridecafluoro-1,1,2,2-tetrahydrooctyl)trichlorosilane (FTS) to ensure that the PDMS mould could be easily released after it had been cured. The glass slide was carefully lifted from the wafer using a razer blade. The PDMS stuctures were then plasma treated at 20W power and 60mTorr oxygen chamber pressure for 30s in order to make them hydrophylic.

For an 8 μm cavity, the experimental process is illustrated in Figure 1. Measurements were carried out using an inverted microscope (Nikon Ti) under bright-field illumination, through a 100× oil-immersion objective. For imaging, ~35 μL cell culture was pipetted onto a prepared PDMS sample and placed on a coverslip holder. Then, a sample cover was placed over the PDMS sample, creating a sealed chamber. The assembly was placed inside a closed microscopic chamber maintained at 30°C. We found that *E. coli* cells that settled inside the cavities swam continuously in the clockwise direction along the cavity wall. Figure 1c,d shows a typical trace, where a single *E. coli* cell was swimming inside an 8μm microcavity with a linear speed of $v \approx 3.5\ \mu ms^{-1}$. It can be observed that the cell performs harmonic motion. This persistent periodic behavior was observed even up to 13 min in some cases, effectively making the *E. coli* cells behave as harmonic oscillators.

By devising sets of microcavities that were pairwise connected by channels, we showed that *E. coli* cells can coordinate their motion to neighboring cells, thus exhibiting coupled oscillatory behavior. The channels could be engineered to induce strong enough hydrodynamic coupling that led to rich dynamic phenomena, including slow-fast motion and synchronous oscillations in the presence of noise, as shown in Figure 2. We showed that the synchronization of these *E. coli* oscillators was due to hydrodynamic coupling forces caused by fluid exchange in the channel. In the future, by shape optimization of the microcavities and channels, to enhance the coupling strength, we envision that bacterial oscillators can evolve into large arrays of synchronous microbial matter with adjustable couplings, paving the way to controllable micro-organism-based oscillator networks and confined active matter.

[1] A. Japaridze, V. Struijk, K. Swamy, I. Rosłoń, O. Shoshani, C. Dekker, F. Alijani, Small 21 (2025) 2407832.
[2] D. Nishiguchi, I.S. Aranson, A. Snezhko, A. Sokolov, Nat. Commun. 9 (2018) 4486.
[3] P. Sharan, A. Nsamela, S.C. Lesher-Pérez, J. Simmchen, Small 17 (2021) 2007403.

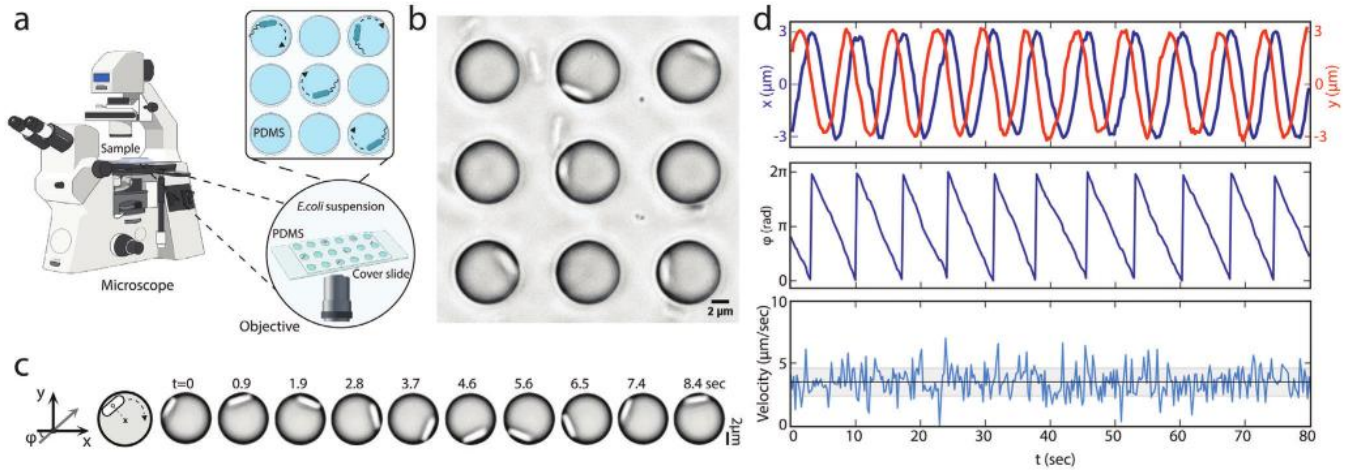

Figure 1. Measuring cell motility in confinement. a) Schematic of microscope setup for phase contrast imaging. b) Image of *E. coli* cells trapped in microcavities. c) Motion of a cell inside a microcavity (8µm diameter). Left schematic depicts the coordinate system. Right images show a time sequence of cell positions. d) Cell coordinates and velocity. Top traces indicate x (in blue) and y (in orange) coordinates versus time; middle shows the cell phase angle; bottom show the tangential velocity, with the black line indicating the mean speed and the grey area the standard deviation. [1]

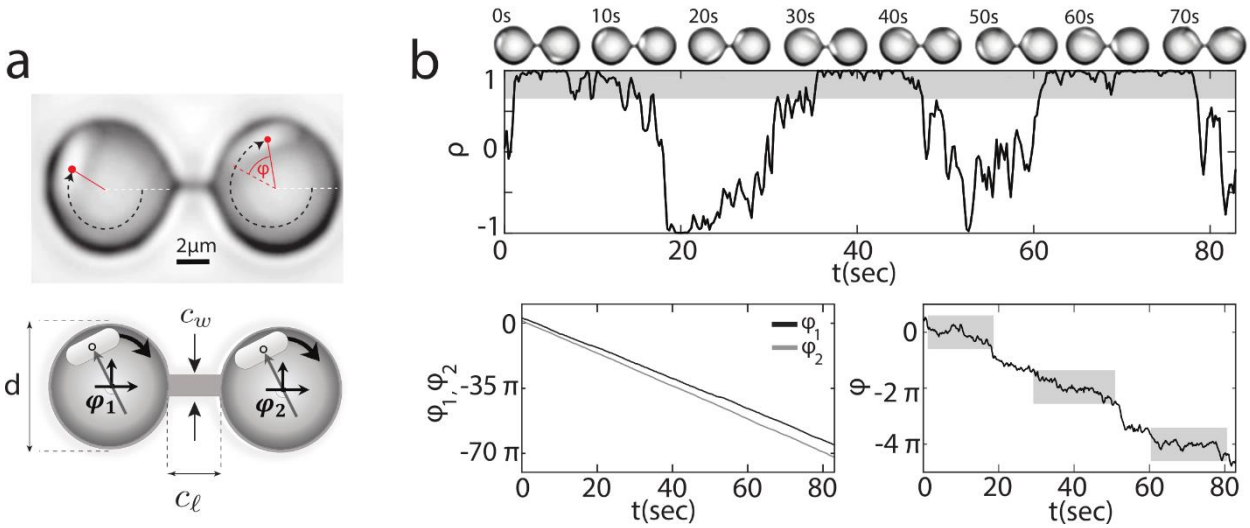

Figure 2. Coupled *E. coli* oscillators. a) Two identical circular microcavities of diameter d are connected with channels of length c_ℓ = 0.5,1,2 µm and width c_w = 0.5,0.7,0.9 µm. b) Strong coupling is observed for the bacterial motions for c_w = 0.5µm, c_ℓ = 0.5µm, where $\rho = \cos\varphi$ oscillates non-periodically with $\langle\rho\rangle \neq 0$. The phase difference φ shows slow-fast dynamics analogous to the motion of an overdamped particle with an alternating slow-fast speed on a washboard potential. Here, grey shaded windows show the phase-locked regions. [1]

Manipulation of Liquid Marbles via Triboelectric Charging

Yuan Hsuen Chou [a], Jiann Shieh [a]
[a] Department of Materials Science and Engineering, National United University, Miaoli, 36063 Taiwan

e-mail address: jshieh@nuu.edu.tw

Liquid marbles (LMs) are formed by encapsulating liquid droplets with a layer of hydrophobic particles [1]. Due to their non-wettability, mechanical stability, and ability to retain liquid, they have attracted significant attention. Their unique properties enable diverse applications in digital microfluidics, biosensing, and chemical microreactors. Although various external stimuli—including gravity, vibration, magnetic fields, electric fields, and heat [2]—have been employed to manipulate LMs, electrostatic-based approaches remain relatively underexplored. Electrostatic charges generated through triboelectric effects offer a simple, energy-efficient, and remote method for driving liquid marbles, without the need for electrode fabrication. In our previous work, we observed that the small electric charges present on pure water droplets could cause mutual repulsion on superhydrophobic glass surfaces [3]. We also demonstrated that triboelectric charging can effectively induce rapid droplet motion [4]. Building on these findings, here we propose a novel method for manipulating LMs using triboelectricity. By introducing a charged PTFE rod, we demonstrate controllable manipulation of LMs on a superhydrophobic glass surface. These results offer a new perspective on non-contact control of LMs and pave the way for simple and scalable manipulation strategies in open-surface digital microfluidics.

The superhydrophobic glass was fabricated by growing silica nanowires on its surface, followed by modification with F_{13}-TCS silane [5]. This treatment resulted in a contact angle greater than 150°, enabling LMs to move with minimal resistance. LMs were created by rolling deionized water droplets on the surface dispersed with 5-μm PTFE particles, as shown in Figures 1a and 1b. For LMs smaller than 15 μL, the sliding angle remained constant at approximately 4.5°, regardless of size (Figure 1c) [6]. However, as the LM volume increased beyond this threshold, the sliding angle decreased—a trend commonly observed in water droplets rolling on inclined surfaces.

The charge carried by the LMs was measured using a nano-Coulomb meter (Figure 1d), revealing a net positive charge. Interestingly, the charge decreased with increasing LM size, likely due to the growing influence of negatively charged PTFE particles. As a result, LMs can be manipulated using a negatively charged controller. To generate such a charge, a PTFE rod was rubbed against a glove (Figure 1e), reaching charge saturation within 5 seconds—significantly exceeding the charge carried by the LMs. This allows effective manipulation via Coulomb's law, enabling the LMs to follow the movement of the PTFE rod (Figure 1f).

We demonstrated two examples of LM manipulation. First, two 5-μL LMs were guided and merged into a single 10-μL LM. Since their sliding angles were similar (Figure 1b) but the charge approximately doubled (Figure 1c), the resulting larger LM remained controllable, as shown in Figure 1g. Second, we showed that LMs could be manipulated from the backside of the glass (Figure 1h). These results confirm that LMs can be effectively controlled using triboelectric charges, supporting the advancement of LM-based applications.

REFERENCES

[1] P. Aussillous, D. Quéré, Liquid Marbles, Nature 411 (2001) 924.
[2] T. Tong, H. Hu, Y. Xie, J. Jin, Droplet 4 (2025) e160.
[3] K. T. Chen, Y. P. Wu, Y. F. Huang, C. C. Hsu, and J. Shieh, Langmuir 40 (2024) 13219.
[4] W. C. Huang, M. Y. Chang, J. Shieh, C. H. Lin, C. C. Hsu, Adv. Mater. Interfaces (2025) in press.
[5] J. Shieh, G. F. Huang, J. Y. Tsai, B. W. Huang, Y. F. Huang, STAR Protocols 3 (2022) 101066.
[6] P. Jin, K. Zhao, Z. Blin, M. Allais, T. Mouterde, D. Quéré, J. Chem. Phys. 158 (2023) 204709.

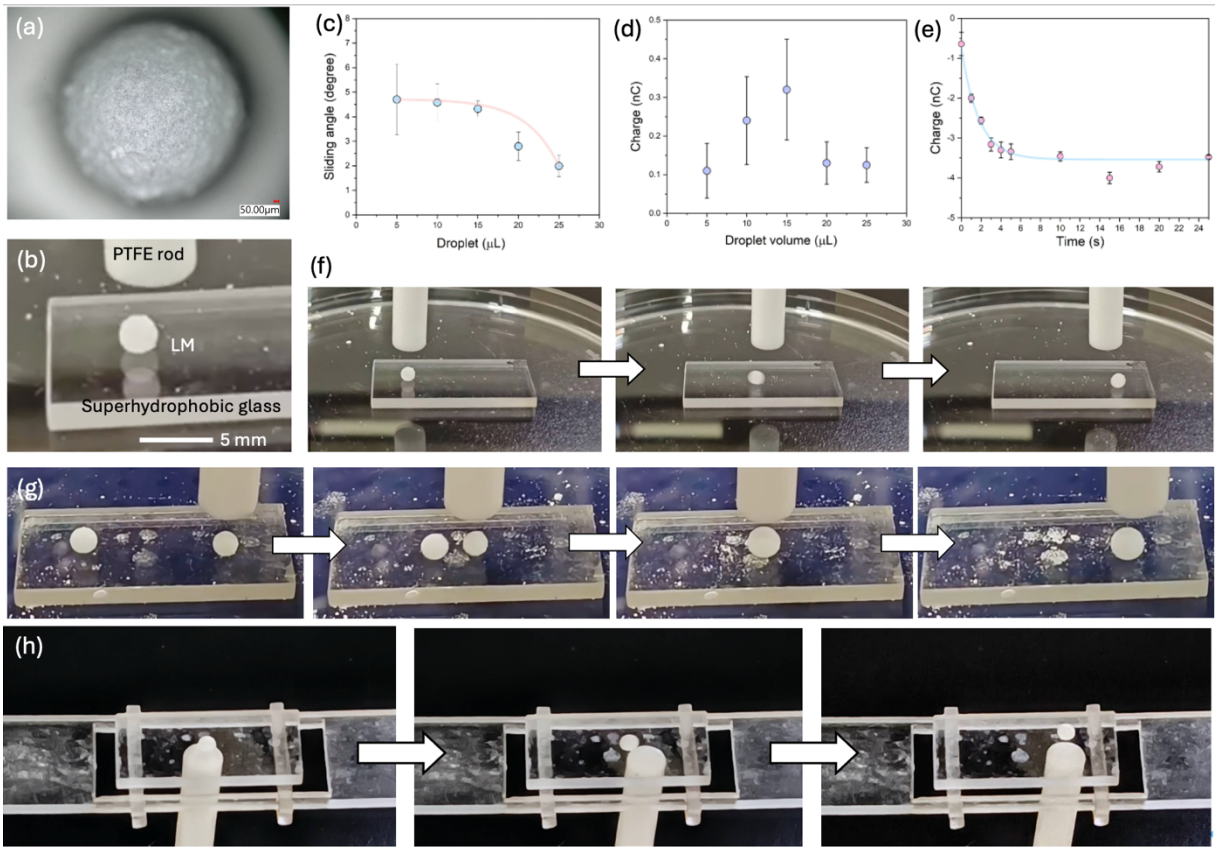

Figure 1. (a) OM image of a LM. (b) Photograph of a LM resting on the superhydrophobic glass surface. (c) Sliding angles of LMs with varying volumes. (d) Measured charge carried by LMs of different sizes. (e) Accumulated charge on a PTFE rod as a function of rubbing time. (f) LM moves follows the guidance of a PTFE rod. (g) Sequential images showing the merging of two LMs guided by a PTFE rod. (h) Demonstration of LM manipulation from the backside of the superhydrophobic glass.

An Extrusion Printed Lorentz Force Actuated Electromechanical Relay

Desmond Lagace[a], Cyrus Shafai[a]
[a]Dept. of Electrical and Computer Engineering, University of Manitoba, Winnipeg, MB, Canada
e-mail: lagaced1@myumanitoba.ca

Keywords: *printed electronics, flexible electronics, relay*.

Abstract: This work presents a millimeter-scale microelectromechanical (MEM) relay fabricated via extrusion printing techniques. The proposed relay features double-sided extrusion printing of silver conductive ink on a polyimide substrate. It utilizes a spring-suspended Lorentz actuator crossbar released via laser micromachining on one side and a relay contact on the other. This method of fabrication realizes a rapidly manufacturable and low-cost alternative to traditional lithographic processes used for MEMS development. The relay exhibits comparable, and, in some cases, superior performance metrics compared to commercially available relays, including switching time, power consumption, contact resistance, and maximum dc load current.

Materials/Methods: The relay utilizes a crossbar Lorentz actuator (see Fig 1) suspended by two folded-beam springs [1] to actuate a normally-open relay contact. For a crossbar of length L carrying current i in the presence of static magnetic flux density B, the force on the crossbar is given by:

$$\overrightarrow{F_L} = L\left(\vec{\imath} \times \vec{B}\right) \quad (1)$$

which simplifies to $F = iLB$ when $\vec{B}$ and $\vec{\imath}$ are normal to each other. This force is balanced by the spring restoring force given by Hooke's law:

$$F_S = k\Delta z = iLB \quad (2)$$

where k is the spring constant and Δz is the displacement of the crossbar. Crossbar length, spring geometry, and actuation current were chosen such as to maximize deflection given the constraints of the extrusion printing process and the available permanent magnets. Fig 2 shows the structure of the device. The top layer contains a 10 mm Lorentz actuator crossbar which carries the actuation current and handles the deflection of the relay. The bottom layer contains a contact pad and lead which strikes a fixed pad placed below the device to close some connection. This design was simulated in COMSOL Multiphysics and yielded a resonance of 27 Hz and deflection of roughly 1 mm for 100 mA actuation current in a 0.2 T field. Joule heating effects were also examined and deemed negligible for actuation currents below 500 mA. The relay was then fabricated using a Voltera NOVA [2] electronics extrusion printer, with dispense pressure 700 (arb. units) and dispense speed 650 mm/min (see Fig 3). Voltera Conductor 3 silver ink [3] was printed on one side of 25 μm polyimide film for the crossbar, cured for 5 min at 120 °C, flipped, printed on again for the relay contact, and then cured for 15 min at 120 °C. The actuator was then released using a laser micromachining tool with a 335 nm, 1.6 mW laser. The fixed relay contact was printed similarly on FR4 circuit board material, including a small dollop of ink roughly 150 μm in height to aid in contact. Fig 4 shows the complete device.

Results: The relay was tested for metric such as switching time, power consumption, contact resistance, dc load current, and resonant frequency using 100 mA actuation current and 0.2 T field. Table 1 shows the results, along with some commercially available relays. Compared to a commercially available electromechanical relay [4], this work exceeds in regard to power consumption and switching time, with values of 36 mW and 0.5 ms, respectively. For a commercially available solid-state optoelectronic relay [5], this work benefits in max dc load current (210 mA), and has comparable contact resistance and switching time. This work shows that extrusion printing is a viable method for rapidly prototyping and fabricating MEMS devices.

[1] B. Park et al., Large displacement bi directional out-of-plane Lorentz actuator array for surface manipulation, J. Micromech., 27 (2017).
[2] Voltera Inc., NOVA - A flexible and printed electronics platform, www.voltera.io/products/nova.
[3] Voltera Inc., Conductor 3 technical datasheet, Rev. 2 (2023).
[4] Songle, SRD-05VDC-DL-C Datasheet.
[5] Littelfuse, CPC1017N Datasheet, Rev. A (2024).

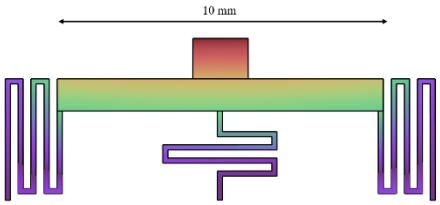

Figure 1. Crossbar Lorentz actuator suspended by folded-beam springs.

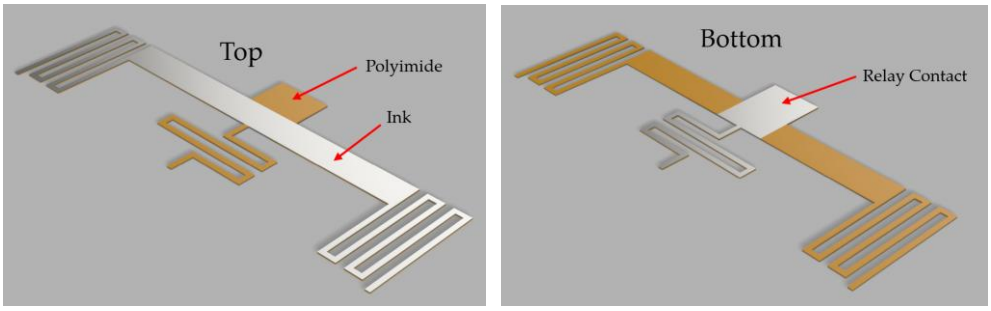

Figure 2. Two-layer structure of the device; top (left) and bottom (right).

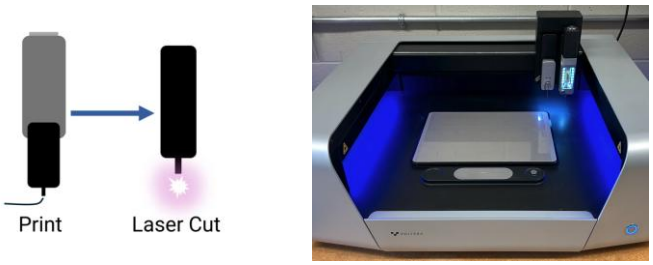

Figure 3. Voltera NOVA extrusion printer.

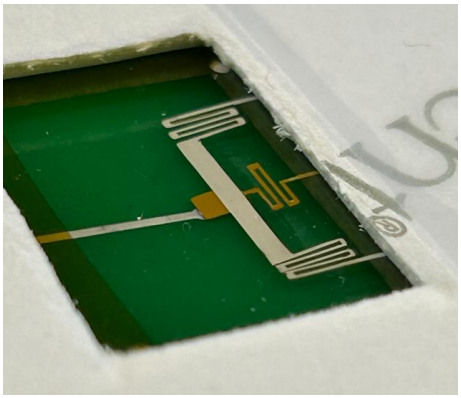

Figure 4. Released relay shown in complete test setup.

Table 1. Comparison of this work to other relays.

	Power Cons. (mW)	Switch Time (ms)	Contact Res. (Ω)	Max Current (A)
This Work	36	0.5	7.65	0.21
[4] (mech.)	450	10	0.1	10
[5] (solid-state)	0.5	1.2	7.1	0.1

Integrating Surface-Confined Molecular Motors into Microfluidic Platforms: Toward Automated, High-Throughput analysis of Actinomyosin in vitro motility Assays

Erichlandwehr, Tim[1,2]; Mieites, Veronica[3,4]; Teuber, Jeremy P.[1,5]; Nasri, Rukan H.[1,6]; Usaj, Marko[7]; Månsson, Alf[7]; Conde, Olga M.[3,8]; Fernandez-Cuesta, Irene[1,6]

[1] Institut für Nanostruktur- und Festkörperphysik, Universität Hamburg, 20146 Hamburg, Germany
[2] Deutsches Elektronen-Synchrotron (DESY), 22607 Hamburg, Germany
[3] University of Cantabria, Photonics Engineering Group, Spain
[4] Valdecilla Health Research Institute (IDIVAL), Cantabria, Spain
[5] Max Planck Institute for the Structure and Dynamics of Matter, 22457 Hamburg, Germany
[6] Hamburg Centre for Ultrafast Imaging, 22607 Hamburg, Germany
[7] Department of Chemistry and Biomedical Sciences, Linnæus University, Kalmar, Sweden
[8] CIBER-BBN, C. de Melchor Fernández Almagro, 3, Madrid, 28029, Madrid, Spain
e-mail: tim.erichlandwehr@desy.de

Lab-on-a-chip devices miniaturize complex laboratory functions onto portable platforms, with promising applications in biomedical diagnostics and environmental monitoring. However, implementing active, selective transport of nanoscale cargo independent of bulk fluid flow remains a major challenge.[1-3] We address this by integrating surface-adsorbed molecular motor systems with microfluidic channels capable of analyte capture and directed transport. Myosin motors bound to hydrophobic surfaces propel actin filaments (AFs), which are partially biotinylated (5–20%) to enable the transport pick-up of biotinylated cargo—such as fluorescently labeled DNA oligos—via a biotin-streptavidin-biotin linkage (**Fig. 1**). To facilitate high-throughput and reproducible surface preparation, we developed and improved a rapid, gas-phase silanization protocol[4] using silanes such as TMCS, FOTCS, and FDDTCS, achieving uniform hydrophobic functionalization of silicon-based glass or polymeric substrates in under 10 minutes. The successful functionalization was assessed via AFM and water contact angle (WCA) measurements (**Fig. 2**). The resulting surfaces support robust AF motility, with average sliding velocities 3.5 ± 1.1 µm/s and motile filament ratios of up to 91% (**Fig. 3**). These conditions enabled reliable cargo capture without compromising filament motility—a key requirement for on-chip transport. Filament confinement was achieved using a fast UV-nanoimprint lithography process, producing polymeric microchannel structures in under two minutes. Motility was retained within these topographically and chemically defined channels, expanding the applicability of the system to complex chip geometries, fabricated in previous studies.[6,7] To address the longstanding bottleneck of low-throughput, manual filament analysis, we implemented an automated analysis pipeline capable of tracking hundreds of filaments per assay (**Fig. 4, Fig. 5**). IVMAs analyzed in this way were performed on different surface coatings and at different temperatures. This workflow was benchmarked against manual annotations and provides scalable, unbiased quantification of filament motility and cargo interaction. Automation significantly boosts statistical power, facilitates quality control of protein preparations and surface treatments, and enables rapid feedback during assay development. This integration of functional bio transport with microfluidic structures together with high-throughput analysis, lays a foundation for scalable, surface-based diagnostic systems that merge molecular precision with robust, unbiased data acquition.

REFERENCES:

[1] M. Persson, 1 Maria Gullberg, C. Tolf, A. Michael Lindberg, A. Månsson, A. Kocer "A Transportation of Nanoscale Cargoes by Myosin Propelled Actin Filaments," PLoS One. 8(2), Feb 21st 2013.
[2] P. Surendiran, C. R. Meinecke, A. Salhotra, G. Heldt, J. Zhu, A. Månsson, S. Diez, D. Reuter, H. Kugler, H. Linke, and T. Korten, "Solving Exact Cover Instances with Molecular-MotorPowered Network-Based Biocomputation" ACS Nanosci. Au June 23rd 2022, 2, 5, 396–403.
[3] A. Salhotra, J. Zhu, P. Surendiran, C. R. Meinecke, R. Lyttleton, M. Ušaj, F. W. Lindberg, M. Norrby, H. Linke, A. Månsson, "Prolonged function and optimization of actomyosin motility for upscaled network-based biocomputation", New Journal of Physics, 23(8), 085005, Aug 16th 2021.
[4] F. W. Lindberg, M. Norrby, M. A. Rahman, A. Salhotra, H. Takatsuki, S. Jeppesen, H. Linke, A. Månsson "Controlled surface silanization for actin-myosin based nanodevices and biocompatibility of new polymer resists", Langmuir, 34(30), 8777-8784, July 3rd 2018.
[5] Esmek, F. M., Grzybeck, P., Nasri, R., Tiwari, S. & Fernandez-Cuesta, I. Flow Behavior Characterization of DNA Molecules in Passive Nanofluidic Devices†. IEEJ Transactions ElecEngng 19, 840–844 (2024).
[6] F. M. Esmek, T. Erichlandwehr, D. H.B. Mors, M. Czech-Sioli, M. Therrem, T. Günther, A.Grundhoff, N. Fischer, I. Fernandez-Cuesta "Real time, in-line optical mapping of single molecules of DNA", Bios and Bioel X, 9, 2021.
[7] Müller, M. et al. Suspended Nanochannel Resonators Made by Nanoimprint and Gas PhaseDeposition. in 2023 IEEE 36th International Conference on Micro Electro Mechanical Systems (MEMS), 2023, 1041–1044.

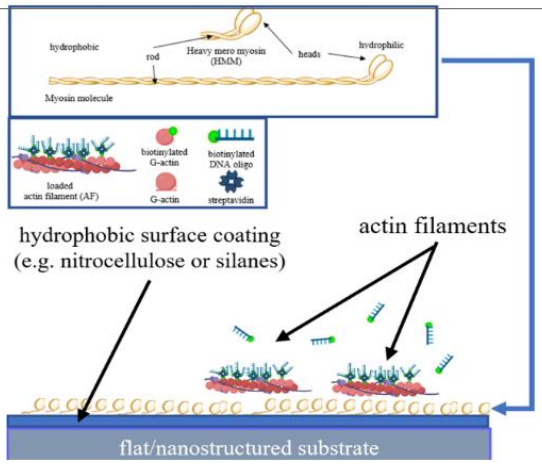

Fig. 1 Schematic of basic cargo capturing platform. The substrate surface is coated with myosin II subunit heavy mero myosin (HMM). These molecules are produced by digesting full myosin II molecules with α-chemotrypsin and bind actin filaments, which can capture biotinylated cargo after incubation with streptavidin.

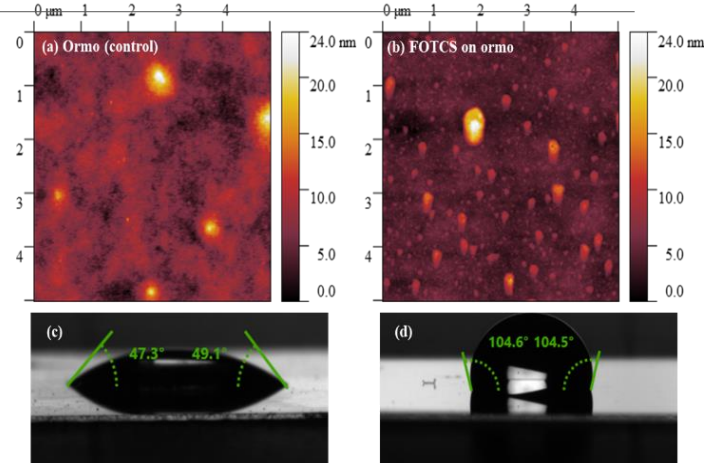

Fig. 2 (**a**) Atomic force microscopy (AFM) images of Ormostamp (polymer) surfaces without coating (RMS = 1.3 nm) and (**b**) functionalized with FOTCS (RMS = 2.8 nm). (**c**) WCA measurements on an Ormostamp surface without coating and (**d**) after functionalization with FOTCS.

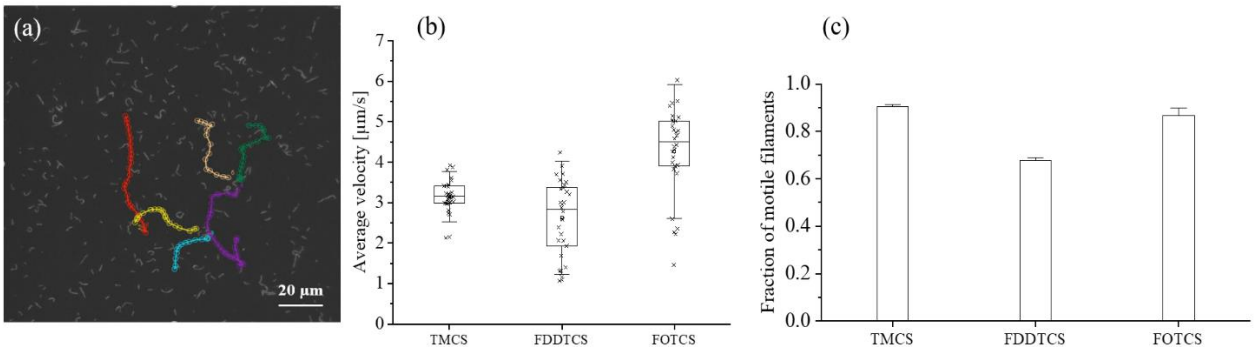

Fig. 3 (a) Manual motility analysis of filaments via evaluation of sliding tracks of individual actin filaments performed in Imagej (using theplugin MtrackJ). **(b)** Box-plot of average sliding velocities of 30 actin filaments,where the box gives the middle two quartiles of the data, the central line represents the median. (**c**) Fraction of motile filaments measured on glass surfaces functionalized with three different silane compounds using the gas phase deposition method. Data and error bars in (c) represent the standard deviation from average of three individual samples. IVMA performed at 22°C.

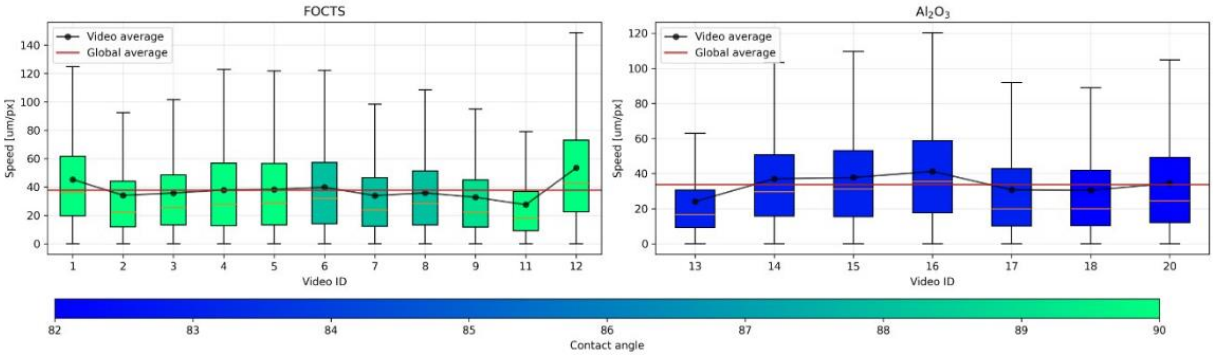

Fig. 4 Box-plots of 20 individual experiments on 2 different surface coatings (FOTCS and Al_2O_3), showing average speed between different experiments, while taking hundreds of filaments into account. IVMAs performed at 22°C.

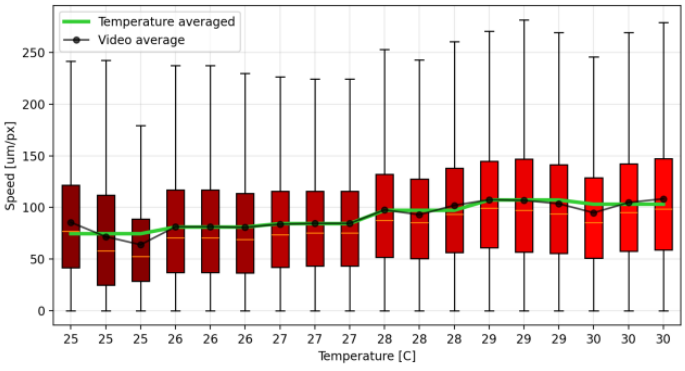

Fig. 5 Box-plots of average sliding velocities of all actin filaments in the FOV (>100) at different temperatures to benchmark against manual analyiss. IVMAs were performed at temperatures between 25 and 30°C. Per temperature three independent IVMAs where performed.

Tuning fork optomechanical NIR antenna with integrated optical transmission line

Daniyal Khosh Maram[a], Xavier Borrisé[b], Joan Garcia[a], Raul Ruiz[a], Xavier Cartoixà[a], Gabriel Abadal[a]
[a] Departament d'Enginyeria Electrònica, Universitat Autònoma de Barcelona, 08193-Bellaterra, Barcelona, SPAIN
[b] Catalan Institute of Nanoscience and Nanotechnology (ICN2) and Barcelona Institute of Science and Technology (BIST), Barcelona, SPAIN
e-mail: Daniyal.Khosh Maram@uab.cat

MEMSTENNAS merge radiofrequency (RF) antennas with electrostatic microactuators to directly convert microwave power into mechanical motion, eliminating local power sources [1]. While promising for wireless relays, IoT wake-up circuits, and batteryless sensors, their RF operation restricts use in optical/nanophotonic systems. Recent advancements introduced NEMSTENNAS, employing plasmonic nanoantennas and microcantilevers to transduce near-infrared (NIR) radiation into mechanical deflection via nonlinear electrostatic forces in the antenna feed gap, enabling remote actuation without on-chip power [2]. Challenges associated to fabrication complexity (precise alignment of dual cantilevers), or to detection of limited displacement from vertical deflection still remain to be addressed. Additionally, impedance-matched nanophotonic transmission lines will be eventually needed to efficiently transfer induced voltage at the antenna feed gap to a rectifier [3]. Here, we present a redesigned NEMSTENNA architecture that simplifies fabrication and enhances performance (Fig1.a). Unlike previous vertical deflection designs, our device employs a dual nano-cantilever with lateral displacement in a tuning fork configuration, eliminating two-component alignment. A monolithic optical transmission line (OTL) patterned on the nano-cantilever based tuning fork has been defined in a Au(35nm)/Si_3N_4(600nm) bilayer substrate. The length of the nano-cantilever tuning fork which constitutes at the same time the OTL is L_{Arm}. An adjacent Au/Si_3N_4 nanodipole antenna with length and width L and W respectively, designed to resonate at 1.55 µm, is coupled to the OTL (Fig1.a). The separation between both nanodipole arms, g_0, defines the size of the feed gap and is kept constant along the whole OTL length. When a 1.55 µm IR laser beam is focused in the nanoantenna, the electric field of the EM radiation is enhanced in the nanoantenna feed gap and propagated along the OTL, inducing a voltage associated to this electric field. This voltage, V, results in an electrostatic force, F_{ee}, that contains a DC component due to the nonlinear dependence of F_{ee} on V, inducing an attraction between the two nano-cantilever components of the tuning fork and their corresponding lateral deflection (Fig1.b). The tuning fork's nanoscale features are defined via a 6-step nano-milling process based on Focus Ion Beam (FIB) lithography as described in Fig. 2: a) The OTL gap is opened by etching a trench 150–200 nm wide at 50 pA and 30 kV, b) Same dose and energy are used to remove material in the nanoantenna region and prepare the feed gap final cut. c) two steps, with 300 pA for etching and 50 pA for polishing are used to define the nanocantievers of the OTL/tuning fork structure. d) Resolution is increased by stepping up magnification to more than 1000X and reducing current to 2 pA to define the feed gap of the nanodipole antenna. e-f) An etching step again at 50 pA allows to fine-tune length (L) and width (W) of the nanodipole antenna. SEM images of Fig2.g confirm well-defined nanoscale gaps and structural integrity, validating the FIB based strategy. A COMSOL model of the NEMSTENNA has been used to predict the electromagnetic and mechanical deflection response. The RF Module resolves near-field enhancement in the feed gap, while a electrostatic-mechanical coupled study calculates DC electrostatic forces from induced voltages, predicting lateral motion of the structure. The COMSOL simulation considers a 1.55 µm IR Gaussian beam focused in an 8 µm spot radius with scattering boundary conditions and PMLs to minimize reflections. A fine mesh near the feed gap/nanoantenna resolves field gradients, while coarser meshes optimize computational efficiency. Resonance peaks occur when the dipole length approximately matches half or full effective wavelength of the EM waves propagating in the nanodipole metal-on-dielectric medium (Fig3.a), maximizing V_{gap} at 1.55 µm. Reducing the feed gap, g_0, from 100 nm to 10 nm enhances the electric field at the nanodipole feed gap ($E_{x,gap} = 3 \cdot 10^6$ V/m) (Fig3.b), but reduces OTL transmission (Fig. 3c) as indicated by a shortening of the transmission line decay length. Conversely, larger gaps offer better transmission, i.e. larger decay lengths, with lower field enhancement at the feed gap. On the other hand, field profiles show minimal fluctuations of $|E_x|$ along the mid-OTL, while impedance mismatch at the termination induces standing waves oscillations of $|E_x|$ (Fig. 3c). Finally, stronger $E_{x,gap}$ in narrower gaps generates higher voltages, V_{gap}, and higher electrostatic forces, enabling larger lateral deflections. Besides, the contribution of the OTL to the attractive electrostatic force improves the actuation response. Thus, when the power of the laser source is increased to 7.5 mW, corresponding to our experimental setup limit, and focused in an 8 µm spot radius on a 100 nm gap NEMSTENNA, a lateral displacement up to more than 13 nm is expected (Fig3.d). Optimizing gap size and dipole length is essential to balance enhancement and transmission for efficient NIR actuation and sensing. This work was funded by Spain's Ministerio de Ciencia e Innovación under Grant No. PID2021-127840NB-I00 (MICINN/AEI/FEDER, UE).

[1] R. Ruiz, J. Bonache, and G. Abadal, Sensors Actuators A Phys. 340 (2022), 113536.
[2] D. K. Maram, X. Borrisé, J. Garcia-Garcia, R. Ruiz, X. Cartoixà, and G. Abadal, Micro Nano Eng. 23, (2024), 100241.
[3] J. S. Huang, T. Feichtner, P. Biagioni, B. Hecht, Nano letters 9(5), (2009), 1897-1902.

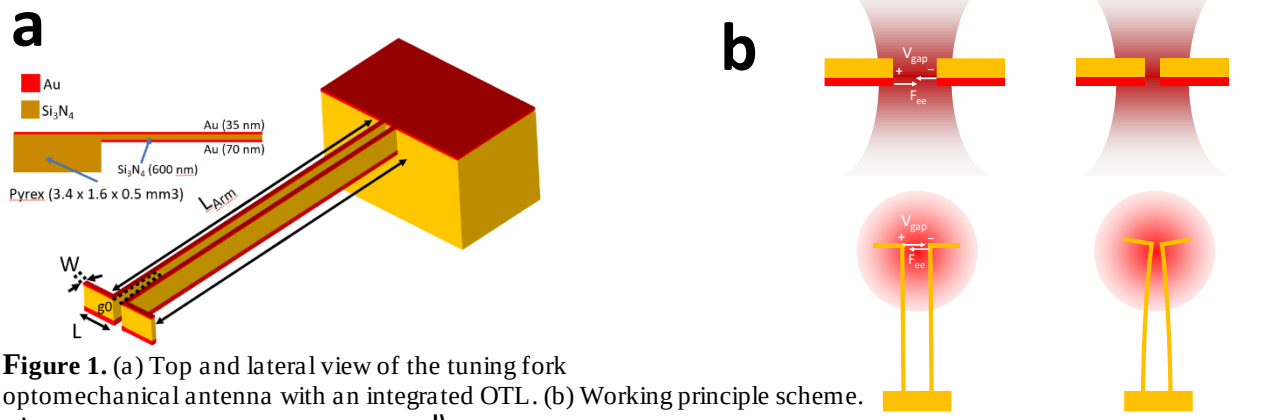

Figure 1. (a) Top and lateral view of the tuning fork optomechanical antenna with an integrated OTL. (b) Working principle scheme.

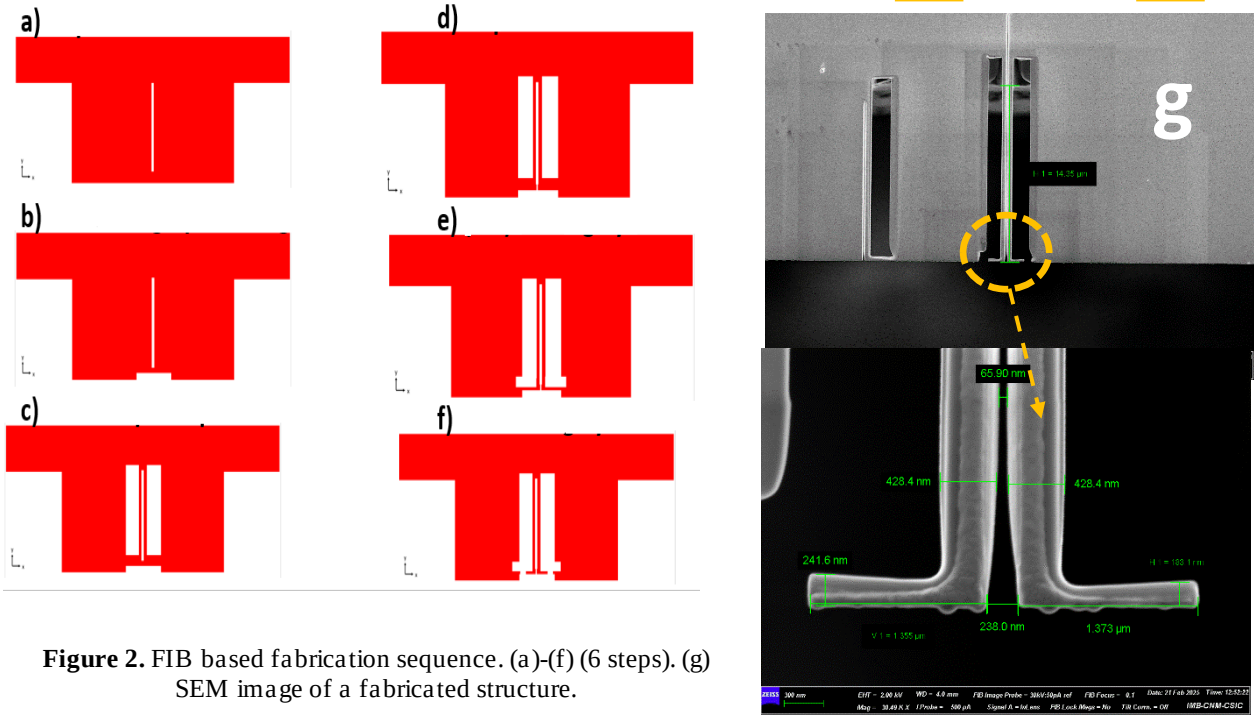

Figure 2. FIB based fabrication sequence. (a)-(f) (6 steps). (g) SEM image of a fabricated structure.

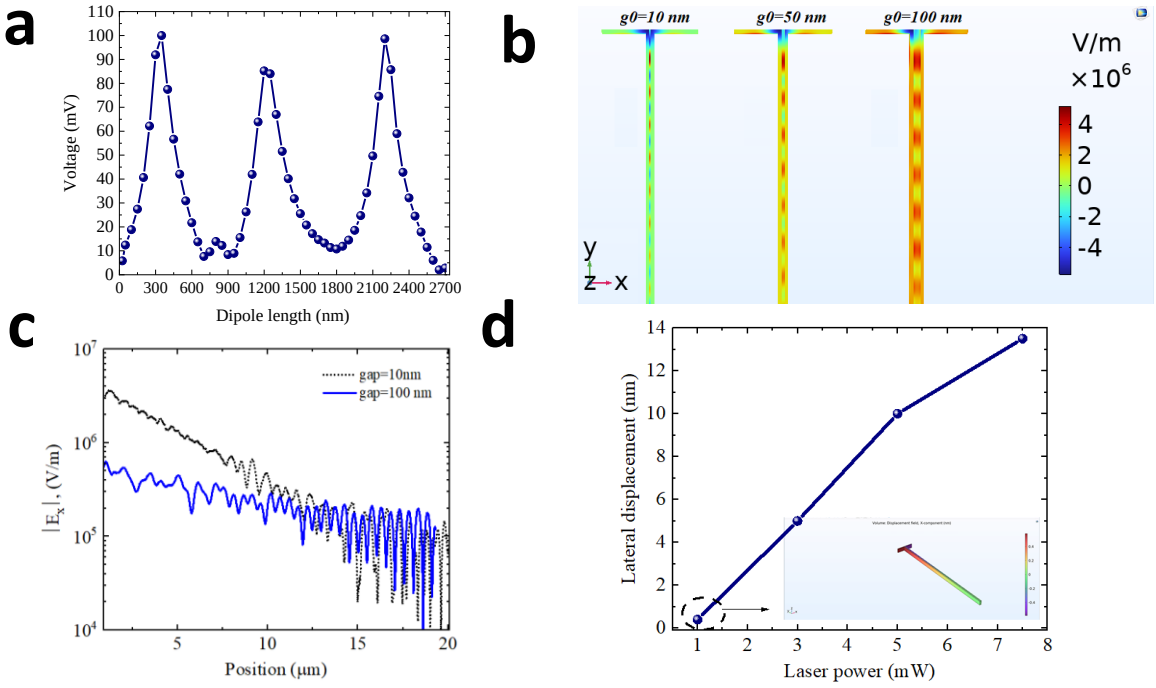

Figure 3. (a) Vgap vs. nanodipole length, (b) color map of E_x, (c) profile of E_x magnitude ($|E_x|$) vs. y position for different, gap distances for g_0=10 nm and g_0=100 nm and (d) lateral displacement with OTL contribution vs. laser power.

Low-Temperature Deposition of Metal Chalcogenides via Single-Source Precursors for Flexible Electronics

Sayali Harke [a], Suprabha Dixit [a], Chitra Gurnani [a], Ruomeng Huang [b], Omesh Kapur [b]

[a] Department of Chemistry, Ecole Centrale School of Engineering, Mahindra University, Hyderabad-500043, India
[b] School of Electronics and Computer Science, University of Southampton, Southampton SO17 1BJ, UK
e-mail: chitra.gurnani@mahindrauniversity.edu.in

Abstract
The development of neuromorphic and flexible electronic systems requires memory devices that combine low energy consumption, scalability, and mechanical adaptability[1]. Memristors, resistive switching devices that mimic synaptic behavior, are at the forefront of this effort due to their capability to unify data storage and computation in a compact form[2]. However, fabricating high-performance memristive materials on flexible substrates remains a key challenge due to the limitations of conventional high-temperature processing methods.
Layered metal chalcogenides such as Bi_2S_3 and SnS_2 offer excellent switching properties, mechanical flexibility, and low activation energies, making them promising candidates for next-generation memory applications[3]. To overcome the scalability and thermal budget limitations associated with traditional deposition methods, we have employed a single-source precursor (SSP)-based *in-situ* solvothermal route to synthesize Bi_2S_3 and SnS_2 films at temperatures <200 °C. The use of $[Bi(S_2P(OC_3H_7)_2)_3]$ and $[Sb(S_2P(OC_3H_7)_2)_4]$ as SSPs provides controlled, stoichiometric film growth and is compatible with flexible and rigid substrates[4,5].
Bi_2S_3 films deposited on both Si/SiO_2 and polyimide substrates exhibit uniform nanocrystalline morphology and excellent resistive switching behavior. Memristor devices show reproducible bipolar switching with an ON/OFF ratio of *ca.* 30, low operation voltages, and endurance exceeding 60 cycles. Importantly, devices on flexible substrates retain their electrical performance under repeated bending, demonstrating robust mechanical flexibility[6]. Neuromorphic properties such as analog conductance modulation, long-term potentiation/depression, and paired-pulse facilitation were clearly observed and will be discussed. A simulated MNIST digit classification task will be performed to confirm the applicability of Bi_2S_3-based memristors for neuromorphic computing systems.
Moreover, Sb_2S_3 films were deposited on FTO substrates and integrated into memristor devices[4]. These devices demonstrated stable bipolar resistive switching characterized by high ON/OFF ratios, low switching voltages, and reliable endurance, as will be presented. Future work will target the deposition and integration of other metal chalcogenides to expand the scope of memory and neuromorphic computing applications, particularly for wearable and flexible electronic platforms.
These findings underscore the potential of SSP-derived metal chalcogenides for enabling scalable, low-temperature fabrication routes. The successful integration of Bi_2S_3 on flexible substrates, along with the promising resistive switching behavior of Sb_2S_3 on rigid platforms, establishes a strong foundation for next-generation intelligent memory and neuromorphic devices. Furthermore, this approach opens up avenues for exploring a broader class of metal chalcogenides[7], expanding the material landscape for high-performance, flexible, and energy-efficient computing technologies.

References:

(1) S. Yao et al., *Adv. Mater.* 2020, *32* (15), 1902343.
(2) B. Zhu et al., *Adv. Mater.* 2016, *28* (22), 4250–4265.
(3) Q. Zhang et al., *ACS Nano* 2021, *15* (2), 2165–2181.
(4) S. S. Harke et al., *Mater Adv* 2023, *4* (18), 4119–4128.
(5) S. S. Harke et al., *ACS Appl. Electron. Mater*. 2025, *7* (3), 1291–1304.
(6) S. S. Harke et al., *ACS Appl. Mater. Interfaces.* [Under communication].
(7) S. Dixit et al., *ACS Appl. Mater. Interfaces.* [Under preparation].

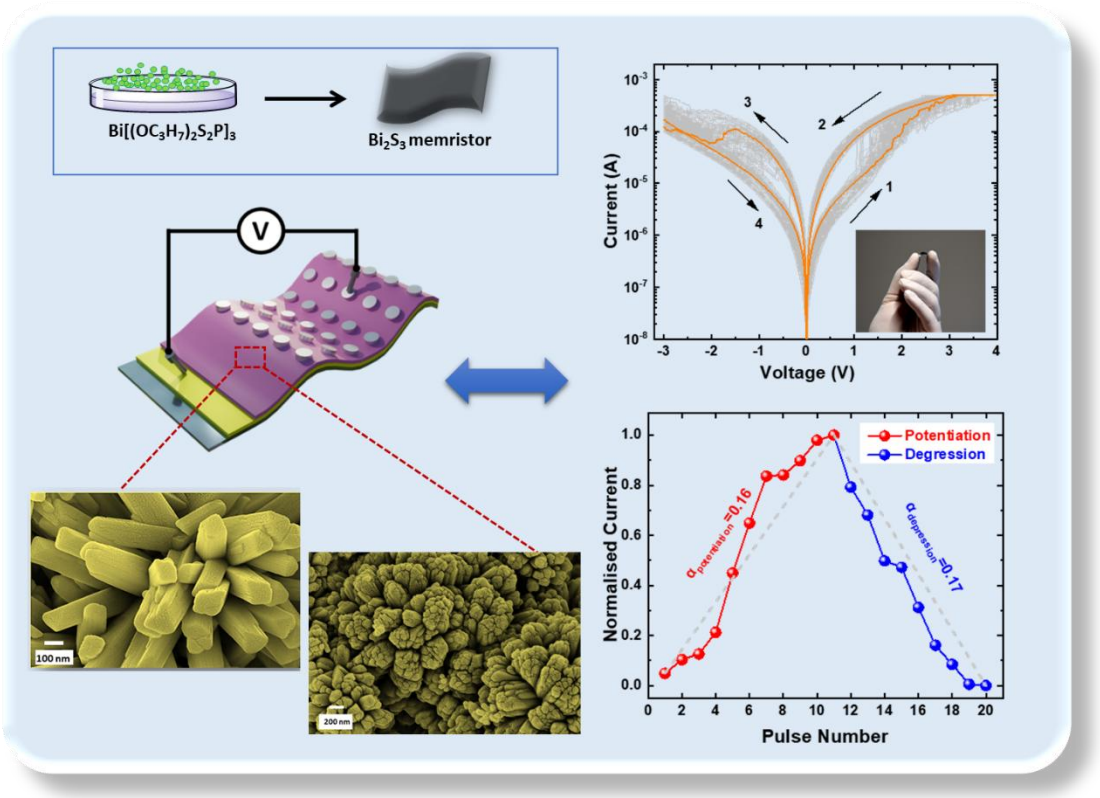

Figure 1. Single-source precursor enabled Bi_2S_3 nanostructures for resistive switching memristors and neuromorphic computing.

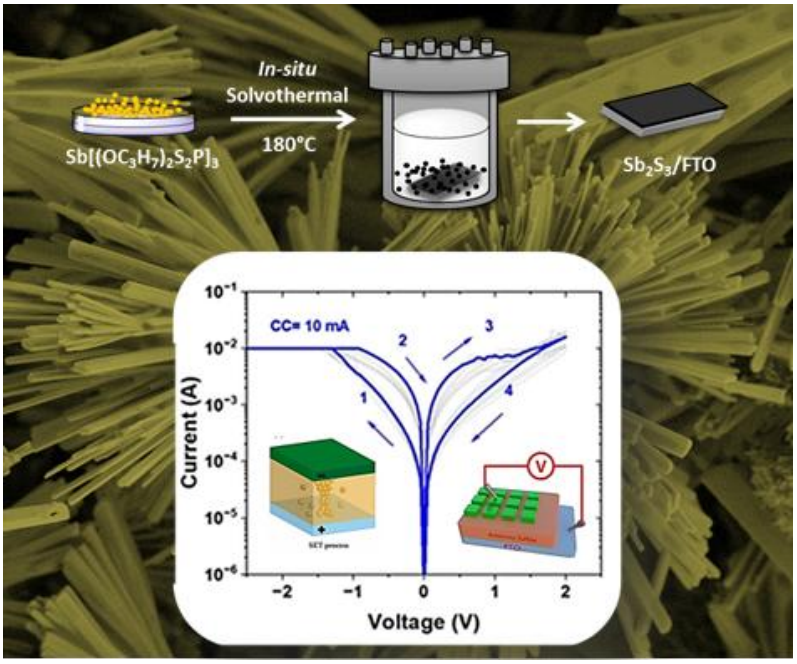

Figure 2. Single-source precursor enabled Sb_2S_3 nanostructures for resistive switching memristors.

Application of Integrated Electrode Fabrication Technique in Microfluidic lab-on-a-chip Devices for Single-Cell Analysis

Herbert Atrian Garcia [a,b], Louise von Lacroix [a,b], Irene Fernandez-Cuesta [a,b], Rukan Nasri [a,b]

[a] Universität Hamburg, Physics Department, Hamburg, 22761, Germany
[b] The Hamburg Centre for Ultrafast Imaging – CUI, Hamburg, 22761, Germany
e-mail: herbert.atrian.garcia@uni-hamburg.de

In this work we present the fabrication of a microfluidic device for the analysis of the mechanical properties of single cells (Figure 1 (a)) integrating microelectrodes with microfluidic channels. Cancer and healthy cells have different mechanical properties. For example, circulating tumor cells have been shown to be less stiff than epithelial healthy cells, meaning that they can contract and expand multiple times without cellular or membrane damage [1]. This increased deformability can be measured and the signal used to differentiate cancer cells apart from healthy ones, which offers useful insights into the heterogeneity of the cellular phenotype in a cell population, and, in addition, a great chance for diagnosis. In our device, the deformability of the individual cells will be tested as they flow along several microchannels and expansion chambers, to force them to squeeze and expand. And the signal will be measured electrically, by sensing the drop of electrical current as the cell flows through the channels, impacting the electrical current flow from the solution in which it is suspended (coulter counting). For this, we will use four gold electrodes integrated in the device, which should be in contact with the liquid. As the size of the cell changes in shape in the chambers, so will the obtained signal. For such sensitive measurements, it is crucial to have electrodes in close proximity to the microchannels, in direct contact with the liquid, and without leaking of liquid along the metal structures, to avoid noise and artifacts in the signal.

Our proposed device consists of two parts (Figure 1(b)): (1) the fluidic device with the microchannels and (2) the coverslip, with the electrodes. The fluidic device was fabricated in Ormostamp® via direct UV nanoimprinting by transferring the microchannel system design from a PDMS master mould. Flow-tests were conducted in the fluidic device with both fluorescent beads (Figure 3 (a,b)) and colon cancer cells (CaCo cell line, incubated in-house) to analyse both the flow path and speed and the behaviour of the cells as they travel the fluidic channel and expansion chambers (Figure 3(c,d)). To integrate the electrodes in the coverslip, we used a newly developed technique that facilitates the integration of the sensing components in the ultra-flat coverslips of the microfluidic device (Figure 1 (b))without compromising its biocompatibility, functionality nor surface roughness [2]. Furthermore, the technique allows to incorporate the metal structures without increasing the complexity of the fabrication of the fluidic device itself. Figure 2 (a) shows the fabrication process. The gold electrodes are structured first on a flat silicon substrate (coated with a fluorosilane film by CVD) by sputter coating, photolithography, and selective chemical wet etching. Then, a drop of Ormostamp® was casted on the substrate, a glass substrate brought on top and firmly pressed under heat until the complete structure was covered by the liquid polymer and then exposed to UV-light for 30 seconds for curing. The substrates can be separated, and the polymer coverslip with the embedded metal structures will stick to the glass substrate, thanks to the antiadhesion properties of the silane monolayer on the silicon. The coverslip can then be peeled from the glass and used for sealing the fluidic device. The thickness of the coverslip can be controlled by the temperature used before curing (Figure 2(b)). For these specific devices, we chose a temperature of 85 °C to achieve a coverslip thickness lower than 100 µm, since this is the most common working distance of objectives with high magnifications. Figure 2 shows the electrodes patterned on glass (d) and then transferred and embedded into the flat polymer coverslip (e). Profilometry and AFM images showed that the coverslip is completely flat, even while measuring at the polymer-gold interface, proving that the method yields relieve-free coverslips, suitable for leakage free liquid sealing [1]. The gold electrodes were used for electrical measurements, confirming that they can be used to detect changes in the conductivity of liquids. Figure 2(c)) shows IV curves for electrodes in a coverslip, where a drop of liquid with different ionic concentrations were placed in between them.

In summary, our work proposes a device consisting of two parts: the fluidic device with the microchannels and the coverslip, with the electrodes. With it, the deformability of the individual cells will be tested in the next steps as they flow along several microchannels and expansion chambers, to force them to squeeze and expand and the drop of the electrical current measured with the integrated electrodes. These results will be presented at the conference.

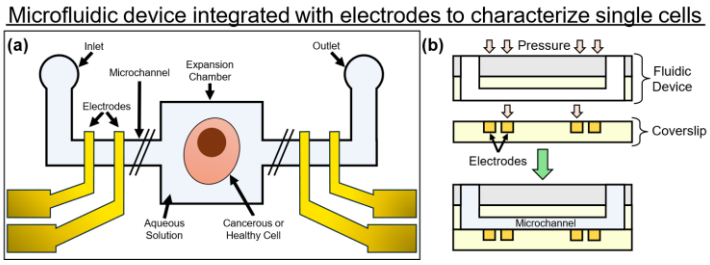

Figure 1. Schematical representation of the microfluidic device for single-cell analysis. (a) An aqueous solution containing cells is flown in the device. The cells get compressed inside a narrow contraction channel and then reaches the expansion chamber. The mechanical deformation of the cells can be measured electronically, using a coulter counter. The electric signal can be measured by using gold electrodes. (b) The microfluidic system was fabricated with Ormostamp® on an acrylic substrate and subsequently sealed with the functionalized coverslip, where the electrodes were embedded. This integration technique facilitates sensing applications on chip without compromising liquid confinement.

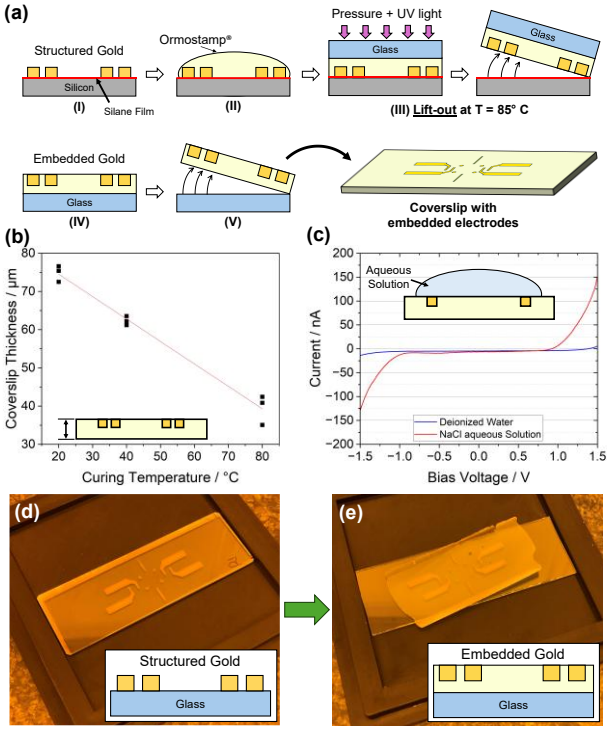

Figure 2. Integration of electrodes into a flat coverslip. The electrodes are first patterned on a substrate. Then, (II) a drop of liquid polymer was cast on the centre of the electrode design, (III) then a second glass substrate was pressed against the substrate where the electrodes were structured and cured with UV-light for 30 s at 85 °C. (IV) The top glass substrate was removed with the imprinted electrodes integrated in the polymer. The thickness of the polymer coverslip depends on the temperature used for baking just before the exposure and curing. (b) The curing temperature was chosen to obtain coverslips with a thickness < 50 um. (c) The electrodes are functional and measure different currents in solution with different ionic concentrations. (d) and (e) demonstrate the technique for embedding the structured gold in a coverslip (sealing component).

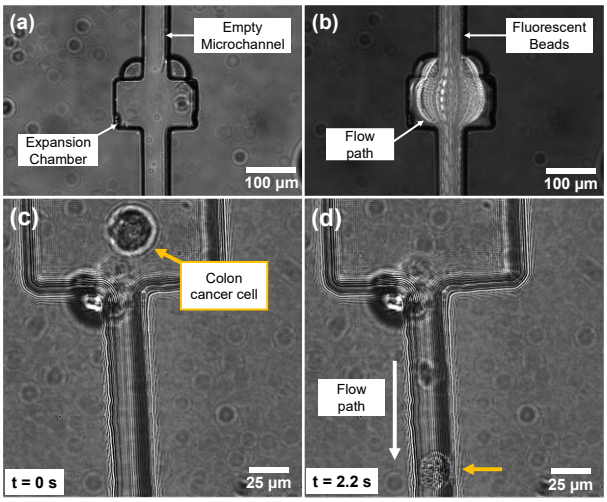

Figure 3. Flow-tests in microfluidic system with fluorescent beads and colon cancer cells (left) and sealing component (right). (a) and (b) show the path the fluorescent beads take when traveling through the contraction channel and expansion chambers. (c) and (d) display the mechanical deformation of a colon cancer cell as it navigates through the contraction channel.

[1] Swaminathan V, et al. *Mechanical stiffness grades metastatic potential in patient tumor cells and in cancer cell lines.* Cancer Research 2011; **71**: 5075–5080.

[2] Atrian-Garcia, H., Nasri, R., Fernandez-Cuesta, I. *Easy fabrication of functional coverslips with electrodes for micro- and nanofluidic lab-on-a-chip devices*. Presented at **MNE** 2024.

Preparation of Biocompatible Ag/Nylon Yarns Fabricated by Supercritical CO_2-assisted Ag Electroless Plating toward Weavable Devices

Tomoya Higashi[a], Tomoyuki Kurioka[a], Kazuhiro Shibata[a], Satoru Egawa[b], Toshitaka Yoshii[b], Chun-Yi Chen[a], Tso-Fu Mark Chang[a], Katsunari Sato[c], Hiromichi Kurosu[c], Masato Sone[a]

[a] Institute of Innovative Research, Institute of Science Tokyo, Yokohama, 226-8503, Japan
[b] Department of Orthopaedic Surgery, Institute of Science Tokyo, Bunkyo-Ku, 113-8503, Japan
[c] Department of Clothing Environmental Science, Nara Women's University, Nara 630-8506, Japan
e-mail: higashi@ames.pi.titech.ac.jp

Weavable devices fabricated by integrating multiple functional yarns are promising next-generation wearable devices. The integrated various functional yarns impart multiple functions to a single piece of fabric, realizing the wearable devices with multiple functions that a one conventional wearable device cannot provide. The electrical conductivity is a one of the key parameters to fabricate the weavable devices. The metallization of polymer yarns is a straitforward approach to fabricate the yarns with good electrical conductivity. On the other hand, the metallization of the polymer yarns is challenging due to their complex three dimentional structures derived from the tightly packed each filament, which hampers uniform their metallization, and results in low adhesion between the coated metal layers and the polymer yarns.

To address this problem, the electroless plating facilitated by supercritical carbon dioxide ($scCO_2$)-assisted catalyzation is a powerful approach [1]. We have developed the $scCO_2$-assisted Ni-P electroless plating of various polymer yarns, such as polyethylene (PE) [1], and polyethylene telephthalate (PET) [2]. We have discovered that the quality of the metalliztion is affected by their Twist number [2], which is defined as a number of twists per meter (T/m), and known as a paramter to tune their mechanical properties. Considering the application of the metallized yarns to weavable devices, their biocompability is also important to decrease the risk of inflammation and allergen. On the other hand, the biocompability of such Ni-P-coated polymer yarns is not enough. Therefore, the fabrication of the electrical conductive yarns with sufficient biocompability is required to realize the biocompatible weavable devices. To this end, the combination of silver (Ag) and Nylon yarns is promising because of their good biocompability, and high electrical conductivity of Ag. In this work, we report Ag/Nylon yarns with different Twist number fabricated by $scCO_2$-assisted Ag electroless plating, and the effects of their Twist number on the electrical conductivity of the Ag-coated Yarns.

Nylon yarns (Twist number [T/m] = 455, 550, 665, 740, and 865) were fixed with zig made from PEEK polymer, and then subjected to the $scCO_2$-assisted catalyzation in the presence of 50 mg of $Pd(hfa)_2$ used as a catalyst for the Ag electroless plating at 80 °C and 15 MPa for 2 hours. Ag electroless plating was performed using glucose as a reductant at 70 °C for 1 hour (Fig. 1).

The electrical resistance of the fabricated Ag/Nylon yarns was measure with the two-probe method. Fig. 2 shows the relationship between their electrical resistance and their Twist number. As the increase in their Twist number, the electrical resistance of the Ag/Nylon yarns, and the deviation of the measured resistance gradually decreased. The same effects of the Twist number of the Nylon on the electrical resistance of the Ni-P/Nylon were recently observed [3]. Fig. 3 shows the optical microscope images of the pristine Nylon yarns with 455 T/m of Twist number or 865 T/m of Twist number, and the Ag/Nylon yarns with the same Twist number. The pristine Nylon yarns showed white colors, whereas the Ag/Nylon yarns showed gray colors due to the deposition of the Ag onto the Nylon yarns. The presence of the Ag onto the Nylon yarns was confirmed by the lased induced breakdown spectroscopy method. The Nylon yarns with greater Twist number were found to be coated by more amount of Ag, and the deposition of Ag seemed to be more uniform. The greater Twist numbers of the Nylon yarns increased the interaction between the immobilized Pd catalysts into the Nylon yarns and the amide group of the Nylon yarns, which would improve the catalytic properties of the Pd catalysts, and facilitated the Ag electroless plating onto the Nylon surface [3].

In conclusion, we have successfully demonstrated the Ag/Nylon yarns with different Twist number via the $scCO_2$-assisted Ag electroless plating. Their electrical conductivity can be tuned by changing their Twist number, which would manipulate the electrical properties of the Ag/Nylon yarns.

References

[1] H. Kondo et al., *Electrochem* **2024**, *5*, 213–222; [2] H. Kondo et al., *J. Supercrit. Fluids* **2025**, *218*, 106501; [3] K. Shibata et al., *Micro Nano Eng.*, *submitted.*

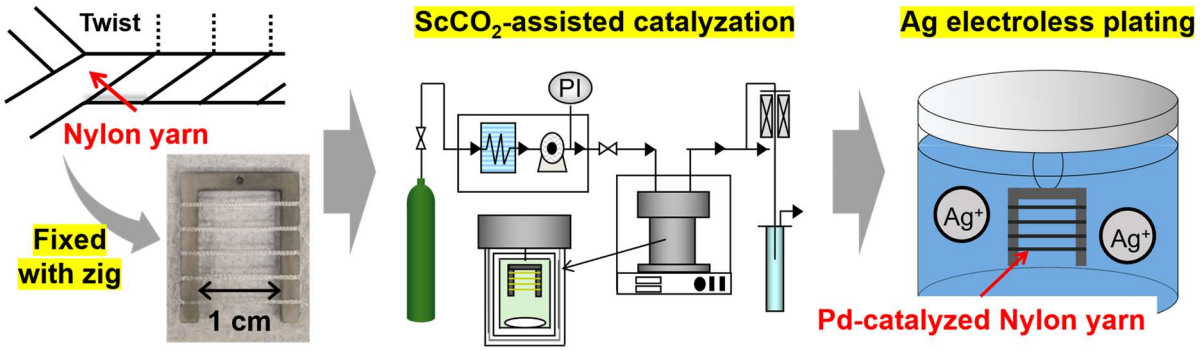

Fig. 1. Schematic illustration of the experimental procedures of the $scCO_2$-assisted Ag electroless plating.

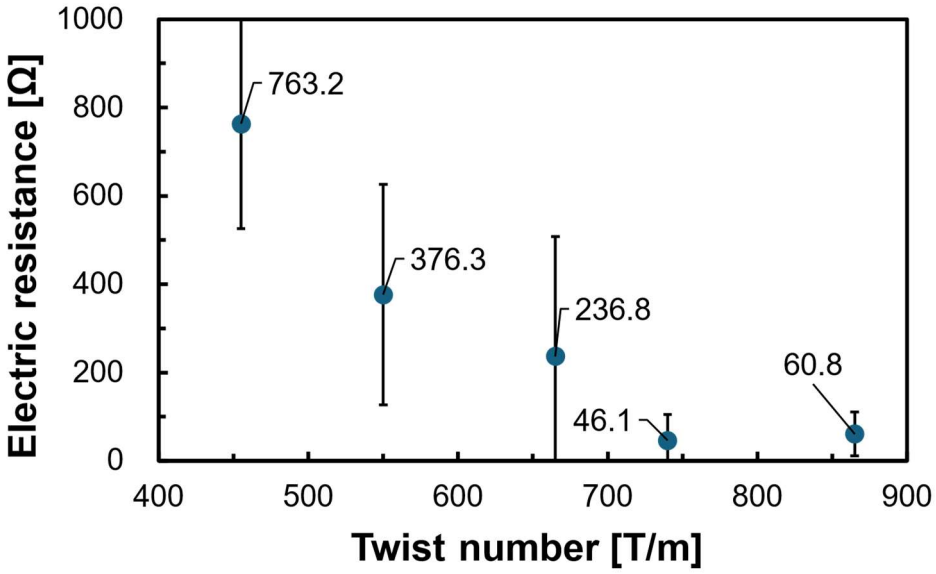

Fig 2. The relationship between the electrical resistance of the Ag/Nylon yarns and their Twist number.

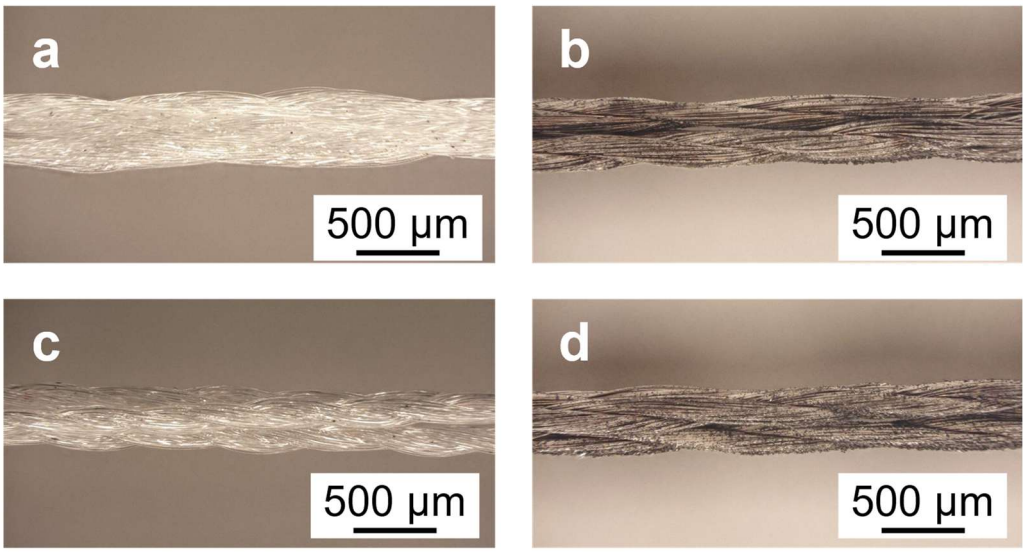

Figure 3. Optical microscope images of (a,c) the pristine Nylon yarns and (b,d) the Ag/Nylon yarns for (a,b) 455 T/m of the Twist number, and (c,d) 865 T/m of the Twist number.

Flexible AlScN Piezoelectric Films for Next-Generation Smart Biomedical Sensors

Padmalochan Panda [a], Gaia de Marzo [a,c], Luciana Algieri [b], Antonio Qualtieri [a], Francesco Rizzi [a], Michele Scaraggi [a,b], Vincenzo Mariano Mastronardi [a,b], Massimo De Vittorio [a,b,c]

[a] Center for Biomolecular Nanotechnologies, Istituto Italiano di Tecnologia (IIT), 73010 Arnesano, LE, Italy
[b] Department of Innovation Engineering, University of Salento, Lecce, LE, 73100, Italy
[c] IDUN section, Department of Health Technology, Technical University of Denmark, DK-2800 Kongens Lyngby, Denmark
e-mail: padmalochan.panda@iit.it

With the growing demand for non-invasive and continuous health monitoring, flexible and wearable biomedical sensors have drawn substantial interest. Over the past two decades, the evolution of micro- and nanoscale devices has been driven by functional materials capable of strong electromechanical coupling [1]. Among them, piezoelectric materials such as aluminum nitride (AlN) are particularly attractive due to their self-powered sensing capability, biocompatibility, and mechanical robustness. AlN-based microelectromechanical systems (MEMS) have shown potential in biosensors, RF resonators, actuators, acoustic devices, and energy harvesters [2-4]. However, the relatively low intrinsic piezoelectric response of AlN limits its performance in sensing applications.

This limitation can be overcome by doping with transition metals, with scandium (Sc) emerging as one of the most effective dopants. Scandium-doped AlN (AlScN) offers significantly enhanced piezoelectric coefficients (d_{33}) and electromechanical coupling (k^2), while remaining compatible with CMOS technology [5,6]. Despite these advantages, integrating AlScN onto flexible substrates remains a challenge due to issues such as high residual stress, brittleness, and the thermal incompatibility of polymer-based materials, all of which hinder the deposition of stable, crack-free films [7,8].

In this work, we report the development and characterization of AlScN films on both rigid silicon and flexible Kapton substrates. AlScN films with 7 at% Sc were successfully deposited at room temperature using pulsed DC sputtering onto AlN/Mo interlayers, employing an AlSc alloy target. Structural and morphological analysis via X-ray diffraction (XRD), scanning electron microscopy (SEM), and energy-dispersive X-ray spectroscopy (EDX) confirmed a *c-axis* oriented wurtzite structure with uniform elemental distribution. Piezoresponse force microscopy (PFM) revealed an enhanced out-of-plane piezoelectric coefficient (d_{33}) of 8.5 ± 0.1 pm/V for AlScN, compared to 5.5 ± 0.1 pm/V for AlN and approximately 7.7 pm/V for previously reported AlScN films with 7 at% Sc [8]. The optimized AlScN films on Kapton, incorporating AlN/Mo interlayers, were further utilized to fabricate a preliminary flexible smart patch sensor using standard photolithography and inductively coupled plasma (ICP) etching. The AlScN films exhibited good adhesion, low stress without any cracks, confirming their suitability for flexible microdevice applications. The mechanical flexibility and electrical performance of the device will be evaluated, demonstrating its potential for real-time physiological signal detection such as respiration and pulse monitoring. These results underscore the promise of AlScN as a high-performance, flexible piezoelectric material for next-generation surface and bulk acoustic wave sensors in biomedical and smart health monitoring applications.

Reference

[1] S. Haider et al., IEEE Access 11 (2023) 58779-58795.
[2] V. Gaddam et al., Adv. Electron. Mater. 11 (2025) 2400849.
[3] M. Cinquino et al., Biosensors and Bioelectronics 267 (2025) 116790.
[4] L. Natta et al., Sci. Rep. 9 (2019) 8392.
[5] C. Zhou et al., IEEE Trans. Electron Dev.71 (2024) 6329.
[6] S. Barth et al., Microsyst Technol 22 (2016) 1613-1617.
[7] S. Qureshi et al., Results in Engineering 22 (2024) 102323.
[8] M. Akiyama et al., Adv. Mater. 2009, 21, 593–596.

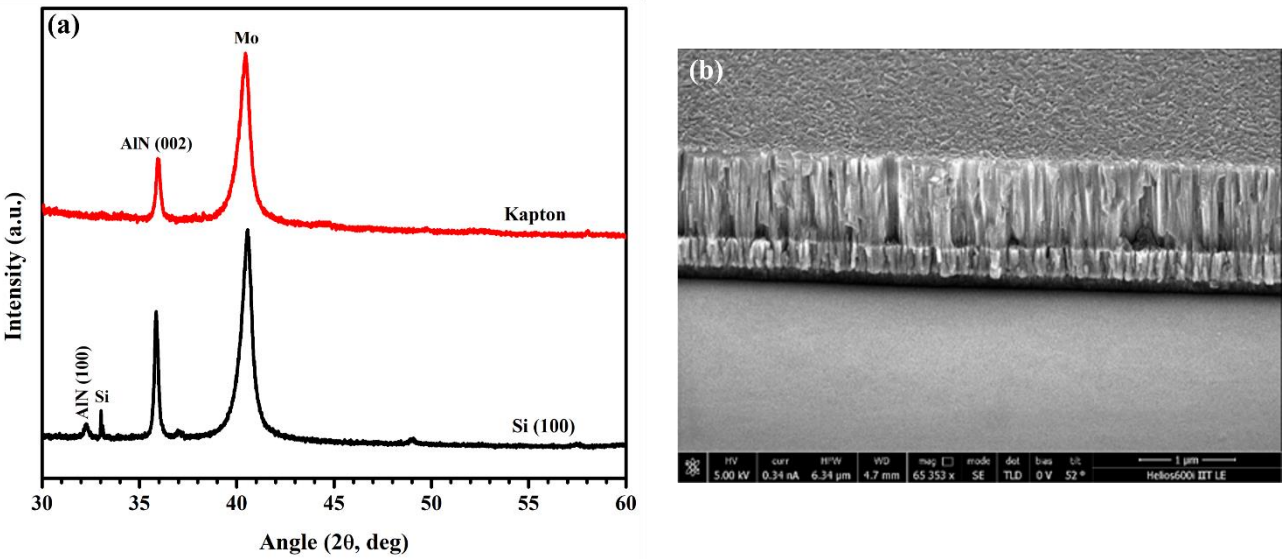

Figure 1. (a) XRD pattern of AlScN films (7 at% Scandium deposited on AlN Interlayer/Mo stack) on Si and Kapton substrates. **(b)** A representative cross-sectional SEM image of AlScN film on Si Substrate.

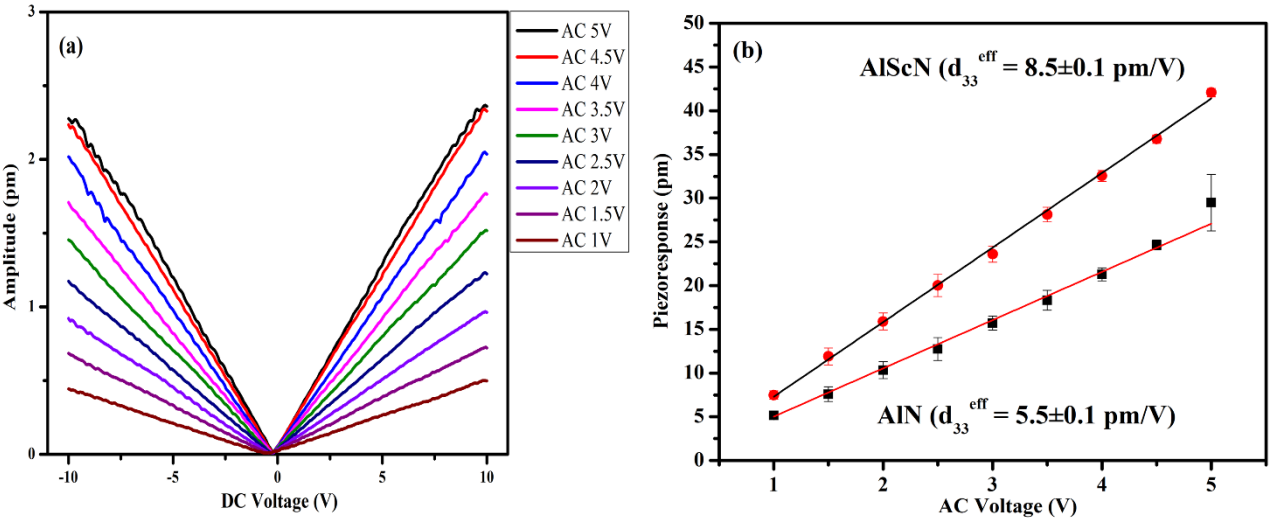

Figure 2. (a) PFM amplitude expansion (butterfly curve) in function of bias voltage at various tip ac voltage for AlScN films with 7 at% Sc. **(b)** Average piezoresponse versus the applied tip ac voltage with the linear fit used for piezoelectric coefficient d_{33}^{eff} evaluation of both AlN and AlScN films.

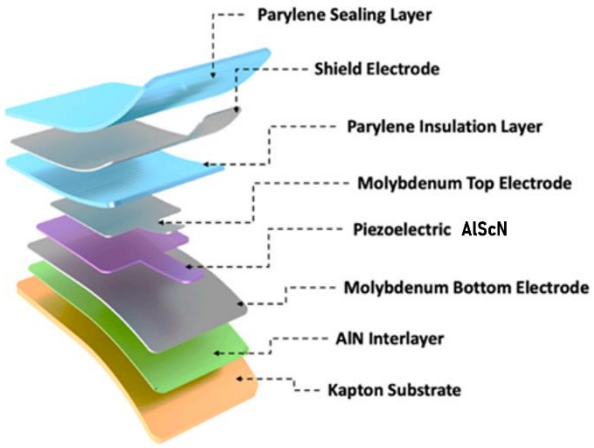

Figure 3. Schematic illustration of flexible AlScN piezoelectric sensor structure.

Monolithic All-Silicon Ring Resonator for Optical Modulation and Detection

Yifu Chen, Weiwei Zhang, Tzu-Yun Chang, Hanuushah Vizabaskaran, James Le Besque, Xingzhao Yan, Martin Ebert, Callum G. Littlejohns, David J. Thomson
Optoelectronics Research Centre, University of Southampton, Southampton SO17 1BJ, UK
e-mail: yc19n22@soton.ac.uk

The silicon photonics platform has become an ideal solution to meet the growing data throughput needs of data centers and high-performance computing systems with its excellent scalability, high compatibility with CMOS processes and low-cost manufacturing potential [1]. Some studies have demonstrated high-speed optical modulation in silicon by leveraging the plasma dispersion effect, achieving modulation rates exceeding 100 Gbaud without resorting to heterogeneous integration of materials such as lithium niobate or III-V compounds, thereby preserving CMOS process compatibility and reducing fabrication complexity [2]. In the realm of photo detection, although Germanium remains the mainstream solution, recent research has shown that specially engineered PN junctions can enable high-responsivity silicon detectors [3]. Building on this, we experimentally validate a co-designed silicon PN junction device with integrated modulation and detection functions. The device can operate at different biases and supports high-speed modulation and detection modes. Its micro-ring structure allows multiple devices to be placed along a single bus waveguide to form high-bandwidth WDM systems, while its reconfigurability makes it a promising candidate for simplifying programmable photonic circuit architectures.

The device fabrication is based on the CORNERSTONE open-source platform and custom doped on a 220 nm silicon-on-insulator (SOI) platform. The lithography steps are performed using a 248 nm deep ultraviolet (DUV) scanner. The manufacturing process begins with a 70 nm silicon etch using a Plasmatherm Versaline ICP device to define the grating coupler. Subsequently, boron ion implantation is performed to form a background p-type doping, on which a shallow phosphorus ion implantation is performed to introduce a light n-type doping, and then a second silicon etch is performed using the same device to define a 100nm high slab and 220 nm high rib waveguide. After that, a second 45-degree tilted phosphorus implantation is performed to form an L-shaped PN junction, and in particular, the position of the pn junction was optimized for the micro-ring structure to achieve greater overlap with the optical mode. Further high-dose boron and phosphorus implants were used to form highly doped regions to ensure low-resistance ohmic contacts with the electrodes. A rapid thermal annealing (RTA) step was performed to activate the dopants and repair lattice damage. A 1μm thick silicon dioxide cladding was then deposited using an Oxford Instruments System 100 PECVD reactor, and finally, ICP etching was used to create vias in the contact areas, followed by metal deposition and patterning to define the electrodes. The device structure is shown in Figure 1.

Figure 2 shows the DC characteristics of the device. The transmission spectrum in (a) shows the resonance peak shift at different voltages. An extinction ratio of 7.7 dB can be achieved under 2.5 Vpp signal drive. (b) shows that the modulation efficiency increases from 5.3 V mm at 0.5 V to 7 V mm at 3.5 V, which is close to the simulation results. (c) shows the dark current and photocurrent of the device when the detector is strongly reverse biased. At -5.7V, the device can maintain a dark current of less than 720nA and a responsivity of 0.3 A/W. At -5.9V, the responsivity can reach up to 0.97A/W. The modulation efficiency and responsivity compare favorably with the state-of-the-art for carrier depletion devices as well as our previous MOS junction devices. [4][5] Figure 3 shows the high-frequency characteristics of the device. (a) and (b) show 56Gb/s modulation eye diagrams without any signal processing and a 78Gb/s eye diagram with 3-tap Feed-Forward Equalization (FFE) added at the receiving end. (c) shows the EO bandwidth up to 55GHz tested using a network analyzer. As a detector, the high-speed detection eye diagrams of 24Gb/s and 48Gb/s (with 3-tap FFE) are shown in (d) and (e), respectively. The OE bandwidth up to 23GHz was measured, as shown in (f).

[1] S. Shekhar, et al., “Roadmapping the next generation of silicon photonics,” Nature Communications, vol. 15, no. 1, p. 751, Jan. 2024.
[2] G. Reed, et al., “Optical modulators,” Integrated Photonics for Data Communication Applications, vol. 3, pp. 69–121, 2023
[3] Y. Yuan, et al., “Mechanisms of Enhanced Sub-Bandgap Absorption in High-Speed All-Silicon Avalanche Photodiodes,” Photonics Research, vol. 11, Dec. 2022.
[4] J. Zhu, et al., “Universal Silicon Ring Resonator for Error Free Transmission Links,” Photonics Research, vol. 12, no. 4, pp. 701–711, Apr. 2024.

[5] W. Zhang, et al. “Harnessing plasma absorption in silicon MOS ring modulators,” Nature Photonics, vol. 17, pp.273–279,2023.

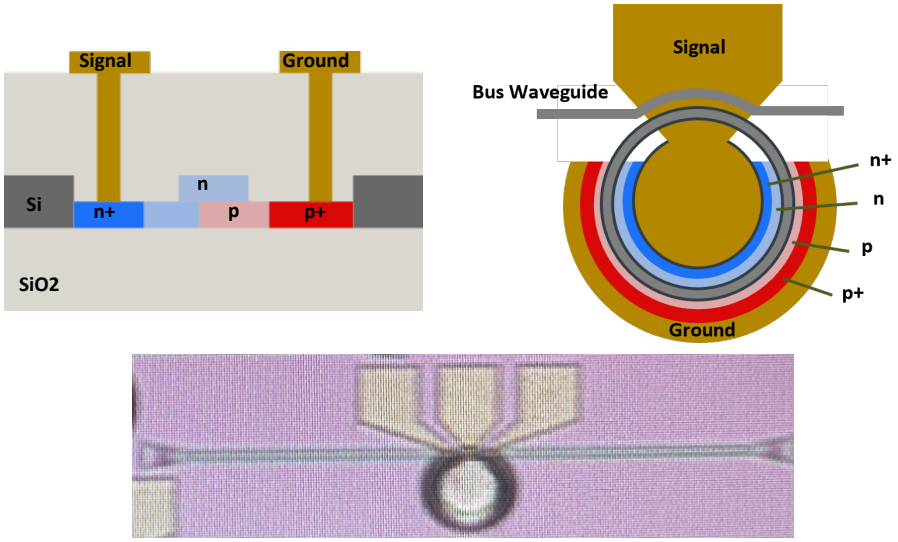

Figure 1. Cross-sectional view of the L-shaped PN junction (top left), layout of ring resonator modulator (top right) and device top view (bottom).

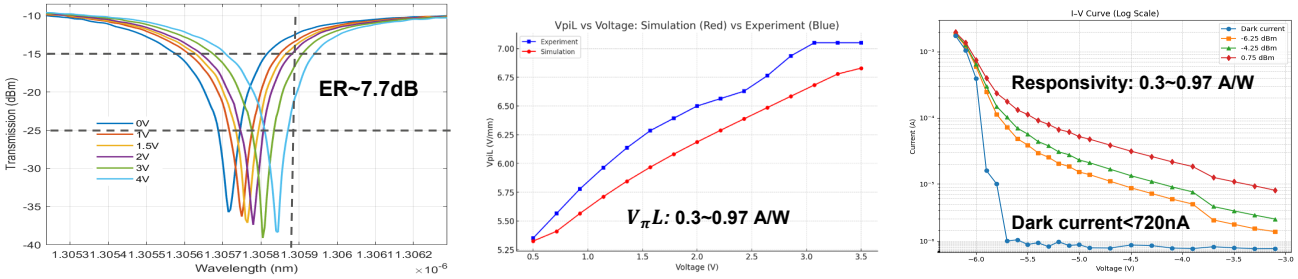

(a) (b) (c)

Figure 2. Measured (a) Optical transmission spectrum (b) Modulation efficiency of simulation and experiment (c) Dark current, photocurrent and responsivity versus bias.

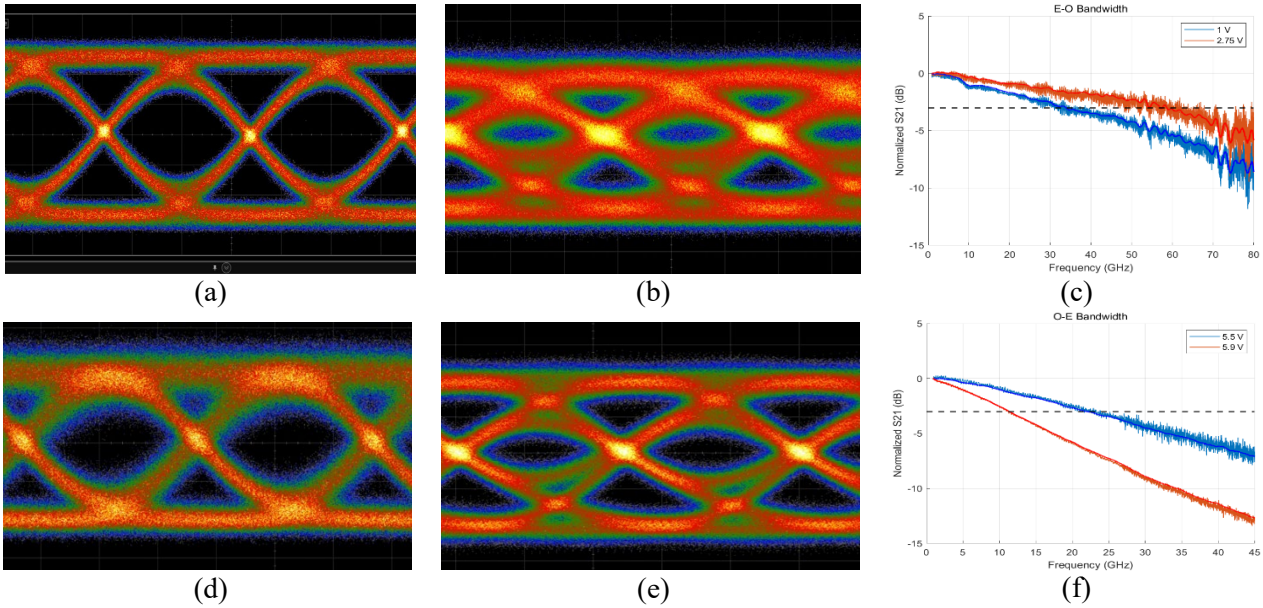

(a) (b) (c)

(d) (e) (f)

Figure 3. High-speed modulator testing (a) Eye diagram at 56Gb/s without FFE (b) Eye diagram at 78Gb/s with FFE (c) E-O Bandwidth. High-speed detector testing (d) Eye diagram at 24Gb/s with FFE (e) Eye diagram at 48Gb/s with FFE (f) O-E Bandwidth.

InP Nanowire-Based Photoelectrical Detection of Single Particles and DNA in Nanofluidic Systems

Leon Seggering [a,b], Vidar Flodgren [c], Abhijit Das [c], Thomas K. Jensen [c], Joachim E. Sestoft [d], Jesper Nygård [d], Anders Mikkelsen [c], Irene Fernandez-Cuesta [a]

[a] University of Hamburg, Physics Department, Hamburg, 22761, Germany
[b] Deutsches Elektronen-Synchrotron (DESY), Hamburg, 22607, Germany
[c] Lund University, Department of Physics and NanoLund, Lund, 223 63, Sweden
[d] University of Copenhagen, Niels Bohr Institute, Copenhagen, 2100, Denmark
E-mail: lseggeri@physnet.uni-hamburg.de

We present a nanofluidic sensing platform that integrates photo-excitable InP nanowires for the electrical detection of single particles and, ultimately, DNA. The approach enables distributed sensing within nanochannels using nanowires that convert optical excitation into measurable electrical signals. This method aims to overcome the limitations of current fluorescence-based single-molecule detection systems that require delicate optical alignment and are restricted to one or two excitation zones per device [1].

The device is fabricated on a Si wafer with a 1000 nm thermal SiO_2 layer and incorporates individually contacted InP nanowires [2] aligned beneath nanochannels (Figure 1, left). Figure 2 outlines the fabrication sequence: a bilayer resist (LOR10B/S1813) is spin-coated and patterned via maskless laser lithography, followed by Ti/Au deposition and lift-off to define large contacts. A bilayer PMMA resist structure (200K / 950K) is then used for EBL to define alignment markers and fine contacts. Shallow trenches (5 × 0.4 µm and 100 nm deep) are etched into the oxide layer by RIE (CHF_3/Ar) to hold the nanowires. The nanowires are individually placed into the trenches using a micromanipulator. SEM imaging of the nanowires is used to align them with the design by referencing the alignment markers. This enables precise definition of individual or parallel nanowire contact electrodes via further EBL and metal lift-off. The entire device is insulated by a conformal 20 nm Al_2O_3 layer deposited by ALD.The fluidic structure is sealed with a transparent coverslip featuring microchannels and liquid inlets. This coverslip is fabricated via direct nanoimprinting of a UV-curable polymer (Ormostamp) onto a glass slide, with inlet holes cut by laser ablation.

The microchannel guides the analyte into vertical nanochannels that cross the nanowires, allowing the fluid to flow directly over the nanowire sensors. The zoomed-in image on the right highlights the precise overlap between nanowires and nanochannels. As seen in the image in Figure 2 on the right, the contacts can address either a single nanowire or multiple nanowires in parallel to enhance the detection region. The continuous fluidic path from inlet hole to microchannel to nanochannel to outlet microchannel ensures stable flow during extended measurement periods. To support multiplexed electrical readout, we developed a custom PCB-based system comprising a daughterboard and a motherboard. The daughterboard is the size of a standard microscope glass slide and holds the sample with fluidics and nanowires (Figure 3). The nanowires are contacted by wirebonding to the PCB, and the daughterboard slots into a microscope-compatible motherboard equipped with BNC connectors. Each nanowire can be measured individually. This modular setup enables rapid measurement cycles and easy sample replacement. First measurements using this complete setup demonstrate that single nanowires respond clearly to laser excitation (Figure 4, right). The photocurrent increases proportionally with laser power, and returns immediately to the dark current level when the laser is no longer aligned. This response confirms the proper functioning of the nanowire readout system under fluidic conditions.

In the near future, measurements will focus on detecting single particles flowing through the nanochannels. The device platform has been successfully demonstrated in terms of fabrication, electrical readout, and fluidic integration. Further optimization will target improved signal stability and sensitivity for future single-DNA analysis applications.

[1] F.M. Esmek et al., IEEJ Trans (2024) 19 840-844.
[2] V. Flodgren et. al., ACS Photonics (2025) 12, 655-66

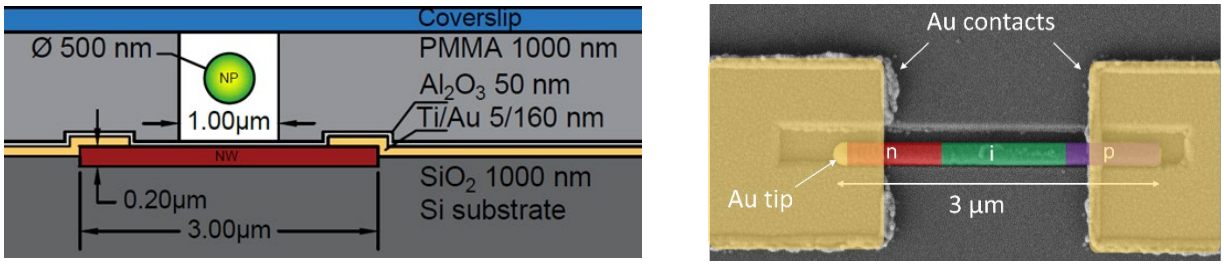

Figure 1. (left) Cross-sectional schematic of the nanofluidic detection system. A 500 nm particle flows through a PMMA nanochannel aligned above a photoexcitable InP nanowire. (right) The SEM image shows the p-i-n doping of the nanowire and is embedded in a shallow trench and contacted with Ti/Au for electrical readout.

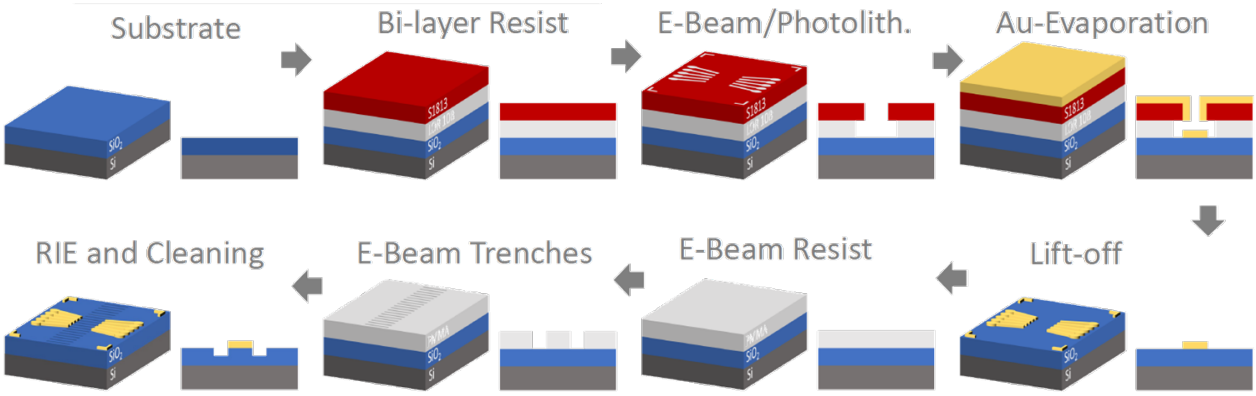

Figure 2. Fabrication steps from Si/SiO_2 (1000 nm) substrate to bilayer resist patterning, metallization, and trench etching by RIE.

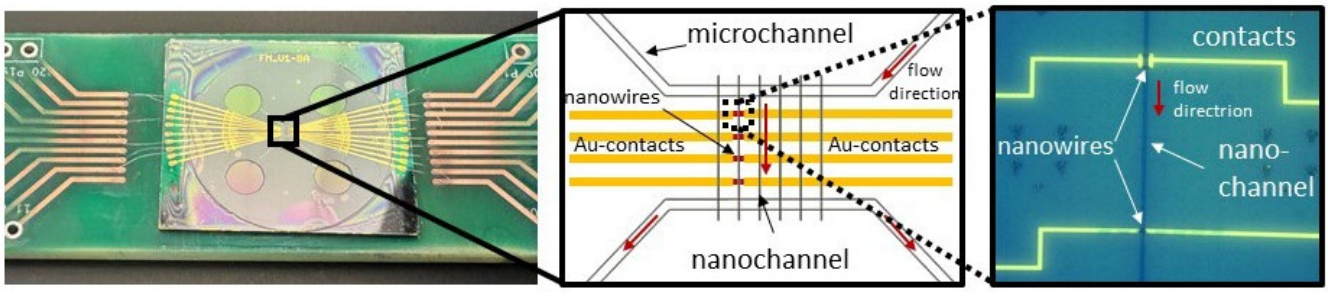

Figure 3. left to right. Overview of sample mounted to PCB for easy readout. The image shows the PMMA layer (visible as rainbow fringes), the transparent coverslip, and large contacts with wirebonds. A schematic illustrates the microchannel-to-nanochannel transition. A zoom-in shows two nanowire–nanochannel crossings with yellow gold contacts.

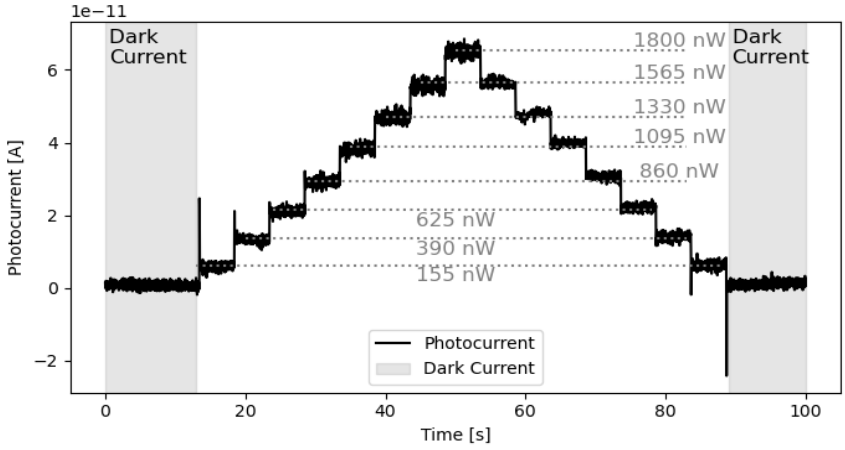

Figure 4. Photocurrent measurement of a nanowire embedded under nanochannels and coverslip. Laser power is stepwise increased showing equal steps.

Ultrasensitive Raman Detection via Electrostatic Droplet Manipulation and Laser-Patterned Pinhole Concentration

Jia Yi Chen [a], Cheng Han Yu [a], Jiann Shieh [a]
[a] Department of Materials Science and Engineering, National United University, Miaoli, 36063 Taiwan

e-mail: jshieh@nuu.edu.tw

The "hot spots" generated by aggregated metal nanoparticles significantly enhances the Raman signal, attracting considerable interest for molecular detection applications. However, identifying few molecules at very low concentrations remains challenging under a microscope. To improve the probability of detection and reduce the time spent searching for these molecules, we previously developed a sticky superhydrophobic silicon nanograss that concentrates analytes at the perimeter of a coffee-ring-like stain, enabling reliable ultrasensitive molecular sensing [1]. However, this method requires precise, sequential droplet placement at the same location and does not support flexible droplet manipulation. In contrast, we recently demonstrated that the rapid movement of water droplets on superhydrophobic glass surfaces can be effectively controlled using electrostatic forces [2]. In this study, we integrate the strengths of both approaches by manipulating and positioning water droplets—containing silver nanoparticles and Rhodamine 6G (R6G) molecules—into laser-patterned microholes via electrostatic manipulation. Upon drying, the droplets form coffee-ring patterns that concentrate the molecules at the ring edge, thereby enhancing the surface-enhanced Raman scattering (SERS) signal.

Quartz glass plate was used as the substrate. Silica nanowires were first grown via chemical vapor deposition (CVD) at 830 °C on the glass to introduce the surface roughness necessary for superhydrophobicity, followed by surface modification with F_{13}-TCS silane to reduce the surface energy [3]. The hydrophilic pinholes were then fabricated using CO_2 laser (10 W power, 10.6 μm wavelength) ablation (Figure 1a). As shown in Figures 1b-1d, the 0.3-mm pinhole reliably retains droplets smaller than 15 μL, even against gravity when the chip is inverted. However, when droplet volume exceeds this threshold, the sliding angle decreases markedly, indicating that anchoring ability depends on droplet size.

To drive droplet motion, we generated an electrostatic charge by rubbing a PTFE rod against a nitrile butadiene rubber glove, then positioned the charged rod on the backside of the superhydrophobic substrate. The resulting electrostatic field was strong enough to manipulate the motion and coalescence of positively charged droplets [2], guiding them toward a laser-defined hydrophilic pinhole (Figure 2a). At this site, the droplets quickly dried by heating, leaving behind a tiny coffee-ring-like stain around the pinhole (Figure 2b). This method enables precise droplet positioning for subsequent analysis, as shown in Figure 2c. Raman measurements revealed a significantly enhanced R6G signal due to the surface-enhanced Raman scattering (SERS) effect, which is attributed to both the concentrated analyte distribution within the coffee ring stain and the formation of localized SERS hot spots from Ag nanoparticles. The measurements performed on the various R6G concentrations confirmed the detection of characteristic Raman peaks down to 10^{-12} M (Figure 2d), demonstrating the ultra-high sensitivity of this approach. These results highlight the potential of integrating laser-patterned superhydrophobic surfaces with electrostatic manipulation for precise droplet control and ultrasensitive molecular detection. This platform shows promise for applications in droplet-based digital microfluidics and molecular sensing.

REFERENCES

[1] H. L. Ho, J. Y. Yang, C. H. Lin, J. Shieh, Y. F. Huang, Y. H. Ho, T. S. Ko, C. C. Hsu, K. Ostrikov, Adv. Mater. Interfaces 10 (2023) 2300291.
[2] W. C. Huang, M. Y. Chang, J. Shieh, C. H. Lin, C. C. Hsu, Adv. Mater. Interfaces (2025) in press.
[3] J. Shieh, G. F. Huang, J. Y. Tsai, B. W. Huang, Y. F. Huang, STAR Protocols 3 (2022) 101066.

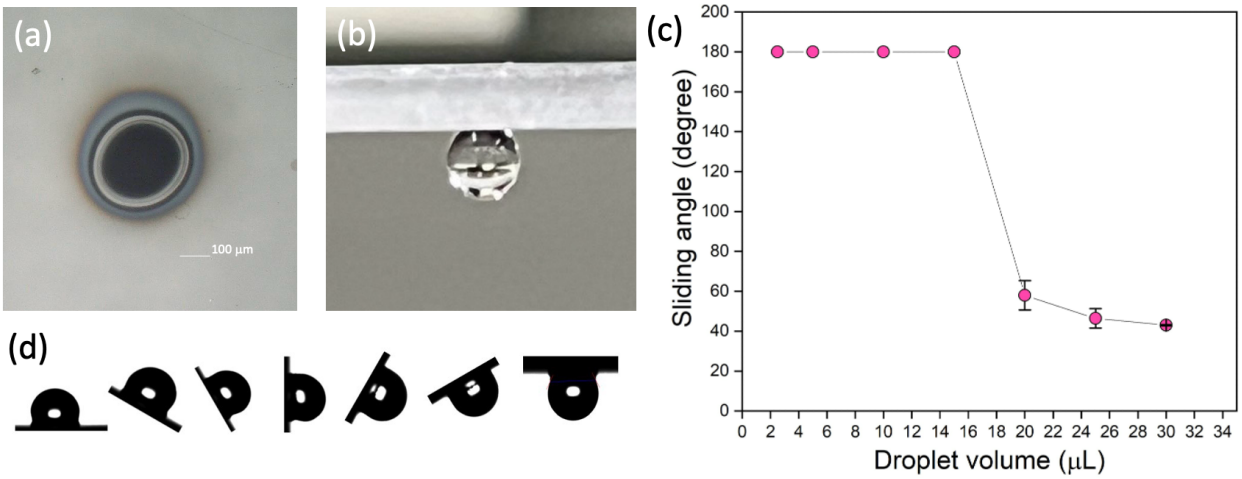

Figure 1. (a) Optical microscopy image of a pinhole fabricated by CO_2 laser ablation. (b) Image of a 5-µL water droplet anchored on the pinhole. (c) Sliding angles of water droplets with varying volumes on the pinhole. (d) Sequential images showing a water droplet anchored on the pinhole during substrate rotation.

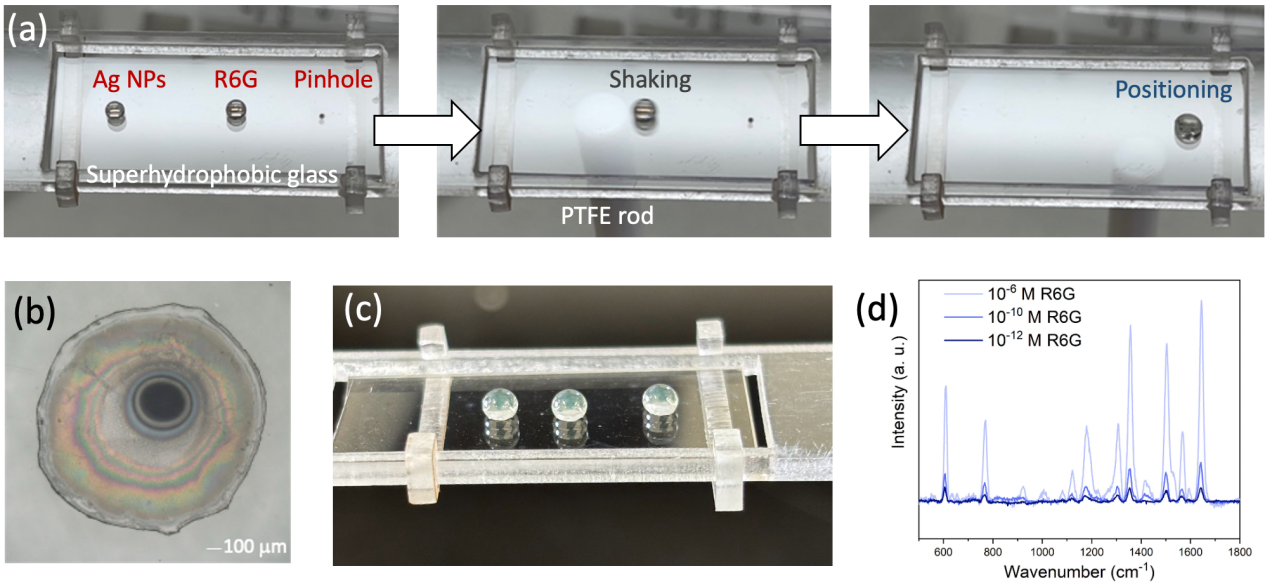

Figure 2. (a) Electrostatic manipulation of Ag nanoparticles and R6G molecules on a superhydrophobic glass surface for precise positioning at a hydrophilic pinhole. (b) Optical microscopy image showing a coffee-ring-like stain formed around the pinhole. (c) Image demonstrating the ability to position droplets with various components through custom design. (d) Raman spectra of R6G molecules detected at the ring edge, highlighting the ultra-high sensitivity achieved using this approach.

Scalable integration of III-V nanowire transistors for NMOS logic

Faris Abualnaja [a], Ibtisam Abbasi [a], Xiaofan Lin [a], Hoe Tan [b], Chennupati Jagadish [b], Hannah J. Joyce [a], Jack Alexander-Webber [a]
[a] University of Cambridge, Cambridge, CB3 0FA, United Kingdom
[b] The Australian National University, Canberra ACT 2600, Australia

e-mail: fa465@cam.ac.uk

Semiconducting III-V nanowires are increasingly attractive for nanoscale device fabrication due to their physical properties and ability to transfer to arbitrary substrates for heterogeneous integration, supporting the development of compact, low-power, and flexible optoelectronic systems. Among them, InAs nanowires exhibit high sensitivity to electrostatic control, due to their high carrier mobility and surface-to-volume ratio, each of which is strongly influenced by nanowire diameter [1]. Designing a suitable device architecture and circuit configuration are critical in enabling logic and memory functionalities in nanowire-based systems.

In this work, we integrate pairs of InAs nanowires in an inverter configuration for NMOS logic circuit applications. Large arrays of single-nanowire transistor devices are fabricated using customised coordinate markers and automated device design based on computer-vision and high-throughput microscopy [2]. A typical device is illustrated in Fig. 1a, where source and drain-terminals are connected to an imaged and detected InAs nanowire, with the *p*-type silicon substrate acting as a global back gate (V_{bg}). Figure 1b shows a scanning electron microscopy (SEM) image of the device. Current-voltage ($I_{sd} - V_{bg}$) characteristics for devices of different nanowire diameter are plotted in Fig. 1c. Here, each device is swept from V_{bg} = –10 V to +10 V with a fixed source-drain voltage, V_{sd} = 0.01 V. All nanowire devices exhibit *n*-type transistor behaviour, where the device turns off at negative gate voltages. Larger diameter (> 50 nm) nanowire transistors show depletion-mode characteristics while smaller diameter (< 50 nm) devices show enhancement-mode behaviours.

These results allow us to construct an inverter device consisting of load and driver nanowire field-effect transistors (NWFET) using a pair of different nanowire diameters (Fig. 2a). Here, each component of the inverter has a local top gate. For $NWFET_{load}$, source and drain terminals are rail-voltage (V_{dd}) and output voltage (V_{out}) respectively, while the gate is supplied by V_{out}. For $NWFET_{driver}$, source and drain terminals are V_{out} and ground (GND) respectively, while the input voltage (V_{in}) acts as the local top gate. Figure 2b shows the schematic for the inverter device. Figure 2c shows the voltage transfer characteristics (VTC) for multiple inverters, where each device has a different diameter for $NWFET_{load}$. Using the results from Fig. 1c, we determined that all devices use a 45 nm diameter nanowire for the $NWFET_{driver}$ as it operates in enhancement mode, allowing for our inverter design. We optimise VTC by controlling the channel and gate geometries and by reducing dielectric thickness. The gate length determines the inverter's switching voltage. The optimised inverter device can achieve a full rail-to-rail output voltage swing, with an RC-limited frequency response.

The partially automated fabrication process and resulting inverter logic presented in this work, demonstrate initial steps towards scalable nanowire devices and potential formation of more complex integrated circuits.

References:

[1] J. A. Alexander-Webber *et al.*, *ACS Appl. Mater. Interfaces*, (2017) 9, 43993 – 44000.
[2] T. Potočnik *et al.*, *ACS Nano*, (2022), 16, 18009 – 18017.
[3] I. Abbasi *et al.*, Nanotechnology, (2025) – accepted.

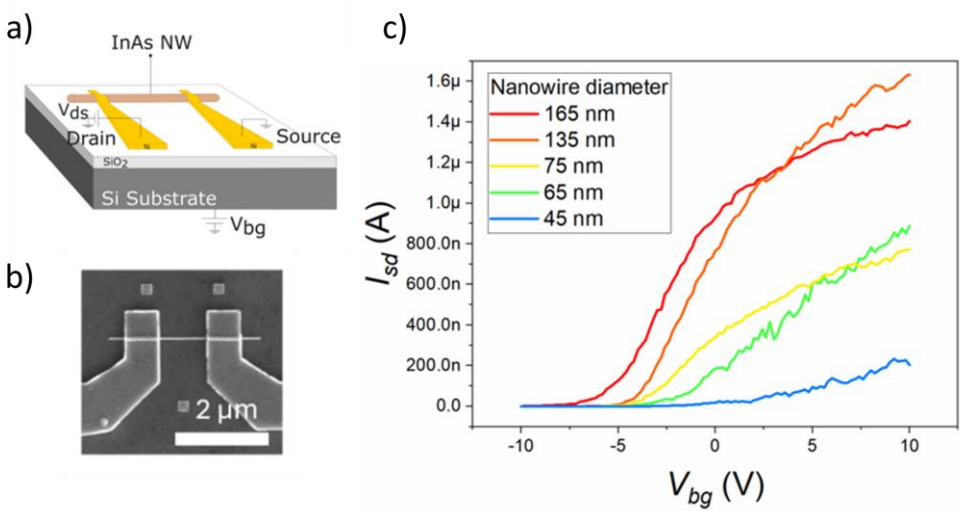

Figure 1. a) Schematic of a nanowire transistor with source-drain terminals, and global back gate (V_{bg}). b) SEM images of the nanowire device. c) Transfer-curves at constant V_{sd} = 0.01 V for different nanowire diameters.

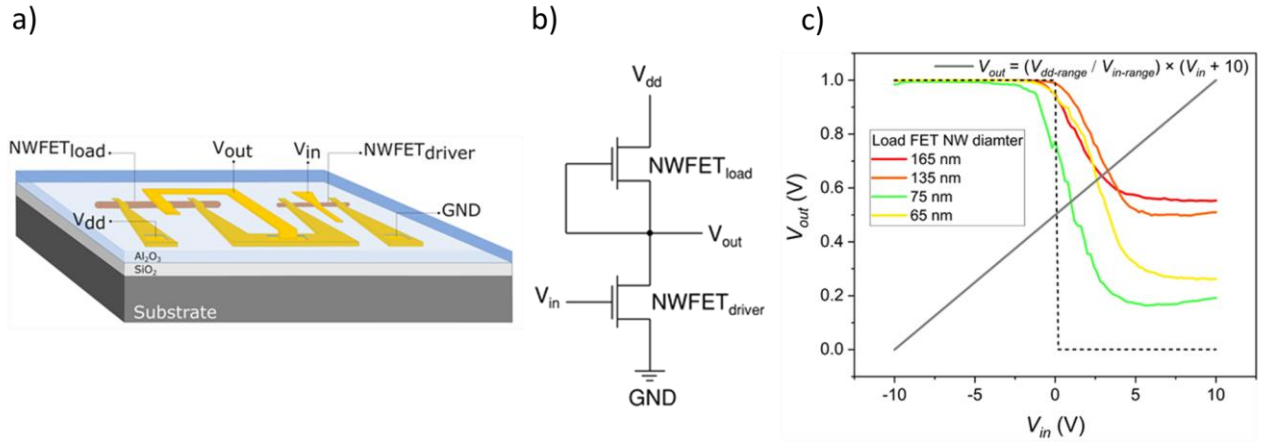

Figure 2. a) Schematic of nanowire-based inverter. $NWFET_{load}$ drain and source/gate terminals correspond to inverter supply power (V_{dd}) and output (V_{out}) ports, while $NWFET_{driver}$ drain and source terminals correspond to inverter V_{out} and ground, and inverter input (V_{in}) as gate. (b) Circuit schematic of a NMOS inverter. (c) Inverter VTC for different NW diameters acting as the $NWFET_{load}$, ($NWFET_{driver}$ diameter = 45 nm). The channel lengths of load and driver transistors were 4 µm and 1 µm, respectively. Intersection of the VTCs and $V_{out} = (V_{dd\text{-}range} / V_{in\text{-}range}) \times (V_{in} + 10)$ indicates inverter output switch between logic "1" to "0".

Piezoelectric microdevices for single-cell stimulation via ultrasound-driven ZnO nanosheets

Laura Lefaix [a], Marc Navarro [a], Jaume Esteve [a], Carme Nogués [b], Andreu Blanquer [b], Gonzalo Murillo [a]

[a] Institute of Microelectronics of Barcelona, Cerdanyola del Vallès (Barcelona), 08193, Spain
[b] Universitat Autònoma de Barcelona, Cerdanyola del Vallès (Barcelona), 08193, Spain
e-mail: laura.lefaix@imb-cnm.csic.es

Purpose of the work:

This research focuses on the study of smart materials through a novel bioinspired approach that promotes microscale-to-nanoscale interactions, inspired by the natural cell–matrix interface. It falls within the field of bioelectronics, which leverages electrical stimulation of biological systems for various applications. Our ultimate goal is to develop materials capable of delivering cellular-level stimuli without causing harm to the organism or requiring invasive procedures. In this work, we harness the properties of piezoelectric materials, which generate a piezopotential in response to mechanical stress (such as cell attachment or acoustic pressure), to enable mechanoelectrical stimulation of cells. We introduce a novel, cytocompatible microdevice, smaller than a cell, designed for precise single-cell stimulation.

Novelty of the work with respect to the state of the art:

The design of this microdevice, which integrates nanostructures onto a microparticle, is inspired by cell–cell and cell–matrix interactions. In such interactions, a cell (typically tens of micrometers in size) engages with external systems through membrane biomolecules (on the scale of tens of nanometers). While piezoelectric materials have previously been used for electrical stimulation in the form of scaffolds or nanoparticles,[1, 2] they have not been explored at this intermediate micrometer scale. This approach enables higher spatial resolution, making single-cell stimulation possible. Moreover, the system also emulates the natural delivery of electrical stimuli in certain tissues, such as bone. In contrast to other miniaturized electrical stimulation devices, usually on the millimeter scale, that rely on electrodes to deliver current or voltage to the target tissue,[3] our microdevice offers a novel strategy. It stimulates cells via actuated piezoelectric ZnO nanosheets (NSs), representing a new direction in therapeutic applications.

Results of the work:

First, the morphology of ZnO NSs was studied by varying the hydrothermal growth conditions.[4] Hexagonal nanosheets with diameters ranging from less than 1 µm to 4 µm and thicknesses between 15 and 40 nm were synthesized. Selected ZnO NSs were then integrated into microdevices of three different sizes (3×3, 6×10, and 12×18 µm²), which had been previously fabricated using microfabrication techniques (**Figure 1**).[5,6] These ZnO NSs were also incorporated into a test device for electrical characterization. When actuated with ultrasound in the biomedical frequency range (3 MHz, up to 2.0 W/cm²), a voltage in the millivolt range was measured. No changes in the integrity of the microdevices were observed after ultrasound actuation.

Subsequently, the experimental phase focused on testing the microdevices for biological applications, including cytotoxicity, internalization, and cell stimulation studies. Both the microdevices and the ultrasound actuation were found to be cytocompatible. Internalization was observed in 52% of cancerous cells for the smallest devices (**Figure 1D**), but only in 8% of healthy cells.[6] This percentage decreased as the size of the microdevices increased. Two other orientations of the microdevices were observed, ZnO NSs facing either toward or away from the cell membrane (**Figure 1E**). As a result, microdevice arrays were used for calcium imaging tests to assess the percentage of stimulated cells. Upon ultrasound actuation at 3 MHz and varying intensities, an increase in the number of cells exhibiting calcium transients was observed. At an intensity of 1.0 W/cm², the percentage of excited cells increased from a basal level of 22% (without ultrasound) to 35% after stimulation (**Figure 2A** and **Figure 2B**). In contrast, the control sample without microdevices showed 12% excitation both before and after ultrasound exposure. Furthermore, a simplified model was developed to investigate the origin of the Ca^{2+} involved in the calcium transients. Using channel blockers and calcium-deprived conditions, it was determined that Ca^{2+} primarily entered the cells from the extracellular environment via voltage-gated calcium channels (VGCCs) and stretch-activated calcium channels (SACCs), particularly in cells interacting with ZnO NSs (**Figure 2C**).[7] Finite element modeling further supported the experimental findings by providing insights into the cell–ZnO NS interaction. Collectively, these results validate the use of these microdevices for their intended purpose: single-cell electrical stimulation.

[1] Y. Ikada et al., J. Biomed. Mater. Res. (1996), 30, 553.
[2] G. Ciofani et al., ACS Nano (2010), 4, 6267. https://pubs.acs.org/doi/10.1021/nn101985a
[3] R. M. Neely et al., Curr. Opin. Neurobiol. – ScienceDirect (2018), 50, 64. https://dx.doi.org/10.1016/j.conb.2017.12.010
[4] G. Murillo et al., Nano Energy (2019), 60, 817-826. https://doi.org/10.1016/j.nanoen.2019.04.017
[5] N. Torras et al. Adv. Mater. (2016), 28, 1449. https://doi.org/10.1002/adma.201504164
[6] Lefaix et al., Adv. Sci. (2025), 2415028. https://doi.org/10.1002/advs.202415028
[7] G. Murillo et al., Ad. Mater. (2017), 29, 1605048. https://doi.org/10.1002/adma.201605048

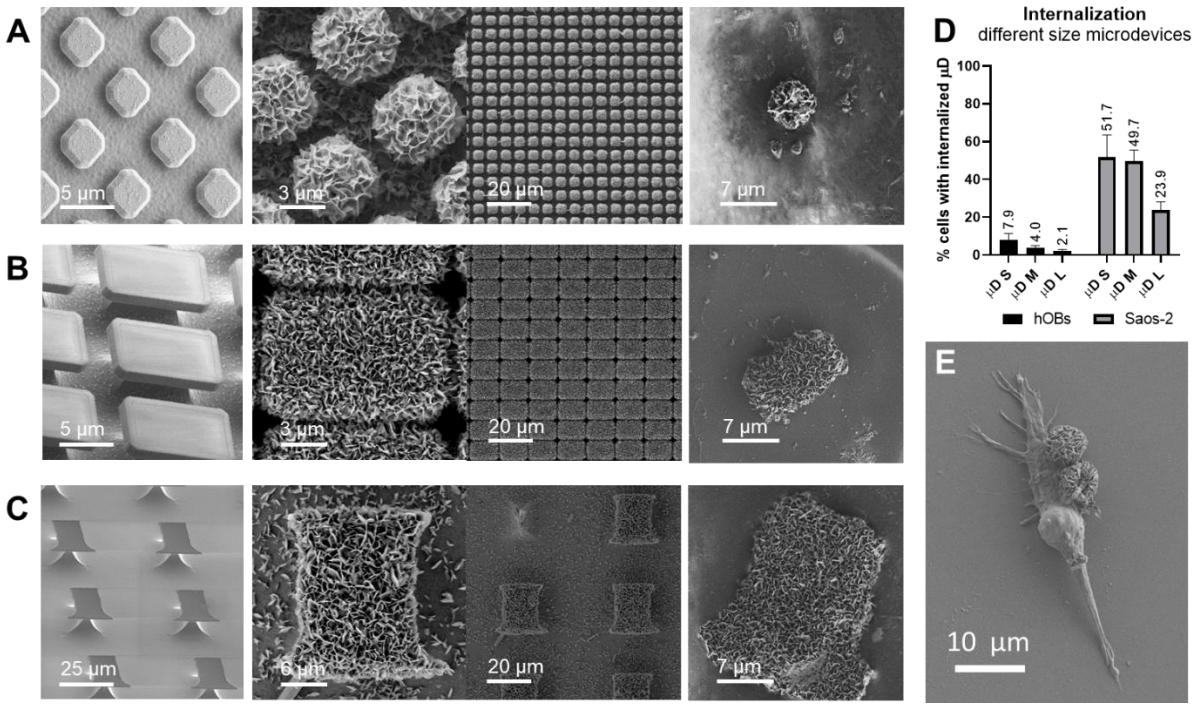

Figure 1. Microdevices at different stages of the fabrication process and biological experiments. Scanning electron microscopy (SEM) images of microdevices of different sizes, (A) 3×3, (B) 6×10, and (C) 12×18 µm² are depicted. In the first column, the microparticles after the microfabrication process. In the second column, the microdevices after a hydrothermal growth of ZnO NSs of 9 h. (D) Graph showing the internalization results both for hOB healthy bone cells and Saos-2 osteosarcoma cells. (E) Saos-2 cell with three small (3×3 µm²) microdevices in three orientations. From left to right, (i) with ZnO NSs facing away from the cell membrane, (ii) with ZnO NSs towards the cell mebrane and (iii) internalized.

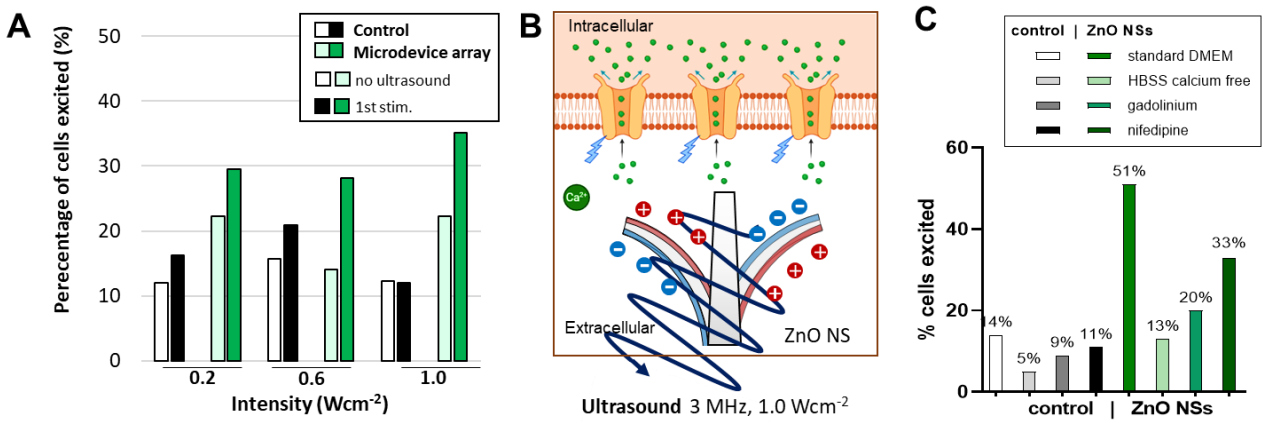

Figure 2. Cell stimulation experiments using Saos-2 cells. (A) Graph of cells excited before and after the ultrasound actuation (3 MHz, different intensities) of control samples and microdevice arrays. (B) Scheme of cell-ZnO NS interaction. The ZnO NS piezopotential in response to ultrasound actuation produces an electric field that reaches the cell membrane and opens membrane channels. This allows the entrance of extracellular Ca^{2+}. (C) Graph depicting the results obtained after using channel blockers and calcium-deprived conditions.

Technological platforms for manufacturing semiconductor qubits

A. del Moral, I. Uranga-Granados, G. Petitto, P. Gaya, G. Aizpurua-Iraola, J. Antoja-Lleonart, E. Amat, J. Llobet, M. Fernández-Regúlez, J. Bausells and F. Perez-Murano

Institute of Microelectronics of Barcelona (IMB-CNM, CSIC), E-08193 Bellaterra, Spain
e-mail: alberto.delmoral@imb-cnm.csic.es

In this work, an overview of the quantum platforms for the development of semiconductor qubits is presented, defining the framework of the state-of-the-art technology with particular interest in qubits based on quantum dots induced electrostatically.

Quantum computing offers the potential to carry out exponentially more efficient algorithms than classical computing, and with that purpose the manufacturing technology is currently facing great challenges in scaling qubits. Semiconductor-based platforms are very suitable, as they inherit extreme parallelization and uniformity characteristics from the well-established semiconductor industry, but due to the loss of coherence of quantum states the implementation of qubits into semiconductor devices is not trivial. Among the most common architectures for a semiconductor qubit system, two groups are identified (Fig. 1). Those that use atoms to implement the qubit, for instance with the qubit implemented in the spin state of the nucleus of the atom [1], and those using engineered fields to confine charge carriers, known as electrostatic qubit systems: architectures using strained SiGe heterostructures grown epitaxially [2], devices based on FDSOI substrates [3], or based on a GeMOS architecture [4]. One key advantage of electrostatic qubits is their capability to be integrated into CMOS technology. The morphology of a MOS-based qubit device is similar to a conventional MOSFET, but still the small feature sizes and high pattern densities necessary for large-scale qubit devices make the building of electrostatic qubit systems challenging, being one of the topics in which quantum computing research is recently more focused [5 – 12].

In this work we report the progress of the qubit device fabrication platform developed at the IMB-CNM, consisting in an MOS channel where multiple planar gates are defined, creating the potential wells, while a second metal layer controls their energy levels. This approach requires the adaptation of conventional CMOS technology towards qubit requirements: a 6.6 nm gate oxide is formed through a dry chloride oxidation ramp at 850ºC (Fig. 2a); AFM was used to characterize the S/D implanted regions and the channel, with special attention to surface roughness analysis. In addition, the patterning of multi-gates by EBL, e-beam evaporation of 30 nm Al and lift-off is optimized (Fig. 2b), with resulting dimensions of ~40 nm wide gates with separation of ~30 nm. These nominal dimensions are validated from calculations by Sentaurus TCAD [13], ensuring the creation of an electrostatic quantum dot (Fig. 3). The starting point of the process flow (Fig. 4) are p-type epitaxial wafers with a 200 nm field; S/D regions are implanted with phosphorus through a sacrificial oxide *(i)*; Fig. 4b shows an optical image of the active area and the S/D regions. Then the gate oxidation is done *(ii)* and S/D contacts fabricated *(iii)*. Barrier gates are patterned in the channel (iv), as shown in Fig. 4c, followed by 5 nm Al_2O_3 dielectric layer deposited by ALD *(v)*, and the lead gate patterned on top of the barrier gates *(vi)*; an AFM image of the resulting device is presented in Fig. 4 D, showing the S/D regions, the barrier electrodes and the gate. In parallel, a conventional MOSFET is structurally (Fig. 5a) and electrically characterized (Fig. 5b), validating the suitability of the channel in low-temperature conditions.

[1] D. Holmes *et al.*, *Adv. Quantum Technol.*, 7.3 2300316 (2024).
[2] S. Neyens *et al.*, *Nature* 629, 80–85 (2024).
[3] T. Bédécarrats *et al.*, *IEEE (IEDM)*, 1-4 (2021).
[4] A. Ciocoiu, *Doctoral Dissertation* University of British Columbia (2023).
[5] A. M. J. Zwerver *et al*., *Nat. Electron.* 5(3) 184-190 (2022).
[6] A. R. Mills *et al*., *Sci. Adv.* 8(14) (2022).
[7] T. Tanttu *et a*l., *Nat. Phys.* 1-6 (2024).
[8] S. Geyer *et a*l., *Appl. Phys. Lett.* 118(10) (2021).
[9] F. Borsoi *et al*., *Nat. Nanotechnol.* 19(1) 21-27 (2024).
[10] A. Noiri *et al*., *Nature* 601 (7893) 338-342 (2022).
[11] X. Xue *et al*., *Nature* 601(7893) 343-347 (2022).
[12] N. S. Lai *et al*., *Sci. Rep.*1(1). 110 (2011).
[13] Sentaurus Device, v. K-2018.06-SP2, 2018.

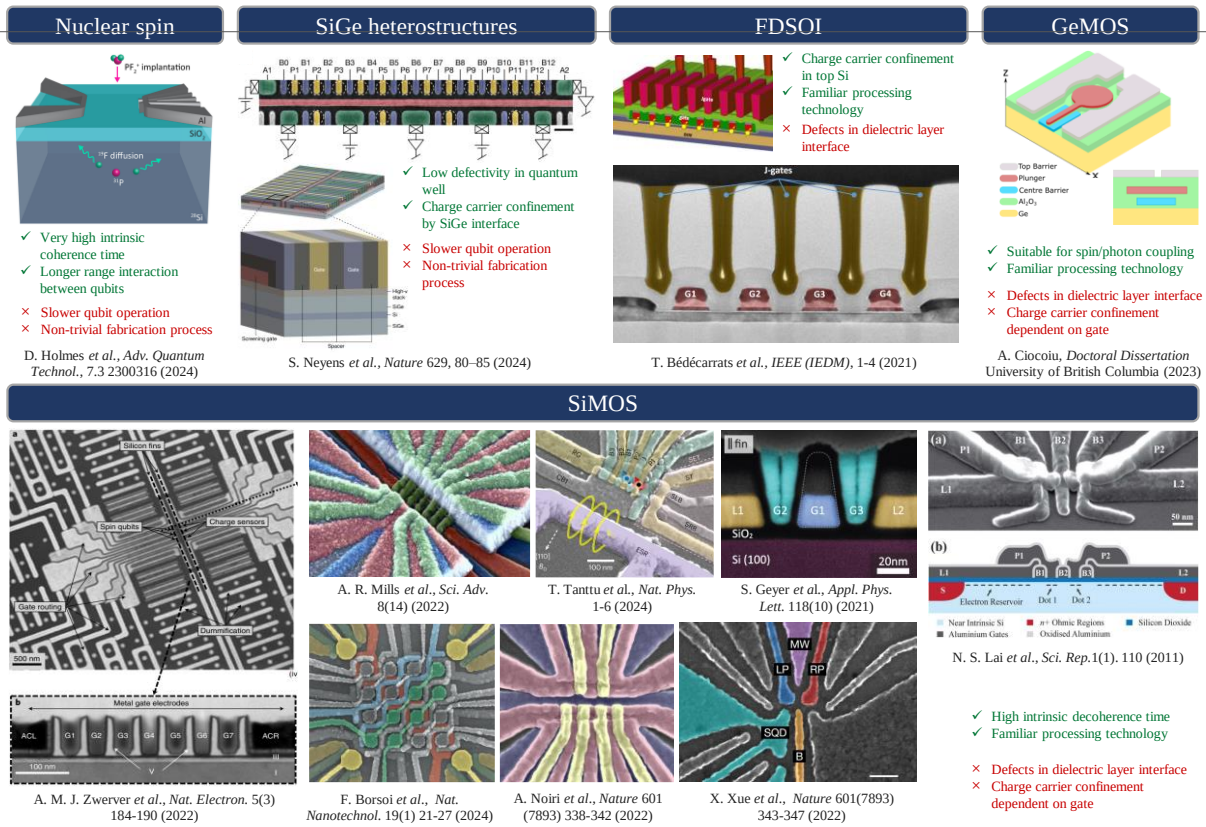

Fig. 1. Concept map of the most relevant technology platforms for qubits based on semiconductor qubits: based on nuclear spin [1], SiGe heterostructures [2], FDSOI substrates [3], GeMOS [4] and SiMOS structures [5 – 12].

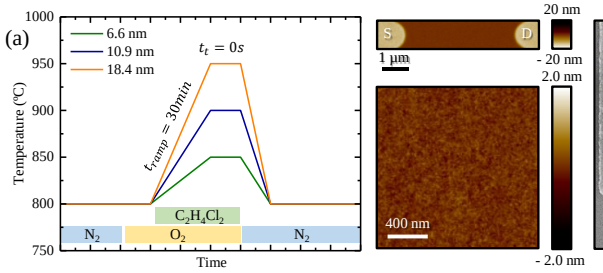

Fig. 2. (a) Dry chloride oxidation ramp adapted for the oxidation process and AFM image of the S/D terminals with detail of the gate oxide in the channel; (b) metal gates patterned by EBL and lift-off.

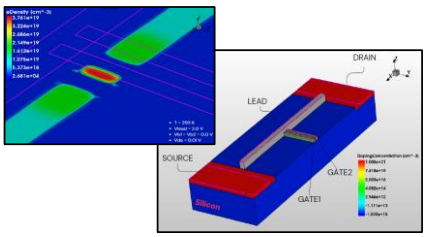

Fig. 3. Electron density map from TCAD 3D simulation of the barrier gates, with the electrostatically induced QD.

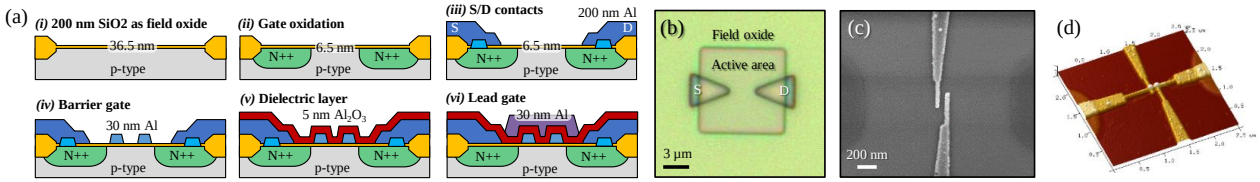

Fig. 4. (a) Schematic of the main process steps with (b) an optical image of the active area with S/D regions after *(ii)*, (c) SEM image of the barrier gate patterned in the channel after *(iv)* and (d) AFM image after lead gate definition *(vi)*.

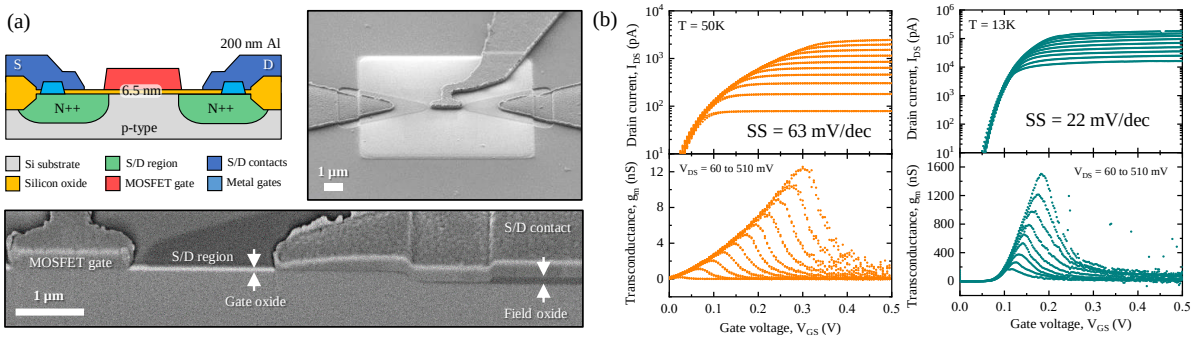

Fig. 5. (a) Schematic of a MOSFET section with (b) tilted SEM image with active area and S/D contacts and (c) cross-section of the channel; (d) corresponding $I_{DS} - V_{GS}$ and transconductance characteristics at 50K and 13K.

Double-Spot Detection in Nanochannels Enables Precise Velocity Profiling and Long-Term Stability Monitoring in Passive Micro- and Nanofluidic- Systems

Phil Grzybeck [a], Lucjan Grzegorzewski [a], Leon Seggering [a, b], Franziska Esmek [a], Irene Fernandez-Cuesta [a]

[a] University of Hamburg, Physics Department, Hamburg, 22761, Germany
[b] Deutsches Elektronen-Synchrotron (DESY), Hamburg, 22607, Germany

E-mail: phil.grzybeck@uni-hamburg.de

Recent progress in micro- and nanofabrication techniques has led to sophisticated nanofluidic devices capable of detecting and characterizing individual particles such as DNA and other biomolecules [1]. In a flow device consisting of two separate microchannels connected by nanochannels, DNA molecules, which are usually coiled, flow through the very confined cross-sections of a nanochannel to enter the other microchannel. To do so, the DNA must untangle (Fig. 1) and move predominantly in a stretched fashion through the nanochannel [2]. With a single laser spot focused on a nanochannel, this DNA produces a fluorescence trace over time, which allows to distinguish between DNA molecules of different lengths. While this laser-assisted detection of molecules (LADOM) provides valuable information, it is inherently limited due to its reliance on peak shape, which is sensitive to a variety of external factors, including variations in the liquid flow. These factors can influence the shape and intensity of the detected peaks, making it difficult to distinguish whether variations arise from changes in particle speed or due to their length. This becomes increasingly problematic when a large number of events should be collected, which requires scans along long times (1 hour), where flow fluctuations and changes can be significant. Long-term measurements are essential for assessing the operational robustness of passive micro- and nanofluidic systems, particularly in view of their potential integration into lab-on-a-chip technologies for biomedical diagnostics.

In this work, we present a novel approach to accurately resolve the velocity of individual DNA molecules flowing in nanochannels using double-spot detection [3]. The measurement setup is designed with two laser excitation spots, spaced a few micrometers apart along a single nanochannel (Fig. 2), enabling us to determine the translocation speed of a passing particle. Incorporating the velocity information enables correction of the peak width. By decoupling velocity from these peak shape artifacts, we obtain a more robust and interpretable metric of particle transport and on the molecular length, conformation and flow dynamics.

We made micro-nano fluidic devices by UV direct imprinting, using a silicon or polymer (Ormostamp) stamp to imprint Ormostamp, dropcasted on an acryl-glass plate, with four pre-drilled holes, serving as liquid inlets and outlets. Fig. 1 shows an SEM picture of the nanochannels in one of the devices. To investigate temporal stability and buffer-dependent effects on flow dynamics, we performed continuous measurements of DNA flow along the nanochannels for up to 60 minutes under passive flow conditions. The experiment was conducted with short DNA molecules (linearised pUC18/19 with 2686 bp) suspended in 0.5x, 0.25x and 0.1x TBE buffer. By varying the buffer concentration, we aimed to assess how ionic strength influences particle velocity and flow stability in the nanochannels. Using our double-spot configuration, we collected raw fluorescence data from 28 long-term measurements (50 to 60 min) and thousands of individual translocation events. A custom Python analysis script was used to extract the peak-to-peak time intervals for each event, allowing us to calculate the velocity of each individual molecule and monitor its evolution over time. By factoring in this velocity information, we were able to correct the average peak width from the different buffer concentrations (0.5x: 11.4 ms ± 0.42, 0.25x: 5.9 ms ± 0.39, 0.1x: 8.1 ms ± 0.41 (with ± indicating relative standard deviation)), resulting in three distributions centered around a consistent mean value of 6.5 ms ± 0.45 ms.

Our measurements reveal that during long-term experiments, significant variations in signal characteristics can occur. By using our double-spot measurement configuration, we ensure that results remain reproducible and comparable across a wide range of buffer concentrations and extended measurement durations. This robustness paves the way for future applications of such systems in simple, mobile, amplification-free and pump-independent single-molecule DNA detection platforms.

[1] Franziska M Esmek et al., Biosensors and Bioelectronics: X (2021) 9 100087.
[2] Franziska M Esmek et al., IOP Science (2022) 33 385301.
[3] Franziska M Esmek et al., IEEJ Trans (2024) 19 840-844.

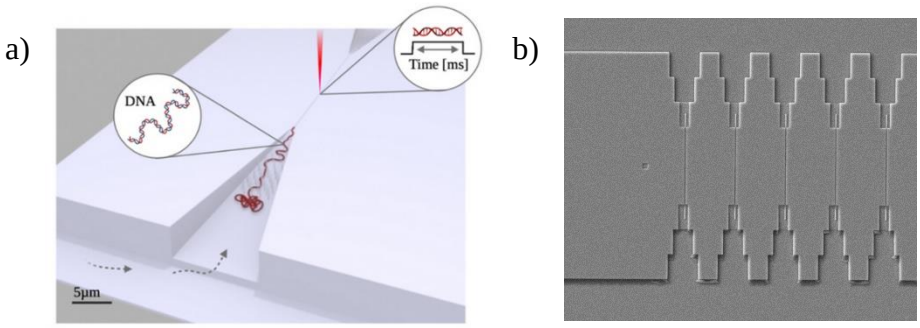

Figure 1. a) Schematic of a DNA molecule uncoiling before entering a nanochannel in a nanofluidic, Ormostamp device made by UV nanoimprinting. b) SEM image of a micro-nano fluidic fabricated device.

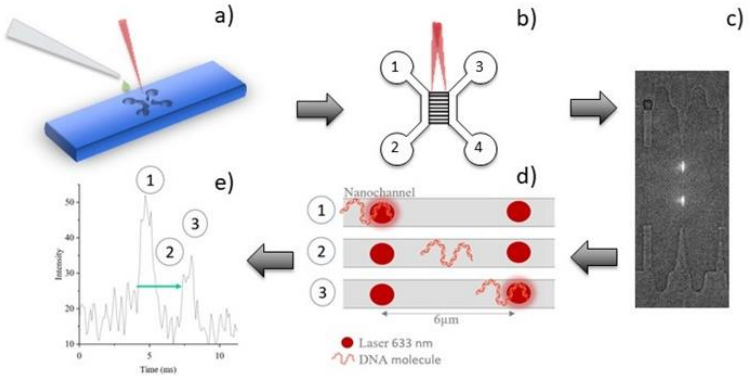

Figure 2. Workflow of laser-assisted DNA optical mapping (LADOM) in steps.
a) Buffer and fluorescent particles or molecules are pipetted into an inlet reservoir of one microchannel of the polymer device. b) Schematic overview of the fluidic device with two laser spots positioned onto the nanochannel. c) Two bright spots indicating the laser spots positioned along a nanochannel. d) Translocation event of a DNA molecule inside the nanochannel and e) its corresponding double-peak signature obtained at the photodetector.

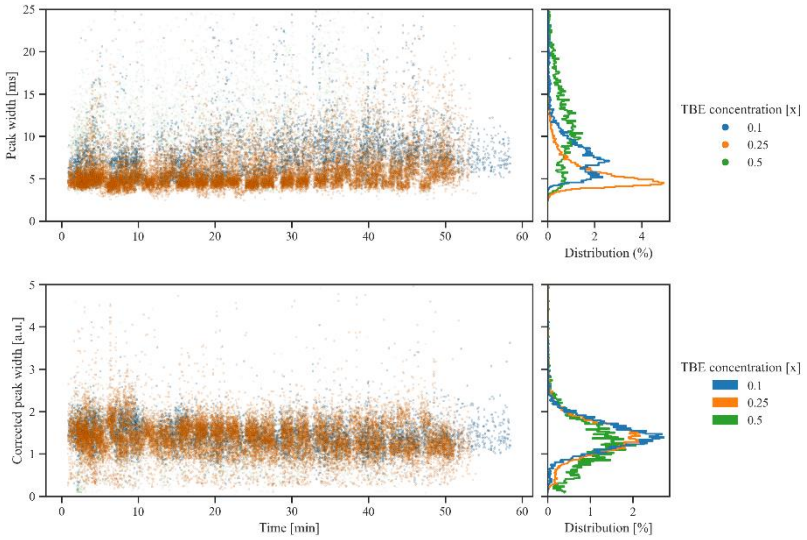

Figure 3. Measured peak widths of thousands of DNA molecules in different buffers, obtained along tens of minutes scans. The upper panel shows the uncorrected peak width of 28 individual long-term measurements, exhibiting high variability. The lower panel displays the same data after velocity correction, resulting in a narrower and more uniform distribution centered around a consistent mean value of 6.5 ms ± 0.45 ms, as shown in the corresponding histograms on the right.

Synchronization of autonomous vibrating electrostatic MEMS torsional mirrors

Yuta Kawashima [a], Mikiya Oki [a], Masaki Shimofuri [a], Amit Banerjee [a],
Jun Hirotani [a] and Toshiyuki Tsuchiya [a]
[a] Kyoto University, Kyoto, 615-8540, Japan
e-mail: y_kawashima@nms.me.kyoto-u.ac.jp

We report synchronization of electrostatic MEMS torsional mirrors by using forced synchronization for high-performance optical systems of large scan angle, high speed, and high resolution. To improve these performance indices together with ensuring the mechanical reliability, we have proposed a system using an array of 4×4 micromirrors, each with a diameter of 150 µm square. However, synchronized oscillation of arrayed mirror is difficult because of variations in the resonant frequencies due to fabrication errors. In this study, we propose a synchronization method for a micromirror array using forced synchronization. By phase locked loop, we autonomously oscillated the micromirrors at its resonance. Then, we applied an external force signal to this autonomous oscillator and confirmed that the vibration frequencies of both mirrors are matched.

Background

MEMS mirror is used in spatial light scanning systems such as laser display, endoscopy, and LiDAR [1]. In these applications, it is demanded to improve the performance such as scan range, framerate, and resolution. Therefore, MEMS mirrors with large deflection angle, high resonant frequency, and large mirror size are needed. To meet this requirement, we have proposed a system using an array of tiny micromirrors [2]. Achieving a large aperture with a single mirror is challenging because of the mechanical reliability issue [3]. A smaller mirror has higher resonant frequency and larger deformation angle without increasing the stress on the torsional beams and reduces optical aberration caused by deformation of the mirror plate. The small aperture is compensated by arraying mirrors, but the variation of the resonant properties of mirrors is an issue.

Description of synchronization method

As a synchronization method, we used forced synchronization, which refers to the phenomenon in which the vibrating frequency of an autonomous oscillator—an oscillator that vibrates at a constant frequency solely through internal energy supply—is pulled toward the frequency of an external periodic force. The experimental setup is shown in Figure 1. We autonomously oscillated each micromirror at a constant frequency employing phase locked loop and applied minute ac voltage as an external periodic force to each autonomously vibrated mirror to induce forced synchronization. The vibration state of each mirror was monitored by measuring the output voltage from the detection electrode, which reflects the capacitance change corresponding to the mirror's velocity. Figure 2 shows schematic design drawings and optical microscope image of electrostatic MEMS torsional mirror. A mirror plate of 150 µm square is suspended by a pair of 2-µm-thick and1.5-µm-wide torsional beams on a 10-µm-thick silicon on insulator (SOI) wafer.

Results

Figures. 3a and 3b show the waveforms and frequency spectrums of the output signals of the left and right mirrors before and after adding external signal. From Fig. 3b, there is a 40 Hz frequency difference between the two mirrors. However, after adding the external force signal, as shown in Figure 3c, forced synchronization occurs, and the vibration frequencies of both mirrors are entrained to the external signal frequency. Furthermore, to investigate the synchronization region, the initial frequencies of the left and right mirrors (f_1, f_2) were detuned symmetrically from the external frequency f_e , with f_1 shifted downward and f_2 upward, under various values of the external signal amplitude ε. Fig. 3c shows the measured synchronization region. As the amplitude of the external signal increased, the synchronization region expanded. As a future work, we plan to compare the scanning performance of a single mirror with that of an array mirror employing this synchronization method, in order to evaluate the effectiveness of the array configuration.

Acknowledgements: This work is partially supported by KAKENHI Grant JP25K22077.

[1] S. T. S. Holmström, et al, *J. Microelectromech. Syst.* 23 (2014), pp. 259-275.
[2] T. Nakamura, et al., *Proc. IEEE MEMS 2020*, pp. 1157-1160.
[3] P. J. Brosens, Applied Optics, 11.12 (1972), pp. 2987-2989.

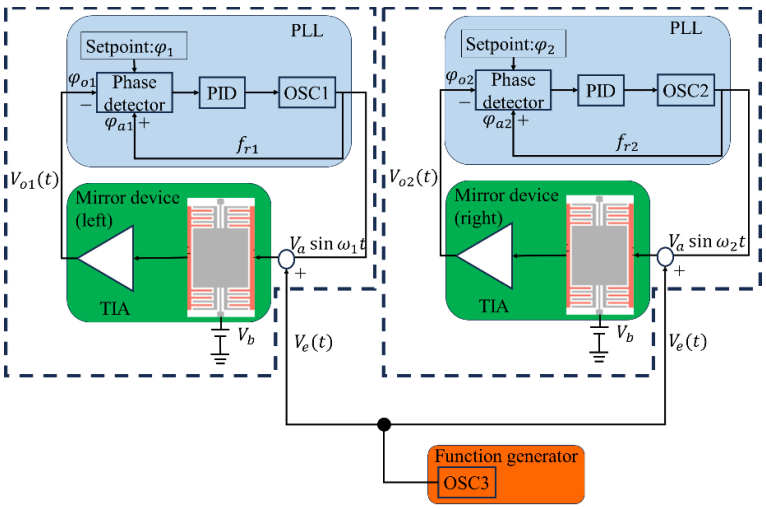

Figure 1. Schematic diagram of synchronization experiment with external force.
(The dotted line represents an autonomous vibration system.)

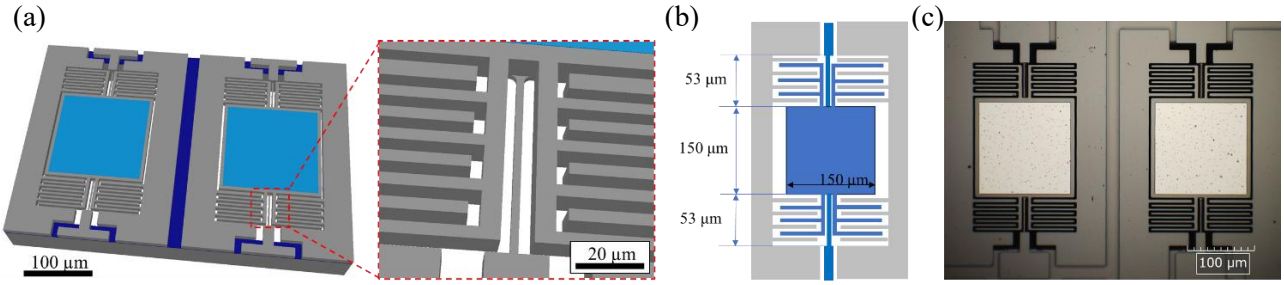

Figure 2. Electrostatic MEMS torsional mirror. (a) Schematic view of 1× 2 MEMS mirror array.
(b) Dimensions of single mirror. (c) Optical microscope image of fabricated mirror array device.

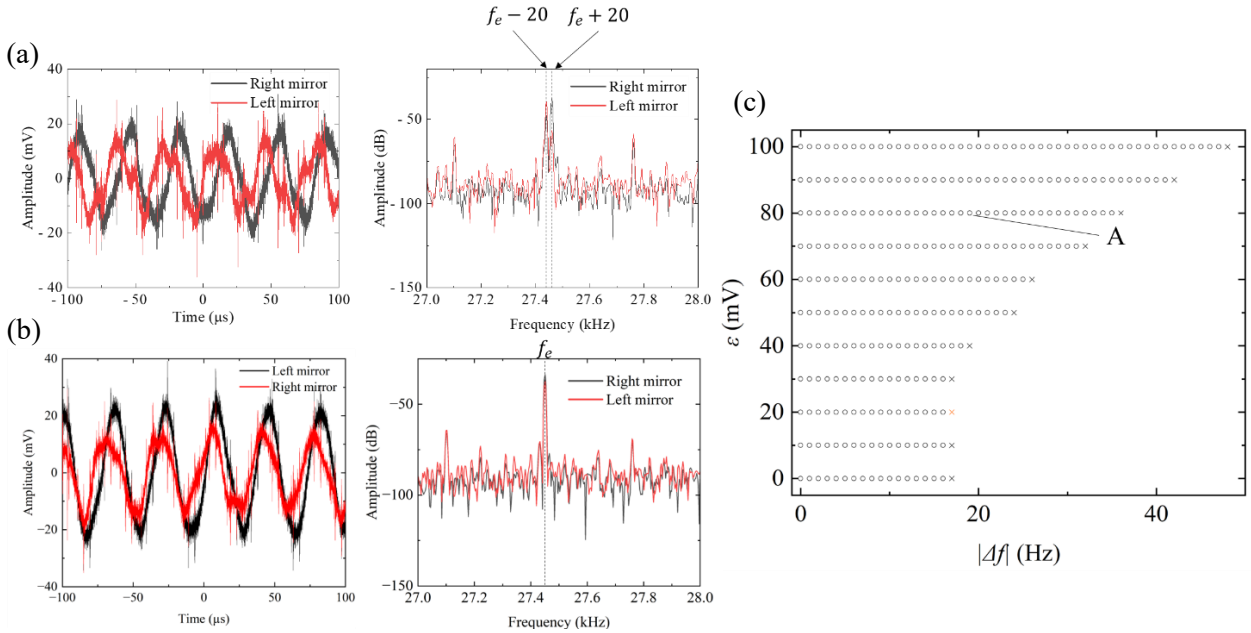

Figure 3. Synchronization results. (a), (b) Raw waveform and FFT spectrum of left and right mirrors at point A in Fig. 3c (a) before and (b) after adding external signal.
(c) Synchronization region. Δf: Frequency difference of f_1 and f_2 from f_e.
○: Both mirrors were synchronized; ×: At least one mirror was unsynchronized.

Solution-Processed UV-Vacuum-Heat (UVVH) Treated Mixed Size Zinc Oxide Nanoparticle Diode-like Device for Ion Sensing Applications

M. Qu [a], H. Dai [a], O. R. Kapur [a], S. P. Beeby [a], and H. M. H. Chong [a]

[a] School of Electronics and Computer Science, University of Southampton, SO17 1BJ, UK
e-mail: mq1g19@soton.ac.uk

Introduction

Zinc oxide nanoparticles (ZnO NPs), as an n-type semiconductor, have garnered significant research interest due to their low toxicity, environmentally friendly fabrication processes, and wide bandgap [1]. The deposition of ZnO NP films can be achieved via solution-based methods that eliminate the need for high-temperature processes. Such solution-processing techniques offer broad applicability, suitable for fabricating electronic devices on various substrates. However, solution-deposited ZnO NPs typically exhibit high resistivity and limited electrical stability, primarily attributed to the adsorption of atmospheric oxygen molecules, which trap electrons within the nanoparticles and reduce carrier concentration [1,2].

The UV-Vacuum-Heating (UVVH) process has been demonstrated to remove adsorbed ionized oxygen, thereby decreasing the film's resistivity. When combined with ethylene-vinyl alcohol (EVOH) passivation, this low-resistivity state can be maintained for up to two months [3]. Li et al. have further reported that the adsorption process can be modulated by an applied electric field [4]. Consequently, it is hypothesized that the resistivity at the interface between low- and high-resistivity ZnO NPs films can be influenced by the bias voltage, which modulates the adsorption and desorption of oxygen molecules on the nanoparticle surfaces. The fabrication process achieves a diode-like ZnO NPs device, which has potential applications for ion sensing.

Fabrication

Figure 1a) shows the schematic fabrication process diagram of the ZnO NPs diode-like devices. A dispenser printer was employed to deposit carbon electrodes onto a glass substrate. The electrodes had a width of 2 mm and a length of 15 mm. Following deposition, the electrodes were cured at 70 °C. ZnO NPs with a diameter of 100/20 nm (with a ratio of 1:1, 0.2 g) were dispersed in 1.8 mL of methanol using ultrasonication. The resultant ZnO NPs solution was spin-coated onto the pre-patterned glass substrate with carbon contacts at 2000 rpm. The ZnO NPs film was coated with 15 wt% Ethylene Vinyl Alcohol (EVOH) solution in DMSO. The EVOH/DMSO was printed on the ZnO NPs film with a 10 mm width and 15 mm length, and the samples were dried at 80 °C for one hour. The samples were then placed in a vacuum chamber under 365 nm UV irradiation for one hour at 110 °C, then cooled for another hour (UVVH process). The pump was maintained throughout the process to ensure a vacuum environment.

Results

Figure 1b) shows the cross-section of the ZnO NPs film covered by the TiOx and SiO_2 film. **Figure 2** demonstrates the IV response for the diode-like ZnO NPs pH sensors, where the voltage was swept from -1.5 V to 3V. The threshold voltage of the device was positively shifted when the lower pH solution was applied. **Figure 2 a) – e)** shows the 2 pH measurement results done from the one device, and repeated 3 times, then calculates the average and the error bar. **Figure 2 f)** shows the IV curve of 6 pH measurements on a single device. The sensor used pH 9 as the reference. For the pH 9 measurement, the diode-like devices exhibit an off-state current on the order of 10^{-8} A and a turn-on current of approximately 8 x 10^{-5} A, achieving an on/off ratio of 8 x 10^3 at 2.5 V. The threshold voltage of the device was 1.3 V for pH 9 measurement and 2.7 V for the pH 4 measurement, achieving a sensitivity of 233 mV/pH.

Conclusions

We successfully demonstrated a diode-like ZnO NPs through a solution-based deposition method and a UVVH process. The device's diode-like behavior was attributed to the adsorption and desorption of the oxygen molecules on the interface between low- and high-ZnO NPs films. The threshold voltage was 1.3 V for pH 9 solution applied and increased with the low pH solution applied, achieving a sensitivity of 233 mV/pH.

[1] M. A. Franco, et al., Sensors and Actuators Reports, 4, 100100 (2022), doi: 10.1016/j.snr.2022.100100
[2] C. B. Jacobs et al., Sci Rep., 7, 1 (2017), doi: 10.1038/s41598-017-05265-5
[3] M. Qu, et al., *ACS Appl. Electron. Mater*., (2024), doi: 10.1021/acsaelm.4c00355
[4] C. Li et al., *Journal of Applied Physics*, 121, 14, 144503 (2017), doi: 10.1063/1.4979973

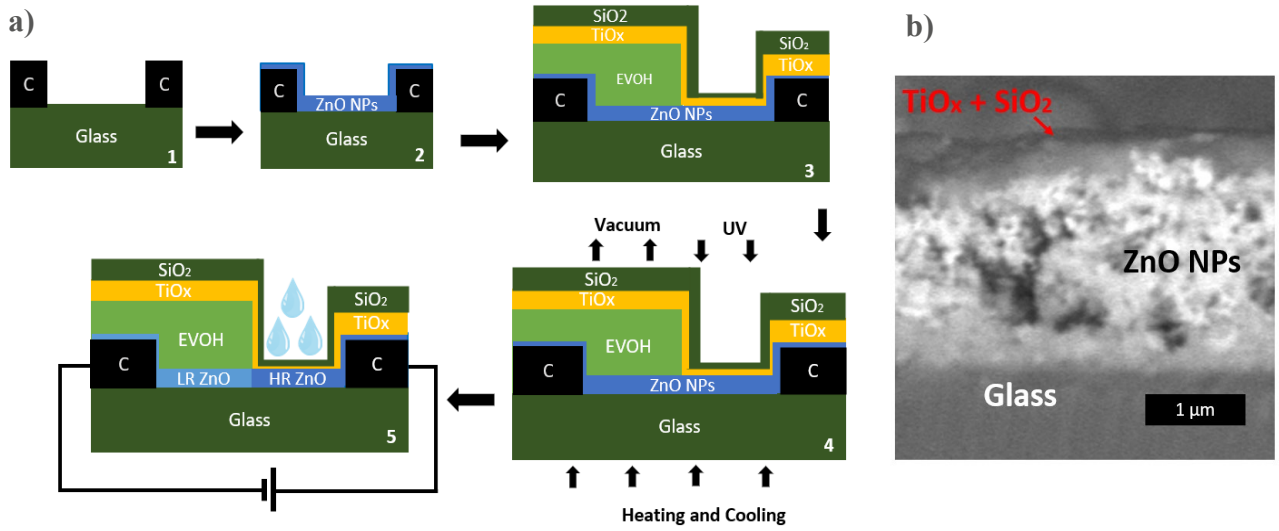

Figure 1.a) Fabrication process of the diode-like ZnO NPs devices. Starting from the dispenser printing the carbon electrode. **b)** Cross section of the ZnO NPs film covered by the TiOx and SiO_2 film.

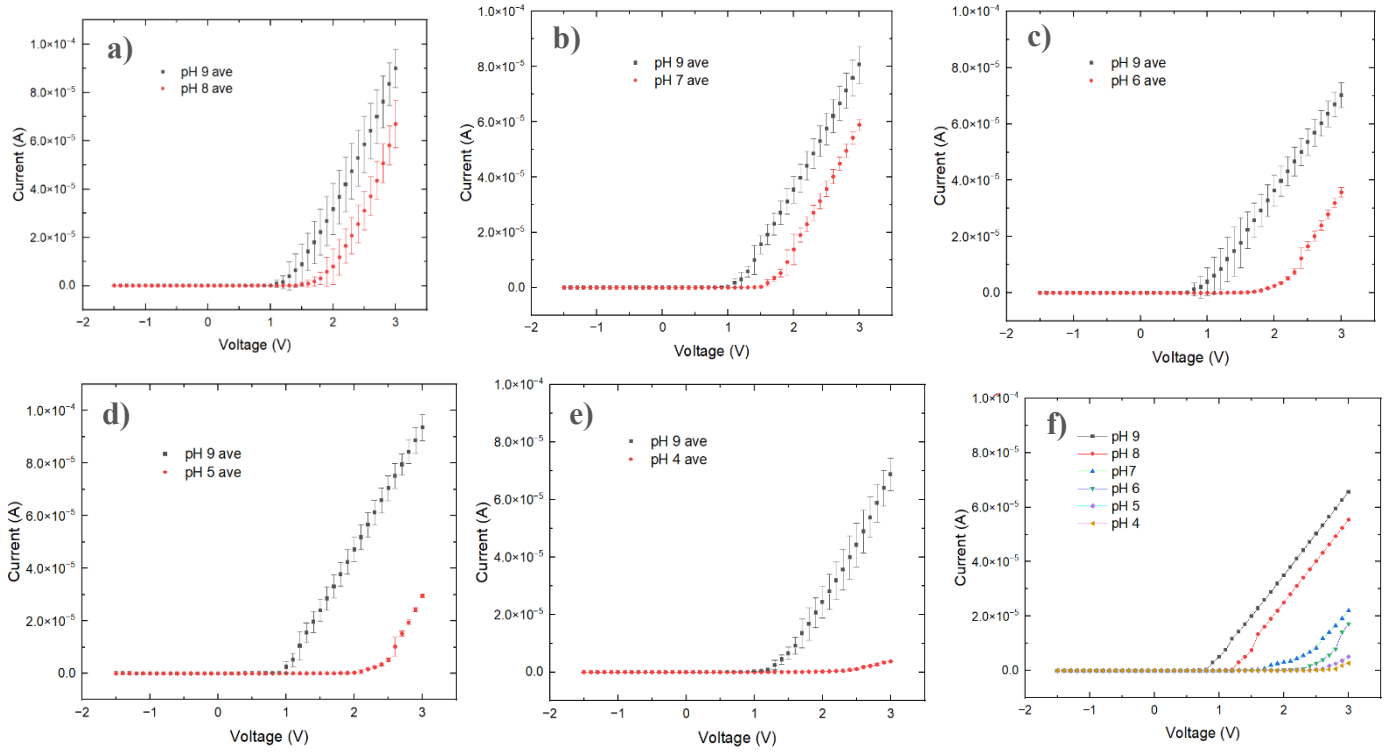

Figure 2. a)-e) IV response for the diode-like pH sensor from 5 individual devices using 100/20 nm ZnO NPs semiconductor film. **f)** IV response from a single device for all the pH measurements.

PEGDA Microfluidic-device featuring a Y-type shape for Hydrogel Microspheres Synthesis Analysis

Villatoro Guillen Anayancy Itzel[1], González Reynoso Orfil[1*], Gomez Salazar Sergio[1], Villalvazo Hidalgo Andrea[1], Martínez Gómez Álvaro de Jesús[1], Romero Estrada Antonio[2] and García Ramírez Mario Alberto[3]

[1] Chemical Engineering Department, CUCEI, Universidad de Guadalajara, Blvd.M. García Barragán #1451, Guadalajara C.P. 44430, Jalisco, México.
[2] Professional Area, Universidad Tecmilenio, Calle Milenio # 8640, Fracc. panorámica Cerro del Tesoro, San Pedro Tlaquepaque C.P. 45530, Jalisco, México.
[3] Electronics Department, CUCEI, Universidad de Guadalajara, Blvd.M. García Barragán #1451, Guadalajara C.P. 44430, Jalisco, México.
[*] Correspondence: mario.garcia@academicos.udg.mx

Abstract:

The microfluidics devices offer remarkable flexibility, integration capability, improved precision and efficient raw materials use [1]. Implementation of different channel sizes and geometries is key to generate monodisperse droplets. The microfluidics operation relies on the viscous forces interplay, capillary forces, nozzle diameter, surface tension between the dispersed and continuous phases. Polyethylene glycol diacrylate (PEGDA) is a polymeric material used in tissue engineering and biomedical applications due to its biocompatibility and ability to form three-dimensional networks through photopolymerization. In this study a numerical analysis was performed in order to find the ideal conditions for the PEGDA hydrogel microspheres formation by using different flow rates featuring a Y-microfluidic device by considering a prepolymer PEGDA hydrogel solution as the dispersed phase and mineral oil as the continuous one. As a result, the numerical analysis shows that the small-size microspheres diameter (200 to 600 µm) is inversely proportional to the flow rate increase for the continuous phase while the dispersed-phase flow rate is kept constant. On the other hand, by decreasing the continuous flow rate, it does not generate the microsphere due to it agglomerates the dispersed phase [2-4]. In contrast, the increment on the continuous flow rate allow to form ovals due to the drift that present the dispersed phase. The application milestone is focused on drug delivery such as in cancer treatments in order to improve the efficiency and reduce the side effects such as cytotoxic ones. By having the smaller the particle, the most efficient it can be.

[1] M. Chen et. al. Molecules, 27, (2022)

[2] D. Debroy et al., Journal of Colloid and Interface Science, 510 (2018) 334–344

[3] M. N. Singh et al, Research in Pharmaceutical Sciences, 5 (2010) 65–77

[4] Y. Wu et al., Journal of Visualized Experiments, 137 (2018)

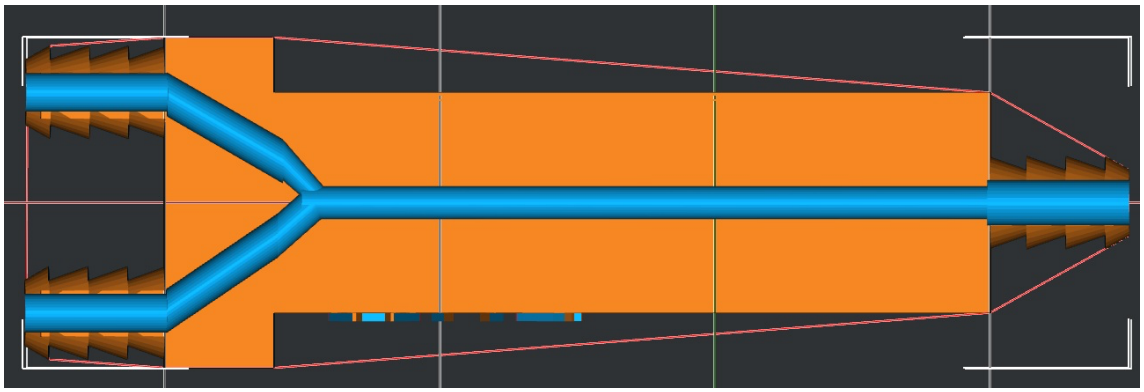

Figure 1. Schematic diagram that features a Y-shaped microfluidic device.

Piezoresistivity in FEBID nanowires imaged via opMEMS straining

Bartosz Pruchnik[a], Magdalena Kucharska[b], Krzysztof Kwoka[a], Tomasz Piasecki[a], Soraya Sangiao[c], José M. De Teresa[c], Ewelina Gacka[a], Dominik Badura[a], Piotr Kunicki[a], Andrzej Sierakowski[b], Paweł Janus[b], Teodor Gotszalk[a]

[a)] Department of Nanometrology, Wrocław University of Science and Technology, 50-370, Wrocław, Poland
[b)] Institute of Microelectronics and Photonics, Łukasiewicz Research Network, Warsaw 02-668, Poland
[c)] Laboratorio de Microscopías Avanzadas (LMA), Instituto de Nanociencia de Aragón (INA), Universidad de Zaragoza, 50018 Zaragoza, Spain

e-mail: bartosz.pruchnik@pwr.edu.pl

Keywords: opMEMS, Lab-in-SEM, giant piezoresistivity, FEBID

Piezoresistivity is the property that enables the resistive measurement of mechanical displacement in solid structures. Electrical strain measurements are used in nanoscopy, nanomechanical sensors and environmental and embedded devices. Piezoresistivity is characterised by the gauge factor (GF), which relates the change in resistance to strain. Typically, it does not exceed 100. However, it is predicted that it may be elevated in one-dimensional structures, namely nanowires [1]. The term 'giant piezoresistivity' is used for a GF greater than 1000.

Conversely, bottom-up nanofabrication enables the development of localised nanowire structures. Focused electron beam induced deposition (FEBID) allows multiple materials to be deposited, including metal-carbon composites (Me(C)). The spatial resolution is better than 2 nm, with a minimal nanostructure diameter of 8 nm. Me(C) materials consist of carbon nanograins embedded in a carbon matrix. This non-uniform structure is predicted to exhibit piezoresistivity and potentially giant piezoresistivity [2].

Here, we report the measurement of giant piezoresistivity in FEBID-developed tungsten-carbon (T(C)) nanowires. GF values exceeding 1000 and reaching 6700 were encountered with a few-fold change in resistance over elongation under 1000 ppm (Fig. 1). We compare the piezoresistive properties of these materials with those of platinum-carbon (Pt(C)) and cobalt (Co), which also exhibit significant GF values, reaching 400. We discuss the possible underlying physical mechanism, which we believe to be the composite nano-grain structure of the materials combined with their heavily limited physical dimensions.

The measurement setup was based on the opMEMS design [3], which operates within the Lab-in-SEM [4]. Nanowires with diameters below 20 nm and lengths below 100 nm were deposited in the area of interest of the opMEMS. The opMEMS was then statically actuated, while the resistance of the nanowire was simultaneously measured. All electrical signals were controlled by a source measurement unit (SMU). The elongation was derived by measuring the displacement of the opMEMS with a laser Doppler vibrometer (LDV). The displacement difference across the region of interest was measured and normalized.

[1] R. He, P. Yang, Nat. Nanotechnol. 1 (2006) 42–46.
[2] G. Ausanio et al., S&A: A Phys. 127 (2006) 56–62.
[3] B. Pruchnik et al., Beilstein J. of Nanotechnol. 15 (2024) 1273–1282.
[4] T. Piasecki et al., Nanotechnol. 35 (2024) 115502.

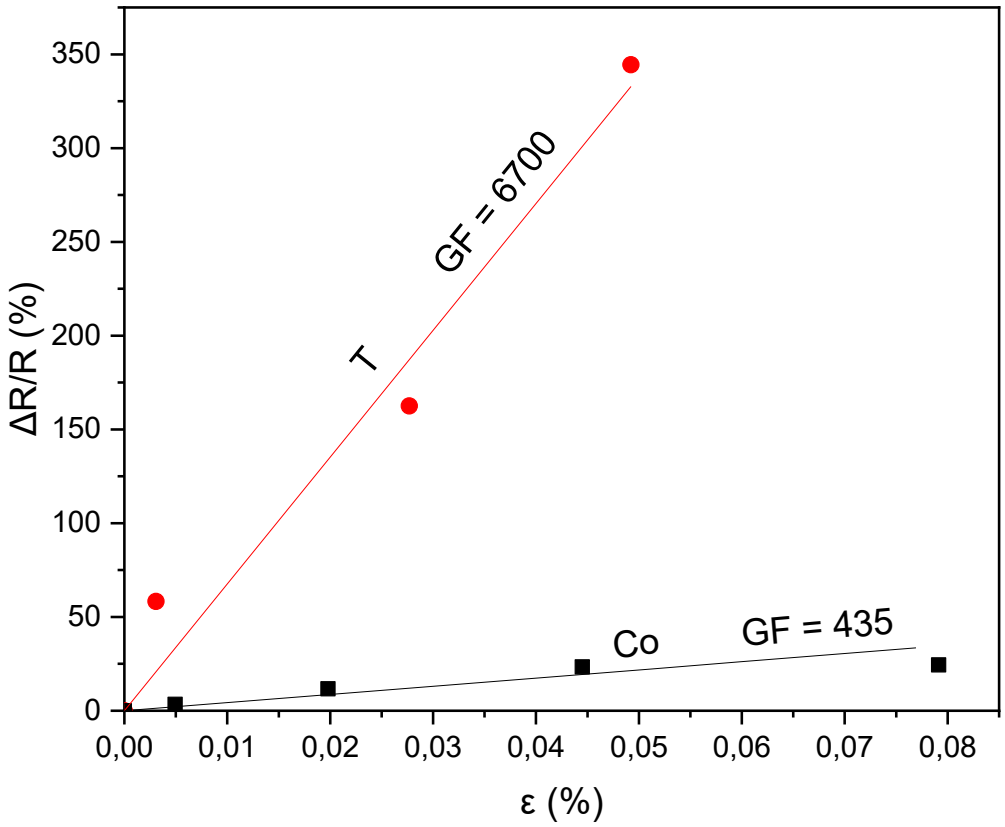

Figure 1. Relative change in resistance over the NW elongation.

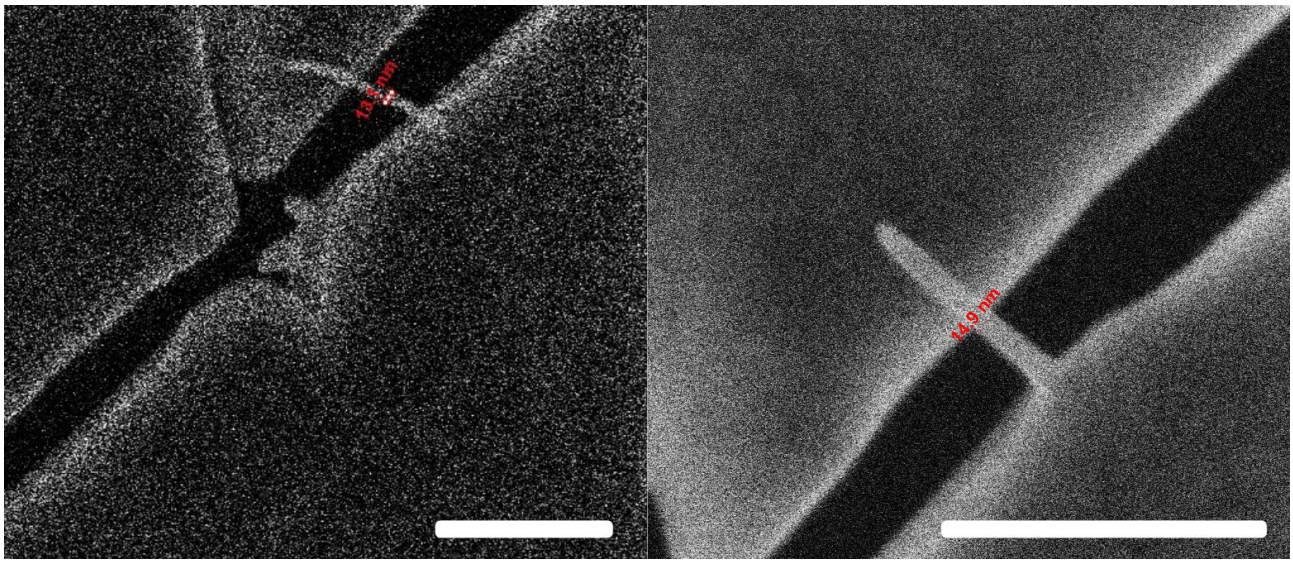

Figure 2. Cobalt (left) and tungsten (right) nanowires deposited in the region of interest of the opMEMS device. Scale bar is 200 nm.

Simulation of contact forces associated with contact wear in MEMS switches

Nasser Aldhahri [a], John W. McBride [b], and Yoshishige Tsuchiya [a]

[a] School of Electronics and Computer Science, University of Southampton, Southampton SO17 1BJ, UK
[b] School of Engineering, University of Southampton, Southampton SO17 1BJ, UK
e-mail: nmaa1n23@soton.ac.uk

Micro-electro-mechanical systems (MEMS) switches offer lower power consumption, excellent isolation, and reduced insertion loss compared to traditional semiconductor switches, and can be used for either RF or DC applications. One of long-standing issues on the MEMS switch technology is to enhance the reliability extending the cycle counts of their switching events. However, a number of issues such as stiction, fatigue, or surface contamination restrict their lifetime, particularly in hot switching scenarios where the transition happens while current is flowing through the switch [1]. Various materials were evaluated to determine their suitability for MEMS switches to extend their lifetime. Among them, the Au on Au-coated multi-wall carbon nanotube (Au/CNT) contact exhibits to maintain a low stable contact resistance for 4 billion cycles in cold switching [2], suggesting significant potential for MEMS contact switch applications. This paper concentrates on simulation of a MEMS switch that utilizes the Au/CNT contact. A particular focus is given onto the simulation of the contact force with consideration of wear of the contact.

Figure 1 illustrates a schematic of a MEMS switch and the dimensions of the beam are as follows: a length L = 300 μm, a width W = 200 μm, and a thickness t = 4 μm, and an initial gap g_0 = 2 μm. We use Au as the structural material with Young's modulus E of 80 GPa. The spring constant $k = 2EW(t/L)^3 \cdot (1\text{-}X)/(3\text{-}4X^3\text{-}X^4)$, where $X = L_g/(L_g + L_e)$ [3], and L_e and L_g are defined in Fig.1.

The contact force $F_c = F_e - F_r$, where the electrostatic force $F_e = \varepsilon_0 A V^2/2g_m^2$, the restoring force $F_r = k(g_0 - g)$, ε_0 is the vacuum permittivity, V is the applied voltage to the electrode, and g and g_m are the gap distance at the contact electrode and at the actuation electrode, respectively. The g_m is defined as $g_m = g_0 - g_0(2L_g + L_e)/2$ [3]. When g = 0 as shown in Fig. 2(a), corresponding to just after contacting, the contact force $F_c = F_e - F_r$ = 0. We obtain the voltage at F_c = 0 of $V_0 \sim$ 15 V. When the V increases, F_e becomes larger as plotted in Fig. 3 (a). According to Ref. [4] for the Au-Au/CNT contact, F_c = 500 μN is required to achieve the contact resistance of less than 1 ohm. From Fig. 3(a), an applied voltage of 54 V is estimated to achieve the desired contact force.

After multiple cycles of contact event, deflection and surface wear are expected on the contact area. For example, experimental results demonstrate that repeated cycles of Au-Au/CNT contact under hot switching conditions result in deflection and wear and exhibit a deflection of 0.545 μm during hot switching of 50 mA after 7 million cycles [5]. Here we attempt to model the surface wear and study how the wear affects the contact force. Figure 2 (b) illustrates how the wear is implemented in the model. After the wear, the initial gap at the contact electrode is changed to $g_0 + g_c$, where g_c corresponds to the depth of the surface deflection. This increment of the contact gap affects the restoring force to be $F_r = k(g_0+g_c)$ at the contact, while the actuation electrode gap is expressed as $g_m = g_0 - (g_0+g_c)\cdot(2L_g+L_e)/2$. Figure 3(c) shows how the contact force F_c is changed with respect to the contact gap increment g_c under the same voltage of 54 V is applied. The results show that an increase of the contact gap as a consequence of deflection leads to an escalation of the contact force. The underlying cause is that the beam moves closer to the actuation electrode, resulting in an increase of the electrostatic force which is larger than an increase of the restoring force. As a result, the contact force increases. This calculation result suggests that after the wear is increased, less voltage is required to achieve the threshold contact force to maintain the low and stable contact resistance, leading to saving the energy by considering gradual reduction of the applied actuation voltage along with the progress of wear in MEMS switch operation.

References:

[1] A. Basu et al., Journal of Micromechanics and Microengineering, 26 (2016) 104004.
[2] J. W. McBride and T. G. Bull, in IEEE Holm Conference on Electrical Contacts, 14-18 September 2019, Milwaukee, WI, USA, pp. 149–155.
[3] I. V. Uvarov and I. A. Belozerov. Micro 4 (2023) 1–13.
[4] M. P. Down et al., Applied Physics Letters 106 (2015) 101911.
[5] J. W. McBride et al., *unpublished.*

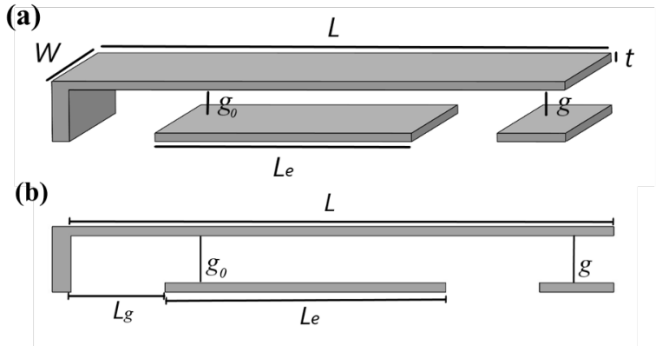

Parameter	Value
Length (L)	300 μm
Width (W)	200 μm
Thickness (t)	4 μm
Electrode Area ($A = W \times L_e$)	200 × 240 μm
Initial Gap (g_0)	2 μm
Distance to the left edge of electrode (L_g)	20 μm

Figure 1: (a) A 3D schematic of a MEMS contact switch. (b) A cross section of the MEMS switch with the symbol definition for the actuation electrode. The dimensional parameters are listed in the table.

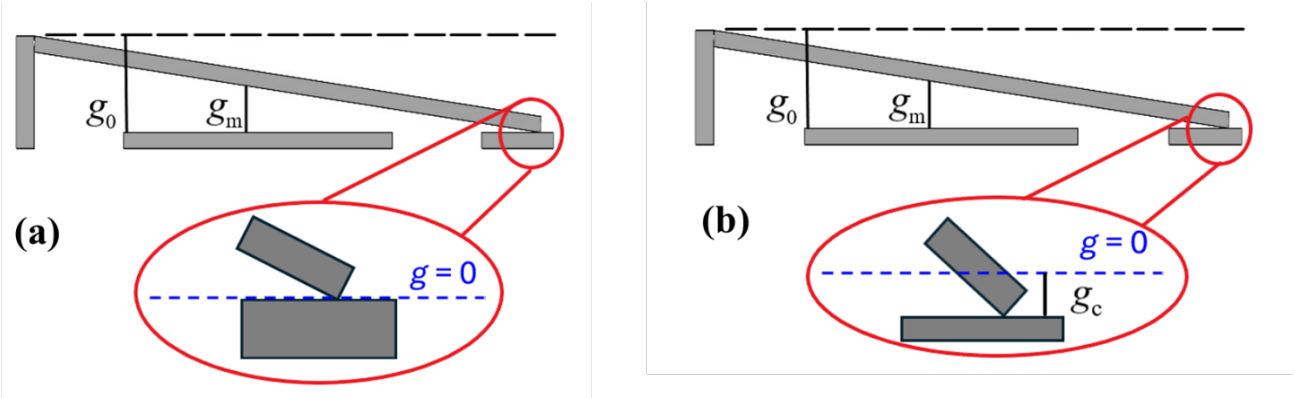

Figure 2: (a) A schematic drawing of the MEMS switch when the contact gap g = 0. (b) A schematic of the model considering the surface wear. The total initial gap at the contact increases to g_0+ g_c after the wear increases.

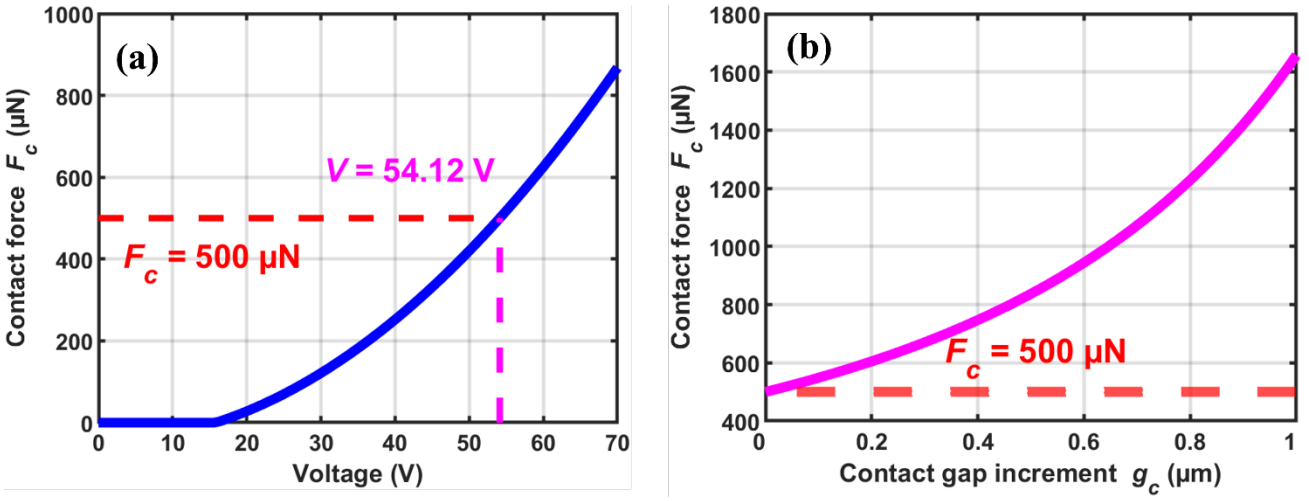

Figure 3: (a) Contact force in response to applied actuation voltage, based on a cantilever structure with L = 300 μm, W = 200 μm, t = 4 μm and g_0 = 2 μm. (b) Contact force corresponding to an increase in contact gap beyond the initial position.

A Hybrid Superconductor/Nanomechanical Magnetic Field Detector for Biomagnetism

L. Pellegrino [a,b], N. Manca [a,b], A. Plaza [a,b], L. Cichetto [a], D. Marré [a,c], F. Maspero [d,e], S. Cuccurullo [e], R. Bertacco [d,e], E. Wahlberg [f], A. Kalaboukhov [f], F. Lombardi [f], T. Hänke [g], D. Mungpara [g], A. Schwarz [g], I. Hilschenz [h], E. Ragucci [a,b,h], S. Spadone [h], W. J. Venstra [i], S. Della Penna [h]

[a] CNR-SPIN, Genoa, 16152, Italy
[b] RAISE Ecosystem, Genoa, 16122, Italy
[c] University of Genoa, Genoa, 16146, Italy
[d] CNR-IFN, Milano, 20133, Italy
[e] Politecnico di Milano, 20133, Milano, Italy
[f] Chalmers University of Technology, SE 41296, Gothenburg, Sweden
[g] University of Hamburg, Hamburg, 22761, Germany,
[h] University of Chieti "G. d'Annunzio", Chieti, 66100, Italy
[i] Quantified Air BV, Leiden, 2312NV, The Netherlands
e-mail: luca.pellegrino@spin.cnr.it

Current commercial setups for magnetoencephalography (MEG) use helmets comprising superconducting quantum interference devices (SQUIDs) made of low critical temperature superconductors. SQUID sensors are barely robust to static and pulsed magnetic fields, such as the ones used in Ultra-Low Field Magnetic Resonance Imaging (MRI) and especially Transcranial Magnetic Stimulation (TMS). For this reason, integration of MEG with these techniques in a unique system at present has not yet been achieved.

Our purpose is to develop a magnetic field sensor with sensitivity of the order of 10fT/sqrt(Hz) to measure the magnetic field of the human brain and at the same time quickly recovering in a strong applied field (» 1 T). This sensor would be suitable for an on-scalp MEG system integrated with multiple imaging modalities to image brain activity and connectivity with high spatial and temporal resolution. We are developing a hybrid device by coupling a high-Q micro/nanomechanical (M/NEMS) resonator having a magnetic element to a high-Tc superconducting magnetic field focuser in series to a pick-up loop that collects the external magnetic field. The biomagnetic field induces a supercurrent in the loop, which has a geometry designed to generate a strong non-uniform magnetic field in the proximity of the magnetic element of the resonator. The resonance frequency of the resonator is modified by this magnetic coupling and detected by a fiber-optic interferometer. Optomechanical detection of biomagnetic fields has the advantage of reducing the crosstalk between the channels with respect to electrical detection. This feature requires the development of a cheap, robust and scalable optomechanical platform for a future M/NEMS-based helmet. We discuss the basic working principle of this hybrid sensor and the advancements made so far for the realization and characterization of the first device prototypes as well for the realization of the optomechanical platform that will host the first magnetometer to be characterized in operative environment.

This project has received funding from the European Union's Horizon 2020 research and innovation programme under Grant Agreement No. 828784 (www.oxinems.eu). This work was also funded by the European Union - NextGenerationEU and by the Ministry of University and Research (MUR), National Recovery and Resilience Plan (NRRP), Mission 4, Component 2, Investment 1.5, project "RAISE - Robotics and AI for Socio-economic Empowerment" (ECS00000035).

[1] Patents no. US11415642 and EP3896470B1 "A device for sensing a magnetic field".

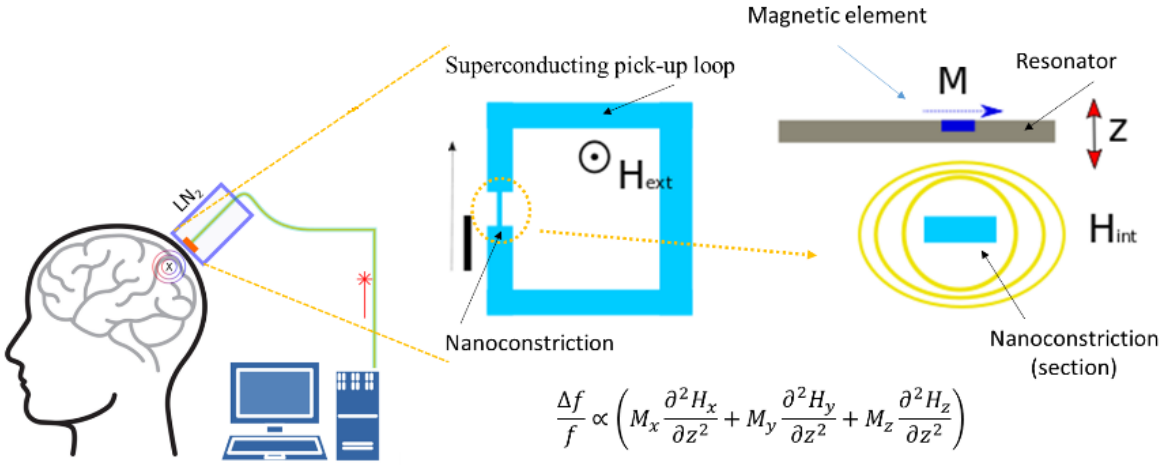

Figure 1. The principle of the OXiNEMS hybrid magnetometer.

Development of a 3-Channel Solar-Blind UV-C Sensor for Determining Source Location and Intensity

Keekeun Lee[a]

[a]Ajou University, Suwon, 16499, S. Korea
e-mail: keekeun@ajou.ac.kr

Abstract: This study presents a high-performance solar-blind UV-C corona sensor using β-Ga_2O_3/Al_2O_3 integrated with a surface acoustic wave (SAW) platform, achieving sub-second response times and a detection limit of 0.1 μW/cm² . A 3-channel electronic interface enables real-time localization and intensity mapping of corona discharges. The sensor demonstrates excellent sensitivity, stability, and long-term reliability, validated through multi-channel testing for accurate UV-C corona detection and positioning.

Introduction: Partial discharge (PD), often caused by insulation defects, contamination, or aging, poses serious risks including power outages, equipment failure, and electrical fires. Corona discharge, a form of PD, emits UV-C light and other signals due to ionization in strong electric fields. While UV cameras are effective for corona detection, their high cost and bulk limit widespread use. Compact UV-C sensors offer affordability but struggle with accuracy, durability, and interference. To overcome these limitations, this study introduces a SAW-based UV-C sensor array that enables real-time detection of corona direction, intensity, and location in the solar-blind UV-C range. The 3×1 angled sensor array features enhanced material stability, rapid response, and built-in environmental compensation, offering a significant advancement over existing methods.

Optimal Design and Experimental Methods: The system comprises three SAW sensors, a reference device, and integrated interface electronics. Each sensor detects 254 nm UV-C light by measuring frequency shifts caused by changes in SAW velocity due to interaction with a Ga_2O_3/Al_2O_3 sensing layer (Fig. 1). A 222 MHz two-port SAW delay line enhances sensitivity and reduces insertion loss. A 3D-printed scaffold orients the sensors at specific angles for directional detection and provides electromagnetic shielding. Interface electronics—comprising oscillators, a multiplexer, mixer, low-pass filter, comparator, FPGA, and PC—process the sensor outputs and display real-time, temperature- and humidity-compensated results (Fig. 2). SAW sensors were fabricated on 128° YX $LiNbO_3$ substrates using lithography and Ti/Pt deposition. The sensing film was applied via RF sputtering, optimized with rapid thermal annealing, and passivated with an ultrathin Al_2O_3 layer for improved surface quality and electronic performance. The system was tested using a controlled UV setup with xenon lamps and wavelength-specific filters.

Results and Discussion: The fabricated sensor, with a 20 nm Ga_2O_3 and 2 nm Al_2O_3 sensing layer, operated at 222 MHz and showed clear, direction-specific frequency shifts under UV-C exposure. When mounted on a 3D-printed scaffold, the 3-channel system accurately identified the direction and intensity of incoming UV-C signals. Sequential and simultaneous exposure tests confirmed rapid, repeatable responses, with visual warnings displayed using a color-coded system (Fig. 3). Built-in compensation using the reference SAW device ensured stability against temperature and humidity variations. The sensor maintained high sensitivity and consistent performance under varied environmental conditions.

Conclusion: This study demonstrates the first integration of a Ga_2O_3/Al_2O_3 sensing layer with a SAW platform for real-time, solar-blind UV-C corona detection using a multichannel sensor array. The system offers ultrafast response, high sensitivity, and accurate directional sensing, with successful field validation confirming its potential for practical corona monitoring applications.

[1] K. Lee et al., ACS sensors, 6 (2021) 4145-4155.
[2] K. Lee et al., IEEE Sensors Journal, Complexity, 25 (2024), 343 – 353.

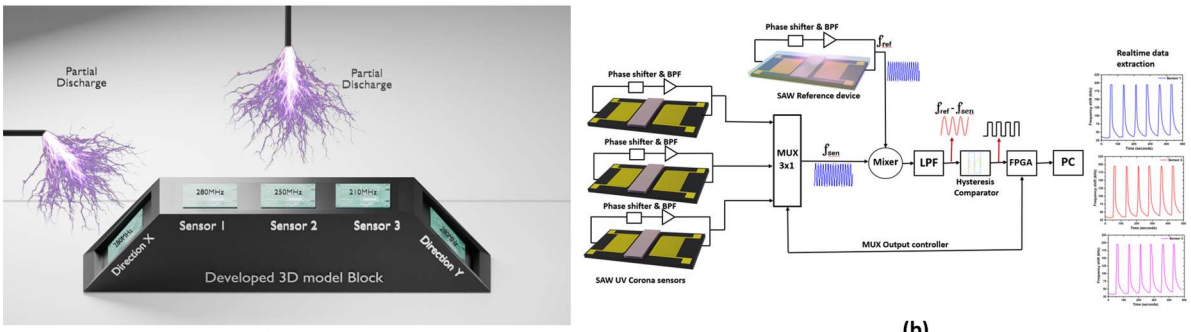

(a) (b)

Figure 1. (a) Overall view of the sensor system and (b) 3-channeled sensor's interface electronics

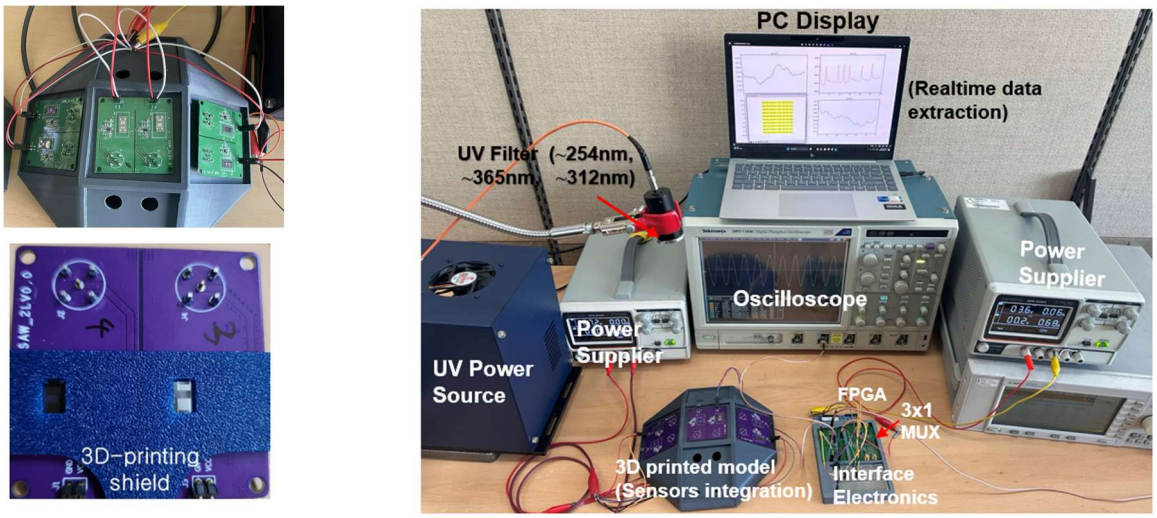

(a) (b)

Figure 2. (a) Optical views of the fabricated sensor and sensor's scaffold and (b) testing setup.

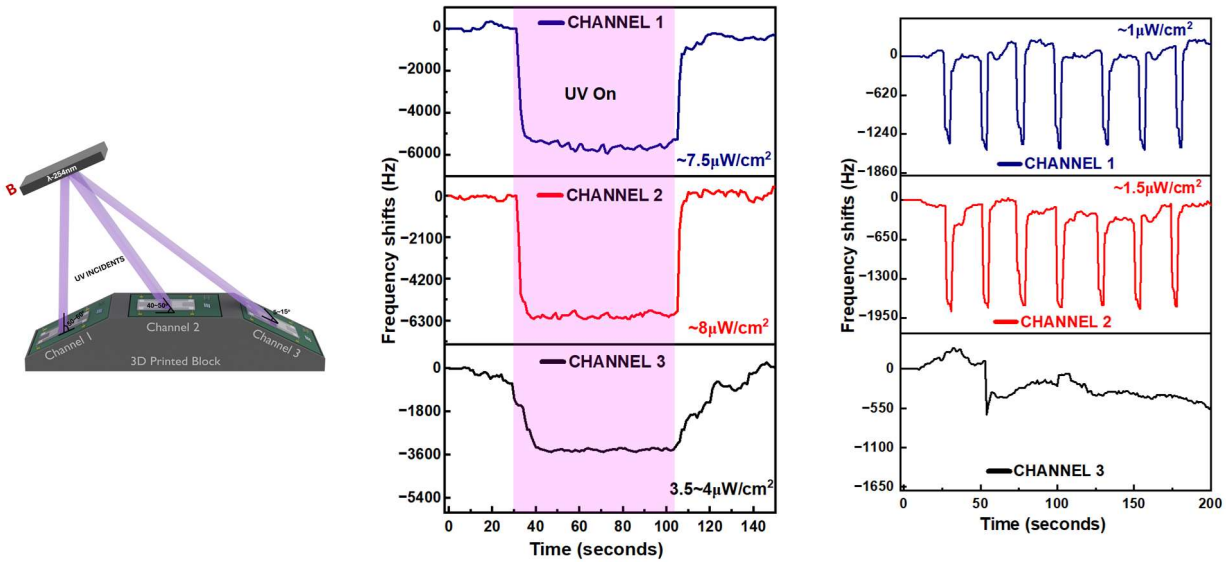

(a) (b)

Figure 3. (a) UV-C illumination at skewed angles and the measured results for each channel.

Electrostatic Manipulation of Low Surface Tension Liquids on Silica Nanowire-based Slippery Liquid-infused Porous Surfaces

Ching Chi Lin [a], Yueh Tse Lin [a], Jiann Shieh [a],

[a] Department of Materials Science and Engineering, National United University, Miaoli, Taiwan
e-mail address: jshieh@nuu.edu.tw

Slippery liquid-infused porous surfaces (SLIPS) were first introduced by Wong et al. [1]. Compared to conventional superhydrophobic surfaces, SLIPS replace the air pockets with a lubricating liquid, resulting in a more stable and durable surface. Furthermore, due to the use of low-surface-energy liquids, droplets with various surface tension can move freely on SLIPS, expanding their range of applications. The working principle of SLIPS involves infusing a lubricant into a porous surface. The surface roughness helps to lock the lubricant in place. To create such rough and porous structures, techniques such as polymer coatings, photolithography, or laser processing are commonly used [2]. However, challenges remain in terms of surface adhesion of coating and process complexity. In addition, typical SLIPS surfaces are not transparent, which also limits their practical applicability.

Previously, we developed a method to fabricate silica nanowires that provides glass substrates with both high optical transparency and superwetting properties [3]. This nanowire-coated glass also serves as an ideal platform for triboelectric manipulation of water droplets [4]. In the present study, we apply this substrate to create a SLIPS surface, where the extremely tiny nanowires help to stably retain the lubricant. As a result, the surface exhibits low sliding resistance for droplets of water, alcohol, and acetone, enabling precise electrostatic control over their movement.

Figure 1a shows that growing silica nanowires on quartz glass increases the contact angles of water, ethanol, and acetone on a surface with silicone lubricant (KF96-50CS). This enhancement leads to significantly lower sliding angles for the droplets—approximately 1° for water, 1.31° for ethanol, and 1.65° for acetone (Figure 1b)—compared to the untreated control surface, where droplet sliding angles reached up to 30°. These low sliding angles are essential for effective triboelectric manipulation. To evaluate the electrical properties of the droplets, we used a nanocoulomb meter (Monroe 284) to measure their net charge. The results (Figure 2a) show that all droplets carry a positive charge that increases with droplet size. Moreover, the charge magnitude follows the order: water > ethanol > acetone, suggesting a correlation with the polarity of the liquids. It is worth noting that low-polarity liquids with low surface energy and minimal charge are typically difficult to manipulate on conventional superhydrophobic surfaces. The use of SLIPS with silica nanowires overcomes this limitation, enabling reliable electrostatic control even for such challenging liquids.

To manipulate droplets, triboelectric charging was generated by rubbing a PTFE rod against a glove, reaching charge saturation within 5 seconds (Figure 2b). This electrostatic charge enabled Coulombic attraction, causing droplets to follow the movement of the PTFE rod (Figure 2c). For programmable and precise control, we modified a commercial 3D printer to serve as an automated manipulation platform. The PTFE rod was mounted on the printer head, with its motion governed by a custom Arduino program. This setup allowed droplets to trace predefined paths with high repeatability and programmability (Figure 2d). Notably, effective droplet manipulation was also achieved from the backside of the glass substrate (Figure 2e). An additional advantage of SLIPS is its ability to mitigate the influence of surface defects. For instance, even in the presence of laser-etched grooves on the glass surface, droplets could still be guided across the track via electrostatic forces (Figure 2f). In summary, incorporating nanowires into SLIPS surfaces enhances contact angles and reduces sliding angles, thereby enabling effective electrostatic manipulation of various liquids. This approach demonstrates a simple strategy for achieving programmable droplet motion using triboelectric charging.

Reference

[1] T. S. Wong, S. H. Kang, S. K. Y. Tang, E. J. Smythe, B. D. Hatton, A. Grinthal, J. Aizenberg, Nature 477 (2011) 443.
[2] J. Li, Z. Zhou, X. Jiao, Z. Guo, F. Fu, Surf. Interf. 53 (2024) 105037.
[3] J. Shieh, G. F. Huang, J. Y. Tsai, B. W. Huang, Y. F. Huang, STAR Protocols 3 (2022) 101066.

[4] W. C. Huang, M. Y. Chang, J. Shieh, C. H. Lin, C. C. Hsu, Adv. Mater. Interfaces (2025) in press.

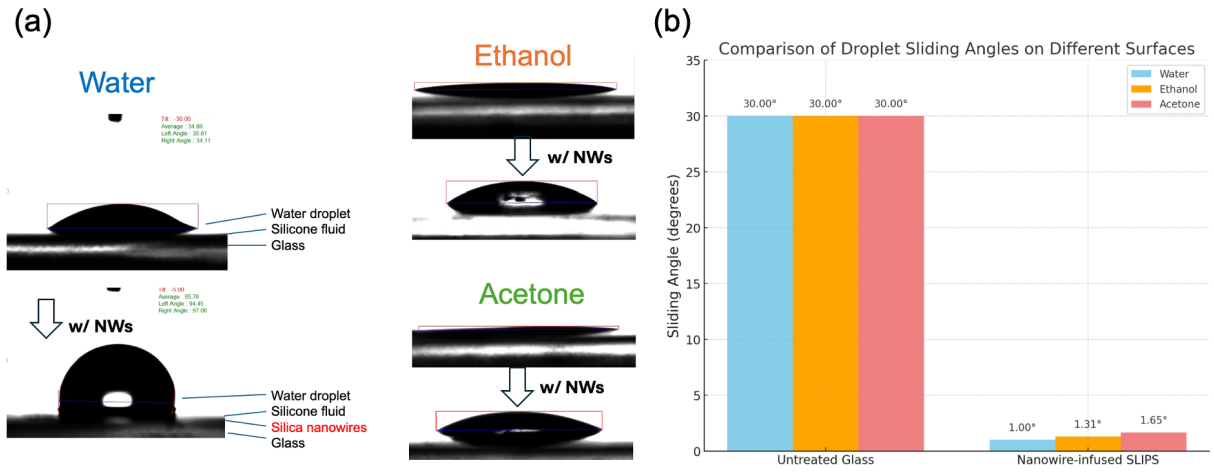

Figure 1. (a) Contact angles and (b) sliding angles of water, ethanol, and acetone on SLIPS with and without silica nanowires introduced between the glass substrate and the lubricant layer.

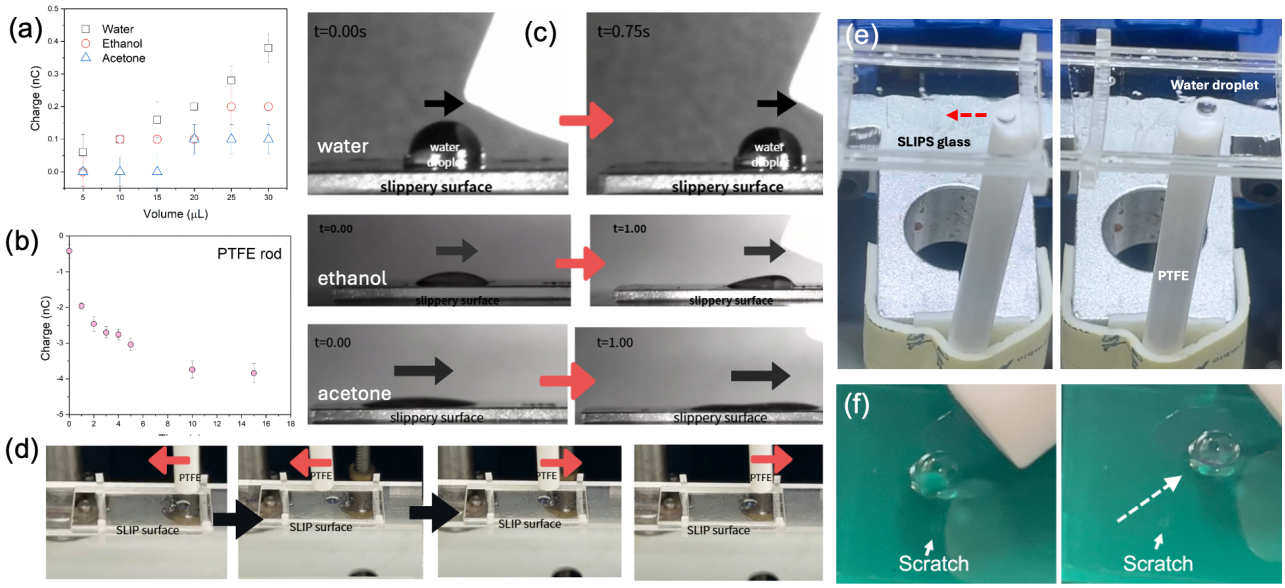

Figure 2. (a) Measured charge carried by water, ethanol, and acetone droplets of varying volumes. (b) Accumulated triboelectric charge on a PTFE rod as a function of rubbing time. (c) Motion of various liquid droplets on the SLIPS surface. (d) Bidirectional movement of an ethanol droplet guided by a PTFE rod controlled by a programmable motor. (e) Demonstration of water droplet manipulation from the backside of the SLIPS substrate. (f) Electrostatic-guided motion of a water droplet across a laser-etched groove on the SLIPS glass.

Edge Engineering for Intrinsic Cold-metallic Injection Source in 2D FETs

Zhirong Peng [a], Ning Ji [b], Jinchen Wei [a], Kwok-Ho Wong [a], Tin Shing Ho [a], Lining Zhang [b], Mansun Chan [a]

[a] ECE Department, The Hong Kong University of Science and Technology, Hong Kong SAR, China
[b] School of Electronic and Computer Engineering, Peking University, Shenzhen, China
e-mail: zhirong.peng@connect.ust.hk

For further improving the energy efficiency of modern transistors, suppressing thermionic carrier injection is a potential strategy against Boltzmann limit. Two-dimensional (2D) devices have remarkable eletrostatic controllability while off-state leakage current is still limited by conventional "hot" metal contacts with thermal broadening of the Fermi-Dirac distribution [1]. Cold metal sources filter out high-energy carriers by sharp decline in density of states (DOS) near the Fermi level (E_F), thus suppressing the thermal tail effect [2]. Experimentally, the graphene nanoribbon has demonstrated its potential as cold source [3], while MoS2 nanoribbons are still mainly applied to channel [4]. Herein, the cold metal characteristics of zigzag-oriented (ZZ) MoS_2 NR is realized by edge engineering. With a significant conduction gap above the Fermi level, the hot electrons can be filtered out at off-state, leading to low electronic transmission.

The ZZ MoS_2 NRs are established as shown in Fig. 1a. Both edges of ZZ MoS_2 NR are ended at sulfur (S) atoms for a better stability, and passivated with pseudo-hydrogen to eliminate dangling bonds while preserving the metallic character of pristine ZZ edges. The ZZ MoS_2 NRs with different width, in the range of 1 nm to 10 nm, are constructed and named as ZZ_N (N=1, 2, 3…), where N denotes the number of Mo-S hexagon rings along x direction. Both un-passivated and passivated ZZ MoS_2 NRs structures exhibit metallic characteristics (Fig. 1b and 1d), which are different from their host 2D structures. In the passivated structure, a conduction gap (E_{CG}) of ~0.467 eV emerges, endowing the ZZ MoS_2 NR with cold source characteristics in n-type devices. The E_{CG} is caused by the pulled-down energy level (marked in green and orange respectively in the band structure), corresponding to the partial charge density plotted in Fig. 1c and 1e. The edge S atoms exhibit two types of coordination: S_1 atoms bonded to one Mo atom and S_2 atoms bonded to two Mo atoms. Upon passivation, a sharper downward energy shift of S_1-derived states can be witnessed than that of S_2-related states due to additional bond formation, consequently results in E_{CG} and thus the cold metallic characteristic.

It is notable that the cold metal properties of ZZ MoS_2 NRs can be extended ranging from 1 nm to 10 nm with the same cold metal formation mechanism (see Fig. 2a and 2b). This band originates from the Mo edge near the S_1 sites (Fig. 1c and 1e), giving further assurance of the metallicity of the ZZ MoS_2 NRs. Fig. 2c plots the lower (E_L) and upper (E_H) bounds of the E_C as a function of width. The presence of a clear E_{CG} above the Fermi level across all widths confirms that the cold metallic feature persists over a wide range of lateral dimensions. Fig. 2d shows the total energy of each structure as a function of nanoribbon width. The total energy of the ZZ MoS_2 NR is linearly correlated with the width, implying similar electronic structure as it scales.

With metallic ZZ_5 as intrinsic source, the cold-sourced device can be constructed as shown in Fig. 3a. Due to a distinct energy window above the Fermi level where the DOS are significantly low, the hot electrons are cut with small gate voltage (Fig. 3b), leading to suppressed hot thermal tail effect. As a result, an electrons filter window can also be observed in the transmission spectrum (Fig. 3c). This energy-selective transmission mechanism underpins the superior performance of cold-metallic sources in minimizing off-state leakage current. To conclude, we proposed that intrinsic cold-metallic ZZ MoS_2 NR can function as the source in MoS_2-based transistors via edge engineering. With an energy gap of ~0.467 eV above the Fermi level, the high-energy electrons can be effectively filtered out at off state. Its robustness is well maintained across a width range of 1 nm to 10 nm, underscoring its potential for continuously scaled low-power device applications.

Acknowledgement: This work was supported by the General Research Fund (GRF) 16203222 from the Research Grants Council (RGC) of Hong Kong.

[1] Y. Zhao et al., *The Journal of Physical Chemistry C* 126 (2022) 12100-12112.
[2] F. Liu et al., *2018 IEEE International Electron Devices Meeting* (2018).
[3] C. Qiu et al, *Science* 361 (2018) 387-392.
[4] P. Ramesh et al., *Micro and Nanostructures* 190 (2024) 207845.

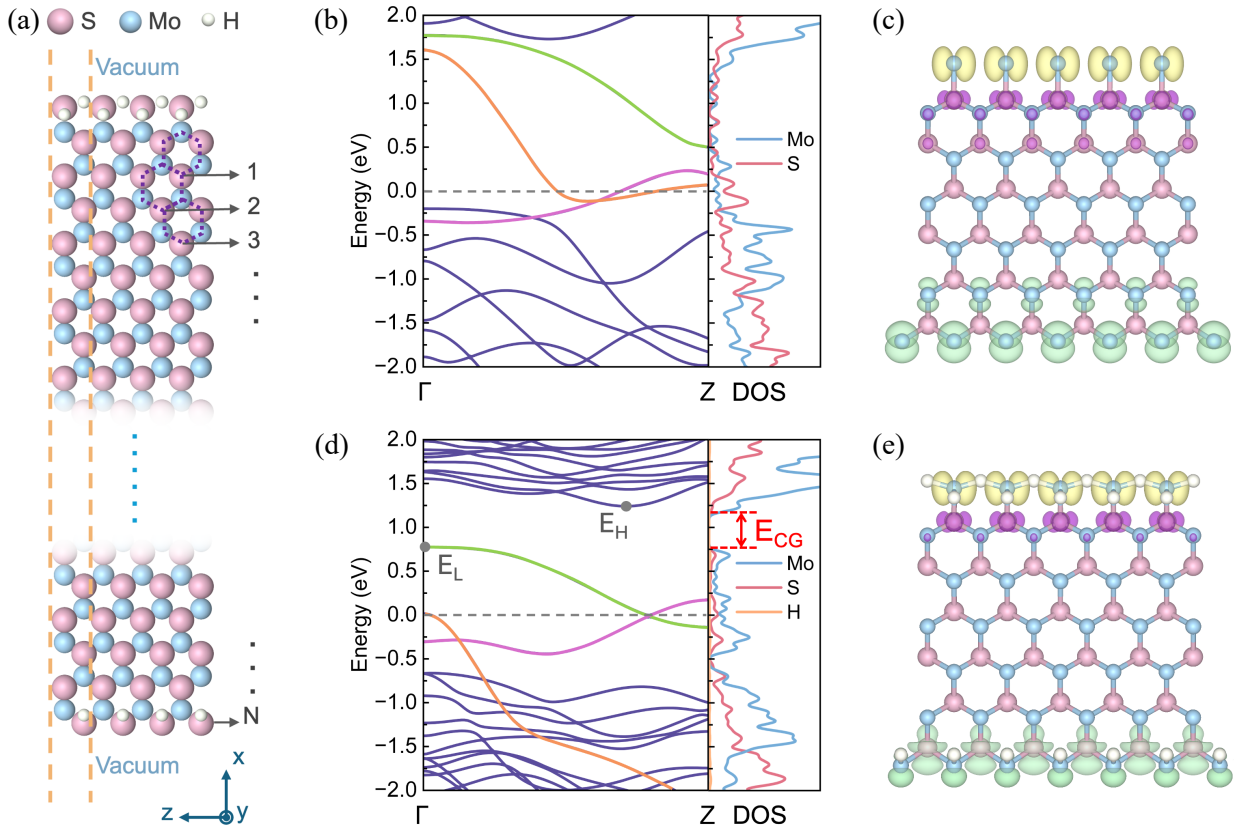

Figure 1. (a) Schematic illustration of ZZ MoS_2 NRs, and the dashed orange line denotes the nanoribbon unit cell. The band structures with DOS diagram, and partial charge density of the bands around Fermi level of ZZ_5 (b, c) without and (d,e) with edge engineering. The Fermi level is set to zero.

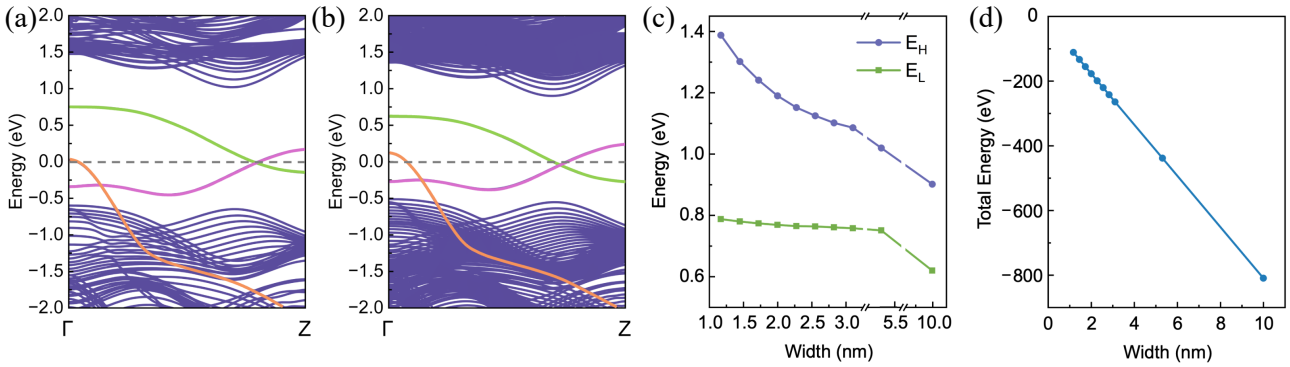

Figure 2. Band structures of (a) ZZ_{18} with ~5 nm width and (b) ZZ_{35} with ~10 nm width. (c) The lower (E_L) and upper (E_H) bounds of the E_{CG}, and (d) the total energy as a function of nanoribbon width.

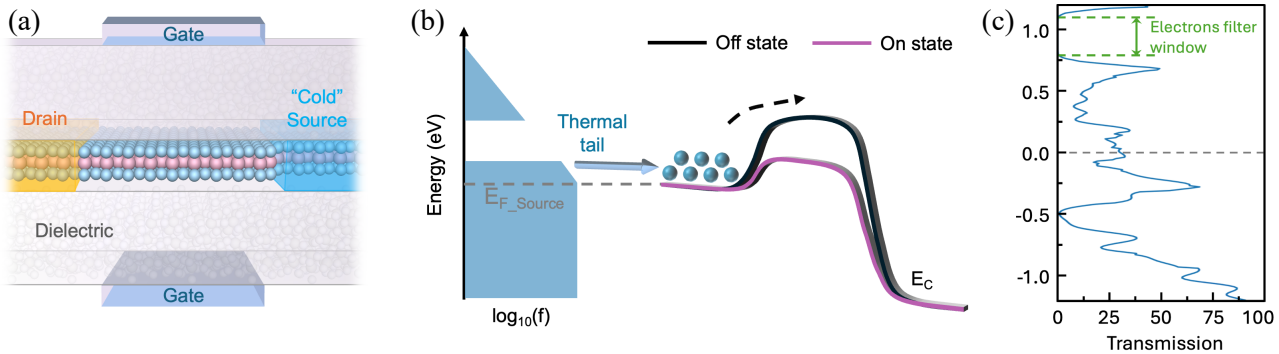

Figure 3. (a) Device construction and (b) working mechanism of FETs with cold sources. The DOS-weighted transmission of cold metal ZZ_5, and the Fermi level is set to zero.

Plasmonic antenna-VO_2 hybrid metasurface for all-optical nonlinearity

D.I. Trubacs[a*], K. Sun[a], I. Zeimpekis[b], and O. L. Muskens[a]

[a]School of Physics and Astronomy, University of Southampton, SO17 1BJ, UK
[b]School of Electronics and Computer Science, University of Southampton, SO17 1BJ, UK
[*]e-mail: D.I.Trubacs@soton.ac.uk

Key words: Vanadium Dioxide, Metasurfaces, Plasmonic Antennas, Optical Nonlinearity

Abstract

The benefits brought by the current Artificial Intelligence (AI) come at a great energy cost, with AI systems demanding ever-increasing computational power. A solution to this problem is photonic computing, which promises to have a much smaller carbon footprint than electronics. While many photonic devices have already been developed to emulate their electronic counterparts, all-optical non-linearity in their design - which is a key requirement for implementing AI algorithms – remains a challenge.

Vanadium dioxide (VO_2) is a promising candidate in this area, as its ultrafast metal-insulator transition (MIT) can be induced all-optically [1] and its switching behavior can be tuned when combined with plasmonic antennas [2]. In this work, we demonstrate that a plasmonic antenna-VO_2 hybrid metasurface exhibits a strong and tunable all-optical nonlinear response to the power of incident light measured on the sample. Unlike many other past works, where many external stimuli are required to induce the MIT, we have used a single source of light: a 1550 nm laser.

A full fabrication flow process of the VO_2 device is shown in Figure 1. Fabrication started with a 1 mm thick glass substrate, onto which electron-beam resist (ZEP520A) was spin-coated and patterned to form the antenna shapes. Next, a gold (Au) layer of thickness 45 nm was formed using electron-beam evaporation. The deposited Au layer was then lifted-off in N-Methyl-2-pyrrolidone (NMP) solvent at room temperature. Afterward, VO_2 with a thickness of about 40 nm was deposited through atomic layer deposition (ALD). The ALD growth parameters were reported in a previous publication [3]. After deposition, the VO_2 was annealed in oxygen to crystallize VO_2 into VO_2(M1), giving the material its crucial phase-transition capabilities.

The fabricated devices consist of 36 square arrays each in size of 120 µm × 120 µm (Figure 2 left), with the length (L) and dimer gap (DG) of the antennas being varied between the square arrays, whilst the width of the antennas (W) and the gap (G) between them stayed constant (Figure 2 right).

Optical characterization, using Fourier Transform Infrared Spectroscopy, shows that the C21 antennas are resonant at ~2 µm, while the C22-C25 antennas are resonant at ~1.2 µm. By modulating the power of a 1550 nm pump laser polarized along the antenna's long axis (Figure 3), optical switching is induced with the MIT in VO_2 being observed at ~30 mW. When the bare film is patterned with Au antennas, the switching threshold can be reduced to as low as ~10 mW. More interestingly, in the C21 array, which has a lower frequency resonance than the other antennas, the MIT happens continuously. Unlike the other sharp transitions, this response can be more suited to emulate smooth nonlinear functions.

The development of a reliable optical nonlinearity is crucial for advancing photonic computing. Our results indicate that VO_2-based plasmonic metasurfaces can provide a strong and tunable optical response to devices working at telecom wavelength. Moreover, by carefully tuning the antenna's shape for specific resonances, the nonlinear optical response can be made into a smooth function, more closely matching activation functions used in neural networks.

[1]. J. Parra et al, Scientific Reports 15, 5608 (2025).
[2]. K. Sun et al, Nanophotonics 11, 17, (2022): 4101-4114.
[3]. O.Muskens et al, Light Science and Applications 5, e16173 (2016)

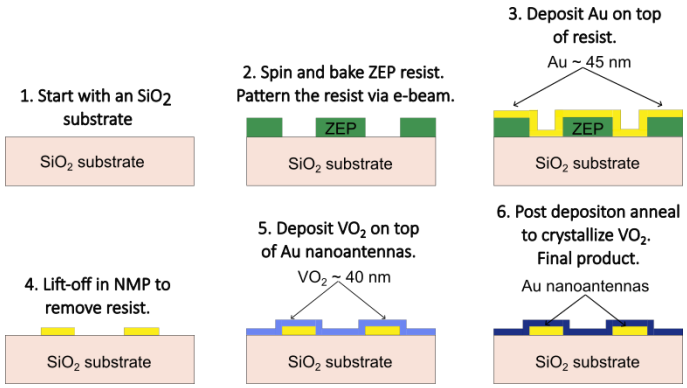

Figure 1. The fabrication process flow of the plasmonic antenna-VO_2 hybrid metasurface. **1,** Initial glass substrate. **2**, Patterning of EB resist. **3**, Au deposition by e-beam evaporation. **4**, Lift-off in NMP. **5**, Deposition of VO_2 by ALD. **6**, Post-deposition anneal in oxygen.

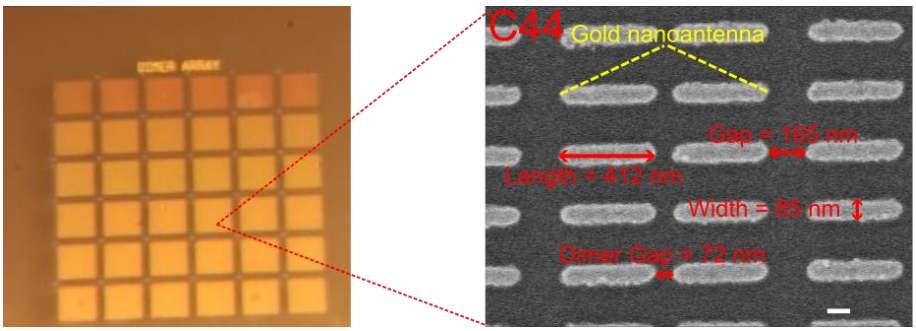

Figure 2. (Left) Micrograph showing 36 arrays of plasmonic antenna-VO_2 hybrid metasurface. (Right) SEM image of one antenna-VO_2 with L=400 nm and DG=100 nm design. The SEM bar is 100 nm. C44 represents the name of the square array based on the column and row in the metasurface.

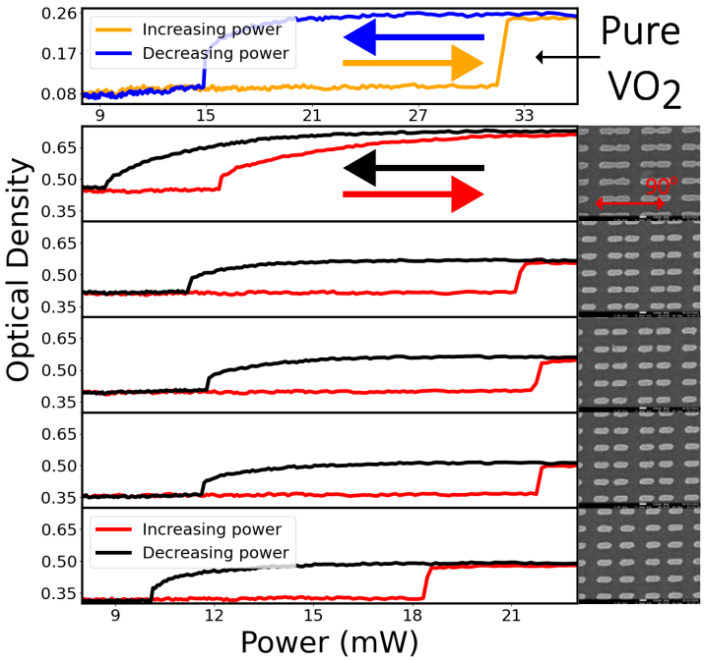

Figure 3. Optical density vs the power of incident light on the metasurface. The source of light is a single 1550 nm laser. The polarization of light is set to 90°. The data is presented from top to bottom, starting with the response of the plain VO_2 and followed by arrays C21 to C25. SEM images of each antenna array are shown on the right.

A massive-scale droplet microfluidic platform based on an active matrix of high-voltage thin-film transistors

Hongjun Liu, Rongyue Liu, Kaicheng Huang, Shaohu Zhan, Jiaze Liu, Qin Luo, Haiyue Ye, Senlin Yan, Qi Guo, Zhen Liu, Yaru Xing, Chunhui Wu, and Xing Cheng
Department of Materials Science and Engineering, Southern University of Science and Technology
Email: chengx@sustech.edu.cn

Droplet-based digital microfluidics are useful alternative to channel-based continuous flow microfluidics. Particularly, droplets actuated by EWOD or DEP forces allow facile manipulation of droplets in large scale using microfabricated electrode arrays. In recent years, electrode arrays driven by active-matrix thin-film transistors (TFTs) are gaining increasing attention due to its automatic operation and potential in scalability. However, current TFTs from flat panel display industry operates at a voltage of 40-60 volts, and this voltage level is often insufficient in driving droplets with less polarity, which sometimes requires a driving voltage of more than 100 volts. Additionally, droplet heating required in applications such as on-chip PCR often expedite the threshold voltage shift in TFTs and render the TFTs unusable after prolonged period of heating and electrical biasing.

To address the limitations of current TFTs in actuating digital microfluidic platform, we design, fabricate and tested a new architecture of TFTs. The cross-sectional view of the new design and a fabricated device based on a-Si is shown in Fig. 1. By splitting channel into two sections and employing internal floating back gates, the new device can withstand high source-drain voltage while approximately maintains the same source-drain current level. Electrical characterizations of the device are shown in Fig. 2. The transfer curve (top left) and the output curve (top right) show a well-behaved a-Si TFT. The high-voltage biasing in Fig. 2 (bottom left) shows the new device can withstand up to ~ 390 volts before breakdown, which has much better high-voltage performance compared to conventional device structure. The device after breakdown is shown in Fig. 2 (bottom right).

A 400x400 AM array of electrodes driven by our high-voltage TFTs is fabricated through a multi-project on glass (MPG) program from Tianma (Fig. 3). With custom-built peripheral electronics and user-interface software, we build a droplet microfluidic platform, which is capable of fully automatic actuation of hundreds of droplets. By utilizing AI imaging sensing, we achieve droplet splitting with high accuracy (~2% CV). We also demonstrate that biologically meaningful applications such as sample preparations for genomics and proteomics analysis can be completed reliably on our platform.

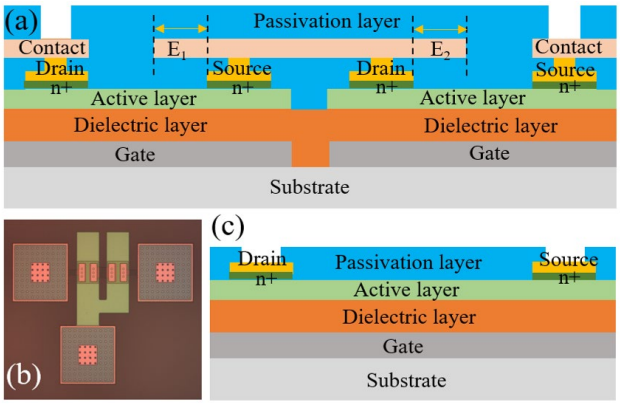

Fig. 1. (a) Device structure schematic for high-voltage TFT. (b) Optical image of high-voltage a-Si TFTs. (c) Device structure schematic of conventional a-Si TFTs for comparison.

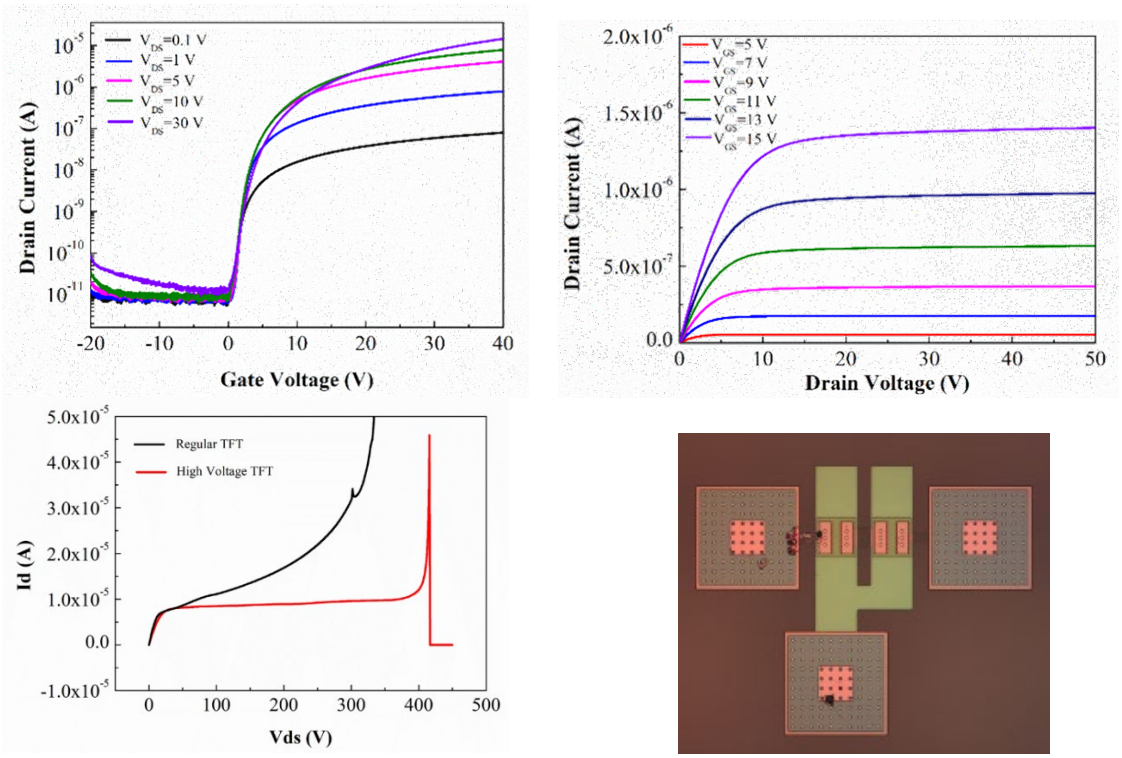

Fig. 2. Electrical performance of high-voltage a-Si TFTs. Top left: transfer curve; Top right: output curve; Bottom left: high-voltage performance; Bottom right: optical image after electrical breakdown.

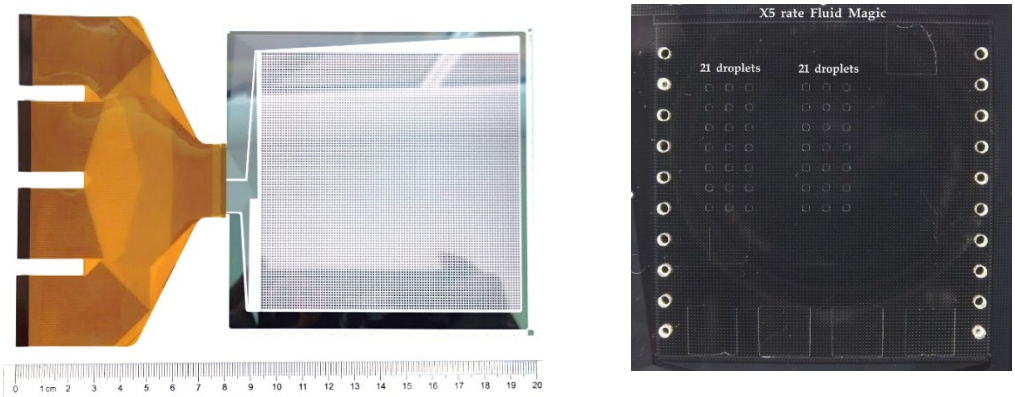

Fig. 3. Left: Optical image of an AM electrode array with high-voltage a-Si TFTs; Right: Parallel droplet actuation on digital microfluidic platform.

Vertically-Integrated VRRAM-Based Hardware Reservoir Computing System

Jihee Park[a], Sungjun Kim[a,*], Hyun Kim[b], Soo Youn Kim[c], Myounggon Kang[d], and Seongjae Cho[e]

[a]Division of Electronics and Electrical Engineering, Dongguk University, Seoul 04620, Republic of Korea
[b]Department of Electrical and Information Engineering, Seoul National University of Science and Technology, Seoul 01811, Republic of Korea
[c]Department of System Semiconductor, Dongguk University, Seoul 04620, Republic of Korea
[d]Department of Intelligent Semiconductor Engineering, School of Advanced Fusion Studies, University of Seoul, Seoul 02504, Republic of Korea
[e]Department of Semiconductor Engineering, Ewha Womans University, Seoul 03760, Republic of Korea

[*]E-mail: sungjun@dongguk.edu

Recent advances in neuromorphic computing have highlighted the urgent need on hardware-driven energy-efficient architectures capable of learning and inference with lower energy consumption and smaller signal latency [1]. Also, recently, reservoir computing has emerged as a highly influential paradigm that enables fast and simple training while maintaining the capability to process input data with high uncertainty [2,3]. Traditional implementation of reservoir computing systems, however, often rely on separated hardware elements to emulate short-term memory in the reservoir layer and long-term memory in the readout layer, respectively, and has a high dependency on software and algorithmic operations. This approach not only increases system complexity and footprint but also poses limitations for integration in a single-process batch. In this research, a fully-hardware-based reservoir computing system in which both reservoir and readout functionalities within a single physical unit are integrated is presented.

The core of our system is a memory technology that inherently exhibits dual-switching behaviors including both volatile and nonvolatile operations depending on bias conditions. These dual-mode characteristics allow a single memory cell to serve as a dynamic reservoir and a stable readout element at the same time, dramatically simplifying fabrication process and system configuration. The volatile operation mode demonstrates the essential properties required for reservoir computing, including information fading and nonlinearity. These features allow the system to transform input data into high-dimensional rich states that preserve temporal dependencies and encode meaningful dynamics. Unlike conventional artificial neural networks which usually require extensive training of all the layers, the reservoir computing architecture proposed in this work does not necessitate weight updates within the reservoir, significantly reducing training complexity and resource consumption at the same time. For the readout layer, the memory cell is operated in the nonvolatile operation mode, realizing gradual and linear conductance modulation across multiple levels. This enables robust vector-matrix multiplication operations and accurate mapping of reservoir states to output responses. In order to enhance weight tunability and precision, pulse techniques such as incremental pulse schemes and feedback algorithms were employed. These strategies significantly improve linearity, reduce device-to-device variation, and ensure higher stability over repeated operation cycles. Furthermore, our system has been benchmarked using classification tasks the more realistically reflect the demands on pattern recognition in the daily lives. Through the application of adaptive programming algorithms, higher accuracy comparable to fully-software-based reservoir computing models has been plausibly achieved, while realizing substantial reductions in power consumption and system complexity. Also, the integrated architecture gets rid of the need for either additional selection devices or external storage elements, which are required in the large-scale neuromorphic systems in many recently reported cases. Beyond the functional performances, the proposed architecture offers key advantages in scalability and manufacturability. The compact vertical design of the cell array facilitates high-density integration for vertical resistive-switching random-access memory (VRRAM) [4], making it well-suited for embedded systems aiming the edge AI applications with portability. In addition, batch fabrication over both reservoir and readout layers improves volume and power efficiencies.

This work demonstrates a novel hardware-oriented reservoir computing architecture that simultaneously satisfies the requirements for short-term temporal processing and long-term state retainability. By leveraging the dual-mode behavior of a single memory cell, the system achieves high computational efficiency, reduced training overhead, and minimal power usage, in a highly scaled physical area. These technological advancements lay the groundwork for manufacturable realization of compact, reliable, and energy-efficient neuromorphic processors capable with higher autonomy in the resource-limited environments.

Acknowledgments This work was supported by National Research Foundation (NRF) of Korea funded by the Korean Ministry of Science and ICT (MIST) under Grants RS-2023-00258527 and RS-2024-00402495.

References

[1] S. Cho, Volatile and Nonvolatile Memory Devices for Neuromorphic and Processing-in-Memory Applications, *J. Semicond. Technol. Sci.* 22 (2022) 30.
[2] A. Senanian, *et al*., Microwave signal processing using an analog quantum reservoir computer, *Nat. Commun.* 15 (2024) 7490.
[3] G. Tanaka, *et al*., Recent advances in physical reservoir computing: A review, *Neural Networks* 115 (2019) 100.
[4] S. Yang, *et al*., Demonstration of Synaptic Characteristics in VRRAM with TiN Nanocrystals for Neuromorphic System, *Adv. Mater. Interfaces* 10 (2023) 2300290.

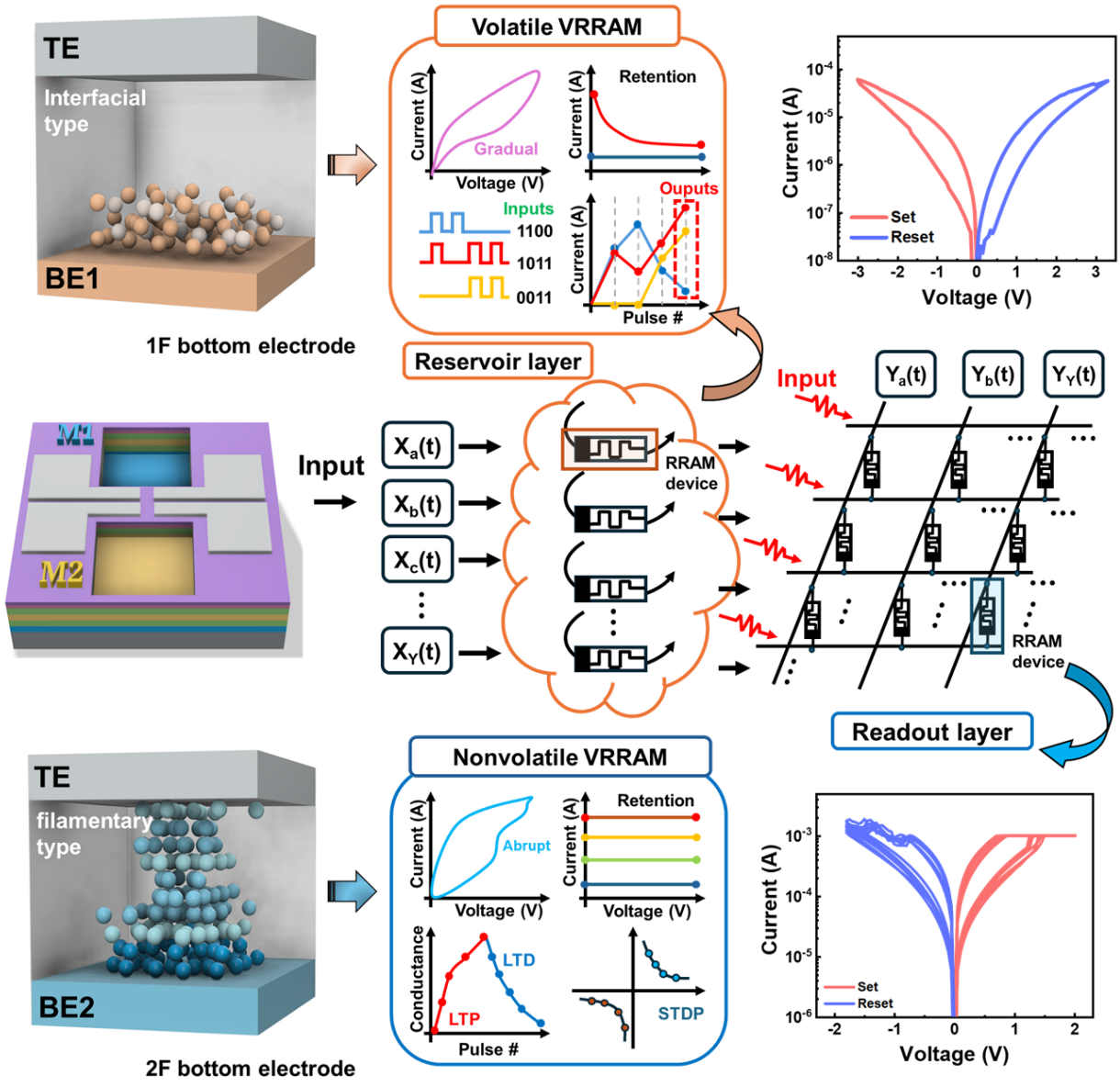

Figure 1. Hybrid reservoir computing system based on VRRAM with volatile and nonvolatile dual-mode operation capability. Volatile VRRAM (top) with interfacial switching forms the reservoir layer, enabling dynamic temporal processing. Nonvolatile VRRAM (bottom) with filamentary switching serves in the readout layer, providing stable weight storage. The system architecture with integrated reservoir and readout layers can be schemed in a batch integrated fabrication. It is notable that the dual-mode operations are realized in a single synaptic memory cell, with the modes switchable simply by bias conditions, which makes the overall system implementation highly simple in terms of fabrication processing, and reduces cost, volume, and energy.

Optoelectronic Synaptic IGZO Transistor and Its Demonstration of Electrical and Optical Plasiticity for Light-Susceptive Processing-in-Memory

Suyong Park[a], Sungjun Kim[a], Hyun Kim[b], Soo Youn Kim[c], Seongjae Cho[d], and Myounggon Kang[e,*]

[a]Division of Electronics and Electrical Engineering, Dongguk University, Seoul 04620, Republic of Korea
[b]Department of Electrical and Information Engineering, Seoul National University of Science and Technology, Seoul 01811, Republic of Korea
[c]Department of System Semiconductor, Dongguk University, Seoul 04620, Republic of Korea
[d]Department of Semiconductor Engineering, Ewha Womans University, Seoul 03760, Republic of Korea
[e]Department of Intelligent Semiconductor Engineering, University of Seoul, Seoul 02504, Republic of Korea

[*]E-mail: mgkang@uos.ac.kr

This work introduces an optoelectronic synaptic transistor having an indium-gallium-zinc-oxide (IGZO) channel and a high-κ gate oxide (TaO_x), designed to emulate key synaptic functions for advanced neuromorphic systems. The gate stack and device structure in the cross-sectional views by transmission electron microscopy (TEM) and the material compositions were analyzed by *in-situ* energy-dispersive spectroscopy (EDS), by which clean and uniform interfaces and expected layer compositions were revealed. Also, X-ray photoelectron spectroscopy (XPS) confirms the high concentration of oxygen vacancies, particularly at the IGZO/TaO_x interface, providing the sites for effective charge trapping and de-trapping under a proper set of electrical biases. Under electrical stimulations, the fabricated synaptic transistor displays reliable long-term memory (LTM) behavior with clear hysteresis window and excellent cycle-to-cycle endurance with repeated gate voltage sweeps. Charge storage-mediated operations are confirmed via gate-voltage-dependent modulation, which effectively emulates synaptic potentiation and depression [1,2]. Notably, the fabricated device demonstrates high stability in weight retention and outstanding repeatability in learning operations, underscoring its suitability for standalone memory solution as well as synaptic device in the neuromorphic integrated circuits. In addition to its characteristics accommodating electrical weight tunability (Fig. 1), the IGZO channel of the proposed synaptic transistor shows strong photosensitivity under 405-nm light illumination (Fig. 2), realizing dynamic modulation in the light-initiated electrical conductance. Most of the research on neuromorphic system focus on the neuronic and synaptic functions for signal transmission, but this optically electrically operational synaptic transistor can be positioned at the input layer for more realistic neuromorphic systems processing the light signals as the input. More specifically, the optical stimulation mimics biological short-term synaptic behaviors such as excitatory postsynaptic current (EPSC) and paired-pulse facilitation (PPF), with the device exhibiting characteristics of nonlinear temporal response and exponential decay. By increasing the number of repetitions of optical pulses, the transient EPSC gradually transits to LTM, validating its potential for biologically-inspired memory systems. Synaptic efficacy is further modulated by controlling the number, width, and interval constructing the optical pulse train, which confirms the capability of synaptic device to emulate spike-timing-dependent plasticity (STDP) (Fig. 3). Further, the IGZO synaptic transistor plausibly replicates nociceptive functionalities, including threshold-triggered responses and pathological sensitization phenomena such as allodynia and hyperalgesia [3]. These behaviors are characterized by elevated photocurrent following injury-like stimuli and persistent response to normally innocuous optical signals. The capability to simulate sensory learning and pain perception underscores the versatility of the invented synaptic device as the fundament to hardware platform for bio-inspired sensing.

The optoelectronic IGZO synaptic transistor in this work has exhibited stable and reproducible dual-mode operations through electrical and optical pathways, effectively emulating the essential synaptic functions. Highlights are shed on its strong potential for integration into low-power, hardware-oriented neuromorphic systems requiring multi-modal input sensitivity and cognitive adaptability, while offering high compatibility with processing-in-memory (PIM) architectures presumably having optical input layer capable of improving the system compactness, minimizing the amount of data transmission, and reducing energy consumption. Through the results, it has been demonstrated that it is possible to move beyond conventional research on electrical neuron and synaptic devices enabling broader applicability across various domains by PIM AI.

Acknowledgments This work was supported by National Research Foundation (NRF) of Korea funded by the Korean Ministry of Science and ICT (MSIT) under Grants RS-2023-00258527 and RS-2024-00402495.

References
[1] J. Jang, J. Lee, J.-H. Bae, S. Cho, and S. Kim, "InGaZnO-based synaptic transistor with embedded ZnO charge-trapping layer for reservoir computing," *Sens. Actuators A Phys.*, 373 (2024) 115405.
[2] J. Jang, S. Park, D. Kim, and S. Kim, "Synaptic plasticity and associative learning in IGZO-based synaptic transistor," *Sens. Actuators A Phys.*, 376 (2024) 115641.
[3] D. Ju, J. Lee, and S. Kim, "Nociceptor-Enhanced Spike-Timing-Dependent Plasticity in Memristor with Coexistence of Filamentary and Non-Filamentary Switching," *Adv. Mater. Technol.*, 9 (2024) 2300956.

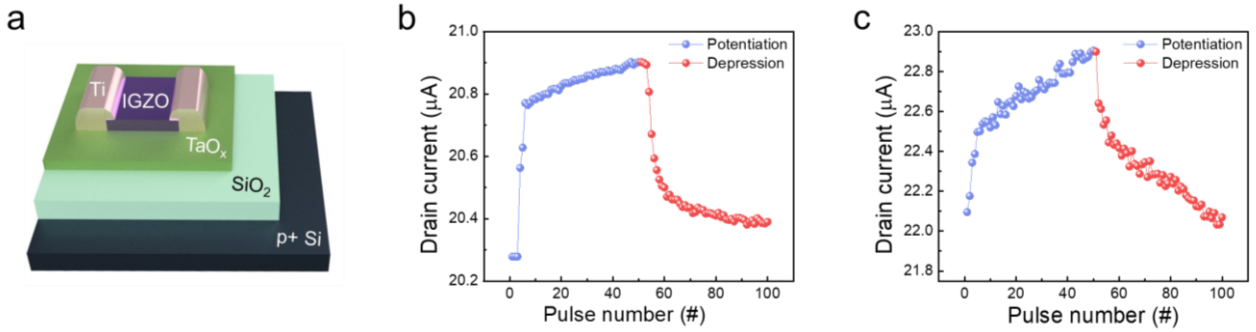

Figure 1. Three-terminal IGZO transistor and its electrical synaptic operations. (a) Schematic illustration of the optoelectronic synaptic IGZO transistor featuring Ti/IGZO/TaO_x gate stack on the SiO_2-isolated Si substrate. Electrical synaptic behaviors of potentiation and depression functions under consecutive pulse stumulations. The fabricated device effectively emulates LTM through (b) identical and (c) incremental pulses.

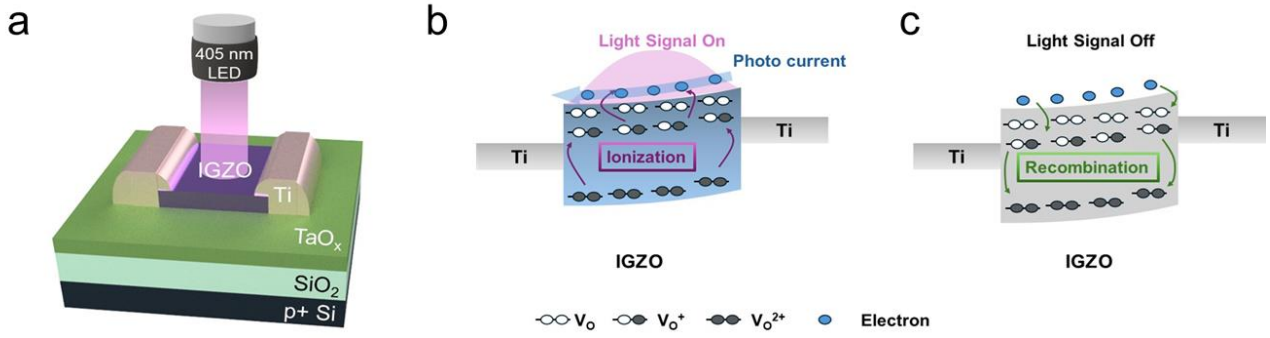

Figure 2. Optical operations of the synaptic IGZO transistor. (a) Optical setup for the device characterization. (b) Photocurrent generation by the 405-nm light illumination. (c) Energy-band diagram under no illumination.

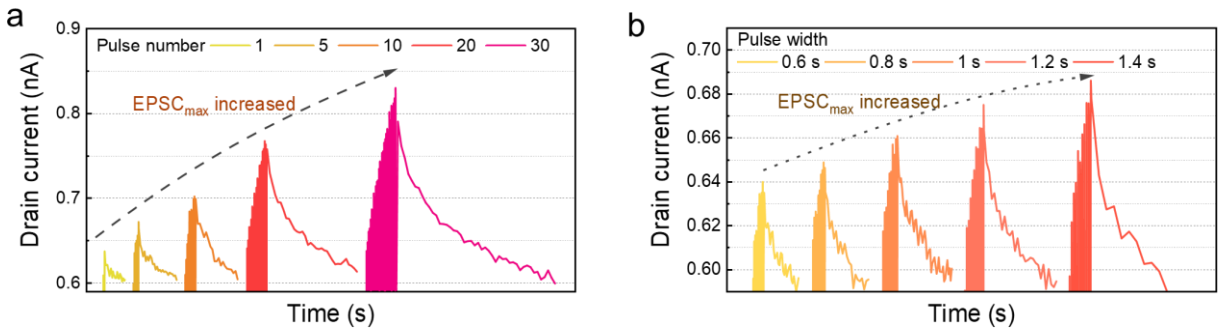

Figure 3. Measurement results for optically-initiable synaptic behaviors. (a) Optical synaptic response under repeated light pulses (405 nm) as a function of time, demonstrating an increase in maximum EPSC with pulse number, emulating synaptic facilitation. (b) Maximum EPSC increases with time as the optical pulse width increases, which reveals the evidence for STDP of the invented synaptic device under optical excitations.

Superhydrophobic Multifocal Microlens Array with Depth-of-Field Detection for Humid Environment

Hao Cao [a*], Yu Shu [a], Yue Zhang [a], Ruiqi Cheng [a], Chengqun Gui [a*]

[a] The Institute of Technological Sciences, Wuhan University, Wuhan, 430072, China
e-mail: 2021106520024@whu.edu.cn (Hao Cao) or cheng.gui@whu.edu.cn(Chengqun Gui)

Abstract

Microlens array (MLA) has been widely applied in augmented reality and optical imaging. When used in humid environment or medical endoscopy, MLA needs to be both superhydrophobic and multifocal. However, it is not easy to achieve both superhydrophobic and multifocal function by integrating superhydrophobic and multifocal structures on the same surface by means of a simple, efficient and precise method. In this paper, the superhydrophobic multifocal MLA with superhydrophobic property and multifocal function is successfully designed for preparation based on a method of 3D lithography and soft lithography. The 3D lithography can further help the preparation of multifocal MLA with varying aperture and multi-step superhydrophobic structure with round doom. The superhydrophobic multifocal MLA with periods 50 μm and 120 μm has perfect superhydrophobic property. The water droplet can slide and bounce off the surface at a roll angle of less than 12.9° with both multifocal and integrated imaging function, as well as up to 397 μm Depth-of-Field (DOF) detection range, this greatly exceeds the conventional MLA. The perfect superhydrophobic and optical property can be achieved in extremely humid environment. The superhydrophobic multifocal MLA proposed in this paper has a promising prospect in actual practices.

Figures

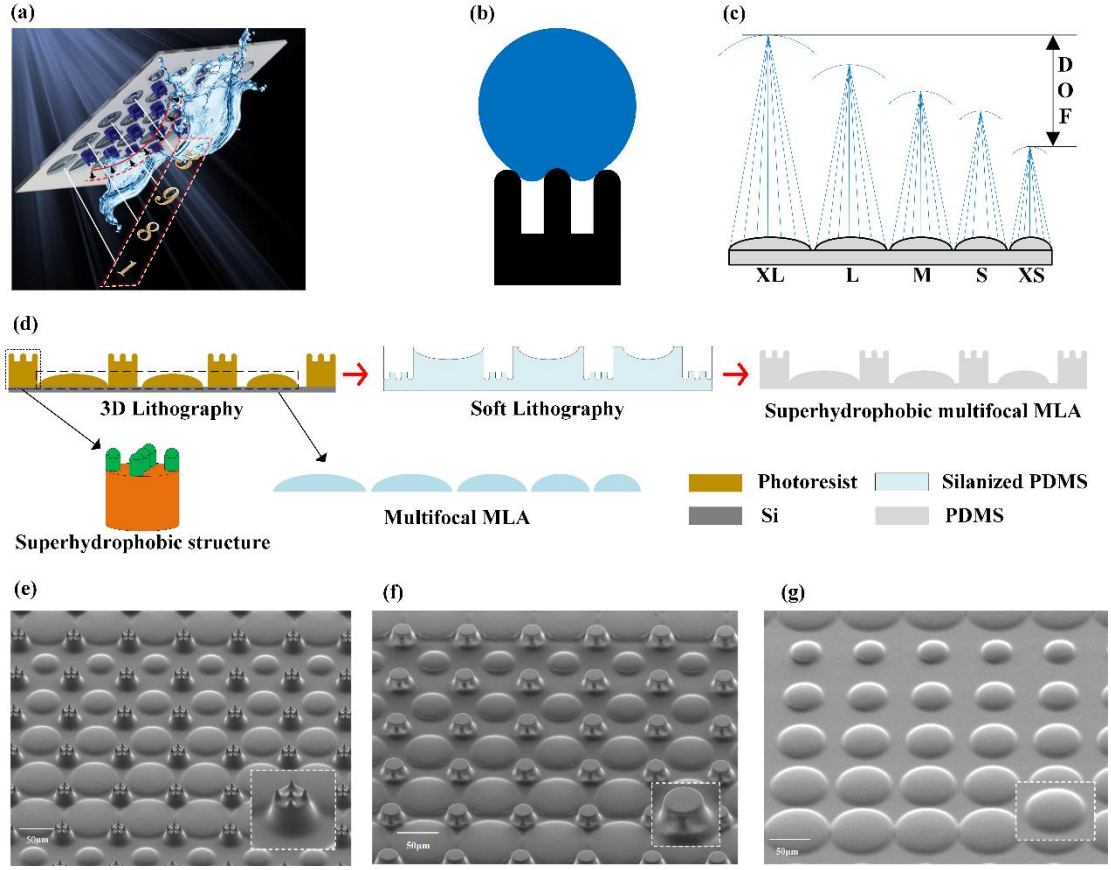

Figure 1. Design and Preparation: (a) Diagram of superhydrophobic multifocal MLA functions; (b) Diagram of superhydrophobic principles; (c) Diagram of multifocal function principles; (d) Diagram of preparation process; (e)~(g) are SEM photos of the microlenses.

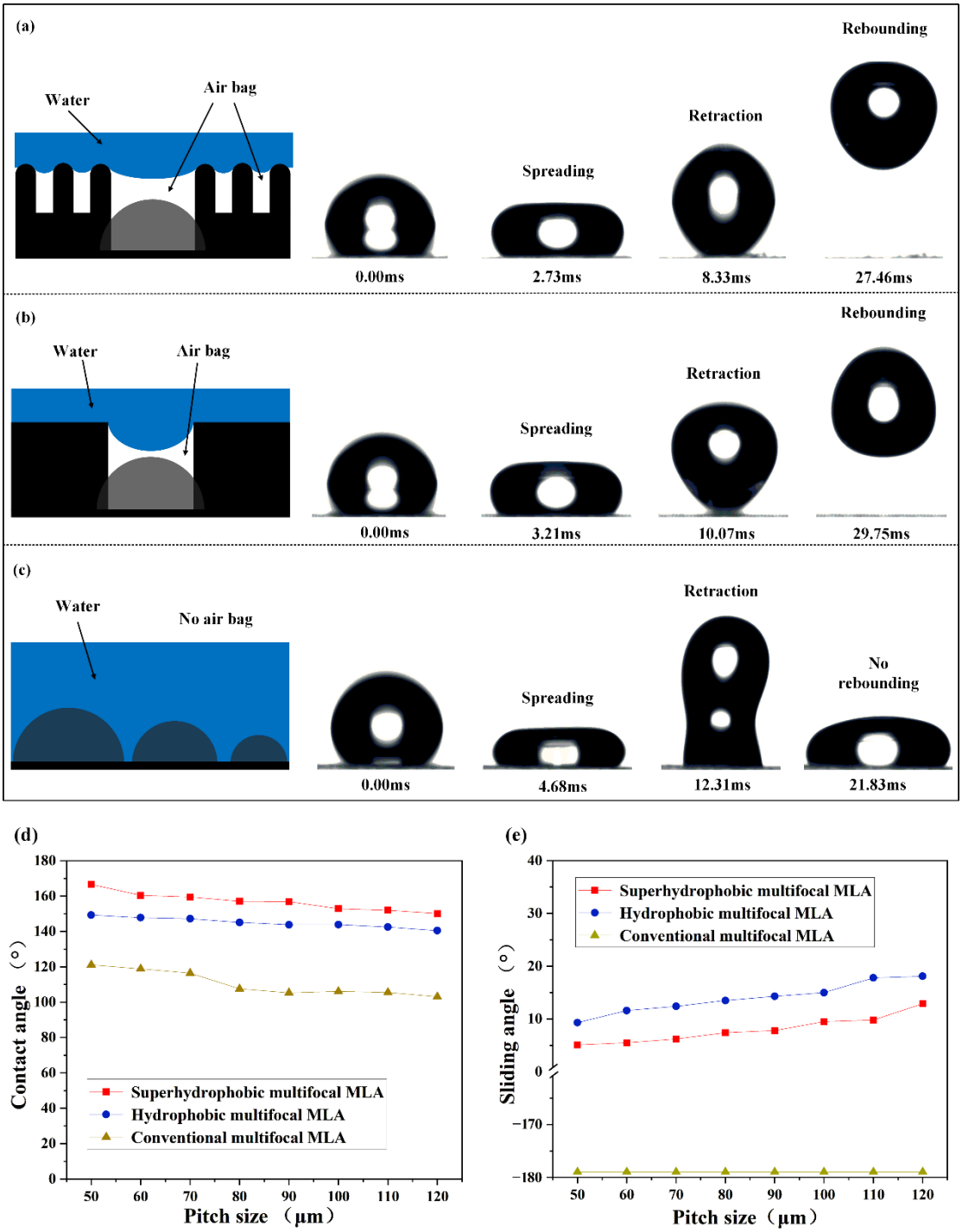

Figure2. Hydrophobicity test and analysis: (a)~(c) are the dynamic performance of different types of MLAs; (d) refers to the contact angle of different types of MLAs; (e) refers to the sliding angle of different types of MLAs.

References

[1] H. Pahlevaninezhad et el., Nano-optic endoscope for high-resolution optical coherence tomography in vivo. Nature Photon. 12 (2018) 540–547.
[2] Y. Zhou et el., Light-field micro-endoscopy using a fiber bundle:a snapshot 3d epi-fluorescence endoscope. Photonics Research. 10 (2022) 2247-2260.
[3] Y. Zhong et el., In Situ Electrohydrodynamic Jet Printing-Based Fabrication of Tunable Microlens Arrays. ACS Appl. Mater. Interfaces, 13 (2021) 39550-39560.
[4] X. Jing et el., Design and Fabrication of Double-Layer Curved Compound Eye via Two-Photon Polymerization. IEEE Photonics Technol. Lett. 33 (2021) 231-234.
[5] H. Liu et el., High-aspect-ratio crack-free microstructures fabrication on sapphire by femtosecond laser ablation. Light: Sci. Appl. 10 (2021) 1.
[6] B. Dai et el., Biomimetic apposition compound eye fabricated using microfluidic-assisted 3D printing. Nat. Commun. 12 (2021) 6458.
[7] J. Li et el., Rapid fabrication of microlens arrays on PMMA substrate using a microlens array by rear-side picosecond laser swelling. Opt. Laser Eng. 126 (2020) 105872.
[8] J. Hua et el., Convex silica microlens arrays via femtosecond laser writing. Opt. Lett. 45 (2020) 636-639.

Prediction of Photo Lithography Equipment Wafer Moving Robot Errors Using ARIMA model

Kyunghwan Joo [a, b], Prof. Jae Wook Jeon [c]

[a] Department of Semiconductor and Display Engineering, Sungkyunkwan University, Suwon, 16419, Korea
[b] Samsung Institute of Technology, Samsung-ro 1, Giheung-gu, Yongin-si, Gyeonggi-do, 17113, Republic of Korea
[c] Department of Electrical and Computer Engineering, Sungkyunkwan University, Suwon, 16419, Korea

e-mail: okata2000@g.skku.edu

• Purpose of the work;

The purpose of this study is to develop a method for predicting unexpected failures of the wafer load robot of semiconductor exposure equipment in advance and improve the operational efficiency and productivity of the equipment. In the semiconductor manufacturing process, the photo process is a key process that accurately forms a circuit pattern on a thin film-formed wafer, and in particular, the stability and accuracy of the exposure process directly affect the product quality and production yield. The wafer load robot of the photo lithography DUV model mainly uses a 3-DoF SCARA type robot, and is responsible for repeatedly moving the wafer to an accurate position. Since this robot has a structural weakness in the vertical (Z-axis) load when the robot extends in the direction of wafer movement, lightweight and durable ceramic materials are used, but fatigue accumulation and tilt phenomenon of the robot arm and gripper occur due to continuous mechanical load and repetitive movement. Such mechanical deterioration and tilt phenomenon of the robot cause a decrease in overlay accuracy and unexpected downtime of the equipment, which affects the operational efficiency of the production line.

• Novelty of the work with respect to the state of the art;

Previously, facility maintenance was focused on periodic inspections and responses to equipment failures, which limited the ability to recognize and respond to sudden and rapid component deterioration early. To overcome these problems, this study developed a deterioration prediction system for a wafer transfer robot based on the ARIMA (Autoregressive Integrated Moving Average) model. The core of this system is the wafer exchange safety sensor, which measures the tilt of the robot and gripper in real time and stops the equipment when the error limit is exceeded. However, the existing method collected wafer exchange safety sensor data only during periodic inspections, making it difficult to respond immediately to changes in the positions of the robot arm and gripper. However, in this study, we implemented a technology to collect the measurements of the wafer exchange safety sensor in real time, visualize them in the form of time series data, and monitor and predict changes. To this end, the robot and gripper tilt values were extracted from the error log, and in this process, it was recognized that the tilt change occurred rapidly when a failure occurred along with the drift due to mechanical deterioration, so the extracted values were plotted as a line chart in time series to detect the tilt change, and the ARIMA model was applied to predict the abnormally fluctuating results. In order for the ARIMA model to improve the prediction accuracy, the equipment predicted to be defective was selected as a model, and the performance of the failure prediction model was evaluated through the prediction results according to the parameter setting values of the three main parameters (p: AR, d: difference, q: MA) and actual observation data, and as a result, the Forecast (5,2,1) model, which showed the most similar prediction performance to the actual operation data, was selected and applied to the equipment, and the prediction accuracy was improved through this.

• Results of the work.

Based on the prediction system developed through this study, a preemptive response standard for replacing the robot in advance was established when the monthly tilt change of the wafer robot exceeds 0.5 mrad. After applying the system to the production site, it contributed to reducing the sudden stoppage of the equipment through prediction-based activities. These results led to increased operational efficiency of the production line and reduced maintenance costs, and it is expected to greatly contribute to improving the stability and productivity of equipment operation in the long term. We plan to conduct continuous research to further improve the accuracy and reliability of the future sudden failure prediction system, and in particular, we will

consider ways to contribute to the establishment of autonomous manufacturing based on real-time cause analysis of predicted problems and an automated response system.

[1] Y. He et al., "Research on Motion Simulation of Wafer Handling Robot Based on SCARA," 2018 19th International Conference on Electronic Packaging Technology (ICEPT), Shanghai, China, 2018, pp. 734-739, doi: 10.1109/ICEPT.2018.8480663

[2] J. Liu, F. Jian and J. Liu, "Four Degrees of Freedom SCARA Robot Modeling and Simulation," 2014 International Symposium on Computer, Consumer and Control, Taichung, Taiwan, 2014, pp. 410-412, doi: 10.1109/IS3C.2014.113

[3] S.L. Ho, M. Xie, "The use of ARIMA models for reliability forecasting and analysis", Computers & Industrial Engineering, Volume 35, Issues 1–2, 1998, Pages 213-216, ISSN 0360-8352, https://doi.org/10.1016/S0360-8352(98)00066-7

SYSTEM EVENT:
WEX safety sensor diagnostics
WEX safety sensor diagnostics for robot WHARxROxTYPE_ROBOT_LOAD
z_final=0.000481275 m,
gripper_tilt = 0.000284817 rad, robot_tilt = -0.00120538 rad

SYSTEM EVENT:
WEX safety sensor diagnostics
WEX safety sensor diagnostics for robot WHARxROxTYPE_ROBOT_UNLOAD
z_final=1.3515e-05 m,
gripper_tilt = -0.000902014 rad, robot_tilt = -0.00048215 rad

Figure 1. Example of error log output after measuring wafer exchange safety sensor

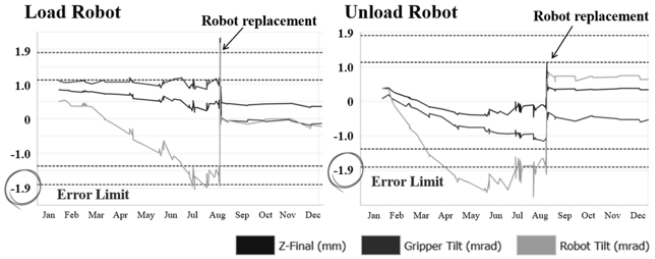

Figure 2. Example of wafer exchange safety sensor log trend

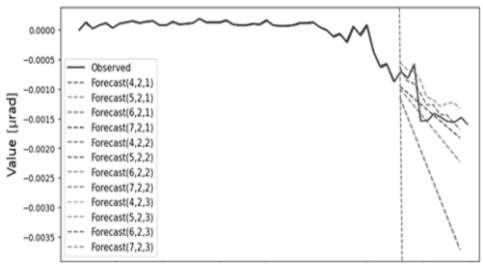

ARIMA (p,d,q)	MAE	MSE	RMSE
Forecast (4,2,1)	3.73.E-04	6.82.E-07	8.26.E-04
Forecast (5,2,1)	4.20.E-04	5.93.E-07	7.70.E-04
Forecast (6,2,1)	6.73.E-04	1.05.E-06	1.03.E-03
Forecast (7,2,1)	4.83.E-04	8.29.E-07	9.10.E-04
Forecast (4,2,2)	1.49.E-03	2.96.E-06	1.72.E-03
Forecast (5,2,2)	1.49.E-03	2.96.E-06	1.72.E-03
Forecast (6,2,2)	1.49.E-03	2.96.E-06	1.72.E-03
Forecast (7,2,2)	1.49.E-03	2.95.E-06	1.72.E-03
Forecast (4,2,3)	1.48.E-03	2.94.E-06	1.71.E-03
Forecast (5,2,3)	1.49.E-03	2.94.E-06	1.72.E-03
Forecast (6,2,3)	1.49.E-03	2.95.E-06	1.72.E-03
Forecast (7,2,3)	1.49.E-03	2.95.E-06	1.72.E-03

Figure 3. Comparison of the differences between observations and ARIMA forecasts

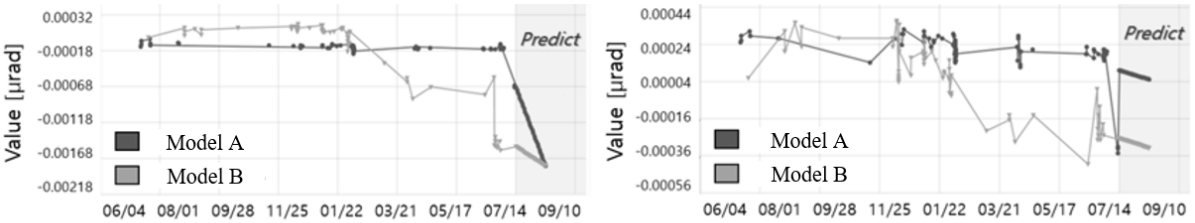

<Wafer Handler Gripper Tilt Predict> <Wafer Handler Load Robot Tilt Predict>

Figure 4. Application examples of failure prediction system

Optimisation of a Microfluidic Electrochemical Biosensor for *E. coli* Detection via ssDNA Hybridization and CRISPR/Cas-Based Sensing to Combat Sepsis

Eleonora Quasso [a], Isabelle Le Potier [a], Hiu Mun Man [a], Hervé Jacquier [b], David Bikard [c], Laurent Thouin [d], Jean Gamby [a]

[a] Université Paris-Saclay, CNRS, Centre de Nanosciences et de Nanotechnologies, Palaiseau, 91120, France
[b] Unité de Bactériologie, Département de Prévention, Diagnostic et Traitement des Infections, Hôpital Henri Mondor, APHP, 94000 Créteil, France
[c] Synthetic Biology, Institut Pasteur, Université Paris Cité, CNRS UMR 6047, Paris, France
[d] CPCV, Département de chimie, Ecole normale supérieure, PSL University, Sorbonne Université, CNRS, 75005, Paris, France
e-mail: eleonora.quasso@universite-paris-saclay.fr
Keywords: biosensors, electrochemistry, microfluidics, Escherichia coli, CRISPR/Cas, antibiotic resistance

Escherichia coli is a Gram-negative bacterium commonly found in the human intestinal microbiome. Most strands are beneficial and necessary for the correct digestion of food, while others have been identified as pathogenic, causing both intestinal and extraintestinal infections of various levels of severity. A major concern for the scientific and medical community has become the increasing and rapidly diffusing resistance that these bacteria are developing toward β-Lactam antibiotics, mainly penicillin derivatives and cephalosporins. These multiresistant strains that produce β-lactamase are the main cause of sepsis cases throughout the world, which 33-35% of the time lead to death [1].

This thesis aims to design, fabricate, and characterise an electrochemical biosensor, able to detect *E. coli* in a patient's sample by coupling thermoelectric and electrochemical measurements to prevent sepsis. We will investigate more in-depth the blaCTX-M-8 resistance gene responsible for the production of β-lactamase enzymes; therefore, our target sequence is one contained in its genome. The device incorporates a microfluidic channel moulded in PDMS and bonded to the glass substrate with the microelectrodes (see Fig. 1A) using oxygen plasma (see Fig. 1B). Through it, we introduce the sample with the target sequence, which will then be detected by probes immobilised on the electrode surface. In this Ph.D. thesis we will follow two techniques for detection: firstly, starting from a previous design [2], the single-stranded DNA (ssDNA) probe will be immobilised on the electrode and it will hybridise and recognise its complementary target (see Fig 2a); secondly we will fabricate a new sensor which utilises the CRISPR/Cas technology to immobilise a Cas protein on the electrode, which will bind to the probe sequence or single guide RNA (sgRNA) and then recognise the target [3]. For both techniques we use platinum electrodes as a base, and for the latter we require a layer of graphene to bond the Cas protein through PBA linker (see Fig. 2b). The usage of the CRISPR/Cas technology yields very high specificity and should therefore improve our device. Whereas most literature deposits graphene on gold electrodes for this purpose, we have decided to use platinum for its greater stability with nucleic acid sequences and for better comparison between the designs.

The two devices are then confronted in their efficiency and specificity through cyclic voltammetry and electrochemical impedance spectroscopy measurements (see Fig. 3), using as targets, according to the device, synthetic sequences and DNA filaments directly extracted from *E. coli* bacteria lysed in our laboratory. Finally, we will optimise the value of surface coverage ratio (θ), defined as the percentage of electrode surface that has been occupied by the probe sequences, by implementing new simulation studies using COMSOL Multiphysics for our application. The correct value of θ is fundamental to have enough probes on the electrode which are free for detection, but avoid excessive crowding effects and non-specific binding, therefore we will analyse it as a trade-off between sensitivity and sensibility: higher probe density leads to higher sensibility, or lower limit of detection (LOD), but lower sensitivity due to steric hindrance; vice versa lower probe density entails higher sensitivity, but lower sensibility.

[1] R. Markwart et al., Epidemiology and burden of sepsis acquired in hospitals and intensive care units: A systematic review and meta-analysis, Intensive Care Medicine, 46(8) (2020) 1536–1551.
[2] H. M. Man et al., Microfluidics-Based Electrochemical Detection of Antimicrobial-Resistant DNA Sequence in Lysed Escherichia coli Medium, ACS Electrochemistry, (2025).
[3] B. Yang, X. Zeng, J. Zhang, J. Kong, and X. Fang, Accurate identification of SARS-CoV-2 variant delta using graphene/CRISPR-dCas9 electrochemical biosensor, Talanta, 249 (2022) 123687.

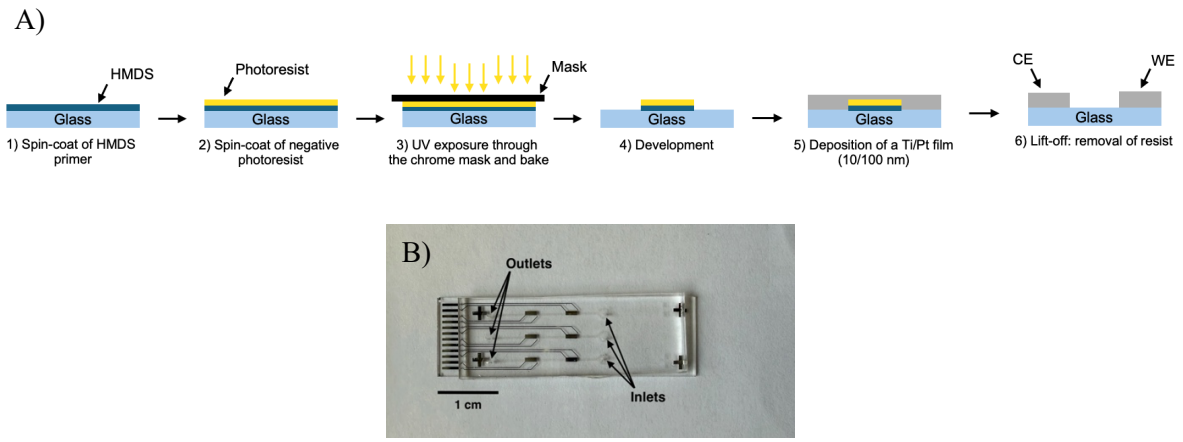

Figure 1. A) Cleanroom fabrication steps for the platinum microelectrodes. B) Complete microfluidic biosensor after oxygen plasma bonding of the PDMS with the microchannels (3 in this case) and the glass substrate with the microelectrodes.

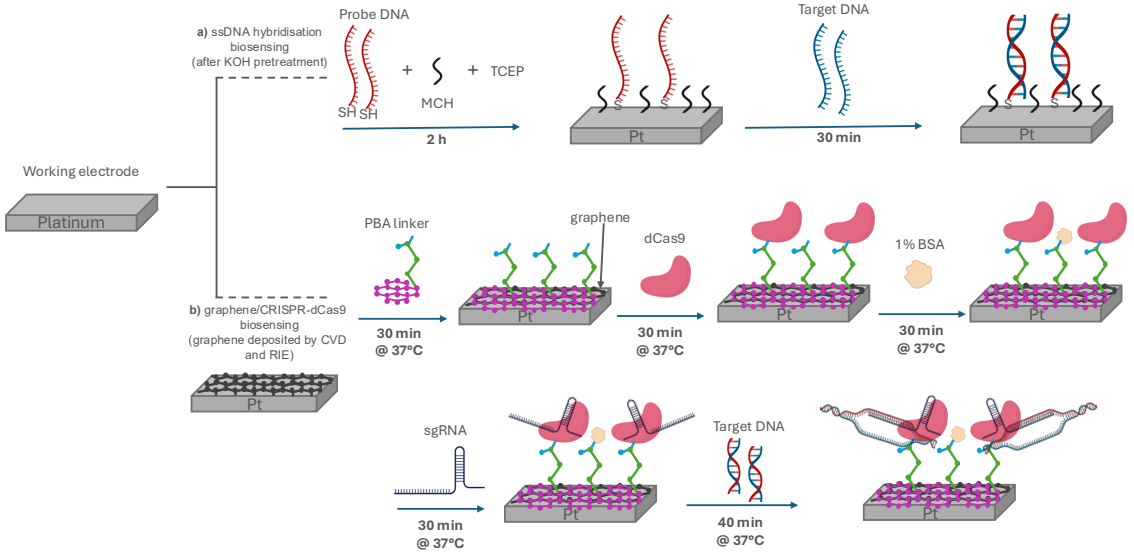

Figure 2. Electrode functionalisation and immobilisation of DNA with two techniques: a) ssDNA hybridisation electrochemical biosensing; b) graphene/CRISPR-dCas9 electrochemical biosensing.

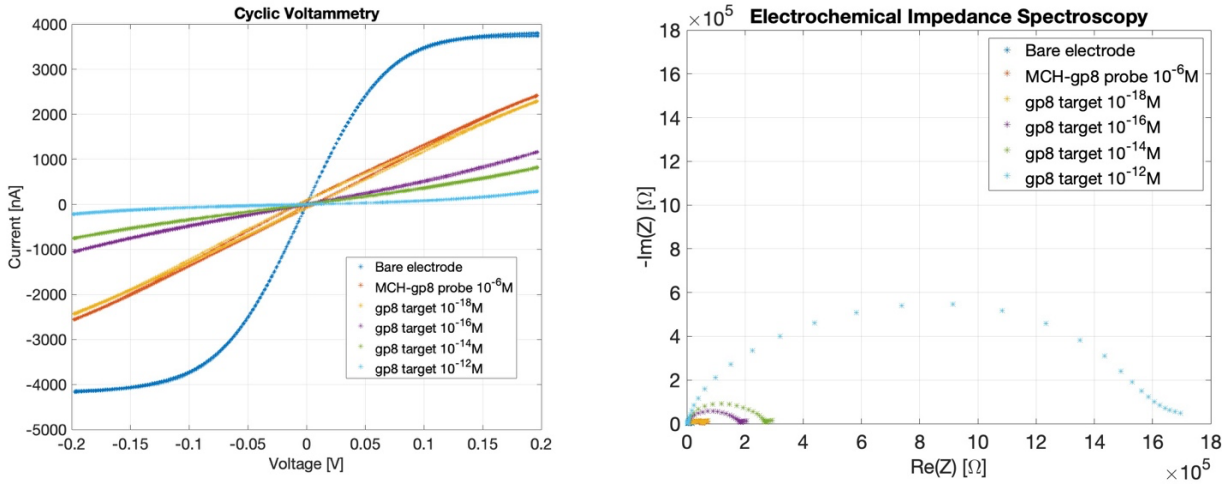

Figure 3. Electrochemical detection methods: cyclic voltammetry and electrochemical impedance spectroscopy.

Scalable Nanobubble Generation Using Centrifugal Micro-Porous Mesh Disc Technology

Bo-Wei Cheng[1], Yuan-Jen Chang[2], Chia-Lung Kuo[1], Kuen-Yi Wu[3], Chao-Ching Ho[1, 2*]

[1] College of Mechanical & Mechatronic Engineering, National Taipei University of Technology, Taipei, Taiwan
[*2] Graduate Institute of Manufacturing Technology, National Taipei University of Technology, Taipei, Taiwan
[3] Rayzher Industrial Co., Ltd., HsinChu, Taiwan,

E-mail: hochao@mail.ntut.edu.tw

Nanobubbles have demonstrated significant potential across various applications, including water treatment, biomedical fields, and industrial cleaning, due to their high surface area and unique physical properties. Conventional methods for nanobubble generation often face challenges in energy efficiency and scalability. To address these limitations, this study introduces a centrifugal-driven mechanism utilizing micro-porous rotational discs for efficient nanobubble production. The primary objective of this study is to develop a centrifugal-based method that enhances gas-liquid interactions through high-speed rotation, forcing gas to pass through the micro-porous structure of the rotating disc. The innovation of this method lies in its ability to regulate gas flow and control bubble size solely through centrifugal force and a flow meter, eliminating the need for additional gas propulsion. The primary motivation behind the design of the centrifugal-driven nanobubble generation system is to overcome the limitations of high energy consumption and limited scalability. The proposed system adopts a micro-porous disc constructed with a mesh-like grid structure (Fig. 1). As the disc rotates, gas is introduced at the center and propelled outward by centrifugal forces. When passing through the fine mesh, the gas is mechanically sheared into smaller bubbles. The system operates based on a rotating micro-porous disc (Fig. 2). Gas is introduced at the center of the rotating disc, where centrifugal force drives it outward at high velocity. As the gas reaches the micro-porous sections, it is forced through micro-scale pores, resulting in the mechanical shearing and dispersion of the gas into nanobubbles. The high rotational speeds ensure uniform distribution and high shearing rates, which are critical for reducing bubble size and enhancing stability. Moreover, similar studies have demonstrated that porous membrane systems can maintain nanobubble stability over extended periods. Nanobubbles maintained consistent size and surface charge over prolonged storage, reinforcing the potential stability of nanobubbles generated through centrifugal mechanisms with micro-porous designs. This approach presents several key benefits: energy efficiency (eliminates the need for high-pressure gas compressors), bubble stability (consistent shear forces generate uniformly sized nanobubbles with enhanced stability), scalability (modular design allows for multi-disc configurations to enhance output), and adjustability (precise control over rotational speed and gas volume enables fine-tuning of bubble characteristics). The centrifugal-driven nanobubble generation system introduced in this study provides an efficient method for producing stable, uniformly sized nanobubbles. Utilizing a micro-porous mesh disc and centrifugal force, high shear rates are achieved to effectively disperse gas into nanobubbles. Experimental results demonstrate high-throughput production with consistent bubble size and stability (Fig. 3). Future work will optimize material properties and explore multi-disc configurations to enhance scalability and versatility. [1][2].

[1] G. Chen, et al., "Effect of different configurations on bubble cutting and process intensification in a micro-structured jet bubble column using digital image analysis," *Processes* 9.12 (2021) 2220.
[2] K. Ulatowski, et al., "Stability of nanobubbles generated in water using porous membrane system," *Chemical Engineering and Processing-Process Intensification* 136 (2019) 62-71.

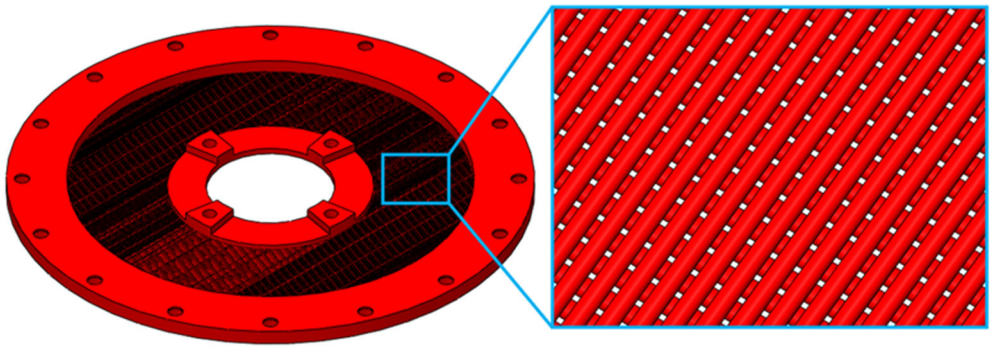

Figure 1. Schematic diagram of microporous structure disk.

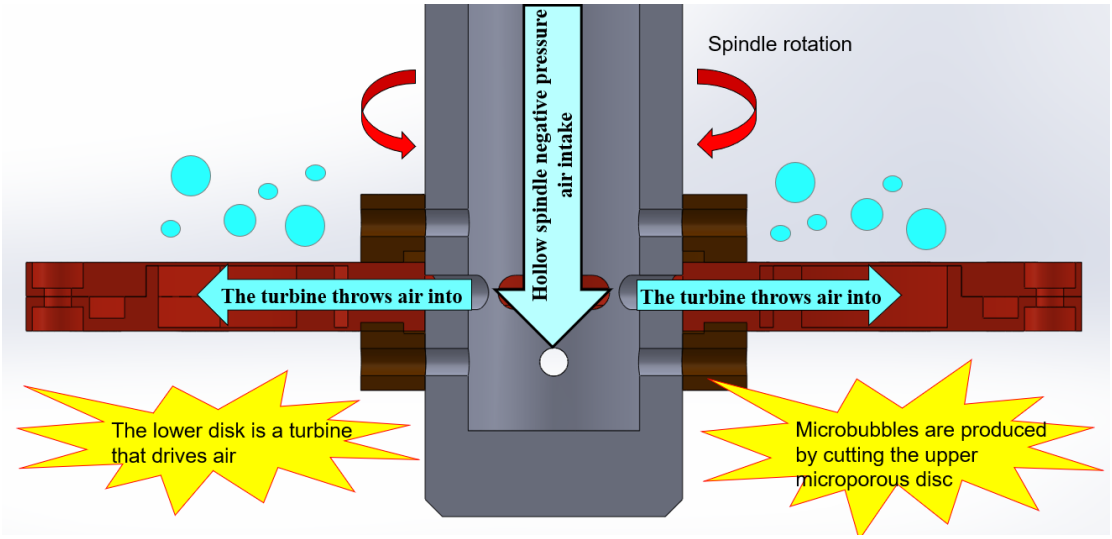

Figure 2. Gas flow diagram.

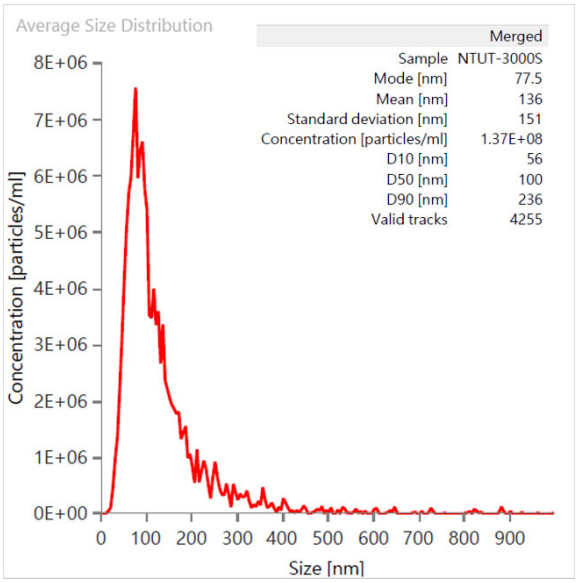

Figure 3. Nanobubble distribution and bubble concentration.

Refractive index controllable plasmonic color metasurfaces fabricated by combination of Nanoimprint lithography and Inkjet Printing

N. Dimogerontaki[1,2], N. Matthaiakakis[2], N. Heidaryan[3], S. Kopp[3], M. Mühlberger[3], N. Kehagias[2]

[1] Department of Physics, School of Applied Mathematical and Physical Sciences National Technical University of Athens, Zografou Campus, GREECE
[2] NCSR Demokritos, Institute of Nanoscience & Nanotechnology, P. Grigoriou 27 & Neapoleos Str., 15341 Ag. Paraskevi, Greece
[3] PROFACTOR GmbH, Im Stadtgut D1, 4407 Steyr, Austria

E-mail: nefelidimogerontaki@mail.ntua.gr
Keywords: metasurfaces; structural colors; nanoimprint lithography, inkjet printing

Plasmonic colors arise from the interaction between light and metallic nanostructures. Their high resolution, color purity, fade resistance and eco-friendliness make them valuable for applications in colored plastics, information security, anti-counterfeiting and more. [1]To enhance the commercial viability of structural color technologies, scalable and cost-effective manufacturing methods are essential. Mass production techniques such as roll-to-roll nanoimprinting, injection molding, and post-processing methods like inkjet printing will play a key role in this advancement.[2] In plasmonic-colored metasurfaces, the resonance frequency—and thus the perceived color—can be tuned by adjusting the structure's shape, size, and surrounding environment. The main challenges in this field involve achieving a broad color range, ensuring large-scale fabrication feasibility, and enabling post-customization for diverse applications.

This work demonstrates plasmonic colors fabricated using ultraviolet (UV) nanoimprint lithography on a transparent PET substrate followed by aluminum (Al) deposition (Fig. 1a–c) and post-processed with inkjet printing. To explore scalable, low-cost approaches for producing different colors on the plasmonic surface, we investigated local color tuning by modifying the effective refractive index of surrounding nanostructures. UV-curable resin cover layers with different refractive indices were deposited on the plasmonic metasurface. A periodic nanopillar geometry with 10nm Al layer (d=230nm, p=450nm, height = 180 nm) initially displayed a vibrant blue color. When a bulk cover layer with a refractive index of 1.39 was applied, a red shift changed the teal color to purple when seen under the microscope. A cover layer with a refractive index of 1.66 shifted the color to green (Fig. 1d). Reflectance spectra measurements and theoretical calculations (Fig. d, f) confirmed these observations.

Applying different materials to the plasmonic surface induced color shifts due to increased refractive index, causing a red shift in plasmonic resonances. This scalable and low-cost method introduces a novel platform for anti-counterfeiting and micro-scale color encoding.

To further investigate color tuning via refractive index changes, inkjet printing was employed. We used a FujiFilm Dimatix inkjet printer with a 1 pL printhead. Three different inks were investigated: an ink with low refractive index based on Fluorolink® MD700 (Syensqo SA), a medium index ink (X30, Stensborg A/S) and an ink with high refractive index (IPO 912, Inkron Oy). Since oxygen inhibition for the inkjet printed materials is prominent and material spreading on the patterned substrate should be minimized, we use a UV-curing unit directly installed next to the inkjet printhead. This pins the droplets directly in the printer and stops movement of the liquid. The X30 was additionally post-cured externally. Figure 3 shows two photographs of inkjet printed samples with different amounts of materials. The advantage of inkjet printing is that as a digital technology it is versatile and material saving, allowing to deposit well defined amounts of material on well-defined positions on a surface.

Acknowledgements
This work has been funded under the 2nd Call for Hellenic Foundation for Research & Innovation Research Projects to support Faculty Members and Researchers. Proposal Number: 02878 Acronym: ALMA.
The authors would also like to thank Nanotypos company for providing necessary equipment for this research. Part of this work has received funding from the European Union's Digital Europe Programme under grant agreement No. 101083472.

[1] Daqiqeh Rezaei, S. *et al.* Nanophotonic Structural Colors. *ACS Photonics* **8**, 18–33 (2021).
[2] Li, G. *et al.* Printable structural colors and their emerging applications. *Mater. Today* **xxx**, (2023).

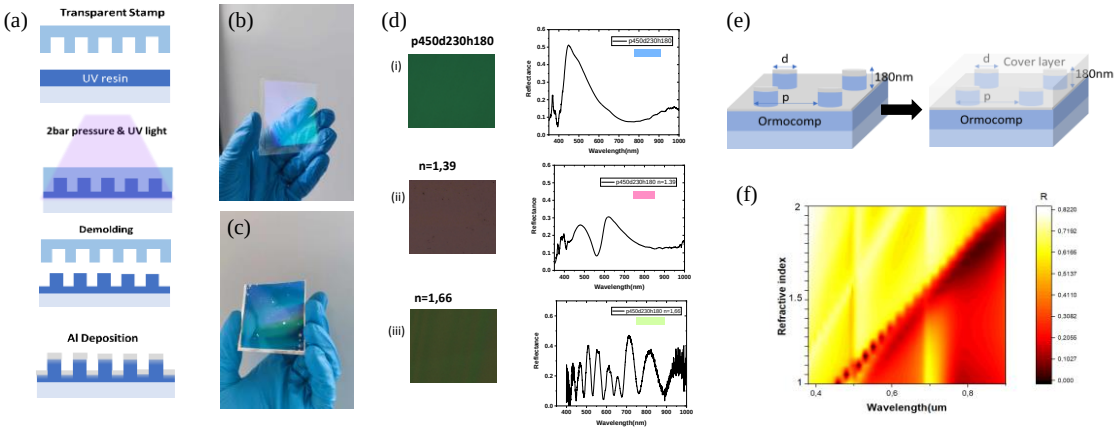

Figure 1. (a)Schematic representation UV-NIL process (b) After UV-NIL (c) After Al 30nm deposition (d) (i) Nanostructured plasmonic surface with periodicity p=450nm and width d=230nm producing a teal color. (ii) Nanostructured plasmonic surface after coating with the of a UV-curable resist (R.I.=1,39) cover. (iii) Nanostructured plasmonic surface after coating with AZ5214E (R.I.=1,66) cover layer. Color on the top left shows the calculated color. (b) Schematic of the plasmonic nanostructures without and with the cover layer. (c) Theoretical parametric scan for a width of w=230nm, period p=450nm and varying refractive index.

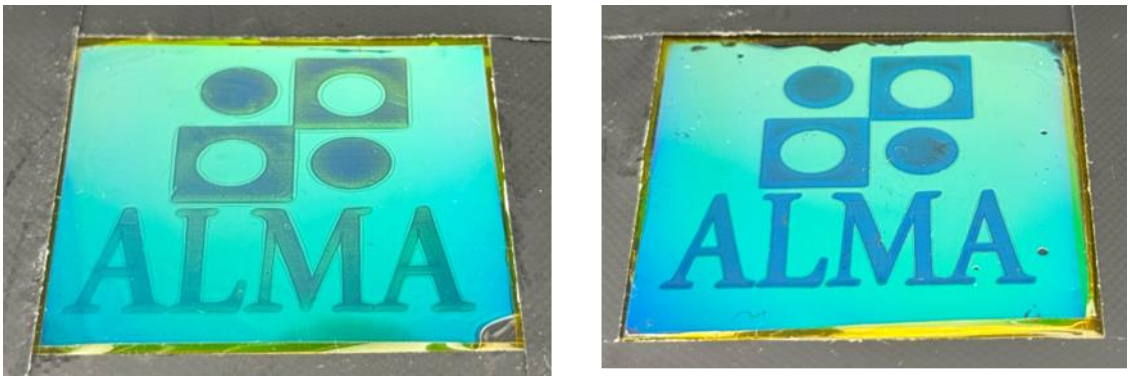

Figure 3. Inkjet printed logo on plasmonic substrate. The Inkron 912 ink was used. The amount of material deposited was doubled on the right samples as compared to the left sample. The sample size is 5x5cm².

Machine Learning Enabled Thermoelectric Device Design and Optimization

Haoji Yang, Yuxiao Zhu, C.H. Kees de Groot, Harold M. H. Chong, Ruomeng Huang
School of Electronics and Computer Science, University of Southampton, Southampton, SO17 1BJ, United Kingdom
e-mail: hy15u22@soton.ac.uk

Thermoelectric (TE) technology has gained significant attention due to its ability to convert heat into electricity and vice versa, offering potential for sustainable energy solutions such as waste heat recovery, clean energy generation, and efficient cooling [1]. TE devices typically consist of n-type and p-type semiconductors connected by metal interconnects and capped with ceramic plates, as shown in Figure 1(a). These devices are classified into thermoelectric generators (TEGs), which convert heat into electricity, and thermoelectric coolers (TECs), which use electrical energy to provide cooling [2]. However, the low efficiency of both TEGs (around 10%) [3] and TECs (often lower than 10%) [4] limits their wider use. Improving the performance of TE devices involves two main approaches: developing better thermoelectric materials and optimizing the device design. While tools like COMSOL Multiphysics, based on the finite element method (FEM), are commonly used for design optimization, they are computationally expensive and time-consuming for iterative simulations [5]. Therefore, more efficient optimization methods are needed to enhance TE device performance.

To address the efficiency limitations of thermoelectric (TE) devices, we present a novel machine learning-based approach that integrates artificial neural networks (ANNs) with genetic algorithms (GAs) to effectively optimize both the geometry and operating conditions of thermoelectric generators (TEGs) and thermoelectric coolers (TECs). As shown in Figure 1(b) and 1(c), the ANN is trained using datasets obtained from COMSOL simulations and achieves prediction accuracy exceeding 98% for TEGs (Figure 2(a)). The model demonstrates excellent agreement with COMSOL results, with R^2 values above 0.999 for both maximum power density (PD_max) and efficiency (η), as illustrated in Figure 2(b–c) [6]. Following training, the GA is employed to explore the design space and determine optimal parameters, with sample results displayed in Figure 3. This approach was also applied to segmented TEGs (STEGs), where the ANN achieved a similar prediction accuracy of 98% and R^2 values over 0.99 for PD_max [7]. Additionally, we extended this method to optimize photovoltaic-thermoelectric generator (PV-TEG) systems, where the ANN reached 98.8% accuracy and R^2 of 0.999 for both power density and the average PV cell temperature [8]. In parallel, we applied the same strategy to TEC optimization, which is equally critical for TE device performance. The ANN developed for TECs achieved over 99% prediction accuracy, with R^2 values surpassing 0.999 for both the cooling and heat dissipation side temperatures. These results demonstrate the effectiveness and versatility of our approach in optimizing various TE systems under different conditions. The optimized device dimensions align with typical fabrication standards for both TEGs and TECs, with TE leg height, width, and depth all within the 0.1–10 mm range, ensuring manufacturability while maximizing thermoelectric performance.

We will present the performance of our artificial neural network model for both TEGs and TECs, comparing the results with those from the COMSOL model under various conditions. Additionally, we will highlight the superior simulation speed by predicting millions of results to generate mapping images. The application of a genetic algorithm in this research to identify optimal parameters will also be discussed. This work bridges the gap between high-fidelity simulation and real-time optimization, providing a scalable framework for next-generation TE device optimization.

[1] Zebarjadi, M., Esfarjani, Chen, G, et al.. Energy & Environmental Science, 2012, 5147-5162.
[2] Twaha S, Zhu J, Yan Y, Li B. Renewable and Sustainable Energy Reviews. 2016;65(698-726):698-726.
[3] Zhang Q, Liao J, Tang Y, et al. Energy and Environmental Science. 2017;10(4):956-963.
[4] DiSalvo FJ. Science. 1999;285(5428):703-706.
[5] Hamid Elsheikh M, Shnawah DA, Sabri MFM, et al. Renewable and Sustainable Energy Reviews. 2014;30(337-355):337-355.
[6] Zhu Y, Daniel W. Newbrook, Dai P, C.H. Kees de Groot, Huang R. Applied Energy. 305 (2022) 117800
[7] Zhu Y, Newbrook DW, Dai P, Liu J, de Groot CHK, Huang R. Energy and AI. 2022;12:100225.
[8] Zhu Y, Newbrook DW, Dai P, Huang R. et al. Case Studies in Thermal Engineering. 2024;61:105053-105053

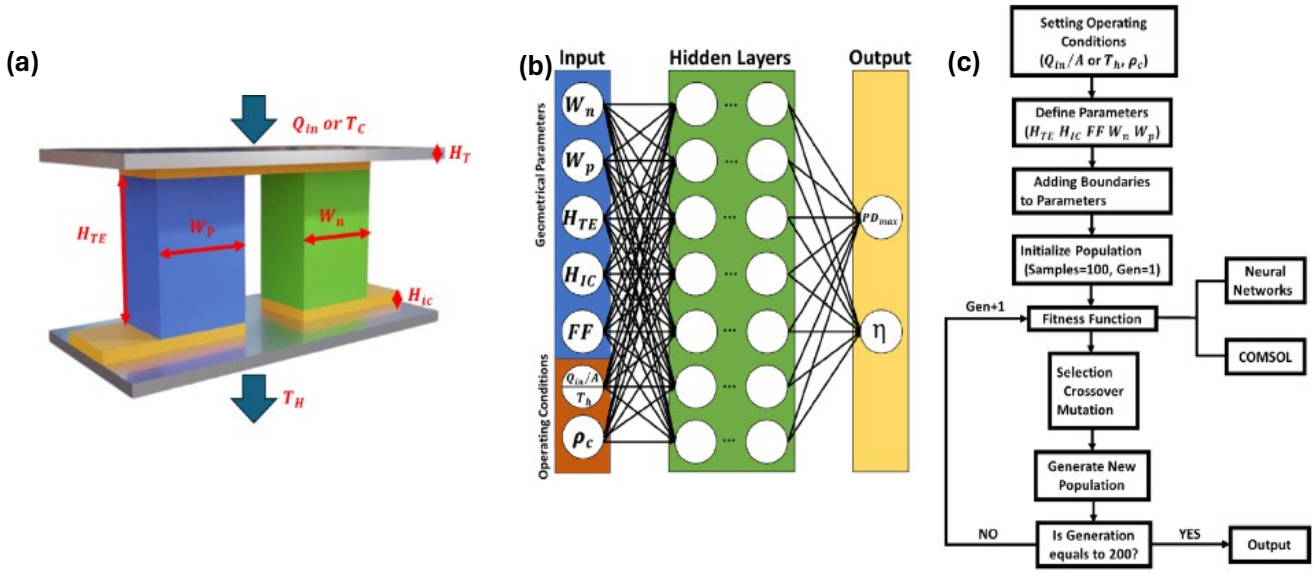

Figure 1 (a) Schematic of a TE device, (b) overall stuucture of an ANN model, and (c) flow chart of GAs process.

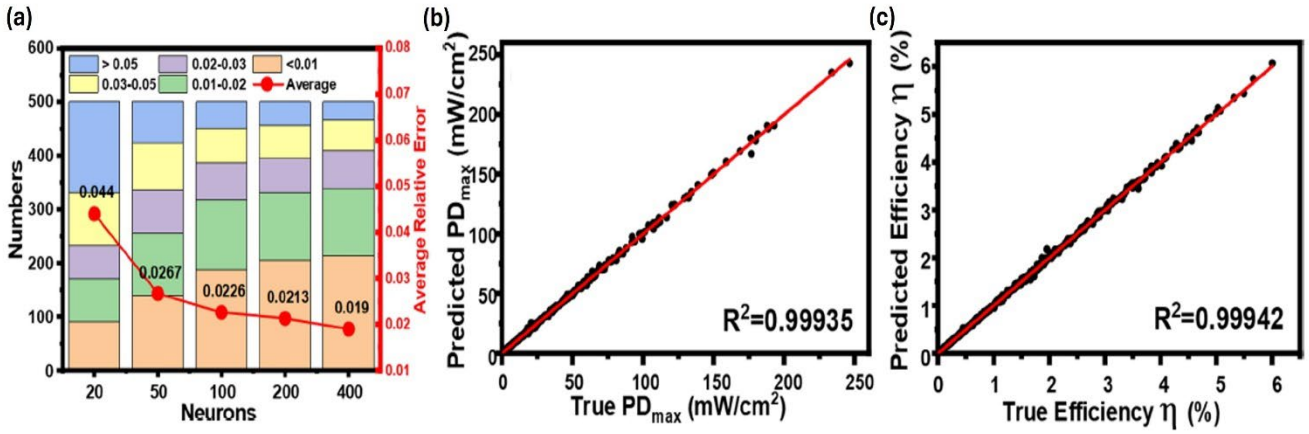

Figure 2 (a) the histogram of the probability and average relative errors of the ANNs with different neurons per layer, (b) Scatter plot of the ANN predicted and the simulated (b) maximum power density, and (c) efficiency under the operating condition of constant temperature difference.

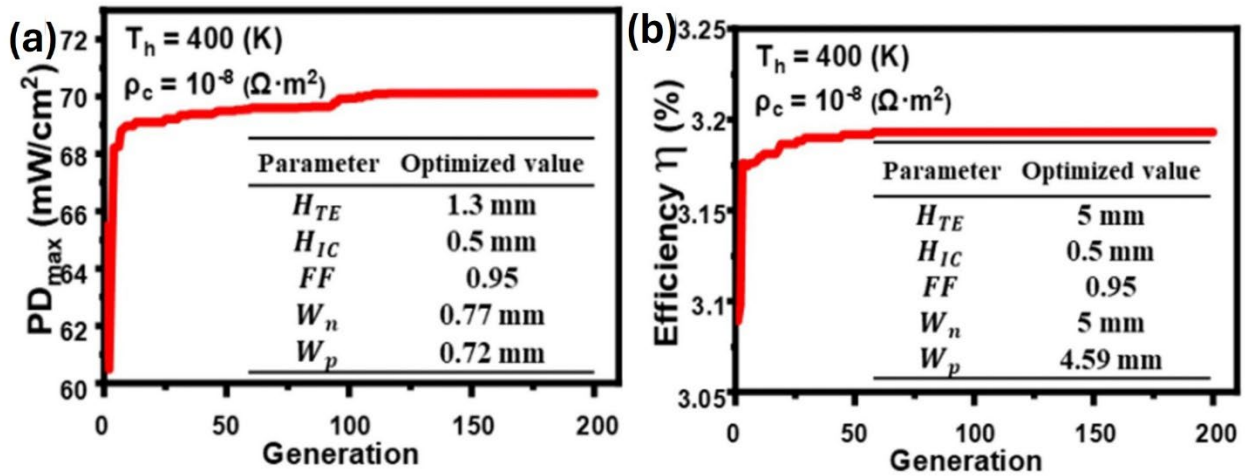

Figure 3 Convergence curve of GA for (a) maximum power density and (b) efficiency under an operating condition of T_h is 400K and ρ_c is $10^{-8}\ \Omega \cdot m^2$.

Flexible, non-toxic SF radiochromic film based on 10,12-PCDA for on-site X-ray dosimetry

Naseer Ahmad[a], Aida Visus[a], Salvador David Aznar[b], Gonzalo Guirado[c], Consuelo Guardiola[a], Xavier Muñoz Berbel[a], Silvia Mena[a]*

[a]Institut de Microelectrònica de Barcelona, IMB-CNM (CSIC), Universitat Autònoma de Barcelona, Cerdanyola Del Vallès, 08193, Barcelona, Spain.
[b]Instituto Murciano de Investigación y Desarrollo Agrario y Medioambiental (IMIDA). C/ Mayor, s/n, 30150 La Alberca, Murcia, Spain
[c]Universitat Autónoma de Bacelona, Bellaterra, 08193, Barcelona, Spain
e-mail: silvia.mena@imb-cnm.csic.es

X-rays play a crucial role in various fields, including medicine, forensic science, security screening, scientific research, sterilization, and industrial applications, due to their ability to penetrate materials and provide detailed information[1-3]. In medicine, X-rays are particularly important for imaging, disease detection, and therapies such as cancer treatment[4]. However, excessive exposure to X-rays poses significant health risks, including tissue damage, DNA mutations, infertility, birth defects, skin burns, impaired vision, and carcinogenesis[5]. Accurate dosimetry is essential to ensure radiation safety. Yet, conventional dosimeters, such as thermoluminescent and semiconductor-based sensors, along with current commercial dosimetry films, often suffer from limitations like rigidity, high costs, and complex fabrication processes, making them less suitable for real-time, on-site detection[6].

In view of these facts, we report a novel flexible and biocompatible X-ray dosimeter based on silk fibroin films incorporating 10,12-pentacosadiynoic acid (PCDA). Upon irradiation, PCDA undergoes topo-chemical polymerization, resulting in changes in the optical density (OD) of the film. A clear linear relationship between absorbed dose (0–50 Gy) and ΔOD after irradiation has been established (Figure 1). Compared to other polymer-based membranes, these films are more biocompatible and mechanically robust: their flexibility has been tested, revealing measurable differences in mechanical properties before and after irradiation (Figure 2). In order to enable real-time, label-free, on-site dosimetry, a conductive sensor has been developed by integrating screen printed electrodes onto the PCDA–silk fibroin film. We explore for the first time the potential correlation between PCDA polymerization and changes in electrical impedance measured by electrochemical impedance spectroscopy (EIS). This correlation between impedance variation and radiation dose highlights the potential of this system for non-optical readout of radiochromic films (Figure 3).

Overall, this work advances the development of flexible, cost-effective, and biocompatible dosimeter films by introducing a new impedance-based readout method. The approach paves the way for integrating similar radiochromic films into portable microfabricated devices for medical dose monitoring and environmental radiation detection.

Keywords: flexible devices, radiochromic film, silk fibroin, X-ray dosimetry

References

[1] Z. Yang et al., Adv. Funct. Mater. 34 (2024) 2406186.
[2] Y. De Deene et al, Radiat. Meas. (2024) 107321.
[3] M. D. Salman et al., J. Radioanal. Nucl. Chem. 333 (2024) 3713.
[4] E. P. Medeiros et al., Expert Syst. Appl. 238 (2024) 122029.
[5] N. K. Lo et al., Mater. Chem. Phys. 319 (2024) 129362.
[6] L. B. Youssef et al., in: 2024 4th Int. Conf. Innov. Res. Appl. Sci. Eng. Technol. (IRASET), IEEE, 2024, pp. 1-6.

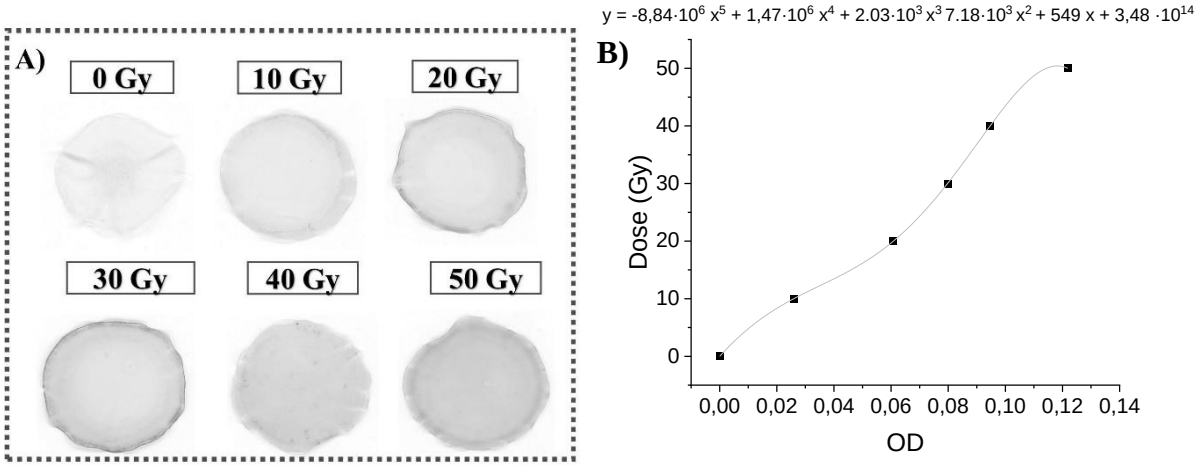

Figure 1. (A) 2D scanner images and (B) Calibration curve response of PCDA-silk fibroin films after X-rays irradiation.

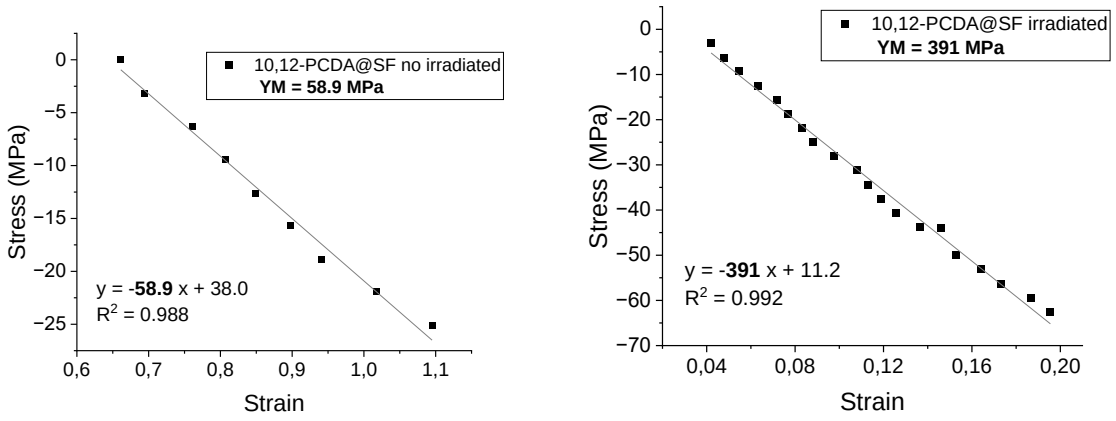

Figure 2. Mechanical properties analysis of PCDA-silk fibroin films before (left) and after (right) X-rays irradiation of 8 Gy.

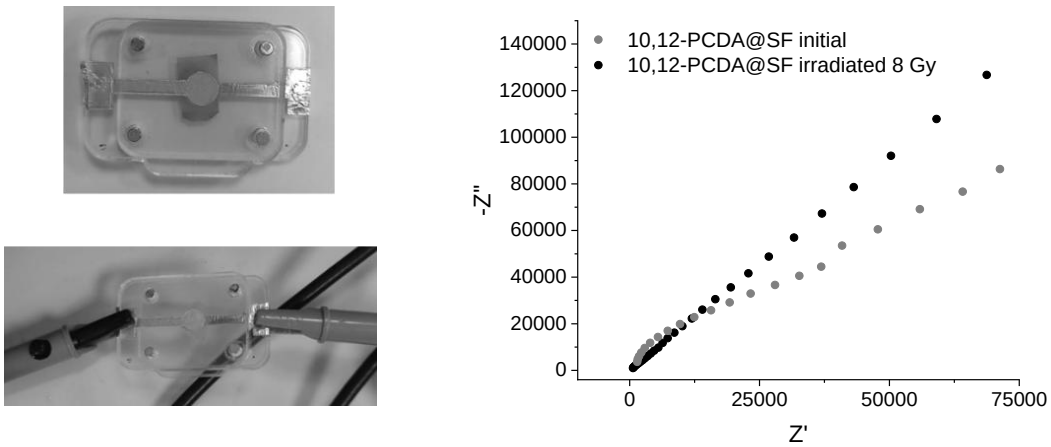

Figure 3: PCDA-silk fibroin film analysis before and after irradiation of 8 Gy by EIS.

Open Science & Technology: Microfluidic fluid handling

Lars Kool[a], Bertrand Cinquin[a]

[a] Institut Pierre-Gilles de Gennes (IPGG), ESPCI Paris - PSL, UAR3750 CNRS, Paris, 75005, France
e-mail: bertrand.cinquin@espci.fr

Keywords: Microfluidics, Automation, µManager, standardization, open-source

Where it gets more and more common to provide (experimental) data alongside research papers, technological developments often only get shared conceptually, leaving many of the non-trivial design decisions to be rediscovered by others. The open science movement strives to improve accessibility, inclusiveness, reproducibility, and transparency of research [1], pushing these technological developments to be directly implemented, improved, and/or extended by others. Such developments have already been observed in the field of microscopy from both the hardware and software side [2, 3]. In microfluidics, ample developments on the hardware side have been done [4, 5]. However, a standardized software approach to fluid handling, and integration with other devices commonly used in microfluidic experiments, is still missing. Here we present our advances on a standardized, open-source approach to fluid handling.

We extended the widely used, open-source, cross-platform microscopy control software µManager [3]. We defined the standard behavior of the pumps. To make a pump compatible with µManager, a translation layer (device adapter) has to be written between this standardized behavior and the pump driver (typically once per manufacturer). The device adapters are shared/supported by µManager making the development available immediately to the µManager community.

This standardization offers great advantages. Researchers interact only with the standardized pumps, meaning that they can mix and match pumps without loss of functionality, e.g. the graphical user interface we developed for pressure and volumetric pumps is completely device agnostic (Figure 1, left). Furthermore, protocols developed using µManager's scripting interface are also device agnostic, meaning that researchers can share their research and protocols with their collaborators without the need to exactly duplicate the hardware part. This is a crucial feature to standardize laboratory protocols. These protocols can also be included in scientific publications, increasing the accessibility and transparency of research. Furthermore, using the excellent support for Multi-Dimensional Acquisition (MDA) of µManager, it has never been easier to explore the parameter space (Flow rate, pressure) of microfluidic devices without manual intervention (Figure 1, right). Lastly, the holistic approach of controlling the entire microfluidic experiment from one central hub allows users to derive the input of one device (e.g. flowrate) from the output of another device (e.g. camera). As a proof of concept, we have made two small applications : (i) the Droplet size controller: diameter is provided by the user and PID controller find the right relative pressure (Figure 2, left). (ii) Pico injection controller : Quantity of pico-injected material is controlled by the user, the system calculates the right fluidic parameters (Figure 2, right). The first example may seem simple, however, the power lies in its interoperability. We successfully transferred this application between microscopes (running different cameras) and switch between pressure controllers and syringe pumps without any additional programming.

[1] *UNESCO Recommendation on Open Science* (UNESCO, 2021)
[2] K.J.A. Martens et al., Nat. Commun. 10 (2019) 3552
[3] A. Edelstein et al., Current Protocols in Molecular Biology 92 (2010) 14-20
[4] R.Z. Gao et al., HardwareX 7 (2020) e00096
[5] S. Baas and V. Saggiomo, HardwareX 10 (2021) e00219

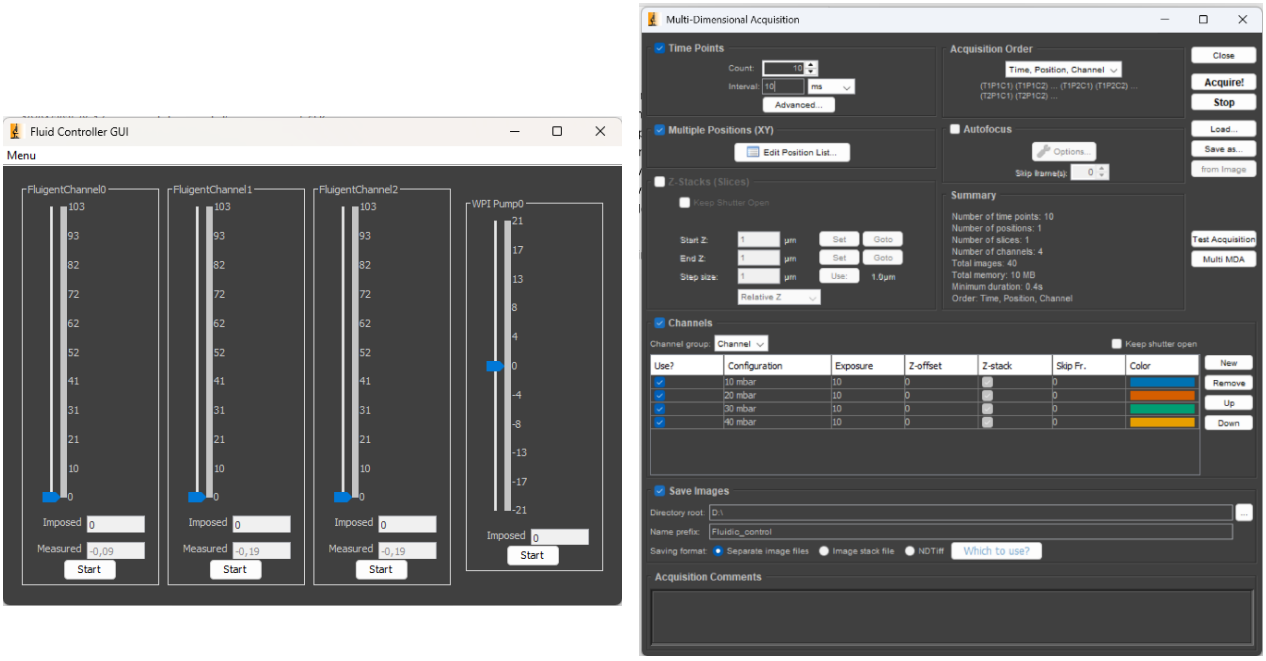

Figure 1. Left: Multi-Dimensional Acquisition using pressure as one of the acquisition dimensions. Right: Simple graphical user interface to control both pressure controllers (first 3 channels), as well as syringe pumps (last channel).

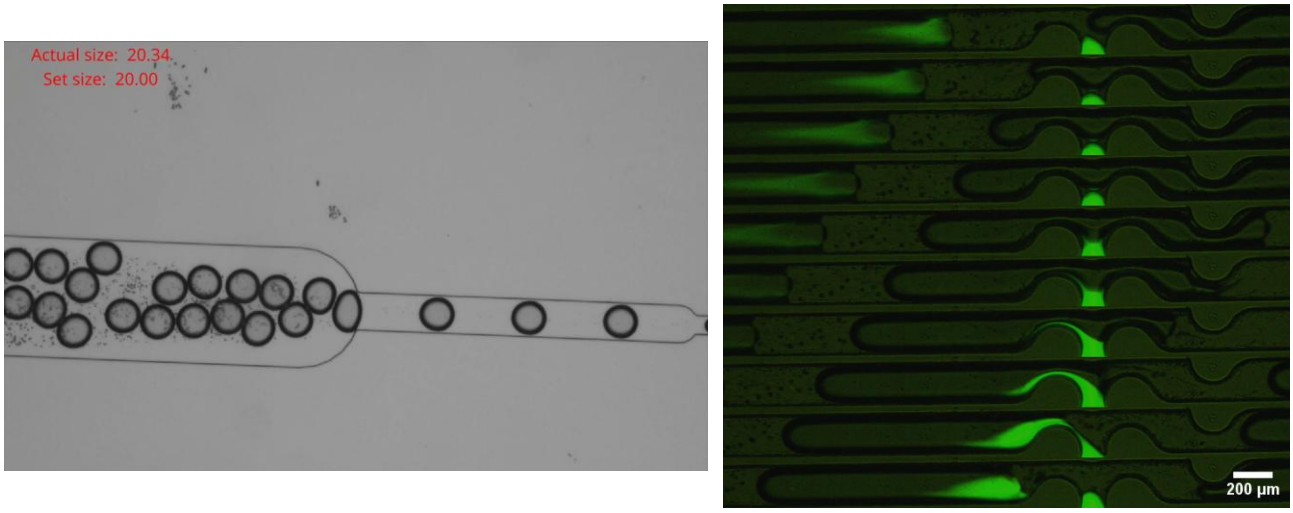

Figure 2. Left: Automatic control of droplet size using a PID protocol. Right: Superposition of fluorescent fluid pico-injected into a droplet using an automated pico-injection application.

Ultrasensitive TDSE/Au/SOD-based Electrochemical Sensing Platform for Real-Time Monitoring of Superoxide Ion at Cellular Level

Pratyusa Mohapatra [a], Soumen Das [a]

[a] Indian Institute of Technology Kharagpur, Kharagpur, 721302, India
e-mail: sou@smst.iitkgp.ac.in

Abstract:- Biological oxidative stress is a critical contributor to the pathogenesis of various life-threatening diseases, such as cancer and neurodegenerative disorders. This oxidative stress is primarily driven by the excessive generation of reactive oxygen species (ROS), among which superoxide anion (O_2^-) serves as the initial form that propagates the formation of more reactive ROS through various interactions. Therefore, detecting superoxide at the cellular level is crucial for controlling the overall ROS-induced stress. However, its detection is particularly challenging due to its short lifespan and high reactivity. Herein, we report the development of an ultrasensitive, planar electrode for the precise detection of superoxide ions in biological systems[1]. The sensor fabrication consists of a thermal vapour deposition-based silver electrode (TDSE) on a polystyrene substrate, which is further functionalized with ultra-small gold nanoparticles (AuNPs) conjugated with superoxide dismutase (SOD) to enhance electrochemical activity and sensitivity[2]. TDSE exhibited superior conductivity and catalytic performance compared to various commercial carbon and gold electrodes, also demonstrated in multiple studies. After completing comprehensive physical and electrochemical characterization, the TDSE/Au/SOD sensor was employed for electrochemical detection. The resulting TDSE/Au/SOD sensor demonstrated a limit of detection (LOD) of 0.1 µM and excellent sensitivity in detecting chemically synthesized superoxide ions. Comprehensive evaluations of selectivity, sensitivity, reliability, and reproducibility were conducted, establishing the sensor as a high-performance platform. Finally, the TDSE/Au/SOD sensor was successfully used to detect superoxide at cellular levels across different cell lines (Hela and L929), exhibiting minimal interference within the cellular environment. The work established the efficacy of TDSE/Au/SOD for real-time monitoring of superoxide concentrations in biological systems, advancing research into ROS-related cellular processes and disease mechanisms[3][4].

[1] E. A. B, I. Arifin, P. Noerrizky, and R. R. Althof, *Proceedings of the 4th International Conference on Life Sciences and Biotechnology (ICOLIB 2021)*, vol. 1. Atlantis Press International BV, 2023. doi: 10.2991/978-94-6463-062-6.

[2] A. M. Pudlarz *et al.*, "The effect of immobilized antioxidant enzymes on the oxidative stress in UV-irradiated rat skin," *Nanomedicine*, vol. 15, no. 1, pp. 23–39, 2020, doi: 10.2217/nnm-2019-0166.

[3] W. Feng *et al.*, "2D vanadium carbide MXenzyme to alleviate ROS-mediated inflammatory and neurodegenerative diseases," *Nat. Commun.*, vol. 12, no. 1, Dec. 2021, doi: 10.1038/s41467-021-22278-x.

[4] M. Hayyan, M. A. Hashim, and I. M. Alnashef, "Superoxide Ion: Generation and Chemical Implications," *Chem. Rev.*, vol. 116, no. 5, pp. 3029–3085, 2016, doi: 10.1021/acs.chemrev.5b00407.

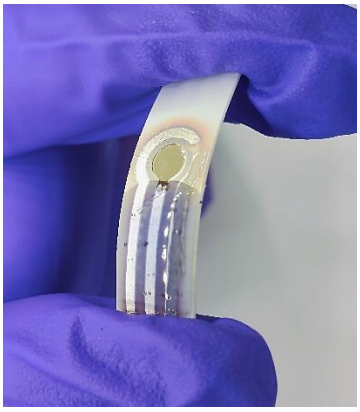

Figure 1. Photograph of fabricated TDSE/Au/SOD

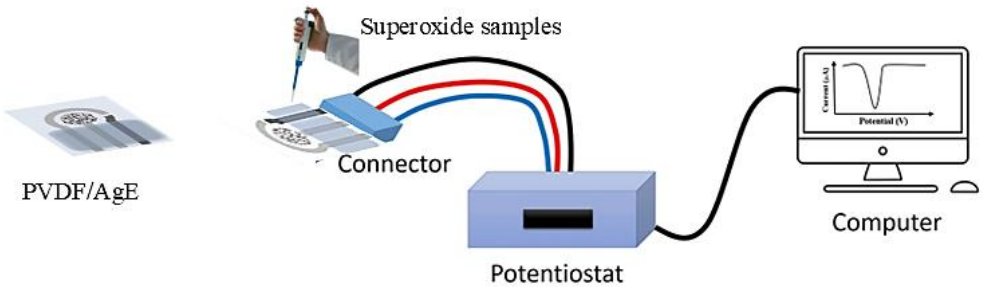

Figure 2. Electrochemical set up using TDSE/Au/SOD

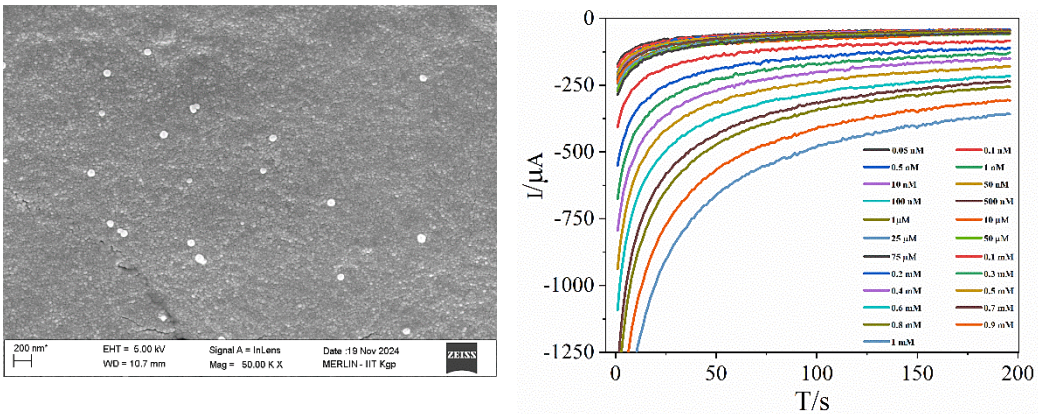

Figure 3. FESEM Image of surface of TDSE/Au/SOD(left) chronoamperometry analysis of superoxide detection using TDSE/Au/SOD(right)

Simulation of physical reservoir computing based on nonlinear dynamics of nanoelectromechanical resonators

Lianghong Ye [a], Klaus-Peter Zauner [a], Mark Vousden [a], Yuta Kawashima [b], Toshiyuki Tsuchiya [b], and Yoshishige Tsuchiya [a]

[a] School of Electronics and Computer Science, University of Southampton, Southampton, SO17 1BJ, UK
[b] Department of Micro Engineering, Kyoto University, Kyoto 615-8540, Japan
e-mail: l.ye@soton.ac.uk

Reservoir computing (RC) is an efficient neuromorphic computing paradigm consisting of a dynamical system, that nonlinearly maps sequential inputs into a high-dimensional space and a readout system that then selects mappings which are useful features to generate the output. As only the readout system is trained, the computational cost is significantly reduced compared to conventional deep networks [1]. The nonlinearity is crucial for such system as it allows linearly inseparable data to be represented in a space where a linear classifier can be applied. In theory, any dynamical system with complex nonlinear behaviour can be used for RC; a hardware implementation is called physical RC. Dion et al. [2] and Takemura et al. [3] have demonstrated physical RC using MEMS resonators, however, physical dimensions of their devices are in microscale, resulting in lower operational speed and higher power consumption.

Nanoelectromechanical (NEMS) resonators feature high frequencies and low power consumption, aligning perfectly with edge computing demands for real-time and low-power processing. This simulation study therefore leverages the NEMS resonators fabricated by Tsuchiya et al. [4] to develop a physical reservoir computing system. Figure 1 shows a schematic model of the NEMS resonator. This resonator is actuated by applying an RF signal on the beam and a DC bias beneath it and reaches a resonance frequency of several hundred MHz. The dimensional and material parameters used in this study are listed in the table in Figure 1.
We employ three types of simulations to evaluate the feasibility of a NEMS-based reservoir computing system: (1) COMSOL finite element analysis is used to model the NEMS resonators response, (2) Mathematical modelling to describe the resonator behaviour, and (3) Reservoir computing simulation to implementing a simulated physical reservoir system based on the modelled behaviours.

Figure 2 shows the resonance behaviour calculated by COMSOL (left). The resonance is consistent with the mathematical model result (right). The mathematical model facilitates batch analysis and easy integration into a software-based reservoir computing framework. This simulation was applied to a parity task, a classic time-series classification benchmark for reservoir computing [2]. In this task, a masked binary step sequence was fed into the system, driving the resonator and generating a non-linear response over time. A Hilbert transform was then applied to the resonator output to extract its envelope, where samples were taken at equal intervals to create virtual nodes, which were subsequently used to generate the output in the readout system, i.e. the parity of the windowed input sequence as shown in Figure 3.The equation for the mathematical model is

$$\ddot{z} + \frac{\omega_0}{Q}\dot{z} + \omega_0^2 z + \omega_0^2 \beta_m z^3 = F_{\text{elec}}/m = \frac{\varepsilon_0 A (V_{DC} + V_{RF})^2}{m(g_0 - z)^2} \quad (Eq.\,1),$$

where z is the beam displacement, m is the beam mass, ω_0 is the eigenfrequency, Q is the quality factor, β_m is the nonlinear coefficient, F_{elec} is the external electrostatic force, ε_0 is the vacuum permittivity, A is the area, g_0 is the initial gap distance, and V_{DC} and V_{RF} are the applied DC and RF voltages, respectively. This model is integrated into the following reservoir computing simulation. The nonlinear velocity response of the resonator to step inputs is shown in Figure 4, along with the parity benchmarking performance, which achieved 100% accuracy (order n=2). 98.5% accuracy (order n=3). 88.1% accuracy (order n=4). The result is consistent with those reported in other mechanical oscillator-based reservoirs [2], effectively demonstrating a cohesive set of models for a real NEMS device, all highlighting the potential of using NEMS in physical reservoir computing.

Acknowledgements
This work is partially supported by UKRI MINDS CDT [EP/S024298/1], Chist-Era NOEMIA (CHIST-ERA-21-NOEMS-004) by EPSRC (EP/X03495X/1), and Royal Society (IEC/R3/233070).

References

[1] G. Tanaka et al., Neural Networks, vol.115, pp. 100123, Jul. 2019.
[2] G. Dion et al., Journal of Applied Physics, vol. 124, no. 15, p. 152132, Oct. 2018.
[3] H. Takemura, et al., 2023 IEEE MEMS, Munich, Germany, 2023, pp. 515-518.
[4] Y. Tsuchiya et al., 2018 IEEE MEMS, Belfast, UK, 2018, pp. 515518.

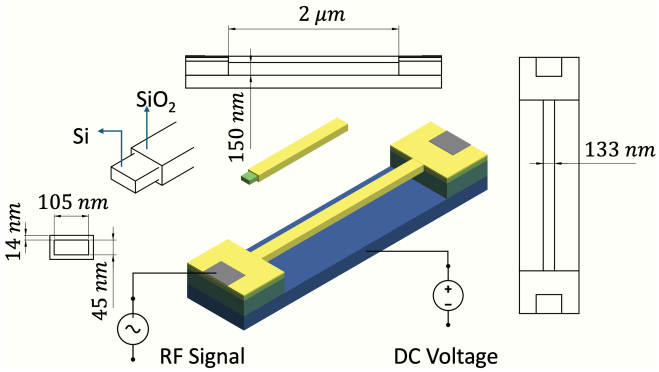

Parameter	Value	Unit
m	3.39×10^{-17}	kg
ω_0	7.36×10^{8}	rad/s
Q	3.30×10^{2}	–
β_m	1.54×10^{-4}	$1/m^2s^2$
ε_0	8.85×10^{-12}	F/m
A	2.66×10^{-13}	m^2
g_0	1.50×10^{-7}	m

Figure 1. Left: Schematic of a NEMS resonator, with its doubly-clamped beam consist of silicon (Si) substrate with a silicon dioxide (SiO_2) layer, actuated by RF and DC voltages. The beam dimensions are 2 μm (length) x 133 nm (width) x 73 nm (height), with a 150 nm gap. Right: Parameters for Eq.1.

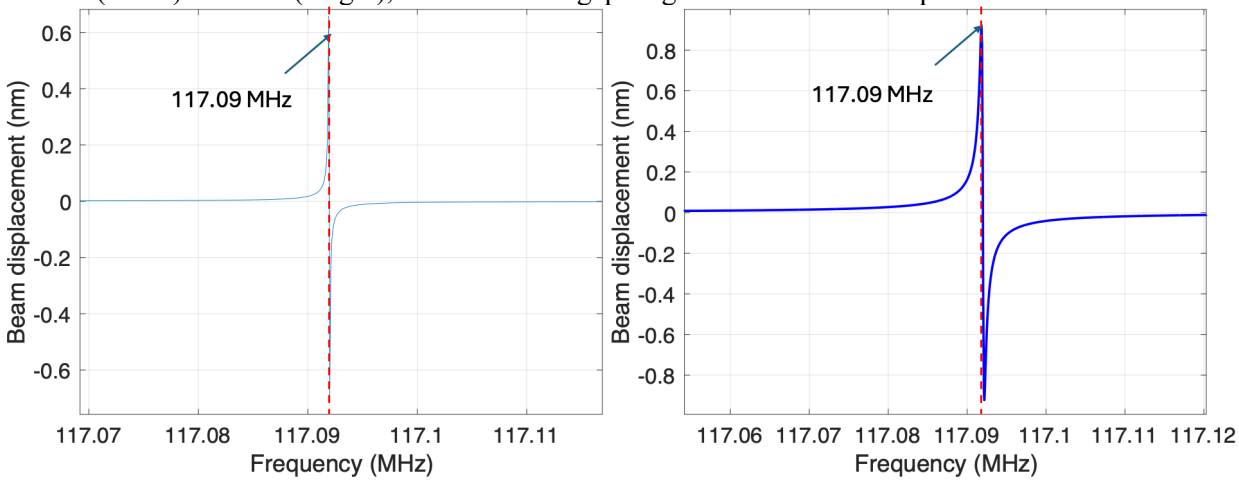

Figure 2. Left: resonance peak from COMSOL simulation. Right, resonance peak from mathematical model

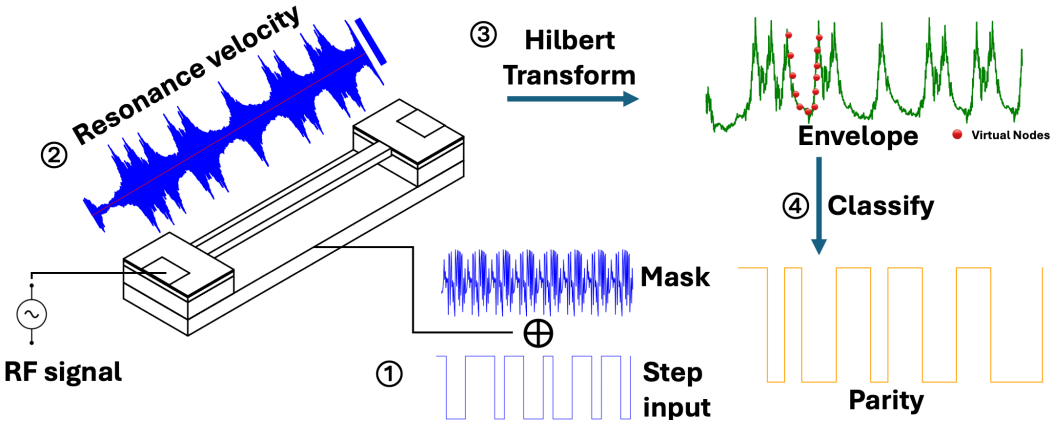

Figure 3. Flow diagram of the reservoir computing using the dynamic response of a NEMS resonator

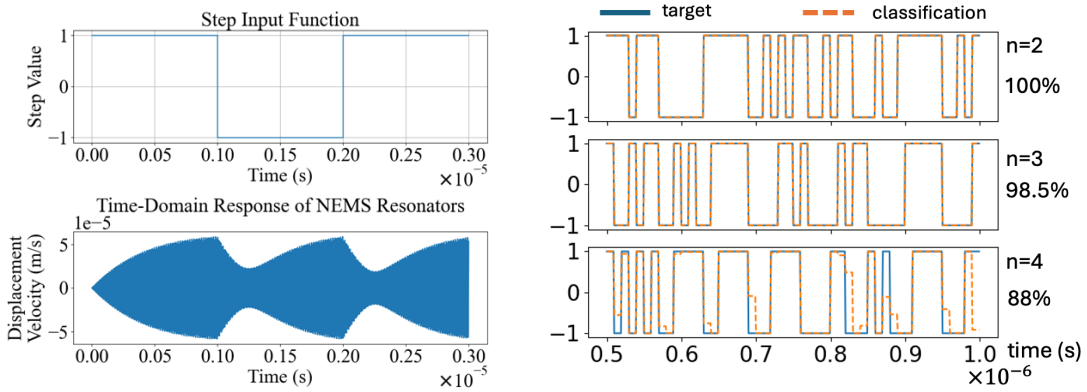

Figure 4. Left: Non-linear velocity response $v(t)$ of the NEMS resonator, driven by changes in actuation voltage. Right: Parity Benchmarking result – with the comparison between classification target and result

Microfluidic chip for electrochemical detection of circulating miRNAs: real-sample testing of cardiac disease biomarkers

A. Tarasova [a], I. Mbomekalle [b], S. Banzet [c], H.M. Man [a], I. Le Potier [a], J. Gamby [a]

[a]Laboratoire Centre de Nanosciences et de Nanotechnologies (C2N), Palaiseau, 91120, France
[b]Institut de Chimie Physique d'Orsay (ICP), Orsay, 91400, France
[c] INSERM UMR-MD-1197, Centre de transfusion sanguine des armées, Clamart, 92140, France
e-mail: anna.tarasova@universite-paris-saclay.fr

Keywords: microfluidics, miRNAs, electrochemical sensor, EIS, CV, biosensing, microfabrication

The quantification of circulating microRNAs (miRNAs), particularly miR-1 and miR-133a, has emerged as a powerful strategy for the early detection and monitoring of cardiac diseases as acute myocardial infarction (AMI) [1]. These muscle-enriched miRNAs are released into the bloodstream during cardiac injury and show strong biomarker potential due to their stability [2], disease specificity, and rapid response to physiological stress [3]. However, existing analytical methods such as real-time quantitative PCR (RT-qPCR) and sequencing remain time-consuming, expensive, and require complex sample processing, which limit their use in point-of-care (POC) or emergency clinical settings.

This work aims to develop and validate a miniaturized microfluidic electrochemical biosensor capable of simultaneous and label-free detection of miRNAs from real samples. The ultimate goal of the platform is to create a profiling map of miRNA expression patterns in different pathologies, allowing for real-time patient monitoring, early diagnosis and therapeutic decision-making.

Our approach builds upon the microelectrode-based reference-free electrochemical detection in portable analytical platforms. The device is shown in **Fig. 1**. [4] Embedding it into microfluidic channel allows uniform distribution of the sample over the detection surface, which minimizes losses due to diffusion limitations. [5] This enhancement results in higher sensitivity, faster response times, lower sample consumption (nanoliters**)** and more accurate quantification of low-abundance miRNAs.

The working electrodes are functionalized with DNA probes complementary to miR-1 and miR-133a. The hybridization event is detected by cyclic voltammetry (CV) and electrochemical impedance spectroscopy (EIS) achieving detection limits in the low attomolar range (**Fig. 2**) with high specificity, even in the presence of similar miRNA sequences. [6]

The approach presented here uses 6-mercapto-1-hexanol (MCH) for a better orientation of immobilized probes and TCEP as a reducing agent for thiols attached to DNAs. [7, 8] The working principle is presented in **Fig.3**. Additionally, we are currently testing alternative strategies for electrode functionalization to improve sensitivity and prevent non-specific adsorption. [9]

To validate our method, we analyzed real plasma samples from mice obtained from our collaborator (INSERM). These samples were collected from mice following notexin-induced muscle injury. Our results were consistent with RT-qPCR findings, confirming that circulating miRNAs, particularly miR-133a, are upregulated in response to muscle damage. In the sample with the lowest degree of muscle lesion, miR-133a was detected at concentrations of 4.9 pM and 620 fM using CV and EIS (via charge transfer resistance, Rct), respectively, while 45 pM for the highest lesion. miR-1, which was detected at low levels by RT-qPCR, also showed lower expression in our measurements (29 fM for lowest and 112 fM for highest), compared to 3 fM in control samples. These findings are summarized in **Fig. 4**. EIS was used also to evaluate the surface coverage dependence.

Our results show a dynamic detection range from attomolar to micromolar concentrations for synthetic miR targets. The varying concentrations of miRNAs in real samples provide a preliminary validation of our approach without the need for PCR amplification. In summary, our device introduces multiple innovations: it operates in a label label-free miR detection platform, supports real-time, and direct analysis of clinical samples without complex preparation steps. These features, together with its compact and low-power design, render the platform ideal for POC diagnostics and continuous patient monitoring.

[1] Y. Kuwabara, et al., Circ. Cardiovasc. Genet. 4 (2011) 446–454.
[2] P.S. Mitchell, et al., Proc. Natl. Acad. Sci. U.S.A. 105 (2008) 10513–10518
[3] J. Siracusa, et al., The American Journal of Pathology, 186 (2016) 1313-1327.
[4] M. Lazerges, et al., Sensors and Actuators B 182 (2013) 510–513.
[5] C. Poujouly, et al., Electrochemistry Communications, 137 (2022) 107262
[6] C. Poujouly, et al., Frontiers in chemistry, 10 (2022).
[7] O. Choyab, et al., Langmuir 2024, 40, 50, 26616–26625
[8] H. H. Man, et al., ACS Electrochem, (2025)
[9] L. Meng, et al., Inorganic Chemistry *63* (46) (2024) 22149-22161
[10] M. Freisa, et al., Electrochimica Acta 505 (2024) 14500

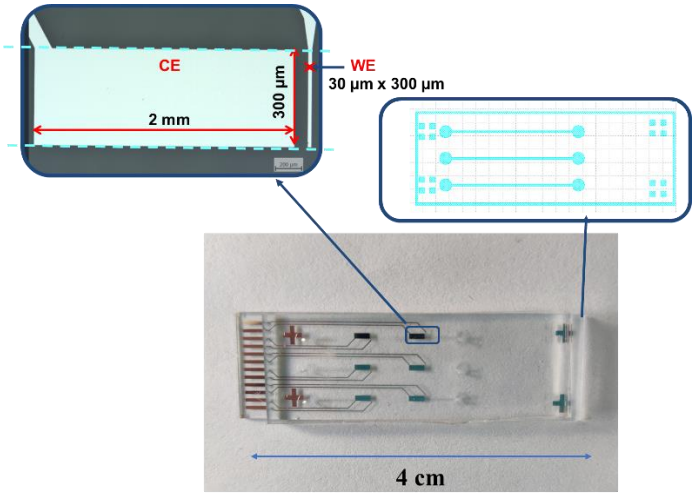

Figure 1. Illustration of the microfluidic device fabricated by UV lithography, platinum deposition and molded PDMS bonding; with dimensions reproduced from reference [10].

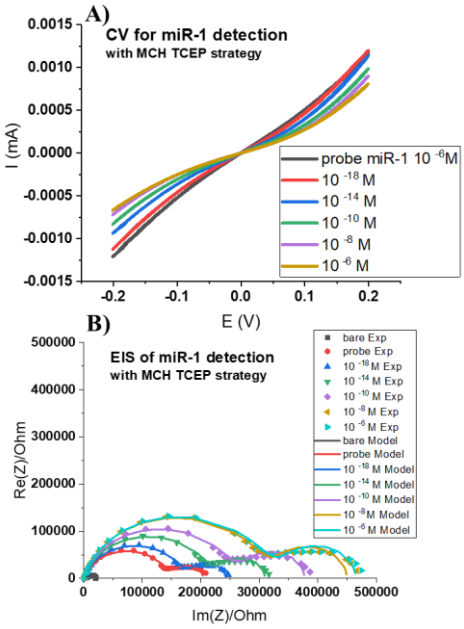

Figure 2. A) Example of CV experiment for detection of miR-1 with 5 synthetics target samples at different concentrations; B) EIS experimental (dots) and fitting (lines) performed by Measurement Model software.

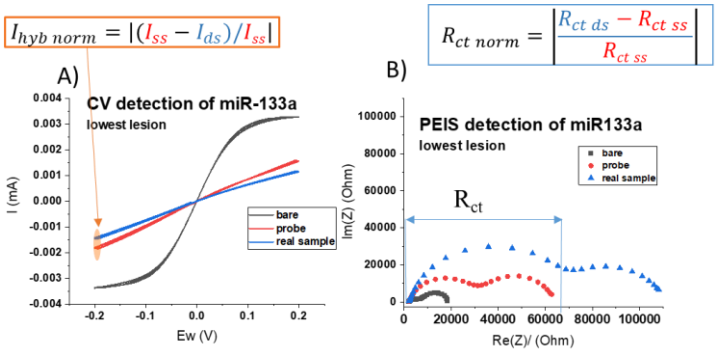

Figure 3. Example of experiments for detection of miR-133a in real sample with the lowest lesion: A) CV showing the current absolute value decreasing after hybridization. B) PEIS showing R_{ct} increase suggesting non-linear mass diffusion due to surface coverage. [10]

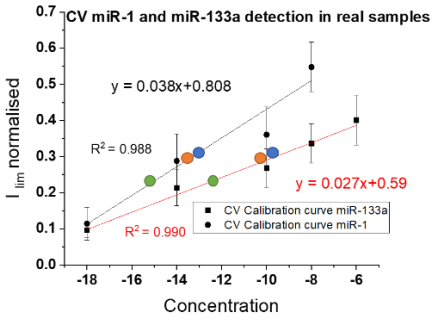

Sample	Repetitions	I norm averaged	Error	Concentration (M)
Control miR-133a	5	0.26	0.02	$3.1\ 10^{-13}$
Lowest lesion miR-133a	3	0.29	0.03	$4.9\ 10^{-12}$
Highest lesion miR-133a	3	0.32	0.02	$4.5\ 10^{-11}$
Control miR-1	4	0.25	0.04	$3.79\ 10^{-15}$
Lowest lesion miR-1	3	0.29	0.05	$2.92\ 10^{-14}$
Highest lesion miR-1	3	0.31	0.03	$1.12\ 10^{-13}$

Figure 4. CV results of detection miR-1 and miR-133a in real samples. Control (green), low lesion (orange), and highest lesion (blue). Table with values.

Optic Fibre Gas Sensor featuring MoS_2 QD as an Active Layer

García-Ramírez Mario Alberto[a], González-Reynoso Orfil[a], Villalvazo-Hidalgo Andrea Carolina[a], Bello-Jiménez Miguel Angel[b], García-Barrientos Abel[b], Carbajal-Arizaga Gregorio Guadalupe[a]

University Centre of Applied Sciences and Engineering, Guadalajara University, Guadalajara, Jalisco, 44430, México
e-mail: mario.garcia@academicos.udg.mx

Bio-related sensors are key for a broad variety of fields such as industrial plants, hospitals, airports, among others [1-3]. Most of them are electronic-based that require a close spot as well as an array to get enough information to be measured and analysed. In this matter, we are proposing a heterodox bio sensor based on an optic fibre array. We are considering an optic fibre featuring a set of four tapers featuring a 60 um thick at 2 cm in length in a transition of 1 cm each whilst a separation among them of 10 cm is presented as schematically is shown in Fig. 1. Once the tapers are generated, through an in-house deposition system, a thin layer of MoS2 quantum dots is deposited (Fig. 2). In order to get the desired biomolecule, we functionalised two taper sections with different bio-receptors and two to measure whole environment as a differential one. MoS2 quantum dots is an in-house synthesised material through a hydrothermal technique where it is possible to get it as a monolayer dispersion. The deposition process is as follows, the optic fibre is covered in a positive photoresist to protect whole fibre, the mask is located at each taper in order to properly deposit the MoS2, once deposited, the photoresist is developed and the material is exposed (Fig. 3). To measure it, we are using a 980 nm laser to read the state for each taper and according to the tuning bio-molecule to analyse. We obtained promising results to measure two different biomolecules in a harsh environment.

[1] M. Bello-Jiménez et al., Optics Continuum, 4 (2025) 778-788
[2] M. A. Garcia-Ramirez et al., KIJM, 8 (2022) 81-87
[3] M. A. Garcia-Ramirez et al., Sensors, 22 (2022) 1806

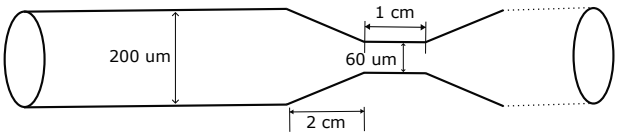

Figure 1. Schematic diagram that features the tapered regions deposited with MoS2 QD.

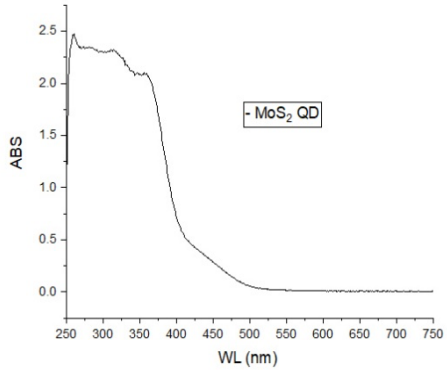

Figure 2. UV–Vis absorption spectrum of MoS_2 quantum dots synthesized via hydrothermal method.

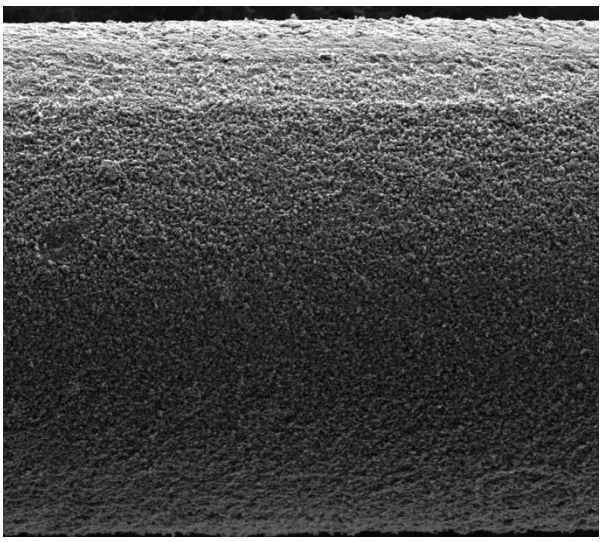

Figure 3. Schematic diagram of the MoS2 QD deposition on the taper

Development kinetics of photoresist films using trimethylammonium hydroxide (TMAH) aqueous developer contaminated with poly(4-hydroxystyrene)

Andreia Santos[a], Masahiko Harumoto[b], Yuqing Jin[c], Takahiro Kozawa[c]

[a] SCREEN SPE Germany, Fraunhoferstrasse 7, D-85737 Ismaning, Germany
[b]SCREEN Semiconductor Solutions Co., Ltd. 480-1 Takamiya-cho, Hikone, Shiga, Japan
[c]SANKEN, Univ. Osaka, 8-1 Mihogaoka, Ibaraki, Osaka, 567-0047, Japan
e-mail: a.santos@screen-spe.eu

The semiconductor industry's pursuit of sustainability requires the reduction of chemical waste and the implementation of greener processes. Tetramethylammonium hydroxide (TMAH) at 2.38 wt% concentration is widely used as a developer in photolithography, but its toxicity and environmental impact pose significant challenges [1]. Recycling TMAH on coater-developer tracks could be a promising solution, but it requires a comprehensive understanding of the interactions between TMAH and photoresist materials, as it is crucial to efficiently remove organic and inorganic impurities that leach to the developer chemical during the development process.

In this work, we initiate a fundamental investigation into the dissolution dynamics of 3 different photoresist polymer models in TMAH solutions using the quartz crystal microbalance (QCM) method [2-4]. The QCM measurement enables real-time monitoring of mass changes on a sensor surface, allowing precise measurements of dissolution rates and the identification of any alterations due to contamination. To simulate a recycling scenario, we checked how TMAH solutions contaminated with different poly(4-hydroxystyrene) (PHS) amounts affect the dissolution behaviour of each photoresist, providing insights into the interactions between the developer and photoresist components.

Our findings reveal that the presence of dissolved PHS in the developer solution significantly influences the dissolution dynamics of each model-resist: the dissolution rate significantly decreases once PHS is added in the developer solution, with higher concentrations of PHS resulting in a corresponding decrease in dissolution (Fig. 1). These results underscore the importance of effective purification strategies to remove organic contaminants from used developer solutions and emphasize the importance of understanding resist-developer interactions to develop recycling protocols that ensure both environmental sustainability and process reliability.

References:

[1] C. Allen, SEMI - Strategic Materials Conference (2012).
[2] Y. Jin et al., , Proc. of SPIE Vol. 13215 (2024)132150J-1.
[3] J. Wang et al., Proc. of SPIE Vol. 13215 (2024) 132150T-4.
[4] K. Machida et al., Proc. of SPIE Vol. 13215 (2024) 1321514-8.

Figures:

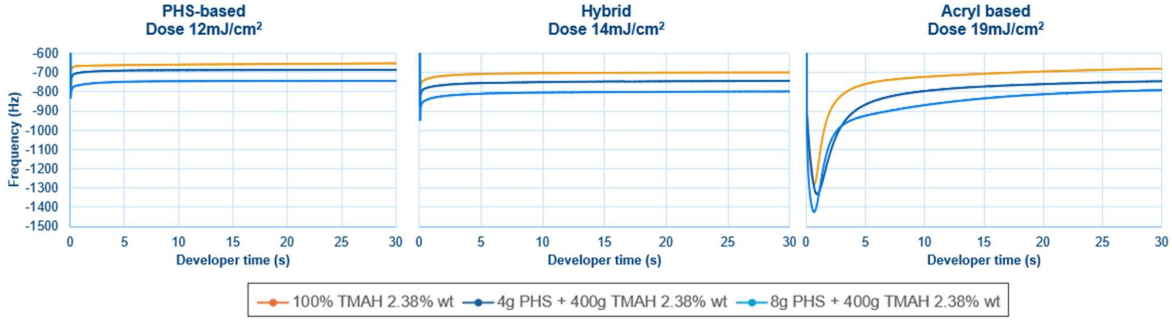

Figure 1. Impact of PHS polymer dissolved in TMAH on the dissolution rate of different model-resists.

Introducing a new era of green and functional biopolymeric surfaces

Dimosthenis Ioannou[a], Kosmas Ellinas[b], Alexandros Banis[a], D.I Koukoumaki[c], D. Sarris[c], Evangelos Gogolides[a]

[a]Institute of Nanoscience and Nanotechnology, NCSR "Demokritos", 27 Neapoleos str & Patriarchou Grigoriou, Ag. Paraskevi, 153 41, Greece
[b]Laboratory of Advanced Functional Materials and Nanotechnology, Department of Food Science and Nutrition, School of the Environment, University of the Aegean, Leoforos Dimokratias 66, Myrina 81400, Lemnos, Greece
[c]Laboratory of Physico-Chemical and Biotechnological Valorization of Food By-Products, Department of Food Science & Nutrition, School of Environment, University of the Aegean, Leoforos Dimokratias 66, Myrina 81400, Lemnos, Greece
e-mail: e.gogolides@inn.demokritos.gr

Polymeric materials have long dominated the market of functional surfaces, accompanied by the rapidly increasing production of disposable plastic products and the excessive use of fossil resources. As a result, the necessity for alternative production models has emerged and the development of integrated biorefinery concepts within the circular bioeconomy era could provide a solution to this urgent problem. Yet, several drawbacks are delaying the adoption of green materials, such as the long cultivation durations, the high cost associated with fermentation feedstocks, and the absence of micro-nanotexturing and surface functionalization tools to tune the properties of biopolymers on demand.

In this work, we demonstrate an approach to fabricate sustainable bacterial cellulose (BC) surfaces, produced using *Komagataeibacter rhaeticus* AAK2 strain (kindly provided by UNIWA), valorizing Brewer's Spent Yeast (BSY), Yeast Extract and Peptone (YE+P), and Brewer's Spent Yeast and Peptone (BSY+P) (FAN content ~ 350 mg/L) and glycose (20 g/L) as nitrogen and carbon source, respectively. In addition, we were able to scale the production of BC in 2L bioreactor, whereas cultivation duration waw kept short 4-8 days.

Taking it one step further, we also tune their structural and chemical properties on demand using plasma nanotechnology, aiming for superhydrophobicity. Surfaces characterized as superhydrophobic are extremely water-repellent, with Water Static Contact Angles (WSCA) higher than 150°, and slippery with hysteresis (WCAH) less than 10°. Delicate substrates such as the ones used in this work require sophisticated methods of surface engineering to prevent large cracks and melting, while ensuring uniform treatment. To this direction, we implement O_2 plasma to create rough surface topography by means of random hierarchical structures, followed by C_4F_8 gas plasma deposition to lower the surface energy. The combination of these plasma processes results in superhydrophobicity.[1–3]

As shown in the SEM images (Figure 1), all plasma-treated samples feature consistent surface topography with dense textures of similar sizes and no large gaps, cracks or voids. In Figure 2, the WSCAs of untreated YE+P and BSY samples are measured in the hydrophilic range, while untreated BSY+P is even in the superhydrophilic range. After only the C_4F_8 plasma deposition step, the WSCAs of all biopolymers increase to 120-140°, indicating a surface energy decrease due to fluorination. However, to reach superhydrophobic levels, both plasma processes are essential. As shown in the same diagram, the WSCAs of all plasma treated samples are measured in the superhydrophobic range, above the black line marking the limit, around 155 - 160°, while the WCAH values are at or below 10°, making the proposed surfaces very promising candidates for a new era of green and functional biopolymeric surfaces.

[1] K. Ellinas et al., Langmuir. 27 (2011) 3960–3969.
[2] E. Gogolides et al., Microelectron. Eng. 132 (2015) 135–155.
[3] D. Ioannou et al., ACS Appl. Mater. Interfaces. 15 (2023) 18493–18504.

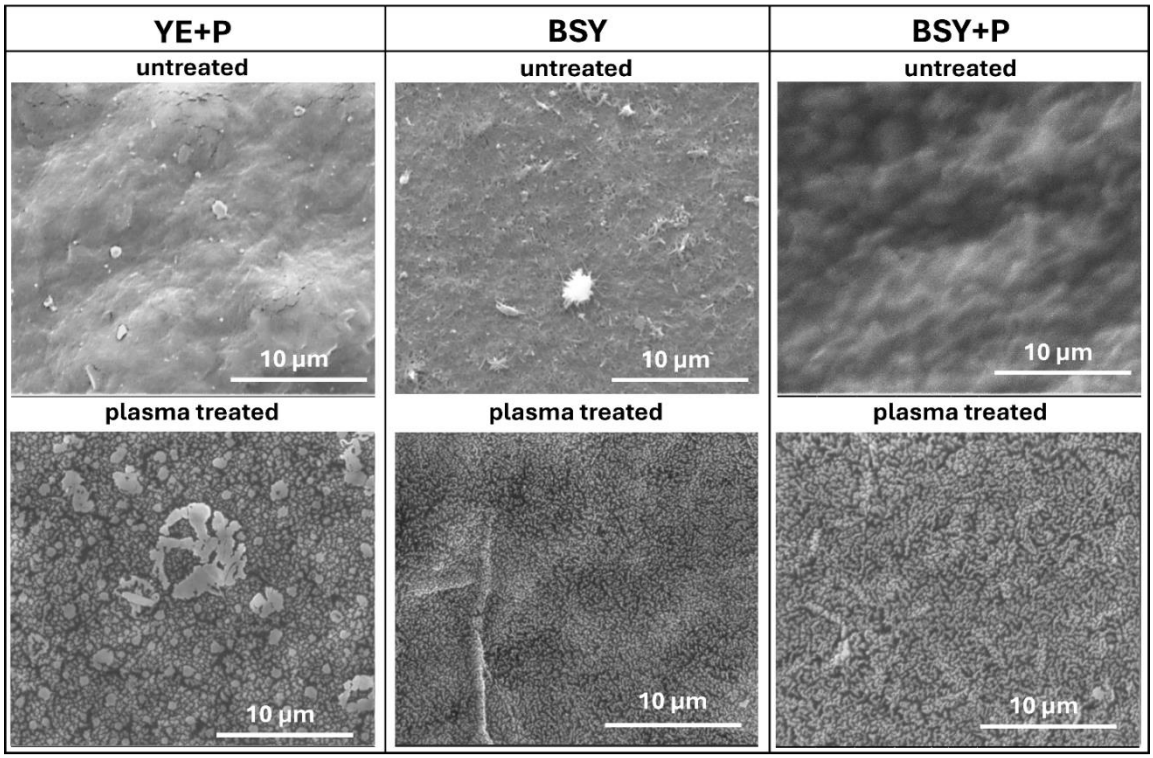

Figure 1. Top-down SEM images of biopolymers (YE+P, BSY and BSY+P) untreated and after 2 minutes of O_2 plasma etching and 1 minute of C_4F_8 plasma deposition. Notice the nanotextured topography formation after plasma treatment which is crucial for achieving the superhydrophobic state.

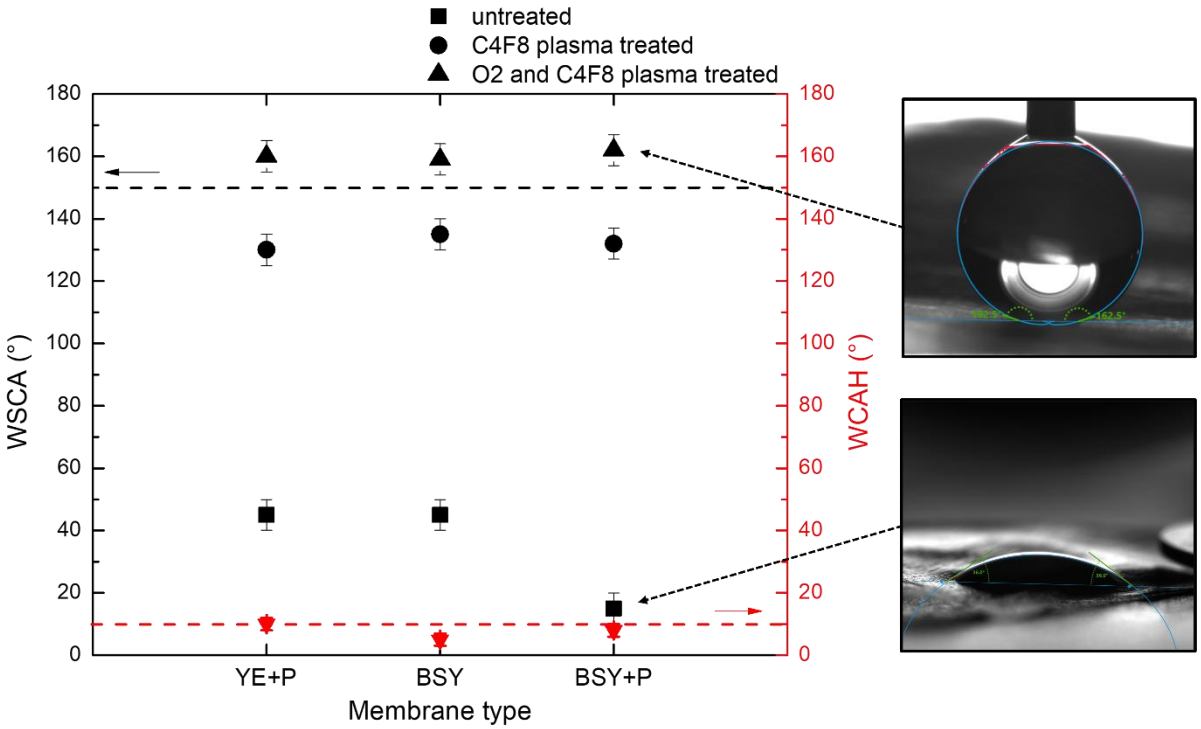

Figure 2. Water static contact angle (WSCA) and hysteresis (WCAH) of YE+P, BSY and BSY+P biopolymeric samples untreated, C_4F_8 plasma treated and O_2 followed by C_4F_8 plasma treated. The lines at 150° (contact angle) and at 10° (hysteresis) mark the limits for superhydrophobicity.

Pattern transfer by laser ablation: demonstration of a vacuumless process for micropatterning from lithographic masks

Klaus Zimmer [a], Joachim Zajadacz [a], Martin Ehrhardt[a], Pierre Lorenz [a],
Tomi Smausz [b], Bela Hopp [b]

[a] Leibniz Institute of Surface Engineering (IOM), Permoserstr. 15 Leipzig, 04318, Germany
[b] Department of Optics and Quantum Electronics, University of Szeged, Dóm tér 9 Szeged, H-6720, Hungary
e-mail: klaus.zimmer@iom-leipzig.de

The transfer of lithographically produced patterns is a key technology in microelectronics and other micro- and nanotechnologies for the definition of functional structures and to localize them precisely for a sufficient overlay. This technology has been improved continuously to meet the actual needs in size and quality. Current pattern transfer processes require vacuum equipment that is expensive and consumes energy and time at operation. Here an atmospheric pressure approach of pattern transfer by laser ablation is proposed and demonstrated. Similar plasma-based pattern transfer approaches, laser beams provide a directed energy impact to the exposed material that may cause directional material removal and with that enabling a directional pattern transfer. Because the material reactions at laser exposure are different from those govern plasma-based techniques, such as RIE or RIBE, other pattern transfer characteristics can be expected. This presentation faces the challenge of demonstrating laser-induced pattern transfer, showing the main characteristics and discussing the primary processes govern the mechanism of laser-induced pattern transfer. Despite laser ablation is well known [1] and the topography development while prolonged laser ablation is studied for polymers [2] the pattern transfer by laser ablation was just demonstrated [3].
Experimentally the transfer of photolithographically fabricated photoresist (PR) pattern with a lateral size below 10 µm and a height of approx. 2 µm into polyimide (PI) films is studied by irradiation with Excimer laser with wavelengths of 193, 248 and 308 nm and a pulse length of approx. 20 ns. The impact of the laser fluence and the pulse number are studied within the experiments. In particular, the patterns characteristics, i.e. the height and width and shape, and the surface roughness are studied in dependence on the laser irradiation parameter and the photolithographically fabricated micron pattern.
Pattern transfer can be achieved once the threshold fluence of the substrate material, here PI, is exceeded but the masking material still withstands the laser irradiation (see Figures 1, 2 and 3). Without mask ablation a binary pattern can be realized. With increasing the strength of the laser irradiation, both the masks as well as the substrate are ablated so that the depth of the transferred pattern is limited, but proportional transfer of pattern can be achieved in principle. The laser ablation-based pattern transfer mechanism comprises (i) optical effects such as laser photon absorption and scattering processes, (ii) thermal processes as materials heating and melting, (iii) mechanical effects such as stress and delamination, and (iv) laser ablation processes. These characteristics cause topographical effects of the pattern transfer process that results in a specific side wall angle of the transferred pattern due to cone formation effects, trench formation related to diffraction and reflection at the mask/patterns side walls and surrounding wavy pattern from light diffraction processes. The results pave the way to a new approach for sustainable economic fabrication processes that do not need vacuum and reactive gases.

References

[1] D. Bäuerle, Laser processing and chemistry, Springer Science, 2013.
[2] P.E. Dyer etal., Excimer laser ablation for micro-machining: geometric effects, Appl. Surf. Sci., 96-98 (1996) 415-419;
J. Jacob etal., Study of excimer laser ablation of photoresist polymer in presence of hydrogen gas environment for micro-fluidic applications, Materials Research Express, 6 (2019) 085316;
J.E.A. Pedder, etal., Improved model for the angular dependence of excimer laser ablation rates in polymer materials, Appl. Phys. Lett., 95 (2009) 174105;
L.G. Reyna, J.R. Soběhart, Laser ablation of multilayer polymer films, J. Appl. Phys., 76 (1994) 4367-4371.
[3] K. Zimmer, J. Zajadacz, M. Ehrhardt, P. Lorenz, T. Smausz, B. Hopp, Transfer of photolithographic patterns by excimer laser ablation of polymers, Appl. Surf. Sci. Adv., 27 (2025) 100754.

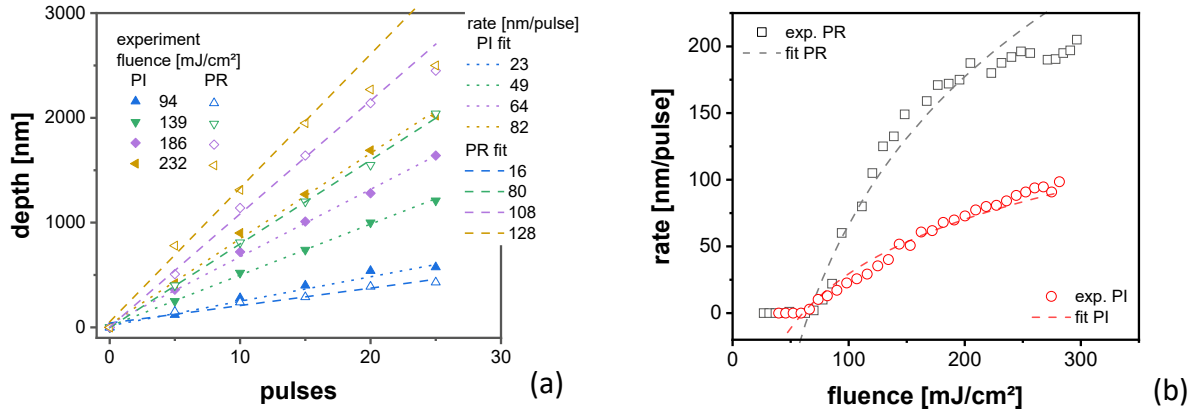

Figure 1: Depth and rate measurements of the involved polymers (photoresist MR 710 and polyimide PI2552) for laser ablation with an Excimer laser at 248 nm. (a) Ablation depth of PR and PI for selected irradiation parameters. In addition, the ablation rates for different laser fluences are given. (b) laser ablation rates in dependence on the laser fluence of PR and PI.

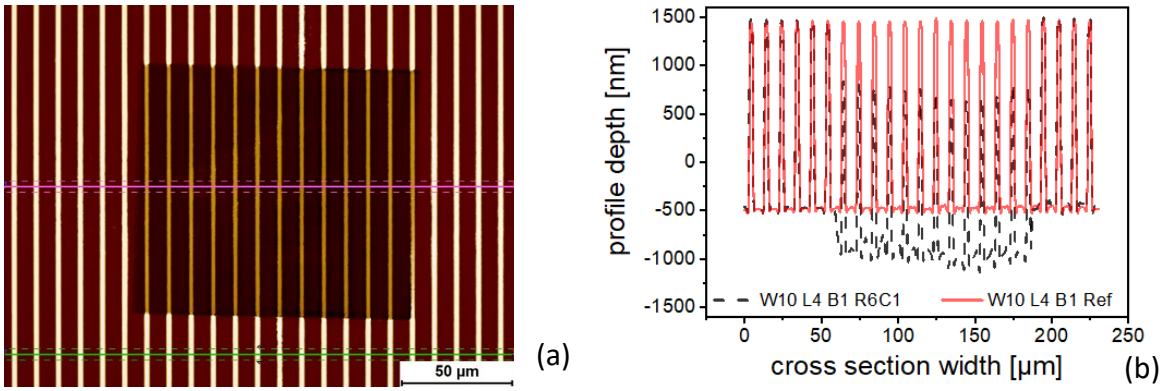

Figure 2: (a) WLIM image of laser spot for local pattern transfer of a lithographically PR mask into PI with an Excimer laser at 248 nm. (b) Cross sections (marked in (a)) of the line patterns for the laser ablated and the reference surface structure.

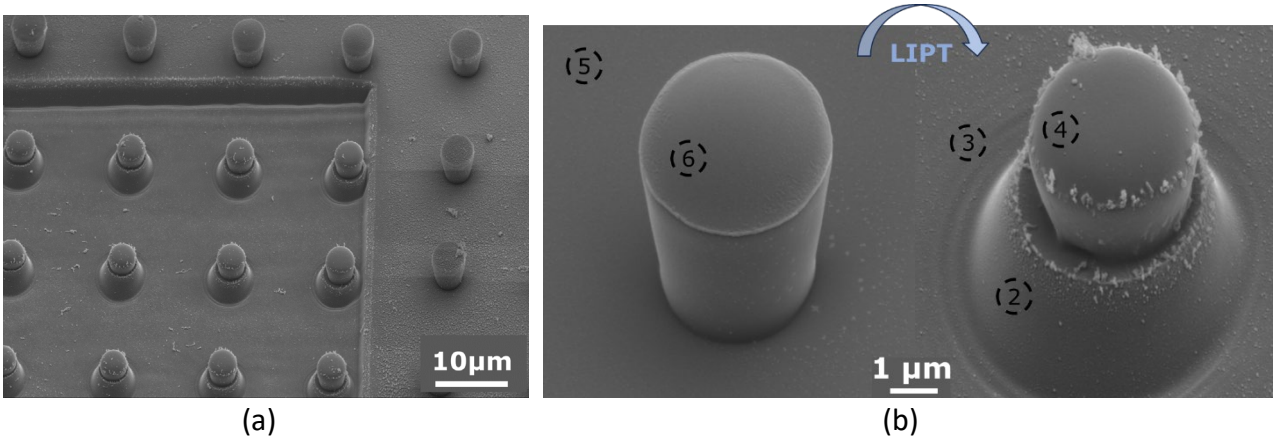

Figure 3: SEM images of (a) a laser irradiated spot with partially transferred cylindrical mask patterns and (b) single cylinder pattern before and with incomplete/partially pattern transfer. The projected 248 nm beam irradiates the substrate perpendicular.

Etching of optical glass by reactive plasmas at atmospheric pressure

Robert Heinke [a,b], Martin Ehrhardt [a], Pierre Lorenz [a], Thomas Arnold [a,b], Klaus Zimmer [a]

[a] Leibniz Institute of Surface Engineering (IOM), Leipzig 04318, Germany
[b] Institute of Manufacturing Science and Engineering, Technische Universität Dresden, Dresden, 01062 Germany
e-mail: klaus.zimmer@iom-leipzig.de

Micropatterning by pattern transfer requires suitable etching methods as a basic process for performing pattern transfer into functional materials or surfaces. Despite plasma etching for electronic materials is well developed the etching of glass for optical applications is still challenging. Another requirement for future fabrication is the development of vacuum-free methods that allow more sustainable machining and further support the enhancement of throughput. With that in mind atmospheric plasma etching technologies are studied, facing these challenges. Both atmospheric plasma jet (APPJ [1]) as well as laser-induced plasmas (LIP [2]) are used to study the etching processes of optical glass with fluorine containing etching gas mixtures (see Fig. 1). In particular, important glass material types such as N-BK7 or Corning 7059 are studied in relation to the etching behavior and the surface morphology after etching. Whereas different studies for APPJ etching of glass approaches were performed [1] the glass processing of optical glass by LIP etching is not well described.
For microelectronic materials, LIP etching is studied. The results show that a low surface roughness, a high surface precision as well as a marginal surface modification characterizes the LIP etching process of these materials. Glass, however, is composed in addition to SiO_2 of various metal oxides which not all form volatile products with fluorine. These effects have been observed for APPJ etching where reaction products stick at the surface and form a residual layer [3]. Therefore, LIP etching as an atmospheric plasma etching technique may show similar effects.
The results of APPJ and LIP etching of different glasses shown in Fig. 2 and Fig 3 cause similar etching results in relation to the surface morphology and the etching depth limitation as well as the residues layer formation.
In the presentation the results of APPJ and LIP etching are compared. Experimental studies of the surfaces after atmospheric pressure plasma etching by SEM, EDX, XRD, TEM and XPS are shown.

[1] H. Paetzelt, G. Böhm, T. Arnold, Etching of silicon surfaces using atmospheric plasma jets, Plasma Sources Science and Technology, 24 (2015) 025002, 10.1088/0963-0252/24/2/025002.
T. Arnold, G. Boehm, Application of atmospheric plasma jet machining (PJM) for effective surface figuring of SiC, Precision Engineering-Journal of the International Societies for Precision Engineering and Nanotechnology, 36 (2012) 546-553, 10.1016/j.precisioneng.2012.04.001.

[2] M. Ehrhardt, P. Lorenz, K. Zimmer, Ultraprecise surface processing by etching with laser-induced plasmas, in: R. Stoian, J. Bonse (Eds.) Ultrafast Laser Nanostructuring — The Pursuit of Extreme Scales, Springer, 2023.
M. Ehrhardt, P. Lorenz, J. Bauer, R. Heinke, M.A. Hossain, B. Han, K. Zimmer, Dry Etching of Germanium with Laser Induced Reactive Micro Plasma, Lasers in Manufacturing and Materials Processing, (2021) 10.1007/s40516-021-00147-1.
M. Ehrhardt, P. Lorenz, B. Han, K. Zimmer, Laser-induced reactive microplasma for etching of fused silica, Applied Physics a-Materials Science & Processing, 126 (2020) 9, 10.1007/s00339-020-04019-x.

[3] R. Heinke, T. Arnold, M. Ehrhardt, P. Lorenz, K. Zimmer, Influence of Fluence and Pulse Number on Laser Cleaning of Atmospheric-Pressure-Plasma-Jet-Etched Optical Glasses, physica status solidi (a), n/a (2023) 2300485, https://doi.org/10.1002/pssa.202300485.
F. Kazemi, T. Arnold, P. Lorenz, M. Ehrhardt, K. Zimmer, Residual Layer Removal of Technical Glass Resulting from Reactive Atmospheric Plasma Jet Etching by Pulsed Laser Irradiation, Plasma Chemistry and Plasma Processing, (2020) 10.1007/s11090-020-10101-2.
F. Kazemi, T. Arnold, P. Lorenz, M. Ehrhardt, K. Zimmer, Combined reactive plasma jet-laser etching method for technical optical glass containing metal oxides, Appl. Surf. Sci., 551 (2021) 149339, https://doi.org/10.1016/j.apsusc.2021.149339.

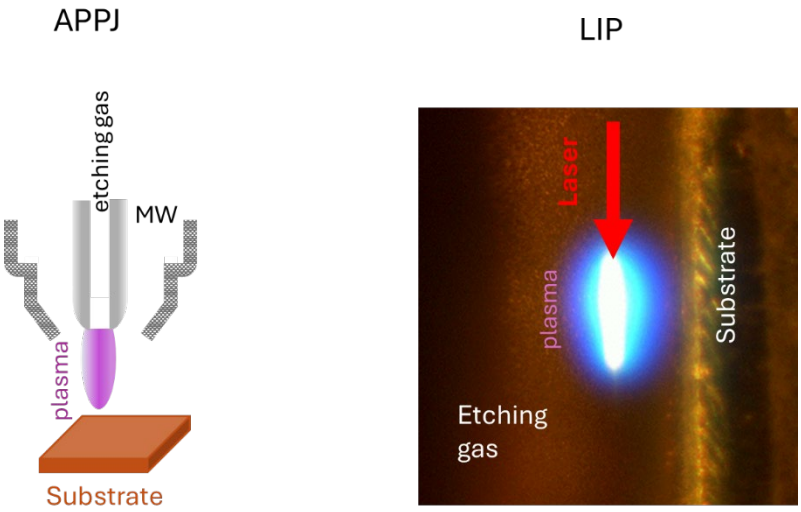

Figure 1. Sketches of the plasma used for etching glass materials.

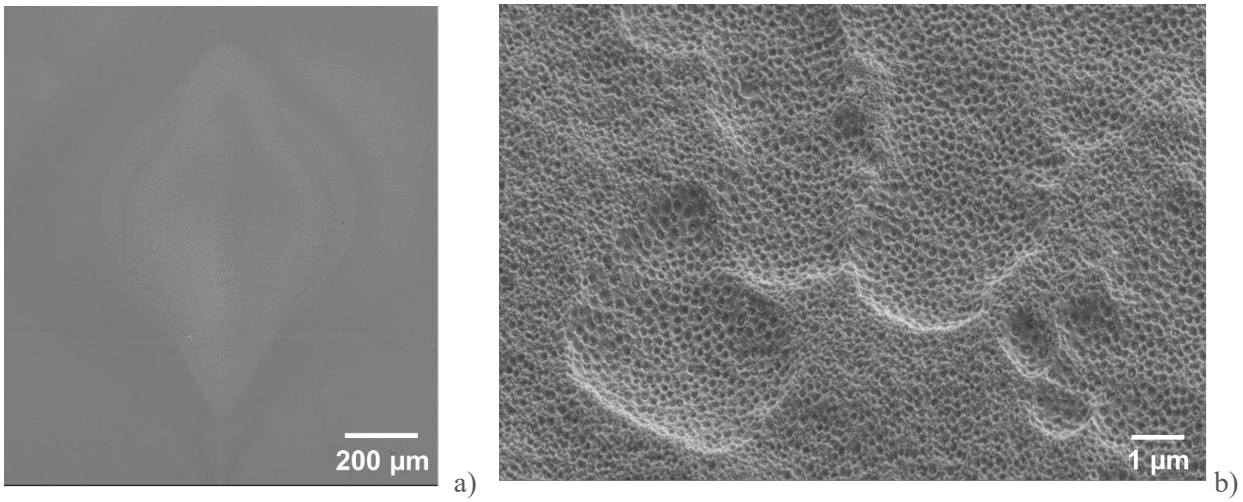

a) b)

Figure 2. Results of LIP of Corning 7059 a) LIP etched groove (footprint), b) morphology of the etched surface.

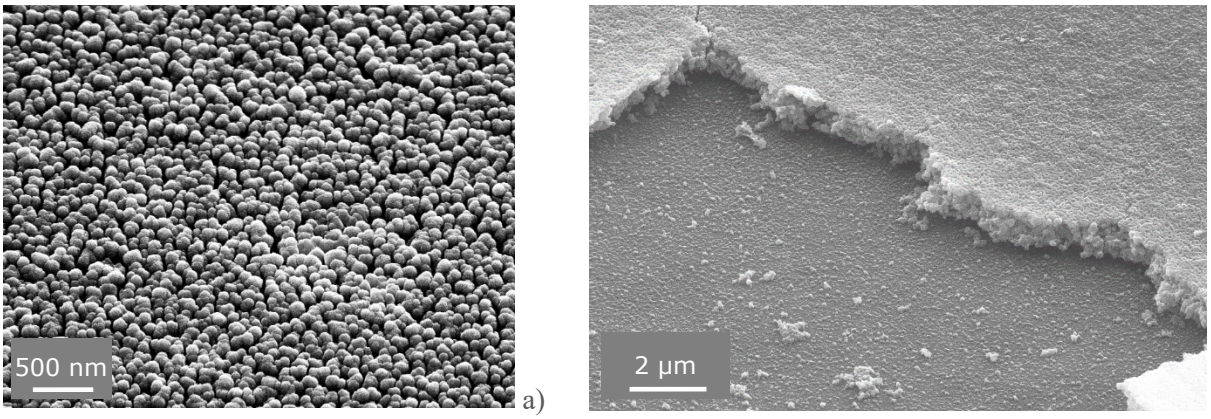

a) b)

Figure 3. Results of APPJ etching of N-BK7 a) morphology of the etched surface. b) delaminated residues layer showing the cross section and the glass surface beneath.

From Waste to Resource: Engineering End-of-Life Graphite Anodes for Solid-State Hydrogen Storage

Mukhammed Kenzhebek[a], Fayil Sultanov[a]*, Almagul Mentbaeyva[a,b]

[a]National Laboratory Astana, Nazarbayev University, Astana, 010000, Kazakhstan;
[b]Department of Chemical and Materials Engineering, School of Engineering and Digital Sciences, Nazarbayev University, Astana, 010000, Kazakhstan.
*Corresponding author (s): fail.sultanov@nu.edu.kz

Key words: Hydrogen storage, graphite, Spent lithium-ion batteries, Physisorption, Chemisorption.

Abstract

The rapid expansion of electric vehicles and portable electronics has driven a surge in lithium-ion battery (LIB) production, with global demand projected to surpass 1100 GWh by 2025. As these batteries reach end-of-life, they generate significant waste-particularly graphite anodes, which constitute 12-21 wt% of LIBs and represent up to 15% of their economic value, yet are largely overlooked in recycling streams *(1)*. This work explores an upcycling strategy that transforms spent graphite anodes into functional materials for hydrogen storage.

Graphite degrades during battery cycling due to lithium intercalation/deintercalation, increasing its interlayer spacing from 0.335 nm to over 0.370 nm and introducing defects such as cracking and SEI instability *(2)*. While detrimental for battery reuse, these structural changes enhance porosity and surface area-favorable for hydrogen adsorption, particularly via physisorption. Hydrogen uptake in carbon materials is strongly influenced by surface characteristics, with storage capacities reported up to 6.5 wt% for carbon nanofibers and 4.48 wt% for graphite *(3)*. Functionalization methods, including doping and composite formation, further improve performance *(4)*.

In this study, we introduce a selective binder-removal process that preserves intercalated lithium ions to facilitate chemisorption-based hydrogen storage. Spent LIB cells were carefully disassembled, and binder removal was performed via two methods: deionized (DI) water washing and heat treatment at 550 °C. Thermogravimetric analysis (TGA) showed similar overall weight loss (Fig 1.), but heat treatment more effectively removed binders while retaining lithium-offering a dual advantage: organic removal without lithium loss, enabling both physisorption and chemisorption of hydrogen.

To enhance hydrogen uptake, the upcycled graphite anode is characterized by expanded interlayer distance (d-spacing), a result of lithium intercalation and structural distortion. This expanded spacing, combined with defect formation, promotes hydrogen sorption. Further modification through exfoliation increases specific surface area and porosity. Additionally, heteroatom doping and metal nanoparticle decoration tailor adsorption energy and introduce active sites, optimizing hydrogen storage behavior. These synergistic effects position spent graphite anodes as multifunctional, high-performance materials for solid-state hydrogen storage.

References:

1. Niu, B.; Xiao, J.; Xu, Z. Advances and challenges in anode graphite recycling from spent lithium-ion batteries. *Journal of Hazardous Materials*. Elsevier B.V. October 5, 2022. doi:10.1016/j.jhazmat.2022.129678.
2. Wang, G.; Yu, M.; Feng, X. Carbon materials for ion-intercalation involved rechargeable battery technologies. *Chem. Soc. Rev.* **2021**, *50*(4), 2388–2443. doi:10.1039/D0CS00187B.
3. Mohan, M.; Sharma, V. K.; Kumar, E. A.; Gayathri, V. Hydrogen storage in carbon materials—A review. *Energy Storage*. John Wiley and Sons Inc April 1, 2019. doi:10.1002/est2.35.
4. Murugan, P.; Nagarajan, R. D.; Shetty, B. H.; Govindasamy, M.; Sundramoorthy, A. K. Recent trends in the applications of thermally expanded graphite for energy storage and sensors - a review. *Nanoscale Advances*. Royal Society of Chemistry November 21, 2021, pp 6294–6309. doi:10.1039/d1na00109d.

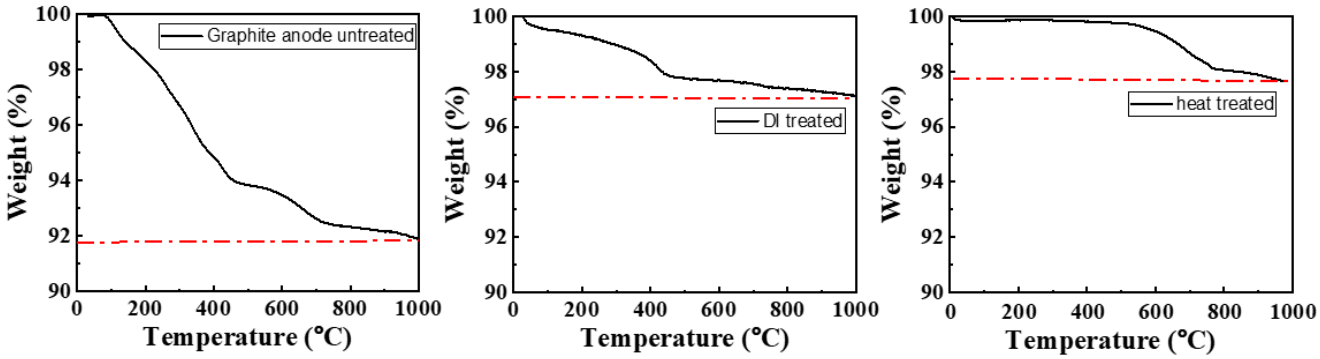

Figure 1. TGA curves of graphite samples.

Low-Waste Fabrication of Flexible Carbon Electrodes: Capacitance Comparison of Inkjet-Printed and Laser-Induced Graphene with Ag Nanoparticles

Rou Xuan Goh [a], Ishant Patil [a], Suan Hui Pu [a], Suhana M. Sultan [b], Harold M. H. Chong [d], Ting Yang Ling [a,d]

[a] Smart Manufacturing and Systems Research Group, University of Southampton Malaysia
[b] Computational Nanoelectronics Research Group, Universiti Teknologi Malaysia (UTM)
[d] Sustainable Electronic Technologies Research Group, School of Electronics and Computer Science, University of Southampton, UK

e-mail: rxg1a15@soton.ac.uk

Inkjet-printing is a contactless, material-efficient, and low-energy fabrication method that has evolved from conventional consumer applications to enable the sustainable production of reduced graphene oxide (rGO) for use in flexible electronic devices. Laser-induced graphene (LIG), similarly, offers an environmentally friendly alternative, formed through direct laser scribing on carbon-rich substrates, eliminating the need for chemical reagents and minimizing process waste. The integration of silver (Ag) nanoparticles onto these carbon-based materials has been shown to enhance electrical conductivity and electrochemical responsiveness, potentially reducing the need for bulky or energy-intensive materials in electrode design [1] [2]. For graphene based electrodes, capacitance enhancement is possible due to the synergistic interaction between Ag nanoparticles and graphene's conductive network [3][4]. This study investigates and compares the capacitance performance of inkjet-printed rGO and LIG electrodes with Ag nanoparticle loading, analyzing their electrical and electrochemical characteristics. This work contributes to the development of sustainable, scalable strategies for flexible electronics.

The rGO electrodes were inkjet printed on a 107 µm-thick polyethylene terephthalate (PET) substrate. Each electrode is in meander geometry of 2 mm thickness and 2mm gap. The ink used was 50 wt.% graphene and 50 wt.% Ag nanoparticles, similar to a previous study [5]. Printed electrodes were cured for 30 minutes at 40°C before measurements. LIG electrodes were fabricated by laser treatment on commercially available 50 µm thick Polyimide (PI) films with a commercial G690 CO^2 IR laser operating at a wavelength of 10.6 µm and laser fluence of 37.58 J/cm^2.The 5 mm by 5 mm electrodes were lasered line-by-line in focus mode, with 0.2 mm gap per adjacent laser pass. Ag nanoparticle solution of 14 µg/ml concentration purchased from Merck (Sigma Alrich) was drop-casted onto LIG and dried for 24 hours before the electrochemical analysis. Cyclic voltammetry (CV) was performed on a standard three electrode configuration in 1 M aqueous KCl to measure the capacitance of the electrodes. Ag/AgCl was the reference electrode while a 5 mm by 5 mm Pt plate was the counter electrode. Electrochemical data was collected through a potentiostat (Autolab PGSTAT101) at scan rates from 5 mV/s to 100 mV/s.

The interfacial capacitances of inkjet-printed rGO and LIG, with and without Ag loading, are obtained and characterized from CV graphs as shown in Figure 1. The capacitance results in Figure 2 show that interfacial capacitances up to 0.0025 mF/cm^2 can be achieved with an offset inkjet printing configuration of rGO electrode with Ag loading. This is a 6.5% improvement over the aligned Ag loading configuration and an improvement of almost five times over the rGO electrode without nanoparticle loading. On the other hand, the Ag loading on LIG improves capacitance by 5.6%. The findings presented here demonstrate the promising pathway for improving the interfacial capacitance of carbon-based flexible electronics, allowing further exploration into environmentally friendly fabrication strategies for graphene-based capacitive flexible electronics.

[1] L. Shi et.al., Sens. Act., B Chem., vol. 256, pp. 938–945, (2018), doi:10.1016/j.snb.2017.10.035.
[2] P. Pinyou et al., Electrocat., vol. 14, no. 4, pp. 648–658, (2023), doi: 10.1007/s12678-023-00826-x.
[3] J. Yao et al., Electrochim. Acta, vol. 441, p. 141719, (2023), doi: 10.1016/j.electacta.2022.141719.
[4] K. Singh et al., J. Electrochem. Soc., vol. 171, no. 10, p. 100501, (2024), doi: 10.1149/1945-7111/ad7bee.
[5] I. G. Patil et al., IEEE Int. Conf. Sensors Nanotechnology, SENNANO, pp. 17–20, (2023), doi: 10.1109/SENNANO57767.2023.10352443.

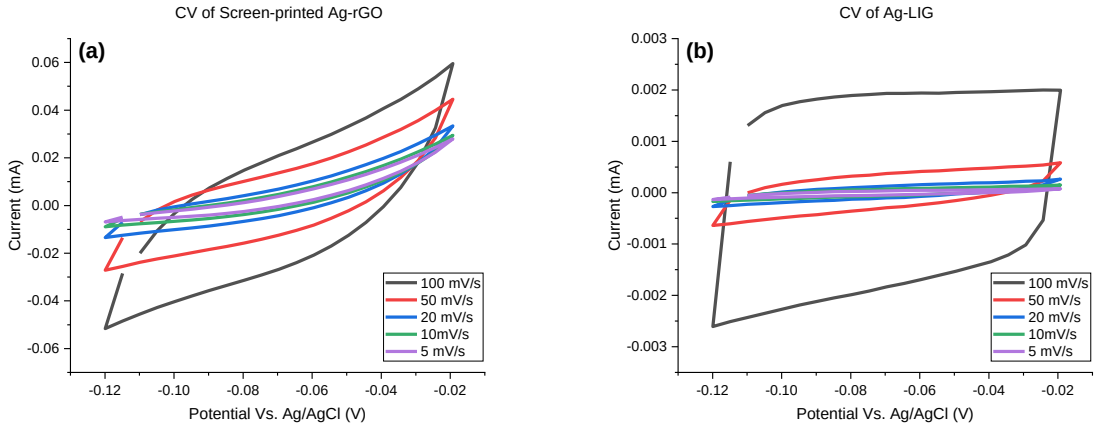

Figure 1. CV plots at various scan rates of (a) inkjet-printed rGO electrode (b) Ag-LIG electrode

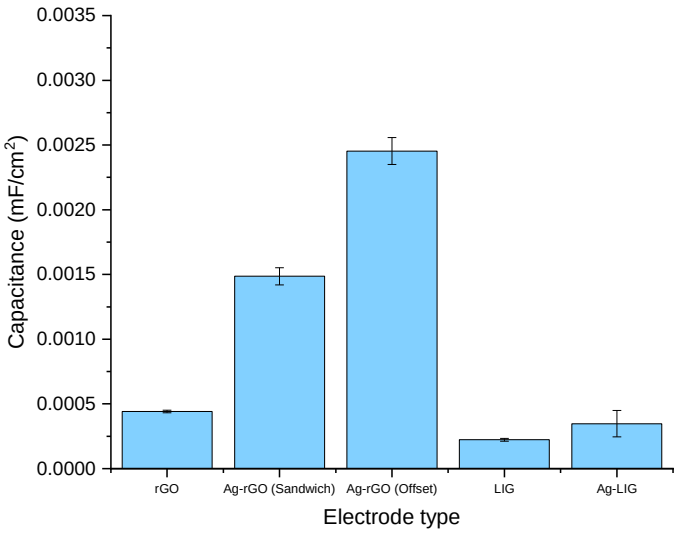

Figure 2. Calculated interfacial capacitance of rGO and LIG with and without Ag nanoparticle loading

Mobile Ions Improve the Power Conversion Efficiency of Perovskite Solar Cells with Large Energetic Offsets

Lucy J. F. Hart [a], Fraser J. Angus [b], Yin Li [c], Abdul Khaleed [c], Philip Calado [a,d], James R. Durrant [a], Aleksandra B. Djurišić [c], Pablo Docampo [b], and Piers R. F. Barnes [a]

[a] Imperial College London, London, SW7 2AZ, UK.
[b] University of Glasgow, Glasgow, G12 8QQ, UK
[c] The University of Hong Kong, Hong Kong S.A.R, China
[d] University of Southampton, Southampton, SO17 1BJ, UK.
e-mail: lucy.hart18@imperial.ac.uk; piers.barnes@imperial.ac.uk

Metal halide perovskites have attracted significant research attention as photovoltaic materials for next generation solar cells, with the best lab-scale devices achieving power conversion efficiencies comparable to incumbent silicon solar cell technology (~26%).[1][2] However, the underlying device physics of perovskite solar cells (PSCs) is substantially different to that of previous generations of photovoltaics, owing to the presence of high concentrations of mobile ionic (Schottky) defects in the perovskite layer, which redistribute to screen internal electric fields.[3][4][5] Consequently, new design criteria must be established to optimise the performance of PSCs.

In this recently published study,[6] we use the open-source mixed ionic-electronic device simulation software Driftfusion[7] to show that, while the inclusion of mobile ionic defects tends to reduce the short-circuit current, it boosts the open circuit voltage (V_{OC}) relative to otherwise identical devices without mobile ions (see Fig 1a). We find that redistribution of mobile ions under steady-state operation leads to the largest improvement in V_{OC} where a large energetic offset exists to the transport layers and when interfacial recombination is the dominant loss pathway (see Fig 1b). These criteria are both met in many high-performing devices. The improvement in V_{OC} arises because, once V_{OC} surpasses the flat-band condition in the active layer (@V_{flat}), ionic carriers screen the reverse electric field that would otherwise drive minority carriers to the interfaces, thus reducing surface recombination currents.

We verified our predictions experimentally by using short voltage pulses to measure the current-voltage characteristics of a set of PSCs (Figs 2a and 2b). By switching rapidly between read and set voltages, the redistribution of mobile ions was minimised during the measurements. Using this technique, we estimated the pre-bias voltage corresponding to V_{flat} and a uniform ion distribution in the perovskite layer. As the performance of a device in this state is theoretically equivalent to an otherwise identical device without mobile ionic defects, these results allowed us to isolate the influence of ionic redistribution on device performance. (Figs 2c-e). Our results demonstrate that ionic modulation of recombination currents increases the range of transport layer energy offsets where it is possible to achieve high performance results and imply new design strategies for PSCs.

References

[1] H. Min et al., Nature, 598 (2021) 444–450.
[2] Park, J et al., Nature, 616 (2023) 724–730.
[3] A. Senocrate et al., Angew. Chem., Int. Ed., 56 (2017) 7755–7759.
[4] N. E. Courtier et al., Energy Environ. Sci., 12 (2019) 396–409.
[5] D. Moia and J. Maier, ACS Energy Lett., 6 (2021) 1566–1576.
[6] L. Hart et al., Energy Environ. Sci., 17 (2024) 7107-7118.
[7] P. Calado et al., J. Comput. Electron., 21 (2022) 960–991.

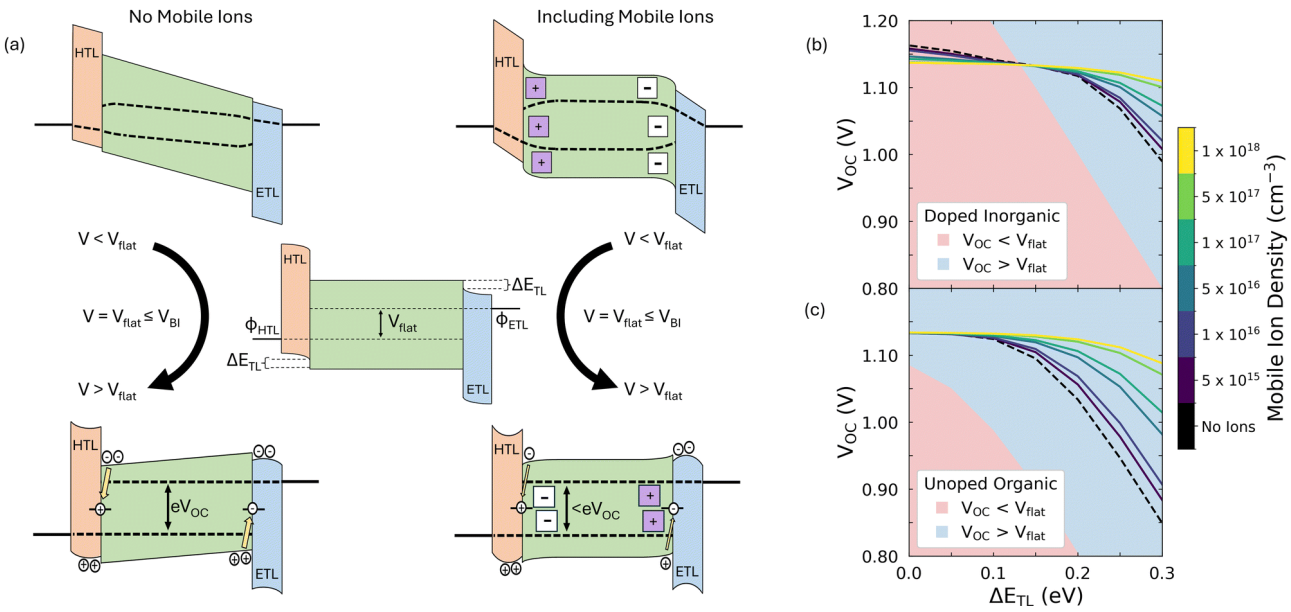

Figure 1. (a) Illustration of the impact of mobile ions on solar cell band diagrams. ΔE_{TL} is the energetic offset between the perovskite's conduction (valence) band and that of the respective transport layer. ETL denotes the electron transport layer and HTL denotes the hole transport layer. The built-in potential V_{BI} is defined as the difference in the anode and cathode work function, φ_{ETL} and φ_{HTL}. (b) and (c) show the dependence of the open circuit voltage V_{OC} on ΔE_{TL} for doped inorganic and undoped organic parameter sets, respectively. The red and blue shaded regions indicate where V_{OC} is less than and greater than V_{flat}, respectively.

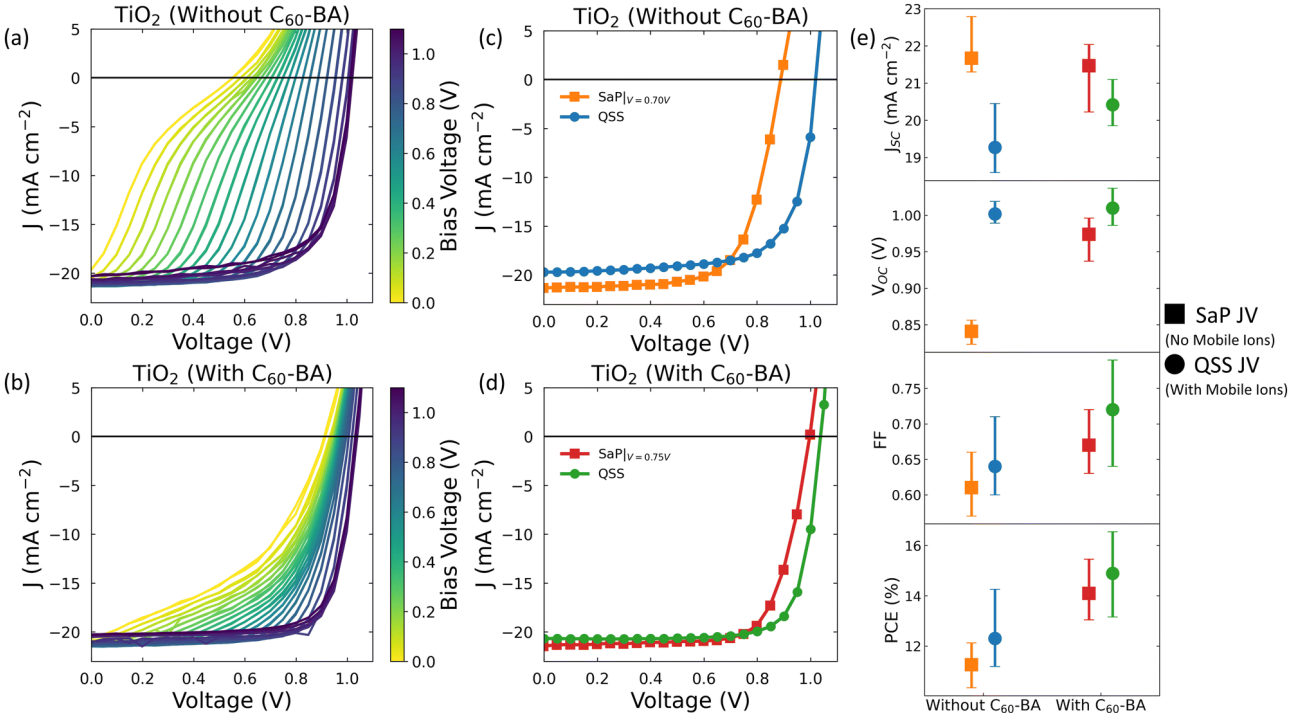

Figure 2. Stabilise and Pulse (SaP) current density-voltage characteristics (*J-V*s) of perovskite solar cells (a) without and (b) with C60-BA. The quasi-steady state (QSS) and Stabilise and Pulse *J-V*s evaluated at $V \approx V_{flat}$ for the devices (c) without and (d) with C60-BA. (e) Summary of the *J-V* parameters extracted from the SaP *J-V*s and QSS *J-V*s for all measured devices.

Heterogeneous Integration of Diamond

Soumen Mandal [a], Jerome A Cuenca [a], Oliver A Williams [a]

[a] School of Physics and Astronomy, Cardiff University, Cardiff, UK, CF24 3AA
e-mail: mandals2@cardiff.ac.uk

The integration of diverse materials opens new possibilities for extreme applications where individual materials alone are insufficient. Diamond, in particular, stands out due to its exceptional combination of properties: unmatched thermal conductivity paired with high electrical resistance, the ability to emit single photons at room temperature, extremely high acoustic wave velocity, and a high Debye temperature. These remarkable characteristics stem from diamond's atomically dense lattice of light carbon atoms. However, this structure also introduces challenges, such as the difficulty of n-type doping and an exceptionally low thermal expansion coefficient.

The low thermal expansion coefficient becomes a critical issue when growing diamond on non-diamond substrates, which typically expand several times more than diamond under heat. As a result, integrating diamond with other materials is a complex, multifaceted challenge that requires tailored approaches—each with its own advantages and limitations.

Our research has focused on growing diamond directly on a variety of substrates [1,2,3,4,5] with or without the use of interlayers. Specifically, we emphasize the self-assembly of diamond nanoparticles onto non-diamond surfaces to serve as seeds for diamond growth [6]. This strategy depends on understanding the zeta potential of both the surface and the diamond particles as a function of pH. Despite achieving high densities of nanodiamond seeds, this alone is insufficient. Issues such as poor adhesion and internal stresses—exacerbated by diamond's low thermal expansion—remain significant.

To be functionally useful after integration, diamond layers typically need to be at least a few microns thick. Our research has demonstrated that diamond can be grown—either directly or with the aid of interlayers—on a range of substrates including GaN [1], h-BN [2], AlN [3], Ga_2O_3 [4], and ferroelectric oxides such as $LiNbO_3$ and $LiTaO_3$ [5]. However, the direct growth of thick diamond films without interlayers has only been successfully achieved on AlN.

This limitation is largely attributed to mismatches in thermal expansion coefficients and the inability of most substrates to form stable carbides with carbon. Even when methods are employed to enhance adhesion between diamond and non-diamond materials, the high temperatures and hydrogen-rich plasma required for high-quality diamond chemical vapor deposition (CVD) often degrade the underlying material, limiting the range of viable integration strategies.

Due to the inherent challenges associated with growing diamond on non-diamond substrates, direct bonding has become a critical strategy for achieving successful heterogeneous integration. This process typically involves activating both surfaces by exposing their dangling bonds using an appropriate ion beam under high-vacuum conditions [7]. A key requirement for effective bonding is the preparation of ultra-smooth surfaces. To address this, we have developed a chemical mechanical polishing (CMP) process for diamond that enables the production of atomically smooth surfaces [8,9,10]. The progressive reduction in surface roughness of a nanodiamond thin film during CMP is illustrated in Figure 1.

Figure 2 presents an example of a partial bond formed between diamond and gallium oxide. For optimal integration, the formation of covalent bonds at the interface is essential [11]. Ongoing work is focused on enabling room-temperature direct bonding of various materials to polished diamond surfaces, which could further expand the applicability of this approach.

References

[1] S. Mandal et al., ACS Omega 2 (2017) 7275
[2] S. Mandal et al., Nanoscale 11 (2019) 10266
[3] S. Mandal et al., ACS Appl. Mater. Interfaces (2019) 40826
[4] S. Mandal et al., Carbon 181 (2021) 79
[5] S. Mandal et al., Carbon 212 (2023) 118160
[6] S. Mandal, RSC Adv. 11 (2021) 10159
[7] J. Liang and N. Shigekawa, Direct bonding of diamond and dissimilar materials for fabricating high performance power devices, in: S. Mandal and N. Yang, ed., Novel Aspects of Diamond II. Topics in Applied Physics, vol 149, (Springer, Cham. 2024) , 237-268
[8] E. Thomas et al., Carbon 68 (2014) 473
[9] E. Thomas et al., Sci. Tech. Adv. Mater. 15 (2014) 035013
[10] S. Mandal et al., Carbon 130 (2018) 25
[11] W. M. Waller et al., Semicond. Sci. Technol. 35 (2020) 095021

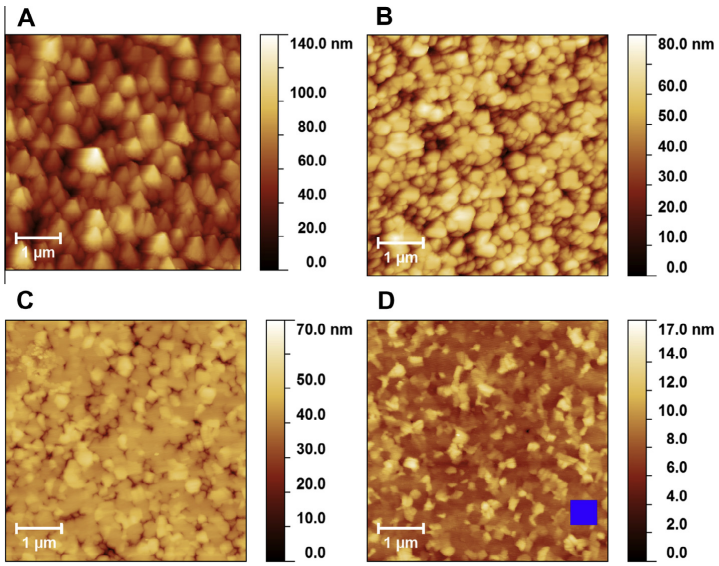

Figure 1. Atomic force microscopy images diamond surfaces as it is polished using CMP for A) unpolished B) 1h, C) 2h and D) 4h reaching a surface roughness below 2nm RMS.

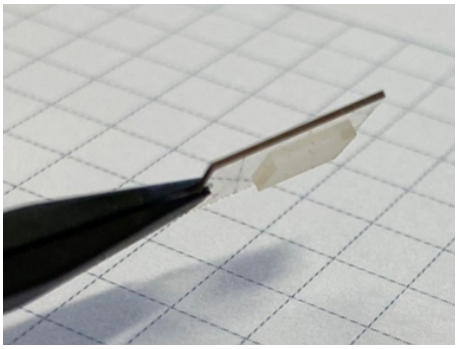

Figure 2. Partial bond between diamond and gallium oxide.

Oral Session 4A: Advanced Nanofabrication II

Geometric optimization improves the performance of organic electrochemical transistors for bio-sensing applications

Noemi Cesario [a], Natalia Malara [b], Nicola Coppedé[c], Francesco Gentile [a]

[a] Nanotechnology Research Center, Department of Experimental and Clinical Medicine, University "Magna Graecia" of Catanzaro, 88100 Catanzaro (Italy)

[b] Department of Health Sciences, University Magna Graecia, Catanzaro, Italy

[c] IMEM-CNR Institute of Materials for Electronic and Magnetism, National research council, Parco area delle scienze 37/a 43124 Parma

e-mail: noemi.cesario@unicz.it

In recent years, there has been a growing demand for miniaturized sensors capable of discriminating between different biomolecules in complex solutions – to correctly identify a number of different physiological states, pathological states - including cancer - and the transition between the two [1]. Among the several different sensors available for measurement, organic electrochemical transistors (OECTs) are especially promising, in that they (i) generate a well-defined, (ii) easily processable, (iii) precise and accurate, signal: i.e. a current (I) over time. Moreover, OECTs can be obtained using simple fabrication process, do not require expensive instrumentation or set-up, that are scalable – and that OECTs can be easily shaped in different forms and size, including the micro–scale [2]. OECTs offer the additional advantage of tunable electrode-electrolyte interface via various materials [3], such as conductive polymers (CPs). An OECT consists of a conducting polymer layer connected to two electrodes, source and drain, in contact with an electrolyte. A third electrode, the gate, is immersed in the same electrolyte. By applying a voltage between the source and the gate, the conductivity of the polymer film can be modulated through a reversible doping/de-doping process (**Figure 1**). The result is a current proportional to ionic concentration of the solution [4]. Here, we investigate the p-doped organic conductive polymer PEDOT:PSS, known for its semiconductor properties and high sensitivity [5]. Previous studies have demonstrated that OECTs can identify four different ionic species (Na^+, Mg^{2+}, K^+ and Zn^{2+}) in a mixture based on their charge and mass [6]. We have examined whether the thickness of the PEDOT channel, i.e. a geometry parameter, can be tuned to modulate the response of the sensor-device and possibly segregate different concentrations of a same electrolyte, i.e. NaCl. In this study, we tested devices varying PEDOT:PSS conductive channel thickness from 400 nm to 3.5 µm on silicon substrates. The PEDOT:PSS layers were fabricated via spin-coating, with the final thickness controlled by adjusting key process parameters: spin speed (RPM), acceleration (RPM/s), and coating duration. After deposition, the substrates underwent a baking process at a fixed temperature for one hour to ensure film stability and solvent evaporation. Subsequently, copper contacts were patterned onto the substrates to complete the device fabrication. Substrates were immersed in NaCl saline solution with varying molar concentration ranging from 1×10^{-3} M to 1.5×10^{-1} M (Physiological Solution, PS). Current signals (**Figure 2**) were recorded using a Keysight B2902B Source/Measure Unit (SMU) controlled via LabVIEW Instrument software. The input voltage applied between drain-source (V_{ds} = -0.1 V) and gate-source (V_{gs} from 0.2 V to 1 V in steps of 0.2 V). Analysis of current-data allowed extraction of key parameters of the process: the modulation (m) and the time constant (τ). Modulation refers to the variation of current over time, defined as the relative change from the initial current value. It is given by the formula: $m = (I_{max} - I_0)/I_0$, where I_{max} is the maximum current and I_0 is the initial current. The time constant τ is the time to reach ~67% of the current signal's steady-state value. Results are reported in the scatter plot in **Figure 3** where we present the values of m and τ relative to different concentrations of NaCl, examined using a sensor device with low ($430\ nm$) and high ($2000\ nm$) thickness. Each point in the diagrams corresponds to a specific applied voltage value. Points associated with the same value of concentration, have been connected to highlight the trend of each individual signal. Diagrams indicate that higher NaCl concentrations correspond to increased modulation and decreased time constants. Additionally, thicker PEDOT:PSS channels yielded improved discrimination between solutions of different molarities. Results suggest that, the larger the thickness, the larger the distance between different measurement points.

These findings suggest that optimizing the conductive channel thickness enhances sensor performance. Future research will investigate how variations in channel thickness influence the response of a range of biomolecules, including cancer biomarkers, with the goal of enabling earlier, more accurate, and effective detection—starting from complex biological fluids.

Keywords: organic electrochemical transistor; conductive polymer; micro-scale; electrolyte solution; geometry optimization; biosensing.

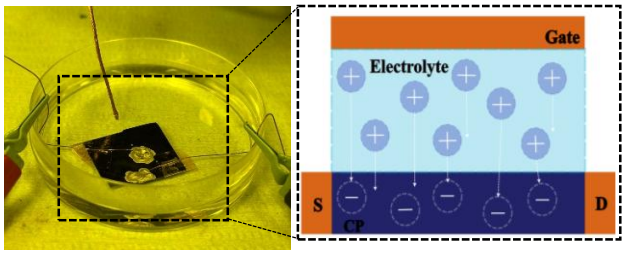

Figure 1. Setup with device prototype and de-doping process of the OECT under $V_{gs} > 0$: cations from the electrolyte enter the PEDOT:PSS channel, bind to PSS^- sites, and reduce conductivity.

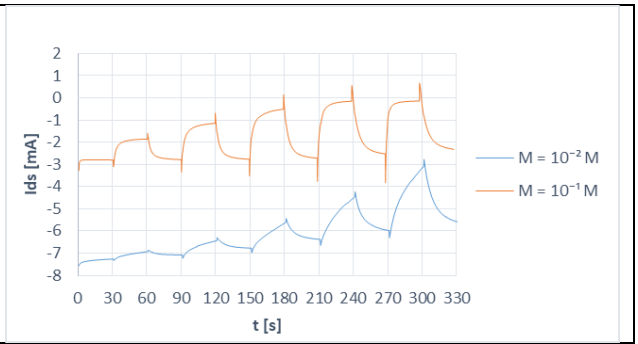

Figure 2. I_{ds} current acquired by sensor device for different concentrations of NaCl in solution.

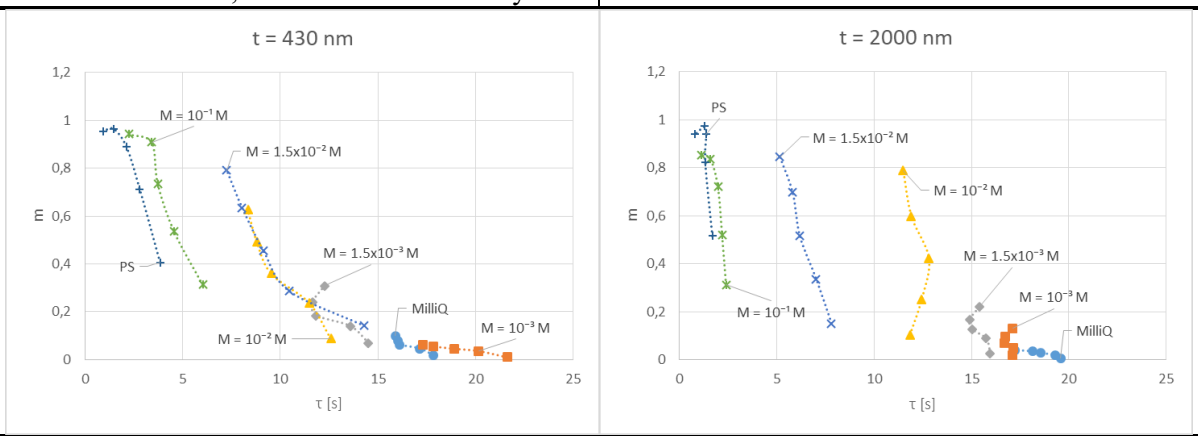

Figure 3. Scatter plots m-τ of Si substrate with PEDOT:PSS thicknesses t = 430 nm and t = 2000 nm with different molar concentrations (Ms).

References

[1] A. Banerjee et al., 2021, Nanotechnology for biosensors: A Review
[2] Yue Niu et al., 2023, Expanding the potential of biosensors: a review on organic field effect transistor (OFET) and organic electrochemical transistor (OECT) biosensors
[3] N. Blel et al., 2017, Ultrasensitive Electrochemical Sensors for PSA Detection: Related Surface Functionalization Strategies, Volume 17, Issue 26, Page: [2913 - 2925].
[4] A. Shirinskaya et al., 2018, Numerical Modeling of an Organic Electrochemical Transistor.
[5] Gaetano Randazzo. Fabbricazione e caratterizzazione di MOSFET organici. Tesi di laurea. Università degli studi di Palermo – Facoltà d'Ingegneria, corso di laurea in Ingegneria Elettronica, a. a. 2011-2012.
[6] N. Coppedè et al., 2014, Diffusion Driven Selectivity in Organic Electrochemical Transistors.

Introducing thermal scanning probe lithography into the fabrication of semiconductor quantum devices

Iker Uranga-Granados [a], Robin Erne [b], Jana Chaaban [b], Marta Fernández-Regúlez [a], Joan Bausells [a], Guido Rademaker[c], Emine Cagin[b] , Francesc Pérez-Murano[a]

[a] Instituto de Microelectrónica de Barcelona (IMB-CNM/CSIC), Bellaterra, 08193, Spain
[b] Heidelberg Instruments Nano AG, Zurich, 8048, Switzerland
[c] University of Grenoble Alpes CEA-Leti, Grenoble, F-3800, France
e-mail: iker.uranga@imb-cnm.csic.es

In the upcoming field of quantum device fabrication lithography processes are among the most critical steps, which typically require state-of-the-art or even beyond resolution and pattern placement accuracy. At the research level, electron beam lithography (EBL) is the most widely used lithography tool whose resolution limit is appropriate for semiconductor quantum device fabrication. However, pattern placement control of typical EBL systems is not enough for these applications. In contrast to EBL, probe-based lithography techniques like thermal scanning probe lithography (t-SPL) offer superior pattern placement control (sub-5 nm pattern placement control demonstrated for t-SPL [1]) while being more accessible than typical EBL systems. The high pattern placement control of t-SPL comes thanks to *in situ* writing and reading of patterns possible in these lithography systems. The purpose of this work is to benchmark the pattern placement accuracy of the NanoFrazor t-SPL tool for use in semiconductor quantum devices.

For this work, two types of samples were supplied from the semiconductor quantum device fabrication lines from both CSIC [2] and CEA-Leti [3] and patterned by NanoFrazor using automatic overlay alignment in the t-SPL system. The stages of the automatic overlay alignment are shown in Figure 1. First, a reference design of the patterns to be aligned over is loaded into the tool software and a model of the expected view of the patterns under the resist layer is calculated. Then, the area of interest is imaged and the patterns to be aligned over are located. Finally, t-SPL patterning is done using the previously mentioned *in situ* read and write cycle. After patterning, contact patterns are transferred to a PMMA layer and the placement error of t-SPL contact patterns are analyzed by SEM imaging.

Results on patterning over CSIC samples are summarized in Figure 2. Figure 2a shows a SEM image with contacts patterned on top of metal structures and ellipses fitted into both circular metal gates and contact patterns to determine t-SPL placement error. Figure 2b shows a map of placement error seen for all analyzed contacts, in which it can be seen that 64% of analyzed contacts have a placement error below 10 nm. Figures 2c and 2d show histograms of the X and Y placement error of the well-aligned contacts, where we obtain a X placement error of **2.6 ± 3.6 nm** and Y placement error of **1.3±4.6 nm** for 95 out of 136 total measured contacts.

Figure 3 shows the results on patterning over CEA-Leti samples. Figure 3a shows a SEM image of a FDSOI mesa isolation sample fabricated at CEA-Leti with metal lines patterned by t-SPL. Figure 3b shows the result of processing the SEM image using a MATLAB script to determine the position of the contact patterns. Figure 3c shows a section of the SEM image used to identify the X position of each of the metal lines. Finally, in figure 3d a histogram of the X placement error of well-placed contacts (placement error below 10 nm) is shown from which we obtain a **1.4±5.3 nm** overlay placement error for 306 out of the total 635 contacts analyzed.

From the results obtained from both CSIC and CEA-Leti samples, we can conclude that the NanoFrazor tool provides pattern placement control suitable for semiconductor quantum device fabrication processes. In the future, the patterning and pattern transfer steps will be optimized to increase the yield of low placement error contacts and to complete metal structure contacting.

[1] S. T. Howell et al., Microsyst Nanoeng. 6 (2020) 21
[2] J. Bausells et al., in 2023 14th Spanish Conference on Electron Devices (CDE), Valencia, Spain: IEEE, jun. 2023, pp. 1-4
[3] T. Bedecarrats et al., in 2021 IEEE International Electron Devices Meeting (IEDM), San Francisco, CA, USA: IEEE, dic. 2021, pp. 1-4.

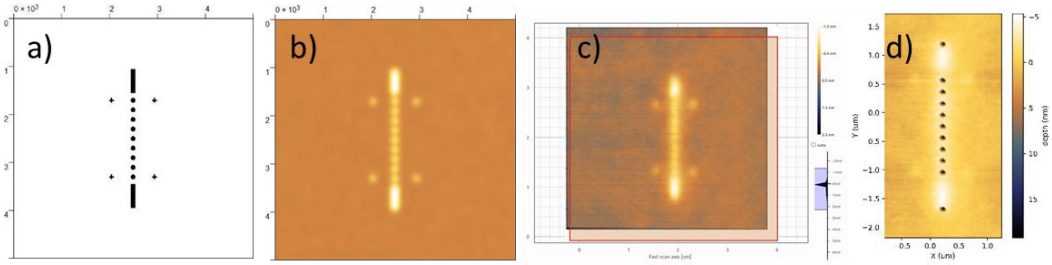

Figure 1. Stages of automatic pattern placement in NanoFrazor software. a) Reference design on patterns to be aligned over. b) Model of pattern t-SPL image under resist layers. c) Automated overlay over patterns. d) t-SPL patterning image.

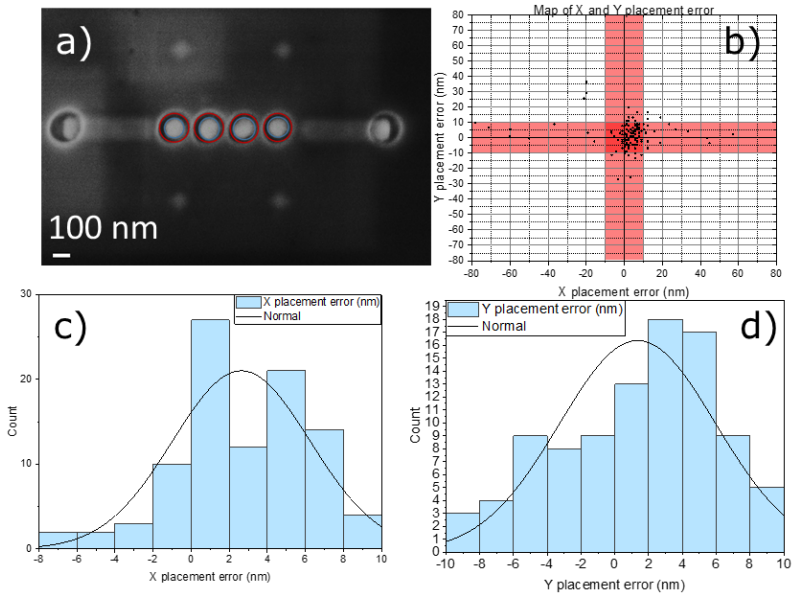

Figure 2. Pattern placement accuracy analysis on CSIC samples. a) SEM image of a CSIC device patterned with t-SPL: blue ellipse fit to metal gates red ellipse fit to t-SPL contacts. b) Map of (x,y) placement error of t-SPL contacts in CSIC samples. c)/d) Histogram of X/Y placement error for CSIC samples.

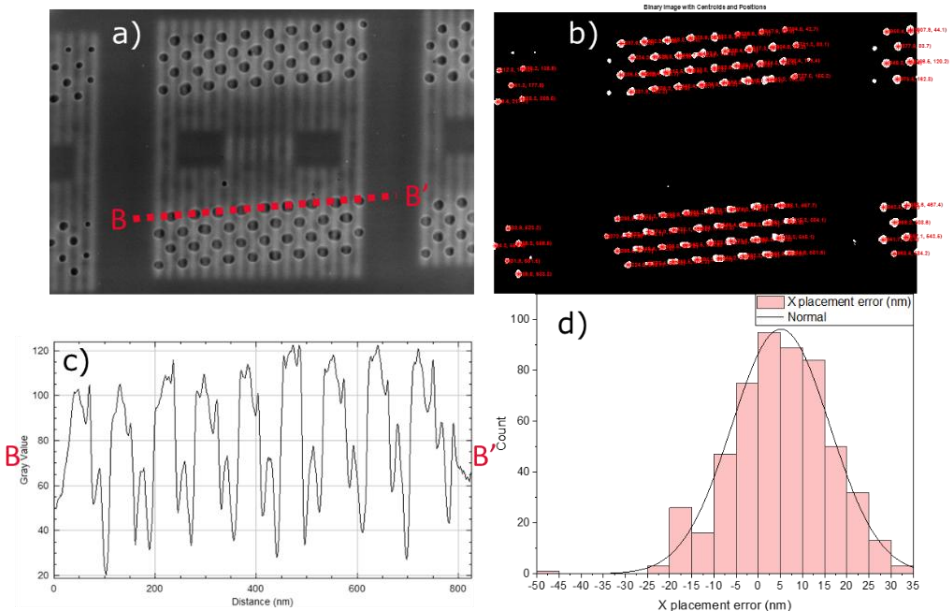

Figure 3. Placement accuracy analysis on CEA-Leti samples. a) SEM image of CEA-Leti devices patterned with t-SPL. b) Processed SEM image to find t-SPL contact placement using a MATLAB script. c) Section of SEM image over the t-SPL contact array to find X position of metal lines d) t-SPL contact and metal line X placement error for CEA-Leti samples.

Fabrication of Vanadium Dioxide Resistors on Fully-released Polyimide Thin Films for High Strain Studies

Lahaye Loïc [a], Raskin Jean-Pierre [a], Flandre Denis [a]

[a] Institute of Information and Communication Technologies, Electronics and Applied Mathematics (ICTEAM) UCLouvain, Louvain-la-Neuve, 1348, Belgium
e-mail: loic.lahaye@uclouvain.be

Vanadium dioxide (VO_2) is a promising material that is well known for its phase change properties, i.e. a reversible insulator-to-metal transition (IMT) near room temperature (more precisely ≈ 68°C) [1]. Across the transition, many of its physical properties undergo an abrupt variation notably its electrical resistance, optical absorption or Young's modulus [2]. The transition of the material between its monoclinic (M1) and rutile (R) phases can be triggered by electrical, thermal or mechanical stimulation [2]. Additionally, vanadium dioxide has been identified for its outstanding gage factor (GF) with authors reporting values from 259 [3] to 534 [4] at a strain level below 0.1%. These results position VO_2 devices as promising candidates for strain sensing with sensitivity beyond silicon (GF ≈120) [5].

This work presents a novel fabrication scheme based on [6] that allows the integration of VO_2 resistors on fully-released polyimide thin film for high strain studies ($\varepsilon > 0.1\%$). The proposed fabrication process, shown in Fig. 1, follows a conventional top-down approach and allows the integration of high-performance VO_2 devices on a flexible substrate. The main processing steps include: (i) the deposition of vanadium dioxide on a Si substrate via reactive sputtering off a vanadium target, (ii) RIE patterning of the VO_2 thin film, (iii) metallization by thermal evaporation and lift-off of chromium and gold, (iv) spin coating and patterning of HDMicroChemical PI2545 and finally (v) XeF_2 etch of the Si substrate and thin film transfer onto a four-point-bending (4P-bending) setup to conduct strain studies.

Fig. 2 shows the as-fabricated resistors. The final stack is made of a 2.5 µm-thick polyimide (PI) layer, 50 nm-thick PECVD SiO_2, 100 nm-thick VO_2, 200 nm-thick Cr/Au contact and a final layer of 50 nm-thick thermal SiO_2. A macroscopic picture of the PI film transferred on office tape is visible in Fig. 2a. Fig. 2b shows a microscopic picture of a complete VO_2 resistor from the same film and Fig. 2c presents the grains forming the VO_2 thin film. Fig. 3a shows the Raman spectrum of the patterned VO_2 thin film to prove its stoichiometry. Finally, Fig. 3b. shows a typical IV characteristic over successive IMTs of one of the fabricated resistors on the polyimide film. Colors from dark to light blue represent the first and last transitions, respectively. As can be seen in the figure, the device showcases a voltage-driven IMT that settles in the sub-five-volts region after a few transitions due to electroforming [7]. This IMT proves that the transfer of the VO_2 devices to the released thin PI film did not hinder the material properties. The success of this fabrication process paves the way to new experimental studies of the material under high strain. The proposed process will allow us to study multiple properties of highly-strained VO_2 resistors including the linearity of the gage factor, the mechanical limits of polycrystalline-VO_2 devices or the impact of strain on the transition temperature or voltage.

[1] F. J. Morin, "Oxides Which Show a Metal-to-Insulator Transition at the Neel Temperature", *Physical Review Letters* 3 (1) (1959) 34–36, doi:10.1103/PhysRevLett.3.34

[2] Y. Ke, S. Wang, G. Liu, M. Li, T. J. White, Y. Long, "Vanadium Dioxide: The Multistimuli Responsive Material and Its Applications", *Small* 14 (39) (Sept. 2018), doi:10.1002/smll.201802025

[3] N. Inomata, N. Van Toan, M. Toda,T. Ono, "Evaluation of piezoresistive property of vanadium oxide thin film", in: *2018 IEEE Micro Electro Mechanical Systems (MEMS)*, Belfast, 2018, pp. 1044–1047, doi:10.1109/MEMSYS.2018.8346738

[4] Z. S. Somaehsofla, C. Masserey, A. Varini, D. Flandre and A. M. Ionescu, "Wafer-Scale Demonstration of a Highly Sensitive Strain Sensor Based on Polycrystalline VO_2", *2025 IEEE 38th International Conference on Micro Electro Mechanical Systems (MEMS)*, Kaohsiung, Taiwan, 2025, pp. 635-638, doi: 10.1109/MEMS61431.2025.10917570

[5] Kaajakari, Practical MEMS, Las Vegas, NV, USA: Small gear Publishing, 2009, pp.74-75.

[6] L. Lahaye, N. Roisin, N. André, D. Flandre, J.-P. Raskin, "Design, Fabrication, Modeling and characterization of a Polyimide-Based Membrane for High Strain Studies in Micro-fabricated Devices", *IEEE Transactions on Materials for Electron Devices* 2 (2025) 26–33, doi:10.1109/TMAT.2025.3557763

[7] A. G. Shabalin *et al.*, "Nanoimaging of Electrical Failure in VO_2 Resistive-Switching Nanodevices", *ACS Applied Electronic Materials*, vol. 2, no. 8, pp. 2357–2362, Aug. 2020, doi:10.1021/acsaelm.0c00382

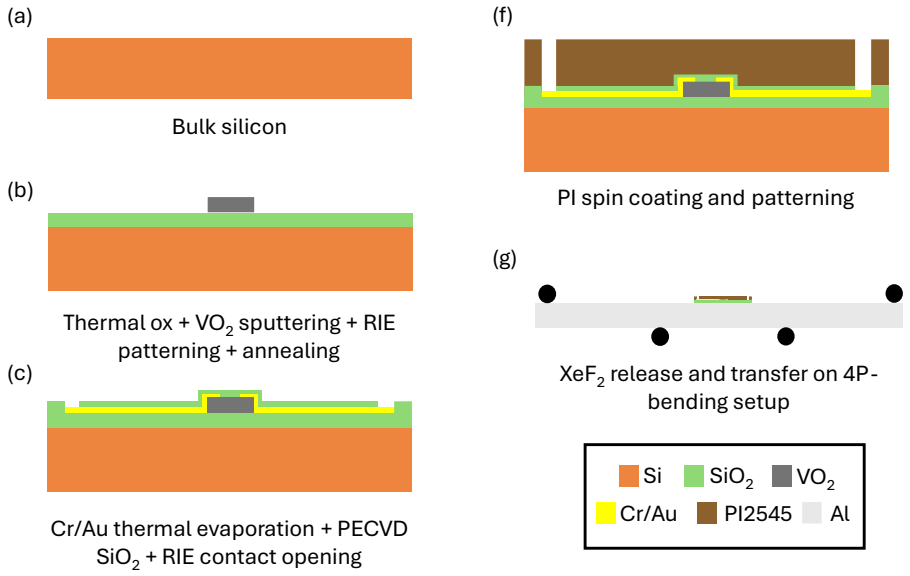

Figure 1. Fabrication process of VO_2 resistors on polyimide thin film for high strain studies

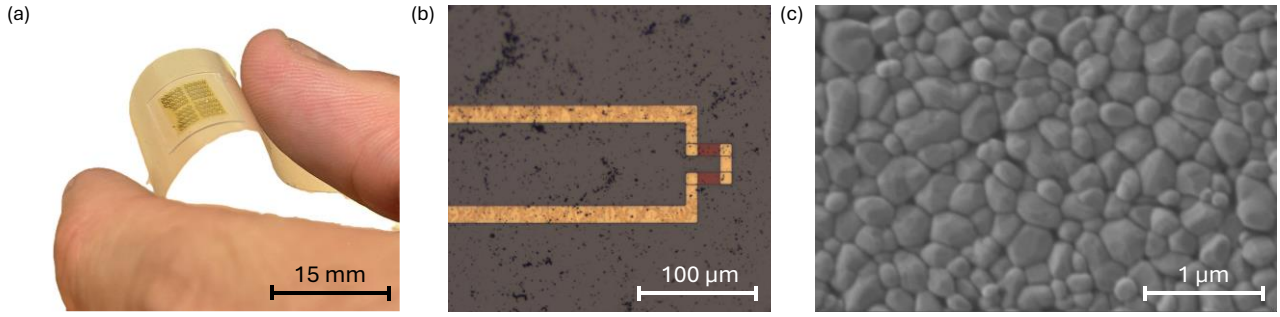

Figure 2. (a) Photography of the fully-released polyimide thin film with VO_2 resistors. (b) Microscopic picture of a VO_2 resistor on a fully-released polyimide thin film. (c) SEM photography of the polycrystalline patterned VO_2 film.

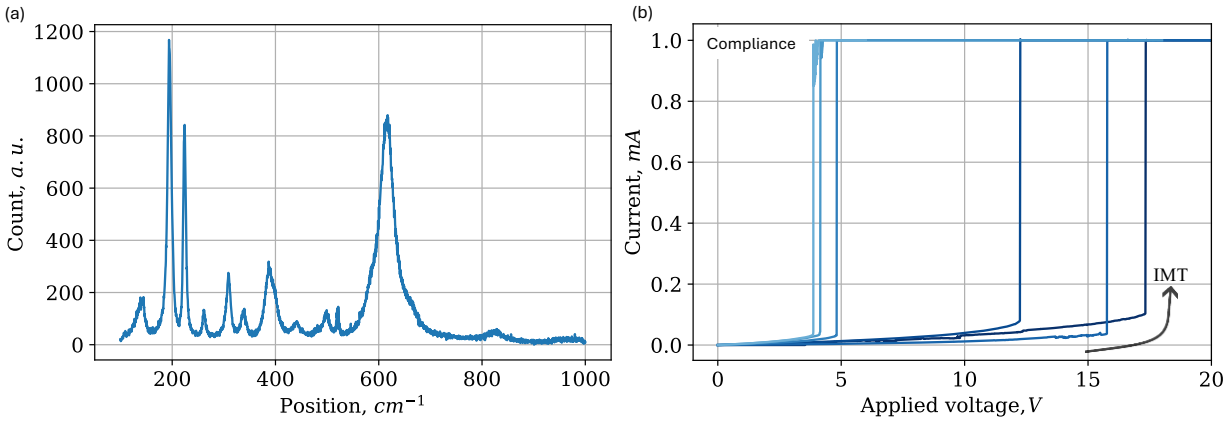

Figure 3. Raman spectrum of the deposited and patterned VO_2 film. (b) IV measurement of a VO_2 resistor on a fully-released polyimide thin film. Colors from dark to light blue indicate the order of the IMT measurement from first to last, respectively.

FabuBlox – An AI-driven Platform Connecting the Nanofabrication World

Jan Tiepelt [a], Josh Perozek [a], Jack Muller [a], Eyal Perry [a]

[a] FabuBlox, Inc., Boston, 02116, USA
e-mail: jan@fabublox.com

Keywords: Process design, cross-facility collaboration, knowledge management, AI optimization, simulation

Abstract

The nanofabrication world faces a critical challenge: the **lack of standardized frameworks for process data, design, and knowledge management** leads to repeated problem-solving, stifling innovation. This fragmentation also hinders modern R&D efforts that require multi-facility, flexible, and custom fabrication workflows. Crucially, this gap impedes effective use of AI/ML tools that could transform semiconductor and nanofabrication development.

Developed by MIT engineers, the FabuBlox cloud platform (www.fabublox.com) provides an accessible, cross-facility data standard that integrates process design, simulation, knowledge management, and collaboration. Since its first release in 2023, it has gained 1,500 users across over 100 fabrication facilities, R&D teams, and tool vendors in 15 countries.

Individual platform users, facilities, and teams can leverage FabuBlox to create **private and secure GitHub-like repositories of process flows and standard processing modules**. A key feature of the FabuBlox process design interface is its ability to algorithmically generate cross-sectional sketches of fabricated structures on the fly, significantly lowering the barrier for process planning, design, and communication. Seamlessly integrated into the design interface is a rapid prototyping 2D device stack simulation tool, harnessing state-of-the-art ray tracing algorithms and supporting automated feature extraction from GDS design files.

Beyond standardizing process data management, **FabuBlox Facility Portals** (launching Q2 2025) will standardize the documentation and management of tool infrastructure. These Portals enable association of templated “tool blox” with real-world tool capabilities and restrictions, thereby helping facilities prevent tool downtimes due to contamination and accelerating user and technician onboarding while optimizing tool usage and process execution. Embedded within Facility Portals is the FabuBlox AI Assistant enabling algorithmic tool-process compatibility analysis, predictive supplier and inventory management, and AI-assisted troubleshooting — forming the foundation for the next generation of AI-enhanced Digital Cleanrooms.

With its AI-driven **fab tracking features** in development, FabuBlox will accelerate lab-to-fab & fab-to-fab transitions, automate process-design co-optimization, and revolutionize fab service coordination. In the long-term vision, the platform will evolve into an AI-powered marketplace connecting foundries, R&D fab facilities, fabless customers, tool vendors, and material suppliers.

Leveraging its platform infrastructure, FabuBlox enables nanofabrication networks to unify processing capabilities into shared, **intelligently managed Hub databases**. This fosters cross-facility collaboration, enhances fab coordination, and creates an end-to-end centralized Hub node for coordination of nanofabrication services — providing faster access to expertise and unlocking opportunities for innovation. In short, **FabuBlox connects the nanofabrication world**.

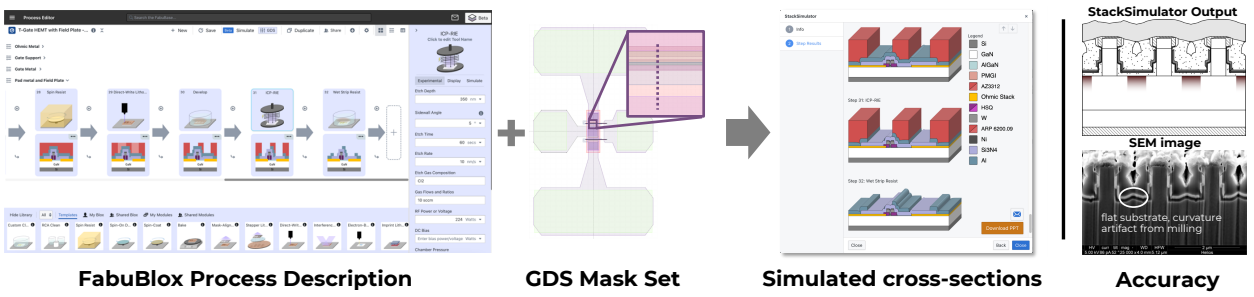

Figure 1. The FabuBlox StackSimulator – A rapid prototyping simulation tool, originally developed for GaN transistor development at MIT, delivering highly-accurate 2D simulations of fabricated device cross-sections from GDS design files in under a minute.

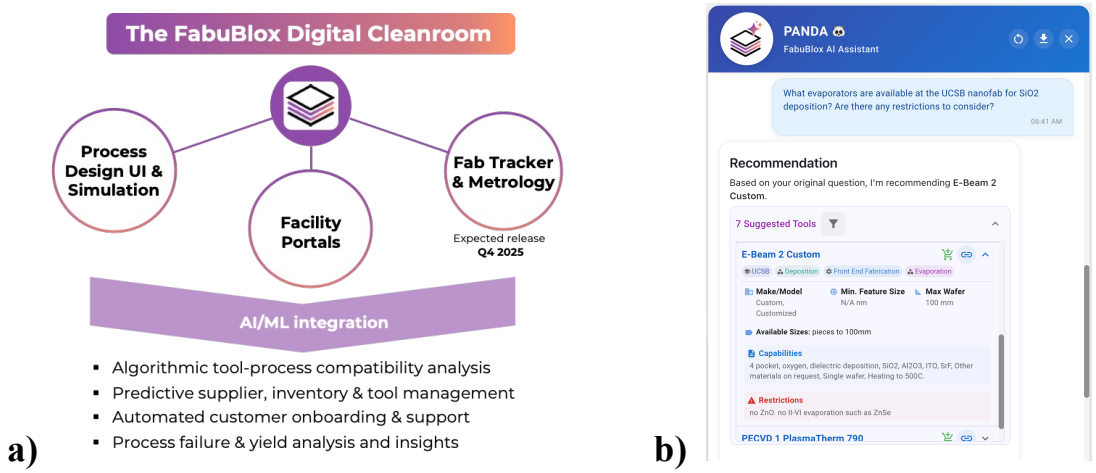

Figure 2. a) FabuBlox building the next generation of AI-enhanced Digital Cleanrooms by combining intuitive process design & database building with its Facility Portals, standardizing tool capability management, and fab run tracking capabilities. **b)** The FabuBlox AI Assistant embedded in the Facility Portal Interface helping, for example, to match tools with processing requirements.

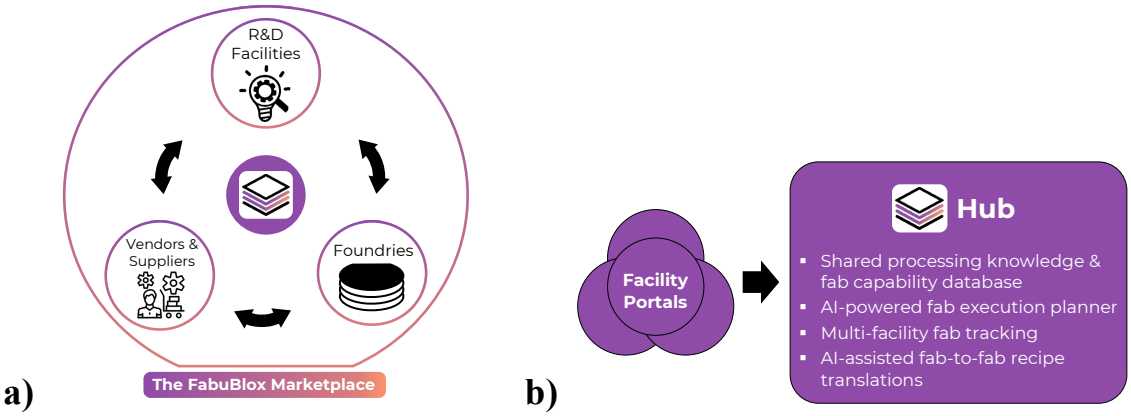

Figure 3. a) The long-term vision – An AI-powered design, marketplace & collaboration platform for automated nanofab service and supply chain management. **b)** FabuBlox Hub Portals centralizing knowledge and fab coordination management.

Fabrication of Seamless, Homogenous Al_2O_3 Membranes by Gas-Phase-Deposition for highly stable Liquid Cells for Transmission Electron Microscopy

Nathalie P. Pranzner[a], Judith Estengre Pérez[a], Jeremy P. Teuber[b], Rukan Nasri[a], Prof Dr. Arwen Pearson[a], Dr. Irene Fernandez-Cuesta[a]

[a] *Institute for Nanostructure and Solid State Physics, University of Hamburg, 22761 Hamburg, Germany;*
[b] *Max-Planck-Institute for the Structure and Dynamics of Matter, 22761 Hamburg, Germany*

nathalie.pranzner@uni-hamburg.de

Liquid cells are valuable tools that allow imaging of soft-matter inside transmission electron microscopes (TEMs), both in situ and at room temperature. The resolution is critically influenced by the thickness of the cell area transmitted by the electron beam. Balancing electron transparency and stability under vacuum is one of the greatest challenges in the fabrication of liquid cells for TEM. Typically, a sub-micron electron-transparent membrane is used for the measurement window. Most currently available devices are fabricated from silicon as a substrate and silicon nitride as a membrane, typically manufactured in two parts and subsequently sealed [1]. This manual sealing process causes interfaces to act as breaking points, often leading to leakage, especially under the vacuum conditions of a TEM. We present here a fabrication method enabling the production of polymer-based liquid chambers sealed by a continuous Al_2O_3 membrane, effectively eliminating the fracture-prone interfaces and providing a foundation for high stability under vacuum conditions. This method also allows the fabrication of intricate fluidics designs with varying depths, including ultra-thin nanochambers allowing electron transmission.

The liquid cell layout was first designed on a silicon wafer using photolithography followed by reactive ion etching (RIE) to establish the desired channel depths. This master structure was subsequently transferred to polymer substrates via direct nanoimprinting using OrmoStamp® as the imprint material [2]. As a substrate, a polycarbonate (PC) chip with pre-drilled inlet holes is used. The samples are sealed using a multilayer coverslip composed of a PC carrier foil, a separation layer of polyvinyl alcohol (PVA), and a polymer layer (3Dresyn R190D90), which is bonded to the sample chip. Following the GPD process, this coverslip can be selectively or entirely removed using RIE to expose the Al_2O_3 membrane underneath.

The fabrication of the Al_2O_3 membrane that confines the liquid inside the cell is based on gas-phase-deposition (GPD). To achieve conformal coating of the inner walls of high-aspect-ratio microchannels and nanochambers, a custom-built GPD system was operated in flow-through mode [3]. To ensure highly controlled material growth, the precursor gases trimethylaluminium (TMA) and water are alternately introduced into the chamber and directed through the fluidic structure using nitrogen as a carrier gas. The desired layer thickness is achieved by adjusting the number of deposition cycles.

The design presented in Fig.1 and is based on several nanochambers with a depth of approximately 380 nm, which in the final application, will hold the samples and serve as the focus point for the imaging. The nanochambers are connected to the four in- and outlets by microchannels with a depth of 5.6 µm to allow a sufficient flow of the sample. After structuring by photolithography and RIE, the chips were coated in the flow-through GPD mode. The corresponding GPD setup and the fabricated membrane is presented in Fig.2. To reveal the Al_2O_3 membrane the coverslip was removed by RIE. A homogeneous and mostly intact Al_2O_3 membrane was revealed. For the Al_2O_3 membrane, a layer thickness of approximately 100 nm was achieved as measured by EDX and SEM. This shows, that flow-trough GPD of Al_2O_3 is a valuable method for the fabrication of vacuum-stable liquid cells with intricate fluidic designs.

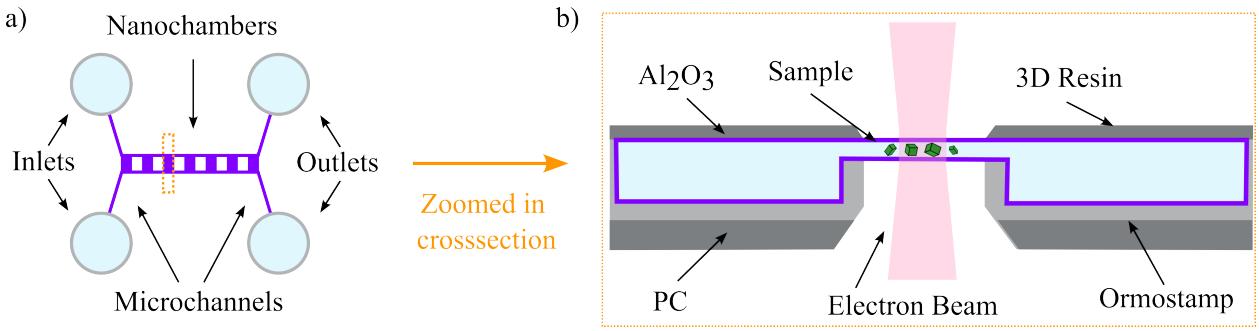

Figure 1: Overview of the chip design and its intended application: a) Schematic of the designed flow structure including the nanochambers being connected to the in- and outlets by microchannels. b) Schematic of a zoomed-in cross-section showing a shallow nanochamber connected to deeper microchannels on both sides, including the materials used. In the final application, the nanochamber will hold the sample and will be the focus point for the imaging.

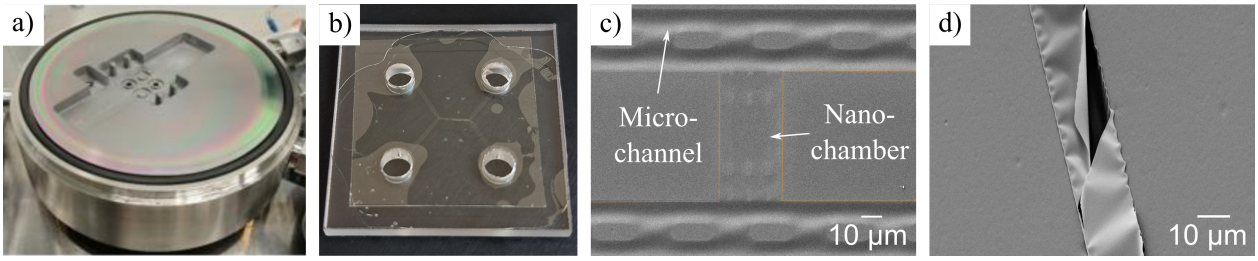

Figure 2: Overview of the GPD device in flow-through mode and the resulting Al_2O_3 membranes: a) Customized GPD chamber allowing the deposition in a flow-through mode. b) Structured PC chip with inlets and outlets before coating by GPD. The chip is sealed by a multi-layer coverslip. The dimensions of the chip are matched to the dimensions of the customized GPD chamber and the inlet holes match the holes in the reactor facilitating an ideal flow of the precursors through the channels. c) Section of the flow structure, showing one nanochamber connected to two microchannels after GPD and removal of the coverslip by RIE. An intact and homogeneous Al_2O_3 membrane can be seen. d) A ripped open portion of the Al_2O_3 membrane covering a microchannel, allowing the analysis of layer thickness by SEM as well as an analysis of the coating of the other sides of the channel by EDX.

[1] K. He, T. Shokuhfar, and R. Shahbazian-Yassar, *Journal of Physics: Condensed Matter*, vol. 31, no. 10, p. 103 001, 2019.

[2] I. Fernandez-Cuesta, A. Laura Palmarelli, X. Liang, *et al.*, *Journal of Vacuum Science & Technology B*, vol. 29, no. 6, 2011.

[3] M. Müller, "De 102020102076a1," *Deutsches Patent- und Markenamt*, Hamburg, Germany, 2020.

Localised O_2 Plasma Treatment of AZO and Zn for Broadband Modulation of Optical and Radio Frequency Response.

T. M. Howe[a*], K. Sun[b], O. L. Muskens[b], C. H. de Groot[a].

a. Electronics and Computer Science, University of Southampton, Southampton, SO17 1BJ, UK.
b. Physics and Astronomy, University of Southampton, Southampton, SO17 1BJ, UK.
*Email: T.M.Howe@soton.ac.uk

The modern world relies heavily on electronic devices for communication and sensing. However, the emitted electromagnetic radiation can cause electromagnetic interference (EMI), which prevents the development of smart cities [1, 2]. Metals can be employed as a broadband shielding material, but they lack the optical transparency desired in certain applications. Metamaterials are comprised of periodically arranged structures with a unique optical response not found naturally, which can further be controlled by changing the structural parameters [3, 4]. In our previous works, we have showcased the ability to form embedded, planar, metamaterial devices which can be easily integrated into multilayer stacks [5, 6]. The embedded metasurface structures are formed through a localised O_2 plasma treatment with contrasting areas of high and low conductivity. In this work, we extend this idea to the key radio-frequency (RF) regime.

The reflection coefficient of a planar AZO back reflector is presented in Figure 1A as a function of wavelength and plasma treatment time. The O_2 plasma treatment was carried out at 300 °C. This exhibits how the optical properties of AZO can be engineered using an O_2 plasma treatment. Figure 1B provides a schematic of the O_2 plasma treatment process, in which a pattern can be transferred to the material through localised oxidation, allowing for a planar metasurface to be produced with a high degree of accuracy. Figure 1C shows the optical magnitude of AZO metasurfaces measured through scattering-type scanning near-field optical spectroscopy (s-SNOM). By using a metalised AFM tip and a laser to interact with the sample surface, the optical amplitude can be extracted at a resolution of 10 nm. The s-SNOM image shows that AZO metasurfaces can be formed with a clear, high contrast in the optical properties.

For RF operation, AZO has too high sheet resistance of ca. 70 Ω/□. Zn is proposed as an alternative compatible material wherein the localised oxygen plasma treatment can form contrasting areas of high conductivity Zn and low conductivity ZnO. The sheet resistance is given as a function of thickness in Figure 2A for various Zn films. An exponential decrease in sheet resistance with thickness is observed. The optical and RF transmission is shown for a planar Zn film, before and after an O_2 plasma treatment, in Figures 2B and 2C respectively. The O_2 plasma treatment was carried out at 400 °C for one hour on a 60 nm Zn film, deposited at 500 W. Before plasma treatment, the as-deposited Zn films show low transmission across the visible, infrared, and RF regimes. After plasma treatment, high transmission values close to the substrate material are seen in the visible and infrared regimes of interest, and the transmitted power loss is equal to the CaF_2 substrate in the RF regime.

In conclusion, this work presents the effect of O_2 plasma treatment on both AZO and Zn. We demonstrate the local optical property modulation of the selective O_2 plasma treatment of AZO through transmission and s-SNOM measurements. A clear difference between the optical properties and local contrast changes is highlighted. We further demonstrate the ability to engineer the optical response of Zn through a similar O_2 plasma treatment. This shows its potential for metamaterial applications where the localised O_2 plasma technique is applied to metallic Zn to generate novel, embedded Zn metamaterials where the response can be engineered to form optically transparent broadband EMI shielding.

[1] K. Wiklundh and P. Stenumgaard, IEEE Electromagnetic Compatibility Magazine 8(2) (2019) 65-74.
[2] Y. Liang et al., Appl. Sci. 13(8) (2023) 4846.
[3] A. K. Iyer et al., IEEE Transactions on Antennas and Propagation 68(3) (2020) 1223-1231.
[4] R. K. Mishra et al., Plasmonics 16(6) (2021) 2061-2071.
[5] K. Sun et al., ACS Photonics 5(2) (2018) 495-501.
[6] K. Sun et al., Advanced Materials 32(25) (2020) 2001534.

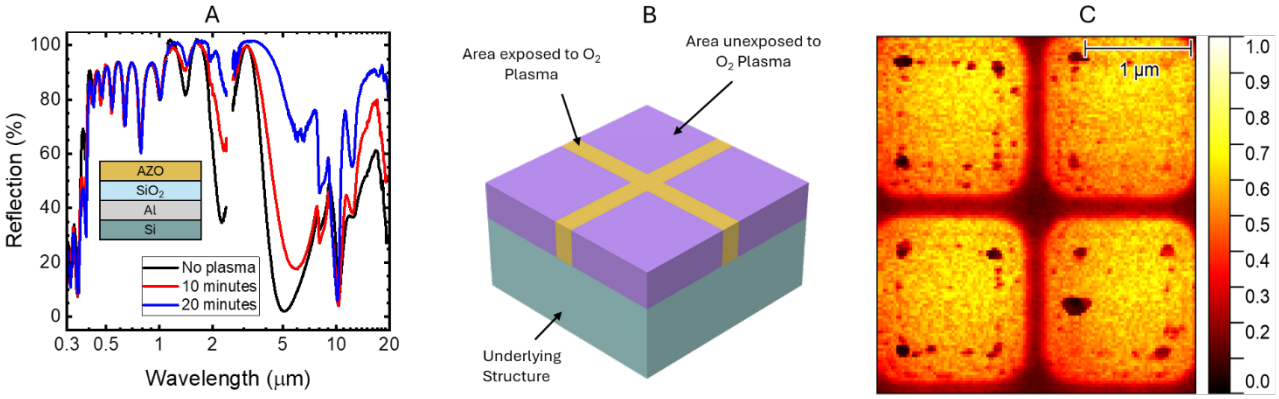

Figure 1: (A) Reflection coefficient as a function of wavelength for planar AZO back reflectors. Samples were treated for two O_2 plasma treatment times. (B) Schematic of the AZO metamaterial design, with exposed and unexposed areas labelled. (C) S-SNOM images of the optical amplitude of an AZO metamaterial. High contrast between the exposed (high optical amplitude) and unexposed (low optical amplitude) areas is seen.

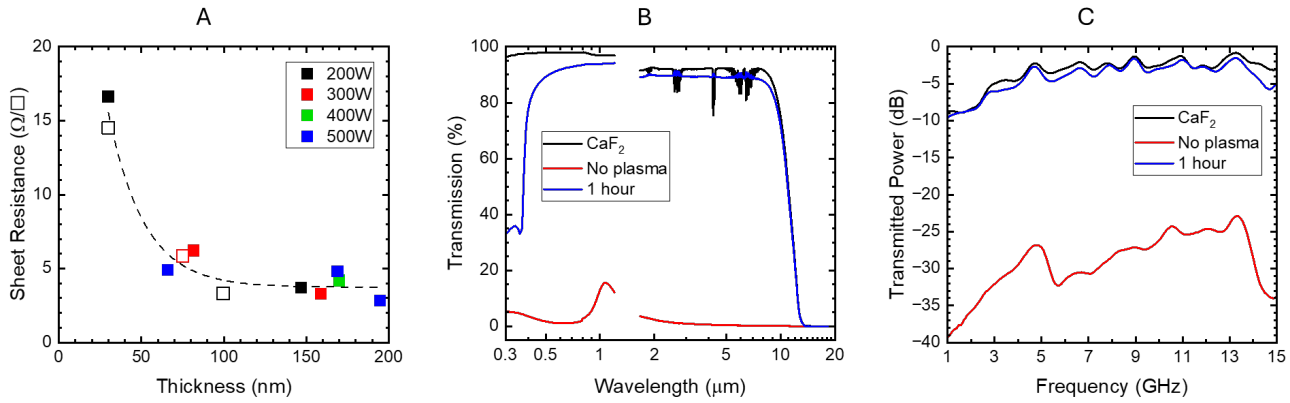

Figure 2: (A) Sheet resistance as a function of Zn thickness for varying RF powers during deposition. An exponential fit of all data is shown with the dashed line. (B) Transmission of a planar Zn film before and after O_2 plasma treatment. (C) Transmitted power in the RF regime of a planar Zn film before and after O_2 plasma treatment. The transmission of the CaF_2 substrate is given in black.

Single-Molecule Identification Using Plasmonic Nanopores and Ultrafast SERS

Kirill Khabarov [a], Ilaria Micol Baldi [a], Maria Blanco Formoso [a], Foroogh Khozeymeh Sarbishe [a], Giulia Bruno [a], Francesco Gentile [b], Francesco Tantussi [a], Francesco De Angelis [a]

[a] Italian Institute of Technology, Genova, 16163, Italy
[b] University of "Magna Graecia" of Catanzaro, Catanzaro, 88100, Italy
e-mail: kirill.khabarov@iit.it, francesco.deangelis@iit.it

Surface-Enhanced Raman Spectroscopy (SERS) has emerged as a powerful tool for biosensing and medical applications due to its single-molecule sensitivity, high accuracy, and rapid response. By leveraging light-matter interactions, SERS provides unique vibrational fingerprints for molecular identification, overcoming the limitations of existing methods, such as high costs and complex sample preparation and treatment. Despite recent studies showing that SERS can distinguish individual molecules, reliable and high-throughput applications remain challenging [1]. The fast and accurate detection and sequencing of biopolymeric molecules, such as DNA and proteins, represent one of the promising applications that holds great potential for disease diagnosis, treatment, and prevention.

The **purpose of this work** is to develop a novel approach for single-molecule identification and biopolymer sequencing using permeable plasmonic membranes combined with real-time microsecond SERS detection. To do that, we establish a system with extreme spatial and temporal resolution, utilizing the latest generation of Single-Photon Avalanche Diode (SPAD) cameras, enabling ultrafast spectral acquisition and paving the way for advanced molecular diagnostics and sequencing technologies [2], [3].

A key **novelty of this work** is the use of permeable plasmonic membranes (Figure 1a) that allow molecules to pass through nanopores while their Raman spectra are recorded with a SPAD camera. Unlike conventional SERS methods, where molecules are immobilized on metal surfaces, our approach enables spectral acquisition in a free-moving state, investigating molecules one after another. This implements a sequential readout concept for DNA and peptides, where Raman spectra are recorded in a sequence as molecules translocate through the nanopore, preserving the molecular order along the chain and enabling unambiguous identification. Consequently, this innovation provides several advantages: (i) it allows real-time, label-free detection of a broad range of molecular species, (ii) relies on a simple and cost-effective fabrication process, (iii) achieves picomolar sensitivity, and (iv) improves molecular discrimination by capturing transient spectral variations rather than relying on averaged spectra. Additionally, it opens the possibility of investigating the molecular solution content from perspectives of quality and quantity and currently has no analogs.

To validate our approach, we conducted a series of experiments with DNA and proteins, demonstrating its **effectiveness and results**. Here, we successfully recorded and distinguished the spectra of individual nucleosides (A,T,G,C) translocating through the nanopores at nanomolar concentrations (Figure 1b). Exploiting machine learning methods, allowing to work on an enormous amount of data collected, we achieved a classification accuracy exceeding 89% (Figure 1c). Furthermore, we demonstrated the spatial resolution of our plasmonic "hot spot" at the level of a few nucleotides, utilizing 10 nb single-stranded DNA (ssDNA) oligos with the sequence AAAAACCCCC, confirming its potential for sequencing applications (Figure 1d). Expanding beyond nucleotides, we applied our approach to peptides and successfully differentiated oxytocin from vasopressin, which are structurally similar peptides differing by only two residues on 3^{d} and 8^{th} positions, at the single-molecule level (Figure 1e). Importantly, our findings highlight that single-molecule SERS spectra reveal fine spectral features that are lost in conventional averaged spectra due to peak broadening, emphasizing the importance of real-time spectral acquisition.

These **results** demonstrate that our method lays the foundation for the next-generation single-molecule detection and sequencing platform. By enabling precise molecular identification with ultrahigh spatial and temporal resolution, this technology has the potential to revolutionize the diagnostics of genomic and proteomic disorders, facilitate toxin detection, and allow the precise quantification of biomolecular concentrations with unprecedented accuracy.

[1] M. M. Schmidt et al., ACS Nano 18.38 (2024) 25930-25938
[2] W. Li et al., ACS Nano 18.29 (2024) 19200–19207
[3] M. Wojtkiewicz et al., IEEE Trans Electron Devices (2024) 3470–3477

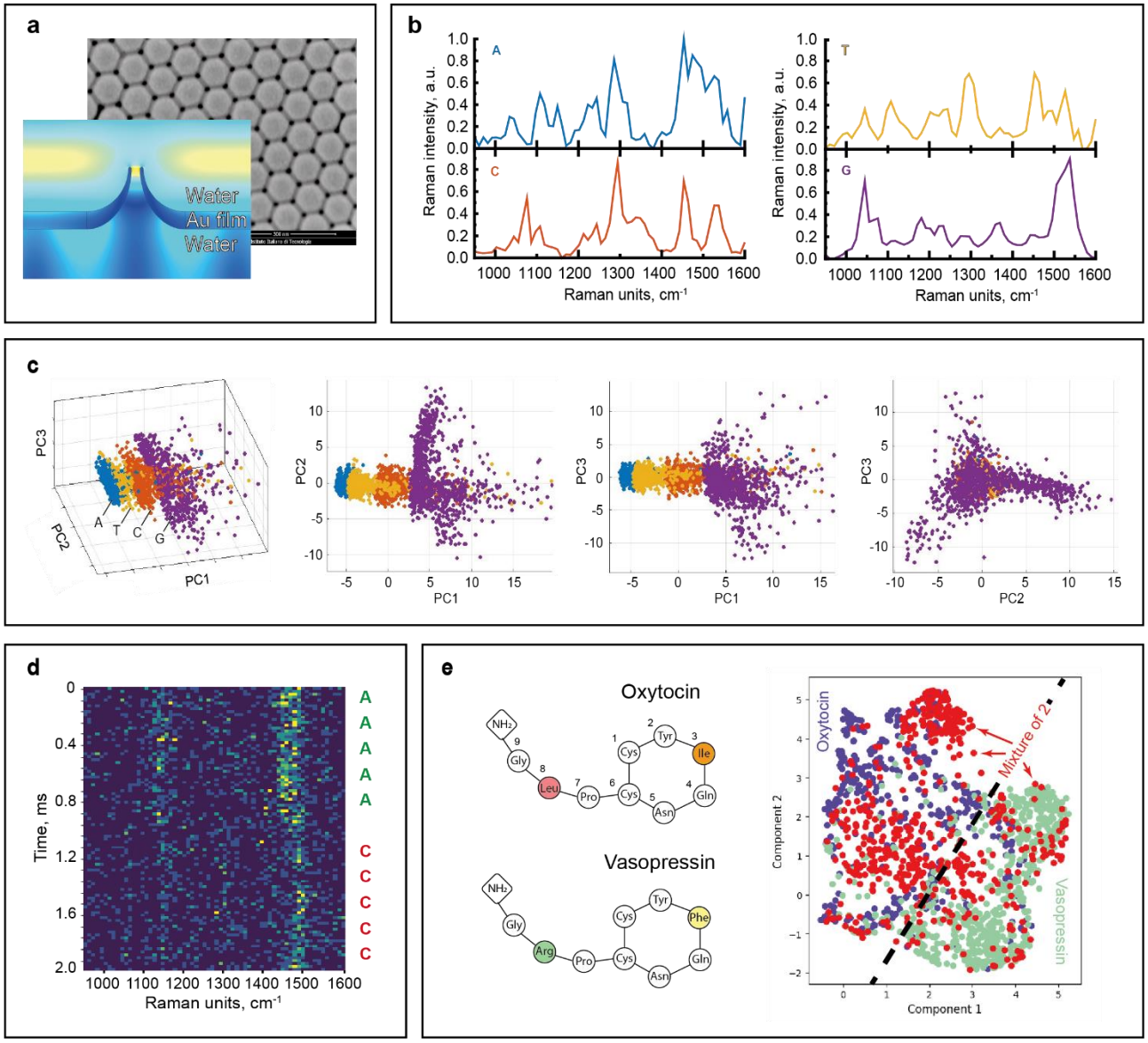

Figure 1. SEM image of a permeable plasmonic membrane used and its cross-sectional E-field distribution simulation with 532 nm laser irradiation using COMSOL Multiphysics **(a)**; Averaged spectra of single nucleosides, collected with single-molecule translocations through the membrane **(b)**; Principle Component Analysis (PCA) of single-molecule spectra, showing a high discriminability between nucleosides **(c)**; Waterfall graph showing SERS spectra inside a nanopore in time for an AAAAACCCCC molecule demonstrating the shift from A to C part **(d)**; PCA for oxytocin and vasopressin molecules showing a good level of discrimination **(e)**.

Oral Session 4B: Advanced Nanofabrication and Characterisation

International Micro- and Nano Engineering (MNE2025) Conference
Track 1: Micro-Nano Fabrication | 1.1 Processes

Ti-Ni-Cu shape memory alloy thin films with improved adhesion and controlled residual stress for MEMS applications

Elaheh Akbarnejad [a], Alan Savan [a], Gowtham Arivanandhan [b], Manfred Kohl [b], Alfred Ludwig [a]
[a] Material Discovery and Interfaces, Ruhr University Bochum, Bochum, 44801, Germany
[b] Institute of Microstructure Technology, Karlsruhe Institute of Technology (KIT), Karlsruhe, Germany

e-mail: elaheh.akbarnejad@ruhr-uni-bochum.de

This work investigates the possibility of coating Ti-Ni-Cu SMA film onto Si nanohinges with properties investigations and enhancing the SMA film adhesion to the selected substrate by reducing residual stress levels using substrate bias during the magnetron sputtering deposition process. Sputtered shape memory alloy (SMA) thin films have gained significant attention in MEMS due to their superior actuation force and displacement compared to other actuator types [1]. The thickness of these films plays a critical role, directly affecting their performance and overall efficiency [1]. The ternary SMA system Ti-Ni-Cu is suitable for MEMS applications like microactuators, microgrippers and microvalves, since Cu enhances functional stability [2], adjusts the transformation temperature ranges and also reduces the width of the thermal transformation hysteresis, so enabling operation at higher frequencies [3]. Transformation temperatures are strongly composition dependent and can be increased by the substitution of Ni with Pd [4], or Ti with Hf [5]. Ti-Ni-X thin films usually require heat treatment at elevated temperature (around 500°C) in order to activate shape memory alloy behavior [2].
Ti-Ni-Cu thin film is directly deposited from an alloy target with a composition of $Ti_{54}Ni_{31}Cu_{15}$ (99.9% purity, FHR, Germany). The sputter system used was a load-locked, multi-UHV-chamber magnetron sputter deposition system (DCA Instruments, Finland). Films were deposited in thicknesses of 150, 300, 600, 800, and 1000 nm on Si/SiO_2 substrates. Also here, all deposited SMA films were amorphous in the as-deposited state and so had a post-deposition annealing treatment in a vacuum of 7.6×10^{-5} Pa at 600 °C for 2 hours and then cooled to room temperature. Temperature-dependent four-point probe electrical resistance measurements were done within a range of -20 °C to 120 °C (5 K per minute, 100 mA applied current). Figs. 1a-e reveal the characteristic phase transformation temperatures and thermal hysteresis for the SMA films deposited in different thicknesses. Fig. 1f shows the phase transformation temperatures for the film with 600 nm thickness were M_s=68.2°C, M_f=28.4°C, A_s=38.2°C, and A_f=77.8°C, while films with thicknesses below 600 nm exhibited lower transformation temperatures due to size effects. Fig. 1g shows the crystallographic results measured by X-ray diffraction. The films with different thicknesses exhibit peaks that predominantly correspond to either the cubic Austenite (B2) phase, the orthorhombic Martensite (B19) phase, or the intermetallic Ti2Ni precipitation phase and C11b-type Ti(Ni,Cu)2 precipitates. A 600 nm SMA film with the composition of $Ti_{50}Ni_{34}Cu_{16}$ was deposited on Si nano-hinges and then was crystallized by annealing at 600°C for 2 hours. Fig. 2 shows scanning electron microscopy (SEM) images of the adhesion problem of the deposited SMA film on 300 nm wide Si hinges fabricated using SOI technology with a Si device layer of 2 µm. To address the delamination issue, a 20 nm tantalum (Ta) adhesion layer was deposited before the SMA layer. During deposition, a 30 W RF substrate bias was applied. The residual stress of the films was measured using the Michelson interferometer method by determining the radius of curvature of a cantilever, which served as the substrate with the SMA film deposited on it. Fig. 1h shows the measurement results in both the as-deposited and annealed states. The data indicate a transition from compressive stress in the as-deposited state to tensile residual stress after crystallization. By employing the adhesion layer and substrate biasing, the delamination and high residual stress issues were effectively mitigated. The SMA film deposited on the fabricated silicon hinge showed no signs of delamination. Figs. 3a and 3b illustrate the hinge design and its coverage with the SMA film, respectively. This result enables the development of TiNiCu-based actuators down to the scale of 150 nm.

[1] K. Tsuchiya et al., Proc. IEEE 24th Int. Conf. Micro Electro Mech. Syst. (MEMS), 2011, pp. 398–401.
[2] D. König et al., Acta Materialia 60 (2012) 306–313.
[3] Y.T. Hsu et al., Journal of Alloys and Compounds 997 (2024) 174937.
[4] R. Zarnetta et al., Applied Surface Science 254 (2007) 743–748.
[5] R. Vitushinsky et al., JMEMS 18 (2009) 1.

Acknowledgements: This research was funded by the German Research Foundation within the Priority Program “Cooperative Multistage Multistable Microactuator Systems” (SPP2206, www.spp-kommma.de).

International Micro- and Nano Engineering (MNE2025) Conference
Track 1: Micro-Nano Fabrication | 1.1 Processes

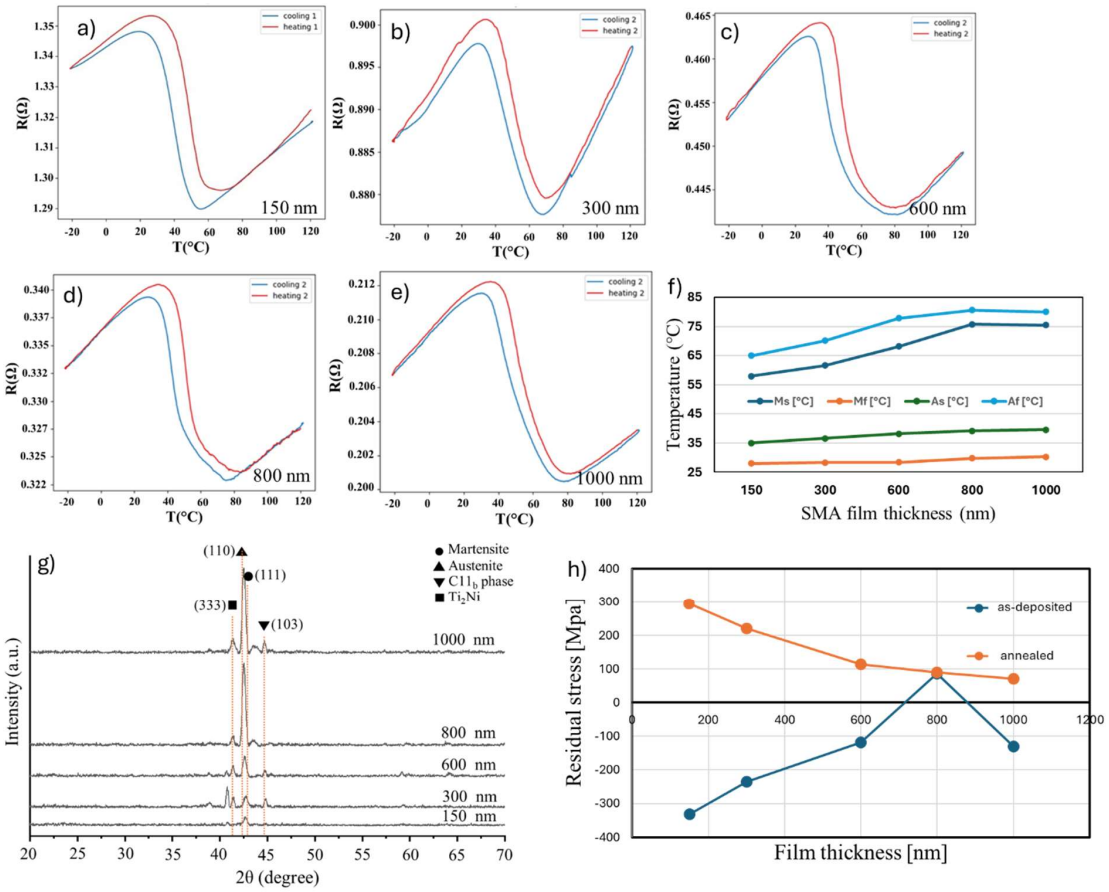

Figure 1: a)-e) shows temperature-dependent resistivity measurement curves for SMA films with different film thicknesses. The red part of each curve indicates heating of the sample, whereas blue indicates cooling. f) XRD spectra of SMA films annealed at 600°C for 2 h, and g) Stress level of the film vs. the film thickness in as-deposited state and after annealing.

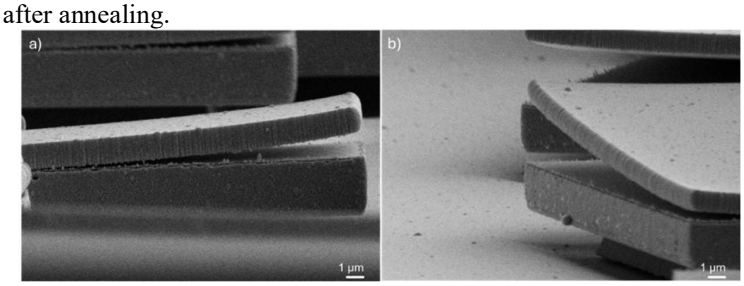

Figure 2: SEM images of SMA film after deposition and annealing on the Si hinges. Here, undesired delamination was observed. This could be avoided by an adhesion layer, see Fig. 3.

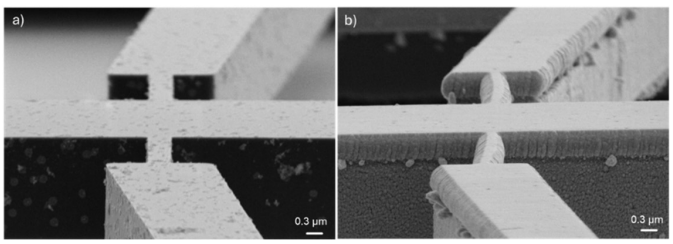

Figure 3: SEM images of a) fabricated Si hinges from SOI wafer, b) after deposition and annealing of 600 nm SMA film with 20 nm Ta adhesion layer on Si hinge.

Temperature Homogenization for Local Electro-Thermal Annealing of Shape Memory Alloy Microstructures

Gowtham Arivanandhan[1], Elaheh Akbarnejad[2], Alfred Ludwig[2], and Manfred Kohl[1]
[1]Institute of Microstructure Technology, Karlsruhe Institute of Technology (KIT), Karlsruhe, Germany
[2]Material Discovery and Interfaces, Ruhr-Universität Bochum (RUB), Bochum, Germany
e-mail: manfred.kohl@kit.edu

We present a novel design strategy for achieving uniform temperature profiles upon direct Joule heating required for local electro-thermal annealing of shape memory alloy (SMA) microstructures. This strategy is validated for a Ti–Ni–Cu/Si microactuator consisting of coupled microbridges and co-integrated heating circuits fabricated by electron beam lithography and magnetron sputtering. Our research is motivated by the need for ultra-compact, bidirectional, and bistable actuators capable of producing large strokes in the order of several percent of the actuator length. Although antagonistic SMA beams have enabled buckling bistable actuation at the macroscale [1], scaling down to micrometer dimensions poses significant challenges. These include fabrication limitations, inhomogeneous temperature profiles, and difficulties in achieving antagonistic shape setting of SMA microbridges. In particular, conventional high-temperature annealing procedures being essential for shape setting of SMA microstructures induce undesired thermal stress in the neighbouring silicon microstructures. Local electrothermal annealing may overcome these issues, however, Joule heating may cause large temperature gradients [2]. Here, we mitigate these challenges by introducing a design that enables temperature homogenization during local annealing to confine the heat treatment to target regions and later on during selective actuation of antagonistic SMA microstructures with enhanced phase transformation.

Layout: The bistable microactuator is designed with a central moving platform suspended by microbridges featuring narrow hinges of width w_h with a pre-deflection offset x_o. Two distinct layouts are implemented, as shown in Fig. 1. The first layout is a conventional design, in which the microbridges are directly fixed to contact pads. Joule heating in this configuration leads to large temperature gradients due to a large heat sink present at the onset of the microbridges, as shown in Fig. 2, which will result in non-uniform crystallization. The second layout is a temperature-homogenized design that incorporates co-integrated heating circuits at the onsets to minimize these gradients. This design not only achieves more uniform crystallization (see Fig. 2) but also reduces thermal coupling to the lower bridge, preventing unintended crystallization.

Fabrication: The developed process flow is summarized in Fig. 3. It comprises electron-beam lithography (EBL), wet etching and reactive ion etching (RIE) making use of the ultra-high precision of the silicon cryo-etching process. Next, an SMA layer is deposited onto the prestructured Si by magnetron sputtering, achieving aspect ratio larger than 5 (Fig. 3f). The deposition is performed at room temperature, whereby the SMA layer remains in amorphous state.

Local shape setting and characterization method: The microbridge 1 is locally annealed in its as-fabricated shape by Joule heating directly using contact pads or integrated heaters. Power levels between 19-23 mW raise temperatures above the crystallization threshold of 600 °C, resulting in crystallized volume fractions $\emptyset_{cry}$ of approximately 30-80%. However, the estimated peak temperature can reach above 1000 °C. In contrast, the temperature-homogenized design achieves nearly 100% of the material volume within the optimal crystallization range of 600-800 °C at a power of 37 mW. After crystallization, a lateral displacement is applied to the central platform in x-direction, and local annealing is performed again but this time to shape-set the microbridge 2. The annealing process is monitored by measuring the electrical resistance. SEM images of the fabricated microactuators in both layouts are depicted in Figs. 4 and 5. Low-power Joule heating and cooling cycles reveal phase transformation behaviour and associated thermal hysteresis (Fig. 6), which demonstrates successful crystallization. The phase transformation of the crystallized Ti–Ni–Cu microbridges and the microactuator performance will be compared for conventional and temperature homogenized designs.

[1] X. Chen et al., *Actuators.* 12(11), 422 (2023).
[2] M. Kohl et al., *Appl. Phys. Lett*. 104, 43111 (2014).

Acknowledgements: This research was funded by the German Research Foundation within the Priority Program "Cooperative Multistage Multistable Microactuator Systems" (SPP2206, www.spp-kommma.de). This work was partly carried out with the support of the Karlsruhe Nano Micro Facility (KNMFi, www.knmf.kit.edu), a Helmholtz Research Infrastructure at Karlsruhe Institute of Technology (KIT, www.kit.edu).

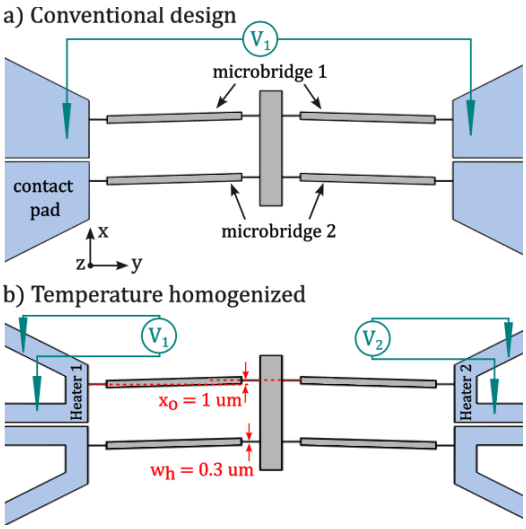

Fig. 1: Schematic layout of the Ti–Ni–Cu/Si microactuator consisting of coupled microbridges and electrical interconnections for local Joule heating. (a) conventional design with contact pads and (b) temperature homogenized design with co-integrated heating circuits 1 and 2. The microactuator has a footprint of 80 × 40 µm² with layer thicknesses of 0.6 µm Ti–Ni–Cu and 2 µm Si.

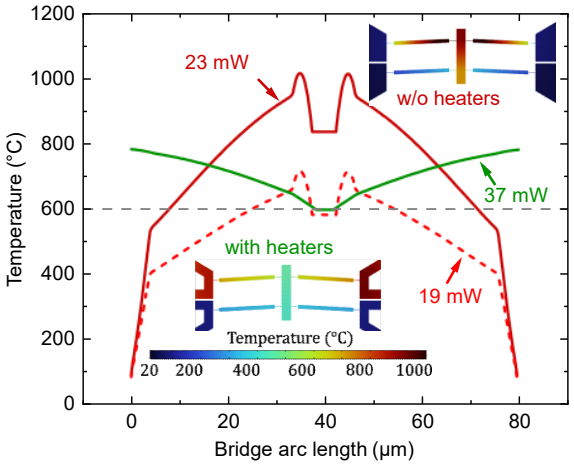

Fig. 2: Simulated temperature profiles across the microbridges of Ti–Ni–Cu/Si microactuator during local annealing. The initial design with contact pads exhibits a large temperature gradient upon Joule heating at P = 23 mW, while the temperature homogenized design operated at total heating power of P = 37 mW allows for an almost uniform temperature profile.

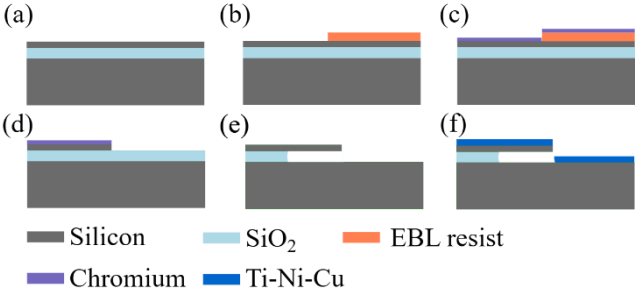

Fig. 3: Schematic process flow for monolithic fabrication of Ti–Ni–Cu/Si microactuator. (a) SOI-wafer with 2 µm device layer, (b) 30 nm Cr layer patterned by EBL, (c,d) lift-off and cryogenic RIE etching of Si, (e) Cr removal and wet etching of SiO_2, (f) DC magnetron sputtering of Ti–Ni–Cu layer.

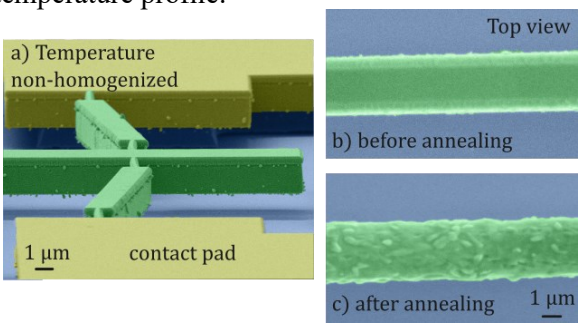

Fig. 4: False-colour SEM images of Ti–Ni–Cu/Si microbridges for (a) initial design with contact pads, (b) surface of microbridge in amorphous state, (c) in crystalline state after local annealing.

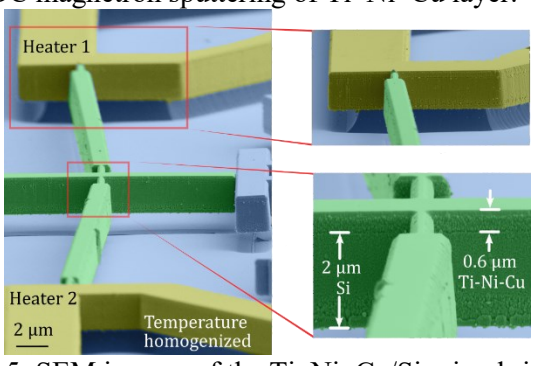

Fig. 5: SEM images of the Ti–Ni–Cu/Si microbridges and heating circuits 1 and 2, co-integrated at both ends. The heater structures are wider than the microbridges and carefully released to remain mechanically fixed by the SiO_2 layer, preventing displacement when heated. The Ti–Ni–Cu film is in the amorphous state and requires local annealing to induce crystallization.

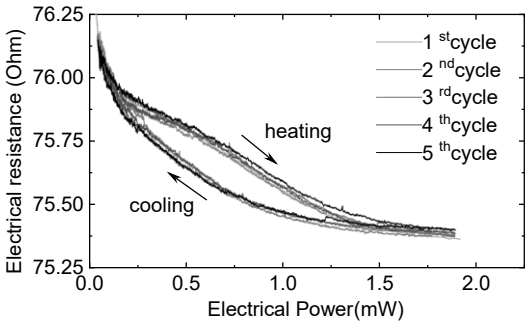

Fig. 6: Electrical resistance measurements of crystallized Ti–Ni–Cu microbridges of the conventional design after local annealing by high-power Joule heating. Subsequent low-power Joule heating and cooling cycles reveal phase transformation behavior and associated thermal hysteresis.

3D Printing of MEMS Devices

Frank Niklaus
KTH Royal Institute of Technology, Division of Micro and Nanosystems, Stockholm, Sweden

Abstract
Traditional semiconductor manufacturing processes enable mass production of MEMS (Micro-Electro-Mechanical Systems) with high efficiency. However, these methods are not well-suited for fabricating complex MEMS components in smaller quantities, making it challenging to serve applications that require fewer than 5,000 to 10,000 units annually. To address this gap, 3D printing offers a promising alternative for producing MEMS with complex structures at low to medium volumes. In this talk, we will share our work on 3D-printing microstructures using polymer and glass materials, and explore how these techniques can be applied to develop functional MEMS devices for specialized use cases.

Lightweight Machine-Learned Surrogate Models for Carrier Transport using Gradient-Boosted Feature Selection

Ben D. Rowlinson [a], Alexandros Keros [a], Subramanian Ramamoorthy [b], Jacqueline M. Cole [c], and Themis Prodromakis [a]

[a] Centre for Electronic Frontiers, University of Edinburgh, Edinburgh, EH9 3BF, U.K.
[b] Institute of Perception, Action and Behaviour, University of Edinburgh, Edinburgh, EH8 9AB, U.K.
[c] Cavendish Laboratory, Department of Physics, University of Cambridge, Cambridge, CB3 0HE, U.K.
e-mail: ben.rowlinson@ed.ac.uk

Keywords: *machine learning; material design; material optimization, carrier transport; interpretable ML*

Introduction

Machine learned (ML) surrogate models of material properties have gathered increasing attention in the engineering community in recent years, primarily due to beneficial scaling properties (O(n)), compared to first-principles approaches which often range from $O(n^3)$ to $O(n^7)$ [1]. An ML surrogate model is inherently only as effective as the underlying training dataset. As such, recent progress in large-scale standardised datasets has enabled increasingly accurate thermodynamic stability and property predictions using ML surrogate models. As semiconductor device engineers, arguably the most critical electronic property is hole and electron mobility (μ_h and μ_e). However, carrier transport is significantly more computationally intensive than properties such as energy above convex hull of stability (E_{hull}) and electronic bandgap (E_g). Therefore, lightweight surrogate models for mobility are becoming desirable for material screening and high-throughput "inverted pyramid" design-to-device pipelines. In this work, we propose interpretable ML surrogate models for E_g, μ_h and μ_e prediction based on chemically-relevant compositional features.

Methodology

Machine readable features are generated using elemental and compositional descriptors from Matminer [2], such as electronegativity and element ratios. By training an ML model on data from the MatHub-3d electronic transport database [3, 4], with a focus on methodical feature selection, the accuracy of the predictive models is evaluated. Gradient-boosted feature selection (GBFS) is employed to rank and prune the features based on their predictive power, identify non-linear feature interactions, and accommodate feature sparsity [5]. Recursive feature elimination (RFE) is used to reduce the model to only the most relevant features. These properties enhance generalizability to unseen test data and while avoiding overfitting. The full pipeline is illustrated in Fig. 1. A separate predictor is trained for E_g, μ_h, and μ_e. Materials are screened for $E_{hull} < 0.05$ eV/atom and $E_g > 0.2$ eV to a set of 6943 predicted stable semiconductors (60%/20%/20% training/cross-validation/test split). Then, two classifiers are trained to predict for $\mu_e > 50$ cm^2/(Vs) and $\mu_h > 10$ cm^2/(Vs). Thresholds are determined by median values of the training dataset.

Results and Analysis

The regression model for E_g uses 70 input features selected by GBFS, feature engineering and RFE, performing with a mean absolute error (MAE) of 0.536 eV. The RFE curve, feature relevance plot, regression plot, and residuals plot for the E_g predictor are shown in Fig. 2. The classifier for μ_e uses 59 input features and performs with an F_1-score of 0.798. The classifier for μ_h uses 47 input features and performs with an F_1-score of 0.809. RFE curves, feature relevance plots, receiver-operator characteristics (ROC), and confusion matrices for μ_e and μ_h prediction are shown in Fig. 3 and 4, respectively. The μ_e and μ_h predictors perform well on the test set of given the relatively small training/cross-validation set of 5554 materials.

Conclusions

We demonstrate lightweight carrier transport property predictors leveraging GBFS, feature engineering, and RFE to improve model interpretability and generalizability. The surrogate models predict E_g with MAE of 0.536 eV, with high μ_e and μ_h classification achieving F_1-score of 0.798 and 0.809, respectively. Carrier transport models form part of inverted pyramid materials screening. Further accuracy improvements can be made by inclusion of structural feature descriptors at the expense of increased complexity.

References

[1] E. O. Pyzer-Knapp *et al.*, *npj Computational Materials*, vol. 8, (2022), doi: 10.1038/s41524-022-00765-z.
[2] L. Ward *et al.*, *Computational Materials Science*, vol. 152, (2018), doi: 10.1016/j.commatsci.2018.05.018.
[3] X. Li *et al.*, *Computational Materials Science*, vol. 186, (2021), doi: 10.1016/j.commatsci.2020.110074.
[4] M. Yao *et al.*, *Sci Data*, vol. 8, no. 1, p. 236, (2021), doi: 10.1038/s41597-021-01022-6.
[5] S. G. Jung, G. Jung, and J. M. Cole, *J Chem Phys*, vol. 159, no. 19, (2023), doi: 10.1063/5.0171540.

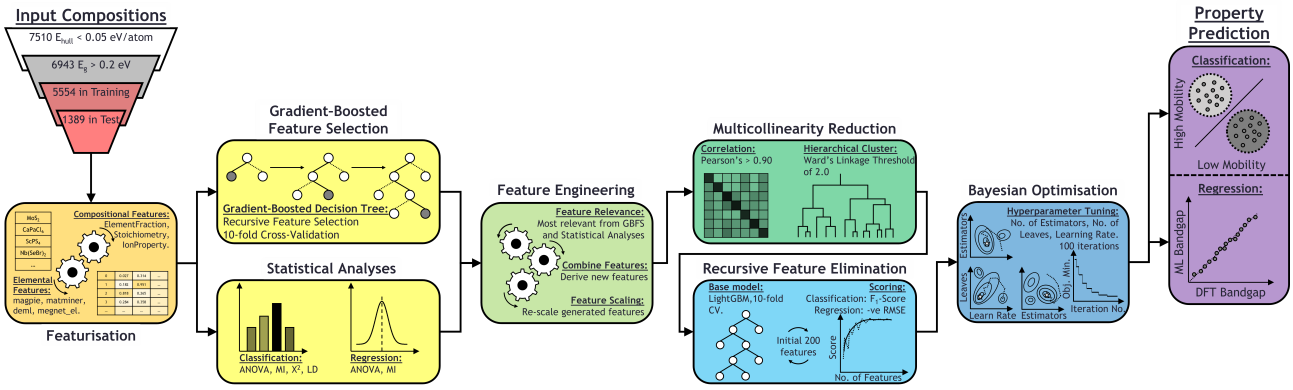

Figure 1. Overview of the gradient-boosted feature selection pipeline for constructing predictive models for carrier transport. The model can be tailored for classification or regression problems.

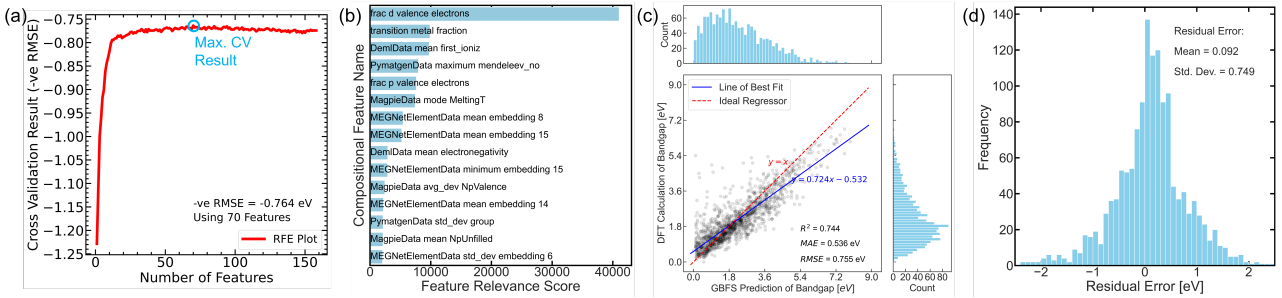

Figure 2. Evaluation of regression model for E_g trained on 5554 materials with 70 feature descriptors, **(a)** recursive feature elimination plot on cross-validation dataset, **(b)** top-15 feature relevance plot, **(c)** regression plot on unseen test dataset of 1389 materials (MAE = 0.536 eV), and **(d)** residuals plot.

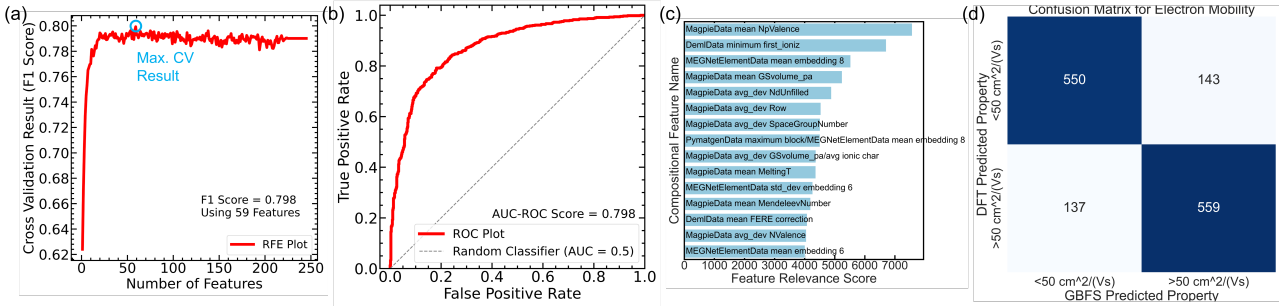

Figure 3. Evaluation of classification model for μ_e trained on 5554 materials with 59 feature descriptors, **(a)** recursive feature elimination plot on cross-validation dataset, **(b)** receiver-operator characteristic, **(c)** top-15 feature relevance plot, and **(d)** confusion matrix on unseen test dataset of 1389 materials (F_1-Score = 0.798).

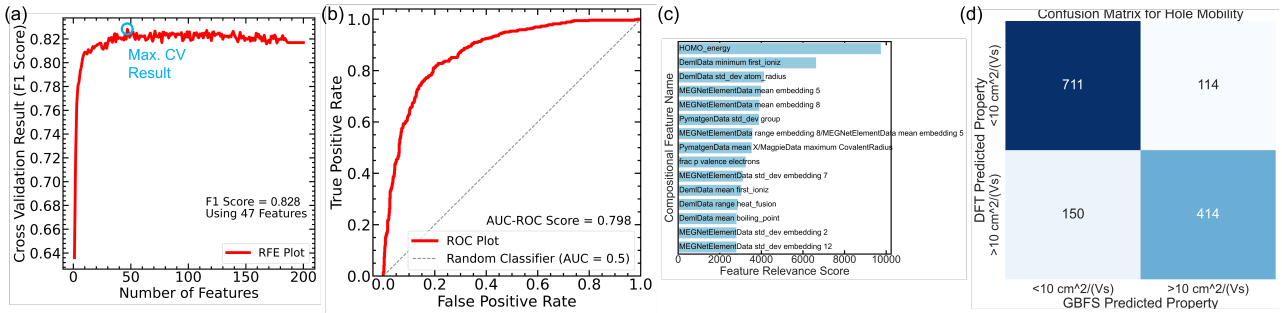

Figure 4. Evaluation of classification model for μ_h trained on 5554 materials with 47 feature descriptors, **(a)** recursive feature elimination plot on cross-validation dataset, **(b)** receiver-operator characteristic, **(c)** top-15 feature relevance plot, and **(d)** confusion matrix on unseen test dataset of 1389 materials (F_1-Score = 0.809).

Breaking the Resolution Barrier: Phased Exposure Methodology for Precision Microfluidic Injection Moulding Tools

Euan McDonald [a], Pedro Duarte Menezes [a], Hojjat Madadi [b], Xin Li [b], Alysha Hunter [a], Nikolaj Gadegaard [a]

[a] Biomedical Engineering, University of Glasgow, G12 8QQ, Scotland
[b] Sphere Bio LTD, Cambridge, CB21 6AL, United Kingdom

e-mail: nikolaj.gadegaard@glasgow.ac.uk

Masked Stereolithography (mSLA) 3D printing offers numerous advantages for microfluidic applications, including design flexibility and rapid prototyping capabilities suitable for injection moulding [1]. However, conventional mSLA approaches utilise uniform exposure calibration regardless of feature size and geometry, fundamentally limiting resolution and feature accuracy for high-precision microfluidics. With standard techniques, features below 100µm in the XY plane are particularly challenging to reproduce accurately, regardless of Z resolution capabilities. This work presents an optimised phased exposure methodology that significantly extends the capabilities of commercial mSLA systems to achieve previously unattainable feature sizes—down to 30µm—and accuracy without specialised equipment.

Our approach introduces three key innovations: feature-specific exposure control, component-wise exposure of intersecting features, and critical sequencing of exposure order. Building upon previous work demonstrating how spatially controlled exposure can enhance resolution in fully 3D printed microfluidics [2], we apply and extend these principles specifically for injection moulding tooling. Unlike conventional methods that expose entire layers uniformly, we selectively control exposure parameters for specific feature sizes and geometries. More importantly, we demonstrate that intersecting microfluidic features (such as droplet generator nozzles) can be decomposed into separate components and exposed sequentially for superior dimensional control. Critical features are prioritised in the exposure sequence, with smaller, geometry-sensitive features exposed first, followed by less critical larger features.

Experimental validation with 60µm droplet generator nozzles demonstrated that phased exposure produced channels with mean height of 62.2µm (±0.258µm) and width of 66.9µm (±10µm), compared to non-optimised approaches yielding 43.2µm (±1.2µm) height and 97.0µm (±12.7µm) width. Microscopy confirmed elimination of rounded corners at channel intersections, achieving sharp junctions critical for consistent droplet generation. The resulting injection moulding tools enabled same-day production of fully functional high accuracy microfluidic devices in commercial thermoplastics (PS and COC). From initial design to testable device, the entire process requires just over 3.5 hours—1 hour for design and exposure planning, 2 hours for mould fabrication, 1 minute cycle for injection moulding, and 30 minutes for assembly and bonding. This represents a paradigm shift compared to traditional injection moulding tooling, which typically requires weeks to months of lead time at costs orders of magnitude higher.

This methodology seamlessly integrates into an end-to-end manufacturing workflow for microfluidic devices, supporting production of up to 500 devices per mould. Current limitations include the need for material-specific calibration and manual exposure editing, presenting opportunities for future automation and further miniaturisation beyond the current 30µm feature size achievement.

[1] Menezes, P.D., Hunter, A., Dickson, T., Hecht, S., Kumar, C., Busek, M., Krauss, S. and Gadegaard, N., 2024. Scalable, Transparent, and Micro: 3D-Printed Rapid Tooling for Injection Molded Microfluidics. Advanced Engineering Materials, 26(20), p.2400276.
[2] Sanchez Noriega, J.L., Chartrand, N.A., Valdoz, J.C., Cribbs, C.G., Jacobs, D.A., Poulson, D., Viglione, M.S., Woolley, A.T., Van Ry, P.M., Christensen, K.A. and Nordin, G.P., 2021. Spatially and optically tailored 3D printing for highly miniaturized and integrated microfluidics. Nature communications, 12(1), p.5509.

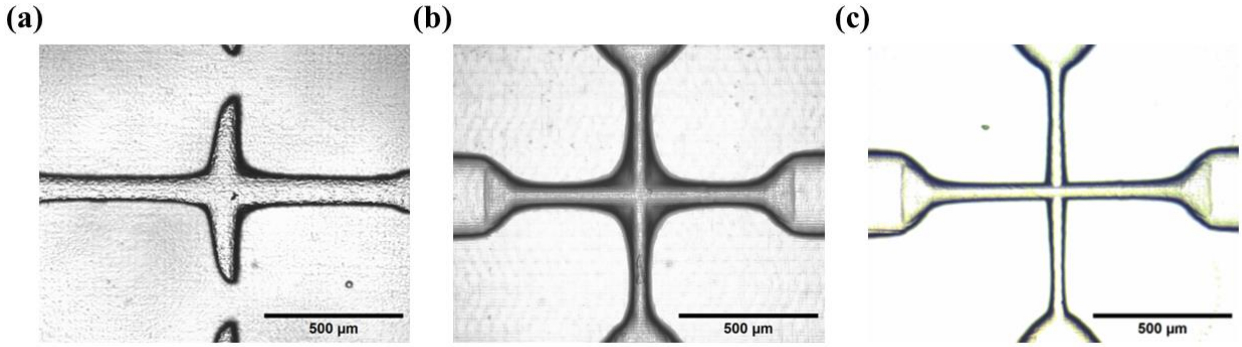

Figure 1. Comparison of exposure strategies for 3D printed 60µm droplet generator nozzles: (a) Conventional single exposure, (b) Two-stage phased exposure, (c) Three-stage phased exposure

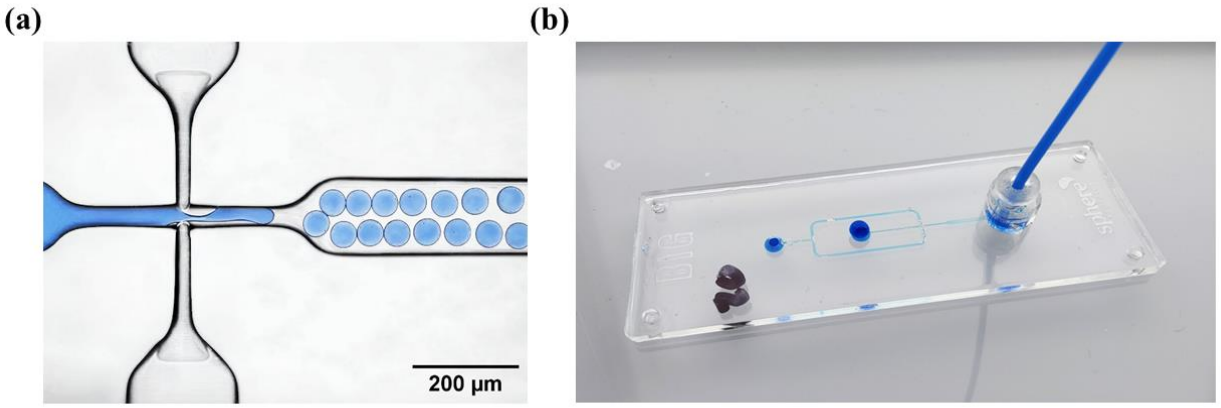

Figure 2. Droplet Generator in PS. (a) Droplet generation in a 30x40x40µm nozzle device. (b) assembled and bonded PS device featuring bespoke fluid connector integration.

Ultra-precision diamond micro-grinding of integrated mirrors in silicon for quantum atomic technologies

Paul C. Gow, Joel M.N. Keen, Glenn M. Churchill, Corin B.E. Gawith, James C. Gates

Optoelectronics Research Centre, University of Southampton, Southampton, SO17 1BJ, UK
e-mail: p.gow@soton.ac.uk

Components for quantum technologies (QT) often leverage fabrication techniques from the sophisticated field of semiconductor processing, including near-perfect substrate wafers, cleanroom infrastructure, and nanometer-scale lithography and deposition. However, many components such as atom/ion traps used in quantum clocks and sensing, superconducting devices, and nonlinear optical components frequently require 3-dimensional structures with a complex combination of centimetre-length scales, sub-micron precision, and nanometre roughness that is difficult to achieve with standard semiconductor tools. These applications require the development of novel, scalable manufacturing techniques to become commercially viable.

The main body of a microfabricated atom trap or vapor cell is typically fabricated in silicon or glass. Etching is suitable for thinner substrates, with materials >2mm thick requiring alternative techniques such as waterjet cutting [1] or multilayer stacked fabrication [2]. With fabrication moving to thicker substrates, there is also interest in improving optical access to the trap. One method is by using a transparent substrate to couple through the sides of the cell, requiring optical quality internal sidewalls, which can be achieved through moulding [3]. Alternatively, the addition of mirrors within the cell can aid optical coupling, though the angles of these are limited to crystal planes when etching [4].

Over the last 10 years, our team has demonstrated optical quality machining in various substrate materials, including milling of high-purity silica glass [5], manufacture of ridge waveguides in lithium niobate with 0.29nm surface roughness [6], and machining optical quality facets and waveguides in a layered silicon nitride composite [7]. This work applies a state-of-the-art ultra-precision micro milling system with nanometre precision (Loxham Precision Ltd. µ6 micro turn/mill machine, Fig. 1c) towards producing components for the QT industry. Using diamond grain micro grinding tools (Fig. 1a) and carefully controlled machining parameters, it is possible to machine thick, brittle materials such as silicon in a rapid and scalable way, whilst achieving nanometre surface roughness through ductile material removal [8]. This method surpasses what is achievable by techniques such as deep reactive ion etching, is not limited to producing features along crystal planes, and does not require a cleanroom.

We will present our work on the fabrication of vacuum cell and atom trap components in up to 6mm thick silicon wafers, with low surface chipping suitable for anodic bonding (Fig.1b), as well as apertures for optical interaction, and vias for transport of atomic species. We will also present ductile machining of silicon to produce optical-grade mirrors internal to the atom trap frames, allowing for in/out-coupling of light for interaction with trapped atom clouds (Fig.2). Machining is not restricted to crystal planes like etching; therefore, mirrored geometries can be produced at any angle. We will also show how this wafer-based machining technique is complementary to cleanroom processing, as well as its suitability for both rapid prototyping and scaling towards volume production.

[1] S. Dyer, et. al., *J. Appl. Phys.* **132** (13), 2022.
[2] Y.Pétremand, et. al., *JMM*, **22** (2), 2012.
[3] Yu, Mingzhi, et. al., *Engineering*, **35**, 2024.
[4] Han, Runqi, et. al., *Micromachines*, **9** (4), 2018.
[5] L.G. Carpenter, PhD Thesis, University of Southampton, 2013.
[6] L.G. Carpenter et al., *Elec. Lett.* **53** (25), 2017.
[7] P.C. Gow et al., *Elec. Lett.* **60** (5), 2024.
[8] T.G. Bifano, et.al., *Advances in fabrication and metrology for optics and large optics*, **966**, 1989.

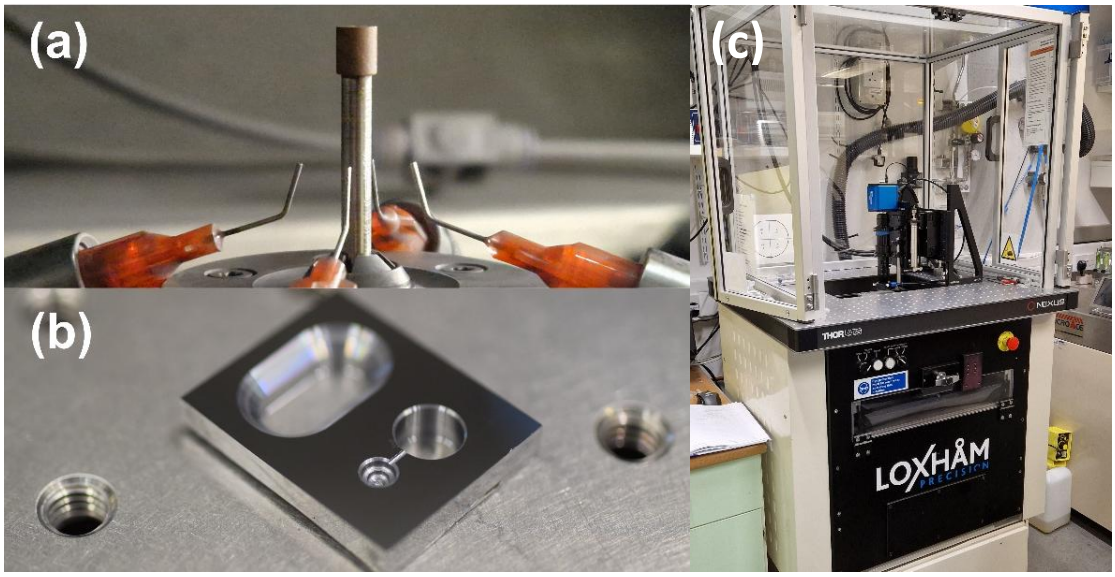

Figure 1. (a) shows a 4mm diameter diamond tool mounted in the air bearing spindle of the Loxham system. (b) shows an example of an atomic vapour cell design in silicon, featuring tapered sidewalls for optical access, main aperture, recess for material source, and a 500-micron channel. (c) shows an image of the Loxham Precision Ltd. µ6 micro turn/mill machine

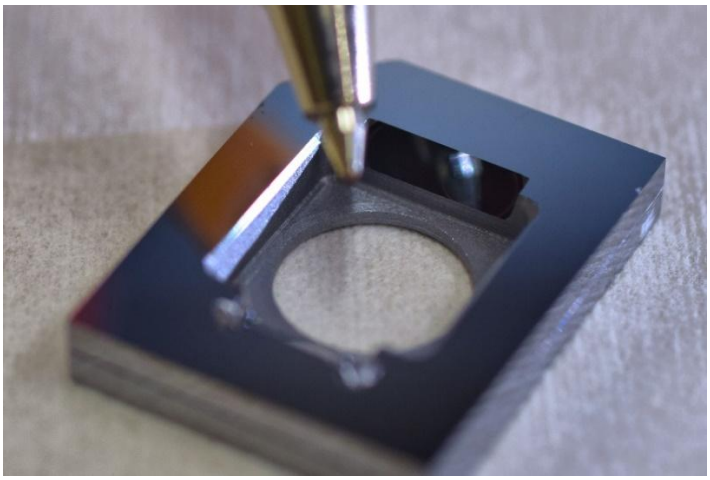

Figure 2. A 4 mm-thick machined silicon atom trap cell. The cell comprises a 15x15mm chamber and a through hole for optical access. Shown is the reflection from mirrors machined at an angle of 45 degrees into the silicon to allow light coupling into the cell for atomic interactions.

Magnetic artificial cilia to steer the locomotion of microswimmers

Zhiwei Cui [a], Kushal Swamy [a], Jaap den Toonder [b], Farbod Alijani [a]

[a] Mechanical Engineering, Delft University of technology, Delft, 2628CD, The Netherlands
[b] Mechanical Engineering, Eindhoven University of technology, Eindhoven, 5612AZ, The Netherlands
e-mail: z.cui-1@tudelft.nl

Abstract

Magnetic artificial cilia (MAC) are flexible, hair-like microactuators inspired by the function of biological cilia [1]. Under the influence of an external magnetic field, MAC exhibit controlled motion and have been utilized in various applications, including flow generation, particle transportation, and self-cleaning surfaces [2]. In this study, we integrate MAC within microfabricated cavities to investigate their effect on the dynamics of microswimmers. When actuated, the MAC generate an external harmonic force inside the cavities, which alters the behavior of the microswimmers. These findings contribute to the understanding of microscale actuation mechanisms and the development of active microenvironments for biomedical microrobotics.

Experiment method

To achieve this objective, we fabricated microscale cavities of varying dimensions, each embedded with a centrally positioned magnetic artificial cilium. When actuated by an external magnetic field, the cilia follows a conical path whose amplitude can be controlled. This in turn leads to dynamic modulation of local fluid flow patterns and generates hydrodynamic forces in confined environments. The cavity design parameters are illustrated in Figure 1.
The fabrication method involves a micro molding process as illustrated in Figure 2. In particular, we fabricate the mold from a fused silica glass slide by Femtosecond laser machining. The properties of the glass are changed locally during exposure to a scanning focused femtosecond laser beam, so that the etching rate in KOH is enhanced; hence, after exposure, the written features are removed in a KOH ultrasonic bath at 85 °C. We treat the surface of the obtained glass molds with silane before using them such that the designed pattern can be easily peeled off the mold. A uniform magnetic precursor mixture of polydimethylsiloxane (PDMS, Sylgard 184, Dow Corning, base to curing agent weight ratio is 10: 1) and magnetic microparticles is then casted onto the mold, followed by a degassing procedure. Excess magnetic composite outside the patterned area is removed, and a layer of pure PDMS is poured over the mold. After further degassing, spin coating is used to achieve a final PDMS layer thickness of approximately 75 μm. The sample is then cured in an oven at 80 °C for 3 hours. Upon completion, the patterned magnetic microstructures are carefully peeled from the mold. We use a homemade actuation setup to drive the central cilia within the fabricated cavities. The setup is comprised of a motor and a permanent magnet mounted off-axis of the motor. The samples are positioned above the central plane. The rotary motion of the cilia can be precisely controlled. The The swimming behavior of the microswimmers within the designed patterns is then observed using a Leica biomicroscope.

Preliminary results

The fabricated devices are biocompatible with bacteria, allowing bacterial cells to be employed as microswimmers in our experiments as shown in Figure 3. By analyzing their swimming behavior, we identify and select cavity dimensions that are best suited to support effective microswimmer dynamics control.

References

[1] Zhang, S., Wang, Y., Lavrijsen, R., Onck, P. R., & den Toonder, J. M. J. Versatile microfluidic flow generated by moulded magnetic artificial cilia. Sensors and Actuators B: Chemical, 2018, 263, 614–624.
[2] Z. Cui,Y. Wang,S. Zhang,T. Wang,& J.M.J. den Toonder, Miniaturized metachronal magnetic artificial cilia, Proc. Natl. Acad. Sci. U.S.A. 2023, 120 (35) e2304519120,

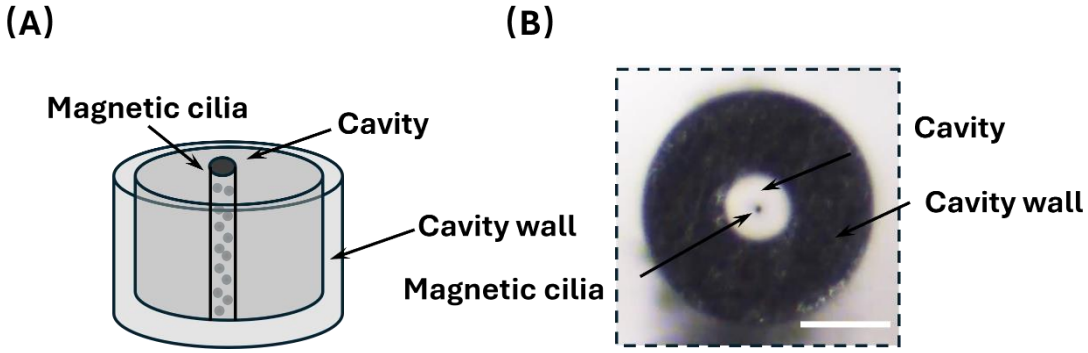

Figure 1. (A) Schematic of the designed pattern. (B) Fabricated pattern from top view. The central white part is the space of the cavity. And the ring shape black part is the thickness of the cavity wall. The black dot at the center is the magnetic artificial cilia. The scale bar is 50 μm.

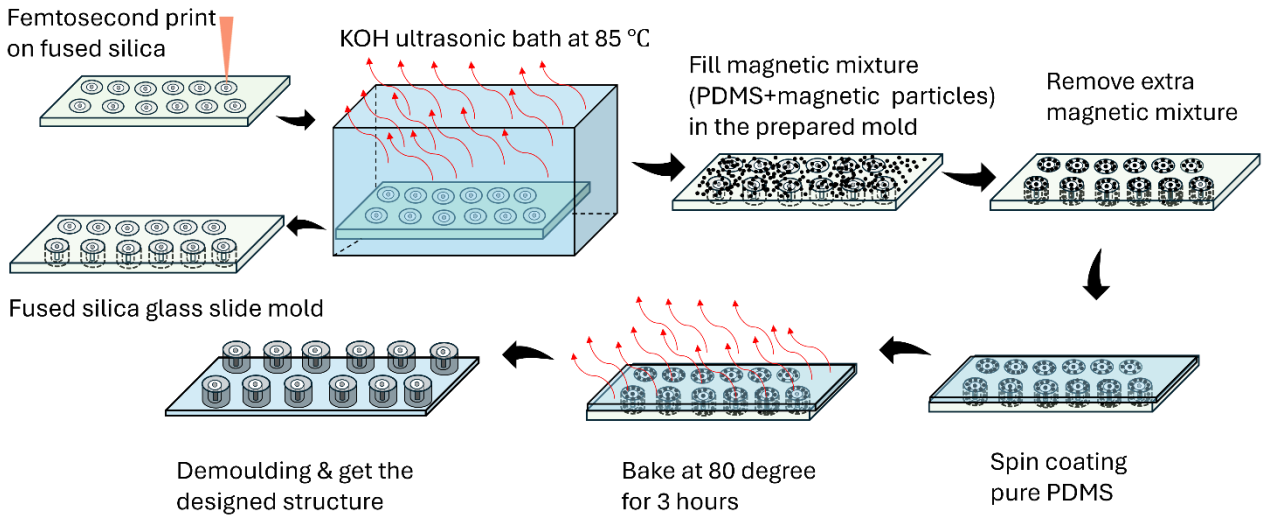

Figure 2. The fabrication process of the designed pattern. The mold is fabricated by the femtosecond laser writing and the designed pattern is made by the micromolding.

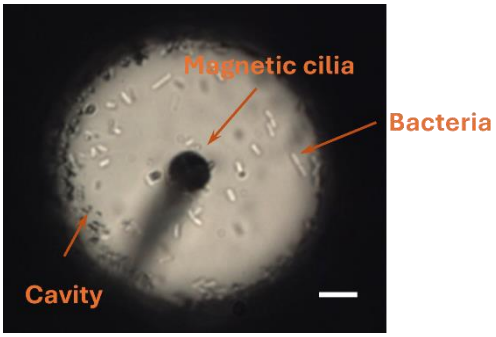

Figure 3. The bacteria as microswimmers moving inside the designed cavity. The scale bar is 10 μm.

Oral Session 4C: Electronics II

Mesoporous silica-based memristor for neuromorphic computing

Bohao Ding [a], Tongjun Zhang [a], Li Shao [b], Ayoub H. Jaafa [a], Andrew Hector [b], and Ruomeng Huang[1*]

[a] School of Electronics and Computer Science, University of Southampton, Southampton, SO17 1BJ, United Kingdom
[b] School of Chemistry, University of Southampton, Southampton, SO17 1BJ, United Kingdom
e-mail: R.Huang@soton.ac.uk

Neuromorphic computing has emerged as a novel branch of computing inspired by structural and functional paradigms of neurons and synapses in the human brains through specialized hardware and software [1]. This approach seeks to overcome the bottleneck of conventional Von Neumann architectures, which separate CPUs and memory units, thereby enhancing energy efficiency in computational processes. This is particularly beneficial for data-intensive applications such as machine learning and neural networks [2]. Within this domain, memristors—specifically diffusive memristors—have gained significant attention due to their ability to emulate the rich and complex dynamics of both short- and long-term synaptic plasticity [3]. Mesoporous materials, notable for their fast electron transport and high surface-to-volume ratios, provide superior properties as active layers in memristors. The introduction of porous structure into the electrolyte layer also enables precise ion dynamics regulation through controlled pore geometry, facilitating the nano/atomic-scale control essential for diffusive memristors.

In our study, we developed a diffusive memristor on 3D-structured mesoporous silica ($mSiO_2$) using a vacuum-free, cost-effective, and rapid sol–gel processing method (Figure 1a-1b) [4]. This device exhibits both volatile and non-volatile resistive switching behaviors, adjustable through the applied compliance current (CC), as shown in Figures 1b and 1c. The fast mobility and diffusivity of Ag^+ ion species migrating within the porous structures enable the demonstration of the short-term memory behaviour (Figure 2a). In addition, such temporal dynamics can also be controlled via the engineering of mesoporous film porosities [5], as well as the pore orientation and selection of active electrodes. For example, as porosity increases, discernible changes in postsynaptic current (PSC), facilitation ratios, and relaxation times are observed (Figure 2b-2c), which can be ascribed to the modulation of hydrogen-bonded networks within the porous structure of the silica layer which significantly influences both anodic oxidation and ion migration processes during switching events (Figure 2d).

To further advance neuromorphic computing, we fabricated devices with crossbar structures as detailed in Figures 3a to 3j, designing various crossbar sizes for performance comparison (Figure 3k). A reservoir computing system utilizing this $mSiO_2$ diffusive memristor achieved high accuracy in classification tasks, showcasing the potential of our approach in implementing scalable and efficient neuromorphic systems. Our findings underscore the viability of mesoporous silica-based memristors in advancing neuromorphic computing, offering a promising avenue for future research and development of energy-efficient, data-centric computational architectures.

[1] D. Ham et al., Nature electronics, 4.9 (2021): 635-644.
[2] D. Ielmini and H.-S. P. Wong, Nature electronics, 1.6 (2018): 333-343.
[3] Y. Ushakov et al., Chaos, Solitons & Fractals, 149 (2021): 110997.
[4] A. H. Jaafar et al., Nanoscale, 14.46 (2022): 17170-17181.
[5] T. Zhang et al., ACS Applied Materials & Interfaces, 16.13 (2024): 16641-16652.

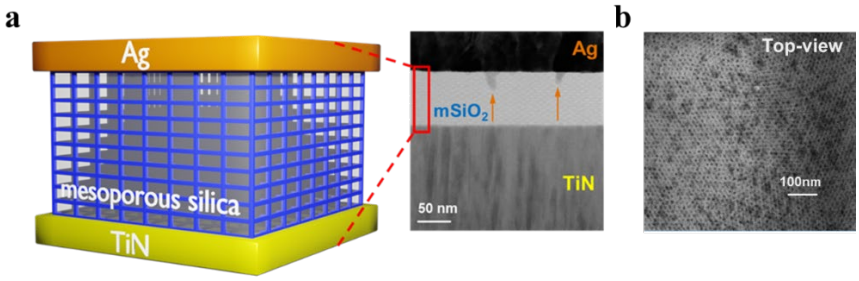

Figure 1. (a) Schematic and the cross-sectional TEM image of the $mSiO_2$ based memristor [4]. (b) The top view SEM image of the $mSiO_2$ film.

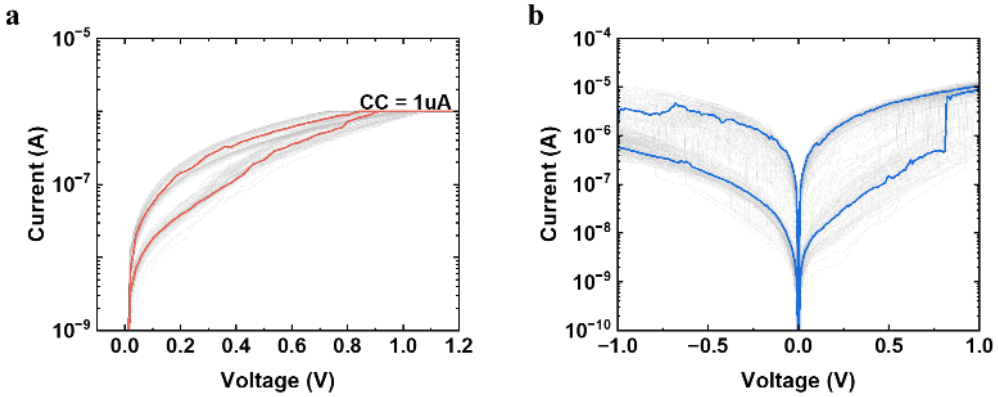

Figure 2. Consecutive volatile (b) and non-volatile (c) switching I–V characteristics of the $mSiO_2$ memristor.

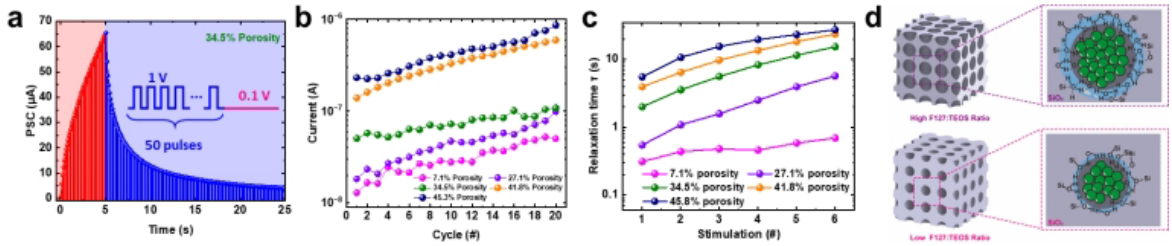

Figure 2. (a) PSC potentiation and subsequent decay showing STP behavior. Control of (b) PSC and (c) relaxation time with different film porosities. (d) Illustration of an internal atom dynamics of devices with different porosities [5].

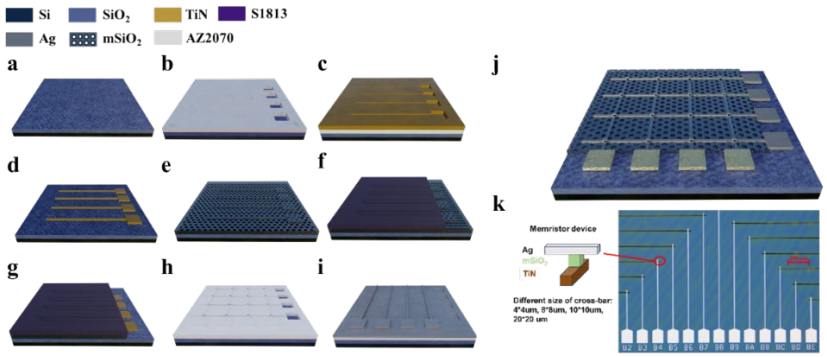

Figure 3. The fabrication process of crossbar structure memristors based on mesoporous silica: (a) Initial wafer with 100nm SiO_2 on Si. (b) The 1st lithography. (c) The deposition of TiN. (d) Lift-off. (e) The deposition of mesoporous silica. (f) The 2nd lithography. (g) RIE. (h) The 3rd lithography. (i) The deposition of silver. (j) Lift-off. (k) The optical Nomar ski micrograph of crossbar structured memristors

Novel Reagents for the Solution-processible Deposition of Low-dimensional Materials and their Composites for Flexible Memristors and Smart Sensors

Trishala R. Desai[1] and Chitra Gurnani[1]
[1]Department of Chemistry, Ecole Centrale School of Engineering, Mahindra University, Hyderabad-500043, India
Email: chitra.gurnani@mahindrauniversity.edu.in

Abstract
Soft, flexible electronics with robust multifunctionality and bending stability are garnering significant interest for applications in e-skin, smart bionic sensors, and human-machine interfaces.[1] The increasing demand for wearable healthcare devices necessitates the cost-effective, wireless, and portable physiological monitoring systems.[2] Among 2D materials, MXenes and transition-metal dichalcogenides (TMDs) stand out due to their exceptional electrical, mechanical, and optoelectronic properties. However, traditional fabrication techniques, such as chemical vapor deposition (CVD) are energy-intensive, costly, and incompatible with flexible substrates.
To address these limitations, novel reagents have been developed to enable the solution-processable synthesis and deposition of low-dimensional materials. These reagents are designed to allow the growth at lower temperatures, compatible with the thermal budget of flexible substrates such as PET and polyimides. Two key approaches are explored: (1) Cellulose-MXene composite hydrogels (CMCH) as multifunctional materials for memory storage, artificial synapses, and wearable sensors. The cellulose-MXene composite hydrogels (CMCH) combine renewable cellulose hydrogels with 2D MXene nanosheets (Figure 1), leveraging their exceptional electrical conductivity, mechanical flexibility, and biocompatibility. The as-fabricated device demonstrates reliable and reproducible bipolar resistive switching at low operating voltages (±0.5V to ±1V) with multilevel switching capabilities (Figure 2).[3] Synaptic functionalities such as spike time-dependent plasticity and potentiation/depression properties were observed, mimicking the Hebbian learning rule of biological synapses. In addition to memory applications, the CMCH exhibited multifunctionality as a biodegradable, wearable smart pressure sensor and piezoelectric nanogenerator, capable of detecting human gestures and breath patterns, paving the way for self-powered, flexible devices.
(2) Nickel disulfide (NiS_2) nanostructures as a bifunctional platform for memory and breath monitoring applications (Figure 3). Using in-situ deposition method via a pre-designed single-source molecular precursor, NiS_2-based memristors demonstrate stable bipolar resistive switching, excellent data retention (10^4 s), and low power switching under both flat and bending conditions, making it suitable for neuromorphic computing.[4] Furthermore, the NiS_2-based breath sensor demonstrated ultra-fast response and recovery times, high sensitivity, and durability over 1000 cycles. It enables real-time, smartphone-integrated monitoring, emphasizing its practicality for IoT and healthcare applications.[5] By integrating innovative material designs with solution-processable fabrication methods, this work establishes a new paradigm for cost-effective, scalable, and multifunctional wearable electronics. These breakthroughs bridge advanced nanomaterials with practical IoT and healthcare applications, paving the way for the next generation of flexible and sustainable electronic systems.

References:

1. G. Yuan et al., ACS Appl Electron Mater. 5(2023) 4451–4461.
2. X. Hu et al., Coord Chem Rev. 499 (2024) 215504.
3. T. Desai et al., ACS Appl. Bio Mater. 6 (2023) 1763–1773.
4. T. Desai et al., ACS Omega 8 (2023) 48873–48883.
5. T. Desai et al., Philos Trans R Soc A. 382 (2024) 2281.

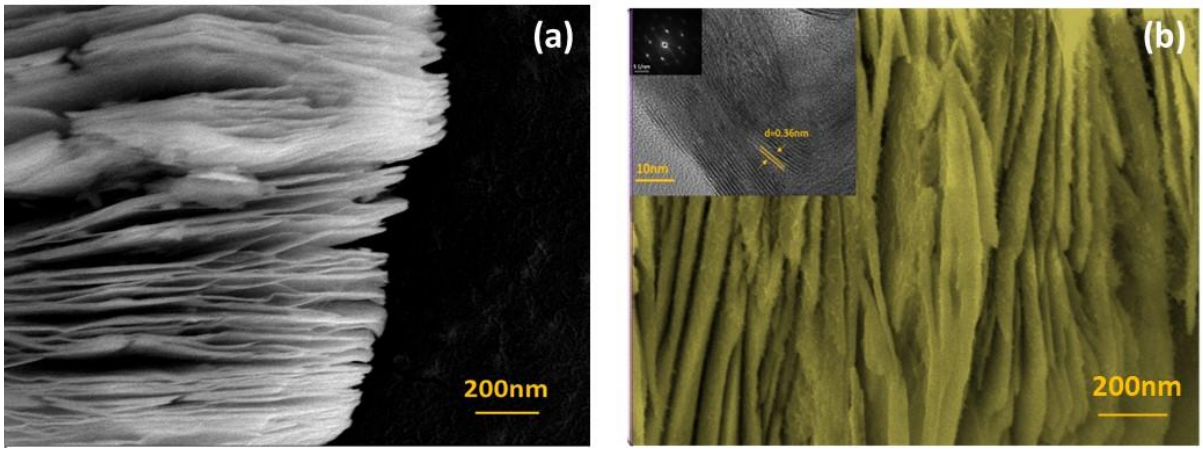

Figure 1. SEM images of synthesized (a) MXene nanosheets and (b) Cellulose-MXene composite hydrogels (CMCH).

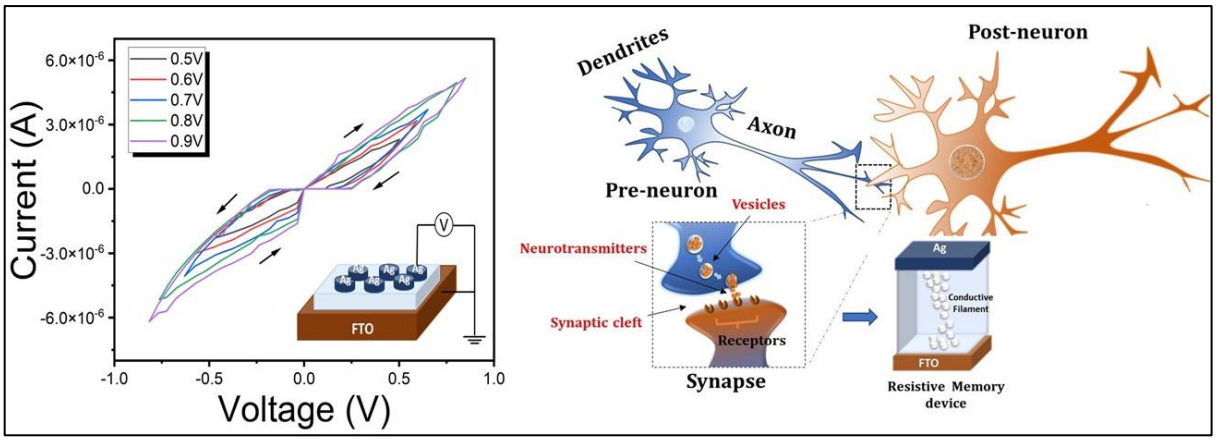

Figure 2. Multilevel resistive switching and synaptic learning functionalities of CMCH memristive device.

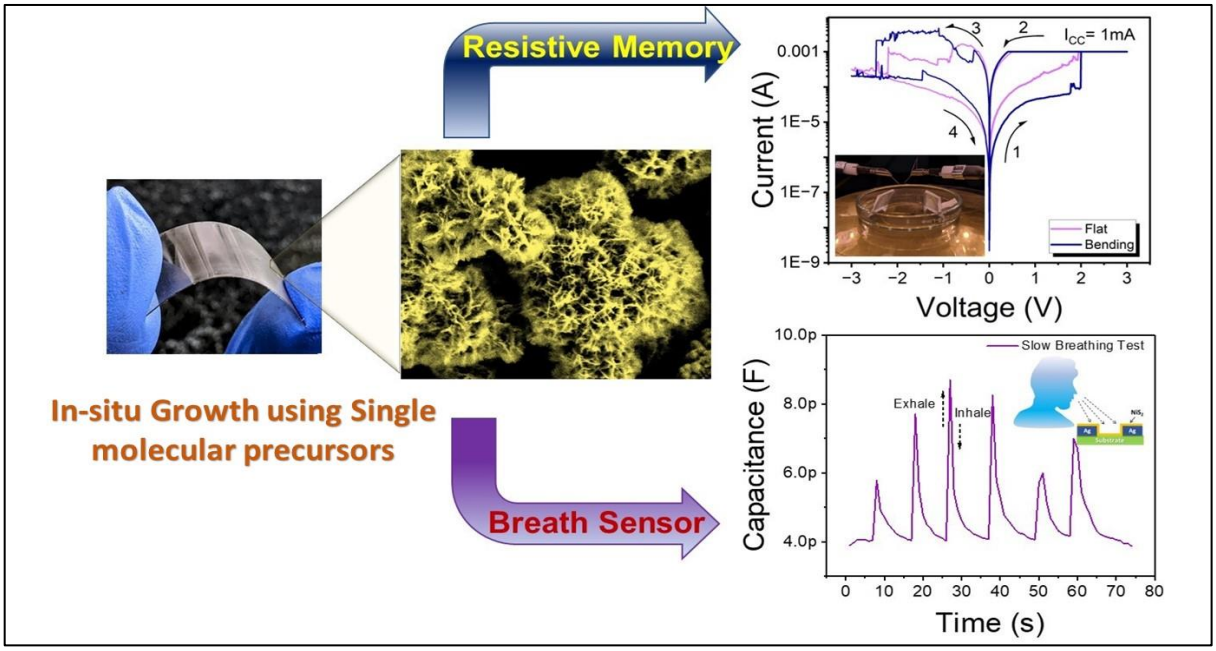

Figure 3. Designed single molecular precursors (SSP) for the direct growth of bifunctional nickel disulfide on flexible PET for resistive switching memristors and human respiration monitoring.

Non-planar patterning of an Organic Electrochemical Transistor (OECT) on a tapered optical fiber-based neural interface

Sneha Pottekkad[a,b*], Stella Aslanoglou[a], Barbara Spagnolo[a], Antonio Qualtieri[a], Claudia Latte Bovio[a], Michele Di Lauro[c] , Federico Rondelli[c,d], Fabio Biscarini[c,e], Massimo De Vittorio[a,b,f,†], Ferruccio Pisanello[a,†]

[a] Istituto Italiano di Tecnologia, Center for Biomolecular Nanotechnologies, 73010 Arnesano, Italy
[b]Dip. di Ingegneria dell'Innovazione, Università del Salento, 73100 Lecce, Italy
[c]Istituto Italiano di Tecnologia, Center for Translational Neurophysiology, 44121 Ferrara, Italy
[d]Sezione di Fisiologia, Dip. di Neuroscienze e Riabilitazione, Università di Ferrara, 44121 Ferrara, Italy
[e]Dip. di Scienze della Vita, Università di Modena e Reggio Emilia, 41125 Modena, Italy
[f]IDUN section, Dept. of Health Technology, Technical University of Denmark, Lyngby, Denmark
[†] These authors jointly supervised the presented work.
[*]Corresponding author. E-mail: sneha.pottekkad@iit.it

Abstract

The use of multifunctional neural interfaces for sensing and actuating neural activity in the living mouse brain is driving the development of a wide range of innovative experimental paradigms for neuroscientists. This progress is made possible by the integration of multiple functionalities into minimally invasive neural implants, capable of probing deep brain regions with high temporal and spatial resolution [1]. A widely used stimulation technique involves visible light radiation to induce action potentials in genetically modified neurons that express light-sensitive ion channels, leveraging optogenetics to activate specific neuronal populations [2]. Depth-resolved light delivery is achieved through implantable optical devices such as micro light-emitting diode (µLED) arrays [3], semiconductor waveguides [4], and tapered optical fibers (TFs) [5]. Neural activity readout is usually conducted using extracellular recording electrodes, which measure electrical signals via capacitive coupling [6]. However, neuronal function is not only governed by electrical signals. Neurochemical signals including neurotransmitters, ions and reactive oxygen species also play a significant role in physiological and pathological processes in the living brain, fact that renders their sensing equally important [7]. In this context, the perspective of adding the capability of electrochemical detection onto an optical neural interface would allow for a better understanding of the multifaceted nature of neural signaling and related functions deep in the brain. Active devices, such as Organic Electrochemical Transistors (OECTs), have emerged as a promising tool for neurochemical sensing due to their high sensitivity, amplification capability and high signal-to-noise ratio (SNR) [8]. However, OECTs are typically fabricated on planar substrates [9].
In this work, we demonstrate, for the first time, a strategy for the integration of an OECT on the highly non-planar surface of a TF-based neural interface for simultaneous performance of optogenetic stimulation and neurochemical sensing. To this aim, we employed two-photon lithography (TPL) – exploiting its high versatility and high spatial resolution – enabling precise fabrication of custom, non-planar metallic and/or dielectric patterns [10]. Therefore, using an original TPL approach [11], source and drain electrodes with respective tracks and connection pads were realized as a protective resist mask onto a metallized (Cr/Au) TF, which was then subjected to metal lift-off and wet etching for resist removal (**Figure 1.a**). Following the deposition of protective Pt pads on the Au electrodes *via* focused ion beam (FIB) (**Figure 1.b**), devices were encapsulated with a conformal film of Parylene-C *via* chemical vapour deposition. Next, a recess on the electrodes and channel between was performed (**Figure 1.c**) to allow for the subsequent potentiostatic electrodeposition of PEDOT:PSS. The applied charge required for successful electrodeposition was calculated with respect to the active area of the device, and as a result PEDOT:PSS grew outwards from the electrodes and subsequently bridged the channel (**Figure 1.d**). After discussing the challenges encountered during OECT integration and the approaches we took to overcome them, we present the electrical characterization of our devices. Electrical characterization was performed in a common source - common ground configuration using an external gate electrode. Our preliminary OECT device on a TF exhibited a transconductance of 300 nS (**Figure 2**), validating its functionality. The versatility of TPL patterning approach allows for further enhancement of the performance of the OECT device *via* tuning of the geometrical characteristics of the channel (W/L), thereby advancing the development of implantable multifunctional optoelectronic neural interfaces.

References

[1] C. Sung, et al., Journal of Materials Chemistry B 8.31 (2020): 6624-6666.
[2] V. Emiliani, et al., Nature Reviews Methods Primers 2.1 (2022): 55.
[3] M. Vöröslakos et al. Advanced Science (2022), 9.18: 2105414.
[4] A. Mohanty et al., Nature Biomedical Engineering (2020), 4.2: 223-231.
[5] B. Spagnolo, et al., Nature materials (2022), 21.7: 826-835.
[6] L. Guo, et al., *J. Neural Eng.* (2020),17, 013001.
[7] Y. Liu, et al., JACS Au (2023), 3.6: 1572-1582.
[8] K. Tang, *et al.*, *ACS Appl. Polym. Mater.* (2022),4, 2337–2345.
[9] K. Xie, et al., Elife (2020), 9: e50345.
[10] A. Balena, et al., Advanced Functional Materials (2023) 33.39: 2211773.
[11] A. Balena, *et al.*, *Nat Protoc* (2025) doi:10.1038/s41596-024-01105-9.

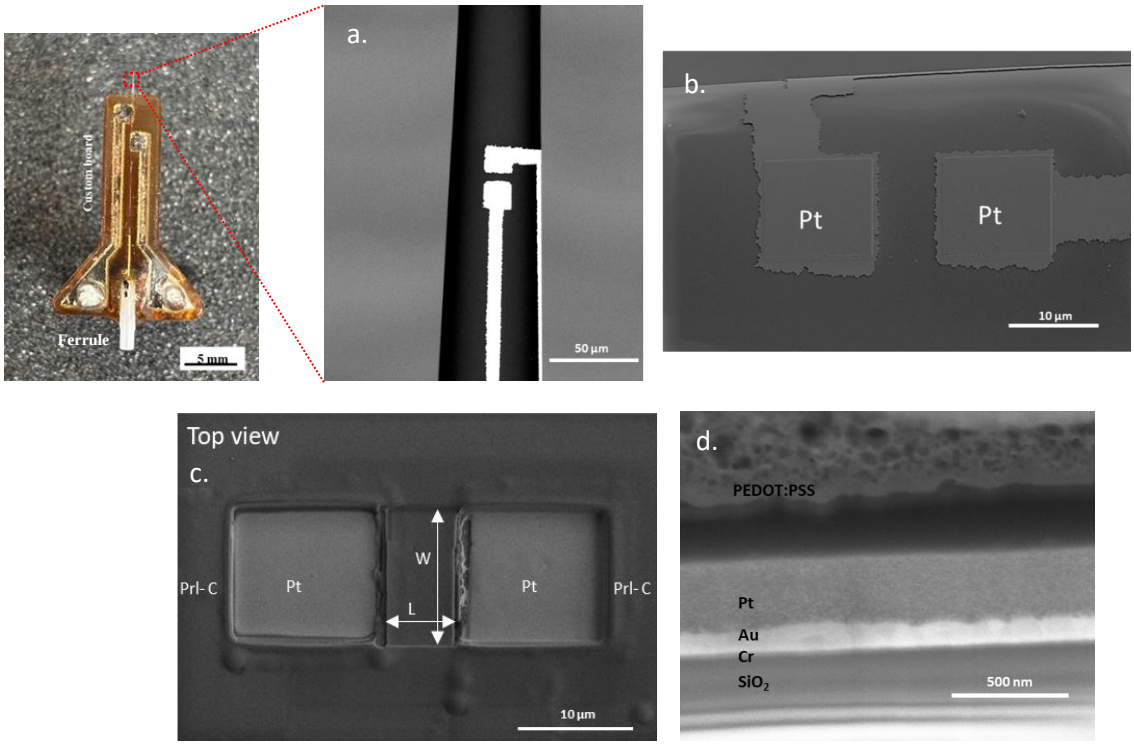

Figure 1. (a) SEM image of TPL realized Au electrodes and tracks on a TF connectorized on a customized PCB. (b) Pt deposition on top of Au electrodes (c) Selective milling of Parylene-C on top of the electrodes and channel (d) Cross sectional image of OECT with porous PEDOT:PSS grown on top of the electrodes.

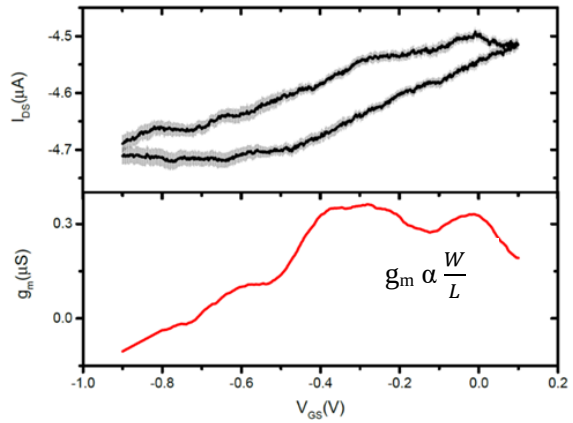

Figure 2. Transfer characteristics and transconductance curve of the OECT on TF.

Towards Additive Manufacturing and Conformal Metallization of 3D-Printed Antennas for Radar Applications

Michael J. Haslinger [a], Vaclav Prochazka [a], P. Bauer [b], D. Holzinger [b], Jean Temga [c], Saeid Karamzadeh [c]

[a] PROFACTOR GmbH, Im Stadtgut D1, 4407 Steyr-Gleink, Austria

[b] TIGER Coatings GmbH & Co KG, Wels, 4600, Austria

[c] Millimeter Wave Technologies, Intelligent Wireless System, Silicon Austria Labs (SAL), 4040 Linz, Austria.

e-mail: Michael.Haslinger@Profactor.at

Additive manufacturing offers transformative potential for radar component development, enabling rapid prototyping, complex geometries, and significant weight reduction—capabilities often unattainable with traditional subtractive techniques [1]. In particular, polymer-based stereolithography (SLA) enables the fabrication of volumetric waveguide and antenna structures, which, when combined with subsequent metallization [2], facilitate enhanced electromagnetic confinement, tailored radiation patterns, and seamless integration into compact platforms. These features are increasingly critical for modern radar applications—from automotive sensing to ground-penetrating and stationary systems—where performance, miniaturization, and design flexibility are key [3].

In this work, we present the design and fabrication of polymeric waveguide and antenna components, including a WR12 air-filled waveguide Butler matrix, using SLA-based 3D printing. Post-processing metallization was carried out using dip coating, electroplating, and electroless plating with silver or copper to achieve continuous, conductive coatings necessary for efficient wave propagation. Key challenges remain, particularly in achieving uniform metal coatings within high-aspect-ratio channels and extending operational performance into the millimetre-wave regime.

We report advances in SLA-based additive manufacturing for radar applications, including novel metallization techniques and SLA resin formulations optimized for high-frequency performance. Comprehensive electromagnetic characterizations are presented and analyzed. Our results demonstrate that the integration of additive manufacturing with state-of-the-art metallization enables the rapid prototyping of volumetric radar components with performance comparable to conventionally manufactured systems

The authors acknowledge funding from the PrintedRadar project (FFG 901694), by the FFG and Upper Austria.

[1] Carvalho, Saúl S., et al. "Exploring design approaches for 3D printed antennas." *IEEE access* 12 (2024): 10718-10735.

[2] A. Jammes, E. des Gayets, K. Staelens, R. Feger, T. Lampersberger and A. Stelzer, "Silver metallization of 77 GHz 3D printed horn antennas," 12th European Conference on Antennas and Propagation (EuCAP 2018), London, UK, 2018

[3] Helena, Diogo, et al. "Antenna design using modern additive manufacturing technology: A review." IEEE Access 8 (2020): 177064-177083. (n.d.).

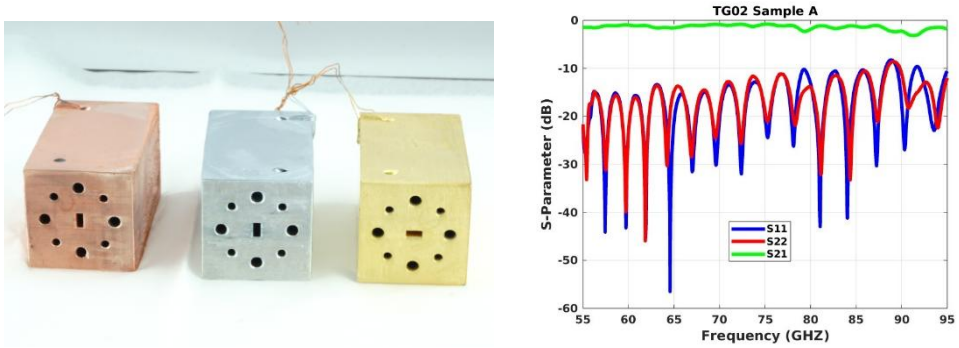

Figure 1. 3D printed waveguide elements with various electroplated metal coatings (left). Transmission measurement of one of the samples (right).

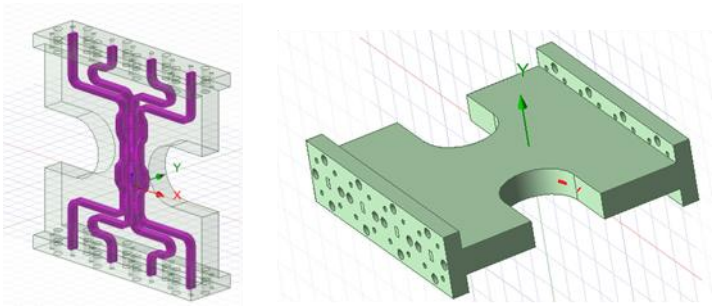

Figure 2. 3-D printable crossover-free WR12 butler matrix for a 1x4 beamforming antenna array

Additive manufacturing via stereolithography (SLA) enables rapid, lightweight fabrication of volumetric waveguides, antenna structures, and a WR12 Butler matrix. Post-print metallization—using dip coating, electroplating, and electroless plating with silver or copper—yields continuous conductive surfaces essential for wave propagation. We introduce SLA resins optimized for millimeter-wave operation and evaluate coating uniformity in high-aspect-ratio channels. High-frequency measurements demonstrate return losses, bandwidths, and radiation patterns. These results demonstrate that SLA combined with advanced metallization delivers rapid prototyping of volumetric waveguide antennas.

Adaptive Reservoir Computing with Electro-Optical and 3D Structured Memristor Hardware Platforms

Sungjun Kim
Division of Electronics and Electrical Engineering, Dongguk University, Seoul 04620, Republic of Korea
e-mail: sungjun@dongguk.edu

The reservoir computing (RC) is an emerging neuromorphic paradigm designed to efficiently process temporal and sequential data by projecting inputs into a high-dimensional dynamic state space using a nonlinear, fixed reservoir. Unlike traditional recurrent neural networks, RC simplifies training by decoupling memory and learning; only the readout layer is trained, significantly reducing computational cost. To implement RC at the hardware level, our research focuses on developing adaptive memory-based platforms with coexisting short-term and long-term memory capabilities. These platforms leverage various emerging memory technologies, including 2D planar resistive switching memories (RRAM), ferroelectric tunnel junctions (FTJs), and 3D vertically stacked RRAM and ferroelectric capacitor arrays.

Volatile memory elements exhibiting tunable short-term memory (STM) dynamics were implemented using oxygen-rich TiO_x layers and metastable defect configurations. These devices showed conductance decay characteristics modulated by the magnitude and duration of electrical or optical stimuli. We demonstrated their potential as nonlinear dynamic reservoirs capable of capturing complex temporal features. On the other hand, non-volatile memory arrays served as readout layers, where precision weight updates were achieved via an Incremental Step Pulse with Verify Algorithm (ISPVA), enabling up to 4-bit multilevel conductance states with high yield (>98%) across memristor arrays (e.g., 24×24 cells).

Moreover, we explored RGB-sensitive optical reservoir computing by integrating light-activated memristors with gold nanoparticles and ferroelectric switching layers. These devices enabled wavelength-dependent modulation of conductance and supported direct color image classification without pre-processing, achieving 97.99% accuracy on the Fruits-360 dataset and 96.37% on MNIST using simple MLP classifiers. Additionally, the monolithic integration of STM (TiN-BE) and LTM (W-BE) VRRAM cells within a unified 3D array offers a scalable architecture for full RC implementation.

Overall, our hardware platforms represent a holistic approach to physical reservoir computing, combining materials engineering, device design, and circuit integration. These systems are highly applicable to energy-efficient neuromorphic processors for edge computing, real-time biosignal analysis, and intelligent sensing systems. By tailoring volatility, optical sensitivity, and structural integration, we pave the way toward fully functional, hardware-implemented reservoir computing systems.

VO_2-based memristor grown by ALD for neuromorphic computing

Bingkai Ding,[a] Kai Sun[a,b], C. H. (Kees) de Groot,[a] and Ruomeng Huang[a]*

[a]School of Electronics and Computer Science, University of Southampton, Southampton, SO17 1BJ, United Kingdom
[b]School of Physics and Astronomy, University of Southampton, Southampton, SO17 1BJ, United Kingdom
e-mail: r.huang@soton.ac.uk

Artificial intelligence technologies are undergoing rapid advancements, leading to increased demands for improved information storage and faster computing. Inspired by the high efficiency of the human brain, neuromorphic computing, which mimics the interconnected neural network of biological systems, presents a promising solution for energy-efficient data processing [1]. Notably, the volatile and threshold-switching memristor possesses a unique combination of distinct physical mechanisms and high similarity to biological neurons and synapses, making it an excellent candidate for mimicking synaptic functions.

VO_2 with its electrically driven metal-insulator transition (MIT) near room temperature, is highly attractive for neuromorphic computing [2]. In this work, we successfully fabricated a vertical Pt/VO_2/Pt crossbar memristor (Fig.1). Optical microscopy and scanning electron microscopy (SEM) images of the device are presented in Fig. 2. The VO_2 layer was grown onto a patterned platinum electrode through atomic layer deposition (ALD) ALD enables precise atomic-level control of the film thickness, ensuring excellent uniformity and scalability. The VO_2 thin films were grown using tetrakis(ethylmethylamino) vanadium (TEMAV) as the precursor using our previous reported process [3], demonstrating cycle-by-cycle self-limiting atomic growth characteristics. Following deposition, an annealing process was conducted to crystallize the VO_2 layer, crucial for achieving optimal device performance.

Electrical characterisation demonstrates volatile threshold switching behavior, which effectively mimics neuronal activity, achieving an on/off ratio greater than two orders of magnitude and showing good reproducibility over 100 DC cycles (Fig. 3a,b). Moreover, the MIT can be triggered by external voltage pulses at a nanosecond scale at room temperature as shown in Figure 3c. The observed cumulative discharge triggered by voltage pulses simulating neuron signals suggests potential applications in Leaky Integrate-and-Fire (LIF) artificial neuron models.

The development of artificial neurons and synapses is crucial for advancing neuromorphic computing. These components are designed to emulate the intricate dynamics of critical neural and synaptic functions, such as the charge accumulation through cell membranes that trigger neuron firing. Our findings indicate that VO_2 memristors can be engineered to process spike signals in a manner that emulates both the facilitation and depression of synapses, mimicking biological neurons, thereby simulating the threshold-driven firing behavior of biological neurons.

[1] P. Schofield *et al*., Advanced Materials. 35.37 (2023): 2205294.
[2] Z. Zhao *et al*., Advanced Physics Research. 4.4 (2025): 2400129.
[3] K. Sun *et al*. Advanced Optical Materials. 10.23 (2022): 2201326.

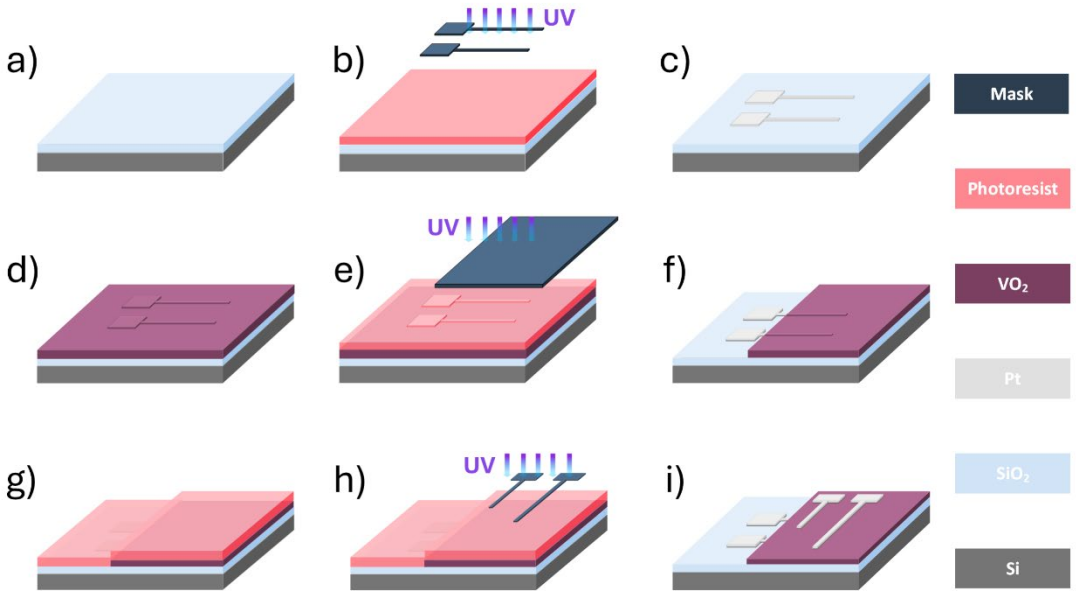

Figure1. The fabrication process flow of VO_2-based memristor: (a) thermal oxidation, (b) UV exposure using photomask1, (c)bottom electrode formation by lift-off, (d)VO_2 layer deposited by ALD, (e)UV exposure using photomask2, (f)etching VO_2 to expose the bottom electrode, (g)photoresist coating, (h)UV exposure using photomask3, (i)top electrode deposition.

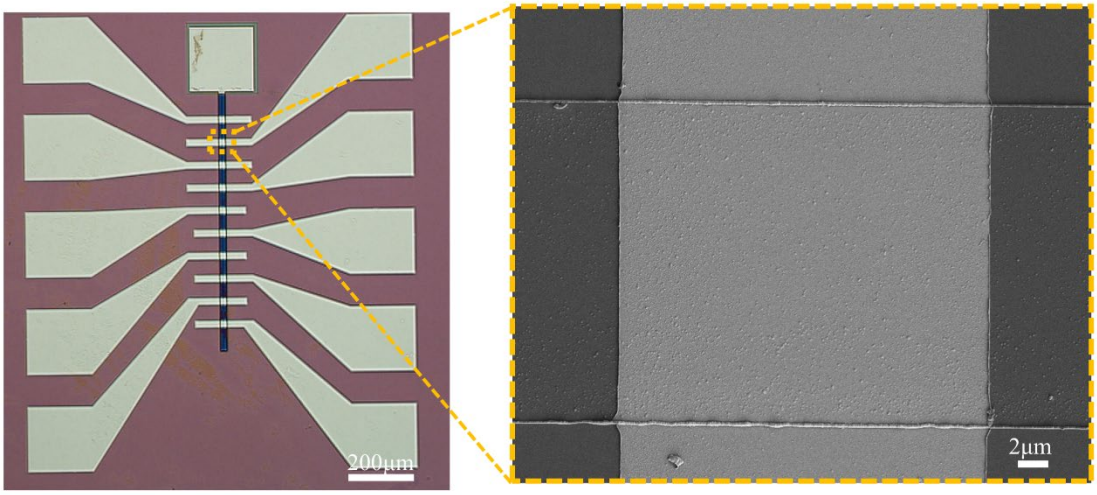

Figure2. The microscope image of the device and the SEM image of the crossbar structure.

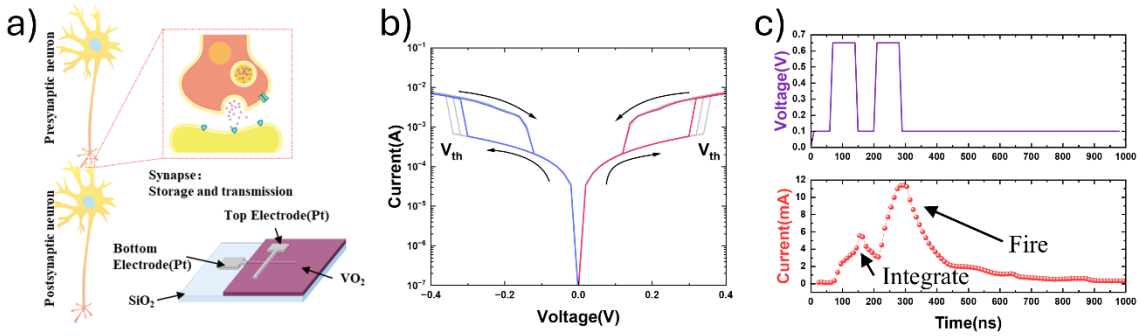

Figure3. (a)The schematic structure of the VO_2 memristor. (b)100 cycles of I-V characteristic for VO_2 memristor. (c) The response of devices under pulses voltage.

Enhancement of Data Retention Characteristics in 2D and 3D NAND Flash via Hydrogen Trap Engineering

JoongHo Yoon [a], MinSung Song [a], HyunSuk Kim [a], EunJin Baek [a], KeeJeong Rho [a], JungGyu Kim [a], Jong Kwang Lim [a], YoungHo Kwon [a], YongSik Yim [a]

[a] Flash Process Integration, Memory Division, Semiconductor Business Division, Samsung Electronics Co., Ltd, Banwol-dong Hwasung-City, 455-701, Gyeonggi-Do, Republic of Korea
e-mail: joongho.yoon@samsung.com

In this study, we investigate the impact of hydrogen on data retention characteristics in both planar (2D) and vertical (3D) NAND flash memory. Through modeling of hydrogen behavior and implementation of trap engineering techniques, we achieved significant improvements in data retention. Hydrogen incorporation prior to cell contact formation serves to suppress cell-to-cell interference by increasing charge traps. Subsequently, outgassing processes are applied post cell contact formation to remove excess hydrogen, thereby stabilizing long-term data retention. Structural modifications—such as partial removal of the blocking SiN layer—facilitate hydrogen exhaust pathways. Experimental results down to sub-2xnm technology nodes demonstrate that this approach is effective in enhancing retention characteristics and is highly applicable to advanced vertical NAND architectures.

NAND flash memory reliability deteriorates as device 2D scaling & 3D stacking intensifies, mainly due to increased trap formation. Non-linear, hard-to-control trap behavior significantly impacts data retention and threshold voltage distribution [1]. Near-interface traps, strongly influenced by hydrogen bonding, are less manageable than oxide traps. Prior hydrogen engineering approaches, applied on a case-by-case basis, have limited effectiveness in advanced nodes [2]. To address this, we propose a hydrogen behavior model focusing on the role of hydrogen-blocking SiN for optimizing data retention.

Figure 1 illustrates 2D and 3D NAND flash cell. As 2D scaling and 3D stacking continues, trap effects intensify at the gate and tunnel edge, degrading cell states during program/erase cycling. After high-temperature baking, distinguishing cell states becomes harder, leading to more retention failures (Figure 2). This HTDR (hot temperature data retention) degradation correlates with hydrogen-dependent interface traps, as confirmed in prior studies [3]. In this study, MLC NAND cells at 4xnm, 3xnm, and 2xnm were cycled 3,000 times and baked at 250 °C for 2 hours. Cell transistors and the chip top layer are encapsulated in SiN to block charge loss and external defects. However, as shown in Figure 3, heat from ILD (inter-layer dielectric) formation perturbs hydrogen bonds at the channel interface. Trapped hydrogen beneath the SiN forms unstable interface traps. Lowering ILD heat improves HTDR by limiting hydrogen reactivation. In contrast, Figure 4 shows that removing SiN during cell contact formation allows hydrogen out-gassing. Under this condition, increased heat improves HTDR, indicating that hydrogen escape pathways reduce trap density. Figure 5 validates this hydrogen model: the program-3 state, highly sensitive to retention loss, exhibits improved HTDR when more time is allowed for hydrogen out-gassing before BEOL contact metal deposition. Conversely, Figure 6 demonstrates that heat before hydrogen path formation—when SiN still blocks hydrogen—leads to degraded HTDR, especially in scaled devices where trap density is higher. Program-3 state shifts post-bake confirm a stronger hydrogen effect at smaller nodes.

In summary, we demonstrate that hydrogen out-gassing, enabled by selective SiN removal after cell contact, significantly improves HTDR. In contrast, blocking hydrogen under SiN leads to increased trap formation and data loss. This hydrogen behavior model offers an effective approach to improving retention characteristics in both 2D and 3D NAND architectures, particularly as devices continue to scale and stacking.

[1] Won-Seong Lee. ICSICT 9th International Conference, 2008, pp.1-4.
[2] Z. S. Wang et al., Electron Devices, IEEE Transactions on, 2013, 60(1), pp.254-259.E. Borger, Computability, Complexity, Logic (North-Holland, Amsterdam, 1989).
[3] A.K. Lenstra and H.W. Lenstra, Jr., Algorithms in number theory, in: J. van Leeuwen, ed., Handbook of Computer Science, Vol. A (Elsevier, Amsterdam, 1990) 673-715.

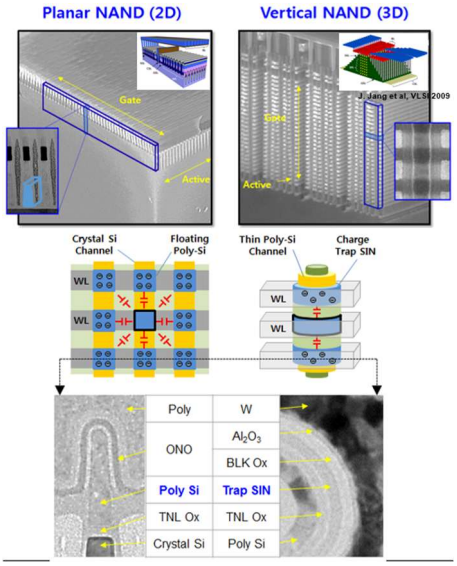

Figure 1. 2D and 3D Nand Flash Memory Flash

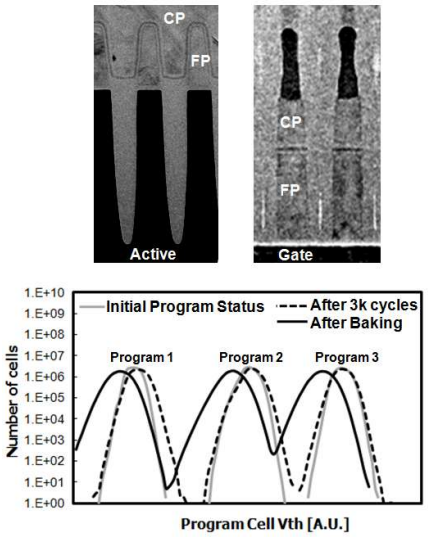

Figure 2. Initial program state and program states after 3k cycling and after 250C, 2hr bake.

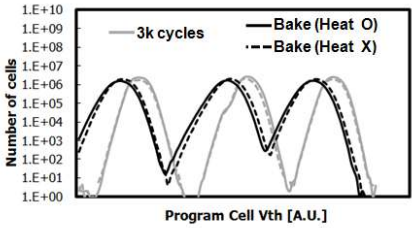

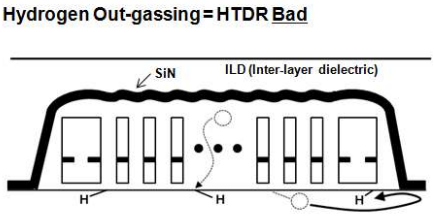

Figure 3. In condition of cell transistor covered with SiN, HTDR difference with & without heat of 300~400OC range of ILD layer. Hydrogen perturbation by heat degrades HTDR.

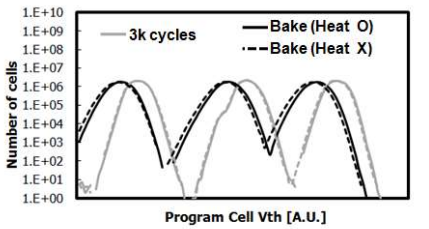

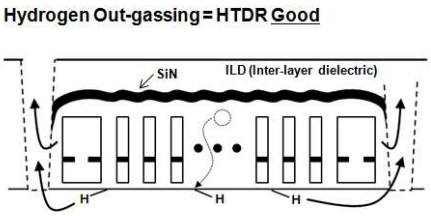

Figure 4. HTDR difference by temperature of of barrier metal deposition after hydrogen path formation by cell contact. Hydrogen out-gassing by heat improves HTDR.

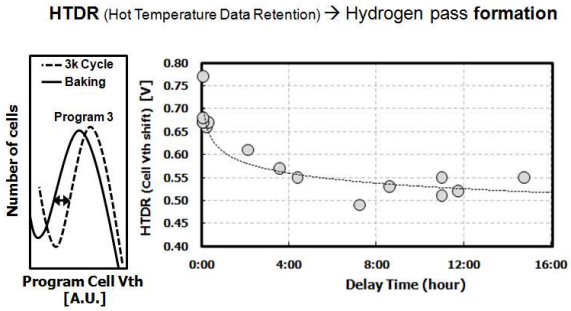

Figure 5. HTDR difference by delay time before upper VIA contact barrier metal deposition in BEOL process. Long delay time helps hydrogen out-gassing resulting in HTDR improvement.

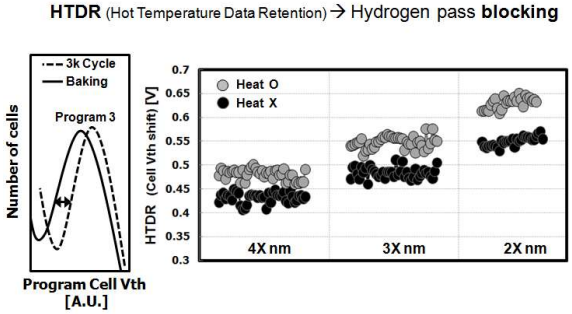

Figure 6. Hydrogen perturbation effect by NAND flash cell size. As cell transistor size becomes smaller, hydrogen influence becomes bigger and HTDR difference becomes bigger due to heat.

Oral Session 4D: Sustainable Fabrication Processes I

Pattern transfer using atmospheric pressure plasma processes

Martin Ehrhardt [a], Robert Heinke [a,b], Pierre Lorenz [a], Joachim Zajadacz [a], Thomas Arnold [a,b], Visar Demiri [a], Klaus Zimmer [a]
[a] Leibniz Institute of Surface Engineering (IOM), Permoserstraße 15, Leipzig 04318, Germany
[b] Technische Universität Dresden, Dresden 01062, Germany

e-mail: martin.ehrhardt@iom-leipzig.de

The generation of microstructures on substrate surfaces using photolithography combined with plasma or ion beam-based dry etching techniques has been extensively studied and is now widely applied in various industrial and research applications. However, these conventional methods require vacuum conditions, which impose significant limitations regarding substrate size, throughput, and process flexibility. These constraints can hinder the scalability and economic efficiency of surface structuring techniques. To overcome these limitations, atmospheric pressure plasma processes have emerged as a powerful alternative. Due to significant technological advancements in recent years, these processes now enable high-precision surface treatment under ambient conditions, eliminating the need for costly vacuum infrastructure [1]. In this context, two atmospheric pressure plasma etching processes are utilized for pattern transfer: the reactive atmospheric pressure plasma jet (APPJ), in which plasma is ignited using microwaves [1], and laser-induced plasma etching (LIPE), where high-energy photons are used to initiate plasma formation [2]. In both cases, the plasma interacts with a reactive etching gas such as CF_4 that is decomposed, forming reactive species that can chemically react with the substrate surface. Volatile compounds formed during this reaction cause etching. Due to the physical nature of plasma generation and confinement in both methods, the lateral spread of the plasma is limited, making these techniques suitable for localized surface modification and structuring. The effective tool size of the APPJ lies in the millimeter to sub-millimeter range, while LIPE achieves resolutions down to the micrometer scale. Both methods have demonstrated their capability to directly write high-quality patterns onto surfaces with excellent precision and flexibility. However, the minimum achievable feature size is inherently limited by the lateral extent of the plasma. To address this limitation and to show the suitability of these methods for fabricating microstructures in the lower micrometer range, a pattern transfer from lithographically structured masks into SiO_2 surfaces was carried out. In this process, various masking materials were tested for their compatibility with each plasma etching technique. The interaction between the masking material and the reactive plasma plays a crucial role in the quality of the pattern transfer, as it influences the selectivity and durability of the masking layer during plasma exposure. Using this approach, periodic linen structures with feature sizes between 2.5 micrometers and 50 micrometers were successfully transferred into SiO_2 surfaces. The presented results highlight the specific etching behavior and process characteristics of both APPJ and LIPE under atmospheric conditions. Furthermore, the localized nature of these processes enables the structuring of non-planar or freeform surfaces, which broadens the range of potential applications [3, 4]. In addition to their technical advantages, atmospheric pressure plasma processes offer several benefits: no vacuum systems and related infrastructure are needed, energy consumption is significantly reduced throughput can be increased. This not only lowers operational costs but also contributes to more sustainable and environmentally friendly manufacturing practices. In conclusion, APPJ and LIPE represent innovative and viable alternatives to conventional vacuum-based etching technologies. Their ability to produce high-resolution microstructures on a variety of substrates, combined with process flexibility and environmental compatibility, makes them highly attractive for applications in microfabrication, optics, electronics, and advanced surface engineering.

[1] Boehm, Georg, Heike Mueller, and Thomas Arnold. "Manufacturing of Freeform Optics completely based on Plasmajet Machining." Optical Fabrication and Testing. Optica Publishing Group, 2021.
[2] Heinke, R., Ehrhardt, M., Lorenz, P., & Zimmer, K. (2021). Dry etching of monocrystalline silicon using a laser-induced reactive micro plasma. Applied Surface Science Advances, 6, 100169.
[3] Ehrhardt, M., Lorenz, P., & Zimmer, K. (2023). Ultraprecise Surface Processing by Etching with Laser-Induced Plasmas. In Ultrafast Laser Nanostructuring: The Pursuit of Extreme Scales (pp. 653-689). Cham: Springer International Publishing.
[4] M. Ehrhardt, P. Lorenz, J. Zajadacz, R. Heinke, T. Arnold, K. Zimmer, Transfer of micron pattern with reactive atmospheric plasma jets into fused silica, Appl. Surf. Sci. Adv., 23 (2024) 100636

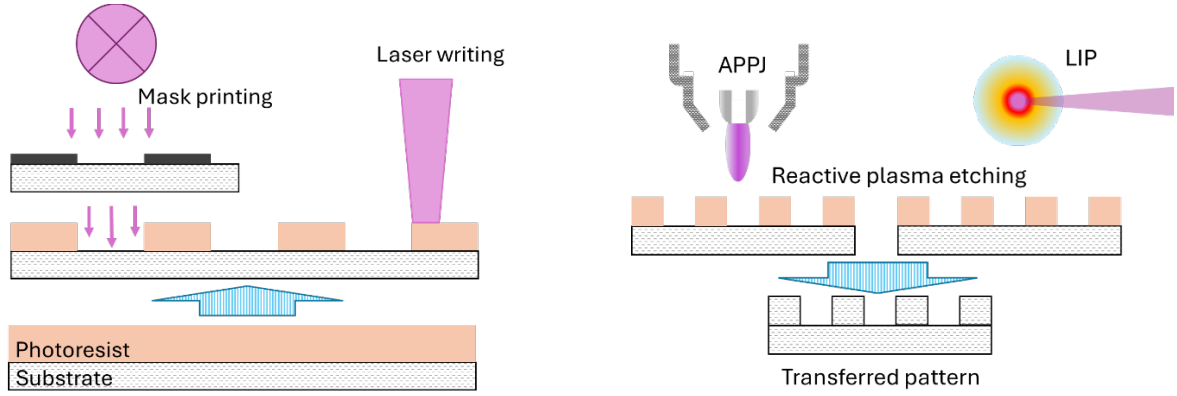

a) b)

Figure 1: Sketch of the process of pattern transfer by reactive atmospheric plasma jets and laser plasma ignited in a reactive gas. a) Pattern

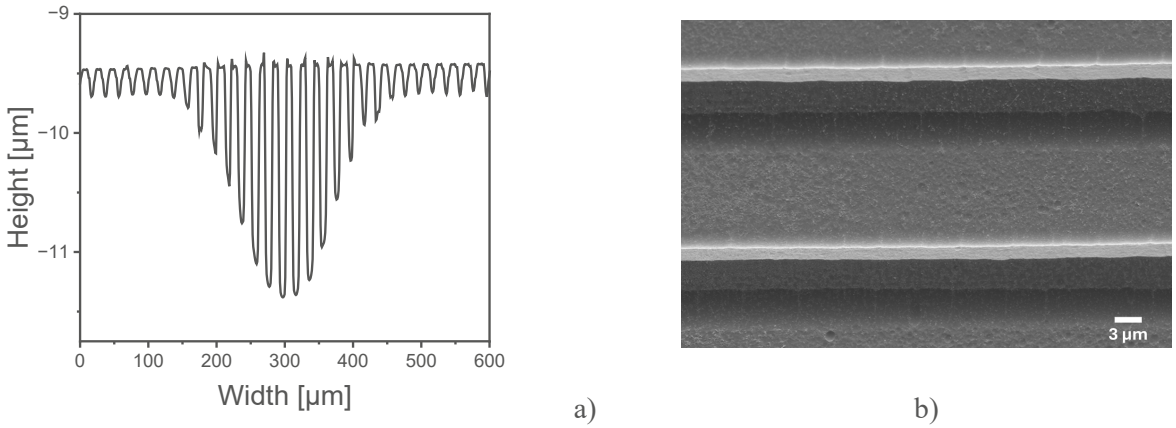

a) b)

Figure 2: Pattern transfer by laser-induced plasma etching. Cross section from WLI measurements. b) SEM image of pattern transferred in SiO_2 with Al mask.

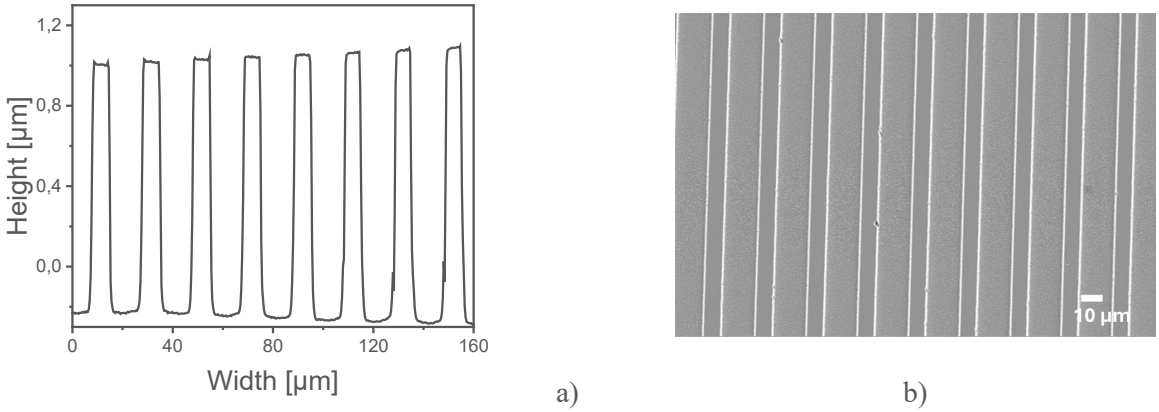

a) b)

Figure 3: Pattern transfer by APPJ. Cross section from WLI measurements. b) SEM image of pattern transferred in SiO_2 with Al mask.

Towards Sustainable Electronics: Wafer-Scale Fabrication of Fully Biodegradable CMOS Devices

Laura Cavedoni [a], Zhengwei Liao [a], Yukun Lian [a], Francesco Stallone [b], Filipe A. Cardoso [a*], Clementine M. Boutry [a*]
[a] Department of Microelectronics, Delft University of Technology, The Netherlands
[b] Else Kooi Laboratory, Delft University of Technology, The Netherlands
e-mail: C.M.F.Viellard-Boutry@tudelft.nl, f.arroyocardoso@tudelft.nl

The rapid turnover of consumer electronic devices, coupled with their environmentally harmful components, underscores the urgent need for sustainable alternatives. Although transient transistors have been demonstrated using both organic and inorganic materials, these approaches remain limited to laboratory-scale fabrication and lack integration into a complete CMOS process flow, significantly limiting scalability [1]. In this work, we present a wafer-scale, fully biodegradable CMOS fabrication method that is fully compatible with standard foundry processes.

Material selection is a key challenge in the development of biodegradable electronics. The biodegradability of silicon, with a dissolution rate of 2-5 nm day^{-1} [1], enables wafer-scale processing. By thinning the wafer to a thickness of 1–10 µm through backside etching, using standard techniques such as wet etching, reactive ion etching (RIE), or polishing, a tunable degradation lifetime ranging from 1 to 10 years can be achieved. To ensure the biodegradability of the device stack (Fig. 1a), phosphorus and boron were selected as dopants, molybdenum (degradation rate = 0.7 nm day^{-1} [1]) as the interconnect material, and silicon oxide (degradation rate = 0.1 nm day^{-1} [1]) and silicon nitride (degradation rate = 0.16 nm day^{-1} [1]) as dielectric layers.

Sentaurus process simulations were performed to optimize implantation parameters, targeting a depth of less than 1 µm to ensure effective biasing in the ultra-thin silicon substrate and high surface dopant concentrations to ensure ohmic contact between the metal and silicon. As shown in Fig. 2, both phosphorus and boron achieved relatively shallow implantation profiles with sufficiently high surface concentrations when calibrated to our process conditions, despite their high diffusivity at elevated temperatures [2]. Simulations indicate that arsenic could offer a shallower and more stable profile, although its high toxicity raises serious concerns for its use in biodegradable electronics, even at trace levels [3].

The fabrication of the NMOS transistor (Fig. 1b) began with ion implantation into a highly doped p-type silicon wafer (~10^{17} cm^{-3}), based on the parameters from the simulations in Fig. 2. A 100 nm SiO_2 layer for via isolation and a 20 nm gate oxide layer were both grown by wet oxidation at 1000 °C. A 20 nm Si_xN_x layer was deposited using LPCVD at 806 °C. The vias to the doped regions were opened by dry etching with SF_6/CHF_3 gases for the Si_xN_x layer and C_4F_8/H_2 gases for the thermal oxide. Molybdenum was deposited by magnetron sputtering and patterned via dry etching using Cl/HBr gases. A 600 nm TEOS passivation layer was then deposited and the pads opened with BHF 7:1. The process concluded with an alloying step, involving a 5 °C/min ramp from 250 °C to 400 °C, followed by a 60-minute anneal at 400 °C.

The transfer length method (TLM, Fig. 3) was used to measure the contact resistivity between molybdenum and doped-Si implants, resulting in values of 35 µΩ cm^2 for p^+-doped Si and 9.56 µΩ cm^2 for n^+-doped Si. For comparison, aluminum, commonly used in standard IC fabrication, can achieve contact resistivities as low as 1 µΩ cm^2 for n-type contacts, with even lower values observed for p-type contacts [2]. The NMOS transistor, with a gate length of 20 µm and a width of 400 µm, exhibited a threshold voltage of ~2.8 V and an on/off current ratio >10^3 (Fig. 4a). The experimental results with molybdenum closely matched the device behavior predicted by mathematical calculations (Fig. 4b). The elevated threshold voltage is mainly due to the relatively thick gate dielectric (20 nm SiO_2 and 20 nm Si_xN_x) and the larger work function of Mo compared to standard polycrystalline Si. Performance could be enhanced by reducing the gate oxide thickness, adopting polysilicon as the gate material, or improving contact resistance through the introduction of silicide interfaces (e.g., $MoSi_2$ or WSi_2) between molybdenum and doped silicon.

In conclusion, a CMOS-compatible fabrication process for a fully biodegradable NMOS device was demonstrated. Although further material investigations are required to improve the transistor's performance (i.e., threshold voltage and contact resistivity), this work represents a promising step towards scalable and sustainable electronics.

[1] Y. Zhang et al., Chem. Rev. 123 (2023) 11722–11773.
[2] R.C. Jaeger, Introduction to Microelectronic Fabrication, Vol. 5, Prentice Hall, 2002.
[3] Y. Liu et al., Adv. Funct. Mater. 29 (2019) 1805402.

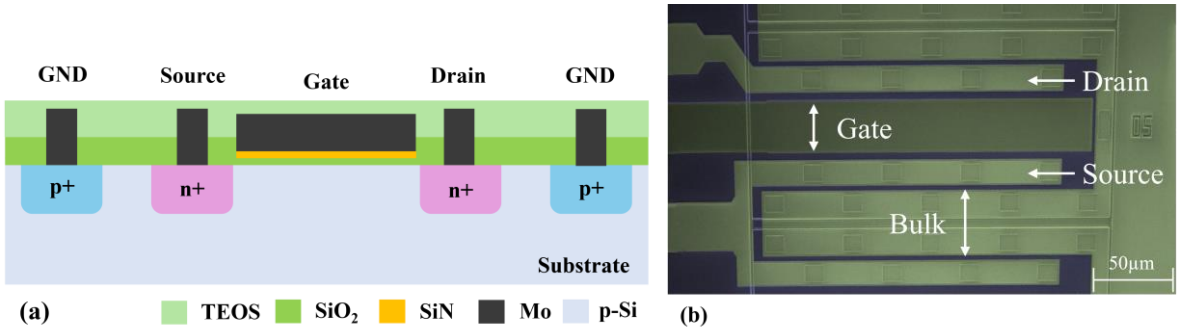

Figure 1. (a) Simplified cross-sectional view of NMOS. (b) Image of the fabricated NMOS device.

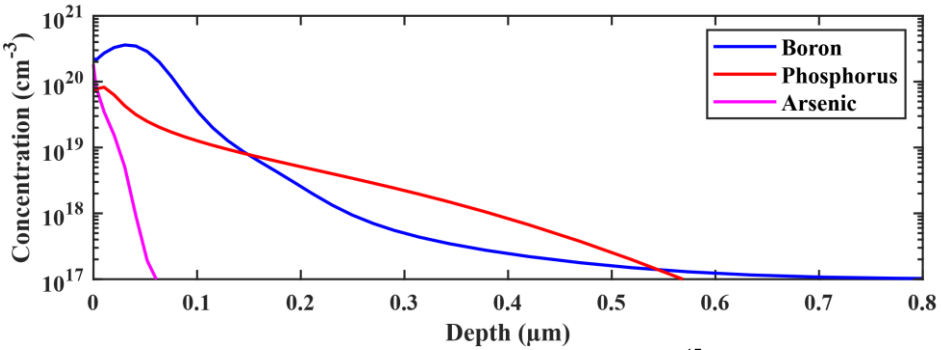

Figure 2. Simulated implantation profiles for boron (20 keV, 6×10^{15} ions cm^{-2}), phosphorus (45 keV, 8×10^{14} ions cm^{-2}), and arsenic (20 keV, 6×10^{15} ions cm^{-2}).

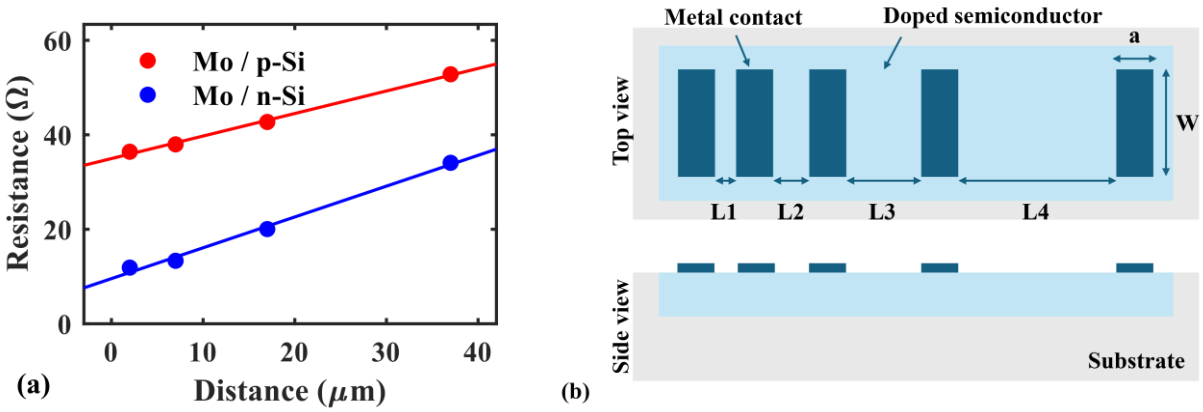

Figure 3. (a) TLM measurements for molybdenum contacts on p-type and n-type silicon. (b) Schematic of the TLM structure.

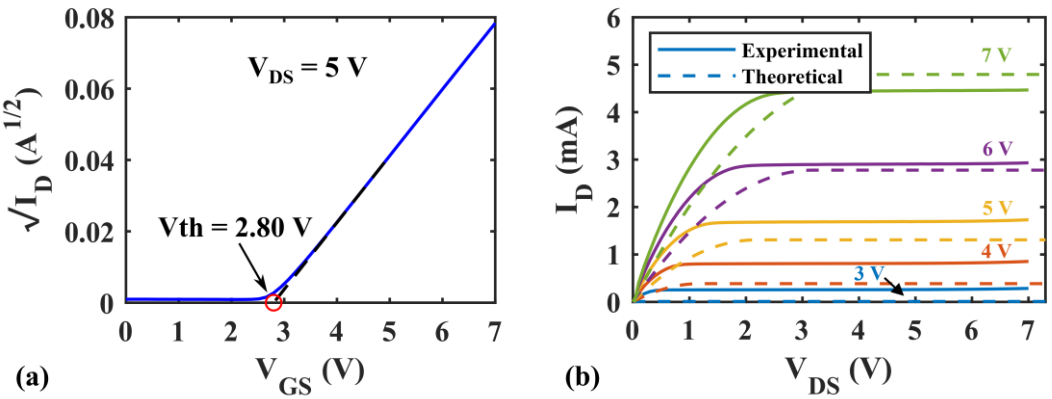

Figure 4. (a) Threshold voltage extraction using the saturation extrapolation method. (b) I-V characteristics at various gate bias voltages for experimental and theoretical results.

Conductive carbon film growth from recycled plastics

Carlos Barbero-Rodriguez, Geoff D. Fowler, Kristel Fobelets

Imperial College London, London, SW7 2AZ, UK
e-mail: carlos.barbero19@imperial.ac.uk

Plastic waste is a global issue, with 6.9 Mt of post-consumer plastic waste discarded to landfills between 2018 and 2020 in Europe alone [1]. To tackle this problem, new paths for recycling common plastics need to be found. In 2023, Zhang et al. [2] presented a way to recycle polystyrene by pyrolyzing it to coat quartz with a conductive carbon layer. The purpose of our research is to further develop this carbon layer growth technique focusing on its use for electronic devices, particularly for the fabrication of high surface area electrodes for capacitors, electrochemical sensors and batteries. The viability of this technique as a method for upcycling waste plastics into high-value devices could give an economic incentive to process waste rather than leaving it in landfills. This technique also benefits from potentially low energy consumption because pyrolysis byproducts (oil and gas) can be used for generating the heat required to deliver the process.

The process used in this work has been adapted from that in [2], with a tube furnace (Carbolite, 50 mm inner diameter) serving as the reactor. Two ceramic boats are placed inside the furnace, one containing a plastic precursor and another one downstream containing the substrate. Nitrogen flow is maintained in the furnace to prevent combustion. The furnace is heated to a fixed temperature, where it remains for a given dwell time. The result is the formation of a carbon layer on the substrate and flammable oil and gas as a byproduct extracted at the exhaust (see Fig 1). Afterwards the furnace is left to cool to room temperature and the sample is extracted. Two changes have been implemented with respect to [2]: i) n-Si and p-Si substrates are used, ii) the device properties of deposited carbon on silicon are studied.

We further develop the technique by assessing the carbon surface formed at a microscopic level as a function of the processing parameters. This involves characterization of the microstructure by scanning electron microscopy (SEM), the crystalline order by Raman spectroscopy, as well as four-point probe resistivity measurements (4pp).

In our work, carbon layers have been deposited on p-Si and n-Si using polystyrene as a precursor whilst maintaining a nitrogen flow rate of 0.5 l/min. Different peak temperatures were tested: 700 °C, 800 °C, and 900 °C, with a dwell time of 2 hours and a heating rate of 20 °C/min. The carbon layers deposited are smooth in appearance, but micrographs such as those for carbon on n-Si (Fig 2) show surface features are present, with higher temperatures resulting in smaller surface features. Dwelling at 900 °C results in the smoothest surface, covered in round features with an average size of 200 nm. Raman spectra of the deposited layers (such as those in Fig 3) show broadened graphite D and G bands at 1581 and 1360 cm^{-1}. These spectra suggest the presence of amorphous carbon with sp2 bonded regions [3]. The absence of the silicon band when dwelling at 900 °C (Fig 3C) points to higher temperatures resulting in thicker carbon layers which do not allow the substrate bands to be excited. 4pp measurements of the films show lower sheet resistance for higher dwell temperatures, with values of 3 kΩ/□, 500 Ω/□ and 100 Ω/□ for 700 °C, 800 °C and 900 °C, respectively. The drop of resistivity at higher temperatures could be explained by a higher quality carbon layer forming with a higher proportion of sp2 bonded carbon.

Our results show that waste polystyrene can be used to deposit conductive carbon on Si, useful for a wide variety of applications such as supercapacitors, batteries and sensors.

[1] "The Circular Economy for Plastics – A European Overview 2022", Plastics Europe. Available: https://plasticseurope.org/knowledge-hub/the-circular-economy-for-plastics-a-european-overview-2/
[2] Y. Zhang, W. Li, J. Hu, and M. Yue, Materials Chemistry and Physics, vol. 309, p. 128380, Nov. 2023, doi: 10.1016/j.matchemphys.2023.128380.
[3] Dennison, JR; Holtz, Mark; and Swain, Greg, Spectroscopy, vol 11, issue 8, pp 38-45, 1996

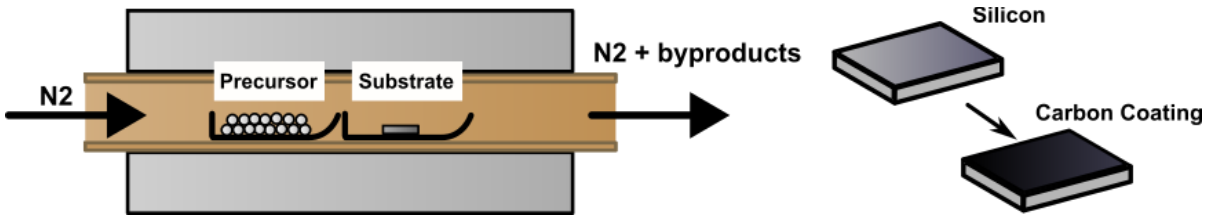

Figure 1. Simplified schematic of the carbon deposition method.

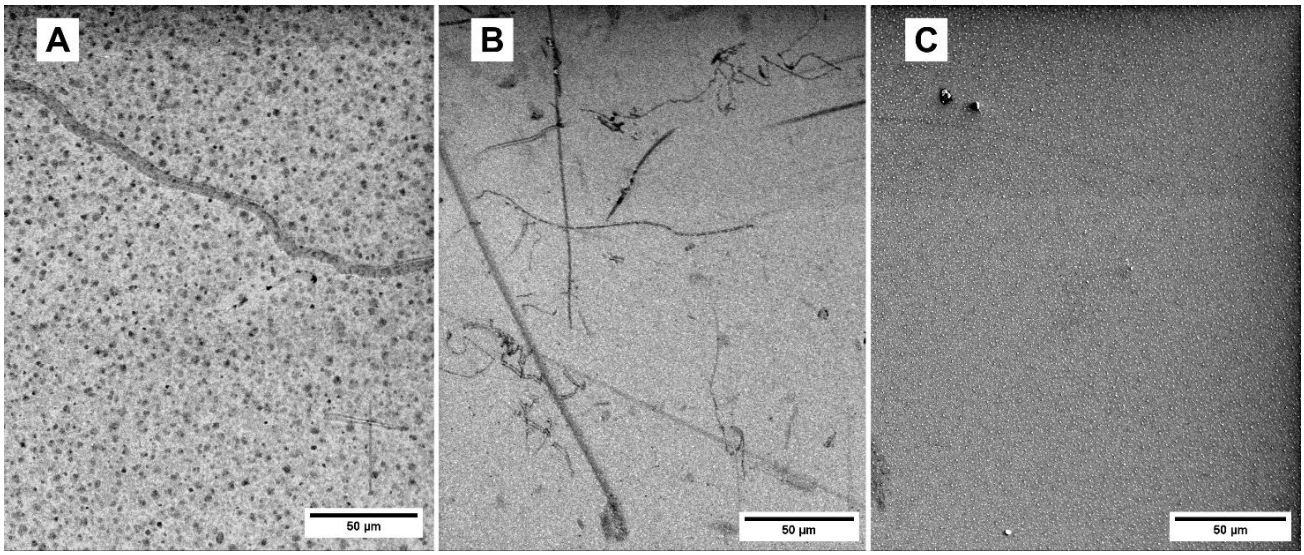

Figure 2. Secondary electron SEM images of carbon layers grown on n-Si at **A**) 700 °C, **B**) 800 °C and **C)** 900 °C. Higher dwell temperatures result in smaller surface feature size. An accelerating voltage of 5kV is used.

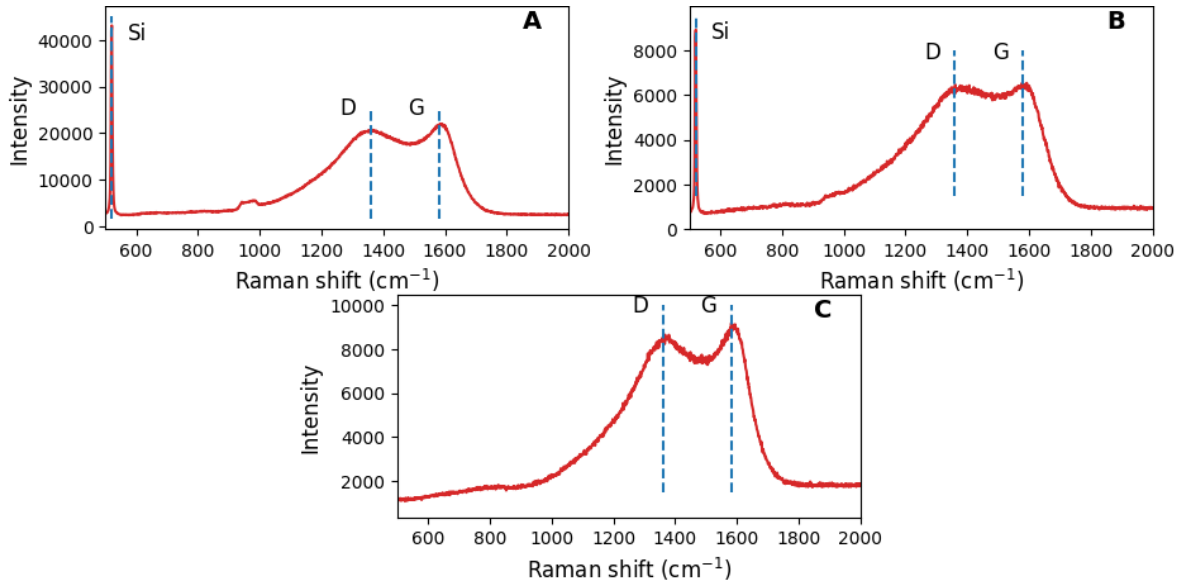

Figure 3. Raman spectra of layer grown on p-Si at **A)** 700 °C, **B)** 800 °C and **C)** 900 °C. Graphitic G and D bands marked at 1581 and 1360 cm^{-1} on all graphs and Silicon band at 521 cm^{-1} marked for **A** and **B**, where it is present.

Development of sustainable machining processes to manufacture vacuum cells for Quantum Technology

Joel M. N. Keen[a], Paul C. Gow[a], Glenn M. Churchill[a], Corin B. E. Gawith[a], James C. Gates[a]

[a] Optoelectronics Research Centre, University of Southampton, SO17 1BJ, UK
e-mail: j.keen@soton.ac.uk

Miniature vacuum cells provide a potential route to producing smaller, more versatile atom traps for use in quantum technologies [1]. The combination of millimetre scale devices with nanometric surface quality requirements on arbitrarily orientated side wall surfaces mean that chemical etching techniques are challenged on capability, time and sustainability grounds. Wafer scale processing of compact vacuum cells is necessary to meet future production volume requirements. We apply techniques from the semiconductor, bulk optics and industrial machining industries to present an optimised hybrid machining process with demonstrable sustainability gains. Our wafer scale demonstration is a 100mm diameter, 6.35mm thick double side polished borosilicate glass wafer, projected to produce nine cell bodies after eventual assembly, shown in Figures 1 & 2.

Deep reactive ion etching in borosilicate has been reported at 750 nm/min [2] and deep wet etch using HF has a similar etch rate of 875 nm/min [3]. At best, this translates to 120 hours of etching for our wafer layout, with potential undercutting and quality issues. While improvements in eco-friendly glass etching have been reviewed recently [4], it remains a process with significant sustainability issues. Abrasive Waterjet Technology (AWT) has been proven for vacuum cell fabrication [5]. AWT cannot produce an optical grade surface (Sa 3.4 µm) and is also hard to align to existing features, however these factors are not critical for initial processing. In theory, the AWT cut surfaces could be polished, but internal walls of a compact cell are very challenging to access. For our design, AWT was used to rough the internal cavities in demonstration wafer in under 30 minutes, a highly significant improvement to etching or even rough grinding over multiple hours.

We have shown diamond micro-grinding (Loxham Precision µ6, see Fig. 2c) of optical finish surfaces in atom traps [6] comparable to, or better than, etched glass. Combining AWT with subsequent finish grinding provides a more sustainable vacuum cell by zero etching and reduced mechanical processing time compared to rough/finish grinding or AWT followed by polishing. Our resulting ~80x surface quality improvement after grinding to 40 nm Sa, shown in Figure 3, allows us to move towards 3D optical access with optical surfaces on each orthogonal axis, Figure 1(a). Our prototype loss measuring setup shows finish ground surfaces transmitting at least three times better than AWT surfaces and only having a 15% loss compared to free space. Exact numerical comparisons between the different fabrication technologies are difficult due to the widely ranging process dynamics. Prototyping is significantly more efficient by mechanical machining, but etching does not take any longer for larger batches. Our initial sustainability analysis will evaluate process time, batch size dynamics and wider environmental impact.

We will present the latest in sustainable mechanical machining techniques applied to enable mass-producible vacuum cells in optical materials. Our waterjet process has significant potential for optimisation; by characterising and reducing sub-surface damage at the initial stage, the finish grinding passes can be cut down significantly. We intend to apply innovative grinding techniques such as axial oscillation and UV laser tool dressing to improve our potential device specification while still ensuring high sustainability compared to conventional micro-fabrication methods.

[1] Y. Petremand et al., JMM, 22(2012), p.025013
[2] J. H. Park et al., Microelectron. Eng., 82(2005), pp.119-128
[3] J.-Y. Jin et al., JMM, 24(2013), p.015003
[4] K. Choi et al., JACerS, 107(2024), pp. 6497-6515
[5] S. Dyer et al., J. Appl. Phys. 132(2022), p.132401
[6] P. C. Gow et al., Physical Machining of Chambers, Vias, and Monolithic Mirrors in Silicon for Quantum Technologies, CLEO Europe 2025, poster accepted

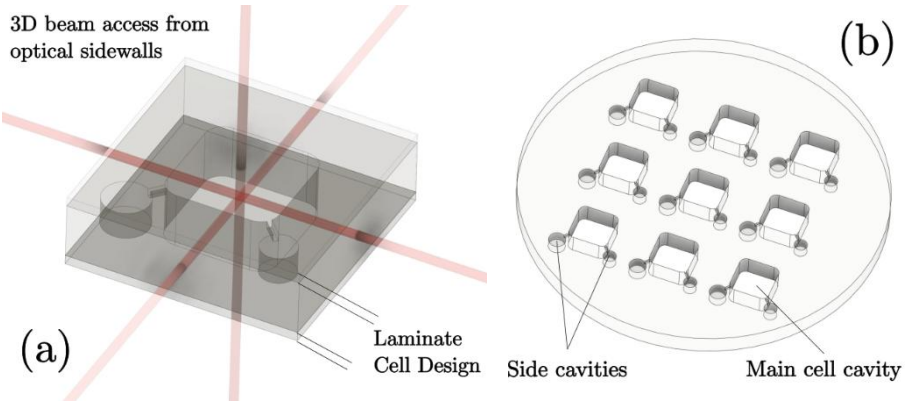

Figure 1. Schematics: 3D Optical Accessible Vacuum Cell (a) Wafer Scale Production Layout (b)

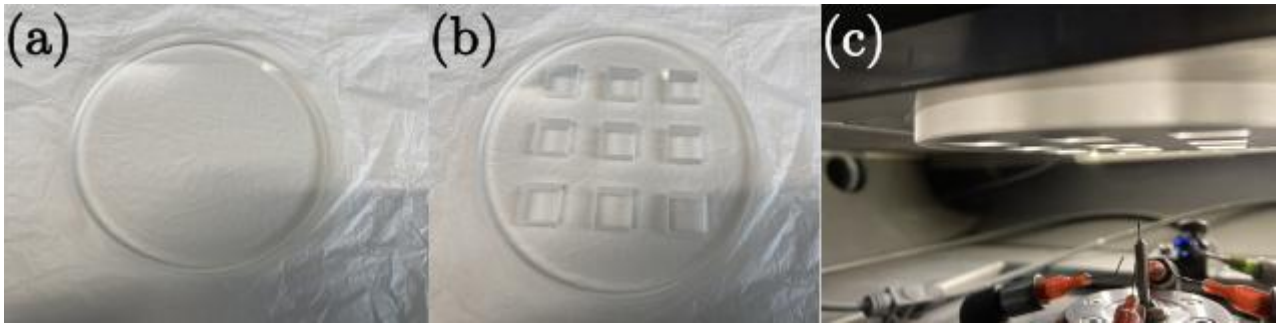

Figure 2. Borosilicate demonstration wafer before (a), after (b) waterjet roughing, before micro-grinding (c)

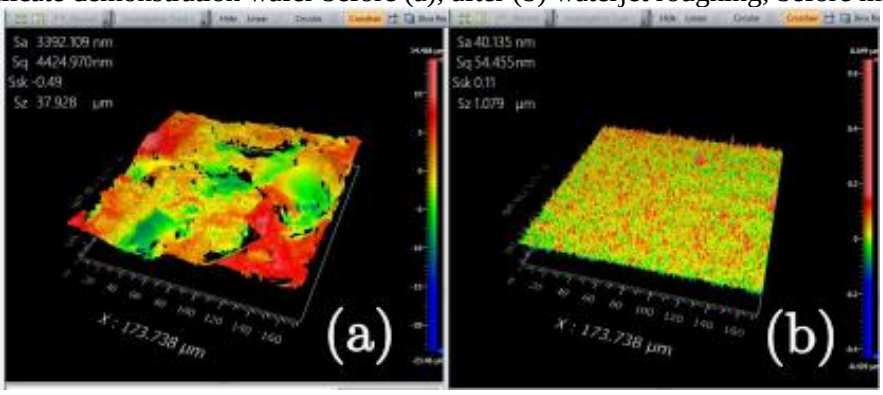

Figure 3. White Light Interferometry of waterjet (a) and micro-ground (b) surfaces (Plane fitted, unfiltered, measured area: 174 x 174 µm)

Energy-efficient optical crosslinking system for sustainability in ArFi lithography

Seungjoo Baek[a], Elke Caron[a], Wesley Zanders[a], Andreia Santos[a], Masahiko Harumoto[b], Seonggil Heo[c], Jelle Vandereyken[c], Veerle Van Driessche[d], Douglas J. Guerrero[d]

[a]SCREEN SPE Germany, Fraunhoferstrasse 7, D-85737 Ismaning, Germany
[b]SCREEN Semiconductor Solutions Co., Ltd. 480-1 Takamiya-cho, Hikone, Shiga, Japan
[c]imec, Kapeldreef 75, 3001 Leuven, Belgium
[d]Brewer Science, Inc., 2401 Brewer Drive, Rolla, MO 65401, USA
e-mail: s.baek@screen-spe.eu

With increasing global emphasis on climate change and sustainability, the semiconductor industry is actively seeking ways to minimize its environmental impact. Reducing greenhouse gas (GHG) emissions and adopting greener processes have become essential priorities in achieving long-term sustainability. Energy efficiency is a critical focus area in the chip manufacturing, as electricity consumption is recognized as one of the most significant challenges due to its resource-intensive nature. Lithography tools, in particular, contribute heavily to energy usage, requiring substantial power to operate effectively. The conventional lithographic process for curing underlayer materials relies on heat applied through a hotplate, which is dependent on elevated temperatures to achieve film densification. The high temperatures required for thermal baking of underlayer materials and the need to maintain elevated target temperatures significantly contribute to energy consumption in track systems, raising concerns about energy usage.

SCREEN introduced an innovative energy-saving process utilizing light, integrated into SCREEN's DT-3000 track, as an energy-efficient alternative to conventional baking process for baking underlayer materials using heat on the hotplate in exposure extreme ultraviolet (EUV) lithography [1-3]. This novel technique has successfully demonstrated significant energy-conservation and rapid processing at room temperature while maintaining lithographic performance. Following this initial success, we have extended the evaluation of this technology to ArF immersion (ArFi) lithography, which remains widely used in the semiconductor industry. By applying optical crosslinking to ArFi processes, we aim to demonstrate that this approach is not limited to EUV but can also deliver environmental and process integration advantage across multiple lithography platforms.

In this work, we assessed the patterning performance of the optical crosslinking system using light-curable underlayer materials, which achieved full crosslinking at 200mJ/cm^2, in ArFi lithography. The patterning results from the after-development inspection (ADI) process on a pitch 90 nm line-and-space (L/S) structure with a critical dimension (CD) of 41 nm demonstrate that the optical crosslinking process shows competitive patterns compared to the conventional thermal crosslinking system (Fig 1). To further validate this approach, we advanced the study to contact hole (CH) patterns on a pitch 100 nm targeting a CD of 50 nm and observed improved pattern performance, including dose to size, depth of focus (DOF) and exposure latitude (EL), as shown in Fig 2. Fig 3 shows that the optical crosslinking process demonstrated energy savings of 75% for spin-on carbon (SOC) and 60% for spin-on glass (SOG) compared to thermal-curable underlayers, without compromising lithographic performance. These findings highlight the potential of optical crosslinking as a sustainable and process-compatible solution for next-generation lithography, enabling reduced environmental impact while maintaining pattern quality.

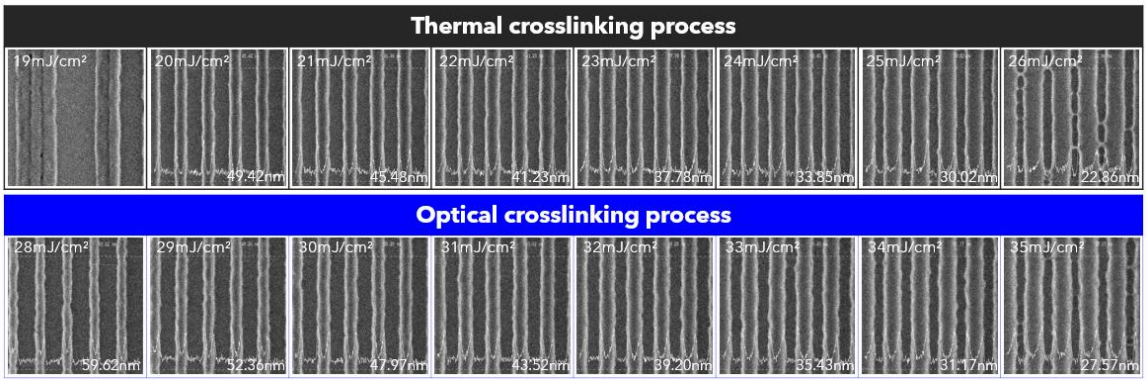

Figure 1. Comparison of L/S patterning performance for the ADI process between thermal crosslinking and optical crosslinking process.

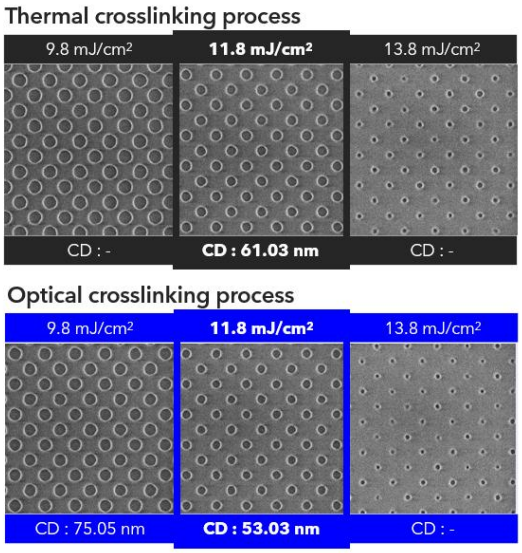

	Thermal crosslinking	Optical crosslinking
Dose to size (mJ/cm²)	11.4	10.57
DOF (nm)	104	127
EL (%)	6.32	10.86

(at a CD of 62nm)

Figure 2. Assessment of CH patterning performance for the ADI process.

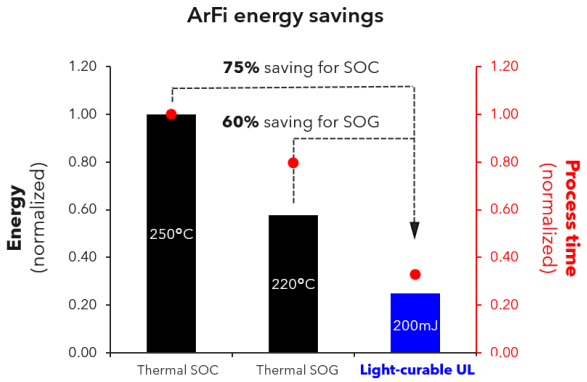

Figure 3. Energy savings of SOC and SOG underlayers for ArFi lithography.

Reference:

[1] S. Baek et al., J. Micro/Nanopattern. Mater. Metrol. Vol. 23(3) (2024) 034602-9.
[2] S. Baek et al., Proc. of SPIE Vol. 12957 (2024) 129572G-7.
[3] A. Santos et al., Proc. of SPIE Vol. 12957 (2024) 12957A-9.

Isotropic etching of suspended Si structures using a single-step, single-mask deep reactive ion etching process

Sarah Günther-Müller[a], Marius Hillebrand[b], Martin Hoffmann[b], Steffen Strehle[a]

[a] Institute of Micro- and Nanotechnologies (IMN) MacroNano®, Microsystems Technology Group Technische Universität Ilmenau, D-98693 Ilmenau, Germany
[b] Chair of Microsystems Technology, Department of Electrical Engineering and Information Science, Ruhr University Bochum, D-44801 Bochum, Germany
e-mail: sarah.guenther-mueller@tu-ilmenau.de

In the field of microelectromechanical systems (MEMS), the development of efficient and cost-effective fabrication techniques is a fundamental aspect. Traditional methods for creating complex silicon structures often involve multiple process steps and masks, which increase production time and cost. Here, we introduce a fabrication approach to produce suspended silicon structures that significantly simplifies the process. By combining a single-mask process and deep reactive ion etching (DRIE), we demonstrate how intricate, multi-level released structures can be produced by modifying the alternation of isotropic and anisotropic etching steps. This efficient approach not only reduces manufacturing complexity but also opens new possibilities for the design and application of MEMS.

Recently, a method was presented to release suspended structures using a combination of isotropic and anisotropic etching steps [1-3]. Using this method, floated structures with widths down to 5 µm and aspect ratios up to 20 were realized. Here, we present a new approach in which the isotropic etching process is extended by a subsequent deep etching step. This enables the production of structures at multiple levels. Only a single mask is required and the subsequent etching steps can be integrated into a simple process run.
To demonstrate the approach, microfabrication was carried out on silicon substrates (<100>, thickness 525 µm). As mask, a layer of AZ® ECI 3027 resist was spin-coated onto the substrates at 2000 rpm leading to a thickness of approximately 4 µm. Dry etching was performed using an Oxford Instruments PlasmaPro® Estrelas 100 etching tool. The process sequence for producing the suspended structures first involves a conventional DRIE etching step (Fig. 1(a), step (i)). Next, a thick polymer layer is deposited by C_4F_8 plasma onto the structures and the so-called breakthrough at the bottom of the trenches is carried out using an anisotropic etching step (Fig. 1 (a), steps (ii) and (iii)). Subsequently, the structures are underetched in an isotropic etching step until complete release is achieved (Fig. 1 (a), steps (iv) and (v)). The height of the structures released in this way can be precisely adjusted by the etching depth of the first DRIE process.
To generate functional structures on different levels, the described steps are transferred to a silicon on insulator (SOI) substrate (Fig. 1 (b), steps (i) and (ii)). A further DRIE process is now introduced after isotropic release (Fig 1. (b), step (iii)). By etching the SiO_2 layer using hydrofluoric acid (HF), multi-level elements are obtained (Fig 1. (b), step (iv)).

Defined and fully released structures are generated in this manner in a single-mask, single-level process. Figure 2 illustrates the fabricated structures based on scanning electron microscopy images. Regarding trenches, widths down to 3 µm at depths of 18 µm could be released (Fig. 2 (a)). With regard to freestanding comb structures, bar widths down to 5 µm are attainable, as shown in Fig. 2 (b). The multi-level structures, as provided in Fig. 2 (c) and (d), demonstrate successful stepwise release and vertical separation, creating different levels of suspended and supporting structures. The experimental results indicate that the limiting factor is most likely not the aspect ratio but rather the width of the released structures. This might apparently be a result of the high thermal stress acting on the material during isotropic etching. Adjustments to the individual process steps can counteract this by shortening the etching times and introducing cooling pauses. In conclusion, the presented method enables efficient and scalable fabrication of both, single- and multi-level suspended silicon structures, offering substantial potential for cost-effective MEMS production. The investigations also reveal new findings regarding the feasible lateral dimensions and the aspect ratio.

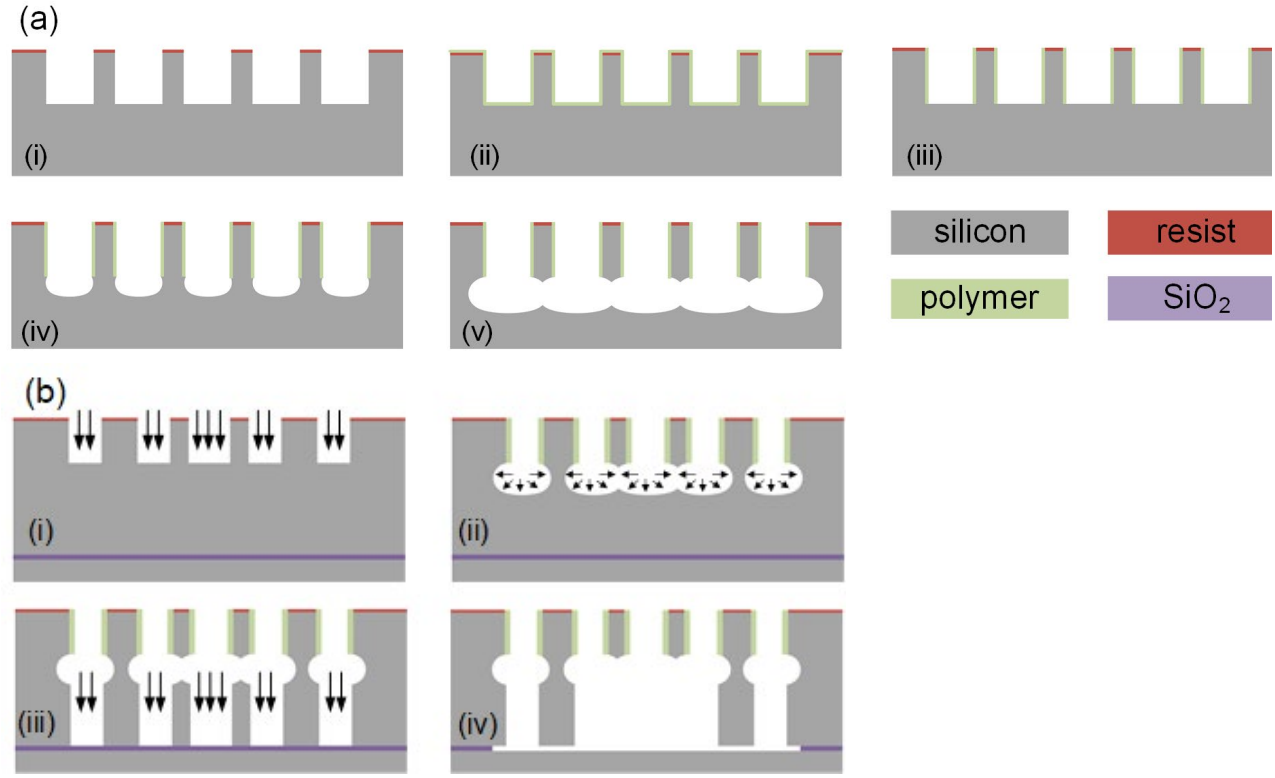

Figure 1. Schematic process flow to generate suspended structures by combination of DRIE and isotropic etching on single level (a) and multi-level using silicon-on-insulator substrates (b).

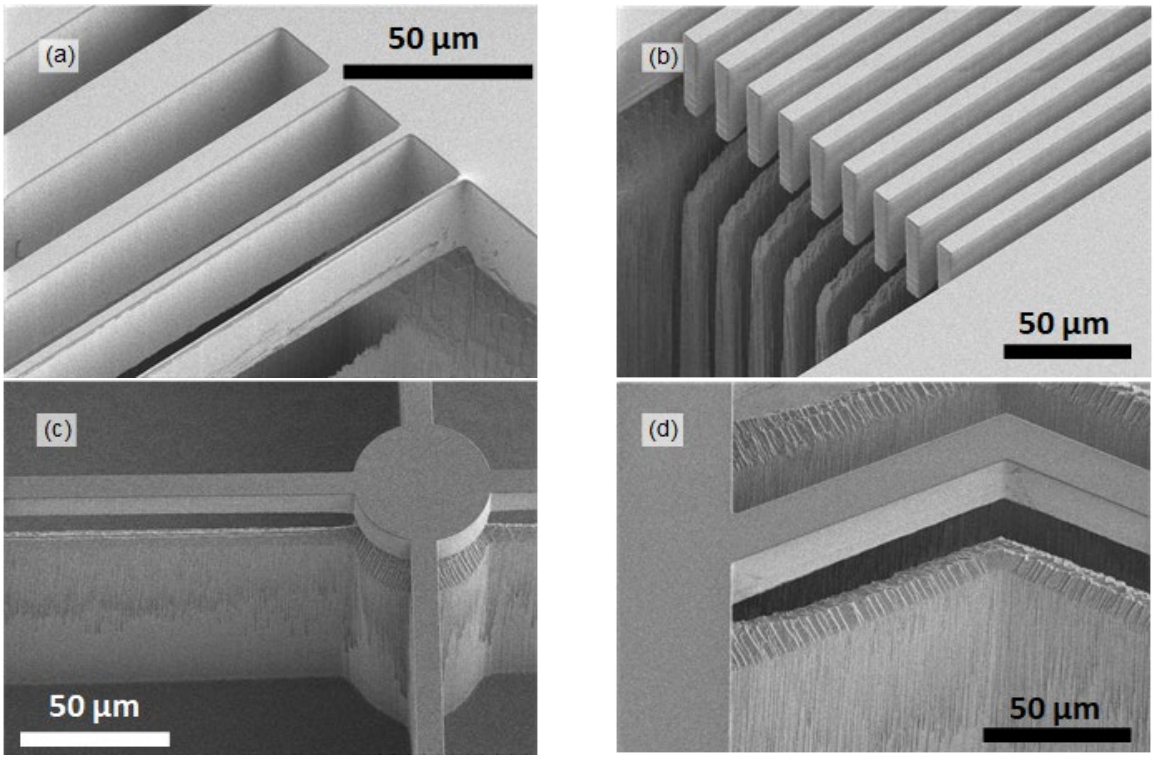

Figure 2. Scanning electron microscope images showing examples of suspended structures in silicon that were created by the combination of conventional DRIE and isotropic etching.

[1] Hamid Mazraati, et al., 2014 J. Vac. Sci. Technol. B1 (6): 062002
[2] Yao-Joe Yang and Wen-Cheng Kuo 2005 J. Micromech. Microeng. 15 2184
[3] Yu-Hsin Lin and Wensyang Hsu 2012 J. Micromech. Microeng. 22 045015

Designing for End-of-Life Electronics: Additive Manufacturing of conductive materials to enable 99% degradable High-Performance Printed Circuit Boards

Jonathon Harwell, Jeff Kettle
James Watt School of Engineering, University of Glasgow, G12 8QQ, Glasgow, Scotland
Email; jeff.kettle@glasgow.ac.uk

For more than 50 years, advances in electronics have transformed every socioeconomic sector. However, this progress has largely been driven by technical or economic requirements rather than sustainability, leading to unsustainable practices with unintended consequences. In response, interest has grown in recyclable, or degradable electronics to address the escalating e-waste challenge, which is anticipated to grow significantly over the next decade and beyond. Yet, achieving high-resolution circuits with bulk-metal performance and environmentally benign end-of-life (EoL) pathways has remained a significant challenge.

Here, we report printed circuit board (PCB) assemblies in which 99.7% of the mass degrades into benign products under both controlled laboratory and soil environments, enabling circularity of integrated circuits (ICs) and reducing significantly the waste generated by the electronics. Our approach uses a “growth-and-transfer” method, where a conductive zinc (Zn) layer is electroplated onto a sacrificial carrier substrate and subsequently transferred onto a biodegradable substrate. This process yields track resolutions as fine as 5 µm, a sheet resistance of 3 mΩ/square, and a shelf life exceeding one year; an order of magnitude higher resolution than conventional subtractive PCBs made using Copper.

To demonstrate viability, we fabricated PCB-based touch sensor circuits embedding a microcontroller and amplifier to drive an LED. Their functionality, lifetime performance, and degradability were evaluated. Results show that the PCBs fully degrade within 450 hours in a soil composter or within 30 minutes under laboratory conditions using an acetic acid solution. Life Cycle Assessments (LCAs) of this manufacturing approach, benchmarked against conventional FR-4 copper (FR-4-Cu) PCBs, reveal a 79% reduction in Global Warming Potential and significant improvements across other environmental impact categories.

Moreover, this method facilitates the recovery of high-value components such as ICs and LEDs for recycling. Our findings demonstrate a scalable and new pathway to reduce e-waste, enhance component recovery and lower the overall environmental footprint of electronics throughout their entire lifecycle, while ensuring that, even if discarded in landfills, PCBs degrade into harmless end products.

Plenary Sessions

Plenary 6 - Dr Feras Alkhalil

Flexible Integrated Circuits Revolution: Innovative Manufacturing, Materials and Roadmaps

Feras Alkhalil

PragmatIC Semiconductor, 400 Cambridge Science Park, CB4 0WH, UK

Abstract:

Pragmatic Semiconductor's innovative approach to semiconductor manufacturing enables ultra-thin, flexible, low carbon and low-cost integrated circuits. In this talk we will provide an overview of our vision, our unique technology and will showcase how our innovative approach to manufacturing drives our flexible integrated circuit products and applications roadmap.

Elsevier YIA Talk - Dr Alexandros El Sachat

Engineering thermal and thermoelectric transport in two-dimensional (2D) semiconductors and devices

Kai Xu[1,2], Stefania Skorda,[1] Stuart Finch[3], Polychronis Tsipas,[1] Athanasios Dimoulas,[1] Juan Sebastián Reparaz[2], Oleg Kolosov[3] and Alexandros El Sachat[1]

[1]Institute of Nanoscience and Nanotechnology, National Center for Scientific Research "Demokritos," 15341 Agia Paraskevi, Athens, Greece

[2]Institut de Ciència de Materials de Barcelona, ICMAB-CSIC, Campus UAB, 08193 Bellaterra, Spain

[3]Department of Physics, Lancaster University, Lancaster, UK

*Email: a.elsachat@inn.demokritos.gr

We present a comprehensive overview of three interrelated scientific investigations that collectively address the engineering of thermal and thermoelectric transport in two-dimensional (2D) materials and devices. The first study demonstrates the successful realization of large area cross-plane thermal insulation by engineering ultra-thin lattice mismatched epitaxial van der Waals heterostructures [1]. In the second study, we systematically study the temperature-dependent in-plane and cross-plane thermal conductivity in nanopatterned suspended MoS_2 and supported WS_2 films with varying thickness in a wide temperature range (80-460 K). The research uncovers that nanopatterning is an efficiency approach to create 2D heat-routing structures that effectively confine and guide heat flow in prespecified directions [2]. Additionally, we find that WS_2 exhibits an exceptionally high in-plane thermal conductivity, ~1000 $Wm^{-1}K^{-1}$ at 80 K and tunable thermal anisotropy, i.e. increases from 30 (460 K) to 78 (80 K), which is observed to originate from the strong reduction of the out-of-plane component triggered by the onset of the quasi-ballistic transport regime. Last, we investigate local thermal and thermoelectric transport [3] on devices based on nanopatterned $SnSe_2$. We found that while thermal transport varies on distances of a few tens of nanometres, the modification of Seebeck coefficient expands on much larger distance with the characteristic Seebeck exponential "decay length" being on the order of 1 μm. By selecting appropriate density and diameter of the nanofabricated patterns, we demonstrate the possibility to create large areas of Seebeck coefficient modification. Collectively, these works advance thermal management technologies and foster the design of customized thermoelectric devices.

References

[1] E. Chavez-Angel et al., *Nano Letters* 23, 6883–6891 (2023)
[2] P. Xiao et al. *Science Advances*, 10, 13, (2024)
[3] Harzheim et al. *Nano Letters* 18 (12), 7719-7725 (2018)

Oral Session 5A: Integrated System Processes

Microscale Patterning of Transparent Conductive Oxides (TCOs) Using High Precision Capillary Printing for Display Applications

Marc Pascual [b], Ludovic Hahn [a], Frederic Raynal [b], Nathan Bigan [b], Achille Guitton [b], Amin M'Barki [b], Tony Jullien [a], Chloé Guerin [a], Vincent Jousseaume [a]

[a] Univ. Grenoble Alpes, CEA, LETI, F-38000 Grenoble, France
[b] Hummink, Paris, 75003, France
e-mail: marc.pascual@hummink.com

Keywords: Capillary Printing, Transparent Conductive Oxide, Repair

Thin films of Transparent Conductive Oxides (TCOs) are critical components in modern display devices, where they function both as electrodes and optical filters [1]. While Indium Tin Oxide (ITO) is the industry standard, there is growing interest in alternative materials such as Zinc Oxide (ZnO) and Tin Dioxide (SnO_2) due to potential benefits in cost, performance, and environmental impact. However, a significant challenge remains in achieving precise patterning of these alternative TCOs at the micrometer scale, which is essential for advanced device applications and repair strategies.

To address this challenge, we introduce an innovative approach using Hummink's High Precision Capillary Printing (HPCaP) technology. Inspired by the precision of atomic force microscopy, HPCaP enables the direct printing of thin polymer masking layers onto a silicon substrate (Fig.1) [2,3]. This is followed by the deposition of the TCO layer via Atomic Layer Deposition (ALD), a process that ensures uniformity and high-quality film formation while preserving the integrity of the substrate.

In our study, we evaluated the performance of three different polymers—PMMA (15k molecular weight), PVP (40k molecular weight), and SU8 2002—as masking materials to inhibit the ALD growth of ZnO [4]. Our experiments demonstrate that PMMA and PVP effectively prevent unwanted ZnO deposition in the masked areas. After removing the polymer masks, we achieved well-defined patterns with pixel sizes smaller than 5 µm (Fig.2).

These results underscore the potential of HPCaP as a powerful tool for prototyping and repairing TCO-based display devices. Although the current approach may not yet be ready for mass production, its ability to produce precise microscale patterns provides a promising avenue for future research and development. By combining high-resolution printing with the controlled deposition of alternative TCOs, this work paves the way for more versatile and cost-effective manufacturing processes in the electronics and display industries. Overall, our findings contribute to advancing the state of the art in TCO patterning technology, highlighting a novel method that enhances both the prototyping and repair of high-performance display devices.

References:

[1] Miao, W.-C., Hsiao, F.-H., Sheng, Y., Lee, T.-Y., Hong, Y.-H., Tsai, C.-W., Chen, H.-L., Liu, Z., Lin, C.-L., Chung, R.-J., et al., "Microdisplays: Mini-led, micro-oled, and micro-led," Advanced Optical Materials 12(7), 2300112 (2024).

[2] Pascual, M., Bigan, N., M'Barki, A., Mental, R., Allegro, I., and Lemmer, U., "All-printed su8-perovskite dfb laser," in [Advanced Fabrication Technologies for Micro/Nano Optics and Photonics XVI], 12433, 87–89, SPIE (2023).

[3] Guitton, A., Pascual, M., Farmand, K., Haddada, M. B., Bigan, N., Al Kamand, S., and M'barki, A., "Cap- illary printing of fine structures on flexible and hybrid substrates," in [2024 IEEE International Conference on Flexible and Printable Sensors and Systems (FLEPS)], 1–4, IEEE (2024).

[4] Feougier, R., Guerin, C., and Jousseaume, V., "Inhibition of the atomic layer deposition of zno and sno2 using a vapor-based polymer thin film," Journal of Vacuum Science & Technology A 41(1) (2023).

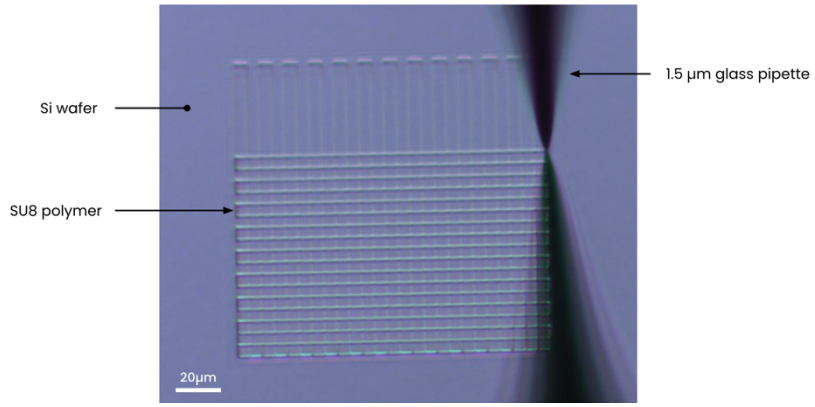

Figure 1. Printing of a SU8 grid with a 1.5 µm using High Precision Capillary Printing.

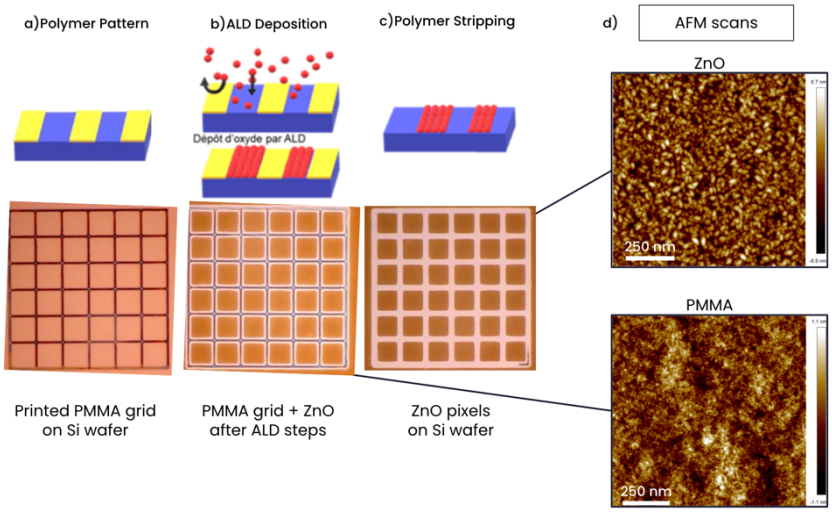

Figure 2. a) Illustration and image of the printed PMMA grid on Si wafer; b) Illustration of the ALD deposition of ZnO and image of the PMMA grid and ZnO after the ALD steps; c) Image of the ZnO pixels on Si wafer after the polymer stripping step; d) AFM scans of ZnO after polymer stripping (top image) and before polymer stripping (bottom image).

MULTILAYER POLYMER-BASED CANTILEVERS WITH MULTIPLE EMBEDDED PIEZORESISTIVE SENSORS FOR HIGH-SENSITIVITY ATOMIC FORCE MICROSCOPY

Ekin A. Ozek[a], Nahid Hosseini[a] and Georg E. Fantner[a]
[a] Laboratory for Bio- and Nano- Instrumentation, EPFL, Lausanne, 1015, Switzerland
e-mail: ekin.ozek@epfl.ch

We present a self-sensing AFM cantilever based on a polymer–semiconductor–ceramic trilayer architecture integrating two embedded layers of piezoresistive strain sensors. Previous trilayer cantilever designs integrated four piezoresistors on a single SiN–polymer interface; the process presented here introduces a second set of polysilicon strain gauges at the opposite interface—resulting in a dual-layer architecture with eight independently addressable sensors symmetrically distributed at both the top and bottom SiN–polymer interfaces [1], [3]. The sensor layers are vertically aligned at the cantilever base and fully encapsulated via low-temperature, wafer-scale bonding using BCB 3022-35, enabling differential readout and full-bridge configurations while remaining compatible with standard MEMS batch processing.

Trilayer cantilevers with polymer cores offer mechanical advantages over monolithic silicon counterparts. The low Young's modulus of BCB (2.9 MPa) allows fabrication of thick cantilever beams with reduced spring constants while maintaining high deflection sensitivity due to enhanced strain localization away from the neutral axis [1]. Prior work demonstrated that embedding a single piezoresistor at one interface improved force sensitivity by utilizing strain gradients in the multilayer stack [2]. However, such single-layer designs lack the ability for differential sensing and full-bridge configurations, which are critical for mitigating thermal drift and suppressing common-mode noise.

This work extends the trilayer platform by embedding polysilicon piezoresistors at both SiN–polymer interfaces, each fabricated independently on separate wafers. The sensors are symmetrically positioned to maximize axial strain and enable differential signal acquisition across matched piezoresistors. To preserve dopant profiles and electrical performance, wafer bonding is performed below 250 °C using spin-coated BCB. The completed cantilevers feature hermetically sealed multilayer sensor stacks, buried metal interconnects, and integrated silicon tips formed via crystallographically aligned KOH etching.

Fabrication begins with thin-film depositions of low-stress silicon nitride (LSNT), polysilicon, and borosilicate glass (BSG) on double-side polished silicon wafers. Polysilicon strain gauges are patterned using photolithography and etched with KOH while the BSG layer serves as an etch mask. Contact pads are defined via lift-off using Cr/Au metal stacks. One wafer is spin-coated with BCB, soft-baked, and aligned to the second wafer using backside alignment. The stack is then bonded to form a sealed trilayer structure. The handle wafer is patterned and etched to define the chip body, and the front side is selectively thinned to facilitate tip formation. A crystallographically selective KOH etch is then used to fabricate the silicon tip [4], yielding apex radii below 40 nm.

SEM and optical inspection confirm the structural integrity and alignment of the fabricated cantilevers. A scanning electron microscopy (SEM) overview image of a single device is shown in Fig. 1a, highlighting the chip body, trilayer cantilever, and buried metal traces leading to the sensor pads. An SEM close-up of an individual cantilever showing chip body, trilayer cantielver and integrated silicon tip (Fig. 1b). Optical micrographs verify the vertical alignment of the piezoresistive sensor layers, while also indicating a minor lateral misalignment during bonding (Fig. 1c). AFM imaging performed using the developed cantilever—with sensors connected in a full-bridge configuration—demonstrates operational performance with a resonance frequency of 335 kHz and a deflection sensitivity of 40 nm/V (Fig. 1d). This matches the performance of optical beam deflection (OBD) systems and doubles the sensitivity of prior single-sensor-layer trilayer designs.

This multilayer sensor integration strategy advances self-sensing probe technology by combining high strain sensitivity, differential readout, and scalable MEMS fabrication. The resulting probes support compact, laser-free AFM operation in ambient and fluidic environments and provide a versatile platform for multi-sensor integration in next-generation scanning probe systems.

[1] N. Hosseini, S. H. Andany, M. Neuenschwander, M. Kangul, J. D. Adams, and G. E. Fantner, "A polymer–semiconductor–ceramic cantilever for high-sensitivity fluid-compatible microelectromechanical systems," *Nature Electronics*, vol. 7, no. 7, pp. 567–575, Jul. 2024, doi: 10.1038/s41928-024-01195-z.

[2] J. D. Adams, S. H. Andany, N. Hosseini, and G. E. Fantner, "Analysis of local deformation effects in resistive strain sensing of a submicron-thickness AFM cantilever," in *Proc. SPIE 8763, Smart Sensors, Actuators, and MEMS VI*, 2013, p. 876327.

[3] N. Hosseini, O. Peric, M. Neuenschwander, S. H. Andany, J. D. Adams, and G. E. Fantner, "Batch fabrication of multilayer polymer cantilevers with integrated hard tips for high-speed atomic force microscopy," in *Proc. Transducers & Eurosensors XXXIII*, Berlin, Germany, 2019, pp. 2033–2036, doi: 10.1109/TRANSDUCERS.2019.8808606.

[4] J. Li, Y. Sun, and W. Pang, "Fabrication of cantilever with self-sharpening nano-silicon-tip for AFM applications," *Microsystem Technologies*, vol. 19, pp. 285–290, 2013.

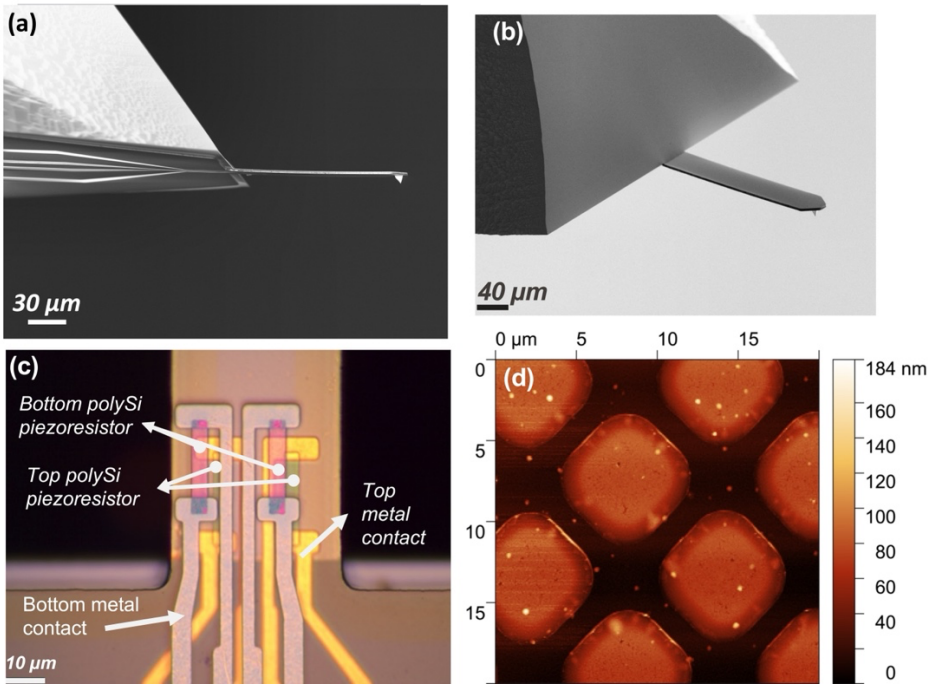

Figure 1: Characterization of the multilayer trilayer cantilever: (a) SEM overview image of a fabricated device showing the chip body, trilayer cantilever, and buried metal interconnects leading to contact pads and piezoresistors; (b) SEM image of an individual cantilever, showing the silicon chip body, trilayer cantilever, and integrated silicon tip; (c) Optical image showing the polysilicon piezoresistive strain sensors and corresponding metal contacts, showing alignment after wafer bonding and device release; (d) AFM image acquired using the developed probe, where embedded strain sensors are connected in a full-bridge configuration, with data collected from the bridge output and a resonance frequency of 335 kHz

Pattern dependent micro needle formation in the SPPW process using a digital mask

Myung Seo Kim [a], Jun Ho Song [a], Seo Rim Park [a], Young Tae Cho [a]

[a] Changwon National University, Changwon, 51139, Republic of Korea
e-mail: ytcho@changwon.ac.kr

keywords : SPPW(Self Propagating Polymer Waveguide), High aspect ratio, Digital mask, Micro needle

Micro- and nanoscale structures have proven essential in a wide range of fields, including fuel cells, electronics, and electrical engineering. In particular, the demand for high-resolution microfabrication has increased due to the miniaturization of mechanical and electronic components driven by advances in artificial intelligence (AI). Among these, high-aspect-ratio structures, characterized by large surface area-to-volume ratios and tall profiles relative to their diameter, have demonstrated significant utility in applications such as gas sensors [1] and micro-lattices [2]. Various fabrication methods have been explored for producing such structures, including nanoimprint lithography (NIL) and 3D printing, but these approaches present limitations in achievable aspect ratio, production speed, or structural precision.

The Self-Propagating Polymer Waveguide (SPPW) process, a nonlinear photopolymerization technique, has recently gained attention for its ability to fabricate high-aspect-ratio structures in a single exposure. This is achieved by exploiting refractive index variations generated during the UV curing of photopolymer resins [3]. However, the SPPW process requires masks to spatially modulate UV exposure. Since traditional physical masks must be redesigned for each pattern change, this presents a significant drawback in terms of scalability and flexibility.

In this study, we replace conventional physical masks with a digital mask implemented via a Digital Micromirror Device (DMD) engine, enabling programmable and selective UV exposure (**Figure 1**). Additionally, we utilize a phenomenon typically considered undesirable in polymer structures, namely the spontaneous aggregation of high-aspect-ratio features (above ~5:1 aspect ratio), as a means of shape control to explore their potential application as microneedles. Experiments were conducted using the DMD engine of a Digital Light Processing (DLP) 3D printer under darkroom conditions due to the photosensitivity of the resin. A circular layout, known for its mechanical stability, was used as the base geometry. Four polygonal patterns, ranging from triangle to hexagon, were tested, each inscribed in a circumscribed circle with a fixed radius of 300 μm. For each pattern, the center of aggregation, the minimum structure height required for aggregation, and the tilt angle of the structures were quantitatively analyzed.

The fabricated structures were observed from the side using a USB microscope, and each experiment was repeated three times to ensure reproducibility (**Figure 2**). High-aspect-ratio structures were successfully fabricated across all pattern types, and the structure height increased with increasing UV dose over time. The hexagonal pattern, which had the largest circumradius and thus the lowest required aggregation angle, exhibited the lowest height threshold for aggregation. However, it showed a lower aggregation rate compared to the triangular pattern, which required a greater aggregation height. This outcome was attributed to the higher number of units required for aggregation in the hexagonal pattern, approximately twice as many as in the triangular case, and the concurrent increase in resin hardness at higher UV doses.

Overall, this study demonstrates the feasibility of employing a DMD-based digital mask in the SPPW process and proposes a novel approach for high-precision microstructure fabrication by repurposing polymer aggregation as a shape control strategy for microneedle formation.

Acknowledgement

This work was supported by the National Research Foundation of Korea(NRF) grant funded by the Korea government(MSIT)(NRF 2023R1A2C3006499) and the Korea Institute for Advancement of Technology (KIAT) grant funded by the Korean government (MOTIE) (141588607, Additive Manufacturing Technology Innovation Alliance for Aerospace/Small modular reactor/Defense industry).

References
[1] S.G. Higgins et al., Adv. Mater. 32 (2020) 1903862.
[2] A.J. Jacobsen, W. Barvosa-Carter, S. Nutt, Adv. Mater. 19 (2007) 3892–3896.
[3] A.A. Sukhorukov et al., J. Nonlinear Opt. Phys. Mater. 11 (2002) 391–407.

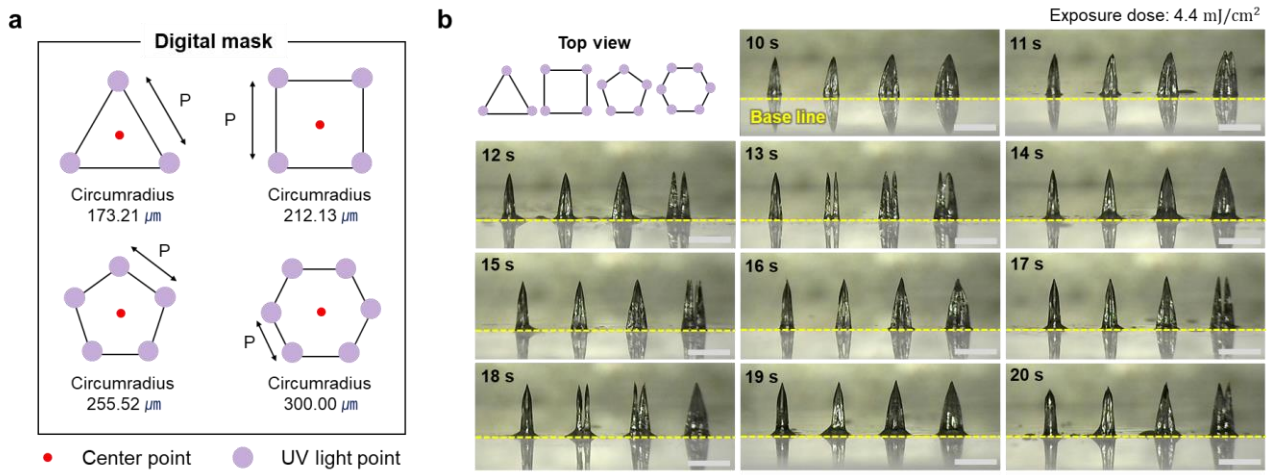

Figure 1. a) A digital mask generated via a DMD engine. b) A side view of the structure fabricated through the SPPW process using the digital mask.

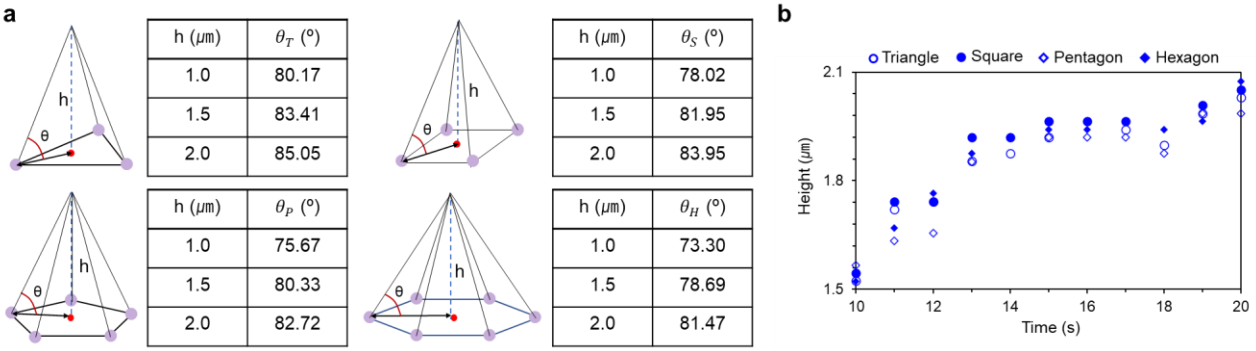

h (μm)	θ_T (°)
1.0	80.17
1.5	83.41
2.0	85.05

h (μm)	θ_S (°)
1.0	78.02
1.5	81.95
2.0	83.95

h (μm)	θ_P (°)
1.0	75.67
1.5	80.33
2.0	82.72

h (μm)	θ_H (°)
1.0	73.30
1.5	78.69
2.0	81.47

Figure 2. a) Isometric views of each structure fabricated via the SPPW process and the angle of each strut required for aggregation. b) Comparison of structure heights over time in the SPPW process.

Fabrication of Ultra-Scaled Back-End TiN Contacts in Silicon-Rich Oxide for High Density Memory Applications

C. Charpin-Nicolle [a], G. Navarro [a], A. Salvi [a], C. Pellissier [a], P. Sixt [a], E. Nguyen Gia Can [a], F. Baudin [a], C. Beluffi [a], R. Souil [a], J.P. Nieto [a], D. Despois [a], F. Laulagnet [a], T. Magis [a], R. Blanc [a], O. Glorieux [a], G. Boniface [a], J. Rottner [a], T. Jimbo [b], T. Kojiri [b], V. Barral [a], F. Andrieu [a]

[a] CEA-Leti, Uni. Grenoble Alpes, 38000 Grenoble, France
[b] Zeon Corporation R&D Center, 1-2-1 Yako, Kawasaki-ku, Kawasaki, Kanagawa, 210-9507, Japan
e-mail: christelle.charpin@cea.fr

Fabrication of ultra-scaled contacts is a main challenge to improve the memory array density in particular in embedded applications targeting sub-30 nm technology nodes [1].
To avoid delamination of some advanced memory stacks, a dedicated oxide is required, so-called "SRO", Silicon-Rich Oxide, or SiO_x ($x<2$) before the deposition of memory materials. In this study, we fabricated ultra-scaled contacts on 200 mm silicon substrates <100>, with a diameter down to 30 nm, using a damascene integration approach: fabrication of vias in SRO, metal filling and removal of the metallic surplus by using chemical mechanical polishing process. To our knowledge, it is the first time such tiny contacts could be fabricated in a Silicon-Rich Oxide material.
We firstly developed SRO material, using Applied Materials Centura 5200 tool, equipped with a DxZ PECVD chamber. SRO is a non-stoichiometric Silicon Oxide, obtained by incomplete dissociation of a silicon precursor. SRO has to fulfill the following specifications: a refractive index of 1.50 ± 0.01 at a wavelength of 633 nm; a thin thickness of about 40 nm (due to damascene integration constraints, i.e. filling); a non-uniformity of less than 5%, and a good stability (index and thickness) over time and within temperature, to overcome Back-End thermal budget. The impact of SiH_4, He and N_2O flows were investigated to deposit thin thicknesses, improve uniformity and get a refractive index of 1.5 (**Fig. 1**). SRO 40 nm film could be developed, reaching all specifications. Deposition rate is less than 200 nm/min and thickness uniformity is about 2% (1 - sigma standard deviation). Impact of ageing and annealing is evaluated, demonstrating a good stability of SRO.
Various sizes, shapes and densities of devices were designed, ranging from 30 nm to 300 nm, and single devices as well as double, quadruple devices and even mini-arrays (9×8 devices) were implemented. Electron beam lithography was used to define devices down to 30 nm. A thin positive tone resist (TOK CAP164) was chosen to define holes [2], and a dedicated etching process was tuned in a CCP reactor with a low RF power in order to minimize the etch rate (lower than 100 nm/min) and to correctly open the patterns. A combination of two TiN deposition processes (process A + process B) was found to correctly fill small vias. Conformity of the deposited material was verified using TEM analyses after partial deposition of TiN. Chemical Mechanical Polishing (CMP) process was specifically adapted, using Applied Materials Mirra tool, to minimize the TiN removal rate (lower than 100nm/min) and increase selectivity towards to SRO. CMP was performed on standard hard polymeric pad and alumina-based slurry.
In particular, various combinations of thicknesses for TiN deposition processes A and B were investigated to minimize SRO thickness consumption. T_R is defined as $T_B/(T_A+T_B)$. T_A and T_B are thicknesses deposited respectively using Process A and Process B. T_A+T_B is hence the total TiN deposition thickness. Optimized range could be found for T_R lower than 0.7, with an average SRO consumption lower than 3.3 nm, as demonstrated in **Fig. 2**.
In-depth morphological characterizations (SEM, TEM, EDX and AFM analyses) were conducted. After polishing process, TiN consumption in vias is less than 5 nm whatever the dimension of the via, which is also confirmed by AFM measurements (**Fig. 3**). EDX measurements highlight no oxidation at the surface of the via, and show homogeneity of Ti and N elements inside the vias.
Electrical functionality was demonstrated, measuring the resistance as a function of the via surface. The preservation of the TiN resistivity independently from the size/surface of the device was confirmed (**Fig. 4**).

[1] H. Saito et al., IEEE International Memory Workshop (IMW), 2021.
[2] A. Goodyear et al., Proc. SPIE, Vol. 9428, Advanced Etch Technology for Nanopatterning IV, 2015.
Acknowledgements: NEDO's Green Innovation Fund Projects / Next Generation Digital Infrastructure Construction Project / Next Generation Green Data Center Technology Development

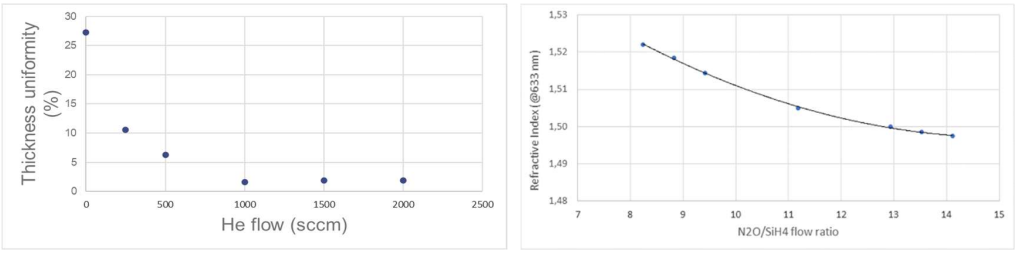

Fig. 1. Impact of He flow on thickness uniformity of SRO film (left). Impact of the N_2O/SiH_4 flow on the refractive index (@ 633nm) (right).

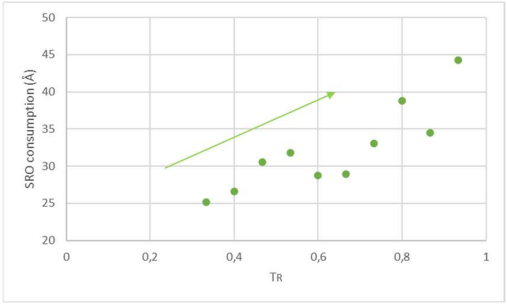

Fig. 2. Impact of Thickness Ratio (T_R) on the consumption of SRO during CMP process. T_R is defined as $T_B/(T_A+T_B)$. T_A and T_B are TiN thicknesses deposited respectively using Process A and Process B.

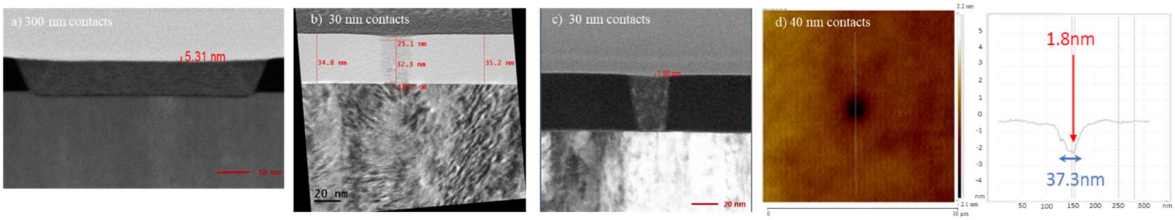

Fig. 3. a): SEM observation after TiN polishing. Via dimension is 300 nm, recess is less than 6 nm. b) and c): TEM observations after TiN polishing. Via diameter is roughly 30 nm, recess is less than 2 nm. d): AFM measurements on smallest contacts confirm the depth lower than 2 nm.

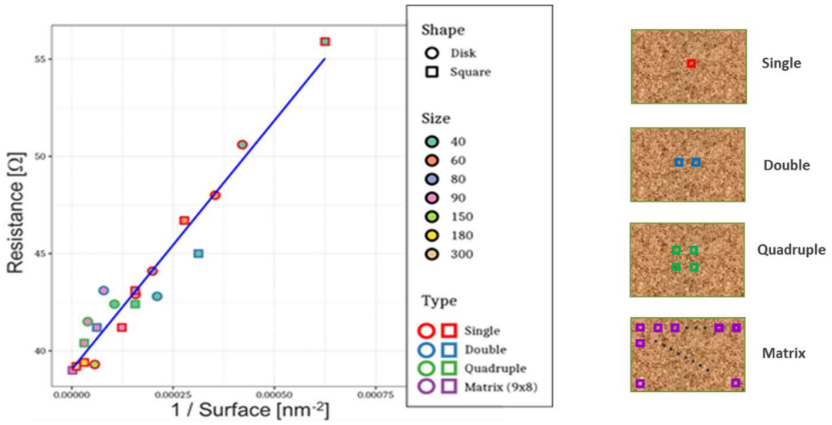

Fig. 4. Resistance as a function of the nominal surface of the fabricated TiN plugs (left). Various types of patterns were considered (square patterns are schematized on the right).

Oral Session 5B:
Biodevices and Systems II

Fabrication of Low-cost Microfluidic Devices for Point-of-Care Bacterial Diagnostics

Maria Szola[a], Peng Tian[a], Chang Liu[a], Aysegül Develioglu[a], Gabriel Weber[a,b], Marceau Brisselian Kamary[a], Thomas Mortelmans[a,b], Dimitrios Kazazis[a], Philipp Berger[c], Yasin Ekinci[a]

[a] Laboratory for X-ray Nanoscience and Technologies, Villigen, 5232, Switzerland
[b] Swiss Nanoscience Institute, University of Basel, Basel, 4056, Switzerland
[c] Laboratory of Multiscale Bioimaging, Paul Scherrer Institute, Villigen, 5232, Switzerland

e-mail: maria.szola@psi.ch

Keywords: Microfluidic device, bacterial identification, nano-imprint

Rapid and reliable detection, enumeration, and identification of bacteria remain vital across various fields, including clinical diagnostics and food safety [1]. Among the many bacterial infections impacting global health, urinary tract infections (UTIs) represent a particularly widespread and recurrent challenge [2]. This issue is further intensified by the rising threat of antimicrobial resistance [3], which continues to complicate treatment strategies and necessitates the development of innovative diagnostic tools. While conventional culture-based microbiological methods remain the golden standard, they are often hindered by long processing times, the need for specialized personnel, and reliance on costly instrumentation.

In this work, we present a novel microfluidic platform designed to facilitate rapid, on-site bacterial analysis. The device is fabricated using a combination of advanced micro- and nanofabrication techniques, including grayscale electron beam lithography, nanoimprint lithography, and plasma-assisted bonding [4]. These methods enable the creation of a poly(methyl methacrylate) (PMMA)-glass hybrid device (Fig. 1 (a)) incorporating precise microfluidic channel geometries suited for efficient bacterial manipulation. The system is engineered for broad-range bacterial trapping (Fig. 2) and supports multiplexed identification through immunoassay-based approaches [5, 6]. The device operates based on size-dependent trapping, achieved through a microfluidic architecture featuring a gradually decreasing channel height in the trapping region (Fig 1 (b)). This geometry enables physical retention of bacterial cells according to their size, facilitating effective separation and concentration without the need for external labeling or forces.

In this presentation, we will showcase cost-effective device fabrication and experimental results demonstrating the platform's ability to trap and differentiate between multiple bacterial species. By introducing controlled mixtures and varying initial concentrations, we will assess the trapping efficiency of the device for each species. Quantitative analyses will be presented to compare the concentration profiles post-trapping. This microfluidic device offers a promising alternative to conventional diagnostic workflows by combining portability, scalability, and cost-effectiveness. Its design accommodates a wide spectrum of bacterial concentrations and lays the groundwork for species-level discrimination.

Looking forward, future efforts will focus on validating the platform with clinical UTI samples and investigating its applicability for antibiotic susceptibility testing and mechanobiological studies, aiming to extend its utility across both research and diagnostic contexts. In parallel, we are currently pursuing process transfer to grayscale laser lithography region (Fig 1 (c)) to enable faster, more scalable prototyping and reduce reliance on electron beam lithography for microstructure definition.

[1] Davis, C. J. Microbiol. Methods, 103 (2014) 9–17.
[2] Schmiemann G et al., Dtsch Arztebl Int. (2010), 107(21):361-7.
[3] Larsson, D.G.J., Flach, CF. Nat Rev Microbiol 20 (2022) 257–269.
[4] Mortelmans, T. et al., Microelectron. Eng., 225 (2020) 111272.
[5] Mortelmans, T. et al., ACS Appl. Nano Mater. 5 (2022) 517−526.
[6] Mortelmans, T. et al., ACS Sens. 9 (2024) 2455−2464.

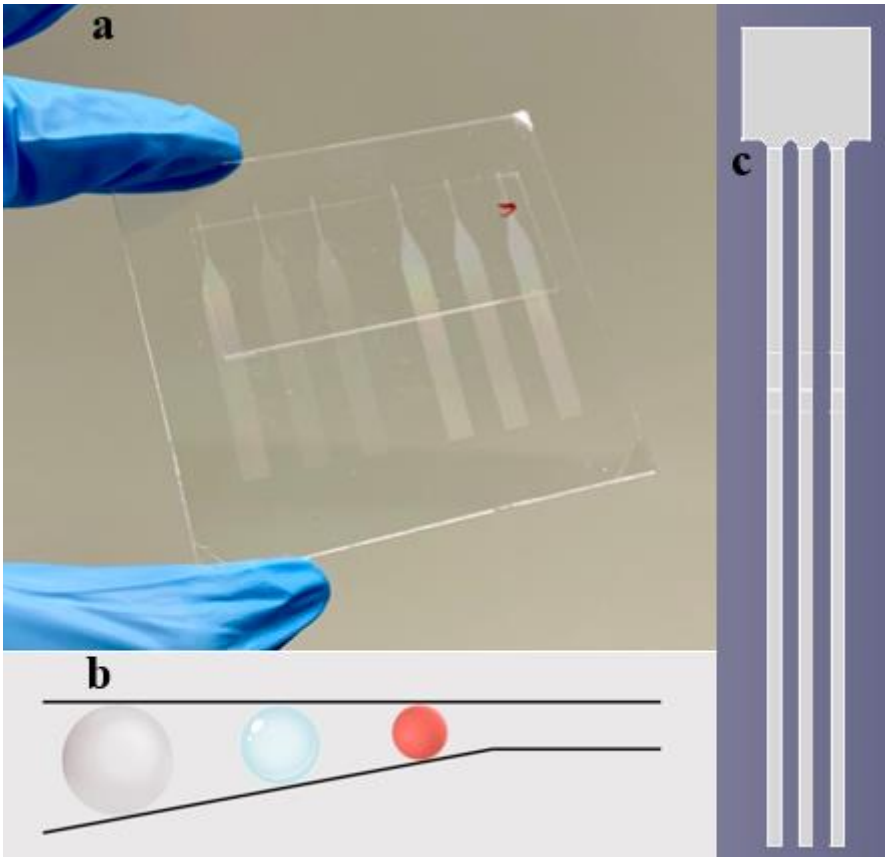

Figure 1. (a) Photograph of the fabricated PMMA-glass microfluidic device featuring patterned channels designed for bacterial analysis. (b) Schematic cross section of the device's trapping region. (c) Top view of the upgraded channel design for grayscale laser lithography.

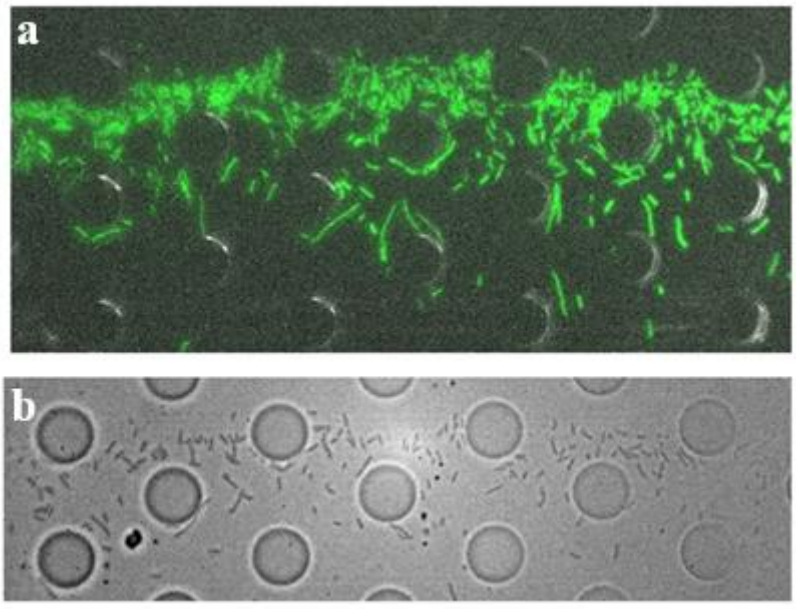

Figure 2. (a) Fluorescence (with DNA staining) and (b) brightfield microscopy images of bacteria (~1 μm) captured in the microfluidic channel.

Non-Invasive Label-Free Electrical and Optical Parallel Recordings of Electrophysiological Action Potentials of hiPSC Cardiomyocytes

Julien Hurtaud[1], Alessio Boschi[1], Giuseppina Iachetta[1], Michele Dipalo[1], Francesco De Angelis[1]
[1] Istituto Italiano di Tecnologia, Plasmon Nanotechnologies, Genova, Italy
(francesco.deangelis@iit.it)

Abstract:

Among the many molecules tested every year as potential drugs, 90% fail to reach the market despite sometimes more than 12 years of development and over two billion individual costs. As rejections are often related to cardiovascular issues, some cell-lines such as hiPSC cardiomyocytes have been extensively used to model drug toxicity *in vitro*, translating efficiently to clinical trials afterward. However, at the current state of art, parameters such as mechanical contractility, electrophysiological signals and calcium fluxes must be measured separately, on different types of devices and often on different *in vitro* cultures. This makes the interpretation of results difficult and therefore reduces their relevancy. In that context, we developed a novel device that: i) is able to optically record electrophysiological signals in a label-free and non-invasive manner. ii) has embedded electrodes for direct recordings of field potentials and for cell stimulation at the electrode location iii) is transparent enough to enable calcium imaging using fluorescence microscopy. Moving beyond the simple sum of these data, the device couples these modes that can be used independently and simultaneously. Thus, it provides a platform on which relevant and time-efficient studies of cardiotoxicity can be performed. One can use electrodes to pace the surrounding cells and detect discrepancies in cardiac frequency due to assayed drugs. The cardiotoxic effect can be detected at the whole culture level using the high-density optical sensors. In this work, we could observe for example the modification induced by isoprenaline in action potential duration and frequency. To conclude, this device exploits and combines microfluidics, fluorescent dyes, complex nanofabrication and pass-through electrodes to transduce the cardiac action potentials into optical signals. Using the same structure, it can also perform basic electrical recordings and stimulation, allowing deep studies of drugs cardiotoxicity, necessary to improve drug approval rates.

Keywords:
biosensor, cardiomyocyte, contractility biomedical engineering, nanofabrication, membranes, multi-electrode array, label-free detection.

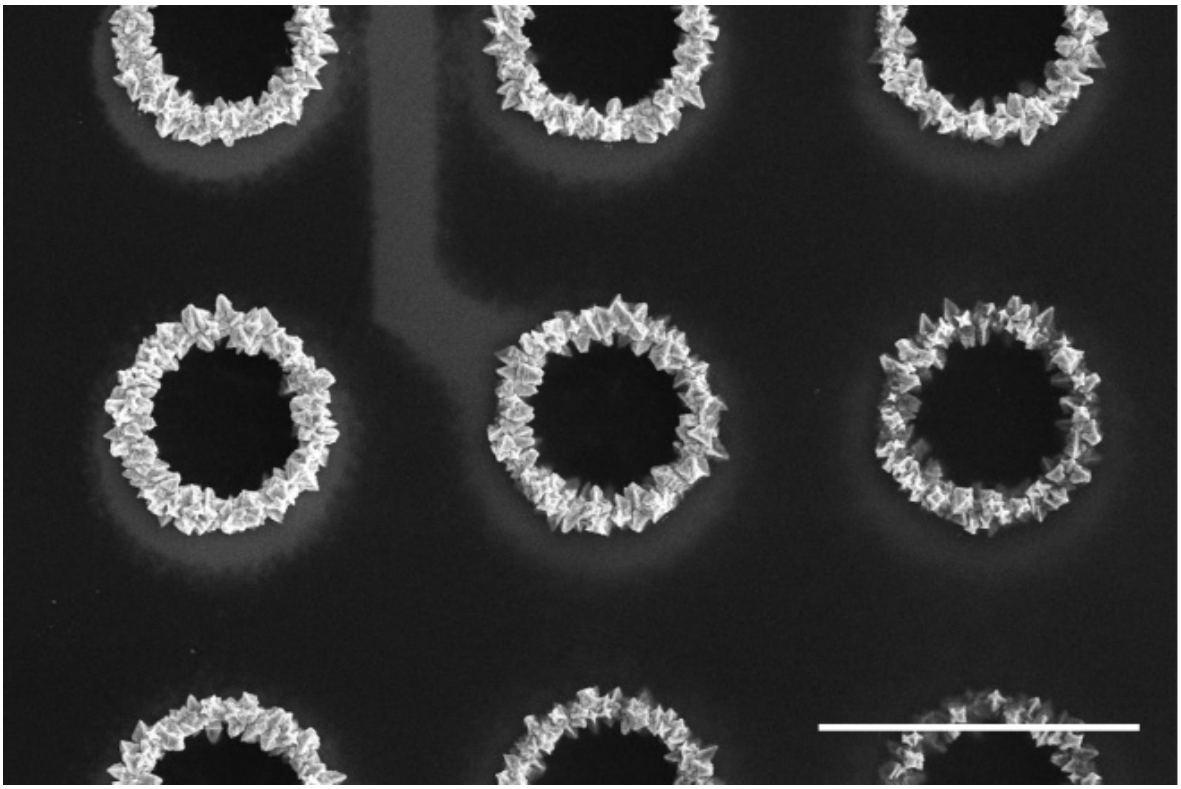

Figure 1: SEM image showing the all-in-one microstructures used on TOXFREE devices to detect in a label-free, non-invasive manner, and at whole culture scale, the contraction of hiPSC cardiomyocytes. On some of the structures, electrodes functionality is embedded as seen at the center. Scale bar 50 µm.

Biodegradable silk fibroin nanofiber-based microparticles for wound regeneration

Marc Navarro[a], Laia Bagur[a,b], Lasse Højlund Eklund Thamdrup[c], Fatemeh Ajalloueian[c], S.D. Aznar-Cervantes[d], Xavier Muñoz-Berbel[a] , Anja Boisen[c], Andreu Blanquer[b], Gonzalo Murillo[a]

[a] *Institute of Microelectronics of Barcelona (IMB-CNM, CSIC), Barcelona, 08193, SPAIN*
[b] *Departament de Biologia Cel.lular, Fisiologia i Immunologia, Universitat Autonoma de Barcelona, 08193, Barcelona, SPAIN*
[c] *Center for Intelligent Drug Delivery and Sensing Using Microcontainers and Nanomechanics (IDUN), Department of Health Technology, Technical University of Denmark, 2800, Kgs. Lyngby, Denmark*
[d] *Instituto Murciano de Investigación y Desarrollo Agrario y Alimentario (IMIDA), Department of Biotechnology, Murcia, 30150, SPAIN*
e-mail: marc.navarro@imb-cnm.csic.es

The development of green electronics is increasingly driven by the need to reduce e-waste and develop sustainable alternatives to conventional materials. As the silicon chip industry continues to expand, with projected e-waste reaching 75 Mt by 2030 [1], biodegradable and biocompatible materials are gaining relevance for applications such as transient electronics and bio-integrated devices. Particularly within the biomedical field, materials that combine functionality with low environmental impact are essential for designing implantable or resorbable systems capable of interfacing with biological tissues [2,3]. Silk fibroin (SF) has emerged as a leading biodegradable piezoelectric polymer for biomedical applications, uniquely combining sustainability with functional efficacy. Its intrinsic piezoelectricity stems from the orientation of β-sheet domains, which can be enhanced through post-processing, and enables mechano-electrical stimulation for tissue regeneration [4]. This effect is particularly pronounced when SF is processed into nanofibers via electrospinning, which promotes domain alignment due to the high electrical field. Facing other biodegradable polymers like chitosan, SF exhibits a higher and more tunable piezoelectric coefficient (d_{33}) [5,6].

In this work, we present biodegradable microparticles, made of piezoelectric SF nanofibers, designed to generate cell electrical stimulation when actuated by an ultrasound stimulus in the medical application range (1-20 MHz). The main target is to promote skin cell differentiation, thus enhancing wound regeneration. The scaffold-like architecture and submicron dimensions of the fibers forming the microparticles enable efficient mechano-electrical stimulation for tissue regeneration.

A 17% (w/v) SF solution was used to electrospin a membrane of nanofibers in a Fluidnatek LE-10 electrospinner. This SF solution was doped with 0.5% (w/w) of glycerol. Elecostrpining conditions are shown in Figure 1. The electrospun membranes were crystalized by vacuum annealing in H_2O saturated atmosphere overnight or by methanol immersion during 45 min [7]. The microparticles were cut down using a patented procedure (WO2024184189) [8] at 30 kN for 5 min. Figure 1 shows the microparticle fabrication process, from electrospinning to cutting.
FTIR spectra confirms sample crystallization with both methods. Figure 2A shows SEM images of cut SF microparticles. Regarding cell adhesion and morphology, Figure 2B and 2C display human keratinocytes (HaCaT) and normal human dermal fibroblasts (NHdF) cultured on electrospun SF nanofibers. Figure 3 shows the cell viability of HaCaT and NHdF cells cultured for 3 days under standard conditions. For both crystallization methods, cell viability remained above 88%. We are now assessing the cell viability of the microparticles and validating cell stimulation by ultrasound-driven mechanical actuation.

[1] B. Tansel et al., Environment International 98 (2017) 35–45.
[2] R. Wang et al., ACS Nano 16 (2022) 17708–17728.
[3] J. Hwangbo et al., Cell Reports Phys. Sci. 5 (2024) 102099.
[4] A. Veronica et al., ChemPhysChem 22 (2021) 2266–2280.
[5] V. Sencadas et al., Nano Energy 66 (2019) 104106.
[6] G. de Marzo et al., Adv. Electron. Mater. 9 (2023) 2200069.
[7] S. Aznar-Cervantes et al., Materials Science and Engineering C 79 (2017) 315–325.
[8] F. Ajalloueian et al., Heliyon 10 (2024) e30844.

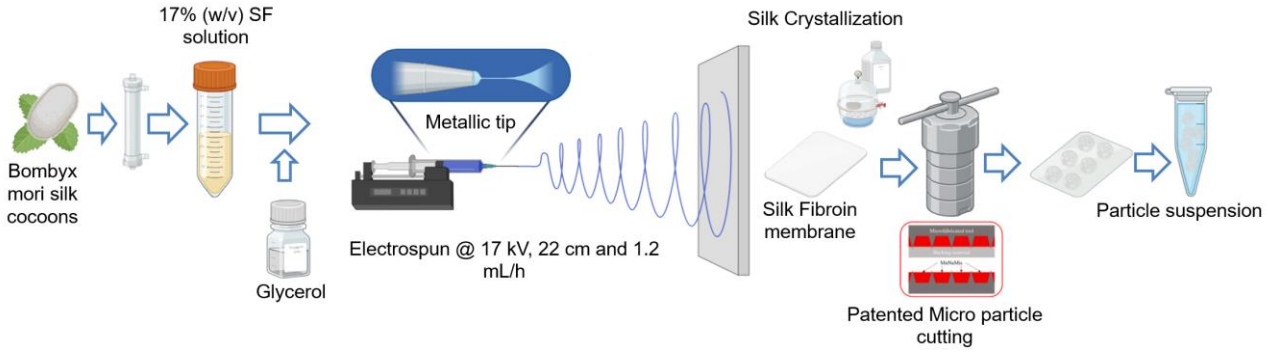

Figure 1. Fabrication process of the biodegradable SF microparticles, with electrospinning, and cutting.

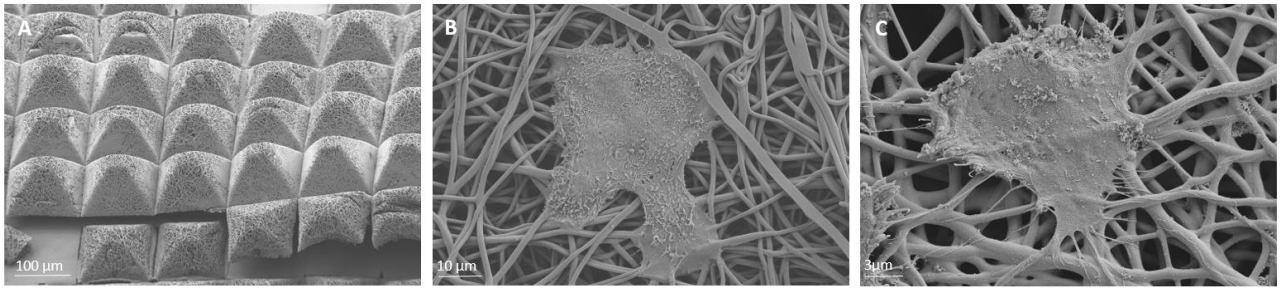

Figure 2. SEM images of (A) fabricated SF microparticles, (B) HaCaT cell adhesion on electrospun SF nanofibers (meOH crystallization) and (C) NHdF cell adhesion on electrospun SF nanofibers (H_2O crystallization).

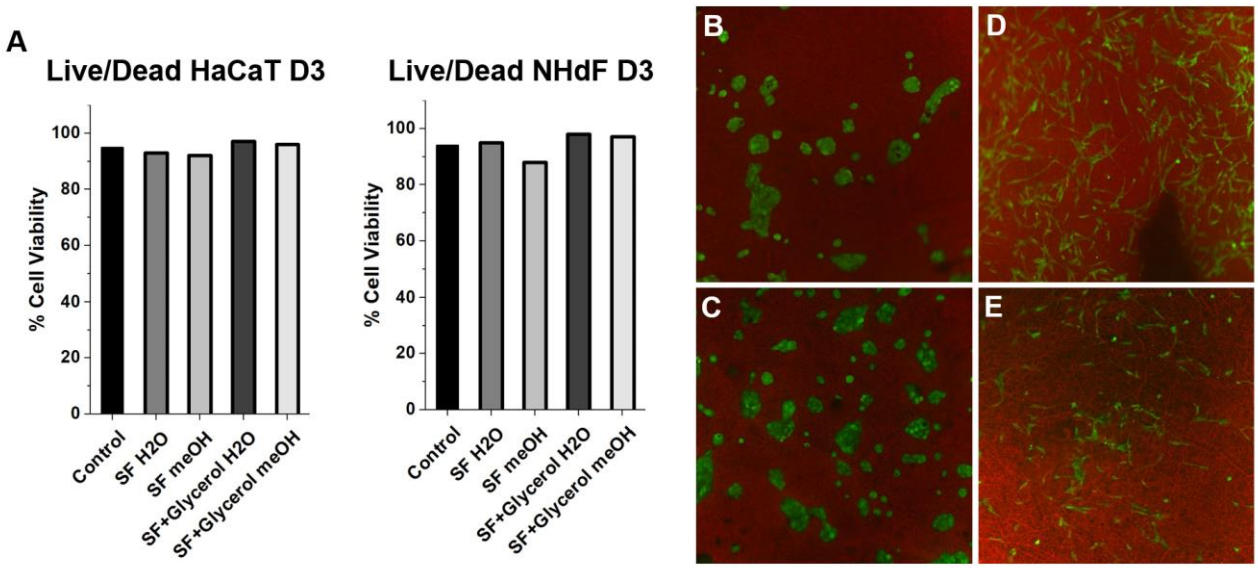

Figure 3. (A) Live-dead cell viability assay (3 days) for HaCaT and NHdF cells in electrospun SF (different crystallization methods), HaCaT cells Live-dead (3 days) in electrospun SF crystalized by (B) methanol immersion and (C) H_2O annealing, NHdF cells Live-dead (3 days) in electrospun SF crystalized by (D) methanol immersion and (E) H_2O annealing.

Development of micron mist generating nebulizer

Taki Watanabe [a], Sho Amano [a], Yuichi Utsumi [a], and Kazuhiro Kanda [a]

[a] Laboratory of Advanced Science and Technology for Industry, University of Hyogo, Kamigori, Hyogo 678-1205, Japan
e-mail: kanda@lasti.u-hyogo.ac.jp

Technologies for atomizing liquids into fine droplets using micro-nozzles [1] are widely applied across various industries. Particularly in the medical field, atomizing technology has evolved for use in nebulizers, which are devices designed to generate and deliver mist into the respiratory system. In the treatment of respiratory diseases, including COVID-19, nebulizers have played a vital role in generating mist and delivering medication deep into the lungs. It has been reported that the deposition location of mist in the respiratory tract varies depending on the particle size, and only particles with a diameter of 2 μm or less can reach the deep regions of the lungs, such as the alveoli [2]. One such system for generating mist is the mesh nebulizer. A mesh nebulizer consists of a filter with micro-sized holes, a liquid medication, and a vibrating element. When the vibrator pushes the liquid, the medication is ejected through the micro-apertures in the mesh filter. The diameter of the ejected droplets is determined by the properties of the liquid, the aperture diameter of the nozzle, and the operation of the vibrator. The droplet size distribution is often evaluated using the D50 value, which represents the droplet size at which the cumulative number of droplets in the volume fraction-based size distribution reaches 50% of the total. Previous studies have reported D50 values no smaller than 3.65 μm [3], which are still too large to effectively reach the alveolar regions of the lungs. Therefore, the objective of this study is to develop a nebulizer capable of generating mist with droplet diameters of 2 μm or less at high yield, making it suitable for deep lung delivery. This study is meaningful as it enables the generation of mist with a particle size distribution that has not been achieved by conventional technologies, thereby offering new value in the advancement of inhalation therapy.

In our previous work, we reported a fabrication technique for micro-perforated filters intended for use in mesh nebulizers [4]. By employing a two-axis piezoelectric actuator stage with nanometer-scale positioning resolution, we precisely controlled the X-ray exposure dose distribution, enabling the formation of submicron-order apertures. Furthermore, by strictly controlling the exposure process and development time on the order of minutes, we successfully fabricated a nozzle array with submicron-order aperture diameters. In the present study, we conducted mist generation experiments using the micro-perforated filter fabricated in the previous report. Figure 1 shows a cross-sectional image of the filter holes and a histogram summarizing the measured aperture diameters. The filter contains approximately 500 holes, with a median aperture diameter of about 1.36 μm. Each nozzle has a tapered shape designed to efficiently pressurize the liquid medication. This micro-perforated filter was mounted onto the nebulizer unit shown in Figure 2. The nebulizer unit consists of the micro-perforated filter, a liquid reservoir, and an actuator. A piezoelectric actuator (AE0505D16F, NEC Corp.) was used to pressurize the liquid, generating sinusoidal vibrations with an amplitude of approximately 2.0 μm at 60,000 Hz. The particle size distribution of the generated mist was measured using a particle size analyzer (LDSA-SPR 3500A, MicrotracBEL Corp.). Water was used as the test liquid, and the measurements were performed 100 times at intervals of 50 msec.

Figure 3 shows the measured particle size distribution of the mist. The figure presents the volume fraction at each particle diameter, and the D50 value was found to be 1.53 μm. This value closely matches the aperture diameter of the filter nozzles, suggesting that the droplets ejected from the nozzles travel without significant coalescence or breakup. According to the measured particle size distribution, droplets with diameters of 2 μm or less—corresponding to the target range for effective pulmonary drug delivery—accounted for 72% of the total volume. In addition, submicron-sized droplets constituted approximately 20% of the mist. These results demonstrate that the developed nebulizer is capable of producing fine mist with a high yield of sub-2 μm droplets, representing a significant improvement in droplet generation efficiency compared to conventional nebulizers. Future work will focus on applied research for the use of this nebulizer as a medical device for treating respiratory diseases.

Keywords : Mesh nebulizer, micron, mist, atomization

[1] N. Hailu, et al., Fluids. 5 (2020) 91.
[2] J.M. Borghardt, et al., Can. Respir. J. (2018) 2732017.
[3] Q. Yan, et al., Appl. Sci. 9 (2019) 1836.
[4] T. Watanabe, et al., Jpn. J. Appl. Phys. 64 (2025).

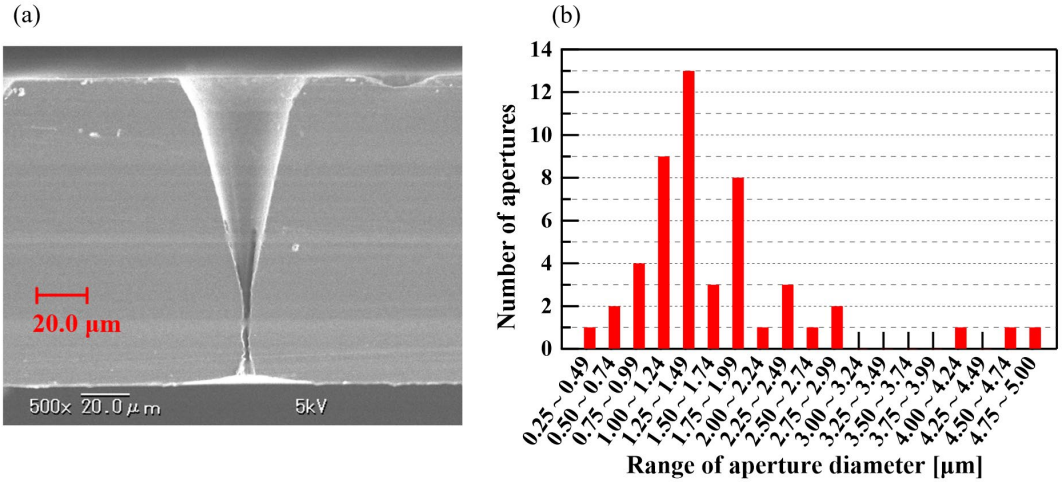

Figure 1. (a) Cross-sectional shape of the nozzles. (b) Histogram of the measured aperture diameters[4].

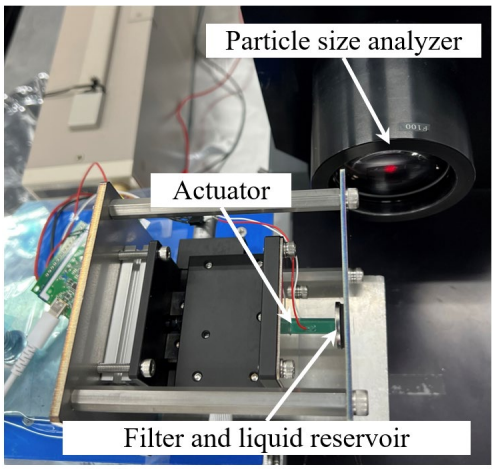

Figure 2. Nebulizer unit composed of a micro-perforated filter, liquid medication, and a piezoelectric vibrator.

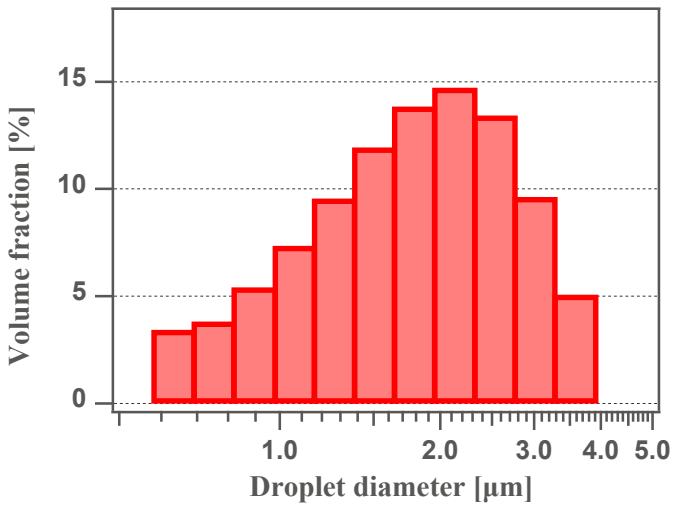

Figure 3. Volume-based particle size distribution of the mist measured using the particle size analyzer.

Three-Dimensional Manipulation of Water Droplets via Spatially Patterned Triboelectric Charging

Yu Chia Chen [a], Cheng Han Yu [a], Chin Chi Hsu [b], Jiann Shieh [a]
[a] Department of Materials Science and Engineering, National United University, Miaoli, 36063, Taiwan
[b] Department of Mechanical Engineering, National United University, Miaoli, 36063, Taiwan

e-mail: jshieh@nuu.edu.tw

With the rapid advancement of nanotechnology, droplet manipulation has emerged as a critical technology in areas such as microfluidic chips, biomedical diagnostics, self-cleaning surfaces, and precision manufacturing. Conventional droplet control methods largely rely on microchannel designs, surface energy gradients, or contact-based force mechanisms. These approaches are typically constrained to planar configurations and require physical contact, thereby limiting their applicability in non-planar or open, multidimensional environments. Although previous studies have explored light-thermal effects, magnetic fields, and mechanical deformation for droplet actuation, most systems still fall short in enabling real-time, contactless, and fully three-dimensional directional control.

To address these limitations, we propose a droplet transfer platform that utilizes tunable electrostatic charges in combination with a superhydrophobic glass substrate to enable contactless, spatially programmable droplet manipulation in 3D space. Polytetrafluoroethylene (PTFE) was employed as a low-adhesion material capable of accumulating negative charges via triboelectric friction, and a custom-built, automated control system was developed to manipulate water droplets with high precision. Experimental results demonstrate that this platform enables droplets to move precisely in multiple orientations—including horizontal sliding, vertical elevation, and lateral transfer between substrates—and can successfully facilitate the mixing of multiple droplets.

A key component of this platform is the superhydrophobic glass, fabricated using our CVD-based technique for growing silica nanowires on various substrates [1]. These silica nanowires enable a range of remarkable behaviors, including self-jumping metal [2], superwetting surfaces [3], mutual repulsion between pure water droplets [4], and the rapid, directional control of droplet motion [5]. A schematic of the 3D droplet manipulation process is shown in Figure 1. As demonstrated in Figure 2a, even pure deionized water droplets acquire a positive charge upon being dispensed from a pipette. We then introduced negative charges on the superhydrophobic glass surface by injecting water onto specific regions [6], with the accumulated charge being tunable based on the volume of water applied (Figure 2b). To further enhance electrostatic control, a PTFE plate was rubbed for a few seconds to generate additional negative charges, producing an electrostatic field capable of influencing the droplet (Figure 2c). The amount of generated charge depends on the rubbing duration and could be modulated using PTFE plates of varying sizes to alter the surface charge density.

For automated manipulation, the PTFE plate was mounted onto a 3D printer for precise motion control. Using this setup, we first guided droplets horizontally across the glass surface to mix two droplets. Then, by lifting the PTFE plates vertically, we were able to pick up droplets and transfer them onto a different substrate. Finally, by positioning the droplet above a region with a higher surface charge, we achieved targeted droplet release, completing a full cycle of contactless, three-dimensional droplet manipulation (Figure 2d). Using this platform, we demonstrated several microscale chemical reactions, including precipitation and color-change processes. This novel approach offers a versatile and contact-free strategy for manipulating droplets in open-space microfluidic systems, opening new avenues for microscale chemical processing and lab-on-a-chip applications.

[1] J. Shieh, G. F. Huang, J. Y. Tsai, B. W. Huang, Y. F. Huang, STAR Protoc. 3 (2022) 101066.
[2] J. Y. Tsai, G. F. Huang, J. Shieh, C. C. Hsu, K. Ostrikov, iScience 24 (2021) 102746.
[3] Y. C. Tsai, J. Shieh, Appl. Surf. Sci. 479 (2019) 619.
[4] K. T. Chen, Y. P. Wu, Y. F. Huang, C. C. Hsu, J. Shieh, Langmuir. 40 (2024) 13219.
[5] W. C. Huang, M. Y. Chang, J. Shieh, C. H. Lin, C. C. Hsu, Adv. Mater. Interf. (2025) in press.
[6] Q. Sun, D. Wang, Y. Li, J. Zhang, S. Ye, J. Cui, L. Chen, Z. Wang, H. J. Butt, D. Vollmer, X. Deng, Nat. Mater. 18 (2019) 936.

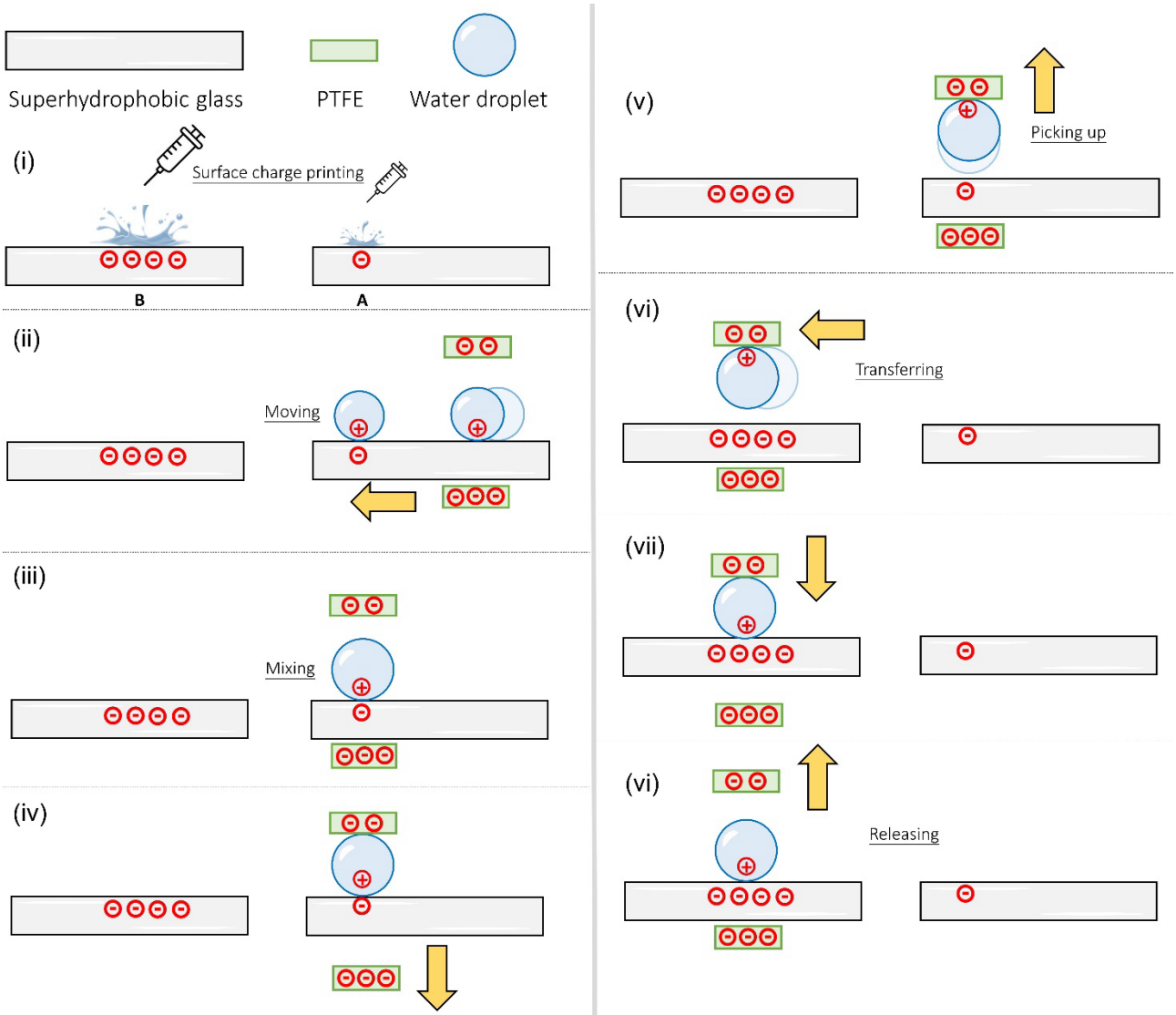

Figure 1. Schematic illustration of the three-dimensional manipulation of a water droplet.

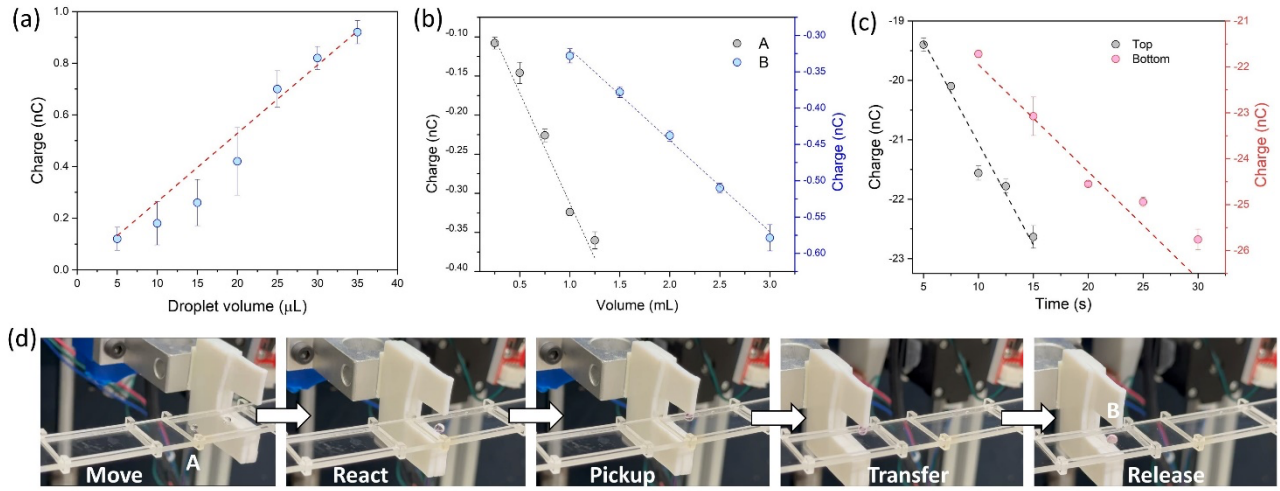

Figure 2. Manipulating water droplets in 3D space using static charge. (a) Positive charges carried by pure water droplets of various volumes. (b) Accumulation of negative charges at sites A and B via spraying water droplets of different volumes. (c) Generation of negative charges on PTFE through triboelectric friction over varying durations. (d) Snapshot demonstrating 3D manipulation by this platform.

Zero-power MEMS sensors for trees health monitoring

Zarina Nazyrova, Emile Martincic
C2N, Centre de Nanosciences et de Nanotechnologies, UMR9001 Univ. Paris-Saclay, CNRS, 91120 Palaiseau, France
e-mail: zarina.nazyrova@universite-paris-saclay.fr

***Abstract* — Global warming provokes stronger heat waves causing damages to the agricultural sector. Extreme heat exposure causes multiple stress responses in crops that threaten agricultural productivity. Innovative solutions are becoming important for real-time monitoring and adaptive management due to the growing challenges.**

Applications based on Micro-Electro-Mechanical Systems (MEMS) can provide important solutions to monitor heat wave effects due to compact, low-cost, and energy-efficient tools for precision agriculture. The integration of MEMS sensors into agricultural systems allow to monitor key environmental parameters such as soil temperature, moisture levels, plants health and atmospheric conditions with higher accuracy. These sensors enable farmers to detect early signs of heat stress, optimize irrigation and implement timely interventions, ultimately increasing resilience to the adverse effects of extreme heat events.

The created tension in the xylem vessels due to transpiration makes sap inside the plants to move from the roots to the leaves. However, during drought or freezing temperatures the tension in xylem vessels increases leading to cavitation. If the tension reaches the cavitation threshold, ultrasonic emissions occur from 100 kHz to 500 kHz that can be monitored allowing access to the health state of the trees. In this work, ZnO based on passive MEMS resonators for acoustic emissions detection are presented. The performance of the resonators set has been measured and compared to the predicted ones.

Key words - ZnO, piezoelectric MEMS, zero-power, water-stress, cavitation, ultrasonic emissions, mechanical resonators, MEMS resonators, FEM

I. Introduction

Persistent droughts impact on the agriculture sector affecting crop productivity, soil quality, water availability, and the overall economic stability of farming [1], [2]. Drought reduces photosynthetic activity, slows plant growth, and causes significant yield losses. Water stress can degrade soil health by reducing microbial activity and increasing salinity, which further reduces land productivity over time. Adaptive technology strategies such as plant health monitoring are critical to mitigating the impacts of drought and increasing the resilience of the agricultural sector [3]. It is important to monitor plants during strong and long heatwaves to prevent early-stage wilting process. High temperatures increase evapotranspiration rates, leading to rapid water loss from both soil and plant tissues. Therefore, early detection of such physiological changes is critical, especially in drought conditions which accelerates the stress response. Real-time monitoring of various parameters such as leaf temperature, stem diameter variations, sap flow rate, and stomatal conductance can provide valuable information about the water balance status of plants. These indicators allow timely adjustments to the irrigation system, preventing long-term damage and improving water use efficiency.

Plants transport water from roots to leaves through the xylem vessels due to transpiration pull, capillary action, and cohesion between water molecules. The heat waves provoke high stress in the xylem vessels leading to water evaporation and formation of cavitation bubbles which produce cavitation events [4], [5] Plants begin to experience water stress which can lead to irreversible cellular damage, impaired photosynthesis and ultimately plant death.

Every single cavitation event generates an acoustic wave that can be detected by acoustic microphone [6]. The acoustic cavitation emissions appear for grape trees in the frequency range between 100-500 kHz and the experiments of Oletic *et al.* [7] showed that the frequency and time density of the cavitation events can be used to diagnose the health state of the tree. However, long term monitoring electronics uses batteries which have a limited lifetime and produce chemical waste. One mitigating solution is to harvest energy to power the electronics [8], [9]. Advanced sensing technologies, particularly those based on MEMS enable non-invasive, continuous monitoring of cavitation events. By capturing subtle physiological changes before visible symptoms appear. These sensors support precision farming practices and help protect crops during increasingly frequent and intense heat waves associated with climate change.

The zero-power MEMS sensors can sense powerless and be used as wake-up systems for readout electronics, saving batteries and extend the battery lifetime. The system will be in sleep mode, waking up only when a sensing signal is detected [10]. Previous work [7] presented the initial version of FEM designed cavitation event sensor resonators. In present work, we describe the first fabricated prototype of the Zero-power MEMS sensor for trees health monitoring based on ZnO piezoelectric material due to the non-toxic origin and excellent piezoelectric properties. [9], [11]

II. SENSORS DESIGN AND FABRICATION

A. Sensors design

The design parameters of MEMS sensors consist of different types of cantilevers from 160 to 300 um long and 100-200 um width and shapes (Fig.1). Each cantilever is designed to resonate at a specific frequency determined by its shape, dimensions, and position within the sensor structure. Both rectangular and triangular cantilevers are used with unique mechanical characteristics. Rectangular cantilevers provide uniform stiffness and suitable for a stable deflection response, while triangular cantilevers have variable stiffness along their length, providing higher sensitivity in localized areas. Some microcantilevers were integrated within a shared cavity, while others were placed in isolated cavities to eliminate interactions. This configuration was designed to investigate and quantify the coupling effect between cantilevers and evaluate how these interactions influence their resonance frequencies and output voltages. The dimensions of the piezoelectric layer also varied from localized regions to full coverage across the cantilever surface.

These parameters have been carefully analyzed and optimized in previous work to ensure high sensitivity and reliability in various application scenarios. [7].

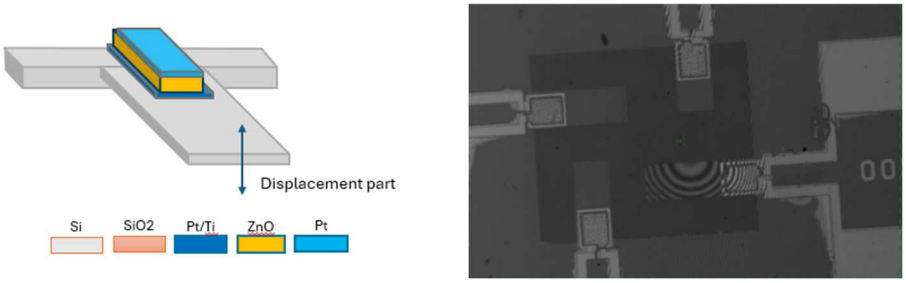

Figure 1. *MEMS resonator layered structure representation (left) and optical interferometric microscope view (right).*

However, during fabrication process the design was modified. The fundamental resonance frequencies of the first mode were calculated by FEM analysis and analytically to match the range of 100 kHz to 500 kHz measured cavitation event of grape trees. The fabrication process was carried out on 10 um SOI wafer, featuring ZnO for piezoelectric material [12]. SOI wafer was thermally oxidized by 1 µm of SiO_2 and covered by bottom electrode Pt/Ti (100nm/10nm) which were sputtered by Electron Beam Evaporator (Plassys MEB550S) using a lift-off process. ZnO piezoelectric layer was deposited by RF reactive sputtering.

The etching process of ZnO was complicated due to continuous electrical connection. ZnO can be etched by dry etching methods such as RIE, ion milling or wet chemical etching by various acids: BHF, HCl, HBr, HNO3, HF, H2O2, H3PO4, H2SO4. Wet etching process is faster and more cost-effective. However, many etchants are unsuitable for controlled MEMS processes due to the significantly higher lateral than vertical etch rates. As a result, the mixed solution was used: pre-etching by ion milling (IBE Roth & Rau Ionsys 500) and final etching by HCl acid solution diluted at 1%[13].

Then top electrodes were deposited, and the resonators were realized by DRIE using Bosch process (ICP-SPTS).

III. RESULTS AND DISCUSSION

The set of MEMS resonators was analyzed and compared with the calculated and simulation results. The resonance frequency and impedance measurements were made respectively by optical interferometry (homemade setup) and impedance analysis (Hioki IM3570). Resonators were electrically connected to an oscilloscope while the mechanical behavior was observed by interferometry (Fig. 1).

The resonance frequency was calculated by the following equation:

$$f = s.\frac{1}{2\pi}.(\beta_1 L)^2 \frac{1}{L^2}\sqrt{\frac{E.(b.t)^3}{12.\rho.b.t}} \quad (1)$$

where E is the material Young's modulus (169 GPa), ρ represents density (2700 kg/m3), L, b and t the length, width (100 µm) and thickness (10 µm) of the cantilever respectively, $(\beta_1 L) = 1.875$, a constant depending of the vibration mode and s is a shape factor related to the layered structure.

The measurements presented here consist in measuring at the same time the electrical and mechanical response of the resonators.

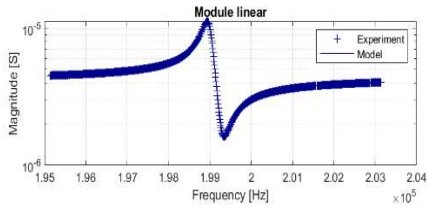

№	Length, um	Width, um	Dimensions of piezo, um	Frequency (th) (kHz)	Frequency (ex) (kHz)	Vmax (th), mV	Vmax (ex), mV	Quality factor, Q
1	280	100	295x95	145,65	178,84	6,5	1,5	1010,7
2	280	200	110x195	160,53	198,9	7	3	746,42
3	280	200	295x195	144,37	177,24	5	6	634,38
4	280	200	295x195	144,37	179,11	5	4	622,69

Figure 2. *impedance plot of one 280um length resonator (left) and measured features of 4 resonators with 280 µm long (right).*

We present here the results for 280 um long resonators. Fig. 2 (left) shows the impedance curve for resonator #2 and Fig. 2 (right) the results for several resonators of the same length, but with different surface of piezoelectric material at the top of the cantilever.

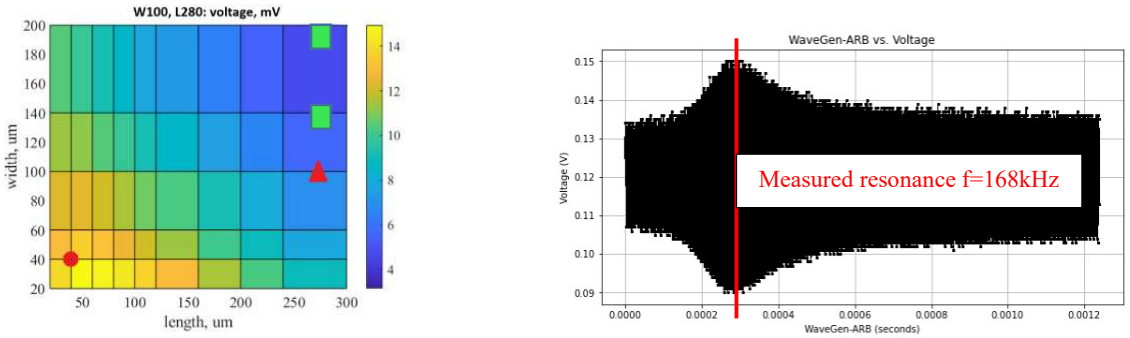

Figure 3. *a) electrode area for frequency and max. piezo-voltage. (figure adapted from [5]) b) Electrical output Voltage.*

Simulation results predicted 145 to 160 kHz and generated piezoelectric voltage of 4 to 9mV, while experimental voltage is 3mV. Depending on the area of piezoelectric surface the cantilevers perform different voltage, at larger surface the output signal showed higher signal and lower at the smaller surface. The result of the mode analysis of the resonators shows the first mode between 100kHz to 500kHz with error from 3 to 10% according to the theoretical and experimental parameters, the output voltage ranges from 1.5 to 6mV depending on the width of the resonator and dimensions of the piezoelectric material. Quality factors were measured between 600 to 1600. The highest quality factor was obtained by the thinner resonator with 100um width. However, the highest output voltage was performed by wide cantilevers with entire covering of piezoelectric material.

IV. Conclution

In this study the first fabricated prototype of ZnO-based MEMS resonators for monitoring trees health was presented. The results indicate that MEMS resonators operating within the frequency range of 100 kHz to 500 kHz produce output voltages between 1.5 and 6mV depending on the dimensions of the piezoelectric material and cantilever structure. The quality factors measured between 600 to 1600 indicate the reliability and sensitivity of the sensors.

By providing early detection of cavitation events, these sensors offer a promising solution for real-time monitoring of plant health, particularly under extreme heat conditions due to climate change. Future work will focus on the optimization of sensor design conducting experiments on real trees to validate the effectiveness of the MEMS resonators in detecting cavitation events under natural conditions and to enhance the sustainability of the monitoring system.

Acnowledgment

This work was done on the C2N micro-nanotechnologies platforms and partly supported by the RENATECH network and the General Council of Essonne.

ZnO depositions were made at Institut Jean Lamour, Univ. Lorraine by Prince Mengue and Sami Hage-Ali.

References

[1] A. J. Gabric, “The Climate Change Crisis: A Review of Its Causes and Possible Responses,” Jul. 01, 2023, *Multidisciplinary Digital Publishing Institute (MDPI)*. doi: 10.3390/atmos14071081.

[2] A. Rawat, D. Kumar, and B. S. Khati, “A review on climate change impacts, models, and its consequences on different sectors: a systematic approach,” *Journal of Water and Climate Change*, vol. 15, no. 1, pp. 104–126, 2024, doi: 10.2166/wcc.2023.536.

[3] K. Mohan, “Scientometric Analysis-based Review of Drought Indices for Assessment and Monitoring of Drought,” *Geographica Pannonica*, vol. 27, no. 2, pp. 104–118, 2023, doi: 10.5937/gp27-41531.
[4] H. Cochard, “Cavitation in trees,” Nov. 2006. doi: 10.1016/j.crhy.2006.10.012.
[5] A. Ponomarenko, O. Vincent, A. Pietriga, H. Cochard, E. Badel, and P. Marmottant, “Ultrasonic emissions reveal individual cavitation bubbles in water-stressed wood,” *J R Soc Interface*, vol. 11, no. 99, Oct. 2014, doi: 10.1098/rsif.2014.0480.
[6] L. De Roo, L. L. Vergeynst, N. J. F. De Baerdemaeker, and K. Steppe, “Acoustic emissions to measure drought-induced cavitation in plants,” 2016, *MDPI AG*. doi: 10.3390/app6030071.
[7] D. Oletic and V. Bilas, “Designing Micro-Mechanical Cantilever Resonator Arrays for Wideband Detection of Ultrasonic Xylem Cavitation Emissions Related to Plant Water-Stress.”
[8] I. Kanno, “Piezoelectric MEMS for energy harvesting,” in *Journal of Physics: Conference Series*, Institute of Physics Publishing, Dec. 2015. doi: 10.1088/1742-6596/660/1/012001.
[9] A. Kumar, M. Prasad, V. Janyani, and R. P. Yadav, “Design, fabrication and reliability study of piezoelectric ZnO based structure for development of MEMS acoustic sensor,” *Microsystem Technologies*, vol. 25, no. 12, pp. 4517–4528, Dec. 2019, doi: 10.1007/s00542-019-04524-x.
[10] V. Pinrod *et al.*, “Zero-power sensors with near-zero-power wakeup switches for reliable sensor platforms,” in *2017 IEEE 30th International Conference on Micro Electro Mechanical Systems (MEMS)*, 2017, pp. 1236–1239. doi: 10.1109/MEMSYS.2017.7863640.
[11] M. A. Borysiewicz, “ZnO as a functional material, a review,” *Crystals (Basel)*, vol. 9, no. 10, Oct. 2019, doi: 10.3390/cryst9100505.
[12] P. P. Deshpande, R. S. Pande, and R. M. Patrikar, “Fabrication and characterization of zinc oxide piezoelectric MEMS resonator,” *Microsystem Technologies*, vol. 26, no. 2, pp. 415–423, Feb. 2020, doi: 10.1007/s00542-019-04509-w.
[13] Z. Nazyrova, P. Mengue, S. Hage-Ali, and E. Martincic, “Piezoelectric ZnO Chemical Etching for Zero-Power MEMS Applications,” Feb. 2024, pp. 1–5. doi: 10.1109/DTIP62575.2024.10613113.

Oral Session 5C:
Micro-Nano Systems I

CFET novel implementation to enhance IC integration level by stacking devices in a single vertical nanowire

E. Amat, A. del Moral, J. Bausells and F. Perez-Murano

Institute of Microelectronics of Barcelona (IMB-CNM, CSIC), 08193 Bellaterra, Spain.
e-mail: esteve.amat@imb-cnm.csic.es

Abstract. CFET circuit implementation has emerged as a promising option to increase the ICs integration level. 3D configurations using vertical device topology are considered the next step to improve the performance of electronic devices/circuits. Relevant reduction in area and power consumption can be achieved.

Introduction. Nanosheet devices are a clear candidate to replace FinFETs beyond the 7-nm technology node [1], thanks to their better electrostatic and dynamic behavior, due to the use of gate-all-around (GAA) configuration. Nevertheless, IRDS forecast that the use of horizontal devices can reach its limit in terms of contact pitch dimensions [2]. In this context, vertical structures, such as vertical nanowires (vNWs), may be more suitable for further scaling down technology nodes beyond 3-nm. In contrast to horizontal arrangement, vNWs exhibit better performance in terms of low parasitic capacitance and large output current [3].

For 2.5-nm and beyond, the predicted device implementation is complementary FET (CFET), where n- and p-devices can be implemented by stacking both horizontal structures on top of each other. Recently, the vertical stacking of nanosheets has been considered to implement circuits using a CFET configuration [4]. However, we present an alternative proposal, where we stack n- and p-type transistors along a single silicon vNW implementing a circuit-in-pillar (CiP) strategy. By using our vNWs proposal a relevant reduction in parasitic elements [3] and power consumption can be obtained. Vertical structures are gaining relevance to implement low-power circuits, bio-sensors [5] and Internet of Things (IoT) circuits [6].

Device structure. Individual vNWs have already been used to implement a CMOS inverter [7]. In contrast, our novel concept proposes a step forward in technology integration evolution by stacking both transistor types in the same silicon pillar (Fig. 1). This can achieve large area reduction (>50%) and minimize to the limit the number of structures needed to implement integrated circuits (ICs). For further comparison, a SRAM cell is used as a baseline circuit to validate new technologies at advanced nodes. Fig. 2 illustrates the forecast reduction in area consumption for the case of a standard SRAM layout when it is designed using: a) nanosheet devices, b) CFET configuration, and c) our proposal. While the CFET option shows a 50% reduction in cell area compared to the conventional one [8], our proposal predicts larger area footprint reduction (~80%).

Circuit simulation. First, the entire CiP structure and its behavior were simulated using Sentaurus 3D TCAD Synopsys software [9]. To prove the feasibility of our proposal, we simulated a CMOS inverter as baseline circuit (Figs. 3. a-b). CiP structure can be implemented by using both the "conventional" inversion device mode (p-n junction, imFET) and junctionless (JLFET) option [6]. The main difference lies in the number of vertical epitaxial layers required, i.e. 7 and 3 doped regions (Fig. 3.c), respectively. The fabrication process would be valid for both configurations; although the JLFET proposal is more flexible, less accuracy is required as there is no specific region where the device channel is placed as is the case with the imFET one. Fig. 3.d presents its feasibility performance, and future applications have been presented in a previous paper [10].

Structure fabrication. The structures require a vNW diameter of tens of nanometers with a high aspect ratio. Fabrication is not trivial and can usually require the use of very expensive lithographic tools. However, a cheaper process can be explored by using colloidal lithography [11]. Fig. 4.a shows the two possible approaches to obtain the silicon vNWs: a) Reactive Ion Etching (RIE) or b) Metal-Assisted Chemical Etching (MACE). Fig. 4.b shows a Scanning Electron Microscope (SEM) image of the obtained vNW structures. Fig. 4.c depicts the integration process to be carried out based on multi-layer deposition required to make our pillar become an electronic device [12]. Fig. 4.d shows a first tentative to integrate the obtained colloidal pillar, by using the RIE approach, as a vertical electronic devices by implementing the different device regions properly separated. A key issue will be to achieve good device contacts. The use of silicide layers will be an interesting option. The use of Titanium silicide (TiSi) will be investigated as a valid material. Fig. 4.e presents a study to obtain a good source terminal based on TiSi, by considering the influence of the silicide layer thickness.

Conclusions. We present a novel approach to the implementation of CMOS integrated circuits. The basis of our proposal is to stack two devices in a silicon vNW. Its feasibility is demonstrated by simulating a CMOS inverter as a proof of concept. The device integration requires a relevant process development. Our proposal will result in a large reduction in area footprint and power consumption.

References. [1] D. Jang *et al.*, IEEE TED, vol. 64 (6), pp. 2707–2713, 2017. **[2]** IRDS 2023. **[3]** D. Yakimets *et al.*, IEEE TED, vol. 62 (5), pp. 1433–1439, 2015. **[4]** C.-Y. Huang *et al.*, IEEE IEDM, pp. 20.6.1-20.6.4, 2020. **[5]** P. Saha *et al.*, Solid. State. Elec., vol. 161, pp. 107637, 2019. **[6]** D. L. Kwong *et al.*, J. Nanotech., vol. 2012 (49212), pp. 1–21, 2012. **[7]** G. Larrieu *et al.*, Solid. State. Elec., vol. 130, pp. 9–14, 2017. **[8]** H.-H. Liu *et al.*, Proc. SPIE, vol. 12495, pp. 124950Z, 2023. **[9]** Sentaurus v. K-2018.06-SP2, 2018. **[10]** E. Amat *et al.*, IEEE Trans. Nanotech., vol. 23, pp. 435-440, 2024. **[11]** Y. Wang *et al.*, Nanotoday, vol. 22, pp. 36-61, 2018. **[12]** A. del Moral *et al.*, Solid. State. Elec., vol. 37, pp. 125014, 2012.

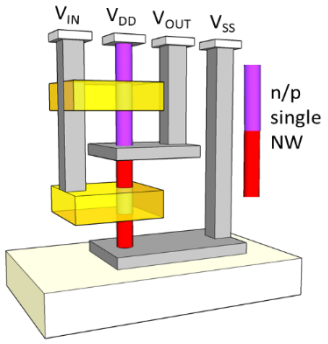

Fig. 1. Conceptual drawing of a CMOS inverter based on our CiP proposal.

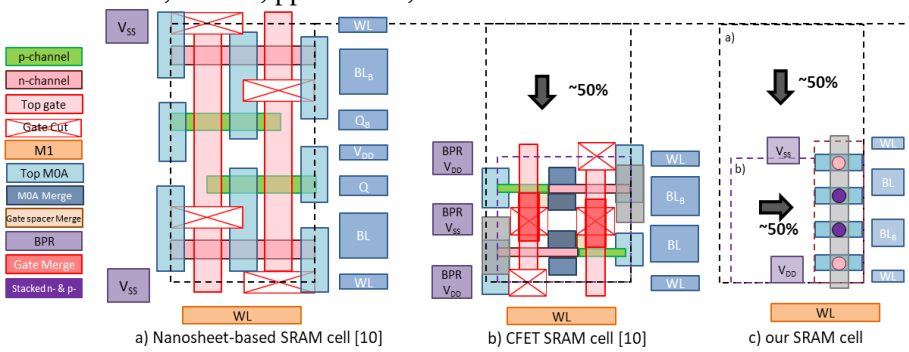

Fig. 2. Impact of device technology on SRAM cell layout design by using: **a)** nanosheet devices [8], **b)** CFET configuration [8], and **c)** prediction for our CiP proposal.

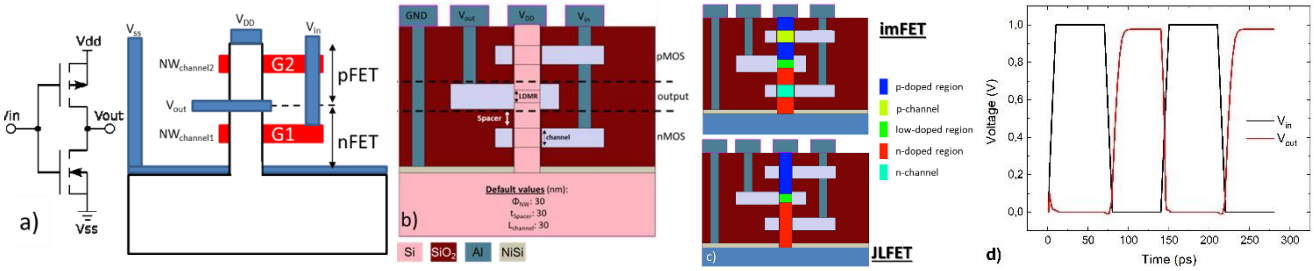

Fig. 3. **a)** CMOS inverter implementation by using our stacking device approach; **b)** Proposal of the stacked CMOS inverter with the different regions shown; **c)** different CiP implementation by using imFET or JLET options; **d)** proof of the feasibility of our CMOS inverter based on CiP implementation (transient regime).

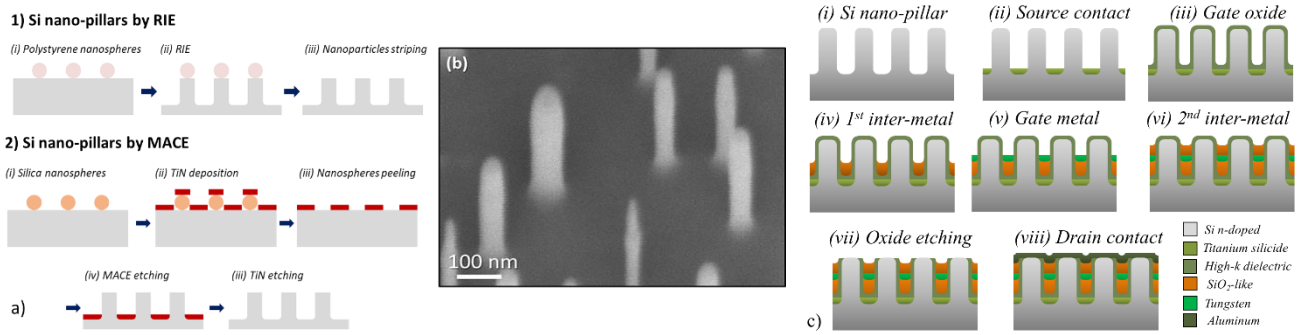

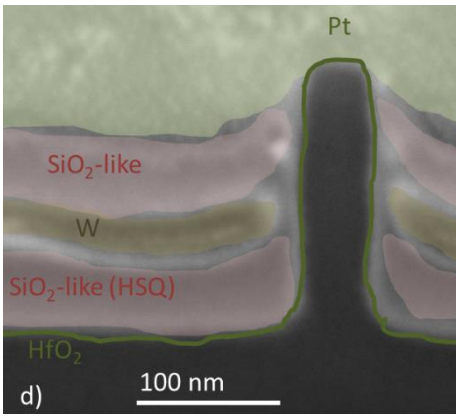

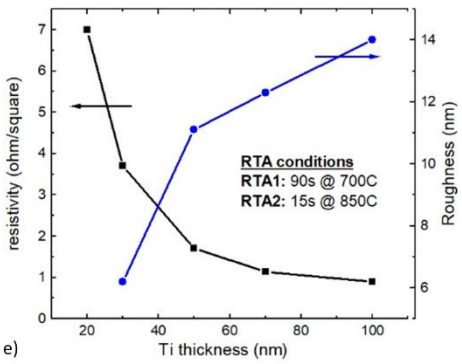

Fig. 4. a) Manufacturing process to carry on. Two approximations are explored: 1) RIE and 2) MACE. **b)** SEM image of vNWs obtained by RIE approach. **c)** Process flow to integrate the vNW as an operational FET device. **d)** vNW integration. **e)** TiSi layer optimization by studying their thickness influence.

Replaceable micromixer agitated by surface acoustic wave

Akinobu Yamaguchi [a], Masatoshi Takahashi [b], Satoshi Amaya [c], Tsunemasa Saiki [d]

[a] Toyo University, Kawagoe, 350-8585, Japan
[b] University of Hyogo, Kamigori, 678-1205, Japan
[c] University of Tokyo, Tokyo, 113-8656, Japan
[d] University of Fukuchiyama, Fukuchiyama, 620-0886, Japan

e-mail:yamaguchi054@toyo.jp

Lab-on-a-Chip (LOC) has attracted much attention in the fields of medicine, environmental measurement, and biochemistry etc. In LOC, the micropumps commonly used in unit chemical operations include mechanical diaphragm pumps and non-mechanical electro-osmotic pumps. These pumps are simple to use, but have the disadvantages of residual fluid in the tubing and pump and a larger system. A new pump proposal is therefore requested. Pumping mechanisms using surface acoustic waves (SAWs) are attracting attention as new pumps. [1, 2] Until now, many research groups demonstrated fluid drive, droplet transfer, continuous fluid pumping on a single chip and mixing. However, depending on the fluid used, the substrate can become contaminated and cannot be used again, because the microfluidic channels are directly formed on the piezoelectric substrate for SAW excitation and the liquid is directly manipulated on the substrate.

In the present study, a mixing system with SAWs was fabricated by means of interdigital transducer (IDT) electrodes arranged with a shifted central axis, and a coupling liquid was introduced between the SAW-excited substrate and the mixing vessel to enable separation of the substrate and vessel, as shown in Fig. 1(a). A jig was arranged to transmit the SAW propagation to the mixing vessel via the coupling solution and at the same time to position the mixing vessel so that it is not driven out of position by the SAW. An optical photograph of the completed system is shown in Fig. 1(b). When the aluminium (Al) vessel is placed on top of the coupling solution and jig and the SAW is driven, longitudinal wave propagation of the SAW occurs and the liquid in the Al vessel is driven as shown in Fig. 1(c). The driving force from the opposing SAW exerts a swirling force on the liquid in the Al vessel, so that the liquid in the Al vessel can mix. The system was fabricated onto the 500-μm-thick piezoelectric $LiNbO_3$ substrate using a combination of semiconductor lithography, a lift-off process and 3D printer jig fabrication. The pitch and aperture width of IDT are set to be 200 μm and 6.0 mm with log 20, respectively.

To demonstrate and characterise the mixing system, water was used as the coupling liquid and zirconia ball with a diameter of 900 μm were floated in an Al vessel. Figure 2(a) shows snapshots of the swirling behaviour at an input power of 0.1 W. Figure 3(b) shows the time dependence of the area velocity for the input power of 0.1, 0. 3, and 0.5 W. The area velocity of the ball becomes stable and almost constat in about 3 seconds after the start of power application to the IDT.

From the snapshots, kinetic energy due to swirling behaviour is evaluated as physical energy. Based on the law conservation of angular momentum, the kinetic energy, K_c, is given by $K_c = \frac{2m}{r^2}\left(\frac{dS}{dt}\right)^2$, where m, r, and dS/dt are the mass of zirconia ball, radius of ball rotation assumed that the ball is swirling in a nearly circular motion, and area velocity, respectively. The input power dependence is measured by applying powers of 0.1, 0.2, 0.3, 0.4, and 0.5 W to the IDT. We estimated input power dependence of kinetic energy, as plotted on Fig. 2(c). The results show that the output can have a nearly linear rotation behaviour with the respect to the input power. Next, in order to consider the optimisation of the coupling liquid, the mixing characteristics of different specific gravities of the coupling liquid were investigated. The method of investigation was based on the previous evaluation method, where NaCl was dissolved in the coupling liquid and the swirling characteristics of the zirconia balls in relation to the specific gravity of the coupling liquid were evaluated. The dependence of the evaluated physical energy on NaCl is shown in Fig. 3. The results show that there was almost no change in the swirling properties in the 0 - 20% concentration range where the evaluation was carried out.

This study shows that by introducing a SAW propagation mechanism with coupling liquids, a contamination-free and interchangeable mixing system can be achieved.

[1] L. Schmid and T. Franke, Lab Chip 13, 1691 (2013).
[2] M. Takahashi, A. Yamaguchi, Y. Utsumi, M. Takeo, S. Amaya, H. Sakamoto, and T. Saiki, J. Photopolym. Sci. Technol. 35, 147 (2022).

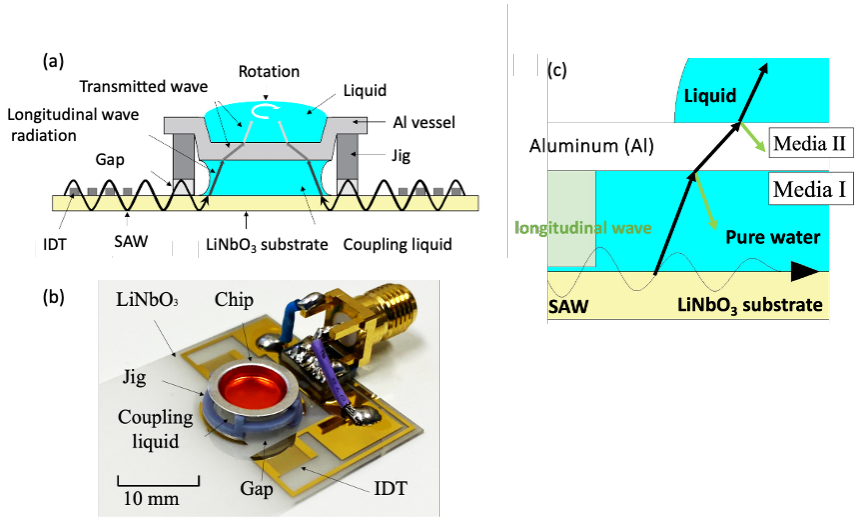

Figure 1. (a) Cross-sectional schematic of the SAW excitation mixing system. (b) Photograph of the fabricated system. (c) Schematic diagram of SAW propagation near the interface on SAW propagation.

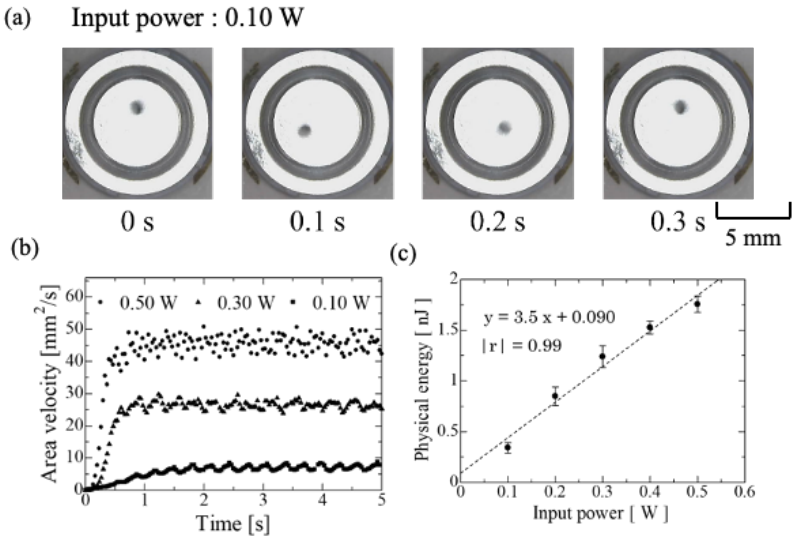

Figure 2. (a) Observed image of a zirconia ball in rotation. (b) Time dependence of area velocity. (c) Dependence of physical energy on input power.

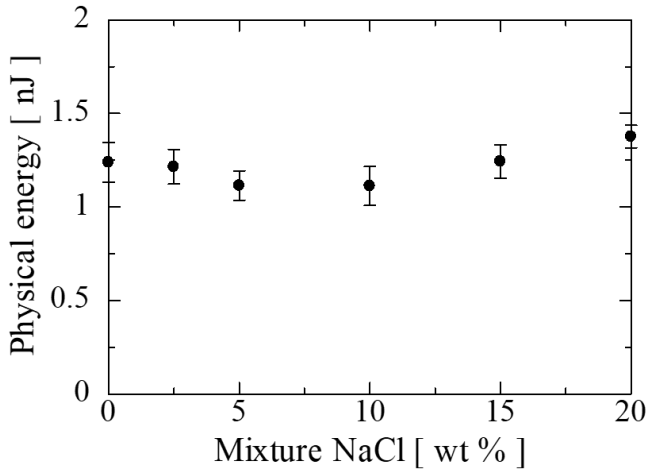

Figure 3. Dependence of physical energy on coupling solution NaCl concentration.

Characterization and Thermo-mechanical Analysis for a Light-driven Liquid-crystal-elastomer-based Crawling Robot

Yen-Chun Chen [a] and Yao-Joe Yang [a*]
[a] National Taiwan University, Taipei, 106319, Taiwan
e-mail: amelia@mems.me.ntu.edu.tw

Novelty / Progress Claim(s)

This work presents the thermo-mechanical analysis and characterization of a light-driven crawling soft robot. The device is made of liquid crystal elastomer (LCE) coated with an efficient photothermal film, and is capable of rapid locomotion and turning directions. The proposed LCE device consists of two small front legs, two large rear legs, and a concave cargo platform connecting the legs. The device locomotion, which is inspired by the principle of snake rectilinear movement, is generated by activating the rear legs with periodic NIR illumination. The thermo-mechanical analysis was performed using a commercially-available finite element tool. Thermal response of the device was also measured using an infrared imager. The simulated results were also validated by measurement. The performance of the device locomotion under different NIR intensities was also characterized and discussed.

Background / State of the Art / Results

LCEs exhibit large and reversible deformation when subjected to external stimuli, and have been employed as actuating materials in developing various novel devices such as reconfigurable structures, soft microactuators, miniaturized medical devices, and soft robotics [1]. Thermal actuation of LCE devices using near-infrared (NIR) light facilitates high degree of deformation control and temporal resolution. Fig. 1 shows the schematic of the NIR-driven LCE-based crawling robot developed by our research group recently [2]. Its capabilities of multidirectional locomotion and cargo transport have been demonstrated. However, transient thermo-mechanical behaviors have yet been fully understood so that the appropriate operating conditions for optimal device design and performance cannot be estimated at this moment. In [3], a simple 2D model for modeling the bending and curling characteristics of LCE beams was presented. Experimental validation of the LCE beam behaviors was also described. In [4], an analytical transient thermo-mechanical model for a soft robot consisting of a bimorph strip of LCE and a thermal inert polymer was developed. The results evaluated by the analytical model also revealed the key design parameters for generating transient bending deformation. In this work, we employed finite-element analysis to estimate the transient behaviors of the LCE-based crawling robots [2], and the measurement of the devices was performed to validate the simulated results. Preliminary studies on optimal device operating conditions based on the simulated results were also reported.

Figure 1 shows the schematic of the proposed LCE device, which consists of two small front legs, two large rear legs, a concave cargo platform connecting the legs, and a liquid-metal-based photo-thermal film (PTF) for improving thermal absorption efficiency. The picture of fabricated LCE devices is shown in Fig. 2(a). The SEM image of the top surface of the PTF is presented in Fig. 2(b). Numerous liquid metal micro-droplets are clearly shown in the picture. Fig. 3 illustrates the operational principle of the device locomotion [2], which mimics the rectilinear locomotion of snakes in succession. Fig. 4 shows the photo-thermal properties of PTF coated on the LCE crawling robot, measured using an infrared imager. The inset shows the measurement setup. The LCE temperature reaches above the LC-to-isotropic phase transition temperature (80 °C) within 0.8 s with an NIR power of 1.8 W/cm^2. Series of snapshot images of the device locomotion under NIR intensities of 1.8 W/cm^2 and 2.4 W/cm^2 are shown in Fig. 5(a) and (b), respectively. The snapshot series present the locomotion for a full actuation cycle, in which the device is heated by vertically incident NIR illumination upon the PTF for 0.8 s, and then passively cooled down for 3 s. The associated FEM simulated results and infrared snapshot images are also shown in the figure. The simulated temperature distributions were reasonably close to the measured results. Fig. 6(a) presents the transient device temperature on the top surface of PTF for one actuation cycle. Fig. 6(b) shows the transient displacement of the rear leg. The simulated temperature followed the measurement very well, while there was a little discrepancy between the simulated displacement and measured results. Fig. 7 demonstrates the transient displacement of the crawling robot for five actuation cycles under different input incidence power. The reversible and repeated motion of the rear legs generated to steady and successive locomotion. In addition, with higher NIR intensity, the device generated a larger stride for each actuation cycle. The figure also shows that the maximum device speed exceeds 2 body lengths per minute.

[1] H. Zeng et al., Advanced Materials 30 (2018) 1703554.
[2] Y. Chen et al., Sensors and Actuators A: Physical 378 (2024) 115777.
[3] A. Potekhina and C. Wang, Applied Physics Letters 118 (2021) 241903.
[4] Y. Cui et al., Applied Mathematics and Mechanics 40 (2019) 943-952.

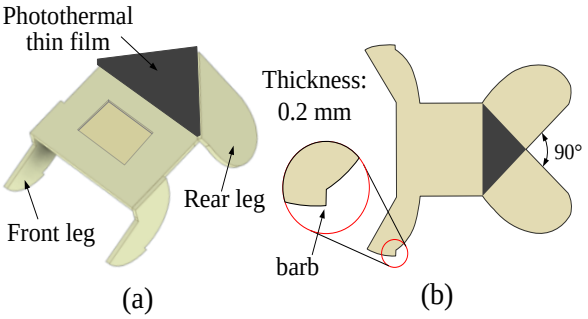

Figure 1. (a) 3D schematic of the proposed soft climbing robot. (b) The device top view prior to LCE shape memory programming.

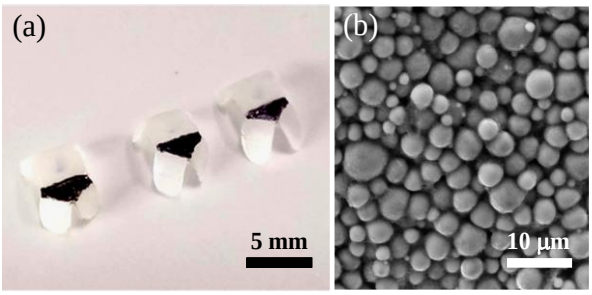

Figure 2. (a) Picture of the proposed LCE-based devices. (b) SEM image of the top surface of the PTF deposited on LCE.

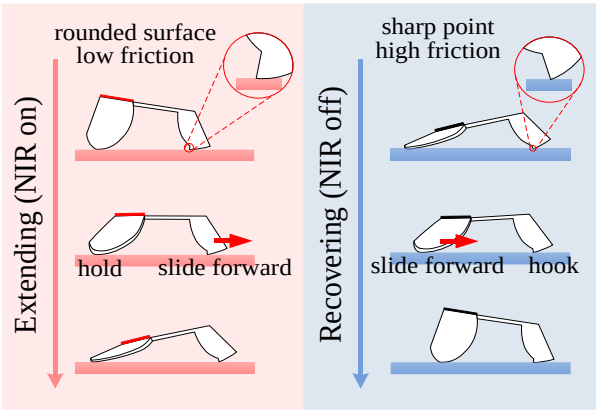

Figure 3. Schematic of the operational principle of the proposed device.

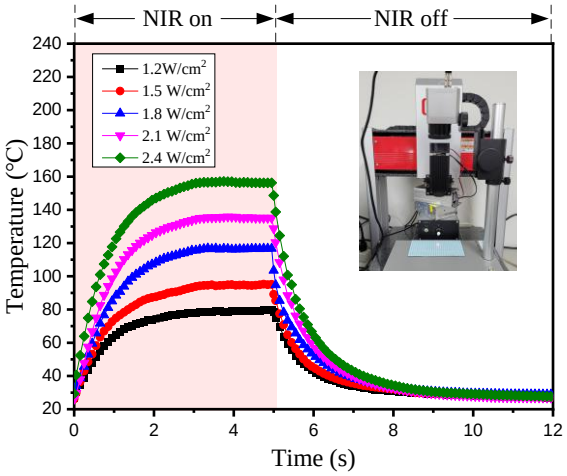

Figure 4. Heating and cooling temperature curves of the LCE films coated with PTF. The inset shows the experimental setup of infrared imager.

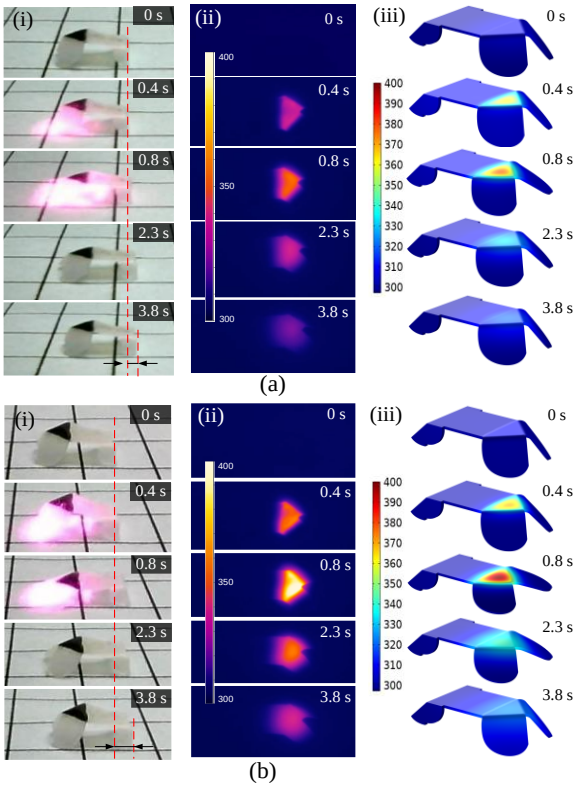

Figure 5. Measured and simulated transient behaviors under two NIR intensities: (a) 1.8 W/cm^2 and (b) 2.4 W/cm^2. Series of snapshot images (extracted from the videos taken by a CCD camera and an infrared camera) are also shown.

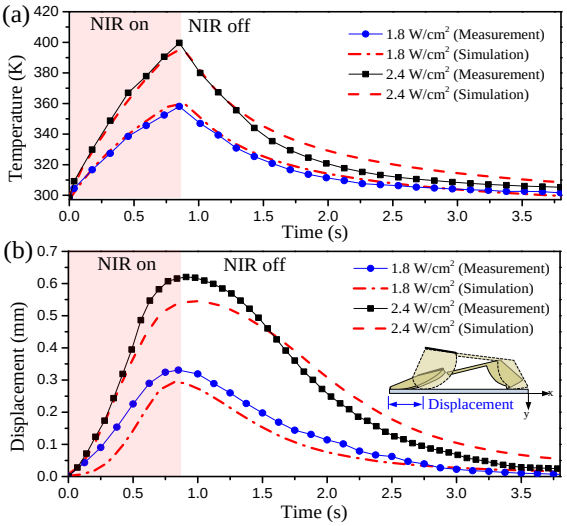

Figure 6. Comparison between the simulated and experimental results over one actuation cycle: (a) temperature on top of PTF, and (b) displacement.

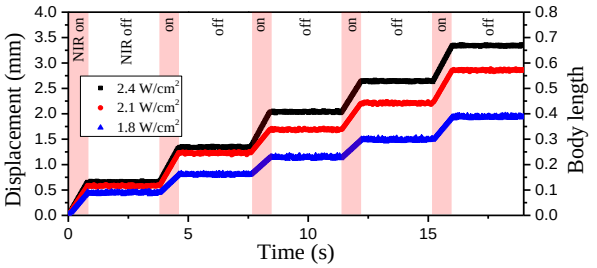

Figure 7. Measured transient displacement of the device under various NIR intensities

A MINIATURIZED KIRIGAMI SOFT GRIPPER INTEGRATED WITH SELF-SENSING CAPABILITY

Chia-Yu Cho [a] and Yao-Joe Yang [a]

[a] National Taiwan University, Taipei, 106, TAIWAN
e-mail: chiayucho@mems.me.ntu.edu.tw

This work presents a miniaturized electrothermally-driven soft actuator based on Kirigami structure. The proposed device is capable of generating large deformations, but also possesses self-sensing capability for structure deformation. The device comprises a liquid crystal elastomer (LCE) layer serving as the active material for generating deformation, and a conductive composite layer (CCL) serving as a piezoresistive sensing material for detecting deformations. Inspired by the art of Kirigami, monolithically micromachined flat structures can smoothly transform between 2D and 3D shapes. The gripper was capable of grasping and lifting objects of different sizes. The relationships between structure deformation and resistance change were measured. The capabilities of displacement tracking and touch detection were also demonstrated.

In recent years, soft actuators have shown significant progress because of their rapid development and intriguing applications in the fields of soft robots and flexible machines. Liquid crystal elastomer (LCE) has emerged as a promising material for soft actuators because of its capability of generating large and reversible actuation [1]. Untethered electrothermal LCE actuators based on wireless power transfer technology were reported in [2]. Multiple devices simultaneously actuated by the wireless technique was also demonstrated. In [3], graphene-based actuators on paper substrates with integrated-sensing function were proposed. The composite consisting of graphene oxide and paper substrate enables the actuation and sensing functions of the devices. In this study, we present a miniaturized soft actuator based on Kirigami structure, which is capable of generating large forces and deformations, but also possesses self-sensing capability for loadings.

Figure 1(a) shows the schematic of the proposed device, which consists of an active LCE Kirigami structure and a CCL composed of graphite microparticles and carbon nanotubes (CNTs). By pulling on the edge sides of the structure, which induces the out-of-plane motion due to the proposed Kirigami design, the structure transforms from the 2D shape patterns into a 3D grasping shape. The LCE structure is capable of reversibly exhibiting large deformations by employing a shape-programming process using UV illumination. Figure. 1(b) depicts the monolithically-fabricated planar Kirigami LCE structure prior to the shape memory programming process. Figure 1(c) illustrates the device operational principle. Figure 1(c-i) is the schematic view of the LCE structure after encoding with shape information (the folded shape). Upon application of a voltage across the two terminals of the CCL, the temperature of the actuator is elevated. When the temperature is above the LC–isotropic phase transition temperature (T_I), the actuator deforms from the folded shape to the flat shape (Fig. 1(c-ii)). While~~When~~ the voltage is turned off, the temperature decreases, and the actuator reverses to the folded shape. By controlling the concentrations of conductive particles, it is possible to obtain a CCL with near-zero temperature coefficient of resistance (TCR), which can be employed as a strain sensing element with self-temperature compensation. Also, the tip displacement of the gripper can be estimated based on the CCL resistance values (R_{CCL}), subject to the size of the grasped object (Fig. 2(a)). A simple circuit with a divider resistor was employed to measure R_{CCL} via the same pair of leads to actuate the device (Fig. 2(b)). Figure. 3 illustrates the fabrication process. The CCL was realized by the standard soft-lithography technique and a novel vacuum filtration process (Fig. 3(a)-3(e)). The LCE structure, bonded with the CCL, was then cured in a PMMA mold (Fig. 3(f)-3(h)). Finally, the bilayer structure was encoded into the folded shape (Fig. 3(i)-3(j)). Figure. 4(a) shows the picture of the fabricated actuator. Figure 5 presents the measured TCR behaviors of CCLs with different CNT/graphite mass ratios. The CCL with 10 wt% exhibited the lowest TCR value, and was employed for the implementation of the proposed device. Figure. 6 shows the transient responses of the actuator for three cycles. For each cycle, the device is actuated by a step voltage of 12 V for 6 s, and cools down for 44 s. Figure 7 shows the transient resistance values when the Kirigami soft actuator is grasping objects of different sizes (i.e., 0 mm, 2 mm, and 3 mm). These results also indicate that the self-sensing capability allows the device to detect its deformations as well as the size of the grasped objects.

[1] Y. Wang et al., Appl. Phys. Rev., 9 (2022), 011301.
[2] H. Zhang et al., ACS Appl. Mater. Interfaces, 15 (2023), pp. 27195-27205.
[3] L. Chen et al., Adv. Funct. Mater., 29 (2019), p. 1806057.

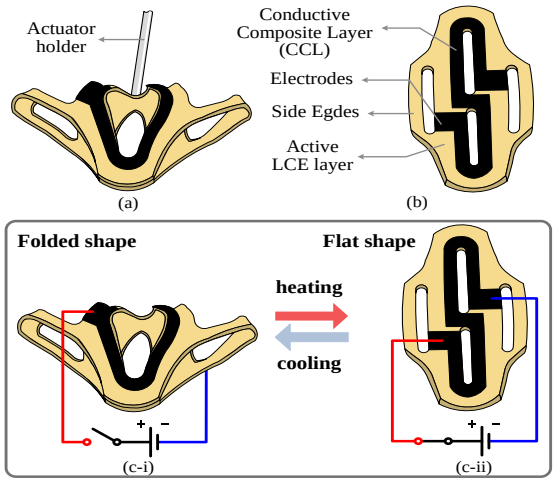

Figure 1. Schematics of (a) the proposed LCE actuator and (b) the proposed LCE actuator before shape programming. (c) The device operating principle.

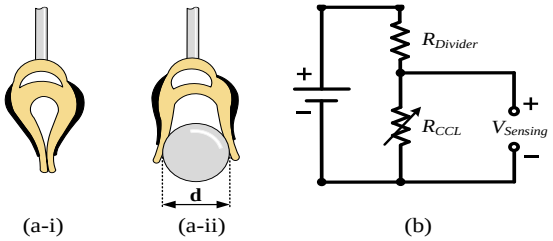

Figure 2. (a) Schematic of operational principle of the gripper when touches an object. (b) Diagram of the circuit for device actuating and sensing.

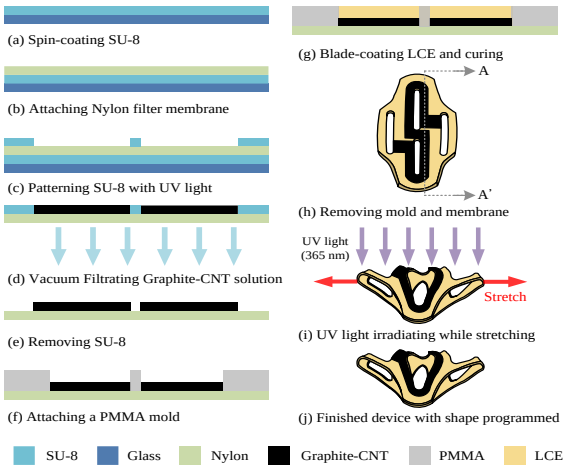

Figure 3. The fabrication process of the proposed actuator (the A-A' cross-sectional view of Fig 3(h)).

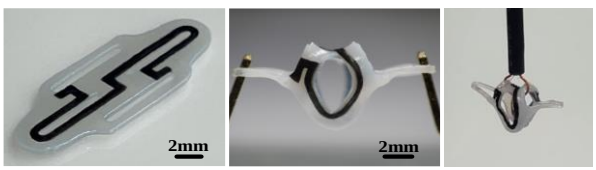

Figure 4. The fabrication of the Kirigami soft actuator (a) before shape programming and (b) after shape programming. (c) The fabrication soft gripper.

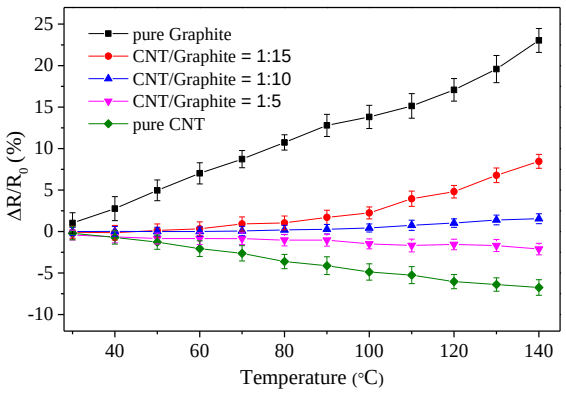

Figure 5. Temperature dependence of relative resistance change of CCL with different ratios of CNT and Graphite.

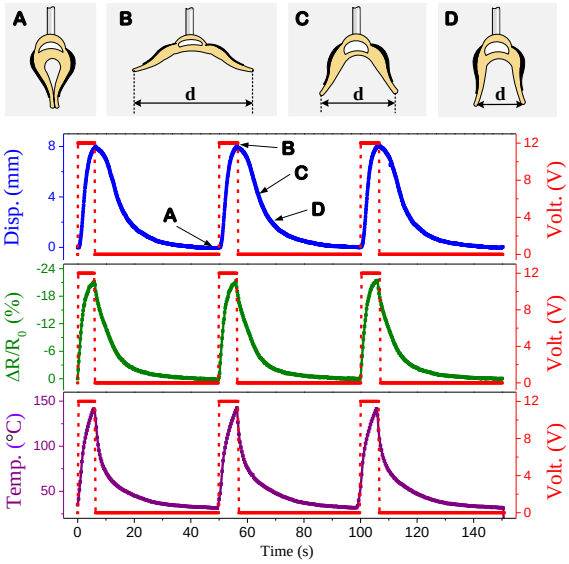

Figure 6. Transient responses of the displacement, resistance, temperature upon the given voltage for 3 actuation cycles.

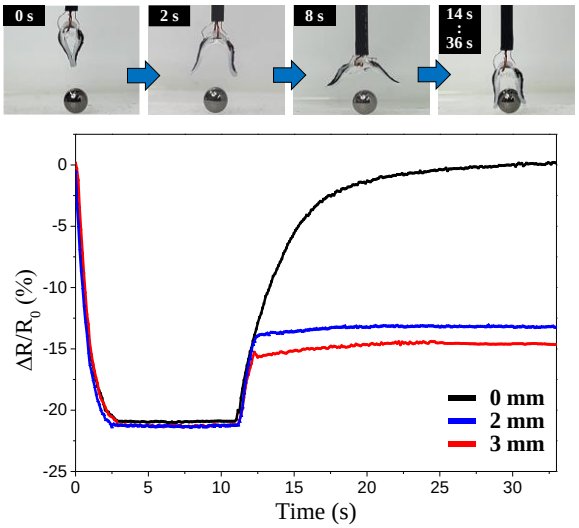

Figure 7. Transient responses of resistance when the gripper grasps an object. A series of snapshot images (taken at 0, 2, 8, and 14 s) are also shown.

Short-Channel Junctionless Nanowire Transistors

Sayantan Ghosh [a,b], Alessandro Puddu [a,b], Slawomir Prucnal [a], Ahmad Echresh [a], Artur Erbe [a,b], Yordan M. Georgiev [a,c]
[a] Institute of Ion Beam Physics and Materials Research, HZDR, Dresden, 01328, Germany
[b] Technische Universität Dresden, Dresden, 01069, Germany
[c] Institute of Electronics at Bulgarian Academy of Sciences, 72, Sofia, 1784, Bulgaria
E-Mail: s.ghosh@hzdr.de

Keywords: Junctionless nanowire transistor, ambipolar, unipolar, short-channel

The relentless demand for miniaturized, high-speed, and energy-efficient electronic systems continues to drive the semiconductor industry's pursuit of aggressive device scaling, as projected by Moore's Law [1]. However, the physical and technological limitations of traditional planar transistors at sub-nanometer nodes necessitate the exploration of alternative device architectures. Junctionless nanowire transistors (JNTs) have emerged as a promising candidate owing to their superior electrostatic gate control, intrinsic scalability, and simplified fabrication requirements. Silicon (Si) nanowires, with their reduced dimensionality, enhance gate controllability and enable higher sensitivity, making them ideal for next-generation applications. A defining characteristic of JNTs is the absence of pn-junctions within the channel, which allows for a uniformly doped active region [2]. This eliminates the need for complex doping profiles, thereby simplifying the fabrication process and improving manufacturability. Furthermore, short-channel JNTs offer the potential for high-density integration with reduced power consumption, primarily due to their inherently low leakage currents [3].

In this work, short-channel Si JNT devices are fabricated and characterized using a top-down approach. The devices are created on silicon-on-insulator (SOI) substrates with a 20 nm-thick n-doped (~5 x 10^{18} cm^{-3}) Si layer and a 100 nm buried oxide. Nanowires with a fixed width and height of 20 nm and channel lengths from 1000 nm to 50 nm are patterned by electron beam lithography (EBL) and etched using reactive ion etching. A 3 nm SiO_2 layer is grown by rapid thermal oxidation (RTO) for surface passivation, followed by deposition of a 7 nm Al_2O_3 gate dielectric via atomic layer deposition (ALD). Nickel (Ni) source/drain contacts (100 nm) are sputtered, and TiN top gates are defined using EBL, metal sputtering, and lift-off process [4]. Figure 1 presents the schematic of the short-channel JNT device, along with SEM images of the smallest device (50 nm channel length) and a 1000 nm device featuring a TiN top gate. Electrical characterization of short-channel JNT is initially performed using back-gate modulation. Transfer characteristics, obtained by sweeping the back-gate voltage (V_{BG}) from –30 to 30 V at the constant drain bias (V_{DS}) of 0.5 V, exhibit pronounced ambipolar behaviour (Figure 2a) across all channel lengths (1000 nm to 50 nm). This ambipolarity is observed to resemble reconfigurable FET (RFET) behavior more than that of conventional JNTs [5]. The 50 nm device exhibits an I_{ON}/I_{OFF} ratio exceeding 10^7, indicating strong gate control at scaled dimensions. A positive threshold shift is consistently observed, likely due to charge trapping introduced during the ALD process. To investigate the origin of ambipolarity, output characteristics are analyzed. Schottky barrier-limited conduction is confirmed for electron conduction (Figure 2c), while predominantly ohmic conduction is observed for holes (Figure 2d), suggesting Fermi level pinning near the valence band due to interface traps. Top-gated characteristics measured for the 50 nm device (Figure 2b) further validate the true junctionless mode of operation, with prominent unipolar behaviour with strong electrostatic modulation. Extracted parameters across various channel lengths (Figure 3) show that device performance improves with scaling. The 50 nm JNT demonstrates an I_{ON}/I_{OFF} ratio of 1.1 x 10^5 and a subthreshold swing (SS) of 231 mV/dec—among the best reported for CMOS-compatible, top-down fabricated short-channel JNTs. In conclusion, scaling to shorter channel lengths significantly enhances electrostatic control, demonstrating that JNTs are a promising solution for continued transistor miniaturization. Their simplified fabrication process and effective gate modulation at nanoscale dimensions make them well-suited for future technology nodes. As a next step, these short-channel devices will be investigated for gas sensing applications under various gaseous environments [6], leveraging their high sensitivity and strong electrostatic control for real life practical deployment.

[1] Moore, G.E., Proceedings of the IEEE, 1998. 86(1).
[2] Duffy, R., ECS Transactions, 2016. 72(4).
[3] Colinge, J.-P., et al., Nature Nanotechnology, 2010. 5(3).
[4] Ghosh, S., et al., Device Research Conference, 2024.
[5] Ghosh, S., et al., ACS Applied Electronic Materials, 2023.
[6] Vardhan, V., et al., ACS Applied Materials & Interfaces, 2023.

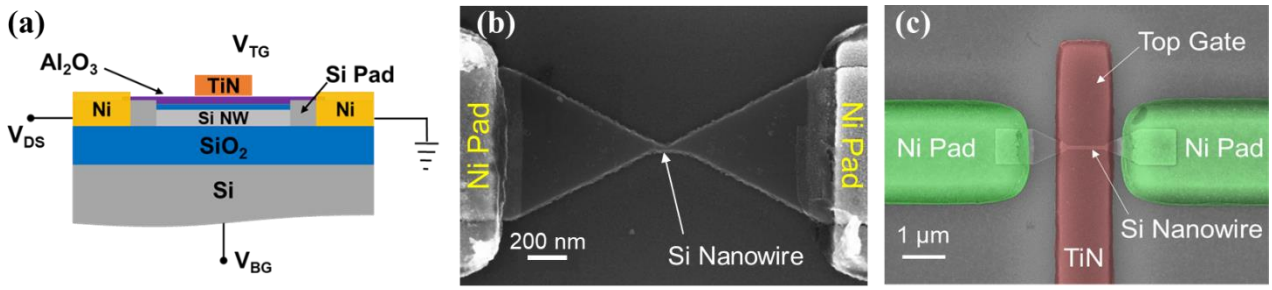

Figure 1. Schematic representation of the short-channel JNT device. (b) SEM micrograph of the shortest 50 nm channel device. (c) SEM micrograph of the 1000 nm device with TiN top gate.

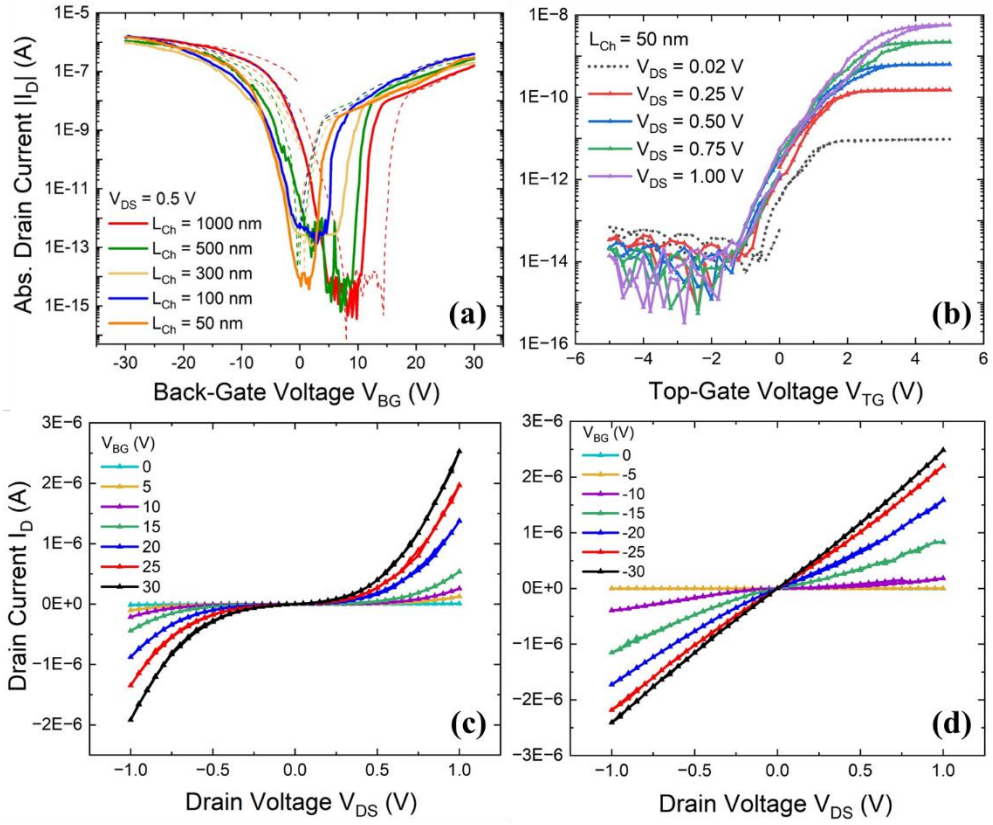

Figure 2. (a) Back-gated transfer characteristics for channel lengths ranging from 1000 nm to 50 nm. (b) Top-gated unipolar transfer characteristics of the 50 nm JNT for varying V_{DS}. Output characteristics of the 50 nm device demonstrating (c) Schottky-electron conduction and (d) ohmic hole conduction.

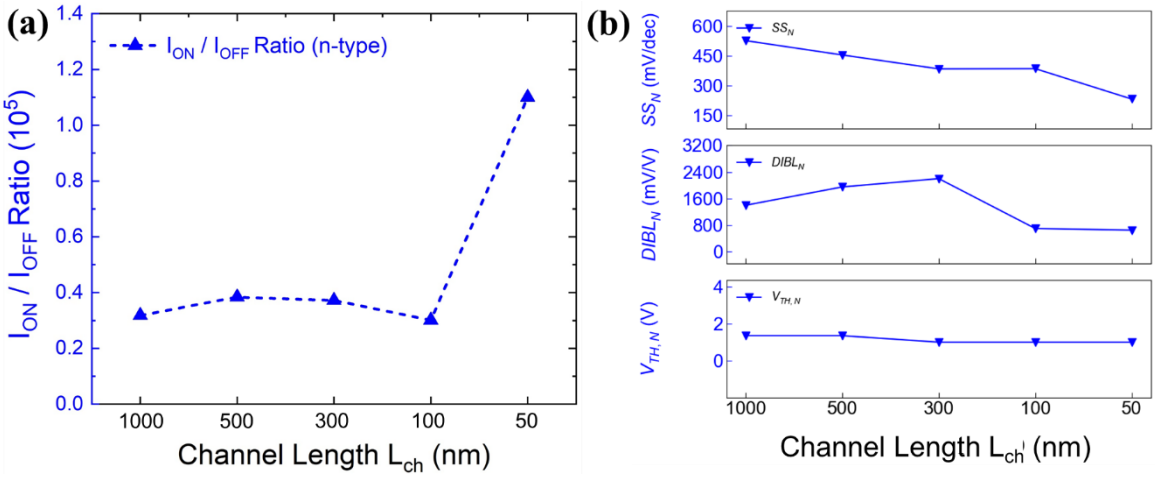

Figure 3. Graphical representation of comparison of top-gated characteristics across channel lengths from 1000 nm to 50 nm showing (a) I_{ON}/I_{OFF} ratio (b) Variation of subthreshold swing (SS), drain-induced barrier lowering (DIBL), and threshold voltage (V_{TH}) as a function of varied channel length.

Oral Session 5D: Electronic Sensors

A Saw-Tooth Slot Antenna Sensor for Dielectric Sensing

Hilary Scott Nkimbeng Cho and Jin W. Choi

Department of Electrical and Computer Engineering
Michigan Technological University, Houghton, MI 49931, USA
e-mail: choijw@mtu.edu

This work introduces a novel saw-tooth slot antenna sensor designed to enhance electric field concentration within the sensing region, addressing the critical need for high-sensitivity performance in dielectric sensing applications. Although slot antennas have been widely developed for various sensing applications [1–3], improving the sensitivity of the slot area itself has not been fully explored. Specifically, in [1], an array of narrow rectangular slots was employed for yeast detection, but without any modifications to enhance the electric field concentration within the slots. In [2], a wide slotted region of 11 mm was introduced into a patch antenna to improve sensitivity; however, increasing the slot width was found to reduce electric field concentration, thereby diminishing sensing effectiveness. Similarly, in [3], a wide slot was used for sweat sensing, which again resulted in lower E-field confinement and reduced sensing performance. Based on the aforementioned designs, there remains a need for a new approach that effectively enhances electric field localization within the sensing region.

The proposed antenna consists of a saw-tooth slot etched into the ground plane on the top surface of a single-layer Rogers RO4003 substrate, which has a thickness of 0.508 mm and dimensions of 48 × 48 mm². A microstrip feedline with a matching stub is placed on the bottom side to efficiently excite the slot and improve impedance matching, as shown in Fig. 1(a) and (b), respectively. Rogers RO4003 was chosen for its low dielectric loss, stable permittivity, and excellent mechanical properties, ensuring consistent sensor performance and minimal signal degradation. In the sensing setup illustrated in Fig. 1(c) and (d), a dielectric layer representing the material under test is placed above the slot to simulate different sensing conditions.

To evaluate the effect of slot geometry on sensing performance, three slot configurations were compared: a rectangular slot, a wide saw-tooth slot, and a narrow saw-tooth slot as shown in Fig. 2(a), (b) and (c) respectively. Among them, the narrow saw-tooth slot demonstrated superior resonance characteristics and improved impedance matching, as shown in Fig. 2(d). Electric field analysis in Fig. 3 further revealed that the narrow saw-tooth configuration achieved the highest relative field concentration approximately 7.4 times greater than the rectangular slot and 1.5 times greater than the wide saw-tooth slot. This enhancement is attributed to the sharp, confined geometry of the narrow saw-tooth slot.

Sensing performance was tested by placing various porous polymer materials—polyimide (ε_r=4.3), polystyrene (ε_r=2.6), and polyethylene (ε_r=2.25) as well as liquid materials such as distilled water(ε_r=81), and vinegar (ε_r=24.1) over the slot region, as shown in Fig.1(c). Each material caused a shift in the resonance frequency shift due to changes in the effective dielectric constant as illustrated in Fig.4. This frequency shift occurs because the material near the slot alters the effective dielectric constant, thereby modifying the electrical length of the antenna. As the effective permittivity increases, the resonant frequency decreases, based on $f_r^2 \propto 1/\varepsilon_{ff}$ where f_r is the resonance frequency and ε_{ff} is the effective dieletric constant.

This work presents a novel narrow saw-tooth slot antenna sensor designed to enhance electric field confinement and achieve high sensitivity for dielectric sensing applications. The proposed structure demonstrates improved field localization and distinct resonance frequency shifts in response to different dielectric materials, confirming its effectiveness. Future work will focus on experimental validation of the simulation results, fabrication of the antenna prototype, and integration into compact wireless sensing platforms for potential applications in environmental monitoring and gas sensing.

References

[1] S. J. Park, B. H. Son, S. J. Choi, H. S. Kim, and Y. H. Ahn, Sensitive detection of yeast using terahertz slot antennas, *Opt. Express*, vol. 22 (2014) 30467–30472.

[2] A. A. Al-Mudhafar and R. A. Malallah, High-Precise Microwave Active Antenna Sensor (MAAS) formulated for sensing liquid properties, *Sensors and Actuators A: Physical*, vol. 341 (2022) 113567.

[3] A. R. Eldamak and E. C. Fear, Conformal and disposable antenna-based sensor for non-invasive sweat monitoring, *Sensors*, vol. 18, no. 12 (2018) 4088.

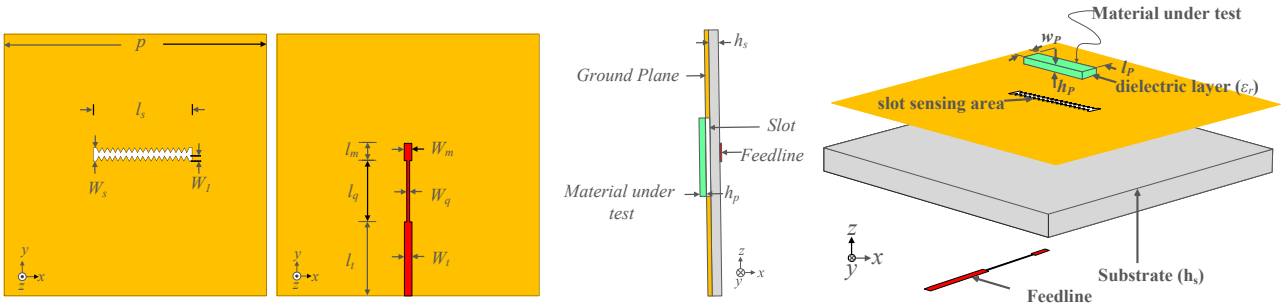

(a) (b) (c) (d)

Fig. 1. Geometry of the proposed saw-tooth slot antenna sensor : (a) Top view of the topside , (b) bottom view of the bottom side and (c) side view, and (d) 3D-view of the antenna sensor system.

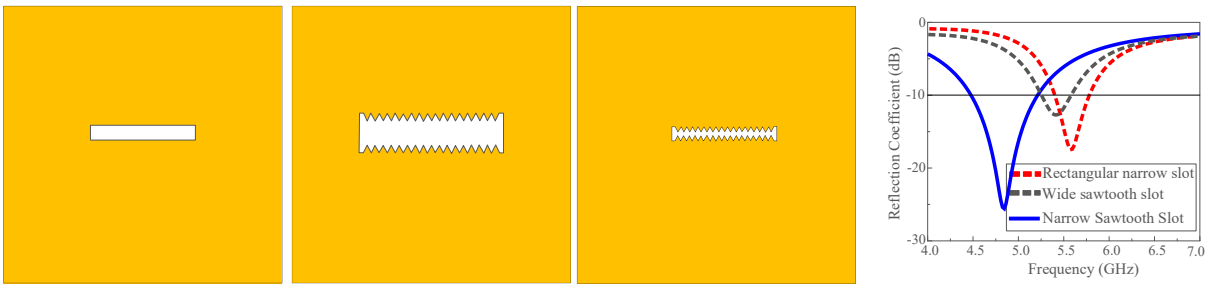

(a) (b) (c) (d)

Fig. 2. Various antenna sensor geometries: (a) rectangular slot antenna (b) wide saw-tooth slot antenna sensor , (c) narrow saw-tooth slot antenna , and (d) reflection coefficient.

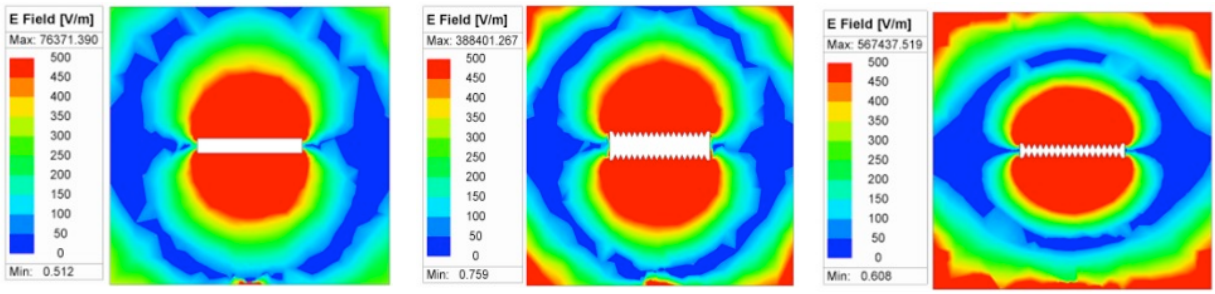

(a) (b) (c)

Fig. 3. Electric field distribution of various antenna sensors :(a) rectangular slot, and (b) wide saw-tooth slot and (c) narrow saw-tooth. The preliminary optimized design parameters are found as follows: P = 48 mm, l_s= 18mm, l_q= 13 mm, l_t= 10 mm, l_m= 3 mm, W_s=2.5 W_t=1.5mm, W_t= 2 mm, W_q = 0.15 mm, W_p =0.2 mm, l_p= 6mm, h_p = 0.5 mm, W_m = 1 mm, and h_s = 0.508 mm.

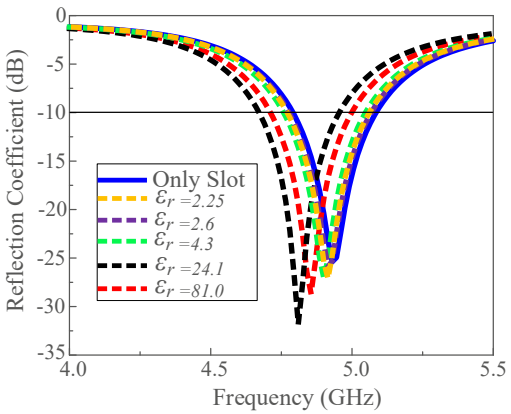

Fig. 4. Reflection coefficient variation for different dielectric constants (ε_r) of the sensing elements.

Exploitation of Surface Acoustic Waves for the implementation of innovative sensing devices applied to the measurement of gas phase pollutants

Meddy VANOTTI [a], Ghida FAWAZ [a], Margerie LOZE [b], Sacha POISSON [a], Stéphane BRANDÈS [b], Laurie ANDRÉ [b], Nicolas DESBOIS [b], Claude P. GROS [b], Virginie BLONDEAU-PATISSIER [a]

[a] Université Marie et Louis Pasteur (UMLP), FEMTO-ST Institut - UMR CNRS 6174,
Time and Frequency Department, CoSyMA Team, 26 chemin de l'Epitaphe, 25000 Besançon, France
[b] Université Bourgogne Europe, ICMUB - UMR CNRS 6302, EMCAP Team,
9 Avenue Alain Savary, 21000 Dijon, France
e-mail: meddy.vanotti@femto-st.fr

Keywords: SAW sensor, Love wave, Rayleigh Wave, Particulate matter, Ammonia.

The topic of health issues related to air pollution has been taking over international headlines. Gaseous pollutants and Particulate Matter (PM) represent a threat not only to human health but also to that of animals and plants. Here we propose to show how the diverse properties of Surface Acoustic Waves (SAW) can be exploited in different ways to further develop innovative air quality monitoring solutions.
In the past decade, our team has put efforts in the fabrication of an innovative prototype dedicated to the measurement of PM, mainly PM2.5 and PM10 with an aerodynamic diameter less than 2.5 and 10 µm, respectively [1]. In this context we chose to integrate Rayleigh wave based Surface Acoustic Waves (SAW) sensors as impaction plates in a cascade impactor to measure in real time particulate mass through phase velocity analysis of the propagating wave. A limitation of such system lies in the fouling of the sensor's surface with particles that impacts the wave propagation and thus the sensor's sensitivity. In order to address this obstacle, surface acoustic waves have once again been put to use to develop of a self-cleaning system integrated directly on the sensor to remove particles from the sensitive zone. The process relies on the use of Rayleigh waves at low frequency for the manipulation of water droplets [2] on the fooled zone to drag the particles off the active area and restore optimal working conditions of the sensor (Fig.1). This system has been proven efficient and patented for repeatable measurements of PM in ambient air. To assess the capacity of the system to measure and remove various types of PM, solid particules of silicon carbide and visous particules obtained from NaCl solutions have been succesfully measured and removed from the surface.
In a different field, we also have shown the potential of SAW for probing the properties of organic/inorganic or metallic layers for the development of gas sensors [3]. Here we propose to demonstrate this potential through the manufacturing of an ammonia (NH_3) sensor based on the properties of organic layers for early disease detection. EMCAP team has shown that Co corroles can bind two NH_3 molecules on the Co center (Fig. 2) to lead to hexa-coordinated species. More recently, we have shown that the incorporation of corrole complexes in organic polymers leads to new porous materials with similar reactivity [4]. To exploit the adsorption capabilities of corroles, SAW delay lines trading on the high gravimetric sensitivity of Love waves have been functionalized. A differential configuration based on two delay lines has been chosen to get rid of outer parameter variations. The first is covered with the NH_3 sensitive Co corroles and the second with Cu corroles used as a reference layer. An example of phase monitoring is presented in Figure 3. The sensor's sensitivity have been estimated in the presence of the main interferents, namely oxygen and carbon monoxide. Variations up to 30 % maximum have been observed (Fig. 4) and the sensor allowed us to measure NH_3 concentrations in the 1-45 ppm range in nitrogen, air and CO polluted nitrogen media.

[1] Djoumi, Lyes, Meddy Vanotti, and Virginie Blondeau-Patissier. "Real time cascade impactor based on surface acoustic wave delay lines for PM10 and PM2. 5 mass concentration measurement." Sensors 18.1 (2018): 255.
[2] Paquit, Melvin, et al. "Displacement of Microparticles on Surface Acoustic Wave Delay Line Using High RF Power." 2018 IEEE International Ultrasonics Symposium (IUS). IEEE, 2018.
[3] Vanotti, Meddy, et al. "Influence of interfering gases on a carbon monoxide differential sensor based on SAW devices functionalized with cobalt and copper corroles." Sensors and Actuators B: Chemical 332 (2021): 129507.
[4] Brandès, Stéphane, et al. "Porous organic polymers based on cobalt corroles for carbon monoxide binding." Dalton Transactions 48.31 (2019): 11651-11662.

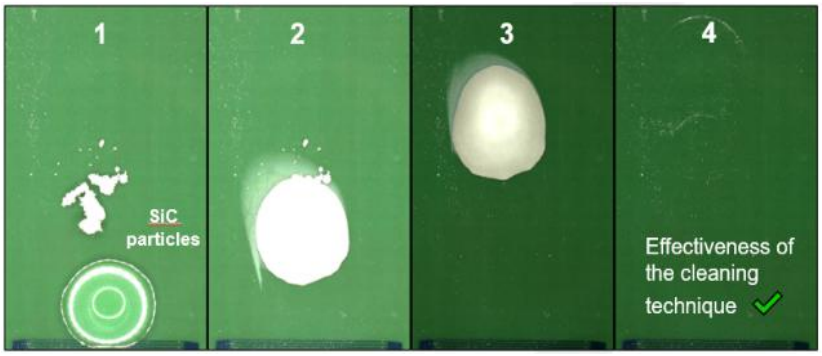

Figure 1. Evidence of the surface cleaning efficiency relying on the displacement of a water droplet by mean of high RF powered Rayleigh waves.

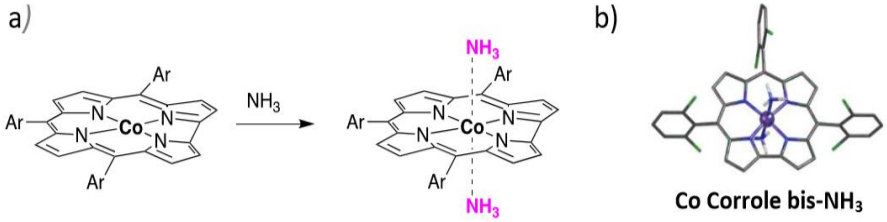

Figure 2. a) Selective NH_3 coordination on cobalt corroles b) X-ray of bis-NH_3 Co corrole.

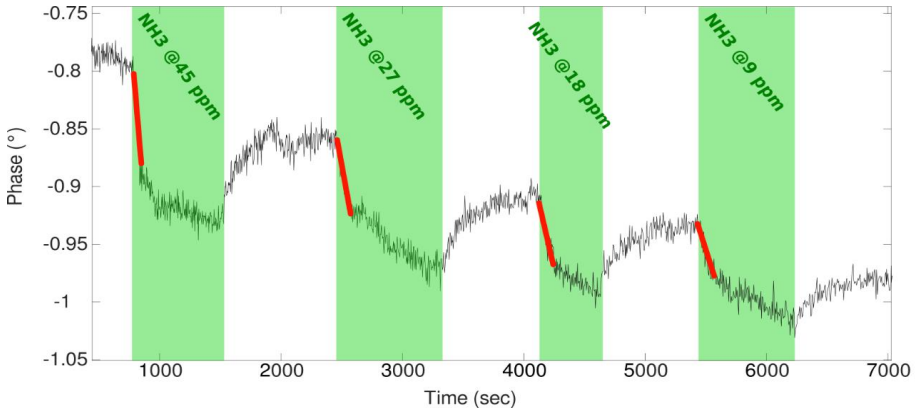

Figure 3. Measurements of NH_3 concentrations in a nitrogen flow in the [9-45] ppm range using a differential Love wave based SAW sensors functionalized with Co/Cu corroles.

	Sensitivity (µ°/s/ppm)	Uncertainty (µ°/s/ppm)
pure N_2	22.1	3.7 (16.7%)
AIR	27.3	3.1 (11.3%)
N_2 + CO@180ppm	32.9	3.9 (11.8%)

Figure 4. Caracterisation of the sensor's sensitivity to ammonia using pure nitrogen and nitrogen polluted with oxygen (AIR) and carbon monoxide (CO@180ppm) as carrier gases.

Tunable Nanoarchitectures in NiO/In_2O_3 Thin Films Sensor: Thickness-Modulated Response Enhancement for Ultrafast Butanone Sensing

Zhongming Guo, Zhenyu Yuan*, Fanli Meng

College of Information Science and Engineering, Northeastern University, Shenyang, 110819, China
e-mail: yuanzhenyu@ise.neu.edu.cn

This study aims to develop high-performance butanone gas sensors by introducing a gas-liquid interfacial self-assembly technique to construct heterojunction-sensitive thin films, addressing the limited gas permeability of traditional thick-film metal oxide semiconductor (MOS) sensors. By synergizing heterojunction interface engineering with interfacial self-assembly innovation, this work provides a novel strategy for designing highly sensitive and integrable gas sensors. The proposed self-assembly technique enables large-area, controllable film fabrication without complex equipment, demonstrating unique potential for flexible sensing and MEMS integration.

Monodispersed $Ni(OH)_2$/InOOH heterojunction microspheres were synthesized via a solvothermal method, with surface oxygen adsorption properties optimized by adjusting the Ni/In atomic ratio (0–5%). Leveraging interfacial engineering at the gas-liquid boundary, surfactant (Hypermer 2296)-mediated modulation enabled the formation of dense monolayer films (>10 cm^2), overcoming the thickness control limitations of conventional spin/dip-coating methods (see Fig 1a). The layer-by-layer (LbL) self-assembly technique was further employed to precisely regulate film thickness, systematically investigating the structure-response relationship between film layers and butanone sensing performance at the test platform (see Fig 1b).

A series of characterizations verified the successful preparation of monolayer and multilayer NiO/In_2O_3 heterogeneous thin films. The heterojunction construction between NiO and In_2O_3 significantly governed the morphological evolution of the monolayer microspheres. SEM analysis (see Fig 2a) revealed that increasing NiO content slightly enlarged microsphere diameters while suppressing surface protrusions and alleviating agglomeration. Optimal heterojunction engineering was achieved at 3% NiO, yielding monodisperse microspheres with minimal aggregation, where surface microprotrusions (40–50 nm height) and nanoscale roughness synergistically amplified the specific surface area, enhancing gas adsorption capacity. XPS analysis revealed that NiO incorporation (3% Ni/In ratio) boosted chemisorbed oxygen (O_C) content from 39.80% to 46.79% (see Fig 2b), creating abundant active sites for gas adsorption. Cross-sectional SEM characterization confirmed the formation of monolayer films and multilayer structures via LbL assembly, achieving thickness control from ~300 nm (1L) to ~3 μm (10L), as shown in Fig 2c.

The 3% NiO/In_2O_3 heterojunction thin film achieved breakthrough gas-sensing performance through synergistic heterojunction engineering and morphology optimization (see Fig 3a). It exhibited an ultrafast response time of 1.3 s to 50 ppm butanone at 220°C, enabled by hierarchical nanoparticle-assembled microspheres with high surface accessibility and reduced agglomeration. Simultaneously, the heterojunction-enhanced specificity delivered a 3.2× higher response to butanone (192.86 vs. 60 for pure In_2O_3) with minimal cross-sensitivity to 10 interfering gases, while microprotrusions and agglomeration-free monolayers facilitated ultrasensitive detection down to 750 ppb butanone (response: 4.66). Furthermore, the sensor demonstrated robust reliability.

The gas-liquid self-assembled NiO/In_2O_3 films exhibited thickness-dependent sensing performance for butanone (see Fig 3b). The optimal 5-layer film (NiO/In_2O_3-5L) achieved a response of 235.7 to 50 ppm butanone at 200°C, outperforming 1L (192.86) and 10L (198) films. This ‘rise-then-fall’ trend stems from a balance between enhanced active sites (increasing layers) and gas diffusion limitations (excessive thickness). The 5L films also demonstrated ultrafast response (1.3 s) and sub-ppm detection (6–750 ppb). Simultaneously, the multilayer films retained robust selectivity and reliability, further validating their adaptability to complex sensing environments.

Thicker films reduced baseline resistance (R_a) by widening conductive channels (1L: ~300 nm; 5L: ~1.5 μm), but excessive layers (10L) caused electron transport saturation. The 5L architecture optimally balances gas accessibility, charge transfer efficiency, and active site density, positioning it as a benchmark for tunable, high-performance sensing interfaces.

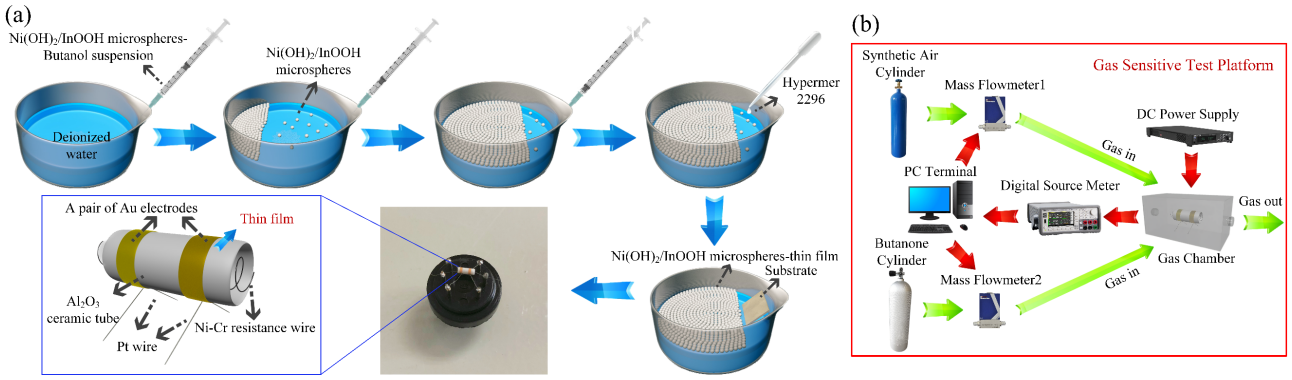

Figure 1. (a) Schematic diagram of the fabrication process for NiO/In_2O_3 thin film and gas sensor devices. (b) Schematic diagram of the gas sensitive test platform setup and workflow.

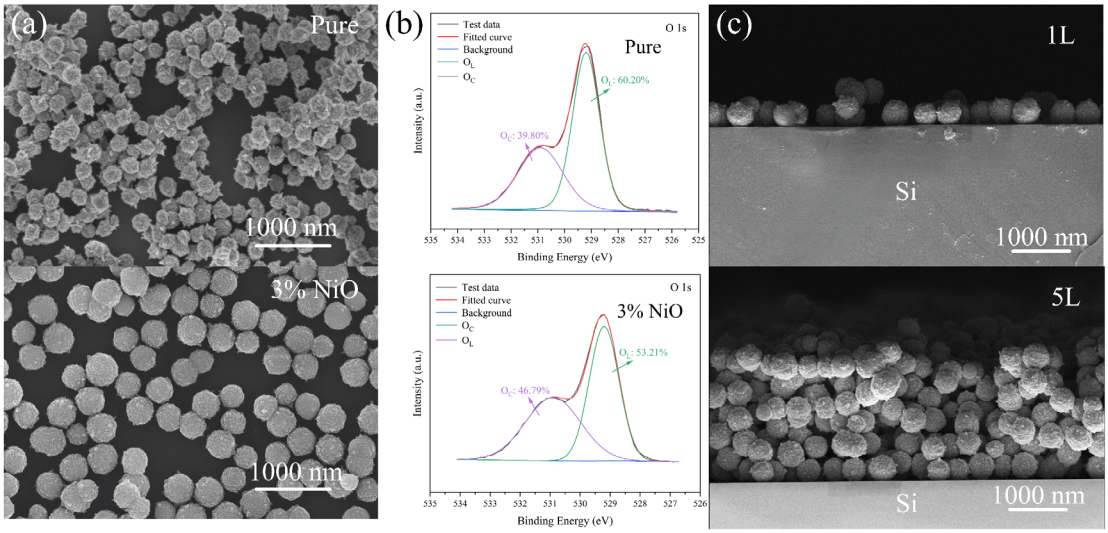

Figure 2. (a) SEM characterizations of monolayer NiO/In_2O_3 films with different NiO doping ratios (0%, 1%, 3% and 5%). (b) XPS spectra of O 1s of pure In_2O_3 and 3%-NiO/In_2O_3. (c) Cross-sectional SEM images of NiO/In_2O_3-1L and NiO/In_2O_3-5L.

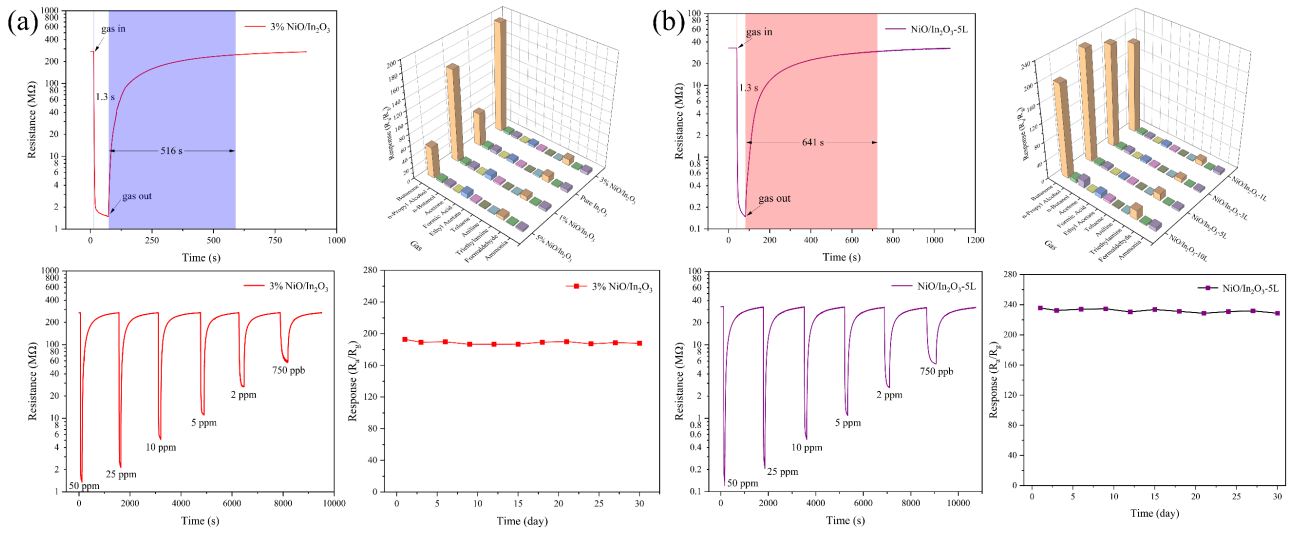

Figure 3. Response-recovery characteristics, selectivity, concentration gradient, and long-term stability tests of (a) 3% NiO/In_2O_3 monolayer thin films and (b) NiO/In_2O_3-5L thin films.

Electric-field Sensor based on Graphene/MoS_2 Heterostructure for Lightning Forecast

Jiali Hu [a], Mohammad Razzakul Islam [a], Afsal Kareekunnam [a], Takeshi Kudo [b], Takeshi Maruyama [b], Masashi Akabori [a], Hiroshi Mizuta [ac]

[a] JAIST, Ishikawa, 923-1211, Japan
[b] Otowa Electric Co., Ltd., Hyogo, 669-1313, Japan
[c] University of Southampton, Southampton, SO17 1BJ, UK
e-mail: mizuta@jaist.ac.jp

Molybdenum disulfide (MoS_2) has shown great potential in next-generation sensing applications such as lightning sensing [1], owing to its high sensitivity to the ambient conditions. However, the practical performance is often limited by poor contact quality at the metal/MoS_2 interface [2]. In this study, we propose a novel device structure based on a van der Waals heterostructure of graphene and MoS_2. The graphene replaces conventional metal contacts to reduce contact resistance while preserving the intrinsic properties of MoS_2 channels. At the graphene edge, the MoS_2 bends and touches the SiO_2 substrate, enabling strain engineering and substrate-induced carrier trapping simultaneously. This work aims to utilize graphene/MoS_2 heterostructures to achieve ultra-high sensitivity in weak electric filed detection.

The device schematic is shown in **Fig. 1**. We fabricated different heterostructure devices with bilayer graphene (BLG) and multilayer graphene (MLG, ~10 layers). MoS_2 and graphene flakes are mechanically exfoliated onto a lightly doped Si/SiO_2 substrate, featuring a 285 nm oxide layer. A nanogap was introduced into the graphene using oxygen plasma etching. Dry transfer technique was used to place the MoS_2 flake across the nanogap. Metal Au/Ti (55 nm/15 nm) contacts were fabricated on the top of graphene.

In contrast to conventional metal/MoS_2 contacts, which typically suffer from Fermi level pinning and high contact resistance, the use of metal/graphene ohmic contacts combined with graphene/MoS_2 van der Waals heterojunctions in this work significantly improves the contact interface. This improved contact quality facilitates more efficient carrier injection and enhances the carrier mobility, as shown in **Fig. 2**. Furthermore, at the MLG edge, tensile strain induced by the bending of MoS_2 channel further enhances carrier mobility by reducing the effective mass and electron-phonon scattering. Thus, the graphene/MoS_2 heterostructure devices could achieve carrier mobility up to ~108 $cm^2V^{-1}s^{-1}$ at room temperature. **Fig. 3a** shows the response of a graphene/MoS_2 device to the applied positive electric field of 1.6 kV/m, which is recorded as the change in drain current. The drain current variation is caused by changes in effective carrier density due to field-induced carrier trapping and de-trapping at the SiO_2/MoS_2 interface [3]. Significantly, the device shows a more pronounced drain current change than the previous MoS_2 device under the same electric field. This is because the enhanced carrier mobility increases the number of carriers moving through the channel at a given time, which in turn increases the probability of carriers being trapped. The number of carriers trapped/de-trapped is proportional to the electric field strength, and the direction of charge transfer depends on the electric field polarity. Thereby, the electric field sensitivity (S_{EF}) is defined as the percentage change in the drain current:

$$S_{EF} = \frac{|I_{ON} - I_{OFF}|}{I_{OFF}} \times 100\%$$

, where I_{ON} is the drain current in the presence of the electric field and I_{OFF} is the drain current in the absence of the electric field. As shown in **Fig. 3b**, S_{EF} has a linear dependence on the electric field strength. Under the same electric field, the graphene/MoS_2 heterostructure device has a much higher electric field sensitivity than the MoS_2 device. Particularly, the detection limit is lowered to ~100 V/m. Prospectively, the graphene/MoS_2 heterostructure offers a new way to build simple, sensitive, and low-power electric field sensors for lightning detection, and also provides a promising platform for high-performance two-dimensional electronics.

[1] M.R. Islam et al., ACS Omega 9 (2024) 29751–29755.
[2] H. Yuan et al., ACS Appl. Mater. Interfaces 7 (2015) 1180–1187.
[3] A. Kareekunnan et al., ACS Omega 6 (2021) 34086.

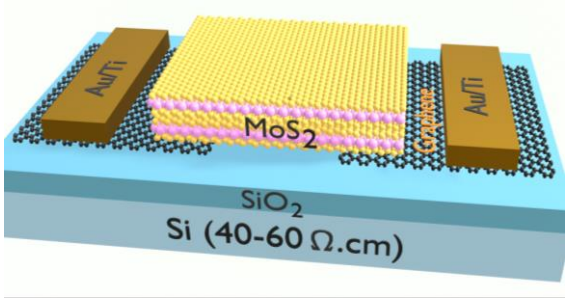

Figure 1. Schematic of the graphene/MoS_2 heterostructure device.

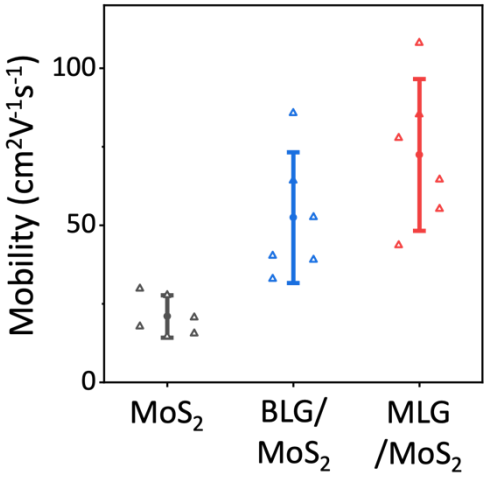

Figure 2. Comparison of carrier mobilities among the BLG/MoS_2 and MLG//MoS_2 heterostructure devices, and MoS_2 devices. All types of devices use MoS_2 channels with similar layers (5~6 layers).

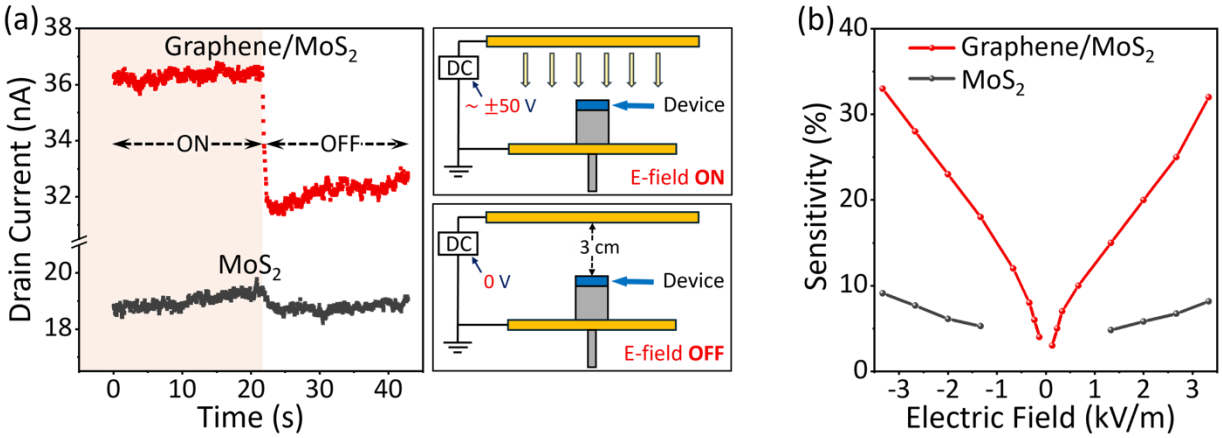

Figure 3. (a) Response of the graphene/MoS_2 heterostructure device under an applied positive electric field of 1.6 kV/m and comparison with MoS_2 device. (b) Comparison of electric field sensitivities between the graphene/MoS_2 heterostructure device and MoS_2 device. The minimum electric field that can be detected by the graphene/MoS_2 heterostructure device is as low as ~100 V/m.

Disposable electrode based iontronic pressure sensors and their potential applications in generative artificial intelligence

Changwoo Cho, Chaeeun Lee, Je Hoon Oh

Department of Mechanical Engineering and BK21 FOUR ERICA-ACE Center, Hanyang University, Ansan, Gyeonggi-do, 15588, Republic of Korea
E-mail: jehoon@hanyang.ac.kr

Cardiovascular disease (CVD) remains a leading global cause of morbidity and mortality, highlighting the importance of detecting those who may be affected at an early stage [1]. Blood pressure (BP), a critical marker for assessing CVD, is commonly monitored using cuff-based or invasive methods. However, these are often unsuitable for frequent or continuous use due to discomfort, infection risk, and limitations in ambulatory or critical care settings [2]. As a result, recent research has increasingly focused on non-invasive BP estimation techniques based on arterial pulse waveforms, particularly those derived from the radial artery.

In clinical settings where hygiene and convenience are essential, the need for disposable sensor platforms is growing. Iontronic capacitive pressure sensors (CPS) are well-suited for such applications due to their high sensitivity, fast response, low power consumption, and mechanical flexibility [3]. To address these needs, a disposable Hanji-based IL/polymer composite (DIP) CPS is introduced. Hanji's fibrous and microstructured surface facilitates electric double layer (EDL) formation, enhancing sensing performance. The fabricated sensor achieved a sensitivity of up to 300 kPa^{-1} and successfully captured pulse signals from the wrist.

Although deep learning has shown promise in estimating blood pressure from pulse waveforms, its practical deployment remains hindered by the limited availability of large-scale, high-quality paired datasets linking waveform data to corresponding BP measurements [4]. To address this, generative artificial intelligence (AI) was introduced as a data augmentation strategy, with the time generative adversarial network (TimeGAN) utilized to synthesize realistic waveform-BP pairs from limited clinical samples. Unlike conventional methods, TimeGAN captures both the temporal dynamics and joint distribution of pulse signals and BP values, generating physiologically meaningful data that can enhance model training for improved prediction accuracy and robustness [5].

In this study, a scalable and personalized approach to continuous cardiovascular monitoring is presented by integrating a low-cost, disposable sensor platform with a generative AI. DIP CPS enables reliable acquisition of radial artery pulse signals, while TimeGAN is employed to generate realistic synthetic waveform-BP pairs from limited data. This combination offers a novel pathway to address data scarcity in biomedical applications and holds promises for future deployment in both clinical and home-care settings.

Figure 1(a) shows a schematic of the DIP CPS, which consists of conductive Hanji electrodes and an IL/polymer composite dielectric layer. The dielectric was prepared by blending [EMIM][OTF] with poly(ethylene glycol) in deionized water, followed by thermal evaporation, and then sandwiched between the Hanji electrodes with adhesive. These features enable rapid contact area modulation with the IL/polymer composite, leading to the formation of nanoscale EDL at the electrode interface, as shown in Figure 1(b).

Figure 2(a) shows the capacitance variation of the DIP CPS measured from the wrist, clearly capturing periodic changes corresponding to radial artery pulse waveforms. The sensor demonstrates reliable responsiveness to arterial pressure fluctuations in real time. Figure 2(b) illustrates the data augmentation and BP estimation pipeline. Original pulse waveform–BP pairs are expanded using TimeGAN, which learns their temporal and statistical structure. The augmented data are intended to train a CNN-LSTM model to estimate systolic and diastolic blood pressure (SYS and DIA).

Figure 3(a) depicts the autoencoder-based architecture of TimeGAN. The model embeds the input time-series x_t, into a latent space using an encoder function $e(x_t)$ and reconstructs it through a recovery function $r(h_t)$, enabling realistic temporal representation and generation. The t-SNE analysis comparing original and synthetic data, as shown in Figure 3(b), reveals a strong distributional overlap between the two datasets. This result indicates that the synthetic data generated by TimeGAN effectively preserves the temporal and statistical properties of the original waveform-BP dataset.

In summary, we fabricated a disposable ionic CPS using IL/polymer composites and Hanji-based electrodes, which exhibited high sensitivity due to the microstructured surface of Hanji and successfully acquired wrist pulse signals. Additionally, generative AI (TimeGAN) was applied to augment limited clinical data, highlighting its potential to support deep learning-based BP estimation.

References

[1] V. Main et al., Biosens. Bioelectron. **216** (2022) 114680.
[2] C. Peng et al., IEEE Sens. J. **21** (2021) 2642-2650.
[3] Z. Feng et al., ACS Appl. Mater. Interfaces **15** (2023) 6219-6227.
[4] N. Bai et al., ACS Nano **16** (2022) 4338-4347.
[5] Y. Zhang et al., Energy **260** (2022) 124919.

Figures

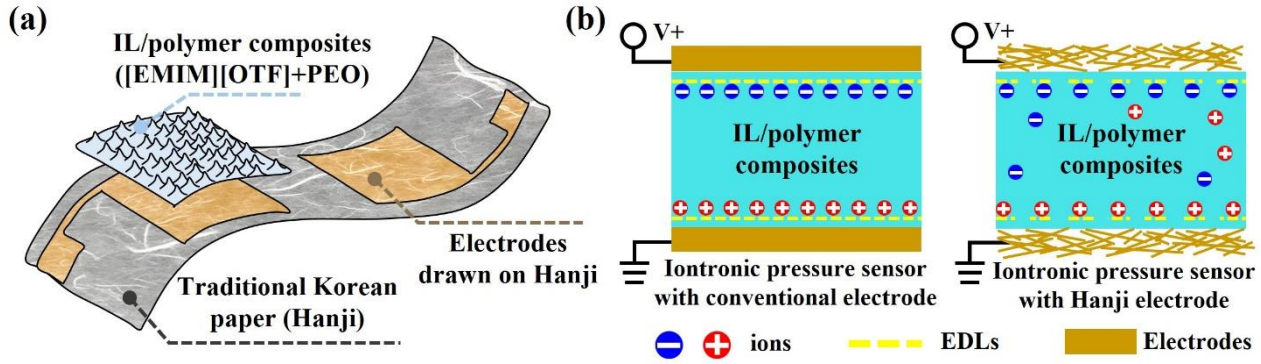

Figure 1. (a) Schematic diagram of the proposed DIP capacitive pressure sensor. (b) The formation mechanism of the EDLs, which is a factor in the capacitance variation of the DIP CPS.

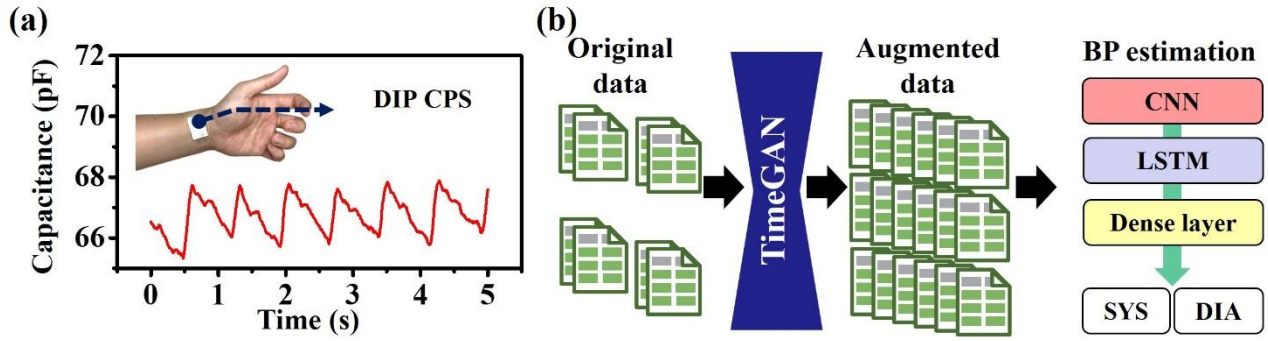

Figure 2. (a) Pulse waveform collected using the DIP CPS attached to the radial artery of the wrist. (b) TimeGAN-based waveform-BP data augmentation and deep learning-based BP prediction

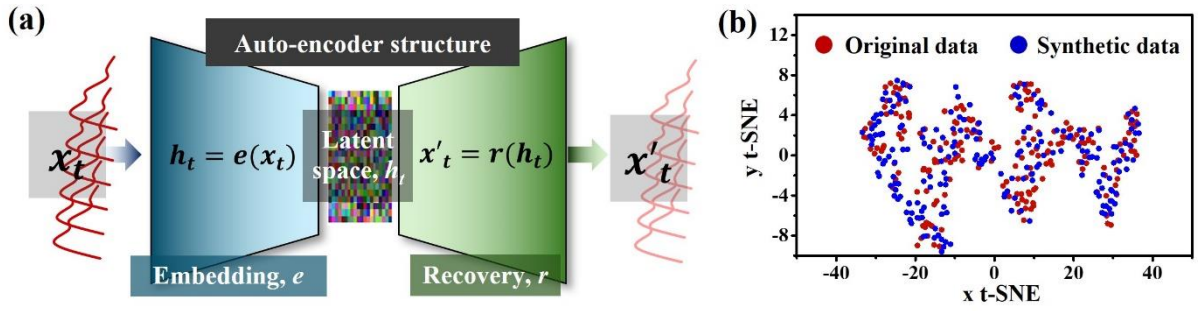

Figure 3. (a) Autoencoder-based structure of TimeGAN for time-series data generation. (b) *t*-SNE comparison of original and synthetic waveform-BP data showing strong distributional similarity.

High-Mobility of Amorphous-Crystalline Phase-Composite Indium Oxide for Thin Film Transistor Applications

Quang Khanh Nguyen [a], Myung Mo Sung [a]

[a] Department of Chemistry, Hanyang University, Seoul 04763, Republic of Korea.
e-mail: khanhnq.vnu@gmail.com

Abstract

Indium oxide (InO_x) exhibits high electron mobility and optical transparency, ideal for advanced thin-film transistors (TFTs). However, its performance is often constrained by excessive carrier concentration and challenges in crystallization control. In this study, we demonstrate the fabrication of exceptionally smooth indium oxide (InO_x) thin films with an amorphous/nanocrystal phase-composite structure using high-pressure atomic layer deposition (ALD) for the first time (Figure 1). By employing bis(trimethylsilyl)amidodiethyl indium (InCA-1) and hydrogen peroxide (H_2O_2) vapor at pressures over 100 times higher than conventional ALD, we achieved ultrafast growth rates at low temperatures [1]. Systematic control of deposition temperature and film thickness enabled precise tuning of carrier concentration and crystallinity. Notably, lower temperatures suppressed both carrier concentration and crystallization, yielding films with enhanced electronic properties. An optimized 7.0 nm-thick InO_x film deposited at 110 °C exhibited excellent field-effect transistor (FET) performance, with an electron mobility (μ_e) of 61.1 $cm^2 V^{-1} s^{-1}$ and an on/off current ratio of ~0.9×10^6 (Figure 2-3). The phase-composite structure, consisting of nanocrystals embedded in an amorphous matrix, facilitates efficient charge transport via resonant hybridization, forming delocalized electronic states [2-3]. These InO_x films also exhibit high optical transparency, uniform surface coverage, mechanical flexibility, and environmental stability. This high-pressure ALD approach overcomes previous limitations in InO_x film processing and unlocks new possibilities for next-generation flexible and transparent electronics.

[1] J. Sheng et al., J. Mater. Chem. C 4 (2016) 7571.
[2] J. Kim et al., ACS Appl. Mater. Interfaces. 15 (2023) 53835–53846.
[3] I. Palani et al., Small Struct. 5 (2024) 2400201.

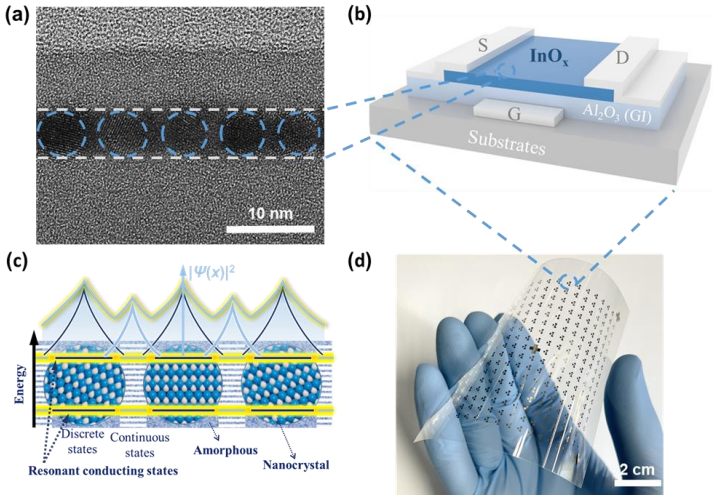

Figure 1. Phase-composite InO_x semiconducting layer for high performance flexible TFT.

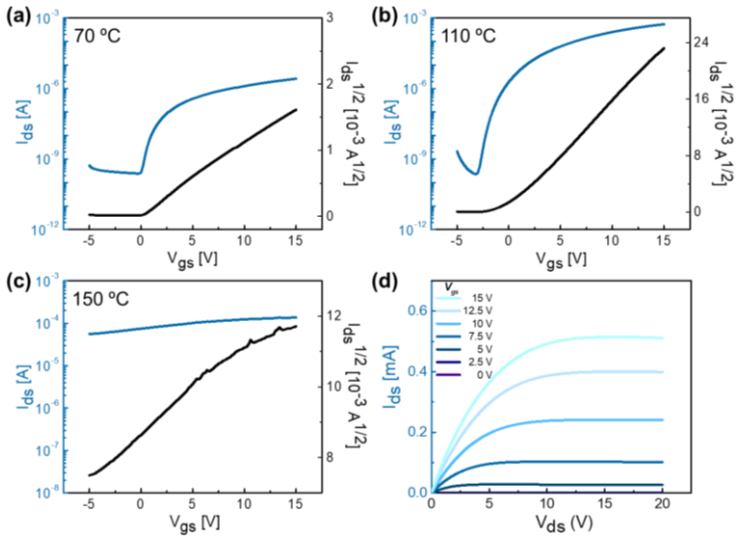

Figure 2. The dependence of electrical performance with phase-composite InO_x deposition temperature.

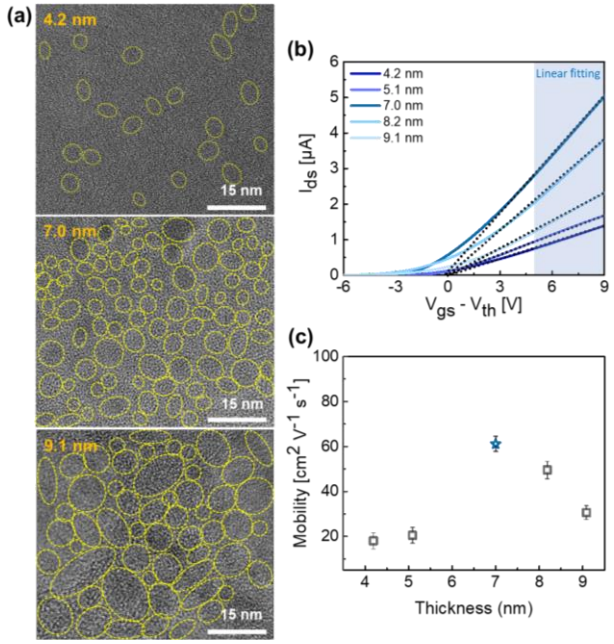

Figure 3. The dependence of electrical performance with phase-composite InO_x thickness.

Oral Session 6A: Advanced Nanofabrication III

Sequential Infiltration Synthesis for Organized Nanostructure Fabrication

G. Seguini, IMM-CNR, Unit of Agrate Brianza, Via C. Olivetti 2, I-20864 Agrate Brianza, Italy
gabriele.seguini@mdm.imm.cnr.it

Sequential infiltration synthesis (SIS) is a three-dimensional growth process derived from atomic layer deposition (ALD) on polymers. SIS permits to grow inorganic materials into polymeric films. SIS into self-assembled block copolymers (BCP) offers the possibility to fabricate inorganic nanostructures starting from nanostructured organic templates. The fine-tuning of the dimensions of the resulting nanostructures can be achieved by proper selection of the SIS process conditions. In particular, the sequential reaction steps of the SIS process allow tuning the dimensions of the nanostructured material adjusting the number of SIS cycles. This capability to achieve a fine tuning of the dimensions of the resulting inorganic nanostructures is fundamental to make this technology suitable for the different target applications. At the same time, this step-by-step growth of the inorganic nanostructure allows us to obtain information about the progressive mass uptake of the inorganic component into the polymer matrix and to delve into the growth mechanism. In this work, Al_2O_3 dot, antidot, or lamellae arrays were synthetized by infiltration of trimethylaluminum and water precursors into out of plane cylinder or lamellae forming poly(styrene-*block*-methyl methacrylate) (PS-*b*-PMMA) BCP thin films. Collected data provided information about the mechanism governing the effective incorporation of Al_2O_3 into the PMMA component of the BCP thin films. Overall, this study collects exhaustively the infiltration behavior in different PS-*b*-PMMA nanostructures and consequently improves the application of SIS generated masks from PS-*b*-PMMA in industrial lithographic processes.

This research was partially supported by the project “IONS4SET” funded from the European Union’s Horizon 2020 research and innovation program (Grant No. 688072).

Effect of Binary Mechanical Environment on T Cell Function

Jatin Jawhir Pandit[1,2], Abed Al-Kader Yassin[3], Carlos Ureña Martin[1,2], Guillaume Le Saux[1,2], Angel Porgador[3], Mark Schvartzman[1,2]

[1]Department of Materials Engineering, Ben-Gurion University of the Negev, P.O. Box 653, Beer-Sheva 84105, Israel; [2]Ilse Katz Institute for Nanoscale Science and Technology, [3]The Shraga Segal Department of Microbiology, Immunology, and Genetics Faculty of Health Sciences, Ben-Gurion University of the Negev, P.O. Box 653, Beer-Sheva 84105, Israel
Email id: Panditj@post.bgu.ac.il

Recent studies indicate that T cells are mechanosensitive, and their activation depends on the mechanical properties of their environment, including target cells, professional antigen-presenting cells, and surrounding tissues. This mechanosensing was demonstrated *ex vivo* by showing that T cells activated on surfaces of varying stiffness adjust their responses accordingly. However, in all these studies, T cells were stimulated *ex vivo* by **homogeneous** mechanical environments, whereas their natural environment can be **heterogeneous**, providing multiple mechanical stimuli simultaneously. For example, antigen-presenting cells such as dendritic cells, macrophages, and B cells, as well as endothelial cells within blood vessels, expose T cells to different mechanical cues, often at the same time. In bones, T cells encounter both the cortical bone, with elasticity in the range of tens of GPa, and the bone marrow, with elasticity in the range of a few kPa. Similarly, tumor tissue comprises multiple components with varying elasticities: tumor cells (~1–10 kPa), fibroblasts (~5–10 kPa), immune cells (~100 Pa), and extracellular matrix, whose primary components include fibronectin (~1–15 MPa) and collagen (~5–10 GPa). This raises a long-standing question: **when T cells receive two or more mechanical stimuli simultaneously, do they average their responses to these stimuli, or does one stimulus dominate**? Addressing this question has so far been limited due to the lack of *ex vivo* model environments capable of delivering simultaneous mechanical stimuli.

Here, we engineered a novel model system for T cell stimulation that mimics the mechanical complexity of the T cell environment and studied its effects on T cell activation. The system consisted of a micropattern of alternating soft and stiff microdomains. The micropattern was fabricated by photolithographic patterning of silica lines, which were then mechanically embedded within soft polydimethylsiloxane (PDMS). The pattern was uniformly functionalized with activating and costimulatory ligands essential for biochemical signaling. T cells were plated on these patterns as well as on homogeneous soft and stiff surfaces for comparison. We found that T cells did not average the mechanical signals. Instead, they responded similarly to those on a homogeneously soft surface, exhibiting lower activation compared to those on a stiff surface. Interestingly, long-term exposure to these patterns enhanced the proliferation of central memory and effector T cell phenotypes, similar to the response observed in stiff environments. These findings reveal the non-linear nature of T cell mechanosensing and suggest that mechanical heterogeneity plays a critical role in modulating T cell responses. This provides new insights into T cell activation and has potential implications for immunotherapies.

[1] J.J Pandit., Acta Biomaterialia Volume 195 (2025), 83-93.

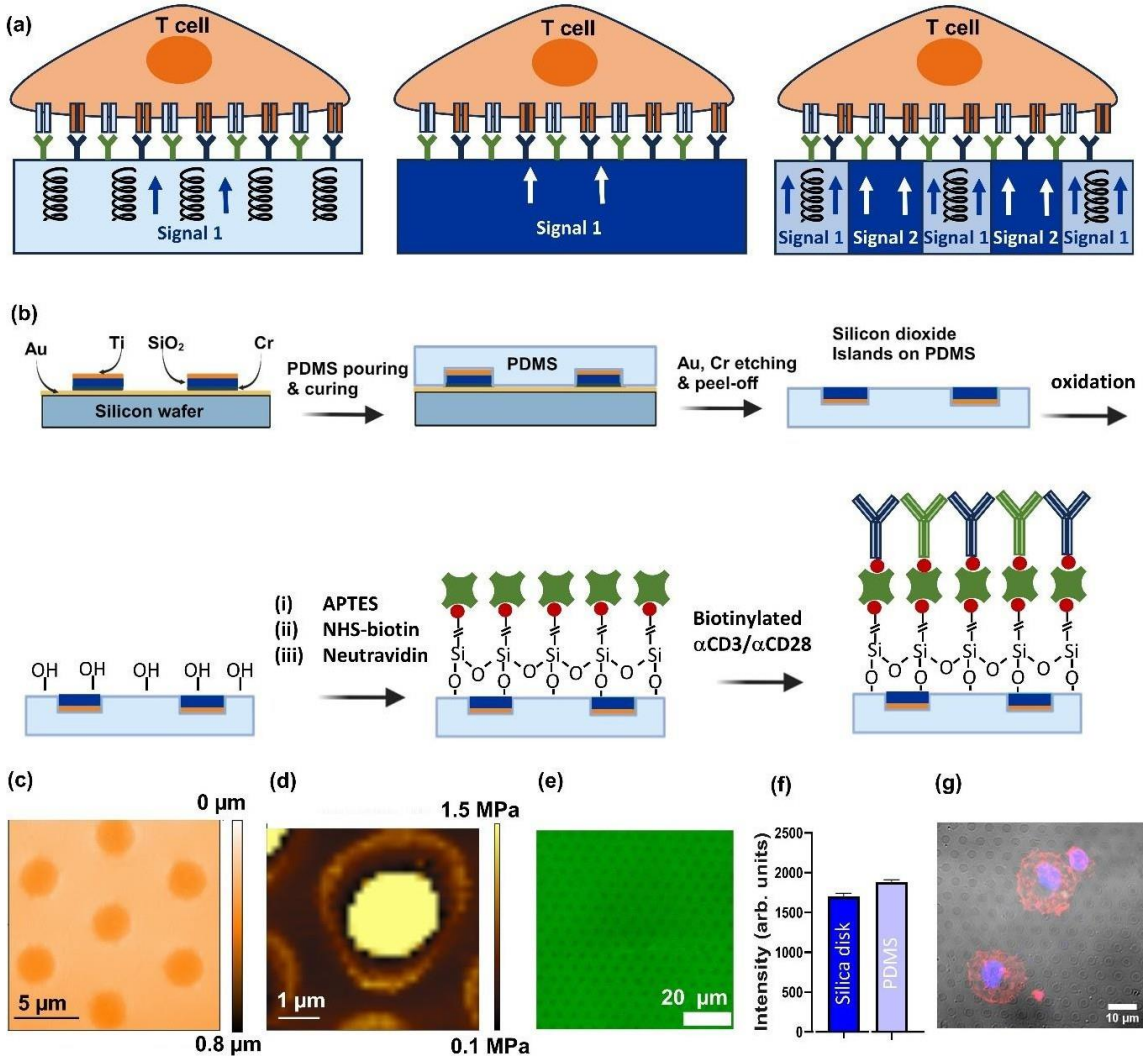

Figure (a) Scheme of two activating microenvironment – soft and stiff, each providing uniform mechanical activating signal, vs. mechanically patterned microenvironment simultaneously providing different mechanical signals to each cell. (b) Fabrication and biofunctionalization process flow of the stiffness pattern. (c) Topography AFM scanning of the stiffness pattern. (d) Modulus AFM mapping of the stiffness pattern. (e) Fluorescence microscopy image of the stiffness pattern after the biofunctionalization, showing the presence of tagged Neutravidin on both PDMS and Silica domains. (f) Quantitative comparison between the fluorescence signals from PDMS and Silica domains. (g) Primary Human T cells spread on fluorescence pattern. The cells were incubated on the pattern for 24 hrs, fixed and stained for cytoskeleton with phalloidin (red) and for nucleus with DAPI (blue).

Published in Acta Biomaterialia Volume 195 (2025), 83-93

Patterning on Living Tardigrades

Zhirong Yang [a], Shan Wu [a], Kang Zhao [b], Ding Zhao [a,b*], Min Qiu [a,b,c*]

[a] Key Laboratory of 3D Micro/Nano Fabrication and Characterization of Zhejiang Province, School of Engineering, Westlake University, Hangzhou 310030, China
[b] Westlake Institute for Optoelectronics, Fuyang, Hangzhou 311421, China
[c] Institute of Advanced Technology, Westlake Institute for Advanced Study, Hangzhou 310024, China.
e-mail: zhaoding@westlake.edu.cn (D.Z.), qiu_lab@westlake.edu.cn (M.Q.)

Micro/nanofabrication techniques have revolutionized modern photonics and electronics. However, conventional methods remain incompatible with living organisms due to inherent constraints including nonconformal coating, radiation damage and toxic solvent requirements [1]. In this study, we integrate semiconductor manufacturing techniques with biology, demonstrating that electron-beam lithography (EBL) can be employed to fabricate micro and nanoscale patterns on extremophilic organisms such as tardigrades. This process must be carried out at cryogenic temperatures in a technique known as ice lithography, an emerging variation of the traditional method [2]. The tardigrade, often called the “water bear,” is renowned for its remarkable resilience in its cryptobiotic state, making it an ideal subject for initial experiments (see Fig 1). In ice lithography, vaporized chemicals condense onto the sample surface to form conformal electron resists, making this technique particularly suitable for micro/nanofabrication on small, delicate, or non-planar objects [3,4]. A key advantage of using ice as an electron resist is its ability to minimize electron radiation damage to the sample. While cryopreservation techniques have advanced significantly, preventing damage caused by ice crystal formation during freezing remains a challenge. Ice lithography circumvents this issue by utilizing ice in its amorphous state, thereby preventing crystal formation and protecting the sample. Using this method, we successfully fabricated in situ micro and nanoscale patterns of arbitrary shapes on living tardigrades, including a line array with a line width of 72 nm (see Fig 2). These patterns remained securely attached to the tardigrade’s body even after stretching, solvent immersion, rinsing, and drying. The insights gained from this work could advance researchers’ ability to detect and manipulate biological entities at the micro and nanoscale, with potential applications in cryopreservation, microbial sensing, and the development of living micro-robotic systems.

Keywords: micro/nanofabrication, ice lithography, living organisms, wearables, biosensors

References:
[1] A. K. Grebenko et al., Small 18 (2022), e2200476.
[2] D. Zhao et al., Sci. Bull. 64 (2019) 865–871.
[3] A. Han et al., Nano Lett. 12 (2012) 1018–1021.
[4] S. Wu et al., ACS Appl. Mater. Interfaces 14 (2022) 1652–1658.

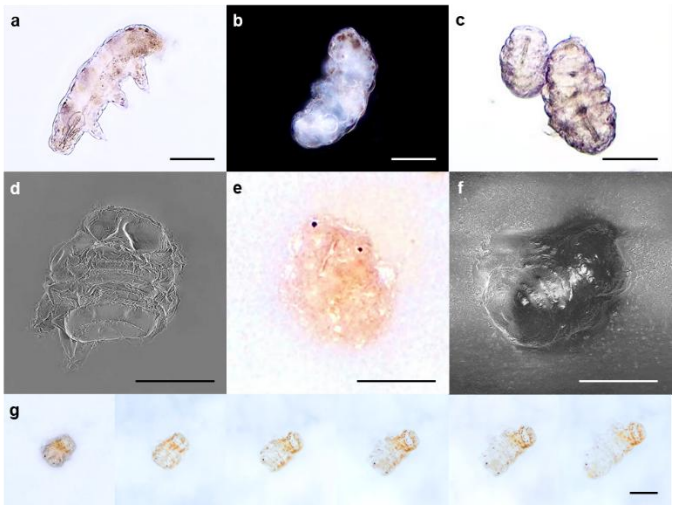

Figure 1. Resilience testing of tardigrades. (a) Optical image and (b) fluorescent image of the extremotolerant tardigrade in a hydrated condition. Optical images (c and e) and SEM images (d and f) of cryptobiotic tardigrades under extreme conditions: desiccation (c), vacuum and electron radiation (d), freezing in liquid nitrogen (e), and covering with solid anisole (f). (g) Revival process from tun state to active state with water. Scale bars: 50 μm.

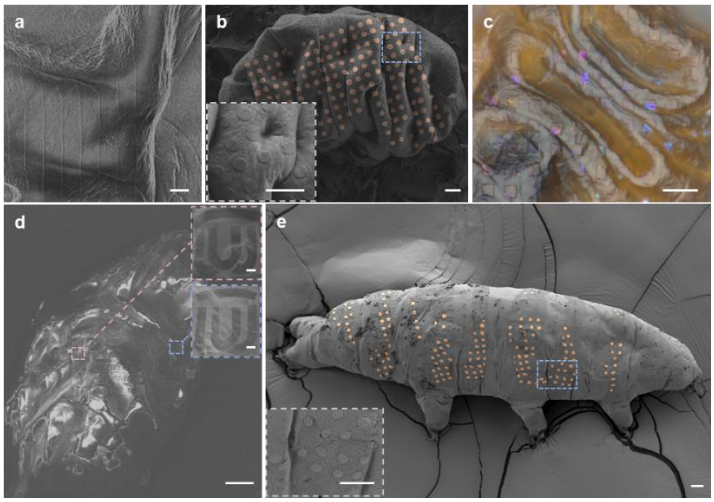

Figure 2. Microstructures created by ice lithography. (a) SEM image of nanolines on a tardigrade (~72 nm line width). (b) False-colored SEM image of a microdisk array (3 μm diameter, 3 μm spacing) on a tardigrade, with a magnified inset of the blue-boxed area. (c) 3D micrograph of a square array (3 μm side length, 3 μm spacing) on a tardigrade. (d) SEM image of the "Westlake University logo" array on a tardigrade. (e) False-colored SEM image of the tardigrade in (b) after rehydration and fixation, with a magnified inset of the blue-boxed area. Scale bars: 2 μm in (a), 20 μm in (d), 1 μm in inset of (d), and 10 μm in (b), (c), and (e).

Electrodeposition of conducting polymers on silicon towards integrated autonomous sensor systems

Tomoyuki Kurioka [a], Punvinai Vinaisuratern [a], Joji Higuchi [a], Keisuke Okamoto [a], Tso-Fu Mark Chang [a], Nasser Aldhahri [b], John W. McBride [c], Yoshishige Tsuchiya [b], Masato Sone [a]

[a] Institute of Integrated Research, Institute of Science Tokyo, Yokohama, 226-8501, Japan
[b] School of Electronics and Computer Science, University of Southampton, Southampton, SO17 1BJ, UK
[c] School of Engineering, University of Southampton, Southampton, SO17 1BJ, UK
e-mail: tkurioka@first.iir.isct.ac.jp

Autonomous sensor systems can be defined as devices that autonomously collect the information from the measurement environment and update these data without the physical connection to external equipment [1]. Such sensing systems are ideal for portable medical devices that can analyze human health conditions by measuring physiological signals. The autonomous sensors and their sensing interfaces can be designed based on advanced Si device technology. However, to address human skins which are mechanically softer than Si without damaging them in operation, coating the Si surface by any softer materials to tune the mechanical properties will be an effective method [2]. Among various materials, conducting polymers (CPs) will be a good candidate because of their moderate softness, good electrical conductivity, biocompatibility and versatility. Furthermore, CPs can be fabricated via electrodeposition, which is compatible with the back-end processes of the advanced Si device technology. So far there are few reports regarding the direct electrodeposition of CPs onto the Si substrate without surface modification.

This paper focuses on developing technology to fabricate CP films on Si substrates via electrodeposition. We report the results of direct electrodeposition of three different CPs, polyaniline (PANI), polypyrrole (PPy), and poly(3,4-ethylenedioxythiophene) (PEDOT) on Si substrates, and discuss the relevance between their electrodeposition parameters and their electrical properties.

P-doped Si wafer substrates (2 cm × 1 cm) were prepared and immersed in 5 wt% HF(aq), and then rinsed with DI water. The surface area of the Si substrate was regulated to 1 cm × 1 cm with insulating tape, and then used as a working electrode for the electrodeposition of CPs. The electrodeposition was performed in electrolytes containing the corresponding monomers as shown in Figure 1. The amount of the electrodeposited CP was controlled by changing the amount of charge passed. The CP films prepared onto the Si substrates were denoted as "CP name@##", where ## represents the amount of charge passed (eg PEDOT@1.0C). Their morphologies and thickness were investigated by scanning electron microscope (SEM) observations. The electrical conductivity was measured using the four-point probe method.

After the passage of 0.1 C of the amount of charge, the Si substrates were covered with the CPs as shown in Figure 1. The PPy and PEDOT films were more uniformly deposited than the PANI films, presumably due to the difference in the hydrophobicity of monomers. We further investigated the effects of the amount of charge passed on the propagation behavior of the PPy films and the PEDOT films. Figure 2 shows the SEM images of the PPy films and the PEDOT films prepared with the passage of 0.1 C or 1.0 C of amount of charge, and the cross-sectional SEM image of PPy(1.0 C) and PEDOT(1.0 C). As the increase in the amount of charge passed, the surface was occupied with more particles, and the particle size became larger. The amount of charge also affected the thickness of the CPs, and their electrical conductivity. Figure 3 shows the relationship between the amount of charge passed and their thickness and electrical conductivity. The more amount of charge was passed, the larger the thickness of the CP films became. The electrical conductivity of the CP films was also improved with the increase in the amount of charge passed, presumably due to the formation of the network structures, which facilitated the electron transfer within the whole CP films.

In conclusion, we successfully coated three types of CPs, PANI, PPy, and PEDOT on Si substrates via the electrodeposition. The thickness and electrical conductivity of the CPs can be manipulated by tuning the amount of charge passed. The developed methodologies would be applicable to the heterogeneous integration of CPs with the Si technologies to manipulate the autonomous sensor interfaces.

Acknowledgement: This work was partly supported by the Cooperative Research Project of the Research Center for Biomedical Engineering and British Counsil Reconnect Travel Grant.

References: [1] M. Serpelloni et al., Sensor 9 (2009) 943–960; [2] G. He et al., Mater. Res. Express 7 (2020) 102001.

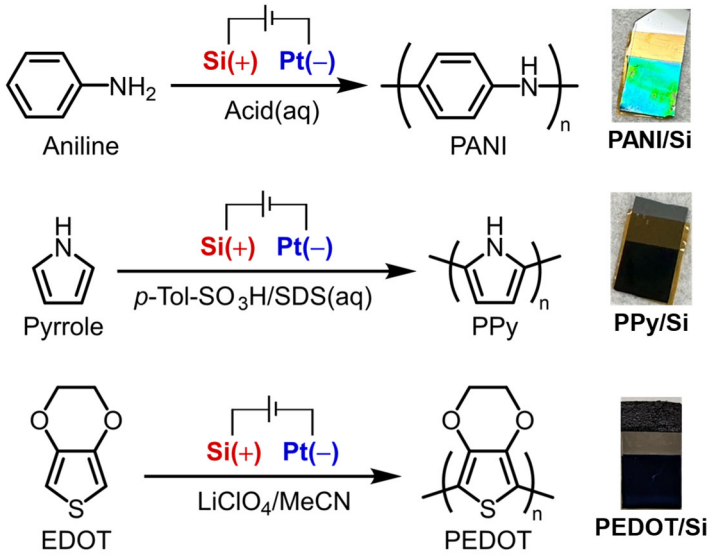

Figure 1. Electrodeposition of various CPs using a Si substrate as a working electrode, and the photos of the deposited CPs onto the Si substrate with the passage of 0.1 C amount of charge.

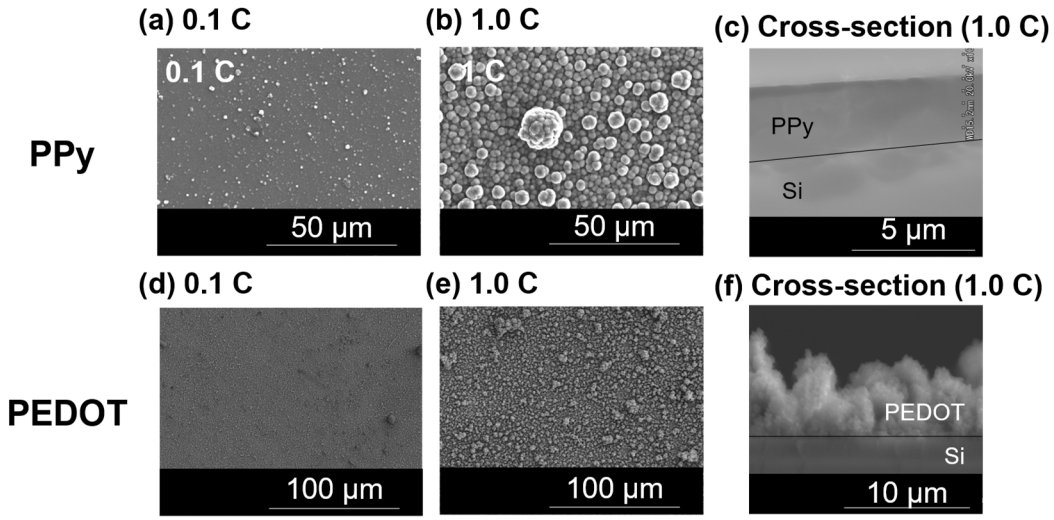

Figure 2. (a, b) SEM images of PPy films prepared with the passage of (a) 0.1 C amount of charge (PPy@0.1 C), and (b) 1.0 C amount of charge (PPy@1.0 C). (c) The cross-sectional SEM image of the PPy@1.0 C. (d, e) SEM images of PEDOT films prepared with the passage of (a) 0.1 C amount of charge (PEDOT@0.1 C), and (b) 1.0 C amount of charge (PEDOT@1.0 C). (c) The cross-sectional SEM image of the PEDOT@1.0 C.

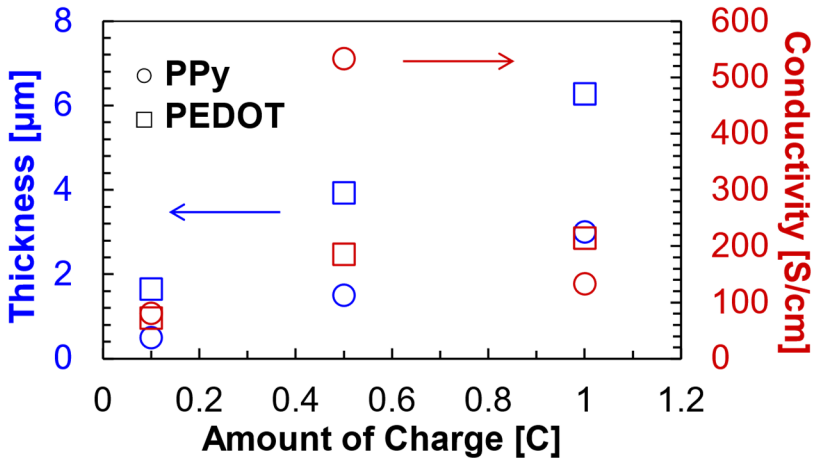

Figure 3. Relationship between the amount of charge passed for the electrodeposition of CPs (PPy (circle) and PEDOT (square)) and their thickness (left in blue) or electrical conductivity (right in red).

A Thick-Film Micro-Patterning Method for Organic Thermoelectric Materials Using O_2 Plasma and Metal Masks

Shota Sawayama [a], Qingshuo Wei [b], Daisuke Yamane [a,c],

[a] Graduate School of Science and Engineering, Ritsumeikan University, Kusatsu, Shiga 525-8577, Japan
[b] Research Institute of Core Technology for Materials Innovation, National Institute of Advanced Industrial Science and Technology (AIST), 1-1-1 Higashi, Tsukuba, Ibaraki, 305-8565, Japan
[c] Department of Mechanical Engineering, Ritsumeikan University, Kusatsu, Shiga 525-8577, Japan
e-mail: dyamane@fc.ritsumei.ac.jp
keywords : Organic thermoelectric materials, micro-patterning, PEDOT:PSS, PBFDO

INTRODUCTION

In the development of organic thermoelectric generators using materials such as poly(3,4-ethylenedioxythiophene) polystyrene sulfonate (PEDOT: PSS), miniaturization through on-substrate patterning has been a key research focus. However, most existing methods rely on techniques such as inkjet printing, which inherently limit the achievable film thickness. Since reducing internal resistance is essential to improving power output, maintaining sufficient film thickness becomes critical. To overcome this limitation, we have developed a new micro-patterning technique for organic thermoelectric materials using reactive ion etching (RIE) and metal masks developed by a physical vapor deposition (PVD). Expanding on prior works using ashing processes to pattern PEDOT: PSS [1] films, this work proposes an optimized process for thicker films and explores its applicability to a different material, polymer polybenzodifuranedione (PBFDO) [2]. The differences from the previous work are summarized in Table 1.

METHOD

PEDOT: PSS and PBFDO were used as organic thermoelectric materials, each deposited via drop-casting to achieve film thicknesses exceeding 15 μm on average. Aluminum was employed as the mask material, and patterning was carried out following the sequence illustrated in Fig. 1. The design dimensions of the pattern are shown in Fig. 2. During the wet etching of the aluminum mask, the high viscosity of the undiluted etchant often caused the organic layers to flow off the substrate. To address this issue, we propose diluting the etchant with deionized (DI) water to reduce viscosity. Furthermore, ethanol was used instead of DI water during the final cleaning step to prevent film delamination.

RESULT

O_2 ashing was performed at a flow rate of 200 sccm and 150 W for 8 hours for PEDOT: PSS, and at 250 sccm and 450 W for 4 hours for PBFDO. As shown in Figs 3 and 4, micro-patterns were successfully developed for both materials. The measurement results are summarized in Table 2 for PEDOT: PSS and Table 3 for PBFDO. Diluting the aluminum etchant significantly improved the adhesion of PEDOT: PSS, while ethanol cleaning effectively prevented delamination. PBFDO exhibited excellent stability, maintaining adhesion even when using undiluted etchant and DI water for cleaning. The measured film thicknesses deviated from the design value (15 μm): ~20 μm for PEDOT:PSS and ~7 μm for OBFDO. These thickness deviations likely result from differences in drying conditions and solution viscosity.

CONCLUSION

We demonstrated that PEDOT: PSS and PBFDO films with high thickness and micro patterns can be processed using O_2 plasma and metal masks with diluted aluminum etchant and ethanol cleaning, minimizing delamination during wet etching. Moreover, we confirmed that PBFDO is compatible with RIE-based patterning and exhibits strong adhesion regardless of etchant concentration or cleaning solvent. Thus, this method can be a promising approach to achieve thick-film organic thermoelectric devices with micro patterning capability.

REFERENCE

[1] Amrita Chakraborty , Daniel Herrera , Payton Fallen , Daniel Hall , Nicholas Bampton , Thomas Olivero & Marius Orlowski : Conductive organic electrodes for flexible electronic devices, Scientific Reports,13 (2023) 4125.
[2] Haoran Tang, Yuanying Liang, Chunchen Liu, Zhicheng Hu, Yifei Deng, Han Guo, Zidi Yu, Ao Song, Haiyang Zhao, Duokai Zhao, Yuanzhu Zhang, Xugang Guo, Jian Pei, Yuguang Ma1, Yong Cao1 & Fei Huang. : A solution-processed n-type conducting polymer with ultrahigh conductivity : Nature, 611 (2022) 271-277.

Table 1. Technology comparison

	Previous Work[1]	**This Work**
Material	PEDOT: PSS	PEDOT: PSS or PEDOT
Thickness	0.085 μm	15 μm
Deposition	Spin coating	Drop casting
Mask	Ag	Al
Etchant	NO_3	PAN[1] etcant

1 PAN (Phosphoric-Acetic-Nitric)

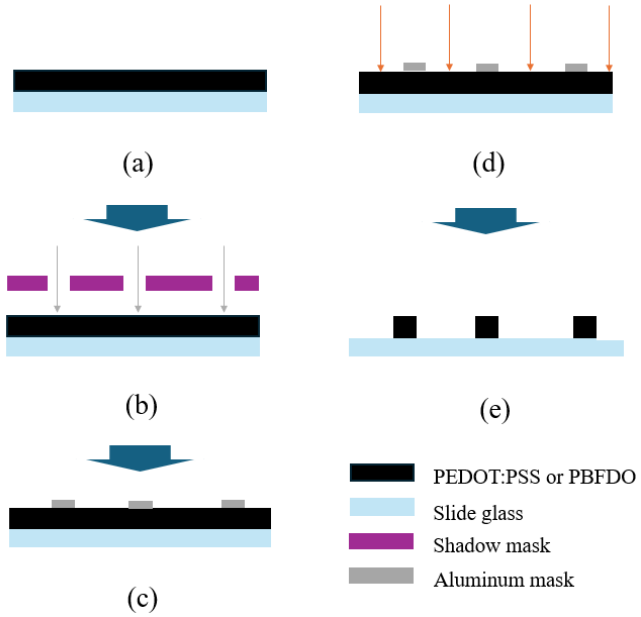

Figure 1. Process diagram. (a) Coating organic thermoelectric materials onto a slide glass, (b) placing a shadow mask and deposit aluminum using PVD, (c) removing the shadow mask, (d) performing ashing using RIE, and (e) removing the aluminum mask using wet etching.

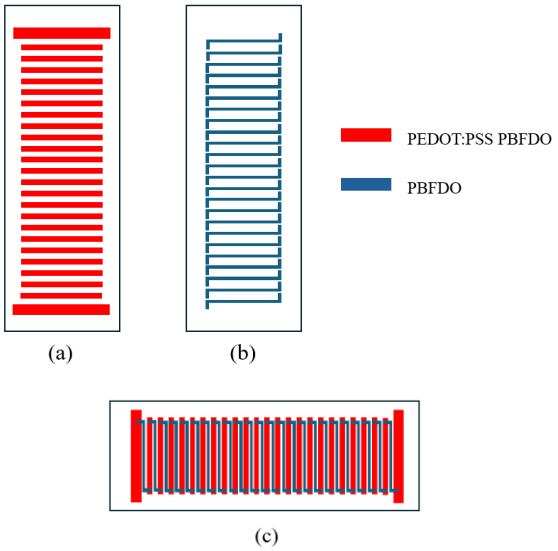

Figure 2. Conceptual Diagram.
(a) P-type, (b) N-type, and (c) thermoelectric device.

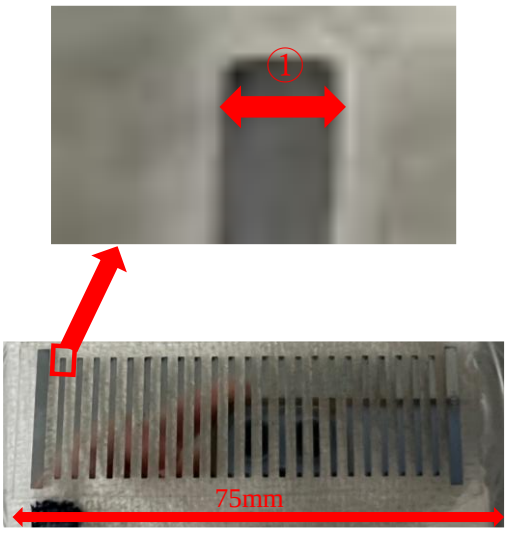

Figure 3. Micro-pattering of PEDOT: PSS.

Table 2. Measurement results for PEDOT: PSS.

	①	**Thickness**
Designed	1000 μm	15 μm
Measured (Shadow Mask)	992 μm	N/A
Measured (PEDOT: PSS)	987 μm	20 μm

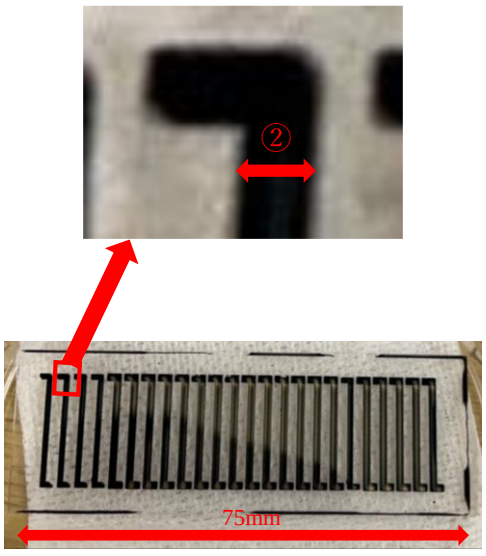

Figure 4. Micro-patterning of PBFDO.

Table 3. Measurement results for PBFDO.

	②	**Thickness**
Designed	1000 μm	15 μm
Measured (Shadow Mask)	1024 μm	N/A
Measured (PEDOT: PSS)	1026 μm	7 μm

Oral Session 6B: Micro-Nano Systems II

Making a Miniature Sun: Ultra High Temperature Carbon Devices

ELH Thomas [a], J Stritt [a], S Mandal [a], M Imboden [b], OA Williams [a]

[a] School of Physics and Astronomy, Cardiff University, Queen's Buildings, The Parade, Cardiff CF24 3AA, UK

[b] 4K-MEMS SA, St Blaise 2072, Switzerland

e-mail: williamso@cardiff.ac.uk

There is an increasing need for miniaturised broadband light emitters as light sources in gas detection and spectroscopy. Commercial Micro-Electro-Mechanical (MEMS) InfraRed emitters are joule heated hot plates, based on thin silicon nitride membranes patterned with metallic heaters, which can operate at temperatures up to 1000 K and be modulated at typically less than 10 Hz. One the critical limiting factors of such incumbent technologies is that they are generally bilayers and thus suffer from differences in coefficients of thermal expansion (C_{TE}) between the two materials. Thus, their maximum temperature is limited.

In this work we demonstrate MEMS hotplates based on boron doped diamond thin film technology (**figure 1**) [1]. The active heating element of these hotplates is diamond alone (dark regions of **figure 1**), significantly reducing the stresses induced by thermal expansion and thus increasing the maximum operating temperature dramatically. Temperatures exceeding 2700 K (**figure 2** shows up to 2275 K) were reached with millisecond response times. At temperatures over 1400 K the devices catastrophically fail on cooling down due to high inhomogeneous stresses buckling the structures. This stress originates from the formation of non-diamond carbon which is an unavoidable consequence of the extreme temperatures. To this end, the development of glass like carbon devices is under way as non-graphitising carbons will not undergo such phase changes up to 3000 K.

[1] E. L. H. Thomas, J. Stritt, S. Mandal, M. Imboden, and O. A. Williams, "Polycrystalline Diamond Micro-Hotplates," *Small,* vol. 19, no. 48, p. e2303976, Nov 2023, doi: 10.1002/smll.202303976.

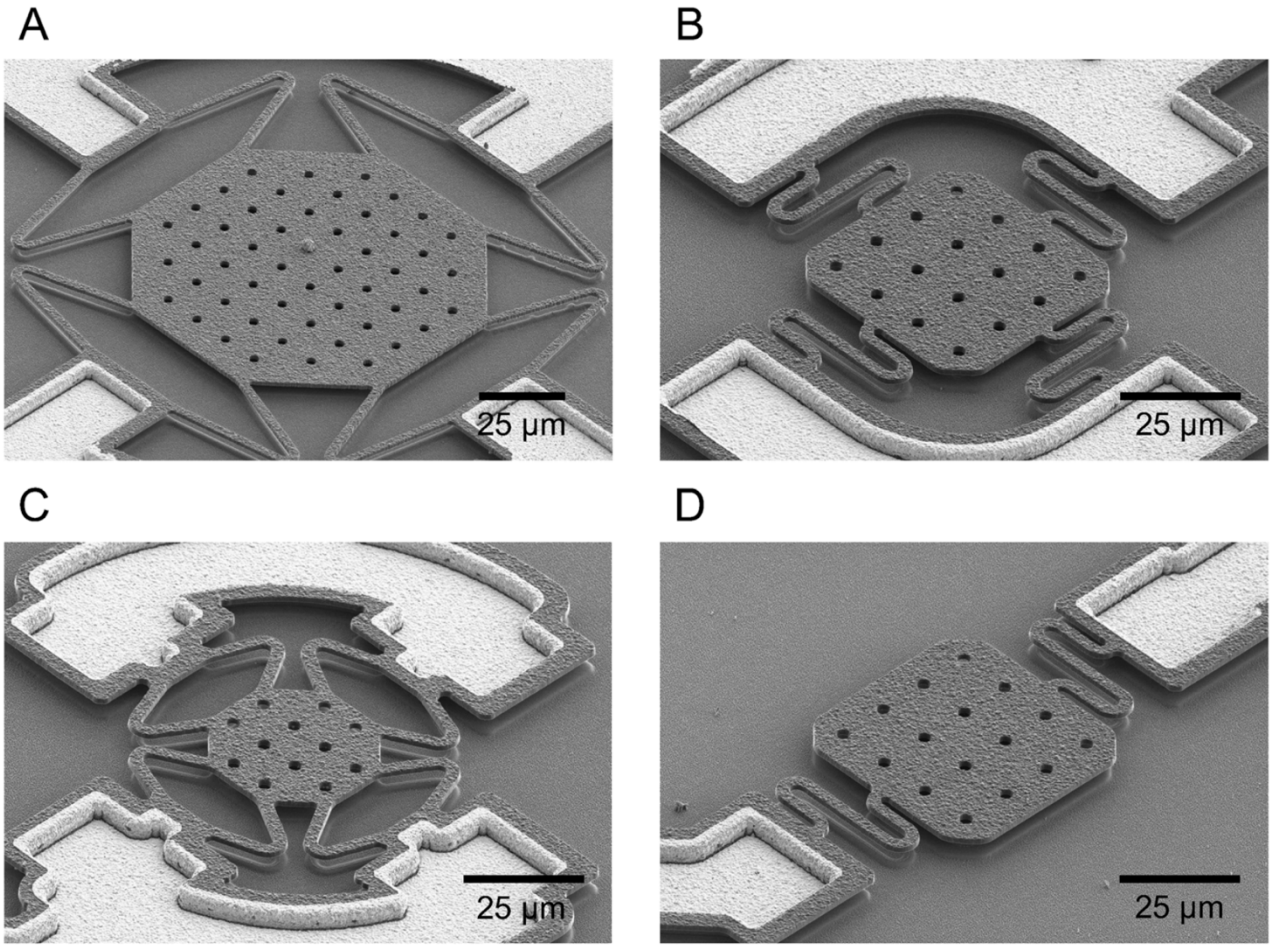

Figure 1. Various Diamond Micro Hotplate structures.

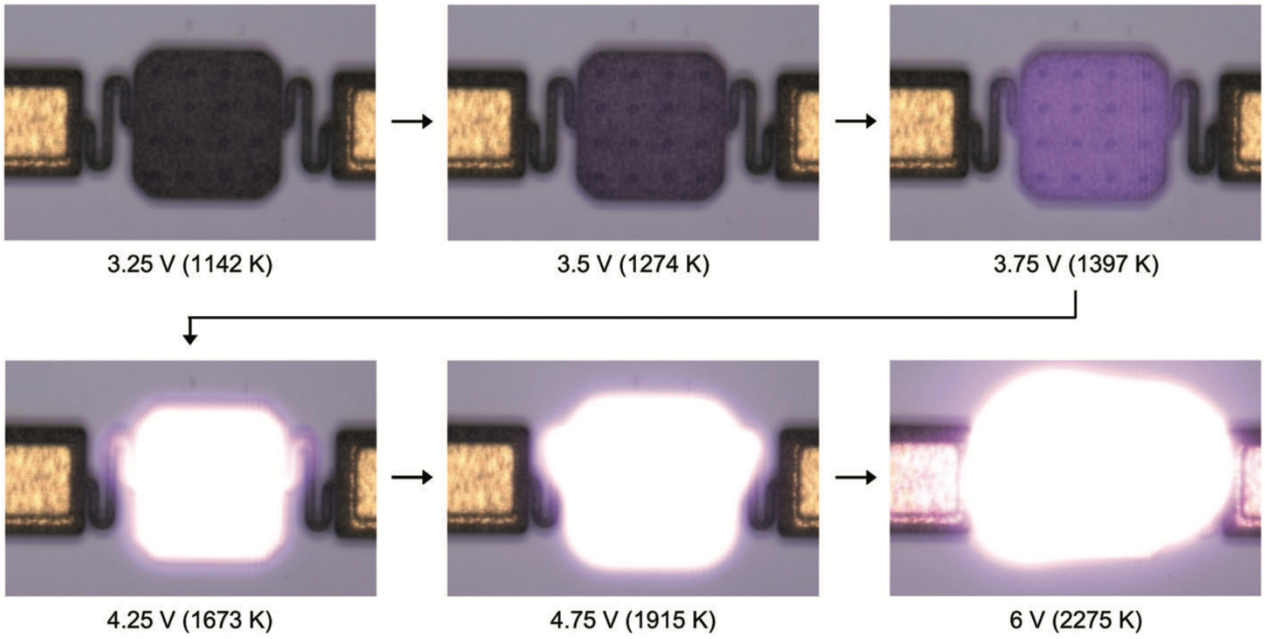

Figure 2. Diamond Micro Hotplates at increasing temperature.

Mechanical and electrical contact testing for Pt/PEDOT/Si layered structures

Yoshishige Tsuchiya [a], Tomoyuki Kurioka [b], Punvinai Vinaisuratern [b], Joji Higuchi [b], Tso-Fu Mark Chang [b], Masato Sone [b], Nasser Aldhahri [a], Liam Boodhoo [a], Thomas Bull [c], Yan Yang [d] and John W. McBride [c,d]

[a] School of Electronics and Computer Science, University of Southampton, Southampton SO17 1BJ, UK
[b] Institute of Integrated Research, Institute of Science Tokyo, Yokohama 226-8501, Japan
[c] School of Engineering, University of Southampton, Southampton SO17 1BJ, UK
[d] TaiCaan Technologies, Southampton, SO16 7NP, UK
E-mail: yt2@ecs.soton.ac.uk

Micro/Nano-Electro-Mechanical Systems (MEMS/NEMS) contact switches use physical contact and separation of a contact pair of conductive materials for their on and off states, and have been known as an ultimate form of micro/nanoscale switches thanks to their excellent isolation at the off state and very low insertion loss at the on state. However, a longstanding issue is optimisation of the mechanical contact structure including usage of materials, and many efforts have been made to improve the contact properties to realise high-speed operation, low contact resistance and long lifetime simultaneously. In Ref. [1] vertically aligned multi-wall carbon nanotubes (CNT) coated by Au (Au/CNT) are reported to improve the switching lifetime under low force and low current switching as the CNT can work as a mechanically compliant subsurface [1]. This work inspires investigation of alternative sets of materials that could be used for the surface/subsurface pair to improve the durability of mechanical contacts. Conducting polymers (CPs) are unique materials: mechanically soft or flexible as a polymer while conductive electrically. Recently, direct electrodeposition of CPs onto silicon have been demonstrated towards development of CP/Si heterogeneous integration technology [2]. Motivated by these works, in this study, we have fabricated a metal/CP/Si layered structure and conducted a contact resistance with force test and a hot switching test for the first time.

Figure 1(a) shows a photo of a sample, where Poly(3,4-ethylenedioxythiophene) (PEDOT) was electrodeposited on a p-doped Si substrate. Detailed deposition procedure was reported elsewhere [2]. A 200-nm-thick Pt is sputtered onto the PEDOT as shown in Fig. 1 (b). The sample is loaded on the stage of the ICE system (TaiCaan Technologies) as shown in Fig. 2(a). Two wires are bonded to the edges of the Pt/PEDOT deposited area. An Au-coated 1-mm-radius ball mounted on a rod with the Au thickness of 500 nm is used to make electrical contact with surface of the sample. Two wires bonded to the rod enables 4-wire contact resistance measurements between the Au and sample surface at contact. Prior to the tests, surface morphology of the sample is measured by a surface profiler XYRIS Ultra 2020 L (TaiCaan Technologies). Figure 2 (b) shows a surface profile of the Pt/PEDOT deposited area. We used a relatively flat area indicated in Fig. 2(b) for the following mechanical and electrical testing. The contact resistance is measured by using a Keithley micro-ohm meter with respect to the contact force measured via a piezoelectric force transducer Kistler 9207. With increasing the contact force up to 1 mN, the contact resistance of down to 120 Ω is observed.

For this site, we conducted hot switching test with the cycle frequency of 250 Hz and the current in hot switching is set 20 mA. Note that due to the high contact resistance, the current is down to approximately 15 mA. Figure 3 (a) shows s surface morphology of the indentation testing site after 50,000 hot switching cycles. A clear dip-like structure formed after the indentation show the depth of about 5-6 μm, suggesting the amount of material has been removed after the cyclic indentation. Figure 3 (b) and (c) show the behaviour of the voltage across the contact and the contact force at an event of hot switching, corresponding to a half cycle. The contact closes at t = -0.6 ms and opens fully again at t = 0.2 ms. While the open circuit voltage is about 4 V, the close circuit voltage is only down to 2 V between t = -0.3 – 0 ms due to the large contact resistance. The maximum contact force is about 0.8 mN at 0.7 ms after the impact event. Note that the steps observed at t = -0.6 – -0.3 ms, and t = 0 – 0.2 ms in Fig. 3 (b) corresponds to the boiling voltage of the Pt conductive surface, suggesting the formation of molten metal bridges both in closing and opening.

Acknowledgements: This work was partially supported by British Counsil Reconnect Travel Grant, the Cooperative Research Project of the Research Centre for Biomedical Engineering, and CHIST-ERA NOEMIA (CHIST-ERA-21-NOEMS-004) by EPSRC (EP/X03495X/1).

References: [1] J. W. McBride and T. G. Bull, in IEEE Holm Conference on Electrical Contacts, 14-18 September 2019, Milwaukee, WI, USA, pp. 149–155; and M. P. Down et al., Applied Physics Letters 106 (2015) 101911. [2] T. Kurioka et al., in ISE 38th Topical Meeting, Manchester, UK, 2024; and MNE2025, Southampton, UK, 2025, *submitted*.

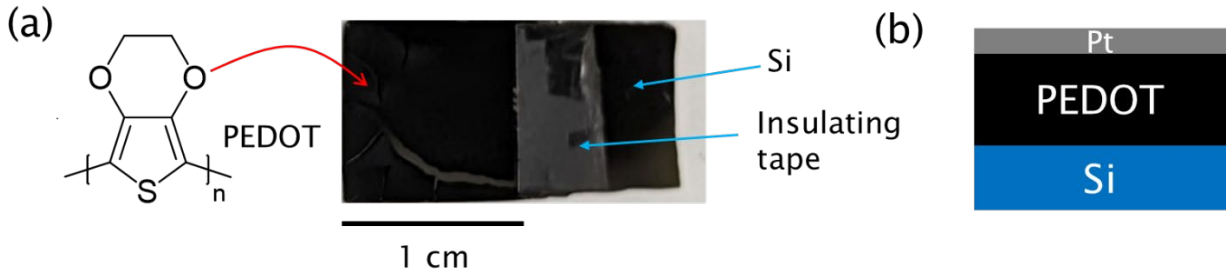

Figure 1. (a) A photo of a sample where Pt/PEDOT/Si structure is formed. The chemical structure of the PEDOT is also shown. Insulating tape is used to define the deposition area and isolate from the electrode in electrodeposition. (b) A schematic of the cross section of the Pt/PEDOT/Si structure. The estimated thickness of the PEDOT layer is 12 µm.

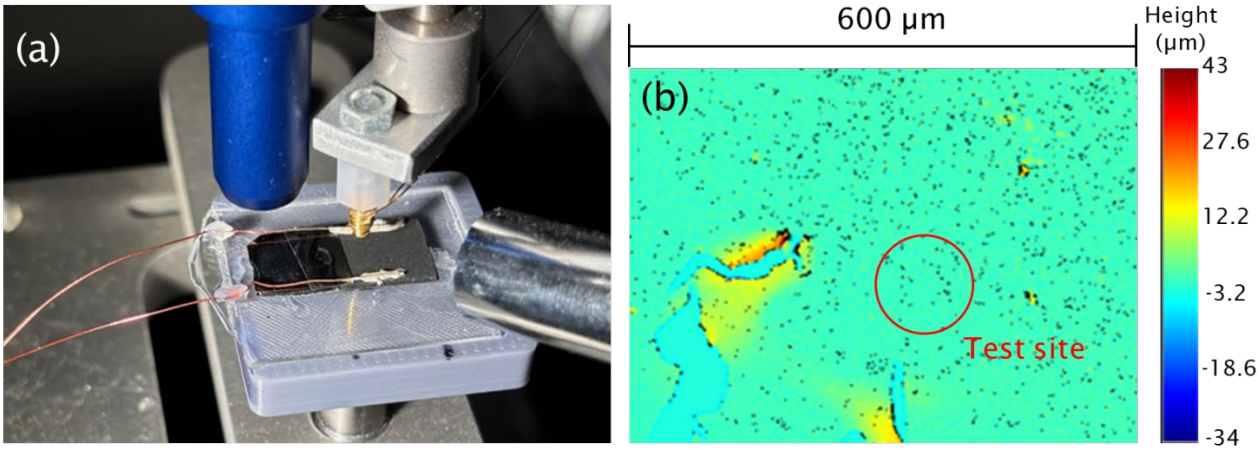

Figure 2. (a) A photograph of the ICE system to characterize mechanical contact properties of a contact pair. The Pt/PEDOT surface with two wire connected is mounted on the stage. (b) A surface profile of the Pt/PEDOT surface taken by XYRIS Ultra 2020 L. The site tested for cyclic hot switching is indicated.

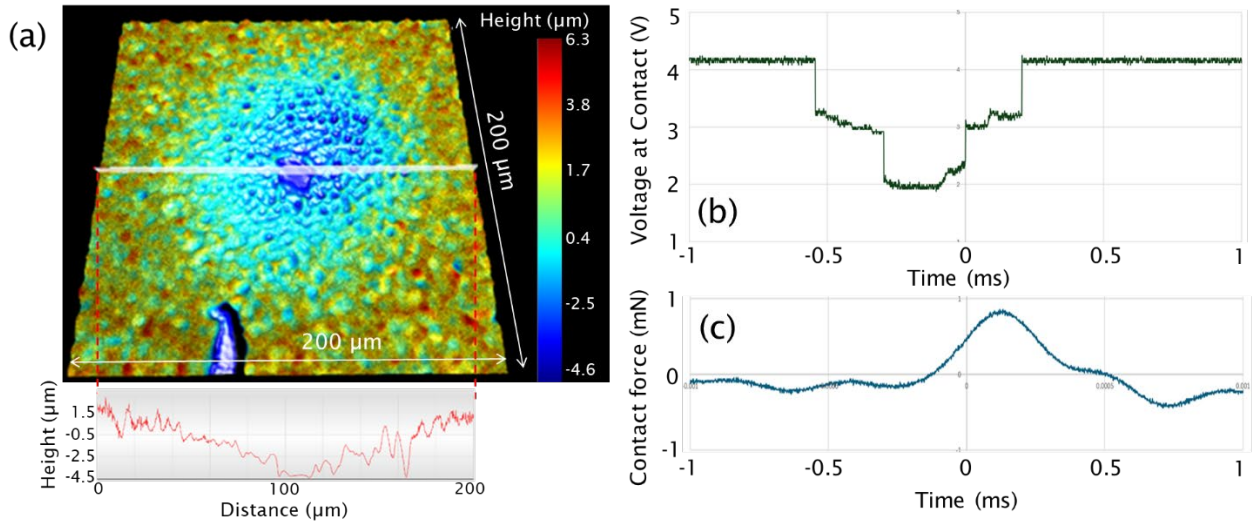

Figure 3. (a) Surface morphology of the Pt/PEDOT surface after 50,000 times hot switching. Clear dip-like structure is observed. The voltage across the contact (b) and the contact force (c) in a contact event are plotted with respect to the time. The time range corresponds to a half cycle. Molten metal bridge behavior is observed both in closing and opening.

Wafer scale fabrication of pyrolytic carbon submicron gap membrane electrodes for electrochemical sensing

Nicolai Støvring [a], Pratik Kusumanchi [a], Estefany Ureta [a], Jenny Emnéus [b], Arto Heiskanen [b], Stephan Sylvest Keller [a]

[a] National Centre for Nano Fabrication and Characterization, Kgs. Lyngby, 2800, Denmark
[b] Department of Biotechnology and Biomedicine, Kgs. Lyngby, 2800, Denmark
e-mail: nicosto@dtu.dk

Submicron gap electrically separated electrodes can be employed to drastically enhance current signals for electrochemical sensors by a phenomenon known as redox cycling[1]. Here, an analyte is repeatedly oxidized and reduced between the electrodes effectively amplifying the signal each time. Redox cycling sensors have been demonstrated as wearable devices [2] and in nanofluidic channels [3]. Realizing submicron gap electrodes in a membrane-based format could further improve these sensor architectures by offering flexible electrodes coupled with higher flow rates through the submicron gaps for redox cycling. Pyrolytic carbon (PyrC) has been shown to offer high structural strength [4] making it ideal for enabling thin membrane electrodes with submicron gaps. In this work we demonstrate the wafer-scale fabrication of large area, 4 mm diameter, membrane PyrC electrodes separated by a submicron insulating layer. Furthermore, we elucidate some of the ongoing challenges in fabrication of these devices due to the high-temperature and reactive ion etching process as well as required through wafer electrical contacts.

Initially, 350 µm thick 4-inch Si wafers with a thermally grown 1 µm thick SiO_2 layer and a polycrystalline Si (pSi) layer with a thickness of 520 nm were prepared. The wafers were anisotropically reactive ion etched (RIE) from the backside using an SF_6-based plasma with a photoresist mask. This resulted in trenches with a diameter of 4 mm and a depth of ~290 µm (Fig. 1A). The remaining ~60 µm thick Si membrane was stable in the subsequent process steps, even when subjected to vacuum fixation in equipment. To ensure proper adhesion of the PyrC electrode to the frontside electrodes, pSi adhesion structures were patterned (Fig. 1B) as described previously [5]. Afterwards, a 9 µm thick mr-DWL photoresist precursor layer was patterned and pyrolyzed at 1050 °C on the wafer frontside. Subsequently the substrate was crystal-bonded to a carrier wafer, the backside oxide was removed and the remaining ~60 µm thick Si at the bottom of the trench was isotropically etched using an SF_6-based RIE (Fig. 1C). To define the backside electrode an ultrasonic spray-coating process was employed to achieve step coverage of the tall vertical sidewall at the trench edge. TI-Spray photoresist was employed to coat the backside in photoresist using two spray coating steps (Fig. 1D). The first step consisted of 4 passes running the spray-coating nozzle back and forth across the wafer with a flow rate of 1mL/min and a 5 mm spacing between spray coated 'lines' followed by a 2 min softbake at 95 °C on a hotplate. In the second step, 32 passes performed with a flow rate of 233 µL/min using the same line spacing and subsequent softbake settings were employed. The resulting thickness of the precursor layer was 11 µm on horizontal flat surfaces. Then, the backside layer was pyrolyzed at 1050 °C (Fig. 1E) to achieve a PyrC backside electrode. Finally, the SiO_2 layer was etched from the frontside using RIE (Fig. 1F).

One challenge of the spray-coating process was the ability to conformally coat convex corners (Fig. 2A). Here, the resulting PyrC layer covering the corner was measured to be ~20 nm thick (Fig. 2B), which could result in large electrical resistances that could inhibit measurements. Vertical and horizontal surfaces were covered well with PyrC using spray-coating for the deposition of the photoresist precursor as is evident from SEM (Fig. 2B-C). The PyrC electrode offered good structural stability during processing and the yield was >90 %, even for 4 mm diameter membranes (Fig. 3A). However, a key challenge remains in that for most chips, there was short-circuiting from the frontside electrode to the backside electrode. One hypothesis is that the large degree of wrinkling of the membrane (Fig. 3B, C) might induce small cracks in the SiO_2 layer. However, the layer seemed intact (Fig. 3D), and thus it serves as a natural problem to solve in the future process development which we are currently working on. So far, we have only achieved etching of the frontside SiO_2 layer for 600 µm diameter membranes (Fig. 3E) and not for the 4 mm diameter membranes which is also a key point we are working on to implement. Finally, we seek to employ this electrode architecture for redox cycling experiments.

[1] F.-R. F. Fan and A. J. Bard, Science 267 (1995), 871–874.
[2] S. H. Park et al., Biosens. Bioelectron. 220 (2023), 114912.
[3] S. Kang et al. , ACS Nano 7 (2013) 10931–10937.
[4] J. Bauer et al., Nat. Mater. 15 (2016) 438–443.
[5] N. Støvring et al., Micro Nano Eng. 23 (2024) , 100257.

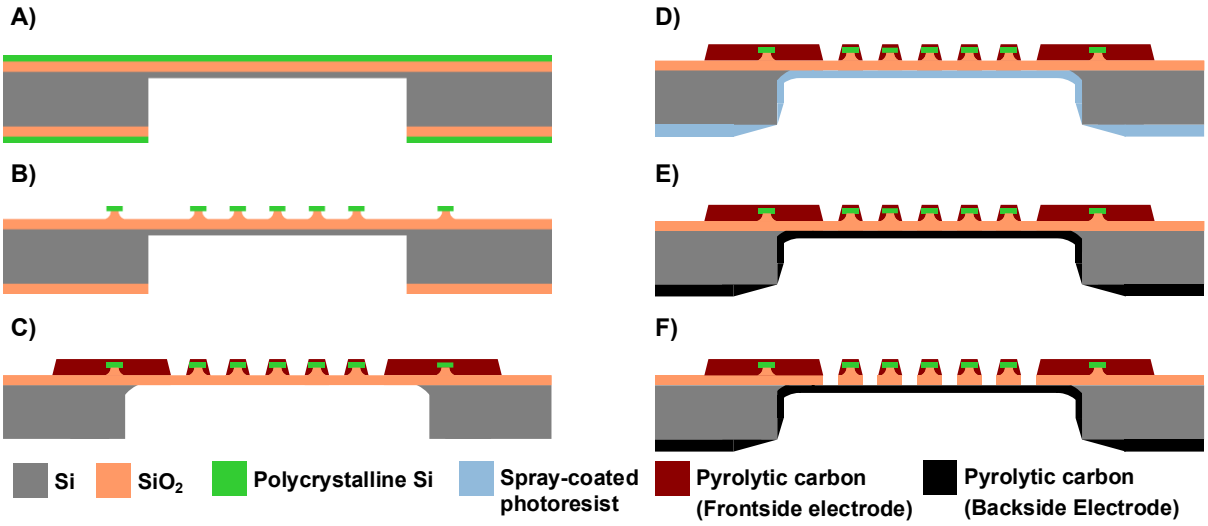

Figure 1. Process flow of the membrane electrodes showing the side view. A) Anisotropic RIE on substrate backside for trenches. B) Fabrication of pSi adhesion structures. C) Photolithography of mr-DWL and pyrolysis on frontside and isotropic Si RIE on backside. D) Spray-coating of photoresist precursor on substrate backside. E) Pyrolysis of spray-coated photoresist. F) Frontside etch of SiO_2 for solute access to backside electrode.

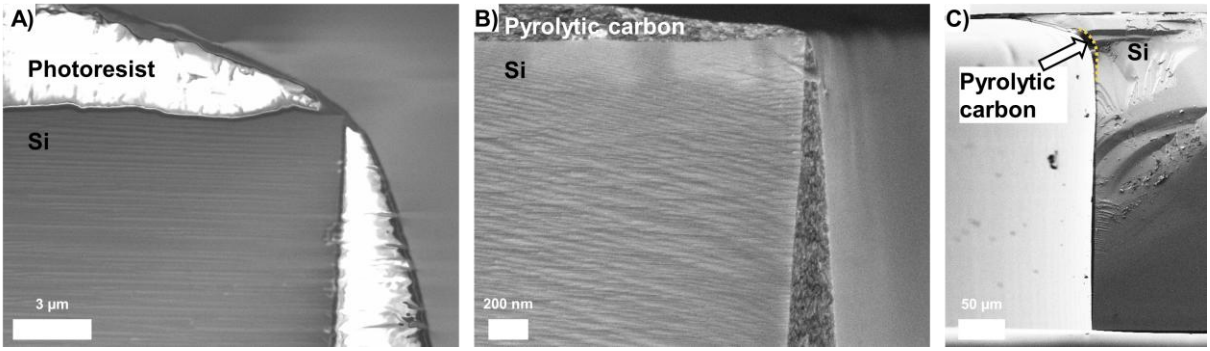

Figure 2. SEM cross sections of the backside trench after A) Spray-coating and B-C) subsequent pyrolysis. The yellow dashed line in C marks the boundary between Si and PyrC.

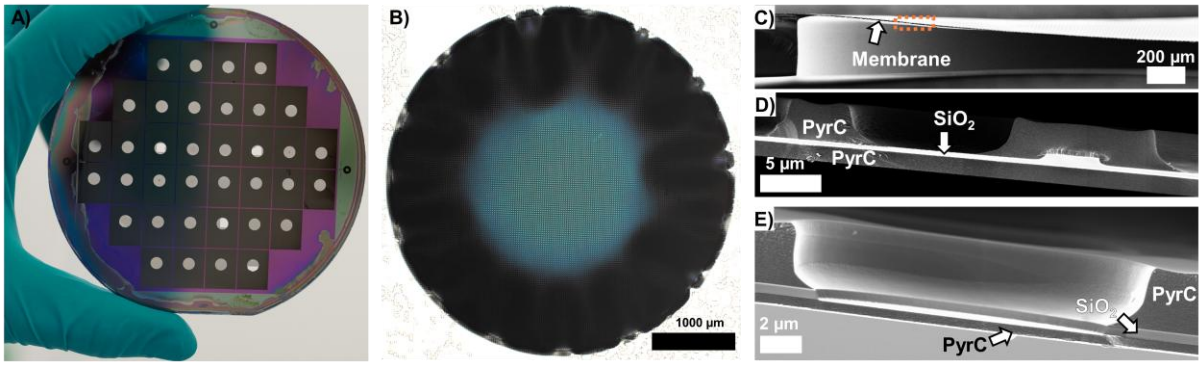

Figure 3. A) Photograph of a full 4-inch wafer with 36 chips before spray-coating. B) Optical micrograph of a single membrane before spray-coating. C) SEM cross section of a portion of a membrane after pyrolysis of the spray-coated photoresist. The orange dashed region corresponds to the image in D. D) Zoom-in on the membrane showing the front- and backside pyrC layers and the SiO_2 layer separating them before etching the insulating layer and E) After etching the insulating layer from the frontside.

Energy-Free Micro-Latching Mechanisms for Bidirectional SMA Actuators

Yizheng Liu [a], Vincent Gottwald [b], Eleonore Stier [a], Manfred Kohl [b], Jürgen Rühe [a]

[a] Department of Microsystems Engineering, University of Freiburg, Freiburg im Breisgau, Germany
[b] Institute of Microstructure Technology, Karlsruhe Institute of Technology (KIT), Karlsruhe, Germany
Email: yizheng.liu@imtek.uni-freiburg.de

Abstract: This work presents the design, fabrication, and performance of polymer-based, reversible and energy-free micro-latching systems, developed to prevent reset motion in bidirectional shape memory alloy (SMA) microactuators [1]. The latching system is specifically designed for the folding of microactuators, paving the way for origami-inspired microsystems and enabling programmable, compact mechanical operations at the microscale. Two different latching strategies are developed: firstly, an active latching mechanism which is based on thermal stimulation using a paraffin-filled container that melts with heat to admit the plunger and then solidifies to mechanically lock it in place. Reheating causes the paraffin to melt again, allowing the plunger to be released (see Figure 1). Secondly, a passive latching mechanism using a sticky polymer surface, where the adhesive interaction holds a plunger in place upon contact. Release is achieved by actuating the opposing directional SMA microactuator, which pulls the plunger off (see Figure 2). Both mechanisms provide reversible, energy-free latching in a microscale actuation system without the need of continuous output energy to maintain the latched state, only an input force is required to 'snap through' between the latched and unlatched states.

In the active latching mechanism, two-photon printing (2PP) is used to fabricate the T-shaped plunger and the container due to its high resolution and fast prototyping [2]. Upthermo® is a commercial resin which is used as the printing material due to its high mechanical stiffness and high heat deflection temperature [3]. To characterize the performance of this system, the latching failure force - defined as the maximum force the system can withstand while latched - was measured using a piezoelectric actuator manipulator system by pulling the plunger out of a fully solidified paraffin container. The results demonstrate the effectiveness of the mechanical interlock.

Pressure-sensitive adhesives (PSAs) are materials that bond instantly to surfaces with light pressure, without the need for heat or solvents. At temperatures above their glass transition temperature (Tg), PSAs change from a glassy, rigid state to a rubbery, elastic state, which is an ideal material for latching the plunger [4]. An 80 µm layer of pressure-sensitive adhesive copolymer P(nBA-AA-MABP) is coated on the other side. Upon UV irradiation, the MABP units in the copolymer generate reactive carbenes that undergo C,H insertion crosslinking (CHic), forming covalent bonds with neighboring polymer chains and the surface[5] . By varying the UV irradiation dose, the crosslinking density of the polymer was tuned, resulting in different binding strength. When the protagonist is actuated, the microactuator folds, bringing the plunger into contact with the adhesive surface to achieve latching by adhesion, which tolerates angular and positional misalignment. Unlatching is achieved by tearing off the plunger by actuating the antagonist.

The two states of the active latching mechanism are shown in Figure 3(a, b), representing the unlatched state and the latched state with the plunger secured by solidified paraffin. Figure 3(c, d, e, f) shows the sequential operation of the passive latching, including: plunger approach to the adhesive surface; latched state on contact; initiation of unlatching; and complete release.

Origami-inspired microsystems actuated by SMA folding microactuators investigate latching angle and force. The paraffin-based design offers strong mechanical locking at similar footprint, while the CHic-able polymer provides tunable, durable adhesion. Future work will integrate these micro-latching strategies directly into microactuator systems, enabling on-demand latching positions at the microscale.

Keywords: Reversible micro-latching, Shape memory alloy, CHic crosslinking, Microactuator, Two-photon printing

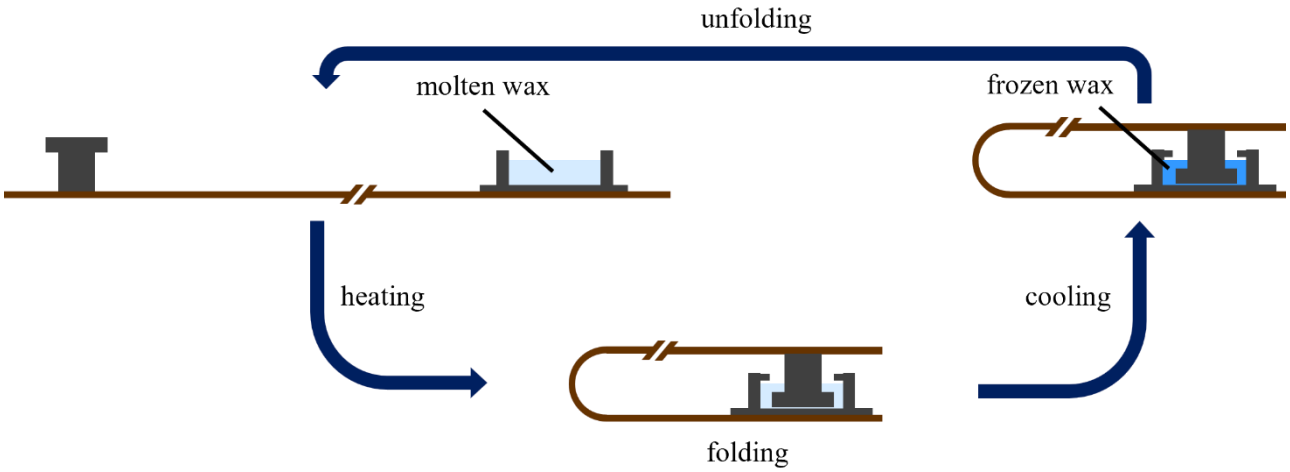

Figure 1. Schematic representation of the active micro-latching mechanism. A micro T-shaped plunger is printed on one side and a micro container filled with paraffin is on the other side. When heated, the microactuator folds, inserting the plunger into the container; when cooled, the paraffin freezes and blocks the plunger in the container. Reheating melts the paraffin and releases the plunger to unfold the microactuator.

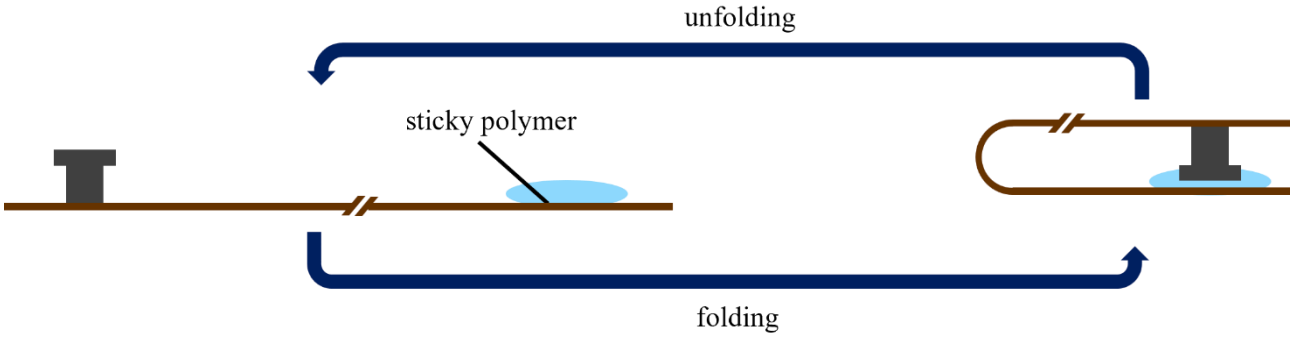

Figure 2. Schematic of the passive micro-latching mechanism. When actuated, the plunger reaches the sticky polymer and is blocked. Actuation of the opposite microactuator rips plunger off and unfold the latching system.

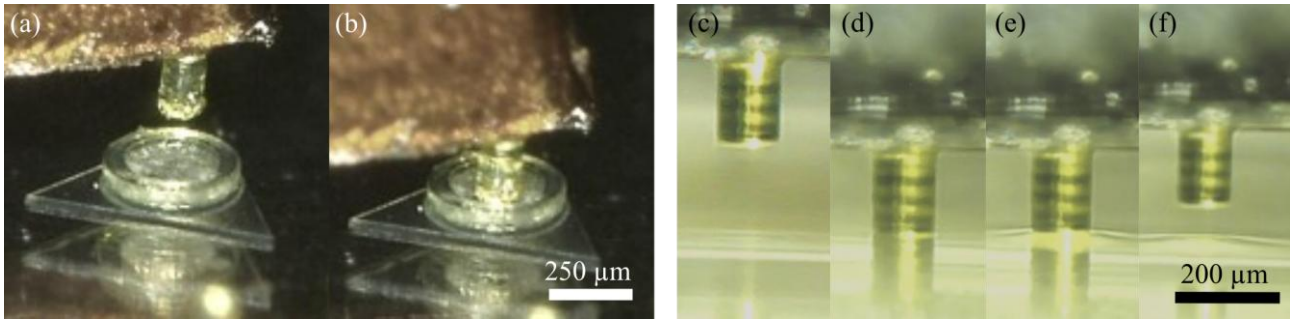

Figure 3. Microscopic images illustrating the setup of active latching mechanisms: (a) the plunger approaching the microcontainer during actuation as the free state and (b) the plunger mechanically locked in place by solidified paraffin after cooling as the latched state in the active latching process. (c-f) Sequential microscopic images illustrating the passive latching process: (c) approach to contact with the polymer surface, (d) initial contact with the surface, (e) initiation of unlatching, and (f) complete release.

Reference:

[1] L. Seigner et al., Actuators. 2021, 10(8), 181.
[2] N. Geid et al., Actuators. 2023, 12(3), 124.
[3] S Yu et al., Advanced Manufacturing 2023, 4, 39.
[4] I Márquez et al., Polymers 2021, 13(16), 2627.
[5] O. Prucker et al., Biointerphases 2018, 13, 010801.

Physical reservoir computing with MEMS torsional mirrors

Yuta Kawashima [a], Mikiya Oki [a], Jun-Yu Ou [b], Yoshishige Tsuchiya [b], and Toshiyuki Tsuchiya [a]
[a] Kyoto University, Kyoto, 615-8540, Japan
[b] University of Southampton, Southampton, SO17 1BJ, United Kingdom
e-mail: y_kawashima@nms.me.kyoto-u.ac.jp

This paper reports on physical reservoir computing (PRC) using an electrostatic MEMS mirror demonstrating enhanced memory capacities at resonance for the first time. The mirror plate supported by torsion beams fabricated on a silicon on insulator (SOI) wafer is acutuated by electrostatic attraction force. We evaluated the learning performance of this novel computing system both numerically and experimentally. Numerical simulation and experiments show similar results that the performance in both the linear and nonlinear tasks has improved at the resonance, demonstrating the effectiveness of physical reservoir computing using a MEMS mirror.

Background

Physical reservoir computing (PRC) is a machine learning algorithm that utilizes nonlinear physical dynamics as computational resources, resulting in low computing cost and low power consumption. A MEMS resonator can be used as a physical reservoir because of its compactness and power efficiency. The previous reports on MEMS PRC [1-3] employ electrical output from the reservoir and it is difficult to connect with each other when the number of resonators increases. In this study, we used torsional resonators for micromirror devices as a physical reservoir. The reservoir state of vibration is detected by projecting the reflected light into space to generate more complex responses through interference between mirrors. The optical detection can avoid degradation in learning performance caused by parasitic capacitance [3].

Description of MEMS mirror PRC

Figure 1 shows a schematic drawing, and an SEM image of electrostatic MEMS torsional mirror used in this study. A 150-µm-square mirror plate which is suspended by a pair of 2-µm-width tortional beams is fabricated on a 10-µm thick SOI wafer. Figure 2a shows the implementation of PRC. The input signal applied to the fixed electrode is binary dc bias voltage, added to the driving square ac voltage. A state matrix X is sampled from the intensity of the reflected light modulated by the oscullation of the MEMS mirror, and a simple ridge regression is used for learning. Optics for detecting mirror vibration is shown in Fig. 2b. The intensity of the reflected light is measured by a photodetector and demodulated using a lock-in amplifier. The real part of the output signal is acquired by synchronous detection. This signal is processed by a PC to extract the envelope.

Results

The memory capacities for a linear task of the short-term memory (STM) and a nonlinear task of the parity check (PC) were evaluated. The memory capacity was calculated as a function of the driving frequency and the input signal hold time. Figure 3(a) shows the frequency response of the in-phase component. The resonance region extends towards lower frequencies, which is considered as a result of nonlinearity caused by the soft-spring effect due to electrostatic attraction between the comb electrodes. Figures 3(b) and 3(c) show the benchmark task results. The input hold time was set around 0.9 ms, corresponding to the measured damping time of the mirror resonator. Both the STM and PC tasks exhibit enhanced performance across a broad frequency range at the resonance. An overall complementary relationship between memory capacities in the linear and nonlinear tasks was observed: regions with longer hold time (T>1.8 ms) showed higher performance in the PC task, while regions with shorter input hold time (T < 1.8 ms) exhibited higher performance in the STM task. Figure 3(d) shows experimental results of the resonance measurement. Figures 3(e) and 3(f) also confirm memory capacities that increased in the resonance region for both the tasks. A complementary relationship between memory capacities is observed, which is well consistent with the simulation results. Unlike the simulation results, some regions exhibit locally degraded performance, which is considered to be due to the influence of noise.

Acknowledgements: This work is partially supported by Royal Society (IEC/R3/233070), CHIST-ERA NOEMIA (CHIST-ERA-21-NOEMS-004) by EPSRC (EP/X03495X/1) and KAKENHI Grant JP25K22077.

[1] G. Dion, et al., *Journal of Applied Physics,* 124 (2018), 152132.
[2] T. Zheng, et al, *Sensors,* 21 (2021), 2961.
[3] K. Shima, et al., Proc. IEEE MEMS 2025, pp. 546-549.

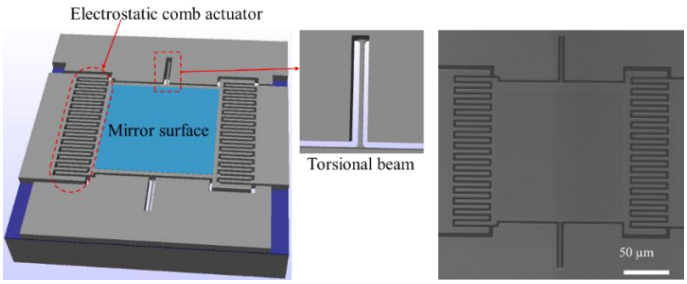

Figure 1. Electrostatic MEMS mirror. (left) Schematic view. (right) SEM image of device.

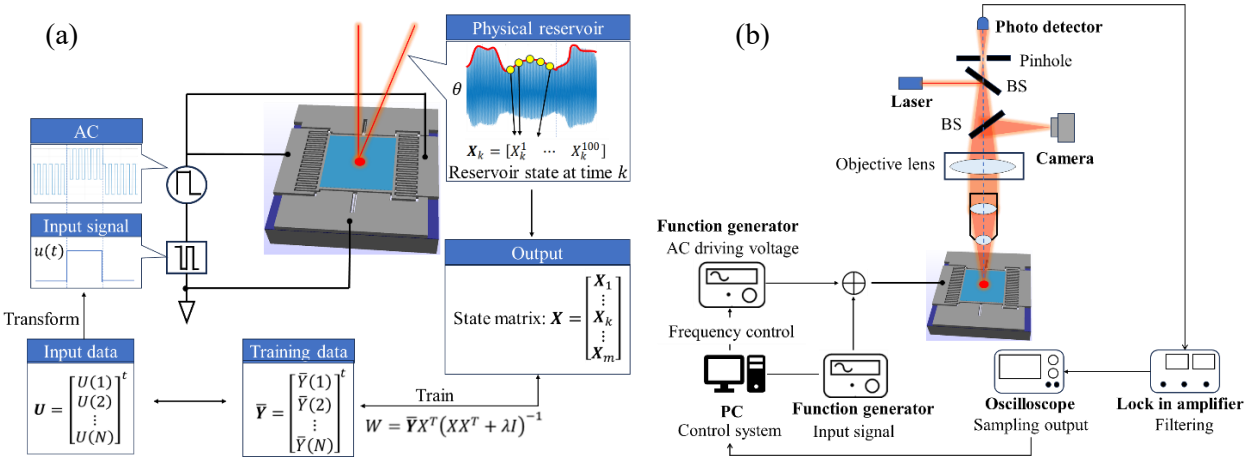

Figure 2. Physical reservoir computing using electrostatic MEMS mirror.
(a) Implementation method. (b) Experimental setups.

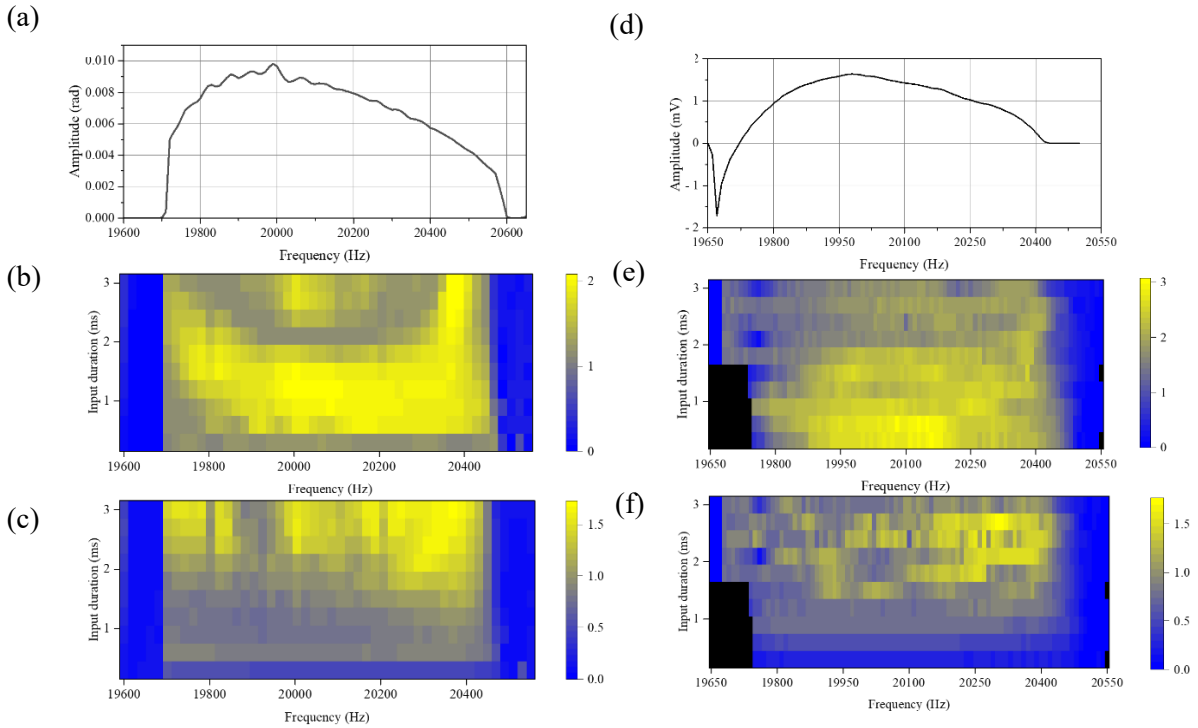

Figure 3. Benchmark task results by numerical simulation ((a) – (c)) and experiment ((d) – (f)).
(a)(d) Frequency responses, (b)(e) heatmaps of memory capacities in STM task and (c)(f) heatmaps of memory capacities in PC task. (black area: missing values)

Oral Session 6C : Optical Sensors

Monitoring vibrational fingerprints of polypeptide monolayers by infrared plasmonic nanoantennas

Santos Merino [a,b], Alberto Villar [a], Ruth Díez-Ahedo [a], Gabriel Ortega [c,d], Mónica García-Mota [e], Anna Kimmel [e], Albert Guerrero [f], Jorge Espina [g], Mario Zapata [h,i], Javier Aizpurua [h,i]

[a] Surface Chemistry and Nanotechnologies Unit, Tekniker, Eibar 20600, Spain
[b] Departamento de Electricidad y Electrónica, Universidad del País Vasco UPV/EHU, 48940 Leioa, Spain
[c] CIC bioGUNE, Bizkaia Science & Technology Park, 48160 Derio, Spain
[d] Ikerbasque, Basque Foundation for Science, Bilbao, Spain
[e] Simune Atomistics. Tolosa Hiribidea, 76. 20018, Donostia-San Sebastián, Spain
[f] Instituto de Microelectrónica de Barcelona – (IMB-CNM, CSIC), Bellaterra (Barcelona), Spain
[g] Servicios Científico-Técnicos, Universidad de Oviedo, C/Fernando Bongera s/n, 33006, Oviedo, Spain
[h] Theory of Nanophotonics Group, Materials Physics Center (CSIC-UPV/EHU), Donostia-San Sebastián, Spain
[i] Donostia International Physics Center, Paseo Manuel Lardizabal 5, 200018 Donostia-San Sebastian, Spain
e-mail: santos.merino@tekniker.es

Infrared spectroscopy is a powerful tool widely used in research and industry for a label-free and unambiguous identification of molecular species. Inconveniently, its application to minute amounts of materials is hampered by the low infrared absorption cross-sections. Surface-enhanced infrared absorption spectroscopy (SEIRA) using resonant metal nanoantennas overcomes this limitation [1]. Resonantly excited, such metal nanostructures feature collective oscillations of electrons (plasmons), provide huge electromagnetic fields on the nanometer scale and infrared vibrations of molecules located in these fields are enhanced by orders of magnitude enabling a spectroscopic characterization with unprecedented sensitivity [2]. This study utilizes resonant SEIRA to detect the vibrational fingerprints of the TRP-cage, one of the smallest proteins known to adopt a stable, cooperative, and compact fold.

To evaluate the potential of resonant SEIRA to detect the TRP-cage protein, *ab-initio* calculation was developed under the formalism of Density Functional Theory (DFT) taking the folded geometry of the structure 1L2Y [3]. DFT calculation was developed by the SIESTA code as the molecule is in a water solvent surrounded by an Au_{55} cluster and a dithiolated alkane acts as the TRP-cage connector with the surface (Fig.1a). The study was mainly focused on the Amide I band, which represents the strongest absorption in the infrared spectrum of proteins. It determines two different frequency ranges: as the C=O stretching is decoupled from the surrounding atoms (Fig.1b) and as the vibration is coupled to a cooperative motion of the R-C=O group (Fig.1c) and it is influenced by the molecular environment of the amide groups. These vibrational frequencies are predicted at 1524-1621 cm^{-1}. From this *ab-initio* calculation, the geometry of the gold antennas was optimized to provide effective coupling between the frequency of the plasmonic modes of the gold nanorod (NRs) antennas and the vibrational frequencies. The optical response was studied by Finite Element Method as NRs were arranged in a square symmetry with a lattice parameter of W=2.8 µm on a CaF_2 substrate. Fig.2 shows a numerical comparison of the reflectivity of the bare NRs and that of the NRs covered by a shell containing the TRP-cage in water deposited on the substrate. Arrays of antennas with varying lengths and widths were fabricated using electron beam lithography followed by gold lift-off (Fig. 3a) and then encapsulated in a microfluidic chamber (Fig. 3b). To enhance the vibrational signal using resonant plasmonic nanoantennas, the TRP-cage must be positioned within the local electric field around the NRs, with appropriate lateral spacing to allow the molecules to vibrate at their natural frequencies. Conversely, ensuring that the protein binds to the surface in a uniform orientation is crucial to prevent varying attachment modes on the gold surface. To achieve this, we used a mixture of two types of thiols: one that binds the protein via a cysteine residue introduced at the terminal position of the TRP-cage, and another that prevents the protein from binding to the surface. (Fig. 3c). The chips were assessed in heavy water solvent through reflection using an FTIR setup. Fig. 4a shows the plasmonic broadband resonance for antennas of different lengths, along with pronounced dips in the spectrum corresponding to the decoupled and coupled vibrational modes of the Amide I band. In addition, the Amide II band, associated with N–H bending and N–C stretching vibrations, is also observed. The absorbance signal was extracted from the spectrum, and the vibrational modes were identified from the 2.1 µm length NRs (Fig 4b) showing a good correspondence with those predicted by DFT calculation.

[1] A. John-Herpin. Advanced Materials 2023, 35, 2110163
[2] T. Neumant et al. J. Phys.Chem. C 2015, 119, 26652-26662
[3] https://www.rcsb.org/structure/1L2Y

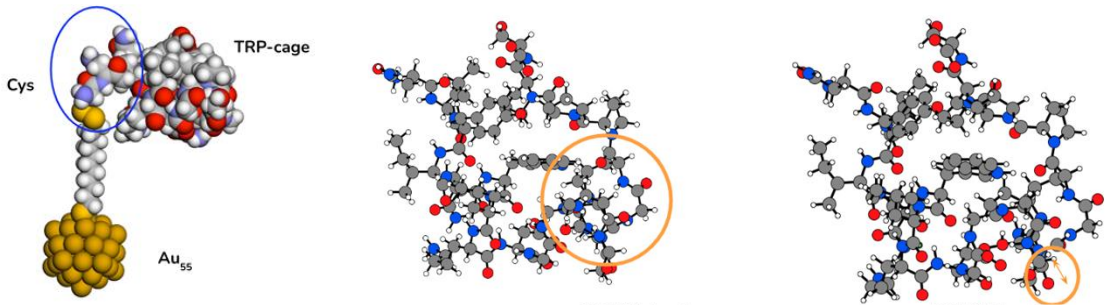

Fig. 1. *Left:* Schematic representation of the TRP-cage protein, where the blue, grey, and red spheres represent nitrogen, carbon, and oxygen atoms, respectively. The dark and light-yellow spheres represent gold and sulfur atoms, respectively. *Centre:* Cooperative vibration of the TRP's R–C=O group. *Right:* Local C=O stretching vibration.

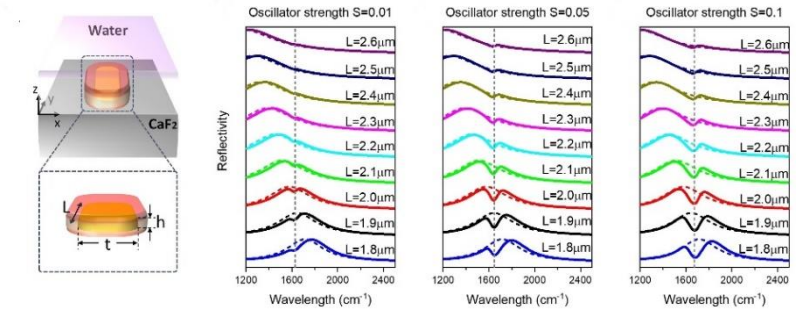

Fig. 2. Numerical comparison of the reflectivity of the bare gold nanorods (dashed lines) and that of the gold nanorods covered by a shell containing the TRP-cage protein in water deposited on a CaF_2 substrate, and illuminated by a plane wave, with the electric field polarized along the main axis of the antennas. *Left:* scheme representing the simulated system. *Right:* Three different scenarios corresponding to low to high TRP concentration of molecules surrounded the antennas. The height (h) and width (t) of the antennas were fixed at 70 nm and 300 nm, respectively while the length (L) was varied between 1.8 µm and 2.6 µm.

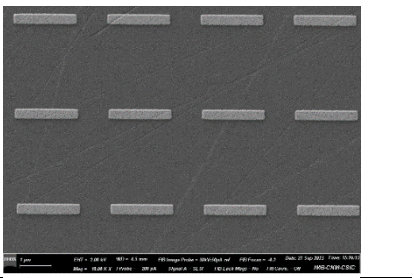

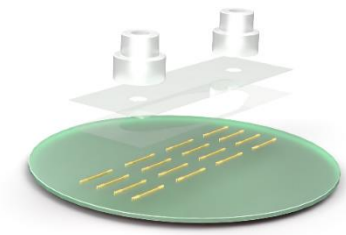

Fig. 3. *Left:* Scanning Electron Microscopy (SEM) of 2.1 µm length gold nanorods antennas fabricated by e-beam lithography. *Right:* scheme of the microfluidic cell used to encapsulate the CaF2 substrate for sample introduction and posterior infrared absorption measurements.

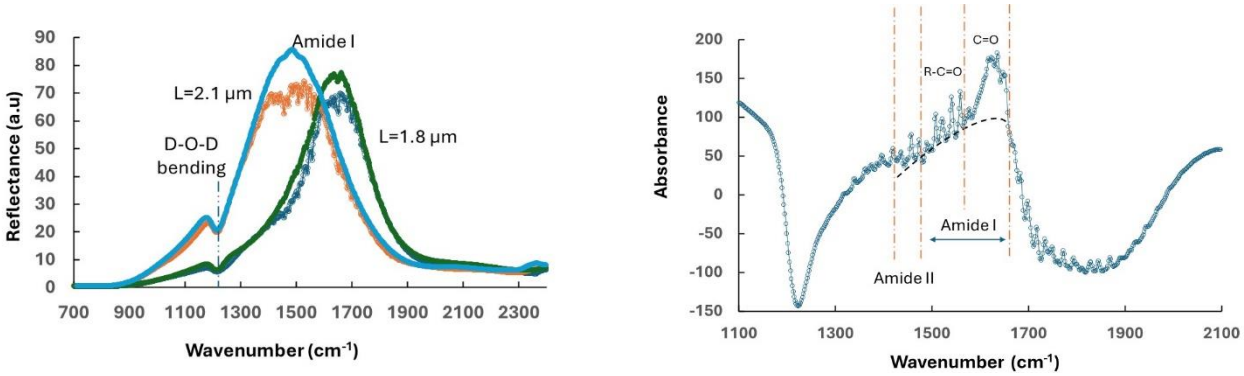

Fig 4. *Left:* Reflectance spectra for different NR lengths of the functionalized TRP-cage in heavy water (orange and dark blue) and of heavy water alone (light blue and green). *Right:* Absorbance signal calculated for the 2.1 µm length NRs.

On-fiber printed polymeric tapers for chronically implantable neural interfaces

Stella Aslanoglou[a,*], Barbara Spagnolo[a], Cinzia Montinaro[a], Alberto Perna[b], João F. Ribeiro[b], Marco Pisanello[c], Luca Berdondini[b], Tommaso Fellin[b], Ferruccio Pisanello[a,†], Massimo De Vittorio[a,d,e,†]

[a] Istituto Italiano di Tecnologia, Center for Biomolecular Nanotechnologies, Arnesano (LE) 73010, Italy
[b] Istituto Italiano di Tecnologia, Center for Convergent Technologies, Genova, 16163, Italy
[c] OptogeniX s.r.l., Arnesano (LE), 73010, Italy
[d] IDUN section, Dept. of Health Technology, Technical University of Denmark, Lyngby, Denmark
[e] Dip. di Ingegneria dell'Innovazione, Università del Salento, Lecce, 73100, Italy
†These authors jointly supervised the presented work.
* Corresponding author. E-mail: stella.aslanoglou@iit.it

Abstract

Capturing the dynamics of brain activity in its multifaceted components can enable a more thorough study of neural functions that will open up the way for new diagnostic and therapeutic approaches. To address this challenging task, the neuroscience community requires the use of bidirectional neural probes able to monitor and modulate neural activity simultaneously at the cellular level [1]. Among them, implantable multimode optical fibers and particularly tapered fibers (TFs) have recently emerged as a promising tool for delivering light and collecting fluorescence to and from the brain tissue, allowing spatially resolved bidirectional optical neural interfaces [2]. Compared to their flat-cleaved counterparts, TFs are less invasive for the brain tissue and offer controlled light emission along the taper by exploiting the modal properties of the gradually narrowing waveguide [3]. Despite their highly non-planar surface, TFs can be patterned to control the modal content and host electric elements for simultaneous performance of optogenetic stimulation and electrophysiological recordings [4]. However, establishing a stable interface between them and the brain tissue is challenging due to the mechanical mismatch in place. The high bending stiffness of glass silica fibers induces inflammation and consequently neuronal death and tissue encapsulation in the implant surroundings, when applied in chronic settings [5]. This adverse immune response could be minimized by replacing silica with a material that matches more closely with the mechanical properties and micro-scale movements of the brain. As a result, over the last years, there has been an increased interest in developing chronically implantable neural probes based on polymer optical fibers (POFs) [6]. The most popular approach for POF fabrication is the thermal drawing process [7]. However, achieving a taper profile in a thermal-drawn fiber requires an additional fabrication step, such as chemical etching, thus rendering the whole process time-consuming and with limited control [8].
Here, we demonstrate a method for the fabrication of soft and flexible polymeric air-clad tapers using two-photon polymerization (2PP) in a single processing step and investigate their prospective use in chronically implantable neural interfaces. 2PP is a highly versatile additive manufacturing technique that enables the fabrication of 3D structures of arbitrary shape with sub-diffraction limit resolution and tunable mechanical properties and has been successfully employed for the fabrication of optical fiber integrated photonic elements [9]. To fabricate soft polymeric tapers, we used the commercially available IP-PDMS photoresin, which is a photocurable type of polydimethylsiloxane (PDMS). IP-PDMS exhibits high transmission in the visible spectral range and a refractive index of 1.45 (@ 589 nm), while it is characterized by a Young's Modulus of 15 MPa. 2PP was performed using Nanoscribe's Photonic Professional system equipped with a femtosecond laser (λ=780 nm). 3D structures were printed in a layer-by-layer sequence using the Dip-in-Liquid Lithography (DiLL) mode on top of polished multimode fiber facets. Following the exposure, not cross-linked material was removed and solid tapers were encapsulated with a thin conformal film of Parylene-C *via* chemical vapor deposition (**Figure 1**). Polymeric tapers were then characterized in terms of light delivery performance *in vitro*. Using an angle-selective injection system, we demonstrated that polymeric tapers exhibit spatially resolved illumination; a favourable feature for optogenetic applications (**Figure 2.a**). We further investigated the prospective use of those tapers in fiber photometry by characterizing their light collection properties (**Figure 2.b**). Polymeric tapers were successfully implanted into phantom brains (0.6 % w/v agar gel), while their impact on mechanically induced trauma was assesed by performing insertion force measurements (**Figure 2.c**). Our results suggest that IP-PDMS tapers hold great promise as chronically implantable neural probes.

References

[1] Li H. et al., Microsystems & Nanoengineering, 2023. **9**: p.4.
[2] Pisano F. et al., Nature Methods, 2019. **16**(11): p. 1185-1192.
[3] Pisanello F., Microelectronic Engineering, 2019. **215**(C): p.10
[4] Balena A. et al., Nature Protocols, 2025
[5] Rivnay J. et al., Science Advances, 2017. **3**(6): p. e1601649
[6] Park S. et al., Nature Neuroscience, 2017. **20**(4): p. 612-619
[7] Meneghetti M. et al., Advanced Optical and Optoelectronic Fibers, Springer Nature (Singapore, 2024)
[8] Meneghetti M. et al., Optics Letters, 2025. **50**(2): p. 670-673
[9] Aslanoglou S. et al., 24th International Conference on Transparent Optical Networks (ICTON), 2024

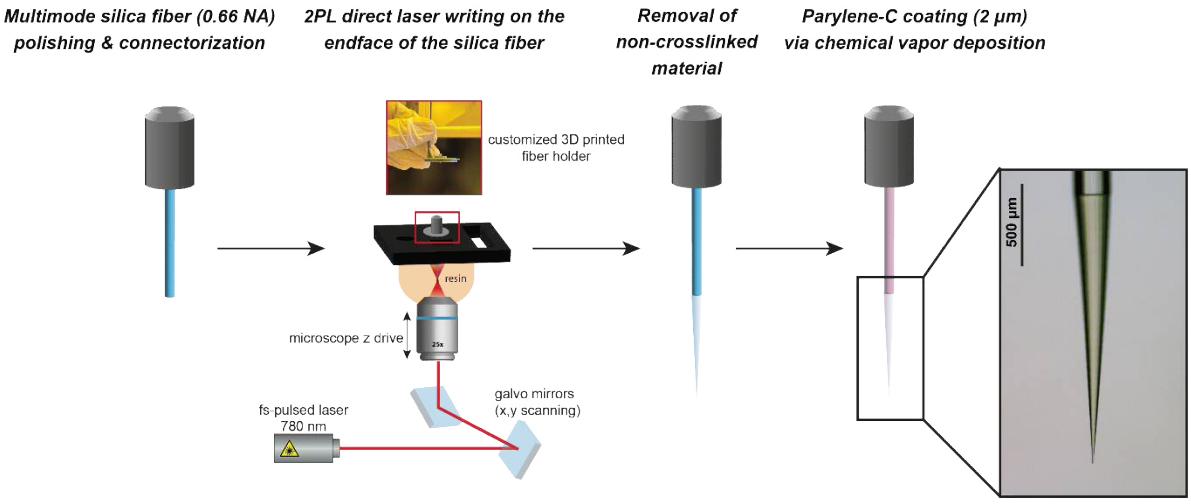

Figure 1. Polymeric tapers fabcrication workflow.

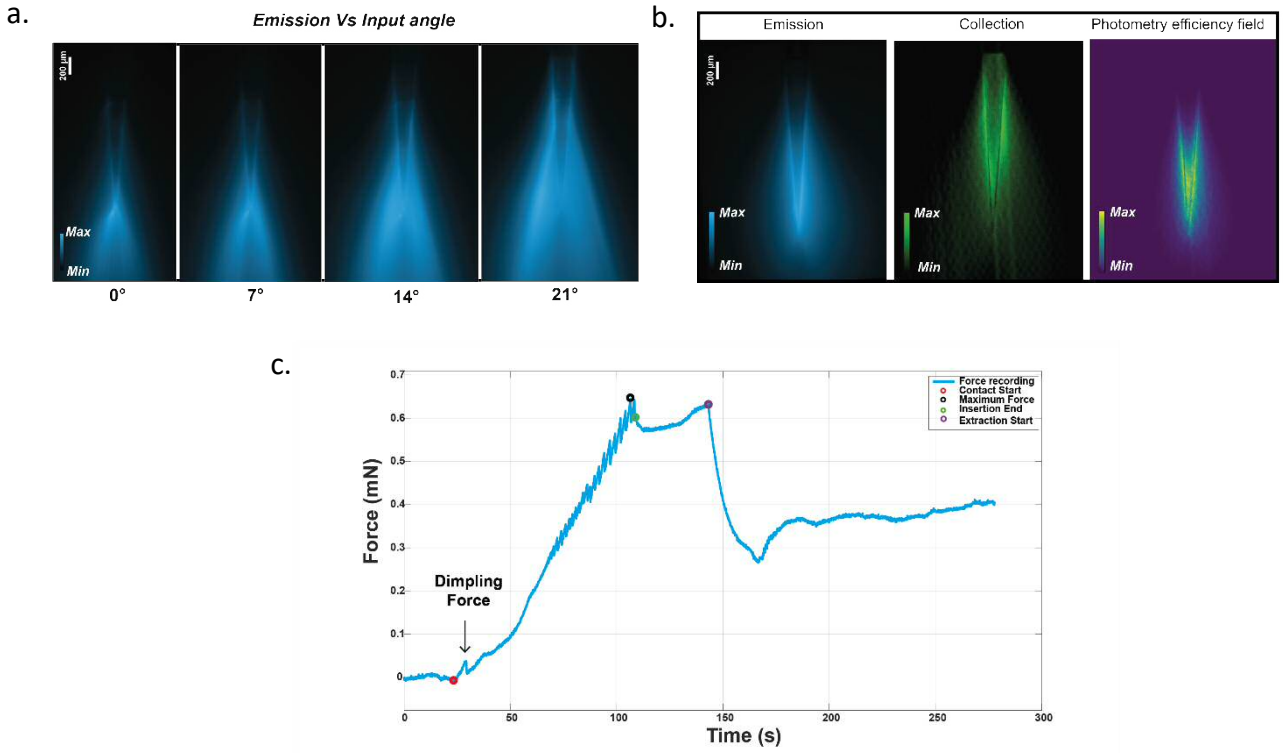

Figure 2. Characterization of polymeric tapers in terms of their emission (a) and collection (b) properties *in vitro*. (c) Representative insertion force measurement, demonstrating minimal gel compression.

Detection of Phtalate release from plastic tubes using a NanoFabricated Surface Enhanced Raman Spectroscopy device

S.Ramos [a], C.Blanc [b], L.Salomé [b], P.Louarn [c], E.Trevisiol [a,d], C.Vieu [a]

[a] LAAS-CNRS, Université de Toulouse, CNRS, INSA, Toulouse, 31400, France
[b] IPBS, Université de Toulouse, CNRS, Toulouse, 31400, France
[c] IRAP, Université de Toulouse, CNRS, Toulouse, 31400, France
[d] TBI, Université de Toulouse, CNRS, INSA, Toulouse, 31400, France
e-mail: sramos@laas.fr

Phthalates are used in the manufacture of various plastic products of our everyday lives for their plasticising properties. They are part of many materials used as liquid containers such as PolyPropylene (PP) tubes employed in many research activities. The question of the contamination of a solution stored in PP tubes during long periods of time by phthalates derivatives has received recent attention. For this type of problematics, there is a need to develop analytical analysis methods of traces of phthalate molecules in water, sufficiently sensitive for small concentration detection and of easy implementation as compared to the standard method of Mass Spectroscopy which cannot be deployed in a systematic way. Recently, phthalate contamination of deionised water stored for several months in a polypropylene plastic tube has been evidenced through the detection of phthalic acid (PA) [1]. In this contribution we present an analytical method of PA traces using Surface Enhanced Raman Spectroscopy (SERS). This method is implemented for analysing the release of PA from conventional PP tubes used in research laboratories.

Our analytical devices comprise a fluidic concentrator based on a superhydrophobic surface that concentrates the analytes contained inside a water droplet [2] onto a small SERS-active area equipped with plasmonic resonators (Ag nanoparticles) which turned out to be suitable for SERS analysis in the sub-femtomolar range [3] (see figure 1). After analyte concentration, the analytical zone is scanned pixel by pixel by micro-Raman and each acquired SERS spectrum is used for molecular identification of molecular traces. In this research work, solutions of PA diluted in Ultra Pure De-Ionized (DI) water at controlled concentrations have been analysed with such devices in order to validate their detection capabilities and in a second step, Ultra Pure DI water stored in PP tubes over days was analysed in order to detect possible traces of PA release form the plastic laboratory tubes. In every case, in order to certify that a SERS spectrum is really a PA signature, we use a reference SERS spectrum of PA from the scientific literature [4]. When an experimental spectrum exhibits some Raman peaks in common with this reference spectrum, we calculate the probability that this correspondence be a random coincidence. Only spectra with a weak random probability (<5%) are labelled as PA traces. This approach increases the reliability of our analytical method by eliminating ambiguous SERS spectra.

In this work, we demonstrate our ability to detect intentionally added phthalic acid molecules in ultrapure DI water (clean room) at concentrations of 1 nM and 1 fM. On the other hand, by analysing ultrapure DI water stored for one week at 37°C in 15 mL and 50 mL polypropylene tubes, we clearly identify in both cases, traces of PA release from the plastic tubes inside the solution (one example is shown in figure 2). For water storage in 15 mL PP tubes, we obtained on average 10 certified spectra of PA molecules, while with the same methodology more than 50 certified signatures of PA molecules were detected for 50 mL tubes. This result seems to indicate that the amount of release of PA molecules depends on the volume of the container. We will present in details at the conference the devices and measurements and the method of SERS spectra analysis. By comparing with pure PA solutions, we will show that we can estimate the concentration of PA molecules inside 50 ml PP tubes after one week of storage in the order of 1 nM.

Our analytical method for the detection of traces of plastic additives is of potential interest for human health issues also and could be deployed to evaluate a possible exposition of people to toxic molecules released from plastic containers.

[1] Z. Xu et al., J. Raman Spectrosc. 42 (2011) 1939–1944.
[2] V Fabre, F Carcenac, A Laborde, J Doucet, C Vieu, P Louarn, E Trevisiol, Langmuir 38 (2022) 14249–14260.
[3] V Fabre, F Carcenac, A Laborde, J Doucet, C Vieu, P Louarn, E Trevisiol, Analytical Science Advances 6 (1) (2025)
[4] S.W. Joo, S et al., J. Raman Spectrosc. 31 (2000) 145–150.

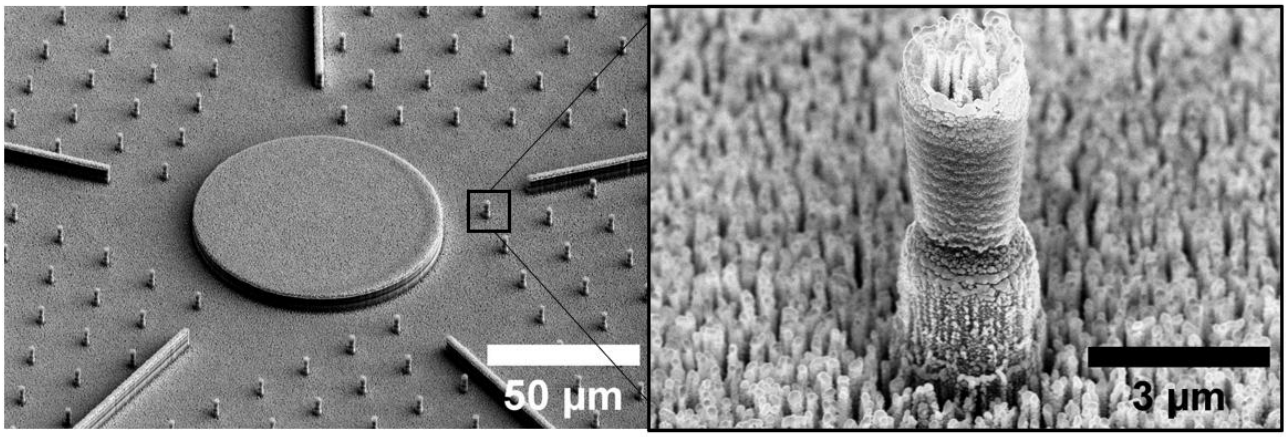

Figure 1. Left: SEM image of the superhydrophobic fluidic concentrator/SERS device used in this study. The central circular region corresponds to the analytical pedestal where all analytes are concentrated. Right: SEM image of one of the silicon micropillars used to create the superhydrophobic surface. The entire surface is covered with plasmonic nano antennas composed of silicon nanopillars (Black Silicon etching process) topped with silver nanoparticles in strong plasmonic coupling (see ref [2] and [3] for details).

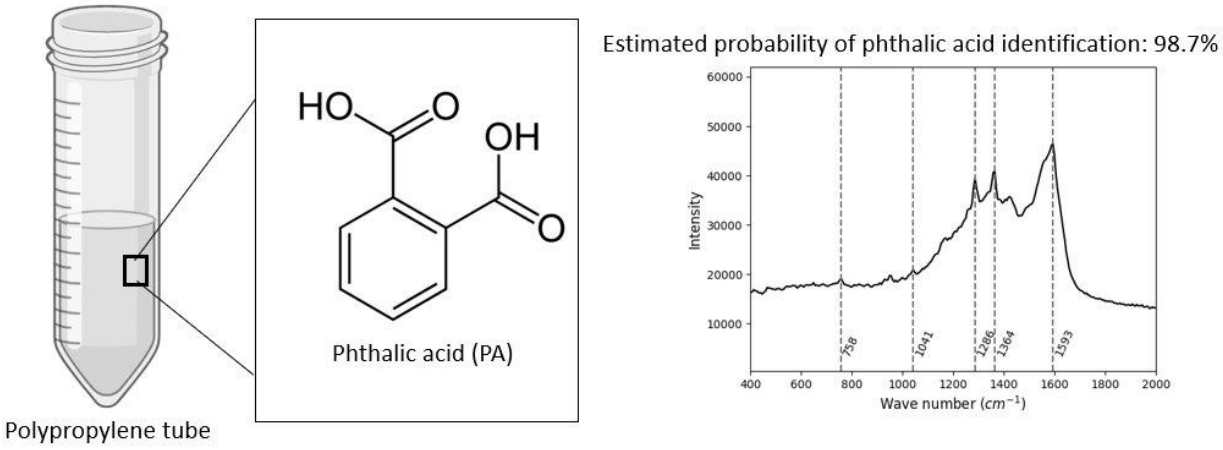

Figure 2. Detection of Phthalic acid release from plastic tubes: Example of a spectrum with a 98.7% probability of being phthalic acid (PA) (<5% of random probability). The spectrum exhibits 5 SERS peaks that can be attributed to PA vibrations. This spectrum has been detected after the evaporation of a drop of water stored for one week in a polypropylene tube of 50 mL.

Detection of Polystyrene Microplastics via Surface-Enhanced Raman Scattering on Sticky Hydrophobic Nanopillar Substrates

Tzu-Yu Chiu [a], Wen-Huei Chang [b]*, Kuan-Ting Kuo [a], Yao-Ming Ku [a], Chih-Chia Huang [a], Chun-Hung Lin [a]*

[a] Department of Photonics, National Cheng Kung University, Tainan 70101, Taiwan
[b] Department of Applied Chemistry, National Pingtung University, Pingtung 90003, Taiwan
e-mail: whchang@mail.nptu.edu.tw, chlin@ncku.edu.tw

Nanoplastic detection poses significant environmental and health challenges due to their small size, chemical stability, and accumulation through the food chain. Their resistance to degradation complicates detection using conventional methods. Surface-enhanced Raman scattering (SERS) offers a promising alternative with ultra-high sensitivity, rapid analysis, and high selectivity. However, effective enhancement occurs primarily at hot spots where localized electromagnetic fields amplify Raman signals. Therefore, optimizing nanoparticle distribution on the substrate is crucial for maximizing sensitivity and reproducibility [1].

This study aimed to enhance SERS sensitivity and reproducibility for nanoplastic detection by optimizing gold nanoparticle (AuNP) size, concentration, and distribution on a hydrophobic patterned substrate. The workflow, illustrated in Fig. 1, involved synthesizing AuNPs, fabricating a hydrophobic hexagonal array substrate, and performing SERS detection of polystyrene (PS) nanoparticles.

We synthesized four sizes of AuNPs from growth step 1 (G1) to growth step 4 (G4) following the protocol of N. G. Bastus [2], as shown in Fig. 2(a). Absorbance measurements showed a redshift at 530 nm, indicating size-dependent localized surface plasmon resonance (LSPR) behavior. Mie-scattering theory was applied to calculate scattering, absorption, and extinction cross-sections of 52 nm AuNPs under identical absorbance conditions, as illustrated in Fig. 2(b). The Beer-Lambert law was then used to accurately determine the concentration of G4 AuNPs, which was subsequently applied to quantify PS nanoparticle concentrations. A key innovation of this study was the development of a sticky, hydrophobic SU-8 hexagonal nanopillar substrate designed to control the coffee ring effect and enhance nanoparticle distribution [3]. Fabricated using nanoimprint lithography and treated with SF_6/C_4F_8 plasma, the substrate's fluorine coating significantly improved hydrophobicity, promoting effective nanoparticle aggregation during solvent evaporation. As shown in Fig. 3(a), evaporating 10 µL of a 500 nm PS mixture at 50°C confined the coffee ring to approximately 1~2 mm. The addition of NaCl as an aggregator enhanced AuNPs clustering around PS microspheres [4], as demonstrated in Fig.3(b), thereby improving SERS performance. SERS detection was conducted by depositing AuNP solutions, NaCl, and PS spheres onto the hydrophobic substrate through controlled evaporation at 90°C. Using a 785 nm laser, SERS detection focused on the PS absorption peak at 998 cm^{-1}.As shown in Figs. 4(a) and 4(b), the optimized substrate achieved a detection limit of 1 µg/mL, demonstrating excellent linearity between SERS intensities and PS concentrations ranging from 100 to 1 µg/mL, with an R^2 value of 0.965.

This study presents a reliable strategy for enhancing SERS detection sensitivity by leveraging a sticky hydrophobic nanopillar substrate, NaCl aggregators, and AuNPs. The scalable nanoimprinted SU-8 substrate, treated with fluorine plasma, ensures effective nanoparticle aggregation during solvent evaporation. Additionally, NaCl-induced AuNP clustering around PS microspheres further boosts SERS performance. This integrated approach offers a promising, robust platform for sensitive and consistent nanoplastic detection, supporting advancements in environmental monitoring and health risk assessment.

[1] X.-X. Zhou, R. Liu, L.-T. Hao, and J.-F. Liu, "Identification of Polystyrene Nanoplastics Using Surface Enhanced Raman Spectroscopy," Talanta 221 (2021) 121552.
[2] N. G. Bastús, J. Comenge, and V. Puntes, "Kinetically Controlled Seeded Growth Synthesis of Citrate-stabilized Gold Nanoparticles of Up to 200 nm: Size Focusing Versus Ostwald Ripening," Langmuir 27 (2011) 11098-11105.
[3] W.-H. Chang, Y.-C. Wu, J. Shieh, K.-T. Kuo, C.-C. Huang, H.-L. Cheng, and C.-H. Lin, "Nanoimprinted Sticky Hydrophobic SU-8 Nanopillars for Ultra-Sensitive Surface-Enhanced Raman Spectroscopy Applications," ACS Applied Nano Materials 8 (2025) 10087-10095

[4] L. Mikac, I. Rigó, L. Himics, A. Tolić, M. Ivanda, and M. Veres, "Surface-Enhanced Raman Spectroscopy for the Detection of Microplastics," Applied Surface Science 608 (2023) 155239.

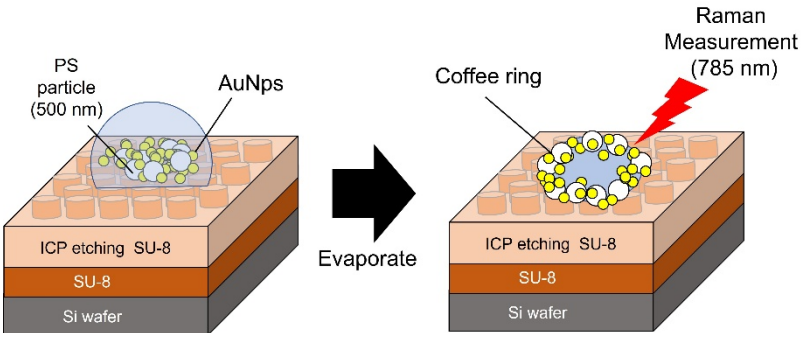

Figure 1. Workflow of SERS detection of PS nanoparticles using sticky hydrophobic nanopillar substrates.

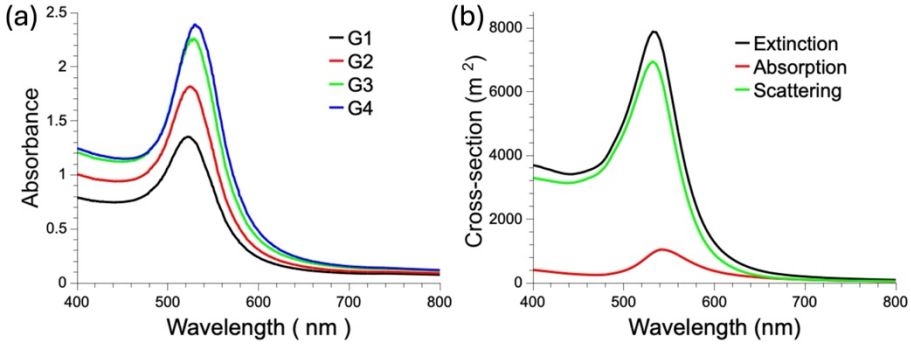

Figure 2. (a) UV–vis absorbance spectra of synthesized AuNPs (G1–G4). (b) Cross-sectional area of AuNPs (G4) calculated using Mie-scattering theory across the 400–800 nm wavelength range.

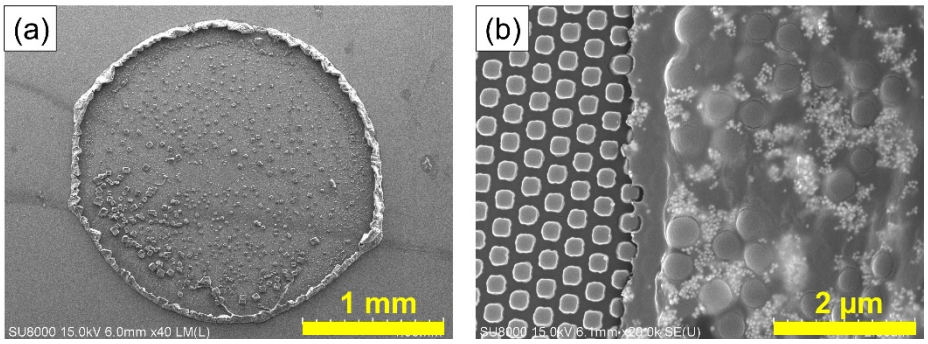

Figure 3. (a) SEM image of the coffee ring formed by a PS nanoparticle mixture. (b) SEM image of AuNps aggregation on PS microspheres within the coffee ring.

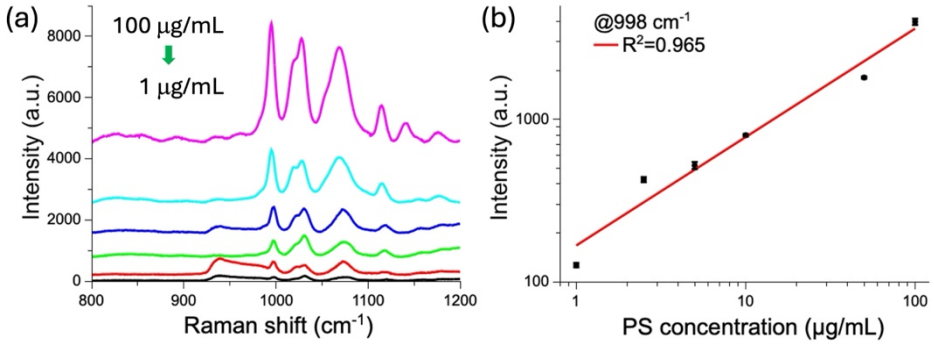

Figure 4. (a) SERS spectra of PS nanoparticles at concentrations of 100, 50, 10, 5, 2.5, and 1 µg/mL. (b) Linear relationship between SERS intensity at 998 cm^{-1} and PS concentration, with an R^2 value of 0.965.

Micro-optics Design and Preliminary Characterization of a Fiber-Optic SERS Probe for *In Vivo* Diagnostics

Yingwei Hou[a], Nilanjan Mandal[a], Belal Ahmad[a], Jang Ah Kim[b], Alex J. Thompson[a]

[a]Department of Surgery & Cancer and [b]Department of Mechanical Engineering, Imperial College London, London, United Kingdom.
e-mail: y.hou20@imperial.ac.uk, j.a.kim@imperial.ac.uk, alex.thompson08@imperial.ac.uk

Abstract: We present a forward-viewing surface-enhanced Raman spectroscopy (SERS) probe designed to improve signal detection and reduce background noise in minimally invasive diagnostics. A gold-coated micro-optical cap with a SERS array was designed and fabricated using two-photon polymerization (2PP) to provide Raman signal enhancement and to enable integration with complex fibers and fiber-tip optics (e.g. hollow core fibers, focusing lenses, etc.). Comparative analysis of three types of fibers demonstrated that the capped design enhanced Raman signal intensity relative to a bare fiber and provided similar performance to a SERS fiber (which is not suitable for integration with complex fibers/optics). These findings validate the probe's feasibility and support future integration with hollow-core fibers for low-background, fiber-optic SERS.

1. Introduction

Surface-enhanced Raman spectroscopy (SERS) has gained widespread use in biomedical diagnostics due to its sensitivity and chemical specificity [1]. Signal enhancement is achieved through localized surface plasmon resonance, which amplifies the electromagnetic field around noble metal nanostructures such as gold or silver, thereby increasing Raman signal intensity.

As real-time diagnostics becomes increasingly important in minimally invasive surgical procedures, there is a growing demand for miniaturized sensing platforms that can be deployed within confined anatomical spaces. Fiber-optic Raman/SERS probes are promising candidates owing to their compact size, mechanical flexibility, and efficient light delivery and collection capabilities, as demonstrated in previous work [2]. However, standard silica fibers introduce a strong intrinsic Raman background, which interferes with weak SERS signals and compromises sensitivity [3].

To address this limitation, hollow-core fibers (HCFs) have been introduced as a promising alternative. HCFs guide light through an air-filled core, thereby significantly suppressing Raman scattering from the fiber material itself [4]. While this property makes HCFs advantageous for noise suppression, incorporating SERS structures is more challenging than with standard silica fibers (where structures can be fabricated using various surface modification/functionalization approaches). To enable effective signal amplification in a forward-viewing format, a micro-optical structure must be incorporated at the fiber tip to support the integration of a SERS-active array. Such designs can enhance signal collection efficiency and enable forward-viewing detection, which is essential for targeted sensing in clinical settings [5].

This study presents the conceptual design and preliminary characterization of a forward-viewing SERS probe suitable for integration with HCFs. Using Rhodamine 6G (R6G) as a model analyte, we compare the performance of a bare optical fiber, a gold-coated fiber with a SERS-active array, and the proposed forward-viewing SERS fiber (fabricated on silica fiber). Initial results demonstrate Raman signal enhancement (relative to a bare fiber) and comparable performance to an existing SERS fiber probe [2], confirming the feasibility of this approach and laying the foundation for further development of miniaturized, fiber-optic SERS probes.

2. Methods

A micro-optical cap structure was designed using SolidWorks to support a SERS-active surface directly above the output face of an optical fibre (200/220 μm core/cladding diameter, 0.22 NA, FG200LEA, Thorlabs). The cap (250 μm diameter) features a flat platform with central SERS array (80×80 μm^2) and four supporting legs for attachment to the fibre tip (Fig. 1(a)). Both the cap and SERS array were produced using 2PP with a Photonic Professional GT system (Nanoscribe). Due to their scale difference, the structures were fabricated sequentially. The cap was printed first using a 25× objective and IP-S photoresist, followed by development in PGMEA for 10 minutes and rinsing with IPA for 1 minute. The SERS array was then printed on the cap interface using a 63× objective and IP-Dip photoresist and developed likewise. Fig. 1(b) presents the fabricated structure on an ITO-coated glass substrate. When printed directly on the fibre tip, the complete structure

appears as shown in Fig. 1(c). Finally, to enable SERS functionality, a 50 nm gold film was uniformly deposited via sputtering over both the cap and the SERS array (Fig. 1(d)).

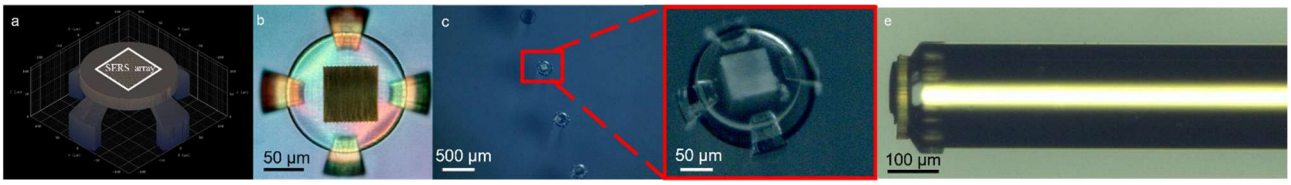

Figure 1. Design and fabrication of the forward-viewing SERS probe. (a) Schematic design of the cap structure. (b) Microscope image of the SERS array printed on the cap structure on an ITO-coated substrate. (c) The cap plus SERS array structure printed onto the tip of a conventional optical fiber (inset shows a magnified view of the cap and array). (d) Microscope image of the final structure after deposition of a 50 nm gold film.

3. Results and Discussion

To evaluate the sensing performance of the forward-viewing SERS probe, we conducted preliminary experiments using three probe configurations: a bare fibre, a gold-coated fibre with SERS array (GS; as reported in [2]), and a gold-coated fibre with cap and SERS array (GCS). We tested R6G at concentrations ranging from 10^{-3} mM to 1 mM. For each concentration, ten Raman spectra were collected, and the mean intensity was calculated. A consistent excitation power of 5 mM was used for all measurements. Baseline correction was applied using the asymmetric least squares smoothing method.

Fig. 2(a) shows the mean Raman spectra obtained using the GCS probe in varying R6G concentrations. As the R6G concentration increased, a corresponding rise in Raman intensity was observed. Baseline-corrected spectra are shown in Fig. 2(b), where characteristic R6G peaks are clearly visible. Fig. 2(c) compares the mean spectra from the three probes at 1 mM R6G (baseline-corrected data shown in Fig. 2(d)). The GS configuration exhibited higher absolute signal intensity than the GCS, due to the inclusion of an air gap between the fiber and the GCS SERS substrate (which introduces some signal losses and additional back-reflections). However, following baseline correction, the GCS structure exhibits comparable sensing performance to the GS as well as considerable higher signal levels than the bare fiber (Fig. 2(d)), thus verifying the signal collection and enhancement capabilities of the GCS probe. These results support continued development of the proposed micro-optic cap and its integration with HCFs to achieve forward-viewing, low-background SERS probes.

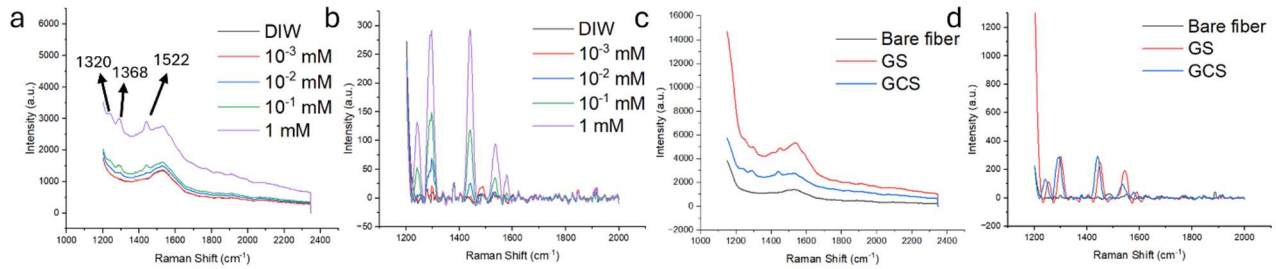

Figure 2. Raman spectral analysis of R6G using different probe configurations. (a) Raw spectra from the GCS probe at R6G concentrations from 10^{-3} mM to 1 mM, showing clear peaks at 1241, 1290, and 1440 cm^{-1}. (b) Baseline-corrected spectra corresponding to (a). (c) Raw spectra comparison of bare fiber, GS, and GCS at 1 mM of R6G. (d) Baseline-corrected spectra of (c), performance was similar for the two probe configurations.

4. Conclusion

In summary, we have presented a forward-viewing, fiber-optic SERS probe – based on a micro-optical fiber cap with central SERS array – suitable for integration with complex fibers (e.g. HCFs) and additional optics (e.g. focusing lenses). Through preliminary experiments using a model chemical analyte and three different fiber configurations, the micro-cap design was validated to preserve signal integrity while enabling effective SERS detection. Future work will focus on integrating this design with HCFs to reduce background noise, thus providing opportunities for real-time, minimally invasive diagnostics.

5. Reference

[1] Schlücker et al., Angew. *Chem. Int. Ed.*, https://doi.org/10.1002/anie.201205748, 2014.
[2] Kim et al., *Adv. Opt. Mater.*, https://doi.org/10.1002/adom.201901934, 2020.
[3] Ochoa et al., *Sensors*, https://doi.org/10.3390/s21196469, 2021.
[4] Debord et al., *Opt. Express*, https://doi.org/10.1364/OE.21.028597, 2013.
[5] Milenko et al., *Sensors*, https://doi.org/10.3390/s21248434, 2021.

Oral Session 6D: Advanced Nanofabrication IV

Ice lithography using Diobalt octa-carbonyl

Limin Qi[a], Dongli Liu[b] , Ding Zhao[a, c], Min Qiu [a, c, d *]

a Key Laboratory of 3D Micro/Nano Fabrication and Characterization of Zhejiang Province, School of Engineering, Westlake University, Hangzhou 310030, China
b Westlake Institute for Advanced Study, Hangzhou 310024, Zhejiang Province, China
c Westlake Institute for Optoelectronics, Fuyang, Hangzhou 311421, China
d Institute of Advanced Technology, Westlake Institute for Advanced Study, Hangzhou 310024, China.
e-mail: qiu_lab@westlake.edu.cn (M.Q.)

Abstract Ice lithography is an emerging, environmentally friendly nanofabrication technique that enables electron beam patterning on curved or irregular surfaces [1]. In recent years, metal-organic precursors such as tungsten hexacarbonyl ($W(CO)_6$) [2] and gold dimethyl acetylacetonate ($Au(acac)Me_2$) [3] have drawn increasing attention for their ability to fabricate metal-containing nanostructures in situ. In this work, we investigate the use of dicobalt octa-carbonyl ($Co_2(CO)_8$) as a novel precursor for metal-organic ice lithography. A low-vibration micromachined Joule-Thomson cryocooler [4] was used to maintain the substrate at approximately 106 K, enabling controlled condensation of thermally evaporated $Co_2(CO)_8$ vapor. Subsequent electron beam exposure followed by thermal desorption produced cobalt-based nanostructures with high resolution. The results demonstrate that $Co_2(CO)_8$ requires an exposure dose on the order 10 mC/cm² and enables patterning with sub-100 nm resolution. Electrical and optical characterizations of the resulting nanostructures confirm their functional properties, highlighting their potential applications in electronic and photonic devices.

Abstract Ice lithography, Diobalt octa-carbonyl, Nanofabrication, Metalorganic ice.

[1] D. Zhao et al., Sci. Bull. 64 (2019) 865–871.
[2] Haque et al., Micro Nano Eng 18 (2023): 100171.
[3] Chang, B et al., Addit. Manuf. 98 (2025) 104645.
[4] Qi, L et al., Microelectron. Eng. 289 (2024) 112180.

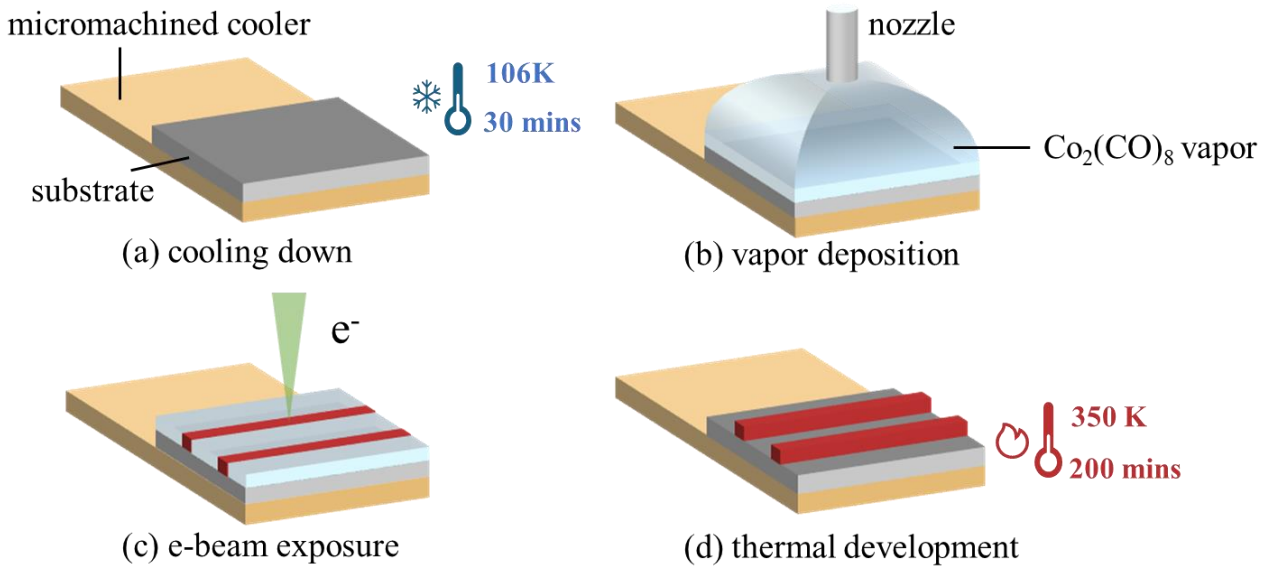

Figure 1. Schematics of the ice lithography process using dicobalt octa-carbonyl. (a) Cooling the substrate to approximately 106 K using the micromachined cooler. (b) Condensing thermally evaporated $Co_2(CO)_8$ vapor onto the cold substrate to form a precursor ice layer. (c) Patterning the ice layer using e-beam. (d) Sublimating unexposed material by heating the substrate to 350 K, resulting in well-defined nanostructures.

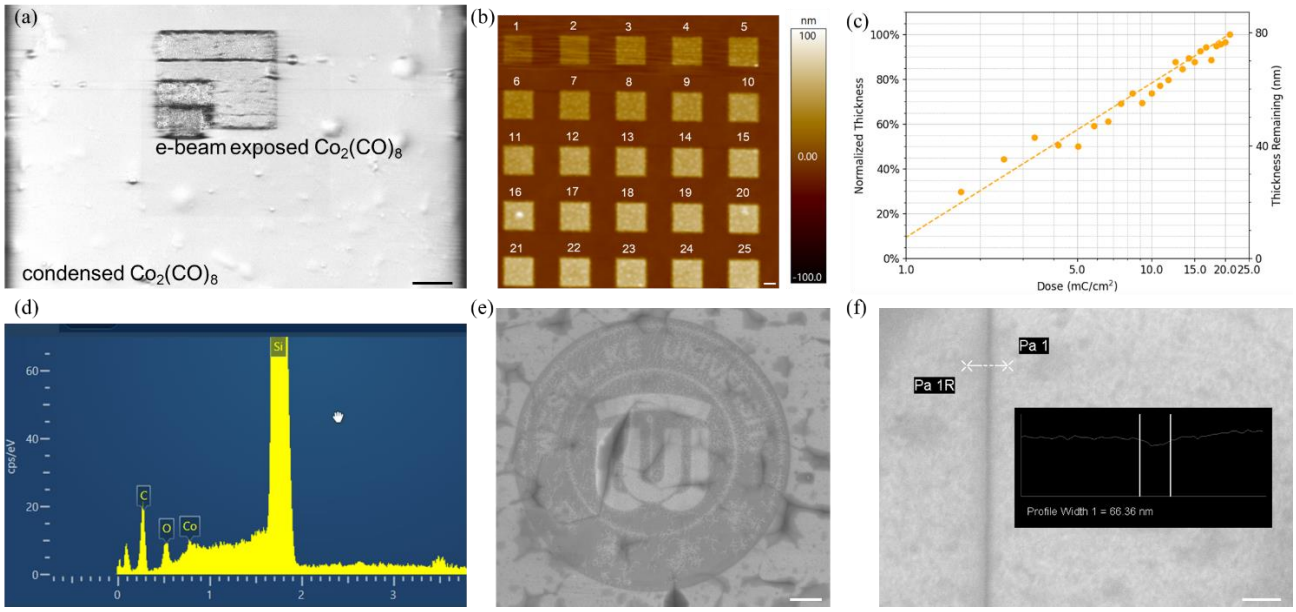

Figure 2. (a) SEM image of condensed $Co_2(CO)_8$. Scale bar is 2 µm. (b) SEM image of patterned square arrays on a 80 nm thick solid $Co_2(CO)_8$ on silicon. The squares of 5 × 5 µm^2 represent different e-beam dose from 1 (top left) to 25 (bottom right) mC/cm^2. Scale bar is 2 µm. (c) Dose curve at 5 keV. The scatters correspond to the thicknesses of the squares in (b). (d) EDS spectrum of a single square pattern in (b) exposed with a dose of 16 mC/cm^2. (e) SEM image of the "Westlake University logo" array on a SiO_2 substrate. Scale bar is 5 µm. (f) SEM image of a single-pixel line patterned on a SiO_2 substrate, with a measured width of 66 nm. Scale bar: 500 nm.

Quasi-3D Nanoscale Fabrication: Precision Patterning and Modelling via Focused Ion Beam Implantation

J Llobet [a], J Antoja-Lleonart [a], A del Moral [a], M de la Vega [a], M Duch [a], A Cian [b], E Scattolo [b], M Crivellari [b], X Borrisé [c], D Giubertoni [b], F Pérez-Murano [a]

[a] Institute of Microelectronics of Barcelona (IMB-CNM CSIC), Bellaterra, 08193, Catalonia, Spain
[b] Center for Sensors and Devices, Fondazione Bruno Kessler (FBK), Trento, 38123, Italy
[c] Catalan Institute of Nanoscience and Nanotech. (ICN2), and BIST, Campus UAB, Bellaterra, 08193, Spain
e-mail: jordi.llobet@imb-cnm.csic.es

In this work, we present recent advances in the development and modelling of quasi-3D silicon nanostructures defined by focused ion beam (FIB) technologies together with tetramethylammonium hydroxide (TMAH) etching. The development of FIB columns equipped with liquid metal alloy ion sources (LMAIS) opens new opportunities for FIB-based processing, enabling multi-species patterning [1]. Here, we report the use of focused Au+ and Ga+ ion implantation to create hard masks for nanolithography on silicon, focusing on the modelling of the implantation and etching processes to control the thickness and height/depth to the ultimate sub-nm range. Our aim is to develop a predictive model for the etching behavior of FIB-implanted volumes, enabling the design of corrugated and 3D suspended silicon structures with tailored dimensions. Previous studies have demonstrated that Ga+ ion implantation in silicon via FIB serves as an efficient and straightforward resistless lithography technique [2-5]. This approach facilitates the fabrication of nanometer-scale structures on silicon and other materials. The implanted Ga+ volume enhances silicon's resistance to both wet and dry etching, enabling its use as an etching hard mask or as a functional device (Figure 1). The resolution of the structures is largely determined by the focused beam's diameter and the ion penetration depth and straggling. Several applications of this method have been reported, including the fabrication of suspended silicon nanowires [6] and single-electron devices [7].

We have modelled the process to precisely control the vertical dimensions (z-direction) of silicon nanostructures, including both suspended and non-suspended configurations. Process-calibration experiments were conducted for Ga+ using a 30 keV Crossbeam 550L system (Zeiss) and for Au+ [8] using a 35 keV Velion FIB-SEM system (Raith). Fluence values ranged from $1 \cdot 10^{14}$ at/cm² to $1 \cdot 10^{17}$ at/cm², avoiding lower doses (insufficient) and higher dose rates (entering milling regimes) [5]. The implanted samples were etched using TMAH at 25% concentration and 80°C. Atomic force microscopy (AFM) was used to characterize the structures post-implantation and post-etching. After calibration, we developed algorithms in Matlab software to predict the etching rates in TMAH and the final etching depth (Figure 2) for both Au+ and Ga+ ion species as a function of implantation dose. A custom Matlab framework was chosen to enable modeling flexibility, integration of experimental parameters and simulations tailored to the specific scope of implantation and etching dynamics. This information is crucial for fine-tuning the dimensions of corrugated and 3D suspended silicon structures. Figure 3 shows the silicon surface after Ga+ implantation and the corrugated silicon surface that results from the subsequent etching step.

In this study, we successfully demonstrated the development and modelling of silicon nanostructures using FIB implantation with both Ga and Au ion species. Through the detailed process-calibration experiments and the development of predictive algorithms, we achieved precise control over the etching behavior of ion-implanted silicon in TMAH, enabling the fabrication of highly defined, suspended 3D nanostructures (Figure 4). Our results show that the combination of FIB implantation and wet etching provides an effective route for creating complex 3D silicon nanostructures, opening new possibilities for fabricating nanoscale electronic and sensing devices.

References:
[1] L. Bischoff et al. *Appl Phy Rev* 3, 021101 (2016);
[2] J. Brugger et al. *Microelect. Eng*, 35, pp. 401-404 (1997);
[3] B. Schmidt et al. *Sens. Actuators Phys*, 61, 369-373 (1997);
[4] G. Rius et al. *J. Vac. Sci. Technol*, 27, 6, p. 2691 (2009);
[5] J. Llobet et al. *Nanotechnology*, 25, 13, p. 135302 (2014);
[6] J. Llobet et al. *Appl. Phys. Lett.*, 107, 7, p. 073104 (2015);
[7] J. Llobet et al. *Appl. Phys. Lett.*, 107, 22, p. 223501 (2015);
[8] E. Scattolo et al. *Micro Nano Eng.* 28, 100308 (2025)

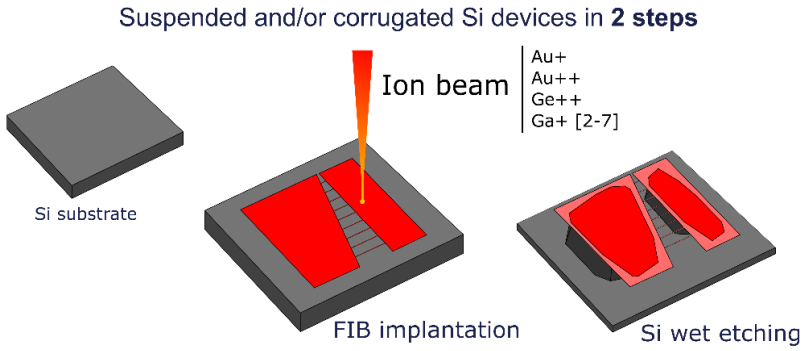

Figure 1. *Schematic representation of the two-step process flow. The diagram illustrates the process used to fabricate suspended silicon nanostructures via FIB implantation and wet etching.*

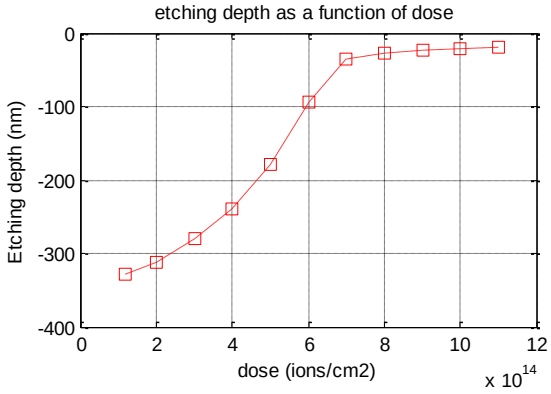

Figure 2. *Simulation of etching depth as a function of implantation dose after FIB implantation predicting the etching depth for silicon implanted with varying doses of Ga+ ions.*

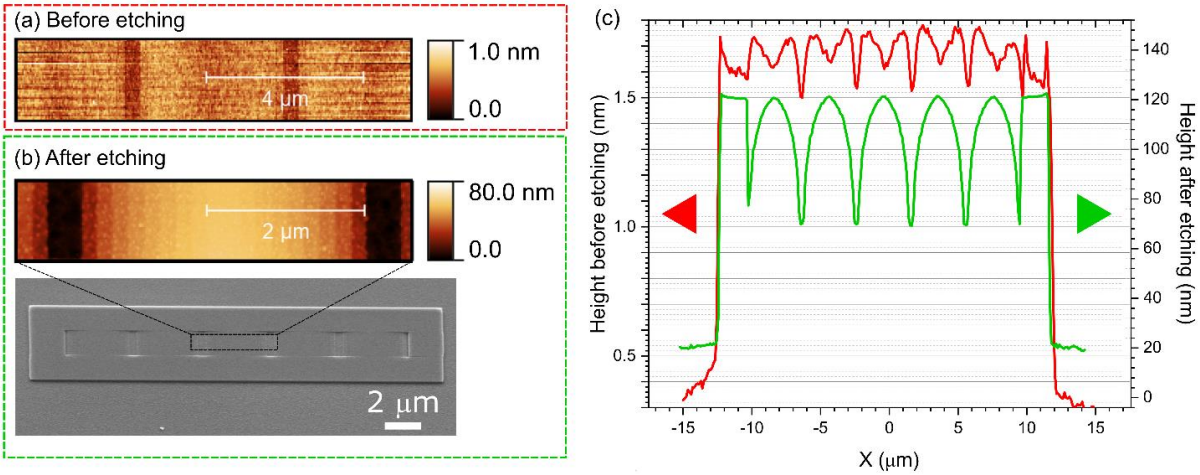

Figure 3. *Corrugated structure defined by Ga+ implantation and TMAH etching. a) AFM image of the silicon surface after FIB implantation, showing two cycles of the corrugated structure. b) AFM and SEM images of the same structure after wet etching, demonstrating the dimensional change and profile amplification induced by etching. c) Graph comparing the height of the full set of the corrugated structure before (left axis) and after the etching process (right axis).*

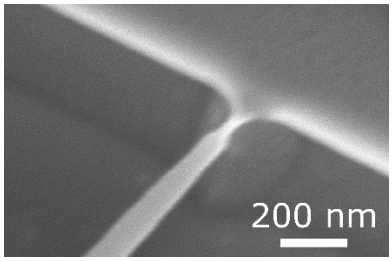

Figure 4. *Tilted SEM image of a suspended Si constriction embedded within a quasi-3D corrugated architecture.*

Investigation of process windows for alternative non-toxic and metal ion free developer choline hydroxide for HSQ resist Medusa 84 SiH

P. Kohlschreiber[a], M. Gottwald[a], C. Helke[a,b], H. Biller[c], M. Sendel[c] and D. Reuter[a,b]
[a] Fraunhofer Institute for Electronic Nano Systems (ENAS), Chemnitz, 09126, Germany
[b] Technische Universität Chemnitz, Center for Micro- and Nanotechnologies (ZfM), Chemnitz, 09126, Germany
[c] Allresist GmbH, Strausberg, 15344 Germany
pia.kohlschreiber@enas.fraunhofer.de

As a high-resolution negative-tone resist for electron beam lithography (EBL), hydrogen silsesquioxane (HSQ) continues to be of relevance. Its advantages include sub-10 nm resolution [1], low line edge roughness and higher etching stability compared to organic resists [2], and it finds applications for example in nanoimprint lithography (NIL) [3]. Several developer chemistries for HSQ resists have been applied: salty developers based on NaOH/NaCl solutions [4], KOH as well as tetramethyl ammonium hydroxide (TMAH) solutions [1]. Specifically, high contrast of HSQ resist has been shown by developing in 25 % TMAH solution [5]. As the toxicity of TMAH introduces additional occupational hazards into clean rooms, finding alternative non-toxic and more importantly, metal ion free developer chemistries is desirable, one such candidate being choline hydroxide, a non-toxic and metal ion free strong aqueous base. This study aims to establish process windows for the novel HSQ resist Medusa 84 SiH using choline hydroxide as a developer. Achieved contrast, sensitivity and minimum critical dimensions (CD) are compared to both KOH- and TMAH-based developer solutions.

The resist Medusa 84 SiH (SX AR-N 8400.08 by Allresist GmbH) was spun onto 6-inch silicon wafers at 4000 rpm to form resist layers of 120 nm. Softbakes were performed at 100 °C for 60. The substrates were exposed using a Vistec SB254 variable-shape-beam system with an acceleration voltage of 50 kV; the exposed layout included isolated (iso) lines as well as line:space arrays with pitches 1:1, 1:2, 1:5 and 1:10 with varying CD of 25 to 500 nm. Exposure doses ranged from 400 to 1600 µC/cm² in steps of 80 µC/cm² as well as 2400 to 3600 µC/cm² in steps of 400 µC/cm². Three different types of developer chemistries as well as varying development times were investigated: TMAH-based developer AR 300-73 (6.5 % TMAH, Allresist GmbH), KOH-based developer AZ 400K (MicroChemicals GmbH) diluted 1:6 with deionized water (DIW), and choline hydroxide (10 and 25 %, Allresist GmbH). Within three hours after exposure, the wafers were developed for a specified development time, flushed with DIW and finally spin-dried. The developed structures were analyzed electro-optically with a Hitachi CS4800 CD-SEM. Contrast curves were measured using a DektakXT stylus profilometer.

The contrast curves (Figure 1) show large differences in selectivity of the Medusa 84 SiH resist depending on the used developer chemistry and concentration. First, a 1:6 dilution of AZ 400K as developer is too strong for the exposed doses, strongly limiting the ability to analyze exposed structures. In contrast, the chosen developers AR 300-73 (6.5 % TMAH) and 10 % choline hydroxide enable a significantly increased sensitivity of the resist below 600 µC/cm². The contrast could be increased further by increasing the concentrations of choline hydroxide developer; no occupational risk would be involved as choline hydroxide continues to be non-toxic even at higher concentrations up to 50% [7]. Due to the trade-off relationship between contrast and sensisivity [3], an optimum between has to be found, as is applicable for any developer. Figure 2 a)-c) shows exemplary CD-SEM images of achieved CDs for the three investigated developer chemistries; a 40 nm iso line was developed with 25 % choline hydroxide at comparatively low exposure dose of 560 µC/cm² (Figure 2b). As the CD-SEM images do not allow conclusions regarding the thickness of the developed feature, CD-AFM measurements will be conducted next to determine the minimum required line width maintaining full resist thickness.

For highest resolution applications, process windows for a thinner HSQ resist layers with thicknesses of 30 nm will be established using appropriate base doses and developer dilutions of choline hydroxide and compared to TMAH- and KOH-based developers, ultimately having the chance to remove one additional occupational hazard in the form of toxic developers by replacing with non-toxic and metal ion free choline hydroxide.

[1] A. E. Grigorescu et al., Microelectron. Eng. 84 (2007), 822.
[2] H. Namatsu et al., J. Vac. Sci. Technol. B 16 (1998), 69.
[3] A. E. Grigorescu et al, (2009) Nanotechnology 20 (2009), 292001.
[4] S.-W. Nam et al., J. Vac. Sci. Technol. B 27 (2009), 2635–2639.
[5] Y.M. Georgiev et al., Vacuum 77 (2005), 2, 117-123.
[6] N. Clark et al., J. Vac. Sci. Technol. B (2006), 24 (6), 3073–3076.
[7] Sigma-Aldrich Chemie GmbH, safety data sheet for choline hydroxide solution (2023).

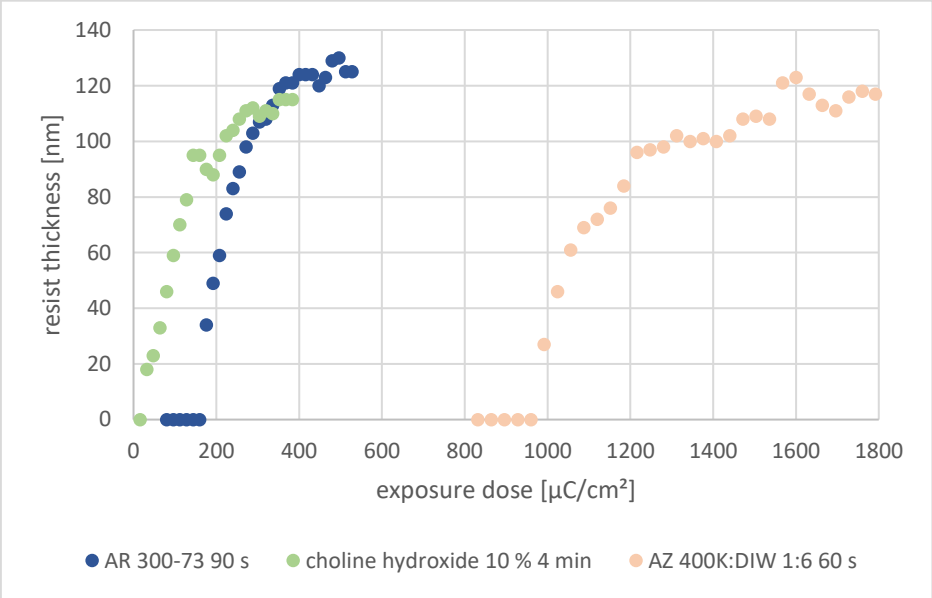

Figure 1. Contrast curves for the three investigated developer chemistries (AR 300-73 (6.5 % TMAH), AZ 400 K diluted 1:6 with de-ionized water (DIW), and 10 % choline hydroxide).

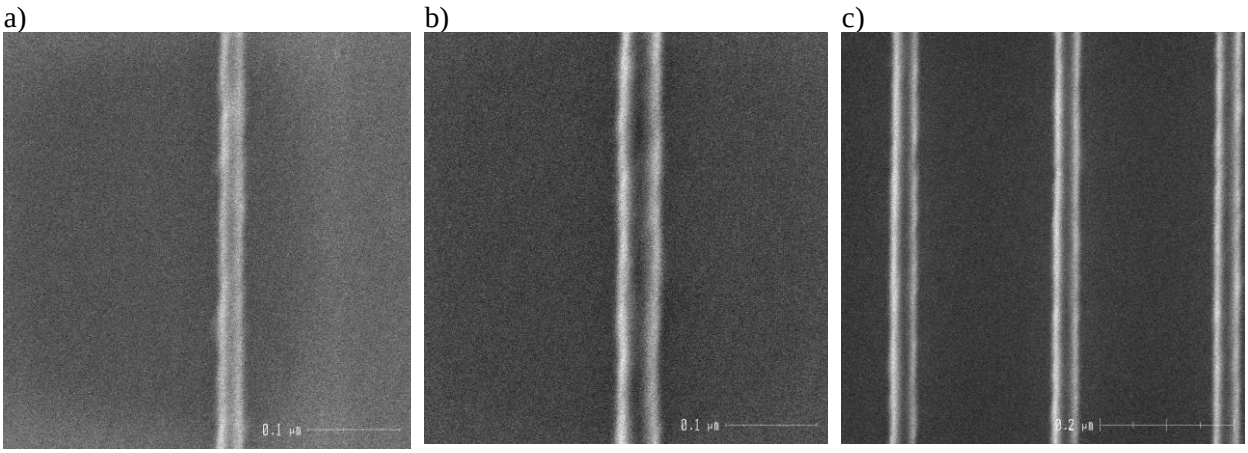

Figure 2. CD-SEM images of a) a 25 nm isolated (iso) line exposed with a dose of 1600 µC/cm² developed for 90 s in AR 300-73 (6.5 % TMAH), b) a 40 nm iso line exposed with 560 µC/cm² developed for 4 min in 25 % choline hydroxide, and c) 40 nm lines (line:space=1:5) exposed with 3600 µC/cm² developed for 60 s in AZ 400K diluted 1:6 with deionized water (DIW). The scale bars correspond to 100 nm for a) and b), and 200 nm for c).

Resist-free and low-temperature micropatterning of IGZO using stencil lithography for electronic applications

Chenxiang Zhang, Giovanni Boero, Arnaud Bertsch, Jürgen Brugger

Microsystems Laboratory, Ecole Polytechnique Fédérale de Lausanne (EPFL), 1015 Lausanne, Switzerland
e-mail: chenxiang.zhang@epfl.ch

Electronic waste (e-waste) is one of the fastest-growing global waste streams, driven by the non-degradability of traditional electronics. A promising solution is to use biodegradable substrates such as Polyvinyl Alcohol (PVA). However, their low thermal stability requires near-room-temperature processing. Indium-Gallium-Zinc Oxide (IGZO), an n-type oxide semiconductor, is well-suited for thin-film transistors (TFTs) in this condition due to its relatively high electron mobility (~20 $cm^2/(V \cdot s)$) and compatibility with room-temperature deposition [1]. Yet, conventional patterning methods like photolithography and wet etching using HCl [2] are incompatible with biodegradable substrates due to their sensitivity to water and acid.

To address this, previous studies have used laser-cut steel shadow-masks for the patterning of IGZO TFTs, reaching a resolution of ~400 µm [3]. Here we explore how SiN_x-based micro-stencils [4] can be used for the resist-free patterning of IGZO by two routes: i) local RF sputter deposition and ii) local ion beam etching (IBE), thereby eliminating wet chemicals and keeping substrate temperatures below PVA's upper limit (~120 °C).

Figure 1(a) outlines the process flow with 2 different methods, using RF sputtering (RF power 200W, Ar flow 30 sccm, working pressure 5×10^{-3} mbar, working distance 80 mm) or IBE (tilt -10°, rotation 10 rpm, working pressure 10^{-4} mbar), with stencil chip shown in (b) and (c). Both methods exhibit edge blurring due to the unavoidable 10 µm-level gap between the stencil and substrate: sputtering causes under deposition due to short mean-free path of IGZO flux, while IBE results in edge slanting due to angled incidence, rotation, and re-sputtering effects. Figure 1(d)-(e) show successful 5 µm patterning, and AFM scans in (f)-(g), with profiles in (h). For both samples, the IGZO thickness is 10 nm. In the IBE-fabricated sample, an additional 15 nm of over-etching into the underlying SiO_2 is observed, resulting in a total depth of 25 nm. The lateral blurring in both cases is approximately 5 µm. However, given the corresponding depth, IBE produces significantly steeper sidewalls compared to RF sputtering. With further optimization of etching parameters (e.g., tilting angle, acceleration voltage) and stencil-substrate contact (e.g., with a firm clamping), even steeper profiles can be achieved. This might help to prevent the so-called "hump phenomenon" caused by parasitic transistor introduced by the slope of IGZO [5].

Stencil-patterned IGZO's electrical properties were characterized using a complete stencil-deposited Van der Pauw structure (Figure 2(a)), with the cross-section shown in (b). Using the same deposition parameters as mentioned above, a linear four-probe I-V curve (Figure 2(c)) indicates Ohmic contacts and an IGZO resistivity of 8.5 mΩ·cm. Hall measurements (Figure 2(d)) yield a carrier density of 3.5×10^{19} cm^{-3} and electron mobility of 20.6 $cm^2/(V \cdot s)$, consistent with literature [6], confirming the process through the stencils retains, as expected, IGZO's intrinsic electrical performance.

Electrical tunability is achieved by varying O_2 partial pressure during RF sputtering (Figure 3(a)). Increased O_2 reduces oxygen vacancies, which are primary electron donors, and thereby lowering the carrier density. Results in (b) show a clear drop in carrier density with increasing O_2. In (c), the mobility shows a slight improvement, consistent with trends reported in previous studies within the carrier density range of 10^{19} cm^{-3} [7].

In summary, SiN_x stencil lithography enables near-room-temperature, resist-free IGZO patterning with micrometer resolution while preserving and tuning electrical properties using oxygen content. This makes it an interesting candidate for biodegradable and flexible TFT applications, contributing to more sustainable electronics manufacturing.

[1] K. Nomura et al., Nature 432 (2004) 488–492.

[2] K.-L. Han et al., ACS Appl. Electron. Mater. 3 (2021) 5037–5047.
[3] Z. Zheng et al., J. Mater. Chem. C 5 (2017) 7043–7050.
[4] O. Vazquez-Mena et al., Microelectron. Eng. 132 (2015) 236–254.
[5] X. Shi et al., IEEE Trans. Electron Devices 67 (2020) 1606–1612.
[6] H. Yabuta et al., Appl. Phys. Lett. 89 (2006) 112123.
[7] K. Nomura et al., Appl. Phys. Lett. 85 (2004) 1993–1995.

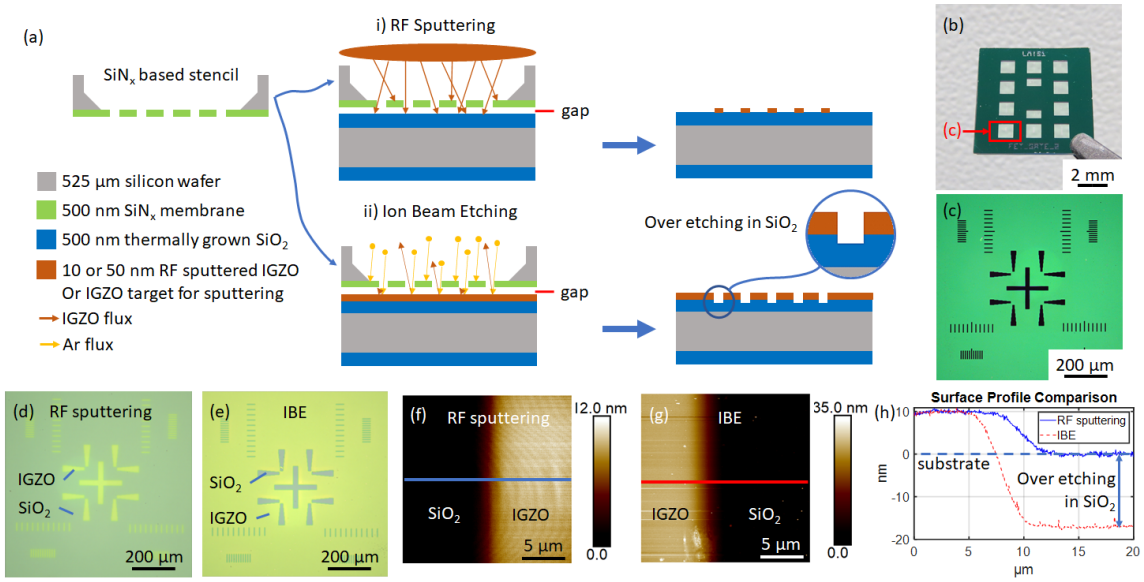

Figure 1. IGZO patterning by stencil lithography. (a) Process flow using SiN_x stencil with i) RF sputtering or ii) IBE, including theoretical principles. (b) Optical image of the stencil chip. (c) Zoom-in of the test structure region. (d, e) Optical images of IGZO (10 nm) patterned by RF sputtering and IBE. (f, g) AFM scans showing edges of IGZO. (h) Surface profiles along lines in (f, g), showing steeper edges with IBE.

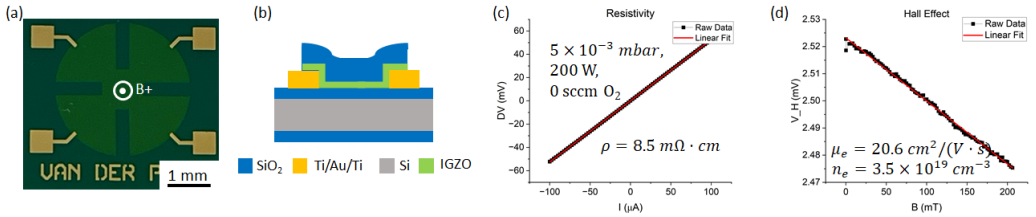

Figure 2. Device and electrical characterization of stencil-patterned IGZO. (a) Optical image of the Van der Pauw structure, fully fabricated using stencil lithography with deposition for electrical characterization. (b) Illustration of the device's cross-section. The thickness of IGZO in this sample is 50 nm. (c) I-V curve of the device. (d) B-V curve obtained from Hall effect measurements on the same sample.

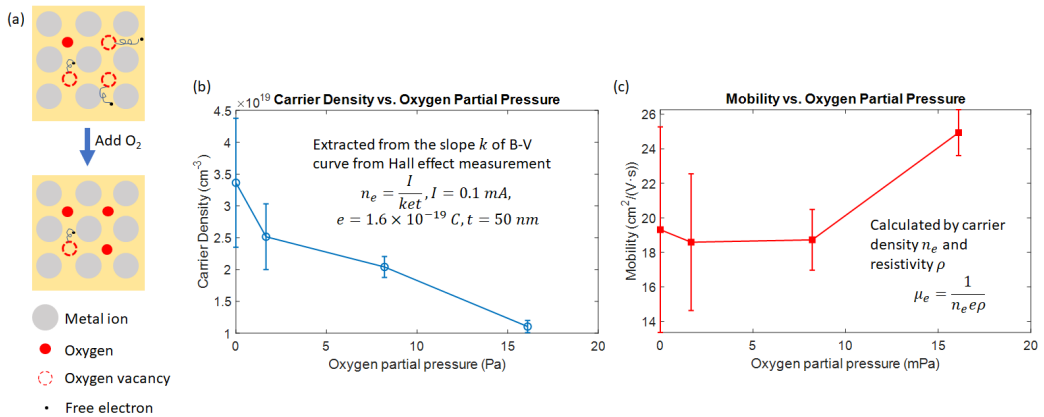

Figure 3. Effect of O_2 partial pressure on the electrical properties of stencil-patterned IGZO. (a) Schematic illustration of the mechanism by which varying O_2 partial pressure influences IGZO's electrical characteristics. (b) Plot of measured carrier density and (c) calculated mobility versus O_2 partial pressure.

Authors Index

Abadal, G. 267, 894
Abadi, E. 71, 524
Abbasi, I. 275, 910
Abdelazim, N. 115, 220, 614, 801
Abualnaja, F. 275, 910
Achleitner, T. 148, 673
Adeyemi, D. 256, 872
Adikimenakis, A. 238, 836
Aggarwal, I. 259, 878
Aggarwal, T. 215, 791
Ahmad, B. 395, 1128
Ahmad, N. 299, 958
Ahn, E. 27, 440
Ai, D. 240, 838
Aida, Y. 85, 555
Aizpurua, J. 391, 1120
Aizpurua-Iraola, G. 277, 914
Ajalloueian, F. 358, 1064
Akabori, M. 375, 1092
Akbarnejad, E. 322, 323, 1003, 1005
akiyama, k. 51, 483
Alan, B. 77, 539
Albrechtsen, M. 164, 700
Aldhahri, N. (School of Electronics and Computer Science, University of Southampton, Southampton SO17 1BJ, United Kingdom) 382, 1104
Aldhahri, N. (University of Southampton) 283, 386, 926, 1111
Alexander-Webber, J. 275, 910
Algieri, L. 229, 271, 819, 902
ALI, A. 204, 769
Ali, S. 115, 614
Alijani, F. 263, 328, 886, 1014
Alkhalil, F. 347, 1047
Amano, S. 359, 1066
Amano, T. 151, 677
Amat, E. 234, 277, 363, 828, 914, 1075
Amaya, S. 364, 1077
Ambar, R. 205, 771
Amirhosseini, S. 107, 600
Ammon, A. 178, 725
An, M. 211, 783
Anderson, D. 212, 785
ANDRIEU, F. 354, 1057
Andrieux-Ledier, A. 58, 62, 68, 497, 505, 517
André, L. 372, 1088
Angus, F. 311, 983
Antoja, J. 234, 277, 398, 828, 914, 1133
Arefi, F. 175, 720
Arivanandhan, G. 322, 323, 1003, 1005
Arnold, T. 308, 338, 977, 1032
Arregui Bravo, G. 164, 700
Arresta, G. 232, 825
Arrigoni, A. 94, 573
Arroyo Cardoso, F. 32, 339, 449, 1034
Ashfield, A. 162, 696
Ashida, T. 145, 667
Ashish, A. 92, 569
Aslanoglou, S. 332, 392, 1021, 1122
Atrian-Garcia, H. 269, 898
Ayela, C. 11, 412
Aznar, S. 299, 358, 958, 1064

Babar, A. 164, 700
Badura, D. 282, 924
Baek, E. 336, 1029
BAEK, S. 342, 1040
Bagur, L. 358, 1064
Baine, P. 104, 117, 594, 617
Bakli, C. 137, 190, 655, 745
Baldi, I. 320, 1000
Balme, L. 52, 485
Banergee, A. 100, 279, 585, 918
Banis, A. 306, 972
Bano, E. 112, 608
Banzet, S. 303, 966
Bao, L. 197, 756
Baraket, M. 187, 741
Barbero Rodriguez, C. 340, 1036
Barnes, P. 311, 983
Baron, T. 58, 62, 497, 505
BARRAL, V. 354, 1057
Barrioz, V. 136, 652

Bartlett, P. 220, 801
BAUDIN, F. 354, 1057
Bauer, P. 333, 1023
Baumann, B. 37, 457
Bausells, J. 234, 277, 315, 363, 828, 914, 990, 1075
Bayat, D. 175, 720
Bazin, A. 76, 537
Beanland, R. 220, 801
Becker, J. 17, 421
Beeby, S. 280, 920
Beier, M. 168, 708
Bell, O. 136, 652
Bello-Jiménez, M. 304, 968
BELUFFI, C. 354, 1057
Benz, B. 21, 212, 429, 785
Berdagué, p. 35, 453
Berdondini, L. 392, 1122
Berencen, Y. 89, 563
Berger, P. 356, 1060
Bermejo, S. 63, 507
Bermudez, D. 236, 832
Bertsch, A. 400, 1137
Bieling, J. 213, 787
Bigan, N. 351, 1051
Bikard, D. 295, 950
Biller, H. 205, 251, 399, 771, 861, 1135
Biscarini, F. 332, 1021
Biswas, S. 56, 493
Blanc, C. 393, 1124
BLANC, R. 354, 1057
Blanquer, A. 276, 358, 912, 1064
Blattert, C. 80, 545
Bleiker, S. 198, 758
Blondeau-Patissier, V. 372, 1088
Boche, K. 237, 834
Boden, S. 228, 817
Boero, G. 400, 1137
Bogdanov, A. 18, 423
Boisen, A. 358, 1064
Bolk, J. 180, 730
Bollani, M. 94, 99, 102, 250, 573, 583, 589, 859
Bolten, J. 20, 80, 81, 198, 427, 545, 547, 758
Bolzonello, L. 99, 583
BONIFACE, G. 354, 1057
Bonitz, J. 213, 787
Bonora, M. 48, 105, 477, 596
Boodhoo, L. 207, 386, 775, 1111
BORGET, L. 52, 485
Borrisé, X. 267, 398, 894, 1133
Borstner, D. 210, 781
Boschi, A. 357, 1062
Bottegoni, F. 102, 589
Boudier, L. 144, 665
Boulouis, A. 138, 657
bourrier, d. 11, 195, 412, 752
Boussey, J. 112, 608
Boutry, C. 32, 339, 449, 1034
Bouville, D. 35, 453
Bowman, R. 104, 117, 162, 594, 617, 696
Brandès, S. 372, 1088
Bravo Larrea, J. 236, 832
Bresson, B. 189, 743
Brisselian Kamary, M. 356, 1060
Bristow, E. 30, 445
Brox, O. 168, 251, 708, 861
Brugger, J. 400, 1137
Bruno, G. 320, 1000
Bruno, L. 253, 865
Bruno, M. 173, 716
Buddha, K. 152, 679
Buitelaar, M. 184, 735
Bull, T. 386, 1111
Buzio, M. 260, 880
Bächtold, B. 178, 725
Bélot, G. 76, 537
Bérard-Bergery, S. 76, 537
Böhm, L. 206, 773

Calado, P. 24, 311, 434, 983
Caneva, S. 163, 698
Cao, H. 292, 944
Carbajal-Arizaga, G. 128, 304, 635, 968
Carcenac, F. 144, 665
Caron, E. 342, 1040
Carré, E. 58, 62, 497, 505
Cartoixà, X. 267, 894
Casals, E. 93, 571
Casimiro, A. 231, 823
Castillo, Y. 93, 571
Catarino, S. 116, 615
catuneanu, m. 89, 563
Cavedoni, L. 32, 339, 449, 1034
Cedeño, M. 63, 507
Celik, S. 43, 467
Cesario, N. 314, 988

Chaaban, J. 152, 315, 679, 990
Chakraborty, S. 108, 109, 190, 602, 604, 745
Chalker, P. 23, 432
Chan, M. 287, 934
Chang, T. (Institute of Science Tokyo) 15, 65, 79, 96, 270, 382, 386, 418, 511, 543, 577, 900, 1104, 1111
Chang, T. (Optoelectronics Research Centre, University of Southampton, SO17 1BJ, UK) 272, 904
Chang, W. 165, 394, 702, 1126
Chang, Y. 216, 296, 793, 952
Charguéraud, A. 138, 657
Charlton, M. 85, 111, 555, 606
CHARPIN-NICOLLE, C. 354, 1057
Chen, C. 15, 65, 79, 96, 270, 418, 511, 543, 577, 900
Chen, H. 165, 702
Chen, J. (Department of Photonics, National Cheng Kung University) 165, 702
Chen, J. (Imperial College London) 174, 718
Chen, J. (National United University) 274, 908
Chen, P. 216, 793
Chen, Q. 86, 87, 113, 200, 201, 258, 557, 559, 610, 761, 763, 876
Chen, X. (Beihang University) 185, 737
Chen, X. (Optoelectronics Research Centre, University of Southampton, SO17 1BJ, UK) 262, 884
CHEN, Y. 360, 1068
Chen, Y. (Fudan university) 86–88, 113, 200, 201, 258, 557, 559, 561, 610, 761, 763, 876
Chen, Y. (National Taiwan University) 366, 1079
Chen, Y. (University of Southampton) 272, 904
Cheng, B. 296, 952
Cheng, X. 289, 938
Chiu, T. 394, 1126
Chmielak, B. 198, 758
Cho, C. (Hanyang University) 29, 376, 443, 1094
Cho, C. (National Taiwan University) 367, 1081
Cho, H. 371, 1086
Cho, Y. 67, 211, 217, 353, 515, 783, 795, 1055
Choi, J. 371, 1086
Chong, H. 98, 227, 228, 255, 280, 298, 310, 581, 815, 817, 870, 920, 956, 981
Chou, Y. 264, 888
Christopher, H. 168, 708
Chu, K. 174, 718
Chung-Che Huang, K. 136, 652
Churchill, G. 327, 341, 1012, 1038
Cian, A. 398, 1133
Ciccacci, F. 102, 589
Cinquin, B. 300, 960
Ciriolo, A. 250, 859
Cole, J. 325, 1008
Coloma Velez, A. 63, 507
Coluccio, M. 253, 865
Conde Portilla, O. 266, 892
Connolly, B. 148, 673
Constantoudis, V. 210, 781
Coppedè, N. 314, 988
Cornu, M. 68, 517
Cox, D. 232, 825
Criscuolo, V. 260, 880
Crivellari, M. 398, 1133
Cuenca, J. 25, 312, 436, 985
Cui, Z. 328, 1014
Curson, N. 184, 735

D'Errico, V. 229, 819
Dague, E. 195, 752
Dai, H. 280, 920
Daniel-Iosif, T. 288, 936
Darlington, J. 207, 775
Das, A. 273, 906
Das, S. 109, 301, 604, 962
DasGupta, S. 247, 853
Dave, S. 180, 730
Davidsen, R. 191, 747
De Angelis, F. 320, 357, 1000, 1062
de Bruijn, R. 252, 863
de Ceglia, D. 99, 583
de Groot, K. (School of Electronics and Computer Science, University of Southampton, Southampton SO17 1BJ, United Kingdom) 220, 801
de Groot, K. (University of Southampton) 26, 319, 438, 998
de la Vega Czarnecki, M. 398, 1133
DE MARCO, C. 253, 865
de Marzo, G. 229, 271, 819, 902
De Teresa, J. 282, 924
De Vittorio, M. 173, 229, 271, 332, 392, 716, 819, 902, 1021, 1122
Decams, J. 68, 517
del Moral, A. 234, 277, 363, 398, 828, 914, 1075, 1133

Della Casa, P. 251, 861
Demiri, V. 338, 1032
DeMoor, S. 213, 787
den Toonder, J. 252, 259, 328, 863, 878, 1014
Deng, F. 82, 549
Desai, T. 331, 1019
Desbois, N. 372, 1088
Deshpande, R. 176, 722
DESPOIS, D. 354, 1057
Despont, M. 175, 720
Develioglu, A. 356, 1060
Dhara, T. 247, 853
Di Lauro, M. 332, 1021
Diewald, S. 225, 811
Dimogerontaki, N. 169, 297, 710, 954
Ding, B. (School of Electronics and Computer Science, University of Southampton, Southampton SO17 1BJ, United Kingdom) 335, 1027
Ding, B. (University of Southampton) 330, 1017
Dipalo, M. 357, 1062
Dixit, S. 268, 896
Djurišić, A. 311, 983
Docampo, P. 311, 983
Domański, K. 245, 848
Domínguez-Pumar, M. 63, 507
Dong, G. 114, 612
Doucet, J. 144, 665
Du, G. 20, 427
Duan, Y. 259, 878
Duch, M. 398, 1133
Dufour, I. 11, 412
Duran, S. 241, 840
Durrani, Z. 174, 718
Durrant, J. 311, 983
Dutta, G. 92, 569
Díez, R. 391, 1120

E. Amirabadi, H. 252, 863
Ebbert, J. 17, 421
Ebert, M. 272, 904
Echresh, A. 89, 368, 563, 1083
Egawa, S. 270, 900
Eggeling, M. 60, 501
Egger, F. 244, 846
Ehlert, L. 81, 198, 547, 758
Ehrhardt, M. 307, 308, 338, 974, 977, 1032
Einsiedler, C. 157, 687
Ekinci, Y. 147, 178, 356, 671, 725, 1060
El Sachat, A. 349, 1049
Elbeshausen Sestoft, J. 273, 906
Elenes Cervantes, M. 241, 840
Ellinas, K. 306, 972
Emnéus, J. 387, 1113
Erbe, A. 89, 368, 563, 1083
Erichlandwehr, T. 53, 261, 266, 487, 882, 892
Erne, R. 315, 990
Esmek, F. 157, 261, 278, 687, 882, 916
Espina, J. 391, 1120
Estengre Pérez, J. 318, 996
Esteve, J. 276, 912
Evangelos, A. 238, 836

Fagiani, L. 99, 583
Fan, Y. 202, 765
Fang, X. 208, 777
Fantner, G. 352, 1053
FATTACCIOLI, J. 138, 189, 657, 743
Fawaz, G. 372, 1088
Fay, A. 76, 537
Fedorov, A. (IFN-CNR) 102, 589
Fedorov, A. (Institute of Photonic and Nanotechnology (IFN) - CNR) 94, 573
Fehres, C. 30, 445
Fellin, T. 392, 1122
Fernandez, I. 53, 157, 218, 261, 269, 318, 487, 687, 797, 882, 898, 996
Fernandez-Cuesta, I. 266, 273, 278, 892, 906, 916
Fernández Contreras, A. 13, 414
Fernández-Regúlez, M. 241, 277, 315, 840, 914, 990
Ferreira, G. 116, 615
Fetisova, M. 60, 501
Finazzi, M. 102, 589
Fischer-Kaszuba, B. 58, 62, 497, 505
FitzGerald, O. 254, 868
Flandre, D. 316, 992
Flewitt, A. 23, 432
Fliervoet, T. 203, 767
Flodgren, V. 273, 906
Florensa, X. 57, 495
Fobelets, K. 340, 1036
Formoso, M. 320, 1000
Fossard, F. 58, 62, 68, 497, 505, 517
Fowler, G. 340, 1036
Francais, R. 52, 485
Frangen, A. 148, 673

Freddi, S. 94, 99, 102, 250, 573, 583, 589, 859
Frederiksen, B. 164, 700
Fricke, J. 168, 708
Frischmann, F. 246, 850
Fujieda, S. 50, 481
Fujiwara, K. 100, 585
Fukuoka, T. 192, 749

Gabriel, G. 93, 571
Gacka, E. 282, 924
Gadegaard, N. 57, 326, 495, 1010
Galiana, B. 242, 842
Gamby, J. 295, 303, 950, 966
Gangnaik, A. 26, 207, 438, 775
Garcia-Garcia, J. 267, 894
García-Barrientos, A. 304, 968
García-García, A. 234, 828
García-Mota, M. 391, 1120
García-Ramírez, M. 128, 281, 304, 635, 922, 968
Gates, J. 327, 341, 1012, 1038
Gawith, C. 327, 341, 1012, 1038
Gaya, P. 277, 914
Gebeyehu, F. 27, 440
Gentile, F. 253, 314, 320, 865, 988, 1000
Georgiadou, D. 72, 98, 124, 526, 581, 629
Georgiev, Y. 89, 368, 563, 1083
Georgiou, P. 59, 499
Gherardi, M. 94, 99, 102, 573, 583, 589
Ghosh, S. 368, 1083
Giani, R. 94, 573
Gieb, K. 43, 467
Gierak, J. 35, 453
Giubertoni, D. 398, 1133
GLORIEUX, O. 354, 1057
Gogolides, E. 210, 306, 781, 972
Goh, R. 310, 981
Goll, G. 225, 811
González-Reynoso, O. 128, 281, 304, 635, 922, 968
Goodwin, A. 35, 453
Goraus, M. 84, 553
Gorb, S. 173, 716
Gotszalk, T. 282, 924
Gottwald, M. 205, 399, 771, 1135
Gottwald, V. 388, 1115
Gourgon, C. 76, 112, 537, 608
Gow, P. 327, 341, 1012, 1038
Graham, A. 98, 124, 581, 629
Gram, L. 57, 495
Granchi, N. 94, 573
Granegger, M. 48, 477
Green, A. 207, 775
Greenacre, V. 220, 801
Greenhorn, S. 112, 608
Grekobi, C. 68, 517
Grimpe, C. 20, 427
Groot, K. 298, 335, 956, 1027
Gros, C. 372, 1088
Grushina, A. 237, 834
Grzegorzewski, L. 243, 844
Grzegorzewski, l. 278, 916
Grzybeck, P. 278, 916
Grützner, G. 84, 160, 553, 693
Gualtieri, F. 253, 865
Guardiola, C. 299, 958
Guerin, C. 351, 1051
Guerrero, A. 234, 391, 828, 1120
Guerrero, D. 342, 1040
Guimerà-Brunet, A. 93, 571
Guirado, G. 299, 958
Guitton, A. 351, 1051
Gujrati, R. 11, 412
Guo, J. 86–88, 113, 200, 201, 258, 557, 559, 561, 610, 761, 763, 876
Guo, X. 235, 830
Guo, Y. 115, 614
Gupta, A. 150, 675
Gurnani, C. 268, 331, 896, 1019
Gómez-Salazar, S. 281, 922
Günther-Müller, S. 343, 1042

Haapala, M. 31, 47, 447, 475
Haase, M. 206, 773
Hagen, K. 203, 767
Hahn, J. 261, 882
Hahn, L. 351, 1051
Hainberger, R. 60, 501
Hajiabadi, Z. 98, 124, 581, 629
Haluska, M. 131, 641
Han, J. 66, 103, 513, 592
HAN, Y. 211, 783
Han, Y. 220, 801
Hanada, K. 41, 465
Hansen, S. 164, 700
Harke, S. 268, 896
Harnisch, M. 246, 850
Harringer, M. 246, 850

Hart, L. 311, 983
Hartmann, F. 175, 720
Harumoto, M. 305, 342, 970, 1040
Harwell, J. 344, 1044
Haslinger, M. 48, 244, 246, 333, 477, 846, 850, 1023
He, W. 174, 718
Heck, M. 215, 791
Hector, A. 330, 1017
Heidaryan, N. 297, 954
Heimgartner, P. 178, 725
Heinke, R. 308, 338, 977, 1032
Heiskanen, A. 387, 1113
Helke, C. 205, 206, 213, 399, 771, 773, 787, 1135
Heller, L. 178, 725
Helm, M. 89, 563
Heo, S. 342, 1040
Hidalgo-Ríos, M. 128, 635
Hierold, C. 131, 641
Higashi, T. 270, 900
Higuchi, J. 382, 386, 1104, 1111
Hilber, W. 39, 40, 461, 463
Hillebrand, M. 343, 1042
Hirata, K. 166, 704
Hirotani, J. 100, 279, 585, 918
Ho, C. 296, 952
Ho, D. 136, 652
Ho, T. (Northumbria University) 136, 652
Ho, T. (The Hong Kong University of Science and Technology) 287, 934
Hoffmann, M. 343, 1042
Holzer-Harringer, D. 246, 850
Holzinger, D. 333, 1023
Hopp, B. 307, 974
Horiguchi, N. 5, 405
Hosseini, N. 352, 1053
Hosseini, V. 212, 785
Hou, T. 197, 240, 756, 838
HOU, W. 15, 418
Hou, Y. 395, 1128
Hougs, N. 164, 700
Howe, T. 319, 998
Hsu, C. 360, 1068
Hu, J. 375, 1092
Huang, C. 394, 1126
Huang, R. 26, 124, 268, 298, 330, 335, 438, 629, 896, 956, 1017, 1027
Huang, Z. 36, 455
Hunt, W. 11, 412
Hunter, A. 326, 1010
Huo, W. 246, 850
Hurtaud, J. 357, 1062
Husain, M. 125, 631

Iachetta, G. 357, 1062
Iacovella, F. 112, 608
Ihle, M. 101, 587
Iima, S. 79, 543
Imeri, F. 43, 467
Inoue, G. 46, 473
inoue, t. 51, 483
Intonti, F. 94, 573
Ioannou, D. 306, 972
Isella, G. 102, 589
Ishida, H. 45, 471
Ishiguro, H. 186, 739
Islam, M. 375, 1092
Israelievitch, E. 138, 657
Itatani, T. 151, 677
Ito, H. 65, 79, 511, 543
Ito, T. 44, 45, 51, 186, 469, 471, 483, 739

Jaafa, A. 330, 1017
Jaccottet, A. 59, 499
Jacquier, H. 295, 950
Jagadish, C. 275, 910
Jakoby, B. 39, 40, 461, 463
Jamshidi, K. 89, 563
Janus, P. 245, 282, 848, 924
Jané, R. 93, 571
Japichino, E. 178, 725
Jeon, J. 120, 293, 623, 948
Jeon, Y. 95, 97, 575, 579
Jespersen, T. 176, 722
JI, N. 287, 934
Jiao, Y. 180, 215, 730, 791
Jimbo, T. 354, 1057
Jin, J. 203, 767
Jin, W. 114, 159, 612, 691
Jin, Y. 305, 970
JO, J. 54, 248, 489, 855
Jo, N. 74, 528
Jofre, L. 236, 832
Johnson, A. 23, 432
Jonaityte, V. 48, 105, 244, 246, 477, 596, 846, 850
Jones, C. 136, 652

Jones, M. 174, 718
Joo, K. 120, 293, 623, 948
Jordan, E. 20, 427
Jousseaume, V. 351, 1051
Joyce, H. 275, 910
JUAN, Y. 223, 224, 807, 809
Juhl, M. 164, 700
Jullien, T. 351, 1051
Jung, S. (GRIT Custom-IC) 119, 621
Jung, S. (Pusan National) 90, 565
Järvinen, P. 31, 47, 447, 475

Kagias, M. 156, 685
Kahilogullari, T. 17, 421
Kahleed, A. 311, 983
Kameramzadeh, S. 333, 1023
Kaminaga, M. 91, 567
Kan, T. 71, 524
Kanade, P. 104, 117, 594, 617
Kanda, K. 359, 1066
Kandra, M. 257, 874
Kang, H. 133, 158, 645, 689
Kang, M. 291, 942
Kanno, S. 79, 543
Kapur, O. 26, 207, 227, 268, 280, 438, 775, 815, 896, 920
Kareekunnam, A. 375, 1092
Karle, S. 181, 732
Kartopu, G. 136, 652
Karvinen, P. 60, 501
Kassem, A. 11, 412
Kastania, A. 210, 781
Kato, H. 85, 555
Kawashima, Y. 279, 302, 389, 918, 964, 1117
Kayser, P. 58, 62, 497, 505
Kazazis, D. 147, 178, 356, 671, 725, 1060
Keeble, L. 59, 499
Keen, J. 327, 341, 1012, 1038
Kehagias, N. 169, 297, 710, 954
Keller, S. 191, 387, 747, 1113
Kempen, P. 57, 495
Kenzhebek, M. 309, 979
Keros, A. 325, 1008
Keskinbora, K. 231, 823
Kettle, J. 344, 1044
Khabarov, K. 320, 1000
Khan, S. 176, 722
Khoshmaram, D. (Department of Electrical Engineering, Amirkabir University of Technology, Tehran, Iran) 107, 135, 600, 650
Khoshmaram, D. (Universitat Autonòma de Barcelona) 267, 894
Khozeymeh Sarbishe, F. 320, 1000
Kiang, K. 85, 114, 159, 208, 226, 240, 255, 555, 612, 691, 777, 813, 838, 870
Kiiski, I. 47, 475
Kim, C. 66, 513
Kim, G. 66, 103, 513, 592
Kim, H. (Pohang University of Science and Technology) 133, 158, 645, 689
Kim, H. (Samsung Electronics) 336, 1029
Kim, H. (Seoul National University of Science and Technology) 119, 621
Kim, I. 54, 489
Kim, J. (Department of Mechanical Engineering, Imperial College London, London, United Kingdom.) 395, 1128
Kim, J. (Korea Institute of Science and Technology) 171, 713
Kim, J. (Pohang University of Science and Technology) 221, 803
Kim, J. (Samsung Electronics) 336, 1029
Kim, J. (SUNG KYUN KWAN University / Samsung Electronics) 118, 619
Kim, M. 217, 353, 795, 1055
Kim, S. 290, 334, 940, 1026
Kim, s. 221, 803
Kim, W. (Changwon National University, Changwon) 67, 515
Kimmel, A. 391, 1120
Kimura, A. 91, 567
Kirchner, R. 181, 732
Kjellberg Jensen, T. 273, 906
Klikovits, J. 43, 467
Knigge, A. 168, 251, 708, 861
Kocun, M. 83, 551
Koenemann, F. 152, 679
Kohl, M. 322, 323, 1003, 1005
Kohlschreiber, P. 205, 206, 399, 771, 773, 1135
Kojiri, T. 354, 1057
Kokkoris, G. 210, 781
Kometani, R. 19, 425
Konstantinidis, G. 238, 836

Kool, L. 138, 300, 657, 960
Kopp, S. 48, 105, 297, 477, 596, 954
Korhonen, O. 31, 447
Korolkov, V. 83, 551
Korsgaard, M. 164, 700
Kotani, A. 91, 567
Koukoumaki, D. 306, 972
Koukouvinos, G. 130, 639
Kozawa, T. 305, 970
Kraiem, I. 131, 641
Kroker, S. 20, 427
Kronawitter, A. 148, 673
Kropf, M. 178, 725
Ku, Y. 394, 1126
Kucharska, M. 245, 282, 848, 924
Kudo, T. 375, 1092
Kuhness, D. 84, 553
Kumar Gautam, M. 72, 526
Kunicki, P. 282, 924
Kuo, C. 296, 952
Kuo, K. 165, 394, 702, 1126
KURASHIMA, Y. 70, 71, 522, 524
Kurioka, T. 15, 65, 79, 96, 270, 382, 386, 418, 511, 543, 577, 900, 1104, 1111
Kurosu, H. 96, 270, 577, 900
Kusumanchi, P. 387, 1113
Kutucu, C. 32, 449
Kuzuya, A. 45, 471
Kwoka, K. 282, 924
Kwon, Y. 336, 1029
Körner, S. 101, 587

Labau, S. 112, 608
Labbe, L. 112, 608
Lachat, T. 178, 725
Lagace, D. 265, 890
Lagrave, J. 68, 517
Lahaye, L. 316, 992
Lale, A. 48, 477
Lang, S. 39, 40, 461, 463
Latte Bovio, C. 332, 1021
LAULAGNET, F. 354, 1057
Lavenus, P. 58, 62, 497, 505
Le Besque, J. 272, 904
Le Potier, I. 295, 303, 950, 966
Le Saux, G. 380, 1100
Lebel, Y. 52, 485
Lee, C. 29, 376, 443, 1094
Lee, E. (Departamento de Física de la Materia Condensada and Condensed Matter Physics Center (IFIMAC), Universidad Autónoma de Madrid, 28049 Madrid) 242, 842
Lee, E. (POSTECH) 167, 209, 706, 779
Lee, J. (Korea Institute of Machinery and Materials (KIMM)) 74, 528
Lee, K. (Ajou Unversity) 285, 930
Lee, K. (Samsung Electronics) 120, 623
Lee, K. (Seoul National University / Samsung Electronics) 126, 633
Lee, T. 54, 489
Lee, W. 126, 633
LEE, Y. 223, 224, 807, 809
Lefaix, L. 276, 912
Lehnert, L. 37, 457
Leibold, A. 80, 545
Leichlé, T. 11, 412
Lemme, M. 20, 80, 81, 198, 427, 545, 547, 758
Lepukhov, E. 60, 501
Lesot, p. 35, 453
Li, J. 83, 551
Li, M. 134, 648
Li, R. 77, 539
Li, X. 326, 1010
Li, Y. (Department of Physics, The University of Hong Kong) 311, 983
Li, Y. (Royal Institute of Technology (KTH)) 198, 758
Lian, Y. 339, 1034
liang, h. 123, 627
Liang, N. 44, 469
Liao, Z. 32, 339, 449, 1034
Lignieres, J. 195, 752
Lim, J. 336, 1029
Lima, R. 116, 615
Lin, C. (National Cheng Kung University) 165, 394, 702, 1126
Lin, C. (National United University) 286, 932
Lin, X. 275, 910
Lin, Y. 286, 932
Ling, I. 310, 981
Lingenfelder, L. 214, 789
Linnemeier, S. 48, 477
Lipinski, A. 104, 117, 162, 594, 617, 696
Lipkin, M. 81, 547
Littlejohns, C. 272, 904

Liu, C. 356, 1060
Liu, D. 397, 1131
Liu, K. 86–88, 113, 200, 201, 258, 557, 559, 561, 610, 761, 763, 876
Liu, Q. 26, 438
Liu, S. 82, 549
Liu, Y. (Institut für Mikrosystemtechnik – IMTEK, Albert-Ludwigs-Universität Freiburg, Georges-Köhler-Allee 102, 79110 Freiburg, Germany) 388, 1115
Liu, Y. (Technical University of Denmark) 57, 495
Liu, Z. 82, 235, 549, 830
Llobet, J. (Institut de Microelectrònica de Barcelona, IMB-CNM (CSIC), Universitat Autònoma de Barcelona, Cerdanyola Del Vallès, 08193, Barcelona, Spain.) 234, 277, 398, 828, 914, 1133
Llobet, J. (Institute of Microelectronics of Barcelona (IMB-CNM, CSIC)) 241, 840
Logan, A. 262, 884
Loiseau, A. 68, 517
Lorenz, P. 307, 308, 338, 974, 977, 1032
Louarn, P. 393, 1124
Loze, M. 372, 1088
Lu, B. 164, 700
Lu, E. 189, 743
LU, J. 70, 522
Ludwig, A. 322, 323, 1003, 1005
Lunzer, M. 105, 596
Luttge, R. 30, 445
Lyu, W. 61, 503

M. Mastronardi, V. 271, 902
Ma, D. 59, 499
Maag, S. 178, 725
Maaßdorf, A. 168, 708
Machida, K. 65, 79, 511, 543
Madadi, H. 326, 1010
Maeda, A. 71, 524
Maeda, J. 151, 677
Maghsoomi Taramsari, S. 132, 643
MAGIS, T. 354, 1057
Maikap, A. 109, 604
Makris, N. 238, 836
Malaquin, L. 195, 752
Malara, N. 314, 988
Mallari, A. 207, 775
Malvicini, G. 64, 179, 509, 727
Man, H. 295, 303, 950, 966
Manca, N. 249, 857
Manda, N. 395, 1128
Mandal, S. 25, 312, 436, 985
Manhica, B. 101, 587
Maqbool, M. 204, 769
Mar, J. 136, 652
Martin, C. 380, 1100
Martina, S. 180, 730
Martincic, E. 361, 1070
Martinez Vazquez, R. 250, 859
Martínez-Gómez, A. 281, 922
Maruyama, T. 375, 1092
Mas, R. 234, 828
Mashanovich, G. 256, 262, 872, 884
Mathieu, F. 11, 412
Matsui, R. 85, 555
Matsumae, T. 71, 524
Matsunobu, K. 202, 765
Mattheakakis, N. 169, 297, 710, 954
Mazzini, G. 30, 445
Mbarki, A. 351, 1051
Mbomekallé, I. 303, 966
Mcbride, J. 283, 382, 386, 926, 1104, 1111
McDonald, E. 57, 326, 495, 1010
Medina Sanchez, M. 142, 663
Mehlstaeubler, T. 20, 427
Meinecke, C. 212, 785
Melchior, P. 210, 781
Mena Fernández, S. 299, 958
Menezes, P. 326, 1010
Mergia, K. 210, 781
Merino, S. 391, 1120
MERMET, O. 52, 485
Meulenbelt, I. 30, 445
Mieites, V. 266, 892
Mikkelsen, A. 273, 906
MILITELLO-MILITELLO, C. 122, 625
Minas, G. 116, 615
Mishra, R. 233, 826
Mitchell, C. 256, 872
Mitteramskogler, T. 40, 463
Miyake, Y. 65, 79, 511, 543
Mizuta, H. 375, 1092
Mochi, I. 178, 725
Moebius, H. 37, 457
Mogilatenko, A. 168, 708

Mohapatra, P. 301, 962
Moheimani, S. 233, 826
Monchablon, M. 252, 863
Monks, J. 155, 683
Montelius, L. 9, 410
Montinaro, C. 392, 1122
Moothedath Sethumadhavan, A. 49, 479
Moradi, E. 31, 447
Moradiani, F. 117, 162, 617, 696
Moraes, G. 242, 842
Morano, C. 253, 865
Mori, T. 65, 511
Moritz, M. 261, 882
Mortelmans, T. 356, 1060
Mortini, B. 52, 485
Moscato, F. 48, 105, 477, 596
Mouchtouris, S. 210, 781
Mrena, D. 84, 553
Muehlberger, M. 48, 105, 244, 246, 297, 477, 596, 846, 850, 954
Muller, J. 317, 994
Mulvihill, D. 326, 1010
Muntada, O. 241, 840
Murayama, M. 38, 459
Murillo, G. 276, 358, 912, 1064
Muskens, O. 155, 288, 319, 683, 936, 998
Muñoz Berbel, X. 299, 358, 958, 1064
Månsson, A. 266, 892
Mérot, J. 58, 62, 68, 497, 505, 517
Möhring, L. 101, 587
Möller, M. 20, 80, 81, 427, 545, 547
Müellner, P. 60, 501

Nakamura, F. 151, 677
Nakatsuka, N. 33, 451
Nam, Y. 221, 803
Namura, K. 192, 749
Napari, M. 98, 581
Nasri, R. (Hamburg Centre for Ultrafast Imaging) 266, 892
Nasri, R. (UHH) 53, 157, 269, 318, 487, 687, 898, 996
NAVARRO, G. 354, 1057
Navarro, M. 276, 358, 912, 1064
Navne, J. 187, 741
Nazyrova, Z. 361, 1070
Nedeljkovic, M. 256, 872
Nees, D. 210, 781
Nelson, D. 3, 403
NGUYEN GIA CAN, E. 354, 1057
Nguyen, L. 196, 754
Nguyen, Q. 377, 1096
Niang, K. 23, 432
Niazi, J. 106, 172, 598, 715
Nicolas, A. 13, 414
Nicu, L. 11, 412
NIEH, G. 223, 224, 807, 809
Nielsen, J. 191, 747
Niemi, T. 60, 501
NIETO, J. 354, 1057
Niklaus, F. 198, 324, 758, 1007
Nishio, T. 38, 459
Nishiyama, N. 197, 756
Niu, J. 82, 549
Noda, D. 71, 524
Nogués, C. 276, 912
Noh, J. 78, 129, 541, 637
Noori, Y. 220, 801
Noy, R. 241, 840
Nygård, J. 273, 906
Nüßlein, J. 36, 455

Oh, J. 29, 376, 443, 1094
Ohta, R. 71, 524
Okada, I. 41, 465
Okado, Y. 50, 481
Okamoto, K. 382, 1104
Okawa, T. 51, 483
Oki, M. 279, 389, 918, 1117
Onck, P. 259, 878
Ortega, G. 391, 1120
Osaki, T. 50, 481
Oshita, M. 71, 524
Osmond, J. 99, 583
Ottapilakkal, V. 11, 412
Ou, J. 155, 159, 197, 240, 389, 683, 691, 756, 838, 1117
Ougazzaden, A. 11, 412
Owen, J. 146, 669

Palakkool, N. 136, 652
Palomas Jiménez, A. 63, 507
Pamunuwa, D. 7, 198, 408, 758
Panda, I. 247, 853
Panda, P. 271, 902
Pandian, S. 60, 501
Pandit, J. 380, 1100
Papanikolaou, N. 169, 710

Paraggio, M. 253, 865
Parish, J. 23, 432
Park, H. 171, 713
Park, J. 78, 129, 541, 637
Park, P. 54, 489
Park, S. 211, 217, 353, 783, 795, 1055
Partsch, U. 101, 587
Pascual, M. 351, 1051
Pasini, M. 94, 573
Pasquardini, L. 94, 573
Patil, I. 310, 981
Patwari, A. 190, 745
Pearson, A. 318, 996
Peek, B. 23, 432
Pellegrino, L. 249, 284, 857, 928
PELLISSIER, C. 354, 1057
Peng, H. 208, 777
PENG, Z. 287, 934
Perak, S. 105, 596
Perdigao, L. 83, 551
PEREZ DOMINGUEZ, C. 122, 625
Perez-Murano, F. 241, 840
Perna, A. 392, 1122
Perozek, J. 317, 994
Perry, E. 317, 994
Peters, M. 178, 725
Petit-Etienne, C. 112, 608
Petitto, G. 234, 277, 828, 914
Petrou, P. 130, 639
Piasecki, T. 282, 924
Piguet, D. 178, 725
Pisanello, F. 332, 392, 1021, 1122
Pisanello, M. 392, 1122
Plucinski, A. 160, 693
Podstránský, J. 257, 874
Poggio, M. 21, 429
Poisson, S. 372, 1088
Porgador, A. 380, 1100
Portaluri, L. 173, 716
Postl, M. 84, 553
Pottekkad, S. 332, 1021
Pound-Lana, G. 112, 608
Prabowo, B. 104, 117, 594, 617
Prajzler, V. 244, 846
Pranzner, N. 318, 996
Prietl, C. 84, 553
Prieto, I. 175, 720
Prochazka, V. 333, 1023
Prodromakis, T. 325, 1008
Proksch, R. 83, 551
Pruchnik, B. 282, 924
Prucnal, S. 368, 1083
Pu, S. 310, 981
Puddu, A. 368, 1083
Pudis, D. 84, 553
Pérez-Murano, F. 234, 277, 315, 363, 398, 828, 914, 990, 1075, 1133

Qi, L. 397, 1131
Qiu, M. 61, 381, 397, 503, 1102, 1131
Qu, M. 280, 920
Qu, Y. 136, 652
Qualtieri, A. 229, 271, 332, 819, 902, 1021
Quan, H. 86, 87, 113, 200, 201, 258, 557, 559, 610, 761, 763, 876
Quasso, E. 295, 950
Qureshi, A. 106, 598

Rademacher, N. 80, 545
Rademaker, G. 315, 990
Ramadan, S. 220, 801
Ramamoorthy, S. 325, 1008
Ramos, S. 393, 1124
Ramos, Y. 30, 445
Randall, J. 146, 669
Rao, P. 32, 449
Raptis, I. 130, 639
Raskin, J. 316, 992
Ravichandar, R. 184, 735
Raynam, F. 351, 1051
Rebohle, L. 89, 563
Reed, G. 262, 884
Reid, G. 220, 801
Ren, Z. 49, 83, 479, 551
Reniers, S. 180, 730
Rentner, D. 251, 861
Reuter, C. 77, 539
Reuter, D. 205, 206, 212, 213, 399, 771, 773, 785, 787, 1135
Revol, I. 144, 665
Reynolds, P. 213, 787
Rho, J. 95, 97, 133, 154, 158, 167, 209, 575, 579, 645, 682, 689, 706, 779
Rho, K. 336, 1029
Ribeiro, J. 392, 1122

Rimböck, J. 148, 673
Ritter, D. 17, 421
Rizzi, F. 271, 902
Rodriguez-Manzano, J. 59, 499
Rois, J. 156, 685
Roman, C. 131, 641
Romano, L. 21, 212, 429, 785
Romero-Estrada, A. 281, 922
Rondelli, F. 332, 1021
Rosiek, C. 164, 700
ROTTNER, J. 354, 1057
Rowlinson, B. 227, 228, 325, 815, 817, 1008
Roy, A. 137, 655
Roy, B. 109, 604
Roy, D. 108, 602
Roy, R. 137, 655
Ruiz, R. 267, 894
Russew, M. 160, 693

saada, k. 195, 752
Sabahi-Kaviani, R. 30, 445
Sacco, L. 125, 631
Sah, P. 20, 427
Saiki, T. 364, 1077
Saito, S. 140, 660
Sakurai, I. 41, 465
Salomé, L. 393, 1124
Salvestrini, J. 11, 412
SALVI, A. 354, 1057
Sammeta, P. 251, 861
Sand, J. 164, 700
Sandbrink-Koblenz, T. 212, 785
Sangiao, S. 282, 924
Santini, R. 146, 669
Santoro, F. 260, 880
Santos, A. 305, 342, 970, 1040
Sari, I. 207, 775
Sarris, D. 306, 972
Satheesh-Babu, R. 72, 526
Sato, K. 96, 270, 577, 900
Sattari, H. 175, 720
Sauer, S. 20, 427
Savan, A. 322, 1003
SAWAYAMA, S. 383, 1106
Scali, F. 102, 589
Scaraggi, M. 173, 271, 716, 902
Scattolo, E. 398, 1133
Schellingerhout, S. 231, 823
Schermer, S. 205, 213, 771, 787
Schider, G. 210, 781
Schift, H. 64, 179, 509, 727
Schirmer, M. 251, 861
Schleunitz, A. 84, 160, 553, 693
Schlüter, H. 261, 882
Schneider, E. 232, 825
Schneider, M. 178, 725
Schuster, C. 84, 553
Schuster, P. 148, 673
Schvartzman, M. 380, 1100
Schwentenwein, M. 48, 477
Schäfer, M. 251, 861
Scott, J. 155, 683
Sczyrba, M. 148, 673
Sebag, E. 35, 453
See, P. 184, 735
Seggering, L. 273, 278, 906, 916
Seguini, G. 379, 1099
Sekiguchi, A. 55, 75, 230, 491, 530, 821
Sekiguchi, H. 41, 465
Selvaggio, G. 83, 551
Sendel, M. 205, 399, 771, 1135
Seok, S. 171, 713
Seong, J. 95, 97, 575, 579
Sequeira, S. 180, 730
Shafai, C. 265, 890
Shaikh, M. 89, 563
Shakeel, H. 204, 769
Shao, L. 330, 1017
Shen, W. 262, 884
Shibasaki, N. 69, 519
Shibata, K. 96, 270, 577, 900
Shieh, J. 264, 274, 286, 360, 888, 908, 932, 1068
Shimizu, T. 44, 45, 51, 186, 469, 471, 483, 739
Shimofuri, M. 100, 585
Shin, D. 163, 698
Shin, M. 66, 103, 513, 592
Shingubara, S. 44, 45, 51, 186, 469, 471, 483, 739
Siampour, H. 162, 696
Sierakowski, A. 245, 282, 848, 924
Sigron, A. 131, 641
Sikanen, T. 31, 47, 447, 475
Silva, D. 215, 791
Sim, G. 119, 621
Simanjuntak, F. 98, 124, 581, 629
Singh, R. 20, 427

SIXT, P. 354, 1057
Smausz, T. 307, 974
Sole, L. 241, 840
Son, Y. 211, 783
Sone, M. 15, 65, 79, 96, 270, 382, 386, 418, 511, 543, 577, 900, 1104, 1111
Song, J. 353, 1055
Song, M. 336, 1029
Song, S. 220, 801
Sorokina, A. 20, 427
SOUIL, R. 354, 1057
Sousa, P. 116, 615
Spagnolo, B. 332, 392, 1021, 1122
Spruce, K. 184, 735
Squeo, B. 94, 573
Stadlober, B. 210, 781
Stagira, S. 250, 859
Stai, E. 210, 781
Stajkovic, N. 260, 880
Stallone, F. 339, 1034
Stampanoni, M. 21, 429
Stark, J. 152, 679
Stavrinidis, A. 238, 836
Steeneken, P. 163, 698
Stephan, O. 13, 414
Sternberg, C. 57, 495
Stettler, S. 175, 720
Stobbe, S. 164, 700
Stock, T. 184, 254, 735, 868
Stockbridge, K. 232, 825
Stokes, K. 83, 551
Stoll, S. 80, 545
Strehle, S. 36, 77, 150, 343, 455, 539, 675, 1042
Støvring, N. 387, 1113
Suckow, S. 20, 81, 427, 547
Suda, T. 96, 577
Sultan, S. 310, 981
Sun, C. 159, 691
Sun, K. 155, 288, 319, 335, 683, 936, 998, 1027
Sun, Z. 234, 828
Sundaram, S. 11, 412
Sung, M. 377, 1096
Sungauer, É. 76, 537
Suzuki, M. 192, 749
Swamy, K. 263, 328, 886, 1014
Szmigiel, D. 245, 848
Szola, M. 147, 356, 671, 1060
Taboryski, R. 57, 176, 495, 722
Tailpied, L. 68, 517
Takada, A. 55, 491
TAKAGI, H. 70, 71, 522, 524
Takahashi, M. 364, 1077
TAKIGAWA, R. 202, 765
Tan, H. 275, 910
Tanaka, M. 55, 491
Taniguchi, J. 50, 69, 145, 166, 222, 481, 519, 667, 704, 805
Tantussi, F. 320, 1000
Tao, S. 88, 561
Tarasova, A. 303, 966
Tasli, N. 218, 261, 797, 882
Taverne, M. 136, 652
Tejedor, P. 236, 242, 832, 842
Temga, J. 333, 1023
teng, x. 123, 627
Termes Español, N. 93, 571
Teuber, J. 53, 266, 318, 487, 892, 996
Thamdrup, L. 358, 1064
Theodosiou, A. 244, 846
Thoelen, R. 37, 457
Thomas, D. 98, 581
Thomas, R. 20, 81, 427, 547
Thomas, S. 220, 801
Thompson, A. 395, 1128
Thomson, D. 255, 262, 272, 870, 884, 904
Thouin, L. 295, 950
Tian, P. 147, 356, 671, 1060
Tian, S. 86–88, 201, 258, 557, 559, 561, 763, 876
Tiepelt, J. 317, 994
Tiwari, S. (UHH) 218, 797
Tiwari, S. (University of Hamburg) 261, 882
Toes, R. 30, 445
Tolin, E. 101, 587
Tong, X. 258, 876
Tortai, J. 13, 414
Tran, Y. 85, 255, 555, 870
Trevisiol, E. 393, 1124
TRUJILLO-SEVILLA, J. 122, 625
TSAI, Y. 223, 224, 807, 809
Tsavalas, P. 210, 781
Tserepi, A. 210, 781
Tsoukalas, K. 164, 700
Tsounidi, D. 130, 639
Tsuchiya, T. 100, 279, 302, 389, 585, 918, 964, 1117

Tsuchiya, Y. 197, 240, 283, 302, 382, 386, 389, 756, 838, 926, 964, 1104, 1111, 1117

Uhlig, P. 101, 587
Ulmeanu, M. 83, 551
Umbria, A. 231, 823
Umlauf, G. 212, 785
Unger, R. 168, 251, 708, 861
Uranga, I. 277, 315, 914, 990
Ureta, E. 387, 1113
Usaj, M. 266, 892
Utsumi, Y. 359, 1066
Uvarov, A. 112, 608

Vajjula, N. 27, 440
van der Sanden, B. 13, 414
van der Sanden, L. 252, 863
Van Driessche, V. 342, 1040
van Hulst, N. 99, 583
Vandereyken, J. 342, 1040
Vanotti, M. 372, 1088
Vanzetti, L. 94, 573
Viat, C. 13, 414
Vieu, C. 393, 1124
Villa, R. 93, 571
Villalvazo-Hidalgo, A. 128, 281, 304, 635, 922, 968
Villanueva, G. 175, 720
Villar, A. 391, 1120
Villar, J. 63, 507
Villatoro Guillen, A. 281, 922
Vinaisuratern, P. 382, 386, 1104, 1111
Vincenti, M. 94, 99, 573, 583
Visser, S. 252, 863
Visus, A. 299, 958
Vizabaskaran, H. 272, 904
Vockenhuber, M. 178, 725
Voigt, A. 84, 213, 553, 787
Vollebregt, S. 14, 56, 125, 416, 493, 631
von Lacroix, L. 269, 898
Vosoughi Lahijani, B. 164, 700
Vostatek, M. 48, 477
Vousden, M. 302, 964
Vsetecka, L. 148, 673
Vuong, P. 11, 412

Wakasa, T. 222, 805
Wang, A. 98, 124, 581, 629
Wang, W. 111, 606
Wang, Y. 259, 878
Wang, Z. (School of Electronics and Computer Science, University of Southampton, Southampton SO17 1BJ, United Kingdom) 159, 691
Wang, Z. (University of Southampton) 114, 240, 612, 838
Warisawa, S. 19, 425
Warsono, A. 76, 537
Watanabe, M. 151, 677
Watanabe, S. 65, 511
Watanabe, T. 359, 1066
Weber, G. 356, 1060
Wei, J. 287, 934
Wei, Q. 383, 1106
Weimann, N. 17, 421
Weis, T. 164, 700
Wenzel, H. 168, 251, 708, 861
Wiggins, J. 104, 117, 594, 617
Wiglenda, T. 160, 693
Williams, K. 180, 730
Williams, O. 25, 312, 385, 436, 985, 1109
Wolf, J. 160, 693
Wong, K. 287, 934
Wong, M. 181, 732
Woo, J. 129, 637
Worsey, E. 198, 758
Wu, H. 235, 830
Wu, K. 296, 952
Wu, Q. 86, 87, 113, 200, 201, 258, 557, 559, 610, 761, 763, 876
Wu, S. 381, 1102

Yamada, T. 91, 567
Yamaguchi, A. 41, 192, 364, 465, 749, 1077
Yamamoto, H. 219, 799
Yamamoto, M. 55, 491
Yamane, D. 383, 1106
Yamashita, K. 45, 471
Yan, J. 114, 159, 208, 226, 612, 691, 777, 813
Yan, X. 155, 262, 272, 683, 884, 904
Yang, H. (School of Electronics and Computer Science, University of Southampton, Southampton SO17 1BJ, United Kingdom) 298, 956
Yang, H. (Techische Universität Ilmenau) 150, 675
YANG, X. 163, 698
YANG, Y. 19, 425

Yang, Y. (National Taiwan University) 366, 367, 1079, 1081
Yang, Y. (Pohang University of Science and Technology) 95, 97, 575, 579
Yang, Y. (TaiCaan Technologies) 386, 1111
Yang, Z. 381, 1102
Yassin, A. 380, 1100
Yasunaga, T. 192, 749
Ye, L. 302, 964
Ye, Y. 208, 777
Yemulwar, P. 181, 732
Yim, Y. 336, 1029
Yin, S. 208, 777
Yoon, C. 67, 515
Yoon, J. 336, 1029
Yoon, S. 67, 211, 515, 783
Yoshida, N. 96, 577
Yoshii, T. 270, 900
Yu, C. 274, 360, 908, 1068
Yu, X. 262, 884
Yu-Sheng, Y. 216, 793
Yuan, W. 86–88, 201, 258, 557, 559, 561, 763, 876
Yuan, Z. 373, 1090
Yun, W. 119, 621

Zajadacz, J. 307, 338, 974, 1032
Zanders, W. 342, 1040
Zanzal, A. 213, 787
Zapata, M. 391, 1120
Zarebidaki, H. 175, 720
Zauner, K. 302, 964
Zeimpekis, I. 72, 288, 526, 936
Zekentes, K. 112, 608
Zeng, J. 227, 815
Zhan, Y. 228, 817
Zhang, C. 400, 1137
Zhang, H. (Components for High Frequency Electronics, Duisburg, 47057, University Duisburg Essen) 17, 421
Zhang, H. (University of Southampton) 220, 801
Zhang, K. (AMO GmbH) 20, 427
Zhang, K. (School of Electronics and Computer Science, University of Southampton, Southampton, SO17 1BJ, UK) 255, 870
ZHANG, L. 70, 522
Zhang, L. 287, 934
Zhang, T. 330, 1017
Zhang, W. 262, 272, 884, 904
zhang, y. 123, 134, 627, 648
Zhao, D. (Westlake Institute for Optoelectronics) 61, 397, 503, 1131
Zhao, D. (Westlake University) 381, 1102
Zhao, K. 381, 1102
ZHAO, X. 51, 483
Zhao, X. 38, 459
Zhao, x. 86, 87, 113, 200, 201, 258, 557, 559, 610, 761, 763, 876
Zhao, Y. (MEMS Center, Harbin Institute of Technology) 134, 648
Zhao, Y. (University of Southampton) 226, 813
Zhao, Z. 44, 469
Zhong, C. 51, 483
Zhou, D. 82, 235, 549, 830
Zhou, S. 89, 563
Zhou, X. 197, 756
Zhou, Z. 156, 685
Zhu, Y. (Institute of Semiconductors, Guangdong Academy of Sciences) 82, 235, 549, 830
Zhu, Y. (University of Southampton) 298, 956
Zielinski, M. 112, 608
Zimmer, K. 307, 308, 338, 974, 977, 1032
Zimmermann, A. 246, 850
Zisis, G. 130, 639
Zschleile, J. 181, 732
Zucchetti, C. 102, 589

Çağın, E. 152, 315, 679, 990
Çoban, B. 43, 467
Özek, E. 352, 1053
Ünal, N. 43, 467

Łaszcz, A. 245, 848

MNE 2025

15 - 18 SEPTEMBER 2025

National Oceanography Centre
Southampton | United Kingdom

Thank You!

See you in MNE 2026!